Springer Handbook of Electrochemical Energy

Breitkopf
Swider-Lyons
Editors

Springer

Springer Handbook of Electrochemical Energy

Springer Handbooks provide a concise compilation of approved key information on methods of research, general principles, and functional relationships in physical and applied sciences. The world's leading experts in the fields of physics and engineering will be assigned by one or several renowned editors to write the chapters comprising each volume. The content is selected by these experts from Springer sources (books, journals, online content) and other systematic and approved recent publications of scientific and technical information.

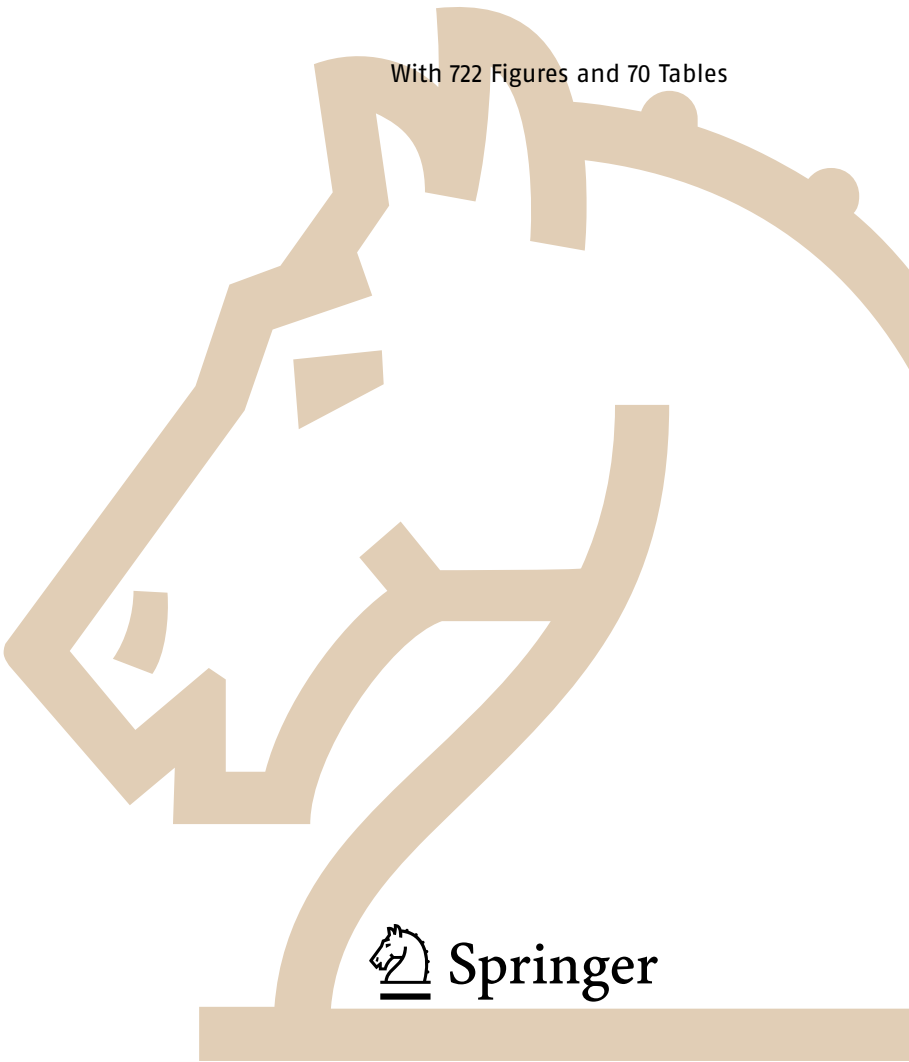
The volumes are designed to be useful as readable desk reference book to give a fast and comprehensive overview and easy retrieval of essential reliable key information, including tables, graphs, and bibliographies. References to extensive sources are provided.

Springer Handbook

of Electrochemical Energy

Cornelia Breitkopf, Karen Swider-Lyons (Eds.)

With 722 Figures and 70 Tables



Springer

Editors
Cornelia Breitkopf
TU Dresden
Dept. Mechanical Engineering
Helmholtzstr. 14
Dresden, Germany
cornelia.breitkopf@tu-dresden.de

Karen Swider-Lyons
US Naval Research Laboratory
Chemistry Division
Washington, D.C. 20375, USA
karen.lyons@nrl.navy.mil

ISBN: 978-3-662-46656-8 e-ISBN: 978-3-662-46657-5
DOI 978-3-662-46657-5
Springer Dordrecht Heidelberg London New York

Library of Congress Control Number: 2016951879

© Springer-Verlag Berlin Heidelberg 2017
This work is subject to copyright. All rights are reserved by the Publisher, whether the whole or part of the material is concerned, specifically the rights of translation, reprinting, reuse of illustrations, recitation, broadcasting, reproduction on microfilm or in any other physical way, and transmission or information storage and retrieval, electronic adaptation, computer software, or by similar or dissimilar methodology now known or hereafter developed.
The use of general descriptive names, registered names, trademarks, service marks, etc. in this publication does not imply, even in the absence of a specific statement, that such names are exempt from the relevant protective laws and regulations and therefore free for general use.
The publisher, the authors and the editors are safe to assume that the advice and information in this book are believed to be true and accurate at the date of publication. Neither the publisher nor the authors or the editors give a warranty, express or implied, with respect to the material contained herein or for any errors or omissions that may have been made.

Production, typesetting and illustrations: le-tex publishing services GmbH, Leipzig
Senior Manager Springer Handbook: Dr. W. Skolaut, Heidelberg
Typography and layout: schreiberVIS, Seeheim
Cover design: eStudio Calamar Steinen, Barcelona
Cover production: WMXDesign GmbH, Heidelberg
Printing and binding: Printer Trento s.r.l., Trento

Printed on acid free paper

This Springer imprint is published by Springer Nature
The registered company is Springer-Verlag GmbH Berlin Heidelberg

Preface

A quick look around your office space tells the importance of electrochemistry. The drinking water in your water or coffee is made safe by electrochemically produced chlorine. Your computer operates seamlessly on solid-state electronics containing electrodeposited thin films and semiconductors. Your cell phone announces the arrival of a text message using energy from a Li-ion battery. Your car outside looks shiny and rust free. If you lose grid power, a flashlight with its two sturdy D-cell batteries will get you around in the dark.

The term electrochemistry is defined in English as

> *the branch of chemistry concerned with the relations between chemical and electrical phenomena, and especially with reactions occurring at the point of contact of an electrical conductor and a conducting liquid.* (Oxford English Dictionary, Oxford University Press 2013)

Electrochemistry is more accurately described by the charge-transfer reaction in Fig. 1.

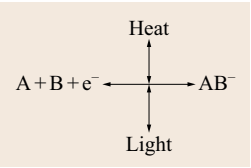


Fig. 1 General scheme for a reversible charge-transfer reaction in which components A and B are reduced by an electron to AB^{-}. Heat is either generated or consumed in the reaction. In some cases, light can be produced or consumed

In this scheme, the forward reaction comprises the reduction of A and B to AB^{-}. In the process, heat and sometimes light is produced or consumed. The reverse reaction would be an oxidation reaction, with an electron created. A and/or B might start as charged species, and constitute a gas, liquid, or solid. In a solid, the species can even be a charged vacancy. Overall, when an electrical path is available to the appropriate reagents or materials, it can release new (wanted or unwanted) chemical species, electricity, and even light. The reactions can occur in any form of matter and a conducting liquid is not required.

The intention of this book is not to cover all aspects of electrochemistry, but rather give a modern portrait of how fundamental electrochemistry is now realized in modern topics in energy. In this respect, we focused on chapters pertaining to the following: thermodynamics, electrodes and electrode processes, mass transport, and electrochemical materials. These aspects of electrochemistry are also examined in polymer, solid oxide and biological fuel cells, batteries, supercapacitors, photoelectrochemistry, and electrochemical hydrogen production, plus other topics including electrometallurgy, electrodeposition and electrochemical machining.

This *Springer Handbook of Electrochemical Energy* is accordingly filled with rich chapters reflecting the complexity of electrochemistry. Chapter 2 on Modern Electrochemistry gives an overview of the chapters and how they are related to electrochemistry and to each other. The invited authors to this book represent an international group of chemists, physicists, materials scientists, biologists, and mechanical and electrical engineers, who tackle both fundamental science and engineering towards the understanding of electrochemistry in energy systems. Each chapter may be treated as a stand alone tutorial or they may be used together to build a more complete picture.

We are grateful to the authors for their contributions and patience in the development of this book, and we hope that the readers find the book a useful research

and development resource for electrochemical theory, governing equations, materials references and methodology.

Cornelia Breitkopf
Karen Swider-Lyons

About the Editors



Cornelia Breitkopf is Full Professor and Chair of Technical Thermodynamics at the Technische Universität Dresden in Germany. She studied chemistry at the Martin-Luther-University Halle-Wittenberg (Germany), where she received the Dipl.-Chem. degree and afterwards the PhD in Physical Chemistry. The main aspects of these graduations had been related to theoretical quantum-chemical calculations of reaction mechanism of enzyme related conversions. After a postdoc position at the Birkbeck College/University of London in the group of Prof. Julia Goodfellow, she joined the Environmental Research Center in Leipzig, where she mainly dealt with the impact of xenobiotics and their distribution in the environment. During this time, she was a Guest Researcher at the Environmental Science Center in Peterborough/Canada in the group of Prof. Don Mackay. At the University of Leipzig she finished her Habilitation in Technical Chemistry. The main aspects of the habilitation work have been the application of transient methods for describing heterogeneously catalyzed reactions. After habilitation she was Professor for Chemical Reaction Engineering in Leipzig and Freiberg. After that she moved to TUM to work as senior scientist also in the field of heterogeneous catalysis. Since 2010 she is Full Professor in Dresden in the Department of Mechanical Engineering. Her main research interests are transient methods for the evaluation of transport and sorption parameters of gases in porous media accompanied with the modeling of complex transport phenomena, the theoretical determination of property data, the characterization of solid porous materials, and modeling of silicon wafer structures.



Dr. Karen Swider Lyons is a Head of the Alternative Energy Section in the Chemistry Division at the Naval Research Laboratory in Washington, D.C. She currently leads research programs on advanced battery materials, low-cost catalysts for use in polymer fuel cells, plus is studying how fuel cells can be used for long-endurance, energy-efficient unmanned air vehicles and unmanned undersea vehicles. She serves as a Technical Advisor to the Defense Advanced Research Projects Agency and the Office of Naval Research. In 2010, she received the Dr. Delores M. Etter Top Scientist Award from the US Navy for her work on the long-endurance Ion Tiger fuel cell unmanned air vehicle. Dr. Swider-Lyons has authored 72 papers in refereed journals, 95 technical articles/chapters and holds 14 patents. She is a member of the Materials Research Society and Electrochemical Society (ECS), for whom she has been an organizing member of the Proton Electrolyte Fuel Cells committee since 2011. She earned her PhD in 1992 in Materials Science and Engineering at the University of Pennsylvania, Philadelphia, PA for her work on mixed conducting materials for solid oxide fuel cells, and holds a BS in Chemistry from Haverford College, Haverford, PA (1987).

List of Authors

Jan Allen
US Army Research Laboratory
Sensors and Electron Devices Directorate
2800 Powder Mill Road
Adelphi, MD 20783, USA
jan.l.allen8.civ@mail.mil

Michael Angelo
University of Hawaii – Manoa
Hawaii Sustainable Energy Research Facility,
Hawaii Natural Energy Inst.
1680 East-West Road
Honolulu, HI 96822, USA
mangelo@hawaii.edu

Dick Bedeaux
Norwegian University of Science and Technology
Dept. Chemistry
Høgskoleringen 5
7491 Trondheim, Norway
dick.bedeaux@chem.ntnu.no

Daniel Bélanger
University Quebec at Montreal (UQAM)
Dept. Chemistry
2101, rue Jeanne-Mance
Montreal, QC H2X2J6, Canada
belanger.daniel@uqam.ca

Keith Bethune
University of Hawaii – Manoa
Hawaii Sustainable Energy Research Facility,
Hawaii Natural Energy Inst.
1680 East-West Road
Honolulu, HI 96822, USA
bethune@hawaii.edu

Nils Brandau
Volkswagen AG
Fuel Cell Research
38440 Wolfsburg, Germany
nils.brandau@volkswagen.de

Cornelia Breitkopf
TU Dresden
Dept. Mechanical Engineering
Helmholtzstr. 14
01062 Dresden, Germany
cornelia.breitkopf@tu-dresden.de

Thierry Brousse
Université de Nantes
Inst. des Matériaux Jean Rouxel IMN, UMR CNRS
6502/Polytech Nantes
rue Christian Pauc
44306 Nantes Cedex 3, France
thierry.brousse@univ-nantes.fr

Colin G. Cameron
Defence Research and Development Canada
Atlantic Research Centre
Dartmouth, NS B2Y 3Z7, Canada
colin.cameron@drdc-rddc.gc.ca

Jeng-Kuei Chang
National Central University
Inst. Material Science and Engineering
300 Jhong-Da Road, Jhong-Li
Taoyuan, Taiwan
jkchang@ncu.edu.tw

George Z. Chen
University of Nottingham Ningbo China
Dept. Chemical and Environmental Engineering
199 Taikang East Road
315100 Ningbo, China
george.chen@nottingham.ac.uk

Kazumi Chiba
Tokyo University of Agriculture and Technology
Laboratory of Bio-organic Chemistry
3-5-8 Saiwai-cho, Fuchu
183-8509 Tokyo, Japan
chiba@carlit.co.jp

Kevin Cooper
Scribner Associates, Inc.
150 E Connecticut Ave.
Southern Pines, NC 28387, USA
kevin@scribner.com

Minato Egashira
Nihon University
College of Bioresource Sciences
1866 Kameino
252-0880 Fujisawa, Japan
egashira.minato@nihon-u.ac.jp

Frédéric Favier
Université Montpellier II
Inst. Charles Gerhardt (ICG)
E. Bataillon, cc1502
34095 Montpellier Cedex 05, France
fredf@um2.fr

James M. Fenton
University of Central Florida
Florida Solar Energy Center
1679 Clearlake Road
Cocoa, FL 32922-5703, USA

Robert J. Forster
Dublin City University
School of Chemical Sciences
Dublin 9, Ireland
robert.forster@dcu.ie

Yannick Garsany
Excet Inc./US Naval Research Laboratory
Chemistry Division
4555 Overlook Ave., SW
Washington, DC 20375, USA
yannick.garsany.ctr@nrl.navy.mil

Isaí Gonzalez Martínez
ThyssenKrupp Electrolysis GmbH
Process Engineering
Vosskuhle 38, Harpen
44141 Dortmund, Germany
isai.gonzalez-martinez@thyssenkrupp.com

Richard Hanke-Rauschenbach
Leibniz University Hannover
Institute for Electric Power Systems,
Electric Energy Storage Systems
Appelstr. 9A
30167 Hannover, Germany
hanke-rauschenbach@ifes.uni-hannover.de

Ting He
Idaho National Laboratory
Energy and Environment Science and Technology
Idaho Falls, ID 83415, USA
ting.he@inl.gov

Dietrich Hebecker
Martin-Luther-University Halle-Wittenberg
Engineering Science Center
06099 Halle (Saale), Germany
dietrich.hebecker@iw.uni-halle.de

Matthias Heim
BMZ GmbH
Zeche Gustav 1
63791 Karlstein, Germany
heimmatthias@hotmail.com

Rudolf Holze
Technische Universität Chemnitz
Institut für Chemie
Str. der Nationen 62
09111 Chemnitz, Germany
rudolf.holze@chemie.tu-chemnitz.de

Di Hu
University of Nottingham Ningbo China
Dept. Chemical and Environmental Engineering
199 Taikang East Road
315100 Ningbo, China
di.hu@nottingham.edu.cn

Jack Huizingh
University of Hawaii – Manoa
Hawaii Sustainable Energy Research Facility,
Hawaii Natural Energy Inst.
1680 East-West Road
Honolulu, HI 96822, USA
huizingh@hawaii.edu

Greg Jackson
Colorado School of Mines
Dept. Mechanical Engineering
1610 Illinois Str.
Golden, CO 8040, USA
gsjackso@mines.edu

Michelle D. Johannes
US Naval Research Laboraty
Center for Computational Materials Science
4555 Overlook Ave.
Washington, DC 20375, USA
michelle.johannes@nrl.navy.mil

T. Richard Jow
US Army Research Laboratory
Sensors and Electron Devices Directorate
2800 Powder Mill Road
Adelphi, MD 20783, USA
t.r.jow.civ@mail.mil

Mahaprasad Kar
Phillips 66 Research Center
Sustainability Technologies
Bartlesville, OK 74003, USA
prasad.kar@p66.com

Tia E. Keyes
Dublin City University
School of Chemical Sciences
Dublin 9, Ireland
tia.keyes@dcu.ie

Chunjoong Kim
Chungnam National University
Department of Materials Science and Engineering
W3-241, 99 Daehak-ro, Yuseong-gu
305-764 Daejeon, Republic of Korea
ckim0218@cnu.ac.kr

Signe Kjelstrup
Norwegian University of Science and Technology
Dept. Chemistry
Høgskoleringen 5
7491 Trondheim, Norway
signe.kjelstrup@ntnu.no

Jürgen Köhler
University of Braunschweig
Thermal Science Laboratory
Hans-Sommer-Str. 5
38106 Braunschweig, Germany
juergen.koehler@tu-braunschweig.de

Andriy Kovalenko
University of Alberta
National Inst. Nanotechnology
11421 Saskatchewan Dr.
Edmonton, AB T6G 2M9, Canada
andriy.kovalenko@nrc-cnrc.gc.ca

Alexander Kuhn
Université de Bordeaux
Ecole Nationale Supérieure de Chimie, Biologie et Physique
16 av. Pey Berland
33607 Pessac, France
kuhn@enscbp.fr

Stuart Licht
George Washington University
Dept. Chemistry
800 22nd Str., NW
Washington, DC 20052, USA
slicht@gwu.edu

Manuel Lohrengel
Heinrich-Heine-Universität Düsseldorf
Inst. Physikalische Chemie
Universitätsstr. 1
40225 Düsseldorf, Germany
manuel.lohrengel@uni-duesseldorf.de

Jeffrey Long
Naval Research Laboratory
Surface Chemistry Branch
4555 Overlook Ave. SW
Washington, DC 20375, USA
jeffrey.long@nrl.navy.mil

Corey T. Love
US Naval Research Laboratory
Chemistry Division
4555 Overlook Ave.
Washington, DC 20375, USA
corey.love@nrl.navy.mil

Cynthia A. Lundgren
US Army Research Laboratory
Sensors and Electron Devices Directorate
2800 Powder Mill Road
Adelphi, MD 20783, USA
cynthia.lundgren@us.army.mil

Neal D. McDaniel
Phillips 66 Research Center
Sustainability Technologies
Bartlesville, OK 74003, USA
neal.d.mcdaniel@p66.com

John R. Miller
JME, Inc.
23500 Mercantile Road
Beachwood, OH 44122, USA
jmecapacitor@att.net

Shelley D. Minteer
University of Utah
Dept. Chemistry and Dept. Materials Science and Engineering
315 S 1400 E
Salt Lake City, UT 84112, USA
minteer@chem.utah.edu

Masayuki Morita
Yamaguchi University
Graduate School of Sciences and Technology for Innovation
2-16-1 Tokiwadai
755-8611 Ube, Japan
morita@yamaguchi-u.ac.jp

Seunghoon Nam
Korea Institute of Machinery & Materials (KIMM)
Dept. of Nano Mechanics, Nano Mechanical Systems Research Division
305-343 Daejeon, Republic of Korea
kwek14@kimm.re.kr

Katsuhiko Naoi
Tokyo University of Agriculture and Technology
Japan Institute of Symbiotic Science and Technology
184-8558 Tokyo, Japan
naoi2@cc.tuat.ac.jp

Yuhong Oh
Samsung Electro-Mechanics
LCR Materials Group
443-743 Suwon, Republic of Korea
yuhong.oh@samsung.com

Byungwoo Park
Seoul National University
Dept. Materials Science and Engineering, and Research Institute of Advanced Materials
1 Gwanak-ro, Gwanak-gu
151-744 Seoul, Republic of Korea
byungwoo@snu.ac.kr

Vijay K. Ramani
Washington University in St. Louis
Dept. Energy, Environmental and Chemical Engineering
One Brookings Drive Campus Box 1180
St. Louis, MO 63130, USA
ramani@wustl.edu

Bruce B. Randolph
Phillips 66 Research Center
Sustainability Technologies
Bartlesville, OK 74003, USA
bruce.b.randolph@p66.com

Tatyana Reshetenko
University of Hawaii – Manoa
Hawaii Sustainable Energy Research Facility, Hawaii Natural Energy Inst.
1680 East-West Road
Honolulu, HI 96822, USA
tatyanar@hawaii.edu

Hans-Hermann Rüttinger
Martin-Luther-University Halle-Wittenberg
Dept. Pharmacy
Langenbeckstr. 4
06120 Halle, Germany
ruettinger@pharmazie.uni-halle.de

Michael Schneider
Fraunhofer IKTS
Dept. Electrochemistry
Winterbergstr. 28
01277 Dresden, Germany
michael.schneider@ikts.fraunhofer.de

Patrice Simon
Université Paul Sabatier
Centre Inter-universitaire de Recherche et d'Ingénierie des Matériaux
CNRS 5085, Toulouse, France
simon@chimie.ups-tlse.fr

Richard O. Stroman
US Naval Research Laboratory
Chemistry Division
4555 Overlook Ave.
Washington, DC 20375, USA
richard.stroman@nrl.navy.mil

Wataru Sugimoto
Shinshu University
Dept. Fine Materials Engineering, Faculty of Textile Science and Technology
3-15-1 Tokida
386-8567 Ueda, Japan
wsugi@shinshu-u.ac.jp

I-Wen Sun
National Cheng Kung University
Dept. Chemistry
No.1, University Road
Tainan, Taiwan
iwsun@mail.ncku.edu.tw

Kai Sundmacher
Max Planck Institute for Dynamics of Complex Technical Systems
Process Systems Engineering
Sandtorstr. 1
39106 Magdeburg, Germany
sundmacher@mpi-magdeburg.mpg.de

Karen Swider-Lyons
US Naval Research Laboratory
Chemistry Division
4555 Overlook Ave.
Washington, DC 20375, USA
karen.lyons@nrl.navy.mil

YuYe J. Tong
Georgetown University
Dept. Chemistry
37th & O Streets, NW
Washington, DC 20057, USA
yyt@georgetown.edu

Tanja Vidaković-Koch
Max Planck Institute for Dynamics of Complex Technical Systems
Process Systems Engineering
Sandtorstr. 1
39106 Magdeburg, Germany
vidakovi@mpi-magdeburg.mpg.de

James J. Walsh
University of Liverpool
Stephenson Institute for Renewable Energy
Liverpool, L69 7ZD, UK
jjwalsh@liv.ac.uk

Kang Xu
US Army Research Laboratory
Sensors and Electron Devices Directorate
2800 Powder Mill Road
Adelphi, MD 20783, USA
conrad.k.xu.civ@mail.mil

Yunfeng Zhai
University of Hawaii – Manoa
Hawaii Sustainable Energy Research Facility,
Hawaii Natural Energy Inst.
1680 East-West Road
Honolulu, HI 96822, USA
yunfeng@hawaii.edu

Sheng S. Zhang
US Army Research Laboratory
Sensors and Electron Devices Directorate
2800 Powder Mill Road
Adelphi, MD 20783, USA
shengshui.zhang.civ@mail.mil

Contents

List of Abbreviations XXI

1 **Electrochemical Science – Historial Review**
Cornelia Breitkopf, Karen Swider-Lyons 1
References 9

2 **Modern Electrochemistry**
Cornelia Breitkopf, Karen Swider-Lyons 11
2.1 Fundamental Components of Electrochemistry 11
2.2 Thermodynamics 14
2.3 Kinetics 17
2.4 Mass Transport 19
2.5 The Charged Electrode Interface/Electrochemical Double Layer 21
2.6 Ionic and Electronic Resistance 23
2.7 Experimentation 24
2.8 Subtopics in Electrochemistry 26
2.9 Summary 28
References 29

Part A Thermodynamics

3 **Thermodynamical Aspects of Electrochemical Reactions**
Dietrich Hebecker 33
3.1 Electrochemical Reactions for Energy Conversion 33
3.2 Electrochemical Reactions and Energy Transformation 54
References 67

4 **Thermodynamics of Electrochemical Systems**
Signe Kjelstrup, Dick Bedeaux 69
4.1 Scope and Premises 69
4.2 Thermodynamic Properties of the Total Cell 72
4.3 Example Cells 73
4.4 Entropy Production in Three- and Two-Dimensions 74
4.5 Alternative Variable Sets 75
4.6 Cell Potentials 80
4.7 The Polymer Electrolyte Fuel Cell 87
4.8 Transport at Interfaces. Perspectives and Conclusion 90
References 91

5 **Multiscale Modeling of Solvation**
Andriy Kovalenko 95
5.1 Integral Equation Theory of Molecular Liquids 96
5.2 Statistical–Mechanical, Molecular Theory of Solvation 99
5.3 Multiscale Coupling of the 3D-RISM-KH Molecular Theory 113
5.4 Multi-Time-Step Molecular Dynamics of Biomolecules 116

5.5 Electrical Double Layer in Nanoporous Materials 123
5.6 Replica Formalism for Fluid Sorbed in a Disordered Matrix 123
5.7 Replica DRISM-KH-VM for Electrolyte Solution Sorbed in Nanoporous Material 124
5.8 Conclusions 133
References 134

Part B Electrodes and Electrode Processes

6 **Highly Ordered Macroporous Electrodes**
Alexander Kuhn, Matthias Heim 143
6.1 Macroporous Electrodes by Infiltration of Colloidal Templates 144
6.2 Macroporous Materials with a Gradient in Pore Diameter 172
6.3 Macroporous Microelectrodes with Cylindrical Geometry 181
6.4 Applications of Macroporous Electrodes 188
6.5 Conclusion 197
References 197

7 **Ion-Sensitive Electrodes**
Hans-Hermann Rüttinger 207
7.1 Fundamentals of Potentiometry 207
7.2 Application of ISE 226
7.3 Amperometric and Voltammetric Methods 227
References 237

8 **Transport in Liquid-Phase Electrochemical Devices**
Richard O. Stroman, Greg Jackson 239
8.1 A General Transport Model for Liquid-Fed Electrochemical Cells 240
8.2 Practical Considerations 246
8.3 Example Cell: Direct Borohydride–Hydrogen Peroxide Fuel Cell 248
8.4 Conclusions 256
8.5 Nomenclature 256
References 257

9 **Catalyst Layer Modeling**
Tanja Vidaković-Koch, Richard Hanke-Rauschenbach, Isaí Gonzalez Martínez, Kai Sundmacher 259
9.1 Gas Diffusion Electrodes 259
9.2 Catalyst Layer Physical Structure 261
9.3 Governing Equations 262
9.4 Macroscale Models 273
9.5 Conclusions and Outlook 282
References 283

10 **Water Management in Proton Exchange Fuell Cells**
Nils Brandau, Jürgen Köhler 287
10.1 Water Management in PEMFC 287
10.2 Thermodynamics and Electrochemistry 289
10.3 Polarization Curve 290
10.4 Gas Humidification 294

10.5 Sensorless Humidification 302
References 311

11 **Calculations in Li-Ion Battery Materials**
Michelle D. Johannes, Corey T. Love, Karen Swider-Lyons 313
11.1 Using DFT to Calculate the Voltage of Layered Materials 315
11.2 PDOS Calculations of Oxygen Stability and Cycling Safety 323
11.3 Summary 326
References 327

Part C Electrochemistry Probes

12 **Electrochemical Energy Generation and Storage as Seen by In-Situ NMR**
YuYe J. Tong 331
12.1 Spatially-Resolved ^{195}Pt NMR Spectroscopy of Pt-Based Electrocatalysts 336
12.2 NMR/MRI Studies of Energy Storage (Batteries) Materials 342
12.3 MRI of Water Distribution in Fuel Cells 352
12.4 Conclusion and Future Perspectives: Sensitivity, Sensitivity and Sensitivity 357
References 360

13 **Spectroscopy of Electrochemical Systems**
James J. Walsh, Robert J. Forster, Tia E. Keyes 365
13.1 General Experimental Considerations 366
13.2 Electronic Spectroscopy 368
13.3 Spectroelectrochemistry of the Excited State 385
13.4 Vibrational Spectroelectrochemistry 393
13.5 Raman Spectroelectrochemistry 404
13.6 Sum Frequency Generation Spectroelectrochemistry 413
13.7 Conclusions and Outlook 414
References 415

14 **Kinetic Activity in Electrochemical Cells**
Yannick Garsany, Karen Swider-Lyons 423
14.1 Evaluation of Pt/VC Electrocatalysts for the ORR 428
14.2 Electrochemical Characterization of the Pt/VC Electrocatalyst Thin-Film Electrodes by RDE and RRDE 435
14.3 Electrochemical Characterization of Mn_xO_y Thin-Film Electrodes 440
14.4 Conclusions 443
References 444

Part D Energy Conversion and Storage

15 **Lithium-Ion Batteries and Materials**
Cynthia A. Lundgren, Kang Xu, T. Richard Jow, Jan Allen, Sheng S. Zhang 449
15.1 Overview – Electrochemical Evaluation of Li-Ion Batteries 449
15.2 Evaluation of Materials and Components in Li-Ion Batteries 451
15.3 Evaluation at the Cell–Battery Level 481

15.4 Beyond Li-Ion 487
15.5 Conclusions 490
References 491

16 **Materials for Electrochemical Capacitors**
Thierry Brousse, Daniel Bélanger, Kazumi Chiba, Minato Egashira, Frédéric Favier, Jeffrey Long, John R. Miller, Masayuki Morita, Katsuhiko Naoi, Patrice Simon, Wataru Sugimoto 495
16.1 Batteries and Electrochemical Capacitors – Basic Concepts 496
16.2 Carbon 504
16.3 Manganese Dioxide 510
16.4 Ruthenium Oxide 523
16.5 Other Pseudocapacitive Materials 529
16.6 Electrolytes 529
16.7 Applications of Electrochemical Capacitors 537
16.8 Electrochemical Capacitor Prospective View 543
References 545

17 **Electrochemical Capacitors**
Colin G. Cameron 563
17.1 The Nature of Capacitance 563
17.2 Test Methods 568
17.3 Configuration 578
17.4 Further Practical Concerns 584
17.5 Summary and Conclusions 586
17.6 Symbols 586
References 587

18 **Kinetics of Fast Redox Systems for Energy Storage**
Rudolf Holze 591
18.1 Overview and Introduction 591
18.2 Flow Batteries – Basic Components 597
18.3 Redox Reactions and their Kinetics 598
18.4 Acceleration of Redox Reactions 600
18.5 Materials for Electrodes in Flow Batteries 601
18.6 Catalysis and Surface Enlargement Effects 605
18.7 Future Directions 606
References 606

19 **Modern Fuel Cell Testing Laboratory**
Jean St-Pierre, Michael Angelo, Keith Bethune, Jack Huizingh, Tatyana Reshetenko, Mebs Virji, Yunfeng Zhai 611
19.1 Fuel Cell Laboratory Evolution 611
19.2 Safety and Test Stations 614
19.3 Fuel Cell Stack Components and Assembly 621
19.4 Testing and Diagnostic Techniques 626
19.5 Conclusion 640
References 641

20 **Polymer Electrolyte Fuel Cells**
Vijay K. Ramani, Kevin Cooper, James M. Fenton, H. Russel Kunz 649
20.1 Experimental Methods 650

20.2 H_2/O_2 or Air Fuel Cell Performance Testing 662
20.3 Application of a Fuel Cell Empirical Model 679
20.4 Fuel Crossover and Electrochemical Surface Area 683
20.5 Impedance Spectroscopy of PEM Fuel Cells 689
References 710

21 **Next-Generation Electrocatalysts**
Seunghoon Nam, Chunjoong Kim, Yuhong Oh, Byungwoo Park 713
21.1 Oxygen-Reduction Reaction – Cathodes 713
21.2 Methanol-Oxidation Reaction – Anodes 724
References 738

22 **Methods in Biological Fuel Cells**
Shelley D. Minteer 743
22.1 Bioelectrocatalysis 744
22.2 Spectroscopic Methods 746
22.3 Electrochemical Methods 749
22.4 Engineering Considerations 752
22.5 Conclusions 753
References 753

23 **Energy Conversion Based on Bio(electro)catalysts**
Tanja Vidaković-Koch 757
23.1 Working Principles of Bioelectrochemical Systems 758
23.2 Bioelectrochemical Systems in Cell-Free Systems 758
23.3 General Aspects 760
23.4 Biotransformation with Redox Enzymes 770
23.5 Conclusions and Outlook 774
References 774

24 **Photoelectrochemical Conversion Processes**
Stuart Licht 779
24.1 Overview and Historical Perspective 779
24.2 Photoelectrochemical Processes 780
24.3 State-of-the-Art and Emerging Technologies 795
24.4 Summary 796
References 796

Part E Electrochemical Processes

25 **Advanced Extractive Electrometallurgy**
Di Hu, George Z. Chen 801
25.1 Conventional Extractive Metallurgy 801
25.2 Innovative Electrolytic Extraction Techniques for Titanium 808
25.3 Direct Electroreduction of Solid Metal Oxides to Metals: The FFC Cambridge Process 814
25.4 Summary 829
References 830

26 **Electrodeposition of Nanomaterials**
I-Wen Sun, Jeng-Kuei Chang 835
26.1 Processes for Electrodeposition of Nanomaterials 836

26.2 Electrodeposited Nanomaterials for Energy Storage/Conversion Devices 865
26.3 Conclusions and Prospects 882
References 882

27 **Electrochemical Hydrogen Production**
Ting He, Mahaprasad Kar, Neal D. McDaniel, Bruce B. Randolph 897
27.1 Theoretical Aspects of Electrochemical Hydrogen Production 899
27.2 Electrochemical Hydrogen Production Methods 905
27.3 Development Perspectives 929
27.4 Conclusions 933
References 934

28 **Electrochemical Machining**
Michael Schneider, Manuel Lohrengel 941
28.1 Introduction and History 942
28.2 Fundamentals of Electrochemical Machining 943
28.3 Experimental Techniques 946
28.4 The Interface Process During ECM 949
28.5 Classification of ECM Processes 952
28.6 Surface Topography, Crystallographic Effects and Surface Quality 952
28.7 Oxygen Evolution 958
28.8 Pulse ECM 959
28.9 Too Difficult-to-Machine: Hard Metals, Carbides and Nitrides 962
References 967

About the Authors 973
Detailed Contents 985
Subject Index 999

List of Abbreviations

3PI	three-phase interline

A

AAM	anodic alumina membrane
AAO	anodic aluminum oxide
ADF	Amsterdam density functional
ADH	alcohol dehydrogenase
AE	acoustic emission
AE	auxiliary electrode
AEM	anion exchange membrane
AFC	alkaline fuel cell
AFM	atomic force microscopy
AHT	anode humidifier temperature
AIR	attenuated internal reflectance
ALD	atomic layer deposition
AN	acetonitrile
AOM	acousto-optic modulator
APD	avalanche photodiode
AQ	anthraquinone
ARC	accelerated-rate calorimetry
ASFE	advanced solvation force extrapolation
ASI	area specific impedance
ASTMI	American Society for Testing and Materials International
ATO	antimony-doped tin oxide
ATP	adenosine triphosphate
ATP	adenosine-5′-triphosphate
ATR-FTIR	attenuated total reflectance infrared
ATR	attenuated total reflection
AU	absorbance unit

B

BCA	bicinchoninic acid
BDD	boron-doped diamond
BET	Brunauer–Emmett–Teller
BHP	Broken Hill proprietary
BJH	Barrett, Joyner, and Halenda theory
BMS	bulk magnetic susceptibility
BOB	bis(oxalato)borate
BP	bypass
BPGG	Ballone–Pastore–Galli–Gazzillo
BPTI	bovine pancreatic trypsin inhibitor
BSA	bovine serum albumin
BS	beam splitter
BSCF	$Ba_{0.5}Sr_{0.5}Co_{0.8}Fe_{0.2}O_{3-\delta}$
BSE	back-scattered electron
BV	Butler–Volmer

C

CA	chronoamperometry
CAPEX	capital expense
CASSCF	complete active space self-consistent field
CCM	catalyst coated membrane
CDC	carbon-derived carbons
CD	circular dichroism
CdS	cadmium sulfide
CdSe	cadmium selenide
CE	coulombic efficiency
CE	counter electrode
CFD	computational fluid dynamics
CHT	cathode humidifier temperature
CIP	contact ion pair
CL	comprising catalyst
CM	crystal modifier
CMOS	complementary metal-oxide-semiconductor
CNC	cellulose nanocrystal
CNT	carbon nanotube
CO	carbon monoxide
COHP	crystal orbital hamiltonian population
COP	coefficient of performance
CP	chronopotentiometry
CP	conducting polymer
CPE	constant phase element
CPMD	Car–Parrinello molecular dynamics
CPV	concentrator photovoltaic cell
CRDS	cavity ring down spectroelectrochemistry
CRP	c-reactive protein
CSI	chemical shift imaging
CTAB	cetyltrimethyl ammonium bromide
CTC	charge transfer complex
CT	cell temperature
CTNFM	4-carboxy-(2,5,7-trinitro-9-fluorenylidene) malonitrile
CVA	cyclic voltabsorptometry
CV	cyclic voltammetry
CV	cyclic voltammogram
CVD	chemical vapor deposition

D

DBFC	direct borohydride fuel cell
DBSA	dodecylbenzene sulfonic acid
DC	direct current
DCIP	dichlorophenolindophenol
DCVA	differential cyclic voltabsorptometry
DEME	diethylmethyl(2-methoxyethyl) ammonium
DET	direct electron transfer
Df	Desulfovibrio fructosovorans
DFG	difference frequency generation
DFT	density functional theory
DHE	dynamic hydrogen electrode

DI	diaphorase
DLM	diffusion layer model
DMC	dimethyl carbonate
DMFC	direct methanol fuel cell
DMF	dimethylformamide
DMS	dimethylsulfone
DMSO	dimethylsulfoxide
DNA	deoxyribonucleic acid
DNP	dynamic nuclear polarization
DoD	depth of discharge
DOS	density of state
DR	diffuse reflectance
DRISM	dielectrically consistent reference interaction site model
DSA	dimensionally stable anode
DSA	dimensionally stable electrode
DSC	differential scanning calorimetry
DSC	dye-sensitized solar cell
DSDH	d-sorbitol dehydrogenase
DSE	dimensionally stable electrode
DVB	divinylbenzene

E

EA-IOW	electroactive integrated optical waveguide
EAD	electro-assisted deposition
EASA	electrochemically active surface area
EBL	electron-beam lithography
EBSD	electron backscatter diffraction
ECDL	external cavity diode laser
EC	electrochemical
EC	electrochemical capacitor
EC	ethylene carbonate
ECL	electrochemiluminescence
ECM	electrochemical machining
ECSA	electrochemical active surface area
EDLC	electrochemical double-layer capacitor
EDL	electric double layer
EDP	electrodeposited paint
EDR	electrolyte distributed resistance
EDS	energy-dispersive spectrometry
EDS	energy-dispersive spectroscopy
EDTA	ethylenediaminetetraacetate
EDAX/EDS	energy dispersive x-ray analysis spectrometer
EDX	electron diffraction x-ray analysis
EDX	energy-dispersive x-ray spectroscopy
EEC	equivalent electrical circuit
EIS	electrochemical impedance spectroscopy
EL	electrochemical lithography
ELISA	enzyme-linked immunosorbant assay
EMC	ethylmethyl carbonate
EM	electromagnetic
EMF	electro motoric force
emf	electromotive force
EMI,TFSI	ethyl-methyl-immidazolium-trifluoro-methane-sulfonylimide
EMIC	ethyl-3-methylimidazolium chloride
EMI	electromagnetic interference
EMI	ethylmethylimidazolium
EMR	electronically mediated reaction
eNMR	electrophoresis nuclear magnetic resonance
EOS	electronic-orbital-specific
EPC	elastic photonic crystal
EPR	electron paramagnetic resonance
EQCM	electrochemical quartz crystal microbalance
ESA	electrocatalytic surface area
ESA	electrochemical surface area
ESED	electrochemical step-edge decoration
ESEM	environmental scanning electron microscopy
ES	enzyme substrate
ESM	electrochemical strain microscopy
ESR	equivalent serial resistance
ET	electron transfer
EV	electric vehicle
EW-BBCEAS	evanescent wave broadband cavity-enhanced absorption spectroscopy
EW-CRDS	evanescent wave cavity ring down spectroelectrochemistry
EW	evanescent wave
EXAFS	extended x-ray absorption fine structure

F

FAD	flavin adenine dinucleotide
FAOR	formic acid oxidation reaction
fcc	face-centered cubic
Fc	ferrocene
FC	fuel cell
FDTO	fluorine-doped tin oxide
FE	field emission
FE	finite element
FESEM	field emission scanning electron microscopy
FET	field effect transistor
FFC	Fray–Farthing–Chen
FMN	flavin mononucleotide
FOM	figure of merit
FOSEC	fiber optic spectroelectrochemical sensor
FRA	frequency response analyzer
FT-EMIRS	Fourier-transform electrochemically modulated infrared spectroscopy
FT	Fourier-transform
FT	Frumkin/Temkin
FTIR	Fourier transform infrared
FTIR	Fourier transform infrared spectroscopy
FV	finite volume
FWHM	full width at half maximum

G

G-OTE	graphene-based optically transparent electrode
GB	generalized Born
GC-MS	gas chromatography-mass spectrometry

GC	glassy carbon
GDC	gadolinium-doped ceria
GDE	gas diffusion electrode
GDH	glucose dehydrogenase
GDL	gas diffusion layer
GGA	generalized gradient approximation
GIC	graphite intercalation compound
GLIC	ligand-gated ion channel
GMRes	generalized minimal residual
GO	graphite oxide
GOx	glucose oxidase
GSFE	generalized SFE
GSFE	generalized solvation force extrapolation
GTT	Ginatta Technologie Titanio
GWE	graphite wax electrode
GWP	global warming potential

H

HAADF	high-angle annular dark field
HAD	hydrogen adsorption/desorption
HA	hard anodization
hcp	hexagonal close-packed
HDWNT	hybrid double-walled nanotube
HER	hydrogen evolution reaction
HEV	hybrid electric vehicle
HFGM	hierarchical flowerlike gold microstructure
HFR	high-frequency resistance
HHV	higher heating value
hNb	human neuroglobin
HNC	hypernetted chain
HOMO	highest occupied molecular orbital
HOPG	highly ordered pyrolytic graphite
HOR	hydrogen oxidation reaction
HPC	high precision coulometry
HPLC	high-performance liquid chromatography
HPPC	hybrid pulse power characteristic
HQBpt	3,5-bis(2-pyridyl)-1,2,4-triazole
HRN	helical rosette nanotube
HRP	horseradish peroxidase
HRTEM	high resolution transmission electron microscopy
HSC	high surface area carbon
HTE	high-temperature electrolysis

I

I/C	ionomer-to-carbon ratio
iCCD	intensified CCD
ICP-AES	inductively coupled plasma-atomic emission spectroscopy
ICP-MS	inductively coupled plasma-mass spectroscopy
ICSD	inorganic crystal structure database
IDC	interparticle diffusional coupling
IEM	ion exchange membrane
IL	interference lithography
IL	ionic liquid
ILS	integrated laboratory scale
INR	isokinetic NH chain RESPA
IR	infrared
ISFET	ion-selective field-effect transistor
IS	impedance spectroscopy
ISS	ion selective sensor
ITO	indium tin oxide
IVCT	inter-valence charge transfer

K

KB	Ketjen Black
KH	Kovalenko and Hirata
KS-DFT	Kohn–Sham density functional theory

L

L-CSA	L-camphorsulfonic acid
LB	Langmuir–Blodgett technique
LC-MS	liquid chromatography-mass spectrometry
LCA	life cycle analysis
LDA	local density approximation
LDOS	local density of state
Li-S	lithium-sulfur
LIB	lithium-ion battery
LN	Langevin
LOPTLC	long optical path thin layer cell
LPNE	lithographically patterned nanowire electrodeposition
LSCF	lanthanum strontium cobalt ferrite
LSM	lanthanum manganite
LSP	localized surface plasmon
LSV	linear sweep voltammetry
LT	low temperature
LUMO	lowest unoccupied molecular orbital

M

MA	mass-specific activity
MA	mild anodization
MAS	magic angle spinning
MBPEC	multiple bandgap photoelectrochemical solar cell
MCD	magnetic circular dichroism
MCE	metallic cavity electrode
MCMB	mesoporous carbon microbead
MDIIS	modified direct inversion in the iterative subspace
MD	molecular dynamics
MEA	membrane–electrode assembly
MER	materials and electrochemical research
MET	mediated electron transfer
MFC	mass flow controller
MG-Si	metallurgical-grade-silicon
MHD	magnetohydrodynamic
MIBK:IPA	methyl isobutyl keton isopropanol
MIP	mercury intrusion porosimetry
MLCT	metal-to-ligand charge transfer

MMCT	metal-to-metal charge transfer
MM	molecular mechanics
MO	methyl orange
MO	molecular orbital
MOR	methanol oxidation reaction
MRI	magnetic resonance imaging
MSA	mean spherical approximation
MSDS	material safety data sheet
MSE	molten salt electrolysis
MS	Martynov–Sarkisov
MS	mass spectrometry
MTS	multiple time step
MWCNT	multiwalled carbon nanotube

N

NADH	reduced nicotinamide adenine dinucleotide
NAD	nicotinamide adenine dinucleotide
NCM	$LiNi_{1/3}Co_{1/3}Mn_{1/3}O_2$
NC	nanocrystal
NET	nonequilibrium thermodynamics
NFRA	nonlinear frequency response analysis
NG	natural graphite
NHE	normal hydrogen electrode
NH	Nosé–Hoover
Ni(II)-NTA	nickel chelating nitrilo-triacetic acid
NiMH	nickel metal hydride
NIR	near-infrared
NMR	nuclear magnetic resonance
NP	nanoparticle
NR	nanorod
NSA	naphthalenesulfonic acid
NTU	number of transfer units
NW	nanowire

O

OCP	open-circuit potential
OCV	open-circuit voltage
OER	oxygen evolution reaction
OFE	orbital-free embedded
OIN	optimized isokinetic Nosé–Hoover
OMC	outer membrane cytochrome
opd	overpotential metal deposition
OPG	ordinary pyrolytic graphite
ORC	organic Rankine cycle
ORC	oxidative and reductive cycle
ORR	oxygen reduction reaction
OTE	optically transparent electrode
OTS	octadecyltrichlorosilane
OTTLE	optically transparent thin layer electrode
OZ	Ornstein–Zernike

P

PALM	photo-activated localization microscopy
PANI	polyaniline
PBG	photonic bandgap
PB	Poisson–Boltzmann
PBS	phosphate buffer solution
PBT	polybithiophene
PC	photonic crystal
PC	polycarbonate
PC	propylene carbonate
PC	pseudocapacitance
PDDA	poly(dimethyldiallylammonium chloride)
PDF	pair-density function
PDOS	partial density of states
PD	packing density
PEC	photoelectrochemical
PECVD	plasma enhanced CVD
PEDOT	poly(3,4-ethylenedioxythiophene)
PEGDE	poly(ethylene glycol) dimethyl ether
PEMFC	proton-exchange membrane fuel cell
PEM	polymer electrolyte membrane
PEM	proton-exchange membrane
PE	polyethylene
PET	poly(ethylene terephthalate)
PFG	pulse field gradient
PFSA	perfluorosulfonic acid
PITT	potentiostatic intermittent titration
PMF	potential of mean force
PMMA	poly(methyl methacrylate)
PM	polarization modulated
PMS	phenazine methosulfate
PMT	photomultiplier tube
POM	polyoxometalate
POPC	1-palmitoyl-2-oleoyl-*sn*-glycero-3-phosphocholine
POT	poly(3-octyl thiophene)
PP	propylene
PPy	polypyrrole
PQQ	pyrroloquinoline quinone
PR	photoresist
PR	production reaction
PRS	porosity ratio shrinkage
PSA	1-pyrenesulfonic acid
PSE-n	partial series expansions of order n
PS	polystyrene
PS	polysulfide
Pt ECSA	Pt electrochemical surface area
PTFE	poly(tetrafluoroethylene)
PT	polythiophene
PVC	polyvinyl chloride
PVDC	carbonized polyvinylidene chloride
PVdF	poly(vinylidene difluoride)
PVD	physical vapor deposition
PV	photovoltaic
PVP	poly(vinylpyrrolidone)
PVP	polyvinylpyridine
PY	Percus–Yevick

Q

QCM	quartz crystal microbalance
QC	quantum chemistry
QIT	Quebec iron and titanium

QM	quantum mechanics
QSE	quantum size effect

R

RAPS	remote area power supply
RDE	rotating-disk electrode
RDF	radial distribution function
RD	rhombic-dodecahedral
REDD	x-ray radial electron density distribution
RE	reference electrode
RESPA	reference system propagator algorithm
RFB	redox flow battery
RF	radio frequency
RHE	reversible hydrogen electrode
RH	relative humidity
RIE	reactive-ion etching
RISM	reference interaction site model
RMS	root mean squared
RNT	rosette nanotube
ROI	regions of interest
rpm	revolution per minute
RRDE	rotating ring-disc electrode
RT	room temperature

S

SA	area-specific activity
SAM	self-assembled monolayer
SAPG	stress-annealed pyrolytic graphite
SA	surface area
SAXS	small angle x-ray scattering
ScCeZ	Sc–Ce-doped zirconia
SCE	saturated calomel electrode
SCE	standard calomel electrode
SCS	single carbon sphere
SC	supercapacitor
ScSZ	scandia-stabilized zirconia
SDA	spatial decomposition analysis
SDBS	sodium dodecyl benzene sulfonate
SDC	samarium-doped ceria
SD	smoothly deposited
SDS	safety data sheet
SDS	sodium dodecyl sulfate
SECQM	spectroelectrochemical quartz crystal microbalance measurement
SEC	spectroelectrochemistry
SEIRAS	surface-enhanced infrared absorption spectroscopy
SEIRA	surface-enhanced infrared absorption
SEI	secondary electrode interface
SEI	secondary electrolyte interphase
SEI	solid electrolyte interphase
SEM	scanning electron microscopy
SERRS	surface-enhanced resonance Raman
SERR	surface-enhanced resonance Raman
SERS	surface-enhanced Raman scattering
SERS	surface-enhanced Raman spectroscopy
SFCE	solvation force coordinate extrapolation
SFED	solvation-free energy density
SFE	solvation force extrapolation
SFG	sum frequency generation
SHE	standard hydrogen electrode
SH	specific humidity
SILD	semi-infinite linear diffusion
SLI	starting, lighting and ignition
SL	sulforane
SMR	steam methane reforming
SM	single molecule
SNIFTIRS	subtractively normalized interfacial Fourier transform infrared spectroscopy
SNOM	scanning near field optical microscopy
SOC	state of charge
SOEC	solid oxide electrolysis cell
SOFC	solid oxide fuel cell
SoG	solar-cell-grade
SOMO	singly occupied molecular orbital
SOM	solid oxide membrane
SOWG	slab optical waveguide spectroscopy
SPE	semiconductor photoelectrode
SPM	scanning probe microscopy
SPP	surface plasmon polariton
SPR	surface plasmon resonance
SSA	specific surface area
SSIP	solvent separated ion pair
STEM	scanning transmission electron microscopy
STEP	solar thermal electrochemical production
STH	solar-to-hydrogen
STM	scanning tunneling microscopy
STORM	stochastic optical reconstruction microscopy
SWCNT	single wall carbon nanotube

T

TaON	tantalum oxynitride
TAS	total analytical system
TBA BF_6	tetrabutylammonium tetrafluoroborate
TBA	*tert*-butyl alcohol
TB	tetragonal bipyramidal
TCNQ	tetracyanoquinodimethan
TCSPC	time-correlated single-photon counting
TEA	tetraethylammonium
TEMA	triethylmethyl ammonium
TEM	transmission electron microscopy
TEOS	tetraethyl orthosilicate
TFSI	bis(trifluoromethanesulfonyl)imide
TFSM	thiol-top-functionalized silane monolayer
TGA	thermogravimetric analysis
THH	tetrahexahedral
TiC	titanium carbide
TIRF	total internal reflectance fluorescence microscopy
TISAB	total ion strength adjustment buffer
TLM-PSD	transmission line model-pore size distribution
TLM	transmission line model

TMC	templated mesoporous carbon
TPB	triple phase boundary
TRLS	time-resolved luminescence spectroelectrochemistry
TTF	tetrathiafulvalane
TU	thiourea

U

UPD	underpotential deposition
UPS	uninterruptible power supply
UV-Vis	ultraviolet–visible
UV	ultraviolet

V

VASP	Vienna Ab initio simulation package
VCD	vibrational circular dichroism
VC	vinylene carbonate
VC	vulcan carbon
VD	vertical deposition
VGCF	vapor-grown carbon fiber
VM	modified Verlet

W

WDS	wavelength dispersive x-ray spectrometer
WE	working electrode

X

XANES	x-ray absorption near-edge spectroscopy
XAS	x-ray absorption spectroscopy
XPS	x-ray photoelectron spectroscopy
XRD	x-ray diffraction

Y

YDC	$Y_{0.2}$,$Ce_{0.8}O_{2-\delta}$
YSZ	yttria-stabilized zirconia

1. Electrochemical Science – Historial Review

Cornelia Breitkopf, Karen Swider-Lyons

Electrochemistry developed from the single contributions of famous researchers and scientists in the 150 years spanning 1776 and 1925. This increasing level of electrochemical knowledge over the 19th century dovetailed with the industrial revolution, turning the electrochemical discoveries of Galvani, Volta, Faraday, Coulomb, and Ohm into familiar principles, infusing their initial discoveries into every aspect of modern science – it is fair to say that no present-day scientist operates a computer or instrument without electrical current. Although modern electrochemists are no longer household names, electrochemistry has indisputably had bridging function in science and industrial applications and is at the basis of all modern sciences, from materials sciences and theoretical chemistry to biochemistry and medicine. A broad swath of electrochemical research still has a rich impact on the world, and the major scientific awards in electrochemistry are now awarded for work in biology/medicine and energy. Galvani would certainly be surprised at the follow on impact of his early studies of frog legs, and where those results leaped to over the last 220 years. This chapter surveys the history from its beginnings.

References 9

The importance of electrochemistry in science and society is clearly summarized by the words of the renowned physical chemist and scientific historian, *Peter Atkins* [1.1]:

> *Electrochemistry – in the broadest sense – will be one of the great achievements in chemistry in the next millennium, and one should prepare our people for it.*

Part of Atkins' enthusiasm for electrochemistry is for its promise in solving the world's energy problems through the use of electrochemical technologies. He also proposes that the path to solving future research challenges is paved by understanding the past [1.2]. Accordingly, the development of electrochemistry is reviewed concisely herein, with a focus on the early and most important developments in the 19th century toward its modern impact in energy technology.

A chronology of important achievements in electrochemistry up to 1945 is summarized in Table 1.1, which is a collection according to different sources [1.1, 3–8]. More in-depth historical reviews are found elsewhere [1.1, 7, 9]. The most ancient example of electrochemical technology is the Baghdad batteries found in Mesopotamian ruins, which comprised copper cylinders surrounding iron rods and was speculated to be for plating gold or silver leaf, although their exact purpose is disputed and they might well have been used for storing sacred papyri. Less historically controversial is the advent of modern electrochemical experiments in 1570, when the medical physician William Gilbert coined the term *electricus* to describe the effects he saw from static electricity.

Research on electricity was causing a great deal of excitement in scientific circles in the 18th century. In parallel with this, modern research on electrochemistry also began in the 18th century, and carried into the 19th century. Famous names as Galvani, Faraday, or Nernst, are associated with this early start of electrochemistry as science and tribute is paid to them today by still naming basic technical terms or scientific laws after these inventors and others, for example, Galvanic cells, Faraday constant, Nernst equation, Ohm's law, and Coulomb's law.

Luigi Galvani (portrait in Fig. 1.1) excited interest in electrochemical phenomena (and electrophysiology) with his experiments on electrical current through frog legs in the 1780s [1.11]. He applied electric field from copper and iron wires connected to a nerve and muscle, respectively, and caused the frog legs to contract. His explanation for the effect was one of a Leyden jar whereby the two dissimilar metals caused the electricity

Table 1.1 History of electrochemistry – from ancient times to 1930 (after [1.1, 3–7, 10])

2750 BC	Ancient Egyptian texts about electric fish appeared.
2650 BC	Ancient Greek, Roman, and Arab texts about electric shocks from catfish and knowledge about transport of these shocks over certain distances are found.
600 BC	Thales of Miletos observed static electricity caused by friction of rods of amber on cat's fur.
200 BC	Archeological remnants suggest primitive batteries used for electroplating in Mesopotamia (Baghdad batteries).
Before 1500	Arab scientists describe identity of lightning and electricity.
Around 1570	W. Gilbert (1544–1603) derived the word *electricus* from *like amber* which was later called electricity.
1646	Sir Thomas Browne (1605–1682) coins the term *electricity*.
1663	O.v. Guericke (1602–1686) created the first electrostatic generator based on application of friction.
1709	F. Hauksbee (1666–1713) created the first gas-discharge lamp.
1733	C.F. de Cisternay du Fay (1698–1739) described two types of static electricity and named them *vitreous* and *resinous* (later positive and negative charge).
1748	J.A. Nollet (1700–1770) developed the electroscope which showed electric charge using electrostatic attraction and repulsion. He first used the name *Leyden jar* for the first apparatus which stored electricity.
1776	H. Cavendish (1731–1810) examined relative conductances of water and salt solutions by using Leyden jar discharging.
1781	C.A. Coulomb (1736–1806) published the law of electrostatic attraction.
1789	F. Aepinus (1724–1802) developed a capacitor after the Leyden jar, where he showed conduction and induction experiments.
1791	L. Galvani (1737–1798) (Figs. 1.1 and 1.2) published his electrical experiments with frogs and marked with his work the birth of electrochemistry.
1800	A. Volta (1745–1827) constructed an electrochemical pile (Fig. 1.3). He demonstrated the possibility of continuous electric current who contacted alternating discs of copper and zinc by damp cardboard, thus creating the first wet battery.
1800	W. Nicholson (153–1815) (Fig. 1.4), A. Carlisle (1768–1840) (Fig. 1.5), and J.W. Ritter (1776–1810) performed the first electrolysis experiments (Fig. 1.6) by using a Volta pile and showed electrolytic conduction. Nicholsen and Carlisle found that water decomposes when brought in contact with Volta's pile (old name for pole) [1.1]. Ritter discovered later the electroplating and observed thermoelectric currents. Ritter also claimed that all galvanic processes comprise of oxidation and reduction, thus founding together with Grotthuß the electrochemical theory. Ritter invented electroplating.
1800–1802	W. Cruikshanks (1745–1800) performed first qualitative analysis of copper by applying electrolysis and designed the first electric battery for mass production.
1803	J.J. Berzelius (1779–1848) and W. Hisinger (1766–1852) also used Volta's pile and observed that in the electrolysis of salts, the solution becomes alkaline near the negative pole and acidic near the positive pole.
1804	W.H. Wollaston (1766–1828) and S. Tennant (1761–1815) tried to refine platinum by electrochemical techniques. Wollaston discovered palladium and rhodium whereas Tennant found iridium and osmium. Wollaston also improved the Galvani battery.

Table 1.1 (continued)

1807	H. Davy (1778–1829) developed a theoretical concept of electrolysis and published it. He used the Volta experiment to decompose solutions and was the first to isolate magnesium, calcium, strontium, sodium, and potassium by using mercury as an electrode. He concluded that electrical attraction was the main force for formation of compounds.
1808, 1812–1819	Based on his former experiments, J.J. Berzelius developed his theory of affinity. He also discovered the use of liquid mercury as an electrode material. He developed a qualitative concept of electrochemical series based on his electrolysis experiments on numerous metal salts and compounds by ordering elements in a series according to their polarity. He proposed that inorganic compounds were held together by electrochemical forces. Combining his polarity theory with the findings of Dalton's atom theory was published as *Theory of Chemical Proportions and the Chemical Influence of Electricity*.
1809	S.T. von Soemmering (1755–1830) applied the electrochemical decomposition of an acid to produce gas which was utilized as telegraph.
1820–1825	H.C. Ørsted (1777–1851) observed a magnetic effect of electrical current, which was further developed later by Ampere. He also prepared aluminum from aluminium chloride electrochemically.
1826–1827	G.S. Ohm (1787–1854) published the law named after him.
1832	W. Sturgeon (1783–1850) improved existing apparatus as the voltaic battery, electric motor, and dealt with theory of thermoelectricity. A.-H. Pixii (1808–1835) was first to transfer the concepts of Faraday into a practical mechanical generator.
1832–1834	M. Faraday (1791–1867) (Fig. 1.7) published, based on numerous experiments, his law and established exact electrochemical nomenclature (ion, anion, cation, electrolyte). He discovered the principles of the electric motor, the dynamo, and the transformer. He formed the basis for coulometric techniques. He also introduced the concept of electric field.
1836	J.F. Daniell (1790–1845) investigated constant sources of electrical current and developed a copper-zinc cell, which showed improved properties in comparison to the voltaic cells.
1838	B. Jakobi (1801–1874) invented the technique of electroforming which was used for printing.
1839	W.R. Grove (1811–1896) described first practical fuel cell collaborated with Schoenbein.
1839	E. Bequerel (1820–1890) published the photovoltaic effect.
1841	R.W.E. Bunsen (1811–1899) developed a zinc–carbon battery (Bunsen cell) and later he prepared metals as chromium, magnesium, barium, calcium, lithium by use of electrolysis.
1841	J.C. Poggendorf (1796–1877) described the use of the potentiometer for measurement of electrical potentials without current draw.
1845	A.W.H. Kolbe (1818–1884) used electrolysis first for organic synthesis.
1846	W.E. Weber (1804–1891) built the electrodynamometer and later he defined the absolute unit of electrical resistance.
1847	E. Hursford (1818–1893) investigated electrode polarization effects by varying the length of the liquid path.
1853–1859	J. Hittorf (1824–1914) presented his results of analysis of solutions around electrodes after electrolysis and defined the transference numbers.
1860	R.L.G. Planté (1834–1889) demonstrated the operation of the lead-acid battery.

Table 1.1 (continued)

1864	W. Gibbs (1822–1908) published the first electrogravimetric analysis.
1866	G. Leclanché (1839–1882) further developed the battery technique and his Leclanché cell was very successful in transportation and telegraphs.
1869	F. Kohlrausch (1840–1910) introduced the a.c. methodology and he did extensive work in the field of electrolytic conductance.
1884	S.A. Arrhenius (1859–1927) published his thesis in the field of electrolytic dissociation and conductance of electrolytes, thus deriving a quantity which describes the actual behavior of solutions – the activity constant.
1880–1900	O. Heaviside (1850–1925) developed the linear systems theory where he laid the foundations for EIS – electrochemical impedance spectroscopy.
1886	Charles Hall (USA) and Paul Hérault (France) independently developed a practical electrolytic reduction process for aluminum (Fig. 1.8).
1889	W.H. Nernst (1864–1941) (Fig. 1.9), as assistant of W. Ostwald (1853–1932) (Fig. 1.10), investigated in his dissertation the relation of potential to the ion activity and published his fundamental equation. He derived first an equation relating the equilibrium potential to the species involved in an electron-transfer reaction. The proportionality factor is the Faraday constant.
1890	W. Ostwald (Fig. 1.10) introduced the calomel electrode which could be calibrated against a dropping mercury electrode and defining by this a standard potential. He also did numerous contributions to electrochemistry especially conductivity and dissociation of acids. Nernst defined the potential of a hydrogen electrode and assigned a potential of zero.
1891	M. LeBlanc (1865–1943), also an associate of Ostwald, studied the decomposition voltages of solutions on platinum electrodes. He introduced a third or reference electrode and was thus able to determine anodic and cathodic potentials separately.
1898	F. Haber (1868–1934) published a textbook about the theoretical basis of technical electrochemistry. Due to his contacts to chemical industry he did much work in the field of electrolytic industrial processes (reduction of nitrobenzene).
1902	Foundation of the Electrochemical Society in the United States, and publication of the first journal dedicated to electrochemistry, the *Journal of the Electrochemical Society*.
1903	Arrhenius awarded 3rd Nobel Prize in Chemistry proving that acids, bases, and salts dissociate when they dissolve in water, forming electrically charged ions.
1907	G. Lewis (1875–1946) developed the concept of ionic activity.
1909	R.A. Mulliken (1868–1953) performed experiments with oil drops to determine the electric charge of a single electron. Ostwald recognized with a Nobel prize for his work on catalysis, chemical reactions, and chemical equilibrium.
1920	Nobel prize awarded to Nernst for determining the relationship between the electromotive forces of chemical cells and the concentration of the electrolyte substances in these cells.
1922	J. Heyrovsky (1890–1967) developed the polarographic method.
1923	J.N. Brønsted (1879–1947) and T.M. Lowry (1874–1936) published a theory of acid and base dissociation based on electrochemical experiments.
1933	Foundation of the Electrochemical Society of Japan, and publication of the journal *Electrochemistry*
1949	Foundation of International Society of Electrochemistry (ISE).



Fig. 1.1 Galvani (after [1.5])

in the muscles to discharge (Fig. 1.2a). But later Galvani discharged potential between the frog legs without using dissimilar metals, an effect which was finally explained through the work of both Nobili and Matteucci to be due to the 50 mV difference in potential between an injured and healthy muscle (Fig. 1.2b) [1.11].

Alessandro Volta in 1794 constructed the first direct current source to a circuit from layers of metal separated by brine-soaked cloth. He realized that two dissimilar metal electrodes coupled by a liquid conducting medium produce an electric voltage, thus inventing the *Voltaic pile* reminiscent of a modern battery (Fig. 1.3). He further found that the type of metal was decisive for the voltage and created an early electrochemical series. Volta also went on to dispute the theories of Galvani about the electrical phenomena occurring in the frog leg experiments, a controversy which *sparked* even more interest in carrying out further in-depth experiments on electrochemical phenomena [1.11, 12].

In 1800, William Nicholson (Fig. 1.4) and Anthony Carlisle (Fig. 1.5) assembled Voltaic piles of silver and zinc plates either 15 or 36 cells, connected metal wires to the positive and negative ends, and studied the interaction of the wires with water. While copper wires in the water turned green, evident of oxidation, they observed the production of H_2 and O_2 when they used platinum wires and had them spaced appropriately. An effusive account of this research was recorded in the journal that Nicholson edited, the *Journal of Natural Philosophy, Chemistry, and the Arts* [1.13]. The setup is shown schematically in Fig. 1.6 and shows the half-cell reactions for hydrogen and oxygen evolution. With this electrochemical experiment, they had unknowingly fulfilled requirements for an electrochemical process: the electrodes were at potential greater than the thermodynamic potential for splitting water (> 1.5 V), and used a Pt electrocatalyst to lower the kinetic losses at the electrodes for oxygen and hydrogen evolution, plus overcome ohmic losses in their cell with the appropriate electrode spacing.

Their discovery was not completely serendipitous, considering the extensive interest at that time in Galvanic apparatuses. Davy soon noticed the link between electricity and chemistry in the liquid phase when he observed that originally neutral solutions changed their composition close to the electrode of a Voltaic pile, essentially by carrying out half-cell reactions with ionic products. *Davy*'s seminar 1807 lecture describing elec-

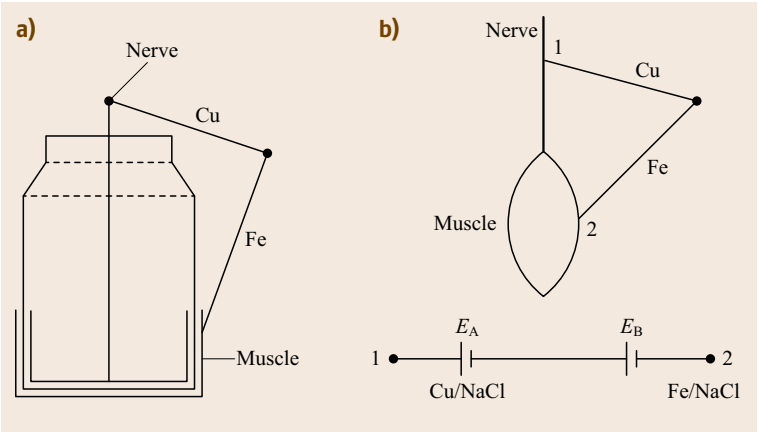


Fig. 1.2 **(a)** Galvani's original explanation of the contraction of frogs muscles, caused by the discharge of the muscle and nerve through external dissimilar metals in a Leyden jar setup and **(b)** later explanation derived from the work of Nobili and Matteucci that the contraction was caused by the voltage difference between the injured and healthy muscle (after [1.11])

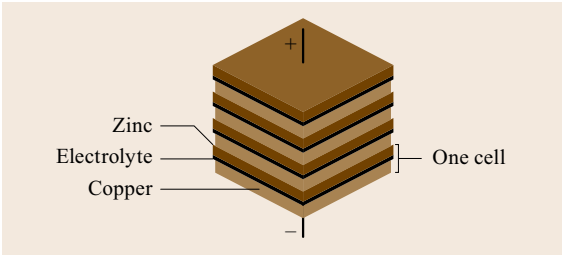


Fig. 1.3 Voltaic pile comprising four repeating cells comprising zinc and copper plates separated by an electrolyte. A voltage is produced across each cell and is built up additively by putting the four cells in series



Fig. 1.4 Nicholsen



Fig. 1.5 Carlisle

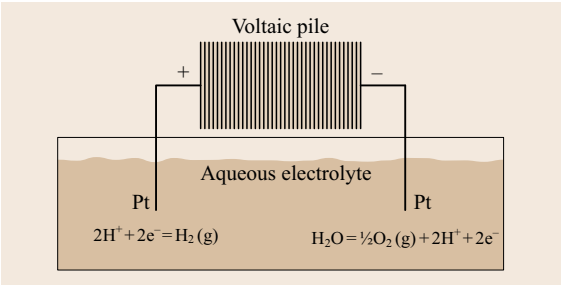


Fig. 1.6 Schematic of early experiments of water electrolysis by Nicholson and Carlisle

trochemistry was published in 1808 [1.14], where he used a voltaic pile of 24 cells of copper and zinc to decompose potash (potassium carbonate/hydroxide) to potassium. He also later isolated sodium and calcium. By Davy's own account, he was the true discoverer of the chemical nature of electricity [1.15].

Davy hired Michael Faraday (Fig. 1.7) in 1813, who went on to make discoveries in electrical phenomena ranging from magnetism to electrochemistry. Faraday was the first to measure *quantitative* changes during electrolysis, and found the exact law that defines the relation between the amount of electric current with respect to the amount of converted matter. These rules are still known as first and second Faraday laws. He reported his research on electricity in a series of 30 chapters called the Experimental Researches in Electricity in the *Philosophical Transactions of London*. See [1.16] for a chapter on his research on the electrochemical decomposition of water. The chapter also includes more history of others contributions to electrochemistry.

Attention was soon turned to applying electrochemistry to processes. Between 1839 and 1868, the fuel cell, or the production of electricity from the electrochemical conversion of gases, was discovered by Christian Friedrich Schoenbein and refined by William Robert Grove [1.17, 18]. By the turn of the century, R. Clausius and S. Arrhenius contributed to the deeper understanding of ion movement in solutions and de-



Fig. 1.7 Faraday (after [1.5])

scribed the concentration change close to electrodes within an electrolysis process. By 1904, there were more than 400 industrial water electrolyzers, 100 years after the initial electrolysis discoveries of Nicholson and Carlisle [1.19].

While commercial processes were being developed, and only with the rudiments of modern electrochemistry understood, Charles Hall of the United States and Paul Hérault of France independently and nearly simultaneously developed electrolytic process for the formation of aluminum metal by electrolysis of aluminum oxide from a cryolite melt, both filing for patents on the process in 1886 [1.20]. Cryolite, Na_3AlF_6, served as an ionic liquid that dissolved the aluminum oxides at high temperature and allowed easy extraction of the aluminum metal by electrolysis, as schematically shown in Fig. 1.8. The resulting aluminum led to a manufacturing revolution by serving as a cheap, lightweight formable metal, further fueling industrial revolution and the soon-to-emerge automobile and aerospace industries. By 1900, 4682 metric tons of aluminum were being produced [1.20], and 1903 marked the first powered flight of an airplane, made possible by the weight savings from using a lightweight aluminum engine.

Electrochemistry was formally recognized when Arrhenius was awarded the third Nobel prize in Chemistry (in 1903) for proving that acids, bases, and salts dissociate when they dissolve in water forming electrically charged ions. Early Nobel prizes were awarded to more electrochemists, with the 1909 one awarded to Ostwald (Fig. 1.9) for his work on catalysis, chemical reactions, and chemical equilibrium. Nernst was then awarded the 1920 prize for his work on thermochemistry and correlation of thermochemistry to electrode potentials (Fig. 1.10).

The portraits in Figs. 1.9 and 1.10 indicate that men were the major early contributors to electrochemical science, which is true for most areas of science. Women played significant but background roles in significant electrochemical milestones, for instance Julia Hall assisted her brother, Charles Hall, in the early experiments electrolysis of aluminum [1.20]. In the 20th century, several women joined the ranks of preeminent electrochemists, particularly in Russia and the Soviet Union where women played key roles in numerous fields and worked along with the renowned electrochemist A. Frumkin on the influence of the structure of the interface between electrode and solution on the rate of electron transfer, the concept of the zero charge potential, plus applied technologies such as industrial electrolysis and anti-corrosion protection. The electro-

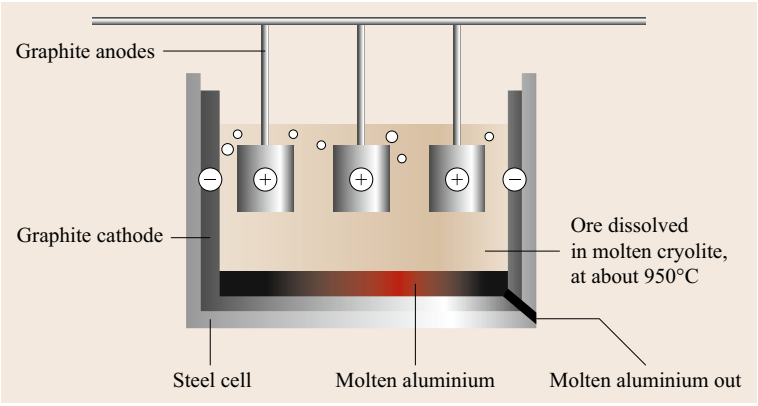


Fig. 1.8 Electrolytic process for the extraction of aluminum metal from cryolite



Fig. 1.9 Ostwald (after [1.5])



Fig. 1.10 Nernst (after [1.5])

chemical contributions of several women have been recently reviewed, including Olga Alfredovna Songina, a leader in solid-state electrochemistry and Yevgeniya Nikolayevna Varasova, a pioneer in electrochemical polarography [1.21]. The first female president of the Electrochemical Society was in 1979, 77 years after its founding, when Joan Berkowitz was elected to that post [1.22].

In 1902, 16 years after the invention of electrolytic reduction of aluminum, the Electrochemical Society formally convened to discuss the new ideas and technology evolving from the *application of electricity to chemical processes* [1.22]. The direction of electrochemistry since 1930 can be gathered from a brief look through the Electrochemical Society's eponymous *Journal of the Electrochemical Society*. The 1930 (Volume 38) *Journal of the Electrochemical Society* captured chapters from a symposium on the *Prevention of Corrosion of Metals in the Automotive Industry*, with papers on how to plate radiators [1.23] and the electrode properties of stainless steel [1.24] and the corrosion of aluminum by alkali [1.25]. Also published in 1930 were papers on *The Engineering Development of Photovoltaic Cell* [1.26], *Hydrolysis in Standard Cells* [1.27] and *Leclanche Cells* (a.k.a. carbon-zinc batteries) [1.28], along with several papers on electrodeposition. The total number of papers in all of 1930 was 28.

By 2012 in Volume 159 of the *Journal of the Electrochemical Society*, issue 1 (of 12 issues published that year) contained a total of 66 articles under the following subheadings or disciplines: Batteries and Energy Storage; Fuel Cells and Energy Conversion; Corrosion, Passivation, and Anodic Films; Electrochemical/Chemical Deposition and Etching; Electrochemical Synthesis and Engineering; Dielectric Science and Materials; Semiconductor Devices, Materials, and Processing; Sensors and Displays: Principles, Materials, and Processing; Nanostructured Materials, Carbon Nanotubes, and Fullerenes. Over those 82 years, electrochemical studies evolved from studies of *electrical conductors in a contacting liquid* to one with a focus on solid-state science, energy technology and materials science.

During this same period of recent history, Nobel prizes were awarded to only four times to electrochemical-related research: in 1948 to A. Tiselius, a biochemist who used electrophoresis to separate charged chemical substances, particularly serum; in 1959 to the electrochemist J. Heyrovksy, for his 1920s discovery and development of the electrochemical polarographic methods of analysis; in 1983 to Taube for the mechanism for electron transfer in solution (or inner sphere electron transfer reactions in re-dox reactions), and lastly in 1992 to R. Marcus, for the development

of theory related to the transfer of electrons between atoms for the determination of electron transfer rates and the probability of an electron jump. Therefore, of the 7 Nobel prizes awarded in electrochemical research, 3 were awarded in the prize's first 19 years (1901 to 1920 to Arrhenius, Ostwald, and Nernst), and only 4 awarded in the following 94 years to the present (to Tiselius, Heyrovksy, Taube and Marcus). Electrochemistry played an important but secondary role in the Nobel awards to Fritz Haber (Chemistry 1918), Peter Debye (Chemistry 1936), Linus Pauling (Chemistry 1954 and Peace 1962), Walter Brattain (Physics 1955), Jaroslav Heyrovsky (Chemistry 1959), and Jack Kilby (Physics 2000).

Notable awards in recent electrochemical history have been for applying early electrochemical discoveries to everything from manufacturing to electronics to biology. The impact of electrochemical research has been recognized well in the last 6 years as with the US National Medal of Science awarded to Marye Anne Fox in 2009 and Allen Bard and John Goodenough in 2011 for their electrochemical research. Adam Heller and Esther Takeuchi received the US National Medals of Technology and Innovation in 2007 and 2008 for using electrochemistry to develop life-saving technologies. Clearly, electrochemistry has provided many major achievements in chemistry and technology and, as noted by Atkins, is poised to do so for years to come.

References

1.1 A.M. Bond: The fundamentals of electrochemistry. In: *Broadening Electrochemical Horizons*, ed. by A.M. Bond (Oxford Univ. Press, Oxford 2001), Chap. 1

1.2 P.W. Atkins: *Galileo's Finger: The Ten Great Ideas of Science* (Oxford Univ. Press, Oxfrod 2003)

1.3 J.S. Stock, M.V. Orna (Eds.): *Electrochemistry, Past and Present* (Oxford Univ. Press, Oxford 1989), Chap. 1

1.4 D.D. Macdonald: Reflections on the history of electrochemical impedance spectroscopy, Electrochim. Acta **51**, 1376–1388 (2006)

1.5 History of electrochemistry: Wikipedia Category, http://commons.wikimedia.org/wiki/Category:History_of_electrochemistry (2015)

1.6 Electricity: Wikipedia, http://en.wikipedia.org/wiki/Electricity

1.7 History of electrochemistry: Wikipedia, http://en.wikipedia.org/wiki/History_of_electrochemistry

1.8 A.K. Shukla, T.P. Kumar: Pillars of modern electrochemistry, Interface **17**, 31–39 (2008)

1.9 F.A. Trumbore, D.R. Turner: *The Electrochemical Society 1902–2002: A Centennial History?* (The Electrochemical Society, Pennington 2002)

1.10 P.H. Rieger: *Electrochemistry*, 2nd edn. (Chapman Hall, New York 1994)

1.11 L.A. Gedes, H.E. Hoff: The discovery of bioelectricity and current electricity, IEEE Spectrum **8**(12), 38–46 (1971)

1.12 M. Pera: *The Ambiguous Frog: The Galvani-Volta Controversy on Animal Electricity* (Princeton Univ. Press, Princeton 1992)

1.13 W. Nicholson, A. Carlisle: Account of the new electrical or galvanic apparatus of Alessandro Volta and experiments performed with the same, J. Nat. Philos. Chem. Arts **4**, 179–187 (1801)

1.14 H. Davy: The Bakerian Lecture, Phil. Trans. R. Soc. Lond. **98**, 1–44 (1808)

1.15 H. Davy: The Bakerian Lecture: On the relations of electrical and chemical changes, Phil. Trans. R. Soc. Lond. **116**, 383–422 (1826)

1.16 M. Faraday: Experimental researches in electricity, Phil. Trans. R. Soc. Lond. **123**, 675–710 (1833)

1.17 U. Bossel: *The Birth of the Fuel Cell* (European Fuel Cell Forum, Oberrohrdorf 2000)

1.18 J.M. Andújar, F. Segura: Fuel cells: History and updating. A walk along two centuries, Renew. Sustain. Energy Rev. **13**, 2309–2322 (2009)

1.19 W. Kreuter, H. Hofmann: Electrolysis: The important energy transformer in a world of sustainable energy, Int. J. Hydrogen Energy **23**, 661–666 (1998)

1.20 T.R. Beck: Hall and Heroult and the discovery of aluminum electrolysis, Interface **23**(2), 36–37 (2014)

1.21 F. Scholz: The role and fate of female electrochemists in the Soviet Union: Ol'ga Al'fredovna Songina – A pioneer of electrochemical solid-state analysis and Yevgeniya Nikolayevna Varasova – A pioneer of polarography, J. Solid State Electrochem. **17**, 1493–1504 (2013)

1.22 M. Yess: The electrochemical society, a forum for electrochemistry and solid state science for 100 years, Interface **11**, 22 (2002)

1.23 O.P. Watts: The plating on radiator shells, Trans. Am. Electrochem. Soc. **58**, 61–87 (1930)

1.24 E. Newbery: The electrode properties of stainless steel, Trans. Am. Electrochem. Soc. **58**, 53–59 (1930)

1.25 O.W. Storey: Unusual corrosion of aluminum by alkali, Trans. Am. Electrochem. Soc. **58**, 43–51 (1930)

1.26 C.G. Fink, D.K. Alpern: The engineering development of photovoltaic cells: I. Some operating characteristics, Trans. Am. Electrochem. Soc. **58**, 275–298 (1930)

1.27 G.A. Hulett: Hydrolysis in standard cells, Trans. Am. Electrochem. Soc. **58**, 299–304 (1930)

1.28 V.A. Kostjejev: Effect of various factors on the output of leclanche cells, Trans. Am. Electrochem. Soc. **58**, 305–325 (1930)

2. Modern Electrochemistry

Cornelia Breitkopf, Karen Swider-Lyons

An overview is given for the factors governing electrochemical reactions and processes: thermodynamics, kinetics, mass transport, ionic and electronic resistance, the charged electrode interface/double layer and the experimentation required to decouple these competing factors. These parameters are discussed in terms of the 28 chapters in the *Springer Handbook of Electrochemical Energy*. Important electrochemical references and resources are provided.

2.1 **Fundamental Components of Electrochemistry** 11
2.1.1 General References 12
2.1.2 Electrochemistry Journals 14
2.1.3 Electrochemistry Conferences 14
2.2 **Thermodynamics** 14
2.3 **Kinetics** 17
2.4 **Mass Transport** 19
2.5 **The Charged Electrode Interface/ Electrochemical Double Layer** 21
2.6 **Ionic and Electronic Resistance** 23
2.7 **Experimentation** 24
2.8 **Subtopics in Electrochemistry** 26
2.8.1 Solid-State Ionics 26
2.8.2 Ionic Liquids 26
2.8.3 Corrosion at Liquid Interfaces 27
2.8.4 Chlor-Alkali Process 27
2.9 **Summary** 28
References 29

In the simplest form, all the electrochemistry subdisciplines, and accordingly the chapters in this book, tackle six fundamental components of research and technology:

1. Thermodynamics
2. Kinetics
3. Mass transport
4. Electric double layer
5. Ohmic losses (a.k.a., electronic and ionic resistance, I^2R)
6. Experimentation to resolve how items 1–5 pertain to electrochemical reactions, such as generally illustrated in Fig. 2.1.

2.1 Fundamental Components of Electrochemistry

In this reaction scheme Fig. 2.1, the forward reaction comprises the reduction of A and B to AB^{-}. The charge balance is met by the contribution of the external electron. In the process, heat and sometimes light is produced or consumed. The reverse reaction would be an oxidation reaction, with an electron created. A and/or B might start as charged species, and constitute a gas, liquid, or solid. In a solid, the species might be a charged vacancy. Overall, when an electrical path is available to the appropriate reagents or materials, it can release new (wanted or unwanted) chemical species, electricity, and even light. As long as it is thermodynamically feasible, the reactions can occur in any form of matter and a conducting liquid is not required.

Each subtopic – thermodynamics, kinetics, mass transport, the electric double layer, electronic and ionic resistance, and experimentation – is a specialty of its own, and each worthy of multiple books. Each topic is also interdependent, as the structure of the electric double layer will affect the electrode kinetics. In the *Springer Handbook of Electrochemical Energy*, these subtopics are the underpinning of chapters describing advanced electrochemical processes, materials, and systems, particularly with a focus on electrochemical energy systems.

This background chapter attempts to give a basic understanding of the issues related to each subtopic. Table 2.1 addresses how each chapter emphasizes which component, noting with a ✓ the electrochemical aspect that it best addresses. Excepting the theoretical chapters at the beginning that delve into details of thermodynamics or mass transport, most chapters touch on all aspects

Table 2.1 Summary of chapters in the Springer Handbook of Electrochemical Energy and how they address issues

Chapter	Title	A Thermo-dynamics	B Kinetics	C Mass transport	D Ionic/electronic resist	E Double layer	F Experimen-tation
1	Electrochemical Science — Historical Review						✓
2	Modern Electrochemistry	✓	✓	✓	✓	✓	✓
3	Thermodynamical Aspects of Electrochemical Reactions	✓	✓			✓	
4	Thermodynamics of Electrochemical Systems	✓	✓	✓		✓	
5	Multiscale Modeling of Solvation	✓	✓	✓		✓	
6	Highly Ordered Macroporous Electrodes			✓		✓	✓
7	Ion-Sensitive Electrodes	✓	✓	✓		✓	✓
8	Transport in Liquid-Phase Electrochemical Devices	✓		✓			✓
9	Catalyst Layer Modeling	✓	✓	✓	✓	✓	
10	Water Management in Proton Exchange Fuell Cells	✓		✓		✓	✓
11	Calculations in Li-Ion Battery Materials	✓			✓		✓
12	Electrochemical Energy Generation and Storage as Seen by In-Situ NMR		✓			✓	✓
13	Spectroscopy of Electrochemical Systems	✓	✓			✓	✓
14	Kinetic Activity in Electrochemical Cells	✓	✓	✓			✓
15	Lithium-Ion Batteries and Materials	✓			✓		✓
16	Materials for Electrochemical Capacitors				✓	✓	✓
17	Electrochemical Capacitors				✓	✓	✓
18	Kinetics of Fast Redox Systems for Energy Storage		✓		✓		✓
19	Modern Fuel Cell Testing Laboratory	✓	✓	✓	✓	✓	✓
20	Polymer Electrolyte Fuel Cells	✓	✓	✓	✓	✓	✓
21	Next-Generation Electrocatalysts		✓		✓		✓
22	Methods in Biological Fuel Cells	✓	✓				✓
23	Energy Conversion Based on Bio(electro)catalysts	✓	✓				✓
24	Photoelectrochemical Conversion Processes	✓	✓		✓		✓
25	Advanced Extractive Electrometallurgy	✓	✓	✓			✓
26	Electrodeposition of Nanomaterials	✓	✓	✓	✓	✓	✓
27	Electrochemical Hydrogen Production	✓	✓	✓	✓		✓
28	Electrochemical Machining	✓	✓	✓		✓	✓

of electrochemistry. That is, research on a fuel cell or battery by definition mandates that all electrochemical aspects are addressed, from understanding the theoretical limits to emphasizing the proper experiments. The basics of each subtopic are covered, and their relevancy of the book chapters explained.

Despite the breadth of this book's 28 chapters, there is much that is not covered and much was not purposely covered because of our focus on electrochemical energy systems. The last section of this chapter gives a brief overview of topics not covered in this book, and provides references where readers may find more information.

2.1.1 General References

As discussed before, this *Springer Handbook of Electrochemical Energy* is focused on electrochemistry rele-

Table 2.2 Some references on electrochemistry fundamental aspects and experimentation

Author(s)	Title	Publication year	References
A.J. Bard, L.R. Faulkner	Electrochemical Methods: Fundamentals and Applications	2000	[2.1]
C. Lefrou, P. Fabry, J.-C. Poignet	Electrochemistry: The Basics, With Examples	2012	[2.2]
A.J. Bard, M. Stratmann, E. Gileadi, M. Urbakh	Encyclopedia of Electrochemistry, Thermodynamics and Electrified Interfaces	2002	[2.3]
J. Newman, K. Thomas-Alyea	Electrochemical Systems	2004	[2.4]
J.O. Bockris, A.K.N. Reddy	Modern Electrochemistry, Vol. 1	1970	[2.5]
J.O. Bockris, A.K.N. Reddy	Modern Electrochemistry, Vol. 2	1970	[2.6]
C.H. Hamann, A. Hamnet, W. Vielstich	Electrochemistry	2007	[2.7]
E. Gileadi	Physical Electrochemistry	2011	[2.8]
C.G. Zoski	Handbook of Electrochemistry	2006	[2.9]
J. Larminie, A. Dicks	Fuel Cell Systems Explained	2003	[2.10]
V.S. Bagotzky	Physical Electrochemistry	2005	[2.11]
D. Pletcher, R. Greff, R. Peat, L.M. Peters, J. Robinson	Instrumental Methods in Electrochemistry	2002	[2.12]
A.M. Bond	Broadening Electrochemical Horizons: Principles and Illustration of Voltammetric and Related Techniques	2003	[2.13]
M. Pourbaix	Atlas of Electrochemical Equilibria in Aqueous Solutions	1974	[2.14]

Table 2.3 Notable electrochemistry journals (2016)

Journal	Publisher
ACS Energy Letters	American Chemical Society
ChemElectroChem	Wiley VCH
Bioelectrochemistry	Elsevier
Corrosion Science	Elsevier
ECS Electrochemistry Letters	Electrochemical Society
ECS Journal of Solid State Science and Technology	Electrochemical Society
ECS Solid State Letters	Electrochemical Society
ECS Transactions	Electrochemical Society
Electroanalysis	Wiley
Electrocatalysis	Springer
Electrochemica Acta	Elsevier
Electrochemical and Solid State Letters	Electrochemical Society
Electrochemistry	Electrochemical Society of Japan
Electrochemistry Communications	Elsevier/International Society of Electrochemistry
Ionics	Springer
International Journal of Hydrogen Energy	Elsevier
Journal of Applied Electrochemistry	Springer
Journal of Electroceramics	Springer
Journal of Electroanalytical Chemistry	Elsevier/International Society of Electrochemistry
Journal of the Electrochemical Society	Electrochemical Society
Journal of Power Sources	Elsevier
Journal of Solid State Electrochemistry	Springer
Solid State Ionics	Elsevier
Fuel cells	Wiley
Russia Journal of Electrochemistry	Springer
Surface Engineering and Applied Electrochemistry	Springer

vant mainly to electrochemical energy processes, where the focus of most electrochemistry lies today. Electrochemistry is a very broad field of research, and notable books on fundamental electrochemistry are listed in Table 2.2. Numerous tutorials are also available on the Internet, as many professors now publish their class notes.

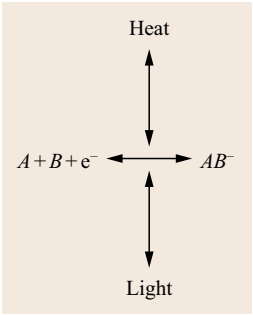


Fig. 2.1 General scheme for a reversible charge-transfer reaction in which components A and B are reduced by an electron to AB^-. Heat is either generated or consumed in the reaction. In some cases, light can be produced or consumed. The reactions take place at charged electrode surfaces

2.1.2 Electrochemistry Journals

There are also numerous journals that specifically focus on electrochemistry. Table 2.3 lists 24 of these journals. Several physical and analytical chemistry journals are also frequent sites of electrochemistry research articles, including the American Chemical Society's *Journal of Physical Chemistry* and *Langmuir* and the Royal Society of Chemistry's *Physical Chemistry Chemical Physics* and *Energy and Environmental Science*. With the ever-present interest in efficient energy storage and production, scientific breakthroughs in electrochemical energy technology often earn publication in the high-profile journals: *Science* and *Nature*. From the broad level of present publications, electrochemical research and technology is clearly vibrant and growing in scope and impact.

Table 2.4 Popular annual/bi-annual electrochemistry meetings

Meeting
Fuel Cell Seminar
Electrochemical Society Meetings (Spring and Fall, Plus Local Chapters)
International Meeting on Lithium Ion Batteries (IMLB)
International Society of Electrochemistry (Topical and Annual Meetings)
Gordon Research Conference: Batteries, Corrosion-Aqueous, Electrochemistry, Electrodeposition, Fuel Cells
Materials Research Society (Special Symposia, Typical Energy Focus)
Solid State Ionics

2.1.3 Electrochemistry Conferences

Some of the more popular annual meetings in electrochemistry are listed in Table 2.4. The dates of locations of the conferences change annually, so readers should consult the Internet for details of upcoming conferences. Many other chemical and physics societies also have symposia related to specific topics of electrochemistry.

2.2 Thermodynamics

This section provides the main technical themes and terms of thermodynamics and points to upcoming chapters for a more detailed reading in the selected field. Many of the chapters touch on issues of thermodynamics. The thermodynamics for equilibrium and nonequilibrium processes are described in detail in Chaps. 3 and 4. Recent progress with respect to multiscale thermodynamics is reviewed in Chap. 5. The practical application of thermodynamics to electrochemical systems is included in detail in many of the chapters (Table 2.1).

Moreover, while thermodynamics are discussed in detail elsewhere in this book (and in the references in Table 2.2), it is compulsory to understand how well-known tools from chemical thermodynamics are used to generally describe equilibrium processes in electrochemistry as well as special features, for example, experimental conditions, provoked by the charged species and potential differences between the phases. For electrochemical half-cells, experimental conditions as constant temperature or pressure, which are valid for standard electrochemical setups, enable the use of the most convenient thermodynamic potential, the Gibbs free energy G

$$G = U + PV - TS = H - TS\,, \tag{2.1}$$

where G is the Gibbs free energy, U is internal energy (equivalent to E in electrochemical cells), P is pressure, V is volume, T is temperature, S is entropy, and H is enthalpy.

Equation (2.1) allows the derivation of all required data related to electrochemical reactions. The Gibbs free energy delivers the information whether a process will proceed spontaneously ($\Delta G > 0$), is at equilibrium ($\Delta G = 0$) or does not proceed ($\Delta G > 0$) [2.11]. Equation (2.1) can be extended for more complex systems, for example, when systems involve two or more phases which cross boundaries/interfaces, as is common in

electrochemical engineering systems such as electrolysis systems which convert liquid H_2O to gaseous H_2 and O_2 (Chaps. 3 and 27), or even more complex systems such as for sodium borohydride fuel cells (Chap. 8). For complex systems, terms are added for the number of moles of the species, their chemical potentials, the surface area, as well as surface tension.

The main question answered by thermodynamics in electrochemistry is related to the maximum work a reaction is able to deliver or how much work is needed to make a reaction occur. It is therefore useful to review the development of the terms electrical work and electrical energy. The application of thermodynamics in electrochemistry is focused on electrical work, which is already reflected by using the thermodynamic potentials at constant pressure. Electrical work and mechanical work obey the same fundamental thermodynamic laws, for example, first and second law; they are thermodynamically equivalent as there are processes which can transform mechanical work completely into electrical energy, and vice versa.

Theoretical aspects with respect to electrical work date back to the early work of Debye and Hückel in the 1920s, as discussed in Chap. 1. They described the molar electrostatic potential energy of an ion based on a molecular kinetic model to understand the influence of electric forces between ions. They calculated the work w_1 of a reversible deionization of ions at infinite dilution and the work w_2 which would be necessary to reload the ion at this concentration. The resulting electric work w_{el} is the sum of w_1 and w_2 (2.2). Textbooks may describe this also in terms of sum of an inner Galvani potential and an outer Volta potential

$$w_{el} = w_1 + w_2 \tag{2.2}$$

w_{el} is delivered if an electric potential an electric charge at one point is transported to another point, which reminiscent of the mechanical definition of work, which is force multiplied by the distance. The higher the electrical charge, the higher is the difference in the electric potential and therefore the electrical work (or force).

A characteristic of all electrode reactions is the fact that no reaction would proceed spontaneously according to the molar-free reaction enthalpy, which is positive. Thus, energy in the form of electrical current is needed to overcome the barrier. The consumed electrical work w_{el} is the product of the amount of the current I and the internal energy U

$$w_{el} = IU > 0\,. \tag{2.3}$$

The energy term U relates here to an *intensity* factor and the current I is a *capacity* factor of the energy denoting a potential difference between two electrodes. For an energetic evaluation of electrochemical processes, the intensity factor, or potential difference, has higher priority compared to the capacity factor (e.g., the current). The intensity factor depends on the prevailing process while the capacity factor is similar for all electrochemical processes when the same amount of moles are converted at an electrode. For electrochemical systems, the intensity factor U is often written as E as the potential between two electrodes. The current relates to the product nF, where n denotes the number of electrons transferred in the reaction and F is the Faraday constant, 96 485 As mol^{-1}.

The substitution of I by nF results in the following expression for the electrical work

$$w_{el} = nFU \quad \text{or} \quad w_{el} = nFE\,. \tag{2.4}$$

The intensity factor further depends on the contact areas of the electrodes in the solution and it can be shown that a minimum of potential is needed to proceed for electrolysis (further details are in Chaps. 3 and 27).

The potential difference or voltage is strongly connected to the equilibrium cell potential E^0. Historically the term electromotive force, emf, was used. This quantity gives the maximum molar effective work of the electrochemical process. The equilibrium cell potential/voltage is related to one fundamental thermodynamic quantity, the Gibbs free energy. This relation of ΔG and U (or E) provides the connection between electrochemical measurements and fundamental thermodynamic properties. If the free energy of the reaction is known, then one can calculate the equilibrium cell potential for a known composition. The value of ΔG is negative in case of a spontaneous reaction which responds to a positive equilibrium cell potential. The driving force of an electrochemical cell is thus proportional to the slope of ΔG when ΔG is displayed as function of the extent of the reaction.

The free energy is further related to the equilibrium constant of the chemical reaction K which delivers the composition of the reaction mixture, where ΔG_0 is the standard value

$$\Delta G = \Delta G^0 + RT \ln K\,. \tag{2.5}$$

In (2.5), R is the universal gas constant, and T is the temperature in Kelvin. The equilibrium constant K is a function of the activities of the products and reactant. It may be noted that ΔG_0 can be created also by knowing values for the formation process, for example, if there is access to ΔH_{form} or ΔS_{form}. Dividing both sides by nF, it follows

$$E = -\Delta G^0/nF - \frac{RT}{nF} \ln K\,. \tag{2.6}$$

The standard free voltage is the free energy of the cell reaction

$$E = E^0 - \frac{RT}{nF} \ln K \,. \tag{2.7}$$

This key relation between cell voltage and composition of the cell reaction is the Nernst equation, which now allows illustrating the change of the cell potential depending on the cell reaction and it includes charged species. The equation is the basis for nearly all applications described in the whole book and was with respect to the development of electrochemistry as a unique discipline of great importance.

To look inside the physical meaning of the Nernst equation, it helps to emphasize the unique features of an electrochemical cell.

The determination of the free energy of a reaction for an ion is available via the concrete application of the standard potential, in (2.8), which shows the exact correlation of the available energy to the cell potential

$$\Delta G^0 = -nFE^0 \,. \tag{2.8}$$

The entropy of a (cell) reaction can be derived via the temperature dependence of ΔG^0

$$\left(\frac{\mathrm{d}G}{\mathrm{d}T}\right)_{\mathrm{P}} = -S \,, \tag{2.9}$$

thus deriving from

$$\left(\frac{\mathrm{d}E^0}{\mathrm{d}T}\right)_{\mathrm{P}} = \frac{\Delta S^0}{nF} \,. \tag{2.10}$$

The temperature dependence of E delivers the entropy of the cell reaction.

The standard enthalpy can be described as

$$\Delta H^0 = \Delta G^0 + T\Delta S^0 = -nF\left[E^0 - T\left(\frac{\mathrm{d}E^0}{\mathrm{d}T}\right)\right], \tag{2.11}$$

which opens an interesting alternative to calorimetric determination of ΔH.

The physical meaning of (2.8)–(2.11) can be derived from electrochemical cells from which thermodynamic data can be derived from standard potentials. While a current flows, an electrochemical cell is a kinetically controlled device. The equilibrium point of the overall reaction is equal to the difference in Gibbs free energy of products and reactants, which is given by ΔG^0, *when the reaction proceeds at standard conditions*. In the electrochemical cell, ΔG^0 is determined by the difference of the two half-cell reactions at standard conditions which are reflected by E^0 (2.8).

Two examples will be described to illustrate how thermodynamic functions may be generated from cell potentials. In this procedure, one has access to equilibrium constants, free enthalpies of reaction and free entropies of reactions. Although readily available in fundamental chemistry texts, the practical relation between electrochemical half-cell reactions and the potential of a full cell, and how it relates to its free energy is given below for a zinc/copper cell. The standard electrochemical potential for a $Zn^+ \mid Zn \mid Cu \mid Cu^{2+}$ cell is in (2.12)–(2.15). The half-cell values for the electrochemical couples can be gathered from standard physical chemistry handbooks [2.15].Then the following reactions calculated to determine the emf of the cell (E), its free energy in joules, and equilibrium constant

Anode:

$$\mathrm{Zn}(s) \rightarrow \mathrm{Zn}^{2+}(\mathrm{aq}) + 2\mathrm{e}^-$$

$$E^0_{\mathrm{ox}} = +0.7996\,\mathrm{V} \,, \tag{2.12}$$

Cathode:

$$\mathrm{Cu}^{2+}(\mathrm{aq}) + 2\mathrm{e}^- \rightarrow \mathrm{Cu}(\mathrm{s})$$

$$E^0_{\mathrm{red}} = -0.3419\,\mathrm{V} \,, \tag{2.13}$$

Total:

$$\mathrm{Zn}(s) + \mathrm{Cu}^{2+}(\mathrm{aq}) \rightarrow \mathrm{Zn}^{2+}(\mathrm{aq}) + \mathrm{Cu}(\mathrm{s})$$

$$E^0_{\mathrm{cell}} = +0.4577\,\mathrm{V} \,, \tag{2.14}$$

$$\Delta G^0 = -(2\,\mathrm{mol\,e^-})(96\,485\,\mathrm{C/mole^-})(0.4577\,\mathrm{J/C}) = -88\,322\,\mathrm{J/mol} \,. \tag{2.15}$$

These potentials are measured with nonbinding counter ions, such as K^+ and Cl^-. Such a measurement is schematically shown in Fig. 2.2, and discussed in more detail for similar cells in Chaps. 4 and 7.

Alternatively, the reactions can be calculated in reverse from thermochemical data. An example is given for the reaction in hydrogen fuel cells, in which gaseous H_2O is made from the combination of gaseous O_2 and H_2 (primarily in Chaps. 10, 19 and 20, but discussed in other chapters as well). In this case, $\Delta G = -237\,141\,\mathrm{J/mol}$ for H_2O at 298.15 K [2.16].

For the two-electron process

$$E^0_{\mathrm{cell}} = \frac{237\,141}{2 \times 96\,485} = 1.228\,\mathrm{V} \,. \tag{2.16}$$

This calculation can also be derived directly from the values of the measured half-cell reactions, found for

instance in the work by *Pourbaix* [2.14]. The cell pH influences the potential at each electrode, but results in no net difference in the full cell:

Anode:

$$H_2 \rightarrow 2H^+ + 2e^- , \quad E^0_{ox} = 0 - 0.0591\text{pH} , \tag{2.17}$$

Cathode:

$$H_2O \rightarrow \frac{1}{2}O_2 + 2H^+ + 2e^-,$$

$$E^0_{red} = 1.228 - 0.0591\text{pH} , \tag{2.18}$$

Total:

$$H_2 + \frac{1}{2}O_2 \rightarrow H_2O(g), \quad E^0_{cell} = +1.228\,\text{V} . \tag{2.19}$$

Note that when the reaction does not proceed at standard conditions, or there is a change of state, the ΔH value of the reaction the predictor of its thermodynamic state, rather than ΔG. A good case is for electrolysis cells (Chaps. 3 and 27), in which liquid water is produced rather than gaseous. In this case, the H^0 value for water is used, which is $-285\,830\,\text{J/mol}$ at 298.15 K [2.16]. Accordingly, the equilibrium cell voltage is higher

$$E^0_{cell} = \frac{285\,830}{2 \times 96\,485} = 1.48\,\text{V} . \tag{2.20}$$

This simple example illustrates that great value in using thermodynamic potentials is the derivation of useful quantities, which can be experimentally extracted. When the reactions become more complex with changes of state and deviations from standard conditions, as in the case with the 8-electron reduction of sodium borohydride (Chap. 8) and catalyst layer modeling (Chap. 9), unraveling the individual reactions contributing to the cell potential becomes challenging, both theoretically and experimentally.

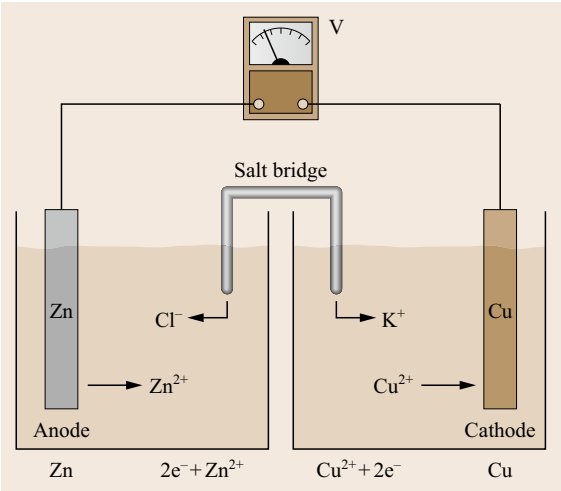


Fig. 2.2 Schematic of measurement of the potential of zinc (Zn^{2+}) and copper (Cu^{2+})

Chapter 4 explains in detail the more complex nonequilibrium thermodynamics associated with electrochemical systems.

Note that as illustrated in Fig. 2.1, an alternative driver to potential in electrochemistry is light or photons, which can also excite internal electron potentials. When energy is supplied in the form of photons the equivalent electric field must still be met (Chaps. 24 and 27).

2.3 Kinetics

Even if a process is thermodynamically favorable with a negative value for ΔG or ΔH, it must also be kinetically favorable to occur, meaning that the individual rate of the electrochemical reactions can be overcome. In most cases, additional energy must be applied to the system to overcome kinetic barriers. The additional energy that must be applied over the equilibrium potential is typically called the overpotential η

$$\eta = E^0 - E . \tag{2.21}$$

Understanding the kinetics of electrochemical surface processes is a crucial step in reducing energy consumption. The books cited in Table 2.2 provide useful introduction to electrochemical kinetics, and other books are dedicated to the topic [2.17]. Reaction processes on surfaces and the practical consideration of kinetics are described in numerous chapters (Table 2.1), with several focusing on the impact of kinetics on the efficiency of fuel cells. The careful experimentation required to isolate the kinetics of the oxygen reduction reaction are described in Chap. 14. A brief overview of electrochemical kinetics is given here.

The reactions required for an electrochemical reactions, like all chemical reactions, are activated and governed by the Arrhenius equation

$$k = Ae_a^{-E/RT} , \tag{2.22}$$

in which k is the rate constant of a chemical reaction, A is the pre-exponential factor, and E_a is the activation energy. The importance of E_a to the overall favorability of the reaction is schematically shown in Fig. 2.3, which shows a thermodynamically favorable reaction of the oxidation of AB^- to products $A + B^-$ (after Fig. 2.1).

The oxidation and reduction reactions at the cathode and anode each have a rate constant, and their ratio forms the value K in (2.5) (e.g., $K = k_{ox}/k_{red}$). The rate constants at the cathode and anode are typically unequal. It follows by substitution into (2.7) that the Nernst equation can be written in terms of the reaction rates at the cathode and anode, and therefore the cell potential can be used to derive reaction rates (2.23). Conversely, any electrode kinetics theory must reduce to the Nernst equation when equilibrium conditions are placed upon it

$$E = E^0 - \frac{RT}{nF} \ln\left(\frac{k_{ox}}{k_{red}}\right) . \qquad (2.23)$$

The theoretical drivers for transfer of charge between an electrode and a species in solution are similar to well-known general concepts as for instance in heterogeneous catalysis, with pressure and temperature playing a role. Electrochemical conversion is controlled by similar several factors. The electrode voltage affects the rate of the electron transfer. The rate of reaction itself is controlled by the rate constant and the actual surface concentration of the reactant. The latter itself is highly influenced by the transport regime. To measure the correct rate, the system has to be in the kinetic regime, for example, the influence of transport needs to be cancelled out by adequate experimental conditions.

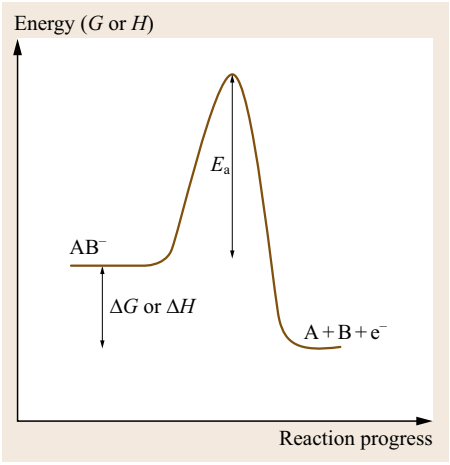


Fig. 2.3 General schematic of the activation energy that must be overcome to allow a thermodynamically favored oxidation reaction. The activation barrier can be overcome by the application of external energy, in the form of potential, heat, or light

Electrocatalysis presents unique conditions, namely that the reaction processes occur at the surface of charged electrode surfaces. These surface reactions generally initiate with or result in charged ions. If the reactant or product is charged it needs to resolvate and diffuse through the charged surface of the surface, the double layer, and adsorb on or desorb from the surface. Sorption and diffusion are activated processes; thus rate constants can be determined by using theoretical approaches as for instance by the theory of activated complex.

Fortunately in electrochemistry, the energy of the system can be changed externally through changing the applied voltage to overcome kinetic limitations (Fig. 2.3). But this extra energy is applied at the cost of inefficiencies. A classic example is water, for which it is thermodynamically favorable for liquid H_2O to split to H_2 and O_2 gases at 1.48 V (2.20). With no applied potential (or excitation by light), water is very stable and does not split. But in an electrochemical cell with an applied potential over 1.48 V, the splitting is thermodynamically favorable. In practice, electrolysis systems are only effective at greater than about 1.7 V because of the kinetic limitations of the experiment. The > 0.22 V of overpotential applied to the system is additional energy and is needed to overcome the kinetic barriers at the electrodes. An objective in industrial electrochemical processes is typically to keep the overpotential low to reduce the amount of energy needed by the system, and increase its efficiency. Sometimes, for instance with corrosion prevention, the objective would be to create a condition in which a very large amount of energy is needed to enable a process, in which case a large over potential would be desired.

The kinetics of electrochemical reactions are governed by the Butler–Volmer equation in (2.24) which reveals the correlation between the current density of the reaction j versus the overpotential. In (2.24), α is an empirical *transfer coefficient* and F, R, and T have their usual meanings (see the section on Thermodynamics). The Butler–Volmer equation reflects the reversibility of the electrochemical reactions, as the first part of the equation is the forward process, and the second is the reverse one. The sum of the forward and backward transfer coefficient is unity, so the reverse reaction is often written with a transfer coefficient of $1 - \alpha$, but can be alternatively written as β,

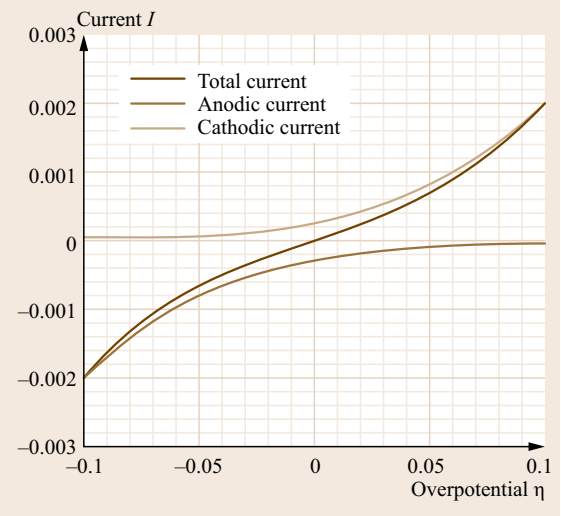


Fig. 2.4 Graphical representation of Bulter–Volmer equation comparing the oxidation and reduction reactions and the total reaction as a function of current and over potential for $\alpha = 0.5$

where $\alpha + \beta = 1$

$$j_k = j_0 \left[\exp\left(\frac{\alpha n F \eta}{RT}\right) - \exp\left(\frac{(1-\alpha) n F \eta}{RT}\right) \right] . \tag{2.24}$$

Figure 2.4 shows a graphical representation of the Butler–Volmer equation, with the competing forward and backward reactions, and the sum of the final reaction. The data is collected on the positive and negative side of current density passing through 0 at E^0 (where $\eta = 0$) so these measurements also carry thermodynamics information.

At high current densities and overpotentials, the I–V plot becomes linear, and this region is studied via Tafel analysis to relate the rate of an electrochemical reaction to its overpotential. The Tafel equation for an anodic reaction is shown in (2.25), where a and b are the Tafel equation constants, a is its y-axis intercept, which is a measure of the exchange current density of the reaction and is directly proportional to the rate constant, b is the Tafel slope, which can be used to determine the order of the reaction (e.g., a slope near $-120\,\mathrm{mV/s}$ is for a two-electron transfer reaction). The slope of a Tafel plot also reveals the value of the transfer coefficient α for the given direction of the electrode reaction

$$\eta = E - E^0 = a + b \log(I) . \tag{2.25}$$

At low overpotentials, the Bulter–Volmer equation is simplified to (2.26), in which D is the diffusion coefficient, δ is the diffusion layer thickness and C is the concentration of electroactive species

$$I_{\text{limit}} = \frac{nFD}{\delta} C . \tag{2.26}$$

Further applications of Butler–Volmer equation is given in Chaps. 4, 7, 10, 18, 19, 23, 27 and 28.

The electron transfer rate constants can also be determined by using theoretical concepts as transition state theory (Chaps. 4 and 5). It is also necessary to describe the rate of an electrochemical reaction in relation to the surface area of the electrode which thus determines the amount of formed products. Electrodes and their use in electroanalysis are described in detail in Chaps. 7 and 14. Special attention to reactions is paid in Chap. 4 for nonequilibrium phenomena, Chap. 23 for bioelectrocatalysts, Chap. 24 with respect to photoelectrochemistry, Chap. 25 for extractive metallurgy and Chap. 27 for hydrogen production.

2.4 Mass Transport

Beside the knowledge of thermodynamic laws and kinetics, transport processes are most decisive for performing efficient electrochemical processes. Mass transport includes the series of steps involved in every electrochemical process where reactants and products are transported to and from the electrode surface. Mass transport issues are also probably the most important part of electrochemical *system* development, as the thermodynamic and kinetic aspects of electrochemistry are not realized unless you can get reactants effectively to and from an electrode.

Mass transport in electrochemical systems takes three forms: diffusion, convection, and migration. These effects are described in detail in numerous chapters (Chaps. 3, 4, 7–10, and 23). and compared in simple graphic in Fig. 2.5. Diffusion in an electrochemical solution is governed by Fick's law, which corresponds to the diffusional flux J from high to low concentrations, over a distance x toward a homogenous solution

$$J_0 = -D_0 \frac{\partial C_0}{\partial x} . \tag{2.27}$$

Simple diffusion parameters can be measured with cyclic voltammetry and application of the Butler–Volmer equation, as discussed earlier. Fick's second law

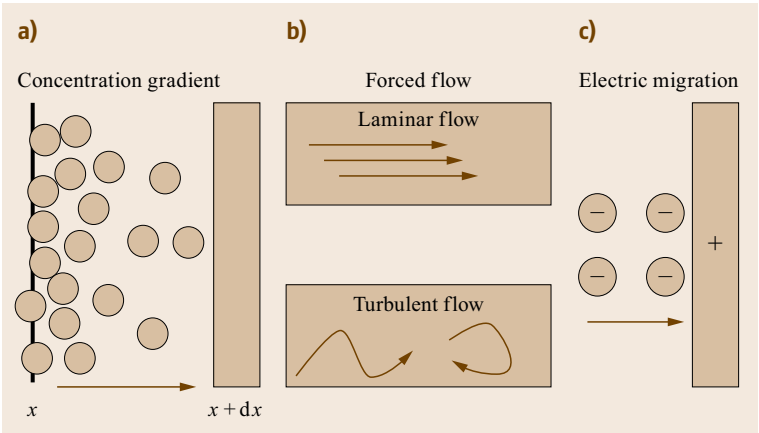


Fig. 2.5a–c Three dominant types of mass transport in electrochemical systems **(a)** diffusion, **(b)** convection, and **(c)** migration

of diffusion is invoked to describe diffusion as a function of time.

Convection is transport to or from a surface that is enhanced by bulk motion of the fluid. The motion is driven by a pressure gradient, which is created by pumping (forced convection) or uneven heating (natural convection). In most electrochemical systems the flows are laminar (low Reynolds number) and easily predicted, but they can be turbulent (high Reynolds number) and be difficult to predict. In either case, rates of convection can be modeled using experiment-derived correlations or by solving the Navier-Stokes equations with the appropriate diffusion and migration relations.

The final source for mass transport is migration due to an electric field, a condition unique to electrochemical systems. The voltage gradient across a cell is a potent force in driving charged ions to and from electrodes. In the operation of a dynamic system with variable voltage, the effect of migration is inconstant. To fully understand mass transport in a system, the diffusion, convection, and migration of the charged species must be accounted for. And solving the transport equations with appropriate boundary conditions opens the root to describe kinetics and energetics of the surface reaction.

Often mass transport issues can be waived in experiments in electrochemical cells, because they are designed to operate at low current where mass transport is negligible. Levich determined that mass transport effects can be eliminated in low current density regions of a reaction, and can be reduced to the convection term by rotating a flat electrode in solution under the appropriate conditions, using the so-called rotating-disk electrode (RDE). As discussed in Chap. 14, rotation is used to increase convection of O_2 in an electrolyte to the electrode, allowing the kinetics to be measured at low current densities. Microelectrodes and ultramicroelectrodes have also been used as tools to study the kinetics of reactions by allowing use of a very fast scan rate, beyond the range for diffusion control [2.18].

In electrochemical systems with gas or liquid flows (fuel cells, air batteries, flow batteries, etc.), the first step is to understand and optimize flow through channels (Chap. 8). Control of the flows is also critical in electrochemical processes, as described in Chap. 28 for electrochemical machining.

The systematic improvement of mass transport is more complicated in real electrochemical systems, which require high surface area electrocatalyst layers or active material typically embedded on a conductive, porous support, as discussed in Chap. 6. The effective diffusion of a species i through a porous material D_i^e is proportional to the diffusion of i through a nonporous system D_i and the porosity of an electrode ϵ as in (2.28) [2.19]

$$D_i^e = D_i \epsilon^{1.5} \,. \tag{2.28}$$

Mass transport is best accomplished through the wide-open spaces found in mesopores that have been optimized for tortuosity. The accurate treatment of diffusion through such porous layers is of critical importance and is discussed briefly in Chap. 8.

2.5 The Charged Electrode Interface/Electrochemical Double Layer

The interaction between the solid electrode and liquid electrolyte is governed by the electrochemical double layer. The double layer consists of a layer of positive charges on the surface of a negative electrode and a surrounding layer of negative charges in solution, or vice versa. Their arrangement on a charged electrode produces an electrical potential difference (Galvani potential) between the bulk of the (metallic) electrode and the electrolyte (solution). Beyond the first layer, there is an additional layer of loosely associated ions attracted to the surface by a coulombic force. The constituents of the double layer are typically ions and polar molecules, such as water. The composition of the charged species at solid–liquid and liquid–liquid interfaces and the accurate measurement of the phenomena has been one of the most heavily studied areas in both fundamental and applied electrochemistry. More detailed discussions of the double layer are abundant, and can be found in the references in Table 2.2 can be found in numerous chapters in this book (Table 2.1) and the references in Table 2.2.

There are two major considerations for the double layer – electrode reactivity and charge storage. Frumpkin proved that this charged structure of ions at the interface between electrode and solution controls the rate of electron transfer, and thus is a major consideration in the kinetics or the rate of electrochemical reactions. The charge at the double layer, or Helmholtz layer, also can store charge electrostatically.

Double-layer effects can be profound in many aspects of electrochemistry, because due to the nature of electrochemistry, charged species are everywhere in electrochemical cells, including the electrolyte, active species, electrodes, and even impurities. Accordingly, the double layer can have a large impact on the performance of any electrochemical reaction and device, and also extends to electroless systems such as the charged interface of colloids. Not only does the double layer affect the kinetics of an electrode reaction, but charge is also a significant driver for the mass transport of ionic species. It must also be considered for its impact on the unintended accumulation of ions or impurities simply by electrostatics at the electrode interface.

The literature includes several models and a wealth of theory regarding the charge storage, reactivity, and behavior of charged particles at an electrode surface. The Gouy–Chapman model improved upon that of Helmholtz by viewing the double layer as a diffuse layer in which the charge dissipates exponentially away from the electrode surface. Stern further improved these models by including the ionic sizes, and thereby including size exclusion. Grahame contended that the solvation spheres of the ions change depending on their proximity to the electrode, allowing the penetration of some ionic and uncharged species. He created the terms inner Helmholtz plane and outer Helmholtz plane. Another improvement was made by Bockris, Devanathan, Müller who included the role of the solvent in Grahame's model. These models are schematically shown in Fig. 2.6. Detailed models for interfaces between electrode and electrolyte as well as their characterization and application are described in Chaps. 3, 5, 6 and 13.

As noted before, the electrochemical double layer is the driving force behind electrochemical capacitors, which is the subject of Chaps. 17 and 18. A typically high surface area is charged, and counter ions are adsorbed. As the potential is decreased or released, the ions at the surface are released and a charge transfer reaction results in a rapid release of electric charge, or power. Research in this area began with simple electrostatic adsorption on high surface area, low cost materials such as carbon, but now materials that store charge internally, for example, MnO_2 and RuO_2, are used as additional sources of stored energy. The specific experimentation for measuring charge storage in capacitors, and distinguishing between charge storage and electrostatic adsorption is described in Chap. 17.

The double-layer effect is also highly variable on the applied potential, or field strength. As the electrode potential is changed, the attraction of the positive and negative species changes respectively on the negatively charged anode or the positively charged cathode [2.20]. The amount that the species is charged also affects its adsorption, as shown schematically in Fig. 2.7 for singly charged A^- ions and doubly charged B^{2-} ions. The higher the charge on the anion, the more it will adsorb on a positive electrode, particularly with increasing potential. Such effects drive the selection of electrolytes. For instance, the electrolyte $HClO_4$ is used for analysis of oxygen reduction electrocatalysts in PEM fuel cell research rather than H_2SO_4, because the $HClO_4^-$ interferes less with the electrode than SO_4^{2-} (Chap. 14). The $HClO_4$ gives a better representative of the oxygen reduction reaction even though H_2SO_4 is chemically closer to the perfluorosulfonic acid electrolyte used in practical cells.

Conversely, as the electrode approaches the point of zero charge of the electrode, adsorbed species can be desorbed. The size and charge of the anion will also affect its solvation layer, or the amount of species that it has attracted to it. The layer of adsorbed anions causes a barrier layer to build up as the external potential of

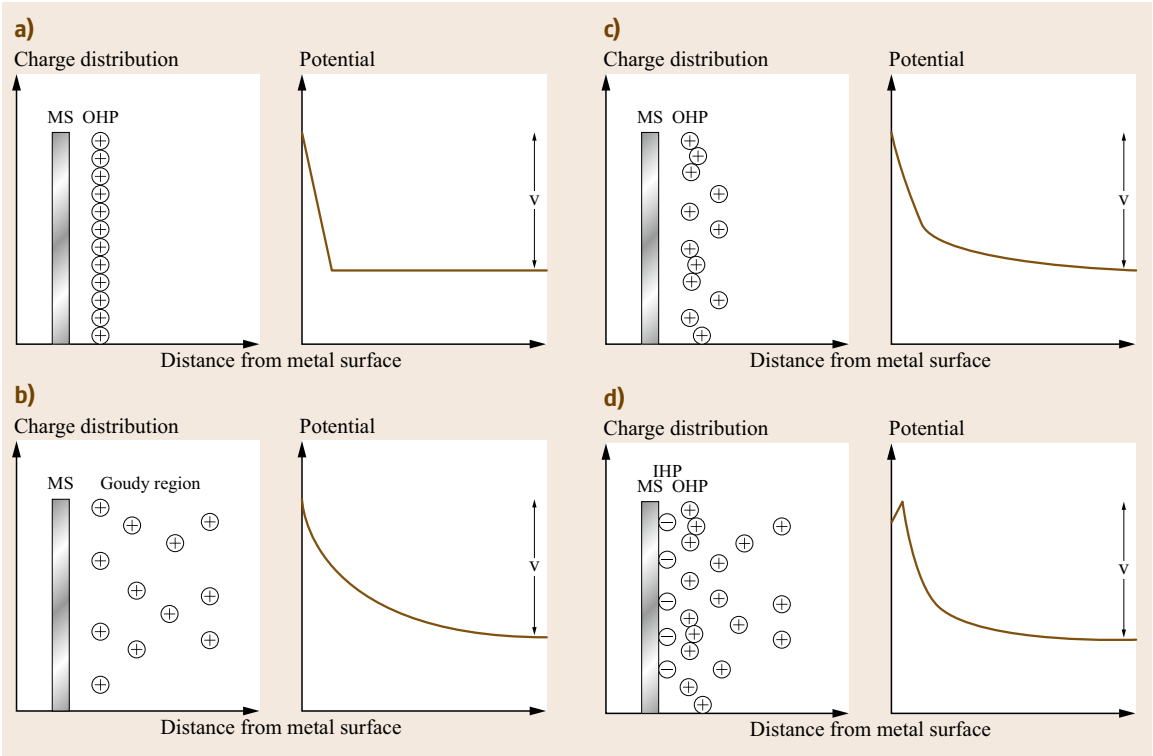


Fig. 2.6a–d Different models for the electric double layer at electrode/electrolyte interface, shown schematically for ion distribution and potential versus distance from the metal surface. **(a)** Helmhotz model; **(b)** Gouy–Chapman model; **(c)** Stern model, and **(d)** composite of models from Esin and Markov, Grahame, and Bockris, Devanathan, Müller model (after [2.21])

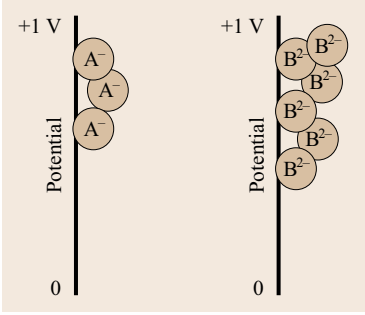


Fig. 2.7 Schematic showing how charged species A^- and B^{2-} might adsorb on a cathode under load. The adsorption of A^- is less and occurs at higher potentials compared to the doubly charged B^{2-} species

the system is increased. This is one reason why the efficiency of a process does not increase linearly with increasing potential – the adsorbed species cause more interference as more energy is supplied.

The reaction of charged species in electrodes becomes particularly dominant in practical electrochemical technologies. For instance, in batteries each electrode material holds a charge inherent to the E^0 of the materials (by comparison in a fuel cell, the cell voltage is driven by external reactants). In a lithium-ion battery, the charged electrode immediately interacts with the electrolyte, and forms a chemical layer called the secondary electrode interface (SEI), as discussed in Chap. 15. The SEI both protects the electrodes, and also introduces I^2R losses, and thus can result in inefficiencies and heat generation in a battery used at high power. Knowledge of this submicrometer layer is scarce, but it is an intense layer of study because of its link to battery stability, power and thermal losses. Understanding the double layer is also highly crucial in electrodeposition processes, in which a new surface is being continuously formed, as discussed in Chap. 26. And efficient electrolytic extraction of metals (Chap. 25) relies on excluding layers of adsorbates in the conversin to pure metal. The electric double layer also controls the processes in electrochemical machining, discussed in Chap. 28.

2.6 Ionic and Electronic Resistance

The materials used in electrochemical cells, and their interfaces, have electronic and ionic resistances which contribute to losses generally in the form of ohmic losses, or I^2R losses. These losses are in addition to mass transport and kinetic losses. Low materials resistance is needed for both ionic and electronic components of the electrochemical reaction, per scheme 1. In the assembly of electrochemical cells, much attention is paid to minimize such I^2R losses through their proper configuration and the proper selection of materials.

The physics relation between resistance and resistivity is shown in (2.29). It clearly shows that during experimentation or technological development of an electrical system, the cell resistance R can be minimized through the use of materials with low resistivity ρ over a large area A over a small length l or electrode thickness

$$R(\Omega) = \rho(\Omega\,\mathrm{cm})\frac{l\,(\mathrm{cm})}{A\,(\mathrm{cm}^2)}\,. \tag{2.29}$$

Because electrochemical cells must contain paths for both ionic and electronic transport, it can be difficult to have each component fully optimized for low resistance. Electronic transport is needed to conduct electrons to and from the electrodes via an external circuit. The electronic resistivity through metals is generally low, so it is less affected by (2.29).

To force electrons through an external circuit and gain work, an electrolyte is chosen with preferably high ionic conductivity, low electronic conductivity. In proton exchange membrane (PEM) fuel cells the typical electrolyte is a proton-conducting solid polymer of perfluorosulfonic acid (PFSA) (Chaps. 19 and 20). Li-ion batteries use carbonate-based electrolyte (Chap. 15). The development of low-resistance solid electrolytes is critical for solid oxide fuel cells (Sec. 8.1), and in solid oxide electrolysis cells (SOECs) (Chap. 27). Another robust field of research is in ionic liquids, which promise high ionic conductivity at elevated temperatures for numerous applications (Sec. 8.2). Such liquid and solid electrolytes used in electrochemistry typically have a ρ that is four times higher than the metals for liquid electrolytes, and much higher for solid electrolytes.

In many cells, the metal electrode is simply in contact with an electrolyte, but in others, particularly for technological cells (batteries, fuel cells, electrolyzers), there is a mixed conducting electrode which transports both ions and electrons. In a battery, this layer would be the active charge storage materials and in a fuel cell or electrolyzer, this would be the electrocatalytic layer. The challenge then is to optimize both ionic and electronic transport, often at what is called the *triple phase boundary* where the electrochemically active material meets the electrolyte or gas phase and a suitable conductor. This is typically done through the formation of composites. In a proton exchange membrane fuel cell (PEMFC), this would be the interface of the carbon-supported nanoscale Pt with the gas phase and a thin PFSA layer for ionic conduction. But such optimization is typically done empirically because the charge-transfer reactions occur at the nanoscale, and imaging the materials at such size levels is still an emerging field of research. Much work is devoted to nanoscale electrochemical materials precisely for the purpose of optimizing such properties (Chap. 21).

To minimize ionic resistance in the overall cell, electrodes tend to have large areas and be thin over their active area, as in Fig. 2.8. Such an electrode is then used for bipolar plates in a fuel cell or electrolyzer, or rolled up in a jelly-roll and put inside a can for a battery.

Contact resistance, or the resistance between interfaces, is another contributor to I^2R losses. This can be avoided simply by ensuring adequate pressure remains on the electrode to the current collector [2.22]. One problem that interferes is corrosion, or the build up of a resistive surface layer, which can result in the formation of resistive oxides on metallic contacts. Therefore resistance is often continually probed in practical electrical systems to ensure that no new sources of losses have occurred. Such cell resistances are often tracked in practical systems by current interrupt methods or a single high-frequency resistance, as discussed in the chapter on battery characterization (Chap. 15) and capacitors (Chap. 17) and PEMFCs (Chaps. 19 and 20).

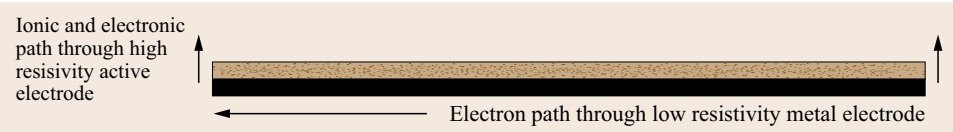


Fig. 2.8 General construction of an electrode material, with electronic transport through the circuit occurring lengthwise through a low-resistance metallic electrode, while the path through a high resistivity active material is kept lengthwise thin over a large area

2.7 Experimentation

It is clear from the discussion that the foundations of electrochemical science and engineering were laid centuries and decades ago. The foundation of electrochemistry in the Nernst and Butler–Volmer equations is well established, and is taught routinely. The general theory of the electric double layer has been known for over a century. What is exciting and new in electrochemistry is the experimental methodology, which is continuously evolving and giving new insights into electrochemical theory, particularly as scientists and engineers move to new frontiers in nanoscience, biology and energy.

The experimental conflicts between the measurement of kinetics, mass transport, and conductivity are often conflicting, as shown schematically in Fig. 2.7. A highly porous electrode may have excellent high surface area for measurement of kinetics, but will have significant mass transport effects, plus may suffer from low electronic conductivity through the web of porous materials. While an ideal high electronic conductor is thin and flat, it might have inadequate surface area for an accurate kinetic measurements.

Accordingly, this book is largely dedicated to experimental methodology and most chapters focus on the specifics of how to correctly carry out modern electrochemical measurements (Table 2.1). We specifically include experimental methodology for energy systems, including PEMFCs, biological fuel cells, capacitors, lithium-ion batteries, and electrolyzers (Fig. 2.9). Likewise, the methodology for electrochemical extraction of metals is included along with electrodeposition.

The idea is to coordinate detailed experimental methodology, which can separate the effects of thermodynamics, kinetics, mass transport, the double layer and ionic/electronic resistances and combine them with spectroscopic and computational tools that provide detailed insights in the materials and electrode processes. As an experiment is set up, the following questions should be asked:

1. What is the E^0 for the full reaction and for each half-cell, and what is the voltage range of their stability?
2. What is the expected kinetics/exchange current density, and can kinetic limitations be removed?
3. Is the system set up to minimize effects of mass transport resistances?
4. Has the electronic and ionic resistances been minimized?
5. Is the impact of electrode charge/attraction of charged species minimized through using reasonable potentials, nonadsorbing electrolytes, and eliminating charged impurities?
6. Are best classical experimental methods being followed, including clean glassware and high purity chemicals, and stable reference electrodes?

The list of 6 items is nontrivial, and is the source of constant experimentation and experimental improvement. But it is worthwhile to think about each category at the beginning of an investigation, and as data is measured. And once the fundamental aspects of an experiment are understood and a question clearly defined, highly complex experiments can be carried out to unravel the electrochemical mysteries of a system.

The most popular electrochemical methods are the transient methods carried out using a potentiostat/galvanostat. Voltage-controlled methods include: single potential step, double potential step, linear sweep

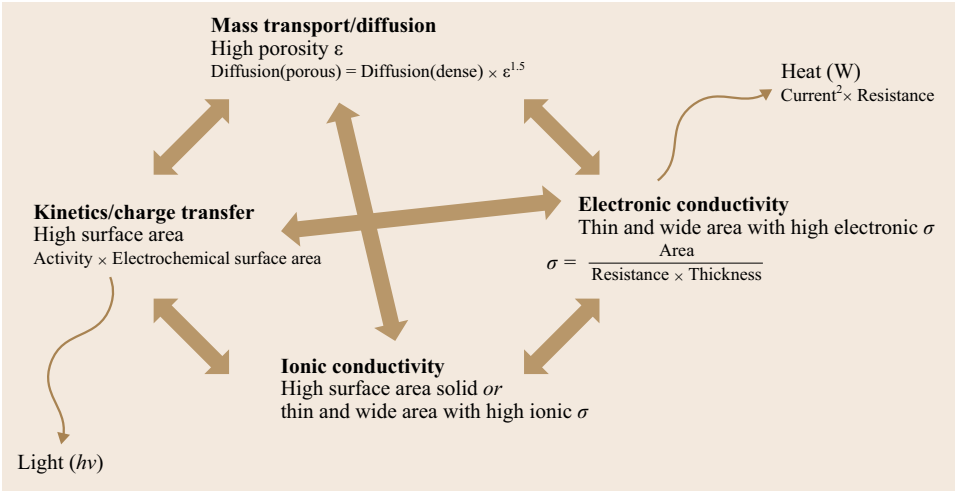


Fig. 2.9 Experimental conditions must strive to separate the competing contributions of kinetics, mass transport, ionic, and electronic conductivity

voltammetry, cyclic voltammetry, and electrochemical impedance (alternating current) measurements with a constant or variable direct current bias. Current-controlled methods include single and double current step methods, plus impedance spectroscopy. Voltammetry is used to detect species in solution and to determine their concentration. The quantitative analysis of coupled transport-reaction phenomena has to address all aspects of double-layer properties, sorption phenomena, and heterogeneous and homogeneous reactions. Experimental dynamic methods which enable a detailed investigation of those coupled processes are impedance spectroscopy, the already mentioned RDE, microelectrodes for fast reactions, cyclic voltammetry, chronoamperometry. These methods are reviewed in this Handbook and extensive details can be found in [2.23–27]. Such electrochemical methods should be carried out to reveal information about thermodynamics (E^0), kinetics, mass transport/diffusion, the double-layer region, and the resistance of the electrode.

A key to any voltammetric experiment is a stable reference electrode. The need for a steady reference electrode arises from the inherent inability to measure the potential across the interface of a single electrode, thus requiring two electrodes to measure a potential difference. The reference electrode is a third electrode in a cell which has a standalone galvanic half cell having a unwavering potential to which the potential of the other two electrodes can be calibrated. The electrochemistry of reference electrodes is discussed in Chap. 7. The proper use and selection of reference electrodes is discussed in a recent Handbook [2.28], and shown in practice in Chap. 14.

For full electrochemical systems containing contributions of bulk and interfacial processes and resistance, the most practical tool for characterization of the ionic and electronic resistances is impedance spectroscopy (IS) and/or electrochemical impedance spectroscopy (EIS). The AC signal used in impedance measurements is able to distinguish between different transport processes because ionic processes have an associated capacitance, while electronic ones have none. Several excellent texts are available on IS, plus tutorials available on the Internet from various equipment vendors [2.29–31]. Impedance spectroscopy is also described in several chapters in this Handbook, including Chaps. 9, 15–20 and 22–23.

A good example of how to characterize materials systems is for PEMFCs, for which a graded series of measurements are now used, as described in several chapters in this book. The activity of the cathode electrocatalysts can be characterized without interference from mass transport effects via RDE measurements of the oxygen reduction reaction, as described in Chap. 14. Note that the isolation of the kinetic measurements from the mass transport limitations required developing methodology to create very thin and uniformly flat electrodes, while choosing an electrolyte with low adsorption on the working electrode. Such methodology took decades to develop across numerous laboratories. Fuel cell characterization becomes more complicated beyond the electrocatalyst characterization. Chapter 9 describes catalyst layer modeling and Chap. 10 discusses the crucial topic of water management. In Chap. 19, *St. Pierre* et al. describe how to set up a proper fuel cell laboratory to operate not only safely but also mainly to distinguish between the competing effects in Fig. 2.7. A further chapter by *Ramani* et al. (Chap. 20) gives more experimental tools for accurately characterizing systems. Through determining the amount of hydrogen cross over under baseline conditions, the resistance via current interrupt methodology, and the humidity/pressure dependence of the system, the effectiveness of a fuel cell membrane electrode assembly can be determined.

The experimental tools are different for the biological systems described by *Minteer* and *Vidakovic* (Chaps. 22 and 23), which have greater environmental vulnerability. The methods are also different for electrochemical capacitors, which must have very low resistance, compared to batteries, which require more emphasis on electrode kinetics, and are vulnerable to overcharge.

In this book, *Walsh* et al. review the vibrational spectroscopy of electrochemical systems (Chap. 13) and *Tong* (Chap. 12) describes the application of nuclear magnetic resonance to electrochemical problems. New experimental methods have worked in tandem with theory to develop the understanding of electrocatalysis at the interface of electrodes [2.32], evolving from the quantum theory of electron transfer reactions which are combined with density functional theory methods and the development of new surface sensitive methods to probe intermediates in solution. Because of its dependence on first principles calculations, studies of kinetics and the electrochemical attributes of materials have been revolutionized by faster computers. The chapters on molecular solvation (Chap. 5) and density functional theory of battery electrodes (Chap. 11) illustrate the benefits of such computational advances.

But the experimental challenges are still daunting. Again for the oxygen reduction reaction in PEM fuel cells, the reaction occurs at a phase boundary with a Pt electrocatalyst in the midst of carbon and a solid electrolyte, and is making a mixture of liquid and gaseous water. Spectroscopically, the challenge of resolving the occupation of Pt by adsorbed OH species in the midst of a sea of aqueous electrolyte and O_2 is daunting. Like-

wise the O_2 and H_2O mass transport through the porous carbon media will be highly dependent upon the fraction of liquid to gaseous water, and not on the pore size of the media. Any impurities in the gas phase will agglomerate at the charged surface of the electrode or in the electrolyte, and cause additional side reactions, affecting the kinetics, and also affecting the resistive losses.

2.8 Subtopics in Electrochemistry

2.8.1 Solid-State Ionics

Solid-state ionics is a subtopic of electrochemistry focusing mainly on electrochemistry within materials, specifically ionic and mixed ionic/electronically conducting materials. This would include the materials used and the processes occurring in solid oxide fuel cells, battery electrodes, high-temperature corrosion, high-temperature sensors, and solid electrolytes. Solid-state ionics affect electrochemical capacitors also, when ions insert beyond the surface into the bulk. Solid electrolyte materials are typically pure ionic conductors, with electronic transference numbers near 0, and electrode materials are typically mixed conductors, requiring both ionic and electronic mobility. Note that the electrodes typically used in battery and fuel cell electrodes are composite electrodes, combining an active material with carbon as the electronic conductor and Nafion in fuel cell electrodes as the ionic conductor. Such composite materials diverge somewhat from the classic consideration of solid-state ionics where the processes are studied in a single material.

A key aspect of solid-state ionics is that there is less emphasis on charge transfer with external reactants and more on charge balance of the ions and electrons within the material, and the conduction of the ions and electrons within the structure. In this respect, Chap. 11 by *Johannes* captures some of the most modern aspects of solid-state ionics research, using first principles calculations to derive the electrochemical materials properties. Other chapters touching on solid-state ionics include Chap. 16 on electrochemical capacitor materials. Also, Chap. 21 describes methodology for characterizing nanomaterial electrocatalysts used in an energy applications. Chapter 27 describes the electrochemistry of SOECs for hydrogen generation.

The other main tool in solid-state ionics is impedance spectroscopy and electrochemical impedance spectroscopy, as described in Fig. 2.10 and specifically for solid-state ionics in references (after [2.33, 34]). The different processes are often characterized by the dependence of conductivity with temperature or oxygen pressure (after [2.35, 36]). Conduction processes often occur over a range of fixed sites, which can be accounted for using Kröger–Vink notation. More recently, nuclear magnetic resonance is being used to measure diffusion in electrochemical systems. Such methodology is described in Chap. 13. Chapter 17 describes the methods to characterize electrochemical capacitors.

More general information of solid-state ionics can be found readily in references, such as the series of books edited by *Kharton* on solid-state ionics [2.37, 38] and a recent handbook on the electrochemistry of mixed ionic-electronic conductors [2.39]. More specific books deal with narrower topics such as the solid-state ionics of batteries [2.40], proton conductors [2.41, 42], general ionic transport processes [2.43], and high-temperature oxidation of metals [2.44].

2.8.2 Ionic Liquids

Ionic liquids are a popular topic in electrochemistry, particularly as electrolytes, where they permit some unusual chemistries. Ionics liquids contain only ionic compounds, yet are in the liquid state at or near room temperature. Common cations include:

1. Alkylammonium
2. Alkylphosphonium
3. *N*, *N*-dialkylimidazolium
4. *N*-alkylpyridinium cations, which have counter (negative ions) such as nitrates.

For electrochemistry, the most common ionic liquid is chloroaluminate for several reasons, as discussed

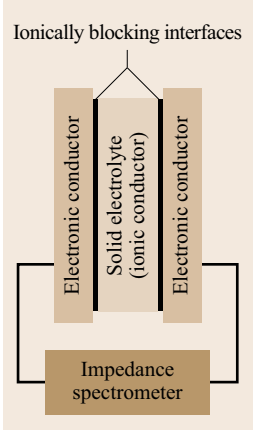


Fig. 2.10 Schematic set up for measuring ionic transport in a solid electrolyte from (after [2.46]). The practical challenge is often decoupling the total electrical properties into individual electronic and ionic components plus isolating the effects of the electrical junction at the materials interface, which requires a great deal of careful experimentation using techniques such as blocking electrodes (after [2.46])

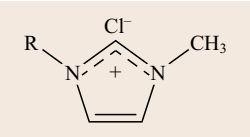


Fig. 2.11 Dialkylimidazolium chloride, where R = methyl, ethyl, propyl, or butyl. These mix with $AlCl_3$ to form chloraluminate ionic liquids (after [2.47])

by *Welton* [2.45], which is schematically shown in Fig 2.11.

Chloroaluminates are good solvents for a wide range of both inorganic and organic materials, permitting the co dissolution of materials not permitted in standard electrolytes. They are often composed of poorly coordinating ions, so can be highly polar yet not create strong double layer effects. Their negligible vapor pressure makes them useful in high-vacuum systems. And they are also highly stable and nonflammable. Their high stability gives them a wide electrochemical voltage window, enabling a range of electrochemical experiments not available to standard liquid electrolyte.

Because of their high thermal and electrochemical stability, ionic liquids are also finding interest in applications, such as lithium-air batteries [2.48] and lithium-ion batteries [2.49], although their relatively high-resistance limits them from high-power applications (high-resistance electrolytes lead to high I^2R heating, as discussed above).

Numerous reviews of various aspects of electrochemistry in ionic liquids are available. *Hussey*'s chapter on *Chemistry of Nonaqueous Solutions* discusses the synthesis and purification of chloroaluminate ionic liquids and also reviews inorganic electrochemistry, organometallic electrochemistry, organic electrochemistry, modified electrodes, and power applications [2.50]. *Electrodeposition from Ionic Liquids* [2.51] includes a very nice series of reviews involving: Electrodeposition of pure metals, alloys, and semiconductors (both bulk and nanocrystalline) as well as the synthesis conducting polymers in chloroaluminate ionic liquids. More recently, the *second edition of Electrochemical aspects of ionic liquids* [2.52] reviews the electrodeposition of metals, electrochemical polymerization, and power applications using chloroaluminate ionic liquids. The benefits of ionic liquids in surface electrochemistry are described by *Liu* et al. [2.53].

2.8.3 Corrosion at Liquid Interfaces

Corrosion is a massive and decisive economic factor and will destroy most products if care is not taken in their design and implementation. The corrosion at low temperatures governs the operation of all interactions with water, including obvious applications such as ocean boating, diving, and deep sea oil exploration, but also affects systems that join dissimilar metals, which with exposure to any water vapor can quickly corrode.

Corrosion occurs simply when it is thermodynamically and kinetically favorable for a material (typically metal) to react with the environment and form another state, such as an oxide. The potential difference between two connecting materials (due to their innately different ΔG values or E^0) is a main source of corrosion, as the more noble metal will withdraw electrons (or oxidize) its less noble partner. Corrosion usually relies on mixed conduction in the metal and at its surface, whereby electrons are transported through a material and then react with water or oxygen in the electrolyte to form either a soluble or insoluble scale on the material surface. The adsorption of ions plays a significant role also, as the materials under corrosion serve as electrodes. Therefore, corrosion can also simply occur at interfaces in contact with a corrosive ionic environment, such as one with chloride. If controlled properly, such as the case with stainless steel and in aluminum, a robust oxide coating can form on the surface and prevent corrosion. If not controlled, defects such coatings can be the point sources for even greater pitting corrosion.

While the *Springer Handbook of Electrochemical Energy* does not specifically address corrosion, the fundamental drivers for corrosion lie in the thermodynamics and kinetics of the reactions. Therefore, those seeking the fundamental underpinnings of corrosion will find value in Chaps. 3, 4, and 7. Corrosion science applied to the process of machining is treated in Chap. 28.

Applied aspects of the electrochemistry of corrosion are covered in books by *McCafferty* [2.54], *Kelly* et al. [2.55], and *Perez* [2.56], with emphasis on corrosion engineering. While it is critical to understand corrosion processes, the prevention of corrosion, typically through cathodic protection is critical, where either an anode is used sacrificially, or a current is applied to hold corrosion at bay. The books in [2.54–56] address cathodic protection, with a more detailed account given by several books focusing specifically on field applications [2.57, 58]. Properties of molecules solvated in ILs are discussed in Chap. 5.

2.8.4 Chlor–Alkali Process

The chlor-alkali process is the foundation of the world's largest industrial electrochemical process, whereby the sodium chloride in brine is electrolyzed to Cl_2, sodium hydroxide, and hydrogen. The drive for chlorine production began with the realization of the power of chlo-

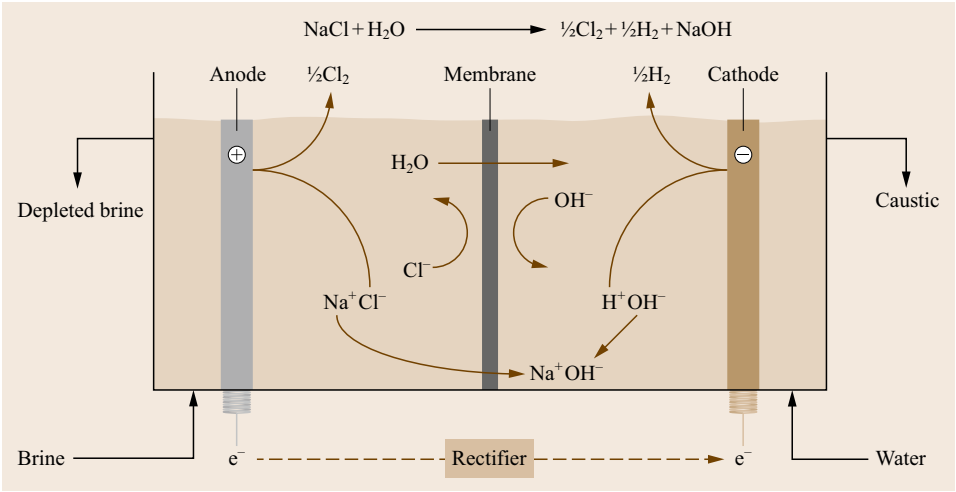


Fig. 2.12 Schematic of modern membrane technology for the chlor-alkali process using sodium perfluorosulfonic membrane separators and dimensionally stable anodes (from Ion Power Inc. data sheet)

rine products as disinfectants and the discovery that it could be used to create safe drinking water. The overall reaction (2.30) and the half-cell reactions (2.31)–(2.32)

$$2\mathrm{NaCl} + 2\mathrm{H_2O} \rightarrow \mathrm{Cl_2} + \mathrm{H_2} + 2\mathrm{NaOH}\,, \tag{2.30}$$

$$\text{Anode reaction: } 2\mathrm{Cl^-} \rightarrow \mathrm{Cl_2} + 2\mathrm{e^-}\,, \tag{2.31}$$

$$\text{Cathode reaction: } 2\mathrm{H_2O} + 2\mathrm{e^-} \rightarrow \mathrm{H_2} + 2\mathrm{OH^-}. \tag{2.32}$$

This process has been a model for incorporating electrochemical advancements. The first industrial processed used a mercury cell (Castner–Kellner process), which used a mercury amalgam to separate the sodium ions. The process evolved to clean the diaphragm process, which used an asbestos fiber porous membrane to separate the NaOH product from the chlorine.

Because of the extremely high electricity needs of the process, there were high motivators to increase the efficiency of the process as the demand for chlorine grew as a bulk material in plastics (e.g., polyvinyl chloride). New technologies were introduced to decrease the overpotential of the electrolysis reactions, increase mass transport, and decrease the I^2R losses in the cell, as prescribed earlier in this chapter. Modern *membrane technology* uses a sodium perfluorosulfonic membrane (e.g., Nafion) separates the cathode and anode, such that only Na^+ can pass between the cathode and anode, allowing for the clean production of Cl_2 gas from the anode, H_2 from the cathode, and NaOH in the cathode compartment, as shown in Fig. 2.12.

Such technological progress has led to high increases in efficiency, along with great improvements in its environmental safety for chlorine gas release. The implementation of a solid ionic-transport membrane in this new efficient electrolysis system laid the foundation for modern proton exchange membrane (PEM) technologies in hydrogen fuel cells and water electrolysis (Chaps. 10 and 27). Also, the chlor alkali process was the first to use gas diffusion electrodes for the efficient transport of gas and liquid at the electrode of an electrochemical cell. Another major development was the dimensionally stable anode (DSA) or dimensionally stable electrodes (DSEs). These comprise ruthenium on titanium to make a corrosion-resistant, highly efficient electrocatalyst that also served as a current collector, the first effective multifunctional bipolar plate [2.59, 60].

Because these developments are now over 40 years old, chlor-alkali technology is only briefly covered in Chap. 3 in favor of focusing on the more modern derivation of the technologies in hydrogen fuel cells and electrolysis. More details of the process can be found in [2.61] and elsewhere [2.62].

2.9 Summary

The book will review all aspects of modern electrochemistry related to energy systems starting with theoretical concepts, basis laws of thermodynamics, nonequilibrium thermodynamics, and multiscale modeling. Basic experimental methods as potentiometry, reference electrodes, ion sensitive electrodes, voltammetry, and amperometry are summarized. Recent developments in experimental approaches as highly ordered macroporous electrodes and nanostructured-tailored electrodes are reviewed.

Special attention is given to Li-ion batteries, electrochemical capacitors, and hydrogen fuel-cell tech-

niques. Moreover, biological fuel cells and bioelectrocatalysts are important recent new developments. Photoelectrochemistry, extractive metallurgy, electrochemical hydrogen production, and elecrodeposition have been chosen out of the variety of applications as they point to the most important aspects of modern electrochemical applications.

Acknowledgments. KSL thanks the Office of Naval Research for support of her time during the development and editing of this book. Robert Mantz provided information for the subsection on ionic liquids.

CB thanks Dr. Maja Glorius for organizing mail contacts to the authors and to Springer.

References

2.1 A.J. Bard, L.R. Faulkner: *Electrochemical Methods: Fundamentals and Applications*, 2nd edn. (Wiley, New York 2000)
2.2 C. Lefrou, P. Fabry, J.-C. Poignet: *Electrochemistry: The Basics* (Springer, Berlin, Heidelberg 2012)
2.3 A.J. Bard, M. Stratmann, E. Gileadi, M. Urbakh (Eds.): *Encyclopedia of Electrochemistry, Thermodynamics and Electrified Interfaces*, Vol. 1 (Wiley-VCH, Weinheim 2002)
2.4 J. Newman, K. Thomas-Alyea (Eds.): *Electrochemical Systems*, 3rd edn. (Wiley-Inderscience, New York 2004)
2.5 J.O. Bockris, A.K.N. Reddy: *Modern Electrochemistry*, Vol. 1 (Springer, Berlin, Heidelberg 1970)
2.6 J.O. Bockris, A.K.N. Reddy: *Modern Electrochemistry*, Vol. 2 (Springer, Berlin, Heidelberg 1970)
2.7 C.H. Hamann, A. Hamnett, W. Vielstich: *Electrochemistry*, 2nd edn. (Wiley-VCH, Weinheim 2007)
2.8 E. Gileadi: *Physical Electrochemistry* (Wiley-VCH, Weinheim 2011)
2.9 C.G. Zoski (Ed.): *Handbook of Electrochemistry* (Elsevier, Amsterdam 2006)
2.10 J. Larminie, A. Dicks: *Fuel Cell Systems Explained*, 2nd edn. (Wiley, Chichester 2003)
2.11 V.S. Bagotzky: *Fundamentals of Electrochemistry*, 2nd edn. (Wiley, New York 2005)
2.12 D. Pletcher, R. Greff, R. Peat, L.M. Peter, J. Robinson: *Instrumental Methods in Electrochemistry* (Elsevier, Amsterdam 2001)
2.13 A.M. Bond: *Broadening Electrochemical Horizons* (Oxford Univ. Press, Oxford 2003)
2.14 M. Pourbaix: *Atlas of Electrochemical Equilibria in Aqueous Solutions* (NACE Int., Houston 1974)
2.15 P. Vanysek: *Handbook of Chemistry and Physics*, 95th edn. (CRC, Boca Raton 2014), Chap.5, pp. 80–88
2.16 M.W. Chase: *NIST-JANAF Thermochemical Tables*, Vol. 14 (NIST, Gaithersburg 1985), suppl.1
2.17 R.C. Alkire, D.M. Kolb, J. Lipkowski: *Electrocatalysis: Theoretical Foundations and Model Experiments*, Vol. 14 (Wiley-VCH, Weinheim 2013)
2.18 J. Heinze: Ultramicroelectrodes in electrochemistry, Angew. Chem. Int. Ed. **32**, 1268–1288 (1993)
2.19 J.S. Yi, T. van Nguyen: Multicomponent transport in porous electrodes of proton exchange membrane fuel cells using interdigitated gas distributors, J. Electrochem. Soc. **146**(1), 38–45 (1999)
2.20 J.M. Bockris, W. Gilead, K. Müller: A molecular theory of the change dependence of the competitive adsorption, Electrochem. Acta **12**, 1301–1321 (1967)
2.21 S. Srinivasan: Electrode/electrolyte interfaces. In: *Fuel Cells*, (Springer, Berlin, Heidelberg 2006), Chap. 2
2.22 C.J. Netwall, B.D. Gould, J.A. Rodgers, N.J. Nasello, K.E. Swider-Lyons: Decreasing contact resistance in proton-exchange membrane fuels cells with metal bipolar plates, J. Power Source **227**, 137–144 (2013)
2.23 D.D. Macdonald: *Transient Techniques in Electrochemistry* (Plenum, New York 1977)
2.24 W. Schmickler, E. Santos: *Interfacial Electrochemistry*, 2nd edn. (Springer, Berlin, Heidelberg 2010)
2.25 F. Scholtz (Ed.): *Electroanalytical Methods*, 2nd edn. (Springer, Berlin, Heidelberg 2010)
2.26 P. Kissinger, W.R. Heineman: *Laboratory Techniques in Electroanalytical Chemistry*, 2nd edn. (Marcel Dekker, Amsterdam 1996)
2.27 R.G. Kelly, J.R. Scully, D. Shoesmith, R.G. Buchheit: *Electrochemical Techniques in Corrosion Science and Engineering* (Marcel Dekker, Amsterdam 2003)
2.28 G. Inzelt, A. Lewenstam, F. Scholz (Eds.): *Handbook of Reference Electrodes* (Springer, Berlin, Heidelberg 2013)
2.29 V.F. Lovovich: *Impedance Spectroscopy* (Wiley, New York 2012)
2.30 M.E. Orazem, B. Tribollet: *Electrochemical Impedance Spectroscopy* (Wiley, New York 2008)
2.31 J.R. MacDonald: *Impedance Spectroscopy Theory* (Wiley, New York 2005)
2.32 M.T.M. Koper: Electrocatalysis: Theory and experiment at the interface, Faraday Discuss. **140**, 11–24 (2009)
2.33 J.T.S. Irvine, D.C. Sinclair, A.R. West: Electroceramics: Characterization by impedance spectroscopy, Adv. Mater. **2**, 132–138 (1990)
2.34 B.A. Boukamp: Electrochemical impedance spectroscopy in solid state ionics: Recent advances, Solid State Ion. **169**, 65–73 (2004)
2.35 H.L. Tuller: *Mixed Conduction in Non Stoichiometric Oxides* (Academic, New York 1981)
2.36 L. Heyne: Electrochemistry of mixed ionic-electronic conductors, Top. Appl. Phys. **21**, 169–221 (1977)
2.37 V.V. Kharton (Ed.): *Solid State Electrochemistry I* (Wiley-VCH, Weinheim 2009)
2.38 V.V. Kharton (Ed.): *Solid State Electrochemistry II* (Wiley-VCH, Weinheim 2011)
2.39 P.J. Gellings, H.J. Bouwmeester: *Handbook of Solid State Electrochemistry* (CRC, Boca Raton 1997)
2.40 T. Minami (Ed.): *Solid State Ionics for Batteries* (Springer, Berlin, Heidelberg 2005)

2.41 P. Colomban (Ed.): *Proton Conductors* (Cambridge Univ. Press, Cambridge 1992)

2.42 P. Knauth, M.L. Di Vona: *Solid State Proton Conductors* (Wiley, New York 2012)

2.43 K. Kontturi, L. Murtomäki, J.A. Manzanares: *Ionic Transport Processes in Electrochemistry and Membrane Science* (Oxford Univ. Press, New York 2008)

2.44 P. Kofstad: *High Temperature Oxidation of Metals* (Wiley, New York 1966)

2.45 T. Welton: Room-temperature ionic liquids: Solvents for synthesis and catalysis, Chem. Rev. **99**, 2071–2083 (1999)

2.46 R.A. Huggins: Simple method to determine electronic and ionic components of the conductivity in mixed conductors, Ionics **8**, 300–313 (2002)

2.47 J.S. Wilkes, J.A. Levisky, R.A. Wilson, C.L. Hussey: Dialkyl-imidazolium chloroaluminate melts: A new class of room-temperature ionic liquids for electrochemistry, spectroscopy, and synthesis, Inorg. Chem. **21**, 1263–1264 (1982)

2.48 T. Kuboki, T. Okuyama, T. Ohsaki, N. Takami: Lithium-air batteries using hydrophobic room temperature ionic liquid electrolyte, J. Power Sources **146**, 766–769 (2005)

2.49 A. Lewandowski, A. Świderska-Mocek: Ionic liquids as electrolytes for Li-ion batteries – An overview of electrochemical studies, J. Power Sources **194**, 601–609 (2009)

2.50 C.L. Hussey: *Chemistry of Nonaqueous Solutions: Current Process* (Wiley-VCH, Weinheim 1994)

2.51 F. Endres, A.P. Abott, D.R. MacFarlane (Eds.): *Electrodeposition from Ionic Liquids* (Wiley-VCH, Weinheim 2008)

2.52 H. Ohno (Ed.): *Electrochemical Aspects of Ionic Liquids*, 2nd edn. (Wiley, New York 2011)

2.53 H. Liu, Y. Liu, J. Li: Ionic liquids in surface surface electrochemistry, Phys. Chem. Chem. Phys. **12**, 1685–1697 (2010)

2.54 E. McCafferty: *Introduction to Corrosion Science* (Springer, Berlin, Heidelberg 2010)

2.55 R.G. Kelly, J.R. Scully, D. Shoesmith, R.G. Buchhiet: *Electrochemical Techniques in Corrosion Science and Engineering* (Marcel Dekker, Amsterdam 2002)

2.56 N. Perez: *Electrochemistry and Corrosion Science* (Springer, Berlin, Heidelberg 2004)

2.57 W. von Baeckmann, W. Schwenk, W. Prinz (Eds.): *Handbook of Cathodic Corrosion Protection*, 3rd edn. (Elsevier, Amsterdam 1997)

2.58 V. Cicek: *Cathodic Protection* (Wiley, New York 2013)

2.59 H.B. Beer, U. Landau, E. Yeager, D. Kortan (Eds.): *in Electrochemistry in Industry* (Plenum, New York 1982)

2.60 P. Duby: History of progress in dimensionally stable anodes, J. Min. Met. Mater. Soc. **45**, 41–43 (1993)

2.61 T.F. O' Brien, T.V. Bommaraju, F. Hine: *Handbook of Chlor-Alkali Technology*, Vol. 1 (Springer, Berlin, Heidelberg 2005)

2.62 D. Pletcher, F.C. Walsh: *Industrial Electrochemistry*, 2nd edn. (Springer, Berlin, Heidelberg 1992)

Part A Thermodynamics

Part A Thermodynamics

3 **Thermodynamical Aspects of Electrochemical Reactions**
Dietrich Hebecker, Halle (Saale), Germany

4 **Thermodynamics of Electrochemical Systems**
Signe Kjelstrup, Trondheim, Norway
Dick Bedeaux, Trondheim, Norway

5 **Multiscale Modeling of Solvation**
Andriy Kovalenko, Edmonton, Canada

3. Thermodynamical Aspects of Electrochemical Reactions

Dietrich Hebecker

The beginning of the transition from fossil fuels to renewable resources is associated with a change in energy conversion technologies and with a growing importance of electricity (Sect. 3.2). The application of electrochemical processes for the use and generation of electricity attains a new position in the energy conversion chain. Electrochemical reactions are associated with heat and electric power (work) exchange and are therefore thermodynamically complicated processes. Chemical and technical thermodynamics are important instruments for the understanding, classification and development of efficient electrochemical reactors and systems. As will be explained in this chapter, the analysis of electrochemical reactions on the basis of the Gibbs–Helmholtz equation allows for the definition of an equivalent temperature, which characterizes the energetic quality of the reaction under equilibrium conditions. The equivalent temperature is the ratio of the molar basic reaction enthalpy and the molar basic reaction entropy. The application of the exergy concept permits the determination of the irreversibilities and of the energetic quality of the exchanged heat as well as of all reaction educts and products (Sect. 3.2). Electrochemical reactions are associated with energy exchange at least at three temperature levels: heat at reaction temperature, work with a normalized exergy of unity, and the chemical conversion itself at its equivalent temperature. Hence, electrochemical reactions can be energy transformations in the sense of thermodynamical cycles, which is of high technological relevance. In addition, each educt and product represents a temperature level or, more precisely, its own normalized exergy. Thus, it is also possible to regard energy transformation processes at the level of substances. Open and closed electrochemical cycles will be considered, evaluated on the basis of their thermodynamical characteristics and compared with conventional processes.

3.1 **Electrochemical Reactions for Energy Conversion** 33
3.1.1 Unity of Material and Energy Conversion 34
3.1.2 Energy Balance of Electrochemical Reactions 35
3.1.3 Equilibrium and Equilibrium Temperature 36
3.1.4 Availability of Chemical Reactions 37
3.1.5 Temperature–Energy Diagram of Chemical Reactions 47
3.1.6 Exotropic Reactions 50
3.1.7 Endotropic Reactions 52
3.2 **Electrochemical Reactions and Energy Transformation** 54
3.2.1 Systematics of Energy Transformation 54
3.2.2 Chemical Energy Transformation 57
3.2.3 Electrochemical Thermodynamic Cycles 60
References 67

3.1 Electrochemical Reactions for Energy Conversion

The development of the electricity production and consumption, and the increase of their efficiency, are of growing importance for productivity, sustainability and eventually for the prosperity of modern societies. For example, thermal power stations achieve coefficient of performance (COPs) of about 60% in spite of the Carnot limitation for the heat-to-power transformation. The development of fuel cell power stations have made this limitation obsolete, at least in principle, and opened the door to fuel cells for the large-scale energy industry. The necessary and planned withdrawal from the use of fossil fuels requires the production of synthetic fuels via

electrolysis. In addition to these two energetic aspects, a growing importance of electrochemical processes for chemical synthesis, for sensor technology and in chemical analysis is to be expected.

Electrochemical reactions are a specific type of chemical reaction associated with the presence of an electrical field and charged particles. Therefore, many microprocesses occur in addition to effects observed in ordinary thermal chemical reactions such as heat conduction, diffusion, convection, turbulence and interface interaction. The electric potential between the electrodes influences the motion of charged species at the electrode surface, in the solution, in membranes and in barriers and other interfacial areas.

Electrochemical reactions are mostly two or more-phase heterogeneous reactions and require a chain of reaction steps with their specific kinetic problems. Each of these transport processes and reaction steps has a driving force. In total, these driving forces lower the useful electrical potential of fuel cells (potential loss) or increase the required electrode potential (overpotential) of electrolysis and battery charge. The multiplicity of such effects requires special design for electrodes, reactors and electrochemical systems. For different chemical processes corresponding types of electrodes have been developed, such as dimensionally stable electrodes, fluid and molten electrodes and porous electrodes for gas reaction. The reactor construction is also very specific for each technology, depending on corrosion requirements, product separation and solution properties [3.1–3]. This all leads to relatively high capital costs. On the other hand the irreversibilities produced by the large number of microprocesses with their driving forces influence the operation costs and the process efficiency in an extreme manner.

This complexity of effects is the reason for the difficulties in investigation, modeling, analysis, design and evaluation, and finally, the management of an electrochemical process. The chemical and technical thermodynamics are, in addition to the heat and mass transfer and the fluid dynamics, important instruments for the understanding and development of such processes [3.4–6]. The importance of the thermodynamics consists of the description of the properties of chemicals, of mixtures and solutions and their dependence on temperature, pressure and composition; the description of the possibility or impossibility of chemical reactions, their equilibrium and the influence of temperature, pressure, composition and electric field on it; the understanding of the nature of the chemical reaction and the necessary interaction of the reacting system with the environment; the description of the quantitative deviation of the real electrochemical process from the reversible one; the description of the thermodynamic losses in each reaction step and of heat, mass and charge transfer; the purpose of which is finding the main causes of loss and the possibilities of their avoidance or reduction, and the analysis and evaluation of the energetic efficiency of electrochemical reactions, processes, devices and plants in comparison to alternative technologies.

The thermodynamics of electrochemical reactions differs from ordinary chemical thermodynamics because of the presence of electrodes and an electric field [3.3, 7]. This is important due to the exchange of electrical energy or work during the reaction. The presence of charged particles alone (as it occurs in many reactions, for instance in water solutions of salts) is not sufficient in this understanding. For the process' thermodynamics, as will be discussed later, there is a fundamental difference between processes with heat exchange only and processes with heat and work transfer.

3.1.1 Unity of Material and Energy Conversion

The unity of material and energy conversion may be obvious in the sense of Einstein's familiar relation between mass and energy. However, here we aim at establishing such a unity for processes where the laws of conservation of mass and energy hold independently. We are not interested in nuclear processes but in chemical conversion and we want to emphasize that each chemical reaction is connected with the simultaneous conversion of chemicals and energy.

Chemical reactions that are an essential part of everyday life and of any modern national economy include the formation of biomass by photosynthesis, the production of life-sustaining heat in combustion reactions, the manufacturing of the immense variety of products of the modern society as well as the destruction of used materials after the end of their life cycle. Of primary interest are usually the chemical properties of the materials involved and, in particular, of the products. Although chemical reactions are aimed at producing material qualities, there is also always a change of the energetic states of the reaction partners and products and the process is thus subject to a unity of material and energy conversion. The energetic effect of a reaction manifests itself in the energy exchange with the environment and, in addition, in the distribution of the energy between the different products. In each case both the quantity and the quality of the energy are of importance. The different qualities of work and heat and the value of the heat as a function of the temperature have to be considered. In addition, the different energetic qualities of the chemical bonds of the materials are essential. Therefore, the quality of the material-bound

chemical energy depends not only on the material itself but also on its relationship to the materials of the natural and/or thermodynamically defined environment. On the one hand, the qualitative aspects of both the material-bound and the material-free forms of energy can be represented using the concept of exergy [3.8]. On the other hand, exergy also permits a distinction between unavoidable expenditures and avoidable losses in connection with the mass and energy conversion [3.9, 10]. In addition to the detailed process and system analysis a relation can be established between the type of reaction, the feasibility, the thermodynamic losses, and the possibilities for their avoidance. This allows identification of pathways to low-loss processing [3.11].

Besides this unity, there are some distinct differences between mass and energy conversion. First, all chemical reactions are reversible in principle by use of energy; i. e., the input materials may be produced again from the products. This is possible by the supply of high quality energy and delivery of waste heat for compensation of the irreversibilities occurring in the reaction process. The measure of irreversibilities of a chemical process must depend on the process conditions and determine the expenditure of work or electricity and heat at a certain temperature for the real process.

3.1.2 Energy Balance of Electrochemical Reactions

For engineering applications it is often convenient to choose temperature and pressure as variables. Therefore enthalpy is suitable for characterizing the energetic state. The energetic effect of a chemical reaction at constant temperature and pressure is consequently the molar reaction enthalpy or the difference between the enthalpy of the products and educts

$$\Delta_R \bar{h} = \sum_k \nu_k \bar{h}_k = \sum_i \nu_{P,i} \bar{h}_{P,i} - \sum_i \nu_{E,i} \bar{h}_{E,i} \,. \quad (3.1)$$

This energy is to be either transferred to the environment (in the case of a constant reaction temperature) or it can serve to change the thermal enthalpy of the reaction products. The delivery of energy from the reaction system may occur as heat (in the case where there is a heat exchange surface), as electric work (for instance on electrodes) or as radiation. Thermodynamically, electric work equals heat at an infinitely high temperature (Carnot factor = 1). In an energetic sense radiation can be described as heat at radiation temperature, which can differ from the reaction temperature. Reactions with work and heat exchange will be named w, q-reactions

$$\Delta_R \bar{h} = \bar{w}_{el} + \sum \bar{q} \,. \quad (3.2)$$

Equation (3.2) holds for any chemical reaction and any chemical reaction is theoretically possible. The only problem is finding out the relation between work and heat and their signs. The theoretical limits of these parameters are given by the second law of thermodynamics.

If (3.2) is interpreted as the first law of thermodynamics, the terms describe real exchanged work and heat. The relation between heat and work depends on the irreversibilities of the reaction system. Irreversibilities always lower the required heat supply to the system or increase the heat delivery

$$\Delta_R \bar{h} = \bar{w}^R_{el,rev} + \bar{w}_{el} - \bar{w}^R_{el,\,rev} + \bar{q} \quad \text{with}$$
$$\bar{q} = \bar{q}_{rev} - (\bar{w}_{el} - \bar{w}^R_{el,\,rev}) \,. \quad (3.3)$$

In photochemical reactions, energy exchange takes place at two different finite temperatures, the reaction temperature and the radiation temperature. The latter is usually very high. Similar to work, the radiation heat $\bar{q}_r$ represents a certain exergy input into the reaction system. The two energy terms may have different signs, for instance photosynthesis uses solar radiation and delivers heat near the surrounding temperature. As we will see later, these reactions are fundamentally similar to the w, q-reactions

$$\Delta_R \bar{h} = \bar{q} + \bar{q}_r \,. \quad (3.4)$$

In ordinary chemical reactions, called thermal reactions or q-reactions, work is not exchanged and energy is delivered or supplied as heat through the heat exchange surface

$$\Delta_R \bar{h} = \bar{q} \,. \quad (3.5)$$

Reactions are either exoenergetic (decrease of chemical energy) or endoenergetic (increase of the chemical energy of the products). At constant temperature and pressure the energy transfer from the reaction system or into the system can take place in the form of heat (exothermic or endothermic reaction) or as work. This is realized by suitable devices, mostly as electric power transfer (exergonic or endergonic reaction). The type of energy transfer (heat or work) influences the equilibrium because of the different qualities of the energy.

The exchanged work or heat can in principle have either sign. An endoenergetic w, q-reaction can be endergonic but exothermic. For instance, the required electrical energy supply of an electrolysis cell can be higher than the reaction enthalpy and some energy must be delivered at low temperature to the environment. On the other hand it is possible that a fuel cell theoretically produces more electric energy than the reaction

enthalpy and therefore requires a low temperature heat input from the environment. This process is exergonic but endothermic.

The possibility of changing the energetic character does not exist for purely thermal reactions, an exoenergetic reaction is always also exothermic and an endoenergetic reaction always endothermic. The irreversibilities may be due to a higher temperature level of the supplied heat or a lower temperature level of produced heat or the deviation of reaction temperature and equilibrium temperature. In this context, the reaction enthalpy in adiabatic exothermic reactions is used to irreversibly heat up the reaction products. By contrast, adiabatic endothermic reactions use energy of the superheated educts irreversibly for the reaction at a lower reaction temperature.

For the analysis of the energetic efficiency of electrochemical reactions, it is useful to write down the first law of thermodynamics in an extended form

$$\sum_i \nu_{\mathrm{E},i}\bar{h}_{\mathrm{E},i} + \bar{w}_{\mathrm{in}} + \sum_i \bar{q}_{\mathrm{in},i} = \sum_i \nu_{\mathrm{P},i}\bar{h}_{\mathrm{P},i} + \bar{w}_{\mathrm{out}} + \sum_i \bar{q}_{\mathrm{out},i}\,. \tag{3.6}$$

Based on the energy balance it is possible to define a thermal or energetic COP or other characteristics. The thermodynamically correct input-output relation is without content and cannot express the thermodynamic losses

$$\eta_{\mathrm{th,td}} = \frac{\sum_i \nu_{\mathrm{P},i}\bar{h}_{\mathrm{P},i} + \bar{w}_{\mathrm{out}} + \sum_i \bar{q}_{\mathrm{out},i}}{\sum_i \nu_{\mathrm{E},i}\bar{h}_{\mathrm{E},i} + \bar{w}_{\mathrm{in}} + \sum_i \bar{q}_{\mathrm{in},i}} = 1\,. \tag{3.7}$$

All other relations are determined by the desired products and therefore depend on technological application conditions, which are subjective. For instance, the COP of a thermal power station with heat and power cogeneration is

$$\eta_{\mathrm{th}} = \frac{\bar{w}_{\mathrm{out}} - \bar{w}_{\mathrm{in}} + \bar{q}_{\mathrm{heat}}}{\sum_i \nu_{\mathrm{E},i}\bar{h}_{\mathrm{E},i} - \sum_i \nu_{\mathrm{P},i}\bar{h}_{\mathrm{P},i}} = \frac{\bar{w}_{\mathrm{out,net}} + \bar{q}_{\mathrm{heat}}}{\Delta_{\mathrm{R}}\bar{h}}\,. \tag{3.8}$$

As seen in this relation, work and heat are added though they are of very different thermodynamic qualities. For this reason the process potential and the loss situation can be analyzed better using the exergy concept rather than just the energy.

3.1.3 Equilibrium and Equilibrium Temperature

As the overwhelming majority of chemical reactions take place at approximately constant values of temperature and pressure, it is convenient to use the molar reaction Gibbs energy $\Delta_{\mathrm{R}}\bar{g}$ as the basis of the thermodynamic analysis of reactions. The negative value of $\Delta_{\mathrm{R}}\bar{g}$ is sometimes also called affinity of a reaction. $\Delta_{\mathrm{R}}\bar{g}$ characterizes the capability of the system to provide work at $T, p = const$ and a given composition of the system $\boldsymbol{x}$ related to the extent of the reaction ξ. If $\Delta_{\mathrm{R}}\bar{g} < 0$ (exergonic reaction), then the reaction is thermodynamically always possible. By contrast, if $\Delta_{\mathrm{R}}\bar{g} > 0$ (endergonic reaction), the reaction is possible only if work is supplied. If the reaction takes place at the equilibrium composition, maintained by the continuous addition of educts and the simultaneous continuous subtraction of products, no work is necessary and no work is performed ($\Delta_{\mathrm{R}}\bar{g} = 0$; equilibrium reaction). The exchange of energy is realized by heat only.

Because the value of $\Delta_{\mathrm{R}}\bar{g}$ is given by the first derivative of the Gibbs energy G of the reacting system with respect to the extent of reaction ξ at $T, p, \boldsymbol{x} = const$, the equilibrium is characterized by the minimum of the Gibbs energy of the system as a function of the extent of the reaction [3.4]

$$\Delta_{\mathrm{R}}\bar{g} = \left(\frac{\partial G}{\partial \xi}\right)_{T,\mathrm{p}} = 0\,. \tag{3.9}$$

Recall that, for a gas phase reaction, the equilibrium constant K_{f} equals the stoichiometric product of the component fugacities f_i (related to the reference pressure), i. e., $\prod_k (f_k/p_0)^{\nu_k}$. Alternatively, K_{a} equals the stoichiometric product of the component activities a_i in the case of condensed phases, $\prod_k (a_k)^{\nu_k}$. This provides a relation between the concentrations of the educts and products. Such equilibrium reactions without any work exchange (w, q-reactions with $\bar{w}_{\mathrm{el}} = 0$, i. e., reversible thermal reactions) are the reference case for the evaluation of either the thermal or the w, q-reactions.

The value of K can be fixed by choosing an appropriate temperature. If the value

$$K = 1, \quad (K_{\mathrm{f}} = 1 \text{ or } K_{\mathrm{a}} = 1) \tag{3.10}$$

at the corresponding equivalent temperature T^* is adopted, the basic Gibbs energy $\Delta_{\mathrm{R}}\bar{g}^{\mathrm{o}}$ calculated from the pure component data alone can be used instead of the reaction Gibbs energy $\Delta_{\mathrm{R}}\bar{g}$.

Since the equilibrium constants K are pressure-independent, or in the case of K_{a} are nearly pressure-independent, the equilibrium can be described using normal pressure data

$$\Delta_{\mathrm{R}}\bar{g} = \Delta_{\mathrm{R}}\bar{g}^{\mathrm{o}}\left(= \Delta_{\mathrm{R}}\bar{g}^{\mathrm{o}}_{\mathrm{p}(0)}\right) = \sum_k \nu_k \bar{g}_{ok} = 0 \quad (\text{at } T^* = T \text{ and } K = 1)\,. \tag{3.11}$$

The equivalent temperature T^* follows using the Gibbs–Helmholtz equation [3.5]

$$\Delta_R \bar{g}^o = \Delta_R \bar{h}^o - T\Delta_R \bar{s}^o \,, \tag{3.12}$$

and the molar basic reaction enthalpy as well as the molar basic reaction entropy, according to the pure component data of the components

$$T^* = \frac{\Delta_R \bar{h}^o}{\Delta_R \bar{s}^o} = \frac{\sum_k \nu_k \bar{h}_{ok}}{\sum_k \nu_k \bar{s}_{ok}} \,. \tag{3.13}$$

In contrast to the reaction enthalpy, the reaction entropy characterizes the change of the disorder in the system. It is also a measure of the thermodynamic quality of the reaction enthalpy. The reaction entropy expresses changes in the structural behavior of the system due to the chemical reaction. The entropy increases (positive reaction entropy, endotropic reaction) if the number of particles in the gas phase increases. This is caused by the stochastic motion of particles. In the opposite case the reaction entropy is negative (exotropic reaction) because gas phase particles disappear and therefore the disorder decreases. In a realistic reacting system, a chemical reaction always leads to an increase in entropy, which is to be transferred to the environment with the products or as heat.

For simplicity, in order to get the correct qualitative conclusions, the relatively unimportant temperature dependence of $\Delta_R \bar{h}^o$ and $\Delta_R \bar{s}^o$ is neglected (1st Ulich approximation, $\Delta_R \bar{c}_p^o = \sum_k \nu_k \bar{c}_p, ok = 0$). This results in a linear temperature dependence of the molar basic reaction Gibbs energy $\Delta_R \bar{g}^o$. It is obtained only from the Gibbs–Helmholtz equation and the standard values of the constituents at T_0 and p_0 (Ø). In most cases, the standard state is $T_0 = 298.15\,\mathrm{K}$ and $p_0 = p_{np} = 101.325\,\mathrm{k\,Pa}$, and the compounds are taken to be in their stable state. Then, for each temperature one has

$$\begin{aligned}\Delta_R \bar{g}^o \equiv \Delta_R \bar{g}^o_{p(0)} &= \Delta_R \bar{h}^{Ø} - T\Delta_R \bar{s}^{Ø} \\ &= -RT \ln K_f(T)\end{aligned} \tag{3.14}$$

and, for the special cases of $T = T_0$ and $T = T^*$,

$$\Delta_R \bar{g}^o_{T(0)} = \Delta_R \bar{h}^{Ø} - T_0 \Delta_R \bar{s}^{Ø} = \Delta_R \bar{g}^{Ø} \tag{3.15}$$

$$\Delta_R \bar{g}^o_{T^*} = \Delta_R \bar{h}^{Ø} - T^* \Delta_R \bar{s}^{Ø} = 0, \quad T^* = \frac{\Delta_R \bar{h}^{Ø}}{\Delta_R \bar{s}^{Ø}} \,. \tag{3.16}$$

In the reversible case, it is also possible to fix the temperature instead of equilibrium constant, $K = 1$. It is then necessary to vary the equilibrium constant. Using (3.14) and (3.16), it is possible to express the ratio of reaction temperature and equivalent reaction temperature as a function of the equilibrium constant

$$\begin{aligned}\frac{T}{T^*} &= \frac{\Delta_R \bar{s}^{Ø}}{\Delta_R \bar{s}^{Ø} - R \ln K_f(T)} \\ &= \frac{\Delta_R \bar{s}^{Ø}/R}{(\Delta_R \bar{s}^{Ø}/R) - \ln K_f(T)} \,.\end{aligned} \tag{3.17}$$

As seen in Fig. 3.1, the influence of the dimensionless reaction entropy on the variation of the reaction temperature for high entropy values is rather small.

If the equilibrium constant is fixed at $K = 1$, the reaction equilibrium can be characterized using only the standard quantities $\Delta_R \bar{h}^{Ø}$ and $\Delta_R \bar{s}^{Ø}$. This corresponds to a well-balanced ratio between educts and products. Furthermore, from an energy-engineering point of view, this choice of system composition gives the possibility to influence the direction of the reaction relatively simply by varying the initial amounts of the reacting components.

If the two quantities $\Delta_R \bar{h}^{Ø}$ and $\Delta_R \bar{s}^{Ø}$ have different signs, and the equivalent temperature is therefore not physical ($T^* < 0$), then the reaction cannot occur under thermal conditions near reversibility. An equilibrium state characterized by $K = 1$ can only be realized via a w, q-reaction.

3.1.4 Availability of Chemical Reactions

Availability is the maximal amount of work which a system is able to perform. It is a convenient generalized measure of the energetic performance of any

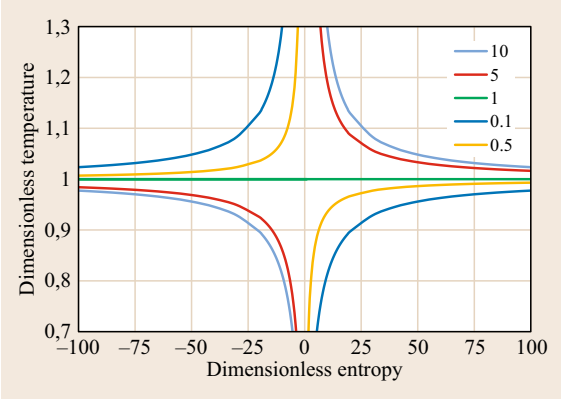


Fig. 3.1 Dimensionless reversible reaction temperature T/T^* as a function of the dimensionless standard reaction entropy $\Delta^R \bar{s}^{Ø}/R$ for various values of the equilibrium constants

technical system expressed in terms of work. All other forms of energy, such as heat, concentration or chemical energy may be expressed in terms of this quantity. This is not entirely correct due to the existence of chemical substances that cannot be produced by the supply of work only. Nevertheless, work remains a well-defined and convenient measure. Another problem is the necessity of defining the environment to calculate the availability. In a first approximation, this simply means pressure and temperature. In comparison with the chemical term, the influence of varying pressure and temperature (within their typical ranges) on the availability is often rather small. While for chemical reactions the differences of enthalpies and entropies are important, the definition of the chemical environment can frequently be neglected. The availability is often called exergy and is a state variable if the environmental conditions are fixed.

For a reversible thermal reaction the reaction Gibbs energy

$$\Delta_R \bar{g} = \Delta_R \bar{g}^o$$

is equal to zero and no chemical work is performed. The whole reaction enthalpy

$$\Delta_R \bar{h} = \Delta_R \bar{h}^o = \Delta_R \bar{h}^{\emptyset}$$

is exchanged with the environment in the form of heat. If the environmental temperature T_{en} is taken to be the standard temperature T_0, as it is common in the consideration of chemical reactions

$$T_{en} = T_0, \tag{3.18}$$

the reaction availability equals the exergy of exchanged heat.

The equation

$$\Delta_R \bar{g}^{\emptyset} = \Delta_R \bar{h}^{\emptyset} \left(1 - \frac{T_0}{T^*}\right) = \Delta_R \bar{h}^{\emptyset} \eta \left(\frac{T_0}{T^*}\right) = \bar{e}_q \tag{3.19}$$

can be obtained by combining the relations (3.15) and (3.16) at T^*, taking into account $K = 1$. This means that the temperature term can be viewed as a Carnot factor with T^* and $T_0 = T_{en}$ as the two relevant temperatures. The reaction Gibbs energy at standard conditions $\Delta_R \bar{g}^{\emptyset}$ corresponds to the availability (possible amount of work that could be performed, work potential) or the exergy of the reaction $\Delta_R \bar{e}_x$ or the reaction heat exergy $\bar{e}_q$ at the equivalent temperature T^*.

The ratio between the reaction Gibbs energy and the reaction enthalpy at standard conditions equals the Carnot factor or the normalized dimensionless exergy

$$\frac{\Delta_R \bar{g}^{\emptyset}}{\Delta_R \bar{h}^{\emptyset}} = \eta \left(\frac{T_0}{T^*}\right) = 1 - \frac{T_0}{T^*} = \hat{e}_q \,. \tag{3.20}$$

For different signs of reaction enthalpy and entropy this ratio becomes greater than one. As heat with a Carnot factor greater than one is not imaginable, it is reasonable to call this coefficient normalized reaction exergy

$$\Delta_R \hat{e}_x^{\emptyset} = \frac{\Delta_R \bar{g}^{\emptyset}}{\Delta_R \bar{h}^{\emptyset}} = \frac{\Delta_R \bar{e}_x^{\emptyset}}{\Delta_R \bar{h}^{\emptyset}} = \frac{\Delta_R \bar{h}^{\emptyset} - T_0 \Delta_R \bar{s}^{\emptyset}}{\Delta_R \bar{h}^{\emptyset}} \,. \tag{3.21}$$

In this case the chemical energy of the reaction is of higher quality than that of work, as was mentioned earlier.

In the majority of industrial applications, chemical reactions involve heat transfer only. In addition, chemical reactions can involve the transfer of work, delivering the availability of the reaction system, at least partially, to the environment (w, q-reactions). The work transfer can be realized under isothermal–isobaric conditions, for example in electrochemical reactions, as the consumption or production of electric power (electric work $\bar{w}_{el}$) since suitable electrochemical equipment exists. The relation to the basic electric potential difference E^o (F Faraday constant, $z_{\pm}$ charge number) at a given temperature is given by the Nernst equation

$$\Delta_R \bar{g}^o = \bar{w}^R_{el,rev} = -z_{\pm} F E^o \,. \tag{3.22}$$

The reversible electric work is the maximal amount of work produced by an exergonic reaction or the minimal amount of work necessary for an endergonic reaction at T, $p =$ constant and pure component flows, or at $K = 1$. The remaining reaction enthalpy is transferred as heat (3.2)

$$\Delta_R \bar{h}^{\emptyset} = \bar{w}_{el} + \bar{q} \,. \tag{3.23}$$

The relation to the Gibbs energy is provided by

$$\Delta_R \bar{g}^o - \bar{w}_{el} = \bar{q} - T \Delta_R \bar{s}^{\emptyset} \,. \tag{3.24}$$

Consider a reversible process, also maintaining the condition $K = 1$. We are interested in the temperature T_q of the heat $\bar{q}$ to be transferred and at which $\Delta_R \bar{g}^o - \bar{w}_{el} = 0$ holds. This temperature can be obtained as

$$T_q = \frac{\bar{q}}{\Delta_R \bar{s}^{\emptyset}} \,, \tag{3.25}$$

and one finally finds

$$\Delta_R \bar{g}^{\emptyset} - \bar{w}_{el} = \bar{q}\left(1 - \frac{T_0}{T_q}\right) . \tag{3.26}$$

In the reversible case, the available potential of a chemical reaction can be used for the production of work as well as heat of a certain temperature. Conversely, a potential required for a chemical reaction to proceed can be realized by the supply of work and heat to the system

$$\begin{aligned}\Delta_R \bar{g}^{\emptyset} &= \bar{w}_{el} + \bar{q}\left(1 - \frac{T_0}{T_q}\right) \\ &= \bar{w}_{el} + \left(\Delta_R \bar{h}^{\emptyset} - \bar{w}_{el}\right)\left(1 - \frac{T_0}{T_q}\right) .\end{aligned} \tag{3.27}$$

The availability of the reaction system is the sum of the electric energy and the exergy of the heat formed at reaction temperature T_q. In a dimensionless form (dividing by $\Delta_R \bar{g}^{\emptyset}$) one can write

$$\begin{aligned}1 &= w + q\left(1 - \frac{T_0}{T_q}\right) \text{ with } w = \frac{\bar{w}_{el}}{\Delta_R \bar{g}^{\emptyset}} \\ &\text{and } q = \frac{\Delta_R \bar{h}^{\emptyset} - \bar{w}_{el}}{\Delta_R \bar{g}^{\emptyset}} .\end{aligned} \tag{3.28}$$

The distribution of the availability between electrical work and heat in w, q-reactions can vary and this variation has a substantial influence on the temperature level of the heat. At $T_q = T_0$ the entire potential can be converted into electrical work or can be supplied as electrical work. The heat transfer, which is then necessary to satisfy the energy balance, is realized at standard temperature, at which there is no availability of heat.

The thermodynamic reaction variables describe only the transformation from educts to products and cannot characterize the thermodynamic quality of the single species involved. The standard state of the species is also not suitable for this as it is calculated from the elements in its stable state, but the expenditure to produce them is very different.

Availability of Chemical Substances

The energetic quality of each substance can be described by its availability. The latter is expressed by the exergy which is necessary to produce this species from the environment. The environmental state is characterized primarily by the environmental temperature T_{en} and pressure p_{en}, but also by the totality of environmental compounds j with molar chemical potential $\bar{\mu}_{j,en}$. The system of the environmental compounds is defined as the exergy-free state of the chemical equilibrium in the so-called thermodynamic environment. For a given set of elements and their ratios, it is obtained by considering the compounds following from these elements minimizing the Gibbs energy of the entire system. For practical reasons the equilibrium state is to be adjusted to the natural environment.

We do not discuss the problems associated with the definition of the environmental compounds in detail and the problem that our reality can be described with a certain degree of subjectivity only. This subjectivity arises because we live in a non-equilibrium world rather than in an equilibrium state. Nevertheless, it is possible to understand the production of each substance from environmental substances and energy in form of heat and work. The thermodynamic functions of these production reactions (PR) then are called production functions instead of formation functions. The exergy of a substance i to be considered is given by the work required for the reversible production of this substance from the environmental compounds [3.12, 13]. At environmental conditions, the exergy follows from the production Gibbs energy $\Delta^{PR}\bar{g}^{\emptyset}_{oi}$ or from the production enthalpy $\Delta^{PR}\bar{h}^{\emptyset}_{oi}$ and production entropy $\Delta^{PR}\bar{s}^{\emptyset}_{oi}$,

$$\begin{aligned}\bar{e}^{\emptyset}_{x,oi} &\equiv \Delta^{PR}\bar{e}^{\emptyset}_{x,oi} \,(= \bar{w}_{el,rev}) = \Delta^{PR}\bar{g}^{\emptyset}_{oi} \\ &= \Delta^{PR}\bar{h}^{\emptyset}_{oi} - T_{en}\Delta^{PR}\bar{s}^{\emptyset}_{oi} .\end{aligned} \tag{3.29}$$

The thermodynamic production quantities are obtained from the formation quantities or from the conventional quantities which are used correspondingly to the data situation [3.14]. This is done considering the stoichiometry of the particular reaction for the compound i (reaction educts, $\nu_{ji} < 0$; reaction products, $\nu_{ji} > 0$; compound i to be considered, $\nu_i = 1$)

$$\begin{aligned}\Delta^{PR}\bar{g}^{\emptyset}_{oi} &= \bar{g}_{conv,\,oi^{\emptyset}} + \sum_{j\neq i}\nu_{ji}\bar{g}^{\emptyset}_{conv,oj(i)} \\ &= \Delta^{F}\bar{g}^{\emptyset}_{oi} + \sum_{j\neq i}\nu_{ji}\Delta^{F}\bar{g}^{\emptyset}_{oj(i)} ,\end{aligned} \tag{3.30}$$

$$\bar{g}^{\emptyset}_{conv,oi} = \Delta^{F}\bar{h}^{\emptyset}_{oi} - T_0\bar{s}^{\emptyset}_{conv,oi} \tag{3.31}$$

$$\Delta^{PR}\bar{h}^{\emptyset}_{oi} = \Delta^{F}\bar{h}^{\emptyset}_{oi} + \sum_{j\neq i}\nu_{ji}\Delta^{F}\bar{h}^{\emptyset}_{oj(i)} , \tag{3.32}$$

$$\begin{aligned}\Delta^{PR}\bar{s}^{\emptyset}_{oi} &= \bar{s}^{\emptyset}_{conv,oi} + \sum_{j\neq i}\nu_{ji}\bar{s}^{\emptyset}_{conv,oj(i)} \\ &= \Delta^{F}\bar{s}^{\emptyset}_{oi} + \sum_{j\neq i}\nu_{ji}\Delta^{F}\bar{s}^{\emptyset}_{oj(i)} \\ \text{with}\quad \Delta^{F}\bar{s}^{\emptyset}_{oi} &= \frac{\Delta^{F}\bar{h}^{\emptyset}_{oi} - \Delta^{F}\bar{g}^{\emptyset}_{oi}}{T_0} .\end{aligned} \tag{3.33}$$

Table 3.1 Reaction of glucose and calcium oxide

Example: glucose	Example: calcium oxide
$6CO_2 + 6H_2O \rightarrow C_6H_{12}O_6(S) + 6O_2$	$CaCO_3(S1) \rightarrow CaO(S2) + CO_2$
$\Delta^{PR}\bar{h}^{\varnothing}_{o\,glu} = 2802.7\,kJ/mol$	$\Delta^{PR}\bar{h}^{\varnothing}_{o\,CaO} = 179.8\,kJ/mol$
$\Delta^{PR}\bar{s}^{\varnothing}_{o\,glu} = -0.2619\,kJ/mol\,K$	$\Delta^{PR}\bar{s}^{\varnothing}_{o\,CaO} = 0.1638\,kJ/mol\,K$
$\bar{e}^{\varnothing}_{x,o\,glu} = \Delta^{PR}\bar{g}^{\varnothing}_{o\,glu} = 2880.8\,kJ/mol$	$\bar{e}^{\varnothing}_{x,o\,CaO} = \Delta^{PR}\bar{g}^{\varnothing}_{o\,CaO} = 130.9\,kJ/mol$
$\hat{e}^{\varnothing}_{x,o\,glu} = 1.028$	$T^{*}_{glu} = -10\,699\,K$
$\hat{e}^{\varnothing}_{x,o\,CaO} = 0.728$	$T^{*}_{CaO} = 1097\,K$
$\bar{w}_{rev} = \Delta^{PR}\bar{h}^{\varnothing} - \bar{q}_{rev} = 2880.8\,kJ/mol$	$\bar{w}_{rev} = \Delta^{PR}\bar{h}^{\varnothing} - \bar{q}_{rev} = 130.9\,kJ/mol$
$\bar{q}_{rev} = -78.1\,kJ/mol$	$\bar{q}_{rev} = 48.9\,kJ/mol$

The following relations hold at any temperature

$$\bar{e}_{x,oi} = \bar{w}_{el} + \bar{e}_q = \bar{w}_{el} + \left(1 - \frac{T_{en}}{T}\right)\bar{q}\,, \tag{3.34}$$

$$\begin{aligned}\bar{e}_{x,oi} &= \Delta^{PR}\bar{g}_{oi} + \left(1 - \frac{T_{en}}{T}\right) T\Delta^{PR}\bar{s}_{oi} \\ &= \Delta^{PR}\bar{h}_{oi} - T_{en}\Delta^{PR}\bar{s}_{oi}\,,\end{aligned} \tag{3.35}$$

$$\begin{aligned}\bar{e}_{x,oi} &= \Delta^{PR}\bar{h}^{\varnothing}_{oi} - T_{en}\Delta^{PR}\bar{s}^{\varnothing}_{oi} \\ &\left(+\int_{T_{en}}^{T}\Delta^{PR}\bar{c}_{p,oi}\mathrm{d}T - T_{en}\int_{T_{en}}^{T}\frac{\Delta^{PR}\bar{c}_{p,oi}}{T}\mathrm{d}T\right).\end{aligned} \tag{3.36}$$

The temperature dependence of the exergy is obtained solely from the temperature dependences of the enthalpy and entropy. By using the 1st Ulich approximation as discussed before

$$\begin{aligned}\bar{e}_{x,oi} &= \bar{e}^{\varnothing}_{x,oi} = \Delta^{PR}\bar{e}^{\varnothing}_{x,oi} = \Delta^{PR}\bar{h}^{\varnothing}_{oi} - T_{en}\Delta^{PR}\bar{s}^{\varnothing}_{oi} \\ &= \Delta^{PR}\bar{g}^{\varnothing}_{oi}\,,\end{aligned} \tag{3.37}$$

the exergy of the compound i follows as a temperature-independent quantity. At each temperature, the analysis can then proceed on the basis of the standard exergies.

A convenient evaluation of the quality of the energy stored in a compound is obtained if the exergy is related to the production enthalpy. This results in a normalized dimensionless exergy $\hat{e}_{x,oi}$. By introducing simultaneously the equivalent temperature T^{*}_{i} of the substance i ($\Delta^{PR}\bar{g}_{oi} = 0$), the equation

$$\begin{aligned}\hat{e}_{x,oi} = \hat{e}^{\varnothing}_{x,oi} &= \frac{\bar{e}^{\varnothing}_{x,oi}}{\Delta^{PR}\bar{h}^{\varnothing}_{oi}} = \frac{\Delta^{PR}\bar{g}^{\varnothing}_{oi}}{\Delta^{PR}\bar{h}^{\varnothing}_{oi}} \\ &= 1 - T_{en}\frac{\Delta^{PR}\bar{s}^{\varnothing}_{oi}}{\Delta^{PR}\bar{h}^{\varnothing}_{oi}} = 1 - \frac{T_{en}}{T^{*}_{i}} \\ \text{with } T^{*}_{i} &= \frac{\Delta^{PR}\bar{h}^{\varnothing}_{oi}}{\Delta^{PR}\bar{s}^{\varnothing}_{oi}}\end{aligned} \tag{3.38}$$

follows as a measure for the quality of the compound energy. Here, *equivalent* means that at this temperature the exergy of the compound is equal to the availability of the heat given by the production enthalpy.

The formulation of the exergy equation in the form

$$\begin{aligned}\bar{e}_{x,oi} = \bar{e}^{\varnothing}_{x,oi} &= \frac{\bar{e}^{\varnothing}_{x,oi}}{\Delta^{PR}\bar{h}^{\varnothing}_{oi}}\Delta^{PR}\bar{h}^{\varnothing}_{oi} = \hat{e}^{\varnothing}_{x,oi}\Delta^{PR}\bar{h}^{\varnothing}_{oi} \\ &= \left(1 - \frac{T_{en}}{T^{*}_{i}}\right)\Delta^{PR}\bar{h}^{\varnothing}_{oi}\end{aligned} \tag{3.39}$$

shows that each compound can be described thermodynamically by a quantitative and a qualitative factor. The qualitative factor corresponds to the Carnot factor formed by using the equivalent temperature. This means that the equivalent temperature is also very important for the evaluation of the quality of the chemical energy of a compound.

In the following scheme, the production reaction of glucose (important in connection with the assimilation) and calcium oxide (calcination process) from the environmental compounds CO_2 (V), H_2O (L), O_2 (V) and $CaCO_3$ (S), CO_2 (V), respectively, are illustrated in Table 3.1.

In contrast to the temperature of a heat or the thermodynamic mean temperature of an isobaric change of state, the equivalent temperature can also take negative values. This occurs whenever the production enthalpy and the production entropy, the ratio of which determine the equivalent temperature, have different signs. A negative equivalent temperature results in a normalized exergy which is greater than one, $\hat{e}_{x,oi} > 1$ (Table 3.1; the example of glucose). This means that the relevant substance cannot be formed solely by the supply of work. Instead, it is necessary to supply work or energy that is able to perform work (such as solar radiation) and simultaneously to deliver heat to the environment. This fact manifests itself for example in the necessary evaporation of water from the leaves of plants for the

transfer of heat, produced in photosynthesis, to the outside of the assimilation system.

The production of substances from environmental compounds can be viewed as the manufacturing of energetically valuable materials. These can then be applied to produce other materials or in energetic procedures, such as chemical reactions. Production enthalpy and production exergy have a double function. On the one hand, they describe quantity and quality of the energy stored in a material. On the other hand, they characterize the quantity and quality of the energy transferred to or from the environment during the reversible process of the production or the disposal of materials. Figure 3.2 displays the normalized production exergies of some compounds in comparison with the exergy of heat and work.

Availability of Electrochemical Reactions

For a reversible thermal reaction, for example exothermic, the whole reaction availability is transformed into the exergy of heat at temperature T^*. A higher temperature is impossible on account of insufficient availability of the reaction system. By increasing the availability through the supply of electrical energy it is possible to raise the reaction temperature. By contrast, if part of the availability of the reaction is converted to electricity, the remaining availability of the system allows only for a lower reaction temperature. It becomes apparent that, except for the point T^*, the whole temperature axis can be covered by electrochemical reactions. Electrochemical reactions are characterized by splitting the reaction availability in the way described above.

Since, in general, several substances are involved in a chemical reaction, the resulting basic reaction Gibbs energy is the combination of the pure component values

$$\begin{aligned}\Delta_R \bar{e}_x^{\varnothing} &= \sum_k \nu_k \Delta^{PR} \bar{e}_{x,ok}^{\varnothing} = \sum_k \nu_k \Delta^{PR} \hat{e}_{x,ok}^{\varnothing} \Delta^{PR} \bar{h}_{ok}^{\varnothing} \\ &= \Delta_R \bar{h}^{\varnothing} - T_{en} \Delta_R \bar{s}^{\varnothing} = \Delta_R \bar{g}^{\varnothing} \,. \end{aligned} \tag{3.40}$$

In addition, the complete reaction is characterized by a quality factor

$$\begin{aligned}\Delta_R \hat{e}_x^{\varnothing} &= \frac{\Delta_R \bar{e}_x^{\varnothing}}{\Delta_R \bar{h}^{\varnothing}} = \frac{\Delta_R \bar{g}^{\varnothing}}{\Delta_R \bar{h}^{\varnothing}} = \frac{\Delta_R \bar{h}^{\varnothing} - T_{en} \Delta_R \bar{s}^{\varnothing}}{\Delta_R \bar{h}^{\varnothing}} \\ &= 1 - \frac{T_{en}}{T^*} \quad \text{with } T^* = \frac{\Delta_R \bar{h}^{\varnothing}}{\Delta_R \bar{s}^{\varnothing}} \,, \end{aligned} \tag{3.41}$$

where T^* characterizes the temperature of an equilibrium reaction with $K = 1$. At each temperature T_q of the reversible w, q-reaction, the reaction exergy is to be compensated on the basis of an exergy balance by the supply of exergy in the form of (electrical) work and exergy of heat from outside. Describing the exergy of heat with the help of the Carnot factor, it follows that

$$\bar{e}_q = \hat{e}_q \bar{q} = \frac{T_q - T_{en}}{T_q} \bar{q} \,. \tag{3.42}$$

By substituting the heat or the work using the energy balance of the reaction, the reaction exergy can be written as

$$\begin{aligned}\Delta_R \bar{e}_x^{\varnothing} &= \bar{w}_{el} + \bar{e}_q = (\Delta_R \bar{h}^{\varnothing} - \bar{q}) + \hat{e}_q \bar{q} \\ &= \bar{w}_{el} + \hat{e}_q (\Delta_R \bar{h}^{\varnothing} - \bar{w}_{el}) \,. \end{aligned} \tag{3.43}$$

The temperature T_q and therefore the exergy of the heat transferred are determined by the ratio of the heat and the work that are exchanged. This ratio has a different influence on the supply of work to the system depending on whether the reaction is exotropic or endotropic. The part of the reaction enthalpy supplied as heat determines the reversible temperature of the w, q-reaction

$$T_q = \frac{\bar{q}}{\Delta_R \bar{s}^{\varnothing}} = \frac{\Delta_R \bar{h}^{\varnothing} - \bar{w}_{el}}{\Delta_R \bar{s}^{\varnothing}} = T^* - \frac{\bar{w}_{el}}{\Delta_R \bar{s}^{\varnothing}} \tag{3.44}$$

and the quality factor $\hat{e}_q$ of the heat transferred in a reaction proceeding near equilibrium. From this, the following three relations can be derived

$$\begin{aligned}&\frac{\bar{q}}{\Delta_R \bar{h}^{\varnothing}} = \frac{T_q}{T^*}, \quad \frac{\bar{w}_{el}}{\Delta_R \bar{h}^{\varnothing}} = \frac{T^* - T_q}{T^*}, \\ &\frac{\bar{w}_{el}}{\bar{q}} = \frac{T^* - T_q}{T_q} \,. \end{aligned} \tag{3.45}$$

These can be interpreted as formulae for the dimensionless heat, dimensionless work and for their ratio. The heat may be larger than the reaction enthalpy, leading to a heat temperature that is higher than the equivalent temperature. The sign of heat and enthalpy may be different, corresponding to a negative sign of the equivalent temperature. If the equivalent temperature is too high for heat exchange, it is useful to deliver part of the availability as work and lower the heat temperature. In order to illustrate the energetic situation, a temperature–energy diagram is suitable.

For chemical reactions with radiation, the availability can be split into exergy of radiation and exergy of heat

$$\begin{aligned}\Delta_R \bar{e}_x^{\varnothing} &= \bar{e}_q + \bar{e}_{qr} = \hat{e}_q \bar{q} + \hat{e}_{qr} \bar{q}_r \\ &= \hat{e}_{qr} \bar{q}_r + \hat{e}_q (\Delta_R \bar{h}^{\varnothing} - \bar{q}_r) \,. \end{aligned} \tag{3.46}$$

The reversible temperature of the heat is calculated using the exergy balance and depends on the radiation temperature and the exchanged heat

$$T_q = T_r \frac{\bar{q}}{\bar{q} - \Delta_R \bar{h}^{\varnothing} \frac{T^* - T_r}{T^*}} = T^* \frac{\Delta_R \bar{h}^{\varnothing} - \bar{q}_r}{\Delta_R \bar{h}^{\varnothing} - \bar{q}_r \frac{T^*}{T_r}} \,. \tag{3.47}$$

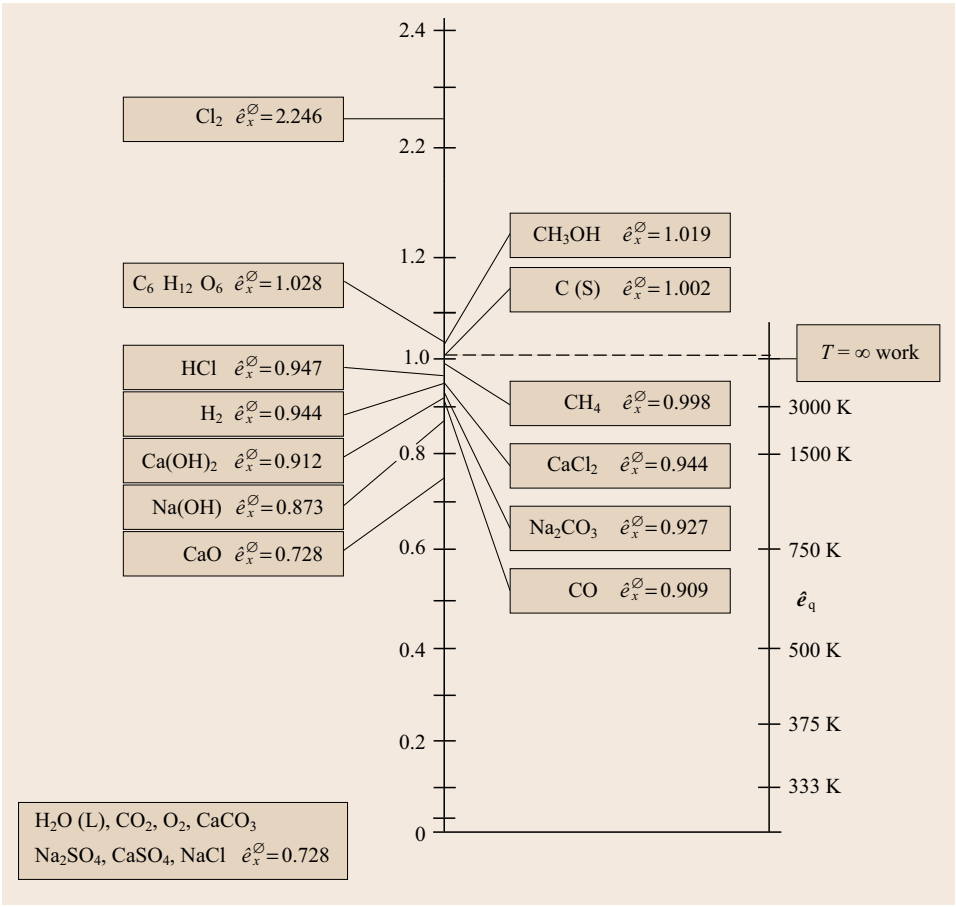


Fig. 3.2 Normalized standard exergy of some substances as well as of work and heat along the dimensionless exergy axis

In analogy to w, q-reactions, the ratio of heat and reaction enthalpy is given by the ratio of two Carnot factors. The first Carnot factor is defined by the equivalent temperature and the radiation temperature, the second by the heat temperature and the radiation temperature

$$\frac{\bar{q}}{\Delta_R \bar{h}^{\varnothing}} = \frac{\frac{T^*-T_r}{T^*}}{\frac{T_q-T_r}{T_q}} . \qquad (3.48)$$

Example of an electrochemical reaction. The relations (3.43)–(3.48) explained before will now be applied to the reaction of O_2 and H_2 (Table 3.2).

$$\frac{1}{2}O_2(V) + H_2(V) \rightarrow H_2O ;$$
$$\Delta_R \bar{h}^{\varnothing} = -241.9\,\mathrm{kJ/mol} ,$$
$$\Delta_R \bar{s}^{\varnothing} = -0.04506\,\mathrm{kJ/mol\,K} ,$$
$$\Delta_R \bar{e}_x^{\varnothing} = \Delta_R \bar{g}^{\varnothing} = -228.4\,\mathrm{kJ/mol} ,$$
$$\Delta_R \hat{e}^{\varnothing} = 0.944, \quad T^* = 5367\,\mathrm{K} .$$

These data are valid for the equilibrium constants

$$K_f = 1 \quad \text{or} \quad K_a = 1$$

and thus provide an impression of process parameters near the equilibrium.

Under realistic reaction conditions, the equilibrium constant is not unity but depends on the species concentrations. The molar reaction Gibbs energy becomes

$$\Delta_R \bar{g} = \Delta_R \bar{g}^{o} + RT \ln \prod_k (f_k / p_0)^{\nu_k} \qquad (3.49)$$

or, for condensed phases

$$\Delta_R \bar{g} = \Delta_R \bar{g}^{o} + RT \ln \prod_k (a_k)^{\nu_k} . \qquad (3.50)$$

Correspondingly, the Nernst equation

$$\Delta_R \bar{g} = -z_{\pm} FE \qquad (3.51)$$

describes the reversible cell potential under realistic process conditions,

$$\Delta_R \bar{g} = \Delta_R \bar{g}^o (= \Delta_R \bar{g}^o_{p(0)}) = \sum_k \nu_k \bar{g}_{ok} = 0$$
$$(\text{ at } T^* = T \text{ and } K = 1) \,. \tag{3.52}$$

The Nernst equation can be written separately for each half-cell reaction, i. e., for anode and cathode

$$\Delta_R \bar{g} = \Delta_R \bar{g}_a + \Delta_R \bar{g}_c \,, \tag{3.53}$$
$$\Delta_R \bar{g}_a = \Delta_R \bar{g}^o_a + RT \ln \prod_{ak} (a_{ak})^{\nu_{ak}} \,, \tag{3.54}$$
$$\Delta_R \bar{g}_c = \Delta_R \bar{g}^o_c + RT \ln \prod_{ck} (a_{ck})^{\nu_{ck}} \,. \tag{3.55}$$

Together with (3.51), the Nernst equation expresses the dependence of the cell potential on the species concentrations. The latter can for example be expressed as fugacities or activities

$$E = E^0 - \frac{RT}{z_\pm F} \ln \prod_k (a_k)^{\nu_k} = E_a + E_c \,. \tag{3.56}$$

Each half-cell reaction occurs on the electrode surface in the electric double layer, where the chemical potential difference is compensated by the electric potential difference

$$\Delta_R \bar{g}_a = -zFE_a, \quad \Delta_R \bar{g}_c = -zFE_c \,. \tag{3.57}$$

The double layer has to be crossed by ions and neutral species moving to or from the electrode. This holds for all electrode types, such as metal–ion, ion–ion, metal-insoluble salt or gas electrodes. The formation of ions or neutral species is associated with the formation of a temporary activation complex. It is kinetically limited.

Exergy

The availability or exergy of chemical substances or reactions or of systems in general is the maximum amount of work that can be produced by transforming the system to the environmental state. This statement implies that in realistic processes the produced amount of work is smaller. The dissipation of part of the availability leads to an exergy loss according to the second law of thermodynamics. By including this exergy loss term, it is possible to express the second law of thermodynamics of realistic or irreversible processes as an exergy equation

$$\sum_i E_{in,i} = \sum_i E_{out,i} + \sum_j \Delta E_{loss,j} \,. \tag{3.58}$$

The exergy input and output can contain the exergy of substances, heat, radiation or work. The exergy loss contains all kinds of irreversibilities. For an electrochemical reaction the general exergy balance is

$$\sum_i \nu_{E,i} \bar{e}_{E,i} + \bar{w}_{in} + \hat{e}_{q,in} \bar{q}_{in} = \sum_i \nu_{P,i} \bar{e}_{P,i} + \bar{w}_{out} + \hat{e}_{q,out} \bar{q}_{out} + \sum_j \Delta \bar{e}_{loss,j} \,. \tag{3.59}$$

A purely thermodynamic efficiency of the process is given by the output–input relation; in the reversible case it equals unity

$$\eta_{ex,td} = \frac{\sum_i \nu_{P,i} \bar{e}_{P,i} + \bar{w}_{out} + \hat{e}_{q,out} \bar{q}_{out}}{\sum_i \nu_{E,i} \bar{e}_{E,i} + \bar{w}_{in} + \hat{e}_{q,in} \bar{q}_{in}} \,. \tag{3.60}$$

In most cases, not all of the outputs are desired. The exergetic process COP is defined as the ratio of the desired output and the exergetic expenditure. This characterization by an exergetic process COP is not an objective one, as in different situations different products are desired. For a hydrogen fuel cell it can be given by

$$\eta_{ex,wq} = \frac{\bar{w}_{out} + \hat{e}_{q,out} \bar{q}_{out}}{\sum_i \nu_{E,i} \bar{e}_{E,i} + \bar{w}_{in} + \hat{e}_{q,in} \bar{q}_{in}} \text{ or}$$
$$\eta_{ex,w} = \frac{\bar{w}_{out}}{\bar{e}_{hy}} \,, \tag{3.61}$$

depending on whether work and heat or only heat are desired. For an electrolysis process with two desired products, for instance hydrogen and sodium hydroxide, one has

$$\eta_{ex,el} = \frac{\nu_{hy} \bar{e}_{hy} + \nu_s \bar{e}_s}{\sum_i \nu_{E,i} \bar{e}_{E,i} + \bar{w}_{in} + \hat{e}_{q,in} \bar{q}_{in}} \,. \tag{3.62}$$

Also in the reversible case, the exergetic process COP can be less than unity because there can be exergetic outputs that are not desired and which therefore represent an external loss. It can also be useful to express

Table 3.2 Reaction of hydrogen and oxygen varation of the part of reversible work and rection temperature

Variant A	Variant B	Variant C
$\bar{w} = 0$	$\bar{w} = 0.5\,\bar{w}_{rev}$ $= -114.2\,\text{kJ/mol}$	$\bar{w} = 0.75\,\bar{w}_{rev}$ $= -171.3\,\text{kJ/mol}$
$\bar{q} = -241.9\,\text{kJ/mol}$	$\bar{q} =$ $-127.7\,\text{kJ/mol}$	$\bar{q} = \bar{q}_{rev}$ $= -70.6\,\text{kJ/mol}$
$T_q = T^* = 5367\,\text{K}$	$T_q = 2834\,\text{K}$	$T_q = 1567\,\text{K}$

the efficiency using a complementary characteristic, the exergy loss coefficient

$$\varepsilon_{\mathrm{ex,td}} = 1 - \eta_{\mathrm{ex,td}} = \frac{\sum_{\mathrm{j}} \Delta \bar{e}_{\mathrm{loss,j}}}{\sum_i \nu_{\mathrm{E},i} \bar{e}_{\mathrm{E},i} + \bar{w}_{\mathrm{in}} + \hat{e}_{\mathrm{q,in}} \bar{q}_{\mathrm{in}}} \,. \tag{3.63}$$

This characteristic has the advantage of making the additive properties of the loss terms manifest

$$\begin{aligned} \varepsilon_{\mathrm{ex,td}} &= \sum_{\mathrm{j}} \frac{\Delta \bar{e}_{\mathrm{loss,j}}}{\sum_i \nu_{\mathrm{E},i} \bar{e}_{\mathrm{E},i} + \bar{w}_{\mathrm{in}} + \hat{e}_{\mathrm{q,in}} \bar{q}_{\mathrm{in}}} \\ &= \sum_{\mathrm{j}} \lambda_{\mathrm{loss,j}} \,. \end{aligned} \tag{3.64}$$

Exergy Loss

There are very different causes for exergy loss in electrochemical reactions, beginning with the educt preparation before the reaction, the electrochemical reaction itself and finally the product separation.

Educt preparation consists of the arrangement of the necessary pressure, concentration and temperature by pumping, mixing or purifying and heating, with the typical exergy losses of these operations. In some cases chemical reactions are necessary, such as the precipitation of dangerous or harmful substances, water treatment, and conversion of the feed to the required reactive components (for instance, the conversion of hydrocarbons to hydrogen and its purification).

Product separation and conditioning is often associated with evaporation, sludge treatment and separation of unreacted components as well as vacuuming, cooling and purification. However, the exergy consumption and, eventually, the exergy loss of these operations are mostly unimportant in comparison to the energy intensive electrochemical reaction step.

An electrochemical reaction can be described by two half-cell reactions. The anodic reaction can be represented as the formation of ions and electrons from neutral species, for instance two protons and two electrons from a hydrogen molecule. This is an oxidation reaction. The cathodic reaction is, by analogy, the recombination of electrons with ions to form neutral species and is, correspondingly, a reduction reaction. Electrode reactions are often associated with phase change (gas–liquid or liquid–solid), which requires a suitable electrode construction. Each of these half-cell reactions takes place in a double layer and all neutral species, ions or electrons involved must pass through these layers.

The double layer appears on all contact surfaces between liquid and solid phases. On electrodes the double layer is of special importance because of the existence of an electrochemical potential. The first layer consists of a thin region of electrons or gaps inside the electrodes. The second layer is situated in the liquid phase, also in a rather small region of charged species. This second layer can be further split in two sublayers. The first of these sublayers is relatively fixed. It is localized near the surface of the electrode due to charge interaction and it is partially surrounded by solvent molecules. The second of these sublayers contains charged species at a certain distance from the surface, which are shifting more or less freely under the influence of thermal motion, diffusion and electrical interaction. An alternative view of the second layer is as follows:

1. Its first sublayer is approximately described as a single layer of adsorbed charged species, the Helmholtz layer
2. The second sublayer is a diffuse layer with an exponential decrease of the electric potential, the Gouy–Chapman layer or a combination of them, the Stern layer [3.7] (Fig. 3.3).

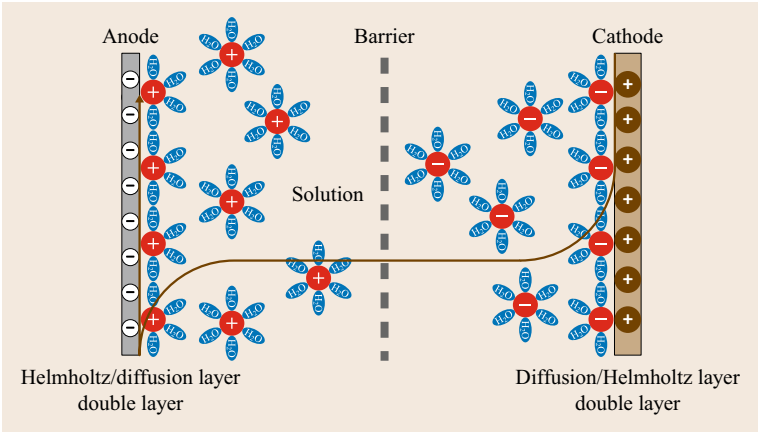


Fig. 3.3 Schematic illustration of an anodic and cathodic double layer in a fuel cell

In most cases, crossing this double layer is the limiting step of the electrochemical reaction and therefore important for the driving force consumption and, eventually, for irreversibilities. The only way to calculate these irreversibilities is the entropy balance. In the simplest case, the transfer of heat $\bar{q}_1 = \bar{q}_2$ from temperature T_{m1} to temperature T_{m2} satisfies the relation

$$\frac{\bar{q}_2}{T_{\mathrm{m2}}} = \frac{\bar{q}_1}{T_{\mathrm{m1}}} + \Delta\bar{s}_{\mathrm{c}} \,. \tag{3.65}$$

Hence, the heat exchange entropy creation is

$$\Delta\bar{s}_{\mathrm{c}} = \bar{q}_1 \frac{T_{\mathrm{m1}} - T_{\mathrm{m2}}}{T_{\mathrm{m1}} T_{\mathrm{m2}}} \,. \tag{3.66}$$

If the exothermic reaction proceeds at temperature $T_{\mathrm{m1}} = T_{\mathrm{R}}$, and the temperature of cooling is $T_{\mathrm{m2}} = T_{\mathrm{mcw}}$, the exergy loss can be calculated as

$$\Delta\bar{e}_{\mathrm{loss}} = T_{\mathrm{en}} \bar{q}_{\mathrm{R}} \frac{T_{\mathrm{R}} - T_{\mathrm{mcw}}}{T_{\mathrm{R}} T_{\mathrm{mcw}}} \,. \tag{3.67}$$

Analogously, the entropy creation of an electrochemical reaction is given by the reaction entropy minus the entropy of the supplied heat

$$\Delta\bar{s}_{\mathrm{c}} = \Delta_{\mathrm{R}}\bar{s}^{\mathrm{o}} - \frac{\bar{q}}{T_{\mathrm{R}}} = \Delta_{\mathrm{R}}\bar{s}^{\mathrm{o}} - \frac{\Delta_{\mathrm{R}}\bar{h}^{\mathrm{o}} - \bar{w}_{\mathrm{el}}}{T_{\mathrm{R}}} \,. \tag{3.68}$$

Using (3.44) and (3.66), one can derive that

$$\Delta\bar{s}_{\mathrm{c}} = \frac{\bar{q}}{T_{\mathrm{q}}} - \frac{\bar{q}}{T_{\mathrm{R}}} = (\Delta_{\mathrm{R}}\bar{h}^{\mathrm{o}} - \bar{w}_{\mathrm{el}}) \frac{T_{\mathrm{q}} - T_{\mathrm{R}}}{T_{\mathrm{q}} T_{\mathrm{R}}} \,, \tag{3.69}$$

i. e., the reaction irreversibilities can be understood as irreversible heat exchange between the reversible reaction temperature and the real reaction temperature, assuming completeness of the reaction. In this case all irreversibilities of chemical and physical kinetics and of electrical resistance are expressed as a temperature difference.

Another possibility to describe exergy loss is to fix the reaction temperature and to express irreversibilities as loss of electrochemical potential or simply as voltage loss (if the cell current is given). The pure reaction loss depends on the driving force and follows from the reaction rate and the current density.

Using the Arrhenius equation, the overall reaction rate k can be expressed as exchange current density $j = l/A$

$$k = K \exp\left(-\frac{\Delta_{\mathrm{R}}\bar{g}}{RT}\right) \,, \tag{3.70}$$

$$j_0 = zFk = zFK \exp\left(-\frac{\Delta_{\mathrm{R}}\bar{g}}{RT}\right) \,. \tag{3.71}$$

Near the equilibrium the current density is proportional to the driving force or the irreversibilities

$$j = j_0 \frac{zF\Delta E_{\mathrm{r,loss}}}{RT} \,. \tag{3.72}$$

These reaction irreversibilities are expressed as potential loss or, in case of electrolysis processes, as overpotential, and represent the reaction resistance

$$R_{\mathrm{r}} = \frac{RT}{j_0 zF} \,. \tag{3.73}$$

Away from the equilibrium, this proportionality is lost and the dependence of the reaction rate on the driving force can be described using the Tafel equation [3.15].

This equation, found by Tafel empirically in 1905, gives a logarithmic correlation between overpotential of anode and cathode and reaction rate or current density, as seen in Fig. 3.4

$$\Delta E_{\mathrm{ar,loss}} = \frac{RT}{\alpha_{\mathrm{a}} zF} \ln\left(\frac{j_{\mathrm{a}}}{j_0}\right)$$

$$\text{and } \Delta E_{\mathrm{cr,loss}} = \frac{RT}{(1-\alpha_{\mathrm{a}})zF} \ln\left(\frac{j_{\mathrm{c}}}{j_0}\right) \,. \tag{3.74}$$

Here α_{a} is the anodic cross factor or symmetry factor and $\alpha_{\mathrm{c}} = 1 - \alpha_{\mathrm{a}}$ the cathodic cross factor. The symmetry factor is usually close to 0.5. The higher the overpotential the more ions are produced or consumed, which implies that their transport to or from the double layer becomes important. If the driving force is very high, the current is not limited by reaction but by diffusion from the electrolyte bulk to the double layer [3.16]. Depending on the electrode design and reactor construction,

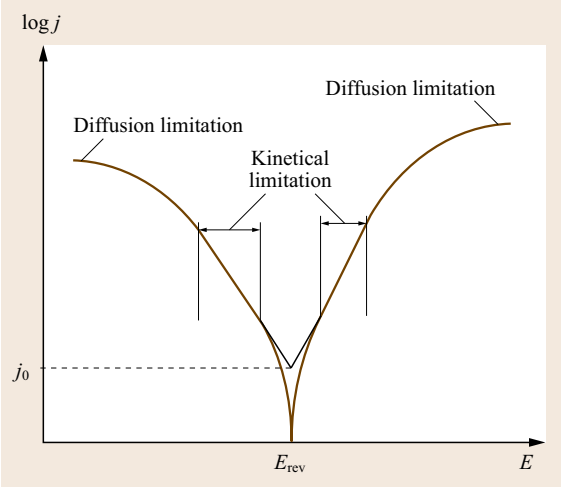


Fig. 3.4 Cathodic and anodic slope as function of the current density, Tafel plot

one observes a limiting current density for both anode and cathode, $j_{a,l}$ and $j_{c,l}$. This limiting current depends on the ion concentration difference between the bulk and the phase interface, as well as on the distance between them, according to Fick's law

$$j = -zFD\frac{\delta c}{\delta x} = -zFD\frac{c_0 - c_{a,l}}{\delta} \,. \tag{3.75}$$

If all ions are consumed, ($c_0 = 0$), the limiting current is

$$j_{a,l} = zFD\frac{c_{a,l}}{\delta} \,. \tag{3.76}$$

The concentration difference, which is also the driving force, leads to additional irreversibilities. These can be expressed in terms of entropy creation or as potential loss (overpotential, Fig. 3.5)

If diffusion is the limiting step, the overpotential is given by the Nernst equation

$$\Delta E_{ad,loss} = \frac{RT}{zF}\ln\left(1 - \frac{j}{j_{a,l}}\right) \,. \tag{3.77}$$

Another cause of potential loss is related to the ohmic resistance of the electrolyte. The electrical conductivity of electrolytes depends on the type and concentration of ions. Important properties in this context are the molar conductivity $\Lambda_m = \chi/c$, the ratio between electrical conductivity and ion concentration, and the ion mobility $u = v/E$, the ratio between ion velocity and electrical field strength. They appear in the relations

$$\Delta E_{ohmic,loss} = jR_{el} = \frac{jx}{\Lambda_m cA} = \frac{jx}{FucA} \,. \tag{3.78}$$

If required, an analogous term for the resistance of a barrier may be added separately. Unfortunately, there are also other causes for current loss, for instance self diffusion. Besides reaction and heat transfer, there are also other reasons for irreversibilities, for instance, mixing entropy creation for ideal gas

$$\Delta\bar{s}_c = \sum_k \Delta\bar{s}_{ck} = \sum_k \nu_k \bar{c}_{p,k} \ln\frac{p}{p_k} \,, \tag{3.79}$$

throttling entropy creation for ideal gas

$$\Delta\bar{s}_c = \sum_k \nu_k R \ln\frac{p_1}{p_2} \,, \tag{3.80}$$

and thermal mixing entropy creation for constant heat capacities

$$\Delta\bar{s}_c = \sum_k \nu_k \bar{c}_{p,k} \ln\frac{T_m}{T_k}, \quad T_m = \frac{\sum_k \nu_k \bar{c}_{p,k} T_k}{\sum_k \nu_k \bar{c}_{p,k}} \,. \tag{3.81}$$

The complete exergy loss is given by

$$\Delta\bar{e}_{loss} = T_{en} \sum_i \Delta\bar{s}_{ci} \,. \tag{3.82}$$

All irreversibilities occurring in the process lead to the increase of entropy export with the heat or to additional consumption of work instead of heat.

Dissipative Work

The dissipative work, also called lost work, is defined as the difference between the actually exchanged work of a process and the work that would be exchanged in the reversible case. In electrolysis reactions, the supplied work is significantly higher than the thermodynamically required minimal work. However, the difference

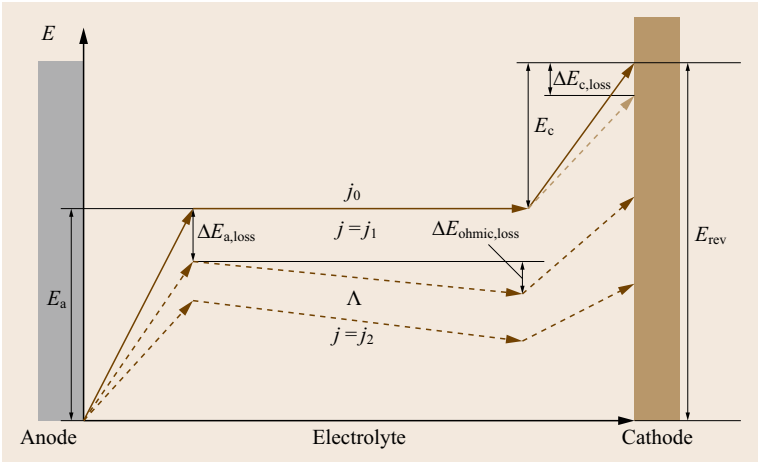


Fig. 3.5 Potential field of a fuel cell in the reversible case and for various current densities

between exchanged work and reversible work it is not equal to the exergy loss of the process. The additional supplied work is dissipated into thermal energy at process temperature. It therefore either substitutes heat that otherwise would have to be supplied to the system or it is transferred to the environment. As the work is entropy-free, the entropy of the dissipated work equals the entropy of the substituted heat

$$\Delta \bar{e}_{\mathrm{loss}} = T_{\mathrm{en}} \Delta \bar{s}_{\mathrm{c}} = T_{\mathrm{en}} \frac{\bar{w} - \bar{w}_{\mathrm{rev}}}{T_{\mathrm{R}}} \,. \tag{3.83}$$

The higher the reaction temperature, the smaller the exergy loss of the supplied work. Equation (3.83) also characterizes the exergy loss of a fuel cell because the sign of the produced work is negative and the produced work is smaller than the reversible work. In the case of a fuel cell, the heat delivered as a result of dissipation has some exergy, which in principle can be transformed into work. This is not the only reason why a higher process temperature is advantageous. It also decreases the overpotential for reaction activation and diffusion. The reduction of dissipation work with growing reaction temperature can be higher than the reduction of the reversible work of a fuel cell. Hence the produced work of a high-temperature fuel cell can be significantly increased by using the high-temperature heat of dissipation in a gas turbine and, subsequently, in a conventional vapor power station for additional work production.

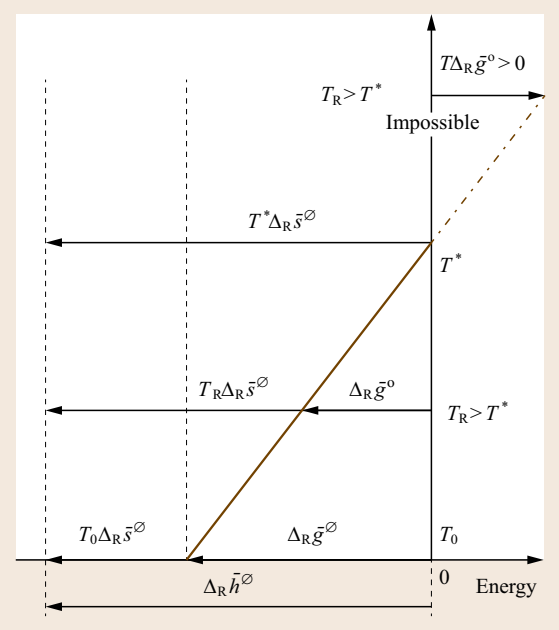


Fig. 3.6 Gibbs reaction energy for an exothermic–exotropic reaction in the temperature–energy diagram (*impossible* means impossible at $K = 1$ without the supply of work)

3.1.5 Temperature–Energy Diagram of Chemical Reactions

In Fig. 3.6, the standard reaction enthalpy $\Delta_{\mathrm{R}}\bar{h}^{\varnothing}$ and the Gibbs basic reaction energy $\Delta_{\mathrm{R}}\bar{g}^{\mathrm{o}}$ are plotted on the x-axis while the corresponding temperature is plotted on the y-axis. The entropy term $T\Delta_{\mathrm{R}}\bar{s}^{\varnothing}$ can be read off as the horizontal distance between the two curves. In our approximation, the linear dependence of the Gibbs basic reaction energy on the temperature, visible in Fig. 3.6, is a generic feature.

If reaction enthalpy and entropy are negative (for example reactions see Table 3.3) both heat and entropy are transferred to the environment. By comparing the standard enthalpy and entropy terms, reactions can be classified into several groups. The first group is defined by demanding

$$\Delta_{\mathrm{R}}\bar{h}^{\varnothing} < T_{\mathrm{R}}\Delta_{\mathrm{R}}\bar{s}^{\varnothing},\ T_{\mathrm{R}} \le T^* > 1000\,\mathrm{K}\,,$$
$$\text{equivalently } \Delta_{\mathrm{R}}\bar{g}^{\mathrm{o}} < 0\,.$$

If the equivalent temperature T^* is much higher than 1000 K, a large irreversibility frequently arises since the reaction heat can only be used with a large temperature difference.

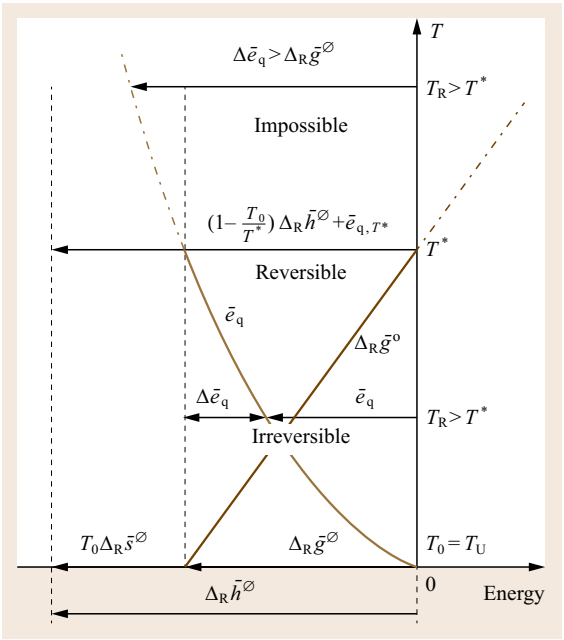


Fig. 3.7 Exergy for an exothermic–exotropic reaction in the temperature–energy diagram

Table 3.3 Exoenergetic–exotropic reactions (after [3.14])

Reaction	$\Delta_R \bar{h}^{\emptyset}$ (kJ/mol)	$\Delta_R \bar{s}^{\emptyset}$ (kJ/molK)	$\Delta_R \bar{g}^{\emptyset}$ (kJ/mol)	T^* (K)	$\Delta_R \hat{e}_x^{\emptyset}$
$2\,Ag\,(S) + 1/2\,O_2 \rightarrow Ag_2\,O\,(S)$	−31.05	−0.06663	−11.18	466	0.360
$1/2\,N_2 + 3/2\,H_2 \rightarrow NH_3$	−45.94	−0.09905	−16.41	464	0.357
$SO_2 + 1/2\,O_2 \rightarrow SO_3$	−98.96	−0.09417	−70.88	1051	0.716
$CO + 3\,H_2 \rightarrow CH_4 + H_2\,O(V)$	−206.1	−0.2153	−142.0	958	0.689
$CO + H_2\,O(V) \rightarrow CO_2 + H_2$	−41.11	−0.04140	−28.76	993	0.700
$C_2H_2 \rightarrow 2\,C\,(S) + H_2$	−228.2	−0.05876	−210.7	3883	0.923
$H_2 + 1/2\,O_2 \rightarrow H_2\,O(V)$	−241.9	−0.04506	−228.4	5367	0.944
$H_2 + 1/2\,O_2 \rightarrow H_2\,O\,(L)$	−285.8	−0.1632	−237.2	1751	0.830
$CO + 1/2\,O_2 \rightarrow CO_2$	−283.0	−0.08652	−257.2	3271	0.909
$CH_4 + 2\,O_2 \rightarrow CO_2 + 2\,H_2\,O(V)$	−802.3	−0.00618	−800.4	129 860	0.998
$CH_4 + 2\,O_2 \rightarrow CO_2 + 2\,H_2\,O\,(L)$	−890.3	−0.2427	−817.9	3669	0.918

Table 3.4 Exoenergetic–endotropic reactions, (after [3.14])

Reaction	$\Delta_R \bar{h}^{\emptyset}$ (kJ/mol)	$\Delta_R \bar{s}^{\emptyset}$ (kJ/mol K)	$\Delta_R \bar{g}^{\emptyset}$ (kJ/mol)	T^* (K)	$\Delta_R \hat{e}_x^{\emptyset}$
$C_6H_{12}O_6(S) + 6\,O_2 \rightarrow 6\,CO_2 + 6H_2O\,(L)$	−2802.7	0.2619	−2880.8	−10 699	1.028
$C_6H_{12}O_6(S) + 6\,O_2 \rightarrow 6\,CO_2 + 6H_2O\,(V)$	−2538.9	0.9708	−2828.3	−2615	1.114
$CH_4 + 1/2\,O_2 \rightarrow CO + 2\,H_2$	−35.67	0.1702	−86.42	−210	2.423
$C_6H_6 \rightarrow 6\,C(S) + 3\,H_2$	−82.93	0.04896	−129.8	−1694	1.565
$C_6H_6(L) \rightarrow 6\,C(S) + 3\,H_2$	−49.04	0.2532	−124.5	−194	2.540
$CH_4 + O_2 \rightarrow CO + H_2O(V) + H_2$	−277.5	0.1252	−314.8	−2217	1.134
$CH_4 + O_2 \rightarrow CO + H_2O(L) + H_2$	−321.5	0.00703	−325.6	−45 732	1.013
$Ca(OH)_2(S) + 2\,HCl \rightarrow CaCl_2(S) + 2\,H_2O(V)$	−108.8	0.02447	−228.4	−4446	1.067
$CH_3OH + 3/2\,O_2 \rightarrow CO_2 + 2\,H_2O(V)$	−546.05	0.36943	−656.88	−1479	1.203
$C\,(S) + O_2 \rightarrow CO_2$	−393.5	0.00288	−394.4	−136 586	1.002
$C\,(S) + 1/2\,O_2 \rightarrow CO$	−110.5	0.08935	−137.2	−1237	1.241

In analogy to Fig. 3.6, the exergy of the supplied or delivered energy can also be plotted in a temperature–energy diagram. This is done in Fig. 3.7, where the behavior of the exergy of the reaction heat in the region between T_0 and T^* is shown. One can also see that, as the reaction temperature approaches the equivalent temperature, the availability of the heat increases and the thermodynamic losses decrease. All of the reaction enthalpy is delivered as heat of a correspondingly lower temperature. The thermodynamic losses can be understood as a temperature devaluation of the heat.

As is also shown in Fig. 3.7, a large reaction potential is available in exothermic–exotropic reactions at the standard temperature. If the chemical conversion takes place at this temperature, this potential is lost completely. This is an exergy loss.

The next group of reactions is defined by

$$\Delta_R \bar{h}^{\emptyset} < T_R \Delta_R \bar{s}^{\emptyset},\ T_R \leq T^* < 1000\,K\,,$$
$$\text{equivalently } \Delta_R \bar{g}^{o} < 0\,.$$

At $T^* < 1000\,K$, a process can be technologically realized near its equivalent temperature since temperature- and corrosion-resistant materials are available in this temperature range for most reaction systems. It is then possible to transfer heat at temperatures close to T^*. If the reaction temperature in a system is $T_R \leq T_0$, the entire availability of the reaction is lost. In case of inequality, there is an additional loss from the cooling system.

If the equivalent temperature of a system is smaller than the temperature of the environment ($T_R = T^* < T_0$), the temperature of the delivered heat must be raised to the environmental level with cooling processes.

The final set of conditions

$$\Delta_R \bar{h}^{\emptyset} > T_R \Delta_R \bar{s}^{\emptyset},\ T_R > T^*,$$
$$\text{equivalently } \Delta_R \bar{g}^{o} > 0\,,$$

corresponds to impossible processes. The reason is that purely thermal processes above the equivalent temperature and with $K = 1$ are impossible. On the one hand, it is impossible to deliver a sufficient amount of entropy with the heat. On the other hand, the exergy of the delivered heat would exceed the availability of the reaction system.

Each reaction with negative reaction enthalpy and positive reaction entropy (for examples see Table 3.4) can be realized in principle. However, such reactions are characterized by very high irreversibilities. On the one hand, there is positive reaction entropy, which is due to the entropies of the products being higher than those of the educts. On the other hand, entropy is delivered to

the environment together with the output of heat. Even at high reaction temperatures the large availability of the reaction system can be delivered to the environment only partially, as exergy of the reaction heat $\bar{e}_q$.

If a reaction takes place at environmental (standard) temperature, the exergy is lost completely. Moreover, if a reaction proceeds below the temperature of the environment, not only does the entire availability of the reaction disappear, but additional work has to be spent to raise the temperature level of the heat to allow its delivery to the environment.

Figure 3.8 shows that, even at a hypothetical reaction temperature $T_R = 0$, the equivalent temperature is not reached due to the different signs of $\Delta_R\bar{h}^{\varnothing}$ and $\Delta_R\bar{s}^{\varnothing}$, an equivalent temperature $T^* < 0$ is obtained, which shows that exothermic–endotropic reactions can never be realized technically as thermal reactions near the equilibrium.

Endothermic reactions need energy, which must be supplied from the outside, for instance by an isothermal process or with preheated educts. With the heat, both entropy and exergy are supplied. All endothermic reactions are in principle reverse reactions of exothermic reactions. However, some of them are of industrial interest as exothermic reactions, while others are of interest as endothermic reactions. For the latter (examples are given in Table 3.5, in addition to the reverse reactions of Table 3.3), there are competing contributions to the chemical potential coming from the enthalpy and the entropy terms. Their balance determines whether the corresponding reaction is possible or impossible.

If both the reaction enthalpy and entropy terms are positive, then enthalpy dominates at low reaction temperatures $T_R < T^*$. Since the availability of the heat supplied is too small to compensate the necessary reaction exergy, the reaction cannot take place at this temperature,

$$\Delta_R\bar{h}^{\varnothing} > T_R\Delta_R\bar{s}^{\varnothing} \text{ and hence } \Delta_R\bar{g}^{o} > 0\,.$$

At high reaction temperatures, $T_R > T^*$, the entropy term dominates and the reaction can proceed in principle, (Fig. 3.9).

If the reaction heat is supplied at the equivalent temperature, a reversible process is conceivable,

$$\Delta_R\bar{h}^{\varnothing} < T_R\Delta_R\bar{s}^{\varnothing} \quad \text{and hence} \quad \Delta_R\bar{g}^{o} < 0\,.$$

If the heat is supplied at a higher temperature, part of the exergy of the heat is lost. At high equivalent temperatures, the heat supply can become a technical problem because of the extreme material properties required.

If the reaction enthalpy is already positive, negative reaction entropy always leads to a positive Gibbs reaction energy. As a consequence, the reaction is impossible as a thermal process. This holds in particular for the reverse reactions of Table 3.4 and some addi-

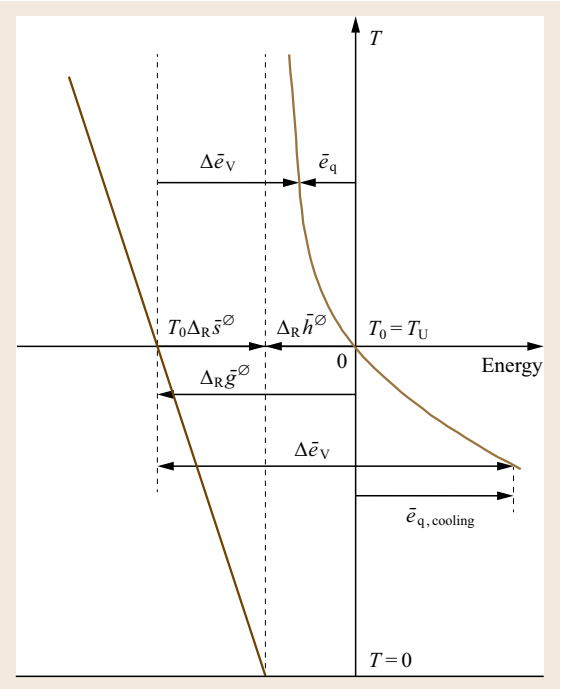


Fig. 3.8 Exothermic–endotropic reactions with heat exchange only

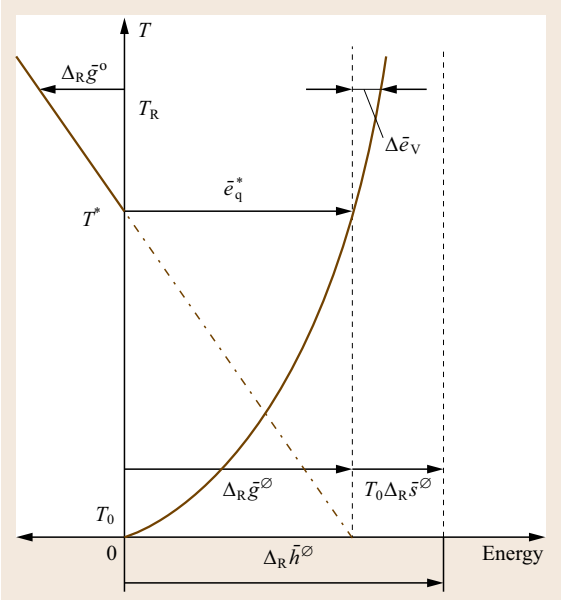


Fig. 3.9 Endothermic–endotropic reactions with heat exchange only

Table 3.5 Endoenergetic–endotropic reactions, (after [3.14])

Reaction	$\Delta_R \bar{h}^{\emptyset}$ (kJ/mol)	$\Delta_R \bar{s}^{\emptyset}$ (kJ/mol K)	$\Delta_R \bar{g}^{\emptyset}$ (kJ/mol)	T^* (K)	$\Delta_R \hat{e}_x^{\emptyset}$
$2\,NaHCO_3(S) \rightarrow Na_2CO_3\,(S) + CO_2 + H_2O\,(L)$	91.52	0.2316	22.46	395	0.245
$2\,NaHCO_3\,(S) \rightarrow Na_2CO_3\,(S) + CO_2 + H_2O\,(V)$	135.5	0.3498	31.21	387	0.230
$MgCl_2(S) + H_2O \rightarrow MgO + 2\,HCl$	97.15	0.1207	61.15	805	0.629
$MgCl_2(S) + H_2O(L) \rightarrow MgO(S) + 2\,HCl$	141.1	0.2389	69.90	591	0.495
$Ca(OH)_2(S) \rightarrow CaO\,(S) + H_2O(V)$	109.1	0.1429	66.54	764	0.610
$CH_4 \rightarrow C(S) + 2\,H_2$	74.87	0.08089	50.76	926	0.678
$CaCO_3(S) \rightarrow CaO(S) + CO_2$	179.8	0.1638	130.9	1097	0.728
$2\,CH_4 \rightarrow C_2H_2 + 3\,H_2$	377.9	0.2205	312.2	1714	0.826
$CH_4 + CO_2 \rightarrow 2\,CO + 2\,H_2$	247.3	0.2567	170.8	963	0.691
$C\,(S) + CO_2 \rightarrow 2\;\;CO$	172.4	0.1758	120.0	981	0.696
$C_2H_6 \rightarrow C_2H_4 + H_2$	137.2	0.1204	101.2	1139	0.738
$C\,(S) + H_2O(V) \rightarrow CO + H_2$	131.3	0.1344	91.24	977	0.695
$1/2\,N_2 + 1/2\;\;O_2 \rightarrow NO$	90.29	0.01227	86.63	7357	0.959
$NaCl\,(S) + H_2O\,(L) \rightarrow 1/2\;\;Cl_2 + 1/2\;\;\;H_2 + NaOH\,(S)$	271.0	0.09915	241.5	2733	0.891
$H_2O\,(V) \rightarrow H_2 + 1/2\,O_2$	241.83	0.04496	228.4	5378	0.945
$H_2O\,(L) \rightarrow H_2 + 1/2\,O_2$	285.83	0.1632	237.2	1751	0.830
$Al_2O_3(S) + 3/2\,C(S) \rightarrow 2\,Al(S) + 3/2CO_2$	1085.4	0.3176	990.6	3418	0.913
$NaCl\,(S) \rightarrow Na\,(S) + 1/2\;Cl_2$	411.1	0.909	384.0	4524	0.934

tional examples presented in Table 3.6. While, as we just explained, the inequality $\Delta_R \bar{g}^o > 0$ makes these reactions impossible as thermal reactions, they can nevertheless in principle be realized as w, q-reactions. The process of photosynthesis, which appears as the fourth reaction in Table 3.5, is also not a thermal reaction. It operates with two temperature levels, the solar radiation temperature and the environmental temperature.

Since thermal reactions can be understood as w, q-reactions with $\bar{w}_{el} = 0$, the reversible reaction temperature can be increased by supplying, or lowered by releasing, work.

If the reaction products have smaller entropy than the raw materials, entropy must be discharged to the outside. However, this can only be realized together with heat transfer. The Gibbs basic reaction energy has a negative gradient in the temperature–energy diagram. From this point of view, it is useful to subdivide electrochemical reactions in exotropic and endotropic reactions.

3.1.6 Exotropic Reactions

Exotropic reactions are associated with the delivery of entropy, which can be realized by heat transfer to the environment. For this reason, exotropic exothermic reactions are preferred with respect to exotropic endothermic reactions.

Exotropic Exoenergetic w, q-Reactions

From an energetic point of view, exothermic reactions are suitable for and are used for combustion processes in heat supply and power generation. Due to the extremely high temperatures T^* achieved, the heat cannot be used reversibly. Of course such reactions are also used for the transformation of materials. In this context the temperature of the heat plays an important role since it affects both the possibilities for using the energy as well as the thermodynamic feasibility of the reaction. If reaction enthalpy and entropy are negative (for examples see Table 3.3), both the heat and entropy are transferred to the environment).

Exoenergetic reactions with work production have gained great technical importance during recent years in connection with the development of fuel cell technology. The fraction of the reaction enthalpy that can be transformed into work or electricity in a reversible process depends on the reaction entropy. In general, the energy delivery partly as work and partly as heat is related to the objective of cogenerating heat and power. The final goal is low-loss production of low-temperature heat. Figure 3.10 illustrates three process cases:

1. Thermal reaction
2. Heat and power production
3. Power production only.

In the case of reversible w, q-reactions, the heat exergy and the corresponding work have a linear temperature dependence. This behavior arises because the delivered heat of a reversible reaction changes with temperature. If the reaction temperature is lower than $T_{q,1}$, the irreversibilities are related to the heat ($\Delta_R \bar{h}^{\emptyset} - \bar{w}_l$) only. The larger the entropy term in compari-

Table 3.6 Endoenergetic/exotropic reactions, (after [3.14])

Reaction	$\Delta_R\bar{h}^{\varnothing}$ (kJ/mol)	$\Delta_R\bar{s}^{\varnothing}$ (kJ/mol K)	$\Delta_R\bar{g}^{\varnothing}$ (kJ/mol)	T^* (K)	$\Delta_R\hat{e}_x^{\varnothing}$
$N_2 + 1/2\,O_2 \rightarrow N_2O$	82.84	−0.07431	104.21	−1104	1.270
$N_2 + 3/2\,O_2 \rightarrow N_2O_3$	82.84	−0.1906	139.67	−434	1.685
$1/2\,N_2 + O_2 \rightarrow NO_2$	33.18	−0.0609	51.33	−545	1.547
$6\,CO_2 + 6\,H_2O(V) \rightarrow C_6H_{12}O_6(S) + 6\,O_2$	2538.7	−0.9713	2828.3	−2614	1.114
$HCl \rightarrow 1/2\,Cl_2 + 1/2\,H_2$	92.310	−0.00952	95.19	−9556	1.031

son to the enthalpy term, the smaller the fraction of energy that can be delivered as electricity (for examples see Table 3.3). When a reaction is modified by allowing for the release of work $\bar{w}_l$ by the system, the reversible temperature decreases from T^* to T_{q1}. Here T_{q1} is the temperature at which the availability of heat corresponds to the remaining potential ($\bar{e}_{q,T(q1)} = \Delta_R\bar{g}^{\varnothing} - \bar{w}_l$). By lowering the reaction temperature the deliverable work increases (graph 1 in Fig. 3.10). In extreme cases the reaction temperature can be lowered to the environmental or standard temperature. In this case the produced work attains its highest value and the remaining heat must be transferred to the environment as shown in graph 2 in Fig. 3.10.

Exotropic Endoenergetic w, q-Reactions

If the reaction entropy is negative and the reaction enthalpy is positive, then the Gibbs reaction energy is positive and consequently a thermal process is impossible ($\Delta_R\bar{g}^{o} > 0$) (Fig. 3.11). Such reactions can only be realized as electrochemical reactions.

In more detail, it is required that the input of work overcompensates the thermal effect, which leads to a corresponding output of heat. Such reactions are exothermic in spite of being endoenergetic (graph 1 in Fig. 3.11). If the supplied work is sufficiently large, the reaction temperature increases and the additional availability can be used as exergy of heat (graph 2 in Fig. 3.11). Unfortunately the entropy production resulting from reaction irreversibilities must also be delivered to the environment. This requires additional work supply.

Examples of Exotropic Reactions

As electrochemical reactions of industrial interest, we consider in the following the oxidation of hydrogen, Table 3.3, and the electrolysis of hydrochloric acid, Table 3.5 (Fig. 3.12).

The hydrogen fuel cell (Fig. 3.12, example A) is the best investigated and most widely applied fuel cell. The corresponding chemical process can be realized between standard temperature and 100 °C in a basic medium (Fig. 3.12, graph 2A), at temperatures of 300–400 °C in an acid medium, and at high temperatures in a molten state (Fig. 3.12, graph 1A). As expected, the reversible electric work decreases with increasing temperature. At 5367 K the reversible work equals zero and the whole reaction availability is contained in the delivered heat (Fig. 3.12, graph A). Note that at such a high-temperature heat exchange is practically impossible and the delivered heat must be used at lower temperatures. The amount of work that can be produced from hydrogen is maximized at standard temperature and equals the chemical potential of hydrogen. In praxis the reaction proceeds in several steps, each

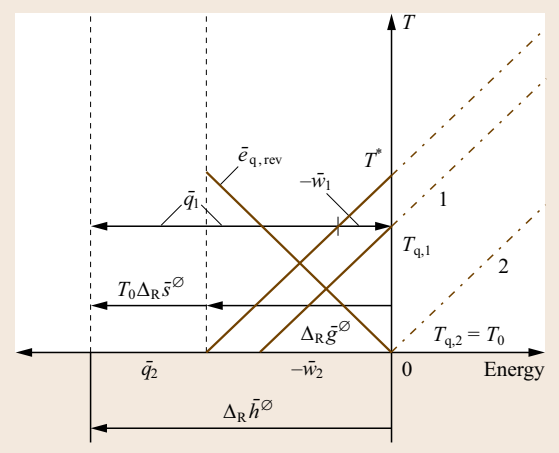


Fig. 3.10 Exotropic–exoenergetic reactions with work and heat exchange

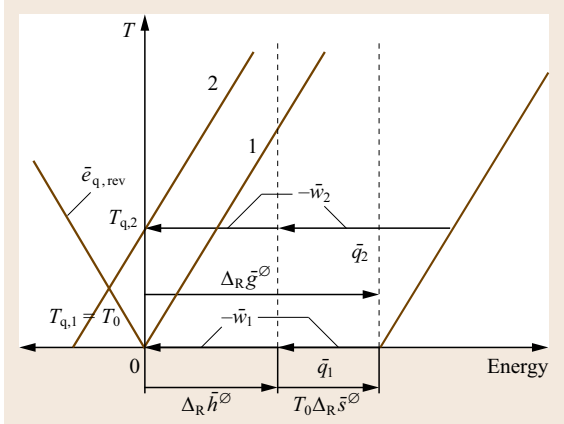


Fig. 3.11 Exotropic–endoenergetic reactions with work and heat exchange

with its corresponding irreversibility. First, the gaseous hydrogen is fed into the porous electrode, distributed within it, and adsorbed onto the surface. The most important and energetically expensive reaction step is the ionization of the molecular hydrogen. Next, the recombination of the hydrogen ions with the hydroxyl ions diffusing through the electrolyte solution leads to the formation of water. In analogy to the hydrogen, the gaseous oxygen is supplied, distributed and adsorbed onto the surface of the electrode. It then forms hydroxyl ions that diffuse through the electrolyte and the barrier to the cathode. Both electrode reactions are associated with high activation energies and double-layer crossing resistance. Hence, different overpotentials exist. As a result, nearly half of the chemical potential is lost in a realistic fuel cell process [3.16], producing low-temperature heat that can eventually be used for heating.

The other example of exotropic reactions is an endothermic reaction. It cannot be realized as a purely thermal reaction for the following reasons. On the one hand, the reaction entropy as well as the additional entropy created under real process conditions have to be delivered to the environment. On the other hand, entropy would have to be supplied with the necessary heat. Thus, the overall entropy balance cannot be satisfied. We now return to our example of the electrolysis of hydrogen chloride: If the positive free enthalpy of about 95.2 kJ/mol is supplied as work (i. e., entropy free) and the difference to the reaction enthalpy of about 2.9 kJ/mol is delivered to the environment together with the reaction entropy at standard temperature, the reversible reaction becomes possible (Fig. 3.12 graph 1B). Due to irreversibilities, the realistic electrolysis of hydrogen chloride requires approximately 230 kJ/mol of electricity and correspondingly delivers approximately 138 kJ/mol of heat. These processes are of some practical interest in the context of chlorine production without additional sodium hydroxide coproduction and of the use of waste hydrochloric acid.

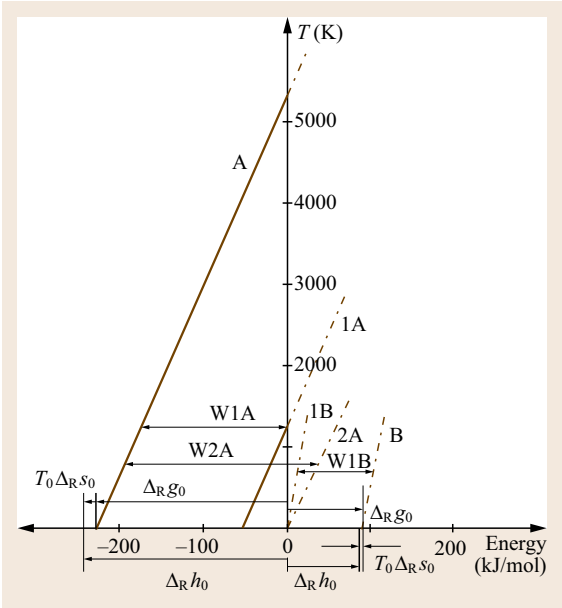


Fig. 3.12 Two examples of exotropic reactions

3.1.7 Endotropic Reactions

If the product entropy is higher than that of the educts, conditions are favorable both for exothermic but also for endothermic chemical reactions. Entropy can not only be delivered with the heat, as in the case of exothermic reactions, but also with the products.

Endotropic Exoenergetic w, q-Reactions

For reactions with negative reaction enthalpy and positive reaction entropy (Table 3.3) the absolute value of the deliverable electric work is larger than that of the reaction enthalpy.

As seen in Fig. 3.13, the high availability of the reaction system can only be used completely if heat is supplied from the environment, for example at the standard temperature, in addition to the amount of energy provided by the reaction enthalpy. In a reversible fuel cell process, this heat is converted into electric power together with the reaction enthalpy (Fig. 3.13, graph 1). These are exoenergetic reactions, which require heating due to the large amount of work de-

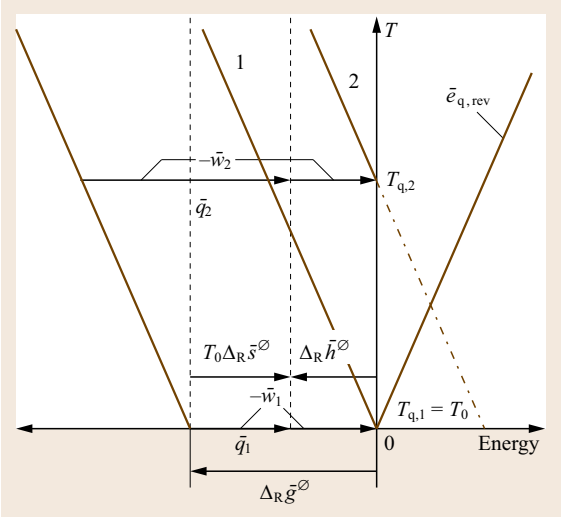


Fig. 3.13 Endotropic–exoenergetic reactions with work and heat exchange

livered. Thus, in spite of being exoenergetic, these processes are endothermic from the point of view of heat transfer.

In principle, this heat supply can be realized at a higher temperature, which can be advantageous for kinetic reasons as seen in graph 2 of Fig. 3.13. In this case the deliverable electric energy increases, wich is given by the reaction Gibbs energy $\Delta_R\bar{g}^o$ at the temperature discussed. The exergy of the supplied heat can also be converted into work. The overall change of the availability of the system in the course of the chemical reaction corresponds to the Gibbs reaction energy at environmental temperature (i. e., $\Delta_R\bar{g}^{\varnothing}$).

Note that electrochemical reactions involve irreversibilities related to the dissipation of part of the conceivable amount of work. Hence the corresponding processes cannot be realized as reversible reactions and the produced work is frequently smaller than the reaction enthalpy.

Endotropic Endothermic w, q-Reactions

Endothermic reactions require not only energy but also availability. Therefore these reactions are preferably realized at high temperatures, as seen in Fig. 3.14, and the availability is supplied with the heat.

This availability can also be supplied as work. In this case the supply of the remaining energy can be realized in the form of heat at a lower temperature (Fig. 3.14, graph 1), or even at standard temperature (Fig. 3.14, graph 2). In this case, the entire reaction entropy can be supplied with the heat from the environment, possibly reduced by the irreversibility that results from the entropy production. The partial or exclusive supply of work makes possible chemical reactions that cannot take place as thermal reactions because their equilibrium temperature T^* is too high.

Theoretically, even an endoenergetic reaction with work delivery is conceivable. In that case, extra heat is supplied at a temperature above T^* and the additional exergy is delivered as work.

Examples of Endotropic Reactions

Methanol is one of the organic fuels that has more availability than energy (Table 3.4). Its high chemical exergy is partially lost if methanol is burned in a burner or in an engine, but also if it is converted into hydrogen by steam reforming. As a liquid fuel with a high energy density, methanol is suitable for transportation, storage and is easy to use. The availability can only be used completely (at least in principle) in the direct methanol fuel cell (DMFC), for instance at standard temperature (Fig. 3.15, case 1A). Such a reversible methanol fuel cell has to be heated.

DMFCs are working at temperatures of 90–150 °C. The exergy of the supplied heat can be theoretically transformed into additional work (Fig. 3.15, case 2A). The electrochemical oxidation reaction of methanol can, for example, also be realized in a potassium hydroxide solution. This requires a complicated reaction scheme with several oxidation steps. In this case, the carbon dioxide that has been formed remains in the solution, which requires the exchange of the electrolyte. A modern DMFC operates with a proton exchange membrane (PEM), made for example from Nafion [3.17]. At the anode, methanol is oxidized to

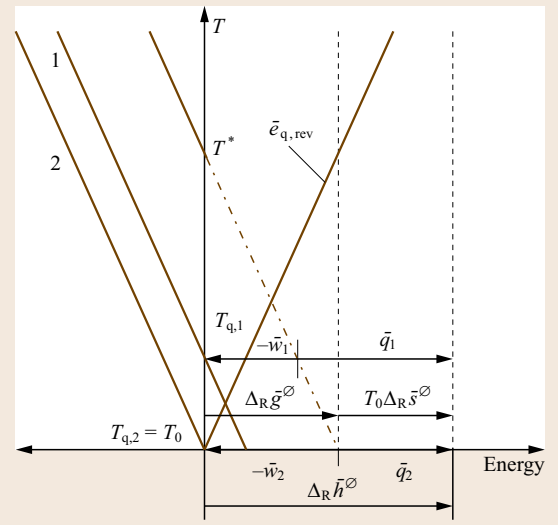


Fig. 3.14 Endotropic–endoenergetic reactions with work and heat exchange

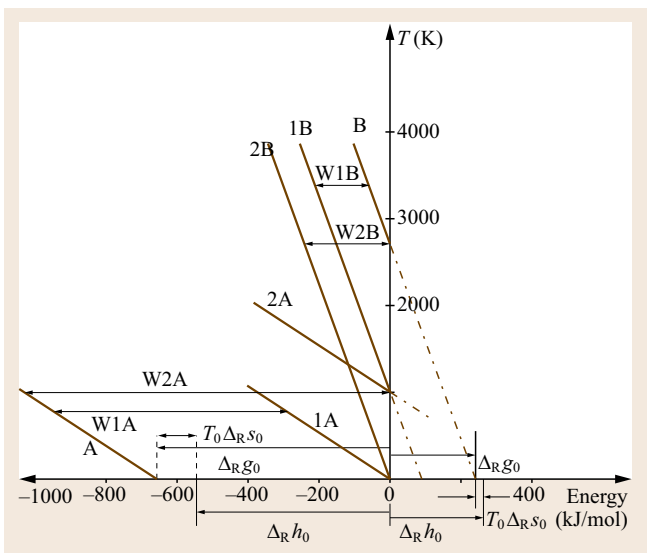


Fig. 3.15 Two examples of endotropic reactions

carbon dioxide and protons

$$CH_3OH + H_2O \rightarrow 6\,H^+ + CO_2 + 6\,e^- \,,$$

with the protons subsequently diffusing to the PEM. The formation of water is realized at the cathode

$$6H^+ + 3/2O_2 + 6\,e^- \rightarrow 3\,H_2O \,.$$

Direct methanol cells usually work with a low methanol concentration to reduce the methanol diffusion to the cathode. The realistic process of the methanol fuel cell is associated with significant irreversibilities and therefore heat has to be delivered rather than supplied.

The second example of an endotropic reaction is the formation of sodium hydroxide from common salt. A thermal process requires unrealistically high reaction temperatures (Fig. 3.15, case B). If part of the required heat is substituted by work, the reaction temperature can be lowered (Fig. 3.15, case 1B). This reaction, realized at standard temperature, is one of the most widely used electrolysis process: the chlorine–alkali electrolysis, (Fig. 3.15, case 2B)

$$NaCl + H_2O \rightarrow 1/2\,Cl_2 + 1/2\,H_2 + NaOH \,.$$

The three different products are used in different branches of industry:

1. Chlorine for polymer chemicals
2. Sodium hydroxide for neutralization and cleaning procedures
3. Hydrogen for hydrogenation and energetic applications [3.18].

The distribution of the reversible exergy between the products is as follows:

1. Sodium hydroxide (72.7%)
2. Chlorine (8.7%)
3. Hydrogen (18.6%).

The two half-reactions can be written schematically as

$$2\,NaCl \rightarrow Cl_2 + 2\,Na^+ + 2\,e^-$$
$$\text{and } 2\,Na^+ + 2\,e^- + 2\,H_2O \rightarrow H_2 + 2\,NaOH \,.$$

In fact, two technical electrolysis processes are in use, with the preference shifting from the mercury-amalgam process to the less dangerous diaphragm process.

3.2 Electrochemical Reactions and Energy Transformation

According to the second law of thermodynamics, processes consisting solely of the transfer of heat from a certain low temperature to a high temperature are impossible. Achieving a higher temperature requires a heat transformation process and a thermodynamic cycle [3.19, 20]. In such a cycle, the temperature increase is realized with the help of additional energy. The temperature level of the latter has to be reduced. This energy may be high temperature heat or work, i. e., energy with an infinitely high temperature level. Hence at least three temperature levels are necessary for heat transformation (Fig. 3.16). Cycles of this type are widely used for the production of electricity, low-temperature heat and refrigeration [3.6].

The above concept of energy transformation and thermodynamic cycles is also applicable to electrochemical reactions. An electrochemical reaction with its reversible reaction temperature T^* represents one temperature level and the exchanged heat and work two other temperature levels. Thus, the conditions for energy transformation are fulfilled. From this point of view, an electrochemical reaction is an open cycle with heat and work transfer: educts and products are entering and leaving the cycle. As a result, electrochemical reactions have a place in the systematics of energy transformation.

3.2.1 Systematics of Energy Transformation

Processes in which the temperature levels of heat flows change play an important role in energy engineering. For instance, in heat exchangers the temperature level of a heat decreases from a high to a low temperature. This is a *simple energy conversion*. Another example is the dissipation of work, with its infinite equivalent temperature, which is devalued to the process temperature. This occurs in every electro–thermal process.

Simple Energy Conversion

There are also chemical reactions representing simple energy conversions. The simplest chemical reaction corresponding to simple energy conversion is the devaluation of a valuable material into environmental materials in a purely thermal process, i. e., the inversion of a basic synthesis. Similar to the heat exchanger, in the case of exothermic or endothermic reactions only two temperature levels are present. The first is the equivalent temperature of the valuable material. The second

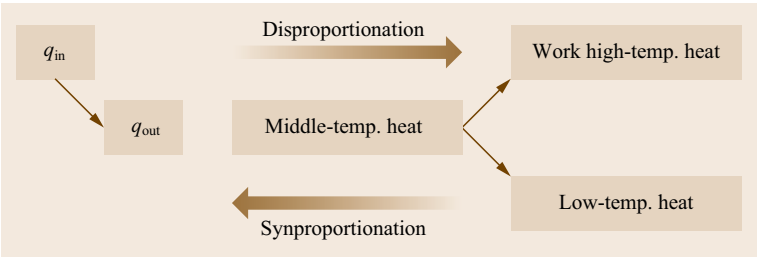


Fig. 3.16 Simple energy conversion and energy transformation

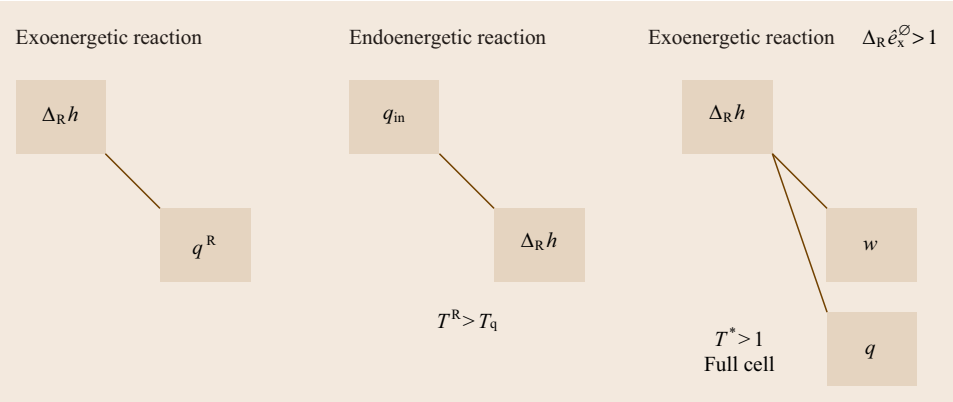


Fig. 3.17 Chemical reactions as simple energy conversions

is the temperature level of the heat delivered by the system or supplied to the system. From this point of view, all thermal reactions with several valuable materials are, in principle, simple energy conversions as well. The temperature of the delivered heat can only be lower than the equivalent reaction temperature because of the presence of irreversibilities. A simple example of such a process is the combustion of hydrogen in a furnace. The normalized exergy of the hydrogen amounts to 0.944; the equivalent temperature T^* is approximately 5370 K. The temperature of the heat delivered by the reaction system in a real technical process would be significantly lower. A simple energy conversion is also realized if a valuable material with a normalized exergy larger than unity, for example methanol or sugar, is converted into the environmental materials carbon dioxide and water steam in a thermal process. This also applies to the combustion of methanol in a realistic fuel cell, i. e., in an irreversible w, q-reaction. The devaluation of methanol, which occurs during the production of work (electric power), is associated with the decrease of the temperature level of the chemical energy. The latter is due to the dissipation into heat, as qualitatively shown in Fig. 3.17.

Analyzing chemical reactions at the level of the substances, one has to remember that each involved educt and product is an energy carrier, in addition to the heat and work. Each substance can be characterized by its normalized exergy. It is characteristic for simple energy conversions that the educt or one of the educts possesses the highest energy level, i. e., the highest normalized exergy, and that all products as well as the exchanged heat have a lower energy-quality level. For the simple energy conversion, the two following basic types of thermal reactions can be identified as illustrated in Fig. 3.18:

- Exothermic–endotropic reactions with simple energy conversion. In such reactions strong irreversibilities are always involved. (More generally, for all exothermic–endotropic reactions, the reverse reaction is impossible as a thermal reaction.) Examples are the thermal conversion of methane to synthesis gas and the conversion of solid carbon with oxygen to carbon monoxide. The realistic methanol fuel cell is also a simple energy conversion if, because of irreversibilities, part of the reaction enthalpy is delivered as heat.
- Exothermic–exotropic reactions with simple energy conversion. For such reactions, one has $\hat{e}^{\varnothing}_{x,\mathrm{P}} < \hat{e}^{\varnothing}_{x,\mathrm{E}}$ and $\hat{e}^{\varnothing}_{x,\mathrm{q}} < \hat{e}^{\varnothing}_{x,\mathrm{E}}$. Examples are the thermal combustion of methane, hydrogen or carbon monoxide.

Energy Disproportionation

In contrast to simple energy conversions, the increase of the temperature level of heat (i. e., an energy transformation) requires at least three temperature levels and the realization of a thermodynamic cycle as in Fig. 3.16.

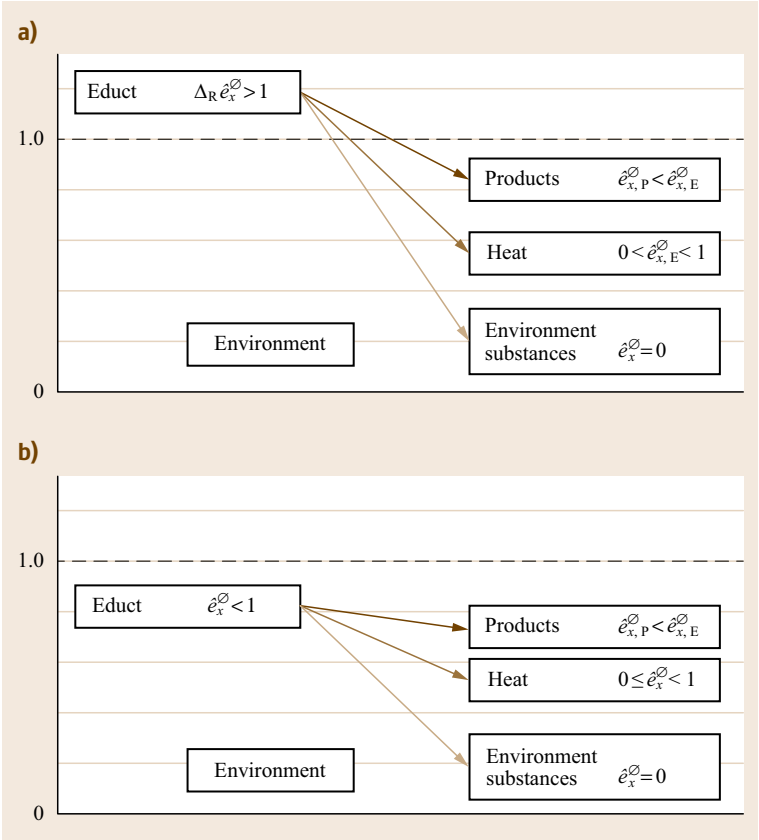


Fig. 3.18a,b Chemical reactions, at the level of substances, with simple energy conversion **(a)** Exothermic–endotropic, **(b)** Exothermic–exotropic

Of course only part of the energy may be lifted to a higher temperature level because an appropriate part of energy has to be transformed to a lower temperature level as a driving force for the transformation process. If some heat is lifted from the middle temperature level to the high level, another part has to be reduced to the low temperature level. This is a disproportionation process. A typical representative of such a thermodynamic cycle is the steam power process. It leads to a disproportionation of middle-temperature heat into work of the turbine and into low-temperature heat of the condenser. The driving force of the process is the transformation of heat from the middle temperature level to the low level, expressed for instance as the difference of Carnot factors

$$
\begin{aligned}
&\Delta e_{\mathrm{driv}} = e_{\mathrm{qml}} - e_{\mathrm{ql}} \,, \\
&e_{\mathrm{qml}} = \hat{e}_{\mathrm{qm}} q_{\mathrm{l}} = \frac{T_{\mathrm{qm}} - T_{\mathrm{en}}}{T_{\mathrm{qm}}} q_{\mathrm{l}} \,, \\
&e_{\mathrm{ql}} = \hat{e}_{\mathrm{ql}} q_{\mathrm{l}} = \frac{T_{\mathrm{ql}} - T_{\mathrm{en}}}{T_{\mathrm{ql}}} q_{\mathrm{l}} \,, \\
&\Delta e_{\mathrm{driv}} = (\hat{e}_{\mathrm{qm}} - \hat{e}_{\mathrm{ql}}) q_{\mathrm{l}} \,, \\
&\Delta \hat{e}_{\mathrm{driv}} = \hat{e}_{\mathrm{qm}} - \hat{e}_{\mathrm{ql}} \,.
\end{aligned}
\tag{3.84}
$$

The remaining part of the middle-temperature heat is transformed into work

$$
\begin{aligned}
&\Delta e_{\mathrm{lift}} = w - e_{\mathrm{qmh}} \,, \quad e_{\mathrm{qmh}} = \hat{e}_{\mathrm{qm}} w = \frac{T_{\mathrm{qm}} - T_{\mathrm{en}}}{T_{\mathrm{qm}}} w \,, \\
&\Delta e_{\mathrm{lift}} = (\hat{e}_{\mathrm{w}} - \hat{e}_{\mathrm{qm}}) w \,, \\
&\Delta \hat{e}_{\mathrm{lift}} = \hat{e}_{\mathrm{w}} - \hat{e}_{\mathrm{qm}} = 1 - \hat{e}_{\mathrm{qm}} \,.
\end{aligned}
\tag{3.85}
$$

In a reversible transformation process, the driving exergy is equal to the lifted exergy. In a realistic process, the driving exergy is higher and the exergetic COP of the transformation process $\eta_{\mathrm{ex,t}}$ becomes less than unity. The expression for the COP contains the transformation ratio ε_{t} between work and low-temperature heat

$$
\begin{aligned}
&1 = \frac{\Delta \hat{e}_{\mathrm{lift}}}{\Delta \hat{e}_{\mathrm{driv}}} \frac{w}{q_{\mathrm{l}}} \,, \\
&\eta_{\mathrm{ex,t}} = \frac{\Delta \hat{e}_{\mathrm{lift}}}{\Delta \hat{e}_{\mathrm{driv}}} \frac{w_{\mathrm{real}}}{q_{\mathrm{l,real}}} \,, \\
&\varepsilon_{\mathrm{t}} = \frac{w_{\mathrm{real}}}{q_{\mathrm{l,real}}} \,.
\end{aligned}
\tag{3.86}
$$

Energy Synproportionation

Analogously, in a synproportionation process low-temperature heat is lifted to the middle temperature level by a driving force, which is either work or heat at a higher temperature. Typical examples of such cycles are heat pumps and refrigeration systems. The transformation efficiency of a compression heat pump reads, similar to (3.86)

$$
\begin{aligned}
1 &= \frac{(\hat{e}_{\mathrm{qm}} - \hat{e}_{\mathrm{ql}})q_{\mathrm{l}}}{(1-\hat{e}_{\mathrm{qm}})w} = \frac{\Delta\hat{e}_{\mathrm{lift}}}{\Delta\hat{e}_{\mathrm{driv}}}\frac{q_{\mathrm{l}}}{w}\,,\\
\eta_{\mathrm{hp,ex,t}} &= \frac{\Delta\hat{e}_{\mathrm{lift}}}{\Delta\hat{e}_{\mathrm{driv}}}\frac{q_{\mathrm{l,real}}}{w_{\mathrm{real}}}\,,\\
\varepsilon_{\mathrm{hp,t}} &= \frac{q_{\mathrm{l,real}}}{w_{\mathrm{real}}}\,.
\end{aligned}
\tag{3.87}
$$

For an absorption heat pump, one has

$$
\begin{aligned}
1 &= \frac{(\hat{e}_{\mathrm{qm}} - \hat{e}_{\mathrm{ql}})q_{\mathrm{l}}}{(\hat{e}_{\mathrm{qh}} - \hat{e}_{\mathrm{qm}})q_{\mathrm{h}}} = \frac{\Delta\hat{e}_{\mathrm{lift}}}{\Delta\hat{e}_{\mathrm{driv}}}\frac{q_{\mathrm{l}}}{q_{\mathrm{h}}}\,,\\
\eta_{\mathrm{ahp,ex,t}} &= \frac{\Delta\hat{e}_{\mathrm{lift}}}{\Delta\hat{e}_{\mathrm{driv}}}\frac{q_{\mathrm{l,real}}}{q_{\mathrm{h,real}}}\,,\\
\varepsilon_{\mathrm{ahp,t}} &= \frac{q_{\mathrm{l,real}}}{q_{\mathrm{h,real}}}\,.
\end{aligned}
\tag{3.88}
$$

The transformation characteristics [3.21] are different from the conventionally used internal exergetic and thermal COPs of thermal power stations and heat pumps. The reason is that these transformation characteristics are based on the energetic or exergetic input rather than on the transformed parts of energy: disproportionation

$$
\eta_{\mathrm{tps,ex}} = \frac{w_{\mathrm{real}}}{\hat{e}_{\mathrm{qm}}q_{\mathrm{m,real}}}\,,\quad \eta_{\mathrm{tps,th}} = \frac{w_{\mathrm{real}}}{q_{\mathrm{m,real}}}\,,
\tag{3.89}
$$

and synproportionation

$$
\begin{aligned}
\eta_{\mathrm{ahp,ex}} &= \frac{\Delta\hat{e}_{\mathrm{lift}}}{\Delta\hat{e}_{\mathrm{driv}} + \Delta\hat{e}_{\mathrm{lift}}}\frac{q_{\mathrm{l,real}} + q_{\mathrm{h,real}}}{q_{\mathrm{h,real}}}\,,\\
\varepsilon_{\mathrm{ahp}} &= \frac{q_{\mathrm{l,real}} + q_{\mathrm{h,real}}}{q_{\mathrm{h,real}}}\,.
\end{aligned}
\tag{3.90}
$$

3.2.2 Chemical Energy Transformation

From the point of view of energy exchange under equilibrium conditions at the equivalent temperature T^*, chemical reactions can be regarded as one entity. In this case, one is not interested in the rearrangement of the energy between the educts and products and the quality of species. Instead, only the reaction enthalpy and reaction entropy are relevant. For example an exotropic and exothermic reaction with delivery of work and heat is a disproportionation process. The reaction enthalpy is in part transformed into low-temperature heat and in part into work. The former part is the driving force

$$
\begin{aligned}
\Delta\hat{e}_{\mathrm{driv}} &= \Delta_{\mathrm{R}}\hat{e}_x^{\emptyset} - \hat{e}_{\mathrm{ql}}\,,\quad \bar{e}_{\mathrm{qml}} = \Delta_{\mathrm{R}}\hat{e}_x^{\emptyset}\bar{q}\,,\\
\bar{e}_{\mathrm{ql}} &= \hat{e}_{\mathrm{ql}}\bar{q}
\end{aligned}
\tag{3.91}
$$

and

$$
\begin{aligned}
\Delta\hat{e}_{\mathrm{lift}} &= \hat{e}_{\mathrm{w}} - \Delta_{\mathrm{R}}\hat{e}_x^{\emptyset} = 1 - \Delta_{\mathrm{R}}\hat{e}_x^{\emptyset}\,,\\
\bar{e}_{\mathrm{qmh}} &= \Delta_{\mathrm{R}}\hat{e}_x^{\emptyset}\,\bar{w}_{\mathrm{el}}\,.
\end{aligned}
\tag{3.92}
$$

As a result, the transformation characteristics are

$$
\eta_{\mathrm{t,ex}} = \frac{\Delta\hat{e}_{\mathrm{lift}}}{\Delta\hat{e}_{\mathrm{driv}}}\frac{\bar{w}_{\mathrm{el}}}{\bar{q}}\,,\quad \varepsilon_{\mathrm{t}} = \frac{\bar{w}_{\mathrm{el}}}{\bar{q}}\,.
\tag{3.93}
$$

This is to be contrasted with the conventional quantities, Tables 3.7 and 3.8

$$
\eta_{\mathrm{ex}} = \frac{w_{\mathrm{el}}}{\Delta_{\mathrm{R}}\hat{e}_x^{\emptyset}\Delta_{\mathrm{R}}\bar{h}^{\emptyset}}\,,\quad \eta_{\mathrm{th}} = \frac{\bar{w}_{\mathrm{el}}}{\Delta_{\mathrm{R}}\bar{h}^{\emptyset}}\,.
\tag{3.94}
$$

Table 3.7 Transformation characteristics and coefficients of performance for disproportionation

Disproportionation	Type I	Type II	Type III
Energy balance	$\bar{w}_{\mathrm{el}} = \Delta_{\mathrm{R}}\bar{h}^{\emptyset} + \bar{q}$	$\Delta_{\mathrm{R}}\bar{h}^{\emptyset} = \bar{w}_{\mathrm{el}} + \bar{q}$	$\bar{q} = \bar{w}_{\mathrm{el}} + \Delta_{\mathrm{R}}\bar{h}^{\emptyset}$
Exergy balance	$\bar{w}_{\mathrm{el}} = \Delta_{\mathrm{R}}\bar{h}^{\emptyset}\Delta_{\mathrm{R}}\hat{e}_x^{\emptyset}$ $+\bar{q}\hat{e}_{\mathrm{ql}} + \Delta\bar{e}_{\mathrm{loss}}$	$\Delta_{\mathrm{R}}\bar{h}^{\emptyset}\Delta_{\mathrm{R}}\hat{e}_x^{\emptyset} = \bar{w}_{\mathrm{el}}$ $+\bar{q}\hat{e}_{\mathrm{ql}} + \Delta\bar{e}_{\mathrm{loss}}$	$\bar{q}\hat{e}_{\mathrm{qm}} = \bar{w}_{\mathrm{el}}$ $+\Delta_{\mathrm{R}}\bar{h}^{\emptyset}\Delta_{\mathrm{R}}\hat{e}_x^{\emptyset} + \Delta\bar{e}_{\mathrm{loss}}$
Transformation ratio reversible	$\varepsilon_{\mathrm{t}} = \frac{\Delta_{\mathrm{R}}\bar{h}^{\emptyset}}{\bar{q}}$	$\varepsilon_{\mathrm{t}} = \frac{\bar{w}_{\mathrm{el}}}{\bar{q}}$	$\varepsilon_{\mathrm{t}} = \frac{\bar{w}_{\mathrm{el}}}{\Delta_{\mathrm{R}}\bar{h}^{\emptyset}}$
Transformation ratio	$\varepsilon_{\mathrm{t}} = \frac{1-\hat{e}_{\mathrm{ql}}}{\Delta_{\mathrm{R}}\hat{e}_x^{\emptyset}-1}$	$\varepsilon_{\mathrm{t}} = \frac{\Delta_{\mathrm{R}}\hat{e}_x^{\emptyset}-\hat{e}_{\mathrm{ql}}}{1-\Delta_{\mathrm{R}}\hat{e}_x^{\emptyset}}$	$\varepsilon_{\mathrm{t}} = \frac{\hat{e}_{\mathrm{qm}}-\Delta_{\mathrm{R}}\hat{e}_x^{\emptyset}}{1-\hat{e}_{\mathrm{qm}}}$
Transformation efficiency	$\eta_{\mathrm{ex,t}} = \frac{\Delta\hat{e}_{\mathrm{lift}}}{\Delta\hat{e}_{\mathrm{driv}}}\frac{\Delta_{\mathrm{R}}\bar{h}^{\emptyset}}{\bar{q}}$	$\eta_{\mathrm{ex,t}} = \frac{\Delta\hat{e}_{\mathrm{lift}}}{\Delta\hat{e}_{\mathrm{driv}}}\frac{\bar{w}_{\mathrm{el}}}{\bar{q}}$	$\eta_{\mathrm{ex,t}} = \frac{\Delta\hat{e}_{\mathrm{lift}}}{\Delta\hat{e}_{\mathrm{driv}}}\frac{\bar{w}_{\mathrm{el}}}{\Delta_{\mathrm{R}}\bar{h}^{\emptyset}}$
COP	$\eta_{\mathrm{th}} = \frac{\Delta_{\mathrm{R}}\bar{h}^{\emptyset}}{w_{\mathrm{el}}}$	$\eta_{\mathrm{th}} = \frac{\bar{w}_{\mathrm{el}}}{\Delta_{\mathrm{R}}\bar{h}^{\emptyset}}$	$\eta_{\mathrm{th}} = \frac{\bar{w}_{\mathrm{el}}}{\bar{q}}$
Exergetic COP	$\eta_{\mathrm{ex}} = \frac{\Delta_{\mathrm{R}}\hat{e}_x^{\emptyset}\Delta_{\mathrm{R}}\bar{h}^{\emptyset}}{w_{\mathrm{el}}}$	$\eta_{\mathrm{ex}} = \frac{\bar{w}_{\mathrm{el}}}{\Delta_{\mathrm{R}}\hat{e}_x^{\emptyset}\Delta_{\mathrm{R}}\bar{h}^{\emptyset}}$	$\eta_{\mathrm{ex}} = \frac{\bar{w}_{\mathrm{el}}}{\hat{e}_{\mathrm{qm}}\bar{q}}$

Table 3.8 Transformation characteristics and coefficients of performance for synproportionation

Synproportionation	Type I	Type II	Type III
Energy balance	$\Delta_R\bar{h}^{\emptyset} + \bar{q} = \bar{w}_{el}$	$\bar{w}_{el} + \bar{q} = \Delta_R\bar{h}^{\emptyset}$	$\bar{w}_{el} + \Delta_R\bar{h}^{\emptyset} = \bar{q}$
Exergy balance	$\Delta_R\bar{h}^{\emptyset}\Delta_R\hat{e}_x^{\emptyset} + \bar{q}\hat{e}_{ql}$ $= \bar{w}_{el} + \Delta\bar{e}_{loss}$	$\bar{w}_{el} + \bar{q}\hat{e}_{ql}$ $= \Delta_R\bar{h}^{\emptyset}\Delta_R\hat{e}_x^{\emptyset} + \Delta\bar{e}_{loss}$	$\bar{w}_{el} + \Delta_R\bar{h}^{\emptyset}\Delta_R\hat{e}_x^{\emptyset}$ $= \bar{q}\hat{e}_{qm} + \Delta\bar{e}_{loss}$
Transformation ratio reversible	$\varepsilon_t = \frac{\bar{q}}{\Delta_R\bar{h}^{\emptyset}}$	$\varepsilon_t = \frac{\bar{q}}{\bar{w}_{el}}$	$\varepsilon_t = \frac{\Delta_R\bar{h}^{\emptyset}}{\bar{w}_{el}}$
Transformation ratio	$\varepsilon_t = \frac{\Delta_R\hat{e}_x^{\emptyset}-1}{1-\hat{e}_{ql}}$	$\varepsilon_t = \frac{1-\Delta_R\hat{e}_x^{\emptyset}}{\Delta_R\hat{e}_x^{\emptyset}-\hat{e}_{ql}}$	$\varepsilon_t = \frac{1-\hat{e}_{qm}}{\hat{e}_{qm}-\Delta_R\hat{e}_x^{\emptyset}}$
Transformation efficiency	$\eta_{ex,t} = \frac{\Delta\hat{e}_{lift}}{\Delta\hat{e}_{driv}}\frac{\bar{q}}{\Delta_R\bar{h}^{\emptyset}}$	$\eta_{ex,t} = \frac{\Delta\hat{e}_{lift}}{\Delta\hat{e}_{driv}}\frac{\bar{q}}{\bar{w}_{el}}$	$\eta_{ex,t} = \frac{\Delta\hat{e}_{lift}}{\Delta\hat{e}_{driv}}\frac{\Delta_R\bar{h}^{\emptyset}}{\bar{w}_{el}}$
COP	$\varepsilon_{th} = \frac{\bar{w}_{el}}{\Delta_R\bar{h}^{\emptyset}}$	$\varepsilon_{th} = \frac{\Delta_R\bar{h}^{\emptyset}}{\bar{w}_{el}}$	$\varepsilon_{th} = \frac{\bar{q}}{\bar{w}_{el}}$
Exergetic COP	$\eta_{ex} = \frac{\bar{w}_{el}}{\Delta_R\bar{h}^{\emptyset}\Delta_R\hat{e}_x^{\emptyset}+\bar{q}\hat{e}_{ql}}$	$\eta_{ex} = \frac{\Delta_R\bar{h}^{\emptyset}\Delta_R\hat{e}_x^{\emptyset}}{\bar{w}_{el}+\bar{q}\hat{e}_{ql}}$	$\eta_{ex} = \frac{\bar{q}\hat{e}_{qm}}{\bar{w}_{el}+\Delta_R\bar{h}^{\emptyset}\Delta_R\hat{e}_x^{\emptyset}}$

In the reversible case, the transformation ratio and the thermal COP are also given, in agreement with (3.45), by

$$\varepsilon_t = \frac{\bar{w}_{el}}{\bar{q}} = \frac{T^* - T_q}{T_q} \text{ and } \eta_{th} = \frac{\bar{w}_{el}}{\Delta_R\bar{h}^{\emptyset}} = \frac{T^* - T_q}{T^*} \,. \tag{3.95}$$

The quality of chemical energy may be visualized on the temperature scale as T^* or, on the Carnot factor scale, as normalized exergy. The three interactions of the (more or less reversible) w, q-reactions are then the chemical reaction itself, the heat, and the work (and/or the radiation effects). Because the normalized exergy of work is equal to unity and the exergy of heat is less than unity, the energy quality of work is always higher than that of heat. The normalized reaction exergy can take values between zero and above unity and is therefore suitable for all three temperature levels of a transformation process. In this way, six transformation possibilities result: three disproportionation processes and three synproportionation processes with the chemical reaction on the high, middle or low temperature level, as is visible in Fig. 3.19.

The disproportionation processes I and II are of particular technical relevance since the photosynthesis of biomass, the fuel cells on the basis of hydrogen and the lead–acid storage battery operate according to this pattern. In the reaction of calcium oxide with carbon dioxide to calcium carbonate, realized in an electrolytic process in a fuel cell, up to 70% of the energy can be delivered as electric power. The remaining 30% is

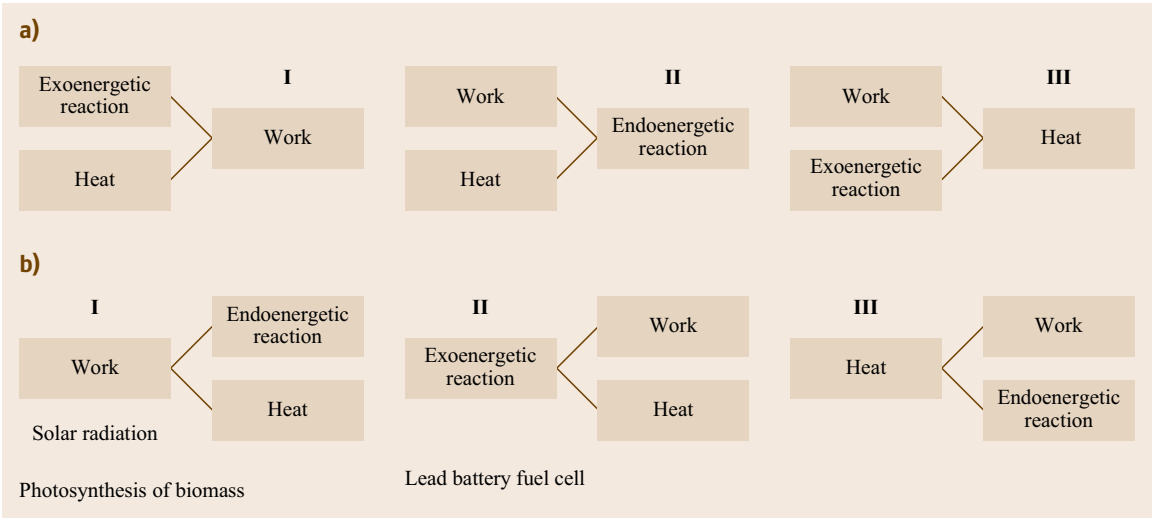


Fig. 3.19a,b Energy transformation from the point of view of the chemical reaction **(a)** Synproportionation, **(b)** Disproportionation

transferred to the environment as heat. This is a disproportionation process since the produced electric power possesses the highest normalized exergy. For the disproportionation process III, no applications are known since, in the low-temperature range, chemical reactions are frequently kinetically limited.

The synproportionation processes I and II are used in the form of the methanol fuel cell (I) and the water electrolysis process (II). In the case of a reversible realization, they are expected to absorb heat from the environment (Fig. 3.15). However, because of internal irreversibilities, so much work is dissipated into heat that no further heat can be absorbed.

An evaluation of chemical reactions can also be performed on the basis of the chemical substances. In this case, each educt or product represents its own temperature level according to the production reaction. As a result, the rearrangement of the energy is evaluated. More than three temperature levels are frequently involved in the energy transformation, similar to the different temperatures of absorber, evaporator, desorber and condenser in absorption–refrigeration cycles.

If at least one reaction product possesses a higher normalized exergy than the highest normalized exergy of the raw materials, then the normalized exergies of further reaction products have to be lower. This is necessary since the entire exergy of the process, including the exergy supply with the process heat, can only remain constant or decrease because of the irreversibility. This situation corresponds to the definition of energy-

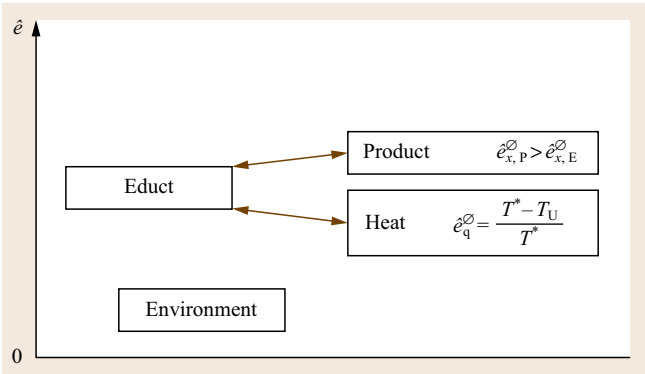


Fig. 3.20 Energy transformation considered on the basis of educts and products

disproportionation processes, in which heat can only be transformed to a higher temperature level if an equivalent heat is devaluated to a lower temperature level as illustrated in Fig. 3.20.

The inversion of this transformation process, the synproportionation, can be realized with the reverse reaction near equilibrium.

Examples of reactions which, depending on the direction, are either disproportionation or synproportionation processes, are the conversion of calcium oxide with water steam and the decomposition of methane, also with water steam (Fig. 3.21a,b). If calcium oxide is converted to calcium hydroxide, the normalized exergy of the calcium oxide of 0.728 increases to that of the calcium hydroxide of 0.912. The heat can be deliv-

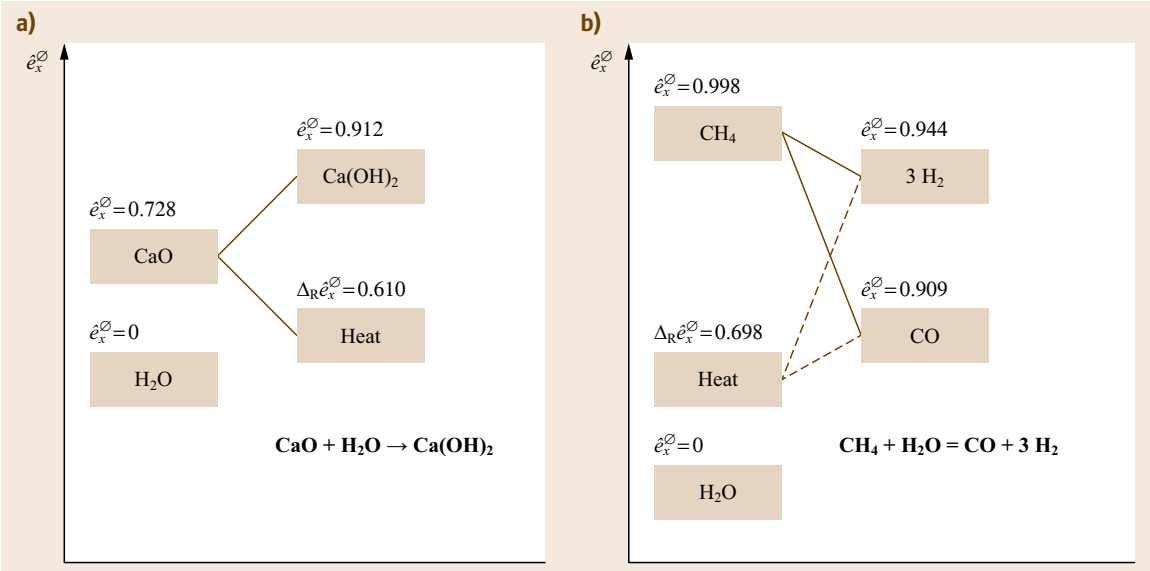


Fig. 3.21a,b Examples of energy transformation considered on the basis of educts and products **(a)** Decomposition of CaO, **(b)** Decomposition of methane

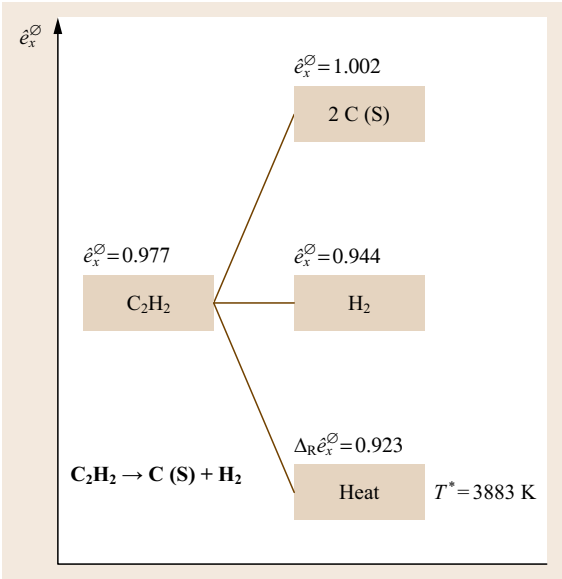


Fig. 3.22 Energy disproportionation in spontaneous reactions such as acetylene decomposition

ered at a temperature level of maximally 764 K. This is a typical disproportionation process.

The inversion of this reaction, the decomposition of calcium hydroxide, is then a synproportionation process in which the temperature level of heat is increased to the product temperature level of calcium oxide. Similarly, the production of synthesis gas on the basis of methane is a synproportionation process, and the methanisation is a disproportionation.

The spontaneous decomposition of acetylene with a normalized exergy of 0.977 into carbon black and hydrogen, which is connected to a considerable energy release of $-228.2\,\mathrm{kJ/mol}$, is a disproportionation as well since the carbon formed has a normalized exergy of 1.002. This value is higher than that of the acetylene to be converted (Fig. 3.22). Furthermore, hydrogen with a lower normalized exergy of 0.944 is a byproduct.

The high equivalent temperature of 3883 K, at which heat would have to be delivered in a reversible process, cannot be achieved in the technical realization. After the initial supply of an appropriate activation energy, the reaction proceeds spontaneously at much lower temperatures. Therefore the reverse reaction cannot be realized in the same way as a synproportionation process.

3.2.3 Electrochemical Thermodynamic Cycles

Usually, in thermodynamic cycles a working fluid continuously passes a closed sequence of states. Thermodynamically, *closed* means that there is no mass but only energy exchange with the surroundings. If this cycle consists simply in going reversibly from state A to state B, then returning from B to A along the same path means no change in the surroundings is induced. By contrast, if the cycle does not take such a degenerate form (i. e., the paths from A to B and from B to A differ), a change in the surroundings occurs even if the process is reversible. During this process, work and heat at different temperature levels are exchanged. The process causes an increase in the quality of part of this energy in the sense of synproportionation or disproportionation. Thus, cycles are fundamentally different from circuits, which also follow a closed sequence of states but cause no increase of the quality of some energy. These include for instance washing circuits, where a solvent circulates. For example, the solvent may absorbs some heat and deliver it again (simple energy conversion). Other examples are heating and cooling circuits between distribution stations and individual consumers.

The different paths from A to B and back may be associated with temperature and pressure changes and/or with concentration and phase state changes, or with chemical and electrochemical reactions. Depending on driving forces, phase changes and thermal or chemical interactions, thermodynamic cycles may be classified into several types [3.22] (Table 3.9).

Closed Electrochemical Cycles

In a closed chemical cycle, a reaction proceeds in the direct and reverse direction under different conditions. Moreover, a chemical cycle may include several different reactions. Some of them may be thermal reactions and, for instance, only one an electrochemical reaction. The understanding of the term closed chemical cycle includes the production of a chemical energy carrier that is converted, in a final reaction, into educts. This final step is associated with the delivery of power or of heat and power.

Since we are concerned with closed cycles, only the exchange of heat and work and the produced irreversibilities are important from the perspective of the environment.

For example, thermochemical hydrogen production is an interesting field of research. In the past, this has been due to the possibility of using the heat of high-temperature nuclear reactors and now with a view on using solar energy. Thermochemical cycles working only with high-temperature heat are very complicated because they require many reaction steps. If part of the energy is supplied as work, then one is dealing with so-called hybrid processes [3.23] and, as a result, the number of steps may be reduced. For instance, the sul-

Table 3.9 Classification of thermodynamic cycles

Transformation type	Disproportionation			Synproportionation		
Cycle type	Application	Driving energy	Generated energy	Application	Driving energy	Generated energy
Mechanical cycles	Gas turbine, Otto engine, Diesel engine	High-temperature heat (fuel)	Work, electricity, cogeneration w and q	Gas compression heat pump, cold gas processes, Ranque–Hilsch vortex tube	Work, electricity	Low-temperature heat, cold
Thermomechanical cycles	Rankine cycles, organic Rankine cycle (ORC) processes	High-temperature heat, (fuel), Solar radiation	Work, electricity, cogeneration w and q	Vapor compression cycle	Work, electricity	Low-temperature heat, cold
Thermophysical cycles	Kalina process, ab-, adsorption heat transformer	Waste heat	Heat, electricity	Ab-, Adsorption heat pump or refrigerator, ejection refrigerator	Heat	Low-temperature heat, cold
Thermochemical cycles	Hydrogen production	Solar radiation, high-temperature heat	Chemical potential	Thermo chemical combustion	Chemical potential	Heat
Photoelectrical cycles	Photovoltaic cell, photosynthesis	Solar radiation	Electricity, chemical potential			
Thermoelectrical cycles	Thermo electrical generator	High-temperature heat	Electricity	Peltier thermoelectric cooler	Electricity	cold
Electrochemical cycles	Hydrogen fuel cell, electrolysis	Chemical potential, electricity	Work, electricity, cogeneration w and q chemical potential,	Direct methanol fuel cell (theoretically), electrolysis	Chemical potential, electricity	Work, electricity cogeneration w and q chemical potential
Magnetoelectrical cycles	Magnetohydrodynamic (MHD) generator	High-temperature heat (fuel)	Work, electricity cogeneration w and q			

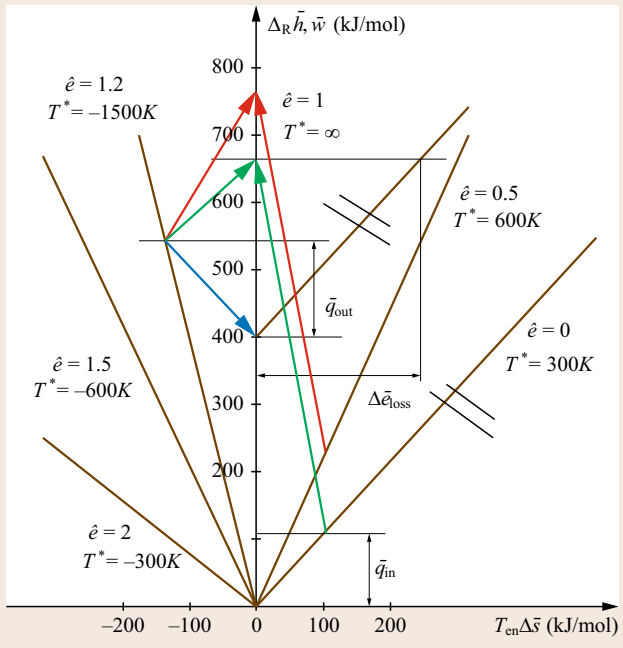


Fig. 3.23 Energy–entropy plot for reversible and irreversible methanol fuel cell. *green lines* reversible methanol fuel cell, heat supply at 300 K, synproportionation; *red lines* reversible methanol fuel cell, heat supply at 600 K, synproportionation; *blue lines* irreversible methanol fuel cell, heat delivery at 300 K, simple conversion

fur acid process requires, in principle, only two steps. However, for technological reasons, it is better to use the following three steps:

1. The high temperature decomposition of sulfuric acid
2. The thermal dissociation of sulfur three oxide
3. The electrolysis of sulfurous acid to sulfuric acid and hydrogen.

$$H_2SO_4 \rightarrow H_2O + SO_3\,,$$
$$\Delta_R\bar{h}_1^{\emptyset} = 109.8\,\mathrm{kJ/mol},\ \Delta_R\bar{g}_1^{\emptyset} = 66.4\,\mathrm{kJ/mol}\,,$$
$$\Delta_R\hat{e}_1^{\emptyset} = 0.605,\ T_1^* = 754.4\,\mathrm{K}\,;$$
$$SO_3 \rightarrow 1/2O_2 + SO_2\,,$$
$$\Delta_R\bar{h}_2^{\emptyset} = 98.3\,\mathrm{kJ/mol},\ \Delta_R\bar{g}_2^{\emptyset} = 70.0\,\mathrm{kJ/mol}\,,$$
$$\Delta_R\hat{e}_2^{\emptyset} = 0.712, T_2^* = 1034.7\,\mathrm{K}\,;$$
$$SO_2 + 2H_2O \rightarrow H_2SO_4 + H_2\,,$$
$$\Delta_R\bar{h}_3^{\emptyset} = 33.7\,\mathrm{kJ/mol},\ \Delta_R\bar{g}_3^{\emptyset} = 92.2\,\mathrm{kJ/mol}\,,$$
$$\Delta_R\hat{e}_3^{\emptyset} = 2.736\ T_3^* = -171.7\,\mathrm{K}\,.$$

As seen from the reaction data, all three reactions are endothermic. For the first two reactions, the required availability can be supplied with the reaction heat. By contrast, for the third reaction the required heat is significantly smaller than the availability, and therefore the supply of work is necessary. Even for the reversible electrolysis, the required electric work makes up 40% (92.2 from 228.6 kJ/mol) of the produced hydrogen exergy. For this reason, the sulfuric acid hybrid cycle is unfavorable. Moreover, this process has technical problems associated with corrosion, catalyst efficiency, separation and purification requirements, and energetic efficiency. The alternative for hydrogen production is the use of a solar power station together with water electrolysis.

In contrast to closed cycles, such as compression heat pumps or absorption refrigeration cycles, chemical cycles are realized in different installations (possibly at different locations) even when they are closed. Since it is not reasonable to also store and transport the byproducts to the place of the reverse reaction, a chemical cycle can only conditionally be called a closed cycle. For instance, the combustion of hydrogen produced in a thermochemical cycle may be used as the final reaction in a fuel cell or thermal power station. This requires transportation and storage of the hydrogen. The oxygen necessary for the fuel cell or for combustion would be taken from the surroundings of the power station; hence the cycle is only conditionally closed.

The formation and storage of methanol from synthesis gas is a disproportionation process as methanol has a higher normalized exergy than all components of the synthesis gas. In contrast, the combustion of methanol in a reversible fuel cell is a synproportionation with low-temperature heat supply, as shown in Fig. 3.23.

The use of methanol (usually after storage) in a realistic fuel cell is a simple energy conversion. The reason is that the energy of methanol (with normalized exergy 1.2) is devalued to a smaller amount of electricity (with normalized exergy of unity) and low-temperature heat.

From the point of view of energy transformations, the situation could, in principle, be different when the fuel cell pressure is increased with low-temperature heat supply. This is analogous to a heat pump, where the pressure is increased from the evaporator pressure to the condenser pressure. Correspondingly, the evaporator heat is raised to the temperature level of the condenser. Formally, this would also be achieved if the compressor of a heat pump were powered by a methanol fuel cell (Fig. 3.24). This could be viewed as an energy transformation. However, the transformation process occurs in an additional closed cycle. In a realistic fuel cell there is no low temperature heat input and one is still dealing with a simple energy conversion.

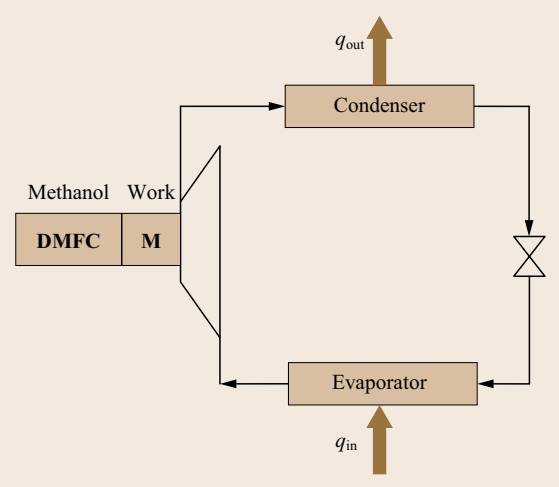


Fig. 3.24 Methanol fuel cell driving a heat pump

Open Electrochemical Cycles

From the standpoint of electrochemistry, two open processes are possible in principle: one with supply, the other with delivery of electrical energy. They correspond to electrolysis and the fuel cell. Both processes may be understood as open cycles. The electrolysis is an open cycle of the production of an energy carrier on the basis of electric power. By contrast, the fuel cell is an open cycle of transformation of chemical energy into electricity. These electrochemical open cycles may be combined with thermochemical open cycles.

Chemical energy carriers may be used in conventional open cycles, which are associated with the combustion of fuel in an engine or a gas turbine. These are the thermodynamic cycles of the well-known Otto and Diesel engines or the Joule process. In the chemical sense, these cycles resemble the fuel cell since educts and products may be the same. But their chemistry, technical devices, driving force, process limitations, efficiency and, eventually, irreversibilities are very different.

The increasing production of renewable-energy-based electricity can also be used for the production of chemicals. This is particularly relevant for the use of cheap electricity (associated, e.g., with periods of high winds or intense solar radiation). This applies to the production of basic chemicals such as sodium hydroxide by chlorine–alkali electrolysis [3.18] or of aluminum by smelting flux electrolysis. Although these processes are aimed at the production of chemicals, they may be understood as open thermodynamic cycles of energy transformation. Using the example of chlorine–alkali electrolysis, it can be shown that there is a difference depending on whether the reaction is considered on the basis of educts and products or as a complete reaction. At the level of educts and products, the produced chlorine has the highest normalized exergy and therefore the transformation process is a disproportionation (Fig. 3.25).

By contrast, the complete electrolysis reaction has a normalized reaction exergy of 0.891 and the supplied work has the highest temperature level. In case of a (nearly) reversible reaction, the process is an endothermic reaction and the supplied heat is transformed to the level of the normalized reaction exergy (Fig. 3.26).

If, due to irreversibilities, the supplied work is higher than the reaction enthalpy, some heat has to be delivered and the process is a simple energy conversion.

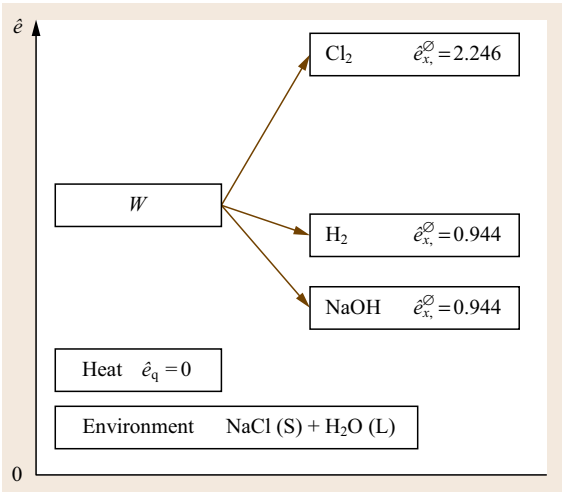


Fig. 3.25 Chlorine–alkali electrolysis at the level of educts and products as an example of energy disproportionation

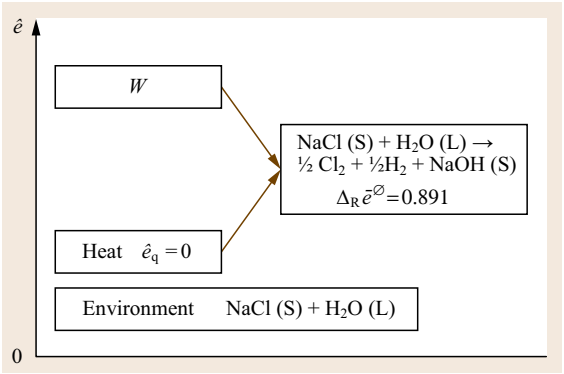


Fig. 3.26 Reversible chlorine–alkali electrolysis as an example of energy synproportionation

Water Electrolysis/Hydrogen Fuel Cell as Closed Circuit

If hydrogen is produced with the help of electric power in an electrolysis process and, after transportation and storage, is converted back into electricity in a fuel cell, one is not dealing with a cycle in the thermodynamic sense but only with a circuit. The quality of energy does not increase but, on the contrary, part of the electric energy is devalued into low-temperature heat, compensating the thermodynamic losses.

The reversible water electrolysis is an endotropic endothermic reaction with synproportionation of electricity and heat (and water) to hydrogen (and oxygen). However, the corresponding realistic electrochemical reaction is an exothermic process. This is caused by the additional supply of electrical energy that is needed to compensate the irreversibilities. Hence only about 80% of the supplied electric power is converted into hydrogen [3.24]. The dissipative work is delivered to the environment with the help of a cooling system, (Fig. 3.27a)

$$\varepsilon_{\mathrm{th}} = \frac{\Delta_{\mathrm{R}}\bar{h}^{\emptyset}_{\mathrm{hy}}}{\bar{w}_{\mathrm{el}}} = 0.8\,.$$

The fuel cell process of hydrogen oxidation [3.25] is a disproportionation process of chemical energy into power, heat and water. Hydrogen with a normalized exergy of 0.944 is transformed, in a PEM fuel cell, into electric energy with a normalized exergy of unity. If 50% of the reaction enthalpy is transformed into work, and the other 50% into low-temperature heat with a normalized exergy of 0.2, then the conventional COP of power production (Fig. 3.27b) is about

$$\eta_{\mathrm{th}} = \frac{\bar{w}_{\mathrm{el}}}{\Delta_{\mathrm{R}}\bar{h}^{\emptyset}_{\mathrm{hy}}} = 0.5\,.$$

The exergetic COP of cogeneration of heat and power is correspondingly

$$\eta_{\mathrm{ex}} = \frac{\bar{w}_{\mathrm{el}} + \bar{q}\hat{e}_{\mathrm{ql}}}{\Delta_{\mathrm{R}}\bar{h}^{\emptyset}_{\mathrm{hy}}\Delta_{\mathrm{R}}\hat{e}^{\emptyset}_{\mathrm{hy}}} = 0.64\,.$$

The transformation ratio of the realistic PEM fuel cell is about unity

$$\varepsilon_{\mathrm{t}} = \frac{\bar{w}_{\mathrm{el}}}{\bar{q}} = 1\,.$$

The reversible transformation ratio is the ratio of the normalized driving exergy $\Delta\hat{e}_{\mathrm{driv}}$ and the lifted normalized exergy $\Delta\hat{e}_{\mathrm{lift}}$

$$\varepsilon_{\mathrm{t,rev}} = \frac{\Delta_{\mathrm{R}}\hat{e}^{\emptyset}_{\mathrm{hy}} - \hat{e}_{\mathrm{ql}}}{1 - \Delta_{\mathrm{R}}\hat{e}^{\emptyset}_{\mathrm{hy}}} = \frac{\bar{w}_{\mathrm{el,rev}}}{\bar{q}_{\mathrm{rev}}} = 13.3\,.$$

The exergetic transformation efficiency is very low because too much hydrogen enthalpy is converted into low-temperature heat

$$\eta_{\mathrm{ex,t}} = \frac{\Delta\hat{e}_{\mathrm{lift}}}{\Delta\hat{e}_{\mathrm{driv}}}\frac{\bar{w}_{\mathrm{el}}}{\bar{q}} = 0.075.$$

In the total sum of these two thermodynamic processes, the supplied electrical energy is converted into a smaller amount of electricity and heat. Even in the case of cogeneration of heat and power in a fuel cell, this is not a cycle in the thermodynamic sense. Strictly speaking, it is an energy storage process with simple energy conversion by storage (power to gas) and an energy transformation during the extraction from storage. But in the sum, it remains a simple conversion.

Consider, for instance, the use of electrical energy (produced e.g., in a wind park) in a water splitting process and the reaction of the resulting hydrogen in a fuel cell for power production. Why can't this be a thermodynamic cycle?

A closed cycle exchanges only work and heat exchange with the environment. If work is the only energy input, representing always a higher temperature level than that of any heat, there is no possibility to increase the temperature level of some energy.

For the same reason, charge and discharge processes in batteries are also, in the sum, only simple energy conversions.

Independently of the classification as transformation process or simple energy conversion, a COP may be defined as ratio between produced electricity after storage of hydrogen (or methane or methanol) and the electricity supplied by the wind park. For instance, if the efficiency of the electrolysis process is 0.8 and that of the fuel cell 0.5, the overall efficiency achieved is

$$\eta_{\mathrm{ex,el-fc}} = \frac{w_{\mathrm{real}}}{w_{\mathrm{wp}}} = \frac{\Delta_{\mathrm{R}}\hat{e}^{\emptyset}_{\mathrm{hy}}}{w_{\mathrm{wp}}}\frac{w_{\mathrm{real}}}{\Delta_{\mathrm{R}}\hat{e}^{\emptyset}_{\mathrm{hy}}} = 0.4\,.$$

When comparing this process with conventional transformation processes and cycles for power production, it is necessary to take into account the energy supply situation of today.

Comparison to Other Conventional Cycles

The beginning of the transition in energy consumption from fossil fuels (coal, petroleum and natural gas), to renewable resources (solar radiation, water power, wind energy and biomass), is associated with a change in energy conversion technologies. In the thermodynamic sense, i. e., with respect to the normalized exergy of the sources, the differences between fossil fuels

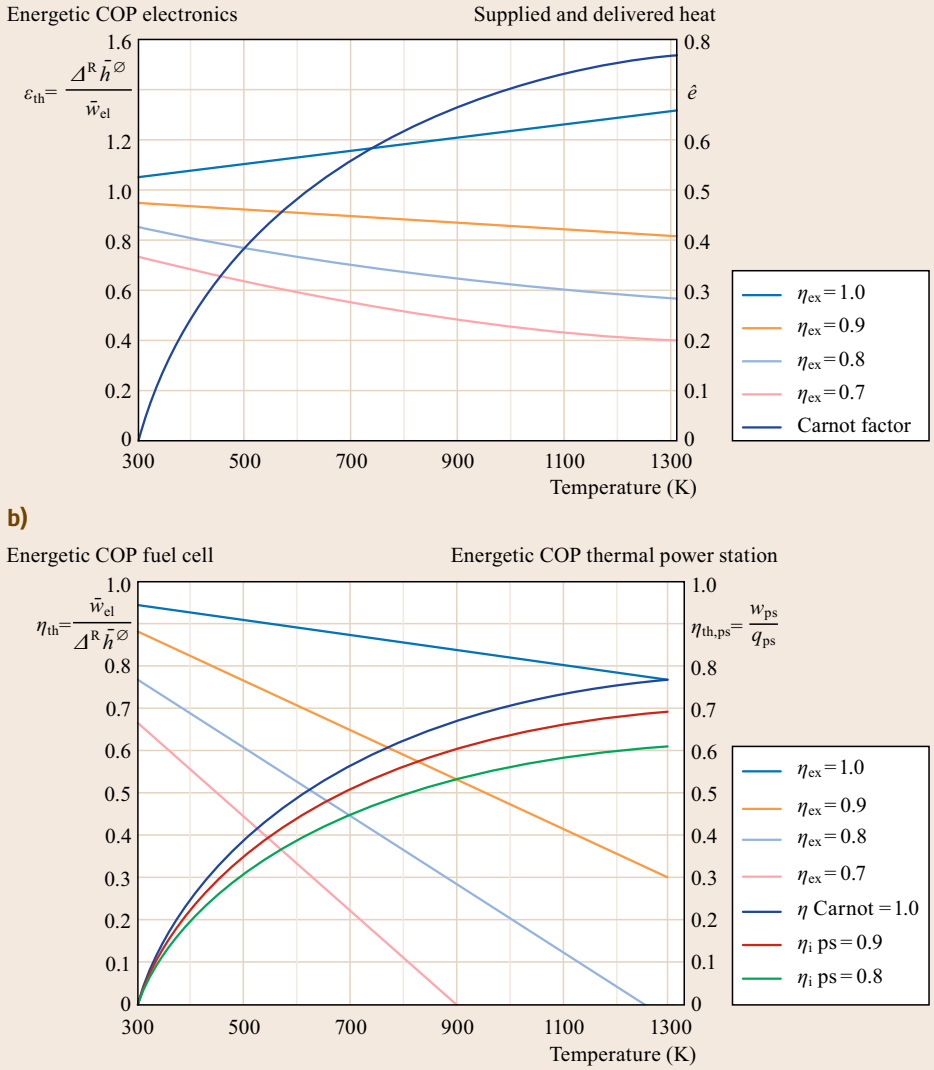


Fig. 3.27a,b COPs of **(a)** water electrolysis and **(b)** hydrogen fuel cell as functions of temperature. The secondary axis of **(a)** illustrates the normalized exergy of the supplied heat in the case $\eta_{ex} = 1$ and of the delivered heat in the case of $\eta_{ex} \leq 0.9$. The secondary axis of **(b)** illustrates the COP of a thermal power station with hydrogen combustion and with different interior COPs of the cycle

and renewable energies are small. All fossil fuels have a normalized exergy near unity. For solid fuels it is somewhat larger, for natural gas somewhat smaller than unity. Renewable sources also have a normalized exergy near unity. For solar radiation it is slightly less than unity, for water and wind (i. e., kinetic energy) it equals unity, and for biomass it is slightly higher than unity. The first step in conversion of renewable energy is the production of electricity, with the exception of solar thermal low-temperature heat generation. In case of water and wind energy, it is a simple conversion. In the case of photovoltaic or solar thermal power stations it is a disproportionation. By contrast, fossil fuels are mainly used for process and communal heating or for traffic in the form of gasoline and diesel oil. This latter use is realized through internal combustion engines, i. e., in open cycles. Fossil fuels are only partly used for power generation with the help of thermodynamic cycles. Correspondingly, for the energy supply on the basis of renewable sources, electricity acquires a new role: it can be viewed as a primary type of energy. On this basis, energy carriers with better storage properties than that of electricity have to be produced. This is even more important because of the fluctuating energy output of solar power stations and wind converters. Such energy carriers are for instance hydrogen, methane, methanol and other chemicals, which may be used as fuel for transporta-

tion and as feedstock for the chemical industry in the future.

Usually, thermal power stations are described as closed cycles, i. e., as water steam Rankine cycles. However, in the combustion of fossil fuel with air the environment is always included. This may also be understood as a combination of a simple energy conversion (thermal combustion) and a closed cycle (the disproportionation of middle-temperature heat into work and low-temperature heat).

There are many important industrial cycles with mass transfer to the surroundings, especially involving coal, gas or liquid fuel combustion in power stations, engines and turbines or a combination of them. Partially, the heat supply at the middle temperature level is substituted by an interior combustion (instead of the use of a heat exchange surface). Such open cycles often require less technical expenditure, but they have more influence on the environment. If natural gas is used, the thermal reaction is

$$
\begin{aligned}
&\mathrm{CH_4} + 2\,\mathrm{O_2} + n\,\mathrm{N_2} \rightarrow \mathrm{CO_2} + 2\,\mathrm{H_2O} + n\,\mathrm{N_2},\\
&\bar{e}^{\,\varnothing}_{\mathrm{o}\,\mathrm{CH_4}} = \Delta^{\mathrm{PR}}\bar{g}^{\,\varnothing}_{\mathrm{o}\,\mathrm{CH_4}} = 800.4\,\mathrm{kJ/mol}\,,\\
&\Delta_{\mathrm{R}}\bar{h}^{\,\varnothing}_{\mathrm{o}\,\mathrm{CH_4}} = -802.3\,\mathrm{kJ/mol},\ \Delta_{\mathrm{R}}\hat{e}^{\,\varnothing}_{\mathrm{o}\,\mathrm{CH_4}} = 0.998\,,\\
&\Delta\bar{h}_{\mathrm{th}} = -342.3\,\mathrm{kJ/mol},\ \Delta\bar{w} = -460\,\mathrm{kJ/mol}\,.
\end{aligned}
$$

A combination of a real gas turbine with a Rankine cycle produces nearly 460 kJ/mol methane of mechanical work. This work is the difference between the power output of the gas and steam turbine and the power required by the compressor. If one includes the combustion reaction, there is only a very small difference between the normalized exergies of methane and work. The combustion irreversibilities are significant because the real reaction temperature is very different from the reversible reaction temperature. The thermal COP of the gas and steam turbine process is ideally 0.6. As the reaction enthalpy and reaction exergy are nearly the same, the thermal and the exergetic COP do not differ significantly

$$
\begin{aligned}
\eta_{\mathrm{th,gst}} &= \frac{w_{\mathrm{real}}}{q_{\mathrm{mreal}}} = \frac{\Delta\bar{w}_{\mathrm{real}}}{\Delta_{\mathrm{R}}\bar{h}^{\,\varnothing}_{\mathrm{o}\,\mathrm{CH_4}}} = 0.573\,,\\
\eta_{\mathrm{ex,gst}} &= \frac{\Delta\bar{w}_{\mathrm{real}}}{\bar{e}^{\,\varnothing}_{\mathrm{o}\,\mathrm{CH_4}}} = 0.575\,.
\end{aligned}
$$

However, taking into consideration the transformation characteristics (the transformation ratio, the reversible transformation ratio, and consequently the exergetic transformation COP), the influence of irreversibilities becomes evident. Theoretically, the normalized exergy of methane is almost unity and the necessary normalized lifting exergy for the transformation is very small. The normalized driving exergy (i. e., the difference between the normalized exergy of methane and low-temperature heat) is very high. Therefore, the reversible transformation ratio is also very high

$$
\varepsilon_{\mathrm{t,rev}} = \frac{\Delta_{\mathrm{R}}\hat{e}^{\,\varnothing}_{\mathrm{o}\,\mathrm{CH_4}} - \hat{e}_{\mathrm{ql}}}{1 - \Delta_{\mathrm{R}}\hat{e}^{\,\varnothing}_{\mathrm{o}\,\mathrm{CH_4}}} = \frac{\bar{w}_{\mathrm{el,rev}}}{\bar{q}_{\mathrm{rev}}} = 499\,.
$$

The realistic transformation ratio is, though it is the best efficiency of modern thermal power stations, only

$$
\varepsilon_{\mathrm{t,gt}} = \frac{\Delta\bar{w}_{\mathrm{real}}}{\Delta_{\mathrm{R}}\bar{h}^{\,\varnothing}_{\mathrm{o}\,\mathrm{CH_4}} - \Delta\bar{w}_{\mathrm{real}}} = 1.5\,,
$$

hence the exergetic transformation COP reads

$$
\eta_{\mathrm{ex,t}} = \frac{\Delta\hat{e}_{\mathrm{lift}}}{\Delta\hat{e}_{\mathrm{driv}}}\,\frac{\bar{w}_{\mathrm{el}}}{\bar{q}} = 0.003\,.
$$

The reason for this catastrophic efficiency is the high energetic quality, which cannot be directly transformed into work. It can only be used after conversion into thermal enthalpy and its subsequent transformation in a gas turbine cycle and in a steam turbine cycle.

Nomenclature

Latin symbols:

A	Surface
a	Activity
$\bar{c}_{\mathrm{p}}$	Molar heat capacity
c	Concentration
$\bar{e}_x$	Molar exergy
$\bar{e}_q$	Molar exergy of heat
$\hat{e}_x$	Normalized exergy
E	Electrical potential, electrical field strength
F	Faraday constant
f	Fugacity
G	Gibbs energy
$\bar{g}$	Molar Gibbs energy
$\bar{h}$	Molar enthalpy
I	Current
j	Current density
K	Thermodynamic equilibrium constant
k	Reaction rate
L	Liquid
P	Pressure
$\bar{q}$	Molar heat
R	Molar gas constant
R_{r}	Reaction resistance
S	Solid
$\bar{s}$	Molar entropy
T	Thermodynamic temperature
T^*	Equivalent temperature
u	Ion mobility

V Gas
$\bar{w}$ Molar work
$\boldsymbol{x}$ Composition of the system
$z_{\pm}$ Number of charges
$\Delta_R \bar{e}_x$ Molar reaction exergy
$\Delta_R \hat{e}_x^{\emptyset}$ Normalized molar reaction exergy
$\Delta \bar{e}_{\mathrm{loss}}$ Molar exergy loss
ΔE Overpotential, potential loss
$\Delta_R \bar{g}$ Molar reaction Gibbs energy (negative value of molar affinity)
$\Delta_R \bar{h}$ Molar reaction enthalpy
$\Delta_R \bar{s}$ Molar reaction entropy
$\Delta \bar{s}_{\mathrm{c}}$ Entropy creation
$\Delta_R \bar{c}_{\mathrm{p}}$ Molar reaction heat capacity

Greek symbols:

α Cross factor
δ Distance
ε Transformation ratio, COP
η COP
λ Loss coefficient
Λ Molar conductivity
$\bar{\mu}$ Molar chemical potential
ν Stoichiometric coefficient, ion velocity
ξ Extent of the reaction
χ Electrical conductivity

References

3.1 J. Newman, K.E. Thomas-Alyea: *Electrochemical Systems* (Wiley, New York 2004)
3.2 F. Goodridge, K. Scott: *Electrochemical Process Engineering: A Guide to the Design of Electrolytic Plant* (Plenum, New York 1995)
3.3 G.G. Trost, V. Edwards, J. Newman: *Electrochemical Reaction Engineering*, Chemical Reaction and Reactor Engineering (Marcel Dekker, New York 1987)
3.4 S.I. Sander: *Chemical, Biochemical and Engineering Thermodynamics* (Wiley, New York 2006)
3.5 J.M. Smith, H.C. Van Ness, M.M. Abbott: *Introduction to Chemical Engineering Thermodynamics* (McGraw-Hill, New York 2005)
3.6 M.J. Moran, H.N. Shapiro, D.D. Boettner, M.B. Bailey: *Fundamentals of Engineering Thermodynamics* (Wiley, New York 2010)
3.7 V.S. Bagotsky: *Fundamentals of Electrochemistry* (Wiley, New York 2006)
3.8 J. Szargut, D.R. Morris, F.R. Steward: *Exergy Analysis of Thermal, Chemical and Metallurgical Processes* (Hemisphere, New York 1988)
3.9 J. Szargut: *Exergy Analysis: Technical and Ecological Applications* (Wittpress, Southampton 2005)
3.10 A. Bejan: *Advanced Engineering Thermodynamics* (Wiley, New York 1990)
3.11 V.M. Brodyansky: *The Efficiency of Industrial Process* (Elsevier, Amsterdam 1994)
3.12 N. Sato: *Chemical Energy and Exergy* (Elsevier Science, Amsterdam 2004)
3.13 I. Dincer, M.A. Rosen: *Exergy* (Elsevier, Amsterdam 2012)
3.14 G. Hradetzky, D.A. Lempe: MerseburgDataBank MDB for Physico-Chemical Data of Pure Compounds. Version 6.4.2. (1992–2008)
3.15 A.J. Bard, L.R. Faulkner: *Electrochemical Methods, Fundamentals and Applications* (Wiley, New York 2001)
3.16 W. Vielstich, A. Lamm, H. Gasteiger: *Handbook of Fuel Cells* (Wiley, Chichester 2003)
3.17 T. Schulz, S. Zhou: Sundmacher: Current status of and recent developments in the direct methanol fuel cell, Chem. Eng. Technol. **24**, 1223–1233 (2001)
3.18 H. Wendt, G. Kreysa: *Electrochemical Engineering* (Springer, Berlin, Heidelberg 1999)
3.19 G. Alefeld, R. Rademacher: *Heat Conversion Systems* (CRC, Boca Raton 1994)
3.20 R.D.H. Hoyle, P.H. Clarke: *Thermodynamic Cycles and Processes* (Longman, New York 1973)
3.21 D. Hebecker, P. Bittrich: Energy and materials conversion with the help of regeneration and energy transformation, Int. J. Therm. Sci. **40**, 316–328 (2001)
3.22 D. Hebecker, P. Bittrich: Classification and evaluation of heat transformation processes, Int. J. Therm. Sci. **38**, 465–474 (1999)
3.23 N. Monnerie, M. Schmitz, M. Roeb, D. Quantius, D. Graf, C. Sattler, D. de Lorenzo: Potential of hybridisation of the thermochemical hybrid-sulphur cycle for the production of hydrogen by using nuclear and solar energy in the same plant, Int. J. Nucl. Hydrogen Prod. Appl. **2**(3), 178–201 (2011)
3.24 M. Carmo, D.L. Fritz, J. Mergel, D. Stolten: A comprehensive review on PEM water electrolysis, Intern. J. Hydrogen Energy **38**, 4901–4934 (2013)
3.25 K. Kordesch, G. Simader: *Fuel Cells and Their Application* (VCH, Weinheim 1996)

4. Thermodynamics of Electrochemical Systems

Signe Kjelstrup, Dick Bedeaux

The aim of this chapter is to show how a new extension of classical nonequilibrium thermodynamics, able to describe heterogeneous systems, can be applied in electrochemistry [4.1]. The aim is also to discuss how a further extension to mesoscopic systems can be used to describe nonlinear regimes, that is, the electrode overpotential. Electrochemical systems are heterogeneous, for instance, because the charge carrier changes across the system. We need to deal with charge transfer through a series of layers; the electrode, the electrolyte material layers, and interfaces between them. The extension of nonequilibrium thermodynamics to heterogeneous systems [4.1] enables us to deal with the variation in chemical potential and temperature across such layers in a systematic manner. We review the method that enables us to integrate across the layers, and explain coupled transfer of heat, mass and charge in such systems. The idea of mesoscopic nonequilibrium thermodynamics is next presented, and perspectives and new possibilities are pointed out.

4.1 **Scope and Premises** 69
4.1.1 The Core Postulates of Non-Equilibrium Thermodynamics 70
4.1.2 Perspectives of NET on Electrochemical Systems 70
4.1.3 Symmetry Rules in Heterogeneous Systems 71
4.1.4 The Basic Assumption: Local Equilibrium 71
4.2 **Thermodynamic Properties of the Total Cell** 72
4.3 **Example Cells** 73
4.4 **Entropy Production in Three- and Two-Dimensions** 74
4.5 **Alternative Variable Sets** 75
4.5.1 Mass Balance and Entropy Production 76
4.5.2 Transference Coefficients and Transport Numbers 77
4.5.3 Externally Controlled Fluxes. The Measurable Electric Potential 78
4.5.4 Ionic Fluxes and Forces: The Planck Potential 79
4.6 **Cell Potentials** 80
4.6.1 An Isothermal Formation Cell with a Concentration Gradient 80
4.6.2 A Nonisothermal Formation Cell 80
4.6.3 The Liquid Junction 82
4.6.4 The Butler–Volmer Equation 83
4.6.5 Power from Reverse Electrodialysis 85
4.6.6 Electrochemical Cells as Thermoelectric Generators 86
4.7 **The Polymer Electrolyte Fuel Cell** 87
4.8 **Transport at Interfaces. Perspectives and Conclusion** 90
References 91

4.1 Scope and Premises

The field of classical nonequilibrium thermodynamics (NET) was established by *Onsager* in 1931 [4.2, 3] and developed during the 1940s and 1950s. Equilibrium thermodynamics describes energy conversion in formation cells or electrolysis cells under reversible conditions. Nonequilibrium thermodynamics gives a systematic dynamic description of energy conversion far from reversible conditions. Conversions between thermal, mechanical, chemical, and electric energies are described through coupled fluxes and forces. The coupling coefficients in electrochemical systems, which are all heterogeneous systems, are large at interfaces. The principles of the theory are illustrated here for concentration and formation cells. We proceed to discuss how the theory becomes useful in the case of thermoelectric energy conversion, a saline power plant, and the polymer electrolyte fuel cell. The theory can be extended to include internal variables, and this gives

a thermodynamic basis to the Butler–Volmer equation. New perspectives are pointed out, given the rules provided by NET for coupling of transport phenomena at interfaces.

4.1.1 The Core Postulates of Non-Equilibrium Thermodynamics

The theory of NET describes transport processes in systems that are out of global equilibrium. This condition applies to electrochemical systems in operation. The theory resulted from the work of many scientists with the aim to find a more useful formulation of the second law of thermodynamics [4.1]. In NET, the second law is formulated in terms of the entropy production σ in a volume or area element of the system. This quantity is positive or zero (if the process is reversible). It is given by the product sum of the so-called conjugate fluxes J_i and forces X_i

$$\sigma = \sum_i J_i X_i \geq 0 \,. \tag{4.1}$$

Each flux is *locally* a linear combination of all forces

$$J_i = \sum_j L_{ij} X_j \,. \tag{4.2}$$

The reciprocal (Onsager) relations

$$L_{ji} = L_{ij} \tag{4.3}$$

were proven for independent forces and fluxes [4.2, 3]. In the context of NET, the word *coupling* refers to a nonzero value of the off-diagonal coefficients (4.3). The word will be used here in this strict sense. The interdependence of variables via other equations, say via the energy, mass, or momentum balances, is not coupling in this sense.

The linearity in (4.2) refers to a position x. We shall deal with example systems, where the transport processes can be regarded as being one-dimensional (1-D). By integrating across a system, nonlinearities will appear, because the coefficients are functions of state variables. One may also integrate over internal variables in the system in a mesoscopic formulation of (4.1)–(4.3) [4.4–9], see Sect. 4.6.4, and obtain nonlinear relations. In this sense NET is now a theory also for nonlinear phenomena. In the application of NET, one has to first identify a complete set of extensive, independent variables A_i and the entropy S. Then the conjugate fluxes and forces obey

$$J_i = \frac{\mathrm{d}A_i}{\mathrm{d}t} \quad \text{and} \quad X_i = \left(\frac{\partial S}{\partial A_i}\right)_{A_j} \,. \tag{4.4}$$

Here t is the time. Some authors have stated that any set of fluxes and forces that fulfill (4.1) also obeys (4.3). This is not correct [4.5]. We also need (4.4). Equations (4.1)–(4.4) contain all information on the nonequilibrium behavior of the system. In practice, the simplest version of σ is chosen for each part of the system for the determination of appropriate laws of transport.

The importance of equilibrium thermodynamics for the design of experiments is well known. The definition, of say a partial molar property, explains what shall be varied, and what shall be kept constant in the experimental determination of a quantity. Equilibrium thermodynamics offers relations between variables, for alternative measurements of these. For instance, the enthalpy of evaporation can be measured in a calorimeter and it can also be determined from the variation in the vapor pressure of the evaporating gas with the temperature.

Nonequilibrium thermodynamics is instrumental for the design of experiments that give transport properties, and the Onsager relations offer alternative routes to the same transport coefficient. For instance, if it is difficult to measure one coefficient $L_{q\phi}$, one may rather measure $L_{\phi q}$ [4.10–13]. A valuable consistency check for the measurements is provided by measuring both coupling coefficients. So, similar to the situation in equilibrium, also nonequilibrium systems have possibilities for control of internal consistency. A second possibility for control is to use the entropy balance (Sect. 4.2) in combination with (4.1).

4.1.2 Perspectives of NET on Electrochemical Systems

The general development of NET was reviewed by *Kjelstrup* and *Bedeaux* [4.1]. The classical form of the theory was early applied to electrochemical systems. Works by *Kedem*, *Katchalsky* and coworkers [4.14] and *Haase* [4.15] were central in that context. Electrokinetic phenomena in membranes were treated by *Laksminarayanaiah* [4.16], *Mikulecky* [4.17], *Staverman* [4.18], and *Førland* et al. [4.19], while *Ito* et al. [4.20] and *Richter* et al. [4.21, 22] studied molten salt electrolytes. Concentration cells with and without membranes were used to test concepts [4.23–26]. Membranes exposed to gradients in concentration, pressure, and temperature were systematically studied by several groups [4.27–31]. Books on electrochemistry have since long contained chapters on NET, see e.g., *Newman* [4.32]. Classical NET was applied to continuous or discrete systems, but the heterogeneity of electrochemical systems was taken systematically into account only after 1996, see [4.1] for further references.

Heterogeneous systems distinguish themselves from homogeneous ones by the presence of interfaces

or phase boundaries. The interface can, according to *Gibbs* [4.33], be regarded as a separate two-dimensional (2-D) thermodynamic system between three-dimensional systems. This is a core element in the extension of classical nonequilibrium theory to deal with interface transport [4.1]. The electrode surface can be treated as a two-dimensional thermodynamic system. Because most of the electrochemical energy conversion takes place here, it is of interest to know the entropy production for two-dimensional systems and the rules of coupling in this context.

Transports at interfaces, or contact lines, possess a different symmetry than transport processes in homogeneous phases. At the surface, the system is no longer isotropic in the direction normal to the surface. The normal component of any vectorial flux is then scalar under rotations and reflections in the plane of the surface, and this component may then couple to scalars, such as a reaction rate, without violating the Curie principle [4.4]. This leads to other rules of coupling for interfaces or contact lines [4.1] than for bulk systems, as demonstrated for biological systems [4.34]. One purpose of this chapter is to present and discuss these rules for the electrode surface. The coupling rules remain to be explored to a large extent in electrochemistry, and we shall point at such possibilities in the end of the chapter.

The typical electrochemical reaction has a nonlinear relation between the reaction rate and its driving force, similar to the case of a chemical reaction. The systematic approach of classical NET was also extended to deal with this situation, by including mesoscale (internal) variables. The probability density along the reaction coordinate is an example of a central internal variable. Linear flux–force relations (4.2), will then apply, but on the scale of the internal variables. To do this, was first suggested by *Prigogine* and *Mazur* [4.35], cf. *de Groot* and *Mazur* [4.4, 5], but the idea has now gained momentum [4.6–9]. The Butler–Volmer equation has thus been derived also with a basis in the entropy production [4.7], but one has not yet fully taken advantage of this line of research opening up in electrochemistry. We shall focus on conditions where the linear laws (4.2), apply on the macroscopic level to the homogeneous phases as well as to the interface, and discuss briefly the mesocopic formulation of the Butler–Volmer equation and the meaning of coupling in this context in Sect. 4.6.4.

Hydrodynamic equations are frequently important for the description of electrochemical measurements and cells in operation. It is also possible to see such descriptions within the framework of NET [4.36]. This represents another branch of NET, which is little explored, but is outside the scope of this chapter.

4.1.3 Symmetry Rules in Heterogeneous Systems

Homogeneous and heterogeneous systems differ in major ways with respect to possibilities for coupling, cf. (4.3). Homogeneous (isotropic) systems have no coupling between vectorial phenomena (transport of heat, mass and charge) and scalar phenomena (chemical reactions). These phenomena belong to separate classes and can be dealt with separately [4.4, 5] (the Curie principle) (Sect. 4.1.2).

A heterogeneous system contains interfaces or surfaces (these words will be used interchangeably). Only the scalar component perpendicular to the interface is relevant for a flux of heat, mass, or charge into or through the interface. This means that coupling can occur directly between transport of heat, mass, charge and (electro)chemical reaction without violating the Curie principle. This fact has mostly been overlooked in the literature. But according to the rules stated, such coupling is possible at electrode surfaces, creating a need for a local, not overall, description of the transport problems.

The coupling between heat and mass fluxes at interfaces was studied for the liquid–vapor transition [4.37–40]. The coupling coefficients were large for this phase transition. They are also large at the electrode surface due to the electrochemical reactions [4.1]. The flux equations for the surfaces predict jumps in intensive variables across or into the surface, and define in this manner dynamic boundary conditions, essential for the integration of variables through the surface. The most important jump is, of course, the electric potential jump. But there are, in principle, also jumps in other intensive variables; the chemical potentials and the temperature. This chapter will present such examples.

4.1.4 The Basic Assumption: Local Equilibrium

The basic assumption of NET, for homogeneous or heterogeneous systems, as well as mesoscopic ones, is the assumption of local equilibrium. Some words on the validity of this crucial assumption are thus important. For homogeneous systems, we *define* local equilibrium by the validity of the classical thermodynamic equations in the volume element considered [4.1, 41, 42]. For interfaces, we obtain a thermodynamic description of the interface, following Gibbs, using excess densities. Local equilibrium is then defined for Gibbs excess quantities which have values that obey equilibrium thermodynamic relations for the area element [4.1, 43]. For mesoscopic systems, local equilibrium means that the Gibbs entropy postulate applies to variables

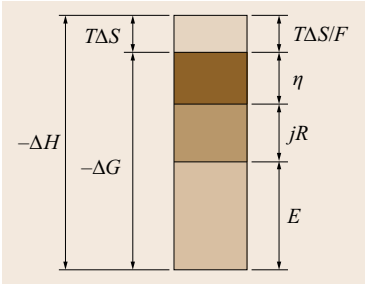


Fig. 4.1 Thermodynamic properties of the total electrochemical cell. The entropy change of the cell contributes to the cell potential, while the total entropy production represents available energy dissipated as heat (after [4.46]). For explanation of symbols (Sect. 4.2)

on the meso-level [4.6]. We distinguish between local *chemical* equilibrium, when the reaction Gibbs energy $\Delta G = 0$, and local *thermodynamic* equilibrium which allows the chemical reaction to be out of equilibrium, as it frequently is at an electrode surface. The first situation is a sub case of the more general second case and need not apply, see [4.44] for an application.

In a heterogeneous electrochemical system, we therefore assume, in spite of gradients or jumps in intensive variables and electric fields, that there is local thermodynamic equilibrium in each homogeneous phase, in each interface, and even along the reaction coordinate of the electrochemical reaction where internal variables are defined (see Sect. 4.6.4 and [4.7] for further comments). In other words, we can use thermodynamic equations in modeling on all relevant scales. This assumption is frequently taken for granted, without explicit reference. In fact, it is used whenever thermodynamic equations are used in the modeling of a system. Evidence for the validity of the assumption of local equilibrium has been obtained under extreme nonequilibrium conditions, using molecular dynamics simulations. Also, linear flux–force relations were often found under such conditions. For an overview, see [4.45].

Surprisingly small systems have well definable thermodynamic properties [4.47–51], and evidence for local equilibrium in small systems (surfaces) is accumulating [4.39, 52–54]. The interface can thus have its own intensive variables, different from the corresponding variables in the adjacent bulk phases. The fact that the law of mass action [4.55], or the Butler–Volmer equation [4.7], can be derived from a mesoscopic thermodynamic basis, gives indirect support to the validity of the assumption of local equilibrium on this scale (Sect. 4.6.4) and so does the fact that biological pumps can be described adequately [4.8, 9, 34, 56, 57].

Classical thermodynamics describes systems in global equilibrium. The equations apply also to molecular sized systems, but then with special additions [4.47–51]. NET describes systems, sometimes exposed to extreme fields, having small volume elements in local equilibrium. It is then natural to ask: What is the similarity and what is the difference between two small volume elements; one in the absence and one in the presence of a field?

The similarity is that thermodynamic equations apply to both types of volume elements. The difference has been found by studying the nature of the fluctuations. In global equilibrium, fluctuations center around the equilibrium value. In local equilibrium, fluctuations of densities and temperature can be enhanced several orders of magnitude [4.58] compared to the value at global equilibrium. In particular, long-range correlations reaching the μm scale develop away from global equilibrium. While the nature of the temperature and density fluctuations changes considerably away from global equilibrium, a local form of the fluctuation-dissipation theorem remains valid [4.42]. This gives another justification for the use of thermodynamic equations in these volume elements. For further discussions on the nature of the long-range fluctuations, we refer to [4.42].

4.2 Thermodynamic Properties of the Total Cell

An electrochemical cell is never in global equilibrium. Using NET, we are seeking a local description of the energy conversion that takes place as charge is transported through the layers. The description has its origin in the second law of thermodynamics and produces in a systematic manner equations that govern the coupled transport of heat, mass, and charge. The local description will, when integrated, agree with the thermodynamic description of the total cell. It is, therefore, useful to first consider the overall description. The energy available for work in an isothermal, isobaric electrochemical cell is the Gibbs energy change of the cell reaction ΔG. This quantity gives the reversible cell potential, or the electromotive force $\Delta\phi_{j\to 0} = -\Delta G/F$, at the temperature T and pressure p in question. Here j is the electric current density and F is Faraday's constant, when one mole of electrons are transferred in the reaction. The Gibbs energy change has a contribution from

the enthalpy change ΔH and the entropy change ΔS. The heat transferred reversibly from the surroundings to the system is $q_{\text{syst, rev}} = T\Delta S = -q_{\text{surr, rev}}$. Its sign depends on ΔS.

Under reversible conditions ($j \to 0$), the entropy change in the system and in the surroundings is zero, and no entropy is produced. When $j \neq 0$, there is heat production, also from irreversible processes. This includes, for instance, Joule heat from the ohmic potential drop jR, where R is the total electric resistance, and heat production due to the sum of overpotentials η at the electrodes. The heat production can be measured in the surroundings at steady state [4.46, 59].

The total entropy production $\mathrm{d}S_{\text{irr}}/\mathrm{d}t$, which is the entropy change in the surroundings plus in the system, is the heat production per unit of time from the irreversible processes. The entropy balance for a system of cross-sectional area Ω and length l in a steady state is

$$\frac{\mathrm{d}S_{\text{irr}}}{\mathrm{d}t} = \Omega \int_0^l \sigma(x)\mathrm{d}x \,, \tag{4.5}$$

where we have assumed that all transport processes take place in the x-direction. At steady state, the entropy production is equal to the net entropy flow into the surroundings. This flow is obtainable from state function properties. But, as explained, the entropy production is also obtained by integrating (4.5), using transport properties (4.1) across the system. This makes a consistency check on the thermodynamic model possible, as mentioned in Sect. 4.4.

We obtain an overall picture of the situation in the cell. The actual power is Ej, while the lost work or exergy loss is $T_0\mathrm{d}S_{\text{irr}}/\mathrm{d}t$, where T_0 is the temperature of the surroundings [4.1]. The contributions to the total entropy production come from $\sigma(x)$. We can use NET to gain an insight into the origin of power losses, knowing local values of the fluxes and forces in (4.1) (Sect. 4.7). Through NET we can answer questions like, will a difference in temperature between the anode and the cathode promote or reduce the cell potential. In a situation where the energy efficiency for power use and power production is in focus worldwide, it may be beneficial to pay more attention to $\mathrm{d}S_{\text{irr}}/\mathrm{d}t$ [4.59].

4.3 Example Cells

We consider for the purpose of illustration, a (theoretical) formation cell [4.1, 60] and its two corresponding concentration cells [4.1, 61]. The formation cell has an electrode reversible to Na^+ to the left and a Ag|AgCl-electrode reversible to Cl^- to the right. Na can be thought of as stabilized by a stirred amalgam. The concentration cells have two electrodes, either reversible to Na^+ or to Cl^-. With standard notation, we write for the cells

$$\mathrm{Na(Hg)|NaCl(aq)|AgCl(s)|Ag(s)} \,, \tag{4.6}$$

$$\mathrm{Na(Hg)|NaCl(aq)|Na(Hg)} \,, \tag{4.7}$$

$$\mathrm{Ag(s)|AgCl(s)|NaCl(aq)|AgCl(s)|Ag(s)} \,. \tag{4.8}$$

The heterogeneity of a cell is shown by vertical bars between the phases. In a local analysis, each homogeneous phase and each interface is a thermodynamic subsystem, a two- or three-dimensional (3-D) one, respectively.

The left-hand side electrode reaction of the formation cell (4.6) is

$$\mathrm{Na(Hg)} \to \mathrm{Na^+(aq)} + \mathrm{e^-} \,. \tag{4.9}$$

One mole of Na^+ moves into the electrolyte from the stirred amalgam per mole of electrons (faraday) passing the external circuit from left to right. At the surface of the chloride layer that faces the electrolyte we have

$$\mathrm{AgCl(s)} \to \mathrm{Cl^-(aq)} + \mathrm{Ag^+(s)} \,. \tag{4.10}$$

One mole of Cl^- is produced in the electrolyte, while one mole of silver ions is produced in the chloride, close to this surface. The silver ions are transported to the surface between the chloride layer and the silver. The right-hand side electrode reaction is

$$\mathrm{Ag^+(s)} + \mathrm{e^-} \to \mathrm{Ag(s)} \,. \tag{4.11}$$

The overall electrode reaction is the sum of (4.10)–(4.11). The overall *cell* reaction of (4.6) is

$$\mathrm{Na(Hg)} + \mathrm{AgCl(s)} \to \mathrm{Na^+(aq)} + \mathrm{Cl^-(aq)} + \mathrm{Ag(s)} \,. \tag{4.12}$$

One mole of Ag(s) and one mole of NaCl(aq) are produced and one mole of Na and one mole of AgCl(s) are consumed per faraday passing the cell. Because of the electroneutral nature of the electrolyte, the concentrations of the sodium and the chloride ions are the same at every position in the electrolyte. When a sodium ion enters the electrolyte from the electrode surface, it is

therefore quickly accompanied by a chloride ion coming into the electrolyte from the AgCl surface. This is not described by the total reaction, but can be captured using NET.

In a concentration cell, there is no *net* accumulation of salt in the cell as electric current passes the cell, because the number and type of ions entering the cell is equal to the number and type of ions leaving the cell. This is true when the two electrodes are reversible to Na^+ or to other ions, for example Cl^-. Local changes in salt concentration take place, however. Deficits on one location are balanced by a surplus on another location in a concentration cell. In a formation cell, this is no longer true. The interplay of all phenomena can be systematically described by NET [4.62–66].

With well conducting metal electrodes, heat can be rapidly conducted away from the cell, and the cell can be regarded as isothermal. Whenever the thermal conduction becomes poor, however, significant temperature gradients arise. This can happen for instance in gas electrodes like in fuel cells. It is a well-known problem in Li batteries. There are always concentration gradients in electrochemical cells, to a smaller or larger degree. NET can be used to find a simultaneous solution to profiles of temperature, concentration, and electric potential. At the start of such an analysis, the most practical formulation of the entropy production is sought.

4.4 Entropy Production in Three- and Two-Dimensions

As explained in Sect. 4.1.1, an analysis in terms of NET starts with a derivation of the entropy production. Electrochemical cells are heterogeneous, and the entropy production can vary largely between the parts, or the subsystems, of the cell. It may be particularly large at surfaces, due to reaction overpotentials. An electrochemical cell has often a mixture of processes, linear, or nonlinear in the driving forces. In the next section, we address the processes that are linear in their driving forces, while the typical nonlinear Butler–Volmer equation is given a thermodynamic basis in Sect. 4.6.4 [4.7]. The entropy production has *in all cases*, however, a bilinear form in fluxes and driving forces [4.67].

The electrolyte and the bulk electrode materials are relatively thick and can therefore be regarded as homogeneous bulk or three-dimensional subsystems. The electrode interfaces are normally much thinner. We shall therefore regard these as two-dimensional thermodynamic systems. It will carry too far to show the derivation of the entropy production for three- and two-dimensional systems. For this, we refer to [4.1, 62, 68–70]. We only stress as that the entropy production, *not the dissipation function*, defines the conjugate forces and fluxes [4.1]. The old literature is not always clear on this point. The purpose here is to demonstrate the use and meaning of the expressions. We give therefore practical forms of the entropy production for all subsystems of the example cells, referring to the literature mentioned for derivations. Notation and symbols follow [4.1] and are illustrated and explained in Fig. 4.2.

Consider thus the simultaneous transport of heat, mass and charge through the formation cell (4.6). The entropy production in a uniform sodium electrode, phase a, is given by

$$\sigma^{\mathrm{a}} = -J_q'^{\mathrm{a}} \frac{1}{T^2}\frac{\partial T}{\partial x} - j\frac{1}{T}\frac{\partial \phi}{\partial x} \,. \tag{4.13}$$

The entropy production has one contribution from the measurable heat flux across the metal and the temperature gradient. The last term contains the electric current density and its conjugate force, the negative gradient in the electric potential over the temperature. A similar expression applies to the pure, solid AgCl and Ag phases.

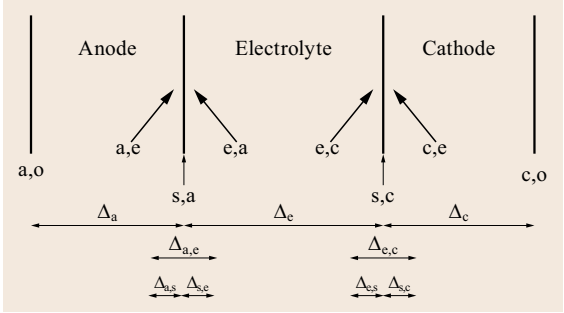


Fig. 4.2 Terminology for electrochemical cells according to [4.1]. The anode, electrolyte, and cathode phases are indicated with superscripts a, e, and c, respectively. The electrode surfaces are denoted by s,a and s,c at the anode and cathode, respectively. A difference is taken between the last (j) and the first (i) phase in a subscript i,j, or across a homogeneous phase (k) with subscript k. Locations are indicated by superscripts (i,j), where the phase is i, and the adjacent phase is j

The entropy production in the bulk electrolyte has three terms

$$\sigma^{\mathrm{e}} = -J_q'^{\mathrm{e}} \frac{1}{T^2} \frac{\partial T}{\partial x} - J^{\mathrm{e}}_{\mathrm{NaCl}} \frac{1}{T} \frac{\partial}{\partial x} \mu^{\mathrm{e}}_{\mathrm{NaCl},T} - j \frac{1}{T} \frac{\partial \phi}{\partial x} \,. \tag{4.14}$$

The contributions are from the measurable heat flux across the electrolyte and the temperature gradient, the flux of NaCl relative to water and the gradient in chemical potential of NaCl at constant temperature, and the electric current density and the gradient in the electric potential. It is practical to choose the same frame of reference for all fluxes involved. The natural frame of reference for an electrochemical cell is an equimolar electrode surface. This becomes equal to the solvent (water) frame of reference in the present case. It is more common to choose ionic fluxes than salt fluxes as variables. We discuss in Sect. 4.5 alternative choices of fluxes to J_{NaCl} and j, namely J_{Na^+} and J_{Cl^-}. All choices must describe the same entropy production, however.

The entropy production in the surface of the Na^+ reversible electrode has two heat flux contributions, the first pointing into the surface on the left-hand side, the other pointing out of the surface on the right-hand side. The number of variables at the surface can very soon become large, if there is transport across both sides of the surface. In the stationary state, the reaction rate is given in terms of the electric current $r^{\mathrm{s,a}} = j/F$. This results in

$$\sigma^{\mathrm{s,a}} = J_q'^{\mathrm{a,e}} \Delta_{\mathrm{a,s}} \left(\frac{1}{T}\right) + J_q'^{\mathrm{e,a}} \Delta_{\mathrm{s,e}} \left(\frac{1}{T}\right) - j \frac{1}{T^{\mathrm{s,a}}} \left(\Delta_{\mathrm{a,e}}\phi + \frac{\Delta_n G^{\mathrm{s,a}}}{F}\right), \tag{4.15}$$

where all sub- and superscripts are defined in Fig. 4.2. The dividing surface is the equimolar sodium interface. The surface of discontinuity includes part of the metal, part of the electrolyte. Metal is consumed, while $t^{\mathrm{e,a}}_{\mathrm{NaCl}}$ moles of NaCl are formed in the electrolyte next to the metal per mole of charge passing the external circuit (Sect. 4.5). The Gibbs energy change $\Delta_{\mathrm{n}}G$ is defined by the changes in content of neutral components in the surface.

The entropy production of the electrolyte-AgCl|Ag-surface becomes in analogy

$$\sigma^{\mathrm{s,c}} = J_q'^{\mathrm{e,c}} \Delta_{\mathrm{e,s}} \left(\frac{1}{T}\right) + J_q'^{\mathrm{c,e}} \Delta_{\mathrm{s,c}} \left(\frac{1}{T}\right) - j \frac{1}{T^{\mathrm{s,c}}} \left(\Delta_{\mathrm{e,c}}\phi + \frac{1}{F}\Delta_n G^{\mathrm{s,c}}\right). \tag{4.16}$$

The position of this interface is the crystallographic interface of AgCl, but the interface of discontinuity extends from the electrolyte phase into the Ag phase. The interface moves to the right as Cl^- is produced in the electrolyte. There is a change in the NaCl content per mole of charge passing the external circuit equal to $t^{\mathrm{e,c}}_{\mathrm{NaCl}}$ moles due to the electrode reaction and migration of ions from the electrolyte to the interface. The Gibbs energy change $\Delta_n G^{\mathrm{s,c}}$ in (4.16) reflects the changes in Ag, AgCl, and NaCl.

The electromotive force is measured in the limit $j \to 0$. All $\sigma^{\mathrm{s,i}}$ are zero in this limit, and

$$\Delta_{\mathrm{a,e}}\phi = -\frac{1}{F}\Delta_n G^{\mathrm{s,a}} \quad \text{and} \quad \Delta_{\mathrm{e,c}}\phi = -\frac{1}{F}\Delta_n G^{\mathrm{s,c}} \,. \tag{4.17}$$

It follows that there are no temperature jumps across the electrode surfaces under reversible conditions. The heat fluxes at these conditions need not be zero, however (Sect. 4.2), as the sum of the heat fluxes out of the cell is given by the cell's entropy change. Even in a concentration cell under reversible conditions, the heat produced at one electrode can be large (the single-electrode Peltier effect [4.20, 71, 72]), but the total heat flux out of the cell is zero in concentration cells (the cell entropy change is zero). This case shall be described in Sect. 4.6.6.

4.5 Alternative Variable Sets

The use of independent variables is mandatory in the proof of (4.3), but independent sets of concentration variables can be chosen in several ways.

In a system with transport of net charges, charge separation occurs because of differences in ionic mobilities. The most common choice is therefore to use ionic fluxes as variables and describe the changes in terms of these. The electric current density is then a dependent variable, equal to the difference between the fluxes of positive and negative charges. The driving forces are gradients in electrochemical potentials.

Kedem and *Katchalsky*, see [4.14], proposed to use operationally defined variables, motivated by the practical consideration that they are directly linked to measurements. The variable fluxes are then those of the neutral salts and the electric current density.

Charge separation can then be described using a time-dependent polarization, for instance, to find a cell's impedance [4.73]. The electric current density is seen as an independent variable, controllable from the outside of the cell. The assumption of local electroneutrality is used to eliminate ionic densities, as this assumption applies very well to time-scales typical for diffusion [4.74].

The last choice was used in the description of the entropy production in Sect. 4.4. We shall stay with the operationally defined variables, but discuss the relation between possible choices in this section, to enable comparisons of the operational approach with expressions in the literature, see also [4.1, 14, 19]. Any choice of mass variables must conform to the system's mass balance and describe all entropy production. We consider therefore the example cells from these perspectives, for the two possible choice of variables; the operationally defined choice and the choice using ionic fluxes and forces.

4.5.1 Mass Balance and Entropy Production

Consider the electrolyte solution of NaCl in water bounded by two electrodes. The time dependence of the salt concentration in the formation- or concentration cell satisfies

$$\frac{\partial}{\partial t} c^{\mathrm{e}}_{\mathrm{NaCl}}(t) = -\frac{\partial}{\partial x} J^{\mathrm{e}}_{\mathrm{NaCl}}(x,t)\,, \tag{4.18}$$

where $J^{\mathrm{e}}_{\mathrm{NaCl}}$ is the salt flux in the electrolyte. The positive direction of transport is from left to right. By integrating this equation across the thickness of the electrolyte, from $x = 0$ to $x = d_{\mathrm{e}}$, we obtain

$$\begin{aligned}\frac{\partial}{\partial t}\int_0^{d_{\mathrm{e}}} c^{\mathrm{e}}_{\mathrm{NaCl}}(t)\mathrm{d}x &= -J^{\mathrm{e}}_{\mathrm{NaCl}}(d_{\mathrm{e}},t) + J^{\mathrm{e}}_{\mathrm{NaCl}}(0,t)\\ &= J^{\mathrm{e,a}}_{\mathrm{NaCl}}(t) - J^{\mathrm{e,c}}_{\mathrm{NaCl}}(t)\,.\end{aligned} \tag{4.19}$$

Equation (4.19) describes that the accumulation of salt in the electrolyte per unit cross-sectional area is the difference of the salt fluxes at the two electrodes. In the two concentration cells, the difference is zero. In the formation cell, the integrated salt content in the electrolyte increases with j/F moles of NaCl per unit time and per unit cross-sectional area. The increase in the salt content in the electrolyte is therefore

$$\frac{\partial}{\partial t} c^{\mathrm{e}}_{\mathrm{NaCl}}(t) = -\frac{\partial}{\partial x} J^{\mathrm{e}}_{\mathrm{NaCl}}(x) = \frac{j}{d_{\mathrm{e}}F}\,. \tag{4.20}$$

Equations (4.18)–(4.20) imply that the salt flux is independent of time, but depends on position.

The relation between the ion fluxes and the salt flux depends, however, on the boundary conditions (the electrodes). When both electrodes are reversible to Cl^-, the component flux of NaCl is everywhere defined by the flux of Na^+. When both are reversible to Na^+, the flux of NaCl is everywhere defined by the flux of Cl^-

$$J^{\mathrm{e}}_{\mathrm{NaCl}} = J^{\mathrm{e}}_{\mathrm{Na^+}}$$

Concentration cell, Cl^--reversible electrodes, (4.21)

$$J^{\mathrm{e}}_{\mathrm{NaCl}} = J^{\mathrm{e}}_{\mathrm{Cl^-}}$$

Concentration cell, Na^+-reversible electrodes. (4.22)

In the formation cell, fluxes are position dependent (4.20), and (4.21)–(4.22) do not apply. The relation between salt and ion fluxes for this case will be given in Sect. 4.5.4.

The relation between the electric current density and the ionic fluxes is

$$\frac{j}{F} = J^{\mathrm{e}}_{\mathrm{Na}^+} - J^{\mathrm{e}}_{\mathrm{Cl}^-}\,, \tag{4.23}$$

meaning that possible position-dependent terms in the ionic fluxes cancel.

The entropy production due to NaCl transport in this solution, in terms of operationally defined variables (4.14) is

$$\sigma^{\mathrm{e}} = -J^{\mathrm{e}}_{\mathrm{NaCl}}\frac{1}{T}\frac{\partial}{\partial x}\mu^{\mathrm{e}}_{\mathrm{NaCl}} - j\frac{1}{T}\frac{\partial\phi}{\partial x}\,. \tag{4.24}$$

The same entropy production can also be written using ionic fluxes and forces

$$\sigma^{\mathrm{e}} = -J^{\mathrm{e}}_{\mathrm{Na}^+}\frac{1}{T}\frac{\partial}{\partial x}\tilde{\mu}^{\mathrm{e}}_{\mathrm{Na}^+} - J^{\mathrm{e}}_{\mathrm{Cl}^-}\frac{1}{T}\frac{\partial}{\partial x}\tilde{\mu}^{\mathrm{e}}_{\mathrm{Cl}^-}\,, \tag{4.25}$$

where the *electrochemical potentials of the ions* are defined as

$$\tilde{\mu}^{\mathrm{e}}_{\mathrm{Na}^+} = \mu^{\mathrm{e}}_{\mathrm{Na}^+} + F\psi\,, \tag{4.26}$$

$$\tilde{\mu}^{\mathrm{e}}_{\mathrm{Cl}^-} = \mu^{\mathrm{e}}_{\mathrm{Cl}^-} - F\psi\,. \tag{4.27}$$

Here, ψ is the electrostatic potential (Maxwell potential).

The fact that these expressions describe the same entropy production gives relations between the driving forces. When (4.21)–(4.22) are introduced into (4.24) and (4.25), we obtain for the concentration cell with sodium reversible electrodes

$$\phi = \psi + \frac{\mu^{\mathrm{e}}_{\mathrm{Na}^+}}{F} = \frac{\tilde{\mu}^{\mathrm{e}}_{\mathrm{Na}^+}}{F}\,, \tag{4.28}$$

and for chloride reversible electrodes

$$\phi = \psi - \frac{\mu^{\mathrm{e}}_{\mathrm{Cl}^-}}{F} = -\frac{\tilde{\mu}^{\mathrm{e}}_{\mathrm{Cl}^-}}{F} \,. \tag{4.29}$$

The expression for the formation cell will be given in Sect. 4.5.4. Similar relations can be written for other cells. They enable us to refer all variables to measurements and provide opportunities for consistency tests of theoretical descriptions. The measurable properties are $\Delta\phi, j, \Delta_{\mathrm{e}}\mu_{\mathrm{NaCl}}$ and $J^{\mathrm{e}}_{\mathrm{NaCl}}$. The measured electric potential is the sum of contributions from the various parts of the cell, $\Delta\phi = \Delta_{a,\mathrm{e}}\phi + \Delta_{\mathrm{e}}\phi + \Delta_{\mathrm{e},c}\phi$. Other properties can be derived or calculated from these. For instance, for concentration cells we have for the respective electrodes [4.1, 14]

$$\Delta\tilde{\mu}_{\mathrm{Na}^+} = F\Delta\phi = F\Delta_{\mathrm{e}}\phi \,, \tag{4.30}$$

$$\Delta\tilde{\mu}_{\mathrm{Cl}^-} = -F\Delta\phi = -F\Delta_{\mathrm{e}}\phi \,. \tag{4.31}$$

4.5.2 Transference Coefficients and Transport Numbers

From the mass balance, we can find the transference coefficients of neutral components in terms of transport numbers of ions. The well-known transport number of a cation and an anion is defined for a system without boundaries

$$t^{\mathrm{e}}_{\mathrm{Na}^+} \equiv F\left(\frac{J^{\mathrm{e}}_{\mathrm{Na}^+}}{j}\right)_{\partial c^{\mathrm{e}}_{\mathrm{NaCl}}/\partial x=0,\partial T/\partial x=0} \,,$$

$$t^{\mathrm{e}}_{\mathrm{Cl}^-} \equiv -F\left(\frac{J_{\mathrm{Cl}^-\mathrm{e}}}{j}\right)_{\partial c^{\mathrm{e}}_{\mathrm{NaCl}}/\partial x=0,\partial T/\partial x=0} \,. \tag{4.32}$$

It is the fraction of the electric current carried by the ion. The transport numbers do not depend on the position.

The transference coefficient of the salt in an electrolyte is defined by

$$t^{\mathrm{e}}_{\mathrm{NaCl}}(x,t) \equiv F\left(\frac{J^{\mathrm{e}}_{\mathrm{NaCl}}(x,t)}{j}\right)_{\partial\mu^{\mathrm{e}}_{\mathrm{NaCl}}/\partial x=0,\partial T/\partial x=0} \,. \tag{4.33}$$

A constant chemical potential and a constant temperature mean that the salt concentration is uniform or independent of the position in the electrolyte. Depending on the electrodes that supply the electric current density j, the transference coefficient can still be position dependent.

For the concentration cells, we have, from (4.21)–(4.22),

$$t^{\mathrm{e}}_{\mathrm{NaCl}} = t^{\mathrm{e}}_{\mathrm{Na}^+} \quad \text{for} \quad \mathrm{Cl}^- \text{-reversible electrodes} \,, \tag{4.34}$$

$$t^{\mathrm{e}}_{\mathrm{NaCl}} = -t^{\mathrm{e}}_{\mathrm{Cl}^-} \quad \text{for} \quad \mathrm{Na}^+ \text{-reversible electrodes} \,. \tag{4.35}$$

In order to find the transference coefficient for the formation cell, we start with the gradient of the transference coefficient. From (4.20) and (4.33), we have

$$\frac{\partial}{\partial x} t^{\mathrm{e}}_{\mathrm{NaCl}}(x,t) = \frac{F}{j}\frac{\partial}{\partial x} J^{\mathrm{e}}_{\mathrm{NaCl}}(x,t)$$
$$= -\frac{F}{j}\frac{\partial}{\partial t} c^{\mathrm{e}}_{\mathrm{NaCl}}(t) = -\frac{1}{d_{\mathrm{e}}} \,. \tag{4.36}$$

For all conditions, the electroneutrality condition gives $c^{\mathrm{e}}_{\mathrm{Na}^+}(t) = c^{\mathrm{e}}_{\mathrm{Cl}^-}(t) = c^{\mathrm{e}}_{\mathrm{NaCl}}(t)$. It follows that

$$\frac{F}{j}\frac{\partial}{\partial x} J^{\mathrm{e}}_{\mathrm{Na}^+}(x,t) = -\frac{F}{j}\frac{\partial}{\partial x} J^{\mathrm{e}}_{\mathrm{Cl}^-}(t) = -\frac{1}{d_{\mathrm{e}}} \,. \tag{4.37}$$

But in the formation cell [4.1, 60]; $J^{\mathrm{e}}_{\mathrm{Na}^+}(x,t) \neq t^{\mathrm{e}}_{\mathrm{Na}^+}(j/F)$ and $J^{\mathrm{e}}_{\mathrm{Cl}^-}(x,t) \neq t^{\mathrm{e}}_{\mathrm{Cl}^-}(j/F)$. In the formation cell, the salt flux is given by

$$J^{\mathrm{e}}_{\mathrm{NaCl}} = t^{\mathrm{e}}_{\mathrm{Cl}^-} J^{\mathrm{e}}_{\mathrm{Na}^+} + t^{\mathrm{e}}_{\mathrm{Na}^+} J^{\mathrm{e}}_{\mathrm{Cl}^-} \,. \tag{4.38}$$

In combination with (4.23) this implies that

$$J^{\mathrm{e}}_{\mathrm{Cl}^-} = J^{\mathrm{e}}_{\mathrm{NaCl}} - \frac{t^{\mathrm{e}}_{\mathrm{Cl}^-} j}{F} \quad \text{and}$$
$$J^{\mathrm{e}}_{\mathrm{Na}^+} = J^{\mathrm{e}}_{\mathrm{NaCl}} + \frac{t^{\mathrm{e}}_{\mathrm{Na}^+} j}{F} \,. \tag{4.39}$$

By introducing these expressions into (4.25), we obtain the correct entropy production (4.24) with the relation

$$\phi = \psi + \frac{t^{\mathrm{e}}_{\mathrm{Na}^+}\mu^{\mathrm{e}}_{\mathrm{Na}^+}}{F} - \frac{t^{\mathrm{e}}_{\mathrm{Cl}^-}\mu^{\mathrm{e}}_{\mathrm{Cl}^-}}{F} \,. \tag{4.40}$$

In the formation cell, the natural boundary conditions are

$$J^{\mathrm{e}}_{\mathrm{Cl}^-}(0) = 0 = J^{\mathrm{e}}_{\mathrm{Na}^+}(d_{\mathrm{e}}) \,. \tag{4.41}$$

This means that

$$J^{\mathrm{e}}_{\mathrm{Cl}^-}(d_{\mathrm{e}}) = -\frac{t^{\mathrm{e}}_{\mathrm{Cl}^-} j}{F} \quad \text{and} \quad J^{\mathrm{e}}_{\mathrm{Na}^+}(0) = \frac{t^{\mathrm{e}}_{\mathrm{Na}^+} j}{F} \,. \tag{4.42}$$

These boundary conditions in combination with (4.20) give for the salt flux

$$J^{\mathrm{e}}_{\mathrm{NaCl}}(x) = -\left[t^{\mathrm{e}}_{\mathrm{Na}^+}\frac{x}{d_{\mathrm{e}}} - t^{\mathrm{e}}_{\mathrm{Cl}^-}\left(1 - \frac{x}{d_{\mathrm{e}}}\right)\right]\frac{j}{F} \,. \tag{4.43}$$

This gives the expression for the position-dependent transference coefficient

$$t^{\mathrm{e}}_{\mathrm{NaCl}}(x) = -\frac{x}{d_{\mathrm{e}}} t^{\mathrm{e}}_{\mathrm{Na}^+} + \left(1 - \frac{x}{d_{\mathrm{e}}}\right) t^{\mathrm{e}}_{\mathrm{Cl}^-} , \tag{4.44}$$

at the anode and cathode surface in the formation cell we then have

$$\begin{aligned} t^{\mathrm{e,a}}_{\mathrm{NaCl}} &= t^{\mathrm{e}}_{\mathrm{Cl}^-} , \\ t^{\mathrm{e,c}}_{\mathrm{NaCl}} &= -t^{\mathrm{e}}_{\mathrm{Na}^+} . \end{aligned} \tag{4.45}$$

In [4.1, 60] the transference coefficient was obtained using wrong boundary conditions. The average value was still correct (Sect. 4.5.4) The average transference coefficient over the electrolyte in a formation cell becomes equal to $-\frac{1}{2}(t^{\mathrm{e}}_{\mathrm{Na}^+} - t^{\mathrm{e}}_{\mathrm{Cl}^-})$. This expression appears in the Planck potential (Sect. 4.5.4) and confirms in another way the choice of boundary values.

4.5.3 Externally Controlled Fluxes. The Measurable Electric Potential

Each flux in the entropy production is a linear combination of all conjugate forces. The flux equations that follow from (4.24) for isothermal conditions are

$$\begin{aligned} J^{\mathrm{e}}_{\mathrm{NaCl}} &= -L^{\mathrm{e}}_{\mu\mu} \frac{1}{T} \frac{\partial}{\partial x} \mu^{\mathrm{e}}_{\mathrm{NaCl}} - L^{\mathrm{e}}_{\mu\phi} \frac{1}{T} \frac{\partial \phi}{\partial x} , \\ j &= -L^{\mathrm{e}}_{\phi\mu} \frac{1}{T} \frac{\partial}{\partial x} \mu^{\mathrm{e}}_{\mathrm{NaCl}} - L^{\mathrm{e}}_{\phi\phi} \frac{1}{T} \frac{\partial \phi}{\partial x} . \end{aligned} \tag{4.46}$$

The coefficients L_{ij} are transport coefficients in a symmetric matrix of coefficients. In electrochemical cells, the off-diagonal terms, the coupling coefficients are of the same order of magnitude as the main (diagonal) coefficients. Simple laws of transport, like Fick's or Ohm's law, are then not sufficient. The transference coefficient is related to the off-diagonal coefficient. From the definition

$$t^{\mathrm{e}}_{\mathrm{NaCl}} = F \frac{L^{\mathrm{e}}_{\mu\phi}}{L^{\mathrm{e}}_{\phi\phi}} , \tag{4.47}$$

in the reversible limit ($j \to 0$) we find, using the symmetry of the coefficient matrix (the Onsager relation), the contribution from the electrolyte to the potential gradient

$$\left(\frac{\partial \phi}{\partial x}\right)_{j \to 0} = -\frac{t^{\mathrm{e}}_{\mathrm{NaCl}}}{F} \frac{\partial}{\partial x} \mu^{\mathrm{e}}_{\mathrm{NaCl}} , \tag{4.48}$$

$r^{\mathrm{e}} = T/L_{\phi\phi}$ is the resistivity of the electrolyte. The measurable potential difference with a constant transference coefficient is

$$\Delta_{\mathrm{e}} \phi_{j \to 0} = -\int_{\mathrm{e,a}}^{\mathrm{e,c}} \frac{t^{\mathrm{e}}_{\mathrm{NaCl}}}{F} \mathrm{d}\mu^{\mathrm{e}}_{\mathrm{NaCl}} = -\frac{t^{\mathrm{e}}_{\mathrm{NaCl}}}{F} \Delta_{\mathrm{e}} \mu_{\mathrm{NaCl}} . \tag{4.49}$$

The effects of boundary conditions (electrodes) on the transference coefficient can now be compared. For illustration, we introduce ideal expressions for the chemical potentials. When both electrodes are reversible to the Na^+ ion, the contribution from the electrolyte is

$$\Delta_{\mathrm{e}} \phi_{j \to 0} = t^{\mathrm{e}}_{\mathrm{Cl}^-} \frac{2RT}{F} \ln\left(\frac{c^{\mathrm{e,c}}_{\mathrm{NaCl}}}{c^{\mathrm{e,a}}_{\mathrm{NaCl}}}\right) . \tag{4.50}$$

When the electrodes are reversible to the Cl^- ion, the contribution from the electrolyte is

$$\Delta_{\mathrm{e}} \phi_{j \to 0} = -t^{\mathrm{e}}_{\mathrm{Na}^+} \frac{2RT}{F} \ln\left(\frac{c^{\mathrm{e,c}}_{\mathrm{NaCl}}}{c^{\mathrm{e,a}}_{\mathrm{NaCl}}}\right) . \tag{4.51}$$

The expressions describe the possible electric energy that can be obtained from the concentration cell, when the salt content varies through the electrolyte.

For the formation cell, we obtain from (4.44) and (4.49)

$$\begin{aligned} \Delta_{\mathrm{e}} \phi_{j \to 0} &= \frac{1}{F} \int_{\mathrm{e,a}}^{\mathrm{e,c}} \left[\frac{x}{d_{\mathrm{e}}} t^{\mathrm{e}}_{\mathrm{Na}^+} - \left(1 - \frac{x}{d_{\mathrm{e}}}\right) t^{\mathrm{e}}_{\mathrm{Cl}^-}\right] \mathrm{d}\mu_{\mathrm{NaCl}} \\ &= \frac{1}{2F} \left(t^{\mathrm{e}}_{\mathrm{Na}^+} - t^{\mathrm{e}}_{\mathrm{Cl}^-}\right) \Delta_{\mathrm{e}} \mu^{\mathrm{e}}_{\mathrm{NaCl}} \\ &= \frac{RT}{F} \frac{u_{\mathrm{Na}^+} - u_{\mathrm{Cl}^-}}{u_{\mathrm{Na}^+} + u_{\mathrm{Cl}^-}} \ln \frac{c^{\mathrm{e,c}}_{\mathrm{NaCl}}}{c^{\mathrm{e,a}}_{\mathrm{NaCl}}} , \end{aligned} \tag{4.52}$$

where we introduced the relation between transport number and ionic mobilities, $u^{\mathrm{e}}_{\mathrm{Na}^+}$ and $u^{\mathrm{e}}_{\mathrm{Cl}^-}$

$$t^{\mathrm{e}}_{\mathrm{Na}^+} = \frac{u_{\mathrm{Na}^+}}{u_{\mathrm{Na}^+} + u_{\mathrm{Cl}^-}} \quad \text{and} \quad t^{\mathrm{e}}_{\mathrm{Cl}^-} = \frac{u_{\mathrm{Cl}^-}}{u_{\mathrm{Na}^+} + u_{\mathrm{Cl}^-}} . \tag{4.53}$$

In order to find the integral in (4.52), we also used that $\mu^{\mathrm{e}}_{\mathrm{NaCl}}$ is a linear function of x, meaning that $\mathrm{d}\mu^{\mathrm{e}}_{\mathrm{NaCl}} = \Delta_{\mathrm{e}} \mu^{\mathrm{e}}_{\mathrm{NaCl}} \mathrm{d}x/d_{\mathrm{e}}$. The expression for the full cell potential is obtained by adding the potential drops at the electrodes (Sect. 4.6).

The magnitude of all potential contributions from the electrolyte is some mV. By introducing the transport number of Na^+ equal to 0.396, or a transport number of

Cl^- equal to 0.604, (4.52) gives 12 mV with a tenfold increase in concentration across the cell at 300 K. This value is negligible compared to the electromotive force of most formation cells. A membrane electrolyte can significantly increase the contribution from the electrolyte. With a transport number of a cation equal to 1, the concentration cell potential of (4.51) becomes −120 mV for the same concentration gradient and temperature. Expressions (4.50) and (4.51) can be used to describe contributions to the power in saline power plants (Sect. 4.6.5).

4.5.4 Ionic Fluxes and Forces: The Planck Potential

Planck [4.75, 76] derived the expression for the potential that bears his name from a description using ions as components. The linear flux–force relations for the electrolyte that follow from the entropy production (4.25) are

$$\begin{aligned} J^{\mathrm{e}}_{\mathrm{Na}^+} &= -L^{++}\frac{1}{T}\frac{\partial}{\partial x}\left(\mu^{\mathrm{e}}_{\mathrm{Na}^+} + F\psi\right) \\ &\quad -L^{+-}\frac{1}{T}\frac{\partial}{\partial x}\left(\mu^{\mathrm{e}}_{\mathrm{Cl}^-} - F\psi\right), \\ J^{\mathrm{e}}_{\mathrm{Cl}^-} &= -L^{-+}\frac{1}{T}\frac{\partial}{\partial x}\left(\mu^{\mathrm{e}}_{\mathrm{Na}^+} + F\psi\right) \\ &\quad -L^{--}\frac{1}{T}\frac{\partial}{\partial x}\left(\mu^{\mathrm{e}}_{\mathrm{Cl}^-} - F\psi\right). \end{aligned} \tag{4.54}$$

The ionic conductivities in dilute solutions are proportional to the ion concentration

$$\begin{aligned} L^{++} &= Tc^{\mathrm{e}}_{\mathrm{NaCl}}u_{\mathrm{Na}^+}, \\ L^{-+} &= L^{+-} = 0, \\ L^{--} &= Tc^{\mathrm{e}}_{\mathrm{NaCl}}u_{\mathrm{Cl}^-}, \end{aligned} \tag{4.55}$$

where we used $c^{\mathrm{e}}_{\mathrm{Na}^+} = c^{\mathrm{e}}_{\mathrm{Cl}^-} = c^{\mathrm{e}}_{\mathrm{NaCl}}$. This gives the Nernst–Planck flux equations for Na^+ and Cl^-

$$\begin{aligned} J^{\mathrm{e}}_{\mathrm{Na}^+} &= -c^{\mathrm{e}}_{\mathrm{NaCl}}u_{\mathrm{Na}^+}\frac{\partial}{\partial x}\left(\mu^{\mathrm{e}}_{\mathrm{Na}^+} + F\psi\right), \\ J^{\mathrm{e}}_{\mathrm{Cl}^-} &= -c^{\mathrm{e}}_{\mathrm{NaCl}}u_{\mathrm{Cl}^-}\frac{\partial}{\partial x}\left(\mu^{\mathrm{e}}_{\mathrm{Cl}^-} - F\psi\right). \end{aligned} \tag{4.56}$$

In a concentration cell, we can calculate the electrostatic potential gradient at zero electric current $J^{\mathrm{e}}_{\mathrm{Na}^+} = J^{\mathrm{e}}_{\mathrm{Cl}^-}$ to be

$$\begin{aligned} \frac{\partial}{\partial x}\psi = &-\frac{1}{F\left(u_{\mathrm{Na}^+} + u_{\mathrm{Cl}^-}\right)} \\ &\times\left(u_{\mathrm{Na}^+}\frac{\partial}{\partial x}\mu^{\mathrm{e}}_{\mathrm{Na}^+} - u_{\mathrm{Cl}^-}\frac{\partial}{\partial x}\mu^{\mathrm{e}}_{\mathrm{Cl}^-}\right). \end{aligned} \tag{4.57}$$

By introducing the conditions for the neutral electrolyte

$$\mu^{\mathrm{e}}_{\mathrm{Na}^+} = \mu^{\mathrm{e}}_{\mathrm{Cl}^-} = \frac{1}{2}\mu^{\mathrm{e}}_{\mathrm{NaCl}}, \tag{4.58}$$

we obtain the Planck potential gradient

$$\frac{\partial}{\partial x}\psi = -\frac{\left(u_{\mathrm{Na}^+} - u_{\mathrm{Cl}^-}\right)}{2F\left(u_{\mathrm{Na}^+} + u_{\mathrm{Cl}^-}\right)}\frac{\partial}{\partial x}\mu^{\mathrm{e}}_{\mathrm{NaCl}}. \tag{4.59}$$

Expression (4.59), named after Planck [4.75, 76], was obtained already in 1890 using the electroneutrality condition, $J^{\mathrm{e}}_{\mathrm{Na}^+} = J^{\mathrm{e}}_{\mathrm{Cl}^-}$ and the Nernst–Planck flux equations, (4.56). The equations have been tested in cation-exchange membranes [4.24].

Equation (4.43) shows that there is no salt flux if $j = 0$ in a formation cell. The condition $J^{\mathrm{e}}_{\mathrm{Na}^+} = J^{\mathrm{e}}_{\mathrm{Cl}^-}$, used to derive the electrostatic potential gradient across the electrolyte in a concentration cell (4.40) is not appropriate for a formation cell, as both ionic fluxes are zero when $j = 0$ (4.42). It follows from (4.40) that

$$\Delta_{\mathrm{e}}\phi = \Delta_{\mathrm{e}}\psi + \frac{1}{2F}\left(t^{\mathrm{e}}_{\mathrm{Na}^+} - t^{\mathrm{e}}_{\mathrm{Cl}^-}\right)\Delta_{\mathrm{e}}\mu^{\mathrm{e}}\mathrm{NaCl}. \tag{4.60}$$

In view of (4.52), we have for the formation cell

$$\Delta_{\mathrm{e}}\psi = 0. \tag{4.61}$$

The measured cell potential of the formation cell is related to the total Maxwell potential difference [4.1, 4], by

$$\Delta\phi = \Delta\psi - \Delta\mu_{\mathrm{e}^-}. \tag{4.62}$$

The Maxwell potential jumps at the electrodes are $\Delta_{a,\mathrm{e}}\psi$ and $\Delta_{\mathrm{e},c}\psi$. These jumps follow from the condition of a reversible process, $\Delta\psi + \Delta_{\mathrm{r}}G/F = 0$, where for the sodium electrode

$$\begin{aligned} \Delta_{\mathrm{r}}G^{\mathrm{s,a}} &= -\mu^{\mathrm{a,e}}_{\mathrm{Na}} + \mu^{\mathrm{e,a}}_{\mathrm{Na}^+} + \mu^{\mathrm{a,e}}_{\mathrm{e}^-}, \\ \Delta_{\mathrm{r}}G^{\mathrm{s,c}} &= -\mu^{\mathrm{c,e}}_{\mathrm{AgCl}} + \mu^{\mathrm{c,e}}_{\mathrm{Ag}} + \mu^{\mathrm{e,c}}_{\mathrm{Cl}^-} - \mu^{\mathrm{c,e}}_{\mathrm{e}^-}. \end{aligned} \tag{4.63}$$

The jumps in the Maxwell potentials are accordingly

$$\begin{aligned} \Delta_{a,\mathrm{e}}\psi &= \frac{\left(\mu^{\mathrm{a,e}}_{\mathrm{Na}} - \mu^{\mathrm{e,a}}_{\mathrm{Na}^+} - \mu^{\mathrm{a,e}}_{\mathrm{e}^-}\right)}{F}, \\ \Delta_{\mathrm{e},c}\psi &= \frac{\left(\mu^{\mathrm{c,e}}_{\mathrm{AgCl}} - \mu^{\mathrm{c,e}}_{\mathrm{Ag}} - \mu^{\mathrm{e,c}}_{\mathrm{Cl}^-} + \mu^{\mathrm{c,e}}_{\mathrm{e}^-}\right)}{F}. \end{aligned} \tag{4.64}$$

With (4.61), the cell potential is the sum of these two terms

$$\begin{aligned} \Delta\psi &= \Delta_{a,e}\psi + \Delta_{e,c}\psi \\ &= \frac{1}{F}\left[\mu^{\mathrm{a,e}}_{\mathrm{Na}} - \mu^{\mathrm{c,e}}_{\mathrm{Ag}} + \mu^{\mathrm{c,e}}_{\mathrm{AgCl}}\right. \\ &\quad \left. -\frac{1}{2}\left(\mu^{\mathrm{e,a}}_{\mathrm{NaCl}} + \mu^{\mathrm{e,c}}_{\mathrm{NaCl}}\right) + \Delta\mu_{\mathrm{e}^-}\right]. \end{aligned} \tag{4.65}$$

Using the relation (4.62) with this result, we recover (4.70) below.

4.6 Cell Potentials

In the preceeding sections, we have described how the entropy production is set up, and how one can choose independent variable sets to describe the various parts of the electrochemical cell. We proceed using the sets of operationally defined variables, as they are more directly amenable to experimental control, and do not depend on the state of dissociation of the electrolytes in solution. In other words, the description can be used for molten salts as well as concentrated solutions. If wanted, an ionic description can be found using the transformation rules given above.

Not much has been done to describe formation cells using NET of heterogeneous systems, see however [4.1, 60]. (The transport numbers were incorrectly interchanged in (4.43) in this reference). We describe therefore the scheme to obtain the cell potential under reversible conditions (the electromotive force), in the absence and presence of a temperature gradient. We also give sets of flux equations that can be solved when the electric current is nonnegligible. An example of solutions of a full set of equations is described for a fuel cell in Sect. 4.7.

4.6.1 An Isothermal Formation Cell with a Concentration Gradient

Return therefore to the example formation cell. The cell potential under various conditions is of interest, first with the restriction $j \to 0$. The reaction Gibbs energy was defined by the change in Gibbs energy of the neutral components in the interface [4.1]

$$\begin{aligned}\Delta_{\mathrm{n}}G^{\mathrm{s,a}} &= -\mu^{\mathrm{a,e}}_{\mathrm{Na}} + t^{\mathrm{e}}_{\mathrm{NaCl}}\mu^{\mathrm{e,a}}_{\mathrm{NaCl}}\,,\\ \Delta_{\mathrm{n}}G^{\mathrm{s,c}} &= -\mu^{\mathrm{c,e}}_{\mathrm{AgCl}} + \mu^{\mathrm{c,e}}_{\mathrm{Ag}} - t^{\mathrm{e}}_{\mathrm{NaCl}}\mu^{\mathrm{e,c}}_{\mathrm{NaCl}}\,.\end{aligned} \tag{4.66}$$

The cell potential under reversible conditions is found by adding potential jumps as we pass across the cell

$$\Delta\phi = \Delta_{\mathrm{a,e}}\phi + \Delta_{\mathrm{e}}\phi + \Delta_{\mathrm{e,c}}\phi\,. \tag{4.67}$$

We introduce the reaction Gibbs energies of the neutral components and obtain the electrode potential jumps

$$\Delta_{\mathrm{a,e}}\phi = \frac{1}{F}\left(\mu^{\mathrm{a,e}}_{\mathrm{Na}} - t^{\mathrm{e}}_{\mathrm{Cl}^-}\mu^{\mathrm{e,a}}_{\mathrm{NaCl}}\right), \tag{4.68}$$

$$\Delta_{\mathrm{e,c}}\phi = \frac{1}{F}\left(\mu^{\mathrm{c,e}}_{\mathrm{AgCl}} - \mu^{\mathrm{c,e}}_{\mathrm{Ag}} - t^{\mathrm{e}}_{\mathrm{Na}^+}\mu^{\mathrm{e,c}}_{\mathrm{NaCl}}\right). \tag{4.69}$$

The contribution from the electrolyte was given in (4.60) and (4.61). By adding all contributions, we obtain after some reshuffling

$$\begin{aligned}\Delta\phi = \frac{1}{F}\Bigg[&\mu^{\mathrm{a,e}}_{\mathrm{Na}} - t^{\mathrm{e}}_{\mathrm{Cl}^-}\mu^{\mathrm{e,a}}_{\mathrm{NaCl}} - \mu^{\mathrm{c,e}}_{\mathrm{Ag}} + \mu^{\mathrm{c,e}}_{\mathrm{AgCl}}\\ &- t^{\mathrm{e}}_{\mathrm{Na}^+}\mu^{\mathrm{e,c}}_{\mathrm{NaCl}} + \frac{1}{2}\left(t^{\mathrm{e}}_{\mathrm{Na}^+} - t^{\mathrm{e}}_{\mathrm{Cl}^-}\right)\Delta_{\mathrm{e}}\mu^{\mathrm{e}}_{\mathrm{NaCl}}\Bigg].\end{aligned}$$

We see that the expression reduces to the Nernst equation

$$\begin{aligned}\Delta\phi &= \Delta_{\mathrm{a,e}}\phi + \Delta_{\mathrm{e,c}}\phi\\ &= \frac{1}{F}\left(\mu^{\mathrm{a,e}}_{\mathrm{Na}} - \mu^{\mathrm{c,e}}_{\mathrm{Ag}} + \mu^{\mathrm{c,e}}_{\mathrm{AgCl}} - \mu^{\mathrm{e}}_{\mathrm{NaCl}}\right)\\ &= \frac{1}{F}\left[\mu^{\mathrm{a,e}}_{\mathrm{Na}} - \mu^{\mathrm{c,e}}_{\mathrm{Ag}} + \mu^{\mathrm{c,e}}_{\mathrm{AgCl}} - \frac{1}{2}(\mu^{\mathrm{e,a}}_{\mathrm{NaCl}} + \mu^{\mathrm{e,c}}_{\mathrm{NaCl}})\right].\end{aligned} \tag{4.70}$$

We have used the fact that the transport numbers of the ions add to unity. This expression confirms the relations of the preceeding section.

4.6.2 A Nonisothermal Formation Cell

Heat conducts well in metal electrodes and many electrolytes, but an electrochemical cell does not need to have a uniform temperature. The temperature can become important in two ways: as a variable for the properties involved and as a gradient or a thermal driving force.

In order to evaluate a chemical potential, one must specify the temperature. The appropriate temperature is indicated by setting the temperature in parenthesis behind the chemical potential. The chemical potential of the sodium in the bulk anode close to the surface, $\mu^{\mathrm{a,e}}_{\mathrm{Na}}(T^{\mathrm{s,a}})$, is therefore evaluated at the temperature of the surface.

We continue to describe the cell potential when the cell is exposed to a temperature gradient. The possible temperature variation in the transport coefficients shall be neglected.

The Homogeneous Anode Phase

The flux–force relations that result from (4.13) are

$$\begin{aligned}J'^{\mathrm{a}}_q &= -L^{\mathrm{a}}_{qq}\frac{1}{T^2}\frac{\partial T}{\partial x} - L^{\mathrm{a}}_{q\phi}\frac{1}{T}\frac{\partial\phi}{\partial x}\,,\\ j &= -L^{\mathrm{a}}_{\phi q}\frac{1}{T^2}\frac{\partial T}{\partial x} - L^{\mathrm{a}}_{\phi\phi}\frac{1}{T}\frac{\partial\phi}{\partial x}\,.\end{aligned} \tag{4.71}$$

The Peltier coefficient is defined by

$$\pi^{\mathrm{a}}(x) \equiv F\left(\frac{J'^{\mathrm{a}}_q}{j}\right)_{\partial T/\partial x=0,} = F\frac{L^{\mathrm{a}}_{q\phi}}{L^{\mathrm{a}}_{\phi\phi}} \equiv -T(x)(S^{\mathrm{a,e}}_{\mathrm{Na}} + S^{*,\mathrm{a}}_{\mathrm{e}^-}) \,, \tag{4.72}$$

and is given by the transported entropy of electrons. Using the Onsager relation, the Peltier coefficient and the entropy of sodium, we find for the reversible contribution to the electric potential gradient

$$\left(\frac{\partial\phi}{\partial x}\right)_{j\to 0} = -\frac{1}{F}\frac{\pi^{\mathrm{a}}(x)}{T(x)}\frac{\partial T}{\partial x} = \frac{1}{F}(S^{\mathrm{a,e}}_{\mathrm{Na}} + S^{*,\mathrm{a}}_{\mathrm{e}^-})\frac{\partial T}{\partial x} \,. \tag{4.73}$$

By integrating across the electrode, we obtain for the potential difference at $j \approx 0$

$$\Delta_{\mathrm{a}}\phi = \frac{1}{F}(S^{\mathrm{a,e}}_{\mathrm{Na}} + S^{*,\mathrm{a}}_{\mathrm{e}^-})\Delta_{\mathrm{a}}T \,. \tag{4.74}$$

Contributions from transported entropies of electrons $S^{*,\mathrm{a}}_{\mathrm{e}^-}$ are frequently negligible.

The Electrolyte

The resulting linear flux–force relations from (4.14) are

$$\begin{aligned}
J'^{\mathrm{e}}_q &= -L^{\mathrm{e}}_{qq}\frac{1}{T^2}\frac{\partial T}{\partial x} - L^{\mathrm{e}}_{q\mu}\frac{1}{T}\frac{\partial}{\partial x}\mu^{\mathrm{e}}_{\mathrm{NaCl},T} \\
&\quad - L^{\mathrm{e}}_{q\phi}\frac{1}{T}\frac{\partial\phi}{\partial x} \,, \\
J^{\mathrm{e}}_{\mathrm{NaCl}} &= -L^{\mathrm{e}}_{\mu q}\frac{1}{T^2}\frac{\partial T}{\partial x} - L^{\mathrm{e}}_{\mu\mu}\frac{1}{T}\frac{\partial}{\partial x}\mu^{\mathrm{e}}_{\mathrm{NaCl},T} \\
&\quad - L^{\mathrm{e}}_{\mu\phi}\frac{1}{T}\frac{\partial\phi}{\partial x} \,, \\
j &= -L^{\mathrm{e}}_{\phi q}\frac{1}{T^2}\frac{\partial T}{\partial x} - L^{\mathrm{e}}_{\phi\mu}\frac{1}{T}\frac{\partial}{\partial x}\mu^{\mathrm{e}}_{\mathrm{NaCl},T} \\
&\quad - L^{\mathrm{e}}_{\phi\phi}\frac{1}{T}\frac{\partial\phi}{\partial x} \,.
\end{aligned} \tag{4.75}$$

The transference coefficient $t^{\mathrm{e}}_{\mathrm{NaCl}}(x)$ was given in (4.44). The definition of the position-dependent Peltier coefficient is in analogy with (4.44)

$$\begin{aligned}
\pi^{\mathrm{e}}(x) &\equiv F\left(\frac{J'^{\mathrm{e}}_q}{j}\right)_{\substack{\partial T/\partial x=0,\\ \partial\mu^{\mathrm{e}}_{\mathrm{NaCl}}/\partial x=0}} = F\frac{L^{\mathrm{e}}_{q\phi}}{L^{\mathrm{e}}_{\phi\phi}} \\
&\equiv T(x)\left[-t^{\mathrm{e}}_{\mathrm{NaCl}}(x)S^{\mathrm{e}}_{\mathrm{NaCl}} + \frac{x}{d_{\mathrm{e}}}t^{\mathrm{e}}_{\mathrm{Na}^+}S^{*,\mathrm{e}}_{\mathrm{Na}^+} \right. \\
&\quad \left. -\left(1-\frac{x}{d_{\mathrm{e}}}\right)t^{\mathrm{e}}_{\mathrm{Cl}^-}S^{*,\mathrm{e}}_{\mathrm{Cl}^-}\right] .
\end{aligned} \tag{4.76}$$

The Peltier coefficient is given by the entropy of NaCl and transported entropies of the ions. The transported entropies enter the analysis as integration constants at the surfaces, just as the transport numbers did in the expression for transference coefficient of the salt. With T as a linear function of x, the contribution to the cell potential from the electrolyte nonuniformities becomes

$$\begin{aligned}
\Delta_{\mathrm{e}}\phi &= \frac{1}{2F}\left(t^{\mathrm{e}}_{\mathrm{Na}^+} - t^{\mathrm{e}}_{\mathrm{Cl}^-}\right)\Delta_{\mathrm{e}}\mu^{\mathrm{e}}_{\mathrm{NaCl},T} \\
&\quad + \frac{1}{2F}\left[\left(t^{\mathrm{e}}_{\mathrm{Na}^+} - t^{\mathrm{e}}_{\mathrm{Cl}^-}\right)S^{\mathrm{e}}_{\mathrm{NaCl}} \right. \\
&\quad \left. + t^{\mathrm{e}}_{\mathrm{Na}^+}S^{*,\mathrm{e}}_{\mathrm{Na}^+} - t^{\mathrm{e}}_{\mathrm{Cl}^-}S^{*,\mathrm{e}}_{\mathrm{Cl}^-}\right]\Delta_{\mathrm{e}}T \,.
\end{aligned} \tag{4.77}$$

In the last expression, the difference $\Delta_{\mathrm{e}}\mu^{\mathrm{e}}_{\mathrm{NaCl}}$ is taken at the temperature $T^{\mathrm{e,c}}$, as prescribed in (4.75). The transported entropies were taken constant in the integration. The first contribution is probably larger than the second. We did not introduce Soret equilibrium in the electrolyte.

The Anode and its Surface

The electrode reaction at the interface between the anode and NaCl(aq) was given in (4.9). The flux equations are from (4.15)

$$\begin{aligned}
J'^{\mathrm{a,e}}_q &= L^{\mathrm{s,a}}_{aa}\Delta_{\mathrm{a,s}}\left(\frac{1}{T}\right) + L^{\mathrm{s,a}}_{ae}\Delta_{\mathrm{s,e}}\left(\frac{1}{T}\right) \\
&\quad - L^{\mathrm{s,a}}_{a\phi}\frac{1}{T^{\mathrm{s,a}}}\left(\Delta_{\mathrm{a,e}}\phi + \frac{\Delta_{\mathrm{n}}G^{\mathrm{s,a}}}{F}\right) , \\
J'^{\mathrm{e,a}}_q &= L^{\mathrm{s,a}}_{ea}\Delta_{\mathrm{a,s}}\left(\frac{1}{T}\right) + L^{\mathrm{s,a}}_{ee}\Delta_{\mathrm{s,e}}\left(\frac{1}{T}\right) \\
&\quad - L^{\mathrm{s,a}}_{e\phi}\frac{1}{T^{\mathrm{s,a}}}\left(\Delta_{\mathrm{a,e}}\phi + \frac{\Delta_{\mathrm{n}}G^{\mathrm{s,a}}}{F}\right) , \\
j &= L^{\mathrm{s,a}}_{\phi a}\Delta_{\mathrm{a,s}}\left(\frac{1}{T}\right) + L^{\mathrm{s,a}}_{\phi e}\Delta_{\mathrm{s,e}}\left(\frac{1}{T}\right) \\
&\quad - L^{\mathrm{s,a}}_{\phi\phi}\frac{1}{T^{\mathrm{s,a}}}\left(\Delta_{\mathrm{a,e}}\phi + \frac{\Delta_{\mathrm{n}}G^{\mathrm{s,a}}}{F}\right) ,
\end{aligned} \tag{4.78}$$

where the reaction Gibbs energy of the neutral components was given by (4.66). The Peltier coefficients for the bulk phases at the anode surface are transference coefficients for heat

$$\begin{aligned}
\pi^{\mathrm{a,e}} &\equiv \left(\frac{J'^{\mathrm{a,e}}_q}{j/F}\right)_{\substack{\Delta_{\mathrm{a,s}}T=\Delta_{\mathrm{s,e}}T=0,\\ \Delta_{\mathrm{s,e}}\mu_{\mathrm{NaCl}}=0}} = F\frac{L^{\mathrm{s,a}}_{a\phi}}{L^{\mathrm{s,a}}_{\phi\phi}} \\
&\equiv -T^{\mathrm{a,e}}\left(S^{\mathrm{a,e}}_{\mathrm{Na}} + S^{*,\mathrm{a,e}}_{\mathrm{e}^-}\right) , \\
\pi^{\mathrm{e,a}} &\equiv \left(\frac{J'^{\mathrm{e,a}}_q}{j/F}\right)_{\substack{\Delta_{\mathrm{a,s}}T=\Delta_{\mathrm{s,e}}T=0,\\ \Delta_{\mathrm{s,e}}\mu_{\mathrm{NaCl}}=0}} = F\frac{L^{\mathrm{s,a}}_{e\phi}}{L^{\mathrm{s,a}}_{\phi\phi}} \\
&\equiv T^{\mathrm{e,a}}\left(-t^{\mathrm{e}}_{\mathrm{Cl}^-}S^{\mathrm{e,a}}_{\mathrm{NaCl}} - t^{\mathrm{e}}_{\mathrm{Cl}^-}S^{*,\mathrm{e,a}}_{\mathrm{Cl}^-}\right) .
\end{aligned} \tag{4.79}$$

We have that $\pi^{a,e} = \pi^{a}(0)$ and $\pi^{e,a} = \pi^{e}(0)$, cf. (4.72) and (4.76). As mentioned before, the transported entropy of the electron can be neglected. By using the Onsager relations, the potential difference across the anode surface becomes

$$\begin{aligned}\Delta_{a,e}\phi &= -\frac{1}{F}\left[\Delta_n G^{s,a} + \pi^{a,e}\left(\frac{T^{s,a}-T^{a,e}}{T^{a,e}}\right)\right.\\ &\quad \left.+\pi^{e,a}\left(\frac{T^{e,a}-T^{s,a}}{T^{e,a}}\right)\right]\\ &= -\frac{1}{F}\left[-\mu^{a,e}_{Na}(T^{s,a}) + t_{Cl^-}\mu^{a,e}_{NaCl}(T^{s,a})\right.\\ &\quad -S^{a,e}_{Na}(T^{s,a}-T^{a,e})\\ &\quad \left.-t^{e}_{Cl^-}\left(S^{e,a}_{NaCl}+S^{*,e,a}_{Cl^-}\right)(T^{e,a}-T^{s,a})\right]\\ &= -\frac{1}{F}\left[-\mu^{a,e}_{Na}(T^{a,e}) + t_{Cl^-}\mu^{e,a}_{NaCl}(T^{e,a})\right.\\ &\quad \left.-t^{e}_{Cl^-}S^{*,e,a}_{Cl^-}(T^{e,a}-T^{s,a})\right]. \end{aligned} \tag{4.80}$$

The main contribution to the surface potential drop is given by the reaction Gibbs energy. We see that the entropy of Na and NaCl refer to different temperatures. In the first equality, the expression contains the temperature of the surface while in the second equality the expression contains the temperature of the anode near the electrolyte (for Na) and of the electrolyte near the anode (for NaCl). In the derivation of the final result, we have used the temperature dependence of the chemical potentials. For constant temperature, the expression reduces to the one given in (4.68).

The Cathode and its Surface

The chemical reaction in the cathode surface produces Cl^- in the electrolyte, while Ag^+ conducts charge in AgCl (4.10). The Peltier coefficients are now

$$\begin{aligned}\pi^{e,c} &\equiv F\left(\frac{J'^{e,c}_q}{j}\right)_{\substack{\Delta_{e,s}T=\Delta_{s,c}T=0,\\ \Delta_{e,s}\mu^{e}_{NaCl}=0}} = F\frac{L^{s,c}_{e\phi}}{L^{s,c}_{\phi\phi}}\\ &\equiv T^{e,c}\left(t^{e}_{Na^+}S^{e,c}_{NaCl} + t^{e}_{Na^+}S^{*,e,c}_{Na^+}\right),\\ \pi^{c,e} &\equiv F\left(\frac{J'^{c,e}_q}{j}\right)_{\substack{\Delta_{e,s}T=\Delta_{s,c}T=0,\\ \Delta_{e,s}\mu^{e}_{NaCl}=0}} = F\frac{L^{s,c}_{c\phi}}{L^{s,c}_{\phi\phi}}\\ &\equiv T^{c,e}\left(S^{*,c,e}_{Ag^+} + S^{c,e}_{AgCl} - S^{c,e}_{Ag}\right). \end{aligned} \tag{4.81}$$

The contribution to the cell potential is accordingly

$$\begin{aligned}\Delta_{e,c}\phi &= -\frac{1}{F}\left(\Delta_n G^{s,c} + \frac{\pi^{e,c}}{T^{e,c}}\Delta_{e,s}T + \frac{\pi^{c,e}}{T^{c,e}}\Delta_{s,c}T\right)\\ &= -\frac{1}{F}\left[-\mu^{c,e}_{AgCl}(T^{c,e}) + \mu^{c,e}_{Ag}(T^{c,e}) + t^{e}_{Na^+}\mu^{e,c}_{NaCl}(T^{e,c})\right.\\ &\quad \left.+t^{e}_{Na^+}S^{*,e,c}_{Na^+}\Delta_{e,s}T + S^{*,c}_{Ag^+}\Delta_{s,c}T\right]. \end{aligned} \tag{4.82}$$

Entropies and transported entropies were again taken constant in the integration.

The Sets of Flux Equations

We have seen above, using a simple formation cell as example, how the cell potential profile can be derived using NET. Depending on experimental conditions, one can introduce various levels of precision in the formulation. With operationally defined variables, one can control by experiment the assumptions, which are introduced in the theory (Sect. 4.6.3). The operational approach makes use of position dependent transference coefficients for mass transport and position dependent Peltier coefficients for heat transport. The detailed expressions were derived from the boundary conditions imposed by the electrodes.

The contributions from each part of the cell to the cell potential was expressed. In sequence, they give the potential profile across the cell

$$\Delta\phi = \Delta_{a,e}\phi + \Delta_{e}\phi + \Delta_{e,c}\phi\,.$$

The sets of equations given for each subsystem apply not only to the limit of zero current density, used here, but also to conditions far from global equilibrium. Local temperature gradients may not be large in a cell made of good conductors. But the use of porous gas electrodes, ceramic electrolytes, semiconductors and large current densities, may change this situation.

The sets of equations give the possibility to calculate heat and mass fluxes that arise from varying and large electric currents and find simultaneous solutions of several variable profiles. For sizable current densities, one can find temperature and concentration profiles in addition to electric potential profiles. At the end of this chapter, we return to such profiles (Sect. 4.7) obtained for the polymer fuel cell [4.1, 77, 78].

4.6.3 The Liquid Junction

We reported in Sect. 4.5.3 expressions for the potential gradient that arise in a concentration cell. The integral of this potential gradient has been called the liquid junction potential. Commonly, there are more than one component in a junction, but KCl is frequently one of them for well-known reasons, see below. As mentioned in Sect. 4.5.4, it is common to neglect liquid junction potentials, and we shall see in more detail what that means. Consider therefore a junction made up of solutions of two electrolytes, KCl and HCl, as in the following cell

$$\begin{aligned}&\mathrm{Ag(s)|AgCl(s)|KCl(aq}, c_{HCl})||\mathrm{HCl(aq}, c_{KCl})|\\ &\mathrm{AgCl(s)|Ag(s)}\,.\end{aligned} \tag{4.83}$$

The cell potential has three terms, two from the electrodes and one from the electrolyte

$$\Delta\phi = \Delta_{a,e}\phi + \Delta_e\phi + \Delta_{e,c}\phi\,, \tag{4.84}$$

because $\Delta_{a,e}\phi = -\Delta_{e,c}\phi = \left(-\mu^{c,e}_{AgCl} + \mu^{c,e}_{Ag}\right)/F$, $\Delta\phi = \Delta_e\phi$. The cell potential is

$$\Delta_e\phi = \int \left(t_{KCl}\mathrm{d}\mu_{KCl} + t_{HCl}\mathrm{d}\mu_{HCl}\right), \tag{4.85}$$

The chemical potentials of the strong electrolytes are

$$\begin{aligned}
\mu^e_{KCl} &= \mu^0_{KCl} + RT\ln a^e_{KCl} = \mu^0_{KCl} \\
&\quad + RT\ln\left[c^e_{Cl^-}c^e_{K^+}(\gamma^e_{\pm,KCl})^2\right], \\
\mu^e_{HCl} &= \mu^0_{HCl} + RT\ln a^e_{HCl} = \mu^0_{HCl} \\
&\quad + RT\ln\left[c^e_{Cl^-}c^e_{H^+}(\gamma^e_{\pm,HCl})^2\right],
\end{aligned} \tag{4.86}$$

where the mean activity coefficient for the salt has been given the symbol $\gamma^2_\pm$.

The cell potential is due to the electrolyte contribution only. The contribution from the electrolyte is obtained by introducing the chemical potentials and integrating an equation corresponding to (4.48) for the two electrolytes

$$\begin{aligned}
&(\Delta_e\phi)_{j=0} \\
&= -\frac{1}{F}\int_{e,a}^{e,c}\left(\frac{u^e_{K^+}c^e_{K^+}\mathrm{d}\mu^e_{KCl} + u^e_{H^+}c^e_{H^+}\mathrm{d}\mu^e_{HCl}}{u^e_{K^+}c^e_{K^+} + u^e_{H^+}c^e_{H^+} + u^e_{Cl^-}c^e_{Cl^-}}\right) \\
&= -\frac{RT}{F}\int_{e,a}^{e,c}\mathrm{d}\ln c^e_{Cl^-} \\
&\quad -\frac{RT}{F}\int_1^2\left\{\left[\left(u^e_{K^+} - u^e_{Cl^-}\right)\mathrm{d}c^e_{K^+}\right.\right. \\
&\quad \left.\left. + \left(u^e_{H^+} - u^e_{Cl^-}\right)\mathrm{d}c^e_{H^+}\right] \right. \\
&\quad \left.\times\left(u^e_{K^+}c^e_{K^+} + u^e_{H^+}c^e_{H^+} + u^e_{Cl^-}c^e_{Cl^-}\right)^{-1}\right\} \\
&\quad -\frac{RT}{F}\int_{e,a}^{e,c}\left(\left[u^e_{K^+}c^e_{K^+}\mathrm{d}\ln y^e_{KCl}\right.\right. \\
&\quad \left.\left. + u^e_{H^+}c^e_{H^+}\mathrm{d}\ln y^e_{HCl}\right] \right. \\
&\quad \left.\times\left[u^e_{K^+}c^e_{K^+} + u^e_{H^+}c^e_{H^+} + u^e_{Cl^-}c^e_{Cl^-}\right]^{-1}\right).
\end{aligned} \tag{4.87}$$

The three integrals on the right-hand side that contribute to the liquid junction potential (the cell potential) are for easy reference denoted

$$\begin{aligned}
\Delta\phi &= (\Delta_e\phi)_{j=0} \\
&= \Delta_e\phi_{Nernst} + \Delta_e\phi_{mobility} + \Delta_e\phi_{activity}\,.
\end{aligned} \tag{4.88}$$

In order to determine these terms, one has to know the concentration profiles through the electrolyte. For the results in Table 4.1, linear concentration profiles were constructed [4.79]. The first and the largest contribution is due to the concentration difference of Cl^-. This has the form of an electrode potential jump, but the electrode potential jump is no part of the $\Delta_e\phi$! The remaining two contributions have the same order of magnitude. They may represent significant corrections to the overall potential, like when $c_{HCl} = 0.1$ and $c_{KCl} = 0.5\,\mathrm{kmol/m^3}$.

The equation shows that KCl will not contribute much to $\Delta\phi_{mobility}$ because the mobility of potassium is near that of chloride. This is the reason why KCl is used in salt bridges. Still, the table shows that $\Delta\phi_{mobility}$ can add up to 15 mV to the cell potential at high HCl concentrations. The last term is of the same order of magnitude. It was calculated using constant ionic mobilities in (4.87) [4.79]. The variation in this term in Table 4.1 reaches an upper limit as $c_{HCl} \to 0$. The comparison with experimental results for the total cell potential is very good.

A contribution of the order of 10 mV is negligible compared to the potential of a formation cell. But in an accurate description of concentration cells, which are relevant for saline power plants (Sect. 4.6.5), it is essential to be able to model liquid junctions. Such terms may also play a role when the liquid junction is used for electro-analytical purposes, like in calomel electrodes [4.27]. The assumptions of linear concentration profiles and constant mobilities were checked and found to give good estimates of measured values [4.79].

4.6.4 The Butler–Volmer Equation

Electrode reactions are generally not reversible. They may create large resistances to the electric current, giving a characteristic nonlinear relation between the current density and the overpotential (the potential difference needed to overcome the resistance). The famous Butler–Volmer equation

$$j = -j_0\left(\mathrm{e}^{(1-\alpha)F\eta/RT} - \mathrm{e}^{-\alpha F\eta/RT}\right) \tag{4.89}$$

relates j to the exchange current density, j_0, the electrode overpotential η and the transfer factor α. The

Table 4.1 Calculated contributions to the liquid junction potential at 298 K in the cell, Ag(s)| AgCl(s)| KCl(aq, c_{HCl}) | | HCl (aq, c_{KCl}) | AgCl(s)| Ag(s). The liquid junction has a linear variation in concentrations. The sum is compared to experimental results. The uncertainty in the experimental results is below ±0.2 mV

c_{HCl} (kmol/m^3)	$\Delta\phi_{\mathrm{Nernst}}$ (mV)	$\Delta\phi_{\mathrm{mobility}}$ (mV)	$\Delta\phi_{\mathrm{activity}}$ (mV)	$\Delta\phi_{\mathrm{calc.}}$ (mV)	$\Delta\phi_{\mathrm{exp}}$ (mV)	c_{KCl} (kmol/m^3)
0.1	94.78	−4.03	−2.33	88.42	88.3	4
0.01	153.94	−3.59	−8.56	141.79	143.1	–
0.001	213.09	−4.47	−9.99	198.68	199.0	–
0.1	41.4	−13.53	−4.53	22.2	–	0.5
0.01	100.5	−4.66	−9.16	86.6	–	–
0.001	159.7	−3.33	−10.41	146.0	–	–

equation is normally derived from kinetic considerations, but we shall see how it can also be derived from NET. Consider therefore the entropy production in Sect. 4.4 at isothermal conditions for a simple electrochemical reaction A goes to $A^+ + e^-$. We have in the ionic formulation

$$\sigma^s = -j\frac{1}{T}\left(\Delta\psi + \Delta_r G/F\right). \tag{4.90}$$

Only the beginning and the end state of products and reactants enter the expression for $\Delta_r G$. Such a two-state description can be too coarse, when the process is activated. The reaction occurs on a finer scale, a mesoscale, which can be represented by a reaction coordinate. As variable, we must rather use the probability density of states $\Gamma(\gamma)$ along the reaction coordinate. The entropy production is invariant, however. With constant j and T, we are seeking a variation in ψ and G that obeys

$$\sigma^s = -\frac{1}{T}j\int_0^1\left(\frac{\partial\psi(\gamma)}{\partial\gamma} + \frac{1}{F}\frac{\partial g(\gamma)}{\partial\gamma}\right)\mathrm{d}\gamma\,. \tag{4.91}$$

We see that we obtain (4.90) by integrating over γ. On the mesoscale, we can express the Gibbs energy of the reacting mixture $g(\gamma)$ by the enthalpy $h(\gamma)$ and entropy

$$g(\gamma) = h(\gamma) + RT\ln\Gamma(\gamma)\,. \tag{4.92}$$

At any coordinate γ, we can now define the effective Gibbs energy as the combination [4.7]

$$\begin{aligned}\tilde{\mu}(\gamma) &= g(\gamma) + F\psi(\gamma)\\ &= [h(\gamma) + F\psi(\gamma)] + RT\ln\Gamma(\gamma)\,.\end{aligned} \tag{4.93}$$

Doing this, we have implicitly assumed that there is local equilibrium for each value of γ, meaning that we picture an ensemble of particles for each γ, with the effective chemical potential $\tilde{\mu}$, as in the discussion in Sect. 4.1.4.

The electric potential will modify the enthalpy barrier and make the reaction go forward. The driving force conjugate to the electric current density in γ-space is $-(1/TF)\partial\tilde{\mu}/\partial\gamma$. The assumption is now that linear relations can be written for the fluxes and forces in the internal variable space, giving

$$j = -\left(\frac{L}{TF}\right)\frac{\partial\tilde{\mu}}{\partial\gamma}\,, \tag{4.94}$$

where L is the transport coefficient. Under reversible conditions $\partial\tilde{\mu}/\partial\gamma = 0$ so that $\tilde{\mu}$ is constant. The probability distribution across the barrier becomes

$$\Gamma_{\mathrm{rev}}(\gamma) = \exp\left[\tilde{\mu}_{\mathrm{rev}} - h(\gamma) - \frac{F\psi(\gamma)}{RT}\right]. \tag{4.95}$$

The phenomenological coefficient is generally proportional to the density of the conducting species (4.55). In the present context, this means that

$$L(\gamma) = uF\Gamma(\gamma)\,, \tag{4.96}$$

where u is the constant mobility of the reaction complex along the reaction coordinate. By introducing (4.93) and (4.96) into (4.94), we obtain

$$j = -uR\exp\left(\frac{-[h(\gamma) + F\psi(\gamma)]}{RT}\right)\frac{\partial}{\partial\gamma}\exp\frac{\tilde{\mu}(\gamma)}{RT}\,. \tag{4.97}$$

If the enthalpy barrier is high compared to RT, the reaction is slow. The reaction is activated. A gradient in electric potential does not alter this much. It then follows that j is constant and independent of γ (the process is quasi-stationary). The first exponential factor can be brought to the left-hand side, and (4.97) can be integrated from 0 to 1. The result is

$$j = -l\left(\exp\frac{[\tilde{\mu}(0) - \tilde{\mu}_{\mathrm{rev}}]}{RT} - \exp\frac{[\tilde{\mu}(1) - \tilde{\mu}_{\mathrm{rev}}]}{RT}\right), \tag{4.98}$$

where

$$l = uR\left[\int_0^1 \mathrm{d}\gamma \exp\left(\frac{h(\gamma)+F\psi(\gamma)-\tilde{\mu}_{\mathrm{rev}}}{RT}\right)\right]^{-1} \tag{4.99}$$

has Arrhenius-type behavior. Equation (4.98) has the form of the Butler–Volmer equation, if we make the following identifications

$$\begin{aligned}\tilde{\mu}(0)-\tilde{\mu}_{\mathrm{rev}} &= (1-\alpha)F\eta\,,\\ \tilde{\mu}(1)-\tilde{\mu}_{\mathrm{rev}} &= -\alpha F\eta\,,\end{aligned} \tag{4.100}$$

meaning that the value of the effective chemical potential under these conditions is positioned a fraction α of the total distance between the two states, away from state 1, and that the overpotential can be associated with $\Delta\tilde{\mu}$, the effective driving force. The Butler–Volmer equation obtains a thermodynamic basis through mesoscopic NET. In fact, the law of mass action can be similarly derived [4.55].

An equivalent form of (4.98) is

$$\begin{aligned} j &= l_0\left(1-\exp\frac{[\tilde{\mu}(1)-\tilde{\mu}(0)]}{RT}\right)\\ &= l_0\left(1-\exp\frac{(-F\eta)}{RT}\right), \end{aligned} \tag{4.101}$$

where the coefficient is

$$l_0 = l\exp\frac{[\tilde{\mu}_{\mathrm{rev}}-\tilde{\mu}(0)]}{RT}\,. \tag{4.102}$$

The overpotential appears as an effective driving force in (4.101). The expression for j can be used as the flux in the expression for the entropy production (4.90). It shows the dissipative nature of the term. For small driving forces, we obtain a linear flux–force relation.

Fluxes and forces for mass and charge couple to thermal driving forces, as described in (4.79). We know that the coupling coefficients can be large at interfaces [4.40]. This coupling has not yet been described in any detail for electrochemical systems, see however [4.8, 34, 80]. A task will be to integrate expression (4.91) into the expressions of Sect. 4.4.

4.6.5 Power from Reverse Electrodialysis

A power plant that uses (only) the electrolyte concentration difference to give electric current as expressed by (4.48) is called a saline power plant. The idea is old, but has gained new momentum. One possible technology for such a plant is reverse electrodialysis [4.55, 81–83] as is illustrated in Fig. 4.3.

Sea water and fresh water are fed into alternating compartments which are separated by ion-exchange membranes. The membranes alternate between anion- and cation-exchange membranes. One unit cell consists of a salt water compartment (concentration $c_{\mathrm{NaCl}}(1)$), a cation-exchange membrane, a fresh water compartment ($c_{\mathrm{NaCl}}(2)$), an anion-exchange membrane and a salt water compartment ($c_{\mathrm{NaCl}}(1)$). The gradient in chemical potential of salt (NaCl) drives chloride ions through the anion-exchange membrane and sodium ions through the cation-exchange membrane.

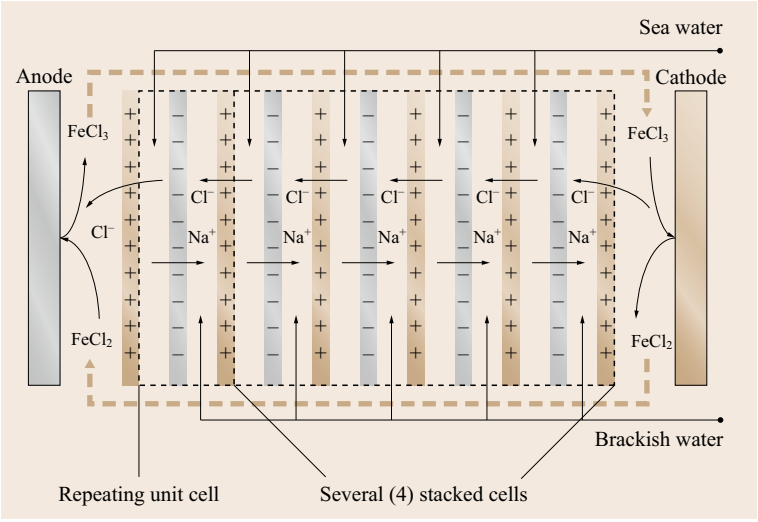


Fig. 4.3 The principle of a saline power plant that uses reverse electrodialysis. The figure shows four unit cells in series. The chemical potential difference of sodium chloride, between sea water and the fresh water, drives an electric current and creates electric power and brackish water

There are concentration jumps at the solution–membrane interfaces, as the ion-exchange membrane can be seen as a concentrated ionic solution. Donnan equilibrium at the solution–membrane interface means that the interface is in equilibrium with its adjacent bulk phases. There is no contribution to the measurable cell potential from these parts of the cell, and the sole contribution comes from transport across the membrane. The membrane transport numbers for Na^+ and Cl^-, respectively, are near unity. The electric field that arises, causes an electric current in the external circuit.

Because most ion-exchange membranes are not perfect at the salt concentrations in question, salt may leak (diffuse) into the fresh water compartment and reduce the potential difference. But some salt is also required there to give an acceptable ohmic resistance in this compartment. The concentration profiles across the membranes and the compartments can be solved using the expressions for the diffusion and charge transfer. The transference coefficient for NaCl in the membranes is equal to the transport number of Na^+ corrected for the electro-osmotic contribution of water [4.19]

$$t^m_{\mathrm{NaCl}} = t^m_{\mathrm{Na}^+} - \frac{c_{\mathrm{w}}}{c_{\mathrm{NaCl}}} t^m_{\mathrm{w}} \quad \text{for} \quad m = c, a \,. \tag{4.103}$$

The main part of the electric potential can therefore be attributed to the cation-exchange membrane. In the cation exchange membrane, $t^m_{\mathrm{Na}^+}$ is near 1, while in the anion membrane it is close to zero. We use (4.48) and obtain the electromotive force for a unit cell

$$(\Delta\phi)_{j=0} = -\frac{2RT}{F}\left(t^c_{\mathrm{Na}^+} - t^a_{\mathrm{Na}^+}\right) \ln\left(\frac{c_{\mathrm{NaCl},2}\gamma_{\pm,2}}{c_{\mathrm{NaCl},1}\gamma_{\pm,1}}\right), \tag{4.104}$$

where the salt activity is $a_{\mathrm{NaCl}} = c^2_{\mathrm{NaCl}}\gamma^2_{\pm}$. When the membranes are perfect and the water transference coefficient is negligible, $t^c_{\mathrm{Na}^+} = 1$ and $t^a_{\mathrm{Na}^+} = 0$. A salt concentration ratio of 1 : 10 at 300 K gives −240 mV from this formula, for these conditions, with electrodes reversible to the chloride ion. The low value means that unit cells must be stacked like indicated in Fig. 4.3 to obtain a reasonable stack voltage. Clearly, the selectivities of the membranes are important. It may also be good to pay attention to the water contribution. The electric potential of the membrane plant is proportional to the number of unit cells. Power densities around $4\,\mathrm{W/m^2}$ stack unit cell cross-sectional area can be expected. Expression (4.104) must not be confused with the Planck potential, as the front factors and the path of integration differ.

It has been proposed that the cell potential can be further enhanced by applying pressure and/or temperature gradients across the membranes [4.84]. The conversion of mechanical energy to electric energy, called friction electricity production, has not yet been systematically studied in membrane systems.

4.6.6 Electrochemical Cells as Thermoelectric Generators

According to the International Energy Agency [4.85], the industrial sector is responsible for about 40% of the power consumption worldwide. Large amounts of waste heat is generated in conventional power plants, in the process industry, in the metallurgicall industry, and so on. All processes are now under scrutiny for better use of energy resources. The use of waste heat, even at low temperatures, is then of interest. Thermoelectric generators convert thermal energy to electric energy directly. Most of the research effort has been concentrated on solid-state generators, where a Seebeck effect is generated by change in charge carriers between semiconductors. The transported entropy in semi-conductors, seem to reach an upper limit, see review of *Sootsman* et al. [4.86]. Seebeck coefficients are typically in the order of a few hundred microvolts per Kelvin, for example, $240\,\mu\mathrm{V/K}$ for a Bi Te-based device. It is therefore interesting to look to ionic conductors, and some have been examined [4.87–89]. The change in entropy due to an electrode reaction, in particular reactions which include gases, may give a Seebeck coefficient one order of magnitude larger.

To illustrate the principle, let us examine a possible thermoelectric converter made from the hydrogen electrode of the fuel cell [4.72] (Sect. 4.7). With standard notation, the cell is denoted

$$\begin{aligned}&(\mathrm{Pt,C})\ \mathrm{H_2}(p^a, T^a)|\mathrm{H_2O}(p_w, T^{\mathrm{a}})|^{\mathrm{m}}|\mathrm{H_2}(p^c, T^{\mathrm{c}}),\\ &\mathrm{H_2O}(p_{\mathrm{w}}, T^{\mathrm{c}})|(\mathrm{Pt,C})\,.\end{aligned} \tag{4.105}$$

The cell reaction, which includes electroosmosis, can be written as

$$\frac{1}{2}\mathrm{H_2(a)} + t_{\mathrm{w}}\mathrm{H_2O(a)} \rightarrow \frac{1}{2}\mathrm{H_2(c)} + t_{\mathrm{w}}\mathrm{H_2O(c)}\,, \tag{4.106}$$

where the transference coefficient for water (electro-osmotic drag) t_{w} is the number of water molecules

transported by each proton moving through the membrane. There are three independent fluxes in the membrane, the heat flux, the water flux, and the electric current density. The flux–force relations for the membrane can be written as

$$\frac{\mathrm{d}T}{\mathrm{d}x} = -\frac{1}{\lambda^m}\left[J_q'^{,m} - q^{*,m}\left(J_\mathrm{w}^m - t_\mathrm{w}^m\frac{j}{F}\right) - \pi^m\frac{j}{F}\right], \tag{4.107a}$$

$$\frac{\mathrm{d}\mu_{\mathrm{w},T}}{\mathrm{d}x} = -\frac{q^{*,m}}{T}\frac{\mathrm{d}T}{\mathrm{d}x} - \frac{RT}{D_\mathrm{w}^m c_w}\left(J_\mathrm{w}^m - t_\mathrm{w}^m\frac{j}{F}\right), \tag{4.107b}$$

$$\frac{\mathrm{d}\phi}{\mathrm{d}x} = -\frac{\pi^m}{TF}\frac{\mathrm{d}T}{\mathrm{d}x} - \frac{t_\mathrm{w}^m}{F}\frac{\mathrm{d}\mu_{\mathrm{w},T}}{\mathrm{d}x} - r^m j\,, \tag{4.107c}$$

with the stationary state thermal conductivity λ^m, the electric resistivity r^m, the heat of transfer $q^{*,m}$, the Peltier coefficient π^m, the water transference number t_w^m and the diffusion coefficient of water in the membrane on a concentration basis is D_w^m. The relation between the membrane water activity and membrane water concentration c_w is known [4.90]. The Peltier coefficient for the membrane is

$$\frac{\pi^m}{T} = S_{H+}^* - t_\mathrm{w}^m S_\mathrm{w}^m\,. \tag{4.108}$$

In Seebeck coefficient determination, one measures the cell potential $\Delta\phi$ as a function of the temperature difference between the electrodes at $j \to 0$. At the start of the experiment, there is no gradient in chemical potential, and the Seebeck coefficient contains the first term of (4.107c). As the temperature difference across the membrane becomes stable, one obtains from (4.107b) that the gradient $\mathrm{d}\mu_{\mathrm{w},T}/\mathrm{d}x$ is proportional to the temperature gradient via the heat of transfer over the temperature $q^{*,m}/T$. It can be shown that this ratio is equal to the entropy of water, when there is also equilibrium for water across the membrane [4.72]. From (4.107c) and (4.108), we obtain the Seebeck coefficient of the cell

$$\left(\frac{\Delta\phi}{\Delta T}\right)_{j\approx 0, t=\infty} = \frac{1}{F}\left(\frac{1}{2}S_{\mathrm{H}_2} - S_{\mathrm{H}^+}^*\right). \tag{4.109}$$

Measurements [4.72] give the Seebeck coefficient $670 \pm 50\,\mu\mathrm{V/K}$ for a hydrogen pressure of 1 bar, in agreement with the results of [4.91]. Lower hydrogen pressures give higher values, as $S_{\mathrm{H}_2} = S_{\mathrm{H}_2}^0 - R\ln(p/p^0)$. The value for 1 bar is already more than twice the value for a Bi Te-based device. Electrochemical cells with (large) heat production at the single electrodes could be used for thermoelectric energy conversion [4.13, 89].

In a cell with identical electrodes, clearly one electrode is heated, while the other is cooled equally much, when electric current is passing the cell. In the same manner as semiconducting devices are used for cooling purposes, also electrochemical systems can be used in this manner. In the aluminum electrolysis, the Peltier cooling effect is an unwanted effect, as it can lead to local freezing of the molten salt electrolyte [4.13, 92].

4.7 The Polymer Electrolyte Fuel Cell

The purpose of NET for heterogeneous systems is to provide in a systematic way, a method for integration of intensive variables across the system. We shall sketch how this has been done for the polymer electrolyte fuel cell, taking a part of the cell as example. For a calculation of the whole cell, see *Kjelstrup* et al. [4.1, 78] and *Siemer* [4.77].

The chemical energy added to the cell is converted in the different parts of the cell. A conversion takes place to electric energy, heat and other chemical energies. For the membrane in the stationary state, energy conservation means that the energy flux is constant

$$\frac{\mathrm{d}}{\mathrm{d}x}J_u = \frac{\mathrm{d}}{\mathrm{d}x}(J_q'^m + j\phi^m + J_\mathrm{w}^m H_\mathrm{w}^m) = 0\,. \tag{4.110}$$

We see that a gradient in electric potential can develop under these conditions, only on the cost of a gradient in heat flux or, at constant water flux J_m^m from a variation in the enthalpy of water H_w. The entropy production defines how that exactly happens. The entropy production is given by (4.14) with water (w) replacing NaCl. The corresponding flux equations were given in Sect. 4.6.6. Replacing the activity in the expression for the water flux with the water content $\Lambda = c_\mathrm{w}M/\rho$ (M is the molar mass of polymer and ρ is the membrane dry density), we obtain

$$J_\mathrm{w}^m = -\frac{q^{*,m}D_\mathrm{w}^m\Lambda\rho}{RMT^2}\frac{\mathrm{d}T}{\mathrm{d}x} - \frac{D_\mathrm{w}^m\rho}{M}\frac{\mathrm{d}\Lambda}{\mathrm{d}x} + \frac{t_\mathrm{w}^m j}{F}\,. \tag{4.111}$$

The last term gives the electro-osmotic transport of water, while the term in front of it describes diffusion. We see also how the water flux due to coupling obtains a contribution from the temperature gradient (thermal osmosis [4.93]) in addition to the contributions that are common to take along.

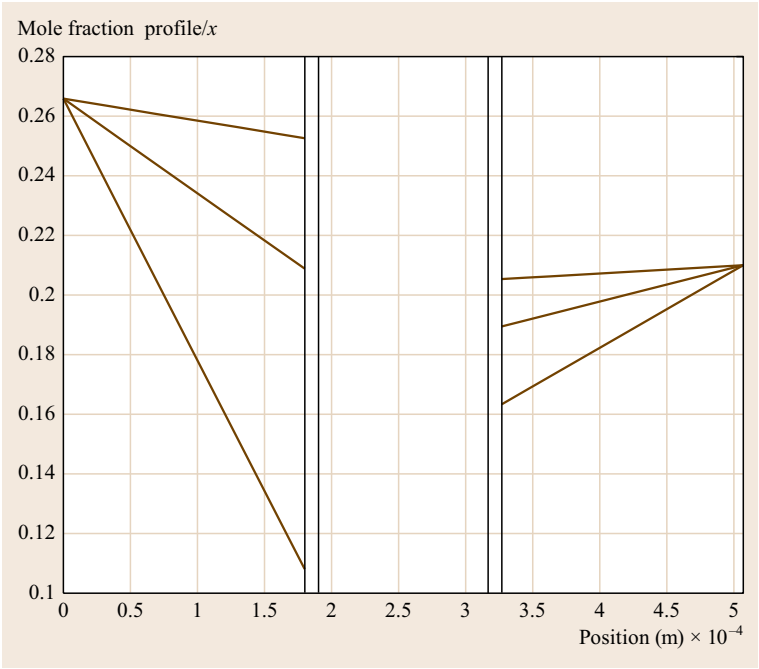


Fig. 4.4 The concentration of water (*left*) and oxygen (*right*) in the anode and cathode boundary layers, respectively, as a function of the electric current densities 500, 2500, and 5000 $\mathrm{A/cm^2}$ (counted from above). The center of the figure is the membrane–electrode assembly

The temperature profile and the gradient in electric potential are accordingly

$$\frac{\mathrm{d}T}{\mathrm{d}x} = -\frac{J_q'^m}{\lambda^m} + \frac{q^{*,m}}{\lambda^m}\left(J_\mathrm{w}^m - t_\mathrm{w}^m\frac{j}{F}\right) + \frac{\pi^m j}{\lambda^m F}\,,$$
$$\frac{\mathrm{d}\phi}{\mathrm{d}x} = -\frac{\pi^m}{TF}\frac{\mathrm{d}T}{\mathrm{d}x} - \frac{t_\mathrm{w}^m RT}{F}\frac{\mathrm{d}\mu_\mathrm{w}}{\mathrm{d}x} - r^m j\,. \tag{4.112}$$

We see that the heat flux cannot be replaced by Fourier's law, not even in the balanced situation where $J_\mathrm{w}^m = t_\mathrm{w}^m j/F$, because the Peltier coefficient contributes with a term that contains the nonnegligible entropy of water and is proportional to the current density. Likewise, it is not so that the electric potential gradient is given by the ohmic resistance of the membrane only. There are contributions from the Peltier coefficient, and possible changes in the chemical potential of water.

The form of the equations for the other parts of the cell contains the same type of terms. The set of equations for the anode backing, anode surface, membrane, cathode surface, and cathode backing were solved for some simplifying conditions [4.78]. In addition to standard thermodynamic data, we used

$$q^{*,m} = -TS_\mathrm{w}^m\,. \tag{4.113}$$

The membrane density and molar mass were $1.64\times 10^3\,\mathrm{kg/m^3}$ and $1.1\,\mathrm{kg/mol}$, respectively. The water transference coefficient of water in Nafion 115 in equilibrium with vapor was 1.2 [4.94]. The $\pi^m/T^{m,c}$ was taken from the literature [4.95]. The membrane diffusion coefficient was $D^m = 1.5\times 10^{-10}\,\mathrm{m^2/s}$. The electric resistivity, r^m, and diffusion coefficient, D^m, were taken from *Springer* et al. [4.90]

$$(r^m)^{-1} = \exp\left[1268\left(\frac{1}{303}-\frac{1}{T}\right)\right](0.5139\Lambda - 0.326)\,. \tag{4.114}$$

For the thermal conductivity of the membrane, we used $\lambda^m = 0.2\,\mathrm{W/K\,m}$ [4.96]. The results of the computations of the concentration profiles, the electric potential profile and the heat flux variation are shown in Figs. 4.4–4.6.

Figure 4.4 shows the variation in the mole fraction of water (left) and oxygen (right) in the anode and cathode backing as a function of the electric current density. We see how the sink for the gases in the electrodes creates concentration gradients. It is the nonnegligible water transference coefficient in the membrane that creates the sink for water.

The electric potential profile across the cell becomes nonlinear in the membrane, as shown in Fig. 4.5. This can be understood from the dependence of r^m on the water content (4.114). As the membrane water content sinks at the anode surface (Fig. 4.4), the resistance

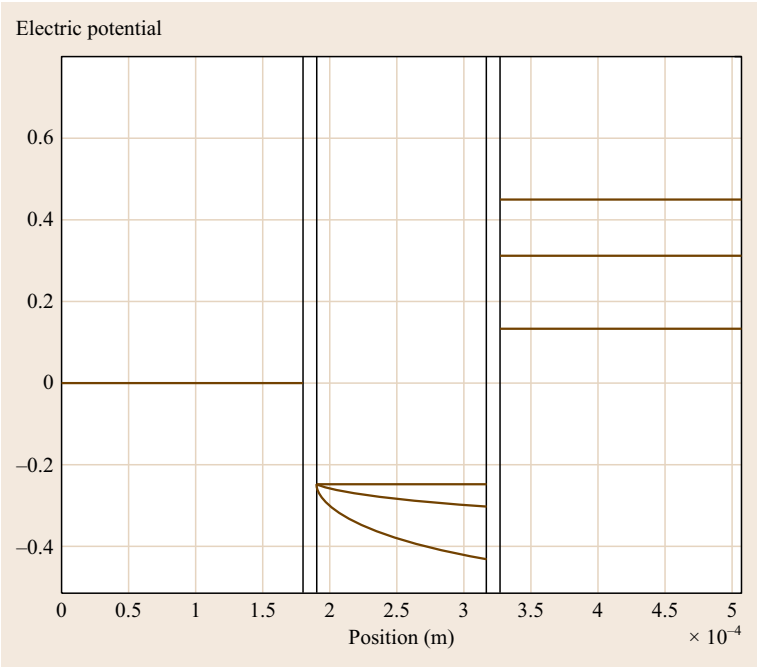


Fig. 4.5 The electric potential profile across the polymer electrolyte membrane fuel cell as a function of the electric current density (Fig. 4.4). Five layers are pictured: the anode backing, the anode surface, the membrane, the cathode surface, and the cathode backing

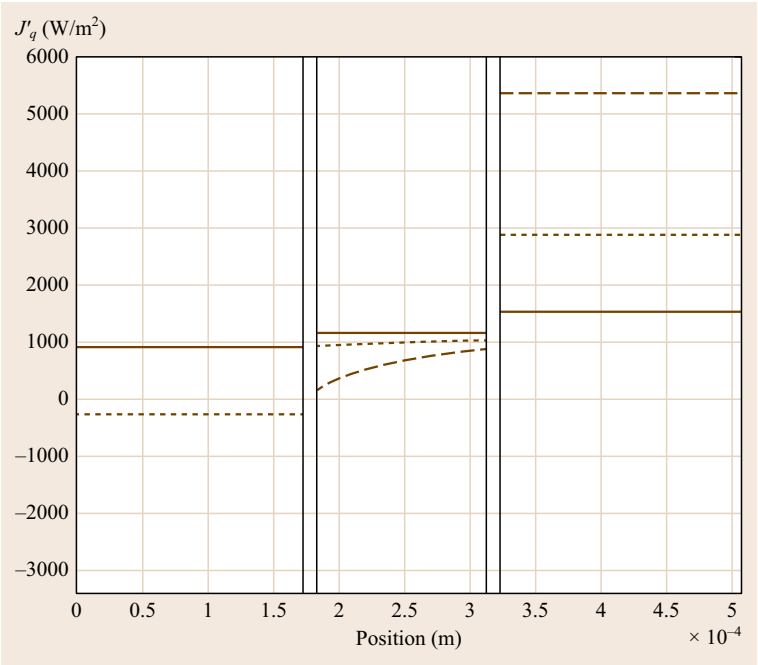


Fig. 4.6 The measurable heat flux in various layers of the polymer electrolyte fuel cell as a function of the electric current density (Fig. 4.4). The heat flux is negative on the anode side and positive on the cathode side, meaning that positive heat is leaving the cell on both sides

increases, and so does the electric potential. This gives the biggest contribution to the electric potential variation across the membrane. The contribution from the water chemical potential is not big in the present calculation, because we have assumed equilibrium for water at both electrode surfaces. This condition may not be true under typical operating conditions, however [4.72]. The local temperature may rise or fall, depending on j. The variation in $j\phi^m$ leads indeed to large changes in J'^m_q (Fig. 4.6). The heat flux in Fig. 4.6 is negative on the anode side and positive on the cathode side, meaning that positive heat is leaving the cell on both sides.

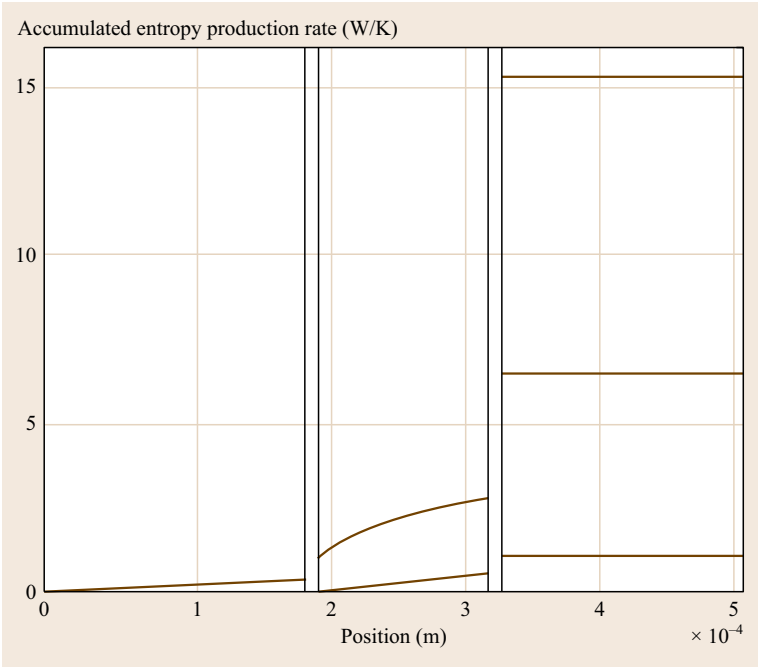


Fig. 4.7 The variation in the accumulated entropy production across the polymer electrolyte fuel cell, for the examples illustrated by Figs. 4.4–4.6. The *higher level lines* refer to the high current densities

For reversible conditions, the heat leaving the cell divided by the constant temperature, sums to the entropy of the reaction.

Knowing the profiles across each layer in the fuel cell, one can find the variation in the entropy production. The accumulated entropy production obtained by integration from 0 to the position in the cell is shown in Fig. 4.7. The figure shows that the major dissipation of energy takes place at the electrode surfaces and in the membrane. The concentration profiles in the backings do not lead to significant dissipation, not even at high electric current densities. By integrating across the cell over the local entropy production, using (4.5), we obtain the total entropy production, compatible with Fig. 4.1.

4.8 Transport at Interfaces. Perspectives and Conclusion

We have seen in the preceeding sections how NET and its extension to the mesoscopic scale can be used in a systematic way to define independent fluxes and conjugate forces for each part of a heterogeneous system. From this definition by the entropy production, one can explore the electrochemical properties of a complete cell. We have seen that the theory is not restricted to transport phenomena which are globally linear. Extensions into the nonlinear area are little explored in NET, however. This gives a possibility for future developments. The reason why a further exploration may be fruitful can be captured in one statement: The coupling of fluxes at interfaces is significant. The coupling at electrochemical interfaces was only recently understood and formulated [4.1]. Through the development of NET to also deal with heterogeneous systems, one has obtained general boundary conditions for these important interfaces. These boundary conditions are fluxes, in contrast to most of the commonly chosen ones. They allow us to deal in a systematic manner with situations, when interface transport becomes rate-limiting.

With such boundary conditions available, one can calculate with high precision the profiles of intensive variables across the cell. NET is absolutely essential to describe the performance of power plants, like the saline one, or the thermoelectric one. An example, not described here, is a membrane plant that converts mechanical energy to electric power (friction electricity) [4.84]. In this context, it may be beneficial to include also the momentum balance in the entropy production [4.55]. All these power plants take direct advantage of coupling coefficients being different from zero. The simple transport laws of Fick, Fourier, and Darcy become obsolete in these situations.

We have also seen how the entropy production can be described in detail, and how one can use the expression in consistency checks, in modeling and experimental work [4.59, 72]. The entropy production gives the only general measure of the deviation from reversible operation, through the dissipated energy (lost exergy). It can be used to localize power losses, adding to the information obtained from polarization curves. It can also be used to compare different technologies. With a general basis available, it is possible to check effects of assumptions introduced in the theoretical description, like was done for the liquid junction potential.

Acknowledgments. The authors acknowledge support for their sabbatical stay at the University of Barcelona with J.M. Rubi. The comments of J.K. Sengers on the section of local equilibrium are appreciated, and O.S. Burheim is thanked for general comments on a late version of the ms.

References

4.1 S. Kjelstrup, D. Bedeaux: *Non-equilibrium Thermodynamics for Heterogeneous Systems*, Advances in Statistical Mechanics, Vol. 16 (World Scientific, Singapore 2008)

4.2 L. Onsager: Reciprocal relations in irreversible processes. I, Phys. Rev. **37**, 405–426 (1931)

4.3 L. Onsager: Reciprocal relations in irreversible processes. II, Phys. Rev. **38**, 2265–2279 (1931)

4.4 S.R. de Groot, P. Mazur: *Non-equilibrium Thermodynamics* (North-Holland, Amsterdam 1962)

4.5 S.R. de Groot, P. Mazur: *Non-equilibrium Thermodynamics* (Dover, London 1984)

4.6 J.M.G. Vilar, J.M. Rubi: Thermodynamics 'beyond' local equilibrium, Proc. Natl. Acad. Sci. USA **98**, 11081–11084 (2001)

4.7 J.M. Rubi, S. Kjelstrup: Mesoscopic nonequilibrium thermodynamics gives the same thermodynamic basis to Butler-Volmer and Nernst equations, J. Phys. Chem. B **107**, 13471–13477 (2003)

4.8 S. Kjelstrup, J.M. Rubi, D. Bedeaux: Energy dissipation in slipping biological pumps, Phys. Chem. Chem. Phys. **7**, 4009–4018 (2005)

4.9 S. Kjelstrup, J.M. Rubi, D. Bedeaux: Active transport: A Kinetic description on thermodynamic grounds, J. Theor. Biol. **234**, 7–12 (2005)

4.10 T.S. Brun, D. Vaula: Correlation of measurements of electroosmosis and streaming potentials in ion exchange membranes, Ber. Bunsenges. Physik. Chem. **71**, 824–829 (1967)

4.11 B. Flem, S. Kjelstrup, Å. Sterten: Peltier heats in cryolite melts with alumina, Light Metals (TMS, Warrendale 1996) pp. 203–209

4.12 B. Flem: Peltier Heats in Cryolite Melts with Alumina, Ph.D. Thesis (Department of Physical Chemistry, Norwegian Institute of Technology, Trondheim 1996)

4.13 B. Flem, Q. Xu, S. Kjelstrup, Å. Sterten: Thermoelectric powers of cells with NaF-AlF_3-Al_2O_3 melts, J. Non-Equilib. Thermodyn. **26**, 125–151 (2001)

4.14 A. Katchalsky, P. Curran: *Nonequilibrium Thermodynamics in Biophysics* (Harvard Univ. Press, Cambrigde 1975)

4.15 R. Haase: *Thermodynamics of Irreversible Processes* (Addison-Wesley, Reading 1969)

4.16 N. Laksminarayanaiah: *Transport Phenomena in Membranes* (Academic Press, New York 1969)

4.17 D.C. Mikulecky, W.A. Wiegand, J.S. Shiner: A simple network thermodynamic method for parallel coupled flows I. The linear case, J. Theor. Biol. **69**, 471–510 (1977)

4.18 A.J. Staverman: Non-equilibrium thermodynamics of membrane processes, Trans. Faraday Soc. **48**, 176–185 (1952)

4.19 K.S. Førland, T. Førland, S. Kjelstrup Ratkje: *Irreversible Thermodynamics. Theory and Application*, 1st edn. (Wiley, Chichester 1988)

4.20 Y. Ito, H. Kaiya, S. Yoshizawa, S. Kjelstrup Ratkje, T. Førland: Electrode heat balances of electrochemical cells: Application to water electrolysis, J. Electrochem. Soc. **131**, 2504–2509 (1984)

4.21 J. Richter, A. Heller, W. Vreuls: Investigations of non-isothermal molten salts-initial values of thermoelectric-power for systems $AgNO_3$, $LiNO_3$+ $AgNO_3$, and $NaNO_3$+ $AgNO_3$ as a function of temperature and composition, Ber. Bunsenges. Phys. Chem. **81**, 375–380 (1977)

4.22 J. Richter, U. Prüser: Untersuchungen des stationären Zustandes der Thermodiffusion in Thermoketten mit Nitratschmelzen, Ber. Bunsenges. Phys. Chem. **81**, 508–514 (1977), in German

4.23 T. Førland, S. Kjelstrup Ratkje: Entropy production by heat, mass, charge transfer and specific chemical reactions, Electrochim. Acta **25**, 157–163 (1980)

4.24 S. Kjelstrup Ratkje, T. Holt, M.G. Skrede: Cation membrane transport: Evidence for local validity of Nernst-Planck equations, Ber. Bunsenges. Physik. Chem. **92**, 825–832 (1988)

4.25 K.S. Førland, T. Førland, A. Makange, S. Kjelstrup Ratkje: The coupling between transport of electric charge and chemical reaction, J. Electrochem. Soc. **130**, 2376–2380 (1983)

4.26 S. Kjelstrup Ratkje, H. Rajabu, T. Førland: Transference coefficients and transference numbers in molten salt mixtures relevant for the aluminium electrolysis, Electrochim. Acta **38**, 415–423 (1993)

4.27 M. Tasaka, S. Morita, M. Nagasawa: Membrane potential in non-isothermal system, J. Phys. Chem. **69**, 4191–4197 (1965)

4.28 T. Okada, S. Kjelstrup Ratkje, S. Møller-Holst, L.O. Jerdal, K. Friestad, G. Xie, R. Holmen: Water and ion transport in the cation-exchange membrane systems NaCl-$SrCl_2$ and KCl-$SrCl_2$, J. Membr. Sci. **111**,

159–167 (1996)
4.29 T. Okada, S. Møller-Holst, O. Gorseth, S. Kjelstrup: Transport and equilibrium properties of Nafion membranes with H^+ and Na^+ ions, J. Electroanal. Chem. **442**, 3313–3319 (1998)
4.30 T. Suzuki, R. Kiyono, M. Tasaka: Solvent transport across anion-exchange membranes under a temperature difference and transported entropy of water, J. Membr. Sci. **92**, 85–93 (1994)
4.31 T. Suzuki, Y. Takahashi, R. Kiyono, M. Tasaka: Non-isothermal membrane phenomena across perfluorosulfonic acid-type membranes, Flemions S: part I. Thermoosmosis and transported entropy of water, Colloid Polym. Sci. **272**, 971–978 (1994)
4.32 J.S. Newman: *Electrochemical Systems*, 2nd edn. (Prentice-Hall, Englewood Cliffs 1991)
4.33 J.W. Gibbs: *The Scientific Papers of J.W. Gibbs* (Dover, New York 1961)
4.34 A. Lervik, S. Kjelstrup, D. Bedeaux: Kinetic and mesoscopic non-equilibrium description of the Ca^{2+} pump: A comparison, Eur. Biophys. J. **41**, 437–448 (2012)
4.35 I. Prigogine, P. Mazur: Sur l'extension de la thermodynamique aux phénomènes irréversibles liés aux degrés de liberté internes, Physica **19**, 241–254 (1953), in French
4.36 G.D.C. Kuiken: *Thermodynamics for Irreversible Processes* (Wiley, Chichester 1994)
4.37 D. Bedeaux, S. Kjelstrup: Transfer coefficients for evaporation, Physica A **270**, 413–426 (1999)
4.38 A. Røsjorde, D. Bedeaux, S. Kjelstrup, B. Hafskjold: Non-equilibrium molecular dynamics simulations of steady-state heat and mass transport in condensation II: Transfer coefficients, J. Colloid Interface Sci. **240**, 355–364 (2001)
4.39 J.-M. Simon, S. Kjelstrup, D. Bedeaux, B. Hafskjold: Thermal flux through a surface of n-octane. A non-equilibrium molecular dynamics study, J. Phys. Chem.B **108**, 7186–7195 (2004)
4.40 J. Ge, S. Kjelstrup, D. Bedeaux, J.M. Simon, B. Rousseau: Transfer coefficients for evaporation of a system with a Lennard-Jones long range spline potential, Phys. Rev. E **75**, 061604–61610 (2007)
4.41 B. Hafskjold, S. Kjelstrup Ratkje: Criteria for local equilibrium in a system with transport of heat and mass, J. Stat. Phys. **78**, 463–494 (1995)
4.42 J.M. Ortiz de Zárate, J.V. Sengers: *Hydrodynamic Fluctuations in Fluids and Fluid Mixtures* (Elsevier, Amsterdam 2006)
4.43 T. Savin, K. Glavatskiy, S. Kjelstrup, H.C. Öttinger, D. Bedeaux: Local equilibrium of the Gibbs interface in two-phase systems, Eur. Phys. Lett. **97**, 40002 (2012)
4.44 J. Xu, S. Kjelstrup, D. Bedeaux: Molecular dynamics simulations of a chemical reaction; conditions for local equilibrium in a temperature gradient, Phys. Chem. Chem. Phys. **8**, 2017–2027 (2006)
4.45 S. Kjelstrup, D. Bedeaux, I. Inzoli, J.-M. Simon: Criteria for validity of thermodynamic equations from non-equilibrium molecular dynamics simulations, Energy **33**, 1185–1196 (2008)
4.46 O. Burheim, P.J.S. Vie, S. Møller-Holst, J. Pharoah, S. Kjelstrup: A calorimetric analysis of a polymer electrolyte fuel cell and the production of H_2O_2 at the cathode, Electrochim. Acta **55**, 935–942 (2010)
4.47 T.L. Hill: *Thermodynamics of Small Systems. Part I* (Benjamin, New York 1963)
4.48 S.K. Schnell, T.J.H. Vlugt, J.-M. Simon, D. Bedeaux, S. Kjelstrup: Thermodynamics of a small system in a μT reservoir, Chem. Phys. Lett. **504**, 199–201 (2011)
4.49 S.K. Schnell, X. Liu, J.-M. Simon, A. Bardow, D. Bedeaux, T.J.H. Vlugt, S. Kjelstrup: Calculating thermodynamics properties from fluctuations at small scales, J. Phys. Chem. B **115**, 10911–10918 (2011)
4.50 S.K. Schnell, T.J.H. Vlugt, J.-M. Simon, D. Bedeaux, S. Kjelstrup: Thermodynamics of small systems embedded in a reservoir: A detailed analysis of finite size effects, Mol. Phys. **110**, 1069–1079 (2012)
4.51 D. Bedeaux, S. Kjelstrup, T.J.H. Vlugt, P. Kruger, S.K. Schnell, J.-M. Simon: Kirkwood–Buff integrals for finite volumes, J. Phys. Chem. Lett. **4**, 235–238 (2013)
4.52 A. Røsjorde, D.W. Fossmo, D. Bedeaux, S. Kjelstrup, B. Hafskjold: Non-equilibrium molecular dynamics simulations of steady-state heat and mass transport in condensation I: Local equilibrium, J. Colloid Interface Sci. **232**, 178–185 (2000)
4.53 E. Johannessen, D. Bedeaux: The non-equilibrium van der Waals square gradient model. II. Local equilibrium and the Gibbs surface, Physica A **330**, 354–372 (2003)
4.54 K. Glavatskiy, D. Bedeaux: Numerical solution of the nonequilibrium square-gradient model and verification of local equilibrium for the Gibbs surface in a two-phase binary mixture, Phys. Rev. E **79**, 031608 (2009)
4.55 S. Kjelstrup, D. Bedeaux, E. Johannessen, J. Gross: *Non-equilibrium Thermodynamics for Engineers* (World Scientific, Singapore 2010)
4.56 S. Kjelstrup, L. de Meis, D. Bedeaux, J.-M. Simon: Heat transport from the sarcoplasmic reticulum by the Ca-ATPase, Eur. Biophys. J. Biophys. Lett. **38**, 59–67 (2008)
4.57 S. Kjelstrup, D. Barragan, D. Bedeaux: Transport coefficients for heat and ion transport in Ca^{2+}-ATPase isoforms, Biophys. J. **96**, 4376–4386 (2009)
4.58 P.N. Segre, R.W. Gammon, J.V. Sengers, B.M. Law: Rayleigh scattering in a liquid far from thermal equilibrium, Phys. Rev. A **45**, 714–724 (1992)
4.59 O. Burheim, S. Kjelstrup, J.G. Pharoah, P.J.S. Vie, S. Møller-Holst: Calculation of reversible electrode heats in the proton exchange membrane fuel cell from calorimetric measurements, Electrochim. Acta **56**, 3248–3257 (2011)
4.60 D. Bedeaux, S. Kjelstrup: Local properties of a formation cell as described by non-equilibrium thermodynamics, J. Non-Equilib. Thermodyn. **25**, 161–178 (2000)
4.61 S. Kjelstrup, D. Bedeaux, E.M. Hansen: Surface contributions to emf and half cell potentials of non-isothermal cells, Period. Polytech. Ser. Chem. Eng. **41**, 11–27 (1997)

4.62 A.M. Albano, D. Bedeaux: Non-equilibrium electro-thermodynamics of polarizable multicomponent fluids with an interface, Physica A **147**, 407–435 (1987)

4.63 V. Blinov, S. Kjelstrup, D. Bedeaux, V.S. Sharivker: The role of the transported entropy of lead in partially thermostatted and adiabatic cells, J. Electrochem. Soc. **148**, 364–371 (2001)

4.64 S. Kjelstrup, D. Bedeaux: Jumps in electric potential and in temperature at the electrode surfaces of the solid oxide fuel cell, Physica A **244**, 213–226 (1997)

4.65 S. Kjelstrup Ratkje, D. Bedeaux: The overpotential as a surface singularity described by nonequilibrium thermodynamics, J. Electrochem. Soc. **143**, 779–789 (1996)

4.66 D. Bedeaux, S. Kjelstrup Ratkje: The dissipated energy of electrode surfaces. Temperature jumps from coupled transport processes, J. Electrochem. Soc. **136**, 767–779 (1996)

4.67 J. Ross, P. Mazur: Some deductions from a statistical mechanical theory of chemical kinetics, J. Chem. Phys. **35**, 19–28 (1961)

4.68 D. Bedeaux, A.M. Albano, P. Mazur: Boundary conditions and nonequilibrium thermodynamics, Physica A **82**, 438–462 (1976)

4.69 A.M. Albano, D. Bedeaux, J. Vlieger: On the description of interfacial electromagnetic properties using singular fields, charge density and currents at a dividing surface, Physica A **102**, 105–119 (1980)

4.70 D. Bedeaux: Nonequilibrium thermodynamics and statistical physics of surfaces, Adv. Chem. Phys. **64**, 47–109 (1986)

4.71 M. Kamata, Y. Ito, J. Oishi: Single electrode Peltier heat of a hydrogen electrode in NaOH solutions at high concentrations, Electrochim. Acta **33**, 359–363 (1988)

4.72 S. Kjelstrup, P.J.S. Vie, L. Alkyacin, P. Zefaniya, J.G. Pharoah, O. Burheim: The Seebeck coefficient and the Peltier effect in a polymer electrolyte cell with hydrogen electrodes, Electrochim. Acta **99**, 166–175 (2013)

4.73 A.K. Meland, D. Bedeaux, S. Kjelstrup: Rate-limiting proton hydration in the anode of the polymer electrolyte fuel cell, J. Membr. Sci. **282**, 96–108 (2006)

4.74 J.L. Jackson: Charge neutrality in electrolyte solutions and the liquid junction potential, J. Phys. Chem. **78**, 2060–2064 (1974)

4.75 M. Planck: Über die Erregung von Electricität und Wärme in Electrolyten, Ann. Phys. Chem. **39**, 161–186 (1890), in German

4.76 M. Planck: Über die Potentialdifferenz zwischen zwei verdünnten Lösungen binärer Electrolyte, Ann. Phys. Chem. **40**, 561–576 (1890), in German

4.77 M. Siemer: Lokale Entropieproduktionsraten in der Polymerelektrolyt-Membran-Brennstoffzelle, Ph.D. Thesis (Fachbereich Maschinenbau der Helmut-Schmidt-Universität, Universität der Bundeswehr, Hamburg 2007), in German

4.78 S. Kjelstrup, A. Røsjorde: Local and total entropy production and heat and water fluxes in a one-dimensional polymer electrolyte fuel cell, J. Phys. Chem. B **109**, 9020–9033 (2005)

4.79 J. Breer, S. Kjelstrup Ratkje, G.F. Olsen: Control of liquid junctions: The system HCl-KCl, Zeitschr. Phys. Chem. **174**, 179–198 (1991)

4.80 D. Bedeaux, S. Kjelstrup: The measurable heat flux that accompanies active transport by Ca-ATPase, Phys. Chem. Chem. Phys. **48**, 7304–7317 (2008)

4.81 R.E. Pattle: Production of electric power by mixing fresh and salt water in the hydroelectric pile, Nature **174**, 660 (1954)

4.82 J.W. Post, J. Veerman, H.V.M. Hamelers, G.J.W. Euverink, S.J. Metz, K. Nijmeijer, C.J.N. Buisman: Salinity-gradient power: Evaluation of pressure-retarded osmosis and reverse electrodialysis, J. Membr. Sci. **288**, 218–230 (2007)

4.83 O. Burheim, F. Seland, J.G. Pharoah, S. Kjelstrup: Improved electrode systems for reverse electro-dialysis and electro-dialysis, Desalination **285**, 147–152 (2012)

4.84 A. Bentien, T. Okada, S. Kjelstrup: Evaluation of nano-porous polymer membranes for electrokinetic energy conversion in power applications, J. Phys. Chem. C **117**, 1582–1588 (2013)

4.85 E.A. Abdelaziz, R. Saidur, S. Mekhilef: A review on energy saving strategies in industrial sector, Renew. Sustain. Energy Rev. **15**, 150–168 (2011)

4.86 J.R. Sootsman, D.Y. Chung, M. Kanatzidis: New and old concepts in thermoelectric materials, Angew. Chem. Int. Ed. **48**, 8616–8639 (2009)

4.87 T. Jacobsen, G.H.J. Broers: Single electrode heat effects, J. Electrochem. Soc. **124**, 207–210 (1977)

4.88 S. Kjelstrup Ratkje, Y. Tomii: The transported entropy of oxygen ion in zirconia with 3–12 mole percent yttria, J. Electrochem. Soc. **140**, 59–66 (1993)

4.89 Q. Xu, S. Kjelstrup: Reversible heat effects in the aluminium electrolysis, Proc. TMS Ann. Meet. (1998) pp. 539–546

4.90 T.E. Springer, T.A. Zawodzinski Jr., S. Gottesfeld: Polymer electrolyte fuel cell model, J. Electrochem. Soc. **138**, 2334–2342 (1991)

4.91 Z. Fang, S. Wang, Z. Zhang, G. Qiu: The electrochemical Peltier heat of the standard hydrogen electrode reaction, Thermochim. Acta **473**, 40 (2008)

4.92 S. Kjelstrup, J. Qian, G.M. Haarberg: The Peltier heating of the aluminium cathode in contact with cryolite-alumina melts, Electrochim. Acta **45**, 2707–2717 (2000)

4.93 J.G.P.K. Glavatskiy, S. Kjelstrup: Thermal phenomena associated with water transport across a fuel cell membrane: Soret and Dufour effects, J. Membr. Sci. **431**, 96 (2013)

4.94 M. Ottøy: Mass and Heat Transfer in Ion-Exchange Membranes, Ph.D. Thesis (Norwegian University of Science and Technology, Department of Physical Chemistry, Trondheim 1996)

4.95 S. Kjelstrup Ratkje, M. Ottøy, R. Halseid, M. Strømgård: Thermoelectric power relevant for the solid-polymer-electrolyte fuel cell, J. Membr. Sci. **107**, 219–228 (1995)

4.96 P.J.S. Vie: Characterisation and Optimisation of the Polymer Electrolyte Fuel Cell, Ph.D Thesis (Norwegian University of Science and Technology, Department of Chemistry, Trondheim 2002)

5. Multiscale Modeling of Solvation

Andriy Kovalenko

Statistical-mechanical, reference interaction site model (RISM) molecular theory of solvation is promising as an essential part of multiscale methodology for chemical and biomolecular nanosystems in solution. Beginning with a force field of site interaction potentials between solution species, it uses a diagrammatic analysis of the solvation free energy to construct integral equations for 3-D spatial correlation functions of molecular interaction sites in the statistical-mechanical ensemble. With the solvation structure so obtained at the level of molecular simulation, 3D-RISM-KH further yields the solvation thermodynamics at once as a simple integral of the correlation functions which is obtained by performing thermodynamic integration analytically. The latter allows analytical differentiation of the free energy functional and thus self-consistent coupling in various multiscale approaches. 3D-RISM-KH has been coupled with the KS-DFT and CASSCF quantum chemistry methods in a self-consistent field description of electronic structure, geometry optimization, nanochemistry, and photochemistry in solution. The multiple time step molecular dynamics of biomolecules steered by effective solvation forces obtained from the 3D-RISM-KH theory, accelerated by the generalized solvation force extrapolation, and stabilized by the optimized isokinetic Nosé-Hoover chain (OIN) thermostat, enables gigantic outer time steps up to tens picoseconds to accurately calculate equilibrium properties.

5.1 **Integral Equation Theory of Molecular Liquids** 96

5.2 **Statistical-Mechanical, Molecular Theory of Solvation** 99
5.2.1 3D-RISM-KH Integral Equations for the Solvation Structure 99
5.2.2 Analytical Expressions for the Solvation Thermodynamics 102
5.2.3 Analytical Treatment of Electrostatics 103
5.2.4 Examples of 3D-RISM-KH Calculations of Solvation Structure. 103
5.2.5 Molecular Recognition and Protein-Ligand Binding 112
5.2.6 Post-Processing of the Thermodynamics of MD Trajectories 112

5.3 **Multiscale Coupling of the 3D-RISM-KH Molecular Theory** 113
5.3.1 Self-Consistent Field Coupling of KS-DFT with 3D-RISM-KH 113
5.3.2 Example of Multiscale KS-DFT/3D-RISM-KH Calculations ... 115

5.4 **Multi-Time-Step Molecular Dynamics of Biomolecules** 116
5.4.1 Molecular Dynamics Coupled with 3-D Molecular Theory of Solvation 116
5.4.2 Calculation of Solvation Forces by 3D-RISM-KH MTS-MD 118
5.4.3 MTS-MD/SFCE/3D-RISM-KH Method for Biomolecular Solvation 120

5.5 **Electrical Double Layer in Nanoporous Materials** 123

5.6 **Replica Formalism for Fluid Sorbed in a Disordered Matrix** 123

5.7 **Replica DRISM-KH-VM for Electrolyte Solution Sorbed in Nanoporous Material** 124
5.7.1 Thermodynamics of Sorbed Solution 126
5.7.2 Electric Double Layer in the Nanopores of Host Matrix.... 127
5.7.3 Molecular Mechanism of Electrosorption and Capacitance 128
5.7.4 Illustration for a Supercapacitor 129

5.8 **Conclusions** 133

References 134

The replica RISM-KH-VM theory for electrolyte solutions sorbed in disordered nanoporous materials which is based on the replica formalism in statistical mechanics of quenched-annealed systems yields the solvation structure, thermochemical, and electrochemical properties averaged over both the thermal motion of sorbed solution and the quenched distribution of host nanoporous material (morphology and functionalization of nanopores). It predicts such sorption effects as solvent-specific wetting and water depletion in hydrophobic nanopores of activated carbon, asymmetry in solvation and adsorption of cations and anions, desalination of simple ions in hydrophobic nanopores and its reversal with external voltage, and specific adsorption at surface functionalities of carbon nanopores. The replica RISM-KH-VM theory reveals that the mechanisms of purification efficiency of an electrosorption cell and specific capacitance of a supercapacitor with nanoporous carbon electrodes are much more involved than the common view of an equivalent planar electrical double layer mapped onto the nanoporous morphology, and are determined by an interplay of several factors in the Nernst equation. The chemical potentials comprise the ideal term for the different concentrations of solution species in the nanoporous cathode and anode and in the bulk electrolyte solution outside these (osmotic effect); the free energy of solvation in sorbed electrolyte solution modified by nanoporous confinement and of effective interaction with the bulk of functionalized nanoporous material, all statistically averaged over the nanoporous morphology (nanoporous material volume effect); the electric potential step of Gibbs–Donnan type across a diffuse double layer arising at the boundary of the nanoporous electrode in contact with the bulk solution to keep the chemical balance (electrode boundary effect). On the other hand, the voltage between the charged carbon frameworks of the cathode and anode electrodes and the bulk solution outside the electrodes are determined by the electrostatic potential change from the surface of carbon nanopores to the mean potential level inside the nanoporous electrode (across the Stern surface layer and the analog of the Gouy–Chapman diffuse layer statistically averaged over the nanoporous morphology), plus the above Gibbs–Donnan electric potential step from the nanoporous electrode volume across its boundary to the solution bulk. This generalizes the conventional description of nanoporous electrodes based on an equivalent planar electric double layer (EDL) and the Donnan potential to a molecular description with an interplay of electrostatics, molecular specificity of solvent and electrolyte, adsorption at functionalized surface of nanopores, accommodation of ions and their solvation shells in nanoporous confinement, and osmotic effects.

5.1 Integral Equation Theory of Molecular Liquids

Nanoscale properties, phenomena, and processes are profoundly different from the macroscopic laws governing the behavior of continuous media and materials. Functional features of nanostructures all stem from microscopic properties of the atoms and chemical groups they are built of, but manifest on length scale from one to hundreds nanometers and time scale up to microseconds and more. By changing size, composition, and fabrication protocol, the properties of nanostructures and processes involving them can be tuned up in a wide range. Predictive modeling of nanosystems should operate at length scales from an Angström to hundreds nanometers and microns and time scales to miliseconds and seconds (e.g., in the description of various biological cellular systems acting as nanomachines operating in crowded environment), and yet derive their properties from the chemical functionalities of the constituents. Explicit molecular modeling of such nanosystems involves millions and billions of molecules and is by far not feasible in a *brute force* approach employing just ab initio quantum chemical methods and/or molecular simulations. A proper way thus requires multiscale methods coupling several levels of description, from electronic structure methods for building blocks and classical molecular simulations for critical aggregates in the system, to statistical–mechanical theories for their large assemblies and mean properties in a statistical ensemble over characteristic size and time scales, to eventually come up with macroscopic scale properties of the nanostructures and related processes showing up in the *real observable world*. A true, genuine challenge of multiscale modeling is a theoretical framework that couples methods at different scales, so that observables at lower level scales are *analytically* linked to force fields of more coarse-grained models at higher level scales. Statistical mechanics itself is an example of such a theoretical coupling between microscopic molecular variables and thermodynamic, macroscopic properties.

Integral equation theory of liquids [5.1] is becoming increasingly popular, as it provides a firm platform to handle complex chemical and biomolecular systems in solution. The methodology that has shown substantial success for a number of systems in solution is based on the first principles foundation of statistical mechan-

ics and Ornstein–Zernike (OZ)-type integral equation theory of molecular liquids [5.1], also known as reference interaction site model (RISM) molecular theory of solvation [5.1, 2]. As distinct from molecular simulations that explore the phase space by direct sampling, RISM theory operates with spatial distributions rather than trajectories of molecules and is based on analytical summation of the free-energy diagrams which yields the solvation structure and thermodynamics in the statistical–mechanical ensemble. It yields the solvation structure by solving the RISM integral equations for the correlation functions and then the solvation thermodynamics analytically as a single integral in terms of the correlation functions obtained. Its three-dimensional (3-D) version, 3D-RISM theory, gives the 3-D maps of distributions of solvent around a solute macromolecule of arbitrary shape [5.2–11]. An important component of 3D-RISM theory has been the closure proposed by Kovalenko and Hirata (KH approximation) [5.8, 11]. For simple and complex solvents and solutions of a given composition, including buffers, salts, polymers, ligands, and other cofactors at a finite concentration, the 3D-RISM-KH molecular theory of solvation properly accounts for chemical functionalities by representing in a single formalism both electrostatic and nonpolar features of solvation, such as hydrogen bonding, structural solvent molecules, salt bridges, solvophobicity, and other electrochemical, associative and steric effects. For real systems, solving the 3D-RISM-KH integral equations is far less computationally expensive than running molecular simulations, which must be long enough to sample all relevant exchange and binding events. This enables handling complex systems and processes occurring on large space and time scales, problematic and frequently not even feasible for molecular simulations. The 3D-RISM-KH theory provides a successful description of both simple and complex associating liquids with various chemical functionalities [5.12–15] in the whole range of fluid thermodynamic conditions [5.16, 17] and a variety of local environments in different systems, such as interfaces with metal [5.8, 11], metal oxide [5.18], zeolite [5.19], and clay [5.20], and in confinement of carbon nanotubes [5.13], synthetic organic rosette nanotubular architectures [5.21–25], and biomolecular systems [5.26–35]. The latter range from structural water and xenon bound in the pocket of lysozyme protein [5.26, 27], permeation of water and ions through aquaporin channels [5.27], ligand efflux in the multidrug transporter AcrB [5.28], aggregation of amyloid (A)β oligomers and fibrils [5.29–31] and prion proteins [5.29, 31], binding modes for inhibitors of the pathological conversion and aggregation of prion proteins [5.31], and thiamine against the extracytoplasmic thiamine binding lipoprotein MG289 [5.32, 33], to biomolecular systems as large as the *Gloebacter violaceus* pentameric ligand-gated ion channel (GLIC) homologue in a lipid bilayer [5.31, 32] and the GroEL chaperone/GroES co-chaperone complex [5.34]. The RISM/3D-RISM-KH approach provided an insight into a number of experimentally observed phenomena in soft matter systems, including the structural transitions and related thermodynamic anomalies for the formation of micromicelles and tetrahedral-to-zigzag transformation of the hydrogen bonding network in water–alcohol mixtures in the whole range of concentrations [5.36, 37], microscopic structure of interfaces of nonpolar and polar hydrogen bonding forming molecular liquids [5.38, 39], and microscopic structure of gels formed by oligomeric polyelectrolyte gelators in different solvents [5.35].

The MM/3D-RISM-KH approach introduces statistical–mechanical evaluation of the solvation thermodynamics along molecular dynamics (MD) trajectories in replacement of the MM/PB(GB)SA post-processing using the Poisson–Boltzmann (PB) or generalized Born (GB) continuum solvation model with the solvent accessible surface area (SA) empirical terms representing nonelectrostatic effects [5.29–31].

Furthermore, the 3D-RISM-KH molecular theory of solvation has been coupled with multiple time-step molecular dynamics (MTS-MD) simulation of a solute biomolecule steered by effective solvation forces (or potential of mean force (PMF)) obtained analytically from the 3D-RISM-KH theory [5.40–44]. This allows one to contract the degrees of freedom of solvent molecules and perform MD evolution of just the solute molecule on a multidimensional landscape of a quasi-equilibrium solvation free energy. In this respect, it is similar to MD using the continuous implicit solvent models of Poisson-Boltzmann or Generalized Born with hydrophobic solvent accessible surface area (PBSA or GBSA). implicit solvent. As distinct, 3D-RISM-KH effective solvation forces obtained from the first principles of statistical mechanics provide the full molecular picture of solvation structure, as if full-scale equilibrated MD of all-atom explicit solvent were run at each conformation of the solute molecule. In this approach, solvent can be a mixture including counterions and any other constituents, such as co-solvent and ligands, and effective solvation forces obtained from 3D-RISM-KH allow for structural solvent, preferential solvation and attachment, specific and nonspecific binding. While decoupling the dynamics of the solute from that of solvent and contracting the latter, MTS-MD/3D-RISM-KH accounts for statistics of slow and/or rare solvation events, such as exchange and localization of solvent molecules and ions in function-related confined spaces of biomolecules, and ligand

binding. Unlike short-range forces between molecular repulsive cores steeply changing in space and time with the movement of explicit solvent molecules, effective solvation forces vary smoothly in space and time with solute evolution. This enables the use of solvation force extrapolation (SFE) techniques of different complexities [5.41–44] at inner time steps, based on a set of stored vectors of 3D-RISM-KH effective solvation forces updated at outer time steps. The MTS-MD procedure is stabilized using the new algorithm of the optimized isokinetic Nosé–Hoover chain (OIN) thermostat. The multiscale MTS-MD/OIN/SFE/3D-RISM-KH approach of MD steered by effective solvation forces was implemented in the Amber MD package and illustrated on a fully flexible model of alanine dipeptide and protein G in aqueous solution [5.42–44]. With the generalized SFE approach (GSFE) and the stabilizing effect of OIN thermostatting, gigantic outer time steps up to tens of picoseconds can be employed to accurately calculate equilibrium and conformational properties, which provides a 100- to 500-fold effective computational speed-up relative to conventional MD with explicit solvent.

Further to the above acceleration of solute time evolution in a plain step-to-step comparison of the MTS-MD/OIN/ASFE/3D-RISM-KH method to explicit solvent MD, the 3D-RISM-KH molecular theory of solvation produces 3-D density distributions and effective forces of solvent equilibrated for a current solute conformation and thus samples over a variety of solvent configurations around the solute molecule as if a multitude of explicit solvent MD were run simultaneously. The use of 3D-RISM-KH provides a dramatic acceleration of sampling over slow and/or rare solvation events in complex biomolecular systems, such as exchange and localization of solvent and ions in pockets and other function-related inner spaces of biomolecules, and in various processes of biomolecular recognition, including protein–ligand binding, DNA association, and protein–protein interactions.

To address the electronic structure in solution, the 3D-RISM-KH molecular theory of solvation was coupled with quantum chemistry methods, in particular, complete active space self-consistent field (CASSCF) ab initio method [5.12], Kohn–Sham density functional theory (KS-DFT) [5.8, 45], and orbital-free embedded (OFE) KS-DFT [5.14], in a self-consistent field description of electronic properties, optimized geometry, and chemical reactions in solution. The (OFE)KS-DFT/3D-RISM-KH multiscale method was implemented in the Amsterdam density functional (ADF) computational chemistry package [5.14, 45] and extensively validated against experiment for solvation thermochemistry, photochemistry, conformational equilibria, and activation barriers of various nanosystems in different solvents [5.13, 14, 45] and for ionic liquids (ILs) [5.15].

Nanoporous materials find wide application in chemistry for a possibility of modulating local environment to optimize and enhance reaction yield due to nanoporous confinement and surface functionalization, and for a drastic increase of efficiency of heterogeneous processes due to a huge specific area of nanopores. Control over these effects and rational design of nanoporous materials requires full understanding of molecular mechanisms and driving forces in functionalized nanoporous confinement. Meanwhile, thermochemistry and electrochemistry of liquids and solutions sorbed in nanoporous media are drastically different from bulk systems and planar interfaces. For example, the properties of an electric double layer (EDL) formed by electrolyte solution sorbed in a nanoporous carbon electrode are very different from a conventional, planar electrode–solution interface of equal SA due to mutual influence and hence substantial distortion of EDLs densely packed in nanoporous confinement. A widely used empirical model simply *maps* the EDL of electrolyte solution at the internal surface of nanopores onto an equivalent *unfolded* planar EDL of the same SA. With the effective *insulator layer* thickness given by the radii of adsorbed ions in the Stern layer, the SA capacitance and specific capacitance of a nanoporous EDL supercapacitor predicted by this mapping turn out to be an order of magnitude higher than the typical experimental values of SA capacitance $15{-}20\,\mu\mathrm{F/cm^2}$ and the correspondingly specific capacitance $100{-}200\,\mathrm{F/g}$ in real devices. To match the experimental value of area capacitance, the effective thickness of an EDL has to be empirically set about 5 nm, an order of magnitude thicker than the Stern layer in a planar EDL of equivalent area.

At present, molecular simulations of electrolyte solution with complex molecular solvent (such as water, methanol, acetonitrile, or ILs) sorbed in nanoporous electrodes with realistic morphology is virtually unfeasible due to severe challenges with representative sampling. Conventional modeling approaches typically involve either analytical description and molecular simulation of an EDL formed by finite-size ions in slit-like pores but without molecular solvent with chemical specificities [5.46] or molecular simulation with full atomistic models of ions and solvent but in confinement of simplified geometry [5.47]. Meanwhile, essential effects include:

1. A strong interplay of long-range electrostatic and short-range steric interactions on large space and long time scales.

2. Formation of locally distributed phases of enhanced/depleted fluid mixtures of solvent and electrolyte species (e.g., surface wetting/dewetting and solvent expulsion/condensation in the nanopores depending on the surface functionalities, salination/desalination of sorbed solution depending on the nanoporous electrode charge, condensation of electrolyte ions at charged nanoparticles of the nanoporous matrix), and moreover
3. A necessity to satisfy the conditions of chemical and mechanical balance between the species in the bulk electrolyte solution and those sorbed in the nanoporous spaces of the electrodes.

A generalization of RISM molecular theory of solvation to solutions sorbed in disordered nanoporous materials using the replica method for statistical mechanics of quenched-annealed systems, the so-called replica RISM-KH-VM theory, provides full microscopic details of the solvation structure and thermodynamics averaged over the thermal motion of sorbed solution and over the quenched distribution of host nanoporous material (morphology of nanopores) [5.17, 48, 49]. This theory enables predictive molecular modeling of thermochemistry and electrochemistry of electrolyte solutions sorbed in functionalized nanoporous materials. It predicts, from the first principles of statistical mechanics, such effects as solvent-specific wetting [5.17] and water depletion in hydrophobic carbon nanopores [5.50–52], asymmetry in solvation and adsorption of cations and anions [5.49–52], desalination of simple ions in hydrophobic nanopores and its reversal with external voltage applied [5.49–52], efficient removal of ionic impurities from an aqueous waste stream by a nanoporous carbon electrosorption cell [5.51], and specific adsorption at chemical functionalities on the surface of carbon nanopores [5.48]. In particular, the replica RISM-KH-VM theory reveals the mechanisms of sorption and supercapacitance in nanoporous carbon electrodes [5.17, 48–52] which appear to be more involved than in the case of a planar EDL capacitor. They are determined by the interplay of the EDL potential drop across the Stern layer at the surface of nanopores and the Gouy–Chapman diffuse layer statistically averaged over the morphology of the nanoporous material, the osmotic forces arising due to the difference between the ionic concentrations in the nanoporous cathode and anode electrodes and in the bulk electrolyte solution outside these, the excess chemical potentials of sorbed electrolyte solution species due to solvation in the nanoporous confinement and interaction with the nanoporous material, and the Gibbs–Donnan electric potential step across a diffuse double layer arising at the electrode boundary to keep chemical balance between the sorbed solution in the nanoporous electrode volume and the bulk solution outside. These factors are strongly affected by chemical specificities of ions, solvent, surface functional groups in nanopores, and steric effects for solvated ions in nanoporous confinement. Note that solvation shells of ions can enlarge their effective size due to stiffening at low operational temperature and hinder ions them from entering small pores. The excess chemical potential components due to such steric and short-range effective solvation interactions with the nanoporous confinement (in general different for cations and anions) cause a chemical potential bias with respect to the bulk solution and bring about, in addition to the internal EDL at the surface of nanopores inside the electrode, an extra EDL at the electrode boundary in contact with the bulk solution to keep the chemical balance. The resulting Gibbs–Donnan electric potential steps at the boundaries of the cathode and anode electrodes become asymmetric with charging the supercapacitor device, because of a significant difference between cations and anions in size (and geometry for molecular ions), solvation (hydration), and adsorption at carbon surface and functional groups. This substantially contributes to the supercapacitor voltage and thus constitutes a major factor affecting the specific capacitance.

5.2 Statistical–Mechanical, Molecular Theory of Solvation

The solvation structure is represented by the probability density $\rho_\gamma g_\gamma(\boldsymbol{r})$ of finding the interaction site γ of solvent molecules at 3-D space position $\boldsymbol{r}$ around the solute molecule (which can be both a macromolecule and supramolecule), as determined by the average number density ρ_γ in the solution bulk times the normalized density distribution, or the 3-D distribution function, $g_\gamma(\boldsymbol{r})$. The values of $g_\gamma(\boldsymbol{r}) > 1$ or $g_\gamma(\boldsymbol{r}) < 1$ indicate areas of density enhancement or depletion, respectively, relative to the average density at a distance from the solute in the solution bulk where $g_\gamma \to 1$.

5.2.1 3D-RISM-KH Integral Equations for the Solvation Structure

The 3-D distribution functions of solvent interaction sites around the solute molecule are obtained from the

3D-RISM integral equation [5.3–11]

$$h_\gamma(\boldsymbol{r}) = \sum_\alpha \int d\boldsymbol{r}' c_\alpha(\boldsymbol{r}-\boldsymbol{r}')\chi_{\alpha\gamma}(r') \,, \tag{5.1}$$

where $h_\gamma(\boldsymbol{r})$ is the 3-D total correlation function of solvent site γ related to the 3-D site distribution function by $g_\gamma(\boldsymbol{r}) = h_\gamma(\boldsymbol{r}) + 1$, and $c_\gamma(\boldsymbol{r})$ is the 3-D direct correlation function which has the asymptotics of the solute–solvent site interaction potential, $c_\gamma(\boldsymbol{r}) \approx -u_\gamma(\boldsymbol{r})/(k_\mathrm{B}T)$; the site–site susceptibility of pure solvent $\chi_{\alpha\gamma}(r)$ is an input to the 3D-RISM theory; and indices α and γ enumerate all sites on all sorts of solvent species. Another relation between the 3-D total and direct correlation functions, called a closure, is necessary to complement the 3D-RISM integral equation (5.1). The exact closure can be formally expressed as a series in terms of multiple integrals of the combinations of the total correlation functions. However, it is extremely cumbersome, and in practice is replaced with amenable approximations. The KH closure approximation [5.8, 11] accounts in a consistent manner for both electrostatic and nonpolar features (associative and steric effects) of solvation in simple and complex liquids, nonelectrolyte and electrolyte solutions, and complex macromolecular and supramolecular solutes in chemical [5.8–19, 45], synthetic organic [5.21, 23–25], biomolecular [5.26–35], and soft matter [5.35–39] systems. The 3D-KH closure reads

$$g_\gamma(\boldsymbol{r}) = \begin{cases} \exp\left[\dfrac{-u_\gamma(\boldsymbol{r})}{k_\mathrm{B}T} + h_\gamma(\boldsymbol{r}) - c_\gamma(\boldsymbol{r})\right] \\ \qquad \text{for } g_\gamma(\boldsymbol{r}) \le 1 \,, \\ 1 - \dfrac{u_\gamma(\boldsymbol{r})}{k_\mathrm{B}T} + h_\gamma(\boldsymbol{r}) - c_\gamma(\boldsymbol{r}) \\ \qquad \text{for } g_\gamma(\boldsymbol{r}) > 1 \,, \end{cases} \tag{5.2}$$

where $u_\gamma(\boldsymbol{r})$ is the 3-D interaction potential between the whole solute and solvent site γ specified by the molecular force field, and $k_\mathrm{B}T$ is the Boltzmann constant times the solution temperature. The 3D-KH closure (5.2) couples in a nontrivial way the so-called mean spherical approximation (MSA) and the hypernetted chain (HNC) approximation [5.1], the former being applied to spatial regions of solvent density enrichment $g_\gamma(\boldsymbol{r}) > 1$, such as association peaks and critical enhancement long-range tails, and the latter to regions of density depletion $g_\gamma(\boldsymbol{r}) < 1$, including the repulsive core. The distribution function and its first derivative are continuous at the joint boundary $g_\gamma(\boldsymbol{r}) = 1$ (or equivalently $d_\gamma(\boldsymbol{r}) = 1$) by construct. A substantial advantage of the 3D-KH closure approximation is that it properly accounts for the solvation structure in complex systems with significant association effects. For comparison, the 3D-HNC closure strongly overestimates such associative effects and therefore the 3D-RISM-HNC equations diverge in many practical applications for macromolecules with considerable site charges solvated in polar solvents or electrolyte solutions. Other approximations such as, for example, the Percus–Yevick (PY), modified Verlet (VM), Martynov–Sarkisov (MS), and Ballone–Pastore–Galli–Gazzillo (BPGG) closures do not properly account for the electrostatic asymptotics of the interaction potential.

The 3D-KH closure underestimates the height of strong associative peaks of the 3-D site distribution functions because of the MSA linearization applied to them [5.8, 53] However, it somewhat widens the peaks and so 3D-RISM-KH quite accurately reproduces the coordination numbers of the solvation structure in different systems, including microheterogeneities (micromicellar aggregates) in water–alcohol solutions [5.36]; solvation shells of metal–water [5.8, 11], metal oxide–water [5.18], and organic solvent–clay [5.20] interfaces; and structural water solvent localized in biomolecular confinement [5.27, 34]. For example, the coordination numbers of water strongly bound to the MgO surface are calculated from the 3D-RISM-KH theory with a 90% accuracy and the peak positions within a 0.5 Å deviation, compared to MD simulations [5.18]. The 3-D solvation map $g_\gamma(\boldsymbol{r})$ of function-related structural water in the GroEL chaperon complex (shown to be strongly correlated with the rate of protein folding inside the chaperon cavity) obtained in an expensive MD simulation with explicit solvent involving ≈ 1 million atoms is reproduced from the 3D-RISM-KH theory in a relatively short calculation on a workstation with an accuracy of over 90% correlation for the 3-D density map and about 98% correlation for the 3-D density maxima [5.34].

Note that different approximate 3-D bridge functions, or bridge corrections, to the 3D-HNC approximation can be constructed, such as the 3D-HNC bridge-corrected closure (3D-HNC) which reproduced MD simulation results for the height of the 3-D distribution peaks of water solvent around the bovine pancreatic trypsin inhibitor (BPTI) protein [5.53]. A related promising approach is the partial series expansions of order n (PSE-n) of the HNC closure [5.54]. The PSE-n closures interpolate between the KH and HNC approximations and therefore combine numerical stability with enhanced accuracy, as demonstrated for aqueous solutions of alkali halide ions [5.54, 55]. However, a particular appeal of the 3D-KH closure is that it provides adequate accuracy and existence of solutions if expected from physical considerations for a wide class of solution systems *from the wild*, including various chem-

ical and biomolecular solutes in solution with different solvents, co-solvents, and electrolytes [5.8–39, 45, 56–60], and moreover, with ligand molecules or fragments considered as part of solvent for efficient 3-D mapping of binding affinities in such problems as molecular recognition and fragment-based drug design [5.27, 28, 33]. Construction of bridge functions for such systems with different solvent components other than water constitutes a significant challenge not addressed so far, and the 3D-KH closure constitutes a reliable choice for a given system.

The site–site susceptibility of solvent breaks up into the intra- and intermolecular terms

$$\chi_{\alpha\gamma}(r) = \omega_{\alpha\gamma}(r) + \rho_\alpha h_{\alpha\gamma}(r)\,, \tag{5.3}$$

where the intramolecular correlation function $\omega_{\alpha\gamma}(r)$ normalized as $\int \mathrm{d}\boldsymbol{r}\omega_{\alpha\gamma}(r) = 1$ represents the geometry of solvent molecules. ($\omega_{\alpha\gamma}(r) = 0$ for sites α and γ on different species.) For rigid species with site separations $l_{\alpha\gamma}$ it has the form $\omega_{\alpha\gamma}(r) = \delta(r - l_{\alpha\gamma})/(4\pi l_{\alpha\gamma}^2)$ specified in the reciprocal k-space in terms of the zeroth-order spherical Bessel function $j(x)$ as

$$\omega_{\alpha\gamma}(r) = j_0(kl_{\alpha\gamma})\,, \tag{5.4}$$

and $h_{\alpha\gamma}(r)$ is the intermolecular, radial total correlation function between sites α and γ enumerating all sites on all sorts of molecules in bulk solvent. The site–site total correlation functions $h_{\alpha\gamma}(r)$ to be input in (5.3) and then (5.1) are obtained in advance to the 3D-RISM-KH calculation from the dielectrically consistent RISM theory [5.61] coupled with the KH closure (DRISM-KH approach [5.11]), which can be applied to bulk solution of a given composition, including polar solvent, co-solvent, electrolyte, and ligands at a given concentration. The DRISM integral equation reads as

$$\begin{aligned}\widetilde{h}_{\alpha\gamma}(r) = {} & \widetilde{\omega}_{\alpha\mu}(r)\cdot c_{\mu\nu}(r)\cdot\widetilde{\omega}_{\nu\gamma}(r) \\ & + \widetilde{\omega}_{\alpha\mu}(r)\cdot c_{\mu\nu}(r)\cdot\rho_\nu\widetilde{h}_{\nu\gamma}(r)\,,\end{aligned} \tag{5.5a}$$

where $c_{\alpha\gamma}(r)$ is the site–site direct correlation function of bulk solvent, and both the intramolecular correlation functions $\widetilde{\omega}_{\alpha\gamma}(r)$ and total correlation functions $\widetilde{h}_{\alpha\gamma}(r)$ are renormalized due to a dielectric bridge correction in a particular analytical form [5.61] that ensures the given value and consistency of the dielectric constant obtained for solvent–solvent, solvent–ion, and ion–ion effective interactions in electrolyte solution

$$\widetilde{\omega}_{\alpha\gamma}(r) = \omega_{\alpha\gamma}(r) + \rho_\alpha\chi_{\alpha\gamma}(r)\,, \tag{5.5b}$$

$$\widetilde{h}_{\alpha\gamma}(r) = h_{\alpha\gamma}(r) - \chi_{\alpha\gamma}(r)\,. \tag{5.5c}$$

The renormalized dielectric correction enforcing the given phenomenological value of the dielectric constant and the proper orientational behavior and consistency of the dielectric response in the electrolyte solution is obtained in the analytical form specified in the reciprocal k-space as follows [5.61]

$$\begin{aligned}\chi_{\alpha\gamma}(k) = {} & j_0(kx_\alpha)j_0(ky_\alpha)j_1(kz_\alpha)h_\mathrm{c}(k)j_0(kx_\gamma) \\ & \times j_0(ky_\gamma)j_1(kz_\gamma)\,,\end{aligned} \tag{5.6}$$

where $j(x)$ and $j_1(x)$ are the zeroth- and first-order spherical Bessel functions, respectively, $\boldsymbol{r}_\alpha = (x_\alpha, y_\alpha, z_\alpha)$ are the Cartesian coordinates of partial site charge q_α of site α on species s with respect to its molecular origin, both sites α and γ are on the same species s, and its dipole moment $\boldsymbol{d}_s = \sum_{\alpha\in s} q_\alpha\boldsymbol{r}_\alpha$ is oriented along the z-axis, $\boldsymbol{d}_s = (0, 0, d_s)$. Note that the renormalized dielectric correction (5.6) is nonzero only for polar solvent species of sorbed electrolyte solution which possess a dipole moment and thus are responsible for the dielectric response in the DRISM approach. The envelope function $h_\mathrm{c}(k)$ has the value at $k = 0$ determining the dielectric constant of the solution and is assumed in the smooth nonoscillatory form quickly falling off at wavevectors k larger than those corresponding to characteristic size l of liquid molecules [5.61]

$$h_\mathrm{c}(k) = A\exp\left(\frac{-l^2k^2}{4}\right)\,, \tag{5.7}$$

where the amplitude A is related to the dielectric constant ε of the electrolyte solution

$$A = \frac{1}{\rho_\mathrm{polar}}\left(\frac{\varepsilon}{y} - 3\right)\,. \tag{5.8}$$

The form (5.6)–(5.8) is extended to mixed solvents [5.62] by using the total number density of solution polar species

$$\rho_\mathrm{polar} = \sum_{s\in\mathrm{polar}}\rho_s \tag{5.9}$$

and the solution dielectric susceptibility

$$y = \frac{4\pi}{9k_\mathrm{B}T}\sum_{s\in\mathrm{polar}}\rho_s\,(d_s)^2\,. \tag{5.10}$$

The parameter l specifies the characteristic separation from a liquid molecule below which the dielectric correction (5.6) is switched off so as not to distort the short-range solvation structure. It can be chosen to be about $l = 1$ Å for water solvent; however, in solvent of larger molecules, such as octanol or in the presence of

such co-solvent it should be increased to about $l = 10$ Å so as to avoid *ghost* associative peaks appearing in the radial distributions if the dielectric correction (5.6) interferes with the intramolecular structure of the large solvent species.

The DRISM integral equations (5.5) with the KH closure [5.11]

$$g_{\alpha\gamma}(r) = \begin{cases} \exp\left[\dfrac{-u_{\alpha\gamma}(r)}{k_\mathrm{B}T} + h_{\alpha\gamma}(r) - c_{\alpha\gamma}(r)\right] \\ \qquad \text{for } g_{\alpha\gamma}(r) \le 1\,, \\ 1 - \dfrac{u_{\alpha\gamma}(r)}{k_\mathrm{B}T} + h_{\alpha\gamma}(r) - c_{\alpha\gamma}(r) \\ \qquad \text{for } g_{\alpha\gamma}(r) > 1\,, \end{cases} \tag{5.11}$$

keep the same dielectrically consistent asymptotics (5.6) and (5.7) as the originally derived DRISM-HNC theory [5.61] but extend the description to solutions with strong associative species in a wide range of composition and thermodynamic conditions not amenable to HNC, which overestimates attraction in associative forces and phase transition phenomena.

5.2.2 Analytical Expressions for the Solvation Thermodynamics

As mentioned before, 3D-RISM is an integral equation theory of OZ type based on analytical summation of the free-energy diagrams, which yields the 3-D solute–solvent site correlation functions and the solvation thermodynamics. The KH and HNC closure approximations to the 3D-RISM integral equation have an exact differential of the solvation free energy, and allow one to analytically perform Kirkwood's thermodynamic integration gradually switching on the solute–solvent interaction. The solvation free energy of the solute macro- or supramolecule in multicomponent solvent following from the 3D-RISM-KH integral equations (5.1)–(5.2) is thus given in the closed analytical form as a single integral of the correlation functions [5.8, 11]

$$\mu_\mathrm{solv} = \sum_\gamma \int_V \mathrm{d}\boldsymbol{r} \Phi_\gamma(\boldsymbol{r})\,, \tag{5.12a}$$

$$\Phi_\gamma(\boldsymbol{r}) = \rho_\gamma k_\mathrm{B}T \left[\frac{1}{2}h_\gamma^2(\boldsymbol{r})\Theta(-h_\gamma(\boldsymbol{r})) - c_\gamma(\boldsymbol{r}) - \frac{1}{2}h_\gamma(\boldsymbol{r})c_\gamma(\boldsymbol{r})\right], \tag{5.12b}$$

where $\Theta(x)$ is the Heaviside step function. The integrand $\Phi_\gamma(\boldsymbol{r})$ in (5.12a) is interpreted as the solvation-free-energy density (3D-SFED) coming from interaction site γ of solvent molecules around the solute. The solvation free energy of the solute macromolecule $\Delta\mu$ is obtained by summation of the 3D-SFED partial contributions from all solvent species and spatial integration over the whole space. (Note that the integration volume V in the form (5.12a) comprises both the solvation shells and the solute–solvent molecular repulsive cores, since the direct correlation functions $c_\gamma(\boldsymbol{r})$ inside the latter are related to the free energy of creation of a cavity to accommodate the solute excluded volume.) In this way, $\Phi_\gamma(\boldsymbol{r})$ characterizes the intensity of effective solvation forces in different 3-D spatial regions of the solvation shells and indicates where they contribute the most/least to the entire solvation free energy.

Other thermodynamics quantities can be derived from the solvation free energy (5.12) by differentiation. In particular, the solvation chemical potential is decomposed into the energetic and entropic contributions at constant volume

$$\Delta\mu = \Delta\varepsilon^\mathrm{uv} + \Delta\varepsilon^\mathrm{vv} - T\Delta s_V \tag{5.13}$$

by calculating the solvation entropy at constant volume as

$$\Delta s_V = -\frac{1}{T}\left(\frac{\partial\Delta\mu}{\partial T}\right)_V \tag{5.14}$$

and the internal energy of the solute ('u')–solvent ('v') interaction as

$$\Delta\varepsilon^\mathrm{uv} = k_\mathrm{B}T\sum_\gamma \rho_\gamma \int \mathrm{d}\boldsymbol{r} g_\gamma(\boldsymbol{r})u_\gamma(\boldsymbol{r})\,, \tag{5.15}$$

with the remaining term $\Delta\varepsilon^\mathrm{vv}$ giving the energy of solvent reorganization around the solute. Further, the partial molar volume of the solute macromolecule is obtained from the Kirkwood–Buff theory [5.63] extended to the 3D-RISM formalism [5.27, 56, 57]

$$V = k_\mathrm{B}T\chi_\mathrm{T}\left(1 - \sum_\gamma \rho_\gamma \int \mathrm{d}\boldsymbol{r} c_\gamma(\boldsymbol{r})\right), \tag{5.16}$$

where χ_T is the isothermal compressibility of bulk solvent obtained in terms of the site–site direct correlation functions of bulk solvent as

$$\rho k_\mathrm{B}T\chi_\mathrm{T} = \left(1 - 4\pi\sum_{\alpha\gamma}\rho_\alpha \int_0^\infty r^2 \mathrm{d}r c_{\alpha\gamma}(r)\right)^{-1}, \tag{5.17}$$

where $\rho = \sum_s \rho_s$ is in general the total number density of the bulk solvent mixture of molecular species s.

Note that the solvation free energy (5.12) and its derivatives (5.13)–(5.15), as well as the partial

molar volume (5.16) can be decomposed into partial contributions of the interaction sites of the solute macromolecule, providing a basis for spatial decomposition analysis (SDA) of association effects in solution [5.58, 59], as illustrated for supramolecular complexation [5.58] and proteins [5.59].

The PMF $W_\gamma(\boldsymbol{r})$ acting on the site γ of solvent species near the solute macro- or supramolecule can be defined in terms of the 3-D site distribution function as

$$W_\gamma(\boldsymbol{r}) = -k_\mathrm{B}T \ln g_\gamma(\boldsymbol{r}) \,. \tag{5.18}$$

The form (5.18) gives a 3-D map of the effective potential between each solvent species and the solute macromolecule, and determines the binding strength and most probable locations (binding modes) of structural solvent molecules at the solute macromolecule, averaged over the statistical mechanical ensemble of mutual arrangements and orientations.

5.2.3 Analytical Treatment of Electrostatics

To properly treat electrostatic forces in electrolyte solution with polar molecular solvent and ionic species in 3D-RISM/1D-RISM theory, we analytically handle the long-range electrostatic asymptotics of the radial site–site total and direct correlation functions of bulk solvent in the DRISM-KH equations (5.5)–(5.11) and the 3-D site total and direct correlation functions in the 3D-RISM-KH equations (5.1) and (5.2), as well as in the thermodynamics expressions for the solvation free energy (5.12) and its derivatives [5.9–11, 14, 64]. The analytical forms for the nonperiodic electrostatic asymptotics are separated out in the direct and reciprocal space from all the correlation functions and the remaining short-range terms are discretized for the DRISM-KH equations on a uniform radial grid with resolution 0.01−0.1 Å and for the 3D-RISM-KH equations on a uniform 3-D rectangular grid with resolution 0.1−0.5 Å in a 3-D box large enough to ensure decay of the short-range terms at the 3-D box boundaries [5.14, 64]. The convolution of the short-range terms in the 3D-RISM integral equation (5.1) is calculated using 3-D fast Fourier transform (3D-FFT) in the 3-D box of size including at least 2–3 solvation shells around the solute. This cancels out the aliasing effects since the resulting short-range solvation shells of the total correlation functions usually decay at this distance and the remaining electrostatic asymptotics is separated out and handled analytically [5.64]. Accordingly, the electrostatic asymptotics terms in the thermodynamic integral (5.4) are handled analytically and reduced to one-dimensional integrals easy to compute [5.14, 64].

The 3D-RISM-KH integral equations (5.1) and (5.2) are converged typically to a relative root mean square accuracy of 10^{-4}−10^{-5} and the DRISM-KH equations (5.5) and (5.11) to an accuracy of 10^{-8}−10^{-10} by using the modified direct inversion in the iterative subspace (MDIIS) numerical solver which is an iterative procedure achieving accelerated convergence for integral equations of liquid state theory by optimizing each iterative guess in a Krylov subspace of typically last 10−20 successive iterations [5.9–11, 65]. It is closely related to Pulay's DIIS approach for quantum chemistry equations [5.66] and other similar algorithms like the generalized minimal residual (GMRes) solver [5.67]. Note that the GMRes method applied on the fine grid discretizing the 3D-RISM integral equations has also been coupled with a Newton–Raphson-type numerical scheme on a coarse grid [5.53] which can be limited to the solute repulsive core area as well [5.68]. Direct methods of Newton–Raphson type to solve integral equations provide a quadratic convergence when approaching the solution. However, they require calculating and inverting the Jacobian matrix in one or another way, which is prohibitively wasteful for fine 3-D grids and very slow for coarse 3-D grids even if performed just once and used for preconditioning [5.68]. The MDIIS solver combines the simplicity and relatively small memory usage of an iterative approach with the efficiency of a direct method. Compared to damped (Picard) iterations, MDIIS provides substantial acceleration with quasiquadratic convergence practically throughout the entire range of root mean square residual, and is robust and stable. Of particular importance is that MDIIS ensures convergence (provided a solution exists) for complex charged systems with strong associative and steric effects, which is usually not achievable by Picard iterations and constitutes a challenging task in the case of 3-D integral equations. Further, a core-shell-asymptotics technique coupling MDIIS for the excluded volume core with iteration of the solvation shells has been developed, which provides 6- to 16-fold memory reduction and corresponding CPU load decrease in MDIIS [5.65]. Although being of benefit for solutes of any size, this memory reduction becomes critical in 3D-RISM calculations for large solvated systems, such as macromolecules in solution with ions, ligands, and other cofactors.

5.2.4 Examples of 3D-RISM-KH Calculations of Solvation Structure

One of the basic cases of electrolyte solution systems is aqueous solution of sodium chloride. Figures 5.1–5.3 show the 3D-RISM results for the solvation structure

and PMF of the Na^+ and Cl^- ion pair in aqueous solution at infinite dilution and at a high concentration of 1 mol/l [5.9, 10]. This generic system presents a very illustrative test for a solvation theory to reproduce most of the essential features of a variety of chemical and biomolecular effects in solution, and the 3D-RISM theory succeeds in that.

Simple Ions in Aqueous Electrolyte Solution

Figure 5.1 shows the 3-D site distributions of the water oxygen (O) and hydrogen (H) site distributions around the pair of the Na^+ and Cl^- ions in aqueous solution at infinite dilution. Both the O and H distributions form high crowns of the first solvation shell around the ions, with the high O and lower H peaks near the contacts of the crowns corresponding to water molecules bridging the ions. This structure is then followed by the shallow second solvation shells. The corresponding potential of mean force (PMF) is shown in Fig. 5.2. The H distribution has two crowns around the Cl^- ion; their separation from the ion shows that the inner H crown gives the water hydrogens in contact with the Cl^- ion while the outer H crown corresponds to the other water hydrogens looking outward but at the angle determined by the tetrahedral hydrogen bonding structure of the water. On the other hand, there is a single H crown around the Na^+ ion and the separations of the O and H crowns from Na^+ show that both the water hydrogens are looking outward Na^+, tilted at the same angle. These are typical arrangements of dipole-like oriented water around a cation and water hydrogen bonded with one hydrogen to an anion. The arrangements are visualized in the cartoons in the lower part of Fig. 5.1, with the left and right columns corresponding to the 3-D water site distributions around the Na^+ and Cl^- contact ion pair (CIP) and solvent-separated ion pair (SSIP), respectively. Water molecules in contact with both the cation and anion form the dipole-like association with the former and the hydrogen bonding with the latter, thus creating a water bridge of strongly associated water molecules located in a ring between the ions. This bridge strongly deepens the solvation contribution to the PMF at the CIP arrangement; interplayed with the ion–ion core repulsion, this results in a significant shift of the first minimum on the PMF to a shorter ion–ion separation, compared to the primitive solvation model just uniformly reducing the Coulomb attraction between the ions by the water dielectric constant $\varepsilon = 80$ (dashed line in Fig. 5.2a). At the SSIP arrangement, the water bridge strengthens the association between the ions and results in the second minimum on the ion–ion PMF (Fig. 5.2). The oscillations diminish with distance and the PMF goes to the limit of the pure dielectrically screened electrostatic potential (dashed line). At

Fig. 5.1a,b Solvation structure of the contact ion pair (CIP) and solvent separated ion pair (SSIP) of the Na^+ and Cl^- ion pair in aqueous solution at infinite dilution (*left and right columns*, respectively), obtained from 3D-RISM theory (after [5.9, 10]). **(a)** Section of the 3-D distribution functions of water oxygen (O) and hydrogen (H) in the plane passing through the ion–ion axis. **(b)** Visualization of the water-solvent arrangements around the CIP and SSIP, as well as the ions separated by a gap corresponding to the barrier at their potential of mean force (*lower part*) ►

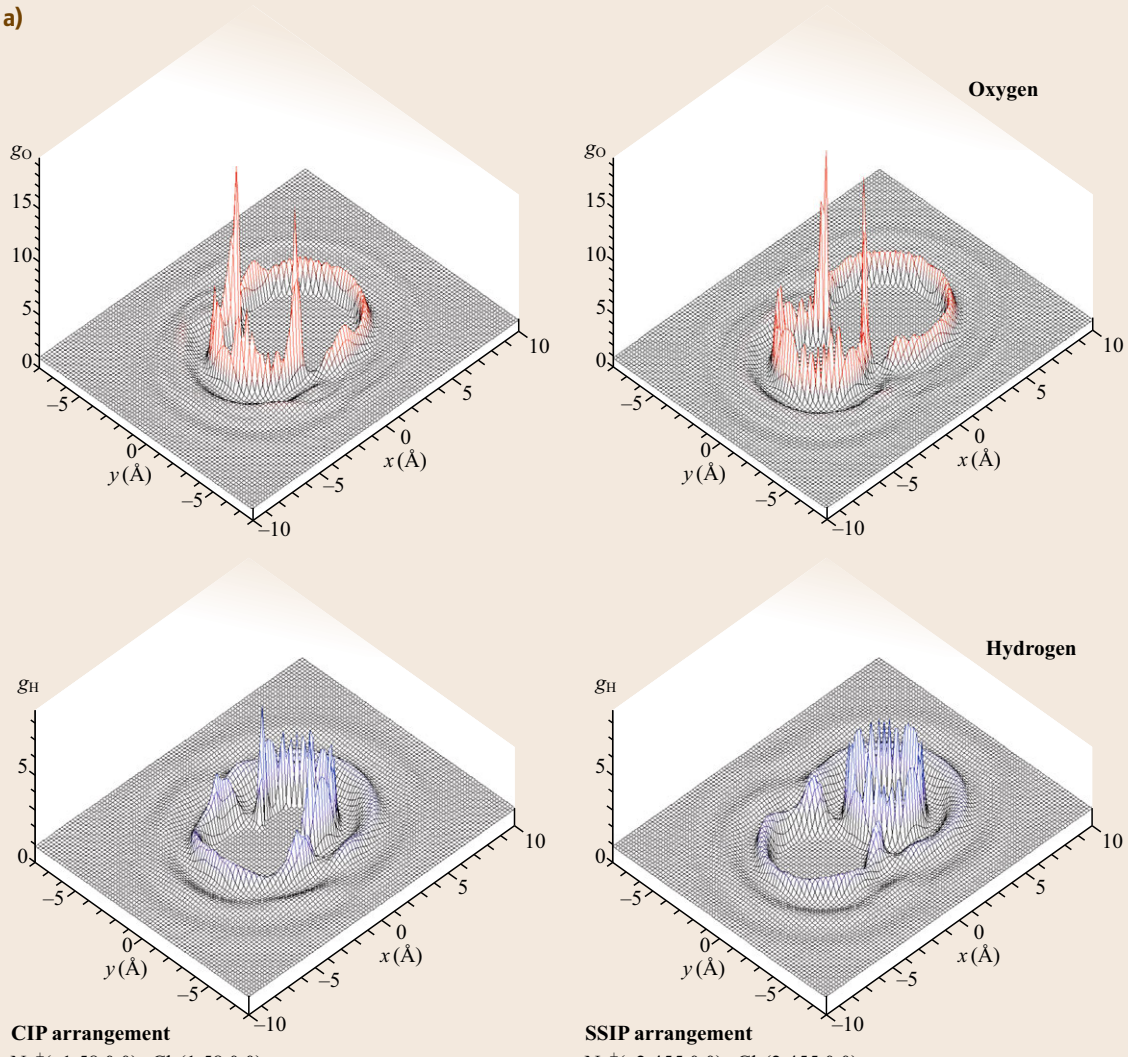
an intermediate separation between the ions, a desolvated gap forms because of the steric effect of expulsion of solvent molecules by the repulsive cores of the ions (Fig. 5.1). The work against the solvent environment to expel the solvent and create the desolvation gap results in a barrier between the PMF first and second minima corresponding to the CIP and SSIP arrangements (Fig. 5.2a).

The PMFs in the Na^+–Na^+ and Cl^-–Cl^- pairs of like ions have the same features of the first and second minima and the barrier between them due to the interplay of the associative forces and molecular structure of the ions and solvent molecules. However, at infinite dilution the strength of the solvent bridges is not sufficient to overcome the electrostatic repulsion and to stabilize the like ion pairs, and both the first and second minima are local (Fig. 5.2a). (Note that this can be very different for large molecular ions with weaker electrostatic attraction at the separation determined by their size.) The picture changes for the electrolyte solution at a high concentration of 1 mol/l; numerous salt bridges form in addition to water hydrogen bridges, and the like ion pairs get stabilized in both CIP and SSIP arrangements (Fig. 5.2b) For example, the Cl^-–Cl^- ion pair in the aqueous solution at this concentration is bridged by several Na^+ ions and water molecules, forming a cluster depicted in Fig. 5.3. The structure of such a cluster follows from the analysis of the 3D-RISM results for the 3-D distribution functions of solution species and the corresponding coordination numbers of Na^+, Cl^-, and water around each ion pair (Na^+–Cl^-, Cl^-–Cl^-, and Cl^-–Cl^-).

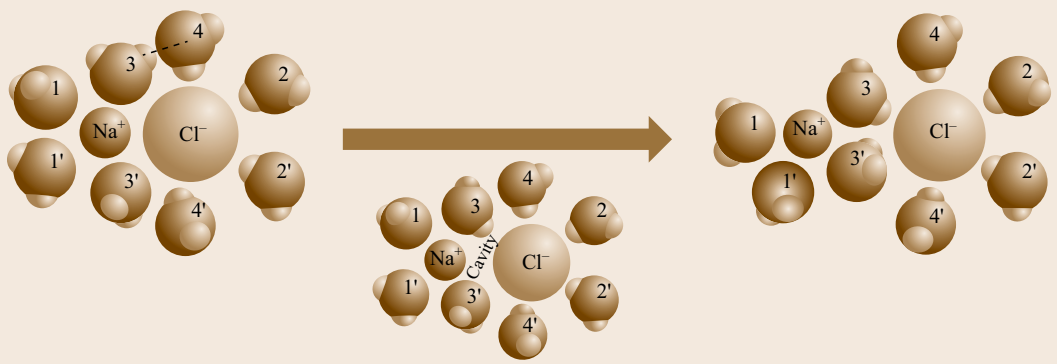
Water–Alcohol Mixtures

A further important example of crucial importance in chemistry and biomolecular nanosystems is the formation of nanostructures in solution driven by hydrophobic attraction. Figure 5.4 illustrates the RISM theory predictions for the structure of the ambient mixtures of water and *tert*-butyl alcohol (TBA) in the whole range of concentrations [5.36, 37]. TBA is a generic example of primitive surfactant with a hydrophobic head of

a)


Oxygen
g_O
15
10
5
0
–5
0
y (Å)
–5
–10
–5
0
x (Å)
5
10
Hydrogen
g_H
5
0
CIP arrangement
Na^+(–1.58,0,0) Cl^-(1.58,0,0)
SSIP arrangement
Na^+(–2.455,0,0) Cl^-(2.455,0,0)

b)


1
1'
2
2'
3
3'
4
4'
Na^+
Cl^-
Cavity

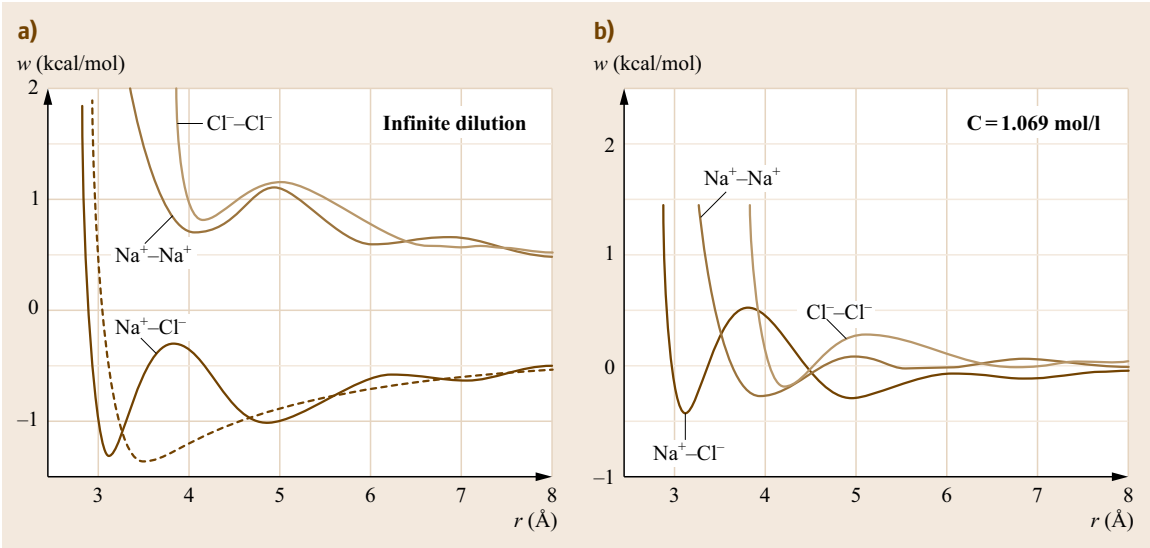


Fig. 5.2a,b Potential of mean force between Na^+ and Cl^- ions in aqueous solution at infinite dilution **(a)** and concentration 1 mol/l **(b)**, obtained from 3D-RISM theory (after [5.9, 10]). Section of the 3-D distribution functions of water oxygen (O) and hydrogen (H) in the plane passing through the ion–ion axis (3-D graphs in **(a)**). Shown in **(a)** for comparison is also the PMF obtained with the primitive model of water solvent as structureless dielectric continuum (*dashed line*)



Fig. 5.3 Cl^- ions (*gray*) in a stabilized CIP arrangement bridged by Na^+ ions (*blue*) as well as by hydrogen bonding bridges of water molecules (O in *red*, H in *white*) in aqueous electrolyte solution of concentration 1 M. The visualization is made based on the peaks positions on the 3-D site distribution functions between the species of this system obtained from 3D-RISM theory (after [5.9, 10])

four carbons and a hydrophilic *tale* represented by the hydroxyl group. The solvation structure of this system successively goes through several stages with TBA concentration in water changing from infinite dilution pure TBA: a separate TBA molecule embedded in a water tetrahedral hydrogen bonding cage at infinite dilution changes to micromicelles of four to six TBA molecules in the head-to-head arrangement incorporated in a water hydrogen bonding cage at about 4% TBA molar fraction; then, the tetrahedral hydrogen bonding structure of water gets disrupted at about 40% TBA molar fraction to be replaced by the zigzag hydrogen bonding structure of alcohol, with separate water molecules embedded in it at infinite dilution of water in TBA. The RISM theory predicted both the structure and thermodynamics of these mixtures in full agreement with experiment, in particular, the concentration and temperature dependence of the compressibility, including the isosbestic point and minimum corresponding to the formation of micromicelles [5.36, 37].

Functionalized Cellulose Nanocrystals

Cellulose nanocrystals (CNC), the smallest building blocks of cellulose that carry its physical properties, are a biocompatible and biodegradable material with mechanical properties comparable to these of reinforcement materials, such as carbon fibers, carbon nanotubes, and steel [5.69, 70]. The CNC can be produced in a sustainable and viable bulk process, unlike other nanomaterials (e.g., carbon nanotubes) that are typically produced in small amounts and at a very high cost [5.71]. The outstanding mechanical properties of CNC make it very attractive as reinforcing additive in nanocomposite materials [5.72–76], hydrogels [5.77–81], and foams [5.82, 83], as well as specialized security inks [5.84, 85]. Suspensions of CNCs display a phase

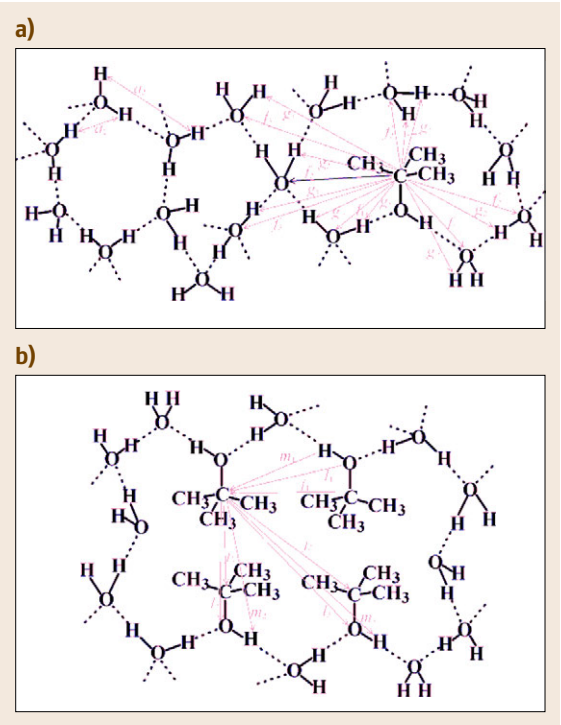


Fig. 5.4 Structural transitions with concentration in a mixture of water and TBA and predicted by the RISM-KH molecular theory of solvation. **(a)** *tert*-Butyl alcohol molecule at infinite dilution incorporated in a cage of water tetrahedral hydrogen bonding. **(b)** Micromicelle of four *tert*-butyl alcohol molecules in a cage of the water hydrogen bonding

separation into clear isotropic and structured chiral nematic phases above critical concentration [5.86] and upon drying from iridescent chiral nematic films [5.87–89].

Large-scale applications of CNC in nanocomposites require modifications to tune up its surface properties thus enhancing its solubility in nonpolar solvents and compatibility with polymer matrices [5.90]. The CNC have been extensively manipulated to provide a rich suite of new materials and platforms for further transformations [5.91]. Several methods for CNC surface modification have been developed, including grafting [5.92–94], self-assembly [5.95], and surfactants [5.96]. Effective surface modifications must provide sufficient solubility tune up without altering the CNC inter- and intramolecular hydrogen bonding network and deteriorating crystallinity and mechanical properties.

Despite the extensive experimental research effort, progress toward the development of effective surface modifications has been rather slow, mainly because (i) extensive chemical modifications destabilize the hydrogen bonding network of cellulose, causing deterioration of the mechanical properties, and (ii) relationship between surface modifications and solvation thermodynamics has not been thoroughly studied. As briefly overviewed below, the 3D-RISM-KH theory presents an insight into CNC–water hydrogen bonding interactions relevant to relaxation and right-hand twist, and predicts the effective forces that control the dispersion of pristine and modified CNC particles in a variety of solvents [5.97, 98].

A model for the computer simulation of CNC is based on the I_α crystal structure [5.99] containing 34 chains forming a three-layered cellulose fibril, as shown in Fig. 5.5. The fibril cross section is approximately 4.3 nm in its longest direction and each chain in the fibril consists of 16 glucose units making 8 nm long particles.

For this model particle, structure relaxation is performed using MD simulation in a periodic box with dimensions 14.9 nm × 8.9 nm × 8.3 nm [5.98]. The distance between particle surface and the box edges is 2 nm and the space in the box around the particle is filled with water molecules. The aim of this simulation is to relax and equilibrate the model structure in the presence of solvent, mimicking as close as possible the experimental conditions of pristine CNC solvation in aqueous solution. In this neutral particle, the initial charge distribution in the cellulose fibril is inhomogeneous over different faces of

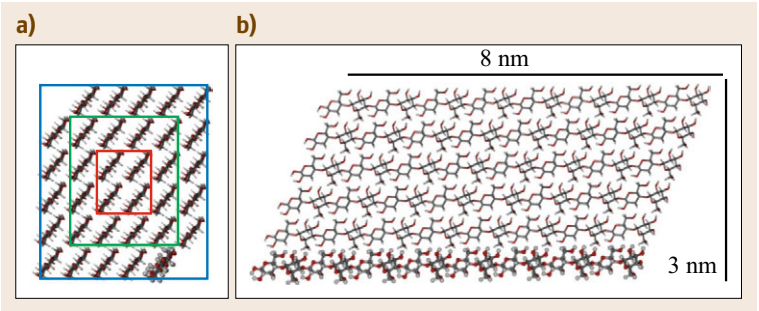


Fig. 5.5a,b Cellulose fibril containing 34 glucan chains: **(a)** cross section showing inner (*red*), intermediate (*green*), and outer (*blue*) layers; **(b)** CNC particle dimensions

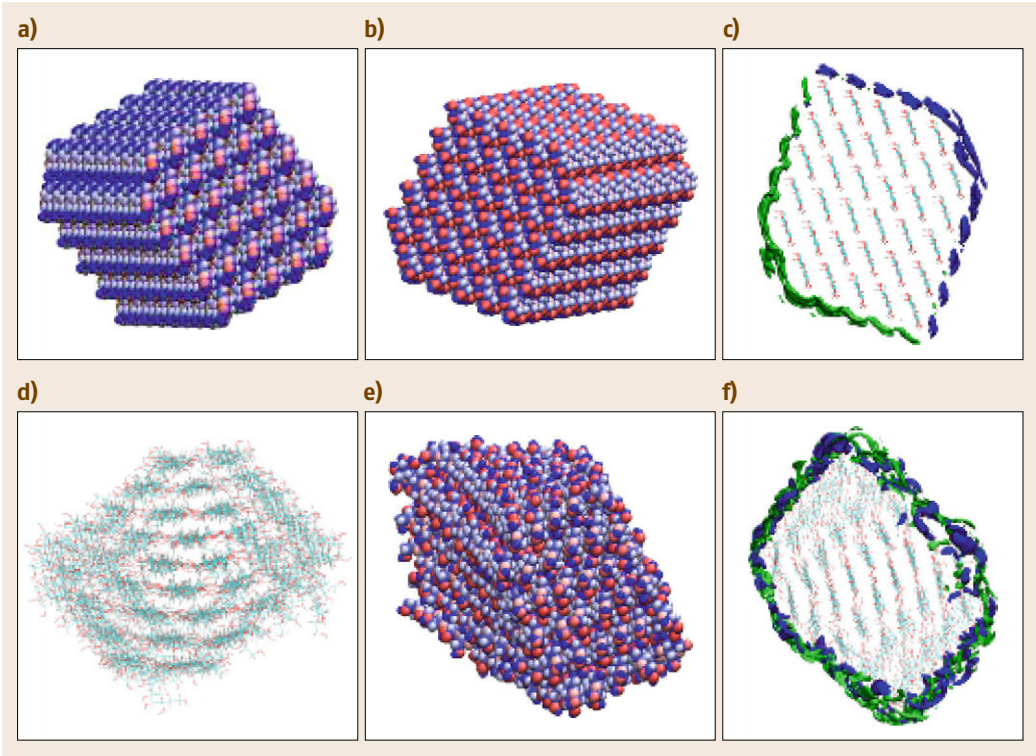


Fig. 5.6a–f Pristine CNC particle relaxation in explicit water solution simulated with MD, showing positively (*blue*) and negatively (*red*) charged atoms. *Top*: Surface charge distribution of the unrelaxed CNC particle. **(a)** Faces exposing positively charged groups are predominantly *blue colored*. **(b)** Faces exposing negatively charged groups are predominantly *red colored*. **(c)** 3-D distributions of Na^+ (*blue*) and Cl^- (*green*) around an unrelaxed fibril in aq. NaCl. *Bottom*: Surface charge distribution of a relaxed CNC particle after 5 ns MD simulation. **(d)** CNC particle cross section showing right-hand twist. **(e)** Charge distribution in the relaxed particle. **(f)** 3-D distributions for Na^+ (*blue*) and Cl^- (*green*) around a relaxed fibril in aq. NaCl

the particle (Fig. 5.6a,b). In the crystal, cellulose layers are stacked so that the positively charged groups face the negatively charged groups giving a *crystal-like* charge distribution. The 3-D density distributions of solvent species around an unrelaxed CNC particle clearly shows that anions (Cl^-) are concentrated around the particle surface with exposed positively charged groups, while positively charged ions (Na^+) are localized on the opposite side of the particle (Fig 5.6c).

On relaxing the CNC particle in explicit water solution for 6 ns and analyzing the structure after relaxation, we observe a smearing of the charge over the faces (Fig. 5.6d,e) which noticeably affects the distribution of the ions around the fibril (Fig 5.6f). The relaxed particle charge is weakly polarized, as evidenced by the rather even distribution of cations and anions around it. In both unrelaxed and relaxed particles, the ions distributions are calculated using the 3D-RISM-KH theory for a particle in aqueous solution of NaCl at concentration 0.040 mol/kg. One can hypothesize that the initial *crystal-like* highly polarized charge distribution in the CNC particle is one of the driving forces leading to the fibril twisting.

The next step taken toward the development of representative CNC models is to build a charged sulfonated particle model, which is accomplished by grafting sulfate groups to some of the cellulose's surface chains at the surface density taken from elemental analysis [5.100]. The model contains 16 modified glucose units at the C6 position with sulfate groups so as to have four substitutions on each face. Each sulfonate group bears one unit of negative charge and the total CNC particle charge is $16e$. The estimated surface charge density is $0.3e/\mathrm{nm}^2$ in accordance with the experimental values for sulfonated CNC [5.101]. The MD system setup for the particle relaxation is similar to that of the neutral particle,

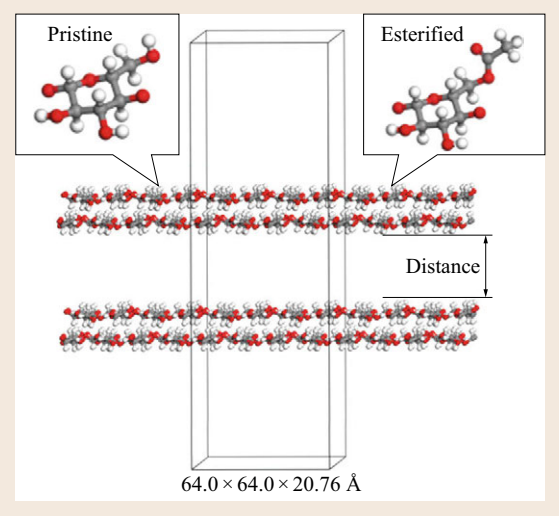


Fig. 5.7 Pristine and esterified periodically extended I_β CNC

the only difference being the addition of 16 Na^+ into the simulation box to achieve overall electrostatic neutrality.

The 3D-RISM-KH theory has been further applied to CNC surface modifications to tune-up the effective forces acting on CNC particles in solution. The I_β pristine and esterified cellulose were considered in a hydrophilic solvent (water), a hydrophobic solvent (benzene) and an ionic liquid (IL) (1-methyl-3-methylimidazolium chloride). ILs are a novel class of nonvolatile environmentally friendly solvents that have attracted the interest of synthetic chemists due to the fundamentally different reaction thermodynamics and kinetics compared to typical molecular solvents [5.102]. The 3D-RISM-KH method predicts the properties of IL in a remarkable agreement with conclusions drawn from Car–Parrinello high-level ab initio modeling [5.15].

Figure 5.7 shows a periodically extended I_β CNC rod model that is particularly suitable for prediction of interaction among particles with uniform surface and large aspect ratio, using the pristine structure from [5.103]. The esterified structure that contains acetate groups at every primary surface hydroxyl group (O6 atom, Scheme I) is partially relaxed using molecular mechanics (MM) with constrained cellulose backbone. Figure 5.8 presents the effective interaction (PMF) plots for pristine and esterified CNC in the top and bottom panels, respectively. Similar to I_α cellulose, the I_β cellulose is stabilized by a hydration shell. The pristine CNC disaggregation barrier increases in the order water < benzene < IL, indicating that dispersion in water is favorable, whereas in benzene and IL it is not. This is typical for hydrophilic surfaces.

For esterified CNC, the PMF in benzene and IL have lower disaggregation barrier than in water, suggesting facilitated dispersion in hydrophobic solvents. The lack of significant solvent expulsion barriers in benzene and IL suggest a weak solvent–solute interaction. This example demonstrates how surface modifications are employed to tune-up dispersion properties of CNC in various solvents. For every dispersion configuration, our methodology predicts the solvent orientation based on the solvent distribution function, as presented in Fig. 5.9 for the IL $mmim^+$ Cl^-. In addition to addressing the type of the surface modification, this

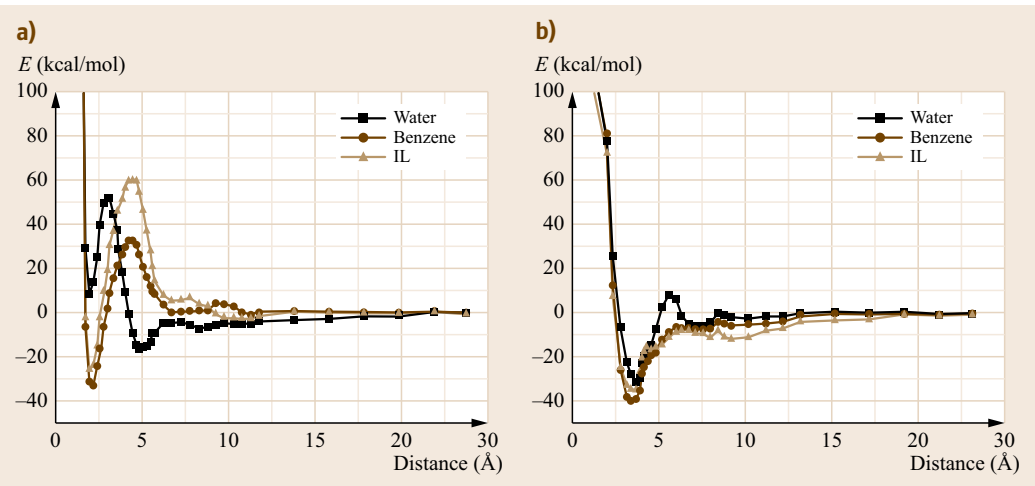


Fig. 5.8a,b PMF of the pristine (**a**) and esterified (**b**) periodically extended I_β CNC in water, benzene, and IL

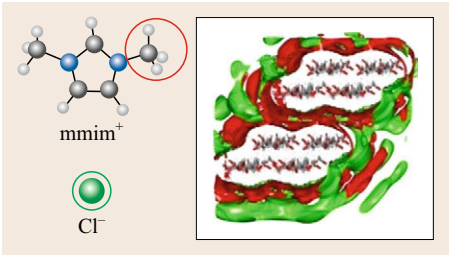


Fig. 5.9 Solvation structure of the methylmethyl-imidazolium ($mmim^+$) Cl^- ionic liquid around the periodically extended pristine I_β CNC particle

methodology allows the prediction of the degree of surface modification necessary to achieve a certain dispersion effect. This is particularly important in industrial processing, where achieving high degrees of surface modification could be costly.

Supramolecular Rosette Nanotubular Architectures in Solution

One complex example from supramolecular organic chemistry is synthetic organic supramolecular rosette nanoarchitectures, or rosette nanotubes (RNTs) [5.21–25]. The 3D-RISM-KH molecular theory of solvation revealed the molecular mechanisms of self-assembly and conformational stability of RNTs forming in different solvents and held through noncovalent forces. The molecular building block, Cytosine∧Guanine motif decorated with various functional groups, undergoes a hierarchical self-assembly process in solution to form a six-membered supermacrocycle (rosette ring) maintained by 18 hydrogen bonds between its complementary sites, which in turn self-organizes into a linear stack (a nanotube with an open central channel), an aggregate which in general is highly stable and readily withstands boiling and drying (Fig. 5.10). Any functional

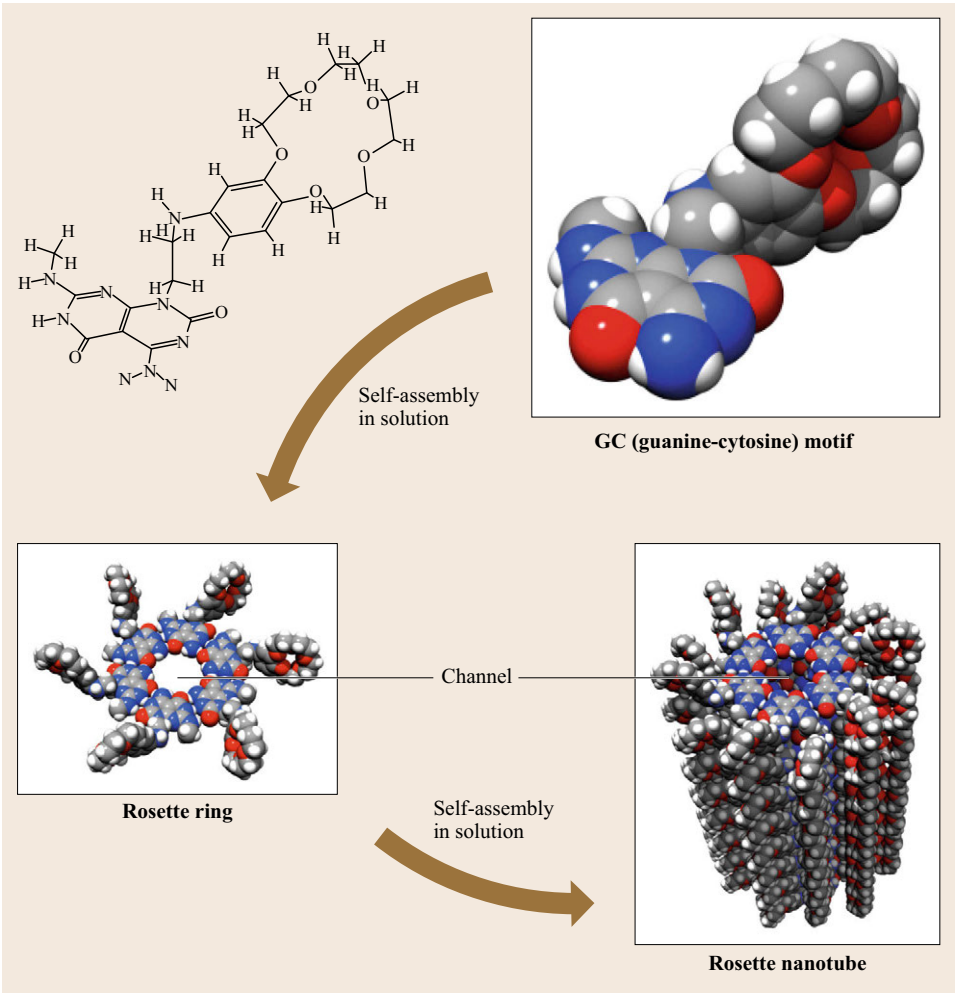


Fig. 5.10 Formation of supramolecular organic RNTs (after [5.21, 23–25]). Shown is RNT functionalized with crown ethers expressed on the outer RNT surface

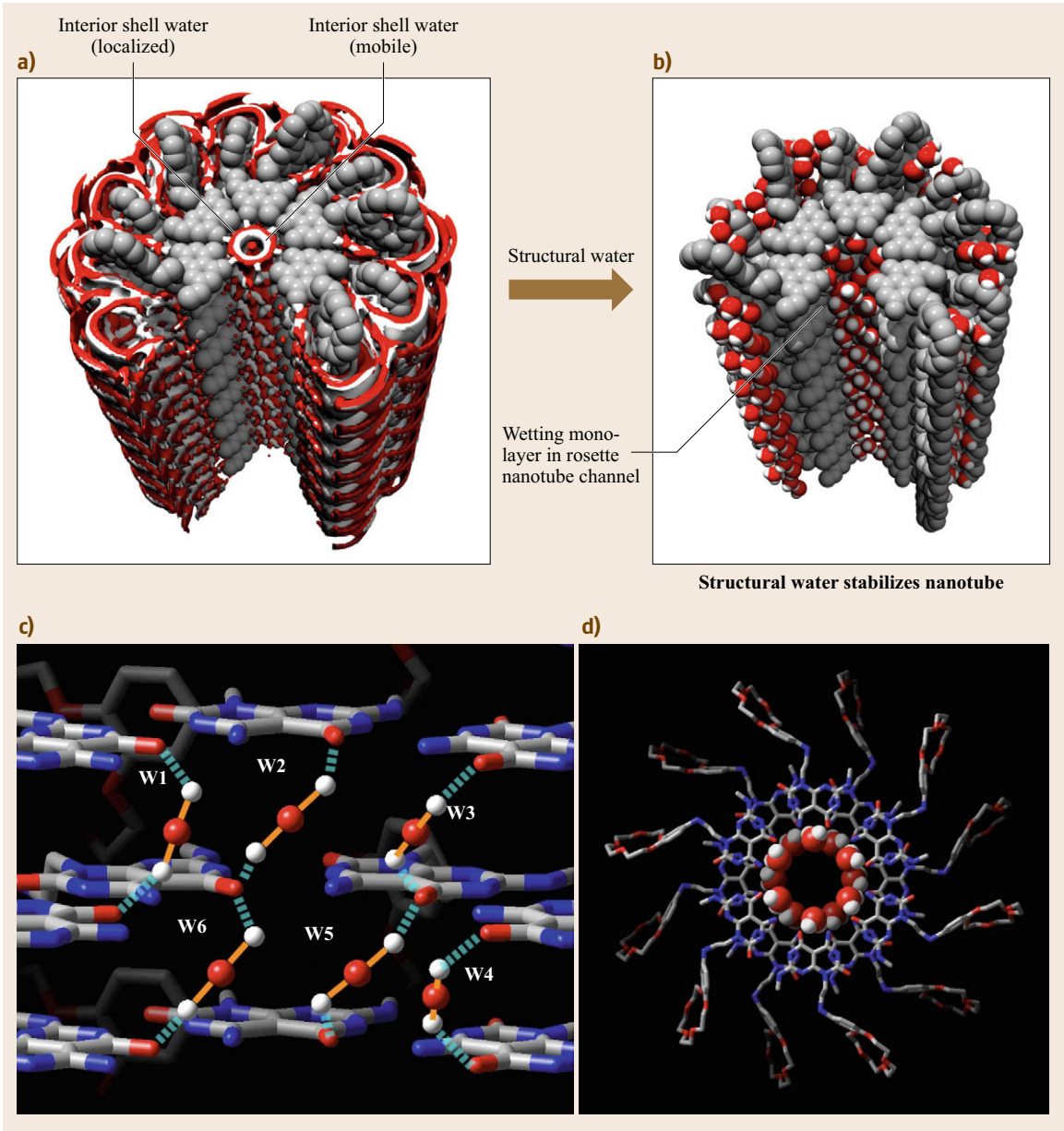


Fig. 5.11a–d Hydration structure of the RNT functionalized with crown ethers in aqueous electrolyte solution with Cl^- counterions [5.24]. 3-D distributions of water oxygen (*red*) and hydrogen (*white*) in the inner and outer hydration shells of the RNT predicted by the 3D-RISM-KH molecular theory of solvation **(a)**. Visualization of the structural molecules in the channel and outer pockets of the RNT **(b)**. Structural water molecules of the interior shell water in the RNT channel attach to the RNT motifs with hydrogen bonds stabilizing the RNT **(c)** and form a wetting monolayer **(d)**

group covalently attached to the motif, for example, crown ether, alkyl chains, and lysine tails, could be expressed on the RNT surface, thereby offering a general *built-in* strategy for tailoring the physico-chemical properties of RNTs. The 3D-RISM-KH theory uncovered the pathways of the step-by-step self-assembly of RNTs from motifs into rosettes and then nanotubes, showing that the thermodynamically preferred mechanism of RNT growth is attachment of motifs to the nanotube end to form and complete a new rosette ring, rather than growth of a separate ring in solution and then its attachment to the nanotube end [5.24]. Fig-

ure 5.11 depicts the inner and outer hydration structure of the RNT with crown ether functionalities on its outer surface. The theory exhibited that the RNT channel is covered with a wetting monolayer of structural water molecules strongly bound to its surface and crucially contributing to the RNT stability, holds a chain of loosely bound water molecules at the channel center, and can also hold host molecules of inert gases or drugs inside [5.24]. This suggests potential use of RNTs as artificial channels for molecular transport in nanoengineered bioorganic systems and as drug delivery vehicles. The 3D-RISM-KH theory predicted that a G–C base bearing two C12 alkyl chains undergoes a solvent-controlled multistep hierarchical self-assembly process into lamellar prolate nanospheroids [5.23]. The theory explained how the stability of the helical rosette nanotubes (HRNs) self-assembling from the C–G motif decorated with the lysine tail can be tuned (significantly increased) by adding a covalent linker pairing adjacent G∧C bases in neighboring rings, and how HRNs undergo further hierarchical self-organization into superhelices [5.21]. The theory predicted the molecular mechanism of solvent-driven supramolecular chirality in HRNs: structural solvent molecules localized in the pockets between the lysine tails on the HRN surface play a role of molecular switches causing the tails to form a right-hand supramolecular helix in water, the conformation with the lowest free energy (thermodynamic formation), but a left-hand supramolecular helix in methanol, the conformation preferred due to a kinetic barrier for the right-hand one at the beginning of HRN self-assembly in methanol (kinetic formation), but undergoing subsequent conversion to the right-hand one under heating, in full agreement with experiment [5.22]. The 3D-RISM-KH theory predicted the most stable conformation of the RNTs made of twin G–C module bearing the lysine side chain, with the *nests* consisting of four side chains used for one-pot nucleation, growth, morphogenesis, and passivation of 1.4 nm Au nanoparticles, one of the possible applications of RNTs [5.25].

To conclude this part, the examples represent generic forces acting in chemical and biomolecular systems in solution. They demonstrate how this theory captures and resolves in the molecular origin of the solvation structure shells and the PMFs between the solution species three dimensionally. Note that the molecular picture provided by 3D-RISM theory is completely at the level of molecular simulation, and is not achievable otherwise by a continuum solvation semi-empirical treatment; the latter can be parameterized to represent, for example, the effect of hydrogen bonding in pure water but is not transferable to solution with other components, such as electrolyte, co-solvent, not speaking of such complex co-factors as different ligand compounds.

5.2.5 Molecular Recognition and Protein–Ligand Binding

The PMF (5.18) defined in terms of the 3-D site distribution functions as a 3-D map of the effective potential between each solvent species and the solute biomolecule determines the binding strength and most probable locations (binding modes) of structural solvent molecules at the solute macromolecule, averaged over the statistical mechanical ensemble of mutual arrangements and orientations. With the solvent mixture also including ions and other co-factors, such as co-solvent and ligands, this constitutes an approach to predict molecular recognition in supramolecules and biomolecules from the first principles of statistical mechanics, with full account of their molecular specificities [5.27]. It gives a new computational method of mapping ligand molecules on protein surfaces for protein–ligand binding and fragment-based drug design [5.27, 28]. This approach has been realized in the 3D-RISM based ligand mapping (3D-RISM-LM) algorithm [5.60] applied to identify the drug efflux pathway in the membrane protein and multidrug transporter AcrB [5.28], and in the ligand docking (3D-RISM-Dock) algorithm [5.31, 33] implemented in the AutoDock package and validated on the experimental data for the binding modes and binding free energy of the antiprion compound GN8 against mouse PrP protein [5.31] and those of thiamine against the extracytoplasmic thiamine binding lipoprotein MG289 [5.59, 60]. The 3D-RISM-Dock approach properly accounts for molecular specificity of the ligand and solvent and allows one to study concentration effects on protein–ligand binding in fragment-based rational drug design.

5.2.6 Post-Processing of the Thermodynamics of MD Trajectories

The popular approach of MM/PB(GB)SA post-processing of the thermodynamics of MD trajectories uses the PB or generalized Born (GB) continuum solvation model combined with the solvent-accessible SA empirical term to account for nonpolar interactions in solution, such as hydrophobic hydration and hydrophobic attraction. There is growing evidence that the PB(GB)SA continuous solvation models cannot describe the nonelectrostatic effects accurately [5.104–106], especially for small proteins. This follows from the fact that for small peptides there is no proportionality between solvent-accessible SA of a protein and

the nonpolar part of the solvation free energy [5.107]. In addition, such models do not account correctly for the dispersion interactions and excluded volume effects [5.104, 105]. This raises questions about the applicability of PB(GB)SA to describe quantitatively the hydrophobic effects in biomolecular systems. An alternative to account accurately for nonpolar effects is to use the following combined approach: MD is used to generate trajectories, followed by MM to calculate the peptides internal energy and conformational entropy, and the 3D-RISM-KH molecular theory of solvation to characterize the solvation free energy. It is worth noting that the continuous solvation models, such as PB(GB)SA require phenomenological parameters, such as ionic radii and surface tension coefficients to be used as input or modeling [5.106], which makes them less reliable, compared to the molecular theory of solvation.

The MM/3D-RISM-KH post-processing method was applied to study the thermodynamics and volumetrics of the hydration and aggregation of the HET-s prion and amyloid-β fibril [5.29, 31], and the conformational stability and association thermodynamics of small wild-type Aβ(17–42) oligomers with different protonation states of Glu(22) versus the E22Q (Dutch) mutants [5.30, 31].

5.3 Multiscale Coupling of the 3D-RISM-KH Molecular Theory

The 3D-RISM-KH molecular theory of solvation has been coupled with quantum chemistry methods, including KS-DFT [5.8, 11, 13, 14, 45] and ab initio CASSCF method [5.11, 12], in a multiscale approach to electronic structure and chemical reactions in solution [5.11, 13, 14, 45] and at solid–liquid interfaces [5.8]. Note that 3D-RISM-KH can be combined in a self-consistent field approach with any multireference electronic structure theory. The closed analytical form for the solvation free energy stemming from the 3D-RISM-KH equations allows one to obtain its analytical gradients with respect to nuclei coordinates, or analytical solvation forces acting on nuclei in solution, which gives access to geometry optimization and evaluation of reaction pathways in solution. The self-consistent field, KS-DFT/3D-RISM-KH multiscale theory, including analytical gradients, for the electronic structure in solution are implemented in the ADF computational chemistry package [5.13, 14, 45]. Further, the orbital-free embedding (OFE) KS-DFT method with Wesolowski and Warshel's two-density functionals separately representing the electronic structure of the solute and that of environment [5.108] was coupled with 3D-RISM-KH for an improved description of the effect of solution environment on the solute electronic structure properties, such as photochemistry in solution; the OFE-DFT/3D-RISM-KH multiscale method is also implemented in the ADF package [5.14]. The KS-DFT(OFE-DFT)/3D-RISM-KH multiscale theory of electronic structure in solution has been extensively validated against experiment for thermochemistry, conformational equilibria and activation barriers for different solutes in various solvents [5.13, 14, 45], solvated carbon nanotubes [5.13], chemical reactions [5.13] and photochemistry [5.14] in solution, structure and work-function of metal–water interface [5.8], and structure of ILs [5.15].

5.3.1 Self-Consistent Field Coupling of KS-DFT with 3D-RISM-KH

KS-DFT in the Presence of Solvent

The electronic structure of the solute is calculated from the self-consistent KS-DFT equations modified to include the presence of solvent. The whole system of the solute and solvent has the Helmholtz free energy defined as [5.8, 11]

$$A\left[n_{\mathrm{e}}(r),\{\rho_{\gamma}(r)\}\right] = E_{\mathrm{solute}}\left[n_{\mathrm{e}}(r)\right] + \Delta\mu\left[\{\rho_{\gamma}(r)\};n_{\mathrm{e}}(r)\right] , \tag{5.19}$$

where E_{solute} is the internal energy of the solute macromolecule including the standard components of electronic structure theory, $\Delta\mu$ is the solvation free energy determined by the expression (5.12) which comes from the solute–solvent interaction and solvent reorganization around the solute macromolecule, $n_{\mathrm{e}}(\boldsymbol{r})$ is the electron-density distribution of the solute macromolecule, and $\rho_{\gamma}(\boldsymbol{r}) = \rho_{\gamma} g_{\gamma}(\boldsymbol{r})$ is the classical density distributions of solvent interaction sites γ of solvent molecules obtained from the 3D-RISM-KH integral equation. In the KS-DFT of electronic structure, the electronic internal energy of the solute is written in atomic units as

$$E_{\mathrm{solute}}\left[n_{\mathrm{e}}(r)\right] = T\left[n_{\mathrm{e}}(r)\right] + \int \mathrm{d}r n_{\mathrm{e}}(r)\upsilon_{\mathrm{i}}(r) + \int \mathrm{d}r\mathrm{d}r' \frac{n_{\mathrm{e}}(r)n_{\mathrm{e}}(r')}{|r-r'|} + E_{\mathrm{xc}}\left[n_{\mathrm{e}}(r)\right] , \tag{5.20}$$

where $T[n_e(\boldsymbol{r})]$ is the kinetic energy of a noninteracting electron gas in its ground state with density distribution $n_e(\boldsymbol{r})$, $\upsilon_i(\boldsymbol{r})$ is the attractive potential of the nuclei, and $E_{xc}[n_e(\boldsymbol{r})]$ is the exchange-correlation energy. The minimization of the free-energy functional (5.19) by functional variation with respect to the electron density

$$\frac{\delta A\left[n_e(r),\{\rho_\gamma(r)\}\right]}{\delta n_e(r)} = 0 \tag{5.21}$$

subject to the normalization condition for N_e valence electrons of the solute

$$\int \mathrm{d}r n_e(r) = N_e \tag{5.22}$$

leads to the self-consistent KS-DFT equation modified due to the presence of solvent [5.8, 11, 13, 45]

$$\left[-\frac{1}{2}\Delta + \upsilon_i(r) + \upsilon_H(r) + \upsilon_{xc}(r) + \upsilon_{solv}(r)\right]\psi_j(r) = \varepsilon_j\psi_j(r)\,, \tag{5.23}$$

where the Hartree potential of the electrostatic interaction with the electron cloud is

$$\upsilon_H(r) = \int \mathrm{d}r' \frac{n_e(r')}{|r-r'|}\,, \tag{5.24}$$

the electron density is determined by summation over the N_e lowest occupied eigenstates with account of their double occupancy by electrons with opposed spins

$$n_e(r) = \sum_{j=1}^{N_e} |\psi_j(r)|^2\,, \tag{5.25}$$

the exchange-correlation potential is the functional derivative

$$\upsilon_{xc}(r) = \frac{\delta E_{xc}\left[n_e(r)\right]}{\delta n_e(r)}\,, \tag{5.26}$$

and the solvent potential acting on the valence electrons of the solute is defined as

$$\upsilon_{solv}(r) = \frac{\delta\Delta\mu\left[n_e(r),\{\rho_\gamma(r)\}\right]}{\delta n_e(r)}\,. \tag{5.27}$$

In the ADF package implementation, calculation of $\upsilon_H(\boldsymbol{r})$ is simplified by using the fitted density

$$n_e(r) \approx \sum_{j=1}^{N_e} c_j f_j(r) \tag{5.28}$$

expressed in terms of the single-center Slater functions f_j with the coefficients c_j determined by least-square fitting [5.109, 110]. Substituting (5.28) in the Hartree form (5.24) and using the locality properties [5.111] dramatically reduce the computational load for evaluation of the potentials and matrix elements [5.13, 45].

Finally, the total free energy is calculated as

$$\begin{aligned} A_{total} = {} & \sum_{j=1}^{N_e} \varepsilon_j T - \frac{1}{2}\int \mathrm{d}r\mathrm{d}r' \frac{n_e(r)n_e(r')}{|r-r'|} \\ & + E_{xc}\left[n_e(r)\right] - \int \mathrm{d}r n_e(r)\upsilon_{xc}(r) \\ & + \Delta\mu\left[\{\rho_\gamma(r)\}; n_e(r)\right] \\ & - \int \mathrm{d}r n_e(r)\upsilon_{solv}(r)\,. \end{aligned} \tag{5.29}$$

Effective Potentials Coupling the Electronic and Classical Subsystems

With the free-energy functional in the form (5.19) allowing functional differentiation analytically, the effective potentials of the self-consistent field coupling the electronic and classical subsystems are obtained in the closed analytical form.

The classical effective potential of the whole solute acting on solvent site γ

$$u_\gamma(r) = u_\gamma^{sr}(r) + q_\gamma\left[\varphi^n(r) + \varphi^e(r)\right]\,, \tag{5.30}$$

is broken up [5.8, 11, 13, 45] into the short-range interaction term $u_\gamma^{sr}(r)$ and the electrostatic energy of the solvent site charge q_γ in the electrostatic potential of the solute valence electrons $\varphi^e(r)$ and that of nuclei charges Z_i

$$\varphi^n(r) = \sum_i \frac{Z_i}{|r-R_i|}\,. \tag{5.31}$$

The short-range interaction is given by the sum of the pairwise contributions from the solute nuclei represented by the 12-6 Lennard-Jones potential

$$u_\gamma^{sr}(r) = \sum_i 4\varepsilon_{i\gamma}\left[\left(\frac{\sigma_{i\gamma}}{r_{i\gamma}}\right)^{12} - \left(\frac{\sigma_{i\gamma}}{r_{i\gamma}}\right)^{6}\right]\,, \tag{5.32}$$

where $\sigma_{i\gamma}$ and $\varepsilon_{i\gamma}$ are the Lennard-Jones cross-term diameter and energy parameters obtained from those of solute nucleus i and solvent site γ by using the standard mixing riles $\sigma_{i\gamma} = (\sigma_i + \sigma_\gamma)/2$ and $\varepsilon_{i\gamma} = (\varepsilon_i\varepsilon_\gamma)^{1/2}$, and $r_{i\gamma} = |r_\gamma - R_i|$ is the nucleus–site separation. Within the ADF package implementation, the potential of valence electrons acting on a single solvent site $\varphi^e(r)$ is

calculated from the valence electron density $n_e(r)$ in the density-fitting procedure (5.28) [5.110].

With the solvation free energy given by the 3D-RISM-KH analytical expression (5.12), the effective potential of the solvent acting on the solute valence electrons given by the functional derivative (5.27) is derived as [5.8, 11, 13, 45]

$$\upsilon_{\text{solv}}(r) = \frac{\delta \Delta\mu}{\delta n_e(r)} = \sum_\gamma \rho_\gamma \int \mathrm{d}r' h_\gamma(|r-r'|)\upsilon_\gamma^{\text{ps}}(r') \,, \quad (5.33)$$

where $\upsilon_\gamma^{\text{ps}}(r)$ is the contribution of solvent site γ to the pseudopotential of a solvent molecule acting on an external electron which is in general given by the variational derivative of the classical site potential with respect to the valence electron density [5.8, 11]

$$\upsilon_\gamma^{\text{ps}}(r-r') = \frac{\delta u_\gamma(r)}{\delta n_e(r')} \,. \quad (5.34)$$

The potential (5.33) implies the mean field approximation, which follows essentially from the use of the solvation free energy in the form (5.12).

Analytical Gradients in Solution

The analytical first derivative with respect to the coordinates of the solute nuclei $\boldsymbol{R}_i$ is obtained by differentiation of the whole system free energy (5.19)

$$\frac{\mathrm{d}A\,[n_e(r),\{\rho_\gamma(r)\}]}{\mathrm{d}\boldsymbol{R}_i} = \frac{\mathrm{d}E_{\text{solute}}\,[n_e(r)]}{\mathrm{d}\boldsymbol{R}_i} + \frac{\mathrm{d}\Delta\mu\,[\{\rho_\gamma(r)\}\,;n_e(r)]}{\mathrm{d}\boldsymbol{R}_i} \,, \quad (5.35)$$

where the former term has the same structure as in the gas-phase case [5.112] and the latter term is derived from the solvation free energy (5.12) as follows

$$\frac{\mathrm{d}\Delta\mu}{\mathrm{d}\boldsymbol{R}_i} = \sum_\gamma \rho_\gamma \int \mathrm{d}r g_\gamma(r) \frac{\partial u_\gamma^{\text{sr}}(r)}{\partial \boldsymbol{R}_i} + \int \mathrm{d}r \upsilon_{\text{solv}}(r) \frac{\partial n_e(r)}{\partial \boldsymbol{R}_i} + q_i \frac{\partial \upsilon_{\text{solv}}(r)}{\partial r}\bigg|_{r=\boldsymbol{R}_i} \,. \quad (5.36)$$

The calculation of (5.36) requires little computational effort. The second term is calculated together with the gradients of the exchange-correlation potential [5.112], and the rest is calculated in the 3D-RISM procedure. Notice that the first term in the square brackets does not contribute much to the gradients because the large magnitude of the derivatives of the short-range potential $u_\gamma^{\text{sr}}(r)$ at the repulsive core edge is suppressed by the distribution function $g_\gamma(r)$ exponentially decaying there.

5.3.2 Example of Multiscale KS-DFT/3D-RISM-KH Calculations

Novel applications of green chemistry involve ionic liquids (ILs) as tunable solvent environment, including organic synthesis and other applications, such as electrodeposition. Properties of molecules solvated in ILs, including ions constituting IL itself are strongly affected by solvent environment. In bulk liquid, the solvent environment affects physicochemical characteristics of ILs constituents, including nuclear magnetic resonance (NMR) chemical shifts, relaxation times, IR frequencies, as well as such important chemical behavior as acidity of aromatic protons. To give reliable results, ab initio calculations for such systems have to self-consistently account for the change in both electronic and classical solvation structure. This can be achieved in principle by using a Car–Parrinello molecular dynamics (CPMD) method in which MD is driven by the forces obtained from electronic structure DFT for the whole system or at least by using a QM/MD approach in which quantum mechanics (QM) treats one selected ion and MD handles the classical solvation structure of IL. However, both the approaches, particularly the former, are extremely computationally demanding, especially to obtain the solvation thermodynamics. A simpler alternative is a QM/MM approach; however, for many systems, molecular mechanics (MM) cannot adequately represent the solvation structure and thermodynamics in the statistical ensemble average. Meanwhile, the 3D-RISM-KH molecular theory of solvation properly resolves a 3-D spatial map of solvation structure and reliably describes solvation effects for macromolecules of the complex geometry and different chemical specificities, such as hydrogen bonding and/or solvophobic solvation and solvophobic interaction. The self-consistent field KS-DFT/3D-RISM-KH multiscale method provides a first-principle physical view on electronic structure in solution and thus offers an accurate and computationally efficient procedure to perform ab initio calculations on species solvated in ILs.

Figure 5.12 depicts the KS-DFT/3D-RISM-KH results for the solvation structure of the mmim ion in bulk liquid of [mmim][Cl] at $T = 400\,\text{K}$ [5.15]. The method predicts the IL properties in remarkable agreement with the conclusions drawn from CPMD simulations for the three-dimensional solvation structure and the solvent environment effect of the IL constituents. This includes

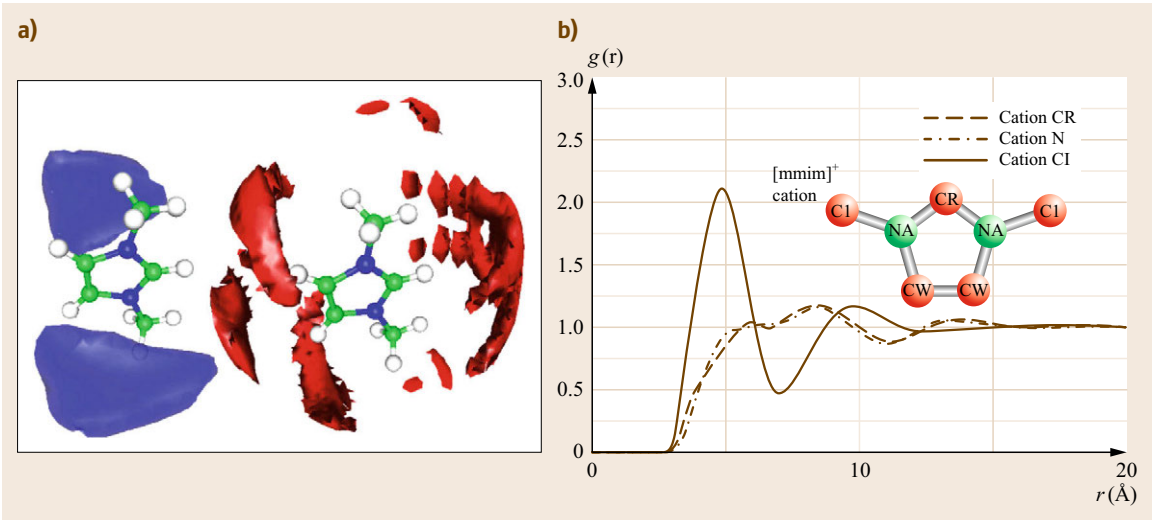


Fig. 5.12a,b Solvation structure of the mmim ion in bulk liquid of [mmim][Cl] at $T = 400\,\mathrm{K}$, obtained by the self-consistent field KS-DFT/3D-RISM-KH multiscale theory of electronic structure in solution. **(a)** Isosurfaces of the nitrogen of $[\mathrm{mmim}]^+$ cations at $g_N(r) > 2$ (*blue*) and of Cl^- anions at $g_{Cl}(r) > 5$ (*red*). **(b)** Radial distribution functions of Cl^- anions (*solid line*), cation CR site (*dashed line*), and cation N site (*dash-dotted line*) around the center of mass of the $[\mathrm{mmim}]^+$ cation in the IL

such effects as the polarization due to electronic effects in the IL environment, the dipole moment enhancement from $\mu = 2.10\,\mathrm{D}$ for the isolated cation to 2.59 D in the bulk IL ($\mu = 2.10$–$2.59\,\mathrm{D}$ from CPMD), the antiparallel stacking of adjacent cations with the central CR hydrogens of neighboring sites pointing in the opposite directions, the coordination number of 7.4 anions around the cation (versus 7.5 from CPMD), and the solvation free energy of $-22.1\,\mathrm{kcal/mol}$ for the $[\mathrm{mmim}]^+$ cation and $-49.1\,\mathrm{kcal/mol}$ for the Cl^- anion in the IL [5.15].

Another example of the performance of the KS-DFT/3D-RISM-KH method at the level of CPMD simulation is the self-consistent electronic and classical solvation structure of a (100) copper–water interface [5.8]. The predicted shift of the Fermi level of the metal due to the presence of water matches the values typically found in experiment. Dense water substantially affects the electron distribution around a water molecule adsorbed at the metal surface and changes the metal–water effective potential. The latter follows the shapes of the metal-effective electrostatic potential which for this interface is strongest at the hollow site adsorption positions. Therefore, both CPMD and KS-DFT/3D-RISM-KH predict the 3-D water density distributions with the maxima at the hollow and bridge adsorption positions, unlike classical MD predicting the maxima at the on-top site positions. The layering and orientations of water molecules near the surface found with DFT/3D-RISM-KH are in agreement with experiment.

The above examples demonstrate the capability of the KS-DFT/3D-RISM-KH multiscale method to predict electronic structure in solution, including solid–liquid interfaces, essentially at the level of CPMD simulation.

5.4 Multi-Time-Step Molecular Dynamics of Biomolecules

The statistically averaged effective forces of solvent acting on each solute atom produced by the 3D-RISM-KH molecular theory of solvation can then be used together with the direct solute–solute interactions to drive molecular dynamics (MD) simulation of the solute macromolecule.

5.4.1 Molecular Dynamics Coupled with 3-D Molecular Theory of Solvation

Solving the 3D-RISM integral equations is computationally expensive compared to a single-MD step, and it naturally leads to resorting to multiple time step

(MTS) MD techniques. One of the first attempts toward the hybrid MD/3D-RISM method [5.40] when studying acetylacetone in aqueous solution, the consideration was limited to the reference system propagator algorithm (RESPA) in the microcanonical ensemble, making possible to perform outer time steps up to 5 fs. The outer time step in microcanonical simulations of ambient liquids cannot exceed 4−8 fs because of resonance instabilities arising due to an interplay in an MTS procedure between strong intramolecular forces handled with an inner spacing of 0.5−1 fs and weak long-ranged intermolecular interactions. It was proven that in the microcanonical ensemble the maximum allowed length of the outer time step cannot exceed the theoretical limit of 20 fs [5.113]. Therefore, such an ensemble is very inefficient for complex systems, including large macromolecules in solution, characterized by time scales spanning up to micro- and milliseconds.

It is often much more convenient for compatibility with experiment to sample configurations from the canonical (constant temperature) ensemble, instead of the microcanonical (constant energy) one. Many thermostats have been devised to handle the canonical distributions within MTS dynamics. In the popular Langevin (LN) approach [5.114–118], artificial friction and random forces are incorporated to stabilize the solutions. Although these forces satisfy the fluctuation–dissipative theorem, the target temperature is not guarantied. On the other hand, employing a large viscosity coefficient to ensure the stability can deviate the system from the true canonical state corresponding to real interactions between particles. In addition, the LN dynamics does not possess any conserved quantity, and so it is difficult to examine the quality of the trajectories obtained. The latter drawback is absent in the well-established Nosé–Hoover (NH) chain method [5.119–122]. Here, the canonical behavior is reproduced by introducing extra phase-space variables associated with a thermostat, while the ergodicity is ensured by its chain counterparts. A famous feature of this method is that the temperature can be controlled without involving random numbers. Moreover, the NH equations of motion can be derived within the Hamiltonian formalism using the extended energy function, which is conserved during the time evolution. A great advantage of the canonical description is the possibility to postpone the appearance of unphysical MTS effects to outer time steps significantly longer than in the case of the microcanonical ensemble. For instance, the maximal applicable time steps can reach 50 fs [5.123] within the NH thermostat and can further increase up to 75 fs [5.123] in the isokinetic ensemble [5.124]. Here, employing Gauss' principle of least constraint, the total kinetic energy is kept strictly constant. This causes a modification of the real dynamics but holds the correct canonical distributions of position-dependent functions. A better efficiency can be observed by combining the canonical NH chain method [5.119] with the isokinetic ensemble [5.124]. This yields the so-called isokinetic NH chain RESPA (INR) approach [5.125, 126] in which the heat baths are coupled individually to each degree of freedom in the system. The INR algorithm was applied to MD simulations of water to certify that the outer time step size of 100 fs is workable [5.125].

The coupled MD/3D-RISM-KH approach was extended to the canonical ensemble by employing the LN thermostat [5.41]. Using the solvent-induced forces calculated by 3D-RISM-KH at outer time steps and the solvation force coordinate extrapolation (SFCE) at inner time steps of LN, it was demonstrated on an example of alanine dipeptide in aqueous solution that larger outer time steps up to 20 fs are possible with the LN/SFCE/3D-RISM-KH approach. Such steps, however, are still smaller than 100 fs ones achievable within MD simulation using the INR algorithm [5.125].

A more general formulation of the canonical-isokinetic NH chain approach [5.42] consists in a special splitting of the total kinetic energy into its partial components. Such components are first collected into groups with a chosen number of either translational degrees of freedom of atoms or translational, orientational, and vibrational degrees of molecules. Then each of these groups is coupled to its own set of chain thermostats characterized with given lengths and relaxation times. This allows us to optimize and further significantly increase in efficiency the integration of motion, resulting in the optimized isokinetic Nosé–Hoover chain (OIN) algorithm [5.42]. The standard isokinetic [5.124] or INR [5.125, 126] ensembles appear from the generalized formulation as particular cases. With the stabilizing effect of OIN thermostatting in MTS-MD, gigantic outer time steps up to picoseconds can be employed to accurately calculate equilibrium and conformational properties, both in pure OIN and multiscale OIN/SCFE/3-DRISM-KH simulations [5.42]. In the atomic version of OIN for MTS-MD of a biomolecule in a solvent PMF, the solvation forces are obtained analytically by converging the 3D-RISM-KH integral equations once per several OIN outer time steps, and are calculated in between by using SFCE in the subspace of previous successive solutions to 3D-RISM-KH. While the computational rate of solvent sampling in OIN/SFCE/3D-RISM-KH is already about 20 times faster than standard MD with explicit solvent, further substantial acceleration of sampling stems from making solute evolution steps in a statistically averaged PMF obtained from 3D-RISM-KH. The latter efficiently samples the phase space for essen-

tial events with rare statistics, such as exchange and localization of solvent and ligand molecules in confined spaces, pockets, and at binding sites of the solute macromolecule, as distinct from MD with explicit solvent which requires enormous computational time and number of steps in such cases.

5.4.2 Calculation of Solvation Forces by 3D-RISM-KH MTS-MD

In the coupled MTS-MD/3D-RISM-KH method implemented in the Amber MD package [5.41, 42], MD is applied to the biomolecule driven by effective solvation forces which are obtained analytically by the 3D-RISM-KH molecular theory of solvation. 3D-RISM-KH yields the solvation structure of the biomolecule, the solvation free-energy landscape dependent on its conformation, and the corresponding effective solvation forces acting on its interaction sites. The latter are derived by differentiating the Kirkwood thermodynamic integration formula analytically, also valid for the solvation free energy (5.12) in the 3D-KH approximation (5.2)

$$f_i(\boldsymbol{R}_i) \equiv -\frac{\mathrm{d}\Delta\mu}{\mathrm{d}\boldsymbol{R}_i} = \sum_\gamma \rho_\gamma \int \mathrm{d}r g_\gamma(r) \frac{\partial u_{i\gamma}(\boldsymbol{r}-\boldsymbol{R}_i)}{\partial \boldsymbol{R}_i} \,, \tag{5.37}$$

where $u_{i\gamma}(\boldsymbol{r}-\boldsymbol{R}_i)$ is the pairwise interaction potential between the biomolecule site i located at position $\boldsymbol{R}_i$ and solvent site γ at position $\boldsymbol{r}$. To obtain meaningful sampling of solute conformations, the computational expense of the 3D-RISMKH calculations is reduced with several optimization strategies:

1. Creating a high-quality initial guess for the direct correlation function $c_\gamma(\boldsymbol{r})$ from previous successive solutions.
2. Accelerating pre- and post-processing of the solute–solvent potentials, long-range asymptotics, and forces by using a cutoff scheme and a varying solvation box of smallest size containing two–three solvation shells around the current conformation of the protein.
3. Avoiding the direct calculation of solvation forces (5.37) with solving 3D-RISM-KH at every inner time step δt but rather doing that at each outer time step $h \gg \delta t$ and extrapolating the solvation forces at inner time steps in between based on previous successive vectors of solvation forces calculated with 3D-RISM-KH.

The extrapolation of solvation forces can be performed by using the so-called force-coordinate approximation [5.41, 42], or the solvation force coordinate extrapolation (SFCE). The main idea is that solvation forces acting on each atom of the solute macromolecule do not have strong repulsive cores and vary smoothly in space and time with solute evolution, and therefore can be extrapolated at subsequent inner time steps $\delta t \ll h$ until the next 3D-RISM-KH calculation at outer time step h with sufficient accuracy by using the solvation forces and solute atomic coordinates at previous outer time steps h. Let $f^{(k)} = \{f_i^{(k)}\}$ be a $3M$-dimensional vector of effective solvation forces acting on all solute atoms $i = 1, \ldots, M$ at locations specified by a $3M$-dimensional vector of coordinates $R^{(k)} = \{R_i^{(k)}\}$ for each of $k = 1, \ldots, K$ previous successive outer time steps of length h at which the solvation forces were calculated by using 3D-RISM-KH. Then the solvation forces $\boldsymbol{f}(t)$ at current time t within the next outer time step interval can be extrapolated in the subspace of the previous $k = 1, \ldots, K$ vectors of forces by the linear combination

$$f(t) = \sum_{k=1}^{K} a_k(t) f^{(k)} \,, \tag{5.38}$$

where the weight coefficients $a_k(t)$ are obtained by best representating the vector of solute atomic coordinates $\boldsymbol{R}(t)$ at time t in terms of its projections onto the *basis* of the previous ones $\boldsymbol{R}^{(k)}$, $k = 1, \ldots, K$ to minimize the norm of the residual

$$\min \left| R(t) - \sum_{k=1}^{K} a_k(t) R^{(k)} \right| \,. \tag{5.39}$$

A further improvement of SFCE [5.42] over its genuine version [5.41] is achieved with imposing an additional condition of normalization on the weight coefficients of the expansion (5.38)

$$\sum_{k=1}^{K} a_k = 1 \,. \tag{5.40}$$

The solute–solvent forces (5.36) can be expanded in the power series of a deviation of the current coordinate vector $\boldsymbol{R}$ from the closest basis point $R^{(*)} \in \{R^{(k)}\}$

$$f(\boldsymbol{R}) = f(\boldsymbol{R}^{(*)}) - \left.\frac{\partial f}{\partial \boldsymbol{R}}\right|_{\boldsymbol{R}^{(*)}} \left(\boldsymbol{R} - \boldsymbol{R}^{(*)}\right) + O\left(\boldsymbol{R} - \boldsymbol{R}^{(*)}\right)^2 \,, \tag{5.41}$$

where $\partial f / \partial \boldsymbol{R}$ denotes the Hessian matrix, and the second and higher order spatial inhomogeneities are neglected. Imposing the condition (5.40) automatically reproduces the zero-order term of the expansion, while the first-order one linear in coordinate is extrapolated

by minimizing the coordinate norm (5.39). Note that putting $K = 1$ reduces to the simplest case of constant-force extrapolation. The minimization procedure (5.39) with the normalization condition (5.39) leads to the set of $K + 1$ linear equations for the weight coefficients

$$\begin{pmatrix} S_{11} & \dots & S_{1K} & -1 \\ \vdots & & \vdots & \vdots \\ S_{K1} & \dots & S_{KK} & -1 \\ -1 & \dots & -1 & 0 \end{pmatrix} \begin{pmatrix} a_1 \\ \vdots \\ a_K \\ \lambda \end{pmatrix} = \begin{pmatrix} S_{1t} \\ \vdots \\ S_{Kt} \\ -1 \end{pmatrix} , \quad (5.42)$$

where S_{kl} is the inner scalar product of the $3M$-dimensional vectors of atomic coordinates for solute conformations $\boldsymbol{R}^{(k)}$ and $\boldsymbol{R}^{(l)}$ at outer time steps k and l, as well as S_{kt} is that for $\boldsymbol{R}^{(k)}$ and running conformation $\boldsymbol{R}(t)$

$$S_{kl} = \left\langle R^{(k)} | R^{(l)} \right\rangle \equiv \sum_{i=1}^{M} \left(R_i^{(k)} \cdot R_i^{(l)} \right) ,$$

$$S_{kt} = \left\langle R^{(k)} | R(t) \right\rangle \equiv \sum_{i=1}^{M} \left(R_i^{(k)} \cdot R_i(t) \right) , \quad (5.43)$$

and λ is a Lagrangian multiplier yielding the squared norm of the minimized approximation residual (5.38). At each inner step δt within the outer time step interval h, (5.42) are being solved by using standard numerical methods of solving a set of linear equations and the extrapolation (5.38) is being computed. After the next 3D-RISM-KH calculation, the basis set is updated with the new vector of forces and coordinates and the oldest one is discarded. In practical calculations, we found optimal to perform extrapolation with about $K = 20$ coordinate-force pairs. A further increase of the basis size gives no significant improvement in the extrapolation accuracy since the current conformation and forces get too different from the earliest ones in a larger basis set, but eventually leads to the accumulation of numerical errors when (5.42) become ill-conditioned for larger K.

A recent development of solvation force extrapolation for efficient sampling of biomolecules in solution resulted in the advanced solvation force extrapolation (ASFE) that couples a number of techniques: non-Eckart transformation of coordinate space, modified least-squares minimization of the residuals between the extrapolated and original coordinates/forces in the transformed space, maintaining an extended force-coordinate pair set while selecting the best subset for the smallest force residual minimum, balancing the normal equations, and incremental increase of the extrapolation interval [5.43]. Complemented with the OIN thermostat, these techniques allow increasing the outer time step by about three orders of magnitude and thus to dramatically improve the efficiency of MTS-MD steered by 3D-RISM-KH effective solvation forces. As demonstrated on a fully flexible model of alanine dipeptide in aqueous solution, the hybrid MTS-MD/OIN/ASFE/3D-RISM-KH integrator is able to handle effective solvation forces in huge outer time steps up to tens of picoseconds without affecting the equilibrium and conformational properties [5.43]. This provides a speedup by a factor of 100−500 with respect to explicit solvent MD simulations.

To obtain the desired speedup for larger solute molecules like proteins, ASFE has been further extended to the generalized solvation force extrapolation (GSFE) algorithm which includes the following: performing an individual non-Eckart-like transformation for each solute atom with a smooth weight function rather than a global rotational transformation of the whole molecule; the least-squares minimization; extension of the force-coordinate pair set to select the best subset; modified balancing of the normal equations; the so-called frequency scheme to reduce the extra computational costs without loss of extrapolation precision [5.44].

Further to the acceleration of solute time evolution in a plain step-to-step comparison of OIN/ASFE(GSFE)/3D-RISM-KH to explicit solvent MD, the 3D-RISM-KH molecular theory of solvation produces 3-D density distributions and effective forces of solvent quasi-equilibrated for a current solute conformation and thus samples in effect over an ensemble of solvent configurations around the solute molecule as if a multitude of explicit solvent MD simulations were run simultaneously. This efficiently samples biomolecular processes with slow and/or rare solvation events, for example, conformational transitions of hydrated alanine dipeptide with the mean life times ranging from 30 ps up to 10 ns for *flip–flop* conformations. The use of 3D-RISM-KH provides a dramatic acceleration of sampling over slow and rare solvation events in complex supramolecular and biomolecular systems, such as exchange and localization of solvent and ions in pockets and other function-related inner spaces and in various processes of molecular recognition, including protein–ligand binding, selective ion binding and gating, association and salt-induced conformational transitions of DNA, protein–protein interaction, and nanoparticles aggregation. In particular, the hybrid OIN/ASFE(GSFE)/3D-RISM-KH method is well suited to evaluate effective interactions (potentials of mean force) between biomolecules and nanoparticles in solution, which are computationally very expensive to get from MD simulations but are efficiently calculated from the 3D-RISM-KH theory.

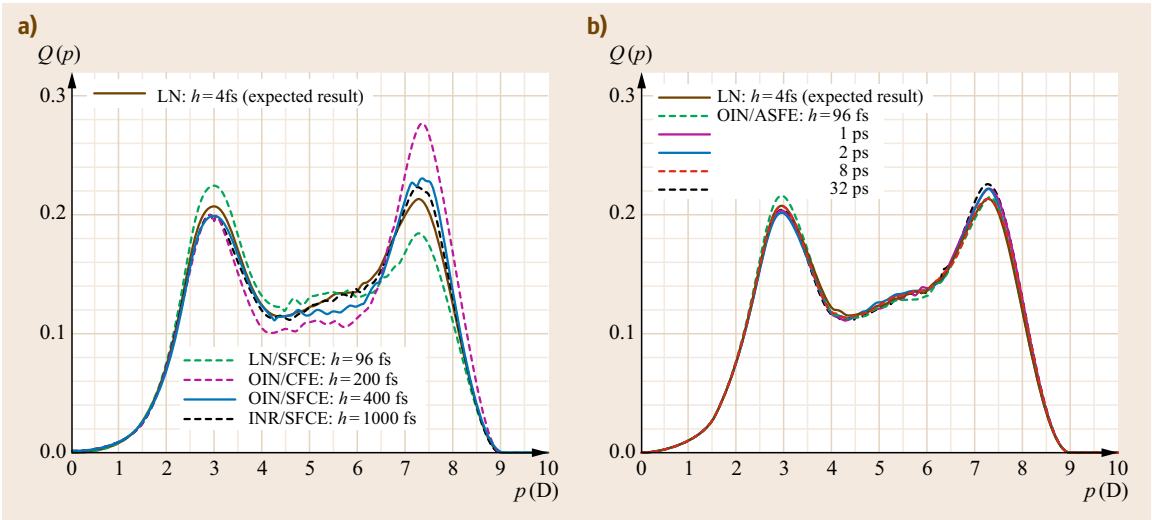


Fig. 5.13a,b Dipole moment distribution of alanine dipeptide in aqueous solution, obtained in MTS-MD/3D-RISM-KH simulations with different integrators versus the *expected* result from LN/3D-RISM-KH at $h = 4$ fs (*solid blue line*). **(a)** LN/SFCE integrator at outer time step $h = 96$ fs (*dashed green*), OIN/CFE at $h = 200$ fs (*dashed magenta*), OIN/SFCE at $h = 400$ fs (solid cyan), and INR/SFCE at $h = 1$ ps (*dashed black*). **(b)** OIN/ASFE integrator at outer time steps $h = 96$ fs; 1; 2; 8; 32 ps (*dashed green, solid magenta, solid cyan, dashed red,* and *dashed black,* respectively)

5.4.3 MTS-MD/SFCE/3D-RISM-KH Method for Biomolecular Solvation

A simple system that nevertheless has some essential biomolecular properties and thus allows one to test and validate simulation and modeling methods is alanine dipeptide in aqueous solution. This simple molecule has often been used as a model in theoretical studies of backbone conformational equilibria in proteins [5.127]. For hydrated alanine dipeptide, there are several transitions between different conformational states characterized by the mean life time of order varying from 30 ps, through 250 ps, and up to 10 ns [5.128]. Thus, even for such a relatively simple organic molecule as alanine dipeptide, a long observation time of at least $t \approx 100$ ns is necessary to gain proper statistic and average out the statistical noise in explicit solvent MD simulation. The accuracy of the MTS-MD/SFCE/3D-RISM-KH algorithms was estimated by measuring the dipole moment distribution function $f(p)$ of the hydrated alanine dipeptide [5.42]. Such a function is very sensitive to the conformational sampling and the effect of solvent, and comparing $f(p)$ with its *exact* counterpart is a reliable way of testing an MD integrator. To estimate the accuracy of the MTS thermostats and SFCE approach, the *expected* values of $f(p)$ were obtained by using the LN/3D-RISM-KH run with no solvent force extrapolation and a small friction coefficient $\gamma = 5$ fs with small inner time step $\delta t = 1$ fs for MD and outer time step $\Delta t = 4$ fs for solvation forces from 3D-RISM-KH in order to minimize all possible uncertainties.

Figure 5.13 presents the dipole moment distribution $Q(p)$ of the alanine dipeptide molecule in cSPC/E water [5.41] obtained in the MTS-MD/3D-RISM-KH method with different integrators versus the reference run with LN/3D-RISM-KH [5.42, 121]. The *expected* dipole moment distribution function $Q(p)$ (solid blue line on both the upper and lower parts) has two clear peaks on the left at $p \approx 3$ D and on the right at $p \approx 7.5$ D, as well as an enhancement in the intermediate region at $p \approx 5.5$ D; a similar pattern is observed experimentally in the real system of hydrated alanine dipeptide, which stems from the coexistence of different conformational states [5.128]. The SFCE performed within the OIN and INR ensembles for up to $\kappa = 20$ time steps provides an accuracy high enough at $h \leq 200$ fs for OIN and up to 1 ps for INR. The deviations become visible for OIN/SFCE at $h = 400$ fs (solid cyan curve in Fig. 5.13a) and achieve a value of about 10% which can still be acceptable. When OIN/3D-RISM-KH with the constant force extrapolation (referred to as OIN/CFE) is employed, that is, $\kappa = 1$ and the solvation forces stay the same during the full outer time interval h instead of the SFCE with $\kappa = 20$, a much larger uncertainty of 30% is exhibited in OIN/CFE already at $h = 200$ fs (dashed magenta curve in Fig. 5.13a). Such uncertainties exceed even those in the INR/SFCE algorithm at $h = 2000$ fs (dashed black curve in Fig. 5.13a). Approximately the

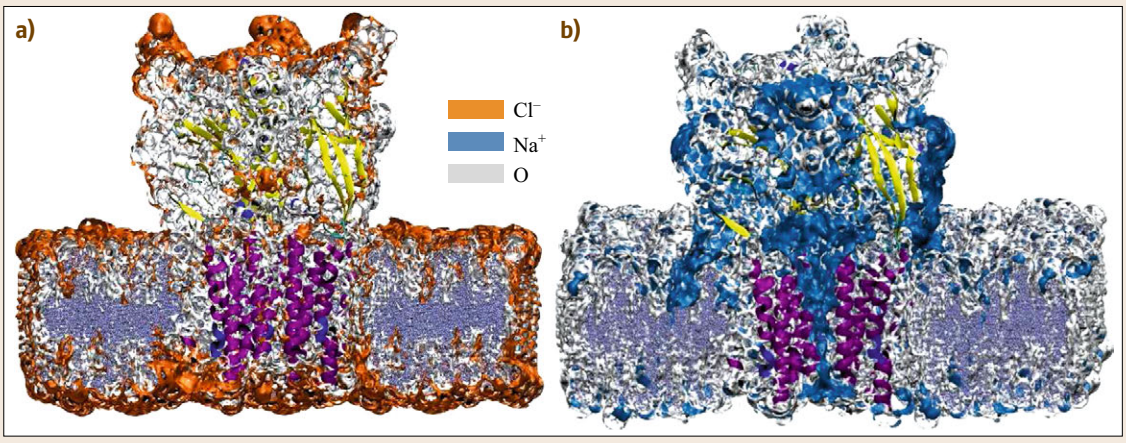


Fig. 5.14a,b 3-D distributions of water oxygen (*gray*, **(a,b)** parts), Cl^- (*orange*, **(a)**) and Na^+ (blue, **(b)**) ions around the GLIC channel embedded in the POPC lipid bilayer membrane. The channel protein is shown as β-sheet (*yellow*) and α-helices (*magenta*), and the lipids are shown in the *ball-and-stick representation*

same level of accuracy of 30% is inherent in the LN/SFCE/3-DRISM-KH integration at $h = 96$ fs, despite the use of the extrapolation with the same $\kappa = 20$. This indicates an evident advantage of the generalized canonical-isokinetic OIN/INR approach over the Langevin scheme. Note that the maximal acceptable outer time step reported earlier [5.41] was $h = 20$ fs, as achieved in the LN/SFCE/3D-RISM-KH scheme with the extrapolation. This time step size is more than one order of magnitude smaller than steps of $h =$ 200–400 fs feasible with the OIN/SFCE/3D-RISM-KH algorithm. It is worth recalling that the outer time step in the explicit microcanonical MTS-MD/3D-RISM simulations cannot exceed 5 fs [5.40, 41]. Thus, the use of the generalized canonical-isokinetic OIN ensemble coupled with the 3D-RISM-KH molecular theory of solvation and solvent force coordinate extrapolation in the multiscale OIN/SFCE/3D-RISM-KH integrator allowed to exceed this value by at least 40–80 times.

The use of the advanced extrapolation approach in the OIN ensemble leads to the best results, which remain of high quality even at extremely large outer time steps. Indeed, it is readily seen in Fig. 5.13b that the OIN/ASFE/3D-RISM-KH curves related to $h = 96$ fs (green), 1 ps (magenta), 2 ps (cyan), and 8 ps (red) are practically indistinguishable from the *exact* one (blue). (Some uncertainties can be attributed to statistical noise.) Only at $h = 32$ ps, the OIN deviations become noticeable and reach about 10%, which is still tolerable. Thus, outer time steps of order of tens of picoseconds are applicable, indeed. Thus, the OIN ensemble coupled with the ASFE approach and the 3D-RISM-KH molecular theory of solvation produces the equilibrium properties, including slow motion like the *flip–flop* conformational transitions and partitioning, with a high accuracy of better than 5% by using a large outer time step up to to $h = 8$ ps. This provides a speedup of by a factor of 100–500 with respect to explicit solvent MD simulations [5.44].

Ion channels belong to an important class of biomolecular systems where solvent (ions, protons, water, and ligands) performs the biological functions in confinement. Ion translocation through the channel is a rare event on the time scale of bulk solvent relaxation, and explicit solvent simulations require extensive computations to achieve statistically reliable results. Furthermore, the study of selectivity mechanisms and permeation properties of channels under physiological conditions may require modeling of complex solvent conditions, including low ionic concentration environments, which is currently beyond the scope of explicit solvent MD simulations. To alleviate these difficulties, coarse-grained models of a channel were proposed and used to study the physical properties and functioning of ionic channels [5.129–131], such as the importance of protein polarization and side chains mobility on the selectivity of sodium channels [5.129]. However, they neither account for the atomic structure of the real ion channels nor allow one to include in a transferable manner more complex solvent compositions with different cofactors, ligands, and other small molecules. This can be done with the 3-D molecular theory of solvation which provides a natural bridge between the coarse-grained description and all-atom explicit solvent MD simulations.

The structure of the bacterial *G. violaceus* pentameric GLIC homolog in an open conformation was resolved in the X-ray experiments [5.132]. It was also

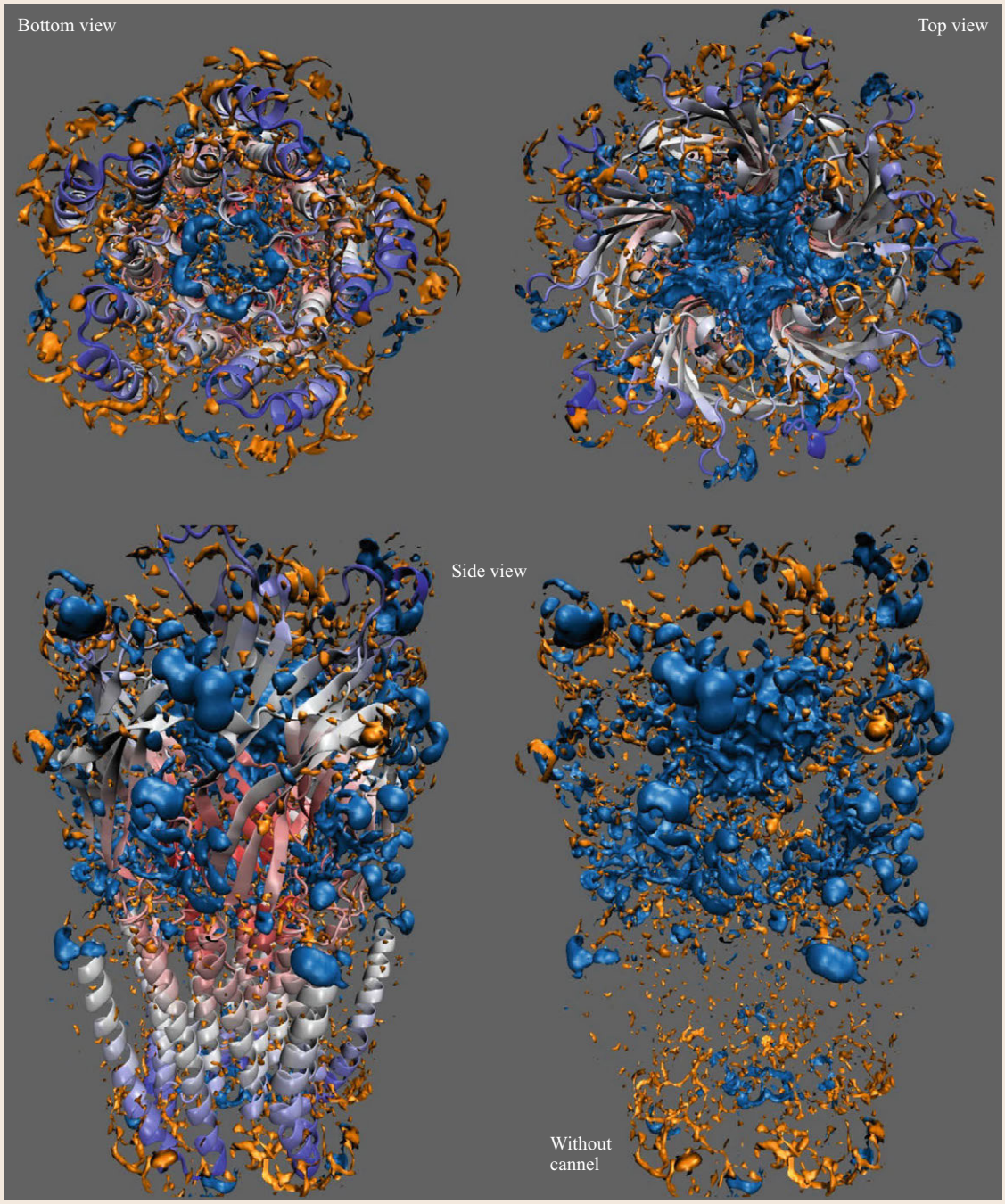


Fig. 5.15 3-D distribution functions of Na^+ (*blue*) and Cl^- (*orange*) ions inside the GLIC ion channel, obtained from 3D-RISM-KH. Isosurfaces of $g(r) \geq 5$. Bottom and top view of the channel (*upper left* and *right parts*), and side view with and without the channel protein (*lower left* and *right parts*, respectively)

demonstrated that this channel is sensitive to general anesthetics [5.133]. Figures 5.14 and 5.15 present the results for the solvation structure of the GLIC channel inserted in the 1-palmitoyl-2-oleoyl-*sn*-glycero-3-phosphocholine (POPC) lipid bilayer obtained by the LN/SFCE/3D-RISM-KH modeling [5.31, 32]. The 3-D

density distributions obtained from 3D-RISM-KH for water oxygen (O) and sodium (Na^+) and chloride (Cl^-) ions of solvent around the channel protein embedded in the cellular membrane are shown in Fig. 5.14; and those of Na^+ and Cl^- are detailed in Fig. 5.15 for the top, bottom, and side views of the channel with isosurfaces of $g(r) \geq 5$. It is seen that the Cl^- anions are mostly expelled from the pore of this cationic channel, whereas there are nonzero densities of Na^+ ions throughout the channel pore, in agreement with experimental data. The solvent distributions in the proximity of the protein are characterized by some features. For example, the preferable solvation sites for Cl^- ions are located along the external ring of the channel funnel, facing the extracellular space above the membrane. Inside the funnel, right before the entrance to the channel pore, the distributions of water and Na^+ ions are complementary. There is a pocket of Cl^- ions which separates the upper and lower parts of the funnel, the area above the level of the lipid bilayer. The lower part being adjacent to the channel pore is characterized by the preferable solvation of Na^+ ions much as the rest of the channel pore. The exit from the channel pore from the intracellular side below the membrane is surrounded by the solvation sites of Cl^- ions. In general, both the extra and intracellular surfaces of the lipid bilayer are characterized by the enhanced densities of the anions. The sodium distribution inside the channel pore correlates with the channel radius and the pattern in the distributions of the hydrophobic and hydrophilic residues in the channel pore. The above illustrates how the ion charge distribution over the pore space contributes to the selectivity and permeation properties of the ion channel.

5.5 Electrical Double Layer in Nanoporous Materials

The properties of an electric double layer (EDL) formed in inner spaces of nanoporous electrodes are very different from a conventional, planar electrochemical capacitor of equal SA due to an overlap of adjacent EDLs. The EDL at the surface of carbon nanopores gets substantially distorted, compared to that at a planar electrode in contact with electrolyte solution, resulting in the specific capacitance per SA by up to 1–2 orders of magnitude less than for the planar electrode. At present, molecular simulation description of these effects is virtually unfeasible due to the interplay of long-range electrostatic and short-range steric interactions on large-space and long-time scales, and the necessity to satisfy the conditions of chemical and mechanical balance between the species in the bulk electrolyte solution and those sorbed in the nanoporous electrodes.

A generalization of RISM molecular theory of solvation to solutions sorbed in disordered nanoporous materials using the replica method for statistical mechanics of quenched-annealed systems, the so-called replica RISM-KH-VM theory, provides full microscopic details of the solvation structure and thermodynamics averaged over the thermal motion of sorbed solution and over the quenched distribution of host nanoporous material (morphology of nanopores) [5.17, 48, 49]. This theory enables predictive molecular modeling of thermochemistry and electrochemistry of electrolyte solutions sorbed in functionalized nanoporous materials. In particular, it reveals the mechanisms of sorption and supercapacitance in nanoporous carbon electrodes [5.17, 48–52]. The replica RISM-KH-VM theory predicts, from the first principles of statistical mechanics, such effects as solvent-specific wetting [5.17] and water depletion in hydrophobic carbon nanopores [5.50–52], asymmetry in solvation and adsorption of cations and anions [5.49–52], desalination of simple ions in hydrophobic nanopores and its reversal with external voltage applied [5.49–52], efficient removal of ionic impurities from an aqueous waste stream by a nanoporous carbon electrosorption cell [5.51], and specific adsorption at chemical functionalities on the surface of carbon nanopores [5.48].

5.6 Replica Formalism for Fluid Sorbed in a Disordered Matrix

The replica formalism of statistical–mechanical, integral equation theory of quenched-annealed systems treats *annealed* fluid with equilibrium temperature T_1 (species 1) sorbed in a porous matrix of *quenched* particles with a spatial distribution corresponding to an equilibrium ensemble with temperature T (species 0). Note that, in general, $T_0 \neq T_1$ because the matrix and liquid subsystems are not in equilibrium and do not exchange with energy. This has implications on the thermodynamic expressions in the replica RISM theory involving density and temperature derivatives of matrix material [5.48, 49]; however, for the purpose of typical systems and calculations with rigid unchangeable matrix, T affects only its structure obtained beforehand and can be reduced to $T_0 = T_1 = T$ at the beginning by scaling the interaction potential used for the matrix model

(if this is not a purely hard core model.) The mean free energy of the sorbed annealed fluid is obtained as a statistical average of the free energy with the canonical partition function $Z_1(\boldsymbol{q}_0)$ of the fluid sorbed in the matrix with a particular spatial configuration of quenched particles $\boldsymbol{q}_0$ over the ensemble of all realizations of matrix configurations $\boldsymbol{q}_0$

$$\overline{A}_1 = A_1^{\mathrm{id}} - k_\mathrm{B}T_1 \left\langle \ln Z_1\left(\boldsymbol{q}_0\right)\right\rangle_{\boldsymbol{q}_0} , \tag{5.44}$$

where A_1^{id} is the ideal gas free energy. The statistical average of a logarithm is not amenable to standard evaluation and is obtained by using the so-called replica identity similar to the theory of spin glasses that relates the logarithm to the analytic continuation of moments Z^s as follows:

$$\ln Z_1 = \lim_{s\to 0} \frac{\mathrm{d}Z^s}{\mathrm{d}s} .$$

For integer values of s, the statistical average of the moments takes the form of the equilibrium canonical partition function of a fully annealed $(s+1)$-component liquid mixture consisting of matrix species 0 and s equivalent replicas of fluid species 1, with no interaction between the fluid replicas. The average free energy of the annealed fluid is then obtained in the assumption of no replica symmetry breaking in the analytic continuation of the free energy of the annealed replicated system $A_{\mathrm{rep}}(s)$ as

$$\overline{A}_1 = \lim_{s\to 0} \frac{\mathrm{d}A_{\mathrm{rep}}(s)}{\mathrm{d}s} . \tag{5.45}$$

Using the above formalism to evaluate in terms of Meyer diagrams, the free energy and statistical sum of *mobile* atomic fluid sorbed in a *frozen* matrix of spherical obstacles generates the so-called replica OZ integral equations for a quenched-annealed atomic system [5.134–137]. This formalism was generalized to replica RISM for simple and complex associating molecular systems [5.17, 48, 49].

5.7 Replica DRISM–KH–VM for Electrolyte Solution Sorbed in Nanoporous Material

Applying this replica formalism to the dielectrically consistent reference interaction site model (DRISM) integral equations of *Perkyns* and *Pettitt* [5.61], we get after some algebra the replica DRISM integral equations for annealed molecular liquid (or equally for liquid mixture) sorbed in a quenched matrix

$$\begin{aligned}
h^{00}_{\alpha\gamma}(r) &= \omega^{00}_{\alpha\mu}(r) * c^{00}_{\mu\nu}(r) * \omega^{00}_{\nu\gamma}(r) \\
&\quad + \omega^{00}_{\alpha\mu}(r) * c^{00}_{\mu\nu}(r) * \rho^0_\nu h^{00}_{\nu\gamma}(r) , && (5.46a)\\
h^{10}_{\alpha\gamma}(r) &= \widetilde{\omega}^{11}_{\alpha\mu}(r) * c^{10}_{\mu\nu}(r) * \omega^{00}_{\nu\gamma}(r) \\
&\quad + \widetilde{\omega}^{11}_{\alpha\mu}(r) * c^{10}_{\mu\nu}(r) * \rho^0_\nu h^{00}_{\nu\gamma}(r) \\
&\quad + \widetilde{\omega}^{11}_{\alpha\mu}(r) * c^{(\mathrm{c})}_{\mu\nu}(r) * \rho^1_\nu h^{10}_{\nu\gamma}(r) , && (5.46b)\\
h^{01}_{\alpha\gamma}(r) &= \omega^{00}_{\alpha\mu}(r) * c^{01}_{\mu\nu}(r) * \widetilde{\omega}^{11}_{\nu\gamma}(r) \\
&\quad + \omega^{00}_{\alpha\mu}(r) * c^{00}_{\mu\nu}(r) * \rho^0_\nu h^{01}_{\nu\gamma}(r) \\
&\quad + \omega^{00}_{\alpha\mu}(r) * c^{01}_{\mu\nu}(r) * \rho^1_\nu \widetilde{h}^{(\mathrm{c})}_{\nu\gamma}(r) , && (5.46c)\\
\widetilde{h}^{11}_{\alpha\gamma}(r) &= \widetilde{\omega}^{11}_{\alpha\mu}(r) * c^{11}_{\mu\nu}(r) * \widetilde{\omega}^{11}_{\nu\gamma}(r) \\
&\quad + \widetilde{\omega}^{11}_{\alpha\mu}(r) * c^{10}_{\mu\nu}(r) * \rho^0_\nu h^{01}_{\nu\gamma}(r) \\
&\quad + \widetilde{\omega}^{11}_{\alpha\mu}(r) * c^{(\mathrm{c})}_{\mu\nu}(r) * \rho^1_\nu h^{10}_{\nu\gamma}(r) \\
&\quad + \widetilde{\omega}^{11}_{\alpha\mu}(r) * c^{(\mathrm{b})}_{\mu\nu}(r) * \rho^1_\nu \widetilde{h}^{(\mathrm{c})}_{\nu\gamma}(r) , && (5.46d)\\
\widetilde{h}^{(\mathrm{c})}_{\alpha\gamma}(r) &= \widetilde{\omega}^{11}_{\alpha\mu}(r) * c^{(\mathrm{c})}_{\mu\nu}(r) * \widetilde{\omega}^{11}_{\nu\gamma}(r) \\
&\quad + \widetilde{\omega}^{11}_{\alpha\mu}(r) * c^{(\mathrm{c})}_{\mu\nu}(r) * \rho^1_\nu \widetilde{h}^{(\mathrm{c})}_{\nu\gamma}(r) , && (5.46e)
\end{aligned}$$

where ρ^1_γ is the number density of interaction site γ of liquid species and ρ^0_γ is that of matrix nanoparticles, $h^{ij}_{\alpha\gamma}(r)$ and $c^{ij}_{\alpha\gamma}(r)$ are respectively the total and direct correlation functions between site α of species i and site γ of species j ($i,j = 0$ for matrix nanoparticles and 1 for liquid molecules). In the replica formalism, the liquid–liquid total and direct correlation functions are subdivided into the so-called connected and blocking (or disconnected) parts

$$\begin{aligned}
\widetilde{h}^{11}_{\alpha\gamma}(r) &= \widetilde{h}^{(\mathrm{c})}_{\alpha\gamma}(r) + h^{(\mathrm{b})}_{\alpha\gamma}(r) , && (5.46f)\\
c^{11}_{\alpha\gamma}(r) &= c^{(\mathrm{c})}_{\alpha\gamma}(r) + c^{(\mathrm{b})}_{\alpha\gamma}(r) , && (5.46g)
\end{aligned}$$

with the connected correlations denoted by superscript (c) stemming following from the corresponding correlations between the particles of the same replica of the liquid and the blocking ones denoted by (b) stemming from those between different replicas of the liquid in the analytical continuation limit of $s \to 0$. In terms of Mayer diagrams, the blocking correlations are identified as a subset of diagrams in which all paths between the two root vortices pass through at least one field vortex of matrix, that is, such liquid–liquid diagrams that are completely blocked/disconnected by matrix vortices. In other words, this is the indirect, matrix-mediated part of the liquid–liquid correlations. The remaining portion constitutes the connected part

of the liquid–liquid correlations. Further, within the DRISM approach both the intramolecular and total liquid–liquid correlation functions are renormalized due to a dielectric bridge correction introduced to ensure the given value and consistency of the dielectric constant obtained for solvent–solvent, solvent–ion, and ion–ion effective interactions in electrolyte solution

$$\widetilde{\omega}^{11}_{\alpha\gamma}(r) = \omega^{11}_{\alpha\gamma}(r) + \rho^1_\alpha \chi^{11}_{\alpha\gamma}(r)\,, \tag{5.47a}$$
$$\widetilde{h}^{11}_{\alpha\gamma}(r) = h^{11}_{\alpha\gamma}(r) - \chi^{11}_{\alpha\gamma}(r)\,, \tag{5.47b}$$
$$\widetilde{h}^{(c)}_{\alpha\gamma}(r) = h^{(c)}_{\alpha\gamma}(r) - \chi^{11}_{\alpha\gamma}(r)\,. \tag{5.47c}$$

The renormalized dielectric correction enforcing the given phenomenological value of the dielectric constant and the proper orientational behavior and consistency of the dielectric response in the electrolyte solution is obtained in the same analytical form (5.6) as for bulk electrolyte solution but now for annealed liquid species

$$\chi^{11}_{\alpha\gamma}(k) = j_0(kx^1_\alpha) j_0(ky^1_\alpha) j_1(kz^1_\alpha) h_c(k) \\ j_0(kx^1_\gamma) j_0(ky^1_\gamma) j_1(kz^1_\gamma)\,, \quad \alpha,\gamma \in s\,, \tag{5.48}$$

where $\boldsymbol{r}^1_\alpha = (x^1_\alpha, y^1_\alpha, z^1_\alpha)$ and $\boldsymbol{r}^1_\gamma = (x^1_\gamma, y^1_\gamma, z^1_\gamma)$ are the Cartesian coordinates of partial site charges q^1_α and q^1_γ at sites α and γ of the same solution species s with respect to its molecular origin, the dipole moment $\boldsymbol{d}^1_s = \sum_{\alpha\in s} q^1_\alpha \boldsymbol{r}^1_\alpha$ is oriented along the z-axis, $\boldsymbol{d}^1_s = (0,0,d^1_s)$, the envelope function $h_c(k)$ is assumed in the same form

$$h_c(k) = A \exp\left(-l^2 k^2 4\right)\,,$$

the amplitude A is related to the dielectric constant ε of the electrolyte solution

$$A = \frac{1}{\rho^1_{\text{polar}}}\left(\frac{\varepsilon}{\text{y}} - 3\right)\,,$$

the total number density of solution polar species is

$$\rho^1_{\text{polar}} = \sum_{s\in\text{polar}} \rho^1_s\,,$$

and the solution dielectric susceptibility is

$$y^1 = \frac{4\pi}{9k_BT} \sum_{s\in\text{polar}} \rho^1_s \left(d^1_s\right)^2\,.$$

The parameter l specifying the characteristic separation from which the dielectric correction is switched on is chosen according to the maximal repulsive core size of liquid species (e.g., $l = 1$ Å for water solvent, and $l = 10$ Å for octanol).

The average number densities of sorbed electrolyte solution species ρ^1_s substantially differ from those in bulk solution ρ^{bulk}_s and so does the dielectric constant of sorbed solution ε compared to that of bulk solution $\varepsilon^{\text{bulk}}$. This is taken into account by smoothly interpolating in density between the gas form $\varepsilon = 1 + 3y$ and the bulk solution value $\varepsilon^{\text{bulk}}$ as follows

$$\varepsilon = 1 + \left(3 + \rho^1_{\text{polar}} A^{\text{bulk}}\right) y\,, \tag{5.49}$$

where the correction amplitude for the sorbed solution with densities ρ^1_s keeps the same value as for the bulk solution with ρ^{bulk}_s

$$A = A^{\text{bulk}} = \frac{1}{\rho^{\text{bulk}}_{\text{polar}}}\left(\frac{\varepsilon^{\text{bulk}}}{\text{y}^{\text{bulk}}} - 3\right)\,. \tag{5.50}$$

The replica DRISM integral equations (5.46) have to be complemented with appropriate closure relations that properly account for both electrostatic and non-electrostatic features of molecular specificities of the species of both the matrix nanoparticles and the sorbed liquid. The closure proposed by Kovalenko and Hirata (KH approximation) [5.8, 11] accounts for both electrostatic and nonpolar features of solvation, such as hydrogen bonding, solvophobicity, structural solvent molecules, salt bridges, and other steric, associative, and electrochemical effects in simple liquids and complex solutions of a given composition, including buffers, salts, polymers, ligands, and other co-factors at a finite concentration. Further, the KH closure describes associating molecular fluids and solutions in the whole density range from gas to liquid [5.16, 17], and is thus suitable for such a system with strong associative effects as electrolyte solution sorbed in nanoporous materials [5.17, 48, 49], in particular, in a charged nanoporous electrode [5.50–52]. It is used for the matrix–matrix, liquid–matrix, and liquid–liquid correlation functions

$$g^{ij}_{\alpha\gamma}(r) = \begin{cases} \exp\left[\dfrac{-u^{ij}_{\alpha\gamma}(r)}{k_BT} + h^{ij}_{\alpha\gamma}(r) - c^{ij}_{\alpha\gamma}(r)\right] \\ \qquad \text{for } g^{ij}_{\alpha\gamma}(r) \le 1\,, \\ 1 - \dfrac{u^{ij}_{\alpha\gamma}(r)}{k_BT} + h^{ij}_{\alpha\gamma}(r) - c^{ij}_{\alpha\gamma}(r) \\ \qquad \text{for } g^{ij}_{\alpha\gamma}(r) > 1\,, \end{cases} \tag{5.51}$$

where $g^{ij}_{\alpha\gamma}(r) = h^{ij}_{\alpha\gamma}(r) + 1$ is the radial distribution function (RDF) between interaction sites α and γ of species $i, j = 0, 1$ (matrix, liquid), and $u^{ij}_{\alpha\gamma}(r)$ is the site–site pairwise interaction potential, scaled by the Boltzmann constant k_B times solution or matrix temperature T. Note that, in general, $T = T_0$ for $i, j = 0$ and $T_1 \neq T_0$ otherwise; however, one can put $T_0 = T_1 \equiv T$ simply by scaling the matrix model interaction potential $u^{00}_{\alpha\gamma}(r)$, as explained at the beginning of the previous section.

It was shown that the application of linearized closures of MSA type to blocking correlations leads to trivial solutions with $c^{(b)}(r) = 0$ [5.134–137]. On the other hand, the HNC approximation strongly overestimates the blocking correlations in the presence of charged species and leads to the divergence of the Replica RISM equations for electrolyte solution sorbed in nanoporous material [5.17, 48–52]. To work at the advanced level with nontrivial blocking correlations, we complement (5.46e)–(5.46g) for the blocking correlations with the modified Verlet (VM) closure

$$g^{(b)}_{\alpha\gamma}(r) = h^{(b)}_{\alpha\gamma}(r) + 1 = \exp\left(h^{(b)}_{\alpha\gamma}(r) - c^{(b)}_{\alpha\gamma}(r) + b^{(b)}_{\alpha\gamma}(r)\right) , \tag{5.52a}$$

$$b^{(b)}_{\alpha\gamma}(r) = -\frac{1}{2}\frac{\left(t^{(b)}_{\alpha\gamma}(r)\right)^2}{1 + a\max\left(t^{(b)}_{\alpha\gamma}(r), 0\right)} , \tag{5.52b}$$

where the VM bridge correction (5.52b) is expressed in terms of the nodal correlation function

$$t^{(b)}_{\alpha\gamma}(r) = h^{(b)}_{\alpha\gamma}(r) - c^{(b)}_{\alpha\gamma}(r) ,$$

and the parameter value $a = 0.8$ is the same as in the original Verlet correction. (Note that it can be adjusted with liquid density for self-consistency, for example, to satisfy the zero-separation theorem [5.138].) Note that there is no interaction potential in the closure (5.52) for the blocking correlations as they stem in the limit $s \to \infty$ from the correlations between different replicas of liquid which do not interact with each other. The VM approximation (5.52) accounts reasonably well for the nonlinearity of blocking correlations in such strongly associating systems as polar solvents and electrolyte solutions sorbed in nanoporous matrices, both neutral and with external electric charge [5.17, 48–52, 134].

Solving the replica DRISM-KH-VM equations (5.46)–(5.52) at particular forcefield and thermodynamic parameters requires the analytical treatment of all the electrostatic asymptotics and is done similarly to the bulk DRISM-KH equations (5.5)–(5.11). The equations are converged by using the MDIIS accelerated numerical solver [5.9–11, 65].

5.7.1 Thermodynamics of Sorbed Solution

For the replica DRISM-KH-VM integral equations (5.46), the excess chemical potential $\Delta\mu^1_s$ of sorption of liquid species s in the frozen matrix of nanoparticles is readily decomposed into the contributions from the host matrix due to the liquid–matrix ($ij = 10$) correlations and from the sorbed liquid due to the liquid–liquid ($ij = 11$) correlations less an additional term due to the blocking (b) correlations [5.48, 49]

$$\Delta\mu^1_s = \Delta\mu^{10}_s + \Delta\mu^{11}_s - \Delta\mu^{(b)}_s . \tag{5.53}$$

The KH closure (5.51) to the replica DRISM integral equations (5.46) leads to the corresponding components of the excess chemical potential expressed in a closed analytical form in terms of the liquid–matrix and liquid–liquid correlation functions

$$\Delta\mu^{1j}_s = k_B T \sum_{\alpha\in s}\sum_{\gamma\in j}\rho^j_\gamma 4\pi\int_0^\infty r^2 dr \times\left[\frac{1}{2}\Theta\left(-h^{1j}_{\alpha\chi}(r)\right)\left(h^{1j}_{\alpha\chi}(r)\right)^2 - \frac{1}{2}h^{1j}_{\alpha\chi}(r)c^{1j}_{\alpha\chi}(r) - c^{1j}_{\alpha\chi}(r)\right] , \tag{5.54}$$

where the summation is over interaction sites α of liquid species s, and over all sites γ of matrix for $j = 0$ and liqud for $j = 1$. The chemical potential term due to the blocking correlations can be obtained from the VM closure (5.52) to the replica DRISM integral equations (5.46e)–(5.46g) by performing the thermodynamic integration in an approximate analytical form

$$\Delta\mu^{(b)}_s = k_B T \sum_{\alpha\gamma\in 1}\rho^1_\alpha 4\pi\int r^2 dr \times\left[\frac{1}{2}\left(h^{(b)}_{\alpha\chi}(r)\right)^2 - \frac{1}{2}h^{(b)}_{\alpha\chi}(r)c^{(b)}_{\alpha\chi}(r) - c^{(b)}_{\alpha\chi}(r) + \left(h^{(b)}_{\alpha\chi}(r) + 1\right)b^{(b)}_{\alpha\chi}(r) - s^{(b)}_{\alpha\chi}(r)\right] , \tag{5.55}$$

where the so-called star function obtained in the assumption of the so-called unique functionality of the

correlations [5.138] is written as

$$s^{(b)}_{\alpha\gamma}(r) = \begin{cases} -\frac{1}{2a^3}\left[\ln\left(1+at^{(b)}_{\alpha\gamma}(r)\right) \right. \\ \left. -at^{(b)}_{\alpha\gamma}(r)+\frac{1}{2}\left(at^{(b)}_{\alpha\gamma}(r)\right)^2\right]\frac{t^{(b)}_{\alpha\gamma}(r)}{h^{(b)}_{\alpha\gamma}(r)} \\ \qquad \text{for } t^{(b)}_{\alpha\gamma}(r) > 0\,, \\ -\frac{1}{6}t^{(b)}_{\alpha\gamma}(r)h^{(b)}_{\alpha\gamma}(r) \\ \qquad \text{for } t^{(b)}_{\alpha\gamma}(r) \le 0\,. \end{cases} \tag{5.56}$$

Also, the compressibility of the sorbed solution is exactly expressed in terms of the connected part of the correlations [5.48, 49]. Other thermodynamic derivatives of the free energy of the sorbed solution are available as well [5.48, 49].

5.7.2 Electric Double Layer in the Nanopores of Host Matrix

The sorbed electrolyte solution forms an EDL at the surface of nanopores of the host material even in the absence of external specific electric charge on the nanoporous electrode due to the asymmetry between the density distributions of cations and anions at the surface, as well as the preferential orientation of polar solvent molecules at the surface. The statistically averaged electrostatic potential of the EDL is obtained as follows [5.50–52]. The statistical distribution of charge density around a labeled matrix nanoparticle of sort $c \in 0$ due to interaction site charges q^1_γ on electrolyte solution species of sort $\gamma \in 1$ as well as q^0_f on chemical functional groups of sort $f \in 0$ grafted to matrix nanoparticles is obtained as

$$\tau^0_c(r) = \sum_{f\in 0} q^0_f \rho^0_f g^{00}_{cf}(r) + \sum_{\gamma\in 1} q^1_\gamma \rho^1_\gamma g^{01}_{c\gamma}(r)\,. \tag{5.57}$$

(Note that matrix nanoparticles and chemical functional groups grafted to them, both belonging to matrix species $j = 0$, are now denoted separately with roman subscript indices of sort c and f, respectively.) The corresponding statistically averages electrostatic potential $\psi^0_c(r)$ of sorbed solution species and nanoporous material surrounding matrix nanoparticle c is determined from the Poisson equation

$$\nabla^2\psi^0_c(r) = -4\pi\tau^0_c(r)\,. \tag{5.58}$$

The full local electrostatic potential $\varphi^0_c(r)$ around a conducting matrix nanoparticle of radius R^0_c also includes the contribution from an externally induced charge q^0_c on the nanoparticle

$$\varphi^0_c(r) = \psi^0_c(r) + \frac{q^0_c}{\max\left(r, R^0_c\right)}\,. \tag{5.59}$$

The external charge of density

$$q_{\text{ex}} = \sum_{c\in 0} q^0_c \rho^0_c \tag{5.60}$$

induced on the electrode and the corresponding opposite external charge $-q_{\text{ex}}$ on the other electrode of the supercapacitor cause the separation of cations and anions of the electrolyte diffusing across the separator between the electrodes to the EDLs in their pores, until the bias of the ionic concentrations in each electrode satisfies the condition of electroneutrality for the whole system

$$q_{\text{ex}} + \sum_f q^0_f \rho^0_f + \sum_\gamma q^1_\gamma \rho^1_\gamma = 0\,. \tag{5.61}$$

Note that for symmetric electrodes with charges functional groups of atomic charges q^0_f and specific densities ρ^0_f there is a symmetric concentration of counterions (or a bias between the concentrations of cations and anions) sorbed in each electrode initially, at zero voltage of the device. For asymmetric densities of charged functional groups in the two electrodes, the initial concentrations of counterions or the bias between the concentrations of cations and anions change due to diffusion exchange between the electrodes and the bulk solution bath until the electroneutrality is satisfied in each electrode. For the nanoporous carbon material formed by connected carbon spheres of several sorts α with in general different sizes R^0_c, the external charge q_{ex} is distributed among the charges q^0_c on spheres of each sort subject to the electrostatic potential inside the sphere being equal for all carbon spheres

$$\varphi_{\text{C}}(q_{\text{ex}}) \equiv \varphi^0_c(r < R^0_c; q_{\text{ex}}) \quad \text{for all } c \in 0\,, \tag{5.62}$$

whereas the electrostatic potential (5.59) at a distance from each sphere of sort c by definition gives the average potential level in the electrode including both carbon spheres and sorbed solution

$$\varphi_{\text{av}}(q_{\text{ex}}) \equiv \varphi^0_c(r = \infty; q_{\text{ex}}) \quad \text{for all } c \in 0\,. \tag{5.63}$$

The value $\varphi_{\text{C}}(q_{\text{ex}})$ of the electrostatic potential on each carbon sphere gives the potential level of the carbon conducting framework of the nanoporous electrode. The potential change from the carbon framework level $\varphi_{\text{C}}(q_{\text{ex}})$ to the average electrode potential

level $\varphi_{av}(q_{ex})$ comprises (i) the potential step across the internal EDL at the nanoparticle surface (Stern surface layer), and (ii) the mean electric field of the diffuse layer including also all surrounding carbon nanoparticles together with their EDLs (an analog of a Gouy–Chapman diffuse layer, averaged over the nanoporous morphology). The average value of the electrostatic potential over the whole nanoporous electrode (including both the nanoporous carbon framework and the sorbed electrolyte solution) $\varphi_{av}(q_{ex})$ is a constant of integration of the Poisson equation (5.58), or the *electrode bulk level* from which the statistically averaged, radial electrostatic potential (5.59) is counted. The electrode bulk level is positioned with respect to the vacuum level of the electrostatic potential by an external electric field in the solution outside the electrode, and the solution to the Poisson equation yields the potential of the carbon conducting frame with respect to the electrode bulk level $\varphi_C(q_{ex}) - \varphi_{av}(q_{ex})$ caused by all electric charges inside the electrode, that is, the external specific charge on the electrode and EDL charges of ions and polar solvent molecules sorbed inside the nanopores.

5.7.3 Molecular Mechanism of Electrosorption and Capacitance

The molecular mechanisms determining the high specific capacitance of the supercapacitor device and purification efficiency of the electrosorption cell with nanoporous electrodes are much more complex than in a planar EDL of equivalent area. As explained below, they include the internal EDL at the surface of nanopores, the Gouy–Chapman layer statistically averaged over the volume of the nanoporous material, the osmotic term arising due to the difference between the ionic concentrations in the two nanoporous electrodes and in the bulk electrolyte solution outside, and the solvation chemical potentials of sorbed solvated ions statistically averaged over the nanoporous material [5.50–52].

The chemical potential μ_s of sorbed solution species s of density ρ_s consists of the ideal gas contribution

$$\mu_s^{id} = k_B T \ln(\rho_s \Lambda_s)$$

with the de Broglie thermal wave length

$$\Lambda_s = \sqrt{2\pi\hbar^2/(m_s k_B T)}$$

of ideal monatomic particles with molecular weight m_s, the excess term $\Delta\mu_s$ due to liquid–liquid and matrix–liquid intermolecular interactions inside the nanoporous material (electrode volume effect), and the electrostatic energy of species s with charge q_s in the electrostatic field between the two electrodes (electrode boundary effect)

$$\mu_s = \mu_s^{id} + \Delta\mu_s + q_s\varphi_{av} \,. \tag{5.64}$$

The first term is the osmotic contribution, the second one arises from the interactions inside the nanoporous material, and the third one gives the electrode bulk level of the electrostatic potential averaged over the whole nanoporous electrode with respect to the gas phase outside the system. The presence of the third term in the chemical potential (5.64) directly follows from the Nernst equation.

The excess chemical potentials $\Delta\mu_s$ of ionic species s inside a charged electrode are strongly different from those in the bulk solution. For the electrode in contact with the bulk solution, this causes the diffusion of ions across the separator until the electric field of ionic dipoles forming at the boundaries of the electrodes counterbalances the difference between the *interior* chemical potential terms $\mu_s^{id} + \Delta\mu_s$ of electrode I, as well as those of electrode II, and thus equalizes the chemical potential in the two electrodes, $\mu_s^{I} = \mu_s^{II}$. Using the decomposition (5.65) of the chemical potential inside the electrode yields the bias between the statistically averaged bulk levels $\varphi_{av}^{II}(q_{ex})$ and $\varphi_{av}^{I}(-q_{ex})$ of the two electrodes with opposite external charges $\pm q_{ex}$

$$q_s\left(\varphi_{av}^{II}(q_{ex}) - \varphi_{av}^{I}(-q_{ex})\right) = k_B T \ln\left(\frac{\rho_s^{I}}{\rho_s^{II}}\right) + \Delta\mu_s^{I}(-q_{ex}) - \Delta\mu_s^{II}(q_{ex}) \,. \tag{5.65}$$

The same bias of the electrostatic potential levels $\varphi_{av}^{II} - \varphi_{av}^{I}$ must satisfy the relation (5.65) for each solution species s, including ions and neutral solvent molecules. A discrepancy between the bias values required to counterbalance the *interior* part of the chemical potential $k_B T \ln(\rho_s \Lambda_s) + \Delta\mu_s$ for cations as well as that for anions causes diffusion of each of the ionic species to the corresponding electrode with the lower chemical potential. This changes the osmotic and excess terms in the chemical potential (5.64) for cations and anions in the opposite directions until the relation (5.65) is satisfied for both cations and anions. Similarly, diffusion of solvent molecules between the two electrodes occurs until the osmotic term as well as the excess chemical potentials for the changed densities of solvent in the electrodes, dependent on the densities of both solvent and ions, satisfies the chemical equilibrium condition (5.65), which for the neutral solvent molecules with

$q_s = 0$ reduces to the equality of the *interior* terms $k_B T \ln(\rho_s \Lambda_s) + \Delta\mu_s$.

The voltage of the supercapacitor device given by the electrostatic potential difference between the conducting carbon matrix frameworks of electrodes I and II is thus obtained by summing up the statistically averaged electrostatic potential steps across the whole device. (Note that all losses due to equivalent serial resistance (ESR), including electric conductivity of the carbon nanoparticles and their contacts as well as electrolyte diffusion resistance are not considered here and can be incorporated separately.) The supercapacitor voltage comprises the potential step $\varphi^{\mathrm{I}}_{\mathrm{av}}(-q_{\mathrm{ex}}) - \varphi^{\mathrm{I}}_{\mathrm{c}}(-q_{\mathrm{ex}})$ across the internal EDL in nanopores of electrode I from its conducting carbon framework to the electrode bulk, next the potential step $\varphi^{\mathrm{II}}_{\mathrm{av}}(q_{\mathrm{ex}}) - \varphi^{\mathrm{I}}_{\mathrm{av}}(-q_{\mathrm{ex}})$ from the bulk level of electrode I across the EDL at its outer edge to the solution bulk and then similarly across the EDL at the outer edge of electrode II to its bulk level, and then $\varphi^{\mathrm{II}}_{\mathrm{c}}(q_{\mathrm{ex}}) - \varphi^{\mathrm{II}}_{\mathrm{av}}(q_{\mathrm{ex}})$ from the electrode bulk across the internal EDL in nanopores of electrode II to its conducting carbon framework. Using the relation (5.65) to express $\varphi^{\mathrm{I}}_{\mathrm{av}} - \varphi^{\mathrm{II}}_{\mathrm{av}}$ in terms of the number densities ρ_s and excess chemical potentials $\Delta\mu_s$ of sorbed ions s, the supercapacitor voltage is written as

$$U(q_{\mathrm{ex}}) = \left(\varphi^{\mathrm{I}}_{\mathrm{av}} - \varphi^{\mathrm{I}}_{\mathrm{c}}\right) - \left(\varphi^{\mathrm{II}}_{\mathrm{av}} - \varphi^{\mathrm{II}}_{\mathrm{c}}\right) + \frac{1}{q_s}\left(k_B T \ln\left(\frac{\rho^{\mathrm{I}}_s}{\rho^{\mathrm{II}}_s}\right) + \Delta\mu^{\mathrm{I}}_s - \Delta\mu^{\mathrm{II}}_s\right) \tag{5.66}$$

for any ionic species s (with $q_s \neq 0$). The number densities ρ_s and excess chemical potentials $\Delta\mu_s$ of sorbed species s are obtained by converging the chemical equilibrium conditions (5.65) for ρ_s by using iterations or any other accelerated solver, in turn with solving at each step the replica DRISM-KH-VM integral equations (5.46)–(5.52) at current ρ_s and calculating the excess chemical potentials from the expressions (5.53)–(5.56). The potential steps $\varphi_{\mathrm{av}} - \varphi_{\mathrm{c}}$ in electrodes I and II are then calculated at the densities ρ_s for the converged equations (5.65) as the difference of the boundary values (5.63) and (5.62) from solving the Poisson equation (5.58).

Finally, applying the chemical equilibrium condition between the electrodes and the bulk solution yields the relation for the purification efficiency of the electrosorption cell at voltage $U(q_{\mathrm{ex}})$ which holds sorbed electrolyte at high concentrations ρ^{I}_s and ρ^{II}_s of cations and anions inside the corresponding nanoporous electrodes I and II with the opposite external charge, against the osmotic forces for a significantly lower concentration ρ^{blk}_s of electrolyte in the bulk solution efflux [5.51]

$$\frac{\rho^{\mathrm{blk}}_s}{\rho^{\mathrm{I}}_s} = \exp\left[-\frac{1}{k_B T}\left(\Delta\mu^{\mathrm{blk}}_s - \Delta\mu^{\mathrm{I}}_s(-q_{\mathrm{ex}}) - q_s\varphi^{\mathrm{I}}_{\mathrm{av}}(-q_{\mathrm{ex}})\right)\right] \quad \text{for } q_s > 0 \text{ (cations)}, \tag{5.67a}$$

$$\frac{\rho^{\mathrm{blk}}_s}{\rho^{\mathrm{II}}_s} = \exp\left[-\frac{1}{k_B T}\left(\Delta\mu^{\mathrm{blk}}_s - \Delta\mu^{\mathrm{II}}_s(q_{\mathrm{ex}}) - q_s\varphi^{\mathrm{II}}_{\mathrm{av}}(q_{\mathrm{ex}})\right)\right] \quad \text{for } q_s < 0 \text{ (anions)}, \tag{5.67b}$$

where $\Delta\mu^{\mathrm{blk}}_s$ is the excess chemical potential of species s at concentration ρ^{blk}_s in bulk solution efflux.

5.7.4 Illustration for a Supercapacitor

Carbonized polyvinylidene chloride (PVDC) material attracted both scientific and industrial attention [5.139] because of its uniform nanoporous texture with controlled pore size, and the possibility of a cheaper production cycle for applications in high-energy storage and electrochemical separation devices. A model consisting of a statistical–mechanical mix of hard cores and *cavity* spheres at high packing fraction has been developed [5.50] to represent essential properties of carbonized PVDC material and is so parameterized as to fit the pore size distribution peaks, porosity, pores SA, and the physical density to the experimental data for carbonized PVDC material [5.139].

The replica DRISM-KH-MV integral equations for the correlation functions of NaCl aqueous electrolyte solution (5.46)–(5.52) with the electrostatic asymptotics separated out and treated analytically were discretized on a uniform radial grid of length 1000 Å. The domain of this significant size is necessary to properly represent the interplay of the slowly decaying oscillations in the correlations of the matrix material and the EDL diffuse layers around matrix nanoparticles, resulting in the solvation structure oscillations with at the size of sorbed solution species which last on many sizes of matrix nanoparticles [5.50–52]. The replica DRISM-KH-MV integral equations were converged by using the MDIIS accelerated numerical solver [5.9–11, 65]. The force-field parameters and densities for the ambient electrolyte solution and the matrix nanoparticles of the present system are summarized in [5.50–52]. For a given specific charge q_{ex} on the carbonized PVDC material, the number densities of species of the sorbed solutions were obtained by calculating the excess chemical potentials (5.53)–(5.56), obtaining the electrostatic

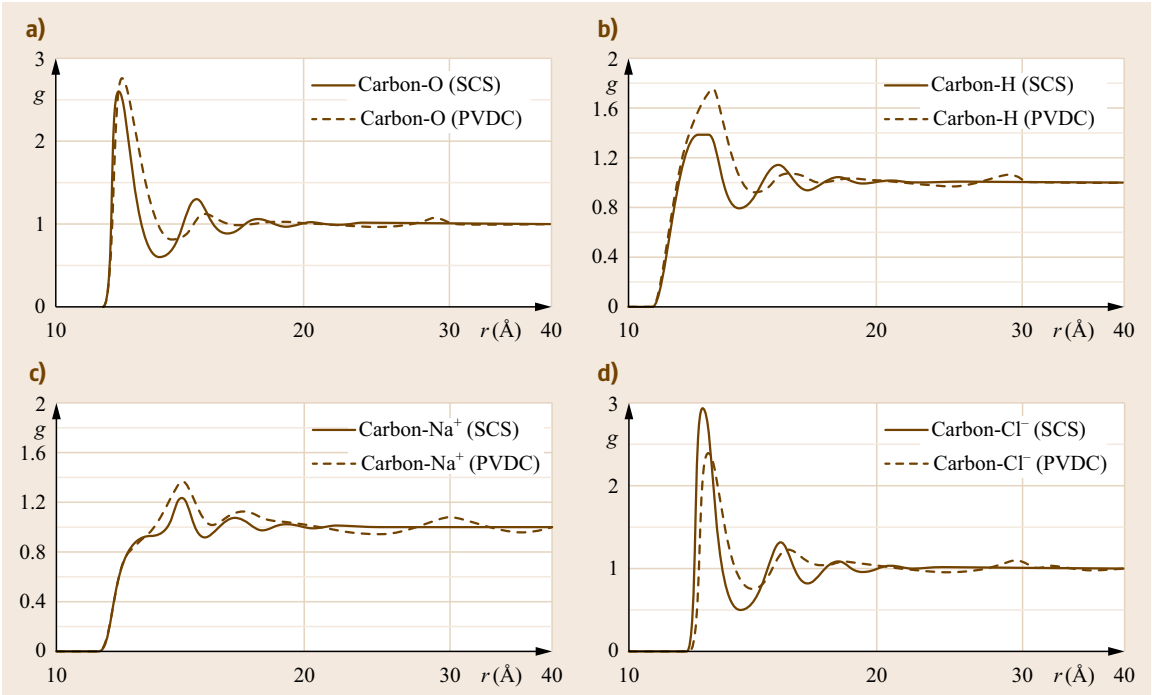


Fig. 5.16a–d Solvation structure of the internal EDL formed by NaCl aqueous solution in nanoporous carbonized PVDC material. RDFs of water O and H sites, and of Na^+ and Cl^- ions **(a–d)** at the surface of a carbon nanosphere in the nanoporous matrix framework (*solid lines*) versus the solvation structure of a single carbon sphere (SCS) immersed in the bulk aqueous electrolyte solution (*dashed lines*). The nanoporous material is in contact with the bulk ambient aqueous solution of NaCl at concentration 1 M

potential from the Poisson equation (5.58), and solving the chemical balance equations (5.65). The supercapacitor voltage for each value of q_{ex} was finally obtained from the expression (5.66).

Figure 5.16 exhibits the radial distribution functions (RDFs) of the solvation structure of electrolyte solution species around a carbon nanoparticle of the nanoporous matrix of carbonized PVDC material, which is in equilibrium with the bulk NaCl aqueous electrolyte solution at concentration 1 M at ambient conditions. Shown for comparison is the solvation structure of a single carbon sphere (SCS) of the same size immersed in the bulk electrolyte solution. In both the cases, the positions and width of the first peaks of water oxygen and hydrogen sites correspond to the typical solvation structure of a hydrophobic nanosphere in aqueous electrolyte solution, with water hydrogens oriented preferentially in parallel to the surface. The nanoporous PVDC confinement enhances the first solvation peaks but depletes the amplitude of the oscillations in the second solvation peak. The positions of the RDF peaks indicate that Cl^- ions are localized in contact with the surface hydrophobic of carbon nanoparticles, while Na^+ ions located at the surface (the highest peak of the carbon-Na^+ RDF) are surrounded by hydration shells.

Figure 5.17 shows the change of the carbon-solution RDFs with charging the nanoporous electrode. The carbon-ion RDFs strongly change due to attraction of counterions and repulsion of co-ions according to the external charge of the electrode. The carbon-water oxygen and hydrogen distributions remain almost unchanged with electrode charge. Figure 5.18 depicts the run of the electrostatic potential with distance from a carbon nanosphere in the nanoporous matrix to the bulk of the nanoporous carbon electrode, which is obtained from the Poisson equation (5.58) with the electric charge density (5.57) following from the carbon-solution distributions shown in Fig. 5.17. (Each curve in Fig. 5.18 is plotted with respect to the average electrostatic potential level ϕ_C inside the nanoporous electrode.) The electrostatic potential is constant for $r < R_C^0$ inside the conducting carbon nanosphere. The carbon nanosphere bears the average external charge which strongly affects the electrostatic potential run next to the nanosphere surface and in the first and second solvation shells. The Stern layer contains no so-

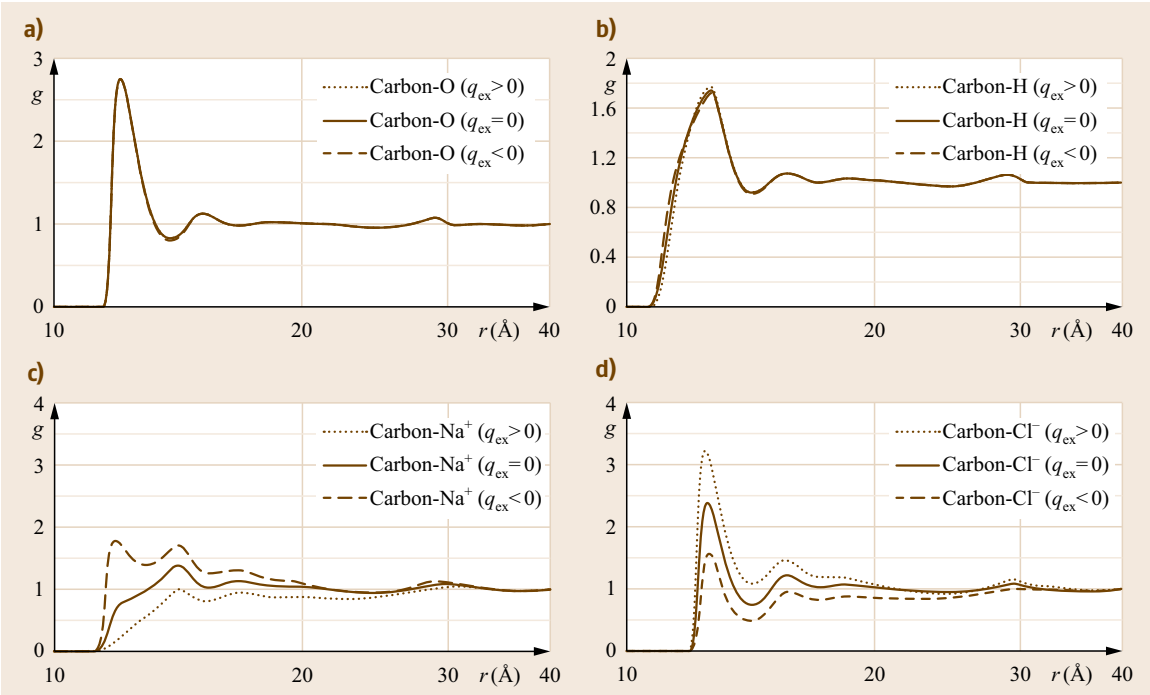


Fig. 5.17a–d Solvation structure of the NaCl aqueous electrolyte solution sorbed in the nanoporous carbonized PVDC electrode at zero charge (*solid lines*), and at positive and negative specific charge $q_{ex} = \pm 12\,C/cm^3$ (*dotted* and *dashed lines*, respectively). RDFs of water O and H sites, and Na^+ and Cl^- ions around carbon matrix nanoparticles **(a–d)**

lution charges due to the steric constraints, and the slope of the curves for $r > R_C^0$ right at the nanosphere surface is caused barely by its Coulomb potential. Then follow the potential drop due to the surface dipole with water hydrogens closer to the surface than oxygens and the potential rise due to the surface dipole with Cl^- ions located closer than Na^+. These potential peaks in the first and second solvation layers are identified as the outer Helmholtz layer. The nanosphere electric charge introduces oscillations with a period of 12 Å close to the size of nanospheres in carbonized PVDC, slowly decaying with distance. The whole range of oscillations includes the diffuse layer around the nanoparticle, as well as the statistical average of the EDLs around other nanoparticles which are closely packed and correlated in the nanoporous carbon matrix. The potential

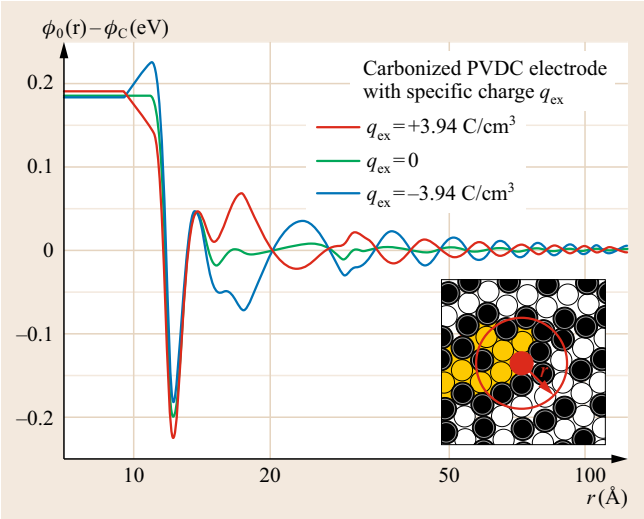


Fig. 5.18 Statistically averaged electrostatic potential $\phi_0(r)$ around a carbon nanoparticle of the carbonized PVDC electrode with respect to its bulk level ϕ_C averaged over the whole nanoporous electrode. The electrolyte solution sorbed in the nanoporous electrode is in equilibrium with the bulk ambient aqueous solution of NaCl at concentration 120 ppm. The electrode is at zero charge (*green line*), and at positive and negative specific charge $q_{ex} = \pm 3.94\,C/cm^3$ (*red* and *blue lines*, respectively). The *inset* schematically illustrates statistical–mechanical averaging (*red circle* and *distance vector*) around a labeled carbon nanoparticle (*red ball*) over the whole nanoporous material, including carbon nanoparticles (*black balls*) and nanopores (*white voids*) ►

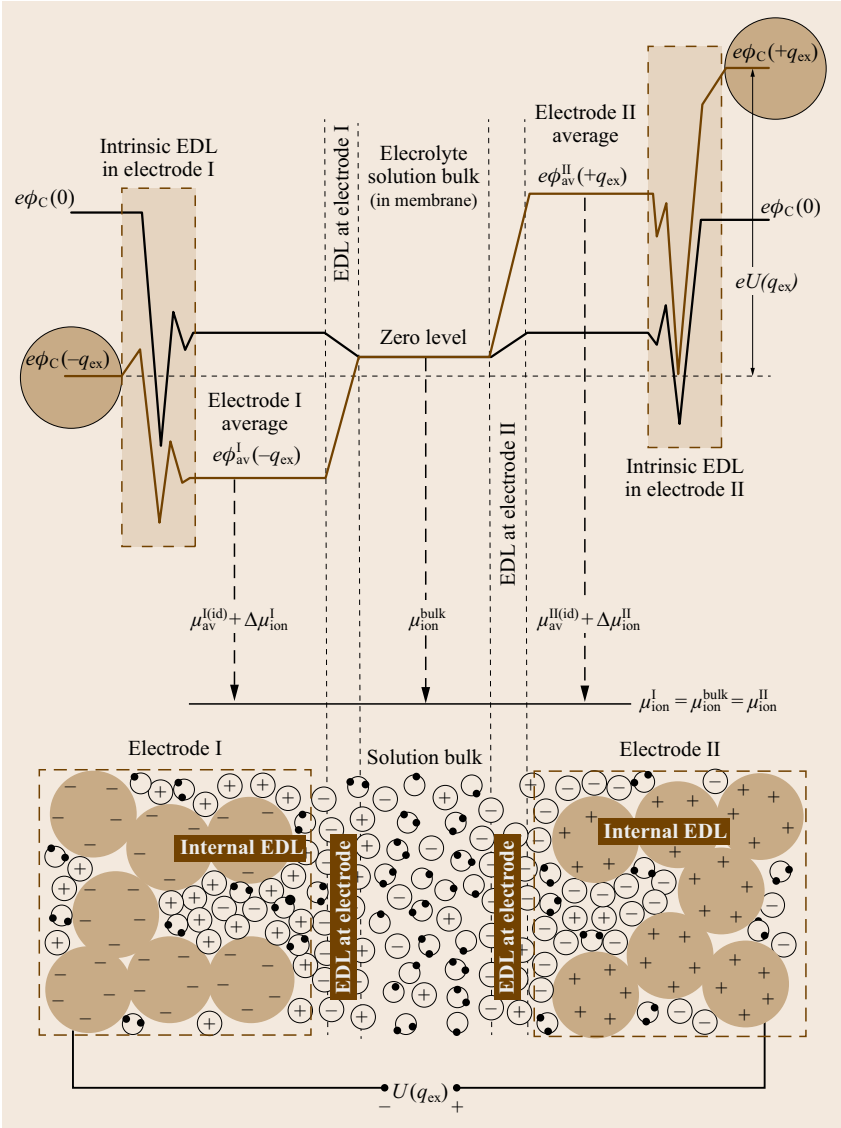


Fig. 5.19 Diagram of the electrostatic potential across the supercapacitor device. From conducting carbon nanospheres in the nanoporous carbon matrix, across the internal EDL at the surface of nanopores, across the external EDL at the edge of electrode I, to the electrolyte solution bulk, and then across the external EDL and internal EDL to the nanoporous carbon matrix of electrode II

drop of the Stern layer is almost completely cancelled out by the electric field of the outer Helmholtz layer and further oscillations which stems mainly from the ionic cloud of the first and second solvation shells screening the external charge of the carbon nanosphere, with Cl^- ions prevailing for positive and Na^+ for the negative external charge.

Finally, Fig. 5.19 presents a diagram of the overall run of the electrostatic potential across the supercapacitor device. The average potential energy level $q_{ex}\phi_C$ of the nanoporous electrode is shifted due to the electric field of the dipole which is formed by solution species outside the electrode at its macroscopic boundary to satisfy the chemical equilibrium conditions (5.65). An additional EDL emerges at the macroscopic boundary of each electrode to counterbalance the difference between the *interior* chemical potential part $k_BT\ln(\rho_s\Lambda_s)+\Delta\mu_s$ of ions inside the two nanoporous electrodes. The potential drop across these EDLs outside the electrodes constitutes a major part of the supercapacitor voltage $U(q_{ex})$ and is determined by the conditions of chemical equilibrium between the solution sorbed in each of the electrodes and the bulk solution outside the electrodes. Calculations performed for the carbonized PVDC nanoporous material in contact with the ambient aqueous electrolyte solution of 1 M NaCl reveal that the electrochemical mechanism of the EDL supercapacitor is determined

largely by the chemical balance for sorbed ions in the Nernst–Planck equation, rather than just by the EDL potential drop at the surface of a nanopore as in the case of a planar electrode [5.50–52]. The same molecular forces determine for the specific sorption capacity and purification efficiency (5.67) of a nanoporous carbon electrosorption cell [5.51]. As demonstrated earlier, the specific capacitance and sorption capacity of nanoporous carbon electrodes are determined by the interplay of the EDL potential drop across the Stern layer at the surface of nanopores and the Gouy–Chapman layer statistically averaged over the volume of the nanoporous material, the osmotic term arising due to the difference between the ionic concentrations in the two nanoporous electrodes and in the bulk electrolyte solution outside, and the solvation chemical potentials of sorbed solvated ions statistically averaged over the nanoporous material [5.50–52]. The latter term is strongly affected by chemical specificity of ions, solvent, surface functional groups, and steric effects for solvated ions confined in nanopores. Note that solvation shells of ions enlarge their effective size and can strongly affect the specific capacitance, which has strong implications for real life supercapacitor devices. For example, a power circuit supercapacitor should function in a wide range of temperatures down to −40 °C, which stiffens the solvation shells of ions and hinders them from entering small pores, thus decreasing the capacitance. Thus, the chemical potentials of solvated ions in nanopores constitute a major factor driving the specific capacitance, as they bring about two extra EDLs at the outer boundaries of the nanoporous electrodes to offset the chemical potential difference between the electrodes and solution bulk, and thus substantially contribute to the supercapacitor voltage.

5.8 Conclusions

Nanoscale properties and processes are profoundly different from the macroscopic laws in continuous media and materials. Functional features of nanostructures stem from microscopic properties of the atoms and chemical groups they are built of, but manifest on length scale from one to hundreds nanometers and time scale up to microseconds and more. The properties of nanostructures and processes involving them can be tuned in a wide range by changing size and composition. Predictive modeling of nanosystems should operate at length scales from 1 Angström to hundreds nanometers and microns and time scales to miliseconds and seconds, and yet derive their properties from the chemical functionalities of the constituents. Explicit molecular modeling of such nanosystems involves millions and billions of molecules and is by far not feasible in a *brute force* approach employing just ab initio quantum chemical methods and/or molecular simulations. A proper way thus requires multiscale methods coupling electronic structure methods for building blocks, classical molecular simulations for critical aggregates in the system, statistical–mechanical theories for their large assemblies and mean properties over characteristic size and time scales, and macroscopic scale properties.

Integral equation theory of liquids which is based on the first principles of statistical mechanics is becoming increasingly popular, as it provides a firm platform to handle the solvation structure and thermodynamics of complex chemical and biomolecular systems in solution. In particular, the statistical–mechanical, 3D-RISM-KH molecular theory of solvation is promising as an essential part of the multiscale methodology for chemical and biological nanosystems in solution. As distinct from molecular simulations that explore the phase space by the direct sampling of a limited subsystem of molecules on space and time intervals substantially restricted by computational feasibility, 3D-RISM-KH operates with spatial distributions rather than trajectories of molecules and is based on analytical summation of the free-energy diagrams which yields the solvation structure and thermodynamics in the statistical–mechanical ensemble. It gives the solvation structure in terms of the 3-D maps of distributions of solvent sites around a solute macromolecule of arbitrary shape and then the solvation thermodynamics analytically as a single integral in terms of the correlation functions obtained. The 3D-RISM-KH theory was employed to explain the molecular mechanisms of self-assembly, conformational stability of synthetic organic RNTs, aggregation of prion proteins and β-sheet amyloid oligomers, protein–ligand binding, and function-related solvation properties of biomolecular complexes as large as the GLIC ion channel in a lipid bilayer and the GroEL/ES chaperon complex.

The 3D-RISM-KH molecular theory of solvation was coupled with ab initio CASSCF, Kohn–Sham and orbital-free embedded (OFE) DFT quantum chemistry methods in a self-consistent field description of electronic structure, optimized geometry, and chemical reactions in solution. The (OFE)KS-DFT/3D-RISM-KH multiscale method is implemented in the ADF computational chemistry package and extensively validated

against experiment for solvation thermochemistry, photochemistry, conformational equilibria, and activation barriers of various nanosystems in different solvents and ILs.

In biomolecular calculations, MM/3D-RISM-KH statistical–mechanical evaluation of the solvation thermodynamics of MD trajectories replaces their conventional MM/PB(GB)SA post-processing involving empirical nonpolar terms. The 3D-RISM-KH molecular theory of solvation has been coupled with MTS-MD of a solute biomolecule steered by effective solvation forces (potential of mean force). The MTS-MD procedure is stabilized using the new algorithm of the OIN thermostat. The solvation forces are obtained analytically by converging the 3D-RISM-KH integral equations once per several OIN outer time steps, and for acceleration they are calculated at inner time steps by using GSFE in the subspace of previous successive solutions to 3D-RISM-KH. With the stabilizing effect of OIN thermostatting, gigantic outer time steps up to tens of picoseconds can be employed to accurately calculate equilibrium and conformational properties. The multiscale MTS-MD/OIN/GSFE/3D-RISM-KH integrator algorithm has been implemented in the Amber MD package, and validated and benchmarked on a fully flexible model of alanine dipeptide and on protein G in aqueous solution. While the computational rate of solvent sampling in OIN/SFCE/3D-RISM-KH is already 100−500 times faster than standard MD with explicit solvent, further substantial acceleration of sampling stems from the 3D-RISM-KH molecular theory of solvation efficiently sampling the phase space for essential events with rare statistics, such as exchange and localization of solvent and ligand molecules in pockets and at binding sites of the biomolecule.

The molecular mechanisms determining high specific capacitance of the EDL supercapacitor with nanoporous electrodes, as well as purification efficiency of the nanoporous electrosorption cell, are much more complex than the naïve picture of just a very large specific SA of pores densely *folded* or *packed* in the volume of nanoporous material. These mechanisms are very different from a planar EDL of equivalent SA. This constitutes the reason why the specific capacitance based on such an equivalent planar EDL capacitor with the *insulator* thickness given by the ionic radii turns out to be by an order of magnitude higher than the typical values in real devices. To amend this empirical model, the effective thickness of the EDL insulator is typically assumed to be up to 5 nm instead, resulting in the empirical value of area capacitance of $15-20\,\mu F/cm^3$ for the model of a planar EDL of equivalent area. Meanwhile, the replica RISM-KH-VM molecular theory for the solvation structure, thermodynamics, and electrochemistry of electrolyte solutions sorbed in nanoporous materials reveals that the driving forces of sorption and supercapacitance in nanoporous carbon electrodes are very distinct from a planar EDL capacitor. They are determined by the interplay of the EDL potential drop across the Stern layer at the surface of nanopores and the Gouy–Chapman layer statistically averaged over the volume of the nanoporous material, the osmotic term arising due to the difference between the ionic concentrations in the two nanoporous electrodes and in the bulk electrolyte solution outside, and the solvation chemical potentials of sorbed solvated ions statistically averaged over the nanoporous material. The latter factor is strongly affected by chemical specificity of ions, solvent, surface functional groups, and steric effects for solvated ions confined in nanopores. Note that solvation shells of ions can enlarge their effective size due to stiffening at low operational temperature and hinder ions them from entering small pores. The chemical potentials of solvated ions in nanoporous confinement thus constitute a major factor driving the specific capacitance, as they bring about two extra EDLs at the outer boundaries of the nanoporous electrodes to offset the chemical potential difference between the electrodes and solution bulk, which substantially contribute to the supercapacitor voltage.

Acknowledgments. This work was supported by the National Research Council of Canada, Alberta Prion Research Institute, and ArboraNano – the Canadian Forest NanoProducts Network. The computations were supported in part by WestGrid and Compute/Calcul Canada.

References

5.1 J.-P. Hansen, I. McDonald: *Theory of Simple Liquids*, 3rd edn. (Elsevier, Amsterdam 2006)

5.2 F. Hirata (Ed.): *Molecular Theory of Solvation*, Understanding Chemical Reactivity (Kluwer, Dordrecht 2003)

5.3 D. Chandler, J.D. McCoy, S.J. Singer: Density functional theory of nonuniform polyatomic systems. I. General formulation, J. Chem. Phys. **85**, 5971–5976 (1986)

5.4 D. Chandler, J.D. McCoy, S.J. Singer: Density functional theory of nonuniform polyatomic systems.

II. Rational closures for integral equations, J. Chem. Phys. **85**, 5977–5982 (1986)
5.5 D. Beglov, B. Roux: Numerical solution of the HNC equation for solute of arbitrary geometry in three-dimensions, J. Chem. Phys. **103**, 360–364 (1995)
5.6 D. Beglov, B. Roux: An integral equation to describe the solvation of polar molecules in liquid water, J. Phys. Chem. B **101**, 7821–7826 (1997)
5.7 A. Kovalenko, F. Hirata: Three-dimensional density profiles of water in contact with a solute of arbitrary shape: A RISM approach, Chem. Phys. Lett. **290**, 237–244 (1998)
5.8 A. Kovalenko, F. Hirata: Self-consistent description of a metal–water interface by the Kohn–Sham density functional theory and the three-dimensional reference interaction site model, J. Chem. Phys. **110**, 10095–10112 (1999)
5.9 A. Kovalenko, F. Hirata: F. Potentials of mean force of simple ions in ambient aqueous solution. I. Three-dimensional reference interaction site model approach, J. Chem. Phys. **112**, 10391–10402 (2000)
5.10 A. Kovalenko, F. Hirata: Potentials of mean force of simple ions in ambient aqueous solution. II. Solvation structure from the three-dimensional reference interaction site model approach, and comparison with simulations, J. Chem. Phys. **112**, 10403–10416 (2000)
5.11 A. Kovalenko: Three-dimensional RISM theory for molecular liquids and solid-liquid interfaces. In: *Molecular Theory of Solvation*, Understanding Chemichal Reactivity, Vol. 24, ed. by F. Hirata (Springer, Dordrecht 2003) pp. 169–275
5.12 H. Sato, A. Kovalenko, F. Hirata: Self-consistent field, ab initio molecular orbital and three-dimensional reference interaction site model study for solvation effect on carbon monoxide in aqueous solution, J. Chem. Phys. **112**, 9463–9468 (2000)
5.13 D. Casanova, S. Gusarov, A. Kovalenko, T. Ziegler: Evaluation of the SCF combination of KS-DFT and 3D-RISM-KH; Solvation effect on conformational equilibria, tautomerization energies, and activation barriers, J. Chem. Theory Comput. **3**, 458–476 (2007)
5.14 J.W. Kaminski, S. Gusarov, T.A. Wesolowski, A. Kovalenko: Modeling solvatochromic shifts using the orbital-free embedding potential at statistically mechanically averaged solvent density, J. Phys. Chem. A **114**, 6082–6096 (2010)
5.15 M. Malvaldi, S. Bruzzone, C. Chiappe, S. Gusarov, A. Kovalenko: Ab initio study of ionic liquids by KS-DFT/3D-RISM-KH theory, J. Phys. Chem. B **113**, 3536–3542 (2009)
5.16 A. Kovalenko, F. Hirata: First-principles realization of a van der Waals–Maxwell theory for water, Chem. Phys. Lett. **349**, 496–502 (2001)
5.17 A. Kovalenko, F. Hirata: Towards a molecular theory for the van der Waals–Maxwell description of fluid phase transitions, J. Theor. Comput. Chem. **1**, 381–406 (2002)
5.18 V. Shapovalov, T.N. Truong, A. Kovalenko, F. Hirata: Liquid structure at metal oxide–water interface: Accuracy of a three-dimensional RISM methodology, Chem. Phys. Lett. **320**, 186–193 (2000)
5.19 S.R. Stoyanov, S. Gusarov, A. Kovalenko: Multiscale modeling of the adsorption interaction between bitumen model compounds and zeolite nanoparticles in gas and liquid phase. In: *Industrial Applications of Molecular Simulations*, ed. by M. Meunier (CRC, Boca Raton 2011) pp. 203–230
5.20 J. Fafard, O. Lyubimova, S.R. Stoyanov, G.K. Dedzo, S. Gusarov, A. Kovalenko, C. Detellier: Adsorption of indole on kaolinite in non-aqueous media: Organoclay preparation and characterization, and 3D-RISM-KH molecular theory of solvation investigation, J. Phys. Chem. C **117**, 18556–18566 (2013)
5.21 J.G. Moralez, J. Raez, T. Yamazaki, R.K. Motkuri, A. Kovalenko, H. Fenniri: Helical rosette nanotubes with tunable stability and hierarchy, J. Am. Chem. Soc. **127**, 8307–8309 (2005)
5.22 R.S. Johnson, T. Yamazaki, A. Kovalenko, H. Fenniri: Molecular basis for water-promoted supramolecular chirality inversion in helical rosette nanotubes, J. Am. Chem. Soc. **129**, 5735–5743 (2007)
5.23 G. Tikhomirov, T. Yamazaki, A. Kovalenko, H. Fenniri: Self-assembly of prolate nanospheroids from hydrophobic rosette nanotubes, Langmuir **24**, 4447–4450 (2007)
5.24 T. Yamazaki, H. Fenniri, A. Kovalenko: Structural water drives self-assembly of organic rosette nanotubes and holds host atoms in the channel, ChemPhysChem **11**, 361–367 (2010)
5.25 R. Chhabra, J.G. Moralez, J. Raez, T. Yamazaki, J.-Y. Cho, A.J. Myles, A. Kovalenko, H. Fenniri: One-pot nucleation, growth, morphogenesis, and passivation of 1.4 nm Au nanoparticles on self-assembled rosette nanotubes, J. Am. Chem. Soc. **132**, 32–33 (2010)
5.26 T. Imai, R. Hiraoka, A. Kovalenko, F. Hirata: Water molecules in a protein cavity detected by a statistical-mechanical theory, J. Am. Chem. Soc. **127**, 15334–15335 (2005)
5.27 N. Yoshida, T. Imai, S. Phongphanphanee, A. Kovalenko, F. Hirata: Molecular recognition in biomolecules studied by statistical-mechanical integral-equation theory of liquids, J. Phys. Chem. B **113**, 873–886 (2009)
5.28 T. Imai, N. Miyashita, Y. Sugita, A. Kovalenko, F. Hirata, A. Kidera: Functionality mapping on internal surfaces of multidrug transporter AcrB based on molecular theory of solvation: Implications for drug efflux pathway, J. Phys. Chem. B **115**, 8288–8295 (2011)
5.29 T. Yamazaki, N. Blinov, D. Wishart, A. Kovalenko: Hydration effects on the HET-s prion and amyloid-β fibrillous aggregates, studied with three-dimensional molecular theory of solvation, Biophys. J. **95**, 4540–4548 (2008)
5.30 N. Blinov, L. Dorosh, D. Wishart, A. Kovalenko: Association thermodynamics and conformational stability of β-sheet amyloid β(17-42) oligomers:

Effects of E22Q (Dutch) mutation and charge neutralization, Biophys. J. **98**, 282–296 (2010)
5.31 N. Blinov, L. Dorosh, D. Wishart, A. Kovalenko: 3D-RISM-KH approach for biomolecular modeling at nanoscale: Thermodynamics of fibril formation and beyond, Mol. Simul. **37**, 718–728 (2011)
5.32 A. Kovalenko, N. Blinov: Multiscale methods for nanochemistry and biophysics in solution, J. Mol. Liq. **164**, 101–112 (2011)
5.33 D. Nikolic, N. Blinov, D. Wishart, A. Kovalenko: 3D-RISM-DOCK: A new fragment-based drug design protocol, J. Chem. Theory Comput. **8**, 3356–3372 (2012)
5.34 M.C. Stumpe, N. Blinov, D. Wishart, A. Kovalenko, V.S. Pande: Calculation of local water densities in biological systems: A comparison of molecular dynamics simulations and the 3D-RISM-KH molecular theory of solvation, J. Phys. Chem. B **115**, 319–328 (2011)
5.35 A. Kovalenko, A.E. Kobryn, S. Gusarov, O. Lyubimova, X. Liu, N. Blinov, M. Yoshida: Molecular theory of solvation for supramolecules and soft matter structures: Application to ligand binding, ion channels, and oligomeric polyelectrolyte gelators, Soft Matter **8**, 1508–1520 (2012)
5.36 K. Yoshida, T. Yamaguchi, A. Kovalenko, F. Hirata: Structure of *tert*-butyl alcohol–water mixtures studied by the RISM theory, J. Phys. Chem. B **106**, 5042–5049 (2002)
5.37 I. Omelyan, A. Kovalenko, F. Hirata: Compressibility of *tert*-butyl alcohol–water mixtures: The RISM theory, J. Theor. Comput. Chem. **2**, 193–203 (2003)
5.38 A. Kovalenko, F. Hirata: A molecular theory of liquid interfaces, Phys. Chem. Chem. Phys. **7**, 1785–1793 (2005)
5.39 A. Kovalenko, F. Hirata: A molecular theory of solutions at liquid interfaces. In: *Interfacial Nanochemistry: Molecular Science and Engineering at Liquid–Liquid Interfaces*, Nanostructure Science and Technology, ed. by H. Watarai, N. Teramae, T. Sawada (Springer, Berlin, Heidelberg 2005) pp. 97–125
5.40 T. Miyata, F. Hirata: Combination of molecular dynamics method and 3D-RISM theory for conformational sampling of large flexible molecules in solution, J. Comput. Chem. **29**, 871–882 (2008)
5.41 T. Luchko, S. Gusarov, D.R. Roe, C. Simmerling, D.A. Case, J. Tuszynski, A. Kovalenko: Three-dimensional molecular theory of solvation coupled with molecular dynamics in Amber, J. Chem. Theory Comput. **6**, 607–624 (2010)
5.42 I.P. Omelyan, A. Kovalenko: Generalized canonical-isokinetic ensemble: Speeding up multiscale molecular dynamics and coupling with 3D molecular theory of solvation, Mol. Simul. **39**, 25–48 (2012)
5.43 I.P. Omelyan, A. Kovalenko: Multi-time-step MD/3D-RISM-KH simulation in the optimized isokinetic ensemble, accelerated with advanced extrapolation of effective solvation forces, J. Chem. Phys. **139**, 244106 (2013)
5.44 I.P. Omelyan, A. Kovalenko: Multi-time-step molecular dynamics of biomolecules in the optimized isokinetic Nosé-Hoover ensemble, steered by 3D-RISM-KH effective solvation forces with generalized extrapolation, J. Comput. Chem. **11**, 1875–1895 (2013)
5.45 S. Gusarov, T. Ziegler, A. Kovalenko: A. self-consistent combination of the three-dimensional RISM theory of molecular solvation with analytical gradients and the Amsterdam density functional package, J. Phys. Chem. A **110**, 6083–6090 (2006)
5.46 B. Skinner, T. Chen, M.S. Loth, B.I. Shklovskii: Theory of volumetric capacitance of an electric double-layer supercapacitor, Phys. Rev. E **83**, 056102–56111 (2011)
5.47 G. Feng, D. Jiang, P.T. Cummings: Curvature effect on the capacitance of electric double layers at ionic liquid/onion-like carbon interfaces, J. Chem. Theory Comput. **8**, 1058–1063 (2012)
5.48 A. Kovalenko, F. Hirata: A replica reference interaction site model theory for a polar molecular liquid sorbed in a disordered microporous material with polar chemical groups, J. Chem. Phys. **115**, 8620–8633 (2001)
5.49 A. Kovalenko, F. Hirata: Description of a polar molecular liquid in a disordered microporous material with activating chemical groups by a replica RISM theory, Condens. Matter Phys. **4**, 643–678 (2001)
5.50 A. Tanimura, A. Kovalenko, F. Hirata: A molecular theory of a double layer formed by aqueous electrolyte solution sorbed in a carbonized polyvinylidene chloride nanoporous electrode, Chem. Phys. Lett. **378**, 638–646 (2003)
5.51 A. Kovalenko: Molecular description of electrosorption in a nanoporous carbon electrode, J. Comput. Theor. Nanosci. **1**, 398–411 (2004)
5.52 A. Tanimura, A. Kovalenko, F. Hirata: Structure of electrolyte solutions sorbed in carbon nanospaces, studied by the replica RISM theory, Langmuir **23**, 1507–1517 (2007)
5.53 J.S. Perkyns, G.C. Lynch, J.J. Howard, B.M. Pettitt: Protein solvation from theory and simulation: Exact treatment of coulomb interactions in three-dimensional theories, J. Chem. Phys. **132**, 064106 (2010)
5.54 S.M. Kast, T. Kloss: Closed-form expressions of the chemical potential for integral equation closures with certain bridge functions, J. Chem. Phys. **129**, 236101–236103 (2008)
5.55 I.S. Joung, T. Luchko, D.A. Case: Simple electrolyte solutions: Comparison of DRISM and molecular dynamics results for alkali halide solutions, J. Chem. Phys. **138**, 044103–44115 (2013)
5.56 Y. Harano, T. Imai, A. Kovalenko, M. Kinoshita, F. Hirata: Theoretical study for partial molar volume of amino acids and poly-peptides by the three-dimensional reference interaction site model, J. Chem. Phys. **114**, 9506–9511 (2001)
5.57 T. Imai, Y. Harano, A. Kovalenko, F. Hirata: Theoretical study for volume changes associated with the helix-coil transition of polypeptides, Biopolymers **59**, 512–519 (2001)

5.58 T. Yamazaki, A. Kovalenko: Spatial decomposition analysis of the thermodynamics of cyclodextrin complexation, J. Chem. Theory Comput. **5**, 1723–1730 (2009)

5.59 T. Yamazaki, A. Kovalenko: Spatial decomposition of solvation free energy based on the 3D integral equation theory of molecular liquid: Application to miniproteins, J. Phys. Chem. B **115**, 310–318 (2011)

5.60 T. Imai, K. Oda, A. Kovalenko, F. Hirata, A. Kidera: Ligand mapping on protein surfaces by the 3D-RISM theory: Toward computational fragment-based drug design, J. Am. Chem. Soc. **131**, 12430–12440 (2009)

5.61 J.S. Perkyns, B.M. Pettitt: A site–site theory for finite concentration saline solutions, J. Chem. Phys. **97**, 7656–7666 (1992)

5.62 B. Kvamme: Interaction-site representation of polar mixtures and electrolyte solutions, Int. J. Thermophys. **16**, 743–750 (1995)

5.63 J.G. Kirkwood, F.P. Buff: The statistical mechanical theory of solutions. I, J. Chem. Phys. **19**, 774–777 (1951)

5.64 S. Gusarov, B.S. Pujari, A. Kovalenko: Kovalenko, efficient treatment of solvation shells in 3D molecular theory of solvation, J. Comput. Chem. **33**, 1478–1494 (2012)

5.65 A. Kovalenko, S. Ten-no, F. Hirata: Solution of the three-dimensional RISM/HNC equations for SPC water by the modified method of direct inversion in the iterative subspace, J. Comput. Chem. **20**, 928–936 (1999)

5.66 P. Pulay: Convergence acceleration of iterative sequences. The case of SCF iteration, Chem. Phys. Lett. **73**, 393–398 (1980)

5.67 Y. Saad, M.H. Schultz: GMRES: A generalized minimal residual algorithm for solving nonsymmetric linear systems, J. Sci. Stat. Comput. **7**, 856–869 (1986)

5.68 N. Minezawa, S. Kato: Efficient implementation of three-dimensional reference interaction site model self-consistent-field method: Application to solvatochromic shift calculations, J. Chem. Phys. **126**, 054511–54515 (2007)

5.69 R.R. Lahiji, X. Xu, R. Reifenberger, A. Raman, A. Rudie, R.J. Moon: Atomic force microscopy characterization of cellulose nanocrystals, Langmuir **26**, 4480–4488 (2010)

5.70 W. Hamad: On the development and applications of cellulosic nanofibrillar and nanocrystalline materials, Can. J. Chem. Eng. **84**, 513–519 (2006)

5.71 M.T. Postek, A.E. Vladar, J. Dagata, N. Farkas, B. Ming, R. Sabo, T.H. Wegner, J. Beecher: Cellulose nanocrystals the next big nano-thing?, Proc. SPIE **7042**, 70420D (2008)

5.72 G. Siqueira, J. Bras, A. Dufresne: Cellulosic bionanocomposites: A review of preparation, properties and applications, Polymers **2**, 728–765 (2010)

5.73 S.Y.Z. Zainuddin, I. Ahmad, H. Kargarzadeh, I. Abdullah, A. Dufresne: Potential of using multiscale kenaf fibers as reinforcing filler in cassava starch-kenaf biocomposites, Carbohydr. Polym. **92**, 2299–2305 (2013)

5.74 J.P. de Mesquita, C.L. Donnici, I.F. Teixeira, F.V. Pereira: Bio-based nanocomposites obtained through covalent linkage between chitosan and cellulose nanocrystals, Carbohydr. Polym. **90**, 210–217 (2012)

5.75 R.A. Khan, S. Beck, D. Dussault, S. Salmieri, J. Bouchard, M. Lacroix: Mechanical and barrier properties of nanocrystalline cellulose reinforced poly(caprolactone) composites: Effect of gamma radiation, J. Appl. Polym. Sci. **129**, 3038–3046 (2013)

5.76 D. Chen, D. Lawton, M.R. Thompson, Q. Liu: Biocomposites reinforced with cellulose nanocrystals derived from potato peel waste, Carbohydr. Polym. **90**, 709–716 (2012)

5.77 T. Abitbol, T. Johnstone, T.M. Quinn, D.G. Gray: Reinforcement with cellulose nanocrystals of poly(vinyl alcohol) hydrogels prepared by cyclic freezing and thawing, Soft Matter **7**, 2373–2379 (2011)

5.78 A. Dorris, D.G. Gray: Gelation of cellulose nanocrystal suspensions in glycerol, Cellulose **19**, 687–694 (2012)

5.79 J.A. Kelly, A.M. Shukaliak, C.C.Y. Cheung, K.E. Shopsowitz, W.Y. Hamad, M.J. MacLachlan: Responsive photonic hydrogels based on nanocrystalline cellulose, Angew. Chem. Int. Ed. Engl. **52**, 8912–8916 (2013)

5.80 N. Lin, A. Dufresne: Supramolecular hydrogels from in situ host-guest inclusion between chemically modified cellulose nanocrystals and cyclodextrin, Biomacromolecules **14**, 871–880 (2013)

5.81 J. Yang, C.-R. Han, J.-F. Duan, F. Xu, R.-C. Sun: Mechanical and viscoelastic properties of cellulose nanocrystals reinforced poly(ethylene glycol) nanocomposite hydrogels, ACS Appl. Mater. Interfaces **5**, 3199–3207 (2013)

5.82 V.M. Wik, M.I. Aranguren, M.A. Mosiewicki: Castor oil-based polyurethanes containing cellulose nanocrystals, Polym. Eng. Sci. **51**, 1389–1396 (2011)

5.83 B.L. Holt, S.D. Stoyanov, E. Pelan, V.N. Paunov: Novel anisotropic materials from functionalised colloidal cellulose and cellulose derivatives, J. Mater. Chem. **20**, 10058–10070 (2010)

5.84 Y.P. Zhang, V.P. Chodavarapu, A.G. Kirk, M.P. Andrews: Nanocrystalline cellulose for covert optical encryption, J. Nanophotonics **6**, 063516 (2012)

5.85 G. Picard, D. Simon, Y. Kadiri, J.D. LeBreux, F. Ghozayel: Cellulose nanocrystal iridescence: A new model, Langmuir **28**, 14799–14807 (2012)

5.86 X.M. Dong, T. Kimura, J.F. Revol, D.G. Gray: Effects of ionic strength on the isotropic-chiral nematic phase transition of suspensions of cellulose crystallites, Langmuir **12**, 2076–2082 (1996)

5.87 S. Beck, J. Bouchard, R. Berry: Controlling the reflection wavelength of iridescent solid films of nanocrystalline cellulose, Biomacromolecules **12**, 167–172 (2011)

5.88 K.E. Shopsowitz, W.Y. Hamad, M.J. MacLachlan: Flexible and iridescent chiral nematic mesoporous organosilica films, J. Am. Chem. Soc. **134**, 867–870

(2012)
5.89 J.A. Kelly, K.E. Shopsowitz, J.M. Ahn, W.Y. Hamad, M.J. MacLachlan: Chiral nematic stained glass: Controlling the optical properties of nanocrystalline cellulose-templated materials, Langmuir **28**, 17256–17262 (2012)
5.90 M. Hasani, E.D. Cranston, G. Estman, D.G. Gray: Cationic surface functionalization of cellulose nanocrystals, Soft Matter **4**, 2238–2244 (2008)
5.91 Y. Habibi, L.A. Lucia, O.J. Rojas: Cellulose nanocrystals: Chemistry, self-assembly, and applications, Chem. Rev. **110**, 3479–3500 (2010)
5.92 J. Araki, M. Wada, S. Kuga: Steric stabilization of a cellulose microcrystal suspension by poly(ethylene glycol) grafting, Langmuir **17**, 21–27 (2007)
5.93 S. Montanari, M. Roumani, L. Heux, M.R. Vignon: Topochemistry of carboxylated cellulose nanocrystals resulting from TEMPO-mediated oxidation, Macromolecules **38**, 1665–1671 (2005)
5.94 N. Wang, E. Ding, R. Cheng: Surface modification of cellulose nanocrystals, Front. Chem. Eng. China **1**, 228 (2007)
5.95 E.D. Cranston, D.G. Gray: Formation of cellulose-based electrostatic layer-by-layer films in a magnetic field, Sci. Technol. Adv. Mater. **7**, 319–321 (2006)
5.96 C. Gousse, H. Chanzy, G. Excoffier, L. Soubeyrand, E. Fleury: Stable suspensions of partially silylated cellulose whiskers dispersed in organic solvents, Polym. **43**, 2645–2651 (2002)
5.97 S.R. Stoyanov, S. Gusarov, A. Kovalenko: Multiscale modeling of solvation and effective interactions of functionalized cellulose nanocrystals. In: *Production and Application of Cellulose Nanoparticles*, ed. by M.T. Postek, R.J. Moon, A. Rudie, M. Bilodeau (TAPPI, Peachtree Corners 2013) pp. 147–150
5.98 S.R. Stoyanov, O. Lyubimova, S. Gusarov, A. Kovalenko: Computational modeling of the structure relaxation and dispersion thermodynamics of pristine and modified cellulose nanocrystals in solution, Nordic Pulp Paper Res. J. **29**(1), 144–155 (2014)
5.99 Y. Nishiyama, J. Sugiyama, H. Chanzy, P. Langan: Crystal structure and hydrogen bonding system in cellulose I_α from synchrotron X-ray and neutron fiber diffraction, J. Am. Chem. Soc. **125**, 14300–14306 (2003)
5.100 Y. Boluk, L. Zhao, V. Incani: Dispersions of nanocrystalline cellulose in aqueous polymer solutions: Structure formation of colloidal rods, Langmuir **28**, 6114–6123 (2012)
5.101 F. Jiang, A.R. Esker, M. Roman: Acid-catalyzed and solvolytic desulfation of H_2SO_4-hydrolyzed cellulose nanocrystals, Langmuir **26**, 17919–17925 (2010)
5.102 T. Welton, P. Wasserschield: *Ionic Liquids in Synthesis* (VCH-Wiley, Weinheim 2007)
5.103 Y. Nishiyama, P. Langan, H. Chanzy: Crystal structure and hydrogen-bonding system in cellulose $I\beta$ from synchrotron X-ray and neutron fiber diffraction, J. Am. Chem. Soc. **124**, 9074–9082 (2002)
5.104 J.A. Wagoner, N.A. Baker: Assessing implicit models for nonpolar mean solvation forces: The importance of dispersion and volume terms, Proc. Natl. Acad. Sci. USA **103**, 8331–8336 (2006)
5.105 R.M. Levy, L.Y. Zhang, A.K. Felts: On the nonpolar hydration free energy of proteins: Surface area and continuum solvent models for the solute-solvent interaction energy, J. Am. Chem. Soc. **125**, 9523–9530 (2003)
5.106 H. Gohlke, D.A. Case: Converging free energy estimates: MM-PB(GB)SA studies on the protein-protein complex Ras-Raf, J. Comput. Chem. **25**, 238–250 (2004)
5.107 K. Lum, D. Chandler, J. Weeks: Hydrophobicity at small and large length scales, J. Phys. Chem. B **103**, 4570–4577 (1999)
5.108 T.A. Wesolowski, A. Warshel: Frozen density functional approach for ab initio calculations of solvated molecules, J. Phys. Chem. **97**, 8050–8053 (1993)
5.109 E.J. Baerends, P. Ros, D.E. Ellis: Self-consistent molecular Hartree–Fock–Slater calculations I. The computational procedure, Chem. Phys. **2**, 41–51 (1973)
5.110 G. te Velde, F. Bickelhaupt, S. van Gisbergen, C. Fonseca Guerra, E. Baerends, J. Snijders, T. Ziegler: Chemistry with ADF, J. Comput. Chem. **22**, 931–967 (2001)
5.111 C. Fonseca Guerra, J. Snijders: G. te Velde, E. Baerends: Towards an order-N DFT method, Theor. Chem. Acc. **99**, 391–403 (1998)
5.112 L. Verslus, T. Ziegler: The determination of molecular structures by density functional theory. The evaluation of analytical energy gradients by numerical integration, J. Chem. Phys. **88**, 322–328 (1988)
5.113 I.P. Omelyan, A. Kovalenko: Multiple time scale molecular dynamics for fluids with orientational degrees of freedom. I. Microcanonical ensemble, J. Chem. Phys. **135**, 11410–11419 (2011)
5.114 E. Barth, T. Schlick: Overcoming stability limitations in biomolecular dynamics. I. Combining force splitting via extrapolation with Langevin dynamics in LN, J. Chem. Phys. **109**, 1617–1632 (1998)
5.115 J.A. Izaguirre, D.P. Catarello, J.M. Wozniak, R.D. Skeel: Langevin stabilization of molecular dynamics, J. Chem. Phys. **114**, 2090–2098 (2001)
5.116 R.D. Skeel, J.A. Izaguirre: An impulse integrator for Langevin dynamics, Mol. Phys. **100**, 3885–3891 (2002)
5.117 Q. Ma, J.A. Izaguirre: Targeted mollified impulse: A multiscale stochastic integrator for long molecular dynamics simulations, Multiscale Model. Simul. **2**, 1–21 (2003)
5.118 S. Melchionna: Can short-range hybrids describe long-range-dependent properties? J. Chem, Phys. **127**, 044108–44109 (2007)
5.119 G.J. Martyna, M.E. Tuckerman, D.J. Tobias, M.L. Klein: Explicit reversible integrators for extended system dynamics, Mol. Phys. **87**, 1117–1157 (1996)

5.120 A. Cheng, K.M. Merz Jr.: Application of a multiple time step algorithm to biomolecular systems, J. Phys. Chem. B **103**, 5396–5405 (1999)

5.121 J. Komeiji: Ewald summation and multiple time step methods for molecular dynamics simulation of biological molecules, J. Mol. Struct. THEOCHEM **530**, 237–243 (2000)

5.122 W. Shinoda, M. Mikami: Rigid-body dynamics in the isothermal-isobaric ensemble: A test on the accuracy and computational efficiency, J. Comput. Chem. **24**, 920–930 (2003)

5.123 I.P. Omelyan, A. Kovalenko: Multiple time scale molecular dynamics for fluids with orientational degrees of freedom. II. Canonical and isokinetic ensembles, J. Chem. Phys. **135**, 234107–234112 (2011)

5.124 P. Minary, G.J. Martyna, M.E. Tuckerman: Algorithms and novel applications based on the isokinetic ensemble. I. Biophysical and path integral molecular dynamics, J. Chem. Phys. **118**, 2510–2526 (2003)

5.125 P. Minary, M.E. Tuckerman, G.J. Martyna: Long time molecular dynamics for enhanced conformational sampling in biomolecular systems, Phys. Rev. Lett. **93**, 150201–150204 (2004)

5.126 J.B. Abrams, M.E. Tuckerman, G.J. Martyna: Equilibrium statistical mechanics, non-Hamiltonian molecular dynamics, and Novel applications from resonance-free timesteps to adiabatic free energy dynamics. In: *Computer Simulations in Condensed Matter Systems: From Materials to Chemical Biology Volume 1*, Lecture Notes in Physics, Vol. 703, ed. by M. Ferrario, G. Ciccotti, K. Binder (Springer, Berlin, Heidelberg 2006) pp. 139–192

5.127 D.J. Tobias, C.L. Brooks III: Conformational equilibrium in the alanine dipeptide in the gas phase and aqueous solution: A comparison of theoretical results, J. Phys. Chem. **96**, 3864–3870 (1992)

5.128 D.S. Chekmarev, T. Ishida, R.M. Levy: Long-time conformational transitions of alanine dipeptide in aqueous solution: Continuous and discrete-state kinetic models, J. Phys. Chem. B **108**, 19487–19495 (2004)

5.129 D. Boda, W. Nonner, M. Valiskó, D. Henderson, B. Eisenberg, D. Gillespie: Steric selectivity in Na channels arising from protein polarization and mobile side chains, Biophys. J. **93**, 1960–1980 (2007)

5.130 D. Boda, M. Valiskó, B. Eisenberg, W. Nonner, D. Henderson, D. Gillespie: The effect of protein dielectric coefficient on the ionic selectivity of a calcium channel, J. Chem. Phys. **125**, 034901–34911 (2006)

5.131 D. Boda, M. Valiskó, B. Eisenberg, W. Nonner, D. Henderson, D. Gillespie: Combined effect of pore radius and protein dielectric coefficient on the selectivity of a calcium channel, Phys. Rev. Lett. **98**, 168102–168104 (2007)

5.132 N. Bocquet, H. Nury, M. Baaden, C. Le Poupon, J.-P. Changeux, M. Delarue, P.-J. Corringer: X-ray structure of a pentameric ligand-gated ion channel in an apparently open conformation, Nature **457**, 111–114 (2009)

5.133 Y. Weng, L. Yang, P.-J. Corringer, J.M. Sonner: Anesthetic sensitivity of the *gloeobacter violaceus* proton-gated ion channel, Anesth. Analg. **110**, 59–63 (2010)

5.134 J. Given: Liquid-state methods for random media: Random sequential adsorption, Phys. Rev. A **45**, 816–824 (1992)

5.135 J. Given, G. Stell: Comment on: Fluid distributions in two – phase random media: Arbitrary matrices, J. Chem. Phys. **97**, 4573–4574 (1992)

5.136 J. Given, G. Stell: The replica Ornstein–Zernike equations and the structure of partly quenched media, Physica A **209**, 495–510 (1994)

5.137 J. Given, G. Stell: Liquid-state theory for some nonequilibrium processes, Condens. Matter Theor. **8**, 395–410 (1993)

5.138 L.L. Lee: Chemical potentials based on the molecular distribution functions. An exact diagrammatical representation and the star function, J. Chem. Phys. **97**, 8606–8616 (1992)

5.139 M. Endo, T. Takeda, Y.J. Kim, K. Koshiba, K. Ishii: High power electric double layer capacitor (EDLC's); From operating principle to pore size control in advanced carbons, Carbon Sci. **1**, 117–128 (2001)

Part B Electrode

Part B Electrodes and Electrode Processes

6 **Highly Ordered Macroporous Electrodes**
Alexander Kuhn, Pessac, France
Matthias Heim, Karlstein, Germany

7 **Ion-Sensitive Electrodes**
Hans-Hermann Rüttinger, Halle, Germany

8 **Transport in Liquid-Phase Electrochemical Devices**
Richard O. Stroman, Washington, USA
Greg Jackson, Golden, USA

9 **Catalyst Layer Modeling**
Tanja Vidaković-Koch, Magdeburg, Germany
Richard Hanke-Rauschenbach, Hannover, Germany
Isaí Gonzalez Martínez, Dortmund, Germany
Kai Sundmacher, Magdeburg, Germany

10 **Water Management in Proton Exchange Fuell Cells**
Nils Brandau, Wolfsburg, Germany
Jürgen Köhler, Braunschweig, Germany

11 **Calculations in Li-Ion Battery Materials**
Michelle D. Johannes, Washington, USA
Corey T. Love, Washington, USA
Karen Swider-Lyons, Washington, USA

6. Highly Ordered Macroporous Electrodes

Alexander Kuhn, Matthias Heim

In recent years, the field of highly ordered macroporous thin films coated onto solid electrode surfaces has received increasing attention, on the one hand, due to interesting fundamental questions, and, on the other hand, because of a large variety of potential applications of such designer structures, ranging from electrocatalysis to biosensors and energy storage/conversion. This chapter describes the synthesis, the characterization, and the features of such organized layers, with a special emphasis on an increasingly sophisticated and rational design, which is possible when using colloidal crystal structures as templates. Some possible applications of such modified electrodes are also highlighted in the last section of the chapter, illustrating their beneficial effects in various domains, going eventually far beyond pure electrochemical aspects.

In this chapter, we present the elaboration of highly-ordered macroporous electrodes using colloidal crystal templating. A structure is considered as macroporous, when the pore size exceeds 50 nm; pores with 2—50 nm are considered as mesopores, whereas pores smaller than 2 nm are termed microporous. Several techniques allowing the self-assembly of microspheres into colloidal crystal templates will be discussed in Sect. 6.1.1. After giving an overview in Sect. 6.1.2 over existing methods to infiltrate colloidal templates, Sects. 6.1.3 and 6.1.4 will focus on the controlled electrodeposition of metals and conducting polymers (CPs) into colloidal templates, and the electrochemical characterization of the resulting macroporous electrodes. Section 6.2 illustrates an approach to fabricate macroporous electrodes with complex pore architectures, including gradient pore structures. Assembly of colloidal microspheres into complex colloidal crystal architectures in a layer-by-layer deposition process using the Langmuir–Blodgett technique followed by infiltration of the template by electrochemical deposition enabled us to obtain this objective. In Sect. 6.3, we focus on miniaturized macroporous gold electrodes with a cylindrical geometry and their utility with respect to the electrocatalytic reduction of oxygen. The broad field of applications, in which macroporous electrodes can be used for, is presented in Sect. 6.4.

6.1 **Macroporous Electrodes by Infiltration of Colloidal Templates** 144
6.1.1 Assembly of Colloidal Crystals 144
6.1.2 Overview over Different Infiltration Techniques 151
6.1.3 Electrodeposition of Metals in Colloidal Templates 156
6.1.4 Electrodeposition of Conducting Polymers in Colloidal Crystals 165
6.2 **Macroporous Materials with a Gradient in Pore Diameter** 172
6.2.1 Gradient Pore Diameter Template Fabrication 173
6.2.2 Electrodeposition of Metals and Conducting Polymers 176
6.3 **Macroporous Microelectrodes with Cylindrical Geometry** 181
6.3.1 Fabrication of Colloidal Crystal Templates on Gold Wires 182
6.3.2 Electrodeposition of Metals and Conducting Polymers 183
6.3.3 Characterization of Macroporous Gold Cylinders 188
6.4 **Applications of Macroporous Electrodes** 188
6.4.1 Electrocatalysis 189
6.4.2 Energy Storage 189
6.4.3 Sensing Applications 190
6.4.4 Electrosynthesis 191
6.4.5 Optical Applications 193
6.5 **Conclusion** 197
References 197

Electrochemical devices occupy an important part of our life. Among the most well-known and broadly used electrochemical cells are batteries or fuel cells, allowing us to store and convert energy, respectively [6.1, 2]. Electrochemical sensors allow the concentration of various biological or chemical species to be determined [6.3, 4]. These are just some of the numerous examples in which electrochemical reactions serve for useful purposes. In many respects, the characteristics of the electrode play a crucial role, affecting the performance of these devices. A strategy to improve the efficiency of electrochemical setups in different fields of applications consists in using electrodes with a nanostructured surface [6.5–7]. Improvement of the performance of macroscopic electrodes can be achieved by modifying their surface with particles of nanoscopic dimensions, for example, metal nanoparticles or carbon nanotubes. The high surface-to-volume ratio of nanoparticles provides an efficient way to increase the active surface area of electrodes. Another approach for achieving the same goal consists in using porous electrodes. Efforts have been made in the field of porous electrodes, since their introduction more than a century ago [6.8], to develop new synthesis procedures allowing us to control their microstructure and organization. In this regard, the use of templates has proved to be particularly well suited to generate porous materials with a well-defined morphology. Owing to the structure directing properties of different types of templates, porous materials can be produced, which are a cast of the template. The possibility of using a wide range of different materials for the infiltration of a template also makes it a very versatile method.

Various up-to-date templates, that can be divided into hard and soft templates have been employed to create porous films on electrode surfaces. Hard templates include track etched or anodized alumina and polycarbonate membranes, which were among the first templates that have been successfully used to produce nanostructured conductive films on the surface of an electrode [6.9]. Furthermore, also mesoporous silica membranes or colloidal microspheres assembled into colloidal crystals belong to this category. Examples for soft templates are surfactant molecules, block copolymers, polymer gels, and emulsions. The particular benefit in using templates rather than other nanofabrication techniques, for example, chemical dealloying [6.10], resides in the high level of control over the microstructure in the porous material offered by the template-based approach.

6.1 Macroporous Electrodes by Infiltration of Colloidal Templates

In the following sections, different steps for the elaboration of ordered macroporous electrodes by colloidal crystal templating are discussed. In Sect. 6.1.1, the most current methods employed for assembling microspheres into ordered colloidal crystal structures are presented. Section 6.1.2 compares existing techniques for the infiltration of colloidal templates relying on a gaseous (e.g., CVD) or liquid (e.g., sol–gel) precursor and electrochemical deposition. In the following, the focus is centered on the controlled electrochemical deposition of metals (Sect. 6.1.3) and (CPs) (Sect. 6.1.4) in colloidal templates. Temporal current oscillations observed during the amperometric electrodeposition in colloidal crystals result from the periodic variation of the electroactive area during the infiltration of such templates. They enabled us to follow the filling process of the template with material and, hence, to precisely control the thickness of the macroporous electrodes. The macroporous metal and CP electrodes are further characterized using scanning electron microscope (SEM) and electrochemical techniques. A linear increase of the active surface area for increasing numbers of pore layers in macroporous gold electrodes could be experimentally confirmed.

6.1.1 Assembly of Colloidal Crystals

Self-assembly represents a process where structures organize into ordered patterns without human intervention. It can be found at all scales in the natural or the artificial domain of our world. Examples for self-assembly are living cells, molecules, self-assembled monolayers (SAMs), liquid and colloidal crystals, bacterial colonies, and even animal swarms (e.g., ants) [6.13]. In crystalline materials, the atoms or molecules are arranged in defined locations building up a highly ordered crystal lattice. The same degree of order is found in colloidal crystals (Fig. 6.1b). Here the building blocks are colloidal spheres with dimensions typically three orders of magnitude larger than atoms. A natural form of colloidal crystals represents gem opals attracting one's attention by their intense coloration (Fig. 6.1a) that changes when the opal is observed under different angles. This phenomenon, known as opalescence, is caused by a diffraction of light at the periodic crystal lattice, generally being composed of sub-μm sized spherical particles. Even though colloidal crystals can be used directly for different kinds of applications, several others arise from the possibility

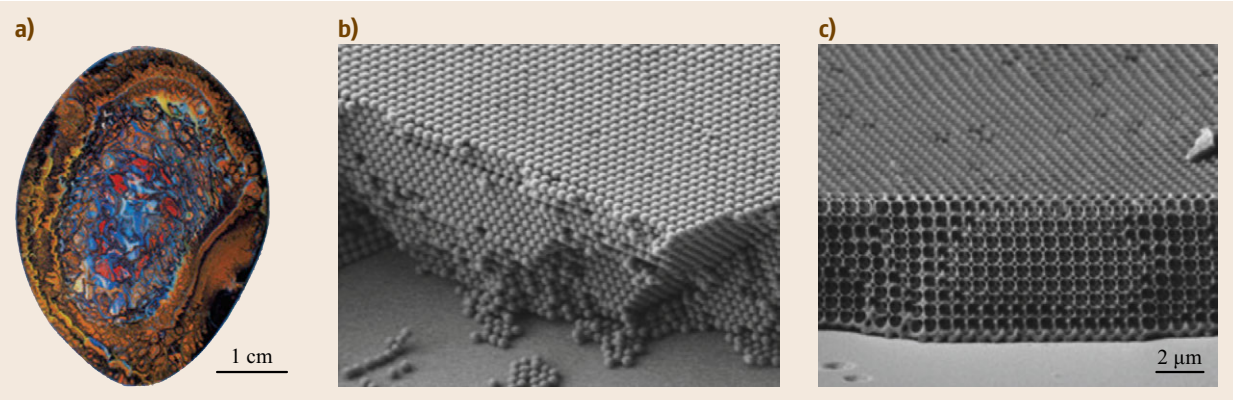


Fig. 6.1 **(a)** Top view of a natural iron oxide-containing matrix opal (after [6.11]). **(b)** Cross-sectional SEM image of a colloidal crystal made up from silica spheres with a diameter of 1000 nm (after [6.12]). **(c)** Silicon inverse opal obtained from a colloidal crystal like the one shown in **(b)**. Those structures show optical properties consistent with a photonic bandgap (PBG) (after [6.12])

of fabricating inverse opals of various materials. Infiltration followed by the dissolution of the colloidal template is employed in order to produce negative replicas of colloidal crystals. Those inverse opals resemble *honeycomb structures* and are characterized by a 3-D periodic arrangement of interconnected voids in a host material (Fig. 6.1c). Inverse opals offer great potential in application fields including photonic crystals (PCs), metamaterials, or macroporous materials.

Colloidal crystals are generally build up from spherical building blocks of organic or inorganic nature with either metallic, semiconducting, or electrical isolating character. In the following, the focus will be directed on nonconductive particles that are used as an inert template for a subsequent infiltration, for example, by electrochemical deposition. A crucial parameter in the assembly of colloidal crystals represents the monodispersity of the colloidal building blocks. The narrower the size distribution of the colloids, the better the resulting quality and the lower the number of stacking faults in the colloidal crystal [6.14]. The key feature in particle synthesis therefore consists in controlling the process in such a way that nucleation on one side and the growth of the nuclei on the other are distinct processes that are well separated from each other [6.15]. Focusing on organic matter, poly(methylmethacrylate) (PMMA) and polystyrene (PS) microspheres with diameters ranging from 20 nm to 1 µm are obtained by a range of different techniques (e.g., emulsion polymerization) [6.16]. Inorganic silica spheres with diameters ranging from 50 nm to a 1 µm and a very narrow size distribution are obtained by a method described by *Stöber* et al. in 1968, relying on the hydrolysis and polycondensation of a dilute siloxane precursor (in general tetraethyl orthosilicate – TEOS) in an alcoholic solution under basic conditions [6.17]. Since then much effort has been put in investigating the influence of different reaction parameters on the size and the distribution of the particles [6.18, 19]. For the synthesis of bigger particles, a two-step process can be used. In a first step, silica colloids of submicrometer dimensions are produced by the Stöber method. These *seeds* can be grown to their final size by a controlled addition of the precursor [6.20, 21].

A condition for forming stable aggregates in colloidal systems presents the establishment of a balance between attractive and repulsive forces that act on the particles. Besides the Van der Waals attraction and the electrostatic repulsion, resulting from an interaction of counterions in the electric double layer, steric, hydrophobic, and solvation forces are to be considered in colloidal systems as internal forces. A second group, not directly depending on intermolecular interactions, includes capillary forces, surface tension, wetting and adhesion on interfaces, gravity, diffusion, Brownian motion, osmotic pressure, force by flow as well as electrokinetic, and magnetophoretic forces. Self-assembly that relies strictly on the internal forces described earlier presents a rather random process in colloidal systems [6.22]. Much effort has been dedicated to explore various routes allowing the self-assembly of colloidal crystals to become directional and highly controllable via the involvement of different external forces. A considerable part of the research performed in this field focused on achieving high quality colloidal crystals with a low number of defects. Especially for an application in the field of PCs, a big challenge is the control of the assembly in such a way that defects can be integrated into the colloidal crystal structure in a precise manner. Finally, the scale-up and the acceleration of the self-assembly process represent important goals in order to allow an economic manufacturing at the industrial scale. In recent works, detailed overviews are given

over principal methods used for the self-assembly of colloidal spheres into colloidal crystals [6.11, 23, 24].

Probably the most straightforward technique to produce colloidal crystals consists in using sedimentation of colloidal microspheres in suspensions [6.25]. Forces acting on the particles are gravity, Brownian motion, and also the electrostatic repulsion in the case of charged particles. The more favorable lattice structure for opals obtained from sedimentation or other self-assembly methods tends to be face-centered cubic (fcc) rather than hexagonal closed packed (hcp) [6.23, 26, 27]. However, sedimentation represents only a well-adapted method for a very limited range of particle sizes. Using big particles leads to a very fast sedimentation, which prevents well-ordered colloidal crystals from being formed [6.28]. On the other hand, this technique can't be employed when the particle size is getting too small, because the efficient settling of the particles takes too much time. Adding centrifugal forces allowed to accelerate the sedimentation process [6.29], whereas electrophoretic forces could be used to either slow down or speed up the natural sedimentation of charged particles depending on the bias of an electric field with respect to the gravitational force [6.30]. The ordering and the structural quality in colloidal crystals could be improved by using prestructured substrates [6.31] or oscillatory shear [6.32].

Colloidal spheres also self-assemble during evaporation of solvent from a colloidal suspension, the substrate being either in a horizontal [6.33–35] or a vertical position [6.36]. In both configurations, capillary forces induced by the evaporation of solvent are at the origin of the self-assembly process (Fig. 6.2) In the horizontal deposition method, the flow-induced assembly of colloidal particles starts at the outside of a drop moving continually toward its center (Fig. 6.2a). As a result, the thickness of the colloidal crystal is not homogeneous throughout the sample showing thicker deposits in the outer than in central regions. With a controlled air flow, it was possible to guide the self-assembly and to achieve a more homogeneous thickness throughout the sample [6.37]. Sonication-assisted evaporation resulted also in a better crystal quality by equally speeding up the evaporation process [6.38].

In the vertical deposition (VD) method gravity acts on the particles by pulling them away from the growth interface of the crystal. Therefore, this method was in its original configuration not well adapted for assembling big colloidal particles into colloidal crystals, as the sedimentation rate of these spheres was too high. This limitation could be overcome by introducing a permanent flow in the solution by heating [6.39, 40] or mechanical agitation [6.41], keeping the spheres in suspension. The influence of a range of different process parameters on the assembled colloidal crystals was studied and optimized including temperature [6.42], sphere size [6.43], volume fraction of particles in solution [6.44], relative humidity [6.45], application of negative pressure [6.46], and also the pH and the ionic strength of the solution [6.47]. In terms of the structural quality of the assembled colloidal crystals, VD leads to better results compared to the sedimentation or the horizontal deposition.

Well-ordered crystals with a low number of defects can be obtained in that way; an example of that is given in Fig. 6.3a. Residual defects as the ones illustrated in Fig. 6.3b are mostly due to insufficient monodispersity in the size distribution of the colloidal spheres. The intrinsically slow process of the natural evaporation of aqueous solutions could be accelerated by using ethanol instead of water as the solvent [6.46, 50]. The thickness of the deposited film can roughly be

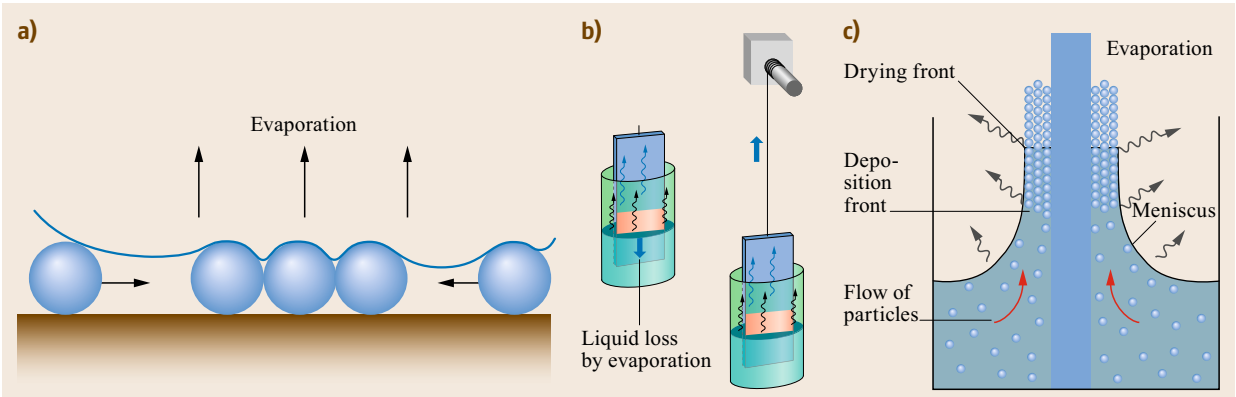


Fig. 6.2 (a) Self-assembly of colloidal spheres on a horizontal substrate due to evaporation-induced capillary forces (after [6.16]). (b) The VD method. *Left*: Original configuration of the VD method. *Right*: Additional slow lifting of the sample. (c) Processes occurring at the air–liquid–substrate interface during solvent evaporation (after [6.11])

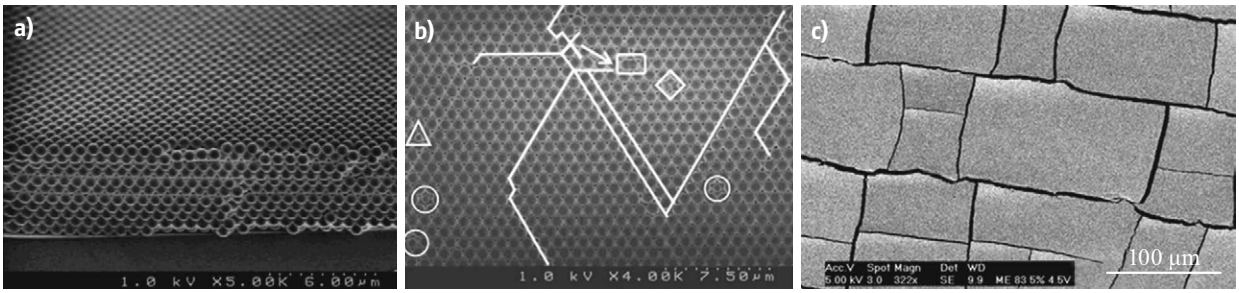


Fig. 6.3a–c SEM images of colloidal crystals produced by VD under isothermal heating **(a,b)** or horizontal deposition **(c)**. In panel **(b)**, different kinds of defects are shown, including bigger or smaller particles, doublet or missing spheres. **(c)** Typical crack formation observed in the colloidal crystal assembly based upon solvent evaporation (after [6.40, 48])

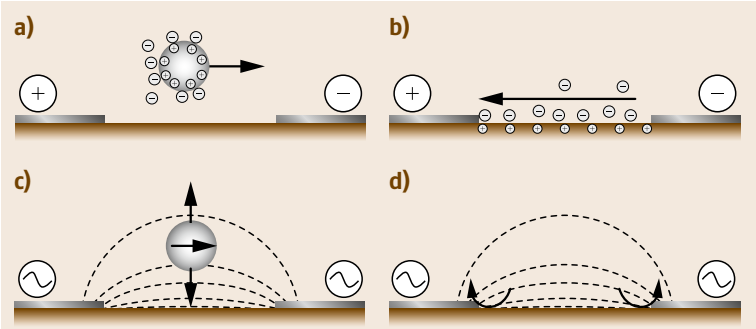


Fig. 6.4a–d Different forces acting on a colloidal particle upon application of a DC **(a,b)** or an AC **(c,d)** electric field. **(a)** DC electrophoresis. **(b)** DC electroosmosis. **(c)** AC dielectrophoresis. **(d)** AC electro hydrodynamics (after [6.49])

adjusted by controlling the particle concentration of the suspension. Also, a change in the tilt angle of the substrate could serve the same purpose [6.51]. However, the film thickness generally was found to vary throughout the sample, as particle concentration increases with proceeding evaporation of the solvent. By pulling the substrate slowly out of the solution (Fig. 6.2b right), the method was accelerated and variations in film thickness throughout the sample could be avoided [6.52, 53].

A general issue of colloidal crystals formed from particle suspensions represents the cracking of the structure that occurs during the drying process (Fig. 6.3c) [6.53, 54]. Here, the shrinking of individual particles and/or the solvent evaporation between the spheres leads to a stress in the lattice domains of the colloidal crystal adhering to the substrate. This stress is released in the form of cracks splitting the colloidal crystal into different crystalline domains. Only very few techniques exist that allow producing crack-free colloidal crystals directly from a particle suspension making use of flexible [6.48] or prestructured substrates [6.55].

The self-assembly of colloidal particles can also be controlled by using electric fields [6.49]. When colloidal suspensions are exposed to an electric field, a movement of particles results from forces that either act directly on them or cause a liquid flow that drags the particles along. An overview of different forces and the underlying mechanism is given in Fig. 6.4.

By applying a constant DC electric field between two electrodes in a suspension-containing colloidal spheres with a charged surface, colloidal crystals can be assembled on the electrode surface (Fig. 6.4a). In this way, colloidal crystals have been assembled from silica [6.61, 62] and latex [6.56, 63, 64] beads (Fig. 6.5a). However, the application of a DC electric field may result in effects disturbing the assembly process of colloidal particles, including electroosmotic flow (Fig. 6.4b) and faradaic reactions occurring at the electrode surface. For example, adding ethanol to aqueous solutions was reported to enable higher electric fields to be applied without water decomposition reactions taking place [6.56].

In contrast to DC, AC electric fields offer the advantage that higher electric fields can be applied without causing electrolysis or electroosmotic water motion, given that the employed frequency is high enough. As shown in Fig. 6.4c, the dielectrophoretic force attracts colloidal particles to areas of higher electric field intensity as a result of the interaction of induced dipoles with the nonuniform electric field. Whereas highly polarizable particles (e.g., metal particles) are attracted to regions of higher field intensity in the whole frequency range, less polarizable (e.g., polymer beads)

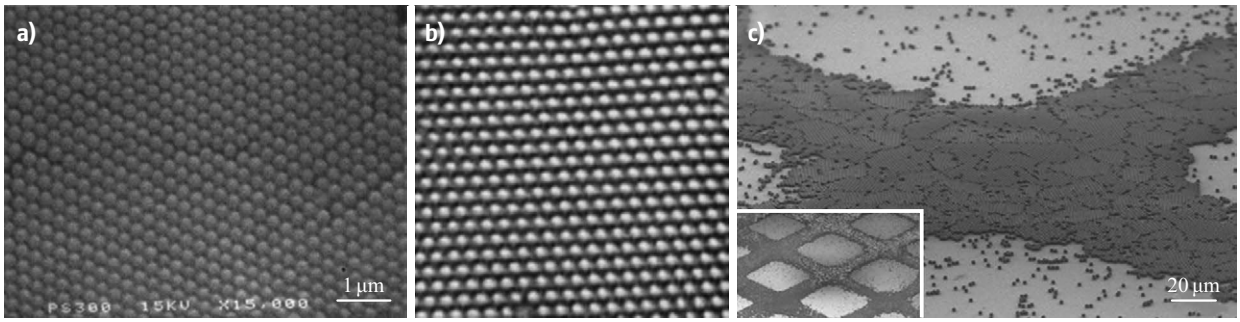


Fig. 6.5a–c SEM images of colloidal crystals obtained by applying electric fields. **(a)** Colloidal assembly obtained by DC electrophoresis (after [6.56]). **(b)** Colloidal crystal formed by AC dielectrophoresis from latex spheres with a diameter of 1.4 µm (after [6.57]). **(c)** Colloidal crystal patterns on ITO (indium tin oxide) obtained by applying a DC electric field with simultaneous illumination of the ITO through a mask (after [6.58])

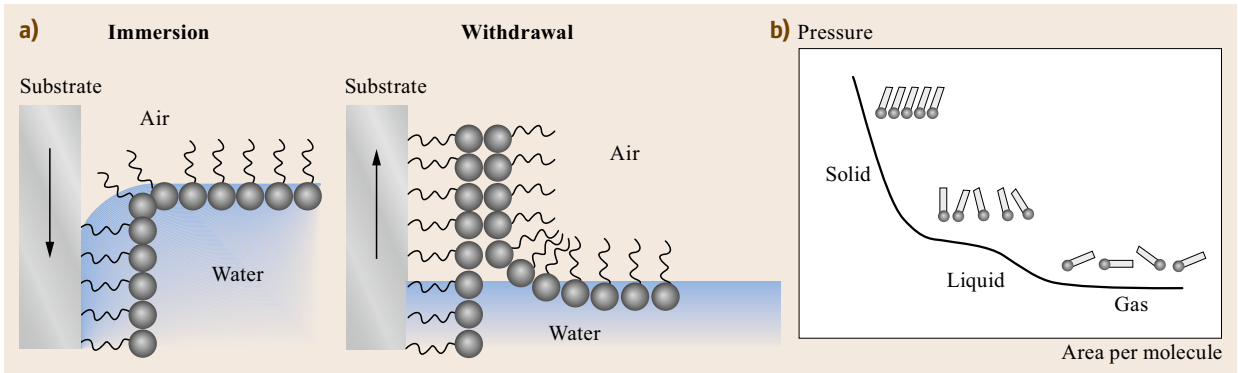


Fig. 6.6 **(a)** Principle of transferring a molecular Langmuir film onto a bulk substrate (after [6.59]). **(b)** Schematic representation of a compression isotherm for a molecular Langmuir film. The surface pressure is plotted as a function of the area per molecule (after [6.60])

can be directed either to regions of higher or lower field intensities in the low- and high-frequency regime, respectively. A setup with two parallel electrodes separated by a thin gap of the order of the particle diameter allows us to assemble 2-D colloidal crystals by applying an AC electric field [6.65–71], whereas the setup shown in Fig. 6.4c can be used to build up 3-D colloidal crystals from polymer [6.57, 72] or silica [6.73] particles. Local modification of the conductivity of the electrode by using photoresist- [6.74, 75] or a mask [6.58, 76] gives rise to nonuniform electric fields when a DC [6.74, 76] or an AC [6.75, 77] electric field is applied, leading to colloidal crystal patterns (Fig. 6.5c).

Colloidal crystals may also be build up by a layer-by-layer deposition method using the Langmuir–Blodgett (LB) technique. Originally, this technique was conceived to transfer molecular films composed of amphiphilic molecules from the water surface onto solid samples [6.78, 79]. Multiple layers of molecular films, the polar head groups pointing into the water, and the hydrocarbon tails toward the air, can be transferred to solid substrates upon repeated immersion and withdrawal cycles (Fig. 6.6a). Before the transfer, Langmuir films are compressed by means of movable barriers in order to obtain dense and well-ordered monolayers. A typical compression isotherm shown in Fig. 6.6b is obtained from recording the surface pressure of the water as a function of film area or area per molecule. In analogy to different phases of matter, three distinct states can be distinguished for molecular films during their compression, including a gaseous, liquid, and solid state, where the film is typically transferred to a substrate. Any further compression would lead to a collapse of the film with layers being stacked on top of each other.

LB can also be employed with microspheres, silica being the most widely used material [6.80]. Changing the surface chemistry of silica beads from a hydrophilic to a more hydrophobic state by silylation prevents them from sinking into the aqueous subphase when spread onto the water surface (Fig. 6.7a) [6.81, 82]. For a limited range of particle sizes from 180 to 360 nm, stable

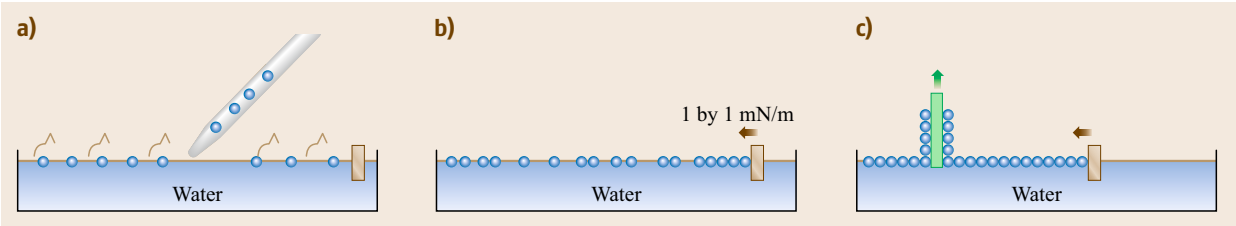


Fig. 6.7a–c Different steps involved in the LB process with colloidal particles. **(a)** Spreading of the particles on the water surface. **(b)** Compression of the Langmuir film. **(c)** Transfer of the colloidal film to a hydrophilic substrate at constant surface pressure

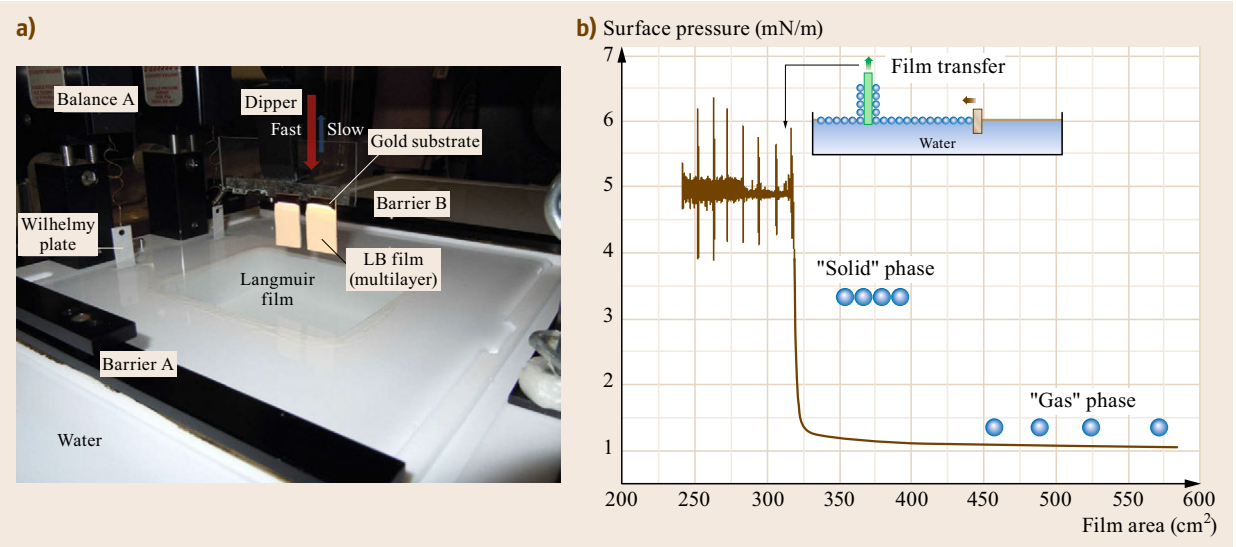


Fig. 6.8 **(a)** Side view on a LB experiment with silica microspheres. Several monolayers of silica beads have been transferred onto the gold-coated glass substrate (ca. 1.5 cm × 2.5 cm). **(b)** Surface pressure as a function of the area occupied by the particle film in the LB trough. Compression of the particle film (silica, 470 nm diameter) to a surface pressure of 5 mN/m and subsequent transfer of seven layers onto a bulk sample

Langmuir films also were obtained without a functionalization process [6.83].

The compression of colloidal Langmuir films (Fig. 6.7b) is similar to that of molecular films (Fig. 6.6b), without the occurrence of a corresponding liquid state in the compression curve (Fig. 6.8b) [6.84]. While the film is transferred to a substrate, the surface pressure is kept constant (between 5 and 10 mN/m for silica microspheres) further reducing the area occupied by the Langmuir film by means of the movable barriers. The transfer of a sphere monolayer (Fig. 6.7c) occurs exclusively during the upstroke of a hydrophilic substrate [6.80], so that the number of dipping events, involving one down and one up cycle, corresponds to the number of deposited particle layers. In this way, colloidal crystals could be successfully built up on glass microscope slides by a successive deposition of particle monolayers [6.84–87]. Figure 6.8a shows the general setup used in an LB experiment including two movable barriers, a piece of paper (Wilhelmy plate) attached to a balance to measure the surface pressure during compression of the film and a substrate attached to a dipper mechanism.

The specific layer-by-layer deposition leads to some important advantages when LB is used to assemble colloidal crystals instead of competing methods. As every individual deposited layer is given enough time to dry, no cracks are present in the colloidal crystal. Furthermore, very few techniques are reported in the literature allowing to deposit only a single monolayer of particles onto different substrates [6.88], bearing a particular interest for applications in nanosphere lithography [6.89]. LB allows a perfect control over the number of deposited layers, including the possibility of combining spheres of a different diameter or chemical composition in different layers of a colloidal crystal. This characteristic will be taken advantage of in Sect. 6.2 to assemble colloidal templates that consist of very so-

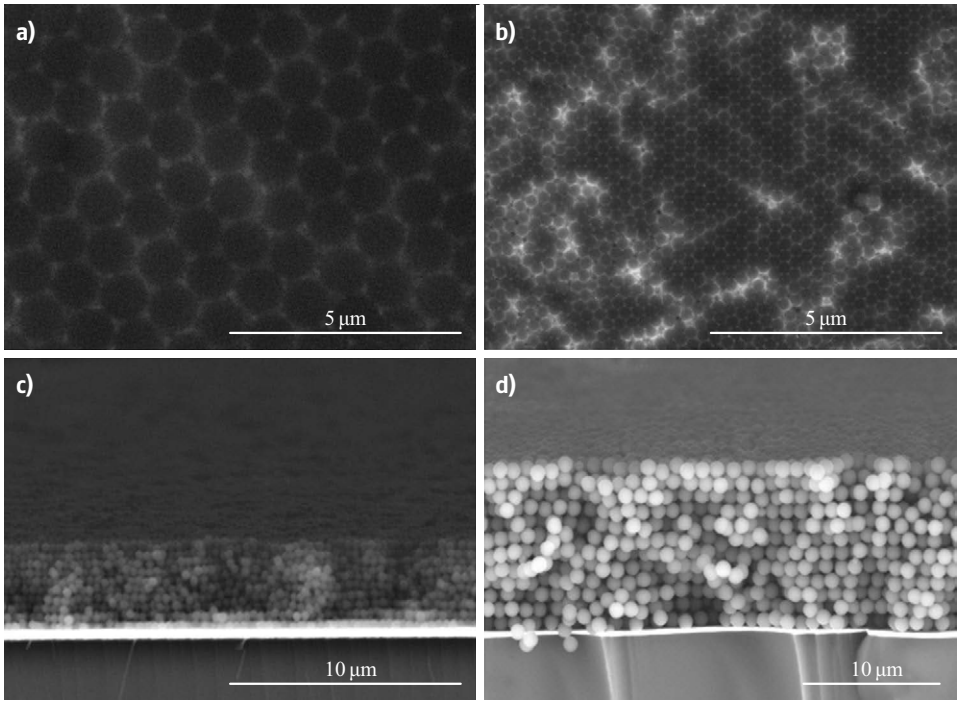


Fig. 6.9a–d SEM images of colloidal crystals produced by the LB technique. **(a,b)** Top view of different magnifications of a monolayer of silica spheres (diameter 1 µm) deposited onto a gold substrate. Cross-section of colloidal crystals composed of **(c)** 10 layers of silica beads ($d = 325$ nm). **(d)** 12 layers of silica beads ($d = 1$ µm)

phisticated architectures including sphere gradients or defect layers. Finally, the maximal film size that can be transferred onto a sample is only limited by the dimensions of the Langmuir trough, in particular the dipping well, and not by the process itself. However, stacking sphere monolayers one after the other results in a higher packing factor c ($c \geq 0.9$) and less ordered sphere layers than in colloidal crystals obtained from evaporation or sedimentation methods with a fcc lattice ($c = 0.816$) [6.80]. The enlarged layer spacing in the z-direction is accompanied by optical properties that are different from those observed in fcc colloidal crystals [6.90–92]. Figure 6.9 shows SEM images of colloidal crystals that have been produced using the LB technique. A monolayer deposit of silica spheres shows domains with a perfect crystalline order (Fig. 6.9a), that might be perturbed by several defects including grain boundaries, missing spheres, or empty space between the spheres (Fig. 6.9b). Investigating the cross-section in multilayer samples in Fig. 6.9c,d confirms that the thickness of the colloidal crystal is uniform throughout the sample.

Colloidal crystals may also be assembled in capillaries. A straightforward setup is shown in Fig. 6.10a. Here, two glass plates that are separated by thin spacers are placed into a colloidal suspension. Capillary forces will transport spheres into the cell toward the edges, where evaporation of solvent and the crystallization of particles takes place. An alternative setup, using a bi-capillary system is illustrated in Fig. 6.10b, which was reported to allow a good control over thickness and crack arrangements in colloidal crystals [6.93]. The thickness of the growing crystal is defined by the distance between the two planar plates of the cell. An SEM image of a sample produced with this setup can be seen in Fig. 6.10c [6.94]. The crystal is very homogenous over large distances with a very low number of defects. For bigger particle diameters, less well-ordered structures resulted, which is probably due to the influence of gravity acting opposite to the capillary force.

Very similar setups to the ones shown in Fig. 6.10 are used when colloidal crystals are formed by confinement. *Park* et al. were the first presenting a confinement cell in order to assemble colloidal crystals from particle suspensions [6.97]. However, in their configuration, the particle flow was driven by the application of positive pressure transporting the particles to the cell edges. Microstructured membranes at the cell edges allowed the solvent to evaporate by retaining the particles in the cell.

Another way of producing ordered colloidal crystal arrays consists in using shear forces. The spin-coating process represents an example for shear-induced ordering. Therefore, colloidal silica particles were suspended in nonvolatile triacrylate monomers and the mixture was spin-coated onto different substrates [6.86]. Ordering of the spheres is observed due to shear forces, occurring when the suspension smears along the rotating substrate. The photopolymerization of the monomer

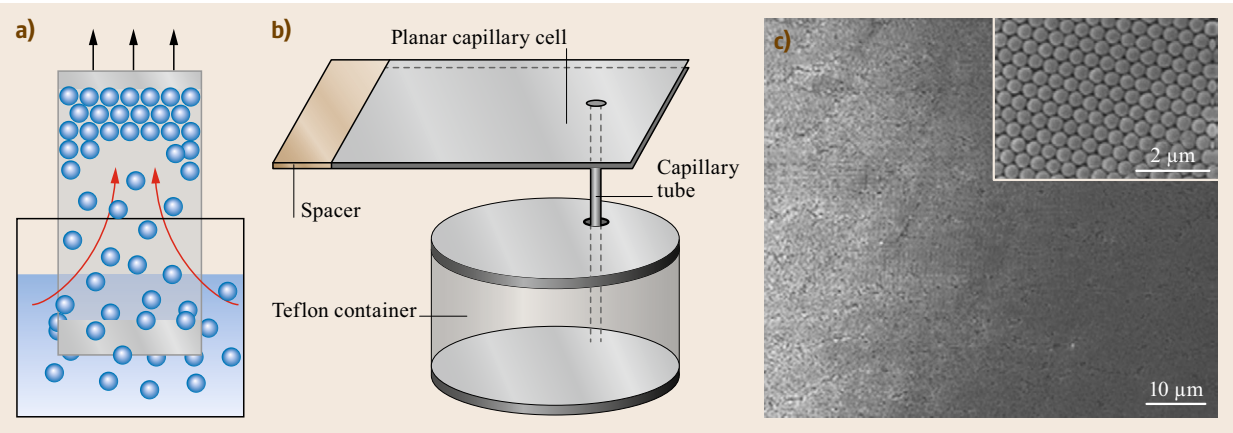


Fig. 6.10a–c Capillary method. **(a)** Schematic representation of the vertical capillary cell (after [6.94]). **(b)** Setup containing a capillary tube for the transport and a capillary cell for the crystallization of colloidal spheres (after [6.93]). **(c)** Colloidal crystal fabricated with the setup shown in **(a)**; particle diameter was 423 nm (after [6.94])

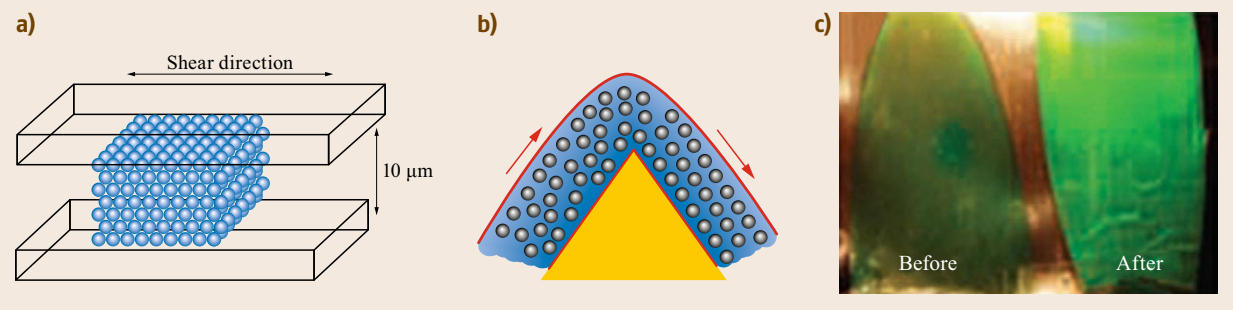


Fig. 6.11a–c Ordering of colloidal assemblies by shear forces. **(a)** Scheme of the shear alignment-based process (after [6.95]). **(b)** Ordering in opaline films by edge-induced shearing. **(c)** Opal films before and after edge-induced shearing (after [6.96])

gave stable composite films where individual particles, however, were not necessarily in contact with each other. The use of volatile solvents as a suspension medium enabled to produce colloidal crystals with touching spheres that did not have to be enclosed in a polymer matrix [6.98]. Apart from spin coating, different other setups can be employed to apply shear forces to a colloidal assembly.

In Fig. 6.11a, a colloidal film is confined in a thin cell composed of two parallel plates, of which one is sheared against the other [6.95]. The resulting shear forces produce well-ordered colloidal crystal arrays. Generally core–shell particles with a soft polymer shell grafted on a hard silica or polymer core are employed in techniques based on a shear alignment. By using polymer core–shell particles well-established processing methods in polymer fabrication including extrusion or hot pressing can be employed to fabricate colloidal crystals [6.96, 99]. Recently, a possibility was presented to enhance the crystalline quality in these core–shell opaline films. First crystalline films made out of polymer particles composed of a polystyrene core and a soft polyethylacrylate shell have been produced by extrusion, followed by a rolling procedure of the produced ribbons. In a second step, these films were drawn over a heated edge, which is schematically shown in Fig. 6.11b. This process resulted in significant improvements in terms of the crystalline order of these films. This finding is supported by the brighter colors seen for the opaline film shown in Fig. 6.11c on the right, where edge-induced shearing has been performed.

6.1.2 Overview over Different Infiltration Techniques

The general steps involved in transforming a colloidal crystal into its inverse structure are shown in Fig. 6.12. After assembling an ordered array of spheres on a substrate, the void space present in the colloidal template can be filled with another material. Different techniques exist that allow efficient infiltration relying on precursors either in a liquid or gaseous form. The choice

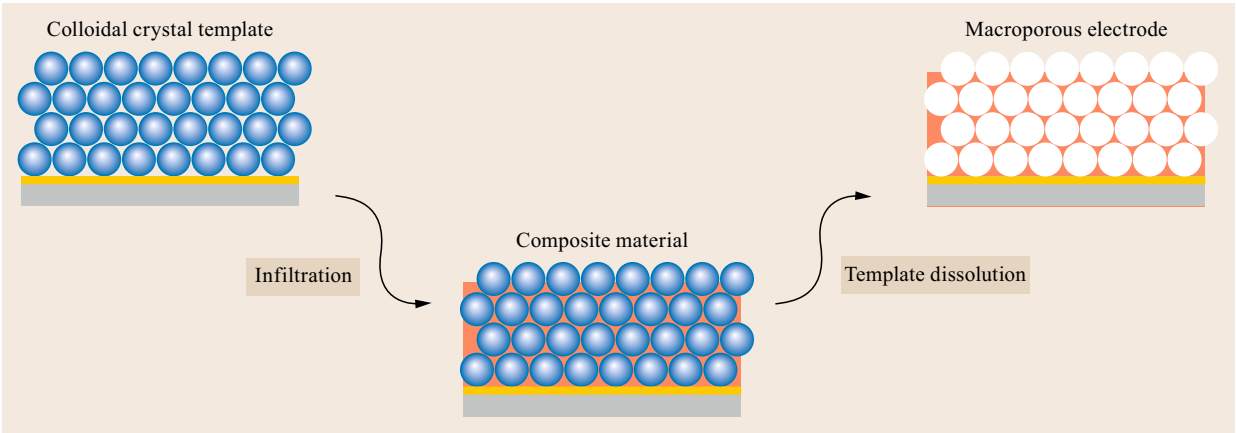


Fig. 6.12 Fabrication steps in colloidal crystal templating. The void space in a colloidal crystal is infiltrated with another material. Removal of the template is achieved by calcination or dissolution of the colloidal spheres. As a result, an inverse opal structure composed of interconnected air spheres, which are embedded in the infiltrated material, is obtained

of the adequate technique here is crucial for the final properties of the inverse structure as they will depend strongly on the employed infiltration method. Once the infiltration is terminated, the template can be removed by calcination or dissolution revealing a three-dimensional-ordered macroporous material.

Some general points regarding colloidal crystal templating may be addressed before discussing different infiltration techniques. It has to be assured that the colloidal sphere template provides enough stability to allow its infiltration in liquid environments. To further stabilize the template structure it may be sintered. This results in a neck formation between neighboring spheres, driven by surface energy minimization, and eventually to a merging of the spheres. It is important to control this step by adapting the temperature and sintering time, because otherwise the void space can get too reduced to allow infiltration of the template. Combining sintering with a subsequent etching step also leads to nonclosed packed opals [6.100]. In order to allow the spheres to be removed after the infiltration, the etching solution has to be able to access the beads. Therefore, the colloidal crystal should only be partly filled with material not exceeding the top layer of the template. This may be difficult to control in certain top-down-based infiltration methods. The removal of the template generally occurs in dilute hydrofluoric acid for silica spheres and in appropriate solvents (e.g., toluene, dichloromethane or acetone) or by calcination for latex spheres.

In Fig. 6.13, two different inverse opal structures, which are obtained by colloidal templating, are shown schematically.

The structure in Fig. 6.13a shows a surface-templated structure. Here the precursor interacts strongly with the spheres during the infiltration resulting in skeletal walls that follow the curvature of the original spheres [6.101]. In this case, only part of the template is filled by the infiltrated material.

Figure 6.13b shows a typical example for a volume-templated material. In contrast to surface templating, all the available void space is filled by the infiltrating material, so that the inverse structure is the exact cast of the original colloidal template. Which of both structures is present in inverse opals depends on both, the employed infiltration method and the degree of interaction of the precursor with the sphere material. Also, mixtures of both cases are possible. For a given infiltration technique, one may switch from one structure to the other by changing either the precursor or the chemical nature of the spheres. These small structural differences also have an influence on the optical properties of inverse opals, for example, the band structures in PCs, and, hence, have been subject of detailed research [6.101–103].

Gaseous Precursor Infiltration

Among the techniques that employ precursors in the gaseous form, the standard method for the infiltration of opals represents chemical vapor deposition (CVD). CVD is widely used in semiconductor processing to deposit thin coatings of silicon, metals, and insulation layers on semiconductor wafers. In order to deposit thin films by CVD, at least one gaseous precursor is introduced into a reaction chamber and condenses at the surface of a heated substrate. Substrate temperatures typically are in the range of 500–1000 °C. CVD is equally known to result in uniform deposits even on complex 3-D cavities, which makes it a suitable technique for the infiltration of colloidal crystals.

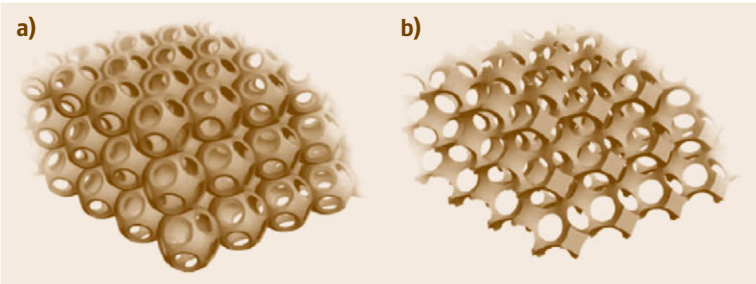


Fig. 6.13a,b Schematic diagrams of a surface-templated material **(a)** and a volume-templated material **(b)** (after [6.101])

In contrast, standard physical vapor deposition (PVD) methods, including sputtering or e-beam evaporation, would result only in film deposition on top of the colloidal crystal which were used in the fabrication of two-dimensional (2-D) nanostructured metal films [6.104]. CVD generally is performed under reduced pressure in order to avoid undesirable reactions to take place in the gas phase including condensation reactions of gas molecules before they reach the surface of the substrate. The high temperatures involved in the process necessitate a temperature stability of the substrates. This excludes polymer particle assemblies from being infiltrated by CVD and bringing into focus silica-based colloidal crystals. A variation of the process employs a plasma to increase the chemical reaction rates of the precursors, allowing lower reaction temperatures in plasma-enhanced CVD (PECVD). Figure 6.14 shows some examples for inverse opals that were produced by CVD methods. Figure 6.14a–c all reveal the typical structure observed for surface-templated inverse opals (Fig. 6.13a).

Gaseous precursor flows through the substrate and reacts at the surface of the spheres leading to a uniform coating. However, colloidal templates are not filled completely by CVD, as access to the void space in the template gets restricted for the gas flow as soon as a certain deposition thickness is reached. Figure 6.14a shows an example in which only a thin tungsten film has been deposited onto the colloidal template. After removal of the latter, a crystalline assembly of hollow spheres with air cavities at the points where the colloidal spheres have been in contact is obtained. Figure 6.14b depicts a graphitic inverse opal with similarly low filling fractions, showing the inner surface of a hollow sphere array. High filling ratios using CVD are generally accompanied by an overgrowth of material covering the top layer of the colloidal template shown in Fig. 6.14c. This makes the removal of the template difficult as the access for the etching solution to reach the spheres is blocked. The excessively deposited material, therefore, first has to be removed. Ion milling using a focused ion beam provides a costly but well-suited technique to ablate nanometer-thick films in a controlled manner [6.106]. The materials deposited by CVD are amorphous, which requires heat treatment for several hours at temperatures where recrystallization in the material occurs [6.39]. Using CVD, a range of materials can be infiltrated into opals including semiconductors (Si, Ge, InP, etc.) [6.11, 39], carbon-based materials [6.105, 107], or oxides [6.108, 109]. Recently, a variation of the CVD process has been applied for the infiltration of colloidal crystals, permitting high control over the thickness of the deposited material [6.106, 110, 111]. In atomic layer deposition (ALD), different gaseous precursors are alternatively applied by a pulsed deposition. In between of the pulses, a purging step

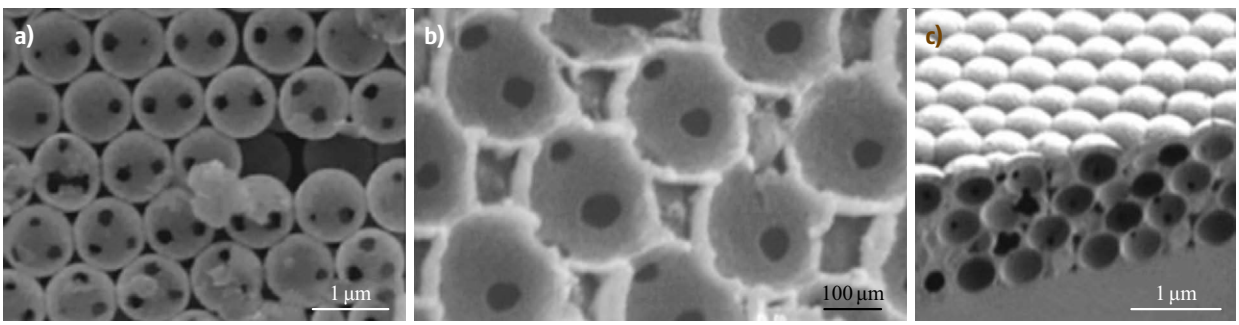


Fig. 6.14 SEM images of inverse opal structures produced by CVD. **(a)** Tungsten inverse opal showing the typical surface-templated structure (after [6.101]). **(b)** Graphitic replica of an opal prepared by PECVD (after [6.105]) **(c)**. Si inverse opal obtained by low-pressure CVD at temperatures slightly below 580 °C (after [6.39])

allows us to remove nonchemisorbed material. For example, a $TiCl_4$ layer, which has been chemisorbed at the surface of the substrate in a previously applied pulse, will react with the H_2O precursor provided by a second pulse, resulting in an ultrathin layer of TiO_2 [6.106]. In this way, the desired final thickness is reached by layer-by-layer deposition. As the process is self-limiting, ALD allows us to deposit materials including TiO_2, WN, and ZnS at a resolution of atomic layers [6.11].

Liquid Precursor Infiltration

Inverse opals of various materials can also be obtained by infiltrating opals with liquid precursors. One can distinguish different techniques by the type of the medium used to infiltrate the opal, including molecular precursors, sols, nanoparticle suspensions, and molten media. The sol–gel process represents a versatile and commonly used technique in order to infiltrate opals. Here, metal alkoxide precursors infiltrate the void space of the opal and start a sol–gel process [6.112, 113]. Alternatively, the sol can be prepared before the infiltration and the sol–gel process is completed in the opal [6.11, 114]. The infiltration and reaction mechanism can be repeated several times in order to increase the filling fraction in the opal [6.113]. Once the infiltration is terminated, the polymer template is removed by calcination which eliminates eventual remains of solvent and stabilizes the inverse opal structure. This process is accompanied by shrinkage of the structure (up to 40%) [6.11] and mass transport leads to a reorganization of material in the structure. Typical inverse opal structures obtained by a sol–gel-based infiltration technique are shown in Fig. 6.15a,b. In these examples, volume-templating, in combination with material reorganization during the sintering produced a skeletal structure with nearly rod-like struts [6.101]. Volume-templated inverse opal structures also could be obtained using sol–gel-based infiltration [6.116]. The electrostatic interactions between the colloidal template and the precursor solution as well as the conditions during hydrolysis, drying, and condensation represent important parameters influencing the final structure of the inverse opal [6.101]. Despite considerable drawbacks of the process involving the roughness of the inverse structure (≈ 10 nm), low filling fractions (about 12%) and the volume loss associated with the shrinkage, sol–gel-based infiltration represents a very versatile technique. Besides the well-studied oxide systems including TiO_2, ZrO_2, SiO_2, and Al_2O_3 [6.112, 113, 117] also carbides [6.118] and even inverse opals doped with metals can be realized [6.118, 119].

Polymer inverse opals can be fabricated by infiltrating colloidal crystals with monomers followed by a polymerization of the monomers by exposure to UV light [6.115, 120], heating [6.121], or catalyzed polymerization [6.122]. Using this approach, different polymers including PU (polyurethane), PMMA, and PS can easily be fabricated [6.115, 120–122]. The same strategy was employed to produce inverse opals of conjugated polymers leading to electrochromic devices with enhanced switching times [6.123]. A simplification toward a one-step process was proposed by *Yan* and *Goedel* who mixed the precursor directly with the colloidal suspension in order to form an ordered crystalline assembly of the mixture on a water surface [6.124]. The cross-sectional image of a PMMA polymer inverse opal is depicted in Fig. 6.15c. A shrinkage of 20–30% was reported to result from the polymerization of the monomers [6.115].

Alternatively, metallic or semiconducting materials can be infiltrated in the molten state into opals when the melting temperature is low enough. The infiltration of molten selenium into a colloidal crystal led to inverse opals with a high refractive index contrast, interesting for an application in PCs [6.125].

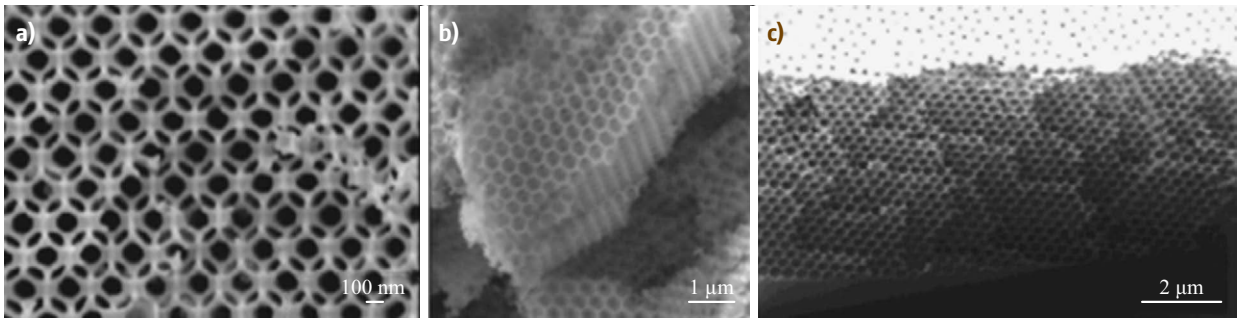


Fig. 6.15 SEM images of inverse opals produced by infiltration with liquid precursors. **(a)** Tungsten inverse opal with a skeletal structure (after [6.101]). **(b)** Inorganic skeleton of a macroporous zirconium oxide sample after calcination (after [6.112]). **(c)** PMMA inverse opal with 24 layers after monomer infiltration, UV polymerization, and removal of the silica template (after [6.115])

Another strategy consists in using nanoparticles to infiltrate colloidal crystals. The nanoparticles have to be sufficiently small to allow the penetration of the void channels in the opal (about a tenth of the diameter of the void channels) [6.11]. In this way, the shrinkage is considerably reduced, as the nanoparticles already are in their final chemical form. This approach enables inverse opals to be fabricated from a variety of materials including metals, oxides, or semiconductors [6.117, 126, 127]. Recently, transparent macroporous electrodes from antimony-doped tin oxide (ATO) have been fabricated in this way [6.127]. This technique may further be simplified by mixing colloidal spheres with nanoparticle suspensions in order to co-assemble *filled* opals from bi- or multimodal dispersions [6.128, 129]. A heating step may provide structural stability to the crystalline assembly prior to the template removal. With this method, very complex metallodielectric inverse opals can be obtained by using core shell nanoparticles, possessing a metallic core and a dielectric shell or the other way round [6.130]. The use of microfluidic devices allowed to break bi-modal suspensions of polystyrene and silica spheres into separate droplets resulting in very uniform porous microspheres after the drying and calcination of the samples [6.131].

Infiltration via Electrochemical Deposition

The void space in a colloidal crystal template equally may be filled using electrochemical deposition. A typical setup for electrodeposition experiments consists of three electrodes – a working (WE), a counter (CE) and a reference electrode (RE) – that are connected to a direct current power supply. The electrodes are immersed into an electrolyte solution which contains species that may be deposited by reduction (e.g., metal ions) or oxidization (e.g., monomers) on the WE. The driving force for the redox process is provided by a potential or a current which is applied to the working electrode in potentiostatic, potentiodynamic, or galvanostatic mode, respectively. The substrate containing the colloidal template serves as the WE and thus needs to be electrically conductive. The application of adequate potentials at the WE leads to a film growth at the surface of the electrode. In contrast to the previously described infiltration methods, the filling of the void space starts in this case at the bottom of the template, proceeding toward the outer surface. This is quite convenient as it allows to stop the electrodeposition at the desired filling level and avoids the overgrowth of material over the top surface of the template. In most cases, the entire void space of a colloidal crystal is filled by the electrodeposited material, hence leading to volume-templated inverse opal structures (Fig. 6.13b). As a consequence, high filling fractions are achieved during the electrochemical infiltration of opals. Additionally, the shrinkage, if involved in the process, is insignificantly small compared to sol–gel techniques, as the electrodeposited material already is in its final chemical form. This results in inverse opals with a good mechanical stability.

In some CP inverse opals also surface-templated structures were observed [6.133, 135]. Figure 6.16b shows a poly(3,4-ethylenedioxythiophene) (PEDOT) inverse opal possessing small air gaps at the connecting points between neighboring air cavities. These gaps are due to the preferential growth of the polymer around the sphere template guiding the film deposition. This guiding effect was attributed to the electrostatic interactions between the radicals formed during the polymerization and the surface groups of the colloidal spheres [6.133]. Figure 6.16c gives an example of a volume-templated inverse opal structure in which the electrodeposition was stopped exactly at a half height of a sphere layer. The three dark spots inside each macropore correspond to the areas where spheres of an underlying layer were in contact with the top-layer spheres. Here the colloidal template has been completely filled with germanium. Figure 6.16a shows the cross-section of a macroporous nickel electrode with highly interconnected pores.

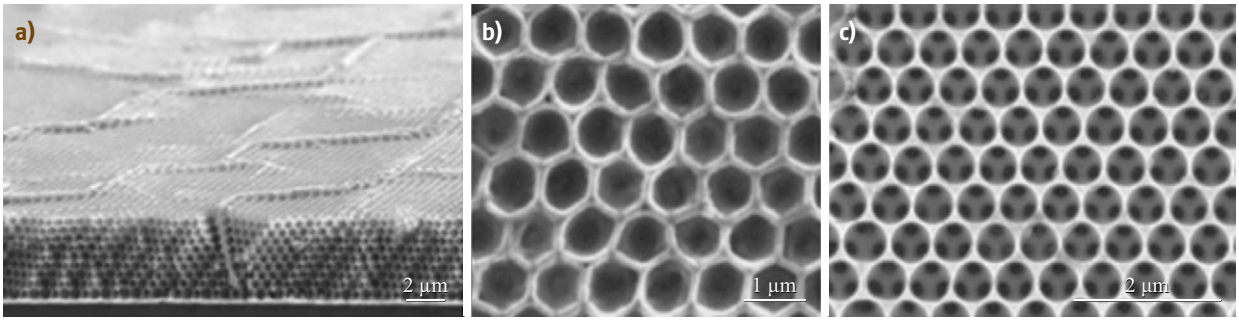


Fig. 6.16 Inverse opals produced by electrochemical deposition. **(a)** Cross-section of a nickel inverse opal with nine and a half-layers (after [6.132]). **(b)** Top view of a CP inverse opal produced by the electrodeposition of PEDOT (after [6.133]). **(c)** Top view of a germanium inverse opal fabricated by electrochemical deposition in an ionic liquid (after [6.134])

A wide range of materials can be electrodeposited and was used to infiltrate colloidal crystals. The biggest group among them are metallic deposits owing to the commercial availability of ready-to-use plating solutions providing a uniform film deposition in the colloidal template. Inverse metallic opals have been prepared by the electrochemical deposition of platinum [6.136–138], gold [6.126, 129, 138–141], silver [6.142, 143], copper [6.136], nickel [6.132, 136, 144–149], cobalt [6.137, 145], palladium [6.137], bismuth [6.150], antimony [6.151], and iron [6.145]. Conducting polymers can also be grown into a colloidal template by electrochemical deposition. Inverse opals of CPs, were obtained for polypyrrole (PPy) [6.135, 152, 153] polyaniline (PANI) [6.135, 154], polythiophene (PT) [6.135, 153], and PEDOT [6.133]. Some semiconducting materials including Ge [6.134], CdS [6.155], and CdSe [6.155] have also been used to infiltrate opals by electrodeposition. Additionally a range of metal oxide inverse opals has been fabricated by electrodeposition including ZnO [6.156, 157], WO_3 [6.158], PbO_2 [6.159], IrO_2 [6.160], RuO_2 [6.161], MnO [6.162], and NiO [6.163], completed by some inorganic/organic hybrid derivatives [6.164].

6.1.3 Electrodeposition of Metals in Colloidal Templates

The fabrication steps to produce macroporous electrodes are schematically illustrated in Fig. 6.17a including the assembly of a colloidal template (e.g., silica) on a gold-coated glass slide, metal electrodeposition, and the removal of the inorganic template (e.g., in hydrofluoric acid). A typical setup for the electrochemical deposition is illustrated in Fig. 6.17b and includes the working (e.g., gold substrate with the colloidal template), the reference (e.g., Ag/AgCl), and the counter electrode (e.g., a high surface area Pt mesh). By applying a sufficiently negative potential to the WE, the electrodeposition process was initiated, provoking the reduction of metal ions leading to the growth of a metallic film at the surface of the WE. Once the desired thickness of the deposit is reached, the electrodeposition can be stopped to remove the template, resulting in the final macroporous metal electrode. Figure 6.17c

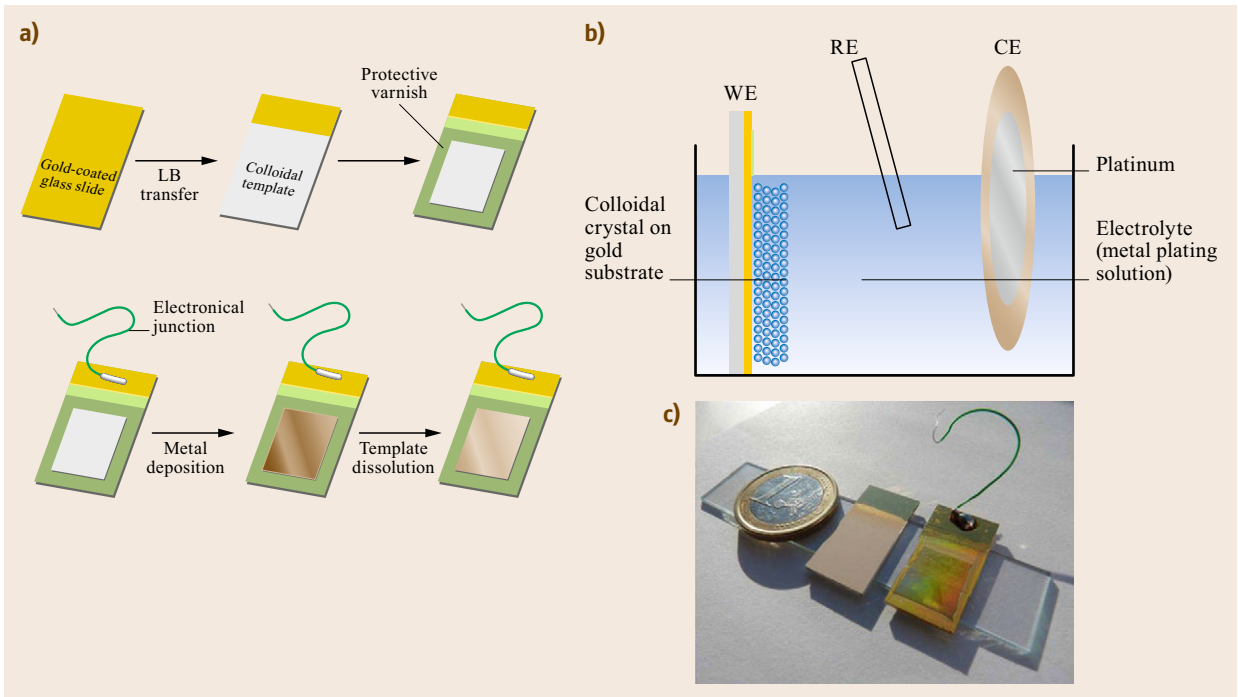


Fig. 6.17 **(a)** Different steps involved in the fabrication of macroporous metal electrodes. Varnish is used in order to delimit the accessible area for the electrochemical deposition on the sample. **(b)** Setup for the infiltration of colloidal crystals with various metals by electrochemical deposition. WE: working electrode; RE: reference electrode; CE: counter electrode. **(c)** Optical photograph of the gold-coated glass slides after the deposition of the colloidal template (*middle*) and after metal deposition and template removal (*right*)

shows a gold-coated glass slide with the colloidal template, (*middle*) and the macroporous gold electrode after electrodeposition and removal of the silica template (*right*).

Gold Electrodeposition Into Colloidal Templates

For the electrodeposition of gold into the void space of colloidal templates the commercial gold bath ECF 60 (Metalor) was used, as it favors a smooth 2-D growth process instead of uncontrolled 3-D growth obtained for solutions containing only chloroauric acid. A potential of −660 mV versus Ag/AgCl allows to reduce $[Au(SO_3)_2]^{3-}$ ions, contained in the plating solution to metallic gold [6.140, 141, 165]. The intensity of the faradaic current during amperometric deposition was measured as a function of the electrodeposition time and is shown in Fig. 6.18a. During the infiltration of the colloidal templates with gold very regular current oscillations were observed. The main parameters, which affect the current intensity during potentiostatic deposition, are the applied electrode potential, the composition and temperature of the plating solution and the active area of the WE. As a constant potential was used and the electrolyte composition and temperature do not change significantly in the course of an experiment, the faradaic current response depends exclusively on the active surface area of the WE. The deposition performed on a smooth electrode without the presence of a colloidal crystal hence is expected to result in a constant response of the current intensity after an initial current drop due to nucleation. However, the presence of a colloidal template on the surface of the electrode leads to current oscillations (Fig. 6.18a) that are caused by a periodic variation of the surface area which is available for the electrodeposition in the colloidal template (Fig. 6.18b).

During the early stages of the electrodeposition in Fig. 6.18a, a fast drop followed by an increase in the absolute value of the current is observed during the nucleation of metal film growth. The value of the absolute current increases due to the surface roughness of the metal nucleation sites and reaches an extremum, corresponding to the first local minimum in the plot since the current is negative. As the metal film begins to fill the void space of the first bead layer, the value of the absolute current decreases. Here, the surface area accessible for the growing film gets more and more restricted in the colloidal template and finally reaches a minimum, when the growth front reaches the half-height of the first bead layer (Fig. 6.18b). Consequently, also the absolute current attains a minimum at this point, corresponding to the first local maximum in Fig. 6.18a. The half-layer gold-filling level in the colloidal template is illustrated by the corresponding inset in Fig. 6.18a. From this point on, the upper half of the first bead layer in the template will be filled with electrodeposited gold.

Contrary to the previously described period, the space between the neighboring spheres here continually increases providing a bigger surface area for the growing metal film (Fig. 6.18b). The absolute value of the current consequently increases, up to the point, where

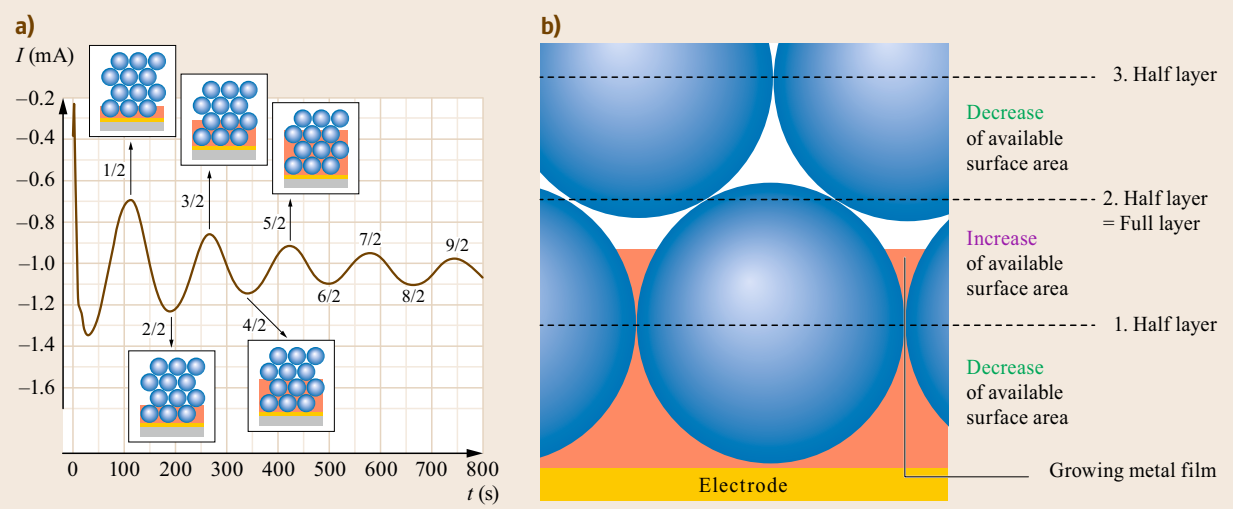


Fig. 6.18 **(a)** Current oscillations observed during potentiostatic gold deposition at $E = -660$ mV into a colloidal crystal template with a sphere size of 395 nm. Absolute current minima correspond to different half-layer gold filling levels in the template and absolute current maxima to full-layer filling levels with gold. **(b)** Schematic representation of the periodic variation of the surface area available for the electrodeposition in a colloidal template

the film reaches the bottom of the second sphere layer in the template. This results in an absolute current maximum which corresponds to the second local minimum in Fig. 6.18a. The void space of the first bead layer here is almost completely filled with gold (see corresponding inset in Fig. 6.18a). The whole process, here described in detail for the infiltration of the first bead layer, continues for the filling of succeeding sphere layers and results in well-pronounced oscillations of the recorded current response. Infiltration into colloidal crystals therefore can be regarded as an electrochemical deposition where the surface area of the WE periodically changes throughout the experiment.

These oscillations represent a very convenient feature, because they allow us to perfectly control the filling of the void space in colloidal crystals with an accuracy that can reach a few nanometers. Obviously, as illustrated by different insets in Fig. 6.18a, one can stop the electrodeposition at half- or full-layer filling levels which results either in completely open or almost fully closed pore structures, respectively. As the electrodeposition can be stopped at any time between the local extrema, very good control is provided over the final structure of the inverse opal. In order to ensure best possible access of the solution to the macroporous structure, the electrodeposition often is stopped at a half-layer filling level, resulting in a complete opening of the pore mouths at the electrode surface.

Oscillating currents during amperometric electrodeposition into colloidal crystal templates have been reported before by several authors including preceding work performed in our group [6.132, 140, 144, 147, 165]. The appearance of this phenomenon is coupled to two crucial parameters requiring both a well organized colloidal crystal structures and the uniform growth of the electrodeposited material. As shown by the oscillations in Fig. 6.18, the amplitude decreases the longer the electrodeposition time and the more void space in the template gets filled by the metal. The cause for the gradual decrease of the oscillation amplitude can be twofold. A lack of organization in the sphere layers and electrodeposited material not growing homogeneously throughout the template are both leading to the situation that the synchronization between the factors increasing or decreasing the global current response gets lost in the course of the infiltration. Therefore, the oscillations are finally *canceled out* after a certain time. Nevertheless, we were able to observe an oscillating current response during the infiltration of colloidal templates for up to 25 sphere layers and deposition times exceeding 1 h (Fig. 6.19a,b). Such results confirm that the packing of sphere layers in colloidal templates produced by the LB technique is very regular. In other literature work, the oscillations cancel out much faster and could be observed in the best case only up to a filling level of 10 sphere layers [6.132]. In Fig. 6.19, the current density j, which corresponds to the measured current intensity divided by the geometric surface area of the sample, has been plotted as a function of the electrodeposition time facilitating the comparison of the results obtained for samples with different surface areas.

By comparing Fig. 6.19a,b, one notes that the frequency of the current oscillations changes when the sphere size of the colloidal template changes. By geometrical considerations, the oscillation frequency

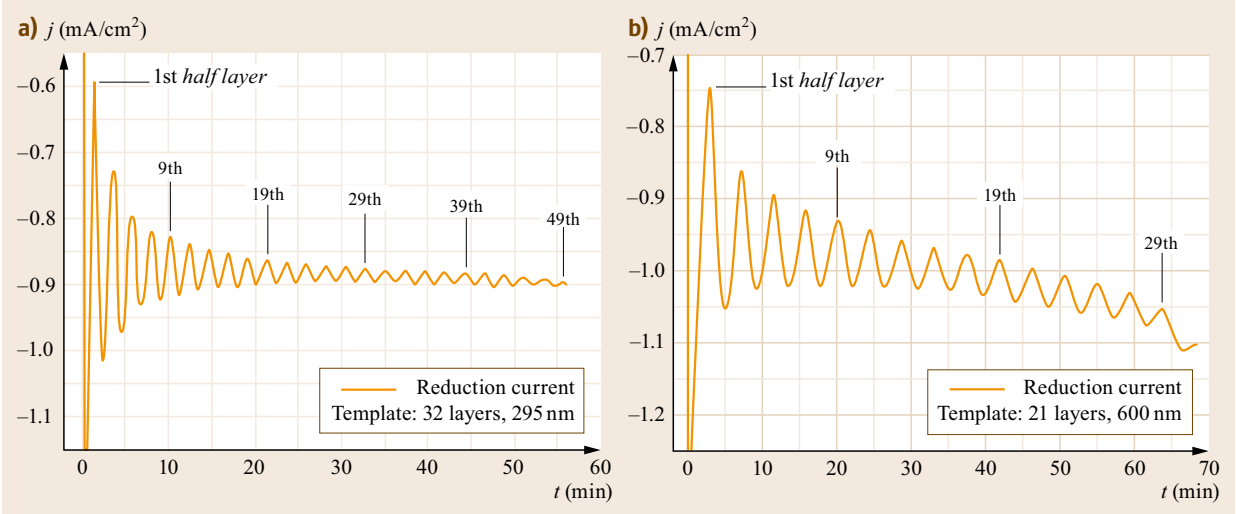


Fig. 6.19a,b Amperometric electrodeposition of gold into colloidal crystal templates at $E = -0.66$ V. Oscillations obtained for the infiltration of **(a)** 49 half-layers (bead size 295 nm) and **(b)** 31 half-layers (bead size 600 nm) of gold into the templates

should be doubled when spheres with a two times smaller diameter form the template, supposing a constant metal deposition rate during different template infiltrations. In Fig. 6.20a, four different chronoamperometric curves are compared showing the infiltration of gold into different colloidal templates that are composed of spheres with different diameters. It is found that the frequency of the oscillations decreases when templates composed of bigger spheres are infiltrated. The arrows added in Fig. 6.20a indicate that three (1st *arrow*) and eleven (2nd *arrow*) half-layers of the template have been filled with gold. For bigger sphere sizes, the corresponding arrows are shifted toward longer times, the frequency decreases and the oscillation period increases. Based on the data of Fig. 6.20a, one can plot the oscillation period as a function of the sphere size in the template shown in Fig. 6.20b. A linear relation found between sphere size and oscillation period (or frequency) is in good agreement with theoretical considerations.

Figure 6.21 illustrates SEM images of several macroporous gold electrodes. In Fig. 6.21a, an electrode cross-section of a two-layer template is shown which has been filled with gold. As expected, the available volume in the sphere template has been filled with gold, resulting in volume-templated structures (Fig. 6.13b). At the black spots present inside the macropores, no metal deposition occurred because touching spheres prevented the electrolyte solution from accessing these areas. After template removal, these spots will become the interconnection points between neighboring macropores. Figure 6.21b provides a top view of a macroporous gold electrode with a thickness corresponding to one and a half pore layers. Here, macroporous domains with a perfect organization are disturbed by some defects in the structure, which is in agreement with the colloidal template structure discussed previously in Fig. 6.9b. Figure 6.21c,d shows the cross-section of the macroporous gold electrode which corresponds to the amperometric deposition curve in

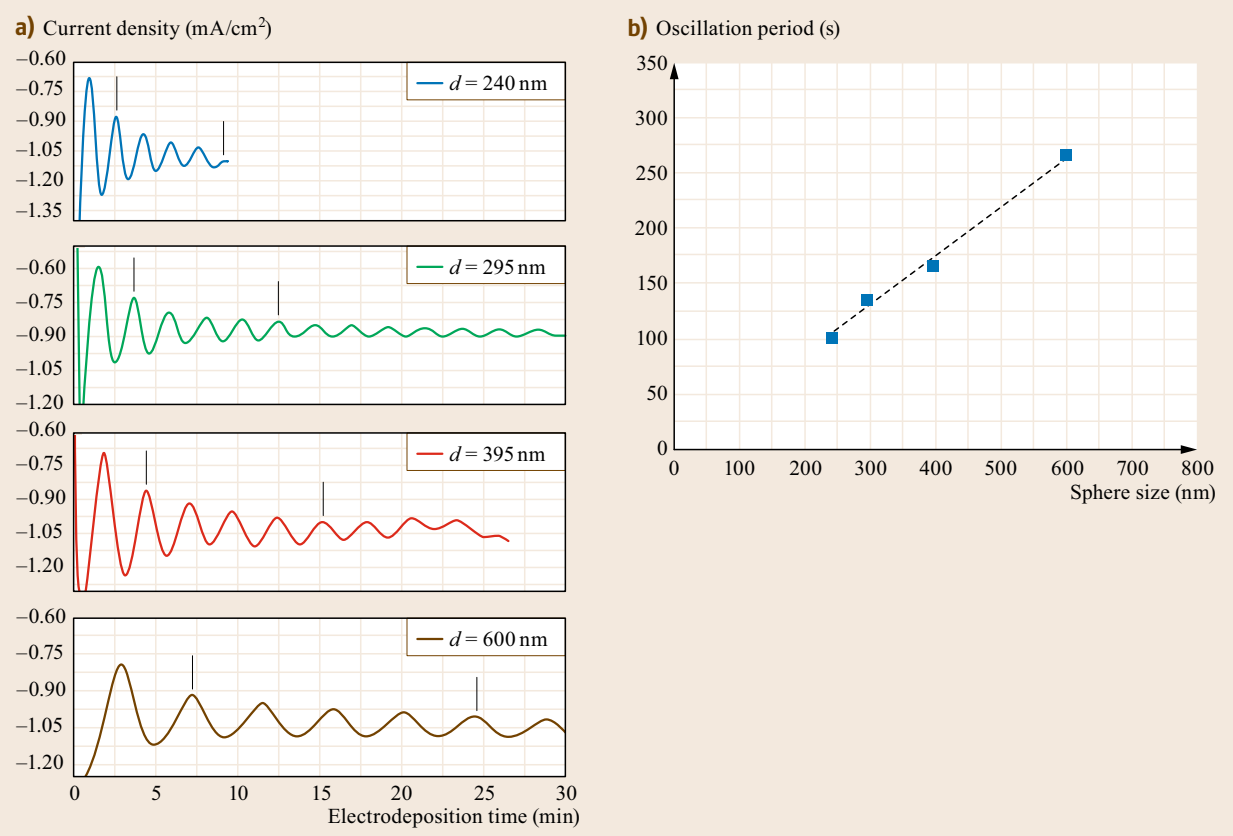


Fig. 6.20 **(a)** Chronoamperometric curves for the electrodeposition of gold into colloidal crystals with a different sphere size. The *two arrows* represented in each curve correspond to the filling of 3/2 (1st *arrow*) and 11/2 layers (2nd *arrow*) of the template with gold. **(b)** Plot of the oscillation period obtained from the results shown in **(a)** as a function of the colloidal sphere size of the template

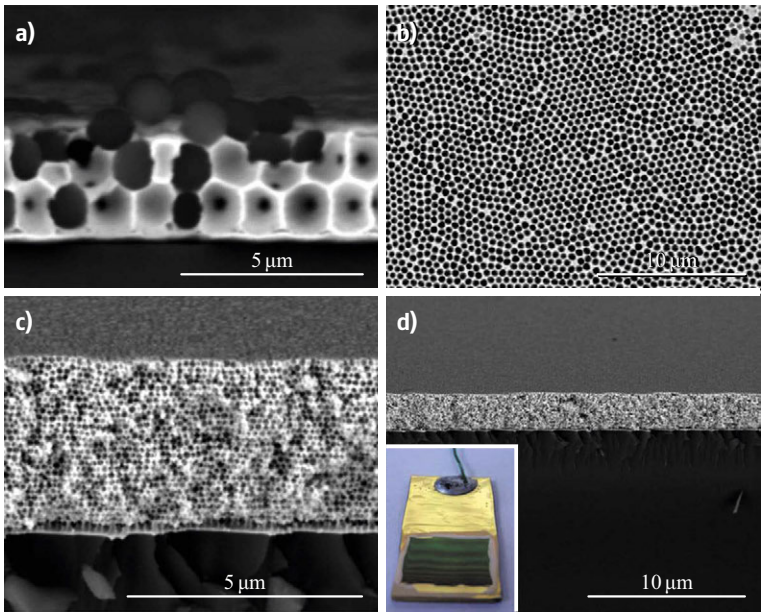


Fig. 6.21a–d SEM images of macroporous gold electrodes obtained by electrochemical deposition. **(a)** Cross-section of a structure ($d = 1200$ nm) where two layers have been filled with gold. **(b)** Top view onto three half-layers of macroporous gold ($d = 600$ nm). **(c)** Cross-section of a macroporous gold electrode with 49 half-layers ($d = 295$ nm); the corresponding amperometric curve is shown in Fig. 6.18a. **(d)** Larger view of **(c)** with the *inset* showing a picture of the sample (geometric area of the macroporous deposit $\approx 1\,\mathrm{cm}^2$)

Fig. 6.19a. Both SEM images confirm the uniform thickness of the electrode which consists of 49 half-layers of macroporous gold.

Electrodeposition of Nickel and Platinum in Colloidal Templates

As mentioned in Sect. 6.1.2, a wide range of different metals may be electrodeposited into colloidal templates. In this section, we focus on nickel and platinum deposits into a colloidal crystal template. For the electrodeposition of nickel, a commercially available plating solution has been employed (Crystal 501; Coventya). Platinum was electrodeposited from an aqueous solution containing 60 mM hexachloroplatinic acid (H_2PtCl_6) and 0.1 wt % of the anionic surfactant sodium dodecyl sulfate (SDS) [6.166]. In order to find the adequate potential leading to smooth and homogeneous film growth, electrodeposition at different applied potentials was performed for each electrolyte solution. Straightforward conditions were found for the applied potentials of −0.93 and +0.142 V [6.167] versus Ag/AgCl for the deposition of nickel and platinum, respectively. Owing to the smooth film growth, oscillations in the current response could be observed for nickel and platinum deposits into colloidal templates. In Fig. 6.22a, a colloidal template composed of 10 layers with a sphere diameter of 325 nm was filled with 17 half-layers of platinum. The measured current here showed similarly regular oscillation profiles as the ones previously observed during potentiostatic gold infiltration. As a consequence, the filling level of the colloidal template with platinum could be perfectly controlled. Figure 6.23a shows the cross-sectional image of the same electrode after platinum had been deposited into the template. It turns out that exactly eight and a half-layers of the template have been infiltrated with platinum, which is in perfect agreement with the results shown in Fig. 6.22a. In Fig. 6.23b, the silica template has been etched away, resulting in the macroporous platinum film electrode. The thickness of the film is perfectly uniform and the pore layers are well organized in the sample. By looking closely, one can see black air spots inside the macropores that interconnect adjacent pores.

In Fig. 6.22b, the current oscillations observed during the nickel infiltration into a colloidal template are illustrated. Here, as in the case of Pt, 17 half-layers of the template should be filled with nickel. The sphere size of the colloidal template, however, was with 740 nm more than double the size of the one used in Fig. 6.22a. At the beginning of the electrodeposition, the first two oscillations show a very regular form with high amplitudes. Already the third oscillation is less pronounced and a big part of the oscillation amplitude is lost. Nevertheless, oscillations are visible until the deposition process is stopped corresponding to a filling level of slightly more than eight sphere layers. The relatively fast loss in oscillation amplitude during the electrochemical infiltration may be caused by an irregular sphere layer stacking or the uneven progress of the nickel growth front in the colloidal template. Figure 6.23c shows the electrode cross-section after the filling of the template

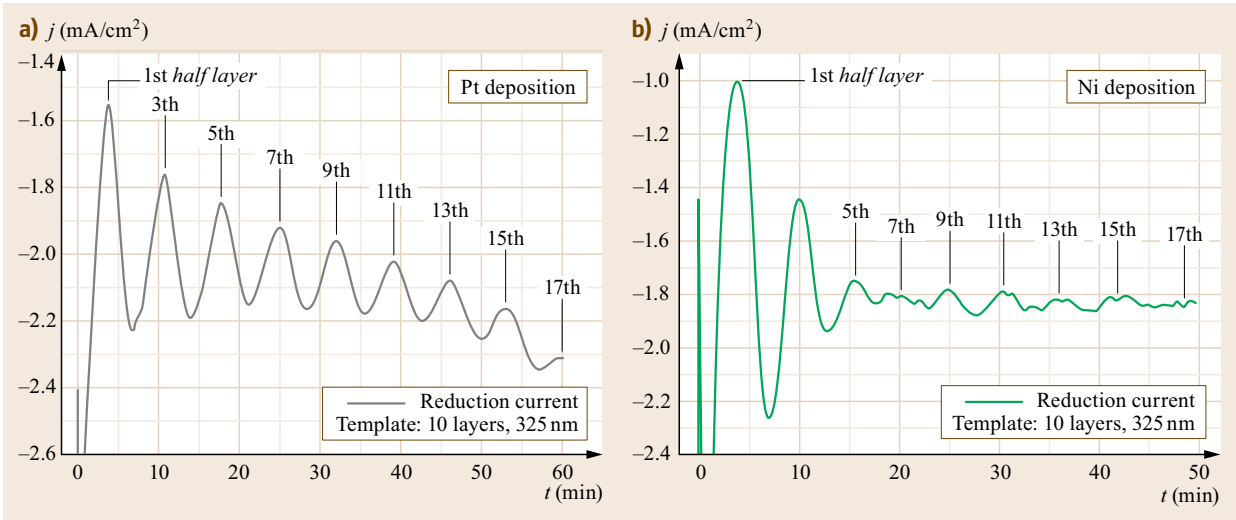


Fig. 6.22a,b Amperometric electrodeposition of **(a)** platinum into a colloidal crystal template (10 sphere layers, diameter 325 nm) at an applied potential of $E = 0.142$ V; **(b)** nickel into a colloidal template (10 sphere layers, diameter 738 nm) at an applied potential of $E = -0.93$ V

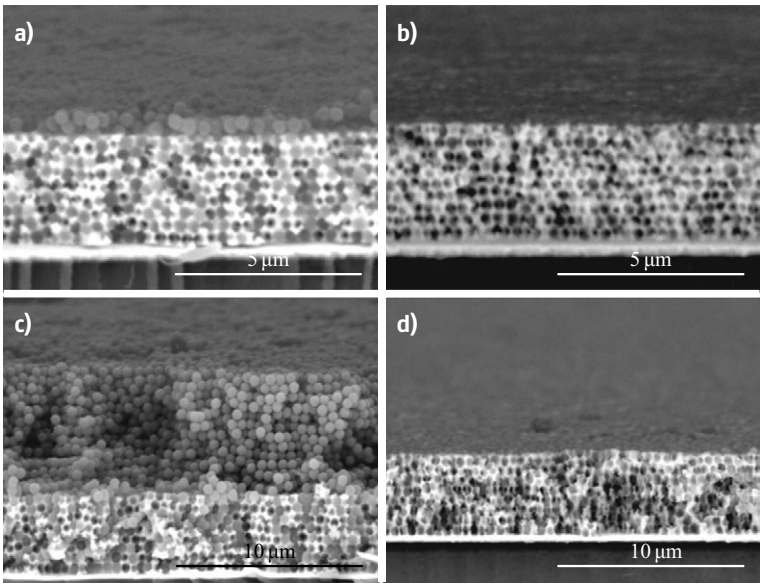


Fig. 6.23a–d Cross-sectional SEM images of nickel and platinum films electrodeposited in colloidal templates assembled by LB. **(a)** Platinum film infiltrated into a colloidal crystal (10 layers of 325 nm). **(b)** Same structure as in **(a)** but without the colloidal template. **(c)** Nickel film electrodeposited into a colloidal crystal (20 layers of 738 nm). **(d)** Same as in **(c)** but without colloidal template (after [6.168])

with nickel. The top surface of the template is found to be uniform providing no direct evidence of irregular packing of the sphere layers in the colloidal crystal. In Fig. 6.23d, the macroporous nickel electrode is shown after the dissolution of the template. The thickness as well as the organization of the pore layers here seems less uniform than in the case of porous platinum films. As the gold-coated glass electrodes are broken in order to allow cross-sectional images to be made, the fracture surface may be more or less intact after the breaking process providing rarely a view of a single plane in the sample. In the case of the macroporous nickel film shown in Fig. 6.23d, the cross-sectional image contains different planes of the sample indicating that the structure is less ordered.

Electrochemical Characterization of Macroporous Metal Electrodes

Macroporous metal electrodes have a greater surface area than their nonporous analogs. It is this gain in the

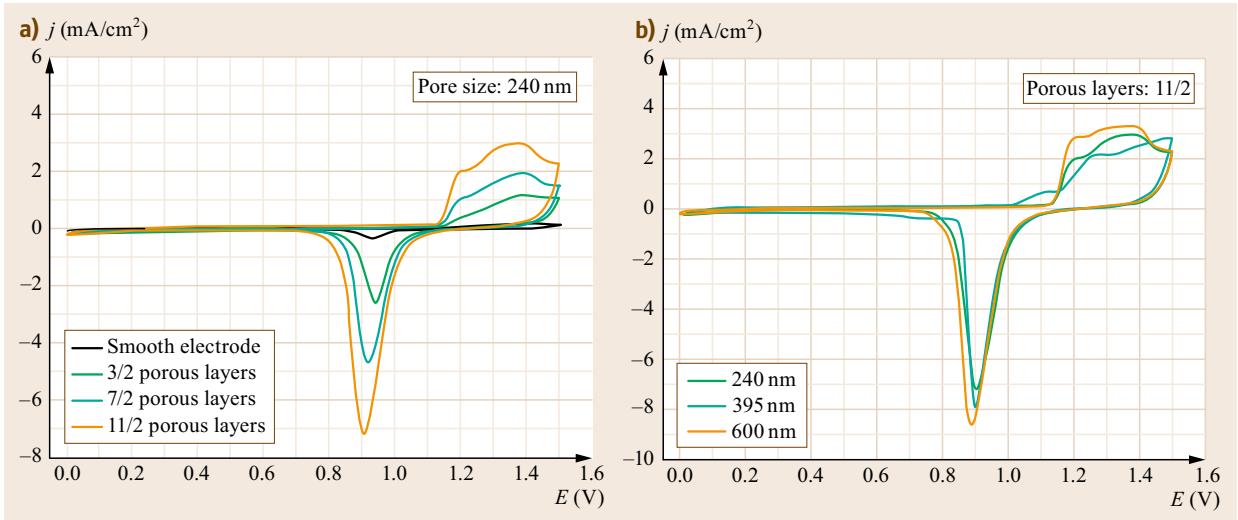


Fig. 6.24a,b Characterization of macroporous gold electrodes by cyclic voltammetry in 0.5 M sulfuric acid. **(a)** Comparison of macroporous gold electrodes with increasing number of pore layers (3, 7, and 11 half-layers) with a nonporous gold electrode. **(b)** Three macroporous electrodes with the same number of pore layers (11 half-layers) but different pore sizes are compared

active electrode surface, together with good diffusion kinetics in the open macropore network, which makes them interesting for different kinds of applications, including energy storage and conversion, electrocatalysis, and electroanalysis. Examples for applications of macroporous electrodes will be given in Sect. 6.4. In this context, the determination of the active surface area is very important in order to characterize the macroporous material. There are different ways to determine the real surface area of metal electrodes by using electrochemical techniques [6.169]. The choice of the most appropriate method depends on the type of metal that is characterized. For metals including Pt, Rh, and Ir, hydrogen adsorption is typically used to determine the real electrode area. Prior to H_2 evolution at sufficiently negative applied potentials a monolayer of hydrogen atoms is adsorbed onto the electrode surface. Assuming the adsorption of one hydrogen atom on each metal atom, the charge associated with the hydrogen adsorption or desorption peak allows us to calculate the number of metal ions at the surface of the electrode and hence its active surface area. In a similar way, oxide monolayer formation and its reduction on electrode surfaces can be used to determine active electrode areas. This represents the standard method that is used for the electrochemical characterization of gold electrodes. Therefore, the potential is cycled between fixed values, so that a complete oxide layer is formed on the gold surface during the anodic scan, which is then fully reduced in the cathodic cycle. The charge which is associated with the reduction of the oxide layer allows us to calculate the real surface area of the electrode, assuming a value of $390 \pm 10\,\mu C/cm^2$ for a smooth polycrystalline gold surface [6.169].

Cyclic voltammograms performed in 0.5 M sulfuric acid with smooth and macroporous gold electrodes are shown in Fig. 6.24a. Macroporous electrodes with the same pore size but a different number of pore layers have been compared with a smooth gold electrode in this plot. The potential was cycled in between 0 and +1.5 V. Gold oxide formation starts slightly above +1.1 V and the reduction peak in the cathodic scan is situated around +0.9 V. The measured current is divided by the geometric surface area of the sample in order to compare the obtained results quantitatively.

As one would expect, the intensities of the oxidation and the reduction peaks are considerably higher for the macroporous electrodes compared to the flat gold sample and gradually increase as the number of pore layers in the sample increases. In Fig. 6.24b, the cyclic voltammograms (CVs) of three macroporous gold electrodes with the same number of pore layers but different pore sizes are compared. Although the absolute film thickness is by more than a factor of 2 higher for the sample with 600 nm pores compared to the one with 240 nm pores, the observed peak intensities in different curves all are approximately at the same level. In accordance with this result, the pore density and hence the gain in the surface area in a given volume of porous material are increased when the pore size decreases. By geometrical considerations, the factor by which the active surface area is increased in macroporous materials can be determined [6.141]. This factor will be referred as to

the theoretical roughness factor R_{th}, which is given in (6.1)

$$R_{th} = \sqrt{\frac{4}{3}\pi n}\,. \tag{6.1}$$

As n in (6.1) corresponds to the number of pore layers in the macroporous material, the increase of the surface area in macroporous materials consequently depends only on the number of porous layers and not on the pore size. This is in perfect agreement with the results shown in Fig. 6.24. The active surface area of samples with a higher number of porous layers (31 and 49 half-layers) was also determined, as shown in Fig. 6.25a. Here the peak currents are further increased for the macroporous samples, which results in barely visible peaks for the bare gold sample at this scale (see the inset in Fig. 6.25a).

In order to evaluate the increase in the active surface area in a quantitative way, the roughness factor R and the active surface area has been determined for different samples as shown in Table 6.1. For a 49 half-layer-thick macroporous gold film, the roughness factor reached a value of 88, meaning that the initial geometric surface area of 0.64 cm^2 has been multiplied by this value resulting in an active surface area of more than 55 cm^2 in the macroporous gold electrode.

In Fig. 6.26, the experimentally determined roughness factors are plotted as a function of pore layers in the material. An excellent correlation is found between the experimental and the theoretical values, the latter being represented by a straight line derived from (6.1).

In some cases the electrolyte solution did not penetrate the whole existing pore volume and lower values are obtained for the active surface area than would have been expected theoretically (Fig. 6.25b). The rather hydrophobic nature of gold might hinder the wetting of the whole interior pore volume. Hence, the air that is present in dry macroporous samples is *entrapped* inside the pores and a considerable part of the pore volume remains inaccessible to the solution. As illustrated in

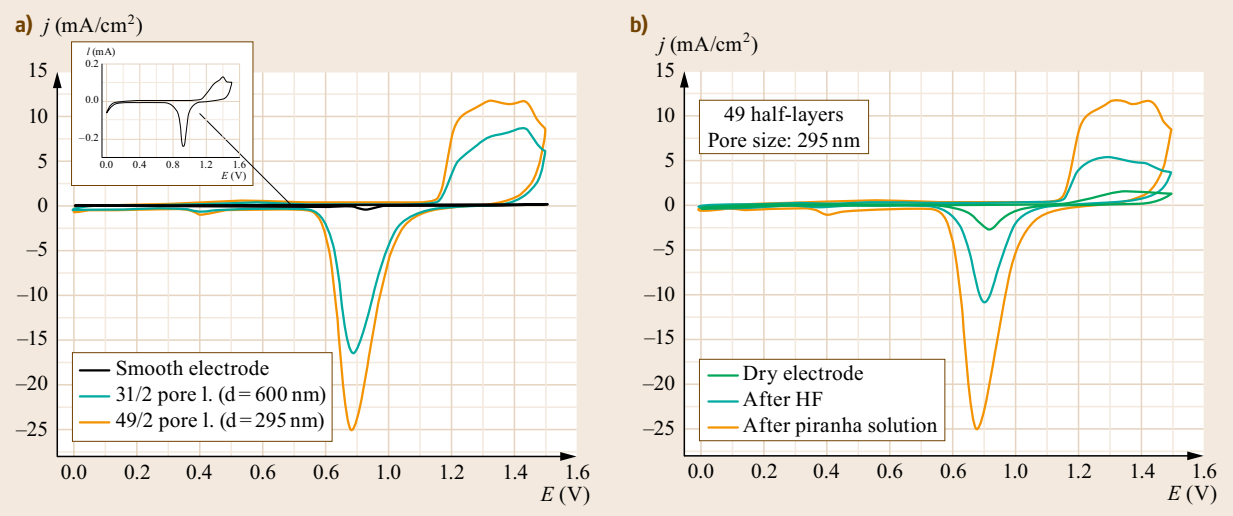


Fig. 6.25a,b Characterization of macroporous gold electrodes by cyclic voltammetry in 0.5 M sulfuric acid. **(a)** Compared are a smooth electrode and two macroporous electrodes composed of 31 and 49 pore half-layers. **(b)** Wetting effect in macroporous electrodes: CVs of the sample composed of 49 half-layers after storage for more than a month in air (*dry*), after immersion for 5 min in HF (5 vol%), and for 1 min in the piranha solution (75 vol% H_2SO_4, 25 vol% H_2O_2)

Table 6.1 Calculation of the roughness factor R and the real active surface area S_r for macroporous gold samples with different number of pore layers

Pore layers on the sample (pore size in nm)	Geometric sample area A (cm^2)	Charge of the gold oxide reduction peak Q (μ C)	Roughness factor $R = Q/A \div 390\,\mu C/cm^2$	Real active surface area $S_r = A \cdot R$ (cm^2)
3/2 (240)	0.7	1800	6.6	4.6
7/2 (240)	1.68	8470	12.9	21.7
11/2 (240)	1.68	14 200	21.6	36.4
31/2 (600)	0.96	21 500	57.4	55.1
49/2 (295)	0.64	22 000	88.1	56.4

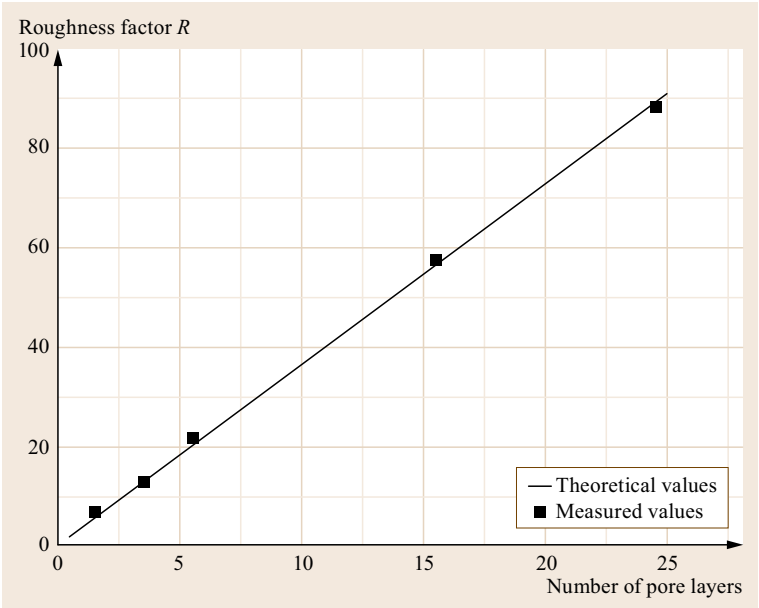


Fig. 6.26 The roughness factor as a function of the number of pore layers for macroporous gold electrodes. Correlation between the theoretically expected value (from purely geometric consideration, see (6.1)) and the measured values

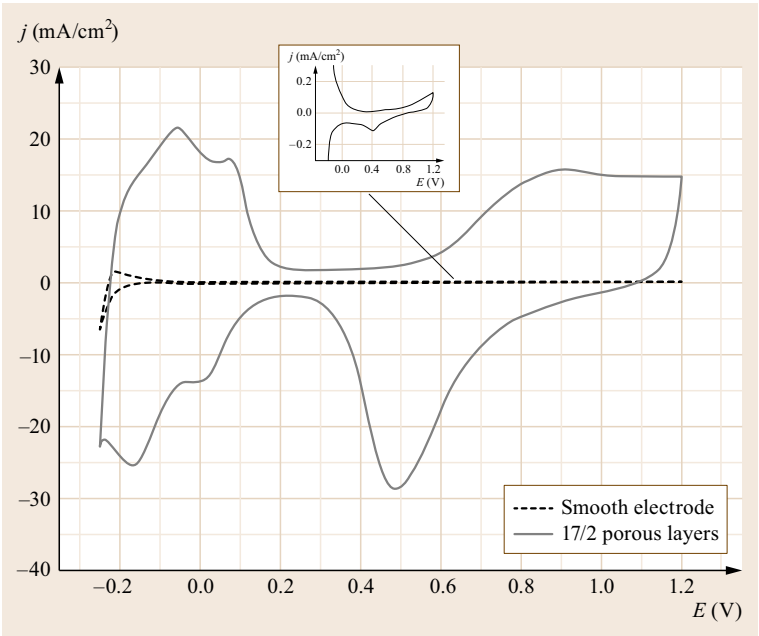


Fig. 6.27 CV of a smooth (see also the *inset*) and a macroporous platinum electrode with 17 pore half-layers (pore size: 325 nm). A hierarchical porosity with mesopores penetrating the walls of the macroporous platinum may be the reason for the extremely high active surface area, resulting in a roughness factor of 267 (theoretically expected value for a purely macroporous Pt electrode: 30)

Fig. 6.25, only a very small percentage of the real surface area is detected by CV in samples that have been stored in air for longer periods of time. Exposing these samples to the hydrofluoric acid solution leads to a partial wetting of the inner pore structures and the redox peaks in the CV increase. Immediate wetting of the whole pore structure is observed when immersing the samples into the piranha solution, so that peak amplitudes in the CV reach the theoretically expected values.

It was also found during the CV measurements that the template not necessarily had to be removed in order to measure the active surface area in the sample. Silica spheres synthesized by the Stöber method contain a certain microporosity that allows the electrolyte solution to reach the gold surface by passing through these pores. The CV shown for a sphere size of 395 nm in Fig. 6.24b actually was obtained for a composite structure of gold deposited into the silica template. Despite the silica

template still being present, it was possible to determine the correct surface area by CV. For thick composite structures composed of gold and silica spheres, the redox peaks of gold, however, were found to be shifted, indicating that diffusion through the pores in the silica can become a limiting factor in the reaction. Additionally, the amount of porosity present in silica spheres is a function of synthesis conditions and generally is the lower the bigger the size of the spheres.

The active surface area of macroporous platinum films was also determined using cyclic voltammetry. In Fig. 6.27, the CVs of a smooth and a macroporous platinum electrode composed of 17 half-layers are compared. The CV obtained for the macroporous electrode shows typical features of polycrystalline platinum with well-defined hydrogen ad- and desorption peaks for potentials lower than 0.1 V. In order to resolve the peaks on the flat platinum sample, the scale had to be adapted for this curve, which is shown in the inset of Fig. 6.27. Assuming $210\,\mu C/cm^2$ as the conversion factor, a roughness factor of 267 was determined for the porous Pt electrode from the charge associated with the hydrogen adsorption [6.169]. By using (6.1), the active surface area of a purely macroporous electrode composed of 17 pore half-layers, however, should be increased only by a factor of roughly 30. This difference between theoretical and experimental values may be explained by the presence of additional (smaller) pores in the macroporous structure. The process for platinum electrodeposition was adopted from a work on mesoporous platinum electrodeposits by *Choi* et al. [6.166]. The authors reported that the potential-controlled assembly of surfactant molecules at the solid–liquid interface can be employed to produce organized mesoporous structures. Although a different potential for the platinum electrodeposition was used with respect to the original report, the difference observed between the theoretically expected and the measured roughness factors strongly suggests the presence of a hierarchical pore system composed of additional mesopores in the macropore network. In order to provide a clear evidence of the presence of the hierarchical porosity, transmission electron microscopy (TEM) images of porous platinum thin films should be performed in future works.

6.1.4 Electrodeposition of Conducting Polymers in Colloidal Crystals

Conducting polymers (CPs) cover a wide spectrum of conductivities ranging from isolating over semiconducting and up to metal-like behavior. CPs are produced by the oxidization of the corresponding monomers. The removal of electrons from the conjugated backbone during the oxidation of the polymer allows for the remaining delocalized electrons to move along the conjugated structure. In this *doped* state, the conductivity of conjugated polymers is increased by several orders of magnitude compared to the *undoped* state. A conversion to the less conducting state is obtained by reducing the polymer, where electrons are reinserted into the structure of the polymer. Analogous to semiconductors, this type of conductivity promoted by nonexisting electrons or positive *holes* in the band structure refers to p-type conductivity. Principally, also n-type conductivity is possible in CPs, which, however, is much less common than the p-type conduction. Polyaniline (PANi), PPy, and PEDOT are among the most widely used CPs. They are employed for different kinds of applications in fields including electroanalysis [6.171], electrochromism [6.172], actuators [6.173–175], energy storage [6.176], bioelectrochemistry [6.177], electrocatalysis [6.178, 179], neural engineering [6.180], corrosion protection [6.181], and sensors [6.177]. The fabrication of a macroporous structure by colloidal templating can add new functionalities [6.182–185] or improve the performance in existing applications, which are based on CPs [6.123, 186, 187].

Polypyrrole Deposition

The electrochemical polymerization of pyrrole is schematically illustrated in Fig. 6.28. The polymer is formed by the oxidation of the pyrrole monomer, whereas counterions (A^-) are incorporated in between the polymer chains to guarantee charge neutrality in the polymer. Figure 6.28 represents a simplified presentation of the electropolymerization process, showing only the educt and the idealized structure of the polymer product. In reality, the polymerization process is more complex and can be divided into several steps [6.170]. When sufficiently positive potentials are applied to

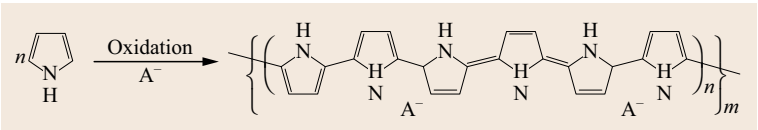


Fig. 6.28 Simplified illustration of PPy formation by oxidation of the pyrrole monomer. A^- is the counterion incorporated into the polymer ensuring charge balance, *m* corresponds to the polymer chain length, and *n* to the molecular weight (after [6.170])

the electrode, the monomer will be oxidized and radicals are formed. Radical–radical coupling now occurs and the growth of the polymer chain proceeds until the charge is such that a counterion is incorporated. When experimental conditions are favorable, the chain reaches a critical length, so that the solubility limit is exceeded and the polymer precipitates at the electrode surface.

The aim was to control the electropolymerization in such a way that smooth polymer film growth would be attained, which eventually could lead to current oscillations during the potentiostatic infiltration of colloidal crystals similar to those previously observed for metallic deposits. In Fig. 6.29a, the electropolymerization of PPy by potential cycling of a smooth gold electrode is shown. An aqueous solution containing the monomer (0.1 M pyrrole) and a supporting electrolyte (1 M KCl, counterion incorporated in the PPy film: Cl^-) was used for the PPy deposition, conditions that are slightly changed with respect to a report found in the literature [6.188].

The potential was cycled between −0.5 and +1.0 V. In the first cycle, PPy is deposited on the pristine gold surface with an onset potential of about +600 mV in the anodic scan. The resulting polymer film is reduced during the cathodic scan. In subsequent cycles, different peaks corresponding to the redox peaks of the polymer and the oxidation of the monomer are observed. As the amount of polymer on the electrode increases with each cycle, the intensity of the corresponding redox peaks also increases. The onset potential for the oxidation of the monomer was found to shift toward lower potentials during the deposition, combined with increasing peak intensities. This effect is due to the polymerization occurring more readily on already deposited PPy than on the electrode substrate [6.170].

However, using cyclic voltammetry for the electropolymerization into colloidal crystals does not allow to control the filling level of the template with sufficient precision. Therefore, potentiostatic deposition was performed at different applied potentials and the resulting polymer films were characterized by their optical aspect and corresponding SEM images. In Fig. 6.29b, the current response for potentiostatic deposition of PPy on a smooth gold sample is shown. A potential of +600 mV versus Ag/AgCl was applied, resulting in smooth polymer films at reasonable deposition rates. Using lower potentials resulted in inhomogeneous film deposition and lower efficiencies. In fact, radicals and polymer chains can diffuse away before they are deposited at the electrode surface, so that part of the totally applied charge is *lost* in this case. For certain conditions, it is, therefore, possible that no film growth is observed, although a considerable amount of charge is applied during the electropolymerization [6.170]. PPy films deposited at higher potentials than +600 mV showed a higher surface roughness in the SEM images.

At the start of the deposition process, as shown in Fig. 6.29b, charging of the double-layer capacity at the electrode together with a nucleation process leads to a steep decrease of the current. In the following, the current increases during polymer film growth at the electrode. In initial stages of the deposition process, the

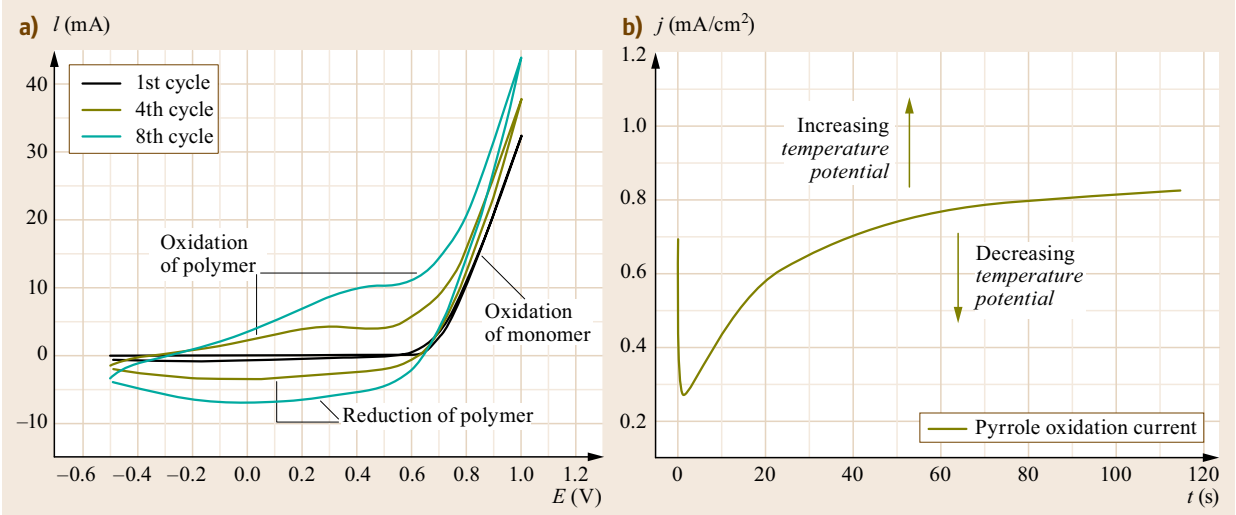


Fig. 6.29 Electropolymerization of pyrrole by **(a)** cyclic voltammetry (scan rate: 100 mV/s) and **(b)** in a potentiostatic mode from an aqueous solution containing 0.1 M pyrrole and 1 M KCl. In **(b)**, a constant potential of +600 mV versus Ag/AgCl was applied

substrate exerts a dominating influence on the kinetics of the electropolymerization. With increasing thickness of the polymer film, the influence of the underlying electrode material decreases and the polymerization occurs more readily, hence leading to continually increasing currents which may reach a plateau for very thick polymer deposits. Changing the potential applied to the electrode or the temperature of the electrolyte solution leads to a similar shape of the deposition curve with a shift to higher or lower current densities, as indicated in the plot. The quality of the PPy films and the reproducibility in the experiments were found to depend strongly on the purity of the monomer, which had to be distilled before use.

The film thickness of the polymer could be controlled by the charge applied during the electropolymerization. Applied charge densities of 400 mC/cm^2 have been reported to result in about 1 µm thick PPy films [6.189]. Figure 6.30a shows gold samples coated with PPy films by applying different charge densities during the electropolymerization. Sample A is the uncoated gold electrode and from sample B (50 nm) to E (300 nm) the thickness of the PPy films increases. As a function of the thickness, the color of the PPy film deposits on gold changed. Continuous color change was observed up to applied charge densities of about 150–200 mC/cm^2, corresponding to about 300–400 nm thick PPy films. Higher values of injected charge resulted in black PPy film deposits. Thus, the optical aspect of PPy thin films can be used as a measure of their thickness and their uniformity. Cross-sectional SEM images of the samples B and C are shown in Fig. 6.31a and confirm that the PPy films exhibit the expected thickness and are uniform throughout the sample.

In the following, colloidal crystal templates were electrochemically infiltrated with PPy. Similarly, as shown for metal deposits in colloidal templates, we were able to observe regular current oscillations during potentiostatic electropolymerization of PPy, illustrated in Fig. 6.32. However, since the formation of PPy results from an oxidation process, the faradaic current has a positive sign. As a consequence, each current density minimum in the plots now corresponds to a minimum of the electroactive surface, equal to a half-layer filling level in the colloidal template.

In Fig. 6.32a, a colloidal template composed of 20 sphere layers with a bead size of 240 nm has been infiltrated with PPy. Well-defined minima and maxima in the recorded current allow us to stop the electrodeposition at different half- or a full-layer filling levels in the template, respectively, similar to the metal deposition. In the present case, 23 half-layers of the template have been filled with PPy.

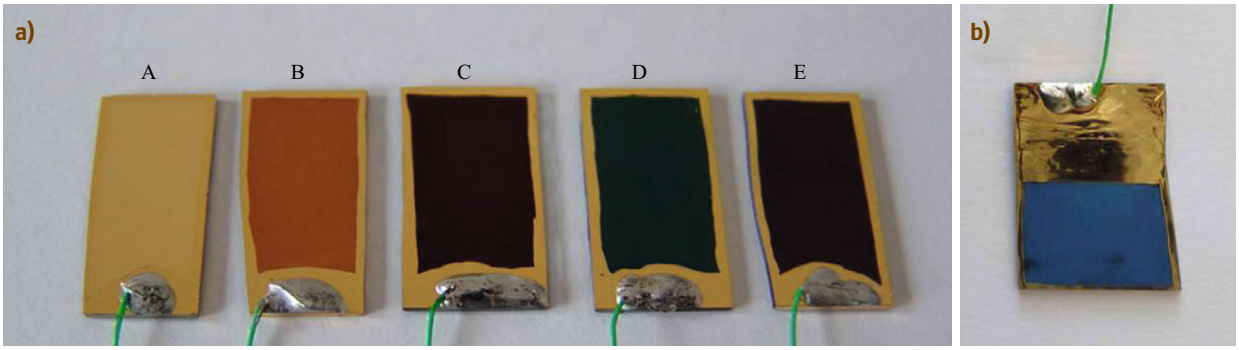


Fig. 6.30a,b Polypyrrole films electropolymerized at an applied potential of +600 mV **(a)** onto smooth gold electrodes with applied charge densities corresponding to (A) 0, (B) 20, (C) 40, (D) 80, (E) 120 mC/cm^2, and **(b)** into a colloidal crystal template (template: 395 nm sphere size with 8 sphere layers; PPy filling level: seven half-layers)

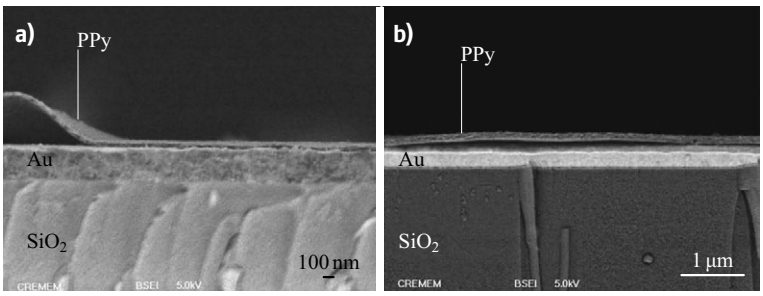


Fig. 6.31a,b SEM cross-sectional images of PPy films electrodeposited on gold slides. **(a,b)** correspond to the samples B and C from Fig. 6.30, respectively. The thickness of the PPy films was found to be **(a)** ≈ 50 nm and **(b)** ≈ 100 nm

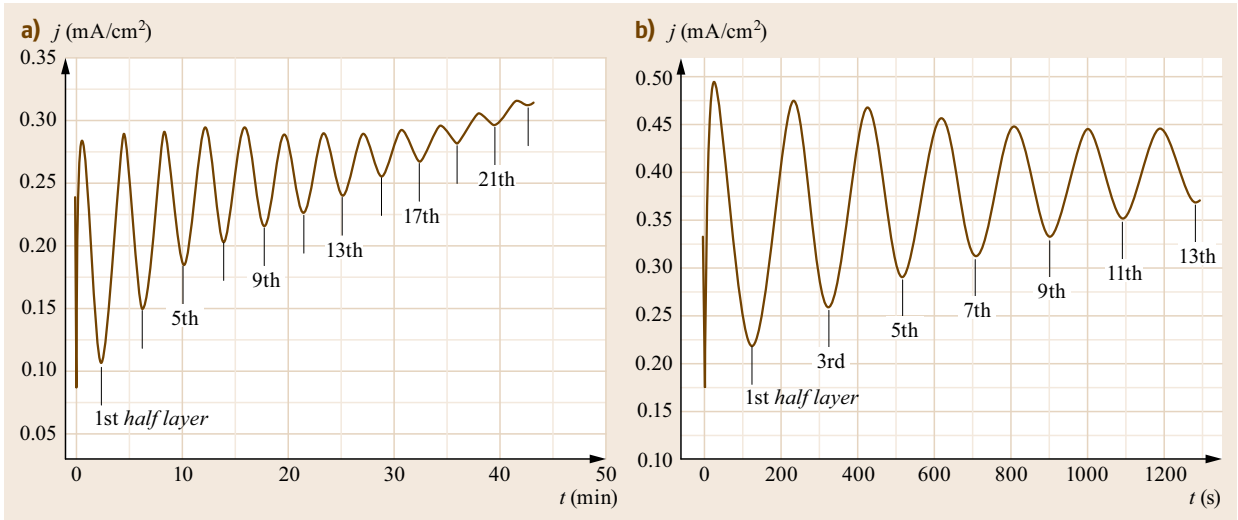


Fig. 6.32a,b Current oscillations observed during potentiostatic electropolymerization ($E = +0.6$ V) of pyrrole in colloidal templates. The templates were filled with PPy up to **(a)** 23 and **(b)** 13 half-layers

In Fig. 6.32b, the observed current oscillations were even more regular than that in Fig. 6.32a as a template composed of 395 nm spheres was filled with PPy up to 13 half-layers. Figure 6.30b shows a digital photograph of a colloidal crystal template which has been partly infiltrated with PPy.

The characterization of different macroporous PPy films by SEM is illustrated in Fig. 6.33. The top surface of a macroporous polymer film with a pore size of 1200 nm is shown at different magnifications in Fig. 6.33a,b. The windows interconnecting the top to the underlying pore layers appear as black spots and are clearly visible in both figures. The PPy struts have different thickness indicating that the silica spheres in this case have not been in a completely close packed arrangement. In Fig. 6.33c, a cross-sectional image of a colloidal template composed of 470 nm beads is shown after the infiltration with PPy. Slightly more than three sphere layers have been filled by the PPy film and reveals a very uniform growth front throughout the template. Figure 6.33d shows the cross-section of a macroporous PPy film with six and a half-pore layers.

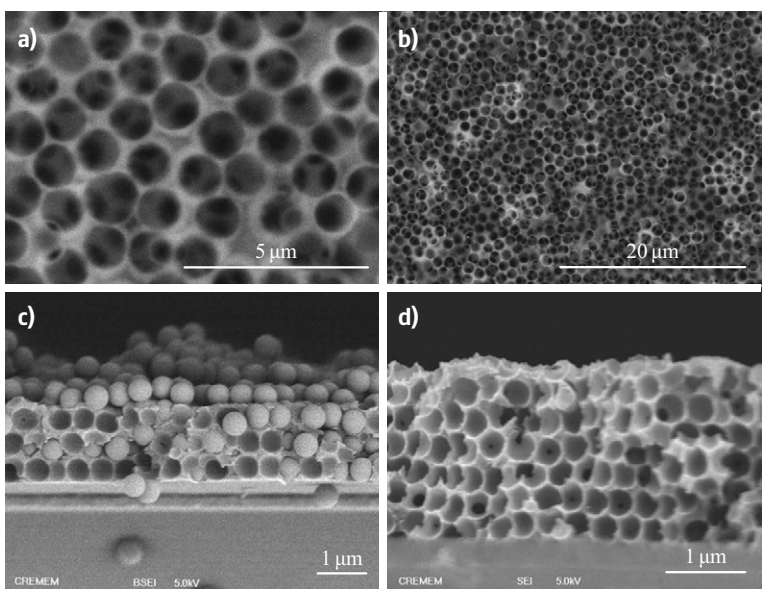


Fig. 6.33a–d SEM images of macroporous and composite polypyrrole films. **(a)** and **(b)**: Top view of a macroporous PPy-film electrode with a pore size of 1200 nm and a thickness of 13 half-layers in different magnifications. **(c)** Cross-section of a colloidal template (sphere size 470 nm) in which 3 layers have been infiltrated with PPy. **(d)** Cross-section of a macroporous PPy film with a thickness of 13 half-layers and a pore size of 395 nm

Polybithiophene Deposition

The electrodeposition of polybithiophene (PBT) into the void space of colloidal crystals has also been examined. Owing to the low solubility of the monomer in aqueous solutions, acetonitrile was used as a solvent [6.190]. Solutions contained 0.1 M tetrabutylammonium tetrafluoroborate (TBA BF_6) with bithiophene concentrations that were varied from 5 to 50 mM. Figure 6.34a shows cyclic voltammograms of flat gold electrodes in a solution containing 50 mM bithiophene.

Similarly, as shown for the PPy deposition in Fig. 6.29b, well-defined redox peaks of the deposited polymer are visible in all cycles after the first one. Compared with pyrrole, potentials higher than $E > 1$ V are required to oxidize bithiophene. In Fig. 6.34b, a chronoamperometric curve for PBT deposition in a colloidal template is shown. Here, no oscillations of the current response were observed and the shape of the curve resembles that for the deposition of PPy on flat gold (Fig. 6.29b).

Directly after the electropolymerization of PBT in the colloidal template, the cross-section of the sample has been characterized by SEM, which is shown in Fig. 6.35a. The same type of volume-templated material as observed for PPy or metal electrodeposits is expected; however, PBT reveals a different growth mechanism in colloidal templates.

Instead of filling the whole available volume in the template, only a thin polymer film is deposited around the spheres. This guidance effect, probably due to electrostatic interactions between the radicals formed during electropolymerization and the surface groups of the colloidal spheres, was mentioned before in Sect. 6.1.2 and results in surface-templated materials. The macroporous PBT electrode can be seen in Fig. 6.35b showing a 3-D network of interconnected hollow spheres on the surface of the gold electrode. Interconnection points between spheres of the original silica template now correspond to black air cavities in the hollow PBT spheres. A collapse of the sphere layers at the top surface of the sample is observed due to a lack of mechanical sta-

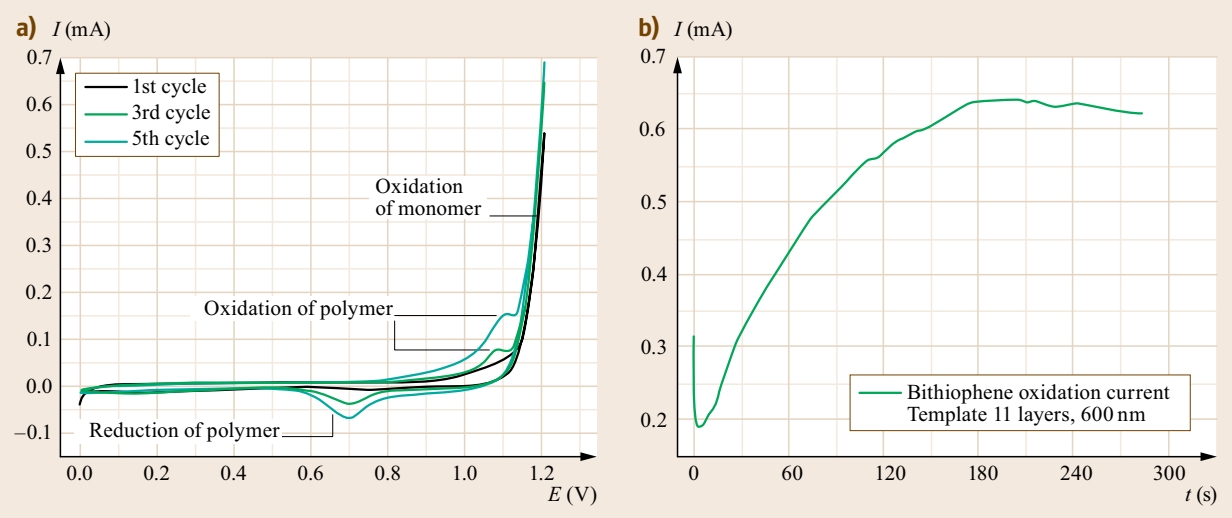


Fig. 6.34a,b **(a)** Electropolymerization of bithiophene by cyclic voltammetry (scan rate: 100 mV/s) in acetonitrile containing 50 mM bithiophene and 0.1 M TBA BF_6. **(b)** Electrochemical infiltration of a colloidal crystal (11 layers, 600 nm sphere diameter) at an applied potential of 1.23 V versus Ag/AgCl. In this case the concentration of the monomer was 5 mM

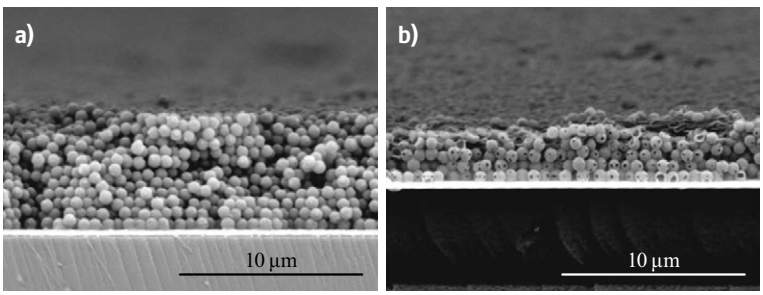


Fig. 6.35a,b SEM cross-sectional images of composite and macroporous PBT films. **(a)** Polybithiophene was deposited in the colloidal template by encapsulating the spheres with a thin polymer film. **(b)** Removal of the inorganic template resulted in a macroporous *hollow sphere* PBT electrode

bility of the hollow polymer spheres. In the illustrated sample, the polymer film, however, has been dried by a rather strong nitrogen flow, more gentle drying conditions resulted in less damage at the macroporous surface layers. A similar surface-templated structure has been observed by *Bartlett* et al. for macroporous PBT films [6.135].

Electrochemical Characterization of Macroporous Conducting Polymers

The macroporous PPy films have been electrochemically characterized using cyclic voltammetry. In Fig. 6.36a, the molecular structure of PPy is shown in its reduced and oxidized form. The switching between both redox states is associated with a movement of electrons and counterions into or out of the polymer structure. When the polymer is reduced, electrons fill the available *holes* in the conjugated structure of the polymer and the counterions move out of the material. Oxidation of the polymer leads to the inverse scenario. The amount of counterions in the polymer will depend on its oxidation state, leading either to a contracted (reduced) or expanded (oxidized) state of the polymer. The reduction (or oxidation) of the polymer proceeds from the point of the electrical contact, as illustrated in Fig. 6.36b [6.170]. It is supposed that the reduction front percolates through the polymer material.

The redox process in CPs significantly differs from that occurring in noble metals which are confined to a thin layer. In CPs, the whole polymer film will get oxidized (reduced) when sufficiently positive (negative) potentials are applied for a certain period of time. Generally, no single redox peak but broad distributions of overlapping peaks are observed in the CVs of CPs. This is caused by different molecular weights of the oligomeric/polymeric species in the CP, all possessing oxidation/reduction peaks at different potentials [6.170]. Figure 6.37 compares the cyclic voltammograms of smooth (Fig. 6.37a) and macroporous (Fig. 6.37b) PPy films. Curves of the same color are standing for samples with the same amount of deposited PPy and, hence, can be directly compared with each other. In both plots, for macroporous as well as for smooth samples, increasing currents are observed as the amount of deposited polymer increases. A thicker film leads to a shift of the oxidation peak toward more positive potentials in smooth PPy samples. A uniform increase of the redox currents with no clearly visible peaks is observed as the thickness of the macroporous PPy films is increased. The observed shift of the oxidation peaks indicates that the exchange of ions with the solution probably is the rate-limiting step in flat PPy films of a certain thickness. Counterions need to diffuse through the polymer film during the redox processes in smooth PPy films. In macroporous films, however, the solution can enter the pore volume so that the diffusion path lengths of the counterions are significantly reduced.

Conducting polymers may be used for many applications that rely on the reversible switching of the polymer between its reduced and oxidized state [6.123, 175, 191]. A fast and reversible redox process is crucial to enable good performance in CP-based devices. In order to compare the kinetics of the ion exchange for flat and macroporous PPy films, CVs were recorded at different scan rates and are shown in Fig. 6.38.

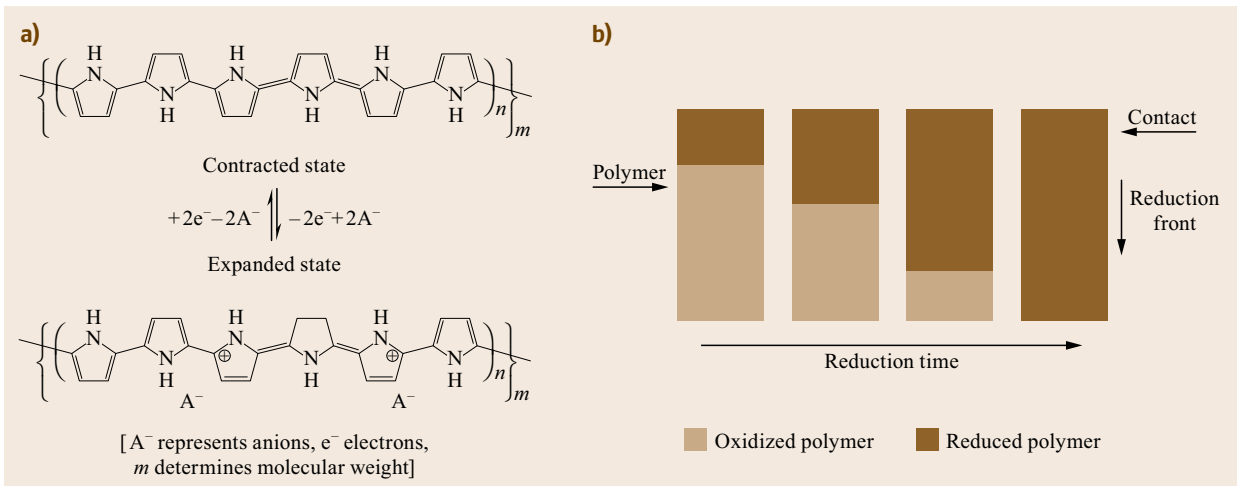


Fig. 6.36 (**a**) Switching of PPy between the reduced (contracted) and oxidized (expanded) state. (**b**) Schematic presentation of the reduction of a CP (after [6.170])

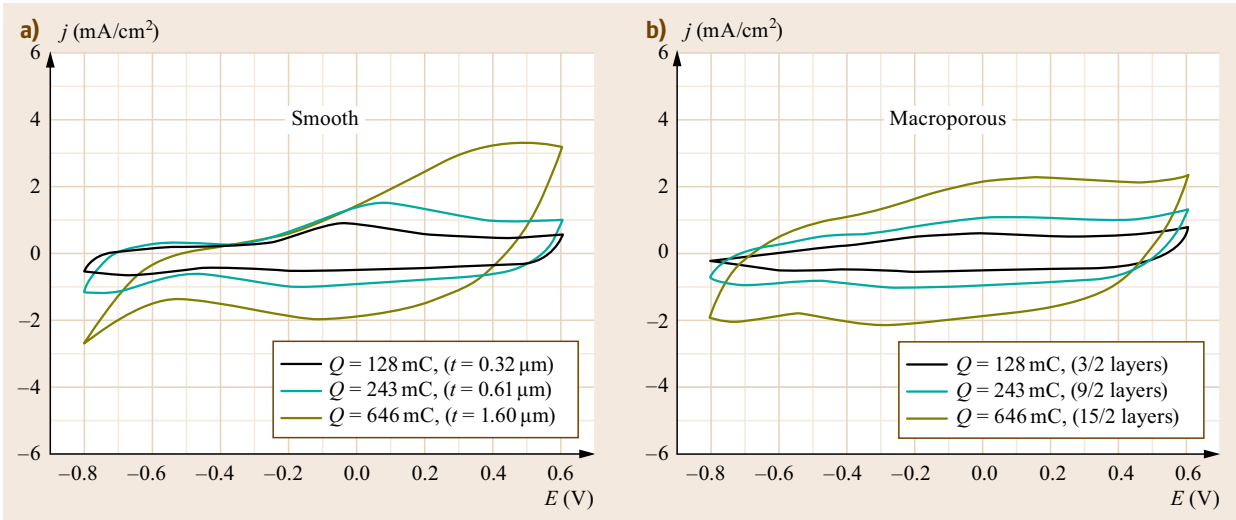


Fig. 6.37a,b Comparison of smooth (a) and macroporous (b) PPy samples by cyclic voltammetry. The scan rate was 50 mV/s in 50 mM KCl aqueous solution. Q represents the charge injected during electropolymerization of PPy. In corresponding smooth and macroporous samples the amount of deposited polymer was equal (t: film thickness, macropore size 430 nm)

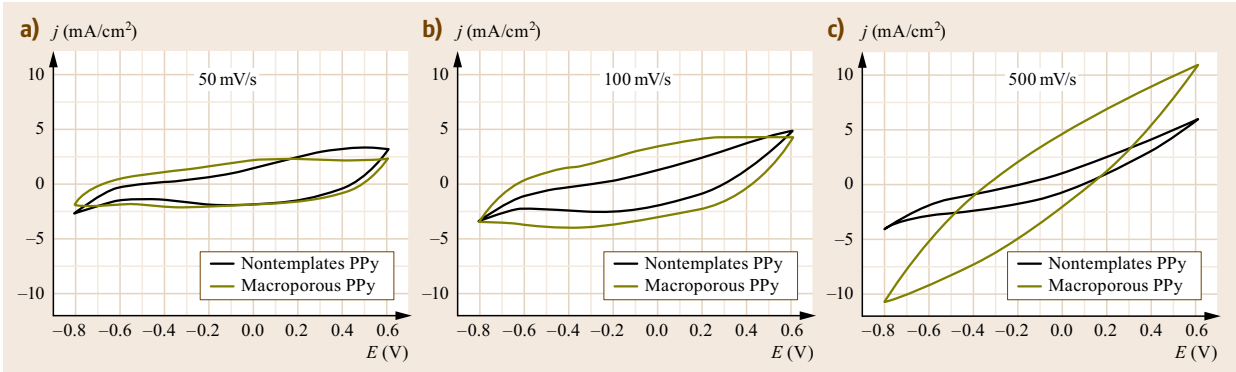


Fig. 6.38a–c Cyclic voltammetry in 50 mM KCl at different scan rates (50, 100, and 500 mV/s). A smooth and macroporous PPy film with the same amount of deposited polymer (injected charge: 646 mC) is compared

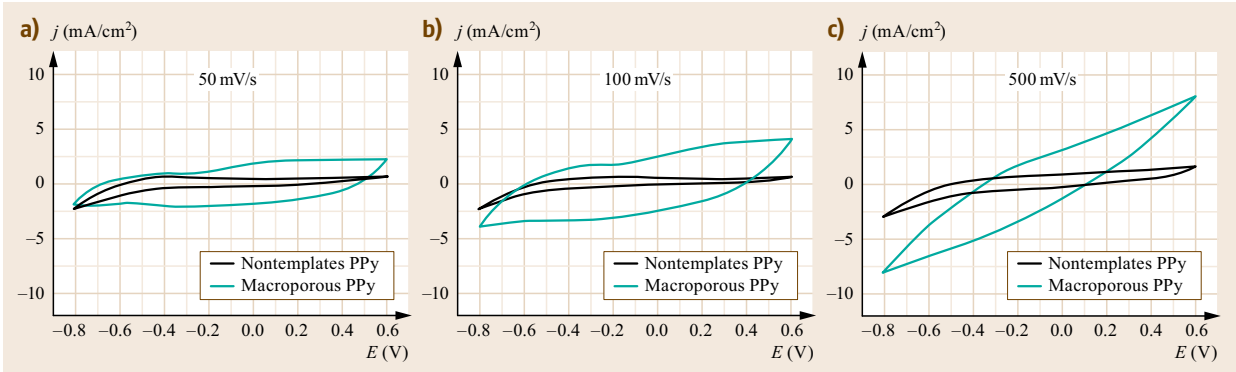


Fig. 6.39a–c Similar scan rate dependent plots as the ones shown in Fig. 6.38 are presented. The same samples but a different electrolyte solution (50 mM KPF_6 aqueous solution) was used here

In each plot, a smooth and a macroporous PPy film are compared containing the same amount of deposited polymer. At a scan rate of 50 mV/s, the redox currents for the templated and the nontemplated films are in a similar range. At 100 mV/s, considerably higher redox currents were observed for macroporous than for flat PPy. This trend was confirmed and even more pronounced at higher scan rates of 500 mV/s.

The results shown in Figs. 6.37 and 6.38 have been obtained by cycling the polymer in a solution which contained the same counterion used during the synthesis of the PPy films. Cl^- is a rather small ion easily diffusing through the polymer structure and facilitating the ion exchange with the solution. Therefore, the same scan-rate-dependent experiments were also performed in equally concentrated solutions which contained a bigger anionic species, PF_6^- in this case.

As shown in Fig. 6.39, a marked difference in the CVs between the flat and the macroporous polymer film is observed in this case at all tested scan rates. The macroporous polymer seems to exchange PF_6^- anions as readily as Cl^- anions, as the current signals are barely reduced compared to Fig. 6.38. In contrast, only small oxidation and reduction currents are observed at different scan rates for the flat PPy samples indicating that PF_6^- anions can hardly penetrate the polymer owing to the restricted diffusion of these species in the film. Improved performance in electrochromic NiO was also attributed to shortened ion pathways in the macroporous structure [6.163].

6.2 Macroporous Materials with a Gradient in Pore Diameter

Macroporous materials with a sophisticated architecture are obtained by the electrochemical deposition of gold or PPy in colloidal-crystal templates. The Langmuir–Blodgett technique enables the assembly of submicrometric silica-particle monolayers on conductive gold substrates, thus leading to colloidal superstructures with an unprecedented control of their features at the single-bead-layer level. This allows the deliberate integration of planar defects or the elaboration of well-defined gradients in terms of sphere size. Controlled infiltration using electrochemical deposition preserves the architecture of the original templates and leads to inverse opals with well-defined pore structures after the removal of the inorganic particles.

In this section, a strategy for the elaboration of macroporous materials with a complex pore gradient architecture will be presented [6.168]. Besides the fabrication of homogeneous colloidal crystals based on one single-bead size, different assembly techniques allowed building up various superstructures combining spheres of different sizes [6.192] or chemical composition [6.193] in one template. Additionally, point [6.194, 195], line [6.196], or planar [6.197–199] defects were successfully integrated in colloidal crystals in order to explore their influence on the photonic properties of the material. *Yan* et al. gave a broad overview over existing strategies to introduce different artificial defects in 3-D colloidal crystals [6.200]. A drawback of most assembly techniques, however, consists in the poor control over the number of particle layers deposited during the assembly process, hence leading to restrictions, for example, when gradients in colloidal crystals with different sphere sizes in successive layers have to be produced. The few attempts made to fabricate graded colloidal crystal structures consisted in top-down modifications of previously assembled polystyrene spheres by heating [6.201] or by plasma etching [6.202] associated with a considerable lack of control over the resulting bead size and structure of the gradient. This limitation can be overcome by using a layer-by-layer assembling process of colloidal particles. As shown in Sect. 6.1.1, LB allows us to elaborate colloidal crystal assemblies with an extremely well-defined geometry. Additionally, Langmuir films can be prepared from silica particles with a range of different diameters. In the past, architectures using two different sphere sizes have been realized using the LB technique [6.203–209]. Here, we have taken advantage of all the benefits of the LB technique to build up colloidal superstructures with an unprecedented degree of complexity using up to six different particle sizes, the sequential deposition of monolayers allowing us to exactly generate a predefined architecture. In a second step, these templates have been infiltrated either with gold or PPy by chronoamperometric electrodeposition, providing a perfect control over the filling level of the colloidal template. Finally, the inorganic template was removed using wet-etching techniques revealing a macroporous electrode with the exact inverse structure of the original template [6.168]. Figure 6.40 illustrates schematically different steps leading to macroporous electrodes with a pore gradient structure.

In the following section, different colloidal templates fabricated by LB are introduced and characterized by SEM imaging, serving in a second step as templates for the electrochemical infiltration.

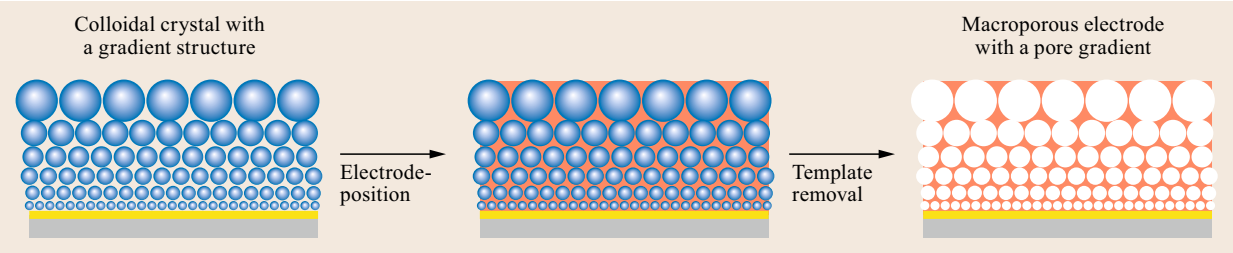


Fig. 6.40 Different steps involved in the fabrication of well-defined macroporous electrodes with a pore gradient. The key steps here are the assembly of the colloidal template using LB and the controlled infiltration by electrochemical deposition

6.2.1 Gradient Pore Diameter Template Fabrication

Among others, one of the great advantages of the LB technique is the possibility of building up colloidal crystals with a control at the single-bead-layer level. As described in Sect. 6.1.1, well-compressed monolayers of silica particles are transferred from the air–water interface onto solid substrates, and this process can be repeated until a desired number of layers, up to several tens of layers, has been deposited on the sample. Following this strategy, colloidal crystal templates with various morphologies were synthesized using silica particles of different diameters. More precisely, three main families of templates with an increasing complexity, which may lead to various types of applications, were generated and are schematically shown in Fig. 6.41.

In *Type A* templates, two sizes of particles were used to build up a colloidal crystal with a well-defined planar defect consisting of a stack of smaller in between two stacks of bigger particles. For the generation of *Type B* templates, three different particle sizes were assembled into *single-gradient* structures. Stacks of bigger particles were here deposited onto those of smaller ones. The most complex architecture is shown in *Type C* templates. Monolayers of up to six different sphere diameters have been assembled into *double-gradient* colloidal crystals. The sphere layers have been symmetrically arranged with respect to the central layer consisting of the largest or smallest particles. In *Type* C_1 templates, the sphere layer succession was *ascending–descending*, whereas a *descending–ascending* architecture was realized in *Type* C_2 samples. All colloidal templates have been assembled on gold-coated glass slides and were uniform over an area of more than 2 cm^2, similar to those shown in Fig. 6.17c. Generally, Langmuir–Blodgett films could perfectly be deposited onto larger surfaces without any restriction, as long as the required equipment – a Langmuir trough with a large working area and a sufficient immersion depth – is available.

After assembling different types of colloidal templates by LB, some samples were broken in order to characterize the sphere layer stacking in the corresponding cross-sectional SEM images. Figure 6.42a shows a *Type A* colloidal template containing a five-layer stack of smaller particles in between two five-layer stacks of bigger particles. Figure 6.42b shows a *Type B* template composed of three successive stacks, each containing 10-particle layers. The thickness and the composition of both templates were very regular.

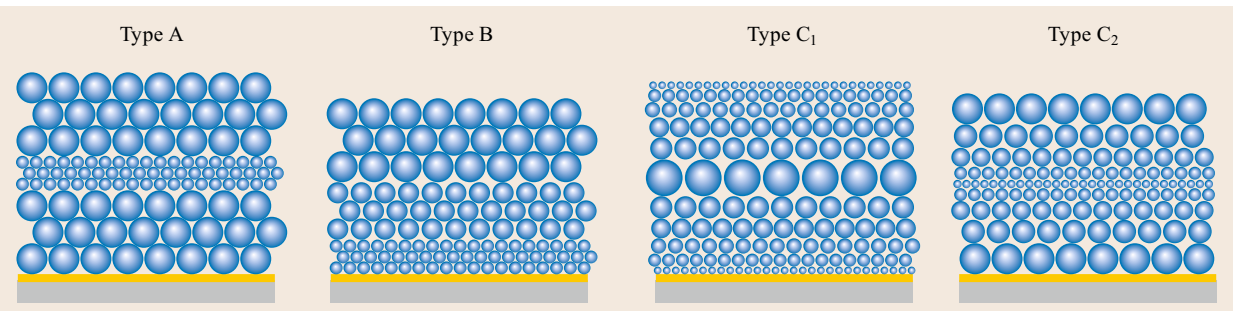


Fig. 6.41 Different template architectures produced. *Type A* templates with two sizes of particles are used to assemble a colloidal crystal with a well-defined planar defect. *Type B* templates with three sizes of particles allowed to build up *single-gradient* structures. *Type* C_1 and *Type* C_2 templates consist of up to six different particle sizes with *ascending–descending* and *descending–ascending* architecture, respectively. Sphere layers in these *double-gradient* structures were symmetrically organized with respect to a central layer of large or small particles

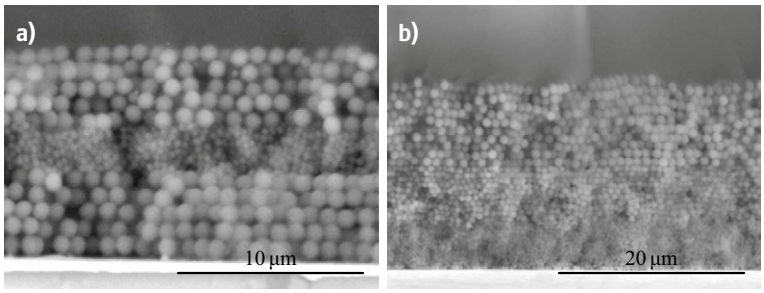


Fig. 6.42a,b SEM side views of silica colloidal templates produced by LB showing **(a)** *Type A* and **(b)** *Type B* structure. In panel **(a)** two 5-layer stacks of 1000 nm particles are separated by a 5-layer stack of 430 nm particles. In panel **(b)** a sample consisting of three 10 layer stacks of 430, 740, and 1000 nm particles are shown

Especially, in templates based on successive stacks of layers with increasing diameters of silica particles (e.g., Fig. 6.42b), the eventual irregularities of the first stackings have little influence on the arrangement of the upper ones.

As mentioned, it is possible to take advantage of the specific *layer-by-layer* iterative process, characteristic for the LB strategy, to get templates with an even higher degree of complexity. Indeed, sequential stacking of single layers of particles with different diameters can lead to structures with a *double-gradient* (*Type C* templates). In Fig. 6.43a,b, a *Type* C_1 template composed of 11 layers comprising particles of six different diameters ranging from 240 to 1200 nm is shown. In this case, the particle diameter was gradually increased for the first six layers and decreased for the following five ones, leading to an *ascending–descending* architecture. By taking a closer look at the template structure (Fig. 6.43a), one can notice that the first six layers are homogeneously organized throughout the colloidal crystal, without any significant variation in thickness. The remaining five layers, however, show a slightly wavy character, which is attributed to the fact that layers of smaller particle size are deposited onto bigger ones. It is found that this effect is particularly pronounced for big variations of the particle size from one layer to the next one (e.g., the step of 1200–600 nm spheres, as shown in Fig. 6.43a).

By selecting particles with diameters varying only slightly from one layer to the next one, it is possible to minimize the influence of this effect. In Fig. 6.44a,b, a reverse type of template (*Type* C_2, descending–ascending) is illustrated: the particle diameter first decreases for five layers from 1000 to 240 nm and subsequently becomes larger for the last four layers. A top view of these samples is shown in Fig. 6.44c,d. The homogeneity of the top surface is noticeable and might be put down to the more regular variation of the particle diameters in the descending or ascending parts (diameter ratios between consecutive layers were always close to 1.25). As shown in Fig. 6.44c, areas with a perfectly close packed sphere arrangement exist in the template, which is remarkable given the complexity of the template architecture. At lower magnifications, some defects including missing spheres or grain boundaries are visible in Fig. 6.44d in the top layer of the colloidal crystal template.

Since they are deposited on a gold substrate, reflectance spectroscopy is a very convenient and nondestructive technique to optically characterize the structure of our templates. Measurements have, therefore, been carried out using a microspectrophotometer working at normal incidence in the UV–Vis–IR range between 250 and 1650 nm. Similar to previous observations, regular oscillations, known as Fabry–Pérot fringes, testify the thickness homogeneity. They can be observed in a certain range of wavelengths (here, between 1200 and 1600 nm), as shown in Fig. 6.45 for three *Type B* samples consisting of three consecutive stacks of N layers of 430, 740, and 1000 nm silica particles (with $N = 3, 5,$ or 10). While the overall reflectance signal becomes more and more attenuated when the sample gets thicker, the number of fringes, resulting from interference phenomena at the air–template and

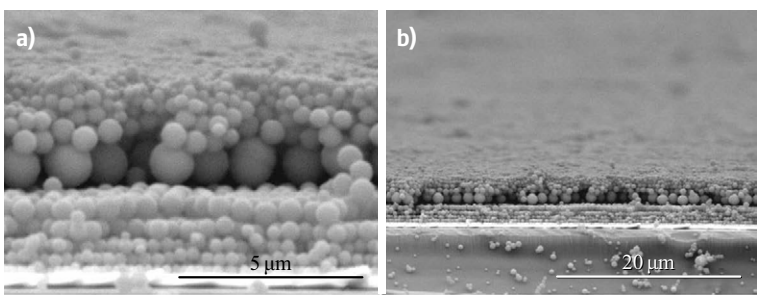


Fig. 6.43 **(a,b)** SEM side views of an double-gradient colloidal template (*Type* C_1) produced by LB at different magnifications. Spheres of six different diameters are symmetrically arranged with respect to the middle layer in the ascending–descending architecture (sphere diameters: 240, 325, 395, 470, 600, 1200, 600, 470, 395, 325, and 240 nm)

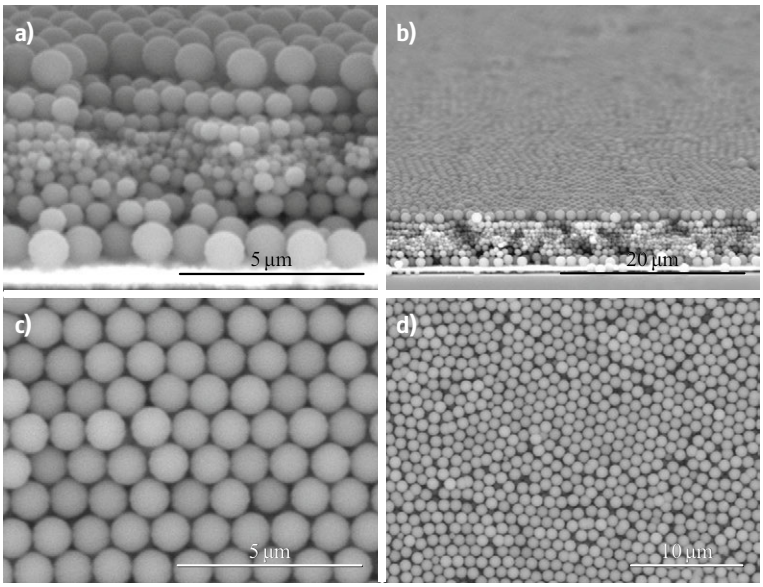


Fig. 6.44a–d SEM side (**a**,**b**) and top (**c**,**d**) views of a double gradient colloidal template (*Type* C_2) produced by LB at different magnifications. Spheres of five different diameters are symmetrically arranged with respect to the middle layer in the descending–ascending architecture (sphere diameters: 1000, 740, 470, 325, 240, 325, 470, 740, and 1000 nm)

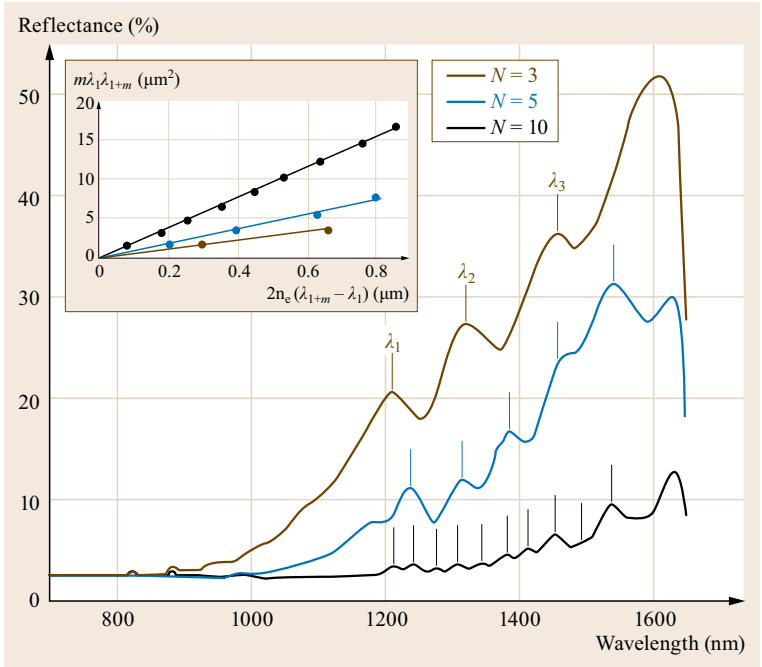


Fig. 6.45 UV–Vis–NIR reflectance spectra of three *Type B* templates consisting of three consecutive stacks of N layers of silica particles with an increasing diameter (430 nm for the first stack, 740 nm for the second and 1000 nm for the third). *Arrows* indicate the positions of the Fabry–Pérot fringes taken into account for calculating the thickness of each sample, given by the slope of the linear fits shown in the *inset*

template–substrate interfaces, increases as a result of a larger optical pathway. The wavelength positions of consecutive reflectance maxima allow us to estimate the thickness Θ of a sample [6.210], following (6.2)

$$m\lambda_1\lambda_{1+m} = 2n_e\,(\lambda_{1+m} - \lambda_1)\,\Theta\,, \qquad (6.2)$$

where λ_1 is the wavelength position of the first visible fringe taken into account and n_e is the mean refractive index for a compact arrangement of silica spheres in air, assumed to be close to 1.33. For each sample, Θ is, therefore, equal to the slope of the linear fits plotted in the inset of Fig. 6.45 and the calculated values are 5.3, 9.4, and 19.4 µm for the three *Type B* examples with three consecutive stacks of N layers ($N = 3$, 5, and 10, respectively). This result is in good agreement with the thicknesses inferred either from the SEM observations

or from geometrical calculations assuming a fcc packing of the spheres in each stack.

As shown in this section, extremely well-defined colloidal crystals of different, very complex architectures have been assembled by LB. In the following, they will serve as templates for the controlled infiltration with gold and PPy using electrochemical deposition.

6.2.2 Electrodeposition of Metals and Conducting Polymers

The templates fabricated in Sect. 6.2.1 served as working electrodes for the electrodeposition of gold and PPy. The electrodeposition was performed in a potentiostatic mode, which already had proven efficient to control the filling level of the infiltration of homogenous colloidal templates, thanks to the oscillating currents caused by periodic variations of the electroactive area in the template (Sect. 6.1.3). The experimental conditions including the electrolyte solutions, the experimental setup, and the applied potential were identical to those previously employed in Sects. 6.1.3 and 6.1.4. In all the figures presented in the following, for the sake of clarity, the intensity of the faradaic current signal that was recorded during the electrodeposition process was divided by the geometrical surface area of the electrode.

A typical example of such a chronoamperometric curve, recorded for the infiltration of the *Type A* colloidal template shown in Fig. 6.42a, is presented in Fig. 6.46a. Similar to the potentiostatic deposition of gold into homogeneous colloidal templates, we were able to observe current oscillations during the infiltration of templates with a more complex architecture.

The chronoamperometric curve in Fig. 6.46a shows that the shape of the oscillations depends on the sphere layer architecture in the template. The first and the last five oscillations of the curve exhibit relatively high amplitudes corresponding to the filling of the two 1000 nm sphere stacks in the template. The infiltration of the intermediate 430 nm sphere stack resulted in oscillations of higher frequency and much smaller amplitude. As explained in Sect. 6.1.3, these current oscillations allow us to follow the growth of the metallic deposit in these homogeneous and crack-free colloidal templates. The absolute minima of the current density correspond to the minima of the electroactive area and hence to half-layer filling levels in the template indicated by the arrows in the plot.

Another remarkable feature is particularly visible when the electrodeposition occurs in templates containing large particles. As expected – but never observed experimentally – by other authors [6.144, 147], the interpenetration of two consecutive layers of particles in an fcc arrangement should generate a local extremum for the current density when the electrodeposition front reaches the middle of the junction between two consecutive layers. As shown in the inset of Fig. 6.46a, the first minimum in current density indeed presents a small local maximum, thus corresponding to a local minimum of the electroactive surface area. This observation is in

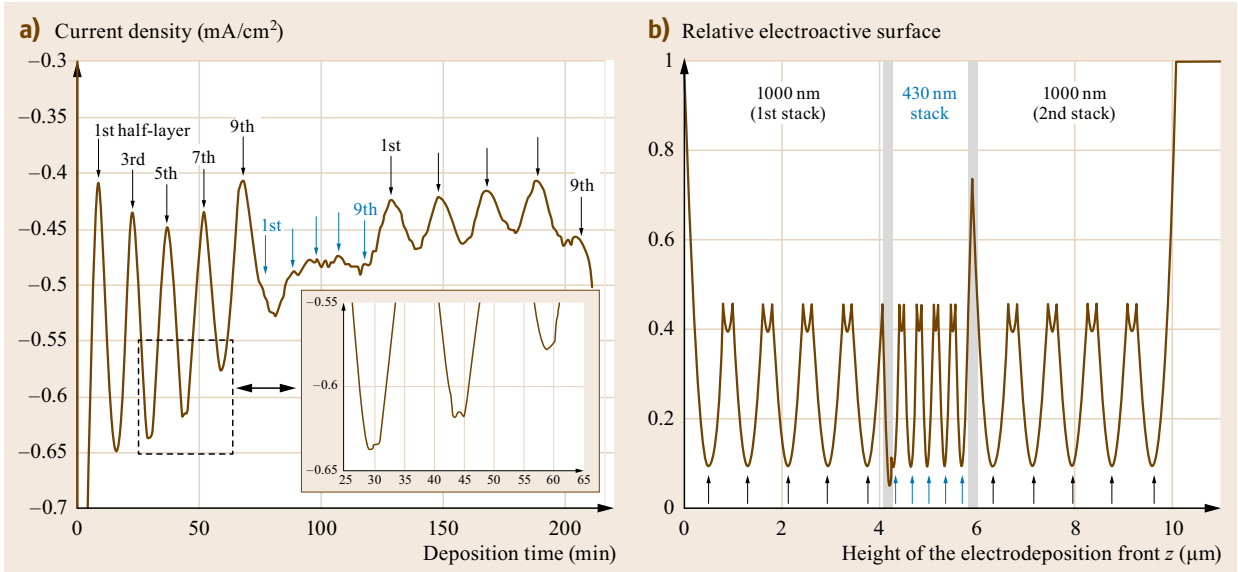


Fig. 6.46 **(a)** Chronoamperometric curves corresponding to the electrodeposition of gold ($E = -0.66$ V) in a *Type A* template presenting an artificial planar defect with two 5-layers stacks of 1000 nm particles separated by a 5-layer stack of 430 nm particles. **(b)** Theoretical calculation of the electroactive area as a function of the position of the progressing electrodeposition front

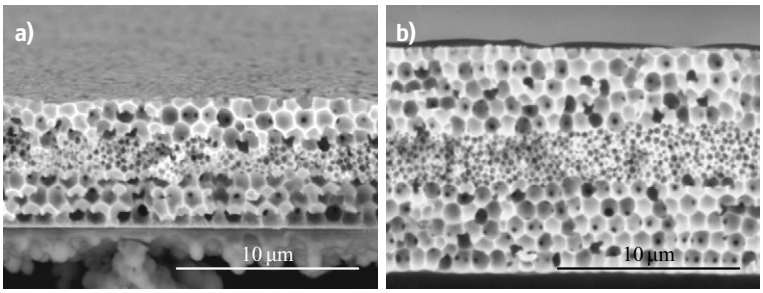


Fig. 6.47 SEM side views of macroporous gold electrodes obtained by infiltration of *Type A* templates and subsequent template removal. Templates were composed of three stacks of **(a)** $N = 3$ and **(b)** $N = 5$ sphere layers (after [6.168])

perfect agreement with the theoretical variation of the available surface area, calculated as a function of the height z of the growth front in the same Type B template (5 layers of 1000 nm, 5 layers of 430 nm, 5 layers of 1000 nm). Assuming that the velocity of the electrodeposition process is constant, this z-dependency, plotted in Fig. 6.46b, can be analyzed as a function of time. Two symmetrical cusps are observed around the extrema for each even number of half-layers, illustrating the antimonotone surface area variation for the overlap zone of two consecutive layers.

Three other characteristics emerge from this theoretical calculation based on pure geometric considerations. First, the absolute minimal area should equal 10% of the whole surface for each half-layer thickness, in agreement with the value of 0.9 for the packing factor expected for a hexagonal pavement of disks. It is worth noting that this minimum value is independent on the diameter of the particles. Second, the variation of the surface in the overlap between two consecutive stacks, around values of z close to 4.2 and 5.9 µm also exhibits local extrema that are not visible experimentally. Finally, when the metallic deposit reaches the top surface of the template, the electrochemically active area increases again until its maximum value, that is, the geometrical surface of the bare substrate. This last feature was, however, not observed in our experiments, since we systematically stopped the electrochemical reaction just before the gold deposit reaches the top surface. To be more precise, the electrodeposition was performed until the observation of the last maximum, corresponding to the 9th half-layer in Fig. 6.46.

Figure 6.47a,b shows the cross-sectional SEM images of macroporous gold electrodes obtained from the infiltration of Type A templates containing (a) three- and (b) five-sphere layers per stack. As intended, the infiltration of the templates has been stopped in the top layer of the template. The experiments show that oscillations had much smaller amplitudes for the infiltration of the stack composed of 470 nm spheres as theoretically would have been expected (Fig. 6.46a,b). This difference is due to the fact that layers of smaller particle size have been deposited onto bigger ones which creates a certain amount of disorder in this region of the template, not being included in the theoretical model. Pore layers in the *defect stack* of the sample are, hence, found to exhibit a slightly wavy character (visible in Fig. 6.47b). This lack of sphere layer alignment in the template is sufficient to suppress well-pronounced oscillating currents with a high amplitude.

In Fig. 6.48, chronoamperometric curves for the infiltration of gold into *Type B* templates, which consisted of three stacks of particles with an increasing diameter, are presented. Certain half-layer filling levels at absolute current minima have been indicated by arrows in the plot, each color corresponding to a different sphere size in different stacks of the *single-gradient* template. In both plots, a decrease of the oscillation frequency is observed when stacks of bigger particles are infiltrated with gold. The electrodeposition was stopped after the 5th and the 19th half-layer of their respective third stack, consisting of three (Fig. 6.48a) or ten (Fig. 6.48b) layers of 1000 nm silica particles.

The characterization of *Type B* templates by SEM images after the infiltration with gold and the removal of the template are shown in Fig. 6.49a,b respectively. The SEM image of the silica–gold composite illustrates well the level of precision provided by potentiostatic electrodeposition during the filling of the colloidal templates. As shown in Fig. 6.49a, the deposition of gold into the void space of the template has precisely been stopped before the metal front began to grow out of the top layer of the template. This allowed us to remove the silica template by dissolution, requiring the diffusion of a dilute solution of hydrofluoric acid from the top surface to the bottom of the electrode.

In Fig. 6.49b, a macroporous *single-gradient* gold electrode with $N = 10$ pore layers per stack is shown, corresponding to the amperometric deposition curve presented in Fig. 6.48b. The final macroporous material presents interconnected pores and a top surface with a remarkable flatness, illustrating the homogeneity of the electrodeposition process due to both, the adequate plating solution and the template quality. This is particularly well illustrated by the registered current transients in Fig. 6.48 where almost every maximum of the current

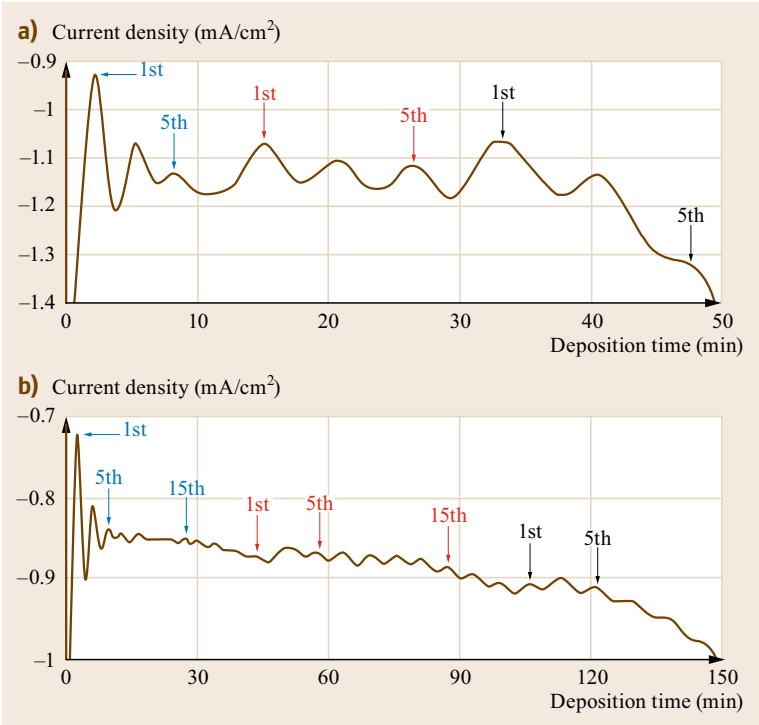


Fig. 6.48a,b Chronoamperometric curves corresponding to the electrodeposition of gold in a *Type B single-gradient* template consisting of three consecutive stacks of $N = 3$ **(a)** or $N = 10$ **(b)** layers of 430, 740, and 1000 nm particles. *Arrows* indicate the maxima corresponding to the half-layer positions in each stack

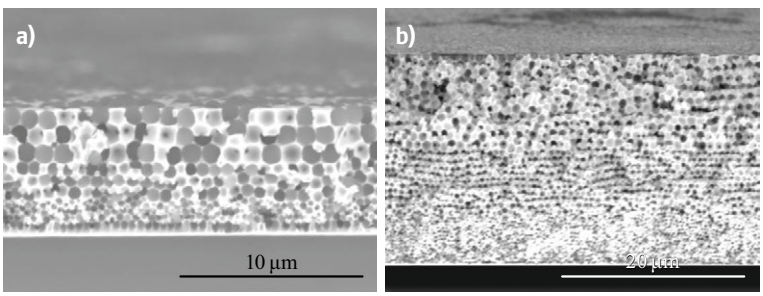


Fig. 6.49a,b SEM side views of macroporous gold electrodes originating from gold deposition into *Type B* templates. **(a)** After infiltration with gold for $N = 3$ and **(b)** after the template removal for $N = 10$ (after [6.168])

was resolved (up to 30 for the *Type B* sample, as shown in Fig. 6.49b), whereas the best results described in the literature quote the detection of a mere 10 maxima of the current density for the infiltration of colloidal crystals composed of a single sphere size [6.132].

Additional experiments were also carried out under similar conditions using the *Type C* templates shown in Figs. 6.43 and 6.44. Again, the variation of the current density versus time has to be correlated with the architecture template, the amplitude of the oscillations decreasing slowly during the electrodeposition process, either due to a laterally inhomogeneous growth front of the gold deposit or a slight imperfection in the ordering of the colloidal particles in the template.

A good example for the last mentioned point is presented in Fig. 6.50a with the *ascending–descending* sequence. For the sake of clarity, the structure of the template was reminded at the top of the figure, using spheres that were positioned symmetrically around each extremum (corresponding to each half-layer) and whose size was exactly proportional to the actual size of the silica particles used experimentally.

Indeed, the corresponding chronoamperometric curve is particularly remarkable, since the first six current oscillations, related to each of the six monolayers of the *ascending* stack, are clearly visible and their period matches almost perfectly the size of the particles. However, electrodeposition in the *descending* stack generates less pronounced oscillations. This result is in good agreement with the SEM images of the resulting inverse material, as shown in Fig. 6.51a,b, where a highly ordered porous structure is observed in the lower part of the sample (until the middle layer), whereas the degree of disorder is higher in the upper

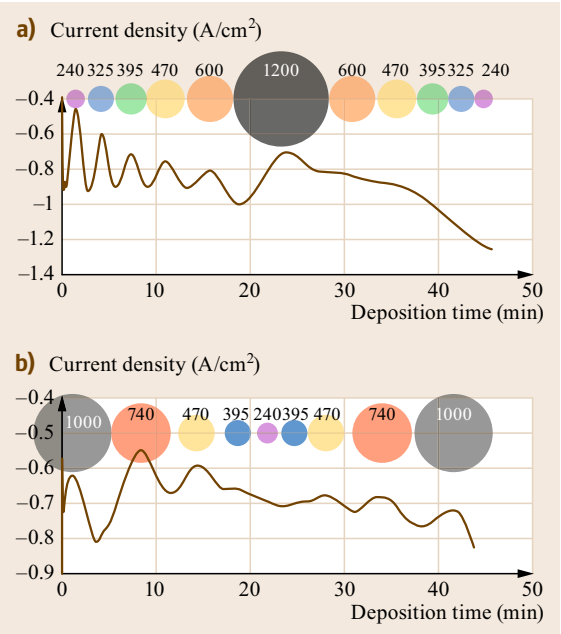


Fig. 6.50a,b Chronoamperometric curves corresponding to the electrodeposition of gold in double-gradient templates with ascending–descending (*Type* C_1, **(a)**) and descending–ascending (*Type* C_2, **(b)**) structures (numbers on spheres indicate the diameter of the particles used in the template) (after [6.168])

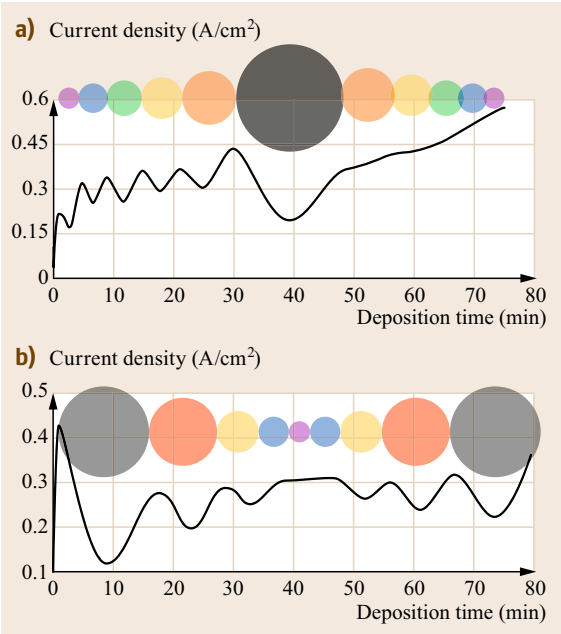


Fig. 6.52a,b Chronoamperometric curves corresponding to the electrodeposition of PPy ($E = +0.6$ V) in double-gradient templates with ascending–descending (*Type* C_1, *top figure*) and descending–ascending (*Type* C_2), **(a)** structures (after [6.168])

five layers, this being directly related to the stacking irregularities observed in the template (Fig. 6.43).

Electrodeposition in the *descending–ascending* structure, where the variation in particle size was more progressive between consecutive layers, leads to a much more symmetrical chronoamperometric profile, the maxima of the current density being still visible in the second *ascending* stack. The SEM images of the corresponding macroporous gold structure is shown in

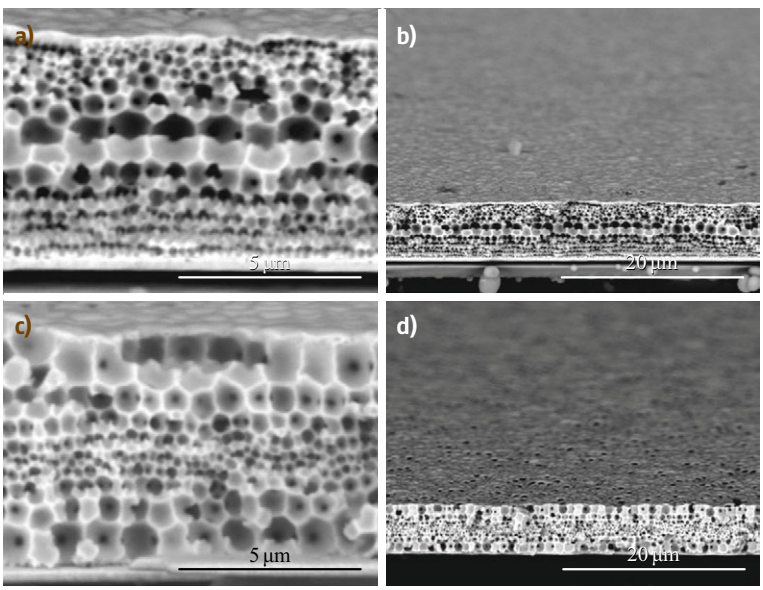


Fig. 6.51a–d SEM side view-images of macroporous double-gradient gold electrodes with ascending–descending **(a,b)** and descending–ascending **(c,d)** pore size structures at different magnifications (after [6.168])

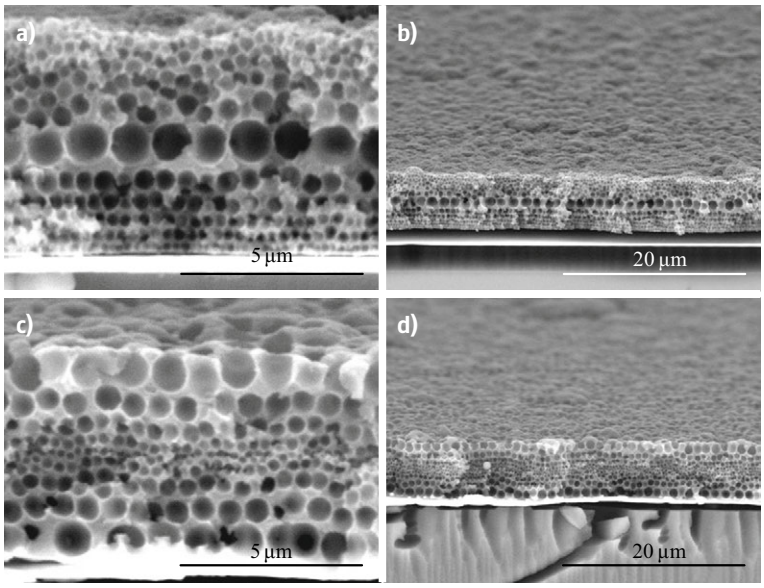


Fig. 6.53a–d SEM side view-images of macroporous double-gradient PPy electrodes with ascending–descending (**a,b**) and descending–ascending (**c,d**) pore size structures at different magnifications (after [6.168])

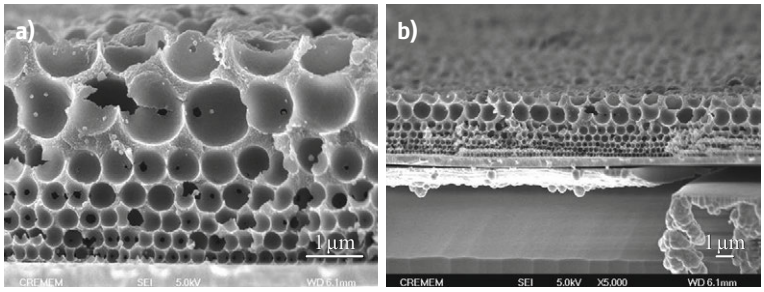


Fig. 6.54a,b Macroporous PPy electrodes with a pore size gradient. Pore sizes are increasing from 240 to 1200 nm. The *top half-layer pore* has the same diameter as the underlying pore layer ($d = 1200$ nm). Images with a (**a**) high and (**b**) lower magnification (after [6.168])

Fig. 6.51c,d. A very regular pore architecture is found in the double-gradient structure, with a remarkable flatness of the top pore layer. As can be seen, the whole template was infiltrated with gold, without growing over the top surface layer, thanks to the control provided by the recorded current oscillations.

As mentioned in Sect. 6.1.2, a wide range of materials including different metals, CPs, oxides, and certain semiconductors can be infiltrated into the void space of colloidal crystals using electrochemical deposition. To illustrate that the results we showed so far are mainly depending on the quality of the template, the electrodeposition of a CP film was performed into the *Type C* templates. Polypyrrole was deposited in a potentiostatic mode as described in Sect. 6.1.4.

Figure 6.52 presents the chronoamperometric curves obtained during the electrodeposition within *Type C* templates, identical to those shown in Figs. 6.43 and 6.44.

Similar to the results obtained with the gold plating solution, we again observe regular oscillations of the current density, here around a mean value of 0.3 mA/cm^2. In the *ascending* stack of the ascending–descending structure, the interdistance between consecutive maxima is again in perfect agreement with the size variation of the particles in consecutive layers. As expected, oscillations are, however, less visible in the *descending stack*. The order in the last five pore layers in Fig. 6.53a is considerably lower than that in the first six layers, explaining the lack of oscillations during the infiltration of the second part of the template. The flatness of the top surface is also less regular in PPy films compared to its gold analogue, as can be seen in Fig. 6.53a,b. On the other hand, electrodeposition in the *descending–ascending* structure leads to an almost perfectly symmetrical chronoamperometric curve, indicating both (i) the good symmetry of the template architecture and (ii) a constant rate of reaction – or film growth velocity – suggesting that the electrochemical oxidation of pyrrole proceeds homogeneously.

Again, the SEM side view pictures in Fig. 6.53c,d, recorded after the dissolution of the silica particles in dilute HF, confirm this statement.

Figure 6.54 illustrates the cross-sectional SEM images showing a macroporous PPy electrode with a pore size gradient in high resolution. It has been obtained from a template consisting of the *ascending* part of the *Type* C_1 structure with one additional layer of 1200 nm spheres deposited on top. Filling this template up to the last half-sphere layer with PPy and removing the template led to the macroporous gradient structure, as shown in Fig. 6.54a,b. The well-ordered and uniform character of the structure found in *ascending* stacks of pore layers is particularly visible in these images.

In this section, we successfully produced macroporous electrodes with complex pore architectures including defect layers and single- and double-gradient structures with a remarkably well-defined structural integrity. Current oscillations observed during the potentiostatic electrodeposition provided excellent control over the filling of the void space in the templates and, hence, the final thickness of the nanostructured electrode films. In the following Sect. 6.3, we will show how macroporous gold microcylinders with a well defined pore size and thickness can be obtained and that their high surface-to-volume ratios present promising features for their further use in miniaturized electrocatalytic devices.

6.3 Macroporous Microelectrodes with Cylindrical Geometry

Porous gold structures with a well-defined pore size and thickness are obtained through electrochemical deposition of gold in a colloidal crystal template synthesized by the LB technique. Cylindrical gold wires were used as substrates for the LB deposition of successive monolayers of silica particles of various sizes, and the electrodeposition of either gold or PPy through this inorganic template led to homogeneous, porous metal, or CP structures. These materials were characterized through typical electrochemical experiments and showed high surface-to-volume ratios with promising features for their further use in miniaturized electrocatalytic devices.

Improving the performances of electrochemical devices for applications ranging from analysis to catalysis and energy conversion has become one of the most important issues of research during the last years [6.6, 211]. In this field, controlling the architecture of an electrode in order to achieve a higher accessibility or a better mass transport and obtaining larger active areas are development strategies of high interest, for example, for analytical [6.8] or optoelectronic applications [6.212]. Macroporous electrodes showed superior performance compared to their nonporous homologs for different applications in fields including analysis, catalysis, and energy storage or conversion. In electroanalysis, they outperformed smooth electrodes offering improved sensitivity toward the detection of different biomolecules [6.140, 164, 213–217] or heavy metal ions [6.150, 151]. Higher catalytic activities for hydrogen peroxide reduction [6.140], NADH [6.139], methanol, or ethanol oxidation [6.218] equally were reported when macroporous instead of flat electrodes were used.

However, the application of these devices is limited due to their macroscopic size and planar geometry. Therefore, a huge application potential still remains for this type of materials, assuming that they can be prepared with a smaller overall size. Miniaturized systems might indeed be really useful for some applications like in vivo measurements, biofuel cells [6.219], and more generally, all devices where confined media with a limited accessibility are involved [6.220]. In this field, cylindrical structures may be very convenient to use and they already proved to be of high interest for analytical purposes [6.221], despite the difficulty of the theoretical aspects since equations for diffusion cannot be solved analytically for a cylindrical geometry, unlike for planar or spherical ones [6.222]. Gold, platinum, or carbon fiber microelectrodes have, for instance, been used successfully for the detection of mercury and copper ions by anodic stripping voltammetry [6.223–226].

In porous cylindrical microwires, which can be produced by colloidal crystal templating, small overall dimensions are combined with high active electrode areas. However, very surprisingly, there are very few reports in the literature dealing with the elaboration of colloidal templates with a nonplanar geometry. In these works, templates were obtained either by the sedimentation of latex or silica dispersions in glass capillaries and PMMA or Kapton tubes [6.227–229], dip-coating onto glass fibers [6.230], or electrophoretic deposition onto carbon fibers [6.231] and were then infiltrated to obtain porous polymeric [6.227–230] or metal replicas [6.231]. In this section, a different strategy is described, allowing us to control both the thickness of the colloidal template and the infiltration of the latter using electrodeposition with a very high accuracy [6.232]. A scheme illustrating different steps involved in the fabrication of macroporous gold cylinders is shown in Fig. 6.55.

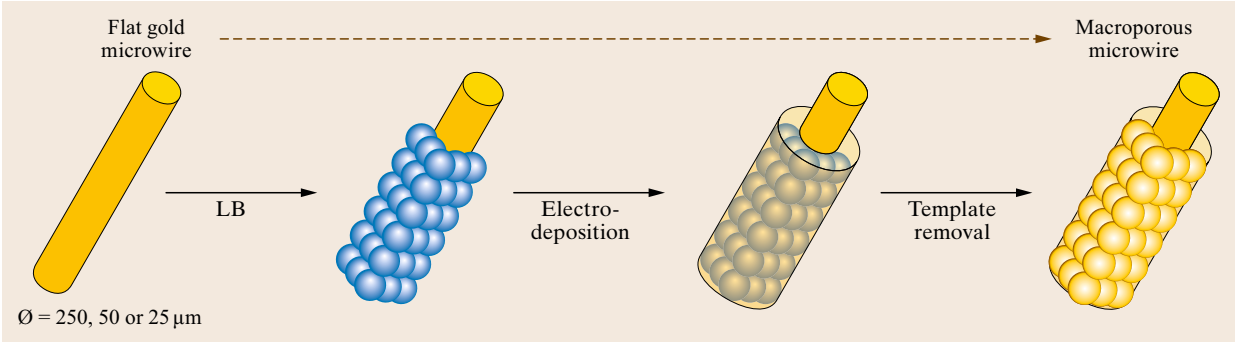


Fig. 6.55 Schematic representation of the fabrication steps involved in the generation of macroporous gold microelecetrodes with cylindrical geometry (after [6.232])

Gold microwires of three different diameters ranging from 25 to 250 µm served as substrates for the deposition of silica colloidal crystals. The desired number of sphere monolayers could be transferred onto the wires by using the LB technique (Sect. 6.3.1). Similar to the electrodes with a planar geometry, the filling ratio of the colloidal template with gold or PPy could be precisely controlled during the potentiostatic electrodeposition due to the oscillating current response. After the removal of the inorganic template, the macroporous wires were characterized by SEM imaging (Sect. 6.3.2). Additionally, the active surface area of the macroporous gold wires was determined electrochemically (Sect. 6.3.3).

6.3.1 Fabrication of Colloidal Crystal Templates on Gold Wires

Synthetic 2-D or 3-D colloidal crystals of silica particles obtained through the LB technique have mainly been considered, if not exclusively, on planar glass substrates. This is due to the interest in the optical properties of the opal films being readily studied in UV–Vis spectroscopic measurements on transparent glass substrates. The transfer of silica Langmuir films on clean hydrophilic glass slides occurs readily and further treatment of the substrates is not required. Similarly, as we have shown in Sect. 6.2.1, reflectance spectroscopy can be used to characterize colloidal crystals assembled on glass slides, covered with a thin gold layer. As mentioned in Sect. 6.1.1, a transfer of silica Langmuir films occurs on sufficiently hydrophilic substrates building up a meniscus at the water–substrate interface during the upstroke. The successful transfer of Langmuir films consequently is not restricted to a planar substrate geometry. In this work, cylindrical LB films with silica particles in the micrometer size range were synthesized. To achieve this, commercial gold wires were first cut in small pieces with a length between 25 and 30 mm and, after a fast cleaning treatment, were used as substrates for the LB deposition. A home-made Langmuir trough (Fig. 6.56b) with two mobile barriers and a maximum interface area of 1000 cm^2 was successfully used to form Langmuir films of silica particles with various diameters. As shown in Fig. 6.56a, the gold wires were fixed to a glass substrate which then was attached to the dipping mechanism (Fig. 6.56b). Fast immersion followed by slow withdrawing cycles allowed us to transfer silica sphere monolayers onto the cylindrical gold wires up to a desired number N of deposited layers.

In Fig. 6.56c,d SEM side view pictures of the so-formed LB films show that the colloidal stacking is regular over very large distances, whatever the diameter of the wire. In order to better illustrate its thickness, a small portion of the template has been removed in these pictures. The cylindrical gold substrate is clearly visible (it appears in white due to its high conductivity) and the thickness of the homogeneous LB film can be measured quite precisely. Due to the small dimensions and the cylindrical geometry of the samples, reflectance spectroscopy was not an adequate technique here to measure the thickness of the colloidal template. The experimental value for the thickness of the template retrieved from SEM observations can then be compared with the theoretical one given by (6.3), assuming a compact stacking of the monolayers

$$e = \left[1 + (N-1)\sqrt{\frac{2}{3}}\right] d \,, \tag{6.3}$$

with d being the diameter of the silica particles, N the number of bead layers, and e the total thickness of the template [6.210]. For the template pictured in Fig. 6.56c, values of $d = 0.69\,\mu m$ and $N = 25$ result in a theoretical thickness of $e = 14.2\,\mu m$. This is in excellent agreement with the thickness estimated from the SEM pictures to be close to 14.1 µm. In other

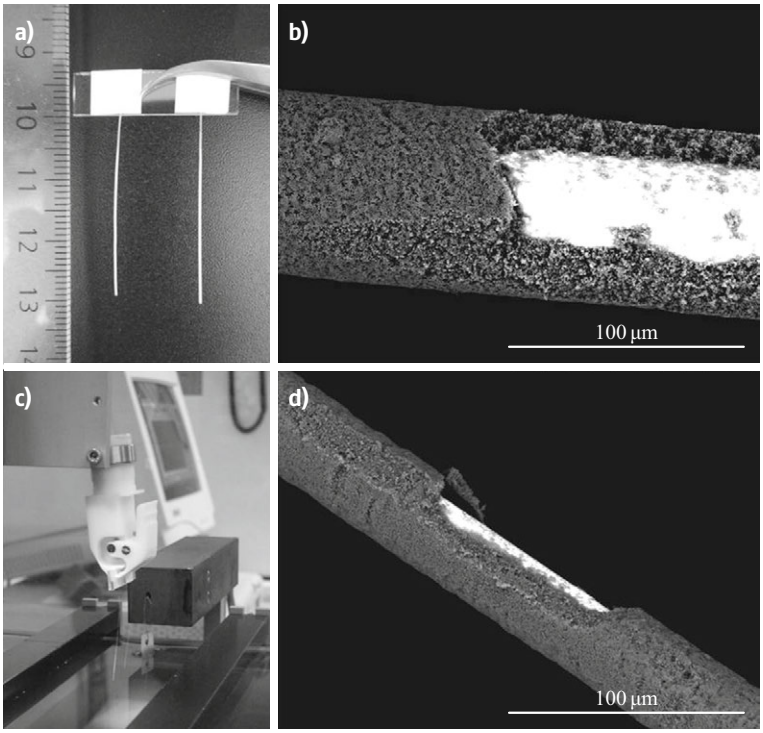


Fig. 6.56a–d Photographs of **(a)** cylindrical gold wires (diameter 250 µm) after the deposition of 50 layers of 420 nm silica particles. **(b)** Home-made Langmuir trough with two mobile barriers, a precut paper as Wilhelmy plate for surface pressure measurement, and a dipping system. On this picture, the dipper holds two pieces (3 cm long) of a 50 µm gold wire as substrates. **(c,d)** SEM images of LB films deposited onto gold wires of different diameters with **(c)** 25 layers of 690 nm silica particles onto a 50 µm wire. **(d)** 25 layers of 420 nm silica particles onto a 25 µm wire (after [6.232])

words, cylindrical colloidal assemblies with a regular thickness and a well-controlled architecture can be obtained by the LB technique with all the interesting features already mentioned before for planar geometries.

6.3.2 Electrodeposition of Metals and Conducting Polymers

The gold wires coated with silica colloidal crystal films were then used in a second step as working electrodes in a conventional three-electrode electrochemical cell, illustrated in Fig. 6.57. Contrary to the setup employed for the electrodeposition onto planar samples (Sect. 6.1.3), a cylindrical platinum mesh served as counterelectrode in order to ensure that the whole cell has the working electrode as a symmetry axis. This enabled a homogeneous deposition with a uniform growth speed throughout the wire. In contrast, using planar CEs was found to lead to a preferential deposition on the side of the wire facing the CE. After a few seconds, to allow the diffusion of the commercial gold-plating solution (ECF 60, Metalor) into the silica deposit, the potentiostatic reduction of the gold sulphite ions, $[Au(SO_3)_2]^{3-}$, contained in the electrolytic bath was carried out at a potential of −660 mV versus Ag/AgCl. The intensity

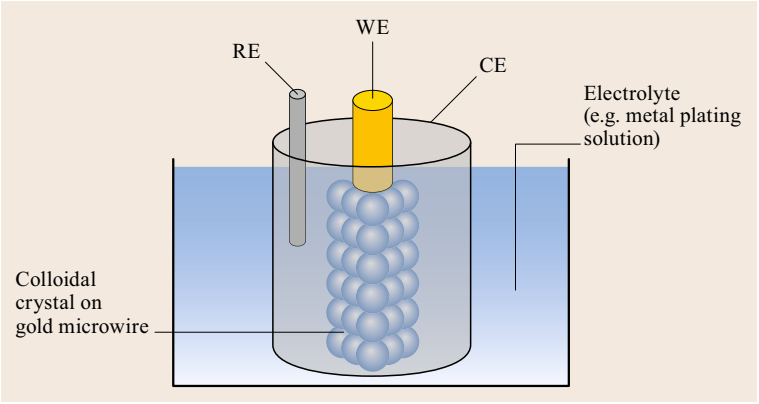


Fig. 6.57 Experimental setup employed for the electrodeposition in colloidal templates on microwire electrodes. A cylindrical platinum mesh (CE) was placed symmetrically around the gold wire (WE) in order to ensure homogeneous film growth on the wire

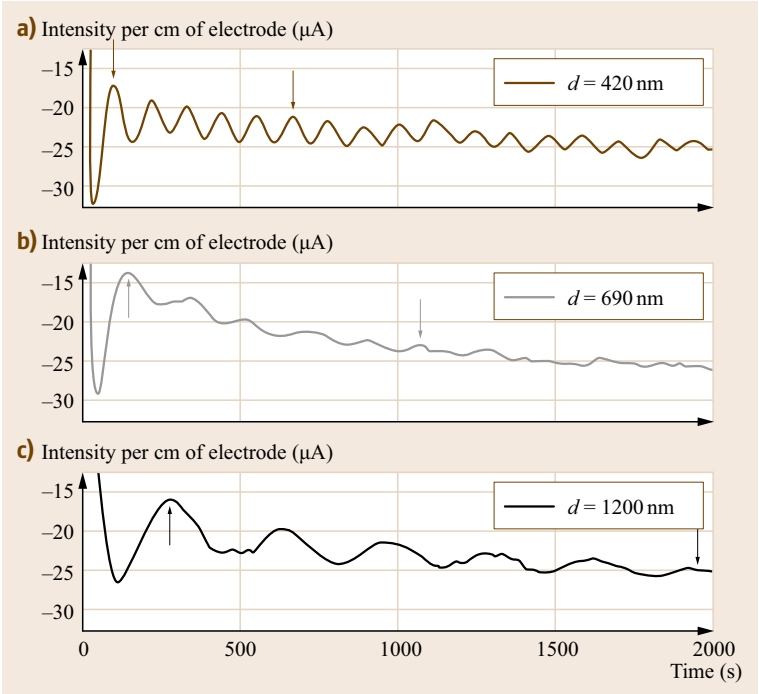


Fig. 6.58 Chronoamperometric curves ($E = -0.66$ V versus Ag/AgCl) corresponding to the electrodeposition of gold within multilayered templates of silica particles with different diameters. *Arrows* indicate the positions of the first and sixth local maxima corresponding to the 1st and 11th half-layer. Diameter of the supporting gold wires: 50 μm (after [6.232])

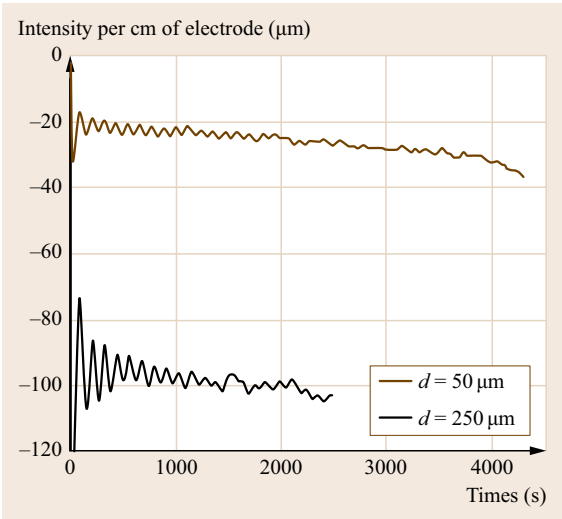


Fig. 6.59 Chronoamperometric curves ($E = -0.66$ V versus Ag/AgCl) corresponding to the electrodeposition of gold in colloidal assemblies of 50 and 25 layers of 420 nm silica particles deposited onto gold wires of 50 and 250 μm, respectively

of the faradaic current was then measured as a function of time.

Similar to samples with planar geometries, it is possible to observe oscillating currents in the chronoamperometric curves during the infiltration of colloidal templates on gold wire electrodes. This can be attributed to a periodic variation of the active surface area of the growing gold deposit during the infiltration of the template voids. In Fig. 6.58, the chronoamperometric curves for the deposition into templates composed of different sphere diameters on 50 μm gold wires are shown.

For the sake of comparison, intensity was normalized to an intensity per electrode length by dividing the experimental $i(t)$ signal by the estimated depth of immersion of the wire in the gold-plating bath (with an accuracy of ±1 mm). The current was found to oscillate more or less regularly around a mean value close to 23 μA during the infiltration of different templates. Such a result already suggests, without any other information, that the top surface of the growing structure is smooth and homogeneous, and that the packing of the colloidal template is regular.

Therefore, each local maximum on this graph should correspond to a minimum of the surface area of the growing film, that is, when the thickness of the gold deposit equals an uneven number of half-layers of particles. In a planar geometry, this would match the equatorial planes of each deposited layer of particles. Assuming a compact stacking and the corresponding geometric considerations, the distance between two consecutive planes is given by (6.4)

$$a = \sqrt{\frac{2}{3}}d\,, \tag{6.4}$$

where d is the diameter of the colloidal particles.

As shown on the plot, the deposition time Δt between the first equatorial plane (first half-layer of particles) and the sixth one (eleventh half-layer) strongly depends on the size of the silica particles. Similar to the results shown in Fig. 6.20a, a decrease in the oscillation frequency was found in templates with bigger spheres. From the peak positions, we can easily estimate, for each particle size, a mean growth speed $\langle v \rangle$ of the gold film in the colloidal crystal structure described by (6.5)

$$\langle v \rangle = \frac{5a}{\Delta t} = \frac{5a}{t_{11/2} - t_{1/2}} \,. \tag{6.5}$$

As summarized in Table 6.2, it seems that the particle size does not affect the growth speed of gold in the templating structure, which is rather constant and close to 3 nm/s under these experimental conditions. This result also suggests that the particle size has no incidence on the diffusion of gold sulphite ions and, therefore, does not affect the deposit growth mechanism. A parameter exhibiting strong influence on the growth speed of the metal deposit is the concentration of metal ions in the plating bath. Due to the depletion of metal ions in the electrolyte, slower growth rates can be observed in the course of the electrodeposition experiments. However, the total amount of deposited gold here was rather small with respect to the employed electrolyte volume, so that this effect was of minor importance for the deposition onto cylindrical microwires.

We have also verified that it was possible to observe this periodic evolution of the faradaic current during longer periods of time, that is, until the gold deposit reaches a large thickness. As it becomes clear from Fig. 6.59, oscillations are visible up to at least 41 half-layers – thus corresponding to over 20 layers of particles – whatever the diameter of the gold wire. It is worth noticing that during the first minutes of the deposition, the current oscillates around a mean value of $-22(\pm 1)\,\mu$A for the 50 µm wire and $-95(\pm 5)\,\mu$A for the 250 µm wire. This result confirms that the electroactive surface is directly proportional to the geometrical surface of the bare substrate.

Gold wires have been characterized directly after the electrodeposition process by cutting the cylindrical wires, allowing us to examine the cross-section of the gold deposit in the colloidal template by SEM imaging. In Fig. 6.60a, the edge of a 250 µm gold wire used as an electrode with 25 layers of 690 nm silica particles as template is observed at low magnification. In this particular case, electrochemical deposition was carried out until the gold deposit became slightly thicker than the template. The surface of the electrode seems homogeneous at this scale without any porosity, but peeling off the porous layer and observing it at higher magnification reveal that there were exactly 25 layers of silica particles deposited onto the gold wire during the LB process, which are completely filled with gold (Fig. 6.60b). On the right side of this image, the bottom surface of the gold–silica layer (which was in direct contact with the wire) looks very smooth, whereas on the left-hand side, it appears that the thickness of the metallic deposit is, as expected, just a few hundreds of nanometers thicker than the original LB film.

When the growth of the gold deposit was stopped before reaching the top surface of the template, the removal of the silica particles was possible by the infiltration of dilute hydrofluoric acid. Under these conditions, SEM side views provide important information about the architecture of the electrodes. First, the homogeneity of the samples is particularly obvious over large distances, not only over half a millimeter as pictured in Fig. 6.61a, but all along the wire electrode. This homogeneity suggests that there were no preferential pathways for the growth of the gold deposit in the sil-

Table 6.2 Calculation of the growth speed $\langle v \rangle$ of the gold deposit in colloidal templates composed of spheres with different diameters d

	$d = 420$ nm	$d = 690$ nm	$d = 1200$ nm
a (nm)	342.9	563.4	979.8
$t_{1/2}$ (s)	94.4	141.6	274.7
$t_{11/2}$ (s)	665.6	1068.0	1953.0
$\langle v \rangle$ (nm/s)	3.00	3.04	2.92

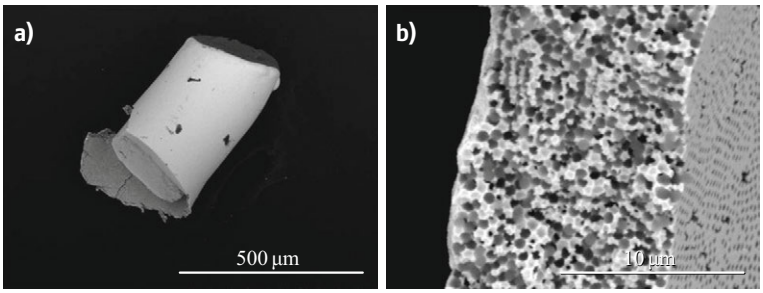


Fig. 6.60a,b SEM pictures of a gold-filled colloidal crystal deposited onto a 250 µm gold wire: **(a)** Top view of the edge of the electrode; **(b)** side view of the gold-silica composite layer with 25 monolayers of 690 nm silica particles as template

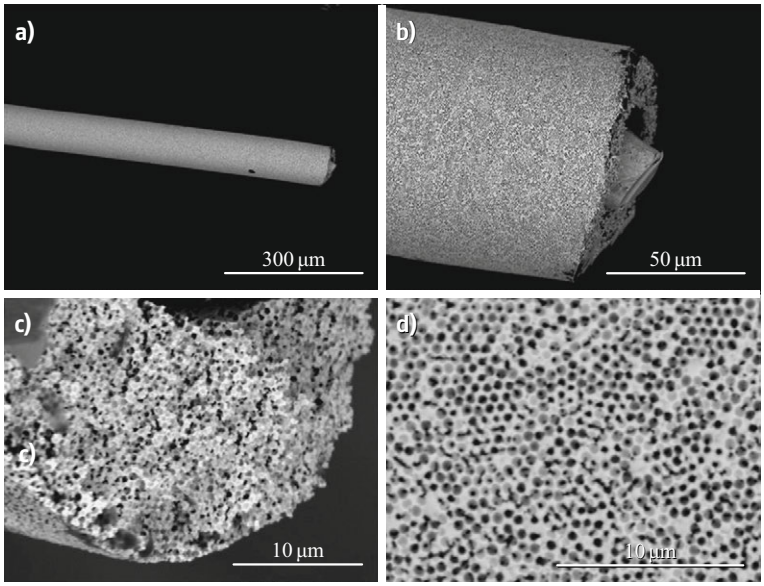


Fig. 6.61a–d SEM pictures of a porous gold electrode based on a 50 µm gold wire. The silica template consisted of 50 layers of 690 nm silica particles. **(a,b)** View of the macroporous wire at different magnifications. **(c)** Cross section image of the macroporous film deposit. **(d)** Surface of the macroporous gold wire (after [6.232])

ica template, which was containing few vacancies and was, most importantly, crack-free. At higher magnifications, as shown in the Fig. 6.61b,c, the thickness of the electrodeposited layer can be measured easily and the original wire used as support is also clearly visible. For instance, in Fig. 6.61c, the thickness of the gold deposit is close to 19.1 µm. Taking $d = 690$ nm, it can be calculated from (6.3) that the gold deposit reached the 34th layer of particles within the 50-layer LB template.

Additional views, such as, in Fig. 6.61d, also provide good information about the morphology of the electrode surface, where macroscopic pores organized in a reasonably compact arrangement – sometimes hexagonal – illustrate the quality of the original silica template. It is also obvious that pores of two consecutive layers are well connected with each other.

Finally, taking advantage of the periodic current oscillations during the gold deposition, we have tested the possibility of controlling precisely the thickness of the porous structure. To do so, the electrochemical reaction was stopped as soon as the faradaic current reached values of the corresponding local maxima of the characteristic chronoamperometric curves. As illustrated by

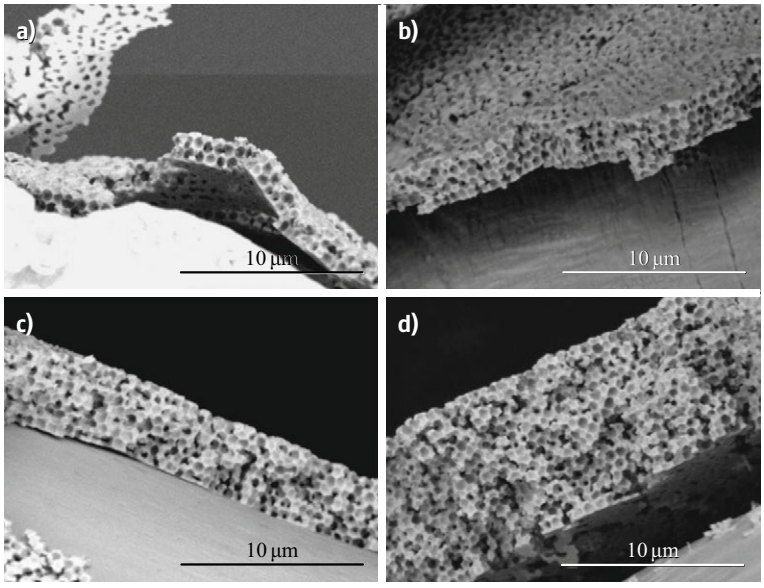


Fig. 6.62a–d SEM pictures of porous gold deposits of various thicknesses on microwires after dissolution of the 690 nm silica particle templates. Images show macroporous gold films with **(a)** 5, **(b)** 9, **(c)** 15 and **(d)** 29 half-layers (after [6.232])

the SEM images of Fig. 6.62, showing side views of the porous gold layer, this feature has also been verified successfully.

As pointed out earlier, besides gold, a range of other materials including CPs can be electrodeposited. In the following example, the void space of the colloidal template on the microwire electrodes has been filled with PPy.

To do so, the same experimental setup as for the gold deposition was used, the electrolyte solution and the potential applied during electropolymerization of pyrrole were adopted from Sect. 6.1.4. Figure 6.63 shows a chronoamperometric curve for the deposition of PPy on a 250 µm gold wire, coated with 10 layers of 1200 nm silica spheres. Although the current oscillations observed during the infiltration of the template with PPy were less regular than shown earlier for the potentiostatic gold deposition, they still enabled us to follow the progression of the PPy growth front in the template and so to control the final thickness of the deposit.

The characterization of the gold wires coated with macroporous PPy by SEM is shown in Fig. 6.64. Cross-sectional views of a 50 µm gold fiber are provided in Fig. 6.64a,b. Despite cutting the fiber using a scalpel, the PPy film adhered well to the substrate showing a uniform thickness all around the gold fiber. Figure 6.64c,d shows a surface view of the PPy-coated microwires at different magnifications. By taking a close look, one can see that the voids in PPy are interconnected similar to what was found in the macroporous gold film deposits.

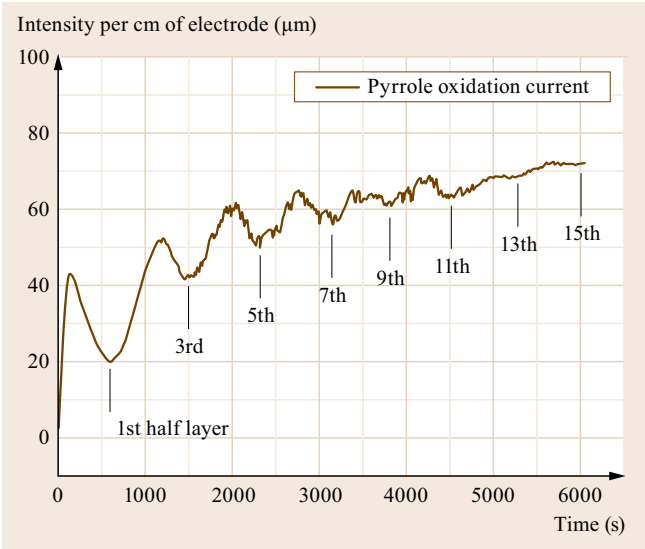


Fig. 6.63 Chronoamperometric curve ($E = 0.6$ V) for the PPy deposition into a colloidal template composed of 10 layers of 1200 nm particles assembled on a 250 µm gold wire

As evidenced by the SEM pictures, it is possible to synthesize macroporous gold and PPy microwires with a highly interconnected pore network. The latter is of special interest considering possible applications of these macroporous wires as miniaturized electrode materials in sensors and catalytic or energy-related devices. Thus, in the following, the active surface area of the gold microwires has been determined using electrochemical methods.

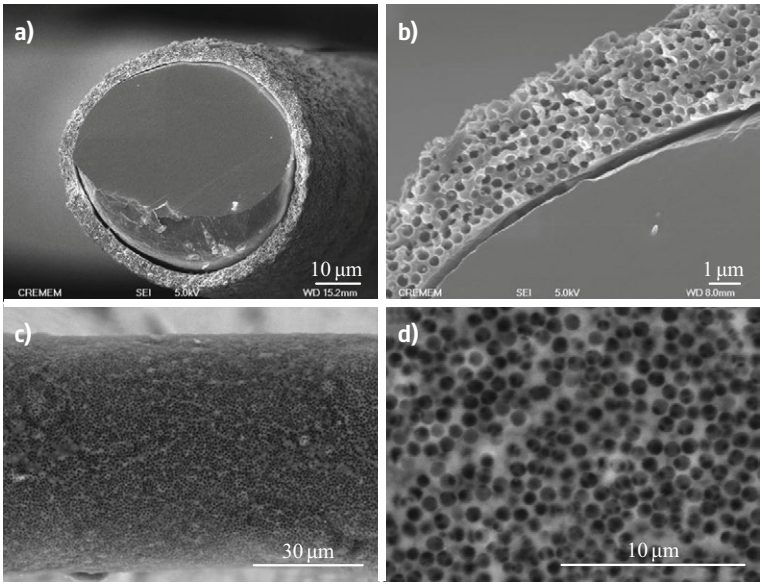


Fig. 6.64a–d SEM characterization of macroporous PPy films on gold microwires (diameter 50 µm). **(a,b)** Cross section images of the gold wire with the macroporous PPy film (pore size 420 nm) at different magnifications. **(c,d)** Surface view of the macroporous PPy film (pore size 1000 nm) deposited on the cylindrical gold wire at different magnifications

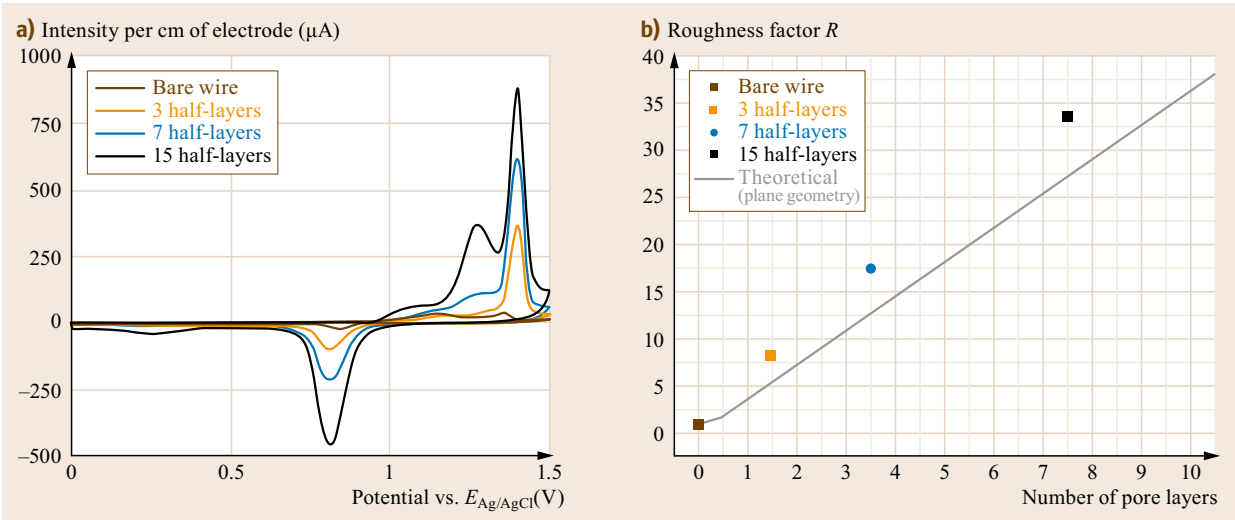


Fig. 6.65 **(a)** CV stripping curves obtained from macroporous gold structures of different thickness (pore size 690 nm) on 250 μm gold wires. A 0.05 M H_2SO_4 aqueous solution together with a scan rate of 100 mV/s was employed. **(b)** Evolution of the roughness factor as a function of the porous layer thickness for macroporous gold microwires

6.3.3 Characterization of Macroporous Gold Cylinders

Similar to their planar homologs (Sect. 6.1.3), macroporous gold wires are likely to possess a much larger active surface area compared to the bare wire substrate. To confirm this statement, stripping of gold oxide using cyclic voltammetry has been carried out in an acidic medium using the porous structure as a working electrode. Figure 6.65a presents the cyclic voltammograms obtained with materials based on a 250 μm wire with porous layers of an identical pore size of 690 nm, but different thicknesses. These stripping curves are typical for a pure gold electrode with a gold oxidation between 1 and 1.5 V (versus Ag/AgCl) and a reduction peak, centered around 0.8 V, related to the gold oxide reduction. As shown in Sect. 6.1.3, the area of this peak is directly proportional to the active surface of the macroporous gold electrodes. From a qualitative point of view, Fig. 6.65a already shows that the intensity of the oxidation and reduction processes increases with the porous layer thickness.

As shown in Sect. 6.1.3, it is possible to calculate the electroactive surface area of macroporous gold samples from the charge associated with the gold oxide reduction peak in the CV, allowing us to further quantify the increase of the surface area by calculating the roughness factor for gold microwires with different numbers of porous layers (Fig. 6.65b). Similar to the samples with plane geometry, a linear increase of the roughness factor with increasing number of pore layers on the gold wires is observed. However, for a cylindrical substrate geometry, the experimental values are higher than theoretically expected for samples with a planar geometry. Due to the increase of the diameter of the wires with increasing number of porous layers, a greater number of pores (spheres) is present in successive layers, explaining the deviation of the experimental from the theoretical values. An overall increase of the electrochemically useful surface area by one or two orders of magnitudes can, therefore, easily be obtained using the above-described strategy. In the following, these improved characteristics will be used for a certain number of applications.

6.4 Applications of Macroporous Electrodes

The previous sections have shown evidence that it is possible to design highly organized porous electrodes on purpose and in a rational way. The perfect control of their electrochemical performance allows us to imagine a wide variety of possible applications, and we will, in the following, discuss a couple of representative examples that should give a first impression of the potential application value of such designed structures in different areas of science ranging from chemistry to optics.

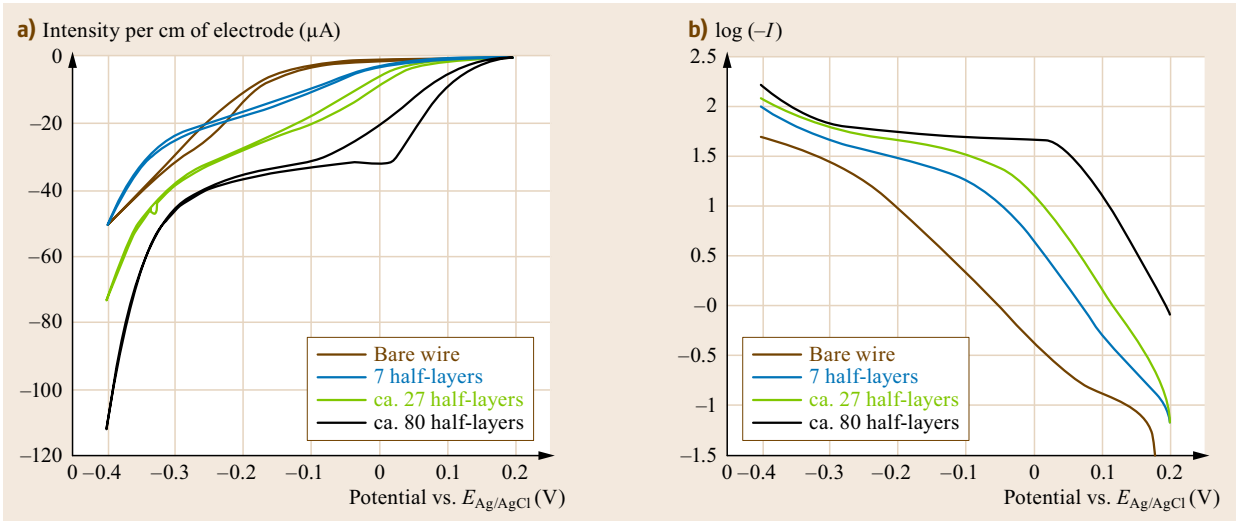


Fig. 6.66 **(a)** CVs obtained with macroporous gold structures of different thickness (pore size 1200 nm) on 50 μm gold wires. The electrodes are exposed to 0.05 M H_2SO_4 aqueous solutions saturated with oxygen (scan rate: 5 mV/s) in order to check their electrocatalytic activity. **(b)** Tafel plots obtained for the same electrodes (after [6.232])

6.4.1 Electrocatalysis

In recent literature work, the ability of nanoporous and/or enzyme-modified gold electrodes to catalyze the reaction of species like oxygen [6.233] or glucose [6.140] has attracted much attention due to their potential application in biofuel cells, [6.234, 235]. It is, therefore, interesting to carry out experiments with the macroporous gold structures described in Sects. 6.3.2 and 6.3.3 in order to estimate the potential usefulness as miniaturized electrochemical devices [6.232]. Because the reduction of oxygen is of great importance as it usually determines the operating voltage, and thereby the efficiency for example of fuel cells, it was chosen as a key test to estimate their catalytic utility. Figure 6.66a presents the cyclic voltammograms recorded in an oxygen-saturated 0.05 M sulfuric acid solution. In the chosen potential window, the only electrochemically active species is oxygen, which is reduced to H_2O_2, and then further to H_2O below −0.4 V.

When the porous gold layer gets thicker, the intensity of the O_2 reduction current becomes significantly higher, similar to what has been previously observed for the reduction of hydrogen peroxide on planar macroporous electrodes [6.140]. However, an even more interesting feature is the evolution of the threshold for the O_2 reduction, defined as the potential at which the electroreduction of oxygen starts. The thicker the porous layer, the more positive this characteristic potential value. Although there is so far no detailed explanation of the underlying mechanism of this observation, one can conclude that the overpotential for oxygen reduction is significantly decreased by around 300 mV when using thick porous electrodes instead of nonporous ones. From the Tafel representation in Fig. 6.66b, it can be furthermore deduced that the kinetics of the reaction, usually expressed by $\log I_0$, is also drastically improved. The identical slopes of the three tested electrodes in the positive potential range indicate that the reaction mechanism (number of exchanged electrons, transfer coefficient) is not affected by the porosity. However, the exchange current I_0 varies by more than one order of magnitude, which is in good agreement with the surface increase obtained from the gold oxide stripping curves. These two aspects, improved overpotentials and increased kinetics, are very encouraging with respect to exploring these types of electrodes as promising candidates for the oxygen reduction in fuel or biofuel cells.

6.4.2 Energy Storage

Due to the high surface areas, combined with good diffusion kinetics, macroporous electrodes are interesting for energy storage or conversion applications, including batteries, supercapacitors, and fuel cells [6.5]. Carbon [6.236] manganese and nickel oxide [6.237, 238], or hybrid materials composed of carbon loaded with a CP [6.239], have been used to fabricate well-ordered macroporous capacitor electrodes. A good pseudocapacitive performance was combined with increased reaction rates in these systems. The latter was attributed to the open pore structures in the inverse opal, allowing a fast and efficient charge transfer even at elevated scan

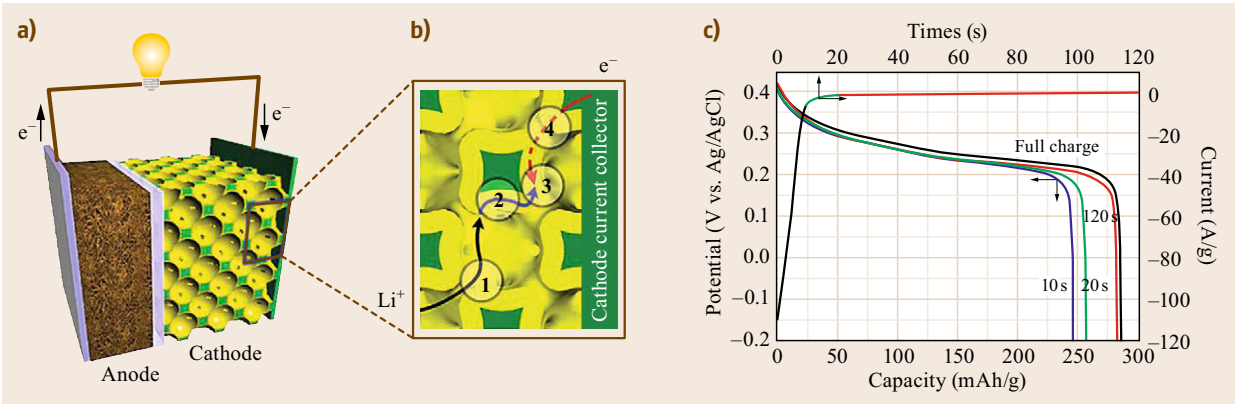


Fig. 6.67 **(a)** Scheme of a battery containing a bicontinuous cathode fabricated by colloidal crystal templating. The electrolytically active phase is *yellow* and the porous metal current collector is *green*. **(b)** Illustration of the four primary resistances in a battery electrode. **(c)** Ultrafast discharge and charge of the NiOOH electrode. Constant potential charge curves (0.45 V versus Ag/AgCl) and 6 C discharge curves after charging at constant potential for the indicated time. The curve labelled *full charge* was charged galvanostatically at 1 C (after [6.149])

rates [6.238]. Using macroporous instead of bulk electrodes as the anodic or the cathodic part in a battery allows us to significantly enhance the charge transfer kinetics with the electrolyte [6.7, 149, 240, 241].

Figure 6.67a schematically illustrates a battery where the cathodic compartment is based on an inverse opal structure. The fabrication of the bicontinuous cathode involved pulsed electrochemical deposition of electroactive materials (NiOOH for nickel-metal hydride and MnO_2 for lithium-ion batteries) into the inverse nickel opal. The pore volume and the interconnecting windows in the opal however first had to be enlarged, to enable high loadings with the active material by simultaneously keeping open the pore windows in the structure. Electropolishing of nickel enabled to increase the overall porosity in the opal to $\approx 94\%$ [6.148, 149]. As illustrated in Fig. 6.67b, the final structure combines fast ionic transport in the electrolyte and an electrode material with high electronic conductivity owing to the metallic nickel phase in the composite material. As a result, the battery could be charged or discharged in a fraction of the time that would have been required for a cell composed of bulk electrodes. Figure 6.67 shows that the electrode is already 85% charged after 10 s, 90% after 20 s, and 99% after 120 s.

6.4.3 Sensing Applications

The higher active surface areas provided by macroporous in contrast to flat electrodes can also be employed to increase the sensitivities and/or to lower the detection limits of conventional electrochemical sensors. As capacitive currents increase parallel to the faradaic currents in highly porous electrodes, improved performance is expected either when analytes are adsorbed on the electrode surface [6.8] or when using differential pulse techniques.

Figure 6.68a shows an example of a macroporous glucose biosensor, where all necessary species including redox mediator (TNF) and cofactor (Ca^{2+}/NAD^{+}) were immobilized on the gold surface [6.140]. Alternatively, only the redox mediator can be immobilized on the surface, whereas other reagents are added in the solution [6.139, 242]. The interconnecting windows between adjacent pores were in this case big enough to allow the glucose to access the whole inner pore volume. The enzymatic oxidation current of glucose increases linearly with the thickness of the macroporous film, as illustrated in Fig. 6.68b. A sensitivity gain by a factor 30, together with a detection limit improvement by a factor 3, was reported in those systems. The stability of the immobilized species on the electrode surface could further be prolonged by encapsulation in electrophoretic paint [6.165, 243]. Several other biosensors based on macroporous electrodes showed improved characteristics for the detection of glucose, adenosine-5′-triphosphate (ATP) and c-reactive protein (CRP) [6.164, 213–217]. It was also possible to use these porous electrodes for sensing the action potential in neurobiological measurements [6.244–246]. Besides biomolecules, other species such as heavy metal ions could be detected with enhanced sensitivity at macroporous bismuth and antimony electrodes [6.150, 151]. Figure 6.68c shows the signal increase for different stripping curves of cadmium and lead for increasing macroporous film thickness.

6.4.4 Electrosynthesis

Dehydrogenases are interesting enzymes for electrosynthesis applications, especially for the production of rare sugars as building blocks for pharmaceutical and food industry [6.247]. One of the main requirements for electro-synthesis involving enzymes is a stable immobilization of a large amount of active proteins on the electrode surface of the reactor [6.248, 249]. A strategy to increase the efficiency and the turnover in the electrosynthesis process consists in using macroporous electrodes which offer higher active surface areas for the immobilization of enzymes with respect to flat electrodes. Methods commonly used for immobilizing biomolecules on electrode surfaces comprise simple adsorption [6.140], the use of an intermediate SAM [6.250] or by cross-linking with glutaraldehyde [6.165]. However, the catalytic performance of the whole system is often limited by the lack of long-term stability or the loss of activity due to the covalent bond. Alternatively, biomolecules can be encapsulated into an organic or inorganic matrix using the electrochemical polymerization of monomers [6.251] or networks electrogenerated from silica precursor molecules [6.252, 253], respectively. In the latter case, the silica layer is produced at the electrode surface by a local modulation of pH. In contrast to conventional sol–gel methods, which rely on evaporation and, hence, are restricted to flat surfaces, the electro-assisted deposition (EAD) of silica films allows us to coat the internal surface of macroporous electrodes in a controlled way. In order to avoid pore clogging and to guarantee a high degree of interconnection between the macropore windows, the silica layers used for the encapsulation of biomolecules must be ultrathin. This objective could be reached by using very dilute tetraethoxysilane (TEOS) precursors in the starting sol [6.253]. Figure 6.69a–d shows TEM images of silica coatings with a thickness below 50 nm which have been uniformly deposited onto the pore walls of a macroporous gold

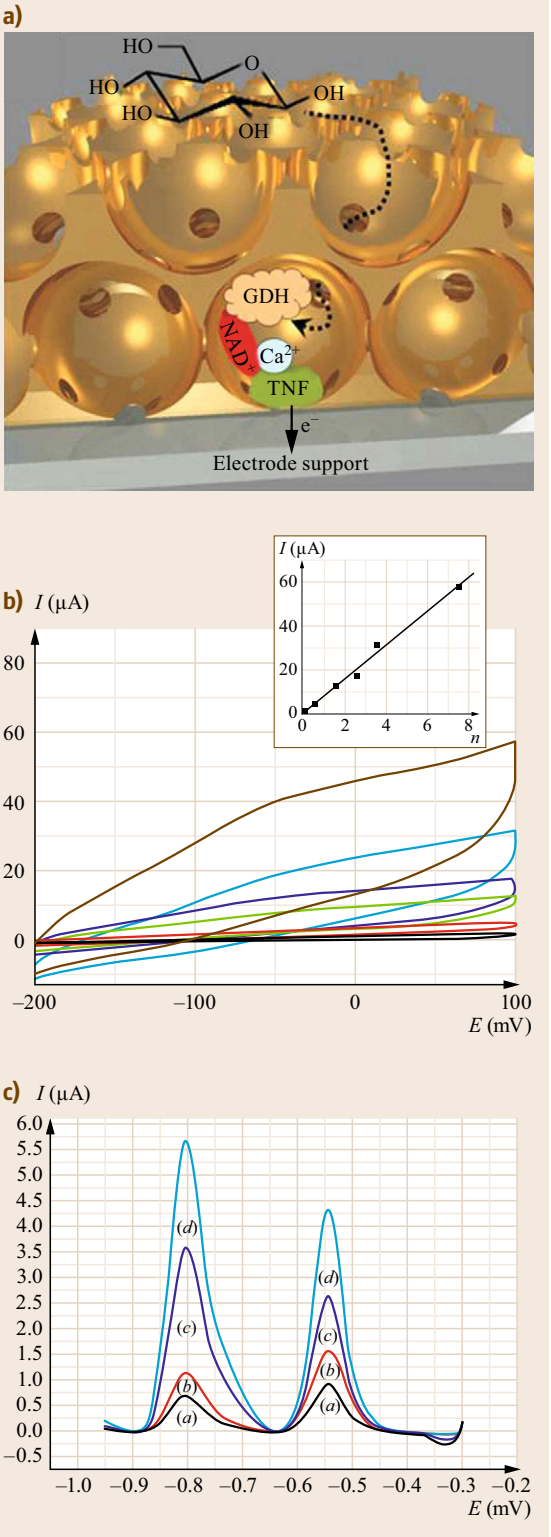


Fig. 6.68 **(a)** Representation of a gold electrode with 3/2 pore layers modified with a mediator monolayer (4-carboxy-2,5,7-trinitro-9-fluorenylidene) malonitrile (CTNFM), Ca^{2+}, NAD^{+}, GDH, and its reaction in a solution containing glucose. **(b)** CVs with macroporous electrodes as shown in **(a)** in the presence of glucose dehydrogenase (3 μM) and glucose (10 mM). The signal increases as the number of pore layers is increased (*inset*: oxidation current at 100 mV) (after [6.140]). **(c)** Comparison of the stripping peaks obtained with a nonporous (curve *a*) and porous bismuth films of increasing thickness (curves *b–d*) for Cd and Pb detection (after [6.150]) ►

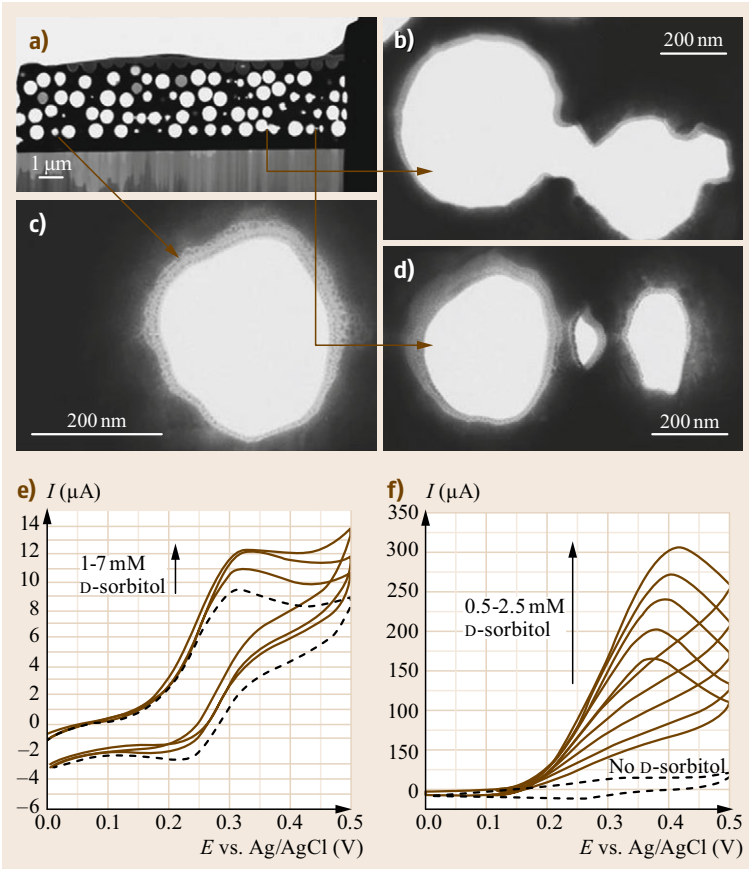


Fig. 6.69a–f High resolution views **(b–d)** of a slice **(a)** of a macroporous gold electrode (9/2 layers) decorated with an ultra-thin electrogenerated silica film (after [6.253]). CV responses to d-sorbitol of flat **(e)** and macroporous **(f)** gold electrodes modified by thin silica films with co-encapsulated DSDH and DI. **(e)** Responses of a flat gold electrode in the absence (*dashed line*) and in the presence of increasing concentrations of d-sorbitol from 1 to 7 mM (*plain lines*). **(f)** Responses of a gold macroporous electrode (three half-layers) in the absence (*dashed line*) and in the presence of increasing concentrations of d-sorbitol from 0.5 to 2.5 mM (*plain lines*) (after [6.254])

electrode. d-Sorbitol dehydrogenase (DSDH) and diaphorase (DI) together with a positively charged polyelectrolyte poly(dimethyldiallylammonium chloride) – PDDA have been successfully co-encapsulated into such a thin silica film on a flat (Fig. 6.69e) and a macroporous gold electrode (Fig. 6.69f) in order to compare their activity toward the oxidation of d-sorbitol. The cofactor (NAD^+) and the mediator (ferrocenedimethanol) in this case were present in the solution. While the current was increased by 16% for the addition of 1 mM of d-sorbitol in the case of a flat electrode (Fig. 6.69e), an increase by 1000% was observed for a macroporous electrode displaying three pore half-layers by adding the same amount of d-sorbitol (Fig. 6.69f).

The bioelectrocatalytic performance can further be optimized by tailoring the electrode features at different length scales [6.255]. The insertion of nanoobjects (e.g., metal nanoparticles) into the encapsulating layer further enlarges the active surface area of the electrode through the formation of a conducting network in the insulating or semiconducting immobilization layer. Figure 6.70a shows experiments conducted on flat gold electrodes with and without gold nanoparticles entrapped in the immobilization layer. In this case, an electrodeposited paint (EDP – Resydrol) in the presence of PDDA was used to encapsulate the enzymatic system (DSDH and DI). CTNFM was used as a mediator, which can be directly adsorbed on gold surfaces by forming an SAM. The highest catalytic signal for the oxidation of d-sorbitol was observed when the mediator was present at both the electrode surface containing the encapsulated biomolecules and the gold nanoparticles, which were adsorbed on the electrode surface (curve (*d*)). The presence of CTNFM on the adsorbed gold nanoparticles (curve (*c*)) leads to higher oxidation currents with respect to the mediator being present exclusively at the electrode surface (curve (*b*)), confirming good electronic communication between the nanoparticles and the electrode. Immobilizing the same system on a macroporous electrode displaying three pore half-layers leads to a significant increase of the d-sorbitol oxidation current (Fig. 6.70d curve (*c*)) compared to a flat gold electrode (Fig. 6.70d curve (*b*)). The enhancement factor determined from Fig. 6.70d for a macroporous electrode with three pore half-layers was found to be higher (determined value: 7.3) than what

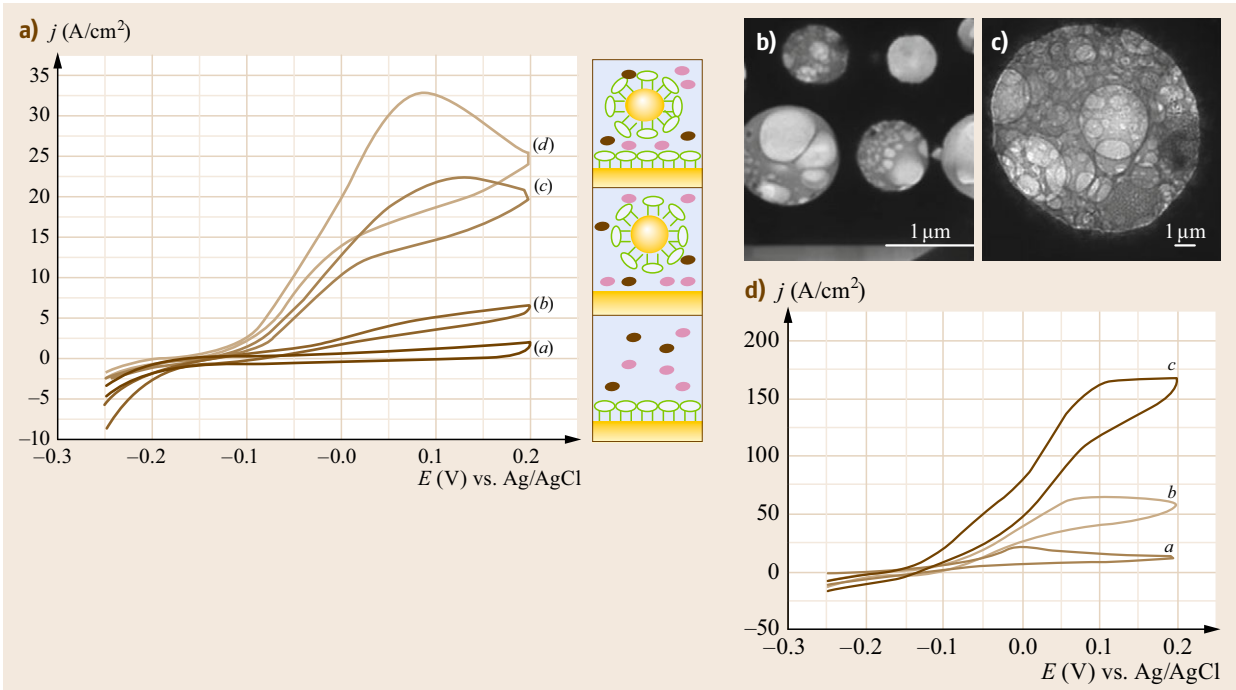


Fig. 6.70 **(a)** Curve (*a*) CTNFM redox signal. (*b*) d-Sorbitol oxidation by the DI/DSDH system (*brown* and *pink*) entrapped in the resydrol/PDDA layer (*light blue background*) on a flat electrode modified with a CTNFM SAM (*green*) on the gold electrode only. (*c*) d-Sorbitol oxidation by the DI/DSDH system entrapped in the resydrol/PDDA layer on a flat electrode with CTNFM adsorbed on the inserted AuNP only. (*d*) Combination of (*b*) and (*c*). **(b,c)** TEM pictures of a section of the macroporous electrode containing the electrodeposited mesoporous resydrol/PDDA/AuNP matrix which hosts the enzymes. **(d)** d-Sorbitol oxidation by DSDH entrapped in a resydrol layer containing CTNFM-modified AuNPs on electrodes modified by a CTNFM SAM on a flat gold electrode (*b*) and on a gold electrode with three pore half-layers (*c*). (*a*) is the background current obtained without d-sorbitol (after [6.255])

would be theoretically expected when using (6.1) (theoretically expected value: 5.4). This was explained by an EDP film which is slightly growing out of the porous structure and the presence of gold nanoparticles in the volume of the macropores, which are additionally increasing the active surface area of the electrode. TEM images of the EDP film deposited in the macropores, as shown in Fig. 6.70b,c, reveal the presence of mesopores in the structure assuring an efficient diffusion of the substrate through the immobilizing layer containing the enzymes and nanoparticles. The fact that the polymer layer is anchored inside the macropores makes it much more resistant against washing away by the hydrodynamic flow (e.g., in a flow-through cells) compared to a layer immobilized on a flat electrode.

6.4.5 Optical Applications

In the above-mentioned examples, macroporous electrodes have been used in the frame of electrochemical applications. However, there is also a pronounced interest in employing these ordered structures in the field of optics and spectroscopy. PCs with a complete PBP are possible when colloidal templates are infiltrated with high refractive index materials. Several applications arise from the structural order present in PCs. If the sphere size in colloidal crystals (or the pore size in the respective inverse opal structures) is in the same order as the wavelength of visible light, Bragg diffraction occurs, leading to their characteristic coloration. The optical response of PCs to electromagnetic radiation depends on structural and also on material parameters. A change of parameters like symmetry, lattice constant or order in PCs will effectively alter the interaction of light with the material. In the same way, a refractive index change of the constituent materials in a PC affects its optical properties. By incorporating stimulus-responsive materials into PCs, at least one of these parameters can be modified due to chemical or physical stimuli so that the diffraction wavelength in the PC changes. In a recent review on responsive PCs, a broad overview is given on the mechanisms and applications

in this field, which includes, besides optical sensors, display units or structural color devices [6.256]. In Fig. 6.71, some examples for optical sensors made from hydrogel inverse opals are shown.

A shift of the reflection peak in PCs may be used to measure the pH (Fig. 6.71a), the temperature (Fig. 6.71b), or the glucose concentration (Fig. 6.71c). The change of the peak wavelength in Fig. 6.71b is due to a temperature-dependent swelling or shrinkage of the hydrogel, causing the lattice constant in the PC to change [6.257, 258]. Recently, it has been shown that the integration of a defect in the inverse opal can lead to increased sensitivities in pH sensing [6.259]. Alternatively, phase transitions occurring in some inorganic materials lead to a refractive index change in a certain temperature range. An example is barium titanate with a phase transition near the Curie temperature ($T_c \approx 120\,^{\circ}\mathrm{C}$). PCs composed of this material equally can serve as a temperature sensor [6.260]. Refractive index change is also observed when a liquid or gaseous component fills the void space in PCs. This effect allows PCs to be employed for the optical detection of various solvents or vapors including a discrimination between different vapor pressures [6.184, 263–265]. Compared to colloidal or PC composite structures, inverse opals provide more volume for the infiltration with a liquid or gaseous analyte, which results in higher shifts of the reflection peaks [6.256]. The principle of ion- or pH-sensitive PCs is based upon a change of the lattice constant in PCs occurring when target ions bind to recognition units that are immobilized in a hydrogel [6.261, 266–268]. The selective recognition of metal ions by crown ethers is an example for ion-sensitive PC sensors [6.266]. The response time of the pH-sensor, as illustrated in Fig. 6.71a, was reported to be strongly decreased when macroporous instead of composite hydrogel PCs were used [6.261]. The same strategy can be employed for the optical detection of biomolecules with responsive PCs [6.182, 183, 262, 266, 268–270]. The example in Fig. 6.71c shows that different levels of glucose concentrations can easily be distinguished by the naked eye using macroporous hydrogel PCs [6.262].

Also, external forces acting on the PC can change the lattice constant and provoke a mechanochromic behavior. Hence, pressure sensors can be realized using porous or composite elastomeric PCs [6.271, 272]. Examples showing an optical pressure sensor based on elastomeric inverse opals are illustrated in Fig. 6.72b,c. The pressure of a finger pressed onto the porous film locally deforms the crystal lattice associated with a color change in the PC. The resolution proved to be sufficiently high to use these PC devices as fingerprint sensors [6.273, 274]. In macroporous films, the pressure required to trigger a color change was sufficiently reduced compared to composite films. Besides sensing, the emission wavelength in organic lasers can be tuned by a mechanochromic PCs. In Fig. 6.72a, uniaxial compression of the PC (PBG) composite film modifies the wavelength of the laser pulse as it propagates through the mechanochromic medium [6.275]. Even though in this report a PC composite material was used, similar results may be obtained with porous PC films. The performance of actuators equally could be increased by introducing a controlled macroporosity into devices based on PPy [6.186]. It was shown that actuation in these materials allowed us to trap and release small particles in/from the pores in a controlled way.

Using electroactive materials in PCs enables us to produce a color change by altering applied potentials.

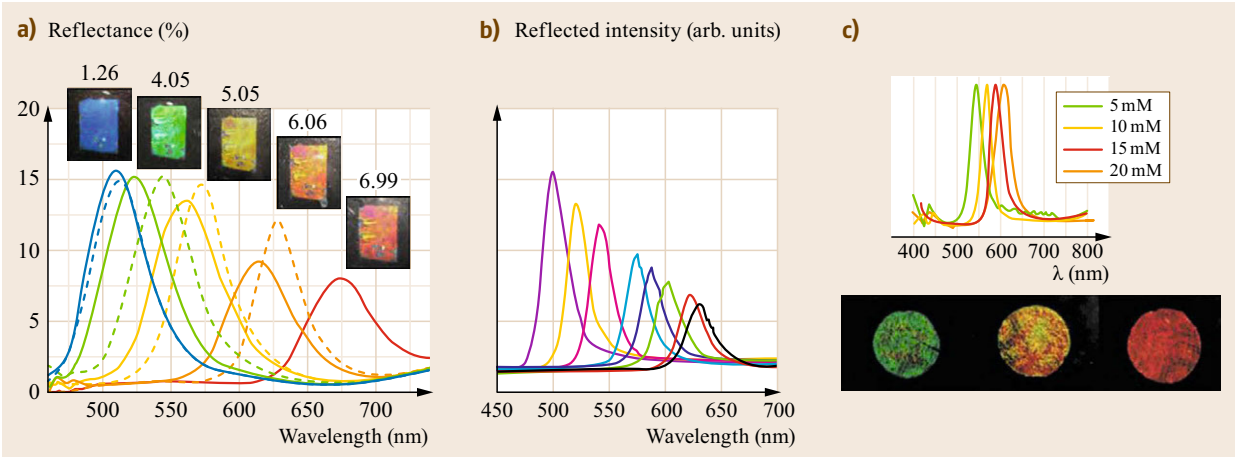


Fig. 6.71a–c Optical sensors based on hydrogel inverse opals. Dependence of the reflection spectra of the hydrogel inverse opal on **(a)** the pH (after [6.261]), **(b)** the temperature (after [6.257]) and **(c)** the glucose concentration (after [6.262])

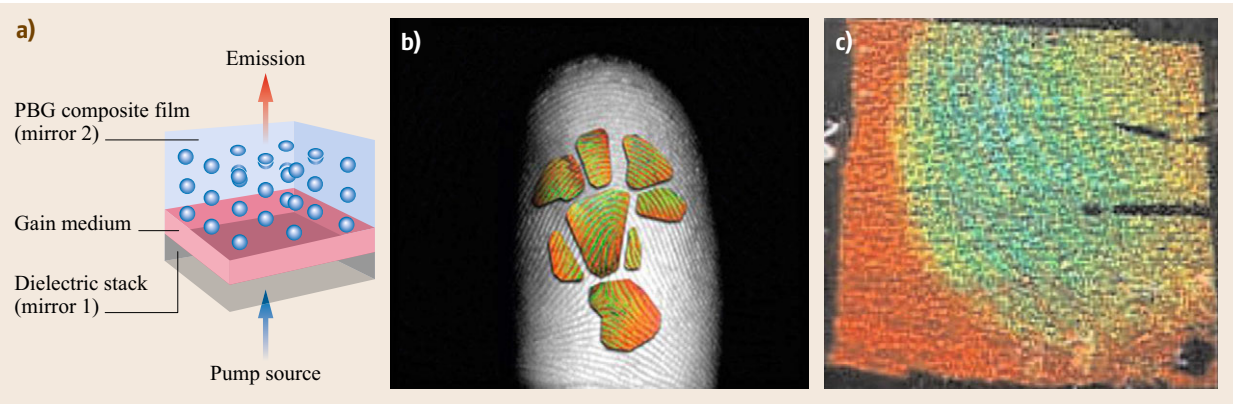


Fig. 6.72a–c Applications of mechanochromic photonic crystals. **(a)** Configuration of a tunable thin-film organic laser: a broadband dielectric stack reflector (mirror 1) is coated with a thin layer of rhodamine B doped PMMA (gain medium) and then laminated with a PBG composite film (mirror 2) (after [6.275]). **(b)** A full-color fingerprint visualized using an elastic photonic crystal (EPC), overlayed onto a grayscale image of an index finger. **(c)** Still image taken during the compression of an EPC film by an index finger (after [6.273, 274])

As illustrated in Fig. 6.73a, the electroactive material can be reduced or oxidized, depending on the applied potential, which is associated with a change in volume and lattice constant of the PC film, consequently leading to a color change. The electroactive media may be a ferroelectric material [6.276] or a CP [6.187, 277]. In this regard, electrically switchable full color displays based on PCs have been fabricated [6.123, 277]. In their first report, *Arsenault* et al. employed a polyferrocenylsilane/silica composite PC to reversibly change the color of the display [6.277]. The use of a macroporous structure resulted in faster switching times combined with lower threshold voltages needed to drive the device [6.123]. As shown in Fig. 6.73b, clear and bright colors are obtained as different potentials are applied to the electroactive inverse opal. The colors are adjustable over the whole range of the visible spectrum in such a device as shown in Fig. 6.73c. Response times in the range of 10 s for a complete color change are still quite high with respect to a commercial application of such PC devices. Instead of electric fields, magnetic fields were used to tune the color in PCs composed of superparamagnetic spheres [6.278, 279].

Coupling PCs to dye-sensitized solar cells (DSCs) based on titanium dioxide have been reported to enhance the light-harvesting performance in the red spec-

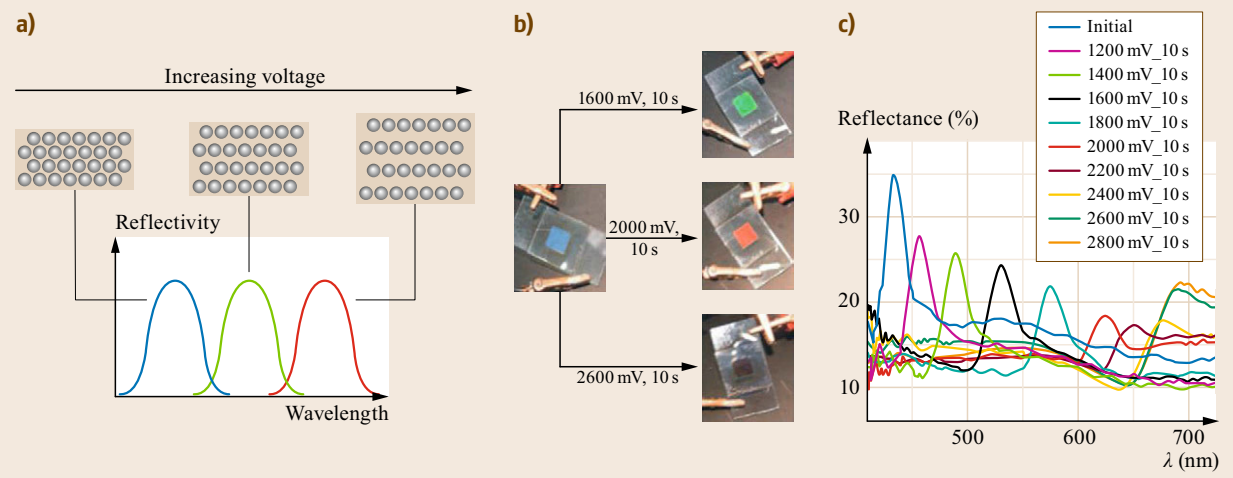


Fig. 6.73 Fabrication of electrically controlled display units based on inverse opals. **(a)** Illustration of the mechanism that leads to a color change in redox-active inverse opals. **(b)** Color tuning in the display upon application of different potentials. **(c)** Reflection spectra for different applied potentials (after [6.123, 274])

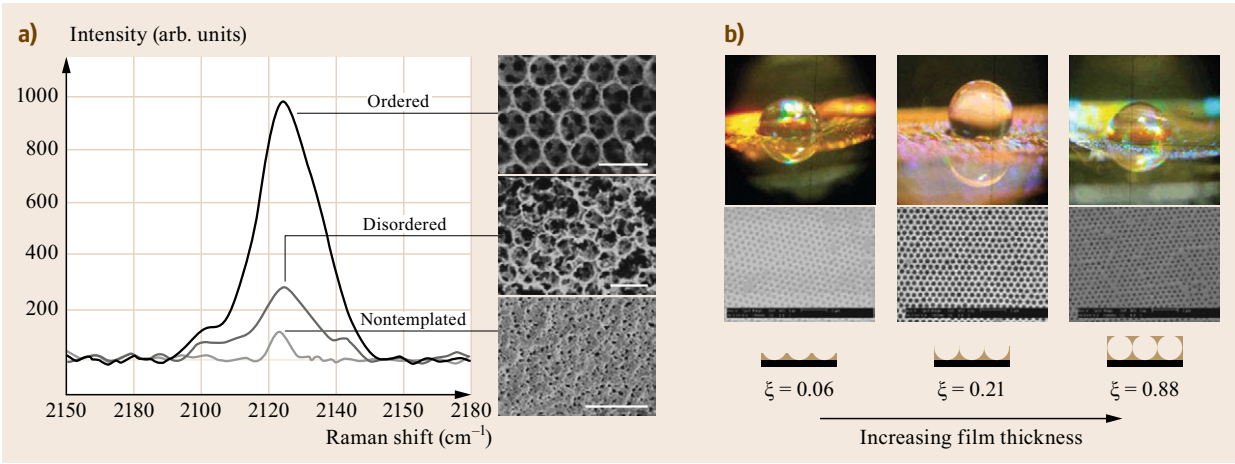


Fig. 6.74 **(a)** Effect of the substrate structure on the SERS signal intensity. Sodium cyanide spectra for nontemplated, disordered and ordered latex-templated Au nanoparticles (10–20 nm). *Scale bars* in SEM images: *top* and *middle* 1 μm, *bottom* 10 μm (after [6.280]). **(b)** Optical images of 5 μl drops of water on macroporous gold films of different thickness with SEM images of the corresponding surfaces below (*scale bar* is 2 μm) (after [6.281])

tral range [6.282]. Different mechanisms can be responsible for the increase of photocurrent in DSCs coupled with a PC film. Higher absorption rates can be due to multidirectional scattering at defects in the PC at short wavelengths[6.283] together with a back reflection of light in the stop band region of the PC [6.284]. The absorption can be also enhanced by increased matter–radiation interaction times due to resonant modes [6.285]. The profile that is required for a nanostructured material to efficiently improve photovoltaic devices due to plasmon-enhanced light absorption has been reviewed by *Atwater* and *Polman* [6.286]. Surface plasmon polaritons (SPPs) are quasiparticles resulting from the interaction of incident light with resonant electronic charge oscillations on a metallic surface [6.287]. In nanostructured materials, SPPs can be locally trapped on the surface producing significantly enhanced optical fields at precise locations. Atwater and Polman mentioned that light scattering and trapping are very sensitive to the shape of plasmonic nanoparticles. The same is true for the nanovoid structures in metallic films produced by colloidal templating.

As shown in Fig. 6.74a, metallic inverse opals can also be used to increase the signal intensity in surface-enhanced Raman spectroscopy (SERS) by several orders of magnitude. A much lower increase of signal intensity was found for disordered compared to ordered inverse opal films templated with Au nanoparticles [6.280, 288]. A similar approach using electrodeposited metallic nanostructures has allowed us to discriminate mutations and to analyze short repeating units in DNA sequences by SERS [6.289, 290]. SERS signals could also be enhanced when macroporous gold structures were directly generated on the surface of optical fiber bundles [6.291]. Furthermore, it has been shown that complete omnidirectional absorption of light can be observed in templated metallic nanovoid films, when the thickness slightly exceeds one void layer [6.292].

Finally, many other interesting properties of such macroporous structures are currently explored by the scientific community. Not all of them can be listed here, but two examples might point out the broad range of potential applications that can be expected for these materials. On the one hand, Fig. 6.74b illustrates the influence of the surface structure of templated gold films on their hydrophobic properties. The contact angle between a water droplet and a nanostructured gold film was found to increase when its thickness approaches a half-sphere layer, whereas decreasing angles were observed for the film thickness, reaching a full pore layer. On the other hand, due to the uniform pore size, highly ordered 3-D macroporous materials also have been used as filters [6.293, 294].

6.5 Conclusion

Ordered macroporous structures at electrode surfaces are obtained by colloidal crystal templating. Various methods have been discussed allowing us to self-assemble microspheres into colloidal crystals and to infiltrate these types of templates with a wide range of different materials. The particular benefit of combining the LB technique for the assembly of colloidal crystals with template-assisted electrodeposition consists in a very high level of control over the final architecture of macroporous electrodes. Besides controlling the number of sphere layers transferred on planar or cylindrical substrate geometries, the LB approach allowed us to create a predefined sequence of layers with different particle sizes to be stacked at will in such a colloidal template. Hence, in addition to templates with a single-particle size, colloidal crystals with on purpose integrated defects and gradients in terms of sphere size with a high structural integrity were obtained. Temporal current oscillations observed during the amperometric electrodeposition of metals and CPs in colloidal crystals result from the periodic variation of the electroactive area during the infiltration of these templates. They enabled us to follow the filling process of the template with material and, hence, to precisely control the thickness of the macroporous electrodes. SEM characterization revealed macroporous films of uniform thickness with interconnected pores on the surface of planar and cylindrical electrodes for both types of structures, composed of a single pore size or more complex architectures, including integrated defect layers or pore size gradients. The active surface area of macroporous gold electrodes could be determined from the gold-oxide stripping peak using CV and was found to be linearly increasing with the number of pore layers on the electrode in accordance with geometrical considerations. Due to the higher active surface area compared to their flat homologs, macroporous electrodes are interesting candidates for improving the performance of devices used in electrocatalysis, energy storage, sensing applications, and electrosynthesis. The structural order which is needed in PCs opens up several possibilities of using macroporous materials also in other fields, such as optics.

References

6.1 D. Linden, T.B. Reddy: *Handbook of Batteries* (McGraw-Hill, New York 2002)

6.2 A. Wieckowski, J. Norskov: *Fuel Cell Science* (Wiley, Hoboken 2010)

6.3 J. Wang: *Analytical Electrochemistry* (Wiley, Hoboken 2006)

6.4 P. Gründler: *Chemical Sensors* (Springer, Berlin, Heidelberg 2007)

6.5 A.S. Arico, P. Bruce, B. Scrosati, J.-M. Tarascon, W. van Schalkwijk: Nanostructured materials for advanced energy conversion and storage devices, Nat. Mater. **4**, 366–377 (2005)

6.6 Y.-G. Guo, J.-S. Hu, L.-J. Wan: Nanostructured materials for electrochemical energy conversion and storage devices, Adv. Mater. **20**, 2878–2887 (2008)

6.7 P.G. Bruce, B. Scrosati, J.-M. Tarascon: Nanomaterials for rechargeable lithium batteries, Angew. Chem. Int. Ed. **47**, 2930–2946 (2008)

6.8 A. Walcarius: Template-directed porous electrodes in electroanalysis, Anal. Bioanal. Chem. **396**, 261–272 (2010)

6.9 C.R. Martin: Nanomaterials: A membrane-based synthetic approach, Science **266**, 1961–1966 (1994)

6.10 Z. Zhang, Y. Wang, Z. Qi, W. Zhang, J. Qin, J. Frenzel: Generalized fabrication of nanoporous metals (Au, Pd, Pt, Ag, and Cu) through chemical dealloying, J. Phys. Chem. C **113**, 12629–12636 (2009)

6.11 F. Marlow, Muldarisnur, P. Sharifi, R. Brinkmann, C. Mendive: Opals: Status and prospects, Angew. Chem. Int. Ed. **48**, 6212–6233 (2009)

6.12 D.J. Norris, E.G. Arlinghaus, L. Meng, R. Heiny, L.E. Scriven: Opaline photonic crystals: How does self-assembly work?, Adv. Mater. **16**, 1393–1399 (2004)

6.13 G.M. Whitesides, B. Grzybowski: Self-assembly at all scales, Science **295**, 2418–2421 (2002)

6.14 P. Ni, P. Dong, B. Cheng, X. Li, D. Zhang: Synthetic SiO_2 opals, Adv. Mater. **13**, 437–441 (2001)

6.15 V.K. LaMer, R.H. Dinegar: Theory, production and mechanism of formation of monodispersed hydrosols, J. Am. Chem. Soc. **72**, 4847–4854 (1950)

6.16 Y. Xia, B. Gates, Y. Yin, Y. Lu: Monodispersed colloidal spheres: Old materials with new applications, Adv. Mater. **12**, 693–713 (2000)

6.17 W. Stöber, A. Fink, E. Bohn: Controlled growth of monodisperse silica spheres in the micron size range, J. Colloid Interface Sci. **26**, 62–69 (1968)

6.18 H. Giesche: Synthesis of monodispersed silica powders I. Particle properties and reaction kinetics, J. Eur. Ceram. Soc. **14**, 189–204 (1994)

6.19 C.G. Tan, B.D. Bowen, N. Epstein: Production of monodisperse colloidal silica spheres: Effect of temperature, J. Colloid Interface Sci. **118**, 290–293 (1987)

6.20 G.H. Bogush, M.A. Tracy, C.F.I.V. Zukoski: Preparation of monodisperse silica particles: Control of size and mass fraction, J. Non-Cryst. Solids **104**, 95–106 (1988)

6.21 K. Nozawa, H. Gailhanou, L. Raison, P. Panizza, H. Ushiki, E. Sellier, J.P. Delville, M.H. Delville:

Smart control of monodisperse Stöber silica particles: Effect of reactant addition rate on growth process, Langmuir **21**, 1516–1523 (2004)
6.22 Y.S. Lee: *Self-Assembly and Nanotechnology* (Wiley, Hoboken 2008)
6.23 J.F. Galisteo-López, M. Ibisate, R. Sapienza, L.S. Froufe-Pérez, Á. Blanco, C. López: Self-assembled photonic structures, Adv. Mater. **23**, 30–69 (2011)
6.24 F. Li, D.P. Josephson, A. Stein: Colloidal assembly: The road from particles to colloidal molecules and crystals, Angew. Chem. Int. Ed. **50**, 360–388 (2011)
6.25 R. Mayoral, J. Requena, J.S. Moya, C. López, A. Cintas, H. Miguez, F. Meseguer, L. Vázquez, M. Holgado, Á. Blanco: 3D Long-range ordering in ein SiO_2 submicrometer-sphere sintered superstructure, Adv. Mater. **9**, 257–260 (1997)
6.26 H. Miguez, F. Meseguer, C. Lopez, A. Mifsud, J.S. Moya, L. Vazquez: Evidence of fcc crystallization of SiO_2 nanospheres, Langmuir **13**, 6009–6011 (1997)
6.27 L.V. Woodcock: Entropy difference between the face-centred cubic and hexagonal close-packed crystal structures, Nature **385**, 141–143 (1997)
6.28 K.E. Davis, W.B. Russel, W.J. Glantschnig: Settling suspensions of colloidal silica: Observations and x-ray measurements, J. Chem. Soc. Faraday Trans. **87**, 411–424 (1991)
6.29 V.M. Shelekhina, O.A. Prokhorov, P.A. Vityaz, A.P. Stupak, S.V. Gaponenko, N.V. Gaponenko: Towards 3D photonic crystals, Synth. Met. **124**, 137–139 (2001)
6.30 M. Holgado, F. Garcia-Santamaria, A. Blanco, M. Ibisate, A. Cintas, H. Miguez, C.J. Serna, C. Molpeceres, J. Requena, A. Mifsud, F. Meseguer, C. López: Electrophoretic deposition to control artificial opal growth, Langmuir **15**, 4701–4704 (1999)
6.31 A. van Blaaderen, R. Ruel, P. Wiltzius: Template-directed colloidal crystallization, Nature **385**, 321–324 (1997)
6.32 O. Vickreva, O. Kalinina, E. Kumacheva: Colloid crystal growth under oscillatory shear, Adv. Mater. **12**, 110–112 (2000)
6.33 C.D. Dushkin, G.S. Lazarov, S.N. Kotsev, H. Yoshimura, K. Nagayama: Effect of growth conditions on the structure of two-dimensional latex crystals: Experiment, Colloid. Polym. Sci. **277**, 914–930 (1999)
6.34 M. Müller, R. Zentel, T. Maka, S.G. Romanov, C.M. Sotomayor Torres: Photonic crystal films with high refractive index contrast, Adv. Mater. **12**, 1499–1503 (2000)
6.35 N. Denkov, O. Velev, P. Kralchevski, I. Ivanov, H. Yoshimura, K. Nagayama: Mechanism of formation of two-dimensional crystals from latex particles on substrates, Langmuir **8**, 3183–3190 (1992)
6.36 P. Jiang, J.F. Bertone, K.S. Hwang, V.L. Colvin: Single-crystal colloidal multilayers of controlled thickness, Chem. Mater. **11**, 2132–2140 (1999)
6.37 Q. Yan, Z. Zhou, X.S. Zhao: Inward-growing self-assembly of colloidal crystal films on horizontal substrates, Langmuir **21**, 3158–3164 (2005)
6.38 Y. Li, T. Kunitake, S. Fujikawa: Efficient fabrication of large, robust films of 3D-ordered polystyrene latex, Colloids Surf. A **275**, 209–217 (2006)
6.39 Y.A. Vlasov, X.-Z. Bo, J.C. Sturm, D.J. Norris: On-chip natural assembly of silicon photonic bandgap crystals, Nature **414**, 289–293 (2001)
6.40 S. Wong, V. Kitaev, G.A. Ozin: Colloidal crystal films: Advances in universality and perfection, J. Am. Chem. Soc. **125**, 15589–15598 (2003)
6.41 S.M. Yang, H. Míguez, G.A. Ozin: Opal circuits of light – Planarized microphotonic crystal chips, Adv. Funct. Mater. **12**, 425–431 (2002)
6.42 Y.H. Ye, F. LeBlanc, A. Haché, V.V. Truong: Self-assembling three-dimensional colloidal photonic crystal structure with high crystalline quality, Appl. Phys. Lett. **78**, 52–54 (2001)
6.43 M.A. McLachlan, N.P. Johnson, R.M. de la Rue, D.W. McComb: Thin film photonic crystals: Synthesis and characterisation, J. Mater. Chem. **14**, 144–150 (2004)
6.44 A. Hartsuiker, W.L. Vos: Structural properties of opals grown with vertical controlled drying, Langmuir **24**, 4670–4675 (2008)
6.45 S.-L. Kuai, X.-F. Hu, A. Haché, V.-V. Truong: High-quality colloidal photonic crystals obtained by optimizing growth parameters in a vertical deposition technique, J. Cryst. Growth **267**, 317–324 (2004)
6.46 J. Zhang, H. Liu, Z. Wang, N. Ming: Assembly of high-quality colloidal crystals under negative pressure, J. Appl. Phys. **103**, 013517–013520 (2008)
6.47 F. Piret, B.L. Su: Effects of pH and ionic strength on the self-assembly of silica colloids to opaline photonic structures, Chem. Phys. Lett. **457**, 376–380 (2008)
6.48 B. Griesebock, M. Egen, R. Zentel: Large photonic films by crystallization on fluid substrates, Chem. Mater. **14**, 4023–4025 (2002)
6.49 O.D. Velev, K.H. Bhatt: On-chip micromanipulation and assembly of colloidal particles by electric fields, Soft Matter **2**, 738–750 (2006)
6.50 V. Kitaev, G.A. Ozin: Self-assembled surface patterns of binary colloidal crystals, Adv. Mater. **15**, 75–78 (2003)
6.51 S.H. Im, M.H. Kim, O.O. Park: Thickness control of colloidal crystals with a substrate dipped at a tilted angle into a colloidal suspension, Chem. Mater. **15**, 1797–1802 (2003)
6.52 A.S. Dimitrov, K. Nagayama: Continuous convective assembling of fine particles into two-dimensional arrays on solid surfaces, Langmuir **12**, 1303–1311 (1996)
6.53 Z.-Z. Gu, A. Fujishima, O. Sato: Fabrication of high-quality opal films with controllable thickness, Chem. Mater. **14**, 760–765 (2002)
6.54 L.K. Teh, N.K. Tan, C.C. Wong, S. Li: Growth imperfections in three-dimensional colloidal self-assembly, Appl. Phys. A **81**, 1399–1404 (2005)
6.55 C. Jin, M.A. McLachlan, D.W. McComb, R.M. de la Rue, N.P. Johnson: Template-assisted growth of nominally cubic (100)-oriented three-dimensional crack-free photonic crystals, Nano Lett. **5**, 2646–2650 (2005)

6.56 A.L. Rogach, N.A. Kotov, D.S. Koktysh, J.W. Ostrander, G.A. Ragoisha: Electrophoretic deposition of latex-based 3D colloidal photonic crystals: A technique for rapid production of high-quality opals, Chem. Mater. **12**, 2721–2726 (2000)

6.57 S.O. Lumsdon, E.W. Kaler, J.P. Williams, O.D. Velev: Dielectrophoretic assembly of oriented and switchable two-dimensional photonic crystals, Appl. Phys. Lett. **82**, 949–951 (2003)

6.58 R.C. Hayward, D.A. Saville, I.A. Aksay: Electrophoretic assembly of colloidal crystals with optically tunable micropatterns, Nature **404**, 56–59 (2000)

6.59 D.H. McCullough III, S.L. Regen: Don't forget Langmuir–Blodgett films, Chem. Commun., 2787–2791 (2004)

6.60 C.G. Zoski: *Handbook of Electrochemistry* (Elsevier, Amsterdam 2007)

6.61 K. Hasegawa, H. Nishimori, M. Tatsumisago, T. Minami: Effect of poly(acrylic acid) on the preparation of thick silica films by electrophoretic sol-gel deposition of re-dispersed silica particles, J. Mater. Sci. **33**, 1095–1098 (1998)

6.62 R.J. Kershner, J.W. Bullard, M.J. Cima: The role of electrochemical reactions during electrophoretic particle deposition, J. Colloid Interface Sci. **278**, 146–154 (2004)

6.63 M. Giersig, P. Mulvaney: Preparation of ordered colloid monolayers by electrophoretic deposition, Langmuir **9**, 3408–3413 (1993)

6.64 M. Böhmer: In situ observation of 2-dimensional clustering during electrophoretic deposition, Langmuir **12**, 5747–5750 (1996)

6.65 P. Richetti, J. Prost, P. Barois: Two-dimensional aggregation and crystallization of a colloidal suspension of latex spheres, J. Phys. Lett. **45**, 1137–1143 (1984)

6.66 S.-R. Yeh, M. Seul, B.I. Shraiman: Assembly of ordered colloidal aggregrates by electric-field-induced fluid flow, Nature **386**, 57–59 (1997)

6.67 T. Gong, D.T. Wu, D.W.M. Marr: Two-dimensional electrohydrodynamically induced colloidal phases, Langmuir **18**, 10064–10067 (2002)

6.68 K.-Q. Zhang, X.Y. Liu: In situ observation of colloidal monolayer nucleation driven by an alternating electric field, Nature **429**, 739–743 (2004)

6.69 A.S. Negi, K. Sengupta, A.K. Sood: Frequency-dependent shape changes of colloidal clusters under transverse electric field, Langmuir **21**, 11623–11627 (2005)

6.70 T.H. Zhang, X.Y. Liu: Configurations and diffusion of point defects in two-dimensional colloidal crystals, Appl. Phys. Lett. **89**, 261914 (2006)

6.71 Y. Liu, R.-G. Xie, X.-Y. Liu: Fine tuning of equilibrium distance of two-dimensional colloidal assembly under an alternating electric field, Appl. Phys. Lett. **91**, 063105–063103 (2007)

6.72 S.O. Lumsdon, E.W. Kaler, O.D. Velev: Two-dimensional crystallization of microspheres by a coplanar ac electric field, Langmuir **20**, 2108–2116 (2004)

6.73 A. Yethiraj, J.H.J. Thijssen, A. Wouterse, A. van Blaaderen: Large-area electric-field-induced colloidal single crystals for photonic applications, Adv. Mater. **16**, 596–600 (2004)

6.74 R.C. Bailey, K.J. Stevenson, J.T. Hupp: Assembly of micropatterned colloidal gold thin films via microtransfer molding and electrophoretic deposition, Adv. Mater. **12**, 1930–1934 (2000)

6.75 R. Xie, X.-Y. Liu: Electrically directed on-chip reversible patterning of two-dimensional tunable colloidal structures, Adv. Funct. Mater. **18**, 802–809 (2008)

6.76 W.M. Choi, O.O. Park: The fabrication of micropatterns of a 2D colloidal assembly by electrophoretic deposition, Nanotechnology **17**, 325 (2006)

6.77 R. Xie, X.-Y. Liu: Controllable epitaxial crystallization and reversible oriented patterning of two-dimensional colloidal crystals, J. Am. Chem. Soc. **131**, 4976–4982 (2009)

6.78 I. Langmuir: The constitution and fundamental properties of solids and liquids. II. Liquids, J. Am. Chem. Soc. **39**, 1848–1906 (1917)

6.79 K.B. Blodgett: Films built by depositing successive monomolecular layers on a solid surface, J. Am. Chem. Soc. **57**, 1007–1022 (1935)

6.80 M. Bardosova, M.E. Pemble, I.M. Povey, R.H. Tredgold: The Langmuir–Blodgett approach to making colloidal photonic crystals from silica spheres, Adv. Mater. **22**, 3104–3124 (2010)

6.81 G. Tolnai, F. Csempesz, M. Kabai-Faix, E. Kálmán, Z. Keresztes, A.L. Kovács, J.J. Ramsden, Z. Hórvölgyi: Preparation and characterization of surface-modified silica-nanoparticles, Langmuir **17**, 2683–2687 (2001)

6.82 Z. Wu, H. Han, W. Han, B. Kim, K.H. Ahn, K. Lee: Controlling the hydrophobicity of submicrometer silica spheres via surface modification for nanocomposite applications, Langmuir **23**, 7799–7803 (2007)

6.83 M. Bardosova, F.C. Dillon, M.E. Pemble, I.M. Povey, R.H. Tredgold: Langmuir–Blodgett assembly of colloidal photonic crystals using silica particles prepared without the use of surfactant molecules, J. Colloid Interface Sci. **333**, 816 (2009)

6.84 M. Szekeres, O. Kamalin, R.A. Schoonheydt, K. Wostyn, K. Clays, A. Persoons, I. Dekany: Ordering and optical properties of monolayers and multilayers of silica spheres deposited by the Langmuir–Blodgett method, J. Mater. Chem. **12**, 3268–3274 (2002)

6.85 M. Bardosova, P. Hodge, L. Pach, M.E. Pemble, V. Smatko, R.H. Tredgold, D. Whitehead: Synthetic opals made by the Langmuir–Blodgett method, Thin Solid Films **437**, 276–279 (2003)

6.86 P. Jiang, M.J. McFarland: Large-scale fabrication of wafer-size colloidal crystals, macroporous polymers and nanocomposites by spin-coating, J. Am. Chem. Soc. **126**, 13778–13786 (2004)

6.87 B. van Duffel, R.H.A. Ras, F.C. De Schryver, R.A. Schoonheydt: Langmuir–Blodgett deposition and optical diffraction of two-dimensional opal, J. Mater. Chem. **11**, 3333–3336 (2001)

6.88 Y. Li, W. Cai, G. Duan: Ordered micro/nanostructured arrays based on the monolayer colloidal

crystals, Chem. Mater. **20**, 615–624 (2007)
6.89 G. Zhang, D. Wang: Colloidal lithography – The art of nanochemical patterning, Chem. Asian J. **4**, 236–245 (2009)
6.90 S.G. Romanov, M. Bardosova, M. Pemble, C.M.S. Torres: (2+1)-dimensional photonic crystals from Langmuir–Blodgett colloidal multilayers, Appl. Phys. Lett. **89**, 043105–043103 (2006)
6.91 M.E. Pemble, M. Bardosova, I.M. Povey, R.H. Tredgold, D. Whitehead: Novel photonic crystal thin films using the Langmuir–Blodgett approach, Physica B **394**, 233–237 (2007)
6.92 S.G. Romanov, M. Bardosova, D.E. Whitehead, I.M. Povey, M. Pemble, C.M.S. Torres: Erasing diffraction orders: Opal versus Langmuir–Blodgett colloidal crystals, Appl. Phys. Lett. **90**, 133101 (2007)
6.93 H.-L. Li, W. Dong, H.-J. Bongard, F. Marlow: Improved controllability of opal film growth using capillaries for the deposition process, J. Phys. Chem. B **109**, 9939–9945 (2005)
6.94 X. Wang, S.M. Husson, X. Qian, S.R. Wickramasinghe: Vertical cell assembly of colloidal crystal films with controllable thickness, Mater. Lett. **63**, 1981–1983 (2009)
6.95 R.M. Amos, J.G. Rarity, P.R. Tapster, T.J. Shepherd, S.C. Kitson: Fabrication of large-area face-centered-cubic hard-sphere colloidal crystals by shear alignment, Phys. Rev. E **61**, 2929 (2000)
6.96 C.E. Finlayson, P. Spahn, D.R.E. Snoswell, G. Yates, A. Kontogeorgos, A.I. Haines, G.P. Hellmann, J.J. Baumberg: 3D bulk ordering in macroscopic solid opaline films by edge-induced rotational shearing, Adv. Mater. **23**, 1540–1544 (2011)
6.97 S.H. Park, D. Qin, Y. Xia: Crystallization of mesoscale particles over large areas, Adv. Mater. **10**, 1028–1032 (1998)
6.98 A. Mihi, M. Ocaña, H. Míguez: Oriented colloidal-crystal thin films by spin-coating microspheres dispersed in volatile media, Adv. Mater. **18**, 2244–2249 (2006)
6.99 O.L.J. Pursiainen, J.J. Baumberg, H. Winkler, B. Viel, P. Spahn, T. Ruhl: Shear-induced organization in flexible polymer opals, Adv. Mater. **20**, 1484–1487 (2008)
6.100 R. Fenollosa, F. Meseguer: Non-close-packed artificial opals, Adv. Mater. **15**, 1282–1285 (2003)
6.101 A. Stein, F. Li, N.R. Denny: Morphological control in colloidal crystal templating of inverse opals, hierarchical structures, and shaped particles, Chem. Mater. **20**, 649–666 (2007)
6.102 W. Dong, H. Bongard, B. Tesche, F. Marlow: Inverse opals with a skeleton structure: Photonic crystals with two complete bandgaps, Adv. Mater. **14**, 1457–1460 (2002)
6.103 F. Marlow, W. Dong: Engineering nanoarchitectures for photonic crystals, ChemPhysChem **4**, 549–554 (2003)
6.104 P. Jiang: Surface-templated nanostructured films with two-dimensional ordered arrays of voids, Angew. Chem. Int. Ed. **43**, 5625–5628 (2004)
6.105 A.A. Zakhidov, R.H. Baughman, Z. Iqbal, C. Cui, I. Khayrullin, S.O. Dantas, J. Marti, V.G. Ralchenko: Carbon structures with three-dimensional periodicity at optical wavelengths, Science **282**, 897–901 (1998)
6.106 J.S. King, E. Graugnard, C.J. Summers: TiO_2 inverse opals fabricated using low-temperature atomic layer deposition, Adv. Mater. **17**, 1010–1013 (2005)
6.107 S. Reculusa, B. Agricole, A. Derré, M. Couzi, E. Sellier, S. Ravaine, P. Delhaès: Carbon membranes of controlled thickness from colloidal crystals, Adv. Mater. **18**, 1705–1708 (2006)
6.108 H. Miguez, N. Tetreault, B. Hatton, S.M. Yang, D. Perovic, G.A. Ozin: Mechanical stability enhancement by pore size and connectivity control in colloidal crystals by layer-by-layer growth of oxide, Chem. Commun., 2736–2737 (2002)
6.109 E. Palacios-Lidón, J.F. Galisteo-López, B.H. Juárez, C. López: Engineered planar defects embedded in opals, Adv. Mater. **16**, 341–345 (2004)
6.110 A. Rugge, J.S. Becker, R.G. Gordon, S.H. Tolbert: Tungsten nitride inverse opals by atomic layer deposition, Nano Lett. **3**, 1293–1297 (2003)
6.111 J.S. King, D.P. Gaillot, E. Graugnard, C.J. Summers: Conformally back-filled, non-close-packed inverse-opal photonic crystals, Adv. Mater. **18**, 1063–1067 (2006)
6.112 B.T. Holland, C.F. Blanford, A. Stein: Synthesis of macroporous minerals with highly ordered three-dimensional arrays of spheroidal voids, Science **281**, 538–540 (1998)
6.113 J.E.G.J. Wijnhoven, W.L. Vos: Preparation of photonic crystals made of air spheres in titania, Science **281**, 802–804 (1998)
6.114 Y. Cao, Y. Wang, Y. Zhu, H. Chen, Z. Li, J. Ding, Y. Chi: Fabrication of anatase titania inverse opal films using polystyrene templates, Superlattices Microstruct. **40**, 155–160 (2006)
6.115 P. Jiang, K.S. Hwang, D.M. Mittleman, J.F. Bertone, V.L. Colvin: Template-directed preparation of macroporous polymers with oriented and crystalline arrays of voids, J. Am. Chem. Soc. **121**, 11630–11637 (1999)
6.116 Z. Zhong, Y. Yin, B. Gates, Y. Xia: Preparation of mesoscale hollow spheres of TiO_2 and SnO_2 by templating against crystalline arrays of polystyrene beads, Adv. Mater. **12**, 206–209 (2000)
6.117 G.I.N. Waterhouse, M.R. Waterland: Opal and inverse opal photonic crystals: Fabrication and characterization, Polyhedron **26**, 356–368 (2007)
6.118 J.P. Bosco, K. Sasaki, M. Sadakane, W. Ueda, J.G. Chen: Synthesis and characterization of three-dimensionally ordered macroporous (3DOM) tungsten carbide: Application to direct methanol fuel cells, Chem. Mater. **22**, 966–973 (2009)
6.119 Y. Ma, J.F. Chen, Y. Ren, X. Tao: Transition metal-doped titania inverse opals: Fabrication and characterization, Colloids Surf. A **370**, 129–135 (2010)
6.120 S.H. Park, Y. Xia: Macroporous membranes with highly ordered and three-dimensionally interconnected spherical pores, Adv. Mater. **10**, 1045–1048 (1998)
6.121 S.A. Johnson, P.J. Ollivier, T.E. Mallouk: Ordered mesoporous polymers of tunable pore size from

colloidal silica templates, Science **283**, 963–965 (1999)
6.122 H. Míguez, F. Meseguer, C. López, F. López-Tejeira, J. Sánchez-Dehesa: Synthesis and photonic bandgap characterization of polymer inverse opals, Adv. Mater. **13**, 393–396 (2001)
6.123 D.P. Puzzo, A.C. Arsenault, I. Manners, G.A. Ozin: Electroactive inverse opal: A single material for all colors, Angew. Chem. Int. Ed. **48**, 943–947 (2009)
6.124 F. Yan, W.A. Goedel: A simple and effective method for the preparation of porous membranes with three-dimensionally arranged pores, Adv. Mater. **16**, 911–915 (2004)
6.125 P.V. Braun, R.W. Zehner, C.A. White, M.K. Weldon, C. Kloc, S.S. Patel, P. Wiltzius: Epitaxial growth of high dielectric contrast three-dimensional photonic crystals, Adv. Mater. **13**, 721–724 (2001)
6.126 O.D. Velev, P.M. Tessier, A.M. Lenhoff, E.W. Kaler: Materials: A class of porous metallic nanostructures, Nature **401**, 548–548 (1999)
6.127 E. Arsenault, N. Soheilnia, G.A. Ozin: Periodic macroporous nanocrystalline antimony-doped tin oxide electrode, ACS Nano **5**, 2984–2988 (2011)
6.128 G. Subramanian, V.N. Manoharan, J.D. Thorne, D.J. Pine: Ordered macroporous materials by colloidal assembly: A possible route to photonic bandgap materials, Adv. Mater. **11**, 1261–1265 (1999)
6.129 P.M. Tessier, O.D. Velev, A.T. Kalambur, A.M. Lenhoff, J.F. Rabolt, E.W. Kaler: Structured metallic films for optical and spectroscopic applications via colloidal crystal templating, Adv. Mater. **13**, 396–400 (2001)
6.130 D. Wang, J. Li, C.T. Chan, V. Salgueiriño-Maceira, L.M. Liz-Marzán, S. Romanov, F. Caruso: Optical properties of nanoparticle-based metallodielectric inverse opals, Small **1**, 122–130 (2005)
6.131 Y. Zhao, X. Zhao, J. Hu, M. Xu, W. Zhao, L. Sun, C. Zhu, H. Xu, Z. Gu: Encoded porous beads for label-free multiplex detection of tumor markers, Adv. Mater. **21**, 569–572 (2009)
6.132 N. Sapoletova, T. Makarevich, K. Napolskii, E. Mishina, A. Eliseev, A. van Etteger, T. Rasing, G. Tsirlina: Controlled growth of metallic inverse opals by electrodeposition, Phys. Chem. Chem. Phys. **12**, 15414–15422 (2010)
6.133 L. Santos, P. Martin, J. Ghilane, P.-C. Lacaze, H. Randriamahazaka, L.M. Abrantes, J.-C. Lacroix: Electrosynthesis of well-organized nanoporous poly(3,4-ethylenedioxythiophene) by nanosphere lithography, Electrochem. Commun. **12**, 872–875 (2010)
6.134 X. Meng, R. Al-Salman, J. Zhao, N. Borissenko, Y. Li, F. Endres: Electrodeposition of 3D ordered macroporous germanium from ionic liquids: A feasible method to make photonic crystals with a high dielectric constant, Angew. Chem. Int. Ed. **48**, 2703–2707 (2009)
6.135 P.N. Bartlett, P.R. Birkin, M.A. Ghanem, C.-S. Toh: Electrochemical syntheses of highly ordered macroporous conducting polymers grown around self-assembled colloidal templates, J. Mater. Chem. **11**, 849–853 (2001)
6.136 P. Jiang, J. Cizeron, J.F. Bertone, V.L. Colvin: Preparation of macroporous metal films from colloidal crystals, J. Am. Chem. Soc. **121**, 7957–7958 (1999)
6.137 P.N. Bartlett, P.R. Birkin, M.A. Ghanem: Electrochemical deposition of macroporous platinum, palladium and cobalt films using polystyrene latex sphere templates, Chem. Commun., 1671–1672 (2000)
6.138 P.N. Bartlett, J.J. Baumberg, P.R. Birkin, M.A. Ghanem, M.C. Netti: Highly ordered macroporous gold and platinum films formed by electrochemical deposition through templates assembled from submicron diameter monodisperse polystyrene spheres, Chem. Mater. **14**, 2199–2208 (2002)
6.139 S. Ben-Ali, D.A. Cook, S.A.G. Evans, A. Thienpont, P.N. Bartlett, A. Kuhn: Electrocatalysis with monolayer modified highly organized macroporous electrodes, Electrochem. Commun. **5**, 747–751 (2003)
6.140 R. Szamocki, S. Reculusa, S. Ravaine, P.N. Bartlett, A. Kuhn, R. Hempelmann: Tailored mesostructuring and biofunctionalization of gold for increased electroactivity, Angew. Chem. Int. Ed. **45**, 1317–1321 (2006)
6.141 R. Szamocki, A. Velichko, C. Holzapfel, F. Mücklich, S. Ravaine, P. Garrigue, N. Sojic, R. Hempelmann, A. Kuhn: Macroporous ultramicroelectrodes for improved electroanalytical measurements, Anal. Chem. **79**, 533–539 (2007)
6.142 A. Altube, Á. Blanco, C. López: Electrodeposition and optical properties of silver infiltrated photonic nanostructures, Mater. Lett. **62**, 2677–2680 (2008)
6.143 P.N. Bartlett, J.J. Baumberg, S. Coyle, M.E. Abdelsalam: Optical properties of nanostructured metal films, Faraday Discuss. **125**, 117–132 (2004)
6.144 T. Sumida, Y. Wada, T. Kitamura, S. Yanagida: Construction of stacked opaline films and electrochemical deposition of ordered macroporous nickel, Langmuir **18**, 3886–3894 (2002)
6.145 P.N. Bartlett, M.A. Ghanem, I.S. El Hallag, P. de Groot, A. Zhukov: Electrochemical deposition of macroporous magnetic networks using colloidal templates, J. Mater. Chem. **13**, 2596–2602 (2003)
6.146 Y.-W. Chung, I.-C. Leu, J.-H. Lee, J.-H. Yen, M.-H. Hon: Fabrication of various nickel nanostructures by manipulating the one-step electrodeposition process, J. Electrochem. Soc. **154**, E77–E83 (2007)
6.147 Y. Hao, F.Q. Zhu, C.L. Chien, P.C. Searson: Fabrication and magnetic properties of ordered macroporous nickel structures, J. Electrochem. Soc. **154**, D65–D69 (2007)
6.148 X. Yu, Y.J. Lee, R. Furstenberg, J.O. White, P.V. Braun: Filling fraction dependent properties of inverse opal metallic photonic crystals, Adv. Mater. **19**, 1689–1692 (2007)
6.149 H. Zhang, X. Yu, P.V. Braun: Three-dimensional bicontinuous ultrafast-charge and -discharge bulk battery electrodes, Nat. Nano **6**, 277–281 (2011)
6.150 V. Urbanová, M. Bartoš, K. Vytřas, A. Kuhn: Porous bismuth film electrodes for signal increase in

anodic stripping voltammetry, Electroanalysis **22**, 1524–1530 (2010)
6.151 V. Urbanová, K. Vytras, A. Kuhn: Macroporous antimony film electrodes for stripping analysis of trace heavy metals, Electrochem. Commun. **12**, 114–117 (2010)
6.152 T. Sumida, Y. Wada, T. Kitamura, S. Yanagida: Electrochemical preparation of macroporous polypyrrole films with regular arrays of interconnected spherical voids, Chem. Commun., 1613–1614 (2000)
6.153 T. Cassagneau, F. Caruso: Semiconducting polymer inverse opals prepared by electropolymerization, Adv. Mater. **14**, 34–38 (2002)
6.154 S. Tian, J. Wang, U. Jonas, W. Knoll: Inverse opals of polyaniline and its copolymers prepared by electrochemical techniques, Chem. Mater. **17**, 5726–5730 (2005)
6.155 P.V. Braun, P. Wiltzius: Microporous materials: Electrochemically grown photonic crystals, Nature **402**, 603–604 (1999)
6.156 T. Sumida, Y. Wada, T. Kitamura, S. Yanagida: Macroporous ZnO films electrochemically prepared by templating of opal films, Chem. Lett. **30**, 38–39 (2001)
6.157 Y. Yang, H. Yan, Z. Fu, B. Yang, J. Zuo, S. Fu: Enhanced photoluminescence from three-dimensional ZnO photonic crystals, Solid State Commun. **139**, 218–221 (2006)
6.158 T. Sumida, Y. Wada, T. Kitamura, S. Yanagida: Electrochemical change of the photonic stop band of the ordered macroporous WO_3 films, Chem. Lett. **31**, 180–181 (2002)
6.159 P.N. Bartlett, T. Dunford, M.A. Ghanem: Templated electrochemical deposition of nanostructured macroporous PbO_2, J. Mater. Chem. **12**, 3130–3135 (2002)
6.160 J. Hu, M. Abdelsalam, P. Bartlett, R. Cole, Y. Sugawara, J. Baumberg, S. Mahajan, G. Denuault: Electrodeposition of highly ordered macroporous iridium oxide through self-assembled colloidal templates, J. Mater. Chem. **19**, 3855–3858 (2009)
6.161 J. Lenz, V. Trieu, R. Hempelmann, A. Kuhn: Ordered macroporous ruthenium oxide electrodes for potentiometric and amperometric sensing applications, Electroanalysis **23**, 1186–1192 (2011)
6.162 T.M. Benedetti, V.R. Goncales, D.F.S. Petri, S.I.C. De Torresi, R.M. Torresi: Macroporous MnO_2 electrodes obtained by template assisted electrodeposition for electrochemical capacitors, J. Braz. Chem. Soc. **21**, 1704–1709 (2010)
6.163 Y.F. Yuan, X.H. Xia, J.B. Wu, Y.B. Chen, J.L. Yang, S.Y. Guo: Enhanced electrochromic properties of ordered porous nickel oxide thin film prepared by self-assembled colloidal crystal template-assisted electrodeposition, Electrochim. Acta **56**, 1208–1212 (2011)
6.164 V.R. Goncales, R.P. Salvador, M.R. Alcantara, S.I.C. De Torresi: On the template synthesis of nanostructured inorganic/organic hybrid films, J. Electrochem. Soc. **155**, K140–K145 (2008)
6.165 R. Szamocki, A. Velichko, F. Mücklich, S. Reculusa, S. Ravaine, S. Neugebauer, W. Schuhmann, R. Hempelmann, A. Kuhn: Improved enzyme immobilization for enhanced bioelectrocatalytic activity of porous electrodes, Electrochem. Commun. **9**, 2121–2127 (2007)
6.166 K.S. Choi, E.W. McFarland, G.D. Stucky: Electrocatalytic properties of thin mesoporous platinum films synthesized utilizing potential-controlled surfactant assembly, Adv. Mater. **15**, 2018–2021 (2003)
6.167 R. Szamocki: Synthèse Contrôllée d'Électrodes Macroporeuses Pour des Applications Électrocatalytiques, Ph.D. Thesis (University Bordeaux I/ Universität des Saarlandes, Bordeaux/Saarbrücken 2006)
6.168 M. Heim, S. Reculusa, S. Ravaine, A. Kuhn: Engineering of complex macroporous materials through controlled electrodeposition in colloidal superstructures, Adv. Funct. Mater. **22**, 538–545 (2012)
6.169 S. Trasatti, O.A. Petrii: Real surface area measurements in electrochemistry, J. Electroanal. Chem. **327**, 353–376 (1992)
6.170 G.G. Wallace, G.M. Spinks, L.A.P. Kane-Maguire: *Conductive Electroactive Polymers: Intelligent Polymer Systems* (CRC, Boca Raton 2009)
6.171 M. Singh, P.K. Kathuroju, N. Jampana: Polypyrrole based amperometric glucose biosensors, Sens. Actuators B **143**, 430–443 (2009)
6.172 E. Smela: A microfabricated movable electrochromic "Pixel" based on polypyrrole, Adv. Mater. **11**, 1343–1345 (1999)
6.173 M.R. Gandhi, P. Murray, G.M. Spinks, G.G. Wallace: Mechanism of electromechanical actuation in polypyrrole, Synth. Met. **73**, 247–256 (1995)
6.174 T.F. Otero, M.T. Cortés: Artificial muscles with tactile sensitivity, Adv. Mater. **15**, 279–282 (2003)
6.175 E. Smela: Conjugated polymer actuators for biomedical applications, Adv. Mater. **15**, 481–494 (2003)
6.176 W. Sun, X. Chen: Preparation and characterization of polypyrrole films for three-dimensional micro supercapacitor, J. Power Sources **193**, 924 (2009)
6.177 U. Lange, N.V. Roznyatovskaya, V.M. Mirsky: Conducting polymers in chemical sensors and arrays, Anal. Chim. Acta **614**, 1 (2008)
6.178 A. Malinauskas: Electrocatalysis at conducting polymers, Synth. Met. **107**, 75 (1999)
6.179 V.G. Khomenko, V.Z. Barsukov, A.S. Katashinskii: The catalytic activity of conducting polymers toward oxygen reduction, Electrochim. Acta **50**, 1675 (2005)
6.180 R.A. Green, N.H. Lovell, G.G. Wallace, L.A. Poole-Warren: Conducting polymers for neural interfaces: Challenges in developing an effective long-term implant, Biomaterials **29**, 3393–3399 (2008)
6.181 A. Mollahosseini, E. Noroozian: Electrodeposition of a highly adherent and thermally stable polypyrrole coating on steel from aqueous polyphosphate solution, Synth. Met. **159**, 1247–1254 (2009)
6.182 T. Cassagneau, F. Caruso: Inverse opals for optical affinity biosensing, Adv. Mater. **14**, 1629–1633 (2002)
6.183 W. Qian, Z.-Z. Gu, A. Fujishima, O. Sato: Three-dimensionally ordered macroporous polymer ma-

terials: An approach for biosensor applications, Langmuir **18**, 4526–4529 (2002)
6.184 C.Y. Kuo, S.Y. Lu, S. Chen, M. Bernards, S. Jiang: Stop band shift based chemical sensing with three-dimensional opal and inverse opal structures, Sens. Actuators B **124**, 452–458 (2007)
6.185 G. Kang, R.B. Borgens, Y. Cho: Well-ordered porous conductive polypyrrole as a new platform for neural interfaces, Langmuir **27**, 6179–6184 (2011)
6.186 L. Zhao, L. Tong, C. Li, Z. Gu, G. Shi: Polypyrrole actuators with inverse opal structures, J. Mater. Chem. **19**, 1653–1658 (2009)
6.187 L. Xu, J. Wang, Y. Song, L. Jiang: Electrically tunable polypyrrole inverse opals with switchable stopband, conductivity, and wettability, Chem. Mater. **20**, 3554–3556 (2008)
6.188 S. Ghosh, G.A. Bowmaker, R.P. Cooney, J.M. Seakins: Infrared and Raman spectroscopic studies of the electrochemical oxidative degradation of polypyrrole, Synth. Met. **95**, 63 (1998)
6.189 T.A. Skotheim, J.R. Reynolds: *Handbook of Conducting Polymers* (CRC, Boca Raton 2007)
6.190 E.A. Bazzaoui, S. Aeiyach, P.C. Lacaze: Electropolymerization of bithiophene on Pt and Fe electrodes in an aqueous sodium dodecylsulfate (SDS) micellar medium, Synth. Met. **83**, 159–165 (1996)
6.191 Y.Z. Wang, R.G. Sun, D.K. Wang, T.M. Swager, A.J. Epstein: Polarity- and voltage-controlled color-variable light-emitting devices based on conjugated polymers, Appl. Phys. Lett. **74**, 2593–2595 (1999)
6.192 P. Jiang, G.N. Ostojic, R. Narat, D.M. Mittleman, V.L. Colvin: The fabrication and bandgap engineering of photonic multilayers, Adv. Mater. **13**, 389–393 (2001)
6.193 Q. Yan, X.S. Zhao, Z. Zhou: Fabrication of colloidal crystal heterostructures using a horizontal deposition method, J. Cryst. Growth **288**, 205–208 (2006)
6.194 Q. Yan, A. Chen, S.J. Chua, X.S. Zhao: Incorporation of point defects into self-assembled three-dimensional colloidal crystals, Adv. Mater. **17**, 2849–2853 (2005)
6.195 Y. Jun, C.A. Leatherdale, D.J. Norris: Tailoring air defects in self-assembled photonic bandgap crystals, Adv. Mater. **17**, 1908–1911 (2005)
6.196 Q. Yan, Z. Zhou, X.S. Zhao, S.J. Chua: Line defects embedded in three-dimensional photonic crystals, Adv. Mater. **17**, 1917–1920 (2005)
6.197 F. Fleischhaker, A.C. Arsenault, Z. Wang, V. Kitaev, F.C. Peiris, G. von Freymann, I. Manners, R. Zentel, G.A. Ozin: Redox-tunable defects in colloidal photonic crystals, Adv. Mater. **17**, 2455–2458 (2005)
6.198 N. Tétreault, A.C. Arsenault, A. Mihi, S. Wong, V. Kitaev, I. Manners, H. Miguez, G.A. Ozin: Building tunable planar defects into photonic crystals using polyelectrolyte multilayers, Adv. Mater. **17**, 1912–1916 (2005)
6.199 R. Pozas, A. Mihi, M. Ocaña, H. Míguez: Building nanocrystalline planar defects within self-assembled photonic crystals by spin-coating, Adv. Mater. **18**, 1183–1187 (2006)
6.200 Q. Yan, L. Wang, X.S. Zhao: Artificial defect engineering in three-dimensional colloidal photonic crystals, Adv. Funct. Mater. **17**, 3695–3706 (2007)
6.201 J. Li, L. Xue, Z. Wang, Y. Han: Colloidal photonic crystals with a graded lattice-constant distribution, Colloid. Polym. Sci. **285**, 1037–1041 (2007)
6.202 G. Von Freymann, S. John, V. Kitaev, G.A. Ozin: Enhanced coupling to slow photon modes in three-dimensional graded colloidal photonic crystals, Adv. Mater. **17**, 1273–1276 (2005)
6.203 K. Wostyn, Y. Zhao, G. de Schaetzen, L. Hellemans, N. Matsuda, K. Clays, A. Persoons: Insertion of a two-dimensional cavity into a self-assembled colloidal crystal, Langmuir **19**, 4465–4468 (2003)
6.204 Y. Zhao, K. Wostyn, G. De Schaetzen, K. Clays, L. Hellemans, A. Persoons, M. Szekeres, R.A. Schoonheydt: The fabrication of photonic band gap materials with a two-dimensional defect, Appl. Phys. Lett. **82**, 3764–3766 (2003)
6.205 P. Massé, S. Reculusa, K. Clays, S. Ravaine: Tailoring planar defect in three-dimensional colloidal crystals, Chem. Phys. Lett. **422**, 251–255 (2006)
6.206 P. Massé, S. Reculusa, S. Ravaine: Elaboration of photonic crystal heterostructures by the Langmuir–Blodgett method, Colloids Surf. A **284/285**, 229–233 (2006)
6.207 J.-F. Dechézelles, P. Massé, E. Cloutet, H. Cramail, S. Ravaine: Building planar defects into colloidal crystals using particles of different chemical nature, Colloids Surf. A **343**, 8 (2009)
6.208 J.F. Dechézelles, G. Mialon, T. Gacoin, C. Barthou, C. Schwob, A. Maître, R.A.L. Vallée, H. Cramail, S. Ravaine: Inhibition and exaltation of emission in layer-controlled colloidal photonic architectures, Colloids Surf. A **373**, 1–5 (2011)
6.209 A. Deák, B. Bancsi, A.L. Tóth, A.L. Kovács, Z. Hórvölgyi: Complex Langmuir–Blodgett films from silica nanoparticles: An optical spectroscopy study, Colloids Surf. A **278**, 10–16 (2006)
6.210 S. Reculusa, S. Ravaine: Synthesis of colloidal crystals of controllable thickness through the Langmuir–Blodgett technique, Chem. Mater. **15**, 598–605 (2003)
6.211 C. Liu, F. Li, L.-P. Ma, H.-M. Cheng: Advanced materials for energy storage, Adv. Mater. **22**, E28–E62 (2010)
6.212 V. Müller, M. Rasp, J. Rathouský, B. Schütz, M. Niederberger, D. Fattakhova-Rohlfing: Transparent conducting films of antimony-doped tin oxide with uniform mesostructure assembled from preformed nanocrystals, Small **6**, 633–637 (2010)
6.213 T. Cassagneau, F. Caruso: Conjugated polymer inverse opals for potentiometric biosensing, Adv. Mater. **14**, 1837–1841 (2002)
6.214 J.-D. Qiu, H.-Z. Peng, R.-P. Liang, M. Xiong: Preparation of three-dimensional ordered macroporous prussian blue film electrode for glucose biosensor application, Electroanalysis **19**, 1201–1206 (2007)
6.215 X. Chen, Y. Wang, J. Zhou, W. Yan, X. Li, J.-J. Zhu: Electrochemical impedance immunosensor based on three-dimensionally ordered macroporous gold film, Anal. Chem. **80**, 2133–2140 (2008)

6.216 X. Yang, Y. Jin, Y. Zhu, L. Tang, C. Li: Inverse opal of polyaniline for biosensors prepared by electrochemical and self-assembly techniques, J. Electrochem. Soc. **155**, J23–J25 (2008)

6.217 J. Zhou, H. Huang, J. Xuan, J. Zhang, J.J. Zhu: Quantum dots electrochemical aptasensor based on three-dimensionally ordered macroporous gold film for the detection of ATP, Biosens. Bioelectron. **26**, 834–840 (2010)

6.218 M.M. Dimos, G.J. Blanchard: Evaluating the role of Pt and Pd catalyst morphology on electrocatalytic methanol and ethanol oxidation, J. Phys. Chem. C **114**, 6019–6026 (2010)

6.219 A. Heller: Miniature biofuel cells, Phys. Chem. Chem. Phys. **6**, 209–216 (2004)

6.220 A. Heller: Potentially implantable miniature batteries, Anal. Bioanal. Chem. **385**, 469–473 (2006)

6.221 S.T. Singleton, J.J. O'Dea, J. Osteryoung: Analytical utility of cylindrical microelectrodes, Anal. Chem. **61**, 1211–1215 (1989)

6.222 M.M. Murphy, J.J. O'Dea, J. Osteryoung: Pulse voltammetry at microcylinder electrodes, Anal. Chem. **63**, 2743–2750 (1991)

6.223 P. Salaün, C.M.G. van den Berg: Voltammetric detection of mercury and copper in seawater using a gold microwire electrode, Anal. Chem. **78**, 5052–5060 (2006)

6.224 L. Fink, D. Mandler: Thin functionalized films on cylindrical microelectrodes for electrochemical determination of Hg(II), J. Electroanal. Chem. **649**, 153–158 (2010)

6.225 J. Wang, N. Foster, S. Armalis, D. Larson, A. Zirino, K. Olsen: Remote stripping electrode for in situ monitoring of labile copper in the marine environment, Anal. Chim. Acta **310**, 223–231 (1995)

6.226 H. Huiliang, D. Jagner, L. Renman: Flow potentiometric and constant-current stripping analysis for mercury(II) with gold, platinum and carbon fibre working electrodes: Application to the analysis of tap water, Anal. Chim. Acta **201**, 1–9 (1987)

6.227 J.H. Moon, S. Kim, G.-R. Yi, Y.-H. Lee, S.-M. Yang: Fabrication of ordered macroporous cylinders by colloidal templating in microcapillaries, Langmuir **20**, 2033–2035 (2004)

6.228 S. Hu, Y. Men, S.V. Roth, R. Gehrke, J. Rieger: Facile preparation of macroscopic soft colloidal crystals with fiber symmetry, Langmuir **24**, 1617–1620 (2008)

6.229 J.H. Song, I. Kretzschmar: Colloid-templated multisectional porous polymeric fibers, Langmuir **24**, 10616–10620 (2008)

6.230 J.H. Moon, G.-R. Yi, S.-M. Yang: Fabrication of hollow colloidal crystal cylinders and their inverted polymeric replicas, J. Colloid Interface Sci. **287**, 173 (2005)

6.231 C.H. Lai, Y.J. Huang, P.W. Wu, L.Y. Chen: Rapid fabrication of cylindrical colloidal crystals and their inverse opals, J. Electrochem. Soc. **157**, 23–27 (2010)

6.232 S. Reculusa, M. Heim, F. Gao, N. Mano, S. Ravaine, A. Kuhn: Design of catalytically active cylindrical and macroporous gold microelectrodes, Adv. Funct. Mater. **21**, 691–698 (2011)

6.233 R. Zeis, T. Lei, K. Sieradzki, J. Snyder, J. Erlebacher: Catalytic reduction of oxygen and hydrogen peroxide by nanoporous gold, J. Catal. **253**, 132–138 (2008)

6.234 L. Deng, F. Wang, H. Chen, L. Shang, L. Wang, T. Wang, S. Dong: A biofuel cell with enhanced performance by multilayer biocatalyst immobilized on highly ordered macroporous electrode, Biosens. Bioelectron. **24**, 329–333 (2008)

6.235 A. Zebda, L. Renaud, M. Cretin, F. Pichot, C. Innocent, R. Ferrigno, S. Tingry: A microfluidic glucose biofuel cell to generate micropower from enzymes at ambient temperature, Electrochem. Commun. **11**, 592–595 (2009)

6.236 H.-J. Liu, W.-J. Cui, L.-H. Jin, C.-X. Wang, Y.-Y. Xia: Preparation of three-dimensional ordered mesoporous carbon sphere arrays by a two-step templating route and their application for supercapacitors, J. Mater. Chem. **19**, 3661–3667 (2009)

6.237 M. Nakayama, T. Kanaya, R. Inoue: Anodic deposition of layered manganese oxide into a colloidal crystal template for electrochemical supercapacitor, Electrochem. Commun. **9**, 1154–1158 (2007)

6.238 J.-H. Kim, S.H. Kang, K. Zhu, J.Y. Kim, N.R. Neale, A.J. Frank: Ni-NiO core-shell inverse opal electrodes for supercapacitors, Chem. Commun. **47**, 5214–5216 (2011)

6.239 S.-W. Woo, K. Dokko, H. Nakano, K. Kanamura: Incorporation of polyaniline into macropores of three-dimensionally ordered macroporous carbon electrode for electrochemical capacitors, J. Power Sources **190**, 596–600 (2009)

6.240 N.S. Ergang, J.C. Lytle, K.T. Lee, S.M. Oh, W.H. Smyrl, A. Stein: Photonic crystal structures as a basis for a three-dimensionally interpenetrating electrochemical-cell system, Adv. Mater. **18**, 1750–1753 (2006)

6.241 N.S. Ergang, M.A. Fierke, Z. Wang, W.H. Smyrl, A. Stein: Fabrication of a fully infiltrated three-dimensional solid-state interpenetrating electrochemical cell, J. Electrochem. Soc. **154**, A1135–A1139 (2007)

6.242 S. Ben-Ali, D.A. Cook, P.N. Bartlett, A. Kuhn: Bioelectrocatalysis with modified highly ordered macroporous electrodes, J. Electroanal. Chem. **579**, 181–187 (2005)

6.243 Y. Bon Saint Côme, H. Lalo, Z. Wang, M. Etienne, J. Gajdzik, G.-W. Kohring, A. Walcarius, R. Hempelmann, A. Kuhn: Multiscale-tailored bioelectrode surfaces for optimized catalytic conversion efficiency, Langmuir **27**(20), 12737–12744 (2011)

6.244 M. Heim, B. Yvert, A. Kuhn: Nanostructuration strategies to enhance microelectrode array (MEA) performance for neuronal recording and stimulation, J. Physiol. Paris **106**, 137–145 (2012)

6.245 M. Heim, L. Rousseau, S. Reculusa, V. Urbanova, C. Mazzocco, S. Joucla, L. Bouffier, K. Vytras, P. Bartlett, A. Kuhn, B. Yvert: Combined macro/mesoporous microelectrode arrays (MEAs) for low noise extracellular recording of neural networks, J. Neurophysiol. **15**, 1793–1803 (2012)

6.246 V. Urbanová, Y. Li, K. Vytras, B. Yvert, A. Kuhn: Macroporous microelectrode arrays for measurements with reduced noise, J. Electroanal. Chem. **656**, 91–95 (2011)

6.247 P. Kornberger, F. Giffhorn, G.W. Kohring: Dehydrogenases, electrochemical cofactor regeneration. In: *Encyclopedia of Industrial Biotechnology, Bioprocess, Bioseparation, and Cell Technology*, Vol. 3, ed. by M.C. Flickinger (Wiley, Hoboken 2010) p. 1888

6.248 R. Wichmann, D. Vasic-Racki: Cofactor regeneration at the lab scale, Adv. Biochem. Eng. **92**, 225–260 (2005)

6.249 C. Kohlmann, W. Märkle, S. Lätz: Electroenzymatic synthesis, J. Mol. Catal. B **51**, 57–72 (2008)

6.250 S. Gaspar, H. Zimmermann, I. Gazaryan, E. Csöregi, W. Schuhmann: Hydrogen peroxide biosensors based on direct electron transfer from plant peroxidases immobilized on self-assembled thiol-monolayer modified gold electrodes, Electroanalysis **13**, 284–288 (2001)

6.251 S. Cosnier, M. Holzinger: Electrosynthesized polymers for biosensing, Chem. Soc. Rev. **40**, 2146–2156 (2011)

6.252 D. Avnir, T. Coradin, O. Lev, J. Livage: Recent bio-applications of sol-gel materials, J. Mater. Chem. **16**, 1013–1030 (2006)

6.253 F. Qu, R. Nasraoui, M. Etienne, Y.B.S. Côme, A. Kuhn, J. Lenz, J. Gajdzik, R. Hempelmann, A. Walcarius: Electrogeneration of ultra-thin silica films for the functionalization of macroporous electrodes, Electrochem. Commun. **13**, 138–142 (2011)

6.254 Z. Wang, M. Etienne, G.-W. Kohring, Y. Bon-Saint-Côme, A. Kuhn, A. Walcarius: Electrochemically assisted deposition of sol–gel bio-composite with co-immobilized dehydrogenase and diaphorase, Electrochim. Acta **56**, 9032–9040 (2011)

6.255 Y. Bon Saint Côme, H. Lalo, Z. Wang, M. Etienne, J. Gajdzik, G.-W. Kohring, A. Walcarius, R. Hempelmann, A. Kuhn: Multiscale-tailored bioelectrode surfaces for optimized catalytic conversion efficiency, Langmuir **27**(2999), 12737–12744 (2011)

6.256 J. Ge, Y. Yin: Responsive photonic crystals, Angew. Chem. Int. Ed. **50**, 1492–1522 (2011)

6.257 Y. Takeoka, M. Watanabe: Tuning structural color changes of porous thermosensitive gels through quantitative adjustment of the cross-linker in pregel solutions, Langmuir **19**, 9104–9106 (2003)

6.258 J.M. Weissman, H.B. Sunkara, A.S. Tse, S.A. Asher: Thermally switchable periodicities and diffraction from mesoscopically ordered materials, Science **274**, 959–963 (1996)

6.259 N. Griffete, H. Frederich, A. Maitre, M.M. Chehimi, S. Ravaine, C. Mangeney: Photonic crystal pH sensor containing a planar defect for fast and enhanced response, J. Mater. Chem. **21**, 13052–13055 (2011)

6.260 J. Zhou, C.Q. Sun, K. Pita, Y.L. Lam, Y. Zhou, S.L. Ng, C.H. Kam, L.T. Li, Z.L. Gui: Thermally tuning of the photonic band gap of SiO_2 colloid-crystal infilled with ferroelectric $BaTiO_3$, Appl. Phys. Lett. **78**, 661–663 (2001)

6.261 J. Shin, P.V. Braun, W. Lee: Fast response photonic crystal pH sensor based on templated photo-polymerized hydrogel inverse opal, Sens. Actuators B **150**, 183–190 (2010)

6.262 D. Nakayama, Y. Takeoka, M. Watanabe, K. Kataoka: Simple and precise preparation of a porous gel for a colorimetric glucose sensor by a templating technique, Angew. Chem. Int. Ed. **42**, 4197–4200 (2003)

6.263 A.C. Arsenault, V. Kitaev, I. Manners, G.A. Ozin, A. Mihi, H. Miguez: Vapor swellable colloidal photonic crystals with pressure tunability, J. Mater. Chem. **15**, 133–138 (2005)

6.264 E. Tian, J. Wang, Y. Zheng, Y. Song, L. Jiang, D. Zhu: Colorful humidity sensitive photonic crystal hydrogel, J. Mater. Chem. **18**, 1116–1122 (2008)

6.265 K.-U. Jeong, J.-H. Jang, C.Y. Koh, M.J. Graham, K.-Y. Jin, S.-J. Park, C. Nah, M.-H. Lee, S.Z.D. Cheng, E.L. Thomas: Colour-tunable spiral photonic actuators, J. Mater. Chem. **19**, 1956–1959 (2009)

6.266 J.H. Holtz, S.A. Asher: Polymerized colloidal crystal hydrogel films as intelligent chemical sensing materials, Nature **389**, 829–832 (1997)

6.267 K. Lee, S.A. Asher: Photonic crystal chemical sensors: pH and ionic strength, J. Am. Chem. Soc. **122**, 9534–9537 (2000)

6.268 J.H. Holtz, J.S.W. Holtz, C.H. Munro, S.A. Asher: Intelligent polymerized crystalline colloidal arrays: Novel chemical sensor materials, Anal. Chem. **70**, 780–791 (1998)

6.269 V.L. Alexeev, A.C. Sharma, A.V. Goponenko, S. Das, I.K. Lednev, C.S. Wilcox, D.N. Finegold, S.A. Asher: High ionic strength glucose-sensing photonic crystal, Anal. Chem. **75**, 2316–2323 (2003)

6.270 Y.-J. Lee, S.A. Pruzinsky, P.V. Braun: Glucose-sensitive inverse opal hydrogels: Analysis of optical diffraction response, Langmuir **20**, 3096–3106 (2004)

6.271 K. Sumioka, H. Kayashima, T. Tsutsui: Tuning the optical properties of inverse opal photonic crystals by deformation, Adv. Mater. **14**, 1284–1286 (2002)

6.272 S.H. Foulger, P. Jiang, A. Lattam, D.W. Smith, J. Ballato, D.E. Dausch, S. Grego, B.R. Stoner: Photonic crystal composites with reversible high-frequency stop band shifts, Adv. Mater. **15**, 685–689 (2003)

6.273 A.C. Arsenault, T.J. Clark, G. von Freymann, L. Cademartiri, R. Sapienza, J. Bertolotti, E. Vekris, S. Wong, V. Kitaev, I. Manners, R.Z. Wang, S. John, D. Wiersma, G.A. Ozin: From colour fingerprinting to the control of photoluminescence in elastic photonic crystals, Nat. Mater. **5**, 179–184 (2006)

6.274 G.A. Ozin, A.C. Arsenault: P-Ink and Elast-Ink from lab to market, Mater. Today **11**, 44–51 (2008)

6.275 J.R. Lawrence, Y. Ying, P. Jiang, S.H. Foulger: Dynamic tuning of organic lasers with colloidal crystals, Adv. Mater. **18**, 300–303 (2006)

6.276 B. Li, J. Zhou, L. Li, X.J. Wang, X.H. Liu, J. Zi: Ferroelectric inverse opals with electrically tunable photonic band gap, Appl. Phys. Lett. **83**, 4704–4706 (2003)

6.277 A.C. Arsenault, D.P. Puzzo, I. Manners, G.A. Ozin: Photonic-crystal full-colour displays, Nat. Photonics **1**, 468–472 (2007)

6.278 J. Ge, Y. Hu, Y. Yin: Highly tunable superparamagnetic colloidal photonic crystals, Angew. Chem. Int.

Ed. **46**, 7428–7431 (2007)
6.279 J. Ge, Y. Yin: Magnetically tunable colloidal photonic structures in alkanol solutions, Adv. Mater. **20**, 3485–3491 (2008)
6.280 D.M. Kuncicky, B.G. Prevo, O.D. Velev: Controlled assembly of SERS substrates templated by colloidal crystal films, J. Mater. Chem. **16**, 1207–1211 (2006)
6.281 M.E. Abdelsalam, P.N. Bartlett, T. Kelf, J. Baumberg: Wetting of regularly structured gold surfaces, Langmuir **21**, 1753–1757 (2005)
6.282 S. Nishimura, N. Abrams, B.A. Lewis, L.I. Halaoui, T.E. Mallouk, K.D. Benkstein, J. van de Lagemaat, A.J. Frank: Standing wave enhancement of red absorbance and photocurrent in dye-sensitized titanium dioxide photoelectrodes coupled to photonic crystals, J. Am. Chem. Soc. **125**, 6306–6310 (2003)
6.283 L.I. Halaoui, N.M. Abrams, T.E. Mallouk: Increasing the conversion efficiency of dye-sensitized TiO_2 photoelectrochemical cells by coupling to photonic crystals, J. Phys. Chem. B **109**, 6334–6342 (2005)
6.284 S. Guldin, S. Hüttner, M. Kolle, M.E. Welland, P. Müller-Buschbaum, R.H. Friend, U. Steiner, N. Tetreault: Dye-sensitized solar cell based on a three-dimensional photonic crystal, Nano Lett. **10**, 2303–2309 (2010)
6.285 A. Mihi, H. Miguez: Origin of light-harvesting enhancement in colloidal-photonic-crystal-based dye-sensitized solar cells, J. Phys. Chem. B **109**, 15968–15976 (2005)
6.286 H.A. Atwater, A. Polman: Plasmonics for improved photovoltaic devices, Nat. Mater. **9**, 205–213 (2010)
6.287 R.M. Cole, J.J. Baumberg, F.J. Garcia de Abajo, S. Mahajan, M. Abdelsalam, P.N. Bartlett: Understanding plasmons in nanoscale voids, Nano Lett. **7**, 2094–2100 (2007)
6.288 P.M. Tessier, O.D. Velev, A.T. Kalambur, J.F. Rabolt, A.M. Lenhoff, E.W. Kaler: Assembly of gold nanostructured films templated by colloidal crystals and use in surface-enhanced Raman spectroscopy, J. Am. Chem. Soc. **122**, 9554–9555 (2000)
6.289 S. Mahajan, J. Richardson, T. Brown, P.N. Bartlett: SERS-Melting: A new method for discriminating mutations in DNA sequences, J. Am. Chem. Soc. **130**, 15589–15601 (2008)
6.290 D.K. Corrigan, N. Gale, T. Brown, P.N. Bartlett: Analysis of short tandem repeats by using SERS monitoring and electrochemical melting, Angew. Chem. Int. Ed. **49**, 5917–5920 (2010)
6.291 M. Zamuner, D. Talaga, F. Deiss, V. Guieu, A. Kuhn, P. Ugo, N. Sojic: Fabrication of a macroporous microwell array for surface-enhanced Raman scattering, Adv. Funct. Mater. **19**, 3129–3135 (2009)
6.292 T.V. Teperik, F.J. Garcia de Abajo, A.G. Borisov, M. Abdelsalam, P.N. Bartlett, Y. Sugawara, J.J. Baumberg: Omnidirectional absorption in nanostructured metal surfaces, Nat. Photonics **2**, 299–301 (2008)
6.293 B. Gates, Y. Yin, Y. Xia: Fabrication and characterization of porous membranes with highly ordered three-dimensional periodic structures, Chem. Mater. **11**, 2827–2836 (1999)
6.294 X. Wang, S.M. Husson, X. Qian, S.R. Wickramasinghe: Inverse colloidal crystal microfiltration membranes, J. Membr. Sci. **365**, 302–310 (2010)

7. Ion-Sensitive Electrodes

Hans-Hermann Rüttinger

In this chapter we introduce the basic methods of electroanalysis that utilize electrochemical reactions at the interface between the solution to be analyzed and different electrodes. Potentiometry, i.e., 7 equilibrium measurements with negligible current is discussed in detail, especially the newer developments of ion-selective electrodes. Experiments that involve charge transfer across the interface are discussed as well, to provide an overview of the most established electroanalytical methods and sensors, comprising constant potential, swept potential, and constant current in quiet solutions or with forced mass transfer.

7.1 **Fundamentals of Potentiometry** 207
7.1.1 Reference Electrodes 208
7.1.2 Simple Indicator Electrodes 210
7.1.3 Membrane Electrodes 210
7.1.4 Characterization of Ion-Selective Electrodes 217
7.1.5 Direct Potentiometric Determination of Concentrations ... 218
7.1.6 Models of ISE Response 218
7.1.7 All Solid-State Electrodes 222
7.1.8 Ion-Selective Field Effect Transistor (ISFET) 225
7.1.9 Drug Sensitive Electrodes 226
7.2 **Application of ISE** 226
7.2.1 Gas-Sensitive Electrodes and Biosensors 226
7.2.2 Detectors in Flow Systems 227
7.3 **Amperometric and Voltammetric Methods** 227
7.3.1 Experimental Methods 227
7.3.2 Electrochemical Reaction Mechanisms 233
References 237

The goal of electroanalysis is to gain chemical information about a sample such as the constituents, its concentration and distribution, and even reactions and state of equilibria directly from electrical measurable readings. Electrical data such as voltage and current are easy to measure and in modern apparatus they may be fed into a powerful microcontroller to calculate the final results. The fundamentals of electroanalysis are more than a hundred years old, but the development still goes on, especially in the field of nanoscaled sensors and their combinations with specific biochemical reactions as immunoassays or enzymatic catalysis.

Ion-selective electrodes (ISE) are an important subgroup of electrochemical sensors. They are small in size, even downscaled to the micrometer range, and easy to interface with low-power consuming inexpensive instruments. They are now commercially available for the determination of a large number of inorganic and organic ions, which are very attractive features concerning practical applications. A huge number of scientific works have been done in the last century and the rate of publication increased steadily up to 1978; since then a constant output of about 400 papers per year has been published [7.1].

7.1 Fundamentals of Potentiometry

Let us consider a simple measurement of a voltage. What is the interface between the instrument and the chemistry in a beaker? In Fig. 7.1 a principal experimental setup is shown.

Both plug-ins of the instrument are connected through a copper wire to a piece of copper or silver, each immersed in a diluted solution of its salts, here copper sulfate and silver sulfate.

A voltage of +0.412 V is measured as the potential difference of the two half cells. Note that the positive plug-in of the instrument is connected to the silver metal, the right electrode; and the common plug-in to

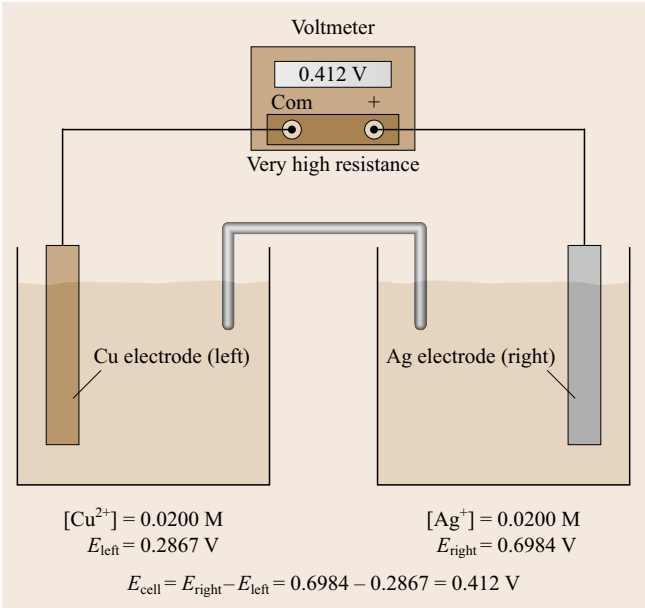


Fig. 7.1 Measurement of the potential between two half cells (after [7.2])

the copper, the left electrode. The observed voltage corresponds to the free enthalpy of the reaction

$$\mathrm{Cu} + 2\mathrm{Ag}^{+} \leftrightarrows \mathrm{Cu}^{2+} + 2\,\mathrm{Ag} \tag{7.1}$$

that would proceed to the equilibrium from left to right. The oxidation of the copper anode and the reduction of the silver cation are separated in space and the charge must be transported through the conductors to make the reaction go. The molar free enthalpy of the reaction equals the electrical energy of the reversible and isothermal charge transfer and is given by the product of voltage and charge

$$\Delta G^{0} = -zFE = -RT \ln K_{\mathrm{eq}} \,. \tag{7.2}$$

By replacing the voltmeter with a resistor, the reaction runs to the right side with a rate of reaction proportional to the electric current, and the setup works as a galvanic element delivering electricity at the cost of the chemical system. The sign of the enthalpy is therefore negative by convention.

The voltage measured by the instrument is the sum of all the differences of potentials that arise at any phase boundary in the electric circuit.

The setup in Fig. 7.1 is therefore symbolized by the scheme

$$\mathrm{Cu}\,|\mathrm{CuSO_4}|\,\text{salt bridge}\,|\mathrm{Ag_2SO_4}|\,\mathrm{Ag}\,|\,\mathrm{Cu}\,.$$

The potential differences at the interface between different metals are small and are mutually compensated, but the transition from metal with electrons as charge carriers to an electrolyte with ions as charge carriers and vice versa involve redox reactions. The free energy of those reactions is related to the potential difference at their interfaces.

In the case of the right half cell

$$\mathrm{Ag}^{+} + \mathrm{e}^{-} \rightarrow \mathrm{Ag}\,, \tag{7.3}$$

δG corresponds to the difference of the chemical potentials of pure silver and the silver ion in the solution

$$\delta G = -zFE = \mu_{\mathrm{Ag}} - \mu_{\mathrm{Ag}^+} = \mu^{\ominus}_{\mathrm{Ag}} - [\mu^{\ominus}_{\mathrm{Ag}^+} + RT \ln(a_{\mathrm{Ag}^+})] \text{ with } z = 1\,, \tag{7.4}$$

$$E = \frac{\mu_{\mathrm{Ag}^+} - \mu_{\mathrm{Ag}}}{zF} + \frac{RT}{zF} \ln(a_{\mathrm{Ag}^+})\,. \tag{7.5}$$

The constant part will be summarized in the standard potential

$$E = E^{0} + \frac{RT}{zF} \ln(a_{\mathrm{Ag}^+})\,. \tag{7.6}$$

This is the well-known Nernst equation. The general form is

$$E = E^{0} + \frac{RT}{zF} \ln \frac{a_{\mathrm{ox}}}{a_{\mathrm{red}}}\,. \tag{7.7}$$

The potential of a half cell can't be measured, because you can't connect the electrolyte to the input of an instrument without establishing a second electrode. A complete cell is needed, and to get thermodynamically defined potential differences between the two electrodes any external charge transfer must be prevented in order to measure a non-disturbed equilibrium potential difference. That means open circuit conditions with a high impedance instrument. Commercial instruments for potentiometric measurements have an input resistance better than $1 \times 10^{12}\,\Omega$. Nevertheless a small charge transfer to achieve the equilibrium must occur to charge the double layer at the electrode and to charge the capacitance of the cables and the input stage of the instrument.

7.1.1 Reference Electrodes

As the Nernst equation implies, direct analytical information can be drawn from potentiometric measurements. For such purposes the second electrode of the cell should remain at a constant and reproducible potential, independent of the analytical matrix. Only then does it work as a proper reference electrode.

A very reproducible half cell is the standard hydrogen electrode, to which all electrode potentials are referenced to by convention.

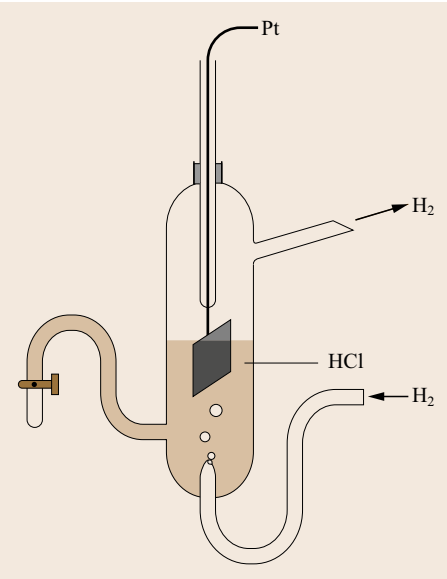


Fig. 7.2 Standard hydrogen electrode. The pressure of hydrogen is 1 bar, the activity of the hydrochloric acid 1N

The standard hydrogen electrode is based on the redox equilibrium between molecular hydrogen and hydronium ions

$$H_{2(g)} \leftrightarrows 2H^+ + 2e^- , \tag{7.8}$$

$$E = E^0_{H_2} + \frac{RT}{2F} \ln \frac{a^2_{H^+}}{p_{H_2}} . \tag{7.9}$$

This reaction is catalyzed on the surface of a rough platinum electrode and the electrons are transferred from the adsorbed hydrogen to the metal. The potential of the hydrogen electrode with $a_{H^+} = 1$ and a hydrogen pressure of 1 bar is defined as $E_{H_2} = 0V$.

Figure 7.2 shows a possible construction of a standard hydrogen electrode.

For practical use the standard hydrogen electrode is cumbersome and can be replaced in the lab by more convenient electrodes. The majority of these reference electrodes are metal electrodes in solution saturated with a low soluble salt of the same metal and an excess of its corresponding anion. These *second type* electrodes exhibit a constant potential against the standard hydrogen electrode and are insensitive against polarization by small currents.

A typical construction of the widely used silver/silver chloride electrode is shown in Fig. 7.3.

The potential of this electrode depends on the concentration of chloride, because the solubility product of the silver chloride determines the activity of the silver ions (Table 7.1). Thus, two equilibria are involved in the potential determination process

$$L = a_{Ag^+} a_{Cl^-} , \tag{7.10}$$

$$E = E^0 + \frac{RT}{F} \ln \frac{L}{a_{Cl^-}} , \tag{7.11}$$

$$E = E^0 + \frac{RT}{F} \ln L - \frac{RT}{F} \ln a_{Cl^-} . \tag{7.12}$$

To prevent contamination of the inner solution an additional salt bridge with a second junction is added in the advanced construction (Fig. 7.3b). Both solutions are separately exchangeable.

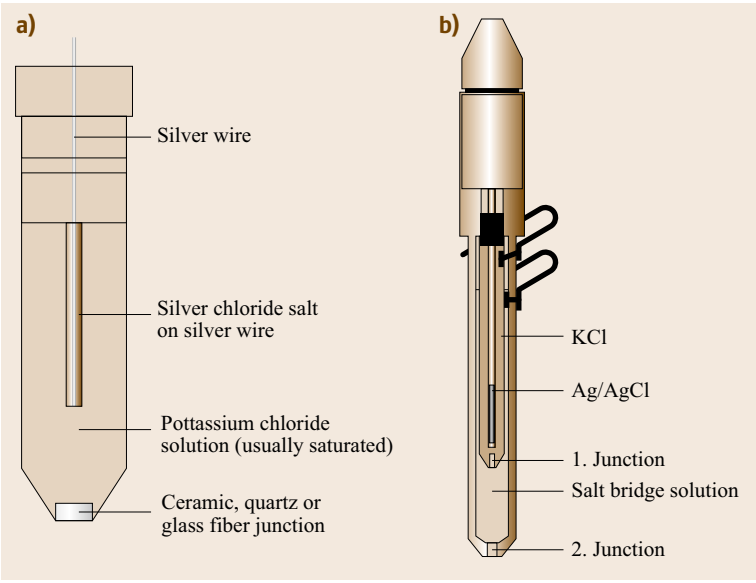


Fig. 7.3a,b Silver/silver chloride electrode. **(a)** Simple reference electrode. **(b)** Double junction reference; the salt bridge solution will be adapted to the analytical problem

Table 7.1 Examples of silver/silver chloride electrodes

Electrolyte	Potential against standard hydrogen electrode (V)	Temperature cofficient at 25 °C (mV/K)
Sat. KCl	+0.197	−1.01
3.5 M KCl	+0.205	−0.73
3.0 M KCl	+0.210	
1.0 M KCl	+0.235	+0.25
0.6 M KCl	+0.250	
Seawater	+0.266	

Table 7.2 Some reference electrodes

Electrode	Potential against standard hydrogen electrode (mV)
Hg/Hg_2Cl_2	+245.0
Hg/Hg_2Br_2	+139.56
Ag/AgBr	+71.31
$Pb/PbSO_4$	−276.0
Ag/AgJ	−152.25

The salt bridge is filled with potassium chloride or nitrate to minimize an additional potential difference at the junction of the salt bridge and the analyte solution. The diffusion coefficients of potassium ions and chloride are nearly the same, thus a minimal diffusion potential is produced.

Other reference electrodes are listed in Table 7.2.

7.1.2 Simple Indicator Electrodes

Whereas the potential of the reference electrode is independent of the analyte, the potential of the indicator electrode should be reliable and be a specific function of the interesting constituent in the solution.

Metal Electrodes

As already shown, the potential of a metal electrode is directly related to the activity of its corresponding ions. The usage of this kind of electrodes is limited because the underlying redox reaction is disturbed if other interfering redox systems are present in the analytical matrix.

Nevertheless, a simple silver wire serves as an indicator in argentometric titrations and since the activity of copper ions is strongly shifted by complexation, a copper wire can be used as indicator for complexometric titrations. It only needs the addition of a small amount of copper ethylenediaminetetraacetate (EDTA)-complex to the solution.

The activity of bismuth ions at the surface of a bismuth electrode is related to the solubility product of the bismuth hydroxide and the hydroxyl ions. In absence of strong oxidizing or reducing agents this electrode is used as a simple and rough pH-electrode. An antimony electrode works analogously.

Inert Electrodes

Noble metal electrodes as well as carbon electrodes are not directly involved in the redox process, but are able to exchange electrons with the redox systems in the surrounding solution. That way the redox potential of a solution is measured and the ratio of a_{ox}/a_{red} of a corresponding redox couple according to the Nernst equation is achieved.

These electrodes are very useful for the registration of redox titrations. The endpoint is indicated as the steepest change of the potential. Contrary to redox titration, the reliability of direct redox potential measurements is often hampered as the electron transition at the electrode is kinetically hindered in many cases, especially in biological systems where redox active macromolecules cannot exchange electrons, because the distance of their redox centers is to far from the surface of the electrode.

7.1.3 Membrane Electrodes

A schematic setup is given in Fig. 7.4 Test solution and reference solution are separated by a permselective membrane and the potential difference is measured by two reference electrodes. Alternatively the inner reference electrode is replaced by a direct metallic contact. As already shown, the transfer of any charge carrier across the border of two separated phases cause a potential difference at the border. If not disturbed, the systems run to an equilibrium where the electrical potential compensates the differences in the chemical potentials of the two phases. Provided the charge transfer is limited to only one ion species, the activity ratio of that ion species is related to the electrical potential between the two phases

$$E = E_{ass} + \frac{RT}{zF} \ln \frac{a_I}{a_{II}} \,. \tag{7.13}$$

In the case of cations z is positive and in the case of anions z is negative. At room temperature (25 °C) the factor RT/F together with a change from the natural to the common decadic logarithm results in a factor of 59 mV. Thus, a tenfold change of activity results in a potential shift of 59 mV in the case of $z = 1$ or 29 mV for $z = 2$. If the two reference electrodes exhibit identical behavior and the membrane is symmetric, then E_{ass} vanishes.

The permeation selectivity of the membrane is crucial for the performance of these ion-selective electrodes.

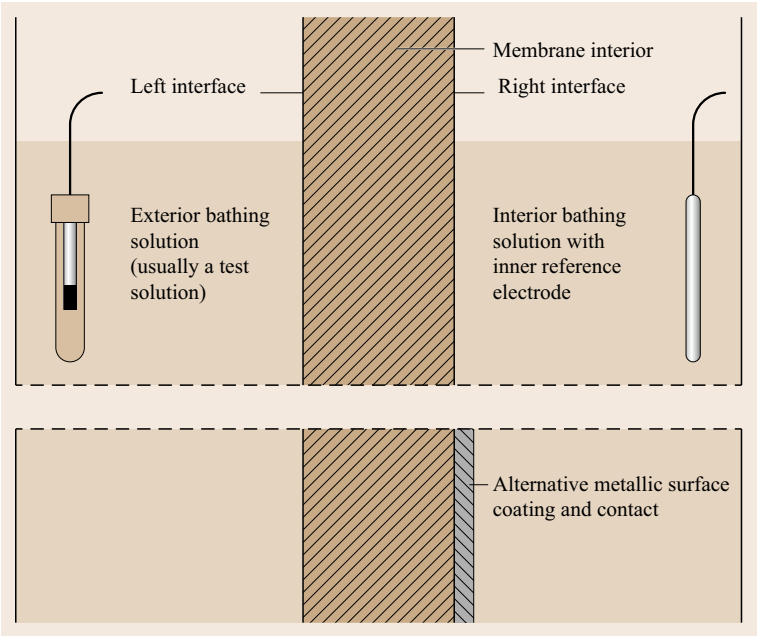


Fig. 7.4 Membrane electrode (after [7.3])

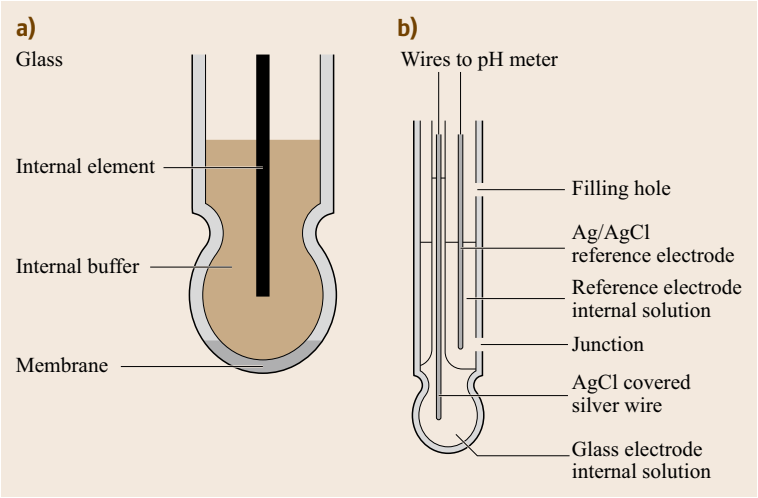


Fig. 7.5 **(a)** A single glass electrode. **(b)** Combined with a silver/silver chloride reference electrode to a one-rod pH sensor

The Glass Electrode

The best selectivity so far is achieved with the H^+ selective glass membranes; nearly all pH measurements are done with this electrode. Since the glass doesn't transport electrons it is insensitive towards oxidizing or reducing agents. The glass electrode is more than hundred years old and a lot of research has been done to gain a closer insight into the potential-forming mechanism as well as to construct robust electrodes for applications in very different media. Often the glass electrode is completed with a reference electrode to a unit in one rod.

A typical construction of a glass electrode is shown in Fig. 7.5.

The best-known glass for pH electrodes is Corning 015 composed of about Na_2O 22%, CaO 6%, SiO_2 72%. In contact with water, the surface layer is hydrated and parts of the sodium ions are exchanged by protons. This gel layer, extending 1–100 nm into the membrane, is responsible for the electrochemical behavior of the electrode.

At high pH values, that means at low hydronium concentrations and high concentrations of univalent cations the glass electrode is even sensitive to sil-

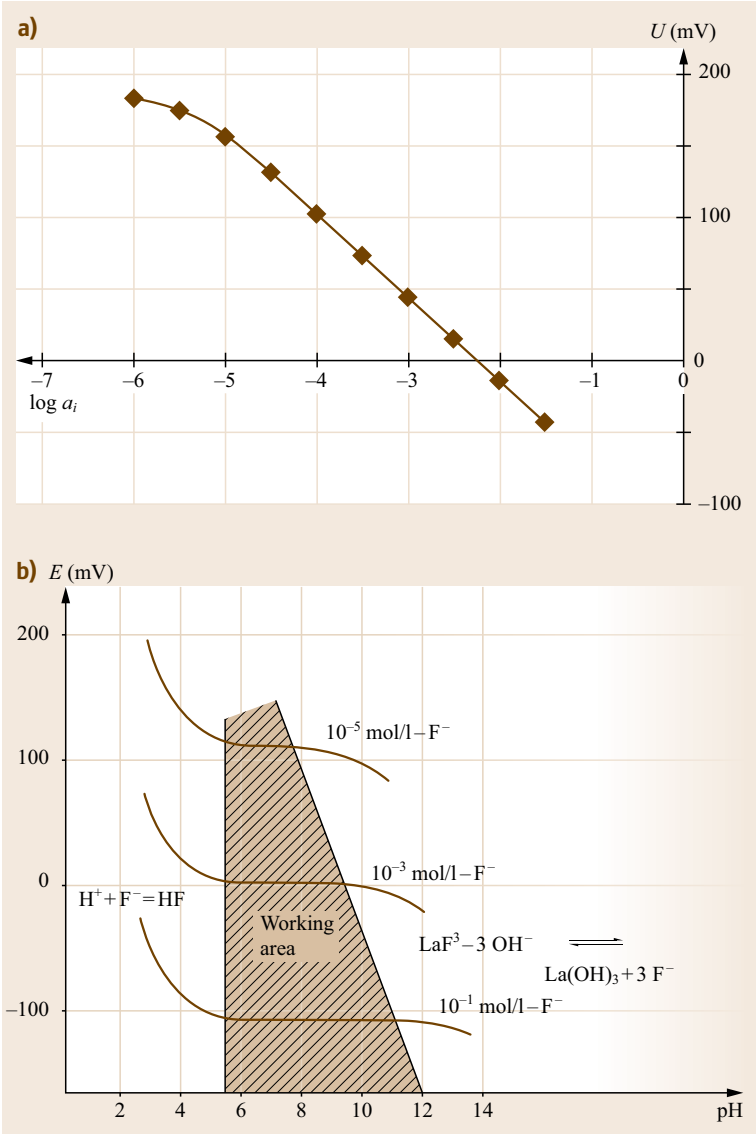


Fig. 7.6a,b Fluoride sensitive electrode. **(a)** Response function. **(b)** Influence of different pH on the working area (after [7.4])

ver, potassium or sodium ions. The sensitivity against sodium ions results in an alkali error in pH measurements. It was found that a part replacement of the sodium component in the glass by lithium diminishes the cross sensitivity towards sodium ions.

On the other side the modification of the glass composition by addition of a certain quantity of alumina results in a sodium-selective electrode. Considering the ion-selective membrane as a selective ion exchanger, the effects of interfering ions can be expressed by the exchange equilibrium between the analyte ion (A_m) at the surface of the membrane and the interfering ion (I_s) from the solution (Sect. 7.1.4)

$$A_m^+ + I_s^+ \leftrightarrows A_s^+ + I_m^+ , \tag{7.14}$$

$$K_{m-s} = \frac{a_{A_s^+} a_{I_m^+}}{a_{A_m^+} a_{I_s^+}} . \tag{7.15}$$

The cross sensitivity of an electrode based on this equilibrium is described by an extension of the Nernst equation introduced by *Nikolsky* and *Eisenmann* [7.5]

$$E = E_{ass} + \frac{RT}{zF} \ln \left[a_A + \sum_{a_I} K_{A-I} (a_I)^{z_A / z_I} \right] . \tag{7.16}$$

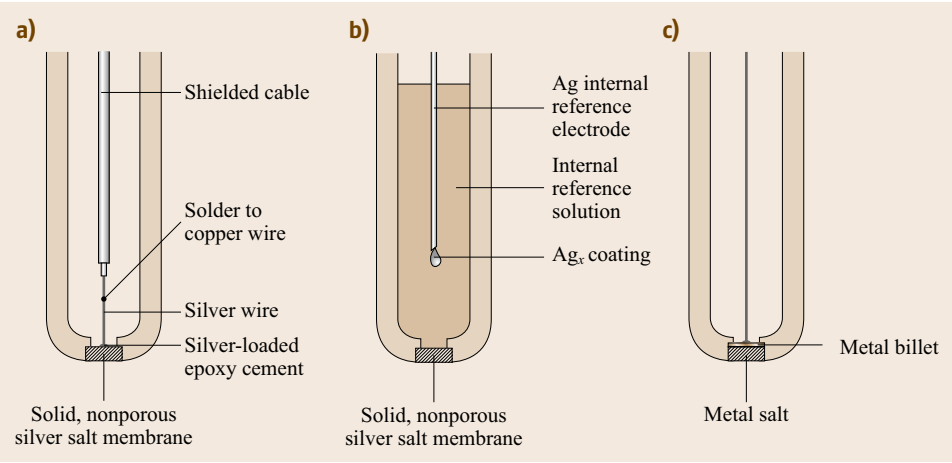


Fig. 7.7a–c Constructions of crystalline membrane electrodes **(a)** All solid state electrode, **(b)** electrode with internal reference solution, **(c)** electrode of the second kind (after [7.3])

This equation is applicable to all ion-selective electrodes.

Crystalline Membrane Electrodes

The membrane of this type of electrodes consists of a single or polycrystalline ion-conducting membrane.

Fluoride Sensitive Electrode

A membrane from a lanthanum fluoride single crystal, doped with EuF_2, transports fluoride ions very selectively. The Eu^{2+} creates lattice vacancies along which the fluoride ions move. Even with a thousand-fold excess of other halide ions and nitrate, phosphate or hydrogen carbonate do not interfere and the electrode shows a Nernstian behavior from concentration ranges $1-1\times10^{-6}\,\mathrm{mol\,l^{-1}}$. In very alkaline solutions the formation of a lanthanum hydroxide layer at the surface of the electrode interferes at low F^- concentrations, and in acidic solutions the fluoride ion associates with the proton, but only the free fluoride ion is measured by the electrode. These two effects define the working area of the electrode as illustrated in Fig.7.6b. As fluoride forms strong complexes with aluminum and ferric ions these ions interfere and must be masked. If true concentrations and not activities are desired as a result, then the electrode must be calibrated and used in solutions of the same ion strength to hold the activity coefficient constant. This is generally realized as in most direct potentiometric determinations by the addition of a total ion strength buffer; it even adjusts the pH to the working range of the electrode.

Silver Sulfide Electrodes

Silver halides and especially silver sulfide exhibit a certain electric conductivity in the solid state. This conductivity is mainly caused by the mobility of the silver ions in this material. Silver sulfide has a very small conductivity for electrons causing a small influence on oxidizing agents. A variety of electrodes are produced on a base of silver sulfide. Selectivity against halides and pseudo halides is achieved by mixing the corresponding silver halides with the basic silver sulfide. The selectivity coefficients of the different halides relate to the solubility product ratio of the incorporated silver salts. Response against other cations such as lead, copper and cadmium is gained by mixing its sulfides to the silver sulfide. The membranes are produced by pressing the powder of the raw material into a tablet or melting it together. This relatively simple procedure results in polycrystalline membranes. Better sensitivity at low concentrations is claimed with a single crystal membrane, due to the lower solubility of the bigger crystals. A typical construction of a solid membrane electrode is shown in Fig. 7.7. The membrane is tightly glued to a plastic (PVC – polyvinyl chloride) tube and the upper part is filled with the reference electrolyte and equipped with a reference electrode. The liquid reference electrolyte in the electrode is regarded as a weak point in the construction of the electrode and there are several attempts to replace it with a solid construction: solidification of the electrolyte by gelling additives, direct contact of the metal, and welded or glued to the membrane. The potential at the direct interface between membrane and metal, the transition from ionic to electronic conductivity, is not well defined and often causes slow drifting of the overall potential. Recently [7.6] these disadvantages have been overcome and very stable all solid-state ion-selective electrodes can now be constructed (Sect. 7.1.6). Table 7.3 shows a collection of some commercial crystal membrane electrodes.

Liquid Membrane Electrodes

These electrodes gain their analytical information from the potential difference at the interface of two immisci-

Table 7.3 A collection of some commercial crystal membrane electrodes

Electrode	Active membrane	Range (mol/l)	Selectivity log[*K*]	Recommended pH-range
Ag^+	Ag_2S	$1-1\times10^{-7}$	Cu^{2+}: −6 Pb^{2+}: −6	2–9
Cu^{2+}	CuS/Ag_2S	$0.1-1\times10^{-8}$	Ag^+, Hg^{2+} must be absent	0–14
Cu^{2+}	CuSe single crystal	$1-1\times10^{-6}$	Pb^{2+}: −3 Cd^{2+}: −5 Ag^+: 6 Hg^{2+}: 4	0–14
Cd^{2+}	CdS/Ag_2S	$0.1-1\times10^{-7}$	Ag^+, Hg^{2+} must be absent Fe^{2+}: 2.3 Pb^{2+}: −0.3 Zn^{2+}: −1	1–14
Pb^{2+}	PbS/Ag_2S	$0.1-1\times10^{-6}$	Ag^+, Hg^{2+}, Cu^{2+} must be absent Zn^{2+}: −3.5 Fe^{3+}: 0 Cd^{2+}: 0	2–14
S^{2-}	Ag_2S	$1-1\times10^{-6}$	Traces of Hg^{2+} interfere, proteins must be absent Cl^-: −15 J^-: −9 CN^-: −2	13–14
Cl^-	$AgCl/Ag_2S$	$1-1\times10^{-7}$	Br^-: 2 J^-: 3	1–5
F^-	LaF_3 single crystal	$1-1\times10^{-6}$	Cl^-: −4 Br^-: −4 NO_3^-, SO_4^{2-}: < −3	4–8

ble liquid phases, the aqueous sample and the organic membrane phase. The liquid organic phase is often fixed in the pores of a hydrophobic porous membrane. Some constructions of such electrode are shown in Fig. 7.8. For better handling the liquid membrane may be solidified by the addition of polymers with no change of the working principle.

Liquid Ion Exchangers

Glass electrodes and the silver sulfide electrodes may be regarded as ion exchangers with fixed ions. On this basis several organic and inorganic solid ion exchangers have been tested as materials for ion-selective electrodes. These tests failed because the mobility of the probed ion is drastically reduced when bound to a fixed

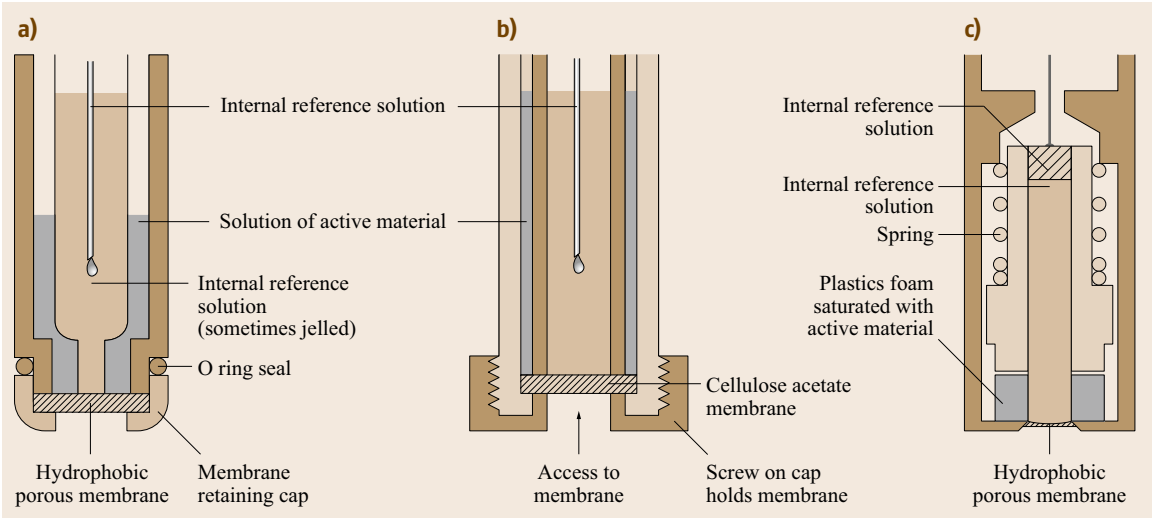


Fig. 7.8a–c Constructions of liquid membrane electrodes (a,b) allow easy replacement of the membranes and (c) contains a reservoir of the active material in a foam (after [7.3])

charge in the ion exchanger. In the liquid phase the complex between the measured ion and the dissolved ion exchanger is mobile. The specific ion exchanger is dissolved in a polar, but not water miscible, organic solvent and the specific charge transfer from the aqueous to the organic phase governs the potential difference at the interface. For stability of the electrode the boiling point of the organic phase should be high to avoid evaporation. The affinity of the ion exchanger to the analyte ion should be high and the ion pair very hydrophobic and nonsoluble in water. The organic phase contains the ion exchanger with the analyte as a counter ion. As solvents, long chain alcohols are used, or nitrobenzene or nitrophenylethers. If the interaction between the liquid ion-exchanger and the analyte ion only consists of electrostatic attraction of the oppositely charged sites, then the selectivity between different sensed ions is dictated mainly by the extraction behavior of the solvating membrane medium. The ionic extraction constants are comparatively small for ions that are strongly hydrated in the aqueous phase and large for lipophilic organic ions.

Therefore the following sequence (Hofmeister row) is obtained for membrane electrodes based on cation exchangers, e.g., tetraphenylborate in nitroaromatic solvents

$$NBu_4^+ > Cs^+ > Rb^+ > K^+ > Na^+ > Li^+ .$$

An analogous sequence is obtained for anion exchangers (e.g., quarternary ammonium salts)

$$Ac^+ > ClO_4^- > I^- > NO_3^- > Cl^- > F^- .$$

A liquid membrane needs a special construction of the electrode to hold the liquid in place.

Therefore their use is limited to special applications such as microelectrodes for intracellular measurements, and most commercial electrodes use solidified liquid membranes working on the same theoretical background.

Tiny glass capillaries with an inner diameter lower than a micrometer are used for monitoring of ion activities in living cells. The ion-selective liquid is placed at the tip and fixed by the capillary adhesion (Fig. 7.9).

Solidification is achieved by addition of polymers such as PVC, polyacrylates or silicon rubber to the liquid. The construction of solidified membrane electrodes is quite simple as shown in Fig. 7.10.

The inner solution with the reference electrode is partly solidified by the addition of a hydrogel like poly(hydroxyl ethyl acrylate). The simplest constructions are the *coated wire electrodes*. They are easy to prepare by dipping a gold, silver or platinum wire into a solution of the ion selective cocktail and isolate the rest of the metal. Unfortunately these electrodes are suffering from drift and other instabilities, because the transition of charge from the membrane to the metal is not really defined. Newer developments successfully overcame these shortcomings and now some all-solid-state electrodes with superior stability and sensitivity are available. The principle of these electrodes will be discussed in Sect. 7.1.6.

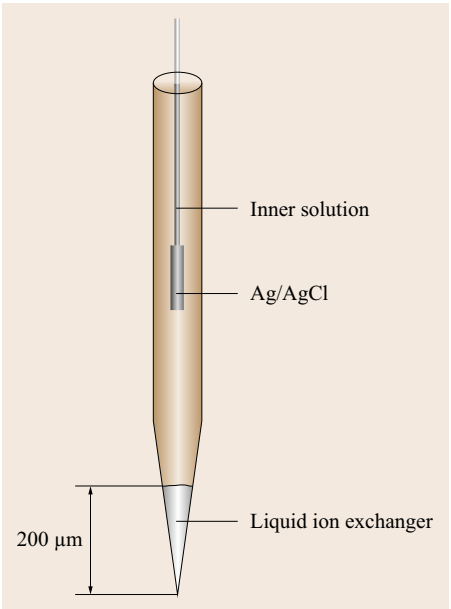


Fig. 7.9 Ion-selective microelectrode with liquid ion exchanger

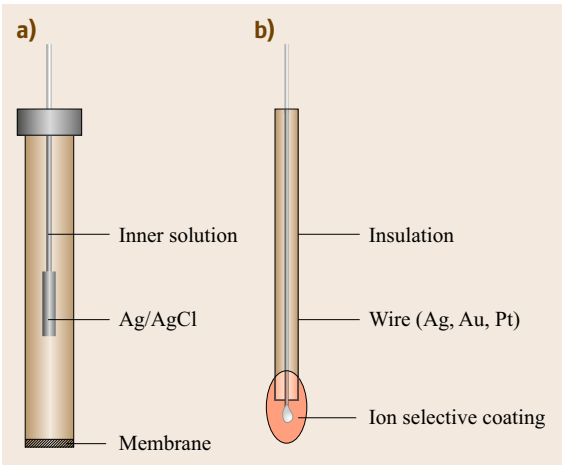


Fig. 7.10a,b Ion-selective polymer membrane electrode. **(a)** With inner reference. **(b)** Coated wire electrode

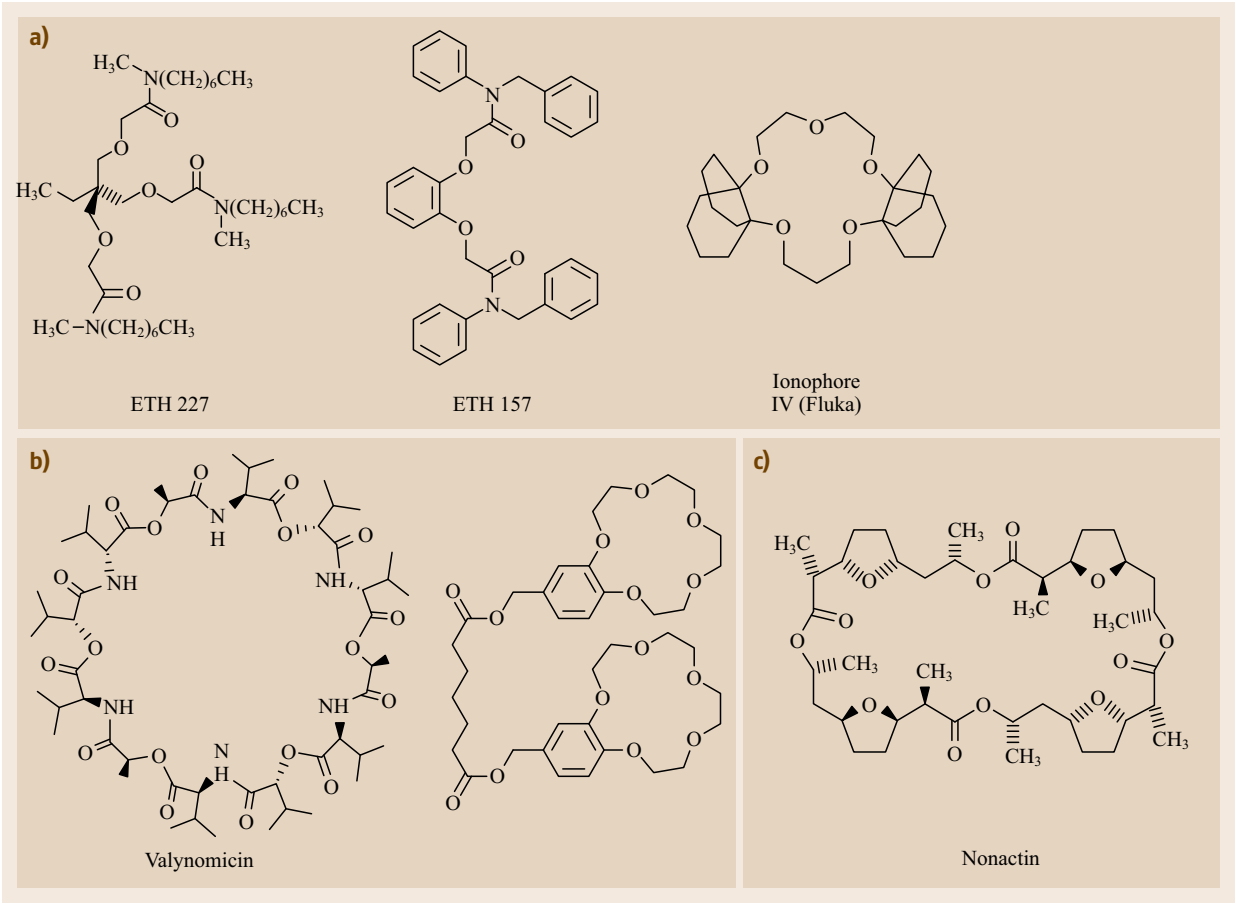


Fig. 7.11a–c Ion carriers for alkali cations **(a)** Na^+, **(b)** K^+, **(c)** NH_4^+ (after [7.7])

A typical recipe for a nitrate sensitive electrode [7.7]:

- 6 wt% Tridodecylmethylammonium nitrate as an ion exchanger
- 65 wt% 2-Nitrophenyl octyl ether as a solvent
- 29 wt% PVC as a solidifier.

Neutral Ion Carriers

Another possibility to specifically force the exchange between the aqueous analyte and the hydrophobic membrane is a complexation of the ion to be measured with a hydrophobic ligand. The selectivity of the electrode then depends on the selectivity of the complex formation. Particularly for the determination of alkali and alkali earth ions, very selective ligands have been designed. Beside the natural antibiotics valinomycin and nonactin, most of the ligands have been tailored in the group of Simon at *ETH Zürich* [7.8]. Some samples are shown in Fig. 7.11 and 7.12.

Table 7.4 Examples of some liquid membrane electrodes

Electrode	Membrane	Solvent
Ca^{2+}	Ca-di(*n*-decyl) phosphate	di(*n*-octylphenyl) phosphonate
Ca^{2+}, Mg^{2+} water hardness	Ca-di(*n*-decyl) phosphate	Decanol
ClO_4^-	Tris(substituted 1,10-phenanthroline) Ni(II)-nitrate	*p*-nitrocymene

The extraction of charged ions into the membrane needs to compensate for this charge. This is done by the addition of a hydrophobic counterion into the membrane.

A typical cocktail of a potassium selective electrode:

- 1.0 wt % Valinomycin as an ionophore
- 0.5 wt % Potassium tetrakis (4-chlorophenyl) borate as a counteranion
- 49.5 wt % Bis (2-ethylhexyl) sebacate as a solvent
- 49.0 wt % PVC 1.8% carboxylated as a solidifier.

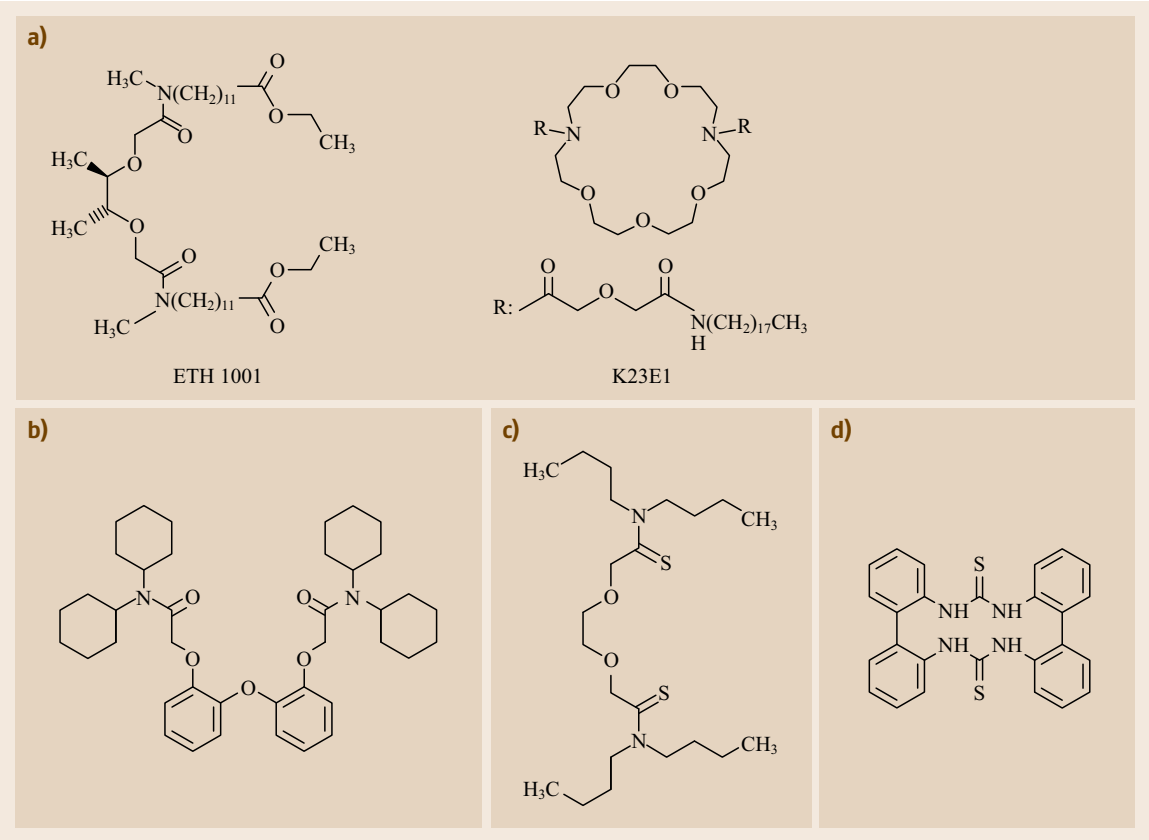


Fig. 7.12a–d Ion carriers for earth alkali cations and nitrate **(a)** Ca^{2+}, **(b)** Ba^{2+}, **(c)** Cd^{2+}, **(d)** NO_3^-

As countercation for the nitrate electrode a small amount of tridodecylammonium (nitrate) is added. A brief selection of liquid membrane electrodes with the used ion carriers is given in Table 7.4.

7.1.4 Characterization of Ion-Selective Electrodes

As already pointed out, the equilibrium potential difference between both sides of an ion-selective membrane strictly corresponds to the difference in the thermodynamically defined chemical potentials on these sides.

This behavior is expressed by the Nernst equation and does not depend on a special structure of the ideal ion-selective membrane.

In practice, however, deviation from this ideal behavior is experienced and a huge amount of research has been undertaken to find out the reasons for this nonideal behavior.

Different levels of theory have been developed for the qualitative and quantitative description of the effects, and resulting theoretical understandings of the potential forming processes at and in the membranes have even resulted in improved sensors and in the last decade to a *new wave of ion-selective electrodes* [7.9].

Potentiometric Response

The most important information for the user of ISEs is the selectivity and the lower limit of detection. Fig. 7.13 shows a typical calibration curve for a univalent cation. Due to leaching of the main ion from the membrane and the influence of interfering ions in the matrix, the electrode becomes more and more insensitive at low concentrations and finally the calibration curve becomes parallel to the activity axis. The detection limit is the intercept of the Nernstian part and the constant part of the calibration curve.

Selectivity Coefficients

The selectivity coefficient can be calculated from the difference between the calibrating curve of the main ion and the interfering ion. Two possible methods of evaluation can be derived based on the Nikolsky equation.

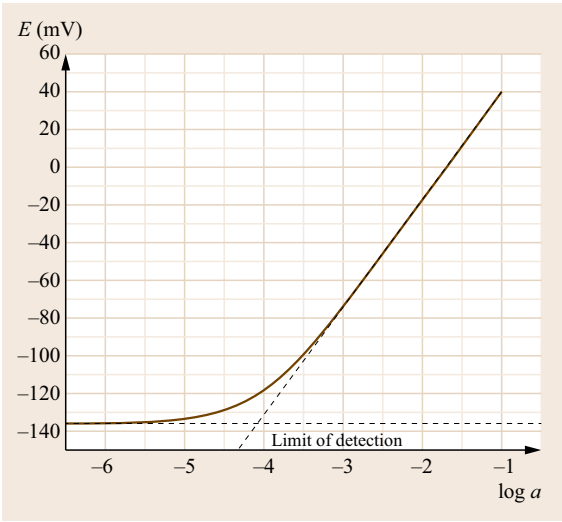


Fig. 7.13 Response function and detection limit of an ion-selective electrode, according to the Nikolsky–Eisenman-equation

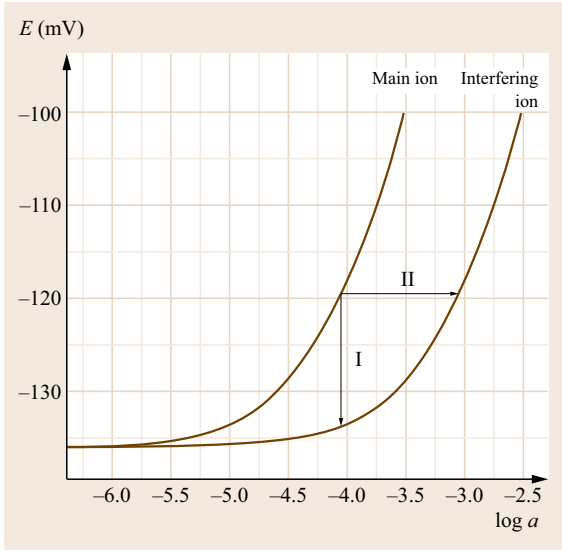


Fig. 7.14 Determination of selectivity coefficients

From the potential difference at the same concentration (I in Fig. 7.14)

$$\log(K_{i,j}) = \frac{E_2 - E_1}{S} , \qquad (7.17)$$

or the ratio of the activities at the same potential (II in Fig. 7.14)

$$\log(K_{i,j}) = \frac{a_i}{a_j} . \qquad (7.18)$$

It is evident that the selectivity coefficient depends on the concentration, because the deviation from Nernstian response of an electrode in a solution of the pure main ion is usually not included in the Nikolsky equation. More realistic data are obtained from calibration curves of the main ion in the presence of constant concentrations of the interfering ions.

After a sudden change of concentration the potential response needs some time to attain the equilibrium value. The response time during which 90% of the final value is reached depends on the concentration and is about five times longer at a transition from concentrated solutions to diluted than vice versa. To establish a new equilibrium at the surface of the ISE, ions must be transported from and to the surface. This process it facilitated by stirring the bathing solution.

7.1.5 Direct Potentiometric Determination of Concentrations

According to the Nernst equation the potential of an indicator electrode is related to the activity of the measured ion in the surrounding solution. This may be a great advantage as very often e.g., in physiology or reaction kinetics and equilibria the field is governed by activities rather than real concentrations. If the concentration data are wanted, then the activity coefficients of the calibration solution and the analytical matrix must be the same. This can be achieved by adjusting the ion strength of sample and standard solutions by the addition of a so-called total ion strength adjustment buffer (TISAB). The additives of this buffer have to be adapted to the analytical problem. In particular, the ions in the buffer should not interfere with the indicator electrode. Not only the ion strength, but the pH is also adjusted by the TISAB to assure a proper working range.

Some examples of ion strength buffers are listed in Table 7.5.

There is no need for ion strength adjustment if calibration and analytical measurement is done in the same matrix. Standard addition is a suitable method to avoid extensive matrix modification and sample preparation.

The addition of inert salts, however, increases the conductivity of the sample, resulting in a short cut of environmental electrical noise and prevents electrokinetic disturbances, caused in streaming media by charge separation at the walls of vessels or tubes.

7.1.6 Models of ISE Response

As the analytical signal is produced at the phase boundary, every change in the bulk analyte composition initiates transport of ions and charge to and from the boundary to establish a new equilibrium. Therefore the potentiometric response is a complex phenomenon that

Table 7.5 Total ion strength adjustment buffer (TISAB) (after [7.10])

Measuring ion	TISAB	For 100 ml solution
Ag^+	$c(KNO_3)$= 1 mol l^{-1}	10.110 g
$BF4^-$	$c[(NH_4 2SO_4]$= 2 mol l^{-1}	26.427 g
Br^-	$c(KNO_3)$= 1 mol l^{-1} or $c(NaNO_3)$= 2 mol l^{-1}	10.110 g 16.999 g
Ca^{2+}	c(KCl)= 1 mol l^{-1}	7.455 g
Cd^{2+}	$c(KNO_3)$= 1 mol l^{-1}	10.110 g
Cl^-	$c(KNO_3)$= 1 mol l^{-1} or KNO_3, Ammonium acetate, Glacial acetic acid or $c(NaNO_3)$= 2 mol l^{-1}	10.110 g 5.06 g 3.85 g 2.8 ml 16.999 g
CN^-	c(NaOH) = 0.1 mol l^{-1}	0.400 g
Cu^{2+}	$c(KNO_3)$= 1 mol l^{-1}	10.110 g
F^-	NaCl G lacial acetic acid Trans-1,2-Diamino-cyclohexane-N,N,N,N-tetraacetic acid monohydrate (CDTA, Komplexon IV)	5.84 g 5.75 ml 0.45 g
I^-	$c(KNO_3)$= 1 mol l^{-1} or $c(NaNO_3)$= 2 mol l^{-1}	10.110 g 16.999 g
K^+	c(NaCl) = 1−0.1 mol l^{-1}	5.844−0.584 g
Na^+ (glass)	Trishydroxymethyl aminomethane $c[(HOH_2 C_3CNH_2]$= 1 mol l^{-1} or triethanolamine	12.114 g 7.5 ml
Na^+ (plastic)	$c(CaCl_2)$ = 1 mol l^{-1}	14.702 g $CaCl_2$ $2H_2O$
NO_3^-	$c[(NH_4)_2SO_4]$= 1 mol l^{-1} or $c[Al_2(SO_4)_3]$= 0.1 mol l^{-1}	13.213 g 3.421 g
Pb^{2+}	$c(NaClO_4$ $H_2O)$= 1 mol l^{-1}	14.046 g
S^{2-}	c(NaOH)= 2 mol l^{-1}	7.999 g
SCN^-	$c(KNO_3)$ = 1 mol l^{-1} or acetate buffer pH = 6, $c(CH_3COO^-)_{tot}$= 1 mol l^{-1}	10.110 g

depends on time, the electroactive material and the bathing solution (the analyte) as well as the membrane–solution interface, and their composition and thermodynamic and kinetic properties. The classical total equilibrium models neglect the kinetic effects and assume the membrane potential as a sum of the phase boundary potential and the diffusion potential in the membrane.

In the simple phase boundary model some idealizing assumptions are used:

- No migration effects in the membrane, resulting in zero diffusion potential
- Electroneutrality in the membrane, except the boundary
- Electrochemical equilibrium at the sample–membrane interface
- Solution and membrane phases are ideally immiscible
- No flux of solvent through the membrane.

The phase boundary potential is then

$$E_{PB} = \frac{RT}{z_i F} \ln k_i + \frac{RT}{z_i F} \ln \frac{a_i}{\overline{a}_i} , \qquad (7.19)$$

with a_i the activity of the main ion in the solution and $\overline{a_i}$ the activity of the main ion in the membrane; k_i is an ion partition constant between solution and membrane.

Introducing the exchange equilibrium constant between the main ion i and the interfering ion j at the membrane surface

$$K_{i,j} = \frac{k_j}{k_i} = \frac{a_i \overline{a}_j}{a_j \overline{a}_i} . \qquad (7.20)$$

Simple calculation results in an expression like the Nikolsky equation

$$\frac{a_i}{\overline{a}_i} = \frac{a_i(\overline{a}_i + \overline{a}_j)}{\overline{a}_i(\overline{a}_i + \overline{a}_j)} = \frac{a_i + \frac{a_i \overline{a}_j}{\overline{a}_i}}{(\overline{a}_i + \overline{a}_j)} = \frac{a_i + K_{i,j} a_j}{(\overline{a}_i + \overline{a}_j)} . \qquad (7.21)$$

Since

$$(\overline{a}_i + \overline{a}_j) = \text{const.} ,$$

$$E_{PB} = \text{const.} + \frac{RT}{z_i F} \ln(a_i + K_{i,j} a_j) . \qquad (7.22)$$

Note that the charge number of the main and interfering ion are the same.

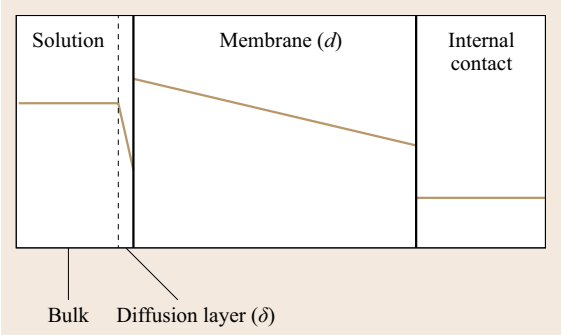


Fig. 7.15 Concentration profiles assumed for the local-equilibrium models (after [7.11])

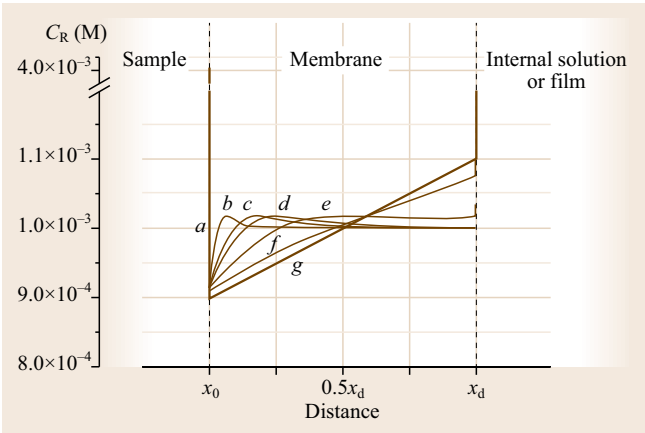


Fig. 7.16 Time-dependent concentration profiles for site $R^-([i^+])$ 1×10^{-4}, $[j^+]$ 1×10^{-3}, $D_i/Dh_j0.5$, $K_{i,j}0.1$, and R_{total} 1×10^{-3}. Curves *a–g* show profiles for: (*a*) 4×10^{-4}, (*b*) 1.64, (*c*) 13.1, (*d*) 26.2, (*e*) 104.8, (*f*) 420, and (*g*) 13 440 s (steady state) (after [7.12])

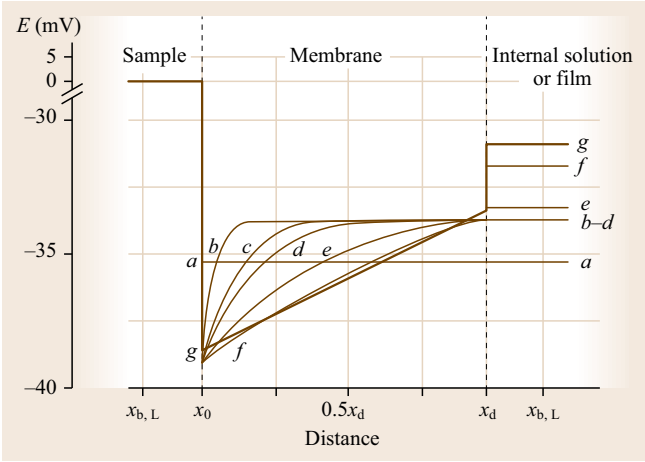


Fig. 7.17 Time-dependent and distance-dependent potential profiles. Curves *a–g* show profiles after the following: (*a*) 4 1×10^{-4}, (*b*) 1.64, (*c*) 13.1, (*d*) 26.2, (*e*) 104.8, (*f*) 420, and (*g*) 13 440 s (steady state) (after [7.13])

Eisenman introduced the migration effect in the phase boundary model. For instance, the equation for the fully dissociated ion exchanger case was derived in the form

$$E_M = E_{PB} + E_D = \text{const.} + \frac{RT}{z_i F}\ln\left(a_i + \frac{\overline{u_j}}{\overline{u_i}}K_{i,j}a_j\right), \quad (7.23)$$

where $\overline{u_i}$ and $\overline{u_j}$ are the mobilities of the respective ions in the membrane.

Despite the simplicity of the total equilibrium model the explicit solution is only possible if the main and interfering ions exhibit the same charge. The often applied Nikolsky–Eisenman equation (7.16) is a (semi) empirical expression, however, it has been proven as very useful in practice. It provides a semiquantitative description of most experiments with ion-selective electrodes and the basis of their evaluation.

Local-Equilibrium Models

In these models, called the diffusion layer models (DLM), ion fluxes result in a steady state concentration profile at the solution–membrane interface. The concentrations depend on the distance perpendicular to the membrane but not on time. See the concentration profile in Fig. 7.15.

Instead of bulk concentrations the local concentrations are used to calculate the potentials. The driving force of the diffusion is the exchange of the main ion and the interfering ion at the solution–membrane interface resulting in a linear concentration profile when the steady state condition is reached. Before the steady state condition is reached potential and selectivity coefficients change with time (Fig. 7.16 and 7.17).

It is predicted that for short readout times the selectivity is a function of the ratio of the diffusion coefficients and not K_{ij}. This can be used for *kinetic discrimination*.

The diffusion layer model was very useful in explaining how poor selectivity and detection limits are caused by increased concentration of the main ion at the membrane surface due to diffusion of this ion from the membrane phase into the solution. *Sokalski* et al. used this approach to find an equation for the detection limit versus concentrations of ions in the inner solution and other parameters [7.13].

The steady state concentration of the main ion at the surface of the membrane is related to the diffusion coefficients of the ion in the membrane and in the bathing solution, respectively

$$c_{io} = c_i + \frac{\overline{D_i}\partial}{D_i d}(\overline{c_{io}} - \overline{c_{id}}) . \quad (7.24)$$

Figure 7.18 shows the calculated (electro motoric force, EMF) functions for the ISE with the same membrane but different primary ion concentrations in the inner solution. It even predicts the way to improve the detection limit of membrane electrodes.

Advanced Nonequilibrium Methods

Despite the merits of the DLM, the kinetic of the sensor is reduced to the diffusion and the influence of the charge- and field distribution on the motion of ions is

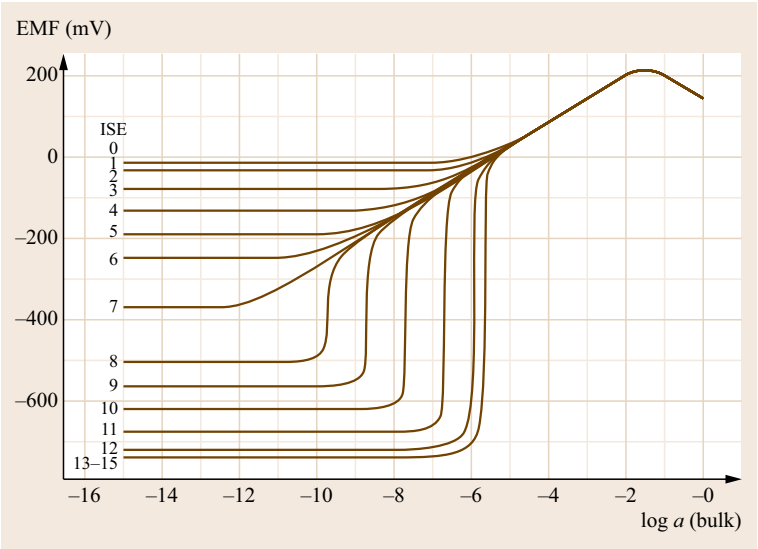


Fig. 7.18 Calculated EMF functions for a series of ISEs having the same membrane but different primary ion concentrations, c_i in the internal solution, from $1-1\times10^{-15}$ M in the inner solution. Curves are labeled with the corresponding negative logarithm (after [7.14])

ignored. The advanced nonequilibrium methods omit the idealizing assumptions of the classical models and regard the motions of ions in the membrane and the adhering solutions as a result of the gradients of concentrations and the local electrical fields that are a result of the charge separation. The condition of electroneutrality is no longer presumed and the equilibrium is replaced by reaction rates.

Sokalski and *Lewenstam* [7.15] used the Nernst–Planck equations to describe the ion fluxes in space (only one dimension perpendicular to the membrane, reduced to the surface area) and time

$$f_i(x,t) = -D_i\left[\frac{\partial c_i(x,t)}{\partial x} - z_i c_i(x,t)\left(\frac{F}{RT}\right)E(x,t)\right], \tag{7.25}$$

where $f_i(x,t)$ is the flux of the i-th ion, $c_i(x,t)$ is the concentration of the i-th ion in space point x and time t, $E(x,t)$ is the electric field, D_i is the diffusion coefficient of the i-th ion, and z_i is the charge of the i-th ion.

The ion fluxes cause an electrical current that is taken into account by the Poisson equation

$$I(t) = F\sum_i z_i f_i(x,t) + \varepsilon\frac{\partial E(x,t)}{\partial t}, \tag{7.26}$$

where $I(t)$ is the total current density and ε is the dielectric permittivity.

The equation system is further completed by mass conservation

$$\frac{\partial c_i(x,t)}{\partial t} = \frac{\partial f_i(x,t)}{\partial x}. \tag{7.27}$$

The kinetic of the ion extraction to and from the membrane is introduced as

$$f_{i0}(t) = \vec{k}_i c_{i,\mathrm{bL}} - \vec{k}_i c_{i,\mathrm{b0}}(t), \tag{7.28}$$

$$f_{id}(t) = -\overleftarrow{k}_i c_{i,\mathrm{bR}} + \overleftarrow{k}_{id}(t), \tag{7.29}$$

where f_{i0}, f_{id}, c_{i0}, and c_{id} are the fluxes and concentrations at $x = 0$ and $x = d$ (where d is membrane thickness), respectively; $\vec{k}_i$ and $\overleftarrow{k}_i$ are the forward and backward rate constants, respectively, and their ratio is a partition coefficient; and $c_{i,\mathrm{bL}}$ and $c_{i,\mathrm{bR}}$ are the concentrations in the bathing solutions on the left (L) and right side (R) of the membrane, respectively.

The numerical evaluation of this complex system of partial differential equations is easily done in the framework of commercial finite element computer programs.

In principle the advanced models are able to simulate all the effects, known from the practical application of these electrodes, especially the time dependence and distortions of the response curve against the main ion and the course of selectivity and the detection limit.

They are valuable tools in the development of new electrodes and improved analytical protocols. Certainly, as seen from the equations above, the models require more data input for calculation. To get such data as permittivity of the membrane or rate constants of ion partitions requires additional instruments of investigation such as voltammetry and impedance spectrometry. Some results may illustrate the utility of these calculations.

Contrary to the assumptions used in the classical models, the distribution of the ion binding sites in the

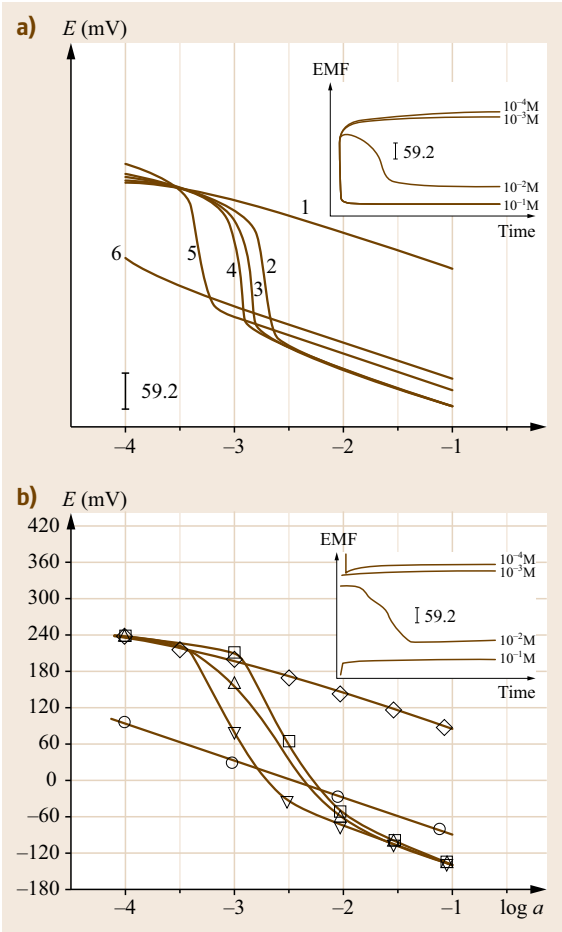


Fig. 7.19a,b Theoretical and experimental calibration curves for the ion-exchanger electrode chloride ion selective sensor (ISS). **(a)** Calibration curves calculated for membrane conditioned in i^- and j^- for solutions of (1) j^- (5 min), (2) i (5 min), (3) i (15 min), (4) i (30 min), and (5) i (60 min), and (6) calibration curve obtained with a membrane conditioned in i^- for a solution of i^- (60 min). i is the preferred ion, and j is the discriminated ion. The *inset* shows the EMF time dependence for an ISE conditioned in discriminated ion for 1×10^{-4}, 1×10^{-3}, 1×10^{-2}, and 1×10^{-1} M. **(b)** Calibration curves obtained with a membrane conditioned in Cl^- for solutions of Cl^- (5 min/conc.), (0) ClO^- (5 min/conc.), (Δ) ClO^- (15 curves obtained with a membrane conditioned in Cl min/conc.), (3) ClO^- (30 min/conc.). Calibration curve obtained with a membrane conditioned in ClO^- for a solution of (O) ClO^- (60 min/conc.) ClO_4 is the preferred ion, and Cl is the discriminated ion. The inset shows the EMF time dependence for an ISE conditioned in Cl^- for 1×10^{-4}, 1×10^{-3}, 1×10^{-2}, and 1×10^{-1} M (after [7.16])

membrane is not constant in space and time, but the ion exchange between the bathing solution and the membrane causes at first a nonlinear profile of the binding sites and only after 7 min is a nearly linear profile reached, (Fig. 7.16).

Whereas in equilibrium models the potential in the membrane is assumed to be locally independent, the advanced theory enabled the potential distribution across the membrane and its dependence on time. The total potential of the electrode corresponds to the integral of the local potential over the membrane

$$E_M(x,t) = \int_{x_{b,L}}^{x_{b,R}} E(x,t)\mathrm{d}x\,, \qquad (7.30)$$

where $x_{b,L}$ and $x_{b,R}$ are the points in the bulk of bathing sample solution (on the left, L) and internal solution/film (on the right, R).

The nonideal behavior of ion-selective electrodes in solutions with an interfering ion is illustrated in Fig. 7.19, where a pretreatment of the electrode with the interfering ion results in a change of the response curve. The comparison of calculated and measured curves proves that the advanced model adequately describes the processes inside the ISE.

7.1.7 All Solid-State Electrodes

To overcome the barrier between the ion conducting membrane and the electron conducting metal and to prevent polarization at the interface, a reversible redox system or a high capacitive layer must be inserted between the metal and the membrane. The conductive organic polymers such as polypyrrol, polyanilin and polythiophene derivatives offer a very convenient transition from electrons to ions (Fig. 7.20). The polymers directly grow from a solution of the monomers on an inert electrode by electrochemical oxidation. Further oxidation generates cationic sites and the corresponding amount of anions is intercalated in the layer.

Thus the uptake of an anion results in a transfer of an electron to the metal and vice versa. The capacity of these polymers is high enough to prevent potential shifts in the case of a low current. The stability of this kind of redox layer is limited by side reactions such as the reaction with oxygen and chemical degradation. If water penetrates the membrane it sometimes destroys the contact between the membrane and the conducting polymer, forming an additional layer; instable interface potentials and a bad performance of the electrode are the consequences. In an effort to optimize these types of all solid-state electrodes a variety of conducting poly-

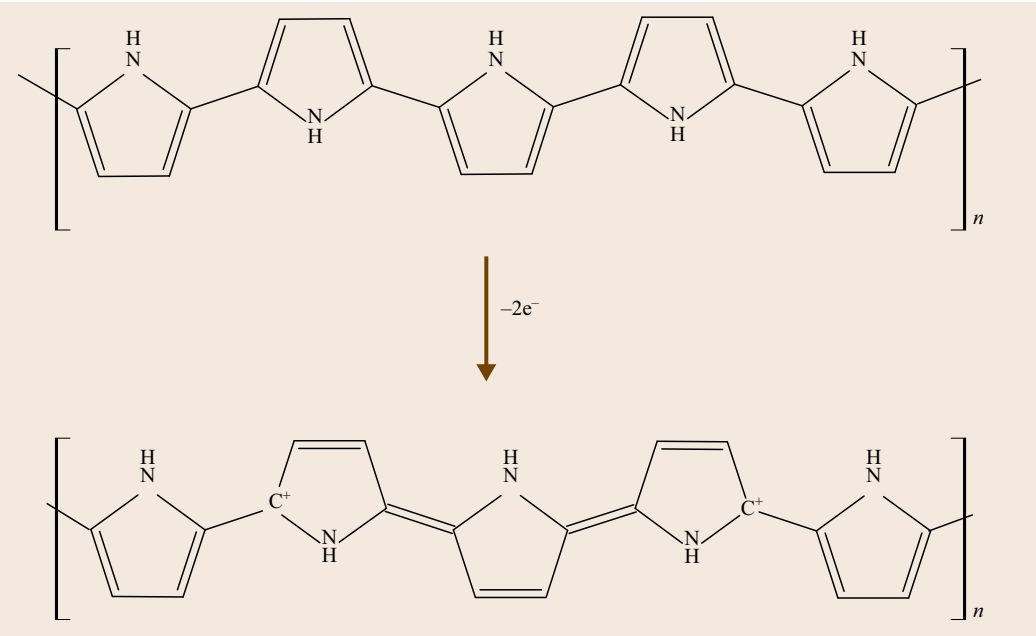


Fig. 7.20 Polypyrrol after polymerization; the polypyrrol is stepwise further oxidized yielding radical cations and dications

mers have been tested. Some examples are given in Fig. 7.21.

Good performance was achieved with polymerized thiophene derivatives such as Poly(3-octyl thiophene) (POT, formula given in Fig 7.21c), which is highly lipophilic and prevents the inclusion of water. Besides the electrochemical grafting the polymer can be dissolved in organic solvents and easily casted onto the metal. As the ion exchange in the conducting polymer in principle is the same as in the overlaying ion-selective membrane, it is also possible to omit the plastic membrane and to incorporate the ion-recognition sites in the conducting polymers as immobilized doping ions. The polymers themselves are used as sensing membranes. On the other side soluble redox polymers have been added to the membrane forming a cocktail to ensure electron transfer in coated wire electrodes. As the redox active polymer comes in direct contact with the sample solution such electrodes are sensitive against redox active agents in the sample.

Another approach to facilitate the ion–electron charge transfer is to enhance the double layer capacity at the interface. This is achieved by the application of carbon black, carbon nanotubes, graphenes, fullerene and other conducting nanoparticles at the interface between the electronic conductor and the membrane. This technique has already been established in the construction of supercapacitors.

All these developments not only bear the possibility of miniaturization, but even the mass production of inexpensive sensors by highly automated processes such as ink jet printing of the sensor materials onto paper, plastics or ceramic [7.17]. All techniques developed for the production of electronic printed boards as well as integrated circuits have been tried as platforms for the preparation of ion-selective electrodes and arrays of them even in combination with other sensors and micromechanics. These sensors are compatible with flow analyzers and micro analytical systems (μ-TAS (total analytical system)).

Beside the indicator electrode the complete sensor system needs an adequate reference electrode. This part of miniaturized sensors causes the most troubles and is often neglected.

The classical silver/silver chloride system often incorporated in a gel and covered by a porous membrane can be used. A plasticized PVC reference membrane containing equimolar amounts of both cation and anionexchanger, potassium tetrakis (4-chlorophenyl) borate and methyltri- dodecylammonium chloride, together with solid potassium chloride and silver chloride with traces of silver over a polymer conductive layer was proposed [7.6].

Depending on the analytical problem, instead of a conventional reference electrode the voltage is alternatively measured against a second ISE. If the sample is buffered to a constant pH, then a pH sensor is a suitable reference. A constant chloride ion concentration allows a Cl^- Sensitrode as reference. In flow systems it is possible to use identical ISEs, one flushed with a standard solution, the other with the sample.

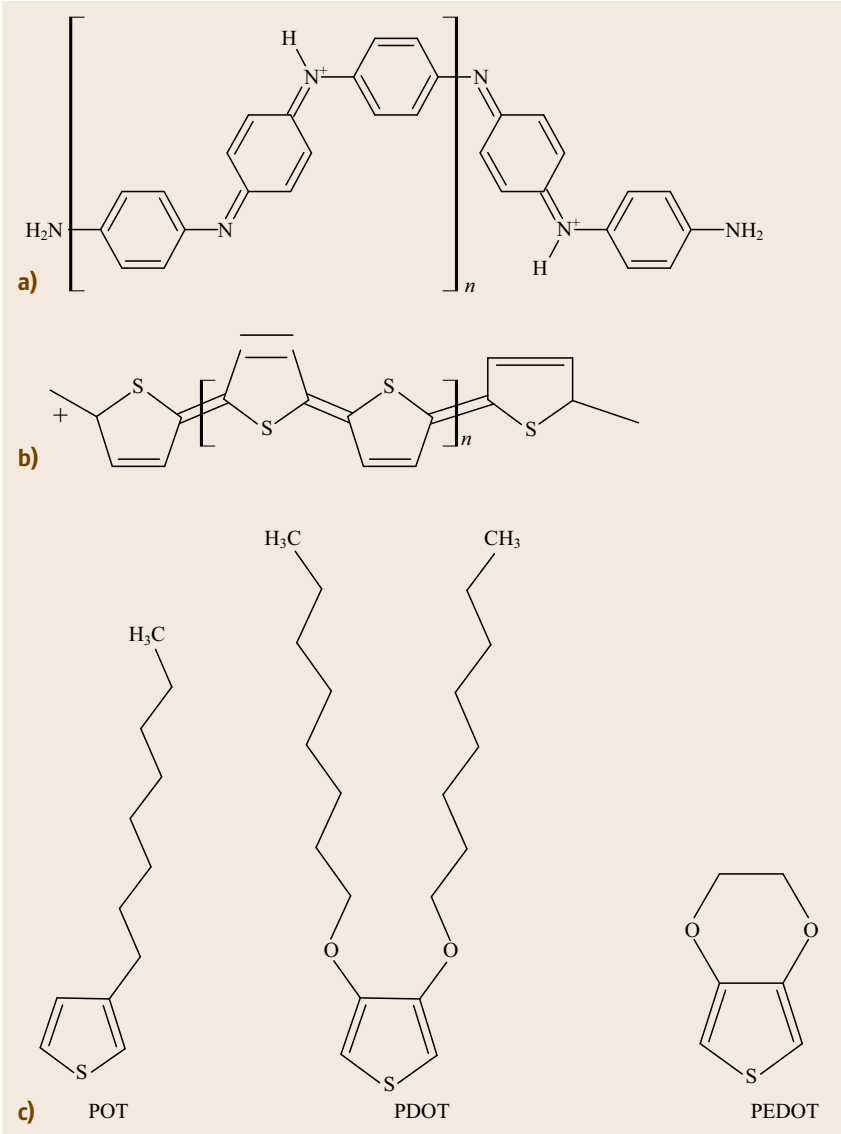


Fig. 7.21 (a) Polyaniline; (b) Polythiophene and (c) Monomer units of conducting thiophene polymer derivatives

Table 7.6 Selection of drug responsive membrane electrode (after [7.15])

Drug	Exchanger	Sample or uses
Amitriptyline	Amitriptyline tetraphenylborate	Response studies
Metoclopramide	Metoclopramide tetraphenylborate	Pharmaceuticals
Amphetamine	Amphetamine dibenzo-crownethers	Selectivity studies
Berberine	Berberine bromomercurate	Tablets
Berberine	Berberine tetraphenylborate	Response studies
Naproxen	Tetraheptylammonium naproxenate	Tablets
5,5 diethylbarbiturate	Tetraoctylammonium 5,5 diethylbarbiturate	Response studies
Cocaine	Cocaine dipicrylaminate	Response studies
Salicylate	Derivatized porphyrine tin dichloride	Biological samples
Benzylpenicillin	Benzyldimethylcetylammonium-benzylpenicilline	Pharmaceuticals
Nicotine	Nicotine tetraphenylborate	Tobacco products
Scopolamine	Scoplamie tetraphenylborate	Response, selectivity studies

7.1.8 Ion-Selective Field Effect Transistor (ISFET)

Already 40 years ago *Bergveld* et al. placed the ion-selective membrane directly at the input transistor of the voltmeter [7.18]. The input stage of most voltmeters uses field effect transistors (FET) to ensure the high input resistance. Figure 7.22 shows the scheme of a FET linked to an ion-selective electrode.

Usually the gate electrode of the FET is connected to the ISE and thereference electrode is connected to the bulk contact. The voltage between the bulk and the isolated gate electrode generates an electric field in the tiny channel below the gate and controls the current between source and drain electrode. Placing the ion-sensitive layer directly above the gate insulator removes all the capacities of the cables and connectors in between, thus the charge that must be transferred following a change of the potential is drastically reduced. This should result in a much better dynamic response and a lower polarization of the membrane–gate interface. Another advantage of the direct capacitive coupling of the ion-selective layer to the gate isolator is that even imperfect layers with holes, which would cause a short cut in conventional ISE, provide a suitable response. Fluoride sensitiveFETs have been produced by vapor deposition of LaF_3 resulting in a nonperfect layer with holes, but that worked perfectly [7.19]. The low output impedance of the transistor prevents the uptake of *electrosmog* and disturbance by electrostatic charges. There are two operation modes using ISFETs:

1. Registration of the source-drain-current. This current is a nonlinear function of the gate potential (Fig. 7.23) and additionally depends on the temperature.
2. The drain current is regulated by an operational amplifier as shown in Fig. 7.24 to a constant value by compensating for the potential difference at the sensing layer by an additional voltage, which is introduced between the reference electrode and the sensor. Here the voltage just corresponds to the potential of a conventional ISE.

The concept of the ion-selective field-effect transistor (ISFET), the link between the very progressive tech-

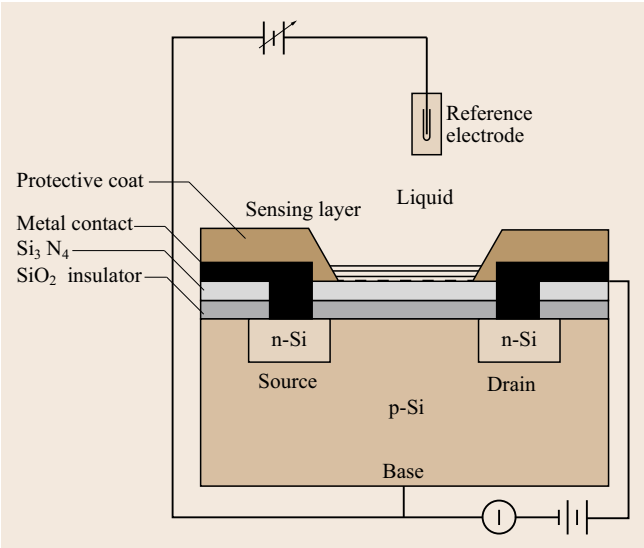


Fig. 7.22 ISFET, ion-selective field-effect transistor

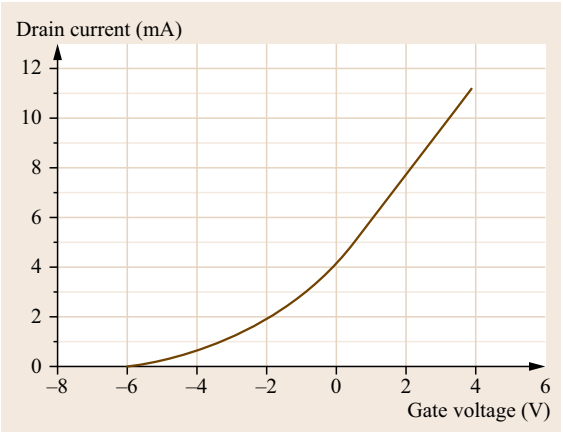


Fig. 7.23 Response function of an-channel depletion FET

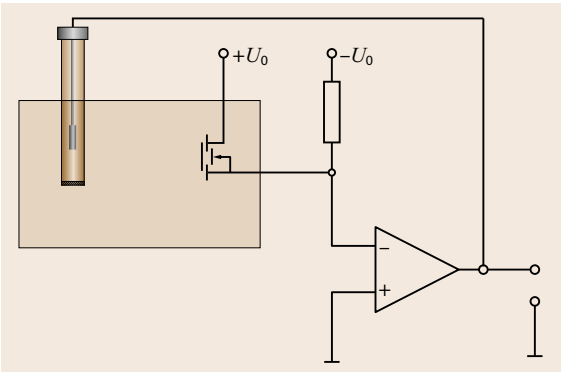


Fig. 7.24 Schematic circuit of constant drain current operating mode with negative feedback to the reference electrode. The current is set by the resistor, which just compensates the current from the ISFET at the inverting input of the operational amplifier. The output voltage results the potentiometric function of the ISFET ►

nique of microelectronics and electrochemical sensing was and is indeed very alluring, but electronic devices are not compatible with water. Except for the sensing layer all other parts must be insulated from the medium. This problem was solved by placing the contacts to the backside and isolating the rest with SiO_2. As in the case of the early *coated wire electrodes* the interface between the membrane and the gate isolator is not well defined. This disadvantage may be resolved by interlayers of conducting polymers or carbon nanotubes as in the all solid-state electrodes. A FET is not an ideal device. In integrated circuits for ionometers all these disadvantages are internally compensated. Therefore the ISFETs did not replace the conventional ISE.

7.1.9 Drug Sensitive Electrodes

The majority of drug molecules bear a basic or acidic function and they are ionized at a suitable pH. The corresponding ions are comparably lipophilic and interact with an ion exchanging membrane. Some drug sensitive electrodes have been constructed for special purposes such as response studies. Contrary to the more complex and only intermittent registration methods such as high performance liquid chromatography (HPLC), the ISE allows for continuous monitoring. Table 7.6 gives some examples of drug sensitive electrodes.

Molecular imprinted polymer membranes promise further progress in selectivity of drug molecules and other xenobiotics.

7.2 Application of ISE

Besides the visual pH strips that allow an estimation of the pH value, the majority of the more exact pH measurements in the laboratory are done with pH meters. This is a standard instrument not only in chemical labs, but also pharmaceutical and biological labs. Small electronic pH sticks also contain a glass electrode as a sensing element. It is very easy to replace the pH electrode against another ISE, switch the pH scale to the mV display and do the job.

To get reliable results, selectivity and working range must be checked, and depending on the analytical problem sample preparation and calibration has to be performed. An abundance of suitable analytical protocols can be found in the application notes of the electrode manufactures [7.10].

For the determination of concentrations the ion strength must be adjusted to the same value for sample and calibration standards and the measurements should be carried out at the same temperature. The electrodes are dipped into the solution and under gentle stirring a stable readout should be arrived at after a few minutes. Continuous drift indicates a failure of the system, often of the reference electrode. If the voltage fluctuates, then the conductivity of the sample is too low or the liquid junction of the reference electrode is clogged. The temperature dependence of the ISE according to the Nernst equation is compensated for in most instruments by a built-in thermometer or the temperature is set manually.

Some comfortable instruments often combined with titrators allow the automation of the whole analytical procedure, including the calculation of the analytical result. After usage the electrode has to be cleaned by distilled water and stored under appropriate conditions.

To compensate for drift, a one-point calibration should be performed before, between and at the end of a series of samples. From time to time the slope has to be checked.

Specialized analyzers such as the AVL 9180 Analyzer for clinical analysis of the electrolytes in blood and urine are equipped with an assembly of flow-through electrodes for K^+, Na^+, Ca^{2+}, pH and Cl^-. These *fool proof* instruments contain self-checking programs that flush the salt bridge of the reference electrode, clean the system and calibrate the electrodes.

Almost all titrations benefit from electrochemical end point detection. It is beyond the scope of this chapter to deal with the numerous variants of potentiometric titrations from acidimetric, redox and complexometric titrations. Chloride-ISEs are used for argentometric titration and Ca-ISE for complexometry. The titration of ionic tensides or ionic biopolymers is demonstrated with tenside electrodes.

7.2.1 Gas-Sensitive Electrodes and Biosensors

An interesting extension of the application of ISEs is achieved by attaching a further reaction layer onto the ion-selective membrane. A thin buffer solution layer in front of a one-rod pH sensor, separated by a (silicone) rubber membrane, which allows the penetration of reactive gases such as CO_2 or NH_3 results in a gas-sensitive electrode. Between the partial pressure of CO_2 for instance and the pH of the carbonate/bicarbonate buffer a secondary equilibrium is established that enables the direct measurement of the partial pressure of CO_2. A typical application is the blood gas analyzer.

The ammonia-sensitive electrode reads the ammonium after alkalization and has found applications in the determination of urea, which is converted by urease to ammonia.

As opposed to a gas-permeable membrane, the separation of the sample solution is also possible simply by placing the electrode above the sample. Then the gas diffuses through the gap between the meniscus of the sample and the electrode.

Highly specific enzyme reactions bound in a layer above the ion-selective membrane producing any detectable species are used as biosensors. The enzyme reaction results in a steady state between product formation and diffusion of this product from the electrode. As the enzyme reaction requires distinct conditions related to temperature, pH and coenzyme concentration the concept of the enzyme electrode seems to be overloaded to some extent. For routine analysis such electrodes are used as disposable sensors or are prepared occasionally on the bench. The stability of the enzymes except from a few cases is very limited, therefore the sensor should be stored in a refrigerator.

Instead of pure enzymes, even small organisms such as bacteria, yeast or algae, different tissues, and parts of cells such as mitochondria have been placed at the sensing site of an ISE.

Immune reactions are indicated using the concept of the enzyme-linked immunosorbant assay (ELISA). The Immune reaction results in an immobilization of the linked enzyme in front of the electrode and the product of the enzymatic reaction is detected. Sometimes nonnatural substrates are used, such as 4-fluorphenol, which releases fluoride upon oxidation, which is sensed by a fluoride electrode.

7.2.2 Detectors in Flow Systems

Flow systems offer a wide variety of automated sample preparation, as HPLC or capillary electrophoresis, dilution or reactions as in flow injection analysis are compatible with ISEs. Their response is independent of the sample volume enabling miniaturization to save reagents and avoid waste.

Some examples are flow injection determination of total concentration of aliphatic carboxyclic acids [7.20]; application of a potentiometric electronic tongue in food analysis [7.21]; or a potentiometric detector in capillary electrophoresis [7.22].

7.3 Amperometric and Voltammetric Methods

A current flowing through an electrode disturbs the equilibria at all interfaces between different phases. Particularly at the interface between electronic conductors and ionic conductors, the transition of electrons involves oxidation in the case of positive (anodic) or reduction in the case of negative (cathodic) charge transfer.

The current corresponds to the reaction rate according to Faradays law

$$\frac{\mathrm{d}n}{\mathrm{d}t} = \frac{1}{zF}\frac{\mathrm{d}Q}{\mathrm{d}t} = \frac{1}{zF}I\,. \tag{7.31}$$

As a heterogeneous reaction the rate is proportional to the area of the electrode where the reaction takes place. As the reaction goes on, the concentration of the educt is depleted at the surface and as a consequence the concentration of the product increases. This causes a concentration gradient near the electrode and forces diffusion of the educt to the electrode and the product from the electrode. If the charge transition is not kinetically hindered, then these transport phenomena control the current, and the potential at the *working* electrode corresponds to the actual surface concentrations of the redox couple according to the Nernst equation.

7.3.1 Experimental Methods

The experimental setup is a little bit more complex than in simple open circuit potentiometric measurements. Although most reference electrodes are stable against small currents it is better to avoid a current through the reference electrode. Therefore an auxiliary electrode as a third electrode is introduced. The current then flows between the auxillary and the working electrode, while the potential at the working electrode is measured against the reference electrode with a high impedance voltmeter.

The inner resistance of the solution causes an ohmic drop, resulting in a potential error.

To counteract this error the reference electrode is placed as near as possible to the working electrode, using a Luggin capillary and the conductivity of the electrolyte is increased by addition of a suitable inert salt. The current is kept low, using a small working electrode. With these small working electrodes the electrochemical conversation related to the bulk of the solution can be neglected.

Different measuring regimes have been established so far.

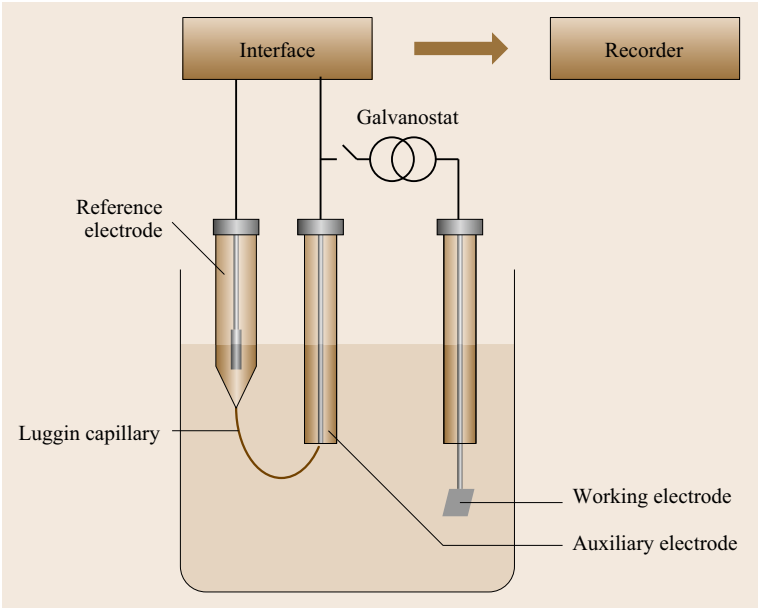


Fig. 7.25 Experimental setup of chronopotentiometry

Quiet solution, no convection:

- *Chronopotentiometry*: Current is switched on, regulated to a constant value, potential is recorded as function of time
- *Chronoamperometry*: Potential is stepped to a defined value, current is recorded as function of time
- *Linear sweep voltammetry*: Potential is set as a linear function of time, current is recorded as function of potential
- *Cyclic voltammetry*: Potential set as a triangular function of time, current is recorded as function of potential.

There are several variants of voltammetry with more complex potential time functions, such as staircase voltammetry, pulse voltammetry, AC-voltammetry, ans stripping voltammetry.

Forced convection:

- *Polarography*: Dropping mercury electrode
- *Rotated disk electrode*
- *Vibrated disk electrode*: Current is recorded as function of potential
- *Streaming solution*: In flow injection analysis and HPLC detectors, current is recorded as function of time or potential
- *Chronopotentiometry*.

The procedure may be illustrated in a simple system. The cell is equipped with a platinum disk working electrode, 3 mm diameter sealed in glass. Prior to usage the electrode is polished with fine ground alumina and carefully cleaned with a mixture of concentrated sulfuric acid and hydrogen peroxide. As shown in Fig. 7.25 the cell is further completed with an auxiliary platinum electrode and a silver/silver chloride reference electrode.

The cell is filled with 1 M KCl and 1 mM potassium hexacyanoferrat (II) in water. The potential is measured with a high-impedance voltmeter interfaced to a computer recording the potential time function. The current is generated by an electronic current source *galvanostat* and adjusted to $+100\,\mu A$.

As the current is switched on, the hexacyanoferrat (II) begins to be oxidized at the electrode to hexacyanoferrat III. Since the coordination sphere of the iron atom is not changed and the charge can be easily distributed, this reaction is almost quick and reversible. The potential of the working electrode is shifted to a positive direction and when almost all of the reduced species is consumed at the surface of the electrode a steep increase in the potential is observed. This point of time is called the *transition time* (τ). Since the current is kept constant anything else must be oxidized; here the chloride of the ground electrolyte is oxidized to chlorine at the end. Provided that any convection during the measurement is prevented and the conductivity of the solution is kept high, the transport of the reduced and oxidized species is governed by a planar diffusion perpendicular to the active surface of the electrode. This can be described by Fick's second law

$$\frac{\partial c}{\partial t} = D\frac{\partial^2 c}{\partial x^2} \,. \tag{7.32}$$

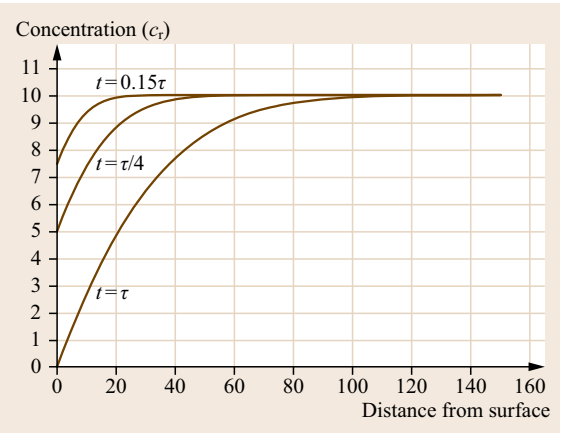


Fig. 7.26 Evolution of concentration gradients at the surface of the working electrode after the current is switched on

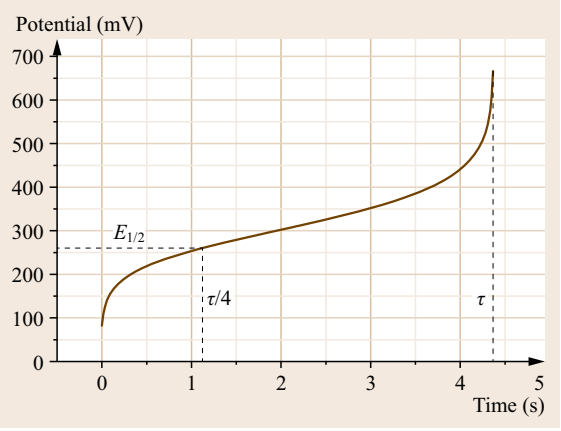


Fig. 7.27 Chronopotentiometric record of the oxidation of hexacyanoferrate (II)

As long as the educt is not exhausted, the oxidation goes on at the surface with a constant rate according to (7.31) and the depletion of the of the hexacyanoferrate (II) extents more and more into the bulk solution, as illustrated in Fig. 7.26.

In the case of a reversible quick reaction the measured potential is determined by the Nernst equation and the standard potential is reached when just the half of the reduced form is oxidized. This is the case at a quarter of the transition time (Fig. 7.27). Solutions of the differential equations (7.31) and (7.32) reveals that the square root of the transition time is proportional to the bulk concentration

$$\tau^{\frac{1}{2}} = \frac{\pi^{\frac{1}{2}} z F D^{\frac{1}{2}}}{2i} c_r \,. \tag{7.33}$$

For simplicity diffusion coefficients of reduced species as well as the activity coefficients are set to be equal.

The current density must be adapted to the concentration to ensure a transition time of a few seconds to avoid onset of spontaneous convection and deviation from planar diffusion. Therefore this old procedure by *Karaoglanoff* [7.23] is seldom used in analytical practice.

Chronoamperometry

In all amperometric or voltammetric methods the potential of the working electrode is set to a defined value. This is done by an electronic controller, the potentiostat. Usually a potentiostat is realized with an integrated operational amplifier. Such amplifiers exhibit a differential input and a high open loop gain of about 1×10^5. A typical schematic setup is shown in Fig. 7.28.

The nominal potential is set at the potentiometer or a digital-analog-converter from a computer. Because of the high amplification of A1, the voltage of the auxiliary electrode is regulated to an appropriate value, which ensures an input difference at A1 near zero. This means that the potential of the reference electrode against ground is just the set voltage. The second amplifier holds the potential of the working electrode at ground and the output voltage of A2 corresponds to

$$U_{out} = -RI_{in} \,. \tag{7.34}$$

The feedback resistor must be adapted to the expected current to ensure a suitable working range of the amplifier and the recorder. There are some other more sophisticated schemes on the instruments market to meet special demands for high regulation speed or higher currents.

Let us consider again a reversible diffusion controlled oxidation, without any complication.

Switching the potential from about 150 mV below the redox potential to a value 150 mV above the standard potential results first in a sharp peak of current to charge the double layer of the working electrode. This capacitive current exponentially decays, depending on the conductivity of the solution. The new potential corresponds to a ratio of c_{ox}/c_{red} of about 0.997. The surface concentration of the reduced species is near zero and a concentration gradient evolves from the surface into the solution. Figure 7.29 shows the concentration profiles $c_{red}(x,t)$ calculated from Fick's second law with the boundary conditions of $c_{t=0} = c_B$ and $c_{x=0} = 0$.

The solution of the differential equation yields

$$c_{red}(x,t) = c_L \mathrm{erf}\left(\frac{x}{2D^{\frac{1}{2}} t^{\frac{1}{2}}}\right) , \tag{7.35}$$

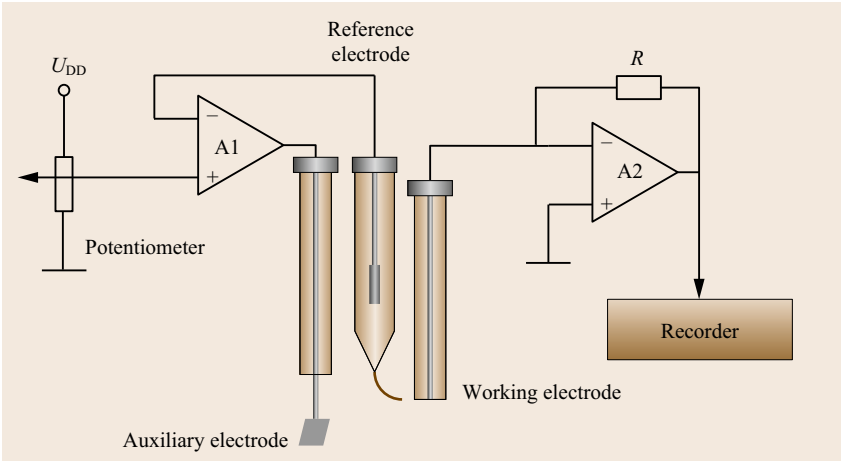


Fig. 7.28 Potentiostat

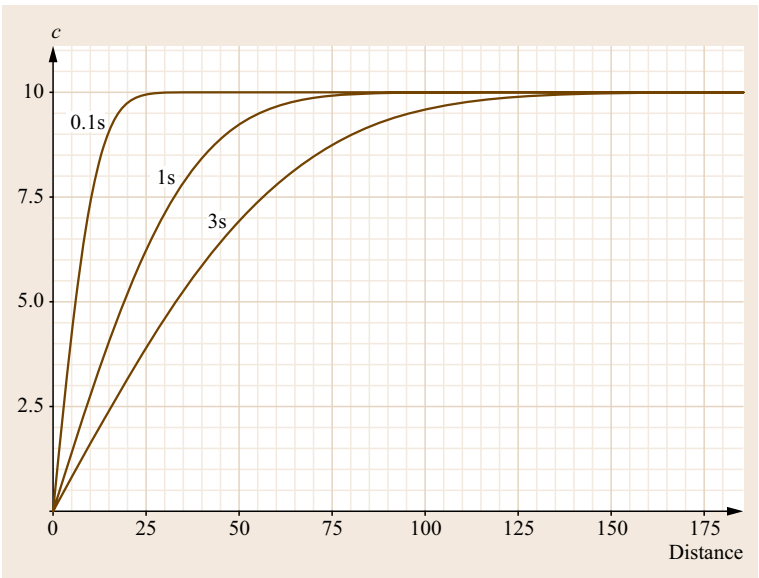


Fig. 7.29 Concentration profile near the surface of the electrode during the chronoaperometric experiment, calculated following (7.35)

where erf = error function.

The current density j decays with the square root of the time

$$j = \frac{zFD^{\frac{1}{2}}c_{\mathrm{L}}}{\pi^{\frac{1}{2}}t^{\frac{1}{2}}} \text{ (Cotrell equation)} . \tag{7.36}$$

Plotting $1/j$ against the square root of time yields a straight line from which the diffusion coefficient conveniently may be derived. Deviation from linearity is indicative of a more complicated kinetic.

Linear Sweep Voltammetry

The experimental setup is just the same as in chronoamperometry, but the set potential is swept with time. A wide variety of potential time functions are used in the practice of electrochemical measuring techniques. Rectangular, sawtooth or staircase functions, linear ramps with overlaid Sin of different frequencies and pulses are used. Linear sweep voltammetry we discuss here to show the principal phenomena. In a typical oxidation experiment we start far below the redox potential and increase the potential with a constant voltage rate. The response curve is shown in Fig. 7.30. A small, ideally constant, current is recorded due to the charging of the double layer. It is proportional to the sweep rate

$$I = Cv, \quad v = \frac{\mathrm{d}U}{\mathrm{d}t} . \tag{7.37}$$

Near the redox potential the oxidation begins, resulting in a Faraday current reaching a maximum above the

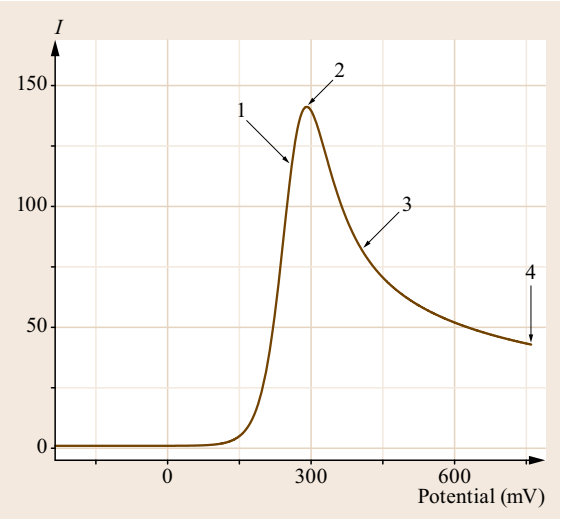


Fig. 7.30 Single-sweep voltammogram, pure diffusion control

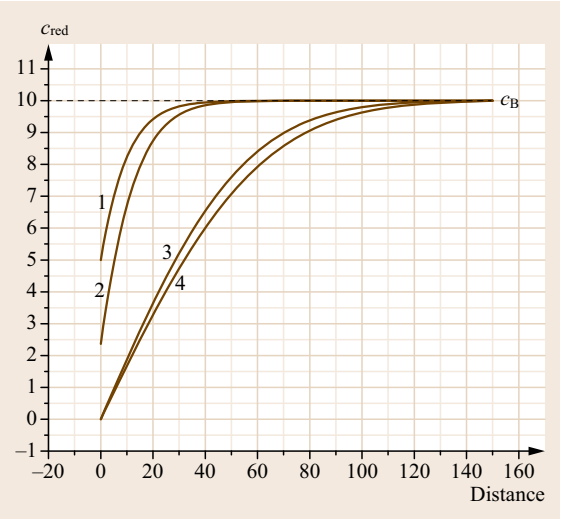


Fig. 7.31 Concentration profile at single-sweep voltammogram

standard potential (7.1) and then decays as the surface of the electrode is depleted of reactive material.

The current decay obeys the square root law as in chronoamperometry. The surface concentration is already zero at point 3 and 4 in Fig. 7.30.

Compare the concentration profiles in Fig. 7.31.

The peak current density is proportional to the bulk concentration and the sweep rate

$$j_p = 2.69 \times 10^5 z^{\frac{3}{2}} D^{\frac{1}{2}} c_L v^{\frac{1}{2}}$$

(Randles–Sevcik equation) , (7.38)

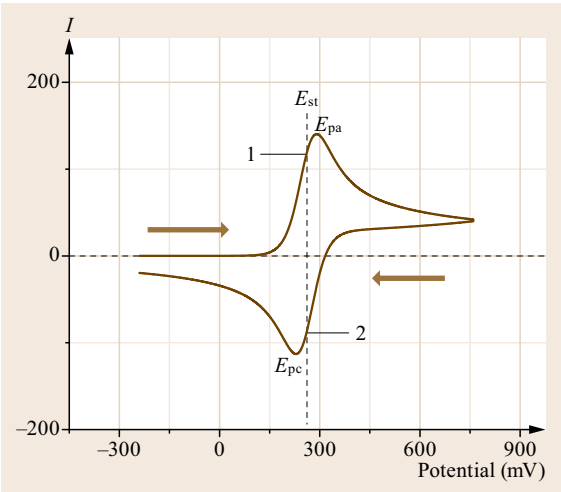


Fig. 7.32 Cyclic voltammetry of a reversible one-electron oxidation

where j_p in A cm^{-2}, D in cm^2 s^{-1}, c in mol cm^{-3}, v in V s^{-1}.

The sweep rate ranges from some millivolts per minute to 1000 V s^{-1}. At very slow sweep rates the convection is difficult to avoid and at high sweep rates the capacitive current (7.37) becomes much higher than the Faraday current. The peak potential does not depend on sweep rate in a pure diffusion-controlled electrode reaction. If any other kinetic effects are involved then a distinct dependence of the peak potential from the sweep rate is observed and the shift of the peak potential serves as diagnostic criteria for a variety of reaction mechanisms. It even provides the kinetic constants.

Cyclic Voltammetry

Much more information can be acquired when the linear sweep is extended, reversing its direction at least after the peak and scan back to the starting potential. This results in a triangular potential time function. In our example the oxidized product of the first positive part of the scan is then reduced again. Because of diffusion, both peaks are separated by 59 mV in the case of a reversible one-electron transition.

The standard potential (points 1 and 2 in Fig. 7.32) situates just in between the two peak potentials

$$E_{st} = \frac{E_{pa} - E_{pc}}{2} , \quad (7.39)$$

where, as the forward part equals the single sweep, there are quite different concentration patterns for the reverse scan at the same potential.

With additional scan cycles a steady state is reached producing nearly identical voltammograms. If only

a few parts of the electrochemical product decay, then the educt is only partly regenerated at the reverse scan and disappears after some time. As the peak current is proportional to the bulk concentration (Fig. 7.33), it is possible to use single sweep or cyclic voltammetry for analytical determination of concentrations, but a much more important application of the method is the investigation of electrochemical reaction mechanisms. The researcher now has a well-developed theoretical background as well as powerful computer programs at hand to interpret the data from cyclic voltammetry. Nevertheless any voltammetric experiment must be carefully designed to avoid distortions of the potential by IR (voltage) drop or undesired blocking of the electrode surface.

The investigation of reaction kinetics needs the application of a wide range of scan rates. At high scan rates the use of microelectrodes ensures low current and thus minimizes the IR drop and capacitive current. When the diameter of the active electrode becomes smaller than the extension of diffusion layers before the surface, then the condition of planar diffusion no longer holds.

Microelectrodes

Typical disk microelectrodes have a diameter from 1−100 µm but there are even downsized ultra microelectrodes in the nanometer range. A spherical diffusion field governs the transport at a microelectrode. Theoretical treatment results in a time-independent additional term of the Cotrell equation

$$j = \frac{zFD^{\frac{1}{2}}c_{\mathrm{L}}}{\pi^{\frac{1}{2}}t^{\frac{1}{2}}} + \frac{zFDc_{\mathrm{L}}}{r} \,. \tag{7.40}$$

At very small electrodes this term is decisive and results in a constant and much higher current. The current itself is relatively low in the pA to nA range. To improve the signal to noise ratio it is also possible to use a bundle of microelectrodes in parallel. The constant diffusion to the surface results in a sigmoid form of a voltammogram as shown in Fig. 7.34. Ferrocen is reversibly oxidized in a solution of 0.1 M tetraethylammonium tetrafluoroborate as a conducting electrolyte resulting a typical voltammogram at the macroeletrode but a sigmoidal voltammogram at a microelectrode. Very small microelectrodes are used in electrochemical microscopy.

Electrochemical Kinetic

Charge transfer from an electrode through the double layer to a molecule in the electrolyte needs some activation energy and the change of its oxidation state involves transformation of bonds in the molecule. These

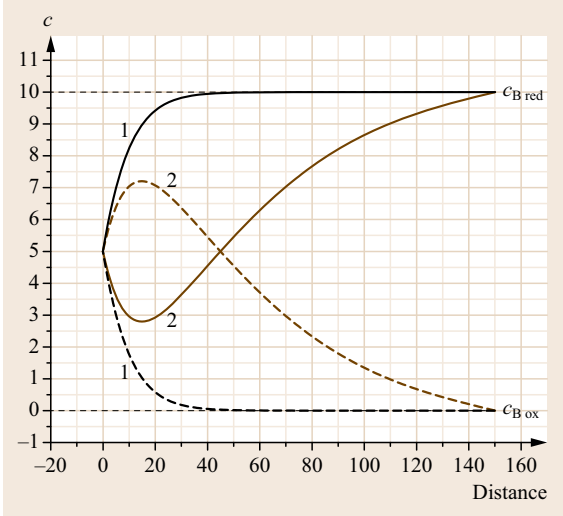


Fig. 7.33 Concentration profiles at the working electrode during cyclic voltammetry (CV) experiment, *black* forward scan, *brown* backward scan

processes take some time and if the rate of the electron transfer is slower than the diffusion, the current is controlled by the reaction rate rather than by diffusion.

The activation energy of a chemical reaction determines the temperature dependence of its rate constants according to the Arrhenius equation

$$k = A\mathrm{e}^{-\Delta G^{\#}/RT} \,. \tag{7.41}$$

In the case of an electrochemical reaction,

$$\mathrm{O} + ze^{-} \leftrightarrows \mathrm{R} \,,$$

the charge transfer across the phase boundary results in an additional electrical energy $zF\Delta E$, which contributes not only to the free energy of the equilibrium reaction but even to the activation energies of the forward and backward reactions.

At equilibrium potential, both anodic and cathodic reaction rates are the same and as the frequency factor A is independent of the direction of the reaction the activation energies are equal too.

A deviation from the equilibrium potential in the positive direction accelerates the oxidation, decreasing its activation energy by a fraction $(1-\alpha)$ of the electrical energy

$$\Delta G_{\mathrm{a}}^{\#} = \Delta G^{\#} - (1-\alpha)zF(E-E^{0}) \,.$$

In contrast the activation energy of the reduction increases by the remaining fraction

$$\Delta G_{\mathrm{c}}^{\#} = \delta G^{\#} + \alpha zF(E-E^{0}) \,, \tag{7.42}$$

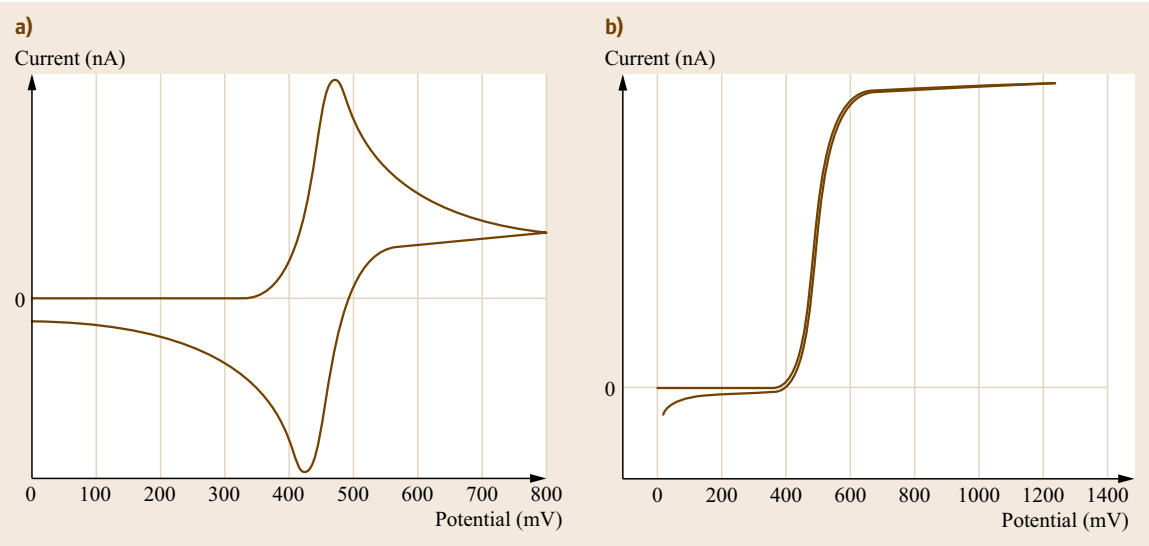


Fig. 7.34a,b Cyclic voltammetry of ferrocen **(a)** At a platinum disk electrode, diameter = 1 mm and **(b)** $d = 10\,\mu m$ (currents not to scale)

where α is the transfer coefficient. It typically ranges from 0.2–0.8.

Introducing the electrical terms into the Arrhenius equation results in

$$k_a = A e^{+[\Delta G^{\#} - (1-\alpha) zF(E-E^0)]/RT} ,$$

$$k_c = A e^{-[\Delta G^{\#} + \alpha zF(E-E^0)]/RT} ,$$

summarizing the potential independent term in k^0

$$k_c = k_c^0 e^{-\alpha zF(E-E^0)/RT}$$

and

$$k_a = k_a^0 e^{(1-\alpha) zF(E-E^0)/RT} .$$

The reaction rate relates to the current density as

$$j = zFkc .$$

At equilibrium, where $E = E^0$, both current densities are the same, and the anodic and cathodic current compensate each other. Its absolute value, representing the dynamic of the equilibrium is called exchange current density

$$k_c = k_a = k^0 , \quad j_0 = zFk^0 c \text{ for } (c = c_O = c_R) .$$

At potentials away from the equilibrium, the net current density is given by the Butler–Volmer equation

$$j = zFk^0 (c_R e^{(1-\alpha) zF(E-E^0)/RT} - c_O e^{-\alpha zF(E-E^0)/RT}) ,$$

inserting j_0 at equivalent concentrations of O and R,

$$j = j_0 (e^{+(1-\alpha) zF(E-E^0)/RT} - e^{-\alpha zF(E-E^0)/RT}) .$$

The potential difference in the exponent is called overvoltage η. At an overvoltage of about 100 mV the cathodic current density vanishes and a plot of $\ln(j)$ against η results in a slope of $(1-\alpha)zF/RT$ from which α can be derived. Analogously, at negative potentials only the cathodic current remains relevant (Fig. 7.35).

7.3.2 Electrochemical Reaction Mechanisms

Most electrochemical reactions involve more than one simple charge transfer step. Prior to the charge transfer we find chemical reactions, equilibria as acid–base reactions, complexations or physical and chemical adsorption at the surface of the electrode. Often the products of the electrolysis are very reactive and they may further react chemically or electrochemically. The electrochemical product can even change the surface of the electrode, corroding the material or forming conducting or isolating layers on it. To gain insight into these processes in principle all the electrochemical methods discussed so far can contribute, but cyclovoltammetry has been established as the most powerful tool. Besides these pure electrochemical techniques, the combination of electrochemistry with other advanced techniques such as spectroscopy and microscopy and a careful analysis of the reaction products are advisable.

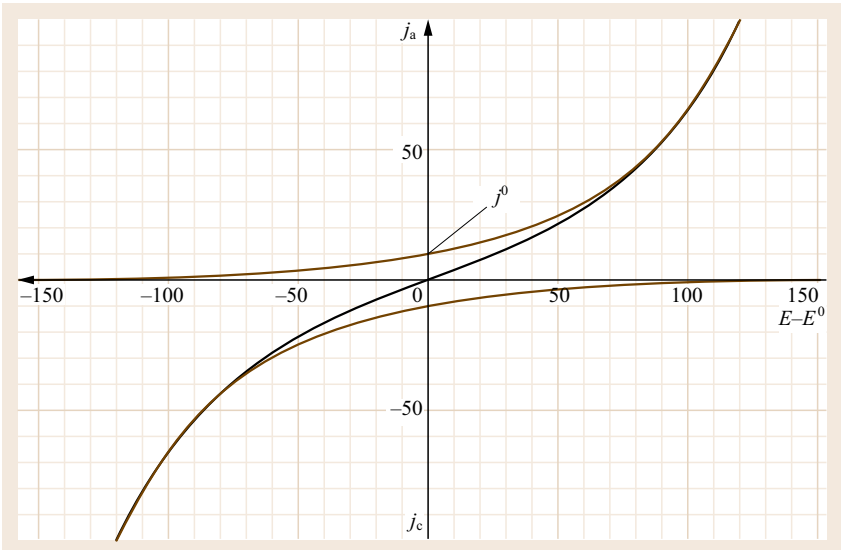


Fig. 7.35 Current density j (mA/cm^2) as a function of overvoltage $(E - E^0)$, $\alpha = 0.5 k_e = 0.1$ cm/s

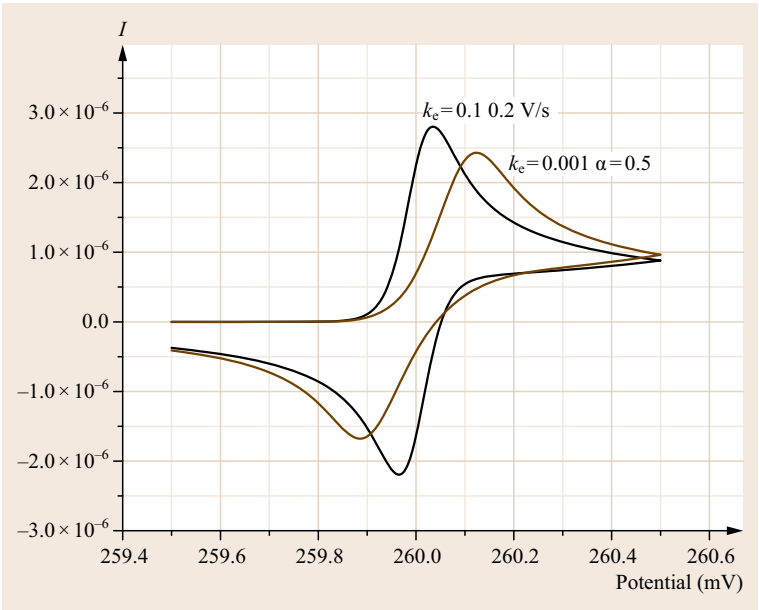


Fig. 7.36 CV with slow electron transfer heterogeneous rate constant 0.1 (*black*) and 0.001 cm/s (*brown*), scan rate 0.2 V/s

In the frame of this chapter a few examples shall be discussed:

1. After the first charge transfer further reversible peaks follow at higher potential. More than two subsequent reversible steps are seldom, because the concentration of high charge makes the molecule instable and a quick irreversible decomposition follows. In C60 fullerene, however, even a six-step reversible reduction is possible: evidently this symmetric molecule enables a uniform distribution of the added electrons.
2. Slow reversible charge transfer. At slow scan rates the reaction rate remains diffusion-controlled, but at higher scan rates the current is limited due to the slow charge transfer. The peak current does not further increase with the square root of the scan rate and according to the Butler–Volmer equation an overvoltage is necessary to achieve a certain current. Thus, the difference between anodic and cathodic peak increases with the scan rate (Fig. 7.36).
3. The charge transfer is irreversible. No peak is found in the reverse part of the scan. Such reactions are of-

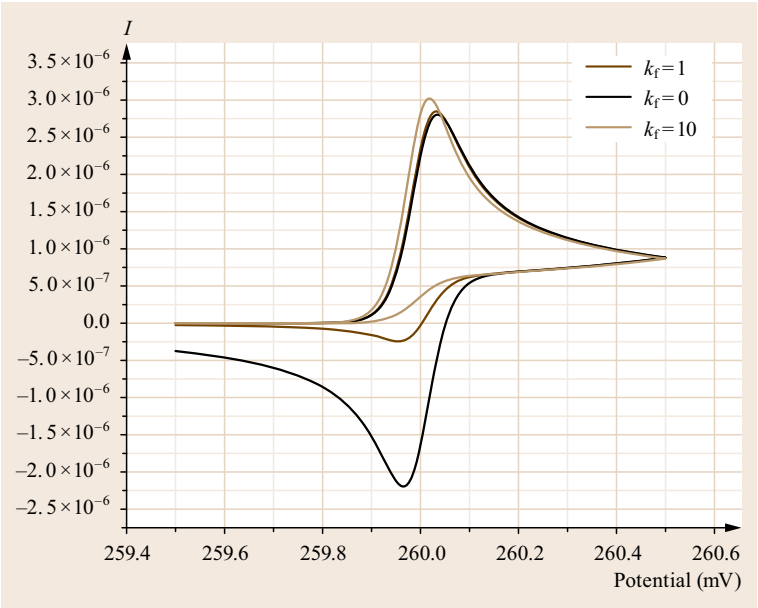


Fig. 7.37 EC mechanism, slow chemical reaction followed by charge transfer $k = 0.1\,s^{-1}$ (*brown*), quick reaction $k = 10\,s^{-1}$ (*tan*), no reaction (*black*) for comparison

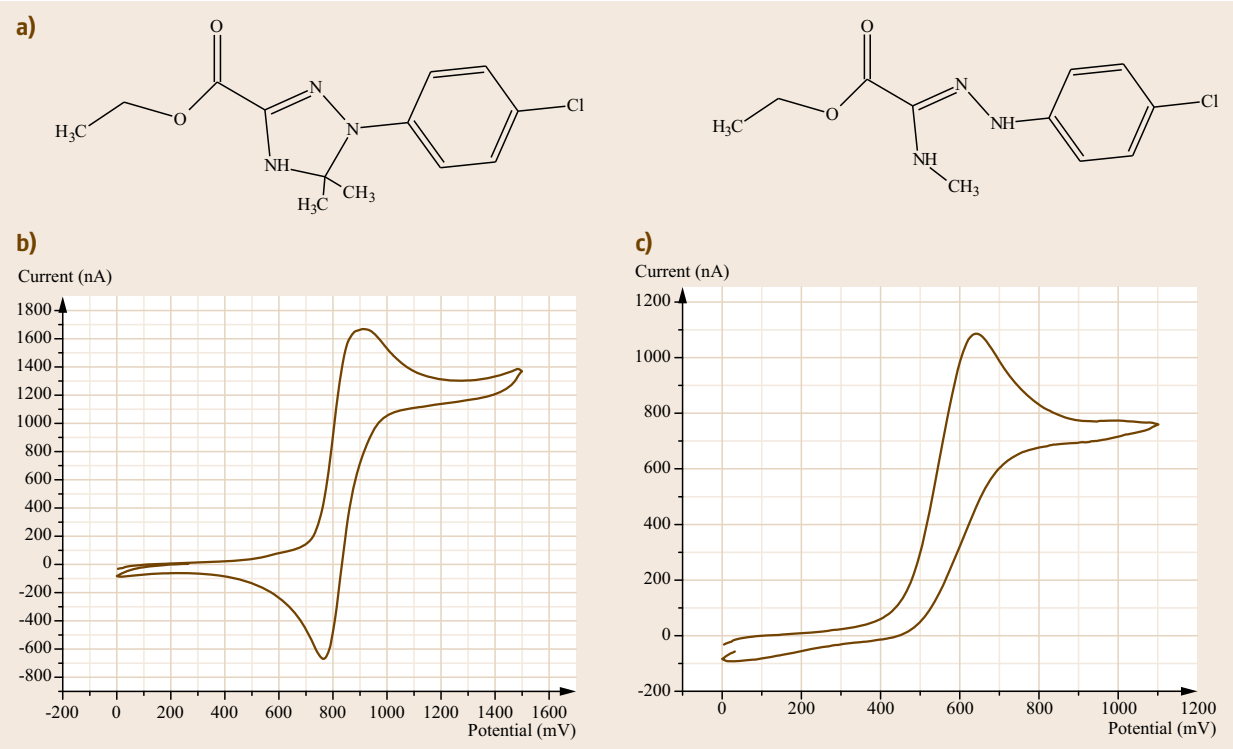


Fig. 7.38a–c Electrochemical oxidation of different amidrazone derivatives **(a)** Reversible oxidation **(b)** rapid decomposition of the primary oxidation product **(c)** presumably because of proton abstraction

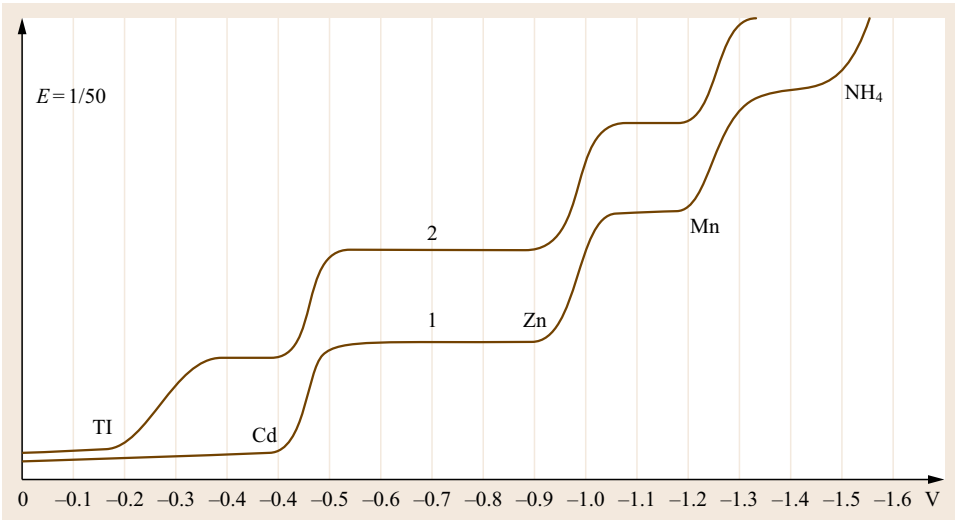


Fig. 7.39 Polarogram of a mixture of different cations. Concentrations 5×10^{-4} M, background electrolyte 0.01 M ammonia/ammonium chloride

ten found when the charge transfer is accompanied by a fission of a bond.

4. The charge transfer is followed by a chemical decomposition of the primary product, known as an EC mechanism. Depending on the reaction rate of the chemical reaction the reverse peak disappears as illustrated in Fig. 7.37. As an example, the oxidation of the triazoline derivative (a) yields a persistent radical cation that is reduced again during the reverse scan; the open-chained amidrazone (b) is readily decomposed after the oxidation.
5. The charge transfer is followed by a chemical reaction resulting in a product more electroactive than the educt. A second charge transfer follows at the same potential, known as an ECE mechanism. The electrochemical active substance is formed in an equilibrium step before the charge transfer (CE mechanism). The peak potential depends on the concentration of other components that are involved in the equilibrium.

The interpretation of CV data is a complex task and there exist several strategies, from correlations of peak currents and peak potential against scan rate to complete simulation of the whole diagram using digital simulation with finite elements. Often these programs are plugged into the instrument's software and allow for automatic parameter optimization to extract the kinetic and equilibrium constants. As an introduction to this field we recommend [7.24].

Amperometry with Convection at the Electrode

Convection strongly enhances the transport of all species from and to the electrode and limits the influence of diffusion to a thin layer immediately at the surface of the electrode. The concentration gradient through this layer comes in a constant steady state, depending on the velocity of the convection. In a single-sweep experiment we find a sigmoidal response function, independent of scan rate. Stirring or pumping the solution against the electrode as in HPLC-detectors or vibrating or rotating the electrode can realize a constant convection. In the case of a rotating disk electrode the limiting current is proportional to the square root of the speed of rotation (Levich equation)

$$j_{\mathrm{L}} = 0.620 z F D^{\frac{2}{3}} w^{\frac{1}{2}} v^{-\frac{1}{6}} c \,,$$

where j_L is the limiting current density, w is the angular rotation rate of the electrode and v is the kinematic viscosity.

The Levich equation is based on a pure diffusion-controlled charge transfer. Deviations can be attributed to a slow heterogeneous rate constant or other reactions linked with the charge transfer.

In polarography the moving boundary of the dropping mercury electrode causes a special form of convection. Together with the changing surface of the electrode, the mean current of this electrode is expressed by the Ilkovics equation. Figure 7.39 shows a typical polarogram.

Voltammetry with the dropping mercury electrode was introduced by Heyrovsky in the 1920s and was by far the most important electroanalytical technique for decades. The surface of the mercury electrode is ideally smooth and because it is renewed with every drop, it remains clean and even adsorption and desorption are reproducible. The high overvoltage of proton reduction enables very negative potentials in

protic solvents such as water. A wide range of analytes, from metal cations, even alkali cations to organic compounds with nitro-, keto- or halogen are suitable for polarographic determination. Since the potential scan in polarography usually begins near zero and extends to the negative direction, the cathodic current is plotted against the negative potential ($-E$ as abscissa).

During the almost hundred years of polarography a huge amount of literature has been published. For an introduction [7.25–29] may provide a non representative selection.

References

7.1 J. Koryta: Theory and application of ion-selective electrodes. Part 8, Anal. Chim. Acta. **223**, 1–30 (1990)

7.2 D.A. Skoog, D.M. West, F.J. Holler, S.R. Crouch: *Fundamentals of Analytical Chemistry* (Thomson Books Cole, New York 2004), Chap. 21

7.3 R. Buck: Electrochemistry of ion-selective electrodes, Sens. Actuators **1**, 197 (1981)

7.4 C.H. Hamann, A. Hamnett, W. Vielstich: *Electrochemistry* (Wiley-VCH, Weinhein 1998)

7.5 G. Eisenmann (Ed.): *Glass Electrodes for Hydrogen and Other Cations* (Marcel Dekker, New York 1967)

7.6 A. Michalska: All solid-state ion selective and all-solid-state reference electrodes, Electroanalysis **24**(6), 1223 (2012)

7.7 Sigma-Aldrich: Handbook Ionophores for ISE, http://www.sigmaaldrich.com (Sigma-Aldrich, St. Louis 2015)

7.8 W.E. Morf: *The Principles of Ion-Selective Electrodes and of Membrane Transport* (Elsevier, Amsterdam 1981)

7.9 E. Pretsch: The new wave of ion-selective, Anal. Chem. **74**(15), 420A–426A (2002)

7.10 Metrohm: Manual Ion selective Electrodes, 8.109.147612, http://www.metrohm.com/en/products-overview (Metrohm, Herisau 2016)

7.11 J. Bobacka, A. Ivaska, A. Lewenstam: Potentiometric ion sensors, Chem. Rev. **108**(14), 329–351 (2008)

7.12 T.R. Brumleve, R.P. Buck: Numberical solution of the Nernst–Planck and Poisson equation system with application to membrane electro-chemistry and solid state physics, J. Electroanal. Chem. **90**(1), 1–31 (1978)

7.13 T. Sokalski, P. Lingenfelter, A. Lewenstam: Numberical solution of the coupled Nernst–Planck and Poisson equations for liquid junction and ion-selective membrane potentials, J. Phys. Chem. **107**, 2443–2452 (2003)

7.14 T. Sokalski, T. Zwickl, E. Bakker, E. Pretsch: Lowering the detection limit of solvent polymeric ion-selective electrods 1. Modeling the influence of steady-state ion fluxes, Anal. Chem. **71**, 1204–1209 (1999)

7.15 R.L. Solsky: Ion selective electrodes, Anal. Chem. **62**(12), 21R–33R (1990)

7.16 P. Lingenfelter, I. Bedlechowicz-Sliwakowska, T. Sokalski, M. Maj-Zurawska, A. Lewenstam: Time-dependent phenomena in the polutial response of ion-selective electrodes treated by the Nernst–Planck and Poisson model-1. Intramembran process and selectivites, Anal. Chem. **78**, 6783–6791 (2006)

7.17 F.X. Rius-Ruiz, G.A. Crespo, D. Bejarano-Nosas, P. Blondeau, J. Riu: Potentiometric strip cell based on carbon nanotubes as transducer layer, Anal. Chem. **83**, 8810 (2011)

7.18 P. Bergveld: Development, operation, and application of ion-sensitive-field-effect-transistor as a tool for electrophysiology, Biomed. Eng. **19**(5), 342 (1972)

7.19 W. Moritz: Ionensensitive Feldeffekttransistoren-Beiträge zum Mechanismus der Potentialbildung und zur Optimierung der sensitiven Schicht, Dissertation (Humboldt Univ., Berlin 1985)

7.20 M. Mroczkirwicz, L. Gorski, A. Zamojska-Jaroszewicz, K.W. Szewczyk, E. Malinowska: Application of flow-injection potentiometric system for determination of total concentration of aliphatic carboxiclic acids, Talanta **85**(4), 2047–2052 (2011)

7.21 J. Gallardo, S. Alegret, M. Del Valle: Application of potentiometric electronic tongue as a classification tool in food analysis, Talanta **66**(5), 1303–1309 (2005)

7.22 J. Tanyanyiwa, S. Leuthardtz, P.C. Hauser: Conductimetric and potentiometric detection in conventional and microchip capillary electrophoresis, Electrophoresis **23**, 3659 (2002)

7.23 V.Z. Karaoglanoff: Über Oxydations- und Reduktionsvorgänge bei Elektrolyse von Eisensalzlösungen, Z. Elektrochem. **12**(1) 5–16 (1906) in German

7.24 D.K. Gosser: *Cyclic Voltammetry* (Wiley, Weinheim 1993)

7.25 P. Bergveld: Thirty years of isfetology, what happened in the past 30 years and what may happen in the next 30 years, Sens. Actuators B Chem. **88**, 1–20 (2003)

7.26 J. Bobacka, A. Ivaska, A. Lewenstam: Potentiometric sensors, Chem. Rev. **108**, 329 (2008)

7.27 G. Henze: *Polarographie und Voltammetrie* (Springer, Berlin, Heidelberg 2001)

7.28 J. Wang: *Analytical Electrochemistry 3* (Wiley-VCH, Weinhein 2006)

7.29 T. Riley, A. Watson: *Polarography and Other Voltammetric Methods* (Wiley, New York 1987)

8. Transport in Liquid-Phase Electrochemical Devices

Richard O. Stroman, Greg Jackson

Transport of reactants and products in liquid-fed electrochemical cells is critical in terms of reactant utilization, concentration polarizations, and coulombic efficiencies. Design of electrochemical flow cells can benefit from adequately detailed models that capture the locally variable impact of reactant depletion and product build-up on electrochemical reactions throughout the cell. This chapter illustrates the importance of transport modeling by presenting a finite-volume, two-dimensional (2-D) model of a liquid-phase electrochemical cell with simple cell geometry, but complex multistep chemistry at each electrode incorporating parasitic reactions and/or mixed potentials. The modeled cell involves two half-cell reactions, borohydride (BH_4^-) oxidation and hydrogen peroxide (H_2O_2) reduction, in planar flow channels with electrodes separated by flowing liquid-phase electrolytes and an ion-exchange membrane. This generic cell topology is representative of many fuel cells and flow batteries. The finite-volume model solves for conservation of mass, momentum, species, and charge in both the cathode and anode flow channels for ideal, dilute, and concentrated electrolytes. The model couples the flows to complex boundary conditions at the electrochemically active electrode surfaces and the selective ion-exchange membrane. Model results show that the balance of advection, diffusion, and migration in the liquid electrolytes results in complex profiles that predict boundary layer build-up and significant advection perpendicular to the flow path. The direct borohydride-hydrogen peroxide fuel cell transport model, used to illustrate these concepts, shows how liquid-phase transport limits conversion and dictates cell voltages within the context of the competing reactions at the two electrodes. The chapter ends by demonstrating how such a model can be implemented in design studies to explore strategies for improving practical cell performance.

8.1 **A General Transport Model for Liquid-Fed Electrochemical Cells** 240
8.1.1 Governing Equations in Liquid Electrolytes 241
8.1.2 Transport in Liquid Electrolytes 242
8.1.3 Transport of Liquids in Porous Media 243
8.1.4 Common Boundary Conditions and Interfaces 244
8.1.5 Reaction Fluxes at the Electrode–Channel Interfaces 245
8.2 **Practical Considerations** 246
8.2.1 Grid Development and Gradient Approximations 246
8.2.2 Implementation of the Governing Equations 246
8.2.3 Numerical Approaches 247
8.2.4 Model Calibration and Validation 248
8.3 **Example Cell: Direct Borohydride–Hydrogen Peroxide Fuel Cell** 248
8.3.1 DBFC Overview 248
8.3.2 Transport in the Channels 250
8.3.3 Transport at the Membrane–Channel Interfaces 250
8.3.4 DBFC Transport Model Calibration 251
8.3.5 Results from the DBFC Transport Model 253
8.4 **Conclusions** 256
8.5 **Nomenclature** 256
References 257

Numerical simulation, using multidimensional finite volume (FV) and finite element (FE) models, has become a valuable tool for understanding electrochemical devices and improving their performance. Advances in numerical simulation techniques and computational power have enabled models to explore processes that couple detailed electrochemistry to transport of species, charge, and energy in increasingly complex geometries.

Models that couple electrochemistry and transport are particularly valuable for the design of electrochemical devices with flowing reactants, in which the extent of reactant depletion or product accumulation near electrode surfaces is related to the fluid velocity. These concentration changes near the electrodes impact reaction cell voltages, reactant utilization, and cell efficiency.

FV methods can be advantageous for electrochemical device modeling because they employ the transport equations in a straightforward way and ensure conservation of conserved properties (mass density, charge density, species concentrations, etc.). Conservation of conserved properties is important for all transport models, but it is critical in electrochemical systems due to the high sensitivity of local potentials in electrolytes and electrodes to any charge imbalances. As such, FV models for electrochemical systems are becoming more common with examples including laminar flow fuel cells [8.1], direct methanol fuel cells (DMFCs) [8.2–5], direct borohydride fuel cells (DBFCs) [8.6, 7], lithium-ion batteries [8.8], and vanadium-redox flow batteries [8.9]. This chapter will discuss and demonstrate the value of FV modeling for electrochemical system design in the limited, but widely applicable, context of liquid-fed electrochemical cells.

FV modeling of liquid flows with chemical reactions has been thoroughly explored by the computational fluid dynamics (CFD) community. However, accurate FV modeling for liquid-phase electrochemical systems is only now becoming feasible in widespread commercial codes, because the presence of ions in solution can complicate reaction and transport calculations substantially. Growing applications for batteries, flow batteries, and fuel cells has motivated the development of these capabilities in commercial and open source software to address the complicated multiphysics simulations of electrochemical systems and bring them into the mainstream of electrochemical cell design.

FV methods divide the model domain into discrete volume elements (computational cells) within which the system state variables are assumed uniform. Governing equations relate the state variables in each cell to the relevant fluxes of mass, momentum, species, and charge crossing the cell boundaries and to any source terms due to body forces, distributed reactions, or other generation terms. A state equation dictates the thermodynamic state of the fluid in each cell, and boundary conditions on the perimeter of the model domain constrain the solution to a unique system state. Steady-state and transient solutions are both possible with the same governing equations. Steady-state models are solved by finding a system state that satisfies the governing equations and respects the boundary conditions. Transient models use the governing equations to estimate the time derivatives of state variables, and then integrate them with respect to time to reveal the time evolution of the system. Since the governing equations relate system state to transport rates, accurate transport models are a prerequisite for an electrochemical system model.

This chapter presents governing equations, transport rate estimation methods, and common boundary conditions for FV models of liquid-fed electrochemical cells. These are discussed in the context of a generic electrochemical cell, and then they are applied with parameters for a detailed model of an all-liquid direct borohydride-hydrogen peroxide fuel cell. Results from the DBFC model are used to illustrate how the general approach can be applied to a specific electrochemical system.

8.1 A General Transport Model for Liquid-Fed Electrochemical Cells

Figure 8.1 illustrates a generic 2-D electrochemical cell, which includes two electrodes, two electrolyte flow channels, and a selective ion-conducting membrane separating them. This cell topology represents a broad class of fuel cells, flow batteries, and conventional batteries. In the case of a conventional battery, the bulk fluid velocity is zero and the inlets and outlets become walls. For the flow-through cell in Fig. 8.1, the x-coordinate originates at the inlets on the left-hand side and increases toward the outlets on the right-hand side. The two y-coordinate systems each originate at an electrode and increase toward the membrane. The channels are separate transport model domains linked by a one-dimensional (1-D) membrane transport model. Mass, momentum, species, and charge can cross the membrane in response to pressure and electrochemical potential gradients, but generally the membrane and liquid flow compositions are chosen to promote the conduction of a particular ion. Chemical and/or electrochemical reactions at the electrode layers produce products and electron fluxes there. In this example, the cell voltage (electric potential difference between the two electrodes) is specified and the electric current is calculated.

In electrochemical cell geometries such as the one illustrated in Fig. 8.1, reactants must flow from the bulk electrolyte to the electrodes, and any products released from the electrode must, in turn, flow from the electrodes back into the bulk flow. In order to com-

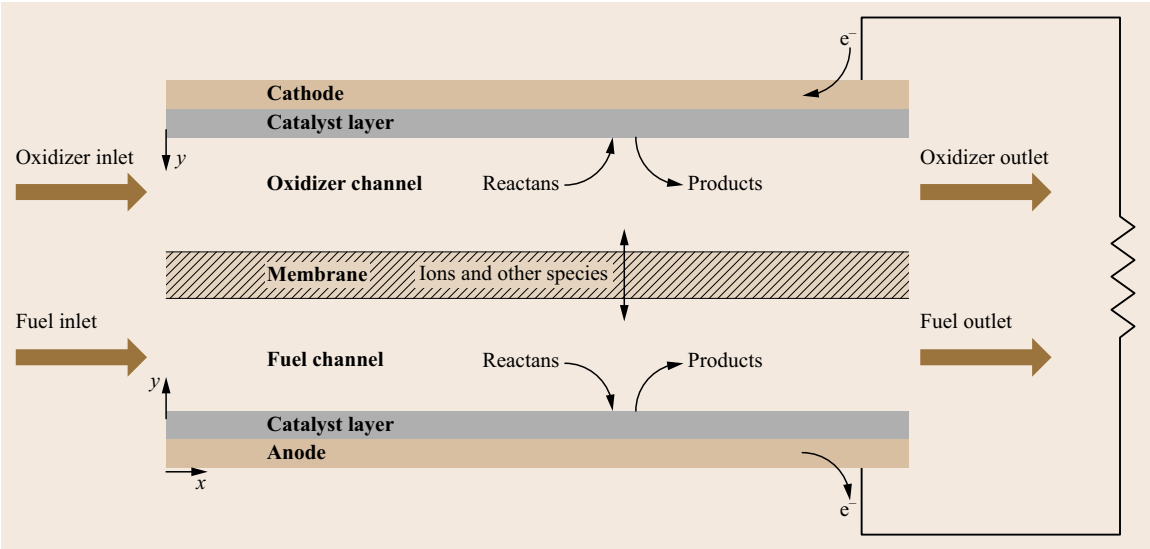


Fig. 8.1 Example electrochemical cell with flowing liquid electrolytes carrying fuel and oxidizer in the anode and cathode channels, respectively

plete the electrochemical circuit between the electrodes, one or more ionic species must cross the channels and membrane. At low current densities, the fluxes of reactants, products, and charge-balancing ions are small and therefore have relatively little impact on cell potential compared to the activation overpotentials that manifest at each electrode due to reaction kinetics. At moderate and high current densities, however, the free energy losses required to drive large fluxes across the membrane and electrolyte channels result in significant drops in cell potential in galvanic cells and large increases in cell potential in electrolytic cells. The changes in cell potential due to transport can be divided into concentration and Ohmic overpotentials. The concentration overpotential is a consequence of concentration changes near the two electrodes as reactants are depleted and products accumulate. These changes produce concentration gradients, which drive reactant and product diffusion and shift equilibrium electrode potentials via the Nernst equation. Ohmic overpotentials are a consequence of the electric potential gradient required to drive a net ionic charge flux between the electrodes. Since concentration and Ohmic overpotentials decrease efficiency, modeling efforts are often motivated by a desire to minimize transport losses.

8.1.1 Governing Equations in Liquid Electrolytes

An isothermal electrochemical system can be described by state variables pressure P, species mass fractions Y_k, velocity $\boldsymbol{v}$, and electric potential ϕ. Pressure is found by enforcing mass conservation (8.1), mass fractions are found by enforcing species conservation (8.2), and the velocity vector is found by enforcing momentum conservation via some form of the Navier–Stokes equation (8.3). Equation (8.3) includes a body force term to capture the influence of electric fields on ions in solution

$$\frac{\partial\left(\rho V\right)}{\partial t} = -\nabla\cdot\left(\sum_k W_k \boldsymbol{J}_k\right), \tag{8.1}$$

$$\frac{\partial\left(C_k V\right)}{\partial t} = -\nabla\cdot\boldsymbol{J}_k\,, \tag{8.2}$$

$$\frac{\partial\left(\rho\boldsymbol{v}\right)}{\partial t} = -\nabla\rho\boldsymbol{v}\cdot\boldsymbol{v} - \nabla P + \mu\nabla^2\boldsymbol{v} - \rho_c\nabla\phi\,. \tag{8.3}$$

Species can also be tracked by mole fraction or concentration, but mass fraction is preferable for systems with flowing electrolyte because it simplifies implementation of (8.3).

Solving for the electric potential presents additional complications. Enforcing charge conservation (8.4) is insufficient because it does not capture the relationship between charge density ρ_c and electric potential–charge could be conserved in a solution with net charge

$$\frac{\partial\left(\rho_c V\right)}{\partial t} = -\nabla\cdot\left(F\sum_k z_k \boldsymbol{J}_k\right). \tag{8.4}$$

Instead, Poisson's electrostatic equation (8.5) must be used. Equation (8.5) shows that deviations from electroneutrality produce electric potential gradients, and

these gradients are oriented to reestablish electroneutrality. Bulk electrolytes are effectively neutral because the small permittivity of free space ($\varepsilon_0 = 8.85419 \times 10^{-12}$ F/m) leads to large electrostatic forces reestablishing electroneutrality [8.10]

$$\nabla E = \nabla^2 \phi = -\frac{\rho_c}{\varepsilon \varepsilon_0} \,. \tag{8.5}$$

The observed electroneutrality of bulk electrolytes can be enforced explicitly to solve for electric potential as in

$$0 = \sum_k z_k C_k \,. \tag{8.6}$$

Equation (8.6) is preferred for bulk electrolytes because it does not require calculation of second derivatives, making it simpler and less computationally expensive. Equation (8.5) must still be used to resolve the steep electric potential gradients and net charge density present in electrochemical double layers adjacent to electrode surfaces [8.11].

An equation of state relating concentration to density is necessary [8.12] to close the governing equations when solute–solvent interactions are significant. One example is shown in (8.7), in which the apparent molar volumes of the solutes δ_k in solvent s are used to calculate the solution mass density

$$\rho = \frac{\rho_s}{Y_s + \rho_s \sum_k (\delta_k Y_k / W_k)} \,. \tag{8.7}$$

8.1.2 Transport in Liquid Electrolytes

Three transport processes occur in the bulk electrolyte of electrochemical systems: advection, diffusion, and migration. Advection is bulk fluid transport due to a pressure gradient ∇P. Diffusion and migration can be viewed as separate processes driven by species activity gradients ∇a_k and electric potential gradients $\nabla \phi$, respectively. Often diffusion plus migration are formulated as a single flux driven by an electrochemical potential gradient $\nabla \tilde{\mu}_k$. The difference in formulation is principally semantic, and in practice the diffusion and migration fluxes are often calculated separately. Nonetheless, the formulation in terms of $\nabla \tilde{\mu}_k$ illustrates the tightly coupled nature of diffusion and migration for ion transport.

The use of slowly flowing liquid electrolytes and relatively narrow flow channels in many electrochemical systems simplifies the advection transport model by making the flows laminar and incompressible and avoiding complications associated with turbulent fluctuations that arise with high-speed and large-scale flows. For conditions in which turbulence cannot be ignored, the grid of computational cells cannot typically resolve turbulent fluctuations. Modeling the turbulent fluctuations of the state variables presents many complications that are beyond the scope of this chapter. While there are many methods to model the increased mixing caused by the turbulent fluctuations, a relatively simple method implements turbulent diffusivities for the conserved species, which depend on the flow characteristics and molecular properties of the fluids. Turbulent diffusion fluxes enhance the standard molecular diffusive fluxes. Turbulence will not be discussed any further here since it is generally not relevant for the small channels and slow flows of most electrochemical cells.

For electrochemical cells, the most appropriate formulation of the migration and diffusion fluxes depends on the solute concentration(s). In ideal and dilute solutions, small solute concentrations (< 1 M) lead to small solute fluxes, which have an insignificant effect on the bulk fluid velocity; therefore the diffusion and migration fluxes can be calculated with respect to the solvent velocity. In concentrated solutions, solute fluxes can be significant compared to the solvent flux, and the diffusion and migration fluxes must be calculated with respect to a mass- or mole-averaged solution velocity. Furthermore, electrostatic ion–ion interactions are absent in ideal solutions, but they influence transport fluxes in dilute and concentrated solutions.

In ideal and dilute solutions, the advection velocity is shared by all species in solution, and the net flux of a species k is equal to the advection flux of k plus the flux of k with respect to the solution, as shown in

$$\boldsymbol{J}_k = \boldsymbol{v} C_k - u_k C_k \nabla \tilde{\mu}_k \,. \tag{8.8}$$

The driving force for the flux of species k with respect to the solution is the electrochemical potential, because it incorporates the influences of both concentration and electric potential gradients. The second term in (8.8) can be expanded to show the contributions from diffusion and migration by replacing $\tilde{\mu}_k$ with (8.9) and (8.10)

$$\tilde{\mu}_k = \mu_k + z_k F \phi \,, \tag{8.9}$$

$$\mu_k = \mu_k^0 + R_{ig} T \ln a_k \,. \tag{8.10}$$

The result is the Nernst–Planck equation (8.11) with separate terms for diffusion, migration, and advection. Note that the Nernst–Einstein relation ($D_k = u_k R_{ig} T$) has been employed to express diffusion in terms of the

binary diffusivity D_k instead of mobility u_k

$$\boldsymbol{J}_k = -D_k \nabla \ln a_k - z_k u_k F C_k \nabla \phi + \boldsymbol{v} C_k \,. \tag{8.11}$$

All terms in (8.11) are physical parameters or state variables except for the activity a_k. The treatment of a_k depends on the extent of species interactions (i. e., nonideality including ion–ion interactions) in solution, and is quantified by an activity coefficient γ_k. The activity coefficient is a concentration-dependent proportionality constant relating the activity and concentration via the following equation

$$a_k = \gamma_k C_k \,. \tag{8.12}$$

In an ideal solution, species interactions are independent of solution composition and γ_k is a constant. Thus, (8.11) simplifies to (8.13) [8.13]. Note the binary diffusivity of k measured with respect to an activity gradient D_k has been replaced in (8.13) by the binary diffusivity measured with respect to a concentration gradient $\mathcal{D}_k$. The diffusion flux is now described by Fick's law

$$\boldsymbol{J}_k = -\mathcal{D}_k \nabla C_k - z_k u_k F C_k \nabla \phi + \boldsymbol{v} C_k \,. \tag{8.13}$$

In a dilute solution, ion–ion interactions are present, therefore the simplification in (8.13) is not appropriate. Instead, (8.11) should be used with an estimate of a_k, which depends on the solute concentration(s). Most thermodynamic models for estimating a_k are arranged to predict γ_k by predicting the excess Gibbs free energy of the mixture. One solution model is the extended Debye–Hückel law. The extended Debye–Hückel law (8.14) models the influence of other ions as a uniform *cloud* of charge surrounding k without addressing the different short-range interactions of specific ion–ion pairs. The effective local charge density is given by the ionic strength I, defined in (8.15)

$$\ln(\gamma_k) = \frac{-A z_k^2 \sqrt{I}}{1 + \bar{a}_k B \sqrt{I}} \,, \tag{8.14}$$

$$I = \frac{1}{2} \sum_k z_k^2 C_k \,. \tag{8.15}$$

Parameters A and B describe properties of the solvent; for water at 25 °C, $A = 0.5092\ \sqrt{\text{kg mol}}$ and $B = 3.283 \times 10^9\ \sqrt{\text{kg mol}}/\text{m}$ [8.14]. A third parameter $\bar{a}_k$ is the effective ionic diameter of species k in water. The standard Debye–Hückel law (numerator only in (8.14)) is appropriate for solutions having $I \lesssim 0.5$ M, but the extended Debye–Hückel law gives better agreement with experiment for solutions with $I \gtrsim 0.5$ M. Equation (8.15) begins to fail at concentrations of several molar.

An alternative to the Debye–Hückel law is the Pitzer equations [8.15], which are virial expansions of the excess Gibbs free energy of ions in solution. The excess Gibbs free energy is a measure of the nonideality of the system, and thus the Pitzer equations capture (to the extent of the expansion) short-range interactions at higher concentration that are omitted by the Debye–Hückel law.

In concentrated solutions, ion–ion interactions result in significant excess free energy in the solution and can add substantial complexity to transport models. Furthermore, the large solute migration fluxes which are possible in concentrated solutions can influence the average solution velocity such that (8.8) is no longer appropriate. More complex transport relations must be used for concentrated solutions to account for ion-ion interactions and the influence of solute fluxes on the average solution velocity. Such transport relations have been discussed in prior work by *Newman* [8.10], so they will not be addressed in greater detail here.

Diffusion does not produce a net mass flux independent of pressure gradients, and, thus, the sum of diffusion mass fluxes must equal zero: $0 = \sum_k \mathcal{D}_k \nabla C_k$. A straightforward and computationally robust way to ensure net zero diffusion mass flux is to calculate the solvent diffusion flux $\boldsymbol{J}_{\text{S,dif}}$ as the negative sum of the solute diffusion fluxes as in (8.16). This approach is accurate for ideal and dilute solutions in which the solute fluxes are small, because the solvent diffusion flux is only a small correction to the much larger solvent advection flux

$$\boldsymbol{J}_{\text{S,dif}} = \frac{1}{W_{\text{S}}} \sum_{k \neq S} (W_k \mathcal{D}_k \nabla C_k) \,. \tag{8.16}$$

With the species fluxes $\boldsymbol{J}_k$ established, the net mass fluxes are the molecular mass weighted sum of the species fluxes (8.1) and the net charge flux $\boldsymbol{J}_{\text{c}}$ (electric current) is the charge-weighted sum over the species fluxes (8.17)

$$\boldsymbol{J}_{\text{c}} = F \sum_k z_k \boldsymbol{J}_k \,. \tag{8.17}$$

8.1.3 Transport of Liquids in Porous Media

The described transport models can be adapted to porous media incorporated into the electrochemical flow paths. In liquid flow cells, porous media can be implemented as an extension of electrode surfaces for spreading out reaction surface areas and for providing improved current collection. For transport modeling within porous electrodes, distributed reactions result in a strong coupling of the distributed reaction rates

with the potential gradients in the electrolyte phase. The potential drop associated with charge transfer reactions between the electrolyte and the solid porous electrode will dictate changes in local potential in the electrolyte. As reactants are depleted and products consumed within the depth of the porous media, the potential difference required to drive charge transfer reactions will be coupled to the activity and potential gradients in the electrolyte necessary to transport reactants and products (charged or neutral) in to and out of the porous electrode. If the charge transfer species between the electrolyte and the electrode is an ion with significant mass (such as in a battery), transport in the porous electrode will include the bulk velocity $\boldsymbol{v}$ that balances the net mass flux to or from the solid electrode. If $\boldsymbol{v}$ through the porous media becomes substantially large, pressure gradients in the porous media may become significant and implementation of an appropriate momentum balance based on an adaptation of Darcy's law or other appropriate porous flow model may be required.

Beyond the complexity of handling the distributed charge-transfer reactions in porous electrodes, an additional challenge is defining the diffusion flux accurately. Porous media inherently change the diffusion flux by adding dispersion to molecular diffusivity to obtain an increased effective diffusion coefficient. Dispersion arises due to bulk motion in porous media because the pores, which in typical electrode or diffusion layer supports have diameters of a few microns or less, cannot be resolved by the computational grid. Dispersion results in an increased effective diffusion coefficient $D_{k,\text{eff}}$ where the added dispersion are functions of porous media properties including porous media diameters, tortuosity, and interconnectedness as discussed in classical reviews like that of *Whitaker* [8.16]. Because dispersion in porous media does not fundamentally alter the nature of the transport equations, it will not be discussed further in this chapter.

Further complexities can arise when nonsoluble products are produced and two-phase flows in porous media become prominent. Such is the case in proton-exchange membrane fuel cells (PEMFCs) and DMFCs. The complexities of two-phase flows in porous distributed electrodes are beyond the scope of this text, but some excellent modeling studies of PEMFCs [8.17, 18] and DMFCs [8.5] provide valuable insight and progress into the significant complexity of this challenge.

8.1.4 Common Boundary Conditions and Interfaces

The computational domain for an FV model must have well-defined boundary conditions for the governing equations. Physical boundaries at the outer perimeter include inlets, outlets, and the thin-film electrodes; these physical boundaries are quantified by specifying the values of state variables (Dirichlet boundary conditions) or by specifying the spatial gradients of state variables (Neumann boundary conditions). The number and type of boundary conditions required in each coordinate direction are related to the spatial derivatives of state variables in the governing equations. A first-order derivative requires one Dirichlet boundary condition while a second-order derivative requires two Dirichlet, two Neumann, or one of each (a mixed boundary condition). Boundary conditions are fixed for steady-state solutions, but they can vary with time to examine transient behavior. Example boundary conditions for the generic electrochemical cell are shown in Fig. 8.2.

Transport models can be divided into subdomains with interfaces defined by boundary conditions, flux-matching constraints, or both. For example, consider one of the membrane–channel interfaces in Fig. 8.2. Electrolyte velocity at the interface is constrained by a no-slip boundary condition ($v_x = 0$) and mass fractions are constrained by a species flux-matching ($\boldsymbol{J}_{k,\text{ch}} = \boldsymbol{J}_{k,\text{mem}}$). The species flux match constraint uniquely defines Y_k at the interface because both fluxes depend on it. Flux-matching constraints can be viewed as links across interfaces that permit variables (in this case Y_k) in different subdomains to share boundary conditions along the outer perimeter of the model. Other locations where flux matches link variables across separate subdomains are the electrode–channel interfaces, where there are species fluxes due to electrochemical reactions on the electrode side of the interface, and species fluxes due to transport on the channel side.

Boundary conditions are established for each of the four state variables in the generic electrochemical cell.

Pressure (P)

A first-order pressure gradient appears in (8.3), so one boundary condition is required in each coordinate direction. In the x-direction, pressure is specified at the outlet, presuming that sufficient pressure is supplied at the inlet to drive a specified flow rate. In the y-direction, $\partial P/\partial y = 0$ at the electrode–channel interface because the electrode is an impermeable barrier (no net mass flux). Pressure is linked across the membrane in the y-direction by mass flux-matching constraints at each membrane–channel interface.

Velocity (v)

Second-order velocity gradients appear in (8.3), so two boundary conditions are required for each velocity vec-

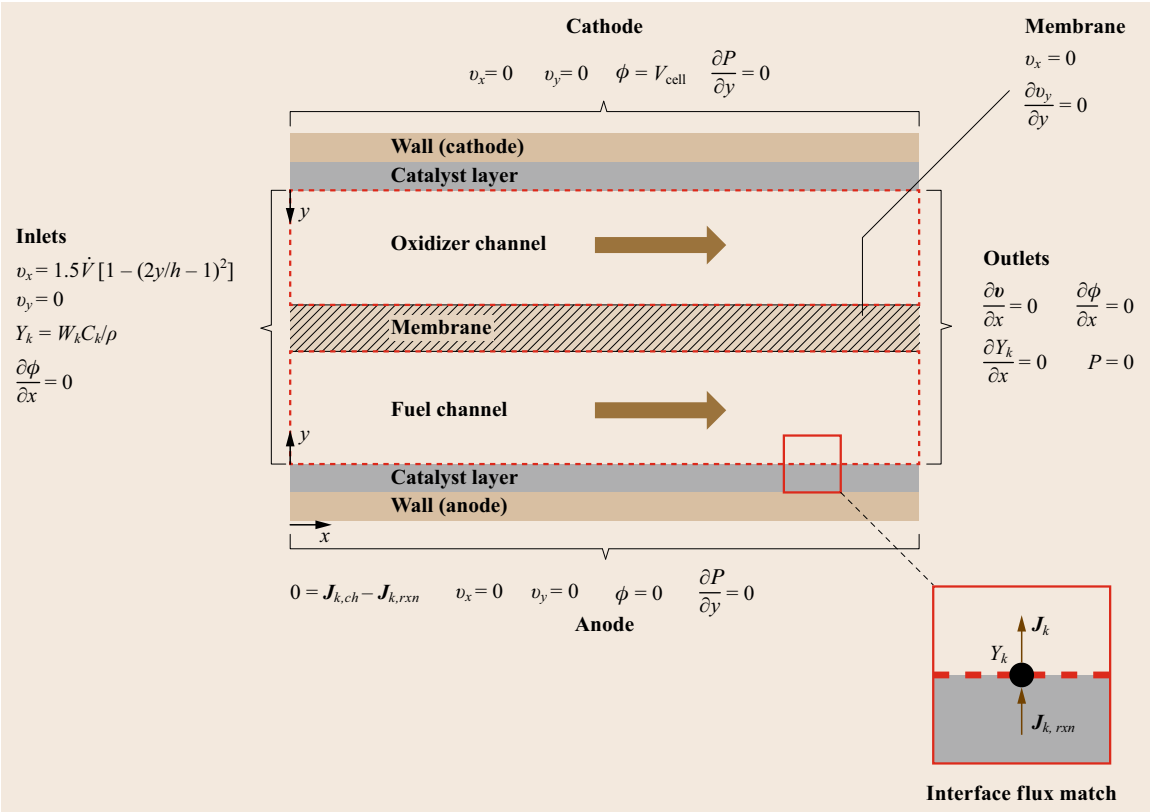


Fig. 8.2 Boundary condition equations at the electrode interface, the membrane interface, and the inlets and outlets of the example electrochemical cell

tor component (v_x and v_y) in each coordinate direction. In the x-direction, fully developed flow at the inlet is specified by $v_x(y) = 1.5\dot{V}[1-(2y/h-1)^2]$ and $v_y = 0$, where h is the channel height. Similarly, fully developed flow at the outlet is specified with boundary conditions $\partial v_x/\partial x = 0$ and $\partial v_y/\partial x = 0$. In the y-direction, $v_x = 0$ at the electrode–channel and membrane–channel interfaces due to the no-slip condition, and $v_y = 0$ at the electrode–channel interface because it is impermeable. Velocity in the y-direction is linked across the membrane by momentum flux-matching constraints at the membrane–channel interfaces.

Mass Fraction (Y_k)

Second-order mass fraction gradients appear in (8.1) and (8.2), and so two boundary conditions are required in each coordinate direction. In the x-direction, mass fractions are specified at the inlet and $\partial Y_k/\partial x = 0$ (fully developed concentration profiles) are specified at the outlet. In the y-direction, species flux matching constraints determine mass fractions at the electrode–electrolyte and membrane–electrolyte interfaces. Mass fractions are linked across the membrane by species flux-matching constraints at the membrane–channel interfaces.

Electric Potential (ϕ)

Electric potential in the electrolyte is governed by (8.5), which includes a second-order derivative, so two boundary conditions are required in each coordinate direction. In the x-direction, zero electric field at the inlet and outlet ($\boldsymbol{E} = \partial\phi/\partial x = 0$) ensures no net electrical current flows through the electrolyte ports. In the y-direction, the anode is assigned an electric potential of zero ($\phi_a = 0$) to form a reference for the rest of the system, and the cathode is assigned the cell potential ($\phi_c = \phi_{cell}$).

8.1.5 Reaction Fluxes at the Electrode–Channel Interfaces

An Arrhenius rate expression is often used to describe the rates of electrochemical charge transfer reactions, where the net rate is the sum of forward and reverse rates (8.18). The forward direction supplying electrons to the electrode is *anodic* (subscript a) and the reverse

direction withdrawing electrons from the electrode is *cathodic* (subscript c)

$$r = k_\mathrm{a} \prod_k a_{k,\mathrm{a}}^{\upsilon_{k,\mathrm{a}}} \mathrm{e}^{n_\mathrm{e}\beta_\mathrm{a} f \Delta\phi} - k_\mathrm{c} \prod_k a_{k,\mathrm{c}}^{\upsilon_{k,\mathrm{c}}} \mathrm{e}^{-n_\mathrm{e}\beta_\mathrm{c} f \Delta\phi} \,. \tag{8.18}$$

The pre-exponential terms include rate constants k and species activities a_k raised to reaction orders equal to stoichiometric coefficients υ_k. The exponential terms are activation energy barriers, which depend on the magnitude of the electric potential difference $\Delta\phi$ between the electrode and electrolyte in the channel, because the reaction must drive a net charge flux through the double layer to proceed. At the anode, for example, oxidation reactions drive a net negative charge flux against the electric potential gradient in the double layer to the lower potential of the anode, doing work in the process. Symmetry factors β describe the slope of the activation energy barrier with respect to the reaction coordinate near equilibrium; $\beta_\mathrm{a} = \beta_\mathrm{c} = 0.5$ implies that the barrier is symmetric. A common assumption in the absence of experimental data is $\beta_\mathrm{c} = 1 - \beta_\mathrm{a}$, that is, the slopes from each direction are nearly linear near equilibrium; n_e is the number of electrons transferred in the rate-determining step.

The net species flux due to reactions at an electrode, $\boldsymbol{J}_{k,rxn}$, is the sum of contributions from all reactions r_q at the electrode multiplied by the appropriate stoichiometric coefficients. A roughness factor ϵ adjusts for the ratio of electrochemical to geometric electrode surface area

$$\boldsymbol{J}_{k,rxn} = \epsilon \sum_q r_q \upsilon_{k,q} \,. \tag{8.19}$$

8.2 Practical Considerations

This section offers suggestions for structuring the model, estimating the required gradients, implementing the governing equations, and calibrating the model.

8.2.1 Grid Development and Gradient Approximations

Each flow channel in Fig. 8.1 is divided into a grid of cells with the electrolyte state in each cell described by state variables P, v_x, v_y, Y_k, and ϕ. For the purposes of estimating gradients at cell boundaries, state variables P, Y_k, and ϕ are colocated at the center of each cell, while v_x and v_y are offset by one half-cell, as shown in Fig. 8.3. Offsetting the velocity from the pressure in this way avoids odd–even decoupling, which can break the causality link between fluid behaviors in adjacent cells and produce unphysical behavior.

Grid density is often increased where gradients are large to resolve them more accurately, and decreased where gradients are small to minimize the computational expense of solving the model. For example, the electrochemical double layers at electrode–channel interfaces can be resolved by solving for the electric potential with (8.5), but only when the grid pitch is much smaller than the width of the double layer [8.3]. Such a dense grid is unnecessary in the rest of the channel, so a grid with varying density is preferred.

Gradients are approximated by finite differences between grid cells and then used to estimate the fluxes of mass, momentum, species, and charge across cell boundaries. Upwind differencing is used for velocity and pressure gradients in the x-direction because transport in the x-direction is dominated by advection, and upstream state variables have more influence over advection than downstream state variables [8.19]. Diffusion, migration, and advection make similar magnitude contributions to transport in the y-direction, and center differencing is more accurate and numerically stable under these conditions, so it is used to approximate gradients in the y-direction.

8.2.2 Implementation of the Governing Equations

The governing equations for an electrochemical flow cell as represented by Fig. 8.1 are employed differently for steady-state and transient simulations, but they have the same basic form. Each conservation equation is rearranged to isolate the time derivative of the associated state variable. The time derivatives in a steady-state simulation are referred to as residuals R and driven to zero. The time derivatives in a transient simulation are evaluated and integrated to plot the trajectory of the system state from a set of initial conditions. The following discussion assumes a steady-state solution.

Pressure is associated with mass conservation because mass fluxes are predominantly driven by pressure gradients. The mass contained by a cell does not change with time at steady state, so to find the steady-state pressure in the channel, mass conservation (8.1) is enforced by driving the residual R_ch^P in (8.20) to zero. Since the net mass flux $\boldsymbol{J}$ includes first-order spatial derivatives of

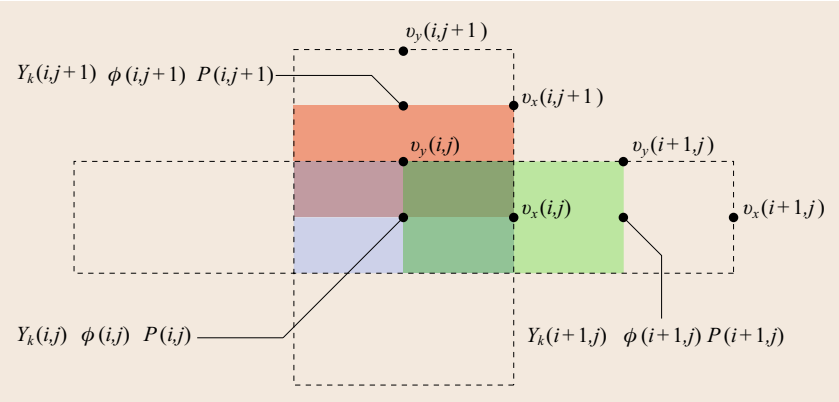


Fig. 8.3 Grid stencil showing relative-state variable locations. Y_k, ϕ, and P cells are demarcated by *dashed lines*. One v_x cell is *shaded green* and one v_y cell is *shaded red*

Y_k and ϕ, (8.20) introduces second-order derivatives of these state variables

$$R^{\mathrm{P}}_{\mathrm{ch}} = -\nabla \cdot \boldsymbol{J} \,. \tag{8.20}$$

The mass flux match used to find the pressure at the membrane–channel interface is given as (8.21). Driving $R^{\mathrm{P}}_{\text{ch-mem}}$ to zero finds the pressure that balances the two mass fluxes and conserves mass across the interface

$$R^{\mathrm{P}}_{\text{ch-mem}} = \boldsymbol{J}_{\mathrm{ch}} - \boldsymbol{J}_{\mathrm{mem}} \,. \tag{8.21}$$

Species conservation (8.2) is rewritten in terms of mass fraction with the relation $C_k = \rho Y_k / W_k$ to simplify the mass and momentum conservation equations. The storage term can then be rearranged to isolate $\partial Y_k / \partial t$ on the left-hand side, which should be zero at steady state and becomes the mass fraction residual. The mass storage term $R^{\mathrm{P}}_{\mathrm{ch}} = \partial \rho / \partial t$ is zero at steady state, but it is retained in the species conservation equation to improve solver convergence by maintaining the link between species and mass conservation. The mass fraction residual for species k in the channel is, therefore, given by (8.22). Since the species flux $\boldsymbol{J}_k$ includes first-order spatial derivatives of Y_k and ϕ, (8.22) introduces second-order derivatives of these state variables

$$R^{\mathrm{MF}}_{k,\mathrm{ch}} = \frac{1}{\rho}\left(-\nabla \cdot \boldsymbol{J}_k - Y_k R^{\mathrm{P}}_{\mathrm{ch}}\right). \tag{8.22}$$

Mass fractions at the electrode–channel and membrane–channel interfaces are found via species flux matching. At the electrode–channel interface, there are fluxes from the channel and electrode (due to reactions) for each species k; thus the residual is given by

$$R^{\mathrm{MF}}_{k,\text{ch-elec}} = \boldsymbol{J}_{k,\mathrm{ch}} - \boldsymbol{J}_{k,\mathrm{rxn}} \,. \tag{8.23}$$

At the membrane–channel interface, there are fluxes from the channel and through the membrane for each species k; thus the residual is given by

$$R^{\mathrm{MF}}_{k,\text{ch-mem}} = \boldsymbol{J}_{k,\mathrm{ch}} - \boldsymbol{J}_{k,\mathrm{mem}} \,. \tag{8.24}$$

Momentum conservation (8.3) can be rearranged to obtain $\partial \boldsymbol{v} / \partial t$, which should be zero at steady state and is therefore the residual. Taking components involved in the x- and y-direction momentum balances separately yields the x- and y-direction velocity residuals in the channels ((8.25) and (8.26)). The mass conservation storage term $R^{\mathrm{P}}_{\mathrm{ch}}$ is retained in (8.23) and (8.24) for the same reasons as in (8.22)

$$R^{x\mathrm{M}}_{\mathrm{ch}} = \frac{1}{\rho}\left[-\frac{\partial}{\partial x}(\rho v_x |v_x|) - \frac{\partial}{\partial y}(\rho v_x v_y) - \frac{\partial P}{\partial x} + \mu\left(\frac{\partial^2 v_x}{\partial x^2} + \frac{\partial^2 v_x}{\partial y^2}\right) - \rho_{\mathrm{c}}\frac{\partial \phi}{\partial x} - v_x R^{\mathrm{P}}_{\mathrm{ch}}\right], \tag{8.25}$$

$$R^{y\mathrm{M}}_{\mathrm{ch}} = \frac{1}{\rho}\left[-\frac{\partial}{\partial x}(\rho v_y v_x) - \frac{\partial}{\partial y}(\rho v_y |v_y|) - \frac{\partial P}{\partial y} + \mu\left(\frac{\partial^2 v_y}{\partial x^2} + \frac{\partial^2 v_y}{\partial y^2}\right) - \rho_{\mathrm{c}}\frac{\partial \phi}{\partial y} - v_y R^{\mathrm{P}}_{\mathrm{ch}}\right]. \tag{8.26}$$

8.2.3 Numerical Approaches

Electrochemical cell models can specify cell voltage and calculate electrical current or specify current and calculate voltage. The governing equations above presume that the example electrochemical system is solved in the voltage → current direction. Both approaches are valid, but specifying the voltage tends to be more numerically robust and physically intuitive because voltage is directly related to the electrochemical potential gradients, which drive electrochemical reactions at the electrodes and charge fluxes through solution. In

order to specify the current, an additional equation is required to relate the specified current to the sum of local current densities over each electrode. Finding a current density distribution, which solves the model and agrees with the specified current, can hinder the progress of typical Newton–Raphson solvers.

8.2.4 Model Calibration and Validation

Calibration and validation are necessary steps following the initial development of a transport model. Models are calibrated by comparing model predictions to physical measurements and then adjusting unknown (or uncertain) parameters until the predicted and measured values agree. Validation compares a broader set of predicted and measured quantities to establish that the model captures the intended physical processes and predicts them accurately. A separate validation may be required for each distinct transport process the model is intended to capture, depending on the level of confidence in the modeling approach.

The relationship between electrode current density and voltage (polarization curve) is often used to calibrate and/or validate electrochemical system models because it is sensitive to the all of the processes (reaction kinetics, charge transport, species transport, etc.) occurring in the system and it is easily measured. If a transport model accurately predicts the polarization curve, then it is likely to correctly capture the internal processes occurring in an electrochemical system. Furthermore, polarization curves govern the interactions between an electrochemical system and the power source driving it or the load it supports, so the polarization curve must be predicted accurately for system-level analysis.

The relationship between limiting current and limiting species flux provides an opportunity for calibration and validation. Larger species fluxes are required to support greater current density, thus the influence of transport on the polarization curve grows with increasing current density. The limiting current density is reached at the end of the polarization curve, when the available driving forces (electrochemical potential gradients, pressure gradients, etc.) are unable to further increase the flux of a key species. Varying the inlet concentrations, flow rates, and other parameters can change the limiting species and vary the limiting flux over a wide range. Current density is easily measured, so comparing the predicted and measured current densities is an excellent way to calibrate and validate a transport model.

8.3 Example Cell: Direct Borohydride–Hydrogen Peroxide Fuel Cell

The FV method of modeling transport in electrochemical cells is illustrated in this section by applying it to a DBFC. DBFCs generate electrical power by oxidizing aqueous BH_4^- and reducing aqueous H_2O_2 or gaseous O_2. Interest in DBFCs has grown due to several prospective advantages over batteries and other fuel cells, including greater energy density and specific energy. (The specific energy and energy density are concentration dependent. For 1 M $NaBH_4$/8 M NaOH fuel and 4 M H_2O_2/8 M H_2SO_4 oxidizer, assuming the full theoretical 3.01 V cell voltage, the specific energy is 210 W h/kg and the energy density 322 W h/l, on a reactants basis that neglects conversion losses. Higher values are possible and limited only by the saturation limits in aqueous solution.) However, the technology remains immature and challenges have inhibited its use in practical applications. Among the challenges are competing parasitic electrochemical reactions and low power density, and both are strongly influenced by transport in the reactant flow channels, as discussed in numerous DBFC review papers [8.20–27]. The strong influence of transport in DBFCs makes them a good case study showing the utility of FV transport models for understanding and designing electrochemical systems.

8.3.1 DBFC Overview

Numerous DBFC configurations have been reported in the literature, but this example focuses on the cell configuration illustrated in Fig. 8.4. Such DBFCs have been considered in experimental studies [8.28, 29] because they are simple to fabricate, resist precipitate accumulation, expose the full membrane area to the electrolyte solutions, and permit migration to aid reactant transport in the channels. Furthermore, this DBFC can be represented in 2-D if the channel side walls are inert (electrochemically inactive) and spaced widely enough to have negligible effect on the hydrodynamics of the reactant flows.

DBFCs with the cell configuration in Fig. 8.4 differ from common low-temperature fuel cells such as the PEMFC and DMFC. These differences stem from the use of aqueous electrolytes for the fuel and oxidizer, in contrast to the gaseous reactants in a PEMFC and the nonelectrolyte aqueous fuel solution in a DMFC. The catalysts in PEMFCs and DMFCs are in contact with an ion-conducting membrane to enable H^+ participation in the electrochemical reactions, but the catalyst in a DBFC can be located on the channel walls because the aqueous electrolytes in each channel sup-

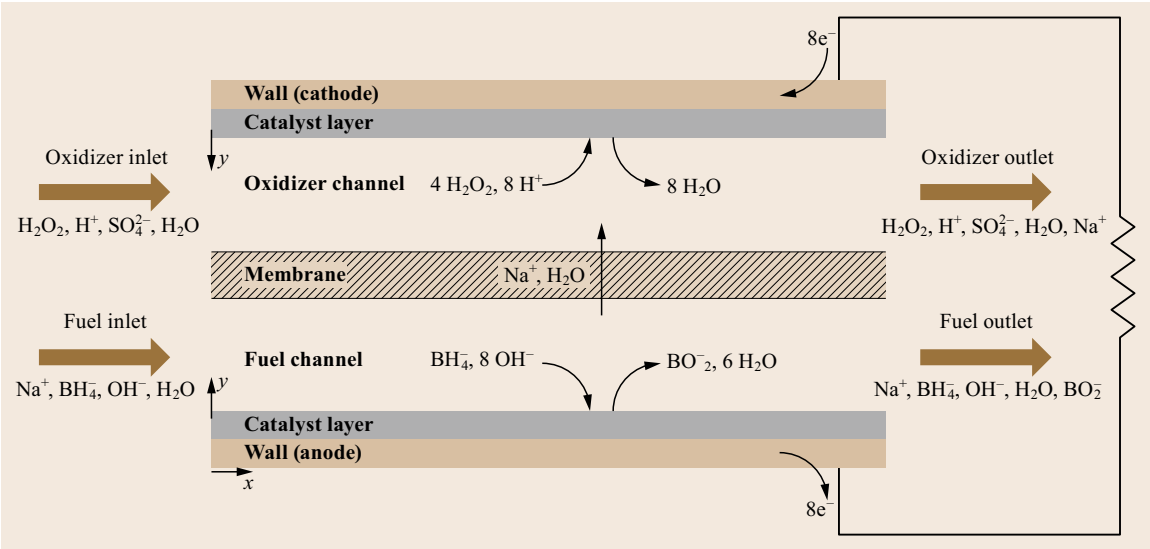


Fig. 8.4 Illustration of a DBFC, showing the cell geometry and ideal electrochemical processes

port ion transport. Channel transport in PEMFCs and DMFCs is governed by convection and diffusion, but in a DBFC migration also contributes to (or inhibits) species transport. Finally, slower diffusion in the liquid phase favors development of steeper concentration gradients in a DBFC, accentuating down-the-channel effects on cell performance.

In this DBFC, the fuel channel carries an aqueous solution containing $NaBH_4$ and NaOH, and the oxidizer channel carries an aqueous solution containing H_2O_2 and H_2SO_4. Each channel wall opposite the membrane is coated with an electrocatalyst; BH_4^- oxidation takes place at the anode (fuel channel wall) and H_2O_2 reduction takes place at the cathode (oxidizer channel wall). Electrons provided to the anode by BH_4^- oxidation travel through an external circuit to the cathode to reduce H_2O_2, while Na^+ ions maintain charge balance in the cell by crossing the membrane from fuel solution to oxidizer solution. The Na^+ ion flux through the membrane induces a H_2O flux due to electro-osmotic drag.

The net reaction (8.27) consumes BH_4^-, H_2O_2, OH^-, and H^+ and forms BO_2^- and H_2O with a standard cell potential of 3.01 V. Eight electrons are liberated by the anode half-cell reaction (8.28) and travel through the external circuit to be consumed by cathode half-cell reaction (8.29).

$$BH_4^- + 8\,OH^- + 4\,H_2O_2 + 8\,H^+ \rightarrow BO_2^- + 14\,H_2O \tag{8.27}$$

$$BO_2^- + 6\,H_2O + 8\,e^- \leftrightharpoons BH_4^- + 8\,OH^- \qquad E^0_{(8.28)} = -1.246\,\text{V versus RHE} \tag{8.28}$$

$$H_2O_2 + 2\,H^+ + 2\,e^- \rightleftharpoons 2\,H_2O \qquad E^0_{(8.29)} = 1.763\,\text{V versus RHE}\,. \tag{8.29}$$

The fuel solution includes OH^- to provide a reactant for BH_4^- oxidation and stabilize the BH_4^- fuel, which is otherwise consumed by homogenous hydrolysis reaction (8.30) to yield BO_2^-

$$BH_4^- + 2\,H_2O \rightarrow BO_2^- + 4\,H_2\,. \tag{8.30}$$

The rate of (8.30) depends on pH and temperature; it occurs more rapidly at low pH and high temperature. Similarly, H^+ in the oxidizer solution provides a reactant for H_2O_2 reduction and stabilizes the H_2O_2, which otherwise decomposes via (8.31). H^+ can also be directly reduced to H_2 via (8.32)

$$2\,H_2O_2 \rightarrow 2\,H_2O + O_2\,, \tag{8.31}$$

$$2\,H^+ + 2\,e^- \rightarrow 2\,H_2\,, \qquad E^0_{(8.32)} = 0.0\,\text{V versus RHE}\,. \tag{8.32}$$

While (8.30) and (8.31) occur slowly in solutions having appropriate pH, the rates are nevertheless accelerated by contact with the anode and cathode catalysts. Heterogeneous catalysis of BH_4^- hydrolysis and H_2O_2 decomposition decreases the number of electrons per oxidized BH_4^- anion to less than 8 and the number of electrons per reduced H_2O_2 molecule to less than 2. The coulombic efficiency η_{ce} of each half-cell reaction is often characterized by proximity to the theoretical number of electrons transferred; an anode that captures 4 electrons (out of the 8 available) per consumed BH_4^- anion would have a coulombic efficiency of 50%.

8.3.2 Transport in the Channels

The advection, diffusion, and migration fluxes of mass, momentum, species, and charge are estimated using the ideal solution approach outlined for the generic electrochemical system. The diffusivities for (8.13) and the apparent molar volumes for (8.7) are provided in Table 8.1.

The electric potential in the channels is found by enforcing electroneutrality (8.6) rather than Poisson's electrostatic equation (8.5) because the electrochemical double layers at each electrode are thin, and therefore assumed to be part of the electrode–channel interfaces. The boundary conditions from the generic electrochemical system are applied to the DBFC, but the fluxes that replace boundary conditions for Y_k at the membrane–channel and electrode–channel interfaces have yet to be defined. The boundary fluxes are provided by the membrane transport and electrode reaction submodels, which are discussed next.

8.3.3 Transport at the Membrane–Channel Interfaces

A 1-D submodel estimates the Na^+ and H_2O mole fluxes across a Nafion membrane at each point down the channel. Table 8.2 lists the relevant transport parameters and Fig. 8.5 illustrates the membrane submodel schematically.

Table 8.1 Diffusivities and apparent molar volumes of fuel and oxidizer solutes in H_2O at infinite dilution and 298 K

Species	Diffusivity ($\times 10^9$ m^2/s)	Apparent molar volume ($\times 10^3$ m^3/kmol)
BH_4^-	2.42 [8.30]	−5.83[a]
BO_2^-	0.814 [8.31]	−14.5 [8.14]
H^+	9.312 [8.10]	0 [8.14]
H_2O_2	1.19 [8.32]	22.17 [8.32]
Na^+	1.334 [8.10]	−1.11 [8.14]
OH^-	5.260 [8.33]	−4.18 [8.14]
SO_4^{2-}	0.625 [8.34]	24.8 [8.35]

[a]Value estimated to be smaller than BO_2^- by the diffusivity ratio

Table 8.2 Summary of thermophysical and transport properties in fully hydrated ($\lambda = 22$) Nafion 115 in the Na^+ form at 298 K

Property	Value
Na^+ mobility, $u_{Na^+,mem}$	2.7×10^{-8} m^2/(V s) [8.36]
H_2O permeability, p_{H_2O}	1.7×10^{-14} m/(Pa s) [8.37]
Na^+ concentration, $C_{Na^+} = C_{SO_3^-}$	1.13 kmol/m^3 [8.38]
Na^+ – H_2O electro-osmotic drag coefficient in fully hydrated Nafion in the Na^+ form, n_d	9.2 kmol H_2O / kmol Na^+ [8.36]

The electric potential gradient in the membrane of an operating DBFC drives Na^+ ions from fuel solution to oxidizer solution, but it also opposes crossover of fuel solution anions and oxidizer solution cations. Studies of BH_4^- crossover through Nafion 117 membranes have shown that the crossover rate diminishes with increasing current density (increasing electric potential gradient) [8.34]. When the cell is at open circuit, however, species other than Na^+ may crossover as the electric potential gradient relaxes. Since this model is intended to simulate *operating* DBFCs and not necessarily predicting the open circuit voltage, only Na^+ and H_2O are assumed to cross the membrane.

Studies of Nafion membranes in contact with aqueous electrolyte solutions containing Na^+ and H^+ have shown that the electronic mobilities and electro-osmotic drag coefficient depend on mole fractions $X_{H^+,mem}$ and $X_{Na^+,mem}$ [8.36, 37]. The electronic mobilities in Nafion 115 are described in terms of mole fraction and interaction parameter k_{int}, in (8.33) and (8.34) [8.37]

$$u_{Na^+,mem} = \frac{u^0_{Na^+,mem}\,(1 - k_{int} X_{H^+,mem})}{F}\,, \qquad (8.33)$$

$$u_{H^+,mem} = \frac{u^0_{H^+,mem}\,(1 - k_{int} X_{Na^+,mem})}{F}\,. \qquad (8.34)$$

Equations (8.33) and (8.34) include Faraday's constant to convert from electronic mobility to standard ion mobility. The electronic mobilities with only one cation species in the membrane are $u^0_{Na^+,mem} = (2.7 \pm 0.1)\times10^{-8}$ m^2/(V s) and $u^0_{H^+,mem} = (1.49 \pm 0.03)\times10^{-7}$ m^2/(V s), and the interaction parameter is $k_{int} = 0.20 \pm 0.02$ [8.36]. The membrane is assumed to be fully hydrated, which in the Na^+ form means the ratio of H_2O molecules to fixed SO_3^- sites in the membrane is $\lambda = 22$ [8.38]. Full hydration is a reasonable assumption in a DBFC, given that both sides are in contact with aqueous solutions, although λ may fall below 22 due to

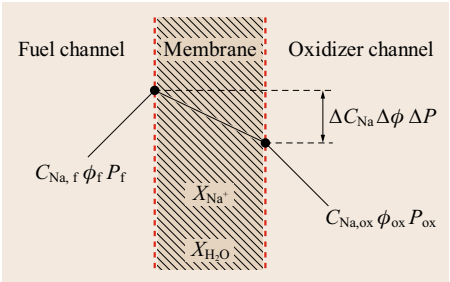


Fig. 8.5 State variable locations and linear gradient estimation in the membrane submodel

the osmotic gradients between the membrane and hypertonic fuel and oxidizer solutions [8.39].

Assuming that the Nafion membrane is thin (N117: 208 μm and N115: 161 μm thick [8.40]) and fully hydrated enables two simplifications. First, gradients in the membrane ($\nabla\phi$, ∇C_k, ∇P) are approximately linear, so the membrane is not discretized in the y-direction. Gradients are estimated as the difference between values at the membrane–channel interfaces divided by the membrane thickness. Second, transport through the membrane in the x-direction is omitted because it is insignificant compared to x-direction flows in the channels. Na^+ is driven through the membrane by migration and diffusion. Thus, the net Na^+ mole flux from fuel channel to oxidizer channel is given by

$$\boldsymbol{J}_{\mathrm{Na,mem}} = -D_{\mathrm{Na}}\frac{\mathrm{d}C_{\mathrm{Na}}}{\mathrm{d}y} - z_{\mathrm{Na}}u_{\mathrm{Na}}FC_{\mathrm{Na}}\frac{\mathrm{d}\phi}{\mathrm{d}y}\,. \qquad (8.35)$$

The concentration of Na^+ must be equal to the concentration of SO_3^- groups in the membrane to maintain electroneutrality. Since $C_{SO_3^-}$ in the membrane is uniform, the Na^+ concentration gradient must be zero: $\mathrm{d}C_{Na^+}/\mathrm{d}y = 0$. Na^+ diffusion through the membrane due to the difference in concentration ΔC_{Na^+} across the membrane does take place, however. The concentration gradient term in (8.35) captures the contribution ΔC_{Na^+} makes to $\Delta\tilde{\mu}_{Na^+}$ by calculating $\mathrm{d}C_{Na^+}/\mathrm{d}y$ based on the concentrations at the membrane–channel interfaces.

Water crosses the membrane due to permeation and electro-osmotic drag induced by the Na^+ flux (8.36)

$$\boldsymbol{J}_{\mathrm{H_2O,mem}} = -p_{\mathrm{H_2O}}\Delta P\frac{\rho_{\mathrm{H_2O}}}{W_{\mathrm{H_2O}}} + n_{\mathrm{d},Na^+}\boldsymbol{J}_{\mathrm{Na,mem}}\,. \qquad (8.36)$$

Water diffusion is neglected because the water concentration is nearly equal on both sides of the membrane.

8.3.4 DBFC Transport Model Calibration

The least certain parameters in the DBFC transport model are the reaction rate parameters. They are not transport parameters per se, but they are necessary to accurately predict species fluxes at the electrode–channel interfaces and solve the model, so they are appropriate fitting parameters. The rate parameters are fitted by comparing five predicted and measured polarization curves.

Rate parameters are fitted by minimizing the 2-norm of errors between the measured and predicted current density at each cell voltage on the polarization curves. Separate parameters k_a and β_a in (8.18) are fitted for each of reactions (8.28) through (8.32). Parameters n_e and β_c are not fitted. Instead, the following values are assumed: $n_e = 1$ for reactions (8.28) and (8.29), $n_e = 2$ for reaction (8.32), and $\beta_c = (1 - \beta_a)$ for all reactions. New values of k_c are chosen for each rate law in each fitting iteration to ensure that the rate laws are thermodynamically consistent, that is, they predict zero net rate at standard conditions with an electrode–channel

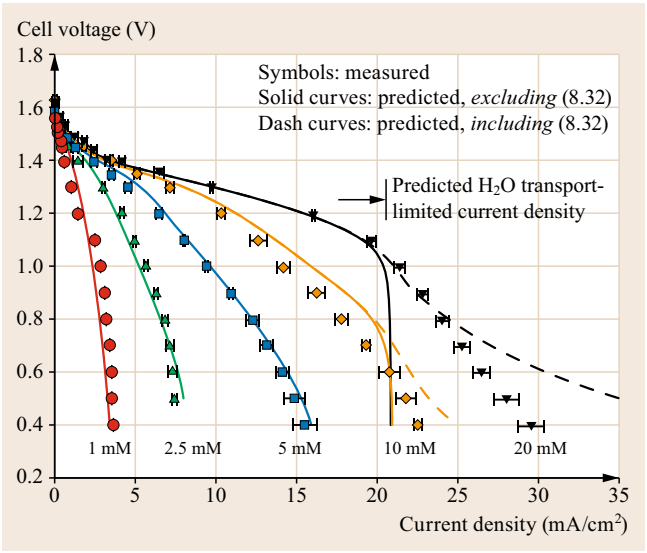


Fig. 8.6 Comparison between measured and predicted DBFC polarization curves with the indicated BH_4^- concentrations in 2 M NaOH, 50 mM H_2O_2/1 M H_2SO_4, and flow rates of 10 ml/min in channels 100 mm long, 0.5 mm high, and 5 mm deep

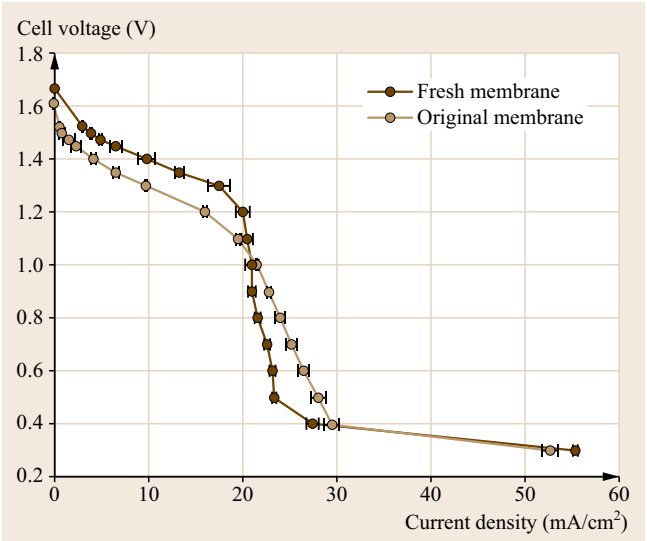


Fig. 8.7 Measured DBFC polarization curves. *Original membrane* is the 20 mM BH_4^- curve replotted from Fig. 8.6 and *fresh membrane* is an additional measurement under the same operating conditions with a higher conductivity membrane

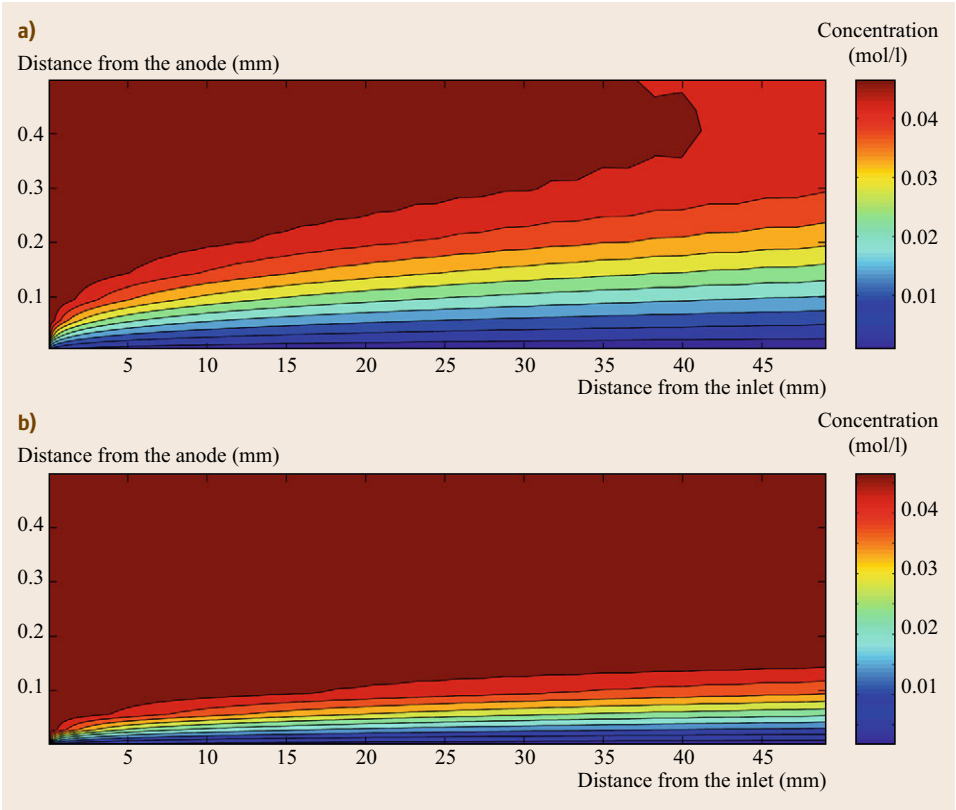


Fig. 8.8a,b Predicted BH_4^- concentration in the fuel channel with baseline operating conditions and flow rates of 1 ml/min **(a)** and 10 ml/min **(b)**. Shows the influence of convection on BH_4^- concentration gradient (and therefore flux) near the anode

interface electric potential difference $\Delta\phi$ equal to the equilibrium value E^0_{rxn}. Equation (8.18) can be solved for k_c with $a_k^{\upsilon_k} = 1$, $T = 298\,\text{K}$, $\Delta\phi = E^0_{\text{rxn}}$, k_a and β_a equal to the guessed values from the fitting algorithm, and $r = 0$. Subsequently replacing k_c and β_c in each rate law yields thermodynamically consistent rates in terms of known and fitted parameters

$$r_{(8.28)} = k_{a,(8.28)} C_{BH_4^-} e^{\beta_{a,(8.28)} f\Delta\phi} - k_{a,(8.28)} e^{fE^0_{(8.28)}} C_{BO_2^-} e^{-(1-\beta_{a,(8.28)})f\Delta\phi}, \tag{8.37}$$

$$r_{(8.29)} = k_{a,(8.29)} e^{\beta_{a,(8.29)} f\Delta\phi} - k_{c,(8.29)} e^{fE^0_{(8.29)}} C_{H_2O_2} e^{-(1-\beta_{a,(8.29)})f\Delta\phi}, \tag{8.38}$$

$$r_{(8.32)} = k_{c,(8.32)} e^{-fE^0_{(8.32)}} C^2_{H^+} e^{2\beta_{a,(8.32)} f\Delta\phi} - k_{c,(8.32)} C_{H_2} e^{-2(1-\beta_{a,(8.32)})f\Delta\phi}. \tag{8.39}$$

The rate laws for (8.28) and (8.29) (see (8.37) and (8.38)) omit the concentrations of OH^-, H^+, and H_2O because they are present in excess and, therefore, have little influence over the rates. The second-order dependence on C_{H^+} and $n_e = 2$ in (8.39) imply that the rate limiting step for (8.32) is H^+ accepting an electron, which must occur twice. The concentration of H^+ was included in (8.39), despite being in excess, because it was the only reactant in the rate equation and omitting it would have permitted a runaway reaction with no H^+ present. This cannot occur in a real cell, but it can cause numerical problems when solving the model. The rates for reactions (8.30) and (8.31) are assumed first order and irreversible (Eqs. (8.40) and (8.41))

$$r_{(8.30)} = k_{f,(8.30)} C_{BH_4^-}, \tag{8.40}$$

$$r_{(8.31)} = k_{f,(8.31)} C_{H_2O_2}. \tag{8.41}$$

The complete set of fitted rate parameters is given in Table 8.3.

Table 8.3 Fitted reaction rate parameters

Anode parameters		Cathode parameters	
$k_{a,(8.28)}$	9.25×10^{-3} m/s	$k_{c,(8.28)}$	7.54×10^{-3} m/s
$\beta_{a,(8.28)}$	0.098	$\beta_{c,(8.28)}$	0.455
$k_{f,(8.30)}$	3.09×10^{-4} m/s	$k_{f,(8.31)}$	6.34×10^{-4} m/s
ϵ_a	2.73	$k_{c,(8.32)}$	1.19×10^{-9} $m^4/(kmol\,s)$
		$\beta_{c,(8.32)}$	0.141
		ϵ_c	4.11

The five measured and predicted polarization curves are shown in Fig. 8.6. The following geometric parameters and operating conditions from the measurements were inputs to the transport model: channels 100 mm long, 0.5 mm high, and 5 mm wide; 1, 2.5, 5, 10, and 20 mM BH_4^-/2 M NaOH fuel with 50 mM H_2O_2/1 M H_2SO_4 oxidizer; flow rates of 10 ml/min. The fuel concentration range was chosen to span from fuel-limited to oxidizer-limited stoichiometry, thereby ensuring that the model captures transport in both the fuel and oxidizer. The model and measurements agree at low BH_4^- concentration and low cell voltage, indicating that the model accurately predicts BH_4^- transport rate in the fuel solution. The measured 20 mM BH_4^- curve does not show the expected H_2O_2 transport limit at 22 mA/cm^2 because H^+ reduction at the cathode also contributes to the current density. The H_2O_2 transport-limited current density is revealed by another experiment, however, using a membrane with higher conductivity. The higher conductivity membrane incurs less Ohmic voltage drop so that the cathode reaches the H^+ reduction onset potential at higher current density, as shown in Fig. 8.7. This offsets the current contributed by H^+ reduction from the current contributed by H_2O_2 reduction, to distinguish the H_2O_2 transport–limited current density at $\approx$ 22 mA/cm^2. The agreement between predicted and measured H_2O_2 transport limited current densities corroborates the predicted H_2O_2 transport rate.

8.3.5 Results from the DBFC Transport Model

The calibrated model is used to investigate the relationships between transport in the channels and DBFC performance. For most of these studies a baseline case was analyzed, consisting of 40 mM BH_4^-/2 M NaOH fuel and 250 mM H_2O_2/1 M H_2SO_4 oxidizer flowing at 10 ml/min.

The influence of flow rate on BH_4^- distribution in the fuel channel is shown in Fig. 8.8, where the BH_4^- concentration boundary layer near the anode is much wider at 1 ml/min (Fig. 8.8a) than at 10 ml/min (Fig. 8.8b). The compact boundary layer with higher flow rate results from greater convection mass transport of BH_4^- to the anode, and has two consequences. First, the DBFC has low single-pass fuel utilization, as often observed in experiments, because most fuel flows through the channel before it can be transported to the anode. Second, the higher flow rate supports greater BH_4^- flux to the anode, and therefore higher peak power density, as shown by the power curves in Fig. 8.9. Figure 8.9 shows that greater flow rates yield greater power density, but with diminishing returns as other processes

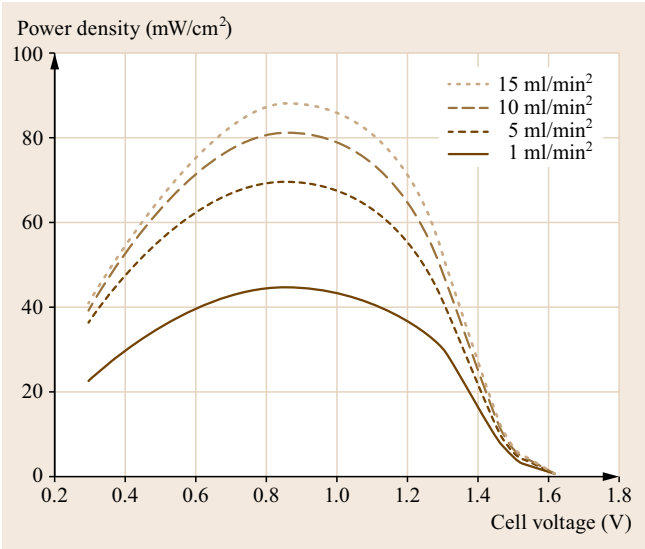


Fig. 8.9 Predicted power density for fuel flow rates from 1–15 ml/min, oxidizer flow rate of 10 ml/min and 50 mM BH_4^-/250 mM H_2O_2

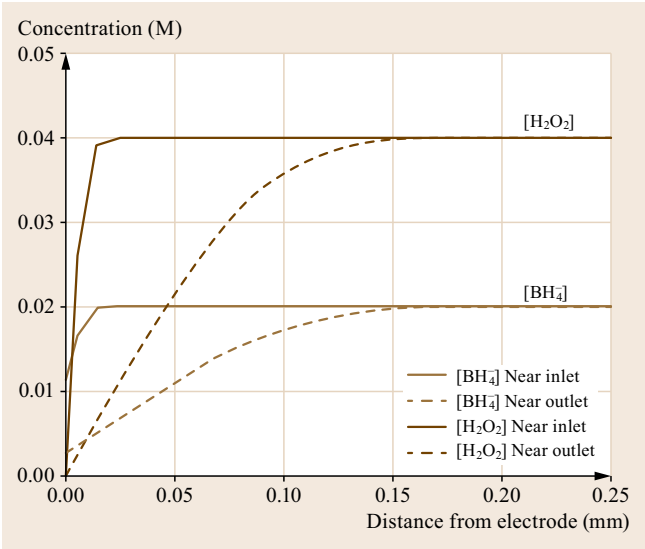


Fig. 8.10 Predicted BH_4^- concentration near the anode and predicted H_2O_2 concentration near the cathode, at the inlet and outlet, given baseline operating conditions

in the DBFC (transport in the oxidizer channel, membrane ohmic losses, etc.) begin to limit power density.

The DBFC current density should be H_2O_2 transport-limited in the baseline case, given the relative concentrations and diffusivities of BH_4^- and H_2O_2. Figure 8.10 plots BH_4^- and H_2O_2 concentration near the electrodes at the inlet and exit of each channel. The H_2O_2 concentration falls to near zero at the end of the

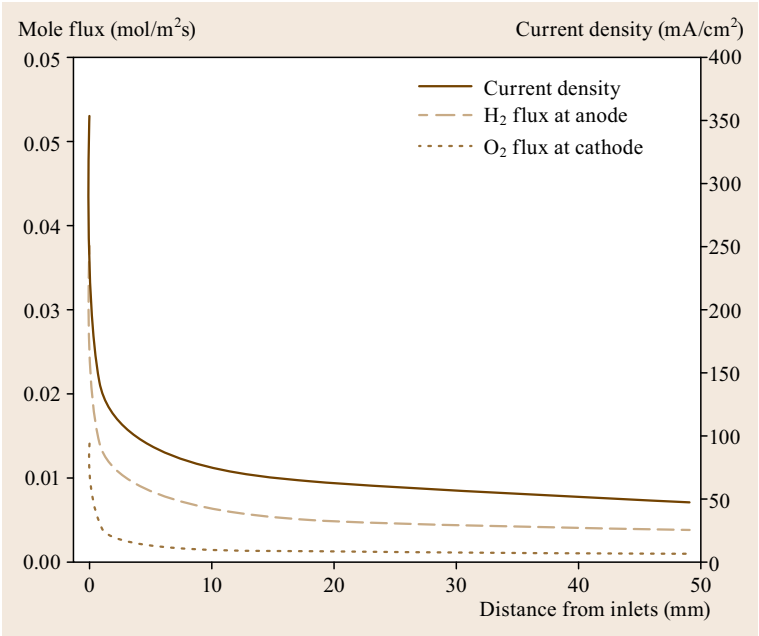


Fig. 8.11 Predicted current density and H_2 and O_2 production rates by parasitic reactions with respect to position in the channel with baseline operating conditions. Demonstrates down-the-channel variation of current production and losses to parasitic reactions due to concentration boundary layer development

oxidizer channel, showing that it does limit the current density.

Transport effects shift concentrations near the electrodes, which lead to changes in cell performance that depend on distance from the inlets. Decreasing reactant concentrations and increasing product concentrations slow the rates of charge transfer reactions so that current density falls from inlet to outlet, as shown in Fig 8.11. The rates of H_2 and O_2 production by parasitic reactions (8.30) and (8.31) at the anode and cathode, respectively, also decrease at points far from the inlet for the same reason. While the current density and parasitic gas production rates both trend lower with distance from the inlets, they change at different rates with respect to distance. The parasitic reaction rates are more sensitive to changes in concentration near the electrodes than the charge transfer reaction rates because the charge transfer reaction rates also depend on the electric potential difference between the electrode and electrolyte.

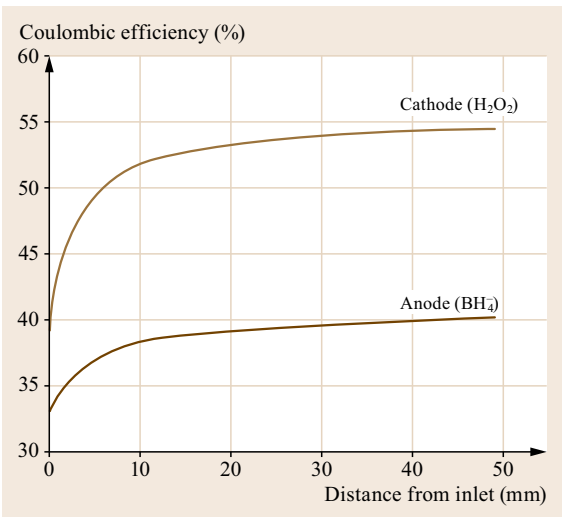


Fig. 8.12 Predicted coulombic efficiencies at the anode and cathode with respect to distance from the channel inlets, for the baseline case at 1.1 V cell

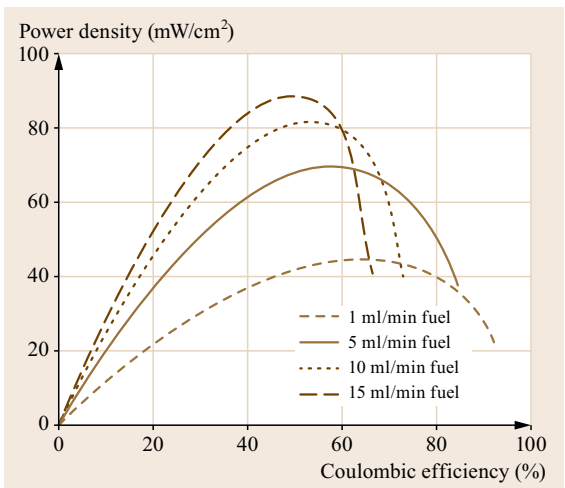


Fig. 8.13 Predicted power density with respect to coulombic efficiency for flow rates ranging from 1 to 15 ml/min, for the baseline case at 1.1 V cell

As a result, the parasitic reactions (8.30) and (8.31) are outcompeted by the charge transfer reactions (8.28), (8.29), and (8.32) at points far from the inlets. These trends are illustrated in Fig. 8.12, which plots coulombic efficiency as a function of distance from the inlets. Figure 8.12 shows how transport processes can affect efficiency by shifting the relative rates of simultaneous electrode reactions.

A similar trend relates coulombic efficiency to flow rate. Higher flow rates increase convective transport of reactants to the electrodes and raise the local reactant concentrations. The higher concentrations favor parasitic reactions over charge transfer reactions, because the parasitic reaction rates are more sensitive to concentration. Figure 8.13 plots predicted power density in the fuel channel with respect to coulombic efficiency for several fuel flow rates to demonstrate this trend and show the trade-off between power density and coulombic efficiency. A similar trend is observed with respect to BH_4^- inlet concentration; higher concentration yields higher power density and lower coulombic efficiency.

A transport model can offer insight unavailable or difficult to acquire from experiments; one example is separating the contributions of diffusion, migration, and advection. Figure 8.14 shows the diffusion, migration, and advection fluxes of BH_4^- at the mid-point of the fuel channel for the baseline case. Transport near the anode is dominated by diffusion due to the large (convection enhanced) concentration gradient there. The migration flux is greatest outside the concentration boundary layer because the migration flux is proportional to BH_4^- concentration. The *y*-direction advection flux is zero at the anode (due to the impermeable electrode) and then increases toward the membrane due to the net mass fluxes of Na^+ and H_2O crossing to the oxidizer channel. The BH_4^- diffusion and migration fluxes grow more negative (oriented toward the anode) near the membrane because of the electroneutrality constraint. Advection carries all species toward the membrane, but because the membrane is impermeable to BH_4^-, the net BH_4^- flux at the membrane–channel interface must be zero.

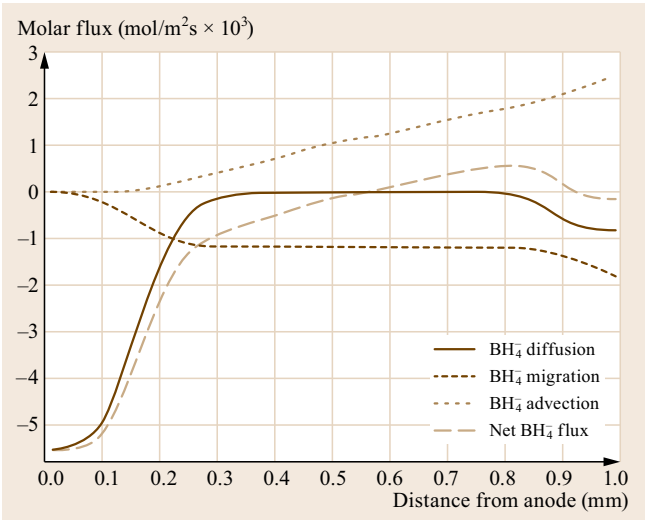


Fig. 8.14 Mole fluxes of BH_4^- in the fuel channel *y*-direction, half way between inlet and outlet, as a profile from anode to membrane. Positive fluxes are toward the membrane and negative fluxes are toward the anode

A BH_4^- concentration gradient develops near the membrane to create BH_4^- diffusion and migration fluxes that oppose the advection flux and yield zero net BH_4^- flux at the membrane.

A similar effect occurs near the anode, where a Na^+ concentration boundary develops near the anode as shown in Fig. 8.15. The net Na^+ flux at the anode must be zero because it does not participate in the anode reactions, but a Na^+ migration flux develops due to the electric field. A Na^+ concentration gradient develops near the anode to drive a diffusion flux that opposes the migration flux and yields zero net Na^+ flux near the anode. Energy is required to maintain the Na^+ concentration gradient, so the DBFC pays a penalty in the form of lower cell voltage–in the baseline case the cell voltage falls by $\approx 1\%$. The Na^+ concentration gradient influences cell voltage by depressing the concentrations of anions near the anode through the

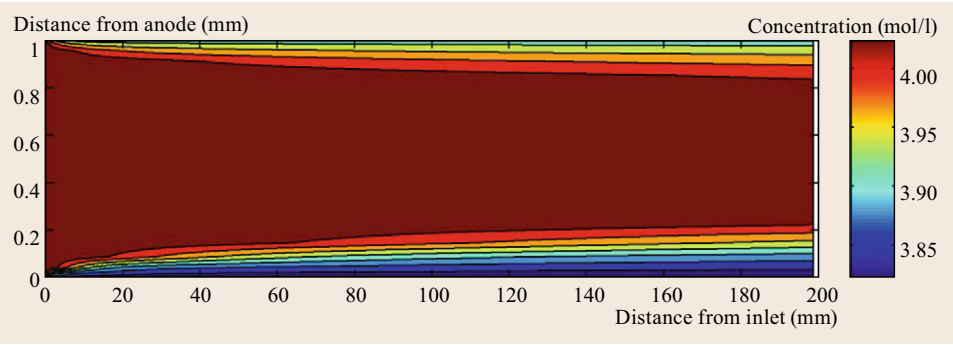


Fig. 8.15 Predicted Na^+ concentration in the fuel channel for the baseline case at 1.1 V cell

electroneutrality constraint. The lower concentrations of reactant anions BH_4^- and OH^- near the anode depress the equilibrium (and therefore the operating) cell voltage. A second, less pronounced Na^+ concentration boundary layer develops near the membrane as Na^+ crosses to the oxidizer channel.

8.4 Conclusions

Discretized computational models using finite volume methods to establish the governing conservation equations for the state variables in electrochemical cells have become valuable tools for understanding the complex coupling of transport and electrochemistry in these devices. The ability to model multidimensional problems with flowing electrolytes as demonstrated in this chapter with a FV model, permits researchers and developers to assess designs with different geometries and to evaluate operating conditions. As shown in this chapter for an all-liquid DBFC with hydrogen peroxide as the oxidizer, FV modeling results provide unique insight into the links between transport fluxes, electrochemical reaction rates, cell efficiency, and reactant utilization. The DBFC example also showed that FV models can predict the spatial variations that arise due to the interactions of electrodes and ion exchange membranes with flowing electrolytes, and these variations can strongly influence performance. The DBFC example focused on species concentrations, but the same FV methods can be applied to capture the influence of other state variables such as temperature. FV models coupling transport and electrochemistry can be used to identify opportunities for improved cell performance with whichever state variables are important for a given electrochemical system. Ultimately, greater computational power and advanced techniques will likely make FV models faster and more sophisticated, which will enable rigorous design optimization of electrochemical cells and larger system-level models with detailed electrochemical components.

8.5 Nomenclature

- a Anodic parameter (subscript)
- a_k Activity of species k
- β Electrochemical reaction symmetry factor
- c Cathodic parameter (subscript)
- C_k Concentration of species k
- $\mathcal{D}_k$ Binary diffusivity of species k with respect to concentration
- D_k Binary diffusivity of species k with respect to activity
- E Electric field strength
- E^0_{rxn} Standard half-cell potential for reaction rxn
- F Faraday's constant
- f $F/R_{\text{ig}}T$
- i Current density
- I Ionic strength of electrolyte
- $\boldsymbol{J}$ Mass flux
- $\boldsymbol{J}_k$ Molar fluxes of species k
- k_q Rate constant for reaction q
- ϵ Electrode roughness factor
- η_{ce} Coulombic efficiency
- μ_k Chemical potential of species k
- $\tilde{\mu}_k$ Electrochemical potential of species k
- n_{e} Number of e^- in rate-limiting reaction step
- ϕ Electric potential
- P Pressure
- p_k Permeability to species k
- ρ Mass density
- ρ_{c} Net charge density
- R Residual (error) in governing equation
- R_{ig} Ideal gas constant
- r_q Rate of reaction q
- t Time
- T Temperature
- u_k Mobility of species k in electrolyte solution
- $u^0_{k,\text{mem}}$ Electronic mobility of species k in membrane
- v, v_x, v_y Velocity components in x- and y-directions
- $\nu_{k,q}$ Stoichiometric coefficient of species k in reaction q
- $\dot{V}$ Volumetric flow rate
- W_k Molar mass of species k
- x Coordinate axis parallel to membrane
- y Coordinate axis perpendicular to membrane
- Y_k Mass fraction of species k
- z_k Charge number of species k
- γ_k Activity coefficient for species k

Acknowledgments. The authors are grateful to the Office of Naval Research, the Naval Research Laboratory Edison Memorial Training Program, and the Naval Research Laboratory Chemistry Division for their support of this research.

References

8.1 I.B. Sprague, P. Dutta: Modeling of diffuse charge effects in a microfluidic based laminar flow fuel cell, Numer. Heat Transf. Part A **59**(1), 1–27 (2011)

8.2 J. Ge, H. Liu: A three-dimensional mathematical model for liquid-fed direct methanol fuel cells, J. Power Sources **160**(1), 413–421 (2006)

8.3 Z.H. Wang, C.Y. Wang: Mathematical modeling of liquid-feed direct methanol fuel cells, J. Electrochem. Soc. **150**(4), A508–A519 (2003)

8.4 J.Q. Zou, Y. He, Z. Miao, X. Li: Non-isothermal modeling of direct methanol fuel cell, Int. J. Hydrogen Energy **35**(13), 7206–7216 (2010)

8.5 V.A. Danilov, J. Lim, I.L. Moon, H. Chang: Three-dimensional, two-phase, CFD model for the design of a direct methanol fuel cell, J. Power Sources **162**(2), 992–1002 (2006)

8.6 R.O. Stroman, G.S. Jackson: Modeling the performance of an ideal $NaBH_4$-H_2O_2 direct borohydride fuel cell, J. Power Sources **247**, 756–769 (2014)

8.7 R.O. Stroman, G.S. Jacksonc, Y. Garsanyd, K. Swider-Lyonsa: A calibrated hydrogen-peroxide direct-borohydride fuel cell model, J. Power Sources **271**, 421–430 (2014)

8.8 J. Christensen, D. Cook, P. Albertus: An efficient parallelizable 3D thermoelectrochemical model of a Li-ion cell, J. Electrochem. Soc. **160**(11), A2258–A2267 (2013)

8.9 G. Qiu, A.S. Joshi, C.R. Dennison, K.W. Knehr, E.C. Kumbur, Y. Sun: 3-D pore-scale resolved model for coupled species/charge/fluid transport in a vanadium redox flow battery, Electrochim. Acta **64**, 46–64 (2012)

8.10 J.S. Newman, K.E. Thomas-Alyea: *Electrochemical Systems*, 3rd edn. (Wiley, Hoboken 2004) p. 647

8.11 I. Sprague, P. Dutta: Role of the diffuse layer in acidic and alkaline fuel cells, Electrochim. Acta **56**(12), 4518–4525 (2011)

8.12 J. Liu, C.W. Monroe: Solute-volume effects in electrolyte transport, Electrochim. Acta **135**, 447–460 (2014)

8.13 R.B. Bird, W.E. Stewart, E.N. Lightfoot: *Transport Phenomena*, 2nd edn. (Wiley, New York 2002)

8.14 G. Ottonello: *Principles of Geochemistry* (Columbia Univ. Press, New York 1997)

8.15 K.S. Pitzer, G. Mayorga: Thermodynamics of electrolytes II. Activity and osmotic coefficients for strong electrolytes with one or both ions univalent, J. Phys. Chem. **77**(19), 2300–2308 (1973)

8.16 S. Whitaker: Diffusion and dispersion in porous media, Am. Inst. Chem. Eng. J. **13**(3), 420–427 (1967)

8.17 H. Wu, P. Berg, X. Li: Non-isothermal transient modeling of water transport in PEM fuel cells, J. Power Sources **165**, 232–243 (2007)

8.18 D.H. Schwarz, N. Djilali: 3D modeling of catalyst layers in PEM fuel cells: Effects of transport limitations, J. Electrochem. Soc. **154**(11), B1167–B1178 (2007)

8.19 E.S. Oran, J.P. Boris: *Numerical Simulation of Reactive Flow*, 2nd edn. (Cambridge Univ. Press, Cambridge 2001)

8.20 J. Ma, N.A. Choudhury, Y. Sahai: A comprehensive review of direct borohydride fuel cells, Renew. Sustain. Energy Rev. **14**(1), 183–199 (2010)

8.21 U.B. Demirci: Direct borohydride fuel cell: Main issues met by the membrane-electrodes-assembly and potential solutions, J. Power Sources **172**(2), 676–687 (2007)

8.22 R. Retnamma, A.Q. Novais, C.M. Rangel: Kinetics of hydrolysis of sodium borohydride for hydrogen production in fuel cell applications: A review, Int. J. Hydrogen Energy **36**(16), 9772–9790 (2011)

8.23 D.M.F. Santos, C.A.C. Sequeira: Sodium borohydride as a fuel for the future, Renew. Sustain. Energy Rev. **15**(8), 3980–4001 (2011)

8.24 B.H. Liu, Z.P. Li: Current status and progress of direct borohydride fuel cell technology development, J. Power Sources **187**(2), 291–297 (2009)

8.25 C.P. de Leon, F.C. Walsh, D. Pletcher, D.J. Browning, J.B. Lakeman: Direct borohydride fuel cells, J. Power Sources **155**(2), 172–181 (2006)

8.26 I. Merino-Jimenez, C. Ponce de León, A.A. Shah, F.C. Walsh: Developments in direct borohydride fuel cells and remaining challenges, J. Power Sources **219**, 339–357 (2012)

8.27 G.H. Miley, N. Luo, J. Mather, R. Burton, G. Hawkins, L. Gu, E. Byrd, R. Gimlin, P.J. Shrestha, G. Benavides, J. Laystrom, D. Carroll: Direct $NaBH_4/H_2O_2$ fuel cells, J. Power Sources **165**(2), 509–516 (2007)

8.28 R.C. Urian, C.J. Patrissi, S.P. Tucker, C.M. Deschenes, F.W. Bielwaski, D.W. Atwater: Direct borohydride/hydrogen peroxide fuel cell development, 43rd Power Sources Conference 2008 (Curran Associates, Red Hook 2011) pp. 295–298

8.29 R.C. Urian: Air independent fuel cells utilizing borohydride and hydrogen peroxide, Mater. Res. Soc. Symp. Proc. (2010), doi:10.1557/PROC-1213-T01-09

8.30 D.M.F. Santos, C.A.C. Sequeira: Chronopotentiometric investigation of borohydride oxidation at a gold electrode, J. Electrochem. Soc. **157**(1), F16–F21 (2010)

8.31 C.R. Cloutier, A. Alfantazi, E. Gyenge: Physicochemical transport properties of aqueous sodium metaborate solutions for sodium borohydride hydrogen generation and storage and fuel cell applications, Adv. Mater. Res. **15–17**, 267–274 (2006)

8.32 W.C. Schumb: *Hydrogen Peroxide*, Am. Chem. Soc. Monogr. (Reinhold, New York 1955)

8.33 J. Newman: Current distribution on a rotating disk below limiting current, J. Electrochem. Soc. **113**(12), 1235–1241 (1966)

8.34 J.M. Nielsen, A.W. Adamson, J.W. Cobble: The self-diffusion coefficients of the ions in aqueous sodium chloride and sodium sulfate at 25-degrees, J. Am. Chem. Soc. **74**(2), 446–451 (1952)

8.35 A. Poisson, J. Chanu: Semi-empirical equations for the partial molar volumes of some ions in water and seawater, Mar. Chem. **8**, 289–298 (1980)

8.36 T. Okada, S. Møller-Holst, O. Gorseth, S. Kjelstrup: Transport and equilibrium properties of Nafion

membranes with H^+ and Na^+ ions, J. Electroanal. Chem. **442**(1/2), 137–145 (1998)

8.37 T. Okada, H. Satou, M. Okuno, M. Yuasa: Ion and water transport characteristics of perfluorosulfonated ionomer membranes with H^+ and alkali metal cations, J. Phys. Chem. B **106**(6), 1267–1273 (2002)

8.38 C.E. Evans, R.D. Noble, S. Nazeri-Thompson, B. Nazeri, C.A. Koval: Role of conditioning on water uptake and hydraulic permeability of Nafion membranes, J. Membr. Sci. **279**(1/2), 521–528 (2006)

8.39 D.M.F. Santos, C.A.C. Sequeira: Effect of membrane separators on the performance of direct borohydride fuel cells, J. Electrochem. Soc. **159**(2), B126–B132 (2012)

8.40 N. Lakshminarayanaiah: *Transport Phenomena in Membranes* (Academic, New York 1969)

9. Catalyst Layer Modeling

Tanja Vidaković-Koch, Richard Hanke-Rauschenbach, Isaí Gonzalez Martínez, Kai Sundmacher

The overall performance of a fuel cell or an electrochemical reactor depends greatly on properties of catalyst layers, where electrochemical reactions take place. Optimization of these structures in the past was mainly guided by experimental methods. For substantial progress in this field, combination of experiments with modeling is highly desirable. In this chapter focus is on macroscale models, since at the moment they provide more straightforward relationship to experimentally measurable quantities. After introducing the physical structure of a catalyst layer, we discuss typical macroscale modeling approaches such as interface, porous, and agglomerate models. We show how governing equations for the state fields, like potential or concentration can be derived and which typical simplifications can be made. For derivations, a porous electrode model has been chosen as a reference case. We prove that the interface model is a simplification of a porous model, where all gradients can be neglected. Furthermore, we demonstrate that the agglomerate model is an extension of the porous model, where in addition to macroscale, additional length scale is considered. Finally some selected examples regarding different macroscale models have been shown. Interface model has low capability to describe the structure of the catalyst layer, but it can be utilized to resolve complex reaction mechanisms, providing reaction kinetic parameters for distributed models. It was shown that the agglomerate models, having more structural parameters of the catalyst layer, are more suitable for catalyst layer optimization than the porous models.

9.1 **Gas Diffusion Electrodes** 259
9.2 **Catalyst Layer Physical Structure** 261
9.2.1 Catalyst and Electron Conducting Network 261
9.2.2 Ionic Conducting Network 262
9.2.3 Void Fraction 262
9.3 **Governing Equations** 262
9.3.1 Porous Electrode Models 263
9.3.2 Interface Models – Neglecting Spatial Gradients 267
9.3.3 Agglomerate Models 269
9.4 **Macroscale Models** 273
9.4.1 Interface Models 273
9.4.2 Porous Electrode Models 276
9.4.3 Agglomerate Models 277
9.5 **Conclusions and Outlook** 282
References 283

9.1 Gas Diffusion Electrodes

Gas diffusion electrodes (GDEs) are frequently applied in different fields of applied electrochemistry like in low and high temperature fuel cells, electrolyzers (chloralkali and water electrolysis, electrocatalytic oxidation of CH_4, C_2H_4), batteries (Zn-air batteries), and sensors (CO, O_2, CH_3OH) [9.1]. They are usually combined with solid electrolyte membranes (for example polymer membranes like Nafion for low temperature fuel cell applications, or ceramic membranes like yttria-stabilized zirconia for high temperature systems), which enables the use of the so-called zero-gap set-up, allowing for very compact electrochemical reactors. GDEs offer high surface area for the electrochemical reactions and provide the possibility of reactant utilization from the gas phase, reducing mass transfer limitations usually observed in reactions taking place from the liquid phase. A schematic representation of a typical electrochemical membrane reactor in Fig. 9.1 shows a solid electrolyte membrane in contact with GDEs comprising catalyst (CLs) and gas diffusion layers (GDLs).

Due to different procedures and materials employed to fabricate GDEs, it is very difficult to establish general

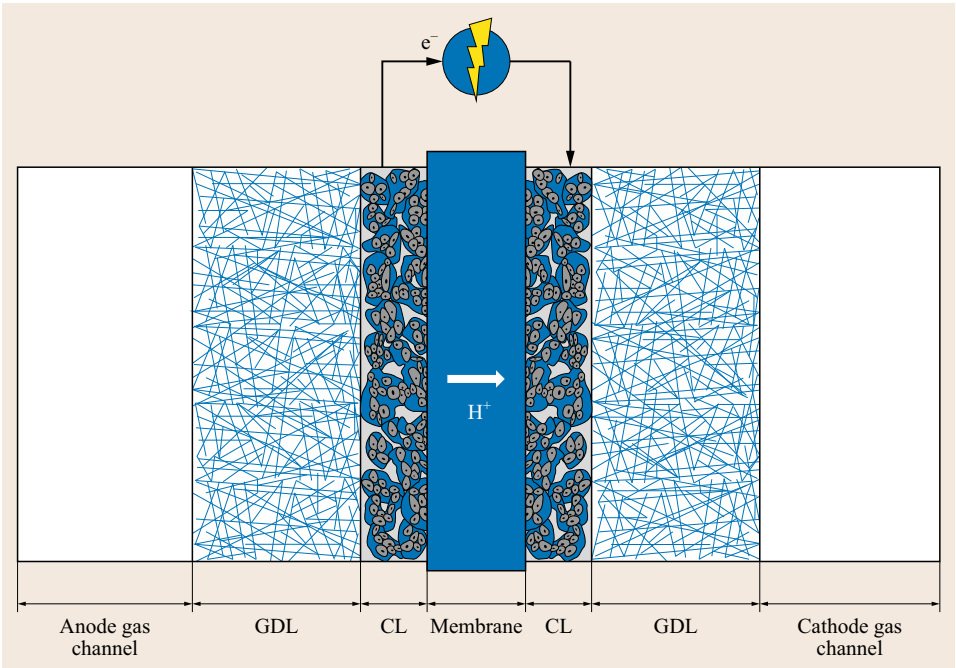


Fig. 9.1 Schematical representation of a polymer-electrolyte-membrane (PEM) reactor

guidelines pointing out the correlation between preparation protocol, GDE structure and its performance. One part of the reason is the lack of GDE structural characterization in most publications. Another part of the reason is that GDE structural characterizations are commonly performed under ex-situ conditions, meaning that a large part of the information regarding GDE structure under operating conditions (like the change of pore size distribution due to pressure conditions in the reactor) is not available. Recently, x-ray tomography has emerged as a new analytical technique to enable for the nondestructive analysis of GDE architecture, liquid water transport, etc. [9.2–4]. The first results are encouraging, and we hope that further applications of this method will follow soon [9.5].

Additionally, modeling comes into play in order to possibly provide a better insight into the interplay between different GDEs physical parameters and its performance, as well as optimization of preparation protocols reducing the amount of expensive, time-consuming, or complicated experiments. In this respect, especially modeling of CL, where electrochemical reactions are taking place, appears important. In order for the reaction to happen, reactants must be transported to the active sites, where electron- and ion-conducting matrixes must be present. This leads to a complex structure where many different phenomena, such as mass, heat, momentum, and charge transport simultaneously occur. Currently only ca. 10–20% [9.6] of the catalyst in the CL is active, which leaves a lot of space for further improvements.

Up to now, CLs have been considered with varying degrees of complexity. They have been modeled as an interface, homogeneous or inhomogeneous layers in 1, 2, or 3-dimensional 1-D, 2-D, 3-D computational domains, as well as in microscopic or macroscopic scales applying density functional theory, Monte Carlo simulations, mean-field theory, or empirical approaches. Morphology, as well as coupled physical processes taking place in the CL, requires enormous computational effort for their proper phenomenological simulation. For this reason, most authors analyzing CLs on an atomistic or microscale concentrate on only small portions of the CL, focusing on specific phenomena to determine commonly transport parameters of involved species, their interaction with the solid matrixes present along its path, or only the electrochemical reaction. In these studies, little or no parameters are freely adjustable. Other authors focus more on the macroscale, for example, through mean field theory and can simulate polarization curves which are readily available experimentally, at the cost of a more empirical description of the phenomena occurring in the system but increased flexibility to adjust simulations to experimental data by means of free parameters. For the systematic optimization and understanding of the CLs, it is required to have a molecular understanding of the phenomena taking place in the CL as well as the capa-

bility to use this information on a macroscale, in order to analyze different scenarios and obtain physically reasonable results of the system as a whole. Ideally, these two approaches should be combined in multiscale modeling approach.

Although in the longer time scale it may be expected that the microscale models will bring major breakthroughs, at present their predictive power is still limited and the macroscale models are still more *practical* for predicting experimental observations. For this reason, special focus will be given to macroscale CL models as well as their applications mainly in low temperature electrochemical systems. For a further insight of microscopic and mesoscale models, the reader is referred to the recent reviews of *Yu* et al. [9.7] and *Shah* et al. [9.8].

In following, first, an overview of the catalyst layer physical structure, its components and interactions are presented. Second, the relevant governing equations for the physical and chemical processes taking place in the CL are explained. Next, the selected results of different macroscopic models are discussed.

9.2 Catalyst Layer Physical Structure

CLs consist of a catalyst, an electron-, and an ion-conducting matrixes (Fig. 9.2). These three components must be tailored in order to obtain high CL performance. In this respect, CL synthesis procedure must provide good interconnection along these three constitutive elements in order to offer pathways for reactants, electrons and ions to be transported as well as active places for the reaction to take place. In addition to the abovementioned phases, in low temperature systems, water is needed in order to provide a proper ionic conductivity of the solid electrolyte and also to enable catalyst activity since only catalyst particles in contact with water are active [9.6, 9].

9.2.1 Catalyst and Electron Conducting Network

Typically applied catalysts, in low-temperature processes, are metals (e.g., platinum, ruthenium, rhodium, and palladium). Their incomplete d-shell render them active for both oxidation and reduction reactions [9.10, 11] and they possess high electron conductivity. The catalyst builds the electron conducting network in the CL. This electron-conducting network can be complemented with other electron conducting materials which usually do not incorporate a catalytic function, like carbon nanomaterials or polymers, but serve as a support. Furthermore, addition of support reduces significantly catalyst loading, provides a better catalyst distribution and prevents its agglomeration [9.12, 13]. The material of choice as catalyst support in the literature is carbon black, due to its price, easy handling and inert behavior toward perfluoro sulfonic acid (PFSA) membranes [9.14]. Carbon black can be mixed with different polymers in order to gain different chemical and physical properties (e.g., improved corrosion resistance, hydrophobicity, etc. [9.15]). One of recently discussed disadvantages of carbon black is its activity toward oxygen reduction. This is kinetically less favored than oxygen reduction on, for example, platinum, but still at higher overpotentials can lead to hydrogen peroxide production causing in addition to an inherent voltage loss, corrosion of the

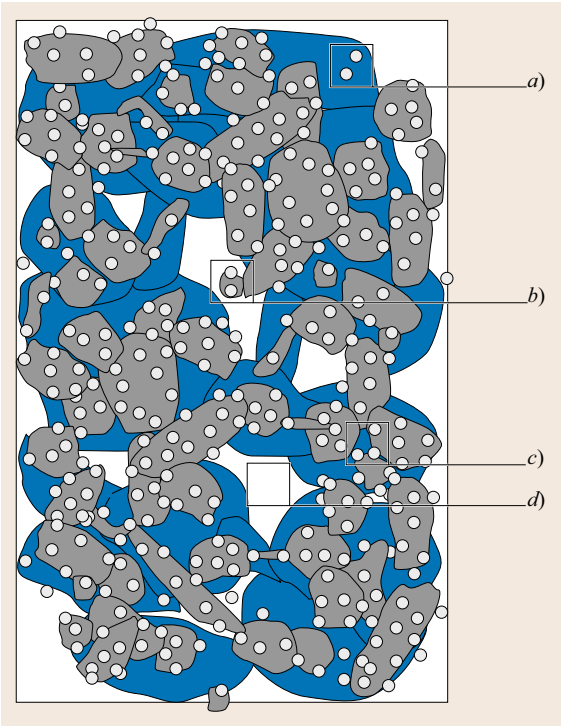


Fig. 9.2 Schematic representation of the real CL structure. *Light gray circles* represent the catalyst, *dark gray circles* represent the support, *blue areas* represent the solid electrolyte. *(a)* Inactive catalyst particles due to lacking electrical connection; *(b)* inactive electrically conductive cluster due to lacking electrolyte contact; *(c)* primary pore; *(d)* secondary pore

support, and Pt liberation [9.16, 17]. For this reason, alternative catalyst support materials have been discussed. Novel proposals for supports are TiO_2 [9.18] and SiO_2 [9.19] because of their improved corrosion resistance even though their electric conductivity is much lower.

Catalysts can be synthesized using different methods (for an overview please refer to [9.20]), which might have an influence on the catalyst activity for a specific reaction. Typical cathode reactions are

$$O_2 + 4H^+ + 4e^- \rightarrow 2H_2O\,, \tag{9.1}$$

$$2H^+ + 2e^- \rightarrow H_2\,, \tag{9.2}$$

while typical anode reactions are

$$H_2 \rightarrow 2H^+ + 2e^-\,, \tag{9.3}$$

$$CH_3OH + H_2O \rightarrow CO_2 + 6H^+ + 6e^-\,, \tag{9.4}$$

$$2HCl \rightarrow Cl_2 + 2H^+ + 2e^-\,. \tag{9.5}$$

All these reactions include mass transfer of reactants and products as well as different chemical and electrochemical steps. In order to perform a systematic analysis and/or optimization of a fuel cell or an electrochemical reactor, the understanding of the reactions taking place in the CLs is of vital importance. In this respect, it is important to choose a proper reaction mechanism, neglecting irrelevant reaction steps or effects (Sect. 9.4.1) which helps us to reduce the computational requirement of the model without losing valuable information. This has a significant effect especially in the case of 3-D and detailed models looking for an entire system optimization.

9.2.2 Ionic Conducting Network

The protons produced by electrochemical reactions, for example, (9.3)–(9.5), must be transported away from the anode to the cathode in order to close the circuit. For this reason, an ion-conducting media must be present in the CL. Usually Nafion is, due to its super acidic and hydration properties, mechanical strength, high conductivity, and inert chemical nature [9.21], added to the CL to ensure good ionic conductivity. However, Nafion in the absence of water has very low conductivity, implying the role of water as a primary ion-carrier. According to the literature the presence of Nafion in the CL can also increase mass transfer resistance of the reactants and products, since Nafion can deposit over the active sites or block CL pores (see Sect. 9.4.3). Nevertheless, Nafion is not impermeable for gases due to its porosity and high degree of liquid uptake [9.21], allowing gas transport in the presence of high driving forces such as concentration (chemical potential) gradients. According to data from different authors [9.22–25], Nafion can absorb water up to 30% v/v, allowing for gas pathways to be present at low-humidification levels. Under high amounts of water – or any other polar liquid-, continuous liquid channels through the Nafion structure are formed. Reactants can still dissolve in Nafion or water (e.g., Henry's constants for oxygen absorption in Nafion and water both lie around $H_{O_2} \approx 10^4$) [9.26–28]. If the concentration of Nafion in the CL is very high, it may even break the electron conducting network, rendering some catalyst inactive, as in Fig. 9.1. Because of this, different catalyst ink and CL preparation techniques [9.9, 29, 30] as well as Nafion loadings [9.31, 32] have been revised in the past in order to optimize CL performance.

9.2.3 Void Fraction

Depending on the CL synthesis method used, pore networks are created between the previously discussed components. Through these void area reactants diffuse to the catalyst sites. The void fraction is the most difficult CL parameter to estimate and predict. Unlike the amount of Nafion, catalyst and support, it cannot be set up beforehand and depends mostly on the CL preparation method and/or mechanical treatments such as hot pressing or screw torque applied to the reactor. It can be possibly estimated knowing other parameters, such as CL thickness, CL component loadings, and assuming a specific packing of inside the CL.

9.3 Governing Equations

In the following, the basic structure of different type of electrode models will be discussed. For the sake of simplicity, all considerations refer to a cathode with the following reactions occurring

$$\sum_{\text{ox}} \nu_{\text{ox},k} \mathrm{S}_{\text{ox}} + n_k \mathrm{e}^- \rightleftharpoons \sum_{\text{red}} \nu_{\text{red},k} \mathrm{S}_{\text{red}} \tag{9.6}$$

In (9.6), S_{ox} and S_{red} are the oxidizing and the reducing agents, respectively. The symbols $\nu_{\text{ox},k}$ and $\nu_{\text{red},k}$ stand for their stoichiometric coefficients in the k-th reaction. The rate of the k-th reaction is denoted with r_k. In general, r_k is different in every location z of the electrode. It can be calculated with an appropriate kinetic

expression

$$r_k(t,z) = r_k(\eta_k(t,z), c_\alpha(t,z), T(t,z)\ldots)\,, \tag{9.7}$$

from the concentration field $c_\alpha(t,z)$, the temperature field $T(t,z)$ and the local overpotential $\eta_k(t,z)$ of the k-th reaction. Per convention throughout the whole section it is assumed that $r_k > 0$ for $\eta_k < 0$. The spatial profile of the overpotential $\eta_k(t,z)$ follows from the potential field within the electron conductor $\varphi_\mathrm{E}(t,z)$ and the potential field within the ion conductor $\varphi_\mathrm{I}(t,z)$ through

$$\eta_k(t,z) = \underbrace{[\varphi_\mathrm{E}(t,z) - \varphi_\mathrm{I}(t,z)]}_{\Delta\varphi(t,z)} - \Delta\varphi_k^0\,, \tag{9.8}$$

with $\Delta\varphi_k^0$ being the equilibrium potential difference of the k-th reaction.

The focus of all derivations in this section is on the governing equations for the description of the relevant state fields appearing in (9.7) and (9.8). Most important are the potential fields $\varphi_\mathrm{E}(t,z)$ and $\varphi_\mathrm{I}(t,z)$ and the concentration field $c_\alpha(t,z)$. Their knowledge and the understanding of their interplay is an important tool to evaluate different approaches to improve the electrode structure and its performance.

Figure 9.3 shows typical macroscale profiles for φ_E, φ_I, and c_α, as well as the corresponding qualitative profile for the reaction rate r. In the first case (left column in Fig. 9.3), the reactant transport is limiting. The concentration sharply drops to rather small values for increasing distances from the GDL–catalyst layer interface ($z = 0$). Consequently, the reaction rate r is high only in the vicinity of this interface, while in the rest of the electrode almost no current is produced. In case II (right column in Fig. 9.3), we find the opposite situation. Here the ion transport is limiting and φ_I sharply drops with increasing distance from the catalyst layer-membrane interface ($z = L$). As a result the overpotential η and consequently the reaction rate r are high only in the vicinity of this interface.

The spatial profiles of the relevant variables on the macroscale are described by porous electrode models. They are subject of Sect. 9.3.1. Afterward a simplification and an extension of the porous electrode models are discussed: in Sect. 9.3.2 the focus is on interface models. They can be easily derived from the porous electrode models by making some simplifying assumptions. In Sect. 9.3.3, agglomerate models are discussed. They apply in situations where it is necessary to describe the state fields in addition on a microscale. For this purpose, the same equations that are valid on the macroscale will be applied to the microscale and solved simultaneously with the macroscale equations.

9.3.1 Porous Electrode Models

Porous electrode models resolve the state fields of interest on a macroscale. They rely on the general assumptions associated with the application of the spatial averaging theorem (for further details [9.33, 34] and sources therein). For this kind of models, the variables of interest are averaged over a representative averaging volume. The exact geometrical details of the electrode are ignored. Instead the electrode geometry is described by the volume fraction ε of the corresponding phase and the internal surface a (in $\mathrm{m}^2_\mathrm{act}/\mathrm{m}^3$). In the balance equations, all fluxes are then typically related to superficial quantities by multiplying the interstitial flux with the corresponding volume fraction ε. For a diffusive flux we get, for example

$$g_\alpha = \varepsilon g_\alpha^\mathrm{interstitial} \tag{9.9}$$

with g_α being the superficial diffusive flux measured in $\mathrm{mol}/(\mathrm{m}^2_\mathrm{(electrode)}\mathrm{s})$ and $g_\alpha^\mathrm{interstitial}$ being the interstitial diffusive flux measured in $\mathrm{mol}/(\mathrm{m}^2_\mathrm{pore}\,\mathrm{s})$.

The phenomenological coefficients appearing in the transport kinetics (e.g., diffusivities D_α, conductivities $\sigma, \ldots$) are typically corrected, considering a tortuosity of the pores within the representative averaging volume, τ (in m/m). For the diffusivity, we get for example

$$g_\alpha^\mathrm{interstitial} = -c_\mathrm{t}\frac{D_\alpha}{\tau}\frac{\partial x_\alpha}{\partial z}\,. \tag{9.10}$$

When inserting (9.10) into (9.9), we find in this example for the superficial diffusive flux

$$g_\alpha = -c_\mathrm{t}\underbrace{\frac{\varepsilon}{\tau}D_\alpha}_{D_\alpha^\mathrm{eff}}\frac{\partial x_\alpha}{\partial z}\,, \tag{9.11}$$

where the quantity D_α^eff is called the effective diffusivity. One of the most common relations used to express this effective diffusivity is Bruggemann's correlation, which assumes $\tau = \sqrt{1/\varepsilon}$ relationship. In the analogous way, all other phenomenological coefficients can be treated.

As mentioned earlier, the most important variables for the understanding of the electrode behavior are the electric potentials of the electron conductor and the ion conductor as well as the concentrations of the involved species. The corresponding balance equations will be discussed in the following Subsections. In some situations also other state fields, such as the temperature, might be of interest. The relevant balance equations will be briefly discussed at the end of this Section.

For the sake of simplicity, a spatially one-dimensional description is considered in the following, with z being the spatial coordinate (Fig. 9.3).

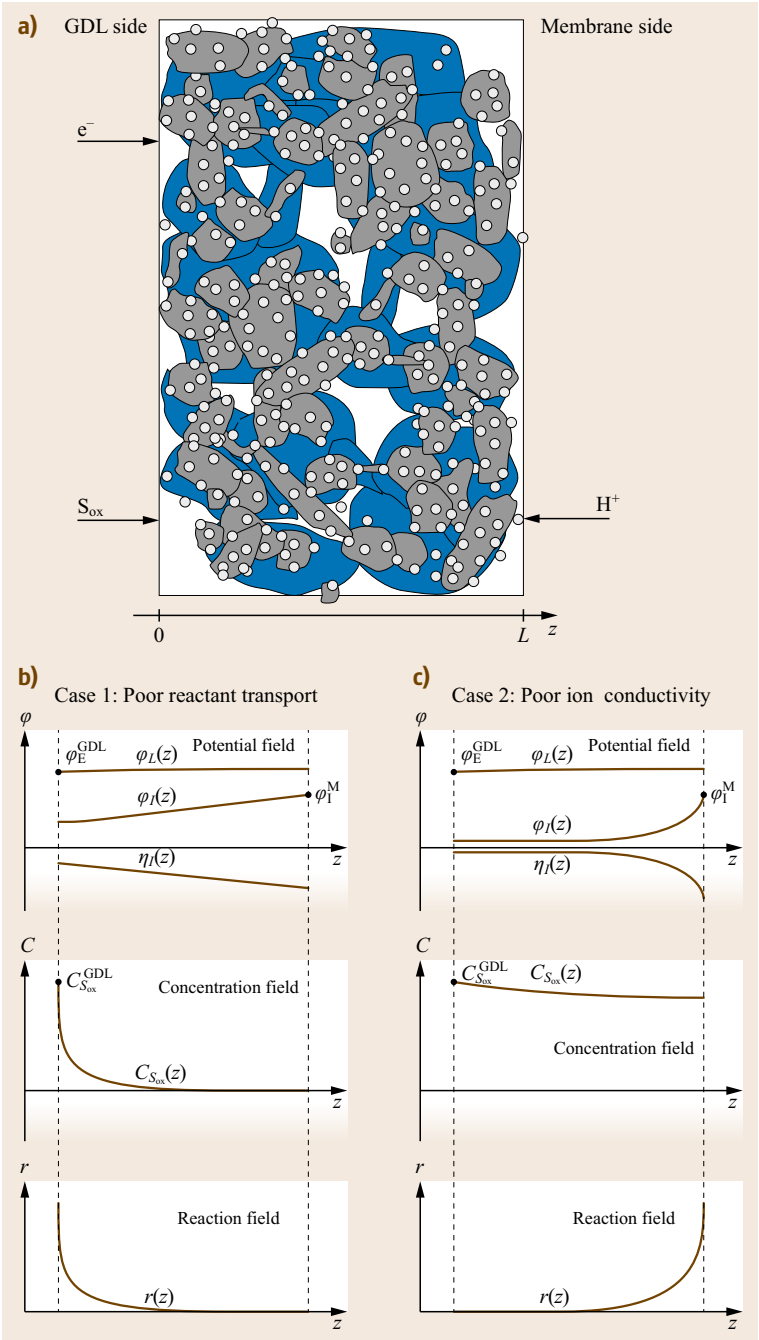


Fig. 9.3 (a) Schematic representation of the CL structure and typical steady-state profiles on a macroscale for potential and concentration fields as well as corresponding spatial profile of the reaction rate for cases of (b) poor reactant transport and (c) poor ion conductivity

Potential Field–Charge Balances

The purpose of the following derivations is to determine the electric potential within the electron conductor $\varphi_\mathrm{E}(t,z)$ (index E = electron) and the ion conductor $\varphi_\mathrm{I}(t,z)$ (index I = ion). From these quantities, the sought after spatial profile of the overpotential $\eta_k(t,z)$ can be easily calculated (9.8).

The first profile, $\varphi_\mathrm{E}(t,z)$, follows from the charge balance for the electron conductor

$$0 = -\frac{\partial}{\partial z}\underbrace{\left(-\sigma_\mathrm{E}^\mathrm{eff}\frac{\partial\varphi_\mathrm{E}}{\partial z}\right)}_{i_\mathrm{E}} + aj\,, \tag{9.12}$$

where σ_E^{eff} (in $1/(\Omega m)$) is the effective conductivity of the electron conductor, i_E (in A/m^2) the superficial current density in the electron conductor and j (in A/m^2_{act}) the local charge production density. The variable a (in m^2_{act}/m^3) is the internal surface of the electrode material, as mentioned earlier. The quantity σ_E^{eff} is given by

$$\sigma_E^{eff} = \frac{\varepsilon_E}{\tau_E}\sigma_E \,, \tag{9.13}$$

with ε_E and τ_E being the volume fraction and the tortuosity of the electron conductor, respectively.

The typical boundary conditions for (9.12) read

$$\varphi_E(t, z=0) = \varphi_E^{GDL}(t),$$
$$-\sigma_E^{eff}\left.\frac{\partial \varphi_E}{\partial z}\right|_{t,z=L} = 0 \quad \forall t \,. \tag{9.14}$$

The first expression represents the fact that the potential at the interface between the GDL and the catalyst layer ($z = 0$) is typically known (Fig. 9.3). The second term ensures that no current leaves the electron conductor at the interface between the catalyst layer and the membrane ($z = L$).

The unknown profiles of the charge production density $j(t, z)$ appearing in (9.12) and the electric potential in the ion conductor $\varphi_I(t, z)$ can be calculated from the following two relations

$$0 = -\frac{\partial}{\partial z}\underbrace{\left(-\sigma_I^{eff}\frac{\partial \varphi_I}{\partial z}\right)}_{i_I} - aj \,, \tag{9.15}$$

$$c_{dl}\frac{\partial}{\partial t}(\varphi_E - \varphi_I) = -j + F\sum_k n_k r_k \,. \tag{9.16}$$

Equation (9.15) is the charge balance of the electrolyte. Herein, σ_E^{eff} (in $1/(\Omega m)$) is the effective electrolyte conductivity and i_I (in A/m^2) the superficial current density in the ion conductor. This equation is formulated under the assumption of a binary electrolyte with only one charged species being considered as mobile. This is a reasonable simplification for most gas diffusion electrodes. In case that more then one charged species are mobile, some extra terms appear in (9.15) [9.35]. The quantity σ_I^{eff} is given by

$$\sigma_I^{eff} = \frac{\varepsilon_I}{\tau_I}\sigma_I \,, \tag{9.17}$$

with ε_I and τ_I being the volume fraction and the tortuosity of the ion conductor, respectively.

Typical boundary conditions for (9.15) read

$$-\sigma_I^{eff}\left.\frac{\partial \varphi_I}{\partial z}\right|_{t,z=0} = 0 \forall t, \quad \varphi_I(t, z=L) = \varphi_I^M(t) \,. \tag{9.18}$$

The first expression represents the physical fact that no current can leave the ion conductor at the interface between the GDL and the catalyst layer ($z = 0$). The second expression considers a fixed potential at the interface between the catalyst layer and the membrane ($z = L$). Alternatively at this interface also the potential gradient can be provided (9.23)

$$-\sigma_I^{eff}\left.\frac{\partial \varphi_I}{\partial z}\right|_{t,z=L} = -i_{electrode}(t) \,, \tag{9.19}$$

in order to solve the model galvanostatically.

Equation (9.16) is the charge balance for the electrochemical double layer. Herein c_{dl} (in F/m^2_{act}) is the local double layer capacitance, F (in As/mol) is the Faraday constant, and n_k and r_k (in $mol/(sm^2_{act})$) are the number of transferred electrons and the reaction rate of the k-th electrode reaction, respectively (9.6).

The solution of (9.12), (9.15), and (9.16) finally delivers the local profiles $\varphi_E(t, z)$, $\varphi_I(t, z)$, and $j(t, z)$. From these, on the one hand, the spatial profile of the overpotential can be calculated (9.8), which is necessary to evaluate the rate expression for r_k (9.7). On the other hand some integral variables of interest can be determined. The polarization of the whole electrode $\Delta\varphi_{electrode}$ (in V) follows from

$$\Delta\varphi_{electrode}(t) = \varphi_E(t, z=0) - \varphi_I(t, z=L) \,. \tag{9.20}$$

For the current produced in the whole electrode $i_{electrode}$ (in A/m^2), we find

$$i_{electrode}(t) = \int_{z=0}^{z=L} aj(t, z)\mathrm{d}z \,, \tag{9.21}$$

or alternatively with (9.12) and (9.15) integrated over the electrode thickness

$$i_{electrode}(t) = -\underbrace{\left(-\sigma_E^{eff}\left.\frac{\partial \varphi_E}{\partial z}\right|_{t,z=0}\right)}_{i_E(t,z=0)} \,, \tag{9.22}$$

$$i_{electrode}(t) = -\underbrace{\left(-\sigma_I^{eff}\left.\frac{\partial \varphi_I}{\partial z}\right|_{t,z=L}\right)}_{i_I(t,z=L)} \,. \tag{9.23}$$

Classical Simplifications of the Charge Balances. In many publications, two simplifying assumptions are considered for the treatment of the equations discussed above. The first assumption is considering the charge balance of the electrochemical double layer (9.16) to be quasi-stationary. The time constant of this equation is typically several orders of magnitude smaller than the one of the material balances or the energy balance. If the corresponding short-term dynamics is not of interest, the assumption is well justified. As a consequence from (9.16), it follows for $j(t,z)$ the straightforward expression

$$j(t,z) = F\sum_k n_k r_k(t,z)\,. \tag{9.24}$$

Inserting (9.24) into the charge balances (9.12) and (9.15) for the electron and ion conductor, respectively, yields the well-known result

$$\frac{\partial i_\mathrm{E}}{\partial z} = aF\sum_k n_k r_k\,, \tag{9.25}$$

$$\frac{\partial i_\mathrm{I}}{\partial z} = -aF\sum_k n_k r_k\,, \tag{9.26}$$

with the boundary conditions (9.14) and (9.18)

$$i_\mathrm{E}(t,z=L) = 0\;\forall t,\quad i_\mathrm{I}(t,z=0) = 0\;\forall t\,. \tag{9.27}$$

The potential of the electron and ion conductor can be calculated from i_E and i_I through (9.12) and (9.15)

$$\frac{\partial \varphi_\mathrm{E}}{\partial z} = -\frac{i_\mathrm{E}}{\sigma_\mathrm{E}^\mathrm{eff}}\,, \tag{9.28}$$

$$\frac{\partial \varphi_\mathrm{I}}{\partial z} = -\frac{i_\mathrm{I}}{\sigma_\mathrm{I}^\mathrm{eff}}\,, \tag{9.29}$$

with the boundary conditions (9.14) and (9.18)

$$\varphi_\mathrm{E}(t,z=0) = \varphi_\mathrm{E}^\mathrm{GDL}(t),\quad \varphi_\mathrm{I}(t,z=L) = \varphi_\mathrm{I}^\mathrm{M}(t)\,. \tag{9.30}$$

From this result, the spatial profile of the overpotential can be calculated by means of (9.8).

For the second simplification, it is considered further that the conductivity of the electron conductor, $\sigma_\mathrm{E}^\mathrm{eff}$ is typically large. As a consequence, we find from (9.28) that the spatial derivative of φ_E can be neglected

$$\frac{\partial \varphi_\mathrm{E}}{\partial z} = 0\quad \forall t,z\,. \tag{9.31}$$

This result allows for the derivation of a differential equation for the overpotential η_k. Spatial derivation of (9.8) gives

$$\frac{\partial \eta_k}{\partial z} = \frac{\partial \varphi_\mathrm{E}}{\partial z} - \frac{\partial \varphi_\mathrm{I}}{\partial z} - \underbrace{\frac{\partial \Delta\varphi_k^0}{\partial z}}_{(\Delta\varphi_k^0 \neq f(z))} = 0\,. \tag{9.32}$$

With relations (9.28) and (9.31), we find the well-known relation

$$\frac{\partial \eta_k}{\partial z} = \frac{i_\mathrm{I}}{\sigma_\mathrm{I}^\mathrm{eff}} \tag{9.33}$$

with the boundary condition

$$\eta_k(t,z=L) = \varphi_\mathrm{E}^\mathrm{GDL}(t) - \varphi_\mathrm{I}^\mathrm{M}(t) - \Delta\varphi_k^0\,. \tag{9.34}$$

Solving simultaneously (9.26) and (9.33) together with the corresponding boundary conditions the sought after spatial profile of $\eta_k(t,z)$ can be obtained.

Concentration Field Within the Gas Phase – Material Balances

The spatial profiles of the component concentrations within the gas phase $c_\alpha(t,z)$ can be calculated from the following material balances

$$\frac{\partial}{\partial t}(\varepsilon c_\alpha) = -\frac{\partial g_\alpha}{\partial z} + a\sum_k \nu_{\alpha,k} r_k\,. \tag{9.35}$$

Herein, ε (in $\mathrm{m}^3_\mathrm{pore}/\mathrm{m}^3$) is the porosity (volume fraction of the gas phase), c_α (in $\mathrm{mol}/\mathrm{m}^3_\mathrm{void}$) the sought after interstitial concentration of the component α and g_α (in $\mathrm{mol}/(\mathrm{m}^2\mathrm{s})$) is the superficial component molar flow rate. Again the symbols a, $\nu_{\alpha,k}$, and r_k stand for the internal surface (in $\mathrm{m}^2_\mathrm{act}/\mathrm{m}^3$), the component stoichiometric coefficient and the reaction rate of the k-th electrode reaction (in $\mathrm{mol}/(\mathrm{sm}^2_\mathrm{act})$), respectively.

The superficial component molar flow rates g_α are typically calculated by means of the dusty gas model [9.36, 37]

$$g_\alpha:\; -c_\mathrm{t}\frac{\partial x_\alpha}{\partial z} = \sum_{\beta=1}^{N}\frac{x_\beta g_\alpha - x_\alpha g_\beta}{D_{\alpha\beta}^\mathrm{eff}} + \frac{g_\alpha}{D_{\alpha\mathrm{M}}^\mathrm{eff}}\,. \tag{9.36}$$

Herein, $D_{\alpha\beta}^\mathrm{eff}$ and $D_{\alpha\mathrm{M}}^\mathrm{eff}$ are the effective Maxwell–Stefan diffusion coefficients (in m^2/s) for the interaction between α and β and α with the solid matrix, respectively. The total interstitial concentration c_t (in $\mathrm{mol}/\mathrm{m}^3_\mathrm{void}$) and x_α, the interstitial mole fraction of component α can

be calculated from the interstitial component concentrations by

$$c_\mathrm{t} = \sum_{\alpha=1}^{N} c_\alpha \,, \tag{9.37}$$

$$x_\alpha = \frac{c_\alpha}{c_\mathrm{t}} \,. \tag{9.38}$$

Typical boundary conditions for (9.35) and (9.36) read

$$c_\alpha(t, z=0) = c_\alpha^{\mathrm{GDL}}(t), \quad g_\alpha(t, z=L) = 0 \;\forall t \,. \tag{9.39}$$

The first expression represents the fact that the concentrations at the interface between the GDL and the catalyst layer ($z = 0$) is typically known (Fig. 9.3). The second term represents a zero material flow at the interface between the catalyst layer and the membrane ($z = L$).

Classical Simplification of the Material Balance. In many publications, only the steady-state solution of the material balances is considered. Under this condition, we find from (9.35)

$$\frac{\partial g_\alpha}{\partial z} = a \sum_k \nu_{\alpha,k} r_k \,. \tag{9.40}$$

Often the molar flow rates g_α are calculated from Fick's law

$$g_\alpha = -c_\mathrm{t} D_\alpha^{\mathrm{eff}} \frac{\partial x_\alpha}{\partial z} \,, \tag{9.41}$$

with D_α^{eff} (in m^2/s) being the (Fickean) diffusion coefficient. Inserting (9.41) into (9.40), we get

$$-\frac{\partial}{\partial z}\left(D_\alpha^{\mathrm{eff}} \frac{\partial c_\alpha}{\partial z}\right) = a \sum_k \nu_{\alpha,k} r_k(\eta, c_\alpha) \,. \tag{9.42}$$

Together with the simplified relations for the potential field (9.26) and (9.33)

$$\frac{\partial i_\mathrm{I}}{\partial z} = -aF \sum_k n_k r_k(\eta, c_\alpha) \,, \tag{9.43}$$

$$\frac{\partial \eta_k}{\partial z} = \frac{i_\mathrm{I}}{\sigma_\mathrm{I}^{\mathrm{eff}}} \,, \tag{9.44}$$

and the reaction kinetics (9.7), we gain a relatively simple and well-structured steady-state model for the determination of the concentration field $c_\alpha(z)$, the potential field $\eta_k(z)$ and the corresponding spatial profiles of the reaction rates $r_k(z)$. For the sake of completeness, the boundary conditions for (9.42)–(9.44) should be given. They read

$$c_\alpha(t, z=0) = c_\alpha^{\mathrm{GDL}}(t) \,, \; \left.\frac{\partial c_\alpha}{\partial z}\right|_{t,z=L} = 0 \;\forall t \,, \tag{9.45}$$

$$i_\mathrm{I}(t, z=0) = 0 \,,$$

$$\left.\frac{\partial \eta}{\partial z}\right|_{t,z=0} = 0 \;\forall t \,,$$

$$\eta_k(t, z=L) = \varphi_\mathrm{E}^{\mathrm{GDL}}(t) - \varphi_\mathrm{I}^{\mathrm{M}}(t) - \Delta\varphi_k^0 \,. \tag{9.46}$$

If finally, only one single reactionoccurs (9.42)–(9.44) can be brought in the following well-known form

$$\frac{\partial i_\mathrm{I}}{\partial z} = -anFr(\eta, c_\alpha) \,, \tag{9.47}$$

$$\frac{\partial \eta_k}{\partial z} = \frac{i_\mathrm{I}}{\sigma_\mathrm{I}^{\mathrm{eff}}} \,, \tag{9.48}$$

$$\frac{\partial c_\alpha}{\partial z} = \nu_\alpha \frac{(i_{\mathrm{electrode}} + i_\mathrm{I})}{D_\alpha^{\mathrm{eff}} nF} \,, \tag{9.49}$$

with the boundary conditions,

$$i_\mathrm{I}(t, z=0) = 0 \;\forall t \,, \tag{9.50}$$

$$\eta_k(t, z=L) = \varphi_\mathrm{E}^{\mathrm{GDL}}(t) - \varphi_\mathrm{I}^{\mathrm{M}}(t) - \Delta\varphi_k^0 \,, \tag{9.51}$$

$$c_\alpha(t, z=0) = c_\alpha^{\mathrm{GDL}}(t) \,. \tag{9.52}$$

Further State Fields to be Considered

Depending on the system under consideration and the question associated with the model, apart from the potential field and the concentration field also other state fields have to be considered. A few examples will be briefly mentioned here and exemplified in Sect. 9.4.2.

A first possible refinement of the model discussed so far is the consideration of the temperature field $T(t, z)$. For this purpose, typically a mutual energy balance is formulated for all involved phases (electron conductor, ion conductor, and gas phase).

Another typical model modification is the consideration of electrode flooding. Such a behavior occurs in PEM fuel cell cathodes, when the product water condensates within the pore network and forms a liquid phase. In such a situation, the model equations will be amended by a liquid water balance to calculate the liquid phase saturation within the pore network.

9.3.2 Interface Models – Neglecting Spatial Gradients

For very thin electrodes or vanishing transport resistances for charge and mass transport, interface models

are applicable. The governing equations can be directly derived from the key equations of the porous electrode model, discussed earlier.

First, the kinetic relations for charge and mass transport (9.12), (9.15) and (9.36) are treated. With the introduction of a dimensionless spatial coordinate $\zeta = z/L$ they can be brought in the following form

$$\frac{\partial \varphi_\mathrm{E}}{\partial \zeta} = -\frac{i_\mathrm{E}}{\sigma_\mathrm{E}^\mathrm{eff}/L}\,, \tag{9.53}$$

$$\frac{\partial \varphi_\mathrm{I}}{\partial \zeta} = -\frac{i_\mathrm{I}}{\sigma_\mathrm{I}^\mathrm{eff}/L}\,, \tag{9.54}$$

$$\frac{\partial c_\alpha}{\partial \zeta} = -\sum_{\beta=1}^{N} \frac{x_\beta g_\alpha - x_\alpha g_\beta}{D_{\alpha\beta}^\mathrm{eff}/L} + \frac{g_\alpha}{D_{\alpha\mathrm{M}}^\mathrm{eff}/L}\,. \tag{9.55}$$

For

$$\sigma_\mathrm{E}^\mathrm{eff}/L \to \infty, \quad \sigma_\mathrm{I}^\mathrm{eff}/L \to \infty\,, \tag{9.56}$$

$$D_{\alpha\beta}^\mathrm{eff}/L \to \infty, \quad D_{\alpha\mathrm{M}}^\mathrm{eff}/L \to \infty\,, \tag{9.57}$$

which is true for thin electrodes ($L \to 0$) or vanishing transport resistances, we find the expected result

$$\frac{\partial \varphi_\mathrm{E}}{\partial z} = 0 \quad \forall z\,, \tag{9.58}$$

$$\frac{\partial \varphi_\mathrm{I}}{\partial z} = 0 \quad \forall z\,, \tag{9.59}$$

$$\frac{\partial c_\alpha}{\partial z} = 0 \quad \forall z\,. \tag{9.60}$$

For the overpotential, we find from (9.8), (9.58), and (9.59)

$$\frac{\partial \eta_k}{\partial z} = 0 \quad \forall z\,. \tag{9.61}$$

As a first conclusion, it can be seen from relations (9.58)–(9.61) that the potentials of the electron conductor and the ion conductor, as well as the reactant concentrations and the overpotential are constant over the electrode. Now, the charge balance for the electrochemical double layer (9.16) can be considered. Multiplication of the whole equation with the internal surface a and subsequent spatial integration gives

$$ac_\mathrm{dl} \int_{z=0}^{z=L} \frac{\partial}{\partial t}(\varphi_\mathrm{E} - \varphi_\mathrm{I})\mathrm{d}z = -a \int_{z=0}^{z=L} j\mathrm{d}z + aF \int_{z=0}^{z=L} \sum_k n_k r_k(\eta_k, c_\alpha)\mathrm{d}z\,. \tag{9.62}$$

For the solution of the first integral, it is considered that φ_E and φ_I are no longer functions of space (9.58), (9.59). Consequently, the time derivative can be taken out of the integral. The second integral can be substituted with the electrode current $i_\mathrm{electrode}$ (9.21) and for the last integral it is considered that c_α and η are constant in space (9.60) and (9.61); that means, the whole sum can be drawn out of the integral. We get

$$ac_\mathrm{dl} \frac{\mathrm{d}}{\mathrm{d}t}(\varphi_\mathrm{E} - \varphi_\mathrm{I}) \int_{z=0}^{z=L} \mathrm{d}z = -i_\mathrm{electrode} + aF \sum_k n_k r_k(\eta_k, c_\alpha) \int_{z=0}^{z=L} \mathrm{d}z\,. \tag{9.63}$$

Solving the trivial integrals and using relation (9.20), we get for the charge balance the final result

$$aLc_\mathrm{dl} \frac{\mathrm{d}\Delta\varphi_\mathrm{electrode}}{\mathrm{d}t} = -i_\mathrm{electrode} + aLF \sum_k n_k r_k(\eta_k, c_\alpha)\,, \tag{9.64}$$

with η_k from (9.8),

$$\eta_k(t) = \Delta\varphi_\mathrm{electrode}(t) - \Delta\varphi_k^0\,. \tag{9.65}$$

The product of the internal surface a and the electrode thickness L, appearing in (9.64), is called the roughness factor. Its unit is $\mathrm{m_{act^2}}/\mathrm{m}^2$, which follows directly from the units of a and L.

Sometimes the roughness factor is combined with the other quantities appearing next to the expression. A typical example would be

$$c_\mathrm{electrode} \frac{\mathrm{d}\Delta\varphi_\mathrm{electrode}}{\mathrm{d}t} = -i_\mathrm{electrode} + F \sum_k n_k r_k^*(\eta_k, c_\alpha) \tag{9.66}$$

with $c_\mathrm{electrode}$ being the electrode capacitance (in $\mathrm{F/m^2}$) defined as

$$c_\mathrm{electrode} = aLc_\mathrm{dl} \tag{9.67}$$

and r_k^* ($\mathrm{mol/(m^2}s)$) given by

$$r_k^*(\eta_k, c_\alpha) = aLr_k(\eta_k, c_\alpha)\,. \tag{9.68}$$

Finally, the material balances (9.35) have to be treated in order to find a relation for $c_\alpha(t)$. These equations can be treated in the same way as the charge balance for the

electrochemical double layer, discussed above. Spatial integration of (9.35) gives

$$\varepsilon \int_{z=0}^{z=L} \frac{\partial c_\alpha}{\partial t} \mathrm{d}z = -\int_{z=0}^{z=L} \frac{\partial g_\alpha}{\partial z} \mathrm{d}z + a \int_{z=0}^{z=L} \sum_k \nu_{\alpha,k} r_k(\eta_k, c_\alpha) \mathrm{d}z \,. \tag{9.69}$$

For the solution of the first and the last integral, it is considered that c_α and η are constant in space (9.60), (9.61). Consequently, the time derivative and the sum can be taken out of the integrals. The second integral can be solved straightforward (fundamental theorem of calculus). We get

$$\varepsilon \frac{\mathrm{d}c_\alpha}{\mathrm{d}t} \int_{z=0}^{z=L} \mathrm{d}z = -\left(g_\alpha|_{z=L} - g_\alpha|_{z=0} \right) + a \sum_k \nu_{\alpha,k} r_k(\eta_k, c_\alpha) \int_{z=0}^{z=L} \mathrm{d}z \,. \tag{9.70}$$

Solving the trivial integrals and considering that $g_\alpha|_{z=L} = 0$ (boundary condition (9.39)), we find for the calculation of $c_\alpha(t)$ the final result

$$\varepsilon L \frac{\mathrm{d}c_\alpha}{\mathrm{d}t} = g_\alpha|_{z=0} + aL \sum_k \nu_{\alpha,k} r_k(\eta_k, c_\alpha) \,. \tag{9.71}$$

9.3.3 Agglomerate Models

Agglomerate models can be seen as an extension of the porous electrode models. They allow for the consideration of geometrical details of the electrode. The state fields of the variables of interest are formulated on a macroscale and a microscale, respectively. The macroscale is identical with the macroscale of the porous electrode models. Its spatial extension is again denoted by the coordinate z. On the microscale, at every location z a representative catalyst particle/agglomerate is considered. The relevant state fields within the agglomerate are resolved over the radial coordinate r. All further explanations should be based on the governing equations. For the sake of simplicity, they are considered here with a quasi-stationary charge balance.

First, the balance equations for the macroscale are given. They are used to calculate the potential fields $\varphi_\mathrm{E}(t,z)$ and $\varphi_\mathrm{I}(t,z)$ and the concentration field $c_\alpha(t,z)$ on the macroscale (please note that no extra index is used for the quantities on the macroscale). On the basis of (9.12), (9.15), and (9.35) with the assumption of a quasi-stationary charge balance (9.16), we can write for the macroscale

$$\varphi_\mathrm{E}(t,z): \quad 0 = -\frac{\partial}{\partial z} \underbrace{\left(-\sigma_\mathrm{E}^\mathrm{eff} \frac{\partial \varphi_\mathrm{E}}{\partial z} \right)}_{i_\mathrm{E}} + a\, i_\mathrm{E}^\mu|_{r=R} \,, \tag{9.72}$$

$$\varphi_\mathrm{I}(t,z): \quad 0 = -\frac{\partial}{\partial z} \underbrace{\left(-\sigma_I^\mathrm{eff} \frac{\partial \varphi_\mathrm{I}}{\partial z} \right)}_{i_\mathrm{I}} - a\, i_\mathrm{I}^\mu|_{r=R} \,, \tag{9.73}$$

$$c_\alpha(t,z): \quad \frac{\partial}{\partial t}(\varepsilon c_\alpha) = -\frac{\partial g_\alpha}{\partial z} + a\, g_\alpha^\mu|_{r=R} \,. \tag{9.74}$$

The meaning of all symbols is identical with the derivations in Sect. 9.3.1. The same is true for the boundary conditions, which are repeated here for the sake of completeness (relations (9.14), (9.18), and (9.39))

$$\varphi_\mathrm{E}(t, z=0) = \varphi_\mathrm{E}^\mathrm{GDL}(t), \quad -\sigma_\mathrm{E}^\mathrm{eff} \left. \frac{\partial \varphi_\mathrm{E}}{\partial z} \right|_{\mathrm{t,z=L}} = 0 \;\forall t \,, \tag{9.75}$$

$$-\sigma_\mathrm{I}^\mathrm{eff} \left. \frac{\partial \varphi_\mathrm{I}}{\partial z} \right|_{\mathrm{t,z=0}} = 0 \;\forall t, \quad \varphi_\mathrm{I}(t, z=L) = \varphi_\mathrm{I}^\mathrm{M}(t) \,, \tag{9.76}$$

$$c_\alpha(t, z=0) = c_\alpha^\mathrm{GDL}(t), \quad g_\alpha(t, z=L) = 0 \;\forall t \,. \tag{9.77}$$

The quantities $i_\mathrm{E}^\mu|_{r=R}$, $i_\mathrm{I}^\mu|_{r=R}$ and $g_\alpha^\mu|_{r=R}$ appearing in (9.72)–(9.74) consider the exchange of electrons, ions and mass between the macro- and the microscale. They can be evaluated from the solution of the balance equations for the microscale, which are formulated in spherical coordinates to account for the spherical shape of the agglomerates. On the basis of (9.12), (9.15), and (9.35) with the assumption of a quasi-stationary charge balance (9.16), we find

$$\varphi_\mathrm{E}^\mu(t,z,r): \; 0 = -\frac{1}{r^2} \frac{\partial}{\partial r} \left[r^2 \underbrace{\left(-\sigma_\mathrm{E}^{\mathrm{eff},\mu} \frac{\partial \varphi_\mathrm{E}^\mu}{\partial r} \right)}_{i_\mathrm{E}^\mu} \right] + a^\mu F \sum_k n_k r_k^\mu(c_\alpha^\mu, \varphi_\mathrm{E}^\mu, \varphi_\mathrm{I}^\mu) \,, \tag{9.78}$$

$$\varphi_\mathrm{I}^\mu(t,z,r): \; 0 = -\frac{1}{r^2} \frac{\partial}{\partial r} \left[r^2 \underbrace{\left(-\sigma_\mathrm{I}^{\mathrm{eff},\mu} \frac{\partial \varphi_\mathrm{I}^\mu}{\partial r} \right)}_{i_\mathrm{I}^\mu} \right] - a^\mu F \sum_k n_k r_k^\mu(c_\alpha^\mu, \varphi_\mathrm{E}^\mu, \varphi_\mathrm{I}^\mu) \,, \tag{9.79}$$

$$c_\alpha^\mu(t,z,r):\ \frac{\partial}{\partial t}(\varepsilon^\mu c_\alpha^\mu) = -\frac{1}{r^2}\frac{\partial}{\partial r}(r^2 g_\alpha^\mu) + a^\mu \sum_k \nu_{\alpha,k} r_k^\mu (c_\alpha^\mu, \varphi_\mathrm{E}^\mu, \varphi_\mathrm{I}^\mu)\,. \tag{9.80}$$

The state fields being considered on the microscale are functions of the radial coordinate r and get the superscript μ not to mix them up with the macroscale quantities. However, the general meaning of all symbols is identical with the meaning of the quantities appearing in the macroscale balances.

The boundary conditions for (9.78)–(9.80) at $r = R$ (with R being the agglomerate radius) couple the microscale with the macroscale. We find

$$\varphi_\mathrm{E}^\mu(t,z,r=R) = \varphi_\mathrm{E}(t,z)\,, \tag{9.81}$$

$$\varphi_\mathrm{I}^\mu(t,z,r=R) = \varphi_\mathrm{I}(t,z)\,, \tag{9.82}$$

$$c_\alpha^\mu(t,z,r=R) = \frac{c_\alpha(t,z)}{k_{\mathrm{H},\alpha}}\,, \tag{9.83}$$

with $k_{\mathrm{H},\alpha}$, is the Henry constant of component α.

The remaining boundary conditions follow for $r = 0$ (center of the agglomerate). For reasons of symmetry, we have

$$i_\mathrm{E}^\mu\big|_{\mathrm{t,z,r=0}} = 0,\ i_\mathrm{I}^\mu\big|_{t,z,r=0} = 0,\ g_\alpha^\mu\big|_{t,z,r=0} = 0\,. \tag{9.84}$$

Simultaneous solution of (9.72)–(9.74) and (9.78)–(9.80) together with the boundary conditions allows for the determination of the state fields on the microscale and macroscale. From these results, again the integral variables of interest, such as $\Delta\varphi_\mathrm{electrode}$ or $i_\mathrm{electrode}$ can be calculated (9.20), (9.23).

Classical Simplifications of the Micro Scale Balances

Two very helpful simplifications are typically applied to the balance equations for the microscale (9.78)–(9.80). The first one concerns the potential field within the agglomerate. The kinetic relations, appearing in the charge balances (9.78) and (9.79), can be brought in the following dimensionless form ($\rho = r/R$)

$$\frac{\partial\varphi_\mathrm{E}^\mu}{\partial\rho} = -\frac{i_\mathrm{E}^\mu}{\sigma_\mathrm{E}^{\mathrm{eff},\mu}/R},\quad \frac{\partial\varphi_\mathrm{I}^\mu}{\partial\rho} = -\frac{i_\mathrm{I}^\mu}{\sigma_\mathrm{I}^{\mathrm{eff},\mu}/R}\,. \tag{9.85}$$

In case $\sigma_\mathrm{E}^{\mathrm{eff},\mu}/R \to \infty$ and $\sigma_\mathrm{I}^{\mathrm{eff},\mu}/R \to \infty$, which is true for small agglomerate radii ($R \to 0$) or high conductivities, we have

$$\frac{\partial\varphi_\mathrm{E}^\mu}{\partial r} = 0\ \forall r\,,\quad \frac{\partial\varphi_\mathrm{I}^\mu}{\partial r} = 0\ \forall r\,. \tag{9.86}$$

With the boundary conditions (9.81) and (9.82), we find

$$\varphi_\mathrm{E}^\mu(t,z,r) = \varphi_\mathrm{E}(t,z)\ \forall r\,,\quad \varphi_\mathrm{I}^\mu(t,z,r) = \varphi_\mathrm{I}(t,z)\ \forall r\,, \tag{9.87}$$

which means that the potentials in the electron and ion conductor are constant over the radial coordinate r. The microscale model (9.78)–(9.80) then simplify to one single differential equation to determine the concentration field $c_\alpha^\mu(t,z,r)$. We have,

$$\frac{\partial}{\partial t}(\varepsilon^\mu c_\alpha^\mu) = -\frac{1}{r^2}\frac{\partial}{\partial r}(r^2 g_\alpha^\mu) + a^\mu \sum_k \nu_{\alpha,k} r_k^\mu (c_\alpha^\mu, \varphi_\mathrm{E}, \varphi_\mathrm{I}) \tag{9.88}$$

with

$$c_\alpha^\mu(t,z,r=R) = \frac{c_\alpha(t,z)}{k_{\mathrm{H},\alpha}}\,,\ g_\alpha^\mu\big|_{\mathrm{t,z,r=0}} = 0 \tag{9.89}$$

The quantities $i_\mathrm{E}^\mu|_{r=R}$ and $i_\mathrm{I}^\mu|_{r=R}$ appearing in (9.72)–(9.74) follow from spatial integration (over r) of (9.78) and (9.79). With the corresponding boundary conditions (9.84), we find

$$a\, i_\mathrm{E}^\mu\big|_{r=R} = a\frac{1}{R^2}\int_{r=0}^{r=R} r^2 a^\mu F \sum_k n_k r_k^\mu (c_\alpha^\mu, \varphi_\mathrm{E}, \varphi_\mathrm{I})\mathrm{d}r\,, \tag{9.90}$$

$$a\, i_\mathrm{I}^\mu\big|_{r=R} = -a\frac{1}{R^2}\int_{r=0}^{r=R} r^2 a^\mu F \sum_k n_k r_k^\mu (c_\alpha^\mu, \varphi_\mathrm{E}, \varphi_\mathrm{I})\mathrm{d}r\,. \tag{9.91}$$

The integrals appearing in both relations can be easily evaluated from the solution of (9.88).

Now, a second simplification can be applied. It concerns the concentration field $c_\alpha^\mu(t,z,r)$. In many studies the mass balance on the microscale is considered to be quasi-stationary. Furthermore, Fick's law with constant diffusivity is considered for the mass transport. Equation (9.88) then turns into

$$0 = -\frac{1}{r^2}\frac{\partial}{\partial r}\left[r^2\left(-D_\mathrm{A}^{\mu,\mathrm{eff}}\frac{\partial c_\alpha^\mu}{\partial r}\right)\right] + a^\mu \sum_k \nu_{\alpha,k} r_k^\mu (c_\alpha^\mu, \varphi_\mathrm{E}, \varphi_\mathrm{I})\,. \tag{9.92}$$

If now only a single irreversible electrode reaction occurs

$$\mathrm{A} + \nu_\mathrm{B}\mathrm{B}^{z_\mathrm{B}+} + n\mathrm{e}^- \xrightarrow{r} \nu_\mathrm{C}\mathrm{C}\,, \tag{9.93}$$

which can be described appropriately with a reaction kinetics of the first order regarding to species A

$$r^\mu = \frac{i_0^\mathrm{ref}}{nF}\frac{c_\mathrm{A}^\mu}{c_\mathrm{A}^\mathrm{ref}}\exp\left(-\frac{\alpha F}{\mathcal{R}T}\eta^\mu\right) \tag{9.94}$$

the material balance (9.92) can be solved analytically. Inserting (9.94) into (9.92), we find

$$0 = -\frac{1}{r^2}\frac{\partial}{\partial r}\left[r^2\left(-D_\mathrm{A}^{\mu,\mathrm{eff}}\frac{\partial c_\mathrm{A}^\mu}{\partial r}\right)\right] - \underbrace{a^\mu\frac{i_0^\mathrm{ref}}{nF}\exp\left(-\frac{\alpha F}{\mathcal{R}T}\eta^\mu\right)}_{k^\mu(\eta^\mu)}\frac{1}{c_\mathrm{A}^\mathrm{ref}}c_\mathrm{A}^\mu\,. \tag{9.95}$$

Herein, $D_\mathrm{A}^{\mu,\mathrm{eff}}$ (in m^2/s) is the effective diffusivity of A on the microscale, a^μ (in $\mathrm{m}^2_\mathrm{act}/\mathrm{m}^3_\mathrm{agglomerate}$) the specific internal area of the agglomerates, i_0^ref (in $\mathrm{A}/\mathrm{m}^2_\mathrm{act}$) the exchange current density at reference concentration $c_\mathrm{A}^\mathrm{ref}$ (in $\mathrm{mol}/\mathrm{m}^3$), α the charge transfer coefficient and η (in V) the local overpotential. The latter follows through (9.8) from the simplified potential field (9.87)

$$\eta^\mu(t,z,r) = \underbrace{[\varphi_\mathrm{E}(t,z) - \varphi_\mathrm{I}(t,z)] - \Delta\varphi^{0,\mathrm{ref}}}_{\eta(t,z)}\ \forall r\,. \tag{9.96}$$

For the quantities $i_\mathrm{E}^\mu|_{r=R}$, $i_\mathrm{I}^\mu|_{r=R}$ and $g_\mathrm{A}^\mu|_{r=R}$ appearing in the macroscale balances (9.72)–(9.74), we now have

$$a\, i_\mathrm{E}^\mu\big|_{r=R} = anFk^\mu(\eta(t,z))\frac{1}{R^2}\int_{r=0}^{r=R} r^2 c_\mathrm{A}^\mu(t,z,r)\mathrm{d}r\,, \tag{9.97}$$

$$a\, i_\mathrm{I}^\mu\big|_{r=R} = -anFk^\mu(\eta(t,z))\frac{1}{R^2}\int_{r=0}^{r=R} r^2 c_\mathrm{A}^\mu(t,z,r)\mathrm{d}r\,, \tag{9.98}$$

$$a\, g_\mathrm{A}^\mu\big|_{r=R} = -ak^\mu(\eta(t,z))\frac{1}{R^2}\int_{r=0}^{r=R} r^2 c_\mathrm{A}^\mu(t,z,r)\mathrm{d}r\,. \tag{9.99}$$

The quantity k^μ

$$k^\mu(\eta^\mu) = a^\mu\frac{i_0^\mathrm{ref}}{nF}\exp\left(-\frac{\alpha F}{\mathcal{R}T}\eta^\mu\right) \tag{9.100}$$

being introduced in (9.95) is a reaction rate constant based on the volume of the agglomerate. Its unit is $\mathrm{mol}/(\mathrm{s}\,\mathrm{m}^3_\mathrm{agglomerate})$, which follows straightforward from the units of the incorporated quantities. For the solution of (9.95), it is important to note that because of (9.96) k is not a function of the radial coordinate. For (9.95), we find after some rearrangement

$$0 = D_\mathrm{A}^{\mu,\mathrm{eff}}\frac{\partial}{\partial r}\left(r^2\frac{\partial}{\partial r}c_\mathrm{A}^\mu(t,z,r)\right) - r^2k^\mu(\eta(t,z))\frac{1}{c_\mathrm{A}^\mathrm{ref}}c_\mathrm{A}^\mu(t,z,r)\,. \tag{9.101}$$

With the given boundary conditions (9.89), (9.101) has the following analytical solution ([9.38] for an instructive explanation)

$$c_\mathrm{A}^\mu(t,z,r) = \frac{c_\mathrm{A}(t,z)}{k_\mathrm{H,A}}\frac{R}{r}\frac{\sinh\left(3M_\mathrm{T}\frac{r}{R}\right)}{\sinh(3M_\mathrm{T})} \tag{9.102}$$

with M_T (dimensionless), the Thiele modulus [9.39] being defined for our problem as

$$M_\mathrm{T} = \frac{R}{3}\sqrt{\frac{k^\mu(\eta)}{D_\mathrm{A}^{\mu,\mathrm{eff}}}}\,. \tag{9.103}$$

Figure 9.4a shows concentration profiles for three different values of the Thiele modulus. For small values of M_T, that is, for small overpotentials η the concentration profile within the particle is rather flat. For large overpotentials η and consequently large M_T most of the reactant is consumed in the external shell of the catalyst particle.

Next, the relations (9.97)–(9.99) can be evaluated by using the analytical solution (9.102). For $i_\mathrm{I}^\mu|_{r=R}$, we get

$$a\, i_\mathrm{I}^\mu\big|_{r=R} = -nF\frac{c_\mathrm{A}(t,z)}{k_\mathrm{H,A}}\left(\frac{1}{k^\mu E}\frac{1}{aR/3}\right)^{-1}\,, \tag{9.104}$$

with E (dimensionless), being the effectiveness factor defined as [9.39]

$$E = \frac{1}{M_\mathrm{T}}\left(\frac{1}{\tanh(3M_\mathrm{T})} - \frac{1}{3}M_\mathrm{T}\right). \tag{9.105}$$

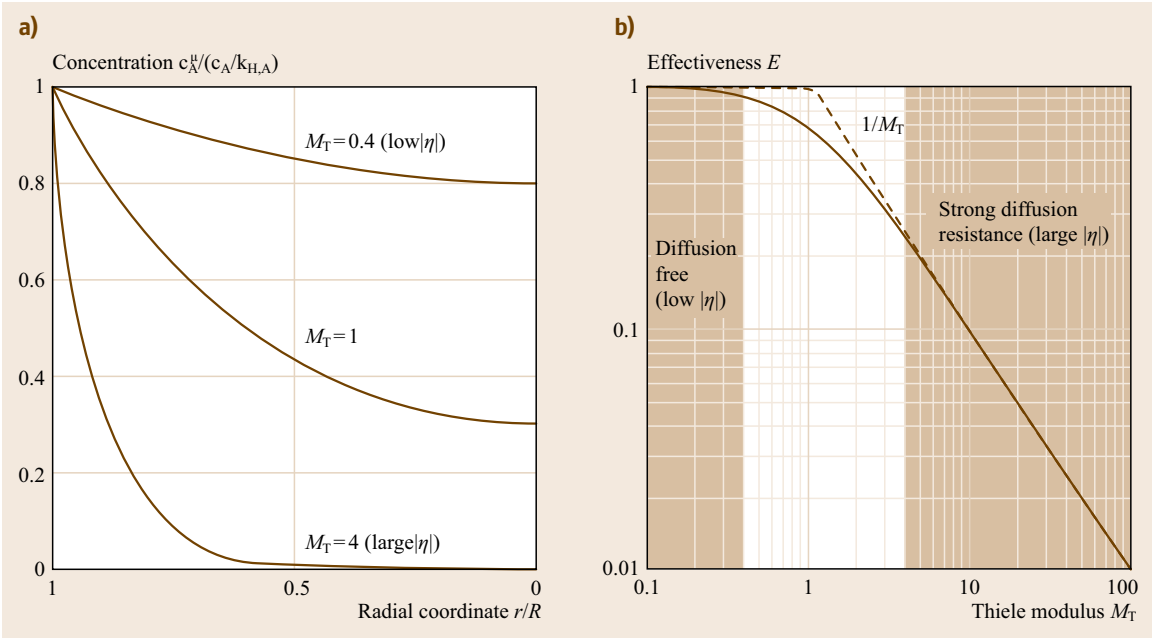


Fig. 9.4a,b Concentration field on the microscale for different values of the Thiele modulus M_T **(a)** and effectiveness factor E as a function of Thiele modulus **(b)**

Figure 9.4b shows the effectiveness factor E as a function of the Thiele modulus M_T.

The term $1/(aR/3)$ appearing in (9.104) can be further treated. With the relation

$$a = \frac{3}{R}(1-\varepsilon)\,, \tag{9.106}$$

which can be derived from geometrical considerations, (9.104) can be brought into the final form

$$a\, i_I^\mu\big|_{r=R} = -nF\frac{c_A(t,z)}{k_{H,A}}\left(\frac{1}{k^\mu E}\frac{1}{(1-\varepsilon)}\right)^{-1}\,. \tag{9.107}$$

In an analogous manner, we find

$$a\, i_E^\mu\big|_{r=R} = nF\frac{c_A(t,z)}{k_{H,A}}\left(\frac{1}{k^\mu E}\frac{1}{(1-\varepsilon)}\right)^{-1}\,, \tag{9.108}$$

$$a\, g_\alpha^\mu\big|_{r=R} = -\frac{c_A(t,z)}{k_{H,A}}\left(\frac{1}{k^\mu E}\frac{1}{(1-\varepsilon)}\right)^{-1}\,. \tag{9.109}$$

Equations (9.107)–(9.109) represent the complete microscale model, which can be solved along with the macroscale balances (9.72)–(9.74) in a straightforward manner.

Finally, a last aspect should be discussed. In some studies, it is considered that the agglomerates (radius R) are composed of a catalyst core (radius R_{core}) that is covered with a thin electrolyte shell of thickness δ^{shell}

$$\delta^{shell} = R - R_{core}\,. \tag{9.110}$$

Under these conditions, the material balance (9.101) needs to be split into two domains. For the shell domain ($R \geq r \geq R_{core}$) we find

$$0 = \frac{1}{r^2}D_A^{shell}\frac{\partial}{\partial r}\left(r^2\frac{\partial c_A^\mu}{\partial r}\right)\,,\quad r: R \geq r \geq R_{core}\,. \tag{9.111}$$

With the boundary conditions

$$c_A^\mu(t,z,r=R) = \frac{c_A(t,z)}{k_{H,A}}\,, \tag{9.112}$$

$$-D_A^{shell}\frac{\partial c_A^{shell}}{\partial r}\bigg|_{t,z,r=R_{core}} = -\frac{1}{R_{core}^2}k^\mu\int_{r=0}^{r=R_{core}} r^2 c_A^\mu(t,z,r)\mathrm{d}r\,. \tag{9.113}$$

For the core domain, we have ($R_{core} \geq r \geq 0$),

$$0 = \frac{1}{r^2}D_A^{\mu,eff}\frac{\partial}{\partial r}\left(r^2\frac{\partial c_A^\mu}{\partial r}\right) - k^\mu\frac{1}{c_A^{ref}}c_A^\mu\,,$$
$$r: R_{core} \geq r \geq 0\,. \tag{9.114}$$

For the concentration field within the particle, we then find

$$c_{\mathrm{A}}^{\mu}(t,z,r)=\begin{cases}\frac{c_{\mathrm{A}}(t,z)}{k_{\mathrm{H,A}}}-\frac{\delta^{\mathrm{shell}}}{D_{\mathrm{A}}^{\mathrm{shell}}}\frac{1}{rR}k^{\mu}\\ \times\int_{r=0}^{r=R_{\mathrm{core}}}r^2c_{\mathrm{A}}^{\mu}(t,z,r)\mathrm{d}r\\ \quad r:R\geq r\geq R_{\mathrm{core}}\,,\\ c_{\mathrm{A}}^{\mu}(t,z,r=R_{\mathrm{core}})\frac{R_{\mathrm{core}}}{r}\\ \times\frac{\sinh(3M_{\mathrm{T}}\frac{r}{R})}{\sinh(3M_{\mathrm{T}})},\\ \quad r:R_{\mathrm{core}}\geq r\geq 0\,.\end{cases}\tag{9.115}$$

When inserting (9.115) into relation (9.98), we find for $i_{\mathrm{I}}^{\mu}|_{r=R}$ after some rearrangement,

$$a\,i_{\mathrm{I}}^{\mu}\big|_{r=R}=-nF\frac{c_{\mathrm{A}}(t,z)}{k_{\mathrm{H,A}}}\times\left[\frac{1}{k^{\mu}E}\frac{1}{(1-\varepsilon)}\left(\underbrace{\frac{R}{R_{\mathrm{core}}}}_{\approx 1}\right)^2+\frac{\delta^{\mathrm{shell}}}{D_{\mathrm{A}}^{\mathrm{shell}}}\frac{1}{a}\underbrace{R_{\mathrm{core}}}_{\approx 1}\right]^{-1}.\tag{9.116}$$

With relation (9.106) and assuming that $R/R_{\mathrm{core}}\approx 1$, we finally have the well-known relation

$$a\,i_{\mathrm{I}}^{\mu}\big|_{r=R}=-nF\frac{c_{\mathrm{A}}(t,z)}{k_{\mathrm{H,A}}}\times\left(\frac{1}{k^{\mu}E}\frac{1}{(1-\varepsilon)}+\frac{\delta^{\mathrm{shell}}}{D_{\mathrm{A}}^{\mathrm{shell}}}\frac{R/3}{(1-\varepsilon)}\right)^{-1}.\tag{9.117}$$

In an analogous manner, we find for $i_{\mathrm{E}}^{\mu}|_{r=R}$ and $g_{\alpha}^{\mu}|_{r=R}$

$$a\,i_{\mathrm{E}}^{\mu}\big|_{r=R}=nF\frac{c_{\mathrm{A}}(t,z)}{k_{\mathrm{H,A}}}\times\left(\frac{1}{k^{\mu}E}\frac{1}{(1-\varepsilon)}+\frac{\delta^{\mathrm{shell}}}{D_{\mathrm{A}}^{\mathrm{shell}}}\frac{R/3}{(1-\varepsilon)}\right)^{-1},\tag{9.118}$$

$$a\,g_{\alpha}^{\mu}\big|_{r=R}=-\frac{c_{\mathrm{A}}(t,z)}{k_{\mathrm{H,A}}}\times\left(\frac{1}{k^{\mu}E}\frac{1}{(1-\varepsilon)}+\frac{\delta^{\mathrm{shell}}}{D_{\mathrm{A}}^{\mathrm{shell}}}\frac{R/3}{(1-\varepsilon)}\right)^{-1}.\tag{9.119}$$

9.4 Macroscale Models

Interface models do not consider the thickness or morphological characteristics of the CL. CL is simply an interface between GDL and a membrane. One of the advantages of interface models is the possibility to integrate more complex reaction kinetics on expense of other phenomena (e.g., disregard of concentration, overpotential, and temperature profiles). These conditions are usually not fulfilled in real fuel cells, therefore interface models provides less reliable predictions of fuel cell operations compared to distributed models as shown in [9.40]. However, these conditions might be fulfilled in some experimental setups such as in the three electrodes setup, using well-defined smooth surfaces or supported or not supported high surface area catalysts in the form of a thin-film layer as working electrodes.

9.4.1 Interface Models

To illustrate the interface modeling approach in more detail, methanol oxidation kinetics has been chosen. This reaction has importance for the development of direct methanol fuel cells. In gross, the methanol oxidation involves the transfer of six electrons and six protons (9.4) implying a very complex reaction mechanism.

In the past, a number of different studies were dedicated to understand the nature of reaction intermediates involved in this reaction and in many studies CO has been identified as a stable intermediate (for example [9.41] and references therein). A lumped reaction mechanism involving CO as an intermediate and a satisfying reaction stoichiometry might be formulated as [9.41, 42] methanol electrochemical adsorption step

$$\mathrm{CH_3OH}\xrightarrow{k_1}\mathrm{CH_3OH_{ads}}\rightarrow\ldots\xrightarrow{-3\mathrm{H}^+-3\mathrm{e}^-}\mathrm{CO_{ads}}+\mathrm{H}^+\,+\mathrm{e}^-\,,\tag{9.120}$$

water disproportionation step

$$\mathrm{H_2O}\overset{k_2/k_{-2}}{\longleftrightarrow}\mathrm{OH_{ads}}+\mathrm{H}^+\,+\mathrm{e}^-\,,\tag{9.121}$$

and surface reaction between adsorbed intermediates

$$\mathrm{CO_{ads}}+\mathrm{OH_{ads}}\xrightarrow{k_{3a}}\mathrm{COOH}\xrightarrow{k_{3b}}\mathrm{CO_2}+\mathrm{H}^+\,+\mathrm{e}^-\,.\tag{9.122}$$

In this mechanism, the methanol and $\mathrm{CO_2}$ diffusion were not considered since it has been shown that the experimentally observed limiting currents are 3 to 5 times lower than the estimated mass transfer limited current [9.43].

The reaction mechanism (9.120)–(9.122) contains still many steps and has to be further simplified to

be operative. Therefore, it was assumed that the first and the last reactions are irreversible, while the second one is reversible. These assumptions appear reasonable since CO_{ads} is a stable intermediate and one of the products of step (9.122) is in the gas phase. Furthermore, in (9.120) it was hypothesized that the methanol adsorption step is rate limiting, which led to the formulation of this reaction rate as a potential independent step (chemical reaction). Before rate expressions for single steps are evolved, the adsorption conditions for adsorbed intermediates have to be set. Usually Langmuir or Frumkin/Temkin (FT) adsorption conditions are used. In the present case, the rate expressions in accordance to the power law kinetics are

$$r_1 = k_1 c_{CH_3OH}(1-\theta_{CO})\,, \tag{9.123}$$

$$r_2 = k_2(1-\theta_{OH}) - k_{-2}\theta_{OH}c_{H^+}\,, \tag{9.124}$$

$$r_{3i} = k_{3i}\theta_{CO}\theta_{OH}\,, \tag{9.125}$$

with c_{CH_3OH} (in mol/m^3) being methanol concentration in the bulk and θ_i (defined as dimensionless), i = CO,OH being surface coverage of adsorbed species. The rate constants k_j, $j = 1, 2, -2, 3i$ are further defined as [9.42]

$$k_1 = k_{1O}\exp[-\beta_{CO}g_{CO}(\theta_{CO}-0.5)]\,, \tag{9.126}$$

$$k_2 = k_{2O}\exp[-\beta_{OH}g_{OH}(\theta_{OH}-0.5)] \times \exp\left(\frac{\alpha_2 F\Delta\varphi_{electrode}}{\mathcal{R}T}\right), \tag{9.127}$$

$$k_{-2} = k_{-2O}\exp[(1-\beta_{OH})g_{OH}(\theta_{OH}-0.5)] \times \exp\left(-\frac{(1-\alpha_2)F\Delta\varphi_{electrode}}{\mathcal{R}T}\right), \tag{9.128}$$

$$k_{3i} = k_{3iO}\exp[(1-\beta_{CO})g_{CO}(\theta_{CO}-0.5)] \times \exp[(1-\beta_{OH})g_{OH}(\theta_{OH}-0.5)] \times \exp\left(\frac{\alpha_3 F\Delta\varphi_{electrode}}{\mathcal{R}T}\right). \tag{9.129}$$

As can be seen in (9.126)–(9.129), adsorption conditions (Frumkin/Temkin) and potential dependences are contained in rate constants, with β_i (dimensionless) and g_i (dimensionless), i = CO, OH defining symmetry and inhomogeneity/interaction factors, respectively. In case that the surface coverage is independent on adsorption energies, the inhomogeneity factors are set to zero, resulting effectively in Langmuir adsorption conditions. Similarly if the transfer coefficient α_3 in (9.129) is set to zero, the reaction step (9.122) will become purely chemical, with an effective rate constant k_{3a}.

To complete the mathematical model, balance equations should be introduced. Here mass balances of dissolved species (methanol, H^+ and CO_2) are not considered since it was assumed that the methanol oxidation kinetics is not mass transport limited. Mass balances of adsorbed species can be formulated as [9.44]

$$c_{cat}\frac{d\theta_i}{dt} = \sum_k \nu_{k,i} r_k\,, \tag{9.130}$$

where c_{cat} is the surface concentration of catalyst (in mol/m^2), θ_i is the surface coverage and $\nu_{k,i}$ are stoichiometric coefficients of species i = CO, OH.

Finally, the charge balance can be defined in accordance to (9.66) [9.42, 44]

$$c_{electrode}\frac{d\Delta\varphi_{electrode}}{dt} = i_{electrode} - F(4r_1 + r_2 + r_3)\,. \tag{9.131}$$

The set of equations (9.123)–(9.131) has to be solved numerically to get the dependence of current on potential and/or time. Under some conditions, an analytical solution for the current can be obtained. For example, under steady-state conditions and by setting the heterogeneity constants g_{CO} and g_{OH} to zero (Langmuir adsorption conditions) one can obtain [9.41]

$$i_{electrode} = \frac{6k_1 c_{CH_3OH}}{1 + \frac{k_1 c_{CH_3OH}}{k_3}\frac{(1+B)}{B}}\,, \tag{9.132}$$

where B is defined as

$$B = \frac{k_2}{k_{-2}c_{H^+}}\,. \tag{9.133}$$

It appears clear that further model varieties based on Eqs. (9.123)–(9.131) can be formulated. Four kinetic models have been developed by introducing two distinctions. The two basic kinetic models have been obtained by introducing the first distinction, which concerns the potential dependence of (9.125) and (9.129). These models have been assigned as the VCS model [9.41] assuming potential dependence of (9.125) and (9.129) and the Kauranen model [9.46] assuming the potential independence of these steps (α_3 is set to zero). The second distinction concerns the adsorption conditions of the adsorbed species (CO and OH), leading to two varieties of the base models, the L-variety for Langmuir adsorption conditions (g_i, i=CO, OH is set to zero) and the FT-variety.

Under steady-state conditions, all of these models were able to reproduce quantitatively the experimental data (Fig. 9.5a) [9.41]. To overcome the lack of model

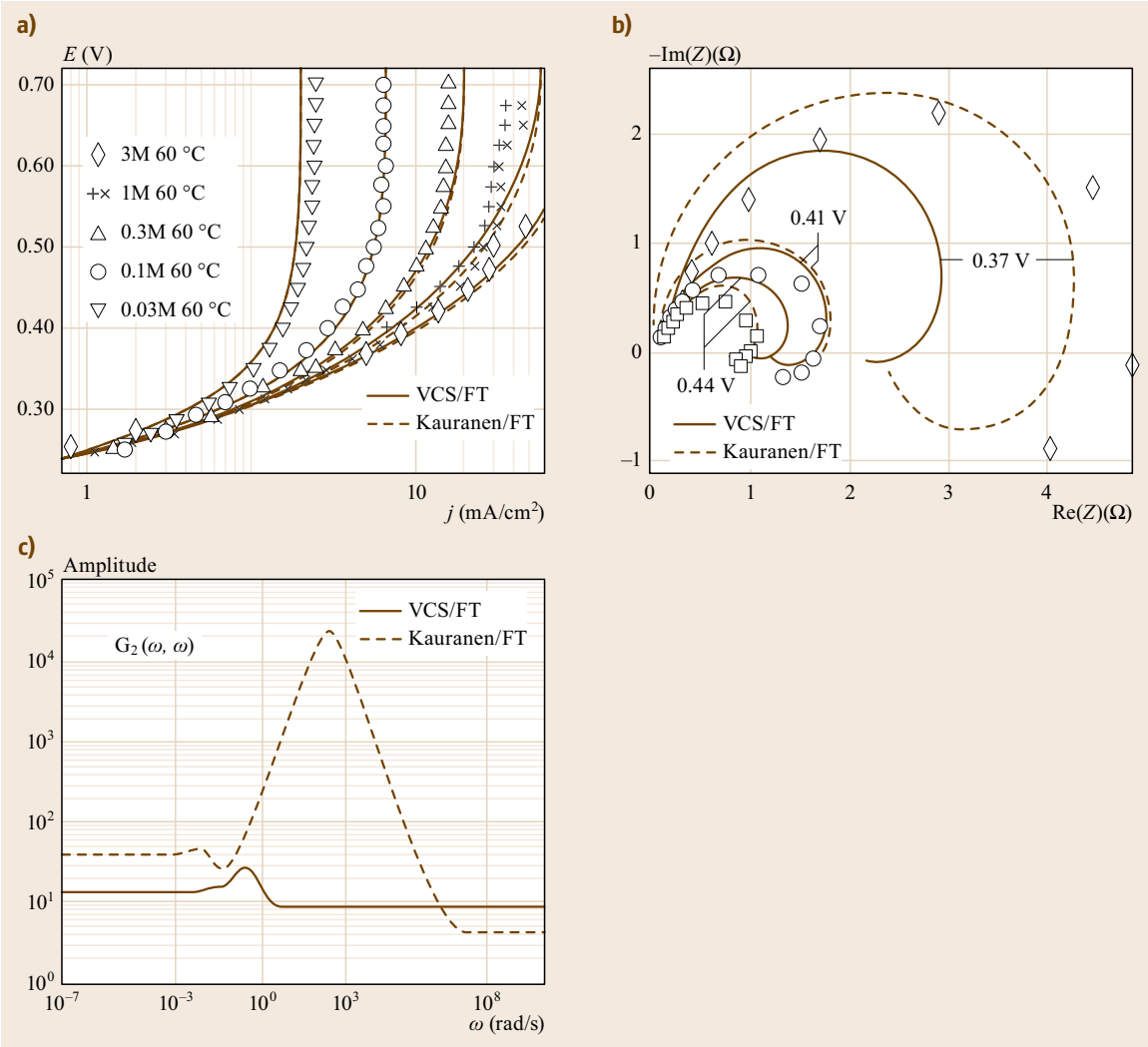


Fig. 9.5a–c Methanol oxidation kinetics (a) steady-state response, (b) EIS and (c) second-order frequency response function. *Concatenated symbols* correspond to experimental data and *lines* correspond to calculated curves for two different model descriptions (after [9.45])

discrimination in the steady-state approach dynamic conditions, such as the electrochemical impedance spectroscopy (EIS) could be considered. The interface modeling approach allows for a relatively easy transformation of a model from the time into the frequency domain [9.42]. In this example, it was shown that only one of four models fits quantitatively the experimental data (Kauranen-FT) (Fig. 9.5b). Still, all models were providing a qualitative fit of the experimental data.

Further insights into the mechanism of this reaction have been obtained by considering the nonlinear part of the frequency response [9.44]. This so-called nonlinear frequency response analysis (NFRA) can be considered as a generalization of EIS; it investigates the quasi-stationary response of a nonlinear system to a high amplitude periodic signal around a steady state. In the frequency domain, the current can be represented as an infinite sum of terms, whereby the first one corresponds to the first-order frequency response function (equivalent to reciprocal of EIS), while further terms are higher order frequency response functions. These higher order frequency response functions contain contributions of the nonlinear parts of the frequency response. For more details on this method and their different applications [9.44, 47, 48] and ref-

erences therein. In the case of the methanol oxidation, the frequency response function have been derived up to second order [9.44] and have shown a significant potential for a qualitative model discrimination (Fig. 9.5c).

Further example of interface modeling approach with respect to determination of electrode kinetics is work by *Wang* et al. [9.49]. These authors derived an analytical expression for the current under steady-state conditions in the case of hydrogen oxidation by assuming a so-called dual-pathway mechanism. First, a reaction mechanism for hydrogen oxidation consisting of three elementary steps has been defined and rate expressions for these steps based on power law kinetics have been evolved. To get an analytical solution for the current density under steady-state conditions assumptions regarding rates of single steps were introduced. With these assumptions, it was possibly to get an analytical expression for the kinetic current which has been further utilized in some works dealing with agglomerate modeling [9.50].

9.4.2 Porous Electrode Models

Porous electrode models can be found in studies on almost all fuel cell types. Therefore, the literature on this topic is rather extensive. A comprehensive review of these works would go beyond the scope of the present contribution. Instead, some selected studies should be discussed in order to exemplify the derivations made in Sect. 9.3.1 and to give a starting point for further reading.

First, a few simpler models, consisting of at least one material balance and the steady-state charge balances, should be discussed. A prototype example can be found in *Broka* and *Ekdunge* [9.51]. The authors consider a PEM fuel cell cathode. The model equations read (nomenclature of [9.51] was used)

Potential field

$$\sigma_{\text{eff}} \frac{\partial \eta}{\partial z} = i \,, \tag{9.134}$$

$$\frac{\partial i}{\partial z} = j_0 a \frac{c_{\text{O2}}}{c^*_{\text{O2}}} \exp\left(-\eta \frac{\beta F}{\mathcal{R} T}\right), \tag{9.135}$$

Concentration field

$$\frac{\partial}{\partial z}\left(-D_{\text{eff}} \frac{\partial c_{\text{O2}}}{\partial z}\right) = -\frac{1}{4F} j_0 a \frac{c_{\text{O2}}}{c^*_{\text{O2}}} \exp\left(-\eta \frac{\beta F}{\mathcal{R} T}\right), \tag{9.136}$$

which are in their structure similar to relations (9.42)–(9.44), discussed in Sect. 9.3.1. One advantage of such models is their simplicity and the relatively low effort for the numerical solution. This feature makes them suitable for numerical optimization. A representative example is the work of *Song* et al. [9.52]. Within this contribution, the authors have employed a model similar to (9.134)–(9.136) and have optimized the Nafion content, the platinum loading, the porosity, and the thickness of a PEM fuel cell cathode.

Further examples come from the field of biofuel cells. *Barton* [9.53] has studied an enzyme-catalyzed oxygen cathode. The current density in such systems is so small that the potential gradients within the electron and ion conductor can be neglected. The model reduces to a single material balance of similar structure as (9.136). Focus of the contribution was the analysis of transport limitations for the substrate and the prediction of the limiting current density. In the work of *Chan* et al. [9.54], the dynamic behavior of a biofuel cell anode was studied. The authors employed transient material balances along with steady-state charge balances for the electron conductor and ion conductor, respectively.

Some final example studies, using material balances and steady-state charge balances, can be found in the field of high-temperature fuel cells. A very simple model was used in the early study of *Fontes* et al. [9.55]. A molten carbonate fuel cell cathode was analyzed. The authors considered the potential field and used the results to clarify some mechanistic aspects for the reactions occurring. *Deseure* et al. [9.56] studied the cathode of a solid-oxide fuel cell. The model is similar to (9.134)–(9.136) and was used to study the influence of the porosity, the volume fraction of YSZ, and the particle diameter on the performance of the electrode. A more comprehensive model was used in the study of *Hussain* et al. [9.57] to analyze a SOFC anode. Here, the authors considered a Maxwell–Stefan approach for the description of the mass transport of the involved species and studied the concentration profiles at different current densities.

Next, a few more comprehensive models should be discussed. Interesting examples can be found in the field of PEM fuel cells. The water being produced at the cathode of a PEM fuel cell typically condensates to the liquid state, partially floods the pore network and hinders the supply of oxygen. In order to capture these conditions adequately, further state fields have to be considered in addition to the potential field and the concentration field. As a first example, the study of *Eikerling* [9.58] should be looked at. The model has the following structure (nomenclature of [9.58] was used).

Potential field

$$\eta(z): \quad \sigma_{\mathrm{el}} \frac{\partial \eta}{\partial z} = j_{\mathrm{p}} \,, \tag{9.137}$$

$$j_{\mathrm{p}}(z): \quad \frac{\partial j_{\mathrm{p}}}{\partial z} = Q^{\mathrm{ec}}(p_{\mathrm{O2}}, \eta, S_r) \,, \tag{9.138}$$

Concentration field gas phase

$$p_{\mathrm{O2}}(z): \quad \frac{\partial}{\partial z}\left(-\frac{D_{\mathrm{O2}}(S_r)}{\mathcal{R}T}\frac{\partial p_{\mathrm{O2}}}{\partial z}\right) = -\frac{Q^{\mathrm{ec}}(p_{\mathrm{O2}}, \eta, S_r)}{4F} \,, \tag{9.139}$$

$$p_{\mathrm{vap}}(z): \quad \frac{\partial}{\partial z}\left(-\frac{D_{\mathrm{vap}}(S_r)}{\mathcal{R}T}\frac{\partial p_{\mathrm{vap}}}{\partial z}\right) = -Q^{\mathrm{lv}}(p_{\mathrm{vap}}, S_r) \,, \tag{9.140}$$

liquid water saturation

$$S_r(z): \quad 0 = f(S_r, p^{\mathrm{l}}) \,, \tag{9.141}$$

$$p^{\mathrm{l}}(z): \quad \frac{\partial}{\partial z}\left(-\frac{K^{\mathrm{l}}(S_r)}{V_m \mu}\frac{\partial p^{\mathrm{l}}}{\partial z}\right) = \frac{Q^{\mathrm{ec}}(p_{\mathrm{O2}}, \eta, S_r)}{2F} - Q^{\mathrm{lv}}(p_{\mathrm{vap}}, S_r) \,. \tag{9.142}$$

Equations (9.137)–(9.139) are the charge balance and the mass balance for oxygen. These equations are similar in their structure to relations (9.134)–(9.136) as discussed earlier. As can be seen, the effective diffusivity and the expression for the reaction rate Q^{ec} are functions of the local liquid water saturation of the electrode $S_r(z)$. In order to calculate this quantity, the water balances for the vapor phase (9.140) and for the liquid phase (9.142) are solved. Both are coupled through the term Q^{lv}, considering evaporation and condensation. From the solution of (9.142), the quantity S_r can be calculated by means of relation (9.141), which considers the pore-size distribution and the wetting properties of the electrode. Models of this kind allow for a comprehensive evaluation of the electrode performance under two-phase flow conditions. In this study [9.58], the author has even found a piecewise analytical solution for the system (9.137)–(9.142), which allowed him to make important conclusions regarding the performance of the cathode in different operating regimes.

Finally, some of the rare studies using transient charge balances should be discussed. In contrast to the formulations given earlier, the charge balance for the electrochemical double layer hast to be considered in a transient formulation. From (9.8), (9.12), (9.15), and (9.16), we have for the potential field

$$\varphi_{\mathrm{E}}(t, z): \quad 0 = -\frac{\partial}{\partial z}\left(-\sigma_{\mathrm{E}}^{\mathrm{eff}}\frac{\partial \varphi_{\mathrm{E}}}{\partial z}\right) + aj \,, \tag{9.143}$$

$$\varphi_{\mathrm{I}}(t, z): \quad c_{\mathrm{dl}}\frac{\partial}{\partial t}(\varphi_{\mathrm{E}} - \varphi_{\mathrm{I}}) = -j + nFr(c_\alpha, \eta) \,, \tag{9.144}$$

$$j(t, z): \quad 0 = -\frac{\partial}{\partial z}\left(-\sigma_{\mathrm{I}}^{\mathrm{eff}}\frac{\partial \varphi_{\mathrm{I}}}{\partial z}\right) - aj \,, \tag{9.145}$$

$$\eta(t, z): \quad \eta = (\varphi_{\mathrm{E}} - \varphi_{\mathrm{I}}) - \Delta\varphi^0 \,. \tag{9.146}$$

Assuming a large conductivity in the electron conductor (9.28) and (9.31) and (9.143)–(9.146) can be easily combined to the following result

$$\eta(t, z): \quad c_{\mathrm{dl}}\frac{\partial \eta}{\partial t} = j - nFr(c_\alpha, \eta) \,, \tag{9.147}$$

$$j(t, z): \quad 0 = -\frac{\partial}{\partial z}\left(\sigma_{\mathrm{I}}^{\mathrm{eff}}\frac{\partial \eta}{\partial z}\right) - aj \,, \tag{9.148}$$

or even more compact (by inserting (9.148) into (9.147))

$$\eta(t, z): \quad ac_{\mathrm{dl}}\frac{\partial \eta}{\partial t} = -\frac{\partial}{\partial z}\left(\sigma_{\mathrm{I}}^{\mathrm{eff}}\frac{\partial \eta}{\partial z}\right) - anFr(c_\alpha, \eta) \,. \tag{9.149}$$

In *Wiezell* et al. [9.59], the formulation (9.147), (9.148) is combined with a material balance to study the impedance of PEM fuel cell anode. Main focus was on the influence of the hydration level of the ionomer on the electrode performance. Therefore, the electrode model was coupled with a simple membrane model and solved simultaneously.

9.4.3 Agglomerate Models

The agglomerate model framework has been used in the literature for the optimization of the catalyst layer structure and for the predictions of the fuel cell behavior under different operating conditions (some examples are studies by *Sahraoui* et al. [9.61] where the influence of different operating parameters, such as cathode inlet pressure, cathode gas humidification, anode gas humidification on PEMFC performance has been studied or by *Chupin* et al. [9.62], where the effect of water formation and distribution on fuel cell performance for control purposes was investigated). In the following, the focus will be on those studies using agglomerate models for the catalyst layer optimization. In this respect several issues, like parameter uncertainty and estimation, approaches in catalyst layer optimization, available kinetic information, as well as the impact of water in models will be discussed.

Agglomerate models assume the formation of so-called agglomerates inside of the catalyst layer. The agglomerates are made of an agglomerate core (consisting of carbon supported Pt nanoparticles) and a shell made of a solid electrolyte polymer film (usually Nafion). They are spatially distributed in the catalyst layer, whereby the void space between them defines the CL porosity (ε) comparable with the catalyst layer porosity in the case of the porous electrode models (Sect. 9.3.1, *Concentration Field Within the Gas Phase – Material Balances*). The existence of this solid electrolyte shell around the agglomerate core is probably one of the major differences compared to porous models. Namely in agglomerate models reacting species (oxygen or hydrogen) prior to the reaction, dissolves in this solid electrolyte film. As a consequence the effective concentration of the reacting species in (9.78)–(9.80) will be given by, for example, Henry's law (9.83), while in the case of porous models (9.35) the local gas phase concentrations are encountered. Therefore, porous models, in general, underestimate mass transport losses in the high current density region [9.40, 51, 63]. Furthermore, agglomerate models introduce more catalyst layer parameters than porous models. In addition to catalyst loading, the platinum-to-carbon ratio, the CL porosity and thickness, agglomerate models bring up further parameters such as the agglomerate size (R), the Nafion volume fraction inside of agglomerates (ε^{μ}), and the Nafion film thickness around agglomerates (δ^{shell}). These new parameters cannot be experimentally determined which makes them debatable.

To illustrate this problem, the determination of the agglomerate size and its shape has been chosen. In the most publications, it is stated that the size of agglomerates is based on the microscopic CL characterization, for example, by using the scanning electron microscopy (SEM). An example of such microscopy characterization has been shown in Fig. 9.6 [9.60]. As can be seen,

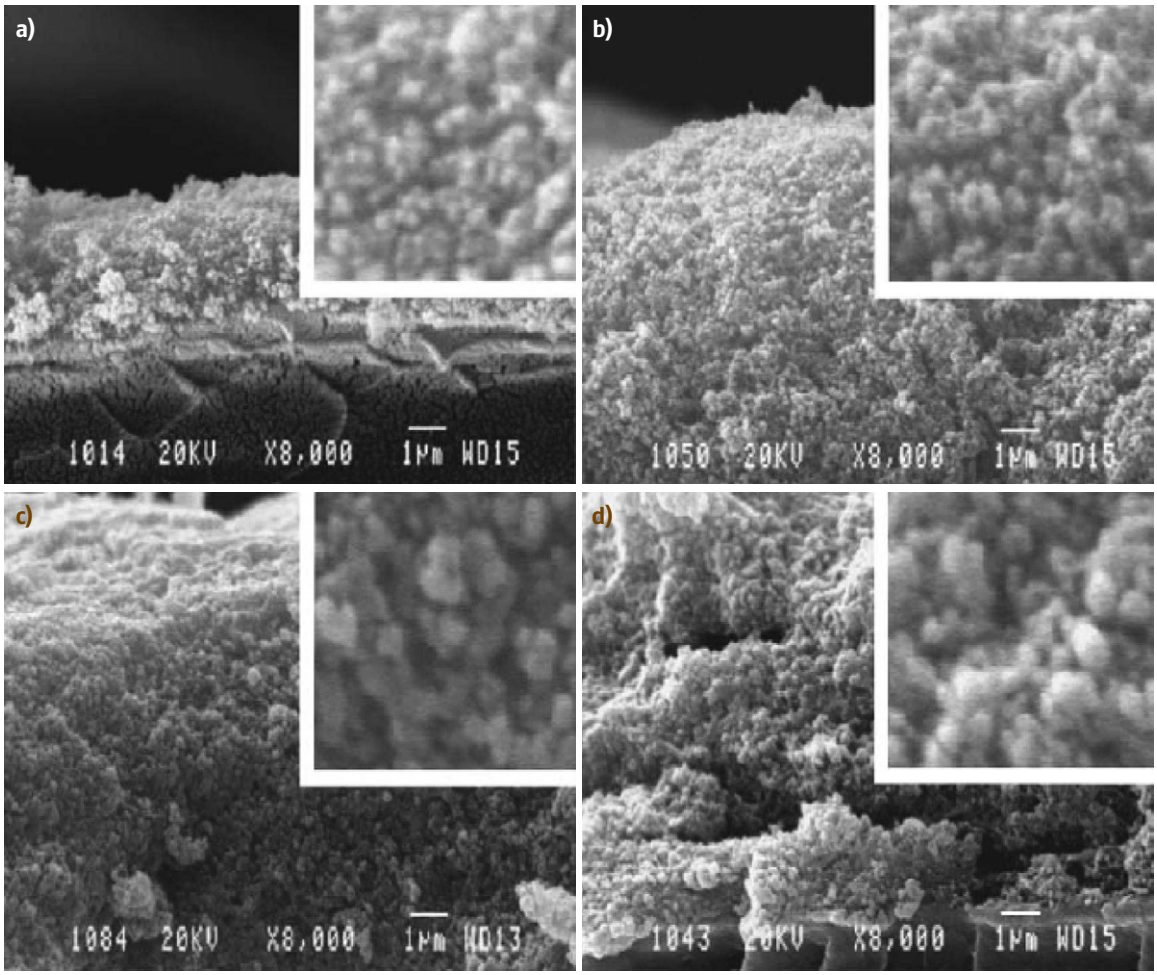


Fig. 9.6a–d SEM micrographs of CLs containing different Nafion contents wt% **(a)** 10, **(b)** 30 **(c)** 50 **(d)** 70 (after [9.60])

Table 9.1 Overview of agglomerate-related parameters

Agglomerate radius, R (nm)	Thickness of Nafion film around agglomerate, δ^{shell} (nm)	Nafion volume fraction inside agglomerates, ε^{μ}	Reference
1000–5000	–	–	[9.45]
3000	–	–	[9.56]
1000	80	0.5	[9.53]
250–1000	0–80	0.5	[9.49]
500	0–50	0.3	[9.54]
190–250	–	0.17–0.24	[9.55]
150	12	0.66–0.77	[9.57]
100	0	0.11–0.45	[9.50]
100	5	0.5	[9.37]

these micrographs evidence the existence of interconnected particle units, which are somewhat irregular in shape. This shape in models is usually approximated as a cylinder [9.64, 65] or a sphere [9.51, 60, 62, 66–68], whereby the models assuming spherical agglomerates are more numerous. The shape of agglomerates has an influence on the equation defining Thiele's modulus (9.103), where the definition of the characteristic length size differs depending on the agglomerate geometry, but it seems that its influence is not very significant.

Unlike agglomerate shape its size has much more impact in simulation studies [9.69–71]. For example, *Marquis* and *Coppens* [9.70] found out that a decrease in the agglomerate radius results in a significant increase of the platinum utilization (it can be improved by factor 30 while maintaining power density). On the other hand, *Kamarajugadda* and *Mazumder* [9.71] point out that the size of agglomerates should not be too small; for very small agglomerates, the CL tortuosity increases significantly causing severe mass transfer limitations in the CL. The agglomerate size values that can be found in the literature are usually based on SEM images. Although these values are partly influenced by the CL preparation protocol, they are somewhat subjected to interpretations, which results in a very broad spectrum of sizes from ca. 50 to 5000 nm. While, the lower limit is obviously specified by a size of a single carbon nanoparticle used as a catalyst support, the upper limit is a subject of perception. *Broka* and *Erkunge* [9.51] were among the first who estimated the agglomerate size based on SEM micrographs, with values between 1 and 5 μm for the CL thicknesses between 10 and 20 μm. *Siegel* et al. [9.69] based on their SEM microscopy images estimated an agglomerate size of ca. 6 μm. Agglomerate size values of ca. 1 μm or more were further adopted in a number of modeling papers [9.51, 66, 69]. Contrary to these studies *Gode* et al. [9.60] estimated the agglomerate sizes based on SEM images for CLs comprising different Nafion loadings and obtained sizes between 159 and 263 nm for Nafion loadings between 10 and 70 wt% Nafion (the employed catalyst was 20 % Pt/C). In addition to SEM, they analyzed agglomerate sizes based on Brunauer–Emmett–Teller (BET) surface areas and obtained a relatively good agreement between two methods especially for higher Nafion loadings. The deviation at low Nafion loadings was ascribed to an overestimation of the agglomerate surface area by BET due to a higher contribution of uncovered Pt/C particles to the measured BET surface area. In recent modeling studies, lower values of the agglomerate radius prevail [9.50, 60, 68, 70].

Similar to the agglomerate size, there is a significant distribution of Nafion film thickness values around the agglomerate as well as of Nafion volume fraction inside the agglomerates. An overview of typical values of all three parameters is presented in Table 9.1. For further values please see [9.68].

In addition to the just discussed uncertainty in determination of agglomerate structural parameters, further uncertainties are brought up by introduction of kinetic and transport parameters. Due to the large number of parameters in agglomerate models, parameter estimation becomes an important point. A few groups addressed this topic explicitly. For example, *Gode* et al. [9.60] determined parameters by fitting impedance spectroscopy data (as more reliable as imposed by nature of dynamic response [9.72]) and used the same parameters to simulate steady-state responses. To achieve a higher reliability of model parameters *Gerteisen* et al. [9.73] fitted simultaneously impedance and steady-state data. Nonlinear least-squares methods have been used by *Guo* et al. [9.74] and *Dobson* et al. [9.68] for parameter estimation. *Dobson* et al. [9.68] applied a gradient based and a global method. The first one is a local method, giving a final solution which might be dependent on the starting point. For further details on these methods, please see [9.68, 74] or for more general literature on parameter estimation in chemical engineering [9.75]. In their work *Dobson* et al. [9.68] let three parameters (agglomerate size, Nafion volume fraction inside ag-

glomerates and the exchange current density) free. All three parameters were bounded to physically meaningful ranges based on previous studies. In the case of the fitting of one polarization curve, parameters estimated by both methods (local and global) were very close. The authors emphasized further in accordance to previous conclusions of *Springer* et al. [9.25] and *Guo* et al. [9.74] that the fitting of a large set of experimental data obtained under different conditions simultaneously is needed in order to obtain reliable parameters (the number of experimental data points has to be much higher than the number of estimated parameters). So, they fitted simultaneously polarization curves obtained at different temperatures, different relative humidifies, and total pressures and obtained a unique set of fitting parameters able to describe the fuel cell behavior under different operating conditions. The values of the agglomerate radius and porosity obtained by simultaneous fitting of several polarization curves obtained under different conditions were 190 nm and 0.17 nm, respectively, while the data obtained from single curves fitting were ca. 250 nm and ca. 0.25.

One of the major foci of agglomerate models in the literature is the structural optimization of the cathode [9.60, 63, 70, 76] and less often of the anode catalyst layers [9.50]. In this respect, one or several CL structural parameters are chosen as design parameters and the optimization is performed by solving single or multivariable optimization problems. For example, *Song* et al. [9.76] used agglomerate models to optimize the distribution of Nafion and platinum in the catalyst layer by formulating a single- or two- variable(s) optimization problem, using the maximization of the current density at single voltage as an objective function and by introducing physically reasonable constrains regarding the volume fractions of components in the catalyst layer. Their results suggest that the nonuniform distribution of Nafion in the catalyst layer, with more Nafion close to membrane and less at the interface with GDL, is more advantageous than a uniform Nafion distribution. The reason is an influence of the Nafion content variation on the CL void fraction, resulting in less mass transport limitations close to GDL. On the other hand, more Nafion in the region close to the membrane reduces the Ohmic resistance in the ionomer phase. The Nafion distribution was also studied by *Sun* et al. [9.66] which in accordance to previous authors concluded that the nonuniform Nafion distribution is better than uniform.

Secanell et al. [9.50, 63] used an agglomerate model framework for optimal cathode [9.63] and anode [9.50] designs by solving multivariable optimization problems. Starting from the base case, the authors formulated a multivariable optimization problem defining similar to [9.76] the maximization of the current density at a certain voltage as an objective function. As design parameters they have chosen the platinum loading, the Pt to carbon ratio, the volume fraction of Nafion inside the agglomerates and the void fraction in the GDL, assuming a constant agglomerate radius and a constant thickness of the Nafion film around the agglomerates. They performed an optimization in different current density regions representing activation, ohmic, and mass-transport-dominated regions and found out that the optimal structure of the catalyst layer is dependent on the current range. For the oxygen cathode at low current densities (activation region) they obtained that higher platinum loadings are preferred, while in the mass transport region the platinum loading can be significantly reduced, but the ionomer content in the agglomerates should increase as well as the void fraction in the GDL [9.63]. In the case of the hydrogen anode, the results suggest that the platinum loading can be reduced by more than one order of magnitude ($0.4-0.018\,mg/cm^2$), at a high Nafion volume fraction inside agglomerates (0.76), low porosity of the GDL (0.27 compared to 0.6 for the base case) and at very high dilution of the Pt/C catalyst (ca. 5% Pt/C) [9.50].

Marquis and *Coppens* [9.70] formulated a agglomerate model of a fuel cell cathode accounting for the effect of liquid water formation and transport in the catalyst layer with the goal to maximize the platinum catalyst utilization by solving a multivariable optimization problem. The objective function was formulated as the ratio between power density and platinum loading, while the design variables were platinum loading, Pt-to-carbon ratio and the catalyst layer void fraction. The optimized catalyst layer was only 1 μm thick (base case was 40 μm), providing the similar power density ($0.36\,W/cm^2$, compared to base case value of $0.46\,W/cm^2$) at a significantly reduced platinum loading ($0.01\,mg/cm^2$ Pt compared to $0.40\,mg/cm^2$ platinum for the base case). Interestingly, according to the simulations the Nafion content in the ultrathin layers is significantly higher than in the base case (ca. 0.6 compared to 0.37 for the base case). An increase of the Nafion loading is at the expense of the CL void fraction which is significantly reduced compared to the base case (ca. 0.25 compared to 0.5 for the base case). These results suggest that a significant catalyst reduction can be achieved even on the cathode side (the values for the cathode reported in this study are similar to those reported previously for the anode [9.50]).

Agglomerate models, due to the mentioned parameter uncertainties are in general less suitable for the determination of electrode kinetics than for example interface models (Sect. 9.4.1). The kinetics of electrochemical reactions in these models is commonly

implemented in terms of lumped kinetics, for example, (9.94) with apparent values of typical electrochemical parameters such as reaction orders, transfer coefficients, and exchange current densities. Ideally this kinetics should be based on results of interface models, where only the exchange current density from the interface model in terms of A/m^2 should be transformed into the volumetric current density (A/m^3) by accounting for the internal surface a (in m^2_{act}/m^3). In the case of ideally flat electrodes (product of aL assigned to electrode roughness in (9.68), equal one), this exchange current density will correspond to *intrinsic* exchange current density in terms of A/m^2_{act}. In case of thin-film electrodes [9.77], which are commonly used to study electrode kinetics on nanoparticle catalysts, the determined exchange current density will have to be corrected for the roughness factor.

In addition, the concentrations of species taking place into reaction should be adjusted in accordance to local concentrations (calculated based on (9.80) at the agglomerate level, which influences further the concentration in the CL (9.74)). The later effect appears to be important since in this way distributed models can provide information on the change of apparent kinetic parameters like the Tafel slope or the apparent reaction order due to for example mass transport limitations. The change of apparent kinetic parameters can also be caused by ion or electron transport limitations (9.72)–(9.73) (these two limitations are usually not an issue in case of interface models and experiments which are typically performed under conditions where these two limitations can be neglected). The abovementioned effects have been indeed observed in the literature. For example, *Jaouen* et al. [9.67] simulations predict the doubling or even the four folding of the Tafel slope under specific conditions. As demonstrated, the doubling of the Tafel slope (from ca. 110–220 mV/dec) could be caused either by mass transport or ion transport limitations. If both of these processes are limited a four folding of the Tafel slope could be observed (440 mV/dec). The doubling of the Tafel slope was also observed by *Gode* et al. [9.60] and commented in terms of mass transfer limitations in the agglomerate.

The effect of liquid water was not always treated in agglomerate models. In general, these models predict some deterioration of the CL performance in the presence of liquid water. *Marquis* and *Coppens* [9.70] predicted based on their simulations the reduction of the CL performance in the presence of liquid water (from 0.47 W/cm^2 without liquid water to 0.36 W/cm^2 with liquid water at the same platinum loading of 0.01 mg/cm^2). *Kamarajugadda* and *Mazumder* [9.71] used a flooded agglomerate model to study the effect of the cathode catalyst layer structure on the PEMFC performance. Their model accounts for influences of Nafion and catalyst loadings, platinum-to-carbon ratio, agglomerate size and the CL thickness. The analysis has been performed by a parameter variation compared to the base case. They concluded that the variation in CL composition affects the performance at intermediate current densities due to local mass transport effects (inside the agglomerate) and electrical conduction, while at high current densities the performance is affected due to global mass transfer limitations.

One of the further important issues is the interrelation of different structural parameters. *Kamarajugadda* and *Mazumder* [9.71] pointed out that the change of the platinum and Nafion loading will cause changes of other structural parameters, most notably volume fractions of pores, Nafion, and solids. These interrelations are in some extent accounted in agglomerate models. For example the internal surface (in m^2_{act}/m^3), utilized for an electrochemical reaction, for example, in (9.74) is usually related to the catalyst loading (m_{Pt}) and the thickness of the CL (L) in accordance to [9.50, 63, 78]

$$a = a_0 \frac{m_{Pt}}{L} , \tag{9.150}$$

where a_0 is the catalyst surface area per unit mass of the catalyst (m^2_{act}/g_{cat}), while m_{Pt} is catalyst loading (in g_{cat}/m^2) and L is the thickness of the CL (in m). This value in some studies [9.63, 78] is based on data provided by catalyst producers (e.g., E-TEK) (Table 9.2).

Alternatively, assuming spherical shape of Pt nanoparticles, a_0 can be estimated by surface area per unit mass of Pt nanoparticles

$$a_0 = \frac{3}{r_{Pt}\rho_{Pt}} , \tag{9.151}$$

where r_{Pt} and ρ_{Pt} are radius (in m) and density of Pt (in kg/m^3).

Some authors account for a so-called three-phase boundary in their models, estimating an effective surface area for example by using a theory of active bonds in dual porous composite materials [9.76]. In some works, the decrease of the surface area due to the

Table 9.2 Catalyst surface area per unit mass of the catalyst (after [9.78])

Type of the catalyst	Platinum to carbon ratio	a_0 (m^2/g)
Carbon supported Pt	0.1	140
catalyst	0.2	112
	0.3	88
	0.4	72
	0.6	32
	0.8	11
Platinum black	1.0	28

formation of a three-phase boundary is accounted by an empirical coefficient [9.66].

The volume fractions of the solid and the ionomer phases are also related to the catalyst loading and the thickness of the catalyst layer in accordance to [9.63, 71]

$$\varepsilon_{\mathrm{S}} = \left(\frac{1}{\rho_{\mathrm{Pt}}} + \frac{100 - \mathrm{Pt/C}}{\mathrm{Pt/C}\rho_{\mathrm{C}}} \right) \frac{m_{\mathrm{Pt}}}{L} \tag{9.152}$$

for the volume fraction of the solid phase where ρ_i stands for densities of solid components (i =Pt, C) as well as for the volume fraction of the ionomer phase

$$\varepsilon_{\mathrm{N}} = \frac{4}{3}\pi N_{\mathrm{agg}} \left\{ R^3 \varepsilon^{\mu} + [(R + \delta^{\mathrm{shell}})^3 - R^3] \right\} , \tag{9.153}$$

where N_{agg} is the number of agglomerates, R the agglomerate radius, ε^{μ} is the Nafion volume fraction in the agglomerate, and δ^{shell} is the thickness of the Nafion film around the agglomerate.

The number of agglomerates N_{agg} can be calculated by assuming an agglomerate radius and its Nafion volume fraction

$$N_{\mathrm{agg}} = \frac{\varepsilon_{\mathrm{S}}}{\frac{4}{3}\pi R^3 (1 - \varepsilon^{\mu})} . \tag{9.154}$$

In all equations, a spherical shape of the agglomerates has been assumed. The void fraction of the catalyst layer can be finally calculated using

$$\varepsilon = 1 - \varepsilon_{\mathrm{S}} - \varepsilon_{\mathrm{N}} . \tag{9.155}$$

9.5 Conclusions and Outlook

A review on macroscale modeling approaches for catalyst layer modeling has been presented. In the first place, the major governing equations for determination of potential and concentration state fields, on an example of a porous electrode model have been developed. In this kind of models the variables of interest are averaged over a representative averaging volume. In addition, instead of the exact geometrical details of the electrode, the volume fraction ε of the corresponding phase and the internal surface a (in $\mathrm{m}^2_{\mathrm{act}}/\mathrm{m}^3$) are considered. In the balance equations, all fluxes are then typically related to superficial quantities by multiplying the interstitial (*pore*) flux with the corresponding volume fraction ε. Similarly, all phenomenological coefficients appearing in the transport kinetics are corrected by considering a tortuosity of the pores inside of catalyst structure (for example by introducing Bruggemann's relation as the most common one). All considered balance equations are formulated as dynamical. In typical simplifications, charge and mass balances are considered quasi-stationary.

By applying common assumptions of interface models (absence of all gradients), it was proven that the interface model governing equations can be derived by spatial integration of the porous electrode model ((9.64)–(9.71)). This showed clear relation between kinetic parameters (rate constants) (9.69) in two different approaches, which has to be taken into consideration when introducing parameters determined by fitting interface models into distributed models.

It was further demonstrated that the agglomerate model is an extension of the porous electrode model. Unlike porous models, the agglomerate models allow for the consideration of some geometrical details of the electrode. The state fields of the variables of interest are formulated on a macroscale and a microscale, respectively, where the macroscale is identical with the macroscale of the porous electrode models. The additional length scale is at the level of agglomerates where the relevant state fields are resolved over the radial coordinate r of the agglomerate. The coupling between these two scales is expressed in terms of $\mathrm{i}_{\mathrm{E}}^{\mu}|_{r=R}$, $\mathrm{i}_{\mathrm{I}}^{\mu}|_{r=R}$ and $g_{\alpha}^{\mu}|_{r=R}$ quantities (9.72)–(9.74), which consider electron, ion and mass exchange between the agglomerate scale and the macroscale. These quantities can be obtained by solving balance equations at the agglomerate level. After applying some simplifications analytical expressions for terms $\mathrm{i}_{\mathrm{E}}^{\mu}|_{r=R}$, $\mathrm{i}_{\mathrm{I}}^{\mu}|_{r=R}$ and $g_{\alpha}^{\mu}|_{r=R}$ and $\mathrm{g}_{\alpha}^{\mu}|_{r=R}$, can be obtained (9.107)–(9.109), which can be then inserted into the balance equations at the macroscale (9.72)–(9.74) and solved.

Some selected examples of different modeling approaches from the literature have been reviewed. In the case on the interface model, its formulation allow for integration of more complex reaction kinetics, as shown on an example of the methanol oxidation. In this way these models are well suited for determination of kinetic constants or derivation and validation of analytical expressions for current, which can be later on integrated into distributed models (porous or agglomerate) to study the influence of structural parameter. The agglomerate models are most conservative with respect to current density, providing the best descriptions of the experimental data compared to other two modeling approaches. One part of the reason is an assumption of a reactant absorption in Nafion film in accordance to Henry's law in the agglomerate model,

while porous electrode models typically uses local concentrations in the gas phase. The other part of the reason is larger number of parameters in the agglomerate model, making them more flexible to fit the experimental data. Some of these parameters cannot be readily measured, which makes them very debatable. Examples are agglomerate radius, Nafion volume fraction inside of agglomerate and Nafion film thickness around the agglomerate. Due to large number of free parameters mathematical tools for parameter estimation and sensitivity analysis should be utilized as emphasized in some studies. Ideally, the parameters should be supplied from the microscale models. This in addition to new experimental methods in studying of the catalyst layers and/or more through applications of existing experimental methods, for more reliable parameter determination will bring further advances in CL simulation and accuracy.

References

9.1 I. Moussallem, J. Jörissen, U. Kunz, S. Pinnow, T. Turek: Chlor-alkali electrolysis with oxygen depolarized cathodes: History, present status and future prospects, J. Appl. Electrochem. **38**, 1177–1194 (2008)

9.2 W.K. Epting, J. Gelb, S. Litster: Resolving the three-dimensional microstructure of polymer electrolyte fuel cell electrodes using nanometer-scale x-ray computed tomography, Adv. Functional Mater. **22**, 555–560 (2012)

9.3 H.-R. Jhong, F.R. Brushett, L. Yin, D.M. Stevenson, P.J.A. Kenis: Combining structural and electrochemical analysis of electrodes using micro-computed tomography and a microfluidic fuel cell, J. Electrochem. Soc. **159**, B292–B298 (2012)

9.4 H. Markoetter, I. Manke, P. Krueger, T. Arlt, J. Haussmann, M. Klages, H. Riesemeier, C. Hartnig, J. Scholta, J. Banhart: Investigation of 3-D water transport paths in gas diffusion layers by combined in-situ synchrotron x-ray radiography and tomography, Electrochem. Commun. **13**, 1001–1004 (2011)

9.5 T. Vidaković-Koch, I. Gonzalez Martinez, R. Kuwertz, U. Kunz, T. Turek, K. Sundmacher: Electrochemical membrane reactors for sustainable chlorine recycling, Membranes **2**, 510–528 (2012)

9.6 M. Eikerling, A.A. Kornyshev, A.R. Kucernak: Water in polymer electrolyte fuel cells: Friend or foe?, Physics Today **59**, 38–44 (2006)

9.7 X. Yu, J.L. Yuan, B. Sunden: Review on the properties of nano-/microstructures in the catalyst layer of PEMFC, ASME J. Fuel Cell Sci. Technol. **8**(3), 034001 (2011)

9.8 A.A. Shah, K.H. Luo, T.R. Ralph, F.C. Walsh: Recent trends and developments in polymer electrolyte membrane fuel cell modelling, Electrochimica Acta **56**, 3731–3757 (2011)

9.9 J. Zhang: *PEM Fuel Cell Catalysts and Catalyst Layers – Fundamentals and Applications* (Springer, Berlin, Heidelberg 2008)

9.10 Y. Wang, X. Feng: Analysis of reaction rates in the cathode electrode of polymer electrolyte fuel cell I. Single-layer electrodes, J. Electrochem. Soc. **155**, B1289–B1295 (2008)

9.11 H. Wendt, H. Vogt, G. Kreysa, D.M. Kolb, G.E. Engelmann, J.C. Ziegler, H. Goldacker, K. Jüttner, U. Galla, H. Schmieder, E. Steckhan: *Ullmann's Encyclopedia of Industrial Chemistry: Electrochemistry*, Vol. 11, 6th edn. (Wiley-VCH, Weinheim 2000) p. 425

9.12 P.K. Das, X. Li, Z.S. Liu: A three-dimensional agglomerate model for the cathode catalyst layer of PEM fuel cells, J. Power Sources **179**, 186–199 (2008)

9.13 N. Khajeh-Hosseini-Dalasm, K. Fushinobu, K. Okazaki: Three-dimensional transient two-phase study of the cathode side of a PEM fuel cell, Int. J. Hydrogen Energy **35**, 4234–4246 (2010)

9.14 C. Song, J. Zhang: Electrocatalytic oxygen reduction reaction. In: *PEM Fuel Cell Electrocatalysts and Catalyst Layers*, ed. by J. Zhang (Springer, Berlin, Heidelberg 2008) p. 1119

9.15 M. Carmo, A.R. Dos Santos, J.G.R. Poco, M. Linardi: Physical and electrochemical evaluation of commercial carbon black as electrocatalysts supports for DMFC applications, J. Power Sources **173**, 860–866 (2007)

9.16 D.J. Jones, J. Peron, Y. Nedellec, J. Roziere: The effect of dissolution, migration and precipitation of platinum in Nafion-based membrane electrode assemblies during fuel cell operation at high potential, J. Power Sources **185**, 1209–1217 (2008)

9.17 W. Bi, G.E. Gray, T.F. Fuller: PEM fuel cell PtC dissolution and deposition in Nafion electrolyte, Electrochem. Solid-State Lett. **10**, B101–B104 (2007)

9.18 S.-Y. Huang, P. Ganesan, S. Park, B.N. Popov: Development of a titanium dioxide-supported platinum catalyst with ultrahigh stability for polymer electrolyte membrane fuel cell applications, J. Am. Chem. Soc. **131**, 13898–13899 (2009)

9.19 L. Wang, B.L. Yi, H.M. Zhang, D.M. Xing: Pt/SiO2 as addition to multilayer SPSU/PTFE composite membrane for fuel cells, Polymers Adv. Technol. **19**, 1809–1815 (2008)

9.20 C. Coutanceau, S. Baranton, T.W. Napporn: Platinum fuel cell nanoparticle syntheses: Effect on morphology, structure and electrocatalytic behavior. In: *The Delivery of Nanoparticles*, ed. by A. A. Hashim, http://www.intechopen.com/books/the-delivery-of-nanoparticles/platinum-fuel-cell-nanoparticle-synthesises-effect-on-morphology-structure-and-electrocatalytic-beha (InTech, 2012)

9.21 K.A. Mauritz, R.B. Moore: State of understanding of Nafion, Chemical Rev. **104**, 4535–4586 (2004)

9.22 J.T. Hinatsu, M. Mizuhata, H. Takenaka: Water uptake of perfluorosulfonic acid membranes from liquid water and water vapor, J. Electrochem. Soc. **141**, 1493–1498 (1994)

9.23 D.R. Morris, X. Sun: Water-sorption and transport properties of Nafion, 117 H, J. Appl. Polymer Sci. **50**, 1445–1452 (1993)
9.24 S. Motupally, A.J. Becker, J.W. Weidner: Diffusion of water in Nafion 115 membranes, J. Electrochem. Soc. **147**, 3171–3177 (2000)
9.25 T.E. Springer, M.S. Wilson, S. Gottesfeld: Modeling and experimental diagnostics in polymer electrolyte fuel cells, J. Electrochem. Soc. **140**, 3513–3526 (1993)
9.26 D.M. Bernardi, M.W. Verbrugge: Mathematical model of a gas diffusion electrode bonded to a polymer electrolyte, Aiche J. **37**, 1151–1163 (1991)
9.27 I. Inchem: *Chemical Safety Information from Intergovernmental Organizations* (WHO, Geneva 2011), IPCS INCHEM
9.28 R.H. Perry, D.W. Green: *Perry's Chemical Engineers' Handbook*, 6th edn. (McGraw-Hill, New York 1984)
9.29 M.S. Wilson, S. Gottesfeld: Thin-film catalyst layers for polymer electrolyte fuel cell electrodes, J. Appl. Electrochem. **22**, 1–7 (1992)
9.30 L. Gubler, G. Scherer: A proton-conducting polymer membrane as solid electrolyte – Function and required properties. In: *Advances in Polymer Science*, Vol. 215, ed. by G. Scherer (Springer, Berlin, Heidelberg 2008) pp. 1–14
9.31 J. Xie, K.L. More, T.A. Zawodzinski, W.H. Smith: Porosimetry of MEAs made by Thin Film Decal method and its effect on performance of PEFCs, J. Electrochem. Soc. **151**, A1841–A1846 (2004)
9.32 E. Antolini, L. Giorgi, A. Pozio, E. Passalacqua: Influence of Nafion loading in the catalyst layer of gas-diffusion electrodes for PEFC, J. Power Sources **77**, 136–142 (1999)
9.33 F.A. Howes, S. Whitaker: The spatial averaging theorem revisited, Chem. Eng. Sci. **40**, 1387–1392 (1985)
9.34 P. De Vidts, R.E. White: Governing equations for transport in porous electrodes, J. Electrochem. Soc. **144**, 1343–1353 (1997)
9.35 J. Newman, K.E. Thomas-Alyea: *Electrochemical Systems*, 3rd edn. (Wiley, New York 2004)
9.36 R.B. Bird, W.E. Stewart, E.N. Lightfoot: *Transport Phenomena* (Wiley, Chichester 1960)
9.37 R. Krishna, J.A. Wesselingh: The Maxwell-Stefan approach to mass transfer, Chem. Eng. Sci. **52**, 861–911 (1997)
9.38 H.S. Fogler: *Elements of Chemical Reaction Engineering* (Prentice Hall, Englewood Cliffs 2005)
9.39 O. Levenspiel: *Chemical Reaction Engineering*, 3rd edn. (Wiley, Chichester 1999)
9.40 D. Harvey, J.G. Pharoah, K. Karan: A comparison of different approaches to modelling the PEMFC catalyst layer, J. Power Sources **179**, 209–219 (2008)
9.41 T. Vidakovic, M. Christov, K. Sundmacher: Rate expression for electrochemical oxidation of methanol on a direct methanol fuel cell anode, J. Electroanal. Chem. **580**, 105–121 (2005)
9.42 U. Krewer, M. Christov, T. Vidakovic', K. Sundmacher: Impedance spectroscopic analysis of the electrochemical methanol oxidation kinetics, J. Electroanal. Chem. **589**, 148–159 (2006)
9.43 T. Vidakovic, M. Christov, K. Sundmacher: Investigation of electrochemical oxidation of methanol in a cyclone flow cell, Electrochimica Acta **49**, 2179–2187 (2004)
9.44 B. Bensmann, M. Petkovska, T. Vidaković-Koch, R. Hanke-Rauschenbach, K. Sundmacher: Nonlinear frequency response of electrochemical methanol oxidation kinetics: A theoretical analysis, J. Electrochem. Soc. **157**, B1279–B1289 (2010)
9.45 U. Krewer, T. Vidakovic-Koch, L. Rihko-Struckmann: Electrochemical oxidation of carbon containing fuels and their dynamics in low temperature fuel cells, ChemPhysChem **12**, 2518–2544 (2011)
9.46 P.S. Kauranen, E. Skou, J. Munk: Kinetics of methanol oxidation on carbon-supported Pt and Pt + Ru catalysts, J. Electroanal. Chem. **404**, 1–13 (1996)
9.47 T.R. Vidaković-Koch, V.V. Panić, M. Andrić, M. Petkovska, K. Sundmacher: Nonlinear frequency response analysis of the ferrocyanide oxidation kinetics. Part I. A theoretical analysis, J. Phys. Chem. C **115**, 17341–17351 (2011)
9.48 V.V. Panić, T.R. Vidaković-Koch, M. Andrić, M. Petkovska, K. Sundmacher: Nonlinear frequency response analysis of the ferrocyanide oxidation kinetics. Part II. Measurement routine and experimental validation, J. Phys. Chem. C **115**, 17352–17358 (2011)
9.49 J.X. Wang, T.E. Springer, R.R. Adzic: Dual-pathway kinetic equation for the hydrogen oxidation reaction on Pt electrodes, J. Electrochem. Soc. **153**, A1732–A1740 (2006)
9.50 M. Secanell, K. Karan, A. Suleman, N. Djilali: Optimal design of ultralow-platinum PEMFC anode electrodes, J. Electrochem. Soc. **155**, B125–B134 (2008)
9.51 K. Broka, P. Ekdunge: Oxygen and hydrogen permeation properties and water uptake of Nafion 117 membrane and recast film for PEM fuel cell, J. Appl. Electrochem. **27**, 281–289 (1997)
9.52 D. Song, Q. Wang, Z. Liu, T. Navessin, M. Eikerling, S. Holdcroft: Numerical optimization study of the catalyst layer of PEM fuel cell cathode, J. Power Sources **126**, 104–111 (2004)
9.53 S.C. Barton: Oxygen transport in composite mediated biocathodes, Electrochimica Acta **50**, 2145–2153 (2005)
9.54 D.-S. Chan, D.-J. Dai, H.-S. Wu: Dynamic modeling of anode function in enzyme-based biofuel cells using high mediator concentration, Energies **5**, 2524–2544 (2012)
9.55 E. Fontes, C. Lagergren, D. Simonsson: Mathematical modelling of the MCFC cathode on the linear polarisation of the NiO cathode, J. Electroanal. Chem. **432**, 121–128 (1997)
9.56 J. Deseure, Y. Bultel, L. Dessemond, E. Siebert: Theoretical optimisation of a SOFC composite cathode, Electrochimica Acta **50**, 2037–2046 (2005)
9.57 M.M. Hussain, X. Li, I. Dincer: Mathematical modeling of transport phenomena in porous SOFC anodes, Int. J. Thermal Sci. **46**, 48–56 (2007)
9.58 M. Eikerling: Water management in cathode catalyst layers of PEM fuel cells: A structure-based model, J. Electrochem. Soc. **153**, E58–E70 (2006)
9.59 K. Wiezell, P. Gode, G. Lindbergh: Steady-state and EIS investigations of hydrogen electrodes and mem-

branes in polymer electrolyte fuel cells: I. Modeling, J. Electrochem. Soc. **153**, A749–A758 (2006)
9.60 P. Gode, F. Jaouen, G. Lindbergh, A. Lundblad, G. Sundholm: Influence of the composition on the structure and electrochemical characteristics of the PEFC cathode, Electrochimica Acta **48**, 4175–4187 (2003)
9.61 M. Sahraoui, C. Kharrat, K. Halouani: Two-dimensional modeling of electrochemical and transport phenomena in the porous structures of a PEMFC, Int. J. of Hydrogen Energy **34**, 3091–3103 (2009)
9.62 S. Chupin, T. Colinart, S. Didierjean, Y. Dubé, K. Agbossou, G. Maranzana, O. Lottin: Numerical investigation of the impact of gas and cooling flow configurations on current and water distributions in a polymer membrane fuel cell through a pseudo-two-dimensional diphasic model, J. Power Sources **195**, 5213–5227 (2010)
9.63 M. Secanell, K. Karan, A. Suleman, N. Djilali: Multi-variable optimization of PEMFC cathodes using an agglomerate model, Electrochimica Acta **52**, 6318–6337 (2007)
9.64 R.M. Rao, D. Bhattacharyya, R. Rengaswamy, S.R. Choudhury: A two-dimensional steady state model including the effect of liquid water for a PEM fuel cell cathode, J. Power Sources **173**, 375–393 (2007)
9.65 G. Lin, W. He, T. Van Nguyen: Modeling liquid water effects in the gas diffusion and catalyst layers of the cathode of a PEM fuel cell, J. Electrochem. Soc. **151**, A1999–A2006 (2004)
9.66 W. Sun, B.A. Peppley, K. Karan: An improved two-dimensional agglomerate cathode model to study the influence of catalyst layer structural parameters, Electrochimica Acta **50**, 3359–3374 (2005)
9.67 F. Jaouen, G. Lindbergh, G. Sundholm: Investigation of mass-transport limitations in the solid polymer fuel cell cathode I. Mathematical model, J. Electrochem. Soc. **149**, A437–A447 (2002)
9.68 P. Dobson, C. Lei, T. Navessin, M. Secanell: Characterization of the PEM fuel cell catalyst layer microstructure by nonlinear least-squares parameter estimation, J. Electrochem. Soc. **159**, B514–B523 (2012)
9.69 N.P. Siegel, M.W. Ellis, D.J. Nelson, M.R. von Spakovsky: Single domain PEMFC model based on agglomerate catalyst geometry, J. Power Sources **115**, 81–89 (2003)
9.70 J. Marquis, M.O. Coppens: Achieving ultra-high platinum utilization via optimization of PEM fuel cell cathode catalyst layer microstructure, Chemical Engineering Science **102**, 151–162 (2013)
9.71 S. Kamarajugadda, S. Mazumder: Numerical investigation of the effect of cathode catalyst layer structure and composition on polymer electrolyte membrane fuel cell performance, J. Power Sources **183**, 629–642 (2008)
9.72 T. Vidaković-Koch, V.K. Mittal, T.Q.N. Do, M. Varničić, K. Sundmacher: Application of electrochemical impedance spectroscopy for studying of enzyme kinetics, Electrochimica Acta **110**, 94–104 (2013)
9.73 D. Gerteisen, A. Hakenjos, J.O. Schumacher: AC impedance modelling study on porous electrodes of proton exchange membrane fuel cells using an agglomerate model, J. Power Sources **173**, 346–356 (2007)
9.74 Q. Guo, V.A. Sethuraman, R.E. White: Parameter estimates for a PEMFC cathode, J. Electrochem. Soc. **151**, A983–A993 (2004)
9.75 E.P. Walter, L. Pronzato: *Identification of Parametric Models: From Experimental Data* (Springer, Berlin, Heidelberg 1997)
9.76 D. Song, Q. Wang, Z. Liu, M. Eikerling, Z. Xie, T. Navessin, S. Holdcroft: A method for optimizing distributions of Nafion and Pt in cathode catalyst layers of PEM fuel cells, Electrochimica Acta **50**, 3347–3358 (2005)
9.77 U.A. Paulus, T.J. Schmidt, H.A. Gasteiger, R.J. Behm: Oxygen reduction on a high-surface area Pt/Vulcan carbon catalyst: A thin-film rotating ring-disk electrode study, J. Electroanal. Chem. **495**, 134–145 (2001)
9.78 P.K. Das, X. Li, Z.-S. Liu: Analytical approach to polymer electrolyte membrane fuel cell performance and optimization, J. Electroanal. Chem. **604**, 72–90 (2007)

10. Water Management in Proton Exchange Fuell Cells

Nils Brandau, Jürgen Köhler

After providing the basic thermodynamic and electrochemical laws and relationships, this chapter investigates the impact of reactant humidification for a polymer electrolyte membrane based fuel cell system. As an example, an air humidifier model operated under coflow, counterflow, and crossflow conditions (independent of separator material) is described. The model includes the operation characteristics of a mass exchanger based on three dimensionless parameters: The dimensionless concentration change, the dimensionless transfer capacity (number of transfer units), and the ratio of the volume flow rates. In this model the whole humidification process (governed by humidifier design and separator material properties) is described based on a single characteristic value, the effective mass transfer coefficient. The model provides a deeper understanding and prediction capability of the transfer processes which is helpful for humidifier design, controlling humidifier operation conditions, and might even make sensors unnecessary.

10.1 Water Management in PEMFC 287
10.2 Thermodynamics and Electrochemistry . 289
10.3 Polarization Curve 290
10.4 Gas Humidification 294
10.4.1 Model of Mass Exchanger 294
10.4.2 Operating Characteristics of Humidifier 301
10.5 Sensorless Humidification 302
References 311

In general, a fuel cell is an electrochemical energy conversion device. Based on an electrochemical reaction, electric and thermal energies are generated from Gibbs free energy of formation (for the case of a polymer electrode membrane fuel cell (PEMFC): Formation of water). An oxidant and a fuel react separately on two electrodes. In PEMFC hydrogen as fuel and oxygen from air as oxidant are typically used. A PEMFC is built around a proton conductive polymer membrane. The anode and cathode electrodes are bonded to either side of the membrane. Both electrodes are composites of a catalyst as well as proton and electron conductive materials. Within the anode electrode, hydrogen is split into protons and electrons. Hydrogen protons diffuse to the cathode electrode through the membrane. An electrical connection from anode electrode to cathode electrode allows the electrons to flow to the cathode electrode. At the cathode electrode oxygen, hydrogen protons and electrons react to form water.

10.1 Water Management in PEMFC

An important physical property of PEMFC is its proton resistance. The proton resistance depends on the water content of proton conductive materials. In addition to the membrane, the electrodes also contain proton conductive materials. In the following text, all proton conductive materials are referred to as ionomers. To minimize proton resistance, the water content of the ionomers should be maximized. To avoid dry out and reach a high water content of ionomers, the fuel cell supply gases are usually humidified. Figure 10.1 shows the proton conductivity of two typical membranes as a function of relative humidity.

In general, proton conductivity increases with higher water content of the membrane caused by ambient humidity of the membrane. During fuel cell operation, certain water transport mechanisms occur

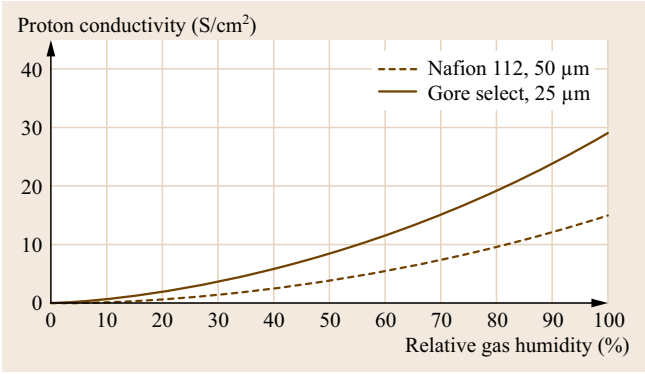


Fig. 10.1 Proton conductivity of Gore-Select (Gore) and Nafion 112 (DuPont) membranes as a function of relative humidity at 80 °C (after [10.1])

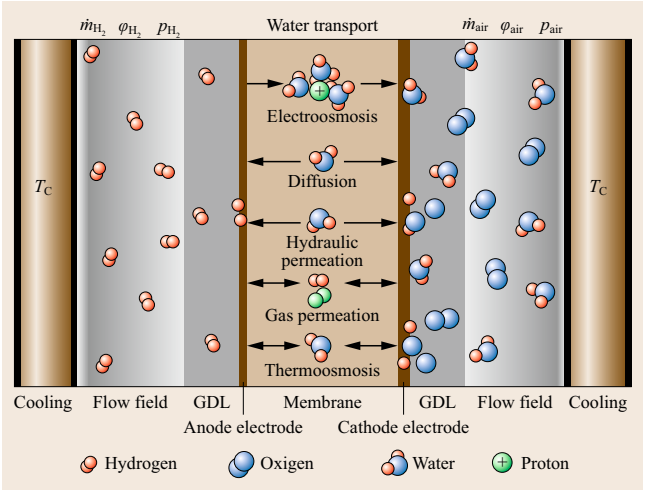


Fig. 10.2 Water transport mechanism in a PEMFC

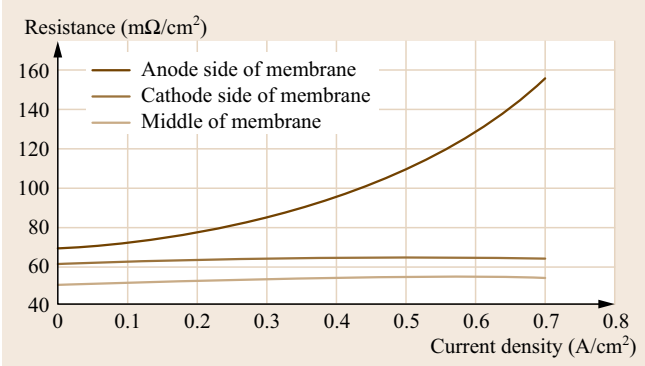


Fig. 10.3 Typical proton resistance of a membrane (Nafion 112) (after [10.2])

between the cathode and the anode side of the membrane. Those mechanisms could dry out the ionomers or flood the fuel cell. Both extremes should be avoided. Figure 10.2 shows the structure of a typical fuel cell as well as different water transport mechanisms for an operating PEMFC. To distribute the supply gases and remove liquid water from the electrodes, gas diffusion layers (GDL) are bonded to the electrodes.

The water content of membrane and electrodes is determined by five dominant water transport mechanisms:

- Electroosmosis
- Water diffusion
- Hydraulic permeation
- Gas permeation
- Thermoosmosis.

Electroosmosis and diffusion are the most significant water transport mechanisms. Electroosmosis describes the behavior of water molecules being dragged by protons on their way from the anode to the cathode. The amount of water molecules transported through the membrane per proton is known as the electroosmotic transport coefficient. Figure 10.3 shows the proton resistance of a Nafion 112-based membrane electrode assembly (MEA) as a function of current density. The increase of proton resistance on the anode side is mostly caused by the electroosmosis effect.

The formation of product water at the cathode electrode results in a water concentration gradient from the cathode side to the anode electrode side. This gradient induces a diffusive water transport from the cathode to the anode electrode. There exist other water transport mechanisms. However, usually they are negligible in comparison to water diffusion and electroosmosis. The pressure difference between the introduced gases, hydrogen and air induces a transport of water which is known as gas permeation. Because the membrane is not fully impermeable, small amounts of reactants are able to diffuse through the membrane and form water on the opposite side. Another water transport mechanism is thermoosmosis, which is caused by temperature gradients across the membrane [10.3]. The water transfer occurs from higher to lower temperatures. Pressure gradients in gas channels allow water to diffuse through the membrane. This process is known as hydraulic permeation. Particularly for dynamic operation of the fuel cell, it is important to maintain high water contents of the ionomers while avoiding flooding of the gas flow field.

10.2 Thermodynamics and Electrochemistry

Thermodynamics and electrochemistry of PEMFC are dependent on water management. The electrochemical reaction of a PEMFC, operated with pure hydrogen and oxygen, can be written as

$$\text{Anode: } H_2 \rightarrow 2H^+ + 2e^- , \tag{10.1}$$

$$\text{Cathode: } \frac{1}{2}O_2 + 2e^- + 2H^+ \rightarrow H_2O , \tag{10.2}$$

$$\text{The overall reaction is: } H_2 + \frac{1}{2}O_2 \rightarrow H_2O . \tag{10.3}$$

The overall reaction is exothermic which means that the molar enthalpy of formation of the product water ΔH is released. Depending on the phase of the product water, two cases have to be distinguished:

- For liquid product water: $\Delta H = -286.0\,\text{kJ/mol}$
- For vapor product water: $\Delta H = -241.9\,\text{kJ/mol}$.

Both enthalpy values are valid at 25 °C and atmospheric pressure or saturation pressure at 25 °C. The difference of enthalpies results from the latent heat of water evaporation. If the chemical reaction of hydrogen and oxygen was imagined as an exothermic combustion, the enthalpy would dissipate almost completely into thermal energy. However, during the reaction in fuel cells, the enthalpy splits into electric and thermal energy. The power of a fuel cell P_{FC} has an electric P_{el} and a thermal contribution $\dot{Q}$. Based on the first law of thermodynamics [10.4] we can write

$$P_{FC} = P_{el} + \dot{Q} = \dot{n}_{fuel} W_{el} + \dot{n}_{fuel} Q = \dot{n}_{fuel} \Delta H_{FC} . \tag{10.4}$$

Here $\dot{n}_{fuel}$ is the molar flow rate of hydrogen. A general thermodynamic relation states that enthalpy (of formation) of the fuel cell ΔH_{FC} is the sum of Gibbs free enthalpy ΔG_{FC} and entropy multiplied by Kelvin temperature $\Delta S_{FC} T_{FC}$

$$\Delta H_{FC} = \Delta G_{FC} + \Delta S_{FC} T_{FC} . \tag{10.5}$$

Based on the second law of thermodynamics, the reversible molar heat Q can be described as

$$Q = \Delta S_{FC} T_{FC} . \tag{10.6}$$

The combination of (10.4)–(10.6) yields the molar electric work of a fuel cell

$$W_{el} = \Delta G_{FC} = \Delta H_{FC} - \Delta S_{FC} T_{FC} . \tag{10.7}$$

The molar Gibbs free enthalpy of formation describes the exergy part of the enthalpy of formation which the fuel cell can deliver as molar electric work W_{el}. Note that the electric work output of the fuel cell has a negative numerical value. Like enthalpy, Gibbs free enthalpy and entropy depend on the phase of the product water (Table 10.1).

The product of voltage and electric current has a positive numerical value which can be equated to the negative electric rate of work

$$U_0 I_{el} = U_0 \left(\dot{n}_{fuel} n F\right) = \dot{n}_{fuel} \left(-W_{el}\right) . \tag{10.8}$$

Hence, electric work and molar Gibbs free energy of formation can be related to Faraday's constant $F = 96\,485\,\text{As/mol}$, theoretical voltage U_0, and number of exchanged electrons of hydrogen $n = 2$

$$-\Delta G_{FC} = nFU_0 . \tag{10.9}$$

Finally, the theoretical voltage of a fuel cell U_0 is given by

$$U_0 = \frac{-\Delta G_{FC}}{nF} . \tag{10.10}$$

The electrical efficiency of the fuel cell that describes the ratio of Gibbs free enthalpy to enthalpy of formation in the fuel cell is given by

$$\eta_{FC} = \frac{-\Delta G_{FC}}{-\Delta H_{FC}} \tag{10.11}$$

For the liquid product water, the theoretical voltage is $U_0 = 1.23\,\text{V}$, and for the vapor product water it is $U_0 = 1.18\,\text{V}$ (both values at 25 °C). The theoretical efficiency for liquid product water is $\eta_{FC} = 0.83$ and for the vapor product water $\eta_{FC} = 0.95$.

The theoretical voltage changes with the operation temperature and operating pressure. As shown in (10.12) the enthalpy and entropy are both dependent on temperature. The following equation shows the theoretical voltage with respect to operation temperature

$$U_0 = -\left(\frac{\Delta H_{FC}\left(T_{FC}\right)}{nF} - \frac{\Delta S_{FC}\left(T_{FC}\right) T_{FC}}{nF}\right) \tag{10.12}$$

Table 10.1 Molar values for Gibbs free enthalpy, enthalpy of formation in the fuel cell and entropy of formation for liquid and vapor product water at 25 °C

Phase product water	ΔG_{FC} (kJ/mol)	ΔH_{FC} (kJ/mol)	ΔS_{FC} (kJ/mol K)
Vapor	−228.7	−241.9	−0.044
Liquid	−237.3	−286.0	−0.163

The effect of pressure is described by the Nernst equation. As a result of the Nernst equation, Gibbs free enthalpy becomes

$$\Delta G_{FC} = \Delta G_{Ref} + RT_{FC} \ln \left(\frac{\frac{p_{H_2O}}{p_0}}{\frac{p_{H_2}}{p_0} \sqrt{\frac{p_{O_2}}{p_0}}} \right) \quad (10.13)$$

with

$$\Delta G_{Ref} = \Delta H_{FC}(T_{FC}) - \Delta S_{FC}(T_{FC})\, T_{FC} \quad (10.14)$$

and p_0 as the reference operation pressure, that is, atmospheric pressure. If liquid product water is generated, then $p_{H_2O} = 1$, otherwise p_{H_2O} is the vapor pressure of water vapor.

Equation (10.15) shows the theoretical voltage of a fuel cell as a function of temperature and pressure.

$$U_0 = -\left(\frac{\Delta H_{FC}(T_{FC})}{nF} - \frac{\Delta S_{FC}(T_{FC})\, T_{FC}}{nF} \right) + \frac{RT_{FC}}{nF} \ln \left(\frac{\frac{p_{H_2}}{p_0} \sqrt{\frac{p_{O_2}}{p_0}}}{\frac{p_{H_2O}}{p_0}} \right) \quad (10.15)$$

10.3 Polarization Curve

Owing to occurring losses, the theoretical voltage of an operated fuel cell given by (10.15) can hardly ever be attained in reality. These losses include:

- Changes in gas properties within the fuel cell
- Kinetic losses
- Electron and proton resistance
- Crossover of reactant gasses.

These losses increase with rising current density. The relationship between voltage and current density is known as the polarization curve, which is shown in Fig. 10.4. Typically, operation losses are categorized as activation loss, ohmic loss, and concentration loss. These losses can be expressed in terms of so-called overpotentials η. The fuel cell operation voltageo U_{FC} then becomes

$$U_{FC} = U_0 - (\eta_{act} + \eta_{ohm} + \eta_{con}). \quad (10.16)$$

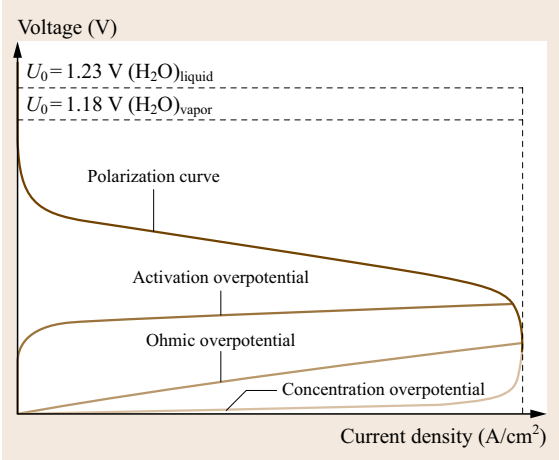


Fig. 10.4 Typical polarization curve and overpotentials of a PEMFC

Note that the fuel cell is an inhomogeneous element. As gases flow along the electrodes, the concentrations of reactants and product water change. Along the electrodes the partial pressure of hydrogen and oxygen decreases and the partial pressure of product water increases. As seen in (10.15), the theoretical voltage depends on partial pressures of the reactants and product water. The consumption of reactants and the generation of product water also changes dependant on current density. Therefore, the fuel cell voltage varies depending on operating current density.

Activation overpotential η_{act} occurs at both the anode electrode and the cathode electrode. Those overpotentials take into account the required energy, before ions and electrons can flow out of the reaction site. Because the oxygen reaction at the cathode electrode is much slower than the hydrogen reaction at the anode electrode, most activation losses come from the cathode electrode. Activation losses can be described with the Butler–Volmer equation. For the anode electrode operating at positive overpotentials, one in two terms of the Butler–Volmer equation becomes predominant. It allows neglecting further parts of the equation. The same is true for the cathode electrode. This simplifies the Butler–Volmer equations to (10.17).

For the anode electrode

$$\eta_{act,A} = \frac{RT_A}{\alpha_A F} \ln \left(\frac{j_{FC}}{j_{0A}} \right). \quad (10.17)$$

For the cathode electrode

$$\eta_{\mathrm{act,C}} = \frac{RT_{\mathrm{C}}}{\alpha_{\mathrm{C}} F} \ln\left(\frac{j_{\mathrm{FC}}}{j_{0\mathrm{C}}}\right). \tag{10.18}$$

The transfer coefficient α takes into account the forward and backward reaction rate of the polarization [10.5].

The exchange current density j_0 can be approximated with [10.6]

$$j_0 = j_0^{\mathrm{ref}} a_{\mathrm{c}} L_{\mathrm{c}} \left(\frac{p_{\mathrm{r}}}{p_{\mathrm{ref}}}\right)^{y} \exp\left[-\frac{E_{\mathrm{c}}}{RT}\left(1 - \frac{T}{T_{\mathrm{ref}}}\right)\right]. \tag{10.19}$$

where j_0^{ref} describes a reference current density, typically given at reference pressure and temperature. The term a_{c} is the electrode area and L_{c} the catalyst loading. Here p_{r} is the reactant partial pressure in relation to a reference pressure p_{ref}, y describes a pressure coefficient from 0.5 to 1 and E_{c} is the activation energy and T is the temperature in relation to a reference temperature T_{ref}.

Ohmic overpotential η_{ohm} in PEMFC is the sum of electrical resistance as well as the sum of proton resistance. Electrical resistances $R_{\mathrm{e}}-$ are barriers for electrons such as contact and material resistances. Proton resistances $R_{\mathrm{p}}+$ are barriers for protons. Ionomers in electrodes and the membrane are the key resistances for protons. The ohmic overpotential is given by the current density multiplied by the sum of ohmic resistances.

$$\eta_{\mathrm{ohm}} = j_{\mathrm{FC}} \left(\sum_i R_{\mathrm{e}^-i} + \sum_j R_{\mathrm{p}^+j}\right) \tag{10.20}$$

As can be seen in Fig. 10.1, the proton resistance/conductivity depends on the water content of ionomer within the electrodes and the membrane.

Concentration overpotential η_{con} describes the effect of depletion of reactants in electrodes. In both anode and cathode electrodes, reactants are consumed. If reactant consumption is higher than delivery, concentration losses occur. These losses are driven by the reactant concentration gradient within the electrodes. The relationship between concentration overpotential and reactant concentration is given by the Nernst equation and Fick's law. Combining those equations and taking into account the reactant consumption (10.8)

$$\dot{n}_{\mathrm{fuel}} = \frac{I_{\mathrm{FC}}}{nF} \tag{10.21}$$

yields the concentration overpotential at the anode electrode

$$\eta_{\mathrm{con,A}} = \frac{RT_{\mathrm{A}}}{nF} \ln\left(\frac{j_{\mathrm{L,A}}}{j_{\mathrm{L,A}} - j_{\mathrm{FC}}}\right). \tag{10.22}$$

The same procedure also yields the concentration overpotential at the cathode electrode

$$\eta_{\mathrm{con,C}} = \frac{RT_{\mathrm{C}}}{nF} \ln\left(\frac{j_{\mathrm{L,C}}}{j_{\mathrm{L,C}} - j_{\mathrm{FC}}}\right). \tag{10.23}$$

The number of electrons that are exchanged per molecule of reactant (H_2 or O_2) is expressed by n. For the cathode reaction $n = 4$ and for the anode reaction $n = 2$. j_{L} characterizes the limiting current density at which the reactant concentration in electrode reaches zero.

The polarization curve of a PEM fuel cell $U_{\mathrm{FC}} = f(j_{\mathrm{FC}})$ can be described ideally by subtracting all the overpotentials from the reversible cell potential. From

$$U_{\mathrm{FC}} = U_0 - (\eta_{\mathrm{act,A}} + \eta_{\mathrm{act,C}} + \eta_{\mathrm{con,A}} + \eta_{\mathrm{con,C}} + \eta_{\mathrm{ohm}}) \tag{10.24}$$

follows

$$\begin{aligned} U_{\mathrm{FC}}(j_{\mathrm{FC}}) = U_0 &- \frac{RT_{\mathrm{A}}}{\alpha_{\mathrm{A}} F} \ln\left(\frac{j_{\mathrm{FC}}}{j_{0\mathrm{A}}}\right) - \frac{RT_{\mathrm{C}}}{\alpha_{\mathrm{C}} F} \ln\left(\frac{j_{\mathrm{FC}}}{j_{0\mathrm{C}}}\right) \\ &- \frac{RT_{\mathrm{A}}}{2F} \ln\left(\frac{j_{\mathrm{L,A}}}{j_{\mathrm{L,A}} - j_{\mathrm{FC}}}\right) \\ &- \frac{RT_{\mathrm{C}}}{4F} \ln\left(\frac{j_{\mathrm{L,C}}}{j_{\mathrm{L,C}} - j_{\mathrm{FC}}}\right) \\ &- j_{\mathrm{FC}} \left(\sum_i R_{\mathrm{e}^-i} + \sum_j R_{\mathrm{p}^+j}\right). \end{aligned} \tag{10.25}$$

Overpotentials on the cathode electrode are much higher than on the anode electrode. Therefore in most cases the anode terms can be neglected. The simplified form of the theoretical polarization curve yields

$$\begin{aligned} U_{\mathrm{FC}}(j_{\mathrm{FC}}) = U_0 &- \frac{RT_{\mathrm{C}}}{\alpha_{\mathrm{C}} F} \ln\left(\frac{j_{\mathrm{FC}}}{j_{0\mathrm{C}}}\right) \\ &- \frac{RT_{\mathrm{C}}}{4F} \ln\left(\frac{j_{\mathrm{L,C}}}{j_{\mathrm{L,C}} - j_{\mathrm{FC}}}\right) \\ &- j_{\mathrm{FC}} \left(\sum_i R_{\mathrm{e}^-i} + \sum_j R_{\mathrm{p}^+j}\right). \end{aligned} \tag{10.26}$$

The mathematically functional expression of the polarization curve is an adequate tool to identify influences on operation voltage as a result of changing water management. By assuming that in a fuel cell liquid water is removed faster than reactant starvation occurs, additional equations can be provided using water vapor only. For gas pressure, Dalton's law shows the

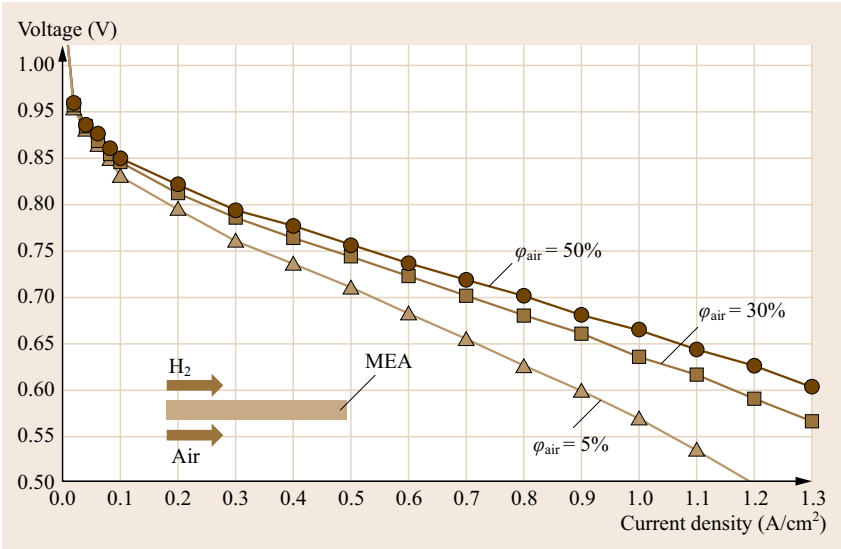


Fig. 10.5 PEMFC polarization curves for different air humidity at fuel cell inlet, measured with a coflow operated fuel cell (*single cell*). MEA thickness 25 µm

relationship of absolute pressure p and partial pressures p_i [10.4]

$$p = \sum_i p_i \,. \tag{10.27}$$

For an isobaric gas, an increase of water vapor content yields a decrease of all other partial pressures in the mixture. As a result, the higher the water vapor content in a fuel cell, the lower the partial pressures of reactants within the electrodes.

For fuel cell applications, a metric to handle water vapor pressure is the relative humidity of supply gases. Relative humidity φ is defined as the ratio of partial vapor pressure p_V to saturated vapor pressure p_S multiplied by 100%

$$\varphi = \frac{p_V}{p_S(T)} 100\% \,. \tag{10.28}$$

Saturated vapor pressure is dependent on gas temperature. The following paragraphs explain the impact of the change in relative humidity on fuel cell operating voltage, compared to (10.26). U_0 depends on the concentration of the reactants as can be seen in (10.15). The higher the relative humidity of the supply gas, the lower the reactant partial pressure within the electrodes and therefore the lower the operating voltage. The limiting current density for which as much reactant as can be supplied is consumed at the electrode is denoted by the term j_L. If the relative humidity of operation gas is high enough that product water is not sufficiently discharged, the product water could condensate to liquid phase and accumulate in pores of the GDL or electrode. Those flooded areas could become inactive or blocked for reactants. In such case and for a given current, other parts of the active area have to deliver a higher current density to compensate for the lower performing areas. The limiting current density would be reached earlier. Resulting losses are shown in Eqs. (10.22) and (10.23). The sum $\sum_j R_{p+j}$ is essentially determined by the water content of the membrane and electrode ionomer fractions. The higher the water content of the ionomer, the higher its proton conductivity. The current density j_{0C} can be calculated by (10.19). The equation shows the dependence on the effective catalytic surface. If product water is not sufficiently discharged from the cathode electrode or collected in the anode electrode, water vapor could condensate to liquid phase and partially block the effective catalytic surface. The result is a decrease in exchange current density. Like reversible cell potential, the exchange current density depends on the partial pressure of reactants at the electrodes. A lower partial pressure results in a lower concentration of reactants at the catalytic surface and therefore in a lower exchange current density. In [10.7], the transfer coefficient α is determined to be in a range of 0.2–2. The transfer coefficient is dependent on membrane water content. This includes the electrode ionomer fractions as well. The higher the humidity around the ionomer, the higher the water content within.

The impact of the air humidity on the polarization curve for a PEMFC is shown in Figs. 10.5 and 10.6. Figure 10.5 shows polarization curves for different air humidity at fuel cell inlet for a coflow operated fuel cell. Coflow means that the reactants (air oxygen and hydrogen) have the same flow direction along the MEA. The fuel cell operation temperature is controlled linearly to the current density from 70 to 80 °C. The operating gas

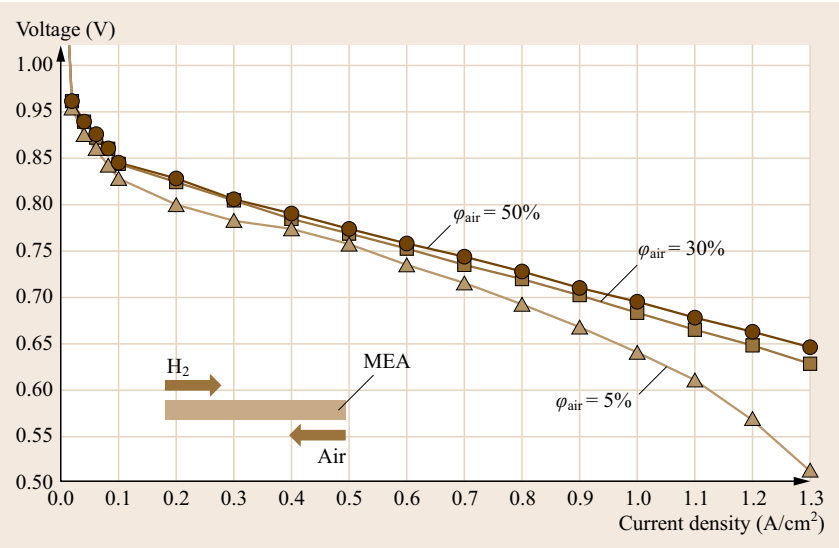


Fig. 10.6 PEMFC polarization curves for different air humidity, measured with a counterflow operated fuel cell (*single cell*). MEA thickness 25 µm

pressures are kept constant to 2 bar. The hydrogen humidity is maintained to 35%. The active area of the MEA is 400 cm^2.

It can be seen that the performance increases with increasing air humidity. It also can be seen that the performance improvement itself diminishes for higher air humidity. The performance gap between the polarization curves of 5 and 30% air humidity is much higher than the performance gap between the polarization curves of 30 and 50% air humidity. It means that the relation between performance and air humidity is an asymptotic function. The asymptotic limit itself depends on fuel cell design and fuel cell operation conditions. Usually the asymptotic limit is between 50% and 80% air humidity at fuel cell inlet.

Figure 10.6 shows experimental results of a counterflow operated fuel cell using the same fuel cell design and operation conditions as the coflow case given earlier. Counterflow means that the flow directions of the reactants (air oxygen and hydrogen) along the MEA are opposite to each other.

The influence of the air humidity on the fuel cell performance is shown clearly. Counterflow operation shows a better performance than the coflow operation. Furthermore, the gap between the polarization curves for different air humidity is smaller compared to the coflow case. This is because a coflow-operated fuel cell does not self-humidify like the counterflow operated fuel cell does [10.8]. Compared to counterflow operation, a coflow operated fuel cell shows dryer fractions of the MEA at the reactant inlets. Each gas flow (reactant flow) accumulates product water while flowing along the MEA, the gas humidity increases in direction to the gas flow outlets. For a counterflow operated fuel cell, the gas flows with high humidity are positioned at the gas flow inlets showing less humidity. So, the exhausting gas flows humidify the MEA fractions at the inflow areas. The polarization curve with 5% air humidity demonstrates the self-humidification clearly. As a result of higher current density, more product water is produced which humidifies the inflow areas. Compared to the coflow operation in Fig. 10.5, the polarizations curve seems to be recovering with an increasing current density.

In addition to that, for the curve of 5% air humidity it seems like high concentration overpotential above 0.5 A/cm^2 occur. For the reaction on the cathode electrode protons, electrons and oxygen must be present at the same time. If one of the three is not present in sufficient quantities, the fuel cell will lose performance according to (10.23). However, in case of too low air humidity the proton conductivity of MEA is insufficient which reduces the performance and seems like oxygen concentration overpotential. However, in reality it is an increasing ohmic resistance of ionomer factions within the MEA.

10.4 Gas Humidification

Gas humidification plays an important role in fuel cell technology. Modern polymer electrolyte membrane (PEM) fuel cells require preconditioned process gases. In particular cases where the fuel cell is to be operated with air instead of pure oxygen, there is a risk of drying-out the MEA due to relative dryness (Sect. 10.3). Gas humidifiers are used to prevent the drying effect. Such air humidifiers are usually passive peripheral elements. This chapter describes the model of a mass exchanger presented by [10.8] and [10.9] which is used to design or characterize the operation characteristics of a gas humidifier. In PEM fuel cells, usually the air humidity is controlled by opening and closing a bypass flow path to the humidifier, as shown in Fig. 10.7.

This form of control includes the actual-state signal from a humidity sensor and a temperature sensor which are both integrated into the path downstream of the humidifier and upstream of the fuel cell. The operating characteristics of the humidifier change with:

- Fuel cell load and product water formation
- Relative air humidity of the ambient
- Dry air mass flow rate provided by the air compressor
- Dry air mass flow rate exhausting the fuel cell
- Air temperatures
- Temperature of the humidifier
- Effective transfer area of the humidifier
- Thickness and properties of the separator
- Operation pressures, and
- Pressure drop within the humidifier.

A dry air mass flow rate is defined as the amount of flow exclusive the water amount. The listed parameters may mutually influence each other, making a dynamic and precise control of the air humidity a challenging task. The following section presents an analytical model to describe the mass transfer within such a humidifier which permits an analytical calculation of the relative humidity at the air-side inlet to the fuel cell. This analytical model of the humidifier might provide options to replace some or even all of the gas humidification sensors. The use of a predictive, model-based pre-control system for gas humidification promises improved dynamic behavior of the humidification control of PEM fuel cells systems.

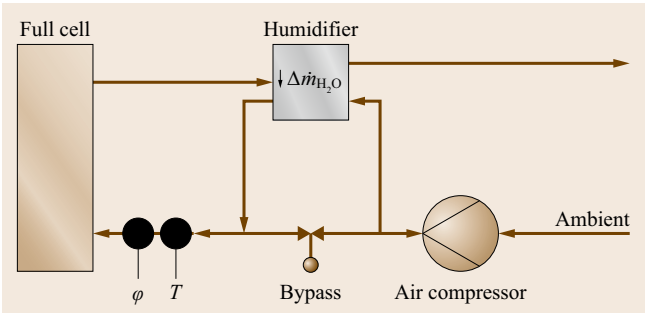


Fig. 10.7 Air humidity control principle of a PEM fuel cell stack

10.4.1 Model of Mass Exchanger

Mass transfer processes are ubiquitous in nature and play an important role in various engineering processes in which the state of a mixture of substances is changed. In particular, these are physical separation processes and numerous chemical reactions. A general challenge of mass transport is that the substance of interest can be unevenly distributed in the carrier medium. This uneven distribution is described by concentration gradients, whereby the gradients themselves are the driving forces for the transport of mass.

According to Fick's law [10.9], the molar flux j_i can be written as

$$j_i = -D\frac{\mathrm{d}c_i}{\mathrm{d}y} \,. \tag{10.29}$$

In (10.29), D is the diffusion coefficient and $\frac{\mathrm{d}c_i}{\mathrm{d}y}$ the molar concentration gradient of the component i. The molar concentration of the component c_i is defined as

$$c_i = \frac{\dot{n}_i}{\dot{V}} \,, \tag{10.30}$$

where $\dot{V}$ denotes the total volume flow rate. The case of transport of mass through a separator is discussed later. Two molar flow rates $\dot{n}_1$ and $\dot{n}_2$ are separated from each other by a separator. These flow rates consist of binary mixtures with the two components a and b

$$\dot{n}_1 = \dot{n}_{1a} + \dot{n}_{1b} = \dot{V}_1\,(c_{1a} + c_{1b}) \quad \text{and} \tag{10.31}$$

$$\dot{n}_2 = \dot{n}_{2a} + \dot{n}_{2b} = \dot{V}_2\,(c_{2a} + c_{2b})\,. \tag{10.32}$$

The separator is permeable for the component b and impermeable for the component a, as seen in Fig. 10.8.

Only $\dot{n}_b$ varies along the transfer area within a mass exchanger. Figure 10.9 shows a general sketch of a mass exchanger. Variables with one prime denote the inlet and those with a double prime denote the outlet of the mass exchanger.

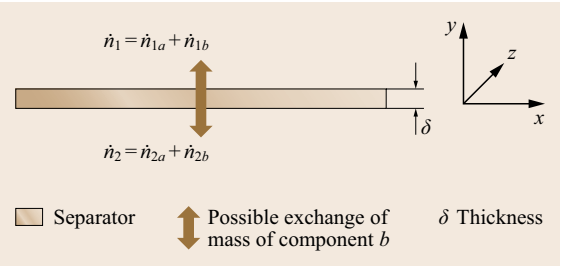


Fig. 10.8 Two molar flows separated by a separator

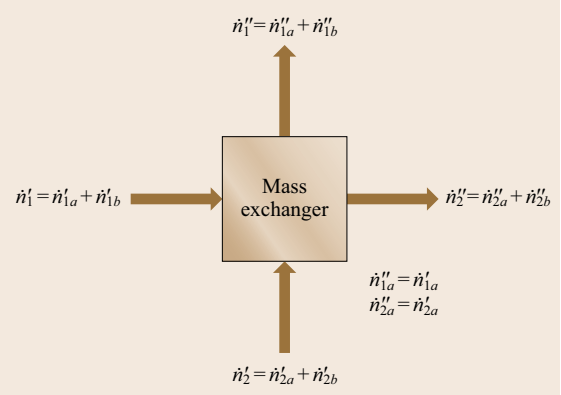


Fig. 10.9 Inlet and outlet flow rates of a mass exchanger

The requirement that the component $\dot{n}_a$ remains constant yields

$$\dot{n}_{1a}'' = \dot{n}_{1a}' \quad \text{and} \tag{10.33}$$

$$\dot{n}_{2a}'' = \dot{n}_{2a}' \,. \tag{10.34}$$

The molar flow rate $\Delta\dot{n}_b$ of the component b transferred by the mass exchanger can be calculated by forming balances for the two molar flow rates $\dot{n}_1$ and $\dot{n}_2$,

$$\begin{aligned}\Delta\dot{n}_{1b} &= \dot{n}_1' - \dot{n}_1'' = \left(\dot{n}_{1a}' + \dot{n}_{1b}'\right) - \left(\dot{n}_{1a}'' + \dot{n}_{1b}''\right) \\ &= \dot{n}_{1b}' - \dot{n}_{1b}'' \,,\end{aligned} \tag{10.35}$$

$$\begin{aligned}\Delta\dot{n}_{2b} &= \dot{n}_2' - \dot{n}_2'' = \left(\dot{n}_{2a}' + \dot{n}_{2b}'\right) - \left(\dot{n}_{2a}'' + \dot{n}_{2b}''\right) \\ &= \dot{n}_{2b}' - \dot{n}_{2b}'' \,.\end{aligned} \tag{10.36}$$

The transfer of mass between $\dot{n}_{1b}$ and $\dot{n}_{2b}$ causes one of the two flows to decrease and the other to consequently increase

$$\Delta\dot{n}_{1b} = -\Delta\dot{n}_{2b} = \Delta\dot{n}_b \,. \tag{10.37}$$

Based on the assumption that the molar flow rates $\dot{n}_1$ and $\dot{n}_2$ remain almost constant, that is, $\dot{n}_1' \approx \dot{n}_1'' = \dot{n}_{1a} + \dot{n}_{1b} \gg \Delta\dot{n}_{1b}$, the transferred molar flow rate can be calculated for (nearly) isothermal and isobaric conditions using (10.30)–(10.32), (10.35), (10.36)

$$\begin{aligned}\Delta\dot{n}_b &= \dot{n}_{1b}' - \dot{n}_{1b}'' = \frac{c_{1b}'}{c_{1a}'}\dot{n}_{1a}' - \frac{c_{1b}''}{c_{1a}''}\dot{n}_{1a}'' \\ &\approx \frac{c_{1b}'}{c_{1a}'}\dot{n}_{1a}' - \frac{c_{1b}''}{c_{1a}'}\dot{n}_{1a}' = \left(c_{1b}' - c_{1b}''\right)\frac{\dot{n}_{1a}'}{c_{1a}'} \,,\end{aligned} \tag{10.38}$$

$$\begin{aligned}-\Delta\dot{n}_b &= \dot{n}_{2b}' - \dot{n}_{2b}'' = \frac{c_{2b}'}{c_{2a}'}\dot{n}_{2a}' - \frac{c_{2b}''}{c_{2a}''}\dot{n}_{2a}'' \\ &\approx \frac{c_{2b}'}{c_{2a}'}\dot{n}_{2a}' - \frac{c_{2b}''}{c_{2a}'}\dot{n}_{2a}' = \left(c_{2b}' - c_{2b}''\right)\frac{\dot{n}_{2a}'}{c_{2a}'} \,.\end{aligned} \tag{10.39}$$

To calculate the infinitesimal mass transfer $\mathrm{d}\dot{n}_b$, an infinitesimal area element $\mathrm{d}A$ of the separator is considered as shown in Fig. 10.10.

The transport of mass $\mathrm{d}\dot{n}_b$ through the area element $\mathrm{d}A$ can be described with

$$\mathrm{d}\dot{n}_b = \mathrm{d}c_{1b}\frac{\dot{n}_{1a}'}{c_{1a}'} \,, \tag{10.40}$$

for the infinitesimal concentration change of $\dot{n}_1$, and

$$\mathrm{d}\dot{n}_b = -\mathrm{d}c_{2b}\frac{\dot{n}_{2a}'}{c_{2a}'} \,, \tag{10.41}$$

for the infinitesimal concentration change of $\dot{n}_2$, and

$$\begin{aligned}\mathrm{d}\dot{n}_b &= -D\frac{\Delta c_{1b,2b}}{\delta}\mathrm{d}x\mathrm{d}z \\ \text{with} \quad \Delta c_{1b,2b} &= c_{1b} - c_{2b} \,,\end{aligned} \tag{10.42}$$

for the transferred molar flow rate across the separator (permeation) from $\dot{n}_2$ to $\dot{n}_1$. The mass transfer from fluid 1 to fluid 2 is governed by three different physical effects, as seen in Fig. 10.11.

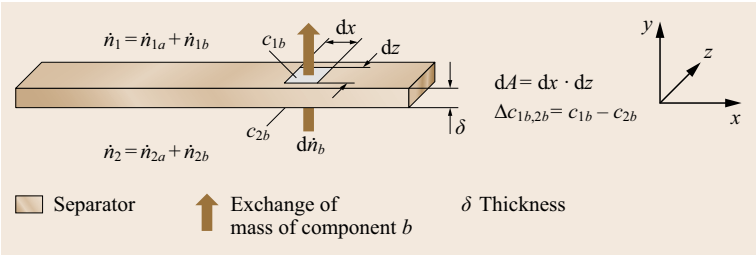


Fig. 10.10 Infinitesimal area element of the separator

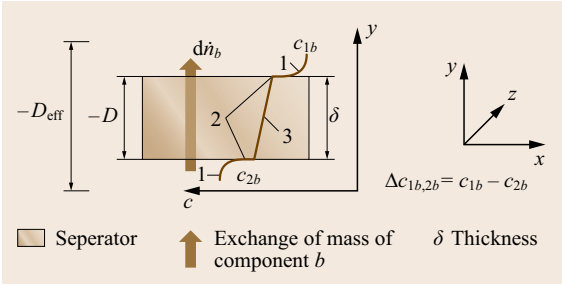


Fig. 10.11 Concentration change through separator

1. Convective mass transfer in the fluid phases from the bulk flow to the surface.
2. Phase equilibrium between the fluid phase and the solid phase at the two surfaces, described by Henry's law.
3. Diffusion through the solid phase, described by Fick's law.

For the sake of simplicity, these three effects are all taken into account by using an effective diffusion coefficient D_{eff} in order to calculate the mass transmission from one fluid to the other.

Accordingly, an effective mass transfer coefficient [10.10] is used

$$\beta_{\text{eff}} = \frac{D_{\text{eff}}}{\delta} \,. \tag{10.43}$$

Eliminating the infinitesimal transfer mass flow rate $d\dot{n}_b$ by equating (10.40) and (10.41) to (10.42) yields two equations for the infinitesimal concentration change of the molar flow rates $\dot{n}_{1b}$ and $\dot{n}_{2b}$

$$dc_{1b} = -\beta_{\text{eff}} \, (c_{1b} - c_{2b}) \, \frac{c'_{1a}}{\dot{n}'_{1a}} dx dz \,, \tag{10.44}$$

$$dc_{2b} = \beta_{\text{eff}} \, (c_{1b} - c_{2b}) \, \frac{c'_{2a}}{\dot{n}'_{2a}} dx dz \,. \tag{10.45}$$

Driven by a concentration change in the x and z direction (Fig. 10.10), the infinitesimal concentration changes. dc_{1b} and $-dc_{2b}$ depends on the direction of the concentration change across the area of the separator. At this point, a distinction regarding the flow direction of $\dot{n}_2$ and $\dot{n}_1$ is necessary.

A crossflow will cause a concentration change with dx and dz. The calculation of this case goes beyond the scope of this work. However, the resulting equations for the crossflow case are shown in Table 10.2. For the counterflow and the coflow, (10.45) is subtracted from (10.44) to determine the differential concentration difference $\Delta c_{1b,2b} = c_{1b} - c_{2b}$

$$d(c_{1b} - c_{2b}) = \left(-\frac{c'_{1a}}{\dot{n}'_{1a}} - \frac{c'_{2a}}{\dot{n}'_{2a}} \right) \beta_{\text{eff}} \, (c_{1b} - c_{2b}) \, dA \,. \tag{10.46}$$

Mathematical manipulation yields a differential equation which describes the behavior of the concentration

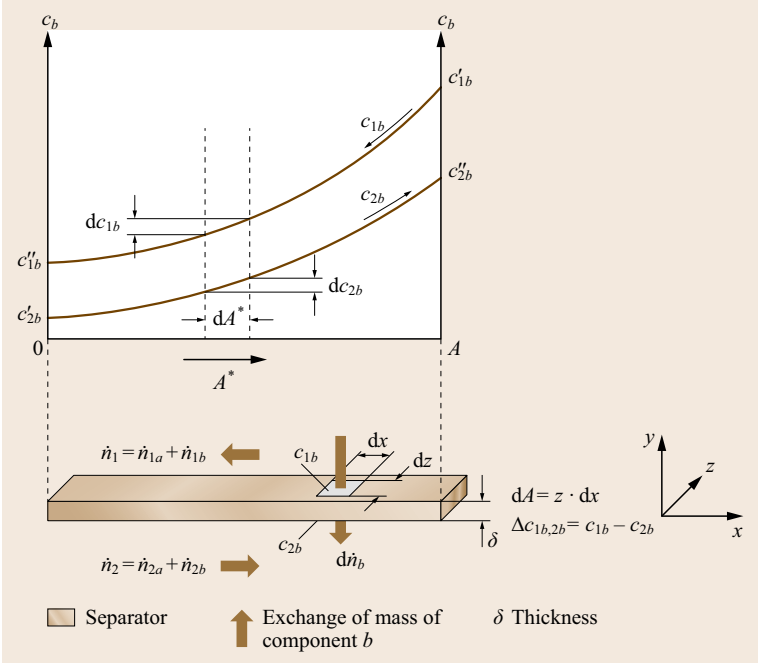


Fig. 10.12 Mass transfer and concentration distribution curves for the counterflow case

change along the x-direction of the separator

$$\frac{\mathrm{d}(c_{1b}-c_{2b})}{c_{1b}-c_{2b}} = \left(-\frac{c'_{1a}}{\dot{n}'_{1a}} - \frac{c'_{2a}}{\dot{n}'_{2a}}\right)\beta_{\mathrm{eff}}\mathrm{d}A\,, \qquad (10.47)$$

where $\mathrm{d}A = z\mathrm{d}x$. Integrating this equation within the limits $0 \to A$ yields the relationship between the area of the mass exchanger, the volume flow rates with

$$\frac{1}{\dot{V}'_1} = \frac{c'_{1a}}{\dot{n}'_{1a}}, \quad \frac{1}{\dot{V}'_2} = \frac{c'_{2a}}{\dot{n}'_{2a}}$$

and the concentration differences at the inlet and outlet of the mass exchanger. With respect to the relative flow direction of $\dot{n}_2$ to $\dot{n}_1$, a counterflow and coflow have to be treated separately.

Counterflow

Figure 10.12 sketches the concentration distribution curves and the integration limits for a mass exchanger in counterflow operation.

The two volume flow rates $\dot{V}'_1$ and $\dot{V}'_2$ have opposite directions. Hence, $\dot{V}'_1$ has a negative sign

$$\int_{0:\,c''_{1b}-c'_{2b}}^{A:\,c'_{1b}-c''_{2b}} \frac{\mathrm{d}\,(c_{1b}-c_{2b})}{c_{1b}-c_{2b}} = \int_0^A \left(-\frac{1}{-\dot{V}'_1} - \frac{1}{\dot{V}'_2}\right)\beta_{\mathrm{eff}}\mathrm{d}A\,. \qquad (10.48)$$

Integration yields

$$\ln\left(\frac{c'_{1b}-c''_{2b}}{c''_{1b}-c'_{2b}}\right) = \frac{\beta_{\mathrm{eff}}A}{\dot{V}'_1} - \frac{\beta_{\mathrm{eff}}A}{\dot{V}'_2}\,. \qquad (10.49)$$

Coflow

Figure 10.13 sketches the concentration curves and the integration limits for mass exchanger in coflow operation.

Here the two volume flow rates $\dot{V}'_1$ and $\dot{V}'_2$ have the same direction

$$\int_{0:\,c'_{1b}-c'_{2b}}^{A:\,c''_{1b}-c''_{2b}} \frac{\mathrm{d}\,(c_{1b}-c_{2b})}{c_{1b}-c_{2b}} = \int_0^A -\left(\frac{1}{\dot{V}'_1} + \frac{1}{\dot{V}'_2}\right)\beta_{\mathrm{eff}}\mathrm{d}A\,. \qquad (10.50)$$

Integration yields

$$\ln\left(\frac{c''_{1b}-c''_{2b}}{c'_{1b}-c'_{2b}}\right) = -\left(\frac{\beta_{\mathrm{eff}}A}{\dot{V}'_1} + \frac{\beta_{\mathrm{eff}}A}{\dot{V}'_2}\right). \qquad (10.51)$$

According to the Buckingham Π theory, n dimensioned physical parameters can be reduced to $n-r$ dimensionless variables, if r basic physical units are needed to completely describe the physical problem [10.11]. In the present case $n = 5$ dimensioned physical parame-

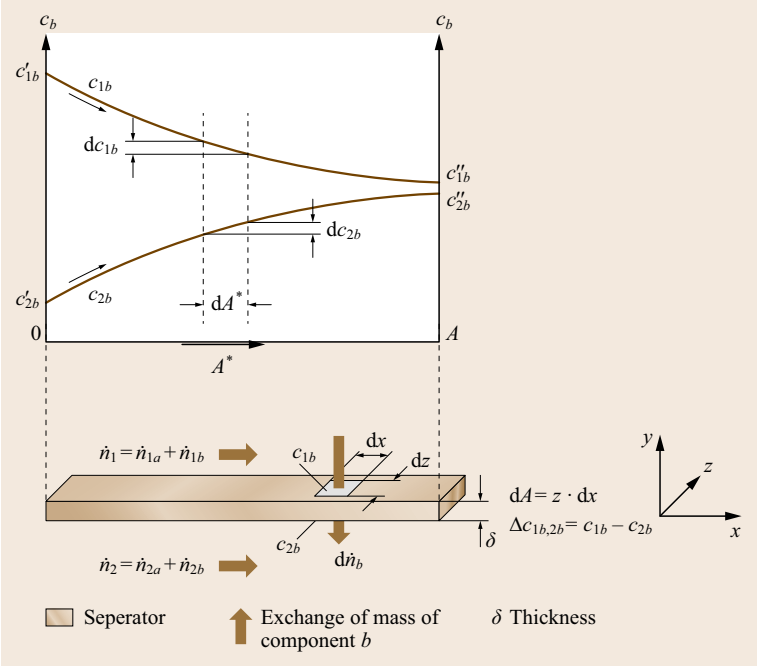


Fig. 10.13 Mass transfer and concentration distribution curves for the coflow case

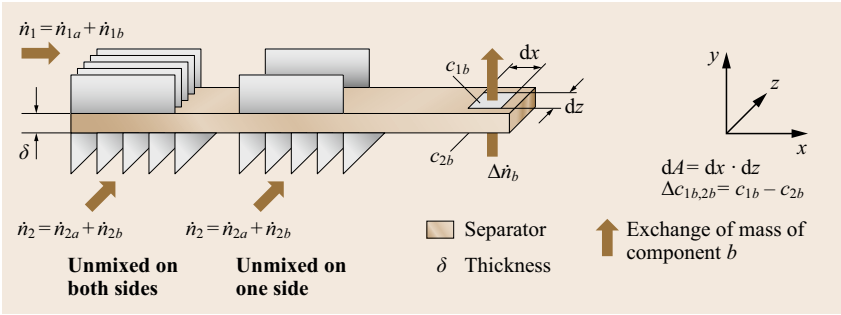


Fig. 10.14 Two mostly used cases of molar flow rates with a pure crossflow operation of a mass exchanger

ters are important:

- $\Delta\dot{n}$ (mol/s)
- $c'_{1b} - c'_{2b}$ (mol/m^3)
- $\beta_{\text{eff}}A$ (m/s m^2 = m^3/s)
- $\dot{V}'_1$ (m^3/s)
- $\dot{V}'_2$ (m^3/s)

with two basic physical units mol/s and mol/m^3 from which the other three-dimensioned physical parameters can be derived. Hence, three dimensionless parameters for the mass transfer can be found:

1. *The dimensionless concentration change*

$$\eta_{\Delta 1} = \frac{\Delta\dot{n}_b}{\dot{V}'_1\left(c'_{1b} - c'_{2b}\right)} = \frac{\left(c'_{1b} - c''_{1b}\right)\frac{\dot{n}'_{1a}}{c'_{1a}}}{\dot{V}'_1\left(c'_{1b} - c'_{2b}\right)} = \frac{c'_{1b} - c''_{1b}}{c'_{1b} - c'_{2b}} \,. \tag{10.52}$$

($\eta_{\Delta 1}$ can also be seen as efficiency)

2. *The dimensionless transfer capacity number of transfer units (NTU)*

$$\text{NTU}_1 = \frac{\beta_{\text{eff}}A}{\dot{V}'_1} \quad \text{with} \quad \frac{1}{\dot{V}'_1} = \frac{c_1}{\dot{n}_1} = \frac{c_{1a}}{\dot{n}_{1a}} \,. \tag{10.53}$$

3. *The dimensionless number of the volume flow rates (Brandau number)*

$$Br_1 = \frac{\dot{V}'_1}{\dot{V}'_2} \,. \tag{10.54}$$

If $\dot{V}'_1 < \dot{V}'_2$, $\eta_{\Delta 1}$ can be considered as a mass transfer efficiency of the mass exchanger. $\eta_{\Delta 1}$ represents the actual transmitted flow rate of component b in gas flow 1 relative to the maximum possible transmitted flow rate of component b. The operating characteristics can also be expressed on basis of the parameters of the second mass flow

$$\eta_{\Delta 2} = \frac{\dot{V}'_1}{\dot{V}'_2}\eta_{\Delta 1} = \frac{\text{NTU}_2}{\text{NTU}_1}\eta_{\Delta 1} = Br_1\eta_{\Delta 1} = \frac{c''_{2b} - c'_{2b}}{c'_{1b} - c'_{2b}} \,, \tag{10.55}$$

$$\text{NTU}_2 = \frac{\beta_{\text{eff}}A}{\dot{V}'_2} \,, \tag{10.56}$$

$$Br_2 = \frac{\dot{V}'_2}{\dot{V}'_1} = \frac{\text{NTU}_1}{\text{NTU}_2} = \frac{1}{Br_1} \,. \tag{10.57}$$

The relationship between the three dimensionless variables $\eta_{\Delta 1}$, NTU_1, and Br_1 can be used to analytically describe the operation characteristics of the mass exchanger. After some mathematical manipulations of (10.49) in order to introduce the three dimensionless parameters, the operation characteristics for the mass transfer in counterflow configuration across a separator can be written as

$$\ln\left(\frac{1 - \eta_{\Delta 1}}{1 - Br_1\eta_{\Delta 1}}\right) = \text{NTU}_1(Br_1 - 1) \,. \tag{10.58}$$

Using (10.51) yields the coflow relation

$$\ln\left[1 - \eta_{\Delta 1}\left(1 + Br_1\right)\right] = -\text{NTU}_1\left(Br_1 + 1\right) \,. \tag{10.59}$$

For crossflow across the separator area, the following results represent the main cases, as seen in Fig. 10.14. The detailed derivation is analogous to that of a crossflow heat exchanger [10.12].

The operation characteristics are for crossflow *unmixed on both sides*

$$\eta_{\Delta 1} = \frac{1}{Br_1\text{NTU}_1}\sum_{m=0}^{\infty}\left[\left(1 - \mathrm{e}^{-\text{NTU}_1}\sum_{j=0}^{m}\frac{\text{NTU}_i^j}{j!}\right) \times \left(1 - \mathrm{e}^{-Br_1\text{NTU}_1}\sum_{j=0}^{m}\frac{(Br_1\text{NTU}_1)^j}{j!}\right)\right] \tag{10.60}$$

Table 10.2 Equations for mass exchanger operation characteristics

	$\eta_{\Delta i} = \eta_{\Delta i}(\mathrm{NTU}_i, Br_i)$	$\mathrm{NTU}_i = \mathrm{NTU}_i(\eta_{\Delta i}, Br_i)$
Counterflow		
$Br_i \neq 1$, $i = 1, 2$	$\eta_{\Delta i} = \dfrac{1 - \mathrm{e}^{(Br_i - 1)\mathrm{NTU}_i}}{1 - Br_i \mathrm{e}^{(Br_i - 1)\mathrm{NTU}_i}}$	$\mathrm{NTU}_i = \dfrac{1}{Br_i - 1} \ln\left(\dfrac{1 - \eta_{\Delta i}}{1 - Br_i \eta_{\Delta i}}\right)$
$Br_i = 1$, $i = 1, 2$	$\eta_{\Delta i} = \dfrac{\mathrm{NTU}_i}{1 + \mathrm{NTU}_i}$	$\mathrm{NTU}_i = \dfrac{\eta_{\Delta i}}{1 - \eta_{\Delta i}}$
Coflow		
$i = 1, 2$	$\eta_{\Delta i} = \dfrac{1 - \mathrm{e}^{-(1 + Br_i)\mathrm{NTU}_i}}{1 + Br_i}$	$\mathrm{NTU}_i = -\dfrac{\ln\left[1 - \eta_{\Delta i}(1 + Br_i)\right]}{1 + Br_i}$
Crossflow		
unmixed $i = 1, 2$	$\eta_{\Delta i} = \dfrac{1}{Br_i \mathrm{NTU}_i} \sum_{m=0}^{\infty} \left[\left(1 - \mathrm{e}^{-\mathrm{NTU}_i} \sum_{j=0}^{m} \dfrac{\mathrm{NTU}_i^j}{j!}\right) \times \left(1 - \mathrm{e}^{-Br_i \mathrm{NTU}_i} \sum_{j=0}^{m} \dfrac{(Br_i \mathrm{NTU}_i)^j}{j!}\right)\right]$	No explicit solution possible
Unmixed on one side, $i = 1, 2$	$\eta_{\Delta i} = 1 - \mathrm{e}^{-\frac{1}{Br_i}\left(1 - \mathrm{e}^{-Br_i \mathrm{NTU}_i}\right)}$	$\mathrm{NTU}_i = -\dfrac{1}{Br_i} \ln\left[1 + Br_i \ln(1 - \eta_{\Delta i})\right]$

$\eta_{\Delta 1} = \dfrac{c'_{1b} - c''_{1b}}{c'_{1b} - c'_{2b}}$; $\eta_{\Delta 2} = \dfrac{c''_{2b} - c'_{2b}}{c'_{1b} - c'_{2b}}$; $\mathrm{NTU}_i = \dfrac{\beta_{\mathrm{eff}} A}{\dot{V}'_i}$ $i = 1, 2$; $Br_1 = \dfrac{\dot{V}'_1}{\dot{V}'_2}$; $Br_2 = \dfrac{\dot{V}'_2}{\dot{V}'_1}$

and crossflow mixed on one side

$$\eta_{\Delta 1} = 1 - \mathrm{e}^{-\frac{1}{Br_1}\left(1 - \mathrm{e}^{-Br_1 \mathrm{NTU}_1}\right)} . \tag{10.61}$$

Table 10.2 summarizes the operation characteristics for counter-, co-, and crossflow conditions of a mass exchanger as described earlier.

With known transferred molar flow rate $\Delta\dot{n}_b$ (e.g., from measurement) the effective mass transfer coefficient β_{eff} can be determined based on equations for NTU given in Table 10.2. For example, the transfer coefficient for counterflow and $Br_1 \neq 1$ can be calculated by

$$\beta_{\mathrm{eff}} = \frac{\ln\left(\dfrac{1 - \eta_{\Delta 1}}{1 - Br_1 \eta_{\Delta 1}}\right)}{(Br_1 - 1)} \frac{\dot{V}'_1}{A} . \tag{10.62}$$

With a known transfer coefficient, the transferred molar flow rate can be calculated by solving (10.52)

$$\Delta\dot{n}_b = \eta_{\Delta i} \dot{V}'_i \left(c'_{1b} - c'_{2b}\right) \tag{10.63}$$

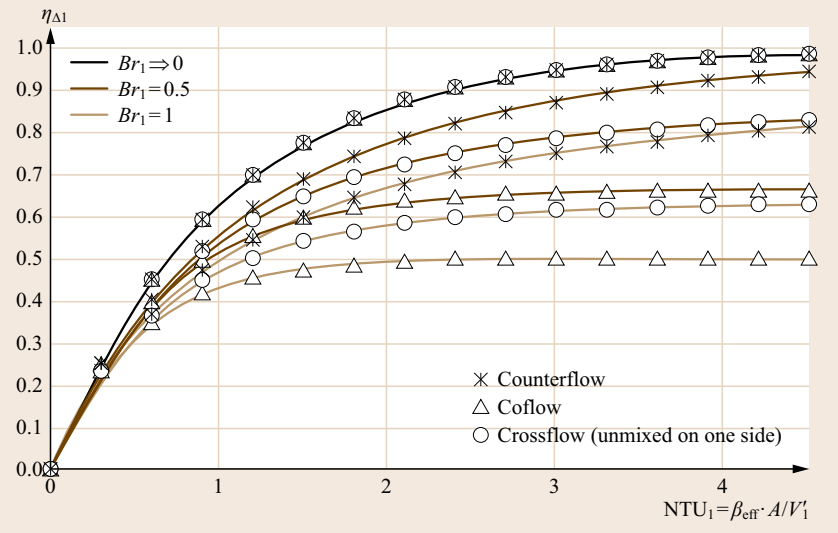


Fig. 10.15 Operation characteristics for crossflow, counterflow, and coflow of a mass exchanger for different Br_1 values

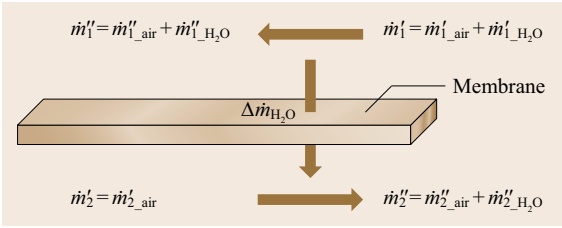


Fig. 10.16 Setup measurement of operation characteristics for planar membrane humidifier in counterflow configuration

and using the equations $\eta_{\Delta i} = f(Br_i,\ \mathrm{NTU}_i = f(\beta_{\mathrm{eff}}))$ from Table 10.2. The graphical representation of relations given in Table 10.2 can be seen in Fig. 10.15. The dimensionless concentration change $\eta_{\Delta 1}$ is plotted over the number of transport units NTU_1 for varying flow ratio Br_1. It can be seen that the concentration change $\eta_{\Delta 1}$ is virtually independent of the flow configuration, if Br_1 approaches zero.

For $Br \neq 0$, the maximum concentration change and thus the maximum efficiency of a mass exchanger is achieved with a counterflow configuration.

For ideal gases, the following relations are valid

$$p_i V = n_i R T_i \Rightarrow c_i = \frac{p_i}{RT_i} = \frac{n_i}{V} \quad \text{or}$$

$$\rho_i = \frac{p_i}{R_i T_i} = \frac{m_i}{V}\,.$$

$$\text{With} \quad \dot{V} = \frac{\dot{m}_i}{\rho_i}\,, \tag{10.64}$$

and

$$p_{\mathrm{Gas}} = \sum_i p_i\,, \tag{10.65}$$

the three dimensionless parameters can also be expressed in terms of the partial pressure p_i, the temperature T_i, the partial density ρ_i, and the mass flow rate $\dot{m}_i$ of the component i. The three dimensionless parameters yield:

The dimensionless concentration change

$$\eta_{\Delta 1} = \frac{\dfrac{\Delta\dot{m}_{1b}}{M_b}}{\dot{V}_1'\left(\dfrac{p_{1b}'}{RT_1'} - \dfrac{p_{2b}'}{RT_2'}\right)} = \frac{\left(\dfrac{p_{1b}'}{T_1'} - \dfrac{p_{1b}''}{T_1''}\right)\dfrac{\dot{V}_1'}{R}}{\dfrac{\dot{V}'_1}{R}\left(\dfrac{p_{1b}'}{T_1'} - \dfrac{p_{2b}'}{T_2'}\right)}$$

$$= \frac{\left(\dfrac{p_{1b}'}{T_1'}\right) - \left(\dfrac{p_{1b}''}{T_1''}\right)}{\left(\dfrac{p_{1b}'}{T_1'}\right) - \left(\dfrac{p_{2b}'}{T_2'}\right)} \tag{10.66}$$

for

$$\left|T_1' - T_1''\right| \ll (T_1' + T_1'')/2\,,$$
$$\left|T_1' - T_2'\right| \ll (T_1' + T_2')/2$$

and

$$\left|p'_{\mathrm{gas_1}} - p''_{\mathrm{gas_1}}\right| \ll (p'_{\mathrm{gas_1}} + p''_{\mathrm{gas_1}})/2\,,$$
$$\left|p'_{\mathrm{gas_2}} - p''_{\mathrm{gas_2}}\right| \ll (p'_{\mathrm{gas_2}} + p''_{\mathrm{gas_2}})/2$$

(see constraint for (10.38) and (10.39)).

The dimensionless transport capacity NTU

$$\mathrm{NTU}_1 = \frac{\beta_{\mathrm{eff}} A}{\dot{V}_1'} = \frac{\beta_{\mathrm{eff}} A}{\dfrac{\dot{m}_{1a}'}{\rho_{1a}'}} = \frac{\beta_{\mathrm{eff}} A \rho_{1a}'}{\dot{m}_{1a}'}\,. \tag{10.67}$$

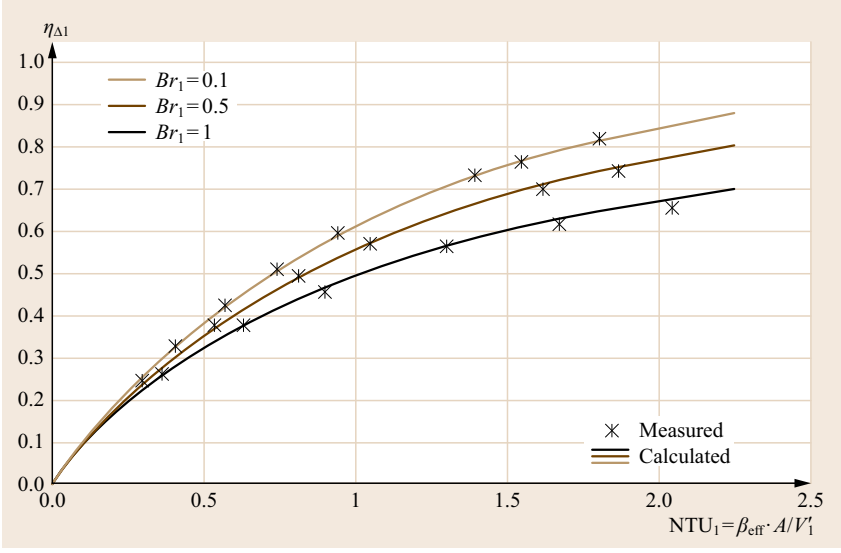


Fig. 10.17 Measured and calculated operation characteristics for a planar membrane humidifier in counterflow configuration

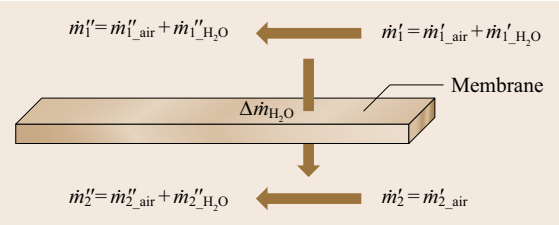


Fig. 10.18 Setup measurement of operation characteristics for a planar membrane humidifier in coflow configuration

The dimensionless ratio of the volume flow rates is

$$Br_1 = \frac{\dot{V}_1'}{\dot{V}_2'} = \frac{\left(\frac{\dot{m}_{1a}'}{\rho_{1a}'}\right)}{\left(\frac{\dot{m}_{2a}'}{\rho_{2a}'}\right)} . \qquad (10.68)$$

10.4.2 Operating Characteristics of Humidifier

In this section, operation characteristics for different humidifiers are discussed. The operating characteristics for a planar membrane humidifier are measured in coflow and counterflow configuration. The operation characteristics for crossflow configuration are measured with a hollow fibre humidifier.

Figure 10.16 shows the setup of measurement of a planar membrane humidifier operated in counterflow. The measured operation characteristics for different NTU values compared with predictions based on the relations provided in Table 10.2 are shown in Fig. 10.17. Figure 10.18 shows the setup of measurement of a planar membrane humidifier operated in coflow. The measured operation characteristics for different NTU values compared with calculations are shown in Fig. 10.19. Figure 10.20 shows the setup of measurement of a hollow fiber humidifier operated in crossflow unmixed on one side. $\dot{m}_2'$ is mixed and $\dot{m}_1'$ is unmixed. The measured operation characteristics for different NTU values compared with calculations are shown in Fig. 10.21. The fundamental properties $\beta_{eff}A$ of gas to gas humidifiers can thus be determined. Once these fundamental properties are known, the water exchange rate can be calculated.

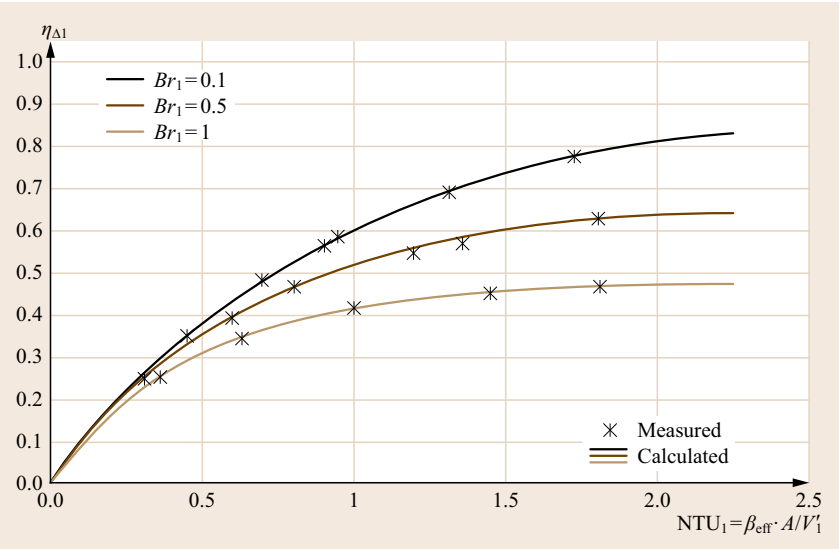


Fig. 10.19 Measured and calculated operation characteristics for planar membrane humidifier in coflow configuration

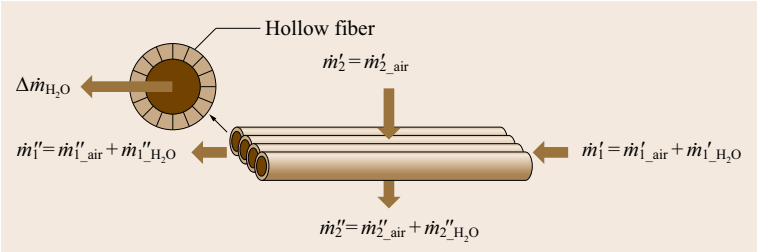


Fig. 10.20 Setup measurement of operation characteristics for a hollow fiber humidifier in crossflow configuration (unmixed on one side)

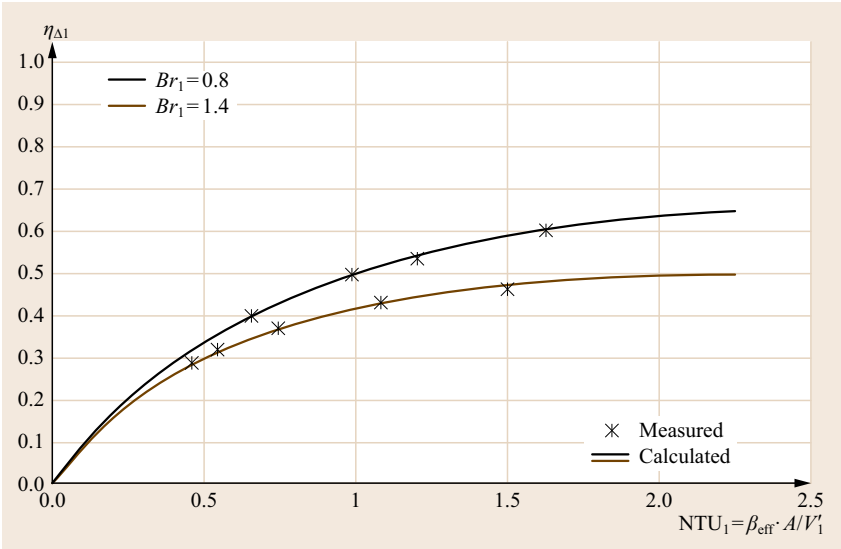


Fig. 10.21 Measured and calculated operation characteristics for a hollow fiber humidifier in crossflow configuration

10.5 Sensorless Humidification

This chapter describes a process of humidification control for fuel cell applications without humidity sensors. With known operation characteristic of the humidifier, sensorless humidification of a PEMFC is possible. The following description is an example of a planar membrane humidifier operated in counter flow configuration. The same procedure can be used for other humidifier configurations. The following procedure covers four steps:

1. Determination of humidifier mass transfer coefficient
2. Calculation of the required gas humidity at the fuel cell inlet.
3. Calculation of the provided gas humidity at the fuel cell inlet.
4. Matching of fuel cell operation conditions so that required and provided gas humidity become equal.

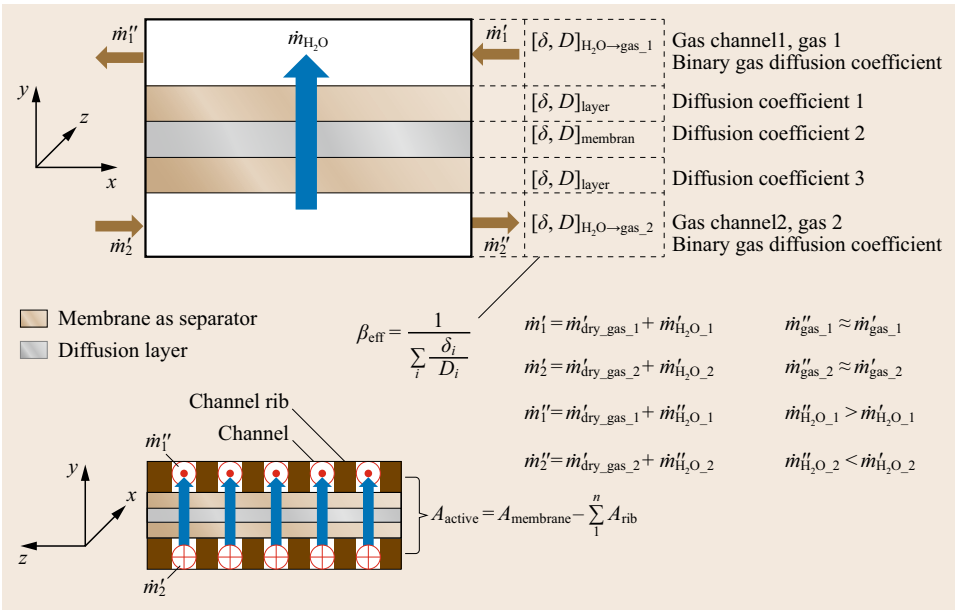


Fig. 10.22 Structure and description of a gas humidifier operated in counterflow

The first step is to get the effective mass transfer coefficient β_{eff} of the humidifier; therefore the active transfer area should be known. Figure 10.22 shows a typical setup of a planar membrane humidifier.

The membrane area A_{membrane} is reduced by the channel ribs to the active membrane area A_{active}. The channel ribs and used diffusion layer keep the membrane in position and ensure a forced flow direction along the membrane. The diffusion layer mechanically supports the membrane and permits gas diffusion under the channel ribs. For this application, only the total diffusion resistance of the humidifier is taken into account. Absorption, diffusion, and desorption processes in each diffusion layer are summarized by the geometrical properties of the flow channels to get the overall mass transfer coefficient β_{eff}.

To determine the mass transfer coefficient, the humidifier mass transfer should be measured for some typical fuel cell operation points. For this purpose, sensors are added to the inlets and outlets of the humidifier. Typical sensors include: Humidity, temperature, pressure, and mass flow rate as seen in Fig. 10.23.

The mass flow rates at the inlets $\dot{m}'_1 = \dot{m}'_{\text{dry_gas_1}} + \dot{m}'_{\text{H}_2\text{O_1}}$ and $\dot{m}'_2 = \dot{m}'_{\text{dry_gas_2}} + \dot{m}'_{\text{H}_2\text{O_2}}$ are defined over the typical fuel cell operating range. Humidifiers for fuel cell applications could be used for hydrogen and air humidification. To cover both, the subscript *gas* is used for the dry mass flow rates, which are gases without water.

The water mass flow rate can be calculated if humidity, dry mass flow rate, temperature and operation pressure are known. According to Dalton's law [10.4], the absolute pressure $p_{_i}$ at point i is the sum of existing partial pressures.

$$p_{_i} = p_{\text{H}_2\text{O_}i} + p_{\text{dry_gas_}i} \,. \tag{10.69}$$

With the definition of the specific humidity or humidity ratio x [10.4],

$$\begin{aligned} x_i &= \frac{\dot{m}_{\text{H}_2\text{O_}i}}{\dot{m}_{\text{dry_gas_}i}} = \frac{p_{\text{H}_2\text{O_}i}}{p_{_i} - p_{\text{H}_2\text{O_}i}} \frac{M_{\text{H}_2\text{O}}}{M_{\text{dry_gas_}i}} \\ &= \frac{\dot{m}_{\text{humid_gas_}i}}{\dot{m}_{\text{dry_gas_}i}} - 1 \,. \end{aligned} \tag{10.70}$$



Fig. 10.23 Required physical values for measurement of humidifiers

the water mass flow rate $\dot{m}_{\text{H}_2\text{O_}i}$, can be determined to

$$\dot{m}_{\text{H}_2\text{O_}i} = \frac{p_{\text{H}_2\text{O_}i}}{p_{_i} - p_{\text{H}_2\text{O_}i}} \frac{M_{\text{H}_2\text{O}}}{M_{\text{dry_gas_}i}} \dot{m}_{\text{dry_gas_}i} \,. \tag{10.71}$$

The water partial pressure is given by

$$p_{\text{H}_2\text{O_}i} = \frac{\varphi_{_i}}{100\%} p_{\text{S}}(T) \,. \tag{10.72}$$

Using Antoine's equation to calculate the saturation pressure as a function of the saturation temperature

$$p_{\text{S}}(T) = \exp\left(A - \frac{B}{C + T\,[\text{K}]}\right) \tag{10.73}$$

the water mass flow rate can be calculated to

$$\begin{aligned} \dot{m}_{\text{H}_2\text{O_}i} = & \frac{\frac{\varphi_{_i}}{100\%} \mathrm{e}^{A - \frac{B}{C + T_i\,[\text{K}]}}}{p_{_i} - \frac{\varphi_{_i}}{100\%} \mathrm{e}^{A - \frac{B}{C + T_i\,[\text{K}]}}} \\ & \times \frac{M_{\text{H}_2\text{O}}}{M_{\text{dry_gas_}i}} \dot{m}_{\text{dry_gas_}i} \,. \end{aligned} \tag{10.74}$$

Based on (10.72) and (10.73), the water partial pressures $p'_{\text{H}_2\text{O_1}}$, $p''_{\text{H}_2\text{O_1}}$, $p'_{\text{H}_2\text{O_2}}$ and $p''_{\text{H}_2\text{O_2}}$ can be calculated with the measured values of humidity and temperature. Equation (10.66) yields the dimensionless concentration change. Using the operation characteristics for a counter flow operated mass exchanger taken from Table 10.2

$$\text{NTU}_i = \frac{1}{Br_i - 1} \ln\left(\frac{1 - \eta_{\Delta i}}{1 - Br_i \eta_{\Delta i}}\right) \tag{10.75}$$

(10.67) provides the effective mass transfer coefficient,

$$\beta_{\text{eff_}i} = \frac{\ln\left(\frac{1 - \eta_{\Delta i}}{1 - Br_i \eta_{\Delta i}}\right)}{(Br_i - 1)} \frac{\dot{m}'_{\text{dry_gas_}i}}{A_{\text{membrane}} \rho_{\text{dry_gas_}i}} \,. \tag{10.76}$$

The ratio of volume flow rates Br is given by (10.68). The same procedure can be used to get the effective mass transfer coefficient for co- and crossflow operated humidifier (Table 10.2).

Measured mass transfer coefficients of humidifiers are effective coefficients, describing the overall mass transfer process of water. It means that the measured effective mass transfer coefficient takes humidifier design factors like flow field geometry, used diffusion layer, separator properties, and channel design into account. The effective mass transfer coefficient depends on laminar or turbulent flow within the humidifier as

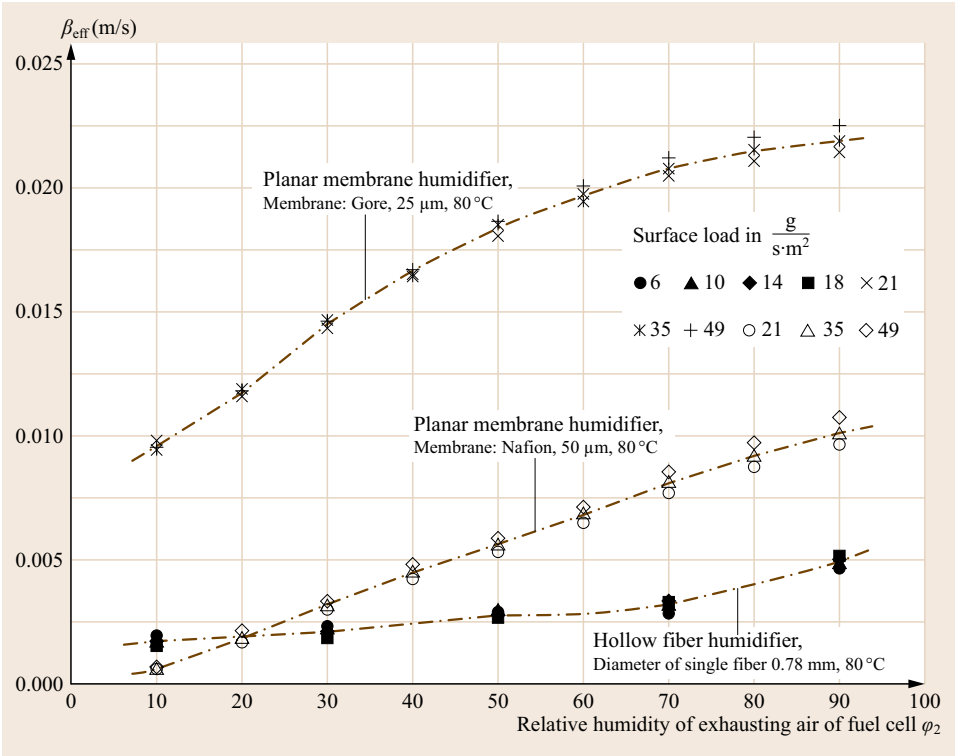


Fig. 10.24 Measured effective mass transfer coefficients for different gas humidifiers as a function of relative humidity of air mass flow 2 at 80 °C, with a constant relative humidity of air mass flow 1 of 5%

well as on temperature and humidity driven diffusion. Figure 10.24 shows measurements of effective transfer coefficient as a function of relative humidity at 80 °C humidifier temperature. Mass flow 1 is humidified with a constant value of 5%, for mass flow 2 the humidity varies from 10% to 90%. In a real fuel cell system, mass flow 1 would be discharged by the compressor and mass flow 2 would be exhausted by the fuel cell, as shown in Fig. 10.25. The ratio of volume flow rates is $Br_1 = 1.4$ ($Br_2 = 0.71$), which is in a typical range for fuel cell applications. Shown are the results of two membrane humidifiers with identical design but different membranes as separator, as well as the result of a hollow fiber humidifier. The effective mass transfer coefficient is plotted as a function of relative humidity of mass flow 2. Each humidifier is measured with different surface loads. The surface load is defined as mass flow rate 1 per transfer area within the humidifier.

Usually planar membrane humidifiers have membrane thicknesses between 10 and 50 µm with corresponding high effective mass transfer coefficients compared to hollow fiber humidifiers which have higher wall thicknesses. The measured effective mass transfer coefficient can be empirically correlated to the relative humidity based on a cubic regression. The resulting equations are listed in Table 10.3.

Humidifier type, separator material, geometry of flow field, laminar or turbulent flow, and operation temperature have also influence on the effective mass transfer coefficient.

When the mass transfer coefficient is known, the transferred water mass flow rate is calculated analyti-

Table 10.3 Empirical correlation functions of the measured effective mass transfer coefficients according to Fig. 10.24, valid for the fuel cell air outlet humidity: $10\% \le \varphi_2' \le 90\%$ and the fuel cell air inlet humidity $\varphi_1' = 5\%$

	Flow field	Equation for the effective mass transfer coefficient
Membrane, Gore	Open, with pillars as points of support, counter flow	$\beta_{eff} = -3.052 \times 10^{-9}\varphi_2^3 - 1.196 \times 10^{-6}\varphi_2^2 + 3.027 \times 10^{-4}\varphi_2 + 6.466 \times 10^{-3}$ ($R^2 = 0.999$)
Membrane, Nafion	Open, with pillars as points of support, counter flow	$\beta_{eff} = -5.012 \times 10^{-9}\varphi_2^3 - 5.089 \times 10^{-7}\varphi_2^2 + 1.122 \times 10^{-4}\varphi_2 + 5.592 \times 10^{-4}$ ($R^2 = 0.999$)
Hollow fiber	Fiber bundle, crossflow	$\beta_{eff} = 1.106 \times 10^{-8}\varphi_2^3 - 1.269 \times 10^{-6}\varphi_2^2 + 6.744 \times 10^{-5}\varphi_2 + 1.121 \times 10^{-3}$ ($R^2 = 0.991$)

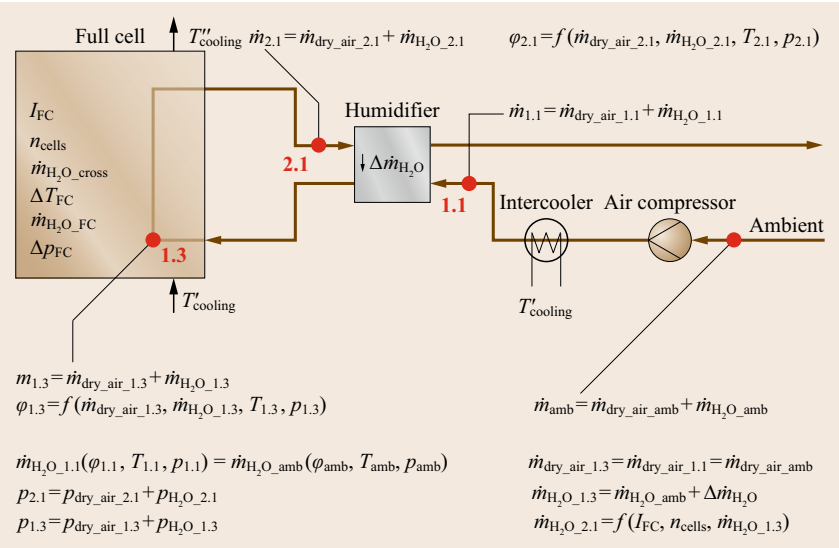


Fig. 10.25 Mass flow rates, humidity, and pressures in typical fuel cell applications

cally based on the relations of Table 10.2. This allows a sensorless humidification control with focus on the air humidity at the fuel cell inlet. The following example shows a counterflow operated humidifier in a typical fuel cell system (Fig. 10.25).

Values marked with subscript 1.*x* describe the air flow parameter at the fuel cell inlet. Values with subscript 2.*x* describe the air flow parameter at the fuel cell exhaust. Hence, within the humidifier water is transferred from mass flow 2 to mass flow 1. The goal is to calculate the relative air humidity $\varphi_{1.3}$ at the inlet of the fuel cell. The air humidity at fuel cell inlet $\varphi_{1.3}$ is controlled to get specified air humidity at the fuel cell outlet $\varphi_{2.1}$. Water management can be facilitated by using this approach. Balanced water management avoids dry-out as well as too much liquid water. In automotive applications too much liquid water is a challenge during cold and freeze start operation. Therefore, $\varphi_{2.1}$ is a known specified set value.

The relative humidity at the fuel cell inlet can be calculated with the help of (10.74)

$$\varphi_{1.3} = \frac{p_{1.3}100\%}{\left(\frac{\dot{m}_{dry_air_1.3}}{\dot{m}_{H_2O_1.3}}\frac{M_{H_2O}}{M_{dry_air}}+1\right)e^{A-\frac{B}{C+T_{1.3}}}} . \tag{10.77}$$

To calculate $\varphi_{1.3}$ the water mass flow rate $\dot{m}_{H_2O_1.3}$, the dry air mass flow rate $\dot{m}_{dry_air_1.3}$, the operation pressure $p_{1.3}$ and the temperature $T_{1.3}$ must be specified. The inlet temperature of the coolant $T'_{cooling}$ can be used to determine the temperature at point 1.3

$$T_{1.3} = T'_{cooling} . \tag{10.78}$$

Usually the coolant temperature is a set value. The gas pressure $p_{1.3}$ is also a known and controlled set value. The dry air mass flow rate depends on the fuel cell current I_{FC} (from Faraday's law), the air-stoichiometric ratio λ_{air}, the oxygen mass fraction of air 23%[(kg O_2)/(kg air)] and the number of cells n_{cells}

$$\dot{m}_{dry_air_1.3} = \frac{I_{FC}}{4F}\frac{1}{0.23}\lambda_{air}M_{O_2}n_{cells} . \tag{10.79}$$

The dimensionless air-stoichiometric ratio is defined as the ratio of actually provided molar air flow rate to the stoichiometrically calculated theoretical molar air flow rate

$$\lambda_{air} = \frac{\dot{n}_{provided_air}}{\dot{n}_{stoichiometry_air}} . \tag{10.80}$$

Usually the air-stoichiometric ratio is a set value in a range between 1.4 (high loads) and 10 (low loads). The water mass flow rate leaving the fuel cell $\dot{m}_{H_2O_2.1}$ is dependent on $\dot{m}_{H_2O_1.3}$, the produced water mass flow rate $\dot{m}_{H_2O_FC}$, and the mass flow rate which is diffusing through the MEA to the hydrogen side $\dot{m}_{H_2O_cross}$

$$\dot{m}_{H_2O_2.1} = \dot{m}_{H_2O_1.3} + \dot{m}_{H_2O_FC} - \dot{m}_{H_2O_cross} . \tag{10.81}$$

With respect to (10.81) the required water mass flow rate (subscript r) at the fuel cell inlet $\dot{m}_{H_2O_1.3r}$ has to be controlled to

$$\dot{m}_{H_2O_1.3r} = \dot{m}_{H_2O_2.1} - \dot{m}_{H_2O_FC} + \dot{m}_{H_2O_cross} . \tag{10.82}$$

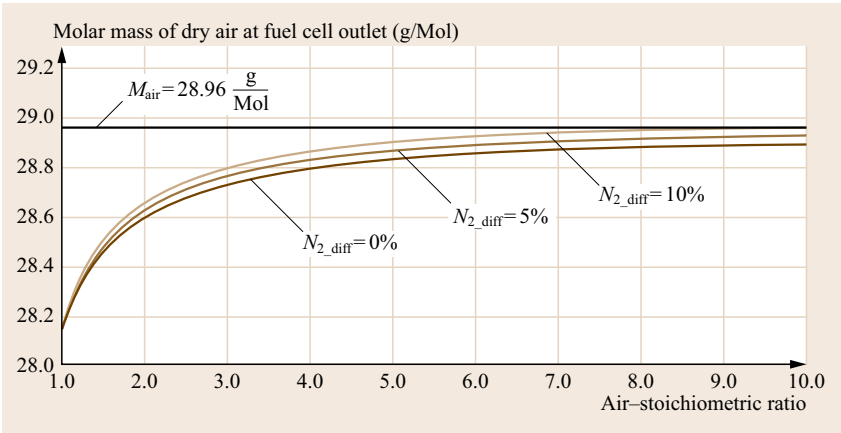


Fig. 10.26 Molar mass constant versus air–stoichiometric ratio for exhausting dry air mass flow rates. Nitrogen, oxygen, and argon are considered as dry air gas mixture

With the help of (10.74), the exhaust water mass flow rate can be calculated

$$\dot{m}_{H_2O_2.1} = \frac{\frac{\varphi_2.1}{100\%} e^{A-\frac{B}{C+T_{2.1}}}}{p_{2.1} - \frac{\varphi_{2.1}}{100\%} e^{A-\frac{B}{C+T_{2.1}}}} \frac{M_{H_2O}\dot{m}_{dry_air_2.1}}{M^*_{dry_air}}$$

$$\text{for } 0\% \le \varphi_{2.1} \le 100\% \,, \tag{10.83}$$

$\varphi_{2.1}$ is a set value usually close to 100%. In reality, exhaust humidity is often above 100%, a mixture of saturated humid air and water droplets. The above presented mass exchanger modeling does not cover a liquid water fraction. However, this does not mean that the liquid amount will not be transferred. To account for the transfer of liquid water, a fictive humidity can be used. In practice, a use of a fictive humidity until 110% often yields realistic results.

The exhaust air temperature $T_{2.1}$ can be estimated to

$$T_{2.1} \approx T''_{cooling} = T'_{cooling} + \Delta T_{FC} \,. \tag{10.84}$$

In most applications, the increase of temperature within the fuel cell ΔT_{FC} is a controlled set value and therefore known. Usually ΔT_{FC} is in a range of 0.5–15 K, depending on load. The exhaust air pressure $p_{2.1}$ can be calculated as controlled operation pressure $p_{1.3}$ minus pressure drop of the fuel cell Δp_{FC}

$$p_{2.1} = p_{1.3} - \Delta p_{FC} \,. \tag{10.85}$$

The pressure drop of a fuel cell basically depends on the mass flow rate and temperature, $p_{1.3}$ is a set value.

The dry air mass flow rate exhausting the fuel cell $\dot{m}_{dry_air_2.1}$ is equal to the inlet dry air mass flow rate minus the consumption of oxygen

$$\dot{m}_{dry_air_2.1} = \dot{m}_{dry_air_1.3} - \left(\frac{I_{FC}}{4F} M_{O_2} n_{cells}\right) . \tag{10.86}$$

Because oxygen is consumed, the molar mass constant for the dry gas mixture at fuel cell outlet is changing. Therefore, the variable $M^*_{dry_air}$ is used for calculations of exhaust dry air mass flow rates. For a simple handling, the subscript *air* for exhausting dry gas flows will be kept. The change of the molar mass constant is dependent on the air-stoichiometric ratio λ_{air} described as

$$\begin{aligned} M^*_{dry_air} \approx \Big[& 0.78\,\mathrm{Mol}_{N_2} M_{N_2} \\ & + 0.21 \left(1 - \frac{1}{\lambda_{air}}\right) \mathrm{Mol}_{O_2} M_{O_2} \\ & + 0.01 \mathrm{Mol}_{air} M_{air} \Big] \Big[0.78 + 0.01 \\ & + 0.21 \left(1 - \frac{1}{\lambda_{air}}\right) \mathrm{Mol} \Big]^{-1} \end{aligned}$$

$$\text{for} \quad \lambda_{air} > 1 \,. \tag{10.87}$$

Note that within the fuel cell, nitrogen could diffuse from the air side to the hydrogen side. This is called nitrogen crossover N_{2-diff} and is not negligible for relatively thin MEAs. Figure 10.26 shows the molar mass constant for exhausting air versus air-stoichiometric ratio.

The produced water mass flow rate can be calculated as

$$\dot{m}_{H_2O_FC} = \frac{I_{FC}}{2F} M_{H_2O} n_{cells} \,. \tag{10.88}$$

Normally $\dot{m}_{H_2O_cross}$ is less than 5% relative to $\dot{m}'_{H_2O_2.1}$ and can be neglected in most applications. However, for greater accuracy the water crossover should be considered. A typical water crossover rate versus current density for a counterflow operated fuel cell is shown in Fig. 10.27.

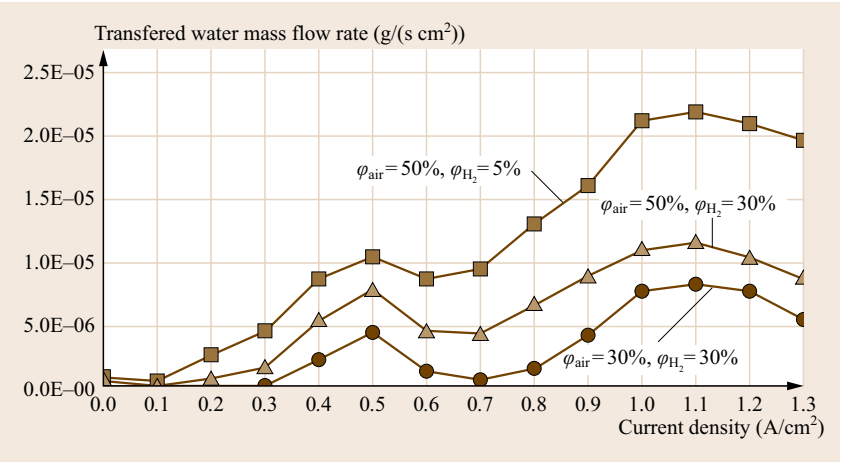


Fig. 10.27 Water crossover from cathode to anode side for different gas humidity. Air-stoichiometric ratio 1.7, H_2-stoichiometric ratio 1.5, air pressure 2 bar, hydrogen pressure 2.1 bar, spend time 10 min/load, temperature 80 °C, counterflow operation of fuel cell, MEA thickness 25 µm, active area 400 cm^2

The water crossover depends on the interaction of many different effects (for example water diffusion, GDL properties, ratio of mass flow rates, and uneven current density distribution within the fuel cell). The water crossover rate for a comparable PEMFC operated in coflow is less than that in counterflow. The behavior of the water crossover rate is related to the operation characteristics of a mass exchanger shown in Fig. 10.15. The difference to a PEMFC is the water source directly at the separator surface.

Equations (10.82)–(10.88) define the required water mass flow rate at the fuel cell inlet. With the help of (10.77), the required air humidity at the fuel cell inlet $\varphi_{1.3r}$ can be calculated. For a sensorless humidification, the provided air humidity at the fuel cell inlet $\varphi_{1.3p}$ has to be equal to the required air humidity $\varphi_{1.3r}$. The same is true for the required and provided water mass flow rates. In the following, the provided (subscript p) water mass flow rate $\dot{m}_{H_2O_1.3p}$ from the humidifier is described. It is the sum of the water mass flow rate $\dot{m}_{H_2O_amb}$ provided by the humid ambient air inlet mass flow rate and the transferred water mass flow rate $\Delta\dot{m}_{H_2O}$ within the humidifier

$$\dot{m}_{H_2O_1.3p} = \dot{m}_{H_2O_amb} + \Delta\dot{m}_{H_2O} \,. \tag{10.89}$$

Changes in climatic conditions, like winter, summer, rain, or freeze could have significant influence on $\dot{m}_{H_2O_1.3p}$ and need to be considered. Equation (10.74) defines the ambient water mass flow rate to

$$\dot{m}_{H_2O_amb} = \frac{\dfrac{\varphi_amb}{100\%} e^{A-\frac{B}{C+T_{amb}}}}{p_amb - \dfrac{\varphi_amb}{100\%} e^{A-\frac{B}{C+T_{amb}}}} \times \frac{M_{H_2O}}{M_{dry_air}} \dot{m}_{dry_air_amb} \,. \tag{10.90}$$

The dry air mass flow rate from ambient is described by (10.79)

$$\dot{m}_{dry_air_amb} = \dot{m}_{dry_air_1.3} \,. \tag{10.91}$$

The humidifier operating characteristic is used to calculate $\Delta\dot{m}_{H_2O}$. Equation (10.66) and the operation characteristics for counter flow operation from Table 10.2 yield

$$\eta_{\Delta 1} = \frac{\dfrac{\Delta\dot{m}_{H_2O}}{M_{H_2O}}}{\left(\dfrac{\dot{m}_{dry_air_1.1}}{\rho_{dry_air_1.1}}\right)\left(\dfrac{p_{H_2O_2.1}}{RT_{2.1}} - \dfrac{p_{H_2O_1.1}}{RT_{1.1}}\right)} = \frac{1 - e^{(Br_1-1)NTU_1}}{1 - Br_1 e^{(Br_1-1)NTU_1}} \,. \tag{10.92}$$

Note that the transferred water mass flow rate is directed from fuel cell outlet (flow 2) to fuel cell inlet (flow 1). Solving (10.92) for the transferred water mass flow rate yields

$$\Delta\dot{m}_{H_2O} = \frac{1 - e^{(Br_1-1)NTU_1}}{1 - Br_1 e^{(Br_1-1)NTU_1}} \left(\frac{\dot{m}_{dry_air_1.1}}{\rho_{dry_air_1.1}}\right) \left(\frac{p_{H_2O_2.1}}{RT_{2.1}} - \frac{p_{H_2O_1.1}}{RT_{1.1}}\right) M_{H_2O} \,. \tag{10.93}$$

For (10.92) the operating characteristic is chosen for $Br_1 \neq 1$. The dry volume flow rates of inflowing and exhausting air flows are mostly different. The reasons are the consumption of gas within the fuel cell and a change in temperature and pressure between fuel cell

inlet and outlet which is responsible for changing densities. Equation (10.68) yields

$$Br_1 = \frac{\left(\frac{\dot{m}_{\mathrm{dry_air_1.1}}}{\rho_{\mathrm{dry_air_1.1}}}\right)}{\left(\frac{\dot{m}_{\mathrm{dry_air_2.1}}}{\rho_{\mathrm{dry_air_2.1}}}\right)} . \tag{10.94}$$

The dry air mass flow rate at humidifier inlet $\dot{m}_{\mathrm{dry_air_1.1}}$ is the same as the mass flow rate at fuel cell inlet $\dot{m}_{\mathrm{dry_air_1.3}}$ which is given by (10.79)

$$\dot{m}_{\mathrm{dry_air_1.1}} = \dot{m}_{\mathrm{dry_air_1.3}} \tag{10.95}$$

The dry air mass flow rate the fuel cell exhausts $\dot{m}_{\mathrm{dry_air_2.1}}$ is provided by (10.86). The partial densities of the dry air $\rho_{\mathrm{dry_air_1.1}}$ and $\rho_{\mathrm{dry_air_2.1}}$ can be calculated with the ideal gas law

$$\rho_i = \frac{n_i M_i}{V} = \frac{m_i}{V} = \frac{p_i M_i}{RT} = \frac{\dot{m}_i}{\dot{V}} . \tag{10.96}$$

For the partial density $\rho_{\mathrm{dry_air_1.1}}$: If an intercooler is integrated upstream of the humidifier T'_{cooling} can be used to estimate the temperature at point 1.1

$$T_{1.1} = T'_{\mathrm{cooling}} . \tag{10.97}$$

According to Dalton's law (10.69), the absolute pressure of the humid air is the sum of the dry air partial pressure and the water vapor partial pressure. The absolute pressure of the humid air at point 1.1 can be calculated with use of the controlled operation pressure at point 1.3 increased by the pressure drop of the humidifier,

$$p_{1.1} = p_{\mathrm{dry_air_1.1}} + p_{\mathrm{H_2O_1.1}} = p_{1.3} + \Delta p_{\mathrm{humidifier}} . \tag{10.98}$$

Using (10.96) to estimate the ratio of the dry air partial pressure to the water partial pressure yields

$$\frac{p_{\mathrm{dry_air_1.1}}}{p_{\mathrm{H_2O_1.1}}} = \frac{\dot{m}_{\mathrm{dry_air_1.1}}}{\dot{m}_{\mathrm{H_2O_1.1}}} \frac{M_{\mathrm{H_2O}}}{M_{\mathrm{dry_air}}} . \tag{10.99}$$

Combining (10.98) and (10.99) gives the partial pressure of dry air at point 1.1

$$\begin{aligned} p_{\mathrm{dry_air_1.1}} &= \frac{p_{1.3} + \Delta p_{\mathrm{humidifier}}}{\frac{\dot{m}_{\mathrm{H_2O_1.1}}}{\dot{m}_{\mathrm{dry_air_1.1}}} \frac{M_{\mathrm{dry_air}}}{M_{\mathrm{H_2O}}} + 1} \\ &= p_{1.1} - p_{\mathrm{H_2O_1.1}} . \end{aligned} \tag{10.100}$$

The water mass flow rate carried by the humid ambient air flow is equal to the water mass flow rate at point 1.1,

$$\dot{m}_{\mathrm{H_2O_1.1}} = \dot{m}_{\mathrm{H_2O_amb}} . \tag{10.101}$$

For the partial density $\rho_{\mathrm{dry_air_2.1}}$: If the humidifier is located in the immediate vicinity of the fuel cell, $T_{2.1}$ can be estimated with (10.84).

Analogous to the derivation of (10.100), the partial pressures of dry air at point 2.1 $p_{\mathrm{dry_air_2.1}}$ can be calculated to

$$\begin{aligned} p_{\mathrm{dry_air_2.1}} &= \frac{p_{2.1}}{\frac{\dot{m}_{\mathrm{H_2O_2.1}}}{\dot{m}_{\mathrm{dry_air_2.1}}} \frac{M^*_{\mathrm{dry_air}}}{M_{\mathrm{H_2O}}} + 1} \\ &= p_{2.1} - p_{\mathrm{H_2O_2.1}} . \end{aligned} \tag{10.102}$$

The number of transfer units can be calculated with the help of (10.67)

$$\mathrm{NTU}_1 = \frac{\beta_{\mathrm{eff}} A_{\mathrm{membrane}} \rho_{\mathrm{dry_air_2.1}}}{\dot{m}_{\mathrm{dry_air_2.1}}} . \tag{10.103}$$

Finally, the water partial pressures $p_{\mathrm{H_2O_1.1}}$ and $p_{\mathrm{H_2O_2.1}}$ can also be calculated with the help of (10.100) and (10.102).

To get the specified relative air humidity at fuel cell outlet $\varphi_{2.1}$, the required water mass flow rate must be the same as the provided water mass flow rate

$$\dot{m}_{\mathrm{H_2O_1.3r}} = \dot{m}_{\mathrm{H_2O_1.3p}} . \tag{10.104}$$

The same is true for the required air humidity $\varphi_{1.3\mathrm{r}}$ and $\varphi_{1.3\mathrm{p}}$ the provided air humidity

$$\varphi_{1.3\mathrm{r}} = \varphi_{1.3\mathrm{p}} . \tag{10.105}$$

Solving (10.104) and (10.105) is a challenge because a multidimensional optimization is needed. The fuel cell operation conditions like:

- Temperatures
- Pressures
- Pressure drops
- Mass flow rates
- Fuel cell load
- Air-stoichiometric ratio

have an impact on the resulting air humidity as well as on the humidifier operation characteristic. Furthermore, the air humidity at fuel cell outlet is dependent on the air humidity at fuel cell inlet which in turn depends on the humidity at fuel cell outlet caused by the water transfer within the humidifier.

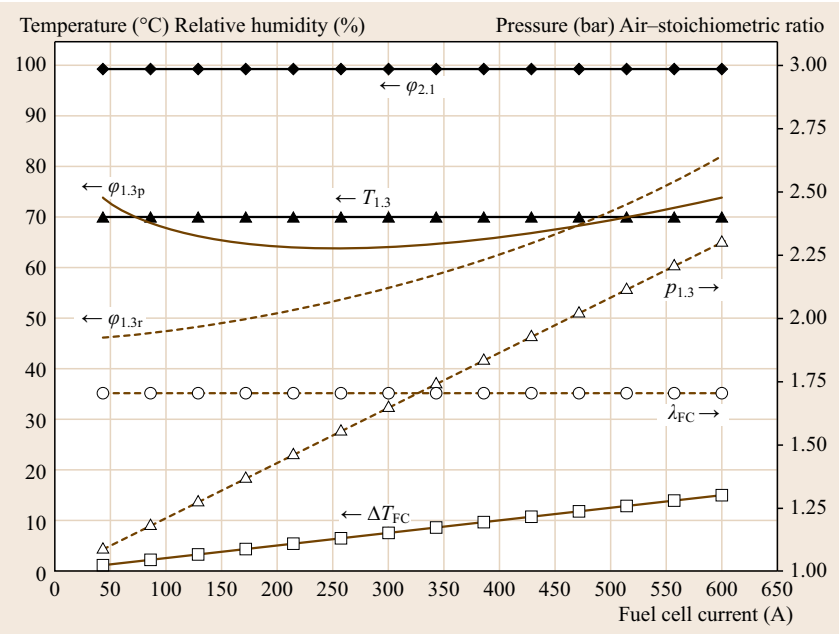


Fig. 10.28 Required and provided air humidity (*bold*) dependent on fuel cell operation conditions. *Left arrow* for the left vertical axis, *right arrow* for the right vertical axis

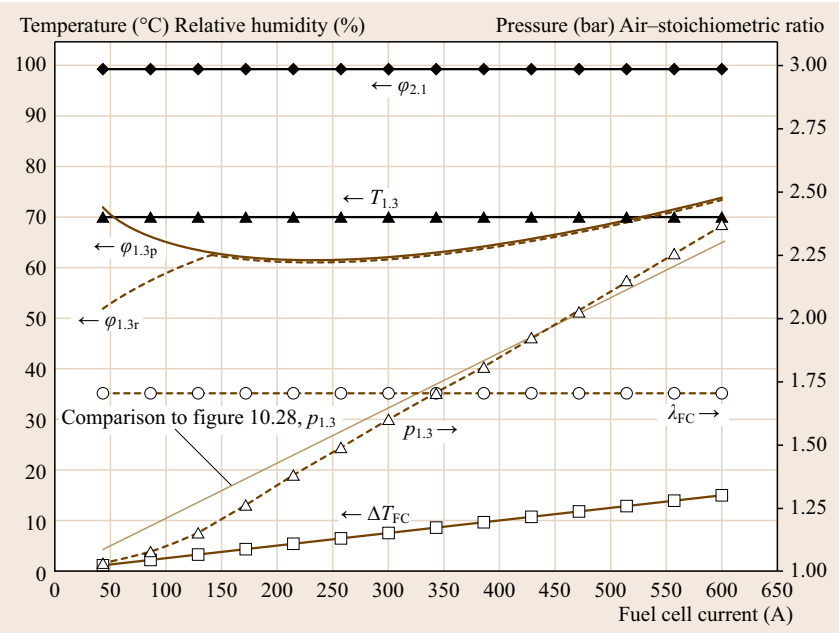


Fig. 10.29 Equating required and provided relative air humidity (*bold*) by changing the operation pressure. *Left arrow* for the left vertical axis, *right arrow* for the right vertical axis

A practical application to solve (10.105) is to consider the requested and the provided relative humidity separately from each other. $\varphi_{1.3r}(\dot{m}_{H_2O_1.3r})$ and $\varphi_{1.3p}(\dot{m}_{H_2O_1.3p})$ can be calculated in two ways. Plotting the required and provided humidity as function of the fuel cell current shows the difference of both. For example, Fig. 10.28 shows a typical case. Plotted are the required air humidity and the provided air humidity versus fuel cell current. Additionally, the corresponding key fuel cell operation conditions are shown.

For the humidifier an active membrane area of 3 m^2 with a constant mass transfer coefficient of 0.01 m/s is assumed. In addition, a linear interpolated water crossover to the anode side of 1 g/s at 600 A is assumed. Pressure drops of humidifier and fuel cell are interpolated as well with maximums of 300 mbar for the fuel

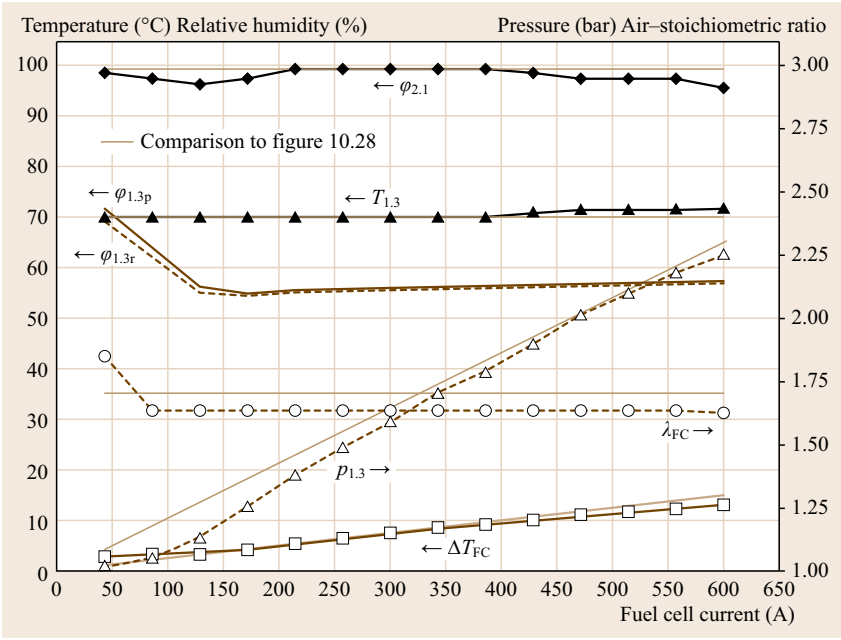


Fig. 10.30 Adjustment of required and provided air humidity (*bold*) due to changing fuel cell operation conditions. *Left arrow* for the left vertical axis, *right arrow* for the right vertical axis. *Small lines* represent the initial case shown in Fig. 10.28

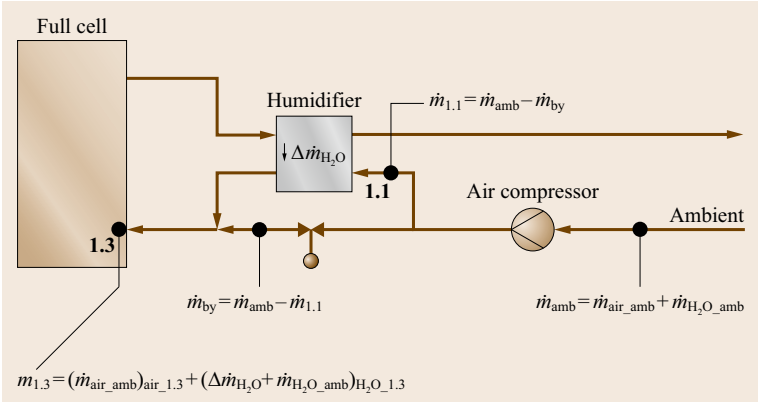


Fig. 10.31 Humidification control by bypassing the humidifier

cell and 100 mbar for the humidifier. The total fuel cell stack has 300 cells. Assumed ambient conditions are 20 °C, 50% air humidity and pressure 1.013 bar.

Below 470 A, the provided humidity is higher than the required. For currents higher than 470 A the required humidity cannot be achieved with the assumed fuel cell operation conditions and humidifier. However, by changing the fuel cell operation conditions, the provided air humidity can be fit to the required air humidity over a wide range of currents. Figure 10.29 shows the same case as depicted in Fig. 10.28 only with a modified operation pressure.

The fuel cell operation conditions can be used to fit the provided air humidity to the required air humidity depending on the humidifier parameters. The reverse is also true. With known humidifier parameters, the fuel cell operation conditions can also be determined.

In the example shown in Fig. 10.29, the operation pressure is the only changed parameter. For currents higher than 430 A, the operation pressure is increased in comparison to Fig. 10.28. However, an increase in operation pressure means also an increase in parasitic losses because the compressor needs more power. The operation pressure should be as low as necessary. Therefore the other fuel cell operation conditions should also be changed with focus on a decrease of operation pressure. Note that there is a trade-off between low pressure operation for minimization of parasitic load and high pressure operation for maximizing the fuel cell performance. Figure 10.30 shows the adjustment of required and provided air humidity due to the

change of the fuel cell operation conditions. The operation pressure is always kept below the initial case shown in Fig. 10.28 in order to reduce parasitic losses. The air-stoichiometric ratio is also reduced for a wide operation range, which also saves parasitic loss. Except for very low loads, where the air-stoichiometric ratio exceeds the initial case presented in Fig. 10.28. To ensure that water droplets are always discharged out of the fuel cell flow field together with the exhaust air mass flow rate, a minimal air mass flow rate is needed, which requires a minimal pressure drop for water removal. Usually air-stoichiometric ratios between 2 and 10 are used for very low loads. Compared to the case shown in Fig. 10.28, the air humidity at fuel cell outlet is lower for relatively low and relatively high currents. The required and the provided relative humidity are almost constant for the whole operation range. Because the relative humidity at fuel cell outlet is also nearly constant, the fuel cell can be operated with an almost constant water balance.

Fuel cell operation conditions affect required humidifier capacity. The results shown in Figs. 10.28 and 10.29 were calculated using a humidifier active membrane area of $3\,m^2$. Using the fuel cell operation conditions from Fig. 10.29, the average provided relative humidity results in around 64%. If a relative humidity of 55% at fuel cell inlet was also sufficient, it would be possible to reduce the active membrane area of the humidifier. For the example shown in Fig. 10.30, the active membrane area of the humidifier is even reduced from 3 to $2.3\,m^2$.

The humidifier could show degradation based on aging of used membrane or hollow fiber. In that case the efficiency decreases which leads to a lower transferred water mass flow rate. The fuel cell operation conditions could be used to counteract a decrease of efficiency. Less operation temperature, less air-stoichiometric ratio, or a higher operation pressure yield to higher humidifier efficiency. In addition, the fuel cell could also degrade with age. As seen in (10.15), higher operating pressures can counter the decrease of fuel cell voltage. A higher operation pressure is preferred to lower operation temperatures, because a higher operation pressure can cover both degradation of humidifier and degradation of fuel cell. However, the parasitic power of the fuel cell system will be higher. The system volume itself will be the same. With use of a reduced air-stoichiometric ratio, the water transfer losses also can be countered. A decrease of air-stoichiometric ratio results in a lower parasitic load of the air compressor. Combined with a higher operation pressure and a lower air-stoichiometric ratio, an increase of parasitic power can be kept at an acceptable level to counter degradation effects of humidifier and fuel cell. To indicate the degradation, the performance loss of the fuel cell polarization curve can be used.

A second way to counteract a decrease of efficiency is to increase the active membrane area of the humidifier. In that case, the cost and volume of the humidifier will increase. More active membrane area means a difference in provided and required air humidity, if the humidity of the air exhausting the fuel cell is kept at a desired level. To keep the required and provided air humidity mutually adjusted, usually a valve is integrated into the system. The valve allows a fraction of mass flow rate to bypass the humidifier. The bypassed mass flow rate will not be humidified. The mass flow rate through the humidifier can be controlled by opening and closing that valve as can be seen in Fig. 10.31.

The humidity at point 1.3 can be calculated by estimating the ratio of humidified air to bypassed air.

References

10.1 S. Cleghorn, J. Kolde, W. Liu: Catalyst coated composite membranes. In: *Handbook of Fuel Cells*, ed. by W. Vielstich, A. Lamm, H.A. Gasteiger (Wiley, Chichester 2003)

10.2 F.N. Buchi, G.G. Scherer: Investigation of the transversal water profile in nafion membranes, J. Electrochem. Soc. **148**, A183–A188 (2000)

10.3 W. Dai, H. Wang, X.-Z. Yuan, J.J. Martin, D. Yang, J. Qiao, J. Ma: A review on water balance in the membrane electrode assembly of proton exchange membrane fuel cells, Int. J. Hydrogen Energy **34**, 9461–9478 (2009)

10.4 B. Weigand, J. Köhler, J. von Wolfersdorf: *Thermodynamik Kompakt*, 3rd edn. (Springer, Berlin, Heidelberg 2013), in German

10.5 K.C. Neyerlin, W. Gu, J. Jorne, H. Gasteiger: Determination of catalyst unique parameters for the oxygen reduction reaction in a PEMFC, J. Electrochem. Soc. **153**, A1955–A1963 (2006)

10.6 H. Gasteiger, W. Gu, R. Makhari, M.F. Matthias: Catalyst utilization and mass transfer limitations in the polymer electrode fuel cells, Electrochem. Soc. Meet., Orlando (2003)

10.7 J.S. Newman: *Electrochemical Systems*, 2nd edn. (Prentice Hall, Englewood Cliffs 1991)

10.8 N. Brandau: Analyse zur Zellinternen Befeuchtung eines Polymer-elektrolytmembran-Brennstoffzellenstapels (Logos, Berlin 2013)

10.9 R.B. Bird, W.E. Stewart, E.N. Lightfoot: *Transport Phenomena* (Wiley, New York 1960)

10.10 E.U. Schlünder: *Einführung in die Stoffübertragung* (Thieme, Stuttgart 1984), in German
10.11 E. Buckingham: On physically similar systems; Illustrations of the use of dimensional equations, Phys. Rev. **4**, 345–376 (1914)
10.12 H.D. Baehr, K. Stephan: *Wärme- und Stoffübertragung* (Springer, Berlin, Heidelberg 2006)

11. Calculations in Li-Ion Battery Materials

Michelle D. Johannes, Corey T. Love, Karen Swider-Lyons

Density functional calculations, or first principles calculations, are emerging as a critical tool for the evaluation of new lithium-ion battery materials. Density functional theory (DFT) is ideal for battery materials because it can be used to calculate critical materials properties, such as electronic and ionic conductivity, phase stability with lithium intercalation, and the roles of defects and dopants. The methods are illustrated herein by the evaluation of charge/discharge properties of two Li-ion battery cathode materials, $LiNi_{1/3}Co_{1/3}Mn_{1/3}O_2$ (NCM) and $LiNi_{1/3}Co_{1/3}Al_{1/3}O_2$ ($NCA_{1/3}$) and their comparison to a $LiCoO_2$ standard. We investigate the effect of substituting Al for Mn on the structural and electronic properties of the compounds at various levels of Li deintercalation and correlate these to performance properties observed in the laboratory. We find a calculated and observable upward shift in the voltage with Al substitution due to a shift in the oxidation levels of the electrochemically active ions during cycling. The results are corroborated by experimental results, in which we observe much lower specific capacity for NCA (despite its higher theoretical value) that can be attributed to a restricted voltage window during deintercalation. There is also a strong increase in resistive losses for NCA. A comparison of our density functional calculations and measured data indicates that this loss is due mainly to disruptive Ni/Li cation disorder. The partial density of states of the materials can be used to calculate their propensity to evolve O_2 when overcharged. DFT gives key insights into changes occurring at the atomistic level and can be used toward physical insights into both new and traditional materials.

11.1 **Using DFT to Calculate the Voltage of Layered Materials** 315
11.1.1 Background 315
11.1.2 Computational Methods 316
11.1.3 Experimental Methods 317
11.1.4 Experimental and DFT Results for NCM and $NCA_{1/3}$ 317
11.1.5 Conclusions 323

11.2 **PDOS Calculations of Oxygen Stability and Cycling Safety** 323
11.2.1 DFT Methods 324
11.2.2 PDOS of $LiCoO_2$ 324
11.2.3 PDOS of NCA 326
11.2.4 Conclusions 326

11.3 **Summary** 326

References 327

The ideal battery materials have high capacity, good stability in affordable materials, yielding high energy storage in a compact, long-lived battery. The energy of a battery is proportional to its operational voltage (power (P) = voltage (V) × current (I), energy = $\int P\mathrm{d}t$). The cathode (or positive electrode) materials should have high voltage and the anode materials should have low voltage to make a battery cell with the highest voltage. Additionally, they must have good electronic and Li-ion mobilities.

The numerous requirements of battery materials, coupled with advances in computational methods and computer speed, are making density functional theory (DFT) a cornerstone in battery research. DFT is a mean-field approximation to the many-body Schrödinger equation. Recent approximations that better account for non-mean-field or so-called *correlation* effects have been developed to accurately estimate electrode potentials and their interplay with the materials structure. The application of DFT is now being used to reveal information on battery materials properties, such as Li^+ conductivity, the impact of phase transformations, and understanding the effects of defects and dopants [11.1, 2], as illustrated schematically in Fig. 11.1

In this chapter, we focus on the application of DFT to metal oxide cathodes. The metal oxides used in lithium-ion battery cathodes require the hybridization of the d-bands from the metal cations with the s–p

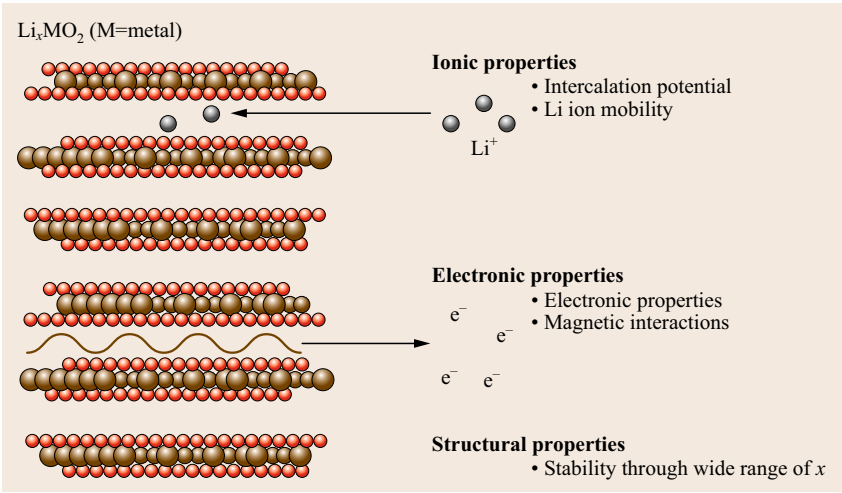


Fig. 11.1 Density functional theory can be used to determine and understand the ionic, electronic, and structural attributes of lithium metal oxide battery materials

bands of the oxygen anions. The crystal field splitting is dependent on the crystal structure, for example, octahedral or tetrahedral. An idealized energy level structure for a cation with 3d valence electrons in the presence of an octahedrally coordinated anion is shown in Fig. 11.2. The creation of such conceptual bonding structures has been discussed extensively by *Goodenough* [11.3], and is used as the first concept in the development of new battery materials [11.4]. The operational voltage is a function of changes in oxidation states of the transition metals with Li^+ content, and thereby changes in their hybridization, particularly with the s–p bands of the oxygen anions in oxide-based cathodes and anodes. The changes in lithium content, plus changes in metal oxidation state, result in mechanical strain and ultimately phase transformations. The voltage parameter is critical because of its above-mentioned correlation to power and energy.

DFT methods were applied by *Aydinol* and colleagues to lithium metal oxides and lithium metal sulfides [11.5]. They derived a simple relationship between the chemical potential of the Li^+ in the lattice and the open circuit voltage (OCV) of the cell as a function of the lithiation state of the anode and cathode materials. Their method provides a prescription for calculation of the OCV via relatively simple DFT calculations of total energy. Their work showed that long- and short-range order of the lithium ions influences the lithium chemical potential through differences in its free energy, as does the expansion/contraction of the host lattice.

Using this powerful methodology, this group went on to predict that doping the standard $LiCoO_2$ cathode material with Al to form $Li(Co, Al)O_2$ solid solutions would increase its voltage [11.1], albeit at the expense of capacity as Al cannot contribute electrons. They subsequently predicted the superior performance of a $LiMn_{0.5}Ni_{0.5}O_2$ material which, when created in the laboratory, matched the DFT predictions [11.6]. These predictions, subsequently verified by experiment are a demonstration of the power and usefulness of DFT in understanding and developing battery materials.

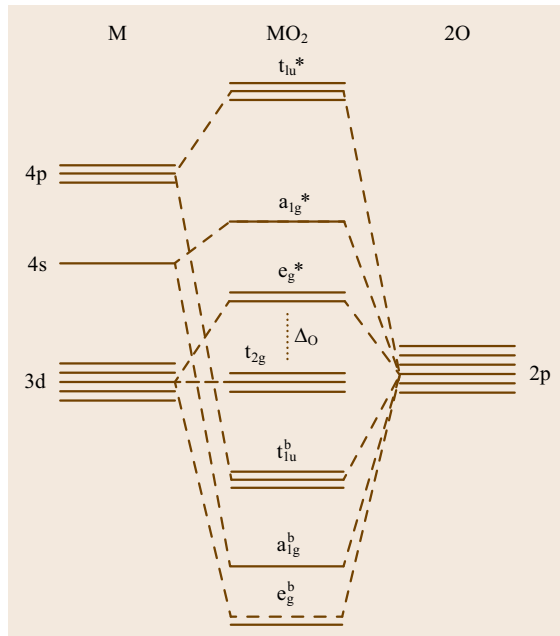


Fig. 11.2 Idealized band structure of an octahedrally coordinated metal oxide. The energy levels in the materials change as the Li content of materials changes and oxidation states of the metal cations change (after [11.5])

Some further materials properties that can be calculated using the DFT methodology include: electronic structure (band structure and density of states (DOS)), oxidation states, cell volumes, bond lengths, ionic mobility, and possibly even phase diagrams. Using the common DFT pseudopotential code, the Vienna Ab initio Simulation Package (VASP) [11.7, 8], DFT calculations have been carried out on 33 000 compounds by The Materials Project, a collaboration of the Massachusetts Institute of Technology and Lawrence Berkeley Laboratory. The results of these calculations are publicly available and are heavily sorted and cross-referenced for easy data mining [11.9]. The lithium battery explorer is a module associated with the materials project and uses crystal structures from the Inorganic Crystal Structure Database (ICSD) which are rapidly evaluated computationally for their voltage, stability, and lithium diffusivity using high-throughput computing many of which can be used for Li-ion batteries [11.9]. With the implementation of the Materials Project, a possible class of new cathode materials based on lithium carbonophosphate [11.10] has been discovered. Discovery of practical materials with the approach of large-scale computational modeling has not yet occurred, possibly due to the complexity of the environment that the material experiences in the battery and the inability of DFT to predict the kinetic activity of Li-ion charge transfer.

Aside from the high throughput and data mining approach to materials development, we contend that a major strength of the DFT methodology is its ability to help explain observable properties of batteries and pinpoint the microscopic origins of measurable performance metrics. Our own research on the application of DFT to battery materials stemmed from research on transition-metal-oxide superconductors, for example $LaFeAsO_{1-x}F_x$ [11.11] and $Na_xCoO_2 \cdot yH_2O$ [11.12–14]. The main difference between research on high-temperature superconductor materials and battery materials, which often overlap, are the variations in potential and lithium content that the materials experience during charging and discharging, which can now be dealt with by the methods developed initially by *Aydinol* [11.5].

In this chapter, we will show how DFT can be used to resolve the origin of ambiguous data, such as the voltage of a discharge curve, the source of capacity (or of capacity fade) and the loss of oxygen from a structure with overcharging. The application of DFT to the study of cathode battery materials with the $R\bar{3}m$ structure are illustrated herein with two practical examples: (1) understanding the impact of doping on the voltage and capacity of the nickel–cobalt derivatives of $LiCoO_2$ by replacing the manganese with aluminum in $LiNi_{1/3}Co_{1/3}Mn_{1/3}O_2$ (NCM) to make $LiNi_{1/3}Co_{1/3}Al_{1/3}O_2$ ($NCA_{1/3}$), and (2) predicting the stability of $LiCoO_2$ and $LiCoO_2$-derived materials to oxygen loss at high voltages. In both cases, observable experimental results are better understood through the computational picture of the electronic states of the materials, particularly as they change in Li content during charging and discharging. As is common in the DFT of Li-ion battery materials, all calculations are carried out with VASP [11.7] in the PAW [11.8, 15] formulation. We use the HSE06 hybrid functional as an approximation to the exchange-correlation functional [11.16].

11.1 Using DFT to Calculate the Voltage of Layered Materials

11.1.1 Background

$LiCoO_2$ is the standard material for Li-ion battery cathodes, and has a layered rhombohedral $R\bar{3}m$ structure with planes containing CoO_6 octahedra separated by planes of Li^+ as can be visualized in Fig. 11.3 and a nominal operational potential of 3.7 V [11.17].

The planar aspect of the materials allows electronic conduction through the network of CoO_6 octahedra and ionic mobility through the Li planes. The capacity of $LiCoO_2$ is somewhat limited because only 0.5 e^- can be intercalated per Co^{3+}/Co^{4+} couple without irreversible structural transformation. The global equation for charging and discharging $LiCoO_2$ to its full capacity is

$$Li_1Co^{3+}O_2 \underset{\text{Charge}}{\overset{\text{Discharge}}{\leftrightarrows}} Li_{0.5}(0.5)Co^{4+}(0.5)Co^{3+}O_2 + 0.5Li^+ + 0.5e^- . \quad (11.1)$$

The same planar $R\bar{3}m$ structure is shared by NiO_2, a nominally 4 V cathode material with the promise of higher capacity due to the availability of both the Ni^{2+}/Ni^{3+} and Ni^{3+}/Ni^{4+} couples [11.18]. $LiNiO_2$ has not found applicability as a practical material because of lack of cyclability caused by the Jahn–Teller

distortion imposed by low-spin Ni^{3+} on the NiO_6 octahedra, causing both structural and electronic changes as the Ni oxidation state changes during charge and discharge [11.19]. There is also interchange between the Li and Ni due to the extremely similar ionic radii of Li^+ and Ni^{3+} [11.20].

In layered oxide compounds with a single electrochemically active ion (Co or Ni), Al substitution can increase the voltage [11.21] and improve the capacity as a function of cycle [11.22]. Both these observed improvements could have their origin in greater Li-ion mobility due to an increase in the *c*-axis length that allows easier deintercalation of Li^+ and less resistance. For doped $LiNiO_2$, the Al has been shown to stabilize the layered structure [11.21] against Li/Ni interchange [11.20].

The benefit of the reversibility of the Co and the capacity and high voltage of Ni in the $R\bar{3}m$ structure are combined in NCM. $LiMnO_2$ is unstable toward transition to a spinel structure due to mobile Mn^{3+} ions [11.23]. However, when included as a partial component in NCM, the Mn takes a much more stable 4^+ valency and the compound can be cycled without a structural transition [11.24].

Aside from already good cycleability and capacity, NCM is very promising as a *manipulable* starting material. The proportions of each transition metal, Ni, Co, and Mn, can be adjusted and various other elements, such as Fe, Ti, or Al, can also be incorporated [11.25, 26]. NCM has been lightly doped with Al to produce $LiNi_{0.8}Co_{0.15}Al_{0.05}$, commonly called NCA, another potentially useful cathode material, particularly for high-power applications [11.25]. The rich possibilities for improvements through selective substitution make NCM an exciting starting point for manipulating materials with DFT, as the impact of cation substitution can be readily predicted with calculational methods.

More recently, a full substitution of Al for Mn in NCM has been achieved to make $LiNi_{1/3}Co_{1/3}Al_{1/3}O_2$ and shown to cycle successfully [11.27]. While this new form of NCA is not a practical material, our objective is to compare it to NCM using DFT to discover what effects full substitution of Mn^{4+} by Al^{3+} has on cycling properties and electronic structure, as the Mn^{4+} remains in its $4+$ state is not involved in charge storage in the NCM [11.28], but does impact its electronic structure. To provide charge balance, the $NCA_{1/3}$ adopts Ni^{3+} rather than Ni^{2+}, making more changes to the electronic structure of NCM. We designate the new $LiNi_{1/3}Co_{1/3}Al_{1/3}O_2$ material as $NCA_{1/3}$ to distinguish it from its practical predecessor, $LiNi_{0.8}Co_{0.15}Al_{0.05}$. Replacing Al^{3+} for Mn^{4+} should shift the sequence of redox couples and raise the voltage of the material, and should be predicted by DFT and measurable on the actual material.

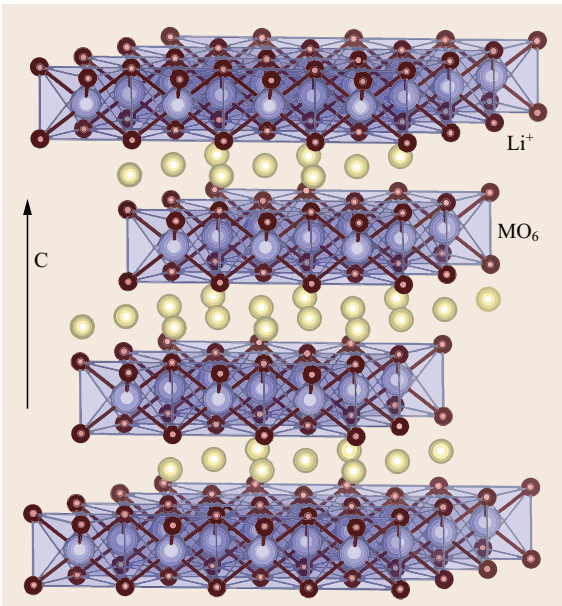


Fig. 11.3 $R\bar{3}m$ structure of $LiCoO_2$, $LiNiO_2$, NCM, and $NCA_{1/3}$ noting the direction of the *c*-axis. Planes of M-O_6 octahedra are separated by planes of Li^+

11.1.2 Computational Methods

For all calculated materials, crystal structures (as visualized in Fig. 11.3 for $LiCoO_2$) were created using the standard $R\bar{3}m$ space group. From this starting structure, both lattice constants and ionic positions were fully relaxed. The creation of a crystal structure and subsequent structural relaxation is done separately for each Li concentration. Total energies are calculated using a $10 \times 12 \times 10$ *k*-point mesh in the Brillouin zone of the six-atom unit cell. For NCM and $NCA_{1/3}$, our full formula units are $Li_6Ni_2Co_2Mn_2O_6$ and $Li_6Ni_2Co_2Al_2O_6$. With no experimental evidence to guide our choice of the transition-metal cation positions within the plane, we chose a simple ordered structure in which each triangular unit within the plane contains one of each cation type. A previous computational study [11.29] has shown that this cation configuration has a lower energy than other ordered configurations, making it more thermodynamically favorable, though there is no guarantee that any long-range order between cations necessarily exists experimentally.

The voltage is best calculated using the method developed by *Aydinol* et al. [11.5]. The material voltage is calculated by taking the difference between the total

energies of compounds with two different Li concentrations, and then subtracting the total energy of metallic Li. This gives the average voltage in the range of Li contents with the two chosen compounds as endpoints.

The central approximation in the DFT methodology is the exchange-correlation potential energy term. For materials with delocalized or itinerant electrons, the standard local density approximation (LDA) or generalized gradient approximation (GGA) is sufficient. However, in materials with very localized electrons, such as the 3d electrons of the metal ions that serve as redox centers in Li-ion battery materials, these approximations can fail badly, yielding voltages and bandgaps that are significantly lower than experimental values. Several remedies are available, most notably the LDA+U methodology [11.30, 31], which provides an element-specific shift of the localized bands that, when applied to metal-oxide cathode materials, gives good results for computational voltages and structural parameters [11.5]. The LDA+U procedure is computationally efficient, but requires the choice of an input parameter U, which varies with chemical element and valency and to which the position of the d bands in materials containing 3d elements is extremely sensitive. Erroneous establishment of these U values can shift the bands relative to one another and misrepresent the sequence of redox couples in the material and badly skew the degree of metal/oxygen covalency.

A recent development is that of so-called *hybrid functionals* that calculate the exchange part of the potential *exactly* for the part of charge density near the ion core where electrons are localized and use the standard GGA approximation farther away where electrons are delocalized. Although hybrid functionals are at least an order of magnitude more computationally expensive than other approximations, they have been shown to correctly reproduce voltages in metal-oxide materials and to correctly establish the position of d bands relative to one another and relative to oxygen bands [11.32], all quantities of importance to this work. Therefore, all calculations presented here employ the HSE06 hybrid functional [11.16] as implemented in the VASP code.

11.1.3 Experimental Methods

The preparation of the materials and experimental methods were straightforward and have been described elsewhere but are included here for clarity [11.33]. The NCM and $NCA_{1/3}$ were synthesized from hydroxide coprecipitates and heated to 800 °C under ultrahigh purity O_2 using previously described methods as guidelines [11.34, 35] and then made into pouch cells versus Li^+/C anodes.

Three separate electrochemical experiments were performed on the NCM and $NCA_{1/3}$ pouch cells for comparison to the DFT results:

1. Charge/discharge data. The cells were cycled at a constant C/5 current rate between cutoff voltages of 2.5 and 4.5 V at room temperature using a Maccor 2300 battery tester. The charge/discharge current was adjusted according to the mass of active material and the theoretical capacities of NCM (280 mAh g^{-1}) and $NCA_{1/3}$ (309 mAh g^{-1}).
2. Differential capacity versus voltage. The NCM and $NCA_{1/3}$ pouch cells were cycled up to 10 cycles at a slow rate of 0.1 mA cm^{-2} (approx. C/20) between 2.5 and 5.0 V. The slow discharge rate was used to account for variations in reactions kinetics, as the $NCA_{1/3}$ is expected to have slower kinetics than the NCM. Increasing the operating voltage for similar materials above 4.7 V has been shown to allow significantly higher utilization of the active material [11.36]. The voltage window increased to 5.0 V to elucidate redox features occurring near the upper cutoff voltage.
3. Cyclic voltammetry. The cells were cycled five times between 2.5 and 4.6 V (versus the Li metal reference electrode) at a constant voltage sweep rate of 0.1 mV s^{-1} to identify changes in the redox peaks with cycling, using a PAR236 potentiostat.

11.1.4 Experimental and DFT Results for NCM and $NCA_{1/3}$

The X-ray diffraction (XRD) results for both the NCM and $NCA_{1/3}$ were indexed according to the $R\bar{3}m$ structure. The separation of 006/102 and 108/110 peaks indicate a well-crystallized structure observed for both compounds. The measured unit cell volumes were 101.3 and 97.9 $Å^3$ for NCM and $NCA_{1/3}$, respectively, indicating that the substitution of Al^{3+} with an ionic radius of 0.53 Å in an octahedral site [11.37] for the slightly larger Mn^{4+} ions (ionic radius of 0.54 Å [11.37]) causes the unit cell to collapse slightly in both the a- and c-directions. The main reason for the smaller volume of the $NCA_{1/3}$ unit cell is attributable to the replacement of Ni^{2+} ions in the NCM (with Mn^{4+}) by smaller Ni^{3+} ions in the $NCA_{1/3}$ to offset the 4+ oxidation state of the Mn in the NCM with the 3+ oxidation state of the Al in the NCA. The swap causes a contraction in the in-plane (a) direction. Ni^{2+} has an ionic radius of 0.7 Å versus 0.56 Å for low-spin Ni^{3+}. This same structural contraction has been reported previously for $NCA_{1/3}$ prepared both via a water-in-oil emulsion technique [11.27] and by a sol–gel method [11.38]. Table 11.1 shows that the

Table 11.1 Experimental and theoretical structural parameters for NCM and $NCA_{1/3}$

	a (Å)	c (Å)	Volume (Å^3)
NCM (exp)	2.86	14.26	101.3
NCM (theory)	2.83	14.00	97.17
$NCA_{1/3}$ (exp)	2.82	14.18	97.90
NCA (theory)	2.78	13.89	93.37

experimental results match well versus the measured lattice parameters calculated for the idealized crystal structures with uniformly distributed cations.

The structural changes induced by replacing the Mn in NCM with Al are relatively minor, resulting only in a structural contraction. Importantly, the incorporation of Al in NCM shrinks the lattice along the *c*-axis, whereas in $LiNiO_2$ or $LiCoO_2$, Al induces a *c*-axis expansion. The mobility of Li ions within the two dimensional *a*–*b* plane is related to the interplanar distance along the *c*-axis, with greater distance giving rise to greater mobility. Thus, the Al-induced contraction is counterproductive in terms of increasing the Li-ion diffusion during charge/discharge.

The Electronic Structure of NCM

The basic electronic structure of NCM has been presented several times in the literature [11.28, 29] and our results for the DOS, identification of redox couples, and magnetic properties are in excellent agreement with these previous works. The known basic deintercalation properties are shown in Fig. 11.4, and written in (11.2)–(11.5). When NCM is at full lithiation, or fully discharged, its formulation is $LiNi_{1/3}Co_{1/3}Mn_{1/3}O_2$ and the cation valencies are Ni^{2+},Co^{3+} and Mn^{4+}. The half-filled Ni e(g) complex is at the top of the one-electron energy spectrum, which gives $Ni^{2+/3+}$ as the first redox couple accessed at the beginning of the charge cycle. Once all Ni has been oxidized to 3+, further electrons are withdrawn from the Ni^{3+}/Ni^{4+} couple. When all Ni ions are 4+, the Co becomes the electrochemically active ion, oxidizing to 4+. This progression of redox couples has also been demonstrated using XANES spectra [11.27, 28, 39] and is well accepted to be correct. As $Li_x < 0.1$, the O^{2-} can serve as a source of electrons and be reduced to O_2, as has been confirmed experimentally in related materials, such as $LiCoO_2$ [11.40, 41] and layered Mn–Ni–O compounds [11.42]. Computational prediction of this irreversible oxidation step at very high-oxidation states when the Co^- 3d and O 2p states approach the same energy level is an important application of DFT [11.43] and will be discussed below.

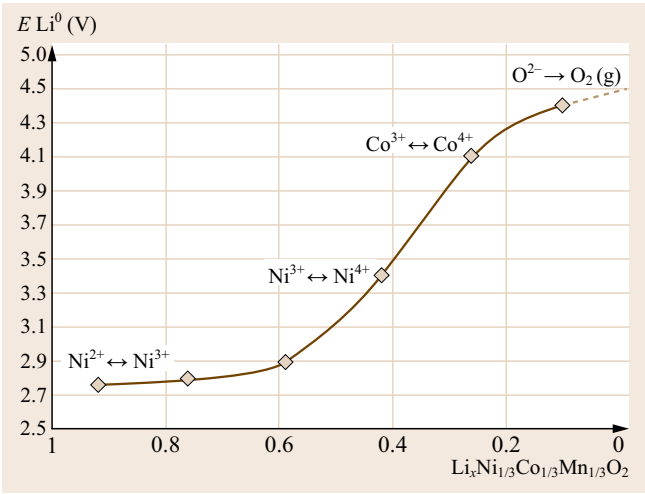


Fig. 11.4 Progression of metal oxidation states in NCM as the material is charged (progression from $Li_x = 1{-}0$) (after [11.28])

The Mn^{4+} does not contribute to the NCM capacity. As $Li_x < 0.1$, electrons can be withdrawn from the O^{2-} sites and be oxidized to O_2 gas [11.43],

$$Ni^{2+} = Ni^{3+} + Li^+ + e^- , \quad (11.2)$$

$$Ni^{3+} = Ni^{4+} + Li^+ + e^- , \quad (11.3)$$

$$Co^{3+} = Co^{4+} + Li^+ + e^- , \quad (11.4)$$

$$2O^{2-} = O_2 + 2e^-(g) . \quad (11.5)$$

The electronic states belonging to the 3d elements in NCM are well localized to their respective elemental sites and the crystal field split energy levels are known. Therefore, one can deduce the valency of each component cationic element by examining its magnetic moment. For instance, a low-spin Ni^{3+} ion will have a single unpaired electron in the e_g complex, giving rise to a spin moment of $\frac{1}{2}$, whereas a Co^{3+} ion will have a completely filled t_{2g} complex yielding no moment at all. Each integer change in valency produces a half-spin change in the calculated moment. Using this method, we find that our calculations reproduce the Ni^{2+}/Ni^{3+} and Ni^{3+}/Ni^{4+} sequence of redox couples previous seen by *Hwang* et al. [11.28] with a simpler DFT methodology. It is interesting to examine the physical structure of the compound when the Ni ions are in the 3+ valency state. For the ground state low-spin configuration, the e_g antibonding complex is half filled. This is a canonical Jahn–Teller state in which the system responds to the high-energy half-filled configuration of the electronic structure by physically distorting to change the energy level hierarchy. The calculations show that the octahedra surrounding the Ni ion indeed distort, forming two long bonds and four short bonds. This lowers the symmetry and splits the e_g doublet; the lower state is filled and the upper state is emptied. The calcu-

lated Ni–O bond lengths are 4×1.88 Å and 2×2.05 Å. The calculated Mn–O and Co–O bonds are more uniform, between 1.88 and 1.91 Å, reflecting the non-Jahn–Teller electronic configurations of the Mn and Co ions.

It is important to note that, without applying some kind of correction to the standard GGA/LDA functional, a local Jahn–Teller symmetry breaking, such as is necessary to correctly reproduce the experimental electronic structure cannot be reproduced in DFT. In cases where both Ni^{2+} and Ni^{3+} or Ni^{3+} and Ni^{4+} exist simultaneously, these functionals yield unphysical $Ni^{2.5+}$ or $Ni^{3.5+}$ valencies and an erroneously metallic ground state that badly skews the voltage calculation. The HSE06 functional, on the other hand, produces the local distortion in good agreement with experimental measurements of bond lengths and for all combinations of Ni valencies.

In addition to understanding the redox sequence, we can gain significant insight into the charge/discharge process by looking at the DOS. The DOS measures the number of states available at each energy in the material. Electrons in the system fill these states, starting with those at the lowest energies and proceeding up to the Fermi energy (E_F). In our calculations, we shift all energy values such that E_F is at 0 eV. When a Li^+ ion is withdrawn during charging, its associated e^- comes from the highest filled energy state, located just below E_F (to the left of 0 eV in the DOS plots). The most recently emptied states are the lowest unfilled states above E_F (to the right of 0 eV in the DOS plots). The DOS can be projected onto each ion separately, yielding a partial DOS or PDOS. One can therefore look at the states below E_F to see from which constituent ion electrons will be withdrawn from in the next step of charging. Similarly, one can look above E_F to see where electrons in the previous step of charging have come from.

In Fig. 11.5, we show the fully discharged PDOS of NCM with spin majority (*up*) states plotted on the positive *y*-axis and spin minority (*down*) states plotted on the negative *y*-axis. The highest filled state (from which electrons will be withdrawn during charging) is mainly spin up Ni with an admixture of spin up Co.

The mixed Ni and Co character of the highest occupied state reflects the fact that the in-plane metal ions are bonded together [11.28] and that this bonding affects the state from which electrons will presumably be withdrawn. However, the actual extraction of electrons at the beginning of the charge cycle changes the valency of the Ni ion *only*, leaving the Co oxidation state unchanged. This can be seen by looking at the magnetic moment of Ni and Co and noting that the Ni moment changes from spin 1 to spin $\frac{1}{2}$, while the Co moment remains unchanged at 0. In Fig. 11.6, the PDOS for a compound of stoichiometry $Li_{0.875}Ni_{1/3}Co_{1/3}Mn_{1/3}O_2$ is shown, where it can be clearly seen that the now empty states located about above E_F contain negligible Co character. It must be the case that, as the electron is removed from this highly mixed state, some combination of one-electron localization and structural relaxation causes the Co-derived levels to fall in energy faster than the Ni levels, re-establishing the Co^{3+} valency. The states at E_F again show strongly hybridized character, but again, once fur-

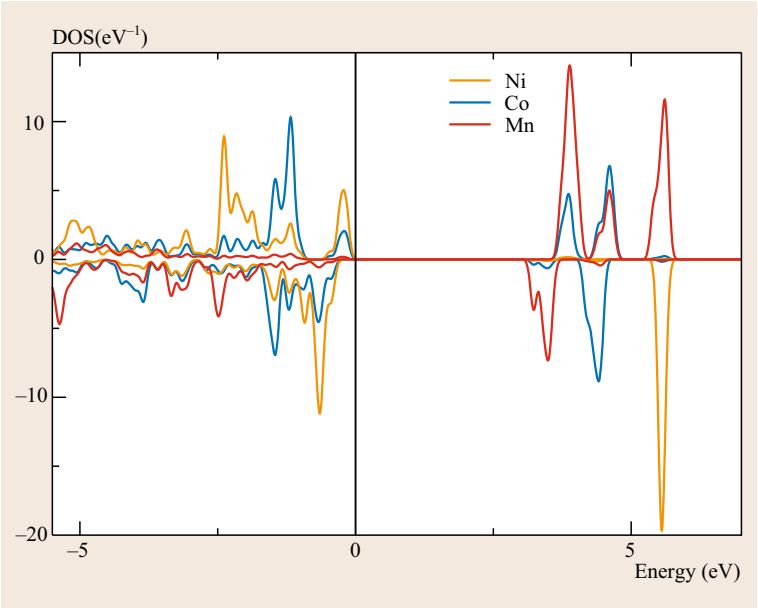


Fig. 11.5 Density of states for Co, Mn, and Ni in $LiNi_{1/3}Co_{1/3}Mn_{1/3}O_2$ with spin *up* plotted on the positive *y*-axis and spin *down* on the negative *y*-axis. All energies have been shifted such that E_F appears at 0 eV. The highest filled states correspond to Ni (hybridized with Co)

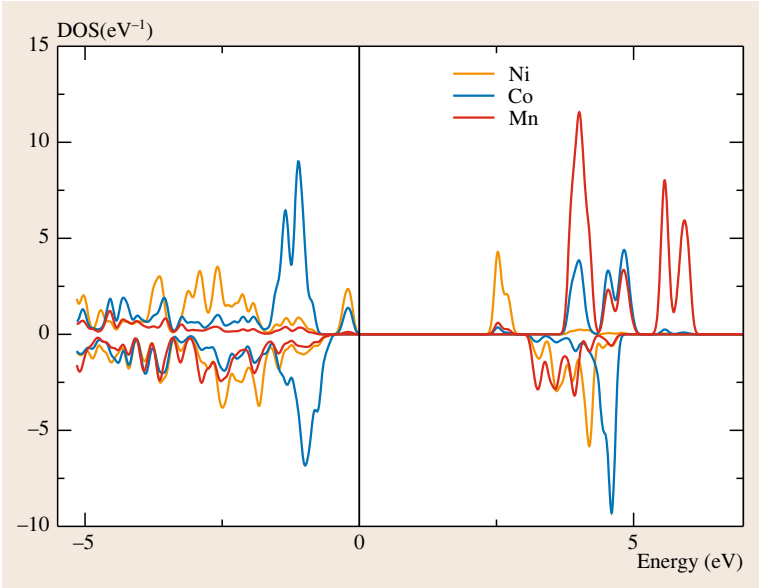


Fig. 11.6 Density of states for Co, Mn, and Ni in $Li_{2/3}Ni_{1/3}Co_{1/3}Mn_{1/3}O_2$ with spin *up* plotted on the positive *y*-axis and spin *down* on the negative *y*-axis. All energies have been shifted such that E_F appears at 0 eV. Hybridization with Co is still relatively strong in the lower (filled) state

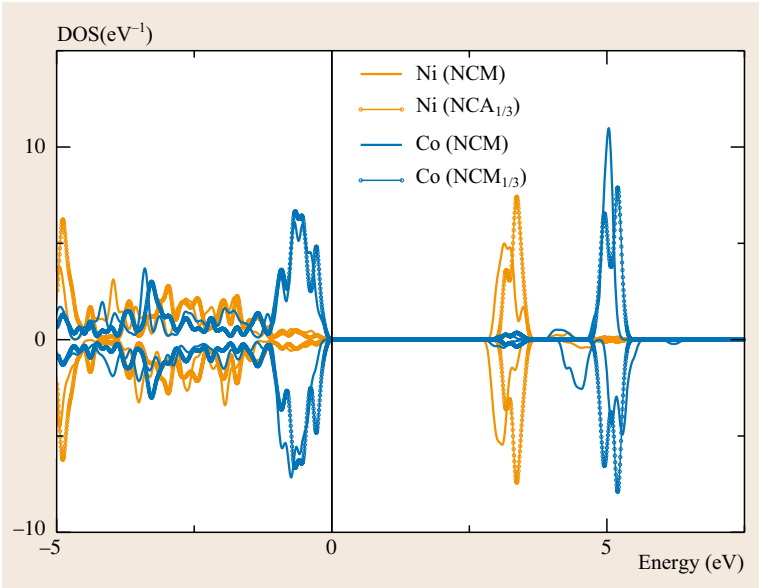


Fig. 11.7 The DOS for $Li_{1/3}Ni_{1/3}Co_{1/3}Mn_{1/3}O_2$ (*solid*) and $Li_{2/3}Ni_{1/3}Co_{1/3}Al_{1/3}O_2$ (*dashed*). Both compounds contain Ni^{4+} and Co^{3+} ions, shown in *orange* and *blue*, respectively (the Mn/Al states present in NCM/$NCA_{1/3}$ are left out for reasons of clarity). Ni and Co complexes of each compound lie nearly precisely on top of one another, indicating that the substitution of Al^{3+} for Mn^{4+} has almost no effect on the electronic structure except to shift the system by one electron

ther electrons are removed, only the Ni ion changes valency.

Electronic Structure of NCA

The substitution of Al (3+) for Mn (4+) requires further oxidation of either the Co or Ni ion compared to the states found in NCM. We know from the delithiation studies of NCM (previous section) that Ni will be oxidized before Co. Therefore the discharged $NCA_{1/3}$ compound is expected to have valencies: Ni^{3+}, Co^{3+}, and Al^{3+}, and indeed, our calculations show exactly this configuration. The addition of Al, therefore, essentially shifts the de-lithiation sequence by one step in the charging progression. Since the Ni^{2+} oxidation state does not exist in $NCA_{1/3}$, the first redox couple is Ni^{3+}/Ni^{4+} and the second couple is Co^{3+}/Co^{4+}, corresponding the second- and third-redox couples of NCM. To demonstrate this fact, we show the PDOS for $Li_{2/3}Ni_{1/3}Co_{1/3}Al_{1/3}O_2$ in comparison to $Li_{1/3}Ni_{1/3}Co_{1/3}Mn_{1/3}O_2$in a single plot in Fig. 11.7. Ni and Co ions in these two compounds have the same oxidations states and their complexes lie

nearly directly atop one another. Thus, our calculations suggest that NCM compound and the $NCA_{1/3}$ compound should have extremely similar voltage profiles during steps [11.3, 4], though these are shifted from each other with respect to Li content.

The final charge step in $NCA_{1/3}$ would be withdrawal of electrons from the Co^{4+}/Co^{5+} couple. Our calculations show that the final 4+/5+ couple is outside the experimental voltage window, that is, above the 5 V cutoff of the electrolyte, and therefore inaccessible. As we will discuss in a later section, the states at E_F prior to the final charge step are predominantly oxygen-like, with minority Co character which is an indication of electronic instability and safety issues. $NCA_{1/3}$ therefore has *less* accessible electrons and a *lower* practical capacity than NCM, even if a higher electrochemical window electrolyte could be found.

Comparison of Calculated and Measured Voltage Profiles

Figure 11.8a,b shows the actual voltage versus Li content as extracted from differential capacity versus voltage (dQ/dV) measurements and compares against the DFT calculated voltages at several values for Li_x. We expect to see plateaus corresponding to the three redox couples accessed during charge/discharge; three for NCM (11.2)–(11.4) and two for $NCA_{1/3}$ (11.3)–(11.4). These can be reasonably identified in the experimental curves. The computational points are in excellent agreement with the measured values at the discrete points where they have been placed. DFT voltages are computed as an average between two specific Li concentrations; we place the calculated point at the midpoint between the two selected Li contents. We use Li concentrations Li_x of $x = 1$, 0.833, 0.667, 0.500, 0.333, 0.167, and 0.0, resulting in placement of the calculated voltages at $x = 0.917$, 0.75, 0.584, 0.417, 0.250 and 0.084. For NCM, the $Ni^{2+/3+}$ plateau is represented by the lowest point (in this case no error is incurred in calculation), and the $Co^{3+/4+}$ plateau is can be seen in the final two data points. In the computational data, the various voltage plateaus are quite obvious for both compounds and the corresponding redox couples, as identified from changes in the individual magnetic moments of the constituent ions, are given above their respective plateaus. For both compounds, our calculated values fall mainly between the charge and discharge lines of the experimental curves. DFT calculations more properly correspond to open-circuit voltage measurements than to cyclic voltammetry measurements since the former lack any IR loss information, while the latter naturally contain all IR loss that exists in the system. Despite this conceptual difference, it is quite clear that the DFT voltage calculations have captured the essential underlying electronic mechanism by which redox couples are accessed and has accurately assessed the redox sequence as well as the voltage profile.

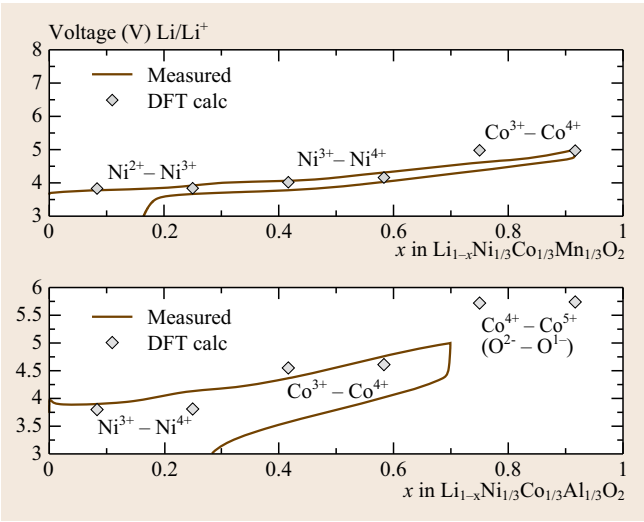


Fig. 11.8a,b Voltage versus Li content for NCM and $NCA_{1/3}$. *Solid lines* are experimental data extracted from dQ/dV measurements and discrete points are density functional calculations

As expected from the DOS calculations, the shape of the calculated NCA curve looks very much like the calculated NCM curve with a rightward shift along the x-axis (signifying the one less original valence electron). It is interesting to note that, according to calculation, the voltage window, even when opened to 5.0 V is still too low to fully access the Co^{4+}/Co^{5+} couple that sits at around 5.5 V or higher. This, then, is the origin of the lower measured specific capacity, rather than any intrinsic limitation (such as structural transition or collapse), though our calculations also reveal that oxygen loss will be a significant problem during this part of the charge cycle, as we discuss in the safety section.

In contrast to the good agreement achieved between calculation and dQ/dV experiments for the voltage profile, we see large differences in IR loss between the two compounds. Our calculations directly address only the electronic conductivity (see discussion above) and not ionic mobility. A compression of the c-axis can in principle be detrimental to Li-ion mobility, but the very small decrease we calculate and observe (only about 0.6–0.7%) to produce the more than factor of twofold increase we measure in IR loss. The effect of Al (compared to Mn) could also have a deleterious effect by increasing the diffusion barrier for Li to move through the plane (calculations to determine this effect are currently underway). However, the most obvious culprit is Ni/Li disorder, as is always observed in $LiNiO_2$. The replacement of Mn by Al results in an initial valency

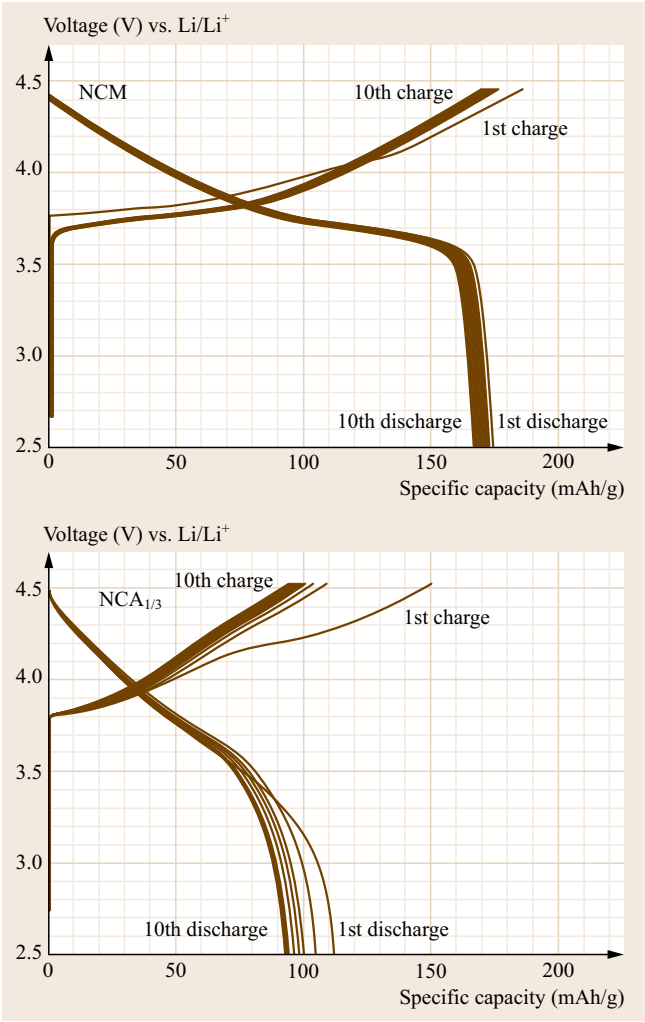


Fig. 11.9 The first 10 charge and discharge cycles for NCM and $NCA_{1/3}$ between 4.5 and 2.5 V. $NCA_{1/3}$ has significant capacity loss on the first charge cycle. NCM is stable with respect to its capacity and voltage plateau. The voltage of the $NCA_{1/3}$ increases as its capacity decreases

of 3+ for Ni ions (instead of 2+ as in NCM). During synthesis or during deintercalation, this leads to easy switching of Ni/Li positions or to Ni migration into the Li plane. Once located in the Li plane, even a small amount of Ni can severely reduce the efficiency of Li-ion withdrawal.

Having inferred from the comparison between our data and our calculations that Ni/Li disorder is likely to exist, we carefully re-analyzed our x-ray diffraction (XRD) data for evidence of Ni in the Li plane. The amount of Ni in the Li plane can be gauged by the ratio I003/I104. The higher this ratio, the less cation disorder between planes [11.44]. A previous evaluation of NCM found I003/I104 between 1.38 and 1.42 depending on the annealing temperature [11.44]. Our value is I003 /I104 = 1.20 for NCM and 1.14 for $NCA_{1/3}$. This indicates that the Ni/Li mixing in $NCA_{1/3}$ is indeed stronger than in NCM, confirming our hypothesis. It is worth noting that other studies, in which Al was substituted for Co in NCM showed a decrease in site disorder [11.36, 45]. This shows that the presence of Al^{3+} ions probably tends to stabilize the ordered, layered structure. Unfortunately, this desirable effect is offset (and in fact overwhelmed) when Al is substituted at the Mn site due to the *side effect* of shifting stable Ni^{2+} ions to unstable Ni^{3+} ions. An increased site disorder as a function of Ni^{3+} ions was also seen by *Kosova* et al. In mixed transition metal compounds without Al [11.44]. Because the difference between NCM and $NCA_{1/3}$ is obvious even prior to cycling, the disorder likely occurs during synthesis and not during cycling, and there is hope that a different synthesis method could result in a more ordered compound, thereby reducing the IR loss, as was shown for instance by *Kang* et al. [11.6].

Cycling Behavior

Figure 11.9 shows the first 10 cycles for NCM and $NCA_{1/3}$. The initial charge curves for both NCM and $NCA_{1/3}$ were uniquely different from the 2–10 charge profiles. The first-charge specific capacities of 148 and 191 mAh g^{-1} for $NCA_{1/3}$ and NCM and first discharge capacities of 111 and 178 mAh g^{-1} for $NCA_{1/3}$ and NCM correlate to an irreversible capacities of 25 and 6.8%, respectively. Such irreversibility is common for electrochemical cycling and is likely due to the existence of a two-phase de-insertion mechanism. However, it should be noted that the voltage window was not great enough to extract the same number of Li ions from $NCA_{1/3}$ as from NCM (see 3 where even at 5 V, only ≈ 0.8 electrons are removed from $NCA_{1/3}$). This explains most, though not all, of the lower first charge capacity of $NCA_{1/3}$ despite its higher theoretical capacity. $NCA_{1/3}$ had a greater degree of specific capacity loss on the 10th cycle and 16% compared to 3.4% for NCM. However, both coulombic efficiencies on the 10th cycle were relatively high 98.8% for $NCA_{1/3}$ and 98.7% for NCM as can be seen in Fig. 11.10.

Two charge peaks appear in the cyclic voltammetry (not shown) initial cycle for $NCA_{1/3}$ (3.90 V, 4.17 V) and NCM (3.80 V, 4.04 V). For NCM, this second charge peak slowly diminishes with cycling until it ultimately vanishes during the 10th cycle. A single discharge peak is for NCM at 3.75 V while a single identifiable discharge peak for $NCA_{1/3}$ is indistinguishable. The polarization inferred from the change in peak voltage during charging and discharging for NCM is

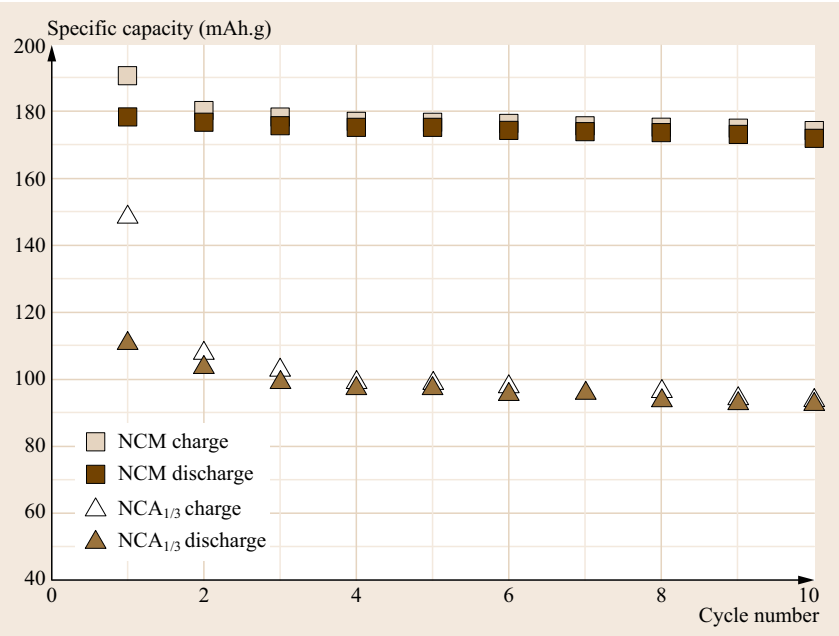


Fig. 11.10 Specific capacity fade (loss) as a function of cycle number for NCM and $NCA_{1/3}$. Losses after the first cycle are predictably large for both materials but subsequent losses are small

small, 0.06 V, indicating the existence of a stable structure. The IR loss associated with charging to 5 V is 210–540 mV for NCM and $NCA_{1/3}$, respectively. It is notable that the charge peak shifts right (upward) for $NCA_{1/3}$ with each successive charge, but is extremely stable for NCM. This is reflected in Fig. 11.9 where the plateau of the $NCA_{1/3}$ charge curve rises as its discharge capacity decreases, while both the plateau and capacity remain very steady for NCM. The shift in voltage indicates that the Li is increasingly difficult to remove from $NCA_{1/3}$ with repeated cycling. This could be attributed to Ni in the Li layer that becomes less mobile as it finds the lowest energy configuration. Density functional calculations reported elsewhere [11.46] show that such Ni anti-site defects in layered $R\bar{3}m$ structures have a very low formation energy when Ni has a 3+ valency, but have a higher formation energy when Ni has a 2+ valency. These defects are known to be extremely prevalent and perhaps even unpreventable in $LiNiO_2$ [11.47] making their presence in $NCA_{1/3}$ highly likely.

11.1.5 Conclusions

We conclude through this process that the advantage of the higher voltage of the $NCA_{1/3}$ versus NCM is offset by the decrease in capacity and a greater IR loss shown in Fig. 11.7. Our calculations indicate that the voltage window used during cycling is too restrictive, though necessarily so because of electrolyte stability, to allow withdrawal of all Li ions from NCA, resulting in the smaller specific capacity. The IR loss cannot be attributed to any change in electronic or macroscopic structural properties and is therefore very likely due to interplanar cationic disorder (Ni ions found in the Li plane). The DFT results are buttressed by the observable results from XRD analysis of the materials, which confirms that cationic disorder is increased in $NCA_{1/3}$ compared to NCM. As we will show, in the mixed-element compounds studied here, Al induces a contraction of the *c*-axis, making improvement through increased Li-ion mobility unlikely, as seen in previous theoretical studies [11.21, 22].

11.2 PDOS Calculations of Oxygen Stability and Cycling Safety

Another valuable capability provided by DFT is to determine the M versus O PDOS with decreasing lithium content, which can be used to predict a material's propensity toward O_2 loss during overcharge [11.43]. Layered transition metal materials may have the propensity to lose O_2 when over charged because of increasing overlap of the metal 3d states band with the top of the O^{2-} 2p band as the metal is oxidized as illustrated for Co in Fig. 11.11. Once metal bands are equal or lower in energy than oxygen bands, the O^{2-}

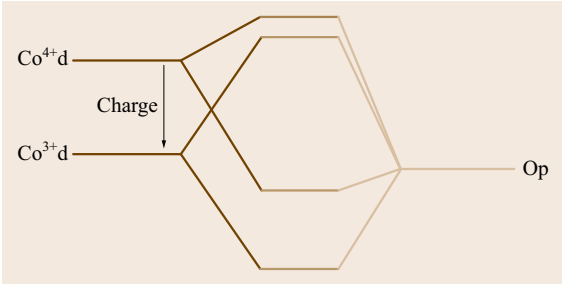


Fig. 11.11 The energy levels of the Co ions decrease as they are oxidized and approach that of the O p bands, making both ions available for oxidation (after [11.43])

states, rather than the desired metal redox couple, become available for oxidation and are oxidized to O_2 (g) (11.5). Liberated O_2 can exothermically react with the organic electrolyte, ultimately leading to a catastrophic fire [11.48]. The O_2 loss is also irreversible, which results in capacity fade as O is lost from the structure, even if only a small fraction of the structural O is oxidized. Since the position of metal 3d bands decreases with increasing atomic number Z, due to increased Coulomb attraction with the nucleus, this undesirable oxidation of O^{2-} states becomes more likely as one moves right along the 3d transition metal row of the periodic table. For $LiCoO_2$, such oxidation has been observed at very high charge states [11.41]. Even when the Co-containing compound contains Mn and Ni fractions, the same limitation of Co–O covalency occurs during charging [11.49].

11.2.1 DFT Methods

In order to be a useful tool to determine how the M–O covalency changes with charging (delithiation), DFT must accurately reproduce the energy positions of the metal and oxygen bands, especially in relationship to one another. Unfortunately, this relative position can depend rather sensitively on the necessary approximation to the exchange-correlation portion of the potential [11.5], as discussed in Sect. 11.1.2. For maximum accuracy, we again choose the HSE06 hybrid functional. This method applies a correction to *all* the electronic states within a material, avoiding a problem with the LDA+U methodology wherein only the metal states are shifted and covalency is often overestimated. A previous work, using valence band X-ray photoemission spectroscopy in comparison to DFT spectra, demonstrates that applying this shift correctly has important ramifications for the states at E_F and that the HSE06 functional outperforms the LDA+U methodology and rather spectacularly reproduces the experimental spectra [11.32].

Previously, *Laubach* et al., reported the PDOS for $LiCoO_2$ and $LiNiO_2$, noting the change in the M and O contributions with changes of lithiation, and validating the results with valence band measurements [11.50]. By their calculations, the Co PDOS was always above the O PDOS at the Fermi level, but there was extensive hybridization between the Co 3d and O 2p states at $x < 0.5$, suggesting the opportunity for the removal of electrons from Co–O d–p hybrid states and the oxidation of O^{2-} anions. We have reported elsewhere the PDOS contribution of the M and O states in four cathode materials ($LiCoO_2$, Li_2RuO_3, Li_2CuO_2, and $LiFePO_4$) in two states of lithiation (charge): fully lithiated (discharged) and highly delithiated (charged) [11.43]. We find that PDOS calculations predict that oxygen bands overhybridize with metal bands resulting in oxygen-like character at E_F in Li_2CuO_2, which is known to lose O_2 [11.51]. On the other hand, the PDOS of LiFePO4, which is known to be very safe during over charging and not susceptive to O_2 loss [11.52, 53], indicate that states at E_F are solidly Fe-like with very minor oxygen character. The correspondence between the measured tendency toward oxygen instability and the calculation of dominant oxygen character at E_F demonstrates that a relatively simple calculation of the PDOS using DFT with a suitable exchange correlation functional can provide valuable safety information about potential transition metal-based cathode materials.

Herein we summarize our previous work for $LiCoO_2$ along with calculations of the PDOS of $NCA_{1/3}$ compounds. For simplicity in these calculations, we combine spin-up and spin-down states into a single spectrum along the positive *y*-axis. For the $NCA_{1/3}$ calculations, we also combine the PDOS of Co, Ni, and Mn together and distinguish only between metal and oxygen states.

11.2.2 PDOS of $LiCoO_2$

While typically only 0.5 Li ions and associated electrons are removed experimentally from $LiCoO_2$ (11.1), we computationally extract all the electrons to investigate what happens to the electronic stability. As shown in Fig. 11.12, the resulting PDOS indicates that for $LiCoO_2$, the states at E_F are predominantly Co-derived. As electrons begin to be removed, the hybridization (covalency) between Co and O increases (not shown), but the Co states remain the majority. At full *delithiation*, as seen in Fig. 11.10 (middle panel), the emptied states above E_F that represent the Co^{3+}/Co^{4+} redox couple are mostly Co-like, indicating that the electrons have been removed safely. However, the new states at E_F have a very high mixture of O. Although there is no Li left to remove from the system, we can use a com-

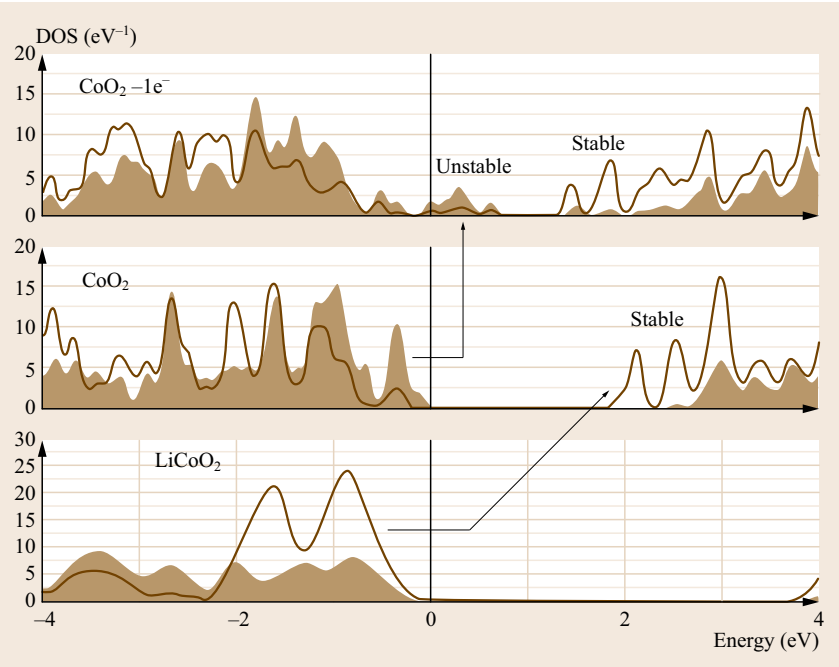


Fig. 11.12 Calculated progression of PDOS of Co and O with Li_x as a battery cathode is charged. The energy of the Co 3d band is well above the O band for Li_1CoO_2 and $Li_{0.66}CoO_2$, but they appear equivalent in the overcharged $Li_{0.33}CoO_2$

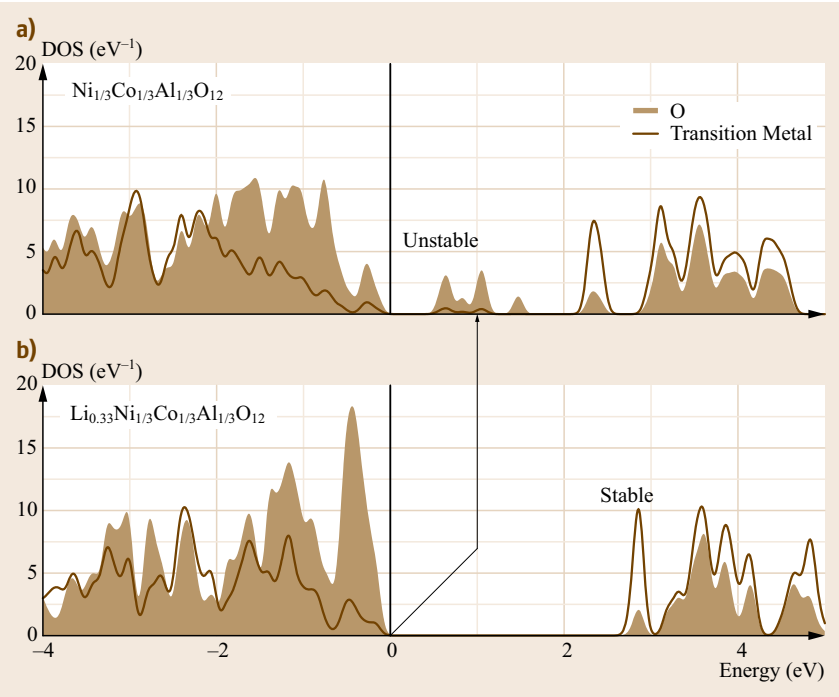


Fig. 11.13 **(a)** PDOS of the deep charge states of $NCA_{1/3}$, **(b)** shows the electronic structure just prior to removing electrons from the Co^{4+}/Co^{5+} redox couple, which is the onset of the electronic instability

putational trick to remove another electron and thereby examine the stability of the Co^{4+}/Co^{5+} couple, even though it is not available experimentally. The top panel of Fig. 11.10 shows that the now emptied states are majority O and therefore these removed electrons will lead to an electronic or chemical instability. Such Co–O covalency might also explain why nanoscale forms of $LiCoO_2$ suffer from irreversibility, as Co may be over-coordinated with O at surface faces and edges and therefore experience a higher valency and more sus-

ceptibility to O_2 loss [11.54]. Our calculations show definitively that the Co^{4+}/Co^{5+} redox couple would be inaccessible in $LiCoO_2$, with further charging resulting in O^{2-} oxidation.

11.2.3 PDOS of NCA

In $NCA_{1/3}$, however, the end of the charge cycle pulls electrons from exactly the Co^{4+}/Co^{5+} redox couple electronic configuration that was inaccessible in $LiCoO_2$. In Fig. 11.13, we calculate the very end of the charge cycle and show oxygen destabilization is highly likely at exactly the point that the Co^{4+}/Co^{5+} would ostensibly be accessed. Figure 11.13b shows a highly, but not fully, charged PDOS calculation. At this charge level, the unfilled states above E_F correspond to Ni^{3+}/Ni^{4+} and Co^{3+}/Co^{4+} redox couples (combined for clarity). As can be clearly seen, the transition metal states dominate over oxygen states, indicating that withdrawal of charge up to this point is likely safe. As discussed in Sect. 11.2.2, the electronic configuration of $NCA_{1/3}$ at $x = 0.33$ is equivalent to NCM at $x = 0.67$ and our experimental measurements show that electrons are indeed removed at approximately the same voltage for each of these x respectively. In contrast to the empty state, the filled states directly below E_F, from which electrons will be removed in the subsequent charging step, are dominated by oxygen states. Further charging would remove electrons not from the Co^{4+}/Co^{5+} redox couple, but rather from oxygen and is therefore likely to precipitate oxygen instability. Figure 11.13a shows the PDOS after this removal has been accomplished. The empty states above E_F are almost entirely of oxygen character and an analysis of the Co magnetic moment shows no change from the higher Li content calculation. This indicates oxidation of the O^{2-} and points toward an electronic and/or chemical instability in the material. Our voltage calculations have indicated that this final step in $NCA_{1/3}$ is outside the electrochemical window of the electrolyte, which gives rise to the lower capacity compared to NCM. The metal and oxygen PDOS calculations show that, even for a very high-voltage electrolyte to be developed, the withdrawal of the final electron would be unsafe in the $NCA_{1/3}$ system due to an intrinsic electronic instability at very deep charge.

11.2.4 Conclusions

We conclude that PDOS calculations are a useful tool for discerning whether oxygen or metal sites contribute to electron withdrawal. Once the oxygen ions become electronic sources, the materials are likely unstable, as the oxygen is irreversibly lost to O_2, although some are proposing reversible oxygen withdrawal as additional sources of charge storage.

11.3 Summary

DFT is a powerful tool for the evaluation of battery materials. We demonstrate how DFT can be used to understand the impact of swapping the Mn^{4+} in $LiNi_{1/3}Co_{1/3}Mn_{1/3}O_2$ (NCM) with Al^{3+} to make $LiNi_{1/3}Co_{1/3}Al_{1/3}O_2$ ($NCA_{1/3}$). Comparison of the theoretical and experimental results show that the substitution of Al for Mn shifts the voltage upward, but decreases the capacity and increases IR loss. By comparing our experimental and theoretical curves, we can attribute the capacity loss to the voltage window which cuts off at 5 V, leaving 0.25 Li ions still within the $LiNi_{1/3}Co_{1/3}Al_{1/3}O_2$ structure. The large difference between IR losses in the two compounds cannot be explained through the calculated electronic structures or through lattice changes. However, since calculations show that the substitution of Al shifts the Ni ion from 2+ to 3+, we can infer that Ni impurities in the Li plane are likely the source of the problem. XRD data confirms that a higher degree of interplanar disorder exists in $NCA_{1/3}$ compared to NCM. Lastly, we discussed that calculating the PDOS of the M and O bands with delithiation can give important information about oxygen instabilities and safety at a materials level. When the metal-oxygen covalency is such that electrons are withdrawn from metal-dominated states, the material exhibits safe and reversible cycling behaviors. If the metal states drop beneath the oxygen states, however, removal of electrons oxidizes the O^{2-} ions leading to oxygen loss and irreversibility as well as possibly dangerous electronic and chemical instabilities.

The examples in this chapter clearly show that DFT is an invaluable modern tool for the understanding of electrochemical materials, giving insights into materials changes that are difficult to discern from global electrochemical tools and even in situ spectroscopies.

Acknowledgments. The authors are grateful to the Office of Naval Research for support of this research.

References

11.1 G. Ceder, Y.M. Chiang, D.R. Sadoway, M.K. Aydinol, Y.I. Jang, B. Huang: Identification of cathode materials for lithium batteries guided by first-principles calculations, Nature **392**(6677), 694–696 (1998)

11.2 Y.S. Meng, M.E. Arroyo-de Dompablo: First principles computational materials design for energy storage materials in lithium ion batteries, Energy Environ. Sci. **2**(6), 589–609 (2009)

11.3 J.B. Goodenough: Metallic oxides, Prog. Solid State Chem. **5**, 145–399 (1971)

11.4 J.B. Goodenough, K.S. Park: The li-ion rechargeable battery: A perspective, J. Am. Chem. Soc. **135**(4), 1167–1176 (2013)

11.5 M.K. Aydinol, A.F. Kohan, G. Ceder, K. Cho, J. Joannopoulos: Ab initio study of lithium intercalation in metal oxides and metal dichalcogenides, Phys. Rev. B **56**(3), 1354–1365 (1997)

11.6 K.S. Kang, Y.S. Meng, J. Bréger, C.P. Grey, G. Ceder: Electrodes with high power and high capacity for rechargeable lithium batteries, Science **311**(5763), 977–980 (2006)

11.7 G. Kresse, J. Furthmuller: Efficient iterative schemes for ab initio total-energy calculations using a plane-wave basis set, Phys. Rev. B **54**(16), 11169–11186 (1996)

11.8 G. Kresse, D. Joubert: From ultrasoft pseudopotentials to the projector augmented-wave method, Phys. Rev. B **59**(3), 1758–1775 (1999)

11.9 A. Jain, S.P. Ong, G. Hautier, W. Chen, W.D. Richards, S. Dacek, S. Cholia, D. Gunter, D. Skinner, G. Ceder, A.K. Persson: Commentary: The materials project: A materials genome approach to accelerating materials innovation, Appl. Mater. **1**(1), 011002 (2013)

11.10 H.L. Chen, G. Hautier, A. Jain, C. Moore, B. Kang, R. Doe, L. Wu, Y. Zhu, Y. Tang: Carbonophosphates: A new family of cathode materials for li-ion batteries identified computationally, Chem. Mater. **24**(11), 2009–2016 (2012)

11.11 I.I. Mazin, D.J. Singh, M.D. Johannes, M.H. Du: Unconventional superconductivity with a sign reversal in the order parameter of $LaFeAsO_{(1-x)}F_{(x)}$, Phys. Rev. Lett. **101**(5), 057003 (2008)

11.12 M.D. Johannes, I.I. Mazin, D.J. Singh, D.A. Papaconstantopoulos: Nesting, spin fluctuations, and odd-gap superconductivity in $Na_xCoO_2yH_2O$, Phys. Rev. Lett. **94**, 169901 (2005)

11.13 M.D. Johannes, I.I. Mazin, D.J. Singh, D.A. Papaconstantopoulos: Erratum: Nesting, spin fluctuations, and odd-gap superconductivity in Na_xCoO_2y H_2O, Phys. Rev. Lett. **93**, 097005 (2004)

11.14 M.D. Johannes, I.I. Mazin, D.J. Singh, D.A. Papaconstantopoulos: Erratum: Nesting, spin fluctuations, and odd-gap superconductivity in Na_xCoO_2y H_2O, Phys. Rev. Lett. **94**, 169901 (2005)

11.15 P.E. Blochl: Projector augmented-wave method, Phys. Rev. B **50**(24), 17953–17979 (1994)

11.16 J. Heyd, G.E. Scuseria, M. Ernzerhof: Hybrid functionals based on a screened coulomb potential, J. Chem. Phys. **118**(18), 8207–8215 (2003)

11.17 K. Mizushima, P.C. Jones, P.J. Wiseman, J.B. Goodenough: Li_xCoO_2 (Oless-Thanxless-Than-or-Equal-To1) – A new cathode material for batteries of high-energy density, Mater. Res. Bull. **15**(6), 783–789 (1980)

11.18 J.R. Dahn, U. VonSacken, M.W. Juzkow, H. Al-Janaby: Rechargeable $LiNiO_2$ carbon cells, J. Electrochem. Soc. **138**(8), 2207–2211 (1991)

11.19 T. Ohzuku, A. Ueda, M. Nagayama: Electrochemistry and structural chemistry of $LiNiO_2$ ($R\bar{3}M$) for 4 volt secondary lithium cells, J. Electrochem. Soc. **140**(7), 1862–1870 (1993)

11.20 J.N. Reimers, J.R. Dahn, J.E. Greedan, C.V. Stager, G. Liu, I. Davidson, U. von Sacken: Spin-glass behavior in the frustrated antiferromagnetic $LiNiO_2$, J. Solid State Chem. **102**(2), 542–552 (1993)

11.21 Y.I. Jang, B. Huang, H. Wang, G.R. Maskaly, G. Ceder, D.R. Sadoway, Y.-M. Chiang, H. Liu, H. Tamura: Synthesis and characterization of $LiAl_yCo_{1-y}O_2$ and $LiAl_yNi_{1-y}O_2$, J. Power Sources **81**, 589–593 (1999)

11.22 T.A. Ohzuku, A. Ueda, M. Kouguchi: Synthesis and characterization of $LiAl_{1/4}Ni_{3/4}O_2$ ($R\bar{3}m$) for lithium-ion (shuttlecock) batteries, J. Electrochem. Soc. **142**(12), 4033–4039 (1995)

11.23 J. Reed, G. Ceder: Role of electronic structure in the susceptibility of metastable transition-metal oxide structures to transformation, Chem. Rev. **104**(10), 4513–4533 (2004)

11.24 M.M. Thackeray, S.H. Kang, C.S. Johnson, J.T. Vaughey, S.A. Hackney: Comments on the structural complexity of lithium-rich $Li_{1+x}M_{1-x}O_2$ electrodes (M = Mn, Ni, Co) for lithium batteries, Electrochem. Commun. **8**(9), 1531–1538 (2006)

11.25 C.H. Chen, J. Liu, M.E. Stoll, G. Henriksen, D.R. Vissers, K. Amine: Aluminum-doped lithium nickel cobalt oxide electrodes for high-power lithium-ion batteries, J. Power Sources **128**(2), 278–285 (2004)

11.26 J. Xiao, N.A. Chernova, M.S. Whittingham: Layered mixed transition metal oxide cathodes with reduced cobalt content for lithium ion batteries, Chem. Mater. **20**(24), 7454–7464 (2008)

11.27 Y.K. Lin, C.H. Lu: Preparation and electrochemical properties of layer-structured $LiNi_{1/3}Co_{1/3}Mn_{1/3}$-$yAl_yO_2$, J. Power Sources **189**(1), 353–358 (2009)

11.28 B.J. Hwang, Y.W. Tsai, D. Carlier, G. Ceder: A combined computational/experimental study on $LiNi_{1/3}Co_{1/3}Mn_{1/3}O_2$, Chem. Mater. **15**(19), 3676–3682 (2003)

11.29 Y. Koyama, I. Tanaka, H. Adachi, Y. Makimura, T. Ohzuku: Crystal and electronic structures of superstructural, $Li_{1-x}[Co_{1/3}Ni_{1/3}Mn_{1/3}]O_2$ ($0 \leq x \leq 1$), J. Power Sources **119**, 644–648 (2003)

11.30 V.I. Anisimov, J. Zaanen, O.K. Andersen: Band theory and mott insulators - hubbard-U instead of stoner-I, Phys. Rev. B **44**(3), 943–954 (1991)

11.31 V.I. Anisimov, O. Gunnarsson: Density-functional calculation of effective coulomb interactions in metals, Phys. Rev. B **43**(10), 7570–7574 (1991)

11.32 M.D. Johannes, K. Hoang, J.L. Allen, K. Gaskell: Hole polaron formation and migration in olivine phosphate materials, Phys. Rev. B **85**(11), 115106 (2012)

11.33 C.T. Love, M.D. Johannes, K.E. Swider-Lyons: Thermal stability of delithiated Al-substituted $LiNi_{1/3}Co_{1/3}Mn_{1/3}O_2$ cathodes in rechargeable lithium-ion batteries, ECS Transactions **25**(36), 231–240 (2012)

11.34 S. Jouanneau, J.R. Dahn: Preparation, structure, and thermal stability of new $Ni_xCo_1-2xMn_x(OH)_{(2)}$ $(0 \leq x \leq 1/2)$ phases, Chem. Mater. **15**(2), 495–499 (2003)

11.35 W.B. Luo, J.R. Dahn: Preparation of $Co_{1-z}Al_z(OH)_{(2)}(NO3)_{(z)}$ layered double hydroxides and $Li(Co_{1-z}Al_z)O_{-2}$, Chem. Mater. **21**(1), 56–62 (2009)

11.36 J. Wilcox, S. Patoux, M. Doeff: Structure and electrochemistry of $LiNi_{1/3}Co_{1/3}$-$yM_yMn_{1/3}O_2$ (M = Ti, Al, Fe) positive electrode materials, J. Electrochem. Soc. **156**(3), A192–A198 (2009)

11.37 R.D. Shannon, C.T. Prewitt: Effective ionic radii in oxides and fluorides, Acta Crystallographica Section B-Structural Crystallogr. Cryst. Chem. B **25**, 925–946 (1969)

11.38 X.M. Zhao, F. Zhou, J.R. Dahn: Phases formed in Al-doped $Ni_{(1/3)}Mn_{(1/3)}Co_{(1/3)}(OH)_{(2)}$ prepared by coprecipitation: Formation of layered double hydroxide, J. Electrochem. Soc. **155**(9), A642–A647 (2008)

11.39 H. Kobayashi, Y. Arachi, S. Emura, K. Tatsumi: Investigation on lithium de-intercalation mechanism for $LiNi_{0.45}Mn_{0.45}Al_{0.1}O_2$, Solid State Ionics **178**(15–18), 1101–1105 (2007)

11.40 J.R. Dahn, E.W. Fuller, M. Obrovac, U. von Sacken: Thermal-stability of Li_xCoO_2, Li_xNiO_2 and λ-MnO_2 and consequences for the safety of Li-ion cells, Solid State Ionics **69**(3–4), 265–270 (1994)

11.41 R. Gupta, A. Manthiram: Chemical extraction of lithium from layered $LiCoO_2$, J. Solid State Chem. **121**(2), 483–491 (1996)

11.42 A.R. Armstrong, M. Holzapfel, P. Novák, C.S. Johnson, S.H. Kang, M.M. Thackeray, P.G. Bruce: Demonstrating oxygen loss and associated structural reorganization in the lithium battery cathode, $Li[Ni_{0.2}Li_{0.2}Mn_{0.6}]O_2$, J. Am. Chem. Soc. **128**(26), 8694–8698 (2006)

11.43 M.D. Johannes, C.T. Love, K.E. Swider-Lyons: Oxygen character in the density of states as an indicator of the stability of Li-ion battery cathode materials, Solid State Ionics **286**, 83–89 (2014)

11.44 N.V. Kosova, E.T. Devyatkina, V.V. Kaichev: $LiNi_{1-x-y}Co_xMn_yO_2$ $(x = y = 0.1, 0.2, 0.33)$ cathode materials prepared using mechanical activation: Structure, state of ions, and electrochemical performance, Inorg. Mater. **43**(2), 185–193 (2007)

11.45 S.K. Hu, S.B. Tang, L. Lu, Y.S. Meng, G. Ceder: Effect of Co content on performance of $LiAl_{1/3}$-$xCo_xNi_{1/3}Mn_{1/3}O_2$ compounds for lithium-ion batteries, J. Power Sources **160**(2), 1287–1293 (2006)

11.46 K. Hoang, M.D. Johannes: Defect chemistry in layered transition-metal oxides from screened hybrid density functional calculations, J. Mater. Chem. A **2**(15), 5224–5235 (2014)

11.47 G. Dutta, A. Manthiram, J.B. Goodenough, J.-C. Grenier: Chemical Synthesis and Properties of, $Li_{1-\delta-x}Ni_{1+\delta}O_2$ and $Li[Ni_2]O_4$, J. Solid State Chem. **96**(1), 123–131 (1992)

11.48 Q.S. Wan, P. Ping, X.J. Zhao, G.Q. Chu, J.H. Sun, C.H. Chen: Thermal runaway caused fire and explosion of lithium ion battery, J. Power Sources **208**, 210–224 (2012)

11.49 Z.Q. Deng, A. Manthiram: Influence of cationic substitutions on the oxygen loss and reversible capacity of lithium-rich layered oxide cathodes, J. Phys. Chem. C. **115**(14), 7097–7103 (2011)

11.50 S. Laubach, S. Laubach, P.C. Schmidt, D. Ensling, S. Schmid, W. Jaegermann, A. Thißen, K. Nikolowski, H. Ehrenberg: Changes in the crystal and electronic structure of $LiCoO_2$ and $LiNiO_2$ upon Li intercalation and de-intercalation, Phys. Chem. Chem. Phys. **11**(17), 3278–3289 (2009)

11.51 C.T. Love, W. Dmowski, M.D. Johannes, K.E. Swider-Lyons: Structural originations of irreversible capacity loss from highly lithiated copper oxides, J. Solid State Chem. **184**(9), 2412–2419 (2011)

11.52 L.X. Yuan, Z.-H. Wang, W.-X. Zhang, X.-L. Hu, J.-T. Chen, Y.-H. Huang, J.B. Goodenough: Development and challenges of $LiFePO_4$ cathode material for lithium-ion batteries, Energy Environ. Sci. **4**(2), 269–284 (2011)

11.53 K. Zaghib, A. Guerfi, P. Hovington, A. Vijh, M. Trudeau, A. Mauger, J.B. Goodenough, C.M. Julien: Review and analysis of nanostructured olivine-based lithium recheargeable batteries: Status and trends, J. Power Sources **232**, 357–369 (2013)

11.54 C.J. Patridge, C.T. Love, K.E.S. Lyons, M.E. Twigg, D.E. Ramaker: In-situ x-ray absorption spectroscopy analysis of capacity fade in nanoscale-$LiCoO_2$, J. Solid State Chem. **203**, 134–144 (2013)

Electroch Part C

Part C Electrochemistry Probes

12 **Electrochemical Energy Generation and Storage as Seen by In-Situ NMR**
YuYe J. Tong, Washington, USA

13 **Spectroscopy of Electrochemical Systems**
James J. Walsh, Liverpool, UK
Robert J. Forster, Dublin 9, Ireland
Tia E. Keyes, Dublin 9, Ireland

14 **Kinetic Activity in Electrochemical Cells**
Yannick Garsany, Washington, USA
Karen Swider-Lyons, Washington, USA

12. Electrochemical Energy Generation and Storage as Seen by In-Situ NMR

YuYe J. Tong

This chapter will provide a concise review/snapshots of the development of in situ electrochemical nuclear magnetic resonance spectroscopy (including magnetic resonance imaging), in both solution and solid state, and its current state of applications to understanding chemical processes for electrochemical energy generation and storage. This will include pedagogical descriptions of involved principles and techniques and discussions of representative case studies that showcase the technical prowess of the methodologies, particularly in investigating nanomaterials used in electrocatalysis for fuel cells and energy storage devices (batteries) and associated water distribution in the former and Li metal deposits in the latter.

12.1 **Spatially-Resolved ^{195}Pt NMR Spectroscopy of Pt-Based Electrocatalysts** 336
12.1.1 ^{195}Pt NMR of Pt Nanoparticles 336
12.1.2 Study of Ru@Pt Versus Au@Pt M (Ru/Au) Core-Pt Shell NPs 338
12.2 **NMR/MRI Studies of Energy Storage (Batteries) Materials** 342
12.2.1 Toroid Resonator: Near-Electrode Imager Versus Compression Coin Cell 344
12.2.2 Bellcore-Like Flexible NMR Cells .. 347
12.2.3 NMR/MRI Studies of Formation of Li Dentrites 350
12.3 **MRI of Water Distribution in Fuel Cells** .. 352
12.3.1 In-Plane Water Distribution 353
12.3.2 Through-Plane Water Distribution 356
12.4 **Conclusion and Future Perspectives: Sensitivity, Sensitivity and Sensitivity** ... 357
References 360

This chapter concerns in situ applications of nuclear magnetic resonance (NMR) spectroscopy, including magnetic resonance imaging (MRI), to the current research in the fields relevant to electrochemical (EC) energy generation (fuel cells) and storage (Li-ion batteries). Despite that NMR is probably the least sensitive one among all spectroscopic techniques in terms of mass detection (its Achilles' heel), its unmatchable chemical specificity and elemental accessibility to almost all elements in the Periodic Table, its exquisite technical versatility (i. e., the noninvasiveness, applicability to almost all forms of matters, ability to see the buried interfaces and access to both static and dynamic information) and its imaging capability have continued to inspire and attract courageous and ingenious practitioners to expand its application horizon [12.1]. This includes novel applications to studying EC energy generation and storage systems [12.2, 3] even though the technical incompatibility between having a good NMR detection and conduction materials of and electrical conduction in the EC systems would further worsen the NMR mass detection sensitivity. The reason for the latter is that the electrical conduction, although indispensable to any operational EC systems, would significantly diminish the quality factor (Q-factor) of the NMR detection circuitry. While only a handful of research groups have been constantly working in this niche of frontier research with well known technical challenges, the last decade has indeed witnessed substantial progress in the in situ applications of NMR/MRI to investigating fundamental chemical processes involved in the EC energy generation and storage [12.2–4].

The earliest application of NMR to electrochemistry was in the context of traditional electroanalytical chemistry and probably goes back to the work by *Richards* and *Evans* [12.6] in which the diamagnetic product of electrolysis (of *trans*-1-phenyl-1-buten-3-one) could be followed by solution NMR using a two-electrode flow-cell setup that enabled the EC products to be transported to and from the NMR detection coil. The work was driven by *the ability of NMR to distinguish quite similar species making its application to electrochemical inves-*

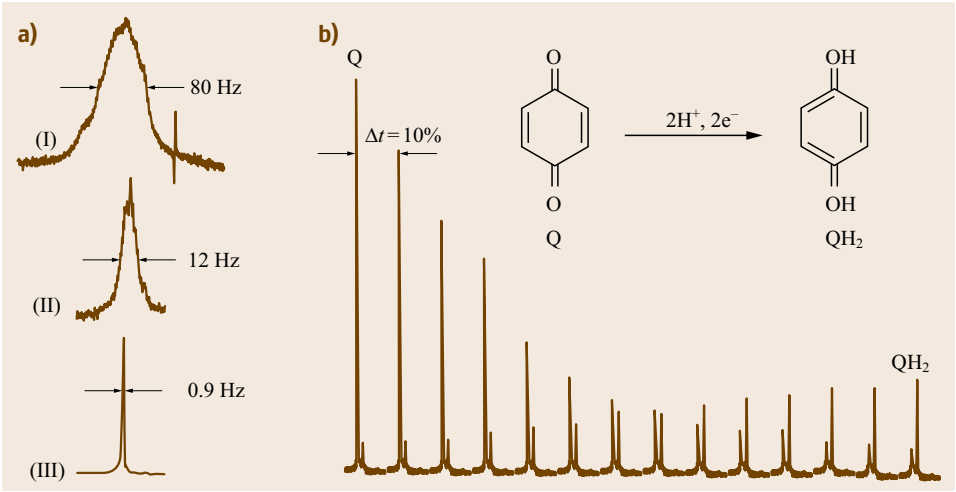
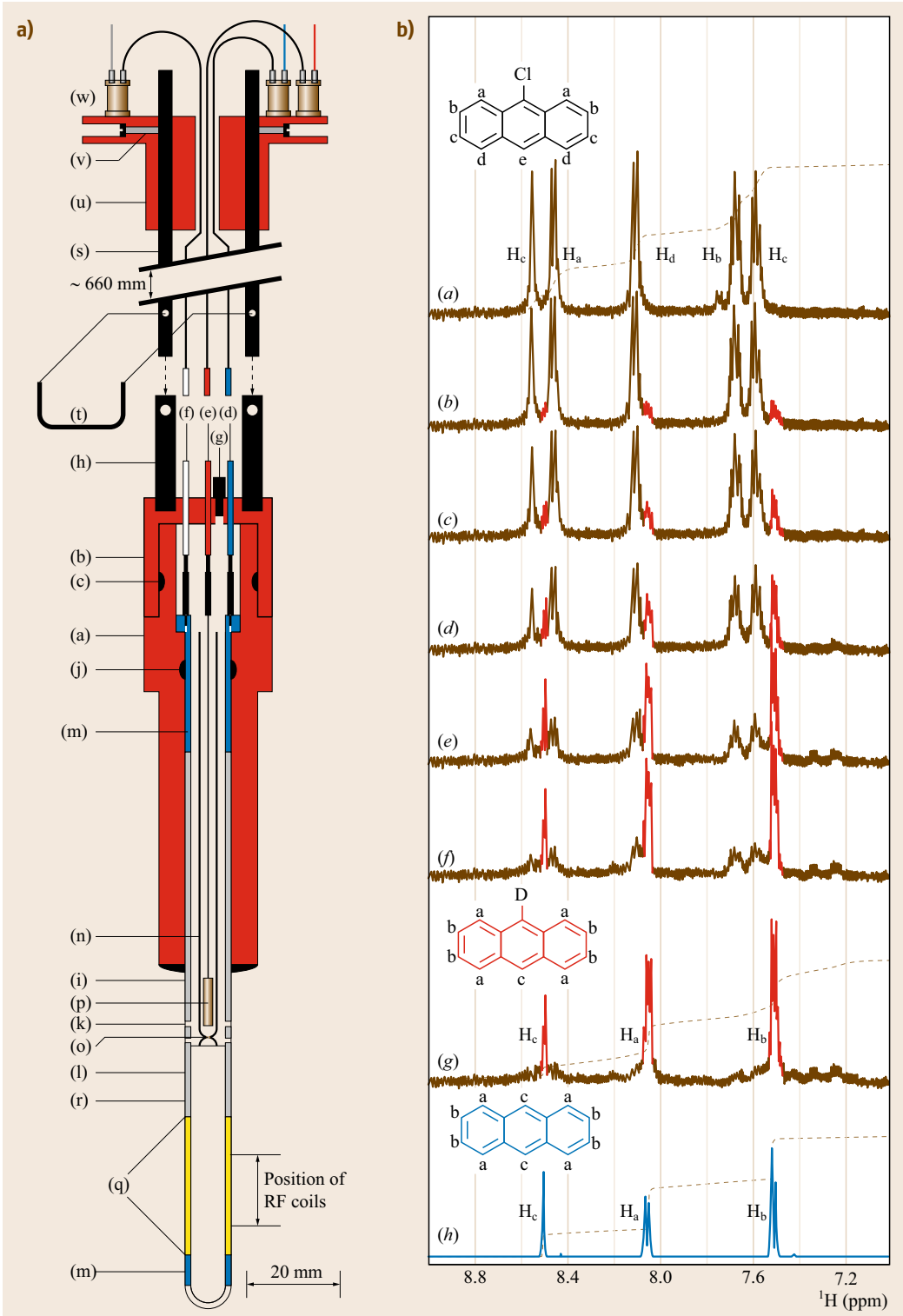


Fig. 12.1 **(a)** Geometric configuration and metal skin-depth effects of a working electrode inside the NMR detection coil on the quality of NMR spectra: (*I*) a spiral Pt wire whose noncylindrical symmetry and metal skin-depth effect caused significant broadening (≈ 80 Hz) of the ^{1}H (300 MHz) spectrum of half-deuterated water (HOD); (*II*) the cylindrical symmetry of a Pt gauze enabled ≈ 7 times reduction in line-broadening as compared to that in (*I*); (*III*) a cylindrical ultrathin Au film whose thickness was much less than the metal skin depth enabled an additional 13 times reduction in line-broadening. **(b)** The high-quality, time-dependent ^{1}H spectra obtained using the cylindrical ultrathin film Au electrode during the electrolytic reduction of *p*-quinone (0.1 M Q in 0.1 M KCl/ 0.3 M DCl at 0.5 V versus Ag/AgCl) into dihydroquinone (after [12.5])

tigations quite attractive [12.6]. While the developed flow cell was integrated into a standard 5 mm NMR tube in a quite sophisticated fashion, the electrodes were placed far enough away from the NMR detection coil so the Q-factor of the latter was not significantly affected. It was expected that the setup, which was originally designed for the unsuccessful observation of chemically induced dynamic nuclear polarization (DNP) using EC-generated radical pairs, would enable the NMR detection of diamagnetic EC products having half-lives greater than a few seconds (longer than NMR acquisition time). It is interesting to note that DNP [12.7], a NMR signal enhancement technique that was initially predicted theoretically by *Overhauser* [12.8, 9] in 1953 and proved experimentally by *Carver* and *Slichter* [12.10], has been reinvigorated recently [12.11] and is becoming one of the most promising NMR signal enhancement techniques. As the DNP NMR signal enhancing techniques become mature, a broad spectrum of NMR applications, including these that are the topics of this chapter, are expected to benefit from their further development.

The ensuing development in coupling electrochemistry with solution NMR, however, has been rather sporadic (probably deterred by the anticipated technical difficulties caused by placing a conducting electrode in NMR detection coil) and largely focused on improving NMR response to EC products by incorporating working electrode inside NMR detection coil [12.5, 12–16]. As NMR is a technique that *welcomes every bit of extra signal* [12.1], an important technical advancement in these endeavors was the realization that cylindrically-symmetric ultrathin metal film ($\approx$ tens nanometers) as a working electrode can significantly reduce energy dissipation/loss caused by the skin-depth effect of metals that degrades the Q-factor of NMR detection coil and lower the interference to NMR ra-

Fig. 12.2 **(a)** Schematic of the electrolytic NMR cell: (*a*)/(*b*) Delrin NMR tube holder/lid, (*c*)/(*j*) O-ring, (*d*) to (*f*) connections to working, counter, reference electrodes respectively, (*g*)/(*m*) Teflon stopper/spacers, (*h*) hollow aluminum rods, (*i*) 10 mm NMR tube, (*k*)/(*l*) holes/air pocket in 7.49 mm NMR tube, (*n*) 6 mm Pyrex tube, (*o*) porosity no.2 glass frit, (*p*) Pt mesh counter electrode, (*q*) Au film (≈ 10 nm) working electrode, (*r*) Ag/Ag^+ pseudo reference electrode, (*s*) Al rods, (*t*) stainless steel spring clip, (*u*) Delrin support block, (*v*) stainless steel screws, and (*w*) RF chokes. **(b)** 500 MHz ^{1}H NMR spectra (*a–g*) obtained in situ during the electrolytic reduction of 9-chloroanthracene that led to anthracene with Cl replaced by D: (*a*) prior to electrolysis, (*b*) 7–12 min, (*c*) 17–22 min, (*d*) 25–30 min, (*e*) 40–45 min, (*f*) 47–52 min, (*g*) 60–65 min, and (*h*) 25 mm anthracene in CD_3CN obtained in a 5 mm NMR tube (after [12.12], courtesy of Am. Chem. Soc. 2004) ►


a)
(w)
(v)
(u)
(s)
~ 660 mm
(t)
(f) (e) (d)
(g)
(h)
(b)
(c)
(a)
(j)
(m)
(n)
(i)
(p)
(k)
(o)
(l)
(r)
(q)
Position of RF coils
(m)
20 mm
b)
Cl
a
b
c
d
e
H_c
H_a
H_d
H_b
(a)
(b)
(c)
(d)
(e)
(f)
D
(g)
(h)
8.8
8.4
8.0
7.6
7.2
^{1}H (ppm)

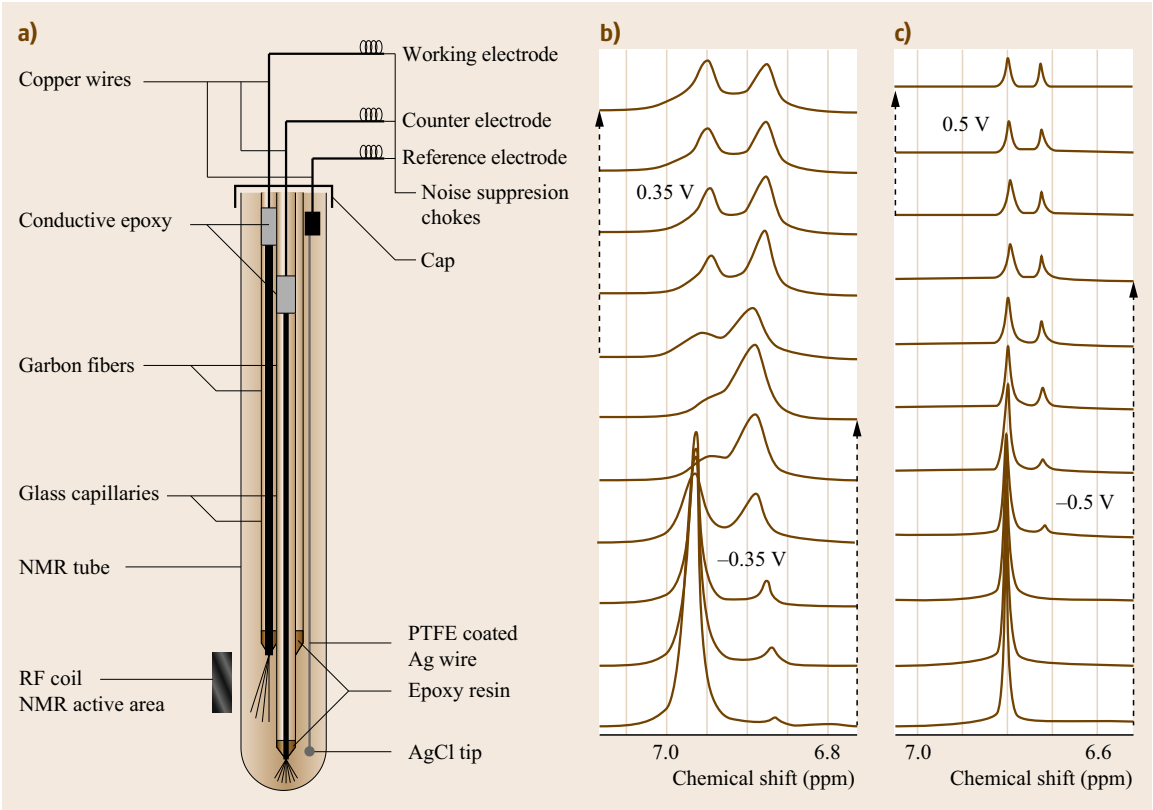


Fig. 12.3 **(a)** Diagram illustrating the configuration of the electrolytic NMR cell. **(b)** ^{1}H NMR spectra of *p*-benzoquinone at -0.35 and 0.35 V respectively at pH=1. **(c)** ^{1}H NMR spectra of *p*-benzoquinone at -0.5 and 0.5 V respectively at pH=7. Deuterated aqueous solution of Li_2SO_4 was used as the supporting electrolyte and Ag/Ag^+ as pseudo reference electrode, with the pH being adjusted with H_2SO_4 for NMR measurements (after [12.17], courtesy of Am. Chem. Soc. 2009)

diation/detection as well as to field homogeneity due to eddy currents [12.5, 12, 15]. Figure 12.1a illustrates that a severe line-broadening by an intruding metal wire (a spiral Pt wire, Fig. 12.1a(I): ≈ 80 Hz for the full width at half maximum–FWHM for the ^{1}H peak of HOD) could be reduced significantly (≈ 7 times) by using a cylindrically-symmetric Pt mesh (Fig. 12.1a(II): FWHM ≈ 12 Hz) and further reduced (≈ 13 times) by using a cylindrically-symmetric thin ($\ll$ skin depth) Au film (Fig. 12.1a(III): FWHM ≈ 0.9 Hz). The latter enabled a time-dependent, high-quality solution NMR spectra to be recorded during the electroreduction of *p*-benzoquinone into (di)hydroquinone, as presented in Fig. 12.1b [12.5].

Taking the cues (i. e., cylindrical symmetry and ultrathin working electrode) from the work by *Mincey* et al. [12.14] and *Prenzler* et al. [12.5], *Webster* probably made the most robust and sophisticated multicomponent electrolytic NMR cell that was assembled inside a standard 10 mm NMR tube, Fig. 12.2a [12.12]. According to *Webster*, there were four major criteria that he tried to achieve in his electrolytic NMR cell [12.12], to:

1. Function in a moisture- and oxygen-free environment and at variable temperatures
2. Be assembled and set up quickly and not require a dedicated NMR instrument
3. Operate with low solution volumes to minimize the amount of deuterated solvents and
4. Minimally interfere with the NMR line widths.

Excellent applicability of this electrolytic NMR cell was convincingly demonstrated by studying the in situ reduction of 9-bromoanthracene, 9-chloroanthracene, and 4-bromobenzophenone in deuterated acetonitrile with tetrabutylammonium hexafluorophosphate as the supporting electrolyte. As an illustrative example, Fig. 12.2b presents the high-quality ^{1}H NMR spectra recorded during the in situ electroreduction of 9-chloroanthracene that led to the formation of anthracene

with Cl replaced by D. Remarkably, the field homogeneity of both the static (B_0) and RF (B_1) fields was almost not affected at all by the presence of the electrolytic NMR cell inside the NMR detection coil as can be clearly seen by comparing Fig. 12.2b(*g*) with Fig. 12.2b(*h*).

On the other hand, only a few more papers on the in situ solution spectro-electrochemical NMR [12.17–22] have been published since Webster's *tour-de-force* showcase of the in situ electrolytic NMR [12.12]. *Zhang* and *Zwanziger* developed a similar but simpler 5 mm electrolytic NMR cell [12.20] that was expected to be applicable to any commercial NMR spectrometers equipped with a 5 mm probe. A much simpler and more versatile version of a 3-electrode electrolytic NMR cell was developed by *Dunsch* and co-workers [12.17] in which the protruding tips of capillary-guided/protected carbon fibers were used as both working and counter electrodes. The ends of capillaries where the carbon fibers protruding out from the capillary and being in contact with electrolyte were sealed by epoxy resin, as shown in Fig. 12.3a. The cell is actually very simple to make, consisting simply of a standard commercial (5 or 10 mm) NMR tube and three easily-arranged electrodes inside the tube, with the working electrode located within the RF coil region, the reference electrode closeby, and the counter electrode placed further to the bottom of the NMR tube for avoiding physical contact among the three electrodes.

The prowess of this simple electrolytic NMR cell is in full display by the ^{1}H NMR spectra shown in Fig. 12.3b,c [12.17]. The ^{1}H NMR spectra in Fig. 12.3b were recorded at pH = 1 but those in Fig. 12.3c were at pH = 7. In the acidic environment, the ^{1}H NMR peak of *p*-benzoquinone appeared at 6.95 ppm. When molecules were subjected to reduction at −0.35 V (versus Ag/Ag^+ pseudo reference), the ^{1}H NMR peak of hydroquinone appeared at 6.85 ppm and became overwhelmingly dominant after 6 h reduction. If the fully reduced solution being subjected to oxidation at 0.35 V, the *p*-benzoquinone peak at 6.95 ppm reappeared and got stronger as time went. On the other hand, it was quite a different story at pH = 7 (Fig. 12.3c). After the application of reduction potential at −0.5 V, the *p*-benzoquinone at 6.80 ppm started decreasing but no new NMR line appeared due to the formation of semiquinone radical. A second peak at 6.72 ppm did appear but only after 1 h reduction and the rate of its growth was much slower than the disappearing rate of the initial peak at 6.80 ppm. The electrolysis ended when the amplitudes of both peaks showed very low intensity, indicating a low concentration of both species in solution.

When subjecting the latter to 0.5 V potential for re-oxidizing what remained in the solution, no changes in the NMR spectrum were observed even after the electrolysis went on for several hours. This was due to the formation of sparsely soluble quinhydrone complex whose precipitates (observable by eyes) made the back reaction at the electrode impossible. The NMR-transparent semiquinone radical underwent a disproportionation reaction to benzoquinone and hydroquinone at the same ratio. Both led to the formation of quinhydrone that became unavailable for the ensuing EC reactions.

While further and more detailed discussion of the in situ solution spectro-electrochemical NMR is outside the scope of this chapter, it is hoped that the qualitative and quantitative investigative power of the technique as impressively showcased in the brief discussion of the three illustrative cases before [12.5, 12, 17], would stimulate or/and entice more interest and therefore use of the technique by a wider variety of researchers than currently are, particularly when considering that the electrolytic NMR cell developed by *Dunsch* et al. [12.17] (Fig. 12.3a) is so simple that almost any research lab could make it.

As to the topics pertinent to the main focus of this chapter, i. e., in situ applications of NMR/ MRI to research relevant to EC energy generation and storage, no attempt will be given to make this chapter an exhaustive account of the field simply because there are several excellent reviews out there [12.2–4, 23–26], particularly the most recent, rather exhaustive one by *Han* on NMR investigations of EC fuel cell reactions in acidic environment [12.2] and a concise account of in situ solid-state NMR spectroscopy of EC cells by *Grey* et al. [12.3]. Instead, in the following, we will discuss three specific topics of *recent* interest to various degrees of detail: In situ spatially-resolved ^{195}Pt NMR spectroscopy applied to Pt-based electrocatalysts (Sect. 12.1), in situ NMR spectroscopy/MRI applied to batteries (Sect. 12.2), and MRI to image water distribution in operating fuel cells (Sect. 12.3).

12.1 Spatially-Resolved ^{195}Pt NMR Spectroscopy of Pt-Based Electrocatalysts

Historically, the association of NMR spectroscopy with nanomaterials goes back to as early as the 1960s in an early quest to understand quantum behavior of conduction electrons in a confined space of nanometer size, i. e., the QSE [12.27], long before *nanoscience* and *nanotechnology* became contemporary buzz words. Over the ensuing two decades, NMR had indeed been one of the major spectroscopic techniques employed to study the QSE because of the direct relationships that the two major NMR observables, the Knight shift K and the nuclear spin-lattice relaxation time T_1, have with the electronic properties of metal nanoparticles (NPs), which would be affected by the QSE as predicted by the classic Kubo theory and its later variants [12.27].

12.1.1 ^{195}Pt NMR of Pt Nanoparticles

In the 1980s, *Slichter* and co-workers, in collaboration with *Sinfelt* from the then Exxon Research Center (now ExxonMobile Research and Engineering Company), pioneered a new line of research by demonstrating the unique aptness of ^{195}Pt and ^{13}C NMR in unraveling some of the fundamental aspects of heterogeneous catalysis of transition metal-based (including Pt) real-world, nanoscale catalysts [12.28]. The refinement of NMR techniques and their theoretical interpretations have advanced to a point where connections with other experimental techniques and with some theories of chemisorption can be made explicitly [12.4, 29, 30].

Since the early 1990s, a new development in combining interfacial electrochemistry and NMR, i. e., EC-NMR, which was largely inspired by Slichter's and others' NMR work in gas-phase nanoscale systems, has been put in motion due to the pioneering work of *Wieckowski* and co-workers [12.31]. The unique feature of EC-NMR is that it combines the elegance of electrochemistry in controlling chemical environments with the exquisite chemical specificity and electronic structural sensitivity of NMR, although overcoming the intrinsic low mass detection sensitivity and incompatibility between electrical conduction of electrochemistry and NMR detection continues to be a challenging perspective.

Among others, it is indeed a happy coincidence that ^{195}Pt NMR of Pt NPs possesses a unique spatially-resolved spectral feature and the Pt-based NPs are still the state-of-the-art electrocatalysts. Thereby, the former can be utilized *advantageously* to probe the chemistry of the latter. The spatially-resolved spectral feature of ^{195}Pt NMR of Pt NPs arise from the electronic alterations caused by the presence of the NP surface where the Pt surface atoms see an electronic environment that is very different from the one as seen by Pt atoms inside the NPs. This is illustrated by the ^{195}Pt NMR spectra of commercial (E-Tek) 2.5 nm carbon-supported Pt NPs, Pt/C (20 wt% Pt loading, transmission electron microscope (TEM) image, d), as presented in Fig. 12.4 [12.32].

In Fig. 12.4a, the surface of the as-received Pt/C sample was shown to be fully covered by Pt oxide by the broad peak at 1.089 G/kHz (G stands for magnetic field unit of Gauss), indicated by the arrow. The fraction of the area under the Pt oxide peak is about 45% of the total spectral area, which is a good measure of the sample's dispersion (defined as the ratio between the number of surface atoms and that of total atoms in a NP). Once EC cleaned, the Pt oxide peak disappeared and the ^{195}Pt NMR spectrum of the cleaned 2.5 nm Pt NPs appeared (Fig. 12.4b), with S indicating the center of the peak (1.1000 G/kHz) at which the clean Pt surface atoms resonate and B the Pt bulk position (1.1380 G/kHz). The whole spectrum spreads over a range of $\approx$ 34 000 ppm. It is this wide spectral range and the *monotonic* recovery of the resonance frequency towards the bulk position as a Pt atom moves inwards the NP from surface that make the unique spatially-resolved analysis possible, as illustrated by the layer-model analysis in Fig. 12.4c. In other words, a Pt NP can be decomposed by surface layer, sub-surface layer, sub-sub-surface layer, etc. and the resonances of Pt atoms of a given layer are combined into a Gaussian that reflects our inability to distinguish them. The central frequency of the Gaussian, however, is distinguishable layer-by-layer that usually obeys an experimentally-observed exponential recovery function and is therefore encoded with the spatial information of the given layer along the NP radius. As can be seen in Fig. 12.4c, decent spatial layer resolution can be achieved for the top most 3 to 4 atomic layers, which is sufficient for most (if not all) Pt-based electrocatalysis problems. It should be emphasized that despite its major limitation, i. e., no Pt atoms within a given layer can be distinguished, such layer-by-layer spatial resolution ($\approx$ 0.3 nm) for the top most few layers of Pt-based NPs is indeed quite unique among all available in situ spectroscopic methods, including the powerful synchrotron x-ray based techniques whose current state-of-the-art spatial resolution is about 10 nm [12.33].

In addition to the spectral position (i. e., the Knight shift K [12.35]) that encodes the spatial atomic layer

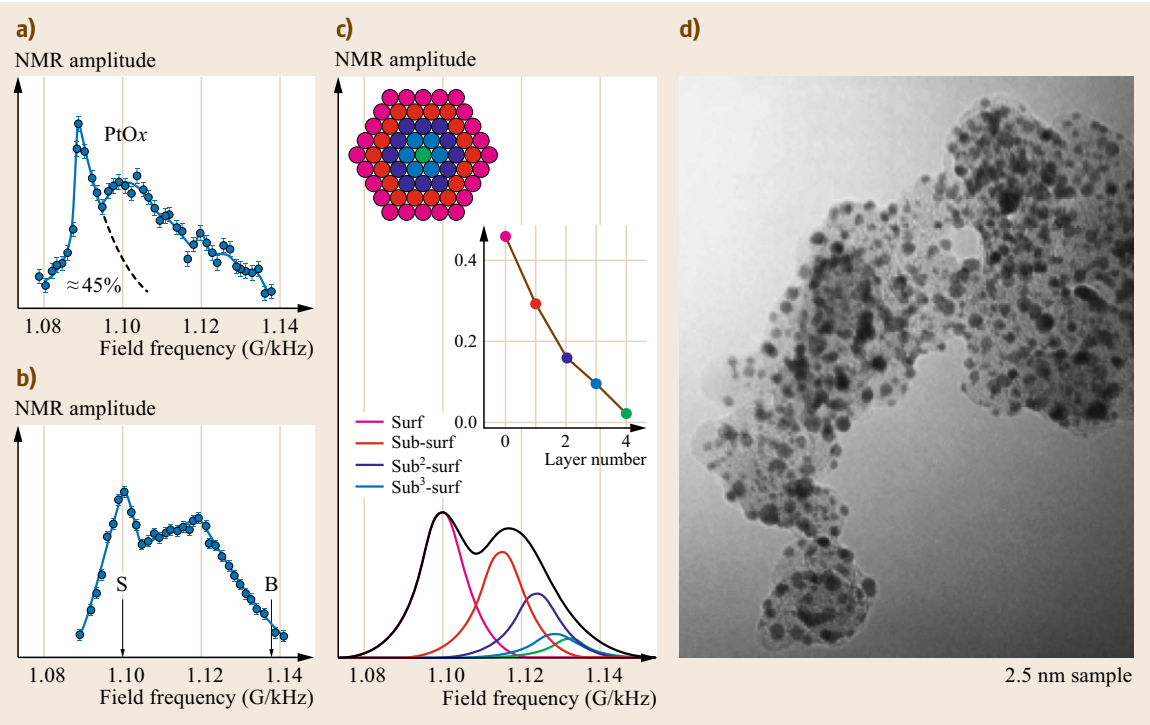


Fig. 12.4a–d Point-by-point ^{195}Pt NMR spectra of the 2.5 nm commercial carbon-supported Pt NPs (TEM image, **(d)**): **(a)** as-received, **(b)** EC-cleaned and **(c)** layer-model simulation (after [12.32], courtesy of Am. Chem. Soc. 1999)

information, there are two other NMR observables: T_1 and spin-spin relaxation time T_2. The former follows the so-called Korringa relationship [12.36] with temperature T if the Pt atoms under observation are in a metallic state (Fig. 12.7c). The latter T_2 relaxation curve can be modulated by a J-coupling interaction (the same interaction also causes the ubiquitously observed J-coupling satellites in solution NMR) with the next-nearest neighboring Pt atoms provided that the neighboring atoms resonate at very different frequencies with a difference that is much larger than the J value (i. e., they are magnetically different species in the NMR sense), which is almost always the case for the Pt-based NPs [12.34]. An experimental observation of such modulation is illustrated in Fig. 12.5.

To understand better how the modulation (also called slow beat) as observed in Fig. 12.5 happens, let us look first at two next-nearest neighboring nuclear spins I_j and I_k with a spin value of 1/2 (like ^{195}Pt) and assume that I_k is the observing nuclear spin. If the difference in their resonance frequencies Δf is larger than the J-coupling strengthen J, i. e., $\Delta f \gg J$, then the contribution of J-coupling to the Hamiltonian of I_k can be truncated in a *secular* form of JI_kI_j. For a given spin orientation of I_j, J-coupling thus leads to spin f_k resonating either at $f_k + J/2$ or $f_k - J/2$, depending on whether the orientation of I_k is parallel or anti-parallel to that of I_j (where f_k is the resonant frequency of I_k without J coupling). This leads to a frequency difference of $J/2$ for either the parallel or anti-parallel spins of I_k with respect to f_k. For a normal T_2 measurement, the classic Hahn $\pi/2$–π-echo pulse sequence, as shown in the inset of Fig. 12.5, is usually used. So a phase difference of $J\tau_d/2$ will be developed in the first τ_d period for the parallel spin I_k with respect to the reference frequency f_k. If the ensuing π can also flip I_j, then the relative spin orientation between the original pair of I_j and I_k will be intact and another phase difference of $J\tau_d/2$ will be developed in the second τ_d period, leading to a total accumulative phase difference of $J\tau_d$. As τ_d varies in a T_2 measurement, so does the phase difference $J\tau_d$, consequently the modulation of the echo amplitude as observed in Fig. 12.5 (the same can be said for the anti-parallel I_k).

Mathematically [12.34], the spin echo modulation is proportional to $\cos(J\tau_d)$ if I_k is only couple to one I_j. For two I_js, the situation becomes a little more involved: a total phase shift of $2J\tau_d$ will be developed if the two I_js are parallel but zero phase shift if they are anti-parallel. Consequently, the spin-echo modulation follows $1/2\cos(2J\tau_d) + 1/2 = \cos^2(J\tau_d)$. Similarly, for r I_js, the amplitude modulation of spin echo of I_k is pro-

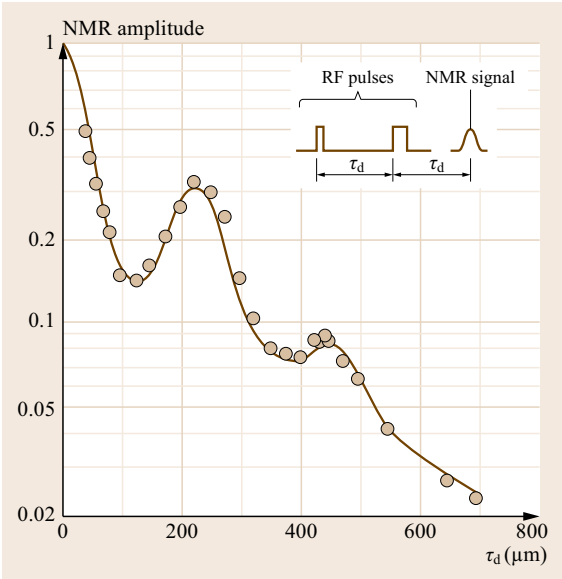


Fig. 12.5 J-coupling induced spin-echo amplitude modulation as measured by the Hahn spin echo sequence (*inset*) on Pt NPs of size between 5−10 nm at the spectral position of 1.138 G/kHz (Fig. 12.4 for more information) and temperature of 4.2 K. The *solid line* is a fit to (12.2) (after [12.34])

portional to $\cos^r(J\tau_d)$. These considerations lead to the first formula in (12.1) (Fig. 12.5) with P_r represents the probability that spin I_k J-couples to r neighboring I_js. Since the strength of J coupling falls rapidly as distance between two coupling spins increases [12.37], and considering that a Pt atoms can only have up to 12 next-nearest neighboring Pt atoms, the first formula in (12.1) can be simplified into the second one. Practically, (12.2) in Fig. 12.5 has been proven to be adequate to describe the experimentally-observed spin-echo modulations, assuming that the spread in J values follows a Gaussian (the $\exp[-(\tau_d/T_{2J})^2]$ term in the formula)

$$S = S_0 \exp\left(-\frac{2\tau_d}{T_2}\right) \sum_{r=0}^{\infty} P_r \cos^r(J\tau_d)$$

$$= S_0 \exp\left(-\frac{2\tau_d}{T_2}\right) \sum_{m=0}^{12} B_m \cos(mJ\tau_d) \qquad (12.1)$$

$$S = S_0 \exp\left(-\frac{2\tau_d}{T_2}\right) \left\{B_0 + \exp\left[-\left(\frac{\tau_d}{T_{2J}}\right)^2\right] \times [B_1 \cos(J\tau_d) + B_2 \cos(2J\tau_d)]\right\} \qquad (12.2)$$

There, B_0, B_1, and B_2 account for the probability of having zero (^{195}Pt has a nature abundance of $\approx 34\%$), one, and two J-coupled neighboring (^{195}Pt) spins, respectively. So the most salient point here is that the amplitude of the J-coupling modulation observed in T_2 curves (i. e., B_0, B_1, and B_2) depends on the number of the next-nearest neighboring ^{195}Pt atoms. With this connection, local (spatially atomic layer-resolved) Pt fraction can in principle be deduced for a Pt-based bimetallic alloy system by measuring the J-coupling modulated T_2 relaxation curves [12.38].

Finally, once the T_1 is measured at a spectral position K, we can use a well-established Pt two-band phenomenological/parameterized model [12.39] to deduce the electronic partition between the s- and d-like Fermi level local density of states (E_F-LDOSs) at the K, i. e., at a spatially atomic layer-resolved position.

12.1.2 Study of Ru@Pt Versus Au@Pt M (Ru/Au) Core–Pt Shell NPs

We now discuss a comparative study of Ru@Pt versus Au@Pt M(Ru/Au) core-Pt shell NPs [12.40] to illustrate how we can harness the investigative power of the in situ spatially-resolved ^{195}Pt EC-NMR for achieving a better understanding of fundamentals of electrocatalysis on Pt-based electrocatalysts.

Figure 12.6 shows the point-by-point ^{195}Pt NMR spectra of the as-received (*red*) and EC-cleaned (*blue*) samples of Au@Pt (with Pt packing density (PD) = 3.8, a) and of Ru@Pt (with Pt PD = 0.4, d) core-shell NPs in comparison with that of the pure Pt/C NPs [12.32] (black dashed lines and open circles, the same as in Fig. 12.4b), all recorded in a supporting electrolyte (0.1 M $HClO_4$) at 80 K. The vertical dashed line indicates the surface peak position (1.1000 G/kHz,) of the EC-cleaned pure 2.5 nm Pt/C NPs (Fig. 12.4b). Although the frozen electrolyte at 80 K prevented active potentiostatic control, the tightly vacuum-sealed sample cell ensured that the sample surface potential would not change during the NMR measurements. This was verified by measuring open circuit potentials before (0.25 V versus Ag/AgCl) and after each NMR measurement that always indicated that a constant potential was indeed achieved.

The as-received Au@Pt NPs had a shelf life of more than 48 months [12.42], therefore, the surface was heavily oxidized, as indicated by the peak of Pt oxide at 1.089 G/kHz (Fig. 12.6a). Notice that distinguishing a Pt surface covered by adsorbed oxygen from that by Pt oxide is straightforward. After the EC cleaning, the Pt oxide peak disappeared and a clean-surface peak appeared at 1.0975 G/kHz. The latter amounts to a 2278 ppm *positive* shift with respect to the clean-surface peak position (1.1000 G/kHz) of the pure Pt NPs, manifesting a strong electronic effect of Au on Pt. The

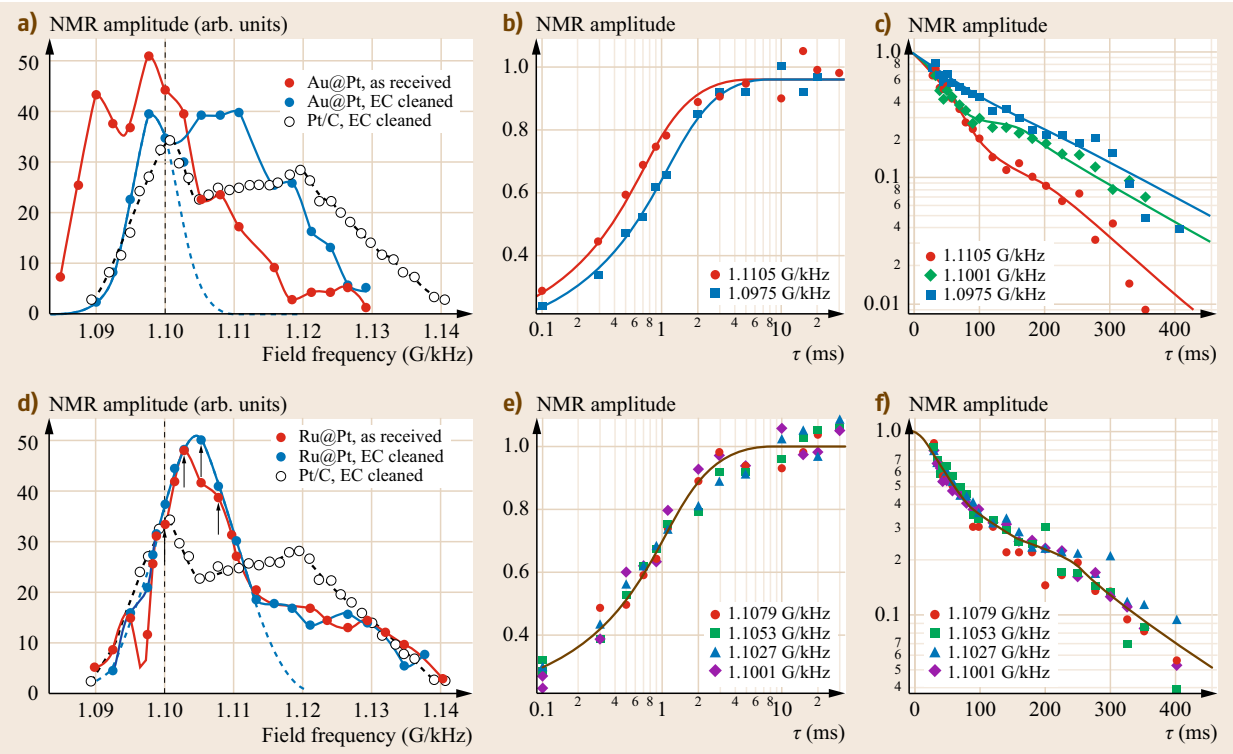


Fig. 12.6 Point-by-point ^{195}Pt NMR spectra **(a,d)**, spin-lattice relaxation curves **(b,e)**, spin-spin relaxation (J-coupling modulation or slow-beat) curves **(c,f)** for the Au@Pt **(a–c)** and Ru@Pt **(d–f)** NPs, respectively. The calculated Pt packing density was 3.8 for the Au@Pt and 0.4 for the Ru@Pt NPs. According to the linear relationship between the Pt fraction on surface and the nominal Pt PD discovered in [12.41], the expected Pt surface fraction would be 1.3, i. e., a fully Pt covered Au core. The % of the total deposited Pt on the surface would be $\approx 1.3/3.8 = 0.34$, in an excellent agreement with the value of 33% determined by ^{195}Pt NMR in **(a)** (after [12.40], courtesy of Am. Chem. Soc. 2012)

significant portion of the ^{195}Pt atoms in the Au@Pt NPs resonating at higher fields (above 1.1000 G/kHz) indicates that many deposited Pt atoms went inside the Au NPs. Indeed, using a Gaussian de-convolution of the surface peak (the dashed blue curve in Fig. 12.6a), we found that only $\approx 33\%$ of all deposited Pt atoms were on the surface of the Au@Pt NPs, which is in agreement with expected atomic exchange between deposited Pt atoms and the underlying Au atoms [12.41]. Notice that such a $\approx 33\%$ value is actually predicted by the linear relationship between the Pt fraction on surface and the nominal Pt PD discovered in [12.41] (Fig. 12.6).

The as-received Ru@Pt NPs were freshly synthesized with a shelf life of only a few hours [12.43]. Under the protection of ethylene glycol, little surface oxidation was expected in such a short time. Indeed, no significant surface oxidation was observed in the corresponding ^{195}Pt NMR spectrum in Fig. 12.6d (red). The clean-surface peak (blue line) now appeared at 1.1053 G/kHz, corresponding to a 4795 ppm *negative* shift with respect to the clean-surface peak position (1.1000 G/kHz) of the pure Pt NPs, revealing a strong electronic effect of Ru on Pt as well, which is *opposite* to that of Au. A Gaussian de-convolution of the surface peak gave a surface atom fraction of $\approx 74\%$, indicating a dominant Ru core Pt shell structure.

The T_1 and T_2 relaxation measurements are presented in Fig. 12.6b,c for the EC-cleaned Au@Pt and in Fig. 12.6e,f for the EC-cleaned Ru@Pt, respectively, at the spectral positions listed in the respective figures. Detailed discussion of the relaxation results is out of scope here due to limited space, but it suffices to demonstrate the most important difference here. Both the T_1 (Fig. 12.6e) and T_2 (Fig. 12.6f) at different spectral positions on Ru@Pt fall into the *same* respective relaxation curves, which is a manifestation of the same chemical environment, i. e., the majority of the Pt atoms were on the surface. Particularly, a J-coupling modulation analysis [12.38] of the data in Fig. 12.6f by fitting to (12.2) gives a Pt atomic fraction of 0.37. Since for a full pseudo-morphic Pt monolayer on a Ru (0001) surface, the Pt atomic fraction among all the possible

Table 12.1 E_F-LDOS values deduced from ^{195}Pt and ^{13}C NMR data (1 Ry = 13.6 eV and mol = molecule)

Samples	$D_s(E_F)$/(Ry atom)	$D_d(E_F)$/(Ry atom)	$D_{5\sigma}(E_F)$/(Ry mol)	$D_{2\pi}(E_F)$/(Ry mol)
Ru@Pt	3.7 (2.9)	13.3 (12.9)	0.7	4.9
Au@Pt	4.3 (3.0)	10.1 (12.7)	0.6	5.8
Pt	5.1 (3.4)	13.5 (15.2)	0.7	6.7

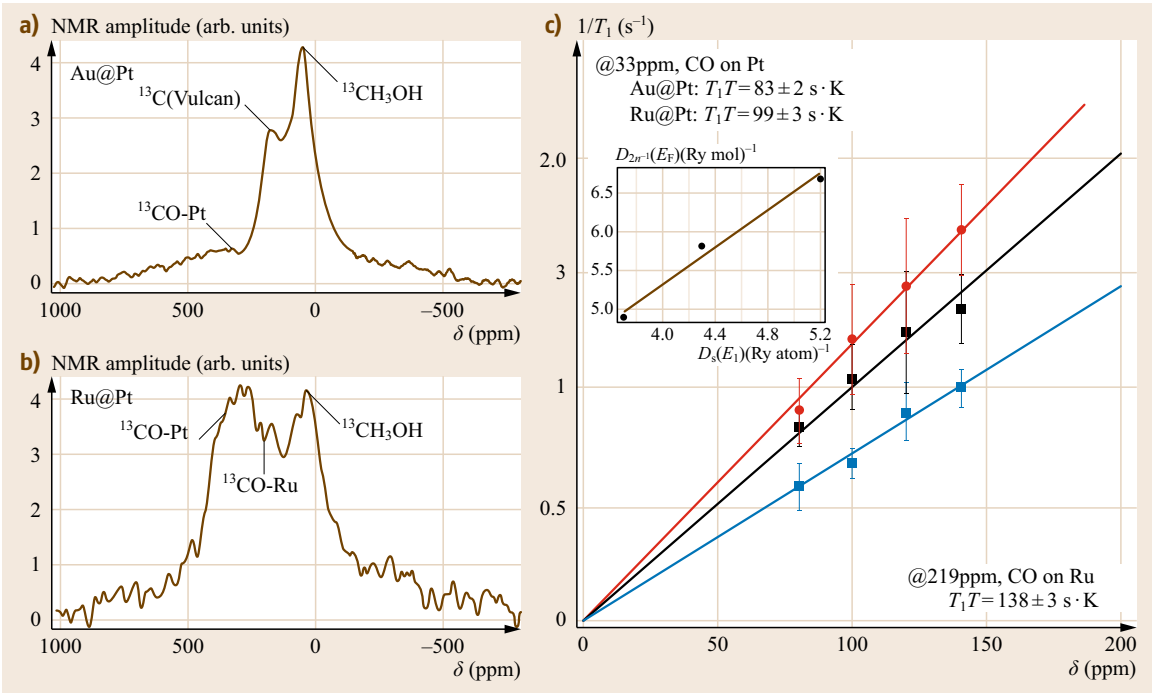


Fig. 12.7 ^{13}C NMR spectra (9.39 T, 80 K) of chemisorbed CO on **(a)** Au@Pt and **(b)** Ru@Pt NPs. Electrodeposition of CO was performed by holding the potential at 0.35 V versus Ag/AgCl (3 M) while immersed in 0.5 M D_2ClO_4 with $^{13}CH_3OH$. $^{13}CH_3OH$ at 49 ppm was also used as an internal shift reference. **(c)** Temperature-dependent T_1 relaxation measurements obtained at 333 ppm for CO-Pt/Ru@Pt and CO-Pt/Au@Pt and at 219 ppm for CO-Ru/Ru@Pt (after [12.40], courtesy of Am. Chem. Soc. 2012) *Inset* in **(c)**: Linear correlation between the $D_{2\pi^*}(E_F)$ and $D_s(E_F)$

next nearest neighbors is $6/9 = 0.67$, a local Pt atomic fraction of 0.37 is thus consistent with a Pt PD of 0.4 of mono-atomic Pt islands. In contrast, both the T_1 (Fig. 12.6b) and T_2 (Fig. 12.6c) at different spectral positions on the Au@Pt were different, which indicates a wider distribution of Pt atoms on surface and inside the NPs as well.

From the T_1 value, the known spectral position and temperature at which the T_1 is measured, one can use the aforementioned two-band model to calculate the s- and d-like E_F-LDOSs, denoted here as $D_s(E_F)$ and $D_d(E_F)$ respectively [12.39]. These values for the surface Pt atoms in Au@Pt and Ru@Pt samples are collected in Table 12.1. As can be clearly seen, Au and Ru cores exert different (opposing) electronic influences on the Pt shell: the former lowers the d-like E_F-LDOSs more while the latter lowers the s-like E_F-LDOSs more.

Also collected (in the parentheses) in Table 12.1 are the average surface values calculated by using the OpenMX density functional theory (DFT package on Pt13@Pt42 (Pt55), Ru13@Pt42 and Au13@Pt42 cubo-octahedral clusters. Considering the very simplified cluster models, it is remarkable that the experiments and theoretical calculations have achieved a good agreement in numerical values and in trend for both $D_s(E_F)$ and $D_d(E_F)$.

How changes in the surface Pt s- and d-like E_F-LDOS induced by the Au and Ru cores influence metal-adsorbate bonding was probed and corroborated by ^{13}C NMR of ^{13}CO adsorbed onto the Au@Pt and Ru@Pt NPs via dissociative adsorption of $^{13}CH_3OH$ (MeOH). The ability to probe the surface electronic properties by using surface-adsorbed molecules, such as adsorbed ^{13}CO, is among the unique investigative strengths of in situ EC-NMR. Figure 12.7 shows the ^{13}C NMR spectra

of ^{13}CO on Au@Pt (a) and on Ru@Pt (b) NPs, with the assigned peaks indicated by the arrows. For the Au@Pt sample, despite the dominant peaks from the remaining MeOH in the electrolyte and the carbon support, the broad and weak – yet still discernable – ^{13}C NMR peak at $\approx$ 333 ppm was assigned to the adsorbed CO, an assignment corroborated by the temperature-dependent T_1 measurements (vide infra). For the Ru@Pt sample, the peaks at $\approx$ 300 ppm and $\approx$ 219 ppm can be assigned to CO on Pt and on Ru sites, respectively, based on the literature values [12.44, 45]. The difference in the signal strength of the adsorbed CO on the Au@Pt and Ru@Pt NPs may reflect the difference in dissociative adsorption of MeOH on the respective surfaces.

The results of temperature-dependent T_1 measurements are presented in Fig. 12.7c. For the CO on Pt, the T_1's were measured at 333 ppm for both Au@Pt and Ru@Pt samples to facilitate comparison, although the peak position for the latter was at $\approx$ 300 ppm. The pass-through-origin straight lines are the hallmark of the Korringa relaxation behavior [12.36], which indicates that the adsorbed CO molecules on three different sites all acquired metallic characteristics through surface bonding. For CO on Ru sites, the shift (219 ppm) and Korringa constant $T_1T = 138\,\mathrm{s} < K$ (where T is the absolute temperature at which T_1 is measured) are very close to those observed on pure Ru [12.45] and on Ru deposited on Pt NPs [12.44], which lends strong support to our peak assignment that is also consistent with the expected exposure of Ru core for a Pt PD of 40%. On the other hand, the Korringa constants measured at the same spectral position (333 ppm) were different for CO on surface Pt atoms of the Au@Pt and on those of the Ru@Pt NPs. The former showed a faster relaxation (i. e., smaller Korringa constant T_1T), and thus a stronger metal-adsorbate bonding. In fact for CO on Pt, we can also deduce the values of the respective 5σ- and $2\pi^*$-like E_F-LDOS, i. e., $D_5\sigma(E_F)$ and $D_2\pi^*(E_F)$, at ^{13}C by using a different two-band model developed for adsorbed CO on Pt [12.46].

As can be seen from the data in Table 12.1, the $D_5\sigma(E_F)$ was essentially constant, while the $D_2\pi^*(E_F)$ decreased proportionally (inset in Fig. 12.7c) with the $D_s(E_F)$ for CO on Pt from pure Pt to Au@Pt to Ru@Pt. This suggests that the electronic alterations on metal-CO bonding, i. e., changes in metal to CO $2\pi^*$ back-donation [12.47] and therefore in bonding strength, were mainly caused by the variations in the $D_s(E_F)$ of the surface Pt atoms. On the other hand, it has been observed that the ability to dissociatively adsorb MeOH that leads to adsorbed CO follows the order Pt $\approx$ Ru@Pt > Au@Pt, which shares the same order in the respective $D_d(E_F)$ as shown in Table 12.1. These results suggest that the d-like electrons are probably responsible for agostic interaction that activates the three methyl protons in MeOH during its dissociative adsorption.

Recent quantum calculations on oxide-supported Pt model systems by *Koningsberger*, *Ramaker* and co-workers [12.48] have (re-)unearthed a potentially important and also more chemically intuitive surface bonding descriptor – the electronic partition, i. e., 6sp versus 5d electrons, at Pt that has been less (if not at all) investigated in electrocatalysis. The calculations predict that the Pt–H bond would be stronger at a Pt site with higher 6sp partition, while the Pt–O bond would be stronger at a Pt site with higher 5d partition, with Pt–CH_3 and Pt–CH_2 in between. The relatively recent application of the crystal orbital hamiltonian population (COHP) formalism [12.49] within the extended Hückel molecular orbital (MO) theory to chemisorption of CO, hydrogen, methyl and ethyl to metal surfaces by *Hoffman* and co-workers [12.50] also highlight the revealing power of such a chemistry-based electronic-orbital-specific (EOS) formalism. For instance, the COHP analysis revealed that the metal *sp* orbitals actually contribute significantly (much more than previously believed) to the overall CO-Ni and CO-Pt chemisorption [12.51–53]. Also, based on the COHP analysis, strong agostic interactions between the C–H bonds of methyl and ethyl groups and the Pt sites of high symmetries were proposed for C–H bond activation [12.50]. This may find useful application in further delineating the mechanism of the formic acid oxidation reaction (FAOR) and the methanol oxidation reaction (MOR) on metal (Pt) surfaces, where C–H bond-breaking is a necessary reaction step.

Indeed, the aforementioned EOS description has long been embodied in the organometallic analogy of surface bonding advocated by *Somorjai* [12.54–56] and in the frontier-orbital formalism by *Hoffmann* [12.57, 58], which has been very successful in rationalizing many reaction mechanisms at solid/gas interfaces of heterogeneous catalysis. It is somewhat surprising that it has not found wide-spread use in electrocatalysis lately, which might have to do with the fact that the powerful valence-electron-orbital-probing ultraviolet photoelectron spectroscopy is not applicable to a solid/liquid interface, so a direct experimental connection with the chemically intuitive EOS description is thus lost. Nonetheless, we strongly believe that an EOS description as briefly mentioned above can complement the highly successful d-band center theory by offering more chemical specificity in terms of surface-bonding-involved electronic orbitals by which the chemistry taking place at an EC interface may be better nuanced. Moreover, FAOR, MOR, and oxygen reduction reaction (ORR) at an electrode surface, all involve elementary reaction steps that will necessarily have Pt–H, Pt–O,

Pt–CH_3, and/or Pt–CH_2 bond formation and C–H, O–H, and/or O=O bond breakings, either sequentially or simultaneously. They can thus serve as a natural and fertile testing ground for the EOS description. Therefore, the EOS description can help parse more insightfully the chemistry of M@Pt core-shell NPs for fuel cell electrocatalysis as a function of core element M at an electronic and molecular level.

Summarizing above, the in situ ^{195}Pt EC-NMR can not only put the opposing core electronic effects by Au and Ru on Pt shell in more specified electronic terms, i. e., Au core lowered its d-like E_F-LDOS while Ru lowered its s-like E_F-LDOS, but also enable the radial distribution of Pt to be discerned: deposited Pt stayed on the Ru core surface with a Pt's atomic fraction of 0.37 but diffused into the Au core. These observations are further complemented by the ^{13}C NMR using CO as a local molecular probe. The linear correlation between the $D_2\pi^*(E_F)$ and $D_s(E_F)$ (inset in Fig. 12.7c) highlights the importance of the Pt's sp electrons in surface bonding, as predicted by the EOS-based theories. Moreover, the correlation between Au@Pts poor ability in dissociating methanol to CO and its substantially decreased d-like E_F-LDOS led us to hypothesize that d-like electrons may be mainly responsible for the agostic interaction between C–H bonds and Pt sites that activates the former. Altogether, these observations exemplify that the unprecedented detailed EOS chemical information about surface bonding can be unraveled by the in situ spatially-resolved ^{195}Pt EC-NMR that is further substantiated by the ^{13}C NMR of adsorbed CO as a local molecular probe.

12.2 NMR/MRI Studies of Energy Storage (Batteries) Materials

NMR, particularly Li NMR [12.59], has played and continues to play an (expanding) important role in offering probably the most versatile tool in characterizing batteries materials. Earlier studies were dominated by ex situ ^{7}Li (MAS) magic angle spinning NMR which has been rather thoroughly reviewed by *Grey* and *Dupré* [12.25]. Despite the plethora of chemical information that can be gleaned by employing ex situ (Li) NMR, the major disadvantage of it is that the electrode materials in an operating battery are always in

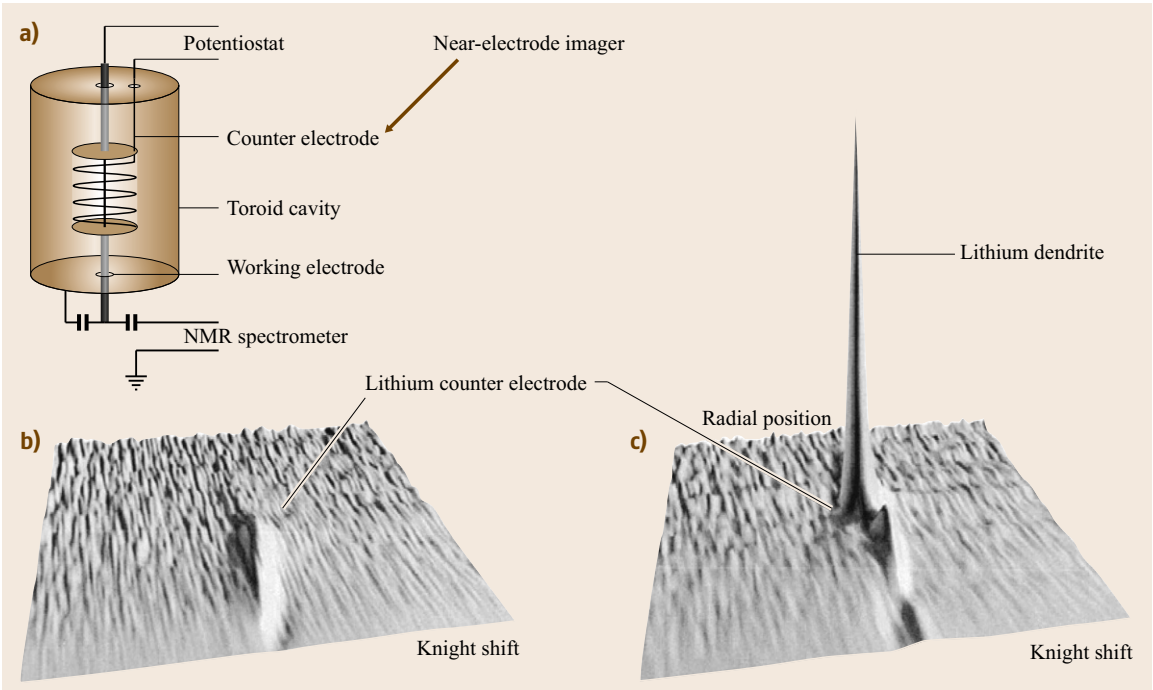


Fig. 12.8 **(a)** Schematic of a near-electrode imager of cylindrical symmetry. **(b,c)** ^{7}Li MRI images of the counter electrode and the Li dentrites that were formed on a hard carbon electrode in the presence of a Li counter electrode before **(b)** and after **(c)** passing current through the cell (after [12.60, 61])

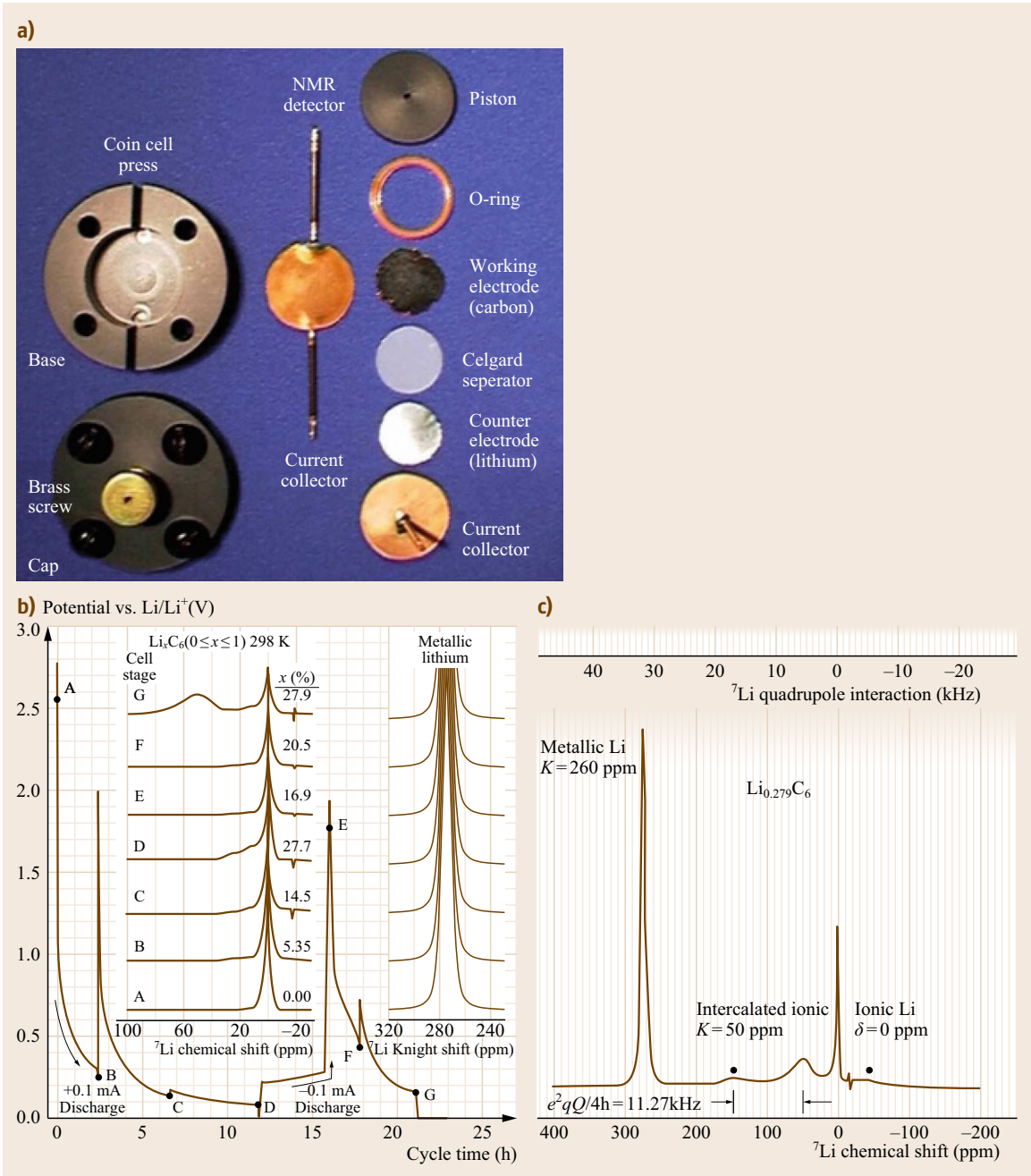


Fig. 12.9 **(a)** Color photo of the real components that made the compression coin cell. **(b)** Step-wise stacked ^{7}Li NMR spectra as a function of x in Li_xC_6 ($0 \le x \le 1$) together with the corresponding EC Li insertion curves (cell potential versus charge capacity). **(c)** A single full-view in situ ^{7}Li NMR spectrum as the one taken at Stage G in **(b)** that shows all the active components in a lithium-ion electrochemical cell: the metallic Li peak of the Li metal counter electrode (anode) at 275 ppm, the Li species in electrolyte at 0 ppm and in solid-electrolyte interface (SEI) at 6 ppm, and the intercalated Li in the carbon electrode (cathode) $Li_{0.279}C_6$ at $\approx$ 50 ppm, which also sees a quadrupolar interaction of $\approx$ 11.27 kHz (after [12.60])

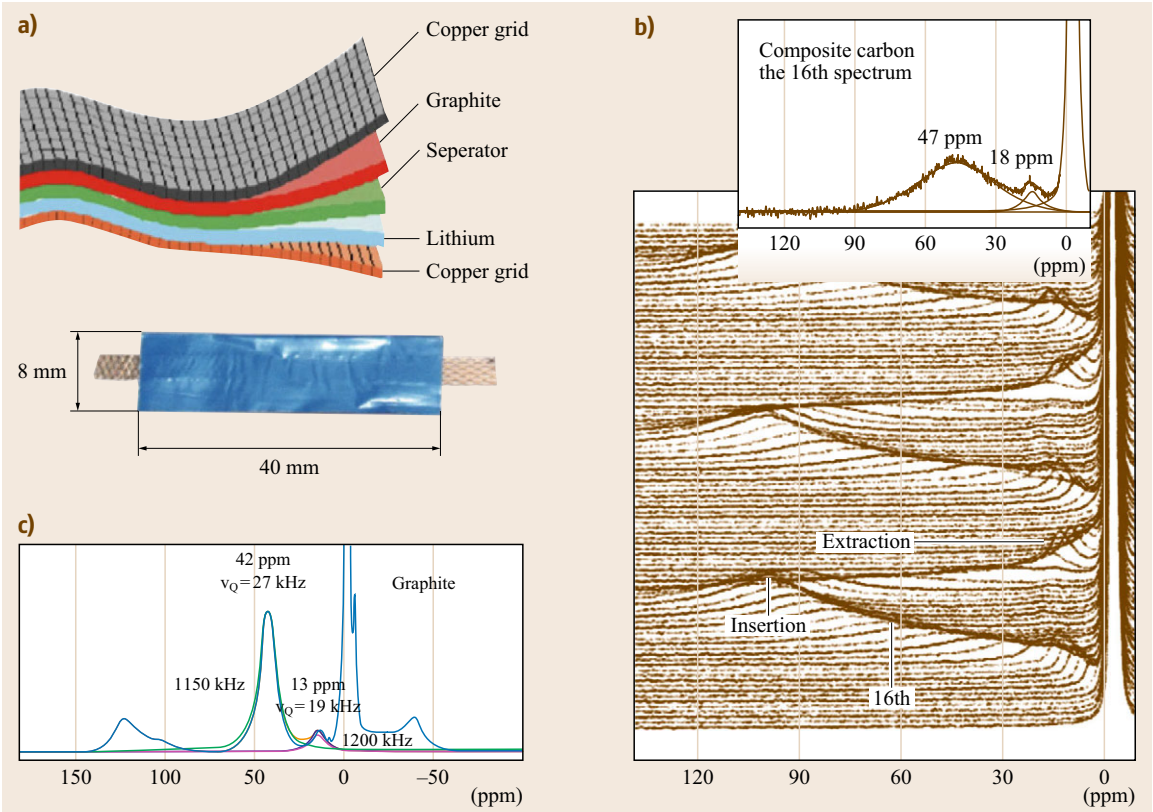


Fig. 12.10 **(a)** Schematic of a Bellcore-like plastic flexible battery cell (*top*) and a photo of a real Bellcore cell hermetically sealed in a blue plastic bag (*bottom*). **(b)** Stacking plot of in situ ^{7}Li NMR spectra as the flexible cell being cycled through Li insertion/discharge into and extraction/charge from disorder composite carbon. The *inset* shows the 16th spectrum as indicated by the *vertical arrow*. The peak at ≈ 18 ppm was assigned to Li *intercalated* between badly stacked graphene sheets and the one at ≈ 47 ppm to 1 and 2 dense insertion stages (i. e., LiC_6 and LiC_{12}. No quadrupolar structures were observed, suggesting fast Li diffusion. **(c)** an in situ ^{7}Li NMR spectrum obtained when Li was inserted into graphite electrode in which quadrupolar spectral structure was observed. The peak at ≈ 42 ppm with $\upsilon_Q = 27$ kHz was assigned to LiC_6 structure [12.62] (after [12.62–65])

an air-tight environment but this is not the case in ex situ NMR measurements, which prevents short lived transient species and structures from being identified and characterized. Yet, probing and understanding these short lived species and structures is critically important in delineating fully the governing chemistry in working batteries and only by which better batteries can be developed in more efficient ways. The latter is indeed the driving force for the development and application of the in situ NMR technique that will be discussed below.

12.2.1 Toroid Resonator: Near-Electrode Imager Versus Compression Coin Cell

Employing toroids detection [12.66], *Gerald* and coworkers were probably the first to pioneer in situ NMR and MRI studies of Li-ion batteries [12.60, 61], as illustrated in Figs. 12.8 and 12.9. Figure 12.8a shows the schematic of a near-electrode imager of cylindrical symmetry in which the central conducting (carbon-coated Cu) rod and the outer metal cylinder forms a toroid resonant cavity for NMR/MRI detection. The central rod also serves as the working (cathode) electrode while the inner symmetrically spiraling Li wire serves as the counter electrode (anode). When the RF current passing through the central conductor, it generates a circling irradiation magnetic field B_1 whose magnitude is proportional to $1/r$ (i. e., $B_1 \propto 1/r$) where r is the radial distance between a point within the outer cylinder and the central conductor. It is this mathematically expressible distance dependence that enables the spatial information along the radius to be encoded with the degree of

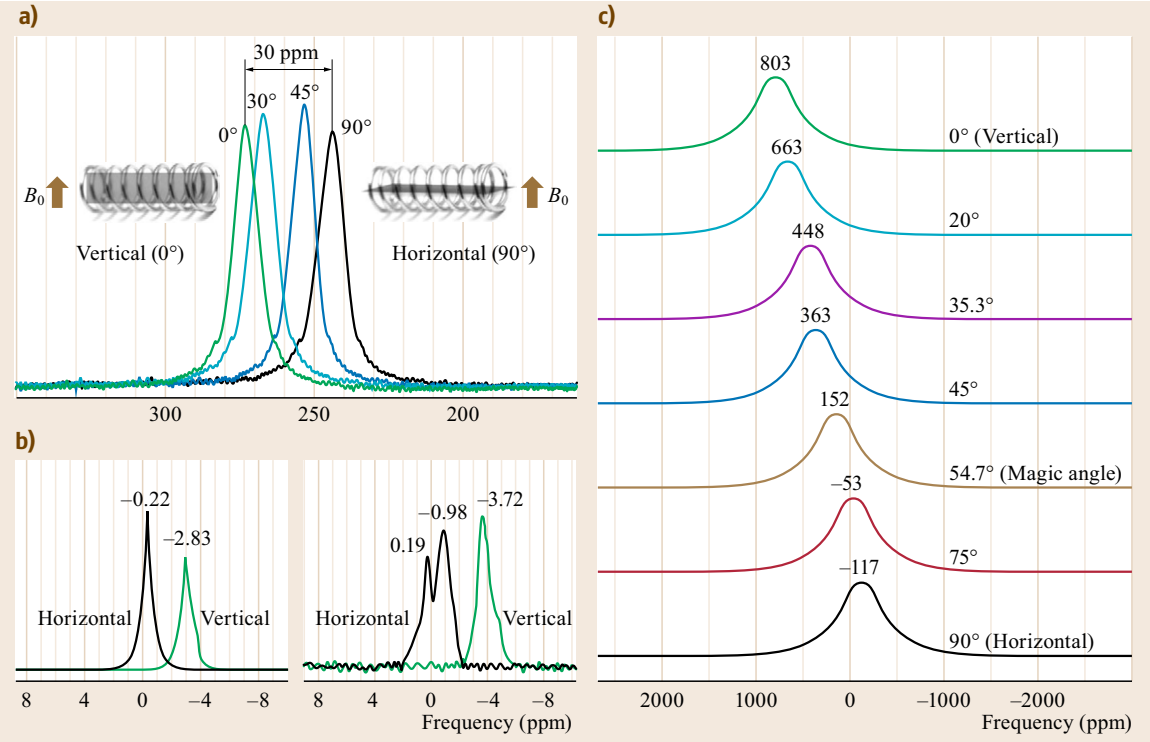


Fig. 12.11 Orientational bulk magnetic susceptibility (BMS) effect on in situ ^{7}Li NMR spectra obtained in **(a)** the Li metal thin film, **(b)** electrolyte (*left*) and an electrolyte-soaked borosilicate glass separator, and **(c)** a paramagnetic spinel $Li_{1.08}Mn_{1.92}O_4$ film (after [12.67])

spin nutation for imaging purposes (called B_1 imaging).

Because $B_1 \propto 1/r$, the closer a location is to the central conductor, the larger the field gradient is and therefore the spatial resolution at that place. This is the reason that a near-electrode imager, that can achieve micron scale spatial resolution, is called that. One advantage of the B_1 imaging as compared to the conventional B_0 imaging method is that the chemical shift information is retained in the former because each spatial point in the toroid cavity experiences the same external field B_0, which is clearly not the case in the latter. The imaging feasibility of the method is clearly demonstrated by the Li MRI images before (Fig. 12.8b) and after (Fig. 12.8c) passing current through the central conductor [12.61]. The former shows only an imaging signal at the position of Li counter electrode but the latter also shows an additional stronger and sharper imaging signal appeared at the inner side of the Li counter electrode and had a different Knight shift, which was assigned to the Li dentrite formed on the central carbon rod surface during operation of the cell. This was the first demonstration showing that Li NMR could be used to follow the growth of Li dentrites which is a safety issue in Li-ion batteries.

However, the configuration of the near-electrode imager not only shares little resemblance with that of real-world Li-ion batteries but also is not ideal for studying Li intercalation processes for it was practically not easy to produce mechanically robust coatings over the central conducting rod, neither to make a symmetrically compact solid-film electrolyte and counter-electrode about the central rod. In an attempt to overcome these shortcomings, an in situ NMR compression coin cell was developed [12.60], as shown in Fig. 12.9. The configuration of the compression coin cell was fashioned like a conventional 2032 stainless steel coin cell, with easily-made circular laminate components detailed in Fig. 12.9a, which were stacked over each other and held together by the base/cap press. The compression coin cell was then placed inside a toroid cavity resonator as shown in Fig. 12.8a, but now with the vertical current collector rod serving as the NMR detector as well.

With the setup of aforedescribed compression coin cell, the processes of Li insertion into disordered graphitic carbon ($LiPF_6$ as the electrolyte) and forma-

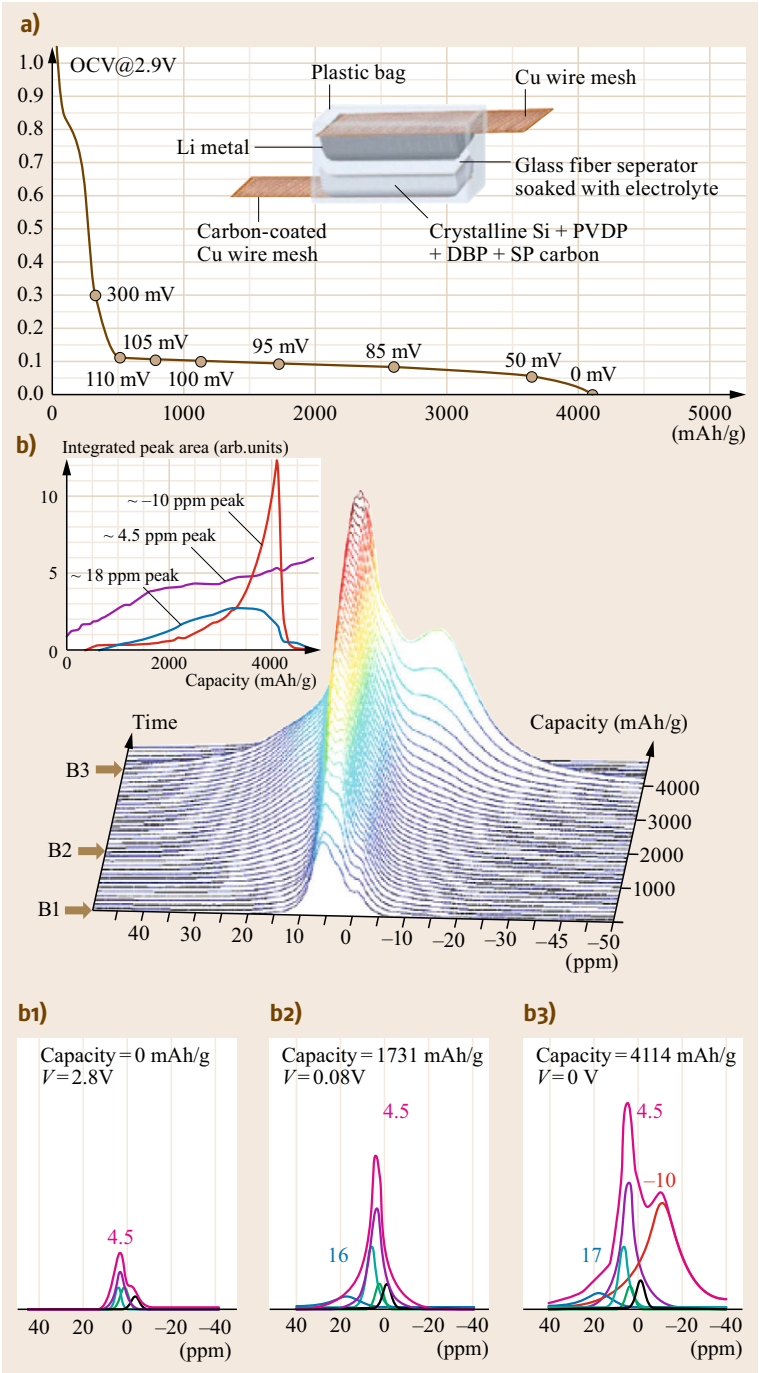


Fig. 12.12 **(a)** The schematic of a Bellcore-like flexible plastic Li-ion battery cell with a silicon electrode used for in situ ^{7}Li NMR studies and its first discharge profile. The initial cell potential, i. e., open circuit voltage (OCV), versus Li/Li^{+} was at 2.9 V (after [12.67–69], courtesy of Am. Chem. Soc. 2009). **(b)** The capacity-dependent in situ ^{7}Li NMR stacking spectra recorded as the battery being discharged and three individual spectra (B1 to B3) at different cell potentials as indicated. Three main peaks were *tentatively* identified via the de-convolution of the spectra: ≈ 18 ppm peak was assigned to the formation of small Si clusters, ≈ 4.5 ppm peak to the formation of isolated Si atoms, and the ≈ −10 ppm peak to the very reactive, metastable $Li_{15}Si_4$ phase. *The upper-left inset* shows their respective peak integrals as a function of capacity (after [12.69], courtsy of Am. Chem. Soc. 2009)

tion of solid-electrolyte interface (SEI) were followed by ^{7}Li NMR in situ (by alternating between EC and NMR experiments without exposing the electrode materials to air) for the first time, as shown by the stacked ^{7}Li NMR spectra in Fig. 12.9b [12.60]. Different Li species associated with different processes were identified (Fig. 12.9c) at different charging stages, particularly the formation of the SEI by the peak at 6 ppm and intercalation of Li into carbon matrix by the peak at 50 ppm. However, the configuration of the compression coin cell in the toroid cavity resonator makes the simple $B_1 \propto 1/r$ relationship no longer applicable, leading

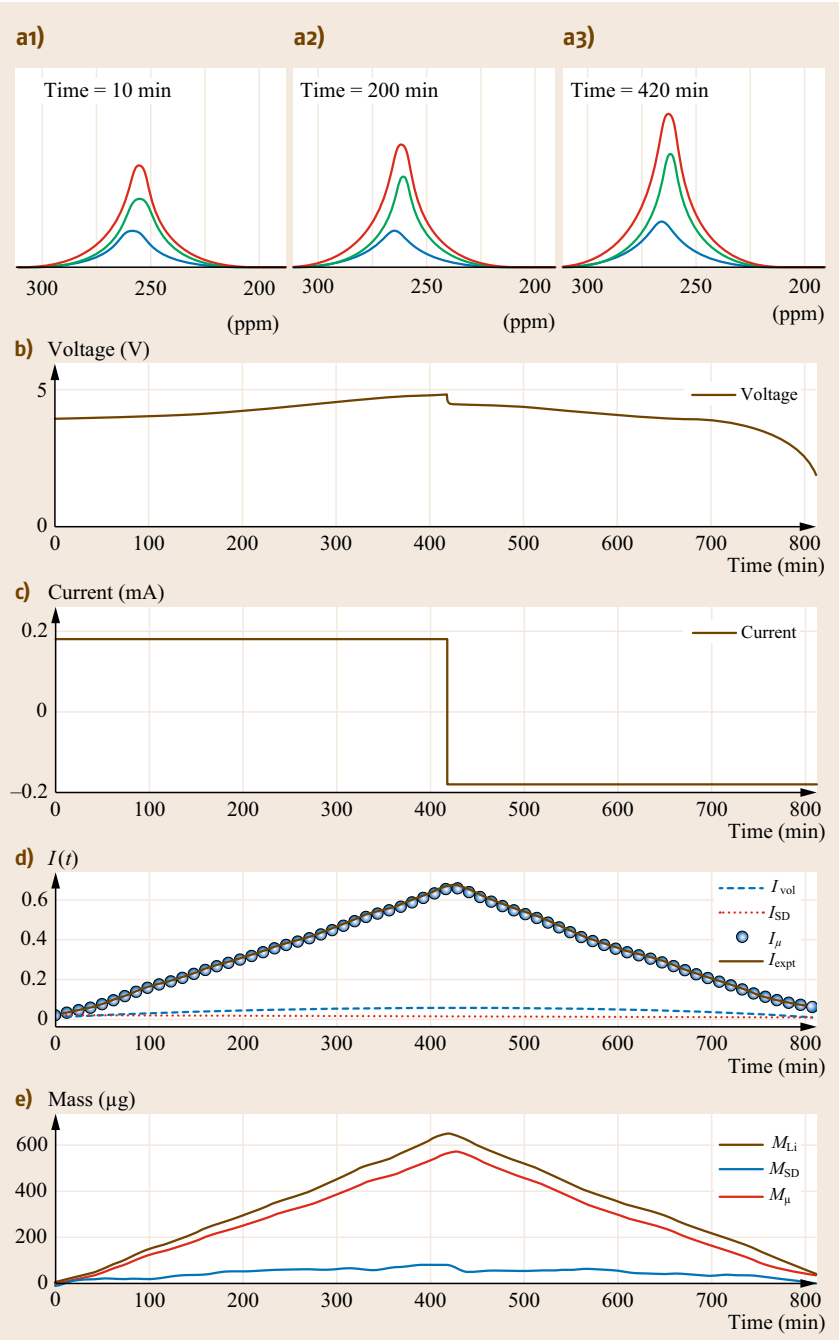


Fig. 12.13 Effect of one battery charge–discharge cycle on the formation of Li dentrite/moss in a $LiCoO_2$–Li cell as seen by in situ ^{7}Li NMR: **(a1–a3)** ^{7}Li NMR spectra with de-convolutions at three different times. **(b,c)**: The measured cell voltage/applied current. **(d)** I_{exp} (*solid black*) is the normalized ^{7}Li NMR signal intensity by $I_{exp} = [S(t) - S(t = 0)]/S(t = 0)$ where $S(t)$ is the raw NMR signal intensity. I_{vol} (*blue dashed line*), I_{SD} (*red dotted line*), and I_{μ} (*blue circles*) are theoretical results calculated under the assumptions that (1) there was no skin but volume (vol) effect, (2) all Li ions generated during the cycles were smoothly deposited (SD) back onto the Li metal surfaces, and (3) all of the lithium deposited/stripped forms microstructures, respectively. Only $I_{\mu}(t)$ provides a good fit to the experimental data. **(c)** M_{SD} (*blue*) is the mass of smoothly deposited or stripped metal and M_{μ} (*red*) is the mass of the microstructures (Li dentrite/moss) as calculated stoichiometrically using I_{exp} and assuming 100% Columbic efficiency (i. e., neglecting any side reactions). M_{Li} (*black*) $= M_{SD} + M_{\mu}$ (after [12.68], courtesy of Macmillan 2010)

to practical difficulties in developing the mathematical formulation for processing images.

12.2.2 Bellcore-Like Flexible NMR Cells

Despite its initial success of being used in investigating in situ Li ion insertion and extraction processes in operating batteries, the toroid cavity resonator setups as discussed above have two main technical inconveniences. The first is that the battery operation and NMR measurements can only be carried out sequentially because the central conducting rod can only be employed for either battery EC cycles or NMR excitation/detection but not both simultaneously. The second is that the

near-electrode imager setup (Fig. 12.8a) is intrinsically of a low-filling-factor thus poor signal-over-noise ratio and the compression coin cell setup (Fig. 12.9a) leads to a complicated distance dependence of B_1 that is mathematically inexpressible. Moreover, the toroid cavity resonator needs to be specially made. These technical inconveniences erect hurdles for a wider adaptation for battery research.

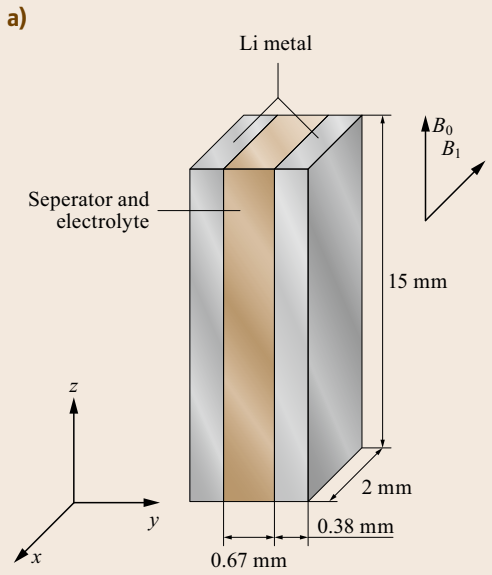
A battery cell in the form of Bellcore's plastic flexible Li-ion rechargeable batteries [12.70], as schematically shown in Fig. 12.10a, was first adapted by *Letellier* and co-workers for in situ NMR studies of Li-ion rechargeable batteries [12.62–65, 71]. The plastic flexible cell can be easily inserted into a conventional solenoid coil for NMR detection. Moreover, it does not physically share conducting parts with the NMR detection coil as it does with the toroids. This means that NMR spectra can be acquired while the battery is being actively charged and discharged. Figure 12.10b presents stack-plotted ^{7}Li NMR spectra so obtained as the battery cell with disordered composite carbon and Li metal sheet being EC cycled [12.65, 71]. There are four peaks of interest in the spectra: First, the peak at 263 ppm which is outside the spectral range used in Fig. 12.10b was from the Li metal electrode and the intense sharp peak at −2 ppm was from the Li ions in the electrolyte $LiPF_6$. As expected, both peaks stayed constant as the battery was being charged or discharged. Second, the peak that appeared soon after the EC cycle started and then varied between 0.8 and 18 ppm was from the fast diffusing Li ions intercalated between badly stacked graphene sheets. Third, the peak that varied between 18−104 ppm was from the *quasi metallic* Li ions that participated in the insertion and extraction processes [12.64]. The inset shows the 16th ^{7}Li NMR spectrum after EC cycle started. Interestingly, no spectral feature of quadrupolar interaction was observed. But when the Li ions were intercalated into a pure graphitic matrix, quadrupolar structures at given frequencies and increasing intensity corresponding to the successive occurrence of LiC_{36}, LiC_{27}, LiC_{18}, LiC_{12} and LiC_6, i. e., stages 4, 3, 2 diluted with chemical shift $\delta < 10$ ppm; then dense stages 2, 1 with $\delta \approx 43$ ppm as shown in Fig. 12.10c.

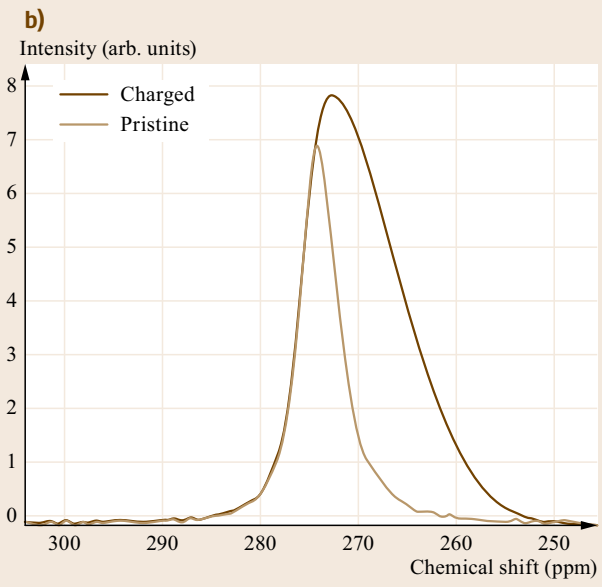
For the quasi 2-D rectangular-shaped Bellcore cell (Fig. 12.10a, bottom), a practically important phenomenon called bulk magnetic susceptibility BMS effect was discovered [12.68] and discussed [12.67] in detail by *Grey* and co-workers, shown in Fig. 12.11. For a Li metal thin film, the spectrum acquired with the Li film parallel to the static magnetic field B_0 is 30 ppm down-field shifted from that acquired with the film perpendicular to B_0 (Fig. 12.11a). This is due purely to sample-shape-caused bulk magnetic susceptibility anisotropy. As shown in Fig. 12.11b, the electrolyte in the cell separator can also experience a BMS effect, although the corresponding orientation-caused shift changes are relatively small. The largest BMS-effect induced orientation dependent shift was observed in paramagnetic spinel $Li_{1.08}Mn_{1.92}O_4$ film where shift difference between vertical and horizontal directions was observed to be as large as 920 ppm (Fig. 12.11c). Therefore, the BMS-effect induced peak changes must be studied, understood, and quantified first before any attempts to have correct peak assignments and to delineate correctly the battery-process caused peak shift.

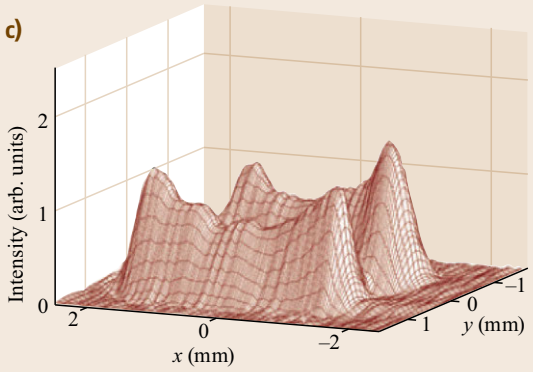
Fig. 12.14 **(a)** Schematic of a Li metal symmetric Bellcore-like flexible plastic cell and its orientation with respect to the static magnetic field B_0 the RF field B_1, and the *xyz* gradient axes used for MRI. **(b)** ^{7}Li NMR spectra of the cell before (*red*) and after being charged (*blue*) at 29 A/m^2 for 4 h. The area under the *blue* (charged) is 2.3 times larger than that under the red (pristine state) spectrum, indicating the substantial formation of the Li microstructures (dentrite/moss). **(c,d)** ^{7}Li 2-D MRI *x*–*y* image (frequency encoding in *x*, phase encoding in *y*) in the pristine **(c)** and charged **(d)** state, respectively. **(e,f)** scanning electron microscope (SEM) images of the pristine **(e)** and charged **(f)** samples (after [12.72], courtesy of Macmillan 2012) ►

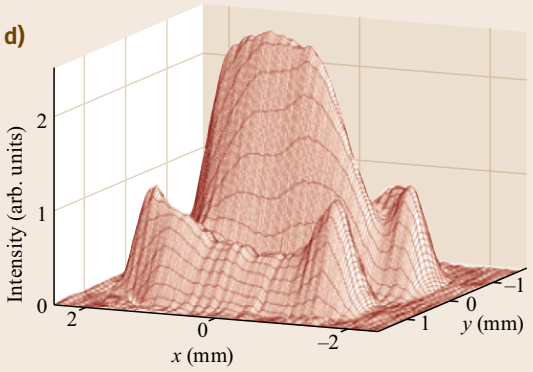
As pointed out at the very beginning of this chapter, one of the features that NMR possesses is its broad applicability to almost all forms of matter, be it a gas, liquid, or solid, or be it a crystalline or amorphous material. This is particularly advantageous when it comes down to investigating electrode materials used in batteries. For instance, silicone is considered a very attractive alternative material to carbon as it could potentially offer ≈ 10 times larger gravimetric as well as volumetric capacity than carbon. But it has been observed that repetitive Li insertion leads to volumetric expansion of the Si lattice to as high as 300% and turns starting crystalline Si into amorphous. In the latter case, NMR has been proven to be informative [12.69], of which a representative case will be discussed below.

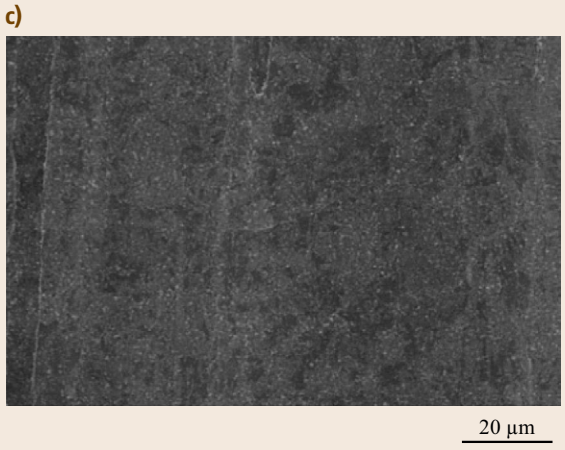
Figure 12.12a shows a schematic of the Bellcore-like battery cell for NMR studies that includes crystalline silicon as part of the negative electrode material [12.69]. Also presented in Fig. 12.12a is the first EC discharging profile of the cell. Notice that it was observed by ex situ ^{7}Li MAS magic angel spinning NMR that the reaction between the crystalline Si and inserting Li took place only after 110 mV because the negative electrode was made by a mix of carbon and silicon [12.69]. Figure 12.12b presents a stacking plot of ^{7}Li NMR spectra recorded during the lithium insertion,

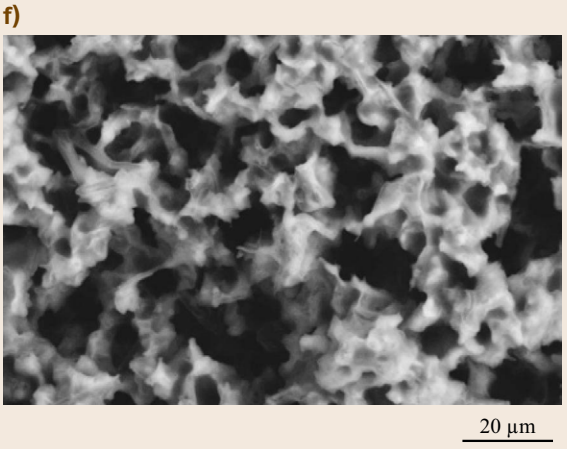

a)
Li metal
Seperator and electrolyte
B_0
B_1
15 mm
2 mm
0.38 mm
0.67 mm
z
y
x


b)
Intensity (arb. units)
Charged
Pristine
8
7
6
5
4
3
2
1
0
300
290
280
270
260
250
Chemical shift (ppm)


c)
Intensity (arb. units)
2
1
0
2
0
−2
x (mm)
−1
0
1
y (mm)


d)
Intensity (arb. units)
2
1
0
2
0
−2
x (mm)
−1
0
1
y (mm)


c)
20 µm


f)
20 µm

together with three individual spectra taken at three representative cell potentials (V)/capacities (mAh/g): 2.8/0 (zero capacity), 0.08/1731 (≈ half capacity) and 0/4114 (full capacity). De-convolution of these peaks enabled three main peaks to be (tentatively) identified: ≈ 18 ppm peak was assigned to the formation of small Si clusters, ≈ 4.5 ppm peak to the formation of isolated Si atoms, and the ≈ −10 ppm peak to the very reactive, metastable $Li_{15}Si_4$ phase, a short lived phase that was missed by the ex situ ^{7}Li MAS NMR but identified by the in situ static ^{7}Li NMR. As shown in the inset of Fig. 12.12b, the increase of the peak at −10 ppm seems to be at the expense of the peak at 18 ppm, although what the exact correlation between the two is is still unclear.

12.2.3 NMR/MRI Studies of Formation of Li Dentrites

Among Li ion batteries, formation of Li dentritic structures is highly hazardous because the formed dentrites can self-detach from the electrode surfaces, migrate from one place to another place, meet other floating dentrite in its journey, and eventually cause short circuits that can lead to fire and/or explosion. Therefore, understanding how and where the dentritic structures are formed inside the battery is of current interest to the energy storage community. Early toroid-based work by Gerald and co-workers (Fig. 12.8c) has already shown that ^{7}Li NMR could be used to observe the Li dentritic structures whose Knight shift was different and distinguishable from that of bulk metal Li.

Grey and co-workers recently made good use of metal skin effect and monitored, in a quantitative fashion, the growth of the Li dentritic structures in Bellcore-like cells by deploying in situ ^{7}Li NMR [12.68]. The idea is pretty straightforward: All conducting materials show skin effect if being subjected to RF irradiation. That is, physical penetration of the RF wave into a metal is limited up to the so-called skin depth d defined by the equation

$$d = \left(\frac{1}{\sqrt{\pi\mu_0}}\right)\left(\frac{\sqrt{\rho}}{\mu_r f}\right),$$

where μ_0 is the vacuum permeability, μ_r the relative permeability, ρ the resistivity of the metal and f is the frequency of the applied RF field (i. e., the Larmor frequency). For ^{7}Li NMR frequency of 77.8 MHz, a simple and straightforward calculation gives $d = 14.7\,\mu$m for Li bulk metal. On the other hand, it turns out that the dimension of Li dentritic structures and/or moss formed during battery operation is $< 5\,\mu$m. Thus, ^{7}Li NMR can in principle see all Li dentritic structures and/or moss formed in the cell but only to the depth of $d = 14.7\,\mu$m for Li metal electrode. To a good approximation, the latter should be a constant. Consequently, the observed increase in ^{7}Li NMR signal should be proportional to the amount of the formed Li dentrites.

This is indeed what was observed experimentally, as shown in Fig. 12.13 where the results of an in situ ^{7}Li NMR study of the formation of metallic Li microstructures in a $LiCoO_2$–Li Bellcore-like Li ion battery cell are presented [12.68]. The amount of growth and decay in the intensity of the Li metal NMR resonance, i. e., the normalized NMR signal $I_{exp}(t)$, is almost linear as presented in Fig. 12.13d. Quantitatively, the spectra (as represented by a1 to a3) could be de-convoluted into two peaks: one at 250 ppm which largely remained constant and one at 270 ppm which changed as the battery cell was being charged and discharged. As suggested by the results in Fig. 12.8c, the former can be assigned to the Li metal electrode and the latter to the Li microstructures formed during the charge-discharge cycle. The latter assignment was confirmed by the following three model analyses. The first model was to assume that all change in intensity of the Li signal was caused by volume but not skin-depth effect (I_{vol} in Fig. 12.13d), which was calculated by normalizing the Li NMR intensity expected for the mass of Li deposited (or stripped), M_{Li} (where the mass can be calculated from the current passed through the cell), by the total mass of the Li metal electrode in the cell. The second model was to assume that M_{Li} was all smoothly deposited back to the surface of Li metal electrode and then calculate the normalized Li NMR intensity by considering the normal skin-depth effect. This gave the value of I_{SD} in Fig. 12.13d. The third model was to assume that all M_{Li} formed Li metal microstructures which led to I_μ in Fig. 12.13d. After these analyses, it becomes arguably clear that neither I_{vol} nor I_{SD} but I_μ accounted the experimental observations well. The best fit was actually achieved if approximately 90% of M_{Li} formed as the microstructures (M_μ) in Fig. 12.13e) and the remaining 10% as a smooth deposition (M_{SD} in Fig. 12.13e) on the Li electrode.

While the above results clearly demonstrate the feasibility of carrying out quantitative studies of the formation of Li microstructures in Li ion batteries by in situ ^{7}Li NMR, which can have great practical ramifications, they still do not address another question of equal importance in practice: where are these Li metal microstructures formed inside the batteries? As already alluded to by the early work of Gerald et al. (Fig. 12.8c), critically insightful information about the geometric location of the formed Li microstructures can in principle be obtained by noninvasive MRI studies. A recent work by *Grey*, *Jerschow* and co-workers did just that [12.72].

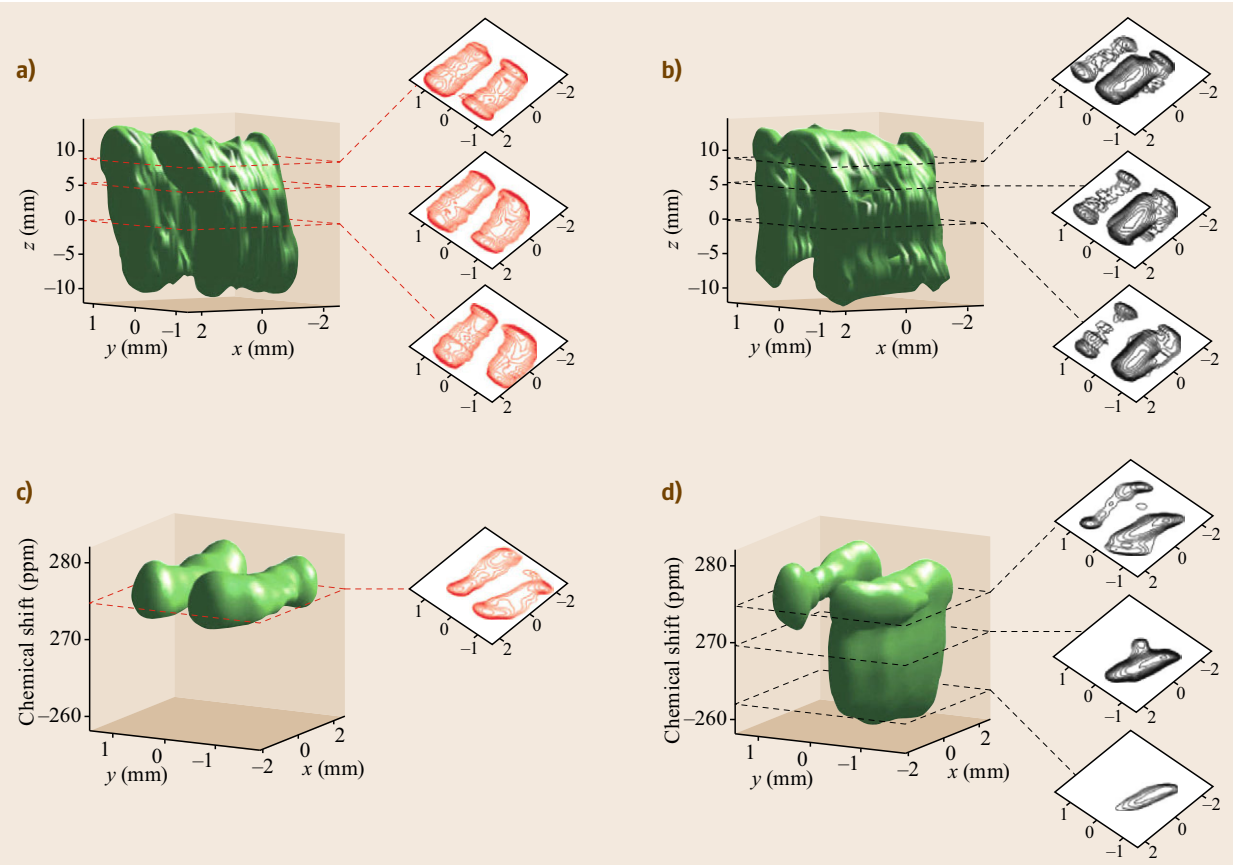


Fig. 12.15 **(a,b)** ^{7}Li 3-D MRI images of the Li-metal cell (frequency encoding in x, phase encoding in y and z) in its pristine **(a)** and charged **(b)** state. The 2-D slices in each panel are horizontal (x–y) cross-sections (perpendicular to the z direction). **(c,d)** Chemical shift imaging of the Li-metal resonance (phase encoding in x and y, chemical shift encoding in the directly observed dimension) in the pristine **(c)** and charged **(d)** state (after [12.72], courtesy of Macmillan 2012)

A symmetrical Li metal cell (in which Li metal is used as both anode and cathode, Fig. 12.14a) was the subject of that study in which not only conventional 2-D and 3-D ^{7}Li MRI images but also chemical shift imaging (CSI) images were obtained for both the initial pristine and subsequent charged states.

Practically, it was discovered that proper orientation of the Li metal cell with respect to the static field B_0 and to the RF field B_1 is critically important for achieving correct and faithful images. Most importantly, the Li metal electrodes must be parallel simultaneously to both the static magnetic field B_0 and the RF field B_1 as illustrated in Fig. 12.14a. Otherwise, the boundary conditions that must be satisfied at the surface of the Li metal electrodes will lead to erroneous images. With such parallel orientations, the initial pristine Li metal electrodes gave the red spectrum shown in Fig. 12.14b, with a peak position of ≈ 275 ppm which is in good agreement with the spectrum of vertical orientation shown in Fig. 12.11a. After being subjected to a unidirectional charging with a current density of 29 A/cm^2 for 4 h, the cell gave the blue spectrum in Fig. 12.14b. Following the case just discussed above (Fig. 12.13), the 130% increase in the detected ^{7}Li NMR signal can be assigned to the formed Li microstructures inside the cell.

The 2-D (xy) ^{7}Li MRI images of the respective pristine and charged cells are compared in Fig. 12.14c and 12.14d compare with a spatial resolution of $60 \times 376\,\mu$m in both the x- and y-directions. As can be seen in Fig. 12.14d, a more-than-2-fold signal build-up at the electrode located on the –y side was observed, together with $\approx 23\%$ decrease in the signal of the electrode located on the +y side. This image shows unambiguously where the formed Li microstructures are located. Notice that the corresponding SEM images (Fig. 12.14e,f) are consistent with the results obtained by ^{7}Li MRI: smooth image for the former but highly microstructured one for the latter.

Further detailed spatial information can be gleaned by full 3-D (*xyz*) MRI images as shown in Fig. 12.15a,b. Additionally, visualized information along the *z*-direction helps present a clearer picture on where and how the Li microstructures were formed and distributed (see the cross-section views/slices at different positions along *z*).

Moreover, the CSI images shown in Fig. 12.15c,d offer more chemical specific information. For instance, the image in Fig. 12.15d shows that the Li microstructures whose *xy* projection overlaps more with that of the Li electrode have a larger Knight shift variation which suggests a broader chemical site distribution. On the other hand, it can also be observed that the larger the Knight shift of a cross-section view is, the broader the area of the cross-section is. This indicates that the farther away the formed Li microstructure is from the Li metal electrode, the larger the Knight shift is but of a narrower distribution. In summary, combining the conventional MRI with CSI offers a powerful noninvasive in situ diagnostic tool of both quantitative analysis and space-resolving capabilities for batteries research.

12.3 MRI of Water Distribution in Fuel Cells

As illustrated by the schematic description of a proton exchange membrane (PEM) fuel cell (FC) in Fig. 12.16, water is an integral part and plays a crucial role in the proper operation of the fuel cell. For instance, the PEM needs to be properly wetted to enable efficient transfer of protons from anode to cathode. Water is also the main by-product of an operating fuel cell. But too much water can flood the gas diffusion layer (GDL), clog the reactants supply lines, swell the PEM too much, and eventually paralyze and/or accelerate the degradation of the fuel cell. Therefore, proper operation of a fuel cell depends critically on how transport and distribution of water in different parts of the fuel cell can be optimally managed, which demands fundamental understanding of many competing and more-often-than-not, interrelated factors such as those just mentioned above. For achieving the latter, developing noninvasive diagnostic tools that can *see* water in an operating fuel cell with adequate temporal and spatial resolution is urgently needed.

In view of its widespread success in diagnostic medical imaging, MRI appears to be an ideal choice for diagnostic applications to *seeing* water in operating fuel cells. Indeed, despite the technical challenge of handling the incompatibility between the necessary conducting components and electrical conduction involved in operating fuel cells and MRI detection, as encountered in any in situ EC-NMR/MRI operations discussed in the previous Sections, impressive progress on this front has been made over the last decade [12.73–88]. However, in the spirit of pedagogy and conciseness adopted here, only a few representative cases will be discussed in the following section. Interested readers are directed to recent reviews [12.2, 26, 89] for more

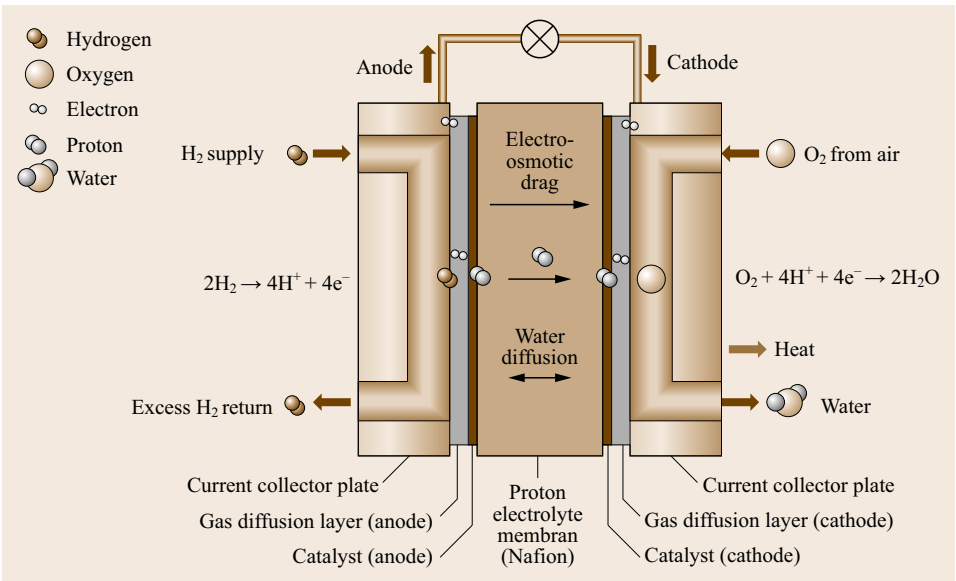


Fig. 12.16 Schematic of a proton exchange membrane fuel cell (PEMFC) whose proper operation depends critically on how water is transported and distributed across the cell (after [12.73])

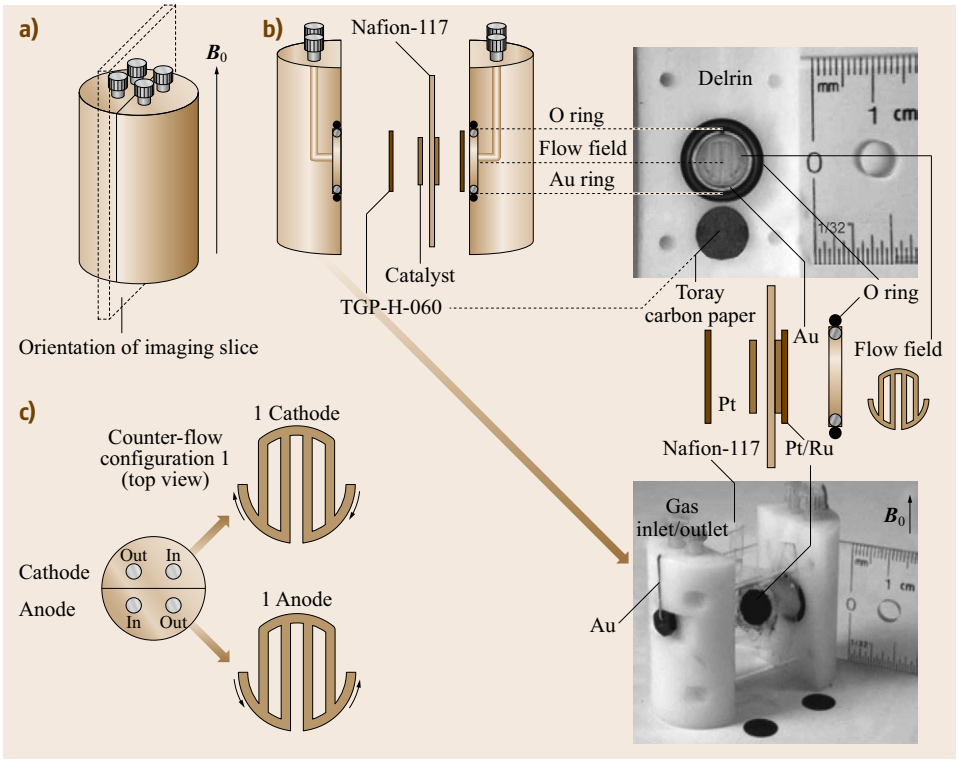


Fig. 12.17 **(a)** Schematic of a cylindrical fuel cell for MRI with imaging plan indicated. **(b)** Graphic description of the components and relative size of the fuel cell. **(c)** One of the four configurations in terms of gas flow direction through the flow field at one electrode versus the other (after [12.82, 83], courtesy of Am. Chem. Soc. 2006)

detailed accounts of the field and original references therein.

12.3.1 In-Plane Water Distribution

Figure 12.17 shows the size, components, configuration, and orientation of an in-plane MRI imaging slice of a cylinder-shaped fuel cell used by *Feindel* and co-workers in their MRI studies of water distribution and associated effect on fuel cell performance [12.81, 82]. A serpentine flow field was machined into each half of the plastic cylinder body and was connected to the gas outlets though well-machined channels. The membrane-electrode assembly (MEA) was constructed via a hot-press decal-transfer method with unsupported HiSpec 1000 Pt black for the cathode and HiSpec 6000 Pt-Ru black for the anode (loadings $\approx 2-3\,\mathrm{mg/cm^2}$, respectively. The geometric area of the catalyst decals was $\approx 5\,\mathrm{cm^2}$. Porous carbon paper was used as GDL and current collector through a contacting Au ring. As such, the use of electrical conducting parts in the fuel cell was reduced to a minimum. A 30 mm birdcage resonator was used for acquiring MRI images. It was observed that water contained in the MEA and resided in the gas flow field could be imaged (Fig. 12.18) but not in the GDLs and catalyst layers.

To illustrate the investigative power of MRI (or called ^{1}H NMR microscopy in the original papers), let us now see how the effects of different gas inlet/outlet configurations (#1 to #4 in Fig. 12.18d) with dry feed of gases (H_2 for the anode and O_2 for the cathode) could be differentiated. Figure 12.18a shows a self-humidifying model for the counter-flow configuration. Since water concentration should be zero at the anode inlet (where dry H_2 enters) but highest at the cathode outlet (where water accumulates preferentially as the product of oxygen reduction [12.82]), the water concentration gradient would be the largest at the anode inlet/cathode outlet side of the cell. This reaction-generated water concentration may be large enough to counter the anode-to-cathode electroosmotic drag and lead to a net water back diffusion from cathode to anode. At the anode outlet/cathode inlet side, the anode-to-cathode electroosmotic drag and the water concentration gradient are expected to go in the same direction, thus leading to the net anode-to-cathode water flow. These opposing net water flows would homogenize water distribution in the PEM. For the co-flow configuration (Fig. 12.18b), on the other hand, different water flow directions would be expected. At the anode inlet/cathode inlet side, entering dry gases would both create water concentration gradients that cause de-hydration of the PEM. At the anode outlet/cathode outlet

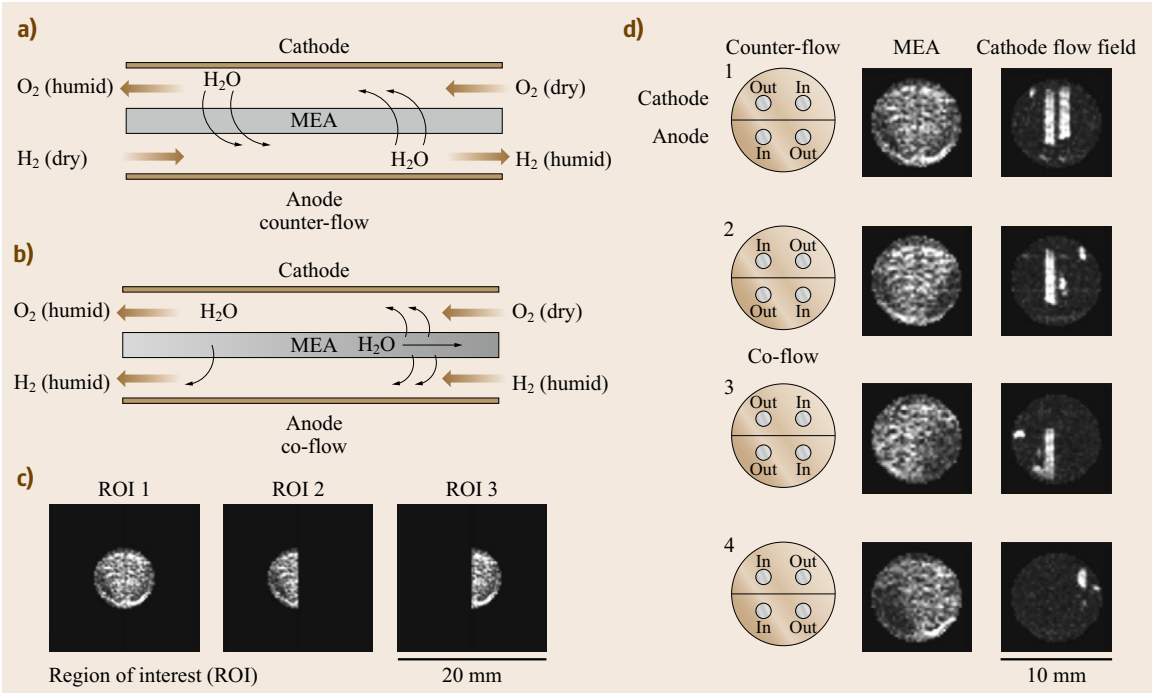


Fig. 12.18 Schematics that illustrate **(a)** counter-flow and **(b)** co-flow of the gases at the cathode and anode. **(c)** Definition of regions of interest ROI for MRI signal integrations over them. **(d)** MRI images of the MEA (membrane-electrode assembly) and the cathode flow field (after [12.81, 82], courtesy of Am. Chem. Soc. 2006)

side, reaction-generated water would still accumulate at the cathode outlet but the water concentration at the anode outlet would not be dry due to self-humidifying. Therefore, the net result may be a weakened back water diffusion, as shown in Fig. 12.18b. The overall effect would be an inhomogeneous water distribution in the PEM: Lower water concentration at the co-inlet side. This was exactly what was observed by the MRI images, as presented in Fig. 12.18d more or less homogeneous water distribution for the counter-flow configuration (#1 and #2) but inhomogeneous water distribution (lower water concentration at co-inlet side) for co-flow configuration (#3 and #4). This was further confirmed quantitatively by numeric integrations of ^{1}H NMR signal over the ROI as defined in Fig. 12.18c: T47461/L22691/R24769 for #1, where T = total (ROI-1), L = left (ROI-2), and R = right (ROI-3); T47751/L24221/R23530 for #2; T44092/L24968/R19125 for #3; and T41365/L15622/R26743 for #4, respectively. The more homogeneous water distribution for #1 and #2 but more preferential water distribution for #3 and #4 are also consistently reflected in the corresponding MRI images of flow field (the right most column in Fig. 12.18d).

In the PEMFC, oxygen reduction at the cathode produces water. Such water could have profound influence on the overall performance of the fuel cell by diffusing back into PEM and influencing the proton conductivity thus the performance of the fuel cell. It could also flood the GDL, clog supplying channels of reactants, and as a result lower the cell performance. The MRI results presented in Fig. 12.19 help unravel some important inter-relationship(s) among several operational parameters discussed above.

According to the original paper, the gas flow configuration was switched from co-flow to counter-flow and the O_2(g) flow rate from 2.5–50 ml/min at t = 0. The intention of switching to 50 ml/min was to flush H_2O(l) from cathode flow field and GDL and to dry the MEA. The rate of 50 ml/min was then maintained until t = 16 min at which point onwards the O_2 flow rate was switched back to 2.5 ml/min. Interestingly, the power density of the cell and water content contained in MEA varied widely, even with a constant O_2(g) flow rate of 50 ml/min. As can be seen in the top panel of Fig. 12.19, the power density and water content contained in MEA were in a remarkable sync between t = 0 to $\approx$ 30 min: Increased first to point A then decreased to point B then increased again.

The initial increase to point A was rationalized by the change of gas flow configuration from co-flow (#3)

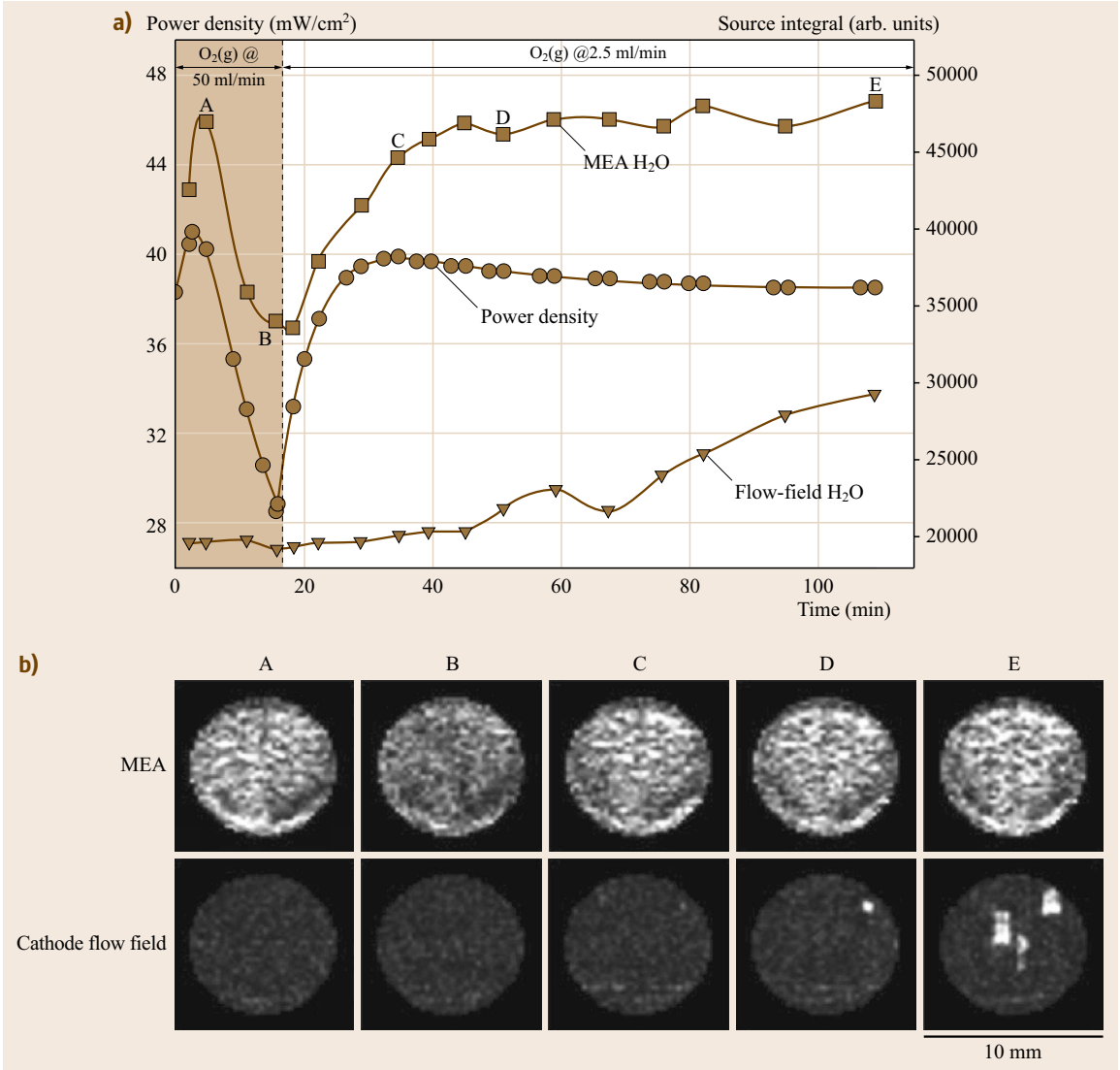


Fig. 12.19 **(a)** Plot of power density and integrated ^{1}H MRI signal intensities versus time showing the effect of changes to the O_2(g) flow rate on: power (*circles*), MEA water content (*squares*), and H_2O(l) in the cathode flow field (*inverted triangles*). **(b)** ^{1}H MRI images (*A–E*) of the MEA and cathode flow field ROI from which the intensities were integrated. From $t = 0–16$ min (*B*) the O_2(g) flow rate was 50 ml/min. The PEMFC was operated in counter-flow gas configuration #2 (Fig. 12.18d) (after [12.81], courtesy of The Owners Soc. 2007)

to counter-flow (#2): the latter configuration produced better cell performance [12.82]. The bright MRI image of the MEA decal and dark image of the flow field in (*A*) indicate that the water content in the MEA was high and water in the flow field was completely flushed out by the high O_2(g) flow. After point A, both cell power density and the water content (proportional to ^{1}H NMR signal integration over ROI-1) decreased until point B (notice that the MRI image of the MEA decal in (*B*) became dark). This decrease was ascribed to reaction-caused dehydration of the PEM.

A decrease in the O_2(g) flow rate to 2.5 ml/min after point B led to an increase in MEA water content as the MRI image of the PEM becoming brighter from (*B*) to (*C*) would indicate, so does the power density. Beyond point C, the increase in water content in the PEM slowed down significantly but still increased. The latter would lead to further improved ionic conductivity and thus, accordingly, cell performance. Yet, a slight

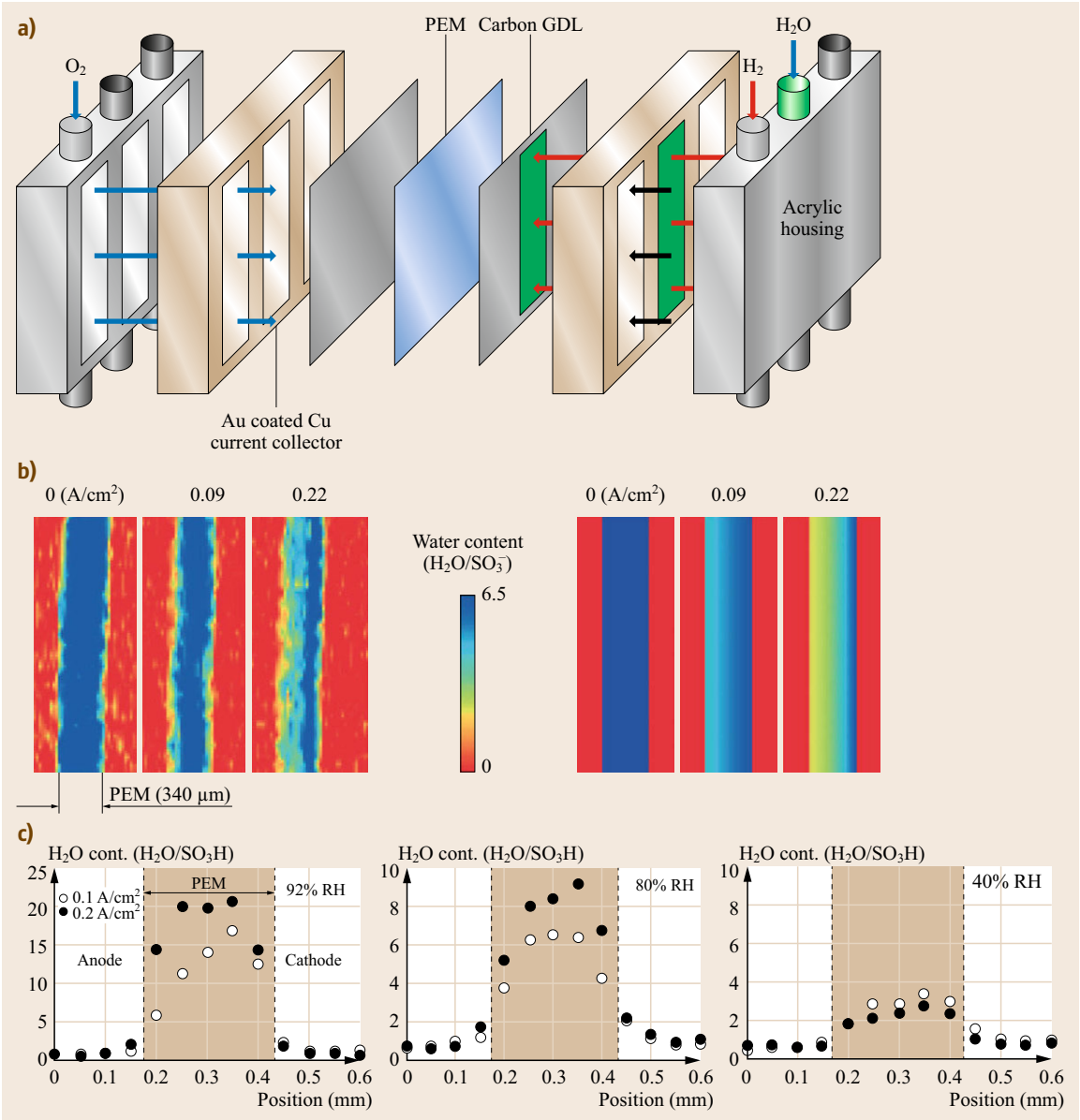


Fig. 12.20 **(a)** Schematic of a fuel cell used for the MRI studies by *Tsushima* et al. The PEM has dimensions of $25 \times 25\,\text{mm} \times 340\,\mu\text{m}$ and the (GDLs) (gas diffusion layers) have dimensions of $20 \times 20\,\text{mm}$ (after [12.78]). **(b)** Room-temperature experimental (*left*) and numerically-simulated (*right*) MRI images of through-plane water content distribution in the fuel cell membrane under operation of different cell currents. The *left side* of each image is the anode side (after [12.26]). **(c)** 1-D through-plane water content profile in the membrane with different relative humidity (RH) (after [12.75])

decrease in power density was observed. This was ascribed to the accumulation of $H_2O(l)$ in the cathode flow field, as confirmed by the MRI image in (*D*), and presumably the GDL, which caused an overall decline of power output.

12.3.2 Through-Plane Water Distribution

The prevailing geometric configuration of practical PEMFCs is like that shown in Fig. 12.16, which dictates the anode-to-cathode proton transport along the

through-plane direction. Consequently, understanding the through-plane water transport processes and so-produced water content distribution, particularly under high current density and low humidity as demanded for automobile applications, is of great practical importance. This involves achieving a fundamental understanding of diverse water transport mechanisms taking place in fuel cells, such as electroosmotic water drag, chemical- and concentration-driven water diffusion, capillary water permeation, and water mass transfer at the MEA interfaces, etc. all of which are of current interest.

MRI is probably the best diagnostic tool currently available to visualize through-plane water content distribution in operating fuel cells. Figure 12.20 illustrates some of the work done by *Tsushima* and co-workers [12.26] with Fig. 12.20a presenting a schematic configuration of the fuel cell used for their MRI studies. The experimentally-observed cell current-dependent MRI visualization of the through-plane water content distribution at room temperature is presented on the left of Fig. 12.20b. As the cell current increased from 0.0 to 0.09 to $0.22\,\mathrm{A/cm^2}$, the anode (left) side of PEM clearly became more dehydrated, indicating that the water transport through the PEM with a water content of $\lambda = [H_2O/-SO_3^-] \approx 6$ was dominated by the anode-to-cathode electroosmotic drag. Results of numerical simulations that did not include effect of capillary pressure or two-phase flow behaviors in the catalyst layers and the GDLs are shown on the right side of Fig. 12.20b. Good agreement with the experimental results on the left side is evident.

Figure 12.20c presents the through-plane 1-D water content distribution profiles in the PEM as the relative humidity (RH) and cell current varied at 70 °C [12.75]. In the standard condition of 80% RH (the middle panel) and a water content of $\lambda \approx 8$, a partial de-hydration at the anode side was observed at the cell current of $0.2\,\mathrm{A/cm^2}$, in agreement with the results presented in Fig. 12.20b and implying a dominant electroosmotic drag. But at cell current of $0.1\,\mathrm{A/cm^2}$, the water profile became much more symmetric, suggesting that the electroosmotic drag and water back diffusion were at similar strengths.

In the dry condition of 40% RH, the overall water content was about $\lambda \approx 3$ (the right panel). Although there was evidence of a slight de-hydration on the anode side, the water content distribution profiles are rather flat and largely independent of the cell current despite the expected increase in electroosmotic drag as cell current doubled. This was ascribed to the fast chemical water diffusion experimentally-observed at relatively low water content [12.90].

In the condition of 92% RH (the left panel), not only was the overall water content much higher than in the other two cases, but also varied substantially when the cell current changed: from $\lambda \approx 15$ at cell current of $0.1\,\mathrm{A/cm^2}$ to $\lambda \approx 22$ at $0.2\,\mathrm{A/cm^2}$. For the latter, the symmetric water content distribution over the PEM implies a water back diffusion that was strong enough to counter the expected strong electroosmotic drag at high cell current. For the former, the decrease of cell current to $0.1\,\mathrm{A/cm^2}$ clearly suppressed the water back diffusion more than the electroosmotic drag and led to de-hydration at the anode side.

In the end, a more nuanced and complex picture emerges from the above discussion in terms of what factors determine the through-plane water content distribution. For instance, the experimental observation suggests that the strength of the electroosmotic drag would be similar to that of water back diffusion at $0.1\,\mathrm{A/cm^2}$ but much stronger in the condition of 92% RH where higher overall water content was observed ($\lambda \approx 15$ versus $\lambda \approx 8$). This suggests that higher water content would induce stronger electroosmotic drag. But one thing that is clear is that many different water transport mechanisms can be operational in a PEMFC, depending on concrete working conditions. However, a full delineation of each and every specific transport mechanism in an operating fuel cell is still far from being accomplished.

12.4 Conclusion and Future Perspectives: Sensitivity, Sensitivity and Sensitivity

It is hoped that the selected cases discussed above, which were the result of personal choices rather than an exhaustive endeavor, can still serve their pedagogical purpose in presenting to interested readers a concise, though limited, overview of the current status concerning applications of in situ EC-NMR/MRI to studies of fundamental chemical processes involved in the EC energy generation and storage. They encompassed the spatially-resolved ^{195}Pt NMR studies of Pt-based electrocatalysts, ^{7}Li NMR/MRI studies of operating Li-ion batteries, and ^{1}H MRI (or NMR microscopy) studies of operating PEMFCs. The unique investigative power of these (and also other) NMR-based methods comes exclusively from NMRs exquisite elemental/chemical

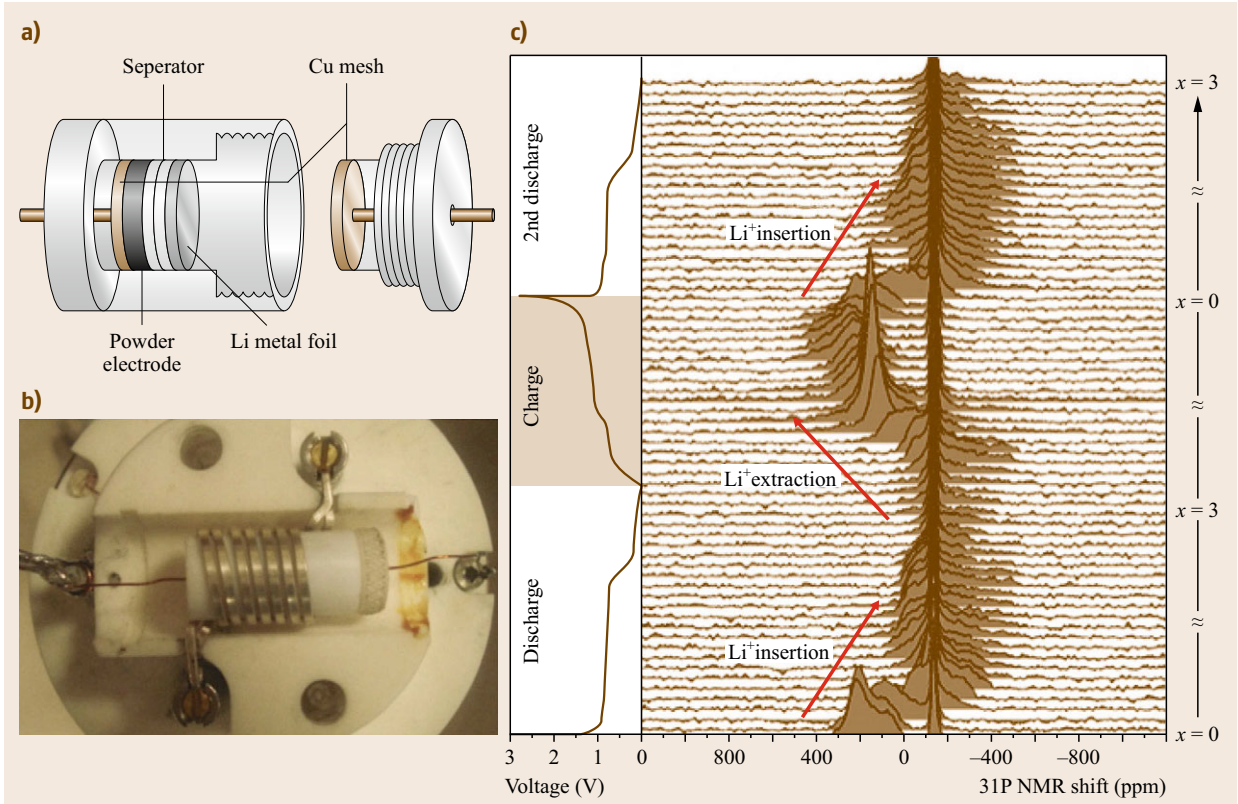


Fig. 12.21 **(a)** Schematic drawing of the cylindrical cell design for in situ NMR. **(b)** Top view of the NMR probe with the cylindrical cell inside a 10 mm solenoid. **(c)** Stack plot of selected in situ ^{31}P NMR spectra recorded during the first and second half cycle of a Cu_3P electrode. The vertical axis represents molar fraction (x) of Li ions (after [12.91])

specificity (easily identifiable/differentiable resonance frequency for each element in the Periodic Table), technical versatility (applicable to samples in the form of solid, liquid, gas, crystalline, or amorphous and therefore easily amenable to in situ requirements), and sensitivity to local chemical/physical environments. Moreover, it is the spectroscopic method that perturbs least electronically the systems under investigation, but with a caveat that a sustained RF radiation could easily cook the samples (think about a microwave oven). Therefore, they will continue to thrive through attracting newcomers and discovering (incremental) new applications. In other words, they will have a rather bright future.

On the other hand, NMR-based methodologies continue their respective perennial struggle with the NMRs Achilles' heel: that is, it has the lowest mass detection sensitivity among all spectroscopic methods. The situation becomes even further exacerbated when the measurements have to deal with conducting materials and associated electrical conduction inside NMR detection coil, as in situ EC-NMR/MRI applications do. Therefore, any future sizable improvements in NMR detection sensitivity will push forwards the frontier of the type of research showcased in this chapter in terms of the quality, depth and scope. Indeed, some of the worthy endeavors have already started. As examples, the recent two cases that are directly relevant to the topics of this chapter will be briefly discussed as follows.

Adapting Bellcore-type flexible plastic bag battery cells for in situ NMR studies of Li-ion batteries by *Letellier* and co-workers [12.71] enabled some significant progress to be made in the arena of in situ NMR investigations of batteries. Due to the easiness of assembling it, its low metal content, and its flexibility that enables the use of normal NMR probes, the overwhelming majority of published in situ NMR work on batteries so far have employed this type of cell. However, its rectangular strip-like shape (Fig. 12.10a) only boasts very small sample filling factor when being inserted into a normal NMR solenoid coil (Fig. 12.11a). Since the signal-to-noise ratio of NMR is linearly proportional to the sample-filling factor, using Bellcore-type cells worsens its mass detection sensitivity. Additionally, the plastic bag cell is not 100% hermetic

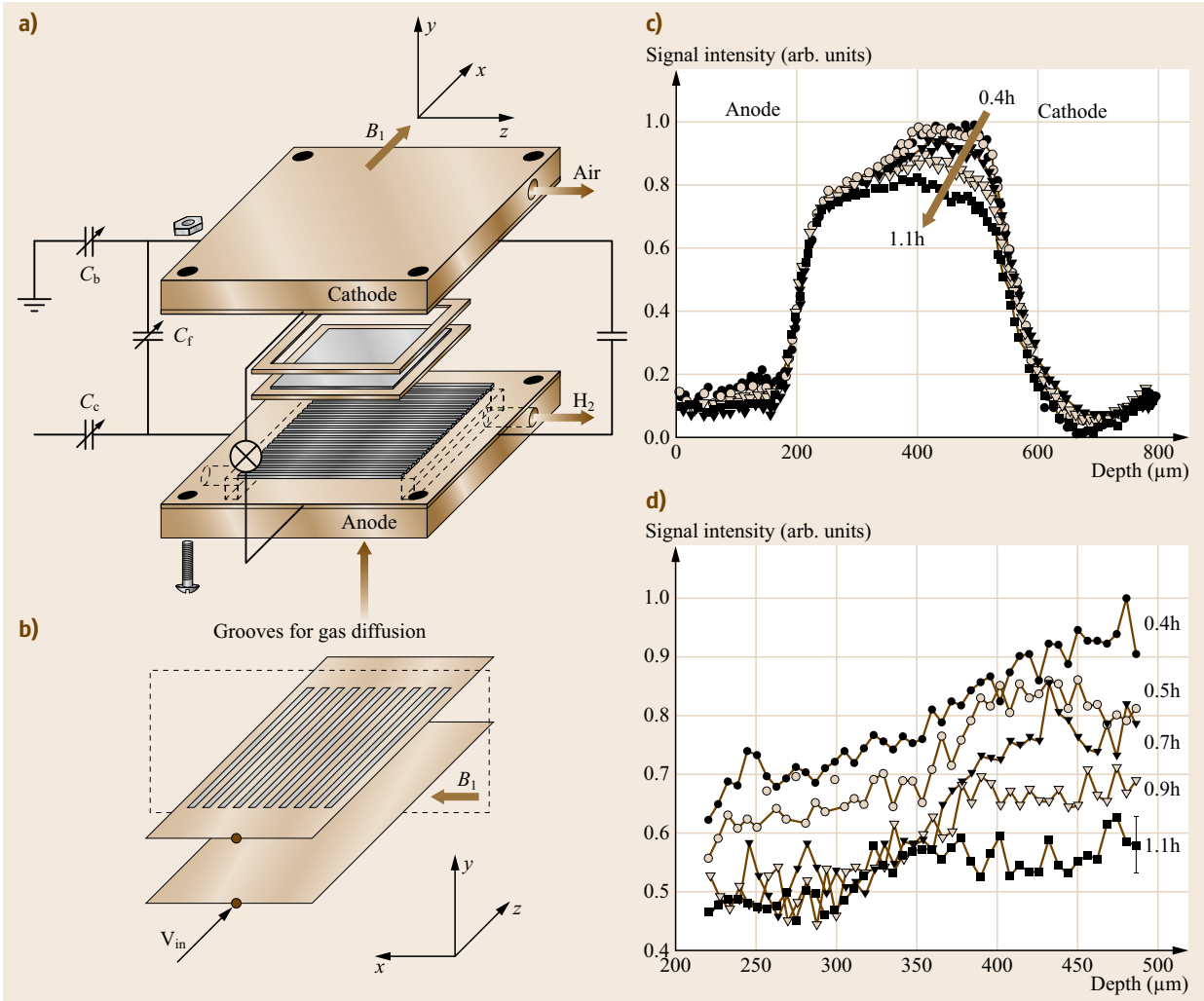


Fig. 12.22 **(a)** Schematic of a parallel-plate resonator incorporated fuel cell for MRI investigations. The up and down plates of the RF-resonator also serve as the current collectors for the fuel cell. **(b)** Schematic shows the grooved up and down resonator plates. **(c)** First echo images of the water content across the Nafion membrane during the full operation stage of fuel cell operation. Five profiles spanning 0.7 h illustrate this process. *Solid circles, open circles, solid inverted triangles, open inverted triangles* and *solid squares* correspond to experimental times of 0.4, 0.5, 0.7, 0.9 and 1.1 h. **(d)** True water content maps of **(c)** determined by relaxation time fitting. Experimental fitting uncertainty is illustrated by the representative *error bars at far right* (after [12.73])

to air and therefore not suitable for long-term studies. To overcome these shortcomings of the Bellcore-type cells, *Letellier* and co-workers developed a cylindrical NMR/battery cell, as shown in Fig. 12.21a,b, that can be snugly fitted into a solenoid coil [12.91]. It boasts a robust cylindrical plastic casing, can be easily assembled and well sealed, and most importantly in terms of filling factor, can accommodate more electrode materials for having a much better filing factor, therefore a much improved sensitivity. The performance of the cylindrical cell is demonstrated by the stacked ^{31}P NMR spectra of Cu_3P electrode recorded during the battery cycles (Fig. 12.21c). It was shown that at least 8 times improvement in sensitivity due both to better sample filling factor and accommodating more electrode material has been achieved. An added bonus of this cylindrical cell, as pointed out recently by *Grey* et al. [12.3], is its potential bearing for being developed into MAS compatible battery cell for high-resolution MAS NMR studies.

The problem of low sample filling factor also exists in the MRI studies of water distribution in PEM-

FCs [12.89]. For both cells shown in Figs. 12.17a and 12.20a, the cumbersome plastic bodies that hold the fuel cell together take most of the sample space when the cell is put into a birdcage resonator for measurements and water-reachable space is only a very small fraction of total sample space. Recently, *Zhang* and co-workers have developed a novel parallel-plate resonator (Fig. 12.22a) as an alternative to the widely used surface coil for high (space) resolution thin film deep imaging [12.73]. The two parallel plates of the resonator also serve as the (anode and cathode) current collectors so grooves were cut through the plates (Fig. 12.22b) to enable the passage of gases to the catalyst layers. In this configuration, the MEA can be snugly sandwiched between the two plates of the resonator, leading to high sample filling factor. In terms of resonance circuitry, the two plates and two capacitors (C_m and C_F) form a closed loop that will generate a RF field B_1 along the x-direction as indicated in Fig. 12.22a,b.

With the much-improved sample filling factor in a small confined space, the authors reported much improved detection sensitivity that enabled them to carry out elaborated, T_2-corrected high spatial resolution ($\approx 6\,\mu m$) imaging of the through-plane water content distribution in the PEM, as presented in Fig. 12.22c,d. The water content profiles were obtained during the full operation stage of the fuel cell, i. e., after the PEM was fully saturated and a steady-state was reached. Five measurements over a span of 0.7 were carried out, with the timing indicated in Fig. 12.22d. The water content was initially relatively high on the cathode size and low on the anode side, indicating a combined electroosmotic drag and accumulation of water as the product of oxygen reduction on the cathode side.

As the reaction continued, water back diffusion became stronger, leading to a gradual homogenization of water content as indicated by the arrow in Fig. 12.21c. True water content maps of data in Fig. 12.21c are presented in Fig. 12.21d, which indicate a gradual water-content homogenization and overall dehydration of the cell.

Notice that in order to obtain the true water contents in Fig. 12.21d, a T_2 relaxation curve of 8 time points was taken so T_2 fitting could be done for each imaging point. Again, these were very measurement intensive exercises and could only be done with good detection sensitivity, as achieved by the parallel-plate resonator.

As to in situ NMR study of metal electrocatalysts, the cry for substantial sensitivity enhancement has also been loud and perennial as well. A potential transformative outlook would be the successful realization of dynamic nuclear polarization (DNP) using conduction electron spin as the polarization transfer source for metal NPs, as *Carver* and *Slichter* achieved for bulk Li metal [12.10] that becomes the first experimental proof of DNP as first proposed by *Overhauser* to a then largely unbelieving audience at the very beginning of the 1950s [12.8, 9]. So the word that would make the future of in situ NMR/MRI even brighter is *sensitivity*, *sensitivity* and *sensitivity*.

Acknowledgments. The research in the Tong Lab at Georgetown University is financially supported by NSF (CHE-0923910 and CHE-0456848) and by DOE-BES (DE-FG02–07ER15895).

References

12.1 A. Trabesinger: Nuclear magnetic resonance: Long live the spin, Nat. Phys. **8**, 781 (2012)
12.2 O.H. Han: Nuclear magnetic resonance investigations on electrochemical reactions of low temperature fuel cells operating in acidic conditions, Prog. NMR Spectrosc. **72**, 1–41 (2013)
12.3 F. Blanc, M. Leskes, C.P. Grey: In situ solid-state NMR spectroscopy of electrochemical cells: Batteries, supercapacitors and fuel cells, Acc. Chem. Res. **46**(9), 1952–1963 (2013)
12.4 Y.Y. Tong: Coupling interfacial electrochemistry with nuclear magnetic resonance spectroscopy. In: *In-Situ Spectroscopic Studies of Adsorption at Electrode and Electrocatalysis*, Vol. 14, ed. by S.G. Sun, P.A. Christensen, A. Wieckowski (Elsevier, Amsterdam 2007) pp. 441–469
12.5 P. Prenzler, R. Bramley, S.R. Downing, G.A. Heath: High-field NMR spectroelectrochemistry of spinning solutions: Simultaneous in situ detection of electrogenerated species in a standard probe under potentiostatic control, Electrochem. Commun. **2**, 516 (2000)
12.6 J.A. Richards, D.H. Evans: Flow cell for electrolysis within the probe of a nuclear magnetic resonance spectrometer, Anal. Chem. **47**, 964 (1975)
12.7 C.P. Slichter: The discovery and demonstration of dynamic nuclear polarization, Phys. Chem. Chem. Phys. **12**, 5741 (2010)
12.8 A.W. Overhauser: Polarization of nuclei in metals, Phys. Rev. **92**, 441 (1953)
12.9 A.W. Overhauser: Paramagnetic relaxation in metals, Phys. Rev. **89**, 689 (1953)
12.10 T.R. Carver, C.P. Slichter: Polarization of nuclear spins in metals, Phys. Rev. **92**, 212 (1953)
12.11 R.G. Griffin, T.F. Prisner: High field dynamic nuclear polarization-the renaissance, Phys. Chem. Chem. Phys. **12**, 5737 (2010)

12.12 R.D. Webster: In situ electrochemical-NMR spectroscopy. Reduction of aromatic halides, Anal. Chem. **76**, 1603 (2004)

12.13 M.E. Sandifer, M. Zhao, S. Kim, D.A. Scherson: In situ nuclear magnetic resonance determination of paramagnetic susceptibilities of electrogenerated species, Anal. Chem. **65**, 2093 (1993)

12.14 D.W. Mincey, M.J. Popovich, P.J. Faustino, M.M. Hurst, J.A. Caruso: Monitoring of electrochemical reactions by nuclear magnetic resonance spectrometry, Anal. Chem. **62**, 1197 (1990)

12.15 V.G. Mairanovsky, L.Y. Yusefovich, T.M. Filippova: NMR electrolysis combined method (NMREL): Basic principles and some applications, J. Magn. Reson. **54**, 19 (1983)

12.16 M.S. Morales-Ríos, P. Joseph-Nathan: NMR studies of indoles and their N-carboalkoxy derivatives, Magn. Reson. Chem. **25**, 911 (1987)

12.17 S. Klod, F. Ziegs, L. Dunsch: In situ NMR spectroelectrochemistry of higher sensitivity by large scale electrodes, Anal. Chem. **81**, 10262 (2009)

12.18 S. Klod, L. Dunsch: A combination of in situ ESR and in situ NMR spectroelectrochemistry for mechanistic studies of electrode reactions: The case of p-benzoquinone, Magn. Reson. Chem. **49**, 725 (2011)

12.19 S. Klod, K. Haubner, E. Jähne, L. Dunsch: Charge stabilization by dimer formation of an endcapped thiophene tetramer – An in situ NMR spectroelectrochemical study, Chem. Sci. **1**, 743 (2010)

12.20 X. Zhang, J.W. Zwanziger: Design and applications of an in situ electrochemical NMR cell, J. Magn. Reson. **208**, 136–147 (2011)

12.21 Z.-R. Ni, X.-H. Cui, S.-G. Sun, Z. Chen: Coupling liquid phase electrochemistry with nuclear magnetic resonance spectroscopy and its applications, Spectrosc. Spect. Anal. **31**, 1 (2011)

12.22 L.L. Williams, R.D. Webster: Electrochemically controlled chemically reversible transformation of α-tocopherol (vitamin E) into its phenoxonium cation, J. Am. Chem. Soc. **126**, 12441 (2004)

12.23 Y.Y. Tong, A. Wieckowski, E. Oldfield: NMR of electrocatalysts, J. Phys. Chem. B **106**, 2434 (2002)

12.24 Y.Y. Tong, E. Oldfield, A. Wieckowski: Exploring electrochemical interfaces with solid-state NMR, Anal. Chem. **70**, 518A (1998)

12.25 C.P. Grey, N. Dupré: NMR studies of cathode materials for lithium-ion rechargeable batteries, Chem. Rev. **104**, 4493 (2004)

12.26 S. Tsushima, S. Hirai: Magnetic resonance imaging of water in operating polymer electrolyte membrane fuel cells, Fuel Cells **9**, 506 (2009)

12.27 W.P. Halperin: Quantum size effects in metal particles, Rev. Mod. Phys. **58**, 533 (1986)

12.28 C.P. Slichter: Probing phenomena at metal surfaces by NMR, Annu. Rev. Phys. Chem. **37**, 25 (1986)

12.29 J.J. van der Klink, H.B. Brom: NMR in metals, metal particles and metal cluster compounds, Prog. NMR Spectrosc. **36**, 89 (2000)

12.30 Y.Y. Tong, J.J. van der Klink: NMR investigations of heterogeneous and electrochemical catalysts. In: *Catalysis and Electrocatalysis at Nanoparticle Surface*, ed. by A. Wieckowski, E.R. Savinova, C.G. Vayenas (Marcel Dekker, New York 2003) p. 455

12.31 P.J. Slezak, A. Wieckowski: Interfacing surface electrochemistry with solid-state NMR. Characterization of surface CO on polycrystalline platinum, J. Magn. Res. A **102**, 166 (1993)

12.32 Y.Y. Tong, C. Rice, N. Godbout, A. Wieckowski, E. Oldfield: Correlation between the Knight shift of chemisorbed CO and the Fermi level local density of states at clean platinum catalyst surfaces, J. Am. Chem. Soc. **121**, 2996–3003 (1999)

12.33 B.M. Weckhuysen: Chemical imaging of spatial heterogeneities in catalytic solids at different length and time scales, Angew. Chem. Int. Ed. **48**, 4910 (2009)

12.34 H.T. Stokes, H.E. Rhodes, P.K. Wang, C.P. Slichter, J.H. Sinfelt: NMR of platinum catalysts. III. Microscopic variation of the knight shifts, Phys. Rev. B **26**, 3575 (1982)

12.35 W.D. Knight, F. Seitz, D. Turnbull: Electron paramagnetism and nuclear magnetic resonance in metals, Solid State Phys. **2**, 93–136 (1956)

12.36 J. Korringa: Nuclear magnetic relaxation and resonnance line shift in metals, Physica. **16**(7–8), 601–610 (1950)

12.37 C.P. Slichter: *Principles of Magnetic Resonance*, 3rd edn. (Springer, Berlin, Heidelberg 1990)

12.38 F. Tan, B. Du, A.L. Danberry, I.-S. Park, Y.-E. Sung, Y. Tong: A comparative in situ ^{195}Pt electrochemical-NMR investigation of PtRu nanoparticles supported on diverse carbon nanomaterials, Faraday Disc. **140**, 139–153 (2008)

12.39 J.P. Bucher, J.J. van der Klink: Electronic properties of small supported Pt particles: NMR study of ^{195}Pt hyperfine parameters, Phys. Rev. B **38**, 11038 (1988)

12.40 D.O. Atienza, T.C. Allison, Y.Y.J. Tong: Spatially resolved electronic alterations as seen by in situ ^{195}Pt and ^{13}CO NMR in Ru@Pt and Au@Pt core-shell nanoparticles, J. Phys. Chem. C **116**, 26480–26486 (2012)

12.41 B. Du, O. Zaluzhna, Y.Y.J. Tong: Electrocatalytic properties of Au@Pt nanoparticles: Effects of Pt shell packing density and Au core size, Phys. Chem. Chem. Phys. **13**, 11568 (2011)

12.42 I.S. Park, K.S. Lee, D.S. Jung, H.Y. Park, Y.-E. Sung: Electrocatalytic activity of carbon-supported Pt-Au nanoparticles for methanol electro-oxidation, Electrochimica Acta **52**, 5599 (2007)

12.43 B. Du, S.A. Rabb, C. Zangmeister, Y. Tong: A volcano curve: Optimizing methanol electrooxidation on Pt-decorated Ru nanoparticles, Phys. Chem. Phys. **11**, 8231–8239 (2009)

12.44 Y.Y. Tong, H.S. Kim, P.K. Babu, P. Waszczuk, A. Wieckowski, E. Oldfield: An NMR investigation of CO tolerance in a Pt/Ru fuel cell catalyst, J. Am. Chem. Soc. **124**, 468 (2002)

12.45 P.K. Wang, J.P. Ansermet, S.L. Rudaz, Z. Wang, S. Shore, C.P. Slichter, J.H. Sinfelt: NMR studies of simple molecules on metal surfaces, Science **234**, 35 (1986)

12.46 Y.Y. Tong, C. Rice, A. Wieckowski, E. Oldfield: A detailed NMR-based model for CO on Pt catalysts

in an electrochemical environment? Shifts, relaxation, back-bonding, and the Fermi-level local density of states, J. Am. Chem. Soc. **122**, 1123 (2000)
12.47 G. Blyholder: Molecular orbital view of chemisorbed carbon monoxide, J. Phys. Chem. **68**, 2772 (1964)
12.48 M.K. Oudenhuijzen, J.A. van Bokhoven, D.E. Ramaker, D.C. Koningsberger: Theoretical study on Pt particle adsorbate bonding: Influence of support ionicity and implications for catalysis, J. Phys. Chem. B **108**, 20247 (2004)
12.49 R. Dronskowski, P.E. Bloechl: Crystal orbital Hamilton populations (COHP): Energy-resolved visualization of chemical bonding in solids based on density-functional calculations, J. Phys. Chem. **97**, 8617 (1993)
12.50 G. Papoian, J.K. Norskov, R. Hoffmann: A comparative theoretical study of the hydrogen, methyl, and ethyl chemisorption on the Pt(111) surface, J. Am. Chem. Soc. **122**, 4129 (2000)
12.51 W.V. Glassey, R. Hoffmann: A Comparative study of the p(2 × 2)-CO/M(111), M=Pt,Cu,Al chemisorption systems, J. Phys. Chem. B **105**, 3245 (2001)
12.52 W.V. Glassey, R. Hoffmann: A molecular orbital study of surface–adsorbate interactions during the oxidation of CO on the Pt(1 1 1) surface, Surface Sci. **475**, 47 (2001)
12.53 W.V. Glassey, G.A. Papoian, R. Hoffmann: Total energy partitioning within a one-electron formalism: A Hamilton population study of surface–CO interaction in the c (2 × 2)-CO/Ni (100) chemisorption system, J. Chem. Phys. **111**, 893 (1999)
12.54 G.A. Somorjai, C. Aliaga: Molecular studies of model surfaces of metals from single crystals to nanoparticles under catalytic reaction conditions. Evolution from prenatal and postmortem studies of catalysts, Langmuir **26**, 16190 (2010)
12.55 G.A. Somorjai, A.M. Contreras, M. Montano, R.M. Rioux: Clusters, surfaces, catalysis, Proc. Nat. Acad. Sci.'06 (2006) p. 10577
12.56 G.A. Somorjai: *Introduction to Surface Chemistry and Catalysis* (Wiley, New York 1994)
12.57 R. Hoffmann: A chemical and theoretical approach to bonding at surfaces, J. Phys. Condens. Matter **5**, A1 (1993)
12.58 R. Hoffmann: Interaction of orbitals through space and through bonds, Acc. Chem. Res. **4**, 1 (1971)
12.59 C.P. Grey, Y.J. Lee: Lithium MAS NMR studies of cathode materials for lithium-ion batteries, Solid State Sci. **5**, 883 (2003)
12.60 I.R.E. Gerald, J. Sanchez, C.S. Johnson, R.J. Klingler, J.W. Rathke: In situ nuclear magnetic resonance investigations of lithium ions in carbon electrode materials using a novel detector, J. Phys. Condens. Matter **13**, 8269 (2001)
12.61 I.R.E. Gerald, C.S. Johnson, J.W. Rathke, R.J. Klingler, G. Sandí, L.G. Scanlon: 7 Li NMR study of intercalated lithium in curved carbon lattices, J. Power Sources **89**, 237 (2000)
12.62 M. Letellier, F. Chevallier, M. Morcrette: In situ ^{7}Li nuclear magnetic resonance observation of the electrochemical intercalation of lithium in graphite; 1st cycle, Carbon **45**, 1025 (2007)
12.63 M. Letellier, F. Chevallier, F. Béguin: In situ ^{7}Li NMR during lithium electrochemical insertion into graphite and a carbon/carbon composite, J. Phys. Chem. Solids **67**, 1228 (2006)
12.64 M. Letellier, F. Chevallier, F. Béguin, E. Frackowiak, J.-N. Rouzaud: The first in situ ^{7}Li NMR study of the reversible lithium insertion mechanism in disorganised carbons, J. Phys. Chem. Solids **65**, 245 (2004)
12.65 F. Chevallier, M. Letellier, M. Morcrette, J.M. Tarascon, E. Frackowiak, J.N. Rouzaud, F. Beguin: In situ 7Li-nuclear magnetic resonance observation of reversible lithium insertion into disordered carbons, Electrochem. Solid-State Lett. **6**, A225 (2003)
12.66 J.W. Rathke, R.J. Klingler, R.E. Gerald, K.W. Kramarz, K. Woelk: Toroids in NMR spectroscopy, Prog. Nucl. Magn. Res. Spectrosc. **30**, 209 (1997)
12.67 N.M. Trease, L. Zhou, H.J. Chang, B.Y. Zhu, C.P. Grey: In situ NMR of lithium ion batteries: Bulk susceptibility effects and practical considerations, Solid State Nucl. Magn. Reson. **42**, 62 (2012)
12.68 R. Bhattacharyya, B. Key, H. Chen, A.S. Best, A.F. Hollenkamp, C.P. Grey: In situ NMR observation of the formation of metallic lithium microstructures in lithium batteries, Nature Mater. **9**, 504–510 (2010)
12.69 B. Key, R. Bhattacharyya, M. Morcrette, V. Seznéc, J.-M. Tarascon, C.P. Grey: Real-time NMR investigations of structural changes in silicon electrodes for lithium-ion batteries, J. Am. Chem. Soc. **131**, 9239 (2009)
12.70 J.M. Tarascon, A.S. Gozdz, C. Schmutz, F. Shokoohi, P.C. Warren: Performance of Bellcore's plastic rechargeable Li-ion batteries, Solid State Ionics **49**, 86–88 (1996)
12.71 M. Letellier, F. Chevallier, C. Clinard, E. Frackowiak, J.-N. Rouzaud, F. Béguin, M. Morcrette, J.-M. Tarascon: The first in situ ^{7}Li nuclear magnetic resonance study of lithium insertion in hard-carbon anode materials for Li-ion batteries, J. Chem. Phys. **118**, 6038 (2003)
12.72 S. Chandrashekar, N.M. Trease, H.J. Chang, L.-S. Du, C.P. Grey, A. Jerschow: ^{7}Li MRI of Li batteries reveals location of microstructural lithium, Nature Mater. **11**, 311 (2012)
12.73 Z. Zhang, J. Martin, J. Wu, H. Wang, K. Promislow, B.J. Balcom: Magnetic resonance imaging of water content across the Nafion membrane in an operational PEM fuel cell, J. Magn. Reson. **193**(2), 259–266 (2008)
12.74 J.Y. Shim, S. Tsushima, S. Hirai: High resolution MRI investigation of transversal water content distributions in PEM under fuel cell operation MEA performance and component diagnostics I: In-situ diagnostics and imaging, ECS Trans. **25**, 523 (2009)
12.75 T. Ikeda, T. Koido, S. Tsushima, S. Hirai: MRI investigation of water transport mechanism in a membrane under elevated temperature condition with relative humidity and current density variation A2.1:Diagnostics, ECS Trans. **16**, 1035 (2008)

12.76 S. Tsushima, S. Hirai, K. Kitamura, M. Yamashita, S. Takase: MRI application for clarifying fuel cell performance with variation of polymer electrolyte membranes: Comparison of water content of a hydrocarbon membrane and a perfluorinated membrane, Appl. Magn. Reson. **32**, 233 (2007)

12.77 S. Tsushima, T. Nanjo, K. Nishida, S. Hirai: Investigation of the lateral water distribution in a proton exchange membrane in fuel cell operation by 3D-MRI membranes, ECS Trans. **1**(6), 199–205 (2006)

12.78 S. Tsushima, K. Teranishi, K. Nishida, S. Hirai: Water content distribution in a polymer electrolyte membrane for advanced fuel cell system with liquid water supply, Magn. Reson. Imaging **23**, 255 (2005)

12.79 S. Tsushima, K. Teranishi, S. Hirai: Magnetic resonance imaging of the water distribution within a polymer electrolyte membrane in fuel cells, Electrochem. Solid-State Lett. **7**, A269 (2004)

12.80 M. Wang, K.W. Feindel, S.H. Bergens, R.E. Wasylishen: In situ quantification of the in-plane water content in the Nafion membrane of an operating polymer-electrolyte membrane fuel cell using ^{1}H micro-magnetic resonance imaging experiments, J. Power Sources **195**, 7316 (2010)

12.81 K.W. Feindel, S.H. Bergens, R.E. Wasylishen: The influence of membrane electrode assembly water content on the performance of a polymer electrolyte membrane fuel cell as investigated by ^{1}H NMR microscopy, Phys. Chem. Phys. **9**, 1850–1857 (2007)

12.82 K.W. Feindel, S.H. Bergens, R.E. Wasylishen: Insights into the distribution of water in a self-humidifying H_2/O_2 proton-exchange membrane fuel cell using 1H NMR microscopy, J. Am. Chem. Soc. **128**, 14192 (2006)

12.83 K.W. Feindel, S.H. Bergens, R.E. Wasylishen: The use of 1H NMR microscopy to study proton exchange membrane fuel cells, Chem. Phys. Chem. **7**, 67–75 (2006)

12.84 K.W. Feindel, L.P.A. LaRocque, D. Starke, S.H. Bergens, R.E. Wasylishen: In situ observations of water production and distribution in an operating H2/02 PEM fuel cell assembly using 1H NMR microscopy, J. Am. Chem. Soc. **126**, 11436 (2004)

12.85 Z. Zhang, A.E. Marble, B. MacMillan, K. Promislow, J. Martin, H. Wang, B.J. Balcom: Spatial and temporal mapping of water content across Nafion membranes under wetting and drying conditions, J. Magn. Res. **194**, 245 (2008)

12.86 K.R. Minard, V.V. Viswanathan, P.D. Majors, L.-Q. Wang, P.C. Rieke: Magnetic resonance imaging (MRI) of PEM dehydration and gas manifold flooding during continuous fuel cell operation, J. Power Sources **161**, 856 (2006)

12.87 Z.W. Dunbar, R.I. Masel: Magnetic resonance imaging investigation of water accumulation and transport in graphite flow fields in a polymer electrolyte membrane fuel cell: Do defects control transport?, J. Power Sources **182**, 76 (2008)

12.88 Z. Dunbar, R.I. Masel: Quantitative MRI study of water distribution during operation of a PEM fuel cell using Teflon flow field, J. Power Sources **171**, 678 (2007)

12.89 Z. Zhang, B.J. Balcom: Magnetic resonance imaging. In: *Handbook of PEM Fuel Cell Durability*, ed. by H. Wang, X.-Z. Yuan, H. Li (CRC, Boca Raton 2012) p. 229

12.90 T.A. Zawodzinski, M. Neeman, L.O. Sillerud, S. Gottesfeld: Determination of water diffusion coefficients in perfluorosulfonate ionomeric membranes, J. Phys. Chem. **95**, 6040 (1991)

12.91 F. Poli, J.S. Kshetrimayum, L. Monconduit, M. Letellier: New cell design for in-situ NMR studies of lithium-ion batteries, Electrochem. Commun. **13**, 1293 (2011)

13. Spectroscopy of Electrochemical Systems

James J. Walsh, Robert J. Forster, Tia E. Keyes

The partnering of electrochemical and spectroscopic methods into a single experiment can yield unprecedented insights into the behavior of redox active materials and into interfacial processes. The application of coupled electrochemical and spectroscopic techniques, collectively called spectroelectrochemistry, has grown dramatically over the past three decades to the point that almost every spectroscopic technique available has been applied under potential control. Spectroelectrochemistry has found application across diverse fields from materials science, corrosion, and electronics to biochemistry and its progress has tracked the advances in microscopy and other optical methods providing increasingly detailed insights into electrochemical processes in diverse environments. This chapter describes the experimental considerations and application of spectroelectrochemistry as applied specifically to optical spectroscopy. We describe the experimental demands of applying electrochemical control to spectroscopic experiments across the most common optical formats. We examine specific applications of absorbance, emission, and vibrational spectroscopies under electrochemical control across a range of of materials, including inorganic, supramolecular structures, and polymers. Application of both steady-state and time-resolved spectroscopies to spectroelectrochemistry are examined and finally we anticipate the growing application of spectroelectrochemistry to some of the most recent advances in optical methods, particularly super-resolution methods and single molecule methods.

13.1 **General Experimental Considerations** 366
13.1.1 Interaction of Light with Electrode Materials 366

13.2 **Electronic Spectroscopy** 368
13.2.1 Optically Transparent Electrodes for Transmittance Spectroscopy ... 368
13.2.2 Thin-Layer Spectroelectrochemistry 370
13.2.3 Reflectance Spectroscopy 381

13.3 **Spectroelectrochemistry of the Excited State** 385
13.3.1 Steady-State Emission Spectroelectrochemistry 386
13.3.2 Transient Luminescence Spectroelectrochemistry 391

13.4 **Vibrational Spectroelectrochemistry** 393
13.4.1 IR Spectroelectrochemistry 393
13.4.2 External Reflectance 399
13.4.3 Vibrational Circular Dichroism SEC 403

13.5 **Raman Spectroelectrochemistry** 404
13.5.1 Resonance Raman Spectroelectrochemistry 407
13.5.2 Surface-Enhanced Raman Spectroscopy 409

13.6 **Sum Frequency Generation Spectroelectrochemistry** 413

13.7 **Conclusions and Outlook** 414

References 415

Spectroelectrochemistry is any experiment that combines an electrochemical method with a spectroscopic method. It is a powerful approach to characterise and quantify chemical structural changes accompanying redox reactions. While electrochemical methods such as voltammetry can provide valuable kinetic and thermodynamic insights into redox processes, they alone can rarely unequivocally resolve the structure of the electrogenerated material. When combined with a spectroscopic method such as electronic or vibrational spectroscopy, however, this limitation can be readily addressed. The earliest examples of spectroelectrochem-

istry combined bulk electrolysis methods initially with electron paramagnetic resonance (EPR) spectroscopy in the 1940s and 1950s with UV-Vis spectroscopy first exploited in spectroelectrochemical methods in the 1960s [13.1, 2]. Over the past 30 years, the range of spectroscopic methods, both optical and nonoptical, combined with electrochemical methods has expanded dramatically to the point where today, most conventional spectroscopic methods have been combined with in-situ electrochemistry. Some spectroelectrochemical methods, such as UV-Vis spectroelectrochemistry are now performed routinely in many laboratories, because of their ease of application and low cost. Others, where for example the combination of spectroscopic method with electrode interface increases the complexity or cost of the experiment, nuclear magnetic resonance (NMR) spectroelectrochemistry being a particular example, remain nonroutine.

This chapter focuses on the method and application of spectroelectrochemistry as applied to optical spectroscopy. Because of the sheer breadth of the subject area, nonoptical methods are excluded from this review. We direct the reader to the following insightful references to learn more on important nonoptical spectroelectrochemical methods such as EPR and NMR [13.3–5].

13.1 General Experimental Considerations

Most spectroelectrochemical experiments employ a three electrode cell comprising a reference, auxiliary, and a working electrode, as for a conventional electrochemical experiment. However, the arrangement of these elements and indeed the material the cell is made from depends critically on the spectroscopic method. The working electrode for most spectroelectrochemical methods should ideally lie within the optical path so that redox changes at the electrode–solution interface can be monitored directly. Parameters such as the cell orientation with respect to light source and the detector as well as the identity of electrode and cell materials are dictated by the method and requirements of transparency for transmission spectroscopy, for example, in transmission UV spectroscopy or in reflectance or light scattering methodologies such as reflectance infrared (IR) or Raman spectroscopy, respectively.

Light impinging on a dielectric interface, can be reflected, scattered, or transmitted through the interface depending on the nature of the material and its optical transparency at the incident wavelength. In general, in a spectroscopic experiment, the intensity of the incident light I_0 is ratioed to the intensity of light transmitted through the cell medium $T = I_0/I$ scattered from the medium $S = I_s/I_0$ or reflected from the medium, where $R = I_r/I$. A material's optical characteristics, that is, reflectivity, transmissivity, and absorbtivity, are described by the Fresnel equations, which describe these properties in the context of the materials complex dielectric constant $\varepsilon' = \varepsilon_r + ik_i$ or refractive index, n', where $n' = n_r + ik_i$ and $n' = \sqrt{\varepsilon'}$. The Fresnel equations also describes the angle dependence of the intensity reflection coefficients and transmission coefficients for the electric field vectors of light which are perpendicularly (s) polarized and parallel (p) polarized relative to the plane of incidence (when light is incident at an angle to the surface which is not normal on a surface) [13.6]. The dominant processes in light interaction at an interface are reflection and transmission as these are first-order optical processes. Inelastic scattering of light, as in the case of Raman scattering, is a higher order optical process and is therefore a weak phenomenon. This is described in more detail below.

13.1.1 Interaction of Light with Electrode Materials

Figure 13.1 illustrates typical optical geometries used in optical transmission and reflectance spectroscopy where the electrode is indicated in the diagram as the dashed line. Transmission spectroscopy in electronic (UV-Vis/near-infrared (NIR)) spectroelectrochemistry is the most widely used optical arrangement as it applies to conventional spectrometers. In the absorbance experiment $A = -\log(I/I_0)$ or $-\log(T)$, the arrangement of the optics minimizes the contribution of scatter and reflection from the sample so that the main contribution to the decrease in I_0 is due to absorbance by the sample.

In a reflectance experiment, light scattered or reflected from a surface is measured and compared with the incident intensity. In general, in a reflectance experiment, the differential reflectance $\Delta R/R$ is quoted which reflects the difference in reflectance between a clean surface and that on which the analyte is placed. In a spectroelectrochemical experiment, it may reflect the difference in reflectance in the absence and presence of applied potential. As this is a differential value, the signal may be very weak, and therefore it is important to limit background contributions to the signal.

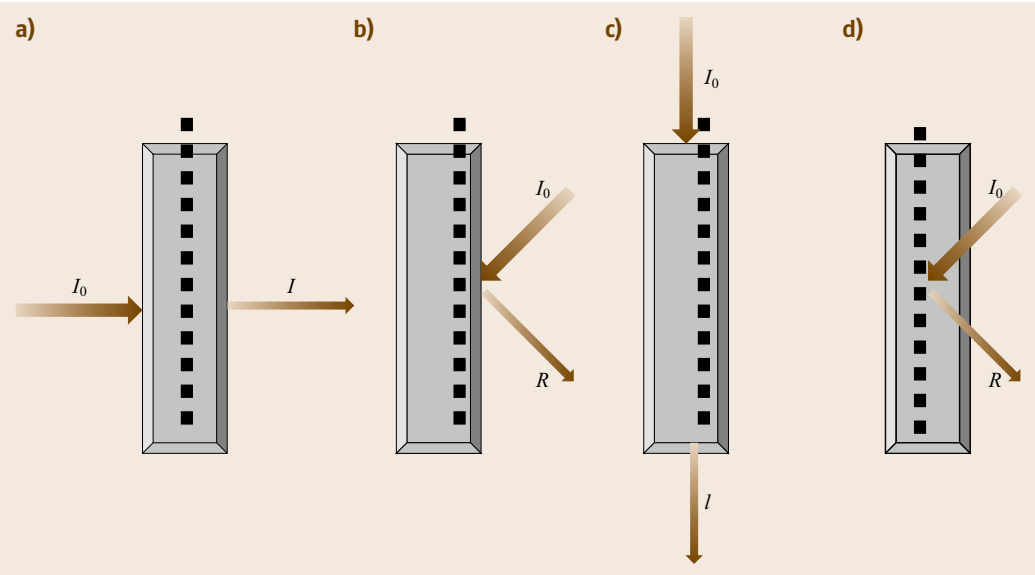


Fig. 13.1a–d The various typical orientations of electrode and cell with respect to the incident I and detected light in UV-Vis spectroelectrochemistry; from left **(a)** conventional transmittance mode typically used with OTE, **(b)** front face reflectance, **(c)** long path transmittance, **(d)** through solution reflectance. The latter three modes **(b–d)** can be used with nontransparent working electrode materials

The majority of reported spectroelectrochemical experiments are qualitative where the spectroscopic method applied is used to structurally characterize an intermediate or final redox state of a given analyte. Quantitative measurements are less common and are often more experimentally challenging, as they require a more rigorous geometric arrangement of the cell to avoid problems such as low current densities or *iR* drop due to the relative size of the working electrode and its orientation with respect to the other electrodes.

Likewise, in absorbance or transmission measurements in spectroelectrochemistry, scattering and reflection must be minimized to provide optimum signal-to-noise ratio. Since in many instances the working electrode presents a reflective surface, minimizing scatter and reflection can be difficult leading to distortion of the absorbance or transmittance signal and thus making quantitative studies difficult. The use of optically transparent electrodes, described below, significantly reduces such interferences.

Thin-Layer Cells

In its simplest manifestation, spectroelectrochemistry involves the bulk electrolysis of the analyte within in a low volume cell combined with simultaneous or succeeding spectroscopic interrogation of the sample. The spectroscopic measurement of the electrochemically generated species occurs in-situ, wherein the sample is held under potential control during the spectroscopic interrogation. The use of low-volume spectroelectrochemistry (SEC) is desirable for two reasons; firstly, because it maximizes the rate at which the cell reaches equilibrium at a given applied potential and secondly keeping the volume small minimizes contributions from solvent and electrolyte to spectroscopic signal. This is commonly achieved in spectroelectrochemistry through the use of a thin layer into which the working electrode is inserted. In some applications, such as UV-Vis spectroelectrochemistry, an optically transparent conducting material, for example, indium tin oxide (ITO) or fluorine-doped tin oxide (FDTO), can be used as working electrode and indeed can form one wall of a cuvette. Frequently though, the working electrode is made of a material, which is not in itself transparent to the frequency of light used in the given experiment. As described, depending on whether the detection strategy is toward transmitted, reflected, or scattered light the requirement for transparent working electrode varies.

13.2 Electronic Spectroscopy

Electronic spectroscopy is probably the most extensively and routinely used spectroelectrochemical analysis. It is cost-effective, straightforward to use, and can provide both quantitative and qualitative information on the analyte species. Electronic spectroscopy is used to probe electronic transitions between different molecular orbitals, and hence is ideal for characterizing redox processes. Electronic transitions lie predominantly in the ultraviolet (190–370 nm) and visible (370–750 nm) regions of the electromagnetic (EM) spectrum, but can also occur into the near-infrared (750–2500 nm). The intensity of electronic absorptions follow the Beer–Lambert law $A = \varepsilon cl$ so that the magnitude of each absorption is directly proportional to the concentration of the analyte in solution. So when operating in absorbance mode, the absorbance is expressed in terms of percentage transmittance where $A = \log(100/\%T) = 2.000 - \log(\%T)$ is the measured absorbance. This means that two absorbance units (AUs) correspond to 100% absorption; hence the peaks under scrutiny should not be permitted to exceed 2 on the ordinate as above this value the Beer–Lambert law deviates from linearity.

13.2.1 Optically Transparent Electrodes for Transmittance Spectroscopy

Electronic spectroelectrochemistry is most frequently carried out in the transmittance mode. This requires the use of optically transparent electrodes (OTEs), which must permit transmittance of light in the region of interest. OTEs must be stable toward cycling in the electrolyte selected and exhibit stability over a suitable voltammetric range.

Thin-Film Electrodes

Thin conducting film electrodes consist typically of a thin layer (100 nm or less) of conducting material, typically a metal or metal oxide, deposited on a nonconducting optically transparent substrate such as glass, quartz, or polyethylene. These materials usually transmit in the visible spectral region with varying degrees of UV transparency. Gold is the most commonly employed conducting substrate and thin film electrodes are available commercially [13.7]. The gold is frequently deposited by CVD or magnetron sputtering. Surface adhesion can be improved by silylation of a glass or quartz substrate with mercaptotrimethoxysilane, as gold bonds strongly to the sulfur-modified surface. Other metals such as Pt, Ag, and Pt–Hg have also been used [13.8–10]. For metal films there is a trade-off between conductivity and transparency which needs to be evaluated for each individual case, for example for gold, a 200 nm film thickness is really the maximum usable for reasonable optical transparency. Thin-film coatings consisting of the optically transparent metal oxides, such as ITO and FDTO do not suffer from such optical transparency issues and are commonly employed in photoelectrochemical water splitting [13.11], photocatalysis [13.12], and electrochromics [13.13]. FDTO and ITO are now far more commonly used than the noble metals. The drawbacks are that indium is very expensive and due to their bandgap absorption in the UV these materials suffer low transparency below 350 nm. For example, a study of the formation of nanotubular J-aggregates of the cyanine dye C8S3 3,3′-bis-(2-sulfopropyl)-5,5′,6,6′-tetrachloro-1,1′-dioctylbenzimidacarbocyanine on ITO reported on the limitations in these studies due to the difficulty in characterizing optical bands generated under potential control in the UV [13.14].

Recently, graphene-based optically transparent electrodes (G-OTE) have been employed to circumvent the problem of UV transparency. The G-OTE electrodes were prepared by exfoliation and oxidation of graphite to form graphite oxide (GO). GO sheets were deposited by spin coating onto quartz substrates that were pretreated by exposure to oxygen plasma to be hydrophilic. The films were then reduced thermally under Ar flow at 800 °C. X-ray photoelectron spectroscopy (XPS) showed that the percent conversion of GO to graphene in these electrodes was 80–95%. Atomic force microscopy (AFM) showed graphene films 6–25 nm thick, which was controllable so that the desired conductivity and transparency parameters could be attained [13.15]. G-OTEs therefore have potential for SEC use across the entire UV-Vis region.

Optically transparent diamond electrodes for use in transmission spectroelectrochemistry can be fabricated via a number of techniques, most notably by chemical vapor deposition (CVD) [13.17]. Polycrystalline diamond can be grown on metal substrates and then separated for use as an optical window [13.18]. Thin-film diamond can be deposited on optically transparent substrates [13.19, 20]. Conducting diamond films have also been employed as a transparent electrode for attenuated total reflectance infrared (ATR-FTIR) spectroscopy [13.21]. High-purity diamond exhibits excellent optical transparency, transmitting from ≈ 225 nm (where it has a bandgap absorption) to the far IR (typically $\approx 50\%$ transparency). However, diamond is a poor conductor and requires doping (often with boron) to produce a sufficiently conducting material for electrode use. Unfortunately, the optical properties are de-

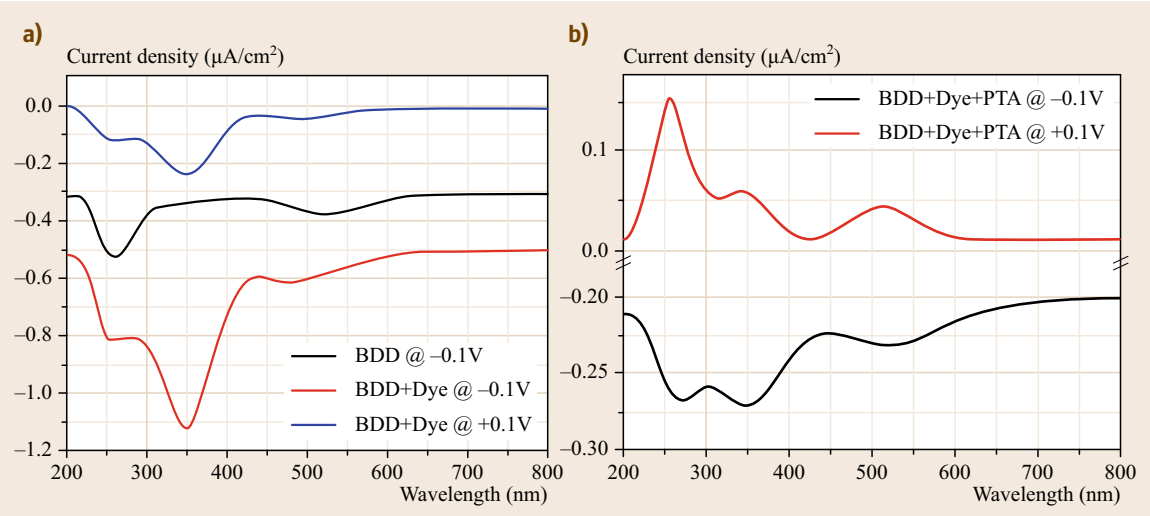


Fig. 13.2 **(a)** Action spectrum of H-terminated BDD (*black*), molecular dye-functionalized BDD (BDD + dye) at −0.1 V (versus Ag/AgCl) bias (*red*) and BDD + dye at +0.1 V bias (*blue*). **(b)** Action spectrum of electrostatically self-assembled POM on molecular dye-functionalized BDD (BDD + dye + POM) at −0.1 V bias (*black*) and at +0.1 V bias (*red*). The light source was a Newport 300 W xenon light source, using a Newport Cornerstone 260 monochromator. The electrolyte was 0.1 M Na_2SO_4 containing 5 mM methyl viologen (MV^{2+}). The reference and auxiliary electrodes (AEs) used were Ag/AgCl (3.0 M KCl) and a Pt mesh, respectively. The BDD electrode area exposed to light was 0.196 cm^2 (after [13.16], courtesy of Am. Chem. Soc.)

graded by doping and the available wavelength range and transparency are considerably reduced. Even so, diamond possesses a wide potential window, is resistant to fouling, and can tolerate extreme solvent conditions. Boron-doped diamond (BDD) substrates have been employed in the photoelectrochemical spectroelectrochemistry of dye/polyoxometalate (POM) hybrid thin films [13.16]. POMs can act as photocatalysts generally under UV irradiation only, and hence require a sensitizer (usually a dye) to extend absorption into the visible [13.22]. BDD films on quartz substrates (160 nm thickness by AFM) were prepared by CVD, and were surface-modified by electrochemically grafting of cationic pyridnium dyes covalently to the surface. An anionic POM layer (phosphotungstic acid, $H_3[PW_{12}O_{40}]$) was electrostatically assembled onto the dye by dip coating. Potential-dependent photocurrent action spectroscopy was used to characterise the relative contributions of both species to current generation.

The action spectrum of H-terminated BDD shows a photocurrent peak at around 250 nm which is attributed to an absorbance characteristic of methyl viologen. A weak, broad peak at 520 nm is attributed to defect-related absorption of CVD diamond. After grafting of the molecular dye, a photocurrent peak appeared at 350 nm attributed to the molecular dye absorption at the diamond–molecular dye–solution interfaces. After electrostatic binding to POM (Fig. 13.2b), the absorption peak of the composite film is slightly broadened and red-shifted to 366 nm with a similar absorption intensity. However, the action spectrum of BDD + dye + POM at the same applied bias (−0.1 V versus Ag/AgCl) shows a significantly reduced photocurrent density compared to BD + dye despite their similar absorption intensity, which implies that the addition of the POM impedes the preferred electron flow. This was attributed to competitive reduction pathways at overlapping potentials between MV^{2+} and the POM. The authors have also reported the potential-dependent photoelectrochemistry of films of cyanothiophene derivatives and buckyballs on CVD BDD surfaces [13.23]. A complete review series dedicated to the electrochemistry of BDD has recently been published [13.24].

Transparent electrodes are important across a wide range of electronics applications outside of spectroelectrochemistry for example in computer and touch screens and other display applications. This has led to a drive to develop transparent electrode materials that will inevitably benefit spectroelectrochemistry. Such materials include graphene [13.25], thin films of carbon nanotubes, and metal nanowires [13.26].

Mesh Electrodes

Mesh or minigrid electrodes are frequently used in transmittance SEC as the working electrode. They con-

sist of a nontransparent metal, frequently platinum or gold [13.27], but also can be of binary materials such as mercury-coated gold or porous glassy carbon. Minigrid electrodes are semitransparent due to their porous nature, which also confers great surface areas which promotes rapid, exhaustive electrolysis of analyte. Mass transport is efficient at such electrodes, and diffusion behavior is dictated by an intricate mixture of temperature, mesh size and wire diameter. Simulation of bidirectional diffusion at a gold minigrid electrode has been reported and the model was demonstrated to be valid for both thin-layer and bulk electrolysis setups [13.28].

Counter and Reference Electrodes in Spectroelectrochemistry

Auxiliary electrodes employed in an SEC measurements are often miniaturized versions of standard reference electrodes such as Ag/Ag^+ or AgCl. Silver-wire electrodes are pseudo-reference electrodes only and must be calibrated versus an internal reference, which is normally the ferrocene–ferrocenium (Fc/Fc^+) redox couple; however, in the special case of ionic liquids the cobaltocence–cobaltocenium couple (Cc/Cc^+) is recommended [13.29]. For voltammetry in acetonitrile and other nonaqueous electrolytes, a commercially available Ag/Ag^+ electrode in a glass casing separated from solution by a porous frit is frequently employed.

13.2.2 Thin-Layer Spectroelectrochemistry

OTTLE Cells

Bulk electrolysis of large sample volumes can be tediously slow, especially in the absence of forced convection. Exhaustive electrolysis of large volume of bulk solutions for SEC analysis (greater than millilitres) is therefore unfeasible. Thin layer cells are therefore widely used in spectroelectrochemistry, to promote fast electrolysis, and an extensive range of such cells have been implemented. Representative cell setups are shown in Fig. 13.3 [13.30–34].

The most basic thin layer cell design employs a short path length quartz cuvette with an electrolyte reservoir at the top where the auxiliary and reference electrodes sit (Fig. 13.3d). The optical path (l, cm) is short so the analyte solution must be of sufficient concentration so that it can be electrochemically detected ($> 1\times10^{-4}$–1×10^{-3} M) but is not so concentrated so that optical behavior deviates from the Beer–Lambert law (Sect. 13.2.1). In an alternative approach side arms can be attached in a glass blown cell to hold the electrodes (Fig. 13.3a). In such an arrangement since the optical pathlengths are typically between 50 and 250 μm optically transparent thin layer electrode (OTTLE) cells electrolysis rate is controlled by finite diffusion. In diffusion-controlled cases, the approximate time required to exhaustively electrolyze the thin layer is given by

$$t = \frac{\delta^2}{\pi D} , \tag{13.1}$$

where δ is the thin layer thickness (cm) and D is the charge transport diffusion coefficient (cm^2/s). If one assumes that a typical D_{CT} value is approximately $1\times10^{-5}\,cm^2/s$ under ambient conditions then (13.1) estimates that a cell of pathlength 25 μm can be exhaustively electrolyzed within roughly 200 ms [13.36]. This electrolysis rate is sufficiently fast to permit the collection of kinetic data.

Thin-layer cells can also be implemented in a flow-through orientation. Figure 13.3c shows a flow cell in which a gold minigrid working electrode is incorporated into a thin layer silica cell. The AE was positioned downstream and the reference upstream. Electrolyte containing the analyte is pumped through the cell and is exhaustively electrolyzed quickly due to the thin layer configuration. The spectrum is recorded and the solution replaced quickly to eliminate spectral contribution from the starting material [13.33].

Another kind of thin layer cell is shown in Fig. 13.3b. In this setup, the cell consists of an OTE and a cell holder. The cell holder is designed to position the OTE, reference electrode, and AE for either absorbance or fluorescence measurements and to standardize the distance between electrodes (see paragraph below). The outer dimensions of the holder are identical to a standard cuvette ($1\times1\times4$ cm) so it is compatible with a conventional benchtop spectrometer. However, unlike a standard cuvette, all four side walls have windows for light passage with two of the inside diagonal corners with slots for the OTE electrode, which positions the thin layer cell at a 45° angle suitable for fluorescence. The cell was custom made from quartz, silicon spacers, and epoxy which avoided more expensive machine milling. Other thin layer cell arrangements include the use of milled polyethylene or Teflon walls into which quartz windows are incorporated. These are designed specifically to replace a standard 1×1 cm sample holder in commercial benchtop spectrometers and can incorporate temperature control through the flow of cooled N_2. Low-temperature OTTLE SEC has been reported (20 °C) [13.37].

Poor arrangement of the auxiliary and reference electrodes relative to the working electrode results in significant ohmic drop which varies across the geometric surface of the working electrode. This ohmic polarization is a serious problem in semi-infinite linear diffusion (SILD) bulk electrolysis and can be challeng-

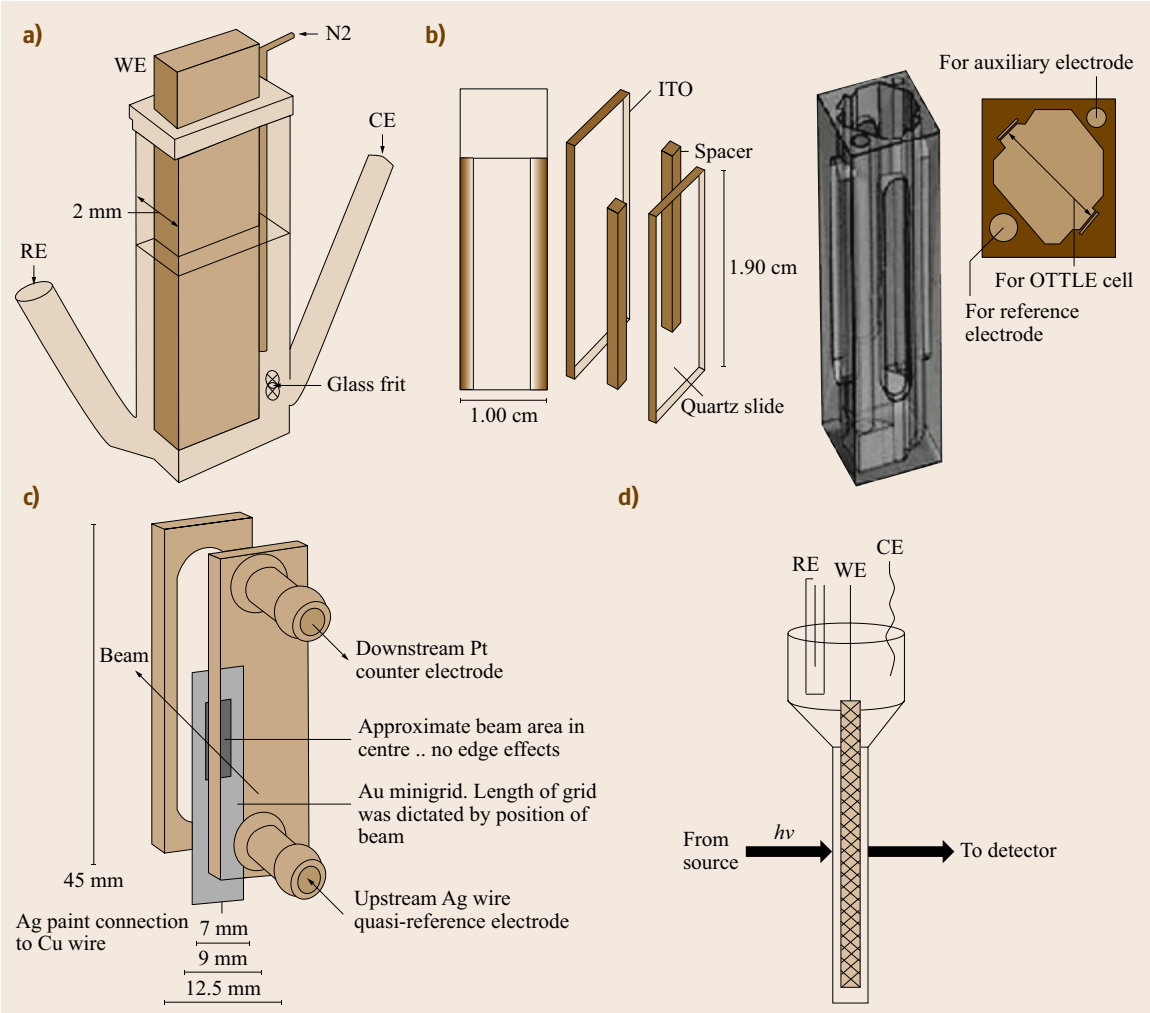


Fig. 13.3a–d OTTLE cells for UV-Vis/NIR: **(a)** thin layer cuvette with side arms for counter and reference electrodes; **(b)** quartz and silicone OTTLE cell suitable for benchtop electronic and fluorescence spectroscopies. Left to right-component assembly, the cell holder and a top–down view; **(c)** a thin layer flow cell; **(d)** a minigrid electrode and conventional thin layer cuvette with reservoir for counter and reference electrodes (**(a)** after [13.34]; **(b)** after [13.35], courtesy of Wiley; **(c)** courtesy of Am. Chem. Soc.; **(d)** after [13.33])

ing to avoid in a thin-layer setup [13.38]. However, this is not a major issue unless quantitative time-dependent data are required. In quantitative measurements, excessive voltage drop can be avoided by careful geometric arrangements of the various electrodes. In placing the counter electrode, in the form of a large surface are Pt flag, near the working electrode the current flow is regulated and an internal reference point is set to alleviate poor potential control [13.39]. For qualitative studies, no such kinetic control is needed, so bulk electrolysis at potentials, previously identified from voltammetry, is sufficient. A very common application of UV-Vis/NIR SEC is in the study of multinuclear transition metal complexes. Mixed valence states in such species are particularly amenable to SEC.

Figure 13.4 illustrates, for example, the spectroelectrochemical response of a heterodinuclear complex $[Os(bpy)_2(bpt)Ru(tpy)Cl]^{2+}$. Voltammetry demonstrated that the two metal oxidations in this asymmetric complex are separated by 210 mV. Such large peak-to-peak separations exceeded what would be expected from electrostatic and statistical effects of oxidizing only one metal centre and was indicative of metal–metal communication. Spectroelectrochemistry provided a convenient avenue to assess the extent of such communication by allowing the isolation

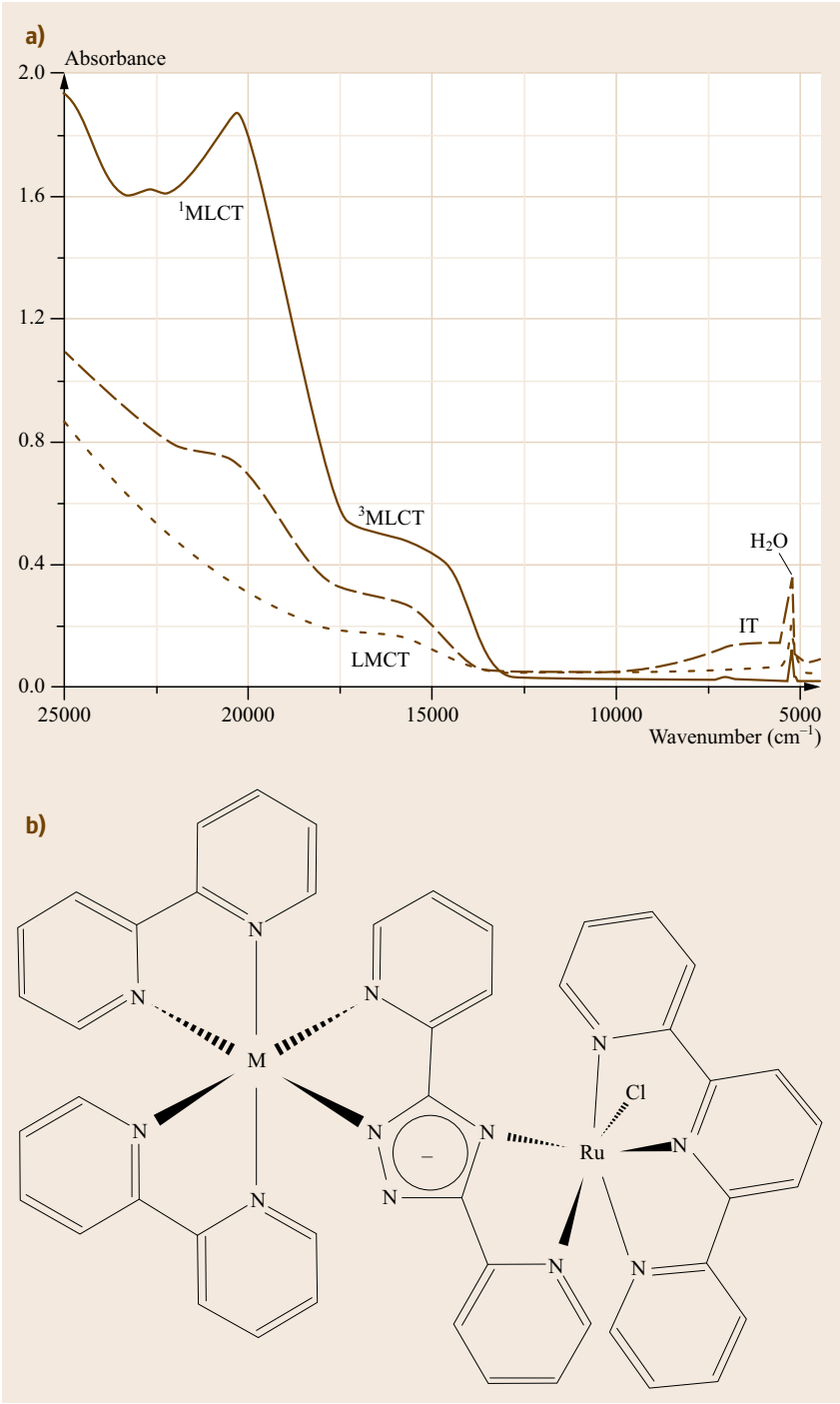


Fig. 13.4 **(a)** UV-Vis/NIR absorption spectra of the dinuclear complex $[Os(bpy)_2(bpt)Ru(tpy)Cl]^{2+}$ in the $M_2^{II,II}$ (*solid lines*), $M_2^{II,III}$ (*dashed lines*), and $M_2^{III,III}$ (*dotted lines*) redox states. A platinum gauze, platinum wire, and SCE were used as the working, counter, and reference electrodes, respectively. A custom-made 2 mm path length 1.2 ml volume quartz cuvette was employed. **(b)** Structure of the compound (M=Os) (after [13.40], courtesy of Am. Chem. Soc.)

and spectroscopic study of the mixed valence state. Oxidation of $[Os(bpy)_2(bpt)Ru(tpy)Cl]^{2+}$ at +0.70 V to form the $Os^{III}Ru^{II}$ redox state resulted in a decrease in intensity of the ^{1}MLCT absorptions at 20 000 and 22 500 cm^{-1} and the ^{3}MLCT absorption (13 000–17 000 cm^{-1}). These changes were accompanied by the appearance of an absorption band at 6000 cm^{-1}. The latter feature was assigned to an intervalence charge transfer (IVCT), also known as a metal-to-metal charge transfer (MMCT) transition on the

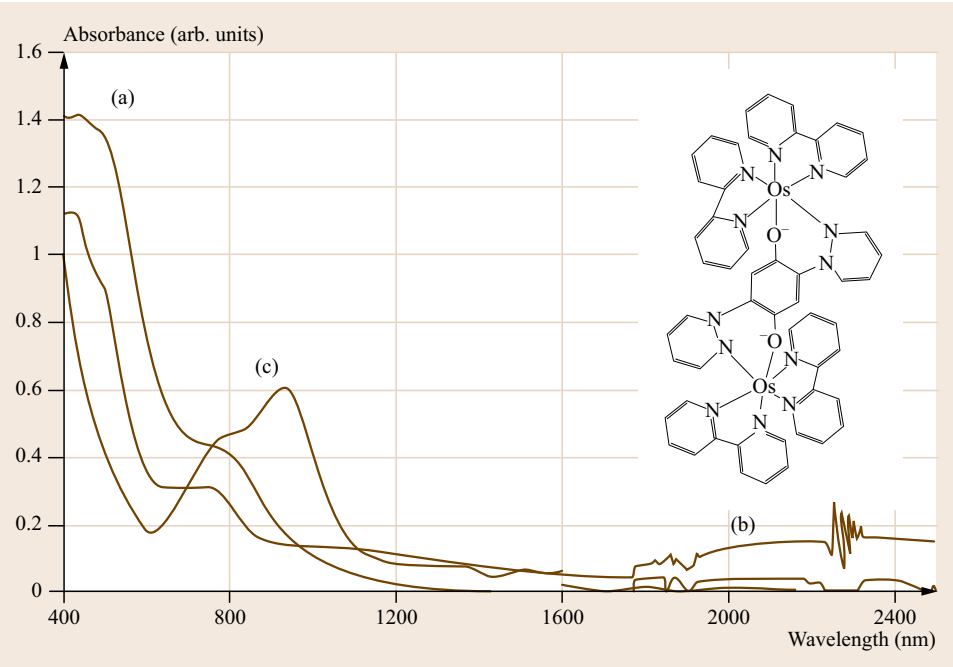


Fig. 13.5 Electronic spectroelectrochemistry of $[(Os(bpy)_2)_2(p\text{-}L)]^{3+}$ (where p-L is 1, 4-dihydroxy-2, 5-bis(pyrazol-1′-yl)benzene) (*inset*) (a) open-circuit potential and upon application of (b) 0.3 V and (c) 0.8 V versus SEC (after [13.41], courtesy of Am. Chem. Soc.)

basis of its subsequent disappearance upon oxidation of the second metal center (Ru) at 0.95 V ($Ru^{II/III}$ centres tends to have higher E_0 values than $Os^{II/III}$ centers in isoelectronic coordination environments) [13.42]. In addition to a decrease in the IVCT band, the MLCT bands decrease further in the fully oxidized state. The optical characteristics of IVCT transitions can be analyzed according to the Hush theory and used to estimate the extent of electronic coupling between two metals across the intervening bridge [13.43]. The full width at half maximum (FWHM, $v_{1/2}$) of the IVCT band reflects the extent of electronic delocalization between the metal centres. For a compound in which electrons on a reduced metal centre are localized, known as a class II system according to the Robin-Day classification [13.44], $v_{1/2}$ can be theoretically predicted from the Hush theory and was estimated to be 4660 cm^{-1} for this complex. The spectroelectrochemistry of electroactive polymer systems has also been extensively studied using OTTLE cells as SEC can give unique insight into electron hopping through a thin layer or thin film [13.45, 46].

Electronic SEC has provided useful insights into the origin of redox processes in transition metal complexes which possess redox active ligands [13.47]. In many such instances voltammetry alone is insufficient to identify the origin of the individual redox steps. For example, a hydroquinone ligand bridged osmium (II) dimer was analyzed by cyclic voltammetry (CV), which revealed three reversible redox waves centred at 0.23, 0.42 and 0.98 V (versus SCE). The SEC of this complex is shown in Fig. 13.5 [13.41].

By employing SEC, the redox waves could be assigned unambiguously, and the two waves at lower potential were identified as ligand based. This conclusion was based on the electronic SEC, which showed the grow-in of a semiquinone to metal CT with increasing applied potential. An IVCT transition appears at 1700 nm and the feature at 2400 nm is attributed to be due to splitting of the nominally degenerate Os 5d π orbitals, a consequence of strong spin–orbit coupling due to the heavy Os center and asymmetry induced by the radical state of the bridge. Overall, the spectroelectrochemistry revealed that the semiquinone state is highly localized whereas there is considerable mixing of quinone and metal states. Such information would be unobtainable from electrochemical measurements alone.

In some cases, electronic spectroelectrochemistry of multinuclear metal complexes is accompanied by other forms of spectroelectrochemistry to yield detailed insights. As described earlier, the polyoxometalates (POMs) are a diverse class of discrete oxo-metal cluster compounds comprised most commonly of tungsten, but also of molybdenum, niobium, and vanadium [13.49]. POMs exhibit very rich redox chemistry, are very stable to voltammetric cycling and reduced forms can be generated both photochemically and electrochemically. Upon one-electron reduction new bands appear in the NIR and visible regions which are attributed to

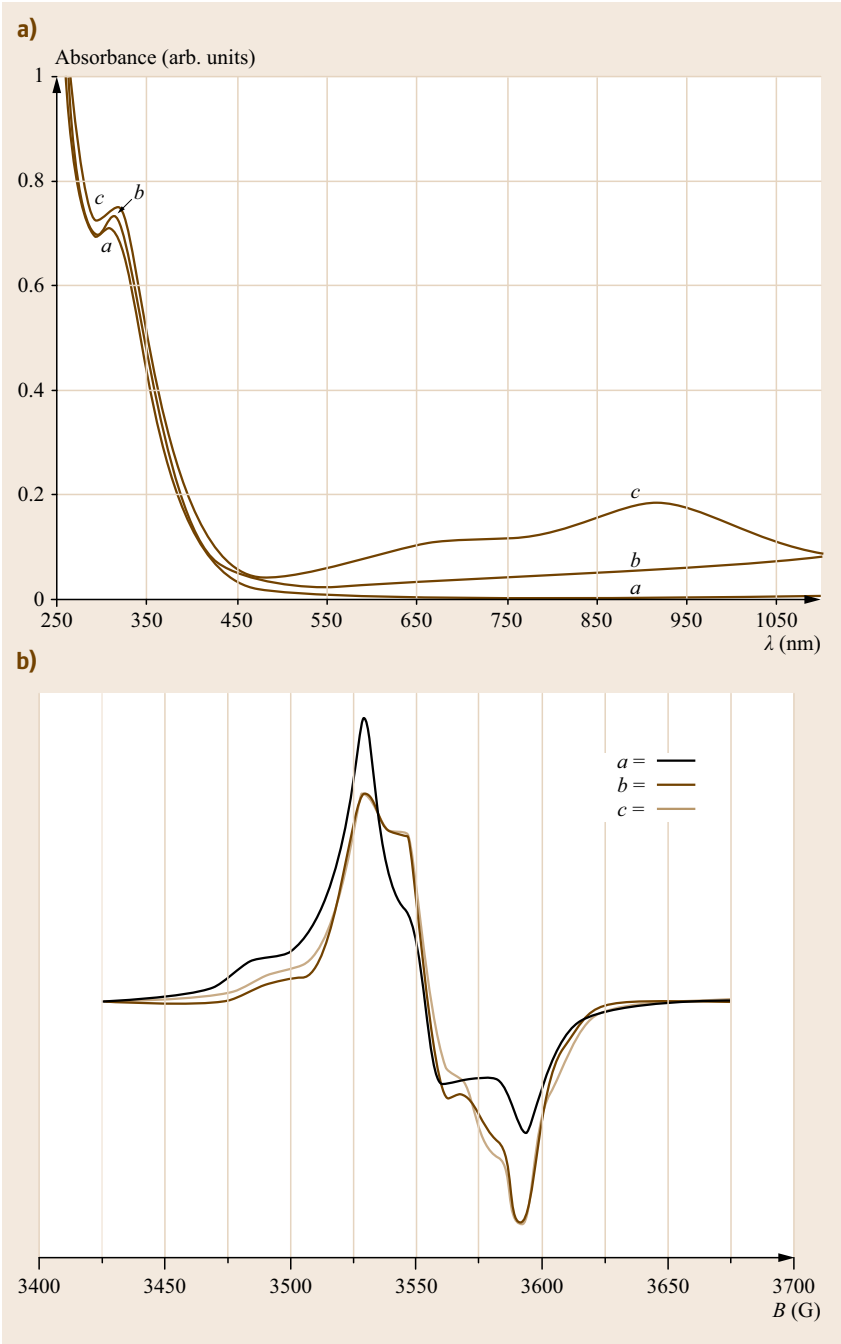


Fig. 13.6a,b UV-Vis/NIR **(a)** spectroelectrochemistry of 0.242 mM β-$[Mo_{18}O_{54}(SO_3)_2]^{4-}$ in CH_3CN $(Hex)_4NClO_4$, in a 1 mm cell (*a*) prior to electrolysis; (*b*) after exhaustive one-electron reduction at -0.205 V and (*c*) after exhaustive two-electron reduction at -0.485 V. **(b)** X-band EPR spectroscopy of the one electron-reduced β-$[Mo_{18}O_{54}(SO_3)_2]^{5-}$ (trace *a*), and simulated spectra of 2 and 3 electron reduced species (*b* and *c*). Conditions: millimolar frozen solutions in CH_3CN, 0.1 M $(Hex)_4NClO_4$, at 2.3 K. Microwave frequency 9.655 GHz, microwave power 209 nW, 100 kHz modulation amplitude 1 G, spectrometer gain 1×10^4, time constant 41 ms, scan rate 250 G/83 s (after [13.48], courtesy of Wiley)

IVCT transitions on the basis of electron paramagnetic resonance (EPR) spectroscopy measurements. These IVCT bands grow in intensity with each subsequent reduction. EPR spectroscopy employs microwaves–radio waves to probe electron spin and electron–nuclear interaction in compounds with unpaired electrons such as radicals, biradicals and other doublet states. The UV-Vis/NIR and X-band EPR spectroelectrochemistry of the polyoxomolybdate β-$[Mo_{18}O_{54}(SO_3)_2]^{4-}$ are shown in Fig. 13.6 [13.48].

The EPR SEC revealed that in the one-electron reduced species, β-$[Mo_{18}O_{54}(SO_3)_2]^{5-}$, the unpaired electron is shared over 3 molybdenum nuclei. Interestingly, SEC shows that the fully oxidized and two-elec-

tron reduced species are almost EPR silent, with any signal contribution attributed to trace amounts of one-electron reduced product. This indicates that electron pairing occurs in the two-electron reduction product. These data are in contrast to the alpha-isomer, where the electron is delocalized over 6 Mo centers [13.35] and the similar structure α-$[Mo_{18}O_{54}(SO_4)_2]^{4-}$, where the electron is delocalized equally over all 18 Mo centers [13.50].

Quantitative Spectroelectrochemistry: The Nernst Plot

Commonly used in thin-layer SEC, the Nernst plot gives the formal redox potential $E^{\circ\prime}$ and the number of electrons n transferred during a reversible electrochemical reaction. For fully reversible voltammetry, the following reaction

$$\mathrm{O} + n\mathrm{e}^- \rightleftharpoons \mathrm{R}$$

exhibits Nernstian behavior. In a thin layer cell, diffusion is rapid so redox equilibrium is established quickly leading to uniform concentrations of oxidized and reduced forms of the analyte in solution and at the interface which can be described by the Nernst equation

$$E_{\mathrm{app}} = E^{\circ\prime} + \frac{RT}{nF}\ln\frac{[\mathrm{O}]}{[\mathrm{R}]}\,. \tag{13.2}$$

A Nernst plot can be generated from a series of CVs by applying potentials over a desired range and recording the electronic spectra when the coulometric response reaches equilibrium. At intermediate potentials, the concentrations of reduced and oxidized species are not equal and can be calculated using a modified Beer–Lambert expression

$$\frac{[\mathrm{O}]}{[\mathrm{R}]} = \frac{\frac{(A_\mathrm{i}-A_\mathrm{R})}{\Delta\varepsilon l}}{\frac{(A_\mathrm{O}-A_\mathrm{i})}{\Delta\varepsilon l}} = \frac{A_\mathrm{i}-A_\mathrm{R}}{A_\mathrm{O}-A_\mathrm{i}}\,, \tag{13.3}$$

where A_O and A_R are the absorbances of the fully oxidized and fully reduced species and A_i is the absorbance at intermediate applied potentials, $\Delta\varepsilon$ is the difference in extinction coefficient between O and R at the monitoring wavelength, and l is the path length. Substituting (13.3) into (13.2) yields

$$E_{\mathrm{app}} = E^{\circ\prime} + \frac{RT}{nF}\ln\frac{A_\mathrm{i}-A_\mathrm{R}}{A_\mathrm{O}-A_\mathrm{i}}\,. \tag{13.4}$$

A plot of E_{app} against $\ln[(A_\mathrm{i}-A_\mathrm{R})/(A_\mathrm{O}-A_\mathrm{i})]$ is linear for a reversible redox reaction so that $E^{\circ\prime}$ and n can be determined from the intercept and slope, respectively. Because the spectra are measured under equilibrium conditions, iR drop does not effect the measurement. The above description assumes that the oxidized and reduced species exhibit absorbance spectra that do not overlap wavelength used to monitor the process. In many instances isolating a single contribution in this way may be difficult and spectral deconvolution is necessary to extract the component spectral contributions to evaluate $E^{\circ\prime}$. Spectropotentiostatic measurements of this type have been used to study multiple redox reactions in complex supramolecular porphyrin systems containing several of the same chromophore units undergoing sequential redox steps. Relative distributions of the oxidized and reduced forms are estimated using iterative algorithms based on (13.2) to obtain $E^{\circ\prime}$ values for each redox process [13.51].

Chronoabsorptometry

Chronoabsorptometry involves recording an absorbance–time curve after the application of a potential step. Applying the data to an integrated form of the Cottrell equation permits the calculation of diffusion coefficients. This approach has been widely used, particularly for systems with slow electron transfer (ET) dynamics [13.52]. For example, in metalloprotein electrochemistry, where slow heterogeneous electron transfer of deeply embedded redox centres yields poor cyclic voltammetric response. More advanced approaches, such as double potential step chronoabsorptometry, have also been used to study electron transfer kinetics in metalloproteins [13.53].

Thin-Layer SEC with Redox Probes

Proteins are frequently rare and difficult to purify and can be expensive; hence they are best studied under low-volume conditions, such as thin-layer techniques as otherwise their study would be prohibitively expensive. Redox probes, either cationic or anionic, must frequently be used to mediate electron transfer between an embedded redox centres within a protein and the electrode surface. Such probes must be sufficiently small to diffuse through the protein to the redox centres, in the common situation where the redox centres of the protein is too far from the interface to be probed directly by heterogeneous electron transfer. The probes must also readily undergo electron transfer with the redox centre under investigation and should ideally not interfere with the spectroscopy under investigation.

A good example of the use of a redox probe in the interrogation of electron transfer in thin films of the protein was demonstrated for histidine-tagged recombinant human neuroglobin (hNb) on gold electrodes. In this study, the Nernst equation was applied to both solution phase protein UV-Vis SEC and immobilized

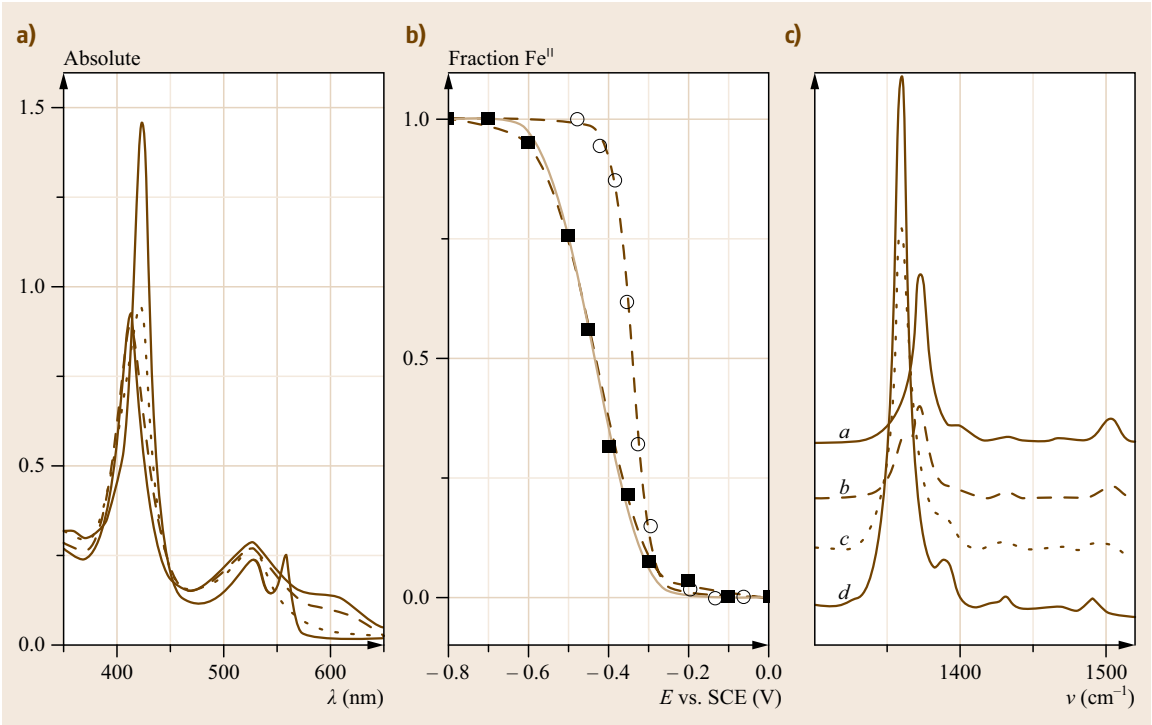


Fig. 13.7 **(a)** UV-Vis spectroelectrochemistry of hNb in solution monitored in the presence of $[Ru(NH_3)_6]Cl_3$. **(b)** Fraction of hNb ferrous form as a function of the potential applied during (O) spectroelectrochemical titration of hNb in solution and (■) SERR spectroscopic titration ($\lambda_{ex} = 406.7$ nm) of hNb immobilized on a nickel chelating nitrilotriacetic acid (Ni(II)-NTA) modified Ag electrode (the data values were obtained from three independent measurements with a standard error of less than 10 mV). *Black* and *brown* fits are of the Nernst equation to UV-Vis and SERRS data, respectively. **(c)** SERR spectroelectrochemistry of hNb immobilized on a Ni(II)-NTA modified Ag electrode. The Soret excitation was 406.7 nm and E_{app} is (*a*) 0.1, (*b*) −0.4, (*c*) −0.5 and (*d*) −0.7 V (after [13.54], courtesy of Am. Chem. Soc.)

thin film protein surface-enhanced resonance Raman (SERR) SEC [13.54]. These data are reproduced in Fig. 13.7.

Using electronic spectroscopic data and the Nernst equation, the authors identified the formal redox potential as – 340 mV, which was in agreement with solution CV data. However, the SERR SEC Nernst plot provided a formal potential of – 440 mV. Despite this shift, the SERR spectra demonstrated that the protein structure remained intact at the interface, and the shift in formal potential was attributed to a range of overlapping values due to an array of heterogeneous binding modes.

In another recent study, the potential-controlled UV-Vis spectra were reported for a multiheme nitrite reductase; *Escherichia coli* NrfA, which had been immobilized on a high surface area mesoporous nanocrystalline SnO_2 electrode [13.55, 56]. Although individual redox reactions involving heme centres have not been detected on conventional metal or graphite electrodes, the authors reported that they are observed fairly readily on the SnO_2 electrode in the absence of substrate especially when the capacitive background current is subtracted. The addition of nitrite yields a well-defined catalytic wave which demonstrates that the immobilized enzyme has not been denatured (i. e., remains catalytically active). UV-Vis spectra show that the immobilized enzyme can be reduced electrochemically, and the fact that the reduced enzyme is rapidly reoxidized by the nitrite substrate confirms that the majority of the film is also catalytically active. UV-Vis absorbance changes track the voltammetric current and peak fitting of normalized CVs allowed the authors to assign the electron transfer processes to low and high spin heme centres. A recent review of metalloprotein spectroelectrochemistry including UV-Vis, Fourier transform infrared (FTIR), magnetic circular dichroism (MCD), fluorescence and Raman methods is recommended for further reading [13.57].

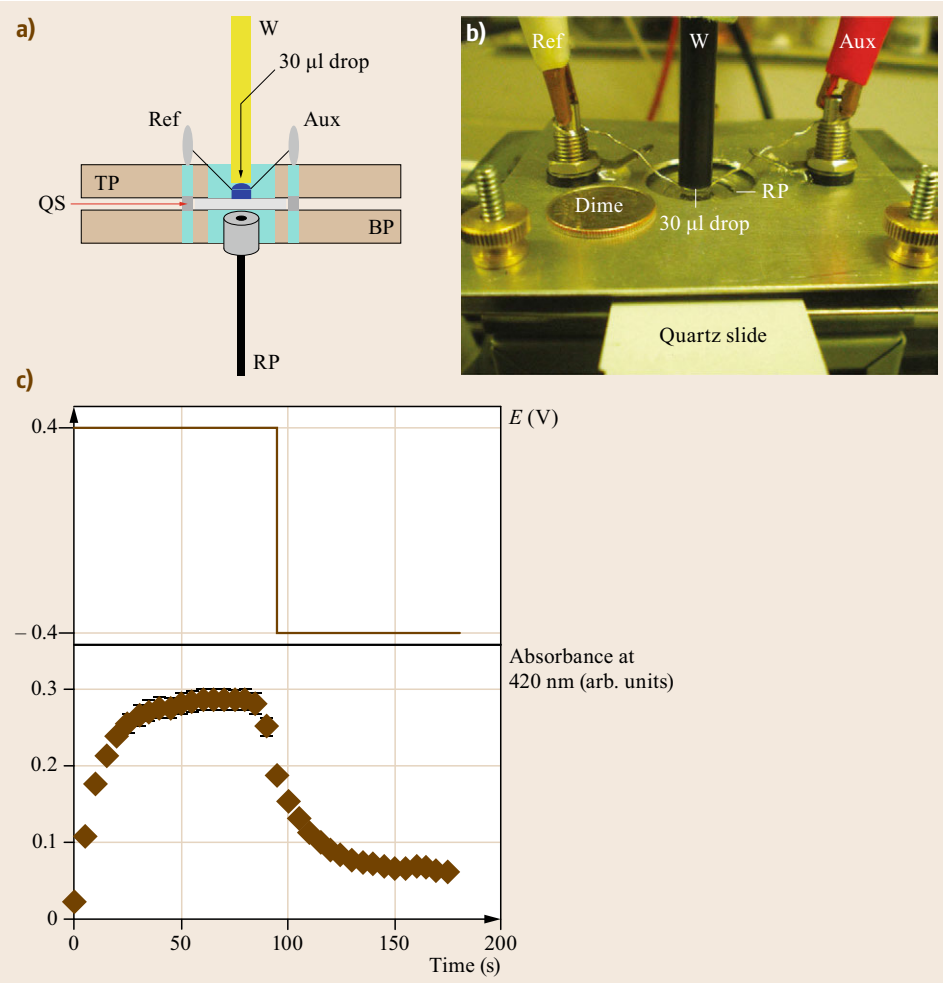


Fig. 13.8 **(a)** Schematic of an SEC setup employing an aqueous microdrop. **(b)** Photo of the cell (W = working electrode, Ref = reference electrode, Aux = auxiliary electrode, TP = top plate, QS = quartz slide, BP = bottom plate, RP = reflectance probe). Dime coin for scale. **(c)** Double potential step chronoabsorptometry ($+0.4$ V and -0.4 V) at 420 nm of 25 mM $Na_4[Fe(CN)_6]$ in aqueous 0.1 M KNO_3 (after [13.58], courtesy of Am. Chem. Soc.)

Semi-Infinite Linear Diffusion Spectroelectrochemistry

Spectroelectrochemistry can be performed in the semi-infinite linear diffusion (SILD) regime under mass transport limitations, and response times can be greatly improved by the use of small solution volumes. In fact, a recent example by *Schroll* et al. demonstrated how an aqueous microdrop can be employed to conduct SILD SEC quantitatively, to permit estimation of diffusion coefficients and electrolysis times [13.58]. A schematic of this experimental setup is shown in Fig. 13.8.

By using the well-defined model $[Fe(CN)_6]^{3-}/[Fe(CN)_6]^{4-}$ redox couple and cyclic voltammetry over a range of scan rates the authors demonstrated a linear relationship between square root of the scan rate and peak current, hence proving SILD control. Furthermore, the diffusion coefficient was estimated from the Randles–Sevçik equation and found to agree with the literature value. Using double potential step chronoabsorptometry, the authors then demonstrated that the estimated electrolysis time (calculated using (13.1)) should take ≈ 60 min. Since the potentials were applied for less than 2 min, only a small fraction of the total volume of the working solution was electrolyzed, and semi-infinite diffusion conditions existed. The authors also reported on the luminescence SEC of a Ru(II) complex in the SILD regime using the same experimental setup, and both absorption and emission were recorded using a 180° back reflectance fiber optic cable.

Potential step measurements such as chronoabsorptometry and chronoamperometry can yield further spectral information from the Cottrell equation. In the above example, the detector is set to monitor at 420 nm only, as at this wavelength a solution of $[Fe(CN)_6]^{4-}$ is spectroscopically silent while $[Fe(CN)_6]^{3-}$ exhibits an intense absorption band ($\varepsilon_{420\,nm} = 1040\,M^{-1}cm^{-1}$). Since only the oxidized product (P) absorbs at the

monitoring wavelength, the time-dependent change in absorbance (dA) across an irradiated area of layer thickness equal to dx is a function of both product concentration (C_P) and its extinction coefficient (ε_P). The total absorbance A is therefore given by the integral

$$A = \varepsilon_P \int_0^\infty C_P(x,t)dx \,. \tag{13.5}$$

This integral represents the total C_P per unit area, which is equivalent to Q/nFA, where Q is the total charge passed (including non-Faradaic charging components) during bulk electrolysis and is described by the integrated Cottrell equation

$$A = \frac{2\varepsilon_0 D^{1/2} C t^{1/2}}{\pi^{1/2}} \,, \tag{13.6}$$

where C and D are the bulk concentration and diffusion coefficient, respectively, of the starting material and ε is the extinction coefficient of the product. Plots of absorbance versus time$^{1/2}$ are therefore linear and can be used to calculate either ε, D or C as desired. In the published example cited above, the reflectance probe surface, which is a 2 mm diameter fiber optic bundle, illuminates the glassy carbon working electrode (3 mm diameter) from a 1 mm distance. At 1 mm distance, the reflectance probe beam divergence is larger than the active area of the working electrode, so the spectroscopic response includes that of bulk solution beyond the diffusion layer. This means that deviation from linear Beer–Lambert behavior is observed in this case. The use of a larger surface area working electrode or a more collimated beam could reduce this effect.

Long Optical Pathway Thin Layer Cells

In instances where the target analyte exhibits low absorbtivity (i. e., a low extinction coefficient), thin layer cells with short optical paths may be unsuitable, particularly where increasing analytic concentration is not feasible, for example, where dimerization may occur or where it is not economical. An option in such instances is to increase the optical pathlength using a long optical path thin layer cell (LOPTLC) [13.59]. In the LOPTLC cell setup, shown in Fig. 13.1, the optical path lies parallel to the working electrode, which means it does not need to be optically transparent. Electrolysis tend to be slower than in the conventional thin layer configuration due to larger solution volumes. Additionally, because the incident light is not transmitted through the electrode, (13.3) and (13.5) no longer apply, meaning LOPTLC cells are unsuitable for dynamic chronocoulometry. Electronic spectra are, in effect, the integral absorption of all absorbing species along the light path. Therefore, as incident light is directed along a length parallel to the front of the working electrode in LOPTLC the spectroscopy is collected from analyte at a set distance from the electrode all along its length (normally within the diffusion layer). This means that if the redox reaction under SEC investigation consists of both surface-confined and diffusion-based processes, the LOPTLC cell arrangement may lead to different spectroscopy than that observed for the corresponding transmittance setup. This is particularly the case for semi-infinite diffusion regimes where the absorbance spectrum recorded in transmittance mode will contain contributions from the bulk solution, the diffuse layer, and the interface. Bidirectional LOPTLC cells can be used in such an experiment.

In a recent example, the electrosynthesis of poly(3,4-ethylenedioxythiophene) (PEDOT) in aqueous media was studied using bidirectional electronic SEC [13.60]. Significant spectral differences were observed between the normal and parallel optical arrangements as shown in Fig. 13.9. In the normal arrangement only surface-based redox processes were observed (Fig. 13.9a). However in the parallel arrangement (Fig. 13.9b), which measures spectroscopic signals in bulk solution only, an extra feature appeared at ≈ 290 nm. The authors attributed this band to the release of oligomer intermediates into solution at cathodic potentials. This provided insight into the mechanism of PEDOT polymerization that could not be provided by conventional thin layer SEC. The authors supported this conclusion by also performing spectroelectrochemical quartz crystal microbalance measurements (SECQM) and mass spectrometry. In other setups, LOPTLC flow-through cells have also been reported by using a peristaltic pump [13.61]. This setup combines low iR drop, high sensitivity, and fast exhaustive electrolysis times. The pump could also be removed and the cell used for nonflow through LOPTLC measurements.

Other examples of LOPTLC spectroelectrochemistry include a fundamental study of chemical versus electrochemical redox processes in flavonoids as a means to identify the nature of the antioxidant behavior of the polyphenolic natural products morin and kaempferol [13.62]. The same group also published LOPTLC SEC of the related antioxidant compound rutin on a graphite wax electrode (GWE) [13.63]. In this study, they used cyclic voltammetry, cyclic voltabsorptometry (CVA) and differential cyclic voltabsorptometry (DCVA) of the thin layer to elucidate competing adsorption and diffusion controlled redox processes. In CVA/DCVA, the absorbance of the product of a surface redox reaction (A_P) is differentiated with respect to the linearly varying potential (dA_P/dE) and is displayed

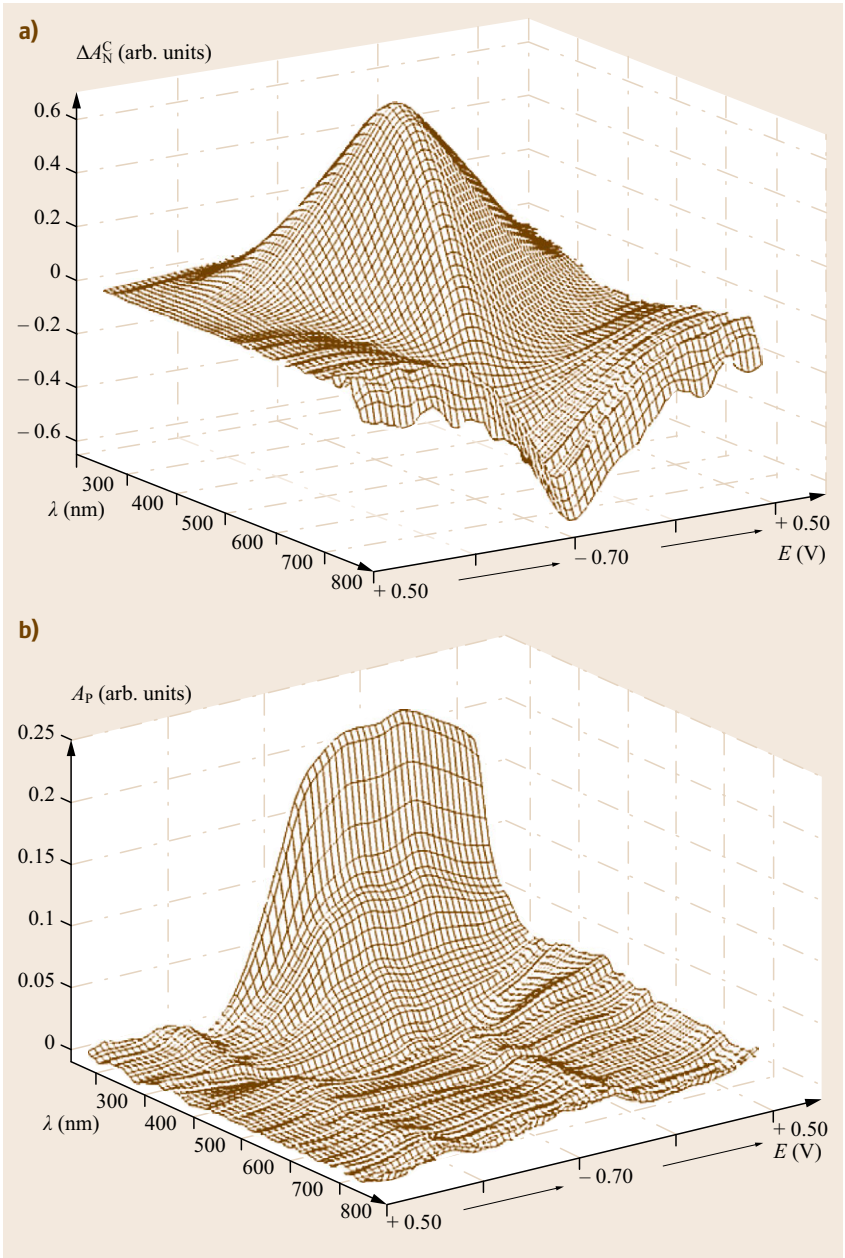


Fig. 13.9a,b Three-dimensional plot of the thin layer spectroelectrochemistry of a PEDOT film. ΔA was measured as a function of wavelength and applied potential in **(a)** the normal optical arrangement and **(b)** parallel optical arrangement. The electrolyte was aqueous 0.2 M $LiClO_4$, scan rate 15 mV/s. A Pt wire auxiliary electrode and a Ag/AgCl reference electrode were employed (after [13.60], courtesy of Elsevier)

as a function of sweep potential. The main advantages of DCVA are its insensitivity to non-Faradaic processes and its ability to permit simultaneous multicomponent analysis with a single potential scan by judicious selection of monitoring wavelength. It has been demonstrated that dA/dt (or dA/dE) versus E is morphologically identical to a cyclic voltammogram and that the dA/dt curve is cleaner than the corresponding cyclic voltammogram [13.54]. Using CVA, DVCA and the Beer–Lambert law the authors deconvoluted a series of complex electrochemical data sets to identify each step in the mechanism of rutin oxidation. This work has implications for investigating electrochemical process involving coupled adsorption–desorption steps.

Slab optical waveguide spectroscopy (SOWG) is an emerging spectroelectrochemical tool which can be used to probe adsorbed species at very low concentrations. A planar waveguide in the form of an evanescent wave is used to probe a self-assembled thin film. *Mendes* and *Saavedra* et al. showed that at visible

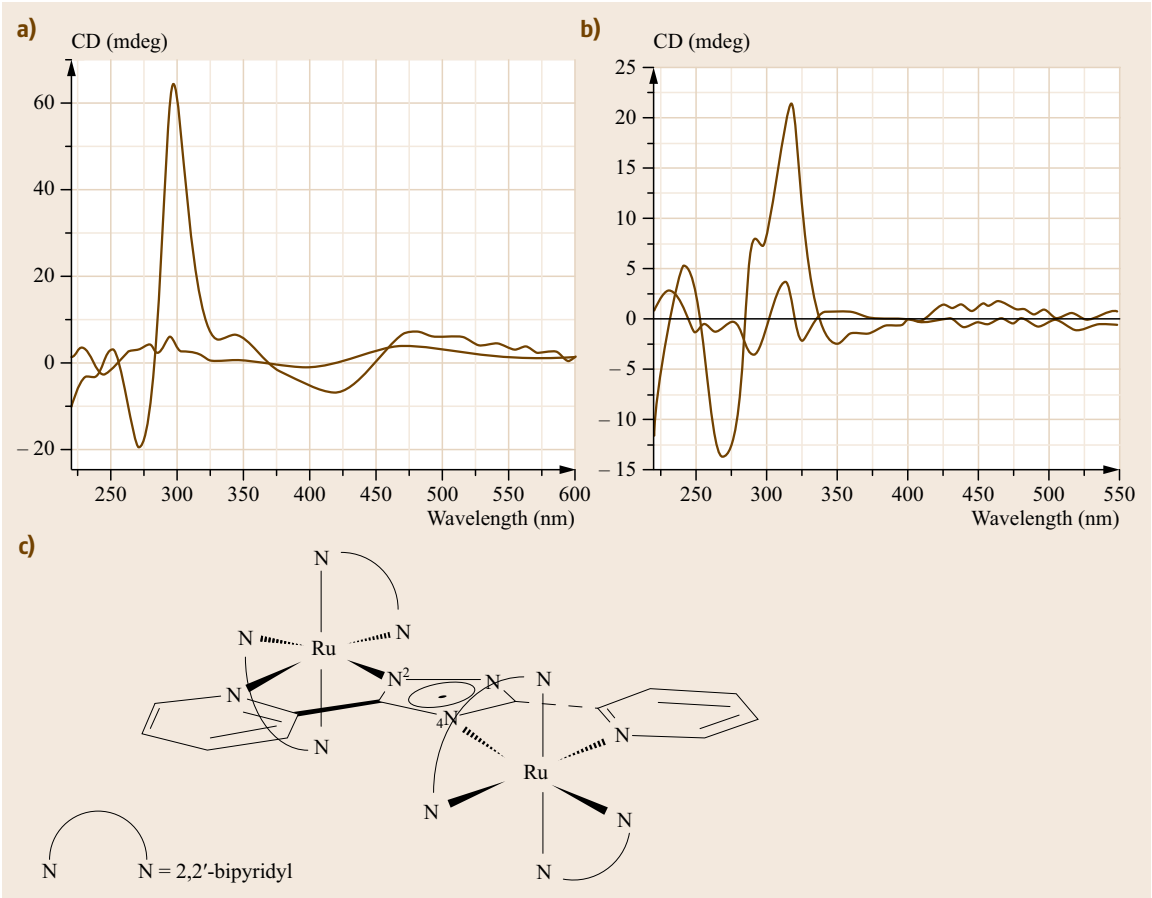


Fig. 13.10a–c CD spectra of (*thick line*) and (*thin line*) diastereoisomers of the complex in $Ru^{II}Ru^{II}$ state **(a)** and the $Ru^{III}Ru^{III}$ state **(b)**. **(c)** Structure of the asymmetric dinuclear ruthenium complex (after [13.64], courtesy of Am. Chem. Soc.)

wavelengths, a single-mode planar waveguide can support up to several thousand reflections per cm of beam propagation [13.65]. This reflection density is about 4 orders of magnitude greater than using bulk optical elements in conventional attenuated total reflection (ATR) techniques and yields a concomitantly much higher sensitivity. The authors employed an achromatic waveguide couple to efficiently couple an incoming light beam of broad spectral width into the waveguide. The evanescent wave of the propagating mode was employed to probe the electronic spectroscopy, in the monolayer regime, of cytochrome c in its oxidized and reduced forms when immobilized. More recently, in-situ SOWG spectroelectrochemical measurements were carried out on the ferroin–ferriin couple as a model reversible redox probe [13.66]. Since the amplitude of the evanescent field decreases with distance from the SOWG/solution interface, the species transiently in the vicinity of the SOWG have their spectroscopic signals selectively enhanced. The authors then used the relative concentration ratios of ferroin and ferriin derived from known ε values and SEC measurements to calculate the penetration depth of the evanescent wave into solution. This could be applied to the fundamental study of diffusion behavior in some colored species.

Circular Dichroism Spectroelectrochemistry

Interestingly, the degree of electron delocalization across a singly occupied molecular orbital (SOMO) in a mixed valence IVCT state has been investigated with UV-Vis circular dichroism (CD) spectroelectrochemistry [13.64]. CD spectroscopy is used to distinguish chiral compounds with identical UV-Vis absorption features based on the fact that the left- and right-handed enantiomers rotate linearly polarized light in different ways. In this study, a dinuclear Ru(II) complex containing an asymmetric bridging triazole ligand was resolved into its four optical isomers using chi-

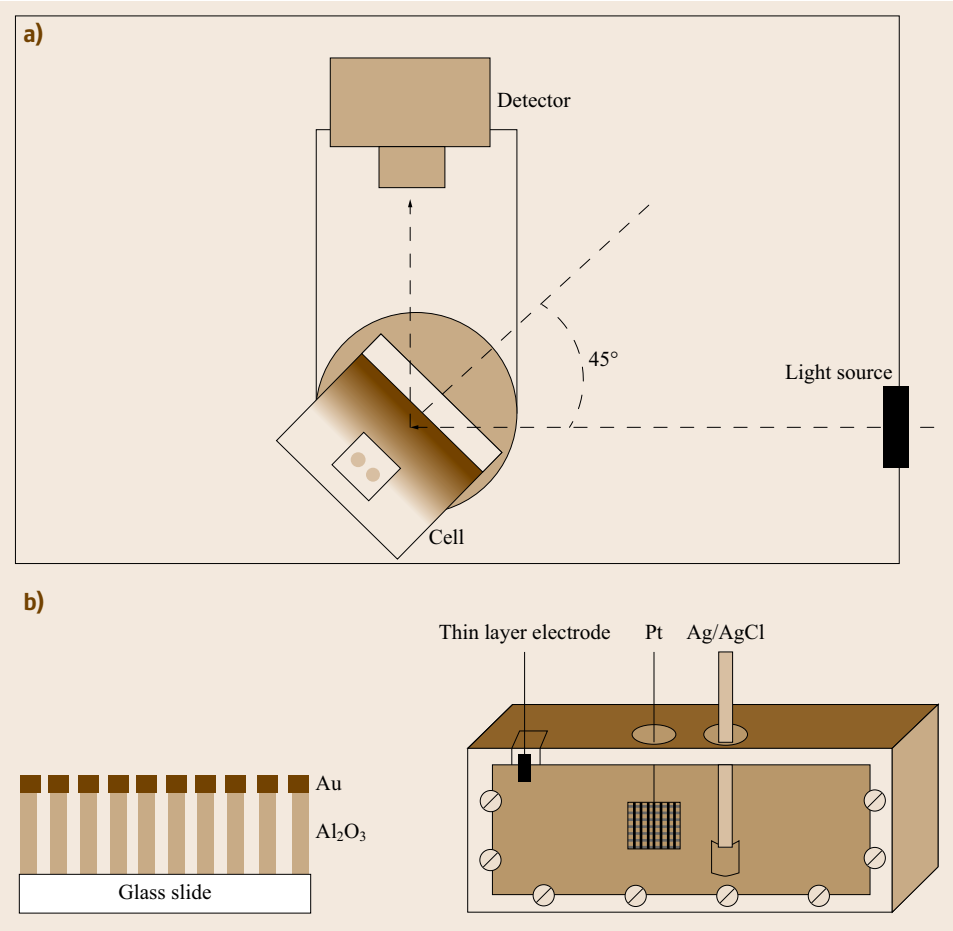


Fig. 13.11a,b Schematic of spectroelectrochemical experiment **(a)** and employing a thin layer optically reflective thin layer cell. **(b)** Side profile of the optically reflective thin layer electrode (after [13.67], courtesy of Elsevier)

ral high-performance liquid chromatography (HPLC). The structure of the complex and the CD spectroelectrochemistry are shown in Fig. 13.10.

CD SEC revealed large differences in the different isomer spectra in the three oxidation states (i. e., $Ru^{II}Ru^{II}$, $Ru^{II}Ru^{III}$, $Ru^{III}Ru^{III}$). The authors demonstrated, on the basis of CD SEC, that the SOMO is localized on one Ru-bound N atom of the bridging triazole ligand (labeled as N^2), and does not hop between the other state ($_4$N bound). Therefore, the optical electron transfer is directional ($_4$N to N^2). CD SEC is useful for study of asymmetric dinuclear complexes where the presence of an IVCT band has not been established or is unclear, as it can provide further information about the nature of the mixed-valence state in such complexes.

13.2.3 Reflectance Spectroscopy

Most studies involving electronic spectroelectrochemistry are performed in the thin-layer transmittance mode, most frequently using an OTTLE cell arrangement. However, reflectance spectroscopy is important in the study of immobilized thin films and solids. Both external reflectance and attenuated internal reflectance (AIR) have been applied in spectroelectrochemistry as well as reflectance microscopy.

External Reflectance Spectroscopy

For external reflectance spectroscopy measurements, light incident on a reflective substrate is partially absorbed by the surface and partially reflected. The reflected beam is detected and the change in intensity compared to that of the incident beam should in large part be attributed to absorption by the analyte. In SEC, reflectance values of a corresponding blank electrode are required for each potential scanned, so that surface and electrolyte features can be subtracted, and typically it is the differential reflectance $\Delta R/R$ which is plotted against wavelength.

Reflectance from an opaque but reflective surface typically contains contributions from both specular and diffuse reflectance (DR) and both can be detected by

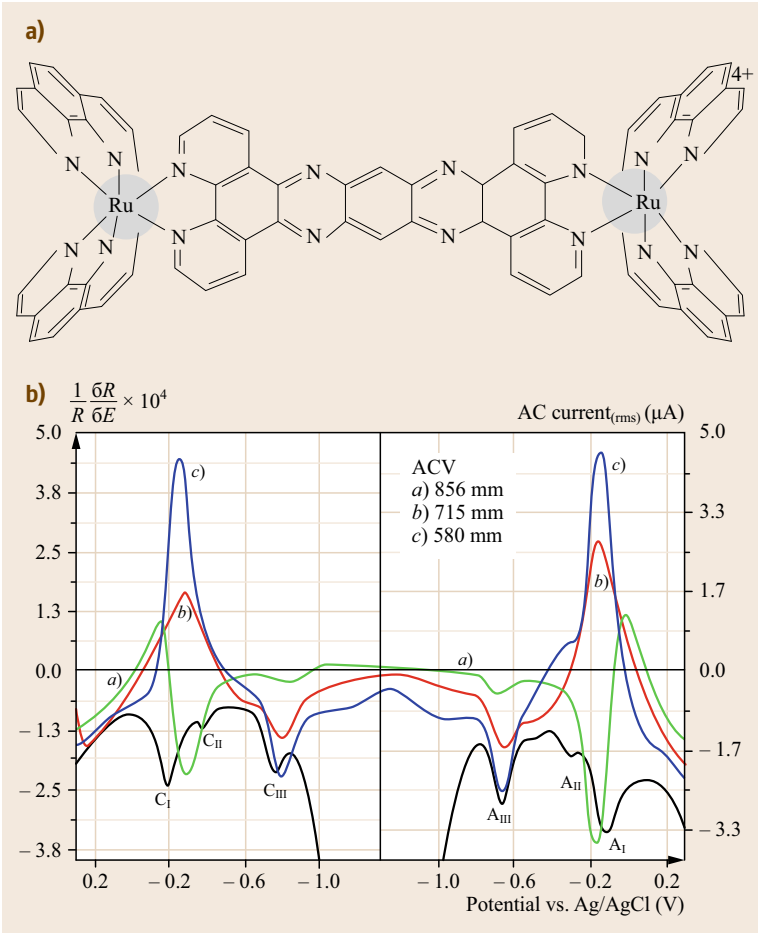


Fig. 13.12 **(a)** Structure of $[(phen)_2Ru(tatpp)Ru\text{-}(phen)_2]^{4+}$ and **(b)** in-phase differential reflectance versus potential curves 2.3×10^{-5} M Ru-tatpp at pH 8.5 during a cyclic linear potential scan at 2 mV/s on a polycrystalline gold disk electrode. Three monitoring wavelengths were used: (*a*) 855, (*b*) 715, and (*c*) 580 nm. The *black trace* is an AC voltammogram shown to underline the correspondence between the optical and electrical signals. The switch potential, (– 1.35 V), was used to separate the plot into two halves (after [13.68], courtesy of Wiley)

different reflectance techniques in electronic reflectance spectroelectrochemistry. Typically specular reflectance is used with metal electrode surfaces which can be polished to give mirror-like reflectance [13.69]. Specular reflectance SEC involves measuring reflectance over a very small range of angles, as such reflectance occurs at discrete angles related to the incident angle, described by Fresnel's equations. Specularly reflected light is polarized and highly anisotropic, therefore variable angle specular reflectance SEC can provide information about film homogeneity, thickness and orientation [13.70]. It has been used in the SEC study of NIR-absorbing electrochromic films [13.71].

DR SEC measures reflected incident light at multiple angles, and is more suited to nonideal reflecting surfaces. In particular, DR predominates with rough surfaces and is isotropic (i. e., not angular dependent, as reflectance naturally occurs in many directions simultaneously); it has frequently been used to study insoluble solid bulk samples. Therefore SR and DR are distinguished experimentally through control of the angle of the incident/reflected beam. Most reports of electronic SEC employ specular reflectance at highly polished metal electrodes such as Au, Ag, or Pt.

Reflectance accessories are routinely available on modern UV-Vis spectrometers and many are available which allow for variation of the incident angle for separation of specular reflectance and diffuse reflectance. Diffuse reflectance, in particular, is commonly performed using an integrating sphere accessory [13.72]. A number of SEC designs have been designed to fit into commercial benchtop spectrometers. An example of a thin film reflectance cell reported by *Miney* et al. [13.67] is shown in Fig. 13.11.

The working electrode was made from a glass microscope slide onto which a layer of aluminium had been sputter coated. The aluminum was treated to form an alumina film ≈ 700 nm thick and conducting but sufficiently thin to be optically transparent. The alumina layer was sputtered over with a thin reflective layer of gold, which did not fill the pores. The pores were sufficiently small for the surface to remain specularly

reflective but large enough to permit solvent/electrolyte diffusion. This cell was employed to study both specular reflectance spectroscopy and chronoamperometry to estimate the onset potentials of water reduction as a function of applied potential from shifts in the interference fringes of the specularly reflected light from the electrode surface. In other thin layer cell designs, temperature control has been integrated [13.73, 74].

The proton-coupled electron transfers of a dinuclear ruthenium complex $[(phen)_2Ru(tatpp)Ru(phen)_2]^{4+}$ (where phen is 1,10-phenanthroline and tatpp is 9,11,20,22-tetraaza tetrapyrido[3,2-a:2′3′-c:3″,2″-l:2‴,3‴]-pentacene) were studied by external reflectance spectroelectrochemistry. The structure (abbreviated to Ru-tatpp) and spectra are shown in Fig. 13.12 [13.68].

In the difference reflectance SEC experiments, the reflectance R data were acquired applying square-wave modulation with the potential limits of the square-wave function selected to cover the desired electrochemical window. Differential reflectance-potential profiles show the optical changes that occur for an electrochemically generated species as a function of a small amplitude potential perturbation (i. e., using AC voltammetry). The monitoring wavelengths, which are established from UV-Vis spectroscopy of the analytes, are held constant during potential modulation. Lock-in detection of the changes in the specularly reflected intensity at this wavelength from the surface of the working electrode surface as a function of small amplitude AC modulation was monitored, after demodulation, as a function of the DC electrode potential. The optical signal generated by such AC modulation is given by

$$\frac{1}{R}\frac{\delta R}{\delta E} = -\frac{1}{R}\frac{\delta A}{\delta c_{\text{int}}}\left|\frac{\delta c_{\text{int}}}{\delta E} + \frac{1}{R}\frac{\delta R}{\delta q}\frac{\delta q}{\delta E}\right|_{\text{AuER}}, \qquad (13.7)$$

where E is the electrode potential, A is the optical absorbance, R the reflectance, and c_{int} is the modulation of the interfacial concentration. A representative optical response from $[(phen)_2Ru(tatpp)Ru(phen)_2]^{4+}$ using this method is shown in Fig. 13.12. These electroreflectance studies permitted characterization of the various interfacial redox and proton-coupled redox processes using the powerful combination of SEC and AC voltammetry, and the authors formulated a complex series of pH-dependent proton and electron transfer steps for the complex, showing the power of these two techniques in elucidating complex electrochemical reaction mechanisms.

Fiber Optic Reflectance SEC

Fiber optic accessories can also be employed in reflectance SEC measurements. In one such arrangement a 180° back-reflectance UV-Vis probe with a bundle of fiber-optic cables was fixed to a clamp directly below the glass slide surface for spectral measurement and focused directly on the surface of the working electrode. The reflectance probe configuration consisted of a concentrically located cable for excitation with six peripheral fiber optic cables arranged for collection of the light transmitted after reflection from the surface of a Pt disk working electrode to the detector. This analysis was performed on a microdrop (30 µl) of 3 mM $[Fe(CN)_6]^{3-}$ probe in aqueous 0.1 M KNO_3 [13.75]. The experimental setup is described in more detail in Sect. 13.2 (Fig. 13.8).

In another approach, fiber optic flow cells were employed as fiber optic spectroelectrochemical sensors (FOSEC) for in-situ heavy metal ion sensors. The fiber optic arrangement could be used for both reflectance spectroelectrochemistry and changing the fiber optic to a bifurcated arrangement, for fluorescence bifurcated, again in a flow cell [13.76].

Reflectance SEC Using Microscopy

Microscopy is particularly useful in reflectance spectroelectrochemical methods because of the high efficiency of optical collection and consequent increased sensitivity and the low sample volume demands. An example of a SEC applied to diffuse reflectance SEC in which a microscope is coupled with a spectrometer as shown in Fig. 13.13. Reflectance in a 180° geometry eliminates interference from incident light. In addition, specularly reflected light was eliminated by using crossed polarizing filters. This low background permitted use of the Kubelka–Munk function for quantitative measurements and the estimation of optical bandgaps [13.77]. Such a setup was also reported in the SEC of silver octacyanomolybdate. The solid powder was mechanically pressed onto a paraffin-impressed graphite electrode and immersed in electrolyte [13.78]. A 200× microscope objective was employed to focus the probe beam onto the solid sample. The SEC data revealed that the electrode reaction started at the solid–electrode interface and slowly proceeded toward the solid–solution interface. The technique is particularly amenable to studying solid-state electrochemistry of electrochromic systems as a transparent working electrode is not required.

Internal Reflectance Spectroscopy

Attenuated total reflectance (ATR) absorption spectroscopy can be used in electronic SEC measurements, although it is far more commonly used in FTIR spectroscopy. The advantage of ATR over conventional transmittance and reflectance measurements is that materials with low molar absorptivities can readily be detected due to the increased optical pathlength of the

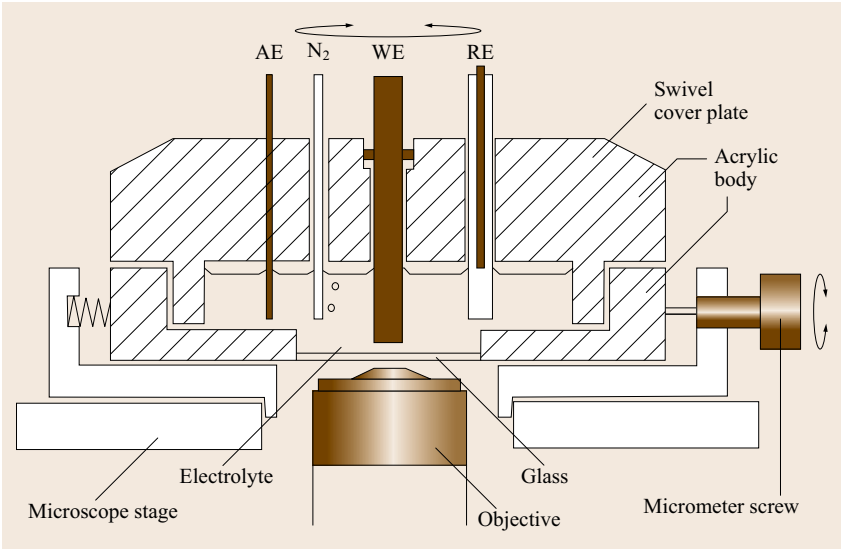


Fig. 13.13 Spectroelectrochemical cell for electronic reflectance studies using a 200× optical microscope objective (after [13.78], courtesy of Springer)

probe beam. ATR occurs at a crystal tip in direct contact with a sample; specifically a beam of light incident on a surface is bent normal from the surface as it passes from a higher to lower refractive index material and this bending is dubbed internal reflection [13.79]. A high refractive index crystal and a high angle of incidence must be used. Germanium and diamond are two commonly used ATR materials. Total reflection of an incident photon at transparent electrode–solution interface is only obtained when the criterion that the incident light passed through the electrode (before interacting with the sample) at an angle that exceeds the critical angle θ_c is fulfilled according to

$$\theta_c = \arcsin\left(\frac{n_1}{n_2}\right) , \tag{13.8}$$

where n_1 and n_2 are the refractive indices of the transmitting and incident media, respectively. When this criterion is met, an evanescent wave perpendicular to the internally reflected beam through the electrolyte with a penetration depth d is generated

$$d = \frac{\lambda}{4\pi(n_1^2 \sin^2\theta - n_1^2)^{1/2}} , \tag{13.9}$$

where θ is the angle of incidence within the substrate. This method increases the sensitivity in the interfacial region where the evanescent field propagates only, as the evanescent wave (EW) decays exponentially away from the surface normal. The penetration of the evanescent wave tends not to exceed 500 nm for the surface, which means that the technique is ideal for studying the interfacial region and eliminating solvent band contributions, which is very useful in FTIR SEC.

A key demand in SEC design in ATR is that the working electrode must be transparent. A common approach is to use a metal or metal oxide thin films deposited on the reflection element (i. e., crystal tip) which is used as the working electrode. Such layers can suffer from poor conductivity; however, this method has been shown to provide sufficient sensitivity and selectivity for studies involving conducting polymer films and self-assembled monolayers [13.80, 81]. In such an experiment, a film of Prussian blue (an iron(III) ferocyanide blue pigment) on an ITO electroactive integrated optical waveguide (EA-IOW) was examined spectroelectrochemically [13.82]. ATR has been exploited even more extensively in FTIR spectroscopy, as discussed in Sect. 13.4.2, where solvent interference is particularly important due to the large number of solvent bands of most solvents.

Evanescent wave cavity ring down spectroelectrochemistry (EW-CRDS) is a relatively new type of internal reflectance electronic spectroelectrochemistry. CRDS is an absorption spectroscopy in which the analyte is housed in a cavity comprising two highly reflective mirrors. After a laser pulse is introduced, the light level within the cavity is monitored via the small fraction of light that leaks through the back mirror every round trip. The decay in the light intensity, known as the *ring down*, is characterized by an exponential decay constant and represents a measure of both the inherent cavity losses and any intracavity absorptions (beam attenuation). The mirror optical coatings used have reflectivities of $> 99.995\%$ across narrow spectral regions of interest. The technique is most usually performed in the gas-phase, which frequently involves an evacuated cavity except for the sample of interest,

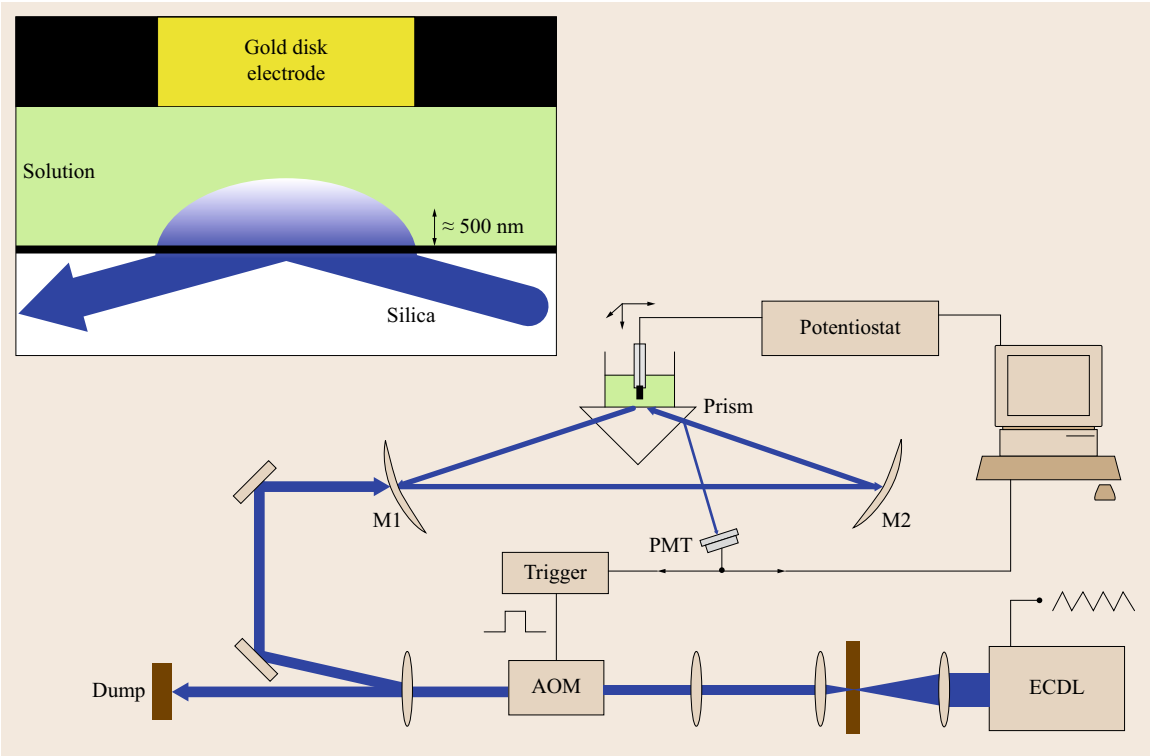


Fig. 13.14 Schematic of thin layer electronic SEC for EW-CRDS. The ring cavity is formed between the two highly reflective mirrors M1 and M2 and the total internal reflection from the back surface of a fused-silica prism. Absorption within the evanescent field is monitored by the ring-down time. External cavity diode laser (ECDL (CW, 417 nm); AOM, acousto-optic modulator; PMT, photomultiplier tube.) Inset: Thin layer configuration for internal reflectance SEC (after [13.83], courtesy of Am. Chem. Soc.)

ring-down times as long as several tens of microseconds are achievable to yield effective path lengths in a typical 1 m diameter cavity of more than 10×10^4 m. The technique has been most widely applied to gas-phase applications at a single wavelength for environmental monitoring, etc. [13.84, 85].

However, *Mazurenka* et al. have reported the use of solution phase EW-CRDS coupled with electrochemistry using the ferrocyanide–ferricyanide couple at a gold-disk working electrode. In this setup they used a thin layer configuration by sandwiching a drop of electrolyte between the total internal reflection prism and the working electrode surface [13.83]. Application of potential resulted in the diffusion-controlled reduction of $[Fe(CN)_6]^{4-}$ to $[Fe(CN)_6]^{3-}$, and due to the differences in molar absorptivity between the two ions, the cavity ring down time changes as a function of [O]/[R] ratio. This experimental setup is shown in Fig. 13.14.

CRDS is severely limited by the fact that generally only one wavelength can be monitored during the experiment. However, the sensitivity afforded is extremely high and the technique may find wider applicability in future; particularly if continuum light source CRD spectrometers become commercially available. The same group has also published thin layer electronic SEC of the $[IrCl_6]^{2-}/[IrCl_6]^{3-}$ redox process using evanescent wave broadband cavity-enhanced absorption spectroscopy (EW-BBCEAS) employing supercontinuum radiation. This technique is similar in principle to CRDS but can be used for a wavelength range [13.86].

13.3 Spectroelectrochemistry of the Excited State

The study of the emission (fluorescence or phosphorescence) from a luminescent material under potential control is one of the less common spectroelectrochemical modes. That luminescence SEC is less commonly reported is likely due to the fact that there are relatively fewer redox active materials which are luminescent in

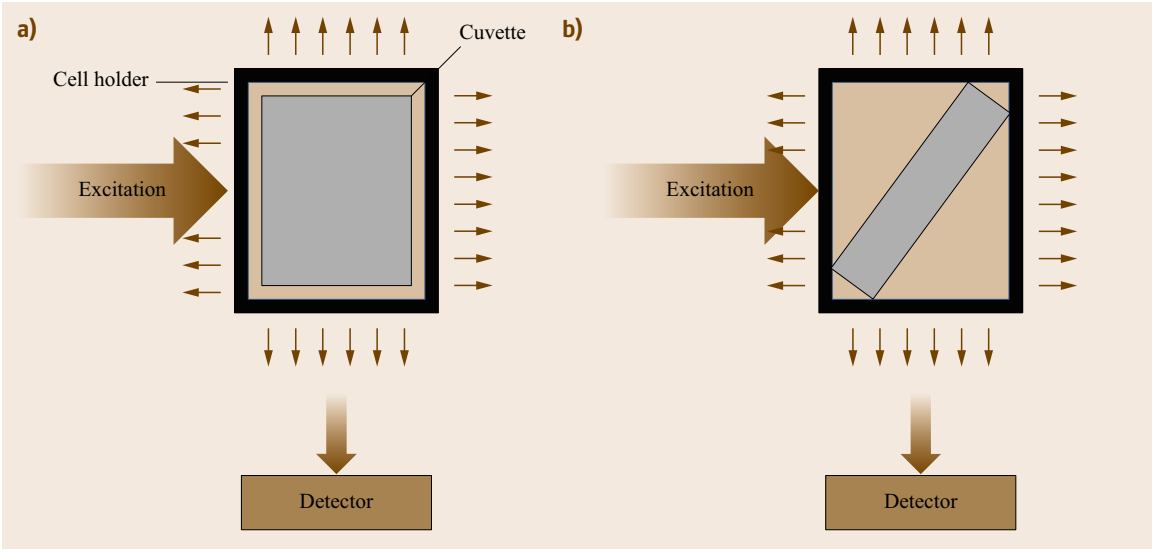


Fig. 13.15a,b Orientation of the cuvette in (a) a conventional luminescence spectrometer, (b) a spectroelectrochemical experiment employing a thin cell

one or more redox state, because in terms of experimental complexity it is not significantly more difficult than UV-Vis spectroelectrochemistry. Luminescence SEC is a very useful method for exploring the role of electron donor or acceptor quenchers in supramolecular structures where the accepting or donating state can be accessed electrochemically. This method can provide useful insights into luminescent states which are not accessible under open-circuit potential (OCP), which may be important in sensing and exploring the behavior of electrochemiluminescent materials [13.87].

13.3.1 Steady-State Emission Spectroelectrochemistry

In a photoluminescence experiment, the sample is excited with a light source, which must be maintained at a 90° angle to the detector to avoid, as much as possible, excitation light reaching the detector. As indicated by the small arrows in Fig. 13.15, this is possible because luminescence in the solution phase is emitted isotropically from the cell and in emission spectroscopy a square, clear sided cuvette is used to facilitate 90° detection from the light source. Such square cuvettes are not suitable for spectroelectrochemistry because of their large volumes. Therefore, a thin layer cell comparable to that used in an OTTLE experiment can be used where the cell must be positioned at a 45° angle relative to the excitation source and detector (Fig. 13.15).

The working electrode can be a semitransparent wire mesh such as gold, platinum, or a rhodium–platinum alloy. However, the reflectivity of the metal and the 45° angle of the cuvette, particularly if orientation of the cuvette is not exact can lead to significant scattering/reflection of the excitation source resulting in stray light interference in the resulting emission spectroscopy. This can be overcome by using a sample holder which will permit reproducible positioning of the cell in the spectrofluorimeter. These typically have to be custom designed. A simple solution is to use a PTFE insert in the conventional instrument cuvette holder which is milled to hold the SEC securely and reproducibly at a 45° angle (Fig. 13.3b). Scatter and reflection from the electrode can be reduced significantly by using an optically transparent working electrode made from for example FDTO or ITO, ideally by making such glass one of the optical windows in the cuvette. Such materials are not transparent in the mid-UV however, so can only be used for visible excitation.

In an alternative approach, one can use a conventional clear-sided square cuvette but reduce its volume either by inserting an electrode that will displace part of the volume of the cuvette by using a shorter cell. In an example of the former approach, *Simone* et al. described a chair-shaped gold-coated Teflon working electrode, which was milled to fit into a conventional fluorescence cuvette. The electrode was large enough that it excluded sufficient volume of the cell that it could be used for spectroelectrochemistry [13.88]. The authors demonstrated its utility by deriving Nernst plots for *o*-tolidine. In an example of the latter approach, *Lee* and *Kirchhoff* reported on a 90° oriented cell is where a small quartz optical cell is mounted in the lower part

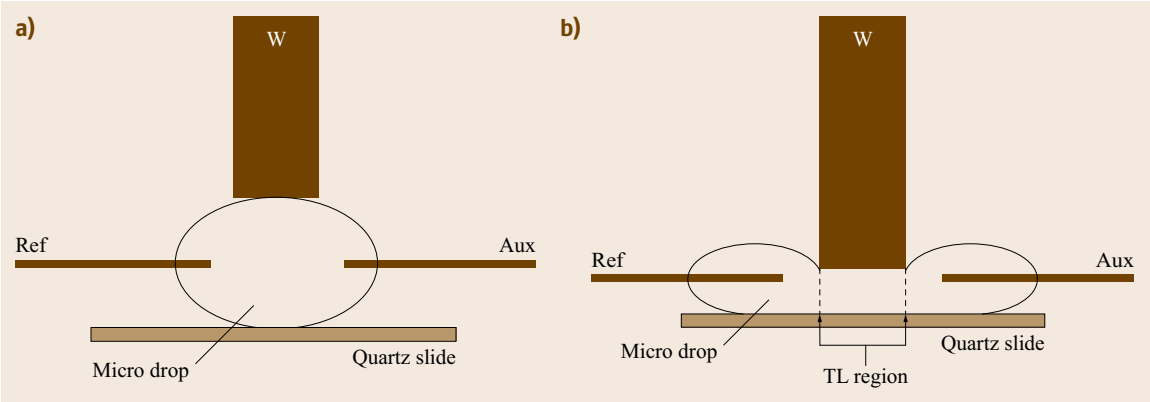


Fig. 13.16a,b Illustration of microdrop technique experiments employing three-electrode components **(a)** semi-infinite linear diffusion and **(b)** thin layer restricted diffusion. (W working electrode; Ref reference electrode; Aux auxiliary electrode; TL region thin-layer region. The surrounding insulating case of the working electrode not shown for simplicity.) (after [13.75], courtesy of Wiley)

of a milled PTFE block to fit tightly into the spectrometer cell holder. The auxiliary and reference electrodes are mounted onto the top of the cell and optical channels drilled through the Teflon mount to permit a 90° angle between excitation and emission pathways and a long optical path for better sensitivity. The working electrode was reticulated carbon and the use of a nonmetal electrode may be advantageous in avoiding luminescence quenching as well as reducing the problems of scattering and reflection. However, the relatively large volume of this cell led to exhaustive electrolysis times of up to 25 min.

An interesting alternative approach to luminescence SEC was described by *Schroll* et al. where they used an aqueous microdrop on a quartz slide to collect both quantitative electrochemistry and absorption and emission [13.75]. The electrode arrangement employed is shown in Fig. 13.16 where the auxiliary and reference electrodes are electrically contacted to alternative sides of an aqueous droplet of the analyte which is sandwiched between the working electrode and the quartz slide so that the total volume was used as the working volume and the dead-volume, in the arrangement shown in Fig. 13.16. The system is under semi-infinite diffusion controlled environment, but by compression of the microdrop by the working electrode the cell volume could be decreased to bring the reaction volume under finite diffusion control and creating a thin layer cell for spectroelectrochemical purposes.

A 180° back-reflectance UV-Vis probe fiber optic bundle clamped directly below the glass slide surface permitted spectroscopic measurement directly from the droplet. $[Ru(bpy)_3]^{2+}$ was used as the model system to demonstrate absorption, emission, and Nernst plots from each method.

Nernst plots analogous to those in UV-Vis spectroelectrochemistry can be obtained from luminescence spectroscopy if the concentrations of oxidized and reduced species can be related to the quantum yields of the oxidized and reduced species according to

$$\frac{[\mathrm{Ox}]}{[\mathrm{Red}]} = \frac{\frac{(I_{\mathrm{red}}-I)}{\varphi L}}{(I-I_{\mathrm{ox}})\varphi L} = \frac{I_{\mathrm{red}}-I}{I-I_{\mathrm{ox}}}\,, \tag{13.10}$$

$$E_{\mathrm{app}} = E^{\circ\prime} + \frac{RT}{nF}\ln\left(\frac{I_{\mathrm{red}}-I}{I-I_{\mathrm{ox}}}\right)\,, \tag{13.11}$$

where I_{red}, I_{ox}, and I are the luminescence intensities of the analyte at potentials where it is fully reduced, fully oxidized and at intermediate potentials, respectively, φ is the luminescence quantum yield and L is the path length. Application of (13.10) to the Nernst equation leads to (13.11), which indicates that a plot of E_{app} versus $\ln\,(I_{\mathrm{red}}-I)/(I-I_{\mathrm{ox}})$ will yield $E^{\circ\prime}$ from the intercept and n from the slope. Another example of a Nernst plot was that constructed for rhodamine 6G at a 4,4′-bipyridine modified gold electrode using a 90° thin layer cell reported by *Yu* and *Zhou* [13.89]. Good agreement was found between the spectroelectrochemically derived value for the formal potential of the rhodamine 6G (-0.787 V) and that obtained from cyclic voltammetry (-0.791 V).

For Nernst plots from luminescence spectroelectrochemistry to be feasible, the two redox states of the analyte should not emit in the same spectral region. Since species capable of emission in two different oxidation states with two mutually exclusive emission spectra are unusual, there are relatively few samples this method will work for. In addition, the oxidized or reduced form of a given analyte can quench the luminescent precursor leading to lower intensity values, an example of this

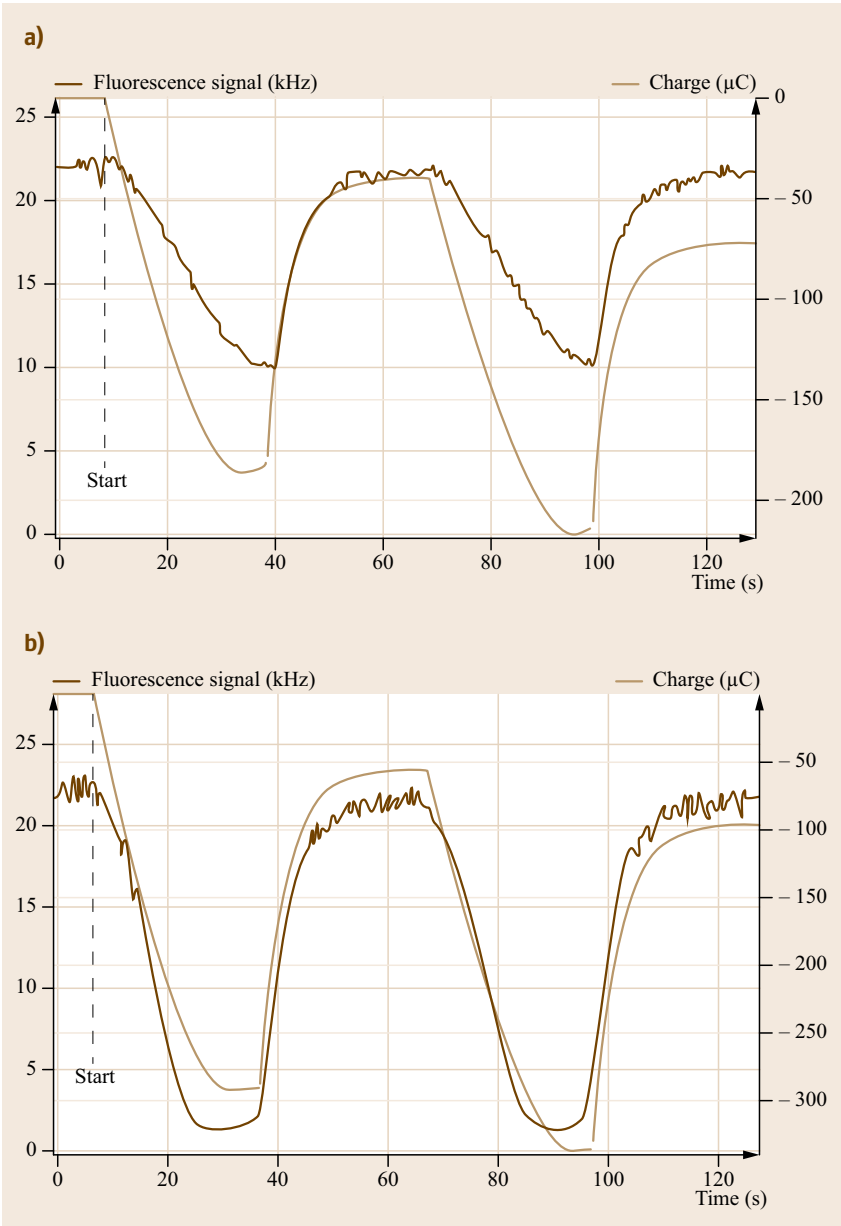


Fig. 13.17a,b Electrochemical modulation of fluorescence intensity (*left axis*) on the one-electron reduction of chloromethoxytetrazine (0.8 mM) in dichloromethane, 1.0 M $(But)_4NPF_6$ in an OTTLE cell positioned under an epifluorescence microscope potential steps from −0.2 V to −0.42 V **(a)** and −0.2 V to −0.48 V **(b)** during 30 s time intervals (after [13.90], courtesy of Elsevier)

investigated by luminescence SEC is discussed below. This can lead to serious errors in the apparent concentrations of the oxidized and reduced species and therefore the values derived from the Nernst plots.

A key strength of spectroelectrochemistry is its ability to generate redox products frequently in quantitative way which may be inaccessible synthetically. *Lee* and *Kirchhoff* reported on the spectroelectrochemistry of such a species; $[Re(dmpe)_3]^+$, where dmpe is 1,2-bis(dimethylphosphino) ethane [13.92]. The reduced d^6 Re(I) complex is colorless and nonluminescent. Oxidation resulted in the formation of the d^5 Re(II) complex, which displays intense emission at 593 nm from an associated absorbance at 530 nm, whose luminescence quantum yield exceeded that of the well-characterized $[Ru(bpy)_3]^{2+}$ complex.

Miomandre reported on the luminescence spectroelectrochemistry of an organic fluorophore, chloromethoxytetrazine, in an SEC cell combined with epifluorescence microscopy which was exploited in total internal reflectance fluorescence mode [13.90]. Reduction of chloromethoxytetrazine led to the extinction of

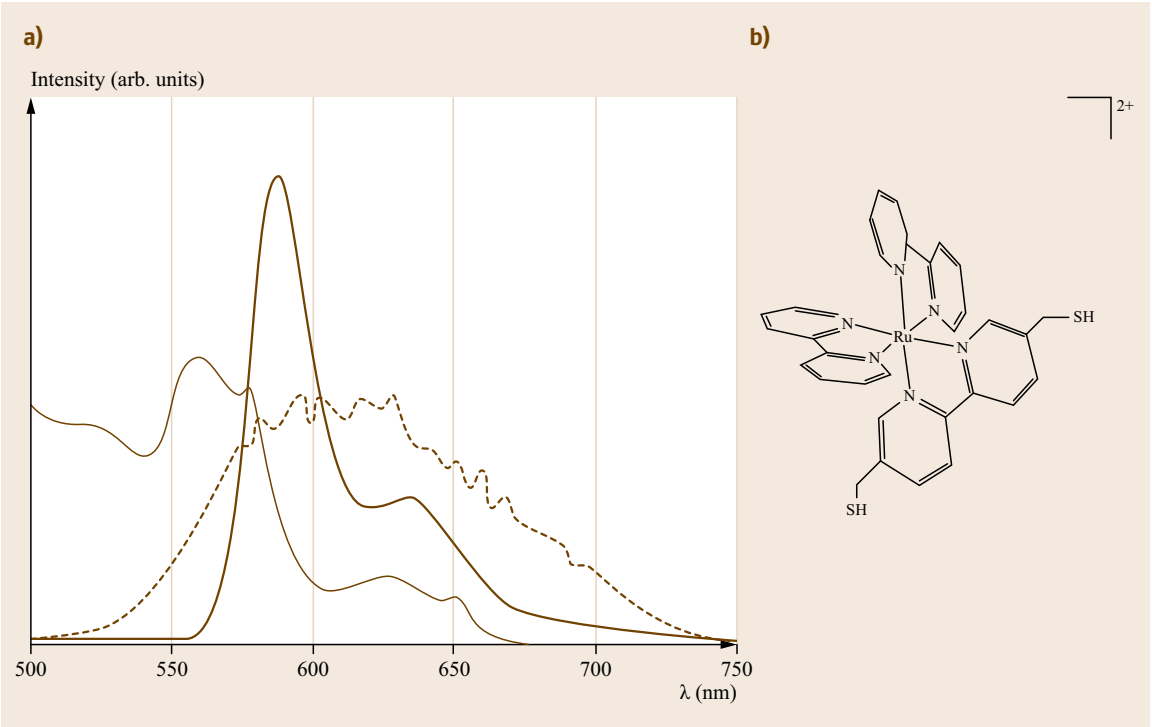


Fig. 13.18 Emission spectrum of a dry RuBpySH monolayer on a 3 mm Pt electrode (*thin solid line*), $\lambda_{ex} = 290$ nm. Emission spectra of RuBpySH **(b)** at 77 K in butyronitrile–acetonitrile 4 : 1 solution (*thick solid line*). ECL spectrum (*broken-line*) from an RuBpySH monolayer (surface coverage) 5×10^{-11} mol/cm^2 recorded following a potential step to 1.20 V. The solution contains 0.1 M $(But)_4NBF_4$ in acetonitrile and 0.1 M tripropylamine (after [13.91], courtesy of Am. Chem. Soc.)

its luminescence centred around 600 nm which was reversibly recovered on its re-oxidation. As shown in Fig. 13.17, the kinetics of the oxidation and reduction processes could be followed simultaneously both coulometrically and spectroscopically.

The mismatch between the two revealed interesting behavior regarding self-quenching of the luminescence by the radical anion generated electrochemically. Quenching of a luminophore by its oxidized or reduced analog can be expected in luminescent films or solutions on thermodynamic grounds and has also been observed previously in luminescent spectroelectrochemistry of metallopolymer films [13.93].

In electrogenerated chemiluminescence, or electrochemiluminescence (ECL), redox intermediates generated under applied potential undergo a highly exergonic reaction with a co-reactant to produce an electronically excited state. These electron-transfer reactions are sufficiently exergonic to allow the excited states of luminophores, including organic fluorophores and metal complexes, to be created without photoexcitation. In an analytical format the co-reactant may be the analyte itself, or it may generate the co-reactant or the ECL luminophore may be bound to an analyte capture species, for example, DNA oligonucleotide. Detailed discussion on mechanism and analytical applications of ECL are beyond the scope of this discussion but the reader is directed to the following reference for more information [13.87].

It is frequently very valuable to understand the spectral features of the resulting ECL signal as they can vary from those of the parent compound and ECL spectroscopy can provide insights particularly from a mechanistic perspective. Such an experiment is little different from conventional optical spectroelectrochemistry in which no exciting light source is required. The electrochemiluminescent species is typically generated from a reaction which occurs under potential control whereas monochromation and detection optics do not require an excitation source. Such measurements may be carried out in a conventional luminescence spectrometer if the excitation source is switched off, but the detector will still run. However, more commonly it is conducted on custom built equipment where the ECL is directed onto a sensitive broad band detector such as a CCD with appropriate optics, a fiber

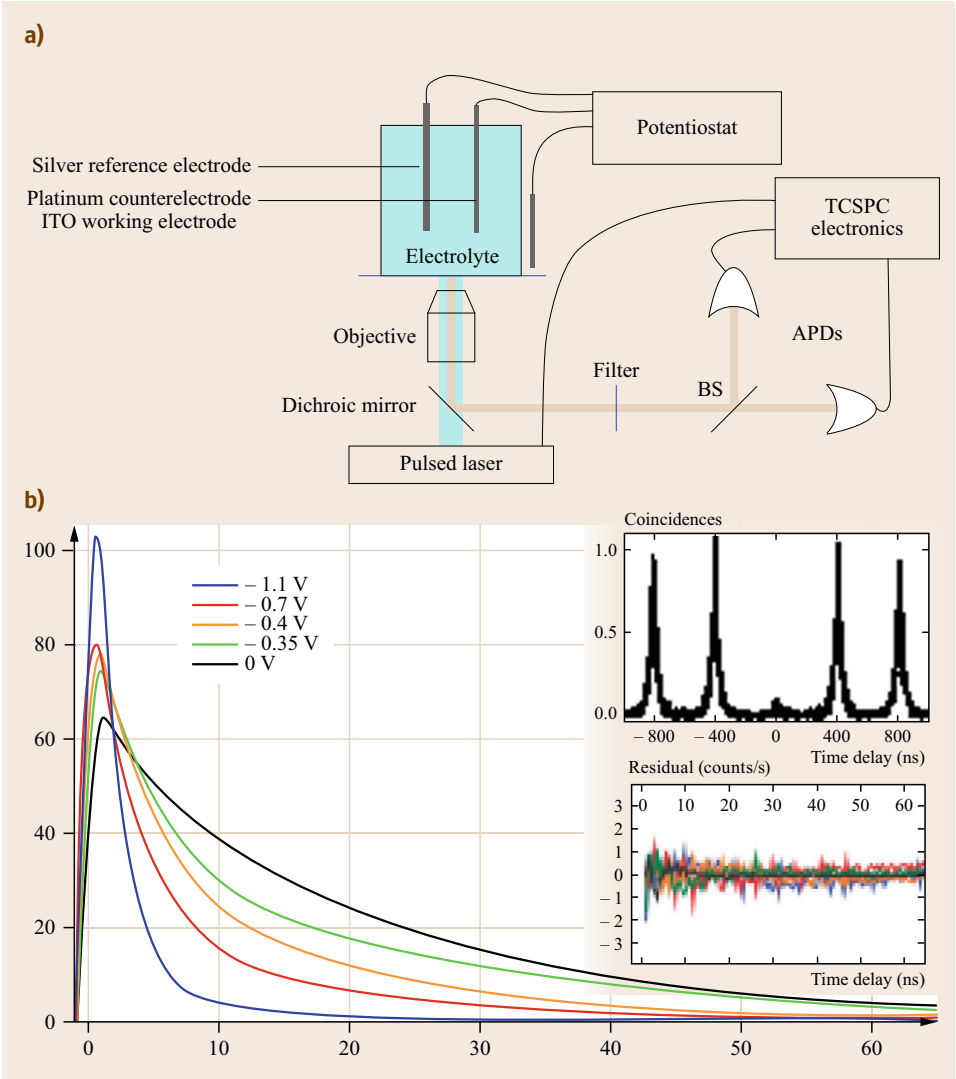


Fig. 13.19a,b Experimental setup described by *Galland* et al. employing time-correlated single-photon counting (TCSPC) to monitor electrochemical charging of quantum dot *nanocrystals*. **(a)** Setup of a single-nanocrystal APD; BS, 50/5 beam splitter; ITO, indium tin oxide; **(b)** The series of photoluminescence decays for a single nanocrystal under increasingly negative applied potentials. The thin gray lines show the best global tri-exponential fits of the luminescence decays, *Top inset*: the second-order photoluminescence intensity correlation function measured for this nanocrystal indicates. *Bottom inset*: residuals of the luminescence decay fits (after [13.94], courtesy of Macmillan)

optic or through a microscope. ECL is carried out most commonly in a three electrode format where ECL agent and co-reactant are in solution. As the emitted light is detected without the need for an excitation source an opaque electrode can be readily used. For example, Fig. 13.18 shows the electrochemiluminescent signal from a monolayer of a thiol-terminated ruthenium polypyridyl complex adsorbed on solid platinum electrode (dashed line), reported by *Bertoncello* et al.. ECL was generated from the monolayer by holding the working electrode at 1.2 V, at which potential the metal centres will be oxidized [13.91]. These oxidized metal complexes then undergo an exerogonic annihilation reaction with the tripropylamine co-reactant which is in solution in contact with the electrode to yield ECL from the monolayer. This was conducted in a three electrode cell held in a dark box, where a fiber optic bundle was directed close to the surface of the working electrode. The fiber optic directed the ECL into a monochromator/iCCD assembly to generate the ECL

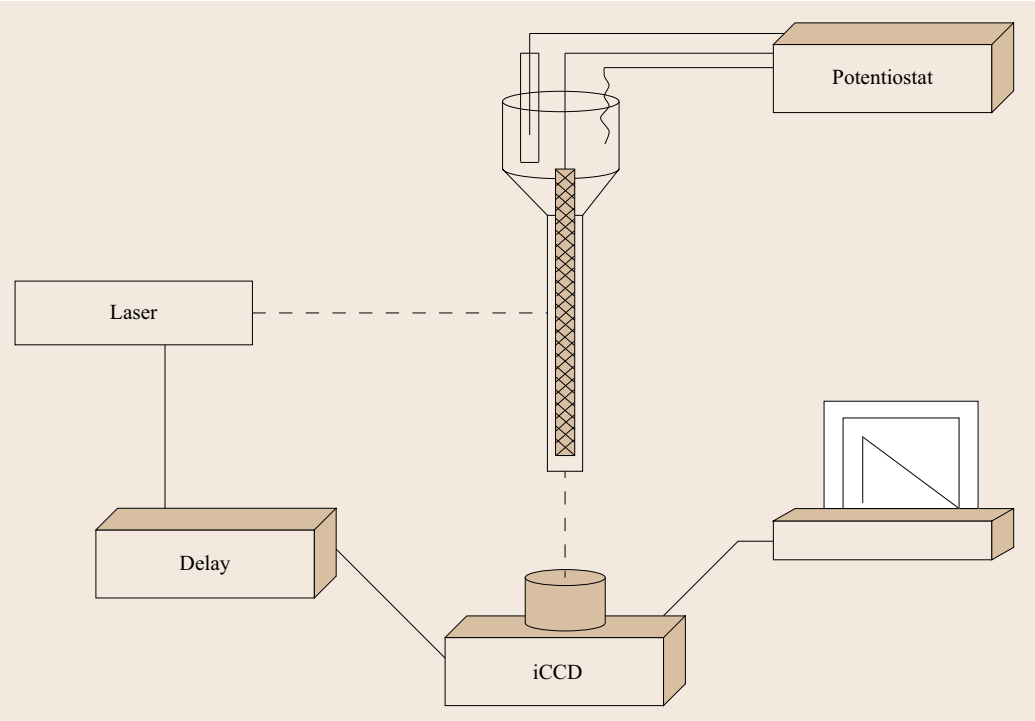


Fig. 13.20 Schematic of a simple instrumental layout for a nanosecond flash photolysis for system of luminescence lifetime under potential control

spectrum. The directly photo excited spectra of this material in solution at low temperature and as a monolayer are compared in Fig. 13.18. It is clear, in the case of the luminescence from the photoexcited monolayer that there is significant interference in the spectrum from scattering/reflection of the exciting radiation from the Pt surface. As there is no excitation source in ECL, the spectrum is much cleaner and appears as a broad Gaussian emission.

13.3.2 Transient Luminescence Spectroelectrochemistry

Time-resolved luminescence spectroelectrochemistry (TRLS) is used to measure the luminescence decay time of a sample under potential control, and although it is less common than steady-state luminescence spectroelectrochemistry it can provide complimentary information. TRLS can be very valuable in providing insights into the photophysics of an electroactive species although emission lifetime is typically insensitive to concentration of a given luminescent analyte.

Methods for studying luminescent lifetimes include time correlated single photon counting and flash photolysis. Phase fluorimetry may also be used to obtain lifetime information. Single photon counting has been recently applied in a spectroelectrochemical experiment reported by *Gallant* et al. aimed at electrochemically controlling the degree of charging of individual quantum dots to elucidate the role of such charging in well-known luminescence blinking phenomena encountered in such luminescent structures [13.94]. Figure 13.19a shows the experimental setup employed and Fig. 13.19b shows the data recorded. A confocal fluorescence lifetime microsocope was used to direct low energy laser pulses (at 405 nm) onto the nanocrystals and to collect the emitted photons. The nanocrystals were directly deposited onto an optically transparent ITO working electrode which was incorporated into a three electrode cell. Time-tagged, time-resolved, single-photon counting studies of the samples under potential control showed that two distinct kinds of blinking occurred which the authors referred to as conventional (A-type) blinking due to charging and discharging of the nanocrystal core, in which lower photoluminescence intensities correlate with shorter photoluminescence lifetimes, and a second sort (B-type), in which large changes in the emission intensity are not accompanied by significant changes in emission decay rates. They found that the type of blinking observed can be controlled or suppressed by applied potential.

Laser flash photolysis has also been used in spectroelectrochemical studies [13.95, 96]. An example of instrumental setup for nanosecond TRLS exploited in our laboratory is shown in Fig. 13.21.

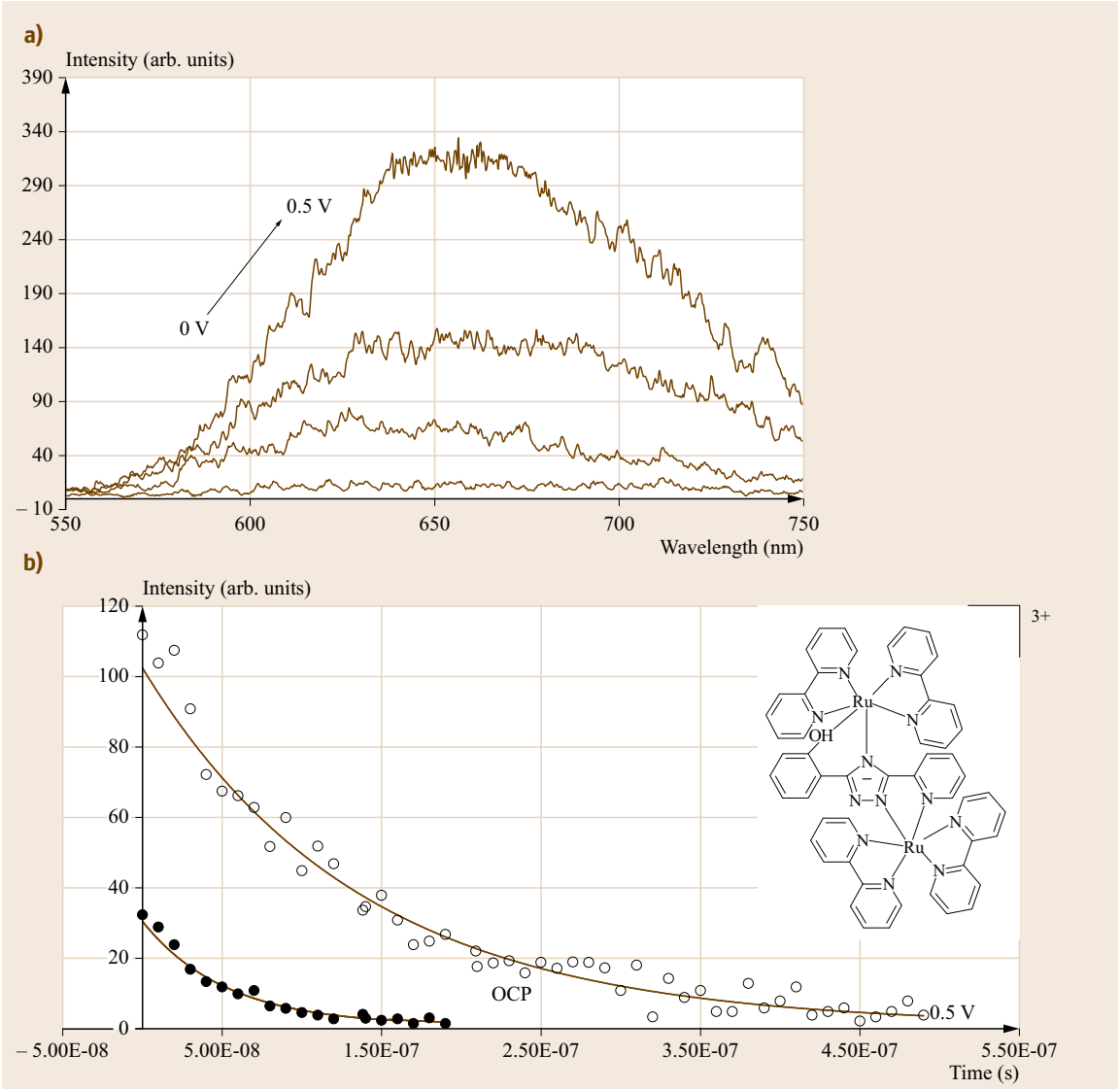


Fig. 13.21 **(a)** Luminescence spectroelectrochemistry and **(b)** TRLS of mixed valence state of dinuclear ruthenium complex. Experiments were conducted in dry acetonitrile containing 0.1 M $TEABF_4$ (TEA: tetraethylammonium) as supporting electrolyte. Emission spectra were collected using iCCD with gate width at 500 ns. Luminescent decays collected using iCCD with gate width at 20 ns (after [13.95], courtesy of the R. Soc. Chem.)

A pulsed light source (e.g., a neodymium YAG laser) is setup at a right angle to the detector which may be a fast photodiode or more complex multichannel detection device such as an intensified CCD (iCCD) or diode array. Multichannel detectors offers significant advantages over single channel devices because they permit acquisition of complete emission spectra (spectral range for a typical iCCD of about 250 nm) within times as short as 10 ns. In addition, by opening the time gate they may also be used for steady-state spectroscopy. This means that both static and dynamic fluorescence studies can be carried out on a single sample using a single experimental instrument. For a time-resolved experiment gate width (i. e., the exposure time of the iCCD) for time-resolved measurements, controlled using a delay generator, should be no more than 5% of the excited state lifetime. The step size (i. e., the time between the acquisition of discrete spectra) is typically between 2% and 5% of the excited state half-life. For steady-state spectra, the gate

width is set to roughly six times the emission lifetime.

An example which exploited both the steady state and time-resolved capability of this luminescence spectroelectrochemistry setup shown in Fig. 13.20 was a study of the dinuclear ruthenium (II) complex bridged by a dianionic ligand shown in Fig. 13.21 [13.95].

In this system, the metals are bound through N,N coordination to the pyridine and triazole and O,N coordination to the triazole and phenolate. In its reduced state the dinuclear compound is weakly emissive with a lifetime of 50 ns. The mixed valence complex was prepared electrochemically through oxidation of the ON bound metal. Application of Hush theory to the electronic spectroelectrochemistry indicated that the metal centres are weakly coupled. Oxidation of the first metal yielded intense luminescence from the complex and an increased luminescent lifetime of 130 ns. This luminescence is reversibly switched on at 0.3 V and reversibly switched off by application of 1.3 or 0 V.

This study was carried out using a thin layer OTTLE cell held at 45° angle to the detector and light source as shown in Fig. 13.15. Time-resolved spectroscopy was carried out using the instrumental setup described in Fig. 13.19. The iCCD allowed collection of both the full luminescence spectrum and the lifetime of the complex with one instrument operated in different time domains [13.97].

Because of the relationship between current passed and concentration of electrochemically generated species, it is possible to *electrochemically titrate* a given redox state of a species present in solution or interfacial film at an electrode. This was illustrated for a thin film of a luminescent metallopolymer $[Ru(bpy)_2(PVP)_{10}]^{2+}$ where PVP is polyvinylpyridine (Fig. 13.22), where the self-quenching of the luminescent Ru(II) centres was explored by titrating in controlled concentrations of oxidized Ru(III) species, electrochemically. The Ru(III) centres behave as electron transfer acceptor states from the electronically excited state Ru(II)*. This strategy was used to gain insight into the extent to which Ru(III) would be likely to quenches the ECL emission in an oxidative–reductive ECL generation scheme. Both steady state and TRLS was carried out to look at the effect of Ru(III) on the emission of the polymer. The experimental setup was similar to that described in Fig. 13.19 wherein an intensified CCD detector permitted collection of both steady-state luminescence spectra and lifetime data whilst the concentration of oxidized metal centres within the film was controlled using chronoamperometry [13.93]. Figure 13.22 shows that the the Ru(III) centers readily quench the luminescence from the Ru(II)* states, as the integrated emission intensity decreases by approximately 80% when approximately 20% of the luminophores within the film are oxidized. The changes to lifetime with increasing Ru(III) concentration were not as dramatic, for example, the luminescence lifetime decreases by $\approx 30\%$ from 129 to 98 ns when $\approx 20\%$ of the film is oxidized. The disparity between the emission intensity and lifetime data indicative of static quenching between the Ru(II) and electrochemically generated Ru(III) centres.

13.4 Vibrational Spectroelectrochemistry

Vibrational spectroelectrochemistry not only encompasses primarily Raman and IR spectroscopy but also some lesser known techniques such as sum frequency generation (SFG). Vibrational spectroelectrochemistry has a key advantage over UV-Vis spectroelectrochemistry in that it can provide direct structural insights into the molecular changes occurring to a species under applied potential. Vibrational spectroscopy has found extensive application in the study of the double layer, redox products in solution, thin films, and surface adsorbed species. Although the underlying mechanism and theory of IR and Raman are fundamentally different, both methods are complementary and each gives detailed vibrational information which may be recorded via spectroelectrochemistry. Unlike electronic spectroscopy, where the majority of spectroelectrochemical experiments are conducted in the transmission mode; for infrared spectroelectrochemistry, the reflectance mode is mainly used. Since Raman is a scattering technique, it is ideally suited to interfacial measurements such as reflectance spectroscopies.

13.4.1 IR Spectroelectrochemistry

The infrared spectral range lies between approximately 50 and 10 000 cm^{-1}, the EM region corresponding chiefly to molecular vibrations which lies between electronic absorptions (visible) and rotational absorptions (microwave). As a type of absorption spectroscopy, IR follows the Beer–Lambert law but is rarely used quantitatively. Absorption of an incident photon by an oscillating dipole results in the formation of a transient excited vibrational state. IR absorption only occurs if it results in a change in the electric dipole moment of the chromophore; bonds that do not fulfil this criterion are dubbed *IR-inactive*.

Modern infrared spectrometers are Fourier-transform (FT) instruments. This technology involves the use of an interferometer and a beamsplitter which splits the incoming infrared signal into two beams. One beam reflects off a flat mirror which is fixed in place, while the other beam reflects off a flat mirror which is on a mechanism which permits movement away from the beamsplitter. The two beams reflect off of their respective mirrors and interfere when reflected back to the beamsplitter to generate an interferogram. The interferogram signal is that which interrogates the sample, and thus all frequencies are being measured simultaneously. The information encoded in the interferogram is a function of mirror positions and undergoes a Fourier transform to convert these data into spectral information (frequency domain). Sluggish continuous wave scanning of the entire infrared region of interest is therefore avoided by applying a short broadband pulse and the FT.

Although absorption FTIR spectroscopy can be conducted in transmission mode, this application is fairly rare due to solvent interference. Common solvents tend to exhibit a multitude of peaks in the mid-IR and near-IR regions, due to both fundamental and overtone bands. Both water and CO_2 have large background absorptions due to their large dipole moments. Despite this significant difficulty, transmission FTIR SEC has been reported [13.98, 99]. Reflectance methods are not only far more common in FTIR SEC, in recent years particularly ATR, but also external reflectance measurements and infrared reflection absorption spectroscopy (IRRAS). FTIR spectroelectrochemistry is a widely reported technique and is continuously expanding [13.100–102].

Internal Reflectance

Internal reflection IR SEC employs a highly polished reflective metal surface as the working electrode that acts as a mirror. Such a smooth surface reflects the probe beam specularly to the detector. However the beam path passes through the solvent, gaining solvent signal, so it is desirable to have a short path length. A reflectance FTIR SEC is shown in Fig. 13.23 [13.103, 104].

The cell is designed for measurements in which a working electrode is pushed through the holder to the electrolyte interface using a plunger, for precise length adjustment. The working electrode surface is made of a reflective metal such as gold or platinum. A large area reference electrode (in Fig. 13.23 as a ring or coil) sits in the bulk solution behind and close to the working electrode tip. The reference electrode is connected via a Luggin capillary, and the cell has an inlet for degassing. The bottom of the cell is sealed and IR transparent. The working electrode is pushed against the window using the plunger to form a thin layer of electrolyte for interfacial measurement.

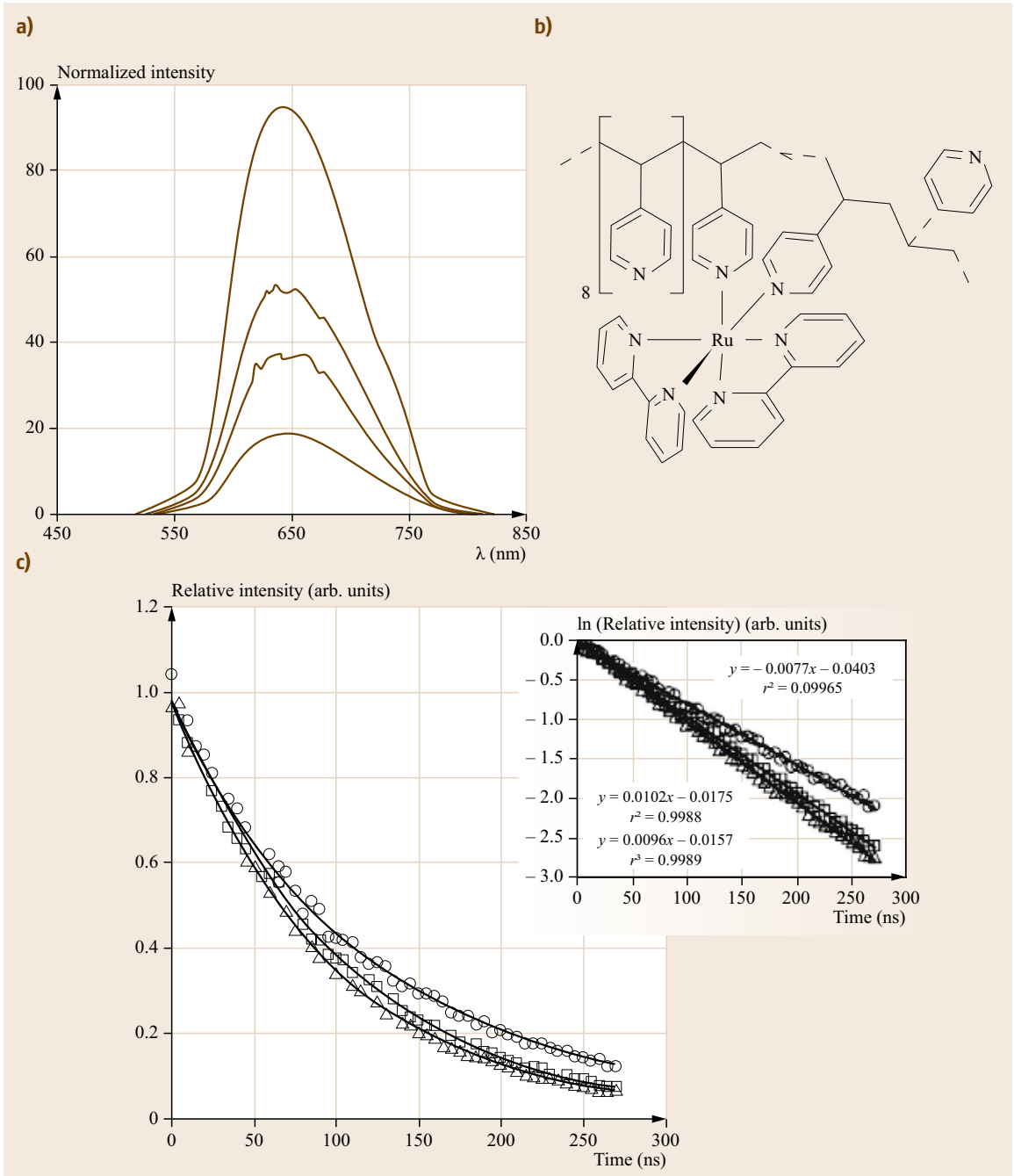
Fig. 13.22a–c Luminescence spectroelectrochemical data; steady-state spectra **(a)** and time-resolved luminescence decays **(c)** from thin films of $[Ru(bpy)_2(PVP)_{10}]^{2+}$ **(b)** deposited onto an ITO working electrode in contact with aqueous 0.1 M H_2SO_4 solution. For the luminescence spectra **(c)**, the percentages of Ru(III) centers are 0, 6, 10, and 20% and for the time-resolved data shown the percentages of Ru(III) are 0(O), 10 (□) and 20% (Δ)(after [13.95], courtesy of Am. Chem. Soc.) ►

The material used for the optical window must permit transmission of IR light and be stable in a variety of common electrolytes. Silicon, CaF_2, and ZnSe are commonly used materials for the optical window in the IR SEC. In aqueous systems, the electrode is typically sealed onto the glass plunger using epoxy resin; however since epoxies are unsuitable for organic electrolytes, the metal is instead sealed directly to the glass. As with all types of FTIR spectroscopy, the electrolyte and solvent are present in large excess relative to the analyte meaning interfering bands are a major issue. However, filtering of this spectral information can be achieved using polarizing filters and difference spectroscopy.

SNIFTIRS

SNIFTIRS (subtractively normalized interfacial Fourier transform infrared spectroscopy) is a difference technique developed for spectroelectrochemistry. It involves collection of a successive series of interferograms at two potential limits E_1 and E_2 where E_1 is a reference potential typically corresponding to a potential at which no faradaic process occurs and E_2 is the potential at which electron transfer occurs. The step between E_1 and E_2 is cycled until an acceptable signal-to-noise ratio is obtained. If R_1 and R_2 are the reflectances measured at E_1 and E_2, respectively, the change of reflectivity $\Delta R/R$ is given as $(R_2-R_1)/R_1 = (R_2/R_1)-1$. Sometimes this is plotted as $\log(\Delta R/R)$. This method has been developed for a commercial FTIR spectrometer [13.105]. The SNIFTIRS method has been used for the in-situ detection of electrogenerated intermediates in the double layer or species adsorbed at the electrode surface. Figure 13.24 shows SNIFTIRS spectra of (bi)sulfate adsorption on a Pt(111) surface in solutions of variable pH while maintaining a constant total bisulfate–sulfate concentration without the addition of supporting electrolyte [13.106].

According to the below equation, the SNIFTIR spectra should consist of negative and positive IR absorbance bands where the negative and positive peaks



represent the IR absorption at E_S and E_R, respectively.

$$\log \frac{R(E_S)}{R(E_R)} = \Gamma\varepsilon(E_R) - \Gamma\varepsilon(E_S)\,. \qquad (13.12)$$

The traces b, c, and d in Fig. 13.24 (left) show the SNIFTIR spectra recorded at the Pt(111) electrode in 0.1 M Na_2SO_4 + 0.001 M H_2SO_4 electrolyte at selected sample potentials E_S, using p-polarized light. The strong negative band shifts from 1238–1258 cm^{-1} when E_S is increased from 0.3 to 0.5 V. This potential dependence demonstrates that this band corresponds to the species adsorbed directly onto the Pt(111) surface. In addition, this negative band also has a shoulder

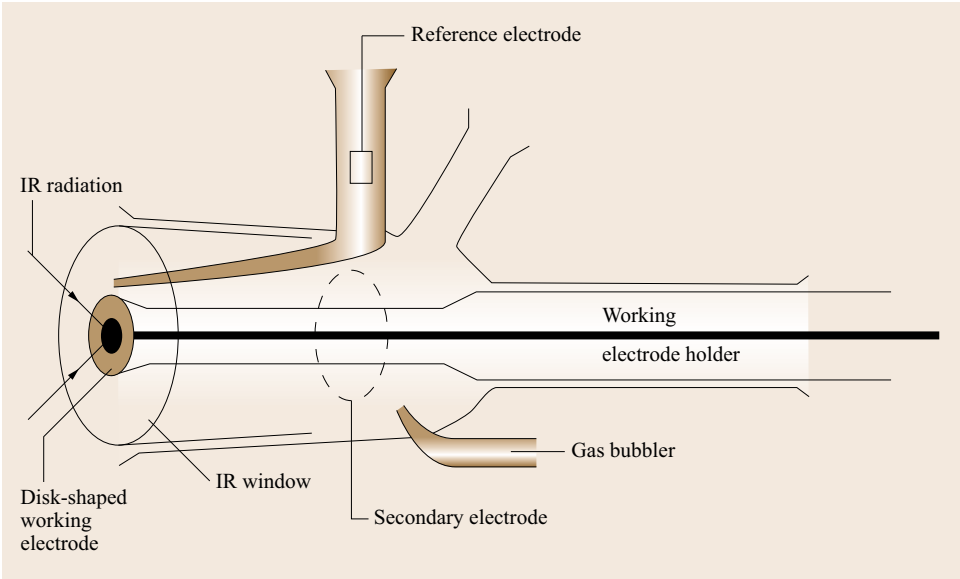


Fig. 13.23 IR SEC for reflectance measurements (courtesy of Elsevier)

around 1200 cm^{-1} which does not shift with modulated potential suggesting that it corresponds to a species in solution. The positive band near 1100 cm^{-1} does not change frequency with changing E_S, indicating that it also corresponds to the solution confined species. The top and bottom spectra in Fig. 13.24 consist mainly of bisulfate (curve *a*) and sulfate (curve *e*) in solution. The transmission spectrum of the HSO_4^- ion, which exhibits C_{3v} symmetry, shows three bands: the totally symmetric S–(OH) stretch at 885 cm^{-1}, the totally symmetric SO_3 stretch at 1050 cm^{-1} and the doubly degenerate SO_3 stretch at 1200 cm^{-1}. In neutral solution tetrahedral sulfate is the predominant species, and the transmission spectrum is dominated by a broad triply degenerate S–O stretch at 1100 cm^{-1}. The second normal mode associated with S–O stretching, the totally symmetric S–O stretch at 980 cm^{-1}, is barely discernible in the spectrum. Using the data obtained from the transmission spectra, the band at $\approx$ 1100 cm^{-1} was assigned to sulfate and the negative shoulder at $\approx$ 1200 cm^{-1} to bisulfate in the SNIFTIR spectra shown in Fig. 13.24. The assignment of the IR bands for adsorbed sulfate and bisulfate bonded to a surface is more complex. For adsorbed species, the only active IR bands are those whose transition dipole moment is oscillating normal to the surface, due to the surface selection rule (*vide infra*). However, direct adsorption lowers the symmetry of the molecule and removes the degeneracy of the SO_3 and S–O stretches. Consequently, the number of bands in the IR spectrum of adsorbed molecules is expected to vary depending on whether bonding to the surface involves one, two, or three oxygen atoms. Curves *b*, *c*, and *d* in Fig. 13.24a are the SNIFTIR spectra acquired using s-polarized light. Using s-polarization, only the IR absorbances of species that are present in the bulk of the thin layer cavity are detected. These SNIFTIR spectra show negative bands at $\approx$ 1100 and $\approx$ 1200 cm^{-1} confirming that the negative shoulder and the positive band observed at these frequencies in the p-polarized spectra correspond to species desorbed into solution. Therefore, in solutions with a pH $\approx$ 3.6, the band at $\approx$ 1250 cm^{-1} can be assigned to anions adsorbed at Pt(111) surface at potentials E_S, whereas the negative signs of the bands at $\approx$ 1200 cm^{-1} in the SNIFTIR spectra in Fig. 13.24a,b indicate an increase of absorbance by bisulfate ions in thin layer cavity at potentials E_S. The SNIFTIR spectra recorded with both p- and s-polarized light were used to calculate the angle of incidence and the thin layer cavity thickness. These values were used to calculate the MSEFS (mean square electric field strength) of IR photons at the electrode surface and within the thin layer cavity. The authors then used the spectra recorded using s-polarized light to eliminate IR bands due to absorption by ions in the thin layer cavity from the p-polarized SNIFTIR spectrum and the resulting spectra contain only the IR bands that arise from anions adsorbed at the single crystal electrode surface, highlighting the power of the SNIFTIRS approach. In this way it was concluded that sulfate is preferentially adsorbed onto Pt(111) over bisulfate species in acidic solution. The SNIFTIRS method has also been used for the in-situ study of self-assembled monolayers of short chain alkyl thiols terminated with electroactive ferrocene (Fc) moieties at Au(111) sur-

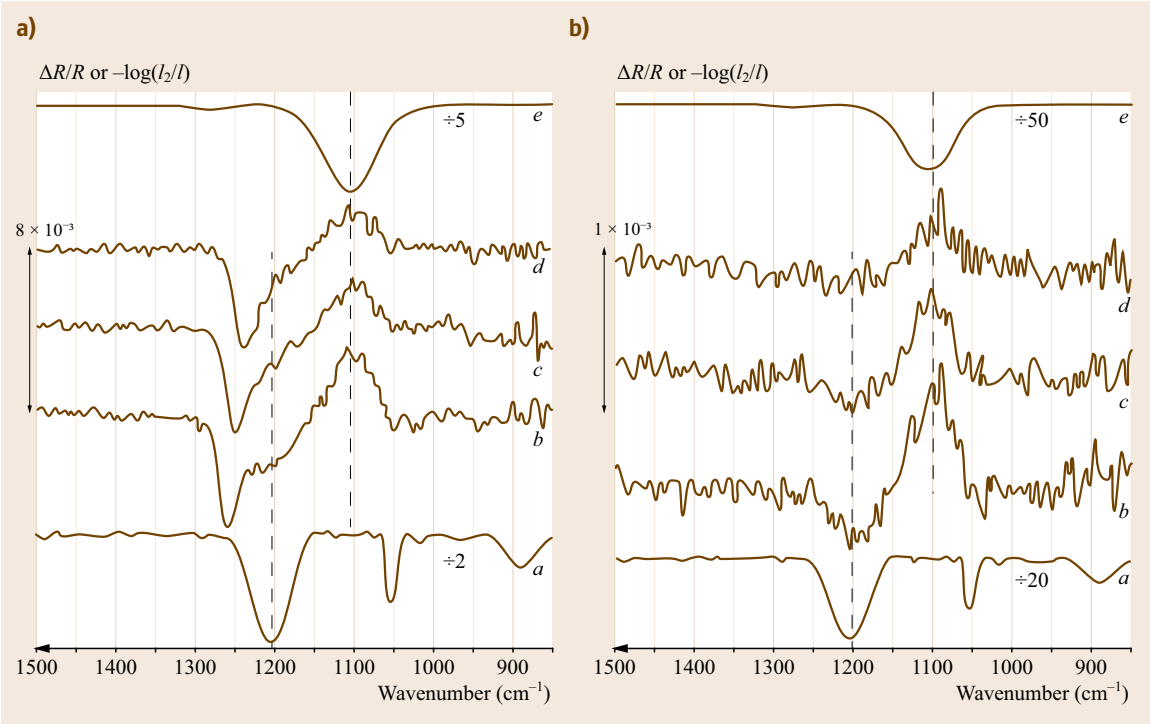


Fig. 13.24a,b SNIFTIR spectra of (bi)sulfate adsorption on a Pt(111) electrode in 0.1 M Na_2SO_4 + 0.001 M H_2SO_4 solution at p-polarized light **(a)**, and s-polarized light **(b)**. E_S is 0.5 V (*b*), 0.4 V (*c*) and 0.3 V (*d*). Traces (*a*) and (*e*) are the transmission FTIR spectra of 0.5 M K_2SO_4 + 3 M HCl and 0.5 M K_2SO_4 solution (after [13.106], courtesy of the R. Soc. Chem.)

faces. Using p-polarized light and exploiting the surface selection rule described, changes in ferrocene orientation were detected upon oxidation of the monolayers. This was attributed to rotation of the ferrocene groups toward a position where the plane of the cyclopentadienyl rings moves into a position normal to the Au(111) surface [13.107].

SNIFTIRS is also used in conjunction with step-scan Fourier-transform electrochemically modulated infrared spectroscopy (FT-EMIRS). Step-scan FT-EMIRS is a potential modulation technique which produces dynamic spectra that are the difference in the optical signal at the two different electrode potentials [13.108].

Infrared Reflection Absorption Spectroelectrochemistry

Infrared reflection absorption spectroscopy (IRRAS, also referred to as RAIRS) has also been applied to measurements in systems under electrochemical control. IRRAS involves the use of s- and p-polarized light sources, which typically generated in cycles by use of a photoelastic modulator. For incident s-polarized light (perpendicular to the plane of reflection), the reflected beam (reflected at the angle of incidence) is out-of-phase with the incident beam and so they destructively interfere, eliminating IR absorption at the surface with s-polarized light. For p-polarized light (parallel to the plane of reflection) the two fields are in phase. This means that s-polarized radiation is completely insensitive to species at the surface but will be absorbed by species in bulk solution; whereas the p-polarized radiation interacts with both surface and solution species. A difference spectrum of (p)–(s) therefore yields a spectrum of the interfacial species only, thus minimizing solvent contributions. In addition, because the exciting radiation at the surface is p-polarized, only those adsorbed species with a dipole moment perpendicular to the metal surface are IR active. In effect, this means that the detected signal can be used to measure the tilt angle of a monolayer as the IRRAS signal tends toward zero as a film moves from vertical to horizontal. This combined with the surface selection rule illustrated in Fig. 13.25 means IRRAS provides highly selective insights into surface bound species. IRRAS has found use in the spectroscopy of thin films of biomolecules, as the absorption bands of water, a very strong and broad IR absorber can be minimized [13.109].

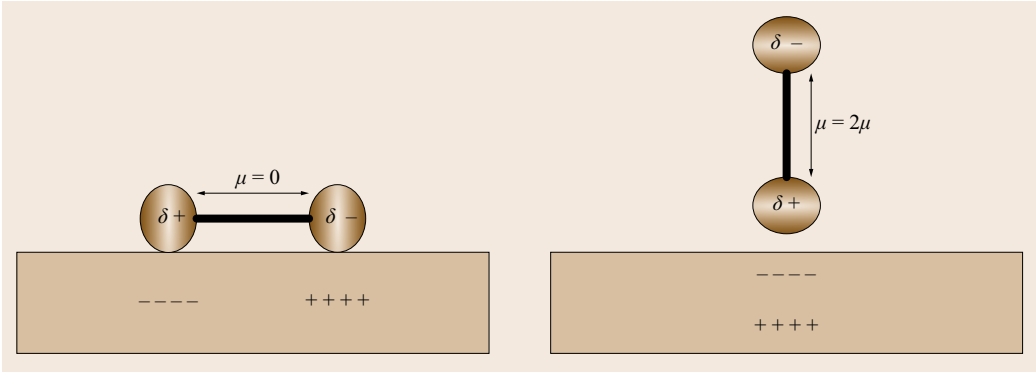


Fig. 13.25 Schematic illustrating the origin of the surface dipole image effect in the surface selection rule for IR spectroscopy. The dipole moment component of a vibrational mode perpendicular to the metal surface is enhanced by the image of the dipole generated within the conducting substrate, whereas those with dipoles oriented parallel to the surface are cancelled by the surface dipole. Therefore, the stretching mode on the right is strongly IR active whereas that on the left is not at all. A dipole at an intermediate angle would be expected to be IR active although will be weaker than a purely the perpendicular mode

In-situ polarization modulated IRRAS (PM IRRAS) was reported in the study of an IR-active redox polymer; PAH-OsCN, a polyallylamine derivatized with the IR-active group $[Os(CN)_5pyX]^{3-/2-}$ (where pyX represents a modified pyridine covalently tethered to the polymer backbone, see polymer structure in Fig. 13.26). The CN bond in the pentacyano redox couple presents different and well-defined stretching bands in its reduced and oxidized forms in contrast to the small shifts observed for the pyridine and bipyridine units in PAH-Os. The study showed how PM IRRAS can be used to determine the oxidation state of Os in a PAH-OsCN/polyacrylic acid multilayer as well as the protonation and hydration states and the content of mobile ions. The PM IRRAS spectroelectrochemistry of a multilayer self-assembled onto a gold mirror surface is shown in Fig. 13.25 [13.110]

The evolution of the CN-Os(II) and CN-Os(III) bands with increasing electrode potentials is shown in Fig. 13.25. It is evident that the molar absorptivity of the CN band of the oxidized complex is lower than that of the reduced species, in agreement with previous observations for the metal cyanide complex $[Fe(CN)_6]^{3-/4-}$ [13.111]. The formal redox potential for the redox couple is expected to be between 0.40 and 0.55 V for this electrode (depending on solution ionic strength) and therefore the lower and upper limits of the electrode potential shown in Fig. 13.26 (0.35 and 0.75 V) correspond to totally reduced and totally oxidized films, respectively. Despite this expectation, the spectra show that this is not true in this case and that an intense CN-Os(II) band is present even at $E = 0.75$ V. It was observed that the CN-Os(II) band did not disappear even when the electrode potential was held at 0.75 V for 90 min, showing that the oxidation of osmium sites was not limited by the diffusion of redox charge. However, upon chemical oxidation with Ce(IV) in H_2SO_4 0.5 M ($E^0 = 1.51$ V) for a few seconds and drying with N_2, the CN-Os(II) peak completely vanished with concomitant appearance of the CN-Os(III) band. The process can be fully reversed by chemical reduction using ascorbic acid ($E^0 = 0.18$ V). These results indicate that, interestingly, certain sections of the polyelectrolyte film are electrochemically inaccessible.

Potential-dependent IRRAS has also been used in CVA and derivative CVA measurements. The first example of FTIR-CVA and FTIR-DVCA were reported in 2009 [13.112]. The authors were studying the redox chemistry of 1,4-benzoquinone and 1,4-bis(2-ferrocenylvinyl) benzene, but also used the well-known ferrocyanide–ferricyanide redox couple to demonstrate the validity of IR CVA and IR DCVA methods. These data are shown in Fig. 13.27.

Figure 13.27a shows the cyclic voltammogram of potassium ferrocyanide. The shape of the CV is in accord with theoretical expectations for a diffusion controlled reversible electron transfer reaction in a thin layer cell. The rapid-scan IR spectra recorded in-situ during the electrochemical process in the range $1800-2300\,cm^{-1}$ are shown in Fig. 13.27b. The spectra were acquired during the CV scan between 0 and 0.4 V using the spectrum recorded at 0 V as the reference spectrum. Two modes at 2116 and $2038\,cm^{-1}$ were employed to track the electrochemical reaction as the peak at $2038\,cm^{-1}$ is due to the disappearance of $[Fe(CN)_6]^{4-}$, and the peak at $2116\,cm^{-1}$ corresponds to the formation of $[Fe(CN)_6]^{3-}$. The cor-

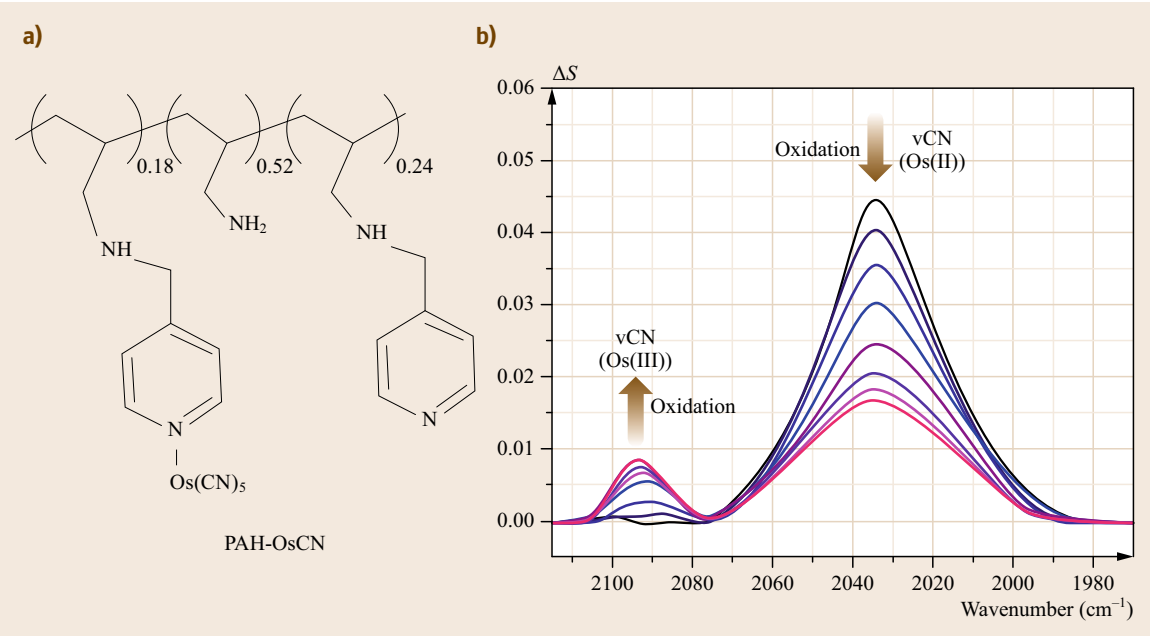


Fig. 13.26 (a) Structure of the redox polymer PAH-OsCN. (b) In-situ PM IRRAS spectra of a (PAH-OsCN/PAA)$_4$PAH-OsCN film in 50 mM aqueous NaF solution for increasing electrode potentials: 0.40, 0.45, 0.50, 0.55, 0.60, 0.65, 0.70, and 0.75 V. Reference electrode was Ag/AgCl (after [13.110], courtesy of Elsevier)

responding cyclic voltabsorptomograms are shown in Fig. 13.27c,d. It is apparent from Fig. 13.27c that there are concomitant increases and decreases of absorbance at 2116 and 2038 cm^{-1} subject to the sweep potential (time), corresponding to the redox process. The absorbance at 2116 cm^{-1} gradually increases in the oxidation process and reaches its maximum at nearly 0.35 V (175 s) after which it starts to decrease in the reduction process and vanish at 0.05 V (375 s). The absorbance at 2038 cm^{-1} gradually decreases during oxidation process and reaches its minimum at nearly 0.35 V (175 s) and begins to increase gradually during the reduction process. First derivatives of CVAs (DCVA, Fig. 13.27d) are morphologically identical to the ideal CV response for electrochemical processes. Figure 13.27d showed that the shapes of DCVA at 2038 and 2116 cm^{-1} both are similar to that of the CV shown in Fig. 13.27a (peak–peak separation, ΔE_P was 35 mV for CV, whereas ΔE_P was 11 mV for DCVA). IRRAS CVA and IRRAS DCVA are likely to find increased use in the fundamental study of heterogeneous electron transfer in future.

13.4.2 External Reflectance

Infrared ATR spectroelectrochemistry is broadly similar to the electronic spectroscopy analog. The main factor to be considered is the maintainance of IR transparency of the working electrode, which doubles as internal reflection component. Again the ATR crystal tip can be made of germanium, silicon, or diamond, which is coated with a thin layer of gold. The trade off between IR transparency and conductivity of the crystal tip is a critical balance that must be achieved. Doped silicon and germanium, alternatively, can be used as both ATR element and electrode. However, doping reduces the transparency of the material [13.100].

Attenuated Total Reflectance

Figure 13.28 shows an example of an ATR setup for potential-modulated FTIR spectroscopy [13.113]. This technique, performed on an electroactive waveguide platform, provides the sensitivity to characterize redox potentials and rates of ET (electron transfer) for thin films at submonolayer surface coverages. Monitoring electrochemically generated optical changes in the redox-active monolayer allows clear differentiation of faradaic versus nonfaradaic events. Thin films (submonolayer coverages) of pyridine-capped CdSe nanocrystals (pyr-CdSe NCs) were chemisorbed onto an ITO working electrode (acting as a planar waveguide) using various chain length mercaptoalkyl acids. Characterization of reversible electron injection into the pyr-CdSe NC layer was performed, and the estimated rate constant of charge injection was found to be inde-

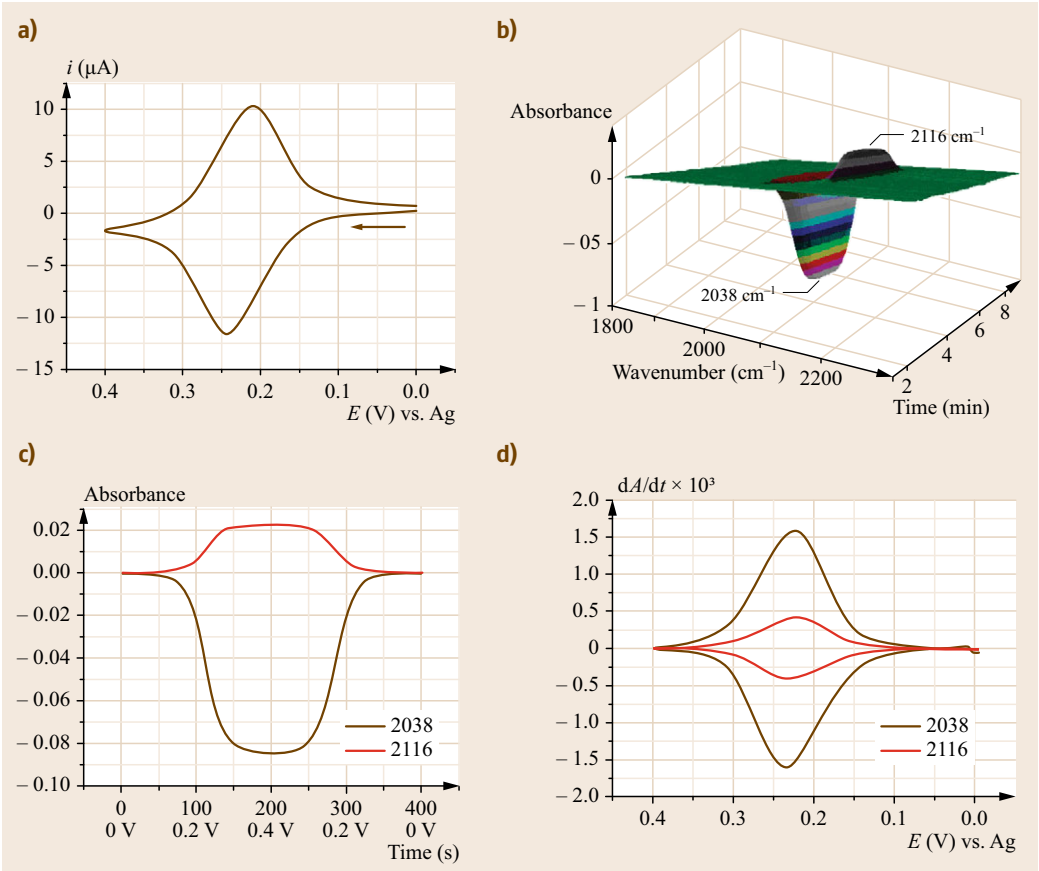


Fig. 13.27 **(a)** Thin-layer CV of 5 mM potassium ferrocyanide in 0.2 M KCl at a scan rate of 2 mV/s. **(b)** Corresponding 3-D spectra of in-situ FT-IRRAS spectroelectrochemistry. CVA **(c)** and DCVA **(d)**, smoothed with a fast Fourier transform algorithm, for the electrochemical reaction at 2038 cm^{-1} (*black line*) and at 2116 cm^{-1} (*red line*). Conditions included a 4 mm diameter Pt disk working electrodes, a platinum wire auxiliary, and a Ag wire or Ag/AgCl reference electrode (after [13.112], courtesy of Am. Chem. Soc.)

pendent of tether alkyl chain length. This novel use of spectroelectrochemistry to study such thin and weakly absorbing films could only be achieved by a technique with the sensitivity of waveguide-based spectroelectrochemistry.

In ATR, the evanescent wave decays exponentially into the signal, which is a distinct advantage in FTIR spectroscopy. This results in reduced solvent contribution and, as multiple reflections occur, the interfacial beam pathlength and hence sensitivity increases. A number of practical limitations for FTIR-ATR have been mentioned previously. For example, theoretical and experimental refraction have been found to differ substantially and these differences have been attributed to the difference in optical properties of the thin metal layers and the bulk, due to either nonideal geometric arrangement of the atoms or through compositional changes caused by inter-diffusion of the phases in the process of film formation [13.116]. Cleaning of the ATR crystal tip can only be done with certain solvents, so care should be taken to avoid permanent contamination.

Surface-Enhanced Infrared Absorption Spectroscopy

A specialized type of ATR spectroscopy known as SEIRAS (surface-enhanced infrared absorption spectroscopy) has been used to study immobilized proteins. In these experiments a thin layer of gold deposited onto an ATR prism serves as the working electrode. Examination of submonolayer protein films is facilitated by a signal enhancement effect (10−100×) at the gold surface which decays rapidly over a distance of about 10 nm from the surface. SEIRA is therefore sensitive to proteins tethered to the surface via a short chain linker, yet relatively insensitive to the bulk elec-

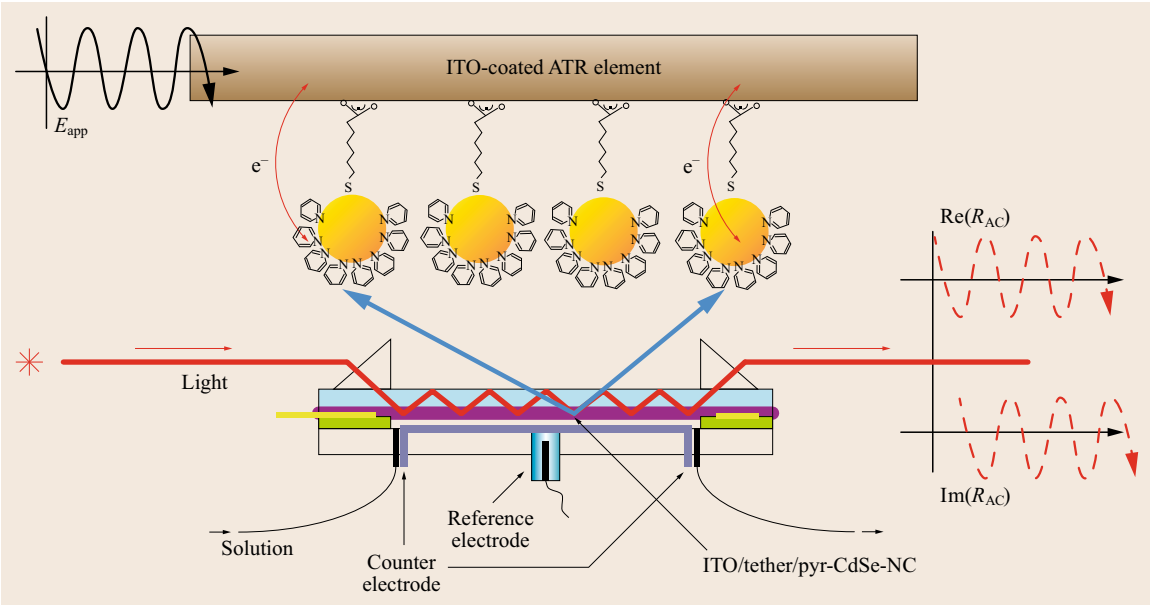


Fig. 13.28 Schematic view of the ATR spectroelectrochemical setup for monolayer-tethered nanocrystals. Light is prism-coupled into and out of an ITO-coated waveguide, with pyr-CdSe NCs chemisorbed at the electrode–solution interface. The ITO working electrode potential is modulated (50 mV about −1.47 V versus Fc/Fc^+, which is the midpoint potential (E_{app}) for reversible electron injection into the tethered NCs. The real (Re) and imaginary (Im) components of the AC portion of the electroreflectance response (R_{AC}) are monitored as a function of the modulation frequency, which is varied from 0.1 Hz to 1 kHz (after [13.113], courtesy of Am. Chem. Soc.)

trolyte, thereby minimizing contributions from water absorption. An example of protein SEIRA spectroelectrochemistry is shown inFig. 13.28 [13.114].

In Fig. 13.28, a rough gold surface used for SEIRA spectroscopy was modified with nickel chelating nitrilo-triacetic acid (Ni(II)-NTA), which selectively binds to the protein sensory rhodopsin II via the C-terminal His-tag to the Ni-NTA modified gold surface, affording signal enhancement. The $10-10\times10^2$ times signal enhancements reported for SEIRAS, though impressive, are orders of magnitude smaller than those reported for surface-enhanced Raman spectroscopy (SERS), where enhancement factors of 10×10^7 are routine (Sect. 13.5). Due to the surface selection rule, the SEIRA spectrum of the SR II protein exhibits a strong amide I and a weak amide II band (Fig. 13.29b) as a consequence of the predominant perpendicular orientation of the transmembrane helices relative to the gold surface. The amide I mode of the α-helix is parallel to and the amide II mode is perpendicular to the helix axis and is therefore normal to the membrane. In contrast, the conventional ATR absorbance spectrum (Fig. 13.29a) shows a strong amide II band. This demonstrates the potential power of the SEIRAS technique in unveiling the nature of protein secondary and tertiary structures.

Far-IR/THz

Reflectance spectroelectrochemistry in the far-infrared region (FIR, approximately $10-400\,cm^{-1}$, also called terahertz region, $1\,THz\approx33\,cm^{-1}$) has to date been relatively uncommon. However, such spectroscopy can be insightful for metal complexes as metal-containing vibrational modes tend to be prominent in this region. For example, *Hahn* et al. used synchrotron far-IR spectromicroscopy at grazing-angle incidence with a thin-layer spectromicroelectrochemical cell to successfully identify in-situ the composition of the oxide film on a copper working microelectrode in 0.1 M NaOH [13.117]. The results indicated the presence of CuO and some $Cu(OH)_2$. This was the first time that synchrotron radiation highly collimated micrometer-size IR probe beam and a microscope fitted with a grazing-angle objective were used in a spectroelectrochemical study of interfacial phenomena in the far-IR region. Far-IR difference SEC has been used to study electron delocalization and symmetry in the redox active multinuclear transition metal complexes $[MS_4Fe_2Cl_4]^{2-}$ (where M = Mo,W) [13.118]. The authors report that dichloromethane, dichloroethane, and THF exhibit low absorption in this region and hence are ideally suited to far-IR SEC. Apart from metallic-based modes, collec-

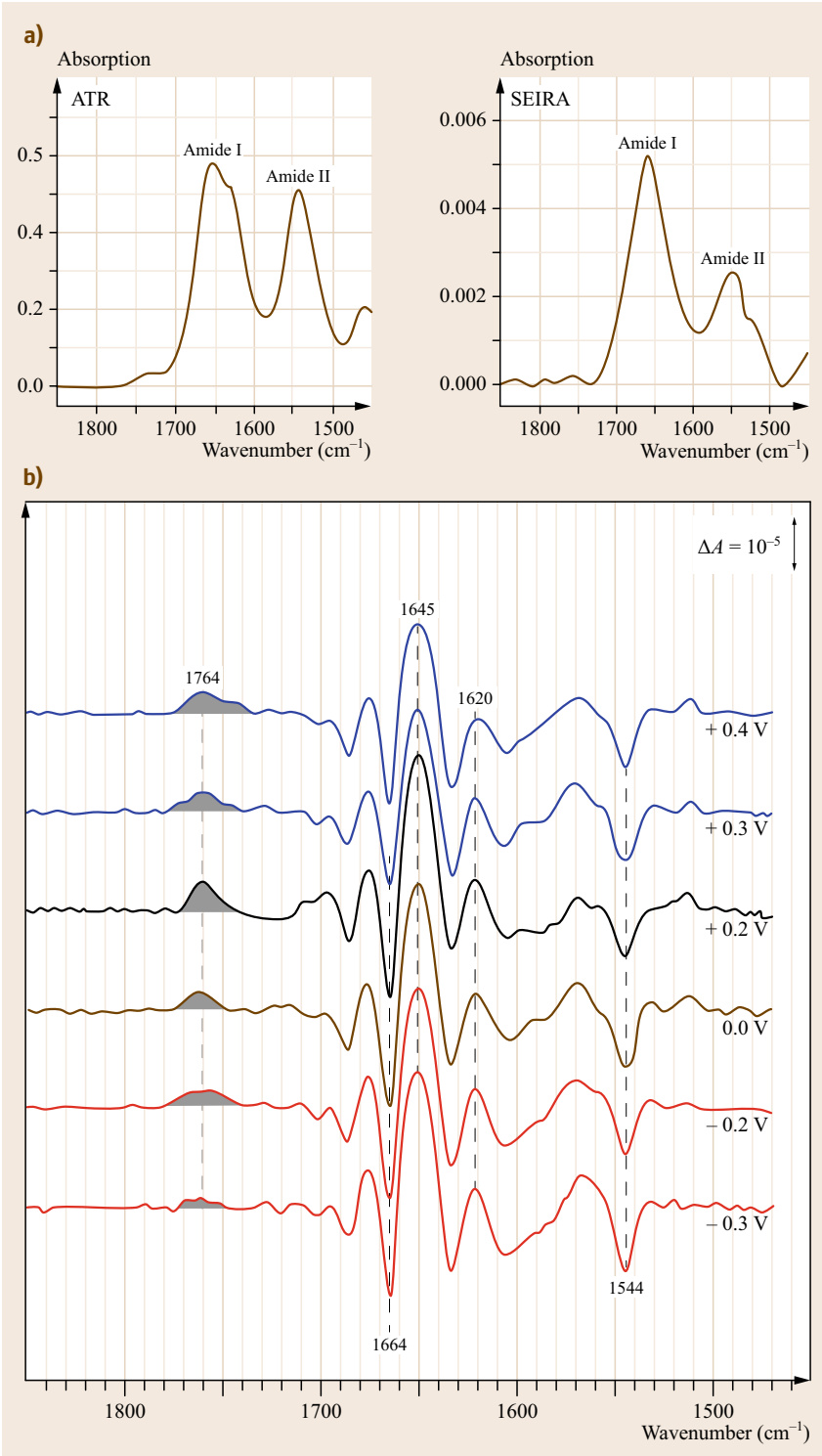


Fig. 13.29 **(a)** ATR/FTIR absorption spectra of a stack of the membrane protein sensory rhodopsin II reconstituted in halobacterial lipids (*left*) in comparison with the SEIRA spectrum of a monolayer of SR II tethered to the modified gold surface via a His-tag (*right*). The spectra have been corrected for vibrational contributions from the solvent water (scissoring mode of H_2O at $\approx 1645\,cm^{-1}$). **(b)** Surface-enhanced IR difference spectra at various transmembrane voltages across a membrane protein monolayer of sensory rhodopsin II from *N. pharaonis* recorded at potentials from $+0.4$ to $-0.3\,V$ **(a,b)**. Applied voltages are given versus the normal hydrogen electrode (NHE) (after [13.114], courtesy of the Nat. Acad. Sci., USA)

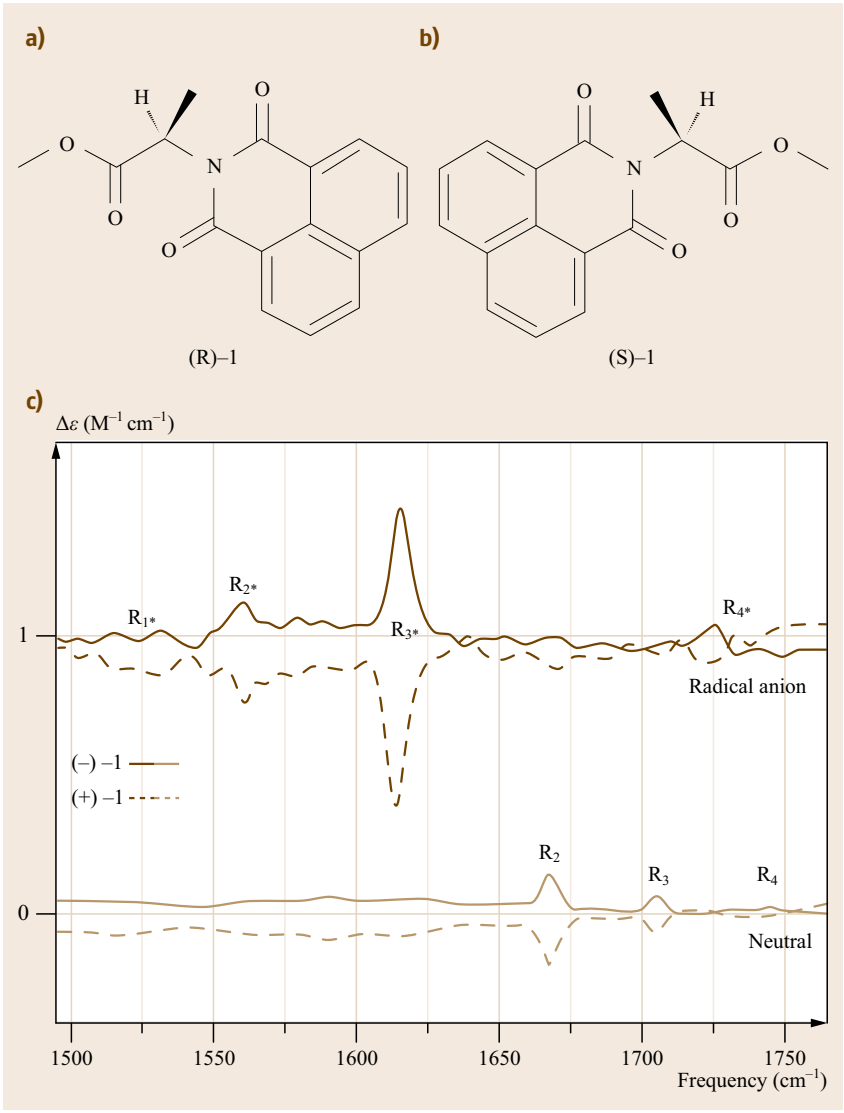


Fig. 13.30 (a,b) Structures of compounds (+)- and (−)-methyl 2-(1,3-dioxo-1H-benzo[de]isoquinolin-2(3H)-yl)propanoate. (c) VCD spectra of 7 mM (−)-1 (*solid line*) and 7 mM (+)-1 (*dashed line*) (OTTLE cell, $l = 0.12$ cm, Pt minigrid electrode) for the neutral (*black*) and radical anion (*brown*) species. The spectra for the radical anion are vertically offset for clarity. Spectra for both enantiomers have been obtained by averaging three consecutive sets of 20 min scans for the neutral and three sets of 2 min scans from independent but consecutive CV cycles for the radical anion (after [13.115], courtesy of the R. Soc. Chem.)

tive H-bonding motions are also observed in the THz region and THz difference spectroelectrochemistry has been employed to study hydrogen bonding in metalloproteins [13.119].

13.4.3 Vibrational Circular Dichroism SEC

Vibrational circular dichroism (VCD) is the infrared CD associated with vibrational transitions of chiral molecules. VCD measurements tend to be difficult because of extremely small signal magnitudes, typically 10^{-5} of the absorption band. Such a small spectral change can be measured but spectral acquisitions tend to be long. However, species with low-lying electronic excited states can exhibit enhanced VCD signals through a vibrational magnetic-dipole transition moment vibronic coupling mechanism [13.120]. Using this insight, *Miomandre* et al. [13.90] used coupled VCD-SEC to modulate the excited-state various excited state potentials of the enantiomers (*R*)- and (*S*)-methyl 2-(1,3-dioxo-1*H*-benzo[*de*]isoquinolin-2(3*H*)-yl)propanoate (hereafter abbreviated to (+)-1 and (−)-1), and hence probe the enhancement effect on VCD signal intensities [13.115]. Cyclic voltammetry revealed that the enantiomers each undergo one fully reversible redox process ($E_{1/2} = -1.3$ V versus Fc/Fc^+), corresponding to the formation of a kinetically stable radical anion. The VCD spectra neutral and electrochemically reduced (+)-1 and (−)-1 are shown in Fig. 13.30.

For neutral (+)-1 and (−)-1, three features R_2, R_3, and R_4 are present in the VCD spectra. The features have identical magnitude but opposite phase. In the radical cation (the electrochemically reduced species) these bands are red-shifted and labeled R_2^*, R_3^*, and R_4^*, respectively. The spectra show another band R_1^* that is not visible in the spectrum of the neutral (i. e., fully oxidized) compounds. In addition the VCD signals are enhanced up to one order of magnitude compared to the neutral species. This enhancement is due to a strong vibronically induced mixing of low-lying electronic excited states with the ground state in the electrochemically generated radical anion species, and the authors provide density functional theory (DFT) evidence to support this claim. Therefore, VCD SEC can be used to identify certain vibrational modes that are otherwise undetectable and also can result in signal enhancement by an order of magnitude.

13.5 Raman Spectroelectrochemistry

Raman spectroscopy is a powerful and extremely versatile vibrational spectroscopic method which has found extensive and growing use in spectroelectrochemical investigations because of its ease of implementation. Detailed description of the Raman effect is beyond the scope of this chapter, although a superficial introduction is provided, the reader is directed elsewhere for background theory [13.121].

In Raman spectroscopy, an intense monochromatic light source (typically of visible wavelength) is directed onto the sample. Although most of the light incident on a sample is reflected or scattered elastically (i. e., with the same frequency as the incident light) a small component of the incident radiation will also be inelastically scattered whereby there is an exchange of energy between an incoming photon and the analyte molecule. This leads to the emission of a second photon with frequency ν which is either higher (i. e., $\Delta\nu = \nu_0 + \nu$) or lower ($\Delta\nu = \nu_0 - \nu$), than that of the incident photon ν_0. This photon is said to be Raman scattered. In vibrational Raman spectroscopy, $\Delta\nu$ corresponds to vibrational quanta and the associated vibrational mode must induce a change in the polarizability of the molecule to be Raman active. As Raman scatter is a two photon process, it is fundamentally weak. In the conventional method less than 1 in every million photons incident on a sample will be Raman scattered. However, the Raman scatter intensity depends inherently on the incident laser power, consequently as a spectroscopic technique it has benefited enormously from the availability of intense laser sources and ultra-sensitive detection which has converted it from a relatively obscure specialist technique to a benchtop method in the last 30 years.

Figure 13.31 illustrates the principle of Raman scattering and for comparison shows the direct vibrational state transition responsible for the spectroscopic signal in IR spectroscopy. In Raman incident light excites the sample to *virtual* electronic state. After excitation to a virtual level, the scattered photon is released and the molecule returns to a higher vibrational level $v = 1$. Stokes scatter originates from a molecule excited to the virtual state from the ground vibrational level $v = 0$. As this is the most likely state to be populated at room temperature, Stokes is the predominant Raman mechanism, and therefore the most intense. Anti-Stokes transitions have weaker intensity because excitation originates from a $v = 1$ vibrational level which will usually be only weakly populated at room temperature. Although broadly the same vibrational transitions can occur, the selection rules for Raman and IR spectroscopy are different and can be mutually exclusive for highly symmetric molecules. For a vibrational mode to be Raman active it must induce a change in a component of the molecular polarizability. Molecules with poor polarizability, i. e., which are highly dipolar, tend to exhibit weak Raman scatter and strong IR absorbance. Therefore those dipoles which exhibit intense IR absorbance tend to be weakly Raman active. This can be a useful advantage of Raman for electrochemical studies in aqueous media the background interference from water which makes IR so difficult in this medium is largely eliminated in Raman.

A further advantage of Raman spectroscopy is that as the excitation source is usually visible or NIR, there is no requirement for IR transmissible optical windows such as the alkali salts, improving further the compatibility of Raman in aqueous media. This opens up the possibility with Raman of exploring biological media accessible only with difficulty in IR spectroscopy.

Raman spectroelectrochemistry has been reviewed in detail previously [13.122, 123]. Selection of the cell used for spectroelectrochemistry depends to some extent on the optical layout of the Raman experiment. The main optical layouts in conventional Raman spectroscopy are front incident and collection mode, 180° backscattering and ATR mode. For solution phase Raman spectroelectrochemistry, a three electrode cell for bulk electrolysis is used and a number of such cells have

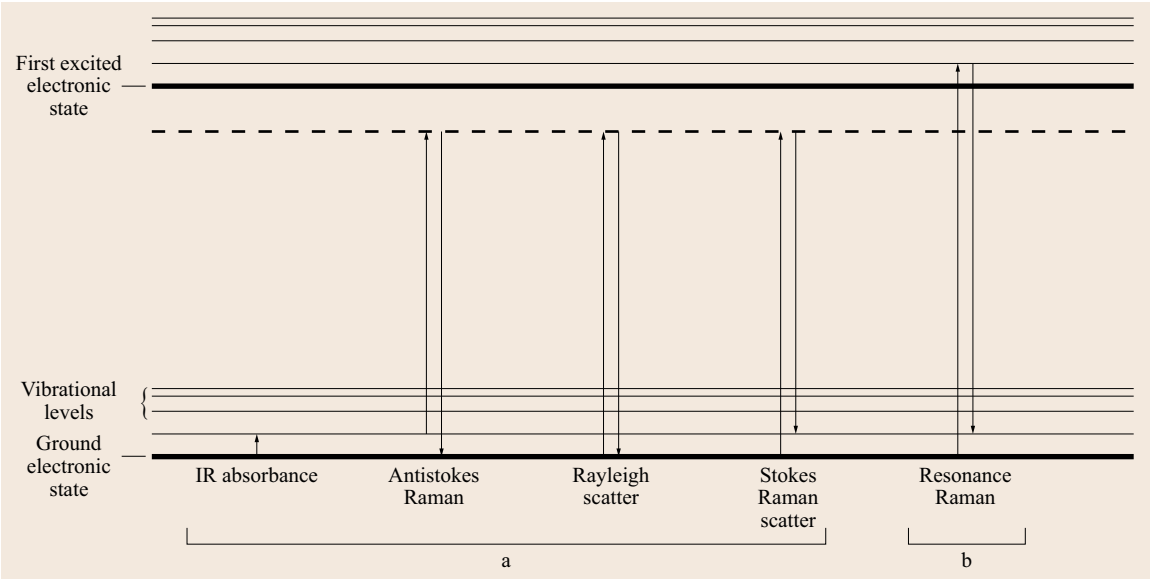


Fig. 13.31 Schematic illustration of the transitions associated with Raman spectroscopy. (*a*) Conventional Raman spectroscopy excitation to a virtual state leads to re-emission of a photo of the same frequency as the excitation source, Rayleigh scattering or inelastic scattering where the re-emitted photon has higher (anti-Stokes) or lower energy (Stokes) than the incident photon. (*b*) Resonance Raman conditions: The frequency of the incident photon matches or is close to the energy of an optical absorbance, resulting in scatter which originates from an excited electronic state

been described [13.124, 125]. The conventional OTTLE cell described for electronic spectroscopy can be used in Raman spectroelectrochemistry. Although, this cell can suffer from solvent interference in nonaqueous media. Thin layer cells like those described for IR are also frequently used.

Pemberton and co-workers described an innovative approach to minimizing solvent background shown in Fig. 13.33. This immersion cell has been used to study self-assembled monolayers and interfacial structure using Raman spectroscopy [13.127, 128]. It operates wherein a slowly rotating electrode making partial contact with a droplet of analyte solution draws a thin film of the analyte solution with it as it rotates out of the solution. The thin film of the solution on the electrodes is of the order of tens of angstroms thick. The interfacial solvent species in this layer retains any preferred orientation that occurred in-situ and electrical contact is maintained across the working electrode and through the droplet. The Raman spectrum is collected from the portion of the working electrode out of solution. This approach reduces the amount of bulk solvent sampled leading to low background interference. Also, because the electrode is rotated during collection of Raman spectra, local heating due to the incident laser is minimized.

Raman spectroelectrochemistry can provide detailed information about structural changes which accompany an electrochemically induced process in solution. In addition, confocal microscopy methods are increasingly being combined with Raman spectroscopy to be used on surfaces, interfaces, and in thin solid films. Because it is a scattering rather than a transmission technique, it can be used for electrochemical studies at solid electrodes and is a valuable means of probing the electrode–solution interface.

With confocal microscopy, spectroscopic signal from out-of-focus region is eliminated by means of a confocal *pinhole* aperture which lies in front of the image plane. In principle, in Raman spectroscopy the confocal geometry permits discrimination of Raman scatter from outside the plane of focus of the laser, limiting the portion of the sample interrogated to a tiny volume, thus allowing depth profiling typically with a resolution of $1-2\,\mu m$. The spatial resolution of a confocal Raman microscope is typically submicron. The resulting tiny sample volume can be used to selectively interrogate the kind of volumes that thin layer cells have been used for spectroelectrochemistry.

A microscope objective fitted to beam turning optics can be used with the cell shown in Fig. 13.34. In this arrangement, the working electrode is inserted into the side of a conventional cuvette; which may be glass or more typically a carbonate cuvette for visible excitation, into which a hole has been bored. The cell is sealed against leakage of electrolyte or solvent with

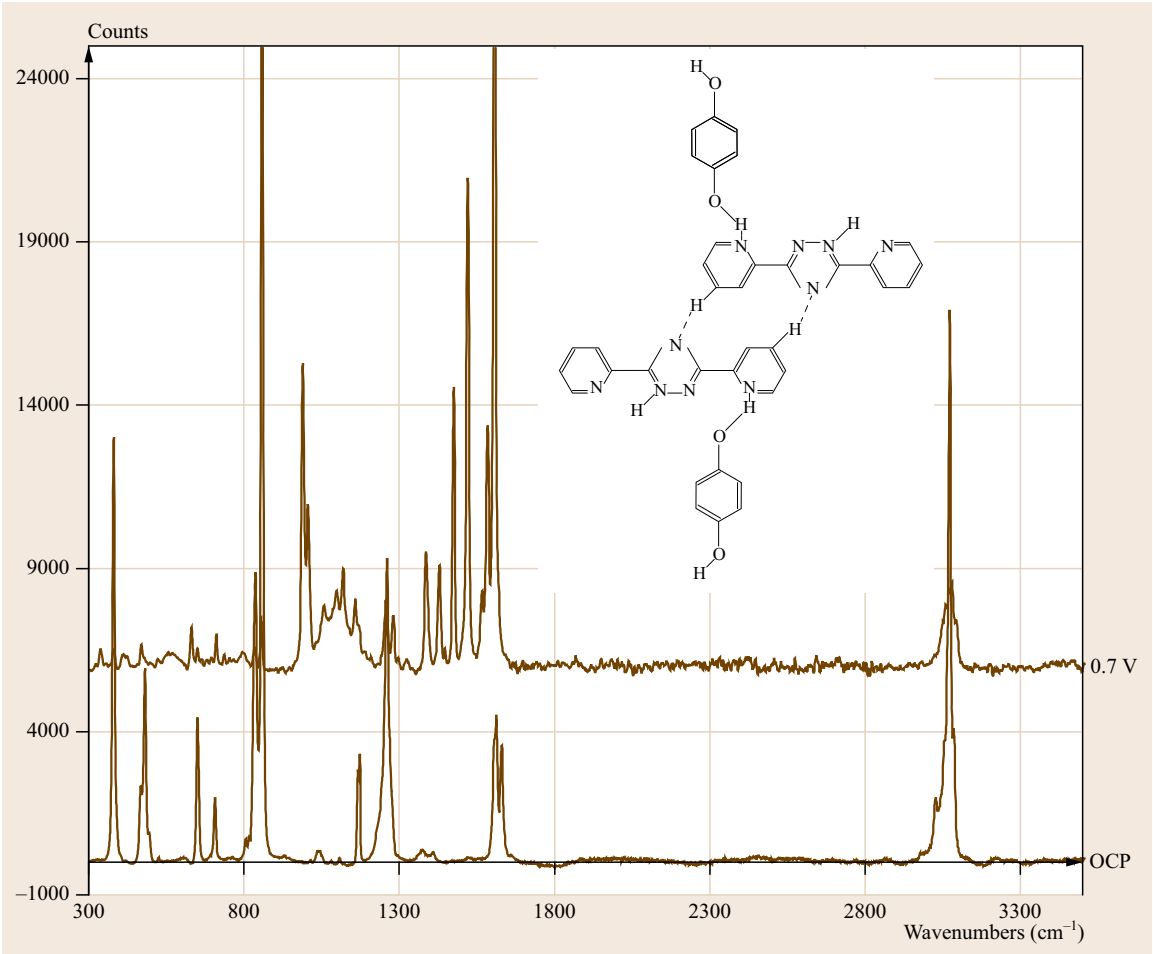


Fig. 13.32 Confocal Raman spectroelectrochemistry of a thin solid film conducted using the arrangement shown in Fig. 13.31, of HQBpt (*inset*) on a glassy carbon electrode at open circuit potential (OCP) and at $+0.7$ V. The supporting electrolyte was aqueous 0.1 M $LiClO_4$ (after [13.126], courtesy of Am. Chem. Soc.)

a rubber o-ring or with wax. A thin layer of solution can then be compressed between the cuvette window and the electrode if it is the solution that is under study. For monolayers or thin films, the compression of the electrode to the window is not a requirement and in fact some distance between them may be an advantage if using a plastic cuvette to avoid signal contamination. The auxiliary and reference electrodes and the solution may be degassed and a blanket of inert gas may be maintained over the top of the cell during spectral acquisition.

Such a cell has been used for confocal Raman microscopy applied to the study of a number of thin solid films and self-assembled monolayers [13.126, 130]. For example, Fig. 13.32 shows the Raman spectroelectrochemistry of solid co-crystalline films of hydroquinone 3,5-bis(2-pyridyl)-1,2,4-triazole (HQBpt) pressed onto a glassy carbon working electrode. Reversible oxidation of the hydroquinone moiety could be followed through Raman spectroscopy following in particular, the appearance and disappearance of quinone C = O modes.

Using the same experimental approach, Raman SEC was applied to the study of solid-state redox transformations of uranyl peroxide studtite, $[UO_2(\eta^2\text{-}O_2)(H_2O_2)] \cdot 2H_2O$, which is a phase alteration product of spent nuclear fuel and has been characterized by solid-state cyclic voltammetry [13.129]. As shown, in Fig. 13.35, following 12 h electrolysis, the Raman spectrum of Studite indicated extensive, irreversible structural change to the mineral, with loss of peroxo marker bands, indicating the product was likely to be UO_2, a very weak Raman scatterer, which yielded an essentially silent spectrum.

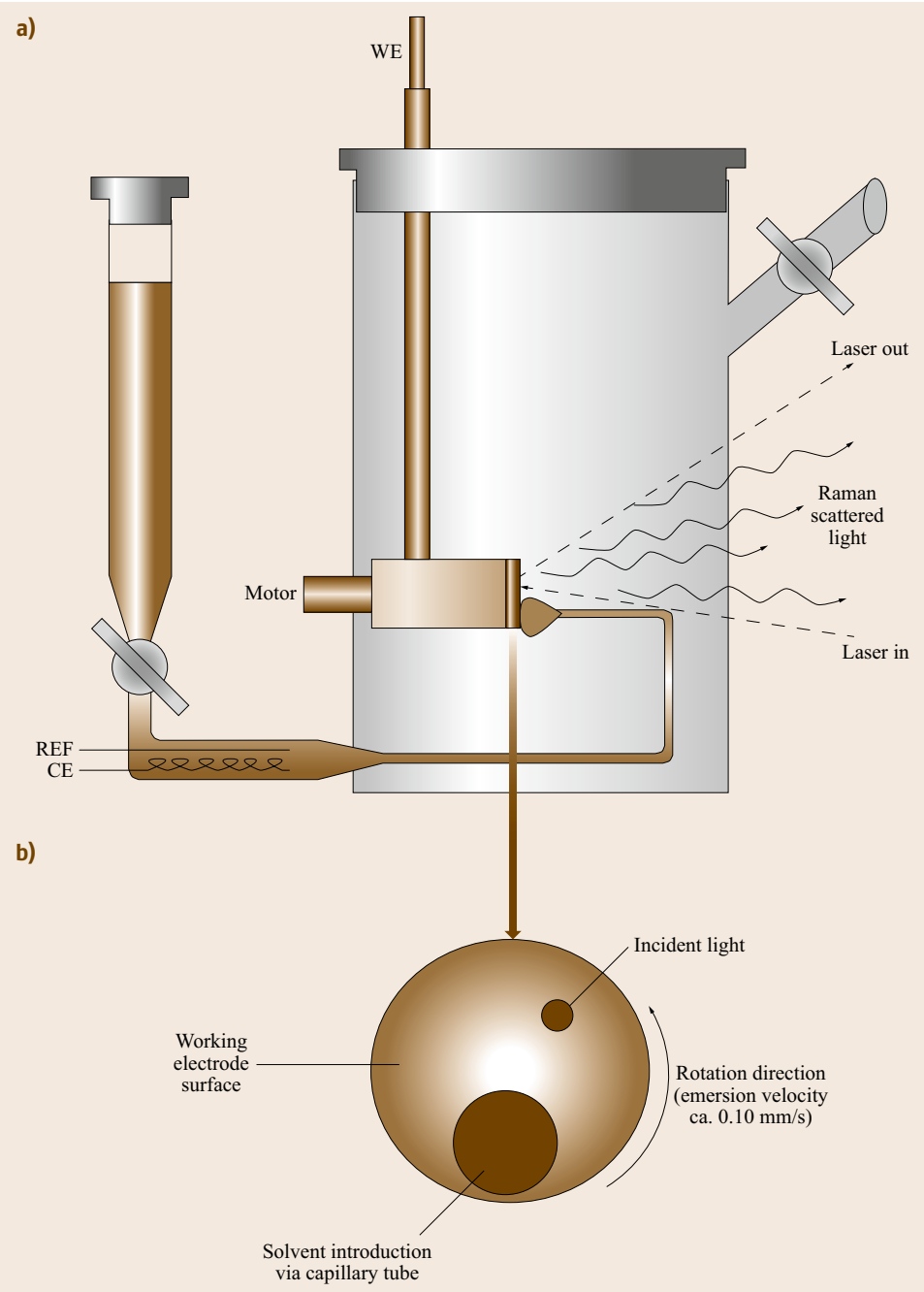


Fig. 13.33 **(a)** Schematic of rotating Raman spectroelectrochemical emersion cell. (REF, reference electrode (Ag wire); CE, counter electrode (Pt wire); WE, working electrode (Ag disk)). **(b)** Face view of working electrode surface (after [13.127], courtesy of Am. Chem. Soc.)

A significant limitation of Raman spectroscopy is that it suffers from low signal intensity. However, exploiting resonance conditions, in resonance Raman spectroscopy and or plasmonic materials in surface-enhanced Raman spectroscopy can lead to significant signal intensity gains.

13.5.1 Resonance Raman Spectroelectrochemistry

In resonance Raman spectroscopy [13.133] by employing excitation wavelengths that are coincident with the electronic absorbances of the species under interroga-

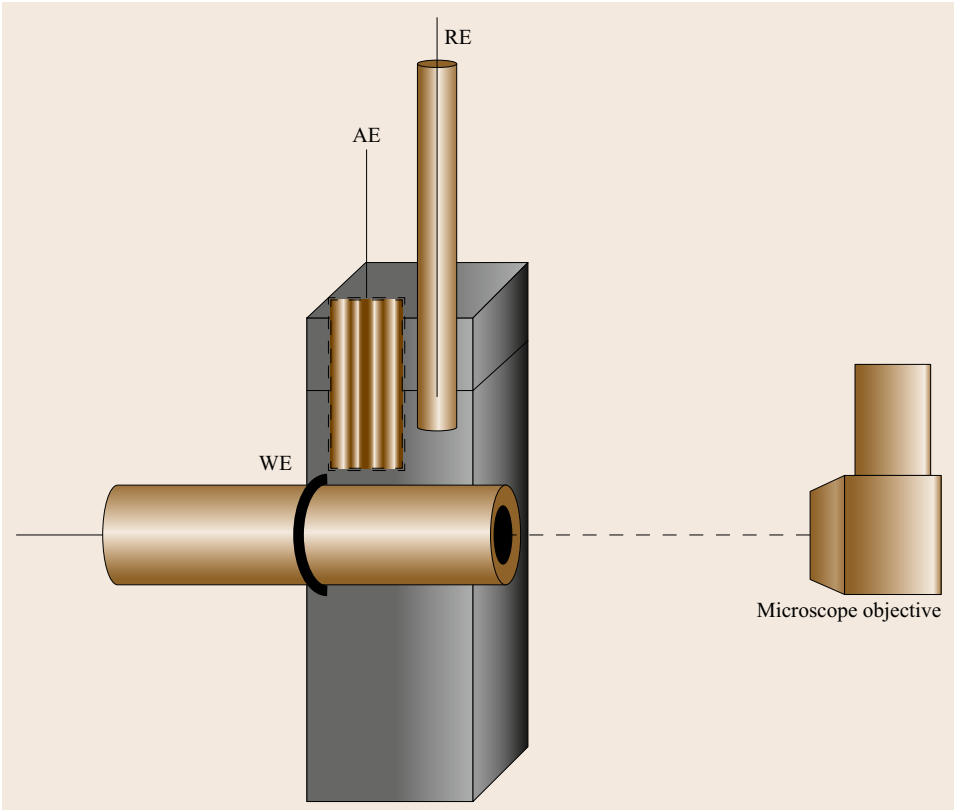


Fig. 13.34 Simple SEC for Raman or fluorescence microscopy of solid films or monolayers. The working electrode (WE) onto which the film or monolayer is adhered, is placed into a cuvette bored through the side and electrolyte/solvent in prevented from leakage by an o-ring. The reference (RE) and auxiliary electrode (AE) are in contact with the solution through the top of the cell and depending on the potential range used, the solution can be maintained under a blanked of inert gas through a needle directed over the top of the cuvette. For Raman, this arrangement is suitable for backscattering and microscope geometries

tion, the Franck Condon modes of the chromophore can be resonantly enhanced by up to 7 orders of magnitude. The theory behind resonance Raman spectroscopy is beyond the scope of this chapter, but is described elsewhere [13.121]. Employing the resonance condition in spectroelectrochemistry provides a highly selective means of unequivocally identifiying new optical transitions resulting from electrode reactions.

The cell formats described for conventional Raman spectroscopy apply. However, the laser excitation wavelength must be coincident with an electronic transition. Figure 13.38 illustrates the utility of this technique wherein it was used to identify if in a family of complexes with redox active ligands, the various redox processes were metal or ligand based. The complexes were $[M(bpy)_2(box)]^+$, where bpy is 2,2-bipyridyl, box is 2-(2-hydroxyphenyl)benzoxazole, and M is either Ru or Os which are coordinated through N of the benzoxazole and through the phenolate O. Electrochemical and electronic spectroelectrochemical behavior suggested the first oxidation was metal based. Whereas, conversely resonance Raman of the native complex suggested the highest energy occupied molecular orbital, HOMO, lay on the phenolate suggesting that this should be site of the most cathodic oxidation [13.131]. The inset of Fig. 13.36 shows the electronic spectroelectrochemistry observed for the first oxidation step of the ruthenium complex, which resulted in loss of the visible MLCT transition with the development of a new optical transition in the NIR.

Resonance Raman spectroelectrochemistry was carried out on $[Ru(bpy)_2(box)]^+$ and the osmium analog in which the bipyridyl units were perdeuterated $[Os(d_8\text{-}bpy)_2(box)]^+$ by holding the cell potential beyond the first oxidation step for each sample. In both cases the resonance Raman were found to be essentially identical, with evidence for participation of the bipyridyl unit in the new optical transition of the oxidized complexes. Resonance Raman spectroelectrochemistry confirmed that for both complexes the metal was oxidized first leading to M(III) to ($d\pi$) ligand to metal charge transfer LMCT transition in each case. Resonance Raman spectroelectrochemistry has also proven extremely useful in the study of solid deposits of POMs on ITO working electrodes [13.134]. In these experiments the electrochemically reduced POM exhibits an intense IVCT band that the fully oxidized form does not, and this mode comes into resonance under 488 nm laser irradiation. The presence of POM modes under 488 nm irradiation therefore confirmed the presence of reduced

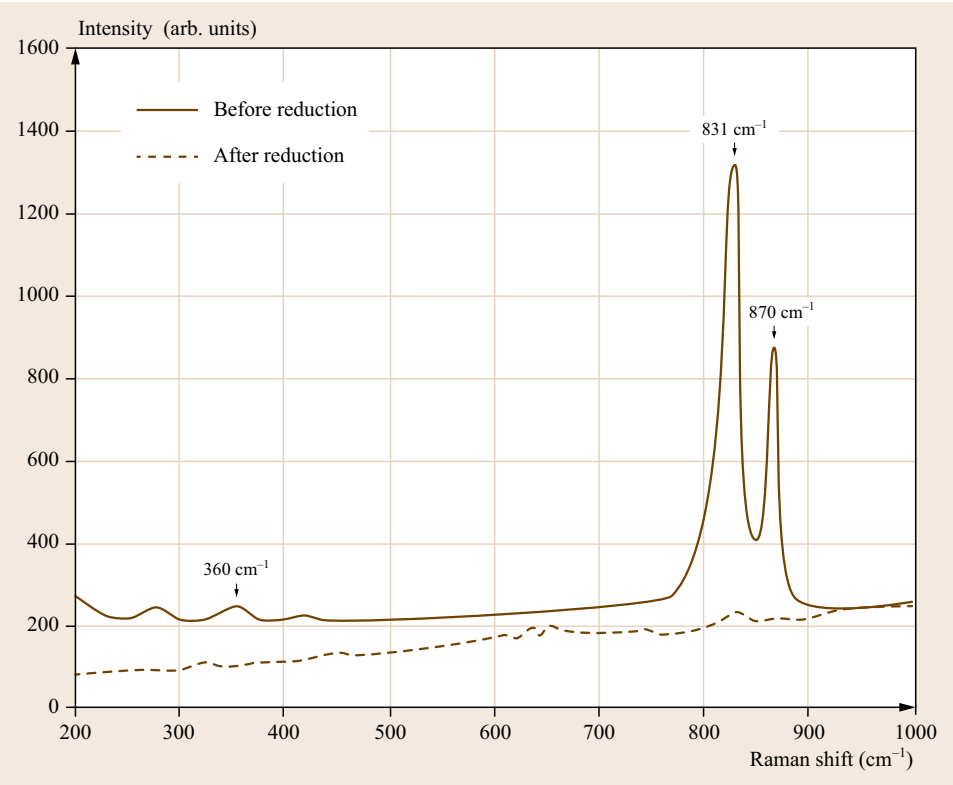


Fig. 13.35 Confocal Raman spectroelectrochemistry of a thin solid films of studtite on FDTO working electrode before and after reduction at −1.2 V for 12 h in 0.2 M $LiClO_4$. The excitation line is 633 nm (after [13.129], courtesy of Am. Chem. Soc.)

POM trace impurities. These trace impurities were not detected by other techniques such as UV-Vis spectroscopy and this highlights the inherent sensitivity of analytical resonance Raman spectroelectrochemistry in trace analysis.

13.5.2 Surface-Enhanced Raman Spectroscopy

In surface-enhanced Raman spectroscopy (SERS), Raman scatter can be enhanced by many orders of magnitude by exploiting the intense interfacial plasmonic fields that can be excited at a roughened or nanoparticulate metal surfaces with resonant incident radiation. The mechanism of SERS has been discussed in detail and remains the focus of intense investigation but is believed to draw on two contributions: electromagnetic and chemical enhancements [13.135–138]. The former arises as described from the excitation of localized surface plasmons at a nanostructured metal interface, the resulting electric field enhances the incident electric field the analyte species experiences. The chemical enhancement is believed to arise from a charge transfer transition occurring between adsorbate and the nanostructured metal. The mechanism of enhancement is somewhat similar to resonance Raman enhancement. Of the two mechanisms, the chemical contribution is the weaker, and is believed to contribute up to two or three orders of magnitude enhancement. It also requires intimate (bonding) contact between adsorbate and substrate.

SERS enhancement is principally limited to the coinage and alkali metals: Ag, Au, Cu, Na, Li, K. Although, in fact, all metals should be capable of plasmonic excitation for example, Pd, Pt, Rh, and Ru will produce enhancements with UV excitation [13.135]. However, UV lasers and the associated optics remain expensive limiting the availability of UV-Raman spectroscopy. The requirement for roughened surfaces for optimal SERS enhancement is well established [13.139]. Surface roughness should be on the order of between 10 and 200 nm and the surface morphology is critical in dictating the quality of SERS achieved. Theory dictates that the highest SERS enhancements of electric field will be achieved where the surface roughness has the highest curvature [13.140]. A range of methods have been explored for development of SERS substrates. This has included electrochemical, chemical and laser-induced roughening of metal surfaces, immobilization of metal particles onto an etched or modified substrate, vapor deposition, metal nanoparticle assembly via lithogra-

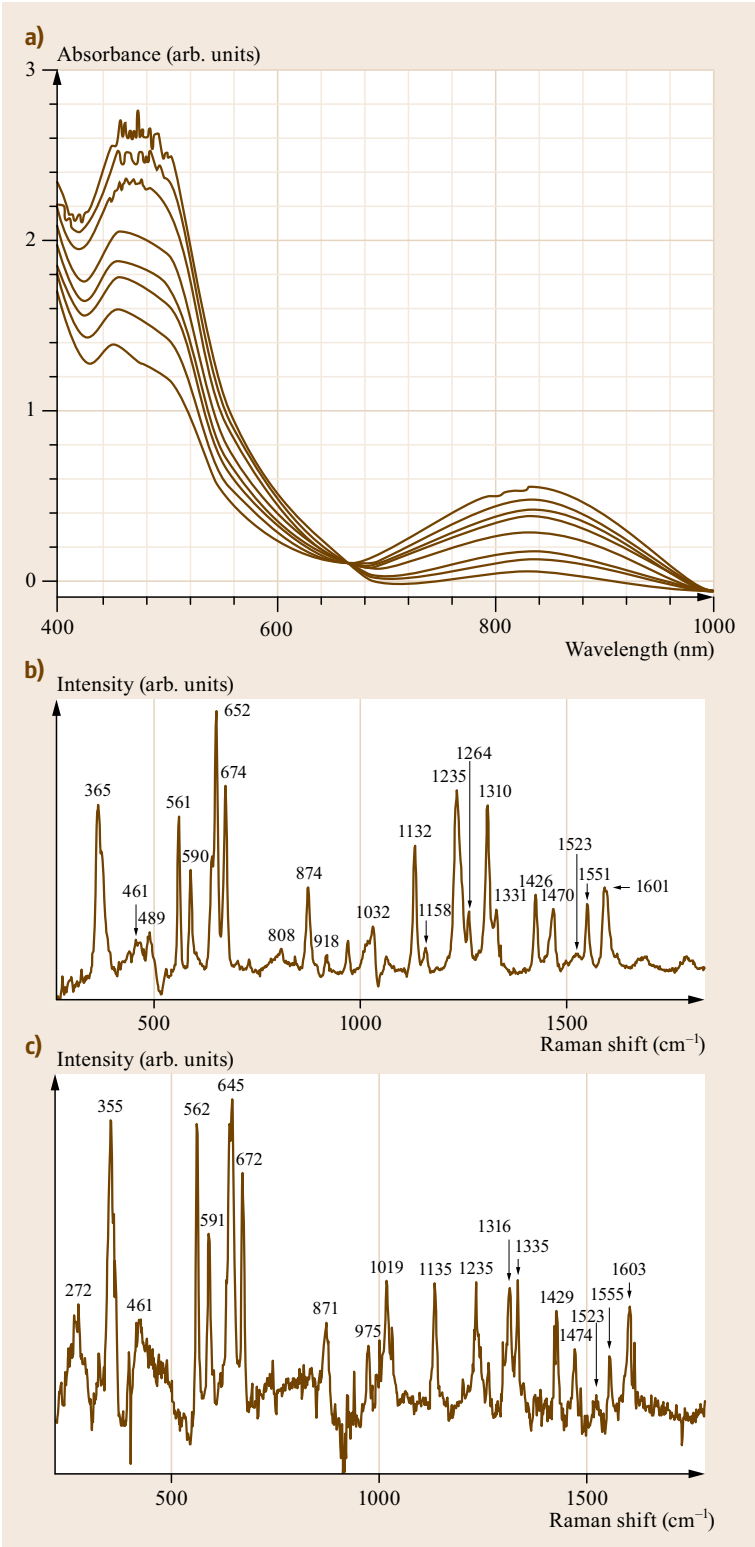


Fig. 13.36a–c Controlled potential spectroscopy of **(a)** $[Ru(bpy)_2(box)]^+$ electronic spectroscopy, **(b)** $[Ru(bpy)_2(box)]^+$ resonance Raman spectroscopy in dichloromethane, excited at 785 nm, **(c)** resonance Raman of $[Os(d_8bpy)_2(box)]^+$ in dichloromethane, excited at 785 nm, the applied potential in each instance was 0.5 V versus Ag/AgCl and the electrolyte 0.1 M $TEABF_4$ (after [13.131], courtesy of the R. Soc. Chem.)

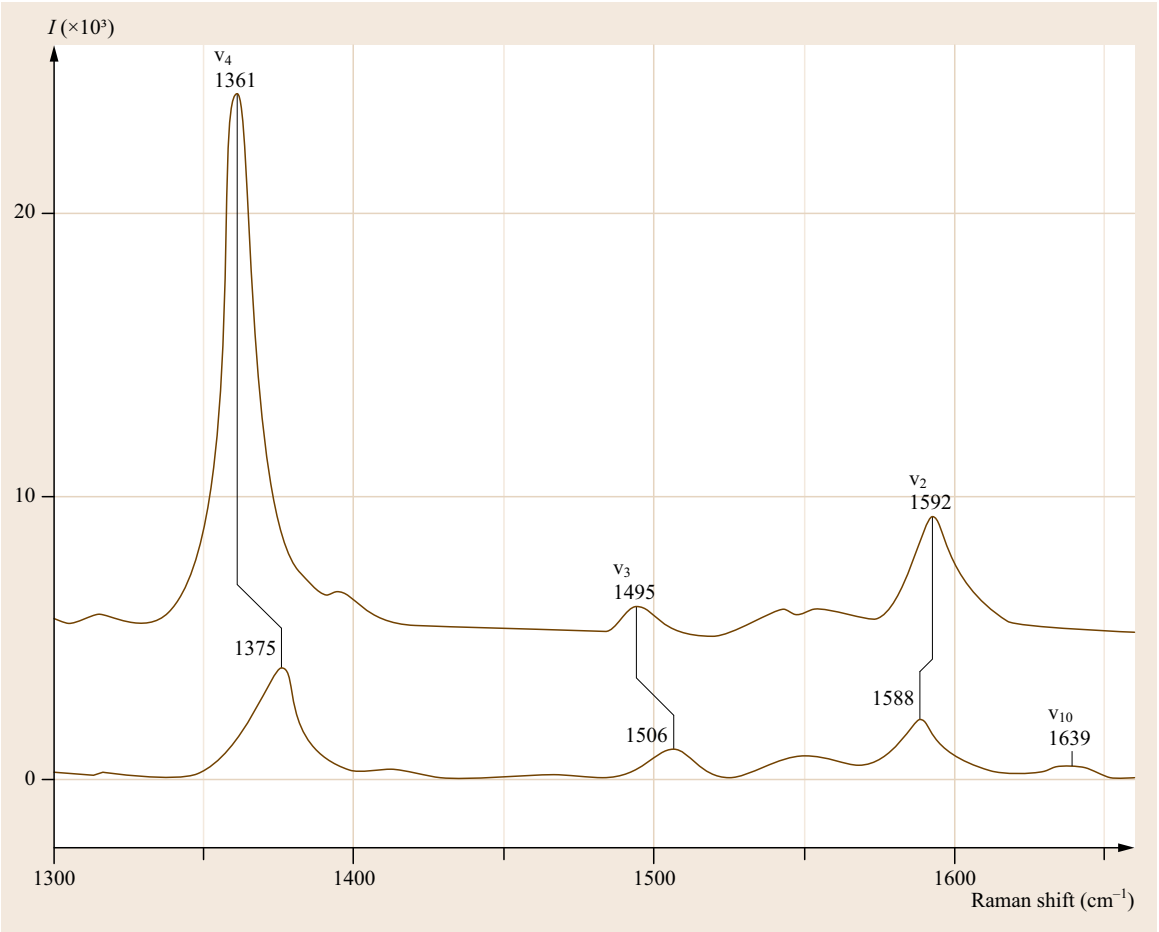


Fig. 13.37 SERR spectra of the reduced (*upper spectrum*) and oxidized (*lower spectrum*) OMCs, obtained at 425 and 0 mV, respectively. The spectra were obtained with excitation at $\lambda = 413$ nm, laser power of 1 mW, and an acquisition time of 90 s. Potentials refer to the Ag/AgCl (KCl 3.0 M) reference electrode (210 mV versus standard hydrogen electrode (SHE)) (after [13.132], courtesy of Wiley)

phy [13.141], colloidal metal nanoparticles, and electrodeposition over polystyrene nanospheres, which can be used to create highly reproducible surface structures [13.142, 143]. All of these methods leave the metal surface with small metal particles or aggregates of particles that behave as rough surface features. Electrochemical roughening is a useful method of surface roughening [13.144]. Typical roughening procedures involve sequential oxidative and reductive cycles (ORC). Typically for gold or silver, this is conducted in Cl^- containing electrolyte [13.145, 146].

The best SERS signal enhancements have been reported for Ag and Au, but these metals, particularly Ag, have very limited working potential windows. This can be overcome by depositing overlayers of platinum group metals such as Pt on a SERS active substrate such as silver or gold, using a range of methods including constant current deposition [13.147] and electrochemical replacement of an underpotential-deposited copper or lead monolayer with a Pt-group metal cation [13.148, 149]. As the main component of the SERS enhancement, the electromagnetic (EM) field from the metal plasmon persists several nanometers from the metal surface, such coatings, once thin enough will not interfere too severely with SERS enhancement.

As described, one of the key experimental advantages of Raman spectroscopy is its insensitivity to the water signal that dominates in IR spectroscopy. It is therefore a valuable technique in biological investigations and has been used in a number of spectro-

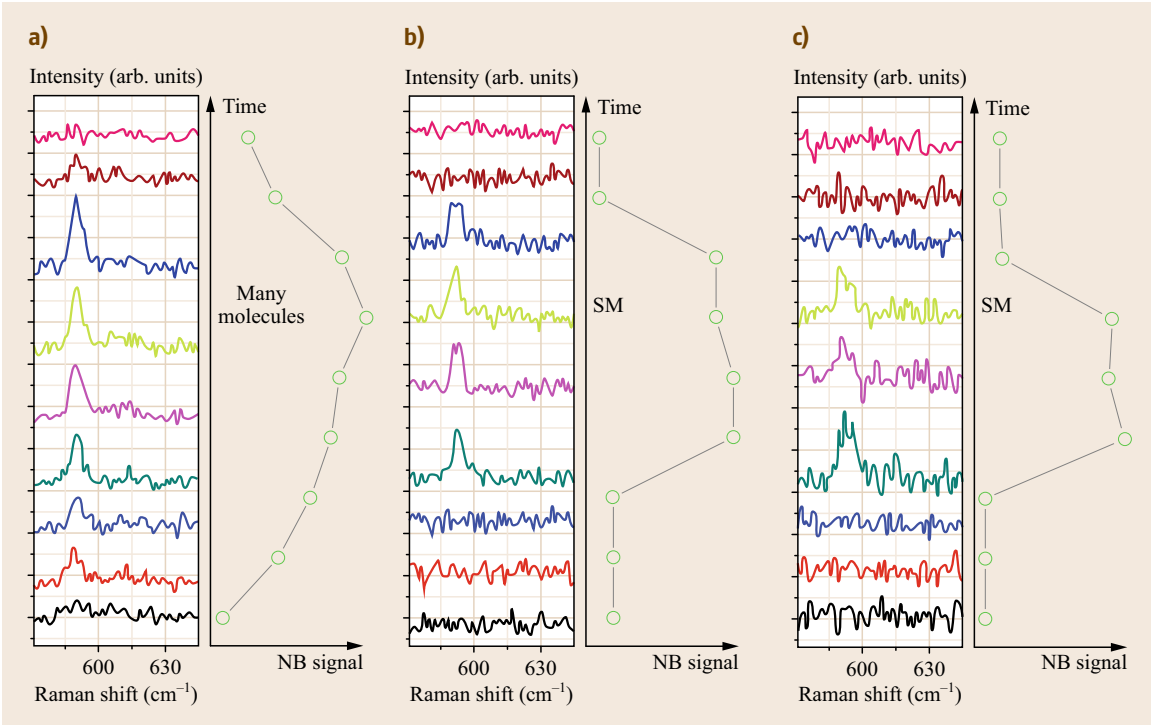


Fig. 13.38a–c Electrochemically modulated bianalyte SERS spectra. Many-molecule and single-molecule SERS electrochemistry. **(a)** Time evolution of SERS spectra over a full electrochemical cycle (scan rate) 0.3 V/s for many molecules. **(b,c)** Two examples of single molecule (SM) events. A smoother time evolution of the signal was obtained for many molecules (25 nM NB with no RH6G in the cell). This is unlike the SM cases (at 2 nM), where a sudden appearance–disappearance of the NB SERS signals was observed (after [13.150], courtesy of Am. Chem. Soc.)

electrochemical studies of biological materials, particularly those involving chromophoric proteins such as cytochrome because of the possibility of using resonant enhancement to improve signal in such materials. The application of spectroelectrochemistry to tissue and cells has been limited to date, but is likely to become more important. In one such study, *Millo* et al. reported on a surface-enhanced resonance Raman spectroelectrochemical study on outer membrane cytochromes (OMCs, Fig. 13.37) in catalytically active microbial biofilms grown under potential control on roughened silver (SERS active) electrodes [13.132]. This is an example of surface-enhanced resonance Raman (SERR), where the Raman excitation line was resonant with the heme iron absorbance in the cytochrome. This enabled selective probing of the heme structure within the OMCs under potential control.

In some instances, the Raman signal achieved using surface enhancement has been so great as to provide single molecule sensitivity to the measurement, a claim that previously had been reserved to fluorescence. This capacity was explored in a spectroelectrochemical experiment by *Etchegoin* et al., using a method developed by this group; the bianalyte SERS method [13.150]. The method is based on the observation that in using two Raman probes with identical Raman cross-sections but different Raman signals one can distinguish a single molecule from ensemble spectrum as the latter will contain signal from both species whereas as single molecule event will contain only signal from one. The method is discussed in detail in the following reference [13.151]. The SERS substrate was prepared from Ag colloids mixed with the two SERS probes, rhodamine 6G and nile blue, each in the range of 2–5 nM concentration. The colloid – dye composite was deposited on a silver working electrode onto which the Raman microscope was trained through an air–water interface. A large area Pt counter electrode and a Ag/AgCl reference electrode were employed. When a single molecule occupies a SERS hot spot, that is, a gap between Ag nanoparticles, this leads to an intense Raman signal that dominates the SERS spectrum. Potential was applied to the working electrode at which

the nile blue but not the rhodamine would be oxidized. Single molecule electrochemistry was then achieved by studying the evolution over time of the spectroscopic change in the nile blue signal at 590 cm^{-1} when it appeared alone in the SERS spectrum. In ensemble measurements that is, mixed events, marker bands for both nile blue and rhodamine 6G appeared within the recorded at 590 and 610 cm^{-1} respectively.

As Fig. 13.38 shows, the response to the applied potential from a single molecule differs from that of an ensemble measurement, where in the former an abrupt transition was observed compared to a broader transition in the ensemble measurement. Figure 13.38 shows the result for a single rhodamine 6G molecular spectrum where this species was followed, via its 610 cm^{-1} over three electrochemical cycles at a scan rate of 1 V/s.

The advantage of this approach is that because the Raman spectra could be unequivocally be assigned to a single molecule the effect of redox cycling on a single molecular species could be studied even though the actual electrochemistry was an ensemble measurement.

SERS has found application across a broad range of electrochemical investigations, including studies of morphological changes associated with redox states [13.152]. It has been used to dynamically determine molecular orientation, and to characterize the structure of adsorbate at an electrode solution interface and has provided insights into how this influences heterogeneous electron transfer [13.153]. Studies focusing on the potential dependence of SERS spectra for water and hydroxyl ions on silver have demonstrated the feasibility of probing solvent molecules within the inner layer of the interface, as well as those associated with the solvation shells of adsorbed cations [13.154, 155]. The relative value of IRRAS and Raman methods in probing the interfacial layer has been discussed. SERS key advantages in this regard arise from:

1. Less restrictive selection rules than IRRAS, which is subject to the surface selection rule that dictates that only adsorbed species with dipole moments perpendicular to the surface are IR active
2. Greater sensitivity, due to electromagnetic and chemical enhancement, and
3. Wider optical ranges [13.156].

Although IRRAS methods can also benefit from surface plasmon enhancement [13.157], the effect is considerably weaker than for SERS. The surface selection rules for RAIRS are not necessarily a disadvantage because they can yield clues to orientation of adsorbates on surfaces. Combination of both techniques to study a single surface can lead to unprecedented structural insights.

13.6 Sum Frequency Generation Spectroelectrochemistry

Sum frequency generation (SFG) is a nonlinear optical process where photons from two lasers undergo coherent mixing. SFG has very high surface selectivity and hence is fundamentally suited to the study of monolayer and submonolayer adsorption. This surface selectivity arises from the fact that even-order nonlinear processes such as SFG are forbidden (in the electric dipole approximation) in media with inversion symmetry: gases, liquids, and crystalline (i. e., isotropic) solids. This symmetry is broken at the interface and hence only surface adsorbates are detected. SFG is sensitive to molecular orientations at an electrode surface. Such analysis is achieved by performing the measurement with different polarizations of the two incoming beams and the generated SFG signal beam. A detailed introduction to SFG is referred to for further reading [13.159].

Since SFG is sensitive to adsorbed species only it is well suited to spectroelectrochemical measurements. For instance, SFG SEC has been used to elucidate the mechanism of the electro-oxidation of ethanol on Pt-black catalyst supported on tungsten carbide (WC) [13.158]. The SFG spectra are shown in Fig. 13.39.

Figure 13.39 shows that two types of resonances were observed. The mode at 1330 cm^{-1} was attributed to the O=C=O asymmetric stretching of acetate, and the mode at 1340–1345 cm^{-1} was identified as the OH and CH wagging combination of EtOH adsorbed via the C atom and the CH_2 wagging of EtOH adsorbed via its oxygen atom. These two modes correspond to the starting reagent and the intermediate. In-situ SFG spectroelectrochemistry demonstrates the co-adsorption of acetate and ethanol, which reveals the power of this technique in mechanistic studies. In a separate publication, the authors also employed sum–difference frequency generation (SFG/DFG) spectroelectrochemistry to the study of the electrodeposition of nitrile compounds from ionic liquids [13.160]. SFG SEC is still in its infancy in relation to FTIR and electronic spectroscopy, but is sure to garner further attention in future.

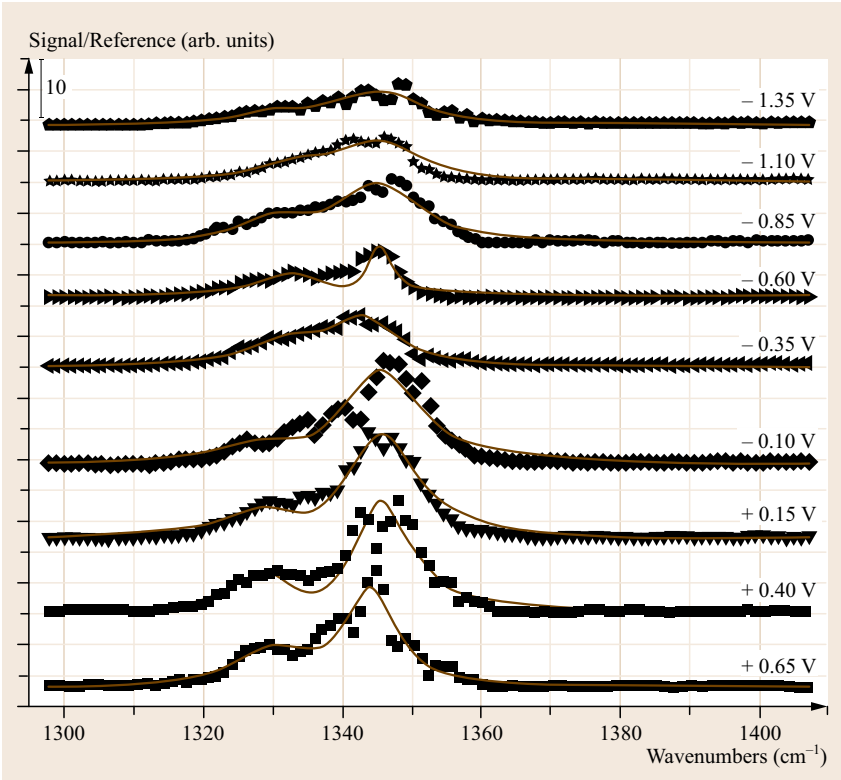


Fig. 13.39 Sequence of SFG spectra measured in the range 0.65 to −1.35 V (versus RHE) on a WC/Pt black electrode in contact with a 0.1 M $HClO_4$ + 0.1 M EtOH solution. The initial spectrum was obtained by prepolarizing the electrode at 0.65 V for 1 h, the potential was set at the desired value just before the acquisition of a spectrum that typically took 20 min (after [13.158], courtsey of Elsevier)

13.7 Conclusions and Outlook

Spectroelectrochemistry has and continues to provide unparalleled structural, mechanistic, and kinetic insights into the redox processes which underlie a range of physical, chemical, and biological systems. Spectroelectrochemistry tends to keep pace with spectroscopic developments and has benefited in particular from the increasing use of microscopy with spectroscopic methods. Interfacial spectroscopic–optical methods such as surface plasmon resonance (SPR) and total internal reflectance fluorescence microscopy (TIRF), can provide very access to study of the electrode interfacial region [13.161] and are likely to find application with potential controlled experiments permitting selective interrogation of the immediate interfacial space within which the redox process is occurring. Spectroscopic imaging under potential control is also likely to expand leading to insights to compliment scanning electrochemical methods but at shorter length scales. Although to date reports of imaging of spectroelectrochemical and interfacial processes using IR and Raman microscopy is limited, this is likely to change as such approaches find application in mapping for example electroactivity and structure of thin films. Z-piezo control on many confocal microscopes allow depth resolved studies which may provide insights into the diffusion fields. Less common spectroscopic methods such as CD have been applied to spectroelectrochemical methods and this is likely to increase, particularly in studies of biological materials where conformational changes in response to electric field or potential responses can be monitored. Spectroelectrochemistry is also likely to see broader application in the investigation of biological applications particularly in the study of biofilms [13.162]. As described in some of the examples given earlier, the variety of problem that is now being addressed by spectroelectrochemistry has diversified enormously from the relatively simple studies of chemical redox reactions which initiated this field. Thus far it has enabled study of single molecule electrochemical switching and the study of charging luminescence blinking of quantum dots.

As new spectroscopic methods develop spectroelectrochemistry tends to follow and the application of electrochemistry to ultra high resolution methods, such as scanning near field optical microscopy (SNOM), are likely to yield interesting outcomes studying interfacial reactions at subdiffraction limit resolutions across materials and biological applications. SNOM can be applied in a range of modes including transmission, reflectance, and emission should be adaptable to potential control. As described, the combination of electrochemistry and single molecule techniques such as SERS and fluorescence is already starting to offer unprecedented insights into redox processes and optical subwavelength methods such as PALM (photo-activated localization microscopy) and STORM (stochastic optical reconstruction microscopy) have emerged over the past 10 years to an extent where they have been commercialized so it is also only a matter of time before such techniques are coupled to electrochemical studies, particularly in the fields of biology and single molecular transistors.

Acknowledgments. The authors gratefully acknowledge the support of Science Foundation Ireland award no. 07/RFP/MASF386 and 10/IN.1/B3025. Thanks to Mary F Fallon for administrative support in preparation of this manuscript.

References

13.1 D.E.G. Austen, P.H. Given, D.J.E. Ingram, M.E. Peover: Electron resonance study of the radicals produced by controlled potential electrolysis of aromatic substances, Nature **182**, 1784–1786 (1958)

13.2 T. Kuwana, R.K. Darlington, D.W. Leedy: Electrochemical studies using conducting glass indicator electrodes, Anal. Chem. **36**, 2023–2025 (1964)

13.3 P.R. Murray, L.J. Yellowlees: EPR spectroelectrochemistry. In: *Spectroelectrochem.*, ed. by W. Kaim, A. Klein (Royal Society of Chemistry, London 2008) pp. 207–231, Chapter 7

13.4 S. Klod, F. Ziegs, L. Dunsch: In situ NMR spectroelectrochemistry of higher sensitivity by large scale electrodes, Anal. Chem. **81**(24), 10262–10267 (2009)

13.5 S. Klod, L. Dunsch: A combination of in situ ESR and in situ NMR spectroelectrochemistry for mechanistic studies of electrode reactions: The case of p-benzoquinone, Magn. Reson. Chem. **49**(2), 725–729 (2011)

13.6 G.R. Fowler: *Introduction to Modern Optics* (Dover, New York 1989)

13.7 I. Ashur, O. Schulz, C.L. McIntosh, I. Pinkas, R. Ros, A.K. Jones: Transparent gold as a platform for adsorbed protein spectroelectrochemistry: Investigation of cytochrome c and azurin, Langmuir **28**, 5861 (2012)

13.8 M.G. Hill, L.D. Rosenhein, K.R. Mann, X. Hai Mu, F.A. Schultz: IR spectroelectrochemical investigation of the disproportionation of bis(benzenemethanethiolato)octacarbonyl-ditungstate(2-), Inorg. Chem. **31**, 4108 (1992)

13.9 B. O'Connor, C. Haughn, K.-H. An, K.P. Pipe, M. Shtein: Transparent and conductive electrodes based on unpatterned, thin metal films, Appl. Phys. Lett. **93**, 223304 (2008)

13.10 W.R. Heineman, T. Kuwana: Mercury platinum optically transparent electrode, Anal. Chem. **43**, 1075 (1971)

13.11 M.G. Walter, E.L. Warren, J.R. McKone, S.W. Boettcher, Q. Mi, E.A. Santori, N.S. Lewis: Solar water splitting cells, Chem. Rev. **110**, 6446 (2010)

13.12 J.J. Walsh, C.T. Mallon, A.M. Bond, T.E. Keyes, R.J. Forster: Enhanced photocurrent production from thin films of Ru(II) metallopolymer/Dawson polyoxotungstate adducts under visible irradiation, Chem. Commun. **48**, 3593 (2012)

13.13 E. Puodziukynaite, J.L. Oberst, A.L. Dyer, J.R. Reynolds: Establishing dual electrogenerated chemiluminescence and multicolor electrochromism in functional ionic transition-metal complexes, J. Am. Chem. Soc. **134**, 968 (2012)

13.14 J.L. Lyon, D.M. Eisele, S. Kirstein, J.P. Rabe, D.A. Vanden Bout, K.J. Stevenson: Spectroelectrochemical investigation of double-walled tubular J-aggregates of amphiphilic cyanine dyes, J. Phys. Chem. C **112**, 1260 (2008)

13.15 C.M. Weber, D.M. Eisele, J.P. Rabe, Y. Liang, X. Feng, L. Zhi, K. Müllen, J.L. Lyon, R. Williams, D.A. Vanden Bout, K.J. Stevenson: Graphene-based optically transparent electrodes for spectroelectrochemistry in the UV-region, Small **6**(2), 184–189 (2010)

13.16 Y.L. Zhong, W. Ng, J.-X. Yang, K.P. Loh: Electrostatically self-assembled polyoxometalates on molecular-dye-functionalized diamond, J. Am. Chem. Soc. **131**, 18293 (2009)

13.17 M.H. Hupert, A. Muck, J. Wang, J. Stotter, Z. Cvackova, S. Haymond, Y. Show, G.M. Swain: Conductive diamond thin-films in electrochemistry, Diam. Relat. Mater. **12**, 1940 (2003)

13.18 J.K. Zak, J.E. Butler, G.M. Swain: Diamond optically transparent electrodes: Demonstration of concept with ferri/ferrocyanide and methyl viologen, Anal. Chem. **73**, 908–914 (2001)

13.19 J. Stotter, S. Haymond, J.K. Zak, Y. Show, Z. Cvackova, G.M. Swain: Optically transparent diamond electrodes for UV-VIS and IR spectroelectrochemistry, Interface **12**, 33–38 (2003)

13.20 J. Stotter, J. Zak, Z. Behler, Y. Show, G.M. Swain: Optical and electrochemical properties of optically transparent, boron-doped diamond thin

films deposited on quartz, Anal. Chem. **74**, 5924–5930 (2002)
13.21 H.B. Martin, P.W. Morrison: Application of a diamond thin film as a transparent electrode for in situ infrared spectroelectrochemistry, Electrochem. Solid-State Lett. **4**, E17 (2001)
13.22 J.J. Walsh, J. Zhu, Q. Zeng, R.J. Forster, T.E. Keyes: Self assembled composites of luminescent Ru(II) metallopolymers and the Dawson polyoxometalate α-$[Mo_{18}O_{54}(SO_4)_2]^{4-}$, Dalton Trans. **41**, 9928–9937 (2012)
13.23 Y.L. Zhong, A. Midya, Z. Ng, Z.-K. Chen, M. Daenen, M. Nesladek, K.P. Loh: Diamond-based molecular platform for photoelectrochemistry, J. Am. Chem. Soc. **130**, 17218–17219 (2008)
13.24 G.R. Salazar Banda, Y. Einaga, C.A. Martinez-Huitle: New trends on the boron-doped diamond electrode: From fundamental studies to applications, Int. J. Electrochem. **2012**, 548504 (2012)
13.25 R.R. Wang, J. Sun, L.A. Gao, J. Zhang: Base and acid treatment of SWCNT-RNA transparent conductive films, ACS Nano **4**, 4890–4896 (2010)
13.26 D. Zhang, R. Wang, M. Wen, D. Weng, X. Cui, J. Sun, H. Li, Y. Lu: Synthesis of ultralong copper nanowires for high-performance transparent electrodes, J. Am. Chem. Soc. **134**, 14283–14286 (2012)
13.27 W. Kaim, J. Fiedler: Spectroelectrochemistry: The best of two worlds, Chem. Soc. Rev. **38**, 3373–3382 (2009)
13.28 A. Colina, J. López-Palacios, A. Heras, V. Ruiz, L. Fuente: Digital simulation model for bidimensional spectroelectrochemistry, J. Electroanal. Chem. **553**, 87–95 (2003)
13.29 E.I. Rogers, D.S. Silvester, D.L. Poole, L. Aldous, C. Hardacre, R.G. Compton: Voltammetric characterization of the ferrocene/ferrocenium and cobaltocenium/cobaltocene redox couples in RTILs, J. Phys. Chem. C **112**, 2729–2735 (2008)
13.30 D.A. Scherson, S. Sarangapani, F.L. Urbach: Thin-layer spectroelectrochemical cell, Anal. Chem. **57**(7), 1501–1503 (1985)
13.31 D. Collison, F.E. Mabbs, E.J.L. McInnes, K.J. Taylor, A.J. Welch, L.J. Yellowlees: Electrochemical and spectroelectrochemical studies on platinum complexes containing 2,2′-bipyridine, J. Chem. Soc. Dalton Trans. **3**, 329–334 (1996)
13.32 X.Q. Lin, K.M. Kadish: Vacuum-tight thin-layer spectroelectrochemical cell with a doublet platinum gauze working electrode, Anal. Chem. **57**(7), 1498–1501 (1985)
13.33 M.B.G. Pilkington, B.A. Coles, R.G. Compton: Construction of an optically transparent thin-layer-electrode cell for use with oxygen-sensitive species in aqueous and nonaqueous solvents, Anal. Chem. **61**, 1787–1789 (1989)
13.34 I. Bedja, S. Hotchandani, P.V. Kamat: Photoelectrochemistry of quantized tungsten trioxide colloids: Electron storage, electrochromic, and photoelectrochromic effects, Phys. Chem. **97**(42), 11064–11070 (1993)
13.35 R.A. Wilson, T.S. Pinyayev, N. Membreno, W.R. Heineman: Rapid prototyped optically transparent thin-layer electrode holder for spectroelectrochemistry in bench-top spectrophotometers, Electroanalysis **22**, 2162–2166 (2010)
13.36 A.T. Hubbard, F.C. Anson: The theory and practice of electrochemistry with thin layer cells. In: *Electroanalytical Chemistry*, Vol. 4, ed. by A.J. Bard (Marcel Dekker, New York 1970) pp. 129–214
13.37 L. van het Goor, P.Th. van Duijnen, C. Koper, L.W. Jenneskens, R.W.A. Havenith, F. Hartl: π-dimerization of pleiadiene radical cations at low temperatures revealed by UV–VIS spectroelectrochemistry and quantum theory, J. Solid State Electrochem. **15**, 2107–2117 (2011)
13.38 T. Chen, S.J. Dong, Y.W. Xie: Influence of the ohmic polarization effect on thin-layer spectroelectrochemistry, J. Electroanal. Chem. **379**, 239–245 (1994)
13.39 R.G. Compton, J. Winkler, D.J. Riley, S.D. Bearpark: Spectrofluorometric hydrodynamic voltammetry – Investigation of reactions at solid–liquid interfaces, J. Phys. Chem. **98**, 6818–6825 (1994)
13.40 Y. Halpin, D. Dini, H.M. Younis Ahmed, L. Cassidy, W.R. Browne, J.G. Vos: Excited state localization and internuclear interactions in asymmetric ruthenium(II) and osmium(II) bpy/tpy based dinuclear compounds, Inorg. Chem. **49**, 2799–2807 (2010)
13.41 T.E. Keyes, R.J. Forster, P.M. Jayaweera, C.G. Coates, J.J. McGarvey, J.G. Vos: Modulation of electronic coupling across dioxolene-bridged osmium and ruthenium dinuclear complexes, Inorg. Chem. **37**(22), 5925–5932 (1998)
13.42 R.J. Forster, J.G. Vos: Synthesis, characterization and properties of a series of osmium- and ruthenium-containing metallopolymers, Macromolecules **23**, 4372–4377 (1990)
13.43 N.S. Hush: Intervalence-transfer absorption Part 2. Theoretical considerations and spectroscopic data, Prog. Inorg. Chem. **8**, 391–444 (1967)
13.44 M.B. Robin, P. Day: Mixed-valence chemistry: A survey and classification, Adv. Inorg. Radiochem. **10**, 247–422 (1967)
13.45 Q. Zeng, A. McNally, T.E. Keyes, R.J. Forster: Three colour electrochromic metallopolymer based on a ruthenium phenolate complex bound to poly(4-vinyl)pyridine, Electrochem. Commun. **10**, 466–470 (2008)
13.46 K. Wagner, R. Byrne, M. Zanoni, S. Gambhir, L. Dennany, R. Breukers, M. Higgins, P. Wagner, D. Diamond, G.G. Wallace, D.L. Officer: A multiswitchable poly(terthiophene) bearing a spiropyran functionality: Understanding photo- and electrochemical control, J. Am. Chem. Soc. **133**, 5453–5462 (2011)
13.47 T.E. Keyes, D. Leane, R.J. Forster, C.G. Coates, J.J. McGarvey, M.N. Nieuwenhuyzen, E. Figgemeier, J.G. Vos: Redox and spectroscopic orbitals in Ru(II) and Os(II) phenolate complexes, Inorg. Chem. **41**, 5721–5732 (2002)

13.48 C. Baffert, J.F. Boas, A.M. Bond, P. Kögerler, D.-L. Long, J.R. Pilbrow, L. Cronin: Experimental and theoretical investigations of the sulfite-based polyoxometalate cluster redox series: α- and β-$[Mo_{18}O_{154}(SO_3)_2]^{4-/5-/6-}$, Chem. Eur. J. **12**, 8472 (2006)

13.49 D.-L. Long, R. Tsunashima, L. Cronin: Polyoxometalates: Building blocks for functional nanoscale systems, Angew. Chem. Int. Ed. **49**, 1736–1758 (2010)

13.50 J.B. Cooper, D.M. Way, A.M. Bond, A.G. Wedd: A green heteropoly blue: Isolation of a stable, odd oxidation level in a Dawson molybdate anion, $[S_2Mo_{18}O_{62}]^{5-}$, Inorg. Chem. **32**(2), 2416–2420 (1993)

13.51 H.E. Toma, K. Araki: Spectroelectrochemical characterization of organic and metal-organic compounds, Curr. Org. Chem. **6**, 21–34 (2002)

13.52 E.E. Bancroft, H.N. Blount, F.M. Hawkridge: *Chapter 2*, Spectroelectrochemical determination of heterogeneous electron transfer kinetic parameters. In: Electrochemical and Spectrochemical Studies of Biological Redox Components, Vol. 201 (American Chemical Society, New York 1982) pp. 23–49

13.53 Y. Astuti, E. Topoglidis, P.B. Briscoe, A. Fantuzzi, G. Gilardi, J.R. Durrant: Proton-coupled electron transfer of flavodoxin immobilized on nanostructured tin dioxide electrodes: Thermodynamics versus kinetics control of protein redox function, J. Am. Chem. Soc. **126**, 8001–8009 (2004)

13.54 V. Balland, S. Lecomte, B. Limoges: Characterization of the electron transfer of a ferrocene redox probe and a histidine-tagged hemoprotein specifically bound to a nitrilotriacetic-terminated self-assembled monolayer, Langmuir **25**, 6532–6542 (2009)

13.55 S.J. Marritt, G.L. Kemp, X. Li, J.R. Durrant, M.R. Cheesman, J.N. Butt: Spectroelectrochemical characterization of a pentaheme cytochrome in solution and as electrocatalytically active films on nanocrystalline metal-oxide electrodes, J. Am. Chem. Soc. **130**, 8588 (2008)

13.56 G.L. Kemp, S.J. Marritt, X. Li, J.R. Durrant, M.R. Cheesman, J.N. Butt: Opportunities for mesoporous nanocrystalline SnO_2 electrodes in kinetic and catalytic analyses of redox proteins, Biochem. Soc. Trans. **37**, 368–372 (2009)

13.57 P.A. Ash, K.A. Vincent: Spectroscopic analysis of immobilised redox enzymes under direct electrochemical control, Chem. Commun. **48**, 1400–1409 (2012)

13.58 C.A. Schroll, S. Chatterjee, W.R. Heineman, S.A. Bryan: Semi-infinite linear diffusion spectroelectrochemistry on an aqueous micro-drop, Anal. Chem. **83**, 4214–4219 (2011)

13.59 N.J. Simmons, M.D. Porter: Long optical path length cell for thin-layer spectroelectrochemistry, Anal. Chem. **69**, 2866–2869 (1997)

13.60 E. Ventosa, A. Colina, A. Heras, A. Martínez, O. Orcajo, V. Ruiz, J. López-Palacios: Electrochemical, spectroscopic and electrogravimetric detection of oligomers occluded in electrochemically synthesized poly(3,4-ethylenedioxythiophene) films, Electrochim. Acta **53**, 4219–4227 (2008)

13.61 D. Daniel, I.G.R. Gutz: Long-optical-path thin-layer spectroelectrochemical flow cell with inexpensive gold electrodes, Electroanalysis **13**, 681–685 (2001)

13.62 J.-B. He, S.-J. Yuan, J.-Q. Du, X.-R. Hu, Y. Wang: Voltammetric and spectral characterization of two flavonols for assay-dependent antioxidant capacity, Bioelectrochem. **75**, 110–116 (2009)

13.63 J.-B. He, Y. Wang, N. Deng, X.-Q. Lin: Study of the adsorption and oxidation of antioxidant rutin by cyclic voltammetry–voltabsorptometry, Bioelectrochem. **71**, 157–163 (2007)

13.64 H.M.Y. Ahmed, N. Coburn, D. Dini, J.J.D. de Jong, C. Villani, W.R. Browne, J.G. Vos: Application of circular dichroism spectroscopy in the study of mixed-valence asymmetric ruthenium polypyridyl complexes, Inorg. Chem. **50**, 5861 (2011)

13.65 S.B. Mendes, S.S. Saavedra: On probing molecular monolayers: A spectroscopic optical waveguide approach of ultra-sensitivity, Opt. Express **4**(2), 449–456 (1999)

13.66 K. Takahashi, F. Kusu: Real time measurement of concentration ratio at an electrode/solution interface by calculating the inverse Laplace transform of SOWG spectroscopy, J. Electroanal. Chem. **628**(1), 1–6 (2009)

13.67 P.G. Miney, M.V. Schiza, M.L. Myrick: A new optically reflective thin layer electrode (ORTLE) window: Gold on a thin porous alumina film used to observe the onset of water reduction, Electroanalysis **16**, 113–119 (2004)

13.68 N.R. de Tacconi, R.O. Lezna, R. Konduri, F. Ongeri, K. Rajeshwar, F.M. MacDonnell: Influence of pH on the photochemical and electrochemical reduction of the dinuclear ruthenium complex, $[(phen)_2Ru(tatpp)Ru(phen)_2]Cl_4$, in water: Proton-coupled sequential and concerted multielectron reduction, Chem. Eur. J. **11**, 4327–4339 (2005)

13.69 R.L. Musselman, R.W. Larsen, B.M. Hoffman: Electronic spectra of porphyrins in the solid state: Newly observed transitions, collective and structural effects and protein-mimicking environments, Coord. Chem. Rev. **257**, 369–380 (2013)

13.70 R.J. Gale (Ed.): *Spectroelectrochemistry, Theory and Practice* (Plenum, New York 1988)

13.71 R. Sydam, M. Deepa, A.K. Srivastava: Electrochromic device response controlled by an in situ polymerized ionic liquid based gel electrolyte, RSC Adv. **2**(24), 9011–9021 (2012)

13.72 C.T. Mallon, R.J. Forster, T.E. Keyes: Fabrication of gold sphere to cuboid nanoarrays using PDMS templates, Chem. Commun. **47**, 7605–7607 (2011)

13.73 I.S. Zavarine, C.P. Kubiak: A versatile variable temperature thin layer reflectance spectroelectrochemical cell, J. Electroanal. Chem. **495**, 106–109 (2001)

13.74 M.G. Hill, J.P. Bullock, T. Wilson, P. Bacon, C.P. Blaine, K. Mann: Infrared spectroelectrochemistry of $[Rh(TM4)_4M(CO)_5]_2^{2+}$ (TM4=2,5-diisocyano-2,5-dimethylhexane; M=Re, Mn): Electron transfer-promoted metal-metal bond cleavage and formation, Inorg. Chim. Acta **226**, 61–68 (1994)

13.75 C.A. Schroll, S. Chatterjee, W.R. Heineman, S.A. Bryan: Thin-layer spectroelectrochemistry on an aqueous microdrop, Electroanalysis **24**, 1065–1070 (2012)

13.76 P.A. Flowers, K.A. Arnett: Fiber optic spectroelectrochemical sensing for in situ determination of metal ions, Spectrosc. Lett. **40**, 501–511 (2007)

13.77 P. Kubelka, F. Munk: Ein Beitrag zur Optik der Farbanstriche, Z. tech. Phys. **12**, 593–601 (1931)

13.78 U. Schröder, F. Scholz: Microscopic in situ diffuse reflectance spectroelectrochemistry of solid state electrochemical reactions of particles immobilized on electrodes, J. Solid State Electrochem. **1**(1), 62–67 (1997)

13.79 J.D. Schuttlefield, V.H. Grassian: ATR-FTIR spectroscopy in the undergraduate chemistry laboratory: Part I. Fundamentals and examples, J. Chem, Ed. **85**, 279–281 (2008)

13.80 J. Tarabek, P. Rapta, M. Kalbac, L. Dunsch: In situ spectroelectrochemistry of poly(N,N'-ethylenebis(salicylideneiminato)Cu(II)), Anal. Chem. **76**(19), 5918–5923 (2004)

13.81 I.T. Bae, M. Sandifer, Y.W. Lee, D.A. Tryk, C.N. Sukenik, D.A. Scherson: In situ fourier transform infrared spectroscopy of molecular adsorbates at electrode-electrolyte interfaces: A comparison between internal and external reflection modes, Anal. Chem. **67**(24), 4508–4513 (1995)

13.82 D.R. Dunphy, S.B. Mendes, S.S. Saavedra, N.R. Armstrong: The electroactive integrated optical waveguide: Ultrasensitive spectroelectrochemistry of submonolayer adsorbates, Anal. Chem. **69**, 3086–3094 (1997)

13.83 M. Mazurenka, L. Wilkins, J.V. Macpherson, P.R. Unwin, S.R. Mackenzie: Evanescent wave cavity ring-down spectroscopy in a thin-layer electrochemical cell, Anal. Chem. **78**, 6833–6839 (2006)

13.84 M.D. Wheeler, S.M. Newman, A.J. Orr-Ewing, M.N.R. Ashfold: Cavity ring-down spectroscopy, J. Chem. Soc. Faraday Trans. **94**, 337–351 (1998)

13.85 G. Berden, R. Peeters, G. Meijer: Cavity ring-down spectroscopy: Experimental schemes and applications, Int. Rev. Phys. Chem. **19**, 565–607 (2000)

13.86 M. Schnippering, P.R. Unwin, J. Hult, T. Laurila, C.F. Kaminski, J.M. Langridge, R.L. Jones, M. Mazurenka, S.R. Mackenzie: Evanescent wave broadband cavity enhanced absorption spectroscopy using supercontinuum radiation: A new probe of electrochemical processes, Electrochem. Commun. **10**, 1827–1830 (2008)

13.87 R.J. Forster, P. Bertoncello, T.E. Keyes: Electrogenerated chemiluminescence, Annu. Rev. Anal. Chem. **2**, 359–385 (2009)

13.88 M.J. Simone, W.R. Heineman, G.P. Kreishman: Long optical path electrochemical cell for absorption or fluorescence spectrometers, Anal. Chem. **54**, 2382–2384 (1982)

13.89 J.-S. Yu, T.-Y. Zhou: The electrochemistry and thin-layer luminescence spectroelectrochemistry of rhodamine 6G at a 4,4'-bipyridine-modified gold electrode, J. Electroanal. Chem. **504**, 89 (2001)

13.90 F. Miomandre, C. Allain, G. Clavier, J.-F. Audibert, R. Pansu, P. Audebert, F. Hartl: Coupling thin layer electrochemistry with epifluorescence microscopy: An expedient way of investigating electrofluorochromism of organic dyes, Electrochem. Comm. **13**, 574 (2011)

13.91 P. Bertoncello, E.T. Kefalas, Z. Pikramenou, P.R. Unwin, R.J. Forster: Adsorption dynamics and electrochemical and photophysical properties of thiolated ruthenium 2,2'-bipyridine monolayers, J. Phys. Chem. B **110**, 10063 (2006)

13.92 Y.F. Lee, J.R. Kirchhoff: Absorption and luminescence spectroelectrochemical characterization of a highly luminescent rhenium(II) complex, J. Am. Chem. Soc. **116**, 3599 (1994)

13.93 L. Dennany, C.F. Hogan, T.E. Keyes, R.J. Forster: Effect of surface immobilization on the electrochemiluminescence of ruthenium-containing metallopolymers, Anal. Chem. **78**, 1412–1417 (2006)

13.94 C. Galland, Y. Ghosh, A. Steinbrük, M. Sykora, J.A. Hollingsworth, V.I. Klimov, H. Htoon: Two types of luminescence blinking revealed by spectroelectrochemistry of single quantum dots, Nature **479**, 203–207 (2011)

13.95 T.E. Keyes, B. Evrard, J.G. Vos, C. Brady, J.J. McGarvey, P. Jayaweera: Electronic and photophysical properties of a novel phenol bound dinuclear ruthenium complex: Evidence for a luminescent mixed valence state, Dalton Trans. **15**, 2341–2346 (2004)

13.96 Z. Ding, R.G. Wellington, P.F. Brevet, H.H. Girault: Spectroelectrochemical studies of $Ru(bpy)_3^{2+}$ at the water/1,2-dichloroethane interface, J. Phys. Chem. **100**, 10658–10663 (1996)

13.97 R.J. Forster, T.E. Keyes: Redox properties of ground and electronically excited states: $[Ru(bpy)_2Qbpy]^{2+}$ monolayers, J. Phys. Chem. **102**, 10004–10012 (1998)

13.98 M. Krejcik, M. Danek, F. Hartl: Simple construction of an infrared optically transparent thin-layer electrochemical cell: Applications to the redox reactions of ferrocene, $Mn_2(CO)_{10}$ and $Mn(CO)_3$(3,5-di-t-butyl-catecholate)$^-$, J. Electroanal. Chem. Interfacial Electrochem. **317**, 179–187 (1991)

13.99 F. Hartl, H. Luyten, H.A. Nieuwenhuis, G. Schoemaker: Versatile cryostated optically transparent thin-layer electrochemical (OTTLE) cell for variable-temperature UV-VIS/IR spectroelectrochemical studies, Appl. Spectrosc. **48**, 1522–1528 (1994)

13.100 J.-N. Chazalviel, B.H. Erne, F. Maroun, F. Ozanam: New directions and challenges in modern electrochemistry: In situ infrared spectroscopy of the semiconductor/electrolyte interface, J. Elec-

troanal. Chem. **502**, 180–190 (2001)
13.101 A.J. Healy, H.A. Reeve, K.A. Vincent: Development of an infrared spectroscopic approach for studying metalloenzyme active site chemistry under direct electrochemical control, Faraday Discuss. **148**, 345–357 (2011)
13.102 S.P. Best, S.J. Borg, K.A. Vincent: Infrared spectroelectrochemistry. In: *Spectroelectrochemistry*, (Royal Society of Chemistry, London 2008), Chap. 1
13.103 S. Pons, T. Davidson, T.A. Bewick: Vibrational spectroscopy of the electrode-electrolyte interface: Part IV – Fourier transform infrared spectroscopy: Experimental considerations, J. Electroanal. Chem. **160**, 63–71 (1984)
13.104 S. Pons: The use of fourier transform infrared spectroscopy for in situ recording of species in the electrode-electrolyte solution interphase, J. Electroanal. Chem. **150**, 495–504 (1983)
13.105 J.D. Mozo, M. Dominguez, E. Roldan, J.M. Rodrigues Mellado: Development of a spectroelectrochemistry assembly (SNIFTIRS) based on a commercial spectrophotometer test with the ferrocyanide/ferricyanide redox couple, Electroanalysis **12**, 767–773 (2000)
13.106 Z. Su, V. Climent, J. Leitch, V. Zamlynny, J.M. Feliu, J. Lipkowski: Quantitative SNIFTIRS studies of (bi)sulfate adsorption at the Pt(111) electrode surface, Phys. Chem. Chem. Phys. **12**, 15231–15239 (2010)
13.107 A.S. Viana, A.H. Jones, L.M. Abrantes, M. Kalaji: Redox induced orientational changes in a series of short chain ferrocenyl alkyl thiols self-assembled on gold(111) electrodes, J. Electroanal. Chem. **500**, 290–298 (2001)
13.108 C.M. Pharr, P.R. Griffiths: Infrared spectroelectrochemical analysis of adsorbed hexacyanoferrate species formed during potential cycling in the ferrocyanide/ferricyanide redox couple, Anal. Chem. **69**, 4673–4679 (1997)
13.109 R. Mendelsohn, G. Mao, C.R. Flach: Infrared reflection–absorption spectroscopy: Principles and applications to lipid–protein interaction in Langmuir films, Biochim. Biophys. Acta **1798**(4), 788–800 (2010)
13.110 M. Tagliazucchi, L.P. Méndez De Leo, A. Cadranel, L.M. Baraldo, E. Völker, C. Bonazzola, E.J. Calvo, V. Zamlynny: PM IRRAS spectroelectrochemistry of layer-by-layer self-assembled polyelectrolyte multilayers, J. Electroanal. Chem. **649**, 110–118 (2010)
13.111 C. Combellas, F. Kanoufi, S. Sanjuan, C. Slim, Y. Tran: Electrochemical and spectroscopic investigation of counterions exchange in polyelectrolyte brushes, Langmuir **25**, 5360–5370 (2009)
13.112 B.-K. Jin, L. Li, J.-L. Huang, S.-Y. Zhang, Y.-P. Tian, J.-X. Yang: IR spectroelectrochemical cyclic voltabsorptometry and derivative cyclic voltabsorptometry, Anal. Chem. **81**, 4476–4481 (2009)
13.113 Z.O. Araci, C.R. Shallcross, N.R. Armstrong, S. Scott Saavedra: Potential-modulated attenuated total reflectance characterization of charge injection processes in monolayer-tethered CdSe nanocrystals, J. Phys. Chem. Lett. **1**, 1900–1905 (2010)
13.114 X. Jiang, E. Zaitseva, M. Schmidt, F. Siebert, M. Engelhard, R. Schlesinger, K. Ataka, R. Vogel, J. Heberle: Resolving voltage-dependent structural changes of a membrane photoreceptor by surface-enhanced IR difference spectroscopy, Proc. Nat. Acad. Sci., Vol. 105 (2008) pp. 12113–12117
13.115 S.R. Domingos, M.R. Panman, B.H. Bakker, F. Hartl, W.J. Buma, S. Woutersen: Amplifying vibrational circular dichroism by manipulation of the electronic manifold, Chem. Commun. **48**, 353 (2012)
13.116 B.W. Johnson, J. Bauhofer, K. Doblhofer, B. Pettinger: Practical considerations of the IR attenuated-total-reflection (IR-ATR) technique for electrochemical investigations, Electrochim. Acta **37**, 2321–2329 (1992)
13.117 F. Hahn, Y.-L. Mathis, A. Bonnefont, F. Maillard, C.A. Melendres: In situ synchrotron far-infrared spectromicroscopy of a copper electrode at grazing incidence angle, J. Synchrotron. Rad. **14**, 446–448 (2007)
13.118 M.D. Ryan, L. Li: Far-infrared spectroelectrochemistry: A study of linear molybdenum/iron/sulfur clusters, Inorg. Chem. Acta **357**, 1332–1336 (2004)
13.119 Y. El Khoury: Mid and Far Infrared Spectroelectrochemical Studies on the Metal-Ligand Interactions in Respiratory Chain Enzymes, Dissertation (Univ. Strasbourg, Strasbourg 2010)
13.120 L.A. Nafie: Theory of vibrational circular dichroism and infrared absorption: Extension to molecules with low-lying excited electronic states, J. Phys. Chem. A **108**, 7222 (2004)
13.121 D.A. Long: *The Raman Effect* (Wiley, Chichester 2002)
13.122 W. Plieth, G.S. Wilson, C.G. De La Fe, C. Gutierrez: Spectroelectrochemistry: A survey of in situ spectroscopic techniques, Pure Appl. Chem. **70**, 1395–1414 (1998)
13.123 Z.Q. Tian, B. Ren: Raman spectroscopy of electrode surfaces. In: *Encyclopaedia of Electrochemistry*, Vol. 3, (Wiley, New York 2014) pp. 572–659
13.124 I.C.G. Thanos: An in-situ Raman spectroscopic study of the reduction of HNO_3 on a rotating silver electrode, J. Electroanal. Chem. **200**, 31–247 (1986)
13.125 A.J. McQuillan, P.J. Hendra, M. Fleischmann: Raman spectroscopic investigation of silver electrodes, J. Electroanal. Chem. **65**, 933–944 (1975)
13.126 T.E. Keyes, R.J. Forster, A.M. Bond, W. Miaou: Electron self-exchange in the solid-state: Cocrystals of hydroquinone and bipyridyl triazole, J. Am. Chem. Soc. **123**, 2877–2884 (2001)
13.127 J.E. Pemberton, A. Shen: Electrochemical and surface enhanced Raman scattering studies of bromide ion adsorption at silver electrodes in a series of normal alcohols, Phys. Chem. Chem. Phys. **1**, 5671–5676 (1999)
13.128 M.H. Schoenfisch, J.E. Pemberton: Effects of electrolyte and potential on the in situ structure of alkanethiol self-assembled monolayers on silver,

Langmuir **15**, 509–517 (1999)
13.129 C. Mallon, A. Walshe, R.J. Forster, T.E. Keyes, R.J. Baker: Physical characterization and reactivity of the uranyl peroxide $[UO_2(\eta(2)\text{-}O_2)(H_2O)_2]2H_2O$: Implications for storage of spent nuclear fuels, Inorg. Chem. **51**, 8509–8515 (2012)
13.130 R.J. Forster, T.E. Keyes, A.M. Bond: Protonation effects on the structure and homogeneous charge transport dynamics of solid state osmium bis(bipyridyl)tetrazine chloride films, J. Phys. Chem. B **104**(27), 6389–6396 (2000)
13.131 T.E. Keyes, D. Leane, R.J. Forster, C.G. Coates, J.J. McGarvey, J.G. Vos: Redox and spectroscopic orbitals in Ru(II) and Os(II) phenolate complexes, Inorg. Chem. **41**, 5721 (2002)
13.132 D. Millo, F. Harnisch, S.A. Patil, H.K. Ly, U. Schröder, P. Hildebrandt: In situ spectroelectrochemical investigation of electrocatalytic microbial biofilms by surface-enhanced resonance Raman spectroscopy, Angew. Chem. Int. Ed. **50**, 2625–2627 (2011)
13.133 We refer here to vibronic resonance Raman spectroscopy
13.134 J.J. Walsh, D.-L. Long, L. Cronin, A.M. Bond, R.J. Forster, T.E. Keyes: Electronic and photophysical properties of adducts of $[Ru(bpy)_3]^{2+}$ and Dawson-type sulfite polyoxomolybdates $\alpha I\beta$-$[Mo_{18}O_{54}(SO_3)_2]^{4-}$, Dalton Trans. **40**, 2038–2045 (2011)
13.135 Z.-Q. Tian, B. Ren, D.-Y. Wu: Surface-enhanced Raman scattering: From noble to transition metals and from rough surfaces to ordered nanostructures, J. Phys. Chem. B **106**(37), 9463–9483 (2002)
13.136 R. Aroca: *Surface Enhanced Vibrational Spectroscopy* (Wiley, Chichester 2006)
13.137 D.J. Maxwell, S.R. Emory, S.M. Nie: Nanostructured thin-film materials with surface-enhanced optical properties, Chem. Mater. **13**(3), 1082–1088 (2001)
13.138 S. Nie, S.R. Emory: Probing single molecules and single nanoparticles by surface-enhanced raman scattering, Science **275**, 1102–1106 (1997)
13.139 T.R. Jensen, M.D. Malinsky, C.L. Haynes, R.P. Van Duyne: Nanosphere lithography: Tunable localized surface plasmon resonance spectra of silver nanoparticles, J. Phys. Chem. B **104**, 10549–10556 (2000)
13.140 M. Moskovits: Surface-enhanced spectroscopy, Rev. Mod. Phys. **57**(3), 783–826 (1985)
13.141 L.A. Dick, A.D. McFarland, C.L. Haynes: Metal film over nanosphere (MFON) electrodes for surface-enhanced Raman spectroscopy (SERS), J. Phys. Chem. B **106**, 853–860 (2002)
13.142 K. Kneipp, H. Kneipp, I. Itzkan, R.R. Dasar, M.S. Feld: Ultrasensitive chemical analysis by Raman spectroscopy, Chem. Rev. **99**, 2957–2976 (1999)
13.143 B. Jose, R. Steffen, U. Neugebauer, E. Sheridan, R. Marthi, R.J. Forster, T.E. Keyes: Emission enhancement within gold spherical nanocavity arrays, Phys. Chem. Chem. Phys. **11**, 10923–10933 (2009)
13.144 D.Y. Wu, Y. Xie, B. Ren, J.W. Yan, B.W. Mao, Z.Q. Tian: Surface enhanced Raman scattering from bare cobalt electrode surfaces, Phys. Chem. Comm. **18**, 89–91 (2001)
13.145 P. Gao, D. Gosztola, L.-W.H. Leung, M.J. Weaver: Surface-enhanced Raman scattering at gold electrodes: Dependence on electrochemical pretreatment conditions and comparisons with silver, J. Electroanal. Chem. **233**, 211–222 (1987)
13.146 S. Byahu, T.E. Furtak: Direct comparison of the chemical properties of single crystal Ag(111) and electrochemically roughened Ag as substrates for surface Raman scattering, Langmuir **7**, 508–513 (1991)
13.147 S. Zou, M.J. Weaver: Surface-enhanced Raman scattering on uniform transition-metal films: Toward a versatile adsorbate vibrational strategy for solid-nonvacuum interfaces?, Anal. Chem. **70**, 2387–2395 (1988)
13.148 M.F. Mrozek, Y. Xie, M.J. Weaver: Surface-enhanced Raman scattering on uniform platinum-group overlayers: Preparation by redox replacement of underpotential-deposited metals on gold, Anal. Chem. **73**, 5953–5960 (2001)
13.149 M.F. Mrozek, S.A. Wasileski, M.J. Weaver: Periodic trends in electrode-chemisorbate bonding: Benzonitrile on platinum-group and other noble metals as probed by surface-enhanced Raman spectroscopy combined with density functional theory, J. Am. Chem. Soc. **123**, 12817–12825 (2001)
13.150 E. Cortés, P.G. Etchegoin, E.C. Le Ru, A. Fainstein, M.E. Vela, R.C. Salvarezza: Monitoring the electrochemistry of single molecules by surface-enhanced Raman spectroscopy, J. Am. Chem. Soc. **132**, 18034–18037 (2010)
13.151 E.C. Le Ru, M. Meyer, P.G. Etchegoin: Proof of single-molecule sensitivity in surface enhanced Raman scattering (SERS) by means of a two-analyte technique, J. Phys. Chem. B **110**, 1944–1948 (2006)
13.152 Y.-Y. Song, Z.-D. Gao, J.J. Kelly, X.-H. Xia: Galvanic deposition of nanostructured noble-metal films on silicon, Electrochem. Solid-State Lett. **8**(10), C148–C150 (2005)
13.153 L.A. Dick, A.J. Haes, R.P. Van Duyne: Distance and orientation dependence of heterogeneous electron transfer: A surface-enhanced resonance raman scattering study of cytochrome c bound to carboxylic acid terminated alkanethiols adsorbed on silver electrodes, J. Phys. Chem. B **104**, 11752–11762 (2000)
13.154 Z.Q. Tian, B. Ren: Adsorption and reaction at electrochemical interfaces as probed by surface-enhanced Raman spectroscopy, Annu. Rev. Phys. Chem. **55**, 197–229 (2004)
13.155 Y.X. Chen, S.Z. Zou, K.Q. Huang, Z.Q. Tian: SERS studies of electrode/electrolyte interfacial water part II–librations of water correlated to hydrogen evolution reaction, J. Raman Spectrosc. **29**, 749–756 (1998)

13.156 M.J. Weaver: Raman and infrared spectroscopies as in situ probes of catalytic adsorbate chemistry at electrochemical and related metal-gas interfaces: Some perspectives and prospects, Top. Catal. **8**(1–2), 65–73 (1999)
13.157 R. Kellner, B. Mizaikoff, M. Jakusch, H.D. Wanzenbock, N. Weissenbacher: Surface-enhanced vibrational spectroscopy: A new tool in chemical IR sensing?, Appl. Spectrosc. **51**, 495–503 (1997)
13.158 B. Bozzini, G.P. De Gaudenzi, B. Busson, C. Humbert, C. Six, A. Gayral, A. Tadjeddin: In situ spectroelectrochemical measurements during the electro-oxidation of ethanol on WC-supported Pt-black, based on sum-frequency generation spectroscopy, J. Power Sources **195**, 4119–4123 (2010)
13.159 F. Vidal, A. Tadjeddine: Sum-frequency generation spectroscopy of interfaces, Rep. Prog. Phys. **68**, 1095 (2005)
13.160 B. Bozzini, B. Busson, A. Gayral, C. Humbert, C. Mele, C. Six, A. Tadjeddin: In situ electrochemical SFG/DFG Study of CN^- and nitrile adsorption at Au from 1-Butyl-1-methyl-pyrrolidinium Bis(trifluoromethylsulfonyl) amide ionic liquid ([BMP][TFSA]) containing 4-[2-[1-(2-Cyanoethyl)-1,2,3,4-tetrahydroquinolin-6-yl]diazenyl] benzonitrile (CTDB) and $K[Au(CN)_2]$, Molecules **17**, 7722–7736 (2012)
13.161 J. Shepherd, Y. Yang, D. Bizzotto: Visualization of potential induced formation of water-insoluble surfactant aggregates by epi-fluorescence microscopy, J. Electroanal. Chem. **524**, 54–61 (2002)
13.162 D. Millo: Spectroelectrochemical analyses of electroactive microbial biofilms, Biochem. Soc. Trans. **40**, 1284–1290 (2012)

14. Kinetic Activity in Electrochemical Cells

Yannick Garsany, Karen Swider-Lyons

The oxygen reduction reaction (ORR) is typically the rate-limiting reaction in electrocatalytic energy systems wherein the oxidizer is air, such as proton exchange membrane fuel cells (PEMFCs) or metal–air batteries. The effectiveness of these air-breathing electrochemical technologies hinges on the use of highly active electrocatalysts that can convert O_2 to H_2O (four-electron reaction) rather than the undesirable product H_2O_2 (two-electron reaction). The evaluation of new electrocatalysts in full cells is not practical due to competing contributions of mass transport and I^2R losses in the electrodes to measurements of kinetic activity. This chapter describes characterization of the electrocatalyst kinetic activity in electrochemical cells by rotating disk electrode (RDE) and rotating ring disk electrode (RRDE) methodologies and describes specifically how to apply the methodology to the porous electrodes used in energy systems. When the experimental procedures are executed properly, RDE and RRDE methodologies can be used to determine electrocatalyst ORR activities as a screening tool prior to full cell testing. Detailed methods are given for the accurate determination of the ORR of two standard materials: platinum/carbon in acid for PEMFC cathode catalysts, and MnO_2 in base for metal–air batteries.

14.1 **Evaluation of Pt/VC Electrocatalysts for the ORR** 428
14.1.1 Glassware Cleaning..... 428
14.1.2 Electrocatalyst Ink Formulation, Preparation of Glassy Carbon Electrode Substrate, and Electrocatalyst Thin-Film Electrodes..... 429
14.1.3 Electrochemical Test Protocol for Evaluation of the Thin-Film Electrocatalyst Electrodes 433
14.2 **Electrochemical Characterization of the Pt/VC Electrocatalyst Thin-Film Electrodes by RDE and RRDE** 435
14.2.1 Influence of Pt/VC Thin-Film Electrodes Quality..... 435
14.2.2 Pt ECSA Calculation in Acid..... 435
14.2.3 Pt ECSA Calculation in Base..... 436
14.2.4 ORR Polarization Curves Versus Film Morphology in Acid Electrolyte by RDE..... 437
14.2.5 ORR Measurements of Pt/C in Acid Electrolyte by RRDE 438
14.2.6 Calculation of Electrocatalyst Mass and Specific Activities 439
14.3 **Electrochemical Characterization of Mn_xO_y Thin-Film Electrodes** 440
14.3.1 Mn_xO_y/VC INK#1 Preparation 440
14.3.2 Mn_xO_y/VC INK#2 Preparation..... 441
14.3.3 Comparison ORR Measured for Mn_xO_y/VC INK#1 to ORR Measured Mn_xO_y/VC INK#2..... 441
14.4 **Conclusions** 443
References..... 444

Electrochemical energy conversion devices, ranging from fuel cells (FCs) to metal–air batteries, require low cost, high activity and durable electrocatalysts for the oxygen reduction reaction (ORR) at their cathodes whereby O_2 is reduced by a four-electron process to H_2O. High activity ORR electrocatalysts are critical to FCs, which make electricity efficiently by the electrochemical of a fuel (hydrogen) at their anodes and the electrochemical reduction of an oxidant (oxygen from air) at their cathodes. The most prevalent type of FCs are proton exchange membrane fuel cells (PEMFCs) that use nanoparticles of platinum (or Pt alloys) as electrocatalysts, usually supported on high surface area carbon (HSC) and a acidic solid polymer electrolyte. In metal–air batteries, the fuel is a metal, such as zinc, instead of hydrogen and the electrolyte is a base. The molecular oxygen serves the same role in each electrochemical cell, by serving as the cathode or electron sink for electrons provided by a more negative anode.

The ORR is a very complex multielectron reaction, the kinetics and mechanism of which are influenced by both the electrocatayst and electrolytes (acid or basic). In acidic electrolyte, it is generally accepted that the overall reaction may proceed by two pathways [14.1–3]: a direct four-electron transfer reaction leading to the formation of H_2O (14.1), or by an indirect two-electron transfer reaction leading to the formation of H_2O_2 (14.2). The hydrogen peroxide may be further electrochemically reduced to water (14.3) or undergo chemical decomposition (14.4)

$$O_2 + 4H^+ + 4e^- \rightarrow 2H_2O \quad E^0 = 1.23\,\mathrm{V}\,, \tag{14.1}$$

$$O_2 + 2H^+ + 2e^- \rightarrow H_2O_2 \quad E^0 = 0.67\,\mathrm{V}\,. \tag{14.2}$$

The H_2O_2 may further be electrochemically reduced via

$$H_2O_2 + 2H^+ + 2e^- \rightarrow 2H_2O \quad E^0 = 1.77\,\mathrm{V} \tag{14.3}$$

or a chemical decomposition via

$$2H_2O_2 \rightarrow 2H_2O + O_2\,. \tag{14.4}$$

The ORR reaction in alkaline electrolyte [14.2, 3] may take a four-electron pathway through which the molecular oxygen is directly reduced to OH^- by accepting four electrons, as described in (14.5), or by a two-electron reaction pathway through which the O_2 is reduced to H_2O^-, followed by further reduction of H_2O^-, or its direct decomposition to OH^- as described in (14.6)–(14.8)

$$O_2 + 2H_2O + 4e^- \rightarrow 4OH^- \quad E^0 = 0.401\,\mathrm{V}\,, \tag{14.5}$$

$$O_2 + H_2O + 2e^- \rightarrow HO_2^- + OH^- \quad E^0 = -0.065\,\mathrm{V}\,, \tag{14.6}$$

$$HO_2^- + H_2O + 2e^- \rightarrow 3OH^- \quad E^0 = 0.867\,\mathrm{V}\,, \tag{14.7}$$

$$2HO_2^- \rightarrow 2OH^- + O_2\,. \tag{14.8}$$

A significant number of reaction mechanisms for the oxygen reduction have been proposed, beginning from the very simple model of *Damjanovic* and *Brusic* [14.4] up to very complicated ones (where intermediates such as superoxide and oxygen ions are included) [14.5, 6]. The details of these different models are beyond the scope of this chapter and can be found in the cited references.

Electrochemists tend to prefer noble metal electrocatalysts such as Pt on which the direct four-electron pathway dominates. Pt is also preferred for PEMFCs because it is acid stable. On other acid-stable materials such as carbon and gold, the predominant reduction pathway is via hydrogen peroxide formation. The latter reaction is undesirable because it produces half the electricity of the full reaction to water, and also produces an aggressive chemical oxidizer. However, noble metals are very expensive, so either their minimization in or elimination from electrochemical technologies is highly desirable. Thus, there are massive numbers of publications dedicated yearly to the pursuit of more efficient, less expensive ORR catalysts. Alkaline fuel cells (AFCs) and metal–air batteries can use metal oxides based on Mn, Ni, and Co, but high efficiency and activity is also desireable in AFCs to increase power density.

A key measure of activity is the potential of the ORR, as more power (and energy) is generated as the voltage difference between the cathode and anode increases. Thus the objective is to decrease the overpotential of the electrocatalyst and approach the ideal potential of 1.23 V (14.1). Of course, the Butler–Volmer equation predicts that the reaction cannot occur at 1.23 V, and the kinetic overpotential will force the electrocatalyst to perform at lower voltages, and convert energy to heat rather than electricity. Typical PEMFC cathodes operate near 0.7 V in practice when using a Pt/C electrode, and much effort has been dedicated to increasing that potential to 0.75 or 0.8 V by implementing new electrocatalysts.

The RRDE is a principal tool used to quantitatively determine the extent of the four-electron ORR reaction versus the two-electron reduction to peroxide [14.4–10]. The concept of this measurement is to use a normal rotating disk electrode (RDE) to eliminate mass transport effects associated with O_2 diffusion to measure the kinetics of the ORR during cycling. An additional ring is attached around the disk electrode to detect the reaction products (H_2O_2). With this setup, it is possible to determine whether the electrocatalytic material under study is active for the ORR, and if active whether the reduction reaction proceeds via the four-electron pathway to H_2O (14.1) or the two-electron path to H_2O_2.

RDE methodology can provide a highly accurate measurement of ORR activity and its fundamental approach leads to estimating the electrochemical activity of electrocatalysts under mass transport conditions. While RDE was used for decades to perform mechanistic studies with single crystal disks, in 1994 *Gloaguen* et al. [14.11] proposed a method for depositing high surface area Pt/C electrocatalysts mixed with 5 wt% Nafion solution onto glassy carbon electrode RDE substrates to use RDE in a liquid electrolyte to study the kinetic properties of the practical high surface area electrocatalysts used in energy systems. *Schmidt* et al. [14.12] modified the method proposed by Gloaguen, by using a smaller amount of the Nafion

ionomer in the form of cap over the Pt/C electrode to minimize the diffusion resistance of the thin Nafion film, and showed that the kinetic current densities can be determined directly from the measured currents without extensive mathematical modeling. *Paulus* et al. [14.13] adapted the thin-film Pt/C RDE methodology to the RRDE methodology for characterizing the ORR electrocatalytic activity of high surface area Pt/C, and quantify the mount of hydrogen peroxide produced during the ORR.

One of the fundamental differences between the conditions that the electrocatalyst experiences in a RDE versus an actual air electrode is the analytically defined mass-transport limiting current. In an FC membrane electrode assembly (MEA), the mass-transport depends on a variety of parameters such as the fuel (H_2) and oxidant (O_2) gas flow rates, operating temperature, relative humidity, pressure, diffusion etc. In contrast, the RDE methodology is a hydrodynamic electrochemistry technique and the ORR occurs on the small concentrations of O_2 dissolved in the electrolyte. The RDE methodology enables *forced convection* to set the transport rate of the active reactant species to the working electrode (WE) surface.

In order to obtain detailed information about electron transfer, it is necessary to reduce and quantify the influence of mass transport on the current-potential curves. This can be achieved by using a well-defined convective flow near the electrode surface which improves the mass transport and thus decrease the Nernst layer δ_N with increasing convection.

Rotating electrodes (e.g., disks, rings, or cylinders) provides the opportunity to carry out electrochemical measurements under defined mass-transport conditions by inducing a forced convective mass-flow into the electrolyte. RDE is the most convenient and widely used method, for which the hydrodynamic equations and the convective–diffusion equation have been solved for steady-state conditions [14.15, 16]. A schematic of a RDE is sketched in Fig. 14.1 [14.14].

The RDE consists of a smooth circular electrode embedded in a circular insulator, such as Teflon. The electrode is cut and polished flush with its holder, so that only the bottom end of the working electrode (metal or glassy carbon) is exposed to the working electrolyte. While rotating, the electrode acts in effect like a pump, pulling the electrolyte up to the disk surface along the rotation axis and flinging it outward radially, following the streamlines illustrated in Fig. 14.1b. Knowing the velocities in both vertical and radial direction allows the determination of the mass-transport rate to the disk electrode surface through the diffusion layer thickness δ calculated according to the following equation [14.2, 14]

$$\delta = \frac{1.61 \nu^{1/6} D^{1/3}}{\omega^{1/2}} , \tag{14.9}$$

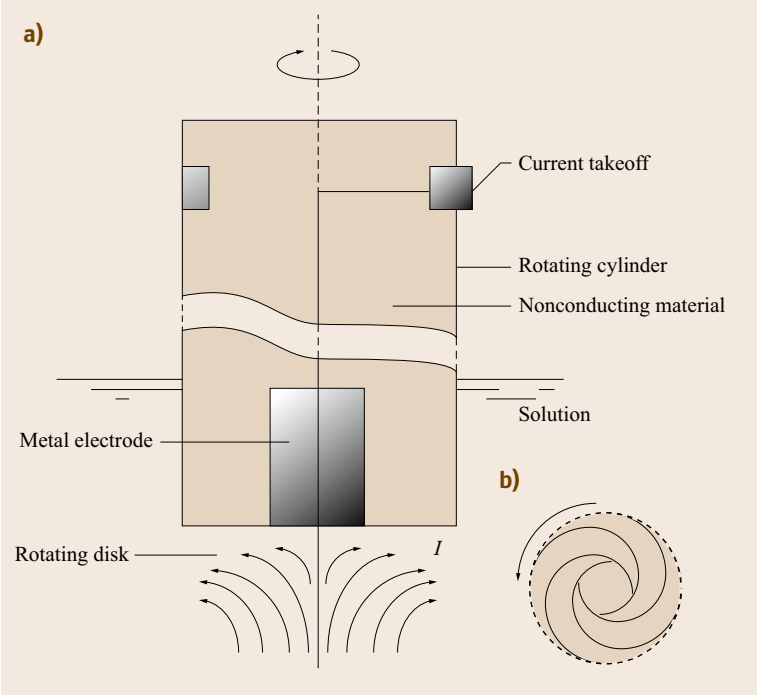


Fig. 14.1 Schematic of hydrodynamic flow over an RDE in solution (after [14.14])

where ν is the kinematic viscosity of the working electrolyte, D is the diffusion coefficient of the reactant in the working electrolyte, and ω is the rotation rate of the disk electrode (rad/s). Consequently, the diffusion layer thickness is dependent on a laminar flow velocity and therefore only depends of the rotation rate of the disk electrode (ω), which can be varied. From this, the thickness of the diffusion layer can be expressed in terms of ω dependence. Assuming Fick's law, the diffusion limiting current density on a working electrode can be described as a function of the diffusion layer thickness as follows

$$j_{\text{lim}} = nFC_0 \frac{D}{\delta} , \tag{14.10}$$

where j_{lim} is the diffusion limiting current density, n is the number of electrons involved in the electrochemical reaction, F is the Faraday constant, and C_0 is the bulk concentration of the reactant. By combining (14.9) and (14.10), an expression for the diffusion limiting current density is found, referred to as the Levich equation, in the following [14.16]

$$j_{\text{lim}} = 0.62nFD^{2/3}\nu^{-1/6}C_0\omega^{1/2} = BC_0\omega^{1/2} , \tag{14.11}$$

B denotes the so-called Levich constant.

When the rotation rate ω of disk electrode is given in revolutions per minute (rpm), (14.11) can be rewritten in the more convenient form as

$$j_{\text{lim}} = 0.20nFD^{2/3}\nu^{-1/6}C_0 \quad [(\text{rpm}^{1/2})] . \tag{14.12}$$

Equation (14.12) shows that the diffusion limiting current density (j_{lim}) is derived directly from the convection of fresh electrolyte to the working electrode surface regardless of the electrode surface properties (electrocatalyst types, surface roughness, etc.) The physical limit of the electrical current generated when using the RDE or RRDE methodology is limited by the delivery rate of fresh electrolyte to the working electrode surface, j_{lim} is strongly dependent on the rotation rate of the disk electrode.

In the absence of any mass transfer effects (i. e., when the current is small in the high potential region $E > 0.90$ V versus reversible hydrogen electrode (RHE)) only kinetic contributions are significant. The relationship between the diffusion limiting, kinetic, and measured current densities is described by the Koutecky–Levich equation as

$$\frac{1}{j} = \frac{1}{j_{\text{k}}} + \frac{1}{j_{\text{diff-lim}}} = \frac{1}{j_{\text{k}}} + \frac{1}{BC_0\omega^{1/2}} , \tag{14.13}$$

where j is the measured current density in the *kinetic region* and j_{k} is the kinetic current density.

Equation (14.13) is very useful for the study of electrode kinetics. A plot of $1/j$ versus $\omega^{-1/2}$ should yield a straight line having an intercept equal to the reciprocal kinetic current (i. e., $1/j_{\text{k}}$). The kinetic current is the current that would be observed in the absence of any mass transport limitations. By repeating the experiment at different potential one can obtain the dependence of j_{k} on potential, and therefore determine the standard rate constant for the electrochemical reaction.

Another suitable method to study multistep electrode reactions is the rotating ring disk electrode (RRDE), first described and theoretically treated by *Frumkin* et al. [14.17]. The RRDE is constructed in such a way that both electrodes are in the same plane, and in close proximity to each other as shown in Fig. 14.2. The RRDE consists of two concentric electrodes: the disk electrode with radius r_1 and a platinum ring electrode with the inner and outer radii r_2 and r_3. The schematic streamlines of the disk electrode in Fig. 14.2 also apply for the RRDE, except there is no external ring. Since both electrodes are in the same flow regime, the equation for the limiting current at both the ring and disk electrode can be solved simultaneously.

The RRDE is calibrated first by determining its collection efficiency N. This parameter is defined as the fraction of a species formed at the inner disk that ar-

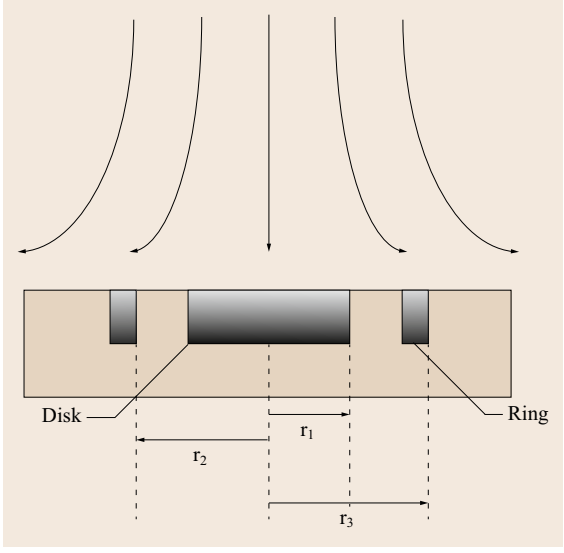


Fig. 14.2 Cross-sectional view of a RRDE with convective flow at its surface. The central disk is surrounded by a Pt ring at a know distance from the disk. The Pt ring converts any H_2O_2 produced at the disk to H_2O via the reaction in (14.3). The cross section of an RDE is similar, except there is no ring (after [14.14])

rives at the outer ring and reacts there. The standard experiment for the evaluation of N is the oxidation of potassium ferrocyanide (Fe^{2+}) on the Pt ring electrode, which was generated by the reduction of potassium ferricyanide (Fe^{3+}) on the working disk electrode. The working disk electrode is set at negative value, where the reduction process occurs at some rate I, while the ring potential is set at very positive value, at which the reduced species is oxidized at its limiting current density. Assuming that there is initially no Fe^{2+} in solution, the ring current results only from the Fe^{2+} ions produced at the working disk electrode and transported to the ring by convection. The ratio of ring current to disk current under these conditions is defined as the collection efficiency N

$$N = \frac{-I_R}{I_D}\,, \tag{14.14}$$

where I_R is the measured ring current (in A) from H_2O_2 oxidation to H_2O and the I_D is measured disk current (in A). Equation (14.14) is used for the experimental determination of the collection efficiency. It should be noted that the collection efficiency is not a function of the rotation rate of the disk electrode, rather it depends exclusively on the dimension of the electrodes.

From the Pt ring currents I_R and the disk currents I_D and the measured collection efficiency of the Pt ring electrode (N), the fraction of hydrogen peroxide produced at the disk electrode is calculated according to (14.15) to obtain quantitative information about hydrogen peroxide formation from an electrocatalyst as well the average number of electrons involved during the ORR over the entire potential range using (14.16) [14.13, 18],

$$\chi_{H_2O_2}(\%) = \left(\frac{\frac{200 I_R}{N}}{I_D + \frac{I_R}{N}}\right)\,, \tag{14.15}$$

$$n_{e^-} = \left(\frac{4 I_D}{I_D + \frac{I_R}{N}}\right)\,. \tag{14.16}$$

The application of RDE to porous electrodes is nontrivial, and a problem was that the activity values reported for Pt/C from different labs tended to be highly variable, calling into question claims of new high activity catalysts when compared to subpar values reported for Pt/C. Since 2001, attempts have been made to establish standard RDE procedures and measurement parameters for standard Pt/C electrocatalysts [14.19–29]. In an effort to streamline the development of advanced electrocatalysts, performance *benchmarking* of commercial electrocatalysts has been reported by a team at General Motors Fuel Cell Activities [14.23]. Their paper showed that cyclic voltammetry (CV) in an inert atmosphere and RDE measurements in the presence of O_2 in a three-electrode electrochemical cell in 0.1 M $HClO_4$ could be used to predict performance trends of practical electrocatalysts in membrane electrode assemblies of PEMFCs. CVs of the Pt/C electrocatalysts in an O_2-free electrolyte were used to measure the Pt electrochemical surface area (Pt ECSA) from the hydrogen adsorption/desorption regions. Thin-film RDE measurements of the electrocatalyst activity in O_2-saturated 0.1 M $HClO_4$ electrolyte performed at different rotation speeds were used to isolate and estimate ORR kinetic currents. The 0.1 M $HClO_4$ electrolyte was chosen over H_2SO_4, because the $HClO_4^-$ anions adsorbs less strongly to the cathode than SO_4^{2-} during cycling and interferes less with O_2 adsorption. Higher concentrations of $HClO_4$ cause Cl-poisoning to the Pt.

Benchmark values were chosen from the calculated kinetic current at 0.90 V from ORR polarization curves measured at an electrode rotation rate of 1600 rpm and potential scan rates of 5 and 20 mV/s in the O_2-saturated 0.1 M $HClO_4$. The results were normalized to the amount of Pt on the electrode and the Pt ECSA to calculate the Pt mass-specific activity (MA) and area-specific activity (SA), which are the accepted measures of true catalyst activity toward the ORR.

Since 2004, many improvements have been made in RDE methodology to improve the implementation of the methods in true cross lab comparison. The methods are also being applied to electrocatalysts for AFCs and metal–air batteries. In this chapter, we will focus on several important aspects of the thin-film electrode RDE and RRDE evaluation of Pt/C standards for the ORR in acidic electrolyte. We will describe both the experimental and electrochemical protocol developed in our laboratory to test the electrocatalytic activity of standard Pt/VC electrocatalysts for the ORR in acid electrolyte using the thin-film electrode RDE or RRDE methodology. The Pt/VC electrocatalytic activity for the ORR will be presented in terms of Pt surface area (Pt ECSA), MA and SA. We briefly describe the (ECSA) calculations necessary for Pt/C in base. A similar experimental and electrochemical protocol is applied to test the electrocatalytic activity of MnO_x electrocatalysts for the ORR in basic electrolyte.

14.1 Evaluation of Pt/VC Electrocatalysts for the ORR

The general procedure for the evaluation of electrocatalyst activity by the RDE or RRDE methodology involves the casting of an electrocatalyst thin film of known concentration on the surface of a glassy carbon (GC) electrode substrate. Once this thin film has dried, the electrocatalyst activity is evaluated in a standard three-electrode electrochemical cell (working electrode (WE), counter electrode (CE) and reference electrode (RE)) as shown in Fig. 14.3, to obtain cyclic voltammograms in a N_2-purged electrolyte, and ORR polarization curves in a O_2-saturated electrolyte.

14.1.1 Glassware Cleaning

For successful RDE or RRDE experiments, the glassware must be as clean as possible. The electrochemical cell, including glassware, stoppers, and O-rings, must be cleaned thoroughly of cationic, anionic, and organic impurities to obtain reproducible measurements and approach what is assumed to be the absolute value of the specific activity of Pt. Any charged species will adsorb electrostatically on the positive electrode, and organic contaminants will chem- or physisorb on the electrocatalyst surface.

The following simple methods are useful for cleaning an electrochemical cell used in the evaluation of high surface area catalysts: The three-compartment electrochemical cell shown in Fig. 14.2 is filled with concentrated sulfuric acid (H_2SO_4, $\approx$ 50 ml) and turned from side to side to make sure that the entire glassware surface is wet and coated with the acid. The interior of three-compartment electrochemical cell is then allowed to soak in the concentrated H_2SO_4 overnight. The three-compartment electrochemical cell is finally rinsed at least eight times with 18 MΩ cm water. An alternative to this method is to wash the three-compartment electrochemical cell thoroughly by one of the following three acid cleaning treatments:

1. Concentrated H_2SO_4 for 8 h;
2. 1 : 1 mixture of H_2SO_4 + HNO_3 for 2–4 h;
3. 1 : 1 mixture of H_2SO_4 + Nochromix$^{\circledR}$ for 4 h.

Following acid treatment, rinse the cell again with 18 MΩ cm water, boil twice in 18 MΩ cm water (1 h each time), rinse well again 18 MΩ cm water, and then finally rinse with the working electrolyte. This more extensive cleaning method is recommended biweekly or monthly if the glassware is contaminated or when testing low surface area electrodes. The success of the cleaning procedure can be benchmarked by evaluating a low-surface area polycrystalline Pt disk electrode in the clean three-compartment electrochemical cell; its specific activity at 0.90 V versus RHE should be $\approx 2000–3000\,\mu A/cm^2$. Polycrystalline Pt disk electrodes are highly sensitive to impurities and obtaining high area-specific ac-

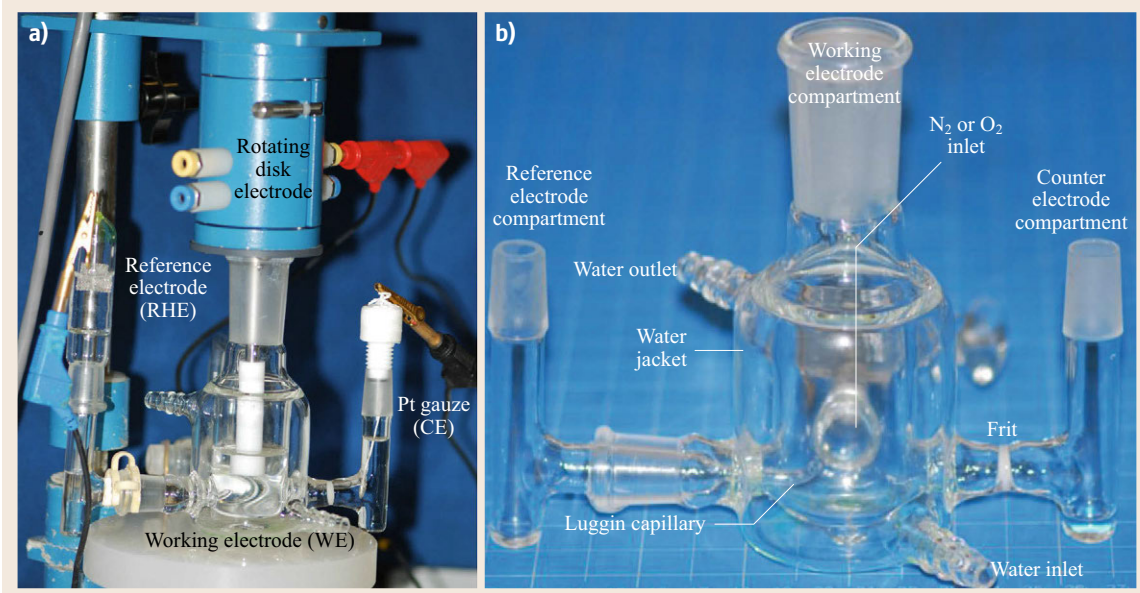


Fig. 14.3 Three compartment electrochemical cell used for thin-film RDE evaluation of electrocatalyst catalytic activity for the ORR in both acidic and basic electrolyte

tivities implies that one has met or exceeded the cleanliness levels needed to obtain good data using thin films of high surface area electrocatalysts as electrodes.

14.1.2 Electrocatalyst Ink Formulation, Preparation of Glassy Carbon Electrode Substrate, and Electrocatalyst Thin-Film Electrodes

Electrocatalyst Ink Formulation

The electrocatalysts (Pt/C standards or other such as MnO_x) are typically dispersed in a water/alcohol/Nafion-ionomer stock solution to form an ink. The ink recipes are highly variable and depend on the type of electrocatalyst. The electrocatalyst ink should be well dispersed and not flocculate or settle. A small amount of Nafion ionomer is added to either the water/alcohol solution or directly to the dry thin-film electrode to improve adhesion of the film to the GC electrode surface. Nafion films thinner than 0.2 μm on solid electrodes [14.3, 30] and Nafion films thinner than 0.1 μm [14.29] on Pt/C-covered GC do not affect oxygen diffusion to the electrode. The alcohol type and content must also be optimized for each electrocatalyst. As discussed extensively [14.27] the ratio of water to alcohol in the ink has a large impact on the ink dispersion, and thus the Pt ECSA measured by CV and ORR electrocatalytic activity. *Takahashi* and *Kocha* [14.27] demonstrated that the addition of isopropanol (IPA) and Nafion ionomer was essential to a well-dispersed Pt/C electrocatalyst ink. An optimal Pt/C electrocatalyst ink formulation of 25 vol.% IPA/75 vol.% water resulted in one of the highest and most reproducible Pt ECSA value reported for a Pt/C (HSC high surface area carbon) of $\approx 105\,m^2/g_{Pt}$. Electrocatalysts that are inherently hydrophobic, such as alloys or heat-treated samples, may require inks with high alcohol (e.g., ethanol or isopropanol) amounts to obtain optimal dispersion. Higher amounts of isopropanol as well as longer ultrasonication times can yield inks that stay well dispersed and result in an electrode having a higher measured electrocatalytic activity. Hydrophilic electrocatalysts can disperse well in solutions with only the Nafion solution and water.

The following is an ink recipe used extensively in our laboratory for preparing thin-film electrode from a standard of 40 wt% Pt/VC (HiSPEC-4000, Johnson Matthey) electrocatalyst yielding an electrode Pt loading of $20\,\mu g_{Pt}/cm^2$ [14.20–22]. Our ink composition and formulation parameters are derived from the basic recipe described in reference [14.23], with a Nafion ionomer-to-carbon ratio (I/C) ratio of about 0.5. It was recently reported by *Kocha* et al. [14.24] that the I/C ratio has a significant effect on the measured activity of Pt/C standards when the I/C ratio is above 1.0. No significant effect was observed for I/C ratio in the range of 0.25−1.0. The choice of an I/C ratio of 0.5 is therefore reasonable choice in terms of sensitivity of activity to ionomer content in the ink formulation. The ink is always prepared the night before:

- A stock solution of 20% isopropanol and 0.02% Nafion ionomer is prepared by mixing 20 ml of isopropanol with 79.6 ml of 18 MΩ cm water, and 0.4 ml of 5 wt% Nafion ionomer solution (Ion Power, Liquion 1100), in a 100 ml volumetric flask.
- Next, 10.4 mg of the 40 wt% Pt/VC electrocatalyst is weighted into a 10 ml borosilicate vial.
- Then, 5 ml of the stock isopropanol/water/Nafion solution is added to the vial containing the Pt/VC electrocatalyst, and then mixed thoroughly with a high shear mixer (IKA, T10-Basic S1) for 1 min.
- The Pt/VC electrocatalyst ink is then transferred to a high-power ultrasonicator (Ultrasonic Power Corp, model N-50-26 549) and sonicated for 60 min, making sure that the water bath temperature does not rise above 40 °C.
- After 60 min of sonication, the Pt/VC electrocatalyst ink is taken out of the high-power ultrasonicator. A small stirring bar is then added to the 10 ml borosilicate vial containing the mixed 10 mg of the Pt/VC electrocatalyst and 5 ml of the stock isopropanol/water/Nafion solution.
- The Pt/VC electrocatalyst ink is then placed on a stirring plate and allowed to stir overnight.

Glassy Carbon (GC) Electrode Substrate Preparation

High-quality electrocatalyst thin-film electrodes can be obtained by casting the electrocatalyst-containing inks on GC electrode substrates. An example of GC electrode is a 5 mm diameter glassy carbon disk, with a geometric area of $0.196\,cm^2$, embedded in a Teflon cylinder (Pine Instruments). The GC electrodes should be polished with a 0.05 μm Al_2O_3 particle suspension on a moistened polishing cloth (Buehler, MicroCloth) in a figure 8 pattern for 4 min to a mirror finish. The polished GC electrode is rinsed well with 18 MΩ cm water, sonicated for 4 min in 18 MΩ cm water, rinsed well again, and then dried at room temperature in air for at least 20 min before use. The result is the mirror-quality finish shown in Fig. 14.4a.

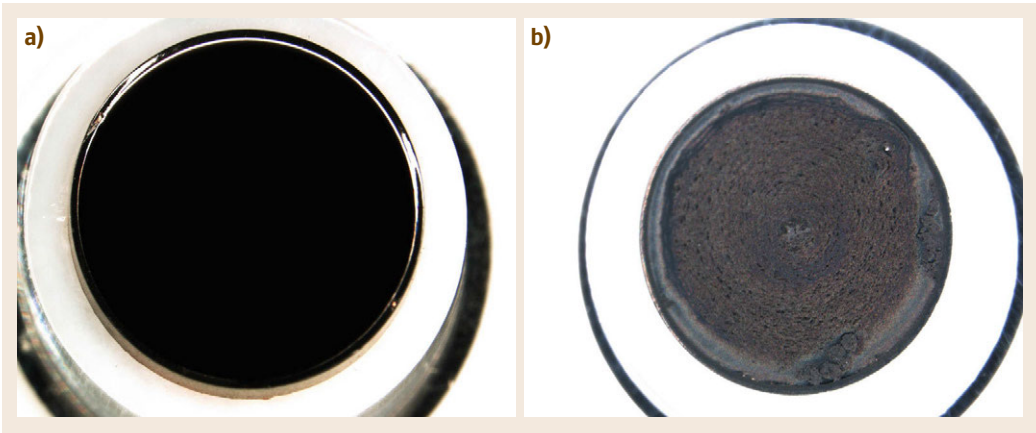


Fig. 14.4 **(a)** Mirror-polished RRDE Glassy carbon substrate prior to casting an aliquot of the Pt/C ink. **(b)** Optical micrograph of the typical thin-film electrode obtained using the stationary drying method for the 40 wt% Pt/VC electrocatalyst

Casting and Drying of the Electrocatalyst Thin-Film Electrodes

Thin-film Pt/C electrocatalyst RDE or RRDE electrodes are typically prepared by casting 7.5–10 µl droplet of the well-dispersed Pt/C ink onto the clean, polished, GC electrode substrate such that it completely covers the GC electrode substrate surface but does not cover any of the Teflon insulator. The ink droplet should be dried in conditions that yield a smooth, uniform, thin Pt/C film that covers the entire surface of the GC electrode substrate. The amount of electrocatalyst should be in the range of 10–20 $\mu g_{Pt}/cm^2$ to assure a sufficiently thin film, plus the film must be uniform after drying. The science of film drying has been studied extensively [14.31, 32] and is a function of alcohol type and content, Pt dispersion, and ambient conditions of the drying (temperature and humidity). Pt/C thin-film RDE or RRDE electrodes have been typically prepared by drying the ink droplet stationary under a flow of N_2 at room temperature or at 40–60 °C for 30 min in air [14.19], but this tends to lead to nonuniform films.

In our own laboratory, we observed that ORR polarization curves measured for thin-film Pt/C RDE or RRDE electrodes are very sensitive to the morphology and uniformity of the electrocatalyst film [14.19–22]. As shown with the optical micrograph in Fig. 14.4b, the typical RRDE thin-film electrode obtained by simply drying the Pt/VC ink aliquot stationary in air leads to a highly nonuniform film with wide discrepancies in film thickness. A *coffee-ring structure* at the edge of the optical micrograph of Fig. 14.4b is clearly visible. Detailed 3-D-profilometry analysis of this typical stationary thin-film Pt/VC electrode can be found in [14.21, 22].

Such agglomeration effects apparent in Fig. 14.4b during drying have been studied extensively for ink-jet related technology and DNA printing. Static drying conditions cause small, round particles to migrate to the edge of a droplet in a nonuniform, unpredictable matter during solvent evaporation, resulting in the familiar coffee ring structure that is left when a solid suspension of cream and coffee particles dries on a table [14.33].

The optical micrograph in Fig. 14.5a illustrates the nonuniformities that are present in the coffee ring structure. Care must be taken to avoid a coffee-ring structure on the thin-film Pt/VC RDE or RRDE electrode and avoid any thick regions on the thin film that limit the mass transport of O_2 [14.34, 35]. Basically, electrocatalyst films that are nonuniform experience higher O_2 mass transport resistance to the thick areas of the electrocatalyst film, preventing full reactivity of the film.

A desired uniform film for accurate RDE is shown in Fig.14.5b. Such films can be prepared by using the rotational drying method [14.20–22], the ink-jet method [14.36], or by using a much lower Pt loading [14.24, 37, 38]. In the case of a low Pt loading, care must still be taken to achieve a uniform thin-film, as even the small amount of electrocatalyst can agglomerate into thick islands on the GC electrode substrate. We have developed a method in which the aliquot of the Pt/VC electrocatalyst ink is rotationally dried on an inverted RDE or RRDE rotator (Fig. 14.6a). The rotational drying method is reminiscent of the RDE method itself. The RDE or RRDE/ink is dropped on an inverted RDE (Fig. 14.6b) and this ensemble is rotated at 700 rpm so that the air flow over the droplet is directed from the center of the film to the outside of the disk, as illustrated in Fig. 14.1 for an electrode rotating in elec-

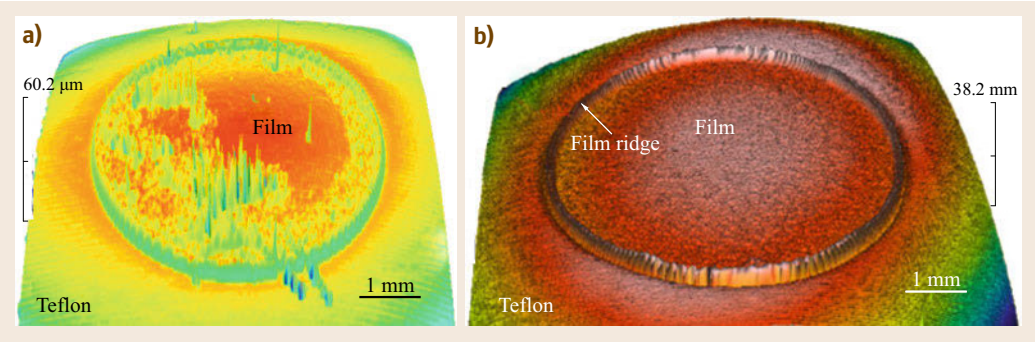


Fig. 14.5a,b Optical profilometry of a Pt/C thin film **(a)** nonuniform film created when Pt/C ink dried statically in open air and **(b)** a uniform film resulting from rotational drying of the ink (after [14.20–22])

trolyte and executed here using an air flow. The result is a uniform and homogenous Pt/VC film on the glassy carbon surface, as shown in Figs. 14.5b and 14.6c (see also videos in reference [14.22] showing that the aliquot ink is not ejected from the GC electrode surface). Figure 14.6c clearly shows that no *coffee-ring* structure is visible when using the rotational drying method.

Another group has come to the same conclusion as us and quantified the mass transport limitations in nonuniform films. *Ke* et al. [14.36] made nonuniform Pt/C electrocatalyst films by stationary drying and uniform films by transferring tiny droplets (≈ 3 nl in volume) of their Pt/C ink to controlled position ($\approx 1\,\mu$m precision) on the glassy carbon electrode surface. Ke's paper quantifies how nonuniform films create mass transport limitations, which affect Koutecky–Levich calculation of the ORR kinetic current and thus lead to subpar ORR activities.

The following is an exact recipe used extensively in our laboratory for preparing uniform thin-film RDE electrode from standard Pt/VC electrocatalyst or other type of electrocatalyst inks using our rotational drying method [14.20–22]:

- The Pt/VC electrocatalyst ink (which has been stirred overnight) is transferred to the high-power ultrasonicator (Ultrasonic Power Corp, model N-50-26 549) and sonicated for 60 min, making sure that the water bath temperature does not rise above 40 °C.
- After 60 min of sonication in the high-power ultrasonicator, the Pt/VC electrocatalyst ink is transferred to a low-power ultrasonicator (Branson, model 2510) and sonicated in a water bath keeping the temperature at below 40 °C.
- After 10 min, while the ink is sonicating in the ultrasonicator (Branson, 2510), a 9.4 µl aliquot of the well-dispersed ink is pipetted and loaded onto the clean, polished, glassy carbon electrode substrate mounted on the inverted rotator (Fig.14.3a) such that it completely covered the glassy carbon but did not cover any of the Teflon (Fig. 14.3b). The electrode is then rotated at 700 rpm until the film is dry. The film should be visually inspected to ensure uniform drying and that the ink is only on the GC disk.

Thin-Film Electrode Pt Loading

The Pt loading of the thin-film electrode must be kept low enough to produce a thin film, but high enough for accurate measurement. The Pt loading on the GC electrode substrate should lie in the range of $5-20\,\mu g_{Pt}/cm^2_{goemetric}$ for electrocatalysts having concentrations in the range of 10–50 wt % Pt/VC, as recommended by *Gasteiger* et al. [14.23] and shown experimentally by *Mayrhofer* et al. [14.25]. This is sufficient Pt to overcome any contributions of background electrical noise, but low enough to allow for casting of a sufficiently thin film that does not suffer from O_2 mass transport losses. The thin-film electrode Pt loading should be adjusted to achieve a thin film on the GC, with lower Pt electrode loadings used for electrocatalysts with low Pt concentrations. Thin films (on the order of $\leq 0.2\,\mu$m) are ideal, as thicker films may result in increased mass-transport resistance through the catalyst layer, giving incomplete access to the electrochemical area of the catalyst and therefore producing incorrect data.

Chemical Grades

All chemicals and gases must be high purity. Ultra-high purity Ar (> 99.9995%), N_2 (> 99.9998%), O_2 (> 99.9995%), double distilled perchloric acid ($HClO_4$), and 18 MΩ cm water must be used. N_2 tends to have higher purity than Ar. Double distilled $HClO_4$ is obtained from GFS chemicals (PPT grade) or EMD Chemicals (PX0397 Omintrace).

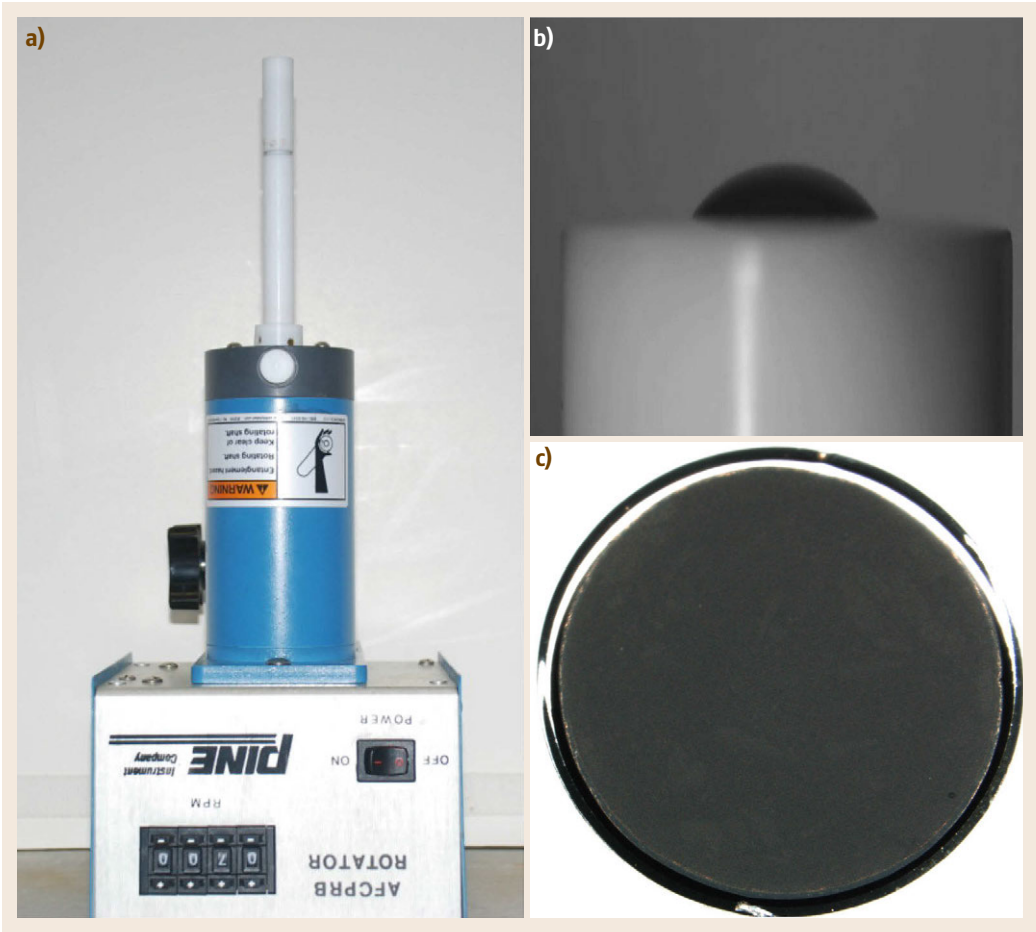


Fig. 14.6 (a) Picture of the inverted AFPCRB rotator used to dry the Pt/VC ink aliquot on the GC electrode substrate surface for the rotational drying method. The GC electrode substrate is rotated at 700 rpm during the drying process. (b) Picture of the Pt/VC ink aliquot covering only the GC electrode substrate. (c) Optical micrograph of the Pt/VC thin-film electrode obtained suing the rotational method

Reference Electrodes

ORR measurements require a stable RE that does not contaminate the experiment, and also is not contaminated by the experiment. Common REs include RHE, dynamic hydrogen electrode (DHE), saturated calomel electrode (SCE), and silver–silver chloride (Ag/AgCl) electrodes. We prefer a RHE consisting of high surface area platinum immersed in H_2-saturated 0.10 M $HClO_4$ electrolyte, because it contains low amount of impurities and also requires no potential correction. An example of a sealed RHE is shown in Fig. 14.7, with a photograph of the RHE connected to the RE compartment in Fig. 14.7b. The surface area of the Pt mesh can be increased significantly by platinization with Pt black. A fresh RHE should be prepared daily, using the same electrolyte in the RE and in the electrochemical cell (i. e., 0.1 M $HClO_4$ or 0.1 M KOH).

Figure 14.7 pictorially describes the procedures to prepare the RHE used in our laboratory. The RHE is filled completely via a syringe with 0.1 M $HClO_4$ with the glass capillary facing up. The RHE is then flipped down, placed into a beaker containing 0.1 M $HClO_4$ and a Pt counter electrode, and the 0.1 M $HClO_4$ is electrolyzed at $\approx$ 30 V to fill the Pt mesh chamber halfway with H_2. The final RHE should have half of the Pt mesh in contact with the H_2 gas and the other half in the 0.10 M $HClO_4$ solution. Commercial SCE and Ag/AgCl REs can also be used successfully by incorporating a salt bridge. The salt bridge minimizes the intrusion of chloride or other ions from the SCE or Ag/AgCl RE into the main compartment of the WE, but can be cumbersome. The SCE and Ag/AgCl REs should be calibrated on a daily basis to ensure that their potential does not drift.

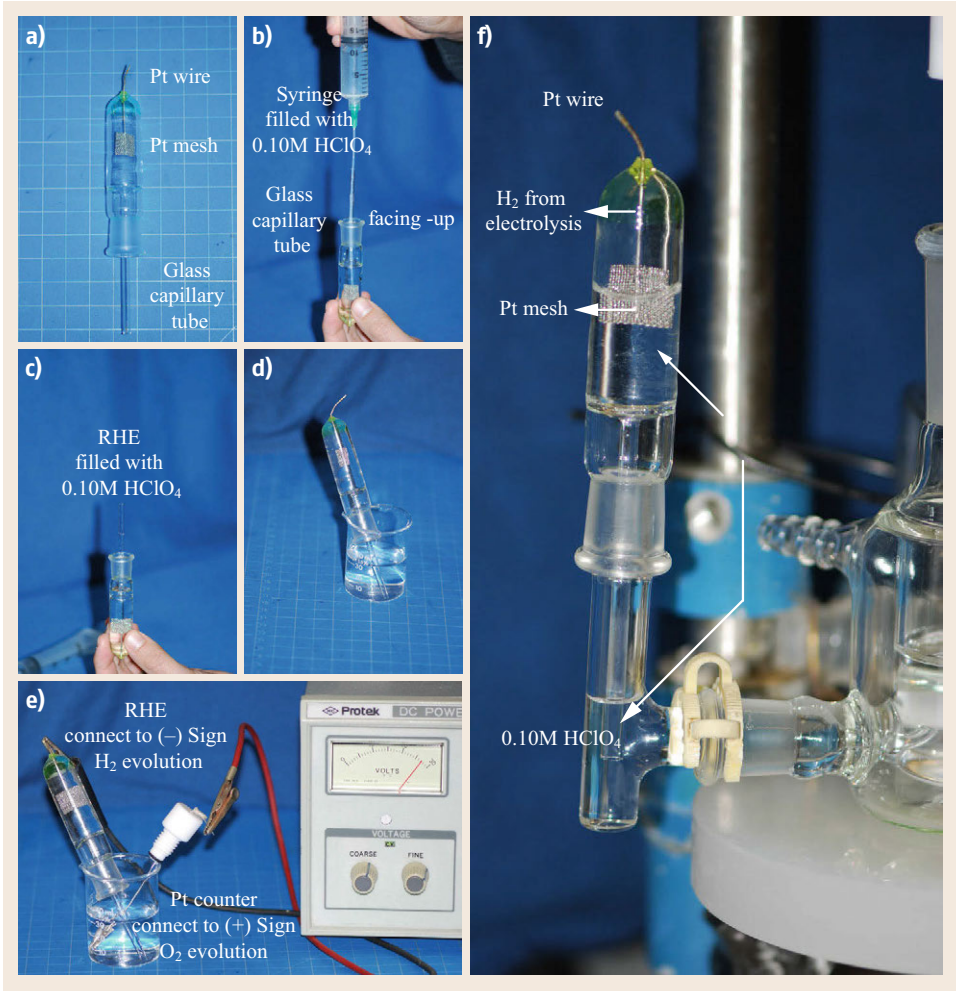


Fig. 14.7 Steps to prepare the RHE

14.1.3 Electrochemical Test Protocol for Evaluation of the Thin-Film Electrocatalyst Electrodes

Figure 14.8 presents the electrochemical protocol developed at the Naval Research Laboratory (NRL) to tests the electrocatalytic activity of Pt/VC standards for the ORR using the thin-film electrode RDE or RRDE methodology. If the RRDE methodology is used, the first step is to determine the collection efficiency N of the Pt ring electrode from the ratio of the oxidation of potassium ferrocyanide (Fe^{2+}) at the ring versus the reduction current of potassium ferricyanide (Fe^{3+}) at the glassy carbon disk electrode (14.9). Prior to casting the Pt/C electrocatalyst ink aliquot on the glassy carbon substrate, the Pt ring is electrochemically clean by potential cycling between 0 and 1.50 V versus the RHE for 100 cycles at 500 mV/s in the 0.10 M $HClO_4$ electrolyte. The RRDE electrode is then rinse well with nanopure water and allowed to dry. The method described earlier is then used to prepare the thin-film Pt/VC RRDE electrodes.

For every measurement, the clean three-compartment electrochemical cell is filled with fresh 0.10 M $HClO_4$ (prepared from double distilled $HClO_4$ (GFS Chemical) and 18 MΩ cm water) and de-oxygenated with a steady stream of ultra-high purity N_2 gas (> 99.9998%) for at least 25 min. Measurements should be carried out near room temperature (25–30 °C). Prior work reports measurements taken at 60 °C, or near the operating temperature of a practical PEMFC, but $HClO_4$ decomposes over time producing Cl^- ions, which inhibit the ORR [14.39]. The lower temperature measurements also put less wear on equipment due to the higher volatility of the acid at elevated temperatures. A baseline temperature can be chosen, such as 30 °C, as *room temperature* can be variable; although the impact of temperature on the results is

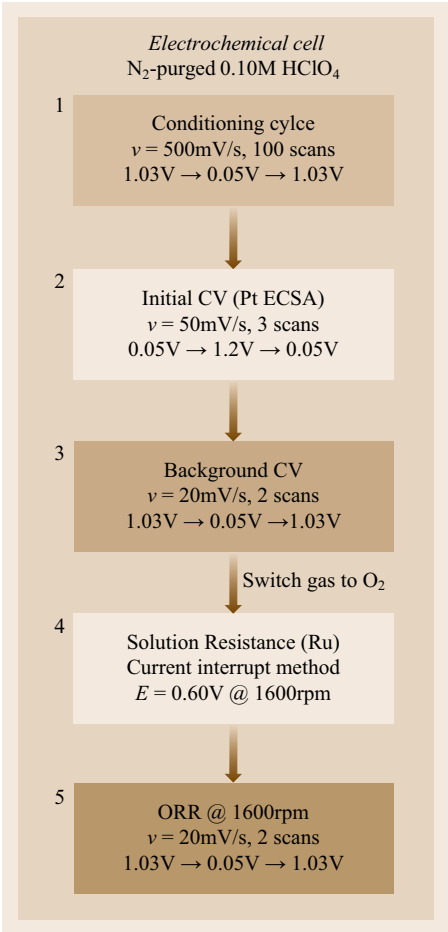


Fig. 14.8 Schematic of the electrochemical protocol used at NRL to study standard Pt/VC electrocatalysts for the ORR using the thin-film RDE or RRDE methodology

very small. The temperature of the cell is controlled by flowing heated/cooled water through the jacket of the electrochemical cell via a circulating water bath.

The electrocatalyst-coated glassy carbon (the working electrode in this experiment) is wetted with 18 MΩ cm water, attached to the shaft of the electrode rotator (Pine, AFMSRX electrode rotator), and guided into the electrolyte. A platinum mesh is used as the counter electrode. All potentials are measured with respect to the sealed RHE as shown in Fig. 14.7. The working electrode is positioned at the same height for each experiment to keep the solution resistance between the working electrode and RHE Luggin capillary similar. Any gas bubbles attached to the working electrode surface are dislodged by rotation at > 3600 rpm. The gas flow rate is reduced during measurements to ensure that no additional bubbles stuck to the working electrode surface. All electrodes are connected to the potentiostat (Autolab bipotentiostat, PGSTAT30) using appropriately shielded cables.

As shown in Fig. 14.8, our electrochemical test protocol consists of five simple steps:

- Step 1. The working electrode is first electrochemically cleaned via potential cycling. The Pt/VC working electrode is cycled between 0 and 1.20 V versus the RHE for 100 cycles at a potential scan rate (ν) of 500 mV/s (conditioning cycle in Fig. 14.8).
- Step 2. The CV measurements for the Pt ECSA determination is carried out by cycling $\geq 3\times$ at a potential scan rate of 50 mV/s between 0.05 and 1.20 V (initial CV in Fig. 14.8). The minimum potential should be just above the potential for hydrogen evolution, which will be scan rate and electrocatalyst dependent.
- Step 3. The background current is measured by running the ORR sweep profile (e.g., 1.03 V → 0.05 V → 1.03 V at a potential scan rate of 20 mV/s and working electrode rotation rate of 1600 rpm) in N_2-purged 0.10 M $HClO_4$ before the ORR measurements to account for capacitive current contributions. This background current is subtracted from the experimental ORR current to eliminate any contributions of capacitive current.
- Step 4. Upon completion of the CV measurements, the saturation gas is switched to O_2 ($> 99.9995\%$) and the 0.10 M $HClO_4$ electrolyte is O_2-saturated for at least 25 min. Prior to each ORR measurement, the solution resistance (R_u) from the working electrode to the Luggin capillary is determined by Current interrupt method integrated in the Autolab bipotentiostat software. The rotator is set to the appropriate rotation rate (i. e., 1600 rpm) and turned on. The electrolyte resistance is determined at a potential that exhibits the diffusion limiting current for the ORR (e.g., 0.60 V), and is assumed constant during measurement. For our setup the typical (R_u) measured for the 0.10 M $HClO_4$ electrolyte is around 20 Ω. This value of (R_u) agree well with values reported in the literature for similar electrolytes [14.28].
- Step 5. The ORR polarization curve measurements are carried out at a working electrode rotation rate of 1600 rpm, a potential scan rate of 20 mV/s in a typical polarization program of 1.03 V → 0.05 V → 1.03 V. A correction voltage proportional to the current is applied during the measurement. Overcompensation for resistance during the measurement of CV can be quickly noted as the potential will start to oscillate. When collecting data for Levich–Koutecky curves, the measurements are

preferably carried out at rotation speeds of 400, 625, 900, 1225 and 1600 rpm. If using the RRDE working electrode, the Pt ring electrode is potentiostated at 1.20 V versus RHE, where the oxidation of hydrogen peroxide is under pure diffusion control.

14.2 Electrochemical Characterization of the Pt/VC Electrocatalyst Thin-Film Electrodes by RDE and RRDE

The following section presents the results obtained when testing a commercially available Pt/VC electrocatalyst standard (40 wt% Pt on VC, HiSPEC 4000, Johnson Matthey) for the ORR using the thin-film RDE and RRDE methodology. The experimental and electrochemical protocol (Fig. 14.8) developed by NRL and described above were used to test the Pt/VC electrocatalyst. The ink and film preparations are described again below. The Pt/VC electrocatalytic activity for the ORR will be presented in terms of Pt surface area, MA and SA calculated at 0.90 V versus RHE. The measurement protocol parameters are based on findings from the literature and our own experimentation. While the Pt/VC ORR electrocatalytic activity is independent of the working electrode rotation rate, comparison of data is best done at one rate. Stemming from the method originally recommended by *Gasteiger* et al. [14.23] in an attempt to correlate RDE of Pt/C to MEA measurements, we recommend to run the ORR polarization curves at the rotation rate of 1600 rpm. While the rotation rate of 1600 rpm is somewhat arbitrary, it is fully adequate. Although the potential scan rate ν does not inherently affect the Pt/VC electrocatalyst ORR electrocatalytic activity, cross lab (or publication) comparison is best achieved when the same potential scan rate conditions are used. Again, we recommend the values originally recommended by *Gasteiger* et al. [14.23]: 5 and 20 mV/s, which are low enough to approach steady-state behavior. At higher scan rates, the concentration gradient does not build up sufficiently giving artificially enhanced kinetics. Scan rates lower than 5 mV/s are not recommended to avoid artifacts imposed by the accumulation of impurities in the electrolyte at the working electrode [14.19], and scan rates higher than 20 mV/s will be more affected by capacitive currents.

Based on the method originally recommended by *Gasteiger* et al. [14.23], activity values for Pt/C are chosen from the calculated kinetic current at 0.90 V from ORR polarization curves measured at an electrode rotation rate of 1600 rpm and potential scan rates of 20 mV/s in O_2-saturated 0.1 M $HClO_4$. As discussed extensively by *Mayrhofer* et al. [14.25] (14.15), the MA and SA must be determined from a potential near the half-wave potential of the scan, which is typically 0.90 V versus RHE for Pt/C. For more active electrocatalysts, a higher potential or a decreased Pt loading might be used. Measuring at the half-wave potential avoids the contribution of diffusion-limited current. *Mayrhofer* et al. recommend within 10–80% of the diffusion limiting current density [14.25]. As discussed in [14.19, 25, 28], iR and background correction methods should be used to help normalize data and remove experimental and equipment artifacts.

14.2.1 Influence of Pt/VC Thin-Film Electrodes Quality

Figure 14.9a compares the average cyclic voltammogram (CV) response obtained for six thin-film Pt/VC electrodes prepared using the traditional stationary drying method to the average CV response obtained for six thin-film Pt/VC electrodes prepared using NRL rotational drying method. The error bars correspond to the standard deviation for the six independent films, respectively. The optical micrograph of the typical film obtained by using both the stationary drying method and the rotational drying method is also added to Fig. 14.9 (Fig. 14.9b). The stationary film presents a fairly smooth and uniform film on the edge of the disk electrode. However, the center of the disk electrode appears nonuniform and rough. A coffee-ring structure on the edge of the disk electrode is visible, clearly indicative of inhomogeneous distribution of the Pt/VC electrocatalyst on the glassy carbon surface. In contrast, the typical film obtained using the rotational method is very uniform over the entire surface of the glassy carbon disk; no coffee ring structure is visible. The CV response obtained for stationary film is very similar to the CV obtained for the rotationally dried film, indicating that the thin-film electrode quality has little impact on the CV measurements.

14.2.2 Pt ECSA Calculation in Acid

The Pt ECSA can be calculated from the hydrogen absorption region from the CVs such as those shown in Fig. 14.9. The reversible mechanism for H adsorption and desorption is written in (14.17) and occurs between 0.4 and 0.0 V versus RHE, above the potential for hydrogen evolution. There is a 1 : 1 correlation between

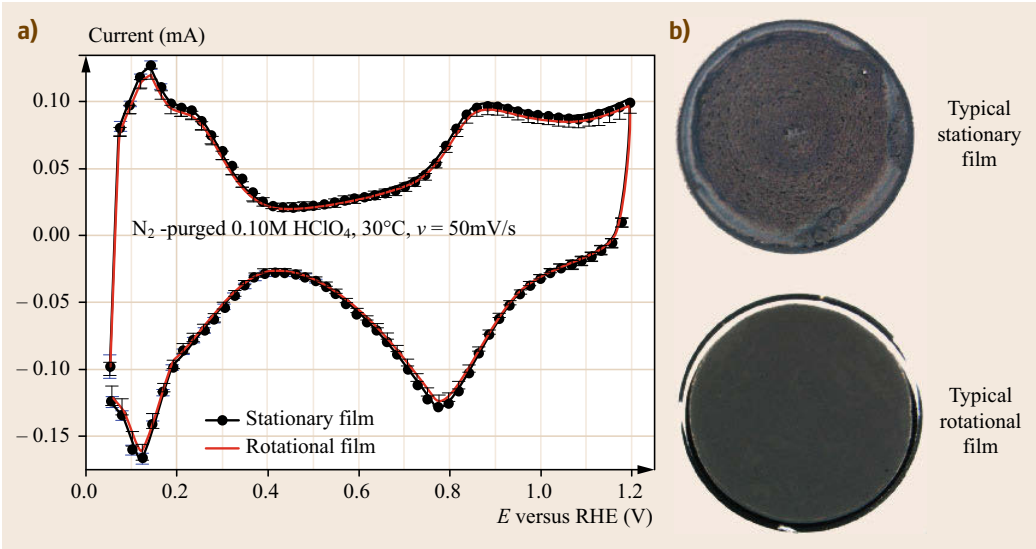


Fig. 14.9 **(a)** Comparison of the average CV curve obtained for six stationary films to the average CV curve obtained for six rotational films. The error bars correspond to the standard deviation for the six independent films, respectively. **(b)** Representative optical micrograph for the typical stationary and rotational film, respectively

the surface Pt and amount of H adsorbed

$$\mathrm{Pt} + \mathrm{e}^- + \mathrm{H}^+ \leftrightarrows \mathrm{Pt-H}\,. \tag{14.17}$$

The charge under the hydrogen adsorption region Q is determined from the negative going potential of a CV scan from 0.40 to 0.05 V and subtracting the current at 0.40 V versus RHE from the total current. The exact equation used to calculate the ECSA is depicted in (14.18). A charge of $210\,\mu\mathrm{C/cm^2_{Pt}}$ is used for adsorption of a monolayer of atomic hydrogen in the acidic electrolyte [14.19].

This method has been validated in our laboratory versus CO adsorption and Cu UPD methods for measuring the Pt ECSA [14.40]. The Pt ECSA is reported in $\mathrm{m^2/g_{Pt}}$, L_{Pt} is the working electrode Pt loading ($\mu\mathrm{g_{Pt}/cm^2}$), and A_{g} is the geometric surface area of the glassy carbon electrode (i. e., $0.196\,\mathrm{cm^2}$)

$$\text{ACID}\quad \mathrm{ECSA_{Pt,cat}} = \left(\frac{Q(C)}{210\mu\mathrm{C/cm^2_{Pt}}L_{\mathrm{Pt}}A_{\mathrm{g}}}\right)10^5\,. \tag{14.18}$$

For the 40 wt% Pt/VC standard (JM), the Pt ECSA measured for the stationary film is equal to $50 \pm 1\,\mathrm{m^2/g_{Pt}}$ compared $49 \pm 1\,\mathrm{m^2/g_{Pt}}$ the rotational film, again indicating that the drying method has a limited impact on the CV responses in N_2-purged 0.10 M $HClO_4$ electrolyte, ostensibly because the H adsorption/desorption reaction in (14.17) is not mass transport limited.

14.2.3 Pt ECSA Calculation in Base

Figure 14.10 presents the typical baseline CV measured for the Pt/VC standard in N_2-purged 0.10 M KOH electrolyte at a potential scan rate of 50 mV/s, with the typical Pt hydrogen adsorption/desorption (H_{upd}) potential region (0.05–0.45 V) separated by the double layer region (0.45–0.60 V) from the oxygen adsorption/desorption region (>0.60 V).

The reaction for H adsorption on Pt in basic electrolyte is given in (14.19)

$$\mathrm{Pt} + \mathrm{e}^- + \mathrm{H_2O} \leftrightarrows \mathrm{Pt-H} + \mathrm{OH}^-\,. \tag{14.19}$$

If the apparent Pt ECSA in alkaline electrolyte is calculated by adaptation of the method developed for the 0.10 M $HClO_4$ electrolyte, i. e., from integration of charge under the hydrogen adsorption region, after correction of the double layer charging assuming a charge of $150\,\mu\mathrm{C/cm^2_{Pt}}$ for adsorption of a monolayer of atomic hydrogen in alkaline electrolyte [14.41, 42], the typical Pt ECSA value calculated using (14.18) is $33\,\mathrm{m^2/g_{Pt}}$. This adaptation of the acid method gives nonsensical Pt ECSA value, which suggest a 1.5 × decrease in surface area just by changing to the acid electrolyte.

For Pt ECSA calculation in alkaline electrolyte we recommend the approach developed by *Vidal-Iglesias* et al. [14.43], by measuring the total voltammetric charge between 0.06 V and 0.90 V versus RHE, without double layer correction, using a reference value of

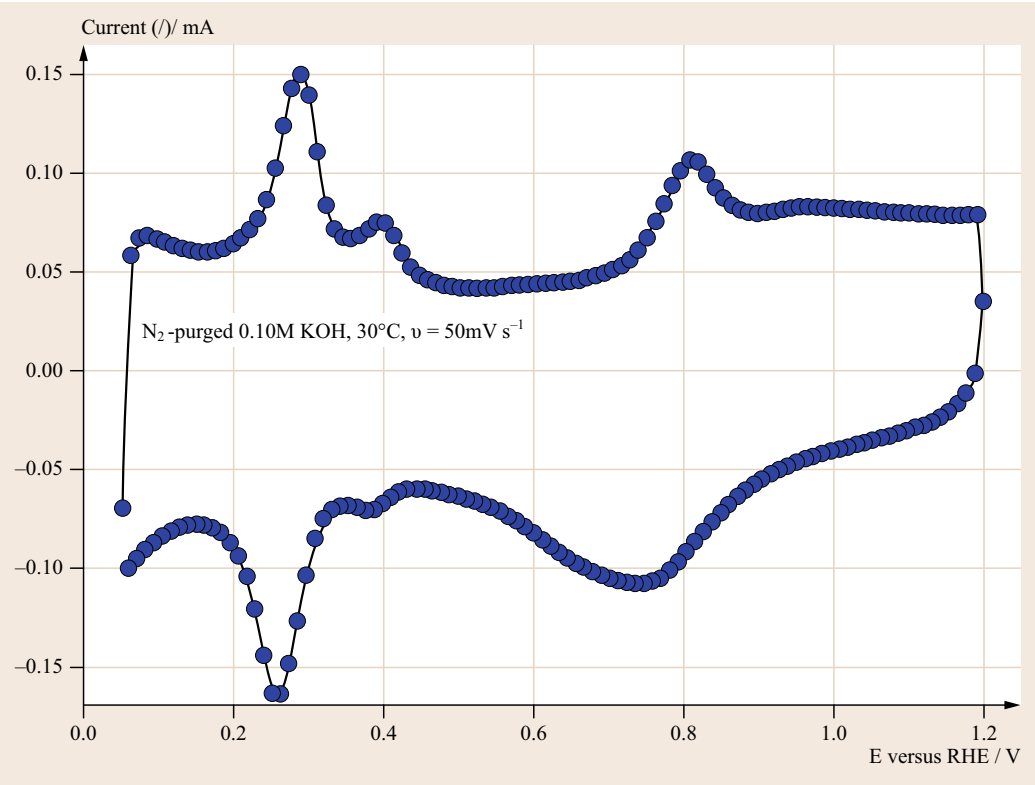


Fig. 14.10 Typical CV recorded for Pt/VC electrocatalyst in N_2-purged 0.10 M KOH electrolyte.

$390\,\mu C/cm^2_{Pt}$. The Pt ECSA in alkaline electrolyte can be calculated as written in (14.20):

$$\text{BASE}\quad \text{ECSA}_{\text{Pt,cat}} = \left(\frac{Q(C)}{390\mu\text{C/cm}^2_{\text{Pt}} L_{\text{Pt}} A_{\text{g}}}\right) 10^5 \,. \quad (14.20)$$

The typical Pt ECSA calculated for the Pt/VC electrocatalyst using (14.20) is $58\,m^2/g_{Pt}$. These differences in the values of Pt ECSA might arise from the difficulty to select a double layer region in the alkaline electrolyte, which is not as wide and well-defined as the corresponding region on acidic electrolyte (Fig. 14.9a).

14.2.4 ORR Polarization Curves Versus Film Morphology in Acid Electrolyte by RDE

The drying method and the resulting film morphology (uniform/homogeneous versus coffee ring structure) has a very substantial effect on the measured ORR polarization curves, as shown in Fig. 14.11a,b, because the film nonuniformities affect the O_2 mass transport in the electrolyte. Figure14.11a,b compares the average iR and background corrected ORR polarization curve obtained for six stationary films to the average iR and background corrected ORR polarization curve obtained for six rotational films in O_2 saturated 0.10 M $HClO_4$ at 30 °C, a potential sweep rate of 20 mV/s and an electrode rotation rate of 1600 rpm (anodic sweep: 0.05 V → 1.03 V). The error bars correspond to the standard deviation for the six independent films, respectively. A single, steep reduction wave with a well-developed limiting current density plateau (j_{lim}) is observed for the average ORR polarization curve obtained by the rotational drying method. The limiting current density plateau is fully reached by $E = 0.70$ V. In contrast, j_{lim} is not as well developed, is only fully reached by $E = 0.50$ V and slightly lower for the average ORR polarization curve obtained using the traditional stationary drying method. The limiting current density of $-5.95\,mA/cm^2$ measured at 1600 rpm is within the 10% margin [14.25] both from the theoretical diffusion limiting current density (i. e., $-5.70\,mA/cm^2$) calculated using the Levich equation and the experimental value obtained on a bare polycrystalline under the same experimental conditions. The Pt/VC electrocatalyst ORR activity can be visually benchmarked from its half-wave potential, $E_{1/2}$, which is the point halfway between zero current and the diffusion limited

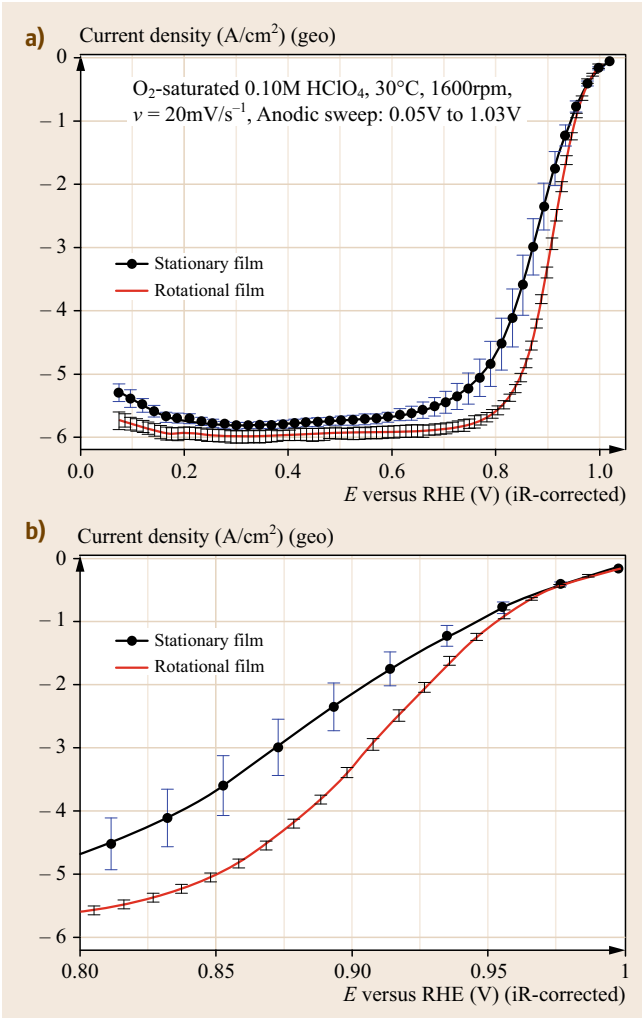


Fig. 14.11 **(a)** Comparison of the average ORR polarization curve obtained for six stationary films to the average ORR polarization curve obtained for six rotational films. The *error bars* correspond to the standard deviation for the six independent films, respectively. **(b)** Zoom in the kinetic region of Fig. 14.11a

current density plateau. The $E_{1/2}$ for the ORR polarization curve obtained for the stationary film is equal to 0.859 V, whereas the $E_{1/2}$ for the ORR polarization curve obtained using the rotational drying method is equal to 0.909 V. The current densities measured for the stationary film are much lower than the rotational film, especially in the mixed kinetic-diffusion controlled region ($0.75\,\mathrm{V} < E < 1.0\,\mathrm{V}$) as shown in Fig. 14.11b. At $E = 0.90\,\mathrm{V}$, the measurement performed on six different electrodes prepared successively using the stationary drying yield an average current density of $-2.15\,\mathrm{mA/cm^2}$, with a standard deviation of $0.34\,\mathrm{mA/cm^2}$ compared to an average current density of $-3.30\,\mathrm{mA/cm^2}$ and a standard deviation of $0.09\,\mathrm{mA/cm^2}$ for the measurement performed on six different electrodes prepared successively using the rotational method.

14.2.5 ORR Measurements of Pt/C in Acid Electrolyte by RRDE

We also tested the ORR electrocatalytic activity of 19.7 wt% Pt/VC electrocatalyst (from E-TeK Inc.) in 0.10 M $HClO_4$ electrolyte using the thin-film RRDE methodology. The electrocatalyst ink formulation is the same as described for the Johnson Matthey 40 wt% Pt/VC electrocatalyst, and five independent films were prepared using the rotational drying method. Figure 14.12a presents the average background corrected ring current measured at the Pt ring when evaluating five independent films prepared with the 19.7 wt% Pt/VC (E-TEK) electrocatalyst using the NRL rotational-drying method, along the average background corrected disk current density data for the same five independent thin-films (Fig. 14.12). The error bars correspond to the standard deviation for the five independent measurements. Figure 14.12b shows that a single, steep reduction wave with a well-developed limiting current density plateau (j_{lim}) is measured at the working electrode rotation rate of 1600 rpm.

Starting at ca. 1.03 V and sweeping the disk potential to 0.05 V, the ring current (Fig. 14.12a) is a very small fraction of the disk currents, implying that the ORR proceeds almost entirely through a direct $4e^-$ pathway. The appearance of hydrogen peroxide oxidation currents on the ring only begins at potential negative to 0.60 V. Increase of peroxide oxidation current is merged with the adsorption of hydrogen ($E <$ 0.20 V versus RHE), approaching a maximum at $E =$ 0.05 V versus RHE. Figure 14.12a,b clearly show that the standard deviations measured for the five independent films are very small, clearly indicating that the rotational drying method consistently produces highly uniform thin films. Using the data from Fig. 14.12a,b, we evaluated the average fraction of hydrogen peroxide produce during the ORR using (14.15) as well the average number of electrons involved during the ORR over the entire potential range using (14.16). The results are presented in Fig. 14.12c,d, respectively. The error bars correspond to the standard deviation for five independent measurements. Figure 14.12c,d confirm that the ORR on the Pt/VC electrode proceeds almost entirely through a four-electrons pathway. The average number of exchanged electrons is close to 4 from 1.03 to 0.4 V versus RHE, and the H_2O_2 fraction (current efficiency) is less than 1%. A maximum of H_2O_2 fraction of ca. 4% is detected at $E = 0.05$ V versus RHE.

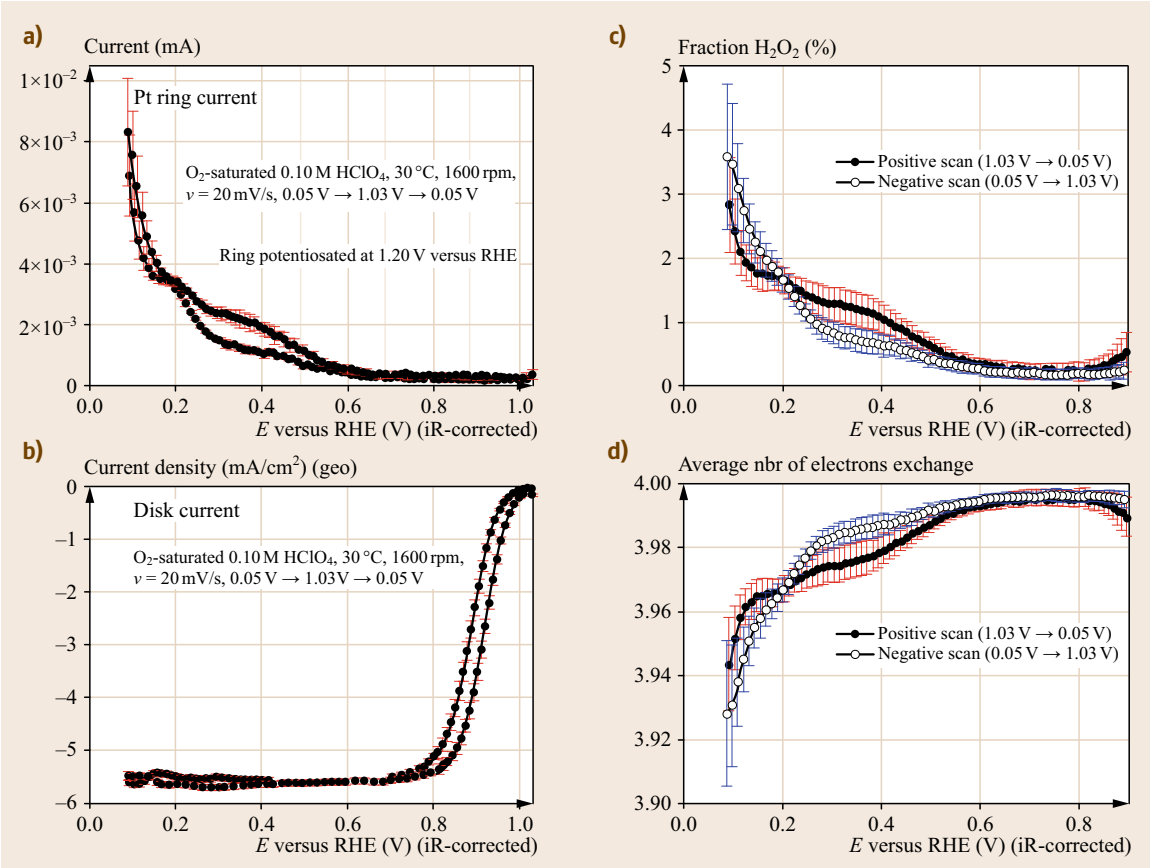


Fig. 14.12 **(a)** Average iR and background corrected ring current recorded for the ORR on a 19.7 wt% Pt/VC electrocatalyst in 0.10 M $HClO_4$. **(b)** Average iR and background corrected disk current density recorded for the ORR on a 19.7 wt% Pt/VC electrocatalyst in 0.10 M $HClO_4$. Error bars correspond the standard deviation for five independent measurements. **(c)** Fraction of H_2O_2 produced during the ORR on the 19.7% Pt/VC catalyst (E-TEK). **(d)** Average number of electrons exchanged during the ORR on the 19.7% Pt/VC catalyst (E-TEK). Errors bars correspond to the standard deviation of five independent measurements

14.2.6 Calculation of Electrocatalyst Mass and Specific Activities

As discussed earlier, the electrocatalytic activity of Pt/C electrocatalysts is best compared by their mass and area-specific activities using the mass transport-correction for thin-film RDEs in [14.19, 21, 23]

$$I_k = \frac{I_{lim} \times I}{I_{lim} - I}\,, \tag{14.21}$$

where I_k is the kinetic current (in A), I_{lim} is the measured limiting current (in A). First the polarization curves are corrected by subtracting background current measured under identical conditions as the ORR polarization curves under N_2 atmosphere without rotation. Then, I is taken from the value of the curve at $E = 0.90$ V and the I_{lim} at $E = 0.50$ V versus RHE. The Pt mass activities (MA, in A/mg_{Pt}) are estimated via calculation of I_k and normalization to the Pt-loading of the disk electrode (i. e., $20\,\mu g_{Pt}/cm^2_{geometric}$ or $\approx 4 \times 10^{-3} mg_{Pt}$). Alternatively, I_k may be calculated using the more rigorous but time-consuming approach of measuring the ORR polarization curves for at least five different rotation speeds (400, 625, 900, 1225, 1600 rpm), from which the current at infinite speed is extrapolated from a Koutecky–Levich plot. The Pt area-specific activities (SA, $\mu A/cm^2_{Pt}$) are estimated via the calculation of I_k and normalization to the platinum surface area, Pt ECSA using

$$I_s(\mu A/cm^2_{Pt}) = \frac{I_k(A)}{\left(Q_{H\text{-adso}}(C)/210(\mu C/cm^2_{Pt})\right)}\,. \tag{14.22}$$

The average MA and SA value at $E = 0.90$ V versus RHE derived from the iR and background corrected ORR polarization curves shown in Fig. 14.6c (anodic sweep: 0.05 V → 1.03 V) for the five independent thin-film Pt/VC RDE electrodes prepared using the traditional stationary drying method is $0.177 \pm 0.042\ \mathrm{A/mg_{Pt}}$ and $356 \pm 81\ \mu\mathrm{A/cm^2_{Pt}}$, respectively compared to $0.359 \pm 0.014\ \mathrm{A/mg_{Pt}}$ and $725 \pm 26\ \mu\mathrm{A/cm^2_{Pt}}$ for five independent thin-film Pt/VC RDE electrodes prepared using the NRL rotational drying method.

14.3 Electrochemical Characterization of Mn_xO_y Thin-Film Electrodes

The same experimental and electrochemical protocol described extensively before for testing Pt/C standards using the thin-film RDE or RRDE methodology was used to test the electrocatalytic activity of three different Mn_xO_y electrocatalysts (i. e., MnO_x, Mn_2O_3, and Mn_3O_4) for their ORR electrocatalytic activity in 0.10 M KOH electrolyte. MnO_2 is attractive because it is naturally abundant, nontoxic and inexpensive. For clarification, what is commonly called MnO_2 or electrolytic MnO_2 is actually a hydrous defective form of $MnO_xH_y \cdot H_2O$.

Two different ink formulations were chosen to evaluate these Mn_xO_y electrocatalysts. The first ink formulation was based on the formulation described by *Tang* et al. [14.44] in their recent publication. This ink formulation is called Mn_xO_y INK#1. The second ink formulation was derived from the typical ink formulation used to test Pt/VC standard for the ORR in our laboratory. This ink formulation is called Mn_xO_y INK#2. The following described the detailed preparation of Mn_xO_y INK#1 and Mn_xO_y INK#2, as well as the method used to cast the thin-film RDE electrodes for the respective inks.

14.3.1 Mn_xO_y/VC INK#1 Preparation

The ink is prepared the day before and stirred overnight before casting the films:

- Approximately, 7 mg of the Mn_xO_y electrocatalyst is weighted into a 10 ml borosilicate vial.
- Next, approximately 5 mg of vulcan carbon (VC) is weighted, and transferred to the vial containing the 7 mg of the Mn_xO_y electrocatalyst.
- Next, 5 ml of ethanol is added to the vial, and mix thoroughly with a high shear mixer (IKA, T10-Basic S1) for 1 min.
- Next, 125 µl of 5 wt% Nafion ionomer solution is added to the vial, and mix thoroughly with a high shear mixer (IKA, T10-Basic S1) for 1 min.
- The Mn_xO_y/VC INK#1 is then transferred to a high-power ultrasonicator (Ultrasonic Power Corporation, model N-50-26 549) and sonicated for 60 min, making sure that the water bath temperature does not rise above 40 °C.
- After 60 min of sonication, the Mn_xO_y/VC INK#1 is taken out of the high-power ultrasonicator. A small stirring bar is then added to the 10 ml borosilicate vial.
- The Mn_xO_y/VC INK#1 is then placed on a stirring plate and allowed to stir overnight.

The thin-film electrodes drying procedure used for the Mn_xO_y/VC INK#1 is the NRL rotational method. However, both the cast ink aliquot volume and the rotation speed of the RDE electrode during the drying process had to be adjusted. Because Mn_xO_y/VC INK#1 uses only ethanol as the solvent, the ink aliquot volume was kept at 7.5 µl. Using only ethanol has the solvent, reduces the surface tension of the ink droplet, and ink aliquot volume > 7.5 µl resulted of ink droplet covering both the GC carbon electrode substrate and the Teflon insulator. The speed of the RDE electrode has to be reduced in order to keep the 7.5 µl ink droplet on the GC electrode substrate. At the typical rotation speed of 700 rpm we used to dry Pt/VC inks, the 7.5 µl Mn_xO_y/VC INK#1 droplet is easily ejected of the surface of the GC electrode substrate. Therefore the rotational speed chosen to dry the Mn_xO_y/VC INK#1 droplet is 100 rpm:

- Glassy carbon disk electrodes ($\phi = 5$ mm, $A = 0.196\ \mathrm{cm^2}$, RDEs) are used as a substrate for the supported electrocatalyst and polished for 4 min to a mirror finish using a 0.05 µm alumina-particle suspension (Buehler) on a moistened polishing cloth. The polished electrodes were rinsed well with nanopure water, sonicated for 4 min in nanopure water, rinsed well again, mounted to the inverted shaft of the electrode rotator (Pine Instrument, AF-PCRB rotator) and then the bare GC electrode was dried at room temperature in air for at least 20 min before use.
- While preparing the RDE electrodes, the Mn_xO_y/VC INK#1 is sonicated in a high-power ultrasonicator for 1 h. After sonication in the high-power

ultrasonicator, the Mn_xO_y/VC INK#1 is then transferred to another ultrasonicator (Branson, 2510) and sonicated for 10 min in a water bath keeping the temperature at $< 40\,^{\circ}C$.

- While the Mn_xO_y/VC INK#1 was sonicated in the ultrasonicator (Branson, 2510), a 7.5 µl aliquot of the well-dispersed ink was pipetted and loaded onto the clean, polished, glassy carbon electrode substrate mounted on the inverted rotator (Fig. 14.3a) such that it completely covered the glassy carbon but did not cover any of the Teflon. The electrode was then rotated at 100 rpm until the film is dry.

14.3.2 Mn_xO_y/VC INK#2 Preparation

The ink is prepared the day before and stirred overnight before casting the films:

- A stock solution containing 40 ml of isopropanol, 59.6 ml of 18 MΩ cm water, and 0.4 ml of 5 wt% Nafion ionomer solution (Ion Power, Liquion 1100), is prepared in a 100 ml volumetric flask.
- Next, approximately 20 mg of the Mn_xO_y electrocatalyst is weighted into a 10 ml borosilicate vial.
- Next, approximately 13 mg of Vulcan carbon (VC) is weighted, and transferred to the vial containing the 20 mg of the Mn_xO_y electrocatalyst.
- Then, 5 ml of the stock isopropanol/water/Nafion solution is added to the vial containing the Mn_xO_y/VC INK#2, and then mixed thoroughly with a high shear mixer (IKA, T10-Basic S1) for 1 min.
- The Mn_xO_y/VC INK#2 is then transferred to a high-power ultrasonicator (Ultrasonic Power Corporation, model N-50-26 549) and sonicated for 60 min, making sure that the water bath temperature does not rise above 40 °C.
- After 60 min of sonication, the Mn_xO_y/VC INK#2 is taken out of the high-power ultrasonicator. A small stirring bar is then added to the 10 ml borosilicate vial containing the mixed Mn_xO_y/VC INK#2 and 5 ml of the stock isopropanol/water/Nafion solution.
- The Mn_xO_y/VC INK#2 is then placed on a stirring plate and allowed to stir overnight.

The thin-film electrodes drying procedure used for the Mn_xO_y/VC INK#2 is the NRL rotational method:

- Glassy carbon disk electrodes ($\phi = 5\,mm, A = 0.196\,cm^2$, RDEs) are used as a substrate for the supported electrocatalyst and polished for 4 min to a mirror finish using a 0.05 µm alumina-particle suspension (Buehler) on a moistened polishing cloth. The polished electrodes were rinsed well with nanopure water, sonicated for 4 min in nanopure water, rinsed well again, mounted to the inverted shaft of the electrode rotator (Pine Instrument, AFPCRB rotator) and then the bare GC electrode was dried at room temperature in air for at least 20 min before use.
- While preparing the RDE electrodes, the Mn_xO_y/VC INK#2 is sonicated in a high-power ultrasonicator for 1 h. After sonication in the high-power ultrasonicator, the Mn_xO_y/VC INK#2 is then transferred to another ultrasonicator (Branson, 2510) and sonicated for 10 min in a water bath keeping the temperature at $< 40\,^{\circ}C$.
- While the Mn_xO_y/VC INK#2 was sonicated in the ultrasonicator (Branson, 2510), a 7.5 µl aliquot of the well-dispersed ink was pipetted and loaded onto the clean, polished, glassy carbon electrode substrate mounted on the inverted rotator (Fig. 14.3a) such that it completely covered the glassy carbon but did not cover any of the Teflon. The electrode was then rotated at 700 rpm until the film is dry.

14.3.3 Comparison ORR Measured for Mn_xO_y/VC INK#1 to ORR Measured Mn_xO_y/VC INK#2

The electrochemical protocol depicted in Fig. 14.13 was used to test the ORR electrocatalytic activity of the Mn_xO_y electrocatalyst samples in 0.10 M KOH electrolyte. A fresh RHE reference electrode as described in Sect. 14.2.6 was used. A typical solution resistance of 35 Ω was measured for the 0.10 M KOH electrolyte at 30 °C, comparable to the literature values [14.45, 46]. For each ink formulation (ca. Mn_xO_y/VC INK#1 and Mn_xO_y/VC INK#2), three RDE thin-film electrodes were prepared for each of the Mn_xO_y samples and tested for their ORR electrocatalytic activity.

Figure 14.13 compares the average iR corrected ORR polarization curves measured for the three RDE thin-film electrodes prepared for each of the Mn_xO_y samples using the Mn_xO_y/VC INK#1 formulation (Fig. 14.13a) to the average iR corrected ORR polarization curves measured for the three RDE thin-film electrodes prepared for each of the Mn_xO_y samples using the Mn_xO_y/VC INK#2 formulation (Fig. 14.13b). Also included in Fig. 14.13 is the typical ORR polarization curve recorded for a Pt/VC RDE thin-film electrode in the same 0.10 M KOH electrolyte as a reference and the ink formulation used for all three Mn_xO_y samples. A single, steep reduction wave with a well-developed limiting current density plateau (j_{lim}) is observed for the ORR polarization curve measured for the Pt/VC

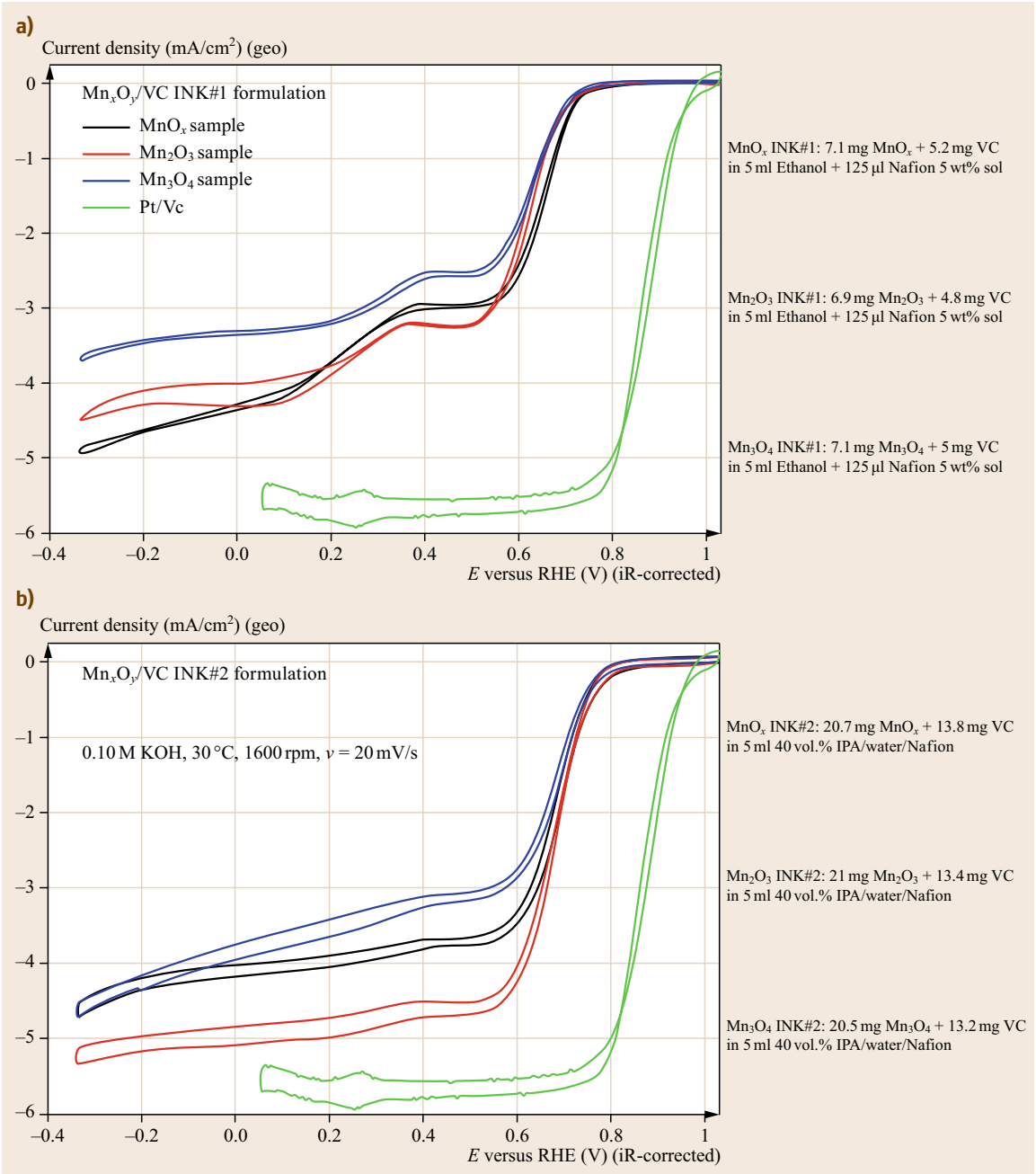


Fig. 14.13 **(a)** Average iR corrected ORR polarization curves measured for three RDE thin-film electrodes prepared for each of the Mn_xO_y samples using the Mn_xO_y/VC INK#1 formulation. **(b)** Average iR corrected ORR polarization curves measured for three RDE thin-film electrodes prepared for each of the Mn_xO_y samples using the Mn_xO_y/VC INK#2 formulation. Typical ORR polarization curve measure for a Pt/VC standard in the same electrolyte is also shown for comparison. Electrolyte 0.10 M KOH, cell temperature of 30 °C, electrode rotation rate of 1600 rpm, potential scan rate ν of 20 mV/s, ORR polarization program: 1.03 V → 0.05 V → 1.03 V

standard in the 0.10 KOH electrolyte. According to the Levich equation, the theoretical limiting diffusion current density is given by (14.12).

For these MnO_2 measurements (and Pt in KOH), the diffusion coefficient (D) of O_2 in 0.10 M KOH is $2\times10^{-5}\,cm^2/s$, [14.47], the kinematic viscosity (v) of the 0.10 M KOH electrolyte is $1\times10^{-2}\,cm^2/s$, [14.47], and the concentration of O_2 in the bulk electrolyte (C_{O_2}) is $1.2\times10^{-6}\,mol/cm^3$, [14.47]. At a working electrode rotation rate of 1600 rpm, for a four-electrons O_2 reduction process and a two-electrons O_2 reduction process, the theoretical diffusion limiting current density can be calculated to be $-5.88\,mA/cm^2$ and $-2.94\,mA/cm^2$, respectively. The j_{lim} experimental value of $-5.91\,mA/cm^2$ measured for the standard Pt/VC RDE thin-film electrode clearly indicates that the ORR takes place on this electrocatalyst via a four-electron process to water.

Figure 14.13a,b also clearly shows that the ORR polarization measured for the different Mn_xO_y are very different that the ORR polarization curve measured for the Pt/VC standard. Several conclusions can be drawn from Fig. 14.13a,b:

- The Mn_xO_y samples are not as active as the Pt/VC electrocatalyst for the ORR. There is a ≈ 250 mV overpotential for all three Mn_xO_y samples compare to the Pt/VC electrocatalyst.
- The ink formulation strongly influences the ORR polarization curves measured for all three Mn_xO_y samples.
- Using the Mn_xO_y/VC INK#1 formulation, two successive reduction waves are visible for the ORR for all three Mn_xO_y samples. There is a steep reduction wave at $E_{1/2} = 0.65$ V versus RHE, followed by a smaller, more drawn out wave at $E_{1/2} = 0.35$ V.
- Using Mn_xO_y/VC INK#1 formulation, the ORR mainly proceed through a two-electrons process for all three Mn_xO_y sample. The limiting current values is about half the value ($-2.85\,mA/cm^2$) measured for the four-electrons process on the Pt/VC electrocatalyst ($-5.88\,mA/cm^2$).
- Using Mn_xO_y/VC INK#1 formulation, the ORR catalytic activity increase in this order: $Mn_3O_4/VC < Mn_2O_3/VC < MnO_x/VC < Pt/VC$.
- Using Mn_xO_y/VC INK#2 formulation, the measured ORR polarization curves for all three Mn_xO_y samples are shaped differently.
- It is more difficult to distinguish the second reduction wave, when using the Mn_xO_y/VC INK#2 formulation.
- The limiting current values measured for all three Mn_xO_y samples are higher than for Mn_xO_y/VC INK#2 formulation
- The ORR take-off potential is the same for all three Mn_xO_y samples when using Mn_xO_y/VC INK#2 formulation (Fig. 14.8b).
- Using Mn_xO_y/VC INK#2 formulation, the ORR catalytic activity increase in this order: $Mn_3O_4 < MnO_x < Mn_2O_3 < Pt/VC$.

Note that the typical method used to characterize such materials is static polarization curves, without rotation. Clearly applying the methods for Pt/C significantly affects the understanding of the relative MnO_2 activities.

14.4 Conclusions

RDE and RRDE methodologies have been developed extensively for Pt/C and related electrocatalysts for PEMFCs because of the desire to find more active electrocatalysts and decrease the catalyst loading in electrodes. In combination with cyclic voltammetry to measure the electrocatalyst electrochemical surface area, RDE methodology has been used for decades to characterize Pt electrocatalysts. RDE methodology has been improved greatly in the last few years as researchers have paid closer attention to background corrections and to the film quality of the electrodes and developed more explicit experimental protocols, enabling the better comparison of electrocatalysts across labs and publications. The film quality has a very high impact, as nonuniform, thick regions have O_2 mass transport limitations, and defeat the benefit of rotating the electrode. The same RDE methods are easily applied to Pt in alkaline conditions, with only a small modification of how the ECSA is calculated. For electrocatalysts used in metal–air batteries, RDE is not yet extensively used because there has been less concern over electrocatalyst cost. But as these technologies drive to requirements for higher efficiencies, accurate comparisons will be needed for electrocatalysts such as MnO_2 as well. While the ultimate performance of an electrocatalyst is determined by its performance in a functional cell, much can be learned about the electrocatalyst kinetics and ORR reaction order from RDE and RRDE methodologies.

References

14.1 K. Kinoshita: *Electrochemical Oxygen Technology* (Wiley, Chichester 1992)

14.2 A.J. Bard, L.R. Faulkner: *Electrochemical Methods* (Wiley, Chichester 1980)

14.3 E. Yeager: Dioxygen electrocatalysis: Mechanisms in relation to catalyst structure, J. Mol. Catal. **38**, 5–25 (1986)

14.4 A. Damjanov, V. Brusic: Electrode kinetics of oxygen reduction on oxide-free platinum electrodes, Electrochim. Acta **12**, 615–628 (1967)

14.5 N.A. Anastasijevic, V. Vesovic, R.R. Adzic: Determination of the kinetic parameters of the oxygen reduction reaction using the rotating ring-disk electrode: Part II applications, J. Electroanal. Chem. **229**, 317–325 (1987)

14.6 N.A. Anastasijevic, V. Vesovic, R.R. Adzic: Determination of the kinetic parameters of the oxygen reduction reaction using the rotating ring-disk electrode: Part I theory, J. Electroanal. Chem. **229**, 305–316 (1987)

14.7 A. Damjanov, M.A. Genshaw, J.O.M. Bockris: The role of hydrogen peroxide in the reduction of oxygen at platinum electrodes, J. Phys. Chem. **70**, 3761–3762 (1966)

14.8 A. Damjanov, M.A. Genshaw, J.O. Bockris: Distinction between intermediates produced in main and side electrodic reactions, J. Chem. Phys. **45**, 4057–4059 (1966)

14.9 V.S. Bagotsky, M.R. Tarasevich, V.J. Filinovskii: Allowance for the adsorption stage in the calculation of kinetic parameters for the reactions of oxygen and hydrogen peroxide, Soviet. Electrochem. **8**, 81–84 (1972)

14.10 H.S. Wroblowa, Y.C. Pan, G. Razumney: Electroreduction of oxygen: A new mechanistic criterion, J. Electroanal. Chem. **69**, 195–201 (1976)

14.11 F. Gloaguen, F. Andolfatto, R. Durand, P. Ozil: Kinetic study of electrochemical reactions at catalyst-recast ionomer interfaces from thin active layer modelling, J. Appl. Electrochem. **24**, 863–869 (1994)

14.12 T.J. Schmidt, H.A. Gasteiger, G.D. Stäb, P.M. Urban, D.M. Kolb, R.J. Behm: Characterization of high-surface-area electrocatalysts using a rotating disk electrode configuration, J. Electrochem. Soc. **145**, 863–869 (1998)

14.13 U.A. Paulus, T.J. Schmidt, H.A. Gasteiger, R.J. Behm: Oxygen reduction on a high-surface area Pt/Vulcan carbon catalyst: A thin-film rotating ring-disk electrode study, J. Electroanal. Chem. **495**, 134–145 (2001)

14.14 C.H. Hamann, A. Hamnett, W. Vielstich: *Electrochemistry* (Wiley-VCH, Weinheim 1998)

14.15 V.G. Levich: Theory of concentration polarization, Zh. Fiz. Khim. **18**, 335–355 (1944)

14.16 V.G. Levich: *Physicochemical Hydrodynamics* (Prentice Hall, Englewood Cliff 1962)

14.17 A. Frumkin, L. Nekrasov, B. Levich, J. Ivanov: Die Anwendung der rotierenden Scheibenelektrode mit einem Ringe zur Untersuchung von Zwischenprodukten elektrochemischer Reaktionen, J. Electroanal. Chem. **1**, 84–90 (1959)

14.18 O. Antoine, R. Durand: RRDE study of oxygen reduction on Pt nanoparticles inside Nafion: H_2O_2 production in PEMFC cathode conditions, J. Appl. Electrochem. **30**, 839–844 (2000)

14.19 Y. Garsany, O.A. Baturina, K.E. Swider-Lyons, S.S. Kocha: Experimental methods for quantifying the activity of platinum electrocatalysts for the oxygen reduction reaction, Anal. Chem. **82**, 6321–6328 (2010)

14.20 Y. Garsany, J. Ge, J. St-Pierre, R. Rocheleau, K. Swider-Lyons: Standardizing thin-film rotating disk electrode measurements of the oxygen reduction activity of Pt/C, ECS Trans. **58**, 3–14 (2013)

14.21 Y. Garsany, J. Ge, J. St-Pierre, R. Rocheleau, K.E. Swider-Lyons: Analytical procedure for accurate comparison of rotating disk electrode results for the oxygen reduction activity of Pt/C, J. Electrochem. Soc. **161**, F628–F640 (2014)

14.22 Y. Garsany, I.L. Singer, K.E. Swider-Lyons: Impact of film drying procedures on RDE characterization of Pt/VC electrocatalysts, J. Electroanal. Chem. **662**, 396–406 (2011)

14.23 H.A. Gasteiger, S.S. Kocha, B. Sompalli, F.T. Wagner: Activity benchmarks and requirements for Pt, Pt-alloys, and non-Pt oxygen reduction catalysts for PEMFCs, Appl. Catal. B-Env. **56**, 9–35 (2005)

14.24 S.S. Kocha, J.W. Zack, S.M. Alia, K.C. Neyerlin, B.S. Pivovar: Influence of ink composition on the electrochemical properties of Pt/C electrocatalysts, ECS Trans. **50**, 1475–1485 (2013)

14.25 K.J.J. Mayrhofer, D. Strmcnik, B.B. Blizanac, V. Stamenkovic, M. Arenz, N.M. Markovic: Measurement of oxygen reduction activities via the rotating disc electrode method: From Pt model surfaces to carbon-supported high surface area catalysts, Electrochim. Acta **53**, 3181–3188 (2008)

14.26 K. Shinozaki, B.S. Pivovar, S.S. Kocha: Enhanced oxygen reduction activity on Pt/C for Nafion-free, thin, uniform films in rotating disk electrode studies Pt-based cathode catalysts, ECS Trans. **58**, 15–26 (2013)

14.27 I. Takahashi, S.S. Kocha: Examination of the activity and durability of PEMFC catalysts in liquid electrolytes, J. Power Sources **195**, 6312–6322 (2010)

14.28 D. van der Vliet, D.S. Strmcnik, C. Wang, V.R. Stamenkovic, N.M. Markovic, M.T.M. Koper: On the importance of correcting for the uncompensated ohmic resistance in model experiments of the oxygen reduction reaction, J. Electroanal. Chem. **647**, 29–34 (2010)

14.29 E. Higuchi, H. Uchida, M. Watanabe: Effect of loading level in platinum-dispersed carbon black electrocatalysts on oxygen reduction activity evaluated by rotating disk electrode, J. Electroanal. Chem. **583**, 69–76 (2005)

14.30 S.K. Zecevic, J.S. Wainright, M.H. Litt, S.L. Gojkovic, R.F. Savinell: Kinetics of O_2 reduction on a Pt electrode covered with a thin film of solid polymer electrolyte, J. Electrochem. Soc. **144**, 2973–2982 (1997)

14.31 R.D. Deegan, O. Bakajin, T.F. Dupont, G. Huber, S.R. Nagel, T.A. Witten: Capillary flow as the cause of ring stains from dried liquid drops, Nature **389**, 827–829 (1997)

14.32 R.D. Deegan, O. Bakajin, T.F. Dupont, G. Huber, S.R. Nagel, T.A. Witten: Contact line deposits in an evaporating drop, Phys. Rev. **E62**, 756–765 (2000)

14.33 P.J. Yunker, T. Still, M.A. Lohr, A.G. Yodh: Suppression of the coffee-ring effect by shape-dependent capillary interactions, Nature **476**, 308–311 (2011)

14.34 F. Gloaguen, P. Convert, S. Gamburzev, O.A. Velev, S. Srinivasan: An evaluation of the macro-homogeneous and agglomerate model for oxygen reduction in PEMFCs, Electrochim. Acta **43**, 3767–3772 (1998)

14.35 S.L. Gojković, S.K. Zečević, R.F. Savinell: O_2 reduction on an ink-type rotating disk electrode using Pt Supported on high-area carbons, J. Electrochem. Soc. **145**, 3713–3720 (1998)

14.36 K. Ke, K. Hiroshima, Y. Kamitaka, T. Hatanaka, Y. Morimoto: An accurate evaluation for the activity of nano-sized electrocatalysts by a thin-film rotating disk electrode: Oxygen reduction on Pt/C, Electrochim. Acta **72**, 120–128 (2012)

14.37 K. Shinozaki, J.W. Zack, S. Pylypenko, R.M. Richards, B.S. Pivovar, S.S. Kocha: Benchmarking the oxygen reduction reaction activity of Pt-based catalysts using standardized rotating disk electrode methods, Int. J. Hydrog. Energ. **40**(46), 16820–16830 (2015)

14.38 K. Shinozaki, J.W. Zack, R.M. Richards, B.S. Pivovar, S.S. Kocha: Oxygen reduction reaction measurements on platinum electrocatalysts utilizing rotating disk electrode technique I. Impact of impurities, measurement protocols and applied corrections, J. Electrochem. Soc. **162**(10), F1144–F1158 (2015)

14.39 V. Stamenkovic, N.M. Markovic, P.N. Ross: Structure-relationships in electrocatalysis: Oxygen reduction and hydrogen oxidation reactions on Pt (111) and Pt (100) in solutions containing chloride ions, J. Electroanal. Chem. **500**, 44–51 (2001)

14.40 O.A. Baturina, B.D. Gould, Y. Garsany, K.E. Swider-Lyons: Insights on the SO_2 poisoning of Pt_3Co/VC and Pt/VC fuel cell catalysts, Electrochim. Acta **55**, 6676–6686 (2010)

14.41 N. Alexeyeva, K. Tammeveski, A. Lopez-Cudero, J. Solla-Gullon, J.M. Feliu: Electroreduction of oxygen on Pt nanoparticle/carbon nanotube nanocomposites in acid and alkaline solutions, Electrochim. Acta **55**, 794–803 (2010)

14.42 Q.S. Chen, J. Solla-Gullon, S.G. Sun, J.M. Feliu: The potential of zero total charge of Pt nanoparticles and polycrystalline electrodes with different surface structure: The role of anion adsorption in fundamental electrocatalysis, Electrochim. Acta **55**, 7982–7994 (2010)

14.43 F.J. Vidal-Iglesias, R.M. Aran-Ais, J. Solla-Gullon, E. Herrero, J.M. Feliu: Electrochemical characterization of shape controlled Pt nanoparticles in different supporting electrolytes, ACS Catalysis **2**, 901–910 (2012)

14.44 Q.W. Tang, L.H. Jiang, J. Liu, S.L. Wang, G.Q. Sun: Effect of surface manganese valence of manganese oxides on the activity of the oxygen reduction reaction in alkaline media, ACS Catalysis **4**, 457–463 (2014)

14.45 Y. Garsany, A. Epshteyn, K.L. More, K.E. Swider-Lyons: Oxygen electroreduction on nanoscale Pt/[$TaOPO_4$/VC] and Pt/[Ta_2O_5/VC] in alkaline electrolyte, ECS Electrochem. Lett. **2**, H46–H50 (2013)

14.46 M. Zhiani, H.A. Gasteiger, M. Piana, S. Catanorchi: Comparative study between platinum supported on carbon and non-noble metal cathode catalyst in alkaline direct ethanol fuel cell (ADEFC), Int. J. Hydrog. Energ. **36**, 5110–5116 (2011)

14.47 G.K.H. Wiberg, K.J.J. Mayrhofer, M. Arenz: Investigation of the Oxygen reduction activity on silver – A rotating disc electrode study, Fuel Cells **10**, 575–581 (2010)

Energy Co Part D

Part D Energy Conversion and Storage

15 Lithium-Ion Batteries and Materials
Cynthia A. Lundgren, Adelphi, USA
Kang Xu, Adelphi, USA
T. Richard Jow, Adelphi, USA
Jan Allen, Adelphi, USA
Sheng S. Zhang, Adelphi, USA

16 Materials for Electrochemical Capacitors
Thierry Brousse, Nantes Cedex 3, France
Daniel Bélanger, Montreal, Canada
Kazumi Chiba, Tokyo, Japan
Minato Egashira, Fujisawa, Japan
Frédéric Favier, Montpellier Cedex 05, France
Jeffrey Long, Washington, USA
John R. Miller, Beachwood, USA
Masayuki Morita, Ube, Japan
Katsuhiko Naoi, Tokyo, Japan
Patrice Simon, Toulouse, France
Wataru Sugimoto, Ueda, Japan

17 Electrochemical Capacitors
Colin G. Cameron, Dartmouth, Canada

18 Kinetics of Fast Redox Systems for Energy Storage
Rudolf Holze, Chemnitz, Germany

19 Modern Fuel Cell Testing Laboratory
Jean St-Pierre, Honolulu, USA
Michael Angelo, Honolulu, USA
Keith Bethune, Honolulu, USA
Jack Huizingh, Honolulu, USA
Tatyana Reshetenko, Honolulu, USA
Mebs Virji, Honolulu, USA
Yunfeng Zhai, Honolulu, USA

20 Polymer Electrolyte Fuel Cells
Vijay K. Ramani, St. Louis, USA
Kevin Cooper, Southern Pines, USA
James M. Fenton, Cocoa, USA
H. Russel Kunz (deceased)

21 Next-Generation Electrocatalysts
Seunghoon Nam, Daejeon, Republic of Korea
Chunjoong Kim, Daejeon, Republic of Korea
Yuhong Oh, Suwon, Republic of Korea
Byungwoo Park, Seoul, Republic of Korea

22 Methods in Biological Fuel Cells
Shelley D. Minteer, Salt Lake City, USA

23 Energy Conversion Based on Bio(electro)catalysts
Tanja Vidaković-Koch, Magdeburg, Germany

24 Photoelectrochemical Conversion Processes
Stuart Licht, Washington, USA

15. Lithium-Ion Batteries and Materials

Cynthia A. Lundgren, Kang Xu, T. Richard Jow, Jan Allen, Sheng S. Zhang

Lithium-ion (Li-ion) batteries are now widely implemented as the power or energy source for everything from portable electronics to electric vehicles. The electrochemical charge storage in the batteries is intimately related to their material properties. This chapter gives an overview of the methods for characterizing battery materials, both ex situ and in situ in practical cells. An important consideration is the interphase between the active charge storage materials and the electrolyte, often called the secondary electrolyte interphase (SEI) layer. Different methodologies unlock different aspects of the battery materials and interphases. Standard test methods are summarized as well as emerging methodologies. Next generation Li-ion batteries, such as Li-sulfur and Li-air are also described.

15.1 **Overview – Electrochemical Evaluation of Li-Ion Batteries** 449

15.2 **Evaluation of Materials and Components in Li-Ion Batteries** 451
15.2.1 Electrode Evaluation 451
15.2.2 Electrolytes and Interphases 454
15.2.3 Separators 470
15.2.4 Advanced/In Situ Spectroscopy 471

15.3 **Evaluation at the Cell–Battery Level** 481
15.3.1 Cell Configurations 481
15.3.2 Performance Characteristics 481
15.3.3 Energy Density 483
15.3.4 Power Capability 483
15.3.5 Cycle Life and Storage Life (or Calendar Life) 485
15.3.6 Safety 486

15.4 **Beyond Li-Ion** 487
15.4.1 Li–S Battery 487
15.4.2 Li–Air Battery 489

15.5 **Conclusions** 490

References 491

Batteries are inherently electrochemical systems undergoing oxidation/reduction reactions. A primary battery is a galvanic cell that converts chemical energy into work. A rechargeable battery combines the galvanic cell with an electrolytic cell, where electrical work is converted into chemical energy upon charging. For a galvanic battery, a positive electrode (cathode) is paired with a negative electrode (anode), which allows a spontaneous oxidation reaction at its surface while sending electrons to the positive electrode through an external circuit, causing a reduction reaction there. Meanwhile within the cell an electrolyte allows the motion of ions in response to an electric field to maintain local and global electroneutrality.

Some figures of merit (FOM) include:

- Storage capacity or charge density (Ah/kg or Ah/l)
- Specific energy (J/kg or Wh/kg)
- Energy density (J/l or Wh/l)
- Specific power (W/kg)
- Power density (W/l)
- Voltage efficiency; ratio of output voltage to E^0.

15.1 Overview – Electrochemical Evaluation of Li-Ion Batteries

Many of these FOM are controlled by the same characteristics that control all electrochemical reactions, including mass loading, surface area, voltage difference between anode and cathode, mobility of ions, resistance of the electrolyte, kinetics and reversibility of the reactions. All modern advances in battery chemistries and components have resorted to various electrochemical methods to evaluate performance and stability. For instance the intrinsic voltage of many battery systems at equilibrium is controlled by the Nernst equation, which

is derived from the Gibb's free energy relationship

$$\Delta G = -nFE\,. \tag{15.1}$$

For any reaction

$$aA + bB = cC + dD\,. \tag{15.2}$$

The voltage of the system can be expressed by

$$E = E^0 - \frac{RT}{nF}\ln\frac{[C]^c[D]^d}{[A]^a[B]^b}\,, \tag{15.3}$$

where E^0 is the standard electrode potential, R is the gas constant, $T =$ is the temperature in K, F is the Faraday constant, n the number of electrons involved in the oxidation/reduction reaction, and [A]–[D] are the concentrations of each species.

The actual voltage produced will always be lower than the theoretical voltage due to voltage loss from parasitic processes and chemistries, and the profile upon discharge is a function of the chemistry, temperature, internal impedance, state of charge (SOC), age of the cell and the kinetics (rate of discharge, often expressed in C-rates). All of these parameters can be studied electrochemically. Some batteries such as lead acid can have the state of charge estimated by voltage at equilibrium; however, some Li-ion cells have a relatively flat voltage profile, indicative of a two-phase system [15.1] (Sect. 15.2.1) during the topotactic intercalation of Li^+. This makes the estimate of state of charge more complicated than just measuring the voltage of the cell at equilibrium. Coulomb counting is a common method to determine the state of charge of these batteries.

Battery components undergo the same electrochemical characterization as other redox systems to determine kinetics, reaction reversibilities, current–voltage behavior, reaction mechanisms and stabilities. These methods include cyclic voltammetry, impedance spectroscopy, coulometry, and so on, and will be discussed in more detail in the subsequent sections. Many of these electrochemical techniques have been augmented by in situ analytical methods, such as in situ extended x-ray absorption fine structure (EXAFS), atomic force microscopy (AFM), IR and nuclear magnetic resonance (NMR) so that chemical and/or structural changes can be observed as a function of real use conditions under an electric field (Sect. 15.2.4).

The development of Li-ion batteries has been spurred by the proliferation of portable electronic devices and the need for higher driving range electric vehicles needing higher energy density batteries that are safe and long lasting. Rechargeable Li-ion batteries have dominated the portable electronics market since their introduction. Due to their relatively high energy density and capacity and good cycle life and storage characteristics, they rapidly replaced Ni–Cd and Ni–metal hydrides, which had been the most widely used in portable electronics prior to Li ion.

The history and advances in Li-ion technology start with the idea of Li metal being used as the source of energy in a battery because of its low weight, high electrochemical potential and stability in nonaqueous electrolytes. Li primary batteries were commercialized in the late 1960s and early 1970s using Li/SO_2, which is still commercially available today. Significant efforts in developing rechargeable Li metal batteries ensued with initial promise shown by Exxon's Li/TiS_2 system [15.2] and then by Ballard Research Inc. and Moli Energy Ltd. However, the problems of Li dendrite formation upon cycling resulted in fires and a NTT recall of Moli batteries in 1989. To date, research is still being actively pursued to develop a rechargeable Li metal or metal–air battery to meet the growing needs of the industry (Sect. 15.4).

The inherent safety issues of using Li metal as the anode led to the development of graphite intercalation materials in the late 1970s by *Basu* and coworkers, *Yazami* and coworkers and patented by Bell Labs [15.3–5]. At the same time, *Goodenough* and *Muzichima* published a report using $LiCoO_2$ as a stable intercalation cathode that can reversibly accommodate Li ions [15.6]. These inventions laid the basis for the modern Li-ion battery, leading to its commercialization by Sony in 1991 [15.7]. The electrochemistry of this new battery is shown in the below equations

$$\mathrm{LiCoO_2} \underset{\text{Discharge}}{\overset{\text{Charge}}{\rightleftarrows}} \mathrm{Li_{1-x}CoO_2} + x\mathrm{Li^+} + x\mathrm{e^-}\,,$$

Positive electrode , (15.4)

$$6\mathrm{C} + x\mathrm{Li^+} + x\mathrm{e^-} \underset{\text{Discharge}}{\overset{\text{Charge}}{\rightleftarrows}} \mathrm{C_6Li_x}\,,$$

Negative electrode , (15.5)

$$\mathrm{LiCoO_2} + \mathrm{C} \underset{\text{Discharge}}{\overset{\text{Charge}}{\rightleftarrows}} \mathrm{Li_{1-x}CoO_2} + \mathrm{CLi_x}\,,$$

Overall cell chemistry . (15.6)

Research into optimizing and developing new chemistries and electrolytes has since grown dramatically. Increasing needs for more energy, higher power, and longer cycle life have led to the development of new materials. The increased interest in hybrid electric vehicles (HEVs) and electric vehicles (EVs) has led to an increased emphasis on safety, especially for

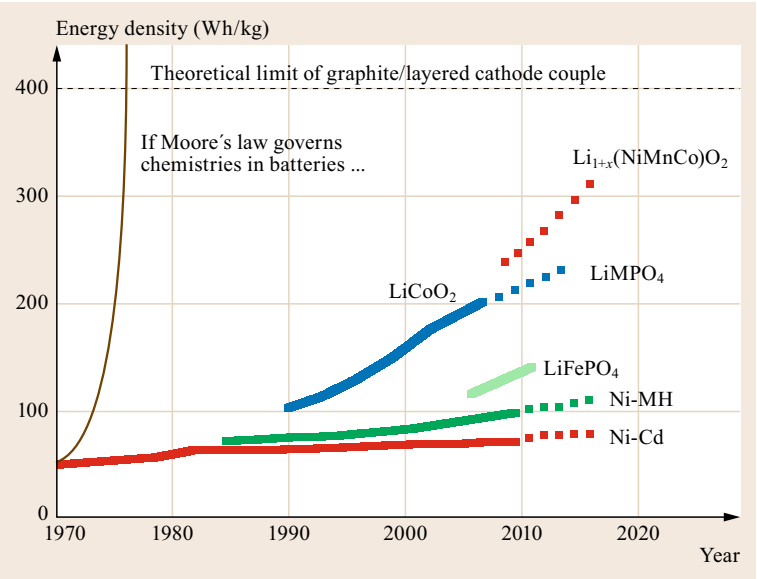


Fig. 15.1 Advancement in advanced battery energy density as a function of time

larger format cells. Figure 15.1 shows the advancement of these Li-ion battery metrics with time. Progress has been steady but incremental, especially compared to the progress in advances of electronics during the same era, which has followed Moore's law (Fig. 15.1).

The rest of this chapter will elaborate the details on the recent advances made in Li-ion batteries and their components and the electrochemical methods that have made them possible, with a foray at the end into what is next, beyond Li ion (Sect. 15.4).

15.2 Evaluation of Materials and Components in Li-Ion Batteries

15.2.1 Electrode Evaluation

Electrode materials can be evaluated by a number of physical methods to predict their performance in a Li-ion cell. Diffraction is a bulk method which gives the average structure over a large number of unit cells.

This has been an important technique for the development of new electrode materials as the typical Li-ion insertion reaction is either a solid solution formation (same phase) or a topotactic transition (meaning there is little change in structure between the charged and discharged state). However, in some cases new phases can be formed. These Li-insertion mechanisms have been more troublesome owing to large changes in the volume between the charged and discharged states. Bulk transitions can be studied by electrochemical methods as well. Beyond this bulk method, local environments have been probed through spectroscopic and electrochemical methods. Thermal methods have shed light on safety considerations. Finally, the potential electrode materials need to be screened in a full electrode pair in order to understand the interactions between the two electrodes and also to determine the behavior when a large surplus of Li reservoir is no longer available, as is the case for a *half* cell. Specific illustrative examples follow.

Diffraction

Diffraction experiments are useful to understand the structural transformations of the electrodes at the bulk level. Diffraction can give information on the crystal structure of the electrodes and changes in lattice constants. The formation of new phases and changes in atomic order can be quantified with high accuracy. For example, *Courtney* and *Dahn* [15.9] used in situ x-ray diffraction to understand the conversion reactions of various Sn oxides including SnO, SnO_3, $LiSnO_3$ and $SnSiO_3$. The diffraction experiments shed light on the mechanism of the conversion. Initially, Li_2O and Sn are formed followed by an alloy formation. *Andersson* and *Thomas* [15.10] used neutron powder diffraction to study the two-phase reaction characteristic of $LiFePO_4$ to $FePO_4$. By using Rietveld refinement the ratio of triphylite ($LiFePO_4$) to heterosite ($FePO_4$) could be quantified and information was gained on the mechanisms for Li insertion and extraction. *Dela-*

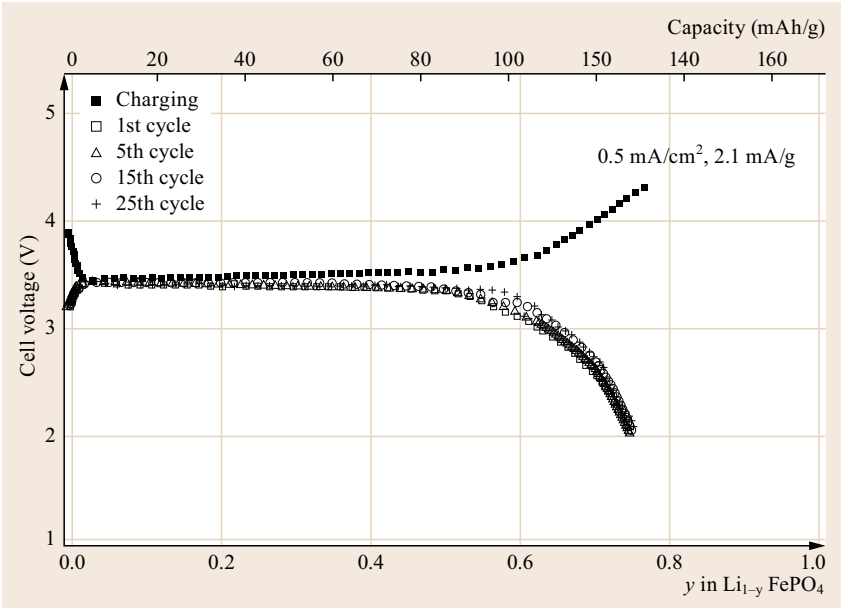


Fig. 15.2 Constant current (2.0 mA/g) discharge and charge curves of $LiFePO_4$ (after [15.8], courtesy of Electrochem. Soc., 1997)

court et al. [15.11] used diffraction to show that the two-phase mechanism changes at temperature above 450 °C to a mechanism where a Li_xFePO_4 ($0 \leq x \leq 1$) solid solution is observed. *Aurbach* et al. [15.12] used diffraction to understand the capacity fading of $LiMn_2O_4$ spinel. The authors observed formation of more disordered phases upon cycling in addition to Mn dissolution, which occurred at voltage > 4.4 V. Understanding of the staging phenomenon in graphite has been heightened by diffraction studies of the intercalation of Li into graphite. *Dahn* [15.13] used in situ x-ray diffraction to determine the phase diagram of Li_xC_6. Another study by *Ohzuku* et al. [15.14] used x-ray diffraction to observe various stages of Li intercalation into graphite such as LiC_6 (stage 1), LiC_{12} (stage 2) and so on up to LiC_{72} (stage 8). Additionally, differences in Li ordering could be discerned.

Spectroscopic

Spectroscopic studies of electrodes are particularly useful for understanding changes in the valence of the active transition metal that occurs during the redox process of a functioning Li-ion battery and to observe the local environment. For example, *Shaju* et al. [15.15] studied the $LiNi_{0.5}Mn_{0.5}O_2$ cathode using x-ray photoelectron spectroscopy (XPS) and observed a $Ni^{2+/4+}$ redox couple and a $Mn^{3+/4+}$ couple. *Johannes* et al. [15.17] used XPS to understand the electronic structures of $LiMPO_4$ olivines by combining the spectroscopy with ab initio computations. Li-6 and Li-7 NMR has been used to study the local environment of Li with cathode materials. For example, *Lee* et al. [15.18] studied $LiMn_2O_4$, $Li_2Mn_4O_9$ and $Li_4Mn_5O_{12}$ through NMR and the resonances could be assigned to different local environments. *Key* et al. [15.19] used in situ Li NMR to study the changes in local structure

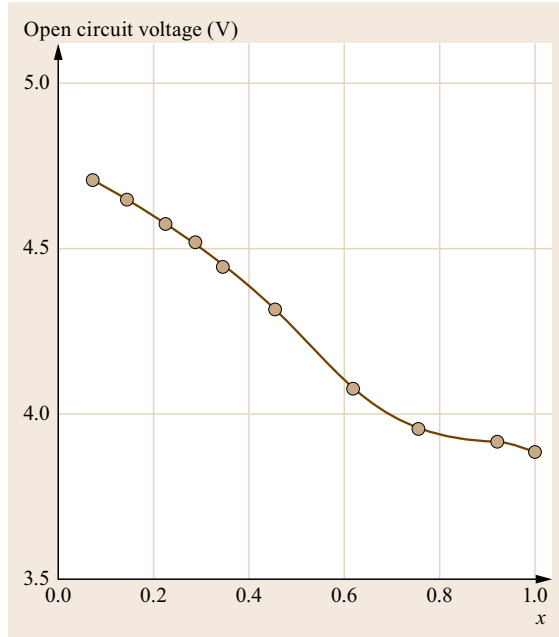


Fig. 15.3 Open-circuit voltage curve for $Li_xCo_{1.01}O_2$ as a function of x. A single-phase region is observed down to about $x = 0.7$, after which a two-phase region is observed (plateau-like behavior) (after [15.16], courtesy of Pergamon Press Ltd, 1980)

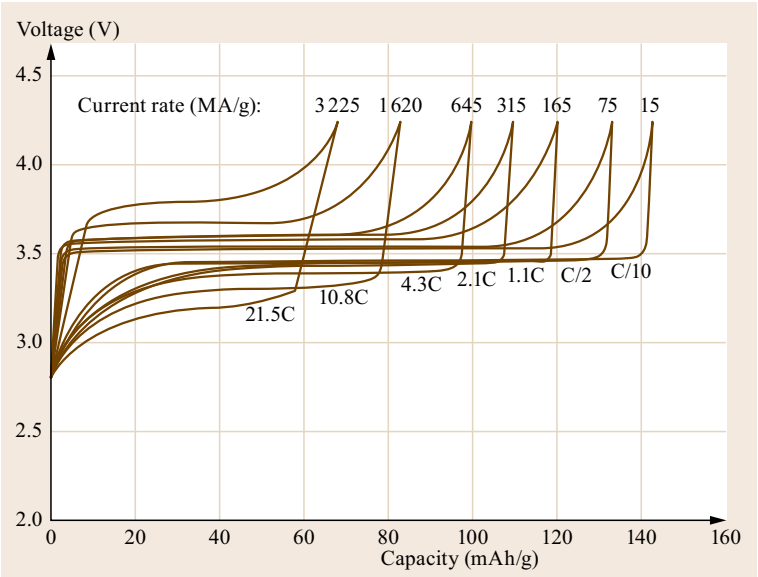


Fig. 15.4 Discharge capacity curves of carbon coated $LiFePO_4$ as a function of discharge capacity (after [15.20], courtesy of Electrochem Soc., 2001)

that occur during the Li intercalation of Si. The authors directly observed formation of isolated Si atoms and a spontaneous side reaction of lithium silicide with the electrolyte via in situ NMR experiments. Mössbauer spectroscopy is another technique which has been used to further the understanding of Li-ion electrode materials. This technique is particularly applicable to materials where the ^{57}Fe nuclei can be studied. For example, *Andersson* et al. [15.21] used the Mössbauer effect to measure the Fe^{3+}/Fe^{2+} ratio during the Li extraction–insertion in $LiFePO_4$. *Allen* et al. [15.22] used Mössbauer to measure the ratio of Fe^{3+}/Fe^{2+} in Fe-substituted $LiCoPO_4$ and to study the local coordination environment. *Dunlap* et al. [15.23] used the ^{119}Sn Mössbauer effect to study the local environment of Sn during Li intercalation.

Electrochemical

Electrochemical techniques have been used to probe the electrode behavior and in particular the diffusion of Li into and out of the electrode material. It can be also used to probe the kinetics of phase transitions. Electrochemical techniques directly measure the battery performance, primarily the amount of energy stored and the rate at which the energy can be utilized. The most simple but informative technique is to build an electrochemical cell, apply a constant current to the cell and monitor the cell voltage as a function of time to a certain cutoff voltage that varies by cathode material. Based on the time of discharge (or charge) the cathode capacity is calculated, which can be expressed in mAh/g or in Wh/kg, which is more useful when comparing materials with different voltage profiles. The rate of the battery or power can be compared by measuring the discharge at different constant currents.

Figure 15.2 shows an example of a galvanosatic discharge and charge curve for $LiFePO_4$ showing the cell voltage as a function of capacity [15.8]. The curve shows a voltage plateau over a large range of Li content, which the authors explain is indicative of a two-phase interface. This method is used to evaluate the capacity (amount of Li that can be removed and reinserted). In this original paper on the use of $LiFePO_4$ as the cathode, a capacity of about 100 mAh/g was shown for the 3.4 V plateau, which corresponds to an energy content of 340 Wh/kg (3.4 V × 100 mAh).

A sloping voltage curve indicating a solid-solution-type behavior for the Li intercalation is shown for Li_xCoO_2 in Fig. 15.3 [15.16]. A single phase region is observed from $1 < x < 0.7$. The capacity obtained for full delithiation is about 274 mAh/g, however in practice the discharge is limited to about $x = 0.5 (\approx 137\,\text{mAh/g})$ in a rechargeable cell because of poor reversibility at high delithiation. The capacity and voltage will vary as a function of rate. As the current increases, the usable capacity of the cell decreases. An illustrative example is shown in Fig. 15.4 [15.20]. In this case the rate capability is determined by measuring the capacity of a $LiFePO_4$ cathode by varying the current during a constant current discharge.

Cyclic voltammetry (CV) is a useful technique in which the voltage is linearly scanned in both directions while measuring the current response. A very small amount of material can be used and it can give insights into many of the physical processes occurring within the cell. For example, *Levi* et al. [15.24]

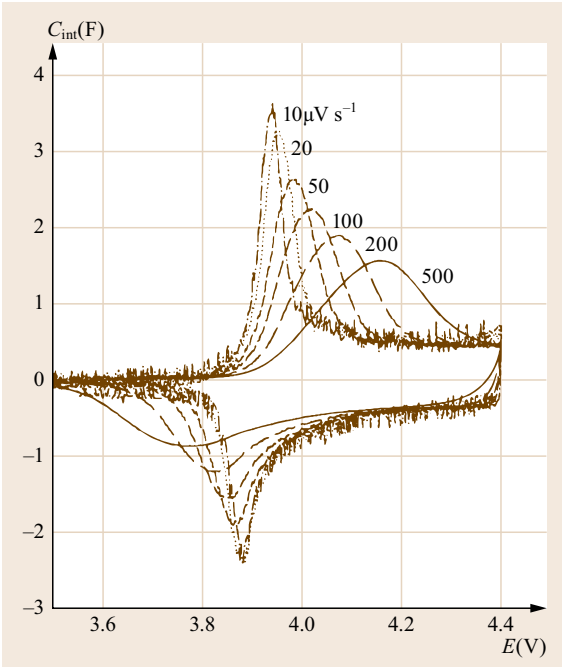


Fig. 15.5 Multiple variable-rate, slow-scan cyclic voltammograms of $LiCoO_2$ showing the differential intercalation capacity C_{int} as a function of the electrode potential. The positive peak and negative peaks indicate intercalation and deintercalation of Li into and out of $LiCoO_2$, respectively (after [15.24], courtesy of Electrochem. Soc., 1999)

combined the use of CV, (Fig. 15.5) potentiostatic intermittent titration (PITT) techniques and electrochemical impedance spectroscopy (EIS) to understand the behavior of $Li_{1-x}CoO_2$ electrodes. This study gave information concerning the solid-state diffusion of Li within the electrode material. The CV technique using a thin sample enabled the use of a Frumkin isotherm to characterize the intercalation process. The PITT technique estimated the chemical diffusion coefficient from application of a potential and measurement of the resultant current. EIS applies a small (AC) potential to the cell and measures the current through the cell. Owing to the small amplitude of the AC potential, the system is close to equilibrium. Levi used an equivalent circuit to obtain information about the Li-ion diffusion coefficient. A further example is that of *Takahashi* et al. [15.25] using cyclic voltammetry (CV) and EIS (Fig. 15.6) to evaluate the activation energy for Li diffusion of $LiFePO_4$.

Phase transformation has been studied using electrochemical methods. For example, the electrochemical $FePO_4$ to $LiFePO_4$ phase transition was studied by *Allen* et al. [15.26]. By measuring the conversion of $FePO_4$ to $LiFePO_4$ by galvanostatic discharge at different temperatures, Avrami plots were obtained enabling an understanding of the dimensionality and the quantification of the activation energy of the phase transition (Fig. 15.7).

Thermal

Thermal studies of electrode materials are particularly useful in order to understand the thermal stability of the electrode and consequently the safety under abusive conditions. An illustrative example of the utility of thermal studies is the work of *Dahn* et al. [15.27]. The authors studied the stability of Li_xCoO_2, Li_xNiO_2 and $Li_xMn_2O_4$ in order to understand the safety of Li-ion cells that utilize these cathodes. The fully lithiated cathodes, $LiCoO_2$, $LiNiO_2$ and $LiMn_2O_4$ were shown to be fully stable in air up to high temperatures. However, partially delithiated samples, Li_xCoO_2, Li_xNiO_2 and $Li_xMn_2O_4$ ($x < 1$) were shown to be only metastable. At moderate temperatures, O_2 was shown to be liberated. Furthermore, $Li_xMn_2O_4$ was suggested to be superior in thermal stability relative to Li_xCoO_2 or Li_xNiO_2. *MacNeil* et al. [15.28] reported on the reaction of electrode materials with electrolyte materials. Differential scanning calorimetry (DSC) was used to show the differences in reactivity with electrolyte between a number of Li-ion cathode materials including $LiCoO_2$, $LiMn_2O_4$ and $LiFePO_4$.

Electrode Pairs

A successful Li-ion cell depends on the interaction of the spatially separated positive electrode (cathode) with the negative electrode (anode). In the Li-ion cell, the first charge involves the net transfer of Li from the cathode to the anode to form a passivation layer, which is a combination of the electrode surface and electrolyte components as is discussed elsewhere in this chapter. Electrochemical methods have been used to study the cathode–anode mass ratio, which is important for long cycle life. For example, *Moshtev* et al. [15.29] studied the effect on performance of the ratio of $LiNiO_2$ to petroleum coke in Li-ion cells. *Tarascon* and *Guyomard* [15.30] reported on the $Li_{1+x}Mn_2O_4$/C system.

15.2.2 Electrolytes and Interphases

The electrolyte is an essential component in any electrochemical device. It acts as the ionic conductor and electronic barrier between the two reactants of the cell chemistry: oxidant (cathode) and reductant (anode). During the cell reaction, the electrolyte should maintain its mechanical, chemical and electrochemical inertness toward both electrodes. In rechargeable batteries, how the electrolyte interacts with electrodes often dictates

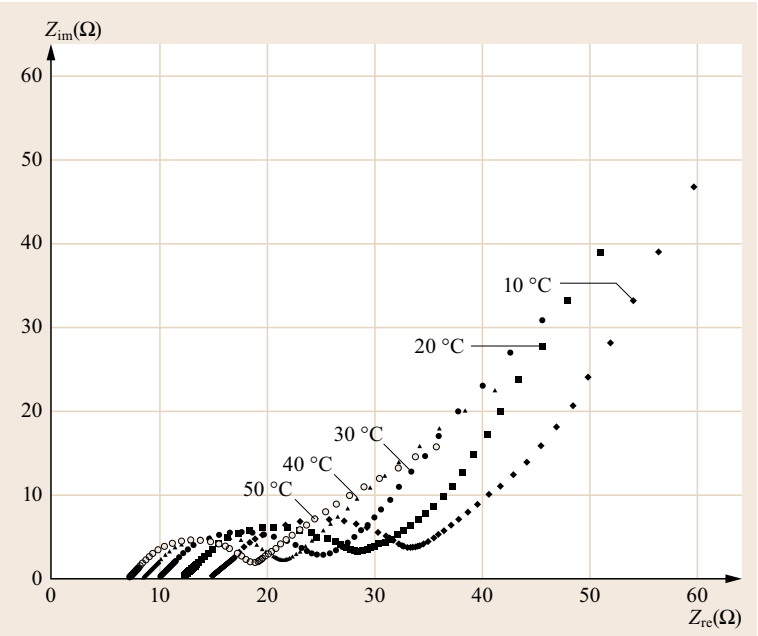


Fig. 15.6 Electrochemical impedance spectrum of $LiFePO_4$, shown as a function of temperature. From this data a plot of the activation energy for Li-ion diffusion was derived (after [15.25], courtesy of Elsevier, 2002)

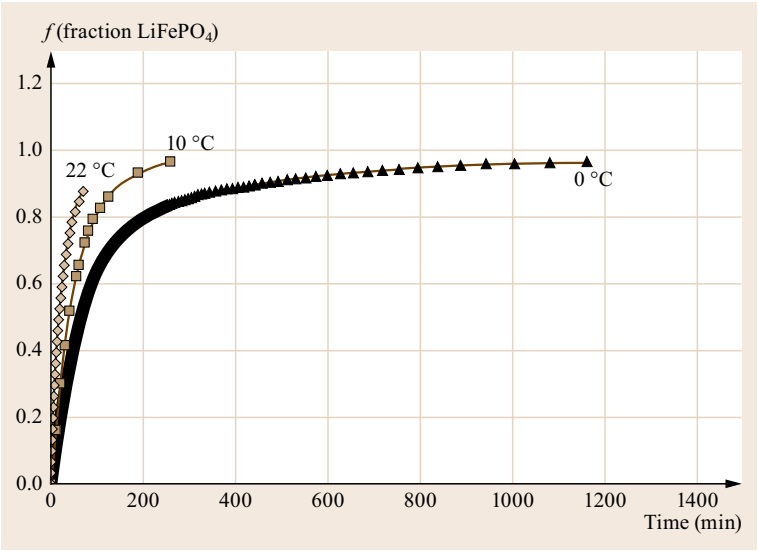


Fig. 15.7 Fraction of $LiFePO_4$ electrochemically formed from $FePO_4$ as a function of time and temperature measured by recording the current as a function of time at a fixed voltage of 3 V. The assumption was that the current measured corresponded to the reaction $FePO_4 + e^- + Li^+ \rightarrow LiFePO_4$. From this data Avrami plots were obtained in order to gain insight into the mechanism of phase transformation (after [15.26])

the cycle life and power density of the device, and an electrochemical stability window is the most important requirement for successful electrolytes besides their capability of conducting ions [15.31].

In devices of low operating voltages (< 2.0 V), such as aqueous-based batteries supercapacitors and fuel cells, etc., the electrochemical inertness of electrolytes is usually realized via the thermodynamic stability of each individual electrolyte component (solvent, salt, additive) against the electrodes. However, when operating voltages of 3.0 V or higher are pursued for the sake of higher energy densities, amost no electrolyte components can remain thermodynamically stable against the strong reducing power of the anode or oxidizing power of the cathode; rather, the stability is achieved through a process called *passivation*, i. e., part of the electrolyte components sacrifice themselves by decomposing, and their products combine to form a protection layer to stop the same decomposition from occurring sustainably. The new interfacial phase is named *interphase* [15.32]. Li-ion batteries rely on such interphases to operate, because

the potential of their graphitic anode sits near 0.20 V for Li (or -3.0 V for SHE), which is far beyond the reduction potential of most known nonaqueous electrolyte components. The interphase on the graphitic anode is also known as the SEI (solid electrolyte interphase) after its Li^+-conducting/electronic insulating nature, and has become a topic of focused research in the past two decades. The existence of the cathode equivalent of the SEI is debated. The potential of the cathode in Li-ion batteries varies between 3.5 V of $LiFePO_4$ to 4.2 V of diversified transition metal oxides LiM_xO_y (M = Co, Ni, Mn etc.), which correspond to 0.5–1.1 V for SHE, which is on the border of oxidation stability limits for most electrolyte components. What is beyond controversy is that, when the cathode potential is pushed higher than 4.5 V with the new 5 V class chemistries (e.g., $LiNi_{0.5}Mn_{1.5}O_4$, $LiCoPO_4$ etc.), the appearance of interphases will become a certainty [15.33, 34].

This section will review the established method of characterizing electrolytes and the resultant interphases, which, unless specified, refer to the SEI on the graphitic anode surface.

Bulk and Transport Properties

The state-of-the-art Li-ion batteries use electrolytes typically consisting of Li salts with fluorinated inorganic anions ($LiPF_6$, $LiBF_4$) dissolved in organic aprotic solvents consisting of carbonic dialkyl-esters or carboxylic esters. With few exceptions ethylene carbonate (EC) is almost an indispensable component due to its role in SEI formation [15.31]. There are also often ingredients at rather small concentrations (from ppm to a few percent), which are called *additives* [15.35]. The role of additives varies from preserving cell safety as *redox shuttles* or *flame retardants*, to assisting interfacial formation chemistry, and remain as unique trade secrets with each manufacture. However, the skeleton composition of most commercial electrolytes is based on solutions of $LiPF_6$ in mixtures of EC with one or more of acyclic carbonic dialkyl esters, such as dimethyl carbonate (DMC) and ethylmethyl carbonate (EMC). The formulation of these state-of-the-art electrolytes is the result of a compromised consideration of the following list of requirements:

1. High ionic and low electronic conductivity
2. Wide liquid range (low liquidus temperature and low vapor pressure)
3. Ability to wet the polyolefin separator whose porous structure is usually lipophilic
4. Inertness to other cell parts such as substrates, binders, current collectors and tabs
5. High safety
6. Low toxicity (therefore of little disposal concern)
7. Low cost.

Phase Diagram. The service temperature range of electrolytes is actually determined by two different sets of standards: the *wider* range by their thermodynamic properties, beyond which the electrolytes would no longer be in the liquid state, and the *narrower* range by the corresponding electrochemical properties, only within which could the desired performances be delivered. The *wider* range is best represented in the form of phase diagrams and serves as the *minimum standard* a nonaqueous electrolyte must meet.

The classical phase diagrams for carbonate-based electrolyte solvent systems were mapped out by *Ding* and coworkers using conventional thermal analysis techniques such as DSC, where all possible combinations of the commonly used carbonates were found to be simple eutectic types [15.36, 37]. The typical binary phase diagram between EC and DMC and how it was constructed by DSC traces is schematically shown in Fig. 15.8a, where the solidus line defines the lower temperature limits for these systems. When mixtures of more than two solvents are used to formulate the electrolytes, the corresponding phase diagrams become increasing complicated. Figure 15.8b shows one such diagram for the ternary system EC/DMC/EMC, in which the ternary liquidus and solidus faces were calculated based on the individual binary phase diagrams [15.38].

While a common feature of binary eutectic systems is the depression of liquidus temperatures for the mixtures, an important discovery by *Ding* et al. is that the effectiveness of such depressions are determined by two factors:

1. Molecular structure similarity
2. Melting point proximity of the two solvents.

For example, the mismatch between the high melting, cyclic EC (mp 37 °C) and low melting, acyclic EMC (mp −53 °C) results in a liquidus line that approaches the mp of EC for most of the compositions, so that the liquid range actually shrinks as compared with the EC/DMC binary system. A similar mismatch exists for almost all electrolyte compositions as long as EC is used, and it has led to a consistent issue of narrow service temperature ranges for all Li-ion batteries [15.36, 37].

Solvation. In order for Li salts to be dissolved into electrolyte solutions, Li^+ must be stabilized by solvent molecules through coulombic coordination, which compensates the free energy increase as result of the

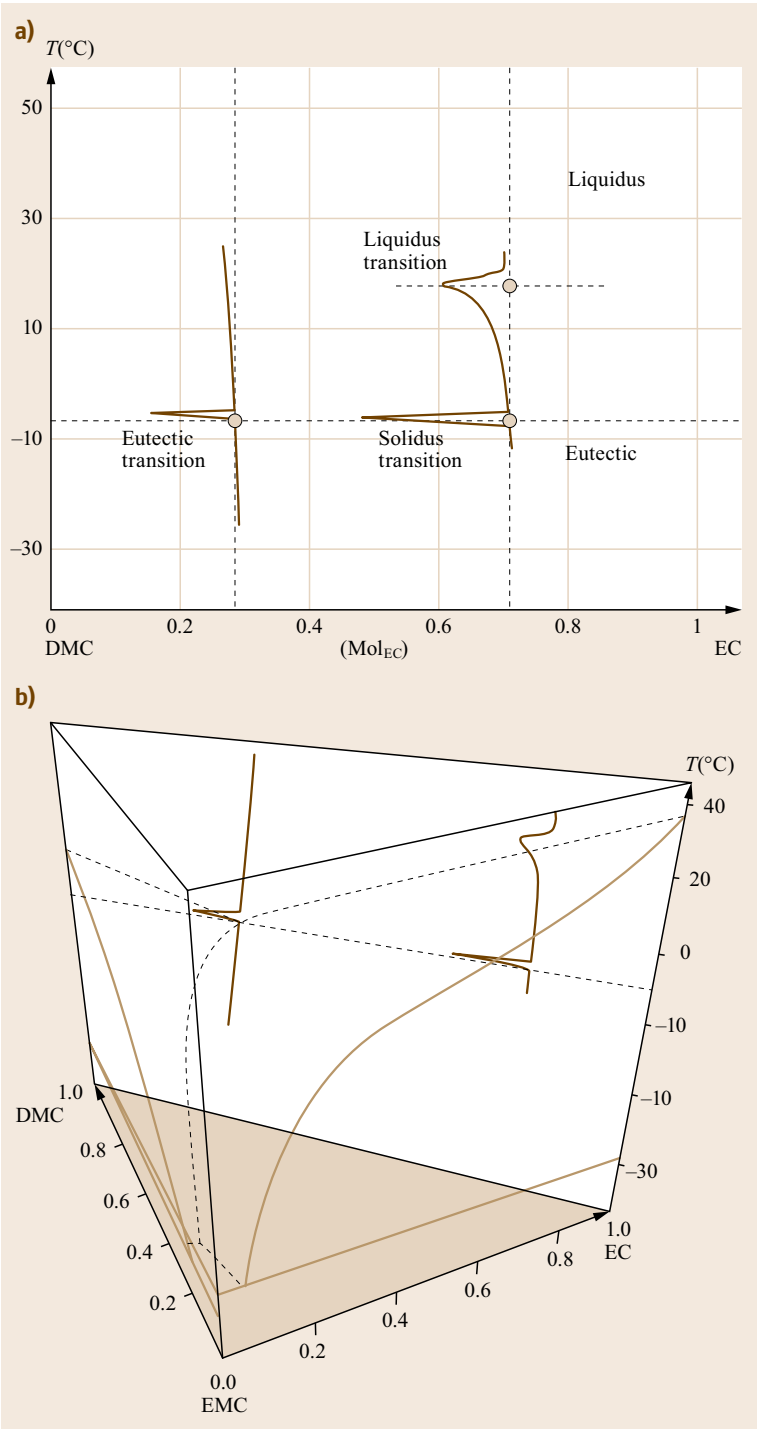


Fig. 15.8 **(a)** Binary phase diagram of EC/DMC constructed by differential scanning calorimetry (DSC) experiments (marked by *red traces*), whose two peaks mark the temperature ranges where liquid and solid phases coexist. Above liquidus line the electrolyte is in true (or thermodynamically stable) liquid state, while in reality the liquid range could be significantly wider due to supercooling (metastable liquid state) **(b)** Ternary phase diagram of EC/DMC/EMC as calculated from thermodynamic non-ideal models based on experimental feedings from corresponding binary phase diagrams. The DSC traces shown in Fig. 15.8 were also shown on the EC/DMC plane. Again, above liquidus surfaces the electrolytes are *true* liquids (after [15.38])

lattice disruption. That is why nonaqueous electrolyte solvents are almost exclusively nucleophilic molecules that have nonpaired electrons. Each Li^+ wrapped in such nucleophilic environments actually forms a solvation sheath. The innermost layer of the sheath is called the *primary solvation sheath*, whose composition is relatively static during ionic movement; while solvent molecules more remote from the central Li^+ consti-

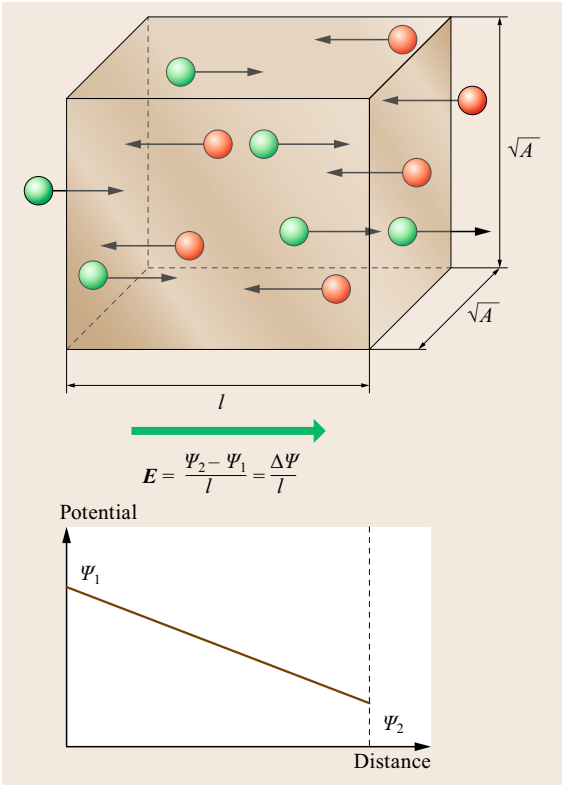


Fig. 15.9 Schematic definition of ion conductivity in an electrolyte block of length l and cross-area A, which is subject to a DC field of E

tute a *secondary solvation sheath*, which is loosely associated with Li^+ and whose composition is more dynamic [15.39]. As described later in this chapter, the structure of such Li^+-solvation sheaths plays critical roles both in defining the interphase chemistry and in dictating Li^+-migration after such interphases are formed.

Based on spectroscopic observations and computation, it is generally accepted that Li^+ can accommodate 3–5 organic solvent molecules in its primary solvation sheath [15.31]. However, little has been known about how Li^+ interacts with those solvent molecules on an atomistic level, or whether Li^+ shows preference toward some of the solvent molecules against others. This latter knowledge becomes critical when one tries to understand the manner in which a solvated Li^+ desolvates in order to intercalate into a host electrode, or a naked Li^+ solvates while leaving a lithiated host electrode [15.40].

Ionic Conductivity. While redox reactions occur within both anode and cathode materials at the influx or exodus of electrons from external circuits during charging or discharging of the batteries, the electrolytes must act as the ionic reservoir or sink to compensate for any disturbance in electroneutrality therein; thus one of the basic requirements for any electrolytes is the capability to transport ions across the device. Such capability is quantified by ionic conductivity σ, which essentially represents the amount of charge carried by the ions through a cubic unit of electrolyte in unit time under unit electric field (Fig. 15.9).

$$\sigma = \frac{l}{RA} = \frac{JzFA}{\Delta\psi}\frac{l}{A} = \frac{JzF}{X}\,, \tag{15.7}$$

where J, z, F and X stand for ion flux, ionic valence, Faraday constant and electric field strength, respectively; ψ is the potential.

Ionic conductivity is defined by an imaginary orientational movement of ions along a (DC) electric field as shown in Fig. 15.10. However, under DC conditions it is very difficult to accurately measure this quantity because of the instantaneous deviation from ideal Ohmic behavior, either caused by the accumulation of charges at electrolyte–electrode interfaces when blocking electrodes are used, or by the slow charge-transfer processes at electrolyte–electrode interfaces when nonblocking electrodes are used. Figure 15.10a,b show the equivalent circuits for both scenarios under DC condition, using a Li^+-containing electrolyte as an example. The ion accumulation at interfaces is represented by a double layer and geometric capacitor (C_{dl} and C_g), and slowed-down ionic migration by additional resistors at interfaces (R_i and R_{ct}).

EIS methodology provides an effective approach to circumvent the unwanted interferences from these electric components, based on the different relaxation time scales with which each of those components responds to an applied AC field [15.41]. For example, the electronic conduction of the circuits and capacitance would respond at extremely high frequencies ($> 10^4$ Hz) due to the rapid movement of electrons in metals and relatively fast formation of electrified double layers, while the much slower ion migration within solid electrodes or charge transfer processes, including either ion movement across the interfaces or reduction/oxidation of ionic species at the interfaces, can only occur at extremely low frequencies ($< 10^2$ Hz). The ion conduction within bulk electrolyte usually lies in the medium frequencies (10^2–10^3 Hz). By applying an AC field at varying frequencies, it is possible to differentiate ion conduction from those above common interferences.

Figure 15.11 graphically shows the basic setup of a typical EIS analysis using blocking electrodes as represented by the equivalent circuit in Fig. 15.10a, where

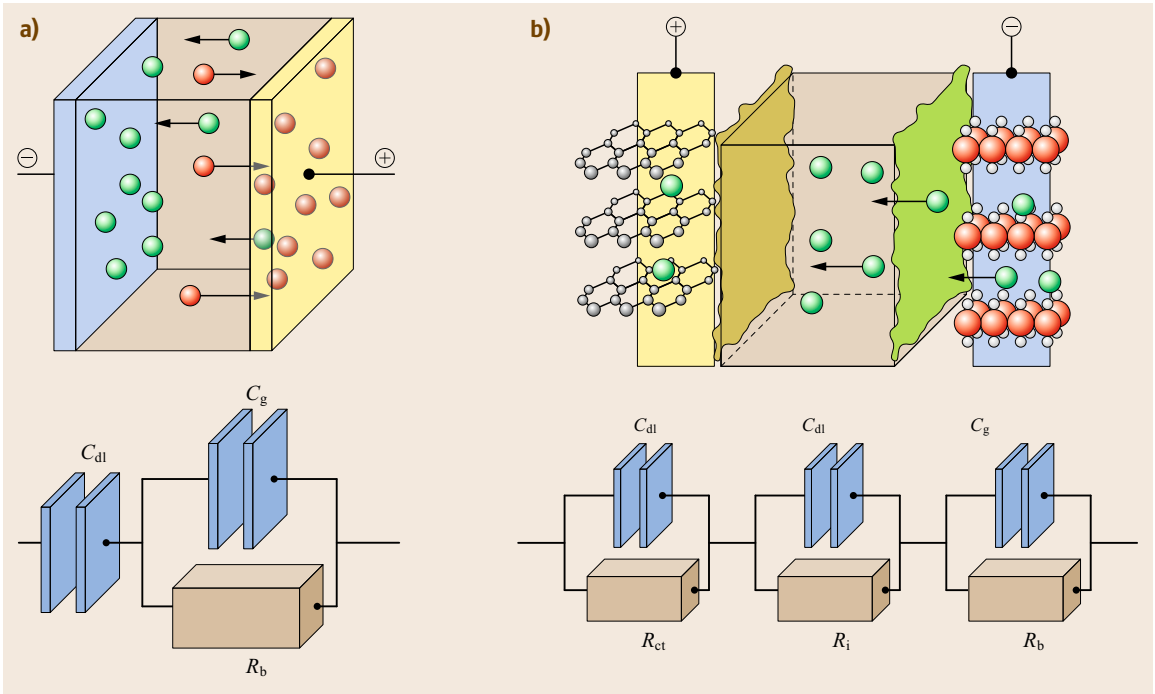


Fig. 15.10a,b Under DC conditions, it is impossible to accurately measure the ionic conductivity of an electrolyte (σ corresponding to bulk resistance component R_b) due to interferences from capacitances (from double-layer C_{dl} and from cell geometry C_g) and other resistor components (R_i and R_{ct}). **(a)** When blocking electrodes are used, neither cation (Li^+) nor anion can travel across the electrode–electrolyte interfaces, thus accumulating opposite charges at the interfaces and forming a double-layer capacitor. **(b)** When nonblocking electrodes are used, such as in a typical Li^+-ion battery, the resistance to Li^+ crossing electrode–electrolyte interfaces far outweighs that of bulk resistance of the electrolyte. If electrode passivation occurs, additional resistance components would arise, such as from interphases (R_i)

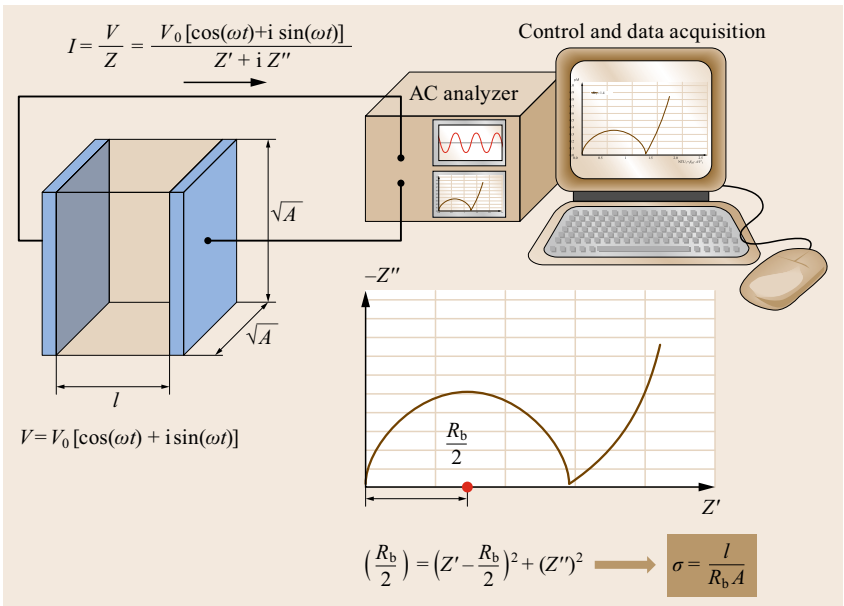


Fig. 15.11 Graphic illustration of a typical AC impedance analysis setup and the evaluation of ionic conductivity σ. Impedance analyses using AC technology can be used to deconvolute the different contributions from various components, enabling accurate measurement of ionic resistance (or conduction)

a symmetrical cell containing the electrolyte under investigation is subject to a sinusoidal voltage of varying frequency ω and constant amplitude V_0,

$$V = V_0[\cos(\omega t) + \mathrm{i}\sin(\omega t)]\,. \tag{15.8}$$

The current response I is recorded as function of V. Since all electric components will contribute to the overall impedance Z, which is now a complex quantity, according to Ohmic law

$$I = \frac{V}{Z} = \frac{V_0[\cos(\omega t) + \mathrm{i}\sin(\omega t)]}{Z' + \mathrm{i}Z''}\,. \tag{15.9}$$

Solution to the complex equation leads to the real (Z') and imaginary (Z'') parts of the overall impedance as

$$Z' = \frac{R_\mathrm{b}}{1 + (\omega C_\mathrm{g} R_\mathrm{b})^2}$$
$$\text{and} \quad Z'' = \frac{\left[1 + (\omega C_\mathrm{g} R_\mathrm{b})^2 \left(1 + \frac{C_\mathrm{dl}}{C_\mathrm{g}}\right)\right]}{\omega C_\mathrm{dl}[1 + (\omega C_\mathrm{g} R_\mathrm{b})^2]}\,, \tag{15.10}$$

where R_b is our goal (bulk electrolyte resistance to ionic movement). Despite their complicated expressions, Z' and Z'' can be rearranged, after reasonable approximations, into a very useful expression that sets the foundation of practical impedance spectroscopy

$$\left(\frac{R_\mathrm{b}}{2}\right)^2 = \left(Z' - \frac{R_\mathrm{b}}{2}\right)^2 + (Z'')^2\,. \tag{15.11}$$

In other words, when $-Z''$ is plotted against Z' on a complex plane, the relation will produce a semicircle that centers at $(\frac{R_\mathrm{b}}{2}, 0)$ on the real axis (Fig. 15.12). Thus the semicircle intercepts the real axis at $(R_\mathrm{b}, 0)$. In reality, deviation from the ideal equivalent circuit distorts the semicircle, but the basic feature remains, and ionic conductivity should always be evaluated from the intercept of Z on real axis

$$\sigma = \frac{l}{R_\mathrm{b} A}\,. \tag{15.12}$$

For most liquid electrolyte at room temperature, whose ionic conductivity remains higher than 1.0 mS/cm, the semicircle corresponding to R_b could *shrink* or entirely merge with the interphase component, and the intercept at the high frequency end is usually used in place of R_b.

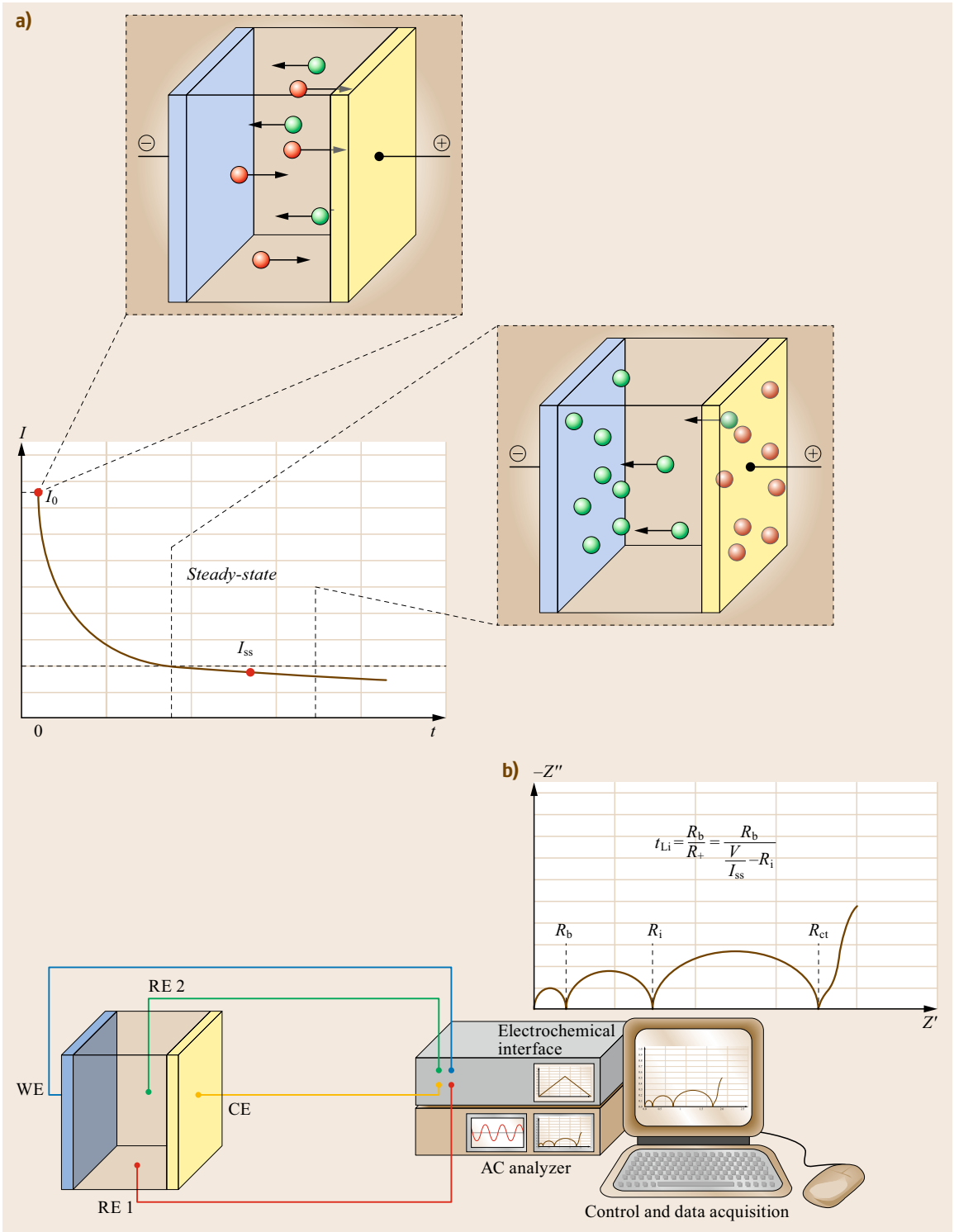
Lithium Ion Transference Number. The ionic conductivity determined before includes the contributions from the movements of both cations and anions. In most electrochemical devices, only one ionic species participates in the cell chemistry. For proton fuel cells this ion would be H^+, for alkaline fuel cells OH^-, and for Li-based batteries Li^+. Therefore, sometimes it becomes necessary to know the portion of current that is solely caused by the movement of that ionic species. Thus, ionic transference number is defined as

$$t_+ = \frac{\sum \sigma_+}{\sigma_\mathrm{i}} = \frac{\sum \mu_+}{\mu_\mathrm{i}} = \frac{I_+}{I_+ + I_-}$$
$$\text{and} \quad t_- = 1 - t_+\,. \tag{15.13}$$

Fig. 15.12 **(a)** Schematic illustration of the *steady-state current* approach to measuring Li^+ transference number. At $t = 0$, both cation and anion migrate under the DC field and contribute to ionic current; at *steady state*, most anions are accumulated at the electrode surface, while Li^+ is the only species carrying ionic current because it can travel across the interphase and enter the nonblocking electrode. **(b)** Typical AC impedance analysis setup and the evaluation of the Li^+-transference number, t_Li. The working electrode (WE) must be a nonblocking electrode to Li^+ so that it can become the only ionic species carrying the current at *steady state* ►

Apparently ion pairs contribute nothing to the overall current and the presence of ion aggregations significantly reduces the available free ions that can carry current.

As one of the smallest cations (radius ≈ 0.09 nm), Li^+ exerts strong Coulombic attraction to solvent molecules in nonaqueous electrolytes, such that on average 4–5 such molecules coordinate with each Li^+. This ion-molecule coordination complex is called the *primary solvation sheath*, which remains intact even when Li^+ moves. Since a solvated Li^+ far outsizes its less-solvated counter ions and is therefore less mobile, most current through nonaqueous electrolytes is not carried by Li^+ itself but by the anion [15.42]. While the presence of anion in the electrolyte is indispensable in maintaining global and regional electroneutrality, anionic current is useless for a Li-ion battery device because anions cannot cross interphases and participate in intercalation chemistries (Fig. 15.13). A direct consequence of this parasitic current is the formation of a concentration polarization, which generates additional resistance against Li^+ conduction. An ideal electrolyte thus should not only show apparent high ion conductivity, but also the maximized Li^+ conduction, although in reality the overall ion conductivity as measured by impedance techniques has been used to characterize and evaluate electrolytes, with an incorrect implication that it is proportional to Li^+ conduction.


a)
I
I_0
Steady-state
I_{ss}
0
t
b)
–Z″
$t_{Li} = \frac{R_b}{R_+} = \frac{R_b}{\frac{V}{I_{ss}} - R_i}$
R_b
R_i
R_{ct}
Z′
RE 2
WE
CE
RE 1
Electrochemical interface
AC analyzer
Control and data acquisition

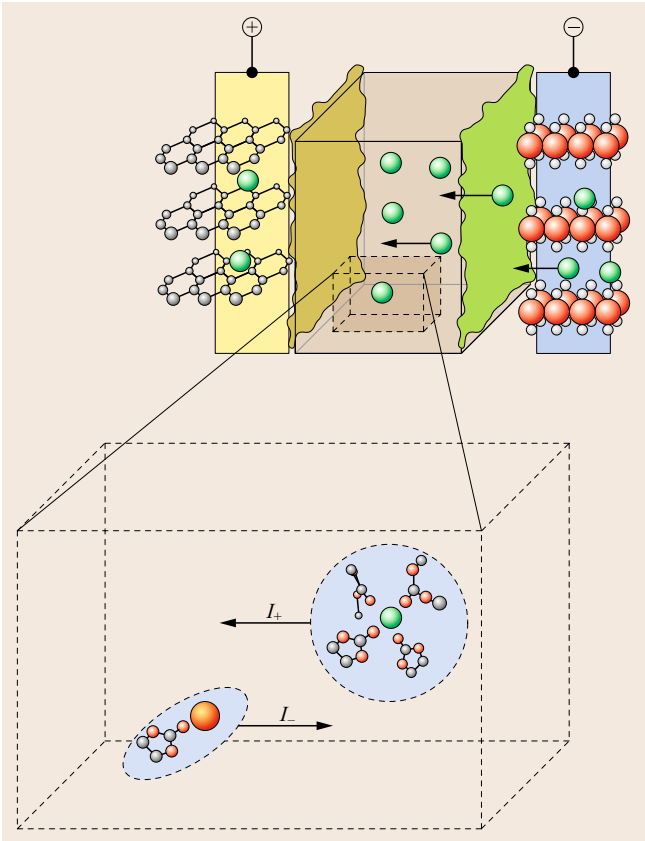


Fig. 15.13 The ionic current consists of contributions from parallel cationic and anionic movements. Solvated Li^+ usually moves much slower than its counter ion in nonaqueous electrolytes due to its much larger solvation sheath, hence the cationic transference number is usually less than 0.5

Accurate measurement of Li^+ transference number is always a topic of controversy. Scattered and even conflicting results are often produced by various methods. The classical *steady-state current approach* was developed by *Evans* et al., who devised a symmetric cell consisting of two identical Li-metal electrodes (Fig. 15.12a) [15.43]. When a small DC field, e.g., 10 mV, is applied to such a cell, Li is oxidized to Li^+ at the positively-polarized electrode (cathode), while Li^+ is reduced to Li at the negatively-polarized electrode (anode). In an ideal scenario, the initial current I_0 consist of both anionic as well as cationic contributions, while after equilibrium is reached, the steady-state current I_{ss} should only be carried by Li^+. Thus,

$$t_{Li} = \frac{I_{ss}}{I_0} \,. \tag{15.14}$$

In reality, various complications, especially surface passivation of metallic Li, cause deviation from the ideal scenario. In order to correct the interference from interphase resistance, Bruce and Vincent coupled the techniques of DC polarization and AC impedance so that the interphase resistances before and after the steady state is accounted for. Figure 15.12b shows the typical setup for the electrochemical impedance spectrum (EIS) to measure interphase resistances, where an additional electrochemical interface is needed to generate and control precisely the DC potential across the test cell. Because nonblocking electrodes are used, the equivalent circuit would be similar to what Fig. 15.11b shows, and the resultant impedance plot, $-Z''$ versus Z' on a complex plane, would consist of two or three adjoining semicircles, depending on the relative magnitudes and characteristic frequencies of bulk and interphase resistor components. Figure 15.12b schematically illustrates an ideal scenario where all three resistor components (R_b, R_i and R_{ct}) are well resolved.

Bruce and Vincent noticed that R_i increases as the cell is being polarized, which reflects the growth of the passivation layer on metallic Li as a consequence of the reaction between the electrolyte and the freshly deposited Li crystal on the anode. They modified the definition of Li^+ transference number

$$t_{Li} = \frac{\frac{1}{R_+}}{\frac{1}{R_+} + \frac{1}{R_-}} \,, \tag{15.15}$$

where R_+ and R_- are resistance to cation (Li^+) and anion movements, respectively. Obviously the overall ion conduction can be viewed as cationic and anionic currents in parallel circuits

$$\frac{1}{R_b} = \frac{1}{R_+} + \frac{1}{R_-} \,, \tag{15.16}$$

then

$$t_{Li} = \frac{R_b}{R_+} = \frac{R_b}{\frac{V}{I_{ss}} - R_i} \,, \tag{15.17}$$

where V is the applied DC potential in both DC and AC experiments, R_b and R_i the first and second intercept on the impedance plot, respectively, and I_{ss} the steady-state current obtained from DC experiment.

A more popular form of the same practice is

$$t_{Li} = \frac{I_{ss}(V - I_0 R_0)}{I_0(V - I_{ss} R_{ss})} \,, \tag{15.18}$$

where R_0 and R_{ss} are the interphase resistances at t = 0 or at steady-state, respectively. For most nonaqueous liquid and polymer electrolytes investigated with this

approach, the Li^+ transference number ranges between 0.2–0.4, confirming the fact that solvated Li^+ is a less mobile species as compared with its counter anion.

Besides the above DC-polarization combined with AC impedance approach, there are several variations based on galvanostatic polarization or electromotive force, but so far none is perfect in terms of accuracy and easiness, while all involve more or fewer assumptions and arbitraries. For example, the determination of I_{ss} value, which constantly decays (Fig. 15.12a), varies depending on the individual judgment by the experimentalist.

Different from electrochemical approaches that consider long-range movement of ions, nuclear magnetic resonance (NMR) can probe local mobility of these ions (as long as the nucleus of each interested ionic species is NMR sensitive), thus providing a means to evaluate the Li^+ transference number

$$t_{Li} = \frac{\mu_+}{\mu_+ + \mu_-} = \frac{D_+}{D_+ + D_-} , \qquad (15.19)$$

where μ and D stand for mobility and diffusivity of individual ionic species, respectively. A commonly used technique, pulse field gradient NMR (PFG-NMR), can directly measure translational self-diffusivities of ^7Li and its anions (such as ^{31}P in hexafluorophosphate PF_6^-, ^{19}F in *bis*(trifluoromethanesulfonyl)imide (TFSI), or ^{11}B in tetrafluoroborate BF_4^- or *bis*(oxalato)borate (BOB) [15.44]. In contrast to the electrochemical methods described above, NMR independently monitors both anion and cation; however, this advantage is somewhat diluted by the fact that all ions in the same species are monitored, whether they are free, in ion pairs or in aggregations. Considering that ion pairs do not contribute to ion conduction and aggregations causes reduction in net ionic current, the ionic self-diffusivities as obtained by PFG-NMR are generally overestimated

$$D_{obs} = xD_{ion} + (1-x)D_{pair} . \qquad (15.20)$$

Unfortunately, this overestimation becomes substantial for electrolytes of practical salt concentration ($\approx$ 1.0 M), where the ion-ion interaction is expected to be significant.

A modified NMR technique, electrophoresis NMR (eNMR), sought to differentiate the mobile ionic species from those not participating in orientational movement by applying a DC field on the investigated solution while monitoring spin-echo relaxation of ^7Li and other nuclei under pulse gradient conditions. Figure 15.14 shows one of the designs for eNMR experiments, in which the drift velocity of Li^+ and a chosen nucleus of its anion can be measured. The Li^+ transference number obtained in this manner should be closer to

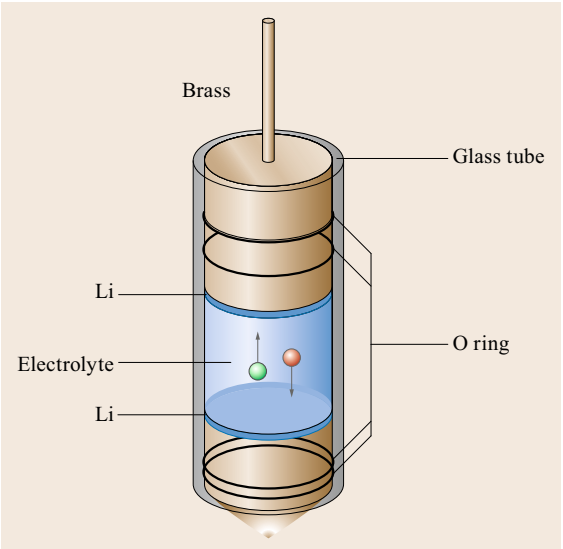


Fig. 15.14 eNMR tube for Li^+-transference number measurement, where the relative diffusivities of each individual nucleus can be directly measured under the DC field based on their relaxation times

reality [15.45]. Despite the widely scattered data available in the literature, the general agreement is that in nonaqueous electrolytes the Li^+ transference number is less than half, reaffirming the knowledge that Li^+ is the less mobile species [15.31, 46].

In addition to the difficulty of measuring the Li^+ transference number accurately, the limited usage of this quantity for characterizing and evaluating electrolytes is also attributed to its insignificant influence over the electrochemical performances of the device. As mentioned above, the concentration polarization built up by transport and accumulation of counter ions introduces additional resistance to Li^+ conduction; however, in most liquid electrolytes, this concentration polarization could be easily eliminated through convection and self-diffusion. Only in more viscous media such as polymer electrolytes, or at subambient temperatures, could the small Li^+ transference number be a factor that significantly affects the device performance.

Interphase Processes: Formation Stage

The characterization of interphase formation has been especially challenging due to the fact that an effective and noninvasive in situ technique is still unavailable. EIS, dilatometry and in situ x-ray diffraction (XRD) are such few rare tools, but each with their individual restrictions. Although most information provided by ex situ techniques such as FTIR, XPS NMR and (TEM)/SEM proved useful and in many cases critical

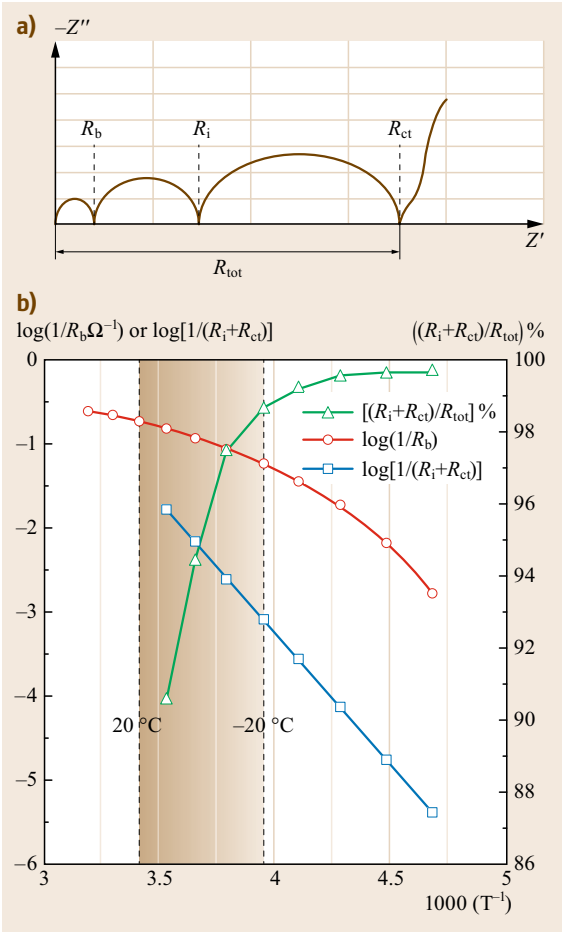


Fig. 15.15a,b Interphase resistance constitutes the main kinetic control over cell chemistry by limiting Li^+ transport rate. **(a)** Schematic breakdown of contributions to overall cell impedance from various bulk and interphase components. **(b)** Resistances of these components measured in a Li-ion cell with $LiCoO_2$ and MCMB chemistry in 1.0 $LiPF_6$/EC/EMC electrolyte at different temperatures

in understanding interphase formation, their invasive nature always cast a shadow of suspicion over the possibility that the actual interphase had been altered during the sample preparation stages, both chemically and morphologically.

From the previous section we have shown that the interphase causes constant interference in the accurate measurement of transport properties in the bulk electrolyte (ion conductivity, ionic transference number). Indeed, more than 90% of the overall cell impedance (R_{tot}) comes from the interphase contribution ($R_i + R_{ct}$), as Fig. 15.15 shows, especially under low temperatures [15.47].

The existence of an interphase on the graphitic anode in Li-ion batteries has been proven beyond any doubt, and in the past two decades ample understanding has been achieved. Early ex situ surface analyses by Aurbach and coworkers established the substantial presence of alkylcarbonates in the anode interphase with spectroscopic signatures (e.g., absorption at 1350 cm^{-1} in FTIR and binding energy at 289 eV for C1s electrons in XPS) [15.48, 49]. The alkylcarbonate is likely the product of an incomplete reduction route pathway from the carbonate solvents. This incomplete reduction was attributed to a single-electron mechanism, primarily due to the poor electron availability during the interphase formation on graphitic anodes [15.50]. More sophisticated diagnosis, performed recently using isotope 13C labeling and high precision FTIR in combination with quantum chemistry (QC) computation, further identified two additional pathways involving acyl-O cleavage and radical recombination, leading to the presence of oxalate and alkoxide species [15.51].

Polymerization might also appear in some scenarios, leading to speculation that interphases actually consist of those inorganic Li salts embedded in the matrix of amorphous polymeric; although it should be pointed out that the polycarbonate structure proposed is actually not thermodynamically stable and tends to lose CO_2 to form the more favored poly(ethylene oxide). Most likely the polymeric species present in interphase is a random copolymer of polycarbonate and polyether. Despite the wide variety of compounds identified, it seems that alkylcarbonate remain the majority interphase species in most cases.

A rather controversial component in the interphase is Li_2CO_3. While organic carbonate can undergo a complete two-electron reduction leading to Li_2CO_3, its presence in the anode interphase has usually been attributed to be the consequence of moisture invasion rather than electrochemical reduction. With an elegant XPS experiment Edstrom et al. showed how the binding energy of carbonyl C1s shifts from 289 eV to > 290 eV upon controlled exposure to ambient , indicating a fast conversion of alkylcarbonate to Li_2CO_3. They suggested that, since alkyl-carbonates are extremely sensitive to moisture, any less than rigorous handling of the samples could lead to misinterpretation [15.52].

Unlike the chemistry, the understanding of the morphology or structure of the interphase is less understood. Peled speculated a mosaic pattern, with inorganic and organic microregimes patterned randomly, while Kanamura proposed a more organized structure of organic and inorganic layers situated closer to or remote from the electrode surface, respectively. The most detailed work was performed by *Bar-Tow* et al. [15.53], whose XPS analysis on basal and edge facets of

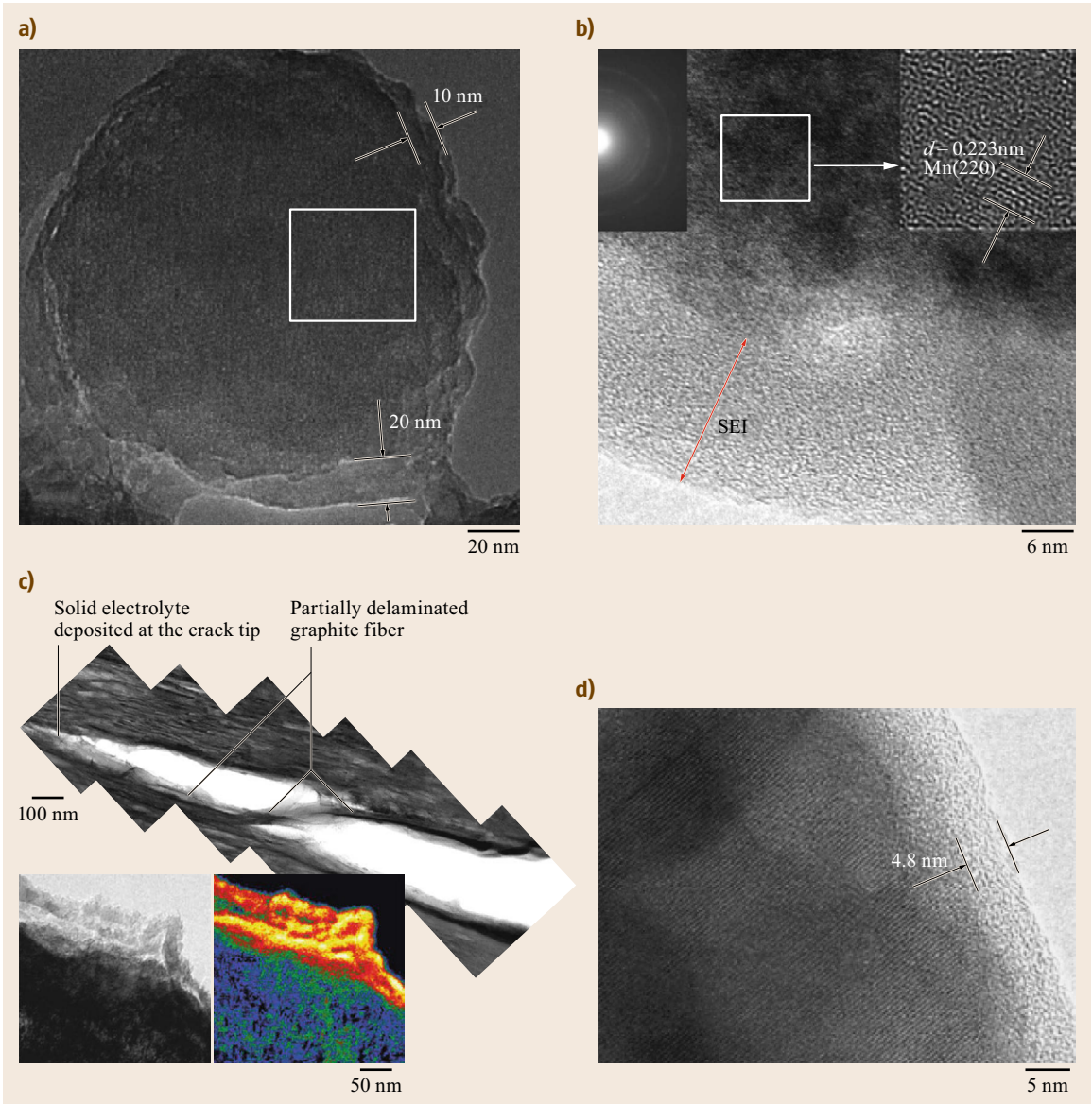


Fig. 15.16a–d TEM images of SEI layers grown on anodes and cathodes after cycling in nonaqueous electrolytes. **(a)** Hard carbon sphere; **(b)** a partially exfoliated graphite sheet still connected by a string of graphene sheets that has been covered with an SEI; and **(c)** bright-field TEM graph of a cycled graphitic anode and its corresponding Li^+-concentration map

graphite placed the former as an inorganic-enriched and the latter as an organic-enriched region.

The structured interphase was further confirmed by recent work by *Lu* and *Harris* [15.54] who employed isotopic ^{6}Li and ^{7}Li to label the interphase and bulk electrolyte, respectively, and found that interphase can be roughly divided into two regions: ≈ 5 nms of *diffuse* layer that is close to the electrolyte side and that can be penetrated with bulk electrolyte, and ≈ 15 nms of *dense* layer on the current collector side that only desolvated Li^+ can migrate into.

In recent years TEM has become an increasingly popular tool employed to image interphases. The amorphous nature of interphases usually appear in strong contrast to the crystalline electrode bulk, however, its instability under electron beam makes the imaging a nontrivial task. Figure 15.16 shows interphases observed on several carbonaceous anodes after cycling in

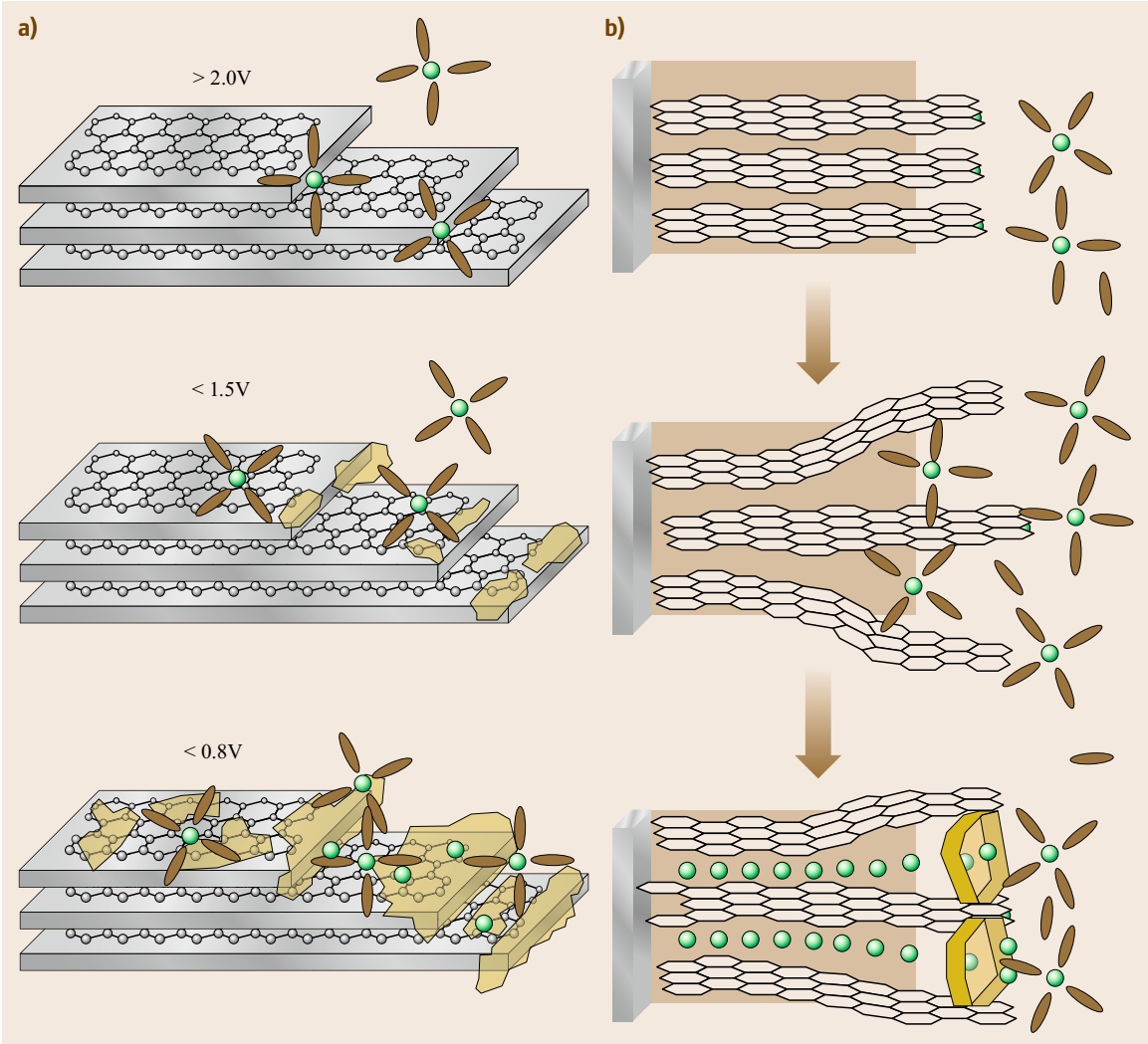


Fig. 15.17 **(a)** Schematic drawing of AFM imaging of interphase formation: Two basic characteristics of interphase formation on graphitic surface, i. e., stepwise and region-differentiation (after [15.55]) **(b)** Schematic drawing of *3-D formation mechanism* proposed by *Besenhard* et al. (after [15.56])

electrolytes, whose thickness of 10−50 nm agrees with the general estimate from other techniques [15.33, 34].

In-depth understanding of the interphase formation mechanism on graphite has been achieved as result of intense investigation since the 1990s. This formation process involves close interaction between graphite and electrolytes; therefore it is specific both to the properties of the electrode (graphitic lattice structure) and electrolyte (Li^+-solvation shell).

Pioneering AFM work by *Farrington* and coworkers [15.55] revealed the two most conspicuous characteristics of interphase formation on graphite that differs from typical electrodes in conventional electrochemistry, i. e., stepwise and regiospecific. Figure 15.17a schematically summarizes their observations. While interphase species start to accumulate at edge sites at high potentials ($\approx$ 1.0 V), the basal plane remains clean until much lower potentials. This stepwise formation provides the possibility that certain electrolyte components could be preferentially reduced at edge sites prior to other components, thus giving the Li-ion industry valuable leverage to manipulate interphase chemistry via the use of additives [15.55].

The early dilatometry studies indicated large volume expansion during the first lithiation process, leading *Besenhard* et al. to propose a *3-D mechanism* that is schematically depicted in Fig. 15.17b [15.56]. The essential element of this model is that a solvated Li^+

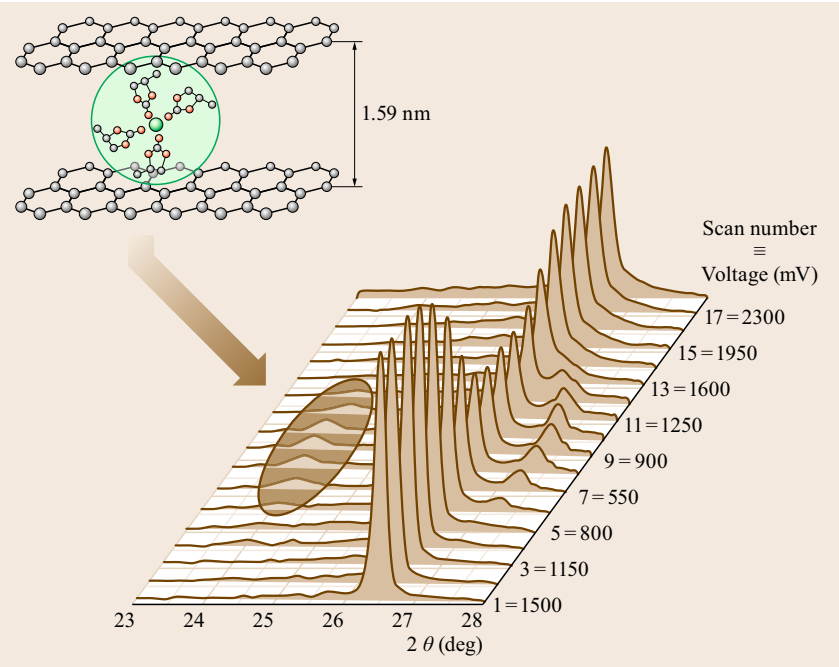


Fig. 15.18 Transient existence of ternary GIC captured by in situ XRD of graphitic anode cycling in PC-based electrolytes. The peaks at $2\theta = 24°$ correspond to an interlayer distance of approximately 1.5 nm, a gap that is wide enough to accommodate a solvated Li^+ with 3–4 solvation sheath members (after [15.57])

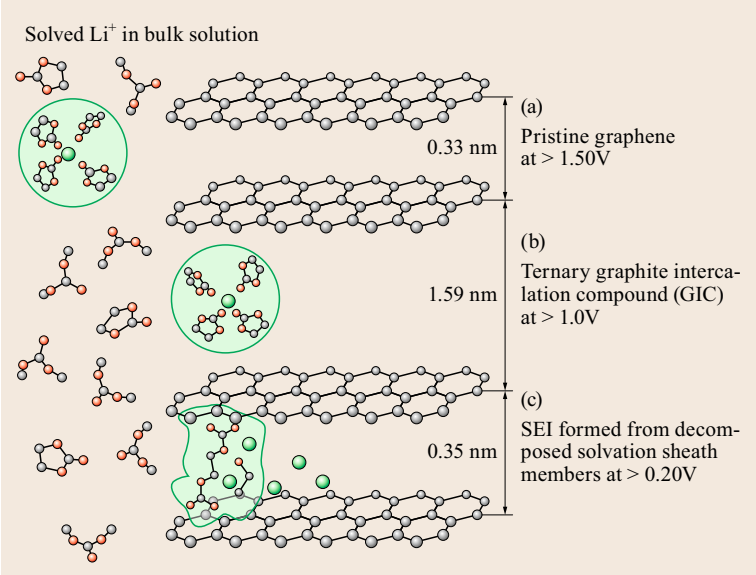


Fig. 15.19 Schematic illustration of the *solvation-driven* model for interphase formation mechanism. (*a*) Above 1.50 V the pristine graphite maintains the original interlayer distance of 0.33 nm; (*b*) While solvated Li^+ intercalates above 1.0 V, this distance widens briefly to ≈ 1.59 nm, accommodating the bulky solvated Li^+ and forming the ternary GIC; (*c*) The solvent members in the solvated Li^+ break down reductively, forming the precursor of SEI, and the interlayer distance of graphite reverts back to ≈ 0.35 nm, which would remain during the subsequent lithiations (after [15.58])

intercalates into graphite before interphase formation, thus the eventual interphase would partially penetrate into the interior of graphite from the edge sites. Although circumstantial evidence from electrochemical impedance studies and surface analyses with FTIR, NMR and Raman already favor this *3-D mechanism*, the most direct support comes from the capture of the intermediate graphite intercalation compound (GIC) by in situ XRD, as shown in Fig. 15.18, in which the smaller angle peaks during the transient cointercalation of propylene carbonate (PC) above 0.5 V versus Li indicates a interlayer distance of ≈ 1.6 nm [15.57]. It was speculated that similar cointercalation by other carbonate molecules should happen, except these ternary GICs are too short-lived before the solvent molecules decompose reductively into interphase. A more recent refinement of the 3-D mechanism was made by *Xu* et al. [15.58], who suggested that the Li^+-solvation-

sheath structure plays a critical role in determining the chemical composition of interphases (Fig. 15.19). Thus, any preferential solvation of Li^+ by an electrolyte solvent would cause unsymmetrical contributions from electrolyte components to the resultant interphase chemical composition. This uneven distribution of the chemical sources of the SEI had been observed earlier via FTIR and NMR [15.58, 59].

The interphase on the cathode remains a topic of debate. Systematic TEM observations made by *Li* and coworkers did reveal the presence of an SEI on certain materials, but absence of it on others (Fig. 15.16) [15.33, 34]. It seems the complication arises not only from the different chemical natures and operating voltages, but also from less controllable factors such as preparation route, porosity, and surface morphology. A surface-catalytic mechanism was speculated, but experimental evidence is still weak, calling for more investigation. What seems to be rational is multiple mechanisms that depends on both chemical state and potential of the cathode, i. e., the interphase nature would be determined by what component of the cathode is exposed to electrolytes: An oxygen layer that nucleophilically attacks solvent molecules at low potential, or a transition metal core layer that reacts electrophilically with solvent molecules at high potential.

Post-Formation: Transport Across Interphases and Growth

Once interphase is formed, it acts as a thin-layer solid electrolyte at the edge sites of graphite, allowing Li^+ migration but insulating electrons (at least under normal operating conditions). Its Li^+ conduction is known but is far from being well understood, as almost no effort has been made to accurately measure the conductivity. The only experiment that sheds light on the Li^+ movement across SEI was performed by *Lu* and *Harris*, who used isotopic ^6Li and ^7Li to form SEI and bulk electrolyte separately, and then monitored the exchange of these two isotopes upon immersion [15.54]. It was observed that after short exposure ($\approx$ mins), $^6Li^+$ already immobilized in interphase can be swapped by $^7Li^+$ in the bulk electrolyte, suggesting a *Grotthuss-like* conducting mechanism as illustrated in Fig. 15.20a. The computational simulation further revealed possible mechanisms as to how a Li^+ is coordinated within the interphase. Using crystalline Li_2CO_3 as a matrix, *Qi* et al. suggested that the transport energy barrier could be significantly reduced if a moving Li^+ sees a series of transition states with penta- or tetra-coordinated O-ligands [15.60]. This would only happen when this Li^+ replaces another Li^+ in its original position, otherwise a longitudal direct diffusion would encounter much higher energetic barriers (Fig. 15.20b).

The dense interphase not only insulates against electron tunneling, but also prevents solvent molecules from diffusing across it; thus, desolvation must occur at the electrolyte–interphase junction when a solvated Li^+ migrates to a graphitic anode during lithiation (charge of Li-ion cell). *Ogumi* et al. were the first to realize that Li^+ desolvation creates additional resistance when a graphitic anode is being charged, thus explaining the unsymmetrical property of Li-ion cells of fast discharging but slow charging [15.61, 62]. *Xu* et al. [15.63] went further to deconvolute the contribution from Li^+ desolvation to the overall cell resistance by using a nearly SEI-free electrode, and concluded that Li^+ desolvation could constitute the significant part of the activation energy barrier to Li^+ migration across the interphase.

Even after SEI formation, it was speculated that SEI does not stop growing all together. This *leaking* nature of the SEI has been confirmed with various evidence of electron tunneling under given circumstances, such as the redox reaction of overcharge-protection shuttles at high voltages, the *Li-ion flow battery* concept, and the ever-increasing impedance at elevated temperatures [15.64, 65]. Even with normal operation, the SEI still continues to grow, at a rate that varies with the voltage, temperature and chemistry of the interphase itself. *Dahn* and coworkers [15.66, 67] developed a high-precision Coulometry technique to monitor this *parasitic* process. Assuming that all irreversible capacities are consumed to make up the SEI, they showed that under a given temperature and similar electrochemical history, the SEI grows at a rate defined by

$$\frac{\mathrm{d}x}{\mathrm{d}t} = \sqrt{\frac{k}{2}} t^{-\frac{1}{2}} \,. \tag{15.21}$$

This parabolic relation states that mathematically the growth of SEI never stops; instead, it can only be slowed down (by reducing k) with effective electrolyte additive use or with better matching between electrode and electrolytes. In reality, *Smith* and *Burns* et al. [15.66, 67] observed with their high-precision coulometry that irreversible loss on most anode materials requires at least 25 cycles to stabilize asymptotically.

Additives

There are many additives used in state-of-the-art electrolytes, but descriptions in the open literature are rather limited. They can be roughly classified into three groups:

1. Interphase additives
2. Overcharge protection additives
3. Safety-trigger additives [15.35].

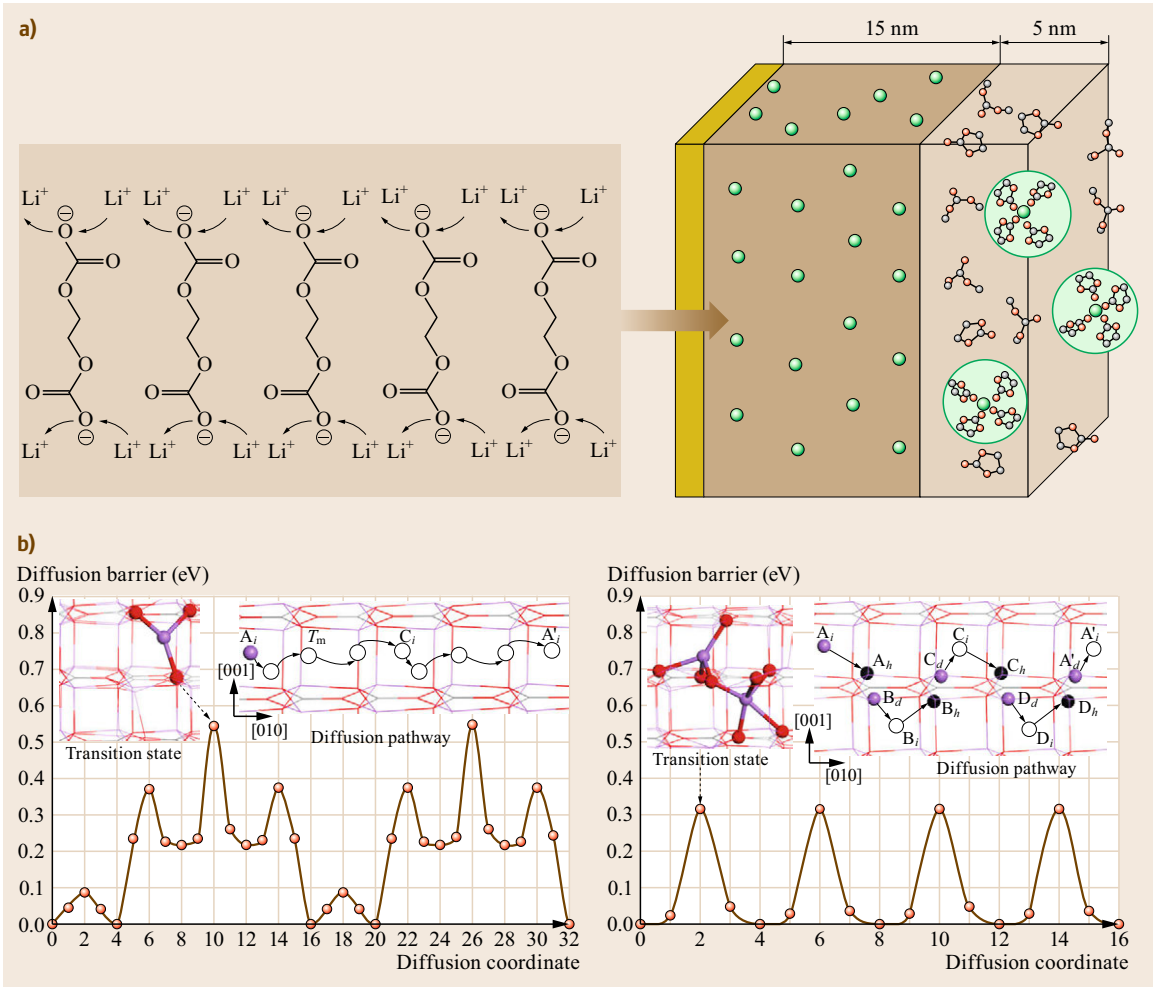


Fig. 15.20 **(a)** *Grothuss-like* transportation mechanism of Li^+ across an interphase. It was proposed that the dense layer of interphase is impenetrable for solvent molecules, so that solvated Li^+ has to desolvate and exchange with the Li^+ already in the interphase (after [15.54]). **(b)** Computation simulations depict the corresponding energy barriers of direct longitudinal Li^+ diffusion through an interphase and *Grotthus-like* mechanism where Li^+ is better stabilized. The tetra- or penta-coordinated transition states available only in the latter case effectively reduce the barrier height (after [15.60])

While interphase additives are almost entirely consumed in the forming cycles of Li-ion batteries, overcharge protection additives exist inertly in the electrolyte and can only be activated at high potentials when the cells are overcharged by creating an internal soft-short within the cell. Safety-trigger additives, on the other hand, are activated only once, whose consequence is to end the cell life under certain conditions (high voltage, elevated temperatures, excessive rate etc.), in order to evade a catastrophic scenario.

The concept of *interphase additives* was established on the basis that an interphase on an electrode in Li-ion batteries is formed when the potential of the electrodes changes gradually. This stepwise nature makes it possible to manipulate the chemistry by using certain ingredients that can react before bulk electrolyte components can. The purpose of manipulating interphase chemistry versus that of a *natural grown* is to make the interphase thinner and more conductive. The sacrificial additives are used at rather small concentrations, so that their presence is completely consumed after the decomposition upon the initial cycling.

Although theoretically additives should have electrochemical signatures upon decomposition, an effective additive leaves little trace behind. Such an example is vinylene carbonate (VC), whose high reduction potential on graphite was only speculated, while neither cyclic voltammetry nor differential capacity derived from gal-

vanostatic experiments yields any evidence of this reduction. Thus, quantum chemistry (QC) computation was usually resorted to to predict their decomposition potential and possible products. A popular approach employed is to calculate energy levels of the highest occupied molecular orbital (HOMO) and lowest unoccupied molecular orbital (LUMO), based on the belief that the ingredient with the lower LUMO serves as a better electron donor and therefore will be selectively reduced, while the higher HOMO makes a better electron acceptor and selective oxidation is expected [15.68]. For SEI chemistry designed for graphitic anodes, compounds of low LUMOs are sought after, and plethora of LUMO/HOMO data have been reported in the literature with different levels of computations, providing useful guidelines. However, it must be emphasized here that, despite the theoretical appearance of this approach, the selection based on HOMO/LUMO information is still semiempirical, because the compound that is reduced at higher potential does not necessarily lead to a more stable interphase. So far computational chemistry still cannot accurately predict the physicochemical properties of the decomposed products.

Compared with its anode counterparts there is less understanding of interphases on cathode surfaces, and in certain cases even its existence is under debate. It was believed though that once the cathode operates at potentials beyond 4.5 V, surface depositions do occur, and probably an interphase-like layer could exist. With the introduction of 5 V class cathode chemistries such as $LiMn_{1.5}Ni_{0.5}O_4$ (LMNO, 4.6 V) and $LiCoPO_4$ (LCP, 4.8 V), the research on additives for cathodes also became active [15.69, 70]. Fluoroalkyl phosphates and alkylthiophenes have been reported as effective in stabilizing nonaqueous electrolytes on these high voltage cathode materials [15.71], while sulfones and nitriles were also used as high voltage stable electrolyte solvents [15.72, 73].

Overcharge protection additives are also known as *redox shuttles*. They were so chosen that their activation potentials rest slightly above the normal operating potentials of the cathode. In case of overcharge, these additives are oxidized on the cathode surface, and the products subsequently migrate to the anode surface where they receive electrons and reduce back to their original form. The overall thermodynamics would dictate that the dissipation of excessive energy would be in the form of heat, so that cathode materials would not be moved to a higher energy level by this excessive energy, otherwise over-delithiation of the cathode would result in hazardous reactive decomposition [15.74, 75]. Most of the reported additives under this category are based on aromatic compounds, whose activation potential can be tuned with the location and the chemistry of ring substitutes. Since the rate of energy dissipation depends on both the solubility and diffusivity of these additives, these additives might not be effectively enough to handle the overcharge under high rates. Additionally, the heat engendered by the *soft short* tends to warm up the device, and the integration of these additives into large format Li-ion cells or battery packs will still need to be thoroughly investigated.

Differing from *interphase* and *overcharge protection additives*, *safety-trigger additives* are designed to be activated only when the cell is on the verge of a catastrophic failure, and the activation marks the end of cell life. These are usually of *gas-generating type*, such as polyphenyl compounds, which build high pressures at high voltages or temperatures and force the cells to open in a mild manner. Many additives under this category remain trade secrets of battery manufacturers or electrolyte suppliers.

15.2.3 Separators

The separator is an essential component for liquid electrolyte and polymer gel electrolyte battery cells. It is generally a porous membrane placed between the positive and negative electrode to prevent physical contact of the electrodes. The liquid and gel electrolytes are absorbed into the pores of the separator and serve as the media for the transport of ions accompanied by the reaction between the two electrodes. The separator itself does not participate in the reaction, however, it critically affects the cell performance, especially the power capability and safety. The essential properties required for a separator are mechanical strength, thickness and porosity for ionic conductivity, and chemical and thermal stability for cycle life and safety. Since many of these properties are fundamentally opposed to each other, a separator with an optimum combination of these properties is needed for Li-ion batteries.

In standard Li-ion batteries, the microporous polyolefin membrane has been most widely used as the separator. In the current market, there are two types of separators, dry-processed and wet-processed, based on the process of pore-forming as shown in Fig. 15.21, both of which are made of either polyethylene (PE) or propylene (PP) [15.76, 77]. The dry-processed membranes have an orientated pore structure and tensile strength, while the wet-processed membranes contain a tortuous pore structure and isotropic tensile strength. From the viewpoint of pore structure, the open and straight pores favor fast ionic transport while the tortuous pores favor preventing the growth of Li dendrites. Therefore, the dry-processed membranes are more suitable for high power batteries, while the wet-processed membranes for long cycle life batteries.

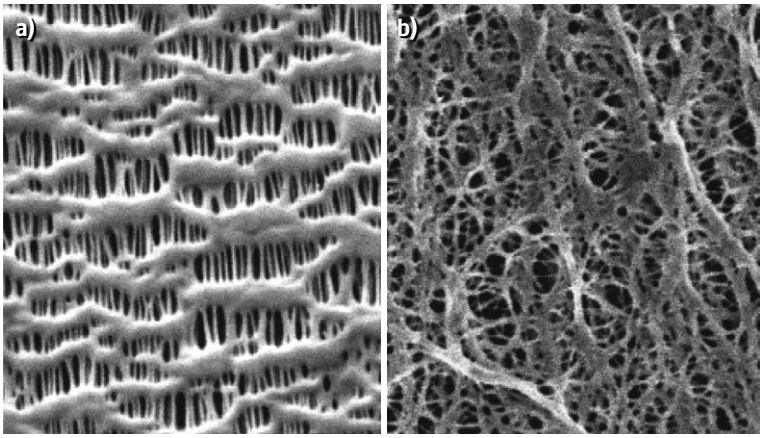


Fig. 15.21a,b SEM images of two types of polyolefin separators. **(a)** Celgard membrane by dry process, and **(b)** tone membrane by wet process (after [15.76, 77])

For safety reasons, thermal shutdown and ceramic separators have been developed for Li-ion batteries. The shutdown separator is a multilayer structural membrane with a PE layer laminated between two PP layers. Its shutdown function is based on a difference in the melting points of PE and PP. Since PE has a lower melting point (mp = 125–135 °C) than PP (mp = 160–165 °C), the PE layer is able to shutdown cell current by closing its pores to prevent ionic transport at the temperatures above the melting point of PE while the PP layers still retains dimensional integrity when the temperature is lower than the melting point of PP. Therefore, the shutdown separator protects the cell only in the temperature range between the melting points of PE and PP. Ceramic separators are also multilayer structural membranes with a porous ceramic layer coated on the surface of one or two sides of a porous polyolefin membrane, where the polyolefin membrane can be a porous membrane or a porous nonwoven cloth. The ceramic separator has excellent dimensional integrity at elevated temperatures because of the negligibly thermal expansion of the ceramic coating.

A variety of evaluations have been applied to the separator of Li-ion batteries, which can be classified as the two aspects of structure and property. The structural evaluations include thickness and porosity. The thickness determines the distance for ionic transport between the two electrodes, whereas the porosity affects uptake of liquid electrolyte and consequently the ionic conductivity in the membrane. The porosity can be evaluated directly by measuring porosity, pore size, pore distribution and orientation of the membrane, or indirectly by measuring gas permeability and gurley across the membrane. Property evaluations include the chemical and electrochemical stability against the cell's conditions, especially at the charged state, the wettability (contact angle), wetting rate, and retention of liquid electrolyte, mechanical stability such as puncture strength and tensile strength, and thermal behavior such as shutdown temperature and dimensional integrity (or shrinkage) at elevated temperatures. Detailed descriptions on the measurements can be found in [15.76, 77].

With advances in technologies and the ever-increasing importance of Li-ion batteries, various in situ techniques have been employed in combination with real-time electrochemistry to observe the dynamic chemistries and processes inside a operational Li-ion battery. The information and the understanding of the failure mechanisms provide valuable feedbacks to the synthesis of new battery materials and cell engineering. This section briefly summarizes this emerging front.

15.2.4 Advanced/In Situ Spectroscopy

There are limited numbers of in situ tools that are noninvasive, noninterfering, and operative in the same chemical environments as Li-ion batteries. As described in the section on ionic conductivity, the AC method of EIS is one of the few that meet these stringent requirements; however, the trade-off is that the information is usually too nonspecific, because a working Li-ion cell is a complicated system that involves many electrochemically-active parts contributing to AC stimulus, such as Li^+ movements in bulk electrolyte, across electrolyte–electrode interphases, and within both cathode and anode bulk, etc. Accurate deconvolution of individual contributions from these components is nearly impossible even with sophisticated model equivalent circuits; therefore so far EIS remains a tool for phenomenological analysis [15.78].

AC Impedance Analyses/Electrochemical Impedance Spectroscopy

Differing from ion conductivity or transference number measurements, the cell impedance for an active battery varies significantly with the chemical state of the elec-

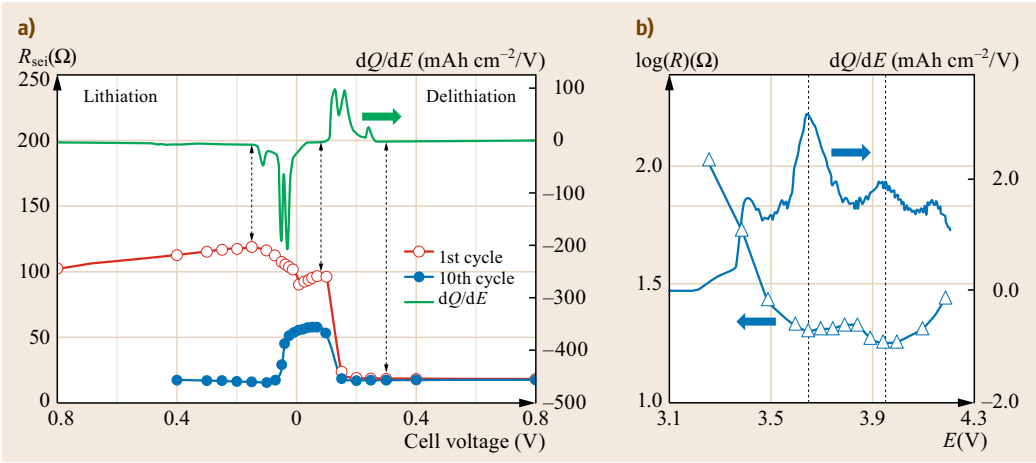


Fig. 15.22a,b In situ impedance spectroscopy of Li-ion electrodes under electrochemical cycling. **(a)** Graphitic anode that shows complete lithiation–delithiation cycles before and after the formation of SEI; and **(b)** a full Li-ion cell based on the same graphite anode and a $LiNi_{0.85}Co_{0.10}Al_{0.05}O_2$ cathode. The overall cell resistance is obviously the combination of the interphase resistance and phase changes within the electrodes, complicated with SEI formation processes (after [15.79, 80])

trodes; therefore it is critical to precisely control the potential of the working electrode (WE) in order for the data be comparable. In the previous section we have shown the basic setup for EIS (Fig. 15.11), in which a four-electrode configuration is recommended for the electrochemical cell (although three- or even two-electrode alternatives are usually adopted experimentally). While the potential between WE and RE 1 is held at certain preset values by the electrochemical interface, an AC signal of varying frequencies is generated by the impedance analyzer, and impedance responses are recorded and analyzed. Figure 15.22a shows the interphase resistance measured on a graphitic anode during a complete lithiation–delithiation cycle, before and after the formation of the interphase, and Fig. 15.22b shows the corresponding full Li-ion cell with the same graphite anode and $LiNi_{0.85}Co_{0.10}Al_{0.05}O_2$ cathode [15.79, 80]. However, it is not always possible to unambiguously separate interphase components. More often than not overall impedance of Li-ion cells was adopted as an indicator of how the kinetics of electrochemical reactions evolves with cell aging. Nevertheless, EIS still provides a rare means to peek into the elusive interphase formation process.

In Situ Synchrotron XRD Studies

In situ diffraction (XRD) studies of an operating Li-ion cell are desirable in order to directly relate the structure of the electrode material to the voltage of the cell and the corresponding level of Li intercalation. However, this level of analyses is often not available through conventional x-ray sources, due to either awkward geometries or low penetration depth of the x-rays. The latter is of particular concern for an intercalation reaction in which the surface may differ significantly from the bulk. Synchrotron facilities, on the other hand, provide high energy x-ray beams that are strong enough to *see* through ordinary stainless steel coin cell hardware, thus making it possible to continuously perform diffraction studies while the Li-ion cells operate. The information revealed paints dynamic pictures of how electrode bulk structure changes when responding to external electrochemical or thermal stimuli, thus allowing us to evaluate cycling stability as well as safety features of these materials more accurately.

An excellent description of the utility of the synchrotron technique relative to a conventional x-ray source has been given by *Mukerjee* et al. [15.81]. The high resolution of the synchrotron enables accurate lattice constant determination along with the observation of the development and disappearance of single- and multiphase regions as Li is intercalated into or out of the electrode material. An example from Mukerjee et al. is shown in Fig. 15.23. From the measurement at many increments along the charge curve, a two-phase region was observed. An example of the electrochemical data and its corresponding XRD pattern as a function of state of charge is shown in Fig. 15.24 [15.82]. In this study the authors documented a *crystallization delay* in which the $FePO_4/LiFePO_4$ ratio appears to be lower than what should be observed based on counting the number of coulombs during the charge. This observation may result from of an unobservable amorphous intermediate phase.

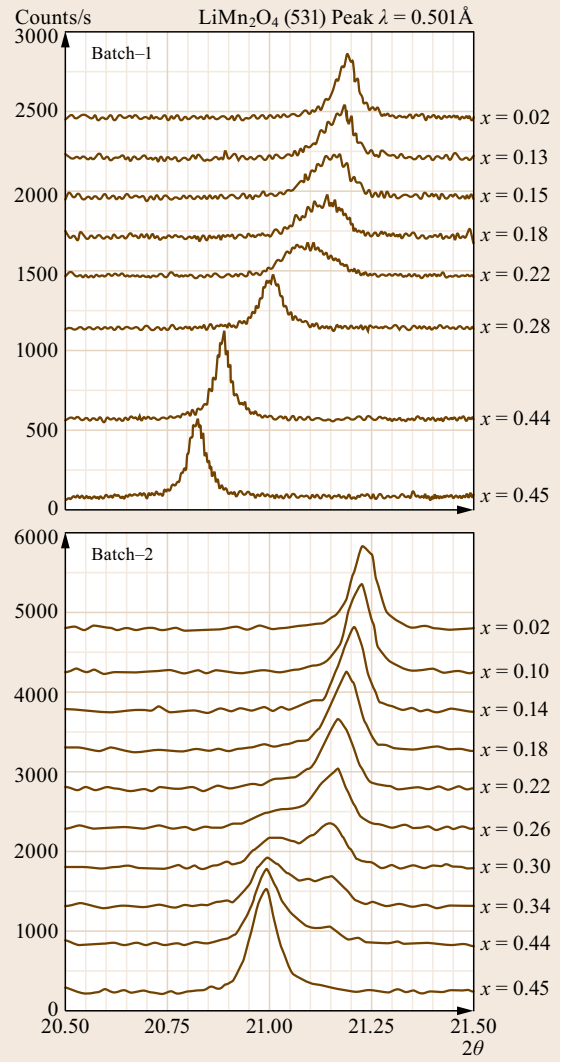


Fig. 15.23 An example of synchrotron x-ray diffraction data showing the 531 peak of $LiMn_2O_4$ during charge of the electrode material. A distinct two-phase region is observed at $x = 0.30$, and $x = 0.34$ (after [15.81])

A more recent example of in situ XRD was conducted by *Sun* et al., in which the thermal stability of concentration gradient cathode material was evaluated. High resolution diffraction peaks were continuously collected on a fully delithiated sample (4.3 V) while the sample experienced a thermal ramping from RT up to 370 °C (Fig. 15.25a) [15.83]. The contour plot in Fig. 15.25b summarizes the structural spectra of such nanostructured Ni-Mn-Co mixed layer oxides in response to the rising temperature. It is clearly seen that (101) peaks (located at 2.57°) start low angle shift at ≈ 110 °C, indicating a major phase transformation of

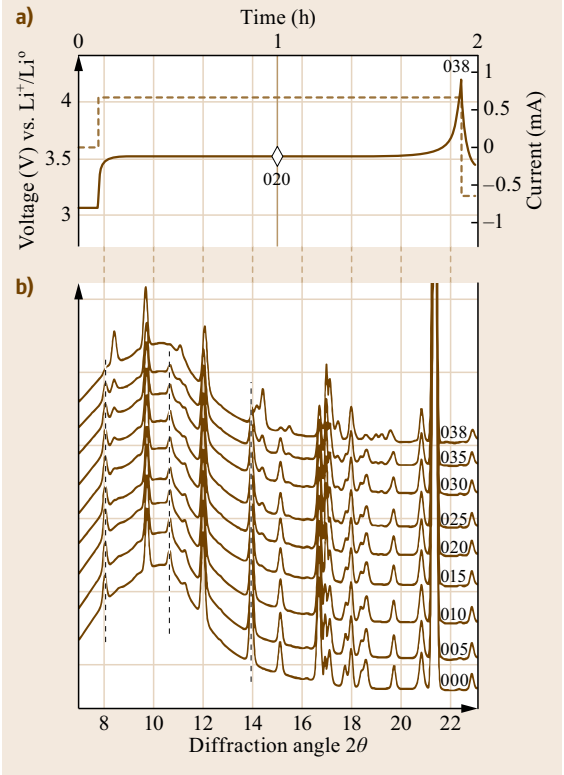


Fig. 15.24a,b An example of synchrotron XRD patterns recorded during the operation of charging $LiFePO_4$ (after [15.82])

these oxides. Although this structural degradation is not necessarily associated with onset of a safety runaway, it could result in loss of electrochemical performance. The level of complexity and relevance of the information obtained on these reactive materials in this single experiment are unprecedented.

In Situ High Resolution Transmission Electron Microscopy

A dream for battery chemists has been to directly observe what transpires at the micro-/nanoscopic scale when electrochemistry proceeds in a battery. In situ transmission electron microscope TEM techniques may have made this dream a reality with reasonable approximations.

Modern high resolution TEM (HRTEM) has enabled visualization at subangstrom scales, but since all electronic microscope must work under high vacuum, the application of it on an operating battery has not been straightforward because of the liquid electrolyte. While state-of-the-art battery packaging may maintain its hermeticity under high vacuum, the packaging materials themselves (stainless steel or aluminum alloy

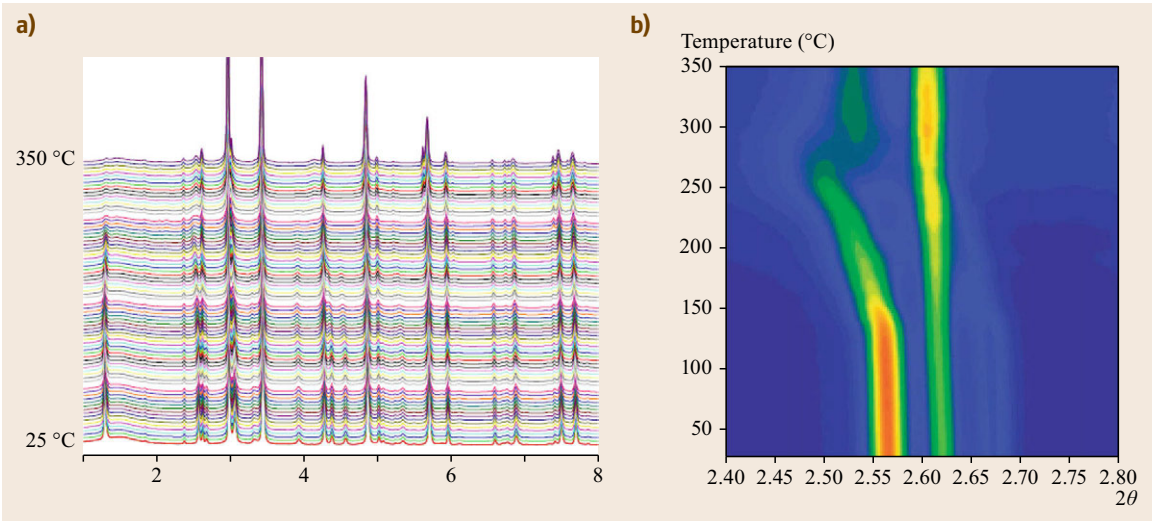


Fig. 15.25 **(a)** In situ high-energy x-ray diffraction profiles of a delithiated cathode in the presence of a nonaqueous electrolyte; **(b)** contour plots showing the phase transformation occurring above 110 °C as indicated by the shift as well as peak abundance of (101) peak (after [15.83])

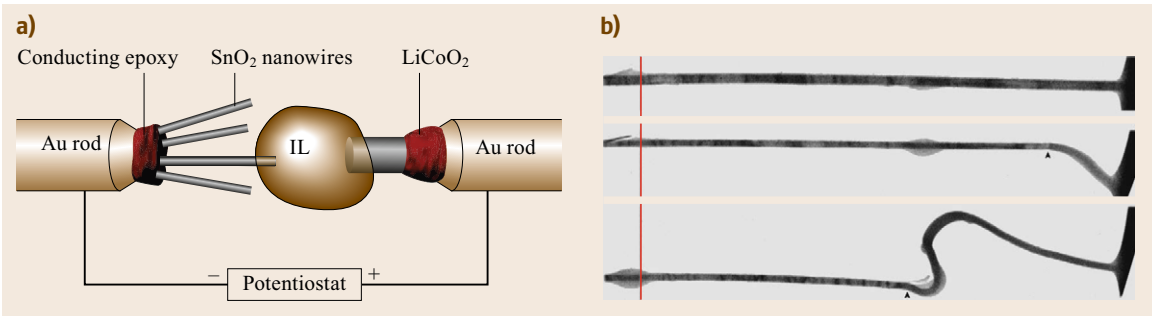


Fig. 15.26a,b In situ TEM graphs showing lithiation of a SnO_2 nanowire in ionic liquid-based electrolyte. **(a)** Instrumental setup; **(b)** volume expansion of SnO_2 nanowire and propagating of amorphous phase upon lithiation (after [15.84])

casing) serve as strong electron barriers that prevent imaging. On the other hand, light plastic packaging materials such as those used in pouch cell configurations cannot survive the high vacuum condition although they do allow electron transmission. To circumvent these issues, *Huang* et al. [15.84] constructed inside a TEM chamber a nanosized battery that employs ionic liquid based on pyrrolidinium *bis*(trifluoromethane sulfonyl)imide salt as electrolyte and SnO_2 nanowire and $LiCoO_2$ nanoparticle as anode and cathode respectively (Fig. 15.26a). The nonvolatile nature of ionic liquid enables direct visualization of this nanosized electrochemical cell without any casing. In the virgin experiment of this technology, they observed real-time images of SnO_2 nanowire during lithiation–delithiation, as shown in Fig. 15.26b, where a reaction front moves longitudinally along the wire, while the swelling caused by lithiation of Sn turns the wire spirally into *Medusa's hair*. This mechanical stress has been responsible for the well-known poor cycling reversibility of SnO_2 anode materials. The same group has used this setup to visualize other anode materials such as aluminum and silicon that face the same challenges.

Because the ionic liquid electrolyte differs from its liquid counterparts used in real-life batteries in terms of electrochemical stability, certain aspects such as interphase chemistry and processes cannot truthfully revealed by the above technique. On the other hand, TEM is not really a noninvasive tool to battery materials, as the electron beam can inflict damage on the target, especially organic materials such as ionic liquids or the SEI grown on the electrode surface. Therefore it should be kept in mind that the in situ observation in this case is under the interference from the observer. Alternative approaches need to be developed so that conditions approximating real-life Li-ion batteries more closely may

be realized while electron beams are shed to image the electrochemical process.

NMR Techniques

Nuclear magnetic resonance (NMR) has been used to study various nuclei in different chemical environments for a long time. With the high abundance of NMR-active ^{7}Li nuclei in nature ($\approx$ 93%), its application in the battery field is well represented by the works of *Greenbaum* et al. and *Grey* et al., with the former reputed for characterization of interphase components and Li^+-transport phenomena in liquid electrolytes, and the latter for local structure of ^{7}Li in transition metal oxide cathode. Chapter 12 by *Tong* also gives a detailed discussion of electrochemical NMR.

NMR is noninvasive to all battery components, but its application on an operating battery is difficult. The earliest such attempt was made by *Gerald* et al. who designed a toroid cavity cell and fit it into a wide-bore magnet so that ^{7}Li-NMR could be recorded to monitor the lithiation–delithiation of carbonaceous materials [15.85]. Such a configuration does not well simulate a realistic Li-ion battery, and also severely restricts the signal-to-noise ratio. Because almost all of the more interesting activities of Li^+ in a live battery are in the solid rather than liquid phases (migration across the interphases or diffusion within cathode and anode bulk materials), the resulting featureless, broad signals often impose hurdles for meaningful analysis and understanding. The effective convention of narrowing solid NMR signals, i. e., magic angle spinning (MAS), is not easily applied to an operating battery, because the need for rotating the sample at high speed (1−70 kHz) not only makes it physically difficult to maintain electric contacts for the current collectors, but will causes cell failures due to electrolyte depletion under the centrifugal force. Nevertheless, efforts are being made to overcome these technical difficulties, and in near future in situ NMR is expected to reveal more helpful information about battery materials in operation.

Grey et al. developed a combined approach of MAS/ex situ as well as static/in situ NMR [15.86]. Their setup is shown in Fig. 15.27a, where a plastic-packaged pouch electrochemical NMR cell was constructed. Using this realistic cell configuration, they have investigated the lithiation process of Si anode materials and attempted to quantify the growth of metallic Li dendrites, respectively. Figure 15.27b describes the dynamic ^{7}Li signal for a crystalline Si anode during its initial lithiation. This study demonstrated that in situ techniques can capture certain Li processes that cannot be resolved with ex situ NMR. The future application of in situ NMR to other battery processes can be expected.

Scanning Probe Microscopy

Scanning probe microscopy (SPM) covers a range of microscopic techniques where a physical tip is moved by piezoelectric actuators to probe the sample surface in a manner of raster scan, so that surface images of the sample could be generated by monitoring and analyzing the tip-surface interaction. The most conspicuous examples from the SPM family are scanning tunneling microscopy (STM), which measures the electronic current between the surface and the tip, and atomic force microscopy (AFM), which measures mechanical force and has been shown to be useful in characterizing the height change of and SEI growth on the graphitic anode in electrolyte.

A more useful variation of the technique is electrochemical strain microscopy (ESM), which records ionic flow between the tip and sample surface with a periodic bias applied, so that the Li^+ distribution can be mapped dynamically on the nanoscale. Figure 15.28a,b shows the basic setup and application of this technology to various Li storage materials [15.87, 88].

One aspect that needs to be emphasized is that the electrochemical conditions under which Li-ion batteries operate cannot be precisely applied to the ESM tip, therefore questions as to whether these measurements simulate real cell situation were often raised. For example, with large bias (12 V) alternating at high frequency, the local electrochemical environment that a Li^+ feels and the subsequent intercalation–deintercalation could involve experimental artifacts. Further development is needed to fully establish ESM as a useful technique for researchers in the community.

Acoustic Emission

A rather unexpected but surprisingly informative in situ technique is acoustic emission measurement. *Ohzuku* et al. were perhaps the first to point out that the acoustic events accompanying the mechanical stress between the reacted and unreacted regions of electrode materials could be used to monitor in situ electrochemical reactions in these materials, and their pioneering work using acoustic emission (AE) on electrolytic manganese dioxide proved that acoustic events are closely associated with particle fracturing upon initial lithiation [15.90]. After a hiatus of a decade, researchers' interest in this technique is renewed due to the advantage of its intrinsic passive nature (hence nondestructive) and high sensitivity. The more interesting work was performed on materials of emerging chemistries such as Sn-, Si- as well as conversion reaction electrodes.

Rhodes et al. applied it to investigate the deleterious volume changes in crystalline Si electrodes and performed the first rigorous waveform analysis (Fig. 15.29a), where the duration, amplitude, counts

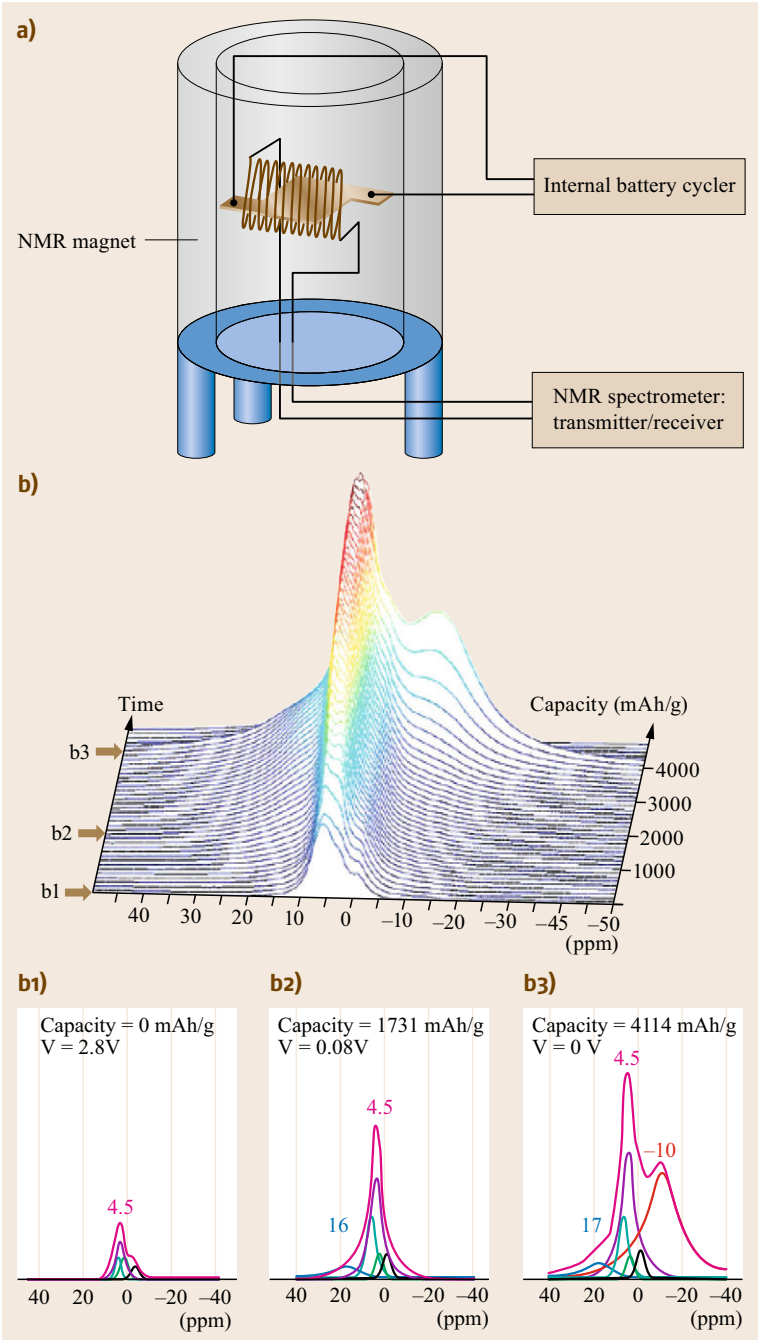


Fig. 15.27 **(a)** Schematic setup of ^{7}Li-NMR study on a crystalline Si anode under electrochemical lithiation. **(b)** Stacked plots of ^{7}Li spectra obtained and the deconvolution at various states of charge (after [15.86])

and frequency were correlated with corresponding electrochemical information so that AES can not only tell when an event occurs but also what it is [15.89]. It was found that the initial lithiation of Si is accompanied with the largest number of emissions, mainly caused by surface fracture of Si particles, while in the subsequent charging–discharging cycles, the emission events are characterized by distinct bursts, reflecting reversible volume expansion–contraction due to formation or disappearance of various Li_xSi alloy phases (Fig. 15.29b). In combination with modeling studies, they concluded that maximum tensile stress occurring at the particle surface is responsible for the largest acoustic events at the initial lithiation. Appar-

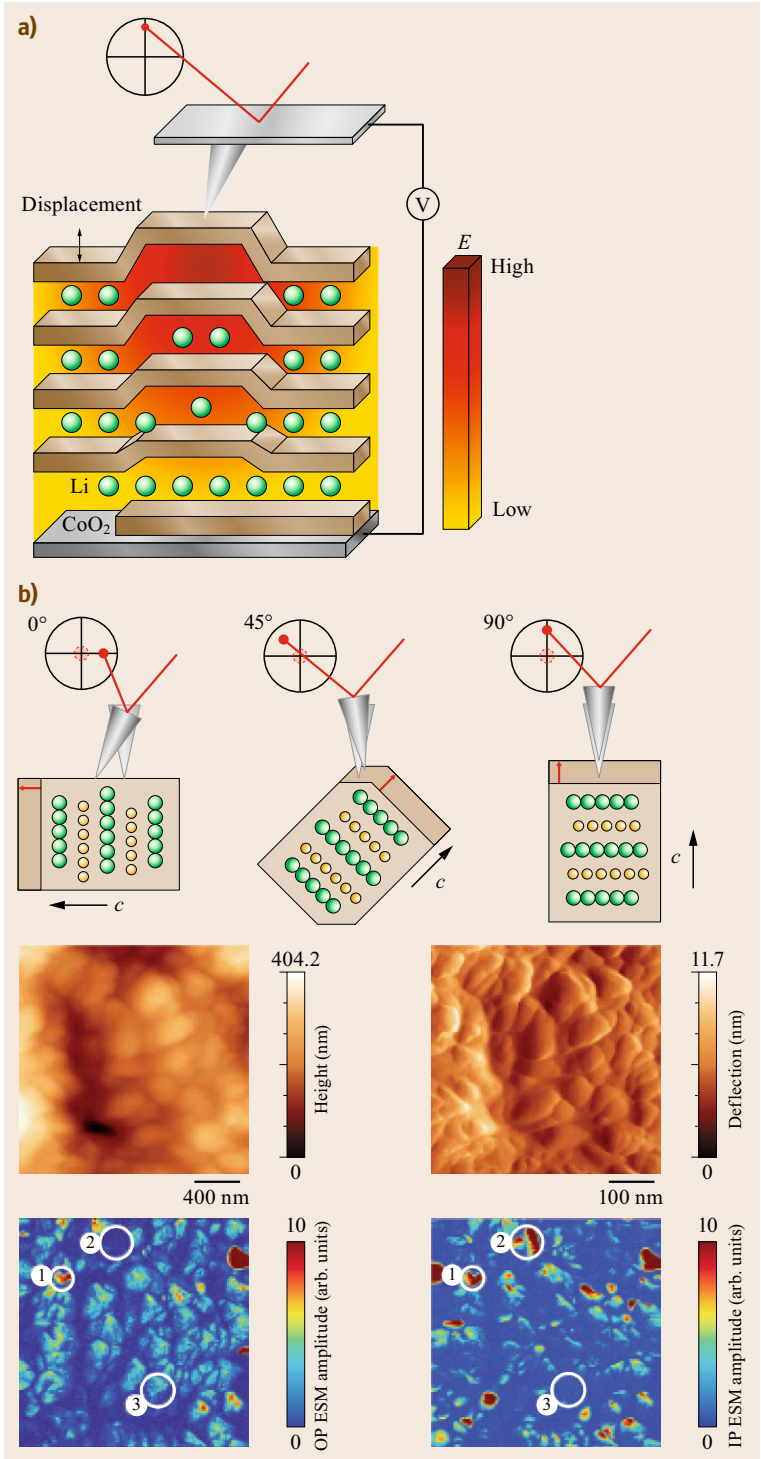


Fig. 15.28 **(a)** Schematic illustration of SPM probe applied on an intercalation electrode; **(b)** SPM experiments on electrode surfaces (after [15.87, 88])

ently, the most severe challenge of Si-based electrodes comes from the initial lithiation process, where not only the crystalline Si turns amorphous to accommodate the incoming Li^+, but also new surfaces created in the process induce consumption of electrolyte solvents and Li^+ as reflected by the irreversible capacity

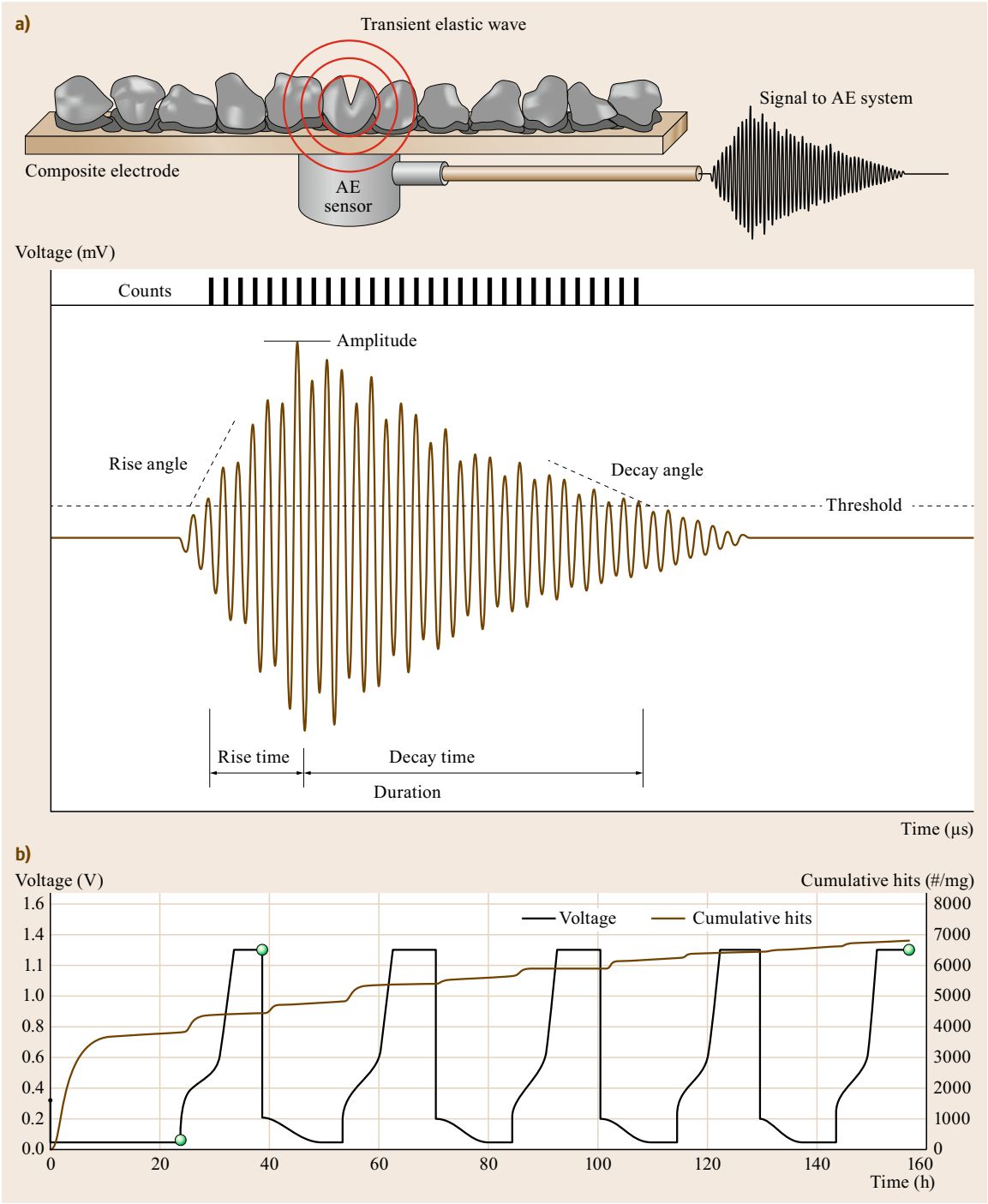


Fig. 15.29 **(a)** Schematic drawing of in situ acoustic emission measurement on an Si electrode and the waveform analysis. **(b)** The voltage profile of an Si electrode cycled in cell and the cumulative acoustic emissions during the cycling (after [15.89])

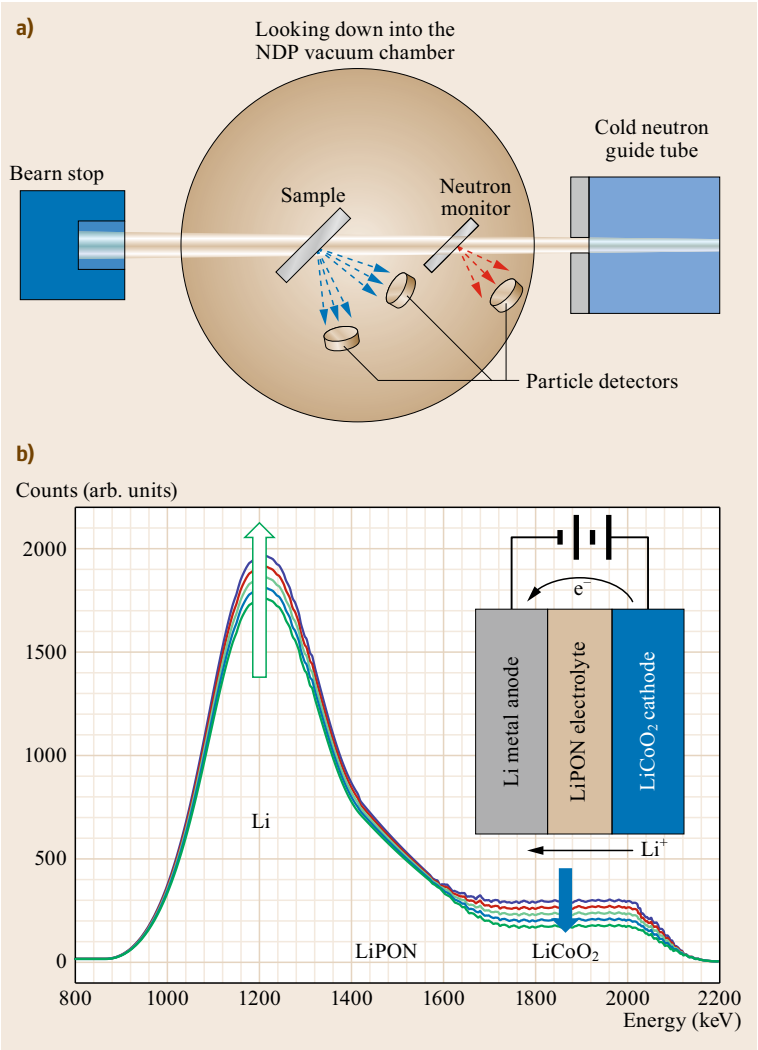


Fig. 15.30 **(a)** The setup of a neutron diffraction experiment. **(b)** Time-resolved in situ neutron diffraction on a thin film battery during charging. The electrode and electrolyte layers are assigned in the spectra. Arrows indicate the flow of Li in each electrode (after [15.91], courtesy of American Chemical Society)

loss. The volume change certainly causes mechanical stress, which can be solved through cell engineering, but to compensate the loss in the first cycle calls for excessive amounts of Li^+ and electrolyte solvents and ultimately leads to high surface impedance. This vicious cycle has to be addressed before practical deployment of Si in actual Li-ion devices can be realized.

Neutron Techniques

An underexplored in situ tool is neutron techniques, apparently due to its limited availability to most potential users. In fact, the sensitivity of neutron techniques to light atoms such as Li makes it a unique complement to TEM, while the low energy (meV) of cold neutrons makes it an essentially nondestructive probing particle that can monitor the dynamic distribution of Li^+ throughout the battery during electrochemical reactions.

In *neutron depth profiling*, space- and time-resolved depth profiles of Li^+ in a Li-ion battery configuration can thus be obtained by bombarding the target with an incoming neutron of 4 meV. Figure 15.30a shows such a typical setup at the National Institute of Standards and Technology (NIST), where the neutron interacts with ^6Li in different electrochemical environments producing a tritium and an α particle

$$^6\mathrm{Li} + n \rightarrow {}^3\mathrm{H} + \alpha\,. \qquad (15.22)$$

Tritium and α particles travel diagonally away from the interaction center, and their energy level reveals the ionic and electronic structures of the matrix where the interaction occurs. The initial locations of the interaction can be traced back using the recorded stopping

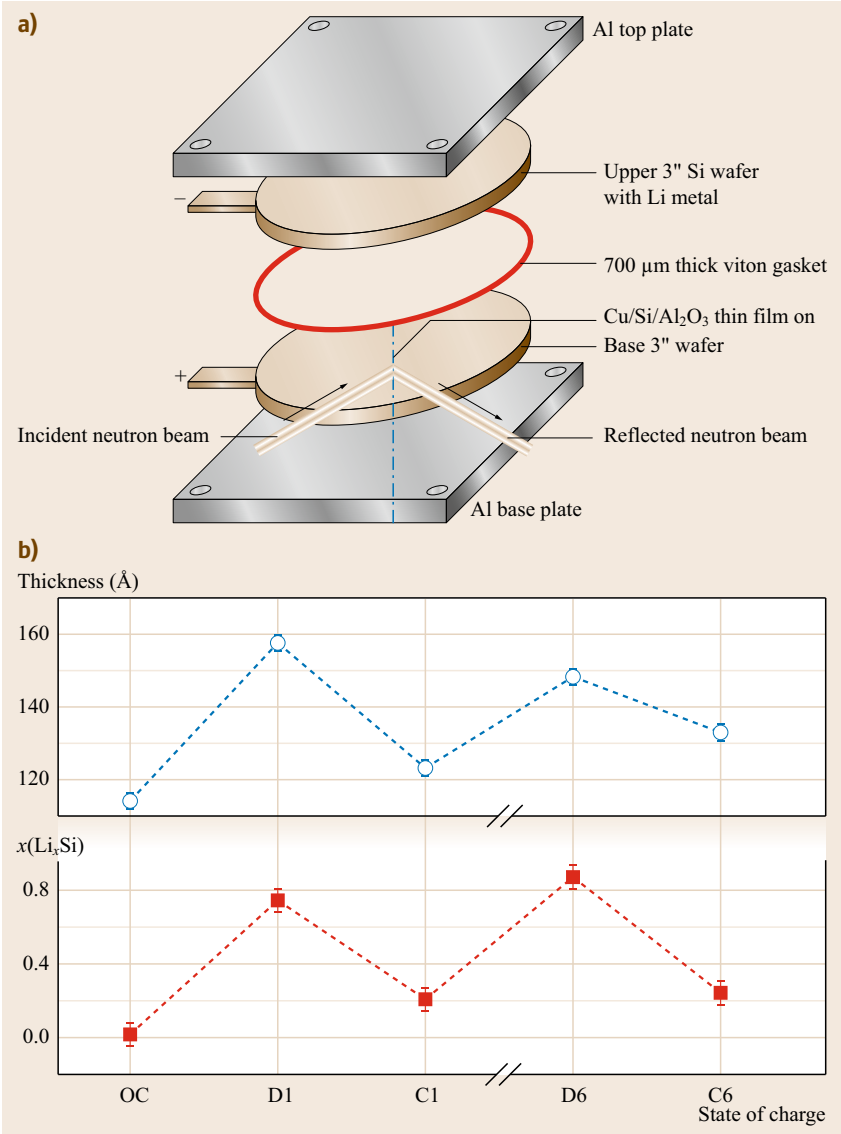


Fig. 15.31 **(a)** Schematic illustration of a battery configuration used for an in situ neutron reflectivity study. **(b)** The thickness of an Si electrode and corresponding Li composition at various states of charge (after [15.91])

power. The relative abundances of ^{6}Li can be calculated using the normalized counts of these charged particles, as shown in Fig. 15.30b, where Li distributions in cathode ($LiCoO_2$), solid electrolyte LiPON and Li metal anode are clearly resolved [15.91].

Another neutron technique variation is its reflectivity on surfaces of different density. While the diffraction is only sensitive to ordered crystalline structures, *neutron reflectivity* sheds rare light on the amorphous phases such as interphase layers on top of bulk electrodes. This high-resolution tool can probe structure and composition with subangstrom accuracy. Typically a monochromatic neutron is directed onto target at a certain angle, and the intensity of the reflecting beam is recorded as the function of the density of isotopes at varying lengths, as Fig. 15.31 shows for a Si-based anode half cell. The atomic dependence established serves as a compositional profile for the interphase, and the dynamic mapping of various interphase layers during charge–discharge provides valuable insight into how interphase thickness changes with the electrochemical states of the batteries. In a recent neutron reflectometry study by *Owejan* et al. the progressive growth of SEI thickness was monitored from 4.0–4.5 to 8.9 nm as a potentiostatic hold was placed on the studied electrode [15.92].

The subangstrom sensitivity of neutron reflectivity proves to be a *double-edged sword*. It could pro-

vide well-resolved information about the targets investigated, but it also imposes stringent, sometimes prohibitive, restrictions on the roughness of the target surface, which could be extremely difficult to satisfy. This latter feature severely limits its application for both materials and environments close to real-life devices. Seeking a technique of both high resolution and low intolerance toward surface roughness, or at least finding a balance in between, remains a challenge for neutron spectroscopists and battery and material scientists.

Other potentially useful neutron tools also include *small angle neutron scattering* and *neutron imaging*. The former is useful in measuring the nanoscale structure of grains and how they behave under the stress induced by lithiation, while the latter provides direct visualization of *hot spots* and nonuniformity in Li^+-distribution in various electrode materials. Both techniques were summarized in a recent rather comprehensive review by *Wang* et al. [15.91]. Their application in Li-ion battery fields are just at the budding stage.

15.3 Evaluation at the Cell–Battery Level

After the Li-ion anode and cathode materials, separator and the compatible electrolyte are evaluated as discussed in Sect. 15.2, and these components need to be evaluated as a complete electrochemical system at a cell or a battery level for a comprehensive assessment of the performance, life and safety. A cell, which is made of anode, cathode, separator and electrolyte, is a system and needs to function well together as a cell or a battery.

15.3.1 Cell Configurations

A cell can be made into a coin cell, pouch cell, prismatic, bobbin or spirally wound cell. For a practical cell, the electrode, either anode or cathode, is typically made by coating a slurry, which is made by blending together a mixture of electrode active material, conductive diluents and binder, which is dissolved in a solvent or solvent mixtures, on both sides of a current collector, copper for anode and aluminum for cathode. Figure 15.32 shows a wound cell assembly with positive electrode, negative electrode and separator, double-side coated porous electrodes, and high surface area particles with small primary particles.

Coin cells [15.93] are also a commonly used testing vehicle for battery materials researchers. These cells can easily be assembled in Argon-filled dry boxes and in dry rooms with simple crimping tools. A test using coin cells will provide information on initial capacity and voltage profile of active anode or cathode materials using half-cell configurations. The electrode-electrolyte stability can also be studied using coin cells with half-cell and full-cell configurations.

Pouch cells are also used for researchers or battery developers for testing battery materials with larger size electrodes. The pouch cells can mimic a practical cell better than coin cells and uncover problems that are hidden in the coin cells such as gas evolution during cycling. A further advantage of using this configuration is that a reference electrode such as Li can easily be incorporated into the cell for the study of electrochemical behavior of both electrodes at the same time [15.94].

The power capability, or the ability to charge and discharge effectively at different rates, is best evaluated in a range of test cells. The cell resistance determines how much energy is lost to heat rather than electricity (I^2R losses). Accordingly, the power performance varies greatly with how the electrodes are fabricated, the thickness of the electrode, and how the cell is packaged, in addition to the inherent materials' ionic and electronic conductivities, its morphology and the contacts' resistance within the electrodes and between the electrodes and the cell.

15.3.2 Performance Characteristics

The evaluation of Li-ion battery materials at the cell level is necessary for assessing the viability of an electrochemical pair for practical use. Well fabricated electrodes assembled in industrial packaged cells such as 18650 cylindrical cells as well as prismatic cells will be ideal for full assessment. At the cell level, the following important data can be obtained:

1. Discharge capacity and voltage profile
2. Discharge capacity at different rates
3. Charge (capacity) retention and recovery
4. Cycle life (endurance in cycles)
5. Internal resistance
6. Safety.

There are international standards published by the International Electrotechnical Commission (IEC) that *define a minimum required level of performance and standardized methodology by which testing is performed and the results of this testing reported to the users* [15.95]. IEC 61960 is an international standard for *secondary cells and batteries containing alkaline or other nonacid electrolytes – secondary Li cells and bat-*

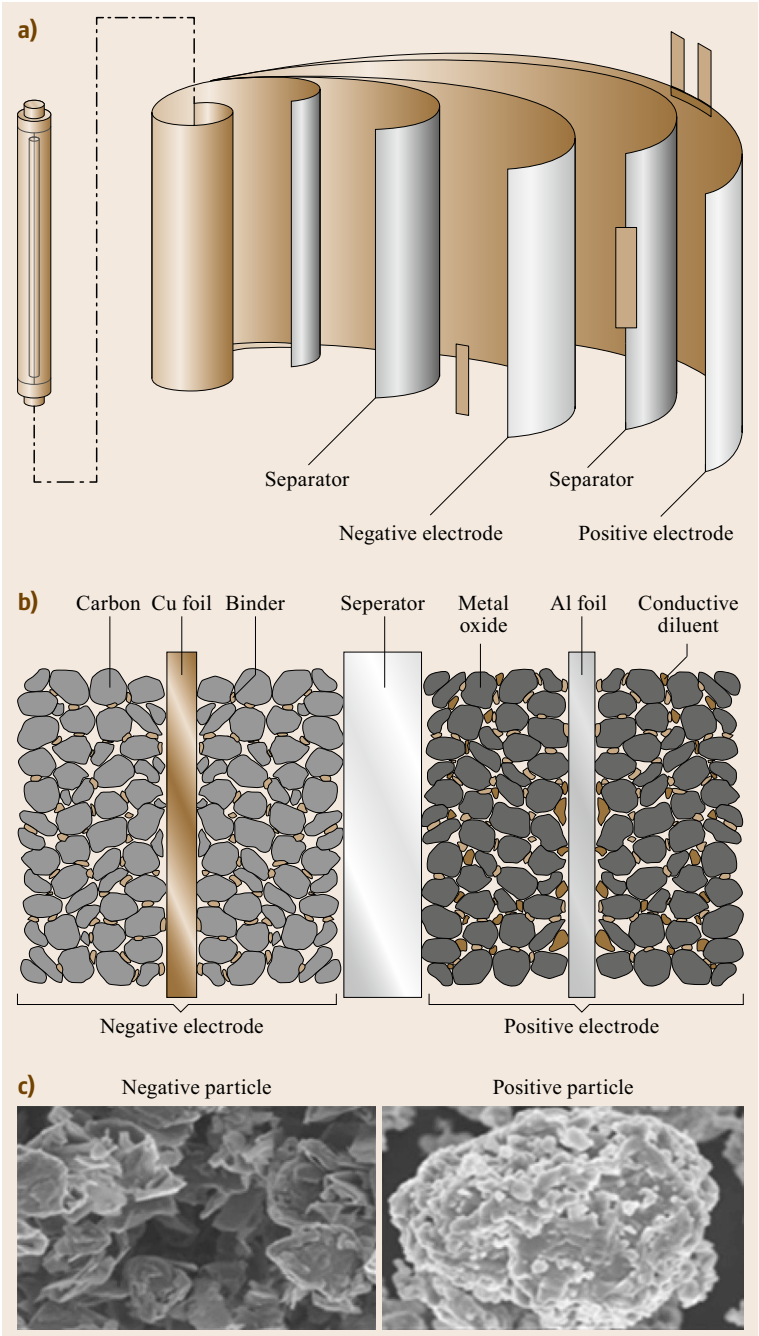


Fig. 15.32 **(a)** Wound cell assembly with positive electrode, negative electrode and separator. **(b)** Double-side coated porous electrodes. **(c)** High surface area particles with small primary particles (courtesy Saft batteries)

teries for portable applications. The standardized tests can also be adopted by researchers for evaluating cells.

The terms and definition used in the standard are also commonly adopted in the electrochemical materials and battery research community. The *rated capacity* is a quantity of electricity C_5 or C in Ah declared by the battery manufacturer that a single cell or battery can deliver during a 5 h period when charged, stored and discharged at a constant current of $0.2\,I_t$ A (ampere) down to a specified end-of-discharge voltage in an ambient temperature of $20\,^{\circ}\mathrm{C} \pm 5\,^{\circ}\mathrm{C}$, where I_t A $= C$ Ah/1 h. The charge or discharge current are expressed as a multiple of I_t A. A rate of 1 I_t is equivalent to $1C$ rate, which means the capacity will be discharged in 1 h

Table 15.1 Theoretical and actual energy densities of selected Li-ion chemistries (after [15.96])

Chemistry	Size	Theoretical (Wh/l)	Actual (Wh/l)	(%)	Theoretical (Wh/kg)	Actual (Wh/kg)	(%)
$LiFePO_4$	54 208	1980	292	14.8	587	156	26.6
$LiFePO_4$	16 650	1980	223	11.3	587	113	19.3
$LiMn_2O_4$	26 700	2060	296	14.4	500	109	21.8
$LiCoO_2$	18 650	2950	570	19.3	1000	250	25.0
Si-$LiMO_2$Panasonic	18 650	2950	919	31.2	1000	252	25.2

The theoretical values in the table assume only the active components, and no volume or weight for Li beside that in the cathode

at this rate. A rate of 0.2 I_t A is often called 0.2 *C* rate and 5 I_t A is equivalent to 5 *C* rate.

Dahn and *Ehrlich* [15.97] have recently provided an excellent overview of the state-of-the-art Li-ion batteries that were available before 2010. New Li-ion batteries of different variations of anode and cathode and configuration have appeared since then. The information regarding these batteries can be found at their websites. The most important characteristics of a Li-ion cell or battery are energy density, power capability, cycle life and storage life, and safety. The related methods for understanding these characteristics are discussed below.

15.3.3 Energy Density

The energy density of an electrochemical pair at the materials level that has been discussed in Sect. 15.2.1 is often called the theoretical energy density of the cell. The energy density of an electrochemical pair at the cell level varies with the tap density of anode and cathode materials, contents of conductive diluents, contents of binder, porosity of the electrode, and tightness of the winding. The inclusion of safety devices in the cell will also affect the energy density of the cell. At the battery level, a battery management system will be installed to ensure the proper operation of the cells or batteries. The energy density values at the cell and the battery levels can be found at the battery manufacturers' websites. Table 15.1 shows the difference between theoretical and actual energy densities of some selected Li-ion chemistries [15.96]. The actual energy density is only a fraction of the theoretical energy density. Further improvement in actual energy density is possible through improvements in materials morphology, processes for fabricating electrodes with reduced nonactive materials contents, and packaging methods.

15.3.4 Power Capability

The power performance is one of the very important performance characteristics of batteries for a number of applications requiring high power including power tools and hybrid electric vehicles. The power performance or rate capability of a cell is determined in part by the internal resistance in the cell as the power is the product of the cell voltage and cell current, which is determined by the cell voltage divided by the cell resistance. In short, the power that can be delivered by a cell is proportional to the square of the voltage and inversely proportional to the cell resistance. The cell resistance is mostly affected by the ability of the electrode materials to conduct electrons and ions. Electrolytes also affect the cells' resistance especially at low temperatures as the charge transfer resistance at the graphite anode–electrolyte interface substantially increases at temperatures below –20 °C [15.94] and their viscosities increase. However, the cell resistance can also be reduced by engineering efforts including the incorporation of conductive diluents, optimization of electrode porosity, reduction of contact resistance between electrode and current collector and between current collector and cell terminals and reduction of electrode thickness.

The cell resistance R_{cell} is the sum of several resistances existing in the cell as expressed in equation

$$R_{cell} = R_e + R_{electrolyte} + R_{SEI} + R_{ct} , \qquad (15.23)$$

where R_e represents all of the contact resistance within the electrodes, electrode–current collector contact resistance and current collector–cell terminals contact resistance; $R_{electrolyte}$ is the resistance of the electrolyte; R_{SEI} is the resistance of the SEI layers on the electrodes; and R_{ct} represents the charge transfer resistance at the electrodes and electrolyte interfaces.

The cell internal resistance can be measured using DC and AC methods. The international standard IEC 61960 [15.95] for secondary Li cells and batteries for portable electronics and IEC 62620 [15.98] for large format secondary Li cells and batteries for industrial applications have described the methods for measuring both resistances in detail. These methods are discussed later.

Internal DC Resistance

The internal DC resistance can be determined by discharging a cell, when the cell is at the 50% SOC, at a specified current I_1 for a period of time, e.g., 30 s, and measuring the voltage, U_1, at the end of 30 s and then

immediately increasing the current to a higher specified I_2 and continued discharge for 5 s and recording the voltage U_2 at the end of 5 s. The internal DC resistance R_{DC} is calculated using

$$R_{DC} = \frac{U_1 - U_2}{I_2 - I_1}(\Omega) , \tag{15.24}$$

where I_1 and I_2 are the constant discharge currents, and U_1 and U_2 are the appropriate voltages measured under load.

For hybrid vehicle applications, the hybrid pulse power characteristics (HPPC) test described in PNGV battery test manual [15.99] is used to determine the pulse discharge or charge resistance or the power capability of cells or batteries. The same relationship as shown in (15.24) is used to determine the pulse discharge resistance or power. But the discharge–charge current and discharge–charge time period are different from that specified in IEC 61960 and 62620.

HPPC Test. The HPPC Test is intended to determine the power capability of a cell or battery at the end of 18 s discharge, as a function of depth of discharge, or the power capability of a cell or battery at the end of a 2 s regeneration as a function of the state of charge (SOC) of the cell or battery for hybrid vehicle applications. For different operational modes, the discharge and charge time periods can be different. The test current selected is 5*C* rate or 25% of the maximum of the manufacturer's absolute maximum allowable pulse discharge or charge current. The discharge power at the specific SOC can be determined using the voltage measured at the end of the 18 s discharge and the discharge current. Figure 15.33 shows one example of the pulse power capability versus depth of discharge of a battery at power assist mode and dual mode. The details of the test procedures can be found in the PNGV battery test manual [15.99].

Pulse discharge resistance and pulse charge resistance, or area specific impedance (ASI) in $\Omega\,\mathrm{cm}^2$, can be obtained using the HPPC test [15.99, 100]. The cell is charged to 100% SOC and allowed to rest for 1 h. Subsequently, the cell is discharged 10% and allowed to rest for 1 h. Next, a 5*C* rate discharge pulse is applied for 10 s. After the pulse, the cell is allowed to rest for 40 s, after which a 10 s charge pulse is applied. After the 10 s charge pulse, the cell is discharged to the next state of charge of 80%. After the cell reaches 90% SOC, it is allowed to rest for 1 h. Subsequently, the discharge and charge pulses are applied again and the cell is then taken to 70% SOC. This continues until the cell can no longer complete the discharge pulse or the cell reaches 0% SOC. The voltages at the end of the 1 h rest and at the end of the discharge pulse are used to calculate the ASI for discharge, and the voltages at the end of the 40 s rest and at the end of the charge pulse are used to calculate the ASI for charge.

Internal AC Resistance and AC Impedance

The AC resistance is determined by measuring the alternating root mean squared (RMS) voltage U_a, while applying an alternating rms current, I_a, at the frequency of 1.0 ± 0.1 kHz, to the battery, for a period of 1–5 s. All voltage measurements should be made at the terminals of the battery independently of the contacts used to carry current. The internal AC resistance R_{AC} is given by

$$R_{AC} = \frac{U_a}{I_a}(\Omega) , \tag{15.25}$$

where U_a is the alternating rms voltage and I_a is the alternating rms current.

Instead of determining the AC resistance at a single frequency, EIS can be used as described in Sect. 15.2.2 and Sect. 15.2.4, whereby an electrochemical pair at the cell level is measured over a wide frequency range from 10^{-3} to 10^6 Hz.

An impedance measurement of commercial 18 650 $LiCoO_2$/graphite based Li-ion cells reveals that the charge-transfer resistance R_{ct} varied with temperature following an Arrhenius relationship [15.101],

$$\frac{I}{R_{ct}} = A_0 e^{-E_a/RT} , \tag{15.26}$$

where the E_a is the activation energy, which is about 70 kJ/mol for this case [15.102]. As identified using Li as a reference electrode in three-electrode Li-ion cells with graphite as an anode and either $LiFePO_4$ or $LiCo_{0.15}Ni_{0.8}Al_{0.05}O_2$ as a cathode, the activation energy for the charge transfer at the graphite anode is also found to be about 67–68 kJ/mol. This suggests that the Li-ion cell is dominated by the charge transfer process across the graphite–electrolyte interface [15.94].

EIS is also a powerful tool in assessing the dynamic power performance dependence on temperature as well as SOC through the impedance measurement at all operating conditions in a wide frequency range. The different electrochemical processes in a cell can also be observed. The study of VL6P, a commercial 6.5 Ah high power Li-ion cell from Saft – a cylindrical cell optimized for the use in hybrid vehicles – using impedance method was recently reported by *Andre* et al. [15.103].

EIS can also be used to study the aging mechanisms of $LiFePO_4$/graphite [15.104] and $Li(Co_{0.2}Ni_{0.8})O_2$/graphite [15.105] Li-ion chemistries by monitoring the impedance evolution over the cell's cycle life.

Srinivasan et al. [15.106] and *Srinivasan* [15.107] demonstrated the existence of an intrinsic relationship

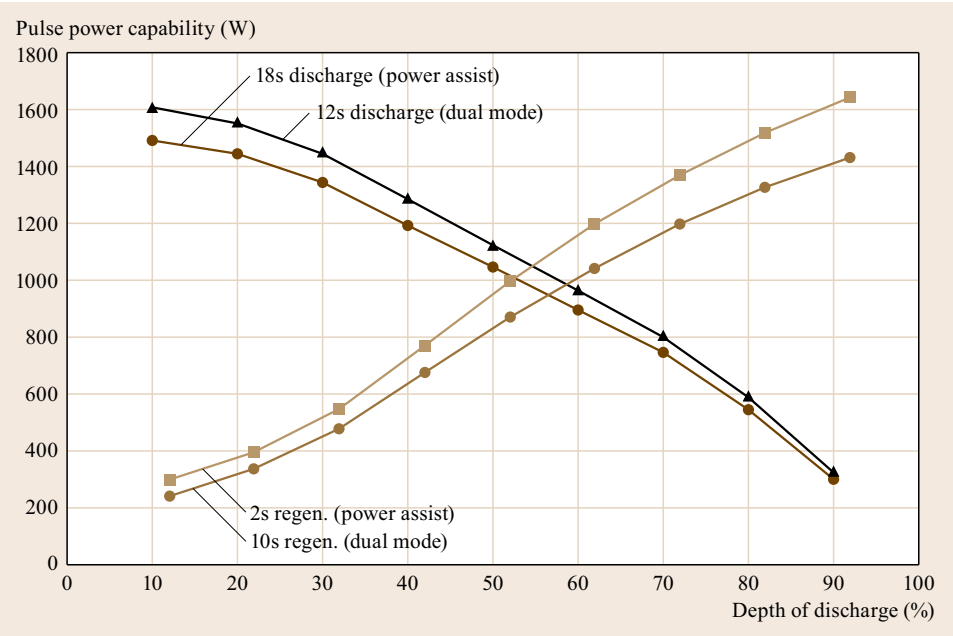


Fig. 15.33 Pulse power capability versus depth of discharge

between a cell's internal temperature and a readily measurable electrical parameter, the phase angle between an applied sinusoidal current and the resulting voltage in three different Li-ion cells, a 53 Ah GS-Yuasa LSE50-002, a 2.3 Ah ANR26650 and a 4.4 Ah Boston Power Swing 4400. This is an interesting application of the EIS method in assessing the thermal behavior inside the Li-ion cells.

15.3.5 Cycle Life and Storage Life (or Calendar Life)

The Li-ion cells lose their capacities during cycling and storage. The cycle life is important for space, automotive and grid energy storage applications, which require services of over 10 years and often involve heavy duty cycling. The storage life is especially important for standby applications including standby power for telecom operations.

The cycling life of a cell or battery is given by the total number of discharge–charge cycles, in which the cell is discharged to the specified end-of-discharge voltage and charged to the specified voltage, performed to reach 60% of the initial capacity at the 0.2 I_t A (or 0.2 C) rate at 25 ± 5 °C based on the IEC 61690 for secondary Li cells and batteries for portable applications and IEC 62620 for large format secondary Li cells and batteries for use in industrial applications. For a 500 cycling life test at a rate of 0.2 C, the test time will be 5000 h, which equals over 208 d. Higher rates can be used for shorter term tests. The storage life test calls for a cell or battery to sustain a minimum of 75% of capacity after 6 months of storage at a constant voltage corresponding to 100% SOC at a temperature specified by the manufacturer.

For different applications such as hybrid electric vehicles, the cycling test profile and the required cycle life could vary and would demand a much longer real life testing. Therefore, the understanding of the capacity fading rate and fading mechanism are the keys in predicting and improving life of the batteries. The life prediction and aging mechanisms are mostly investigated on mature battery chemistries with consistent products available for specific applications in mind.

Electrochemical techniques such as galvanostatic charge–discharge at different rates, AC impedance, and HPPC measurements have been used to characterize the source of capacity fading. The use of a Li reference electrode allows identification of whether the fading is coming from the cathode or anode.

In characterizing the cells made of graphite/$LiCo_{0.15}Ni_{0.8}Al_{0.05}O_2$, *Zhang* et al. [15.108], using a Li reference electrode, identified that the capacity fade during cycling is primarily caused by the positive electrode as shown in the increase in impedance at the cathode, where discharge capacity may be limited by a decrease in active Li intercalation sites in the oxide particles. Different from graphite/$LiCo_{0.15}Ni_{0.8}Al_{0.05}O_2$ batteries, the graphite/$LiFePO_4$ batteries as reported by *Liu* et al. [15.104] do not experience appreciable resistance increase under a variety of cycling conditions.

The loss of active Li results from the repairing of the SEI at the graphite anode [15.104].

High Precision Coulometry

Smith et al. [15.109] of Jeffrey Dahn's group in Dalhousie University, Canada, recently have suggested that high precision coulometry (HPC) can indicate the relative cycle and calendar life of cells by measuring the extent of parasitic reactions in coulombic efficiency (CE) in only a few weeks of testing. Parasitic reaction rate, k (h^{-1}), for $LiCoO_2$, $LiFePO_4$, and $LiMn_2O_4$/graphite Li-ion cells at different temperatures can be determined from CE and the time of one cycle using the relationship

$$1.0000 - \mathrm{CE} = k \quad (\text{time of one cycle}) . \qquad (15.27)$$

High precision coulombic efficiency measurements can detect problems occurring in half cells that do not lead to capacity loss, but would in full cells, and can measure the impact of electrolyte additives and electrode coatings [15.110]. This is a powerful tool for researchers who do not have access to packaged cells.

15.3.6 Safety

Safety has been a concern for the users of Li-ion batteries as a number of incidents of fire have been reported in the news. Safety is also an important area in research and development of Li-ion batteries because it is intimately related to the electrode and electrolyte materials selected and their chemistries under various electrical, electrochemical, thermal and heat conditions.

Commercial Li-ion cells and batteries have to pass a number of safety tests under the conditions of *intended use* and *reasonably foreseeable misuse* as described in IEC 62133 [15.111]. The tests include 1) continuous low-rate charging under *intended use* and 2) external short circuit, thermal abuse, crushing of cells, overcharge, forced discharge, and protection of cells under high rate charging current under the *reasonably foreseeable misuse* conditions. The test conditions and procedures are detailed in the safety standards such as IEC 62133 [15.111], an emerging unified international safety standard at a product level for rechargeable batteries, and UL 1642 [15.112], a standard for safety developed by Underwriters Laboratories Inc. (UL) for Li batteries. IEC 62133 (secondary cells and batteries containing alkaline or other nonacid electrolytes) – general guidelines, is expected to replace UL 1642 by 2012. UL's battery testing laboratories are accredited to do the testing and certification to IEC 62133.

The criteria for passing these tests are that the cells shall not cause fire or explosion under the above test conditions. The commercial Li-ion cells such as VL cells from Saft batteries also feature various redundant safety features (electronic protection circuit, built-in circuit breaker in case of faulty chargers, safety valve, shut down separator), which makes them ideal for demanding applications (military, medical, etc.).

The evaluation of safety aspects of a cell or battery starts by assessing the electrochemical stability of the battery components including electrode materials and electrolytes as discussed in Sect. 15.2.1 and 15.2.2. The ability of the cell or battery to withstand the electrical misuse including short circuit, overcharge, overdischarge, and high rate charging is largely determined by the chemistry and electronic structure of cathode materials. For example, Li can be completely removed from the fully lithiated $LiFePO_4$ of olivine structure at a fully discharged state and leave a stable delithiated phase $FePO_4$ at a fully charged state [15.113] resulting in a much safer $LiFePO_4$/graphite Li-ion cell. A layer structured $LiCoO_2$ would not be able to remove Li completely before the oxygen is removed from the structure and reacted with the flammable electrolyte made of carbonate-based solvents and the Al current collector, causing a thermal runaway.

Physical damage such as crushing, which is similar to a short circuit in the cell, will cause substantial heat generation. Under thermal abuse, the cell or battery is exposed to accelerated reactions between electrode materials and the electrolyte, which will also cause heat generation. Therefore, thermal characterization of Li-ion cells under various electrical conditions is the main characterization tool for the study of the safety of Li-ion at the cells or batteries level.

Thermal characterization techniques including the following are used to assess the safety level of the battery materials and cells:

1. Differential scanning calorimetry (DSC). This technique allows the measure of the thermal response of individual and selected combinations of cell components over a broad temperature range by scanning temperature at a fixed rate. *MacNeil* et al. [15.115] used DSC to compare the thermal stability of seven different charged cathodes in 1 M $LiPF_6$ EC/DEC electrolyte. It was concluded that the cathode materials can be ranked from most safe to least safe in the following order: $LiFePO_4$, $LiNi_{3/8}Co_{1/4}Mn_{3/8}O_2$, $Li_{1-x}Mn_{2-x}O_4$, $LiCoO_2$, $LiNi_{0.7}Co_{0.2}Ti_{0.05}Mg_{0.05}O_2$, $LiNi_{0.8}Co_{0.2}O_2$ and $LiNiO_2$.
2. Accelerated-rate calorimetry (ARC). This technique applies to full cells as well as cell components under adiabatic conditions. Under this condition,

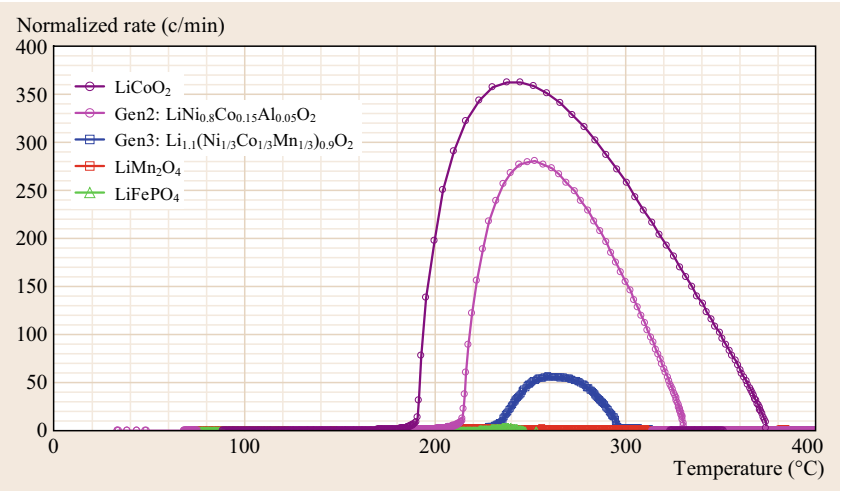


Fig. 15.34 Self-heating rate of 18 650 full cells of different cathodes including $LiCoO_2$, $LiNi_{0.8}Co_{0.15}Al_{0.05}O_2$, $Li_{1.1}(Ni_{1/3}Co_{1/3}Mn_{1/3})_{0.9}O_2$, $LiMn_2O_4$ and $LiFePO_4$ measured by ARC. Improved cathode stability results in higher thermal runaway temperature (increased stability) and reduced peak heating rate (after [15.114])

the cell heating rate is strictly a function of the intrinsic heat generating reactions in the cell and the thermal heat capacitance of the cell components [15.114]. Figure 15.34 shows the self-heating rate of 18 650 full cells of different cathodes measured by ARC. Improved cathode stability results in higher thermal runaway temperature and reduced peak heating rate [15.116].

3. Thermal Ramp Test. The thermal stability of cells can be studied by linear programmed heating to cell failure. In this test, the cells are heated at a programmed heating rate, 5 °C/min is typical, from room temperature to 250 °C or higher, at which temperature the cell fails by initiating a thermal runaway. The flammability of the vent gases and electrolyte solvent vapor can be determined by placing spark ignition sources in critical locations around the cell fixture [15.114].

A series of articles relating to Li-ion battery safety published in 2012 Electrochemical Society Interface Magazine [15.117] provide an excellent overview of the Li-ion battery safety issues, which included how electrolytes influence battery safety [15.118].

15.4 Beyond Li-Ion

The maximum energy density that can be expected for Li-ion batteries is about 275 kWh/kg, which is limited by the stoichiometric Li^+ ion amount of the intercalation electrode materials. In order to meet the emerging energy capacity needs for batteries, alternative chemistries are being proposed. As suggested by the name, the batteries beyond Li-ion do not use Li^+ ion intercalation compounds as the electrode material, instead, these types of batteries are based on the alternative Li-based redox couples with significantly higher specific capacity than Li-ion batteries. Typical examples of the batteries beyond Li-ion are lithium-sulfur (Li-S) battery and Li-air battery (or $Li-O_2$ battery).

15.4.1 Li–S Battery

Lithium-sulfur (Li–S) batteries offer a theoretical specific capacity of 1675 Ah/kg and a theoretical specific energy of 2500 Wh/kg (or 2800 Wh/l) based on the complete reduction from elemental sulfur to lithium sulfide by

$$2Li + S \rightarrow Li_2S\,. \tag{15.28}$$

The high theoretical specific capacity and low cost of sulfur makes Li–S batteries attractive. In nature, sulfur exists mainly in the form of ring-structural cyclooctasulfur (S_8), thus the reduction of sulfur in a Li–S cell is a multistage process through a series of lithium polysulfide (PS, Li_2S_x) intermediates, as [15.118]

$$\begin{aligned} S_8 &\rightarrow Li_2S_8 \rightarrow Li_2S_6 \rightarrow Li_2S_4 \rightarrow Li_2S_3 \\ &\rightarrow Li_2S_2 \rightarrow Li_2S\,. \end{aligned} \tag{15.29}$$

These multistage reductions are reflected in the voltage curve of the first discharge, and can be divided into such four general stages as:

1. A solid-to-liquid phase reaction from sulfur (S_8) to dissolved Li_2S_8, which corresponds to an upper voltage plateau at ≈ 2.3 V

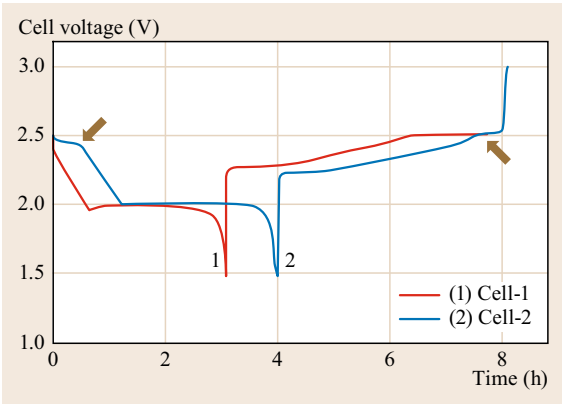


Fig. 15.35 Typical discharge and charge voltage curves of Li–S cells at constant current rate. (1) Baseline cell, and (2) cell with the suppression of redox shuttle reaction by $LiNO_3$ in the electrolyte

2. A single liquid phase reaction from high-order Li_2S_8 to low-order Li_2S_4, which corresponds to a linear voltage decline
3. A liquid-to-solid phase reaction from the soluble Li_2S_4 to insoluble Li_2S_2 or Li_2S, which corresponds to a lower voltage plateau at ≈ 2 V and contributes to the major capacity of a Li-S cell
4. A solid-to-solid phase reaction from insoluble Li_2S_2 to insoluble Li_2S, which corresponds to a steep voltage decline.

Since PS intermediates are soluble in nonaqueous electrolytes and their solubility increases with the length of PS anion chain (i. e., x value in Li_2S_x), the Li–S cell is indeed a liquid electrochemical system. In discharge, sulfur is first reduced into highly soluble Li_2S_8, which dissolves into the electrolyte and serves as the *liquid cathode*. However, the dissolution of PS in liquid electrolyte causes many problems, which include:

1. The dissolution of PS results in a loss in the sulfur active material
2. PS diffuses to the Li anode and reacts with metal Li, which corrodes the Li anode and increases the cell's self-discharge
3. PS is electrochemically reduced on the surface of the Li anode, which reduces charging efficiency
4. PS in electrolyte solution might disproportionate into insoluble species, which precipitates out of the electrolyte to become inactive sulfur.

On the other hand, the dissolution of PS is essential for the kinetics of the cell's reaction. Since sulfur and its reduction intermediates and products are neither electronically conductive nor ionically conductive, the dissolution transfers PS into solution so that the cell's reaction can easily take place on the interface between carbon and electrolyte solution.

While charging, the dissolved PS can be chemically (i. e., directly reacting with metal Li) and electrochemically reduced on the Li anode in addition to being electrochemically oxidized to higher order PS on the cathode. This phenomenon, called a *redox shuttle effect*, significantly affects the charging efficiency and the cell's performance. Figure 15.35 shows typical discharge and charge voltage curves of Li-S cells without and with suppression of redox shuttle by using a $LiNO_3$-contained electrolyte to protect the Li anode (Cell-1 and Cell-2, respectively). Cell-1 can only be charged to 2.5 V, at which point the cell's voltage remains unchanged until the end of the charging process, showing a strong redox shuttle effect. As a result, the following discharge does not show the upper voltage plateau. Cell-2 passes the upper voltage plateau at 2.5 V and reaches the charging cut-off voltage, showing effective suppression of the redox shuttle effect, so that the following discharge shows an upper voltage plateau.

Due to the dissolution of PS and its resulting redox shuttle effect, the theoretical specific capacity and energy density of Li–S cells are not easily obtained, and most of the known problems with Li–S cells are related to the dissolution of PS. Therefore, effective evaluations of Li–S cells are focused on PS-related effects, which include:

1. Cycle life, which reflects the overall effect of the PS dissolution and its resulting effects, including the loss of sulfur active material, Li corrosion, and chemical stability of electrolyte solvents against PS intermediates and metal Li.
2. Charging efficiency, which is a good measure for the redox shuttle reactions of PS in charging process. The redox shuttle reactions not only involve chemical reaction between PS and metal Li but also include electrochemical reduction of PS on the Li surface. High charging efficiency may result from either the suppression of PS diffusion out of the cathode or the protection of Li anode.
3. Self-discharge, which relates to the chemical reactions between the dissolved PS and Li anode, and to the disproportionation of PS in electrolyte solution, which occurs spontaneously during storage.
4. Safety. Direct chemical reactions between the dissolved PS and the Li anode at elevated temperatures is a major source affecting the safety of Li–S batteries, therefore hot-oven storage test is a good measurement for the safety of Li–S batteries.

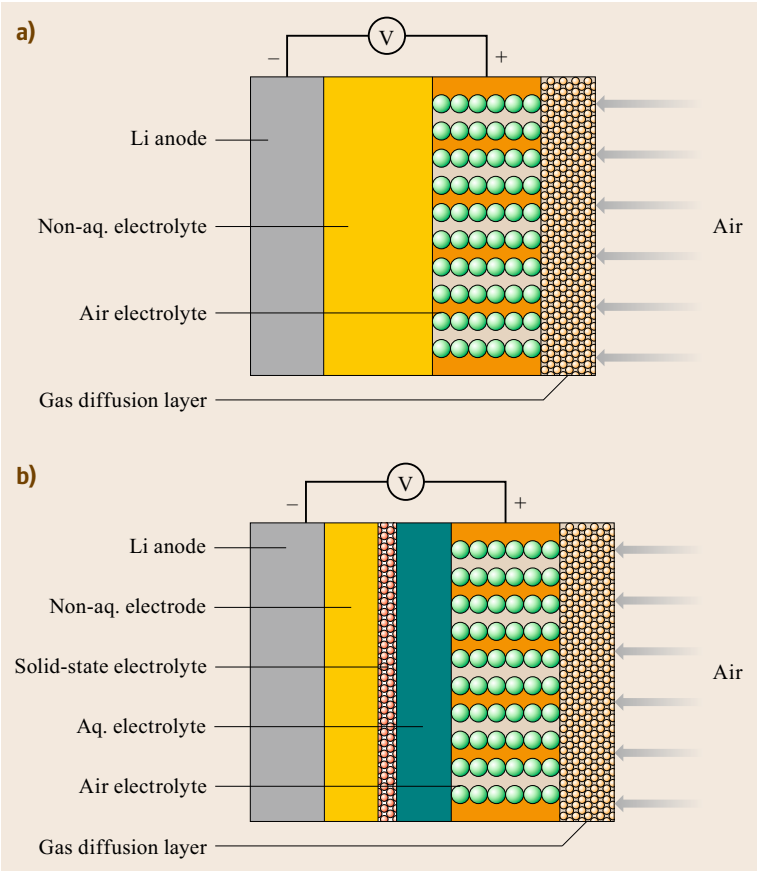


Fig. 15.36a,b Schematic structure of Li–air cells. **(a)** Nonaqueous electrolyte, **(b)** hybrid electrolytes

5. Low-temperature performance. Dissolution of PS increases the viscosity of the electrolyte solution, which mostly affects the power capability and low temperature performance of Li–S cells.

15.4.2 Li–Air Battery

Li–air cells are a class of metal-air batteries. According to the atomic weight of metal Li, the Li–air cell has a theoretical specific capacity of 3862 Ah/kg and a theoretical energy density of 11 425 Wh/kg, which are among the highest values in the known metal-air chemistries. In general, the Li–air cell is composed of a gas diffusion layer (GDL), an air electrode, a separator/electrolyte, and a Li anode. Since metal Li reacts with moisture and CO_2 in the air, the Li anode needs a nonaqueous electrolyte. The Li–air cell can be configured in two electrolyte protocols, i. e., nonaqueous electrolyte system and hybrid nonaqueous–aqueous electrolyte system, as shown in Fig. 15.36.

In the nonaqueous electrolyte Li–air cell, the GDL should be able to isolate moisture and CO_2 from the cell in addition to distributing O_2 evenly into the air electrode and preventing the evaporation of electrolyte solvents out of the cell. The air electrode is a porous carbon sheet without or with the loading of a oxygen reduction reaction (ORR) catalyst. In many cases, the ORR is a mixed process of a two-electron reduction and a four-electron reduction, as described by

$$O_2 + 2Li \rightarrow Li_2O_2, E = 2.959\,V\,, \quad (15.30)$$

$$O_2 + 4Li \rightarrow 2Li_2O, E = 2.913\,V\,, \quad (15.31)$$

which depends on the ORR catalyst, electrolyte solvents, and discharge conditions. The discharge products of Li–air cells are often a mixture of Li_2O_2 and Li_2O. Since both Li_2O_2 and Li_2O are insoluble in nonaqueous electrolytes, they deposit and accumulate on the surface of air electrodes, which consequently clog the access of oxygen into catalytic sites of catalyst and halt the cell's operation. Therefore, the specific capacity and energy density of a Li–air cell are expressed in reference to the mass of carbon. Since the ORR occurs on the *solid–liquid* interface between the catalytic sites and dissolved oxygen, an optimized *solid–liquid* two-phase reaction zone is required for high capacity and

power [15.119]. A general rule is that high capacity requires a large reaction area and high power requires a thin liquid electrolyte film on the catalyst.

For primary Li–air cells, there are no special requirements for ORR catalyst and electrolyte solvents. Especially for low power applications, the catalytic activity of carbon itself is high enough to meet ORR without need of an additional catalyst. For rechargeable Li–air cells, however, there are critical requirements for both the ORR catalyst and electrolyte solvents. First, the reversibility requires a two-electron ORR catalyst because the four-electron ORR product Li_2O cannot be electrochemically oxidized to O_2 once it is formed. Second, the electrolyte solvents are required to be chemically stable against the ORR and oxygen evolution reaction (OER) intermediates. In nonaqueous electrolytes, the ORR and OER involve various oxygen radical anions as the intermediate. These intermediates are highly reactive, which will decompose many organic solvents. For example, the main ORR products in carbonate-based electrolytes are the decomposition products of carbonate solvents, instead of the Li_2O_2 or Li_2O as predicted by (15.30) and (15.31) [15.120]. Therefore, evaluations on the nonaqueous electrolyte rechargeable Li–air cells are mainly focused on the ORR catalyst and electrolyte solvent, including the catalytic activity and selectivity of the two-electron ORR for catalyst and the chemical stability against oxygen radical anions for the electrolyte solvent. Other evaluations include: (1) diffusivity of gaseous oxygen and the efficiency for oxygen separation and blockage of CO_2, moisture, and electrolyte solvent loss for GDL, (2) porosity of carbon material and carbon electrode for the air cathode, and (3) Li stability and cycling efficiency for the electrolyte.

In a hybrid electrolyte Li–air cell, there are two types of electrolytes: one is a nonaqueous electrolyte for the Li anode and the other is an aqueous electrolyte for the air cathode, which are physically isolated by a solid-state Li^+-ion conductive electrolyte film (Fig. 15.34b). Because of the change in the electrolyte system, the overall cell reaction of Li–air cells changes to

$$O_2 + 4Li + 2H_2O \rightleftharpoons 4LiOH, E = 3.446\,V\,, \quad (15.32)$$

in which water becomes a part of the cell's reaction and the ORR is dominated by the four-electron process. More importantly, the ORR product, LiOH, dissociates and dissolves into the aqueous electrolyte, which makes the ORR/OER conversion reversible. In such cells, the solubility and dissolution capacity (relating to the amount of water) of LiOH in the aqueous electrolyte are the important factors for determination of the cell's capacity, and an optimized *solid–liquid–gas* (i. e., catalyst–electrolyte–oxygen) three-phase reaction zone increases the cell's power. In addition to those mentioned in the nonaqueous Li–air cells, the following evaluations are applicable to the hybrid electrolyte Li–air cells:

1. Solid-state electrolyte film: Ionic conductivity, porosity (or called film density), chemical stability against Li metal and two liquid electrolytes, leakage of liquid electrolyte across the film, and mechanical strength for withstanding the cell's stress. Among those, chemical reduction of the electrolyte materials by Li metal and cationic exchange between Li^+ ions in electrolyte film and protons in water are known to be the major challenges for many NASICON (sodium super ionic coductor)-based Li^+ ionic conducting glass ceramics such as LATP ($Li_{1+x+y}Al_xTi_{2-x}Si_yP_{3-y}O_{12}$) glass.
2. Aqueous electrolyte: Ionic conductivity, viscosity, wettability and distribution on the air electrode, and solubility and dissolution capacity of LiOH.
3. Air electrode: Hydrophobicity for optimized three-phase reaction zone, ORR catalyst for cell's power/polarization, and catalyst's chemical stability against the aqueous electrolyte for cycle life.
4. GDL: For fast diffusion of gaseous oxygen, the GDL is required to be highly porous while avoiding water flooding on the GDL and air electrode.

15.5 Conclusions

Electrochemical materials and systems can employ a variety of electrochemical characterization techniques as demonstrated in this chapter on Li-ion batteries, which are not available to nonelectrochemical systems. These techniques, in conjunction with other appropriate characterization methods, result in a powerful suite of characterization tools that aid in the fundamental understanding and advancement of these technologies. Further advances, especially in developing in situ techniques, will allow for more rapid understanding of the nature of the components, their interactions and system behavior.

References

15.1 P.P. Prossini: Modeling the voltage profile for $LiFePO_4$, J. Electrochem. Soc. **152**(10), A1925–A1929 (2005)

15.2 M.S. Whittingham: Electrical energy storage and intercalation chemistry, Science **192**(4244), 1126–1127 (1976)

15.3 S. Basu, C. Zeller, P.J. Flanders, C.D. Fuerst, W.D. Johnson, J.E. Fischer: Synthesis and properties of lithium-graphite intercalation compounds, Mater. Sci. Eng. **38**, 275–283 (1979)

15.4 R. Yazami, P. Touzani: A reversible graphite-lithium negative electrode for electrochemical generators, J. Power Sources **9**, 365–371 (1983)

15.5 S. Basu: assigned to Bell telephone laboratories, Rechargeable battery, US Patent 4 304 825 (1981)

15.6 J. Goodenough, K. Mizuchima: Electrochemical cell with new fast ion conductors, US Patent 4 302 518 (1981)

15.7 T. Nagaura, K. Tozawa: *Progress in Batteries and Solar Cells*, Vol. 9 (JECS, Brunswick 1990) p. 20

15.8 A.K. Padhi, K.S. Nanjundaswamy, J.B. Goodenough: Phospho-olivines as positive-electrode materials for rechargeable lithium batteries, J. Electrochem. Soc. **144**, 1188–1194 (1997)

15.9 I.A. Courtney, J.R. Dahn: Electrochemical and in situ x-ray diffraction studies of the reaction of lithium with tin oxide composites, J. Electrochem. Soc. **144**, 2045–2052 (1997)

15.10 A.S. Andersson, J.O. Thomas: The source of first-cycle capacity loss in $LiFePO_4$, J. Power Sources **97–98**, 498–502 (2001)

15.11 C. Delacourt, P. Poizot, J.M. Tarascon: The existence of a temperature-driven solid solution in Li_xFePO_4 for 01, Nature Mater. **4**, 254–260 (2005)

15.12 D. Aurbach, M.D. Levi, K. Gamulski, B. Markovsky, G. Salitra, E. Levi, U. Heider, L. Heider, R. Oesten: Capacity fading of $Li_xMn_2O_4$ spinel electrodes studied by XRD and electroanalytical techniques, J. Power Sources **81**, 472–479 (1999)

15.13 J.R. Dahn: Phase diagram of Li_xC_6, Phys. Rev. B **44**, 9170–9177 (1991)

15.14 T. Ohzuku, Y. Iwakoshi, K. Sawai: Formation of lithium-graphite intercalation compounds in nonaqueous electrolytes and their application as a negative electrode for a lithium ion (shuttlecock) cell, J. Electrochem. Soc. **140**, 2490–2498 (1993)

15.15 K.M. Shaju, G.V.S. Rao, B.V.R. Chowdari: Performance of layered $Li(Ni_{1/3}Co_{1/3}Mn_{1/3})O_2$ as cathode for Li-ion batteries, Electrochimica Acta **48**, 145–151 (2002)

15.16 K. Mizushima, P.C. Jones, P.J. Wiseman, J.B. Goodenough: Li_xCoO_2 (0_{x-1}): A new cathode material for batteries of high energy density, Mater. Res. Bull. **15**, 783–789 (1980)

15.17 M.D. Johannes, K. Hoang, J.L. Allen, K. Gaskell: Hole polaron formation and migration in olivine phosphate materials, Phys. Rev. B **85**, 115106 (2012)

15.18 Y.J. Lee, F. Wang, C.P. Grey: ^6Li and ^7Li MAS, NMR studies of lithium manganate cathode materials, J. Am. Chem. Soc. **120**, 12601–12613 (1998)

15.19 B. Key, R. Bhattacharyya, M. Morcrette, V. Seznec, J.M. Tarscon, C.P. Grey: Real-time NMR investigations of structural changes in silicon electrodes for lithium-ion batteries, J. Am. Chem. Soc. **131**, 9239–9249 (2009)

15.20 H. Huang, S.-C. Yin, L.F. Nazar: Approaching theoretical capacity of $LiFePO_4$ at room temperature at high rates, Electrochem. Solid-State Lett. **4**, A170–A172 (2001)

15.21 A.S. Andersson, B. Kalska, L. Häggström, J.O. Thomas: Lithium extraction–insertion in $LiFePO_4$: An x-ray diffraction and Mössbauer spectroscopy study, Solid State Ionics **130**, 41–52 (2000)

15.22 J.L. Allen, T.R. Jow, J. Wolfenstine: Improved cycle life of Fe-substituted $LiCoPO_4$, J. Power Sources **196**, 8656–8661 (2011)

15.23 R.A. Dunlap, D.A. Small, D.D. MacNeill, M.N. Obrovac, J.R. Dahn: A Mössbauer effect investigation of the Li Sn system, J. Alloy. Compd. **289**, 135–142 (1999)

15.24 M.D. Levi, G. Salitra, B. Markovsky, H. Teller, D. Aurbach, U. Heider, L. Heider: Solid-state electrochemical kinetics of Li-ion intercalation into $Li_{1-x}CoO_2$: Simultaneous application of electroanalytical techniques SSCV, PITT, and EIS, J. Electrochem. Soc. **146**, 1279–1289 (1999)

15.25 M. Takahashi, S. Tobishima, K. Takei, Y. Sakurai: Reaction behavior of $LiFePO_4$ as a cathode material for rechargeable lithium batteries, Solid State Ionics **148**, 283–289 (2002)

15.26 J.L. Allen, T.R. Jow, J. Wolfenstine: Kinetic study of the electrochemical $FePO_4$ to $LiFePO_4$ phase transition, Chem. Mater. **159**, 2108–2111 (2007)

15.27 J.R. Dahn, E.W. Fuller, M. Obrovac, U. Vonsacken: Thermal stability of Li_xCoO_2, Li_xNiO_2 and λ MnO_2 and consequences for the safety of Li–ion cells, Solid State Ionics **69**, 265–270 (1994)

15.28 D.D. MacNeil, Z.H. Lu, Z.H. Chen, J.R. Dahn: A comparison of the electrode–electrolyte reaction at elevated temperatures for various Li-ion battery cathodes, J. Power Sources **108**, 8–14 (2002)

15.29 R.V. Moshtev, P. Zlatilova, B. Puresheva, V. Manev: Material balance of petroleum coke/$LiNiO_2$ lithium-ion cells, J. Power Sources **56**, 137–144 (1995)

15.30 D. Guyomard, J.M. Tarascon: The carbon/$Li_{1+x}Mn_2O_4$ system, Solid State Ionics **69**, 222–237 (1994)

15.31 K. Xu: Nonaqueous liquid electrolytes for lithium-based rechargeable batteries, Chem. Rev. **104**, 4303–4418 (2004)

15.32 M. Winter: The solid electrolyte interphase – The most important and the least understood solid electrolyte in rechargeable Li batteries, Z. Phys. Chem. **223**, 1395–1406 (2009)

15.33 Y. Zeng, L. Li, H. Li, X. Huang, L. Chen: TG-MS analysis on thermal decomposable components in the SEI film on Cr_2O_3 powder anode in Li-ion batteries, Ionics **15**, 91–96 (2009)

15.34 J. Zhang, R. Wang, X. Yang, W. Lu, X. Wu, X. Wang, H. Li, L. Chen: Direct observation of inhomogeneous solid electrolyte interphase on mno anode with atomic force microscopy and spectroscopy, Nano Lett. **12**, 2153–2157 (2012)

15.35 S.S. Zhang: A review on electrolyte additives for lithium-ion batteries, J. Power Sources **162**, 1379–1394 (2006)

15.36 M.S. Ding, K. Xu, T.R. Jow: Liquid–solid phase diagrams of binary carbonates for lithium batteries, J. Electrochem. Soc. **147**, 1688–1694 (2000)

15.37 M.S. Ding, K. Xu, S. Zhang, T.R. Jow: Liquid–solid phase diagrams of binary carbonates for lithium batteries, Part II, J. Electrochem. Soc. **148**, A299–A304 (2001)

15.38 Z.K. Liu: Thermodynamic modeling of organic carbonates for lithium batteries, J. Electrochem. Soc. **150**, A359–A365 (2003)

15.39 J. O'M Bockris, A.K.N. Reddy: *Modern Electrochemistry*, Vol. 2, 2nd edn. (Plenum, New York 2000)

15.40 K. Xu: Charge-transfer process at graphite/electrolyte interface and the solvation sheath structure of Li^+ in nonaqueous electrolytes, J. Electrochem. Soc. **154**, A162–A167 (2007)

15.41 R.G. Linford (Ed.): *Electrochemical Science and Technology of Polymers*, Elsevier Applied Science, Vol. 2 (Elsevier, London 1990) p. 281

15.42 G.E. Blomgren: Properties, structure and conductivity of organic and inorganic electrolytes for lithium battery systems. In: *Lithium Batteries*, ed. by J.P. Gabano (Academic, London 1983)

15.43 J. Evans, C.A. Vincent, P.G. Bruce: Electrochemical measurement of transference numbers in polymer electrolytes, Polymer **28**, 2324–2328 (1987)

15.44 H. Dai, S. Sanderson, J. Davey, F. Uribe, T.A. Zawodinski: Electrophoretic NMR measurements of lithium transference numbers in polymer gel electrolytes, Proc. Electrochem. Soc., Vol. 96–17 (1996) pp. 111–120

15.45 H.J. Walls, T.A. Zawodinski: Anion and cation transference numbers determined by electrophoretic NMR of polymer electrolytes sum to unity, Electrochem. Solid State Lett. **3**, 321–324 (2000)

15.46 R. Jasinski: *High Energy Batteries* (Plenum, New York 1967)

15.47 K. Xu: *Encyclopedia of Electrochemical Power Sources*, Vol. 5 (Elsevier, Amsterdam 2009) p. 51

15.48 D. Aurbach, M.L. Daroux, P.W. Faguy, E. Yeager: Identification of surface films formed on lithium in propylene carbonate solutions, J. Electrochem. Soc. **134**, 1611–1620 (1987)

15.49 D. Aurbach, A. Zaban, A. Schecheter, Y. Ein-Eli, E. Zinigrad, B. Markovsky: The study of electrolyte solutions based on ethylene and diethyl carbonates for rechargeable Li batteries, J. Electrochem. Soc. **142**, 2873–2882 (1995)

15.50 K. Xu, U. Lee, S. Zhang, T.R. Jow: Syntheses and characterization of lithium alkyl mono- and dicarbonates as components of surface films in Li-ion batteries, J. Phys. Chem. B **110**(15), 7708–7719 (2006)

15.51 M. Onuki, S. Kinoshita, Y. Sakata, M. Yanagidate, Y. Otake, M. Ue, M. Deguchi: Identification of the source of evolved gas in Li-ion batteries using labeled solvents, J. Electrochem. Soc. **155**, A794–A797 (2008)

15.52 S. Malmgren, H. Rensmo, T. Gustafsson, M. Gorgoi, K. Edstrom: Nondestructive depth profiling of the solid electrolyte interphase on LiFePO, Electrochem. Soc. Trans. **25**(36), 201–210 (2010)

15.53 D. Bar-Tow, E. Peled, L. Burstein: A study of highly oriented pyrolytic graphite as a model for the graphite anode in Li-ion batteries, J. Electrochem. Soc. **146**, 824–832 (1999)

15.54 P. Lu, S.J. Harris: Lithium transport within the solid electrolyte interphase, Electrochem. Commun. **13**, 1035–1037 (2011)

15.55 A.C. Chu, J.Y. Josefowicz, G.C. Farrington: Electrochemistry of highly ordered pyrolytic graphite surface film formation observed by atomic force microscopy, J. Electrochem. Soc. **144**, 4161–4169 (1997)

15.56 J.O. Besenhard, M. Winter, J. Yang, W. Biberacher: Filming mechanism of lithium-carbon anodes in organic and inorganic electrolytes, J. Power Sources **54**, 228–231 (1993)

15.57 M.R. Wagner, J.H. Albering, K.C. Moeller, J.O. Besenhard, M. Winter: XRD evidence for the electrochemical formation of in PC-based electrolytes, Electrochem. Commun. **7**, 947–952 (2005)

15.58 K. Xu, Y. Lam, S. Zhang, T.R. Jow, T. Curtis: Solvation sheath of Li^+ in nonaqueous electrolytes and its implication of graphite/electrolyte interface chemistry, J. Phys. Chem. C **111**, 7411–7421 (2007)

15.59 G.V. Zhuang, K. Xu, H. Yang, T.R. Jow, P.N. Ross Jr.: Lithium ethylene dicarbonate identified as the primary product of chemical and electrochemical reduction of EC in 1.2 M $LiPF_6$/EC:EMC Electrolyte, J. Phys. Chem. B **109**, 17567–17573 (2005)

15.60 S. Shi, P. Lu, Z. Liu, Y. Qi, L.G. Hector, H. Li, S.J. Harris: Direct calculation of Li-ion transport in the solid electrolyte interphase, J. Am. Chem. Soc. **134**, 15476–15487 (2012)

15.61 S.K. Jeong, M. Inaba, Y. Iriyama, T. Abe, Z. Ogumi: Electrochemical intercalation of lithium ion within graphite from propylene carbonate solutions, Electrochem. Solid State Lett. **6**, A13–A15 (2003)

15.62 Y. Yamada, Y. Iriyama, T. Abe, Z. Ogumi: Kinetics of lithium ion transfer at the interface between graphite and liquid electrolytes: Effects of solvent and surface film, Langmuir **25**, 12766–12770 (2009)

15.63 K. Xu, A.V. Cresce, U. Lee: Differentiating contributions to ion transfer barrier from interphasial resistance and desolvation at electrolyte/graphite interface, Langmuir **26**, 11538–11543 (2010)

15.64 J. Liu, Z. Chen, S. Busking, I. Belharouak, K. Amine: Effect of electrolyte additives in im-

proving the cycle and calendar life of graphite/$Li_{1.1}$ $[Ni_{1/3}Co_{1/3}Mn_{1/3}]_{0.9}$ O_2 Li-ion cells, J. Power Sources **174**, 852–855 (2007)

15.65 A. Xiao, L. Yang, B.L. Lucht, S.H. Kang, D.P. Abraham: Examining the solid electrolyte interphase on binder-free graphite electrodes, J. Electrochem. Soc. **156**, A318 (2009)

15.66 A.J. Smith, J.C. Burns, J.R. Dahn: A high precision study of the coulombic efficiency of Li-ion batteries, Electrochem. Solid State Lett. **13**, A177–A179 (2010)

15.67 J.C. Burns, J. Gauray, A.J. Smith, K.W. Eberman, E. Scott, J.P. Gardner, J.R. Dahn: Evaluation of effects of additives in wound Li-ion cells through high precision coulometry, J. Electrochem. Soc. **158**, A255–A261 (2011)

15.68 M.D. Halls, K. Tasaki: High-throughput quantum chemistry and virtual screening for lithium ion battery electrolyte additives, J. Power Sources **195**, 1472–1478 (2010)

15.69 L. Yang, B. Lucht: Inhibition of electrolyte oxidation in lithium ion batteries with electrolyte additive, Electrochem. Solid-State Lett. **12**, A229–A231 (2009)

15.70 K. Xu, A. von Cresce: Interfacing electrolytes with electrodes in Li-ion batteries J. Mater, Chem. **21**, 9849–9864 (2011)

15.71 A. von Cresce, K. Xu: Electrolyte additive in support of 5 V Li-ion chemistry, J. Electrochem. Soc. **158**, A337–A342 (2011)

15.72 A. Abouimrane, I. Belharouak, K. Amine: Sulfone-based electrolytes for high-voltage Li-ion batteries, Electrochem. Commun. **11**, 1073–1076 (2009)

15.73 Y. Abu-Lebdeh, I. Davison: High-voltage electrolytes based on adiponitrile for Li-ion batteries, J. Electrochem. Soc. **156**, A60–A65 (2009)

15.74 J.R. Dahn, J. Jiang, L.M. Moshurchak, M.D. Fleischauer, C. Buhrmester, L.J. Krause: High-rate overcharge protection of $LiFePO_4$-based Li-ion cells using the Redox shuttle additive 2,5-Ditertbutyl-1,4-dimethoxybenzene, J. Electrochem. Soc. **152**, A1283–A1289 (2005)

15.75 L.M. Moshurchak, W.M. Lamanna, M. Bulinski, R.L. Wang, R.R. Garsuch, J. Jiang, D. Magnuson, M. Triemert, J.R. Dahn: High-potential Redox shuttle for use in Lithium-ion batteries, J. Electrochem. Soc. **156**, A309–A312 (2009)

15.76 S.S. Zhang: A review on the separators of liquid electrolyte Li-ion batteries, J. Power Sources **164**, 351–364 (2007)

15.77 P. Arora, Z. Zhang: Battery separators, Chem. Rev. **104**, 4419–4462 (2004)

15.78 M.E. Orazem, B. Tribollet: *Electrochemical Impedance Spectroscopy* (Wiley, Hoboken 2008)

15.79 S. Zhang, K. Xu, T.R. Jow: EIS study on the formation of solid electrolyte interface in Li-ion battery, Electrochimica Acta **51**, 1636–1640 (2006)

15.80 S. Zhang, K. Xu, T.R. Jow: Electrochemical impedance study on the low temperature of Li-ion batteries, Electrochimica Acta **49**(1), 1057–1061 (2004)

15.81 S. Mukerjee, T.R. Thurston, N.M. Jisrawi, X.Q. Yang, J. McBreen, M.L. Daroux, X.K. King: Structural evolution of $Li_xMn_2O_4$ in lithium-ion battery cells measured in situ using synchrotron x-ray diffraction techniques, J. Electrochem. Soc. **145**, 466–472 (1998)

15.82 J.B. Leriche, S. Hamelet, J. Shu, M. Morcrette, C. Masquelier, G. Ouvrard, M. Zerrouki, P. Soudan, S. Belin, E. Elkaim, F. Baudelet: An electrochemical cell for operando study of lithium batteries using synchrotron radiation, J. Electrochem. Soc. **157**, A606–A610 (2010)

15.83 Y. Sun, Z. Chen, H. Noh, D. Lee, H. Jung, Y. Ren, S. Wang, C. Yoon, S. Myung, K. Amine: Nanostructured high-energy cathode materials for advanced lithium batteries, Nat. Mater. **11**, 942–947 (2012)

15.84 J. Huang, L. Zhong, C.M. Wang, J.P. Sullivan, W. Xu, L.Q. Zhang, S.X. Mao, N.S. Hudak, X.H. Liu, A. Subramanian, H. Fan, L. Qi, A. Kushima, J. Li: In situ observation of the electrochemical lithiation of a single SnO_2 nanowire electrode, Science **330**, 1515 (2010)

15.85 R.E. Gerald II, R.J. Klingler, G. Sandi, C.S. Johnson, L.G. Scanlon, J.W. Rathke: ^{7}Li NMR study of intercalated lithium in curved carbon lattices, J. Power Sources **89**, 237–243 (2000)

15.86 B. Key, R. Bhattacharyya, M. Morcrette, V. Seznec, J.M. Tarascon, C.P. Grey, B. Key, R. Bhattacharyya, M. Morcrette, V. Seznec, J.M. Tarascon, C.P. Grey: Real-time NMR investigations of structural changes in silicon electrodes for lithium-ion batteries, J. Am. Chem. Soc. **131**, 9239 (2009)

15.87 N. Balke, S. Jesse, A.N. Morozovska, E. Eliseev, D.W. Chung, Y. Kim, L. Adamczyk, R.E. Garcia, N. Dudney, S.V. Kalinin: Nanoscale mapping of ion diffusion in a lithium-ion battery cathode, Nature Nanotech. **5**, 749–754 (2010)

15.88 S. Kalinin, N. Balke, S. Jesse, A. Tselev, A. Kumar, T.M. Arruda, S. Guo, R. Proksch: Li-ion dynamics and reactivity on the nanoscale, Mater. Today **14**, 548–558 (2011)

15.89 K. Rhodes, N. Dudney, E. Lara-Curzio, C. Daniel: Understanding the degradation of silicon electrodes for lithium-ion batteries using acoustic emission, J. Electrochem. Soc. **157**, A1354–A1360 (2010)

15.90 T. Ohzuku, H. Tomura, K. Sawai: Monitoring of particle fracture by acoustic emission during charge and discharge of Li/MnO_2 cells, J. Electrochem. Soc. **144**, 3496–3500 (1997)

15.91 H. Wang, R.G. Downing, J.A. Dura, D.S. Hussey: In situ neutron techniques for studying lithium ion batteries. In: *Polymers for Energy Storage and Delivery: Polyelectrolytes for Batteries and Fuel Cell*, ACS Symp. Ser, Vol. 1096, (American Chemical Society, Washington DC 2012) pp. 91–96

15.92 J.E. Owejan, J.P. Owejan, S.C. DeCaluwe, J. Dura: Solid electrolyte interphase in Li–ion batteries: Evolving structures measured in situ by neutron reflectometry, Chem. Mater. **24**, 2133–2140 (2012)

15.93 *Coin Cell Components and Tools for Making Them are Available from Vendors such as Hohsen Corp.* (Osaka and MTI, Richmond 2016)

15.94 T.R. Jow, M.B. Marx, J.L. Allen: Distinguishing Li^+ charge transfer kinetics at NCA/electrolyte and graphite/electrolyte interfaces, and NCA/electrolyte and LFP/electrolyte interfaces in Li-ion cells, J. Electrochem. Soc. **59**(5), A604–A612 (2012)

15.95 IEC 61960: Secondary cells and batteries containing alkaline or other non-acid electrolytes – Secondary lithium cells and batteries for portable applications, International Electrotechnical Commission (2011) Edition 2.0

15.96 M.S. Whittingham: History, evolution, and future status of energy storage, Proc. IEEE'12, Vol. 100 (2012) pp. 1518–1534

15.97 J. Dahn, G.M. Ehrlich: Lithium ion batteries. In: *Linden's Handbook of Batteries*, 4th edn., ed. by T.B. Reddy (McGraw Hill, New York 2011), Chap. 26

15.98 IEC 62620: Secondary cells and batteries containing alkaline or other non-acid electrolytes – Large format secondary lithium cells and batteries for use in industrial applications, International Electrotechnical Commission (2010) Draft edition 1.0, Dec. 14

15.99 Idaho National Engineering and Environmental Laboratory; United States Department of Energy, Office of Energy Efficiency and Renewable Energy: *PNGV Battery Test Manual* (US Department of Energy, Assistant Secretary for Energy Efficiency and Renewable Energy, Idaho Operations Office, Washington 2001) DOE/ID-10597, Revision 3

15.100 K. Amine, I. Belharouak, Z. Chen, T. Tran, H. Yumoto, N. Ota, S.-T. Myung, Y.-K. Sun: Nanostructured anode material for high-power battery system in electric vehicles, Adv. Mater. **22**, 3052–3057 (2010)

15.101 S.S. Zhang, K. Xu, T.R. Jow: Charge and discharge characteristics of a commercial $LiCoO_2$ based 18650 Li-ion battery, J. Power Sources **160**, 1403–1409 (2006)

15.102 T.R. Jow, S.S. Zhang, K. Xu, J. Allen: Electrolytes for low temperature operations of Li-ion batteries, ECS Trans. **3**(27), 51–58 (2007)

15.103 D. Andre, M. Meiler, K. Steiner, Ch. Wimmer, T. Soczka-Guth, D.U. Sauer: Characterization of high-power lithium-ion batteries by electrochemical impedance spectroscopy. I. Experimental investigation, J. Power Sources **196**, 5334–5341 (2011)

15.104 P. Liu, J. Wang, J. Hicks-Garner, E. Sherman, S. Soukiazian, M. Verbrugge, H. Tataria, J. Musser, P. Finamore: Aging mechanisms of $LiFePO_4$ batteries deduced by electrochemical and structural analyses, J. Electrochem. Soc. **157**(4), A499–A507 (2010)

15.105 I. Bloom, S.A. Jones, E.G. Polzin, V.S. Battaglia, G.L. Henriksen, C.G. Motloch, R.B. Wright: Mechanisms of impedance rise in high-power, lithium-ion cells, J. Power Sources **111**, 152–159 (2002)

15.106 R. Srinivasan, B.G. Carkhuff, M.H. Butler, A.C. Baisden: Instantaneous measurement of the internal temperature in lithium-ion rechargeable cells, Electrochimica Acta **56**, 6198–6204 (2011)

15.107 R. Srinivasan: Monitoring dynamic thermal behavior of the carbon anode in a lithium-ion cell using a four-probe technique, J. Power Sources **198**, 351–358 (2012)

15.108 Y. Zhang, C.-Y. Wang: Cycle-life characterization of automotive lithium-ion batteries with $LiNiO_2$ cathode, J. Electrochem. Soc. **156**, A527–A535 (2009)

15.109 A.J. Smith, J.C. Burns, S. Trussler, J.R. Dahn: Precision measurements of the coulombic efficiency of lithium-ion batteries and of electrode materials for lithium-ion batteries, J. Electrochem. Soc. **157**, A196–A202 (2010)

15.110 J.C. Burns, G. Jain, A.J. Smith, K.W. Eberman, C.E. Scott, J.P. Gardner, J.R. Dahn: Evaluation of effects of additives in wound Li-ion cells through high precision coulometry, J. Electrochem. Soc. **158**, A255–A261 (2011)

15.111 IEC 62133: Secondary cells and batteries containing alkaline or other non-acid electrolytes – Safety requirements for portable sealed secondary cells, and for batteries made from them, for use in portable applications, International Electrotechnical Commission (2002)

15.112 UL 1642: UL Standard for Safety for Lithium Batteries, Underwriters Laboratories (2005) 4th edn., IL 60062-2096

15.113 M.S. Whittingham: Lithium batteries and cathode materials, Chem. Rev. **104**, 4271–4301 (2004)

15.114 D. Doughty, E.P. Roth: A general discussion of Li-ion battery safety, Electrochem. Soc. Interface **21**(2), 37–44 (2012)

15.115 D.D. MacNeil, Z. Lu, Z. Chen, J.R. Dahn: A comparison of the electrode/electrolyte reaction at elevated temperatures for various Li-ion battery cathodes, J. Power Sources **108**, 8–14 (2002)

15.116 E.P. Roth: Effect of cathode composition on abuse response of 18650 Li-ion cells, Proc. 43rd Power Sources Conf., Philadelphia (2008) p. 521

15.117 C. Orendorff, D. Doughty: Lithium ion battery safety, Electrochem. Soc. Interface **21**(2), 35–66 (2012)

15.118 E.P. Roth, C.J. Orendorff: How electrolytes influence battery safety, Electrochem. Soc. Interface **21**(2), 45–49 (2012)

15.119 J.R. Akridge, Y.V. Mikhaylik, N. White: Li/S fundamental chemistry and application to high-performance rechargeable batteries, Solid State Ionics **175**, 243–245 (2004)

15.120 S.S. Zhang, D. Foster, J. Read: Discharge characteristic of a non-aqueous electrolyte Li/O_2 battery, J. Power Sources **195**, 1235–1240 (2010)

16. Materials for Electrochemical Capacitors

Thierry Brousse, Daniel Bélanger, Kazumi Chiba, Minato Egashira, Frédéric Favier, Jeffrey Long, John R. Miller, Masayuki Morita, Katsuhiko Naoi, Patrice Simon, Wataru Sugimoto

The aim of this chapter is threefold. First of all, we will attempt to briefly highlight the differences between batteries and electrochemical capacitors (ECs), describe the general types of ECs (symmetric and asymmetric configurations), and present the electrochemical tools that are available to characterize these systems. Second, an EC is a complex device with many components (current collector, separator, active materials, external management electronics) and design features that ultimately determine the device characteristics. However, the advances in performance for future ECs that will be required for their broader implementation as an energy-storage technology will largely depend on new developments in electrode materials and electrolytes, which will be the focus of this chapter. Thus, this chapter will attempt to present a critical assessment of the materials that are currently being used and developed for hybrid ECs. Third, some current applications of ECs will be described in details and will clearly demonstrate that hybrid ECs are no longer a scientific curiosity and that they have found their place as energy-storage systems due to their unique characteristics. Finally, this chapter will be concluded by a section that presents the major role ECs will be playing in the field of energy storage and conservation.

16.1 **Batteries and Electrochemical Capacitors – Basic Concepts** 496
16.1.1 Electrochemical Characterization of Electrochemical Capacitors 497
16.1.2 Basic Concept of Hybrid Electrochemical Capacitor 500
16.2 **Carbon** 504
16.2.1 Activated Carbons 505
16.2.2 Carbon Aerogels and Related Sol-Gel-Derived Nanoarchitectures 506
16.2.3 Templated Mesoporous Carbons (TMCs) 507
16.2.4 Microporous Carbons 507
16.2.5 Carbon Nanotubes 508
16.2.6 Enhanced Charge Storage 509
16.3 **Manganese Dioxide** 510
16.3.1 Fundamental Structural Properties 510
16.3.2 Pseudocapacitance Mechanisms for Manganese Oxides 511
16.3.3 Thin-Film Electrodes 513
16.3.4 *Bulk* Composite MnO_2 Electrodes 516
16.3.5 Advanced MnO_2-Carbon Electrode Architectures 518
16.3.6 MnO_2-Based Devices 520
16.3.7 Future Outlook 522
16.4 **Ruthenium Oxide** 523
16.4.1 Synthesis, Chemical, and Physical Properties 523
16.4.2 Composites and Other Ruthenium Oxides 524
16.4.3 Charge Storage Mechanism 525
16.5 **Other Pseudocapacitive Materials** 529
16.6 **Electrolytes** 529
16.6.1 Aqueous 529
16.6.2 Organic Solvent Solutions 529
16.6.3 Ionic Liquids 530
16.6.4 Polymer and Gel Electrolytes 531
16.6.5 Stability of the Electrolyte in High Voltage EC 534
16.7 **Applications of Electrochemical Capacitors** 537
16.7.1 Copiers 537
16.7.2 Power Tools 538
16.7.3 Transportation 538
16.7.4 Secondary Uses in Transportation 540
16.7.5 Industrial Applications 541
16.7.6 Stationary Applications for Power and Power Quality 543
16.8 **Electrochemical Capacitor Prospective View** 543
References 545

Over the last century, worldwide energy needs have been primarily satisfied with oil and at the present time about 85% of our total energy consumption comes from fossil fuels (e.g., oil, coal, and natural gas) [16.1]. In recent years, renewable energy technologies, for example wind and solar energies, are becoming more prominent and practical, and the further development of such technologies will be critical to the advancement of modern society. The continued success of renewable energy technologies that harvest their energy from intermittent sources will also depend on the development of new energy-storage systems to capture and deliver the harvested power to satisfy consumer demand. Beyond large-scale stationary power generation, the storage and delivery of electrical energy is required in many applications such as telecommunications devices (e.g., cell phones), electronic devices, stand-by power systems, and electric/hybrid vehicles. A good example is in the transportation sector, which accounts for approximately 19% of global energy use worldwide (primarily derived from the combustion of fossil fuels) [16.2], and is responsible for about 23% of CO_2 emissions – ultimately an untenable situation that will have a severe impact on world economics and ecology. The development of electric/hybrid vehicles, which rely on high-performance electric energy-storage systems to improve the overall energy efficiency of vehicles, would help to reduce the environmental impact of the transportation sector. Likewise, electrochemical energy conversion (e.g., batteries and fuel cells) is now being considered as an alternative energy/power source and an efficient way of storing energy [16.3]. In addition to batteries and fuel cells, a great deal of interest has been focused toward the development of electrochemical capacitors (ECs), also sometimes denoted as *supercapacitors* or *ultracapacitors*, as electrochemical energy-storage systems, as ECs have inherent performance characteristics that are suitable for high-power applications where batteries and fuel cells fall short.

16.1 Batteries and Electrochemical Capacitors – Basic Concepts

Electrochemical capacitors and batteries are related electrochemical energy-storage devices. However, an EC distinguishes from a battery by the charge-storage mechanism, which is typically capacitive rather than faradaic. The faradaic process involves redox reaction at the anode and cathode whereas reversible adsorption of ions occurs at the electrode surface for a capacitive process during charge and discharge [16.4–10]. Capacitors can be classified in two classes: (i) electrolytic capacitors and (ii) ECs, which consist of electric double-layer capacitor (EDLC) and electrochemical pseudocapacitor. On one hand, an electrolytic capacitor stores energy by charge-separation across a thin insulating dielectric oxide layer; on the other hand, an EDLC refers to double-layer charging at a high-surface-area electrode, typically carbon. A carbon-based EC commonly consists of two thick carbon films as the positive and negative capacitive electrodes in contact with an appropriate current collector as well as an electrolyte, which could be either an aqueous or a nonaqueous solution and even an ionic liquid (Fig. 16.1).

The processes involved in the charge-storage mechanism rely on the charge separation at the solid/liquid interface between the carbon and the electrolyte. In the simpler case, anions from the electrolyte compensate the positive charge that builds up in the positive carbon electrode upon charging. Similarly, the negative charges present in the negative electrode upon charging are compensated by cations from the electrolyte. Finally, another type of EC is based on both capacitive charge and faradaic pseudocapacitance of the active material. This class encompasses redox processes in conducting polymers and metal oxides [16.4, 5].

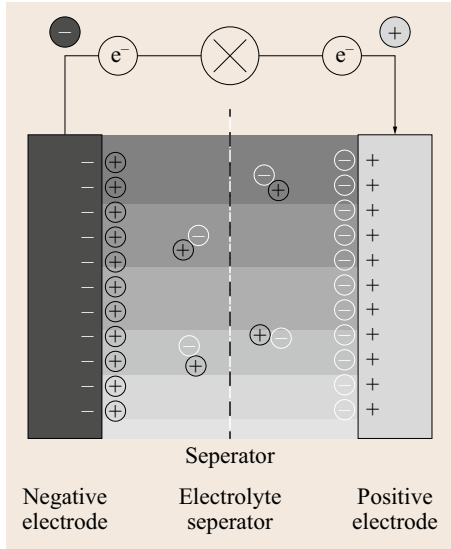


Fig. 16.1 Schematic of an electrochemical capacitor based on two carbon electrodes in the presence of an electrolyte and a membrane. The capacitor is depicted in the charged state with the excess of charge in each electrode that is compensated by ionic species of opposite charge

16.1.1 Electrochemical Characterization of Electrochemical Capacitors

Several tools are available to characterize the performance of individual electrode materials of an EC. A convenient method is cyclic voltammetry, which is commonly used in the three-electrode configuration to characterize the electrode material of interest. The specific capacitance (C) can be estimated by cyclic voltammetry by integrating the cyclic voltammogram curve (Fig. 16.2a) to obtain the voltammetric charge (Q; anodic, Q_a or cathodic, Q_c), and subsequently dividing this charge by the mass of the active material on the electrode (m) and the width of the potential window (ΔE)

$$C = \frac{Q}{\Delta E m} \,. \tag{16.1}$$

Constant current charge–discharge curves (Fig. 16.2b) can also be used to evaluate the specific capacitance of a single electrode by using

$$C = \frac{I t_d}{\Delta E m} \,, \tag{16.2}$$

where I is the total current, t_d the discharge time, and ΔV the potential drop during constant current discharge. Alternately, the capacitance can also be deduced from the slope of the discharge (dV/dt in V/s) curve by dividing the discharge current (I) by the slope

$$C = \frac{I}{\left(\frac{dV}{dt}\right)} \,. \tag{16.3}$$

One should note that for an ideal electrical double-layer capacitor, the discharge curve is almost always distinguished by a *slope* (Fig. 16.2b), whereas batteries more often have *plateaus* in their discharge curves [16.3].

Even though the specific capacitance values of a single electrode are often reported and provide an easy way to compare the performance of various EC materials, it is more relevant to determine the capacitance of the two-electrode EC. In this case, the value that will be estimated for the capacitor (C_{tot}) will be smaller than that found for the single electrode and given by

$$\frac{1}{C_{tot}} = \frac{1}{C_+} + \frac{1}{C_-} \,, \tag{16.4}$$

where C_+ and C_- are the capacitance of the positive and negative electrode, respectively. At this time, it is important to address a point that can sometimes bring some confusion in the literature, the factor of 4 between the capacitance of a single electrode and that of a symmetric two-electrode EC. According to (16.4), if the capacitance (C_+ and C_-) and the weight (m) of both electrodes is the same (which means a total weight of $2m$), then the gravimetric capacitance of the capacitor will become $C_{tot}/2$, thus giving this factor of 4. This issue will also be discussed later.

The real power density P_{real} (W/kg) and the real energy E_{real} (Wh/kg) of a two-electrode capacitor can be determined from the constant current charge/discharge cycles as

$$P_{real} = \frac{\Delta E I}{m} \,, \tag{16.5}$$

where $\Delta E = (E_{max} + E_{min}/2)$, with E_{max} is the potential at the end of charge and E_{min} at the end of discharge, I the applied current, and m the weight of active material of the electrodes

$$E_{real} = P_{real} t \,, \tag{16.6}$$

where t is the discharge time.

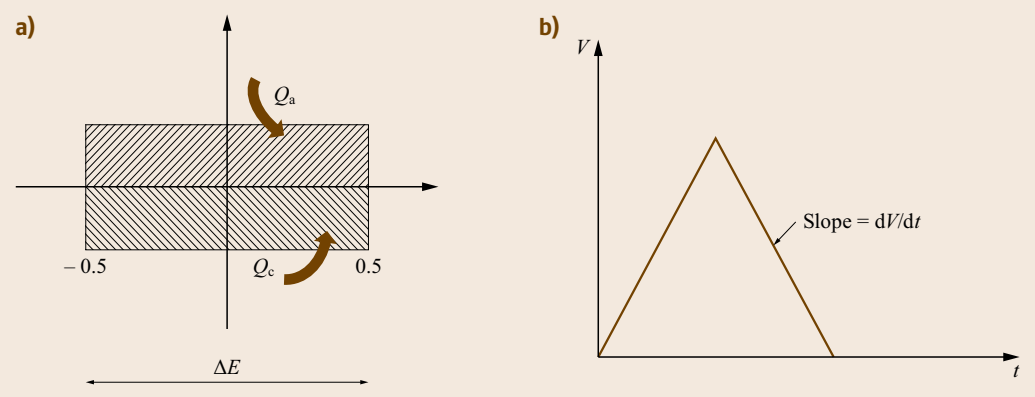


Fig. 16.2 (a) Cyclic voltammogram. (b) Constant current charge/discharge curve

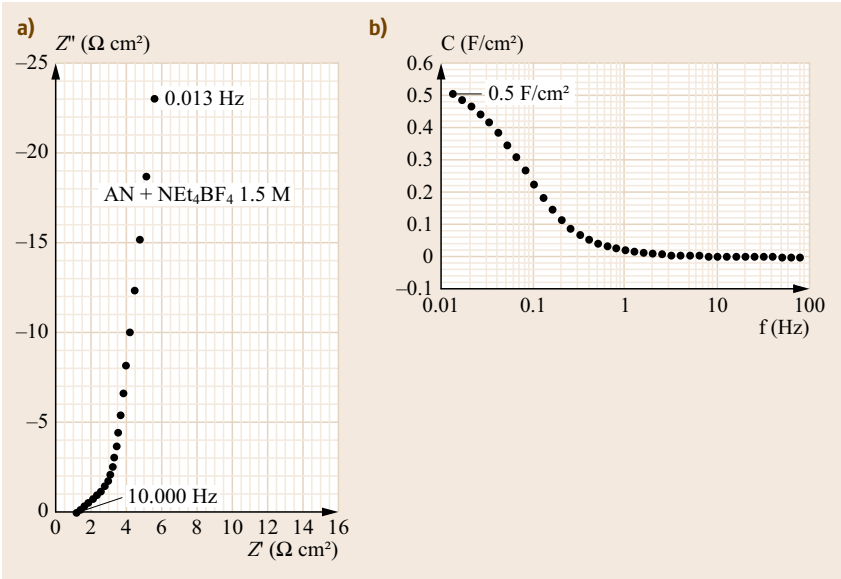


Fig. 16.3 **(a)** Nyquist plot for a laboratory cell assembled with two symmetrical high surface area carbon electrodes, in 1.5 M $(C_2H_5)_4BF_4$ in AN organic electrolyte. Frequency range studied; 10 kHz to 13 mHz. **(b)** Evolution of the real part of the capacitance $C'(\omega)$ versus frequency for a laboratory cell assembled with two symmetrical high surface area carbon electrodes, in 1.5 M $(C_2H_5)_4BF_4$ in AN organic electrolyte (after [16.11])

Alternatively, the maximum specific power, P_{max}, can be calculated from

$$P_{max} = \frac{U_0^2}{4Rm} \quad (\mathrm{W/kg}) \,, \tag{16.7}$$

where U_0 is the potential at the beginning of discharge (after the ohmic drop) and R the internal resistance measured.

The maximum stored specific energy is defined as

$$E_{max} = \frac{C(U_{max})^2}{2} \quad (\mathrm{Wh/kg}) \,, \tag{16.8}$$

where C is the system capacity and U_{max} the potential at the end of discharge.

Other useful parameters that characterize an EC are the coulombic efficiency and the equivalent series resistance (ESR). The coulombic efficiency is given by the discharge time/charge time ratio. A coulombic efficiency of 1 indicates that side reactions are not occurring during either the charge or the discharge step. On the other hand, the ESR can be measured by the current interrupt technique at each end of charge. In first approximation, the cell voltage V_{cell} is described by

$$V_{cell} = \mathrm{ESR}\, I + \frac{Q}{C} \,, \tag{16.9}$$

where C is the capacitance, Q the amount of charge stored at the electrode, and I the constant current used for the galvanostatic experiment. When the current is switched off, the cell voltage drops down to V'_{cell}, expressed as

$$V'_{cell} = \frac{Q}{C} \,. \tag{16.10}$$

A combination of Eqs. (16.9) and (16.10) allows to obtain the ESR value as

$$\mathrm{ESR} = \frac{(V_{cell} - V'_{cell})}{I} \,. \tag{16.11}$$

A series resistance value could also be measured at an AC frequency of 1 kHz by electrochemical impedance spectroscopy.

Capacitance and resistance calculated from (16.1)–(16.3) are obtained from DC measurements. Electrochemical capacitors being high-power devices, it is interesting to know the change of the capacitance and the resistance of the cells with the frequency, that is, under AC polarization; this can be obtained by using the electrochemical impedance spectroscopy technique. Figure 16.3a shows a typical Nyquist plot of a laboratory cell assembled with two symmetrical high surface area carbon electrodes, in 1.5 M $(C_2H_5)_4BF_4$ in acetonitrile (AN) organic electrolyte [16.11]. Starting from the outer interface in contact with the bulk electrolyte solution and going down into the depth of the electrode, the impedance behavior of a porous activated carbon electrode can be described as a succession of series/parallel RC circuits associated with the distribution of pore channels and pore surfaces [16.4, 12]. The change of the capacitance versus frequency can be directly extracted from the Nyquist plots, by using the complex capacitance model

$$C'(\omega) = -\frac{Z''(\omega)}{\omega |Z(\omega)|^2} \,, \tag{16.12}$$

where $|Z(\omega)|^2$ is the modulus of the impedance $Z(\omega)$, and $C'(\omega)$ the real part of the capacitance $C(\omega)$.

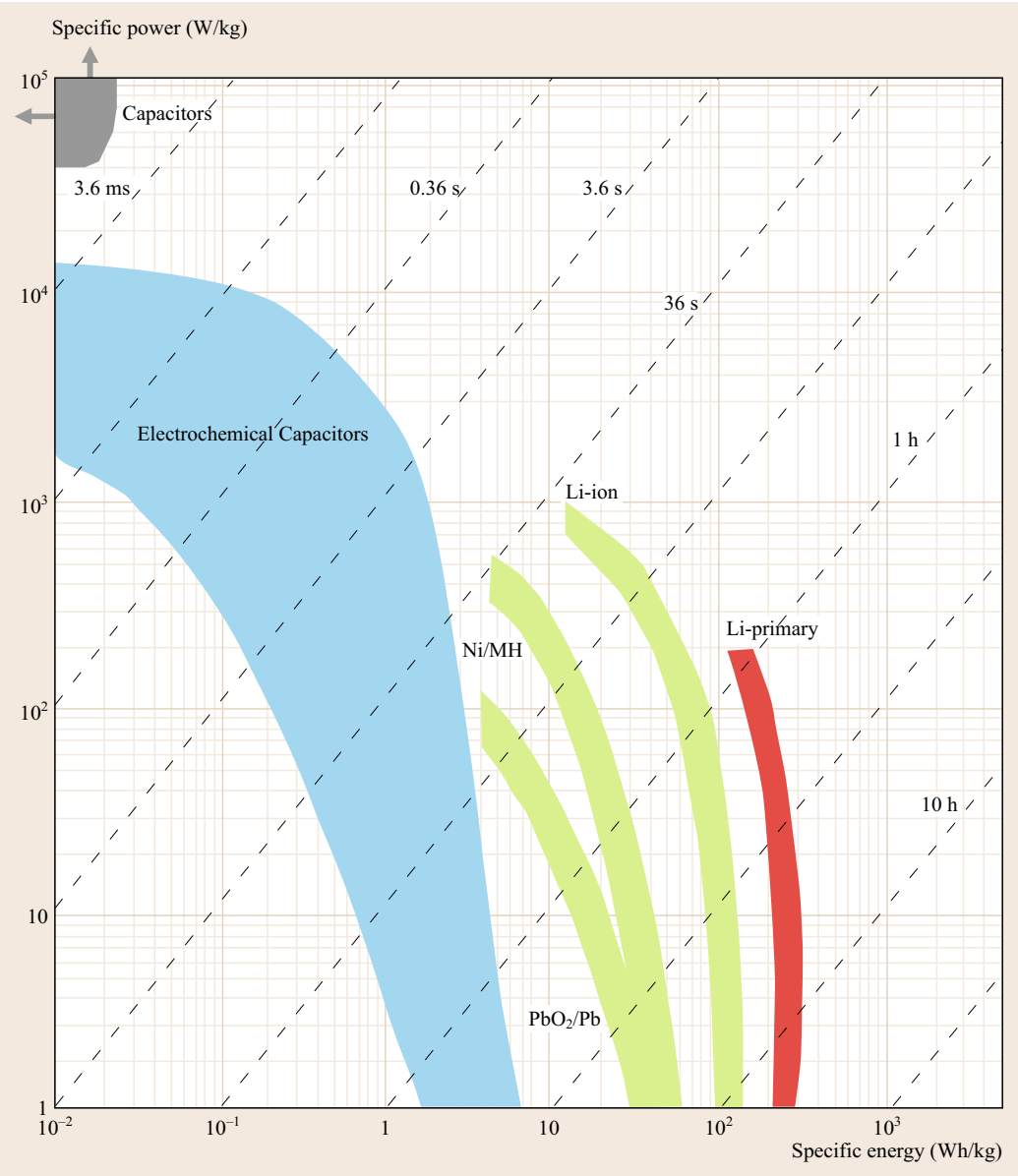


Fig. 16.4 Specific power as a function of specific energy, also called a Ragone plot, for various electrical energy-storage devices. Times shown are the time constants of the devices, obtained by dividing the energy density by the power (after [16.10])

Figure 16.3b shows the change of the real part of the capacitance $C'(\omega)$ versus frequency. The cell capacitance increases when the frequency is decreased since more and more carbon surface is accessible within the depth of the electrode [16.12]; below what is called the *knee frequency* [16.11, 13, 14], the capacitance tends to be less dependent from the frequency, and should be constant at lower frequencies. This knee frequency is an important performance metric of the EDLC; it depends on the type of the porous carbon, the electrolyte, as well as the technology used (electrode thickness, stack). The knowledge of the capacitance change versus the frequency is of great importance for pulse-power applications, and the electrochemical impedance spectroscopy technique is a simple and efficient method to obtain such information.

Electrochemical capacitors are characterized by relatively low energy densities, about 2–5 Wh/kg (com-

pared to a battery), and high power densities up to 20 kW/kg (owing to their fast charge and discharge processes) [16.15]. A Ragone plot, which gives the variation of the specific power with the specific energy, conveniently highlights the difference between batteries and ECs (Fig. 16.4). Another interesting feature of Fig. 16.4 is the time constants of the energy-storage systems, which can be obtained by dividing the energy density by the power. Roughly speaking, when the energy required to activate a device (e.g., power tool, electric car, see also Sect. 16.7) is in the order of the second, an EC is required, whereas a battery can deliver its energy over a much longer time scale of the order of an hour.

16.1.2 Basic Concept of Hybrid Electrochemical Capacitor

A conventional EC usually comprises two identical capacitive electrodes in a symmetric configuration. On the other hand, in an hybrid or asymmetric capacitor, one of the capacitive electrodes is replaced by a faradaic electrode. Several types of hybrid capacitors have been developed and can be classified in four categories. In the first one, the positive electrode of a symmetric carbon/carbon capacitor is replaced by an electrode that is characterized by a much higher charge-storage capability. These include pseudocapacitive electrode materials such as conducting polymers, metal oxides such as MnO_2, RuO_2, or faradaic electrodes such as NiOOH and PbO_2 [16.4–10, 16]. The second type does not use a single carbon electrode but instead metal oxides for both the positive and negative electrodes. For example, an hybrid capacitor based on Fe_3O_4 and MnO_2 have been investigated with an aqueous electrolyte [16.17]. The third and fourth types are based on intercalation compounds as active electrode materials. Even though, they used a capacitive electrode they have been also coined as energy-storage devices. For the third type, an intercalation compound such as $Li_4Ti_5O_{12}$ or disordered carbon is used as negative electrode with an activated carbon or a pseudocapacitive conducting polymer as positive electrode [16.18, 19]. An analogous system in the third category is when the positive electrode of a carbon-based nonaqueous EC is replaced by an intercalation electrode such as $LiNi_{0.5}Mn_{1.5}O_4$ [16.20]. Finally, the fourth type uses a wider potential range of the positive electrode relative to the third type [16.21].

The electrochemical behavior as observed by cyclic voltammetry of an electrode in a three-electrode electrochemical cell gives valuable information on the cell voltage of the electrochemical cell that can be assembled with two similar electrodes (Fig. 16.5a). Typical cyclic voltammograms are shown for a carbon electrode in aqueous and nonaqueous electrolyte. It can be seen that the potential window of electroactivity is much larger (about 3 V) in nonaqueous electrolyte than in either acidic, neutral, or alkaline aqueous solution, for which it is approximately 1 V [16.22]. In the latter case, the electrochemical potential window is limited by the hydrogen- (negative potential) and the oxygen-evolution reactions (positive potential). When the symmetric EC based on two carbon electrodes is assembled and subjected to a constant current charge/discharge cycling, the electrode potential encompasses approximately 50% of the total potential window when using electrodes of the same capacitance. Figures 16.5c,d shows that in the discharge state, the electrochemical cell voltage is 0 V and obviously the potential of each electrode (versus a reference) is the same. Upon charging, the potential of the negative and positive electrodes shift in the negative and positive direction, respectively. In the case of an ideal capacitive electrode material, and assuming that the capacitance of each electrodes of the capacitor is the same, then the change of potential of each electrode will be equal. However, in a practical system, this is very unlikely because the specific capacitance of an electrode material differs in the negative and positive potential domains. The ideal case is represented on the cyclic voltammograms presented in Fig. 16.5a,b, which also shows the potential range over which each electrode is scanned as well as the voltammetric charge upon charge/discharge cycling. In this case, the voltammetric charges involved in the charging process are designated by Q_{-c} and Q_{+c} for the negative and positive electrodes, respectively. Furthermore, Q_{-d} and Q_{+d} represent the voltammetric charges involved in the discharge process for the negative and positive electrodes, respectively.

Hybrid or asymmetric devices mentioned above provide a convenient method to increase the cell voltage and concomitantly the energy and power densities of ECs ((16.6), (16.8)). This can be demonstrated for the four types of hybrid ECs mentioned above by cyclic voltammetry and charge–discharge curves. Figure 16.6 shows the cyclic voltammograms for a capacitive carbon and a pseudocapacitive manganese dioxide electrode that act as the negative and positive electrodes for the first type [16.23]. It can be seen that the potential range over which the two electrodes can be cycled extend to about 2 V, which is much larger than the range expected with a symmetrical capacitor making use of either two carbon or two manganese dioxide electrodes. For the manganese-dioxide-based EC, a maximum cell voltage of only 0.8 V would be expected whereas a slightly larger value of about 1 V

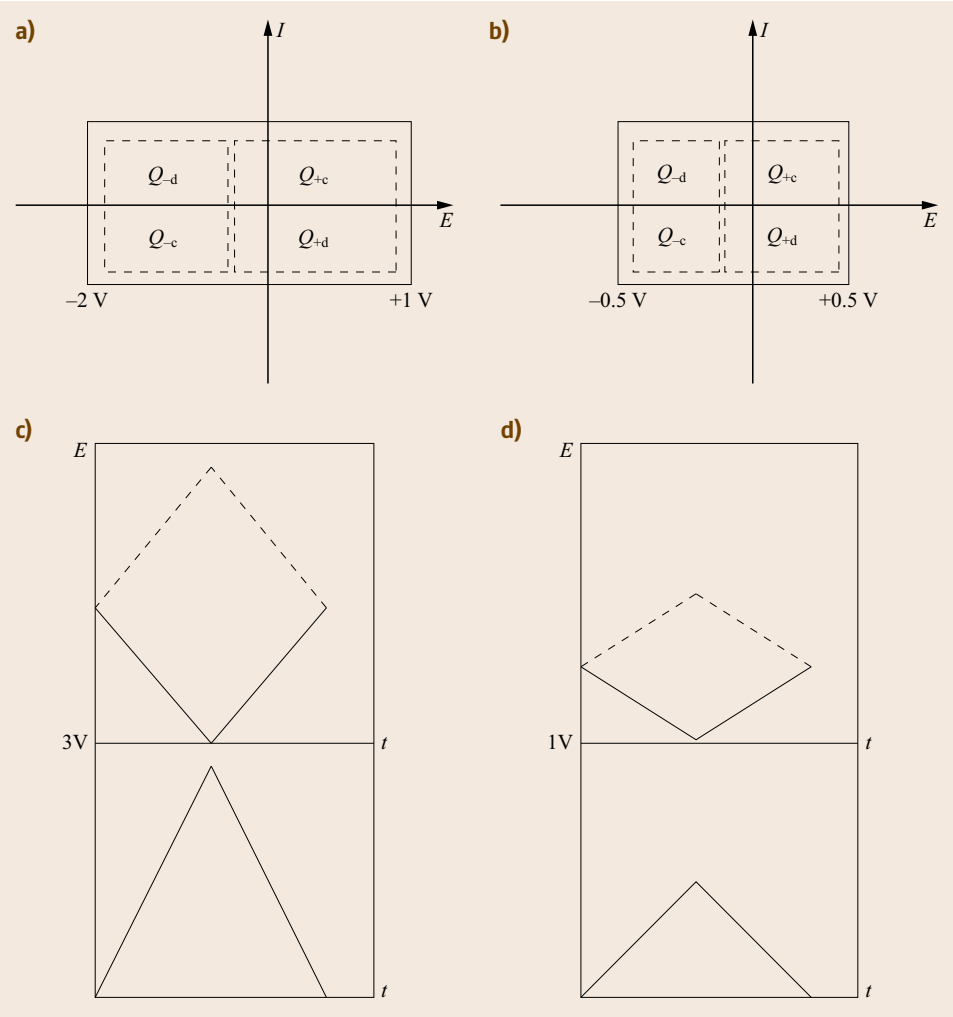


Fig. 16.5a–d Cyclic voltammogram for a carbon electrode in: **(a)** nonaqueous and **(b)** aqueous electrolyte and cyclic voltammograms for the positive and negative electrodes during charge/discharge cycling. Variation of the potential of the positive and negative electrode during constant current charge/discharge cycling for the **(c)** nonaqueous and **(d)** aqueous-based ECs

could be obtained for the carbon-based capacitor. The corresponding constant current charge/discharge curves that show the variation of the cell voltage together with the evolution of the potential of each electrode is presented for this hybrid system. First, it is interesting to see that the variation of the cell voltage is almost linear as expected for an EC. Figure 16.6 also shows that the potential of each electrode will vary over the range presented in the cyclic voltammograms. In the particular case of the manganese dioxide, the potential excursion of the positive electrode should be restricted to both potential limits shown on the cyclic voltammogram to avoid dissolution of the manganese dioxide (e.g., negative potential limit) and oxygen evolution (e.g., positive potential limit). For the negative carbon electrode, care should be taken to avoid a potential excursion to too much negative values during the charging step to avoid the hydrogen evolution reaction. It should be noted that these faradaic reactions will have an effect of the coulombic efficiency of the capacitor and also on its cycling stability. Additionally, the charge–discharge curve will not always be linear for a hybrid EC, as demonstrated in the case of a carbon/conducting polymer asymmetric system.

In this case, the voltammetric charges of the carbon (Q_c) and the polymer (Q_{pol}) are balanced but the range of electroactivity, the mass, and capacitance of the polymer restricts the cycling to high voltage values. As a consequence, an abrupt decrease in the capacitor voltage is seen at the end of the discharge (Fig. 16.7). Such behavior is observed for a carbon/PFPT capacitor [16.25]. It is clear that in some cases, the high-voltage linear region can be extended to a lower V' value, and in these instances the charge involved in the charge/discharge process of the negative electrode will be spread over a slightly wider potential range.

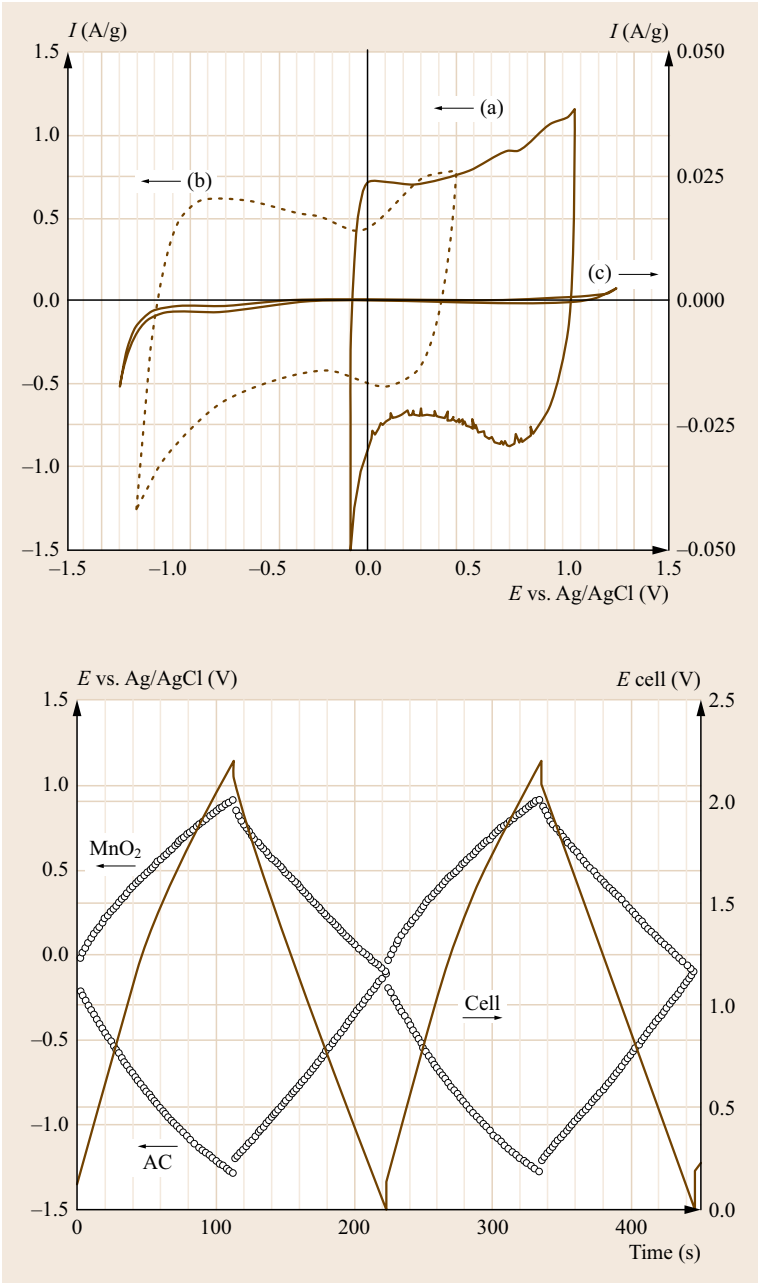


Fig. 16.6 Cyclic voltammograms for activated carbon and manganese dioxide electrode and variation of the potential of each electrode during constant current charge/discharge cycling (after [16.24])

The second type is a natural extension of the first type as the negative carbon electrode is replaced by another pseudocapacitive electrode such as Fe_3O_4. A typical set of cyclic voltammograms is presented in Fig. 16.8 for the Fe_3O_4/MnO_2 EC with an aqueous electrolyte [16.17]. The advantage of this system over the first one can only be seen if the negative potential limit can be extended to more negative values relative to the carbon electrode or if the specific capacitance of the alternative electrode material is larger than that of carbon electrode. Other electrode materials that were investigated with a manganese dioxide positive electrode for this second type include a faradaic or pseudocapacitive negative electrode such as FeOOH [16.26], titanium phosphates [16.27], or conducting polymers [16.28].

In the third asymmetric hybrid type, the capacitive positive electrode is retained and an intercalation

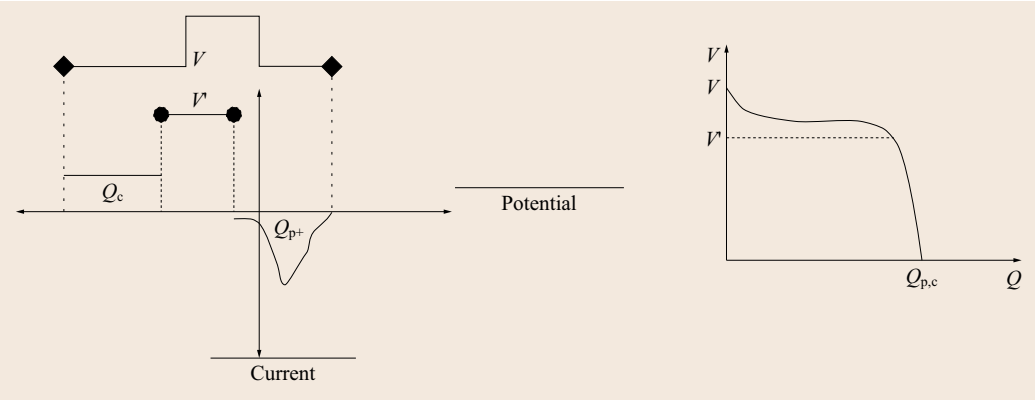


Fig. 16.7 Plot of current as a function of potential giving the discharge charge for a carbon negative electrode (Q_c) and conducting polymer positive electrode (Q_{p+}) and the corresponding voltage-charge profile (after [16.25])

compound replaces the carbon as the negative electrode (Fig. 16.9a). In contrast to the pseudocapacitive electrode, an intercalation is redox active at various potentials with little variation in voltage as a function of the state of charge. As a consequence, the use of the intercalation negative electrode enables an increase in the average voltage of the energy-storage system relative to a conventional electrical double-layer capacitor. In the case of the hybrid capacitor with the $Li_4Ti_5O_{12}$ negative electrode, the average cell voltage is approximately 2.25 V with the end of the discharge occurring at 1.5 V, as opposed to 0 V for a symmetric carbon–carbon EC (Fig. 16.9b) [16.18].

Another system in this category combines a disordered carbon for the negative electrode combined with an activated carbon-positive electrode. In this case, the lower intercalation/desinsertion potential of the carbon-based negative electrode leads to further enhancement of the cell voltage. However, it should be noted that the higher capacity of the lithium-insertion-type negative electrode requires that much more activated carbon must be used for the positive electrode as compared with the negative electrode, which ultimately lowers the energy density of this system. A major limitation of this type of hybrid capacitor with the carbon-based anode, as for lithium-ion battery, is the formation of dendrites of lithium at high charging current, and large volume expansion during the intercalation process, that limits the use of this system in energy-harvesting applications where high charging rates are required. To avoid these phenomena, electrode material such as $Li_4Ti_5O_{12}$ mentioned above is an interesting alternative due to its higher intercalation potential and smaller volume expansion [16.18]. On the other hand, lithium intercalation materials such as $LiNi_{0.5}Mn_{1.5}O_4$ were also used as positive electrode in a lithium battery could be used

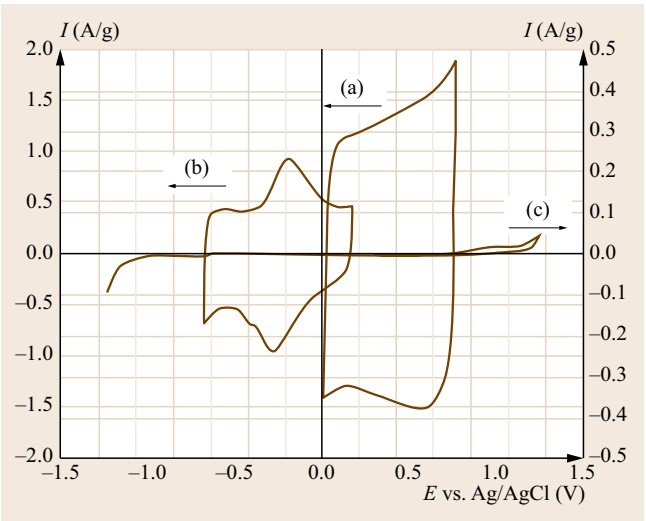


Fig. 16.8 CVs for Fe_3O_4/MnO_2 electrochemical capacitor (after [16.17])

in combination with an activated carbon-negative electrode to produce a hybrid EC [16.20].

The fourth type of EC for which the potential evolution is depicted in Fig. 16.10 comprises a prelithiated intercalation-negative electrode with an activated carbon-positive electrode (curve 2) for which the potential range is extended to a lower value [16.21]. The advantages of this system are an increase in the capacity of the positive electrode due to a wider potential window and a reduced amount of electrolyte required because the lithium ions concentration in the electrolyte will not change in the potential range from 1.5 to 3 V (e.g., lithium desorption at the positive and intercalation in the negative during the charging step). These two factors lead to higher energy and power densities.

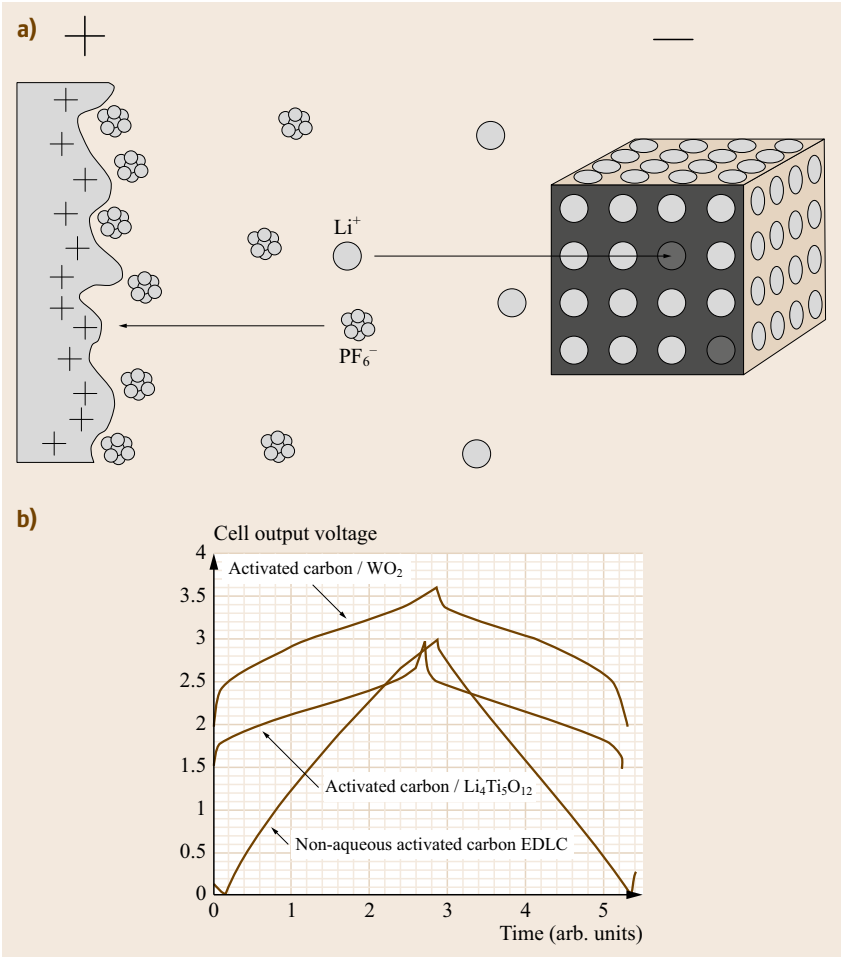


Fig. 16.9 **(a)** Simplified schematic of a hybrid EC with a positive capacitive electrode and an intercalation material as negative electrode. **(b)** Cell outpout voltage comparison for one charge–discharge cycle of an activated carbon/activated carbon nonaqueous EDLC and a $Li_4Ti_5O_{12}$/activated asymmetric hybrid cell. Another example of hybrid EC is shown using tungsten oxide as the positive electrode (after [16.18])

Even if these two categories are of potential interest due to their high energy and power density, they are also plagued by the problems associated with lithium-ion battery materials.

The remainder of this chapter will focus on the materials (e.g., carbon, manganese dioxide, ruthenium dioxide) that are currently the mostly studied for applications in ECs and will not deal with intercalation materials. Information concerning these materials can be found in several recent reviews of materials used for lithium-ion battery [16.29–31]. This chapter will be completed by presenting current applications of EC and a prospective view for these energy storage and harvesting systems.

16.2 Carbon

Charge storage in carbon-based conventional EDLCs rely only on electrostatic interactions between the electrolyte ions and the surface charges of the electrodes, with no charge-transfer reaction – the active material/electrolyte interface functions essentially as a dielectric capacitor. Accordingly, the main requirements that the active materials must meet are as follows:

1. High electrical conductivity
2. High specific surface area
3. Good electrochemical stability.

The electrical conductivity of the active material must be as high as possible to minimize ohmic losses during charge–discharge operation. Finally, the increase

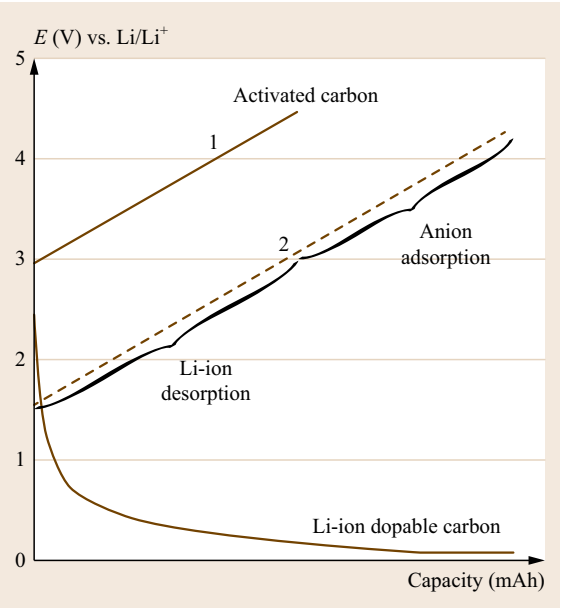


Fig. 16.10 Typical potential profiles for the positive activated carbon electrode (curve 1) and a lithium intercalation carbon for the negative electrode (curve Li-ion dopable carbon) of an asymmetric capacitor (after [16.29])

in the gravimetric capacitance can be done by increasing the active material total surface per footprint area, which is why highly porous materials must be used, with specific surface areas (SSAs) of several hundreds of m^2/g. The charge-storage mechanism being purely electrostatic, the active material must also be electrochemically inert within the operating potential range (i. e., function as a blocking electrode).

Nanostructured forms of carbon satisfy all of these requirements, including high conductivity, electrochemical stability, and open porosity. In addition, carbons can be produced in many different forms, shapes, and pore structures, and this flexibility has made carbon the material of choice for EDLCs. Activated and templated carbons, aerogels, carbon fabrics, fibers, nanotubes, onions, nanohorns, as well as microporous carbons have all been examined for EDLC applications [16.10].

16.2.1 Activated Carbons

Owing to their high SSA and moderate cost, activated carbons are the most widely used materials today for EDLCs [16.32]. Activated carbon is synthesized in a two-step process. First, carbon-rich organic precursors, which can range from organic (shell, wood, coal) to synthetic (polymer), are carbonized at high temperatures (typically $> 800\,^{\circ}C$) in inert atmosphere to obtain a disordered carbon that also contains very short range graphitic zones [16.32]. After grinding the resulting carbon into particles of a few micrometers in diameter ($5-50\,\mu m$), one or more activation treatments (physical-dry route, high-temperature processing in CO_2 or steam atmosphere, or chemical treatments in KOH solution) are applied to increase the SSA and pore volume. The activation treatment creates a porous network within the bulk of the carbon grain, resulting in SSA that ranges from 1000 to $2000\,m^2/g$. The pores that form during the activation step are distributed over a broad size range that includes macropores (pore size $> 50\,nm$), mesopores ($2\,nm < size < 50\,nm$), and micropores ($< 2\,nm$). However, the activation treatment offers relatively poor control over the final porous network, although in general, the longer the activation treatment time, the larger the final mean pore size. Depending on the nature of the carbon precursors used, activated carbon fabrics or powders can be obtained. The carbonization and activation process of a polymer fabric such as rayon result in self-supported activated carbon fabrics [16.32]. However, cost issues have drastically limited the use of this material in EDLCs, and most of the today's commercial devices use activated carbon powder as the active material.

The average gravimetric capacitance of standard activated carbons used in commercial EDLCs is $\approx 100-110\,F/g$ in PC- or AN-based organic electrolytes (compared to $\approx 150\,F/g$ in aqueous KOH electrolytes). In the challenging competition to increase these specific capacitance values, several options have been studied, such as the grafting of acidic, neutral, or basic functional groups on the carbon surface. Many papers have been published on oxygen-functionalized activated carbons, with subsequent capacitance increase [16.32]. However, it is now well established that introducing oxygen functions on the carbon surface leads to an increase in the leakage current as well as a capacitance loss during cycling [16.33–35]. Nitrogen- and boron-doped activated carbons have also been studied [16.36, 37]. The presence of nitrogen groups confers a pseudocapacitive behavior to the carbon that augments the intrinsic double-layer capacitance, while boron is supposed to enhance the oxygen chemisorption in aqueous electrolyte. The cyclability of these modified carbons still appears to be a concern.

Another strategy to increase the carbon capacitance is to control the carbon structure. Initial research on activated carbon was directed toward increasing the pore volume by developing high SSA and refining the activation process. However, it was quickly established that the gravimetric capacitance of activated carbons was limited even for the most porous samples exhibiting very high SSA [16.38–40]. Therefore, beyond simply

the total porous volume or surface area, the pore size and the pore-size distribution were thought to play a key role in optimizing the carbon capacitance.

The double-layer capacitance originates from the adsorption of ions of the electrolyte on each carbon pore walls. The pores must be neither too large to lead to a significant increase in the specific area (m^2/g) nor too small to host, during the capacitor charge/discharge, the solvated ions from the electrolyte (average size between 1 and 2 nm in organic electrolytes) [16.41].

Preliminary progress in this area was to prepare carbon materials with pore structures tailored to the size of the solvated ions in order to optimize charge storage. Today's commercial porous activated carbons have been optimized according to this approach, with a mean pore size centered in the small mesoporosity region (3−5 nm), that is, approximately twice the size of the solvated ions to allow ion adsorption on both pore walls. Further progress toward fine-tuned carbon pore sizes has focused on new synthesis routes that, apart from the activation process, allow more precise control of the final pore size distribution. Sol–gel and template-synthesis routes have been extensively used to prepare such fine-tuned ultraporous carbons.

16.2.2 Carbon Aerogels and Related Sol–Gel–Derived Nanoarchitectures

Sol–gel chemistry is a facile and flexible route for the synthesis of conductive, ultraporous carbon aerogels and related nanoarchitectures, such as cryogels and *nanofoams* [16.42]. Carbon aerogels are produced via the pyrolysis of polymer aerogels that are typically derived from the condensation of phenols (e.g., resorcinol or cresol) with formaldehyde. The structural characteristics of carbon aerogels are primarily determined during the synthesis of the precursor polymer gel. During the gelation process interpenetrated and connected networks of pores and solid spontaneously form. It can be noted that no additional pore-forming agents are required to obtain this peculiar microstructure. The pore-solid architectures of polymer aerogels are easily tailored by varying such parameters as the catalyst:reactant ratio, the total reactant concentration, curing temperature, and drying method (e.g., supercritical-fluid extraction, freeze-drying, or ambient-pressure drying) to produce structures with primary pore sizes ranging from 2 nm up to $\approx 1\,\mu m$ [16.42–44]. The SSA and density of the final carbon aerogel also depend on the conditions used to pyrolyze the polymer precursor aerogel to its conductive carbon form.

Early in the development of carbon aerogels, *Pekala* and others recognized that the innate combination of a conductive, high-surface-area electrifiable interface and a through-continuous void volume made these structures immediately applicable to energy storage in ECs [16.45–48]. Carbon aerogels, aerogel-like structures, and nanofoams are now used as active electrode materials in commercially available carbon–carbon EDLCs. Among the carbons of interest for ECs, carbon aerogels exhibit moderately high specific areas (typically 400−1000 m^2/g), which are sufficient to support specific capacitances of up to 180 F/g in concentrated alkaline electrolytes [16.49]. As mentioned earlier, a key advantage of carbon aerogels over activated carbons is the manner in which their internal surfaces are distributed within a hierarchical pore-solid architecture of macropores, mesopores, and micropores.

For EC applications, the ideal aerogel structure would consist of a primary pore network of mesopores and/or small macropores that serves an effective transport path and reservoir for electrolyte within the interior of the electrode. The mesopore/macropore network of void volume provides access to the micropores that form within the individual carbon particles of the solid network during the carbonization, and which provide a significant fraction of the total aerogel surface area. Micropore formation can be enhanced by additional thermal activation, resulting in carbon aerogels with SSAs exceeding 3000 m^2/g [16.50].

The electrochemical characteristics of carbon aerogel electrodes are further defined by this hierarchical structure, where capacitance contributions at mesopore/macropore surfaces are operative over a wide range of charge–discharge rates, while the additional capacitance provided by surfaces within micropores decreases as the current/frequency demand is increased [16.51, 52]. As with other high-surface-area carbons, thermal/chemical activation procedures and surface functionalization are used to improve the specific capacitance and frequency response of carbon aerogel electrodes. For example, *Fang* and *Binder* recently demonstrated that the accessibility of surfaces within the micropores of carbon aerogels was improved by treatment with the surfactant, vinyltrimethoxysilane, resulting in specific capacitances of ≈ 130 F/g when using propylene carbonate (PC)-based electrolytes [16.53]. However, due to the low density of carbon aerogels, volumetric capacitance are usually not so attractive.

The ability to produce moldable, monolithic forms is another attractive feature of carbon aerogels that can be exploited for fabricating practical electrode structures for ECs and other electrochemical devices, potentially mitigating the need for the polymer binders and conductive additives that are typically used in composite electrode processing. In early electrochemical studies, carbon aerogels were incorporated into prototype ECs in the form of wafers sliced from cylindrical

monoliths [16.45, 47, 48]. The same synthetic methods used to form monolithic aerogels can be adapted to infiltrate carbon-fiber papers with the precursor polymer gel, followed by pyrolysis to form a carbon aerogel/nanofoam paper (Fig. 16.3) [16.46, 54–57]. The supporting carbon-fiber structure provides additional mechanical integrity and electronic conductivity to the resulting carbon aerogel/nanofoam paper, while also defining the electrode thickness in ranges (50−300 μm) that are more typical for high-rate performance in ECs, as compared to monolith wafers.

Carbon aerogels have not received wide use in EDLCs but may become more important in the future. For next-generation EC, carbon aerogels/nanofoams may be more valuable as a base structure for multifunctional electrode nanoarchitectures [16.58, 59] that also include functionalities that exhibit faradaic pseudocapacitance such as conducting or redox polymers [16.60, 61] and mixed electron/ion-conducting metal oxides to amplify the charge-storage capacity of the electrode structure [16.62–64]. Distributing the incorporated polymer or metal oxide moieties as nanoscopic coatings or deposits on an aerogel-like substrate reduces the solid-state transport distances for charge-compensating ions from the electrolyte, and facilitates rapid charging and discharging of the electroactive functionalities. In addition to defining the physical structure of the electrode nanoarchitecture, the carbon aerogel/nanofoam substrate also serves as a massively parallel, 3-D interconnected current collector, shuttling electrons to and from the electroactive phases, which themselves are often poor electron conductors. When properly designed and fabricated, the resulting multifunctional electrode nanoarchitectures will exhibit significantly higher energy densities than typical nanostructured carbons, while also retaining the high-rate charge–discharge characteristics that are facilitated by the conductive framework and through-connected mesopore/macropore network of carbon aerogel/nanofoam structure.

16.2.3 Templated Mesoporous Carbons (TMCs)

Among the synthesis methods proposed to prepare carbons of fine-tuned pore sizes, the *template* route revealed itself as particularly efficient [16.65, 66]. It consists in filling the porous network of an inorganic template matrix with a carbon precursor and the subsequent carbonization of the composite. The inorganic template is removed by acid treatment. One example is the impregnation of a mesoporous silica template substrate with a carbon precursor, either gaseous, liquid, or solid [16.65, 67]; this step is followed by a pyrolysis and finally a dissolution of the silica template in HCl medium. As a result, the obtained carbon has a pore size that is the replica of the templating silica structure. Several groups reported the synthesis of templated carbons using SBA-15 silica templates. Such template allows to synthesize carbons with very narrow pore-size distribution; accordingly, carbons with a mean pore size between 2 and 10 nm have been prepared and characterized in aqueous and organic electrolytes [16.68–70]. A paper from *Centeno* et al. presented a nice overview of the electrochemical performance of more than 25 templated mesoporous carbons (TMCs) [16.71]. The results were somewhat disappointing in that capacitances of only 120 F/g in AN-based electrolyte could be reached, which represents only a 20% increase as compared to the activated carbons. The authors concluded that the expected advantages for TMCs over activated carbons as electrodes were not obvious and these TMCs failed to significantly increase the carbon-specific capacitance.

16.2.4 Microporous Carbons

Although micropore size (< 2 nm) is small as compared to the size of the solvated ions in most of the electrolytes used in EDLCs, some authors reported surprisingly high capacitance with microporous carbons [16.72–74]. *Vix* et al. [16.74] reported a linear relationship between the carbon gravimetric capacitance and the CO_2 volume adsorbed during gas-sorption measurements, establishing a link between the capacitance and the microporous volume. However, there was still no clear evidence of a relationship between micropores – smaller than the size of the solvated ion – and capacitive charge storage.

This was achieved in 2006 by *Chmiola* et al. [16.75] who demonstrated the crucial role played by the micropores in the charge storage mechanism using carbon-derived carbons (CDCs). These CDCs were obtained from the chlorination of a metal carbide (here titanium carbide, TiC) at a temperature range from 400 to 1000 °C according to

$$\mathrm{TiC} + 2\mathrm{Cl_2} \rightarrow \mathrm{TiCl_4} + \mathrm{C_s}\,. \tag{16.13}$$

During the chlorination process, Ti is leached out from the structure leaving behind nanoporous carbon with 50−80% open pore volume with an SSA up to 1600 m^2/g. The main advantage of these carbon materials is that they have a very narrow pore-size distribution with a mean value tunable in the range of approximately 0.6−1 nm, which is smaller than the solvated ion size. Using these CDCs as model materials in $N(C_2H_5)_4BF_4$ 1.5 M in AN organic electrolyte, they demonstrated that ions could enter these narrow pores, and the normal-

ized capacitance ($\mu F/cm^2$) was largely increased when the carbon pore size became less than 1 nm (Fig. 16.4). Accordingly, both the gravimetric (+50%) and volumetric energy (+100%) were increased as compared with standard activated carbons. The proposed hypothesis to explain such an anomalous behavior at pore size less than 1 nm was the deformation of the ion solvation shell [16.75], allowing ions to get closer to the carbon surface, thus increasing the capacitance according to

$$C = \frac{\varepsilon A}{d}\,, \tag{16.14}$$

with A the area, ε represents the electrolyte dielectric constant, and d the distance between the ion and the carbon surface.

These results obtained in AN-based organic electrolyte show the need for micropores of fine-tuned sizes to achieve high energy density in porous carbons for EDLCs. Beyond that, the evidencing of the strong contribution of the subnanometer pores (smaller than 1 nm) to the capacitive storage is questionable since it shows the lack of fundamental understanding in the field of ionic transportation – and charge of the double layer – in subnanometer pores. The effective ion size during the adsorption process in these narrow pores is also questionable and it is not clear if the ions enter the pores partially or fully desolvated. Recent results have been obtained using three-electrodes cell with CDCs in the same electrolyte such that the capacitance at the positive electrode (where anion adsorption occurs) and at the negative electrode (cation adsorption) could be measured independently. Positive capacitance (anion adsorption) and negative capacitance (cation adsorption) were maximum at a pore size of, respectively, approximately 0.7 and 0.8 nm [16.41, 76], that is, values between the bare ion size and the solvated ion size, thus confirming that micropores were accessible to ions owing to partial desolvation. The same conclusions were obtained by *Aurbach*'s group using cyclic voltammetry studies in PC-based electrolyte, who also observed cation trapping [16.77]. *Béguin* et al. nicely confirmed this trend by showing a capacitance limitation when using carbons with more than 85% of the porous volume consisting in pores smaller than the bare cation size [16.78].

A last series of experiment have been achieved in solvent-free electrolytes, that is, ethyl-methyl-immidazolium-trifluoro-methane-sulfonylimide (EMI,TFSI) [16.79]. These two ions have the same dimension in length, and they can be approximated as spheres of approximately 0.8 nm diameter. In the absence of any solvent molecule – without any solvation shell – the maximum capacitance for both the anion and the cation was found for pore sizes close to 0.7 nm (Fig. 16.5), confirming that ions can enter pores of the same dimension [16.10, 79].

The CDC pore size is in the same range as the ion size and there is no space available for more than one ion per pore. Accordingly, it seems that the traditional Helmholtz model used to describe the double-layer capacitance with ions adsorbed on both pore walls cannot apply to these narrow subnanometer pores with no room available for the diffuse layer. It seems that in such confined environment, ions can align along the pore axis, which contribute to the increase in the specific capacitance.

The results published in the literature for the past 3 years on the ion adsorption mechanism in porous carbon offer a new vision of the charge-storage mechanism in EDLC electrodes. First, the small micropores (less than 1nm) that were thought to be inaccessible to ions because of their size greatly contribute to the capacitive storage, thanks to a partial desolvation of the ions; the volumetric energy density is increased by a factor of 2 in such cases. More, from solvent-free electrolytes measurements, the maximum capacitance is obtained when the ion size is in the same range as the pore size, casting doubt on the traditional double-layer charge-storage mechanism. These results highlight the lack of fundamental understanding of the electrochemical interfaces at the nanoscale and the behavior of ions confined in micropores. Some simulation work has been recently done and a mathematical model was proposed to explain these results [16.80–82] where the size of the ion inside the pores was found to be close to the bare ion size. But more fundamental work is needed, including computational modeling, to fully understand the charge-storage mechanism, solvation dynamics, and ion transport in these small micropores. While the results cited above point to the importance of fine-tuned micropores for optimal capacitance, such microporous domains should be designed within a framework of mesopores and/or macropores that are necessary to facilitate efficient long-range ion transport throughout the electrode structure, as reported by *Wang* et al. [16.83]. Synthetic routes that include sol–gel chemistry may be ideal to prepare such hierarchical carbon microporous/mesoporous structures. Improving our fundamental understanding on ion transportation and ion/carbon interaction in nanopores by computational modeling and simulation will be a determining step in the design of the next generation of high-energy density EDLCs.

16.2.5 Carbon Nanotubes

Carbon nanotubes (CNTs) have achieved notoriety for a host of energy-related applications due to their high

electronic conductivity, chemical stability, and moderately high SSAs [16.84]. Over the past decade, numerous reports have described the use of various types of carbon nanotube materials and structures for use of EDLCs. However, a survey of that literature reveals that despite such promise, the reported specific capacitance values for a wide variety of single-walled and multiwalled CNTs rarely exceed 120 F/g in aqueous electrolytes and 50 F/g in organic medium, which is barely competitive with low-cost activated carbons, and would result in limited energy density in EDLCs based on CNT electrodes. The relatively modest specific capacitance of native CNTs can be ascribed to the low area-normalized double-layer capacitance of the basal-plane carbon surfaces [16.85] that comprise the CNT walls and their lower specific surface area (typically 100–500 m^2/g) relative to activated carbon. *Bamboo-type* CNTs [16.86], which have exposed edge-plane graphite walls, may be advantageous as active materials for ECs, because the double-layer capacitance of the edge-plane surface is 3–4 times greater than for the basal plane surface [16.85], but further study of such materials is required. The modification of the CNT walls with specific oxygen and/or nitrogen functionalities will provide additional charge-storage capacity via pseudocapacitance reactions [16.87] but this is generally associated with a decrease in the cycle life.

Even with significant improvements in specific capacitance, the future implementation of CNTs for commercialized devices will require substantial reduction in production costs as well as increased production volume.

Despite their low specific capacitance and energy density in EDLCs, the ability to fabricate CNTs in relatively dense, aligned architectures may ultimately prove beneficial when extremely high power density is required [16.88–93]. Such electrode architectures are also of interest for power sources for microdevices, such as MEMS, where the footprint available for the power source is very limited. Finally, vertically aligned and dense CNT architectures could be efficiently used as support for coating thin films of pseudocapacitive active materials such as recently demonstrated with CNT/MnO_2 composite electrodes [16.94, 95]. Such organized architectures, combining high electrical conductivity and high surface area, have the potential to boost the performance of these oxide-based pseudocapacitors.

16.2.6 Enhanced Charge Storage

As described above, charge storage in symmetric carbon–carbon ECs is based primarily on double-layer capacitance, which in current EDLCs based on activated carbon and nonaqueous electrolytes results in energy densities of 3–5 Wh/kg. Although sufficient for many pulse-power applications, such low energy density limits the broader application of carbon–carbon ECs as stand-alone energy-storage devices. Another route to energy density improvement is based on asymmetric aqueous capacitors [16.96] comprising metal oxide cathodes (e.g., NiO, MnO_2, or PbO_2) paired with high-surface-area carbon anodes, which may ultimately deliver energy densities approaching 40 Wh/kg [16.97], while also provided the safety and cost benefits of aqueous electrolytes. The increased energy density of the asymmetric EC design arises not only from the high capacity of the metal oxide cathode, but also from adventitious pseudocapitance mechanisms that augment the double-layer capacitance at the carbon anode.

Many nanostructured carbons, ranging from activated carbon [16.98, 99] or carbon nanotubes/nanofibers [16.100] to templated mesoporous carbon [16.74], exhibit increasing discharge capacitance (or capacity) as they are progressively charged to more negative potentials in aqueous electrolytes, as shown in Fig. 16.6 for an activated carbon composite electrode, cycled in alkaline electrolyte [16.98]. The origin of this anomalous capacitance behavior is typically ascribed to an electrochemical adsorption/desorption process in which H_2O from the electrolyte is initially reduced at the electrode, followed by adsorption of atomic hydrogen onto and into the carbon structure [16.101, 102]

$$H_2O + e^- \rightarrow H + OH^- , \tag{16.15}$$

$$C + H \rightarrow CH_{ad} . \tag{16.16}$$

Desorbed hydrogen atoms are released from the carbon surface to recombine with OH^- as the electrode is discharged, although typically with considerable hysteresis between the charge and discharge potentials. Because of the similarities to the physisoption/chemisorption of molecular hydrogen on nanostructured carbons, this process is often referred to as *electrochemical hydrogen storage*, and has been extensively explored as alternative form of bulk hydrogen storage [16.103–106].

The pseudocapacitance enhancements observed with carbon anodes are not yet fully understood, but depend on a number of factors including the pore structure [16.74, 98], surface functionality [16.107], the solid-state structure of the carbon [16.108], and the inclusion metals such as Ni that serve as catalytic sites for the hydrogen adsorption/desorption process [16.100]. Fundamental investigations into the underlying mechanisms of the pseudocapacitance process, and their relation to the chemical and physical properties of vari-

ous nanostructured carbon materials, will be required to ultimately exploit this phenomenon for improved performance in asymmetric ECs. The requirements for EC operation are also distinct from those where the electrochemical hydrogen storage mechanism is adapted for the purpose of bulk hydrogen storage. New carbon materials that are developed for use as anodes in asymmetric aqueous ECs should be specifically designed to facilitate charge–discharge time-scales of the order of 1−100 s, while also reducing the charge–discharge hysteresis that is typically observed with the hydrogen adsorption/desorption phenomenon.

16.3 Manganese Dioxide

Manganese oxides have a relatively long history in the field of battery chemistry, beginning with the Leclanché cell in the 1860s, and ultimately evolving to the primary 1.5 V Zn/MnO_2 alkaline cells that are now widely available [16.109]. In the past two decades, manganese oxides, typically in the general form $Li_{1-x}Mn_2O_4$, have also been investigated as cathode materials for rechargeable Li-ion batteries [16.110], which exhibit higher energy densities due to the larger available voltage window of nonaqueous electrolytes (e.g., ≈ 3.5 V for a $Li_xC/Li_{1-x}Mn_2O_4$ cell configuration). In all cases, the primary motivations for using manganese oxides for battery applications are their low cost, low toxicity, and relatively benign environmental impact, particularly when compared to other metal oxides that are commonly used for batteries such as nickel- and cobalt oxides.

Most recently, the interest in manganese oxide electrode materials has extended to the field of ECs, for many of the same motivations described above. In particular, manganese oxides are appealing as a low-cost alternative to the present metal oxide of choice for ECs, hydrous RuO_2 [16.111], which delivers high specific capacitances (> 700 F/g), but at material costs that are prohibitive for all but highly specialized applications. The use of manganese oxides for ECs is focused on asymmetric cell configurations, in which the manganese oxide serves as the active charge-storage component of the positive electrode, and is paired with a negative electrode containing activated carbon or a related high-surface-area carbon [16.112]. Such asymmetric ECs typically use mild aqueous electrolytes, which present several advantages for device manufacturing, safety, and cost, as compared to current EDLCs that are based on symmetric carbon–carbon designs with nonaqueous electrolytes. In addition, the asymmetric electrode design permits the operation of aqueous ECs up to ≈ 2 V, resulting in technologically relevant energy densities.

Lee and *Goodenough* [16.113, 114] were the first to comment on the capacitor-like electrochemical properties of manganese oxide electrodes in mild aqueous electrolytes, reporting a specific capacitance of ≈ 200 F/g, which, even then, was competitive with many high-surface-area carbons. Following this initial report in 1999, the number of publications on manganese oxides as an active material for ECs has grown from only six papers from 1999 to 2001, to more than 1000 papers published from 2002 to the present. The ever-expanding body of literature on this topic covers a wide range of manganese oxide-based materials that differ significantly in terms of crystal structure, morphology, electrode preparation and microstructure, electrolyte composition, etc. In the following sections, we survey the literature from 1999 to the present, compare and contrast the results of published studies with respect to relevant electrochemical properties of manganese oxides for EC applications, and on the basis of such comparisons, outline directions for future research and development efforts on this topic.

16.3.1 Fundamental Structural Properties

The terms *manganese oxide* and *manganese dioxide* describe a class of diverse materials that can be obtained in dozens of crystalline forms, including many tunnel and layer structures that can accommodate cation exchange [16.109, 110, 115]. Many crystalline forms of manganese dioxides occur in minerals [16.116], whose names are often borrowed to describe particular crystal structures. The basic building blocks of crystalline manganese oxides are MnO_6 octahedra subunits sharing vertices and edges [16.117], which can be used to construct one-dimensional (1-D), two-dimensional (2-D), or three-dimensional (3-D) tunnel structures, and combinations thereof [16.118]. The tunnels can be filled with either water molecules, or cations such as Li^+, Na^+, K^+, Mg^{2+}, and Ba^{2+}. The different structures can be described by the size of their tunnel, determined by the number of octahedra subunits ($n \times m$). 1-D tunnels can be found, for example, in β-MnO_2 pyrolusite (1 × 1), ramsdellite (1 × 2), α-MnO_2 hollandite or cryptomelane (2 × 2) or todorokite (4 × 4). δ-MnO_2 compounds (also generally known as *birnessite*) have a layered structure that exhibit infinite 2-D tunnels in between MnO_6 octahedra sheets. λ-MnO_2 is a defi-

cient spinel structure with 3-D tunnels. Among these various MnO_2 structures, the γ-MnO_2 [16.119–122], α-MnO_2 [16.120, 123–125], and δ-MnO_2 [16.113, 119, 120, 126] forms are the most frequently studied for electrochemical applications.

Manganese oxides are also studied as EC materials in so-called *amorphous* forms (often designated as a-MnO_2). Many authors describe such materials as a-MnO_2 even if broad diffraction peaks are observed from x-ray diffraction (XRD) patterns [16.114, 119, 124, 125, 127–133], although resulting diffraction features are difficult to assign to a particular manganese oxide polymorph. Indeed, most of these poorly crystallized compounds consist in a random arrangement of MnO_6 octahedra, which leads to an intergrowth of different structures, alternating tunnels of different size together with water molecules and alkaline cations (Na^+, K^+). Amorphous MnO_2 materials are commonly synthesized by *chimie douce* methods, often by reacting potassium or sodium permanganate with various reducing agents such as Mn^{II} salts (acetate [16.28, 113, 114, 134–141], sulfate [16.127, 133, 142–146], chloride [16.123], etc., borohydrides [16.129], fumaric acid [16.24, 119, 131, 147–149], sodium fumarate [16.130], aniline [16.125], ethanol [16.124, 150–152], ferrocene [16.153], etc.).

The wide range of available crystalline and *amorphous* forms of manganese oxides serve as a basis from which one can select and optimize for particular performance characteristics (stability, capacity, voltage, etc.) for use in aqueous ECs. The presence, adventitious or deliberate, of defects and vacancies within otherwise crystalline polymorphs adds further richness and complexity to manganese oxides. For example, Reutschi previously demonstrated the importance of proton-compensated cation vacancies for the electrochemical performance of manganese oxides in the concentrated alkaline electrolytes of interest for Zn/MnO_2 batteries [16.154–156], a concept that has not been extensively explored in mild aqueous electrolytes. As noted above, manganese oxides are complex, nonstoichiometric oxides, often containing additional metal cations, physisorbed and structural water, and structural vacancies, but for the purposes of this chapter we will denote these materials generally as MnO_2.

16.3.2 Pseudocapacitance Mechanisms for Manganese Oxides

Beginning with the work of *Goodenough* and coworkers [16.113, 114], the importance of faradaic contributions to the observed specific capacitance has been noted, and in the intervening years many studies have been performed in order to elucidate the charge-storage mechanism of MnO_2-based electrodes in mild aqueous electrolytes. A more detailed understanding of the charge-storage process is critical to the design and development of new forms of MnO_2 materials and electrode architectures that demonstrate technologically relevant performance in ECs, in terms of energy and power density, and also cycle life. Fundamental investigations regarding this question have been based on a wide variety of MnO_2 compounds with different structural and microstructural features (thin films, powder-based composite electrodes, amorphous, or crystallized material, etc.), making it difficult to strictly define the pseudocapacitance mechanisms that would be universally applicable to all MnO_2-based electrode materials. However, some general conclusions can be drawn, as detailed in the following sections.

Unlike for activated carbons, where charge storage is primarily ascribed to a capacitive process in the electrochemical double layer at the electrode/electrolyte interface, the charge-storage mechanism in MnO_2 compounds involves the injection/extraction of electrons into/from MnO_2-based electrodes, accompanied by the insertion/intercalation of charge-compensating cations from the electrolyte. Spectroscopy investigations, typically using thin-film forms of MnO_2, have confirmed that the Mn^{3+}/Mn^{4+} redox couple is primarily responsible for the observed pseudocapacitance in mild aqueous electrolytes, as demonstrated for amorphous or poorly crystallized manganese dioxides using in-situ Mn K-edge x-ray absorption spectroscopy (XAS) [16.142, 157, 158] and x-ray photoelectron spectroscopy (XPS) [16.127, 159].

XPS is used as an ex-situ method to probe the Mn3s and O1s core level spectra in order to assess the changes of manganese oxidation state in MnO_2 electrodes that are oxidized and reduced at various potentials [16.127, 159]. The energy splitting between the two peaks of the Mn3s doublet (ΔE_b) shows an inverse linear relationship with the manganese oxidation state (Fig. 16.11), and thus can be used as an ex-situ probe of the MnO_2 redox process [16.160]. The ΔE_b of the Mn3s components for the oxidized MnO_2 thin film is found to be smaller than that of the reduced film and consistent with mean manganese oxidation state of +4. Upon reduction, the value of ΔE_b is increased and the corresponding Mn oxidation state depends on the lower potential limit used. A mean oxidation state of +3.6 is determined for $E = 0.1$ V versus Ag/AgCl; further reduction at $E = 0.0$ V versus Ag/AgCl decreases the manganese oxidation state to to +3.0 for $E = 0.0$ V versus Ag/AgCl (Fig. 16.11) [16.127, 159]. This means that at sufficiently reductive potential all the Mn^{4+} cations of the MnO_2 surface can be reduced to Mn^{3+} at least within the thickness (1–5 nm) of the film that can be probed by XPS analyses. These observations are

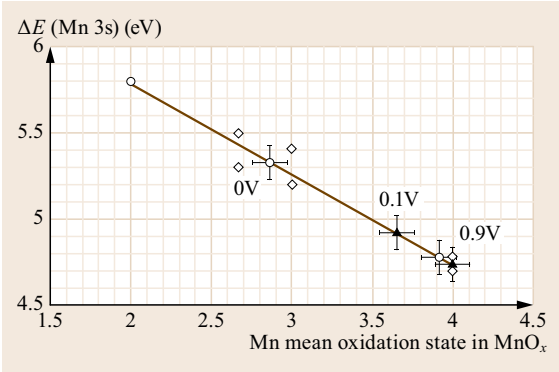


Fig. 16.11 Energy splitting between the two peaks of the Mn3s doublet (ΔE_b) versus the mean manganese oxidation state. Data for MnO, Mn_3O_4, Mn_2O_3, and MnO_2 are extracted from [16.160]. Data for MnO_2 thin film electrode are extracted from [16.127, 159]. The polarization potential versus Ag/AgCl is also given

confirmed by the variation of the different components of the O1s spectra, which is also consistent with such a change in the manganese oxidation state.

In-situ x-ray absorption near-edge spectroscopy (XANES) provides direct evidence for the change of the manganese oxidation state in MnO_2 compounds. The valence state of Mn can be specifically identified by the absorption threshold energy E_0, which is obtained from the first inflection point on the main absorption edge, and progressively shifts to lower energies upon electrochemical reduction of the MnO_2 electrode, in agreement with a decrease in the manganese mean oxidation state [16.157]. For thin-film investigations, the XANES experiments are conducted in-situ using the fluorescence mode [16.157, 158]. As observed with the XPS measurements, a clear change of the manganese oxidation state is observed upon cycling the electrode. In the fully oxidized state, a value close to +4 is deduced from XANES experiments. In the reduced state, the manganese oxidation state is dependent upon the lower potential limit used for the electrochemical tests, and the specific crystal structure of MnO_2 examined. As already noted for XPS analyses [16.127, 159], a potential of +0.1 V versus Ag/AgCl leads to a value of +3.71 while a potential of −0.3 V decreases this value to +3.10. The XANES experiments also seem to indicate that the electrochemically reversible region might be restricted to a thin surface layer [16.157], at least for amorphous or poorly crystallized MnO_2 compounds.

With strong evidence from multiple spectroscopic techniques and various MnO_2 forms that the $Mn^{3+/4+}$ redox couple is responsible for the observed pseudocapacitance, further questions arise with respect to the identity of the cations that must be incorporated from the electrolyte into the solid-state MnO_2 structure to provide charge compensation. Because most of the studies involve the use of mild aqueous-based electrolytes (ACl or A_2SO_4, with A = Li, Na, K), the two obvious candidates are protons or A^+. Anions do not seem to play a major role in charge storage because they are not detected in the compounds at any state of charge [16.127]. Electrochemical quartz crystal microbalance (EQCM) coupled with XPS or XANES measurements are used to follow the electrode mass upon cycling and to correlate the mass change to the manganese oxidation state variation. Two coupled spectroscopy/EQCM studies [16.142, 159] have emphasized the determining role of hydrated protons compared to Na^+ in amorphous or poorly crystallized thin films.

Another work based on XPS [16.127] also reveals that Na^+ cannot be the only cations involved in charge storage, at least for amorphous forms of manganese oxides. The contribution from the alkali cation first decreases then increases with ionic size [16.142]. Two opposing energy considerations can explain this behavior: the preferential insertion of small cations in the MnO_2 lattice, which favors protons and the lower barrier for the removal of solvated water from larger cations. For well-crystallized birnessite, Na^+ is intercalated into the layered structure of the material together with water molecules, thus inducing a change in the Na/Mn molar ratio as detected by energy dispersive x-ray analyses and x-ray diffraction [16.126], but the role of protons cannot be definitively ruled out.

According to the different spectroscopic studies, two main mechanisms can be envisioned. The first one involves the chemisorption of electrolyte cations (A^+) on MnO_2 surface and can be described as

$$(MnO_2)_{surface} + A^+ + e^- \Longleftrightarrow (MnO_2{}^-A^+)_{surface} \quad (16.17)$$

where $A^+ = H^+$, Li^+, Na^+, or K^+. This mechanism is consistent with the typical capacity of composite electrodes made from amorphous compounds (100−300 C/g), which usually exhibit high specific surface area (> 100 m^2/g). This range of charge-storage capacities translates into less than one electron per surface manganese cation ($\approx 5 \times 10^{14}$ atoms/cm^2) thus suggesting that the measured capacitance may be due to a surface mechanism. Additionally, the disordered nature of the a-MnO_2 lattice may be less favorable for cation diffusion, which limits faradic reactions at the surface of the particles.

Early investigations from *Lee* and *Goodenough* [16.113, 114] on a-MnO_2 electrodes have shown that the cyclic voltammetry behavior and the specific capacitance depend on the nature of the cations

(Li^+, Na^+, K^+) in the electrolyte and that there is a competition for chemisorption between these cations and protons when fast charging or cycling rates are used. These trends also emphasize the role of cation's hydration sphere, which is smaller for K^+ and subsequently favors the chemisorption of this cation compared to Li^+ or Na^+. Not only Brunauer–Emmett–Teller (BET) surface area but also pore-size distribution impact the capacitance, especially at fast cycling rates [16.153]. The capacitance appears to correlate to the surface area at low cycling rates, but at fast cycling rates, pores with diameter below 20 nm are less favorable for cations adsorption.

A careful study using AC-impedance spectroscopy, anodic current transient technique, and cyclic voltammetry [16.161] has shown that the pseudocapacitance process of the amorphous manganese oxide electrode can be categorized into two consecutive steps: (i) charge-transfer reaction at the electrode/electrolyte interface and (ii) Na^+/H^+ ion diffusion into the electrode. The charge/discharge of hydrated films is limited by cation diffusion, while removing physisorbed water by annealing leads to a transition from pure diffusion control to a mixed diffusion and charge-transfer reaction control. The electrochemically active region becomes narrower within the electrode with decreasing amount of hydrates, due to fewer hopping sites available for the diffusion of cations in the electrode.

Not all the MnO_2 compounds seem to follow the mechanism proposed in (16.17). Some more crystalline MnO_2 materials exhibit similar capacitance values as high surface area amorphous compounds, despite having significantly lower surface areas ($< 50\,m^2/g$) [16.113, 114, 119, 120, 123, 126]. Subsequently, a second mechanism can be proposed, which involves protons or alkali cation (A^+) intercalation into the *bulk* of the MnO_2 compound

$$MnO_2 + A^+ + e^- \Longleftrightarrow MnOOA\,, \qquad (16.18)$$

where $A^+ = H^+$, Li^+, Na^+, or K^+. This mechanism was also proposed at the beginning of the work on MnO_2 materials for ECs by *Lee* and *Goodenough* [16.113]. Indeed, crystallized compounds with large 1-D or 2-D tunnel structures such as α-MnO_2 (cryptomelane) or δ-MnO_2 (birnessite) exhibit very high capacitance values due to reversible cations intercalation (H^+, Li^+, Na^+, or K^+) into the solid-state lattice [16.119, 120, 126].

The transition between mechanisms depicted in (16.17) and (16.18) can be related to proton diffusion in a subsurface layer by analogy with hydrous RuO_2 [16.162]. *Pang* et al. [16.163] and *Chin* et al. [16.164] proposed a similar mechanism, positing that the reduction of MnO_2 to MnOOH involves the coupled incorporation of protons and electrons into the oxide lattice and in that case the relatively high pseudocapacitance is presumably due to facile proton diffusion into hydrous manganese dioxide films. One should note that mechanisms (16.17) and (16.18) definitely do not neatly divide the MnO_2 compounds in two categories: crystalline and amorphous materials. Some MnO_2 polymorphs such as pyrolusite (β-MnO_2) or nsutite (γ-MnO_2), which have small 1-D tunnels, exhibit limited capacitance values that vary linearly with their surface area [16.121], also in good agreement with the amount of Mn cations at the surface region, thus more likely following mechanism depicted in (16.17). In contrast, some amorphous MnO_2 thin films demonstrate high capacitance values that are only accessible if intercalation takes place in the bulk material [16.163]. Reversible expansion and shrinkage in lattice spacing of poorly crystallized manganese dioxide during charge transfer at manganese sites upon reduction/oxidation was also demonstrated by in-situ synchrotron x-ray diffraction [16.142]. This lattice expansion indicates that the pseudocapacitance of MnO_2 involves the insertion of cations into the bulk of the oxide structure and is not limited only to the surface in contact with the electrolyte (Fig. 16.12).

16.3.3 Thin-Film Electrodes

Thin-film electrodes are often used to determine the intrinsic properties of an electrode material, in the absence of binders and conductive additives and the processing steps required for typical composite electrode fabrication [16.165]. Electrodeposition is the most common and simplest method to fabricate thin films of manganese oxides on conductive substrates (platinum, stainless steel, nickel, titanium, carbon fabrics, carbon nanotubes paper, or transparent conductive oxides (indium tin oxide (ITO))). For example, anodic deposition from a Mn^{2+}-based aqueous solution has been extensively studied, where the typical deposition potential is in the range 0.6–1.0 V versus SCE (standard calomel electrode). The resulting oxide deposits are often amorphous [16.157, 158, 166–174] and present a macroscopic globular morphology. At the microscale, more intricate and complex morphologies are observed. High-resolution scanning electron microscopy of electrodeposited MnO_2 films often reveals that the macroscopic spherical grains are covered with 10–20 nm thick fibers, 50–200 nm long, entangled with one another, delimiting 50–100 nm diameter pores [16.171]. Cross-sections of the same films show petal-shape rather than fibrous nanostructure, with *sand rose* morphology. Tiny spherical particles [16.159] or

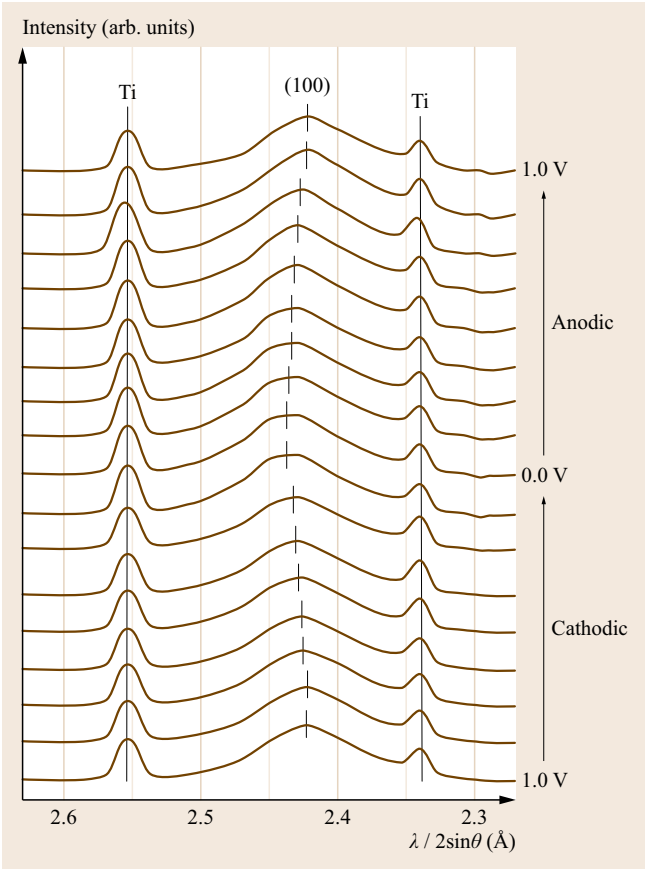


Fig. 16.12 Variation of the (100) reflection of ε-MnO_2 related to cations (H^+ and Na^+) intercalation in the lattice evidenced with synchrotron XRD acquired in-situ during CV cycling in 1 M NaCl(aq) (after [16.142])

nanofibers [16.172] can also be detected. An increase in deposition temperature seems to increase the film porosity [16.175, 176]. The surface area of such films is about 40 m^2/g. Depending on the deposition conditions (Mn^{2+} precursor salt, temperature, additives, etc.) crystallized MnO_2 phase (γ-MnO_2 [16.177], δ-MnO_2 [16.178, 179], ε-MnO_2 [16.142, 180]) can also be obtained.

Potentiodynamic electrodeposition can be used for better control of the porosity, based on the sweep rate [16.181–184]. Low sweep rates ($\approx$ 20 mV/s) result in globular microstructures with spherical grains of 0.4 µm diameter [16.178], while increasing the sweep rate up to 100 mV/s or more increases the roughness and porosity [16.185, 186]. Subsequently, the microstructure is similar to that observed on anodic deposited thin films, and the surface area is also in the range 40–50 m^2/g [16.183]. Constant-current deposition [16.187] or cathodic plating from Mn^{7+} precursor [16.185, 188] does not change significantly the microstructure or the electrochemical performance. Electrophoretic deposition [16.189, 190] of MnO_2 particles or nanofibers also leads to porous microstructure. It is worth noting that very thin layers can be obtained by dip-coating with quite high capacitance values ($\approx$ 700 F/g). The morphological observations suggest a dense microstructure but BET surface area of 50 m^2/g is determined [16.163, 164].

Alternative deposition techniques have been used to prepare dense MnO_2 deposits, which are of interest for determining the influence of surface and subsurface sites, as reported by *Ardizzone* et al. [16.162] for RuO_2 compound. Dense MnO_2 films can be prepared by electrochemical oxidation of Mn metal films that are first deposited by either physical vapor deposition [16.191–195] or electroplating in ionic liquids [16.196–198]. As a result, the films exhibit a heterogeneous microstructure with a dense layer close to the substrate and again a petal-shape top surface layer.

The data collected on all the thin films are summarized in Fig. 16.13 without distinction of the deposition technique. Special thin-film designs using co-deposition with carbon or polymer additives as well as 3-D architecture have not been reported in this plot and will be discussed later on.

From Fig. 16.13 two main trends can be deduced. Above 1 µm, a decrease in capacitance occurs concomitantly with increasing thickness. Even if the capacitance values are close to those observed for composite electrodes (100–300 F/g), the lack of conductive additive such as carbon black seems detrimental to thicker films. The situation is more confused when examining films that are less than 1 µm thick. The scattering of the data can have different origin. For example it was shown that an increase in the Mn^{3+}/Mn^{4+} ratio leads to enhanced capacitance values [16.171]. Annealing at moderate temperatures (below 300 °C) enhances in some cases the electronic conductivity of the film and also leads to an improvement of the capacitance [16.163]. It is very difficult to assume a general trend since high capacitance (e.g., > 500 F/g) can be obtained with various techniques including dip-coating [16.163], oxidation of PVD-deposited metallic manganese films [16.191], potentiodynamic deposition [16.183], or anodic deposition [16.201]. Even higher capacitance values may be obtainable, as some of the reported data are derived at high sweep rates. For example, the films prepared by *Pang* et al. [16.163] exhibit capacitance values from 360 to 700 F/g at 50 mV/s and lower cycling rates usually lead to improved capacitance values, with a typical 50% increase between 50 and 5 mV/s.

Two studies [16.127, 183] report capacitance values above 1200 F/g at low sweep rates (5 mV/s). These

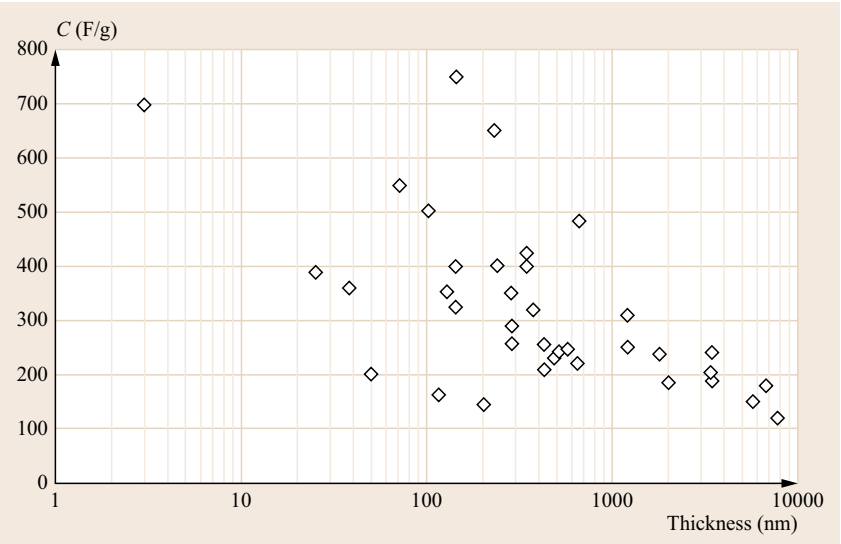


Fig. 16.13 Thin-film capacitance (F/g) versus the thickness of MnO_2 layer. Data are extracted from [16.158, 163, 168–171, 173, 174, 177, 182, 183, 185, 186, 188, 191, 195, 196, 198–201]

values correspond to one electron exchange per manganese atom, which means that all the Mn^{4+} cations in the film are reversibly reduced to Mn^{3+} in Na_2SO_4 aqueous electrolyte between 0 V and 0.9 V/1 V versus SCE. The one-electron reduction is only observed with thin and porous films obtained from the deposition of a limited amount of nanoparticles [16.127] or from the potentiodynamic deposition with a surface-active agent (sodium lauryl sulfate) [16.183], which in both cases enhances the surface area and gives free access of the aqueous electrolyte to all the film surface with no need of long diffusion path for cations inside MnO_2 lattice. However, the cycling behavior of both films is not depicted in the studies and the cyclic volume change of the electrode may be detrimental to cycling ability.

When increasing the sweep rate from 2 to 100 mV/s, capacitance fade is in the same range as for bulk composite electrodes, that is, 20–75% [16.166, 172, 174, 182–184, 186, 188, 190, 191, 196]. The lack of suitable electronic conductivity is detrimental to the film for sustaining fast charge/discharge rates. This confirms the precedent findings on bulk composite electrodes, which indicate that electronic conductivity is an intrinsic limiting factor with particulate-MnO_2 electrodes with respect to achieving high charge/discharge rates capability. Pore-size distribution can also be a hindrance for cation diffusion to the surface of the active material. However it is difficult to evaluate this parameter on such small surface.

Some authors have tried to compensate the drawbacks of *flat* MnO_2 thin films by building 3-D architecture on the substrate. This has been done by performing MnO_2 deposition through different templates [16.200, 202, 203], building nanostructured substrates prior to deposition [16.201, 204] or preparing sandwiched architecture with electroactive layers in between MnO_2 layers [16.205]. Despite the interest in such nanostructured thin films, the electrochemical performances are not significantly enhanced compared to standard thin films.

Doping strategies have also been used for improving capacitance of thin-film electrodes. Anodic plating technique has also been used for doped-MnO_2 deposition. As for MnO_2 powder, nickel [16.181] and cobalt [16.181, 206] have been envisioned. A significant improvement of thin-film capacitance is observed. Cobalt also seems to stabilize the MnO_2 deposit in Na_2SO_4 aqueous electrolyte by suppressing Mn dissolution [16.206, 207].

From all these results, it seems possible to achieve high capacitance values with porous nanostructures combined with very thin layer (< 200 nm), but fast charge/discharge rates are still difficult to achieve while maintaining a reasonable capacitance. The data about thin-film capacitances can be translated into F/cm^2, where the surface is referred to the geometric surface of the substrate and not to the BET surface area of the film. The corresponding plot is depicted in Fig. 16.14. Since only a very tiny mass of active material is mentioned for the films with the highest gravimetric capacitance, the related surface capacitance is very low for thickness below 1 μm (Fig. 16.14). For thicker films, the values of the capacitance increase toward those observed for bulk composite electrodes ($\approx$ 1000–2000 mF/cm^2).

Despite the lack of data on micropower sources based on MnO_2 thin films [16.208], one can calculate the energy density using a symmetrical MnO_2 device in aqueous-based electrolyte. An energy density

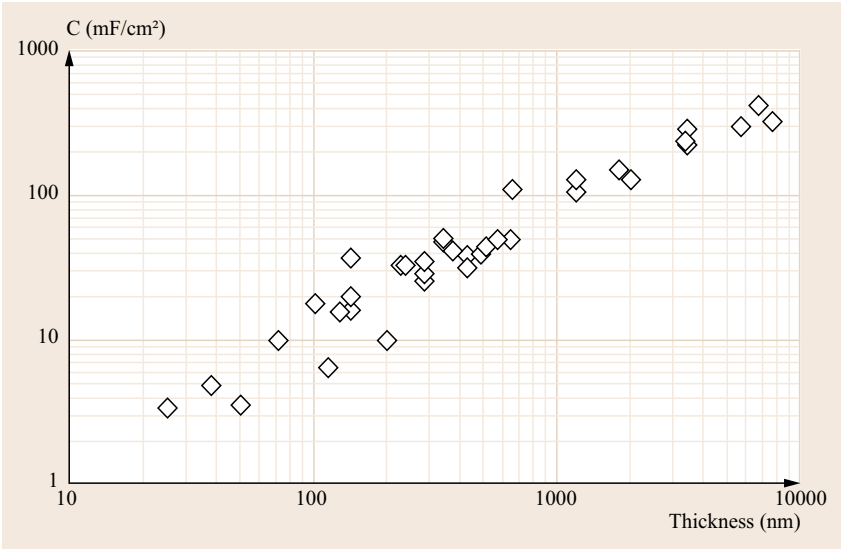


Fig. 16.14 Thin-film capacitance (F/g) versus the thickness of MnO_2 layer. Data are extracted from [16.158, 163, 168–171, 173, 174, 177, 182, 183, 185, 186, 188, 191, 195, 196, 198–201]

of 10 μWh/cm^2 and a power density of 500 μW/cm^2 for 1 μm thick MnO_2 electrodes can be estimated from the data of Fig. 16.14. The low energy density is compensated by interesting power density which compares well with Li-ion-based microbatteries [16.165, 209].

16.3.4 *Bulk* Composite MnO_2 Electrodes

The use of MnO_2 powder as active material for EC requires the preparation of composite electrodes. For this purpose, active material powder (50–90 wt %) is mixed with a carbon conductive additive (e.g., carbon black, graphite, carbon nanotubes 15–40 wt %) in order to enhance the electronic conductivity of the electrode. A binder (e.g., PTFE or PVDF, at 5–20 wt %) is added to the mixture to achieve a self-sustaining mechanically stable electrode that is subsequently pressed onto a current collector grid (stainless steel, titanium, gold, carbon fabric). Alternatively, a slurry of the above-mentioned mixture can be tape-casted onto the current collector. The MnO_2-based composite electrodes are investigated in aqueous-based electrolytes with different electrochemical techniques. Figure 16.15 summarizes literature data on *bulk* electrodes fabricated from different MnO_2 powder. The capacitance values are plotted versus the most commonly indicated parameter, which is the BET surface area. Only the data obtained in almost the same conditions are reported (charge determined from CVs at 2–5 mV/s cycling rate, aqueous Na_2SO_4 or K_2SO_4 salts).

The scattering of the data may be due to the electrode preparation technique. However, other parameters are not taken into account in this plot. The BET surface area is the most accessible parameter from the different papers but pore-size distribution should be more pertinent since, as for activated carbons, all the surface area measured by BET method might not be accessible to the electrolyte cations, especially surface area expressed within micropores. Other parameters such as physisorbed water content or pristine Mn^{3+}/Mn^{4+} ratio also have an influence on the capacitance values.

Despite the scatter of the capacitance data, some general trends can be recoginized. For amorphous compounds, an average capacitance of 200 F/g can be estimated, corresponding to 0.17 electrons per manganese atom involved in charge storage. According to the large surface area, this value fits well with the number of Mn surface atoms as previously emphasized [16.127]. The capacitance seems to reach a limit close to 280 F/g, regardless of the surface area. This limitation has been a driving force for investigating crystalline MnO_2 polymorphs.

For crystallized compounds, the capacitance seems to be related not only to the surface area but also to the crystalline structure, in accordance with cation intercalation mechanism reported above (see mechanism (16.18)). Compounds with small tunnels, namely β, and γ-MnO_2, exhibit low capacitance values even with high-surface-area powders (Fig. 16.15). On the contrary, larger tunnel structures such as δ-MnO_2 (birnessite) or α-MnO_2 (cryptomelane) demonstrate capacitance values above 200 F/g with only moderate surface areas ($< 50\,m^2/g$). In this case, localized surface redox reactions cannot be the only mechanism for charge storage and cations intercalation inside the MnO_2 lattice is predominant, according to the mechanism depicted in (16.18). Again, there is a large discrepancy between the reported data but the nature and the amount of

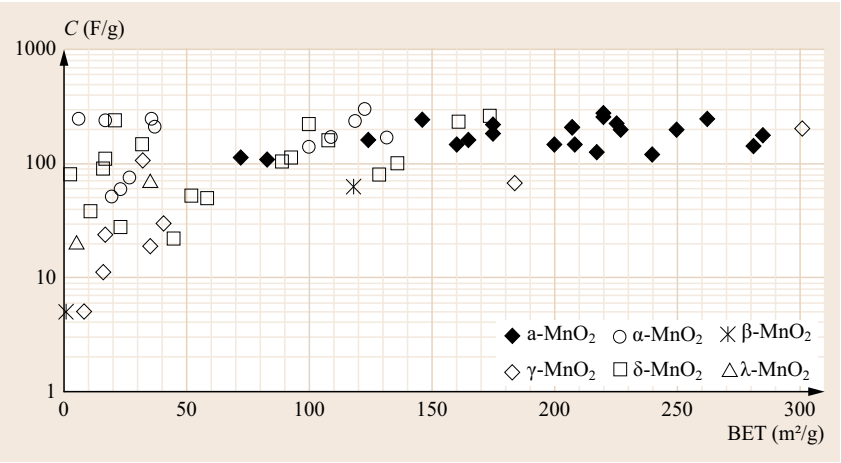


Fig. 16.15 Capacitance versus BET surface area for crystallized (open symbols and crosses) and amorphous (plain symbols) MnO_2 powders (data extracted from [16.24, 113, 114, 119–127, 127, 129–137, 142, 144, 146, 147, 150, 152, 153, 210–219])

alkaline cations in the pristine crystallized phase as well as the amount of physisorbed water molecules should also be considered. The main conclusion about crystalline MnO_2 materials is that, due to cation intercalation, open structures with wide 1-D tunnels (α-MnO_2) or infinite 2-D tunnels (δ-MnO_2) combined with large surface areas can be a pertinent research direction for improving capacitance of MnO_2-based composite electrodes [16.113, 114, 119, 120, 122, 123, 218, 220].

Only few papers deal with the influence of physisorbed water in MnO_2. The first studies of *Lee* and *Goodenough* [16.113, 114] already stated that optimization of the MnO_2 electrode involves the increase of BET surface area, while maintaining a large concentration of electronic charge carriers, that is, a high Mn^{3+}/Mn^{4+} ratio, and excess water, which improves the mobility of intercalating alkaline cations and protons. Indeed, compounds with very low water and Mn^{3+} contents, such as γ-MnO_2, exhibit weak capacitance values even when large surface area are developed [16.121]. Thermal treatments have been used to control the water content in the MnO_2-based electrode, but such treatments also lead to a decrease in surface area, complicating the determination as to which factor is more critical in determining the capacitance value [16.127]. However, as a general rule for bulk electrodes or thin films, the capacitance systematically fades with increasing annealing temperature [16.127, 166]. Only very thin films (< 10 nm) exhibit an opposite behavior due to the great enhancement of electronic conductivity under water removal [16.163]. In all cases, the annealing temperature must not exceed the phase transformation to lower manganese oxidation state compounds (Mn_2O_3 or Mn_3O_4), the temperature of which depends on the structure of the pristine compound [16.221].

A careful investigation of water content using mild annealing treatments (up to 150 °C) [16.215] has also shown a decrease in the capacitance with decreasing water content concomitantly with a decrease in Warburg impedance (lower cation mobility) and an increase in charge-transfer resistance. This was also observed for MnO_2 thin films in which the higher the starting hydrated state, the higher the capacitance value [16.198]. Physisorbed water seems important for preserving hopping sites for electrolyte cations, especially in micro and mesopores, but this parameter has to be coupled with a good electronic conductivity throughout the electrode. The mechanism of charging/discharging at the electrode changes with increasing heat-treatment temperature [16.161], depending upon the amount of hydrates. For hydrated compounds, the charging/discharging mechanism is purely limited by cation diffusion. As the amount of hydrates in the electrodes gradually decreases under annealing, a transition occurs from pure diffusion control to mixed diffusion and charge-transfer reaction control. This trend is emphasized with dehydrated electrodes that only exhibit a charge/discharge mechanism based on charge-transfer reaction at the electrode/electrolyte interface. Furthermore, the electrochemically active region becomes narrower within the electrode with decreasing amount of hydrates, due to fewer hopping sites available for the diffusion of cations in the electrode. Subsequently, capacitance decreases as physisorbed water molecules are removed.

The doping of MnO_2 with various cations has also investigated to enhance the specific capacitance and cycling stability. Doping strategies with either lead, nickel [16.136], cobalt [16.121], aluminum [16.121], or bismuth [16.222] have been performed. Nickel and lead have been found to increase surface area and micropores and to limit the oxygen evolution reaction above $+0.8$ V versus SCE [16.136]. Nickel doping results in an improvement of 20% of the capacitance compared

to undoped MnO_2 prepared with the same procedure. The highest rate capability is also observed for samples doped with nickel. Manganese oxide powders doped with 10% bismuth [16.222] have also demonstrated significant capacitance improvement, up to 308 F/g. Cobalt and aluminum have also been tested as doping agents for increasing the BET surface area of γ-MnO_2 [16.121]. Indeed, specific surface area increases from 17 m^2/g for undoped powder up to 184 m^2/g for 11 at.% Al substitution. The capacitance follows the increase in the surface area but is still limited to 68 F/g due to the small size of tunnels in this phase.

High specific capacitance is not the only parameter required for active materials used in pseudocapacitor. The long-term cycling behavior of MnO_2-based electrodes should also be investigated, particularly at high charge/discharge rates. Most of the studies report cycling ability over 1000 cycles for a-MnO_2 [16.125, 127, 130, 131, 133, 136, 145, 151, 153, 223]. Some authors using special electrode designs where MnO_2 is supported on carbon or incorporated in composites with conducting polymers show improved cycle life up to 10 000 cycles [16.140, 224]. When used inside hybrid devices as the positive electrode versus an activated carbon negative electrode, a-MnO_2 electrode has shown long-term cycling ability over 100 000 cycles [16.144]. Reports on long-term cycling for well-crystallized samples are more scarce, especially those showing at least 1000 cycles [16.121, 216], although a Na-birnessite based electrode has demonstrated 15 000 cycles stability in a hybrid EC device [16.225].

Capacitance fade upon cycling has been studied by different teams [16.145, 153, 157, 180, 216]. The reduction of Mn^{4+} to lower oxidation states is observed below +0.1 V versus SCE [16.157], resulting in manganese dissolution and/or the formation of inactive Mn(III) or Mn(II) oxides or oxohydroxides. These irreversible reactions are responsible for the capacitance fade upon repeated cycling. A dissolution/redeposition mechanism is also observed in different crystalline MnO_2 structures, for which both microstructural and structural changes are depicted concomitantly with the modification of the impedance response [16.180, 185, 186, 198].

The reversibility of the redox reaction generally increases with increasing amount of hydrates and oxidation state of manganese [16.161]. The addition of phosphate and carbonate additives to the electrolyte enhances the cyclability of birnessite by limiting the dissolution of manganese into the electrolyte [16.216]. Capacitance fading has also been attributed to gradual mechanical failure of the electrode structure upon cycling caused by volumetric variations of the oxide particles, resulting in deteriorating electrical contacts among the particles [16.145]. Indeed, microscale cracks appear on the surface of electroplated thin films after cycling, and are assumed to be responsible for 20% capacity fade upon 1000 cycles [16.185]. This effect is exacerbated at high cycling rates.

All these studies suggest that the electrochemical window of MnO_2-based electrode has to be carefully monitored in order to limit capacitance fading upon cycling. Dissolution inhibitor additives can act in a complementary manner to the lower potential limitation. The electrode composition has to be adjusted in order to restrain mechanical failure upon cycling, especially with regard to binders. These three research directions can help MnO_2-based electrodes to meet the requirements of ECs in terms of cycle life (> 100 000 charge/discharge cycles).

The electrode composition is also a conclusive parameter for sustaining fast charge/discharge rates. Electrodes prepared with *standard* composition ($\approx$ 70 wt % MnO_2/20 wt % activated carbon/10 wt % binder) exhibit a large capacitance fade (30–70% of the initial capacitance) when the cycling rate is increased from 2 to 100 mV/s using cycling voltammetry methods [16.119, 122, 125, 127, 131, 133, 146, 217, 222, 224, 226–230], which is ultimately detrimental to the power density, of MnO_2-based electrodes. The same observations are made with galvanostatic charge/discharge cycling, but to a lesser extent, that is, with capacitance decreased from 20 to 50% [16.113, 120]. Some polymorphs such as γ-MnO_2 or λ-MnO_2 even show a more drastic decrease, up to 85%, probably due to high charge-transfer resistance and low water content, limiting cation diffusion [16.119]. Capacitance retention at fast cycling rates can be improved by the use of carbon nanotubes [16.142, 227] or graphite fibers [16.123] as conductive additives, which limit the capacitance drop to 5–25% when the cycling rate is increased from 2 to 100 mV/s. One can conclude that the poor intrinsic electronic conductivity of MnO_2 is responsible for moderate power capability. Unlike carbon-based EC for which capacitive charge storage can be performed at very high charge/discharge rates, the faradic reactions involved in MnO_2-based electrodes may also limit the kinetics of the charge–discharge process.

16.3.5 Advanced MnO_2–Carbon Electrode Architectures

Investigations with planar MnO_2 thin films have demonstrated that the key to achieving maximum specific capacitance is maintaining the MnO_2 phase in a nanoscopically thin form (ideally 10 to 100 s of nm).

The disadvantage of using such submicrometer MnO_2 films is that the geometric area-normalized capacitances are not sufficient to result in relevant energy densities in large-scale packaged EC devices, even with the enhanced specific capacitance observed with ultrathin films. Traditional composite electrodes that incorporate MnO_2 and a conductive carbon additive provide the electrode dimensions that are more typical for energy-storage devices, but the electrochemical utilization of the MnO_2 pseudocapacitance in composite electrodes is less than ideal. In addition, the *brick-and-mortar* approach to composite electrode fabrication with discrete MnO_2 and carbon powder components may ultimately limit the power density that could be achieved in such electrode structures.

A third approach to electrode design combines the best aspects of both the thin-film and composite electrode forms, where the general concept is to incorporate MnO_2 as nanoscale coatings or deposits onto the surfaces of a porous, nanostructured carbon substrate (Fig. 16.16). In such electrode architectures, the nanostructured carbon serves as a three-dimensional current collector, facilitating long-range electron transport to and from the electroactive, but poorly conducting MnO_2 deposits, while also defining a void structure that enables efficient ion/solvent transport when flooded with the electrolyte of interest. Maintaining the MnO_2 as a nanoscale coating on the conductive carbon scaffolding also reduces the solid-state transport distances for charge-compensation cations that are essential to the pseudocapacitance process, enabling rapid charge–discharge of the MnO_2 phase. The ultimate goal for designing and fabricating such MnO_2-carbon nanoarchitectures is not only to maintain the desirable characteristics of nanoscopically thin, planar MnO_2 films (high specific capacitance and high-rate capabilities), but also amplifying those characteristics in a three-dimensional electrode structure that delivers area-normalized capacitances that are relevant for real-world applications.

A variety of nanostructured carbon forms have been investigated as substrates for MnO_2-carbon electrode nanoarchitectures, including many of the same materials that have been explored for EDLCs, as described in a preceding section of this chapter.

Carbon nanotubes are the most common materials reported in the literature as a nanostructured support for MnO_2 [16.95, 137, 151, 210, 231–242], paralleling the proliferation of carbon nanotube research and development over the past several years. Other examples include mesoporous carbons prepared by templating methods (typically resulting in periodic pore structures) [16.243, 244], aperiodic, sol–gel-derived carbon

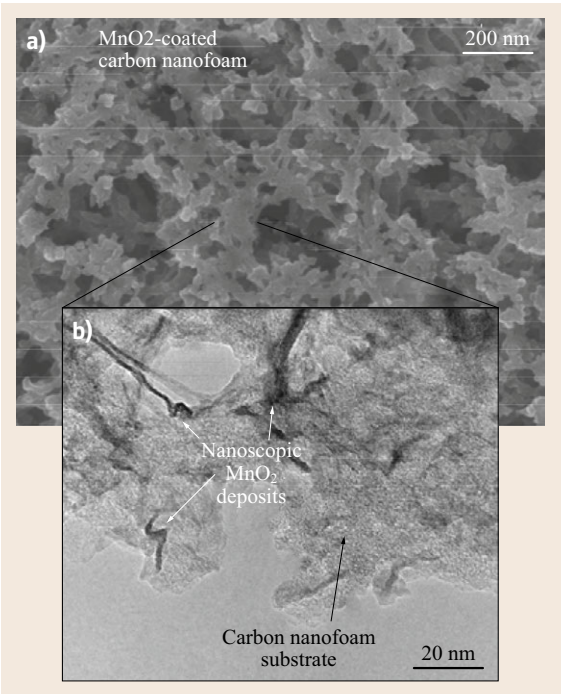


Fig. 16.16a,b Scanning electron micrograph **(a)** and transmission electron micrograph **(b)** of MnO_2-carbon nanofoam hybrid nanoarchitecture (after [16.112])

aerogels and nanofoams [16.28, 62, 63], and also more common carbons, such as carbon blacks [16.245–247].

Common methods for modifying nanostructured carbons with MnO_2 include electroless deposition, electrodeposition, and even simple coprecipitation. Electroless deposition using permanganate as the manganese source has become the most popular technique for coating nanostructured carbons with MnO_2 [16.62, 63, 137, 151, 210, 233, 234, 237, 241–247]. Under the appropriate conditions, permanganate, a strong oxidant, will react with many carbons to generate nanoscale MnO_2 deposits directly on the carbon surface. The efficiency of the permanganate redox process depends on a number of factors, including the functionality of the carbon surface, solution pH, temperature, etc. In some cases additional reducing agents such as Mn(II) salts are added to enhance the deposition process. Electrodeposition is a well-known technique for synthesizing manganese oxides, typically based on anodic deposition from solutions of Mn(II) salts. Electrodeposition has recently been adapted to coat carbon nanotube structures with nanoscale MnO_2 [16.231, 232, 235, 236, 240]. As with electroless deposition methods, electrochemically controlled depositions direct the formation of MnO_2 at the surface of the nanostructured carbon support, re-

Table 16.1 Summary of literature data on MnO_2-based symmetric and asymmetric EC devices. Abbreviations: AC, activated carbon; CNTs, carbon nanotubes; CRF, Carbon aerogel; PANI, polyaniline; Ppy, polypyrrole; PEDOT, poly(3,4-ethylenedioxythiophene; SS, stainless steel; EC, Ethylene carbonate; DEC, diethylcarbonate; C, capacitance; ESR, Equivalent serie resistance (after [16.112])

Negative electrode	Positive electrode	Current collector	Electrolyte salt	Cell voltage (V)	C(F/g)	ESR (Ω cm^2)	Energy density (Wh/kg)	Power density (kW/kg)	Number of cycles
AC	MnO_2	Titanium	KCl	2.0	52	–	28.8	0.5	100
MnO_2	MnO_2	SS	K_2SO_4	1.0	36	–	3.3	3.08	–
Fe_3O_4	MnO_2	SS	K_2SO_4	1.8	21.5	–	8.1	10.2	5000
AC	MnO_2	SS	K_2SO_4	2.2	31	–	17.3	19	10 000
AC	MnO_2	Titanium	K_2SO_4	1.5	–	–	7.0	10	23 000
MnO_2	MnO_2	Gold	KNO_3	0.6	160	1.56	1.9	3.8	–
AC	MnO_2	Gold	KNO_3	2.0	140	0.54	21	123	1000
PANI	MnO_2	Gold	KNO_3	1.2	–	0.57	5.86	42.1	500
Ppy	MnO_2	Gold	H_2SO_4	1.4	–	0.52	7.37	62.8	500
PEDOT	MnO_2	Gold	KNO_3	1.8	–	0.48	13.5	120.1	500
AC	MnO_2	Ni foam	LiOH	1.5	62.4	–	19.5	–	1500
AC	$LiMn_2O_4$	Ni grid	Li_2SO_4	1.8	56	3.3	10.0	2	20 000
AC	MnO_2	SS	K_2SO_4	2.0	21	1.3	11.7	–	195 000

sulting in intimate association of the MnO_2 and carbon components.

Aside from the synthetic methods used to incorporate the MnO_2 component, the assortment of MnO_2-carbon hybrid materials that have been reported can be further classified based on the sequence of fabrication steps en route to the final electrode structure. In many cases, particularly in the case of electroless deposition using permangante, the nanostructured carbon is dispersed in powered form into a liquid, where it is subsequently modified with MnO_2. The resulting MnO_2 powder must then be processed into a finished electrode form, typically using conventional composite electrode methods that include polymer binder and carbon additives. An alternative approach involves first fabricating a carbon electrode structure (e.g., a carbon nanotube array or carbon aerogel/nanofoam paper), which is subsequently coated with nanoscale deposits of MnO_2 [16.62, 63, 231, 232, 235, 236, 240, 242]. Modifying a preformed carbon nanoarchitectures ensures that the long-range electronic pathways of the carbon phase remain continuous, whereas processing MnO_2-coated carbon powders into a composite electrode may introduce junctions between the discrete carbon particles to the electrode conductivity.

The physical and electrochemical characteristics of the MnO_2-carbon nanoarchitectures reported thus far vary widely depending on the particular carbon structure, the MnO_2 loading, and the electrochemical tests performed, but promising trends have been observed. In many cases, distributing the MnO_2 phase as a nanoscopic coating results in enhanced MnO_2-normalized specific capacitance, as observed in some planar thin-film MnO_2 electrodes. For example, *Dong* et al. [16.243] reported a specific capacitance of $\approx 600\,F/g$, normalized to the weight fraction of MnO_2, which was incorporated into the walls of templated mesoporous carbon. The three-dimensional aspects of carbon nanoarchitectures modified with MnO_2 have also been exploited to achieve footprint-normalized capacitance values $> 1\,F/cm^2$ when using structures, such as carbon nanofoam papers, that are prepared in macroscopically thick forms (100–500 μm).

Graphene–MnO_2 nanocomposites have also attracted much attention due to the possibility to couple the high specific capacitance of MnO_2 and the high-power capability of graphene [16.248–250]. However, the reduction of permanganate ions at the surface of grapheme or of RGO leads to the electronic structure of grapheme carbon, which is detrimental to the electronic conductivity of the composite electrode. Additionally, when large amount of MnO_2 are incorporated into the nanocomposite electrode, the benefit of graphene is minimized and the samples exhibit similar energy and power densities as regular carbon/MnO_2 composite electrode.

16.3.6 MnO_2-Based Devices

Not only micropower sources can be envisioned for MnO_2 electrode uses; indeed, the interesting capacitance values displayed by MnO_2 bulk electrodes coupled with their use in mild aqueous electrolytes have led to the fabrication of ECs. The performance of symmetrical MnO_2/MnO_2 devices using

aqueous electrolytes has been reported by several research groups [16.28, 137, 138, 145, 149, 224] (Table 16.1).

The cell voltage is limited to 1 V as maximum and the energy density is in the range 1.9–8 Wh/kg. Indeed, the principal performance limitation of MnO_2-based ECs is the relatively narrow electrochemical window in which MnO_2 is stable. The upper cut-off voltage (≈ 0.9 V vs. Ag/AgCl) for MnO_2 is limited by the oxygen evolution reaction, which adds a nonreversible redox process to the pseudocapacitance process [16.24]. Similarly, the lower cut-off voltage is determined by the onset of the Mn^{4+} *irreversible* reduction and subsequent manganese dissolution, which removes active material at each discharge of the electrode [16.157]. The particular lower potential limit for stability depends on the crystal structure and the microstructure of MnO_2. For standard *amorphous* powder, the lower cut-off voltage is close to −0.1 V versus Ag/AgCl. Subsequently, the cell voltage of a symmetrical MnO_2/MnO_2 device hardly exceeds 1.0 V, which limits both energy and power densities and negates the beneficial effects of high specific capacitance values of this promising metal oxide. Subsequently, the interest in using an aqueous-based device is balanced by the moderate electrochemical performances. Only few hundred cycles are shown in most cases for symmetrical MnO_2/MnO_2 devices.

One strategy to overcome the limited voltage window is to construct asymmetric devices using a positive MnO_2 electrode and a different negative electrode, one with a useful electrochemical window complementary to that of MnO_2 (i. e., with a lower cut-off potential below 0 V vs. Ag/AgCl) [16.251]. Materials that can satisfy this requirement in mild aqueous electrolytes include iron-based oxides (e.g., Fe_3O_4 or FeOOH)[16.26, 147], titanium phosphates [16.141], conducting polymers (e.g., polyaniline, poly(3,4-ethylenedioxythiophene) [16.139], and carbon [16.24, 135, 138, 144, 149, 230, 252–254]. Table 16.1 summarizes the performance of the different asymmetric EC devices which all show extended cell voltage (1.2–2.2 V). These EC devices can be divided into two categories.

The first category uses a faradaic or pseudocapacitive negative electrode (Fe_3O_4 or FeOOH) [16.26, 147], titanium phosphates [16.141], conducting polymers [16.139], together with a pseudocapacitive MnO_2-positive electrode. The second type of asymmetric device combines an activated carbon electrode with a pseudocapacitive manganese dioxide electrode as negative and positive electrodes, respectively [16.24, 135, 138, 144, 149, 230, 252–254]. In this latter case, both the nature of the electrode materials and the nature of the charge-storage mechanisms are different on the negative and positive sides. Typical constant current charge/discharge plot of an activated carbon/MnO_2 2 V EC device is depicted in Fig. 16.17.

From Table 16.1, it can be seen that combining a positive MnO_2 electrode to these negative electrodes produces an increase in the cell voltage up to more than 2.2 V for activated carbon(−)/MnO_2(+) asymmetric device. Because of the expanded voltage range, the activated carbon(−)/MnO_2(+) combination [16.135] provides energy densities up to 28.8 Wh/kg (normalized to the total active material mass), nearly 1 order of magnitude higher than that for symmetrical MnO_2 devices [16.28, 137, 138, 145, 149, 224], and comparable to conventional symmetric carbon/carbon ECs that utilize nonaqueous electrolytes [16.255]. Additionally, the thermal management of aqueous-based asymmetric ECs was compared to standard carbon/carbon AN-based devices, and the superiority of the aqueous device was demonstrated due to higher thermal safety because of a higher vaporization temperature and nonflammability of the cell components, especially the aqueous electrolyte [16.256, 257].

The advantages of increased cell voltage and energy density for MnO_2-based aqueous asymmetric ECs must also be accompanied by long-term cycling stability of the resulting devices. The requirement for commercially viable ECs is between 5×10^3 and 5×10^6 cycles. Unfortunately, most of the MnO_2-based devices presented in the literature only show 100–1000 charge/discharge cycles, highlighting the difficulty to achieve long-term cycling stability for an asymmetric device, unlike the symmetrical carbon/carbon

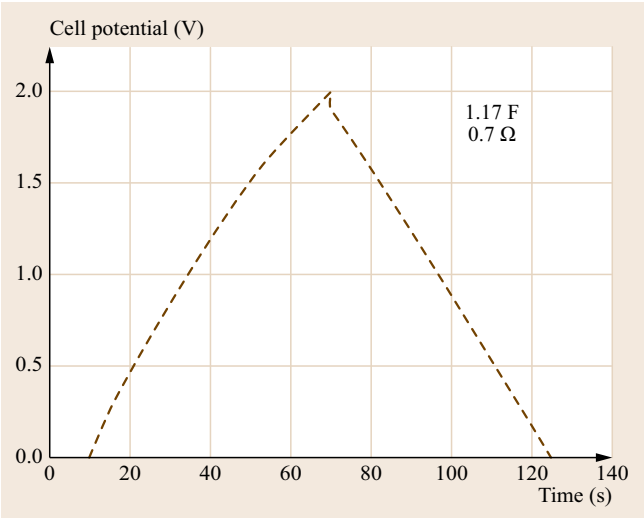


Fig. 16.17 Galvanostatic charge/discharge of an hybrid activated carbon(−)/MnO_2(+) 1.17 F coin type cell

EC, which can sustain several hundred thousand cycles [16.255].

Different factors influence the cycle life of the MnO_2 electrode: (i) manganese dissolution that leads to a progressive loss of active material and a subsequent capacitance fade upon cycling [16.157, 180, 198], (ii) gradual mechanical failure of the electrode structure upon cycling caused by cyclic volumetric variations of the oxide particles [16.145], and (iii) the oxygen evolution reaction, which can affect the electrode/current collector interface and exacerbate corrosion problems [16.144], ultimately increasing the equivalent series resistance (ESR) of the cell. Replacing conventional Na^+ or K^+ aqueous electrolyte with potassium poly(acrylate) hydrogel in a MnO_2/MnO_2 symmetrical cell [16.146] has a significant impact on the capacitance as well as on the power capability, which are greatly improved, probably due to a reduction in the distributed pore-size resistance. This can be a pertinent solution for increasing cycling ability of the hybrid cell while improving power capability. For practical cells, it is important to carefully balance the mass and capacitance of the positive and negative electrodes in order to ensure that MnO_2 does not exceed its stable electrochemical window when cycling the complete asymmetric cell. For example, the potential of an a-MnO_2 electrode must be maintained between 0 and 0.9 V versus Ag/AgCl upon cycling. The problem is even more challenging when a pseudocapacitive or faradic negative electrode is used in combination with MnO_2. In this case, both electrodes have to be carefully monitored in order to avoid capacitance fade upon cycling. Practically, these devices have to be operated within a *safe* cell voltage range, which often results in a limited energy density. In the case of an activated carbon(−)/MnO_2(+) asymmetric EC, the stability of the carbon electrode is a less critical issue. Indeed, nearly 200 000 cycles have been reported for such a device in which precautions were taken to limit the corrosion of the electrode/stainless steel current collector interface [16.144].

Recently, aqueous Li_2SO_4 or LiOH have replaced Na^+ or K^+ salts as the electrolyte. The intercalation of Li^+ may be observed in one or both of the electrodes [16.26, 141, 230, 252, 253]. Reasonable cycling ability has been demonstrated (up to 20 000 cycles [16.252]), with improved energy density up to 36 Wh/kg [16.253]. However, the presence of an *intercalation* compound in the electrode combination obviously limits the power capability (Table 16.1), and the related devices look like *power* batteries rather than conventional EC, as the charge/discharge cycles usually last for several minutes rather than few seconds.

Small amounts of MnO_2 powder can also be added as doping agent to improve the performance of other EC [16.258]. For example, 5 wt % MnO_2 doping in PANI electrode leads to an increase of the energy density from 400 to 650 Wh/kg and a cycling stability over 5000 cycles.

Finally, symmetrical or hybrid devices using MnO_2-based positive electrode and carbon nanotubes in the negative electrode exhibit high cell potential (2.3−2.7 V) in organic-based electrolyte compared to aqueous EC. The energy density reaches 33 Wh/kg [16.150], which is higher than the energy density displayed by MnO_2-based aqueous systems but the advantages of using an aqueous-based electrolyte are lost.

The incorporation of MnO_2-electrodes into asymmetric cell configurations opens the way for safe aqueous-based ECs that deliver technologically with relevant power and energy densities. Aqueous-based ECs present several advantages for device manufacturing: low-cost and environmentally friendly materials and components, no need for special atmospheres during cell assembly, and the use of simple nontoxic salts (e.g., Na_2SO_4). A 620-F activated carbon(−)/MnO_2(+) asymmetric device was recently assembled using this technology [16.144].

16.3.7 Future Outlook

The design of optimized MnO_2-carbon nanoarchitectures for the positive electrode, as well as a more detailed understanding of charge-storage mechanisms in such composite materials, will increase the performance of next-generation asymmetric EC devices. Apart from the scientific quest for high-capacitance MnO_2-based active materials and the search of pertinent complementary negative electrode, the long-term cycling stability of MnO_2 is a technological issue that must be addressed in the near future in order to evaluate and validate the commercial development of aqueous-based asymmetric ECs. Other issues such as self-discharge, corrosion of the current collector, and low-temperature performances should also be examined. Considering that MnO_2-based EC technology is still in its infancy, future research and development should ultimately yield high performance, low-cost, and safe energy-storage devices for applications with challenging energy/power requirements.

16.4 Ruthenium Oxide

Hydrous ruthenium oxide (RuO_2xH_2O) nanoparticles have been extensively studied in recent years as a potential electrode material for ECs owing to its ability to provide high specific capacitance ranging from a few hundred to $\approx 1000\,F/g$ depending on the preparation procedure, measurement conditions, use of support, etc. [16.111, 259–276]. *Trasatti* and *Buzzanca* [16.277] were the first to recognize that the *rectangular*-shaped cyclic voltammogram of a RuO_2 film resembled that of the carbon-based EDLC. The study of hydrous RuO_2 nanoparticles prepared by a sol–gel method constituted a major advance in terms of gravimetric capacitance [16.111, 259], which initiated a worldwide surge in the study of RuO_2-based electrodes for EC application. Much effort has since been devoted to research and development with particular emphasis on structure–property relations. Higher capacitance and enhanced power capability has been achieved by nano- and meso-structural material design, and sophisticated characterization methods have contributed to the understanding of the faradaic behavior of RuO_2-based electrodes. Owing to such extensive studies, the fundamental charge storage properties of RuO_2 are now much better understood, albeit much work is still necessary. RuO_2-based electrodes provide gravimetric capacitance ranging from 100 to $\approx 1200\,F/g$ depending on various parameters including the preparation method, use of conductive supports, etc. [16.278]. Clearly, the high gravimetric capacitance of RuO_2-based electrodes is appealing. The volumetric capacitance is perhaps the most attractive grounds for using RuO_2, as the density of rutile-type RuO_2 is $6.97\,g/cm^3$; roughly three times higher than graphite and 10–15 times higher than most conventional activated carbons. The weakness of RuO_2-based electrodes, besides its lack of abundance and cost, is that these electrodes are better configured in aqueous electrolytes, limiting the voltage window to about 1.0–1.2 V. Thus, much of the technological development has been aimed toward low-voltage miniaturized devices.

A theoretical redox capacitance (C_{redox}) of $1358\,F/g$ can be deduced for $RuO_2\,0.5H_2O$ assuming that the oxidation state of Ru changes from Ru^{2+} to Ru^{4+} within a 1.0 V potential window [16.279–285]. The C_{redox} is $970\,F/g$ if the potential range is 1.4 V [16.259]. If a 4-electron reaction is assumed within a 1.35 V window, then the value exceeds $2000\,F/g$ [16.281, 286]. Note that the earlier given calculations assume that all of the Ru atoms in the crystallite are involved in the reaction and that Ru can take a number of oxidation states, which seems to be an overestimation based on various studies. One should also keep in mind that this calculation neglects the contribution from the electric double-layer capacitance C_{dl}.

The theoretical value of the electric double-layer capacitance C_{dl} of RuO_2 is a matter that is controversial. Most of the C_{dl} values reported in the literature for RuO_2-based electrodes are larger than the C_{dl} value of $\approx 20\,\mu F/cm^2$, which is the value for a mercury electrode in a diluted aqueous electrolyte solution. It is not an easy task to experimentally differentiate between the contribution from the electric double-layer capacitance C_{dl} and redox-related faradaic capacitance C_{redox}, as the (surface) redox related pseudocapacitance for RuO_2 is a fast and reversible process [16.287]. The most widely reported value is $80\,\mu F/cm^2$, [16.287–291] but much higher values have been reported. In the case of hydrous RuO_2 with gravimetric capacitance $\approx 700\,F/g$, specific capacitance can be as high as $1000\,\mu F/cm^2$ using the reported BET surface area [16.111, 259]. Such unusually high surface area normalized capacitance may be a result of a mixture of the electric double-layer capacitance faradaic processes. The surface area of hydrous oxides may also be underestimated by N_2 adsorption measurements depending on the pretreatment.

16.4.1 Synthesis, Chemical, and Physical Properties

Ruthenium, found naturally associated with platinum ores, is one of the less expensive platinum-group metals, typically about 1/10 of platinum. Ruthenium dioxide (RuO_2) is electrochemically stable possessing high electric conductivity ($3\times10^2\,\Omega^{-1}cm^{-1}$) [16.292, 293]. Porous RuO_2 films can be prepared by pyrolysis of ruthenium precursors coated on a conducting substrate by dip-coating or spraying, which is the processes adopted for dimensionally stable electrodes used in industrial electrolysis. Such films are fairly porous with characteristic mud-crack like the surface structure. Heat treatment at moderately high temperature (typically 450–550 °C) is generally performed to prepare stable oxide coatings with RuO_2 crystallites in the range of 20–50 nm in diameter. Smaller, high-surface area RuO_2 nanoparticles can be obtained by soft-solution processing methods including chemical reduction of RuO_4 [16.294], precipitation from various precursors [16.295], sol–gel reactions [16.111, 259, 296] etc. Electrochemical methods such as electro-oxidation of Ru metal [16.264, 265, 297–309] and electrodeposition [16.310–319] have also been applied. Heat treatment at relatively low temperatures (150–200 °C) is often necessary to convert all Ru species to Ru^{4+} and enhance the stability and ca-

pacitance of the hydrous film while maintaining small particle size.

16.4.2 Composites and Other Ruthenium Oxides

Synthesis of RuO_2–MO_x composites and A_xRuO_y complex oxides is a classical approach to increase the utilization of RuO_2. For example, the substitution of Ru^{4+} with other less-expensive transition metal ions such as Sn^{4+}, Ti^{4+}, V^{4+}, Mo^{4+}, etc., has been conducted [16.320]. Incorporation of V^{4+} into the RuO_2 lattice leads to an increase in capacitance with anhydrous $(Ru_{0.35}V_{0.65})O_2$ nanoparticles exhibiting gravimetric capacitance of 1210 F/g of RuO_2, which is 17 times that of RuO_2 nanoparticles prepared under the same conditions [16.321, 322]. Binary hydrous RuO_2–MO_x (M = W, Cr, Sn) [16.323–325] has been prepared by sol–gel methods leading to the capacitance of ≈ 850 F/g of RuO_2. Complex oxides with pyrochlore and perovskite structures have also been prepared, but the high temperature treatment generally leads to low surface area and low capacitance [16.326–328]. Many studies have focused on preparing composite materials with various carbon materials including activated carbon [16.279–281], carbon black [16.282], as well as carbon nanotubes [16.293]. One of the earlier works has shown that a simple physical mixture of acetylene black and sol–gel-derived hydrous RuO_2 can drastically improve the rate performance, which has been discussed based on the increase in mesopores acting as an electrolyte reservoir [16.262]. Carbon-supported RuO_2 materials can be prepared by impregnation or colloidal methods [16.282, 329]. Specific capacitance as high as 800−1300 F/g of RuO_2 has been achieved at relatively low loadings of 10−20 mass % RuO_2. The specific capacitance of hydrous RuO_2 gradually decreases due to particle aggregation and loss of active surface area with increased loading. As the capacitance per electrode material is smaller than pure RuO_2, it is essential that high RuO_2 utilization is achieved at high loadings. Three-dimensional porous nanocomposites consisting of RuO_2 particles with diameter of 20−60 nm and Ketjen Black (KB) which was prepared by an incipient wetness method using fumed silica as template showed a specific capacitance of 647 F/g of composite with 60 wt % RuO_2 loading [16.284]. RuO_2/KB (40 wt % RuO_2) with 2 nm diameter RuO_2 nanoparticles was prepared by a modified sol–gel method and showed 462 F/g [16.330]. By utilizing ultracentrifugal mechanical force, 2 nm RuO_2 particles were encapsulated into the KB network and high capacitance of 821 F/g at 50 wt % RuO_2 was achieved [16.331]. This typical method has a unique nanostructure, where the hydrous RuO_2 nanoparticles in the composites were highly dispersed on the inner (but accessible) surface of KB (Fig. 16.18). The high charge utilization was considered to be due to the facile ionic transport attributed to both the outer and inner hydrous structures of the RuO_2 particles (Fig. 16.19).

High capacitance can also be achieved by using RuO_2 material with a distinctive layered structure. Specific capacitance of ≈ 400 F/g can be obtained by using layered $H_{0.2}RuO_{2.1}xH_2O$ as the electrode material [16.320, 332]. The capacitance is exceptionally large considering the large micrometer size of the particles, which has been attributed to the ability of the

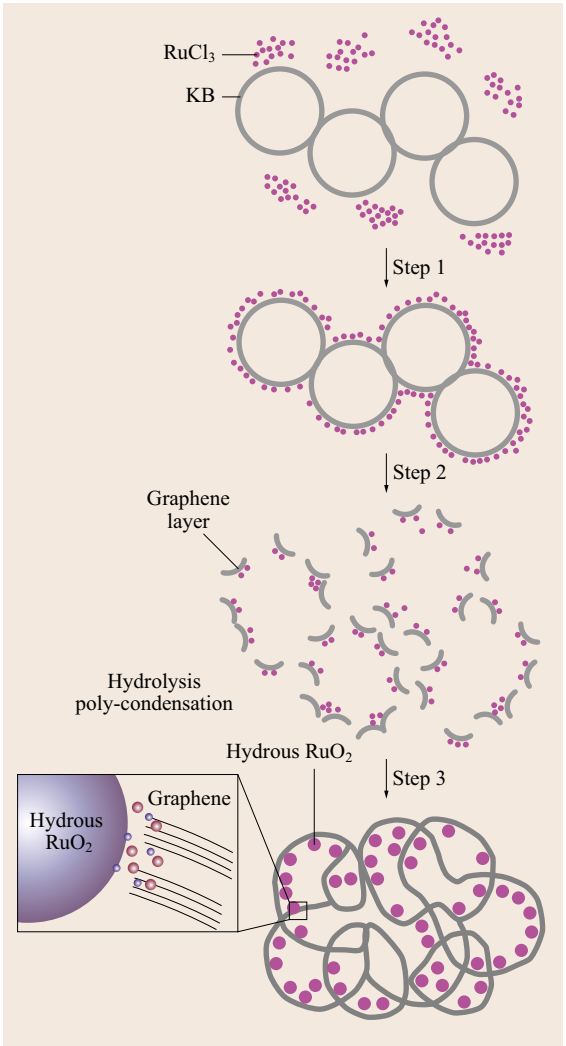


Fig. 16.18 Possible mechanism of ultracentrifugal derived hydrous RuO_2 nanoparticles encapsulated in KB (after [16.331])

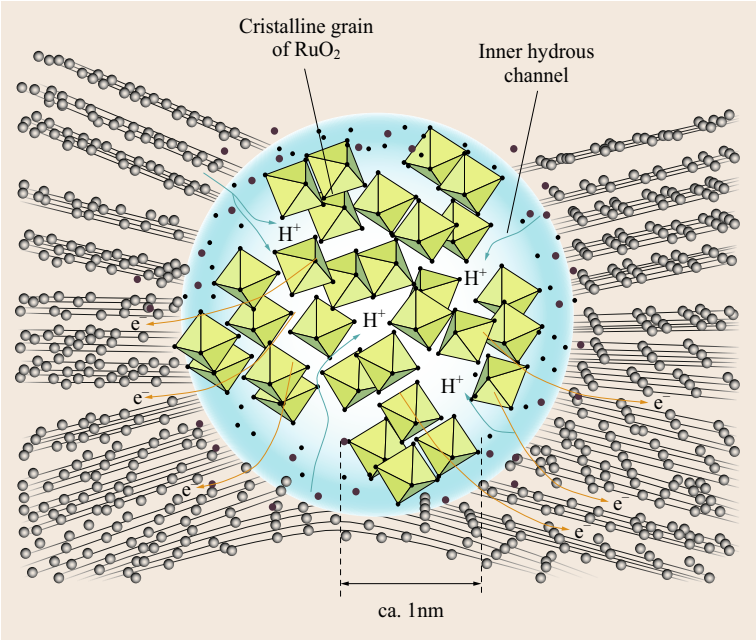


Fig. 16.19 Illustrative models of hydrous RuO_2 nanoparticles accommodated by graphene fragments (after [16.331])

interlayer to swell thereby allowing electrolyte permeation into the two-dimensional structure. Chemical exfoliation and reassembly of the individual nm-thick RuO_2 slabs leads to further enhancement in gravimetric capacitance, as high as 1400 F/g [16.333]. These two-dimensional materials exhibit unique electrochemical properties with remarkably large contribution from pseudocapacitance (as much as 50%), as can be seen from the large redox peaks observed in the CVs (Fig. 16.20).

16.4.3 Charge Storage Mechanism

Cyclic voltammograms of RuO_2 are characterized by a *rectangular*-shaped cyclic voltammogram typical of a reversible system, analogous to an ideal polarizable carbon-based EDLC. The fast and slow charges in thermally prepared RuO_2/Ti DSA-type electrodes have been attributed to the utilization of more accessible, mesoporous surfaces and less accessible, microporous inner surfaces, respectively [16.334]. Based on ellipsometry and electrochemical impedance spectroscopy measurements on anodically and thermally prepared RuO_2, the fast-and slow-charging modes have been ascribed to the charging of the grain surfaces and incorporation of protons into the oxide grains, respectively [16.335]. Similar conclusions were derived by CV and chronoamperometry measurements of anhydrous RuO_2 nanoparticles [16.287]. Figure 16.21 shows examples of cyclic voltammograms of anhydrous RuO_2 (average particle size = 10 nm, $S_{BET} = 42\,m^2/g$, average pore diameter = 16 nm, 90% mesoporosity) acquired at different scan rates (0.5–500 mV/s) in 0.5 H_2SO_4 (25 °C). The pseudocapacitance of anhy-

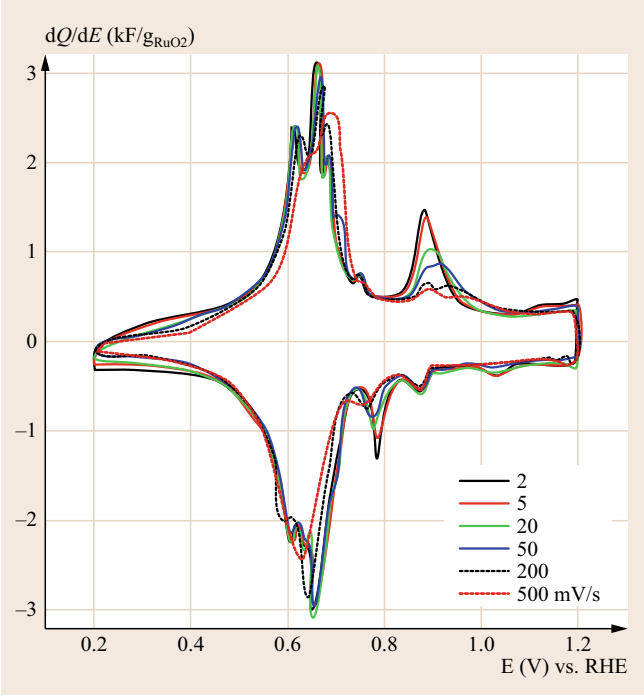


Fig. 16.20 Cyclic voltammograms of restacked ruthenium oxide nanosheet electrodes at various scan rates in 0.5 M H_2SO_4 (25 °C) (after [16.320])

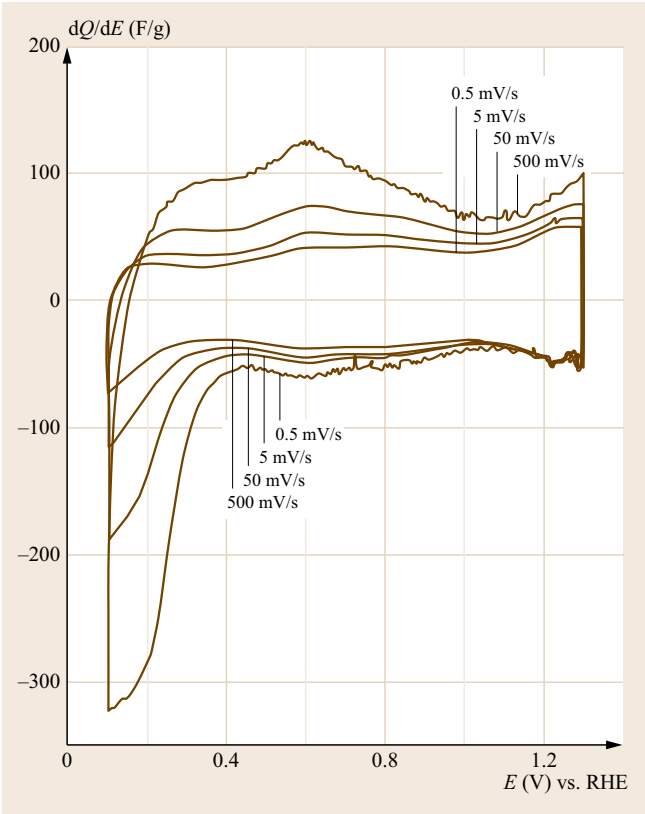


Fig. 16.21 Cyclic voltammograms of RuO_2 thin film electrode at various scan rates in 0.5 M H_2SO_4 (25 °C) (after [16.287])

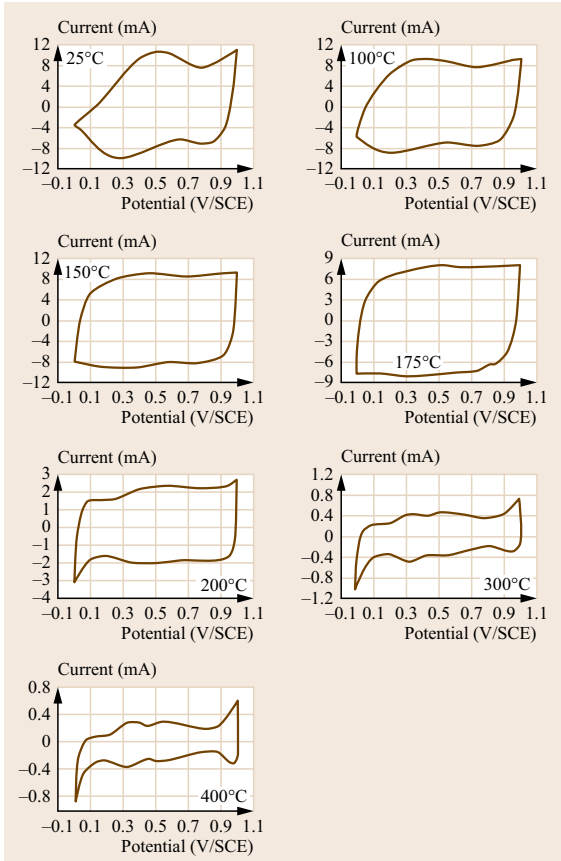


Fig. 16.22 Cyclic voltammograms in 0.5 M H_2SO_4 at 2 mV/s of sol–gel, derived RuO_2xH_2O electrodes annealed at 25, 100, 150, 175, 200, 300, and 400 °C (after [16.259])

drous RuO_2 nanoparticles can be deconvoluted into at least three major components with different kinetics within the potential range of 0.1−1.3 V; that is, the electric double-layer capacitance C_{dl}, a faradaic component attributed to an irreversible redox reaction involving diffusion-limited electroactive species C_{irr}, and a faradaic component attributed to a reversible redox reaction involving electrosorption of ions C_{ad}. The faradaic components are negligible at fast scan rate, but contribute to a substantial amount at low scan rates and low electrode potential. As C_{dl} and C_{ad} are surface sensitive reactions, high surface area nanoparticles yield high capacitance. C_{irr}, which is related to the reduction peak observed below 0.4 V, is a sluggish reaction and is irrelevant to most EC applications.

The cyclic voltammograms of hydrous RuO_2 heat-treated at suitable temperatures are featureless and principally rectangular in shape in comparison to as-prepared or well-annealed material, as shown in Fig. 16.22. Redox peaks are not evident in hydrous RuO_2, which suggests either that the overall capacitance of the system is dominated by the contribution from C_{dl} or the redox reaction is dispersed over the whole voltage range. The influence of the heat-treatment temperature toward the capacitive behavior for sol–gel-derived hydrous RuO_2 as well as the stability of the oxide phase has been discussed in detail by many groups [16.111, 259, 268, 270, 273, 276, 296, 336–346]. At heat-treatment temperatures below 150 °C, poor *i–E* response is observed particularly in the low potential region, which has been associated with the presence of Ru^{3+} in low-temperature annealed materials. Considerable capacitance fading occurs for such materials, as shown in Fig. 16.23, most likely due to the presence of soluble Ru^{3+} [16.295]. When the heat-treatment temperature is raised, highly symmetric and stable *i–E* curves typical of ideally polarizable capacitive behavior is obtained with the capacitance decreasing with increasing temperature.

Various models have been proposed to explain the reasoning behind the observed maximum capacitance and power capability of sol–gel-derived hydrous

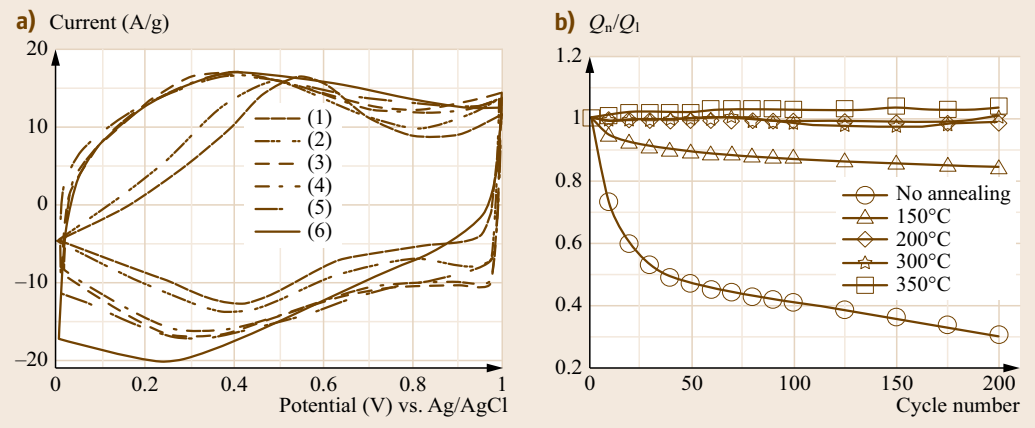


Fig. 16.23 **(a)** Cyclic voltammograms in 0.1 M H_2SO_4 at 25 mV/s of (1) pristine hydrous ruthenium oxide and annealed in air for 2 h at (2) 150, (3) 200, (4) 300, (5) 350, and (6) 400 °C. **(b)** The voltammetric charge ratios between the *n*th and the first cycle (Q_n/Q_1) against the cycle number for pristine and annealed hydrous ruthenium oxide (after [16.295])

RuO_2 as a function of the heat-treatment temperature. The cluster-sized particles for low-temperature annealed hydrous RuO_2 affords high capacitance due to large surface area at the expense of power performance. *Zheng* et al. proposed that the hydrous regions within the nanoparticles allows facile proton permeation for efficient charge storage while the interconnected ruthenium oxide region accounts for the electronic conduction [16.259]. ^{1}H-NMR studies have shown that the specific capacitance is strongly correlated with the proton mobility (Fig. 16.24) [16.270]. An optimum mixed percolation conduction mechanism has also been proposed to explain the volcano-plot behavior [16.273]. Based on impedance spectroscopy, it was shown that the change in the electronic conductivity contributes only slightly to the capacitor frequency response [16.276]. Analysis of the impedance data suggested that the power capability is governed by the proton conduction within the hydrated micropores and the deliverable capacitance is dominated by the particle size. The utilization of micropores not only results in high specific capacitance but also gives low capacitor frequency response. This model is schematically shown in Fig. 16.25. *Kim* et al. have shown that the initial hydrous nature is not a prerequisite for the high capacitance [16.268]. Through electrostatic spray deposition and annealing, a porous anhydrous RuO_2 was synthesized which exhibited capacitance of 640 F/g, one of the highest reported values for anhydrous material.

Various techniques have been implemented to complement standard electrochemical techniques. Rolison and co-workers conducted x-ray absorption near-edge structure (XANES) and atomic pair-density function

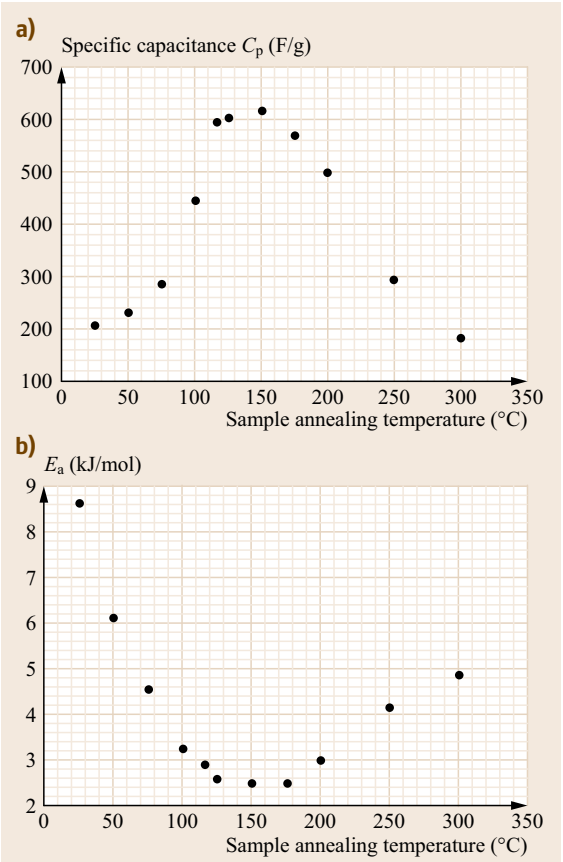


Fig. 16.24 **(a)** Specific capacitance and **(b)** activation energy (E_a) of the RuO_2xH_2O samples as a function of the sample annealing temperature (after [16.270])

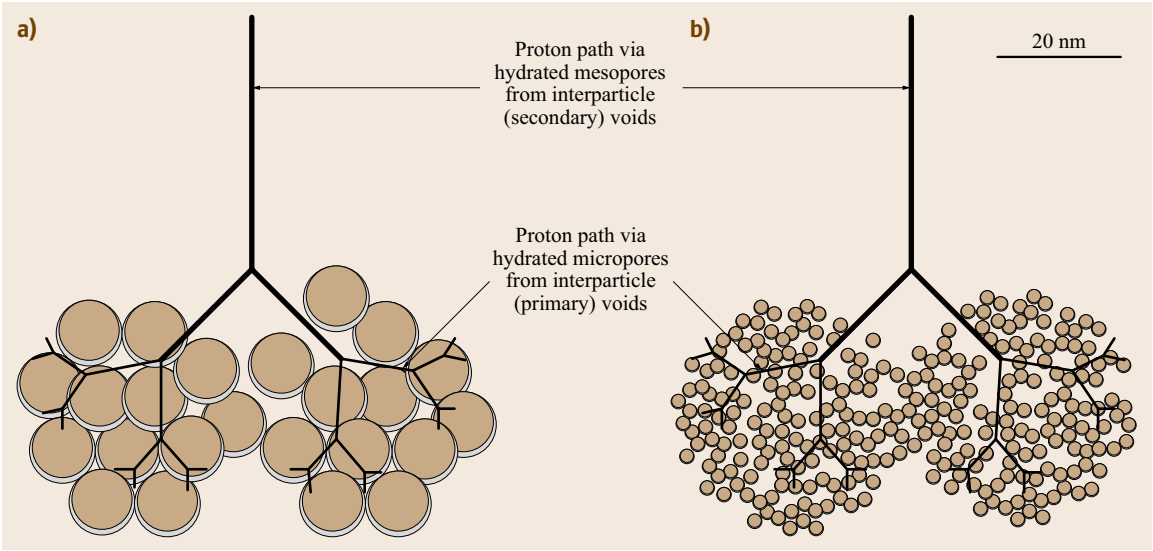


Fig. 16.25a,b A schematic of the fractal tree-root model for **(a)** anhydrous RuO_2 and **(b)** hydrous RuO_2 (after [16.276])

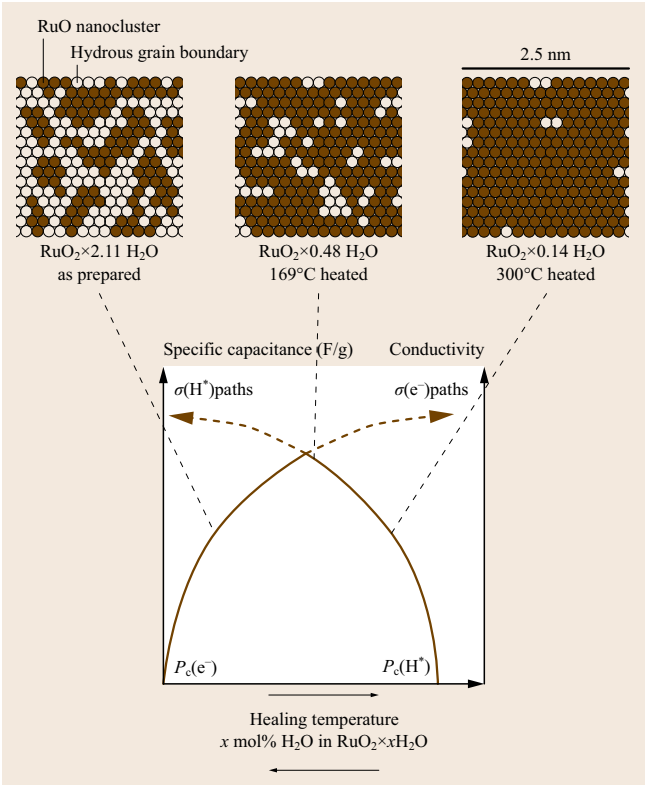


Fig. 16.26 Schematic illustration of the variation of the percolation volumes of the RuO_2 nanocrystals and the hydrous grain boundaries with changes in water content (after [16.263])

(PDF) analysis of synchroton x-ray scattering measurements on a series of hydrous RuO_2 treated at different temperatures [16.273]. Analysis of XANES and PDF analysis showed that hydrous RuO_2 is composed of disordered rutile-like RuO_2 nanocrystals dispersed by boundaries of structural water, in contrast to the apparent amorphousness measured with conventional XRD [16.263]. A parallel electron–proton conduction model, where the rutile-like RuO_2 nanocrystals support electronic conduction and structural water as the boundaries transport protons, was proposed to account for the maximum capacitance of RuO_2xH_2O at $x \approx 0.5$ (Fig. 16.26). *Fu* et al. studied the interaction between the structural water and the rutile crystals by measuring the proton dynamics of hydrous RuO_2 using solid-state proton nuclear magnetic resonance (^{1}H-NMR) spectroscopy [16.270]. A maximum in proton activation energy was observed when the hydrous RuO_2 exhibited the maximum capacitance revealing the correlation between the proton mobility and the charge storage. In addition to the relation between the maximum capacitance and water content in hydrous RuO_2, *Kim* and *Kim* derived a similar model based on electrochemical impedance spectroscopy to explain the frequency response [16.336]. It was suggested that the frequency response (power capability) was dominated by proton conduction within the hydrated micropores between the RuO_2 nanocrystallites. *Foelske* et al. reached similar conclusions based on x-ray photoelectron spectroscopy (XPS) studies [16.337]. Two types of water in hydrous RuO_2 were identified; weakly bound physically adsorbed water and strongly bound chemically bound water. The chemically bound water was correlated to the heat-treatment temperature and increase in particle size.

In-situ techniques have also been exploited to evaluate the effect of the heat-treatment temperature on the charge storage capability of ruthenium oxide. In-situ XPS and XRD data gives evidence that no bulk reduction of anhydrous RuO_2 occurs until the electrode is polarized at potentials where hydrogen evolution occurs [16.338–340]. In-situ resistivity measurements of anhydrous RuO_2 has shown that the resistivity is independent of potential within the hydrogen and oxygen evolution region, complementing the in-situ XPS and XRD data showing that bulk reduction of Ru^{4+} does not take place in the potential region relevant to EC applications [16.341]. For the case of hydrous RuO_2, Ru^{4+} reduction to Ru^{3+} below $E < 0.4\,V$ has been suggested by in-situ EXAFS and XANES [16.313, 343]. The reduction of Ru^{4+} for the case of hydrous RuO_2 leads to a prominent change in resistivity as a function of the potential, in contrast to the case of anhydrous RuO_2 [16.341]. The alteration in oxidation state is thought to be the cause of the change in the Raman spectra and photochromic behavior of the RuO_2 film [16.344–346].

16.5 Other Pseudocapacitive Materials

The power performance of manganese dioxides are limited by their low electronic conductivity. This is not the case for RuO_2. However, many other examples of pseudocapacitive materials can be found in the literature. Oxides such as V_2O_5 [16.149, 347] or Fe_3O_4 [16.149, 348] investigated in mild aqueous electrolytes also demonstrate a more or less pronounced linear relationship between the charge stored and the width of the potential window, thus, enabling to define a constant pseudocapacitance. Many other oxides or hydroxides are presented as pseudocapacitive but typically show faradaic behavior and must be considered as potential electrode for high-power battery (or even hybrid devices) [16.349, 350]. This is the case of lamellar hydroxides $Ni(OH)_2$ and $Co(OH)_2$ and their related oxides (NiO, Co_3O_4) [16.351], which do not show any of the expected properties for pseudocapacitive materials. The difference between faradaic electrode and pseudocapacitive electrode is clearly depicted in a recent paper [16.350].

Recently, metal nitrides such as Mo_xN [16.352, 353], TiN [16.354], VN [16.355], WN [16.356], and RuN [16.357] have been studied and an impressive values of specific capacity until $1340\,F/g$ were reported for VN in thin layers. Due to the metallic conductivity of these nitrides, they can be potential candidates for high power density aqueous-based devices. However, the use of symmetrical designs severely restricts the operating cell voltage and complementary electrodes must be found in order to assemble asymmetrical designs.

16.6 Electrolytes

Possible candidates for electrolyte of hybrid ECs are aqueous solutions, organic solvent solutions, ionic liquids, gel electrolytes including these three kinds of liquids, dry polymer electrolytes, and inorganic ionic conductors. From the viewpoint of the minimization of the series resistance of a capacitor cell, the latter two candidates are not the most adequate materials for this system. The selection of the electrolyte for an hybrid EC system basically depends on the selection of the positive and negative electrodes. A suitable electrolytic solution must meet all the following requirements for application in ECs; (i) high capacitance, (ii) high ionic conductivity, (iii) high solubility of electrolyte salt, (iv) low viscosity, and (v) high thermal and electrochemical stability.

16.6.1 Aqueous

Aqueous electrolytes can be used for various kinds of asymmetric capacitor systems, and in particular, they must be selected for the ones based on inorganic electrode such as ruthenium oxide and manganese oxide [16.17, 23, 24, 135, 253, 255, 358–360]. The limited working voltage of the resulting cell is a drawback of aqueous electrolyte compared with nonaqueous systems. However, for asymmetric capacitors, the working voltage is expected to increase by careful selection of electrodes. In early study of *Hong* et al., the working voltage as high as 2 V was achieved for the cell containing KCl aqueous solution electrolyte combined with activated carbon negative and manganese oxide positive electrodes [16.135].

16.6.2 Organic Solvent Solutions

For a major part of nonaqueous hybrid capacitors, a redox reaction based on reversible lithium intercalation has been utilized in either electrode [16.18, 19, 361–368]. An electrolyte containing lithium ion is required for such a capacitor system. Among them, the

electrolyte system frequently used in lithium-ion battery, $LiPF_6$ is dissolved into mixed solvent of ethylene carbonate with a certain kind of linear alkyl carbonate. $LiPF_6$-based electrolytes show excellent properties such as conductivity as high as 10^{-2} S/cm at room temperature and electrochemical stability toward both oxidation and reduction. However, being different from the case of lithium battery electrolyte, anion species participates in the charge–discharge process on positive electrode, including the formation of double-layer, for hybrid capacitor system.

In contrast, nonaqueous electrolyte containing quaternary ammonium salt, while mainly utilized for an electrical double-layer capacitor, has been less utilized for asymmetric capacitors because only few redox process can occur in this electrolyte. For the activated carbon/conductive polymer capacitor, this electrolyte appeared to be compatible and provide sufficient properties for a practical cell [16.369]. Recently asymmetric capacitor systems including the intercalation reaction of alternative cations and anions into graphitic layers have been proposed [16.365, 370–374]. For these capacitors, nonaqueous electrolyte based on quaternary ammonium salt with tetrafluoroborate or hexafluorophosphate anions have been also applicable.

Today, carbonates represented by PC are the most widely used solvent in Japan whereas AN is a popular solvent in the Unites States and in Europe. By using AN in stead of PC, one would easily achieve excellent rate performances due to triply enhanced ionic conductivity and much lower viscosity of AN compared with PC.

A low-viscosity linear carbonates of ethylmethylcarbonate (EMC) or dimethylcarbonate (DMC) can also solve such problems by mixing them with PC. The DMC was found to be a good co-solvent showing high performance caused by a high solubility of spirobipyrrolydinium tetrafluoroborate (SBP-BF_4) specifically in DMC. However, the withstanding voltage must be limited below 3.0 V in conventional AN system or such carbonate system because of the poor electrochemical stability of solvents.

Morimoto et al. developed an electrolytic solution based on the mixture of sulforane (SL) and EMC, having high withstand voltage of 3.3 V [16.376]. In Fig. 16.27, the electrolyte operable voltages are compared between two systems; PC+EMC and SL+EMC [16.375]. The SL, a ring-structured sulfone, is more tolerate to high-voltage operation than any carbonates. However, this new electrolyte system (SL and EMC mixture) needs to be further improved because the EMC is more volatile than SL and less durable to reflow soldering at elevated temperatures.

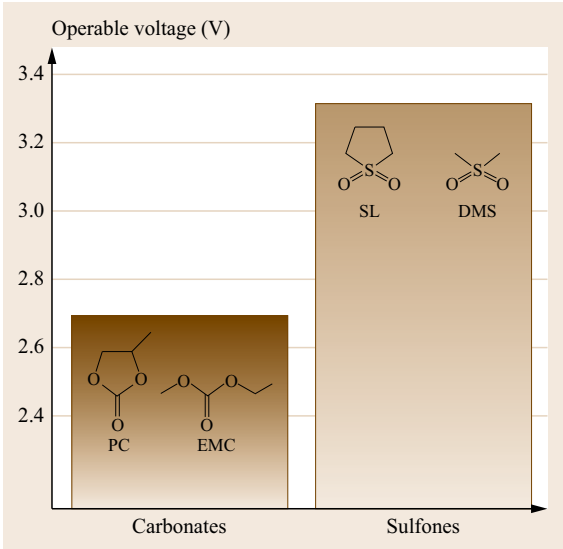


Fig. 16.27 Operable voltages for carbonates and sulfones (after [16.375])

Chiba et al. investigated linear-sulfone co-solvents with SL. One of them, dimethylsulfone (DMS), demonstrated an extremely high withstanding voltage [16.377]. Interestingly, the DMS, the smallest molecule of linear sulfone, has high enough boiling point (> 200 °C) so its durability to the reflow soldering is assured. They also developed a large-sale manufacturing of the SBP-BF_4 for a salt of conventional carbonates and new SL+DMS mixture solvent system. The SBP-BF_4 shows high ionization due to its rigid and comparatively compact size in ion radius. So, the SBP-BF_4 has large maximum solubility for solvents (> 3 M) compared to other commercialized salts like tetraethylammonium (TEA), triethylmethyl ammonium (TEMA), ethylmethylimidazolium (EMI), and diethylmethyl(2-methoxyethyl) ammonium (DEME) systems. The structure of cations and the solubility are indicated in Fig. 16.28 and Table 16.2, respectively.

16.6.3 Ionic Liquids

Ionic liquids have been attracting researchers on capacitor field, because they can be assumed as highly concentrated electrolytes with nonvolatility. The attempts to apply ionic liquids to ECs have been increasing years by years [16.91], [16.379–390]. Some kinds of ionic liquids exhibit specific features on the capacitance [16.375] and the diffusivity in the pore [16.382]. The addition of $LiBF_4$ improves the cathodic stability of ionic liquid ethylmethylimidazolium (EMI) tetrafluoroborate [16.381]. On the other hand, ionic liquids

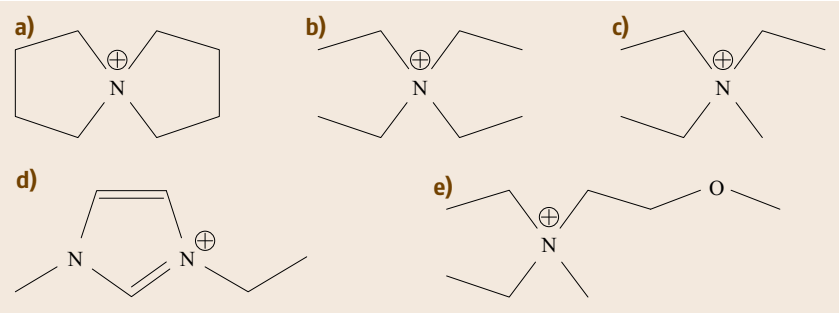


Fig. 16.28a–e Chemical structures of spirobipyrrolidinium (SBP) and other commercialized cations: **(a)** SBP, **(b)** TEA, **(c)** triethylmethylammonium (TEMA), **(d)** ethylmethylimidazolium (EMI), and **(e)** diethylmethyl-(2-methoxyethyl)-ammonium (DEME) (after [16.375])

Table 16.2 Solubility of each electrolyte salts for various solvents. (after [16.378])

Structure of cations	Solubility (mol/dm^3 at 298 K)					
	PC	DMC	EMC	DEC	EC	SL
SBP	3.6	2.1	< 0.0	< 0.1	3.4	3.7
TEMA	2.2	< 0.1	< 0.0	< 0.1	3.3	2.4
TEA	1.1	< 0.1	< 0.0	< 0.1	1.9	0.9

generally suffer from their high viscosity for practical application. Therefore, efforts have been concentrated to increase the fluidity of ionic liquid [16.377, 379, 385, 387], to combine with electrodes having an accessible space of ion, such as aligned carbon nanotube [16.91, 386], or to utilize the cell at high temperature [16.384]. A series of ionic liquid having DEME cation has been investigated for the application to capacitor electrolyte, while the ionic liquid is diluted by carbonate solvent for practical capacitors [16.380]. Asymmetric hybrid EC using pyrrolidinium ionic liquids with a porous carbon/poly(3-methylthiophene) laboratory-scale cells system has shown good energy and power performances [16.391–393].

16.6.4 Polymer and Gel Electrolytes

For most electrochemical devices, liquid electrolytes are expected to be replaced to solid ones in order to improve the reliability of the devices. Both solid polymer electrolyte and inorganic electrolyte are considered to be inadequate for the use in ECs because it is difficult to construct interface between electrolyte and porous electrode. On the other hand, there have been many studies to apply gel polymer electrolytes for ECs, even though a good contact between the electrodes and the electrolyte must be formed in view of practical application. While there have been many efforts on the utilization of gel polymer electrolyte containing conventional nonaqueous electrolytes [16.394–403] or ionic liquids [16.404, 405] for electrical double-layer capacitor, their use in asymmetric hybrid capacitors is limited. On the other hand, proton-conducting gel polymer electrolytes for ECs, both symmetric and asymmetric systems were more widely investigated.

In order to utilize the pseudocapacitance of transition metal oxide, it is necessary to apply a proton conductor as electrolyte. For Nafion, well-known gel polymer electrolyte utilized in fuel cells, attempts have been made for the application to ECs with metal oxide electrodes. Nafion electrolyte has excellent properties for capacitor systems such as good conductivity and long-term stability [16.406–412]. Various polymer gel electrolytes, mainly containing alkali solutions, have also been prepared and applied to symmetric, or asymmetric capacitor systems [16.408–412]. Furthermore, several hydrogel electrolytes containing alkali or acid solutions were also used in an hybrid capacitor [16.413–418]. When water is used as mobile phase of the polymer gel electrolyte, the resulting gel electrolyte limits the electrochemical window of the EC to a value as low as 1.2 V (or slightly higher by using certain kinds of electrodes) and the performance at low temperature as is the case for aqueous liquid electrolyte.

To increase the working voltage of the capacitor device, nonaqueous solvent must be used instead of water.

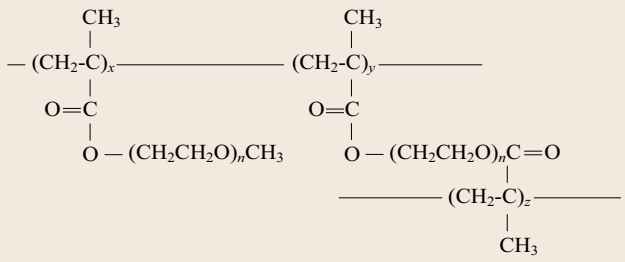


Fig. 16.29 Structural formula of PEO-PMA matrix (after [16.419])

The performance of a capacitor based on Nafion electrolytes containing the solution of H_3PO_4 in ethylene glycol was investigated and compared with those of an EC with Nafion containing water. Nafion containing H_3PO_4/ethylene glycol solution provided typical capacitor performance with a cell voltage of 1.5 V, while an EC containing aqueous Nafion electrolyte exhibited a 1.0 V cell voltage [16.420].

Gel electrolytes based on the combination of nonaqueous acid solution with various polymer matrices have been investigated for not only ECs but also fuel cell application [16.396, 422–427]. Poly(vinylidene difluoride) (PVdF) and poly(methyl methacrylate) (PMMA) have frequently been applied as polymer matrices providing gel electrolyte with good performance. Early works revealed the effect of the components of the gel containing H_3PO_4 on its properties by using both electrochemical and spectroscopic characterizations [16.424, 425]. Several attempts by using similar gel designs have been made for the purpose of the application to various devices. A series of nonaqueous proton conductors based on poly(ethylene oxide)-modified polymethacrylate are shown in Fig. 16.29 [16.419, 428–430]. When containing poly(ethylene glycol) dimethyl ether (PEGDE) plasticizer and H_3PO_4, this gel polymer electrolyte exhibits the conductivity as high as 10^{-3} S/cm at 70 °C. A symmetric double-layer capacitor cell using this gel polymer electrolyte showed the specific capacitance of porous carbon electrode as high as 200 F/g at 90 °C [16.430].

For the use in asymmetric capacitor system based on ruthenium oxide positive electrode and porous carbon negative electrode, gel electrolyte containing PVdF-based polymer matrix and CF_3SO_3H/dimethyl-

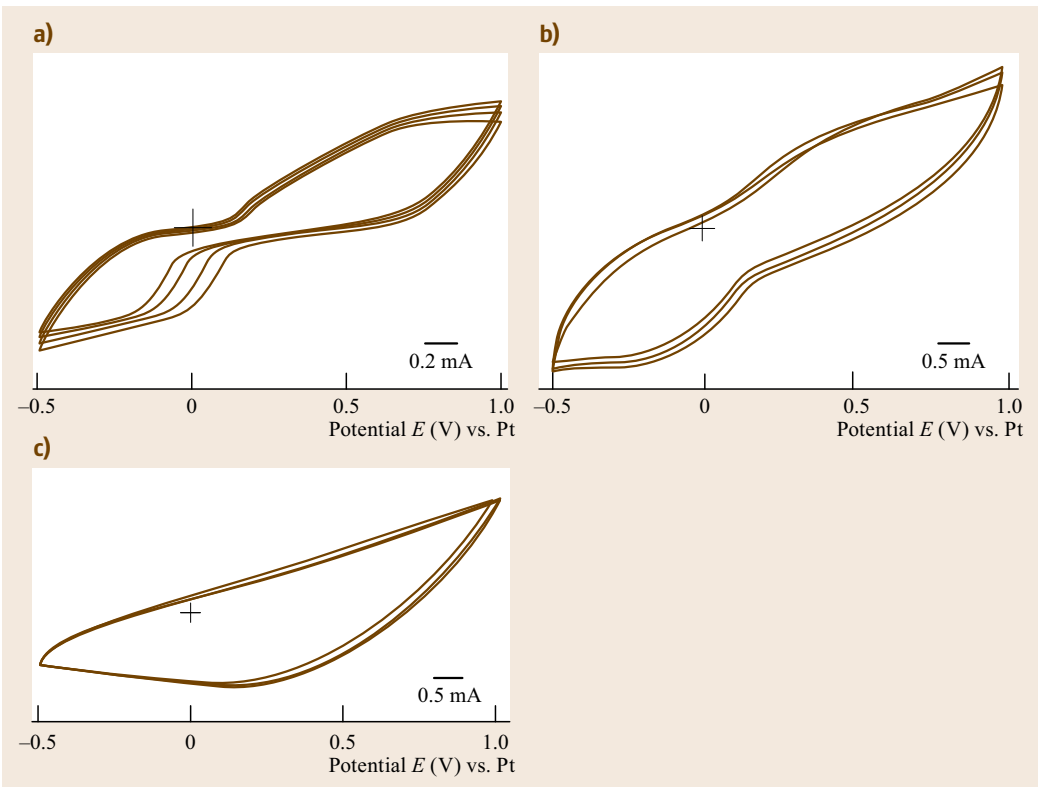


Fig. 16.30a–c Cyclic voltammograms of RuO_2xH_2O electrodes by various preparation procedure in PVdF-HFP/DMF/CH_3SO_3H gel polymer electrolyte **(a)** RuO_2xH_2O/PTFE by the *dry* procedure, **(b)** RuO_2xH_2O/PVdF by the *wet* procedure, and **(c)** RuO_2xH_2O/the gel component composite electrode (after [16.421])

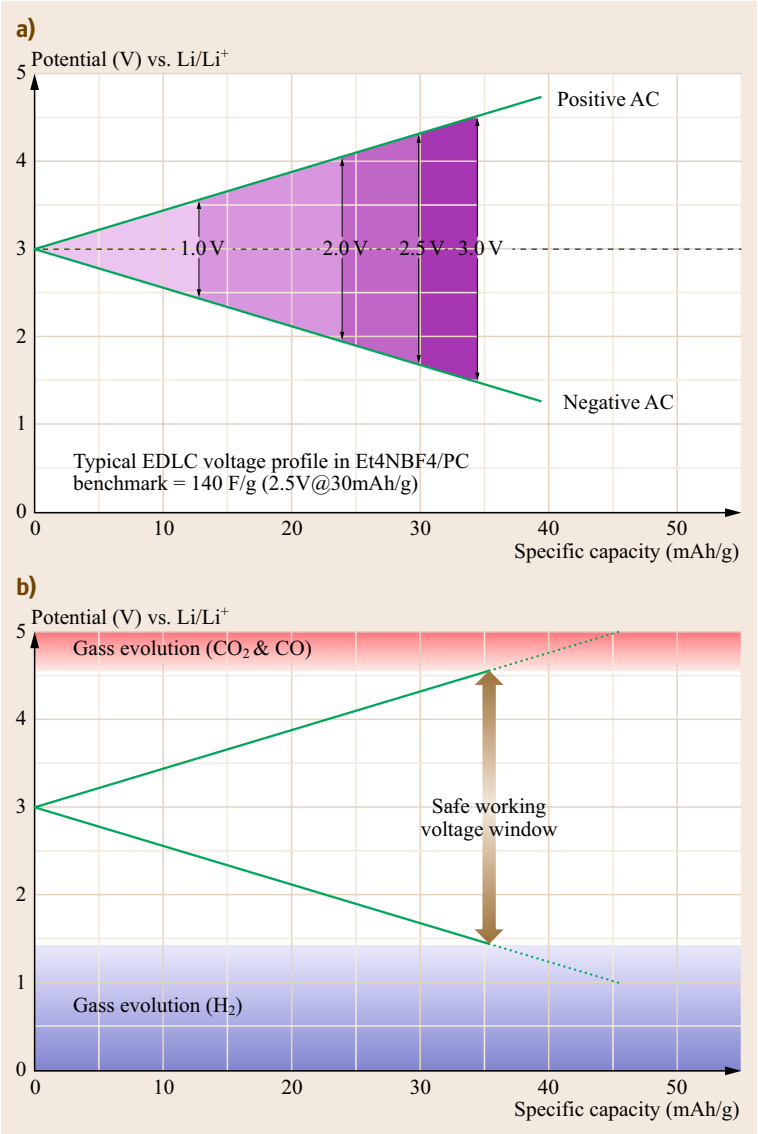


Fig. 16.31 Polarization curves and the cell voltage limit for ECs based on AC electrodes (after [16.375])

formamide (DMF) mobile phase has been proposed. DMF in mobile phase of gel electrolyte is considered to promote Grotthus-like conduction of proton. Therefore, the obtained gel electrolyte exhibits ionic conductivity as high as 6×10^{-3} S/cm at 60 °C. Furthermore, this gel electrolyte is electrochemically stable over 1.0 V, sufficient for application with ruthenium oxide [16.421].

When a gel polymer electrolyte is used in an EC, the interface between the gel electrolyte and electrodes should be designed carefully. The voltammetric behavior of two hydrous ruthenium oxide RuO_2xH_2O electrodes, prepared by different methods, in the CF_3SO_3H/DMF/PVdF gel electrolyte have been compared. The cyclic voltammogram of RuO_2xH_2O electrode made with poly(tetrafluoroethylene) (PTFE) binder by *dry* procedure is shown in Fig. 16.30a, since that of RuO_2xH_2O prepared with PVdF binder by *wet* procedure is shown in Fig. 16.30b at 60 °C. The case of the electrode composite of RuO_2xH_2O with the component of the gel electrolyte is shown in Fig. 16.30c. It is clear that the capacitive current is different by the feature of electrode/electrolyte interface, and an intimate contact between the electrode active material and the gel component provides better capacitance behavior. In an all-solid-state asymmetric capacitor cell with an activated carbon negative electrode, the RuO_2/the gel component composite positive electrode exhibits as

high as 300 F/g of the specific capacitance of RuO_2 over 100 cycles.

From above examples, electrolyte contributes largely to the availability and properties of a certain combination of electrodes. New electrolytes are needed for application in the various kinds of hybrid ECs.

16.6.5 Stability of the Electrolyte in High Voltage EC

Nonaqueous electrolytes consisting of AN or PC solutions with TEA tetrafluoroborate (Et_4NBF_4) [16.6, 431–433] are commonly used in commercial ECs because they permit wide operating voltage (2.5−2.7 V). Increasing the voltage is an effective way to increase the energy density because the energy density increases with the squared voltage (16.8). For the improvement of the voltage characteristics of ECs, it is also essential to develop higher electrochemical durability at electrode/electrolyte interface. This section will focus on phenomenon that is occurring in the electrolyte for high-voltage EC.

Currently, the maximum voltage of ECs is limited to 2.5−2.7 V due to significant decrease in capacitance and continuous increase in internal resistance at applied voltage over 2.7 V (Fig. 16.31b). In fact, the float test revealed that the EDLC cells lose its capacitance (DC $< -13\%$) at the initial stage during 30 days at 2.5 V, whereas over 2.7 V, for example, at 2.9 V the capacitance loss became more significant (DC $= -28\%$) during the same mode of life test for the same duration [16.434]. The undesired faradaic process that leads to a capacitance fade at over a certain cell voltage is the most critical factor that determines the life of ECs. More specifically, the cell voltage between 2.5 and 2.9 V would be the threshold voltage that triggers consecutive and fatal degradation of the EDLC cells.

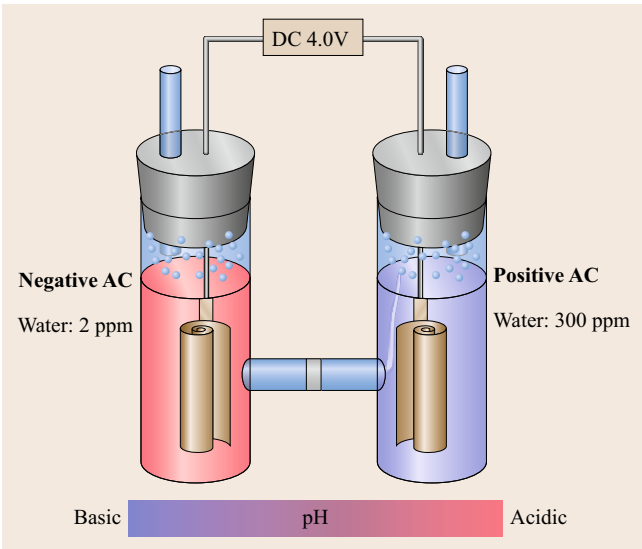


Fig. 16.32 Water released from positive and negative electrodes after 50 h of float test (after [16.375])

There have been few reports concerning such degradation mechanisms. For instance, gaseous products generated from AC electrodes (positive or negative electrode) were analyzed during cyclic voltammetric measurements of EDLC from 0 to 3.5 V in 1 M $TEABF_4$/PC (Fig. 16.31a) [16.435]. According to this report, propylene and H_2 were produced for cell voltages ranging from 2.7 to 3.5 V, and CO_2 started to be released from 2.9 V. It was speculated that propylene and H_2 were formed by reduction of PC solvents at AC negative electrode when it is polarized at 1.5 V versus Li/Li^+ and CO_2 results from the oxidation of PC at AC positive electrode over 4.3 V versus Li/Li^+. In a related study, the surface of a highly oriented pyrolytic graphite (HOPG) negative electrode in 1 M $TEABF_4$/PC as a model electrode of EDLC by careful in-situ AFM and ex-situ SEM observations [16.436]. It was found that TEA^+ insertion, leading toward swelling and exfoliation of graphenes begins at 1.2 V versus Li/Li^+. At a more negative potential of 0.9 V versus Li/Li^+, the SEI of particulate morphology formation starts on the edge planes of the HOPG. From these results [16.435, 436], it is indicated that 4.3 and 1.5 V versus Li/Li^+ are the critical potentials for the positive and the negative electrode, respectively; beyond these limits, the degradation occurs. The considerations and the proposed mechanisms are based on the hypothesis of a water-free electrode.

However, one should take residual or unremoved water in the AC electrodes into consideration. Water is certainly released from the positive and the negative AC electrodes into electrolyte after 50 h of float (Fig. 16.32), and other mechanisms are inferred on the same phenomenon. For example, the CO_2 was generated not only by the oxidation of PC, but also by its hydrolysis mechanism [16.437]. *Kurzweil* et al. [16.438] analyzed the decomposition products in the EDLC cell after aging at 70 °C or 4.0 V in 1 M $TEABF_4$/AN. They detected some derivatives of acetamides via hydrolysis of AN, ethylene, and triethylamines formed by Hoffman elimination in the presence of OH^- from residual waters. This is one of the strong evidences that support the hypothesis that AC electrodes contain much unremoved waters that plays an important role in degradation processes. However, the behavior of unremoved water in AC electrodes has not yet been clarified as a function of the applied cell voltage in PC-based electrolyte.

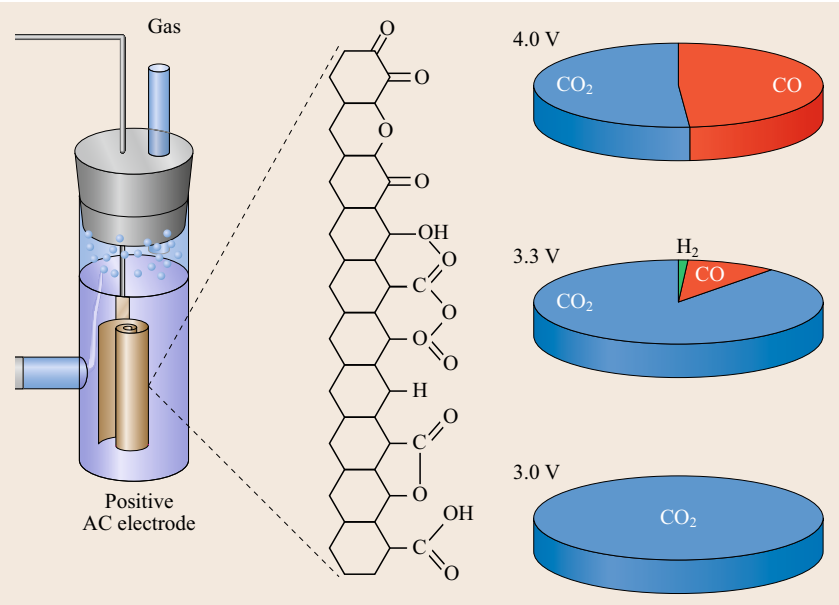


Fig. 16.33 Gases evolved from the positive electrode of ECs (after [16.375])

Using 1.0 M TEMA BF_4/PC as electrolyte, systematic investigations were made on the degradation mechanism of AC electrodes in EDLC cell [16.439]. Gas and water generation were separately characterized from AC positive and negative electrodes as a function of applied cell voltage of 2.5 up to 4.0 V. On the positive electrode, the surface functionality determines the kind of gases evolved (Fig. 16.33): easily oxidizable functional groups give CO_2 at 3.0 V, and at higher voltages above 3.3 V up to 4.0 V, there observed CO evolution. The negative electrode is different (Fig. 16.34). At 3.0 V, water is reduced to give H_2 and at the same time generates OH^- that makes an electrolyte alkaline and triggers a lot of other consecutive degradations. One of them is an alkaline-induced hydrolysis of PC, and the other is a Hoffman elimination of $TEMA^+$ both by the species of $OH^-(H_2O)$.

Also, SEI films formed on positive and negative electrodes were observed separately at the same applied voltages (Fig. 16.35). On the positive electrode, exfoliation and the cracks are observed at 3.0–3.3 V as indicated in the cross-sectional SEM micrographs. At much higher voltages, the AC electrode surface begins to be covered by polymeric products (SEI formation). Much thicker SEI layer is accumulated on the negative electrode that increases the internal resistance of the cells tremendously. The reductive decomposition of the PC solvent is particularly serious on the negative electrode when the water molecule remained in the electrolyte.

We could propose a mechanism for the degradation of the AC electrodes by taking into account the water released. Threshold degradation voltage for each positive and negative electrode could be defined on the basis of SEM observation, incremental-voltage-steps EIS analysis, and minute gases/water detection. The following crucial factors are considered at each cell voltage range (Fig. 16.36). In the cell voltage range of 2.5–3.0 V (region I), no degradation behaviors were observed in the both electrodes. The positive and the negative electrodes are electrochemically stable in the potential range below 4.9 V and over 1.9 V versus Li/Li^+, respectively. On the other hand, for cell voltage range of 3.0–3.7 V (region II), degradation products are observed. At positive electrode beyond 4.9 V versus Li/Li^+, the surface functional groups are electrochemically oxidized and released as gaseous products of CO_2 and CO. At the same time, the adsorbed waters are blasted out by releasing from the surface functional groups. At negative electrode below 1.9 V versus Li/Li^+, the adsorbed waters are slowly reduced and produce H_2 gas as well as generating equi-molar of OH^-. The generated OH^- induces Hoffman elimination of TEMA cations and activates hydrolysis of PC producing PG and CO_2 gas. The activation of PC hydrolysis could result in resistive adsorbed layers composed of organic molecules like PC or PG on the AC surfaces in region II. When the cell voltage reached values of 3.7–4.0 V (region III), PCs are electrochemically oxidized at the positive electrode over 5.2 V versus Li/Li^+ and reduced at the negative electrode below 1.5 V versus Li/Li^+. The electrochemical oxidation and reduction of PCs result in thick and highly resistive fluorinated poly-PC films on both electrodes.

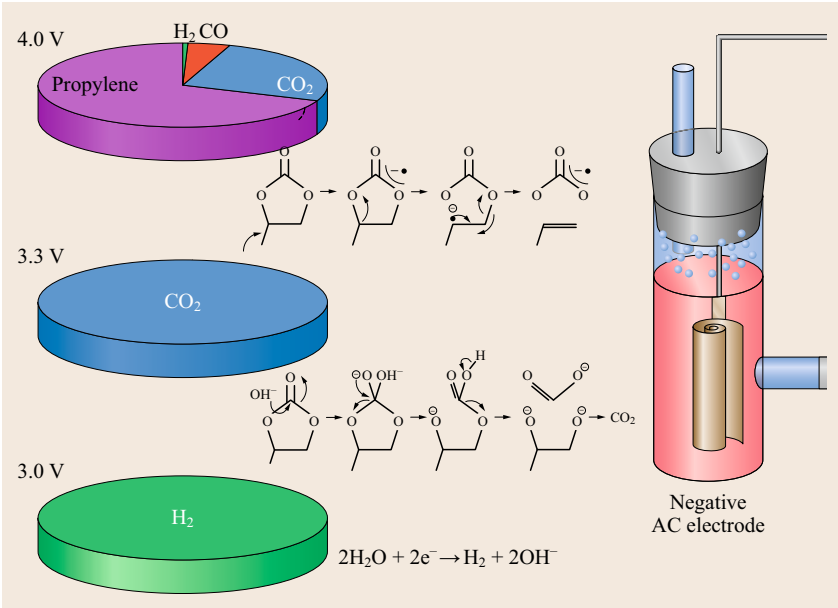


Fig. 16.34 Gases evolved from the negative electrode of ECs (after [16.375])

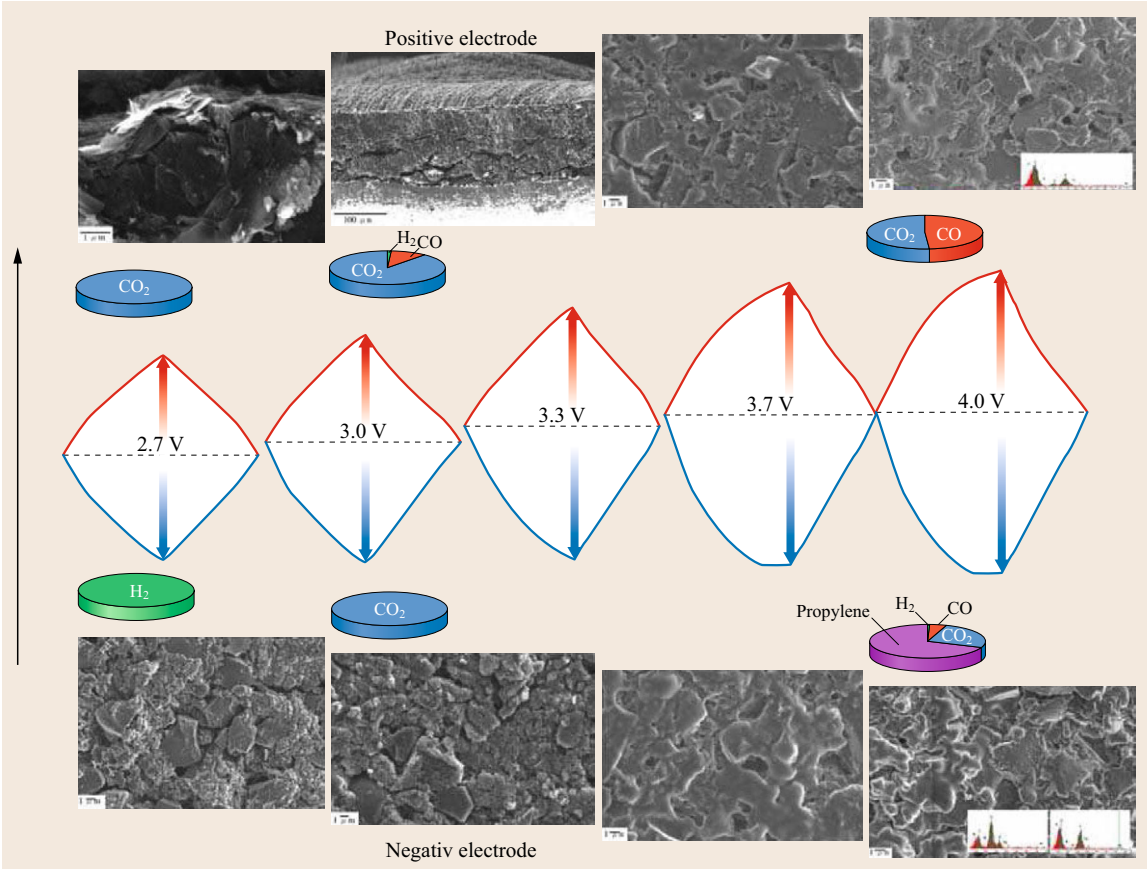


Fig. 16.35 Morphological changes of the surface of positive and negative electrodes of ECs (after [16.375])

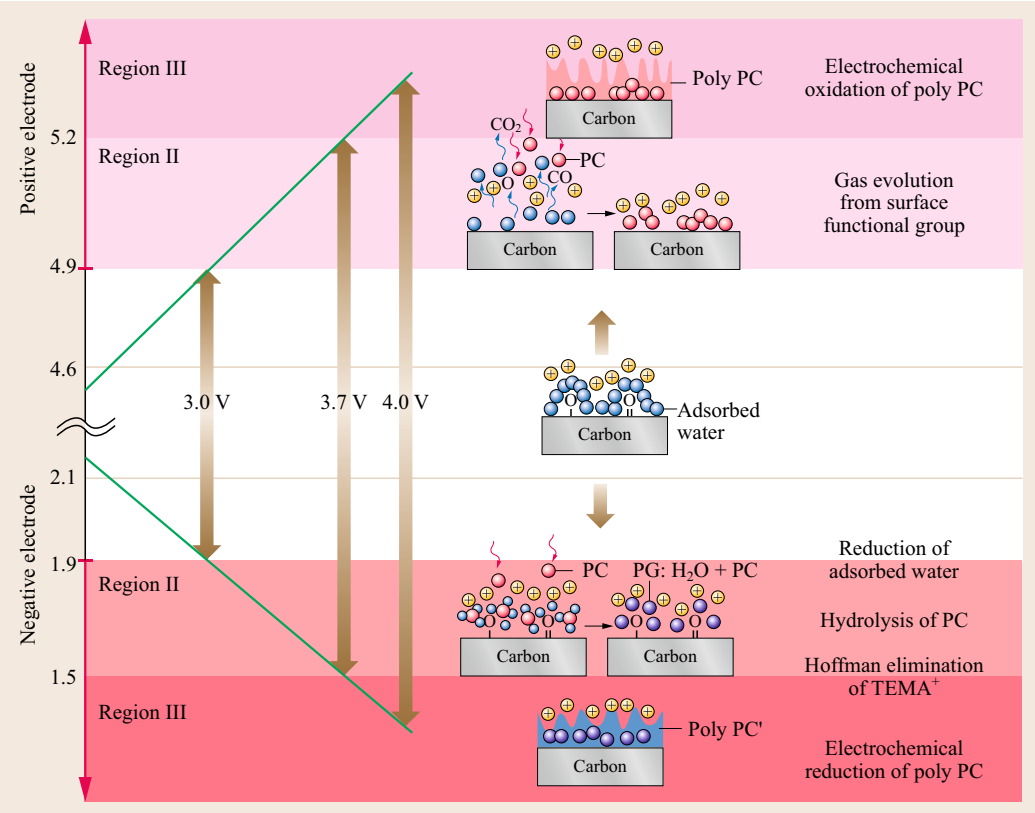


Fig. 16.36 Possible SEI models at each potential ranges of the positive and negative electrodes (after [16.439])

16.7 Applications of Electrochemical Capacitors

Following the commercial introduction of NEC's SuperCapacitor in 1978 under license from SOHIO, ECs have evolved in design. Initially they were used as sources to provide dc power for the backup of volatile clock chips and complementary metal-oxide-semiconductor (CMOS) computer memories. But many applications have emerged over the past 35 years, attributable to product enhancements and emerging applications [16.440]. Such applications include, but are not limited to, portable wireless communication, enhanced power quality for distributed power generation systems, industrial power sources like needed for wind turbine pitch control, load-leveling energy storage for electric vehicles (EVs), and high-efficiency energy storage for energy harvesting as exemplified by hybrid electric vehicles (HEVs). Many applications use ECs in combination with batteries or fuel cells, where the unique attributes of the EC technology complements the weaknesses of the other power source. With the invention of the asymmetric EC [16.441], applications have expanded even further including power for pure EVs, and bulk energy-storage systems developed for the electric utility grid.

16.7.1 Copiers

In a document copier, the fusing roll temperature must be elevated well above the room temperature to set the ink. Continuously maintaining the fusing roll at high temperature, which has been standard practice until recently, consumes a significant amount of energy. Since fusing roll heat up normally requires several minutes but the desire is to have instant copies, the roll is usually continuously maintained at high temperatures even when the copier is in standby. Now some copier models use ECs to provide the power to quickly heat-up the fusing roll before each use [16.442]. Such copiers then do not require a standby mode, since the ECs are able to provide the quick heat-up, typically less than 1 min, thereby reducing energy waste. Energy savings of 50% or greater have been reported.

16.7.2 Power Tools

Electrochemical capacitors are used in several types of portable power tools sold in US market (Fig. 16.37). The UltraCut cordless power tubing cutter produced by the Superior Tool Co. for cutting copper tubing [16.443] and the Coleman FlashCell cordless screwdriver [16.444] are two examples. In the pipe cutter, ECs are wired in parallel with the rechargeable battery to boost power performance, a configuration necessary to power the several second cutting operation. Adding a capacitor to a battery makes it possible for a substantially greater number of tubes that can be cut with each battery charge.

The electric screwdriver is sold for the home market and is unusual, in that a capacitor module is used without a battery. Here the added value with using an EC is the fast charge time. With infrequent use, portable screwdrivers are often in a state of discharge or only partial charge and the first step of any project is thus charging the screwdriver, which can take 30 min or longer with a battery. With the capacitor system, however, the screwdriver is ready in 90 s or less. The energy stored by the EC module is less than would be available with a battery but this deficit is compensated by its fast recharge time.

16.7.3 Transportation

With high oil prices and overall fuel costs difficult to ignore, hybrid vehicles have recently garnered the most attention for possible EC uses. Currently, the basic needs of hybrid automobiles have been well met by the available nickel metal hydride battery (NiMH) technology, with the Toyota Prius – over a million sold to date – being the most notable instance of its use. Even though energy capture with such batteries is perhaps only 50% efficient, this still improves mileage substantially over conventional, nonhybrid designs. Automobile improvements through the use of ECs, however, pale in comparison to those than can be realized in heavy hybrid vehicles like refuse trucks and city transit buses [16.445]. The primary reason for this is the greater amount of energy available to be captured in heavy vehicle applications; for the larger fraction of time these vehicles operate each day, and the very long life expectation held by the owner.

Hybrid Buses

City transit buses are excellent candidates for hybridization because of the large number of stop/start cycles, often with much less time than 1 min between full start and full stop. In the 1990s, there were demonstration projects of hybridized city transit busses, with the first by a group including NASA, which used PSP-Caps made by ECOND in Russia [16.446]. NASA selected ECs for the energy-storage system because of the poor performance offered by then available batteries. Another impetus to hybridize city transit buses, particularly in California, was air quality legislation. ISE Corporation developed a capacitor storage hybrid technology in response to the California Air Resources Board 2005 regulation and their buses are now in commercial service in many cities. ISE has since been selling hybrid buses having 1.5 MJ of stored EC energy [16.447, 448]. BAE Systems developed a hybrid city transit bus with EC storage for New York City, which has shown excellent performance compared with equivalents having battery storage systems [16.449]. Buses with capacitor storage systems offer the advantage of long operational life without maintenance as well as efficient charge/discharge cycling.

Heavy Hybrid Trucks

While it may sound silly to hybridize a refuse truck, in fact the drive cycle and mass of this type of vehicle make it a nearly ideal candidate for hybridization. For the hybrid refuse truck demonstration project led by Oshkosh Truck Corporation for the US Department of Energy [16.450], the energy-storage system was not

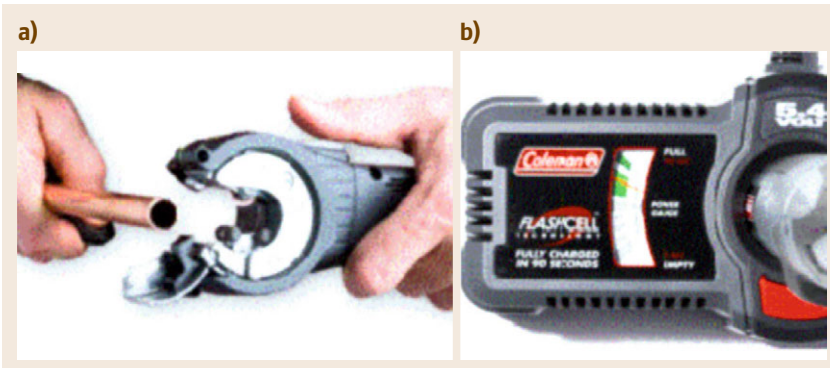


Fig. 16.37a,b Power tools incorporating ECs. The pipe cutter **(a)** uses a capacitor in parallel with a battery to increase the number of cuts possible with each charge. The screwdriver **(b)** is powered completed by energy stored in capacitors, which can be charged in 90 s or less (courtesy of Superior Tool Company and Coleman FlashCell)

specified at the start of the project. After investigation of driving and duty cycles it became clear that ECs were the best option because of their fast and efficient charge/discharge cycling characteristics and their long operational life. During the waste collection part of its route, a trash truck may do as many as two stop/start cycles per minute with a total of 800–1000 cycles per day. Generally, a full start and full stop, with a short run in between, takes 5–10 s, a time period too short for batteries to reclaim much braking energy and operate efficiently plus this number of start stop cycles is outside the range possible for a rechargeable battery system unless it is greatly oversized. The EC modules can also be discharged to 0 V for safer maintenance procedures. The Oshkosh refuse truck achieved established goals for fuel economy and provided the added advantages of lower emissions, quieter operation, and significantly lower brake maintenance.

This application strikingly demonstrates the relationship between size of the energy-storage system in the vehicle and efficiency of operation. Hybrid vehicles using batteries for energy storage must have an oversized battery system to allow only very shallow ($\approx 3\%$) depth of discharge in order to achieve the required operational life and power performance. The refuse truck developed by Oshkosh Truck Corporation weighs 60 000 lbs fully loaded and uses ≈ 2 MJ of EC energy storage. If the vehicle were to use batteries, the system would need to hold considerably more energy. Alternatively, a smaller battery system could be used and frequently replaced.

Hybrid Automobiles

In the early 1990s, ECs were evaluated for power load leveling in electric automobiles but they were never seriously considered, in part, because the USABC (Advanced Battery Consortium LLC) insisted on treating an EC as if it were a battery. Ten years later, when the industry turned toward hybrid instead of electric automobiles, the requirements for ECs in a full hybrid car, as determined for the US FreedomCar, is again that ECs must have as much energy as batteries used in this application, even though that requirement has been determined to be false in heavy hybrid vehicle applications. ECs have been used in demonstration fuel cell-powered cars. More recently the Fukukawa Ultrabattery, an EC and lead acid battery combination, was successfully used in a full hybrid electric automobile demonstration project. Since then the National Renewable Energy Laboratory (NREL) found that replacing the battery pack in a Saturn Vue hybrid with an EC module that stored much less energy provided the equivalent fuel savings and offered the same or better operating performance, even when the capacitor module used power electronics designed and optimized for battery storage [16.451].

ECs are under serious consideration for and very likely will soon be used in stop/start vehicles, a market predicted to grow dramatically, particularly in Europe [16.452]. The EC offers the distinct advantages of high cycle life with power performance that is well matched to the requirements of this application, which should eliminate engine idling during the time when the vehicle is stopped.

Other Heavy Hybrids

Oshkosh Truck offers hybrid drive technology in their heavy vehicles developed for the military. Fuel efficiency is particularly important for operations where the cost and logistics of supplying fuel to vehicles can be very demanding. The military has long been interested in hybrid technology for this reason.

There are also Class 6/Class 7 delivery truck hybrid projects underway that use EC energy-storage systems [16.445]. In addition to fuel savings, lower emissions are another driver for this market because of increased regulations related to air quality. Advantages offered by ECs are the same as for the refuse truck. These vehicles are used for local deliveries with city routes that involve short intervals between delivery stops. One of the innovators of this technology in the United States has been the Eaton Corporation, which has been working with major manufacturers of large trucks.

All-Electric Vehicles

Some of the earliest applications for ECs all-electric vehicles were in Russia with demonstration projects for city transit busses, utility vehicles, and delivery trucks [16.453]. The all-electric bus shown in Fig. 16.38 utilizes an ESMA EC system for drive power, with no internal combustion engine or batteries. This bus is part of a fleet of vehicles that operate on an approximately 10 km loop route in a Moscow park area. The bus uses an asymmetric EC system that stores 30 MJ of energy. The stored energy is sufficient for a circuit on the route and then the capacitor is recharged in 15 min. This may be the largest EC-powered electric vehicle constructed to date. ESMA was the first to power electric vehicles like these strictly using capacitors. They have also powered other all-electric vehicles using capacitors, including utility vehicles and one-ton delivery trucks.

In the United States, there have been some electric vehicle trials using ESMA capacitors. NASA powered a golf cart at one of their facilities as a way to gain experience. Their interest, of course, is in a technology that can provide more reliable operation than is



Fig. 16.38 Electric bus powered solely by an electrochemical capacitors. Range is limited to ≈ 15 km but charge time is less than 15 min, providing near continuous operation over a circular route (courtesy of ELTON Joint Stock Company)

typically available from batteries. The Electric Power Research Institute (EPRI) in the United States conducted several demonstrations with these ESMA capacitors in powering various electric vehicles, including fork lifts [16.454].

Tramway and Light Rail

The use of ECs for transportation applications is probably greater in Europe and Asia than in the United States with use of ECs in both trams and light rail systems. In these applications the interest is in kinetic energy capture upon braking to improve the efficiency of the system, or in specialized situations, where captured and stored energy cannot be effectively returned to the grid. Examples of the latter situation are where power lines are too small to effectively meet peak power demands, at remote stations where the line is too long to efficiently return captured regenerative energy, or with tramways, to allow short off-catenary excursions.

The capacitors can be located at the station where the trains stop, and this stored energy used to accelerate any train that leaves the station. Alternatively, some designs locate the capacitors on the train to permit energy recovery at every stop the train may make, regardless of location and schedule [16.455].

When a tram brakes on a standard tramway line, energy capture is not efficient unless another tram is nearby and has concurrent power draw. Bombardier has developed a system using ECs to recover braking energy and make it available at a later time for vehicle operation – essentially providing *time shifting*. Energy saving of 30% has been reported [16.456].

Siemens has described two energy storage systems, one with ECs alone and one with ECs combined with batteries, for tram applications [16.457]. In one case, the EC module is not located on-board the tram, but near the track, and works primarily to stabilize grid voltage, particularly during a tram's acceleration. The EC module is kept charged. Its energy is delivered to the network only when voltage sag reaches a critical value as might be the case when several vehicles on the same line accelerate at the same time. Thanks to the short response time of capacitor storage, energy can be delivered immediately and efficiently. The storage system is then recharged during braking events or by grid power.

16.7.4 Secondary Uses in Transportation

Except for engine cranking, other EC applications in the transportation industry could be better described as specialty applications that happen to be associated with a form of transportation. Several of this type relate to emergency power, where ECs are used because of their power performance and exceptionally high reliability.

Other applications in use, emerging, and under discussion relate to load leveling a vehicle's power buss [16.458]. With the use of more electronics having transient operation in vehicles, stored energy can be used to stabilize buss voltage. One such application has been in specialized car audio systems [16.459]. Without additional energy storage, the sound system can drain on the electrical system, particularly during play of strong bass notes, even causing headlights to dim in time to the beat of the music. Aluminum electrolytic capacitors rated at 1 F and referred to as *stiffening* capacitors were first introduced into use. Later ECs with ratings of up to 200 F were introduced for this application. While this application may seem silly, it nevertheless demonstrates the effectiveness of using ECs for electric buss load leveling.

There are now newer applications either under discussion or in demonstration that relate to the electric power buss in vehicles. They include electric power steering and active vehicle suspension, where the usual springs and shock absorbers are replaced with linear induction motors to dampen road surface irregularities and create a smoother ride for the vehicle. There have been demonstrations of such systems in Europe using ECs as the power source. Again it is the high power capability as well as the high cycle life and operating efficiency of ECs that makes them attractive in these applications.

Emergency Power

There are two notable emergency power applications for ECs. Capacitor storage technology was selected because it offers exceptional power performance, has high reliability, and provides maintenance-free opera-

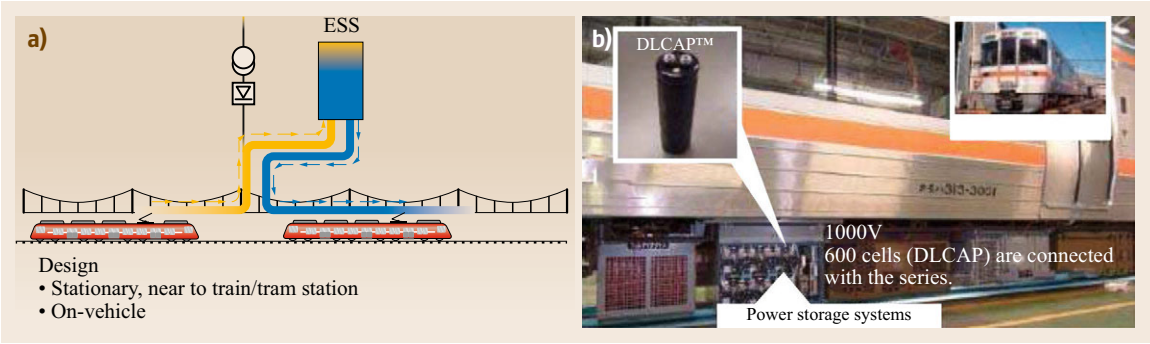


Fig. 16.39a,b Electric train with stationary capacitor energy-storage system near the station **(a)** and with capacitor storage located in the train itself **(b)** (courtesy of Nippon Chemi-Con Corporation)

tion. The first application powers the emergency door opening system of the Airbus A380 jumbo jet, where each of the 16 doors includes a capacitor module for power [16.460]. The second is in the Toyota Prius automobile with its electric brakes, where ECs are reportedly used to provide backup power for braking in the event of loss of normal electrical power.

Engine Cranking

One increasingly popular application of ECs is for engine starting [16.461–467]. Electrochemical capacitors have very high cycle life and, compared to batteries, are very powerful. The very rapid response time, on the order of 1 s, is in line with the short time period typically required for cranking an internal combustion engine. Another important attribute of ECs for this usage is their low-temperature performance, which is dramatically better than that of standard SLI lead acid batteries. Because charge is stored physically in a capacitor rather than chemically like in a battery, reaction kinetics do not impede normal operation at low temperatures. The great reduction in the cranking capability of batteries as temperature is reduced and has no counterpart in the low-temperature operation of capacitors.

Electrochemical capacitors are being used in increasing numbers to provide the cranking power needed to start diesel engines in cold weather or in the case of a depleted battery. A 50 kJ capacitor of the sort often used in this application typically has more cranking power at low temperature than four of the large Group 31 truck batteries. Another advantage is that the capacitor can usually be charged from a functionally *dead* battery and then effect a start. The ESMA asymmetric EC technology has been licensed to Saft for cranking capacitor manufacturing in the United States [16.468].

Two other reasons for growth in the engine cranking application are the high cost of fuel and because of *no idle* laws recently enacted for air quality reasons. A large diesel engine with a displacement of 10–151 consumes approximately one gallon per hour at idle, a costly proposition at high fuel prices. Even so, in the past a vehicle parked for 8 h or more would usually be allowed to idle for that period to provide power for *hotel loads* during the stop and so the driver could be assured of no restarting problem. Now such idling is no longer allowed by law in some locations. *Hotel loads* during stops can drain batteries to the point that an engine cannot be started with them. ECs, because of their great power and since they can even be charged from a nearly depleted battery, are often the most practical option to restart the vehicle.

One of the most outstanding characteristics of the asymmetric capacitor in this application is that its self-discharge rate is among the lowest of all electricity storage technologies. ESMA-developed cranking capacitors have in fact a much lower self-discharge rate than lead acid batteries. They can be charged and still, months later, have sufficient charge remaining to crank a large diesel engine. This is an important characteristic for applications that may see infrequent use, as for instance, in pleasure boats, private airplanes, and military vehicles like those at National Guard facilities. This is also important for use in safety applications that will hopefully only see infrequent use.

Lead oxide-activated carbon asymmetric ECs have been combined with lead acid batteries, sharing a common electrolyte. This Australian development at CSIRO is being commercialized under license by Furukawa Battery Company as an *UltraBattery* [16.469]. This device is claimed to offer four times higher cycle life when compared with a standard SLI ead acid battery having the same depth of discharge as well as 50% more cranking power.

16.7.5 Industrial Applications

Industrial applications broadly fall into the categories of energy harvesting or specialized applications, which

use ECs because of their high power, long life, maintenance-free operation, or other attractive characteristic. Energy harvesting involves the capture and storage of energy that would otherwise be lost during repetitive motions with stop-start, up-down, or back-and-forth motions. The stored energy is subsequently reused, which results in energy savings and ultimately lower emissions. It is much like hybridization in transportation applications where kinetic energy is captured during vehicle braking. More applications of this type are sure to be implemented as a result of higher energy costs or to reduce carbon dioxide and other emissions. The following industrial applications use EC storage systems.

Seaport Gantry Cranes

The use of ECs with rubber-tired gantry cranes allows for efficient capture of the potential energy associated with lowering a cargo container that had previously been raised. Cranes like the one shown in Fig. 16.40 are critical to the operation of many seaports around the world. Such cranes are operated by a diesel engine that powers a generator that in its turn powers electric motors to load containers onto railroad cars or truck beds, or that power another set of motors that translates the crane itself.

There have been a number of hybridization systems for these gantry cranes that make use of ECs [16.470]. Fuel savings of 40% have been documented, which translates into a substantial reduction in emissions and a corresponding increase in air quality, something highly desirable for a seaport environment with its heavy traffic. The power profile for such a crane might involve a 2 min cycle, from lowering the capture mechanism to pick up the container, lifting it, translating it across some distance, and finally lowering it onto a truck bed or railroad car. This 2 min cycle has some very high power requirements, both positive and negative. Because the operation is repetitive, response times are required that are generally much shorter than batteries can easily offer. Batteries, and flywheels as well, have in fact been used for this purpose but their response times are generally measured in minutes and thus they must be greatly oversized to meet operational requirements. In both principle and fact, efficiency is much higher when the storage media response times are considerably less than the duration of features in the application's power profile. Capacitor systems used for this application typically have ≈ 6 MJ of stored energy.

Excavating Machinery

Komatsu has created the next-generation excavator in which turret rotation has been electrified and then hybridized using EC energy storage [16.471]. The excavation cycle involves loading the bucket, lifting the bucket from the excavation ditch to some height, swinging the bucket about 90°, emptying the bucket, rotating the bucket back over the ditch, then dropping it to start another cycle. In the hybrid Komatsu excavator, bucket filling and lifting is still performed using hydraulic power but the repetitive back-and-forth rotation of the bucket has been electrified and hybridized. Fuel savings of 30–40% are reported plus the vehicle has the added benefits of lower emissions and more quiet operation.



Fig. 16.40 Rubber tired gantry crane that has been hybridized using capacitor energy storage. The repetitive-motion operation of this system makes it ideal for energy harvesting. Typical reported fuel saving is 40% (courtesy of Nippon Chemi-Con Corporation) [16.470]



Fig. 16.41 Large EC storage system used to improve power quality. This system delivers 2 MW for 1.5 s (courtesy of Nippon Chemi-Con Corporation)

Forklifts

Electric forklifts represent another industrial application where capacitors are now being used. Some of these forklifts are powered by fuel cells, with capaci-

tors delivering the peak power needed during lifting or vehicle acceleration and absorbing power during lowering or vehicle deceleration [16.472]. Today's capacitors are economically viable in this application because they cost much less than fuel cells. The route to a solution in such situations is usually the choice of using the least expensive fuel cell that provides only the average power required, with capacitors used to provide power levels above that average value and to capture regenerative energy available during load lowering or stopping. Further savings reported are for reducing labor costs associated with changing battery packs that need charging, reducing equipment costs associated with purchasing extra sets of battery packs to provide 24 h operation, and eliminating construction costs for special battery-charging rooms designed to safely vent the gas that may be generated during lead acid battery charging.

16.7.6 Stationary Applications for Power and Power Quality

Uninterruptible Power Supply (UPS) Systems

Another set of emerging applications that involve large-size ECs is related to power quality. Capacitors have the important characteristic of graceful aging. As they grow older, they lose some of their power performance and quantity of stored energy, but very seldom do they fail catastrophically such that they were working yesterday but not today. Their failure behavior is very predictable, and on basis of this reliable energy-storage systems can be created to bridge utility grid power interruptions. There are a number of large storage systems in Japan designed to provide megawatt levels of power for several seconds, like shown in Fig. 16.41 [16.473]. These are found in locations where the economics of losing power for even a fraction of a second would occasion financial losses of great size, as in highly automated manufacturing facilities [16.470].

A bank of ECs can provide limited but extremely reliable power for a time up to several seconds, depending on design. Glitches in the utility grid that have shorter duration can then be powered by the capacitor. Longer duration interruptions are typically handled first by a battery system, then by stored chemical energy (fuel) that is used to power an engine–generator system.

Bulk Energy Storage

There is another new application under development that involves storing electricity in bulk in capacitors [16.474]. This involves storage at night when there is excess generation capability for use the next day when power demand peaks. Day/night energy storage has been used at hundreds of sites around the world in the form of pumped hydro storage. Every night water is pumped uphill into a reservoir from which it can be released the next day to generate electricity. Cycle efficiency generally is 75% or greater. Compressing air inside underground caverns is another approach presently in use. The major difficulty with both of these physical energy storage approaches is that they are completely site specific, requiring a mountain in one case and a cavern in the other. Neither of these may, of course, be available in the middle of a major city. It would, however, be entirely possible to have banks of capacitors in the basement of buildings that could store energy at night to be made available for use in that same building the next day. The plausibility of using capacitors in this way would depend, of course, on the economics of the situation.

Capacitors most suited for such applications would be, of course, the ones with the lowest cost per unit of delivered energy per cycle. Asymmetric ECs having lead oxide/sulfuric acid/activated carbon designs have been most pointedly considered for this purpose [16.475]. Such devices may have limited cycle life, but if they provide as little as 5000 cycles, this still offers at least 13 years of use on the basis of one cycle per day. Since this is a stationary application, once it is settled no further considerations arise about the presence of lead in the system or even of weight. Such asymmetric aqueous electrolyte ECs, reported to have 15–20 Wh/kg storage capability for this particular application, have been under development for the past several years.

16.8 Electrochemical Capacitor Prospective View

There is no denying the reality of global warming. It is clearly evident that negative effects are a direct result of our ever-increasing use of fossil energy without regard for effects to our planet. Although by itself insufficient to halt global warming, one of the most responsible actions we can take is to increase the efficiency of applications that consume major quantities of fossil-fuel-derived energy. The great practicality of improving energy efficiency is easy to see, in that it is often simple to implement, can be widely applied, and is reliably projected to produce significant positive results. Well-known examples include adding thermal insulation to buildings, changing interior lighting from incandescent to fluorescent technology, and increasing

the gas mileage of automobiles. Through such means we can reduce energy waste and temper its dire consequences.

Nonstationary machinery, including vehicles like automobiles, buses, trucks, and trains, as well as industrial equipment like cranes, fork-lifts, and elevators, show great potential for energy efficiency improvement. The key component in energy efficiency improvement is highly reversible energy storage that permits the transformation of kinetic energy to potential energy for reuse as kinetic energy. Hybrid gas–electric vehicle technology, where kinetic energy from braking action is stored for reuse a short time later in acceleration, exemplifies this process.

Electrochemical capacitor technology is well suited for such important energy conservation applications. It offers excellent cycle life, exceptional power performance, and long operational life even in harsh environments. In many of these *energy harvesting* applications electrical storage in a capacitor is far superior to the chemical storage in a battery. The reason is that capacitors can store energy much more efficiently than a battery during the few seconds available for storage system charging. Battery technology has seen great advances in recent years relative to discharge power density but the important property in this application is different, charging efficiency at high-power levels. Nevertheless, battery systems are being used today in such energy conservation applications. But to have value they must be greatly oversized to offer acceptable efficiency and to provide useful cycle life. Use of an oversized battery system means that its effective charge time is extended, which increases efficiency, and that its depth of discharge is reduced, which adds cycle life. A capacitor system, on the other hand, is typically sized to match the energy available for capture since it can be efficiently charged in seconds and does not suffer limitations in cycle life. This means a capacitor storage system is often smaller in size and lower in mass than a battery system offering comparable performance. Thus, EC technology is technically able to lock up much of the market associated with efficiency improvements in nonstationary machinery. Energy conservation by itself is insufficient to alleviate global warming. There is a strong need to increase transmission efficiency of present fossil fuel power generators plus greatly increase reliance on renewable energy sources, solar, and wind. The positive effects of introducing affordable, readily available, easily implemented bulk energy storage is clear in terms of electrical system efficiency. Bulk storage can reduce utility grid transmission losses, which are proportional to the current squared. During the off-peak period at night, current may be a small fraction of what it is during the day. Thus, night time losses may be only a small percentage of those during the day. Filling energy-storage systems at night, when both power demand and losses are much lower, substantially reduces overall grid losses that we otherwise simply tolerate. Energy stored at night would also reduce the need for the peaking generators that the utility industry now uses to meet periodic high power levels. Generation by these is often much less efficient than normal base load generation. Stored energy would reduce the operating time for peaking generators thereby reducing greenhouse emissions while improving grid reliability.

Bulk energy storage will increase the value of renewable energy, which can then be delivered in times quite separate from generation, enhancing the attractiveness and reliability of these as grid power sources. It can also make renewable energy economically viable over a broader geographical area. With wind generation, some locations that are considered unsuitable because the average wind speed is not consistent enough for practical use could benefit from stored energy. Having large amounts of energy-storage capacity available on the grid could substitute storage for generation so existing power plants could be operated at higher capacity, a more optimum condition for both increased efficiency and reduced emissions.

Today's lead acid batteries cost approximately \$0.30/kWh/cycle and are too expensive to gain widespread use in the bulk energy-storage application. Asymmetric ECs presently under development for this bulk energy-storage market are projected to have costs that are three times lower than these batteries. This comes about mainly from providing 10 times higher cycle life. Attractive features for capacitor versus alternate storage technology is that capacitors require no maintenance, have high reliability, are scalable in size, and can be located almost anywhere including in the basements of high-rise office buildings. Although pumped hydro and compressed air storage do arguably operate at lower cost, each is bound to geological features that restrict location. Except for these two examples, the asymmetric EC technology under development appears to offer the lowest energy-storage costs per cycle over a 20 year time of alternative bulk energy-storage technologies.

In recent years capacitor products have evolved to the point where they now satisfy the performance requirements of some of the largest volume applications. More importantly perhaps for practical reasons, continuing efforts at cost reduction are succeeding in driving down the costs of capacitors to levels commensurate with the economics of the applications they are being used in.

The growing challenge to technology developers in the most immediate present is to create capacitor modules and systems that meet the very specific operational requirements of individual applications. Earlier issues like cell performance, durability, cost, and even availability are increasingly being replaced by concerns about thermal management, system reliability, and product safety. In short, technology issues are simply evolving from component engineering to system and reliability engineering, a normal route for any component once it has achieved technical acceptance. Capacitor costs will continue to decline naturally as markets expand and the technology matures. And capacitor performance characteristics will improve continually with research and development efforts that will have grown in step with the technology's demonstrated industrial significance.

A number of important tasks lie on the road to widespread and common EC technology use, particularly the development of configuration architectures that best exploits each and every component in a system to achieve optimal performance. Then this technology can fulfill its natural calling of helping to solve energy inefficiency problems, supplying bulk energy storage for the electrical power grid, offering energy storage to distributed wind and solar generation systems, and providing exceptional solutions to a broad range of emerging applications. The future looks bright for EC technology.

Acknowledgments. This chapter originates from discussion with Dan Scherson, Editor of the *Journal of the Electrochemical Society*, and from the recent Special Issue of JES on Electrochemical Capacitors. It results from a team effort where active researchers in the field have reviewed a specific area. Each section was written by at least a pair of researchers with input from other co-authors. The major contributors for each section are given in parentheses; carbon (Long and Simon), manganese dioxide (Brousse, Bélanger, and Long), ruthenium dioxide (Naoi and Sugimoto), other pseudocapacitive materials (Brousse and Favier), electrolytes (Chiba, Egashira, Morita, and Naoi), applications (Miller and Simon), and prospective views (Miller and Simon). Brousse, Miller, Naoi and Simon would like to acknowledge Global Innovation Research Organization, Tokyo University of Agriculture & Technology, Japan. Finally, we would like to thank Dr. Tarik Bordjiba, Dr. François Moser, Dr. Etsuro Iwama and Dr. Kazuaki Kisu for their help for the final preparation of the manuscript.

References

16.1 EIA: *International Energy Outlook* (Energy Information Admin. DOE, Washington 2009) http://www.eia.doe.gov/oiaf/ieo/index.html

16.2 IEA: *Transport, Energy and CO_2 – Moving Towards Sustainability* (International Energy Agency, Paris 2009)

16.3 M. Winter, R.J. Brodd: What are batteries, fuel cells, and supercapacitors?, Chem. Rev. **104**, 4245 (2004)

16.4 B.E. Conway: *Electrochemical Supercapacitors Scientific Fundamentals and Technological Applications* (Kluwer Academic, Dordrecht 1999)

16.5 B.E. Conway: Transition from "supercapacitor" to "battery" behavior in electrochemical energy storage, J. Electrochem. Soc. **138**, 1539–1548 (1991)

16.6 A. Burke: Ultracapacitors: Why, how, and where is the technology, J. Power Sources **91**, 37 (2000)

16.7 R. Kötz, M. Carlen: Principles and applications of electrochemical capacitors, Electrochim. Acta **45**, 2483 (2000)

16.8 E. Frackowiak: Carbon materials for supercapacitor application, Phys. Chem. Chem. Phys. **9**, 1774 (2007)

16.9 J.W. Long (Ed.): Electrochemical Capacitors, Electrochem. Soc. Interf. **17**, 31–57 (2008)

16.10 P. Simon, Y. Gogotsi: Materials for electrochemical capacitors, Nature Mater **7**, 845 (2008)

16.11 P.L. Taberna, P. Simon, J.F. Fauvarque: Electrochemical characteristics and impedance spectroscopy studies of carbon-carbon supercapacitors, J. Electrochem. Soc. **150**, A292 (2003)

16.12 R. De Levie: On porous electrodes in electrolyte solutions: I. Capacitance effects, Electrochim. Acta **8**, 751 (1963)

16.13 M.A.T. Keddam, F.M. Delnick, D. Ingerssol, X. Andrieu, K. Naoi (Eds.): *Electrochemical Capacitors II*, Electrochem. Soc., Vol. PV96-25 (ECS, Pennington 1996) p. 220

16.14 J.R. Miller: Pulse power performance of electrochemical capacitors: Technical status of present commercial devices, Proc. 8th Int. Semin. Double-Layer Capacitor Similar Energy Storage Devices, Deerfield Beach (1998)

16.15 J.R. Miller, A.F. Burke: Electrochemical capacitors: Challenges and opportunities for real-world applications, Electrochem. Soc. Interf. **17**, 53 (2008)

16.16 D. Bélanger: Polythiophenes as active electrode materials for electrochemical capacitors. In: *Handbook of Thiophene-Based Materials*, ed. by I.F. Perepichka, D. Perepichka (Wiley, New York 2009) pp. 577–594

16.17 T. Brousse, D. Bélanger: A hybrid Fe_3O_4-MnO_2 capacitor in mild aqueous electrolyte, Electrochem. Solid-State Lett. **6**, A244 (2003)

16.18 G.G. Amatucci, F. Badway, A. Du Pasquier, T. Zheng: An asymmetric hybrid nonaqueous energy storage cell, J. Electrochem. Soc. **148**, A930 (2001)

16.19 A. Du Pasquier, A. Laforgue, P. Simon, G.G. Amatucci, J.-F. Fauvarque: A nonaqueous asymmetric hybrid $Li_4Ti_5O_{12}$/poly(fluorophenylthiophene) energy storage device, J. Electrochem. Soc. **149**, A302 (2002)

16.20 H. Li, L. Cheng, Y. Xia: A hybrid electrochemical supercapacitor based on a 5V Li-ion battery cathode and active carbon, Electrochem. Solid-State Lett. **8**, A433 (2005)

16.21 T. Aida, K. Yamada, M. Morita: An advanced hybrid electrochemical capacitor that uses a wide potential range at the positive electrode, Electrochem. Solid-State Lett. **9**, A534 (2006)

16.22 E. Frackowiak, F. Béguin: Carbon materials for the electrochemical storage of energy in capacitors, Carbon **39**, 937 (2001)

16.23 T. Brousse, P.-L. Taberna, O. Crosnier, R. Dugas, P. Guillemet, Y. Scudeller, Y. Zhou, F. Favier, D. Bélanger, P. Simon: Long-term cycling behavior of asymmetric activated carbon/MnO_2 aqueous electrochemical supercapacitor, J. Power Sources **173**, 633 (2007)

16.24 T. Brousse, M. Toupin, D. Bélanger: A hybrid activated carbon-manganese dioxide capacitor using a mild aqueous electrolyte, J. Electrochem. Soc. **151**, A614 (2004)

16.25 D. Villers, D. Jobin, C. Soucy, D. Cossement, R. Chahine, L. Breau, D. Bélanger: The influence of the range of electroactivity and capacitance of conducting polymers on the performance of carbon conducting polymer hybrid supercapacitor, J. Electrochem. Soc. **150**, A747 (2003)

16.26 W.H. Jin, G.T. Cao, J.Y. Sun: Hybrid supercapacitor based on MnO_2 and columned Fe00H using Li_2S04 electrolyte solution, J. Power Sources **175**, 686 (2008)

16.27 J.Y. Luo, J.L. Liu, P. He, Y.Y. Xia: A novel $LiTi_2(P0_4)_3/MnO_2$ hybrid supercapacitor in lithium sulfate aqueous electrolyte, Electrochim. Acta **53**, 8128 (2008)

16.28 J. Li, X. Wang, Q. Huang, S. Gamboa, P.J. Sebastian: A new type of $MnO_2 \cdot xH_2O$/CRF composite electrode for supercapacitors, J. Power Sources **160**, 1501 (2006)

16.29 Y. Wang, G. Cao: Developments in nanostructured cathode materials for high-performance lithium-ion batteries, Adv. Mater. **20**, 2251 (2008)

16.30 P.G. Bruce, B. Scrosati, J.-M. Tarascon: Nanomaterials for rechargeable lithium batteries, Angew. Chem. Int. Ed. **47**, 2930 (2007)

16.31 M.G. Kim, J. Cho: Reversible and high-capacity nanostructured electrode materials for Li-ion batteries, Adv. Funct. Mater. **19**, 1497–1514 (2009)

16.32 A.G. Pandolfo, A.F. Hollenkamp: Carbon properties and their role in supercapacitors, J. Power Sources **157**, 11 (2006)

16.33 B.T. Hsieh, H. Teng: Influence of oxygen treatment on electric double-layer capacitance of activated carbon fabrics, Carbon **40**, 667 (2002)

16.34 T. Morimoto, K. Hiratsuka, Y. Sanada, K. Kurihara: Electric double-layer capacitor using organic electrolyte, J. Power Sources **60**, 239 (1996)

16.35 A. Yoshida, I. Tanahashi, A. Nishino: Effect of concentration of surface acidic functional groups on electric double-layer properties of activated carbon fibers, Carbon **28**, 611 (1990)

16.36 G. Lota, B. Grzyb, H. Machnikowska, J. Machnikowski, E. Frackowiak: Effect of nitrogen in carbon electrode on the supercapacitor performance, Chem. Phys. Lett. **404**, 53 (2005)

16.37 D.W. Wang, F. Li, Z.G. Chen, G.Q. Lu, H.M. Cheng: Synthesis and electrochemical property of boron-doped mesoporous carbon in supercapacitor, Chem. Mater. **20**, 7195 (2008)

16.38 O. Barbieri, M. Hahn, A. Herzog, R. Kötz: Capacitance limits of high surface area activated carbons for double layer capacitors, Carbon **43**, 1303 (2005)

16.39 J. Gamby, P.L. Taberna, P. Simon, J.F. Fauvarque, M. Chesneau: Studies and characterizations of various activated carbons used for carbon/carbon supercapacitors, J. Power Sources **101**, 109 (2001)

16.40 H. Shi: Activated carbons and double layer capacitance, Electrochim. Acta **41**, 1633 (1995)

16.41 R. Lin, P.L. Taberna, J. Chmiola, D. Guay, Y. Gogotsi, P. Simon: Microelectrode study of pore size, ion size, and solvent effects on the charge/discharge behavior of microporous carbons for electrical double-layer capacitors, J. Electrochem. Soc. **156**, A7 (2009)

16.42 S.A. Al-Muhtaseb, J.A. Ritter: Preparation and properties of resorcinolâ formaldehyde organic and carbon gels, Adv. Mater. **15**, 101 (2003)

16.43 N. Job, A. Thery, R. Pirard, J. Marien, L. Kocon, J.N. Rouzaud, F. Béguin, J.P. Pirard: Carbon aerogels, cryogels and xerogels: Influence of the drying method on the textural properties of porous carbon materials, Carbon **43**, 2481 (2005)

16.44 R.W. Pekala, D.W. Schaefer: Structure of organic aerogels. 1. Morphology and scaling, Macromolecules **26**, 5487 (1993)

16.45 S.T. Mayer, R.W. Pekala, J.L. Kaschmitter: The aerocapacitor: An electrochemical double-layer energy-storage device, J. Electrochem. Soc. **140**, 446 (1993)

16.46 R.W. Pekala, J.C. Farmer, C.T. Alviso, T.D. Tran, S.T. Mayer, J.M. Miller, B. Dunn: Carbon aerogels for electrochemical applications, J. Non-Cryst. Solids **225**, 74 (1998)

16.47 R. Saliger, V. Bock, R. Petricevic, T. Tillotson, S. Geis, J. Fricke: Carbon aerogels from dilute catalysis of resorcinol with formaldehyde, J. Non-Cryst. Solids **221**, 144 (1997)

16.48 R. Saliger, U. Fischer, C. Herta, J. Fricke: High surface area carbon aerogels for supercapacitors, J. Non-Cryst. Solids **225**, 81 (1998)

16.49 J. Li, X.Y. Wang, Y. Wang, Q.H. Huang, C.L. Dai, S. Gamboa, P.J. Sebastian: Structure and electro-

chemical properties of carbon aerogels synthesized at ambient temperatures as supercapacitors, J. Non-Cryst. Solids **354**, 19 (2008)
16.50 T.F. Baumann, M.A. Worsley, T.Y.J. Han, J.H. Satcher: High surface area carbon aerogel monoliths with hierarchical porosity, J. Non-Cryst. Solids **354**, 3513 (2008)
16.51 B.B. Garcia, A.M. Feaver, Q.F. Zhang, R.D. Champion, G.Z. Cao, T.T. Fister, K.P. Nagle, G.T. Seidler: Effect of pore morphology on the electrochemical properties of electric double layer carbon cryogel supercapacitors, J. Appl. Phys. **104**, 014305 (2008)
16.52 K.L. Yang, S. Yiacoumi, C. Tsouris: Electrosorption capacitance of nanostructured carbon aerogel obtained by cyclic voltammetry, J. Electroanalyt. Chem. **540**, 159 (2003)
16.53 B.Z. Fang, L. Binder: A modified activated carbon aerogel for high-energy storage in electric double layer capacitors, J. Power Sources **163**, 616 (2006)
16.54 T. Bordjiba, M. Mohamedi, L.H. Dao: New class of carbon-nanotube aerogel electrodes for electrochemical power sources, Adv. Mater. **20**, 815 (2008)
16.55 H. Pröbstle, C. Schmitt, J. Fricke: Button cell supercapacitors with monolithic carbon aerogels, J. Power Sources **105**, 189 (2002)
16.56 H. Pröbstle, M. Wiener, J. Fricke: Carbon aerogels for electrochemical double layer capacitors, J. Porous Mater. **10**, 213 (2003)
16.57 C. Schmitt, H. Pröbstle, J. Fricke: Carbon cloth-reinforced and activated aerogel films for supercapacitors, J. Non-Cryst. Solids **285**, 277 (2001)
16.58 J.W. Long, D.R. Rolison: Architectural design, interior decoration, and three-dimensional plumbing en route to multifunctional nanoarchitectures, Acc. Chem. Res. **40**, 854 (2007)
16.59 D.R. Rolison, R.W. Long, J.C. Lytle, A.E. Fischer, C.P. Rhodes, T.M. McEvoy, M.E. Bourga, A.M. Lubers: Multifunctional 3D nanoarchitectures for energy storage and conversion, Chem. Soc. Rev. **38**, 226 (2009)
16.60 J.W. Long, B.M. Dening, T.M. McEvoy, D.R. Rolison: Carbon aerogels with ultrathin, electroactive poly(o-methoxyaniline) coatings for high-performance electrochemical capacitors, J. Non-Cryst. Solids **350**, 97 (2004)
16.61 H. Talbi, P.E. Just, L.H. Dao: Electropolymerization of aniline on carbonized polyacrylonitrile aerogel electrodes: Applications for supercapacitors, J. Appl. Electrochem. **33**, 465 (2003)
16.62 A.E. Fischer, K.A. Pettigrew, D.R. Rolison, R.M. Stroud, J.W. Long: Incorporation of homogeneous, nanoscale MnO_2 within ultraporous carbon structures via self-limiting electroless deposition: Implications for electrochemical capacitors, Nano Lett. **7**, 281 (2007)
16.63 A.E. Fischer, M.P. Saunders, K.A. Pettigrew, D.R. Rolison, J.W. Long: Electroless deposition of nanoscale MnO_2 on ultraporous carbon nanoarchitectures: Correlation of evolving pore-solid structure and electrochemical performance, J. Electrochem. Soc. **155**, A246 (2008)
16.64 J.M. Miller, B. Dunn, T.D. Tran, R.W. Pekala: Deposition of ruthenium nanoparticles on carbon aerogels for high energy density supercapacitor electrodes, J. Electrochem. Soc. **144**, L309 (1997)
16.65 A.B. Fuertes, G. Lota, T.A. Centeno, E. Frackowiak: Templated mesoporous carbons for supercapacitor application, Electrochim. Acta **50**, 2799 (2005)
16.66 C. Vix-Guterl, S. Saadallah, K. Jurewicz, E. Frackowiak, M. Reda, J. Parmentier, J. Patarin, F. Béguin: Supercapacitor electrodes from new ordered porous carbon materials obtained by a templating procedure, Mater. Sci. Eng. B **108**, 148 (2004)
16.67 A.B. Fuertes: Template synthesis of mesoporous carbons with a controlled particle size, J. Mater. Chem. **13**, 3085 (2003)
16.68 T.A. Centeno, M. Sevilla, A.B. Fuertes, F. Stoeckli: On the electrical double-layer capacitance of mesoporous templated carbons, Carbon **43**, 3012 (2005)
16.69 K. Jurewicz, C. Vix-Guterl, E. Frackowiak, S. Saadallah, A. Reda, J. Parmentier, J. Patarin, F. Béguin: Capacitance properties of ordered porous carbon materials prepared by a templating procedure, J. Phys. Chem. Solids **65**, 287 (2004)
16.70 H. Zhou, S. Zhu, M. Hibino, I. Honma: Electrochemical capacitance of self-ordered mesoporous carbon, J. Power Sources **122**, 219 (2003)
16.71 M. Sevilla, S. Alvarez, T.A. Centeno, A.B. Fuertes, F. Stoeckli: Performance of templated mesoporous carbons in supercapacitors, Electrochim. Acta **52**, 3207 (2007)
16.72 J. Chmiola, G. Yushin, R. Dash, Y. Gogotsi: Effect of pore size and surface area of carbide derived carbons on specific capacitance, J. Power Sources **158**, 765 (2006)
16.73 G. Salitra, A. Soffer, L. Eliad, Y. Cohen, D. Aurback: Carbon electrodes for double-layer capacitors. I. relations between ion and pore dimensions, J. Electrochem. Soc. **147**, 2486 (2000)
16.74 C. Vix-Guterl, E. Frackowiak, K. Jurewicz, M. Friebe, J. Parmentier, F. Béguin: Electrochemical energy storage in ordered porous carbon materials, Carbon **43**, 1293 (2005)
16.75 J. Chmiola, G. Yushin, Y. Gogotsi, C. Portet, P. Simon, P.-L. Taberna: Anomalous increase in carbon capacitance at pore sizes less than 1 nanometer, Science **313**, 1760 (2006)
16.76 J. Chmiola, C. Largeot, P.L. Taberna, P. Simon, Y. Gogotsi: Desolvation of ions in subnanometer pores and its effect on capacitance and double-layer theory, Angew. Chem. Int. Ed. **47**, 3392 (2008)
16.77 D. Aurbach, M.D. Levi, G. Salitra, N. Levy, E. Pollak, J. Muthu: Cation trapping in highly porous carbon electrodes for EDLC cells, J. Electrochem. Soc. **155**, A745 (2008)
16.78 R. Mysyk, E. Raymundo-Piñero, F. Béguin: Saturation of subnanometer pores in an electric double-layer capacitor, Electrochem. Commun. **11**, 554 (2009)

16.79 C. Largeot, C. Portet, J. Chmiola, P.-L. Taberna, Y. Gogotsi, P. Simon: Relation between the ion size and pore size for an electric double-layer capacitor, J. Am. Chem. Soc. **130**, 2730 (2008)

16.80 G. Feng, J. Huang, B.G. Sumpter, V. Meunier, R. Qiao: Structure and dynamics of electrical double layers in organic electrolytes, Phys. Chem. Chem. Phys. **12**, 5468 (2010)

16.81 J.S. Huang, B.G. Sumpter, V. Meunier: Theoretical model for nanoporous carbon supercapacitors, Angew. Chem. Int. Ed. **47**, 520 (2008)

16.82 J.S. Huang, B.G. Sumpter, V. Meunier: A universal model for nanoporous carbon supercapacitors applicable to diverse pore regimes, carbon materials, and electrolytes, Chemistry-A Eur. J. **14**, 6614 (2008)

16.83 D.W. Wang, F. Li, M. Liu, G.Q. Lu, H.M. Cheng: 3D aperiodic hierarchical porous graphitic carbon material for high-rate electrochemical capacitive energy storage, Angew. Chem. Int. Ed. **47**, 373 (2008)

16.84 C. Liu, H.M. Cheng: Carbon nanotubes for clean energy applications, J, Phys. D **38**, R231 (2005)

16.85 T. Kim, S. Lim, K. Kwon, S.-H. Hong, W. Qiao, C.K. Rhee, S.-H. Yoon, I. Mochida: Electrochemical capacitances of well-defined carbon surfaces, Langmuir **22**, 9086 (2006)

16.86 V. Subramanian, H.W. Zhu, B.Q. Wei: High rate reversibility anode materials of lithium batteries from vapor-grown carbon nanofibers, J. Phys. Chem. B **110**, 7178 (2006)

16.87 E. Frackowiak, F. Béguin: Electrochemical storage of energy in carbon nanotubes and nanostructured carbons, Carbon **40**, 1775 (2002)

16.88 D.N. Futaba, K. Hata, T. Yamada, T. Hiraoka, Y. Hayamizu, Y. Kakudate, O. Tanaike, H. Hatori, M. Yumura, S. Iijima: Shape-engineerable and highly densely packed single-walled carbon nanotubes and their application as super-capacitor electrodes, Nat. Mater. **5**, 987 (2006)

16.89 S. Talapatra, S. Kar, S.K. Pal, R. Vajtai, L. Ci, P. Victor, M.M. Shaijumon, S. Kaur, O. Nalamasu, P.M. Ajayan: Direct growth of aligned carbon nanotubes on bulk metals, Nat. Nanotechnol. **1**, 112 (2006)

16.90 Y. Honda, T. Ono, M. Takeshige, N. Morihara, H. Shiozaki, T. Kitamura, K. Yoshikawa, M. Morita, M. Yamagata, M. Ishikawa: Effect of MWCNT bundle structure on electric double-layer capacitor performance, Electrochem. Solid-State Lett. **12**, A45 (2009)

16.91 Y. Honda, M. Takeshige, H. Shiozaki, T. Kitamura, M. Ishikawa: Excellent frequency response of vertically aligned MWCNT electrode for EDLC, Electrochemistry **75**, 586 (2007)

16.92 Y. Honda, T. Haramoto, M. Takeshige, H. Shiozaki, T. Kitamura, M. Ishikawa: Aligned MWCNT sheet electrodes prepared by transfer methodology providing high-power capacitor performance, Electrochem. Solid-State Lett. **10**, A106 (2007)

16.93 H. Zhang, G.P. Cao, Y.S. Yang: Electrochemical properties of ultra-long, aligned, carbon nanotube array electrode in organic electrolyte, J. Power Sources **172**, 476 (2007)

16.94 A.L.M. Reddy, M.M. Shaijumon, S.R. Gowda, P.M. Ajayan: Coaxial MnO_2/carbon nanotube array electrodes for high-performance lithium batteries, Nano Lett. **9**, 1002 (2009)

16.95 H. Zhang, G.P. Cao, Z.Y. Wang, Y.S. Yang, Z.J. Shi, Z.N. Gu: Growth of manganese oxide nanoflowers on vertically-aligned carbon nanotube arrays for high-rate electrochemical capacitive energy storage, Nano Lett. **8**, 2664 (2008)

16.96 W.G. Pell, B.E. Conway: Peculiarities and requirements of asymmetric capacitor devices based on combination of capacitor and battery-type electrodes, J. Power Sources **136**, 334 (2004)

16.97 J.P. Zheng: The limitations of energy density of battery/double-layer capacitor asymmetric cells, J. Electrochem. Soc. **150**, A484 (2003)

16.98 F. Béguin, K. Kierzek, M. Friebe, A. Jankowska, J. Machnikowski, K. Jurewicz, E. Frackowiak: Effect of various porous nanotextures on the reversible electrochemical sorption of hydrogen in activated carbons, Electrochim. Acta **51**, 2161 (2006)

16.99 B.E. Conway, H.A. Andreas, W. Pell: Specific ion effects on double layer capacitance of a C-Cloth electrode showing extended charge acceptance, Proc. 14th Double Layer Capacitor Semin., Deerfield Beach (2004)

16.100 X. Qin, X.P. Gao, H. Liu, H.T. Yuan, D.Y. Yan, W.L. Gong, D.Y. Song: Electrochemical hydrogen storage of multiwalled carbon nanotubes, Electrochem. Solid-State Lett. **3**, 532–535 (2000), pp. 155–176

16.101 K. Jurewicz, E. Frackowiak, F. Béguin: Towards the mechanism of electrochemical hydrogen storage in nanostructured carbon materials, Appl. Phys. A **78**, 981 (2004)

16.102 F. Béguin, M. Friebe, K. Jurewicz, C. Vix-Guterl, J. Dentzer, E. Frackowiak: State of hydrogen electrochemically stored using nanoporous carbons as negative electrode materials in an aqueous medium, Carbon **44**, 2392 (2006)

16.103 F. Béguin, K. Jurewicz, M. Friebe, E. Frackowiak: Advantages of electrochemical hydrogen storage over gas adsorption in nanoporous carbons, Ann. Chim. Sci. Mater. **30**, 531 (2005)

16.104 E. Frackowiak, K. Jurewicz, K. Szostak, S. Delpeux, F. Béguin: Nanotubular materials as electrodes for supercapacitors, Fuel Process. Technol. **77**, 213 (2002)

16.105 K. Jurewicz, E. Frackowiak, F. Béguin: Enhancement of reversible hydrogen capacity into activated carbon through water electrolysis, Electrochem. Solid-State Lett. **4**, A27 (2001)

16.106 C. Nützenadel, A. Zuttel, D. Chartouni, L. Schlapbach: Electrochemical Storage of hydrogen in nanotube materials, Electrochem. Solid-State Lett. **2**, 30 (1999)

16.107 M.J. Bleda-Martínez, J.M. Pérez, A. Linares-Solana, E. Morallón, D. Cazorla-Amorós: Effect of surface chemistry on electrochemical storage of hydrogen in porous carbon materials, Carbon **46**, 1053 (2008)

16.108 D.Y. Qu: Mechanism for electrochemical hydrogen insertion in carbonaceous materials, J. Power Sources **179**, 310 (2008)

16.109 Y. Chabre, J. Pannetier: Structural and electrochemical properties of the proton/γ-MnO_2 system, Prog. Solid State Chem. **23**, 1 (1995)

16.110 M. Thackeray: Manganese oxides for lithium batteries, Prog. Solid State Chem. **25**, 1 (1997)

16.111 J.P. Zheng, T.R. Jow: A new charge storage mechanism for electrochemical capacitors, J. Electrochem. Soc. **142**, L6 (1995)

16.112 D. Bélanger, T. Brousse, J.W. Long: Manganese oxides: Battery materials make the leap to electrochemical capacitors, Electrochem. Soc. Interf. **17**, 49 (2008)

16.113 H.Y. Lee, V. Manivannan, J.B. Goodenough: Electrochemical capacitors with KCl electrolyte, C.R. Acad. Sci. Paris **2**(IIc), 565 (1999)

16.114 H.Y. Lee, J.B. Goodenough: Supercapacitor behavior with KCl electrolyte, J. Solid-State Chem. **144**, 220 (1999)

16.115 Q. Feng, H. Kanoh, K. Ooi: Manganese oxide porous crystals, J. Mater. Chem. **9**, 319 (1999)

16.116 P. Strobel, C. Mouget: Electrochemical lithium insertion into layered manganates, Mater. Res. Bull. **28**, 93 (1993)

16.117 R.G. Burns, V.M. Burns: Manganese Dioxide Symposium, Vol. 2 (Electrochem. Society, Pennington 1981) p. 97

16.118 Q. Feng, K. Yanagizawa, N. Yamasaki: Hydrothermal soft chemical process for synthesis of manganese oxides with tunnel structures, J. Porous Mater. **5**, 153 (1998)

16.119 T. Brousse, M. Toupin, R. Dugas, L. Athouël, O. Crosnier, D. Bélanger: Crystalline MnO_2 as possible alternatives to amorphous compounds in electrochemical supercapacitors, J. Electrochem. Soc. **153**, A2171 (2006)

16.120 S. Devaraj, N. Munichandraiah: Effect of crystallographic structure of MnO_2 on its electrochemical capacitance properties, J. Phys. Chem. C **112**, 4406 (2008)

16.121 E. Machefaux, T. Brousse, D. Bélanger, D. Guyomard: Supercapacitor behavior of new substituted manganese dioxides, J. Power Sources **165**, 651 (2007)

16.122 A. Zolfaghari, F. Ataherian, M. Ghaemi, A. Gholami: Capacitive behavior of nanostructured MnO_2 prepared by sonochemistry method, Electrochim. Acta **52**, 2806 (2007)

16.123 P. Staiti, F. Lufrano: Study and optimisation of manganese oxide-based electrodes for electrochemical supercapacitors, J. Power Sources **187**, 284 (2009)

16.124 M.W. Xu, D.D. Zhao, S.J. Bao, H.L. Li: Mesoporous amorphous MnO_2 as electrode material for supercapacitor, J. Solid State Electrochem. **11**, 1101 (2007)

16.125 P. Ragupathy, H.N. Vasan, N. Munichandraiah: Synthesis and characterization of nano-MnO_2 for electrochemical supercapacitor studies, J. Electrochem. Soc. **155**, A34 (2008)

16.126 L. Athouël, F. Moser, R. Dugas, O. Crosnier, D. Bélanger, T. Brousse: Variation of the MnO_2 birnessite structure upon charge/discharge in an electrochemical supercapacitor electrode in aqueous Na_2SO_4 electrolyte, J. Phys. Chem. C **112**, 7270 (2008)

16.127 M. Toupin, T. Brousse, D. Bélanger: Charge storage mechanism of MnO_2 electrode used in aqueous electrochemical capacitor, Chem. Mater. **16**, 3184 (2004)

16.128 M. Toupin, T. Brousse, D. Bélanger: Influence of microstucture on the charge storage properties of chemically synthesized manganese dioxide, Chem. Mater. **14**, 3946 (2002)

16.129 Y.U. Jeong, A. Manthiram: Nanocrystalline manganese oxides for electrochemical capacitors with neutral electrolytes, J. Electrochem. Soc. **149**, A1419 (2002)

16.130 R.N. Reddy, R.G. Reddy: Sol-gel MnO_2 as an electrode material for electrochemical capacitors, J. Power Sources **124**, 330 (2003)

16.131 R.N. Reddy, R.G. Reddy: Synthesis and electrochemical characterization of amorphous MnO_2 electrochemical capacitor electrode material, J. Power Sources **132**, 315 (2004)

16.132 C. Xu, B. Li, H. Du, F. Kang, Y. Zeng: Supercapacitive studies on amorphous MnO_2 in mild solutions, J. Power Sources **184**, 691 (2008)

16.133 R. Jiang, T. Huang, J. Liu, J. Zhuang, A. Yu: A novel method to prepare nanostructured manganese dioxide and its electrochemical properties as a supercapacitor electrode, Electrochim. Acta **54**, 3047 (2009)

16.134 H.Y. Lee, S.W. Kim, H.Y. Lee: Expansion of active site area and improvement of kinetic reversibility in electrochemical pseudocapacitor electrode, Electrochem. Solid-State Lett. **4**, A19 (2001)

16.135 M.S. Hong, S.H. Lee, S.W. Kim: Use of KCl aqueous electrolyte for 2 V manganese oxide/activated carbon hybrid capacitor, Electrochem. Solid-State Lett. **5**, A227 (2002)

16.136 H. Kim, B.N. Popov: Synthesis and characterization of MnO_2-based mixed oxides as supercapacitors, J. Electrochem. Soc. **150**, D56 (2003)

16.137 E. Raymundo-Piñero, V. Khomenko, E. Frackowiak, F. Béguin: Performance of manganese oxide/CNTs composites as electrode materials for electrochemical capacitors, J. Electrochem. Soc. **152**, A229 (2005)

16.138 V. Khomenko, E. Raymundo-Piñero, F. Béguin: Optimisation of an asymmetric manganese oxide/activated carbon capacitor working at 2 V in aqueous medium, J. Power Sources **153**, 183 (2006)

16.139 V. Khomenko, E. Raymundo-Piñero, E. Frackowiak, F. Béguin: High-voltage asymmetric supercapacitors operating in aqueous electrolyte, Appl. Phys. A **82**, 567 (2006)

16.140 R.K. Sharma, H.S. Oh, Y.G. Shul, H. Kim: Carbon-supported, nano-structured, manganese oxide composite electrode for electrochemical supercapacitor, J. Power Sources **173**, 1024 (2007)

16.141 J.Y. Luo, J.L. Liu, P. He, Y.Y. Xia: A novel $LiTi_2(PO_4)_3/MnO_2$ hybrid supercapacitor in lithium sulfate aqueous electrolyte, Electrochim. Acta **53**, 8128 (2008)

16.142 S.L. Kuo, N.L. Wu: Investigation of pseudocapacitive charge-storage reaction of $MnO_2 \cdot nH_2O$ supercapacitors in aqueous electrolytes, J. Electrochem. Soc. **153**, A1317 (2006)

16.143 Y.K. Zhou, B.L. He, F.B. Zhang, H.L. Li: Hydrous manganese oxide/carbon nanotube composite electrodes for electrochemical capacitors, J. Solid State Electrochem. **8**, 482 (2004)

16.144 T. Brousse, P.L. Taberna, O. Crosnier, R. Dugas, P. Guillemet, Y. Scudeller, Y. Zhou, F. Favier, D. Bélanger, P. Simon: Long-term cycling behavior of asymmetric activated carbon/MnO_2 aqueous electrochemical supercapacitor, J. Power Sources **173**, 633 (2007)

16.145 Y.C. Hsieh, K.T. Lee, Y.P. Lin, N.L. Wu, S.W. Donne: Investigation on capacity fading of aqueous $MnO_2 \cdot nH_2O$ electrochemical capacitor, J. Power Sources **177**, 660 (2008)

16.146 K.T. Lee, N.L. Wu: Manganese oxide electrochemical capacitor with potassium poly(acrylate) hydrogel electrolyte, J. Power Sources **179**, 430 (2008)

16.147 T. Brousse, D. Bélanger: A Hybrid $Fe_3O_4MnO_2$ capacitor in mild aqueous electrolyte, Electrochem. Solid-State Lett. **6**, A244 (2003)

16.148 J.W. Long, A.L. Young, D.R. Rolison: Spectroelectrochemical characterization of nanostructured, mesoporous manganese oxide in aqueous electrolytes, J. Electrochem. Soc. **150**, A1161 (2003)

16.149 T. Cottineau, M. Toupin, T. Delahaye, T. Brousse, D. Bélanger: Nanostructured transition metal oxides for aqueous hybrid electrochemical supercapacitors, Appl. Phys. A **82**, 599 (2006)

16.150 G.X. Wang, B.L. Zhang, Z.L. Yu, M.Z. Qu: Manganese oxide/MWNTs composite electrodes for supercapacitors, Solid State Ionics **176**, 1169 (2005)

16.151 V. Subramanian, H. Zhu, B. Wei: Synthesis and electrochemical characterizations of amorphous manganese oxide and single walled carbon nanotube composites as supercapacitor electrode materials, Electrochem. Commun. **8**, 827 (2006)

16.152 V. Subramanian, H. Zhu, B. Wei: Alcohol-assisted room temperature synthesis of different nanostructured manganese oxides and their pseudocapacitance properties in neutral electrolyte, Chem. Phys. Lett. **453**, 242 (2008)

16.153 X.H. Yang, Y.G. Wang, H.M. Xiong, Y.Y. Xia: Interfacial synthesis of porous MnO_2 and its application in electrochemical capacitor, Electrochim. Acta **53**, 752 (2007)

16.154 P. Ruetschi: Cation-vacancy model for MnO_2, J. Electrochem. Soc. **131**, 2737 (1984)

16.155 P. Ruetschi, R. Giovanoli: Cation vacancies in MnO_2 and their influence on electrochemical reactivity, J. Electrochem. Soc. **135**, 2663 (1988)

16.156 P. Ruetschi: Influence of cation vacancies on the electrode potential of MnO_2, J. Electrochem. Soc. **135**, 2657 (1988)

16.157 K.W. Nam, M.G. Kim, K.B. Kim: In situ Mn K-edge X-ray absorption spectroscopy studies of electrodeposited manganese oxide films for electrochemical capacitors, J. Phys. Chem. C **111**, 749 (2007)

16.158 J.K. Chang, M.T. Lee, W.T. Tsai: In situ Mn K-edge X-ray absorption spectroscopic studies of anodically deposited manganese oxide with relevance to supercapacitor applications, J. Power Sources **166**, 590 (2007)

16.159 M. Nakayama, A. Tanaka, Y. Sato, T. Tonosaki, K. Ogura: Electrodeposition of manganese and molybdenum mixed oxide thin films and their charge storage properties, Langmuir **21**, 5907 (2005)

16.160 M. Chigane, M. Ishikawa: Manganese oxide thin film preparation by potentiostatic electrolyses and electrochromism, J. Electrochem. Soc. **147**, 2246 (2000)

16.161 S.-E. Chun, S.-I. Pyun, G.-J. Lee: A study on mechanism of charging/discharging at amorphous manganese oxide electrode in 0.1 M Na_2SO_4 solution, Electrochim. Acta **51**, 6479 (2006)

16.162 S. Ardizzone, G. Fregonara, S. Trasatti: "Inner" and "outer" active surface of RuO_2 electrodes, Electrochim. Acta **35**, 263 (1990)

16.163 S.C. Pang, M.A. Anderson, T.W. Chapman: Novel electrode materials for thin-film ultracapacitors: Comparison of electrochemical properties of sol-gel-derived and electrodeposited manganese dioxide, J. Electrochem. Soc. **147**, 444 (2000)

16.164 S.F. Chin, S.C. Pang, M.A. Anderson: Material and electrochemical characterization of tetrapropylammonium manganese oxide thin films as novel electrode materials for electrochemical capacitors, J. Electrochem. Soc. **149**, A379 (2002)

16.165 N.J. Dudney: Solid-state thin-film rechargeable batteries, Mater. Sci. Eng. B **116**, 245 (2005)

16.166 J.K. Chang, Y.L. Chen, W.T. Tsai: Effect of heat treatment on material characteristics and pseudo-capacitive properties of manganese oxide prepared by anodic deposition, J. Power Sources **135**, 344 (2004)

16.167 C.C. Hu, T.W. Tsou: Capacitive and textural characteristics of hydrous manganese oxide prepared by anodic deposition, Electrochim. Acta **47**, 3523 (2002)

16.168 M.S. Wu, P.C.J. Chiang: Fabrication of nanostructured manganese oxide electrodes for electrochemical capacitors, Electrochem. Solid-State Lett. **7**, A123 (2004)

16.169 C.C. Hu, C.C. Wang: Nanostructures and capacitive characteristics of hydrous manganese oxide prepared by electrochemical deposition, J. Electrochem. Soc. **150**, A1079 (2003)

16.170 J.N. Broughton, M.J. Brett: Variations in MnO_2 electrodeposition for electrochemical capacitors, Electrochim. Acta **50**, 4814 (2005)

16.171 Y.K. Zhou, M. Toupin, D. Bélanger, T. Brousse, F. Favier: Electrochemical preparation and characterization of Birnessite-type layered manganese oxide films, J. Phys. Chem. Solids **67**, 1351 (2006)
16.172 J. Chang, S. Lee, T. Ganesh, R.S. Mane, S. Min, W. Lee, S.H. Han: Viologen-assisted manganese oxide electrode for improved electrochemical supercapacitors, J. Electroanal. Chem. **624**, 167 (2008)
16.173 C.C. Hu, T.W. Tsou: Ideal capacitive behavior of hydrous manganese oxide prepared by anodic deposition, Electrochem. Comm. **4**, 105 (2002)
16.174 J.K. Chang, W.T. Tsai: Material characterization and electrochemical performance of hydrous manganese oxide electrodes for use in electrochemical pseudocapacitors, J. Electrochem. Soc. **150**, A1333 (2003)
16.175 J.K. Chang, W.T. Tsai: Effects of temperature and concentration on the structure and specific capacitance of manganese oxide deposited in manganese acetate solution, J. Appl. Electrochem. **34**, 953 (2004)
16.176 C.H. Liang, C.L. Nien, H.C. Hu, C.S. Hwang: Charging/discharging behavior of manganese oxide electrodes in aqueous electrolyte prepared by galvanostatic electrodeposition, J. Ceram. Soc. Japan **115**, 319 (2007)
16.177 S. Chou, F. Cheng, J. Chen: Electrodeposition synthesis and electrochemical properties of nanostructured $\gamma-MnO_2$ films, J. Power Sources **162**, 727 (2006)
16.178 M. Nakayama, S. Konishi, H. Tagashira, K. Ogura: Electrochemical synthesis of layered manganese oxides intercalated with tetraalkylammonium ions, Langmuir **21**, 354 (2005)
16.179 M. Nakayama, H. Tagashira: Electrodeposition of layered manganese oxide nanocomposites intercalated with strong and weak polyelectrolytes, Langmuir **22**, 3864 (2006)
16.180 W. Wei, X. Cui, W. Chen, D.G. Ivey: Electrochemical cyclability mechanism for MnO_2 electrodes utilized as electrochemical supercapacitors, J. Power Sources **186**, 543 (2009)
16.181 K.R. Prasad, N. Miura: Electrochemically synthesized MnO_2-based mixed oxides for high performance redox supercapacitors, Electrochem. Commun. **6**, 1004 (2004)
16.182 K.R. Prasad, N. Miura: Potentiodynamically deposited nanostructured manganese dioxide as electrode material for electrochemical redox supercapacitors, J. Power Sources **135**, 354 (2004)
16.183 S. Devaraj, N. Munichandraiah: High capacitance of electrodeposited MnO_2 by the effect of a surface-active agent, Electrochem. Solid-State Lett. **8**, A373 (2005)
16.184 T. Shinomiya, V. Gupta, N. Miura: Effects of electrochemical-deposition method and microstructure on the capacitive characteristics of nanosized manganese oxide, Electrochim. Acta **51**, 4412 (2006)
16.185 N. Nagarajan, H. Humadi, I. Zhitomirsky: Cathodic electrodeposition of MnO_x films for electrochemical supercapacitors, Electrochim. Acta **51**, 3039 (2006)
16.186 N. Nagarajan, M. Cheong, I. Zhitomirsky: Electrochemical capacitance of MnO_x films, Mater. Chem. Phys. **103**, 47 (2007)
16.187 M.S. Wu, R.H. Lee: Nanostructured manganese oxide electrodes for lithium-ion storage in aqueous lithium sulfate electrolyte, J. Power Sources **176**, 363 (2008)
16.188 J. Wei, N. Nagarajan, I. Zhitomirsky: Manganese oxide films for electrochemical supercapacitors, J. Mater. Process. Technol. **186**, 356 (2007)
16.189 S.C. Wang, C.Y. Chen, T.C. Chien, P.Y. Lee, C.K. Lin: Supercapacitive properties of spray pyrolyzed iron-added manganese oxide powders deposited by electrophoretic deposition technique, Thin Solid Films **517**, 1234 (2008)
16.190 J. Li, I. Zhitomirsky: Electrophoretic deposition of manganese oxide nanofibers, Mater. Chem. Phys. **112**, 525 (2008)
16.191 J.N. Broughton, M.J. Brett: Investigation of thin sputtered Mn films for electrochemical capacitors, Electrochim. Acta **49**, 4439 (2004)
16.192 B. Djurfors, J.N. Broughton, M.J. Brett, D.J. Ivey: Electrochemical oxidation of Mn/MnO films: Formation of an electrochemical capacitor, Acta Mater. **53**, 957 (2005)
16.193 B. Djurfors, J.N. Broughton, M.J. Brett, D.J. Ivey: Production of capacitive films from Mn thin films: Effects of current density and film thickness, J. Power Sources **156**, 741 (2006)
16.194 B. Djurfors, J.N. Broughton, M.J. Brett, D.J. Ivey: Electrochemical oxidation of Mn/MnO films: Mechanism of porous film growth, J. Electrochem. Soc. **153**, A64 (2006)
16.195 J.N. Broughton, M.J. Brett: Electrochemical capacitance in manganese thin films with chevron microstructure, Electrochem. Solid-State Lett. **5**, A279 (2002)
16.196 J.K. Chang, C.H. Huang, W.T. Tsai, M.J. Deng, I.W. Sun, P.Y. Chen: Manganese films electrodeposited at different potentials and temperatures in ionic liquid and their application as electrode materials for supercapacitors, Electrochim. Acta **53**, 4447 (2008)
16.197 J.K. Chang, C.H. Huang, W.T. Tsai, M.J. Deng, I.W. Sun: Ideal pseudocapacitive performance of the Mn oxide anodized from the nanostructured and amorphous Mn thin film electrodeposited in BMP-NTf_2 ionic liquid, J. Power Sources **179**, 435 (2008)
16.198 J.K. Chang, C.H. Huang, M.T. Lee, W.T. Tsai, M.J. Deng, I.W. Sun: Physicochemical factors that affect the pseudocapacitance and cyclic stability of Mn oxide electrodes, Electrochim. Acta **54**, 3278 (2009)
16.199 Y.S. Chen, C.C. Hu, Y.T. Wu: Capacitive and textural characteristics of manganese oxide prepared by anodic deposition: Effects of manganese pre-

cursors and oxide thickness, J. Solid State Electrochem. **8**, 467 (2004)
16.200 M. Nakayama, T. Kanaya, R. Inoue: Anodic deposition of layered manganese oxide into a colloidal crystal template for electrochemical supercapacitor, Electrochem. Commun. **9**, 1154 (2007)
16.201 J.K. Tchang, S.H. Hsu, W.T. Tsai, I.W. Sun: A novel electrochemical process to prepare a high-porosity manganese oxide electrode with promising pseudocapacitive performance, J. Power Sources **177**, 676 (2008)
16.202 T. Xue, C.L. Xu, D.D. Zhao, X.H. Li, H.L. Li: Electrodeposition of mesoporous manganese dioxide supercapacitor electrodes through self-assembled triblock copolymer templates, J. Power Sources **164**, 953 (2007)
16.203 B. Dong, T. Xue, C.L. Xu, H.L. Li: Electrodeposition of mesoporous manganese dioxide films from lyotropic liquid crystalline phases, Microporous Mesoporous Mater. **112**, 627 (2008)
16.204 S.J. Pan, Y.J. Shih, J.R. Chen, J.K. Chang, W.T. Tsai: Selective micro-etching of duplex stainless steel for preparing manganese oxide supercapacitor electrode, J. Power Sources **187**, 261 (2009)
16.205 X. Zhang, W. Yang, D.G. Evans: Layer-by-layer self-assembly of manganese oxide nanosheets/polyethylenimine multilayer films as electrodes for supercapacitors, J. Power Sources **184**, 695 (2008)
16.206 P.Y. Chuang, C.C. Hu: The electrochemical characteristics of binary manganese–cobalt oxides prepared by anodic deposition, Mater. Chem. Phys. **92**, 138 (2005)
16.207 J.K. Chang, M.T. Lee, C.H. Huang, W.T. Tsai: Physicochemical properties and electrochemical behavior of binary manganese–cobalt oxide electrodes for supercapacitor applications, Mater. Chem. Phys. **108**, 124 (2008)
16.208 F. Moser, L. Athouël, O. Crosnier, F. Favier, D. Bélanger, T. Brousse: Transparent electrochemical capacitor based on electrodeposited MnO_2 thin film electrodes and gel-type electrolyte, Electrochem. Commun. **11**, 1259 (2009)
16.209 E. Takeuchi: Size does matter: Autonomous micro-power sources, Electrochem. Soc. Interf. **17**, 43 (2008)
16.210 M. Deng, B. Yang, Z. Zhang, Y. Hu: Studies on CNTs–MnO_2 nanocomposite for supercapacitors, J. Mater. Sci. **40**, 1017 (2005)
16.211 D. Jones, E. Wortham, J. Rozière, F. Favier, J.L. Pascal, L. Monconduit: Manganese oxide nanocomposites: Preparation and some electrochemical properties, J. Phys. Chem. Sol. **65**, 235 (2004)
16.212 V. Subramanian, H. Zhu, R. Vajtai, P.M. Ajayan, B. Wei: Hydrothermal synthesis and pseudocapacitance properties of MnO_2 nanostructures, J. Phys. Chem. B **109**, 20207 (2005)
16.213 Q. Zhou, X. Li, Y.G. Li, B.Z. Tian, D.Y. Zhao, Z.Y. Jiang: Synthesis and electrochemical properties of semicrystalline gyroidal mesoporous MnO_2, Chin. J. Chem. **24**, 835 (2006)
16.214 M. Xu, L. Kong, W. Zhou, H. Li: Hydrothermal synthesis and pseudocapacitance properties of α-MnO_2 hollow spheres and hollow urchins, J. Phys. Chem. C **111**, 19141 (2007)
16.215 M. Ghaemi, F. Ataherian, A. Zolfaghari, S.M. Jafari: Charge storage mechanism of sonochemically prepared MnO_2 as supercapacitor electrode: Effects of physisorbed water and proton conduction, Electrochim. Acta **53**, 4607 (2008)
16.216 S. Komaba, A. Ogata, T. Tsuchikawa: Enhanced supercapacitive behaviors of Birnessite, Electrochem. Commun. **10**, 1435 (2008)
16.217 S. Devaraj, N. Munichandraiah: Surfactant stabilized nanopetals morphology of α-MnO_2 prepared by microemulsion method, J. Solid State Electrochem. **12**, 207 (2008)
16.218 J. Zhao, H. Chen, J. Shi, J. Gu, X. Dong, J. Gao, M. Ruan, L. Yu: Electrochemical and oxygen desorption properties of nanostructured ternary compound Na_xMnO_2 directly templated from mesoporous SBA-15, Microporous Mesoporous Mater. **116**, 432 (2008)
16.219 E. Beaudrouet, A. Le Gal La Salle, D. Guyomard: Nanostructured manganese dioxides: Synthesis and properties as supercapacitor electrode materials, Electrochim. Acta **54**, 1240 (2009)
16.220 X. Wang, X. Wang, W. Huang, P.J. Sebastian, S. Gamboa: Sol–gel template synthesis of highly ordered MnO_2 nanowire arrays, J. Power Sources **140**, 211 (2005)
16.221 G. González, J.I. Gutiérrez, J.R. González-Velasco, A. Cid, A. Arnanz, J. Arnanz: Transformations of manganese oxides under different thermal conditions, J. Thermal Anal. Calorim. **47**, 93 (1995)
16.222 S. Li, S. Wang, B. Xu: Dry modification of electrode materials by roller vibration milling at room temperature, Particuology **6**, 383 (2008)
16.223 C. Ye, Z.M. Lin, S.Z. Hui: Electrochemical and capacitance properties of rod-shaped MnO_2 for supercapacitor, J. Electrochem. Soc. **152**, A1272 (2005)
16.224 S.R. Sivakkumar, J.M. Ko, D.Y. Kim, B.C. Kim, G.G. Wallace: Performance evaluation of CNT/polypyrrole/MnO_2 composite electrodes for electrochemical capacitors, Electrochim. Acta **52**, 7377 (2007)
16.225 L. Athouël, F. Moser, R. Duga, O. Crosnier, D. Bélanger, T. Brousse: Birnessite as possible candidate for hybrid carbon/MnO_2 electrochemical capacitor, ECS Trans. **16**, 119 (2008)
16.226 J. Jiang, A. Kucernak: Electrochemical supercapacitor material based on manganese oxide: Preparation and characterization, Electrochim. Acta **47**, 2381 (2002)
16.227 C.Y. Lee, H.M. Tsai, H.J. Chuang, S.Y. Li, P. Lin, T.Y. Tseng: Characteristics and electrochemical performance of supercapacitors with manganese oxide-carbon nanotube nanocomposite electrodes, J. Electrochem. Soc. **152**, A716 (2005)
16.228 Z. Fan, Z. Qie, T. Wei, J. Yan, S. Wang: Preparation and characteristics of nanostructured MnO_2/MWCNTs using microwave irradiation method, Mater. Lett. **62**, 3345 (2008)

16.229 C. Xu, B. Li, H. Du, F. Kang, Y. Zeng: Electrochemical properties of nanosized hydrous manganese dioxide synthesized by a self-reacting microemulsion method, J. Power Sources **180**, 664 (2008)
16.230 A.B. Yuan, M. Zhou, X.L. Wang, Z.H. Sun, Y.Q. Wang: Synthesis and characterization of nanostructured manganese dioxide used as positive electrode material for electrochemical capacitor with lithium hydroxide electrolyte, Chin. J. Chem. **26**, 65 (2008)
16.231 C.Y. Lee, H.M. Tsai, H.J. Chuang, S.Y. Li, P. Lin, Y.T. Tseng: Characteristics and electrochemical performance of supercapacitors with manganese oxide-carbon nanotube nanocomposite electrodes, J. Electrochem. Soc. **152**, A716 (2005)
16.232 Z. Fan, J. Chen, M. Wang, K. Cui, H. Zhou, Y. Kuang: Preparation and characterization of manganese oxide/CNT composites as supercapacitive materials, Diam. Rel. Mater. **15**, 1478 (2006)
16.233 X. Xie, L. Gao: Characterization of a manganese dioxide/carbon nanotube composite fabricated using an in situ coating method, Carbon **45**, 2365 (2007)
16.234 S.-B. Ma, K.-Y. Ahn, E.-S. Lee, K.-H. Oh, K.B. Kim: Synthesis and characterization of manganese dioxide spontaneously coated on carbon nanotubes, Carbon **45**, 375 (2007)
16.235 S.-L. Chou, J.-Z. Wang, S.-Y. Chew, H.K. Liu, S.-X. Dou: Electrodeposition of MnO_2 nanowires on carbon nanotube paper as free-standing, flexible electrode for supercapacitors, Electrochem. Commun. **10**, 1724 (2008)
16.236 Z. Fan, J. Chen, B. Zhang, F. Sun, B. Liu, Y. Kuang: Electrochemically induced deposition method to prepare $\gamma-MnO_2$/multi-walled carbon nanotube composites as electrode material in supercapacitors, Mater. Res. Bull. **43**, 2085 (2008)
16.237 S.-B. Ma, K.-W. Nam, W.-S. Yoon, X.-Q. Yang, K.-Y. Ahn, K.-H. Oh, K.-B. Kim: Electrochemical properties of manganese oxide coated onto carbon nanotubes for energy-storage applications, J. Power Sources **178**, 483 (2008)
16.238 Z. Fan, Z. Qje, T. Wei, J. Yan, S. Wang: Preparation and characteristics of nanostructured MnO_2/MWCNTs using microwave irradiation method, Mater. Lett. **62**, 3345 (2008)
16.239 Z. Fan, J. Chen, B. Zhang, B. Liu, X. Zhong, Y. Kuang: High dispersion of $\gamma-MnO_2$ on well-aligned carbon nanotube arrays and its application in supercapacitors, Diam. Rel. Mater. **17**, 1943 (2008)
16.240 K.-W. Nam, C.-W. Lee, X.-Q. Yang, B.W. Cho, W.-S. Yoon, K.B. Kim: Electrodeposited manganese oxides on three-dimensional carbon nanotube substrate: Supercapacitive behaviour in aqueous and organic electrolytes, J. Power Sources **188**, 323 (2009)
16.241 J.M. Ko, K.M. Kim: Electrochemical properties of MnO_2/activated carbon nanotube composite as an electrode material for supercapacitor, Mater. Chem. Phys. **114**, 837 (2009)
16.242 T. Bordjiba, D. Bélanger: Direct redox deposition of manganese oxide on multiscaled carbon nanotube/microfiber carbon electrode for electrochemical capacitor, J. Electrochem. Soc **156**, A378 (2009)
16.243 X. Dong, W. Shen, J. Gu, L. Xiong, Y. Zhu, H. Li, J. Shi: MnO_2-embedded-in-mesoporous-carbon-wall structure for use as electrochemical capacitors, J. Phys. Chem. B **110**, 6015 (2006)
16.244 S. Zhu, H. Zhou, M. Hibino, I. Honma, M. Ichihara: Synthesis of MnO_2 nanoparticles confined in ordered mesoporous carbon using a sonochemical method, Adv. Funct. Mater. **15**, 381 (2005)
16.245 H. Kawaoka, M. Hibino, H. Zhou, I. Honma: Enhancement of specific capacity of manganese oxide/carbon composite synthesized by sonochemical method, Electrochem. Solid-State Lett. **8**, A253 (2005)
16.246 S.-B. Ma, Y.-H. Lee, K.-Y. Ahn, Ch.-M. Kim, K.-H. Oh, K.-B. Kim: Spontaneously deposited manganese oxide on acetylene black in an aqueous potassium permanganate solution, J. Electrochem. Soc. **153**, C27 (2006)
16.247 X. Huang, H. Yue, A. Attia, Y. Yang: Preparation and properties of manganese oxide/carbon composites by reduction of potassium permanganate with acetylene black, J. Electrochem. Soc. **154**, A26 (2007)
16.248 S. Chen, J. Zhu, X. Wu, Q. Han, X. Wang: Graphene oxide-MnO_2 nanocomposites for supercapacitors, ACS Nano **4**, 2822 (2010)
16.249 J. Yan, Z. Fan, T. Wei, W. Qian, M. Zhang, F. Wei: Fast and reversible surface redox reaction of graphene-MnO_2 composites as supercapacitor electrodes, Carbon **48**, 3825 (2010)
16.250 S.-W. Lee, S.-M. Bak, C.-W. Lee, C. Jaye, D.A. Fischer, B.-K. Kim, X.-Q. Yang, K.-W. Nam, K.-B. Kim: Structural changes in reduced graphene oxide upon MnO_2 deposition by the redox reaction between carbon and permanganate ions, J. Phys. Chem. C **118**, 2834 (2014)
16.251 J.W. Long, D. Bélanger, T. Brousse, W. Sugimoto, M.B. Sassin, O. Crosnier: Asymmetric electrochemical capacitors – Stretching the limits of aqueous electrolytes, MRS Bull. **36**, 513 (2011)
16.252 Y.G. Wang, Y.Y. Xia: Hybrid aqueous energy storage cells using activated carbon and lithium-intercalated compounds: I. The C/Li Mn_2O_4 system, J. Electrochem. Soc. **153**, A450 (2006)
16.253 Y. Xue, Y. Chen, M.L. Zhang, Y.D. Yan: A new asymmetric supercapacitor based on $\lambda-MnO_2$ and activated carbon electrodes, Mater. Lett. **62**, 3884 (2008)
16.254 A. Yuan, Q. Zhang: A novel hybrid manganese dioxide/activated carbon supercapacitor using lithium hydroxide electrolyte, Electrochem. Commun. **8**, 1173 (2006)
16.255 J.R. Miller, P. Simon: Electrochemical capacitors for energy management, Science **321**, 651 (2008)
16.256 P. Guillemet, Y. Scudeller, T. Brousse: Multilevel reduced-order thermal modeling of elec-

trochemical capacitors, J. Power Sources **157**, 630 (2006)
16.257 P. Guillemet, Y. Scudeller, T. Brousse, J.M. Depond: Modèle thermique d'ordre réduit pour la conception de supercondensateur électrique. Détermination de la température de fonctionnement en régime stationnaire, Rev. Int. Génie Electr. **10**, 695 (2007), in French
16.258 K.R. Prasad, N. Miura: Polyaniline-MnO_2 composite electrode for high energy density electrochemical capacitor, Electrochem. Solid-State Lett. **7**, A425 (2004)
16.259 J.P. Zheng, P.J. Cyang, T.R. Jow: Hydrous ruthenium oxide as an electrode material for electrochemical capacitors, J. Electrochem. Soc. **142**, 2699 (1995)
16.260 J.P. Zheng, T.R. Jow: High energy and high power density electrochemical capacitors, J. Power Sources **62**, 155 (1996)
16.261 T.R. Jow, J.P. Zheng: Electrochemical capacitors using hydrous ruthenium oxide and hydrogen inserted ruthenium oxide, J. Electrochem. Soc. **145**, 49 (1998)
16.262 J.P. Zheng: Ruthenium oxide-carbon composite electrodes for electrochemical capacitors, Electrochem. Solid-State Lett. **2**, 359 (1999)
16.263 D.A. McKeown, P.L. Hagans, L.P.P. Carette, A.E. Russell, K.E. Swinder, D.R. Rolison: Structure of hydrous ruthenium oxides: Implications for charge storage, J. Phys. Chem. B **103**, 4825 (1999)
16.264 M. Vuković, D.J. Čukman: Electrochemical quartz crystal microbalance study of electrodeposited ruthenium, Electroanal. Chem. **474**, 167 (1999)
16.265 C.-C. Hu, Y.-H. Huang: Cyclic voltammetric deposition of hydrous ruthenium oxide for electrochemical capacitors, J. Electrochem. Soc. **146**, 2465 (1999)
16.266 J.W. Long, K.E. Swinder, C.I. Merzbacher, D.R. Rolison: Voltammetric characterization of ruthenium oxide-based aerogels and other RuO_2 solids: The nature of capacitance in nanostructured materials, Langmuir **15**, 780 (1999)
16.267 Q.L. Fang, D.A. Evans, S.L. Roberson, J.P. Zheng: Ruthenium oxide film electrodes prepared at low temperatures for electrochemical capacitors, J. Electrochem. Soc. **148**, A833 (2001)
16.268 I.-H. Kim, K.-B. Kim: Ruthenium oxide thin film electrodes for supercapacitors, Electrochem. Solid-State Lett. **4**, A62 (2001)
16.269 J.P. Zheng, C.K. Huang: Electrochemical behavior of amorphous and crystalline ruthenium oxide electrodes, J. New Mater. Electrochem. Syst. **5**, 41 (2002)
16.270 R. Fu, Z. Ma, J.P. Zheng: Proton NMR and dynamic studies of hydrous ruthenium oxide, J. Phys. Chem. B **106**, 3592 (2002)
16.271 J.P. Zheng, Y. Xin: Characterization of $RuO_2 \cdot xH_2O$ with various water contents, J. Power Sources **110**, 86 (2002)
16.272 J.W. Long, K.E. Ayers, D.R. Rolison: Electrochemical characterization of high-surface-area catalysts and other nanoscale electroactive materials at sticky-carbon electrodes, J. Electroanal. Chem. **522**, 58 (2002)
16.273 W. Dmowski, T. Egami, K.E. Swinder-Lyons, C.T. Love, D.R. Rolison: Local atomic structure and conduction mechanism of nanocrystalline hydrous RuO_2 from X-ray scattering, J. Phys. Chem. B **106**, 12677 (2002)
16.274 J.W. Long, K.E. Swider, C.I. Merzbacher, D.R. Rolison: Voltammetric characterization of ruthenium oxide-based aerogels and other RuO_2 solids: The nature of capacitance in nanostructured materials, Langmuir **19**, 2532 (2003)
16.275 W. Sugimoto, H. Iwata, Y. Murakami, Y. Takasu: Electrochemical capacitor behavior of layered ruthenic acid hydrate, J. Electrochem. Soc. **151**, A1181 (2004)
16.276 W. Sugimoto, H. Iwata, K. Yokoshima, Y. Murakami, Y. Takasu: Proton and electron conductivity in hydrous ruthenium oxides evaluated by electrochemical impedance spectroscopy: The origin of large capacitance, J. Phys. Chem. B **109**, 7330 (2005)
16.277 S. Trasatti, G. Buzzanca: Ruthenium dioxide: A new interesting electrode material. Solid state structure and electrochemical behaviour, J. Electroanal. Chem. **29**, A1–A5 (1971)
16.278 K. Naoi, P. Simon: New materials and new configurations for advanced electrochemical capacitors, ECS Interf. **17**, 34 (2008)
16.279 J. Zhang, D. Jiang, B. Chen, J. Zhu, L. Jiang, H. Fang: Preparation and electrochemistry of hydrous ruthenium oxide/active carbon electrode materials for supercapacitor, J. Electrochem. Soc. **148**, A1362 (2001)
16.280 M. Ramani, B.S. Haran, R.E. White, B.N. Popov, L. Arsov: Studies on activated carbon capacitor materials loaded with different amounts of ruthenium oxide, J. Power Sources **93**, 209 (2001)
16.281 C.C. Hu, W.C. Chen, K.H. Chang: How to achieve maximum utilization of hydrous ruthenium oxide for supercapacitors, J. Electrochem. Soc. **151**, A281 (2004)
16.282 H. Kim, B.N. Popov: Characterization of hydrous ruthenium oxide/carbon nanocomposite supercapacitors prepared by a colloidal method, J. Power Sources **104**, 52 (2002)
16.283 J.H. Park, J.M. Ko, O.O. Park: Carbon nanotube/RuO_2 nanocomposite electrodes for supercapacitors, J. Electrochem. Soc. **150**, A864 (2003)
16.284 M. Min, K. Machida, J.H. Jang, K. Naoi: Hydrous RuO_2/carbon black nanocomposites with 3D porous structure by novel incipient wetness method for supercapacitors, J. Electrochem. Soc. **153**, A334 (2006)
16.285 C. Lin, J.A. Ritter, B.N. Popov: Development of carbon-metal oxide supercapacitors from sol-gel derived carbon-ruthenium xerogels, J. Electrochem. Soc. **146**, 3155 (1999)
16.286 C.-C. Hu, W.-C. Chen: Effects of substrates on the capacitive performance of $RuO_x \cdot nH_2O$ and activated carbon-RuO_x electrodes for superca-

pacitors, Electrochim. Acta **49**, 3469 (2004)
16.287 W. Sugimoto, T. Kizaki, K. Yokoshima, Y. Murakami, Y. Takasu: Evaluation of the pseudocapacitance in RuO_2 with a RuO_2/GC thin film electrode, Electrochim. Acta **49**, 313 (2004)
16.288 P. Siviglia, A. Daghetti, S. Trasatti: Influence of the preparation temperature of ruthenium dioxide on its point of zero charge, Colloids Surf. **7**, 15 (1983)
16.289 S. Lavine, A.L. Smith: Theory of the differential capacity of the oxide/aqueous electrolyte interface, Discuss. Faraday Soc. **52**, 290 (1971)
16.290 L.D. Burke, O.J. Murphy: Cyclic voltammetry as a technique for determining the surface area of RuO_2 electrodes, J. Electroanal. Chem. **96**, 19 (1979)
16.291 L.D. Burke, O.J. Murphy: Surface area – Voltammetric charge correlation for RuO_2/TiO_2-based anodes, J. Electroanal. Chem. **112**, 39 (1980)
16.292 M.L. Green, M.E. Gross, L.E. Papa, K.J. Schnoes, D. Brasen: Chemical vapor deposition of ruthenium and ruthenium dioxide films, J. Electrochem. Soc. **132**, 2681 (1985)
16.293 S.H. Kim, J.G. Hong, S.K. Streiffer, A.I. Kingon: The effect of RuO_2/Pt hybrid bottom electrode structure on the leakage and fatigue properties of chemical solution derived $Pb(Zr_xTi_{1-x})O_3$ thin films, J. Mater. Res. **14**, 1018 (1999)
16.294 K.E. Swider-Lyons, C.T. Love, D.R. Rolison: Selective vapor deposition of hydrous RuO_2 thin films, J. Electrochem. Soc. **152**, C158 (2005)
16.295 K.-H. Chang, C.-C. Hu: Oxidative synthesis of $RuO_x \cdot nH_2O$ with ideal capacitive characteristics for supercapacitors, J. Electrochem. Soc. **151**, A958 (2004)
16.296 Y. Murakami, S. Tsuchiya, K. Yahikozawa, Y. Takasu: Preparations of ultrafine RuO_2 and IrO_2 particles by a sol-gel process, J. Mater. Sci. Lett. **13**, 1773 (1994)
16.297 S. Hadži-Jordanov, H. Angerstein-Kozlowska, B.E. Conway: Surface oxidation and H deposition at ruthenium electrodes: Resolution of component processes in potential-sweep experiments, J. Electroanal. Chem. **60**, 359 (1975)
16.298 S. Hadži-Jordanov, H. Angerstein-Kozlowska, M. Vuković, B.E. Conway: The state of electrodeposited hydrogen at ruthenium electrodes, J. Phys. Chem. **81**, 2271 (1977)
16.299 S. Hadži-Jordanov, H. Angerstein-Kozlowska, M. Vuković, B.E. Conway: Reversibility and growth behavior of surface oxide films at ruthenium electrodes, J. Electrochem. Soc. **125**, 1471 (1978)
16.300 M. Vuković, H. Angerstein-Kozlowska, B.E. Conway: Electrocatalytic activation of ruthenium electrodes for the Cl_2 and O_2 evolution reactions by anodic/cathodic cycling, J. Appl. Electrochem. **12**, 193 (1982)
16.301 V. Birss, R. Myers, H. Angerstein-Kozlowska, B.E. Conway: Electron microscopy study of formation of thick oxide films on Ir and Ru electrodes, J. Electrochem. Soc. **131**, 1502 (1984)
16.302 M. Vuković: Rotating ring–disc electrode study of the enhanced oxygen evolution on an activated ruthenium electrode, J. Chem. Soc. Faraday Trans. **86**, 3743 (1990)
16.303 M. Vuković, T. Valla, M. Milun: Electron spectroscopy characterization of an activated ruthenium electrode, J. Electroanal. Chem. **356**, 81 (1993)
16.304 D. Marijan, D. Čukman, M. Vuković, M. Milun: Anodic stability of electrodeposited ruthenium: Galvanostatic, thermogravimetric and X-ray photoelectron spectroscopy studies, J. Mater. Sci. **30**, 3045 (1995)
16.305 T. Liu, W.G. Pell, B.E. Conway: Self-discharge and potential recovery phenomena at thermally and electrochemically prepared RuO_2 supercapacitor electrodes, Electrochim. Acta **42**, 3541 (1997)
16.306 M. Blouiin, D. Guay: Activation of ruthenium oxide, iridium oxide, and mixed Ru_xIr_{1-x} oxide electrodes during cathodic polarization and hydrogen evolution, J. Electrochem. Soc. **144**, 573 (1997)
16.307 Y. Mo, M.R. Antonio, D.A. Scherson: In situ Ru K-edge X-ray absorption fine structure studies of electroprecipitated ruthenium dioxide films with relevance to supercapacitor applications, J. Phys. Chem. B **104**, 9777 (2000)
16.308 V. Horvat-Radošević, K. Kvastek, M. Vuković, D. Čukman: Electrochemical properties of ruthenised electrodes in the oxide layer region, J. Electroanal. Chem. **482**, 188 (2000)
16.309 C.C. Hu, C.C. Wang: Improving the utilization of ruthenium oxide within thick carbon–ruthenium oxide composites by annealing and anodizing for electrochemical supercapacitors, Electrochem. Commun. **4**, 554 (2002)
16.310 H.-M. Wu, P.-F. Hsu, W.-T. Hung: Investigation of redox reaction of Ru on carbon nanotubes by pulse potential electrochemical deposition, Diamond Related Mater. **18**, 337 (2009)
16.311 V.D. Patake, C.D. Lokhande, O.S. Joo: Electrodeposited ruthenium oxide thin films for supercapacitor: Effect of surface treatments, Appl. Surf. Sci. **255**, 4192 (2009)
16.312 Y.Z. Zheng, H.Y. Ding, M.L. Zhang: Hydrous–ruthenium–oxide thin film electrodes prepared by cathodic electrodeposition for supercapacitors, Thin Solid Films **516**, 7381 (2008)
16.313 T.P. Gujar, W.Y. Kim, I. Puspitasari, K.D. Jung, O.S. Joo: Electrochemically deposited nanograin ruthenium oxide as a pseudocapacitive electrode, Int. J. Electrochem. Sci. **2**, 666 (2007)
16.314 Y.R. Ahn, M.Y. Song, S.M. Jo, C.R. Park, D.Y. Kim: Electrochemical capacitors based on electrodeposited ruthenium oxide on nanofibre substrates, Nanotechnology **17**, 2865 (2006)
16.315 B.O. Park, C.D. Lokhande, H.S. Park, K.D. Jung, O.S. Joo: Cathodic electrodeposition of RuO_2 thin films from $Ru(III)Cl_3$ solution, Mater. Chem. Phys. **87**, 59 (2004)
16.316 I. Zhitomirsky, L. Gal-Or: Ruthenium oxide deposits prepared by cathodic electrosynthesis, Mater. Lett. **31**, 155 (1997)

16.317 C.C. Hu, M.J. Liu, K.H. Chang: Anodic deposition of hydrous ruthenium oxide for supercapaciors: Effects of the AcO- concentration, plating temperature, and oxide loading, Electrochim. Acta **53**, 2679 (2008)

16.318 C.C. Hu, M.J. Liu, K.H. Chang: Anodic deposition of hydrous ruthenium oxide for supercapacitors, J. Power Sources **163**, 1126 (2007)

16.319 C.C. Hu, H.R. Chiang, C.C. Wang: Electrochemical and structural investigations of oxide films anodically formed on ruthenium-plated titanium electrodes in sulfuric acid, J. Solid State Electrochem. **7**, 477 (2003)

16.320 Y. Takasu, Y. Murakami: Electrochemical supercapacitor behavior of nanoparticulate rutile-type $Ru_{1-x}V_xO_2$, Electrochim. Acta **45**, 4135 (2000)

16.321 W. Sugimoto, T. Shibutani, Y. Murakami, Y. Takasu: Design of oxide electrodes with large surface area, Electrochem. Solid-State Lett. **5**, A170 (2002)

16.322 K. Yokoshima, T. Shibutani, M. Hirota, W. Sugimoto, Y. Murakami, Y. Takasu: Charge storage capabilities of rutile-type RuO_2VO_2 solid solution for electrochemical supercapacitors, J. Power Sources **160**, 1480 (2006)

16.323 Y.U. Jeong, A. Manthiram: Amorphous ruthenium-chromium oxides for electrochemical capacitors, Electrochem. Solid-State Lett. **3**, 205 (2000)

16.324 Y.U. Jeong, A. Manthiram: Amorphous tungsten oxide/ruthenium oxide composites for electrochemical capacitors, J. Electrochem. Soc. **148**, A189 (2001)

16.325 C.-C. Wang, C.-C. Hu: Electrochemical and textural characteristics of $(Ru-Sn)O_x \cdot nH_2O$ for supercapacitors effects of composition and annealing, J. Electrochem. Soc. **152**, A370 (2005)

16.326 F. Cao, J. Prakash: Performance investigations of $Pb_2Ru_2O_{6.5}$ oxide based pseudocapacitors, J. Power Sources **92**, 40 (2001)

16.327 M. Wohlfahrt-Mehrens, J. Schenk, P.M. Wilde, E. Abdelmula, P. Axmann, J. Garche: New materials for supercapacitors, J. Power Sources **105**, 182 (2002)

16.328 B.-O. Park, C.D. Lokhande, H.-S. Park, K.-D. Jung, O.-S. Joo: Preparation of lead ruthenium oxide and its use in electrochemical capacitor, Mater. Chem. Phys. **86**, 239 (2004)

16.329 T. Nanaumi, Y. Ohsawa, K. Kobayakawa, Y. Sato: High energy electrochemical capacitor materials prepared by loading ruthenium oxide on activated carbon, Electrochemistry **70**, 681 (2002)

16.330 Y.H. Lee, J.G. Oh, H.S. Oh, H. Kim: Novel method for the preparation of carbon supported nanosized amorphous ruthenium oxides for supercapacitors, Electrochem. Commun. **10**, 1035 (2008)

16.331 K. Naoi, S. Ishimoto, N. Ogihara, Y. Nakagawa, S. Hatta: Encapsulation of nanodot ruthenium oxide into KB for electrochemical capacitors, J. Electrochem. Soc. **156**, A52 (2009)

16.332 W. Sugimoto, H. Iwata, Y. Yasunaga, Y. Murakami, Y. Takasu: Preparation of ruthenic acid nanosheets and utilization of its interlayer surface for electrochemical energy storage, Angew. Chem. Int. Ed. **42**, 4092 (2003)

16.333 W. Sugimoto, M. Yonezawa, Y. Takasu: Pseudocapacitance of ruthenium oxide nanosheets derived from layered $NaRuO_2$ with α-NaFe O_2-type structure, Abstr. 214th Electrochem. Soc. Meet. (2008)

16.334 S. Aridizzone, G. Fregonara, S. Trasatti: "Inner" and "outer" active surface of RuO_2 electrodes, Electrochim. Acta **35**, 263 (1990)

16.335 J. Rishpon, S. Gottesfeld: Resolution of fast and slow charging processes in ruthenium oxide films: An AC impedance and optical investigation, J. Electrochem. Soc. **131**, 1960 (1984)

16.336 I.-H. Kim, K.-B. Kim: Ruthenium oxide thin film electrodes prepared by electrostatic spray deposition and their charge storage mechanism, J. Electrochem. Soc. **151**, E7 (2004)

16.337 A. Foelske, O. Barbieri, M. Hahn, R. Kötz: An X-ray photoelectron spectroscopy study of hydrous ruthenium oxide powders with various water contents for supercapacitors, Electrochem. Solid-State Lett. **9**, A268 (2006)

16.338 D. Rochefort, P. Dabo, D. Guay, P.M.A. Sherwood: XPS investigations of thermally prepared RuO_2 electrodes in reductive conditions, Electrochim. Acta **48**, 4245 (2003)

16.339 C. Chabanier, E. Irissou, D. Guay, J.F. Pelletier, M. Sutton, L.B. Lurio: Hydrogen absorption in thermally prepared RuO_2 electrode, Electrochem. Solid-State Lett. **5**, E40 (2002)

16.340 C. Chabanier, D. Guay: Activation and hydrogen absorption in thermally prepared RuO_2 and IrO_2, J. Electroanal. Chem. **570**, 13 (2004)

16.341 O. Barbieri, M. Hahn, A. Foelske, R. Kötz: Effect of electronic resistance and water content on the performance of RuO_2 for supercapacitors, J. Electrochem. Soc. **153**, A2049 (2006)

16.342 I.C. Stefan, Y. Mo, M.R. Antonio, D.A. Scherson: In situ Ru L_{II} and L_{III} edge X-ray absorption near edge structure of electrodeposited ruthenium dioxide films, J. Phys. Chem. B **106**, 12373 (2002)

16.343 Y. Mo, W.-B. Cai, J. Dong, P.R. Carey, D.A. Scherson: In situ surface enhanced raman scattering of ruthenium dioxide films in acid electrolytes, Electrochem. Solid-State Lett. **4**, E37 (2001)

16.344 H. Chol Jo, K.M. Kim, H. Cheong, S.-H. Lee, S.K. Deb: In situ Raman spectroscopy of $RuO_2 \cdot xH_2O$, Electrochem. Solid-State Lett. **8**, E39 (2005)

16.345 S.-H. Lee, P. Liu, M.J. Seong, H.M. Cheong, C.E. Tracy, S.K. Deb: Electrochemical supercapacitors for optical modulation, Electrochem. Solid-State Lett. **6**, A40 (2003)

16.346 S.-H. Lee, P. Liu, H.M. Cheong, C.E. Tracy, S.K. Deb: Electrochromism of amorphous ruthenium oxide thin films, Solid State Ionics **165**, 217 (2003)

16.347 H.Y. Lee, J.B. Goodenough: Ideal supercapacitor behavior of amorphous $V_2O_5 \cdot nH_2O$ in potassium chloride (KCl) aqueous solution, J. Solid State Chem. **148**, 81 (1999)

16.348 N.L. Wu: Nanocrystalline oxide supercapacitors, Mater. Chem. Phys. **75**, 6 (2002)

16.349 Q. Zhou, X. Wang, Y. Liu, Y. He, Y. Gao, J. Liu: High rate capabilities of $NiCo_2O_4$-based hierarchical superstructures for rechargeable charge storage, J. Electrochem. Soc. **161**, A1922 (2014)

16.350 T. Brousse, J.W. Long, D. Bélanger: To be or not to be pseudocapacitive?, J. Electrochem. Soc. **162**, A5185 (2015)

16.351 H. Wang, H. Yi, X. Chen, X. Wang: Facile synthesis of a nano-structured nickel oxide electrode with outstanding pseudocapacitive properties, Electrochim. Acta **105**, 353 (2013)

16.352 B.E. Conway, W.G. Pell, T.C. Liu: Behavior of molybdenum nitrides as materials for electrochemical capacitors: Comparison with ruthenium oxide, J. Electrochem. Soc. **145**, 1882 (1998)

16.353 H. Gao, Y.-J. Ting, N.P. Kherani, K. Lian: Ultra-high-rate all-solid pseudocapacitive electrochemical capacitors, J. Power Sources **222**, 301 (2013)

16.354 R. Lucio Porto, R. Frappier, J.B. Ducros, C. Aucher, H. Mosqueda, S. Shenu, B. Chavillon, F. Tessier, F. Cheviré, T. Brousse: Titanium and vanadium oxynitride powders as pseudo-capacitive materials for electrochemical capacitors, Electrochim. Acta **82**, 257 (2012)

16.355 D. Choi, E. George, E. Blomgren, N. Kumta: Fast and reversible surface redox reaction in nanocrystalline vanadium nitride supercapacitors, Adv. Mater. **18**, 1178 (2006)

16.356 O. Kartachova, A.M. Glushenkov, Y. Chen, H. Zhang, X.J. Dai, Y. Chen: Electrochemical capacitance of mesoporous tungsten oxynitride in aqueous electrolytes, J. Power Sources **220**, 298 (2012)

16.357 S. Bouhtiyya, R. Lucio Porto, B. Laïk, P. Boulet, F. Capon, J.P. Pereira-Ramos, T. Brousse, J.F. Pierson: Application of sputtered ruthenium nitride thin films as electrode material for energy-storage devices, Scr. Mater. **68**, 659 (2013)

16.358 J.H. Park, O.O. Park: Hybrid electrochemical capacitors based on polyaniline and activated carbon electrodes, J. Power Sources **111**, 185 (2002)

16.359 Y.-G. Wang, L. Cheng, Y.-Y. Xia: Electrochemical profile of nano-particle CoAl double hydroxide/active carbon supercapacitor using KOH electrolyte solution, J. Power Sources **153**, 191 (2006)

16.360 C.-Z. Yuan, B. Gao, X.-G. Zhang: Electrochemical capacitance of $NiO/Ru_{0.35}V_{0.65}O_2$ asymmetric electrochemical capacitor, J. Power Sources **173**, 606 (2007)

16.361 A. Du Pasquier, I. Plitz, S. Menocal, G. Amatucci: A comparative study of Li-ion battery, supercapacitor and nonaqueous asymmetric hybrid devices for automotive applications, J. Power Sources **115**, 171 (2003)

16.362 A. Yoshino, T. Tsubata, M. Shimoyamada, H. Satake, Y. Okano, S. Mori, S. Yata: Development of a lithium-type advanced energy storage device, J. Electrochem. Soc. **151**, A2180 (2004)

16.363 T. Brousse, R. Marchand, P.-L. Taberna, P. Simon: TiO_2 (B)/activated carbon non-aqueous hybrid system for energy storage, J. Power Sources **158**, 571 (2006)

16.364 T. Aida, I. Murayama, K. Yamada, M. Morita: An advanced hybrid electrochemical capacitor that uses a wide potential range at the positive electrode, Electrochem. Solid-State Lett. **9**, A534 (2006)

16.365 T. Aida, I. Murayama, K. Yamada, M. Morita: High-energy-density hybrid electrochemical capacitor using graphitizable carbon activated with KOH for positive electrode, J. Power Sources **166**, 462 (2007)

16.366 S.-H. Woo, K. Dokko, H. Nakano, K. Kanamura: Bimodal porous carbon as a negative electrode material for lithium-ion capacitors, Electrochemistry **75**, 635 (2007)

16.367 V. Khomenko, E. Raymundo-Piñero, F. Béguin: High-energy density graphite/AC capacitor in organic electrolyte, J. Power Sources **177**, 643 (2008)

16.368 S. Stewart, P. Albertus, V. Srinivasan, I. Plitz, N. Pereira, G. Amatucci, J. Newman: Optimizing the performance of lithium titanate spinel paired with activated carbon or iron phosphate, J. Electrochem. Soc. **155**, A253 (2008)

16.369 H. Laforgue, P. Simon, J.F. Fauvarque, M. Mastragostino, F. Soavi, J.F. Sarrau, P. Lailler, M. Conte, E. Rossi, S. Saguatti: Activated carbon/conducting polymer hybrid supercapacitors, J. Electrochem. Soc. **150**, A645 (2003)

16.370 H. Wang, M. Yoshio: Graphite, a suitable positive electrode material for high-energy electrochemical capacitors, Electrochem. Commun. **8**, 1481 (2006)

16.371 L.J. Hardwick, M. Hahn, P. Ruch, M. Holzapfel, W. Scheifele, H. Buqa, F. Krumeich, P. Novák, R. Kötz: An in situ Raman study of the intercalation of supercapacitor-type electrolyte into microcrystalline graphite, Electrochim. Acta **52**, 675 (2006)

16.372 P.W. Ruch, M. Hahn, F. Rosciano, M. Holzapfel, H. Kaiser, W. Scheifele, B. Schmitt, P. Novák, R. Kötz, A. Wokaun: In situ X-ray diffraction of the intercalation of $(C_2H_5)_4N^+$ and BF^{4-} into graphite from acetonitrile and propylene carbonate based supercapacitor electrolytes, Electrochim. Acta **53**, 1074 (2007)

16.373 H. Wang, M. Yoshio: Performance of AC/graphite capacitors at high weight ratios of AC/graphite, J. Power Sources **177**, 681 (2008)

16.374 Y. Yokoyama, N. Shimosaka, H. Matsumoto, M. Yoshio, T. Ishihara: Effects of supporting electrolyte on the storage capacity of hybrid capacitors using graphitic and activated carbon, Electrochem. Solid-State Lett. **11**, A72 (2008)

16.375 K. Naoi: Nanohybrid capacitor: The next generation electrochemical capacitors, Fuel Cells **10**, 825–833 (2010)

16.376 T. Kawasato, K. Hiratsuka, T. Morimoto: Development of the coin-type 3.3 V double layer capacitor for back-up power sources of IC memories, AGC Res. Rep. **52**, 39–46 (2002)

16.377 K. Chiba, T. Ueda, H. Yamamoto: Performance of electrolytic solution composed of linear-structure sulfones and electric double-layer capacitor using it, Electrochem. 48th Batter. Symp. Jpn (2007) p. 2C16
16.378 K. Naoi, K. Chiba: High-voltage electrode/electrolyte interface in ECs and hybrid capacitor. In: *Nanotechnology in Advanced Electrochemical Power Sources*, ed. by S.R.S. Prabaharan, M.S. Michael (Pan Stanford Publ., Singapore 2014)
16.379 C. Nunjundiah, S.F. McDevitt, V.R. Koch: Differential capacitance measurements in solvent-free ionic liquids at hg and c interfaces, J. Electrochem. Soc. **144**, 3392 (1997)
16.380 M. Ue, M. Takeda, T. Takahashi, M. Takehara: Ionic liquids with low melting points and their application to double-layer capacitor electrolytes, Electrochem. Solid-State Lett. **5**, A119 (2002)
16.381 M. Ue, M. Takeda, A. Toriumi, A. Kominato, R. Hagiwara, Y. Ito: Application of low-viscosity ionic liquid to the electrolyte of double-layer capacitors, J. Electrochem. Soc. **150**, A499 (2003)
16.382 T. Sato, G. Masuda, K. Takagi: Electrochemical properties of novel ionic liquids for electric double layer capacitor applications, Electrochim. Acta **49**, 3603 (2004)
16.383 I. Murayama, N. Yoshimoto, M. Egashira, M. Morita, Y. Kobayashi, M. Ishikawa: Characteristics of electric double layer capacitors with an ionic liquid electrolyte containing Li ion, Electrochemistry **73**, 600 (2005)
16.384 S. Shiraishi, N. Nishina, A. Oya, R. Hagiwara: Electric double layer capacitance of activated carbon fibers in ionic liquid : EMImBF$_4$, Electrochemistry **73**, 593 (2005)
16.385 Y. Nagao, Y. Nakayama, H. Oda, M. Ishikawa: Activation of an ionic liquid electrolyte for electric double layer capacitors by addition of $BaTiO_3$ to carbon electrodes, J. Power Sources **166**, 595 (2007)
16.386 A. Balducci, R. Dugas, P.L. Taberna, P. Simon, D. Plée, M. Mastragostino, S. Passerini: High temperature carbon–carbon supercapacitor using ionic liquid as electrolyte, J. Power Sources **165**, 922 (2007)
16.387 A. Lewandowski, A. Olejniczak: N-Methyl-N-propylpiperidinium bis(trifluoromethanesulphonyl)imide as an electrolyte for carbon-based double-layer capacitors, J. Power Sources **172**, 487 (2007)
16.388 H. Zhang, G. Cao, Y. Yang, Z. Gu: Comparison between electrochemical properties of aligned carbon nanotube array and entangled carbon nanotube electrodes, J. Electrochem. Soc. **155**, K19 (2008)
16.389 N. Handa, T. Sugimoto, M. Yamagata, M. Kikuta, M. Kono, M. Ishikawa: A neat ionic liquid electrolyte based on FSI anion for electric double layer capacitor, J. Power Sources **185**, 1585 (2008)
16.390 T. Devarajan, S. Higashiya, C. Dangler, M. Rane-Fondacaro, J. Snyder, P. Haldar: Novel ionic liquid electrolyte for electrochemical double layer capacitors, Electrochem. Commun. **11**, 680 (2009)
16.391 A. Balducci, U. Bardi, S. Caporali, M. Mastragostino, F. Soavi: Ionic liquids for hybrid supercapacitors, Electrochem. Commun. **6**, 566 (2004)
16.392 A. Balducci, W.A. Henderson, M. Mastragostino, S. Passerini, P. Simon, F. Soavi: Cycling stability of a hybrid activated carbon/poly(3-methylthiophene) supercapacitor with N-butyl-N-methylpyrrolidinium bis(trifluoromethanesulfonyl)imide ionic liquid as electrolyte, Electrochim. Acta **50**, 2233 (2005)
16.393 C. Arbizzani, M. Biso, D. Cericola, M. Lazzari, F. Soavi, M. Mastragostino: Safe, high-energy supercapacitors based on solvent-free ionic liquid electrolytes, J. Power Sources **185**, 1575 (2008)
16.394 M. Ishikawa, M. Ihara, M. Morita, Y. Matsuda: Electric double layer capacitors with new gel electrolytes, Electrochim. Acta **40**, 2217 (1995)
16.395 X. Liu, T. Osaka: Properties of electric double-layer capacitors with various polymer gel electrolytes, J. Electrochem. Soc. **144**, 3066 (1997)
16.396 S.A. Hashmi, R.J. Latham, R.G. Linford, W.S. Schlindwein: Studies on all solid state electric double layer capacitors using proton and lithium ion conducting polymer electrolytes, J. Chem. Soc. Faraday Trans. **93**, 4177 (1997)
16.397 T. Osaka, X. Liu, M. Mojima: Acetylene black/poly(vinylidene fluoride) gel electrolyte composite electrode for an electric double-layer capacitor, J. Power Sources **74**, 122 (1998)
16.398 Y. Matsuda, K. Inoue, H. Takeuchi, Y. Okuhama: Gel polymer electrolytes for electric double layer capacitors, Solid State Ionics **113–115**, 103 (1998)
16.399 T. Osaka, X. Liu, M. Nojima, T. Momma: An electrochemical double layer capacitor using an activated carbon electrode with gel electrolyte binder, J. Electrochem. Soc. **146**, 1724 (1999)
16.400 M. Ishikawa, L. Yamamoto, M. Morita, Y. Ando: Performance of electric double layer capacitors with gel electrolytes containing an asymmetric ammonium salt, Electrochemistry **69**, 437 (2001)
16.401 X. Liu, T. Osaka: New insights into the carbon/polymer electrolyte interface in the electric double layer capacitor, Electrochemistry **69**, 422 (2001)
16.402 S. Mitra, A.K. Shukla, S. Sampath: Electrochemical capacitors with plasticized gel-polymer electrolytes, J. Power Sources **101**, 213 (2001)
16.403 C.-M. Yang, W.I. Cho, J.K. Lee, H.-W. Rhee, B.W. Cho: EDLC with UV-cured composite polymer electrolyte based on poly[(ethylene glycol) diacrylate]/poly(vinylidene fluoride)/poly(methyl methacrylate) blends, Electrochem. Solid-State Lett. **8**, A91 (2005)
16.404 A. Lewandowski, A. Świderska: Electrochemical capacitors with polymer electrolytes based on ionic liquids, Electrochim. Acta **161**, 243 (2003)
16.405 S. Yamazaki, A. Takegawa, Y. Kaneko, J. Kadokawa, M. Yamagata, M. Ishikawa: An acidic cellulose–chitin hybrid gel as novel electrolyte for an electric double layer capacitor, Electrochem. Commun. **11**, 68 (2009)

16.406 P. Staiti, M. Minutoli, F. Lufrano: All solid electric double layer capacitors based on Nafion ionomer, Electrochim. Acta **47**, 2795 (2002)
16.407 W. Sugimoto, K. Yokoshima, K. Ohuchi, Y. Murakami, Y. Takasu: Fabrication of thin-film, flexible, and transparent electrodes composed of ruthenic acid nanosheets by electrophoretic deposition and application to electrochemical capacitors, J. Electrochem. Soc. **153**, A255 (2006)
16.408 A. Lewandowski, M. Zajder, E. Frackowiak, F. Béguin: Supercapacitor based on activated carbon and polyethylene oxide-KOH-H_2O polymer electrolyte, Electrochim. Acta **46**, 2777 (2001)
16.409 Y.-G. Wang, X.-G. Zhang: Preparation and electrochemical capacitance of RuO_2/TiO_2 nanotubes composites, Electrochim. Acta **49**, 1957 (2004)
16.410 C.-C. Yang, S.-T. Hsu, W.-C. Chien: All solid-state electric double-layer capacitors based on alkaline polyvinyl alcohol polymer electrolytes, J. Power Sources **152**, 303 (2005)
16.411 C. Yuan, X. Zhang, Q. Wu, B. Gao: Effect of temperature on the hybrid supercapacitor based on NiO and activated carbon with alkaline polymer gel electrolyte, Solid State Ionics **177**, 1237 (2006)
16.412 N.A. Choudary, S. Sampath, A.K. Shukla: Gelatin hydrogel electrolytes and their application to electrochemical supercapacitors, J. Electrochem. Soc. **155**, A74 (2007)
16.413 C. Iwakura, H. Wada, S. Nohara, N. Furukawa, H. Inoue, M. Morita: New electric double layer capacitor with polymer hydrogel electrolyte, Electrochem. Solid-State Lett. **6**, A37 (2003)
16.414 H. Wada, S. Nohara, N. Furukawa, H. Inoue, N. Sugoh, H. Iwasaki, M. Morita, C. Iwakura: Electrochemical characteristics of electric double layer capacitor using sulfonated polypropylene separator impregnated with polymer hydrogel electrolyte, Electrochim. Acta **49**, 4871 (2004)
16.415 H. Wada, K. Yoshikawa, S. Nohara, N. Furukawa, H. Inoue, N. Sugoh, H. Iwasaki, C. Iwakura: Electrochemical characteristics of new electric double layer capacitor with acidic polymer hydrogel electrolyte, J. Power Sources **159**, 1464 (2006)
16.416 S. Nohara, T. Asahina, H. Wada, N. Furukawa, H. Inoue, N. Sugoh, H. Iwasaki, C. Iwakura: Hybrid capacitor with activated carbon electrode, $Ni(OH)_2$ electrode and polymer hydrogel electrolyte, J. Power Sources **157**, 605 (2006)
16.417 S. Nohara, T. Miura, C. Iwakura, H. Inoue: Electric double layer capacitor using polymer hydrogel electrolyte with 4M H_2SO_4 aqueous solution, Electrochemistry **75**, 579 (2007)
16.418 H. Inoue, T. Morimoto, S. Nohara: Electrochemical characterization of a hybrid capacitor with Zn and activated carbon electrodes, Electrochem. Solid-State Lett. **10**, A261 (2007)
16.419 J. Qiao, N. Yoshimoto, M. Ishikawa, M. Morita: Acetic acid-doped poly(ethylene oxide)-modified poly(methacrylate): A new proton conducting polymeric gel electrolyte, Electrochim. Acta **47**, 3441 (2002)
16.420 F. Lufrano, P. Staiti: Conductivity and capacitance properties of a supercapacitor based on Nafion electrolyte in a nonaqueous system, Electrochem. Solid-State Lett. **7**, A447 (2004)
16.421 M. Morita, N. Ohsumi, N. Yoshimoto, M. Egashira: Proton-conducting non-aqueous gel electrolyte for a redox capacitor system, Electrochemistry **75**, 641 (2007)
16.422 B. Mattsson, H. Ericson, L.M. Torell, F. Sundholm: Micro-Raman investigations of PVDF-based proton-conducting membranes, J. Polym. Sci. A **37**, 3317 (1999)
16.423 H. Ericson, C. Svanberg, A. Brodin, A.M. Grillone, S. Panero, B. Scrosati, P. Jacobsson: Poly(methyl methacrylate)-based protonic gel electrolytes: A spectroscopic study, Electrochim. Acta **45**, 1409 (2000)
16.424 G. Żukowska, N. Chojnacka, W. Wieczorek: Effect of gel composition on the conductivity of proton-conducting gel polymeric electrolytes doped with H_3PO_4, Chem. Matter **12**, 3578 (2000)
16.425 W. Wieczorek, G. Żukowska, R. Borkowska, S.H. Chung, S. Greenbaum: A basic investigation of anhydrous proton conducting gel electrolytes, Electrochim. Acta **46**, 1427 (2001)
16.426 B.-K. Choi, S.-H. Park, S.-W. Joo, M.-S. Gong: Electrical and thermal properties of poly(vinylidene fluoride-hexafluoropropylene)-based proton conducting gel-electrolytes, Electrochim. Acta **50**, 649 (2004)
16.427 H.P. Singh, S.S. Sekhon: Non-aqueous proton conducting polymer gel electrolytes, Electrochim. Acta **50**, 621 (2004)
16.428 J. Qiao, N. Yoshimoto, M. Morita: Proton conducting behavior of a novel polymeric gel membrane based on poly(ethylene oxide)-grafted-poly(methacrylate), J. Power Sources **105**, 45 (2002)
16.429 J. Qiao, N. Yoshimoto, M. Ishikawa, M. Morita: Proton conductance and spectroscopic characteristics of acid-doped polymer gels based on poly(ethylene oxide)-modified polymethacrylate, Solid State Ionics **156**, 415 (2003)
16.430 M. Morita, J. Qiao, N. Yoshimoto, M. Ishikawa: Application of proton conducting polymeric electrolytes to electrochemical capacitors, Electrochim. Acta **50**, 837 (2004)
16.431 M. Ue, K. Ida, S. Mori: Electrochemical properties of organic liquid electrolytes based on quaternary onium salts for electrical double-layer capacitors, J. Elecrochem. Soc. **141**, 2989 (1994)
16.432 A. Chu, P. Braatz: Comparison of commercial supercapacitors and high-power lithium-ion batteries for power-assist applications in hybrid electric vehicles: I. Initial characterization, J. Power Sources **112**, 236 (2006)
16.433 T. Morimoto: Development and industrialization of electric double-layer capacitors, TANSO **214**, 202 (2004), in Japanese
16.434 O. Bohlen, J. Kowal, D.U. Sauer: Ageing behaviour of electrochemical double layer capacitors: Part I. Experimental study and ageing model, J. Power

Sources **172**, 468 (2007)
16.435 M. Hahn, A. Würsig, R. Gallay, P. Novak, R. Kötz: Gas evolution in activated carbon/propylene carbonate based double-layer capacitors, Electrochem. Commun. **7**, 925 (2005)
16.436 F.P. Campana, M. Hahn, A. Foelske, P. Ruch, R. Kötz, H. Siegenthaler: Intercalation into and film formation on pyrolytic graphite in a supercapacitor-type electrolyte $(C_2H_5)_4NBF_4$/propylene carbonate, Electrochem. Commun. **8**, 1363 (2006)
16.437 L.F. Xiao, Q.F. Yue, C.G. Xia, L.W. Xu: Supported basic ionic liquid: Highly effective catalyst for the synthesis of 1,2-propylene glycol from hydrolysis of propylene carbonate, J. Molec. Catal. A **279**, 230 (2008)
16.438 P. Kurzweil, M. Chwistek: Electrochemical stability of organic electrolytes in supercapacitors: Spectroscopy and gas analysis of decomposition products, J. Power Sources **176**, 555 (2008)
16.439 S. Ishimoto, Y. Asakawa, M. Shinya, K. Naoi: Degradation responses of activated-carbon-based edlcs for higher voltage operation and their factors, J. Electrochem. Soc. **156**, A563 (2009)
16.440 J.R. Miller: A brief history of supercapacitors, Battery Energy Storage Technol. **18**, 61–78 (2007)
16.441 S. Razoumov, A. Klementov, S. Litvinenko, A. Beliakov: Asymmetric Electrochemical Capacitor and Method Of Making, US Patent 6 222 723 (2001)
16.442 H. Uchi: Performance and application – DLCAP, Proc. Adv. Capacitor World Summit, San Diego (2005)
16.443 Superior Tool Company: UltraCut 35278 cordless tubing cutter, http://www.superiortool.com
16.444 J.R. Miller: Capacitor Tech Talk **18**, 121–128 (2007)
16.445 J. Groot: Energy storage systems for heavy-duty HEVs, Proc. Adv. Capacitor World Summit, La Jolla (2009)
16.446 L.A. Viterna: Hybrid electric transit bus, Proc. SAE Int. Truck Bus Meet., Cleveland (1997), paper 973202
16.447 T. Bartley: Ultracapacitors no longer just a technology: Real, safe, efficient, available, Proc. Adv. Capacitor World Summit, Washington (2004)
16.448 G. Willms: Hybrid-electric drive systems for heavy duty vehicles, Proc. Adv. Capacitor World Summit, San Diego (2008)
16.449 T. Apalenek: Advanced energy storage – Field experience, Proc. 9th Int. Adv. Automot. Battery Ultracapacitor Conf. Symp., Long Beach (2009)
16.450 M. Bolton: Energy storage systems for severe duty truck applications, Proc. 9th Int. Adv. Automot. Battery Ultracapacitor Conf. Symp., Long Beach (2009)
16.451 J. Gonder, A. Pesaran, J. Lustbader, H. Tataria: Fuel economy and performance of mild hybrids with ultracapacitors, Proc. 9th Int. Adv. Automot. Battery Ultracapacitor Conf. Symp., Long Beach (2009)
16.452 J. Schneeberger, H. Hakvoort: Requirements and design considerations of automotive double-layer capacitor modules, Proc. 8th Int. Adv. Automot. Battery Ultracapacitor Conf. Symp., Tampa (2008)
16.453 I.N. Varakin, A.D. Klementov, S.V. Litvienko, S.V. Starodubtsev, A.B. Stepanov: Application of ultracapacitors as traction energy sources, Proc. 7th Int. Semin. Double Layer Capacitor Similar Energy Storage Dev., Deerfield Beach (1997)
16.454 T. Geist: A 2000 V ultracapacitor for transmission stability, Adv. Capacitor World Summit, Washington (2004)
16.455 K. Rechenberg, M. Meinert: Requirements on DLC energy storage units for rolling stock, Proc. 9th Int. Adv. Automot. Battery Ultracapacitor Conf. Symp., Long Beach (2009)
16.456 M. Steiner, M. Klohr, S. Pagiela: Energy storage system with ultracaps on board of railway vehicles, Eur. Conf. Power Electronics Appl. (2007), doi:10.1109/EPE.2007.4417400
16.457 M. Meinert: Experiences of the hybrid energy storage system Sitras HES based on a NiMH-Battery and double layer capacitors in tram operation, Proc. 9th Int. Adv. Automot. Battery Ultracapacitor Conf. Symp., Long Beach (2009)
16.458 A. Schneuwly: Efficient energy storage by ultracapacitors to address new demands for electrical power within vehicles, Proc. 8th Int. Adv. Automot. Battery Ultracapacitor Conf. Symp., Tampa (2008)
16.459 J.R. Miller: Boom boom time for ultracaps, Battery Energy Storage Technol. **16**, 61–71 (2007)
16.460 Maxwell Technologies, Inc., San Diego, USA: http://www.maxwell.com/news-events/release.asp?PRID=162
16.461 A.I. Beliakov: Russian supercapacitors to start engines, Battery Int. **102**, 102 (1993)
16.462 A.I. Beliakov: Investigation and developing of double layer capacitors for start of internal combustion engines and of accelerating systems of hybrid electric drive, Proc. 6th Int. Semin. Double Layer Capacitor Similar Energy, Storage Dev., Deerfield Beach (1996)
16.463 J.R. Miller, J. Burgel, H. Catherino, F. Krestik, J. Monroe, J.R. Stafford: Truck starting using electrochemical capacitors, Int. Truck Bus Meet., Indianapolis (1998), SAE Tech. Paper 982794
16.464 J.R. Miller: Engineering battery-capacitor combinations in high power applications: Diesel engine starting, Proc. 9th Int. Semin. Double Layer Capacitor Similar Energy Storage Dev., Deerfield Beach (1999)
16.465 W. Ong, R. Johnston: Electrochemical capacitors and their potential application to heavy duty vehicles, Int. Truck Bus Meet. Portland (2000), SAE Tech. Paper 200-01-3495
16.466 J.R. Miller: Standards for engine-starting capacitors, Proc. 15th Int. Semin. Double Layer Capacitor Hybrid Energy Storage Dev., Deerfield Beach (2005)
16.467 T. Furukawa: Engine cranking with green technology, Proc. Adv. Capacitor World Summit, San Diego (2008)
16.468 SAFT: http://www.saftbatteries.com
16.469 J. Furukawa, T. Takada, H. Sakamoto, L.T. Lam, T. Sugimura, E. Sato, M. Tsuyuki: Development of the flooded-type ultrabattery and battery sen-

sor for micro-HEV applications, Proc. 9th Int. Adv. Automot. Battery Ultracapacitor Conf. Symp., Long Beach (2009)
16.470 T. Furukawa: DLCAP energy storage system multiple application, Proc. Adv. Capacitor World Summit, San Diego (2006)
16.471 Komatsu: Komatsu Introduces the World's First Hydraulic Excavator, Press Release, http://www.komatsu.com/CompanyInfo/press/20080513151136045 88.html
16.472 C. Greenhill: Capacitors in fuel cell forklifts, Proc. Adv. Capacitor World Summit, San Diego (2006)
16.473 T. Yamamoto: The characteristics of MEIDENSHA's bipolar laminate type electric double layer capacitor and its applications, Proc. 9th Int. Adv. Automot. Battery Ultracapacitor Conf. Symp., Long Beach (2009)
16.474 I. Gyuk: Supercapacitors for electricity storage, scope and projects, Proc. Adv. Capacitor World Summit, Washington (2004)
16.475 S. Kazaryan: Characteristics of the $PbO_2|H_2SO_4|C$ ECs, Proc. Adv. Capacitor World Summit, San Diego (2007)

17. Electrochemical Capacitors

Colin G. Cameron

Having power and energy characteristics between batteries and conventional capacitors, electrochemical capacitors offer new opportunities in electrical engineering and a fertile ground for the development and refinement of new electrode materials. This chapter will begin by introducing the fundamentals of electrochemical double-layer capacitors and pseudocapacitors (Sect. 17.1). It will go on to describe the most commonly used methods (Sect. 17.2) for assessing the capacitance, energy, and power of electrochemical capacitors:

- Constant current discharge (Sect. 17.2.1)
- Cyclic voltammetry (Sect. 17.2.2)
- Impedance spectroscopy (Sect. 17.2.3).

Electrode configurations and cell designs will be considered in Sect. 17.2.3, as well as practical concerns such as the electrolyte, the separator, and the current collectors, and common experimental pitfalls will be pointed out.

17.1 **The Nature of Capacitance** 563
17.1.1 Important Capacitor Relationships 565
17.1.2 Double-Layer Capacitance 565
17.1.3 Pseudocapacitance 566
17.1.4 The Role of the Electrolyte 567
17.2 **Test Methods** 568
17.2.1 Constant Current Discharge 568
17.2.2 Cyclic Voltammetry 571
17.2.3 Impedance 573
17.2.4 Self-Discharge and Leak Currents 578
17.3 **Configuration** 578
17.3.1 Three- and Two-Electrode Cells 578
17.3.2 Hybrid Electrochemical Capacitors 581
17.3.3 Two-Electrode Cell Designs 581
17.3.4 Electrode Construction 582
17.3.5 Separators 583
17.3.6 Current Collectors 583
17.4 **Further Practical Concerns** 584
17.4.1 Electrode Area and Pore Size 584
17.4.2 Minimizing Series Resistance 585
17.4.3 Standard Testing 585
17.5 **Summary and Conclusions** 586
17.6 **Symbols** 586
References 587

Electrochemical capacitors (ECs) store energy by means of one of two rapid electrochemical mechanisms, and in doing so take on properties midway between batteries and conventional capacitors. Often known as supercapacitors and ultracapacitor, the less ambiguous term ECs shall be used in this chapter to distinguish these devices from other advanced forms of capacitive energy storage that use unrelated physical phenomena.

17.1 The Nature of Capacitance

Batteries, even advanced Li-ion batteries, are generally unable to sustain rapid power delivery or uptake. Battery chemistry is faradaic, relying on reactions within the bulk of the electrode materials, limited by diffusion and electrochemical kinetics. The same applies to fuel cells, where power limitations are even more urgent due to added problems such as water discharge and gas flow, especially under fluctuating loads [17.2]. On the other hand, ECs are well suited to applications needing transient high-power energy storage or provision, with excellent cycle efficiency. The Ragone plot (Sect. 17.2.1) in Fig. 17.1 illustrates this concept: ECs can provide an order of magnitude more power than the best batteries, but with an order of magnitude

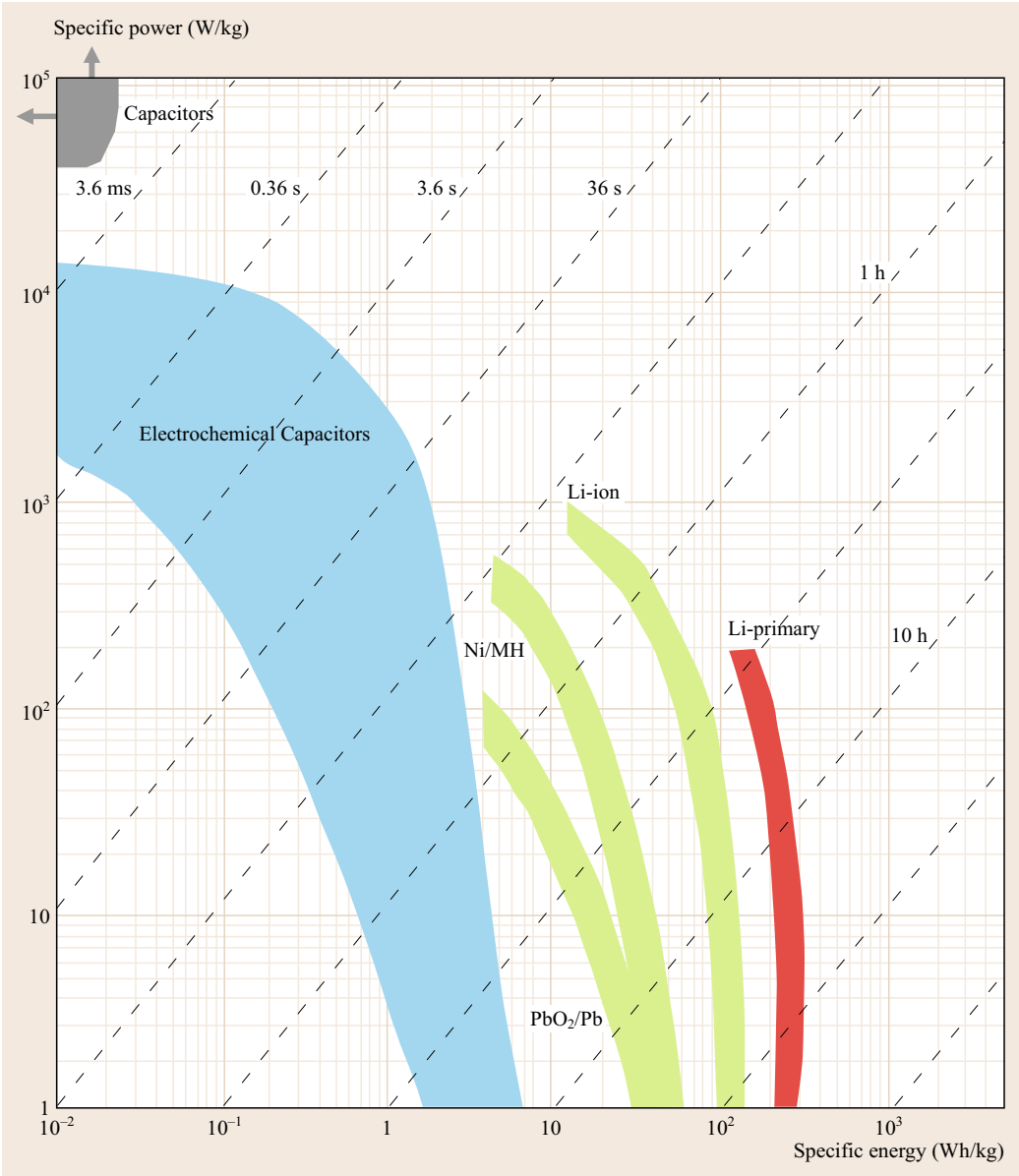


Fig. 17.1 Ragone diagram comparing approximate power and energy ranges of ECs and conventional batteries (after [17.1])

less energy. The diagonal lines denote the time constants of the devices (energy divided by power). ECs operate best in tens-of-seconds or shorter discharges, while batteries drain over minutes or hours. To venture outside of these time scales requires oversizing of the devices to overcome their inherent limitations. A familiar example is the massive lead acid battery that cranks a car engine for only a few seconds. The same function could be fulfilled, in principle, by a much smaller battery coupled to an EC. A current example is found on the Airbus A380, where banks of ECs are used for emergency door opening power, thereby avoiding heavy batteries and/or power cables [17.1, 3]. Therefore, ECs complement conventional electrical energy storage, providing a function somewhere between batteries and dielectric capacitors. They are ideally suited to provide pulse power load leveling in a hybrid arrangement with a high energy source, for example, regenerative braking in a battery-powered car.

Electrochemical capacitors are categorized according to one of two ways that they store energy. The electrochemical double-layer capacitor (EDLC) type (Sect. 17.1.2) works by ion adsorption on large area electrodes. The pseudocapacitance (PC) variety (Sect. 17.1.3) exploits fast electrochemical surface reactions in redox-active materials. The underlying electrochemistry is different, but the overall behavior of the two is similar.

The performance of ECs is usually assessed according to the following key criteria:

1. Power density (power per unit mass, also known as specific power)
2. Energy density (energy per unit mass, also known as specific energy)
3. Specific capacitance (capacitance per unit mass)
4. The voltage range over which the electrodes and electrolyte are stable
5. Self-discharge characteristics.

The reporting of data in a consistent and comparable manner remains a challenge in the study of ECs. There exist test protocols for fully assembled self-contained cells [17.4], but investigation of experimental capacitors at the laboratory scale can be problematic since techniques are not standardized [17.5] and results vary according to experimental conditions [17.6]. This chapter (among others [17.5]) attempts to underline the importance of reporting EC data clearly, and urges researchers to avoid the temptation of using techniques that overstate the potential performance of an electrode material in a working EC cell.

17.1.1 Important Capacitor Relationships

Selected important capacitor relationships and concepts are compiled below. Some derivations can be found later in this chapter, and others can be found elsewhere, such as in *Conway's* book [17.7].

The charge Q, energy E, and power P delivered by an EC are

$$Q = CV\,, \tag{17.1}$$

$$E = \frac{1}{2}CV^2\,, \tag{17.2}$$

$$P = \frac{V^2}{4R_\mathrm{s}}\,, \tag{17.3}$$

where V is the voltage of the capacitor and R_s is the equivalent series resistance (ESR). Power does not depend on C, and energy does not depend on R_s, but the RC time constant τ is a useful parameter that summarizes the discharge characteristics of the device

$$R_\mathrm{s} \times C = \tau\,. \tag{17.4}$$

Two capacitors C_1 and C_2 in series yield a total capacitance C_tot,

$$\frac{1}{C_\mathrm{tot}} = \frac{1}{C_1} + \frac{1}{C_2}\,. \tag{17.5}$$

The current i output of an EC is proportional to its capacitance C and the rate of voltage change $\mathrm{d}V/\mathrm{d}t$

$$i = C\frac{\mathrm{d}V}{\mathrm{d}t}\,. \tag{17.6}$$

The accumulation of charge Q is related to voltage and capacitance by

$$C = \frac{\mathrm{d}Q}{\mathrm{d}V} \tag{17.7}$$

so over range of voltage ΔV,

$$C = \frac{Q}{\Delta V}\,. \tag{17.8}$$

17.1.2 Double-Layer Capacitance

EDLCs store charge electrostatically via the reversible adsorption of electrolyte ions on the surface of chemically stable, high surface area electrodes. Polarization of the electrode leads to adsorption of ions of opposite charge (Fig. 17.2), producing the well-known [17.8] double-layer capacitance C, which is similar in form to the parallel plate capacitor in that energy is stored by separating charge

$$C = \frac{\epsilon_\mathrm{r}\epsilon_0 A}{d}\,, \tag{17.9}$$

where ϵ_r is the dielectric constant of the electrolyte solution, ϵ_0 is the permittivity of a vacuum, A is the surface area of the electrode, and d is the effective thickness of the double layer, the Debye length, $\approx 5-10$ Å in concentrated electrolytes. C ranges from 5 to 50 $\mu\mathrm{F/cm^2}$, depending on the electrolyte [17.9, 10], and is usually $\approx 10-20\,\mu\mathrm{F/cm^2}$ for a smooth electrode in concentrated electrolyte [17.11]. In this way, EDLCs store orders of magnitude more energy than conventional capacitors per unit mass or volume, since d is small, and A can be very large. One can predict the approximate capacitance in an EDLC. For a hypothetical activated carbon with $1000\,\mathrm{m^2/g}$ surface area, an estimated double-layer capacitance of $10\,\mu\mathrm{F/cm^2}$ would

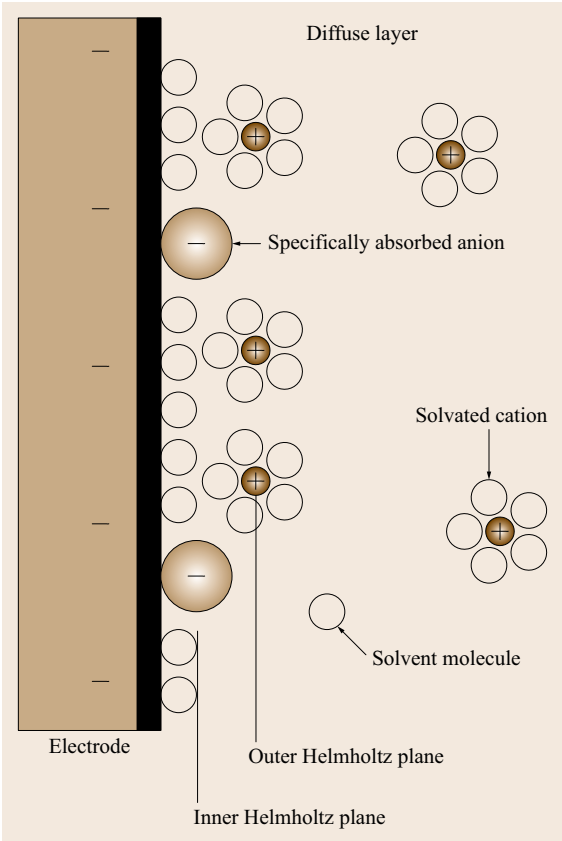


Fig. 17.2 Schematic of the electrochemical double layer

yield 100 F/g. Beyond a simple approximation, this treatment is probably simplistic, and the linear relationship between capacitance and area does not hold because the size of smaller micropores will not permit the ingress of solvated ions (Sect. 17.4.1); the formation of the double layer is inhibited. The surface area of activated carbons measured by Brunauer, Emmett, and Teller (BET) theory (Sect. 17.4.1) can exceed 2000 m^2/g [17.12], but not all of it is necessarily useable by an EDLC.

Since the charge storage is electrostatic, there are no faradaic processes at the electrode. This in turn implies an absence of polarization resistance due to electrochemical kinetics. Furthermore, the lack of redox processes means that the active material is not subjected to deleterious phase changes or swelling that can lead to electrode failure. EDLCs can sustain millions of cycles, while batteries survive only a few thousand at best.

17.1.3 Pseudocapacitance

The phenomenon of PC arises in ECs that exhibit rapid, reversible redox reactions at the electrode surface. Metal oxides, such as RuO_2 and MnO_2, and conducting polymers are widely used. Because the PC process is faradaic, it suffers from long-term instability, like batteries. Unlike the relatively unchanging battery electrode potential, which has its basis in thermodynamics, the pseudocapacitive potential versus state-of-charge profile is linear. The charge transferred is voltage dependent, having the relationship $C = dQ/dV$ (17.7), experiencing potential as a continuous function of state-of-charge [17.13].

One of the most studied pseudocapacitive materials is RuO_2, which undergoes continuous electroadsorption of protons over a window approximately 1.2 V wide (17.10) in which Ru has access to three oxidation states. The process is highly reversible and exhibits good cycle life. Based on electron transfer numbers, the theoretical specific capacitance C_{sp} of $RuO_2 \cdot xH_2O$ is estimated to fall between 1300 and 2200 F/g [17.14], and $C_{sp} > 1000$ F/g is known [17.15, 16]

$$RuO_2 + xH^+ + xe^- \rightleftharpoons RuO_{2-x}(OH)_x \,. \qquad (17.10)$$

Transition metal oxides such as RuO_2 and MnO_2 possess high theoretical PC and as such are attractive candidates for energy storage. However, most of the capacitance – especially in MnO_2 – arises from redox reactions occurring at the surface layer, and bulk material is largely excluded from the process. Consequently, the observed specific capacitance of MnO_2 is consistently lower than the theoretical value [17.17] and depends greatly on the preparation conditions [17.18, 19], influenced by properties such as crystallinity and bonding modes, both of which can be measured by techniques such as x-ray diffraction (XRD) and x-ray photoelectron spectroscopy (XPS) [17.19, 20]. Furthermore, the poor electrical conductivity of MnO_2 will limit the power output of a device based on this material (17.3). The deposition of MnO_2 on high surface area carbon is a promising strategy to improve the effectiveness of the oxide [17.21].

High surface area carbons can also be used as a base for redox-active groups such as carboxylates and quinones bound covalently to the surface. *Pickup* has shown a substantial improvement in capacitance in positive and negative electrodes modified with such functionalities [17.22–24]. The resulting PC provided a boost to the existing large double-layer capacitance.

In general, conducting polymers are more electronically conductive than the metal oxides commonly used for PC (over 300 S/cm for poly(ethylenedioxythiophene) (PEDOT) and polythiophene [17.25, 26]), and they exhibit high specific capacitance, for example, 400–500 F/g for polyaniline (PANI) [17.27]. However, they tend to suffer from poor long-term cycle stabil-

ity owing to the significant volume changes that occur during doping/undoping [17.28]. Typically only a few thousand cycles [17.29] might be useable, compared to 1×10^5 to 1×10^6 for carbon EDLCs, and poor permeability by dopant ions can lead to high internal resistance.

17.1.4 The Role of the Electrolyte

The capacitance of an EC arises from the composition of the electrodes, but the cell voltage and maximum power (via resistance) depend largely on the thermodynamic stability of the electrolyte. Three types of electrolyte are used in EC:

1. Aqueous (commonly H_2SO_4 or KOH)
2. Organic (often tetraalkylammonium salts of BF_4^- or PF_6^- in acetonitrile or propylene carbonate)
3. Ionic liquids.

Pertinent properties are summarized in Table 17.1. The specific capacitance of high area carbon electrodes is much higher in aqueous electrolytes than in nonaqueous due in part to the larger dielectric constant in the former [17.2], but also due to the availability of more pores to the smaller ions. Ideally, the electrode pores should be tailored to a size compatible with the electrolyte ions.

Table 17.1 Typical properties of electrolytes commonly used in ECs. The practical voltage windows might be narrowed by influences such as dissolved oxygen

Electrolyte	Resistivity (Ω cm)	Potential window (V)
H_2SO_4	1.35	1.2
KOH	1.9	1.2
Acetonitrile	17	2.5–3.0
Propylene carbonate	52	2.5–3.0
Ionic liquids	125	3.0–4.0

Organic electrolytes have higher ionic resistance than concentrated aqueous electrolytes. The resistance will typically be a factor of around 10–40 larger, and ionic liquids are more resistive still, 50–100 times greater than aqueous solutions. The maximum avail-

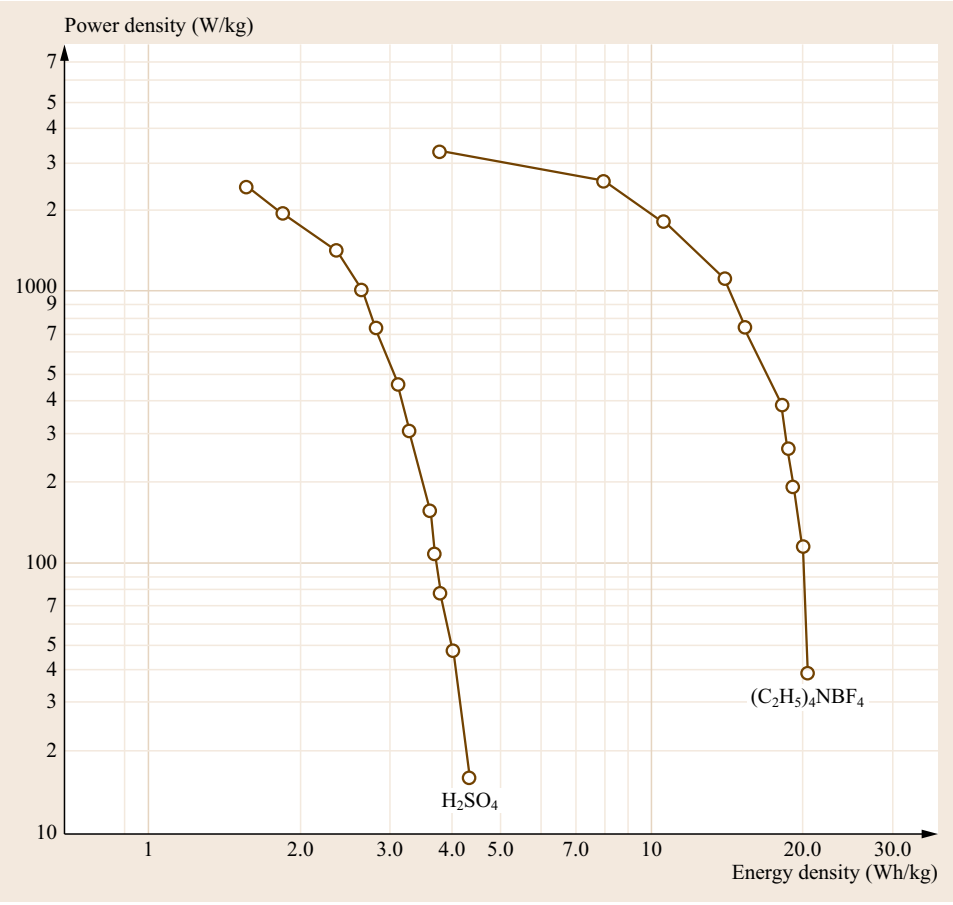


Fig. 17.3 Ragone plots for aqueous (2 M H_2SO_4) and organic (1 M Et_4NBF_4 in acetonitrile) electrolytes for the same type of carbon electrodes (after [17.30])

able power is comparatively lower, in accordance with (17.3). The energy content, however, is significantly increased, since it is proportional to the square of the cell voltage (17.2). Figure 17.3 illustrates the difference on a Ragone plot, where a fivefold increase in specific energy is indicated in the organic electrolyte, consistent with a $\approx 2.2\times$ wider voltage range (specific power is similar in this case, but the aqueous data was not taken to its plateau).

There is continuing concern about the use of acetonitrile due to its flammability and potential toxicity, and propylene carbonate is an attractive substitute. However, its higher resistivity suggests a reduction in the maximum power output of the cell (17.3). Various commercial activated carbon electrodes consistently showed lower specific capacitance in propylene carbonate than in acetonitrile [17.31]. There has also been some interest in developing binary solvent systems such as those used in some Li-ion batteries [17.32].

In choosing an electrolyte, then, one must weigh the importance of power versus energy. Aqueous electrolytes sustain higher power, organic solvents with tetraalkylammonium salts are intermediate, and ionic liquids yield the highest energy. Additionally, if temperature-dependent studies are undertaken, the vapor pressure and freezing point of the system must be considered. For low-temperature aqueous systems, 37% H_2SO_4 represents a good choice, since this concentration gives the greatest freezing point depression.

The concentration of electrolyte ions must be sufficiently high so as not to deplete from the bulk solution during charging when the ions become sequestered by the enormous surface area of the electrodes, but not so high that ion pairing occurs in the bulk solution. *Zheng* and *Jow* have suggested that concentrations above 0.2 M should be adequate [17.33], and *Pell* and *Conway* have shown that 0.08 and 0.2 M NEt_4BF_4 are dilute enough to cause electrolyte starvation effects [17.34]. If the bulk ions do deplete, then the ionic resistance, and hence ESR, increase, and the maximum available power decreases. An electrolyte concentration of at least 1 M is usually safe, although in practical terms, especially in aqueous systems such as H_2SO_4, 3–5 M is usually optimal.

17.2 Test Methods

Three complementary methods encompass the experimental techniques that quantify the most useful parameters of an electrode or a cell. First, constant current (galvanostatic) discharge reveals energy and power properties that most closely mirror those one might expect of an EC in real-world operation, including long-term stability through charge–discharge cycles. Constant power and constant resistance discharges are similar in nature to constant current discharge, but the experiments are slightly more difficult to undertake and/or to interpret, and they do not usually produce any more meaningful data. Second, cyclic voltammetry (CV) highlights potential-specific behavior such as the voltage stability window and redox peaks, and it is also useful for exploring the long-term stability of electrode materials. Third, impedance spectroscopy, which bears little resemblance to real-world conditions, can isolate and quantify individual phenomena that contribute to the overall behavior of an electrode or cell.

Capacitance, energy, and power are usually normalized to mass as specific capacitance, specific energy (energy density), and specific power (power density) by dividing the corresponding results by total active material mass, total electrode mass, or total device mass. See the caveats in Sect. 17.3. In most practical applications, the size of the device, not its mass, is the important consideration. Since the density of the electrode material is rarely of consequence, it might make more sense to express specific capacitance, power, and energy volumetrically, for example, F/cm^3, but this is rarely done.

17.2.1 Constant Current Discharge

The most straightforward method for evaluating EC materials is constant current discharge, and this method forms the basis of the established protocols for testing commercial ECs [17.4] (Sect. 17.4.3). Different discharge rates provide a series of specific energy and average specific power pairs that can be then used to construct a Ragone plot (Sect. 17.2.1).

Figure 17.4 shows the discharge of an ideal capacitor at constant current i, starting from its rated voltage $V_r = 1$ V at time $t = 0$, and ending at 0 V after discharge time $t_D = 4$ s, within the appropriate timescale for an EC (Fig. 17.1). The voltage falls linearly, as predicted by (17.6), and so capacitance C can be calculated from the slope: $C = i/(\mathrm{d}V/\mathrm{d}t)$. Alternatively (17.8), $C = Q/(\Delta V) = (i \times t_d)/(\Delta V)$ can be used to calculate the average capacitance in cases where the discharge is not linear, for example, some pseudocapacitive electrodes.

The product of current and the area under the discharge profile gives energy

$$E = \int_0^{V_r} iV\mathrm{d}t \qquad (17.11)$$

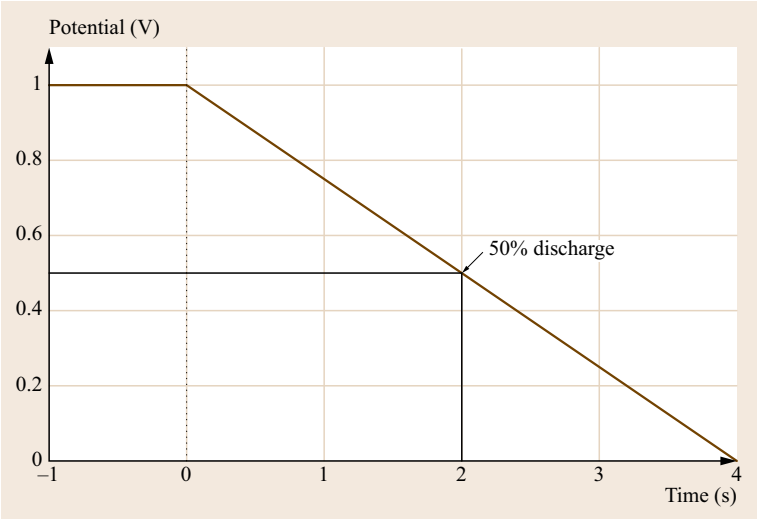


Fig. 17.4 Ideal voltage–time profile of an EC discharged under constant current starting at time $t = 0$

$$= \int_0^{V_r} C\frac{dV}{dt}V dt \tag{17.12}$$

$$= \int_0^{V_r} CV dV \tag{17.13}$$

$$= \frac{1}{2}CV_r^2 . \tag{17.14}$$

Equation (17.14) restates (17.2).

The average power may be obtained by dividing the energy over the duration of the discharge t_D

$$P_{avg} = \frac{E}{t_D} . \tag{17.15}$$

It is often customary to measure the discharge only to one-half the initial voltage; 0.5 V_r. This range contains 75% of the energy of the EC capacitor (Fig. 17.4), since

$$E_{(half\text{-}discharge)} = \int_{0.5V_r}^{V_r} iV dt \tag{17.16}$$

$$= \frac{1}{2}CV_r^2 - \frac{1}{2}C(0.5V_r)^2 \tag{17.17}$$

$$= \frac{1}{2}CV_r^2(1 - 0.5^2) \tag{17.18}$$

$$= \frac{1}{2}CV_r^2 0.75 . \tag{17.19}$$

The discharge time will necessarily be one-half of the duration of the total discharge, leading to an overall increase in average power by 50%

$$P_{avg(half\text{-}discharge)} = \frac{\frac{1}{2}CV_r^2\,0.75}{0.5t_D} \tag{17.20}$$

$$= \frac{\frac{1}{2}CV_r^2}{t_D}\frac{0.75}{0.5} \tag{17.21}$$

$$= P_{avg(full\ discharge)}1.5 . \tag{17.22}$$

Capacitance, energy, and power measured over very long discharge times – beyond the ≈ 100 s useful time domain of ECs (Fig. 17.1) – can be inaccurate because (i) the low discharge rates do not properly reflect realistic conditions and tend to produce overly optimistic predictions of the performance of the material (e.g., by reducing the contribution of ESR at low currents), and (ii) experimental error due to self-discharge becomes more significant.

For the simple RC circuit shown in Fig. 17.5, with the capacitor charged to an initial voltage V_r, the application of discharge current i will produce a voltage drop ΔV_{iR} due to the series resistance R_s

$$\Delta V_{iR} = i \times R_s . \tag{17.23}$$

This is shown in Fig. 17.6 as the 0.2 V drop that appears at the beginning of the discharge. This initial drop is usually abrupt and easily determined. Sometimes the initial drop curves exponentially as in Fig. 17.6. In these cases, the linear region should be extrapolated back to $t = 0$ to determine ΔV_{iR}.

The ESR, R_s, represents the sum of resistances in the system. It includes the electronic resistance of the

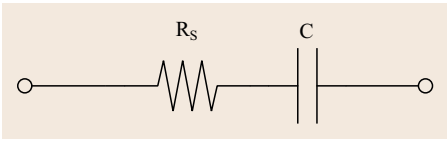


Fig. 17.5 A simple *RC* circuit consisting of a capacitor and a series resistor

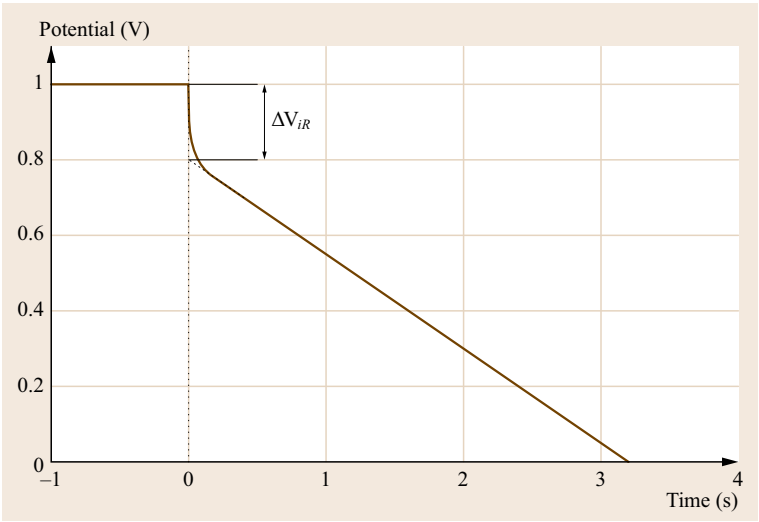


Fig. 17.6 The voltage drop due to series resistance during a hypothetical capacitor discharge. In practice, there is sometimes a precipitous drop followed by a brief curve until the steady discharge becomes established. In such a case, ΔV_{iR} should be taken as the difference between V_r and the extrapolation of the discharge line to $t = 0$ as shown

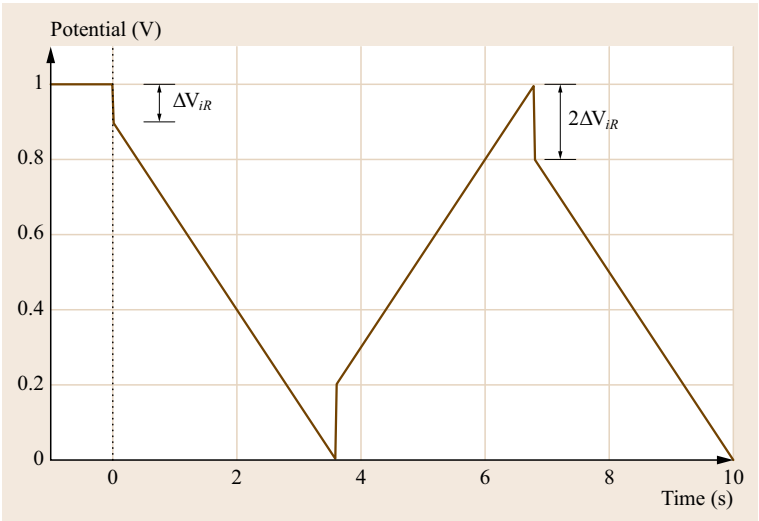


Fig. 17.7 The voltage drop during a charge–discharge cycle switch is twice as large as the voltage drop from a static voltage

electrode, the ionic resistance of the electrolyte, interfacial resistance at the current collector, resistance at the separator, and any resistance due to clips and leads. ESR will be discussed again in Sect. 17.4.2. *Pell* and *Conway* have pointed out [17.34] that some portion of this *iR* drop stems from the redistribution of charge within the electrode pores (Sect. 17.2.3 and Fig. 17.12), though in practice this individual phenomenon is usually not considered separately.

Note that the apparent magnitude of the iR_s drop will be doubled at switching during cyclic charge–discharge experiments (Fig. 17.7), and care must be taken not to interpret this drop incorrectly; the voltage drop upon switching to discharge is twice as great because the true capacitor voltage will lag the applied voltage during charging owing to R_s, which can more generally be calculated from the difference between discharge and charge currents

$$R_s = \frac{\Delta V_{iR}}{i_{\text{discharge}} - i_{\text{charge}}} . \tag{17.24}$$

Equation (17.23) is simply a special case of (17.24); where $i_{\text{charge}} = 0$.

Generally, the cell voltage V established by the application of current i to a capacitor charged to its rated voltage V_r through ESR R_s can be calculated

$$V = V_r - iR_s . \tag{17.25}$$

Multiplying (17.25) by current gives power P as

$$P = iV_r - i^2R_s , \tag{17.26}$$

which reaches a maximum when

$$\frac{\mathrm{d}P}{\mathrm{d}i} = V_\mathrm{r} - 2iR_\mathrm{s} = 0\,, \tag{17.27}$$

that is,

$$i_{(P_\mathrm{max})} = \frac{V_\mathrm{r}}{2R_\mathrm{s}}\,. \tag{17.28}$$

Substituting $i_{(P_\mathrm{max})}$ into (17.25), the cell voltage at $i_{(P_\mathrm{max})}$ is obtained as

$$V_{(P_\mathrm{max})} = V_\mathrm{r} - \frac{V_\mathrm{r}}{2R_\mathrm{s}}R_\mathrm{s} \tag{17.29}$$

$$= \frac{V_\mathrm{r}}{2}\,, \tag{17.30}$$

which implies that the maximum power is generated by a current that causes an iR drop equal to half of the open circuit voltage of the charged capacitor. With $V_{(P_\mathrm{max})}$ and $i_{(P_\mathrm{max})}$ known, P_max, then, is

$$P_\mathrm{max} = V_{(P_\mathrm{max})} \times i_{(P_\mathrm{max})} \tag{17.31}$$

$$= \frac{V_\mathrm{r}}{2}\frac{V_\mathrm{r}}{2R_\mathrm{s}} \tag{17.32}$$

$$= \frac{V_\mathrm{r}^2}{4R_\mathrm{s}}\,, \tag{17.33}$$

which restates (17.3).

Ragone Plots

Ragone plots are charts on which the power and energy characteristics of devices are quantified while providing a straightforward visual assessment of the performance one might expect from a cell under various conditions. Specific power and specific energy are plotted on logarithmic axes, and following the long-standing traditions of electrochemistry, there is no clear convention on which parameter should be on which axis.

Each of a series of galvanostatic discharge experiments at different currents will yield an energy–power pair (from (17.14) and (17.15)) that constitute a single point on the plot. Figure 17.8 presents such data from galvanostatic discharges of a simple carbon cloth EC at two different temperatures. The plot shows that at lower temperature, specific power decreases but specific energy remains unaffected. This is a behavior that one would expect from (17.2) and (17.3), since the increase in the ionic resistance of the H_2SO_4 electrolyte (and the corresponding increase in R_s) will affect power but not energy.

17.2.2 Cyclic Voltammetry

Linear sweep CV is another straightforward method for characterizing EC performance. Equation (17.6) predicts a rectangular voltammogram with current proportional to capacitance and sweep rate $\nu = \mathrm{d}V/\mathrm{d}t$, as shown in Fig. 17.9. In order to be considered capacitive, a material must produce a CV trace resembling the one in Fig. 17.9 in three important respects:

1. Symmetry about the zero current axis
2. Near-vertical current transitions as the extremes of the voltage window
3. Current that is linearly proportional to ν.

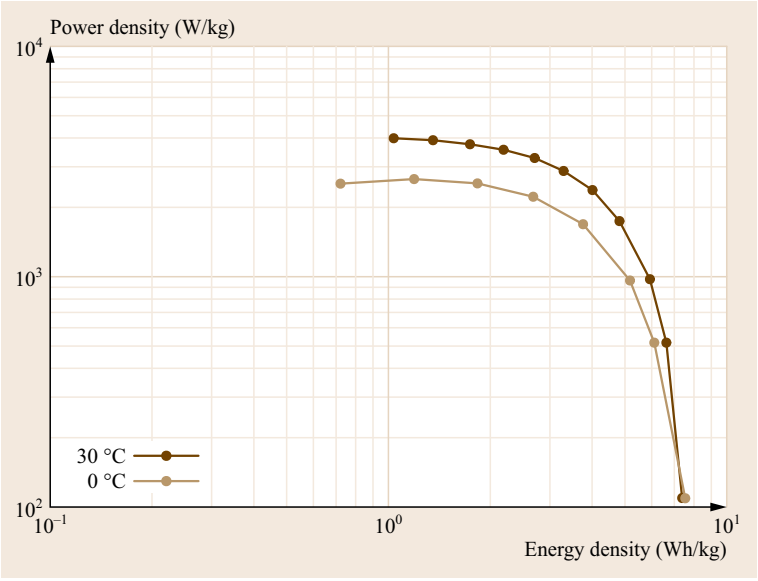


Fig. 17.8 A Ragone plot for the performance of a carbon cloth two-electrode EC at different temperatures

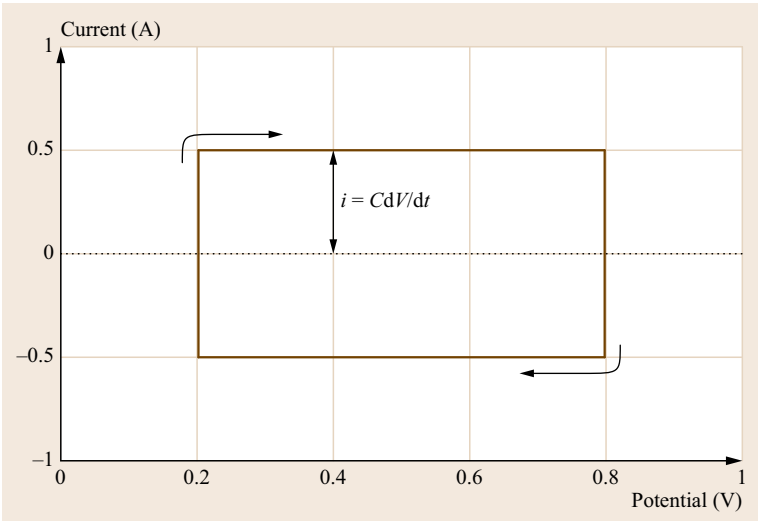


Fig. 17.9 The cyclic voltammogram of an ideal capacitor

Charge symmetry between the two halves of the cycle, that is, $Q_a = Q_c$ is implied, but on its own it is not an adequate indicator of capacitance.

Figure 17.10a shows the CV of a two-electrode carbon cloth EC at various sweep rates. At higher sweep rates the effects of R_s become more pronounced owing to the higher currents, causing a rounding of corners after each direction switch. At the extreme, the CV will begin to resemble the diagonal line of pure resistance. CV, then, is a good qualitative tool for assessing the contribution of ESR under different conditions. Figure 17.10b presents the same data divided by dV/dt to give capacitance on the y-axis. Plateau capacitance – occurring where the current has stabilized to a constant value – decreases with increased scan rate, reflecting the effects of ESR, and a plot of plateau C versus scan rate can provide a useful summary.

Average capacitance can be calculated by integrating the current i over the sweep width ΔV. Since charge $Q = \int i dt$, (17.8) can be re-expressed as

$$C = \frac{\int i dt}{\Delta V} \tag{17.34}$$

$$= \frac{\int i dV}{\frac{dV}{dt}\Delta V} \tag{17.35}$$

$$\equiv \frac{\int i\,dV}{\nu \Delta V}\,. \tag{17.36}$$

$Q = (\int i dV)/\nu$ may be determined from either the anodic or cathodic portions of the sweep, such as in Fig. 17.10c. If $Q_a \neq Q_c$, there is likely some irreversible faradaic reaction involved. Note that some carbon electrodes may be so affected for the first few dozen cycles, and it is thought that this is caused by the irreversible oxidation of unstable surface groups [17.35, 36]. Table 17.2 summarizes plateau and average capacitance for the data in Fig. 17.10.

Certain pseudocapacitive electrode materials can produce more complicated CVs, especially in a three-electrode cell configuration (Sect. 17.3.1). Potential-specific electrochemistry can complicate the interpretation and reporting of the electrode material properties with artifacts such as variances in slope in the galvanostatic discharge. Cyclic voltammetry can reveal such pseudocapacitive redox processes that are not continuous with voltage. An example is presented later in Fig. 17.22. CV can also reveal problems or shortcomings in electrode preparation, such as improperly annealed RuO_2 electrodes that produce a large peak instead of the expected flat capacitance [17.20].

Cyclic voltammetry is the best tool for determining the potential range over which the electrode(s) and electrolyte are stable. Slow sweep rates are desirable so as not to obscure the onset of solvent or electrode degradation current by kinetics-based overpotential. For example, the 2 mV/s CV in Fig. 17.10 shows the onset of electrolyte degradation at the potential extremes as a small increase in current. The

Table 17.2 A comparison of plateau (at 0.3 V) and average capacitance at different sweep rates for a two-electrode carbon cloth EC

dV/dt (mV/s)	Capacitance (F)	
	Plateau	Average
2	0.348	0.328
10	0.330	0.308
20	0.323	0.296
50	0.311	0.262
100	0.302	0.230

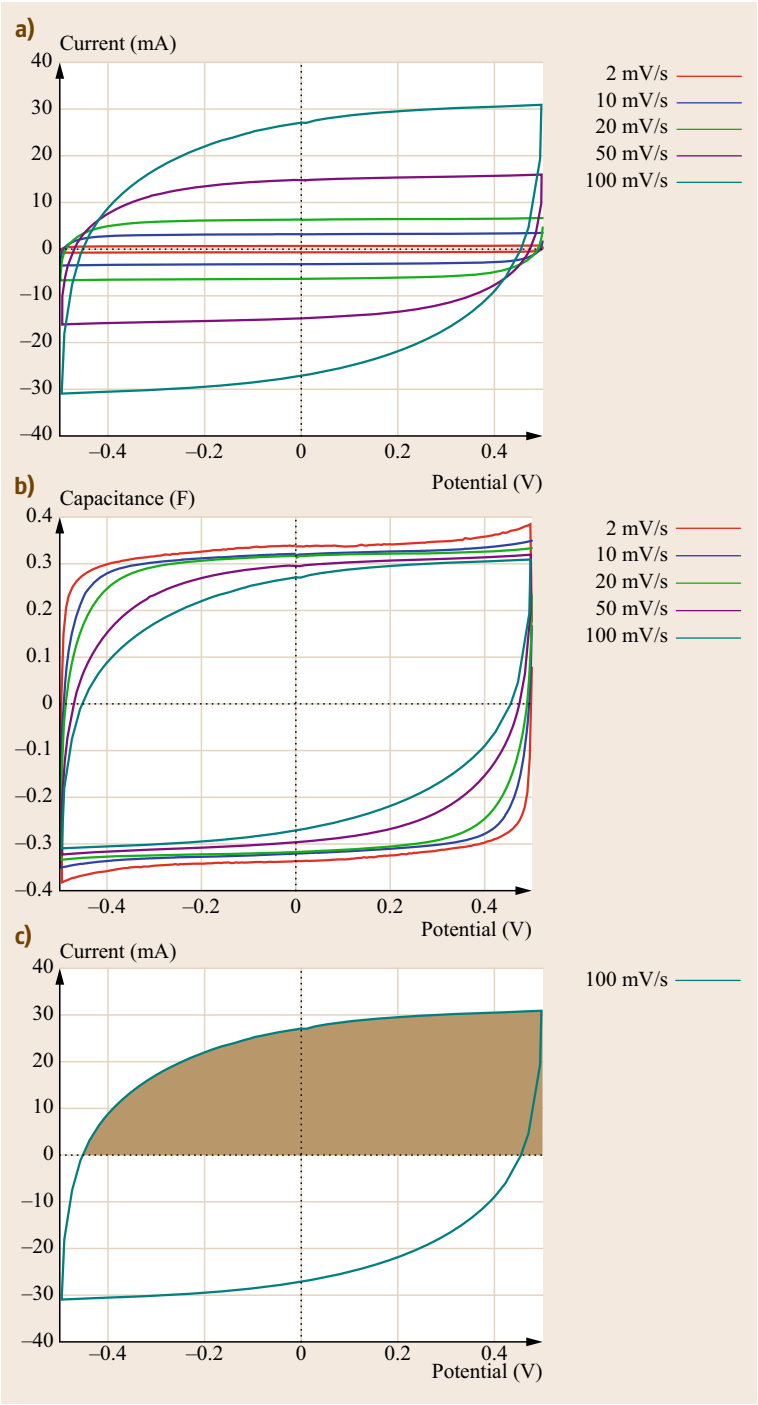


Fig. 17.10 **(a)** Cyclic voltammetry of a two-electrode carbon cloth EC at different sweep rates, **(b)** currents normalized to sweep rate to give capacitance, and **(c)** integration of the anodic current, represented as the shaded area, divided by ν gives Q_a and hence average capacitance

faster voltammograms do not. Finally, CV is an excellent tool for quantifying the stability of an EC over time, since sample results from thousands of cycles can be overlaid for a rapid visual assessment of the cell's performance.

17.2.3 Impedance

Electrochemical impedance spectroscopy (EIS) imposes a sinusoidal perturbation on a DC voltage and records the magnitude and phase angle of the resulting

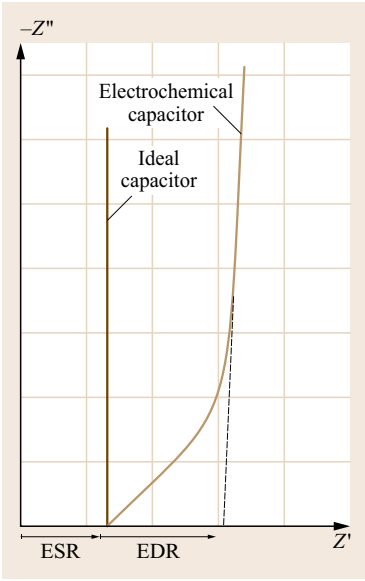


Fig. 17.11 Complex plane (Nyquist) impedance plot of an ideal capacitor and a typical EC. The EDR arises from the restricted motion of ions in the electrode pores

current. The technique is useful for isolating and comparing individual contributions to performance properties for different electrodes or conditions, but methods such as constant current discharge are more useful for determining practical properties such as specific energy. As a general electrochemistry method, EIS is very powerful, and more details of the theory can be found elsewhere [17.8]. For EC work, a zero-to-peak amplitude of 5−10 mV is usually adequate over a frequency range from 5−10 kHz to 5−10 mHz, with five points per decade.

Nyquist Plots

The complex plane (Nyquist) plot summarizes EIS data in a straightforward way. The impedance magnitude and phase angle at each frequency is plotted as a vector from the origin of the plot, thereby isolating the real (Z', x-axis) and imaginary ($-Z''$, y-axis) components, which correspond to resistance and a function of capacitance, respectively. The plots are usually scaled equally on both axes so that the datasets form recognizable shapes that share characteristics with the responses of common circuit elements such as resistors, capacitors, and inductors. Hence, EIS results are often modeled in terms of equivalent electronic circuits where the components correspond to and quantify physical phenomena.

Figure 17.11 contrasts the complex-plane responses of an ideal conventional capacitor in series with a resistor (Fig. 17.5) and a hypothetical EC. The former is typified by a vertical line offset along the x-axis by the ESR of the components of the system and the capacitance is invariant with frequency. The latter shows two distinct regions: A 45° region at higher frequencies and the nearly-vertical capacitive behavior in the low-frequency region. The deviation from vertical can

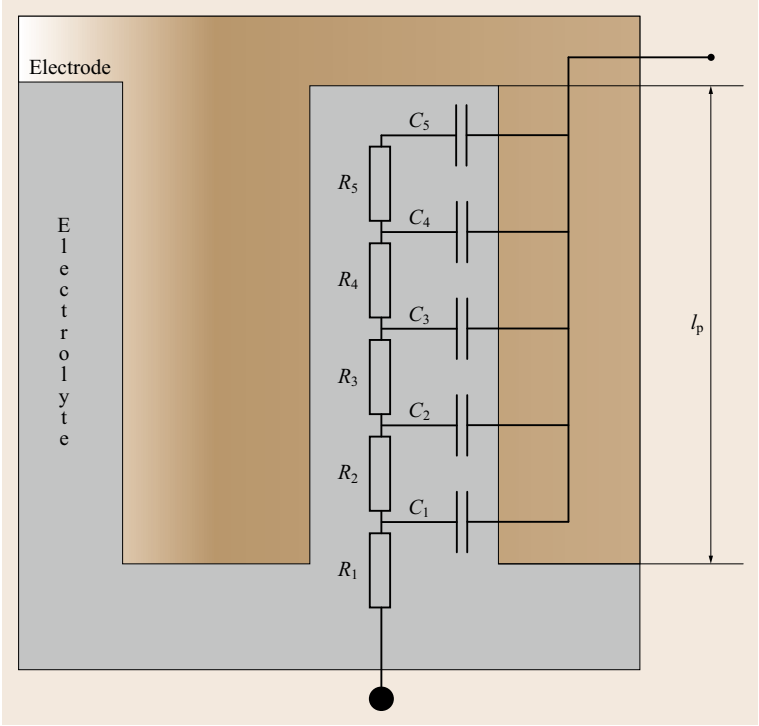


Fig. 17.12 The *RC* transmission line that represents a pore in an electrode (after [17.11])

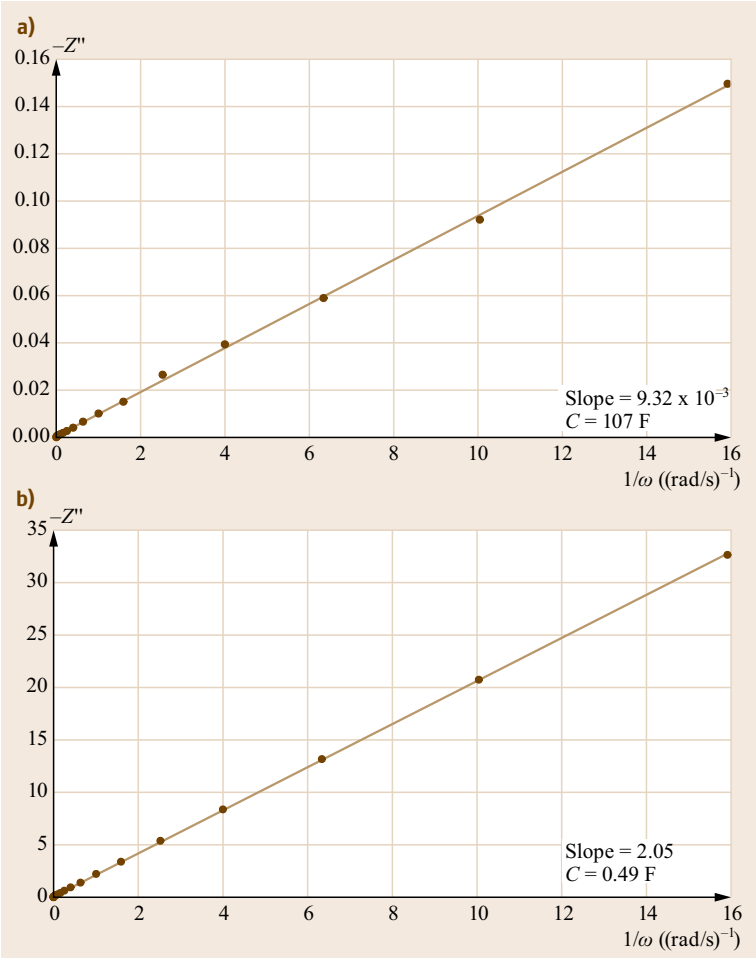


Fig. 17.13 **(a)** $-Z''$ versus reciprocal frequency for a commercial EC with nominal capacitance of 140 F, the same device used for Fig. 17.10, and **(b)** $-Z''$ versus reciprocal frequency for a carbon cloth two-electrode cell

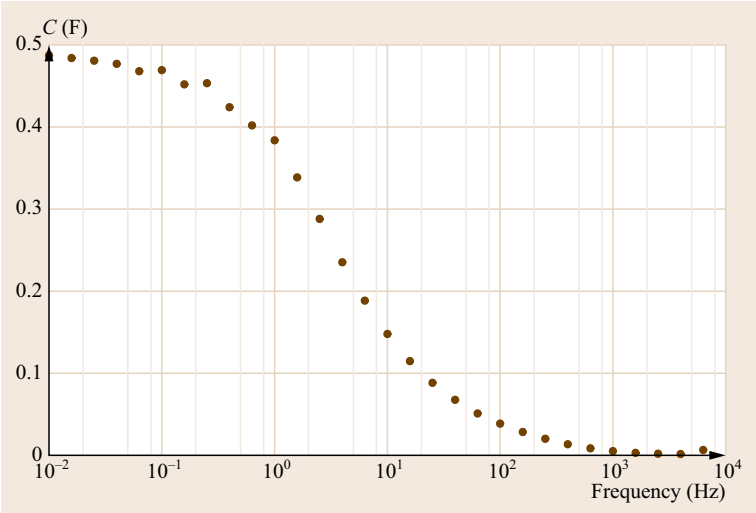


Fig. 17.14 Capacitance versus frequency for a laboratory EC constructed from carbon cloth electrodes, showing the low-frequency limiting capacitance as the *y*-intercept. The same data generated Fig. 17.13b

be modelled by replacing the capacitor with a constant phase element (CPE). Doing so replaces the $(j\omega)$ terms $(j = \sqrt{-1})$ with $(j\omega)^p$, $0 < p < 1$, in the EIS equations; $p = 1$ describes an ideal capacitor. Such behavior is typical of an electrochemical charging process, and may indicate a rough or inhomogeneous surface, including a range of pore depths. The 45° portion – sometimes called the porous region [17.38] in EC work – is generally characteristic of a diffusion-limited process, and for ECs, this applies to the ability of ions to penetrate the pores, leading to an electrolyte distributed resistance (EDR) and distributed capacitance. The knee frequency where these two behaviors meet corresponds approximately to the reciprocal of the *RC* time constant of the cell. Note that any very high frequency data that drops below the *x*-axis is a result of a series inductance that is an experimental artifact introduced by the test leads.

Transmission Line Model

Figure 17.12 shows the *RC* transmission line that models the pores in a high surface area electrode and gives a Nyquist plot consistent with the one in Fig. 17.11. In de Levie's transmission line model (TLM) a pore can be thought of as a uniform cylinder consisting of a sequence of double-layer capacitances extending into the cylinder depth l_p through the resistance of the solution.

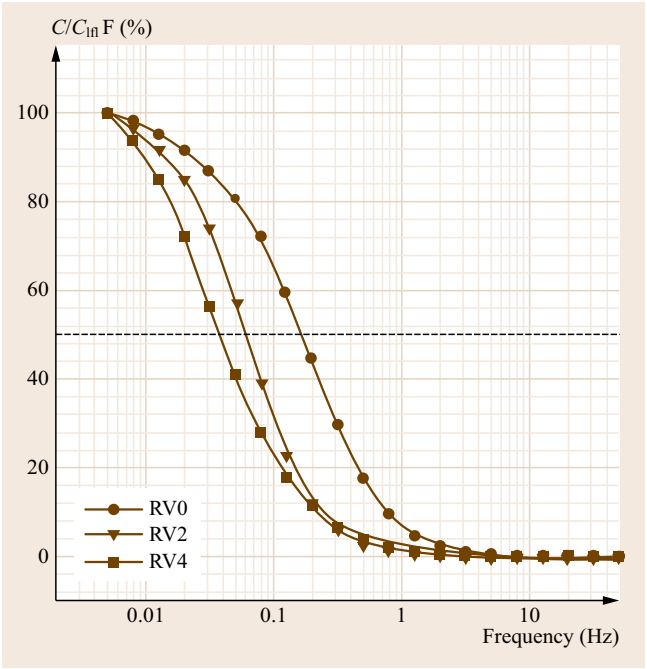


Fig. 17.15 Normalized capacitance versus frequency for three similar carbon materials, revealing 50% utilization and the characteristic frequency from which relative $R'C'$ can be extracted (after [17.37])

The resistance of the bulk electrode is relatively small and can be disregarded. Therefore, at high frequencies, C_1 acts as a shunt, and effectively all the current flows through $R_1 - C_1$ into the bulk, bypassing the pore. Decreasing frequencies permit further penetration into the pore, creating the 45° region that transitions at the knee frequency below which the frequency-independent capacitive behavior dominates.

The penetration depth parameter l arises as

$$l = \left(\frac{\omega R'C'}{2}\right)^{-2}, \tag{17.37}$$

where R' and C' are the pore resistance and capacitance per unit length, respectively. When the frequency is sufficiently high, the penetration depth will be shorter than the pore depth, $l < l_p$. Consequently, only a fraction of the capacitance can be accessed, and a 45° region appears in the Nyquist plot.

Song et al. [17.39] extended the TLM by considering that the pores are not homogeneous but follow a distribution function, as would be expected by the nonvertical, low-frequency portion of an EC Nyquist plot. This transmission line model-pore size distribution (TLM-PSD) model introduces parameters for size and standard deviation, and can accurately predict pore parameters from impedance data, or vice versa.

Low-Frequency Capacitance

Overall capacitance can be quantified from the low-frequency response of the system. Since

$$-Z'' = \frac{1}{\omega C} \tag{17.38}$$

a plot of $-Z''$ versus $1/\omega$ should yield a straight line with slope $1/C$ (Fig. 17.13).

Alternatively, low-frequency limiting capacitance may be obtained from a plot of $-1/(\omega Z'')$ versus $\log(\omega)$ (Fig. 17.14). The sigmoidal region of the plot reveals information about the pores. *Jang* et al. have shown an elegant way to compare the $R'C'$ constants of the pores of similar EDLCs electrodes [17.37]. The fraction of pore utilization at a particular frequency is related to the ratio of capacitance to the low-frequency limiting capacitance. Plots of capacitance normalized to the low-frequency limit (Fig. 17.15) will reveal a characteristic frequency at $C/C_{lfl} = 0.5$. Comparison of these frequencies through (17.37) permits the relative $R'C'$ constants to be extracted, assuming that l_p is equal for the three materials.

Isolating the Contributors to Overall ESR

Charge Transfer Resistance. Impedance spectroscopy can separate charge transfer resistance (R_{ct}) from

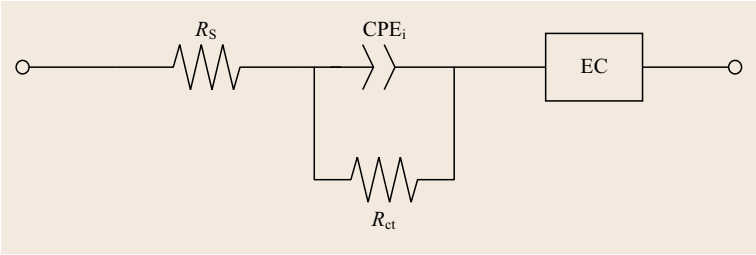


Fig. 17.16 Equivalent circuit showing R_s, the parallel interfacial resistance, and CPE (to permit flattened semicircles). The EC represented as a box corresponds to a transmission line such as the one in Fig. 17.12

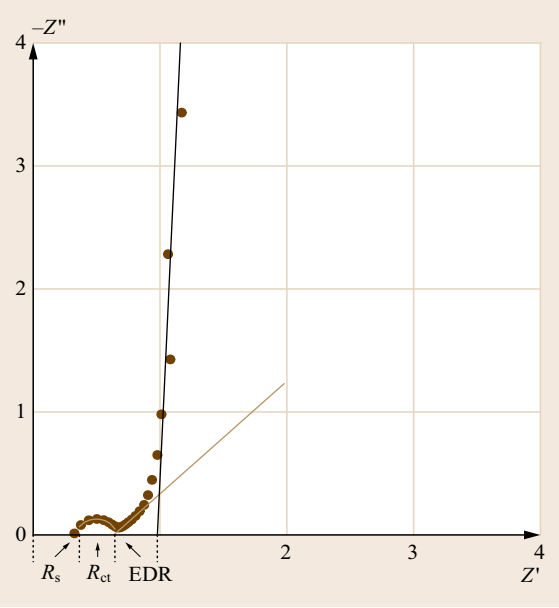


Fig. 17.17 Charge transfer resistance in an EC cell with carbon cloth electrodes

the other series resistances that constitute the overall ESR of a cell. It is manifested as a sometimes-flattened semicircle in the Nyquist plot of the high-frequency data. The equivalent circuit is shown in Fig. 17.16, with R_{ct} in parallel, with an interfacial capacitance (or, rather, a CPE to accommodate the flattened semicircle). Sources of R_{ct} can be the current collector – active material interface [17.41, 42], electronic resistance between layers of graphene [17.43], between electrode particles [17.44], and resistance in the separator [17.34, 45]. As a specific example, *Portet* et al. have linked the charge transfer circle to the aluminum current collectors in a two-electrode cell [17.41]. Untreated, $R_{ct} \approx 50\,\Omega$. Electrochemical etching lowered R_{ct} to $\approx 5\,\Omega$. The addition of a conductive coating to the treated collectors lowered R_{ct} to an insignificant level. This is important since R_{ct} is in series with R_s and will therefore have a significant impact on the power delivery of the capacitor (17.3).

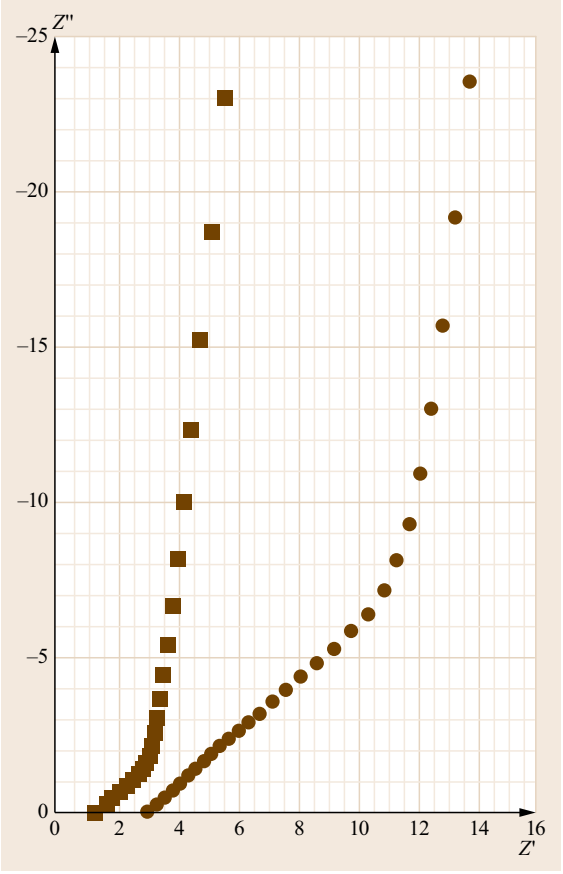


Fig. 17.18 Nyquist plot of identical carbon electrode EC in acetonitrile (*squares*) and propylene carbonate (*circles*) having 1.5 and 1.0 M NEt_4BF_4, respectively (after [17.40])

Figure 17.17 presents data from a carbon cloth capacitor, giving a Nyquist plot that distinctly shows three resistances that contribute to the overall ESR of the cell:

1. The series resistance R_s, which includes solution resistance, separator resistance, and electronic resistance of the electrode
2. R_{ct} due to charge transfer across an interface

3. The distributed resistance associated with the porosity of the electrode material.

The Effect of Electrolyte on EDR. As discussed in Sect. 17.1.4, the main concern with moving from acetonitrile to the safer propylene carbonate is the decreased conductivity. Figure 17.18 shows the complex plane impedance response of identical EC cells in these two solvents. The x-intercept, R_s, roughly doubles in going to the less conductive propylene carbonate. More telling is the pronounced difference in the 45° porous regions, indicating that the latter has its most deleterious influence on charge distribution at the pore scale.

17.2.4 Self-Discharge and Leak Currents

Self-discharge can be easily measured by monitoring the open-circuit potential (OCP) over an extended period with a high input impedance voltmeter or potentiostat. The self-discharge can often be attributed to faradaic processes such as surface functional groups (e.g., carbonyls), metal ions shuttling charge between electrodes, and charge redistribution. The phenomenon acts as a shunt across the capacitor, illustrated in Fig. 17.19. To test the EC for self-discharge, the device should first be charged to its rated voltage and held

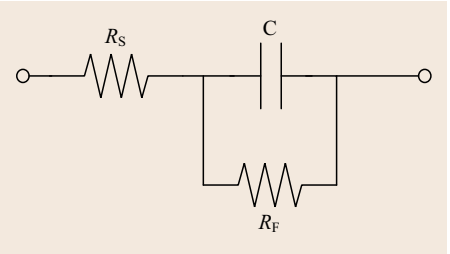


Fig. 17.19 Equivalent circuit showing parallel resistance R_F through which the capacitor self-discharges

for some length of time to stabilize. Then, the OCP should be recorded over the subsequent 72 h. Hold periods of 30–60 min are common and practical. However, *Andreas* has shown that the charge redistribution effects in high-area electrodes occur over much longer timescales, in the tens of hours [17.46]. Therefore, for the comparison of similar materials, it is important that the hold time be at least consistent.

The leak current is the current required to maintain the EC at its rated voltage. It can have some time dependence, so it is best to measure the applied current over several hours. One procedure [17.47] suggests the recording of current at 1 min intervals for 1 h, and at 5 min intervals for a further 2 h.

17.3 Configuration

The reporting of data in a consistent and unambiguous manner remains a challenge in the study of ECs; the literature is plagued with a lack of clarity. There exist test protocols for fully assembled self-contained cells [17.4], but investigation of experimental capacitors at the laboratory scale is complicated by the lack of standard techniques [17.5] and results vary according to experimental details [17.6]. For example, specific energy may refer to the energy per unit mass of the active material, the whole electrode, or even a packaged device. Depending on circumstances, any of the three might be appropriate, but particularly in cases of low loading levels, normalizing to the mass of active material alone may be somewhat misleading. Normalizing results to both active material mass and total electrode mass ought to provide the reader with better perspective. Similarly, unrealistically low galvanostatic discharge currents (Sect. 17.2.1) and very slow potential scan rates (Sect. 17.2.2) risk presenting data in an overly optimistic way. Another source of confusion stems from the important differences in the behavior of three-electrode and two-electrode cells.

17.3.1 Three- and Two-Electrode Cells

Two configurations are possible, and they differ in several important respects. The three-electrode method familiar to electrochemists uses the EC material as the working electrode along with a conventional reference electrode and a counter electrode, all immersed in electrolyte solution. The use of an isolated EC electrode in this way is useful for a careful examination of the electrochemical properties of the electrode material, that is, window of voltage stability or potential-specific redox reactions.

The two-electrode setup is appropriate for fully assembled cells, where one electrode acts as the working electrode and the other is a shunted reference-counter electrode. Some sort of separator inhibits electrical contact between the two while allowing ions to pass freely. Such a cell can either be immersed as an assembly in electrolyte solution or be self-contained, with the electrolyte solution sealed inside the packaging. A cell configuration that resembles a packaged unit geometry will more closely represent the performance of the final design.

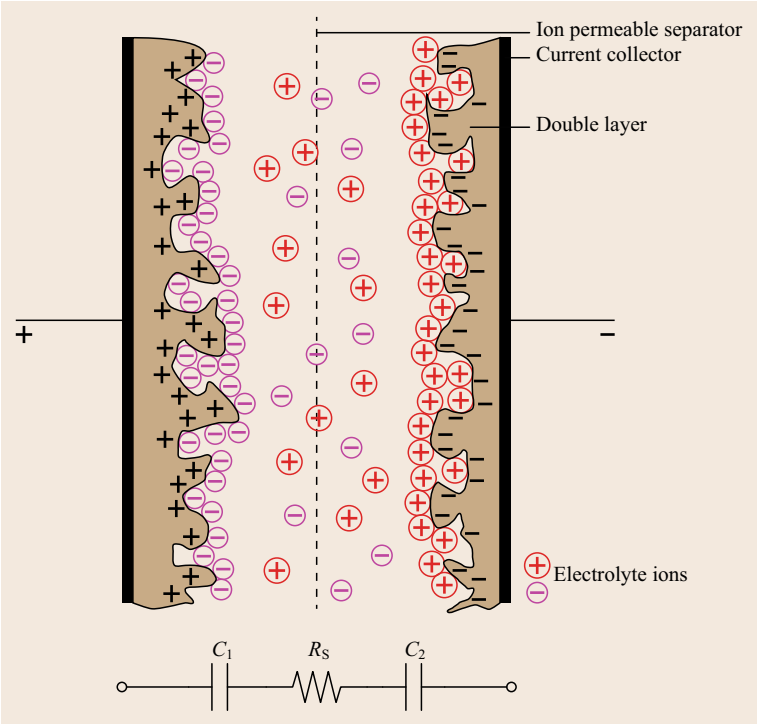


Fig. 17.20 Schematic of a double-layer capacitor in its charged state and the corresponding *RC* circuit. Note that R_s encompasses all series resistances, not just the separator, and that the self-discharge resistances (Sect. 17.2.4) have been omitted (after [17.9])

Important to note in Fig. 17.20 is that a two-electrode EC is really two EDLCs (or PCs) in series, so the measured total capacitance C_{tot} is

$$\frac{1}{C_{tot}} = \frac{1}{C_1} + \frac{1}{C_2} .$$

It follows that the total capacitance is dominated by the smaller of the two constituent capacitances; a capacitor constructed from different materials that independently present good properties risks exhibiting worse overall performance [17.10].

The C_{sp} of an isolated electrode (as measured in a three-electrode cell) is related to the capacitance C of a two-electrode cell with the combined mass of both identical electrodes m_{tot}

$$C_{sp} = \frac{4C}{m_{tot}} . \qquad (17.39)$$

The factor of 4 takes into account the series capacitance of two electrodes and the combined mass of two electrodes. Equation (17.39) also underlines the importance of indicating whether a capacitance measurement corresponds to a single electrode (i. e., in a three-electrode test configuration) or to a pair of electrodes in a two-electrode configuration. For the hypothetical carbon electrode material described in Sect. 17.1.2 with nominal 100 F/g, only 25 F/g would be observed in a symmetric two-electrode configuration.

In a three-electrode configuration, only the working electrode contains active EC material, and it may be subjected to the full range of potentials through which the solvent system is stable. However, in the symmetric two-electrode configuration, both electrodes are identical and active and necessarily the potential on each is equal but opposite in sign. It follows that each electrode may access at best only one-half of the full-potential range of the electrolyte. In practice, the voltage range (and hence important properties like capacitance) obtained in two-electrode mode will depend on the equilibrium potential of both electrodes. This underlines a fundamental problem with two-electrode capacitors: the potential of each electrode floats in the absence of a defined reference. It has been shown, for example, that the OCP of PANI electrodes in a symmetric EC were such that the positive electrode would have access to a decreased potential range, thereby limiting the capacitance of the whole device [17.6]. The OCP of the electrodes, especially in conducting polymer PC, is a reflection of the synthesis conditions, for example, the doping level of the material. It is possible, although inconvenient, to set this value by biasing the pair of electrodes against an external reference electrode and counter-electrode prior to testing, but only in the case where the electrode pair is immersed in a solu-

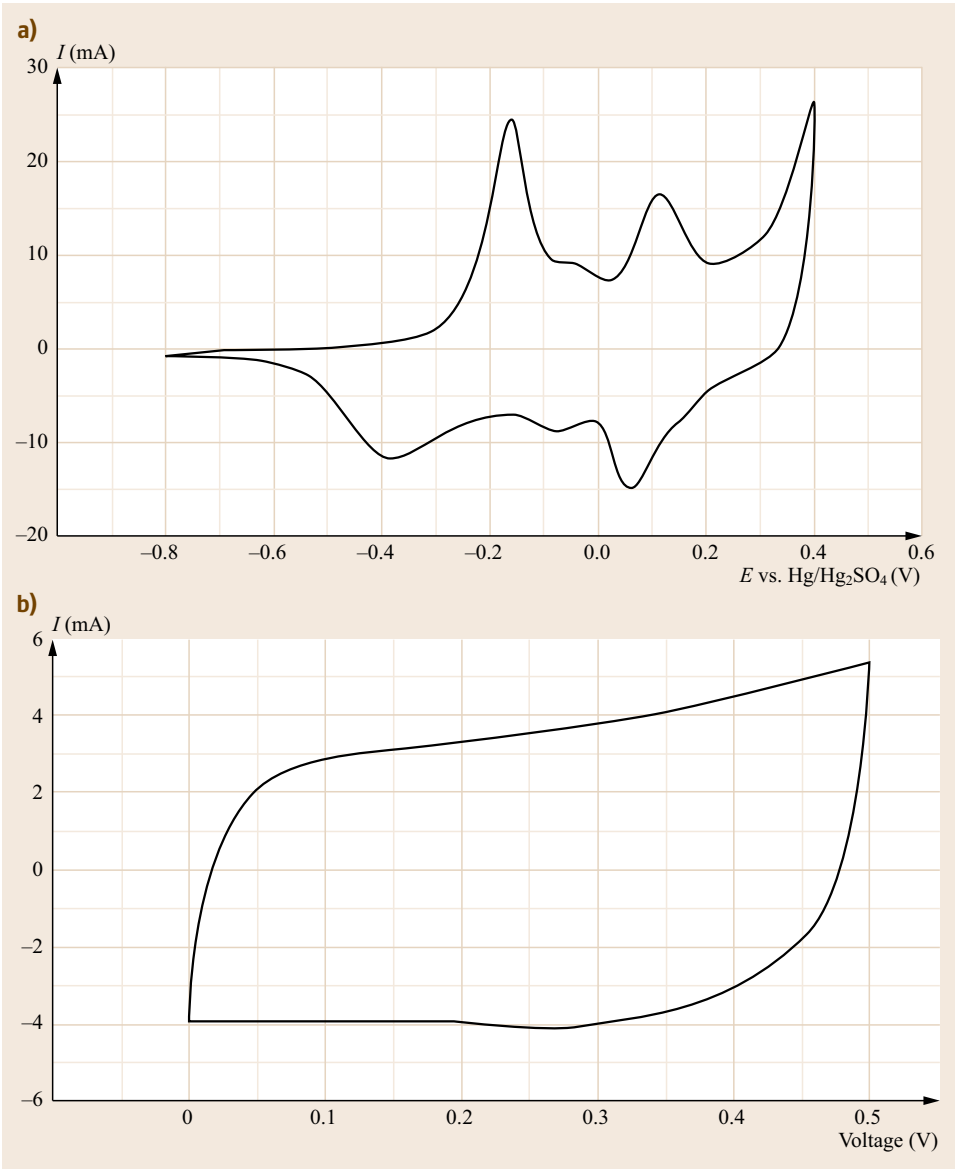


Fig. 17.21a,b Cyclic voltammetry of the same electrode material (PANI/MWNT); **(a)** in a three-electrode cell, and **(b)** in a two-electrode cell (after [17.6])

tion of electrolyte. This approach would not be feasible in a self-contained EC. Alternatively, each electrode can be set to a specific potential in a three-electrode configuration and then removed and assembled into a self-contained two-electrode device. Again, this methodology leaves much to be desired, and it has been shown that the absolute potentials of the electrodes drift over time, leading to decreased performance [17.48].

Dramatically different CV behavior can occur in three-electrode and two-electrode cells. Figure 17.21 shows defined redox peaks due to the active PANI/multiwalled carbon nanotube (MWCNT) material in the three-electrode CV. The peaks were smoothed in the corresponding two-electrode configuration. Another example, Fig. 17.22, had anthraquinone (AQ) modified carbon providing a PC boost to EDLC electrodes [17.22]. Isolated, the AQ exhibited a clear redox peak superimposed on a capacitive background current. In the two-electrode configuration, the sharp peak broadened (and, necessarily, appeared as a positive voltage) when the modified electrode was used as the negative (i. e., reference+counter) electrode. The peak disappeared entirely when the electrode was used as the positive electrode because the electrode potential was no longer able to reach the negative values where the AQ groups are active.

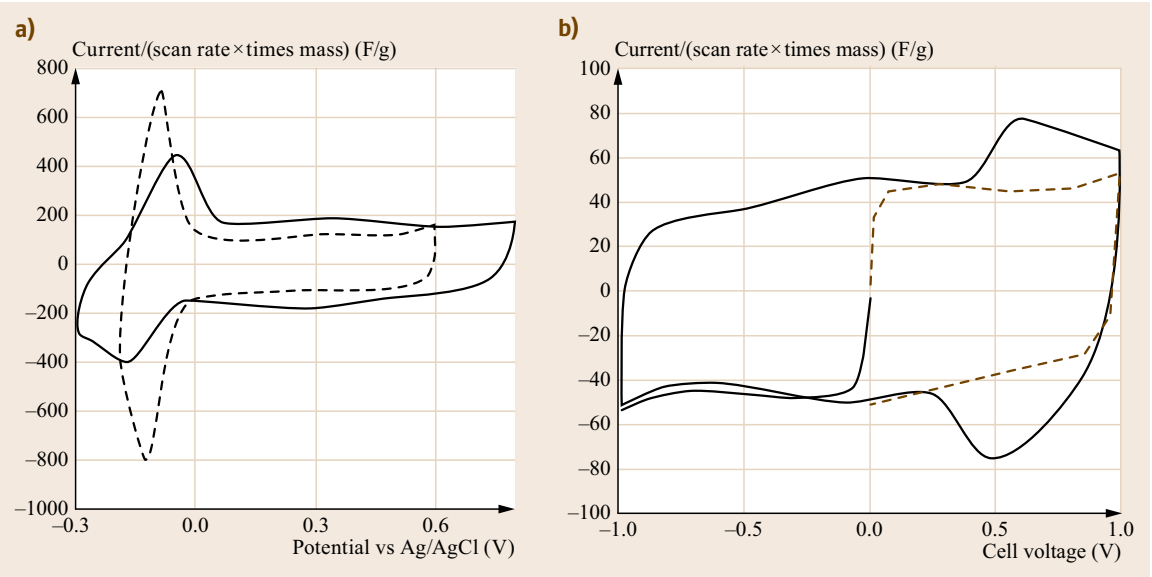


Fig. 17.22a,b Redox PC in an anthraquinone-modified carbon electrode **(a)** as a single electrode, and **(b)** in a two-electrode cell as the negative electrode with an unmodified carbon electrode as the positive electrode (*black line*) and reversed polarity (*brown line*) (after [17.22])

17.3.2 Hybrid Electrochemical Capacitors

This is an EC variant where a single high-power EC electrode (either EDLC type or PC type) is paired with a high-energy faradaic rechargeable battery-type electrode (e.g., $PbO_2/PbSO_4$ or $NiOOH/Ni(OH)_2$) in a single device [17.49]. Consistent with another long-standing tradition in electrochemistry, that is, using confusing and multiply-defined terminology, these devices are often labelled *asymmetric* or *hybrid* ECs. The fundamental premise is that such a device will combine the high power of the EC with the energy density of the battery component, as well as biasing the capacitor electrode against the stable voltage of the battery electrode through its shallow discharge. The advantage of this second point is that the entire charge of the capacitor electrode is available over its full discharge, as opposed to only one-half (or less) in a conventional symmetric configuration. The risk is that a good EC might be transformed into a poor battery.

17.3.3 Two-Electrode Cell Designs

Sandwich Cell

The sandwich cell is a straightforward design appropriate for testing ECs in a two-electrode configuration. The unit consists of a pair of current collectors, the electrode material, and a separator held between a pair of blocks made of an inert material such as poly(tetrafluoroethylene) (PTFE) or polyethylene. The blocks can be bolted together, as in Fig. 17.23, or clamped. Care should be taken to apply a consistent force on the cell since performance is known to be affected by the pressure on the electrodes [17.50]. For a cell such as the one in Fig. 17.23, the bolts should be tightened in a diagonal pattern with a torque wrench. The whole assembly is then immersed in a container of electrolyte solution. Commercial versions are also available.

Compression Union Cell

A popular cell design utilizes inexpensive PTFE compression fittings (e.g., Swagelok type) to form a sealed two-electrode cell (Fig. 17.24). Two metal cylinders act as current collectors for a pair of electrodes contained within the assembly. The cell should be reasonably airtight and is suitable for assembly inside a glovebox.

Coin Cells

Coin cells are a popular configuration for testing batteries and ECs. Hermetically sealed when assembled, the blanks are inexpensive and crimping dies are readily available. However, ECs generally differ from batteries in an important electrical respect: the currents can be expected to be at least 1–2 orders of magnitude greater than would typically be experienced for a battery. Careful control of contact resistances is, therefore, needed in order to minimize ESR in a coin cell. This can be achieved by optimal physical contact between the electrodes, the current collectors, and/or the coin cell

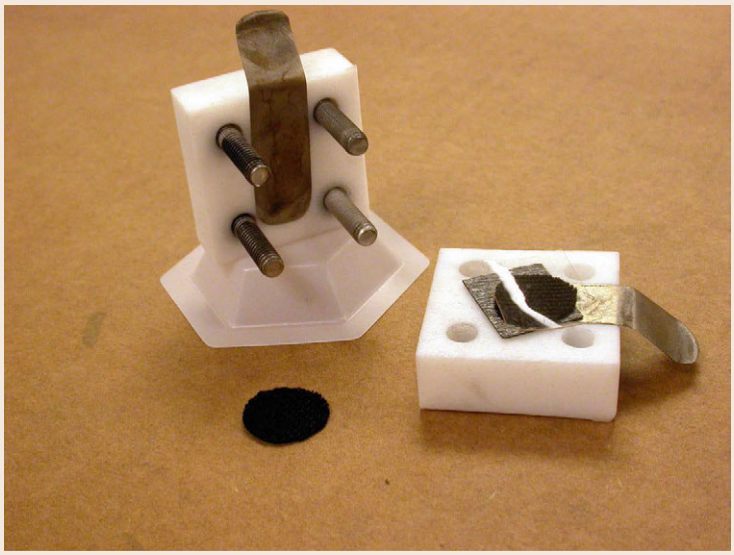


Fig. 17.23 A sandwich cell from the author's laboratory. PTFE blocks and stainless steel fasteners hold together two carbon fabric electrodes with a Nafion 115 separator. In this cell, a square piece of carbon paper was found to lower the charge transfer resistance between each electrode and its titanium current collectors

case [17.50, 51]. It has been pointed out [17.50] that the contact pressure of the cell components inside a coin cell can be difficult to control, thereby affecting the internal ESR in a random way.

An as-assembled coin cell EC will likely not have significant pressure exerted on the electrodes. This can be remedied by the use of internal leaf springs. While insufficient pressure can lead to poor contact and elevated ESR, it has been shown that excessive compression is equally deleterious [17.50], and that a compression ratio in the 1.2–1.3 range in an assembled device produces optimal capacitance and ESR.

Bipolar Stacks

A bipolar configuration consists of a series of electrode pairs packaged in a single monolithic device. Except at the ends, the current collector of one pair's positive electrode is also the current collector of the next pair's negative electrode (Fig. 17.25). In this way, the overall voltage of an n-pair system is boosted to nV_r, at the cost of decreased capacitance, $C_{stack} = 1/(nC)$ (17.5).

Alternatively, discrete cells can be stacked in series to the same effect in a monoblock configuration. The advantage of the bipolar stack is more efficient use of volume and decreased ESR. The disadvantage is that it is more prone to self-discharge and voltage imbalance, and the failure of a single electrode pair will compromise the entire unit. Otherwise, a series of self-contained monopolar EC cells can be wired together to boost overall voltage and has the advantage that the voltage on each cell can be controlled externally.

17.3.4 Electrode Construction

In practical terms for devices, there exists a trade-off between maximizing energy density (requiring thicker,



Fig. 17.24 A pair of stainless steel rods act as current collectors in a cell constructed from a Swagelok-type compression union

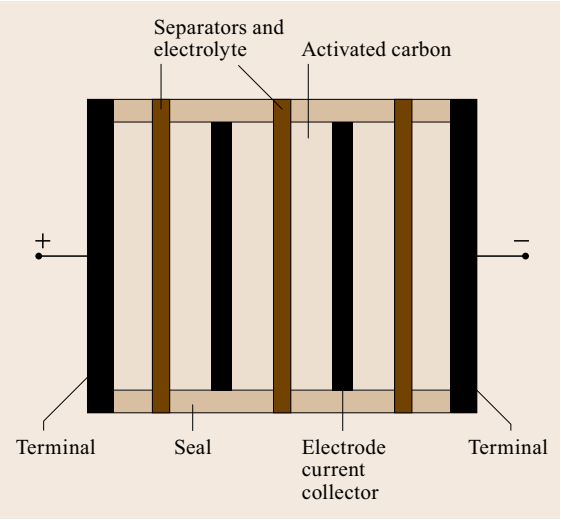


Fig. 17.25 Schematic of a bipolar EC stack (after [17.52])

more resistive electrodes) or power density (requiring thinner, more conductive electrodes). This is particularly true in devices using high resistance, nonaqueous solvents, where the thickness of active material is typically less than 0.1 mm thick [17.12].

Efforts should be made to keep the thickness of the electrodes and/or the active material as close as possible when comparing results. Furthermore, it should be noted that very thin or sparse material may yield overly optimistic power–energy data and capacitance [17.5, 53]. For results to be meaningful, it is important to use reasonable electrode thicknesses and active material masses.

Actual electrode construction depends on the active material, and may require some trial and error. Some constraints will be covered in Sect. 17.4.2. For active carbons as electrode materials, important factors include surface area, pore size and distribution, conductivity, wettability, and the presence of redox-active species. Typical formulations use $\approx 85\%$ active material, 5–10% carbon black or acetylene black for conductivity, and the remainder a binder such as PTFE or polyvinylidene fluoride.

17.3.5 Separators

A separator – either a porous sheet or an ion-exchange membrane – is necessary to prevent electrical shorts between the electrodes in a two-electrode cell. The conductance across a porous separator is related to its porosity p and the conductance of the electrolyte σ_{elec} through its thickness: $\sigma_{sep} = \sigma_{elec} p^{\alpha}$, $1.5 < \alpha < 2$ [17.11, 54]. Other issues include the wettability of the separator material in the electrolyte solution. The separator can be a significant contributor to the ESR of an EC and so it should be chosen judiciously.

Materials commonly used include Nafion 117, Nafion 115, Nafion NRE-211, Celgard 3400, Celgard 3501, other battery separators, glass mat, cellulose-based materials, and filtration membranes.

17.3.6 Current Collectors

Generally, the electrodes used in ECs consist of a thin ($< 300\,\mu m$) layer of active material applied to a metallic current collector. In some cases, a carbon cloth is used as an intermediate support. In order to minimize ESR, the contact resistance between the collector and the active material must be kept low, so some sort of surface treatment of the collector is usually necessary. This can range from simple sanding and polishing to advanced chemical modification. The use of etched or porous current collectors can help lock the carbon in place and increase interface area [17.55].

Stainless steel, titanium, nickel, and carbon cloth are often used. Aluminum foil is a popular choice, though it should be noted that not all alloys are created equal. Many alloys (e.g., Al-7075) have poor corrosion properties, and some are sold in a *clad* state, that is, treated with a thick passivating oxide layer that can lead to undesirable contact resistance. Al-1100 or Al-5005 alloys are reasonable choices.

A selection of current collectors from the literature is as follows:

- Aluminum current collectors, polished, and then coated with a mixture of 30% carbon black in polyurethane [17.40].
- A commercial collector from InteliCoat Technologies: Conducting carbon on an aluminum foil.
- Grafoil: A commercial flexible graphite sheet.
- Sigraflex: Another commercial flexible graphite foil.
- Carbon black filled polypropylene pressed against a stainless steel plate with finely powdered graphite as a contact aid [17.36].
- The deposition of MnO_2 directly on etched current collectors (reviewed in [17.19]).
- The electrochemical etching of aluminum, followed by dipping in a slurry of electrode material [17.41].

17.4 Further Practical Concerns

There exist further practical concerns in assessing EC performance. For example, the porosity of an EC electrode will strongly influence the electrochemical performance of the material, especially in an EDLC configuration, and resistance – including the resistance of the leads and connections – can have a surprising effect on available power. Packaged devices can be tested in accordance with an increasingly accepted straightforward protocol.

17.4.1 Electrode Area and Pore Size

Electrochemical double-layer capacitors are most frequently constructed from high surface area carbon electrodes, with *carbon* having become a catch-all term for a number of different materials ranging from amorphous carbon and highly organized structures such as graphene and nanotubes. Detailed terminology [17.56] and production methods [17.57] can be found elsewhere. The morphology of the carbon materials used in EDLC electrodes influences ion diffusion, electronic resistance, and of course capacitance, and the material must reach a balance between competing properties. Greater surface area implies smaller particles with less contact, and thus fewer paths over which electrons may travel and higher electronic resistance. Small pores lead to higher ESR because of hindered ion transport.

A particularly urgent area of research is the development of inexpensive high surface area carbons that can yield specific capacitance beyond the 150–200 F/g in aqueous electrolytes (80–120 F/g in organic electrolytes) that is the current state-of-the-art. Activation of mesoporous carbons can be done in a number of ways, including by heating a mixture of KOH and the carbon under N_2 at 400–1000 °C. In one example, activated mesoporous carbons showed a post-treatment surface area of 1940 m^2/g and a specific capacitance of 188 F/g; untreated carbon from the same resin was found to have a surface area of 520 m^2/g and a specific capacitance of 71.3 F/g [17.58]. Carbide-derived materials are also showing promise [17.30].

The International Union of Pure and Applied Chemistry (IUPAC) classification of pores has three categories: micropores (< 2 nm), mesopores (2–50 nm), and macropores (> 50 nm) [17.59]. Current beliefs indicate that the ideal electrode contains micropores for elevated charge storage and meso- and macropores that provide facile ion transport within the matrix [17.9].

BET theory is used for measuring the total surface area of an electrode and Barrett, Joyner, and Halenda theory (BJH) gives information on pore size and distribution. Generally, though, there is no linear relationship between the surface area measured by BET and capacitance [17.31, 60, 61]. This is because the measured area includes the monolayer of N_2 gas inside pores too small for solvated ions to penetrate, especially the large ions used in organic electrolytes. BET measurements should therefore be considered at best a semiquantitative predictor of electrode performance. There is the added complication that edge- and basal orientation in graphitic structures present different specific capacitance [17.62]. To complicate things further, recent

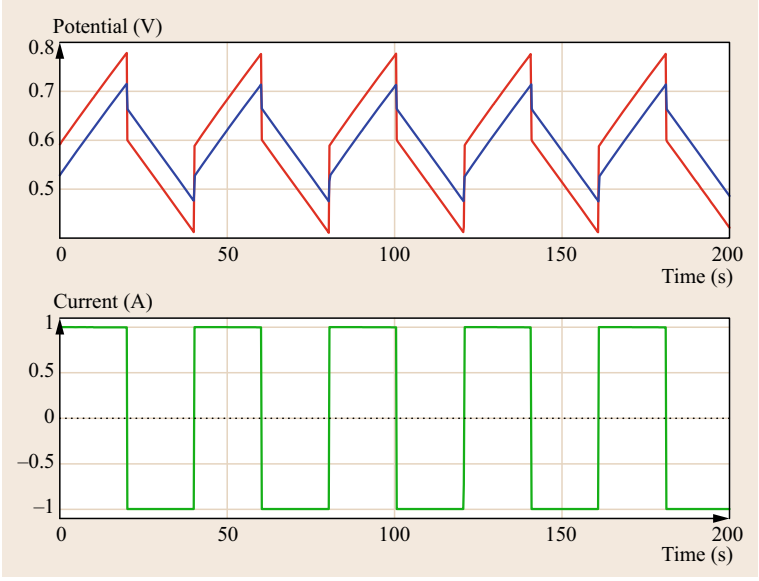


Fig. 17.26 Constant current charge–discharge cycles of a commercial EC at ±1 A illustrating the contribution of cables and connections to the ESR. *Red line*, no special attention paid to connections; *blue line*, after connections and clips were gently sanded with emory cloth

work [17.1, 63] has indicated that ions may partially desolvate in some smaller micropores, underlining that the nature of the electrochemical interface in micropores remains poorly understood, and hinting of the possibility of enhanced capacitance in nanoengineered carbons.

Promising new carbon materials are currently emerging. For example single-walled carbon nanotubes (CNTs) have a surface area of $>1300\,m^2/g$ [17.64, 65], compared to graphite $10–20\,m^2/g$. Graphene is a monolayer of sp^2 carbon – essentially a discrete sheet of graphite – with surface area $> 2600\,m^2/g$ [17.66]. Several methods exist for the preparation of graphene, and the ensuing properties depend on which method was used. A specific capacitance of $205\,F/g$ has been reported [17.67], and an EC cell constructed from graphene electrodes and an ionic liquid electrolyte yielded 85.6 Wh/kg of total electrode weight at room temperature and 136 Wh/kg at 80 °C [17.43]. The results point to an energy storage device with the same capacity as a nickel metal hydride (NiMH) battery, but that can be fully charged in under 2 min and has an exceedingly high cycle life.

17.4.2 Minimizing Series Resistance

The large current densities at which ECs are driven, coupled with the relatively low operating voltage, imply that the effects of ESR are very significant, having a fourfold impact on maximum power (17.3). Series resistance combines a number of different contributions, and each must be minimized. Even a contribution as seemingly trivial as clean alligator and banana clips can have surprising results. Figure 17.26 shows an example where the *iR* drop during galvanostatic discharges was nearly three times greater before the clips were cleaned.

Other concerns include the following:

1. Bulk electrolyte resistance can contribute significantly to the ESR of an EC, so the separation between electrodes can have a profound effect; a thin separator is desirable.
2. A significant problem is the bonding of a thin layer of active material to a current collector and maintaining low ($< 0.1\,\Omega cm$) contact resistance. Conducting paint, that is, carbon black in a support matrix, can be beneficial.
3. The electronic resistivity of the electrode material should be less than $1\,m\Omega cm$ [17.12]. This implies that the material cannot be so macroporous as to restrict electron flow, yet sufficiently macroporous to allow the flow of ions. Also there must be good interparticle contact in the case of particle-based materials. This can be accomplished using a conductive binder or a process that bridges the particles, such as sintering. However, the joining must be done without compromising the high surface area for the electrode. There is a balance to be struck between connectivity and porosity.
4. The resistivity of aqueous electrolytes is much lower ($1–2\,\Omega cm$) than organic electrolytes ($20–60\,\Omega cm$), and the minimum useful pore size is smaller in the former. One ought to consider the electrolyte system in designing electrode materials, and in choosing the separator to assure good wetability.

17.4.3 Standard Testing

International Electrotechnical Commission (IEC) specification IEC 62391-1 is widely accepted as the standard method to characterize the performance of packaged devices, particularly those available commercially. The electrochemical tests are based on concepts presented earlier in the present document (although some refinements have been suggested [17.68]). The protocol gives conditions for ECs intended for different applications (e.g., power output or memory backup), as well as unrelated physical tests (e.g., resistance to soldering heat, tensile tests on the terminals, etc.).

Briefly, the electrochemical testing portion of the protocols consist of the following:

- *Capacitance*: The capacitor is to be held at its rated voltage V_r for 30 min. A constant discharge current is then applied. The current applied depends on the capacitance of the cell (so this process might require a few iterations) and its intended use. For example, a power EC (*Class 3*) is to be discharged at $4CV_r$ mA, while a cell optimized for energy storage (*Class 2*) would be discharged at $0.4CV_r$ mA. The capacitance can then be determined as described in Sect. 17.2.1.
- *ESR from constant current discharge*: Similar to the previous case, but with a tenfold increase in current (which can be scaled back if the initial voltage drop is greater than 20% of V_r). The ESR is calculated by the difference between the initial voltage V_r and the extrapolation of the discharge line to $t = 0$, as described in Sect. 17.2.1: $R_s = \Delta V/i$.
- *ESR from AC measurements*: The root mean squared (RMS) voltage V_{AC} measured from an applied alternating current i_{AC} between 1 and 10 mA RMS at 1 kHz yields an AC resistance R_{AC} through Ohm's law: $R_{AC} = V_{AC}/i_{AC}$. Impedance is not used.
- *Leak current*. This current is measured at V_r (fully charged) after allowing the applied voltage to stabilize after some number of hours.
- *Self-discharge*: After charging to V_r for 8 h, the open circuit ($> 1\,M\Omega$) voltage is monitored for 16 or 24 h.

17.5 Summary and Conclusions

Electrochemical capacitors exhibit unusual energy and power parameters. The large currents that they produce means that special care must be taken to minimize ESR, or the results – especially power results – will be compromised.

Three complementary test methods are most commonly used:

1. Constant current discharge, which largely mimics the conditions that a working device might encounter and provides key power and energy data.
2. Cyclic voltammetry, which reveals potential-specific phenomena and stability.
3. Impedance spectroscopy, which can elucidate and quantify individual components of the cell's overall behavior.

Each method has its strengths, and together they provide valuable information. In reporting this information, it is important to be clear about what is being described. Specific capacitance, for example, could refer to the properties of a single electrode in a three-electrode cell, or an electrode pair in a two-electrode cell. The mass divisor might relate to active material, to a full electrode including binder, to two electrodes, or even to an assembled device including current collectors and packaging. Because this information is often obscure, literature comparisons can sometimes be difficult.

Results also vary widely between two- and three-electrode cells. The three-electrode technique may present features (e.g., peaks in the CV of pseudocapacitors) that are not manifested in the two-electrode configuration. Furthermore, the sensitivity of the three-electrode configuration may lead to findings that are overly optimistic and not representative of the behavior of the same system in a two-electrode configuration. It is, therefore, important that the data clearly indicate the cell configuration.

A two-electrode test cell best represents the expected performance of the electrode materials in packaged devices, since parameters such as separator resistance, charge distribution, and collector interface issues are properly emulated. The configuration of the test apparatus should also be clearly specified. Clamping force should be controlled when appropriate, and/or bolt pitch and torque kept consistent on sandwich cells.

Excessively thin coatings of active material will give overly optimistic results. Electrode thicknesses should be reasonable and consistent with geometry typical for packaged devices, on the order of 10–300 μm. Ideally, the test device should have a capacitance greater than around 0.25 F to avoid errors. Likewise, charge–discharge rates should be reasonable. The effects of high ESR can be masked, for example, by very slow CV sweep rates.

Finally, it is important to keep in mind that different techniques will give different results. For example, the commercial capacitor used as an example throughout this chapter had a nominal capacitance of 140 F. A $-Z''$ versus $1/\omega$ plot from impedance data gave $C = 107\,\mathrm{F}$ (Fig. 17.13). Cyclic voltammetry (not shown) gave average capacitances ranging between 85 and 112 F and 10–20% higher plateau capacitances. The $\mathrm{d}V/\mathrm{d}t$ slope of constant current discharge (Fig. 17.26 and (17.6)) suggests $C = 106\,\mathrm{F}$.

To conclude, there are no clear measurement standards for assessing EC materials and cells at the laboratory scale, and reliable literature comparisons suffer as a consequence. Results are very sensitive to experimental conditions, so it is important to choose methodologies that correspond well to how working devices are used and to keep ESR low. Material loadings and thicknesses should be reasonable, and discharge rates should not be excessively slow (i. e., a full discharge lasting longer than $\approx 100\,\mathrm{s}$) to avoid overstating performance and to avoid straying into the domain of the battery. It is important to be clear what mass-normalized properties like specific capacitance really mean, and also to be mindful that three- and two-electrode cells behave very differently.

17.6 Symbols

ΔV_{iR}	Voltage drop due to iR
ϵ_0	Permittivity of a vacuum
ϵ_r	Dielectric constant
ν	Sweep rate $\mathrm{d}V/\mathrm{d}t$
σ_elec	Electrolyte conductivity
σ_sep	Separator conductivity
τ	RC time constant
ω	Frequency (rad/s)
A	Area
C'	Pore capacitance
C	Capacitance
C_lfl	Low-frequency limiting capacitance
C_sp	Specific capacitance, that is, capacitance per unit mass

C_{tot}	Total capacitance
E	Energy
P	Power
P_{max}	Maximum power
Q	Charge
Q_a	Anodic charge
Q_c	Cathodic charge
R	Resistance
R'	Pore resistance
R_{AC}	Resistance
R_{ct}	Charge transfer resistance
R_s	Series resistance, also used to mean ESR
V	Voltage
V_{AC}	AC voltage
V_r	Rated voltage
Z'	Real impedance
Z''	Imaginary impedance
d	Double-layer thickness
i	Current
i_{AC}	AC current
j	$\sqrt{-1}$
l	Penetration depth
l_p	Pore depth
m	Mass
m_{tot}	Total mass
t	Time
t_D	Discharge time

References

17.1 P. Simon, Y. Gogotsi: Materials for electrochemical capacitors, Nat. Mater. **7**(11), 845–854 (2008)

17.2 B.E. Conway, W.G. Pell: Double-layer and pseudocapacitance types of electrochemical capacitors and their applications to the development of hybrid devices, J. Solid State Electrochem. **7**, 637–644 (2003)

17.3 L.L. Zhang, X.S. Zhao: Carbon-based materials as supercapacitor electrodes, Chem. Soc. Rev. **38**(9), 2520–2531 (2009)

17.4 IEC 62391-1: *Fixed Electric Double-Layer Capacitors for use in Electronic Equipment* (International Electrotechnical Commission, Geneva 2015)

17.5 M.D. Stoller, R.S. Ruoff: Best practice methods for determining an electrode material's performance for ultracapacitors, Energy Environ. Sci. **3**(9), 1294–1301 (2010)

17.6 V. Khomenkoa, E. Frackowiak, F. Béguin: Determination of the specific capacitance of conducting polymer/nanotubes composite electrodes using different cell configurations, Electrochimica Acta **50**, 2499–2506 (2005)

17.7 B.E. Conway: *Electrochemical Supercapacitors* (Kluwer Academic, Dordrecht 1999)

17.8 A.J. Bard, L.R. Faulkner: *Electrochemical Methods: Fundamentals and Applications* (Wiley, New York 2001)

17.9 A.G. Pandolfo, A.F. Hollenkamp: Carbon properties and their role in supercapacitors, J. Power Sources **157**(1), 11–27 (2006)

17.10 E. Frackowiak, F. Beguin: Carbon materials for the electrochemical storage of energy in capacitors, Carbon **39**(6), 937–950 (2001)

17.11 R. Kötz, M. Carlen: Principles and applications of electrochemical capacitors, Electrochimica Acta **45**(15–16), 2483–2498 (2000)

17.12 A. Burke: Ultracapacitors: Why, how, and where is the technology?, J. Power Sources **91**, 37–50 (2000)

17.13 B.E. Conway: Transition from supercapacitor to battery behavior in electrochemical energy storage, J. Electrochem. Soc. **138**, 1539–1548 (1991)

17.14 C.C. Hu, W.C. Chen, K.H. Chang: How to achieve maximum utilization of hydrons ruthenium oxide for supercapacitors, J. Electrochem. Soc. **151**, A281–A290 (2004)

17.15 X. Liu, P.G. Pickup: Ru oxide/carbon fabric composites for supercapacitors, J. Solid State Electrochem. **14**, 231–240 (2009)

17.16 C. Hu, W. Chen: Effects of substrates on the capacitive performance of $RuO_x \cdot nH_2O$ and activated carbon–RuO_x electrodes for supercapacitors, Electrochimica Acta **49**, 3469–3477 (2004)

17.17 Y. Zhai, Y. Dou, D. Zhao, P.F. Fulvio, R.T. Mayes, S. Dai: Carbon materials for chemical capacitive energy storage, Adv. Mater. **23**(42), 4828–4850 (2011)

17.18 C. Xu, F. Kang, B. Li, H. Du: Recent progress on manganese dioxide based supercapacitors, J. Mater. Res. **25**(8), 1421–1432 (2010)

17.19 W. Wei, X. Cui, W. Chen, D.G. Ivey: Manganese oxide-based materials as electrochemical supercapacitor electrodes, Chem. Soc. Rev. **40**(3), 1697–1721 (2011)

17.20 H. Kim, B.N. Popov: Characterization of hydrous ruthenium oxide/carbon nanocomposite supercapacitors prepared by a colloidal method, J. Power Sources **104**, 52–61 (2002)

17.21 T. Bordjiba, D. Bélanger: Direct redox deposition of manganese oxide on multiscaled carbon nanotube/microfiber carbon electrode for electrochemical supercapacitor, J. Electrochem. Soc. **156**, A378–A384 (2009)

17.22 K. Kalinathan, D.P. DesRoches, X. Liu, P.G. Pickup: Anthraquinone modified carbon fabric supercapacitors with improved energy and power densities, J. Power Sources **181**, 182–185 (2008)

17.23 Z. Algharaibeh, X. Liu, P.G. Pickup: An asymmetric anthraquinone-modified carbon/ruthenium oxide supercapacitor, J. Power Sources **187**, 640–643 (2009)

17.24 Z. Algharaibeh, P.G. Pickup: An asymmetric supercapacitor with anthraquinone and dihydroxy-

benzene modified carbon fabric electrodes, Electrochem. Commun. **13**, 147–149 (2011)
17.25 G.A. Snook, P. Kao, A.S. Best: Conducting-polymer-based supercapacitor devices and electrodes, J. Power Sources **196**, 1–12 (2011)
17.26 K. Lota, V. Khomenko, E. Frackowiak: Capacitance properties of poly(3,4-ethylenedioxythiophene)/carbon nanotubes composites, J. Phys. Chem. Solids **65**, 295–301 (2004)
17.27 B. Conway, E. Gileadi: Kinetic theory of pseudo-capacitance and electrode reactions at appreciable surface coverage, Trans. Faraday. Soc. **58**, 2493–2509 (1962)
17.28 B.Z. Fang, L. Binder: Influence of hydrophobisation of carbon surface on electrochemical capacitor performance, J. Electroanal. Chem. **609**, 99–104 (2007)
17.29 H. Talbi, P. Just, L. Dao: Electropolymerization of aniline on carbonized polyacrylonitrile aerogel electrodes: Applications for supercapacitors, J. Appl. Electrochem. **33**, 465–473 (2003)
17.30 J.A. Fernandez, M. Arulepp, J. Leis, F. Stoeckli, T.A. Centeno: EDLC performance of carbide-derived carbons in aprotic and acidic electrolytes, Electrochimica Acta **53**, 7111–7116 (2008)
17.31 J. Gamby, P. Taberna, P. Simon, J. Fauvarque, M. Chesneau: Studies and characterisations of various activated carbons used for carbon/carbon supercapacitors, J. Power Sources **101**(1), 109–116 (2001)
17.32 A. Janes, E. Lust: Organic carbonate-organic ester-based non-aqueous electrolytes for electrical double layer capacitors, Electrochem. Commun. **7**(5), 510–514 (2005)
17.33 J. Zheng, T. Jow: The effect of salt concentration in electrolytes on the maximum energy storage for double layer capacitors, J. Electrochem. Soc. **144**(7), 2417–2420 (1997)
17.34 W. Pell, B. Conway, N. Marincic: Analysis of non-uniform charge/discharge and rate effects in porous carbon capacitors containing sub-optimal electrolyte concentrations, J. Electroanal. Chem. **491**(1–2), 9–21 (2000)
17.35 S. Mayer, R. Pekala, J. Kaschmitter: The aerocapacitor: An electrochemical double-layer energy-storage device, J. Electrochem. Soc. **140**, 446–451 (1993)
17.36 F. Beck, M. Dolata, E. Grivei, N. Probst: Electrochemical supercapacitors based on industrial carbon blacks in aqueous H_2SO_4, J. Appl. Electrochem. **31**, 845–853 (2001)
17.37 J. Jang, S. Han, T. Hyeon, S. Oh: Electrochemical capacitor performance of hydrous ruthenium oxide/mesoporous carbon composite electrodes, J. Power Sources **123**(1), 79–85 (2003)
17.38 A. Janes, L. Permann, M. Arulepp, E. Lust: Electrochemical characteristics of nanoporous carbide-derived carbon materials in non-aqueous electrolyte solutions, Electrochem. Commun. **6**(3), 313–318 (2004)
17.39 H. Song, Y. Jung, K. Lee, L. Dao: Electrochemical impedance spectroscopy of porous electrodes: The effect of pore size distribution, Electrochimica Acta **44**(20), 3513–3519 (1999)
17.40 P.L. Taberna, P. Simon, J.F. Fauvarque: Electrochemical characteristics and impedance spectroscopy studies of carbon-carbon supercapacitors, J. Electrochem. Soc. **150**, A292–A300 (2003)
17.41 C. Portet, P. Taberna, P. Simon, C. Laberty-Robert: Modification of Al current collector surface by sol-gel deposit for carbon-carbon supercapacitor applications, Electrochimica Acta **49**(6), 905–912 (2004)
17.42 J. Chmiola, G. Yushin, R. Dash, Y. Gogotsi: Effect of pore size and surface area of carbide derived carbons on specific capacitance, J. Power Sources **158**(1), 765–772 (2006)
17.43 C. Liu, Z. Yu, D. Neff, A. Zhamu, B.Z. Jang: Graphene-based supercapacitor with an ultrahigh energy density, Nano Lett. **10**, 4863–4868 (2010)
17.44 X. Andrieu, G. Crépy, L. Josset: High power density electrodes for carbon supercapacitor applications, Proc. 3rd Int. Semin. Double Layer Capacit. Similar Energy Storage Devices, Deerfield Beach (1993) pp. 3–5
17.45 C.G. Cameron: Cold temperature optimization of supercapacitors, ECS Trans. **41**, 121–132 (2012)
17.46 J. Black, H.A. Andreas: Effects of charge redistribution on self-discharge of electrochemical capacitors, Electrochimica Acta **54**, 3568–3574 (2009)
17.47 J.R. Miller, A.F. Burke: *Electric Vehicle Capacitor Test Procedures Manual* (U.S. Department of Energy, Idaho Falls 1994)
17.48 G.M. Suppes, C.G. Cameron, M.S. Freund: A polypyrrole/phosphomolybdic acid|poly(3,4-ethylenedioxythiophene)/phosphotungstic acid asymmetric supercapacitor, J. Electrochem. Soc. **157**, A1030–A1034 (2010)
17.49 S.A. Kazaryan, S.N. Razumov, S.V. Litvinenko, G.G. Kharisov, V.I. Kogan: Mathematical model of heterogeneous electrochemical capacitors and calculation of their parameters, J. Electrochem. Soc. **153**, A1655–A1671 (2006)
17.50 M.D. Stoller, S.A. Stoller, N. Quarles, J.W. Suk, S. Murali, Y. Zhu, X. Zhu, R.S. Ruoff: Using coin cells for ultracapacitor electrode material testing, J. Appl. Electrochem. **41**(6), 681–686 (2011)
17.51 G. Gourdin, A. Meehan, T. Jiang, P. Smith, D. Qu: Investigation of the impact of stacking pressure on a double-layer supercapacitor, J. Power Sources **196**, 523–529 (2011)
17.52 Enesite Corp., Coral Springs, FL;http://www.enerize.com/superCap.php
17.53 L.B. Hu, J.W. Choi, Y. Yang, S. Jeong, F.L. Mantia, L.F. Cui, Y. Cui: Highly Conductive Paper for Energy-Storage Devices, Proc. Natl. Acad. Sci., U.S., Vol. 106 (2009) pp. 21490–21494
17.54 D. Fan, R. White: A mathematical-model of a sealed nickel-cadmium battery, J. Electrochem. Soc. **138**(1), 17–25 (1991)
17.55 L. Bonnefoi, P. Simon, J. Fauvarque, C. Sarrazin, A. Dugast: Electrode optimisation for carbon power supercapacitors, J. Power Sources **79**(1), 37–42 (1999)

17.56 E. Fitzer, K.-H. Köchling, H. Boehm, H. Marsh: Recommended terminology for the description of carbon as a solid (IUPAC Recommendations 1995), Pure Appl. Chem. **67**, 473 (1995)
17.57 M. Inagaki, L. Radovic: Nanocarbons, Carbon **40**, 2279–2282 (2002)
17.58 X.Q. Wang, J.S. Lee, C. Tsouris, D.W. DePaoli, S. Dai: Preparation of activated mesoporous carbons for electrosorption of ions from aqueous solutions, J. Mater. Chem. **20**, 4602–4608 (2010)
17.59 K. Sing, D. Everett, R. Haul, L. Moscou, R. Pierotti, J. Rouquerol, T. Siemieniewska: Reporting physisorption data for gas/solid systems with special reference to the determination of surface area and porocity (Recommendations 1984), Pure Appl. Chem. **57**, 603–619 (1985)
17.60 H. Shi: Activated carbons and double layer capacitance, Electrochimica Acta **41**(10), 1633–1639 (1996)
17.61 D. Qu, H. Shi: Studies of activated carbons used in double-layer capacitors, J. Power Sources **74**(1), 99–107 (1998)
17.62 D. Qu: Studies of the activated carbons used in double-layer supercapacitors, J. Power Sources **109**(2), 403–411 (2002)
17.63 J. Chmiola, C. Largeot, P.-L. Taberna, P. Simon, Y. Gogotsi: Desolvation of ions in subnanometer pores and its effect on capacitance and double-layer theory, Angew. Chem.-Int. Edit. **47**(18), 3392–3395 (2008)
17.64 P.M. Ajayan: Nanotubes from carbon, Chem. Rev. **99**, 1787 (1999)
17.65 M. Pumera, B. Smid, K. Veltruska: Influence of nitric acid treatment of carbon nanotubes on their physico-chemical properties, J. Nanosci. Nanotechnol. **9**, 2671 (2009)
17.66 M. Pumera: Graphene-based nanomaterials for energy storage, Energy Environ. Sci. **4**(3), 668–674 (2011)
17.67 Y. Wang, Z. Shi, Y. Huang, Y. Ma, C. Wang, M. Chen, Y. Chen: Supercapacitor devices based on graphene materials, J. Phys. Chem. C **113**, 13103–13107 (2009)
17.68 Y. Cheng: Assessments of energy capacity and energy losses of supercapacitors in fast charging–discharging cycles, IEEE Trans. Energy Convers. **25**, 253–261 (2010)

18. Kinetics of Fast Redox Systems for Energy Storage

Rudolf Holze

Flow batteries (also: redox batteries or redox flow batteries RFB) are introduced as systems for conversion and storage of electrical energy into chemical energy. Their position in the wide range of systems and processes for energy conversion and storage is outlined. Special attention in the discussion of current trends and developments is paid to enhanced electrocatalysis of the electrode processes inside these devices.

18.1 **Overview and Introduction** 591
18.1.1 Flow Batteries and Redox Flow Batteries 592
18.1.2 Chemistry of Redox Batteries 593
18.1.3 Hybrid Systems 595
18.2 **Flow Batteries – Basic Components** 597
18.2.1 Electrodes 597
18.2.2 Separators 597
18.3 **Redox Reactions and their Kinetics** 598
18.3.1 Diffusion, Transport and Flow of Reactants 599
18.3.2 Transport in Porous Electrodes 599
18.3.3 Charge Transfer Reactions 600
18.4 **Acceleration of Redox Reactions** 600
18.4.1 Catalysis by Chemical Surface Treatment 601
18.4.2 Catalysis by Chemical Surface Modification 601
18.5 **Materials for Electrodes in Flow Batteries** 601
18.5.1 Modified Carbons and Graphites 602
18.5.2 Non-Carbon Materials 605
18.6 **Catalysis and Surface Enlargement Effects** 605
18.7 **Future Directions** 606
References 606

18.1 Overview and Introduction

Devices for storage of electrical energy have been needed for quite some time already, definitely since the beginning of the use of electric motors in mobile applications and with all kinds of electric devices at places off the grid. Typical uses of devices are:

- Uninterruptible power supply for, for example, hospitals, traffic supervision, aircrafts
- Starting, lighting and ignition (SLI) in vehicles
- Power supply at places off the grid (remote area power supply RAPS)
- Mobile and portable applications in cameras, mobile phones, electronic gadgets, mobile computers, etc.

More recently the need for storage systems matching the variable supply of electricity from renewable energy sources has been added as a most important application. Because this field of application may become a major challenge, targets for this grid-related application are of general interest. The data concerning grid-related storage presented in Table 18.1 pertains mostly to the US market.

Storage of energy can be achieved basically in mechanical, electrical and in chemical storage systems and processes [18.1–3] such as:

1. Mechanical
   - Pump storage power plants
   - Compressed air storage power plants
   - Flywheels
2. Electrical
   - Capacitors
   - Coils
3. Chemical
   - Hydrogen
   - Hydrocarbons
   - Accumulators (electrochemical)
   - Flow batteries [18.4] (electrochemical)
   - Electrolyzers, regenerative fuel cells (electrochemical)

Because of limited availability, mechanical modes of storage can provide only a partial solution to the ever-growing demand for cheap, reliable and environ-

Table 18.1 Development and performance targets for grid-related storage

Application	Duration	Purpose	Targets
Frequency and area regulation	Short	Matching supply and demand locally (power quality)	Service cost: 20 US$/MW Roundtrip efficiency: 85–90% System lifetime: 10 y Discharge duration: 0.25–2 h Response time: ms
Integration of renewables	Short	Compensating short term fluctuations of photovoltaics energy delivery	Roundtrip efficiency: 90% System lifetime: 10 y Capacity: 1–20 MW Response time: s
Deferral of grid upgrade	Short	Delays or avoids investments in transmission and distribution	Cost: 500 US$/kWh Capacity: 1–100 MW Reliability: 99.9% System lifetime: 10 y
Load following	Long	Enables operation of energy conversion systems with constant high efficiency at all loads	Capital cost: 1500 US$/kW or 500 US$/kWh Running cost: 500 US$/kWh Discharge duration: 2–6 h
Matching daily demand fluctuations	Long	Storage of excess energy during time of high supply, delivery during high demand (load leveling)	Capital cost: 1500 US$/kW or 500 US$/kWh Running cost: 250–500 US$/kWh Discharge duration: 2–6 h Efficiency: 70–80% Response time: 5–30 min
Matching seasonal demand changes	Very long	Storage of excess energy during time of high supply, delivery during high demand (wind, photovoltaics)	–

mentally sustainable conversion and storage of electric energy. Electrical devices are of extremely limited use; only recently have supercapacitors developed into major contributors [18.5, 6]. The chemical options are more versatile, mobile and in most cases widely scaleable. The intimate relation between mode of conversion and mode of storage makes electrochemical options particularly attractive. Among the many available systems, flow batteries are emerging as easily scaleable devices particularly attractive for large-scale stationary operation [18.7–12]. Hybrid systems combining, for example, ideas of redox flow batteries as discussed below with supercapacitors [18.13] or utilizing solid matter as a redox components (e.g., $LiFePO_4$ in a lithium-based flow battery [18.14, 15]) have been described. Financial aspects of all-vanadium systems reported so far [18.16] indicate the dominating influence of costs related to chemical purity of vanadium compounds and the cation exchange membrane.

18.1.1 Flow Batteries and Redox Flow Batteries

When mixing two chemical compounds that may undergo a chemical reaction according to

$$2\,V^{2+} + 2\,VO_2^+ + 4\,H^+ \rightarrow 2\,V^{3+} + 2\,VO^{2+} + 2\,H_2O \qquad (18.1)$$

the free enthalpy (Gibb's energy) released by this reaction is just released as heat. When the process is separated into two electrode reactions it can be recovered as electric energy

$$2\,V^{2+} + H_2O \rightarrow V^{3+} + VO^{2+} + 2\,H^+ + 3\,e^- \qquad (18.2)$$

and

$$2\,VO_2^+ + 6\,H^+ + 3\,e^- \rightarrow V^{3+} + VO^{2+} + 3\,H_2O\,. \qquad (18.3)$$

In the first reaction (18.2), V^{2+} species are converted into V^{3+} and V^{4+} species; the reaction proceeding at an inert electrode only serving as electron source or sink is an oxidation reaction, and the electrode will be called an anode. In the second reaction (18.3) V^{5+} species are converted into V^{3+} and V^{4+} species; this is a reduction reaction and the electrode will be called cathode. Because of the mixture of V^{3+} and V^{4+} species, the solution is also called $V^{3.5+}$ electrolyte.

This is the operating principle of a flow battery, patented for the first time already in 1949 [18.17, 18]. The first proposal of a redox battery was reported only in 1974 [18.19, 20]. Because the reactants are practically always redox systems these devices are sometimes also called redox batteries or redox flow batteries (RFB). Further details of the device may be incorporated when naming it, for example VRB – this is an all-vanadium redox flow battery as in the preceding example. The operating principle and the basic layout can be visualized in Fig. 18.1.

Typical data of elected RFBs enjoying at least some practical success are collected in Table 18.2.

The power capability of a redox battery is given by the cell stack: the larger the electrode areas the higher the possible current, and more cells connected in series provide higher voltage output. The energy storage capability is simply given by the size of the tanks. Actually the amount of redox-active materials determines the storage capacity. Obviously highly soluble materials are preferable. Thus the redox battery provides the unique option to scale an electrochemical energy storage device with respect to both characteristic properties according to the user's requirement. For large-scale storage in terms of energy large tanks may be required, and this scale-up required for seasonal storage comes particularly cheap.

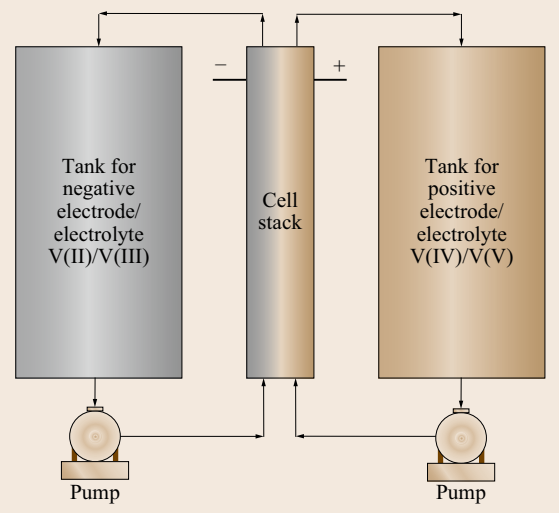


Fig. 18.1 Scheme of a redox flow battery

Self discharge is generally a problem of unwanted chemical reactions between active masses and cell components such as, for example, corrosive dissolution of zinc with associated hydrogen evolution. In case of a RFB, operations of the circulation pump cause a completely different type of *self discharge*. In demonstration plants self-discharge rates of 3% per day have been reported – this should be compared with a rate of 3% per month with a lead-acid accumulator. Suitable cell design enabling a shutdown of the pumps without detrimental effects may reduce this unacceptable rate substantially. Claims of no self-discharge are presumably unrealistic.

For an early general overview see [18.21, 22], for recent reviews [18.7, 23, 24], some typical data are collected in Table 18.3.

18.1.2 Chemistry of Redox Batteries

In the following, the chemical as well as associated technological aspects of flow batteries are briefly reviewed; some common aspects will be discussed in the following chapters.

The Iron/Chromium System

This RFB was the first system proposed and investigated [18.19, 25, 26]. It employs an iron and a chromium redox couple [18.27] according to

$$\mathrm{Fe}^{2+} \underset{\text{discharge}}{\overset{\text{charge}}{\rightleftarrows}} \mathrm{Fe}^{3+} + \mathrm{e}^{-}; \quad E_{0,\mathrm{SHE}} = 0.77\,\mathrm{V} \tag{18.4}$$

and

$$\mathrm{Cr}^{2+} \underset{\text{charge}}{\overset{\text{discharge}}{\rightleftarrows}} \mathrm{Cr}^{3+} + \mathrm{e}^{-}; \quad E_{0,\mathrm{SHE}} = -0.41\,\mathrm{V}\,. \tag{18.5}$$

Table 18.2 Data of selected redox flow batteries

System	Volume energy density (Wh/l)	Current density (mA/cm^2)	Operating temperature (°C)	DC-efficiency[a] (%)
Fe–Cr	40	100	5–60	75
Zn–Br	96	> 100	20–50	65–75
Polysulfide-Br	80	60	n.a.	60–75
V–V	30	80	0–40	70–86
V-Br	35–70	n.a.	n.a.	66–75

[a] Efficiency of devices without periphery

Table 18.3 Comparison of electrochemical storage technologies

Type	Energy efficiency (%)	Life cycle at 80% DOD[a]	Capital cost per unit energy/US$ (kW/h)	Capital cost per cycle/US$ (kW/h)
Lead–acid	72–76	200–1500	250–1000	0.2–1.0
Ni–Cd	60–67	1000–4000	400–900	0.2–1.0
Li–ion	95–98	3000–5000	800–3000	0.2–1.0
Na–S	85–90	1500–3000	250–1000	0.09–0.3
Zn–air	40–50	100–200	500–900	0.9–1.0
Redox battery	60–85[b]	1500–12 000	150–1000	0.05–0.9

[a] Depth of discharge
[b] Data may vary because sometimes energy consumption of pumps etc. are taken into account, sometimes not. This may account for differences of about 10% because the energy consumption of pumps is substantial

An aqueous electrolyte solution of 1–2.5 M HCl with 1–2.5 molar concentrations of the redox couples was used. The iron redox couple showed sufficiently fast kinetics already at carbon cloth, whereas the chromium couple is more sluggish requiring catalysts, adding substantially to the price of the system. The standard electrode potentials provide already a rough estimate of the cell voltage, which is around 0.9–1.2 V in practical setups. Mixing of the redox solutions is avoided by using an ion exchange membrane. Charge transfer at the electrode solution interface causing the redox reaction to proceed, and thus coupling outer electron flow with chemical transformation at the heterogeneous phase boundary, needs to be coupled with ionic flow of current in the electrolyte solution. Only chloride ions can reasonably handle this task. Thus an anion exchange membrane (AEM) is needed. Whereas cation exchange membranes based on functionalized polytetrafluoroethylene (PTFE, Teflon), for example, sulfonated ones (Nafion) or carboxylated ones (Flemion) have been employed commercially with huge success in the chlor-alkaline industry (membrane process), AEMs have so far not been developed to a satisfactory state of the art. Questions of ionic conductivity, longterm stability and permselectivity have not been answered convincingly. The case of the Fe/Cr RFB crossover of metal ions into the *wrong* half cell may happen resulting in losses of efficiency and storage capacity. Acceleration of the chromium redox reaction by adding trace amounts of thallium ions has been reported. Demonstration units up to several 10 kW have been described [18.28].

The Bromine/Polysulfide System

This RFB employs sodium bromide and sodiumpolysulfide as active ingredients. Both chemicals are cheap, abundantly available and highly soluble in aqueous solution. The shared sodium cation can be replaced by another one if necessary. This was the first system proposed and investigated. Electrode reactions are

$$3\,\mathrm{Br}^- \underset{\text{discharge}}{\overset{\text{charge}}{\rightleftarrows}} \mathrm{Br}_3^- + 2\,\mathrm{e}^-; \quad E_{0,\mathrm{SHE}} = 1.09\,\mathrm{V} \tag{18.6}$$

and

$$2\,\mathrm{S}_2^{2-} \underset{\text{charge}}{\overset{\text{discharge}}{\rightleftarrows}} \mathrm{S}_4^{2-} + 2\,\mathrm{e}^-; \quad E_{0,\mathrm{SHE}} = -0.265\,\mathrm{V}\,. \tag{18.7}$$

At the positive electrode a tribromide anion is formed of three bromide ions upon charge whereas at the negative electrode sulfur is moving between sulfide and polysulfide. All redox-active species are anions; consequently a cation exchange membrane permitting only movement of sodium ions is needed. As indicated above already development of CEM has progressed further than that of AEM. Nevertheless crossover may occur resulting in formation of, for example, H_2S or Br_2 – both highly unwelcome byproducts. Actual cell voltages are around 1.5 V, and with activated carbon as electrode material a small increase during charging up to 1.7–2.1 V can be observed, which is assigned to absorption of elemental bromine (Br_2) into the highly absorptive carbon.

Systems with power capacities of 5, 20 and 100 kW have been developed and a 15 MW system has been demonstrated successfully. The latter setup is composed of 120 modules with 200 bipolar electrodes and an energy storage capacity of 12 MWh based on two tanks of 1800 m^3 capacity.

The All-Vanadium System

Both RFBs discussed above are negatively affected by crossover of redox species having detrimental effects. Consequently a system employing only one kind of chemical element in several different states of oxidation was sought. Although numerous metals show this behavior so far only vanadium has been used successfully.

In a RFB briefly discussed already in the introduction (Sect. 18.1.1) the redox couples V(II)/V(III) and V(IV)/V(V) are used in a sulfuric acid electrolyte solution. Electrode reactions are

$$VO^{2+} + H_2O \underset{\text{discharge}}{\overset{\text{charge}}{\rightleftarrows}} VO_2^+ + 2\,H^+ + e^-;$$
$$E_{0,\text{SHE}} = 1.00\,\text{V} \qquad (18.8)$$

and

$$V^{2+} \underset{\text{charge}}{\overset{\text{discharge}}{\rightleftarrows}} V^{3+} + e^-; \quad E_{0,\text{SHE}} = -0.26\,\text{V}\,. \qquad (18.9)$$

The actually observed cell voltage is larger because of pH effects not taken into account in the standard potentials and because of activity coefficients of the participating ions deviating from $\gamma = 1$. The changes of redox state provide the mode of energy storage, and in addition changes of pH proceed. Because all redox-active species are cationic at first glance, an AEM is needed to keep both solutions from mixing. Instead a CEM can be used permitting the flow of protons. Membranes for this purpose are available, although still rather expensive. Crossover of vanadium species will diminish efficiency in a given cycle, but it will not degrade the system and cause reductions in capacity as observed with the systems discussed above.

Prototypes in the MW range of power and MWh range of storage capacity have been demonstrated. Solubility of some of the participating vanadium species (V_2O_5 in sulfuric acid) is limited with the constraints depending on pH and temperature; this causes lower values of energy density of the system. Subsequent precipitation in particular at elevated temperatures may impede operation of the device.

The Vanadium/Bromine System

In order to overcome the solubility limitations of the all-vanadium RFB, addition of halide ions and replacement of the vanadyl couple by a chlorobromine system has been proposed. Electrode reactions in this system are

$$2\,Br^- + Cl^- \underset{\text{discharge}}{\overset{\text{charge}}{\rightleftarrows}} Br_2Cl^- + 2\,e^-;$$
$$E_{0,\text{SHE}} \approx 1.04\,\text{V} \qquad (18.10)$$

and

$$V^{2+} \underset{\text{charge}}{\overset{\text{discharge}}{\rightleftarrows}} V^{3+} + e^-; \quad E_{0,\text{SHE}} = -0.26\,\text{V}\,. \qquad (18.11)$$

The solubility of vanadium species in the presence of bromide ions was found to be about double that found with sulfate anions. Accordingly the energy density of the system could be increased substantially. Because emission of toxic bromine vapors possibly occurring during operation chemicals such as, for example, tetrabutylammonium bromide, *N*-methyl-*N*-ethyl morpholinium bromide or other complexing agents were added to keep bromine in solution.

Numerous other combinations have been suggested and studied with more or less attention to details. In many cases expensive chemicals were needed, efficiencies were low or other drawbacks have so far inhibited successful commercialization.

A major challenge beyond the redox systems is the separator. As already mentioned cation exchange membranes are fairly far developed, although they are still expensive. Anion exchange membrane have been studied intensely also, but so far with much less success. Beyond the permselectivity important in keeping the solutions from mixing with all the associated negative consequences high ionic conductivity and sufficient mechanical stability keeping the membrane in shape when the electrolyte solution is pumped through the half cells fouling of the membrane is an almost permanent topic and problem. Although the term is apparently borrowed from biology, and thus a little imprecise in meaning, it names in general all negative changes of membranes such as coating with undesirable deposits, chemical changes of the polymer etc. Not surprisingly the chemically aggressive, highly oxidizing redox systems are a severe challenge for most membranes.

Nonaqueous RFBs

Cell voltages of RFBs employing aqueous electrolyte solutions are basically limited by the decomposition voltage of water. The use of electrode materials showing only low activity for hydrogen and/or oxygen evolution somehow mitigates the problem, and many redox couples do not decompose water. Nevertheless substantially higher cell voltages may be accessible with nonaqueous electrolyte solutions.

18.1.3 Hybrid Systems

The Zinc/Cerium System

As an example of a nonaqueous RFB this system will be described. Electrode reactions are

$$Ce^{3+} \underset{\text{discharge}}{\overset{\text{charge}}{\rightleftarrows}} Ce^{4+} + e^-; \quad E_{0,\text{SHE}} = 1.75\,\text{V} \qquad (18.12)$$

and

$$\mathrm{Zn} \underset{\text{charge}}{\overset{\text{discharge}}{\rightleftarrows}} \mathrm{Zn^{2+}} + 2\,\mathrm{e^-}; \quad E_{0,\mathrm{SHE}} = -0.76\,\mathrm{V}\,. \tag{18.13}$$

The highly oxidizing cerium ions attack carbon-based electrode materials; so far metallic electrodes such as dimensionally stable electrodes (DSAs) as used in the chlor-alkaline industry have been used.

Beyond systems employing only electrolyte solutions as *carriers of energy*, hybrid systems have been suggested and developed. These devices combine a half cell based on a redox system and a half cell wherein, for example, metal deposition or dissolution proceeds. Among them the zinc/bromine and the zinc/chlorine system have attracted particular attention. In other systems at least one redox system is chemically regenerated using an external fuel and/or oxidant; these systems are called hybrid redox fuel cells.

The Zinc/Bromine System

This hybrid RFB employs a zinc electrode and a bromide/tribromide electrode according to

$$3\,\mathrm{Br^-} \underset{\text{discharge}}{\overset{\text{charge}}{\rightleftarrows}} \mathrm{Br_3^-} + 2\,\mathrm{e^-}; \quad E_{0,\mathrm{SHE}} = 1.09\,\mathrm{V} \tag{18.14}$$

and

$$\mathrm{Zn} \underset{\text{charge}}{\overset{\text{discharge}}{\rightleftarrows}} \mathrm{Zn^{2+}} + 2\,\mathrm{e^-}; \quad E_{0,\mathrm{SHE}} = -0.76\,\mathrm{V}\,. \tag{18.15}$$

As high bromine concentrations are used in this system, a further equilibrium should be mentioned

$$\mathrm{Br_2} + \mathrm{Br^-} \rightleftarrows \mathrm{Br_3^-}\,. \tag{18.16}$$

Although this occurs mostly in liquid bromine it may become effective here because of the large concentration of bromide ions. Addition of bromine-complexing agents as already discussed before is an option to support a high concentration of bromine. The highly corrosive aqueous solution of HBr poses serious materials challenges enhanced by the strongly complexing activity of bromide ions – such as observed with basically all halide ions. Separation of the electrolyte solutions of zinc bromide and bromine, or more precisely, separation of bromine from the zinc metal electrode, is afforded by using an IEM or at least a microporous separator, for example a polyolefine membrane. The use of a solid zinc electrode results in relatively high energy density; unfortunately deposition of solid zinc during charging may result in dendrite formation and internal shortcircuiting. Self discharge by corrosion of zinc in particular is substantial; consequently energy efficiency is low. Although units up to MW size could be demonstrated successfully the various challenges remain substantial. Because of the inherent problems associated with a solid electrode that is dissolved and subsequently regenerated by electrodeposition during the charge, the use of zinc slurries has been proposed. Pumping such slurries is basically possible; it places extreme stress on the mechanical parts of the system, in particular on the pump.

A system somewhat hard to classify is the *soluble lead acid accumulator*. Contrary to the classical lead acid accumulator with all reaction products being solid (except for the trace amount of lead ions in solution controlled by the solubility of $PbSO_4$) this concept employs an electrolyte solution wherein lead ions are highly soluble; for example $HClO_4$, HBF_4 or H_2SiF_6.

The general electrode reactions are

$$\mathrm{Pb^{2+}} + 2\,\mathrm{H_2O} \underset{\text{discharge}}{\overset{\text{charge}}{\rightleftarrows}} \mathrm{PbO_2} + 4\,\mathrm{H^+} + 2\,\mathrm{e^-}; \quad E_{0,\mathrm{SHE}} = 1.49\,\mathrm{V} \tag{18.17}$$

and

$$\mathrm{Pb} \underset{\text{charge}}{\overset{\text{discharge}}{\rightleftarrows}} \mathrm{Pb^{2+}} + 2\,\mathrm{e^-}; \quad E_{0,\mathrm{SHE}} = -0.13\,\mathrm{V}\,. \tag{18.18}$$

The problems associated with deposition and dissolution of $PbSO_4$ in the classical system such as, for example, crystal growth (Ostwald ripening), sulfation, shape change etc., are avoided completely. Because only lead ions are formed (during discharge) and consumed (during charge) no problem of crossover exists. Performance at low temperatures is improved because solid state diffusion in the electrode is avoided. Utilization of the active masses is slightly improved; of course dissolution on both sides must be limited to keep the metal grid or oxide-coated grid functional as current collector and electrode in subsequent recharging. Deep discharge is a smaller problem in comparison with the lead-acid accumulator. Circulation of the lead ion-containing electrolyte solution improves cell performance, beyond this the cell has no similarity with a RFB. The problems associated with deposition and dissolution of solid masses already encountered with

the zinc/bromine system are the same. Unfortunately kinetics of the lead dioxide formation are sluggish.

The term flow battery is sometimes used to designate systems wherein indeed a solution, in most cases the reactant solution, is flowing. Typical examples are supercapacitor *flow cells* proposed to harness electrical energy from salinity gradients between sea water and river water [18.29]. They are alternatively flooded with those waters with this latter mode of operation causing the designation *flow cell*.

18.2 Flow Batteries – Basic Components

Whereas tanks, tubes and pipings are no major challenge – they need to be built with inner linings chemically stable versus the sometimes chemically rather aggressive components of the redox solutions, they should protect the solutions from environmental influence causing, for example, self discharge by chemical reactions with airborne substances – the whole challenge lies in the cell stack.

18.2.1 Electrodes

In the stack the electrode reactions proceed at two electrodes or a number of electrodes connected in series for multiplied output voltage. In case of inherently fast redox reactions, i. e., large values of the exchange current density j_0 and respective heterogeneous rate constant k_0, a graphite plate or a plate of polymer-bonded graphite material may be enough. The redox reaction is a heterogeneous one – thus using a small geometric (and in the case of a smooth graphite plate also real) surface area the current densities may become high resulting in increased charge transfer overpotentials. This results in undesirable loss of efficiency; the heat produced this way is no major problem because of the rapid flow of electrolyte solution. Another potential limitation is transport of redox species. Certainly forced flow of reactants generated by circulating the electrolyte solutions diminishes the problem, but at smooth electrodes and with mostly laminar flow, utilization of the solution will be small, and most of the reactants will pass the cell without getting close enough to the electrolyte-solution interface for charge transfer. This situation changes dramatically when three-dimensional electrodes are employed. Basically cutting some grooves into the graphite plate parallel to the flow of solution will increase the surface area available for the electrode reaction; this will also enhance mixing in the flowing solution slightly, but it will most likely not cause a sufficiently effective change from laminar to turbulent flow. This will be afforded by employing truly three-dimensional electrodes such as carbon paper, graphite cloth or felt and a flow of the electrolyte solution through them. Proper selection of felt in particular with respect to active surface area, flow resistance and effective utilization of reactants has been pointed out early [18.28]. Carbon cloth, paper etc. have been called activation layers [18.30]. The context of this somewhat unusual statement reveals that the result is decreased activation polarization. The latter term has apparently not been defined properly in the literature; it may nevertheless be assumed that it designates either the sum of all electrode overpotentials or the charge transfer overpotential. These almost textile-like materials provide large surface areas, good electronic conductivity, and they enhance turbulent flow. They are not as rigid as graphite plates, thus a sandwich-like structure with a graphite plate acting as support, current collector and flow-guiding structure (flow field) is necessary. The highly porous material must not be compressed too much because this would increase flow resistance, impeding transport of the redox electrolyte solution and increasing required pumping power.

18.2.2 Separators

Because mixing of the electrolyte solutions in the two half cells must be avoided – otherwise self discharge via a homogeneous reaction as outlined above will happen – a separating membrane (IEM) is needed between both half cells. Details will be described below together with particular systems. The basic stack design employs this separator between two porous electrodes of high surface area with two plates acting as current collectors, with flow distributors and mechanical support keeping the sandwich in place (Fig.18.2).

A setup operating without a separator by employing carefully designed and controlled laminar flow has been described [18.31], but the available data do not suggest application in RFB. The use of baffles for improved convection has been proposed [18.32].

The backplates may operate in a bipolar mode in the case of a cell stack constructed of several cells connected in series, supporting on one side the anode of a cell and on the other side the cathode of the next cell. Only the flow field arrangement – usually an array of grooves ensuring effective distribution of the electrolyte solution across the whole porous electrode – needs to

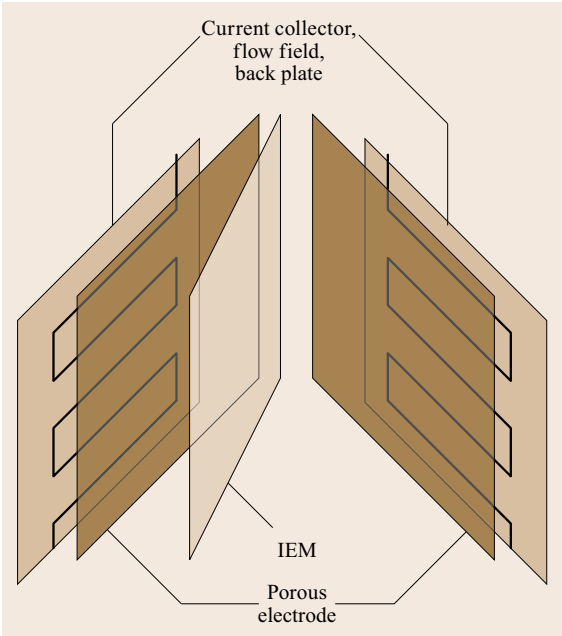


Fig. 18.2 Scheme of a redox flow battery cell stack

be prepared on both sides of the plate. When catalyzed electrodes are used the catalyst is only applied to the porous electrode, not to the current collector. Thus, the bipolar plate can be made highly symmetric resulting in further cost savings.

All systems share common advantages: the electrode reactions proceed at an electrode that acts only as electron source or sink (depending on the mode of operation charging/discharging and the place as positive or negative electrode [18.33]), no deposition or dissolution of matter nor any solid state reaction, intercalation, doping, etc., proceed, and this makes the systems very stable. No degradation of the components such as shape change, loss of contact between particles of active mass or contact to current collector, etc., must be expected. Only when the electrode shows changes because of lacking stability, poisoning, oxidative destruction because of highly oxidizing capability of a redox component, etc., may performance become poorer. Deep discharge that is detrimental with most other accumulators is no problem, neither is overcharge. In this case redox components are completely exhausted during charging gas evolution, in particular hydrogen evolution at the negative electrode, may happen. Since the solution is circulated the gas can be reclaimed from the solution storage tank easily. Systems operate at ambient temperature, so no thermal insulation or heating are necessary. Actually some systems have limitations at higher temperatures because of lower solubility of some redox components. The electrode reactions are simple – beyond the obvious fact of being heterogeneous. Most redox couples show fast kinetics providing low charge transfer overpotentials; sometimes catalysts may be needed to speed up the electron transfer reaction (Sect. 18.3.3). There are some drawbacks: although the cell stack is small and compact in most cases the tanks for storage of the redox solutions are large (of course depending on the planned energy storage capacity) resulting in a size that will presumably exclude the use in mobile and portable applications, perhaps even in densely populated residential quarters. Some of the chemical ingredients are corrosive and/or unhealthy, but none of them are explosive. The pumps are moving parts and need replacement after several years of operation as with pumps in many chemical plant environments. Their operation consumes some energy causing a minor loss in efficiency.

18.3 Redox Reactions and their Kinetics

A heterogeneous reaction taking place at the electrochemical interface, i. e., between an electronically conducting material (this material or phase is frequently somewhat imprecisely called the electrode) and an ionically conducting phase (the electrolyte solution composed of dissolved ions, ionic liquids etc.) is always a sequence of several steps (Fig. 18.3).

The reactant, in case of a RFB a solvated ion, will be present at bulk concentration in the volume of the electrolyte solution, in particular in the reservoir tank. It has to diffuse to the electrochemical interface, where it is consumed or converted in the electrode (charge transfer) reaction.

According to the theory of overpotentials in electrochemical kinetics [18.34] the differences in concentration of species between the bulk value and the interfacial values cause a concentration overpotential η_{conc}, which may be due to insufficient transport or due to slow homogeneous reactions preceding or following the charge transfer step. The former causes a diffusion overpotential η_{diff}, the latter a reaction overpotential η_{react}. Together with the charge transfer overpotential η_{ct} caused by sluggish charge transfer, the adsorption overpotential η_{ad} due to a slow adsorption or desorption step and the crystallization overpotential η_{cryst} caused by slow formation of metal deposits or their dissolution,

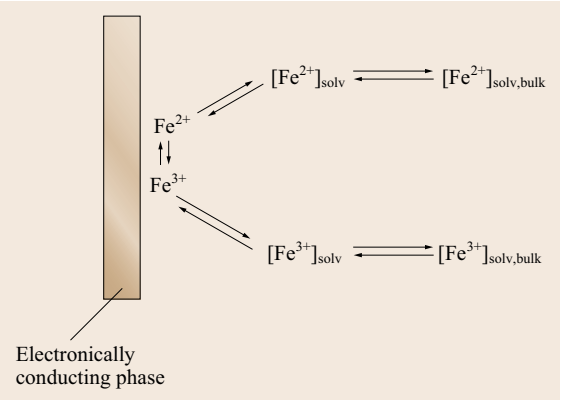


Fig. 18.3 Steps of an electrochemical redox reaction taking the $Fe^{2+/3+}$-redox couple as an example

add up to the difference between the electrode potential at rest E_0 and the electrode potential E at flowing current

$$\eta = E - E_0 = \eta_{conc} + \eta_{ct} + \eta_{ad} + \eta_{cryst} = \eta_{diff} + \eta_{react} + \eta_{ct} + \eta_{ad} + \eta_{cryst} \,. \quad (18.19)$$

For all technical applications small overpotentials are desirable with corrosion reactions being the notable exception.

18.3.1 Diffusion, Transport and Flow of Reactants

Because diffusion is slow and because mass transport through the pipes connecting the cell stack and the reservoir tanks is very limited with stagnant solutions, the reactants are pumped in a close cycle from reservoir to cell and back as depicted in Fig. 18.1. Once the charge transfer reactions have occurred the resulting species have to diffuse away from the electrode, and the same arguments applied to the previous transport step apply here also.

In early research and development work on RFB the need for enhanced mass transport by forced convection, i. e., by circulating the electrolyte solution, was quite obvious. Consequently all work beyond fundamental studies of, for example, electrode reactions or electrolyte solution properties were done with circulating electrolyte solution.

18.3.2 Transport in Porous Electrodes

Even with an electrocatalytically highly active material the required large currents can also be maintained at acceptable electrode overpotentials with high surface area electrodes; otherwise already charge transfer overpotentials will seriously affect stack performance. In many electrochemical applications large electrode surfaces are realized by using porous electrodes of many different designs, structures and compositions. These porous structures help mostly in reducing charge transfer overpotential by increasing the electrochemically active surface and are and thus reducing the current density (which in turn is related to charge transfer overpotential, exchange current density and symmetry factor according to the Butler–Volmer equation [18.34]). In most cases they do not provide enhanced mass transfer. In the case of RFBs this increase is highly desirable because reactants are present in the electrolyte solution only at a limited concentration, mostly in the lower molar range. The flat cell design employed in all reported studies provides only a limited electrolyte solution reservoir, thus electrolyte solution is pumped through the cell. At low rates of flow laminar flow patterns will govern, and accordingly a substantial fraction of the electrolyte solution will pass the cell without having a chance to deliver reactants to the electrode surface. Change to turbulent flow will change this. Such a flow pattern can be effected by increasing the flow rate to values high enough to pass critical Reynolds numbers, this can also be achieved by placing obstacles into the flow resulting in turbulences. In the case of an obstacle serving as active electrode itself an even higher beneficial effect will be reached. This is utilized in technical electrolyzers of the packed or fluidized bed type [18.35, 36]. Designs employing these types of electrode are not suitable for RFB because of costs, complexity and difficulties in scaling up to large stacks. Thus other means of obtaining large surface areas were searched for beyond structuring the graphite plate by cutting slits, etc. Carbon felt and carbon paper have attracted major attention early on. They can be manufactured by pyrolysis from woven, felt-like or paper-like raw materials from natural or synthetic sources. Because of different chemical compositions and pyrolysis conditions, properties of the obtained materials vary wildly. When they are mounted in a cell between a separator (membrane) and a graphite plate they will be flooded with electrolyte solution, actually – depending on design – the solution will flow through them. This results in large active surface areas brought into contact with the electrolye solution and formation of turbulent flow conditions at least on a microscopic and mesoscopic level. These electrodes may thus be called porous electrodes although their porosity differs strongly from that of traditional porous materials.

18.3.3 Charge Transfer Reactions

The intended heterogeneous redox reaction at the electrodes of a RFB includes naturally changes of the redox state of participating ions and – depending on the type of redox species – changes in the arrangement, number and chemical identity of complexing ligands. Even simple redox species like Fe^{2+}/Fe^{3+} ions will be solvated, i. e., complexed, with water molecules. Thus, actually even in this case aquo-complexes will be the reactants.

Electrode reactions are generally classified as inner-sphere and outer-sphere reactions [18.34, 37–39]. In the former case the reacting species has to approach the electrode surface without any molecular species (water molecules, other solvent molecules) or adsorbed species being in between in order for electron transfer to proceed. In the latter case electron transfer proceeds along greater distances even across molecular species and adsorbates in between. A further separation can be made in this case based on the degree of electronic interaction [18.40]. With sufficiently strong interaction the transfer is adiabatic and should be independent of the electrode material. Weak interactions result in a more complicated, less clear-cut picture [18.40]. Because of the more intimate interaction the chemical identity of the electrode and its possibly present particular surface properties will be more effective in the case of inner-sphere reactions and of adiabatic outer-sphere reactions. Generally this matter remains to be subject of strong debate [18.41] and shall not be discussed in more detail here. As will be shown below (Sects. 18.4–18.6) the concepts and models of catalytic activity of materials employed as electrodes or electrode modifiers in RFB is empirical and rather general in most cases. Taking this into account many electrode reactions showing rates of reaction apparently independent of electrode material have been classified as being outer-sphere reactions [18.37], until more recently when experimental methods have been developed enabling precise studies of the reactant–electrode interaction with, for example, spectroelectrochemical methods [18.42]. Many simple redox reactions have been considered as outer-sphere reactions because of the small or even absent dependency on electrode material and because of the absence of any electrode reaction features implying adsorption as a significant reaction step. Because of the arguments available today this oversimplification does not seem to be valid anymore; the consequences will be discussed below (Sects. 18.4–18.6).

Numerous experimental methods are available to obtain kinetic data for redox reactions, i. e., exchange current densities j_0 and the associated heterogeneous rate constants k_0 [18.37]; technological development has definitely passed the stage of early tentative methods [18.43] despite the observation that even nowadays results blithely unaware of modern methods are published.

18.4 Acceleration of Redox Reactions

The numerous redox reactions already mentioned above when briefly characterizing the RFBs proposed so far (the listing may be incomplete) are in many cases rather fast, i. e., the heterogeneous rate constant k_0 is large enough to keep the charge transfer overpotential η_{ct} small enough, i. e., smaller than overpotentials caused by other reaction steps. As also mentioned already some reactions are sluggish causing substantial overpotentials. Prominent among them are

$$Cr^{2+} \underset{\text{charge}}{\overset{\text{discharge}}{\rightleftarrows}} Cr^{3+} + e^- \qquad (18.20)$$

and

$$Cr^{3+}(EDTA) \underset{\text{charge}}{\overset{\text{discharge}}{\rightleftarrows}} Cr^{5+}(EDTA) + 2\,e^- . \qquad (18.21)$$

In addition, redox reactions so far considered to be fast enough have been studied for more fundamental reasons with results being also of technological importance; details will be discussed below.

Surprisingly, exchange of a ligand – in this case water versus EDTA (ethylenediaminetetraacetate) – results in a large increase of k_0 [18.44]

$$Cr^{2+}(EDTA) \underset{\text{charge}}{\overset{\text{discharge}}{\rightleftarrows}} Cr^{3+}(EDTA) + e^- . \qquad (18.22)$$

These statements should be treated carefully because sometimes they are rather unspecific, limited to only the anodic or cathodic electrode reaction, etc.

Sometimes effects of further electrolyte constituents on k_0 have been observed. A prominent example is the *cation effect* of potassium ions on the reaction [18.45]

$$[Fe(CN)_6]^{4-} \rightleftarrows [Fe(CN)_6]^{3-} + e^- . \qquad (18.23)$$

These effects are not catalytic ones; no examples are known related to RFBs. Procedures of reactivation of

electrolyte solution, which as a function of time of operation show sluggish electrode reactions by adding, for example, tetraethylenepentamine, are presumably noncatalytic and they are also not treated here [18.46, 47].

Somewhat surprisingly, truly catalytic effects are sometimes mixed up with terms like current yield [18.48]. Current yield certainly means only the fraction of charge utilized in the desired electrode reaction. Any increase of this yield is certainly not straightforwardly catalysis. It may be assumed that authors had in mind the hydrogen evolution inhibition by some catalytically active materials and the overall increase in stack efficiency with decreasing overpotential-caused losses. Nevertheless confusion should be avoided at this point.

18.4.1 Catalysis by Chemical Surface Treatment

Catalysis in its broadest meaning is acceleration (or less frequently gradual inhibition) of a chemical reaction by an additional substance that participates in the reaction but which is left after the reaction unchanged [18.49]. This applies both to homogeneous and heterogeneous reactions. In the case of RFB catalysis is mostly applied – if at all – to inhibit unwanted side reactions such as hydrogen evolution at the negative electrode and/or to accelerate the desired redox reactions; in the latter case both directions of a given redox reaction may be affected.

Both cases of catalysis require surface treatment of the electrode. In the case of suppression of hydrogen development, in all known cases chemical modification by foreign metal deposition is required. Suppression is important because of both reduced losses by unwanted gas evolution and competition of protons with redox ions for reaction sites on the electrode surface. Preferable are metals with a large hydrogen overvoltage such as, for example, bismuth or lead [18.50–52], mercury [18.48], or RuO_2 [18.30]. For acceleration of the redox reactions at carbon-based electrodes in many cases chemical surface treatment, for example, exposure of the electrode material to a stream of nitrogen gas at high temperatures, may be sufficient.

Catalysis will be subsequently discussed with particular reference to those electrode materials currently considered for technical application.

18.4.2 Catalysis by Chemical Surface Modification

Chemical surface modification implies a change of chemical composition of the electrode surface, and this may result in changes of structure at a molecular or crystallographic level also. Modification processes range from exposure to elevated temperatures in inert gas or in slightly reactive gas (e.g., nitrogen, see also above) to contact with chemically reactive liquids (e.g., oxidizing acids) and to deposition of substances like, for example, metals on the surface by chemical or electrochemical deposition processes.

18.5 Materials for Electrodes in Flow Batteries

As already mentioned, practically all RFB concepts proposed and studied so far have employed preferably carbon-based (graphitic or similar) materials as electrodes; only cerium-containing systems have been an exception because of the extreme oxidizing capability of this ion in its higher state of oxidation. There are several reasons for the dominant use of graphite and similar carbon-based materials. These materials are:

- Cheap and abundantly available
- Easily manufactured into particular shapes and forms
- Chemically stable against practically all reactant solutions encountered in RFB
- Mechanically stable during operation
- Impermeable for electrolyte solution
- Show reasonable electrocatalytic activities for many redox reactions.

There are nevertheless some redox reactions being slow at several electrode materials including carbon-based ones [18.37]. Because of the highly efficient artificially enhanced mass transfer resulting in very small concentration or diffusion overpotentials ($\eta_{conc} = \eta_{diff} + \eta_{react}$) these limitations have become a substantial obstacle requiring improvements of electrocatalytic properties of these materials.

Numerous carbon-based materials have been studied so far. Unfortunately no overview of materials including data of characteristic properties is available so far. Most authors provide no technical data of their samples, sometimes even the source of the material is given incompletely or falsely. Studies of the relationship between precursor materials and the obtained graphite materials, for example felts, are rare. In a typical study felts made from polyacrylonitrile and Rayon have been compared taking an all-vanadium RFB [18.53]. Differ-

ences in electric conductivity (important in particular for power performance) and surface area were found. Rayon-based fibers react more easily with oxygen yielding C=O-surface groups. No significant differences in performance were observed. Table 18.4 lists carbon-based materials by their given trade names, with a generic designation, characteristic properties, the studied redox reaction(s) and references to the study they were used in.

18.5.1 Modified Carbons and Graphites

Electrocatalysis with carbon-based material utilized in RFB can be assigned to three major approaches:

1. Structural modification of carbon itself
2. Mechanical or chemical surface treatment
3. Foreign metal deposits.

1) As already implied with the brief characterization (when available) of the carbon-based materials in the Table 18.4, most materials are either used in the form they are produced in (e.g., plates, with mechanical structure providing a flow field and a slightly increased true surface area) or in polymer-bonded form when produced from powder or flakes. Depending on the process parameters porous or nonporous materials are obtained. The former material is quite obviously not desirable except for applications in, for example, electrolysis, where the whole sample or electrode is immersed in an electrolyte solution. Recently forms of carbon such as carbon nanotubes (CNTs), graphene etc. have been prepared, they have attracted huge interest in both fundamental and applied research. In the case of RFB, nanotubes have attracted particular attention [18.61]. The multiwalled carbon nanotubes were attached in pristine as well as carboxy- and hydroxy-functionalized form. The improved performance of the functionalized MWCNTs (multiwalled carbon nanotubes), in particular of the carboxylated, was attributed to participation of the oxygen-containing surface groups in the redox reaction. In a follow-up study these authors attributed the enhanced performance in addition to increased surface area and number of surface defects [18.62]. Addition of a small amount of graphite oxide to graphite powder subsequently mixed with PTFE as a binder yielded superior electrodes with the improved performance to the added oxygen functional groups provided by he graphite oxide [18.63]. Short carbon nanotubes were attached to carbon felt by *Wei* et al. [18.64] for use as electrodes with both half cells of an all-vanadium RFB. Substantial improvements in terms of higher Coulombic and energy efficiency as well as higher reversibility (i. e., rate) of the redox reactions was attributed o the CNTs, in particular to the catalytic properties of carboxylic surface functional groups on the CNT and the high electronic conductivity of the latter. Vapor-grown carbon fibers (VGCF) deposited on graphite felt have been employed in an all-vanadium RFB [18.65]; addition of nickel and cobalt coatings were evaluated. Beyond increased production costs of the electrode only general efficiency improvements were stated.

For modifications of the surface structure in a topographic sense see 3).

2) Early rather unspecific reports on *activated carbon fiber electrodes* [18.43] apparently confirmed the general and much older experience, that carbon-based electrodes treated in, for example, a nitrogen-containing gas atmosphere, showed significantly enhanced electrocatalytic activity [18.66]. Intentional nitrogen doping has recently attracted attention for electrodes to be used in RFBs [18.67]. Surface oxidation of carbon materials yielding acidic surface functionalities had been reported earlier [18.68]. Both treatments may change the wettability of the surface in addition to creating functional groups and defects. Increased wettability may be desirable in many electrochemical applications because it may help to increase the electrochemically active surface area (EASA). Because most studies pertained to electrocatalysis of dioxygen reduction in fuel cell and related electrolytic applications [18.69, 70] the applicability of these results for RFB needed experimental reappraisal.

Hollax and *Cheng* have reported on kinetics of the $Cr^{2+/3+}$ and $Fe^{2+/3+}$ redox couples at highly oriented pyrolytic graphite after oxidative treatment in air at 600 °C [18.71]. Graphene oxide nanoplatelets heat-treated at various temperatures showed improved performance for both technologically relevant vanadium redox couples [18.72]. Oxygen-containing functional groups as well as hydroxylation were detected on this electrode material; they are invoked as being responsible for the observed improvement. The V^{2+}/V^{3+}-couple depended more significantly on these functional groups than the vanadyl couple [18.73]. In addition, the higher electronic conductivity of graphene oxide (as compared to graphite) and a faster surface diffusion of VO^{2+} have been stated as beneficial effects. A composite of graphene oxide nanoplatelets and muliwalled carbon nanotubes showed improved performance with the vanadyl redox couple [18.74].

The slow redox reaction $Cr^{2+/3+}$ has been studied at heat-treated carbon fibers [18.75]; dependencies on treatment parameters were identified without providing information about catalytic effects. Because of increased cell resistance, efficiency decreased. Although thermal treatments applied so far mostly are simple they

Table 18.4 Carbon-based materials for redox flow batteries

Trade name	Manufacturer	Generic designation[a]	Properties	Studied redox reactions	Reference
ATJ	Le Carbone-Lorraine	Porous bulk graphite		$Fe^{2+/3+}$	[18.54]
BW-309	Toyobo Co. Ltd.	Carbon fiber		$V^{4+/5+}$, $V^{3+/4+}$	[18.55]
GRC	–	Graphite reinforcement carbon		$V^{4+/5+}$, $V^{3+/4+}$	[18.55]
GF-20	Nippon Carbon Co. Ltd.	Carbon fiber		$V^{4+/5+}$, $V^{3+/4+}$	[18.55]
JP845	Le Carbone-Lorraine	Nonporous bulk graphite		$Fe^{2+/3+}$	[18.54]
NG		Natural graphite		$V^{4+/5+}$	[18.56]
PG60	Le Carbone-Lorraine	Porous bulk graphite		$Fe^{2+/3+}$	[18.54]
RVC-45PPI	Electrosynthesis Corp.	Reticulated vitreous carbon		$Fe^{2+/3+}$	[18.54]
RVC-60PPI	Electrosynthesis Corp.	Reticulated vitreous carbon		$Fe^{2+/3+}$	[18.54]
SGF	Stackpole	Graphite felt		$Fe^{2+/3+}$	[18.54]
–	–	Plastic-bonded natural graphite flake		$Cr^{2+/3+}$	[18.48]
–	–	Electrographite		$Cr^{2+/3+}$, $Fe^{2+/3+}$	[18.57]
–	–	Natural graphite		$Cr^{2+/3+}$, $Fe^{2+/3+}$	[18.57]
Electrode graphite EH	Sigri	–		$Fe^{2+/3+}$	[18.58, 59]
OPG	Ringsdorff	Ordinary pyrolytic graphite		$Fe^{2+/3+}$	[18.58, 59]
GC	Sigri, Metrohm	Glassy carbon	Electro-chemically activated	$Fe^{2+/3+}$	[18.58, 59]
Diabon N	Sigri	Graphitized, polymer-bonded material		$Fe^{2+/3+}$	[18.58, 59]
Ridurid V1017	Ringsdorff	Nonporous material bonded with phenolic resin		$Fe^{2+/3+}$	[18.58, 59]
WCA cloth	Union Carbide	Porous graphite		$Cr^{2+/3+}$	[18.60]
Felt	Union Carbide	Porous graphite		$Cr^{2+/3+}$	[18.60]
G 2225 cloth	Hitco	Porous graphite		$Cr^{2+/3+}$	[18.60]
FMI	Fibre Materials Inc.	Rayon-based		$V^{2+/5+}$	[18.53]
GFD 2	Sigri	PAN-based			[18.53]

[a] Designation as stated in the original report

are expensive from an energetic point of view. Fenton's reagent [18.37, 76–78] being a very effective oxidant has been proposed as an alternative way to create catalytically active hydroxylated surfaces [18.79].

Ion etching and sand blasting of both natural graphite and electrographite yielded favorable catalytic effects for both $Cr^{2+/3+}$ and $Fe^{2+/3+}$ redox reaction with the former graphite showing slightly better results [18.57]. The electrocatalytic effects could not be explained alone by invoking increased surface roughness and wettability. The authors suggest participation of acidic surface oxides in the redox reaction by enhanced adsorption of the redox ions at these functions. The lower durability of this effect in case of the $Cr^{2+/3+}$ system was attributed to the fact that during reduction of Cr^{3+}-ions the electrode potential is negative enough to cause reduction of these oxide groups. Effects of thermal oxidation in air of graphite felt on the $Fe^{2+/3+}$-redox couple have been described [18.80]. An optimum burn-off resulting in three-fold enhancement of cell performance was found; surface oxide chemistry was invoked to explain the effect with a minimal amount of quinoid groups being desirable. Graphene as a particular form of carbon has attracted research into numerous applications including use as constituent of electrodes in RFBs.

Addition of various organic compounds (fructose, mannitol, glucose, d-sorbitol) to electrolyte solutions containing the $V^{4+/5+}$ redox couple has been investigated [18.81]. The most effective d-sorbitol apparently caused an increase in surface density of OH groups being involved in the redox reaction; in addition d-sorbitol increases solubility of the V^{5+}-compound. This finding in general corroborates earlier reports by *Sun* and *Skyllas-Kazacos* regarding the effect of surface oxygen functional groups, in particular C-O-H moieties [18.73, 82, 83].

Thermal treatment in the presence of nitrogen results in enhanced electrocatalytic activity for the $V^{4+/5+}$ redox couple [18.84]. The catalytic mecha-

nism influenced by the nitrogen doping was not elucidated. Nitrogen-doped carbon nanotubes in graphite felts have been described [18.67]. The substantially improved performance was attributed to several features of these catalysts: the modification of the electronic structure of the CNTs by embedded nitrogen should change favorably adsorption characteristics for vanadium-species; the doping causes generation of defect sites that are generally catalytically more active; the amount of surface oxygen species, which in many studies has been identified as being critically involved in the redox reactions, is increased; and the doping makes the CNTs more accessible, i. e., the electrochemically active surface is increased presumably because of a more hydrophilic surface. The doping causes also changes in the porous structure supporting diffusion of redox species. As an alternative to thermal treatment in a nitrogen gas-containing atmosphere, a procedure employing aqueous solutions of ammonia has been reported [18.85]. Improvements of Coulombic and voltage efficiency were observed, they were attributed to the improved electrocatalysis of the treated graphite felt, in particular the nitrogeneous surface groups on it.

3) Foreign metal deposits acting as highly efficient catalysts in electrochemical reactions have received considerable attention since the discovery of underpotential metal deposition [18.86, 87] and the associated greatly enhanced electrocatalytic activity of these modified surfaces in, for example, electrooxidation of alcohols at fuel cell electrodes. The formation of foreign metal deposits on metallic substrates at electrode potentials positive to the calculated Nernst potentials involving obviously strong interactions beyond simple metal deposition, i. e., crystallization, has been the subject of a long debate, but the effect appeared initially to be limited naturally to metal electrodes. Large catalytic effects were also observed nevertheless when traces of metal ions were added to electrolyte solutions in systems where carbon-based electrodes were employed (e.g., in the electroreduction of dichloroacetic acid [18.88–90]).

In case of flow batteries catalytic effects were repeatedly observed after addition of small amounts of, for example, thallium [18.91, 92] or of gold [18.93, 94] to the $Cr^{2+/3+}$-couple of a RFB. Metal deposition of the foreign additive was claimed, but neither proven nor studied with respect to the mechanism of catalytic activation. Surprisingly, addition of the same ion may not affect other redox reactions as observed with Tl^{+}-ions not affecting at all the kinetics of the Fe(III/II) couple [18.54]. Acceleration of the oxidation of Cr^{2+}-ions at polymer-bonded graphite electrodes in an HCl-based aqueous electrolyte solution by traces of gold (impregnated on felt with a aqueous gold chloride solution followed by thermal decomposition at 250 °C) and lead were reported [18.22, 51, 95]. Both metals also diminish hydrogen evolution; in the studied case losses due to this undesirable side reaction of about 20% could be reduced to 4–5%. Lead deposits were unstable during the chromium oxidation reaction, but the dissolved lead was redeposited during the Cr^{3+}-reduction when charging the cell. A new catalyst repeatedly mentioned in this report was not specified. An influence of the foreign metal deposition electrode potential with a carbon felt electrode has been mentioned [18.96]. The largest improvement was found with mercury. Acceleration of the V(II)/V(V)-redox reaction by cobalt- and manganese-modification of graphite has been reported [18.97] without a description of the mode of catalytic action.

In later studies metal deposition and catalytic activity were investigated systematically [18.58, 59]. First kinetic and further electrochemical data of the graphite or graphitic material (for details see preceding section) itself were obtained as a benchmark for comparison. The studied metal ions where Ag^{+} (opd), Bi^{3+} (opd), Cd^{2+} (upd), Co^{2+} (upd), Cu^{2+} (upd), Ni^{2+} (upd), Pb^{2+} (opd), Pd^{2+} (opd), Pt^{2+} (opd), Sn^{2+} (upd), Tl^{2+} (upd), and Zn^{2+} (upd), where UPD indicates underpotential deposition and opd indicates metal deposition at electrode potentials negative to the Nernst potential. In all cases numerically submonolayer coverages were found. Scanning electron micrographs show particle deposits. Pyrolytic materials show lowest electrocatalytic activity measured as exchange current density j_0. The increase of EASA due to the metal deposits is usually small; a factor of 2–3 can be deduced from measurements of the double layer capacitance. Changes of j_0 were substantially higher, with palladium increases by a factor of 22–170 observed in some cases. Obviously these enhanced activities are no simple surface enlargement effects (for a further discussion of this aspect see Sect. 18.6). In several cases metal deposits resulted in a decrease of j_0. The studied redox system $Fe^{2+/3+}$ is considered to be an outer-sphere reaction where – at least according to general assumptions – specific adsorption of the reactants on the electrode surface is not significant. Thus the nature of the metal should be of no particular importance. Although kinetic data for a broader discussion of this matter taking into account the metals used here for surface modifications are scant [18.37], it appears likely that metal-specific interactions either directly between metal deposit and redox ion or indirectly via the water molecules or other loosely coordinated species (in the case studied here the redox system was $(NH_4)_2Fe(SO_4)_2/(NH_4)Fe(SO_4)_2$ with either water or

sulfate ions forming the inner ligand sphere of the iron ions) may be effective.

Although electrodes even for technical applications could be made of purely graphitic materials such as ordinary pyrolytic graphite (OPG), stress-annealed pyrolytic graphite (SAPG) or highly ordered pyrolytic graphite (HOPG) (see also: [18.98, 99]), most commercially used materials are composites of carbon and a polymeric binder yielding both compact, nonporous as well as porous materials. Depending on the formation process reticulated, foam-like materials, cloth-like or felt-like products as well as glassy materials can be obtained. Addition of a binder serves mostly an improved processability whereas fibrous structures help in providing large surface areas with electrolyte solution flooding; these structures provide highly turbulent flow. These structural-morphological details became most obvious in a comparative study of carbon felt and polymer-bonded activated carbon as electrode materials with cobalt impregnations. The negative side of a polysulfide/bromine RFB showed significantly larger improvements upon the same surface-specific addition of cobalt with graphite felt [18.100].

In addition to electrochemical deposition of metallic materials further deposition procedures and electrode systems have been described. Cubic nano-Pt and nano-$CuPt_3$ have been deposited on graphene, which in turn had been inkjet-printed on a support [18.101]. The obtained catalyst was useful for the VO^{2+}/VO_2^+ redox couple. The bimetallic system was more active than the platinum system and both were superior to the metal-free graphene. Only surface enlargement effects were invoked to explain the improved performance.

Huang et al. [18.102] have described a modification of graphite felt with platinum-loaded multiwalled carbon nanotubes to be applied in an all-vanadium RFB. No kinetic data enabling an estimate of catalytic effects were provided, but the authors assigned the substantial improvement of system efficiency to the enhanced catalysis of both vanadium half cell reactions. Platinized carbon has been employed in the bromine half cell of a bromine/polysulphide RFBs [18.103]. Good performance was claimed, nothing else beyond the statement, that further reduction in platinum content would be essential requiring further research. Iridium-decorated graphene has been identified as a particularly active electrode material for an all-vanadium RFB [18.104]. The iridium deposits caused an increase of electrolyte solution-accessible area (no explanation of this effect is given, it may be increased wetteability or inhibition of graphene agglomeration, thus both surface area-enlargement effects); its claimed higher affinity to oxygen-containing species [18.105] was assumed to be the cause for more VO^{2+}/VO_2^+-species to participate in redox reactions.

18.5.2 Non-Carbon Materials

Metal-based electrodes – actually metal foils – have been studied only infrequently [18.106]. In this study iron complexes have been studied in nonaqueous electrolyte solutions, and nickel was found to be most active for the $Fe^{2+/3+}$ couple. Iridium-oxide-coated dimensionally stable electrodes have been evaluated as anodes in an all-vanadium RFB [18.107]; no specific catalytic effects were reported. Nickel-based electrodes (e.g., nickel-plated carbon or graphite) of various morphologies have been employed in bromine/polysulphide RFB; no catalytic effects were observed [18.108]. In a study of a high power density sodium polysulfide/bromine RFB, *Ge* et al. found NiS and NiS_2 in the nickel-plating without assigning any specific catalytic role to these inclusions or deposits [18.103].

Natural graphite (NG) and synthetic graphite (MCMB 1028, mesoporous carbon microbeads) have been applied to dimensionally stable electrodes (DSAs) using PTFE as a binder [18.56]. The higher activity of NG was attributed to the greater surface concentration of functional groups; the latter was tentatively assigned to the added conductive carbon black. Zirconium carbide has been suggested as an electrode material for the $Cr^{2+/3+}$ redox couple [18.60]. Addition of lead yielding metallic deposits increased the electrode reaction rate and diminished hydrogen evolution. Tungsten trioxide deposited on carbon paper showed superior performance in terms of Coulombic, voltage and energy efficiency when compared with simple carbon paper [18.109].

18.6 Catalysis and Surface Enlargement Effects

In most reported studies no attempt has been made to clearly assign observed effects to real catalysis, i. e., an increase of the exchange current density j_0, or simply to an increase of electrochemically active surface area. Sometimes a change by several orders of magnitude, when for example going from a flat graphite disc to graphite felt, is stated without even mentioning that most likely this is due simply to the enlarged (three-dimensional) surface area of the electrode [18.110]. Given the large number of methods

available for the determination of electrochemically active surface areas [18.111] this appears to be a minor problem. Beyond this fact, that many authors do not even mention this problem and are thus completely unaware of it means the numbers available from these methods have always been subject of heated debate. At first glance double layer capacity C_{DL} values are the answer. An increase of j_0 or a decrease of η_{ct} at a constant value of C_{DL} would certainly imply true catalysis. In practice this situation is rather unlikely. Any change in surface property – and without such change catalysis is hardly conceivable – may inadvertently result in a change of C_{DL}. Because of lack of data, speculation about such cases is inappropriate here. A change of C_{DL} in turn does not necessarily imply a simple surface enlargement effect because C_{DL} yields information on an atomic or at least nanometer scale – well within the thickness of the diffusion layer. Thus changes in EASA do not necessarily exclude catalytic effects. Changes of EASA with typical surface features in the range of the diffusion layer thickness do not have a measurable effect on values of j_0 in kinetic studies with controlled flow (e.g., turbulent pipe flow [18.112, 113]).

Cases to be discussed in light of these arguments are effects caused by sandblasting and ion etching [18.57]. Certainly sandblasting will result in surface roughening and thus presumably enlargement of EASA. With ion etching chemical changes such as the formation of functional groups catalytically more active and of defects is conceivable. In this study unfortunately not even an attempt is made to address this question.

18.7 Future Directions

The use of electric energy for a number of still-growing purposes will be growing in the foreseeable future absent of any catastrophic developments. Certainly the annual growth rates in highly industrialized countries tend to be smaller than in the past because of substantial improvements in many applications and a slowly changing attitude.

The concept of a RFB based exclusively on two dissolved redox components is slowly extended to a combination of one redox system with a second electrode that can also operate both in charge and discharge mode.

References

18.1 Y. Wu, R. Holze: *Electrochemical Energy Storage and Conversion* (Wiley-VCH, Weinheim 2013)

18.2 N. Chouhan, R.-S. Liu: Electrochemical technologies for energy storage and conversion. In: *Electrochemical Technologies for Energy Storage and Conversion*, ed. by R.S. Liu, L. Zhang, X. Sun, H. Liu, J. Zhang (Wiley-VCH, Weinheim 2012)

18.3 J. Garche, L. Jörissen: Elektrochemische Stromquellen mit externem Speicher, GDCh-Monographie **9**, 63–72 (1996)

18.4 Terminology is confusing, these devices are also called redox batteries or redox flow batteries.

18.5 B.E. Conway: *Electrochemical Supercapacitors: Scientific Fundamentals and Technological Applications* (Springer, New York 1999)

18.6 A. Yu, A. Davies, Z. Chen: Electrochemical supercapacitors. In: *Electrochemical Technologies for Energy Storage and Conversion*, ed. by R.S. Liu, L. Zhang, X. Sun, H. Liu, J. Zhang (Wiley-VCH, Weinheim 2012) p. 317

18.7 M. Skyllas-Kazacos, M.H. Chakrabarti, S.A. Hajimolana, F.S. Mjalli, M. Saleem: Progress in flow battery research and development, J. Electrochem. Soc. **158**, R55–R79 (2011)

18.8 M.J. Watt-Smith, R.G.A. Wills, F.C. Walsh: Secondary batteries – flow systems – Overview. In: *Encyclopedia of Electrochemical Power Sources, Vol. 5*, ed. by J. Garche, C.K. Dyer, P.T. Moseley, Z. Ogumi, D.A.J. Rand, B. Scrosati (Elsevier, Amsterdam 2009) p. 438

18.9 M. Skyllas-Kazacos: Secondary batteries – flow systems: Vanadium redox-flow batteries. In: *Encyclopedia of Electrochemical Power Sources, Vol. 5*, ed. by J. Garche, C.K. Dyer, P.T. Moseley, Z. Ogumi, D.A.J. Rand, B. Scrosati (Elsevier, Amsterdam 2009) p. 444

18.10 A.Z. Weber, M.M. Mench, J.P. Meyers, P.N. Ross, J.T. Gostick, Q. Liu: Redox flow batteries: A review, J. Appl. Electrochem. **41**, 1137–1164 (2011)

18.11 T. Shigematsu: Redox flow battery for energy storage, SEI Tech. Rev. **73**, 4–13 (2011)

18.12 T. Nguyen, R.F. Savinell: Flow Batteries, Interface **19**(3), 54–56 (2010)

18.13 V. Presser, C.R. Dennison, J. Campos, K.W. Knehr, E.C. Kumbur, Y. Gogotsi: The electrochemical flow capacitor: A new concept for rapid energy storage and recovery, Adv. Energy Mater. **2**, 895–902 (2012)

18.14 S. Hamelet, T. Tzedakis, J.-B. Leriche, S. Sailler, D. Larcher, P.-L. Taberna, P. Simon, J.-M. Tarascon: Non-aqueous Li-based redox flow batteries, J. Electrochem. Soc. **159**, A1360–A1367 (2012)

18.15 Q. Huang, H. Li, M. Grätzel, Q. Wang: Reversible chemical delithiation/lithiation of $LiFePO_4$: Towards a redox flow lithium-ion battery, Phys. Chem. Chem. Phys. **15**, 1793–1797 (2013)

18.16 M. Zhang, M. Moore, J.S. Watson, T.A. Zawodzinski, R.M. Counce: Capital cost sensitivity analysis of an all-vanadium redox-flow battery, J. Electrochem. Soc. **159**, A1183–A1188 (2012)

18.17 W. Kangro: Verfahren zur Speicherung von elektrischer Energie, German Patent 914 264 (1949)

18.18 W. Kangro, H. Pieper: Zur Frage der Speicherung von Elektrischer Energie in Flüssigkeiten, Electrochim. Acta **7**, 435–448 (1962)

18.19 L.H. Thaller: Electrically rechargeable redox flow cells, Proc. 9th Intersoc. Energy Convers. Eng. Conf. (1974) pp. 924–928

18.20 N.H. Hagedorn, L.H. Thaller: Redox storage systems for solar applications, J. Power Sources **8**, 227–243 (1981)

18.21 M. Bartolozzi: Development of redox flow batteries. A historical bibliography, J. Power Sources **27**, 219–234 (1989)

18.22 J. Giner, V. Jalan, L. Swette: Redox storage batteries, DECHEMA-Monographie **92**, 381–393 (1982)

18.23 C. Menictas, M. Skyllas-Kazacos: Performance of vanadium-oxygen redox fuel cell, J. Appl. Electrochem. **41**, 1223–1232 (2011)

18.24 H. Zhang: Liquid redox rechargeable batteries. In: *Electrochemical Technologies for Energy Storage and Conversion*, ed. by R.S. Liu, L. Zhang, X. Sun, H. Liu, J. Zhang (Wiley-VCH, Weinheim 2012) p. 279

18.25 L.H. Thaller: Electrically rechargeable redox flow cell, US Patent 3 996 064 (1976)

18.26 L.H. Thaller: *National Aeronautics and Space Administration, US Dept* (of Energy, NASA TM-79143; DOE/NASA/1002-79/3 1979)

18.27 Formulation of the redox equation follows international standards, the reader may notice the accordingly reversed labels charge and discharge.

18.28 H. Izawa, T. Hiramatsu, S. Kondo: Research and development of 10 kW class redox flow battery, Proc. 21st Intersoc. Energy Convers. Eng. Conf., Vol. 2 (1986) p. 1018

18.29 B.B. Sales, F. Liu, O. Schaetzle, C.J.N. Buisman, H.V.M. Hamelers: Electrochemical characterization of a supercapacitor flow cell for power production from salinity gradients, Electrochim. Acta **86**, 298–304 (2012)

18.30 C. Fabjan, J. Garche, B. Harrer, L. Jörissen, C. Kolbeck, F. Philippi, G. Tomazic, F. Wagner: The vanadium redox-battery: An efficient storage unit for photovoltaic systems, Electrochim. Acta **47**, 825–831 (2001)

18.31 R. Ferrigno, A.D. Stroock, T.D. Clark, M. Mayer, G.M. Whitesides: Membraneless vanadium redox fuel cell using laminar flow, J. Am. Chem. Soc. **124**, 12930–12931 (2002)

18.32 M.A. Climent, P. Garces, M. Lopez-Segura, A. Aldaz: Systems for storage of electric energy. II. Filter press-type iron/chromium redox battery, An. Quim. Ser. A **83**, 12–14 (1987)

18.33 This assignment is particularly confusing with RFBs.

18.34 K.J. Vetter, S. Bruckenstein: *Electrochemical Kinetics* (Academic Press, New York 1967)

18.35 G. Kreysa: Elektrochemie in dreidimensionalen Elektroden, Chem. Ing. Tech. **55**, 23–30 (1983)

18.36 B.K. Ferreira: Three-dimensional electrodes for the removal of metals from dilute solutions: A review, Min. Process. Extr. Metall. Rev. **29**, 330–371 (2008)

18.37 R. Holze: Electrochemical thermodynamics and kinetics. *Landolt–Börnstein: Numerical Data and Functional Relationships in Science and Technology – New Series*, Group IV/9A, ed. by W. Martienssen, M.D. Lechner (Springer, Berlin, Heidelberg 2007)

18.38 R.J. Dwayne Miller, G.L. McLendon, A.J. Nozik, W. Schmickler, F. Willig: *Surface Electron Transfer Processes* (VCH, New York 1995)

18.39 W. Schmickler, E. Santos: *Interfacial Electrochemistry* (Springer, Heidelberg 2010)

18.40 N.B. Luque, W. Schmickler: Are the reactions of quinones on graphite adiabatic?, Electrochim. Acta **88**, 892–894 (2013)

18.41 C. Batchelor-McAuley, E. Laborda, M.C. Henstringe, R. Nissim, R.G. Compton: Reply to comments contained in "Are the reactions of quinones on graphite adiabatic?" by N.B. Luque, W. Schmickler (Electrochim. Acta **88**, 892 (2013)), Electrochim. Acta **88**, 895–898 (2013)

18.42 R. Holze: *Surface and Interface Analysis: An Electrochemists Toolbox* (Springer, Heidelberg 2009)

18.43 K. Aoki, H. Kaneko, K. Nozaki: Estimation of charge transfer kinetic parameters from irreversible cyclic voltammograms at carbon fibre, J. Electroanal. Chem. **247**, 29–36 (1988)

18.44 C.-H. Bae, E.P.L. Roberts, R.A.W. Dryfe: Chromium redox couples for application to redox flow batteries, Electrochim. Acta **48**, 279–287 (2002)

18.45 S.A. Campbell, L.M. Peter: The effect of K^+ on the heterogeneous rate-constant for the $(Fe(CN)_6)^{3-}$ $(Fe(CN)_6)^{4-}$ redox couple investigated by AC-impedance spectroscopy, J. Electroanal. Chem. **364**, 257–260 (1994)

18.46 D.S. Cheng, A. Reiner, E. Hollax: Activation of hydrochloric acid-$CrCl{\cdot}6H_2O$ solutions with *N*-alkylamines, J. Appl. Electrochem. **15**, 63–70 (1985)

18.47 A. Reiner, E. Hollax: Verfahren zum Reaktivieren von an Redoxreaktionen beteiligten infolge von Hydratisomere alternden Komplexverbindungen, German Patent DE 3 316 136 (1984)

18.48 H. Cnobloch, H. Nischik, K. Pantel, K. Ledjeff, A. Heinzel, A. Reiner: 250 W/1 kWh iron-chromium redox flow storage battery, Siemens Forsch. Entwickl. Ber. **17**, 270–277 (1988)

18.49 The term catalysis appears sometimes also in the discussion of chemical degradation of electrode materials in RFB, in particular oxidative destruction of carbon-based materials in RFB. Indeed electrolyte solution components may act as cat-

alysts in these unwanted reactions, nevertheless these processes are not treated here.
18.50 R.F. Gahn, N.H. Hagedorn, J.A. Johnson: Cycling performance of the iron-chromium redox energy storage system, Proc. 20th Intersoc. Energy Convers. Eng. Conf., Vol. 2 (1985) pp. 91–97
18.51 H. Cnobloch, H. Nischik, K. Pantel, K. Ledjeff, A. Heinzel, A. Reiner: Eisen-Chrom-Redoxionen-Speicher, Dechema-Monographie **109**, 427–445 (1987)
18.52 C.C. Liu, R.T. Galasco, F. Savinell: Operating performance of an Fe–Ti stationary redox battery in the presence of lead, J. Electrochem. Soc. **129**, 2502–2505 (1982)
18.53 S. Zhong, C. Padeste, M. Kazacos, M. Skyllas-Kazacos: Comparison of the physical, chemical and electrochemical properties of rayon-based and polyacrylonitrile-based graphite felt electrodes, J. Power Sources **45**, 29–41 (1993)
18.54 M.A. Climent, P. Garces, A. Aldaz: Cyclic voltammetric study of Fe^{3+}/Fe^{2+} electrodic reaction for use in a Fe/Cr battery, Bull. Electrochem. **4**, 845–848 (1988)
18.55 H. Kaneko, K. Nozaki, Y. Wada, T. Aoki, A. Negishi, M. Kamimoto: Vanadium redox reactions and carbon electrodes for vanadium redox flow battery, Electrochim. Acta **36**, 1191–1196 (1991)
18.56 H.S. Kim: Electrochemical properties of graphite-based electrodes for redox flow batteries, Bull. Korean Chem. Soc. **32**, 571–575 (2011)
18.57 H. Cnobloch, H. Nischik, K. Pantel, K. Ledjeff, A. Heinzel: Application of carbon as a construction material in redox-flow-storage-batteries, Proc. Carbon 86, 4th Int. Carbon Conf. Baden-Baden (1986) pp. 367–369
18.58 R. Holze: Underpotential deposit electrocatalysis of fast redox reactions for electrochemical energy storage systems, J. Solid State Electrochem. **2**, 73–77 (1998)
18.59 P. Mayer, R. Holze: Electrocatalysis of redox reactions by metal nanoparticles on graphite electrodes, J.Solid State Electrochem. **5**, 402–411 (2001)
18.60 C.Y. Yang: Catalytic electrodes for the Redox Flow Cell energy storage device, J. Appl. Electrochem. **12**, 425–434 (1982)
18.61 W. Li, J. Liu, C. Yan: Multi-walled carbon nanotubes used as an electrode reaction catalyst for VO_2^+/VO^{2+} for a vanadium redox flow battery, Carbon **49**, 3463–3470 (2011)
18.62 W. Li, J. Liu, C. Yan: The electrochemical catalytic activity of single-walled carbon nanotubes towards VO_2^+/VO^{2+} and V^{3+}/V^{2+} redox pairs for an all vanadium redox flow battery, Electrochim. Acta **79**, 102–108 (2012)
18.63 W. Li, J. Liu, C. Yan: Graphite–graphite oxide composite electrode for vanadium redox flow battery, Electrochim. Acta **56**, 5290–5294 (2011)
18.64 G. Wei, C. Jia, J. Liu, C. Yan: Carbon felt supported carbon nanotubes catalysts composite electrode for vanadium redox flow battery application, J. Power Sources **220**, 185–192 (2012)
18.65 H. Yang, C.-H. Hung, S.-P. Wang, I.-L. Chiang: Graphite felt with vapor grown carbon fibers as electrodes for vanadium redox flow batteries, Rare Metals **30**, 1–4 (2011), Spec. Issue
18.66 O. Warburg, W. Brefeld: Über die Aktivierung stickstoffhaltiger Kohlen durch Eisen, Biochem. Z. **145**, 461–480 (1924)
18.67 S. Wang, X. Zhao, T. Cochell, A. Manthiram: Nitrogen-doped carbon nanotube/graphite felts as advanced electrode materials for vanadium redox flow batteries, J. Phys. Chem. Lett. **3**, 2164–2167 (2012)
18.68 H.-P. Boehm: Funktionelle Gruppen an Festkörper-Oberflächen, Angew. Chem. **78**, 617–628 (1966)
18.69 J. Mrha: Katalysatoren für die Elektroden der Brennstoffelemente II. Aktivkohle als Katalysator der Elektroreduktion des Sauerstoffes, Collect. Czechoslov. Chem. Commun. **31**, 715–733 (1966)
18.70 J. Mrha: Study of catalysts for fuel cell electrodes. IV. Active carbon electrodes for oxygen in alkaline electrolyte, Collect. Czechoslov. Chem. Commun. **32**, 708–719 (1967)
18.71 E. Hollax, D.S. Cheng: The influence of oxidative pretreatment of graphite-electrodes on the catalysis of the Cr^{3+}/Cr^{2+} and Fe^{3+}/Fe^{2+} redox reactions, Carbon **23**, 655–664 (1985)
18.72 P.X. Han, H.B. Wang, Z.H. Liu, X.A. Chen, W. Ma, J.H. Yao, Y.W. Zhu, G.L. Cui: Graphene oxide nanoplatelets as excellent electrochemical active materials for VO^{2+}/VO_2^+ and V^{2+}/V^{3+} redox couples for a vanadium redox flow battery, Carbon **49**, 693–700 (2011)
18.73 B.T. Sun, M. Skyllas-Kazacos: Modification of graphite electrode materials for vanadium redox flow battery application – I. Thermal treatment, Electrochim. Acta **37**, 1253–1260 (1992)
18.74 P. Han, Y. Yue, Z. Liu, W. Xu, L. Zhang, H. Xu, S. Dong, G. Cui: Graphene oxide nanosheets/multi-walled carbon nanotubes hybrid as an excellent electrocatalytic material towards VO^{2+}/VO_2^+ redox couples for vanadium redox flow batteries, Energy Environmen. Sci. **4**, 4710–4717 (2011)
18.75 M. Inoue, Y. Iizuka, M. Shimada, Y. Tsuzuki: Carbon-fiber electrode for redox flow battery, J. Electrochem. Soc. **134**, 756–757 (1987)
18.76 Fenton's reagent is an aqueous solution of Fe(II)-salts with hydrogen peroxide. It has a very high oxidation capability (see relevant standard potentials [18.37]) based presumably on the formation of hydroxyl radicals according to $H_2O_2 + Fe^{2+} \rightarrow Fe^{3+} + OH^- + OH^*$ [18.77]. The conversion of Fe(II) into Fe(III) causes the need for either supply of further Fe(II) in order to keep the reaction going or regeneration of Fe(II) from Fe(III) by reduction. This can be elegantly performed electrochemically, accordingly the name of the reagent is now electro-Fenton's reagent [18.78].
18.77 C. Walling: Fenton's Reagent Revisited, Acc. Chem. Res. **8**, 125–131 (1975)

18.78 E. Brillas, I. Sires, M.A. Oturan: Electro-Fenton Process and Related Electrochemical Technologies Based on Fenton's Reaction Chemistry, Chem. Rev. **109**, 6570–6631 (2009)

18.79 C. Gao, N.F. Wang, S. Peng, S.Q. Lin, Y. Lei, X.X. Liang, S.S. Zeng, H.F. Zi: Influence of Fenton's reagent treatment on electrochemical properties of graphite felt for all vanadium redox flow battery, Electrochim. Acta **88**, 193–202 (2013)

18.80 V. Pupkevich, V. Glibin, D. Karamanev: The effect of activation on the electrochemical behaviour of graphite felt towards the Fe^{3+}/Fe^{2+} redox electrode reaction, Electrochem. Commun. **9**, 1924–1930 (2007)

18.81 S. Li, K. Huang, S. Lu, D. Fang, X. Wu, D. Lu, T. Wu: Effect of organic additives on positive electrolyte for vanadium redox battery, Electrochim. Acta **56**, 5483–5487 (2011)

18.82 B.T. Sun, M. Skyllas-Kazacos: Chemical modification and electrochemical behaviour of graphite fibre in acidic vanadium solution, Electrochim. Acta **36**, 513–517 (1991)

18.83 B.T. Sun, M. Skyllas-Kazacos: Chemical modification of graphite electrode materials for vanadium redox flow battery application—part II. Acid treatments, Electrochim. Acta **37**, 2459–2465 (1992)

18.84 Y.Y. Shao, X.D. Wang, M. Engelhard, C.M. Wang, S. Dai, J. Liu, Z.G. Yang, Y.H. Lin: Nitrogen-doped mesoporous carbon for energy storage in vanadium redox flow batteries, J. Power Sources **195**, 4375–4379 (2010)

18.85 T. Wu, K. Huang, S. Liu, S. Zhuang, D. Fang, S. Li, D. Lu, A. Su: Hydrothermal ammoniated treatment of PAN-graphite felt for vanadium redox flow battery, J. Solid State Electrochem. **16**, 579–585 (2012)

18.86 S. Trasatti: Electrocatalysis of hydrogen evolution: Progress in cathode activation. In: *Advances in Electrochemical Science and Engineering*, Vol. 2, ed. by H. Gerischer, C.W. Tobias (VCH, Weinheim 1990) p. 1

18.87 P.N. Ross: The science of electrocatalysis on bimetallic surfaces. In: *Electrocatalysis*, ed. by J. Lipkowski, P.N. Ross (Wiley-VCH, New York 1998) p. 43

18.88 S. Dapperheld: Elektrokatalytisches Verfahren zur Aufbereitung von Mutterlaugen aus der Chloressigsäure-Produktion, DECHEMA-Monographie **112**, 317–324 (1988)

18.89 R. Holze, U. Fette: J. Electroanal. Chem. **339**, 247 (1992)

18.90 R. Holze, U. Fette: Zur Elektrokatalyse der Dichloressigsäurereduktion, DECHEMA-Monographie **125**, 769–775 (1992)

18.91 D. Cheng, E. Hollax: Redox batteries, Ger. Offen. DE 3.333.650 (28.03.1985)

18.92 A. Heinzel: Redox battery, Eur. Pat. Appl. 3.735.992 (23.10.1987), US Patent 4 882 241 (1989)

18.93 L.L. Swette, V.M. Jalan: Characterization of gold electrocatalysts for iron/chromium redox batteries, J. Electrochem. Soc. **133**, C122–C122 (1986)

18.94 L.L. Swette, V.M. Jalan: Characterization of gold electrocatalyst for iron/chromium redox battery, Proc. Electrochem. Soc. **86-10**, 195–201 (1986)

18.95 J. Giner, K. Cahill: Catalyst surfaces for the chromous/chromic redox couple, US Patent 4192910, WO 80/01221, EP 0312875B1 (1980)

18.96 A. Rodes, A. Aldaz, P. Garces, M.A. Climent: Electrocatalysis of the Cr(III)/Cr(II) couple on graphite electrodes, Bull. Electrochem. **5**, 129–133 (1989)

18.97 W. Wang, X. Wang: Study of the electrochemical properties of a transition metallic ions modified electrode in acidic $VOSO_4$ solution, Rare Metals **26**, 131–135 (2007)

18.98 R. Holze: Carbon as electrocatalyst for applications in electrochemical energy conversion – An overview, Proc. Carbon 86, 4th Int. Carbon Conf., Baden-Baden (1986) pp. 361–363

18.99 A. Krüger: *Neue Kohlenstoffmaterialien* (Teubner, Wiesbaden 2007)

18.100 H.T. Zhou, H.M. Zhang, P. Zhao, B.L. Yi: A comparative study of carbon felt and activated carbon based electrodes for sodium polysulfide/bromine redox flow battery, Electrochim. Acta **51**, 6304–6312 (2006)

18.101 C. Flox, J. Rubio-Garcia, R. Nafria, R. Zamani, M. Skoumal, T. Andreu, J. Arbiol, A. Cabot, J.R. Morante: Active nano-$CuPt_3$ electrocatalyst supported on graphene for enhancing reactions at the cathode in all-Vanadium redox flow batteries, Carbon **50**, 2372–2374 (2012)

18.102 R.-H. Huang, C.-H. Sun, T.-M. Tseng, W.-K. Chao, K.-L. Hsueh, F.-S. Shieu: Investigation of active electrodes modified with platinum/multiwalled carbon nanotube for vanadium redox flow battery, J. Electrochem. Soc. **159**, A1579–A1586 (2012)

18.103 S.H. Ge, B.L. Yi, H.M. Zhang: Study of a high power density sodium polysulfide/bromine energy storage cell, J. Appl. Electrochem. **34**, 181–185 (2004)

18.104 H.-M. Tsai, S.-J. Yang, C.-C.M. Ma, X. Xie: Preparation and electrochemical activities of iridium-decorated graphene as the electrode for all-vanadium redox flow batteries, Electrochim. Acta **77**, 232–236 (2012)

18.105 C.H. Chang, T.S. Yuen, Y. Nagao, H. Yugami: Electrocatalytic activity of iridium oxide nanoparticles coated on carbon for oxygen reduction as cathode catalyst in polymer electrolyte fuel cell, J. Power Sources **195**, 5938–5941 (2010)

18.106 J.-H. Kim, K.J. Kim, M.-S. Park, N.J. Lee, U. Hwang, H. Kim, Y.-J. Kim: Development of metal-based electrodes for non-aqueous redox flow batteries, Electrochem. Commun. **13**, 997–1000 (2011)

18.107 M. Rychcik, M. Skyllas-Kazacos: Evaluation of electrode materials for vanadium redox cell, J. Power Sources **19**, 45–54 (1987)

18.108 P. Zhao, H. Zhang, H. Zhou, B. Yi: Nickel foam and carbon felt applications for sodium polysulfide/bromine redox flow battery electrodes, Electrochim. Acta **51**, 1091–1098 (2005)

18.109 C. Yao, H. Zhang, T. Liu, X. Li, Z. Liu: Carbon paper coated with supported tungsten trioxide as novel

electrode for all-vanadium flow battery, J. Power Sources **218**, 455–461 (2012)
18.110 S. Zhong, M. Skyllas-Kazacos: Electrochemical behaviour of vanadium(V)/vanadium(IV) redox couple at graphite electrodes, J. Power Sources **39**, 1–9 (1992)
18.111 J. Ahn, R. Holze: Bifunctional electrodes for an integrated water-electrolysis and hydrogen-oxygen fuel cell with a solid polymer electrolyte, J. Appl. Electrochem. **22**, 1167–1174 (1992)
18.112 J. Herrmann: Entwicklung und Anwendung einer elektrochemischen Methode zur Untersuchung schneller zwischengelagerter Reaktionen an Ringelektroden in turbulenter Rohrströmung, Ph.D. Thesis (Bonn University, Bonn 1983)
18.113 J. Herrmann, H. Schmidt, W. Vielstich: Electrochemical investigations of a fast chemical step between two charge transfer reactions, Z. Phys. Chem. NF **139**, 83–96 (1984)

19. Modern Fuel Cell Testing Laboratory

Jean St-Pierre, Michael Angelo, Keith Bethune, Jack Huizingh, Tatyana Reshetenko, Mebs Virji, Yunfeng Zhai

Elements constituting a fuel cell laboratory are succinctly discussed using the experience developed at the Hawaii Sustainable Energy Research Facility. The information is expected to be useful to organizations with a desire to create or improve a fuel cell laboratory in view of the recent and anticipated fuel cell commercialization activities. Topics discussed cover a wide range with an emphasis on differentiating aspects from other types of laboratories including safety, fuel cell and test equipment, and methods used to characterize fuel cells. The use of hydrogen, oxygen and specifically introduced chemical species, and the presence of high voltages and electrical short risks constitute the most prominent hazards. Reactant purity, cleaning, test station control including data acquisition, and calibration are the most important considerations to ensure fuel cell characterization data quality. Cleanliness is also an important consideration for the fuel cell assembly and integration into the test station. The fuel cell assembly also needs to be verified for faults. Fuel cells need to be conditioned for optimum performance before a purposefully designed test plan is implemented. Many fuel cell diagnostic methods are available but novel techniques are still needed in many areas including through plane temperature distribution, stack diagnostics and mass transfer properties. The emphasis is given to commonly and sparingly used electrochemical techniques. In situ techniques include polarization, impedance spectroscopy, voltammetry and current distribution over the active area. Ex situ techniques include the rotating ring-disc electrode and the membrane conductivity cell. Other nonelectrochemical techniques are also useful to understand fuel cell behavior and include the analysis of reactant streams and condensed water, and spectroscopic measurements in combination with electrochemical cells (spectroelectrochemical cells).

19.1 **Fuel Cell Laboratory Evolution** 611
19.1.1 Background 612
19.1.2 Fuel Cell Laboratory Overview 614
19.2 **Safety and Test Stations** 614
19.2.1 Safety 614
19.2.2 Test Stations 616
19.3 **Fuel Cell Stack Components and Assembly** 621
19.3.1 Hardware Design and Manufacturing 621
19.3.2 Cell and Stack Components Cleaning 621
19.3.3 Single Cell Assembly 623
19.3.4 Cell Assembly Verification 625
19.3.5 Installation into the Test Station 625
19.4 **Testing and Diagnostic Techniques** 626
19.4.1 Conditioning 627
19.4.2 In Situ Tests 628
19.4.3 Ex Situ Tests 638
19.5 **Conclusion** 640
References 641

19.1 Fuel Cell Laboratory Evolution

Developments in fuel cell technology have recently culminated with the commercial release of cars. This evolution as well as progress in similar technologies is expected to continue and will affect the fuel cell laboratory in several ways. An expanding demand for a specialized fuel cell knowledgeable work force will redefine the scope and spreading of fuel cell laboratories and bring to the forefront specific safety risks.

19.1.1 Background

The development of fuel cell technology has significantly progressed during the last few years [19.1]. Fuel cell forklifts are currently being demonstrated and are claimed to already be cost effective in comparison to batteries. Fuel cell cars are also being demonstrated with the anticipation that they will be commercialized on a limited basis during 2015. Fuel cell demonstrations are not limited to motive applications and also include generators for homes. This situation implies that fuel cell laboratories have concurrently been established at companies, national laboratories and universities to sustain research and development activities. In view of the progress achieved and anticipated in fuel cell technology deployment, it is a worthwhile endeavor to reflect on future fuel cell laboratory needs. The education and empowerment of a technically knowledgeable installation, maintenance, diagnosis and repair workforce represents such an example that is supported by a predicted increase in the fuel cell related workforce [19.2]. The resurgence of interest in the development of flow batteries [19.3] for grid energy storage to enhance the penetration of intermittent power sources (solar, wind) represents another incentive to reevaluate future fuel cell laboratory needs. Flow batteries are similar to fuel cells with liquid rather than gaseous reactant streams circulating through the device. The technology has evolved towards a similar fuel cell membrane-electrode assembly (MEA) and bipolar plate design to concurrently enable operation at higher current densities and decrease cost (United States patent application 2012/0258345). A fast recharge is also possible by replacing the depleted electrolytes in the storage tanks rather than by reconstituting the original redox species by reversing the current flow as with a secondary battery recharge.

A comprehensive discussion of a fuel cell laboratory has not been found although examples for other types of laboratories are available. A report recently appeared for an analytical laboratory focusing on measurement techniques [19.4]. However, many fuel cell laboratory elements have already been separately discussed including education material [19.5, 6], standardization of measurement methods [19.7–9], and the relationship between laboratory and application measurements [19.10]. Several measurement method reviews have also appeared [19.11]. Mathematical modeling is also considered as a valid laboratory method in cases where measurements are not possible, are difficult due to space or other constraints, or are expected to create significant artifacts. For instance, a model is needed to generate the current distribution across flow field channels from potential sensing probes (submillimeter dimension [19.12]) and assess the effects associated with the presence of a foreign cation in a membrane [19.13, 14]. In turn, fuel cell measurements are necessary for model validation and to gain confidence in their predictive capabilities. Other important elements include safety (hydrogen, high current electrical shorts, etc.), personnel and fuel cell stack or system fabrication capabilities.

Staffing and Education

The need for education and personnel training cannot be overemphasized especially to increase fuel cell laboratory efficiency and standing. The current Hawaii Sustainable Energy Research Facility (HiSERF) workforce is composed of scientists and engineers with diverse characteristics (age, race, sex, ethnicity, nationality, culture, etc.). Such a group composition has been discussed as one of the elements fostering creativity [19.15]. Interestingly, the group includes a technician who has not received fuel cell training from an academic institution. This statement is symptomatic of a larger issue that has already been identified. There is a significant gap in education about hydrogen and fuel cell technologies below the university level (Fig. 19.1) especially in view of the anticipated increase in the fuel cell related workforce [19.2]. A few topics (Fig. 19.1) are especially relevant to the present discussion including fuel cells, hydrogen production and storage, chemistry, physics and engineering. The inclusion of new technology in public education is important to manage expectations and facilitate technology diffusion (sustainable growth) and commercialization (equipment maintenance). For a fuel cell laboratory, specifically trained technicians would free current fuel cell operators, scientists and engineers, from their duties, allowing them to devote more of their time to their core activities:

- Experimental plan development
- Data analysis
- Reporting functions (presentations, publications, patents) and
- Proposal preparation.

The need for technicians varies with the type of organization. At universities, student education and limited resources constrain the number of technicians whereas at commerce-driven organizations, better resources and the necessity for an optimum efficiency favor a larger technician contingent.

The sustainability trend represents a wider scope opportunity to integrate fuel cell technology into the education curriculum [19.18]. Already, many exam-

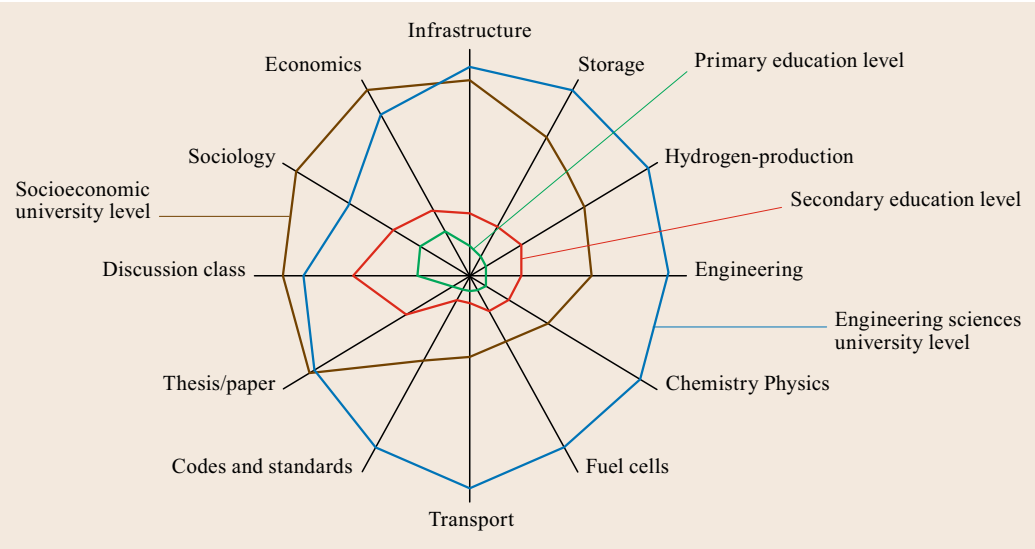


Fig. 19.1 Hydrogen technologies penetration into educational program curricula (after [19.16])

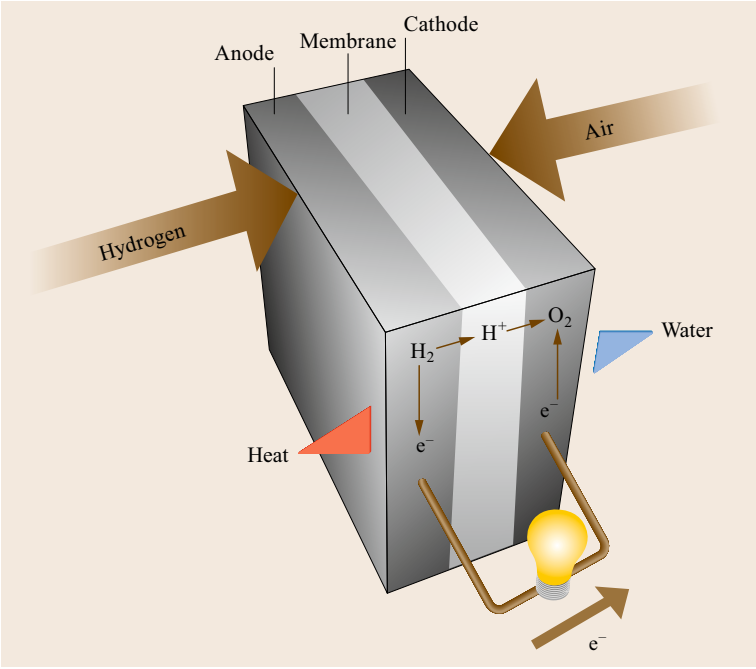


Fig. 19.2 PEMFC operation diagram illustrating key components, reactions ($O_2 + 4H^+ + 4e^- \rightarrow 2H_2O$, $2H_2 \rightarrow 4H^+ + 4e^-$) and output (after [19.17])

ples of fuel cell related material have been proposed to help instructors and teachers [19.19] including the photo-production of hydrogen by algae fed to a proton exchange membrane fuel cell (PEMFC [19.20]), bacteria fuel cells [19.21], a borohydride (hydrogen source) fuel cell [19.5] and a thin layer fuel cell [19.6]. Present educational efforts also mean that future scientists and engineers will be sensitized at a much younger age to fuel cell and related technologies. The impact of this statement on future scientists and engineers' effectiveness remains to be evaluated. Therefore, there is a need to define a clear role for fuel cell laboratories in the educational effort. Also, a complete compendium of all fuel cell laboratory-relevant elements would be valuable to foster the integration of new organizations interested in developing fuel cell technology, evaluating or planning strategic expansions of existing facilities, and identifying gaps.

Key information for many fuel cell laboratory elements is summarized and referenced. Focus will be

given to the PEMFC (Fig. 19.2) to limit the scope. The other main fuel cell technology of commercial interest, the solid oxide fuel cell (SOFC, Fig. 19.2), is expected to still largely benefit from the content by inciting discussions despite distinctive differences associated with higher temperatures (an additional safety risk) and the use of ceramic rather than polymer and other materials. Areas that require improvement are also identified. The information is largely representative of HiSERF with a scope including PEMFC material research, and cell, stack and system characterization. For instance, key electrochemical methods are illustrated with data obtained at HiSERF. The information represents an overview that cannot be comprehensive at the detailed level due in part to the large scope considered but it is hoped that this initial effort will be sufficient to achieve the stated objectives and generate further discussion.

19.1.2 Fuel Cell Laboratory Overview

A fuel cell laboratory is in many respects similar to other laboratories. A fuel cell laboratory is still populated by scientists, engineers and technicians that are concerned with safety aspects including waste disposal, safety devices such as fume hoods and showers, chemicals, analytical equipment, and so on. There are also key differences as high purity fuels and oxidants need to be provided (hydrogen, air or O_2) creating specific safety challenges. In addition, fuel cells need to be assembled, tested and disassembled. These key differences are discussed in more detail in subsequent sections:

- Safety and test stations
- Fuel cell/stack, components and assembly
- Testing and diagnostic techniques.

19.2 Safety and Test Stations

Safety aspects associated with fuel cell technology cannot be overemphasized in view of the negative impact a hydrogen related incident, such as the Hindenburg airship in 1937, could have on public perception. From that standpoint, the fuel cell laboratory infrastructure as well as test station design is of particular importance to minimize safety risks. The test station design is also important to ensure fuel cell characterization is possible under a practical range of conditions and data are acquired and stored at a sufficient rate.

19.2.1 Safety

It is first emphasized that general laboratory safety procedures are assumed to be implemented. The most important additional safety risks associated with a fuel cell laboratory are related to chemicals, reactants, contaminants and tracers, and electricity with high voltages and currents. Hydrogen, oxygen, contaminant and tracer species, electrical shorts and high voltages are discussed with the recognition that other concerns may exist especially if other fuel cell technologies gain prominence. For instance, other oxidants and fuels have been proposed including hydrazine [19.22], dimethyl ether [19.23], peroxide [19.24] and borohydride [19.25] that require different handling and safety procedures. Safety is first addressed at the facility planning stage, which is subsequently followed up by a change management procedure to ensure modifications are made in response to evolutionary trends (new employees, change in research focus, etc.).

Facility Planning, Codes and Regulations

Research and related experimental activities are uncertain in nature and necessitate particular attention to safety and environmental concerns. Safe practices are essential for the protection of personnel, equipment, research integrity and environment. Planning and design of a fuel cell testing laboratory begins with a scope of work, which defines the type and scale of research and testing activities to be conducted, the amount of hazardous materials that might be encountered and the potential risks to personnel and equipment. The scope of work is followed by a sound safety plan that reflects thoughtful consideration of the identification and analysis of safety vulnerabilities (primary and secondary failure modes ranging from benign to catastrophic), hazards prevention, risks mitigation, and effective organization and communication. The safety plan also recognizes the human error factors, equipment life and limitations and the planned or unforeseen changes that occur over the life of the laboratory.

Many sources of information are readily available to support the development and implementation of a safety plan, ranging from promoting organizations and funding agencies (United States Department of Energy, Fuel Cell and Hydrogen Energy Association, etc.) to regulatory organizations codes and standards (National Fire Protection Association, American Society of Mechanical Engineers, American National Standards Institute, International Electrotechnical Commission, Compressed Gas Association, etc.) and safety organizations (Occupational Safety and Health Administration,

etc.). In addition to the wealth of available information, private companies, public agencies, academic institutions and experienced consultants and personnel represent other sources with relevant experience of use for the planning, construction and operation process. Only specific safety risks associated with a fuel cell testing laboratory are discussed in the following sections.

Hydrogen

Hydrogen is considered a likely fuel because it can be produced from water by electrolysis and its consumption in a fuel cell results in the formation of water thus reconstituting the initial stock. Hydrogen is also produced by methane steam reforming. Hydrogen diffuses through solid materials due to its small molecular size. Leaks are also possible near fuel cell and other piping connections. The accumulation of hydrogen in open spaces near ceilings (low vapor density of 0.1 in comparison to air [19.26]) needs to be prevented because little energy is needed to ignite it (low minimum ignition energy of 0.017 mJ [19.26]). This is especially important for leaks because hydrogen warms with a decrease in pressure above the inversion temperature of $\approx 200\,\mathrm{K}$ (Joule–Thomson coefficient) and may spontaneously ignite. Mitigation of the risks is achieved through material selection, detection by sensors linked to an alarm and control system to initiate shutdown procedures and design by adequate ventilation and dilution below the 4% volumetric flammable limit [19.26]. Reactant streams are usually humidified and heating tapes controlled by a thermocouple are used to keep the water in vapor form. Convenient and flexible polymer tubing should not be used as the heating capacity of the heating tapes is sufficient to melt the polymer and create a leak in the event temperature control is lost. The use of an odorant to facilitate leak detection is not recommended as fuel cell operation is likely to be adversely affected.

Other hydrogen sources such as liquid hydrogen or onsite generators (water electrolyzer with additional closed space) add supplementary hazards. Liquid hydrogen is sufficiently cold (boiling point of $-252\,^{\circ}\mathrm{C}$ [19.26]) to create solid oxygen and nitrogen, thermal stresses in system materials and embrittlement of metallic components with hydrogen accumulation in the material microvoids. These risks are minimized by controlled cool down procedures and material selection. A limited liquid hydrogen spill will rapidly disperse but a continuous spill creates an expanding low cloud of dense hydrogen vapors (cold hydrogen is denser than air) that may explode over water. Detailed safety information is readily available (for example, National Fire Protection Association (NFPA) 2 and 55 codes [19.27, 28]).

Oxygen

Air is the preferred oxidant for most applications because it does not need to be stored onboard a system with the exception of air independent devices such as space and underwater vehicles. Oxygen is generally used for diagnostic purposes. A first order estimate of the mass transport overpotentials, gas phase and ionomer phase contributions, is obtained with the sequential use of different oxidant compositions (O_2, 21% O_2/79% He and air [19.29, 30]). This aspect will be more extensively discussed in Sect. 19.4.2. However, additional safety precautions are necessary because combustible material deposits (oils for instance) can ignite as a result of a sudden O_2 compression (gas line pressurization). Gas line and fuel cell materials need to be properly selected and cleaned for O_2 service. Pressurization procedures need to be changed by first pressurizing with an inert gas and subsequently switching to O_2. For long-term O_2 service (life tests), it is advisable to add redundancies for fire detection. Thermocouples located at the reactant stream and coolant outlets as well as H_2 and O_2 sensors in the reactant stream outlets are useful to detect a membrane failure allowing reactants to mix and combust in the presence of the catalyst. These devices need to be linked to the control software to trigger a test station shutdown. An extensive discussion of design aspects for O_2 use is available [19.31] and courses on O_2 systems design and safety are offered.

Contaminant and Tracer Species

A few reasons justify the injection of species that are not reactants into a fuel cell. Ambient air contains hundreds of contaminants that may adversely affect fuel cell performance [19.32–35]. These contaminants originate from a variety of sources but many are generated by the chemical industry and are organic. The fuel stream also contains contaminants that are equally deleterious to fuel cell performance [19.36]. Their nature and concentration depends on the fuel synthesis process (methane reforming, water electrolysis) and purification cost. Although H_2 fuel contaminants may not necessarily include organic species, contaminants leached or evolved from system materials contain organic and other species [19.37]. Finally, tracer species are injected to measure residence time distributions and evaluate fuel cell flow behavior and liquid water content [19.38, 39]. These tracers are commonly colored or radioactive species [19.40]. Contaminants and tracers are usually in low concentrations. Higher contaminant concentrations are used for fuel cell tests to accelerate degradation and minimize the confounding effect of other degradation mechanisms. The toxicity of the reactant gas streams is therefore a con-

cern [19.32–34] and is partially mitigated by using surrogate molecules with the same functionalities but with slightly different structures or less toxic alternatives. It is assumed that the substitute molecules with lower toxicity similarly behave in a fuel cell as the original molecule or are as easily detectable (tracers). The material safety data sheet (MSDS) or equivalent needs to be consulted before tests are initiated, which contains safety information including treatment and disposal (Environment Protection Agency and Occupational Safety and Health Administration regulations). Contaminant and tracer species may be restricted or require special shipment procedures. Other considerations include the need to purge the gas before disconnecting a gas cylinder for replacement and cleaning the gas lines after use to limit carry over to subsequent tests.

Electrical Shorts and High Voltages

In a PEMFC, bipolar plates are only separated by a very short distance that corresponds to the membrane thickness ($\approx 25-50\,\mu m$). The risk associated with electrical shorts cannot therefore be ignored. Also, to achieve higher working voltages cells are usually arranged in series in a fuel cell stack. Stacks operating over 100 V can create a significant electrocution risk that can be lethal [19.41]. The requirement for stack compactness and high power densities reduces the number of options available to decrease short circuit risks. Electrical insulation is effective in preventing contact between adjacent bipolar plates with tools such as screwdrivers and operators wearing metallic rings (Occupational Safety and Health Administration lockout/tagout practices and procedures). Electrical insulation is also effective to reduce electrical shocks. Equally thin battery electrodes also prone to electrical short circuits offer another source of inspiration to improve PEMFC designs [19.42]. The safety risk is not only limited to the external surface of the fuel cell. Polymeric membranes are prone to failure and the creation of pinholes bringing both reactant streams into contact [19.43]. The combustion favored by the presence of a catalyst locally raise the temperature [19.44], which may in severe cases be sufficient to melt the polymer and enlarge the pinhole. This situation may be exacerbated by the short circuit risk between both electrodes especially if they are based on a flexible carbon material (felt, cloth). For this specific case, the risk is mitigated by the presence of thermocouples and O_2 or H_2 sensors mentioned in Sect. 19.2.1. However, the effects of a short circuit develop very rapidly [19.45]. Therefore, mitigation measures may not be sufficient to prevent irreversible damage.

19.2.2 Test Stations

Fuel cells require support equipment (balance of plant) to function including an air compressor or blower, reactant humidifiers, a heat exchanger, a voltage converter, an electrical motor and controls (Fig. 19.3). A fuel cell test station fulfills the same functions as the balance of plant but is more sophisticated and able to provide independently controlled and well-characterized operating conditions for research and development purposes. Test stations are available from a variety of commercial suppliers for both single cells and stacks. Test stations may equally be assembled from commercial parts, however data collection and logging can overwhelm a standard personal computer. The test station is interfaced with reactant supplies in the laboratory emphasizing purity aspects and associated piping cleaning requirements. Test station systems control reactant and diagnostic gas selection, flows, humidification and pressure, cell or stack temperature, voltage-current output and data acquisition. Test stations need to be maintained and regularly calibrated. Test stations are supplemented by other diagnostic equipment to complete additional specific measurements (Sect. 19.4.2) such as current-voltage distributions, liquid water content and outlet gas or liquid water composition.

Reactants Supply and Purity

The performance and durability of PEMFCs is affected by the quality of the reactant gases [19.36, 46]. For the hydrogen fuel, numerous methods exist for its production and purification that result in different contaminants and quality levels. The Society of Automotive Engineers (SAE) recently published a hydrogen fuel quality standard for fuel cell vehicles (SAE J2719, Table 19.1). The hydrogen fuel index is specified as 99.97%, although the primary contributors are inert gases, which are only a concern at these levels if recirculation systems are of interest because contaminants accumulate and reach even higher concentrations [19.47]. The other contaminant concentrations such as for ammonia and sulfur species are ≤ 5 ppm (volumetric basis). Many of these low concentration contaminants still have a significant effect on fuel cell performance [19.36] but are below standard gas analysis detection limits. Therefore, the use of a high efficiency purifier such as a palladium membrane or getter-based devices in combination with a sufficiently high purity source ($\geq 99.995\%$) from a proton exchange membrane electrolyzer for example, is highly recommended to eliminate systematic errors.

Air quality varies around the world and most laboratory air is produced on site with a compressor system. The International Organization for Standard-

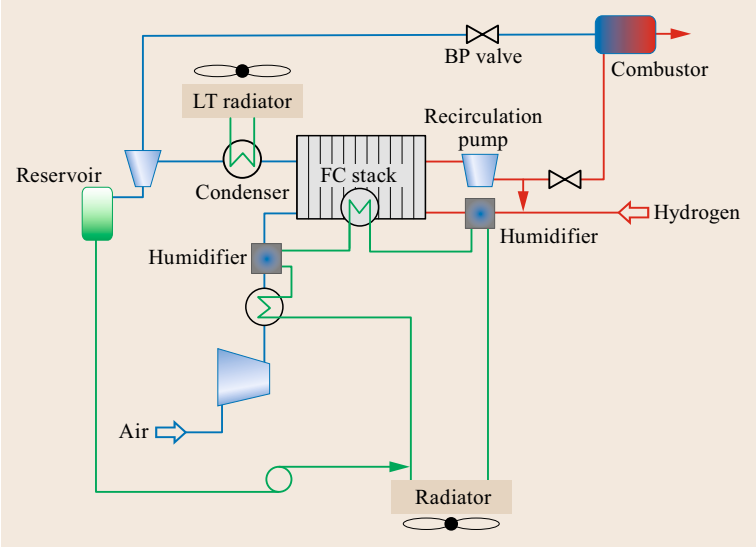


Fig. 19.3 A PEMFC system layout depicting the fuel cell (FC) stack and balance of plant components (BP: bypass, LT: low temperature)

Table 19.1 SAE J2719 hydrogen fuel quality standard

Contaminant	Maximum allowable quantity (ppm by volume unless otherwise specified)
Ammonia	0.1
Carbon dioxide	2
Carbon monoxide	0.2
Formaldehyde	0.01
Formic acid	0.2
Helium	300
Nitrogen and argon	100
Oxygen	5
Particulates	1 µg/l at normal temperature and pressure
Total gases	300
Total halogenated compounds	0.05
Total hydrocarbons	2
Total sulfur compounds	0.004
Water	5

ization (ISO) ISO 8573 series of standards relates to the compressed air quality. ISO 8573-1 describes purity classes that are only distinguished by the maximum oil and water vapor content, and particulate levels. ISO 8573-5 specifies test methods for determining the oil vapor content ($\geq C_6$ hydrocarbons) as well as any organic solvents. ISO 8573-6 specifies test methods for gaseous contaminants consisting of carbon monoxide, carbon dioxide, sulfur dioxide, nitric oxide, nitrogen dioxide and hydrocarbons in the C_1 to C_5 range. However, contaminant level classifications are not included. The most comprehensive classification for ultrahigh purity air quality is contained in the Compressed Gas Association's (CGA) standard CGA G-7.1, Grade J for

Table 19.2 CGA grade J air composition

Species	Concentration (ppm by volume unless otherwise specified)
O_2 (%)	19.5–23.5
Water	1
Carbon monoxide	1
Carbon dioxide	0.5
Total hydrocarbon content as methane	0.5
Halogenated solvents	0.1
Nitrogen dioxide	0.1
Nitrous oxide	0.1
Sulfur dioxide	0.1

specialty air/analytical purposes (Table 19.2). Similar to the SAE standard for hydrogen quality, the maximum limits are very low for the contaminants listed ($\leq$ 1 ppm on a volumetric basis). Trace amounts of contaminants adversely affect fuel cell performance [19.35, 46]. Therefore, the air supply system design needs to surpass the air quality specified in the CGA standard. Table 19.3 describes an air supply and purification system that provides ultrahigh quality air similar to CGA Grade J. Other diagnostic reactant stream gases [19.29, 30] such as nitrogen, helium and oxygen, also need to be of sufficient quality to avoid detrimental effects on fuel cell performance. Thus, high efficiency purification units should also be considered even if research grade gases are purchased.

System Cleaning

The laboratory gas distribution network and PEMFC test stations are composed of piping distribution systems exposed to dry supply gas streams, heated and

Table 19.3 Example of system components for fuel cell laboratory air production

Component (sequentially from upstream)	Description
Oil-free scroll compressor	Initial intake filtration for particles > 10 μm; oil-free compression
Refrigerated dryer	Bulk water vapor removal; gas cooling
Dual stage coalescing filters	Oil and particulate removal for particles > 1 μm (stage 1) and > 0.01 μm (stage 2)
Activated carbon filter	Odor and non-methane hydrocarbon removal
Pressure swing adsorption system	Desiccant for H_2O removal and/or molecular sieve 13X for H_2O and CO_2 removal (achieves < 1 ppm CO_2 and < −70 °C dew point)
Particulate filter	Remove particles from pressure swing adsorption system > 0.01 μm
Mixing tank	Stabilize O_2 concentration swings due to pressure swing adsorption system
Activated carbon filter	Eliminate volatile organic carbons from the coated mixing tank
Semiconductor grade filter	Provides final chemical filtration of acids, bases and organics down to the ppb level

humidified gas streams and deionized water. The selection of piping distribution systems and the test station parts and components materials are first considered to ensure compatibility with gaseous and liquid fluids, and exposure conditions. This step is necessary to prevent contamination issues due to adverse reactions between fluids and materials. For example, metallic corrosion releases ions into the coolant water as well as rust and particulates. Components and assemblies with exposed surfaces need to be cleaned prior to assembly using mechanical and chemical cleaning methods. Several organizations as well as manufacturers provide overview documents for high purity or ultrahigh purity parts design, installation, and cleaning. These guides extend the information contained in CGA (CGA G-4.1, CGA G-5.4, CGA PS-31) and American Society for Testing and Materials International (ASTMI) standards (ASTM A380-06, ASTM G 93-03). For general use fuel cell test stations, material specifications for components do not have to fulfill ultrahigh purity levels such as those required in the semiconductor industry. If contaminants are deliberately introduced into the fuel cell, the system needs to be cleaned before other tests are completed. For that specific case, it is acceptable to at least purge with inert gases under higher temperatures to favor contaminant desorption. In that regard, difficult-to-access dead spaces need to be minimized.

Test Station Control Systems

A fuel cell test system consists of components and subassemblies designed to provide management of the gaseous and liquid fluids being supplied to the fuel cell, to control the electrical output of the fuel cell, and to record and process data from various sensors. The degree of complexity, automation, and dynamic response required depends on the specific application. Station designs range from very basic stations for routine measurements with a limited number of control options (United States Fuel Cell Council document 04-011B) to more complex station designs such as hardware-in-the-loop type stations where fuel cell system components can be simulated and interfaced with an operating stack [19.48, 49], modular test stations allowing for easy exchange of various types of subassemblies [19.50], and even subfreezing stations [19.51]. Figure 19.4 presents a block diagram of the main components and subassemblies that comprise a fuel cell test station.

Gas Selection and Flow Control. The test station gas delivery system provides gas selection, mixing and flow control for various fuel and oxidant mixtures. A basic test station may have only one flow controller for fuel and oxidant delivery. The gas supplied to the flow controller is changed either by switching sources or manually turning valve selectors. Typical test stations have several flow controllers for both the fuel and oxidant mixtures. The number and complexity of the flow controller manifolds depend on the level of flexibility required. Multiple flow controllers are used to create, for example, simulated reformate fuel gas mixtures for testing or oxidant mixtures with different diluent gases for mass transfer studies [19.29, 30]. The turndown ratio is improved by using multiple flow controllers for individual gases to cover a larger range of flow rates. Several types of flow controllers exist. Thermal mass flow controllers are typically used (Brooks Instrument white paper T/021).

Humidification Control. For the majority of PEMFCs especially at the laboratory scale, external humidifiers are used to supply humidified gases and maintain high membrane conductivity [19.52]. A humidification system consists of the humidifier unit as well as heated delivery lines to prevent condensation in the tubing interconnect between the cell and the humidifier. Several types of humidifiers have been utilized in test stations including bubbler dew point saturators, steam injection, flash vaporization, membranes, packed bed/spray chamber contact humidifiers, and so on. The humidifier selection depends on the gas composition, heating and

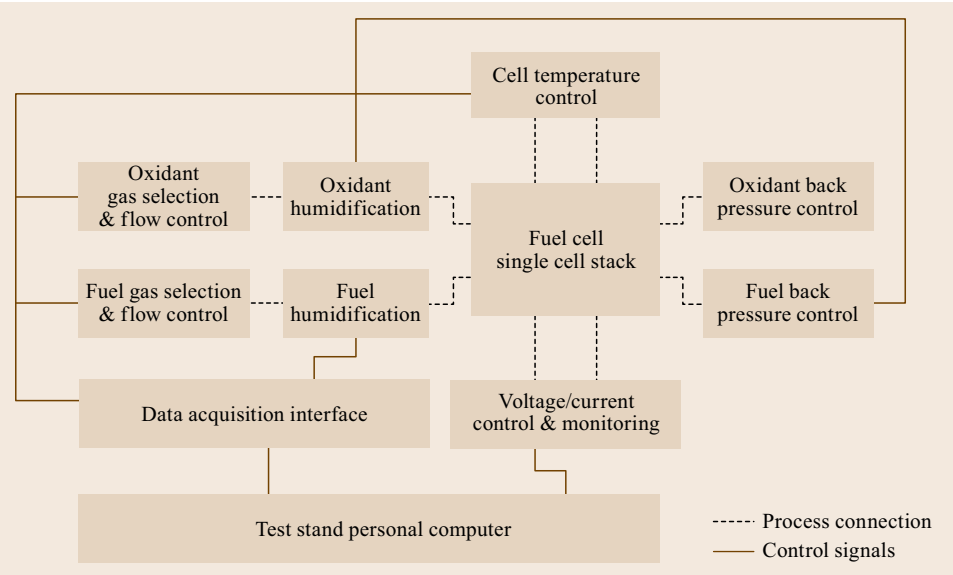


Fig. 19.4 Component subassemblies of a typical fuel cell test stand

cooling rates required, accuracy and stability and the flow range required. For example, for fuel cell tests with water-soluble contaminants, bubbler humidifiers are not acceptable whereas flash vaporization techniques are more suitable. Most test stations also include a dry bypass valve and circuit to provide dry purge gas for safety reasons (shutdown, freezing) or for more complex experiments such as those requiring fast relative humidity cycling.

Back Pressure Control. Thermodynamic, kinetic and mass transfer contributions to the PEMFC performance are affected by the reactant stream pressure [19.53]. The net effect is an increase in performance with pressure [19.54]. As a result, PEMFC operation requires a stable reactant stream pressure. This is accomplished by installing either a back pressure control valve or back pressure regulator on the fuel cell reactant stream outlets. Basic test systems are equipped with a pressure gage and a manual, spring loaded back pressure regulator installed downstream of the fuel cell. In this simple configuration, humidification and product liquid water, and reactant gases pass through the regulator causing instabilities. This system is improved by adding an outlet gas condenser to maintain a single phase gas stream passing through the regulator. Control flexibility is further improved by installing pressure transducers at the reactant inlets and outlets that provide feedback to the pressure control valve or regulator. Even greater flexibility is achieved by adding multiple pressure feedback points in the control software because testing protocol requirements vary (inlet versus outlet pressure control). The most stable systems utilize a dome loaded, back pressure regulator with a current-to-pressure converter controlling the dome pressure and operated by the controller feedback signal. Back pressure control valves are less stable. A back pressure regulator-based control system includes a set point/feedback control loop that interacts with the mechanical feedback loop located within the valve preventing pressure spikes during flow step changes.

Temperature Control. A PEMFC produces a relatively large amount of low-grade heat (50–70 °C) [19.55]. However, a single cell rapidly cools because the heat generated at the approximately two-dimensional thin catalyst layers (a few microns in thickness) is dissipated by contact with good heat conductors (carbon or metallic bipolar plates, metallic end plates). Therefore, the methodology used for cell temperature control depends on the cell or stack under test. Small-scale single cells, $< 50\,\mathrm{cm}^2$ in active area, utilize cartridge heaters installed in the end plates with cooling provided by natural convection. For larger cell sizes, forced cooling is required and is accomplished by attaching fans to the cell, either in a constant flow mode or controlled by the heater feedback controller cooling output. Surface heaters with custom shapes and providing a more uniform heating represent a convenient alternative to cartridge heaters. For specialized single cells and most small stacks, a coolant-based system is used, which also provides a subambient temperature option with the addition of a chiller and adequate cooling fluid [19.56]. A basic coolant system consists of a reservoir, heater, pump and rotameter for constant flow and temperature control. For stack testing,

increased complexity and flexibility are required including coolant flow and pressure, and temperature control. For example, stack testing may require a constant inlet temperature and pressure while maintaining a specific temperature gradient across the stack by varying the flow rate.

Voltage–Current Control. The normal fuel cell operating regime window extends from the open circuit potential to the limiting current ($\approx 0\,V$ or short circuit). A few situations exist that require fuel cell control within (existence of multiplesteady states [19.57, 58]) or outside (fuel starvation leading to cell reversal with a cell potential smaller than 0 V [19.59]) this operating regime window. Therefore, the fuel cell power output controlled by a load bank needs to be carefully assessed and selected from several possible modes: constant potential, current, power or resistance. Resistive load banks are commonly used but inductive load banks are available for more specialized test station needs. For single cells, a power supply may be used in series to boost the voltage level controlled by the load bank. The high current and low voltage output of the fuel cell is typically too low for most load banks. An integrated unit combining this power supply and load bank series arrangement is commercially available and marketed as a *zero volt* load bank. Bidirectional operational amplifiers or booster systems for potentiostats are also used in fuel cell test stands. Load banks are also equipped for the determination of the fuel cell ohmic resistance using current interrupt or frequency response analyzer-based techniques.

Data Acquisition and Hardware and Software Control. The data acquisition input and output hardware represents the test station core (Fig. 19.4). Most test stations include some form of signal conditioning and isolation, and acquisition hardware [19.60]. Information throughput is a function of the number and type of input-output channels, sample rate, and controller processor. Most test stations are also designed for static or quasistatic tests with time constants $\geq 10\,s$ and dwell times of several minutes. Dynamic tests require faster control and acquisition speeds with time constants in the range of milliseconds to seconds [19.48]. Recently, test stations have been designed with embedded controllers improving reliability and safety by reducing the intermediate role of a separate and remote computer working on a high-level operating system. Rather, safety features are integrated into the embedded controllers. Many test stations still rely on a computer for both software control and data visualization. The software provides control and execution of various experimental protocols as well as data storage and visualization. The more elaborate software packages provide flexible scripting features for automation, experiment control, test sequencing, and data processing and visualization.

Calibration

It is emphasized that each fuel cell test station control and measurement device needs to be calibrated. Mass flow controllers, pressure gages, thermocouples, relative humidity sensors and humidifiers, electronic load and data acquisition cards represent the most important elements to be calibrated. The overall test station performance also needs to be assessed with fuel cell tests to determine the synergy between the control and measurement devices.

A standard practice for calibration management involves the selection and identification of the systems and/or instruments requiring calibration, traceability requirements and a calibration frequency. A proper calibration program ensures system and equipment operational integrity and accuracy, and establishes measurements traceability to the United States National Institute of Standards and Technology (NIST) or other approved national measurement standards. Several documents provide guidance in this area (for example, United States Department of Defense standard MIL-STD-1839D). Calibration measurement tolerances and accuracies need to be established for specific equipment. Published standards provide guidance for the measurement uncertainty determination (NIST technical note 1297, American National Standards Institute [ANSI] NCSL Z540.2). At the organizational level, a quality control system for document management and supervision of calibration activities also needs to be established. Accreditation to an international quality standard such as ISO 17025 is not necessary, especially for academic institutions and national laboratories. The ISO 17025 standard is well beyond the level required to ensure the competence of a fuel cell testing laboratory and need to be viewed as a guideline. As a general rule of thumb, equipment calibrations need to be completed with a master meter that is more accurate than the device under test by a factor of ≈ 4 (United States Department of Defense standard MIL-STD-1839D). The master meter needs to be calibrated by an ISO 17025 accredited metrology laboratory, providing traceability to a national standard. The decision to acquire master meters depends on cost (cost and number of calibrations to be completed by an external certification laboratory, master meters cost and calibration cost) and convenience.

The combined system operation also needs to be validated using standardized procedures. The United States Department of Energy and members of the Fuel

Cell and Hydrogen Energy Association initiated programs to establish a standardized test procedure for single-cell PEMFCs. A round robin test series was conducted with several organizational participants with the objective to verify the validity of the proposed standardized test protocols (United States Fuel Cell Council documents 04-011B and 05-014B.2). The European Commission supported similar efforts to address the aspects of prenormative research, benchmarking, and validation through round robin testing under the Fuel Cell Systems Testing, Safety, and Quality Assurance program.

19.3 Fuel Cell Stack Components and Assembly

Fuel cell stack design depends on the application [19.61]. For instance, automotive design is largely dictated by power density whereas stationary design requires durability. For portable applications, design criteria as well as manufacturing methods are much more varied. This is due in part to the restricted space and resulting trend towards a planar stack design that simplifies the compression mechanism and enables the use of manufacturing methods for thin, multiple layers. For each application, it is desirable to avoid the introduction of undesirable species during stack manufacturing and assembly. The assembly of all stack components in the proper sequence is also important to ensure integrity and avoid leaks to the ambient air or from one compartment to another. Therefore, the stack assembly and its interface to the test station or balance of plant need to be verified.

19.3.1 Hardware Design and Manufacturing

A commonly used single fuel cell assembly is discussed as an illustrative and widely representative example. Most fuel cell data are obtained with a single fuel cell. Single cells range from small scale (material evaluation) to full scale size for component evaluation (manifold, flow field, seal, MEA, etc.). For a stack, the assembly procedure is relatively similar with several steps being repeated to achieve the desired number of cells.

An assembled single-cell PEMFC is depicted in Fig. 19.5a and the visible hardware components are identified. A more detailed list of all components and their functions is given in Table 19.4 and discussed in [19.61]. Cited references contain materials used for component production and in several cases methods for performance optimization and durability considerations. A detailed design and manufacturing process review including material selection was also prepared for several PEMFC hardware components [19.62].

An expanded view of the single-cell hardware is given in Fig. 19.5b. Major components are shown with the exception of the gas diffusion media and the MEA, which are located between gas flow field plates. The MEA consists of the anode and cathode catalyst and catalyst support material deposited onto the proton conductive membrane (the catalyst coated membrane or CCM) and the gas diffusion media. If the catalyst layer is deposited onto the gas diffusion medium, the resulting component is referred to as a gas diffusion electrode (GDE). Stacks consist of several single cells with gas flow field bipolar plates that are electrically connected in series to enable higher output voltages. A PEMFC stack design is illustrated in Fig. 19.6 [19.62].

19.3.2 Cell and Stack Components Cleaning

The use of laboratory gloves made of the appropriate material is imperative whenever handling fuel cell components during assembly and cleaning. Gloves provide protection from chemical cleaning agents and avoid contamination of fuel cell components from skin oils. Newly machined fuel cell components need to be cleaned to remove dirt, oil and other residues from the fabrication process. For example, silicon from the gasket migrated to the catalyst layer and membrane and was deemed partly responsible for the observed degradation [19.67]. Additionally, subsequent to fuel cell testing, the test station components may need to be cleaned to remove any residual contaminant that was purposefully added. A number of cleaning strategies and agents are available including from component suppliers.

Fuel cell hardware components are typically removed from the test station and disassembled before cleaning is accomplished using an ultrasonic bath. Cleaning agents are listed in Table 19.5. In general, the use of organic solvents as cleaning agents is limited due to their detrimental effect on cell performance [19.35]. Care should be exercised to avoid damage caused by the ultrasonic bath to sensitive hardware components. For example, the treatment of graphite materials or materials coated with thin anticorrosive layers should be avoided. For these specific cases, alternative cleaning methodologies are necessary such as rinsing with extended durations and compatible cleaning agents.

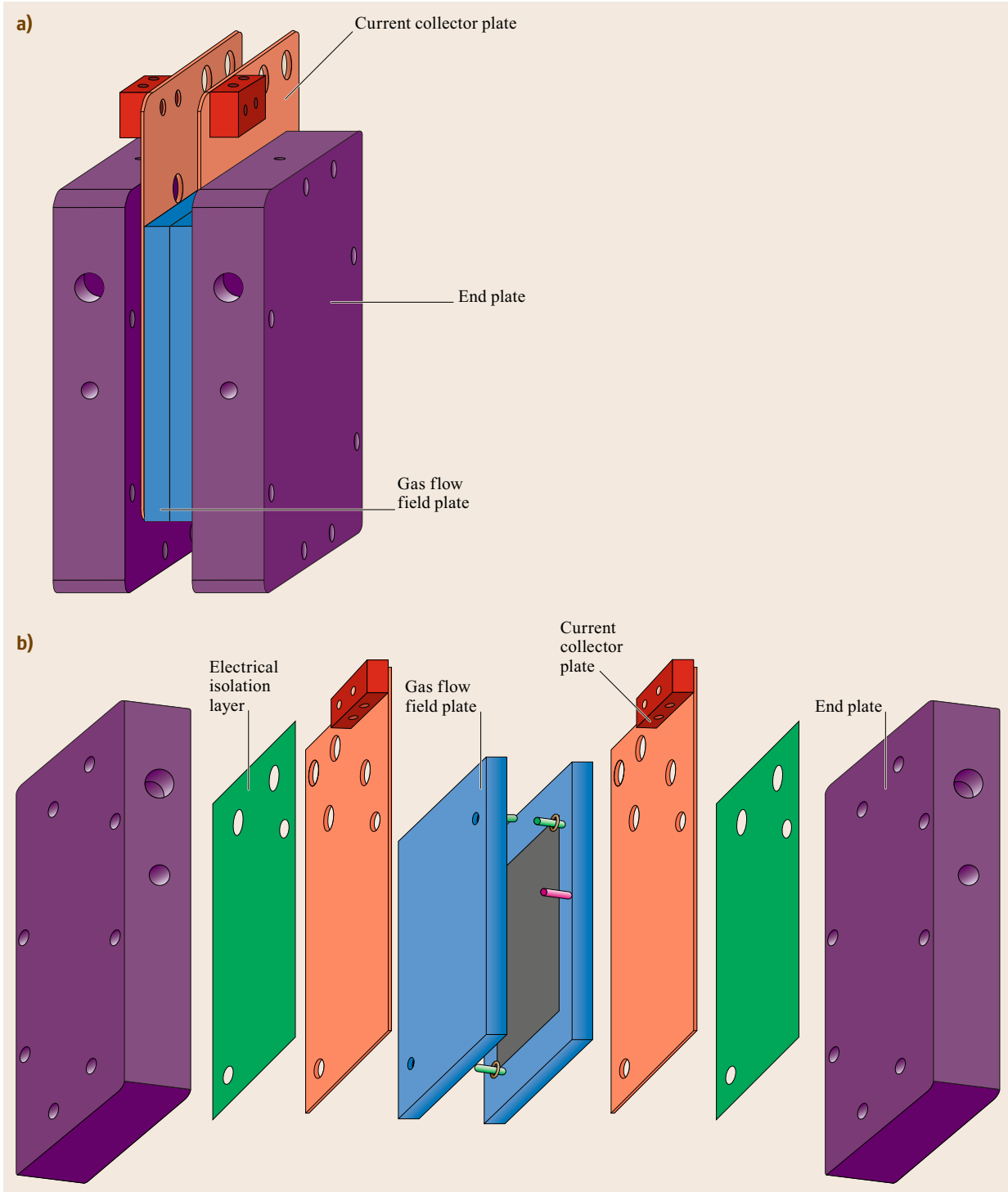


Fig. 19.5a,b PEMFC assembled in a single cell configuration (a). PEMFC expanded view (b). Tie bolts are not displayed for simplicity

Table 19.4 Fuel cell hardware components and functions

Hardware component	Function	References
End plate	Provides compressive force which seals the cell from leaks and minimizes the electrical resistance of the hardware components	*St-Pierre* [19.61]
Bipolar gas flow field plate	Electrically conductive material with channels that enable the gas to flow through the cell	*Mehta* and *Cooper* [19.62], *Tawfik* et al. [19.63]
Seal	Material used to prevent overboard gas leakage	*St-Pierre* [19.61]
Gas diffusion media	Porous media, which is often carbon based, that is placed adjacent to the membrane/electrode assembly to facilitate the transport of gases and water in liquid and vapor phase	*Mehta* and *Cooper* [19.62], *Nam* and *Kaviany* [19.64], *Lin* and *Van Nguyen* [19.65]
Cooling plate	Used for temperature regulation of the fuel cell	*St-Pierre* [19.61, 66]
Membrane–electrode assembly	Consists of anode and cathode electrode catalyst layers deposited onto a proton conductive membrane	*St-Pierre* [19.61], *Mehta* and *Cooper* [19.62]

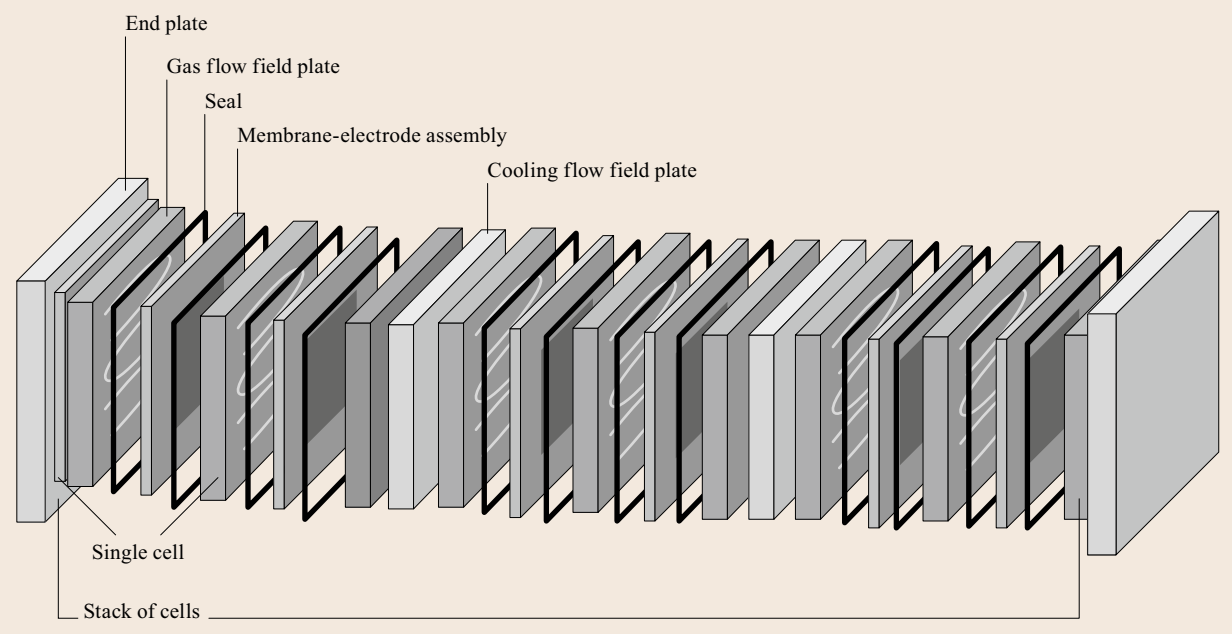


Fig. 19.6 PEMFC stack hardware components. Flow field channels are formed on a bipolar plate noted here as a gas flow field plate (after [19.62])

Table 19.5 Cleaning agents for fuel cell hardware components

Cleaning agent	Examples	Usage precautions	Ultrasonic bath compatibility
Deionized water	–	Can be corrosive to metals	Yes
Organic solvents	Isopropanol, methanol, ethanol, acetone	Possible detrimental effects of solvent residue on PEMFC performance	No
Detergents	Alconox, Liquinox	Materials may be incompatible	Yes
Acidic cleaners	Citranox	Materials may be incompatible	Yes

19.3.3 Single Cell Assembly

The assembly of a single fuel cell with component designs that are commonly used in many fuel cell testing laboratories is discussed as an illustrative example of the design-dependent assembly of a single fuel cell or stack. Commercial fuel cell designs have additional design features that minimize or avoid assembly errors. A successful assembly is achieved with proper component alignment and adequate mechanical compression to mitigate electrical efficiency losses due to contact resistances between components, gas and

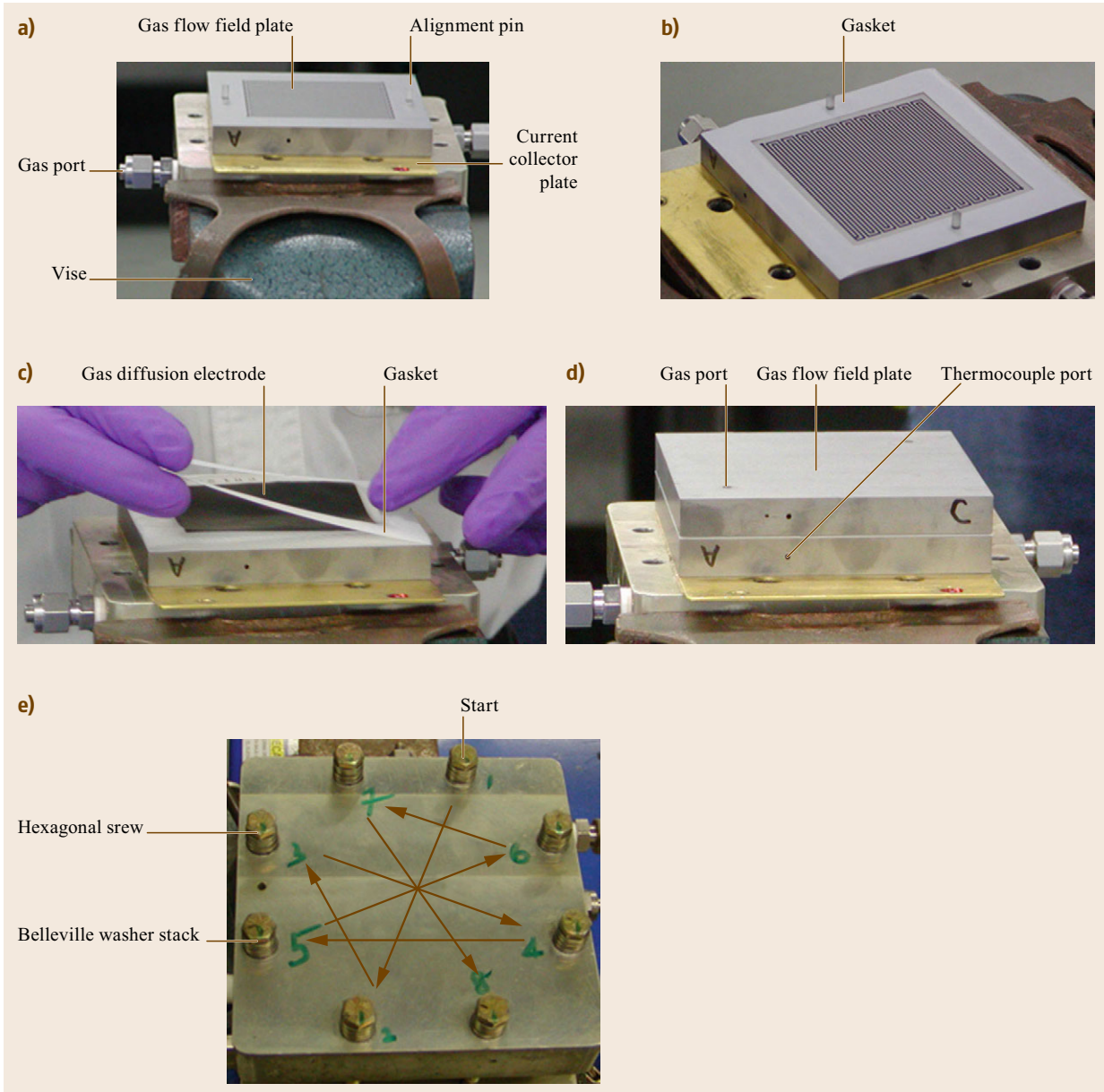


Fig. 19.7a–e Anode end plate, electrical insulation layer, current collector and gas flow field plate **(a)**, gasket seal attached to the anode gas flow field plate **(b)**, MEA and second gasket seal attached to the anode compartment parts **(c)**, cathode gas flow field plate attached to the cell assembly **(d)**, hexagonal head screws sequential tightening scheme to optimize compression across hardware components **(e)**

coolant leakages and to optimize reactant transport and water management within the GDE by avoiding reactant flows bypass and structural collapse of the porous components. This is achieved by selecting the appropriate gasket thickness to match a specific gas diffusion layer (GDL).

Figure 19.7a shows the anode end plate, electrical current collector and anode gas flow field plate during assembly. The gas flow field plate has holes for the attachment of alignment pins which serve to align the anode and cathode flow field plates in addition to the gasket seals and MEA. The end plates are made

of aluminum, the current collector plates of gold-plated copper to minimize the contact resistance and the flow field plates of electrically conductive POCO graphite. The current collector plate is electrically isolated from the end plate by an insulating layer of polymer which is typically polytetrafluoroethylene. The hardware components are assembled by stacking them together so that the inlet and outlet holes on the gas flow field plates align with their counterpart holes on the end plate.

Once the hardware components of the anode side are properly aligned, the first of two gasket seals is applied to the cell. The gasket alignment is maintained by two alignment pins as shown in Fig. 19.7b. After the first gasket is in place, the MEA, which in this case consists of the CCM and a porous carbon layer on both the anode and cathode, is placed onto the assembly while the alignment is still maintained by the pins (Fig. 19.7c). The cathode flow field plate is added to the assembly as demonstrated by Fig. 19.7d. The alignment pins shown in Fig. 19.7a,b serve to maintain the correct placement of the flow field plate. Finally, all fuel cell elements are secured together with screws (Fig. 19.7e). Belleville washers are also added to ensure that compression is maintained at a relatively constant level even if the membrane absorbs water or dehydrates, affecting its thickness [19.68]. Other compression mechanisms are equally adequate [19.61]. The cell assembly proceeds using a calibrated torque wrench with one quarter turns to the hexagonal head screws in a cross tightening pattern until the necessary torque is obtained (Fig. 19.7e).

19.3.4 Cell Assembly Verification

Gas leak rates are determined by using a fixed volume vessel containing nitrogen (or a different inert gas such as helium), pressurized to approximately 5 bar and alternatively connected to the fuel cell anode and cathode inlet reactant gas lines. The 5 bar pressure is suitable for an ambient pressure fuel cell operation, otherwise, for higher pressures, it needs to be adapted. The fuel cell pressure is maintained at approximately 2 bar by a pressure regulator. The 1 l vessel change in pressure is measured over time to calculate the gas leakage rate. The acceptable leakage rate is determined by the cell or stack manufacturer specifications because it is design dependent. A leak is located by submerging a pressurized cell or stack into a deionized water bath. The cell or stack may be subsequently disassembled to determine the cause of the leak and develop preventive measures. If the fuel cell or stack has a coolant circuit, it also needs to be verified for leakage using the same pressurized gas approach. Other leak detection methods exist. For instance, a compartment is pressurized and subsequently isolated with a valve. The subsequent decrease in pressure is monitored and the rate of change indicates the leak size.

Adequate component compression is required to minimize electrical resistance and optimize the GDE performance [19.61, 69]. The optimal compression is dictated by the stack design, component materials and reactant stream pressures. The compression is evaluated by modifying the cell assembly procedure with a pressure-sensitive paper inserted between a flow field plate and the MEA. Subsequently, the cell is dismantled and the pressure-sensitive paper is retrieved for analysis. The resulting color change intensity and distribution is used to estimate the compression magnitude and uniformity across the cell active area.

Electrical short circuits are not desirable because they affect the cell performance evaluation. The presence of an electrical short circuit between the current collector plates and the end plates is easily assessed by measuring the resistance with a multimeter. The presence of a short circuit through the MEA is design dependent and is important to also assess. For flush cut MEA designs where the catalyst and GDLs extend to the membrane edge [19.61], there is a possibility that the thin membrane thickness is bridged by longer GDL carbon fibers. For this specific case, dry inert gases are circulated through the assembled cell and a power supply is used to apply a voltage lower than ≈ 1 V to avoid any electrochemical reactions (water electrolyzer and fuel cell modes) and focus on the electronic conductivity. A multimeter is also used to measure the resulting current allowing the calculation of the electrical resistance. If short circuits are detected, the cell is disassembled to find the cause and devise preventive measures.

19.3.5 Installation into the Test Station

After the cell or stack assembly has been verified, the unit is interfaced with the test station. This step requires the completion of several connections to the reactant gas supplies, coolant supply, load bank and sensors. It is assumed that the test station operation has also been verified especially for fluids leakage using similar methods as described in Sects. 19.2.2 and 19.3.4. Subsequently, the unit is conditioned and tested using methods that are respectively described in Sects. 19.4.1 and 19.4.2.

19.4 Testing and Diagnostic Techniques

The research focus is dependent on many factors that include organization type (academic institutions, national laboratories, companies), resource availability (human, equipment, funds), mission and needs as defined by customers [19.70]. In turn, the research focus defines the selection of testing and diagnostic techniques. These considerations lead to multiple options and underline the variability in research capabilities at fuel cell active institutions.

The HiSERF scope is schematically depicted in Fig. 19.8 and includes fuel cell activities ranging from material, single cell and stack characterization to system level evaluations. Such a wide scope was deemed advantageous and necessary to adapt to customer demands but also to ensure that all different levels effects of interest can be studied and interrelated. For example, a catalyst tested with a rotating ring-disc electrode dipped into a liquid aqueous electrolyte is not representative of the single fuel cell environment with a solid electrolyte. Single cells in a fuel cell stack do not necessarily behave in a similar manner as local operating conditions vary (reactant distribution is not uniform, end cells are cooler in proximity to the heat conductive end plates, etc.). A fuel cell stack is also subjected to different operating conditions in a test station and an application because respective components have different transient response times and operating ranges.

For each activities scope shown in Fig. 19.8, many test options are available and include ex situ tests to generally obtain material related information, and in situ tests with either modified or nonoperating conditions to characterize the fuel cell performance and predict behavior in an application or extract specific parameters to clarify fundamental understanding. A clear purpose needs to be established considering the number of test choices available. From that standpoint, it is useful to consider the different processes taking place in a fuel cell (Fig. 19.9). Mass and heat transfer, charge transfer, reaction kinetics, degradation and other processes take place over a wide range of time scales that do not necessarily overlap thus offering opportunities to focus on specific aspects by tailoring tests. For example, degradation due to contaminants is easily separated from liquid water processes using in situ life tests. However, precautions are still necessary to minimize other degradation mechanisms such as catalyst dissolution and agglomeration. This is achieved with accelerated tests and higher contaminant concentrations, and by maintaining the cell and cathode potential below the Pt oxidation potential. Other test selection considerations include cell voltage loss types, envisaged applications and the existence of standardized protocols with the recognition that many other options exist. For instance, an ex situ membrane conductivity cell is appropriate to understand the effect of gaseous or liquid contaminants on cell voltage ohmic losses. Steady-state performance tests are preferable over hardware in the loop transient tests for stationary applications as the load is expected to slowly vary.

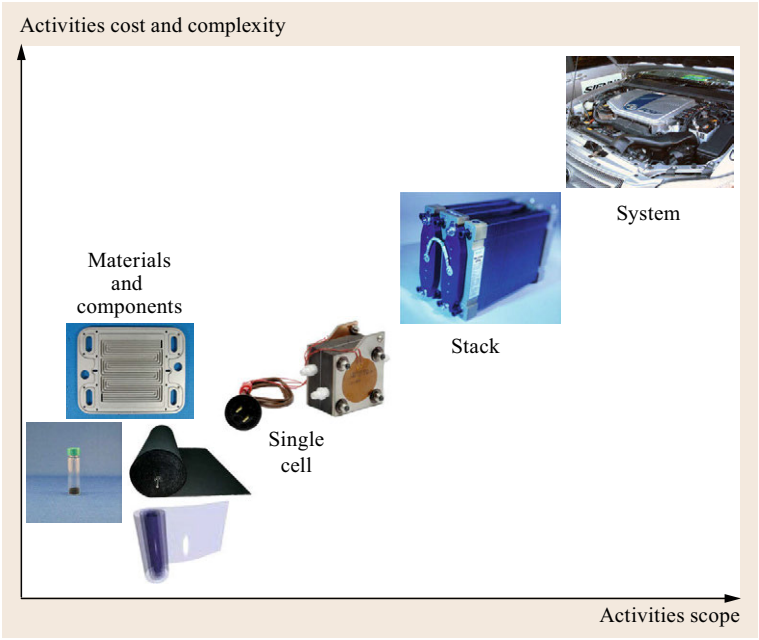


Fig. 19.8 HiSERF PEMFC activities scope

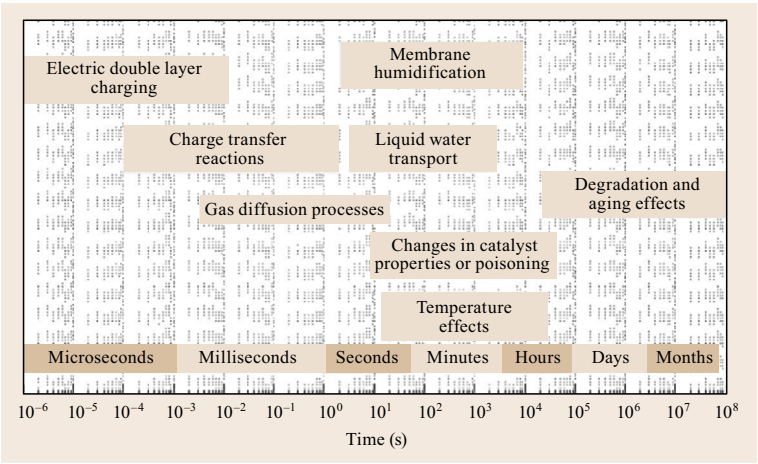


Fig. 19.9 PEMFC processes relaxation time scales

Rather than selecting tests and diagnostic techniques to meet a particular goal, there is also value in assessing gaps. For instance, a large number of techniques have been developed to characterize fuel cell performance. Ten techniques were reviewed for the sole purpose of quantifying the presence of liquid water [19.11]. A detailed review of all techniques irrespective of their purpose is outside the scope of the present chapter. Rather, suggestions for high level analyses are presented to facilitate the identification of gaps in measurement techniques. As a first example, the fuel cell is analyzed at a high level in terms of the fuel cell inputs and outputs: reactants provided and products, power and heat generated (Fig. 19.2). Each technique was classified in these categories using its main objective. Results from this analysis using common and representative techniques without being exhaustive are listed in Table 19.6. Several well-established methods are available to characterize the fuel cell performance, the quantity and nature of the products (main and resulting from side reactions or degradation mechanisms), and reactants (main and present due to imperfections in purification processes). However, few correlations have been established between the different methods especially to take advantage of the potential synergy associated with complementary temporal or geometric resolution. Furthermore, few techniques with sufficient resolution are available to characterize heat transfer (a few ex situ techniques were also presented [19.71–73]). This statement applies to both fuel cell and other operation modes. Thermocouples are approximately of the same dimensions as the thin MEA components (tens to hundreds of microns) creating an accuracy issue. An infrared camera only provides the cell outside temperature. Improved techniques are needed because water management including temperature-driven water transport [19.74] is very sensitive to temperature gradients corresponding to a temperature change of less than a degree Celsius [19.75]. In addition, it was proposed that heat is generated at the cathode whereas heat is consumed at the anode [19.55]. This hypothesis has not yet been experimentally verified. Difficulties associated with the steep temperature gradient measurement is likely responsible for the relatively more numerous modeling activities [19.76]. Supplementary references to Table 19.6 are provided and discussed in Sect. 19.4.2.

Other high level analyses are possible by focusing on other aspects. As a second example, an analysis performed by targeting geometric resolution has revealed that few techniques exist to characterize fuel cells in the cross-channel or through-plane direction [19.98]. Furthermore, many of these geometrically sensitive methods, including those resolving the channel length direction, appear to be seldom used. Another gap exists in relation to methods specifically developed to explore the behavior of stacks, or in other words cell to cell variability, especially in the presence of faults [19.76, 99–101]. Other approaches are possible to identify test and diagnostic technique gaps by focusing on other relevant aspects such as component manufacturing quality control.

In the next section, general test considerations are highlighted. In the subsequent two sections, a few widely applied in situ and ex situ tests are described whereas other more specialized tests are discussed at the high level as detailed descriptions are deemed outside the scope of this chapter.

19.4.1 Conditioning

After the PEMFC is assembled, a conditioning or break-in period is needed to activate and increase catalyst utilization by accessing the catalyst layer inactive regions. This activation normally requires ionomer

Table 19.6 Diagnostic techniques using a PEMFC in different operating modes

Operating mode	Method	Method focus	Reference
Fuel cell	Polarization curve	Electrical power output	*Reshetenko* et al. [19.30]
	Segmented cell	Electrical power output	*Reshetenko* et al. [19.30]
	Impedance spectroscopy	Electrical power output	*Barsoukov* and *MacDonald* [19.77], *Orazem* and *Tribollet* [19.78]
	Current interrupt	Electrical power output	*Büchi* et al. [19.79]
	Residence time distribution	Products	*Diep* et al. [19.38], *St-Pierre* et al. [19.39]
	Neutron imaging	Products	*Mukundan* and *Borup* [19.80]
	X-ray diffraction	Products	*Isopo* et al. [19.81]
	Transparent cell	Products	*Tüber* et al. [19.82], *Yang* et al. [19.83]
	Water collection and analysis	Products	*Young* et al. [19.84]
	Gas chromatography, mass spectroscopy	Reactants, products	*Bender* et al. [19.85], *Schuler* et al. [19.86]
	Thermocouples	Heat	*Vie* and *Kjelstrup* [19.87]
	Infrared camera	Heat	*Matian* et al. [19.88]
Other	Electronic short circuit	Electrical power output	*Kocha* et al. [19.89]
	Cyclic voltammetry	Electrical power output	*Vielstich* [19.90], *Lindström* et al. [19.91]
	Linear sweep voltammetry	Reactants	*Kocha* et al. [19.89], *Inaba* et al. [19.92]
	Segmented cell with different gas diluents	Reactants	*Reshetenko* and *St-Pierre* [19.93]
	Membrane permeability	Reactants	*Kocha* et al. [19.89], *Broka* and *Ekdunge* [19.94]
	Electroosmotic drag	Products	*Choi* et al. [19.95], *Peng* et al. [19.96]
	Water collection and analysis with inlet contaminants	Reactants, products	*Wetton* and *St-Pierre* [19.97]

and membrane humidification. Several reasons explain this situation because reactants reach the catalyst sites but protons cannot, some ionomer sites are less easily hydrated (the ionomer structure is not isotropic) and electrons cannot reach the catalyst sites (partial electronic phase continuity) [19.102, 103]. After conditioning, the fuel cell achieves peak performance with a constant current at a specific voltage that is desirable for research purposes. Rapid and reproducible conditioning methods have been developed by different fuel cell organizations or research institutes (Table 19.7). For instance, the use of a hydrogen pump mode (United States Fuel Cell Council Document 04-003) and CO stripping [19.104] have also been proposed. The conditioning procedure is interrupted after the cell performance for both rated and quarter power reaches a value that is within 2% of the manufacturer's specification or expected value (United States Fuel Cell Council document 04-003).

19.4.2 In Situ Tests

Several categories of in situ tests are distinguished by their objectives. The fuel cell performance is of immediate commercial value as operating conditions change during fuel cell use. As a result, steady-state tests of different duration (short or long term) as well as transient tests including duty cycling are relevant. Hardware in the loop tests aiming at the interactions between fuel cell system balance of plant components and the fuel cell stack are also of interest (Fig. 19.3). Diagnostics are also needed to unravel mechanisms and facilitate the development of improved and more durable fuel cells. Test results are equally needed to validate mathematical models used to predict fuel cell performance and extract model parameters. All three categories are further discussed in the next section. In subsequent sections, the emphasis is given to the use of electrochemical characterization techniques whereas others are only briefly discussed.

Test Types

The performance of PEMFCs is characterized either under constant or varying power conditions. For constant power, the current density of a cell or stack is typically fixed and the resulting voltage is measured. For single cells, a constant potential is easily applied but is problematic for a stack as control is more difficult.

Table 19.7 Standardized conditioning procedures summary

Organization	Operating conditions	First stage	Second stage	Third stage
FCHEA (USA)	80 °C cell temperature H_2/air 1.7/1.7 barg pressure 100/100% relative humidity 1.2/1.5 stoichiometry	Decrease cell voltage until 600 mV is reached and maintain for 1 h	Cycle cell voltage for 6 h between 0.5/0.7 V with a 20 min dwell time	Maintain 0.2 A/cm^2 during 18 h
DOE (USA)	80 °C cell temperature H_2/air, N_2, or O_2 atmospheric pressure 100/75% relative humidity 3/3.6 stoichiometry	Circulate saturated H_2/N_2 on anode/cathode for 3 h	Maintain cell voltage at 0.55 V with H_2/air	Sweep out to the limiting or maximum current density with H_2/air, H_2/O_2
FCTESTNET (European Union)	80 °C cell temperature H_2/O_2 3/3 barg pressure 100/100% relative humidity 1.2/1.5 stoichiometry	Increase current until 1 A/cm^2 is reached and keep cell voltage > 500 mV	Maintain 1 A/cm^2 during 18 h	–
JARI (Japan)	Maintain 0.2 A/cm^2 during 18 h 80 °C cell temperature H_2 or N_2/air or N_2 atmospheric pressure 100/100% relative humidity 1.4/5.5 stoichiometry	Circulate dry N_2/N_2 for 1 min and 22 s at 200/200 ml/min before the cell is heated	Increase current density to 1 A/cm^2 and maintain until cell voltage is stable	–

United States Fuel Cell Council document, 05-014B.2, (after [19.8, 9, 105–107])

Operating parameters such as the reactant gas flow stoichiometries, reactant pressures, cell temperature, and inlet stream relative humidity are held constant. For dynamic measurements, the load across the cell or stack is varied and the corresponding change in voltage is measured. During dynamic measurements, the cell operating parameters change as a result of the changing power output unless the fuel cell test station or system is designed for a rapid response and constant operating conditions.

There are several documents that discuss methods to measure performance. For example, an experimental setup that enables excellent stability of system operating parameters for steady-state performance measurements was described [19.85]. A method for extrapolating performance loss during steady-state operating conditions from a limited amount of performance data was provided [19.108]. Steady-state tests also extend to long durations to establish durability. Such tests typically run from 1000 to 10 000 or more hours [19.109–113]. Such tests are useful but do not necessarily reproduce the observed behavior in the field as operating conditions are not constant. As a result, tests are increasingly completed under dynamic conditions simulating drive or duty cycles in applications [19.114–117]. Furthermore, long-duration tests consume significant resources (low turnover). This additional pressure has led to the development of a number of accelerated tests targeted at specific degradation mechanisms. A consistent set of accelerated protocols is available from the United States Department of Energy for known degradation mechanisms involving key MEA materials: electrocatalyst, catalyst support, and membrane (Table 19.8). An overview of the durability test protocols that were developed through 2011 is available [19.118]. Additional work discussing accelerated testing methods recently appeared [19.119, 120].

A fuel cell requires support components to operate (Fig. 19.3). On the other hand, a fuel cell test station does not mimic the fuel cell system balance of plant behavior. Therefore, it is important to test the fuel cell under system compatible operating conditions. This is achieved with the use of hardware in the loop technique. This concept is illustrated in Fig. 19.10. A fuel cell and optionally a few balance of plant components are integrated into a fast dynamic response test station that is controlled using a model of the remaining balance of plant components [19.48, 49, 121]. In effect, the behavior of the balance of plant is simulated in real time with a combination of a balance of plant components model and the fast response test station. The hardware in the loop technique is useful to evaluate the fuel cell dynamic response under practical, steady-state or long-term operating conditions, control algorithms and controllers, and new system layouts or components. The test station dynamic response needs to be smaller than 100 ms to ensure that the fastest system component is simulated in real time.

Table 19.8 United States Department of Energy accelerated material and component durability tests

Test parameters	Test objective			
	Electrocatalyst	**Catalyst support**	**Membrane/electrode assembly chemical stability**	**Membrane mechanical stability**
Cycle	50 mV/s between 0.6 and 1.0 V, triangular sweep cycle, 25–50 cm^2 single cell	Hold at 1.2 V for 24 h, run polarization curve and electrochemical surface area, repeat for a total of 400 h, 25–50 cm^2 single cell	–	Cycle from 0% relative humidity (2 min) to 90 °C dew point (2 min), 25–50 cm^2 single cell
Number (cycle)	30 000	–	–	–
Cycle time (s)	16	–	–	–
Temperature (°C)	80	80	90	80
Relative humidity (%)	Anode-cathode, 100/100	Anode-cathode, 100/100	Anode-cathode, 30/30	Cycle from 0% relative humidity (2 min) to 90 °C dew point (2 min)
Fuel/oxidant	Hydrogen-N_2 (H_2 at 200 standard cm^3/min and N_2 at 75 standard cm^3/min for a 50 cm^2 cell)	Hydrogen-N_2	Hydrogen-air, 0.2 A/cm^2 and 10/10 stoichiometry equivalent flow	Air-air, 2/2 standard l/min
Pressure (kPa absolute)	0	150	150	0
Total time (h)	–	400 (continuous operation)	500	Until crossover > 2 mA/cm^2 or 20 000 cycles
Diagnostic frequency (h)	–	24	–	–
Test condition	–	–	Steady-state open circuit potential, 25–50 cm^2 single cell	–
Catalytic mass activity[a]	At beginning and end of test (minimum), ≤ 40% loss of initial catalytic activity	Every 24 h, ≤ 40% loss of initial catalytic activity	–	–
Polarization curve[b] from 0 to ≥ 1.5 A/cm^2	After 0, 1 k, 5 k, 10 k and 30 k cycles, ≤ 30 mV loss at 0.8 A/cm^2	Every 24 h, ≤ 30 mV loss at 1.5 A/cm^2 or rated power	–	–
Electrochemical surface area/cyclic voltammetry[c]	After 10, 100, 1 k, 3 k, 10 k, 20 k and 30 k cycles, ≤ 40% loss of initial area	Every 24 h, ≤ 40% loss of initial area	–	–
F^- release or equivalent for non-fluorine membranes	–	–	At least every 24 h, no target (for monitoring purposes)	–
Hydrogen crossover[d]	–	–	Every 24 h, ≤ 2 mA/cm^2	Every 24 h, ≤ 2 mA/cm^2
Open circuit potential	–	–	Continuous, ≤ 20% loss in OCV	–
High frequency resistance	–	–	Every 24 h at 0.2 A/cm^2, no target (for monitoring purposes)	–
Shorting resistance[e]	–	–	Every 24 h, > 1000 Ωcm^2	Every 24 h, > 1000 Ωcm^2

[a] Mass activity in A/mg at 150 kPa absolute back pressure and 857 mV (ohmic loss corrected) on 6 % H_2 (balance N_2)-O_2 (or equivalent thermodynamic potential), 100% relative humidity, 80 °C, normalized to initial mass of catalyst and measured before and after test
[b] Recommended polarization curve protocol
[c] Sweep from 0.05 to 0.6 V at 20 mV/s, 80 °C, 100% relative humidity
[d] Crossover current as described in United States Fuel Cell Council document 05-014B.2, section A3-2
[e] Measured at 0.5 V applied potential with N_2-N_2, 80 °C and 100% relative humidity. Compression to 20% strain on the gas diffusion layer

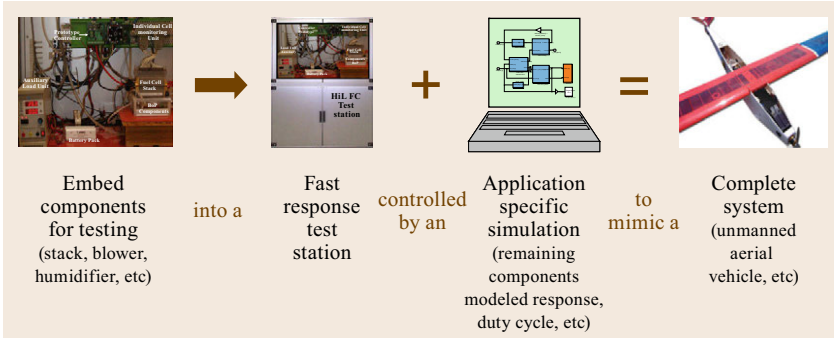


Fig. 19.10 Hardware in the loop operational concept

Diagnostics are added to the main purpose fuel cell performance test to supplement fuel cell characterization data or facilitate interpretation. The selection of the most appropriate diagnostics is crucial to balance time and resources, and information needs. Furthermore, the diagnostics selection may affect the outcome of the main test by introducing artifacts. For example, long term fuel cell tests are relevant to establish the durability of Pt alloy catalysts. However, the measurement of the cell current density or voltage does not yield the evolution of the key metric, the catalyst surface area. A more direct method is needed. Cyclic voltammetry has been used to intermittently evaluate the surface area of Pt catalysts with information obtained in the hydrogen adsorption, hydrogen desorption or CO adsorption regions (voltammetry Sect. 19.4.2). For Pt alloy catalysts, cyclic voltammetry does not lead to the desired active area value because the alloying element either dissolve at a specific potential thus accelerating catalyst degradation or the method is unreliable because the probe molecule adsorption is different on the alloy than on Pt [19.122].

Finally, there are a number of tests typically performed to evaluate MEA properties in situ for modeling validation or diagnostic purposes. For example, a polarization curve is able to provide cathode catalyst kinetic parameters as long as the low current density region is investigated (Tafel behavior) and the membrane crossover H_2 flux is measured for current density correction [19.123]. However, the membrane crossover H_2 flux requires a specific test [19.106]. Other parameters of interest include transport properties (mass and heat) in the gas and solid phases (ionomer/membrane, electrodes, bipolar plates), and main and side reaction rate constants.

Polarization

The H_2–air performance curve, also known as the polarization curve or the current density-voltage ($I-V$) curve, represents the baseline PEMFC performance diagnostic. A polarization curve (Fig. 19.11) generally shows

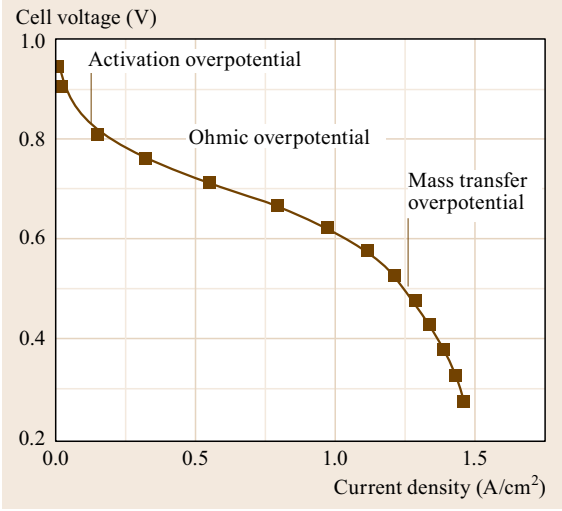


Fig. 19.11 PEMFC polarization curve with three distinct regions

three distinct regions at different current densities, that each indicate the predominance of one process, activation, charge transfer or mass transfer [19.124–126]. Activation losses are associated with slow oxygen reduction kinetics, which are described by the Butler–Volmer equation (19.1). The current density j (A/cm^2) is a function of the exchange current density j_0 (A/cm^2), the electron transfer coefficient α, the number of exchanged electrons n, the Faraday constant F (96 500 C/mol), the activation polarization η_{act} (V), the gas constant R (8.31 J/mol K) and the temperature T (K):

$$j = j_0 \left[\exp\left(\frac{\alpha n F \eta_{act}}{RT}\right) - \exp\left(-\frac{(1-\alpha) n F \eta_{act}}{RT}\right)\right]. \quad (19.1)$$

For large reduction currents leading to an activation polarization that exceeds the limit given by (19.2), the reverse reaction is negligible and (19.1) reduces to the

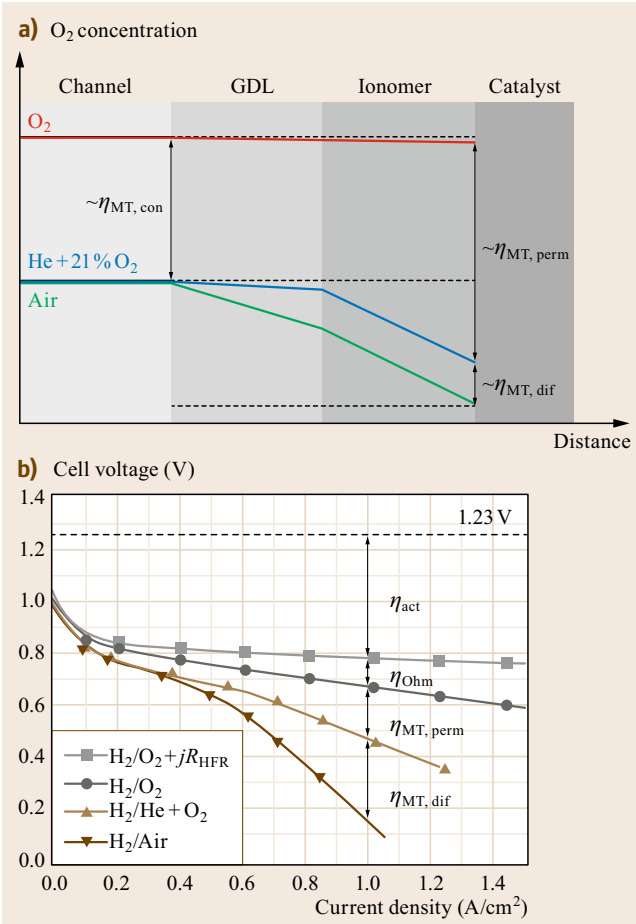


Fig. 19.12a,b O_2 concentration profiles in a PEMFC for different cathode gas supply: O_2, He + O_2, air **(a)**. Polarization curves obtained with H_2-O_2, H_2/He + O_2, H_2-air **(b)**. Anode-cathode conditions: 2/2 stoichiometry, 100/50% relative humidity, 48.3/48.3 kPag, 60 °C

Tafel equation (19.3)

$$|\eta_{act}| \gg \frac{RT}{nF} = \frac{25.7}{n}\text{mV} \quad (\text{at } 25\,^\circ\text{C})\,, \tag{19.2}$$

$$\eta_{act} = \frac{RT}{\alpha nF}\ln j_0 - \frac{RT}{\alpha nF}\ln j\,. \tag{19.3}$$

Ohmic losses η_{Ohm} (V) occur due to limitations associated with protonic and/or electronic charge transport, which linearly increase with the cell current density (Ohm's law, (19.4)). The high frequency resistance denoted by R_{HFR} (or serial resistance, Ωcm^2), is divided into a protonic membrane resistance (R_m, Ωcm^2) and an electronic resistance for electrodes and other electric circuit elements (R_e, Ωcm^2). The high frequency resistance of a fuel cell R_{HFR} is determined during fuel cell operation using electrochemical impedance spectroscopy (EIS):

$$\eta_{Ohm} = R_{HFR}j = (R_m + R_e)j\,. \tag{19.4}$$

The local consumption of O_2 in air, a gas diluted with 79% N_2, creates a local depletion at the catalyst surface and mass transfer losses. Mass transfer losses are described by (19.5) [19.127], which indicates that polarization losses significantly increase when the catalyst surface reactant concentration approaches zero at high current densities j near the limiting value j_l (A/cm^2):

$$\eta_{MT} = -\frac{RT}{nF}\ln\left(1 - \frac{j}{j_l}\right) \tag{19.5}$$

Mass transfer losses are further decomposed into permeability and diffusion components [19.30, 128]. Figure 19.12a illustrates O_2 concentration profiles for different gas compositions. The O_2 concentration is approximately constant from the gas channel to the catalyst surface because only a relatively small amount of water vapor is present in the gas stream. The O_2 polarization curve constant slope at high current densities (ohmic behavior, absence of significant mass transfer losses, Fig. 19.12b) is an alternative to the R_{HFR} measurement with EIS. For a 79% He + 21% O_2 mixture, the O_2 concentration is lower with a small decrease in O_2 concentration in the gas phase, which is limited by the high value of the oxygen diffusion coefficient in He. The decrease in O_2 concentration is more significant in the ionomer phase. For the air case, the O_2 concentration gradient is more significant in the gas phase because the O_2 diffusion coefficient is smaller with a heavier N_2 diluent than with He (diffusion coefficients of an equimolar mixture of O_2–He and O_2–N_2 are 0.723 and 0.202 cm^2/s at 293 K and 101.325 kPa [19.129]). In the ionomer phase, the O_2 concentration profiles for air and the He + O_2 mixture lead to a similar concentration difference (Fick's first law with the same diffusion coefficient and diffusion length). The difference between O_2 and the He + O_2 mixture polarization data defines the permeability overpotential $\eta_{MT,perm}$ (the largest concentration difference is located in the permeable ionomer). The difference between the He + O_2 mixture and air polarization data defines the diffusion overpotential $\eta_{MT,dif}$ (corresponds to the approximate concentration difference in the porous GDE with predominant diffusive transport). The sum of $\eta_{MT,perm}$ and $\eta_{MT,dif}$ corresponds to η_{MT} (19.5).

Figure 19.12b shows polarization curves measured for the three cathode gas compositions and an additional

ohmic loss corrected polarization curve obtained with H_2–O_2. The activation overpotential η_{act} is obtained by subtracting the ohmic loss corrected H_2–O_2 polarization curve $V_{O_2} + jR_{HFR}$ from the theoretical open circuit voltage E of 1.23 V (101.3 kPa) (19.6). The ohmic overpotential η_{Ohm} was obtained by multiplying R_{HFR} with the current density j (19.7). Subtraction of the H_2/He + O_2 data V_{He+O_2} from the H_2–O_2 data V_{O_2} yielded the permeability overpotential $\eta_{MT,perm}$ (19.8) whereas the diffusion overpotential $\eta_{MT,dif}$ was obtained by deducting the H_2-air values V_{air} from the H_2/He + O_2 values V_{He+O_2} (19.9).

$$\eta_{act}(j) = E - [V_{O_2}(j) + jR_{HFR}(j)] , \quad (19.6)$$

$$\eta_{Ohm}(j) = jR_{HFR}(j) , \quad (19.7)$$

$$\eta_{MT,perm}(j) = V_{O_2}(j) - V_{He+O_2}(j) , \quad (19.8)$$

$$\eta_{MT,dif}(j) = V_{He+O_2}(j) - V_{air}(j) . \quad (19.9)$$

It is noted that $\eta_{MT,perm}$ includes a constant contribution owing to the O_2 concentration change $\eta_{MT,con}$ (the oxygen reduction reaction is first order in oxygen concentration [19.130], (19.10)) allowing separation of the concentration change contribution in the ionomer (Fig. 19.12a):

$$\eta_{MT,con} = \frac{RT}{F} \ln \frac{c_{O_2}}{c_{air}} = 45\,\text{mV} \quad (\text{at } 60\,^\circ\text{C}) , \quad (19.10)$$

where c_{O_2} and c_{air} respectively represent the O_2 concentration in the O_2 and air streams (mol/cm^3). Additional analysis refinements were discussed including a current density correction for the hydrogen crossover through the membrane [19.131] and empirical curve fitting relations with alternatives to the mass transfer polarization expression (19.5) [19.132–135].

Impedance Spectroscopy

EIS is a noninvasive diagnostic technique that separates in the frequency domain the individual effects of different processes such as proton transport in the electrolyte, interfacial charge transfer reactions and mass transport in catalyst and backing diffusion layers [19.77, 78, 136]. A small sinusoidal alternating potential or current (V_{AC}^{in},I_{AC}^{in}) is superimposed on the constant fuel cell potential or current (V_{DC}, I_{DC}) and both potential and current responses (V_{AC}^{out},I_{AC}^{out}) are recorded (Fig. 19.13). This operation is repeated for many signal frequencies. The impedance, a complex variable, is calculated by the potential and current signals ratio:

$$Z(\omega) = \frac{\Delta V}{\Delta I} = |Z|\, e^{i\phi(\omega)} = Z_{Re}(\omega) - iZ_{Im}(\omega) , \quad (19.11)$$

where Z is the impedance (Ω), ΔV is the amplitude of the potential perturbation signal (V), ΔI is the amplitude of the current response signal (A), ϕ is the phase angle, ω is the angular frequency (Hz), Z_{Re} is the real part of the impedance (Ω) and Z_{Im} is the imaginary part of the impedance (Ω). There are three necessary requirements to obtain reliable impedance measurements [19.77]. A linear behavior that implies that the perturbation signal amplitude is small in comparison to RT/F (the polarization curve is not linear, Figs. 19.11 and 19.12b), a response that is only due to the applied perturbation (the fuel cell, for instance, is operating at the steady state), and a stable response with the fuel cell returning to its original state after the perturbation is removed.

A frequency response analyzer (FRA) is used to impose the small amplitude alternating current (AC) signal to the fuel cell via the load bank. The AC voltage and current responses are processed by the FRA to determine the complex impedance for all frequencies [19.137]. Physicochemical processes occurring within the fuel cell (Fig. 19.9) have different characteristic time constants and therefore are exhibited in the spectra at different characteristic frequencies. Other options are available to modulate the fuel cell output such as with a high power potentiostat (control unit and booster).

Impedance data are displayed as the negative value of the imaginary impedance as a function of the real impedance (Nyquist plot).The Bode plot is an alternative representation of the impedance data with both the impedance magnitude and phase angle plotted as a function of the perturbation signal frequency. A representative Nyquist plot for a PEMFC is shown in Fig. 19.14. Three distinguishable, depressed semicircles are observed within the 0.1 Hz to 10 kHz frequency range [19.138, 139]. The smaller arc at high frequencies (> 1 kHz) is attributed to the transport of protons and electrons and the anode charge transfer reactions. The larger arc in the mid-frequency range (5 Hz to

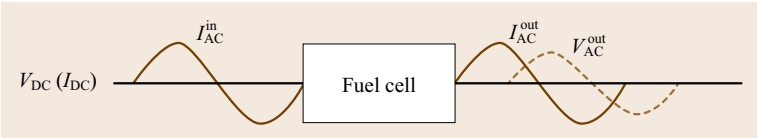


Fig. 19.13 EIS measurement principle

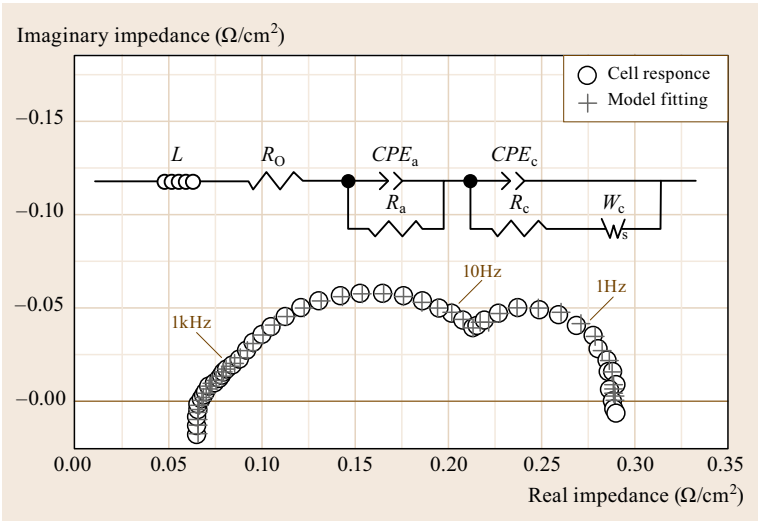


Fig. 19.14 Representative EIS for a PEMFC single cell, corresponding EEC and curve fitting results. Anode-cathode conditions: H_2/air, 2/2 stoichiometry, 100/50% relative humidity, 48.3/48.3 kPa, 80 °C, 0.6 A/cm^2, 15 mA/cm^2 AC perturbation, 0.1 Hz to 10 kHz frequency range

1 kHz) is attributed to the cathode charge transfer reactions. The remaining arc at low frequencies (0.1−5 Hz) is attributed to the reactant transport in the cathode GDE.

Equivalent electrical circuits (EEC) are extensively used to analyze impedance responses and extract physically meaningful fuel cell properties. Common electrical circuit components include resistors, capacitors, inductors, constant phase elements and Warburg elements [19.77]. An EEC for a single PEMFC is shown in Fig. 19.14; L stands for the serial inductance of the cell and system components. The electron and proton transport resistances are combined into the ohmic resistance R_O. Charge transfer resistances of the hydrogen oxidation reaction (HOR) and the oxygen reduction reaction (ORR) are represented by R_a and R_c. A finite length Warburg diffusion element W_c is included for the O_2 transport in the GDE. The H_2 diffusion resistance is negligible, eliminating the need for a Warburg element. Constant phase elements CPE_a and CPE_c represent anode and cathode double-layer capacitances with a rough catalyst layer and a nonuniform catalyst distribution [19.140]. The EEC offers an adequate representation of experimental impedance data (Fig. 19.14). Curve fitting was completed with a commercially available software (ZView, Scribner Associates) with estimated parameter errors < 5% [19.139].

Voltammetry

Cyclic voltammetry (CV) is a potentiodynamic technique for studying thermodynamic and kinetic aspects of electrochemical reactions. The potential of the working electrode (WE) is scanned linearly between two potential limits from an initial value. The current-voltage curve of the WE versus the reference electrode (RE) is referred to as the cyclic voltammogram, as shown in Fig. 19.15. The peak potential and peak currents are important characteristics [19.90, 141]. For a reversible system, the peak current j_p (A) for a reversible couple (at 25 °C) is given by the Randles–Sevcik equation

$$j_p = 2.69 \times 10^5 n^{1.5} A D^{0.5} c v^{0.5} , \qquad (19.12)$$

where A is the electrode area (cm^2), D the diffusion coefficient (cm^2/s), c the concentration (mol/cm^3) and v the potential scan rate (V/s). The corresponding peak potential separation between anode E_p^a and cathode E_p^c peak potentials (V) is

$$E_p^a - E_p^c = \frac{0.059}{n} , \qquad (19.13)$$

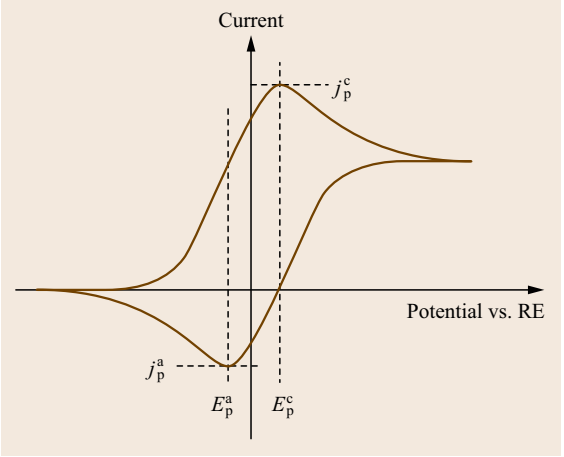


Fig. 19.15 Cyclic voltammogram for a hypothetical reaction and associated peak parameters

which is used as a criterion for a reversible or Nernstian behavior and to determine the number n of electrons transferred. In turn, the diffusion coefficient is determined using n, (19.12) and operating conditions A, c and v. The peak potentials are used to identify specific reactions. Equations (19.12) and (19.13) illustrate qualitative as well as quantitative aspects of cyclic voltammetry. Similar equations were derived for other kinetics including irreversible reactions [19.142].

A potentiostat controls the potential difference between working and reference electrodes at a desired value. An electrometer, a high-input impedance voltmeter that minimizes the reference electrode polarization, measures the voltage difference between reference and working electrodes. The potential scan rate is normally constant. The resulting current passing through the working and the counter electrodes is recorded. The potential limits and the potential scan rate are the adjustable parameters. The potential applied to the working electrode is swept back and forth between the two set voltage limits (triangular wave form).

A cyclic voltammogram for a single PEMFC is shown in Fig. 19.16. The electrode that serves as the PEMFC cathode (GDE with Pt/C as catalyst and Nafion as electrolyte) is fed with humidified N_2 and connected as the WE. The other PEMFC electrode fed with humidified H_2 serves as both counter electrode (CE) and RE. The applied WE potential is scanned between the open circuit voltage (OCV, ≈ 0 V versus the RE) and 1.2 V versus the RE. During the positive scan, the H_2 that permeates from the CE side and adsorbed H_2 on Pt ($Pt\text{-}H_{ads}$) are oxidized within the ≈ 0 to ≈ 0.4 V versus RE potential range according to

$$Pt - H_{ads} \rightarrow Pt + H^+ + e^- \,. \tag{19.14}$$

The presence of two peaks in the ≈ 0 to ≈ 0.4 V versus RE potential range is ascribed to different Pt crystallographic planes ((111) and (100) [19.143]). In the ≈ 0.4 to ≈ 0.6 V versus RE potential range, the positive current is attributed to the oxidation of the H_2 permeating through the membrane and the charging of the double-layer capacitance. Above ≈ 0.6 V versus RE, Pt oxidation takes place with the formation of Pt-OH and Pt-O species [19.144, 145]

$$Pt + H_2O \rightarrow Pt\text{-}OH + H^+ + e^- \,, \tag{19.15}$$

$$Pt\text{-}OH \rightarrow Pt\text{-}O + H^+ + e^- \,. \tag{19.16}$$

During the reverse scan, the Pt oxides are first reduced (≈ 0.77 V peak potential). Subsequently, H_2 is adsorbed on Pt (≈ 0.13 V peak potential versus RE). Below ≈ 0.1 V versus RE, H_2 evolution takes place.

The current measured in the electroinactive region around 0.4 V versus the RE is due to the charging and discharging of the double-layer capacitance associated with the Pt/ionomer interface (a constant phase element in this case, Fig. 19.14). The capacitance C (F) is determined from the charging current j_{dl} (A/cm^2) and the potential scan rate v,

$$Aj_{dl} = C\frac{dV}{dt} = Cv \,, \tag{19.17}$$

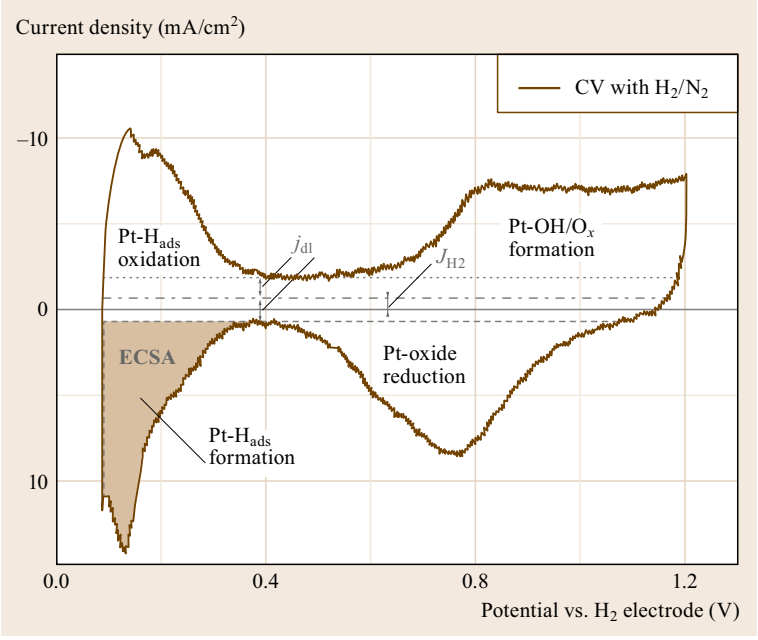


Fig. 19.16 Cyclic voltammogram of a PEMFC MEA. Counter/working electrode compartment conditions: H_2/N_2, 0.5/0.5 l/min at normal conditions, 100/100% relative humidity, 101/101 kPa, 35 °C, 20 mV/s potential scan rate

where V is the electrode potential (V versus the RE) and t the time (s). The electroinactive region around 0.4 V versus the RE is also not centered at a 0 current density because the H_2 permeating through the membrane is oxidized and contributes to a small oxidation current displacing the entire cyclic voltammogram to higher current density values. The permeating H_2 also displaces the entire cyclic voltammogram to higher potentials (diffusion cell polarization of ≈ 0.1 V).

The cyclic voltammogram is used to determine the electrochemical active surface area (ECSA or ECA) by integrating the H_2 adsorption current between ≈ 0.1 and ≈ 0.4 V versus the RE (hashed area in Fig. 19.16). The ECSA is calculated with a charge density of $210\,\mu C/cm^2$, a charge sufficient to reduce a monolayer of H_{ads} on a smooth Pt surface, and the Pt loading

$$\mathrm{ECSA} = \frac{S}{0.021mv}\,, \tag{19.18}$$

where the ECSA is in m^2/g, S is the H_2 adsorption peak area (mW/cm^2) and m the Pt loading (mg/cm^2). The ECSA is essential to compare the activity of different Pt catalyst structures. Alternatively, the H_2 oxidation peaks or CO adsorption were used to estimate the ECSA. The Pt oxides reduction peak was employed to estimate the extent of oxidation [19.146].

Linear sweep voltammetry (LSV) is similar to CV but only one scan is completed between potential limits. Furthermore the scan is completed at a much smaller scan rate equal to or less than 1 mV/s. These precautions are necessary for H_2 crossover and electrical short circuit measurements [19.89, 147] to minimize the effects of preadsorbed H_2 and the double-layer capacitance charging. A LSV curve for a H_2 crossover measurement is shown in Fig. 19.17. The WE potential is scanned at 0.1 mV/s from the ≈ 0.1 to ≈ 0.4 V versus the RE. The upper potential limit is sufficient to obtain a well-defined H_2 oxidation limiting current density. The hydrogen crossover rate J_{H_2} ($mol/s\,cm^2$) is calculated using Faraday's law

$$J_{H_2} = \frac{j_l}{nF}\,. \tag{19.19}$$

The LSV method for the determination of the H_2 crossover is an alternative to the CV method (Fig. 19.16).

In the presence of an electrical MEA short circuit, the H_2 oxidation limiting current density is not constant but rather increases at higher electrode potentials. The electrical short circuit resistance is estimated from the polarization curve slope [19.89, 147].

Other Tests

There are other diagnostic techniques that are used to characterize fuel cells but they are relatively seldom utilized. Although one of these diagnostic techniques is electrochemical, the segmented cell for current-voltage distribution across the cell active area, all the others are not. These diagnostic techniques are briefly and sequentially introduced using the high level framework of

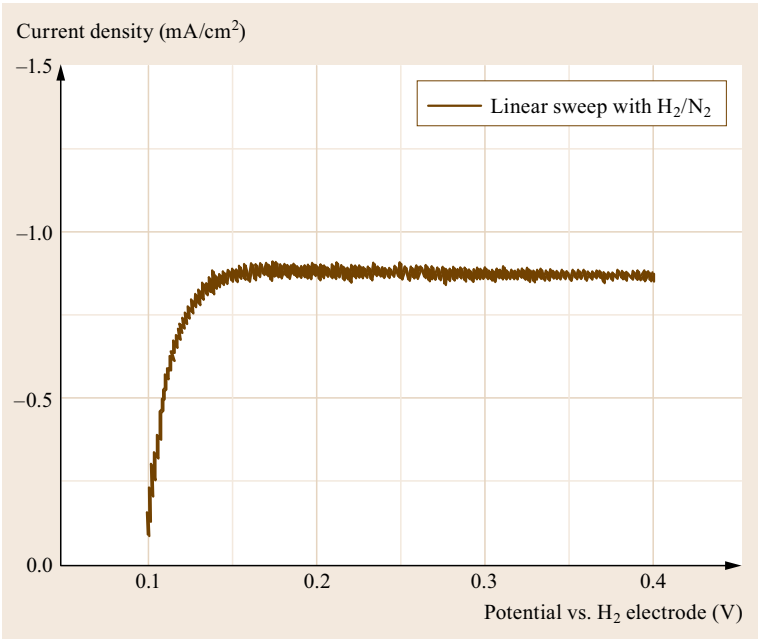


Fig. 19.17 LSV curve of a PEMFC MEA. Counter/working electrode compartment conditions: H_2/N_2, 0.5/0.5 l/min at normal conditions, 100/100% relative humidity, 101/101 kPa, 35 °C, 0.1 mV/s potential scan rate

Table 19.6 (method focus). The section concludes with the hardware-in-the-loop technique.

The consumption of reactants and the generation of products and heat in the fuel cell contribute to the variation of the species concentration and temperature along the flow field length and in turn to the uneven current-cell voltage distribution. The different gradients are impacted by cell design and are thus important to optimize performance and mitigate premature local degradation. Noninvasive measurement techniques rely on the external magnetic field [19.148] whereas invasive techniques require the electrical segregation of one or several active area components including the current collector, the bipolar plate, and the gas diffusion layer and electrode. The invasive techniques are further grouped based on manufacturing techniques including printed circuit boards [19.149] and the addition of multiple sensing or controlling elements. The latter techniques rely on the integration of high precision shunt resistors [19.150, 151], electronic loads [19.150, 152–154] or Hall sensors [19.30, 155–157]. The current-voltage distribution measurements also enable the local use of other electrochemical techniques such as impedance spectroscopy [19.30, 154, 158, 159]. Figure 19.18a illustrates local polarization curves that demonstrate the significantly uneven and interlinked performance and operating condition distributions. The kinetic and ohmic regimes are hardly impacted due to the high stoichiometries and well-humidified reactant streams (Fig. 19.11). However, the mass transfer regime at high current densities is largely modified owing to the progressive effect of product water accumulation. The cell performance decreases along the flow field length. Figure 19.18b shows the evolution of the local cell performance resulting from a temporary CO injection into the H_2 stream. The cell voltage distribution is uniform due to the high bipolar plate electrical conductivity and relatively small active area of 100 cm^2. The cell voltage distribution remains uniform during the CO injection but drops until a steady state is reached (CO adsorption on Pt decreases the catalyst active area) and recovers to its original state after the CO injection is interrupted. By contrast, the current distribution is not uniform with inlet segments relatively more affected by the CO presence with lower than 1 normalized current density values. As the total current is fixed, downstream segments have larger than 1 normalized current density values. The H_2 stream is depleted of CO along the flow field length as it progressively adsorbs on the Pt catalyst or reacts with O_2 diffusing through the membrane from the cathode compartment and creating a much weaker adsorbing CO_2 product.

Several methods are available to quantify the products generated within the fuel cell. Water mapping within the fuel cell has been the subject of extensive studies [19.11]. The most useful and less invasive methods include neutron imaging [19.80], x-ray diffraction [19.81] and residence time distribution [19.38, 39]. Liquid water exiting the fuel cell is also analyzed to obtain information about the membrane degrada-

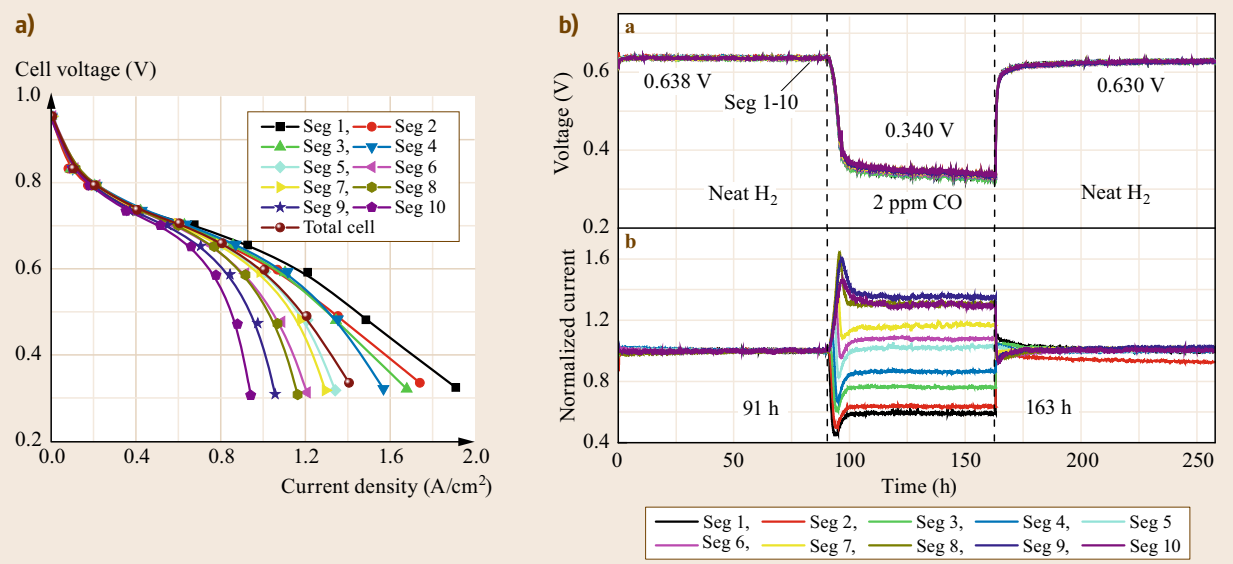


Fig. 19.18a,b Spatially distributed polarization curves for a PEMFC **(a)**. Cell voltage and normalized current density (using the initial performance) distributions at 0.8 A/cm^2 before, during and after a temporary injection of 2 ppm CO in the H_2 stream **(b)**. Anode-cathode conditions: H_2/air, 2/2 stoichiometry, 100/50% relative humidity, 48.3/48.3 kPag, 60 °C

tion rate (fluoride emission rate [19.112, 160, 161]) and assess the contaminant scavenging efficiency [19.97]. Equally, the fuel cell outlet reactant streams are sampled and analyzed to reveal the catalyst support corrosion [19.162, 163], and to establish the presence of side reactions [19.164] and the accumulation of diluents such as N_2 [19.165]. The electro-osmotic drag or number of water molecules transported with the proton in the ionomer is also quantifiable using in situ methods [19.95, 96, 166].

Some reactant properties are also quantifiable within the fuel cell. The limiting current density (Fig. 19.11) is useful to derive overall mass transfer coefficients and separate them into more fundamental contributions [19.93, 167–170]. Permeability coefficients for reactant diffusion in ionomers are also obtainable [19.89, 94]. Heat-related diagnostic methods, although available, have seldom been used. Thermocouples [19.87] as well as an infrared camera [19.88] were employed.

Fuel cell systems also need to be tested to evaluate interactions between the fuel cell and balance of plant components under conditions that mimic the expected transient operating conditions for the selected application (duty cycle). The hardware-in-the-loop technique was developed with that intent (Fig. 19.10) [19.48, 49, 121]). Figure 19.19a displays results for a fuel cell–battery hybrid power system. The total power demand (duty cycle) intermittently exceeds the nominal system power of 300 W with the excess power provided by the battery allowing the fuel cell output to remain relatively constant at ≈ 250 W. Such a control algorithm is expected to extend fuel cell life because, for example, cathode potential changes that lead to Pt catalyst active area loss by Pt dissolution and Pt nanoparticle agglomeration are minimized. This specific fuel cell stack control algorithm can only be implemented with a fuel cell–battery hybrid system. During periods when the total power demand is smaller than the nominal power (< 300 W), the excess fuel cell power is used to recharge the battery. Component sizing is also important to avoid a complete battery discharge and to maintain a reasonable battery state of charge as illustrated in Fig. 19.19a. Figure 19.19b reveals with an expanded timescale the significance of a faster test station control response time (< 100 ms) to measure and observe small and rapid fuel cell and battery dynamic changes with load demand.

19.4.3 Ex Situ Tests

A large number of ex situ tests are also available to characterize fuel cell materials. The information is used to relate freshly synthesized or aged materials parameters to fuel cell performance and degradation mechanisms. More specifically, the correlation between ex situ and in situ tests results is an issue of general relevance because in situ tests require more time and resources. There is a gap in rapid ex situ diagnostic methods that correlate with in situ tests. Tests are first analyzed on the basis of the main fuel cell performance losses (polarizations) to focus and order the discussion. Subsequently, electrochemical cells combined with spectroscopic measurements are introduced (spectroelectrochemical cells). This section leads to other material science characterization methods including spectroscopic measurements.

The rotating ring-disc electrode (RRDE) is the most popular method to obtain kinetic parameters for the main and side electrochemical reactions [19.171]. The ring-disc electrode has a geometry that consists

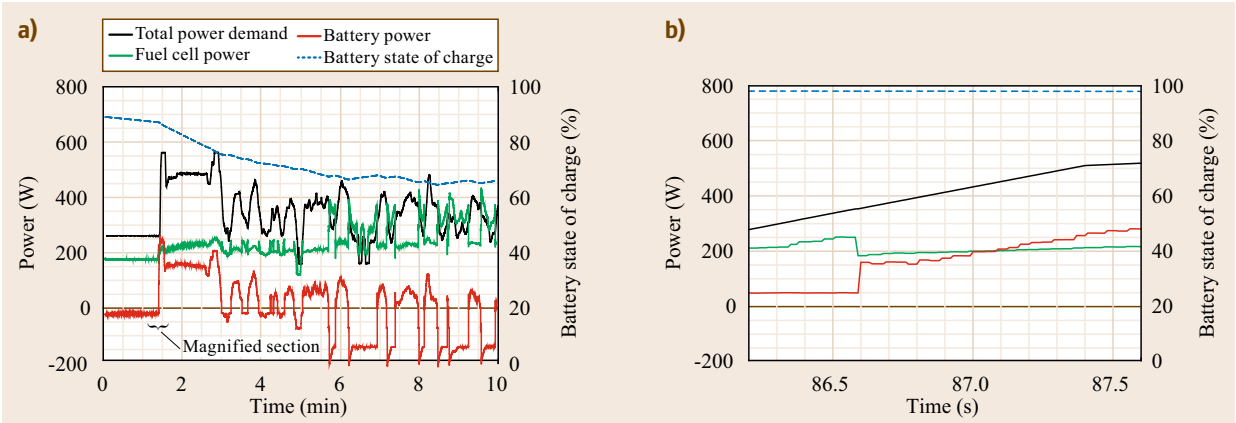


Fig. 19.19a,b Fuel cell–battery hybrid system hardware-in-the-loop duty cycle results displaying the evolution of both power levels and battery state of charge **(a)**. A magnified time scale reveals the test station response time of < 100 ms during a total power demand change that is necessary to measure and observe small and rapid fuel cell and battery dynamic changes **(b)**

of a cylinder inserted in a tube that are both fixed within an inert material and electrically isolated. All parts share the same rotation axis and only one end of the disc cylinder and ring tube assembly is electrochemically active. The ring-disc electrode rotation in an electrolyte solution is a hydrodynamic problem that has been analytically solved. For instance, the limiting current density at the disc is described by the Levich equation

$$j_l = 0.62nFAD^{2/3}\omega^{1/2}\nu^{-1/6}c\,, \tag{19.20}$$

where ν is the kinematic viscosity (cm^2/s). Equation (19.20) leads to the electroactive species diffusion coefficient if other solution properties are known. Separation of the overall current j into kinetic j_k (A/cm^2) and mass transport j_l contributions is also possible with the Koutecký–Levich equation

$$\frac{1}{j} = \frac{1}{j_k} + \frac{1}{j_l}\,. \tag{19.21}$$

A $1/j$ versus $\omega^{-1/2}$ plot yields $1/j_k$ at $\omega^{-1/2} = 0$. At the ring, reaction intermediates that are swept away from the disc surface by the hydrodynamic shearing forces are detected at a potential that is selected to create a current response. The ring potential is not necessarily equal to the disc potential. Only a fraction of the intermediates generated at the disc reach the ring and react. Therefore, in separate experiments, the collection efficiency N needs to be measured to recover the total amount of intermediates

$$N = \frac{-j_{ring}}{j_{disc}}\,. \tag{19.22}$$

A theoretical expression is available to calculate the collection efficiency [19.171]. The RRDE method is especially relevant for the oxygen reduction reaction, which leads to a small amount of peroxide that is affected by the presence of contaminants such as SO_2 [19.172]. An inverted electrode catalyst ink deposition technique was proposed and is preferred in view of an improved reproducibility and a more uniform film thickness [19.173, 174]. Figure 19.20 illustrates the reproducibility achieved for both disc polarization curves and peroxide detection. The amount of peroxide generated during oxygen reduction increases at low electrode potentials and only accounts for a few % of the disc current. However, the peroxide generated has been linked to ionomer and membrane degradation [19.175].

The ionically conductive membrane is the most electrically resistive component material of a PEMFC in comparison to Pt, C and Cu (electronic conductors). A conductivity cell is generally used to measure the membrane resistance and assess ohmic losses. The conductivity cell maintains the membrane sample in contact with a controlled atmosphere or environment and electrodes for current and voltage sensing to eliminate contact resistances (4-point electrodes method [19.176]). Direct or alternating current measurements are used to measure the membrane conductivity. However, alternating current measurements

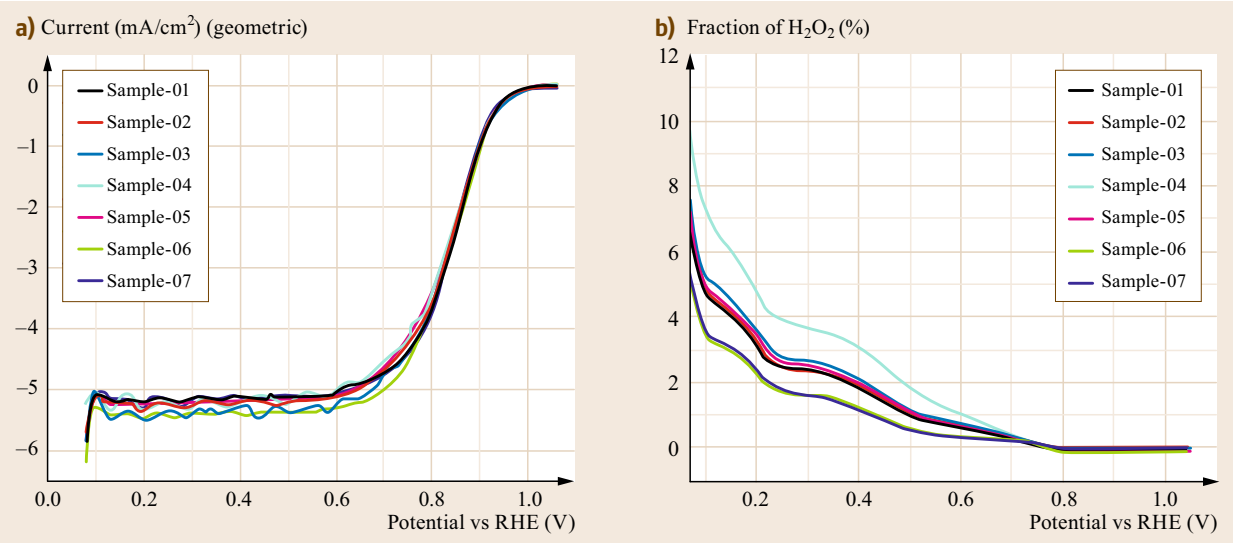


Fig. 19.20a,b Polarization curves for a catalyst ink deposited on a rotating disc electrode **(a)**, corresponding peroxide intermediate detection at the ring electrode **(b)**. Operating conditions: 0.5 M H_2SO_4 saturated with O_2, 30 °C, 20 mV/s potential scan rate, 1.2 V versus the SHE ring potential

such as impedance spectroscopy are preferred to minimize artifacts (absence of a current circulating in the membrane and electrode polarization). Through-plane measurements are also preferred because they correspond to the current and MEA stacking directions [19.61, 177]. Membrane processing affects both ionomer material isotropy and conductivity [19.178, 179]. Therefore, in-plane measurements are not preferred unless they are used for thin ionomer films with isotropic properties.

For mass transfer losses, products as well as reactants and gas and ionomer phases need to be considered. For O_2 and H_2 transport in the gas phase, Gurley measurements were used [19.180] but are not directly comparable to in situ values because the gas flow is circulated (forced convection) rather than being mostly driven by diffusion as in a PEMFC. For O_2 and H_2 diffusive transport in the ionomer phase, a diffusion cell is commonly used [19.94]. For product water vapor, diffusive transport in the gas phase is equally problematic as for O_2 and H_2. Transport of liquid water in the GDE also needs to be considered. However, this is a complex problem that has not yet been satisfactorily resolved. For H_2O transport in the ionomer phase, dynamic vapor sorption is used for diffusion control [19.181] whereas in situ measurements are preferred for electro-osmotic drag control [19.95]. Ultimately, there is a need to relate mass transfer properties to mass transfer polarizations (Sect. 19.4.2). This relationship is not as obvious to develop as for kinetic or ohmic polarizations because other parameters are needed to convert transport properties into mass transfer coefficients, which in turn are used to calculate concentration profiles and mass transfer polarizations. For example, diffusion coefficients are missing for gas-phase reactants (including tortuosity effects) whereas the thickness of the ionomer covering the catalyst is missing precluding the calculation of the concentration profiles.

Electrochemical cells used to study PEMFC reaction kinetics have been modified to include spectroscopic measurements (Raman, x-ray, infrared [19.182–185]). These seldom employed methods are useful to track in situ reaction kinetics and materials evolution that are otherwise not accessible or only obtained for pristine and aged materials.

Other ex situ tests are useful to visualize, analyze the composition, and obtain subsidiary properties for the pristine and aged fuel cell materials to support the development of enhanced and more durable materials. Visualization of surface morphology, characteristic size and other features is achieved using scanning electron microscopy (SEM), environmental scanning electron microscopy (ESEM), transmission electron microscopy (TEM), atomic force microscopy (AFM) and scanning tunneling microscopy (STM) [19.186–188]. Some of these methods have recently been adapted to obtain localized, transient information [19.189, 190]. The bulk phase composition is obtained by x-ray diffraction (XRD), x-ray absorption spectroscopy including x-ray absorption near edge structure (XANES) and extended x-ray absorption fine structure (EXAFS), x-ray radial electron density distribution (REDD) and Fourier transform infrared spectroscopy (FTIR) [19.176, 191]. The surface composition is obtained by Auger electron spectroscopy and x-ray photoelectron spectroscopy (XPS). Electronic microscopes are sometimes equipped with an energy dispersive x-ray analysis spectrometer (EDX or EDAX/EDS), an electron microprobe with wavelength dispersive x-ray spectrometer (WDS) or an energy dispersive spectrometer. Small angle x-ray scattering (SAXS) provides information relative to the ionomer structure as a function of water content (crystallinity, ion clustering, etc.). Subsidiary properties such as pore size distribution, porosity, surface tension and surface groups complement transport properties in porous media. Mercury intrusion porosimetry (MIP), through- and in-plane electrical resistivity and sessile drop are representative of the methods available to characterize GDLs and GDEs [19.192]. A similar statement applies to the ionomer with methods such as differential scanning calorimetry (DSC) and thermogravimetric analysis (TGA) [19.176].

19.5 Conclusion

Fuel cell laboratory constitutive elements were reviewed to better identify gaps including safety aspects, test stations, fuel cell components and their assembly, and in situ as well as ex situ diagnostic techniques. Several opportunities were identified to improve these areas but many other opportunities are possibly left to be discovered until further analysis is completed. For instance, interest in higher and lower operating temperatures for respectively PEMFCs and SOFCs [19.193, 194] may lead to changes in safety, operating conditions and fuel cell materials impacting both test station requirements and operating procedures. This situation equally applies to the recent interest in large-scale flow batteries with circulating liquid electrolytes [19.3]. PEMFCs and SOFCs are the favored technologies for commercialization. Other fuel cell types includ-

ing molten carbonate, phosphoric acid, direct alcohol and alkaline, which were not discussed, may similarly impact the fuel cell laboratory. Fuel cell fabrication aspects were not discussed but are important especially because state-of-the-art commercial designs are not necessarily accessible for testing by academic institutions or national laboratories. For example, the equipment necessary to process bipolar plates and MEAs is relatively extensive and expensive. Therefore, investments need to be carefully assessed especially because the technologies to obtain the best fuel cell performance are still evolving. From that standpoint, it is still unclear if molded, machined carbon-based or stamped metallic bipolar plates will lead to the best overall performance [19.62, 63].

Acknowledgments. Authors are grateful to the Office of Naval Research (award N00014-11-1-0391) and to the Hawaiian Electric Company for their ongoing support of the operations of the Hawaii Sustainable Energy Research Facility. The authors are also grateful to Junjie Ge for Fig. 19.20.

References

19.1 Breakthrough Technologies Inst. Inc.: *2011 Fuel Cell Technologies Market Report*, DOE/EE 0755 (United States Department of Energy, Washington 2012)

19.2 J. Köhler, M. Wietschel, L. Whitmarsh, D. Keles, W. Schade: Infrastructure investment for a transition to hydrogen automobiles, Technol. Forecast. Soc. Change **77**, 1237–1248 (2010)

19.3 Z. Yang, J. Zhang, M.C.W. Kintner-Meyer, X. Lu, D. Choi, J.P. Lemmon, J. Liu: Electrochemical energy storage for green grid, Chem. Rev. **111**, 3577–3613 (2011)

19.4 N. Maximova, O. Dahl: A set up of a modern analytical laboratory for wastewaters from pulp and paper industry, Chem. Soc. Rev. **36**, 1323–1349 (2007)

19.5 M.J. D'Amato, K.W. Lux, K.A. Walz, H. Walter Kerby, B. Anderegg: Introducing new learning tools into a standard classroom: A multi-tool approach to integrating fuel-cell concepts into introductory college chemistry, J. Chem. Educ. **84**, 248–252 (2007)

19.6 M. Shirkhanzadeh: Thin-layer fuel cell for teaching and classroom demonstrations, J. Chem. Educ. **86**, 324–329 (2009)

19.7 P. Lunghi, S. Ubertini: First steps towards fuel cells testing harmonisation: Procedures and parameters for single cell performance evaluation, Fuel Cells **3**, 208–219 (2004)

19.8 R. Cuccaro, M. Lucariello, A. Battaglia, A. Graizzaro: Research of a HySyLab internal standard procedure for single PEMFC, Int. J. Hydrog. Energy **33**, 3159–3166 (2008)

19.9 T. Malkow, A. Saturnio, A. Pilenga, G. De Marco, M. Honselaar, G. Tsotridis: Assessment of PEFC performance by applying harmonized testing procedure, Int. J. Energy Res. **35**, 1075–1089 (2011)

19.10 G. De Moor, C. Bas, F. Lesage, A. Sophie Danérol, E. Claude, E. Rossinot, M. Paris, L. Flandin, N. Dominique Albérola: Understanding the degradation of MEA in PEMFC: Definition of structural markers and comparison between laboratory and on-site ageing, J. Appl. Polym. Sci. **120**, 3501–3510 (2011)

19.11 J. St-Pierre: PEMFC in-situ liquid-water-content monitoring status, J. Electrochem. Soc. **154**, B724–B731 (2007)

19.12 S.A. Freunberger, M. Reum, J. Evertz, A. Wokaun, F.N. Büchi: Measuring the current distribution in PEFCs with sub-millimeter resolution I. methodology, J. Electrochem. Soc. **153**, A2158–A2165 (2006)

19.13 J. St-Pierre: PEMFC contamination model: Foreign cation exchange with ionomer protons, J. Power Sources **196**, 6274–6283 (2011)

19.14 J. St-Pierre: PEMFC contaminant tolerance limit-foreign cations in ionomers, Int. J. Hydrog. Energy **36**, 5527–5535 (2011)

19.15 A.M. Sapienza: *Managing Scientists: Leadership Strategies in Scientific Research*, 2nd edn. (Wiley-Liss, Hoboken 2004) pp. 31–33

19.16 M. Reijalt: Hydrogen and fuel cell education in Europe: From when? and where? to here! and now!, J. Clean. Prod. **18**, S112–S117 (2010)

19.17 Fuel Cell Today, http://www.fuelcelltoday.com

19.18 J. Glassey, S. Haile: Sustainability in chemical engineering curriculum, Int. J. Sustain. High. Educ. **13**, 354–364 (2012)

19.19 L. Diener: Selected online resources for teaching about alternative energy, J. Chem. Educ. **89**, 950–952 (2012)

19.20 R. Wünschiers, P. Lindblad: Hydrogen in education – A biological approach, Int. J. Hydrog. Energy **27**, 1131–1140 (2002)

19.21 B. Briggs, T. Mitton, R. Smith, T. Magnuson: Teaching cellular respiration and alternate energy sources with a laboratory exercise developed by a scientist-teacher partnership, Am. Biol. Teach. **71**, 164–167 (2009)

19.22 A. Serov, C. Kwak: Direct hydrazine fuel cells: A review, Appl. Catal. B **98**, 1–9 (2010)

19.23 A. Serov, C. Kwak: Progress in development of direct dimethyl ether fuel cells, Appl. Catal. B **91**, 1–10 (2009)

19.24 F. Yang, K. Cheng, X. Liu, S. Chang, J. Yin, C. Du, L. Du, G. Wang, D. Cao: Direct peroxide-peroxide fuel cell – Part 2: Effects of conditions on the performance, J. Power Sources **217**, 569–573 (2012)

19.25 J. Ma, N.A. Choudhury, Y. Sahai: A comprehensive review of direct borohydride fuel cells, Renew. Sustain. Energy Rev. **14**, 183–199 (2010)

19.26 G.R. Astbury: A review of the properties and hazards of some alternative fuels, Process Saf. Environ. Prot. **86**, 397–414 (2008)

19.27 Compressed Gas Association: *Handbook of Compressed Gases*, 4th edn. (Springer, Berlin, Heidelberg 1999)

19.28 C.H. Rivkin (Ed.): *The NFPA Guide to Gas Safety* (National Fire Protection Association, Quincy 2005)

19.29 Y.W. Rho, S. Srinivasan, Y.T. Kho: Mass transport phenomena in proton exchange membrane fuel cells using O_2/He, O_2/Ar, and O_2/N_2 mixtures II: Theoretical analysis, J. Electrochem. Soc. **141**, 2089–2096 (1994)

19.30 T.V. Reshetenko, G. Bender, K. Bethune, R. Rocheleau: Systematic study of back pressure and anode stoichiometry effects on spatial PEMFC performance distribution, Electrochimica Acta **56**, 8700–8710 (2011)

19.31 H.D. Beeson, S.R. Smith, W.F. Stewart (Eds.): *Safe Use of Oxygen and Oxygen Systems: Handbook for Design, Operation, and Maintenance*, 2nd edn. (ASTM Intl., West Conshohocken 2007)

19.32 D.K. Berry: Air toxics in the United States – Magnitude of the problem and strategy for control, Toxicol. Ind. Health **6**, 1–12 (1990)

19.33 P.M. Lemieux, C.C. Lutes, D.A. Santoianni: Emissions of organic air toxics from open burning: A comprehensive review, Prog. Energy Combust. Sci. **30**, 1–32 (2004)

19.34 G.M. Woodall, R.L. Smith: The air toxics health effects database (ATHED), Toxicol. Appl. Pharmacol. **233**, 20–24 (2008)

19.35 J. St-Pierre, M.S. Angelo, Y. Zhai: Focusing research by developing performance related selection criteria for PEMFC contaminants, Electrochem. Soc. Trans. **41**(1), 279–286 (2011)

19.36 R. Borup, J. Meyers, B. Pivovar, Y.S. Kim, R. Mukundan, N. Garland, D. Myers, M. Wilson, F. Garzon, D. Wood, P. Zelenay, K. More, K. Stroh, T. Zawodzinski, J. Boncella, J.E. McGrath, M. Inaba, K. Miyatake, M. Hori, K. Ota, Z. Ogumi, S. Miyata, A. Nishikata, Z. Siroma, Y. Uchimoto, K. Yasuda, K.-I. Kimijima, N. Iwashita: Scientific aspects of polymer electrolyte fuel cell durability and degradation, Chem. Rev. **107**, 3904–3951 (2007)

19.37 C.S. Macomber, J. Christ, H. Wang, B. Pivovar, H.N. Dinh: Characterizing leachant contaminants from fuel cell assembly aids, a prelude to effects on performance, Electrochem. Soc. Trans. **50**(2), 603–618 (2012)

19.38 J. Diep, D. Kiel, J. St-Pierre, A. Wong: Development of a residence time distribution method for proton exchange membrane fuel cell evaluation, Chem. Eng. Sci. **62**, 846–857 (2007)

19.39 J. St-Pierre, A. Wong, J. Diep, D. Kiel: Demonstration of a residence time distribution method for proton exchange membrane fuel cell evaluation, J. Power Sources **164**, 196–202 (2007)

19.40 H.S. Fogler: *Elements of Chemical Reaction Engineering*, 4th edn. (Prentice Hall, Upper Saddle River 2006) p. 871

19.41 D. Roberts: 50-V shock hazard threshold, IEEE Trans. Ind. Appl. **46**, 102–107 (2010)

19.42 T.B. Reddy (Ed.): *Linden's Handbook of Batteries*, 4th edn. (McGraw-Hill, New York 2011), Chap. 5

19.43 S. Kreitmeier, M. Michiardi, A. Wokaun, F.N. Büchi: Factors determining the gas crossover through pinholes in polymer electrolyte fuel cell membranes, Electrochimica Acta **80**, 240–247 (2012)

19.44 A.Z. Weber: Gas-crossover and membrane-pinhole effects in polymer-electrolyte fuel cells, J. Electrochem. Soc. **155**, B521–B531 (2008)

19.45 J. Zhang, J. Lee: A review on prognostics and health monitoring of Li-ion battery, J. Power Sources **196**, 6007–6014 (2011)

19.46 J. St-Pierre: Air impurities. In: *Polymer Electrolyte Fuel Cell Durability*, ed. by F.N. Büchi, M. Inaba, T.J. Schmidt (Springer, Berlin, Heidelberg 2009) pp. 289–321

19.47 K. Promislow, J. St-Pierre, B. Wetton: A simple, analytic model of polymer electrolyte membrane fuel cell anode recirculation at operating power including nitrogen crossover, J. Power Sources **196**, 10050–10056 (2011)

19.48 G. Randolf, R.M. Moore: Test system design for hardware-in-loop evaluation of PEM fuel cells and auxiliaries, J. Power Sources **158**, 392–396 (2005)

19.49 R.M. Moore, K.H. Hauer, G. Randolf, M. Virji: Fuel cell hardware-in-loop, J. Power Sources **162**, 302–308 (2006)

19.50 D. Stolten, T. Grube (Eds.): *18th World Hydrogen Energy Conference–WHEC 2010, Parallel Sessions Book 6: Stationary Applications/Transportation Applications* (Forchungszentrum Jülich, Jülich 2010) pp. 115–120

19.51 S. Begot, F. Harel, J.M. Kauffmann: Design and validation of a 2 kW-fuel cell test bench for subfreezing studies, Fuel Cells **8**, 23–32 (2008)

19.52 T.A. Zawodzinski Jr., C. Derouin, S. Radzinski, R.J. Sherman, V.T. Smith, T.E. Springer, S. Gottesfeld: Water uptake by and transport through Nafion 117 membranes, J. Electrochem. Soc. **140**, 1041–1047 (1993)

19.53 F. Barbir: *PEM Fuel Cells: Theory and Practice* (Elsevier, Amsterdam 2005) pp. 55–57

19.54 S. Pischinger, O. Lang: Air-supply components. In: *Handbook of Fuel Cells*, Vol. 4, ed. by W. Vielstich, A. Lamm, H.A. Gasteiger (Wiley, New York 2003) pp. 727–741

19.55 M.J. Lampinen, M. Fomino: Analysis of free energy and entropy changes for half-cell reactions, J. Electrochem. Soc. **140**, 3537–3546 (1993)

19.56 J. St-Pierre, J. Roberts, K. Colbow, S. Campbell, A. Nelson: PEMFC operational and design strategies for sub zero environments, J. New Mater. Electrochem. Syst. **8**, 163–176 (2005)

19.57 R. Hanke-Rauschenbach, M. Mangold, K. Sundmacher: Bistable current-voltage characteristics of PEM fuel cells operated with reduced feed

stream humidification, J. Electrochem. Soc. **155**, B97–B107 (2008)
19.58 T. Kadyk, S. Kirsch, R. Hanke-Rauschenbach, K. Sundmacher: Autonomous potential oscillations at the Pt anode of a polymer electrolyte membrane fuel cell under CO poisoning, Electrochimica Acta **56**, 10593–10602 (2011)
19.59 A. Taniguchi, T. Akita, K. Yasuda, Y. Miyazaki: Analysis of electrocatalyst degradation in PEMFC caused by cell reversal during fuel starvation, J. Power Sources **130**, 42–49 (2004)
19.60 Anonymous: *Fuel Cell Testing – The NI Way*, White Paper 2759 (National Instruments, Austin 2012)
19.61 J. St-Pierre: Stacks. In: *Encyclopedia of Electrochemical Power Sources*, Vol. 2, ed. by J. Garche, C. Dyer, P. Moseley, Z. Ogumi, D. Rand, B. Scrosati (Elsevier, Amsterdam 2009) pp. 879–889
19.62 V. Mehta, J.S. Cooper: Review and analysis of PEM fuel cell design and manufacturing, J. Power Sources **114**, 32–53 (2003)
19.63 H. Tawfik, Y. Hung, D. Mahajan: Metal bipolar plates for PEM fuel cell – A review, J. Power Sources **163**, 755–767 (2007)
19.64 J.H. Nam, M. Kaviany: Effective diffusivity and water-saturation distribution in single- and two-layer PEMFC diffusion medium, Int. J. Heat Mass Transf. **46**, 4595–4611 (2003)
19.65 G. Lin, T. Van Nguyen: Effect of thickness and hydrophobic polymer content of the gas diffusion layer on electrode flooding level in a PEMFC, J. Electrochem. Soc. **152**, A1942–A1948 (2005)
19.66 J. St-Pierre: Overview performance and operational conditions. In: *Encyclopedia of Electrochemical Power Sources*, Vol. 2, ed. by J. Garche, C. Dyer, P. Moseley, Z. Ogumi, D. Rand, B. Scrosati (Elsevier, Amsterdam 2009) pp. 901–911
19.67 S.-Y. Ahn, S.-J. Shin, H.Y. Ha, S.-A. Hong, Y.-C. Lee, T.W. Lim, I.-H. Oh: Performance and lifetime analysis of the kW-class PEMFC stack, J. Power Sources **106**, 295–303 (2002)
19.68 I. Nazarov, K. Promislow: The impact of membrane constraint on PEM fuel cell water management, J. Electrochem. Soc. **154**, B623–B630 (2007)
19.69 C.J. Netwall, B.D. Gould, J.A. Rodgers, N.J. Nasello, K.E. Swider-Lyons: Decreasing contact resistance in proton-exchange membrane fuel cells with metal bipolar plates, J. Power Sources **227**, 137–144 (2013)
19.70 R.K. Jain, H.C. Triandis: *Management of Research and Development Organizations: Managing the Unmanageable*, 2nd edn. (Wiley, New York 1997)
19.71 E. Sadeghia, N. Djilali, M. Bahrami: Effective thermal conductivity and thermal contact resistance of gas diffusion layers in proton exchange membrane fuel cells. Part 2: Hysteresis effect under cyclic compressive load, J. Power Sources **195**, 8104–8109 (2010)
19.72 O. Burheim, P.J.S. Vie, J.G. Pharoah, S. Kjelstrup: Ex-situ measurements of through-plane thermal conductivities in a polymer electrolyte fuel cell, J. Power Sources **195**, 249–256 (2010)
19.73 M. Hamour, J.P. Garnier, J.C. Grandidier, A. Ouibrahim, S. Martemianov: Thermal-conductivity characterization of gas diffusion layer in proton exchange membrane fuel cells and electrolyzers under mechanical loading, Int. J. Thermophys. **32**, 1025–1037 (2011)
19.74 R. Zaffou, J.S. Yi, H.R. Kunz, J.M. Fenton: Temperature-driven water transport through membrane electrode assembly of proton exchange membrane fuel cells, Electrochem. Solid-State Lett. **9**, A418–A422 (2006)
19.75 K. Promislow, J. Stockie, B. Wetton: A sharp interface reduction for multiphase transport in a porous fuel cell electrode, Proc. R. Soc. A **462**, 789–816 (2006)
19.76 K. Promislow, B. Wetton: A simple, mathematical model of thermal coupling in fuel cell stacks, J. Power Sources **150**, 129–135 (2005)
19.77 E. Barsoukov, J.R. MacDonald (Eds.): *Impedance Spectroscopy: Theory, Experiment and Applications*, 2nd edn. (Wiley, New York 2005)
19.78 M.E. Orazem, B. Tribollet: *Electrochemical Impedance Spectroscopy* (Wiley, New York 2008)
19.79 F.N. Büchi, A. Marek, G.G. Scherer: In-situ membrane resistance measurements in polymer electrolyte fuel cells by fast auxiliary current pulses, J. Electrochem. Soc. **142**, 1895–1901 (1995)
19.80 R. Mukundan, R.L. Borup: Visualising liquid water in PEM fuel cells using neutron imaging, Fuel Cells **9**, 499–505 (2009)
19.81 A. Isopo, F. Nobili, V.R. Albertini: Energy dispersive x-ray diffraction applied to laboratory investigation on proton exchange membrane water content in working fuel cells, Fuel Cells **12**, 800–808 (2012)
19.82 K. Tüber, D. Pócza, C. Hebling: Visualization of water buildup in the cathode of a transparent PEM fuel cell, J. Power Sources **124**, 403–414 (2003)
19.83 X.G. Yang, F.Y. Zhang, A.L. Lubawy, C.Y. Wang: Visualization of liquid water transport in a PEFC, Electrochem. Solid-State Lett. **7**, A408–A411 (2004)
19.84 A.P. Young, J. Stumper, S. Knights, E. Gyenge: Ionomer degradation in polymer electrolyte membrane fuel cells, J. Electrochem. Soc. **157**, B425–B436 (2010)
19.85 G. Bender, M. Angelo, K. Bethune, S. Dorn, T. Thampan, R. Rocheleau: Method using gas chromatography to determine the molar flow balance for proton exchange membrane fuel cells exposed to impurities, J. Power Sources **193**, 713–722 (2009)
19.86 G.A. Schuler, A. Wokaun, F.N. Büchi: Local online gas analysis in PEFC using tracer gas concepts, J. Power Sources **195**, 1647–1656 (2010)
19.87 P.J.S. Vie, S. Kjelstrup: Thermal conductivities from temperature profiles in the polymer electrolyte fuel cell, Electrochimica Acta **49**, 1069–1077 (2004)
19.88 M. Matian, A.J. Marquis, N.P. Brandon: Application of thermal imaging to validate a heat transfer model for polymer electrolyte fuel cells, Int. J. Hydrog. Energy **35**, 12308–12316 (2010)

19.89 S.S. Kocha, J.D. Yang, J.S. Yi: Characterization of gas crossover and its implications in PEM fuel cells, Am. Inst. Chem. Eng. J. **52**, 1916–1925 (2006)

19.90 W. Vielstich: Cyclic voltammetry. In: *Handbook of Fuel Cells*, Vol. 2, ed. by W. Vielstich, A. Lamm, H.A. Gasteiger (Wiley, New York 2003) pp. 153–162

19.91 R.W. Lindström, K. Kortsdottir, M. Wesselmark, A. Oyarce, C. Lagergren, G. Lindbergh: Active area determination of porous Pt electrodes used in polymer electrolyte fuel cells: Temperature and humidity effects, J. Electrochem. Soc. **157**, B1795–B1801 (2010)

19.92 M. Inaba, T. Kinumoto, M. Kiriake, R. Umebayashi, A. Tasaka, Z. Ogumi: Gas crossover and membrane degradation in polymer electrolyte fuel cells, Electrochimica Acta **51**, 5746–5753 (2006)

19.93 T.V. Reshetenko, J. St-Pierre: PEMFC GDE oxygen mass transport coefficient separation with different gas diluents, Electrochem. Soc. Trans. **50**(2), 549–555 (2012)

19.94 K. Broka, P. Ekdunge: Oxygen and hydrogen permeation properties and water uptake of Nafion 117 membrane and recast film for PEM fuel cell, J. Appl. Electrochem. **27**, 117–123 (1997)

19.95 K.-H. Choi, D.-H. Peck, C.S. Kim, D.-R. Shin, T.-H. Lee: Water transport in polymer membranes for PEMFC, J. Power Sources **86**, 197–201 (2000)

19.96 Z. Peng, A. Morin, P. Huguet, P. Schott, J. Pauchet: In-situ measurement of electroosmotic drag coefficient in nafion membrane for the PEMFC, J. Phys. Chem. B **115**, 12835–12844 (2011)

19.97 B. Wetton, J. St-Pierre: Liquid water scavenging of PEMFC contaminants, Electrochem. Soc. Trans. **50**(2), 649–657 (2012)

19.98 J. St-Pierre: Section preface. In: *Device and Materials Modeling in PEM Fuel Cells*, ed. by S.J. Paddison, K.S. Promislow (Springer, Berlin, Heidelberg 2009) pp. 3–17

19.99 G.-S. Kim, J. St-Pierre, K. Promislow, B. Wetton: Electrical coupling in proton exchange membrane fuel cell stacks, J. Power Sources **152**, 210–217 (2005)

19.100 P.A.C. Chang, J. St-Pierre, J. Stumper, B. Wetton: Flow distribution in proton exchange membrane fuel cell stacks, J. Power Sources **162**, 340–355 (2006)

19.101 P. Berg, A. Çağlar, K. Promislow, J. St-Pierre, B. Wetton: Electrical coupling in proton exchange membrane fuel cell stacks: Mathematical and computational modelling, IMA J. Appl. Math. **71**, 241–261 (2006)

19.102 X. Cheng, B. Yi, M. Han, J. Zhang, Y. Qiao, J. Yu: Investigation of platinum utilization and morphology in catalyst layer of polymer electrolyte fuel cells, J. Power Sources **79**, 75–81 (1999)

19.103 Z. Qi, A. Kaufman: Activation of low temperature PEM fuel cells, J. Power Sources **111**, 181–184 (2002)

19.104 Z. Xu, Z. Qi, A. Kaufman: Activation of proton-exchange membrane fuel cell via CO oxidation stripping, J. Power Sources **156**, 281–283 (2006)

19.105 H. Tomioka, Y. Hashimasa, N. Yoshimura, M. Akai, S. Watanabe: JARI standard single cell testing protocol, JARI Res. J. **28**, 247–252 (2006)

19.106 Anonymous: *Procedure for Performing PEM Single Cell Testing* (Florida Solar Energy Center, Cocoa 2009)

19.107 T. Malkow, G. De Marco, A. Pilenga, M. Honselaar, G. Tsotridis, S. Escribano, L. Antoni, R. Reißner, O. Thalau, E. Sitters, G. Heinz: *Testing the Voltage and the Power as a Function of the Current Density Following a Dynamic Profile Versus Time–Dynamic Load Cycling Ageing Test for a PEFC Single Cell, Test Module PEFC SC 5-7* (European Commission Joint Research Centre, Institute for Energy, Petten 2010)

19.108 G. Bender, M. Angelo, K. Bethune, R. Rocheleau: Quantitative analysis of the performance impact of low-level carbon monoxide exposure in proton exchange membrane fuel cells, J. Power Sources **228**, 159–169 (2013)

19.109 J. St-Pierre, D.P. Wilkinson, S. Knights, M.L. Bos: Relationships between water management, contamination and lifetime degradation in PEFC, J. New Mater. Electrochem. Syst. **3**, 99–106 (2000)

19.110 J. St-Pierre, N. Jia: Successful demonstration of Ballard PEMFCs for space shuttle applications, J. New Mater. Electrochem. Syst. **5**, 263–271 (2002)

19.111 S.D. Knights, K.M. Colbow, J. St-Pierre, D.P. Wilkinson: Aging mechanisms and lifetime, PEFC and DMFC, J. Power Sources **127**, 127–134 (2004)

19.112 J. Xie, D.L. Wood, D.M. Wayne, T.A. Zawodzinski, P. Atanassov, R.L. Borup: Durability of PEFCs at high humidity conditions, J. Electrochem. Soc. **152**, A104–A113 (2005)

19.113 S.J.C. Cleghorn, D.K. Mayfield, D.A. Moore, J.C. Moore, G. Rusch, T.W. Sherman, N.T. Sisofo, U. Beuscher: A polymer electrolyte fuel cell life test: 3 years of continuous operation, J. Power Sources **158**, 446–454 (2006)

19.114 D. Liu, S. Case: Durability study of proton exchange membrane fuel cells under dynamic testing conditions with cyclic current profile, J. Power Sources **162**, 521–531 (2006)

19.115 R. Borup, J. Davey, F. Garzon, D. Wood, P. Welch, K. More: PEM fuel cell durability with transportation transient operation, Electrochem. Soc. Trans. **3**(1), 879–886 (2006)

19.116 R. Lin, B. Li, Y.P. Hou, J.M. Ma: Investigation of dynamic driving cycle effect on performance degradation and micro-structure change of PEM fuel cell, Int. J. Hydrog. Energy **34**, 2369–2376 (2009)

19.117 B. Li, R. Lin, D. Yang, J. Ma: Effect of driving cycle on the performance of PEM fuel cell and microstructure of membrane electrode assembly, Int. J. Hydrog. Energy **35**, 2814–2819 (2010)

19.118 X.-Z. Yuan, H. Li, S. Zhang, J. Martin, H. Wang: A review of polymer electrolyte membrane fuel cell durability test protocols, J. Power Sources **196**, 9107–9116 (2011)

19.119 S.J. Bae, S.-J. Kim, J.I. Park, C.W. Park, J.-H. Lee, I. Song, N. Lee, K.-B. Kim, J.-Y. Park: Lifetime prediction of a polymer electrolyte membrane fuel cell via an accelerated startup-shutdown cycle test, Int. J. Hydrog. Energy **37**, 9775–9781 (2012)

19.120 T.-C. Jao, G.-B. Jung, S.-C. Kuo, W.-J. Tzeng, A. Su: Degradation mechanism study of PTFE/Nafion membrane in MEA utilizing an accelerated degradation technique, Int. J. Hydrog. Energy **37**, 13623–13630 (2012)

19.121 T.H. Bradley, B.A. Moffitt, D.N. Mavris, T.F. Fuller, D.E. Parekh: Hardware-in-the-loop testing of a fuel cell aircraft powerplant, J. Propuls. Power **25**, 1336–1344 (2009)

19.122 H. Schulenburg, J. Durst, E. Müller, A. Wokaun, G.G. Scherer: Real surface area measurements of Pt_3Co/C catalysts, J. Electroanal. Chem. **642**, 52–60 (2010)

19.123 H.A. Gasteiger, S.S. Kocha, B. Sompalli, F.T. Wagner: Activity benchmarks and requirements for Pt, Pt-alloy, and non-Pt oxygen reduction catalysts for PEMFCs, Appl. Catal. B **56**, 9–35 (2005)

19.124 S.S. Kocha: Principles of MEA preparation. In: *Handbook of Fuel Cells*, Vol. 3, ed. by W. Vielstich, H.A. Gasteiger, A. Lamm (Wiley, New York 2003) pp. 538–565

19.125 F. Barbir: *PEM Fuel Cells: Theory and Practice* (Elsevier, Amsterdam 2005) pp. 449–452

19.126 M.V. Williams, H.R. Kunz, J.M. Fenton: Analysis of polarization curves to evaluate polarization sources in hydrogen/air PEM fuel cells, J. Electrochem. Soc. **152**, A635–A644 (2005)

19.127 F. Barbir: *PEM Fuel Cells: Theory and Practice* (Elsevier, Amsterdam 2005) pp. 45–47

19.128 T.R. Ralph, M.P. Hogarth: Catalysis for low temperature fuel cells Part I: The cathode challenges, Platin. Met. Rev. **46**, 3–14 (2002)

19.129 D.R. Lide (Ed.): *CRC Handbook of Chemistry and Physics*, 89th edn. (CRC, Boca Raton 2008) p. 6-214

19.130 K. O'Neil, J.P. Meyers, R.M. Darling, M.L. Perry: Oxygen gain analysis for proton exchange membrane fuel cells, Int. J. Hydrog. Energy **37**, 373–382 (2012)

19.131 K.C. Neyerlin, W. Gu, J. Jorne, H.A. Gasteiger: Determination of catalyst unique parameters for the oxygen reduction reaction in a PEMFC, J. Electrochem. Soc. **153**, A1955–A1963 (2006)

19.132 J. Kim, S.-M. Lee, S. Srinivasan, C.E. Chamberlin: Modeling of proton-exchange membrane fuel-cell performance with an empirical-equation, J. Electrochem. Soc. **142**, 2670–2674 (1995)

19.133 G. Squadrito, G. Maggio, E. Passalacqua, F. Lufrano, A. Patti: An empirical equation for polymer electrolyte fuel cell (PEFC) behaviour, J. Appl. Electrochem. **29**, 1449–1455 (1999)

19.134 D. Chu, R. Jiang, C. Walker: Analysis of PEM fuel cell stacks using an empirical current-voltage equation, J. Appl. Electrochem. **30**, 365–370 (2000)

19.135 L. Pisani, G. Murgia, M. Valentini, B. D'Aguanno: A new semi-empirical approach to performance curves of polymer electrolyte fuel cells, J. Power Sources **108**, 192–203 (2002)

19.136 A. Bard, L. Faulkner: *Electrochemical Methods: Fundamentals and Applications*, 2nd edn. (Wiley, New York 2000) pp. 383–388

19.137 K.R. Cooper, M. Smith: Electrical test methods for on-line fuel cell ohmic resistance measurement, J. Power Sources **160**, 1088–1095 (2006)

19.138 D. Malevich, E. Halliop, B.A. Peppley, J.G. Pharoah, K. Karan: Investigation of charge-transfer and mass-transport resistances in PEMFCs with microporous layer using electrochemical impedance spectroscopy, J. Electrochem. Soc. **156**, B216–B224 (2009)

19.139 Y. Zhai, K. Bethune, S. Dorn, G. Bender, R. Rocheleau: Analysis of the SO_2 contamination effect on the oxygen reduction reaction in PEMFCs by electrochemical impedance spectroscopy, J. Electrochem. Soc. **159**, B524–B530 (2012)

19.140 J.B. Jorcin, M.E. Orazem, N. Pébère, B. Tribollet: CPE analysis by local electrochemical impedance spectroscopy, Electrochim. Acta **51**, 1473–1479 (2006)

19.141 A.J. Bard, L.R. Faulkner: *Electrochemical Methods: Fundamentals and Applications*, 2nd edn. (Wiley, New York 2001) pp. 239–243

19.142 J. Wang: *Analytical Electrochemistry*, 3rd edn. (Wiley, New York 2006)

19.143 Y. Sun, Y. Dai, Y. Liu, S. Chen: A rotating disk electrode study of the particle size effects of Pt for the hydrogen oxidation reaction, Phys. Chem. Chem. Phys. **14**, 2278–2285 (2012)

19.144 R.M. Darling, J.P. Meyers: Kinetic model of platinum dissolution in PEMFCs, J. Electrochem. Soc. **150**, A1523–A1527 (2003)

19.145 Y. Gu, J. St-Pierre, A. Joly, R. Goeke, A. Datye, P. Atanassov: Aging Studies of Pt/glassy carbon model electrocatalysts, J. Electrochem. Soc. **156**, B485–B492 (2009)

19.146 H. Xu, R. Kunz, J.M. Fenton: Investigation of platinum oxidation in PEM fuel cells at various relative humidities, Electrochem. Solid-State Lett. **10**, B1–B5 (2007)

19.147 K.R. Cooper: In-situ PEM fuel cell: Fuel crossover and electrical short circuit measurement, Fuel Cells **8**, 34–35 (2008)

19.148 K.-H. Hauer, R. Potthast, T. Wüster, D. Stolten: Magnetotomography – A new method for analysing fuel cell performance and quality, J. Power Sources **143**, 67–74 (2005)

19.149 S. Cleghorn, C.R. Derouin, M.S. Wilson, S. Gottesfeld: A printed circuit board approach to measuring current distribution in a fuel cell, J. Appl. Electrochem. **28**, 663–672 (1998)

19.150 J. Stumper, S.A. Campbell, D.P. Wilkinson, M.C. Johnson, M. Davis: In-situ methods for the determination of current distributions in PEM fuel cells, Electrochimica Acta **43**, 3773–3783 (1998)

19.151 M. Noponen, T. Mennola, M. Mikkola, T. Hottinen, P. Lund: Measurement of current distribution in a free-breathing PEMFC, J. Power Sources **106**, 304–312 (2002)

19.152 N. Rajalakshmi, M. Raja, K.S. Dhathathereyan: Evaluation of current distribution in a proton exchange membrane fuel cell by segmented cell approach, J. Power Sources **112**, 331–336 (2002)

19.153 M.M. Mench, C.Y. Wang: An in-situ method for determination of current distribution in PEM fuel cells applied to a direct methanol fuel cell, J. Electrochem. Soc. **150**, A79–A85 (2003)

19.154 D.J.L. Brett, S. Atkins, N.P. Brandon, V. Vesivic, N. Vasileiadis, A. Kucernak: Localized impedance measurements along a single channel of a solid polymer fuel cell, Electrochem. Solid-State Lett. **6**, A63–A66 (2003)

19.155 C. Wieser, A. Helmbold, E. Gülzow: A new technique for two-dimensional current distribution measurements in electrochemical cells, J. Appl. Electrochem. **30**, 803–807 (2000)

19.156 G. Bender, M.S. Wilson, T.A. Zawodzinski: Further refinements in the segmented cell approach to diagnosing performance in polymer electrolyte fuel cells, J. Power Sources **123**, 163–171 (2003)

19.157 A.B. Geiger, R. Eckl, A. Wokaun, G.G. Scherer: An approach to measuring locally resolved currents in polymer electrolyte fuel cells, J. Electrochem. Soc. **151**, A394–A398 (2004)

19.158 A. Hakenjos, C. Hebling: Spatially resolved measurement of PEM fuel cells, J. Power Sources **145**, 307–311 (2005)

19.159 I.A. Schneider, H. Kuhn, A. Wokaun, G.G. Scherer: Fast locally resolved electrochemical impedance spectroscopy in polymer electrolyte fuel cells, J. Electrochem. Soc. **152**, A2092–A2103 (2005)

19.160 A. Pozio, R.F. Silva, M. De Francesco, L. Giorgi: Nafion degradation in PEFCs from end plate iron contamination, Electrochimica Acta **48**, 1543–1549 (2003)

19.161 D.E. Curtin, R.D. Lousenberg, T.J. Henry, P.C. Tangeman, M.E. Tisack: Advanced materials for improved PEMFC performance and life, J. Power Sources **131**, 41–48 (2004)

19.162 S. Maass, F. Finsterwalder, G. Frank, R. Hartmann, C. Merten: Carbon support oxidation in PEM fuel cell cathodes, J. Power Sources **176**, 444–451 (2008)

19.163 H.-S. Oh, J.-G. Oh, S. Haam, K. Arunabha, B. Roh, I. Hwang, H. Kim: On-line mass spectrometry study of carbon corrosion in polymer electrolyte membrane fuel cells, Electrochem. Commun. **10**, 1048–1051 (2008)

19.164 M.S. Angelo, J. St-Pierre, K.P. Bethune, R.E. Rocheleau: Gas chromatography study of reactions of carbon monoxide at different operating temperatures within a PEMFC, Electrochem. Soc. Trans. **35**(32), 167–178 (2011)

19.165 E.A. Müller, F. Kolb, L. Guzzella, A.G. Stefanopoulou, D.A. McKay: Correlating nitrogen accumulation with temporal fuel cell performance, J. Fuel Cell Sci. Technol. **7**, 021013 (2010)

19.166 B.S. Pivovar: An overview of electro-osmosis in fuel cell polymer electrolytes, Polymer **47**, 4194–4202 (2006)

19.167 U. Beuscher: Experimental method to determine the mass transport resistance of a polymer electrolyte fuel cell, J. Electrochem. Soc. **153**, A1788–A1793 (2006)

19.168 J. St-Pierre, B. Wetton, G.-S. Kim, K. Promislow: Limiting current operation of proton exchange membrane fuel cells, J. Electrochem. Soc. **154**, B186–B193 (2007)

19.169 D.R. Baker, D.A. Caulk, K.C. Neyerlin, M.W. Murphy: Measurement of oxygen transport resistance in PEM fuel cells by limiting current methods, J. Electrochem. Soc. **156**, B991–B1003 (2009)

19.170 J. St-Pierre: Hydrogen mass transport in fuel cell gas diffusion electrodes, Fuel Cells **11**, 263–273 (2011)

19.171 A.J. Bard, L.R. Faulkner: *Electrochemical Methods: Fundamentals and Applications*, 2nd edn. (Wiley, New York 2001) pp. 335–353

19.172 Y. Garsany, O.A. Baturina, K.E. Swider-Lyons: Impact of sulfur dioxide on the oxygen reduction reaction at Pt/Vulcan carbon electrocatalysts, J. Electrochem. Soc. **154**, B670–B675 (2007)

19.173 Y. Garsany, O. Baturina, K.E. Swider-Lyons, S.S. Kocha: Experimental methods for quantifying the activity of platinum electrocatalysts for the oxygen reduction reaction, Anal. Chem. **82**, 6321–6328 (2010)

19.174 Y. Garsany, I.L. Singer, K.E. Swider-Lyons: Impact of film drying procedures on RDE characterization of Pt/VC electrocatalysts, J. Electroanal. Chem. **662**, 396–406 (2011)

19.175 D.A. Schiraldi: Perfluorinated polymer electrolyte membrane durability, Polym. Rev. **46**, 315–327 (2006)

19.176 M. Doyle, G. Rajendran: Perfluorinated membranes. In: *Handbook of Fuel Cells*, Vol. 3, ed. by W. Vielstich, A. Lamm, H.A. Gasteiger (Wiley, New York 2003) pp. 351–395

19.177 K.R. Cooper: Progress toward accurate through-plane ion transport resistance measurement of thin solid electrolytes, J. Electrochem. Soc. **157**, B1731–B1739 (2010)

19.178 Z. Siroma, T. Ioroi, N. Fujiwara, K. Yasuda: Proton conductivity along interface in thin cast film of Nafion, Electrochem. Commun. **4**, 143–145 (2002)

19.179 J. Li, K.G. Wilmsmeyer, L.A. Madsen: Anisotropic diffusion and morphology in perfluorosulfonate ionomers investigated by NMR, Macromolecules **42**, 255–262 (2009)

19.180 G. Velayutham: Effect of micro-layer PTFE on the performance of PEM fuel cell electrodes, Int. J. Hydrog. Energy **36**, 14845–14850 (2011)

19.181 D.J. Burnett, A.R. Garcia, F. Thielmann: Measuring moisture sorption and diffusion kinetics on proton exchange membranes using a gravimetric vapor sorption apparatus, J. Power Sources **160**, 426–430 (2006)

19.182 B. Ren, X.-B. Lian, J.-F. Li, P.-P. Fang, Q.-P. Lai, Z.-Q. Tian: Spectroelectrochemical flow cell with temperature control for investigation of electrocatalytic systems with surface-enhanced Raman spectroscopy, Faraday Discuss. **140**, 155–165 (2009)

19.183 R.J.K. Wiltshire, C.R. King, A. Rose, P.P. Wells, M.P. Hogarth, D. Thompsett, A.E. Russell: PEM fuel cell for in-situ XAS studies, Electrochimica Acta **50**, 5208–5217 (2005)
19.184 V. Croze, F. Ettingshausen, J. Melke, M. Soehn, D. Stuermer, C. Roth: The use of in-situ X-ray absorption spectroscopy in applied fuel cell research, J. Appl. Electrochem. **40**, 877–883 (2010)
19.185 M. Heinen, Z. Jusys, R.J. Behm: Ethanol, acetaldehyde and acetic acid adsorption/electrooxidation on a Pt thin film electrode under continuous electrolyte flow: An in-situ ATR-FTIRS flow cell study, J. Phys. Chem. C **114**, 9850–9864 (2010)
19.186 J.R. Anderson: *Structure of Metal Catalysts* (Academic, New York 1975)
19.187 L.A. Kibler, D.M. Kolb: Structure sensitive methods: AFM/STM. In: *Handbook of Fuel Cells*, Vol. 2, ed. by W. Vielstich, A. Lamm, H.A. Gasteiger (Wiley, New York 2003) pp. 266–278
19.188 R. Alink, D. Gerteisen, W. Mérida: Investigating the water transport in porous media for PEMFCs by liquid water visualization in ESEM, Fuel cells **11**, 481–488 (2011)
19.189 K.J.J. Mayrhofer, J.C. Meier, S.J. Ashton, G.K.H. Wiberg, F. Kraus, M. Hanzlik, M. Arenz: Fuel cell catalyst degradation on the nanoscale, Electrochem. Commun. **10**, 1144–1147 (2008)
19.190 Z.Y. Liu, J.L. Zhang, P.T. Yu, J.X. Zhang, R. Makharia, K.L. More, E.A. Stach: Transmission electron microscopy observation of corrosion behaviors of platinized carbon blacks under thermal and electrochemical conditions, J. Electrochem. Soc. **157**, B906–B913 (2010)
19.191 R.R. Adžić, J.X. Wang, B.M. Ocko, J. McBreen: EXAFS, XANES, SXS. In: *Handbook of Fuel Cells*, Vol. 2, ed. by W. Vielstich, A. Lamm, H.A. Gasteiger (Wiley, New York 2003) pp. 279–301
19.192 M.F. Mathias, J. Roth, J. Fleming, W. Lehnert: Diffusion media materials and characterisation. In: *Handbook of Fuel Cells*, Vol. 3, ed. by W. Vielstich, A. Lamm, H.A. Gasteiger (Wiley, New York 2003) pp. 517–537
19.193 N.L. Garland, J.P. Kopasz: The United States Department of Energy's high temperature, low relative humidity membrane program, J. Power Sources **172**, 94–99 (2007)
19.194 E.D. Wachsman, K.T. Lee: Lowering the temperature of solid oxide fuel cells, Science **334**, 935–939 (2011)

20. Polymer Electrolyte Fuel Cells

Vijay K. Ramani, Kevin Cooper, James M. Fenton, H. Russel Kunz

The practical application of theory to experiment and data analysis is a crucial component of effective advancement of electrochemical systems. This chapter takes the fundamental principles of fuel cell operation and the underlying scientific and engineering principles and applies them to laboratory experiments. Topics covered include experiments showing how fuel cell performance varies with test conditions, methodology to fit experimental data to a simple empirical model to extract physically meaningful parameters that govern fuel cell performance, impedance spectroscopy as a diagnostic for fuel cell performance, and data analyses methods to determine the performance of fuel cells. Methods are also given for the practical measurement of relevant items from cell assembly and cell pinch to relative humidity. While the lessons are relevant to all electrochemical systems, this chapter is primarily targeted at new entrants into this arena wishing to learn the basics of fuel cell operation and testing.

20.1 **Experimental Methods** 650
20.1.1 Fuel Cell Testing Safety and Good Lab Practices 651
20.1.2 Handling Instructions for Membrane Electrode Assemblies (MEA) 651
20.1.3 Single Cell PEM Fuel Cell Components 651
20.1.4 Fuel Cell Assembly Instructions ... 653
20.1.5 Calculation of Pinch 655
20.1.6 Fuel Cell Test System Instrumentation 656
20.1.7 Reactant Humidification in Fuel Cell Testing 656
20.2 **H_2/O_2 or Air Fuel Cell Performance Testing** 662
20.2.1 Effects of Oxygen Partial Pressure 663
20.2.2 Temperature and Relative Humidity Effects 672
20.3 **Application of a Fuel Cell Empirical Model** 679
20.3.1 Model Application and Analysis .. 680
20.3.2 Summary 683
20.4 **Fuel Crossover and Electrochemical Surface Area** 683
20.4.1 Hydrogen Crossover and Internal Short Circuit 683
20.4.2 Hydrogen Crossover Test via LSV .. 686
20.4.3 Electrochemically Active Surface Area and Catalyst Utilization Evaluation 687
20.5 **Impedance Spectroscopy of PEM Fuel Cells** 689
20.5.1 Impedance Theory and Practice .. 690
20.5.2 Results and Discussion 699
20.5.3 Impedance of a H_2 PEM Fuel Cell. 701
20.5.4 Effect of Reactant Humidification 704
20.5.5 Electrode Proton Transport Resistance 708
References 710

In Chap. 19, the fundamental principles of fuel cell laboratories and fuel cell operation are described. This chapter provides a series of fuel cell experiments to demonstrate the concepts discussed earlier. Note that the current description is for a proton-exchange membrane (PEM) fuel cell, but the general principles are relevant to most electrochemical cells. The intended audience for this series of laboratories on fuel cells includes undergraduate and graduate science and engineering students and researchers new to the field of fuel cell and electrochemical technology.

The experiments described herein have the following objectives:

- To demonstrate the effect of oxygen concentration and stoichiometry, temperature, and relative humidity (RH) on fuel cell performance.

- To fit experimental data to a simple empirical model to extract physically meaningful parameters that govern fuel cell performance.
- To demonstrate basic experimental diagnostic techniques and data analyses methods to determine properties of fuel cells including:
  1. Fuel crossover rate
  2. Electronic short circuit resistance
  3. Catalytic activity and utilization
  4. Electrolyte (membrane) ohmic resistance
  5. Performance (polarization) curves – voltage versus current density, power density versus current density, and *jR*-corrected voltage
  6. Tafel slope
  7. Transport limiting current
  8. Porous electrode ohmic (ionic) resistance.

To achieve these objectives, this chapter consists besides Sect. 20.1 on experimental methods of four parts (Sects. 20.2–20.5), each designed to address and demonstrate a different aspect of fuel cell performance and characterization:

- Section 20.2 – H_2/O_2 or air fuel cell performance testing. The influence of oxidant (oxygen) concentration on performance is demonstrated for a H_2 PEM fuel cell. Cell voltage, power density, and electrolyte resistance are determined as a function of operating current density. The data obtained is used to examine the performance of the cell at each test condition. The effect of oxygen concentration on the cathode reaction kinetics and on transport limiting current is analyzed. The influence of operating cell temperature and reactant RH is also demonstrated for a H_2 PEM fuel cell operating with either pure oxygen or air as the oxidant.
- Section 20.3 – Application of a fuel cell empirical model. Performance data are fitted using an empirical model to extract physically meaningful parameters such as the cell resistance, Tafel slope, and limiting current density. The benefits, pitfalls, and limitations of using such an empirical model are examined.
- Section 20.4 – Fuel crossover and electrochemical surface area. This section examines the evaluation of two key properties of H_2 PEM fuel cells: (1) hydrogen crossover and internal short through the membrane using linear sweep voltammetry (LSV) and (2) the electrochemically active area of a fuel cell electrode using cyclic voltammetry.
- Section 20.5 – Impedance spectroscopy of PEM fuel cells. This section introduces the theory (entry-level) and practical application of electrochemical impedance spectroscopy as a diagnostic tool for the evaluation of operating PEM fuel cells. The effect of operating conditions such as current density, oxidant concentration (O_2 versus air), and RH are probed to examine their impact on key fuel cell parameters including ohmic resistance, electrode properties, and mass transport resistance. Equivalent circuit models are developed to facilitate extraction of physically meaningful parameters.

These four sections are, as mentioned before, preceded by an experimental section, wherein good laboratory practices are introduced, along with a detailed description of fuel cell handling, assembly, and laboratory testing methods.

Laboratory activities described in the chapter include measurement of the cell voltage and internal resistance as a function of current density at various oxygen concentrations, relative humidities, and temperatures; generation of voltage versus current density curves commonly referred to as performance curves; and calculating cell efficiencies, power densities, and reactant utilizations.

Data analysis activities described in this chapter include fitting performance data to a simple empirical model, estimating ohmic, activation (kinetic), and concentration (transport) polarization losses, and comparing them to experimental and theoretical values.

In an effort to focus on the fundamental processes occurring within fuel cells, the activities described are restricted to single cells, as opposed to stacks or fuel cell power generation systems.

Although the experimental procedures described are applied to a polymer electrolyte membrane fuel cell, in general the methods and concepts are applicable to other types of fuel cells, and readers/instructors are encouraged to adapt the methods presented herein for other fuel cell systems.

20.1 Experimental Methods

The fuel cell test equipment should be operated and maintained only by trained and qualified persons familiar with fuel cell technology and safe laboratory techniques. All users should have adequate training and knowledge of the hazards associated with the use of pressurized flammable gasses and all applicable labo-

ratory techniques before operation of this equipment. Note that the recommendations made below are not comprehensive, but merely highlight certain important factors to be considered. The authors do not accept any responsibility or liability for any accidents or damages that may occur while conducting these experiments.

20.1.1 Fuel Cell Testing Safety and Good Lab Practices

It is strongly recommended that *all* applicable *safety data sheets* (SDSs) be read and understood for the protection of the operator. It is also recommended that due caution be used during all testing procedures. Although safety measures have been applied internally to most commercial fuel cell test stations, there are several regulations that may apply to a facility which uses highly flammable and/or high-pressure gases. It is suggested that a lab structure be used that is not only safe but is fully compliant with the regulations of Occupational Safety and Health Administration (OSHA) regulation for high-pressure gases and flammable materials and with all institutional safety norms.

We recommend using extreme caution during all testing procedures that use hydrogen gas. Gases exiting the fuel cell must be properly vented; placing the test station within a fume hood is recommended.

Precise control and knowledge of the water vapor content (humidity) of reactants is necessary for successful operation and testing of PEM fuel cells.

Fuel cell performance can be severely degraded by impurities in the fuel and oxidant reactant and water feeds. Impurities may be entrained within the feedstock and/or may enter the source steams due to corrosion of the components of the fuel cell test station and the cell itself. Gas fittings and tubing should be either stainless steel or nonmetallic and should be cleaned to remove grease and other debris before use.

Reactants should be of high purity and of known composition. It is strongly recommended that only distilled or deionized water be used in the anode and cathode humidifiers.

Before shutting down, the fuel cell and instrumentation tubing should be purged of reactants by flowing nitrogen through the system on both the anode and cathode sides for 15 min at a high flow rate (e.g., 0.5 l/min).

The conditions under which a fuel cell is operated strongly impact its performance. As such, pertinent test parameters should be reported when presenting fuel cell performance data: anode and cathode reactant composition; anode and cathode reactant moisture content (i. e., RH or temperature of humidifier); anode and cathode reactant stoichiometry (based on consumption rate at 1 A/cm^2); cell temperature; and anode and cathode pressure.

20.1.2 Handling Instructions for Membrane Electrode Assemblies (MEA)

1. Always wear gloves when handling an MEA. The active phase in the MEA (normally carbon-supported platinum) is an extremely active oxidation catalyst that can be dangerous when in direct contact with skin, eyes, or if accidentally swallowed or inhaled.
   Oils normally present in the skin can affect the performance of the MEA if handled with bare hands.
2. Keep the MEA away from alcohols, aromatics and flammable organic compounds. Carbon-supported platinum is a very active combustion catalyst. Exposure of the MEA to flammable compounds in the presence of air can cause combustion and/or fire ignition.
3. Avoid exposing the MEA to sulfur, phosphates, and organic (especially aromatic-based) compounds. Platinum and carbon exhibit strong absorption properties. Sulfur/phosphor compounds and organic compounds common in sealant resins, leak detector fluids, and solvents can act as catalyst poisons and can irreversibly degrade the performance of the MEA.
4. Avoid exposing the MEA to compounds that can release monovalent, divalent or trivalent cations in solution. The PEM in the MEA can be degraded if exposed to cations such as Na^+, Mg^{2+}, and Ca^{2+} all of which are normally found in tap water. Ferrous (Fe^{2+}) and ferric (Fe^{3+}) ions resulting from corrosion of steel and stainless steel can also adversely affect the membrane performance.

20.1.3 Single Cell PEM Fuel Cell Components

A single PEM fuel cell comprises the MEA and supporting cell hardware. The individual components that make up a single cell and an assembled cell are shown in Fig. 20.1.

The MEA consists of the polymer electrolyte membrane, the anode and cathode catalyst layers and the anode and cathode gas diffusion layer (GDL). When the electrocatalyst is directly applied to the GDL (as opposed to application on the membrane), the resulting electrode is often referred to as the gas diffusion electrode (GDE). The nominal active area of the MEA must be known and, on the lab scale, is typically between 5 and 50 cm^2 depending on the capacities and specifications of the test system available.

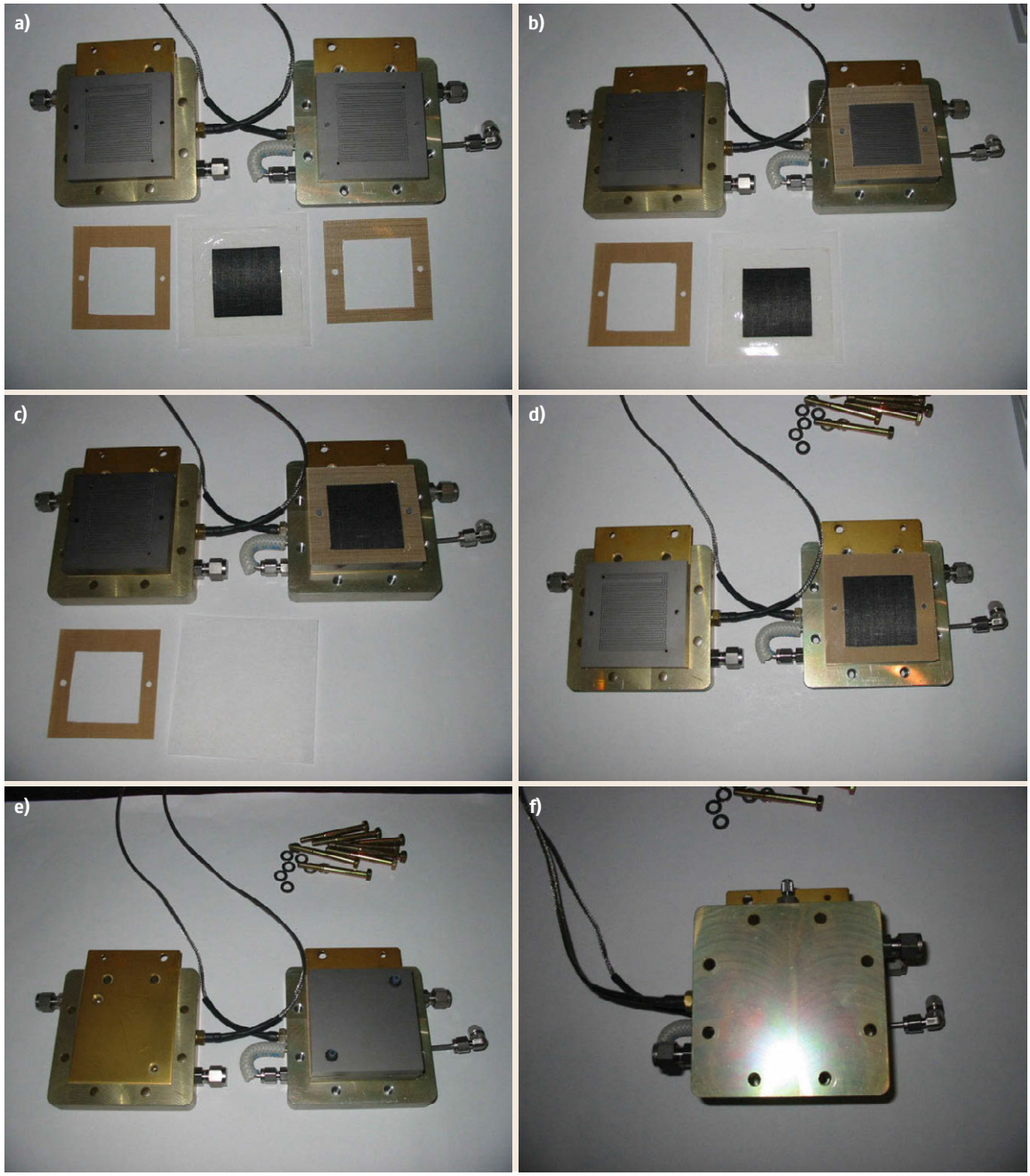


Fig. 20.1a–f Steps to build a single cell PEM fuel cell. **(a)** Ready to assemble – anode is on right, **(b)** Step A – anode gasket in place, **(c)** Step C – five-layer MEA in place, **(d)** Step D – cathode gasket in place, **(e)** Step F – cathode flow field, **(f)** Step G – cathode end plate in place. Steps A–F are described in Sect. 20.1.4

Edge gaskets on either side of the MEA provide a gas-tight seal between the flow channel and the membrane upon compression. The seal prevents reactant gases from leaking from the cell or crossing over from one electrode to the other. Gaskets are often made from polytetrafluoroethylene (PTFE, Teflon) sheet or PTFE-filled fiberglass fabric.

The flow channels deliver reactant gases to the GDL, and because they must be good thermal and electrical conductors, they are typically made from

graphite. Current collector plates made from copper are located on the backside of the graphite flow channels; the cell leads and voltage sense leads are connected to these plates. (The copper current collectors are gold plated to prevent corrosion.) Finally, the end plates are torqued together to provide mechanical compression and connection of the fuel cell components, to seal the cell to inhibit gas leaks, and to reduce contact resistances. In some cell hardware designs, the end plates must be electrically isolated from the current collectors to avoid external short circuiting by the electrical heaters.

Heaters for the cell, located within holes in the end plates (or bonded to outside of the end plates), and a thermocouple also located within the end plate, are used in conjunction with a temperature controller to control the cell temperature.

20.1.4 Fuel Cell Assembly Instructions

This section provides an overview of the basic assembly instructions for a single cell PEM fuel cell using common single cell hardware.

Materials Required

1. Single cell fuel cell hardware – end plates, current collector plates, flow fields, bolts, and washers
2. MEA of the following type:
   - Three-layer: membrane catalyzed on both sides (anode + membrane + cathode)
   - Five-layer: MEA with integrated gas diffusion media (e.g., anode catalyzed GDL + membrane + cathode catalyzed GDL).
3. GDL material if using a three-layer MEA
4. Gasket material – for example, PTFE sheet, PTFE-filled fiberglass sheet (e.g., Furon)
5. Torque wrench – for example, 1.13 to 16.95 Nm torque
6. Knife with sharp tip
7. 11 mm socket
8. Lubricant (nonreactive, nonflammable/combustible, O_2-safe) – for example, PTFE-thickened krytox synthetic grease (DuPont)
9. Ethanol or methanol – residue-free solvent for cleaning hardware
10. Clean gloves for handling catalyzed materials.

Assembly Procedure

1. Calculate the gasket thickness required to achieve the desired pinch (compression of the gas diffusion media or GDL). The calculation procedure is shown in the Fig. 20.2a.
   Note that different gas diffusion media require different compression/pinch to achieve optimum performance. The GDL vendor should be able to provide pinch or percent compression values. As a first approximation, 15–40% pinch is typical.
2. Remove the 8 bolts and flat washers and split the cell in half. The two halves – anode side and cathode side – should stay together fairly easily, separating at the flow fields (Fig. 20.3).
3. Clean the cell hardware, especially the flow fields, with a residue-free solvent such as ethanol or methanol, rinse with distilled or deionized water, and dry.
4. Cut anode and cathode gaskets to size with the Plexiglas template provided. Cut out holes for the alignment pins and the reference electrode (RE), if used (Fig. 20.4).
5. If using a three-layer MEA without integral GDL, cut the anode and cathode GDL material so that it covers all of the catalyzed area. The Plexiglas template can be used to cut the GDL material. Skip this step if using a five-layer MEA with integral GDL.
6. Build-up the cell by layering components. The example below shows assembly of a five-layer MEA so steps b) and e) are omitted:
   a) Anode gasket on anode flow field.
   b) Anode GDL within the cut-out in the gasket (if using bi-layer macro–micro porous GDL, face the microporous surface toward the MEA and the macroporous surface toward the flow field).
   c) MEA on gasket aligned using alignment pins.
   d) Cathode gasket.
   e) Cathode GDL in gasket cut-out (if using bi-layer macro–micro porous GDL, face the microporous surface toward the MEA and the macroporous surface toward the flow field).
   f) Cathode flow field.
   g) Cathode current collector plate and end plate combination.
7. Lightly lubricate the threads of the bolt with a nonreactive/nonflammable lubricant.
8. Feed bolts through the cathode end plate holes and into the anode end plate and finger tighten.
9. Torque to desired level (e.g., 11.3 Nm depending on desired compressive load) using a star/cross pattern (Figs. 20.5 and 20.6) at approximately 1.13–1.7 Nm increments. It has been demonstrated that the torque and the pinch (explained in next section) have a significant impact on the contact resistance. A torque of 2.8–4.5 Nm and a pinch of 25–50 μm usually results in minimal contact resistances; however, it is recommended that an optimization study (wherein cell resistance is measured as a function of torque and pinch using current interrupt or impedance spectroscopy) when using

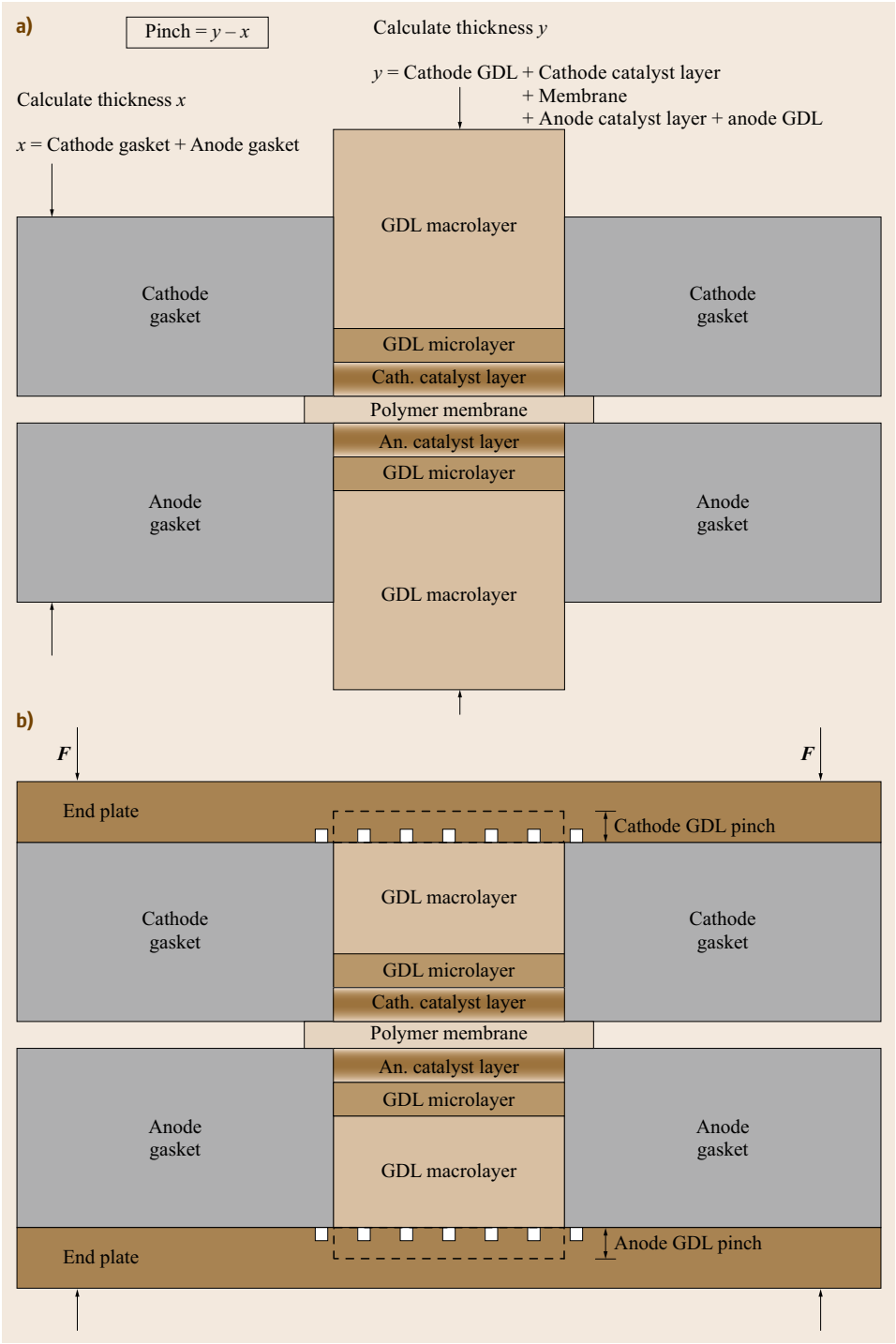


Fig. 20.2a,b Schematic showing calculation of pinch **(a)**, pinch with hardware **(b)**

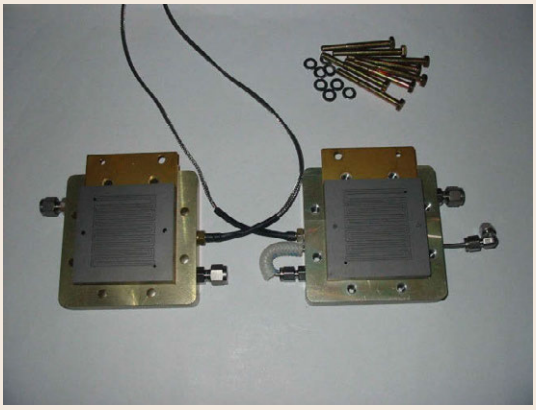


Fig. 20.3 Single cell PEM fuel cell hardware ready for assembly

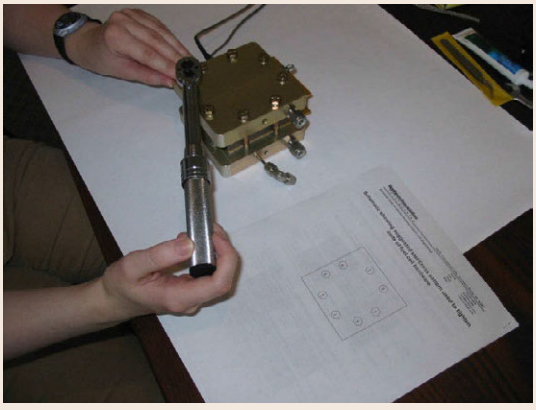


Fig. 20.5 Torquing the cell bolts following a star-like pattern shown in Fig. 20.6

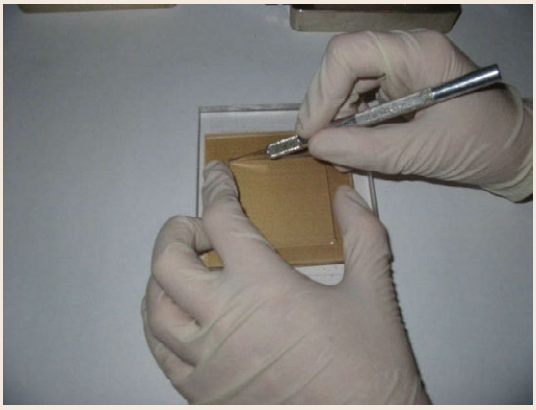


Fig. 20.4 Cutting the gasket using the template

a new set of components, to minimize contact resistances and achieve optimal performance. Netwall and coworkers have recently published a nice article in this regard.

10. Check for gross electrical short circuit in the cell. To do this, determine the resistance by applying a 1 mA current between the anode and cathode current collectors and measuring the voltage across the cell. The cell can be considered free of a gross electrical short if the voltage exceeds 500 $\mathrm{mV/cm^2}$ and therefore the resistance is greater than 500 $\Omega\mathrm{cm^2}$.
11. Check for gross gas leaks. Examples of procedures for gross leak check are available from the US Fuel Cell Council (USFCC) [20.1].
12. Perform a fuel crossover measurement. The principle of and detailed instructions on the electrochemical measurement technique for hydrogen crossover are provided in Sect. 20.4.

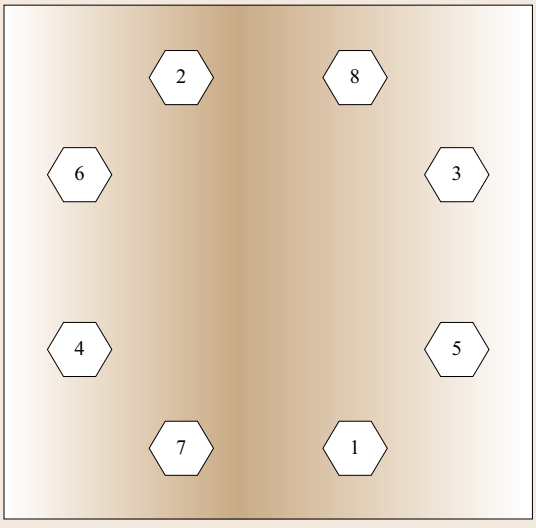


Fig. 20.6 Suggested star/cross pattern used to tighten bolts of fuel cell hardware

13. Perform initial break-in of the cell. If using a commercially available MEA, break in the cell according to the MEA manufacturer's recommended procedure.

20.1.5 Calculation of Pinch

Pinch is defined as the difference between the sum of the thicknesses of the MEA and anode and cathode GDLs and the total thickness of the gaskets. This is shown in Fig. 20.2.

Different GDL products have different optimal pinch values; typical values range from 250 to 500 μm (20–50% of the thickness of the GDL).

20.1.6 Fuel Cell Test System Instrumentation

Primary components of a typical fuel cell test system are shown in Table 20.1.

A schematic of the components and setup for single-cell testing of a H_2 PEM fuel cell is shown in Fig. 20.7. Additional items required to implement the laboratories include:

- Compressed gas with regulators – H_2, N_2, O_2, air (21% O_2), 4% O_2 + 96% N_2 mixture:
  1. N_2 (Regulator code CGA No. 580)
  2. H_2 (Regulator code CGA No. 350)
  3. O_2 (Regulator code CGA No. 540)
  4. Air (Regulator code CGA No. 590)
- Single cell hardware with heating element
- Membrane electrode assembly
- Computer with data acquisition card.

Hydrogen, supplied from a pressurized cylinder, is metered and routed through the heated anode humidifier before being fed through heated tubes to the anode side of the fuel cell. Similarly, oxidant with any desired composition (usually oxygen in nitrogen) is supplied from a pressurized cylinder, metered, and sent to the heated cathode humidifier before being fed through heated tubes to the cathode side of the fuel cell. Humidification of the feed streams is necessary to maintain conductivity of the electrolyte membrane, especially at higher operating temperatures. The desired volumetric flow rates for anode and cathode feeds are controlled by MFCs.

An inert gas such as nitrogen (N_2) is used to purge the anode and cathode chambers of the cell prior to introducing reactants and prior to shutting down the cell. The intent of the former is to prevent mixing the O_2 present within the anode compartment after assembling the cell with H_2, which is potentially dangerous and can cause corrosion of the anode components. Purging with N_2 prior to shutdown is also a safety measure to flush the residual H_2 from the cell.

Heating of the humidifiers, the tubes leading to the fuel cell, and preheating of the fuel cell is accomplished using heating tape. The temperature of the feed streams and fuel cell are maintained using temperature controllers. To avoid flooding the cathode, the humidifier temperature is often maintained slightly below the cell temperature. The RH of a gas exiting a humidifier can be determined manually by flowing it across a temperature controlled, polished metal surface and measuring its dew point. Effluent from the fuel cell is vented to a fume hood for safety purposes.

Table 20.1 Required equipment for fuel cell testing

Quantity	Item
1	Fuel cell load (sink and power supply)
3	Temperature controllers
2	Heated/insulated gas lines
2	Humidifiers
2	Mass flow controllers (MFCs), valves, fittings and tubing (stainless steel)

During a typical experimental run (constant flow rate, oxidant composition, and temperature), the current is manipulated/adjusted on the fuel cell load and the voltage and resistance are recorded from built-in meters in the load. The fuel cell load typically uses the current-interrupt technique [20.2] to measure the total ohmic resistance between the voltage sense leads, which includes ionic and electronic resistances and all contact resistances.

20.1.7 Reactant Humidification in Fuel Cell Testing

The performance of some types of fuel cells, H_2-fuel proton-exchange membrane fuel cell (PEMFC) in particular, may be influenced by its operating conditions, including temperature, pressure, and moisture content of the inlet gases. For a PEMFC these factors all directly affect membrane water content, which in turn impacts fuel cell performance. Hydration of the membrane is a very important determinant of the performance and durability of a PEMFC. If not properly hydrated, the membrane exhibits higher ionic resistance and in extreme cases can be physically damaged. Figure 20.8 demonstrates the effect of the H_2 fuel water vapor content, expressed as dew point and RH, on the resistance of a PEMFC. For this particular cell operating under the indicated conditions, a 2 °C change in the dew point of the anode reactant resulted in a 2–5% change in membrane resistance.

Membrane hydration is affected by the water transport phenomena in the membrane itself, which in turn are affected by the condition of the inlet gases and the operating parameters of the fuel cell. Water is transported through the membrane in three ways: electroosmotic drag by protons from the anode to the cathode, back diffusion due to concentration gradients from the cathode to the anode (or vice versa in limited cases), and convective transfer due to pressure gradients within the stack. At high current densities, where electroosmotic drag of water from the anode to the cathode often exceeds the rate of back diffusion of water, the anode side can dry out if the inlet gases are not sufficiently humidified. Without reactant gas humidification, the fuel cell membrane will become dehydrated leading to high ohmic losses and potential damage to the membrane.

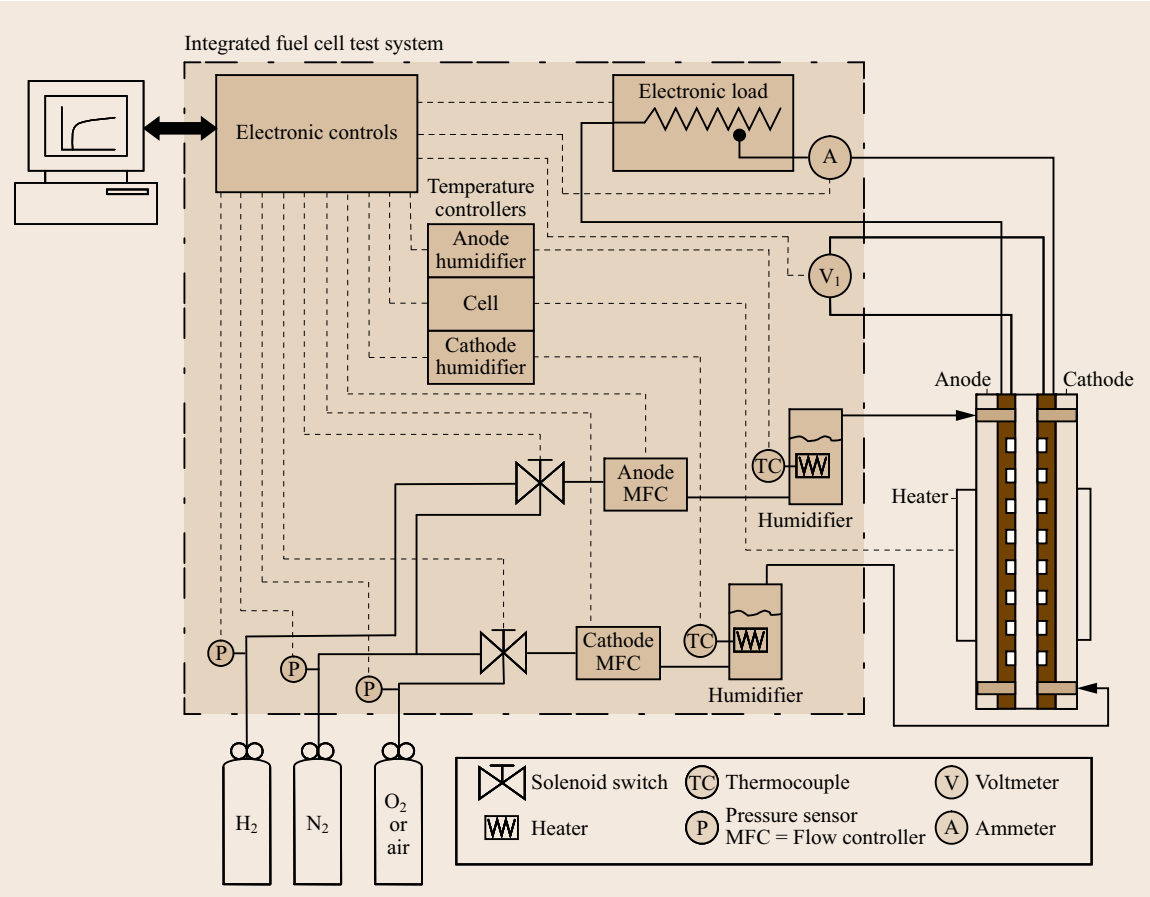


Fig. 20.7 Plumbing and wiring diagram for H_2 PEM fuel cell test station

Definitions and Terms Relating to Humidity

Specific humidity (SH) is the mass of water vapor present in a given mass of gas (e.g., kg water vapor/kg dry air). Relative humidity (RH) is the amount of water vapor present in the gas compared to the amount that could be present in the gas at the same temperature. Thus, RH = SH/saturation SH × 100%. Alternatively, RH is calculated as the fraction of water vapor pressure in the gas (p_v) relative to the saturated water vapor pressure ($p_{v,sat}$) at that temperature: $RH = p_v/p_{v,sat} \times 100\%$. Water vapor pressure is the partial pressure that is due to the water vapor in the gas. Dalton's law of partial pressures states that the total pressure in a gas is the sum of all the partial pressures of the constituents. Ideal or near ideal gases occupy the same volume for the same number of molecules (at the same temperature and pressure). So, the fraction of water vapor pressure relative to the total pressure is the same as the fraction of water molecules relative to the total number of molecules. Multiplying the amount of water and other (carrier) gasses by their respective molecular weights bring us back to SH.

Conceptually, RH is an indication of how close a gas is to being saturated; a gas with 100% RH is saturated in water vapor. Note that SH is unaffected by temperature whereas RH can be changed by changing the temperature of the gas and/or quantity of water vapor present in the gas. RH is empirically useful because most materials respond, absorb or adsorb in proportion to RH rather than SH. Specific humidity is useful when considering chemical equilibrium because it is related to the absolute amount of water vapor in a gaseous mixture.

Dew point is the temperature at which the gas will become saturated. Dew point is a direct measure of vapor pressure (p_v) expressed as a temperature. The dew point temperature is always less than or equal to the temperature of the gas. The closer the dew point is to the temperature of the gas, the closer the gas is to saturation and the higher the RH. If the gas cools to the dew point temperature it is saturated in water vapor and the RH is 100%. Condensation will occur on any surface

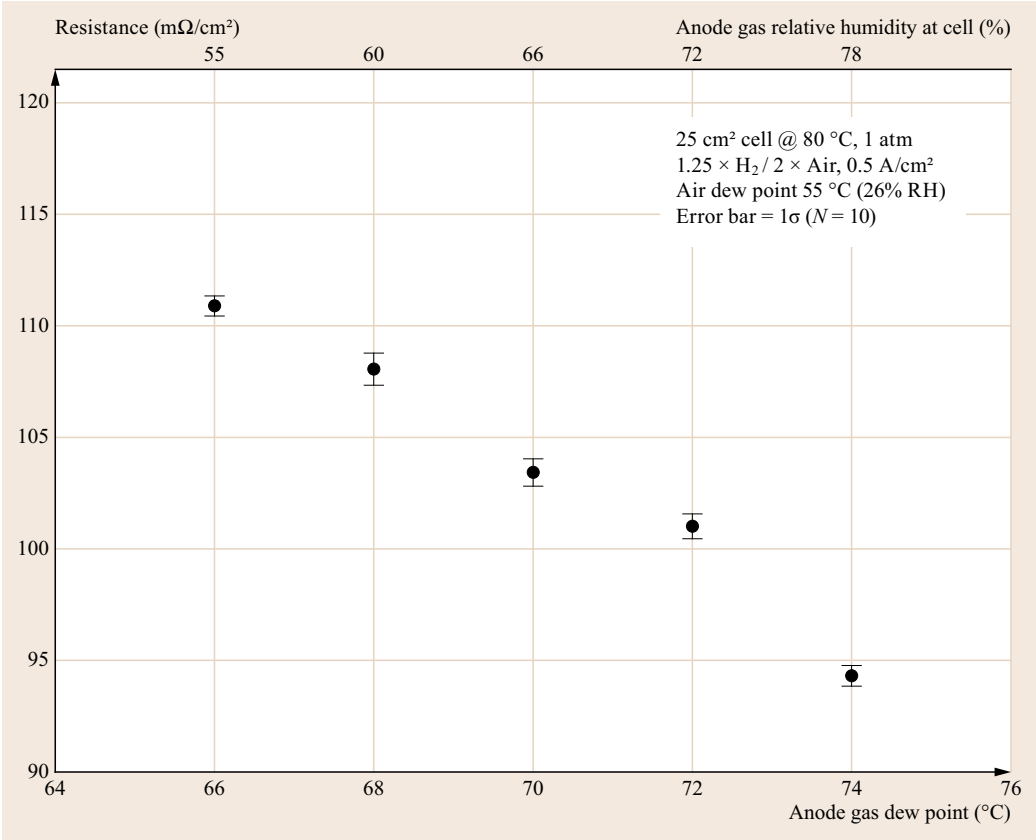


Fig. 20.8 Resistance of a PEM fuel cell as a function of the dew point of the anode reactant (H_2 fuel) highlights the need for accurate, stable, and repeatable control of the water content of fuel cell reactants

cooled to or below the dew point of the surrounding gas.

Dry bulb temperature is the commonly measured temperature from a thermometer. It is called *dry bulb* since the sensing tip of the thermometer is dry (see *wet bulb temperature* for comparison). Since this temperature is so commonly used, it can be assumed that temperatures are dry bulb temperatures unless otherwise designated.

Wet bulb temperature is roughly determined when air is circulated past a wetted thermometer tip. It represents the equilibrium temperature at which water evaporates and brings the air to saturation. Inherent in this definition is an assumption that no heat is lost or gained (i. e., adiabatic system) and the heat loss due to evaporation is balanced by thermal conduction from the air. In practice only carefully constructed systems approach this ideal condition. Wet-bulb temperature differs from dew point. The latter is the balance point where the temperature of liquid or solid water generates a vapor pressure (a tendency to evaporate) equal to the vapor pressure of water in the gas so that no net evaporation occurs. Therefore the dew point is always lower than the wet bulb temperature because at the surface temperature of the wet bulb the water must evaporate to maintain a cooling rate whereas at the dew point temperature the water must be so cold that it will not evaporate (but not so cold that condensation occurs).

Methods for Measuring Humidity

Common approaches employed to measure humidity and dew point temperature are described here; pros and cons of each are summarized in Table 20.2:

- Wet bulb. In the wet bulb method, water is allowed to evaporate and so cool itself to the point where the heat loss through evaporation equals the heat gain through thermal conduction. This method usually involves a wicking material to bring replacement water to the wet bulb, a sufficient wicking distance (with evaporation) to achieve temperature equilibrium for the replacement water, sufficient gas flow rate, and precise temperature measurement.

Table 20.2 Comparison of common humidity and dew point measurement methods

Method	Advantages	Disadvantages
Wet bulb	• Low cost • Easy to perform measurement • Easy to maintain equipment • Robust (not damaged by liquid water) • Accurate at very high humidity where there is little or no evaporation • Response time is moderate	• Relies on established relationships of wet bulb versus water content (function of gas; published tables/formula are for air not H_2 or O_2) • Requires addition of water to the system (problematic for small systems) • Flow rate dependent • Requires a water source and feed • Requires cleaning • Replacement of some components (wick)
Polymer sensor	• Moderate cost ($100s–$1000s) • In-situ, real-time monitoring possible • Rapid response • Little or no maintenance required • Reasonably reliable • Easy to use • Water mist entering the sensor can be evaporated and measured (if super heated chamber is used)	• Probe susceptible to damage on exposure to liquid water • Periodic recalibration required • Periodic replacement of the sensing element required • Accurate local temperature measurement is critical for conversion of %rh to other humidity units.
Chilled mirror	• Very accurate with drift and accuracy comparable to a good thermometer (better than 0.1 °C). • Mirror and sensor can be made from inert materials • Water mist entering the sensor chamber is evaporated and measured • Robust (not damaged by liquid water)	• Relatively expensive ($1000s) • Operation can be temperamental • Mirror must be kept clean • Sensor must be heated to prevent condensation • Gas to be tested must be passed through heated chamber (may not be suitable for in-situ applications)
Optical	• Very rapid response • Sensor cavity can be made from inert materials • Water mist entering the sensor can be evaporated and measured (if super heated chamber is used)	• Relatively expensive • Cavity must be kept clean • Will respond to other gasses which absorb same frequencies of light • Periodic calibration required due to drift in performance of optical components

- Polymer humidity sensor. The operating principle of solid-state humidity probes is measurement of some material property of a water-sensitive material. Polymeric materials are generally used for this type of moisture sensor. Water vapor permeates the plastic and changes its electrical properties such as dielectric constant or conductivity. Sorption or desorption of water from the polymeric material occurs as the humidity of the surrounding environment changes. The change in the materials property are measured and converted to various humidity-related values using established calibration data.
- Chilled mirror. In this approach, a sensor head is heated to a temperature well above the expected dew point and a mirror within the sensor is cooled until dew just begins to form on its reflective surface. An optically controlled servo loop controls the mirror temperature so that the dew neither evaporates nor continues to condense (i. e., the definition of dew point). The temperature at which this equilibrium occurs is measured as the dew point. The chilled mirror technique is a first principles method meaning that the dew point is measured directly as opposed to via correlation of some other measured parameter to a response (calibration) curve.
- Optical. In this method, light of specific frequencies is passed through a cavity of known dimensions. Water vapor absorbs some of the light and the decrease in transmitted light is measured. The reduction in transmitted light is then correlated to the amount of water in the path of the light, and from this the various parameters related to water vapor content of the gas can be calculated.

Methods to Humidify Fuel Cell Gases

In fuel cell operation and fuel cell test equipment, one generally controls the moisture content of the *inlet gas stream*. Water is a product of the fuel cell reaction (Fig. 20.9a). The rate at which it is produced in the cell is a function of the reaction rate, which relates to the electrical current through Faraday's law. Water is also transported from one electrode to the other through the membrane. The direction and rate of net water transport through the membrane is a complex function of the cell

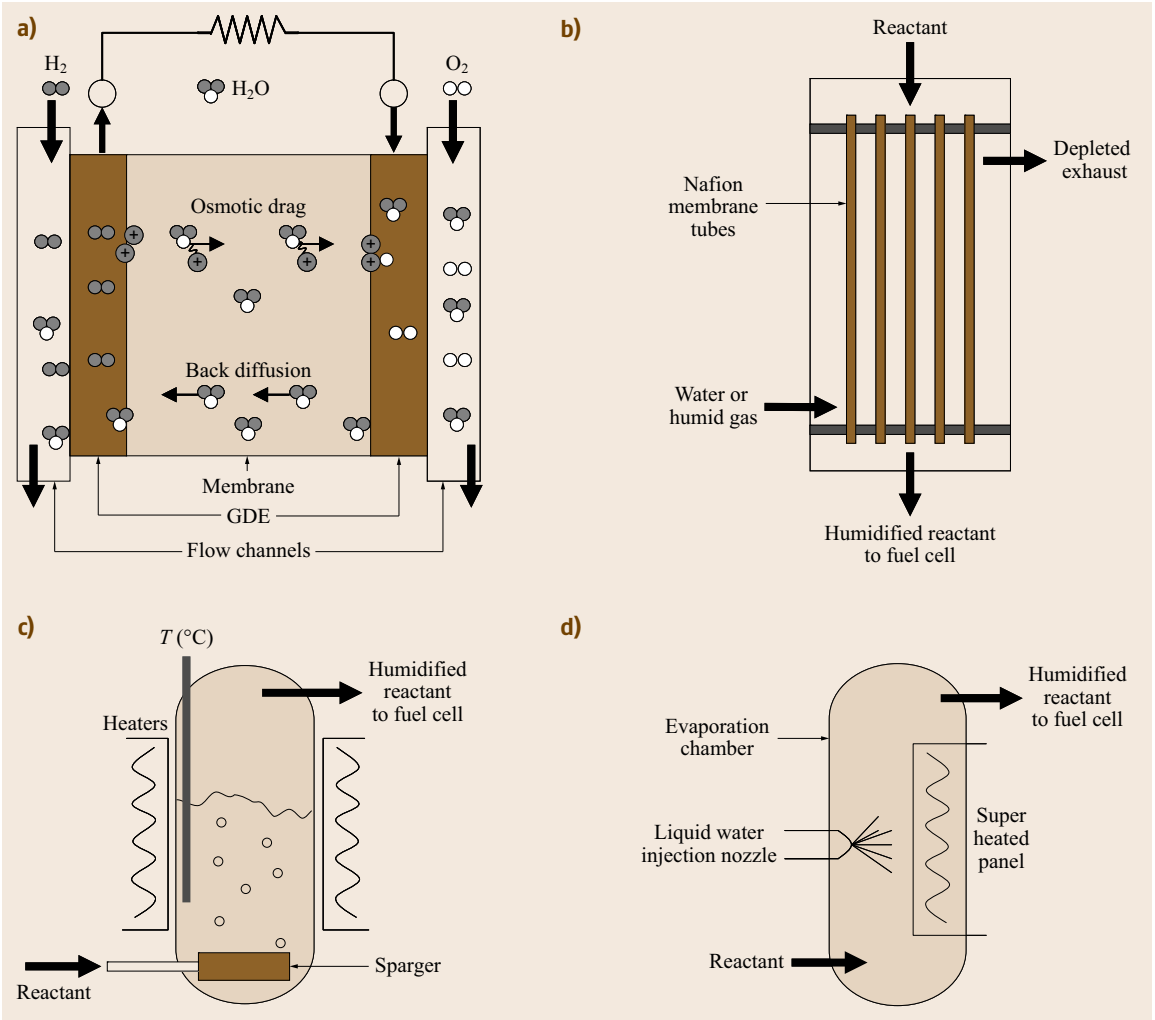


Fig. 20.9a–d Common humidification methods. **(a)** Internal or self-humidification relies on diffusion of cathode-generated water through the membrane, which is at least partially counterbalanced by osmotic drag of water by protons (H^+) from the anode to the cathode. **(b)** Membrane humidifiers are moisture-exchange devices using Nafion tubes. **(c)** For bottle humidifiers, reactant gas is sparged through a temperature-controlled water bath. **(d)** The flash evaporation humidifier produces humidified gas by spraying a stream of water on to a superheated panel where the water very rapidly vaporizes. $T(°C)$ = thermocouple

conditions including anode and cathode RH, current density, and membrane water permeability, among others. For these reasons, the water content of gases within anode and cathode compartments and exit streams can differ from the water content of the respective inlet gas.

Most fuel cell test systems include some method for externally humidifying reactant gases. Three common humidification systems are illustrated in Fig. 20.9b–d: membrane humidifiers, bottle humidifiers, and flash evaporation humidifiers.

Membrane humidifiers are water-exchange devices employing water permeable membrane tubes such as Nafion that allow water transmission but resist transmission of reactant gas or other components. A tube-in-tube membrane humidifier is illustrated in Fig. 20.9b. Membrane humidifiers can operate as either water-to-gas or gas-to-gas humidifiers. In the former, hot, de-ionized water is circulated on one side of the membrane tube and the gas to be humidified on the other. Gas-to-gas humidifiers use a wet gas such as the fuel cell cathode exhaust stream as the water vapor source

for the (dry) gas to be humidified, the two gases being separated by the membrane. In both types, water transport through the membrane is due to the difference in chemical potential (i. e., concentration) of water on either side of the membrane.

Bottle humidifiers, illustrated in Fig. 20.9c, are based on passing the gas to be humidified through a heated water bath. Water vapor is absorbed by the gas as the bubbles rise through the water. Water uptake by the gas is a function of the water–gas interfacial area and therefore a sparger (porous frit) is commonly used to produce fine bubbles thereby increasing the humidification efficiency. Well-designed bottle humidifiers can fully saturate a gas stream, meaning that the dew point of the humidified gas equals the temperature of the water. Bottle-type humidifiers are simple and cost-effective. The primary disadvantages of this humidification method is its limited water transfer capacity and the inability to provide rapid changes in humidity level, although these can be addressed through proportional mixing of wet and dry gases as described below.

As shown in Fig. 20.9d, flash evaporation humidifiers spray water onto a superheated surface to instantly produce water vapor, which mixes with the flowing gas. In some cases, the rate of liquid water injected is dynamically controlled to achieve a desired water vapor content or dew point of the exit gas. When operating in such a mode, the system attempts to produce humidified gas of the user-defined dew point by controlling the liquid water flow rate. This method of operation requires sophisticated feedback control and a built-in, real-time humidity sensor. Alternatively, one can operate under constant flow control mode wherein water is delivered to the hot plate at a rate predetermined to produce the required humidity level. A metering pump injects water into the flash evaporation chamber at the user-specified rate. Precise control of the humidity level can require that corrections to the water injection rate be made to more closely approach the desired dew point.

Steam injection is another common approach, in particular for high-capacity test stands (> 1 kW) where water transfer rates can be significant. In this method, steam is introduced directly to the reactant gas. The steam has enough thermal energy that it heats the reactant gas to a temperature sufficient to entrain all of the water vapor. Temperature-controlled coolers, such a tube-in-tube condensers, are used to decrease the gas temperature to the desired value. As the gas is cooled, excess moisture condenses leaving a water vapor saturated mixture at the desired inlet temperature to the fuel cell. An advantage of the direct steam injection system is its high water transfer capacity.

Proportional mixing of wet or water vapor saturated gas and dry gas is another means to achieving a desired RH of inlet reactant. Computer-controlled MFCs are used to mix in the correct proportion a fully saturated gas and a dry gas to achieve a desired RH. This approach allows the water vapor content of the gases to which the fuel cell is exposed to be quickly changed, which facilitates rapid assessment of fuel cell performance over a range of conditions and measurement of the dynamic response of the fuel cell to changes in reactant humidity.

One issue common to all external humidification systems is that if the gas cools to below its dew point, water will condense out of the gas, which decreases the nominal dew point of the gas and leads to liquid water entering the fuel cell. To counter act this, well-designed external humidification systems employ heated gas transfer lines between the humidifier and the fuel cell.

Reactant humidification is an important consideration in fuel cell test system. The test system needs to be able to maintain stable, accurate reactant humidity and flow levels to the fuel cell at all times. The response time, or the speed at which a desired humidity level can be reached, is also a consideration for some users. As mentioned previously, some humidification methods can more rapidly achieve or change humidification level than other schemes. The test system also needs to be able to supply anode and cathode flow rates sufficient for the cell testing to be performed.

Bottle-type humidifiers provide humidification from a fixed volume of water in a chamber. This water is consumed over time and needs to be replaced. Although a manual fill valve allows the water level to be restored, an automatic filling system reduces the number of tasks required by the test operator and also can provide less disruption to the test conditions when the filling is performed. Automatic water filling also allows long-term unattended operation of the fuel cell test system.

Regardless of the humidification system used, the water from the humid gas will condense on the walls of the tubing exiting the humidifiers unless the lines are heated to a temperature above the dew point of the gas. If the water condenses on the tubing, the dew point is reduced and droplets or *slugs* of liquid water may enter the fuel cell and potentially disturb the cell's operating condition and performance. It is therefore important that the test system heat the entire anode and cathode gas transfer lines up to the point that they enter the fuel cell. Many test systems incorporate heated cell lines for this reason.

While a basic fuel cell demonstration or experiment can allow the unconsumed gases to exit the anode

and cathode outlets of the fuel cell without any restrictions (through a vent to outside the building, for example), many practical fuel cell applications pressurize the anode and cathode compartments. This is typically achieved with a manual or automated regulator on the outlets of both compartments of the fuel cell. The cell is generally not pressurized to more than a few atmospheres.

20.2 H_2/O_2 or Air Fuel Cell Performance Testing

The primary technique for characterizing the performance of fuel cells is measurement of the cell voltage as a function of current density. Voltage (V) versus current density (A/cm^2) and power density (W/cm^2) versus current density curves to a large extent define the performance characteristics of a fuel cell and yield information about cell losses under the operating conditions employed. For a given cell, operating conditions such as the cell temperature, and the composition, flow rate, temperature, and RH of the reactant gases can be readily varied. The effects of such variations on cell performance can be analyzed to better characterize the properties of the fuel cell.

At low current densities, the majority of the losses are due to kinetic limitations at the electrocatalyst surface. In the case of a PEM fuel cell operating with pure hydrogen fuel, the high energy barrier associated with the oxygen reduction reaction (ORR) at the cathode is the dominant source of losses in the fuel cell at low current densities. Cathodic activation losses dominate in this case because the exchange current density, j_o, for O_2 reduction on Pt is approximately 1000 times less than the exchange current density for hydrogen oxidation on the same catalyst. On the other hand, in a direct methanol fuel cell (DMFC), oxidation of the liquid fuel is sluggish and for this type of fuel cell, activation losses on both the anode and cathode are significant.

As the current density increases, the ohmic (jR) voltage drop within the cell becomes significant. This is evident in the linear portion of the polarization curve at intermediate current densities. If current interrupt (or some other method) is used to measure the ohmic resistance (R_Ω in $\Omega\,cm^2$) of the cell, the voltage data can be corrected for the ohmic voltage loss by adding the product of the current density and the ohmic resistance ($\Delta V_\Omega = jR_\Omega$) to the measured cell voltage (V_{cell}) at each current density to generate the jR-compensated polarization curve.

Finally, mass transport effects dominate at high current densities where delivery of reactant gas through the pore structure of the backing layers and electrocatalyst layers becomes the limiting factor. The performance of the cell rapidly decreases when the electrode reaction kinetics are so fast that transport effects become significant. The cell is then stated to be operating under *transport limited* conditions. While such operation is highly desirable in traditional chemical reactors, it is undesirable in fuel cells because the power density (product of current density and cell voltage) typically passes through a maximum some time before limiting current conditions are reached. Even operating at this maximal power density is discouraged, since the corresponding single cell voltage is insufficient from a systems viewpoint.

The performance of the fuel cell depends primarily on the activity of the electrocatalyst layer, the quality of material components, and the flow rate and purity of the reactant gases. Although the best performance is obtained when pure oxygen is fed to the cathode, this is impractical for most applications and generally air is used as the source of oxidant. However, because air is essentially oxygen diluted by N_2 at nearly 1 : 4 ratio, cells that run on air suffer from:

1. Reduced thermodynamic potential (i. e., the Nernst equation reveals that $E_{theor} \propto \log(p_{O_2}^{1/2})$ so decreasing the concentration of O_2 causes decreasing E_{theor})
2. Reduced oxygen reduction kinetics, and
3. Exacerbated mass transport limitations. As a result, cells operated on air exhibit degraded performance in comparison to operation with pure oxygen.

Furthermore, the conductivity of perfluorinated membranes such as Nafion is strongly dependent on the level of hydration in the membrane. Low ionic conductivity due to low membrane water content causes high ohmic voltage loss leading to reduced cell performance. Therefore, in practice, reactant gases are humidified to maintain a well-hydrated membrane and prevent excessive dehydration despite formation of water at the cathode as the product of reaction. An excess of water, however, could flood the electrode, resulting in severe transport limitations and reducing (and/or interrupting) the performance and power output of the cell. Care must be taken to maintain the proper water balance to ensure low ohmic losses and mass transport losses.

When PEMs are subjected to temperatures above 100 °C, at atmospheric pressure, their conductivity decreases significantly due to dehydration. Because water boils at 100 °C at 1 atm, the humidifier dew points

must be below this temperature to ensure that some reactant partial pressure is maintained, thereby lowering the inlet RH to less than 100%. This problem can be alleviated by operating the cell at higher pressures, although pressurization is not desirable for fuel cell systems due to the parasitic compressor power requirement.

The resistance of the membrane can also increase due to dehydration at the anode. This occurs when electroosmotic drag of water by protons migrating through the membrane exceeds transport of neutral water molecules in the opposite direction from the cathode to the anode. This phenomenon is most prominent at high current densities, typically $> 1\,A/cm^2$. The rate of electroosmotic drag of water from anode to cathode depends on the inherent properties of the ionomer and the operating temperature but not on the thickness of the membrane. However, thinner membranes tend to establish a more uniform distribution with the overall effect that thinner membranes tend to less susceptibility to anode dehydration at high current density.

This section will be divided in two parts. In Sect. 20.2.1, we will examine the effect of oxygen concentration and stoichiometry on the performance of a PEM fuel cell operating with hydrogen fuel. In Sect. 20.2.2, a series of experiments will be proposed to demonstrate the effect of temperature and reactant RH on the performance of a hydrogen PEM fuel cell.

20.2.1 Effects of Oxygen Partial Pressure

After cell assembly, the cathode gas composition is selected. Any range of oxygen concentrations in nitrogen that demonstrate the stoichiometry effect is suitable, for example, 4.0%, 10.5%, 21% (air) and 100% O_2.

Then the reactant flow rates based on fixed cathode and anode stoichiometric ratio are calculated:

- Stoichiometric ratio is the inverse of utilization. For example, a stoichiometric ratio of 3 implies a utilization of 33%.
- *Cathode*: As a basis, use a cathode stoichiometric ratio of 1.5× at $1\,A/cm^2$ for the *air* condition. Using the same total volumetric flow rate, determine the O_2 stoichiometric ratio for the other cathode feed gases.
- *Anode*: H_2 stoichiometric ratio of 2.5× at $1\,A/cm^2$ for all tests (constant flow rate) or 1.25× to 1.5× (load-based flow rate). Note that using a load-based flow rate will defeat the purpose of performing H_2 utilization calculations because under these conditions, S_{H_2} and U_{H_2} would be constant once the minimum flow rate has been reached.
- The theoretically required volumetric flow rates using Faraday's law for each cathode oxidant operating condition is determined.

Bring the fuel cell and humidifiers to the following operating condition: 73/80/73 (anode humidifier temperature (AHT) = 73 °C; cell temperature (CT) = 80 °C; cathode humidifier temperature (CHT) = 73 °C; system pressure = 1 atm). Condition the cell until it is well stabilized, that is, constant value of current and resistance over time at a given value of voltage (e.g., 0.55 V).

Measure the cell performance as a function of cathode reactant stoichiometric ratio and O_2 concentration at 80 °C and 75% RH. To obtain the performance curve for Tafel analysis and to generate the full polarization curve, perform a current scan over two current density ranges.

- Tafel analysis: Current density from 0 to $100\,mA/cm^2$ at $10\,mA/cm^2$ increments.
- Full performance curve: Current density $100\,mA/cm^2$ to the limiting current density (or a predefined maximum such as $2000\,mA/cm^2$) in $100\,mA/cm^2$ increments. Data should be acquired after no less than 30 s to 1 min at each current value (although 1 min/step is suitable for instructional purposes, research is typically performed with much longer hold-times at each current increment, for example, 5 min/step). Use current interrupt technique during data acquisition to measure the membrane resistance.

Results and Analysis – Effects of Oxygen Partial Pressure, Stoichiometry

In this section, we analyze the fuel cell performance data acquired for a range of oxygen concentrations (partial pressures).

- Apply the Nernst equation to calculate the theoretical reversible cell potential (E_{theor}) for each operating condition.
- Plot the cell voltage (V) and area-specific cell resistance (in $\Omega\,cm^2$) as a function of current density (A/cm^2) for each operating condition.
- Plot the power density (W/cm^2) versus current density for each operating condition.
- Determine the cathodic Tafel slope (inherent assumption: anode kinetics are very facile) by evaluating the slope of the *jR*-free *V* versus log(*i*) data in the low current density region ($10-100\,mA/cm^2$) for each operating condition.
- Approximate the exchange current density, j_o, for the ORR. Describe the assumptions and likely

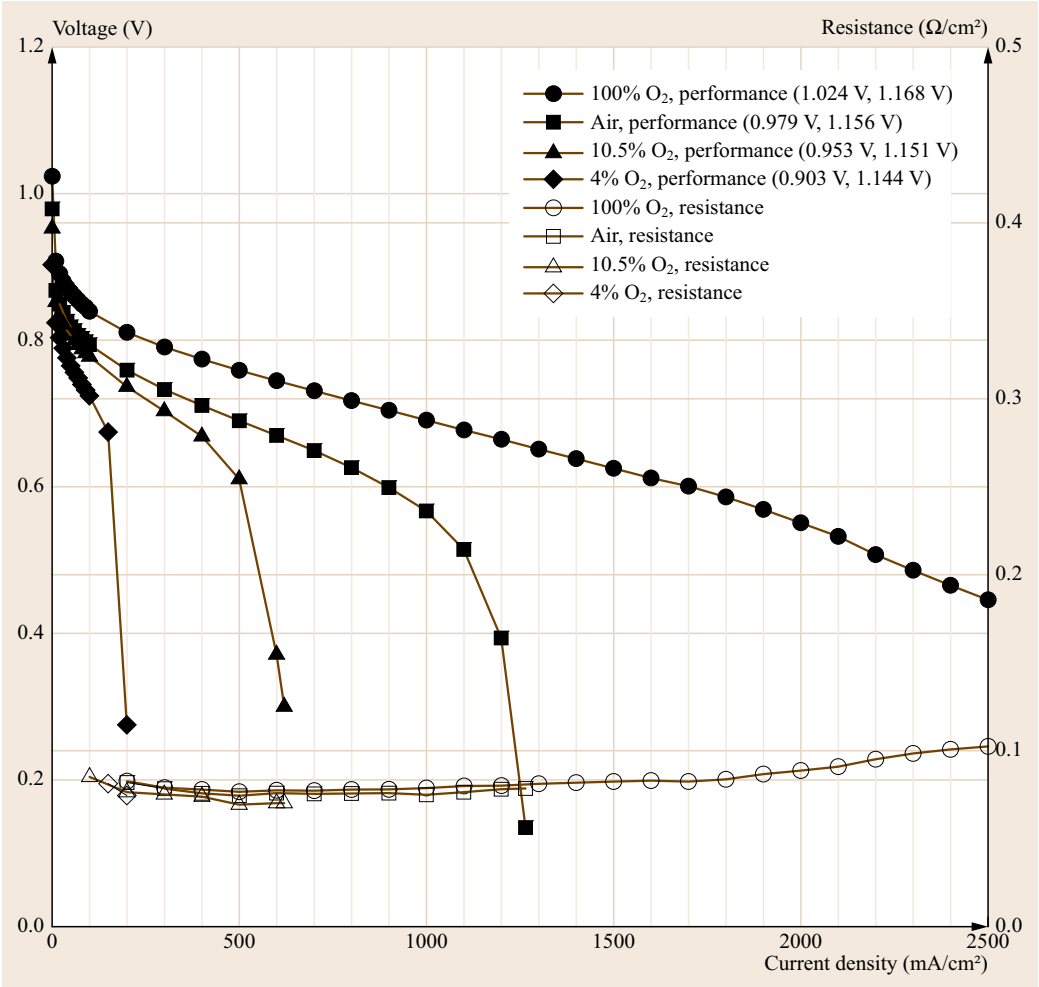


Fig. 20.10 Cell voltage and membrane resistance as a function of current density for a PEMFC operated with a range of oxygen concentrations: 100% O_2, 21% (air), 10.5% and 4%. The legend for the performance curve (V–j) gives the OCV and reversible potential in parenthesis (OCV, E_{theor}). Conditions: 50 cm^2, 80 °C cell/100% RH anode/100% RH cathode. Constant mass flow rate. Anode stoichiometry: 2.5× at 1 A/cm^2. Cathode stoichiometry: 7.14× at 100% O_2, 1.5× at 21% O_2, 0.75× at 10.5% O_2, and 0.29× at 4% O_2; ambient pressure

sources of error in estimating the exchange current density.

- Determine the limiting current density, j_{lim}, for each operating condition.

Polarization Curve Analysis. The performance of the fuel cell is characterized in part by voltage versus current density and resistance versus current density plots. Figures 20.10 and 20.11 summarize the performance data on linear and semi-log plots, respectively; different features of the performance of the fuel cell are highlighted by plotting the data in these two formats. For example, although both figures clearly demonstrate the effect of cathode reactant concentration on the performance of the fuel cell at 80 °C and 100% RH, the V–j plot clearly shows the linear relationship observed at moderate current densities whereas the semi-log V–j format highlights the activation controlled and mass transport controlled regions at low and high current densities, respectively.

Measured open-circuit voltage (OCV) can be compared to the theoretical cell potential (E_{theor}). These values are presented in the legend of the performance curve in Figs. 20.10 and 20.11. The actual OCV is less than the theoretical maximum potential in all cases, and both values decrease with declining oxygen concentration. The OCV is less than E_{theor} because in practice, parasitic oxidation reactions at the cathode cause it

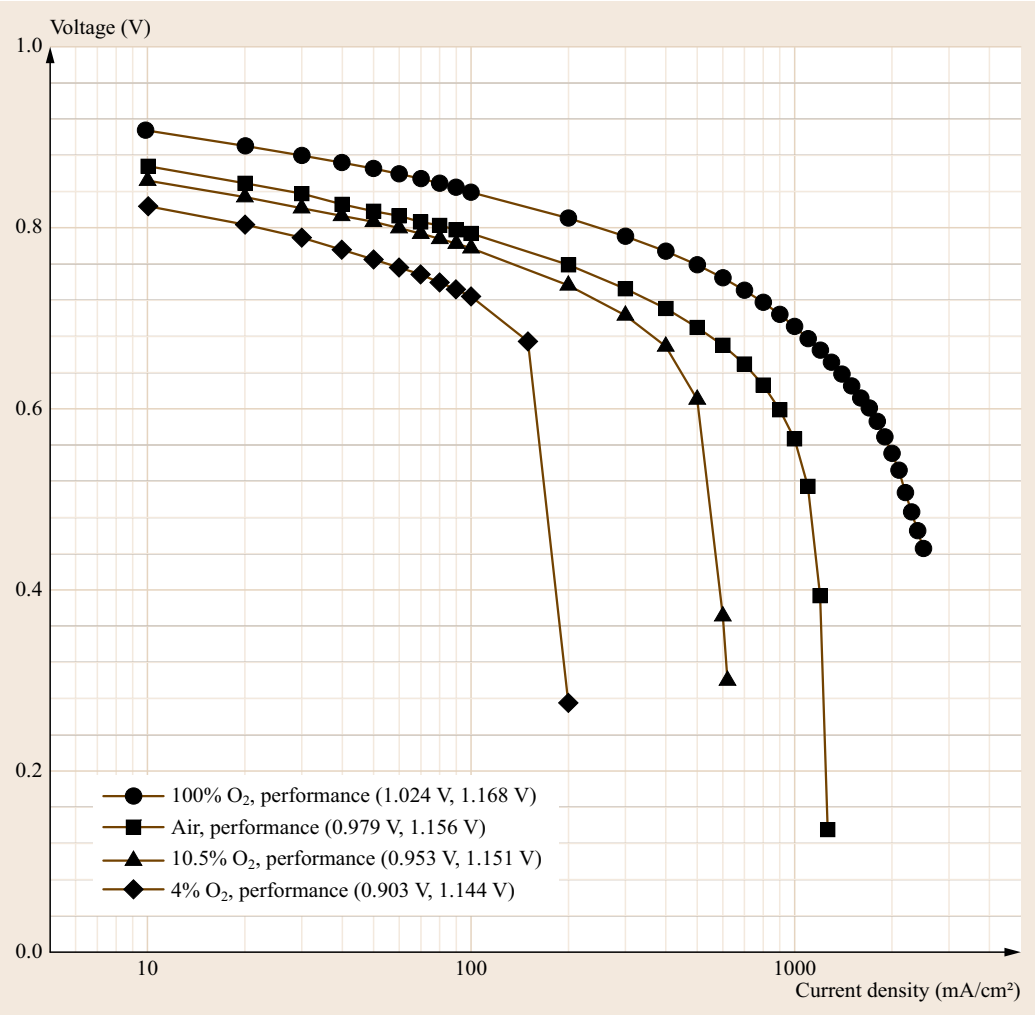


Fig. 20.11 Voltage–current density data shown in Fig. 20.10 plotted on a semi-log format. Shown are the exponential relationship (Tafel behavior) at low current densities where mass transport and ohmic effect are negligible, and the transport limiting current density at high current density. The legend gives the open circuit voltage and reversible potential in parenthesis (OCV, E_{theor}). Conditions described in Fig. 20.10

to attain a mixed potential that is less than predicted based solely on the ORR. Oxidation of fuel that passes through the membrane as well as oxidation of the cathode materials themselves are sources of this mixed potential. (Measurement and analysis of fuel crossover is treated in Sect. 20.4).

Activation polarization due to electrode kinetic limitations is dominant at very low current densities ($0-100\,mA/cm^2$). Looking at the performance curve in the low current density region (most-easily observed on the semi-log format, Fig. 20.11), the slope appears to become more negative with lower O_2 concentration. The larger negative slope suggests that the voltage loss due to reaction kinetics increased as the concentration of the oxidant decreased. However, the Tafel slope itself should, by definition, be independent of oxygen concentration. This apparent contradiction is examined quantitatively below.

Membrane resistance is relatively constant ($0.080\,\Omega\,cm^2$) up to about $1000\,mA/cm^2$ and (as expected) is independent of oxidant composition. At larger current densities, the ohmic resistance of the membrane increases slightly due to dry-out of the membrane on the anode side. Dry-out of the membrane within PEM fuel cells is a common phenomenon at high current densities and occurs because water molecules associated with migrating protons are dragged from the anode to the cathode at a higher rate than they can diffuse from the cathode (where water is produced) to the anode. This phenomenon is more clearly seen with thicker membranes, such as Nafion 117, than with thin membranes such as the one used here.

Mass transport limitations due to insufficient supply of oxygen to the surface of the cathode were observed at higher current densities, especially for gases containing

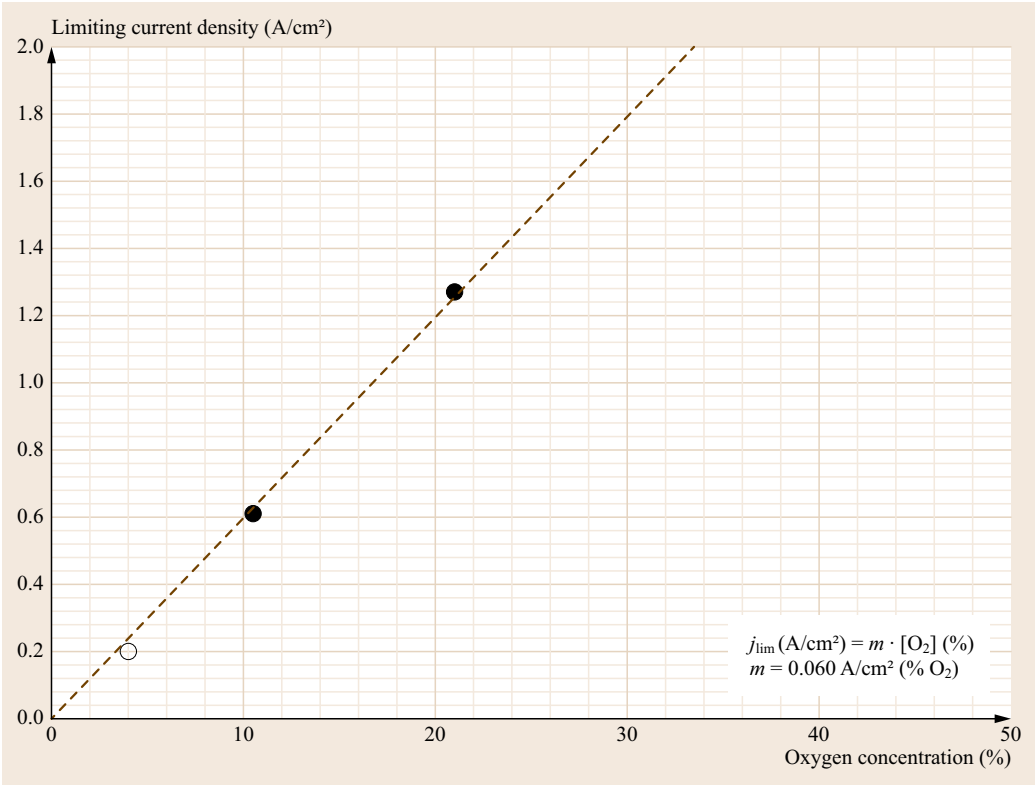


Fig. 20.12 The PEM fuel cell limiting current density was directly proportional to the oxygen concentration of the cathode feed. Slope $= 0.060\,\mathrm{A/cm^2}$ (% O_2) estimated from a linear fit forced through origin (*dashed line*). From performance data presented in Fig. 20.10

low concentrations of oxygen. The mass transport limiting currents were about $200\,\mathrm{mA/cm^2}$, $650\,\mathrm{mA/cm^2}$ and $1200\,\mathrm{mA/cm^2}$ for 4% O_2, 10.5% O_2, and air, respectively. A limiting current density for the pure oxygen condition is not evident ($> 2500\,\mathrm{mA/cm^2}$). Figure 20.12 shows that the limiting current density is directly proportional to oxygen content.

Power density delivered by a fuel cell is defined by the product of current density drawn from the cell and voltage at that current density. The effect of current density on power density for various oxidant compositions is shown in Fig. 20.13. For a given feed composition, maximum power density is achieved approximately two-thirds of the way between the no-load (i. e., OCV) and limiting current density condition. Selection of the optimal operating point depends on the application and how the fuel cell is to be used. For example, for vehicular applications higher power density is required to minimize the weight of the car at the expense of efficiency whereas for residential and other stationary applications a cell with higher efficiency is preferred.

A linear relationship between current density and reactant utilization per Faraday's law is clearly evident in Fig. 20.14. Reactant utilization decreases with increasing inlet oxygen concentration (at constant flow rate) because of the increase in the moles of reactant per unit time.

Analysis of Sources of Polarization and Voltage Loss. To evaluate the three primary sources of voltage loss (activation, ohmic, and mass transfer polarizations) we perform the following analysis:

1. Cathode activation polarization $\eta_{act,c}$ is determined at each current density (j) using the Tafel equation, using the experimentally observed Tafel slope of 67 mV/decade (determined in the next section) and an estimate of the exchange current density (j_o) determined by extrapolating the jR-corrected cell voltage to the theoretical potential, E_{theor}. $\eta_{act,c}$ is calculated by assuming that the ohmic resistance-free H_2/air cell voltage at current densities $< 10\,\mathrm{mA/cm^2}$ is purely controlled by the ORR kinetics with a constant Tafel slope

$$\eta_{act,c} = b_c \log\left(\frac{j}{j_o}\right) . \qquad (20.1)$$

2. Ohmic losses η_Ω is measured using the current interrupt technique. At low current density where the jR-drop may be difficult to measure accurately because of the small voltages, ohmic losses can

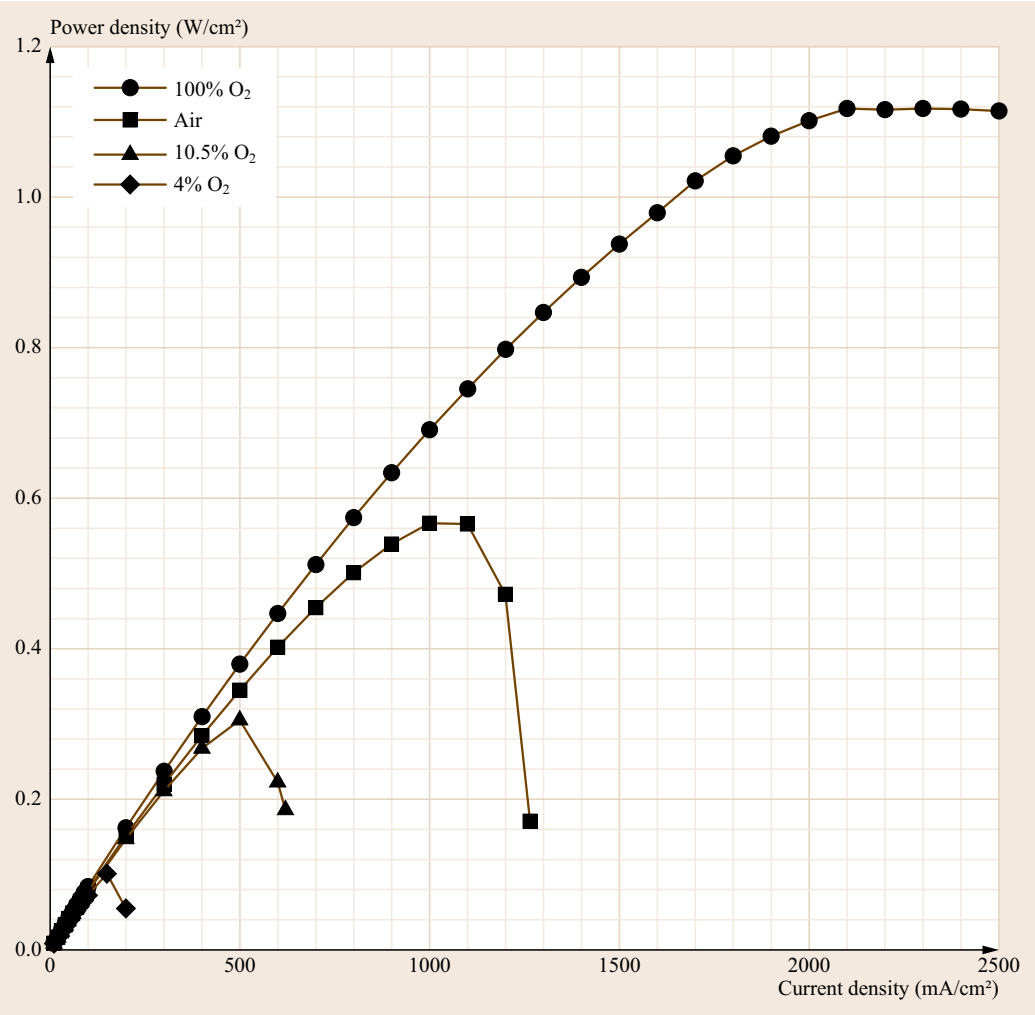


Fig. 20.13 Power density versus current density for the cell and conditions described in Fig. 20.10

be calculated from the cell resistance measured at higher current densities. The latter method assumes that the ohmic resistance of the cell does not change with current density, which is a reasonable assumption at low current densities.

3. Mass transport losses $\eta_{\text{transport}}$ are then calculated from

$$\eta_{\text{mass transport}} = E_{\text{theor}} - E_{\text{cell}} - |\eta_{\text{act,c}}| - \eta_{\Omega} \ , \tag{20.2}$$

where the concentration polarization is now referred to as the mass transport polarization.

The mass transport-induced voltage losses (concentration polarization) may be visualized as the voltage difference between the extrapolated kinetically controlled Tafel behavior (represented by the solid and dashed lines) and the *jR*-corrected cell voltage (plotted data) in Fig. 20.15. Note that mass transport effects are observed at much lower current densities in air than for oxygen. For the air case, mass transport-induced voltage losses are negligible below ca. 0.15 A/cm^2 but grow rapidly with increasing current density. In contrast, mass transport losses were not evident until ca. 0.6 A/cm^2 for the O_2 case. The source of the concentration polarization are generally considered to be flooding of the gas diffusion media, and oxygen concentration gradients/transport resistance in the electrode and thin ionomer film in the catalyst layer [20.3, 4].

An example of the polarization source analysis described above is presented in Fig. 20.16 for the H_2/air PEM fuel cell. The various sources of losses are evident. Clearly, the largest source of voltage loss is due to sluggish oxygen reduction kinetics. Mass transport losses are small relative to activation and ohmic voltage losses at current densities less than ca. 0.15 A/cm^2

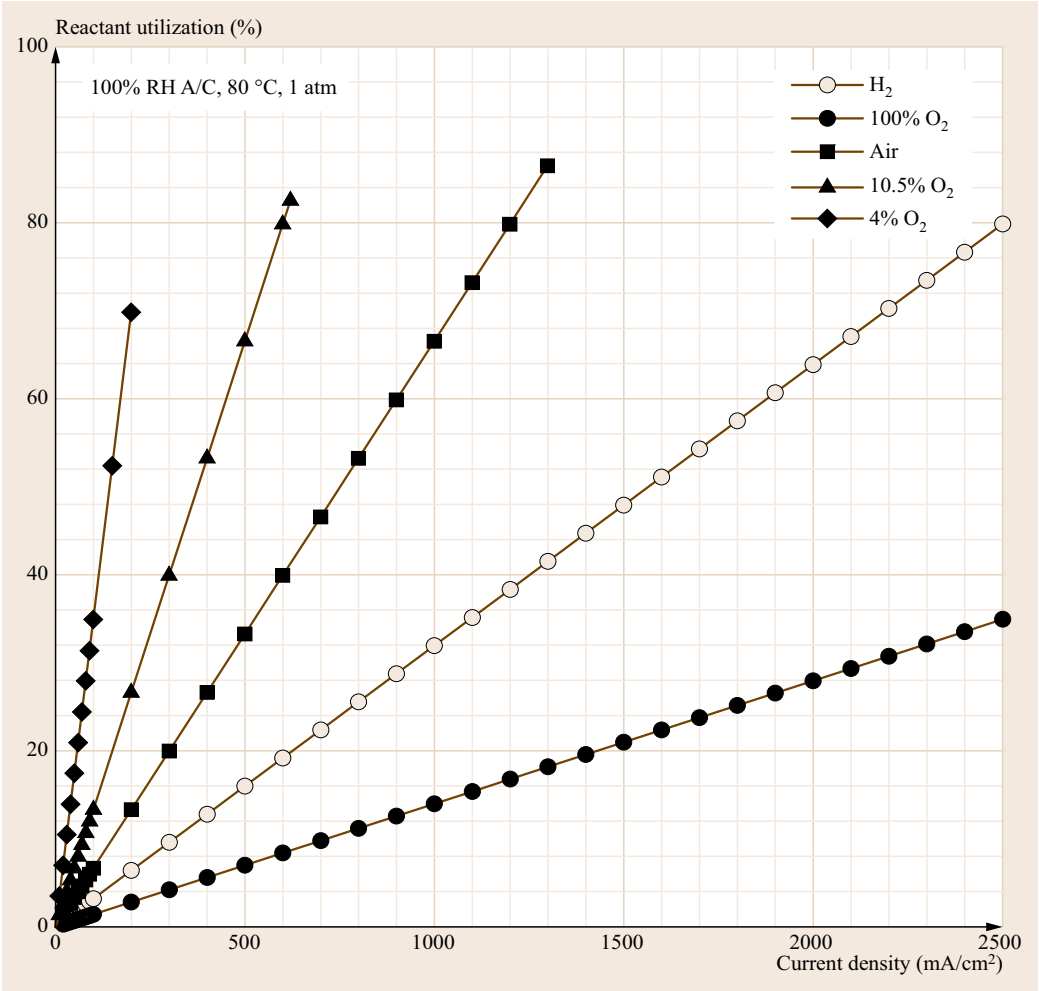


Fig. 20.14 Effect of current density and oxidant composition on reactant utilization at 80 °C, 1 atm

but become significant and indeed dominate the polarization behavior at higher current densities. Prospects for the most significant improvements in overall performance of H_2/air PEM fuel cells lay in increasing the specific catalytic activity through decreasing the Tafel slope and/or increasing the exchange current density, and in reducing mass transport resistances at high current densities through good electrode, gas diffusion media and flow field design and materials selection [20.3].

It should be noted that *Williams* et al. [20.4] expanded upon and enhanced this relatively simple polarization analysis method to extract six different sources of voltage losses in H_2/air PEM fuel cells:

1. Nonelectrode ohmic overpotential
2. Electrode ohmic overpotential
3. Nonelectrode concentration overpotential
4. Electrode concentration overpotential
5. Activation overpotential from the Tafel behavior, and
6. Activation overpotential from the catalyst activity.

The necessary experiments and analysis methods are presented in the referenced paper.

Analysis of Electrode Kinetics. The Tafel slope and the exchange current density are fundamental and important properties that relate to the electrode reaction kinetics. The Tafel slope gives the amount of activation polarization (η_{act}) needed to achieve a given reaction rate (i. e., current density, j). Obviously, the smaller the Tafel slope the better the performance of the cell (i. e., greater cell voltage at a given current density). The exchange current density j_o is the rate of the reaction occurring in the forward and reverse direction at the reversible potential. All else being equal, a larger

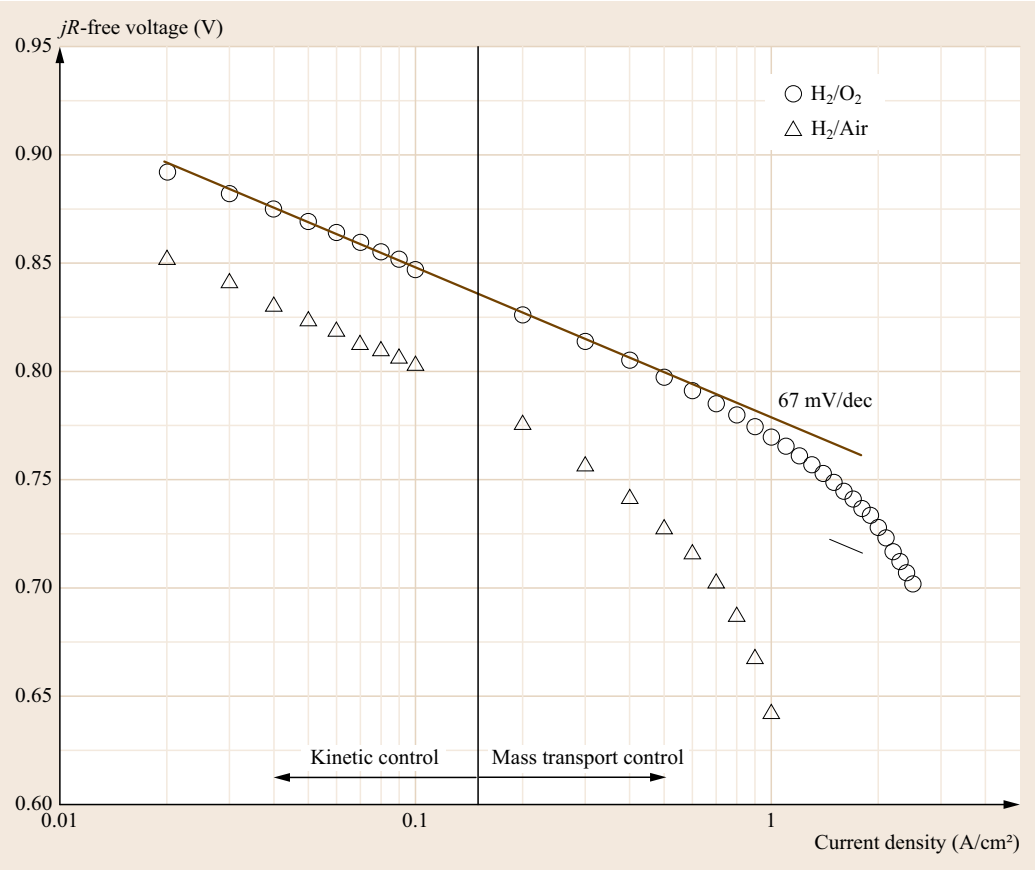


Fig. 20.15 Semi-log plot of *jR*-free voltage versus current density highlighting the difference in minimum current density at which transport-controlled losses (concentration polarization) become significant for a fuel cell operating with either O_2 ($\approx 0.6\,A/cm^2$) or Air ($\approx 0.15\,A/cm^2$) as the oxidant. Conditions: $50\,cm^2$ cell, 80 °C cell, 100% RH anode/100% RH cathode. Constant mass flow rate. Anode: fixed stoichiometric ratio = 1.25× at $1\,A/cm^2$. Cathode: constant mass flow rate = 1.5× O_2 in air at $1\,A/cm^2$; ambient pressure

exchange current density corresponds to a smaller activation loss for a given net current density when the fuel cell is forced from the reversible condition upon application of an external load.

Here we analyze the performance data acquired at low current densities (where mass transport effects are minimized) to determine these electrode parameters. For a PEM cell operating on H_2, we are primarily concerned with the kinetics of the ORR, which is sluggish in comparison to the hydrogen oxidation reaction on Pt catalysts.

The theoretical Tafel slope b in V/dec is

$$b = 2.303\frac{RT}{\alpha_c nF}\,, \tag{20.3}$$

where R is the ideal gas constant ($8.314\,J/(mol\,K)$), T is the absolute temperature (K), F is Faraday's constant (96 485 C/equiv.), α_c is the transfer coefficient, and n is the number of electrons to complete the reaction a single time (equiv./mol). For the ORR, $n = 2$ and we can assume that $\alpha_c = 0.5$ [20.5]. Accordingly, the theoretically calculated cathodic Tafel slope is 70 mV/dec at 80 °C.

In fuel cells, kinetic resistance dominates the low current density portion of the polarization curve, where deviations from equilibrium are relatively small. At these conditions, reactants are plentiful (no mass transfer limitations) and the Tafel equation describes the current density–voltage polarization curve in this region,

$$\eta_{act} = b\log|j| - a\,, \tag{20.4}$$

where a is a kinetic parameter. Linear regression of the *jR*-compensated cell voltage ($V_{cell} + jR$) versus the logarithm of the current density yields the experimentally

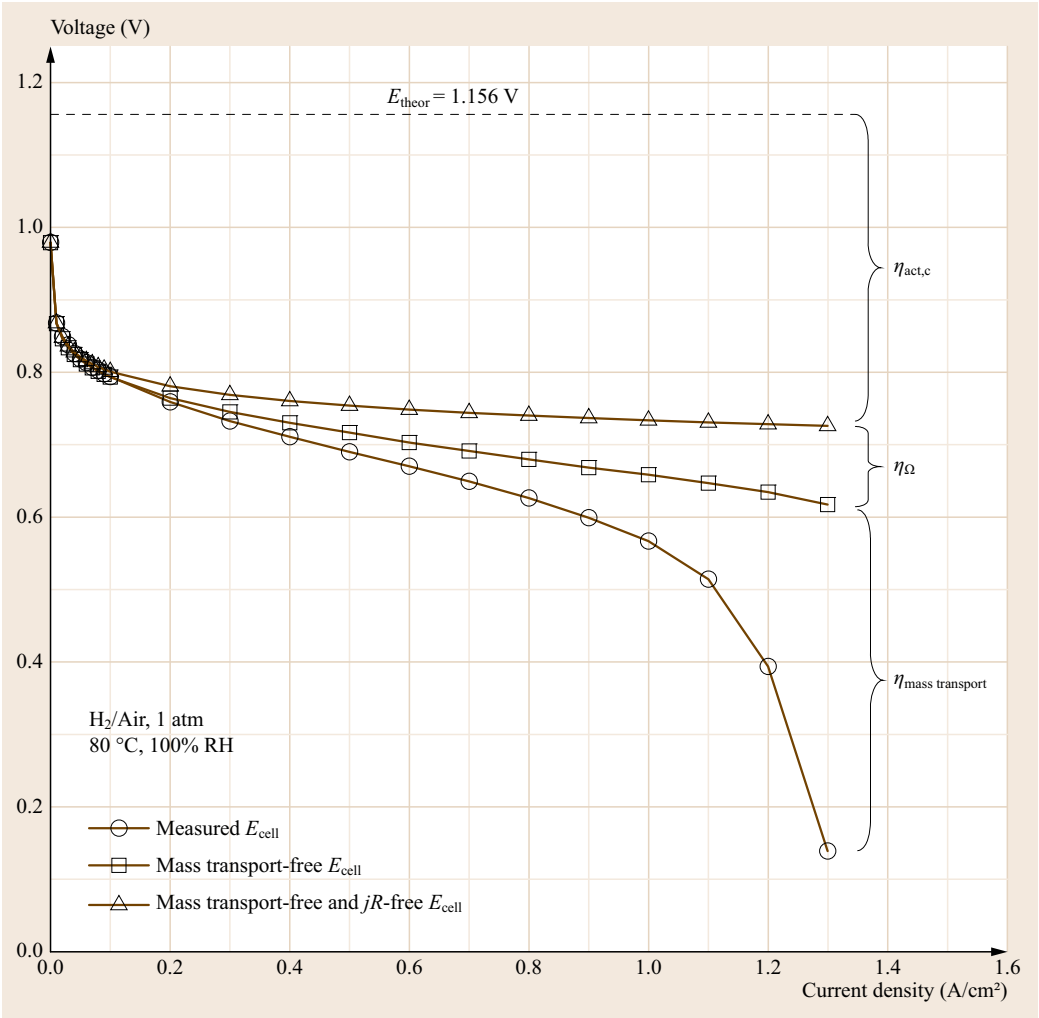


Fig. 20.16 The primary sources of polarization are shown in this voltage versus current density plot for a H_2/air PEM fuel cell. Theoretical cell potential at 1 atm, 80 °C, and 100% RH is 1.156 V assuming vapor-phase water product. Conditions: 50 cm^2 cell, 80 °C cell, 100% RH anode/100% RH cathode. Constant mass flow rate. Anode: fixed stoichiometric ratio = 1.25× at 1 A/cm^2. Cathode: constant mass flow rate = 1.5× O_2 in air at 1 A/cm^2; ambient pressure

observed Tafel slope. Figure 20.17 shows the voltage (corrected for ohmic polarization) plotted as a function of the current density on a semi-log plot. Values for the cathodic Tafel slope, b_c, obtained using this technique are summarized in for each oxidant composition examined here. The values are close to the theoretical value of 70 mV/dec.

In theory, the Tafel slope is independent of reactant concentration. The results, however, indicate a trend of increasing Tafel slope with decreasing O_2 concentration. Although a straight line over the full decade of current density is observed for pure oxygen and air conditions, mass transport effects, such as diffusion of dissolved oxygen through the ionomer layer in the cathode, in fact does influence the apparent Tafel for these high O_2-concentration reactants. The 4% oxygen concentration curve is linear only for 10 through 30 mA/cm^2, above which mass transport resistances are observed as a deviation from linearity. For this data set, only the very lowest current densities are used in the Tafel slope estimation to minimize error in Tafel slope estimation. The influence of mass transport in increasing the apparent Tafel slope with decreasing oxygen concentration is the reason oxygen is typically used for cathode kinetic studies of fuel cells. By using oxygen, we can maximize the current density range over which mass transport effects are minimized.

Having determined the Tafel slope, we can estimate the exchange current density by extrapolating the V–log(j) data to the reversible potential E_{theor}. The results are summarized in Table 20.3. From this data, it is estimated that the exchange current density for oxygen reduction on the cathode catalyst used in this MEA at 80 °C is 4.4×10^{-7} A/cm^2 (standard deviation, $\sigma = 1.2 \times 10^{-7}$ A/cm^2). Note that

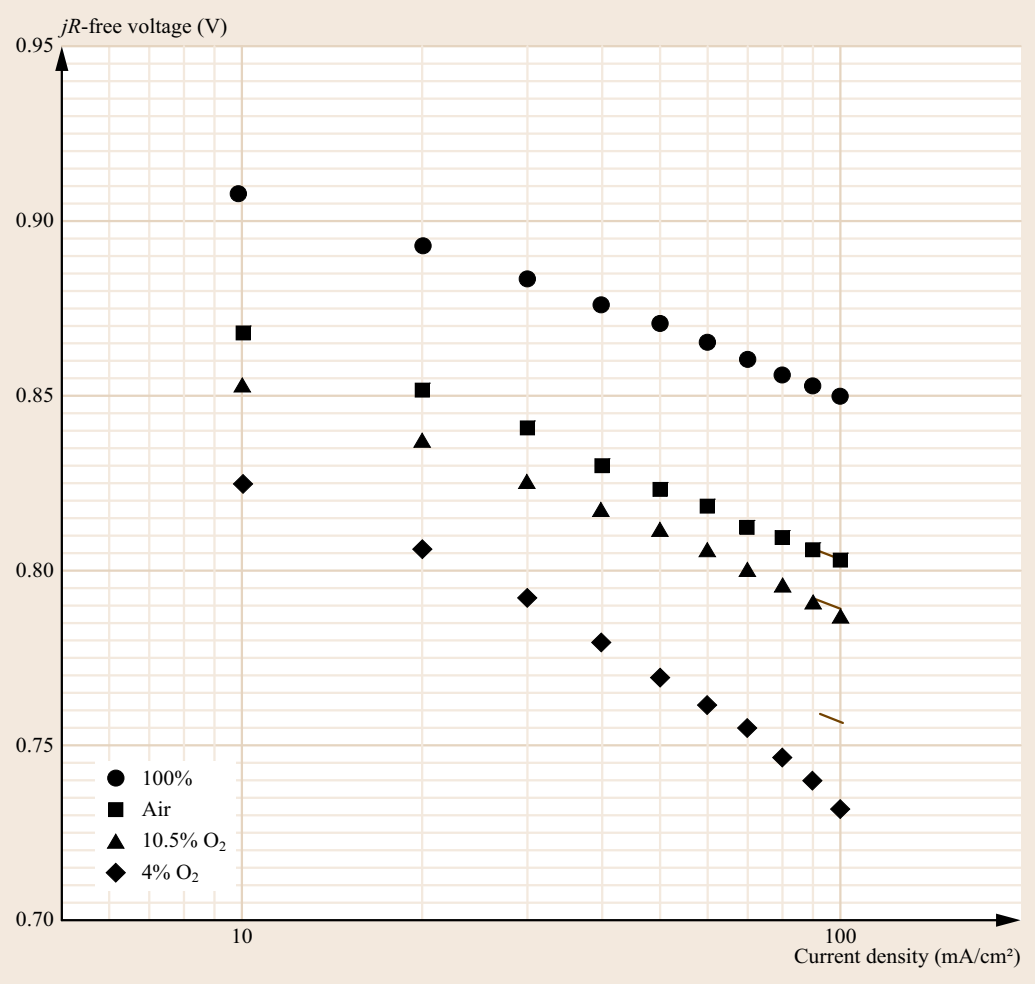


Fig. 20.17 Ohmic-resistance corrected cell voltage versus the current density (semi-log plot) for Tafel analysis of cells operating under different oxygen concentrations. Conditions as described in Fig. 20.10

the extrapolation was extended over several decades where extremely low-current data was unavailable (given that the lowest current density measured was $10\,mA/cm^2$). Such extrapolation invariably leads to large errors in estimating the exchange current density.

Because it is difficult to accurately determine j_o, parameters that can be estimated with better accuracy and precision should be used to assess electrode performance. Typical fuel cell parameters used for kinetic property evaluation shown in Table 20.3 include:

1. Tafel slope
2. Cell voltage at low current density (e.g., $10\,mA/cm^2$) where mass transport effects are negligible
3. Current density at a *jR*-free cell voltage (e.g., 0.85 V).

Table 20.3 Fuel cell electrode performance metrics obtained from *jR*-compensated performance curves measured at 80 °C (Fig. 20.17)

Oxidant	OCV (V)	E_{theor} (V)	E_{cell} at $10\,mA/cm^2$ (V)	b_c (mV/dec)[a]	j at $E_{cell,jR\text{-free}} = 0.85$ V (A/cm^2)	j_o (A/cm^2)
100% O_2	1.024	1.168	0.908	58.6	100	3.6×10^{-7}
Air	0.979	1.156	0.868	67.3	20	5.2×10^{-7}
10.5% O_2	0.953	1.151	0.852	66.5	11	3.2×10^{-7}
4% O_2	0.903	1.144	0.824	75.5	4	5.7×10^{-7}

[a] Theoretical Tafel slope = 70 mV/dec at 80 °C for $\alpha_c = 0.5$, $n = 2$

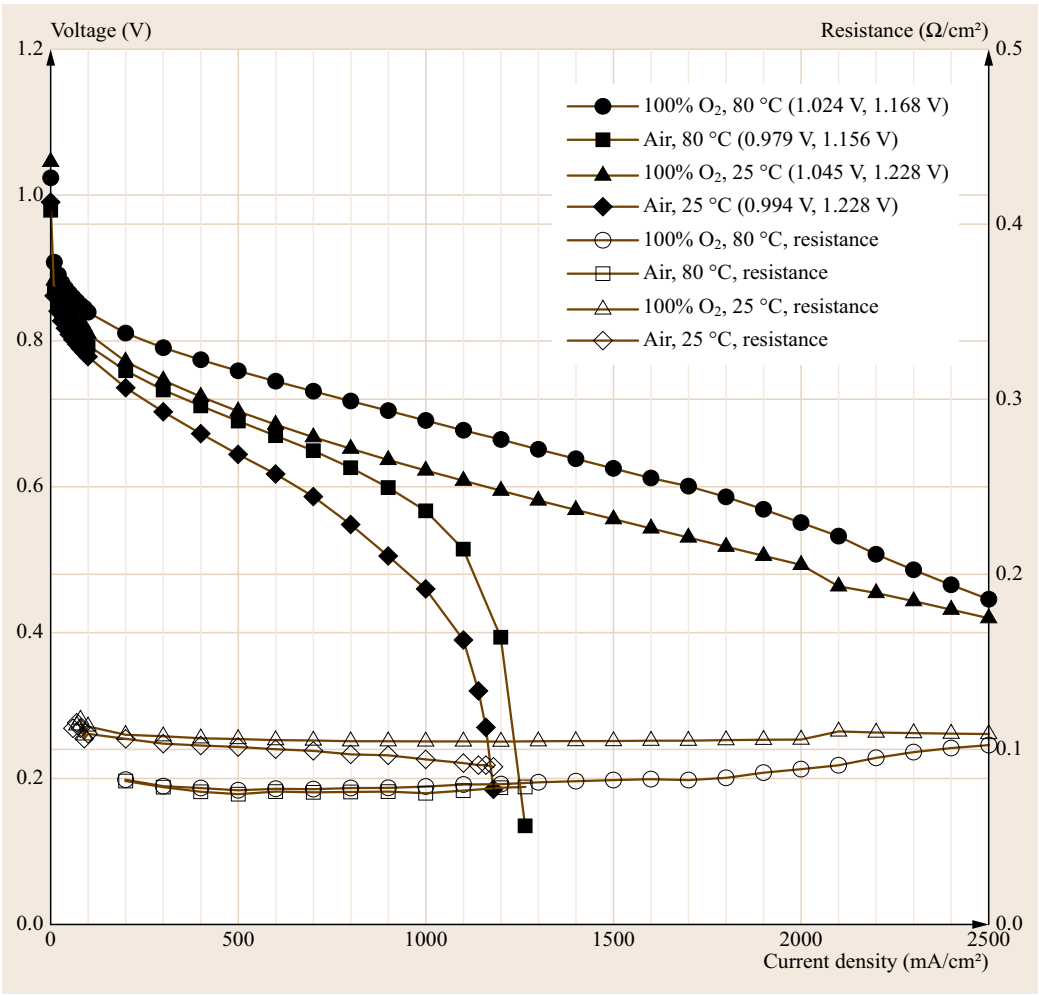


Fig. 20.18 Cell voltage and cell resistance versus current density as a function of temperature for pure oxygen and air cathode reactant. The legend for the performance curve (V–j) gives the measured OCV and theoretical voltage in parenthesis (OCV, E_{theor}). Conditions: 50 cm^2 cell, 100% RH anode 100% RH Cathode at all temperatures. Anode stoichiometry: 2.5×. Cathode stoichiometry: 7.14× at 100% O_2, 1.5× at 21% O_2; stoichiometry based on 1 A/cm^2 and constant flow rate; ambient pressure

Some or all of these parameters can be used to compare the electrode kinetics of the fuel cell as a function of operating conditions, electrode materials, cell components, etc.. For example, the results shown in Table 20.3 indicate that the current density at an jR-compensated cell voltage of 0.85 V is approximately proportional to the oxygen pressure. Additional information on the analysis of the ORR kinetics in PEM fuel cells can be found in [20.6].

Discussion

The described experiments and analyses allow us to compare the performance of the cell operating under different oxygen stoichiometric ratios and to investigate which performance characteristics of the fuel cell are dependent on the oxygen concentration. By comparing the theoretical potential (E_{theor}) to the observed open circuit potential of the cell, one can identify the extent and sources of loss in cell voltage at open circuit. One can also list the sources of losses occurring at any point along the polarization curve and identify regimes (demarcated by current density) wherein activation, ohmic, and mass transport losses dominate.

20.2.2 Temperature and Relative Humidity Effects

After assembling the MEA, setting up the fuel test cell station and connecting all gases, a test for reactant crossover and electronic short within the cell as described in Sect. 20.4 can be carried out. The cell is then conditioned by holding a constant voltage (e.g., 0.55 V) until current density and cell resistance are stable. Cell performance is then determined by measuring the cell voltage as a function of current density, while operating the cell at different conditions.

To obtain the performance curve for Tafel analysis and to generate the full polarization curve, a current

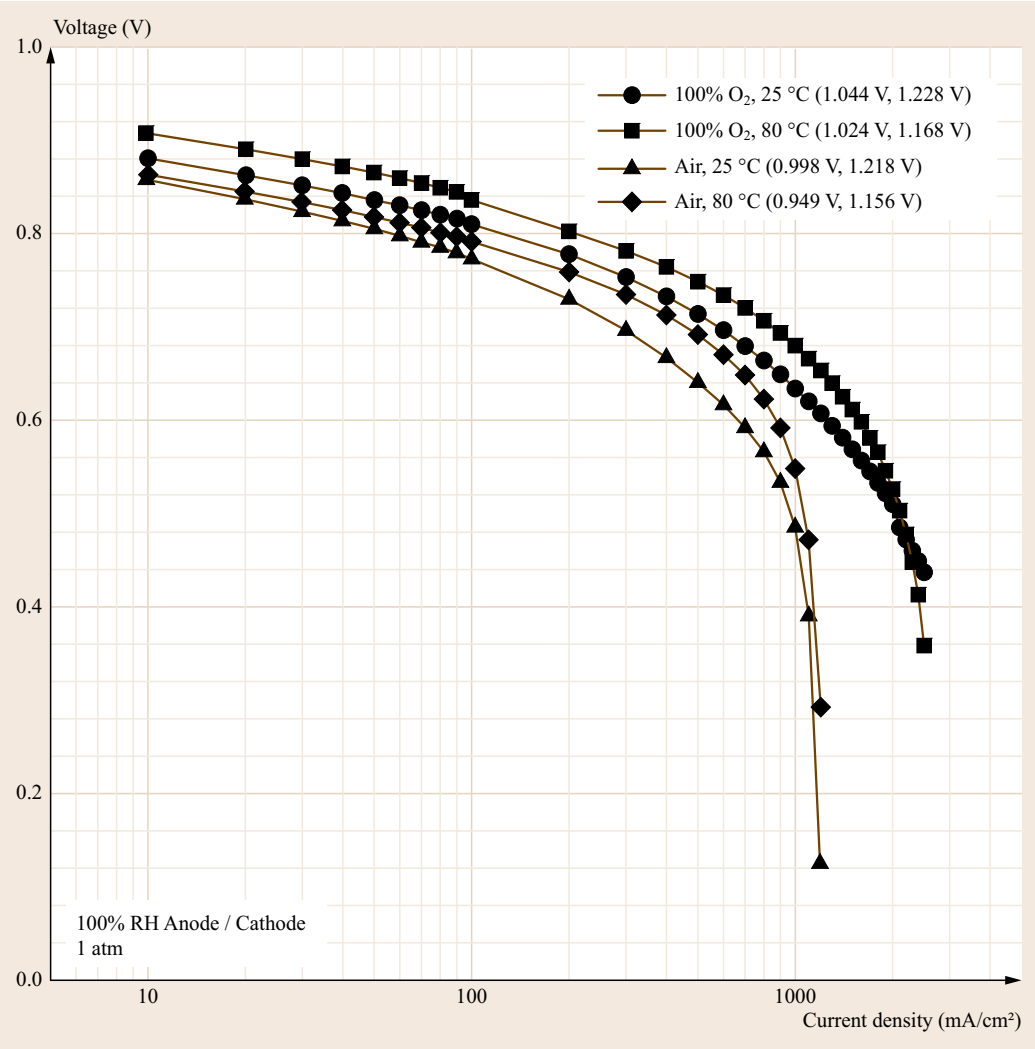


Fig. 20.19 Cell voltage versus current density plotted in semi-log format highlighting the exponential relationship (Tafel behavior) at low current densities where mass transport and ohmic effects are negligible, as well as the transport limiting current density at high current density. OCV and E_{theor} given in the legend (OCV, E_{theor}). Conditions are as in Fig. 20.18

scan experiment over two current density ranges should be performed:

- Tafel analysis: Current density from 0 to 100 mA/cm^2 at 10 mA/cm^2 increments.
- Full performance curve: Current density 100 mA/cm^2 to the limiting current density (or a predefined maximum such as 2000 mA/cm^2) at 100 mA/cm^2 increments. Data should be acquired after no less than 30 s to 1 min at each current value (time/point setting). Although 1 min/step is suitable for instructional purposes, research is typically performed with much longer hold-times at each current increment, for example, 5 min/step. The data are acquired using the current interrupt technique enabled to measure the membrane resistance.

Analysis of Fuel Cell Performance

- The anode and cathode inlet RH, hydrogen and oxygen partial pressure, theoretical reversible potential and Tafel slope at each condition are calculated. Sample results are shown in Table 20.3.
- The theoretical reversible cell voltage E_{theor} is compared to the experimentally observed open circuit voltage.
- The following data can be plotted and analyzed (this is just a representative sample of the data that can be compared – depending on the experimental conditions studied.
  - Performance curves: cell voltage versus current density and membrane resistance versus current density at 25 and 80 °C under fully humidified

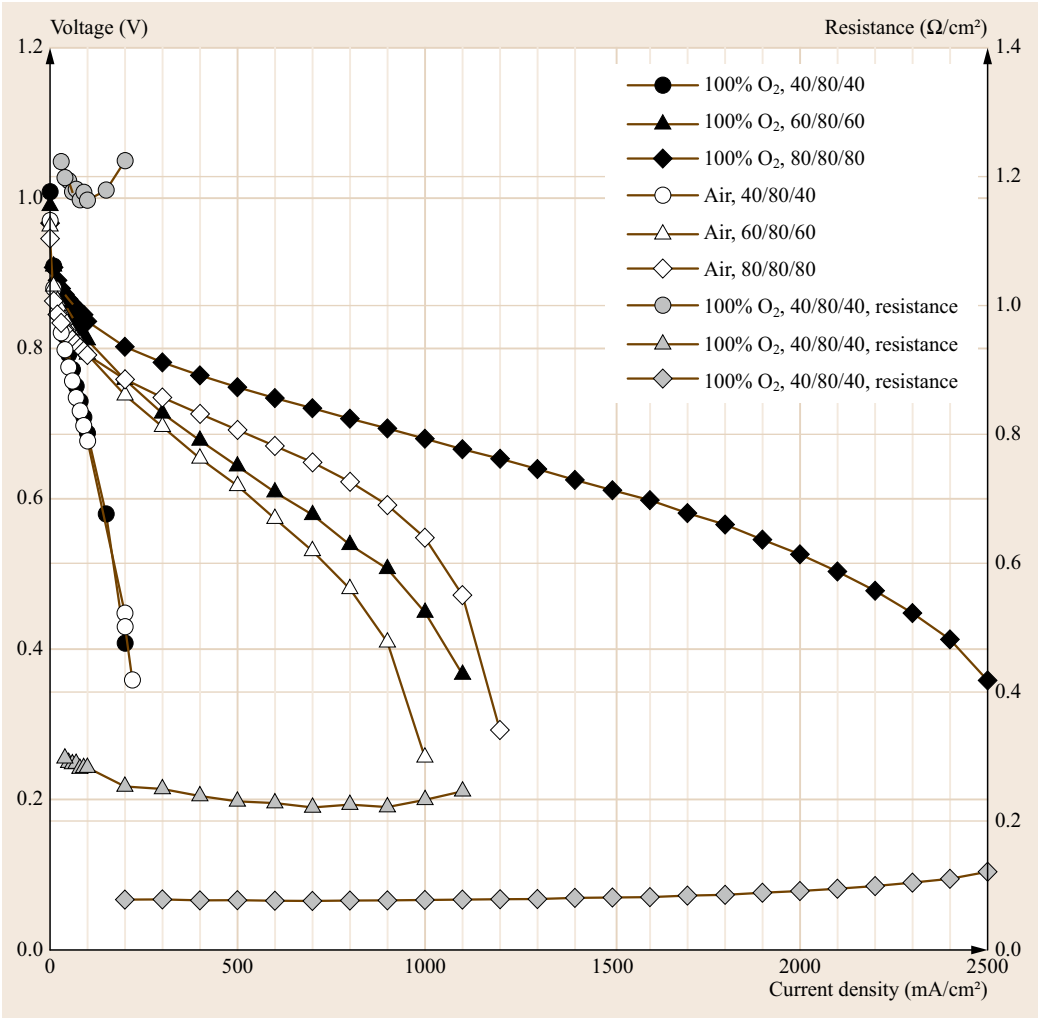


Fig. 20.20 Effect of anode and cathode humidification on the cell performance (V–j) and membrane resistance due to reactant humidification. Conditions: 50 cm^2 cell (AHT, CT, CHT)

conditions (100% RH) for oxygen and air to examine temperature effects (Fig. 20.18).

- Power density curves at 25 and 80 °C under fully humidified conditions (100% RH) for oxygen and air to examine temperature effects (Fig. 20.18).
- Performance curves and membrane resistance for the conditions 40/80/40, 60/80/60, and 80/80/80 for oxygen and air to examine the effect of reactant humidification (Fig. 20.20). Comparison of how the cell resistance changes with reactant humidification can be done.
- Optional: The performance curves and membrane resistance for the conditions 40/80/40, 60/80/40, 60/80/60, 80/80/60, and 80/80/80 for oxygen to examine the effect of *anode* and *anode* + *cathode* reactant humidification (Fig. 20.21). It shows how the cell resistance changes with reactant humidification.
- A plot of the cell voltage and jR-free voltage versus current density for low, medium, and high humidification conditions can be drawn.

- A Tafel (slope) analysis by plotting the jR-free voltage versus log(j) curves and estimate the exchange current density (Figs. 20.22 and 20.23) can be performed. Comparing the Tafel slope and exchange current density obtained for the different cell temperatures and humidity values and the discussion items can be considered at this stage: the electrode reaction resistance (Tafel slope) with decreasing temperature, humidity influence the resistance of the electrode reaction, temperature, or humidity effect on the activation of the oxygen reduction reaction.

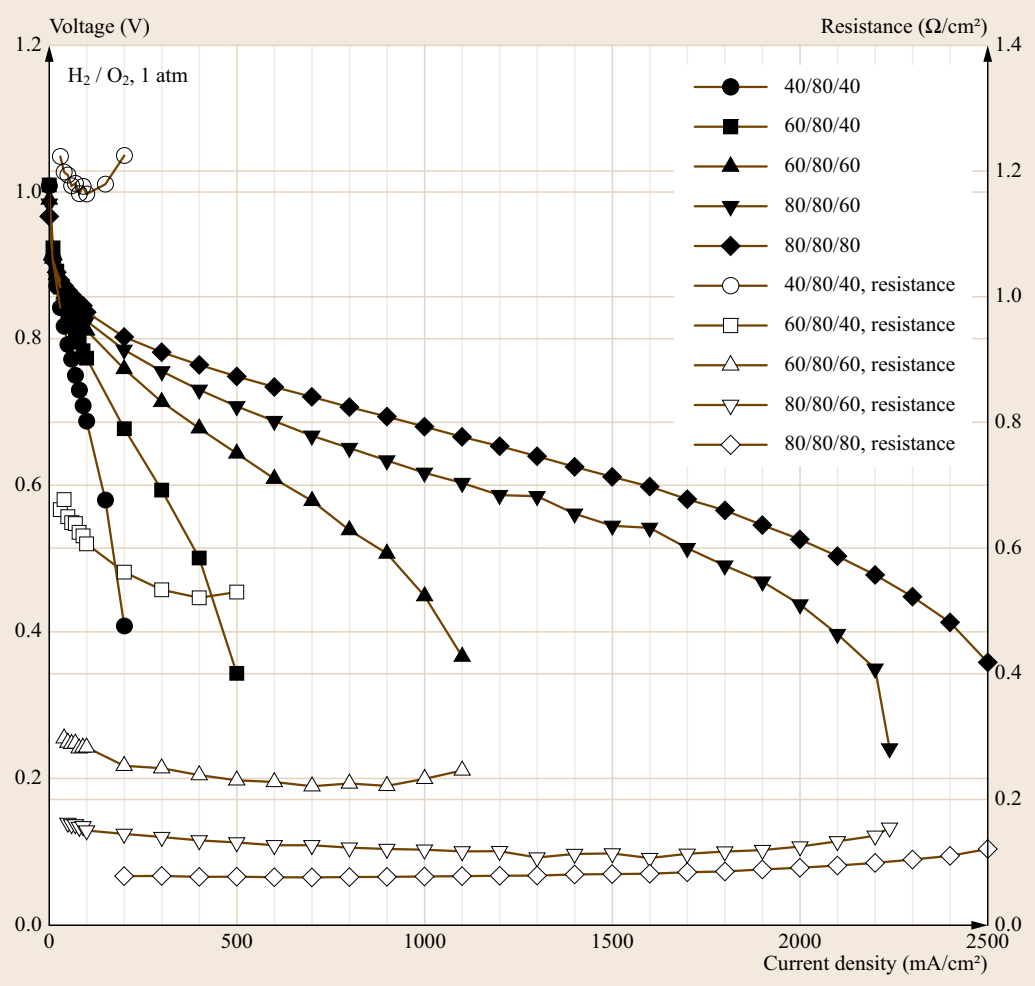


Fig. 20.21 Effect of anode and cathode humidification on the H_2/O_2 cell performance and membrane resistance due to humidification anode-only or anode + cathode reactant. Conditions: 50 cm^2 cell (AHT, CT, CHT)

Figures 20.18 and 20.19 summarize the performance data on linear and semi-log plots, respectively. Different features of the performance of the fuel cell are highlighted by plotting the data in these two formats. The former voltage–current density plot shows the linear relationship observed at moderate current densities whereas the semi-log format highlights the activation-controlled and mass-transport controlled regions at low and high current densities, respectively. Both figures demonstrate the effect of temperature and oxidant concentration on the performance of the cell. For this reason, both types of plots are commonly used when evaluating the *V–j* behavior of fuel cells.

The effect of operating temperature (25 °C versus 80 °C, at 100% RH) on cell performance and membrane resistance for a H_2 PEM cell operating on pure O_2 or air is shown in Fig. 20.18. Measured OCV and theoretical reversible potential at 80 °C are slightly lower than the corresponding values at 25 °C. (There is also the expected oxidant composition effect on OCV and E_{theor}.) The temperature effect on these properties is primarily due to the higher concentration of reactants (H_2 and O_2) when fed at lower temperatures under saturated moisture conditions (100% RH). The absolute water content of a gas increases with temperature; thus, increasing the temperature of the feed gas decreases the relative proportion of reactant in the water-vapor saturated gas. The effect of reduced reactant concentration on E_{theor} can be predicted by examination of the Nernst equation

$$E_{\text{theor}} \propto \log\left(\frac{p_{H_2} p_{O_2}^{1/2}}{p_{H_2O}}\right) . \qquad (20.5)$$

Figure 20.18 shows that under fully hydrated conditions, membrane resistance decreases with increasing

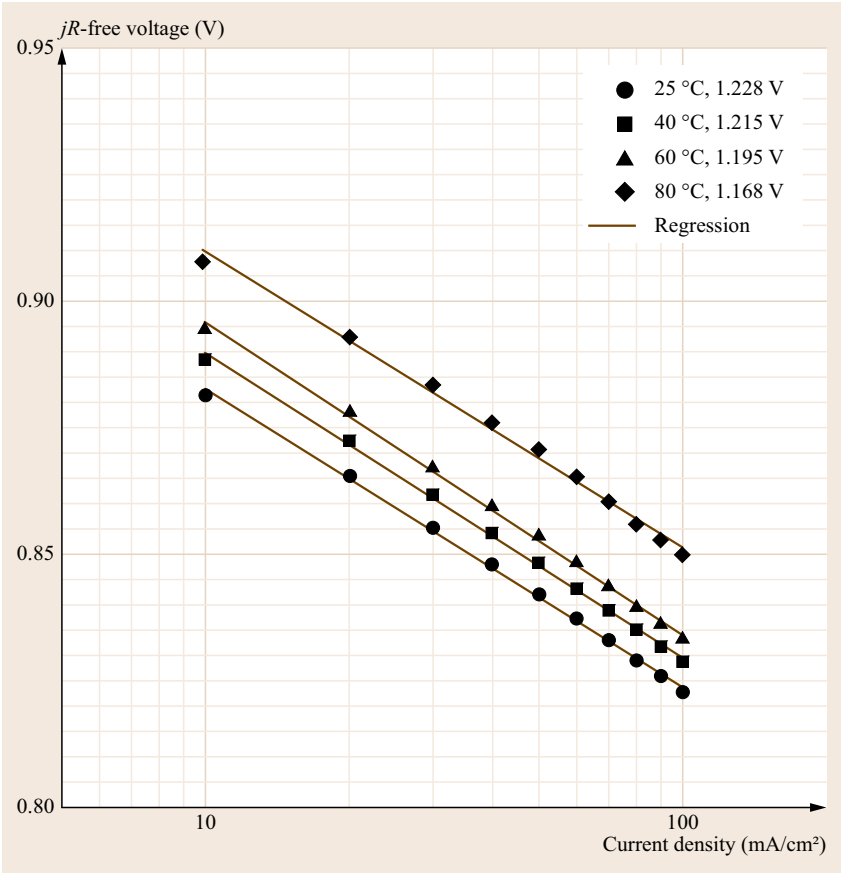


Fig. 20.22 Tafel slope analysis by linear regression of *jR*-free voltage versus log(*j*) data acquired at 4 temperatures. E_{theor} is given in the legend. Conditions: 50 cm^2 cell; anode: 100% RH H_2, cathode: 100% RH O_2; ambient pressure

temperature. The temperature dependence of the ohmic resistance of the membrane is related to the mobility of the protons, which increases with increasing temperature.

Although the OCV and E_{theor} decrease with increasing temperature, elevated temperatures favor faster reaction kinetics on the catalyst surface, increased diffusion through the GDL, and lower membrane resistance. The net result is improved overall cell performance at 80 °C in comparison to 25 °C under fully saturated conditions as demonstrated by the power density curves shown in Fig. 20.24.

The effect of reactant humidity on the performance of the cell is shown in Fig. 20.20. In each case, the cell was operated at 80 °C while the anode and cathode gas humidifier tanks were both set at either 40, 60 or 80 °C, corresponding, respectively, to low (16% RH), moderate (42% RH) and high (100% RH) humidity conditions within the cell. The performance of the cell is a strong function of the humidity of the reactants (Table 20.4).

The performance of the cell at low humidity conditions is independent of the oxidant concentration. That is, the *V*–*j* data are nearly identical using oxygen and air at low humidity (i. e., 40/80/40). A significant improvement in performance when operating with pure oxygen in comparison to air is observed only when the cell was well-humidified indicating that the resistance of the membrane dominates the performance of the cell under dehydrated or low RH conditions.

Figure 20.20 indicates that the membrane resistance, determined using the current interrupt technique, increases by greater than an order of magnitude between the high and low humidity conditions (i. e., 0.1 versus 1.2 Ω cm^2 at 100% RH and 16% RH, respectively). For a given humidity condition, the membrane resistance is independent of the oxidant composition; hence, only resistance data for oxygen is shown.

Figure 20.21 further demonstrates the influence of reactant moisture content on the performance of the PEM fuel cell by showing the effect of just anode as well as anode and cathode reactant humidification. It is evident, for example, that humidification of the fuel alone dramatically improves the performance of the cell by decreasing the resistance of the membrane

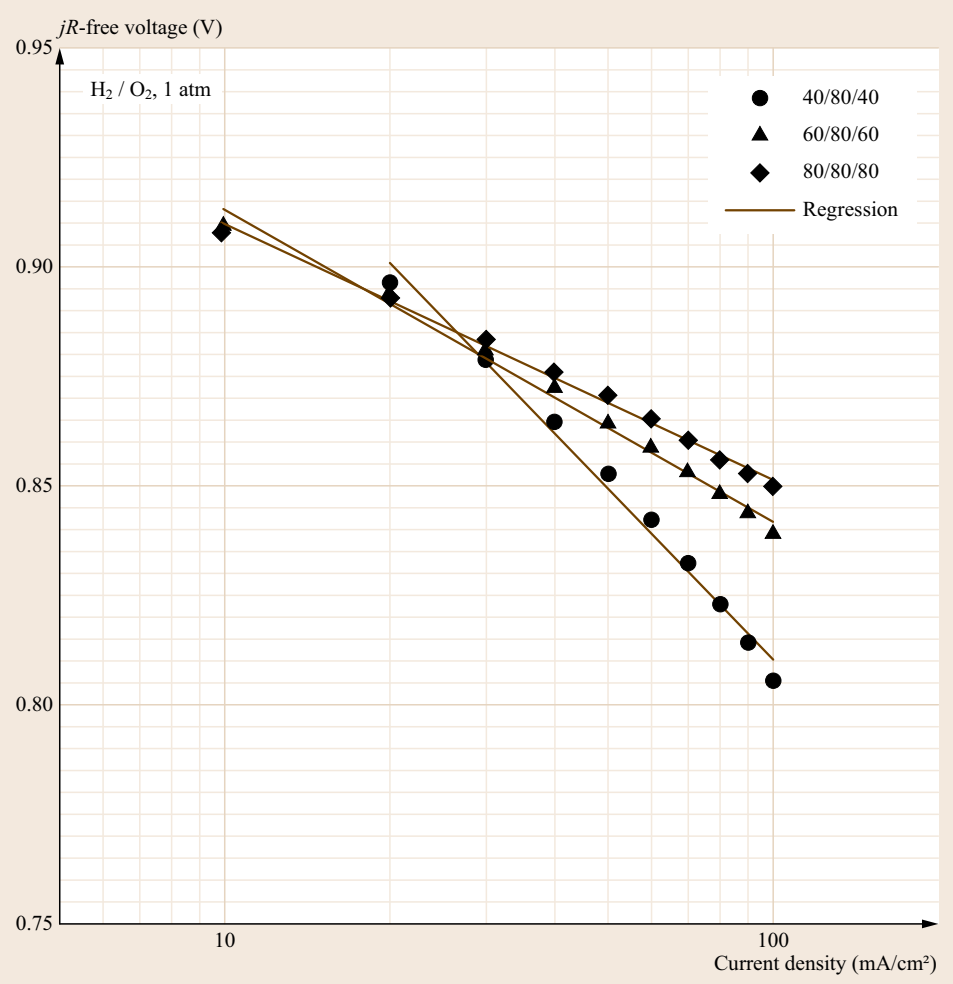


Fig. 20.23 Tafel slope analysis by linear regression of *jR*-free voltage versus log(*j*) data acquired for three reactant humidity levels: low (40/80/40, 16% RH), medium (60/80/60, 42% RH), and high (80/80/80, 100% RH)

(e.g., compare the conditions 60/80/60 and 80/80/60). Arguably, humidification of the hydrogen fuel had a greater impact on the performance of the cell than did humidification of the oxygen. This can be rationalized by considering that water is produced at the cathode whereas it is removed at the anode by osmotic drag through the membrane. In practice, control of the water content of both anode and cathode feed streams is performed to optimize the performance of the cell.

Analysis of Electrode Kinetics

The effect of cell humidification on reaction kinetics is demonstrated by Tafel analysis, which was presented in detail in Sect. 20.2.1. The Tafel slope is given by the slope of the cell voltage (corrected for membrane resistance) plotted as a function of the logarithm of the current density. The Tafel slope is obtained by linear regression of the data.

Figure 20.22 shows the Tafel plots for a fully humidified H_2/O_2 cell operating at four temperatures. Experimental Tafel slopes were 59.0, 60.2, 61.8, and 58.6 mV/dec at 25, 40, 60, and 80 °C, respectively. The low temperature results correspond quite well with theoretical predictions of the Tafel slope although they tend to diverge at the higher temperatures ($b_{c,theor}$ = 59.2, 62.0, 66.1, 70.1 mV/dec, respectively).

The effect of humidity on the electrode kinetics is shown in Fig. 20.23 wherein Tafel analysis is performed on data acquired at low (40/80/40, 16% RH), medium (60/80/60, 42% RH), and high (80/80/80, 100% RH) humidity levels. The apparent resistance to the ORR increased significantly at low humidity levels, as indicated by the large Tafel slope (= 129 mV/dec). With increasing reactant humidity the electrode kinetics became more facile (i. e., 71.2 and 58.6 mV/dec at moderate and high humidity, respectively). This ap-

Table 20.4 Operating conditions, and theoretical and experimental results for PEM fuel cell

Condition AHT/CT/CHT	Theoretical								Experimental					
	Anode		Cathode						Oxygen			Air		
	RH (%)	p (H_2) (atm)	RH (%)	p (O_2) (atm)	E_{theor} (V)	p (O_2) (atm)	E_{theor} (V)	b_c (mV/dec)[a]	OCV (V)	b_c (mV/dec)	j_o (A/cm^2)	OCV (V)	b_c (mV/dec)	j_o (A/cm^2)
25/25/25	100	0.968	100	0.968	1.228	0.203	1.218	59.2	1.044	59.0	1.3×10^{-8}	0.998	–	–
40/40/40	100	0.927	100	0.927	1.215	0.195	1.204	62.0	0.987	60.2	3.6×10^{-8}	0.867	74.0	2.8×10^{-7}
60/60/60	100	0.804	100	0.804	1.195	0.169	1.184	66.1	0.990	61.8	1.3×10^{-7}	0.864	66.0	1.4×10^{-7}
80/80/80	100	0.533	100	0.532	1.168	0.112	1.156	70.1	1.024	58.6	3.6×10^{-7}	0.863	63.4	2.4×10^{-7}
40/80/40	16	0.927	16	0.927	1.181	0.195	1.169	70.1	1.008	129.6	–	0.974	–	–
60/80/40	42	0.804	16	0.927	1.179	0.195	1.167	70.1	1.010	95.7	–	0.976	–	–
60/80/60	42	0.804	42	0.804	1.178	0.169	1.166	70.1	0.990	71.2	1.7×10^{-6}	0.964	–	–
80/80/60	100	0.532	42	0.804	1.171	0.169	1.159	70.1	0.940	63.7	6.4×10^{-7}	0.983	–	–

[a] Tafel slope assuming $\alpha_c = 0.5$, $n = 2$.

parent *increase* in the Tafel slope is perhaps due to enhanced ohmic and mass transport losses within the cathode catalyst layer as the RH is lowered. Data at lower current density would be desirable to define the true cathode kinetics. A change in the mechanism of oxygen reduction cannot be ruled out.

The results attained in these experiments indicate that unless the effects of humidity on the electrode kinetics are specifically being investigated, electrode kinetics should be studied using well humidified conditions and pure oxygen as the oxidant.

Summary

The experiments described in this part are intended to instill understanding and experience in employing electrochemical test methods to determine the performance characteristics of a hydrogen-fueled PEMFC. The performance of the fuel cell has been presented via voltage versus current density and resistance versus current density plots.

A detailed data analysis and discussion is presented to acquaint the reader with concepts related to fuel cell reactant consumption rates and utilization. Some of the experiments proposed allow the reader to evaluate the performance of PEM fuel cell as a function of temperature, reactant gas humidity levels, oxygen concentration and stoichiometry with an emphasis on the effects of varying these parameters on electrode kinetics, mass transport limitations, and cell resistance.

The measured OCV is shown to be less than the theoretical maximum potential (E_{theor}) in all cases, and both values decrease with declining oxygen concentration. The OCV is less than E_{theor} because in practice, parasitic oxidation reactions at the cathode lead to a mixed potential that is lower than the electrode potential predicted based solely on the ORR. Oxidation of fuel that crosses over through the membrane and oxidation of the cathode materials (e.g., carbon support) both contribute to this mixed potential.

Activation polarization due to kinetic limitations dominate at low current densities (0–100 mA/cm^2). Analysis of the polarization data in this activation region allows to estimate the Tafel slope and the exchange current density. Ohmic losses dominate at intermediate current densities (100–1000 mA/cm^2) and are a resultant of ionic and electronic resistances. The membrane resistance is typically relatively constant up to about 1000 mA/cm^2 and is independent of oxidant composition. At larger current densities, the ohmic resistance of the membrane increases slightly due to dry-out of the membrane on the anode side. Dry-out of the membrane within the PEM fuel cells is a common phenomenon at high current densities and occurs because water molecules associated with migrating protons are dragged from the anode to the cathode at a higher rate than they can diffuse back from the cathode (where water is also produced). This phenomenon is more clearly seen with thicker membranes, such as Nafion 117, than with thin membranes such as Nafion 211 used here.

Mass transport limitations due to insufficient supply of oxygen to the surface of the cathode are observed

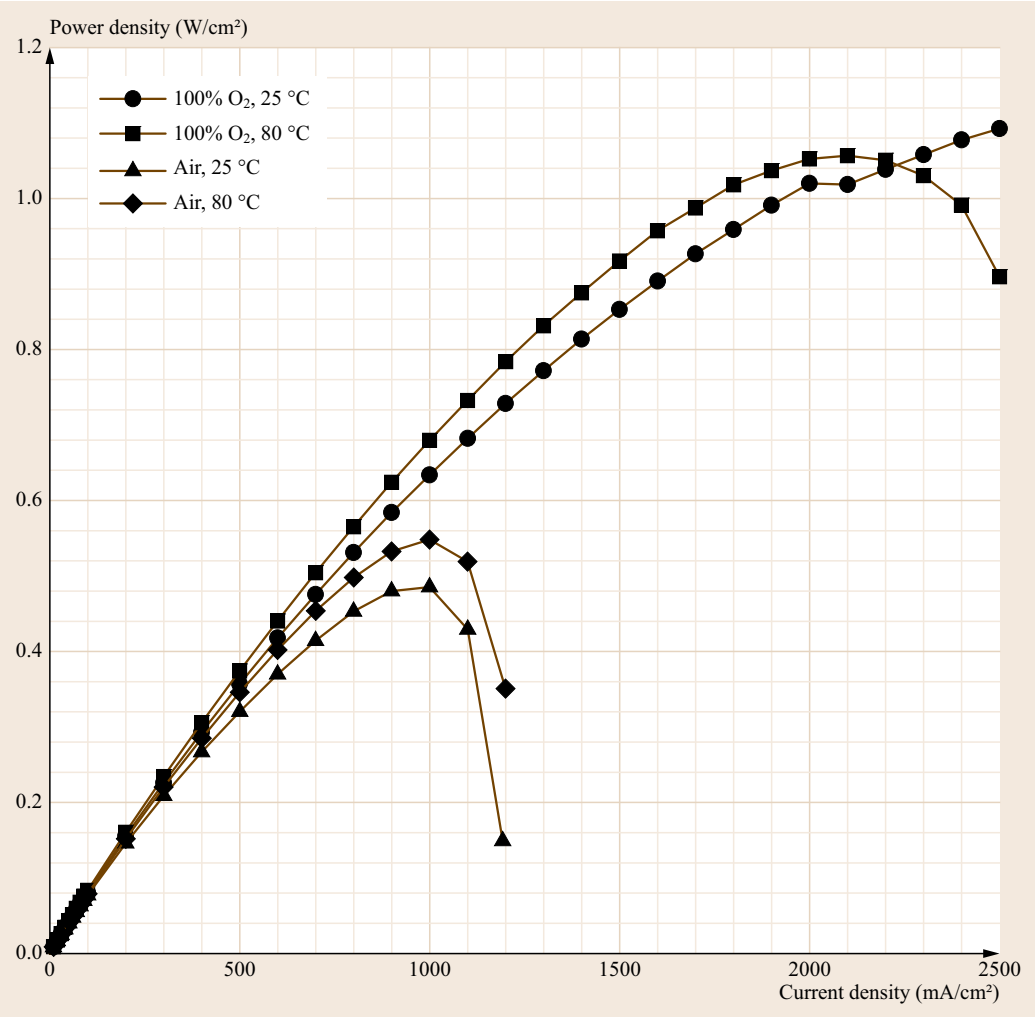


Fig. 20.24 Power density curve at 25 and 80 °C for oxygen and air at 100% RH. Conditions are as in Fig. 20.19

at higher current densities (more than 1000 mA/cm^2) and dominate the polarization in this region. The limiting current density is the maximum attainable current density in this regime and depends on the oxygen concentration in the oxidant stream, the flow rates, the properties of the diffusion media, and the cell design.

20.3 Application of a Fuel Cell Empirical Model

Fuel cell research and development is currently focused on material cost reduction in conjunction with optimization of fuel cell design for improved performance and durability. To achieve the required performance and cost goals, there is a strong need to identify, understand, control, predict, and optimize the various thermodynamic, kinetic and transport processes that occur on disparate length scales during fuel cell operation. Optimization of fuel cell technology will not be achieved by experimental analysis alone because of the large number of interdependent and complex processes and structure–property–performance relationships involved. Modeling of fuel cells is used to reduce development time and cost while increasing the scientific understanding of this complex technology by facilitating identification of the critical parameters that have the largest impact on performance. *Wang* recently reviewed the status of fuel cell modeling efforts [20.7].

Although comprehensive modeling of a fuel cell system is beyond the scope of this book, a simple model describing voltage–current characteristics of the fuel cell can be introduced and implemented to test for 1.) its ability to fit the data, and 2.) its utility as an analytical tool.

A common method to determine cell voltage losses is least squares fitting of an analytical expression incorporating the three main sources of loss to the experimental performance data. The simplified empirical model employed here is based on the work of *Srinivasan* and coworkers [20.8–12].

The complete relationship between the cell voltage and current-dependent polarization losses can be described by

$$V_{\text{cell}} = E_{\text{theor}} - (\eta_{\text{act,c}} + \eta_{\text{act,a}}) - \eta_{\Omega} - (\eta_{\text{conc,c}} + \eta_{\text{conc,a}}) \,, \tag{20.6}$$

where the three primary sources of polarization, previously presented are listed here.

1. *Activation* polarization (η_{act}). The Tafel equation (20.4) describes the relationship between the current density j and activation polarization η_{act} at large overpotentials.
2. Ohmic polarization (η_{Ω}). Voltage losses due to ionic and electronic transport resistance and contact resistance as described by a simplified form of Ohm's law,

$$\eta_{\Omega} = jR_{\Omega} \,, \tag{20.7}$$

where R_{Ω} is the resistance in $\Omega\,\text{cm}^2$.
3. Concentration polarization (η_{conc}). Mass transport polarization losses can be described by

$$\eta_{\text{conc}} = C \log\left(\frac{j_{\text{lim}} - j}{j_{\text{lim}}}\right) \,. \tag{20.8}$$

Here, j_{lim} in A/cm^2 is the maximum achievable current density based on the Fickian diffusion of reactant to the electrode surface at which the concentration of reactant is assumed to be zero [20.13]. The parameter C is related to the Tafel slope by

$$C = 2.303\frac{RT}{nF} \,, \tag{20.9}$$

where R, T, n, and F have their usual meaning. Equation (20.8) indicates that η_{conc} becomes a very large negative number as j approaches j_{lim} and describes the source of the rapid decrease in cell potential in the regime where the reaction consumption rate (given by the current density) is dictated by transport of reactant to the active surface sites.

20.3.1 Model Application and Analysis

To perform the simplified modeling analysis, we make the following assumptions:

- Polarization at the anode (activation, ohmic, and concentration) is negligible in comparison to cathodic contributions. This assumption is generally justified for pure H_2 operation, but will not hold for reformate or direct methanol operation.
- At the cathode, activation-controlled kinetics can be described by Tafel behavior (20.4).
- Mass transport losses (concentration polarization) can be described by (20.8).
- Ohmic resistance is independent of current density. (Resistance is known to increase at high current densities due to dehydration so the validity of this assumption should be regarded with some skepticism, at least under some conditions.)
- All of the polarization losses can be separated and do not interact.
- Ohmic losses in the cathode are negligible.

Equation (20.10) is the result of applying the earlier assumptions and substituting the respective polarization relationships into (20.6),

$$V_{\text{cell}} = E_{\text{theor}} - b_{\text{c}} \log\left(\frac{j}{j_{\text{o,c}}}\right) - jR_{\Omega} + C_{\text{c}} \log\left(\frac{j_{\text{lim,c}} - j}{j_{\text{lim,c}}}\right) \,. \tag{20.10}$$

Here, the subscript c is used to reinforce the assumption that polarization losses are attributed to cathodic processes, either activation or mass transport (in addition to ohmic effects). The exchange current density is a constant for a given reaction–electrode system, and as such (20.10) can be rearranged to give

$$V = E_{\text{theor}} + A_{\text{c}} - b_{\text{c}} \log(j) - jR_{\Omega} + C_{\text{c}} \log\left(\frac{j_{\text{lim,c}} - j}{j_{\text{lim,c}}}\right) \,, \tag{20.11}$$

where $A_{\text{c}} = b_{\text{c}} \log j_{\text{o,c}}$. The five fitted parameters are: $(E_{\text{theor}} + A_{\text{c}})$, b_{c}, R_{Ω}, C_{c}, and $j_{\text{lim,c}}$. From this empirical model, we can estimate physiochemically meaningful parameters including the cathodic Tafel slope and limiting current density, and the cell ohmic resistance.

Table 20.5 summarizes theoretical, experimental, and empirical modeling results for a PEM fuel cell operating at 80 °C, 25 °C, and with a range of oxidant concentrations. Theoretical parameters include the reversible potential and Tafel slope (assuming $\alpha_{\text{c}} = 0.5$). Experimental values include the OCV, cathodic

Table 20.5 Theoretical, experimental, and empirical model fit values for kinetic, ohmic, and transport parameters for a H_2 PEMFC operating at 80 and 25 °C with a range of oxygen concentrations

Temp. (°C)	Cathode reactant	Theoretical		Experimental			Empirical model parameters				
		E_{theor} (V)	b_c (mV/dec)[a]	OCV (V)	b_c (mV/dec)	R_Ω at 0.5 A/cm^2 (mΩcm^2)	$E_{theor} + A_c$ (V)	b_c (mV/dec)	R_Ω (Ωcm^2)	C_c (mV/dec)	$j_{lim,c}$ (A/cm^2)
80	100% O_2	1.168	70	1.024	58.6	76.6	0.790	59.2	63.1	81.6	2.87
	Air	1.156		0.979	67.3	74.4	0.758	49.7	49.7	99.3	1.27
	10.5% O_2	1.151		0.953	66.5	69.3	0.759	85.6	106	163.4	0.61
	4% O_2	1.144		0.903	75.5	–	0.744	92.5	338	89.5	0.20
25	100% O_2	1.228	59	1.045	57.5	105.9	0.743	75.7	118	–	–
	Air	1.218		0.994	72.6	101.4	0.733	64.9	117	86.5	1.191
	10.5% O_2	1.214		0.970	65.0	92.7	0.768	52.0	81.0	92.1	0.536
	4% O_2	1.208		0.930	75.0	–	0.743	47.3	83.8	6.1	0.150

[a] Theoretical Tafel slope based on $\alpha_c = 0.5$

Tafel slope from the analysis of low-current density data regression (e.g., performed in Sects. 20.2.1 and 20.2.2), and the ohmic resistance (R_Ω) from current interrupt.

Values for the adjustable parameters (($E_{theor} + A_c$), b_c, R_Ω, C_c, and $j_{lim,c}$) obtained via regression of polarization data (V versus j) using an equation of the form given by (20.11) are also summarized in Table 20.5. The empirical model was fitted to the experimental data using nonlinear regression software; fitting curves generated using this model had correlation coefficients in excess of 0.992. The model, therefore, is excellent as a fitting function for fuel cell performance curves from which values can be interpolated or extrapolated. For example, one can estimate the limiting current density in cases where data is insufficient to estimate it experimentally. For comparison, the fitted and experimental data are presented in Fig. 20.25. The accuracy of the estimation, however, is in question as is discussed later.

The regression-generated values for R_Ω can be compared to experimentally measured values. Ohmic resistance calculated using (20.7) was consistent (±15%) with experimental values measured by current interrupt at 25 °C; greater discrepancy (−30 to +50%) between predicted and measured values was observed for the 80 °C data set. The discrepancies suggest that R_Ω in (20.7) is not strictly representative of the membrane resistance but in fact includes additional losses other than the ohmic resistance of the membrane. As noted earlier, although R_Ω in the model is assumed to be independent of current density, it is well established that in actual fuel cell operation, membrane resistance is a function of operating conditions such as current density and gas composition. R_Ω is therefore partially determined by mass transport effects [20.11, 12]. Because the ohmic resistance of the cell is not a fixed value, the resistance R_Ω determined from a fit using the empirical model should more appropriately be considered pseudo-ohmic [20.14].

Values for the Tafel slope predicted from theory can also be compared to values obtained via regression using (20.11) (the full empirical model) and (20.4) (the Tafel equation) to test the model's analytical capability. The theoretical cathodic Tafel slope b_c can be calculated using (20.3).

In this equation, α_c is the transfer coefficient and is assumed equal to 0.5 for the ORR [20.5]. According to this theory, the Tafel slope should be 59 mV/dec and 70 mV/dec at 25 and 80 °C, respectively. Tafel slope analysis using experimental data (i. e., jR-free V_{cell} versus $\log j$) based on the Tafel equation was performed as part of Sects. 20.2.1 and 20.2.2.

Table 20.5 shows that b_c values derived from the regression based on the empirical model were ±30% of the theoretical value. In contrast, those obtained from the Tafel equation via linear regression of jR-compensated $V_{cell} - \log j$ data in the low current density region tended to more closely match theoretical predictions. These results indicate that Tafel slopes are more accurately obtained from raw data using the Tafel equation in comparison to the results extracted from a multiparameter empirical model. One might suggest some physical reasons for the discrepancy, such as the existence of diffusion or resistive losses in the cathode catalyst layer of the electrode. We may argue, however, that the model is too flexible to assign any physical significance to the values of the parameters obtained by force fitting to experimental data (i. e., a large range of values for each parameter in the empirical model yield a reasonably good fit). The model exhibits limited reliability in predicting true physical behavior of individual contributions to the polarization curve, and therefore must be used with utmost caution.

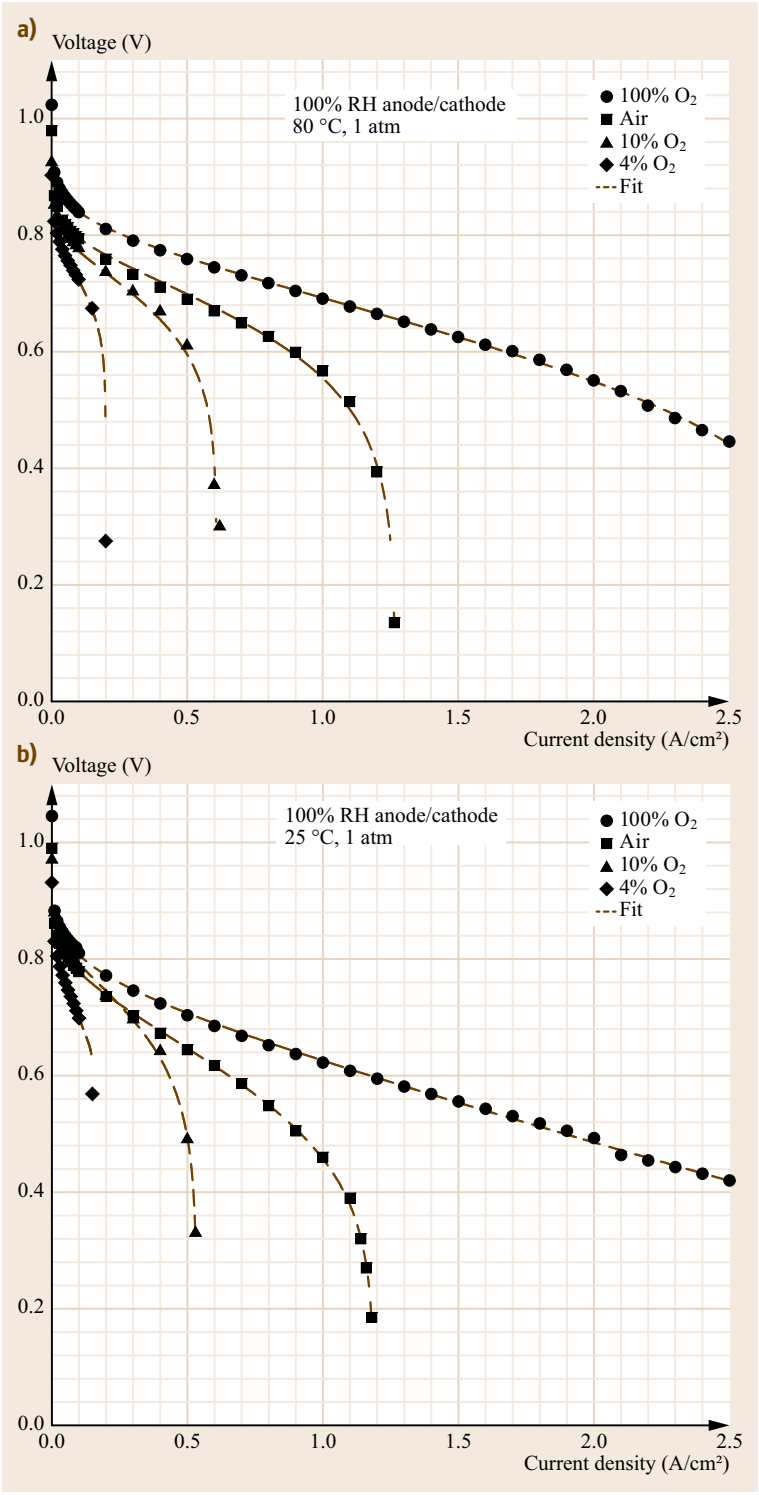


Fig. 20.25a,b Nonlinear regression fits (*dashed line*) of H_2 PEMFC data acquired at 80 °C **(a)** and 25 °C **(b)** for various oxygen concentrations. Conditions: 50 cm^2 cell, 100% RH anode and cathode, 1 atm. Stoichiometry: anode = 2.5×; cathode = 1.5× based on O_2 in air; constant flow rate

Williams et al. presented a more thorough and meaningful methodology to analyze the sources of polarization within PEM fuel cells [20.4].

20.3.2 Summary

In this section, we have examined the application of a simple empirical model to describe the voltage–current density characteristics of the fuel cell, and evaluated the model in terms of its ability to fit the data and its utility as an analytical tool. The model incorporates three main sources of voltage loss: activation polarization (η_{act}), ohmic polarization (η_{Ω}), and concentration polarization. We employ the following assumptions in the application of the model:

1. Polarization at the anode (activation, ohmic and concentration) is negligible in comparison to cathodic contributions.
2. The Tafel equation can be used to describe cathode kinetics.
3. Ohmic resistance is independent of current density.
4. Ohmic losses in the electrodes are negligible.
5. All of the polarization losses are separable and do not interact.

The model fits the experimental data reasonably well. However, given that it is a multiparameter fit, care must be taken to identify whether each parameter is indeed sensitive and can be effectively used to identify main sources of polarization.

20.4 Fuel Crossover and Electrochemical Surface Area

This section examines the evaluation of two key properties of H_2 PEM fuel cells: (a) Hydrogen fuel crossover through the membrane and (b) electrochemically active area of the electrode. These techniques are based on linear potential sweep methods treated in detail by standard texts on electrochemical techniques [20.13, 15].

20.4.1 Hydrogen Crossover and Internal Short Circuit

Crossover of fuel (hydrogen) from one electrode to the other by permeation through the electrolyte degrades the performance of the cell by reducing the OCV of cell through induced mixed potentials and by decreasing fuel efficiency. This phenomenon is referred to as fuel crossover. Oxidant crossover can also occur through a similar mechanism (albeit in the opposite direction).

Direct conduction of electrons between the electrodes through the electrolyte is also a source of loss within a fuel cell. Although the electrolyte of the cell is designed to be electrically insulating and ionically conducting, a finite amount of electron conduction can also occur, especially if small portions of the individual electrode contact one another due to electrolyte thinning. As with crossover, excessive electronic conduction through the electrolyte results in degradation of cell performance.

Fuel crossover and internal short circuits are essentially equivalent. The crossover of one hydrogen molecule resulting in the loss of two electrons is the same as the loss occurring from the conduction of two electrons from the anode to the cathode. A fuel crossover current of $1-2\,\mathrm{mA/cm^2}$ may be acceptable if the operating current density of the system is around $400\,\mathrm{mA/cm^2}$. This proportion equates to a loss of efficiency of 0.25–0.5%.

To experimentally determine the fuel crossover, a suitable inert gas such as nitrogen is used to purge the fuel cell cathode while hydrogen is passed through the fuel cell anode. The potential of the fuel cell cathode (now the working electrode (WE)) is swept by means of a linear potential scan to potentials at which any hydrogen present is instantaneously oxidized. Such experiments are typically referred to as linear sweep voltammetry (LSV) experiments. The output of working electrode (WE) current versus WE potential can be used to derive the hydrogen crossover flux from Faraday's law. The diffusion-limiting current that is attained at electrode potentials is directly related to the hydrogen crossover flux through Faraday's law. The results of such an experiment are shown in Fig. 20.26.

The presence of significant internal shorting within a fuel cell can also be detected from the results of this experiment, and is manifested as a positive slope in the current potential plot (an example of this is shown in Fig. 20.26).

A simpler but less informative approach to detection of crossover is performed by shutting off the cathode oxygen supply and monitoring the OCV of the fuel cell for approximately 2 min [20.16]. Leaking hydrogen gas through membrane to the cathode will react with the available oxygen thereby decreasing the concentration of oxidant. Nernst's law states that the OCV is a function of reactant concentration. Therefore, a decrease in cell voltage arising from the decrease in oxygen concentration indicates fuel crossover. Although relatively

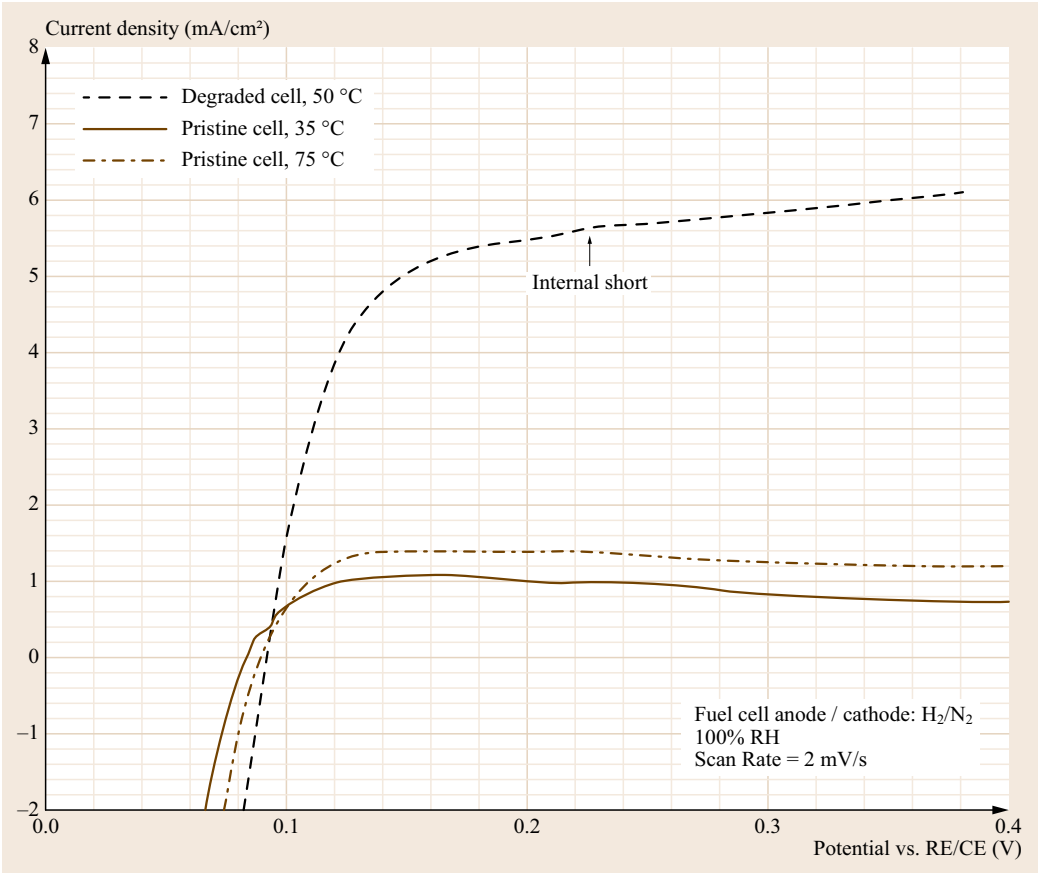


Fig. 20.26 Linear sweep voltammograms for hydrogen crossover in a PEMFC. The limiting current density for the pristine cell at 35 and 75 °C are 1.1 and 1.4 mA/cm^2, respectively, which are indicative of low H_2 crossover flux. In contrast, the limiting current density for the degraded cell was 5.5 mA/cm^2 revealing significantly increased fuel crossover relative to the pristine cell. The positive slope of the degraded cell (not observed for the pristine cell) indicates that an internal short exists within the degraded cell. Test conditions are given in the figure

easy to perform and requiring no special equipment (such as a potentiostat needed for the method described above and performed below), this approach has the disadvantages that the rate of crossover is unknown and the presence or absence of an electrical short is also not indicated.

Electrochemical Surface Area (ECSA) of Electrode Catalyst

Cyclic voltammetry (CV) is a common diagnostic tool for characterizing the electrode properties. A typical PEMFC electrocatalyst layer consists of a mixture of carbon-supported Pt and a proton conducting material such as Nafion (or alternate ionomers). The carbon support enhances the electronic conductivity and provides better Pt dispersions, while the ionomer serves to bind the electrode layer and facilitate proton conduction through the layer. The electrochemical activity of the electrode is dependent on the extent of formation of a three phase boundary where reactants, conducting material and active catalyst sites are in contact with one another.

The technique for determining the electrochemical surface area (ECSA) of a catalyst in an electrode by CV analysis has been used for several decades. The procedure involves cycling the electrode of interest over a voltage range such that charge-transfer reactions are adsorption limited. That is, the electrode potential is such that the number of reactive surface sites can be obtained by recording the total charge required for monolayer adsorption/desorption. Common reactions used when characterizing PEM fuel cell electrodes are the hydrogen adsorption/desorption (HAD) reaction,

$$Pt + H^+ + e^- \leftrightarrow Pt - H_{ads} \qquad (20.12)$$

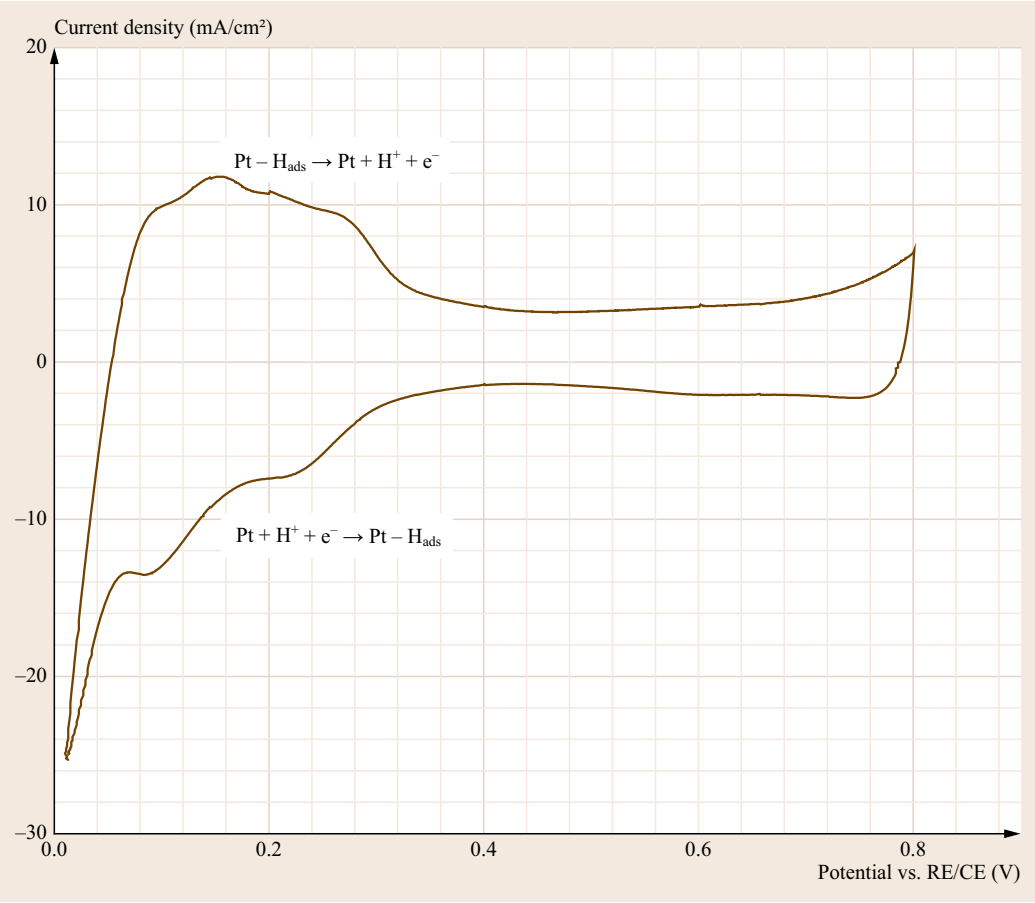


Fig. 20.27 Cyclic voltammogram of PEMFC. Scan rate 40 mV/s; Cell: 50 cm^2, 35 °C; Fuel cell anode/cathode: H_2/N_2, 35 °C humidifier; 1 atm

or the oxidative stripping of adsorbed carbon monoxide (CO) [20.17],

$$Pt - CO_{ads} + H_2O \rightarrow Pt + CO_2 + 2H^- + 2e^- \,. \tag{20.13}$$

Fuel cell electrodes may be examined for their electrocatalytic performance by ex situ or in situ voltammetry experiments. In the case of ex situ experiments (also known as half-cell experiments), the properties of the electrode are evaluated using a standard three-electrode cell with an aqueous solution of acid (typically 0.1 M $HClO_4$) used to simulate the proton-conducting electrolyte in a PEMFC. Half-cell experiments are a convenient and relatively fast method of screening electrocatalysts.

In situ experiments use a two-electrode configuration in which one of the electrodes of the fuel cell serves as both a pseudo-reference electrode and a counter electrode (CE). Typically, the electrochemical activity of the fuel cell cathode is of most interest because of the sluggish kinetics of the ORR. Therefore, this electrode is often chosen to be the WE. The fuel cell anode is used as the CE/RE with the inherent assumption that polarization of this electrode is small relative to the polarization imposed on the fuel cell cathode. The currents obtained in the ECSA tests are small and justify this assumption.

While performing the in situ CV experiment, the fuel cell cathode (WE) is purged with nitrogen, while hydrogen is fed to the anode compartment (counter/reference electrode). Akin to the LSV experiment, the voltage of the WE is swept to high potentials and any hydrogen molecules that cross over through the membrane are instantly oxidized. In contrast to the LSV experiment, in a CV experiment, an additional reverse potential scan is performed. During the reverse potential sweep, proton (H^+) reduction to adsorbed H (H_{ads}) occurs in the potential region 0.4–0.05 V versus the CE/RE (i. e., toward the end of the reverse sweep). An example of such a voltammogram for a Pt electrode is shown in Fig. 20.27.

The reaction of interest [20.18] is the electrochemical reduction of protons (H^+) and subsequent deposi-

tion of atomic hydrogen on the surface of the platinum catalyst. The atomic hydrogen adsorption charge density (q in C/cm^2) due to this reaction can be determined from the CV scan. The ECSA of the Pt catalyst [20.17] is calculated from the charge density, the generally accepted quantity for the charge to reduce a monolayer of protons on Pt ($\Gamma = 210\,\mu C/cm^2$ Pt [20.19, 20]), and the Pt content (i. e., loading) in the electrode (L in g Pt/cm^2 electrode),

$$\text{ECSA cm}^2\text{ Pt / g Pt} = \frac{q}{\Gamma L}\,. \tag{20.14}$$

The ratio of ECSA to the specific area of the Pt used to make the MEA (also in cm^2 Pt/g Pt) is the fraction of catalyst that is electrochemically available to participate in the electrode reactions. This ratio is referred to as *utilization*. Obviously, higher catalyst utilization is better.

Integration of the hydrogen desorption/adsorption peaks that result as a consequence of the forward and reverse scans, respectively, may be used to estimate the electrochemically active surface area of the electrocatalyst. The shaded area represents the total charge arising from hydrogen adsorption. The baseline (current density) is the capacitive current due to charging of the electrode double layer.

During the CV experiment, the potential of the WE is swept first in the anodic direction to oxidize the adsorbed hydrogen (H_{ads}) to H^+ and then in the cathodic direction to electrochemically reduce the H^+ back to H_{ads}. Alternating anodic and cathodic currents occur at the electrode. Experimental results are usually plotted as a graph of current or current density versus the WE potential, and a voltammogram like is obtained. The voltammogram exhibits multiple peaks associated with both the oxidation and reduction reactions. The sweep rate is increased in a CV experiment in comparison to the LSV performed for the crossover experiment to augment the peak size.

Both RH of the gases to which the electrode is exposed, and the electrode temperature impact the measured ECSA. Fully or supersaturated ($\geq$100% RH) are generally used. The ECSA experiment should be conducted on membrane electrode assemblies that have been through a break-in procedure to fully active the electrode.

The flow rate of nitrogen (or other inert gas) on the WE during the voltage sweep can significantly influence the shape of the adsorption/desorption curve and therefore the ECSA measurement [20.21]. The artifact was attributed to the rate of mass transfer of molecular hydrogen (H_2) away from the WE during the voltage scan. With increasing N_2 purge rate, molecular hydrogen is more readily swept from the WE surface, decreasing the partial pressure (concentration) of H_2 at the WE thereby increasing the reversible Nernst potential for hydrogen evolution. Operating conditions that decrease the H_2 concentration at the WE increase the reversible potential for hydrogen evolution, which confounds accurate measurement of the H-adsorption/desorption process. Therefore, relatively low nitrogen flow rate, ≈ 1 sccm/cm^2 of active area is preferred.

Utilization is the fraction of the catalyst's surface area that is electrochemically available in the MEA, obtained by CV on an MEA, to the specific surface area of the catalyst determined by ex situ methods such as particle size analysis. Note that this value represents an idealized condition because the current density is very low and transport resistances that arise at higher current are negligible. In a fuel cell operating at high current density, transport resistances for oxygen and/or protons (H^+) decrease the amount of platinum that participates in the cathode reaction [20.22].

The procedure described here is the most simple for measuring the ECSA in an operating fuel cell. However, it does suffer from some artifacts, such as arising from concentration cell effects and hydrogen crossover. These can be mitigated using modified procedures. Details of those methods can be found in the nice work of *Edmundson* and *Busby* on this topic [20.23].

Procedure

Assemble the MEA, setup the fuel test cell station and connect all gas lines.

The fuel cell anode is purged with 0.20 SLM H_2 at 100% RH, and the fuel cell cathode with 0.5 SLM N_2 at 100% RH.

The potentiostat leads are connected as shown in Fig. 20.28 and any current or sense leads from the test station are disconnected.

To measure hydrogen crossover flux a linear sweep voltammetry LSV or linear polarization experiment from 0 V (vs. open circuit) to 0.8 V (vs. reference) at 2 mV/s is performed.

To determine the ECSA of the electrode catalyst, a CV experiment from 0.05 V (vs. reference) to 1.0 V (vs. reference) at 20 mV/s is performed.

20.4.2 Hydrogen Crossover Test via LSV

Figure 20.26 shows a typical result for an LSV experiment performed under the cell conditions described wherein the current density is shown as a function of voltage. This plot can be used to compare the response of a high-quality pristine cell to that of degraded cell. The pristine cell exhibited a limiting current density

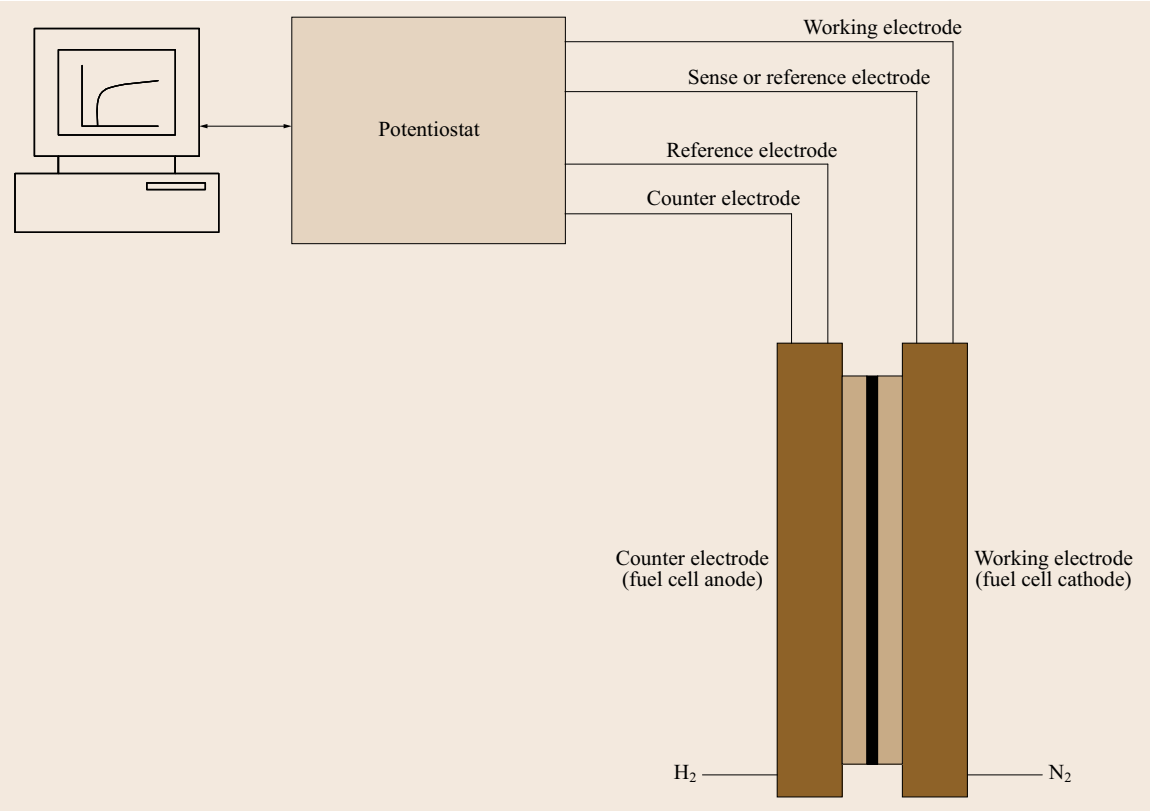


Fig. 20.28 Cell and potentiostat connections for crossover measurement by LSV and ECSA measurement by CV

(j_{lim}) of 1.1 and 1.4 mA/cm^2 at 35 and 75 °C, respectively, which is consistent with an increase in the permeability of hydrogen through the membrane with temperature.

The limiting current density is proportional to the rate of H_2 crossover from the anode to the cathode through the membrane. Applying Faraday's law to determine the limiting hydrogen crossover flux ($\dot{N}_{H_2}$) at 35 °C,

$$\dot{N}_{H_2} = \frac{j_{\text{lim}}}{nF} = \frac{(1.1\times10^{-3}\,\text{A/cm}^2)}{(2\,\text{eq./mol})(96\,485\,\text{C/eq.})}\frac{\text{C}}{\text{As}} = 5.7\times10^{-9}\,\text{mol/(s cm}^2)\,. \tag{20.15}$$

The pristine cell also did not exhibit an internal short as evidenced by the absence of an increasing current with increasing polarization beyond 0.15 V versus RE/CE.

In contrast to the pristine cell, the degraded cell exhibited significant hydrogen flux through the membrane ($j_{\text{lim}} = 5.5\,\text{mA/cm}^2$, $\dot{N}_{H_2} = 2.85\times10^{-8}\,\text{mol/(s cm}^2)$). Figure 20.26 also shows that the degraded cell demonstrated an internal electronic short circuit between the two electrodes. The presence of an internal short within the cell is indicated by the linear, positive slope on the current density versus potential curve. The resistance of the electrical short is estimated to be 333 Ω cm^2 and is obtained from the inverse of the slope of the line in the region 0.2–0.4 V versus CE/RE.

20.4.3 Electrochemically Active Surface Area and Catalyst Utilization Evaluation

Figure 20.27 shows a typical cyclic voltammogram. The reaction of interest is given by (20.12) and the electrochemically active surface area of the platinum catalyst in the cathode which can be estimated from this figure using (20.14).

The cyclic voltammogram of a 50 cm^2 cell is shown in Fig. 20.27, where the data is plotted as current density versus potential. The scan rate (ν) for this experiment was 0.04 V/s. The reduction reaction within the potential range 0.06 to 0.40 V [20.19] which corresponds to a time of 8.5 s (i. e., 0.34 V/0.04 V/s = 8.5 s).

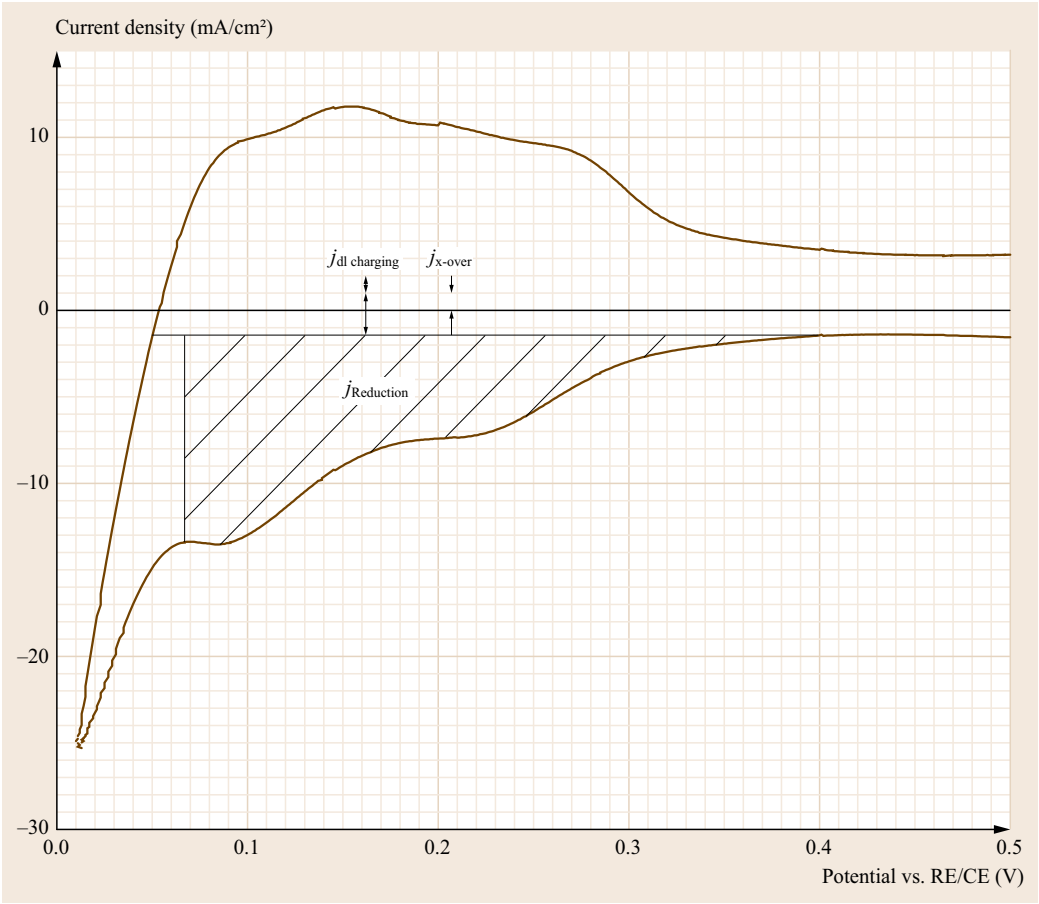


Fig. 20.29 Cyclic voltammogram showing detail of voltage–current density region used for calculation of electrochemically active surface area. The reduction charge density was 43.9 mC/cm^2 (*hatched region*) within the potential window 0.40 to 0.06 V versus RE/CE. The forward and reverse double-layer charging current density, $j_{\text{dl charging}} = 2.3\,\text{mA/cm}^2$, which is offset from the zero current value by the crossover current density, $j_{\text{x-over}} = 0.9\,\text{mA/cm}^2$. Test conditions as described in Fig. 20.27

Recall that the electrode double layer behaves in part like a capacitor. Because the electrode potential is changing with time, non-Faradaic current exists due to charging of the electrode interface, and this current is directly proportional to the scan rate,

$$j_{\text{dl}} = C\frac{\text{d}E}{\text{d}t} = C_{\text{dl}}\nu\,, \tag{20.16}$$

where C_{dl} is the capacitance of the double layer per unit area in C/cm^2.

The charge associated with double-layer charging must be accounted for in the analysis to avoid overestimating the charge attributed to the electrocatalytic activity. From Fig. 20.29, we note that the baseline double-layer charging and discharging current densities ($j_{\text{dl charging}}$) were 2.3 mA/cm^2 in the potential range of 0.4 to 0.06 V where no Faradaic processes are occurring. The double-layer charging charge density over the electrode potential region of interest was 19.6 mC/cm^2 ($= 2.3\,\text{mA/cm}^2 \times 8.5\,\text{s}$). The double-layer charging current density is displaced in the positive direction by an amount equal to the fuel crossover current density ($j_{\text{x-over}}$). Also note that the mean potential at which the oxidation and reduction reaction occurs during, respectively, the forward and reverse scans, is displaced because of the hydrogen crossover.

The net charge density associated with the reduction of protons to adsorbed hydrogen is estimated at 43.9 mC/cm^2, shown as the hatched region in Fig. 20.29. Applying (20.14), the electrochemically ac-

tive surface area of Pt is

$$\begin{aligned}\mathrm{ECSA} &= \left(43.9\,\mathrm{mC/cm^2\,MEA}\right)\\ &\quad\times\left[(210\times10^{-3}\,\mathrm{mC/cm\,Pt})\right.\\ &\quad\left.\times\,(0.4\times10^{-3}\,\mathrm{g\,Pt/cm^3MEA})\right]^{-1}\\ &= 5.23\times10^{5}\,\mathrm{cm^2\,Pt/g\,Pt} = 52.3\,\mathrm{m^2\,Pt/g\,Pt}\,.\end{aligned} \tag{20.17}$$

Assuming that the specific surface area of the Pt used in the manufacturing of the MEA was $70\,\mathrm{m^2\,Pt/g\,Pt}$, this analysis indicates that 75% of the Pt is electrochemically active in the cathode. Thus, catalyst utilization is 75% for this MEA.

Summary

In this part, we examine, through laboratory examples, the evaluation of two key properties of H_2 PEM fuel cells: hydrogen fuel crossover through the membrane and electrochemically active area of the electrode. The techniques used are LSV and CV, and are of high importance for the characterization and proper evaluation of PEM fuel cells.

The method for determining the ECSA of a catalyst in an electrode by CV involves cycling the electrode of interest (mostly the cathode of the PEMFC) typically from 0.05 to 0.8 V versus RE/CE at a scan rate usually in the interval 20–50 mV/s. The atomic hydrogen adsorption charge density can be determined from the CV scan. The ECSA of the Pt catalyst is calculated from the charge density, the generally accepted quantity for the charge to reduce a monolayer of protons on Pt ($210\,\mu\mathrm{C/cm^2\,Pt}$), and the Pt content in the electrode. The charge associated with double-layer charging and hydrogen crossover currents must be accounted for in the analysis, by proper selection of the integration baseline (as shown in Fig. 20.29), to avoid overestimating the charge attributed to the electrocatalytic activity.

Platinum utilization is the ratio of the catalyst surface area that is electrochemically available in the MEA, as obtained by CV on an MEA, to the specific surface area of the catalyst determined by ex situ methods such as particle size analysis or chemisorption measurements.

Fuel crossover through the PEM degrades the performance of the cell by reducing the OCV through induced mixed potentials and by decreasing fuel efficiency. Over time, this also contributes to electrolyte degradation. Direct conduction of electrons between the electrodes through the electrolyte (short circuit) is also a source of loss within a fuel cell. Fuel crossover and internal short circuits are essentially equivalent and can be estimated using LSV (scanning from OCV to 0.4 V versus RE/CE). The diffusion limiting current that is attained at electrode potentials of approximately 0.4 V is directly related to the hydrogen crossover flux through Faraday's law. Typically, a fuel crossover current of 1 to $2\,\mathrm{mA/cm^2}$ is acceptable. The presence of significant internal shorting within a fuel cell can also be detected from the results of this experiment, and is manifested as a positive slope in the current potential plot.

20.5 Impedance Spectroscopy of PEM Fuel Cells

A fuel cell is a complicated electrochemical system. The performance of a fuel cell is a complex interplay of many factors that include structural and operating characteristics of the cell. Some factors are interrelated while others are independent. Furthermore, some properties and processes occurring within the cell are responsive to changes in the cell conditions over a broad range of timescales. For example, diffusion processes occur on the order of subseconds to seconds whereas charge transfer processes (electrode reactions) can occur at much shorter time scale (submilliseconds). Because the time constants differ for different processes that take place in the fuel cell, their effects are revealed at different perturbation frequencies.

Impedance spectroscopy takes advantage of the large spectrum of timescales over which different processes within the fuel cell occur to separate their individual effects. Processes that respond slowly (or not at all) relative to other processes at one time scale can be separated from those that occur at a different timescale based on the measured impedance response of the electrochemical device over a broad range of frequencies.

In short, electrochemical impedance spectroscopy is an experimental technique that involves imposing a small sinusoidal AC voltage or current signal of known amplitude and frequency – the perturbation – to an electrochemical cell and monitoring the AC amplitude and phase response of the cell. The AC perturbation is typically applied over a wide range of frequencies, from 10 kHz or greater to less than 1 Hz; hence, the name impedance *spectroscopy*. The ratio and phase-relation of the AC voltage and current signal response is the complex impedance, $Z(\mathrm{i}\omega)$. The result of an impedance spectroscopy experiment is a rich data set from which many properties of the electrochemical cell may be extracted via application of physically reason-

able equivalent circuit models. Properties of the electrochemical system commonly evaluated using impedance spectroscopy include ohmic (bulk) resistance, electrode properties such as charge transfer resistance and double-layer capacitance, and transport (diffusion) effects.

Theory and concepts critical to understanding impedance spectroscopy and its practical implementation to fuel cells are covered in the following sections. Thorough treatment of this powerful, noninvasive diagnostic technique including its application to fuel cells and other electrochemical power sources are presented in [20.24]. Readers interested in more in-depth description of impedance or those intending to apply this technique for fuel cell studies are encouraged to follow-up with the referenced book as well as applicable technical articles, some of which are referenced here [20.25–27].

20.5.1 Impedance Theory and Practice

A sinusoidal current signal of amplitude I_{AC} and frequency ω can be defined as

$$I(\omega) = I_{AC}\sin(\omega t)\,, \tag{20.18}$$

where t is time. The output AC voltage signal from the electrochemical cell can be defined as

$$V(\omega) = V_{AC}\sin[(\omega t) - \theta]\,, \tag{20.19}$$

where V_{AC} is the amplitude of the output voltage signal and θ is the phase angle. The phase angle is the difference in the phase of the sinusoidal voltage and current signals. Figure 20.30 illustrates the voltage and current responses of a fuel cell that is subject to a sinusoidal AC input signal. In the case of an AC signal, the *resistance* of a circuit or electrochemical device which is not purely resistive will be a function of the frequency of oscillation of the input signal. Ohm's law for the AC case is expressed as

$$Z(\mathrm{i}\omega) = \frac{V(\mathrm{i}\omega)}{I(\mathrm{i}\omega)}\,, \tag{20.20}$$

where $Z(\mathrm{i}\omega)$ is the complex impedance (Ω) and i is the imaginary number

$$\mathrm{i} = \sqrt{-1}\,. \tag{20.21}$$

Equation (20.20) indicates that impedance is a complex value. That is, it can take on both real and imaginary components. Note that the imaginary component of the impedance is a real measurable quantity: the i is for bookkeeping purposes and allows description of the out-of-phase component of the impedance. The complex relationship of impedance is implicit so $Z(\mathrm{i}\omega)$ is normally written as $Z(\omega)$. Although one can think of impedance as *resistance* to current, it is more general than that because it takes into account the phase difference between voltage and current. Equation (20.20) also indicates that impedance depends on the frequency at which it is measured; Z can change as the frequency of the AC signal changes.

Frequency in cycles per second, $f(\mathrm{Hz} = 1/\mathrm{s})$, is obtained through the relation

$$\omega = 2\pi f\,. \tag{20.22}$$

Equation (20.20) can be written in complex notation as

$$Z = Z' + Z''\,, \tag{20.23}$$

where

$$Z' = \mathrm{Re}(Z) = |Z|\cos\theta$$
real (in-phase) component of impedance, (20.24)

$$Z'' = \mathrm{Im}(Z) = |Z|\sin\theta$$
imaginary (out-of-phase) component of impedance. (20.25)

The magnitude of the combined real and imaginary components can be calculated as

$$|Z| = \sqrt{(Z')^2 + (Z'')^2}$$
magnitude of impedance, (20.26)

and

$$\theta = \tan^{-1}\left(\frac{Z''}{Z'}\right)\,. \tag{20.27}$$

Note that the original time-variance of V and I, the input/response signals given by (20.18) and (20.19), have disappeared in (20.23) through (20.27) and the impedance at a fixed frequency itself is time invariant as long as the system itself is time invariant.

Equivalent Circuits – Ideal and Distributed Elements

Although physics-based models for the impedance response of PEM fuel cells have been developed [20.25–31], they are often simplified representations of real systems (e.g., one-dimensional (1-D)), applicable at specific conditions (e.g., open circuit), and they can be complicated, requiring significant computational resources to implement. An alternative approach is to attempt to explain, understand, and extract physically

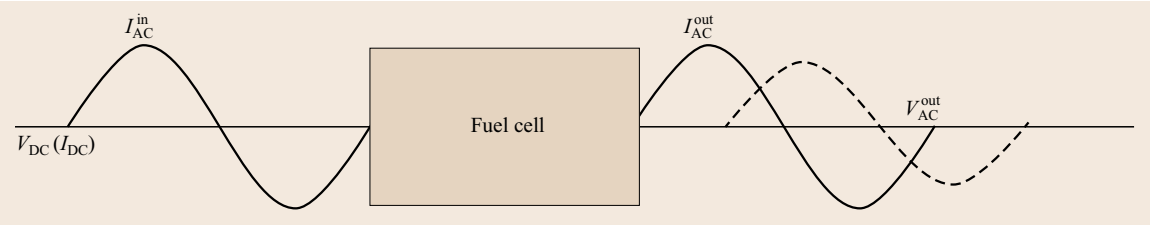


Fig. 20.30 An electrochemical impedance experiment is based on monitoring the AC response of an electrochemical cell that results from imposing a small AC signal. The impedance is the ratio of the AC voltage and current output. In an impedance *spectroscopy* experiment, the frequency of the AC perturbation is swept over a range, from ≈ 10 kHz to less than 1 Hz and the impedance is evaluated as a function of frequency to evaluate the properties of the electrochemical system under investigation

meaningful properties of the electrochemical system by modeling the experimental impedance data in terms of an *equivalent circuit* composed of ideal resistor R, capacitor C, inductor L, and distributed circuit elements. In the equivalent circuit analog resistors represent conductive pathways for ion and electron transfer. As such, a resistor can represent the bulk resistance of a material such as the resistance of the electrolyte to ion transport or the resistance of a conductor to electron transport, or the resistance to the charge-transfer step at the surface of the electrode. Capacitors and inductors are associated with space-charge polarization regions, such as the electrochemical double layer, and adsorption and electrocrystallization processes at an electrode, respectively.

The impedance relationships of ideal electrical elements, commonly used to describe the impedance of electrochemical systems, are:

- Resistor:
  - Defining relationship:

$$V = IR\,,$$

  - Impedance:

$$Z_R = R\,; \tag{20.28}$$

- Capacitor:
  - Defining relationship:

$$I = C\frac{dV}{dt}\,,$$

  - Impedance:

$$Z_C = \frac{1}{i\omega C} = -\frac{i}{\omega C}\,; \tag{20.29}$$

- Inductor:
  - Defining relationship:

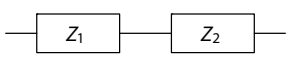
$$V = L\frac{dI}{dt}\,,$$

  - Impedance:

$$Z_L = i\omega L\,. \tag{20.30}$$

We see that the impedance of a resistor Z_R is not a function of frequency whereas the impedance of capacitor Z_C is inversely proportional to ω and the impedance of an inductor Z_L scales linearly with frequency ω. Note the implications of these relationships in the context of an electrochemical system: the impedance of a resistor does not change with frequency; however, the impedance of a capacitor becomes very small at high frequency and very large at low frequency. Therefore, a capacitor or capacitive-like feature of an electrochemical cell behaves as a short circuit with $Z_C \to 0$ as $\omega \to \infty$, and at the other extreme, as an insulator with $Z_C \to \infty$ as $\omega \to 0$. This means that the impedance of a feature or process within an electrochemical device that behaves like a capacitor, such as the electrode double layer, becomes insignificant at high frequency. In effect, the double layer behaves as a short circuit at high frequency, where its impedance becomes negligible. Conversely, the impedance of the double layer becomes very large at very low frequency. Generally, one measures impedance over a range of frequency and it is the analysis of the resulting $Z(\omega)$ versus ω response from which one derives information about the electrical and electrochemical properties of the electrode–material system.

The Ohm's law-like relationship between the complex voltage and current allows the impedance of a circuit with multiple elements to be calculated using the same rules as with multiple resistors. The total impedance of two elements in series is the sum of the impedances of the individual elements



$$Z_{\text{total, series}} = Z_1 + Z_2\,. \tag{20.31}$$

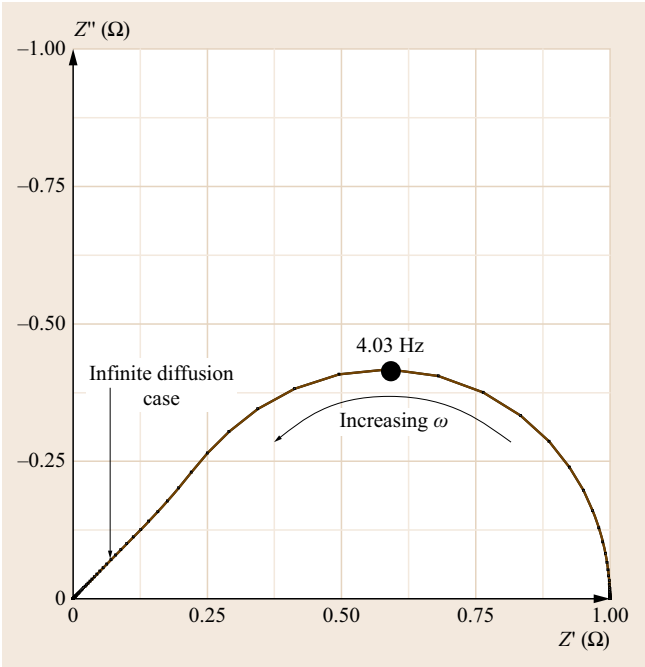
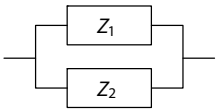


Fig. 20.31 Complex-plane impedance plot of a finite length Warburg element with a short circuit terminus. For example, $R_W = 1\,\Omega$ and $l_{eff}^2/D_{eff} = s/\omega = 0.1$. The frequency at which Z'' is a maximum, $\omega_{max} = 2.53/0.1 = 25.3\,\text{rad/s} = 4.03\,\text{Hz}$

Likewise, the impedance of two elements in parallel is given by



$$\frac{1}{Z_{\text{total, parallel}}} = \frac{1}{Z_1} + \frac{1}{Z_2}\,. \tag{20.32}$$

Note that the order of *series* elements in the equivalent circuit has no influence on the impedance spectrum. In the earlier given figures, the impedance response would be the same whether Z_2 follows Z_1 or Z_1 follows Z_2. While it may be helpful to arrange series circuit elements in a way that is consistent with the physical layout of the electrochemical cell, this is not strictly required. Of course, the impedance of elements arranged in parallel and in series are not the same.

The propriety of using pure resistor, capacitor, and inductor elements, which are lumped-constant quantities with ideal properties, to describe the characteristics of real electrochemical systems is tempered by the complexity of actual cells in which material properties can exhibit a distribution of values and because processes, such as diffusion, occur over a finite distance. For this reason, equivalent circuit models often invoke elements which are intended to mimic the impedance characteristics of processes or reactions which are distributed in nature. A common distributed element is the constant phase element (CPE), the impedance of which is defined as,

$$Z_{\text{CPE}} = \frac{1}{\Gamma(\mathrm{i}\omega)^p}\,, \tag{20.33}$$

where Γ and p are usually assumed to be frequency-independent parameters. The units for Γ are s^p/Ω, while those for capacitance C are s/Ω (= F). Hence, in the case of an ideal capacitor or resistor, $p = 1$ or 0, respectively, and either the magnitude of Γ equals the magnitude of C with the dimension s/Ω or $1/\Gamma$ equals R in Ω (compare (20.33) to (20.29) or (20.28)). Often, a CPE is used in an equivalent circuit model in place of a capacitor to compensate for nonhomogeneity in the system. For example, a rough or porous surface can cause the double-layer capacitance to appear as a CPE with $p \approx 0.8$ to 0.9. This issue is the task of extracting physically meaningful parameters conveyed by the capacitance for impedance data that is best represented in an electrical circuit model by a CPE. Examples of such parameters extracted from ideal interfacial capacitance include electrode area in the case of double-layer capacitance and surface coverage in the case of an adsorption-induced pseudo-capacitance. CPEs can also be used to model diffusional processes under some conditions [20.24].

The Warburg impedance is another common distributed impedance element. It is the electrical analog of diffusion processes in the absence of migration. Various versions of the Warburg impedance exist depending on whether the diffusion can be considered to occur over a finite, semi-infinite or infinite distance. Because of the small distances involved in a fuel cell, the finite length case with a short-circuit (resistive) terminus is typically appropriate. The impedance relationship for this Warburg element is

$$Z_W = R_W \frac{\tanh\left(\sqrt{\mathrm{i}s}\right)}{\sqrt{\mathrm{i}s}}\,, \tag{20.34}$$

where R_W is the effective resistance of the diffusion process and,

$$s = \frac{\ell_{\text{eff}}^2 \omega}{D_{\text{eff}}}\,. \tag{20.35}$$

In (20.35), ℓ_{eff} is the effective diffusion distance and D_{eff} is the effective diffusion coefficient. The term *effective* is applied to these parameters to emphasize that,

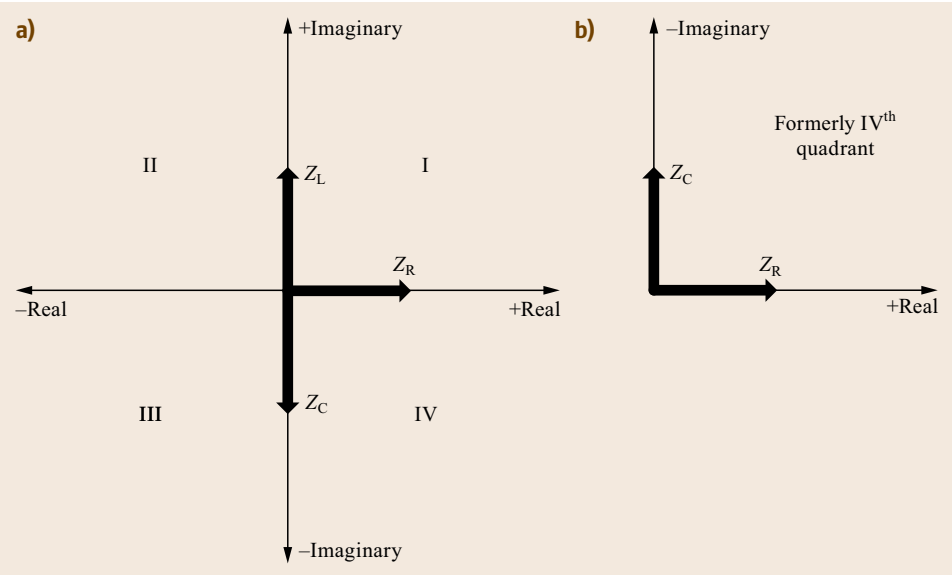


Fig. 20.32a,b Complex plane representation of impedance data. **(a)** Four quadrants are required to show all combinations of real and imaginary impedance. **(b)** Presentation of impedance data for electrochemical cells is typically done by plotting the IVth quadrant in the *top right* (i. e., $-Z''$ versus $+Z'$) because capacitive behavior is more often observed than inductive behavior in electrochemical systems

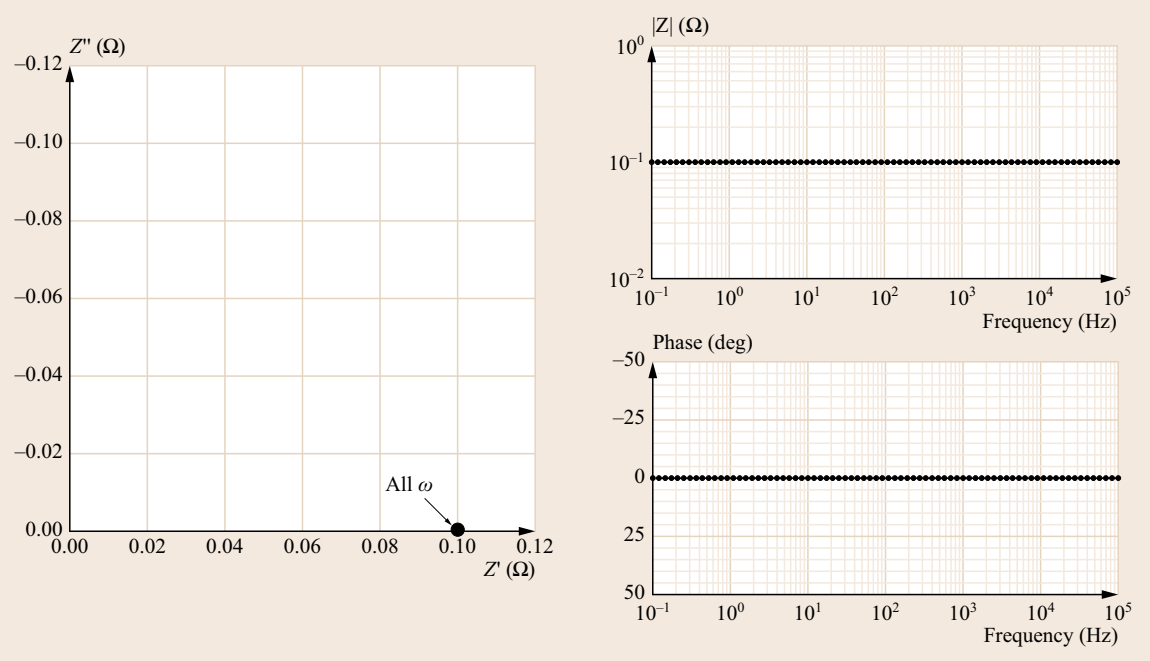


Fig. 20.33 Impedance plots for a pure resistor, $R = 0.1\,\Omega$. $Z' = |Z| = 0.1\,\Omega$ per (20.29) and $Z'' = 0$ and $\theta = 0°$ (in-phase) at all frequencies

depending on the circumstance, nominal properties may not apply. For example, in porous electrodes tortuosity can result in an effective diffusion distance greater than the nominal or straight-line diffusion distance. Likewise, the diffusivity of a pure gas differs from that when mixed with another gas (e.g., $D_{O_2,\text{pure } O_2} \neq D_{O_2,O_2+N_2}$).

The complex plane plot for the finite length Warburg impedance, shown in Fig. 20.31, has two distinct regions: a 45° branch at high frequency and a semicircle or arc at low frequency. Presentation of impedance spectroscopy data is discussed in Figs. 20.32–20.34 The impedance of this finite Warburg diffusion ele-

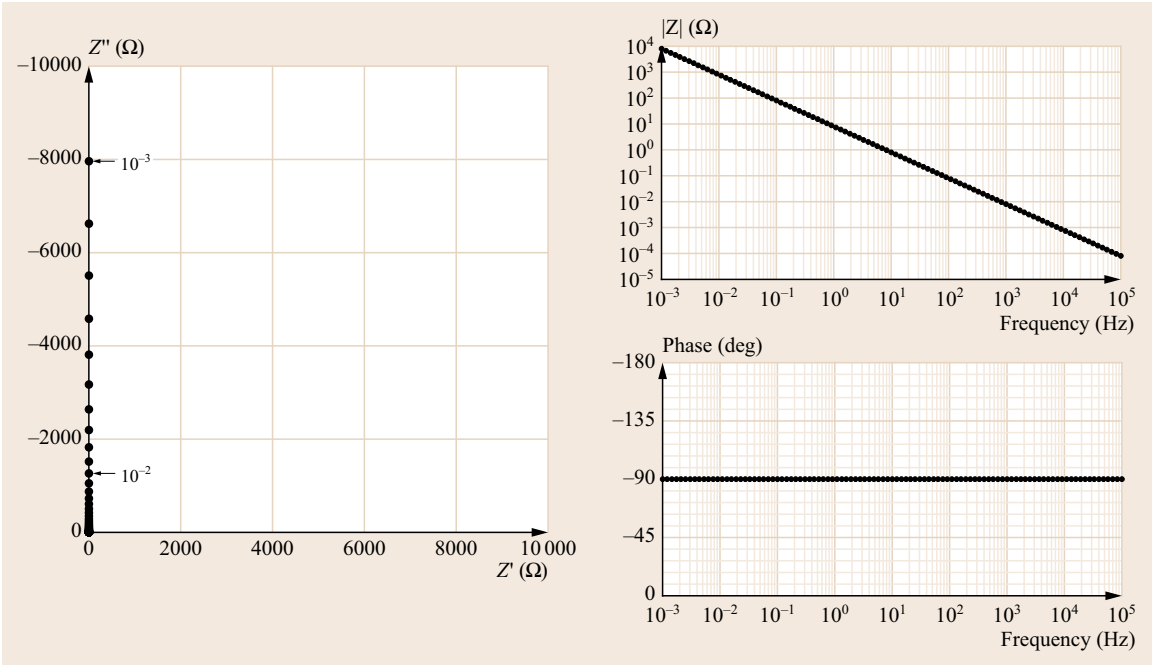


Fig. 20.34 Impedance plots for a pure capacitor $C = 0.02\,\mathrm{F}$. Z'' becomes more negative with decreasing ω according to (20.30); $Z' = 0$ and $\theta = -90°$ (out-of-phase) at all frequencies. Frequency is implicit in the complex plane plot; two frequency labels have been added for clarification (10^{-3} and $10^{-2}\,\mathrm{Hz}$)

ment reaches a peak value of $-Z'' = 0.417\,\mathrm{R_W}$ at $s = 2.53$.

The low-frequency behavior occurs when $s \ll 3$ where Z_W is well-characterized by a parallel resistor–capacitor element combination with values R_W and C_D which can be related by (20.36). Note that $Z_\mathrm{W} \to R_\mathrm{W}$ as $\omega \to 0$.

$$C_\mathrm{D} = \frac{l_\mathrm{eff}^2}{3 D_\mathrm{eff} R_\mathrm{W}} \,. \tag{20.36}$$

At high frequency, where $s \gg 3$, the impedance exhibits the 45° response indicative of the infinite diffusion case. That is, the frequency-dependent diffusion distance, $\ell_\mathrm{D} = (D_\mathrm{eff}/\omega)^{1/2}$, is much smaller than the effective diffusion distance, l_eff, where s can be rewritten as $s = (\ell_\mathrm{eff}/\ell_\mathrm{D})^2$. It is evident that when $\ell_\mathrm{D} \ll \ell_\mathrm{eff}$, which occurs at high frequencies, the diffusion length is much less than the region available for diffusion and the diffusional impedance approaches the infinite case. As ℓ_D approaches ℓ_eff with decreasing ω (i. e., as $s \to 3$), the infinite diffusion impedance response is no longer applicable (observed) because diffusion begins to be limited. Additional discourse on the Warburg impedance is presented in [20.24].

It is worth noting that effective equivalent circuit modeling of a complex electrochemical cell such as a fuel cell requires considerable understanding of the system being studied. Different processes can result in essentially similar impedance response. Care must be taken when developing models to incorporate key features that may influence the impedance response. For example, are the electrodes planar or porous? Is resistance to transport of gaseous or dissolved species likely to be present within the system? Obviously, the relevance of values extracted from an equivalent circuit model that is fit to experimental data is only as good as the model used in the fit.

Furthermore, an equivalent circuit consisting of multiple elements can often be arranged in multiple ways to yield exactly the same impedance behavior. It can debatable as to which specific equivalent circuit out of many should be used to analyze and interpret experimental data in order to gain the appropriate physiochemical insight. Approaches to resolving this complication include applying intuition to the physical system, and, given equally good fits, using the simplest circuit with the smallest number of elements. Executing several measurements using different experimental conditions that one intuitively would expect would exacerbate, reduce, or eliminate some component of the impedance to the system is advantageous. For example, contribution of diffusional processes to the impedance of a system can often be identified by changing the

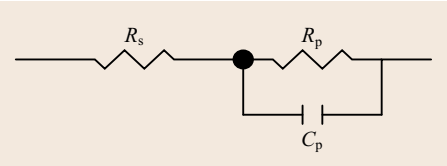


Fig. 20.35 Some simple electrochemical half-cells may be represented by a Randles circuit composed of a resistor (R_s) in series with a resistor (R_p) and capacitor (C_p) in parallel; R_s represents the ohmic resistance of the electrochemical/electrical circuit, R_p represents the resistance to charge transfer at the electrolyte/electrode interface, and C_p represents the double-layer capacitance at that interface

concentration of the transport-limited species and/or its diffusion distance. Finally, one can compare the results of an equivalent circuit model to a physics-based model if the latter is available.

Inductive-like Impedance Behavior

Impedance response that appears inductive in nature ($Z'' > 0$) is sometimes observed at high and low frequencies in electrochemical systems. Inductive behavior at high frequencies is attributed to cell geometry, electrical leads and connectors, and performance characteristics of the analytical instrumentation.

Pseudo-inductive response at low frequency in fuel cells is sometimes reported [20.32] and mechanistic interpretations of the source are emerging. One proposed origin of low frequency (< 3 Hz) inductive or pseudo-inductive behavior in PEM fuel cells is associated with a multi electron-transfer step with an adsorbed intermediate species [20.27, 33]. According to this theory, the ORR on platinum nanoparticles proceeds via a multistep mechanism consisting of a fast oxygen adsorption step that is at equilibrium (the process occurring too fast to be detected in an impedance measurement), a first electron-transfer step that controls the overall rate of reaction (rate determining step), and subsequent chemical and electrochemical steps. Physiochemical-based impedance models predict low frequency pseudo-inductive behavior under some conditions as a result of the multistep process [20.27].

Low frequency inductive-like behavior observed in CO poisoning of a PEMFC anode was attributed to the surface relaxation of the interface although a physiochemical mechanism for interfacial relaxation was not addressed [20.24, 34]. Details of the equivalent circuit and impedance expressions are presented in the references. The same concept of interfacial relaxation was invoked in the model of the Faradaic impedance of DMFC anodes in which methanol oxidation was assumed to proceed by a multistep reaction involving intermediate adsorbed CO [20.35].

Presentation of Impedance Data

Equations (20.23)–(20.27) reveal that there are four parameters that describe impedance at a given frequency: the real and imaginary impedance (Z', Z''), the impedance magnitude ($|Z|$), and the phase angle (θ). These four parameters are related; frequency is an independent variable.

Because of the wealth of information that may be contained within impedance data, graphical presentation typically consists of a plot of the components of the complex impedance (Z'' versus Z') as well as plots of the magnitude of the impedance and phase as a function of frequency ($\log|Z|$ versus $\log\omega$ and θ versus $\log\omega$). The former are often described as complex plane or Nyquist plots and the latter are typically referred to as Bode plots.

A plot of the complex plane is shown in Fig. 20.32a where the real and imaginary components are plotted. Note that frequency is implicit in this representation of data. Because capacitive-like behavior is commonly encountered in electrochemical systems, and inductive-like behavior less so, electrochemical impedance data is generally presented with the IVth quadrant in the right top as indicated in Fig. 20.32b. Inductive-like behavior can be modeled with negative resistor and capacitor elements. The advantage of this format is that individual charge transfer steps and time constants are easily observed; the disadvantage is that the plot contains no frequency information and one can get the exact same graph for different capacitances.

As an example of how circuit elements manifest themselves in graphical form, we now consider the impedance of a pure resistor, a pure capacitor, and a simple electrochemical half-cell resistor–capacitor (R–C) circuit. Figure 20.33 reveals that for a resistor $R = 0.1\,\Omega$, the components of the complex impedance are simply $Z' = |Z| = 0.1\,\Omega$, $Z'' = 0$ and $\theta = 0°$ (in-phase) at all frequency ω. This can be seen by the defining relation for the impedance of a resistor given by (20.28). In contrast to a resistive element, the impedance of a capacitor, given by the (20.29), is inversely proportional to frequency. The Nyquist and Bode plots for a pure capacitor of magnitude 0.02 F are shown in Fig. 20.34. The real component of the impedance is zero and the phase angle is $\theta = -90°$ (out-of-phase) at all frequencies; as frequency increases, Z'' becomes less negative and $|Z|$ decreases.

Finally, we plot the impedance response for a simple circuit often descriptive of an electrochemical half-cell: the Randles equivalent circuit shown in Fig. 20.35. This circuit consists of a resistance in series (R_s) with a parallel resistor–capacitor element ($R_p - C_p$). In an electrochemical half-cell, R_s represents the uncompen-

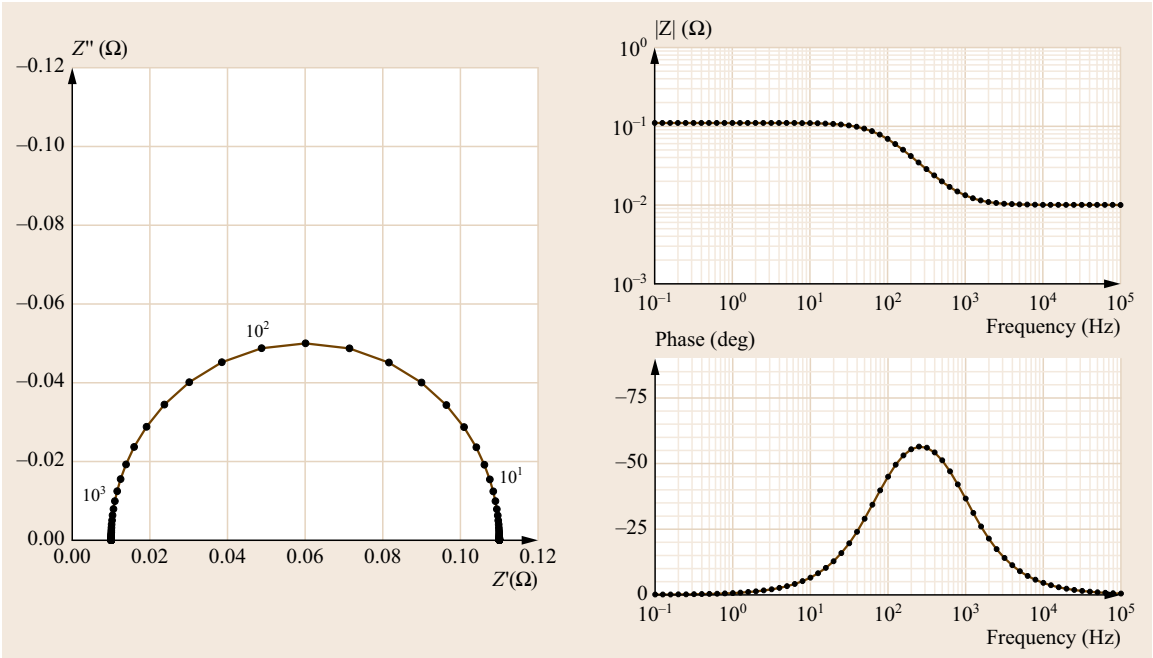


Fig. 20.36 Impedance plots for the Randles circuit depicted in Fig. 20.35 where $R_s = 0.01\,\Omega$, $R_p = 0.1\,\Omega$ and $Cp = 0.02\,\mathrm{F}$. Three frequency labels have been added to the complex plane plot for clarification (10^3, 10^2, and $10^1\,\mathrm{Hz}$)

sated ohmic resistance ($R_s = R_\Omega$) of the electrochemical/electrical circuit, R_p represents the resistance to charge transfer at the electrolyte/electrode interface ($R_p = R_{ct}$), and C_p represents the double-layer capacitance at that interface ($C_p = C_{dl}$).

Impedance plots for this equivalent circuit are shown in Fig. 20.36. In the complex plane plot, the impedance appears as a semicircle or loop with the high-frequency intercept R_{hf} equal to the value of the series resistor ($R_{hf} = R_s = R_\Omega$). The low-frequency intercept R_{lf} is equal to the sum of the series and parallel resistance elements ($R_{lf} = R_s + R_p = R_\Omega + R_{ct}$). The time constant τ for the parallel $R_p - C_p$ element is given by

$$\tau = R_p C_p = R_{ct} C_{dl} \tag{20.37}$$

and

$$\omega_{max} = \frac{1}{\tau}\,, \tag{20.38}$$

where ω_{max} is the frequency at which the imaginary component of the impedance is the most negative (i. e., at the top of the semicircle). Knowledge of R_{ct} and ω_{max} allows one to determine the capacitive component of the electrochemical system ($C_p = C_{dl}$) from (20.37).

The Nyquist plot for the Randles circuit representation of an electrochemical half-cell with finite ohmic resistance is schematically shown in Fig. 20.37.

Criterion for Valid Impedance Measurements

There are four requirements that must be met for valid impedance measurements:

1. Linearity – Impedance measurements are meaningful only when the system under study behaves linearly. That is, doubling the amplitude of the AC perturbation (e.g., AC current ΔI_{AC}) should result in a doubling of the AC response (AC voltage ΔV_{AC}). This can be observed through the use of an oscilloscope. Another measure of linearity is that changing the AC amplitude should not change the impedance response. With that in mind, one can make repeated EIS scans with increasing AC perturbation, for example, $I_{AC} = 0.5$, 1, 2, 5%, etc. of the fuel cell DC (direct current) load current. At very small AC signals, the EIS data will be noisy, because either the AC current or AC voltage will be too small to accurately measure. At large AC signals, the EIS data will start to change because of nonlinearity. Use an AC perturbation that is large enough so that there is little or no noise but small enough that the EIS data is not itself a function of the AC magnitude.

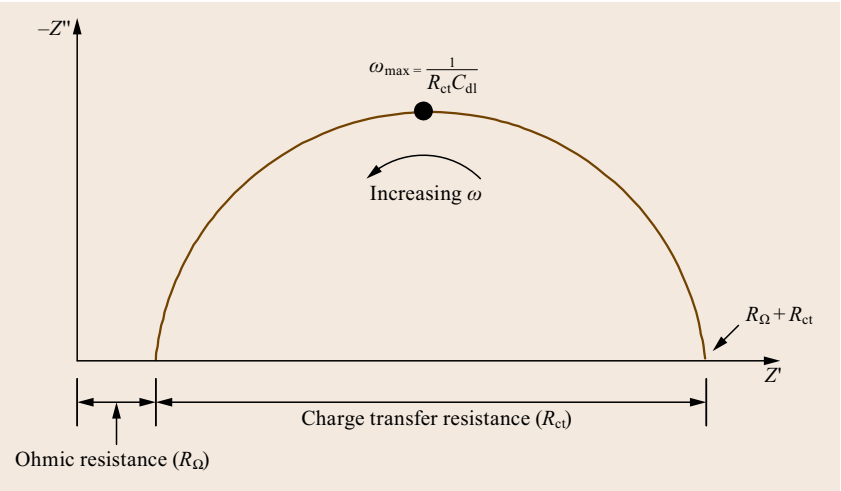


Fig. 20.37 Complex plane representation of impedance data for an equivalent circuit analog to an electrochemical half-cell consisting of an ideal parallel resistor–capacitor ($R_{ct} - C_{dl}$) network in series with a finite ohmic resistance (R_Ω) as shown in Fig. 20.35

As noted by *Orazem* and *Tribollet* [20.36], the amplitude depends on the system under study: large amplitude signals can be tolerated by systems that exhibit a linear current–voltage response whereas for systems that exhibit very nonlinear current–voltage behavior, small amplitude signal is needed. A good rule of thumb advocated by *Orazem* and *Tribollet* [20.36] for satisfying the criteria for linearity is to limit the AC voltage perturbation $\Delta V_{AC,lim}$ to,

$$b\Delta V_{AC,lim} \leq 0.2\,, \qquad (20.39)$$

where $b[V^{-1}] = 2.303/\beta$, and β is the Tafel slope [V/dec]. So, if the Tafel slope of the controlling reaction is known, one can calculate the AC voltage that would ensure that the criteria of linearity are satisfied. We can calculate the maximum ΔV_{AC} that resulted from the imposed AC current during the EIS measurement: $\Delta V_{AC,max} = |Z_{max}| \times \Delta I_{AC}$ and verify that $\Delta V_{AC,max} < \Delta V_{AC,lim}$. The largest impedance $|Z_{max}|$ is generally at low frequency.

Thus, although electrochemical systems are highly nonlinear, this requirement is satisfied for small perturbations. It is imperative that the signal amplitude be sufficiently small such that the interface behaves linearly during the impedance experiment. Typical applied or induced AC voltage amplitudes are 5 to 15 mV. Impedance testing of fuel cells and other electrochemical energy devices under load typically involves applying an AC current signal as opposed to an AC voltage perturbation. The magnitude of the applied AC current should be such that the resulting AC voltage perturbation of the cell is no more than a few tens of millivolts.

2. Causality – The response of the system is only due to the applied perturbation and does not contain significant contributions from spurious sources. This includes artifacts due to the limitations of the measurement electronics or electromagnetic interference (EMI) that corrupts proper functioning of the measurement circuitry, sometimes experimentally observed near line voltage frequencies (50–60 Hz). Cyclic signals generated by associated equipment, such as a peristaltic pump, can also introduce artifacts to the apparent response of the system at specific frequencies.
3. Stability – The system must return to its original state after the perturbation is removed. For systems operated under galvanostatic control (constant current), the cell voltage after the impedance scan should be the same as the cell voltage prior to the impedance sweep. Likewise, for a cell operated in potentiostatic mode (constant voltage), the current should be the same before and after the impedance measurement.
4. Finite – The impedance must be finite at $\omega = 0$ and $\omega = \infty$ and it must be a continuous and finite-valued function at all intermediate frequencies.

Satisfaction of these criteria is necessary for valid and meaningful impedance measurements.

Instrumentation for Impedance Spectroscopy

In an impedance spectroscopy experiment, a small AC signal is applied to the electronic load to modulate the DC load current. The signal generator of the frequency response analyzer (FRA) instrument controls the DC current of the electronic load current such that the load superimposes a small AC signal on DC current.

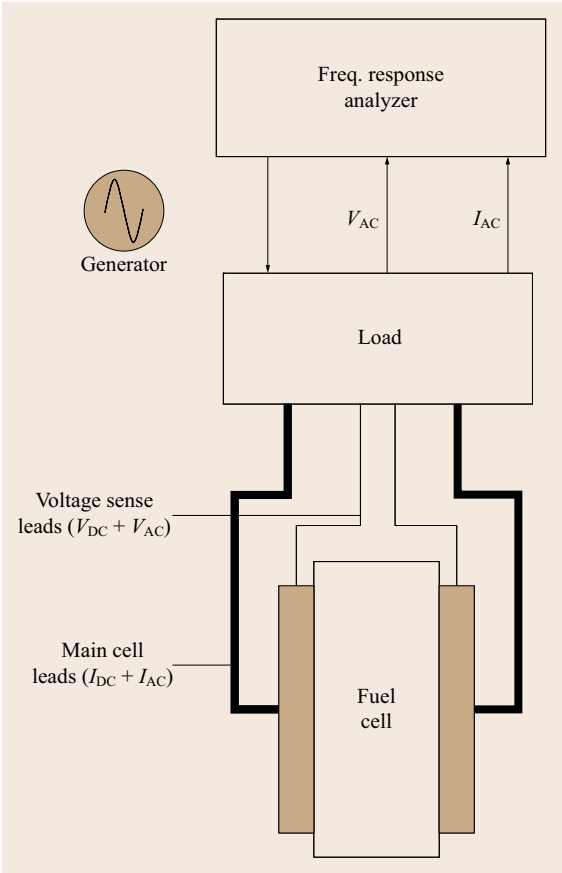


Fig. 20.38 Schematic of the equipment setup for impedance spectroscopy measurements. The AC signal imposed on the cell is done by modulating the load with the FRA. Electrical current is carried in the main leads and the voltage sense leads, connected to a high-input impedance electrometer, measure the voltage of the cell or voltage of one electrode versus a reference electrode

The equipment setup is illustrated in Fig. 20.38. The AC voltage and current signals output from the electrochemical device are analyzed by the FRA to obtain the complex impedance of the device (i. e., magnitude and phase relation) per the relationships presented in (20.20)–(20.27).

High Frequency Resistance

High-frequency resistance (HFR) is a subset of impedance spectroscopy and is used to determine internal or ohmic resistance of the fuel cell. In essence, it is the impedance of the electrochemical cell at a single frequency, usually of the order of 1–10 kHz. Recall that at high frequencies the charge transfer resistance is eliminated by the (short circuiting) capacitive nature of the electrochemical double layer and transport resistances are not evident because of the large time constant of transport-limited processes. Therefore, only the ohmic resistance of the cell is observed as illustrated in Fig. 20.37. It is the real component of the impedance, Z' or $\mathrm{Re}(Z)$, that is of interest in this measurement.

Because the HFR measurement is made very quickly and does not appreciably disturb the operation of the cell, it is suitable for routine, periodic application during normal fuel cell operation.

The appropriate frequency for an HFR measurement varies with the electrochemical system under study. Selection of the proper frequency is best accomplished by examining the phase angle over a range of frequencies. Ideally, the HFR measurement should be made at a frequency at which the phase angle is zero (and, by definition, $Z'' = \mathrm{Im}(Z) = 0$) and therefore the cell is behaving in a purely resistive manner. In terms of a Nyquist plot, this condition exists when the impedance data crosses the real axis at high frequency (Fig. 20.37). In any case, the same frequency must be used for valid data comparison. Note that the method for choosing the HFR frequency requires that the test system should also have EIS capability. This is generally not a problem because a true FRA can measure over a wide range of frequencies, so a test system capable of true HFR measurement will also be capable of performing impedance spectroscopy measurements.

Finally, a cautionary note on the misuse of HFR and impedance spectroscopy for correction of ohmic (jR) drop within the cell is in order. These techniques are sometimes used to correct the cell potential for jR drop by multiplying the high-frequency, real-part of the impedance (Z_{hf}) by the current density to obtain the jR-drop. However, this method of jR-correction is inappropriate if the ohmic resistance is a function of the current density (just such dependence was demonstrated in Sect. 20.2 in which ohmic resistance increased at high current density). This is because the high frequency limit of an impedance spectrum yields the ohmic resistance represented by the slope of the jR-drop versus current density at that steady-state operating point ($R_{\Omega,j}$). But, the product $R_{\Omega,j} \times j$ will differ from the actual jR-drop at that current density unless the jR-drop curve is a straight line (i. e., R_Ω is constant). This limitation of impedance to correct for jR-drop arises because this technique probes the system about a steady-state operating condition. This limitation can be overcome by measuring the resistance as a function of current density and then integrating the measured resistance. The potential for error when using HFR and impedance for

jR-correction is further presented by *Jaouen* and *Lindbergh* [20.28].

Measurement of Low Impedance Electrochemical Cells

Fuel cells, batteries, and ultracapacitors by design have very low impedance. When measuring low impedance cells, the impedance of the connection cables may be of the same order of magnitude as the impedance of the cell itself. Because of the low impedance of fuel cells, measurements using two-terminal or three-terminal connection configurations are susceptible to significant measurement error because the instrumentation will not be able to differentiate between contributions of the cables and the cell to the measured impedance. The four-terminal technique ensures that the actual voltage drop between the two electrodes is observed because it does not contain voltage drop in the current carrying leads, and reduces cable-inductance effects. Accurate measurement of the cell voltage and current using a four-terminal configuration allows accurate characterization of very low impedance electrochemical cells.

Procedure

General Test Conditions. Cell temperature = 80 °C for all tests. Stoichiometry: $1.25 \times H_2/2 \times O_2$ (as pure O_2 and air) at 1 A/cm^2, ambient pressure.

33% Relative humidity (RH): Reactant humidifiers = 55 °C(55/80/55). This is the dry condition (XX/YY/ZZ refers to AHT/cell (CT)/CHT).

100% RH: Reactant humidifiers = 80 °C (80/80/80). This is the fully humidified condition.

Current density: Impedance spectra (IS) are acquired at three current densities to demonstrate the effect of polarization and reactant consumption rate on charge transfer resistance and transport resistance:

- Low current density ≈ 0.1 A/cm^2 small η_{cat}, low consumption rate.
- Moderate current density ≈ 0.5 A/cm^2 moderate η_{cat}, moderate consumption rate.
- High current density ≈ 0.8 to 1.0 A/cm^2 high η_{cat}, high consumption rate.

Most tests are performed with air on the cathode and all tests are performed with H_2 on the anode. Experiments with O_2 are performed to demonstrate the reduction of gas-phase O_2 diffusion resistance when compared to air at the same current density. Experiments with N_2 on the cathode are performed to evaluate the ionic resistance of the electrolyte in the porous electrode under non-Faradaic conditions.

The impedance spectra (IS) were acquired by using an AC current amplitude of 5% of DC current in the frequency range 10 kHz–0.1 Hz. The IS were acquired at each current density after a 5 to 10 min stabilization period.

20.5.2 Results and Discussion

This section presents and discusses the results of the IS acquired using the test conditions described earlier. All tests were conducted using a 50 cm^2 cell which was verified to be free of an internal electrical short and excessive fuel crossover (i. e., $j_{x\text{-}over} \approx 1$ mA/cm^2) using the LSV technique describe in Sect. 20.4.

Equivalent circuit modeling and fitting of experimental impedance data can be performed with most instruments' software. For details of its utilization we refer you to their corresponding manuals.

DC Polarization Data for a H_2 PEM Fuel Cell

The DC polarization scan data (*V–j* performance data) is shown in Fig. 20.39. This data was acquired to demonstrate the steady-state behavior of the fuel cell as a function of cathode reactant (O_2 vs. air) and humidity (33% vs. 100% RH); these effects were presented in Sects. 20.2.1 and 20.2.2, respectively. From the voltage and resistance (by current interrupt) versus current density data presented in Fig. 20.39 we observe that:

- The choice of cathode reactant did not influence the ohmic resistance of the cell although it did influence the total polarization resistance of the cell. This can be seen by comparing the resistance data and slope of the *V–j* curve for the O_2 and air case at high humidity: the resistance is the same but the slope of the non-*jR* corrected *V–j* curve, which represents the total resistance of the cell, is larger for the air case, especially at high current density.
- The resistance of the cell, predominantly the membrane resistance, was much higher at low humidity than at high humidity.
- The dependence of the cell resistance on current density was substantially greater when the cell was at low RH in comparison to the high RH condition.
- The polarization resistance (slope) of the cell was higher at low RH (compare V_{cell} for the two air cases).
- After accounting for the ohmic resistance, the low RH condition exhibited a larger slope than the high RH condition suggesting that there were additional sources of resistance within the cell not accounted for by the ohmic resistance measured by the current interrupt technique.

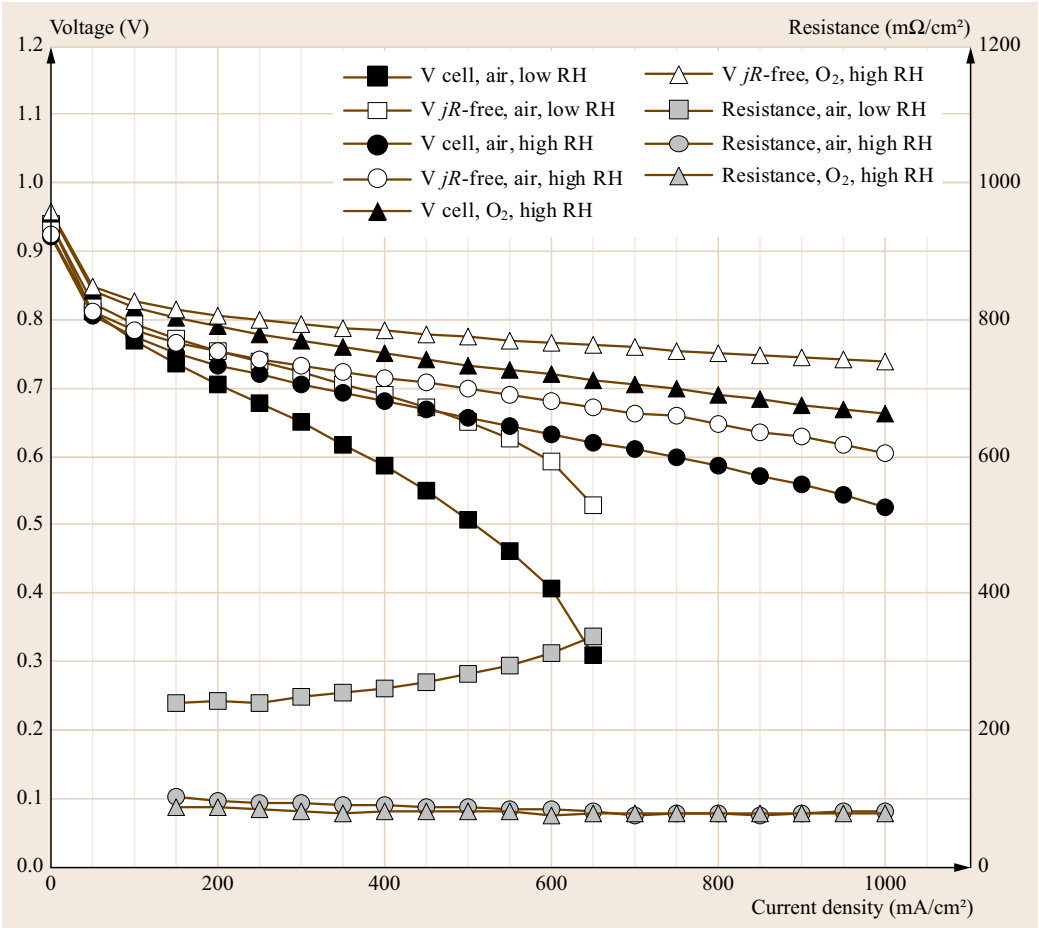


Fig. 20.39 Performance curves for a PEM fuel cell operating on H_2/air at low (33%) and high (100%) RH, and H_2/O_2 at high (100%) RH. Conditions: 50 cm^2, $1.2 \times H_2$, $2.0 \times O_2$ at 1 A/cm^2, 80 °C cell temperature, ambient pressure. Low and high RH conditions defined as humidified reactants with dew point of 55 and 80 °C, respectively

Impedance Data for a H_2 PEM Fuel Cell

We turn our attention to the analysis of the impedance spectroscopy data. Analysis of the effect of oxidant concentration (O_2 versus air), current density, and RH are treated separately. Finally, we present and discuss the results of impedance measurements on a H_2/N_2 cell for the evaluation of the catalyst layer ionic resistance of fuel cell electrodes.

Two of the criteria of valid impedance data are stability and linearity. It is easy and prudent to check that both of these criteria were satisfied. The requirement for a stable system can be verified by comparing the voltage (or current) before and after the impedance experiment. Here, impedance experiments were conducted at fixed DC current, and therefore we confirmed that the cell voltage at that DC current before and after the impedance experiment were within a few millivolts. Similarly, while operating the cell under constant DC potential control, one should confirm that the cell current was the same before and after the impedance experiment.

The requirement for linearity can be confirmed by estimating the AC voltage that resulted from imposition of the AC current signal on the cell. As an example, recall that the impedance experiments were conducted with an AC current equal to 5% of the DC current, and therefore the largest AC current was 0.04 A/cm^2 and existed for the high (0.8 A/cm^2) current density condition. The impedance was largest at low frequency. The low-frequency impedance for the H_2/air condition at 0.8 A/cm^2 (Fig. 20.40) was $\approx 0.51\ \Omega\ cm^2$ and so the AC voltage perturbation of the cell was ≈ 20 mV($= 0.04\ A/cm^2 \times 0.51\ \Omega\ cm^2$). At 80 °C the thermal voltage is 30 mV, so the condition of linearity was met. Performing this calculation at other test conditions revealed that in all cases the AC voltage signal was sufficiently small that the criterion of linearity was satisfied.

Note that the magnitude of the AC voltage changes during an AC current-controlled impedance spectroscopy experiment because the impedance of the cell is a function of frequency. Conversely, during a voltage-controlled impedance sweep, the AC current changes as

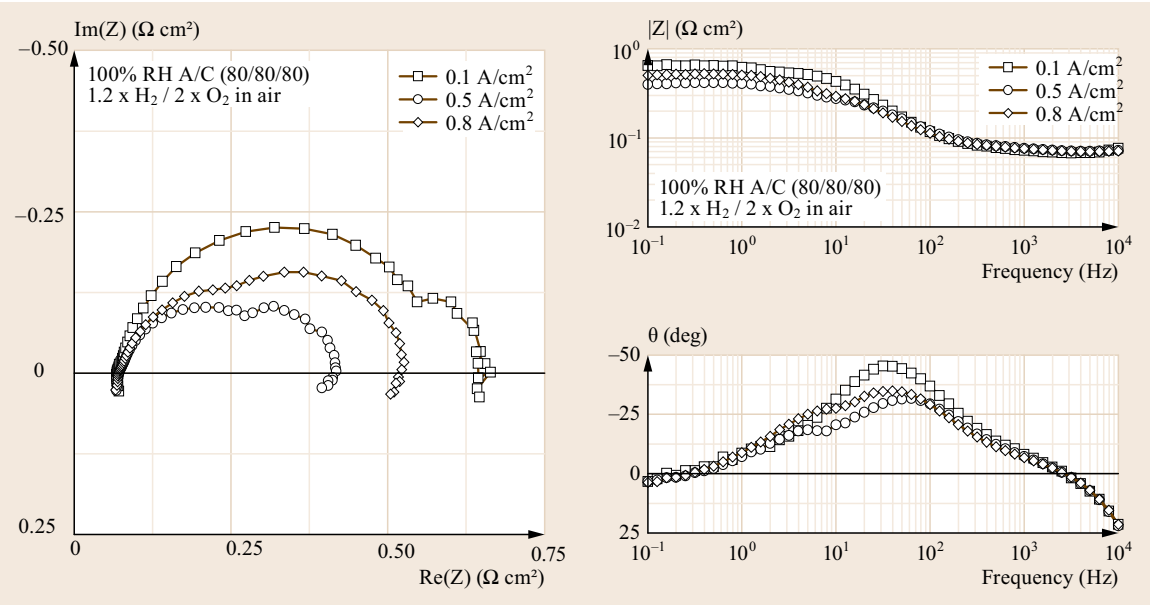


Fig. 20.40 IS for a H_2/air PEM fuel cell as a function of current density under fully humidified conditions. The Nyquist plots indicates that at each current density there are two processes with distinct time constants in series: the charge transfer process has a small-time constant and is evident at high frequency and the larger time constant diffusion-related process evident at low frequency

Table 20.6 Summary of H_2/air-PEMFC properties as a function of current density. Conditions: 80/80/80, 1.2×H_2/2.0×O_2 (in air), ambient pressure. R_{Ω} by current interrupt and R_{pol} from the DC polarization data are shown for comparison

Current density (A/cm²)	Impedance			Current interrupt	DC polarization
	R_{hf} (Ω cm²)	$R_{ct,ORR}$ (Ω cm²)	R_{lf} (Ω cm²)	R_{Ω} (Ω cm²)	$R_{pol,DC}$ (Ω cm²)
0.1	0.070	0.529	0.656	–	0.543
0.5	0.073	0.235	0.418	0.086	0.244
0.8	0.071	0.385	0.522	0.079	0.269

the impedance of the electrochemical cell changes with frequency.

20.5.3 Impedance of a H_2 PEM Fuel Cell

Figure 20.40 shows IS for the H_2/air PEM cell operating on fully humidified reactants. Two distinct arcs or impedance loops are evident. The high-frequency arc is attributed to the combination of an effective charge transfer resistance for the ORR ($R_{ct,ORR}$) and double-layer capacitance within the catalyst layer. The second, low-frequency arc is associated with the mass-transport limitations of gas phase reactant (i. e., O_2) within the gas diffusion media.

Key parameters extracted from the impedance and DC polarization data under the same operating conditions (i. e., current density and oxidant) are summarized in Table 20.6.

The real axis intercept of the impedance plot at the high-frequency end of the high-frequency loop is equal to the total, nonelectrode ohmic resistance of the cell, $R_{\Omega,nonelectrode}$. That is, the high-frequency intercept R_{hf} is the combined ohmic resistance of the cell, and includes contributions from the resistance to proton transport in the bulk membrane (but not within the electrode catalyst layer), electronic resistance of all current-carrying components including the gas diffusion media, flow field, current collector and cell leads (but excludes the contribution from the electrodes), and contact resistances; R_{hf} can be equated to $R_{\Omega,nonelectrode}$. The results summarized in Table 20.6 indicate that the ohmic resistance of the cell measured by current interrupt was close to the high-frequency intercept.

Ohmic resistance of the electrodes does not contribute to the high-frequency intercept because the capacitive nature of the electrode/electrolyte interface shields the presence of the ion and electron transport resistance at frequencies greater than the frequency at which the high-frequency intercept occurs. Under some conditions, the electrode resistance is evident

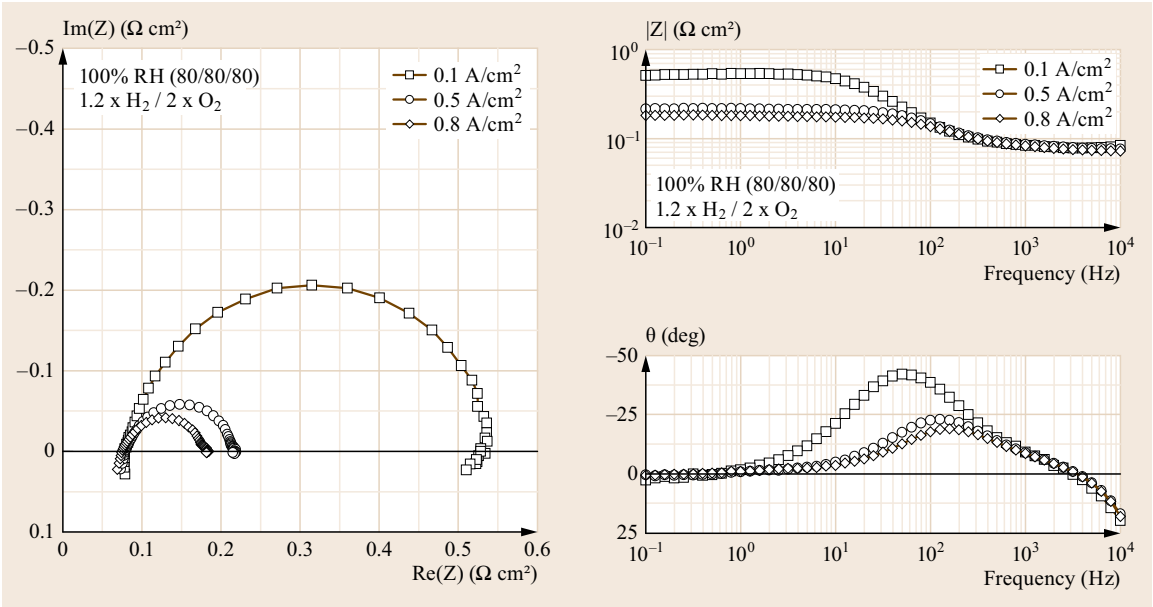


Fig. 20.41 IS for a H_2/O_2 PEM fuel cell as a function of current density at 100% RH. The results contrast with the H_2/air condition shown in Fig. 20.40 in that only a single high-frequency loop associated with charge-transfer is evident

as a 45° branch at the high frequency portion of the charge-transfer impedance loop as discussed in detail in Sects. 20.5.4 and 20.5.5.

At steady state, the intercept of the real axis at low frequency (R_{lf}, where $\omega \to 0$) must equal the total resistance of the fuel cell and therefore equal the slope of the DC polarization curve at the corresponding current density. Table 20.6 indicates that the impedance at the low-frequency intercept was smaller than the cell resistance obtained from the DC polarization curve. The apparent discrepancy in the total polarization resistance obtained from DC and AC methods has been noted [20.27, 32] and attributed to the relaxation of an intermediate species in the multistep ORR [20.33] which manifests as inductive-like behavior at low frequency. Low-frequency inductance, indicated by positive Z'' values, was evident in most impedance scans (Figs. 20.40, 20.41, and 20.42). Impedance measurements at low frequencies reveal this inductive-like behavior and allow reasonable extrapolation of the impedance back to the real axis in order to better estimate the polarization resistance [20.32, 37].

We now examine the IS as a function of current density. Recall that current density, cell voltage, and cathode overpotential are related. Larger current densities are associated with larger cathodic overpotential and lower cell voltage, all else being equal. Thus, we can describe the relative behavior of the fuel cell and the characteristics of the IS either in terms of relative current density, cell potential, or cathodic overpotential.

At low current density, where the cathode overpotential is small, we note that the low-frequency arc is nearly negligible, indicating the near-absence of diffusion-related resistance. This makes sense because at low current density the oxygen consumption rate is small and therefore we would not expect significant losses associated with delivery of reactant to the electrode interface. Under these conditions, the majority of the total cell resistance is due to the resistance of the charge transfer reaction.

As the current and overpotential increases, the diameter of the high-frequency arc decreases, reflecting the increasing driving force for ORR. This can be seen by comparing spectra acquired at current densities of 0.1 and 0.5 A/cm^2. Further increases in the current density, however, result in an increase in the diameter of the high-frequency loop. The increase in the effective charge transfer resistance at the higher cell current and cathode overpotential occurs because the concentration of oxygen within the catalyst layer drops as a result of oxygen transport limitations.

In contrast to the behavior of the high-frequency (kinetic) loop, the low-frequency arc consistently increases in size with current density. This behavior indicates that limitations in mass transport are exacerbated at high reaction rates which impact the oxygen concentration at the GDL/electrode interface. As indicated earlier, at the highest current densities, mass transport resistance is sufficiently large that the effective charge transfer resistance increases because of the reduced oxygen concen-

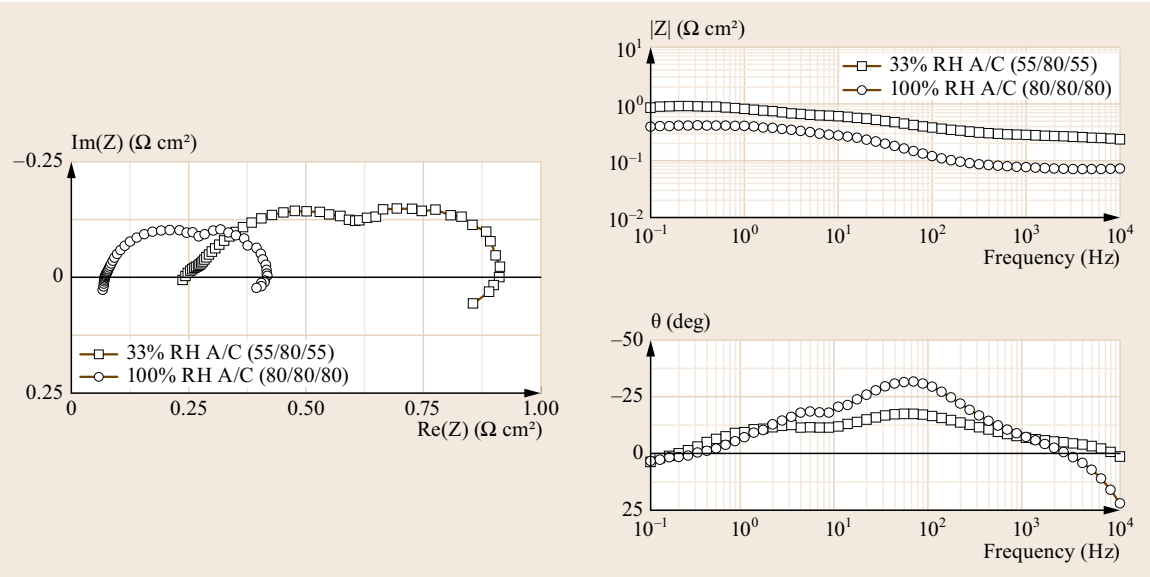


Fig. 20.42 Impedance data for PEM fuel cell operating at 80 °C with relatively dry (33% RH) or wet (100% RH) reactant feeds. Test conditions: 50 cm^2 cell, $1.2 \times H_2/2.0\times O_2$ in air at 1 A/cm^2, ambient pressure. Low and high RH conditions defined as humidified reactants with dew point of 55 and 80 °C, respectively

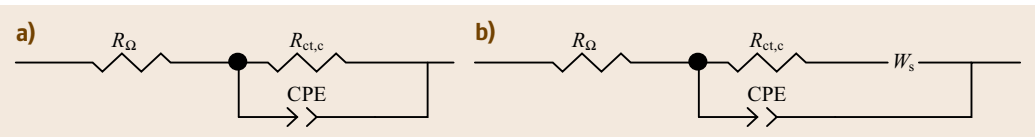


Fig. 20.43a,b Equivalent circuit models used to fit the IS for a PEMFC operating at fully humidified (100% RH) condition. **(a)** A simple *R–C* circuit was used to model the spectra for the H_2/O_2 case at low (0.1 A/cm^2) and moderate (0.5 A/cm^2) current densities for which the spectra consisted of a single high-frequency arc. **(b)** Modeling impedance data for a H_2/air cell at all current densities and the H_2/O_2 at high current density (0.8 A/cm^2) required inclusion of a diffusion resistance term, the finite length Warburg element (W_s), because of the presence of a second, low-frequency loop

tration in the catalyst layer. This can be seen by comparing the respective kinetic-controlled and transport-controlled impedance loops obtained at 0.5 and 0.8 A/cm^2. In each case, the diameter of the respective impedance loop increased at the higher reaction rate.

IS for a H_2/O_2 PEM fuel cell as a function of current density under fully humidified conditions are shown in Fig. 20.41. The results contrast with the H_2/air condition shown in Fig. 20.40 in that only one time constant is evident, the one associated with charge transfer (the high-frequency loop). Although not evident in these figures due to the scale, a very small low-frequency loop was observed at high current density. The absence of a second, low-frequency loop at the low and moderate current densities indicates that there was insignificant resistance due to transport of cathode reactant at these conditions, and only a small diffusional resistance at high consumption rates when operating with pure oxygen.

Equivalent Circuit Models

Simple equivalent circuit models were employed to model the impedance data when the cell was operated with H_2 fuel and either air or pure O_2 oxidant under fully humidified conditions. Figure 20.41 shows that for the H_2/O_2 case, the spectra at low and moderate current densities consisted of a single high-frequency loop displaced along the positive Z' axis (shifted to the right from $Z' = 0$). (For simplicity, we will ignore inductive-like behavior observed at high and low frequencies). This impedance behavior is consistent with a resistor in series with a parallel resistor–capacitor combination. A suitable equivalent circuit for the H_2/O_2 IS at low and moderate current densities is given in Fig. 20.43a. This electrical analog consists of a resistance representing the total nonelectrode cell ohmic resistance (R_Ω) in series with a cathode charge-transfer resistance ($R_{ct,c}$) that is in parallel with a capacitive-

Table 20.7 Summary of O_2-operated PEMFC properties as a function of current density. Conditions: 80/80/80, $1.2\times H_2/2.0\times O_2$, ambient pressure. R_{Ω} by current interrupt and R_{pol} from the DC polarization data are shown for comparison

Current density (A/cm^2)	Impedance				Current interrupt	DC polarization
	R_{hf} (Ω cm^2)	$R_{ct,ORR}$ (Ω cm^2)	R_{diff} (Ω cm^2)	R_{lf} (Ω cm^2)	$R_{\Omega,iR}$ (Ω cm^2)	$R_{pol,DC}$ (Ω cm^2)
0.1	0.081	0.463	–	0.544	–	0.425
0.5	0.081	0.135	–	0.216	0.088	0.218
0.8	0.077	0.100	0.005	0.182	0.087	0.180

Table 20.8 Summary of air-operated PEMFC properties as a function of reactant humidification. Spectra acquired at intermediate current density ($0.5\,A/cm^2$). Impedance data fitted to the models shown in Fig. 20.44 (33% RH) and Fig. 20.46 (100% RH). R_{Ω} by current interrupt and R_{pol} from the steady-state (DC) polarization data are shown for comparison

Relative humidity	Impedance			Current interrupt	DC polarization
	R_{hf} (Ω cm^2)	$R_{ct,ORR}$ (Ω cm^2)	R_{lf} (Ω cm^2)	R_{Ω} (Ω cm^2)	$R_{pol,DC}$ (Ω cm^2)
Low – 33%	0.230	0.317	0.912	0.282	0.857
High – 100%	0.073	0.235	0.418	0.086	0.244

like element representative of the electrode double layer (C_{dl} or CPE).

At high current density ($0.8\,A/cm^2$), a very small second low-frequency arc appeared which was attributed to transport effects. A Warburg impedance element was incorporated into the model to account for this effect, Fig. 20.43b. This equivalent circuit was also used for the H_2/air case at fully humidified conditions because of the presence of the low-frequency arc at all current densities (Fig. 20.40). In all cases, a CPE was found to provide a more accurate fit to the data than when a pure capacitor was used. Detailed results of the equivalent circuit fitting for the H_2/air and H_2/O_2 conditions are presented in the experimental section and summarized in Table 20.7.

Recall that the order of series elements in the equivalent circuit does not affect the impedance spectrum. Therefore, in Fig. 20.43a, one could rearrange the order of the elements, with the parallel $R_{ct,c}$–CPE combination to the left of R_{Ω}. Similarly, the order of the Warburg element W and $R_{ct,c}$ in series in Fig. 20.43b is immaterial.

20.5.4 Effect of Reactant Humidification

IS for the H_2/air cell operating at $0.5\,A/cm^2$ with relatively dry (33% RH) or fully humidified (100% RH) reactants is shown in Fig. 20.42. The spectra indicate that a lack of reactant humidification impacts the properties of the cathode in three different ways, which are well resolved in the IS. It is worth noting that in a steady-state polarization curve, such as the one shown in Fig. 20.39 only the sum of the effects is evident. The relative contributions in voltage loss are not discernible from a simple steady-state performance curve. Three effects with decreasing cell humidification are evident in these spectra:

1. Increase in high-frequency resistance (R_{hf}) reflecting increase in the overall nonelectrode ohmic resistance of the membrane.
2. Increase in the resistance of the ionomeric (proton) component within the cathode catalyst layer indicated by the formation of significant 45° branch at high frequency.
3. Increase in the interfacial impedance for the ORR reflected by the increase in the overall diameter of the high frequency impedance loop. Low water content within the cathode catalyst layer is known to reduce the ORR reaction kinetics [20.6, 38].

The results of equivalent circuit modeling of the IS are summarized in Table 20.8.

Equivalent Circuit Modeling

The equivalent circuit used to fit the impedance data acquired for the fuel cell operating under low humidity conditions is shown in Fig. 20.44.

The equivalent circuit consists of three elements in series:

1. A resistance representing the total nonelectrode ohmic resistance of the cell observed at high frequency

$$R_{hf} = R_{\Omega,\text{nonelectrode}} = R_{\Omega,\text{membrane}} + R_{\Omega,\text{bulk+contact}}\,.$$

2. A two-rail transmission line resistance–capacitor network indicated by the distributed element DX1 and shown in Fig. 20.44b which represents the porous electrode [20.32, 39, 40], and
3. A finite length Warburg impedance with a short-circuit terminus (W_s) which represents the resistance to gas-phase oxygen diffusion.

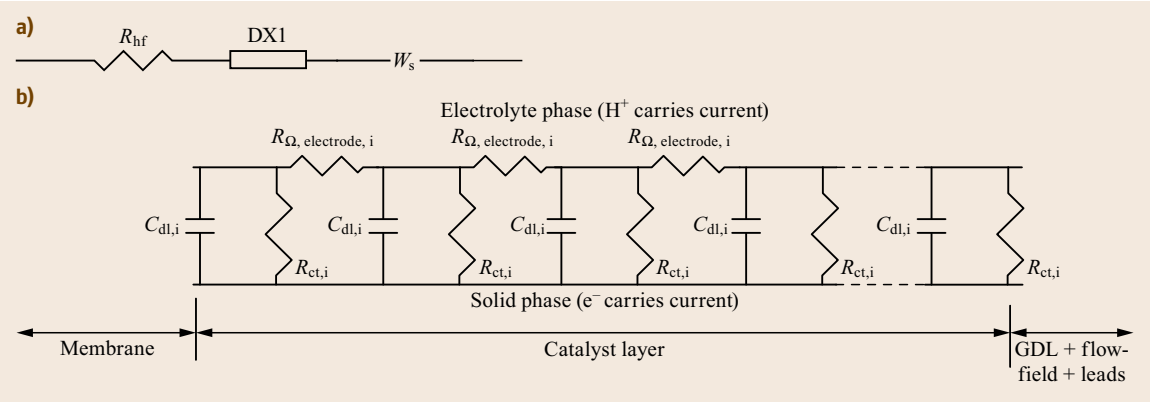


Fig. 20.44 **(a)** Equivalent circuit used to model the impedance data for the low humidity condition, where DX1 represents the distributed element analogous to a transmissive boundary transmission line resistance commonly used for porous electrodes shown in **(b)**. Details of the model elements are given in the text

Low Humidity – 33% RH (55/80/55). The distributed element DX1 is used to model the impedance of the porous electrode including the distributed electrolyte resistance within the electrode ($R_{\Omega,\text{electrode,i}}$), the distributed electrode double-layer capacitance ($C_{dl,i}$) and the distributed charge transfer resistance ($R_{ct,i}$). The electronic resistance of the catalyst layer was assumed negligible. Fitting was performed by estimating the parameters for R_{hf}, DX1 and W_s separately followed by fitting the complete impedance spectrum using the complete model shown in Fig. 20.44a. For this analysis, $n = 100$ repeating units were used in the element DX1.

For a transmission line circuit model with n repeating units,

$$R_{\Omega,\text{electrode}} = nR_{\Omega,\text{electrode,i}}\,;\; C_{dl} = nC_{dl,i}\,;$$
$$\text{and}\quad R_{ct} = \frac{R_{ct,i}}{n}\,. \tag{20.40}$$

The contribution of the proton transport resistance within the electrode catalyst layer to DC polarization resistance (i. e., as $\omega \to 0$) is [20.32, 39, 40],

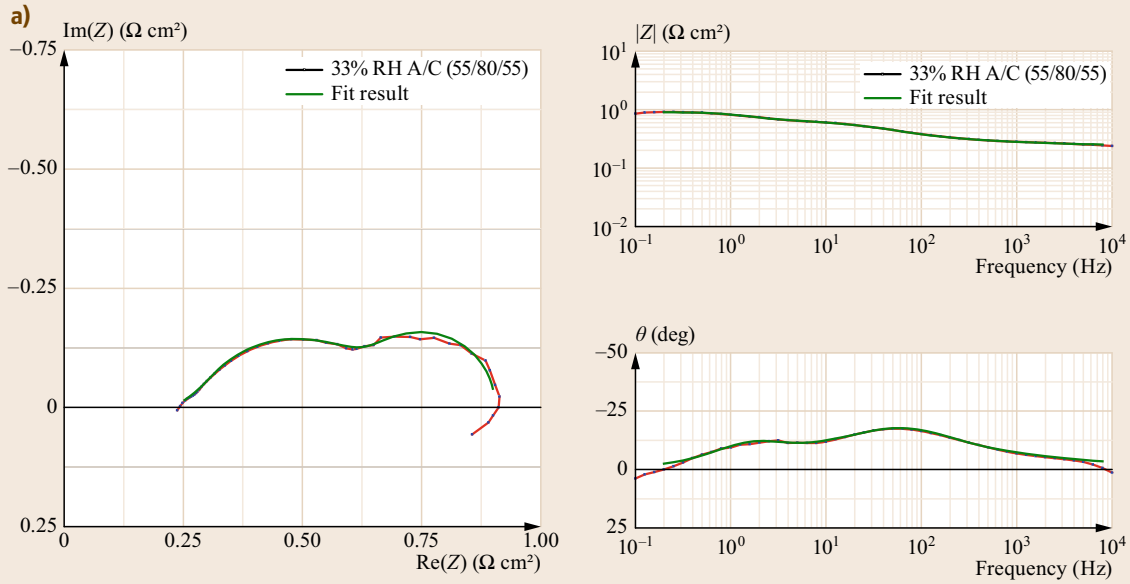
$$R_{\Omega,\text{electrode},\omega\to 0} = \frac{R_{\Omega,\text{electrode}}}{3}\,. \tag{20.41}$$

The goodness of fit can be seen by comparing the calculated and experimental spectra seen in Fig. 20.45. Using the fit results, ohmic losses due to proton resistance in the catalyst layer (electrode) are estimated to be $0.043\,\Omega\,\text{cm}^2$ ($= 0.0013\,\Omega\,\text{cm}^2$/repeating unit $\times$ 100 units $\div$ 3). This analysis indicates that the resistance to proton transport within the electrodes was approximately 20% of the nonelectrode ohmic resistance ($R_{hf} = R_{\Omega,\text{nonelectrode}} = 0.230\,\Omega\,\text{cm}^2$).

It is worth noting that replacing the capacitors, $C_{dl,i}$, with CPEs$_i$, in the transmission line resistance element DX1 results in a slightly improved fit with an estimated exponent for the CPE of $p = 0.67$ (20.34) (recall that for an ideal capacitor, $p = 1$). Physical interpretation of this observation is limited to hand-waving arguments such as a distribution in the properties of the electrolyte/electrode interface at the microscopic level (which is not unreasonable given that there is likely a gradient in the water content and oxygen concentration through the electrode that may impact the local behavior of the electrode and thus cause it to exhibit a distribution in impedance response). A more meaningful and rigorous interpretation of the physiochemical source of the nonideal capacitive behavior is not available.

High Humidity – 100% RH (80/80/80). In contrast to the low humidity condition, in which there was significant resistance to proton transport within the cathode as indicated by the 45° branch at high frequency, IS for the high humidity condition appear to be reasonably well represented by a relatively simple equivalent circuit shown in Fig. 20.46. The high-frequency loop appears to approximate a semicircle; the second low-frequency arc is indicative of a resistance to mass transport. The model consists of a resistor (R_Ω) representing the combined nonelectrode ohmic resistance of the cell in series with an element that contains three components: First, the charge-transfer resistance (R_{ct}) in series with a finite-length Warburg element with a short-circuit terminus (W2) representing a resistance to diffusion in parallel with a term that represents the capacitive behavior of the double layer (C_{dl} or CPE1). Second, model results are presented for this data set to demonstrate the difference between using a pure capacitor (C_{dl}) versus using a CPE to represent the double-layer capacitance. Third, the fit results are presented side-by-side to highlight their similarities and differences.

a)



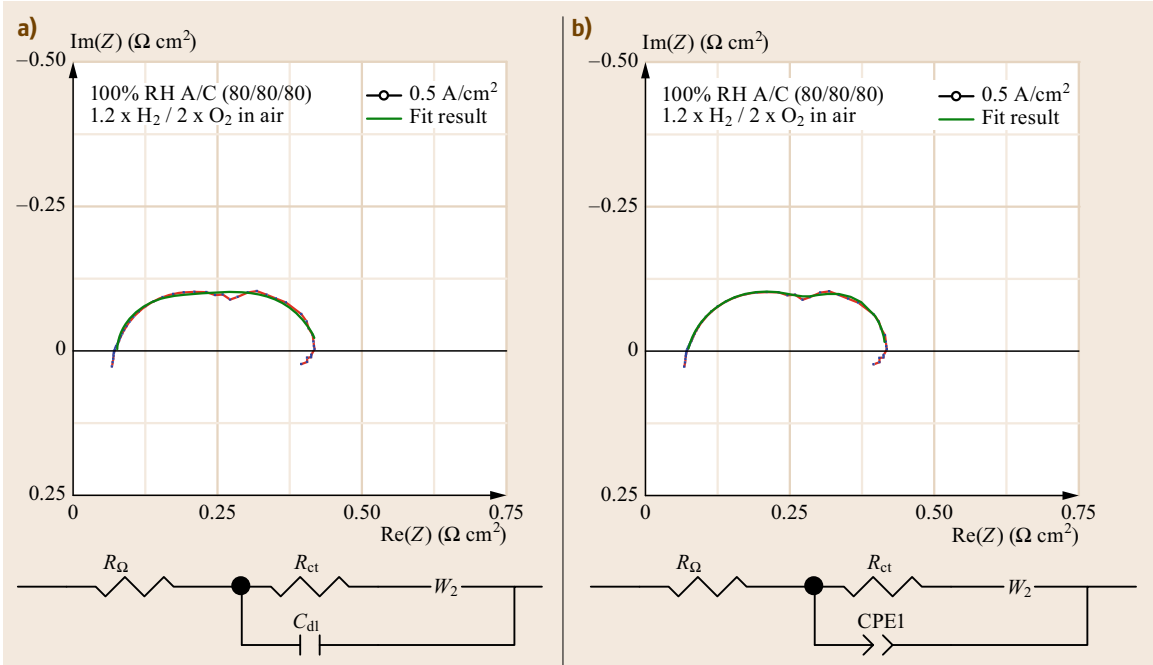
b)

Element	Freedom	Value	Error	Error (%)
R_{hf}	Free(+)	0.23024	0.0017654	0.76677
DX1	Fixed(X)	6 - TL-Open		
DX1-Rs	Free(+)	0.0012897	0.00011784	9.137
DX1-CPE-T	Free(+)	0.00040559	4.4164E-5	10.889
DX1-CPE-T	Free(+)	0.79367	0.023799	2.9986
DX1-N	Fixed(X)	100	N/A	N/A
DX1-Rt	Fixed(X)	0	N/A	N/A
DX1-Rx	Free(+)	31.67	1.7642	5.5706
Ws-R	Free(+)	0.31696	0.019649	6.1992
Ws-T	Free(+)	0.28425	0.012553	4.4162
Ws-P	Free(+)	0.50601	0.017759	3.5096
Chi-squared:		0.00079166		
Weighted sum of squares:		0.0665		

Fig. 20.45 (a) Nyquist and Bode plots showing the experimental impedance data and the fit results using the equivalent circuit model shown in Fig. 20.44 for the low RH (33%) condition. (b) Equivalent circuit model fit results

Both models appear to reasonably replicate the observed impedance over the whole frequency range. We note that the estimated exponent for the CPE, p, was 0.87, and the fit appears to be slightly better when a CPE was used in place of a pure capacitor. (The weighted sum of squares, which is one measure of the goodness-of-fit, was smaller by a factor of 3 for the model that used the CPE). This suggests that the electrolyte/electrode interface did not behave as an ideal capacitor. However, there are significant differences in the *values* of *other parameters* in the model, such as R_{ct} and the Warburg (W) parameters, as a result of using either a C or CPE. Both models appear to be reasonable fits so which set of values *more* accurately describe the fuel cell properties is uncertain.

The results presented in Table 20.8 reveal that R_Ω by current interrupt technique exceeded that of the nonelectrode ohmic resistance determined by the impedance method, the former being about 15–20% greater at both low and high RH conditions. In practice, the results from these two techniques usually correlate reasonably well. There are, however, inherent differ-



Element	Freedom	Value	Error	Error (%)
R_Ω	Free(+)	0.076325	0.00053607	0.70235
R_{ct}	Free(+)	0.13397	0.0090188	6.732
W2-R	Free(+)	0.21478	0.013013	6.0588
W2-T	Free(+)	0.10562	0.0097714	9.2515
W2-P	Free(+)	0.41231	0.023052	5.5909
C_{dl}	Free(+)	0.019958	0.00044433	2.2263

Chi-squared: 0.0025429
Weighted sum of squares: 0.18309

Element	Freedom	Value	Error	Error (%)
R_Ω	Free(+)	0.073462	0.00041384	0.56334
R_{ct}	Free(+)	0.23537	0.0068788	2.9225
W2-R	Free(+)	0.10679	0.007298	6.834
W2-T	Free(+)	0.10745	0.004885	4.5463
W2-P	Free(+)	0.58191	0.021697	3.7286
CPE1-T	Free(+)	0.050022	0.0030788	6.1549
CPE1-P	Free(+)	0.86687	0.0095104	1.0971

Chi-squared: 0.00082525
Weighted sum of squares: 0.058593

Fig. 20.46a,b Nyquist plots, equivalent circuit, and model fit results for the 100% RH condition using either **(a)** an ideal capacitor (C_{dl}) or **(b)** a CPE1 to represent the capacitive behavior of the electrode double layer. The model fit was slightly better when a CPE was used in place of a pure capacitor suggesting that the electrolyte/electrode interface does not behave as an ideal capacitor

ences in the two methods: the current interrupt method introduces a large perturbation to the fuel cell and looks at its time-domain response whereas the impedance method applies a small signal and uses the frequency domain response of the cell. Discrepancies between results obtained from these two methods derive from whether the current distribution present during the current interruption or impedance measurement is the same as the current distribution during standard DC operation of the cell.

In the current interrupt technique, after the external current is rapidly stopped, the *true* cell voltage is only measured if the current is zero everywhere within the cell and on the surface of the electrode; or, in the case of a porous electrode with a reactive layer of finite thickness, the current is zero within the multiphase electrode. This condition exists for a uniform potential distribution on the surface of a planar electrode or within a porous electrode [20.41]. If however, there existed a potential gradient within the electrode under the

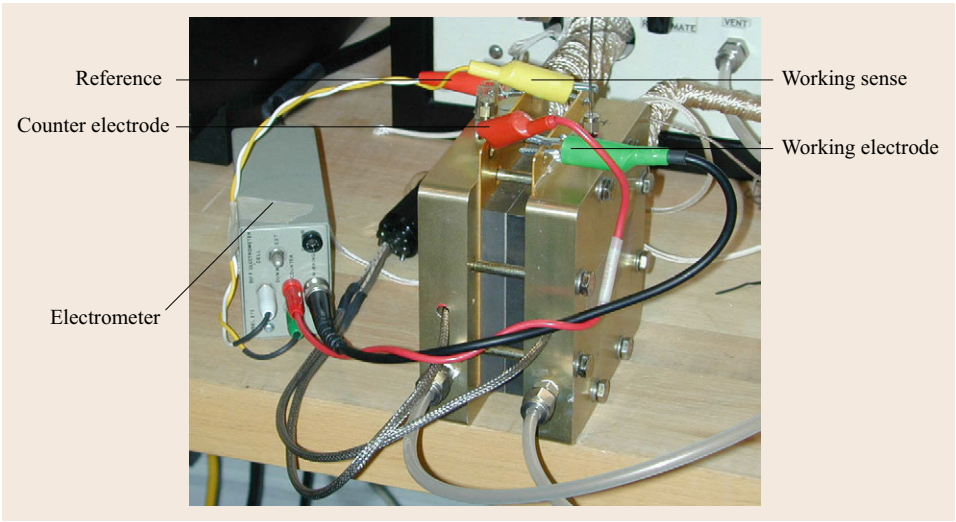


Fig. 20.47 Photograph showing cell connections for impedance measurements performed with a potentiostat + frequency response analyzer combination on a PEM fuel cell operating with H_2 on the anode and N_2 on the cathode. The low impedance of the cell necessitated a four-electrode measurement to minimize the high-frequency inductive behavior from the current-carrying cables that otherwise masked the catalyst layer proton transport resistance. In addition, the reference and working sense leads were twisted together and kept away from the current carrying leads

preinterrupt condition (i. e., $I > 0$), then after the interruption, ionic current will exist within the electrolyte and electronic current within the electrode matrix material to redistribute the nonuniform surface charge. This current just after the interruption will create an additional ohmic voltage drop within the cell, which will introduce an error in the resistance measurement. That is, the measured ΔV will not be equal to the true voltage drop due to ohmic resistance when the cell is operating under DC current. This effect has been described and modeled by *Lagergren* et al. [20.42].

This artifact is most likely to occur in porous electrodes in which the ionic conductivity of the electrolyte is of the same order of magnitude as the electronic conductivity of the electrode matrix [20.43]. The relationship between the magnitude of the error of the ohmic potential drop, $\eta_{\Omega,\text{error}}$, and the electrode properties is

$$\eta_{\Omega,\text{error}} = \frac{L}{\kappa_{\text{eff, electrolyte}} + \kappa_{\text{eff, electrode}}} j \,, \qquad (20.42)$$

where L is the thickness of the catalyst layer, j is the current density, and $\kappa_{\text{eff,electrolyte}}$ and $\kappa_{\text{eff,electrode}}$ are the effective conductivity of the ion conducting pore electrolyte and the electron-conducting matrix material of the reactive layer, respectively. The magnitude of the ohmic potential drop error is directly proportional to the geometric current density and thickness of the electrode, and inversely proportional to the sum of the electrolyte and electrode conductivities. Note that $\eta_{\Omega,\text{error}}$ approaches zero with increasing conductivity of either charge-carrying phase. Furthermore, the phase with the highest conductivity determines $\eta_{\Omega,\text{error}}$.

20.5.5 Electrode Proton Transport Resistance

The ohmic resistance within the ionomer (electrolyte phase) is of interest to electrode designers and for performance diagnostics. The double-layer capacitance shields ohmic losses within the electrode and therefore the ohmic resistance of the electrode does not contribute to the voltage drop measured during a current interrupt event nor does it contribute to the high-frequency intercept. This effect does, however, manifest as a 45° branch at high-frequency during an impedance scan as demonstrated for the low humidity condition in Fig. 20.42. Although the ionic resistance of the electrode can be estimated by employing a complex equivalent circuit model such as the one presented in Fig. 20.44, accurate evaluation of the proton resistance of the electrode is more difficult in this case because of the Faradaic process of oxygen reduction occurring at the cathode.

A number of experimental and modeling papers describe determination of the electrode ohmic resistance, also referred to as the *electrode sheet resistance*, via impedance spectroscopy [20.32, 40, 44, 45]. Typically, the method to assess the catalyst layer electrode resistance using impedance spectroscopy consists of bathing the fuel cell cathode (WE) in N_2 instead of

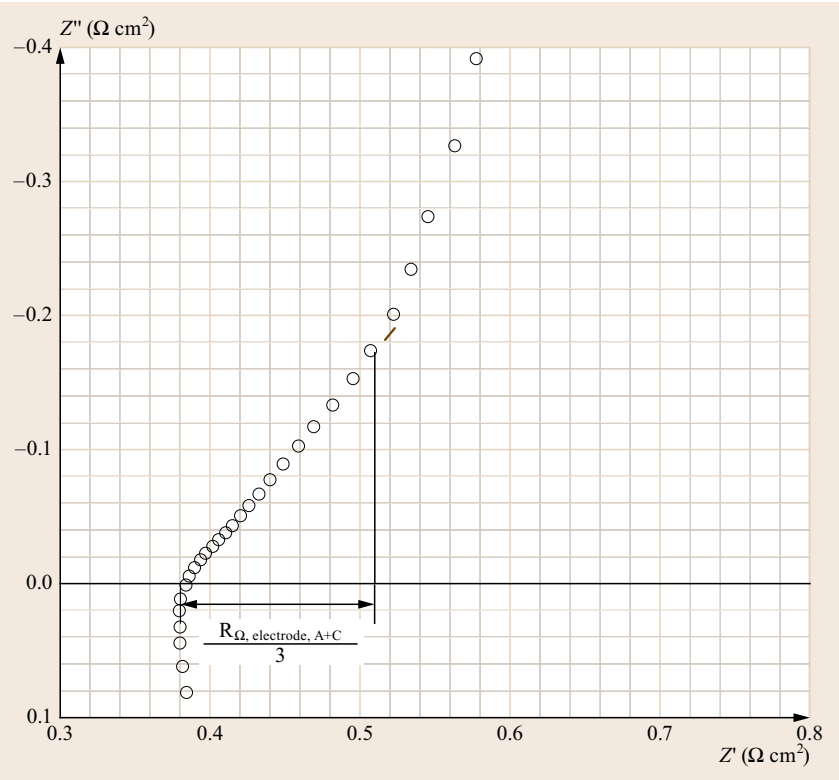


Fig. 20.48 Nyquist plot of PEM fuel cell operated with H_2/N_2 at 33% RH. The combined ionic resistance of the anode and cathode is $R_{\Omega,\text{electrode,A+C}} = 0.390\,\Omega\,\text{cm}^2$. See text for additional discussion

oxygen (or air) so as to minimize charge transfer reactions at the WE. *Liu* [20.45] report that if the N_2-fed WE is potentiostated at ca. $+0.2$ V versus the H_2-fed counter electrode/reference electrode (CE/RE), the H_2 that permeates through the membrane to the WE will be oxidized at the permeation-rate limited current density. As such, during the impedance experiment, the H_2 permeation current does not contribute to the overall impedance. The WE then behaves nearly as a pure capacitor which simplifies evaluation of the impedance data for the electrode ionic resistance, that is, the transition from the high-frequency 45° line to a semicircular arc at low frequency is eliminated in the near-absence of Faradaic reactions. *Murthy* [20.44] noted that in certain instances, a low-frequency arc can be observed due to oxidation on the cathode of H_2 resulting from nonrate limited oxidation of H_2 permeation through the membrane from the CE/RE.

Both the fuel cell anode and cathode were purged with 33% RH gases to accentuate their proton resistance; the cell was operated at 80 °C. After equilibrating the cell for at least 30 to 60 min, an impedance analyzer and potentiostat were used to measure the impedance of the cell at the OCV (ca. 0.10 V). The WE (fuel cell cathode) was scanned from 65 kHz to 0.1 Hz at an AC perturbation of 15 mV.

Measurements of electrochemical cells with impedance on the same order of magnitude as the cell leads are susceptible to corruption at high-frequency by cable inductance. For this reason, attention was given to decrease the effect of cable-inductance on the measured impedance. A four-electrode configuration was used as shown in Fig. 20.47. In this configuration, the voltage sense leads (labeled reference and working sense) are completely separate from the current carrying leads (counter and WE) therefore eliminating the contribution of the inductance in the latter to the measured impedance. In addition, the reference and working sense leads were twisted together and kept away from the current carrying leads.

Figure 20.48 shows the complex plane plot for the H_2/N_2 configuration. When presented as a Nyquist plot, the spectrum exhibits two features worth noting. First, there is a 45° branch at high frequencies which is characteristic of proton transport in the catalyst layer. Second, at lower frequencies, the spectrum becomes nearly vertical (or at least more-so) as the impedance gradually becomes dominated by the capacitance of the electrode. For the results presented in Fig. 20.48, although there is a distinct transition at $Z' = 0.55\,\Omega\,\text{cm}^2$, ideal capacitive behavior at low frequency was not evident. As noted earlier, non-

ideal capacitive behavior at low frequency was likely due to the presence of H_2 oxidation at the cathode due to fuel crossover through the membrane from the anode.

The average ionic resistance of the electrodes can be obtained by projecting the 45° branch onto the real axis. The projected value of the 45° branch equals $R_{\Omega,\text{electrode,A+C}}/3$. From this, we determine that $R_{\Omega,\text{electrode,A+C}}$, the combined resistance to proton transport in the two electrodes, is $0.390\,\Omega\,\text{cm}^2$. Assuming symmetrical electrodes with equal resistance distributed between the anode and cathode, each electrode exhibits $R_{\Omega,\text{electrode}} = 0.195\,\Omega\,\text{cm}^2$.

Although using a four-electrode configuration decreased the magnitude of the inductance at high frequency, this effect was not eliminated. The bulk of the residual inductive behavior was an inherent characteristic of the analytical instruments used to conduct the impedance measurements.

Summary – Diagnostics Using Impedance Spectra and Modeling

In this section, we summarize that the technique of electrochemical impedance spectroscopy is a valuable analysis tool. Data acquired during the laboratory experiments demonstrate the utility of impedance spectroscopy as a diagnostic tool to characterize the source of losses and performance of PEMFC. The interpretation of the data and concepts explored in this laboratory are taken largely from Springer and coworkers' seminal article on impedance spectroscopy of PEMFC [20.26] and can be summarized as follows:

- An impedance spectrum for a PEM fuel cell cathode characterized by a single high-frequency arc which decreases in diameter with increasing cathode overpotential (decreasing voltage) is indicative of the condition where the only source of losses is due to interfacial kinetics of the ORR. The decrease in the diameter of the semicircular impedance loop (i. e., $R_{\text{ct,ORR}}$) with increasing cathode overpotential is consistent with the potential dependence of the ORR interfacial rate constant.
- When the proton resistance in the catalyst layer contributes significantly to the cathode voltage loss, the impedance loop terminates at high frequency with a well-defined 45° branch. The 45° branch at high frequencies reflects coupling of the distributed ionic resistance and distributed capacitance in the catalyst layer. Therefore, the existence of a 45° slope at the high frequency portion of the kinetic (high-frequency) loop can be used as the diagnostic criterion for significant ionic resistance within the electrode catalyst layer.
- Resistance within the GDL is observed at low frequencies. Therefore, the presence of a second, low-frequency impedance loop indicates substantial losses associated with oxygen diffusion through the GDL. The low-frequency loop is generally observed in a PEM fuel cell operating on air as opposed to pure O_2 and arises because of the resistance to oxygen diffusion through nitrogen in the GDL and the porous electrode (catalyst) layer, as well as oxygen diffusion through ionomer films in the catalyst layer.

References

20.1 US Fuel Cell Council (USFCC): http://www.usfcc.com/resources/technicalproducts.html

20.2 G. Hoogers: *Fuel Cell Technology Handbook* (CRC, Roca Baton 2002)

20.3 H.A. Gasteiger, M.F. Mathias (Eds.): *Proceedings of the International Symposium PV 2002-31* (The Electrochemical Society, Pennington 2005)

20.4 M.V. Williams, H.R. Kunz, J.M. Fenton: Analysis of polarization curves to evaluate polarization sources in hydrogen/Air PEM fuel cells, J. Electrochem. Soc. **152**, A635–A644 (2005)

20.5 G. Prentice: *Electrochemical Engineering Principles* (Prentice Hall, New Jersey 1991)

20.6 H. Xu, Y. Song, H.R. Kunz, J.M. Fenton: Effect of elevated temperature and reduced relative humidity on ORR kinetics for PEM fuel cells, J. Electrochem. Soc. **152**, A1828–A1836 (2005)

20.7 C.-Y. Wang: Fundamental models for fuel cell engineering, Chem. Rev. **104**, 4727–4766 (2004)

20.8 S. Srinivasan, E.A. Ticianelli, C.R. Derouin, A. Redondo: Advances in solid polymer electrolyte fuel cell technology with low platinum loading electrodes, J. Power Sources **22**, 359–375 (1988)

20.9 J. Kim, S.-L. Lee, S. Srinivasan, C.E. Chamberlin: Modeling of proton exchange membrane fuel cell performance with an empirical equation, J. Electrochem. Soc. **142**, 2670–2674 (1995)

20.10 R. Mosdale, S. Srinivasan: Analysis of performance and of water and thermal management in proton exchange membrane fuel cells, Electrochim. Acta **40**, 413–422 (1995)

20.11 Y.W. Rho, O.A. Velez, S. Srinivasan, Y.T. Kho: Mass transport phenomena in proton exchange membrane fuel cells using O_2/He, O_2/Ar, and O_2/N_2 mixtures – I. Experimental analysis, J. Electrochem. Soc. **141**, 2084–2089 (1994)

20.12 Y.W. Rho, S. Srinivasan, Y.T. Kho: Mass transport phenomena in proton exchange membrane fuel cells using O_2/He, O_2/Ar and O_2/N_2 mixtures – II. Theoretical analysis, J. Electrochem. Soc. **141**, 2089–2096 (1994)

20.13 A.J. Bard, L. Faulkner: *Electrochemical Methods: Fundamentals and Applications* (Wiley, New York 2001)

20.14 J. Stumper, H. Haas, A. Granados: *In situ* determination of MEA resistance and electrode diffusivity of a fuel cell, J. Electrochem. Soc. **152**, A837–A844 (2005)

20.15 E. Gileadi: *Electrode Kinetics for Chemists, Chemical Engineers and Materials Scientists* (VCH Publishers, Inc, New York 1993)

20.16 S. Srinivasan: *Fuel Cells – From Fundamentals to Applications* (Springer, New York 2006)

20.17 T.R. Ralph, G.A. Hards, J.E. Keating, S.A. Campbell, D.P. Wilkinson, M. Davis, J. St-Pierre, M.C. Johnson: Low cost electrodes for proton exchange membrane fuel cells – Performance in single cells and ballard stacks, J. Electrochem. Soc. **144**, 3845–3857 (1997)

20.18 C.J. Netwall, B.D. Gould, J.A. Rodgers, N.J. Nasello, K.E. Swider-Lyons: Decreasing contact resistance in proton-exchange membrane fuel cells with metal bipolar plates, J. Power Sources **227**, 137–144 (2013)

20.19 J.O.M. Bockris, B.E. Conway (Eds.): *Modern Aspects of Electrochemistry* (Plenum, New York 1977)

20.20 F. Gloaguen, J.-M. Leger, C. Lamy: Electrocatalytic oxidation of methanol on platinum nanoparticles electrodeposited onto porous carbon substrates, J. Appl. Electrochem. **27**, 1052 (1997)

20.21 R.N. Carter, S.S. Kocha, F.T. Wagner, M. Fay, H.A. Gasteiger: Artifacts in measuring electrode catalyst area of fuel cells through cyclic voltammetry, ECS Trans. **11**, 403–410 (2007)

20.22 K.C. Neyerlin, W. Gu, J. Jorne, J.A. Clark, H.A. Gasteiger: Cathode catalyst utilization for the ORR in a PEMFC, J. Electrochem. Soc. **154**, B279–B287 (2007)

20.23 M.D. Edmundson, F.C. Busby: Overcoming artifacts in cyclic voltammetry through the use of multiple scan rates and potential windows, ECS Trans. **41**, 661–671 (2001)

20.24 E. Barsoukov, J.R. Macdonald: *Impedance Spectroscopy – Theory, Experiment, and Applications* (Wiley-Interscience, New York 2005)

20.25 T.E. Springer, I.D. Raistrick: Electrical impedance of a pore wall for the flooded-agglomerate model of porous gas-diffusion electrodes, J. Electrochem. Soc. **136**, 1594–1603 (1989)

20.26 T.E. Springer, T.A. Zawodzinski, M.S. Wilson, S. Gottesfeld: Characterization of polymer electrolyte fuel cells using AC impedance spectroscopy, J. Electrochem. Soc. **143**, 587–599 (1996)

20.27 Y. Bultel, L. Genies, O. Antoine, P. Ozil, R. Durand: Modeling impedance diagrams of active layers in gas diffusion electrodes: Diffusion, ohmic drop effects and multi-step reactions, J. Electroanal. Chem. **527**, 143–155 (2002)

20.28 F. Jaouen, G. Lindbergh: Transient techniques for investigating mass-transport limitations in gas diffusion electrodes – I. Modeling the PEFC cathode, J. Electrochem. Soc. **150**, A1699–A1710 (2003)

20.29 Q. Guo, M. Cayetano, Y. Tsuo, E.S. De Castro, R.E. White: Study of ionic conductivity profiles of the air cathode of a PEMFC by AC impedance spectroscopy, J. Electrochem. Soc. **150**, A1440–A1449 (2003)

20.30 Q. Guo, R.E. White: A Steady-state impedance model for a PEMFC cathode, J. Electrochem. Soc. **151**, E133–E149 (2004)

20.31 S. Devan, V.R. Subramanian, R.E. White: Analytical solution for the impedance of a porous electrode, J. Electrochem. Soc. **151**, A905–A913 (2004)

20.32 R. Makharia, M.F. Mathias, D.R. Baker: Measurement of catalyst layer electrolyte resistance in PEFCs using electrochemical impedance spectroscopy, J. Electrochem. Soc. **152**, A970–A977 (2005)

20.33 O. Antoine, Y. Butel, R. Durand: Oxygen reduction reaction kinetics and mechanism on platinum nanoparticles inside Nafion, J. Electroanal. Chem. **499**, 85–94 (2001)

20.34 B. Müller, N. Wagner, W. Schnurnberger (Eds.): *Proton Conducting Membrane Fuel Cells (2nd International Symposium)* (The Electrochemical Society, Pennington 1999)

20.35 J.T. Müller, P.M. Urban, W.F. Hölderich: Impedance studies on direct methanol fuel cell anodes, J. Power Sources **84**, 157–160 (1999)

20.36 M.E. Orazem, B. Tribollet: *Electrochemical Impedance Spectroscopy* (Wiley, New York 2008)

20.37 D.R. Baker, W. Gu, M.F. Mathias, M. Murphy, K.C. Neyerlin (Eds.): *Diagnostic Methods for Monitoring Fuel Cell Processes* (The Electrochemical Society Inc., Quebec City 2005)

20.38 F.A. Uribe, T.E. Springer, S. Gottesfeld: A microelectrode study of oxygen reduction at the platinum/recast-Nafion film interface, J. Electrochem. Soc. **139**, 765–773 (1992)

20.39 G. Li, P.G. Pickup: Ionic conductivity of PEMFC cathodes – Effect of Nafion loading, J. Electrochem. Soc. **150**, C745–C752 (2003)

20.40 M.C. Lefebvre, R.B. Martin, P.G. Pickup: Characterization of ionic conductivity profiles within proton exchange membrane fuel cell gas diffusion electrodes by impedance spectroscopy, Electrochem. Solid-State Lett. **2**, 259–261 (1999)

20.41 J. Newman: Ohmic potential measured by interrupter techniques, J. Electrochem. Soc. **117**, 507–508 (1970)

20.42 C. Lagergren, G. Lindbergh, D. Simonsson: Investigation of porous electrodes by current interruption, J. Electrochem. Soc. **142**, 787–797 (1995)

20.43 R. Pollard, J. Newman: Mathematical modeling of the lithium-aluminum, iron sulfide battery – Part II. The influence of relaxation time on the charging characteristics, J. Electrochem. Soc. **128**, 503–507 (1981)

20.44 M. Murthy (Ed.): *Proton conducting membrane fuel cells III – Proceedings of the International Symposium* (The Electrochemical Society, Salt Lake City 2005)

20.45 Y. Liu, M. Murphy, D.R. Baker, W. Gu, C. Ji, J. Jorne, H.A. Gasteiger: Determination of electrode sheet resistance in cathode catalyst layer by AC impedance, ECS Trans. **11**, 473–484 (2007)

21. Next-Generation Electrocatalysts

Seunghoon Nam, Chunjoong Kim, Yuhong Oh, Byungwoo Park

In this chapter, we provide a comprehensive review of the most recent advances in the field of efficient catalysts for oxygen reduction reaction (ORR) at fuel-cell cathodes, metal-inorganic nanocomposites. Extensive research has been focused on developing alternative metal-inorganic composites with phosphate compounds. A few examples of ORR catalysts in the aqueous solution will be introduced to help researchers more effectively select composite materials and understand the important reactions involved in fuel cells.

21.1 **Oxygen-Reduction Reaction – Cathodes** 713
21.1.1 Enhancement from Electronic Interactions 714
21.1.2 Improved Structural Stability Against Pt Dissolution 719
21.1.3 Conclusions 724
21.2 **Methanol-Oxidation Reaction – Anodes** 724
21.2.1 Suppression of Ru Dissolution in PtRu Catalyst 725
21.2.2 Enhancement from Various Nanostructured Catalysts 731
21.2.3 Conclusion 738
References 738

The modification of conventional Pt and Au catalysts with metal phosphates can effectively enhance the catalytic activities. The enhancement is attributed to the interactions through charge transfers and/or bifunctional effects. The metal phosphates also prevent the metal catalysts from dissolution and agglomeration by separating the nanoparticle catalysts apart. This role of the physical diffusion barrier is also valid when phosphates are coated onto the PtRu catalysts, similar to the case of the Li-ion battery electrodes. It is found that the dissolution of Ru from PtRu alloy in methanol oxidation is closely related to its oxidation states. Both the catalytic activities and electrochemical stabilities of oxygen reduction or fuel oxidation need to be improved further by identifying the underlying kinetic paths, enabling optimization of the nanostructures and interfaces of catalyst nanocomposites.

21.1 Oxygen-Reduction Reaction – Cathodes

Fuel cells are promising alternative power sources, in which electrical energy is directly converted from the electrochemical reactions with high efficiency and cleanliness [21.1]. Among various types of fuel cells, polymer-electrolyte-membrane fuel cells (PEMFCs) and direct-methanol fuel cells (DMFCs) are of great interest as the power sources for mobile devices due to their low-temperature operation ($< 80\,^{\circ}\mathrm{C}$) [21.2]. In a classical cell design, the catalyst phases, mainly noble metals, are supported by porous carbon layers, which can enable electronic conduction, allow gases to diffuse through the catalyst/membrane interfaces as well as the ability for liquid water to be extracted from the catalyst layer [21.3].

There are two electrochemical reactions occurring at the electrodes: oxidation of fuels (hydrogen or hydrocarbon) at the anode and reduction of oxygen at the cathode. While the fuel-oxidation reaction requires lower oxidation overpotential, the low reaction rate of the oxygen reduction reaction (ORR) at the cathode side leads to higher reduction overpotential, which degrades the overall fuel-cell performance [21.4].

ORR is a process that breaks the bonds of oxygen molecules. ORR in aqueous solutions occurs mainly by two pathways, in which one is the direct four-electron reduction from O_2 to H_2, and the other is two-electron reduction from O_2 to H_2O_2 [21.5, 6]. Since the kinetics involved in ORR are very slow, the enhancement for

highly efficient ORR catalysts is to be achieved for the practical application of fuel cells. At the current stage of technology, platinum and platinum-based nanocomposites have long been considered as the most efficient ORR catalysts. However, the formation of highly stable Pt–O and Pt–OH species act as a limiting factor for the ORR reactions [21.7–9]. Furthermore, these Pt-based catalysts are too expensive to be commercialized.

Apart from highly tailored Pt nanoparticles [21.10, 11], promising advances have been made with new nanocomposite structures (nonprecious metals/heteroatomic polymers) [21.12], or pyrolized metal porphyrins (e.g., cobalt or iron porphyrins) [21.13]. Recently, there are several reports on metal/inorganic nanocomposites, which provide a new approach for making high-performance ORR catalysts with high oxygen-reduction activity and stability [21.14–19].

21.1.1 Enhancement from Electronic Interactions

Concerns about the high cost of Pt-based catalysts led many researchers to focus on the reduction and/or removal of expensive noble metals [21.20–23]. Among the advanced catalyst structures, composite nanostructures are of great interest, which can offer the advantage of an enlarged interfacial area, and also facilitate charge transfers between metal and composite members [21.24]. Therefore, the catalytic activities for ORR can be enhanced or retarded by the d-band modifications.

Charge transfer in the catalysts is a major concern in modifying the electronic structures of catalysts. Tailoring Pt nanoparticles with Au clusters already proved very successful in stabilizing Pt instability against dissolution under potential cycling, where the electronic structures of Pt are changed by the electron transfer with Au clusters [21.25]. Similar charge-transfer effects can be achieved by the metal/metal-inorganic nanocomposites. Through the charge transfer, electrons can be extracted or injected from/to the metals due to the different Fermi energy between the catalytic metal and contacted metal-inorganic compound. Modified d-band electronic structures can induce change in the bonding nature with oxygen molecules, or provide a new reaction pathway to the disproportionation, by which the overall ORR rate can be enhanced with appropriate nanostructural control. Here, gold and aluminum-phosphate composites or bilayer thin-film structures are introduced to identify these charge-transfer effects.

$Au/AlPO_4$ Nanocomposite Catalysts

Since Au has a higher redox potential than Pt, it is more stable during the cathodic reaction. Although the Au catalyst itself shows a moderate electrocatalytic activity, its activity should be further improved to be applicable [21.26], and many investigations are currently underway to make Au more viable. Among them, recent researches on the nanocomposites with inorganic compounds are quite promising since their catalytic activities are proven to be readily controllable.

Metal phosphates are ideal compounds as co-catalysts since they offer resistance to dissolution under the

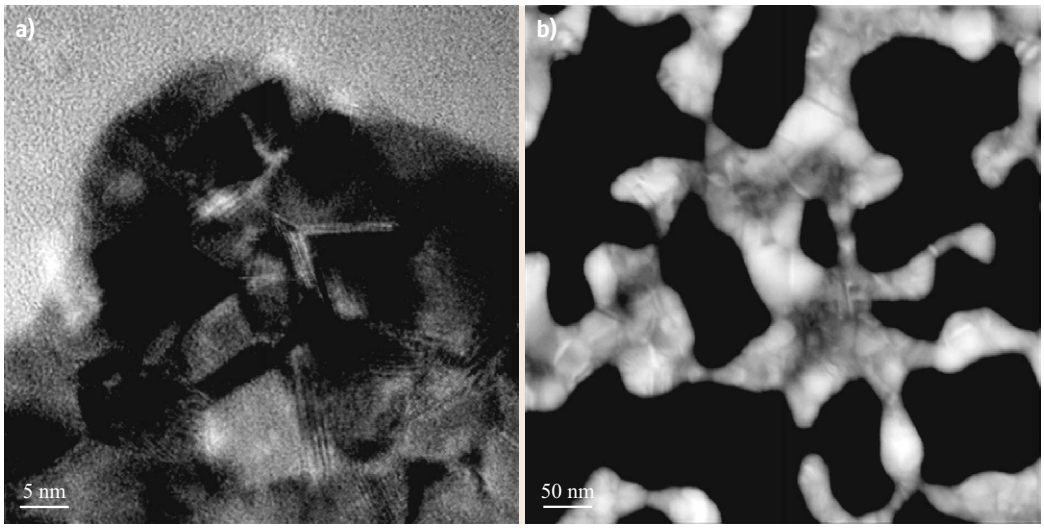


Fig. 21.1 (a) High-resolution TEM image and (b) HAADF (*Z*-contrast STEM) image of the $Au/AlPO_4$ nanocomposites deposited by sputtering (after [21.16])

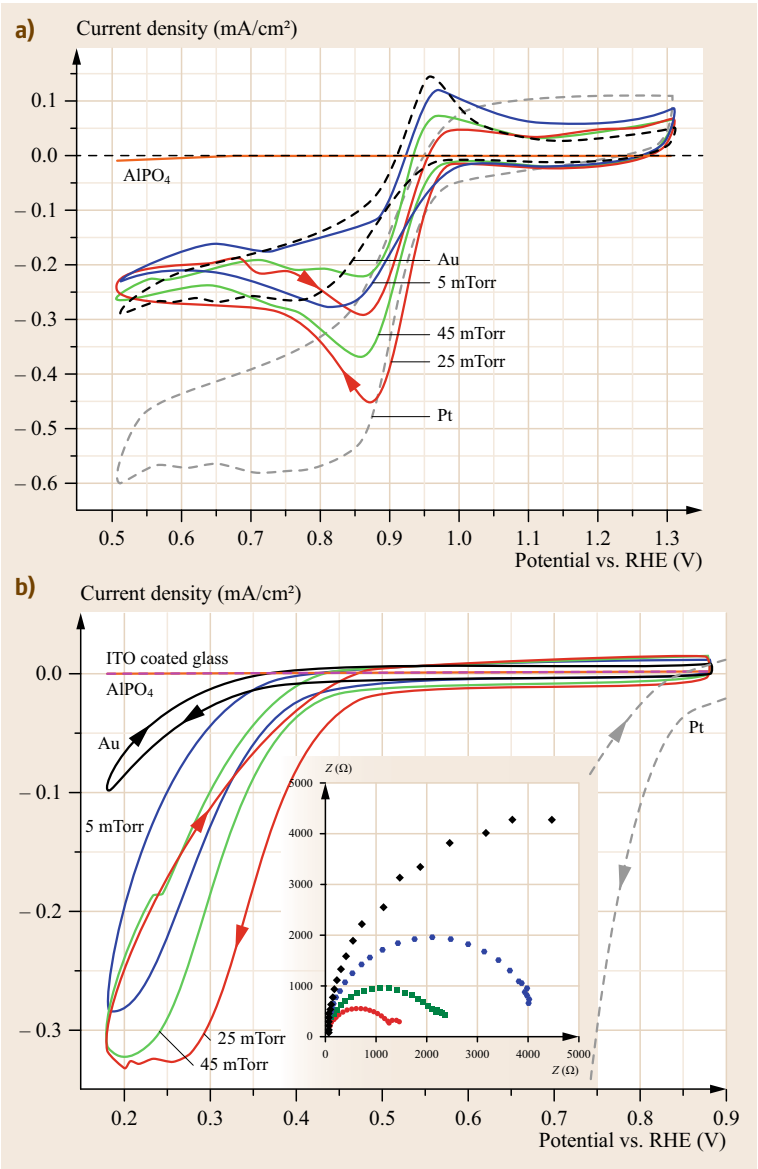


Fig. 21.2a,b Oxygen-reduction activities of the Au/$AlPO_4$ nano composite, Au, and $AlPO_4$ thin-film electrodes, in the oxygen-saturated **(a)** NaOH solution and **(b)** H_2SO_4 solution. The *inset* in **(b)** is a Nyquist plot for the corresponding samples at 0.38 V (after [21.16])

corrosive conditions of the fuel-cell cathode [21.27]. In addition, the nanoporous structures of amorphous (or poor crystalline) metal phosphates allow the facile transfer of protons, hydroxyl ions, water, methanol, or oxygen [21.28–30]. Herein, aluminum phosphate is selected since it has high structural diversity and enables easy hydration for the wide tuning of electrocatalytic properties.

In order to modify the metal phosphate as a matrix material, the working pressure was varied during the deposition in the sputtering chamber. At a high operating pressure, a thermalization of sputtered species occurs from their kinetic energy loss due to an increase in collision frequency. The energy of the arriving atoms is lowered by approximately 1 order of magnitude within the pressure range (5–45 mTorr, 1 mTorr = 1.33 μbar) used in this study, based on the Monte Carlo simulation [21.31]. The sputtered species interact with the ionized/excited gas molecules plus electrons in the plasma, and their chemical or electronic states can be altered depending on the density of the plasma. The various sputtered species at different operating pressures can affect the chemical configurations, defect densities, such as oxygen vacancies, and electronic structures of

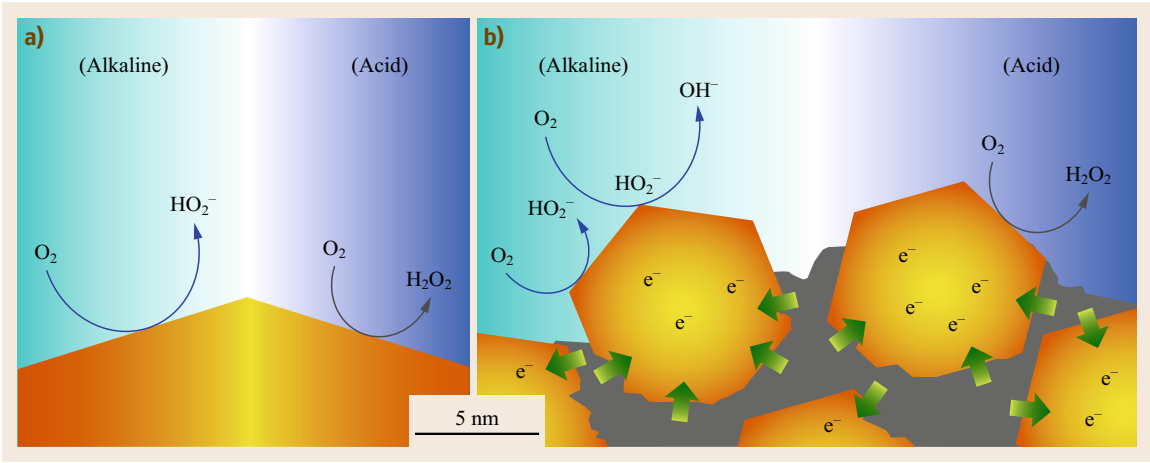


Fig. 21.3a,b Schematic figures of the ORRs on **(a)** Au and **(b)** $Au/AlPO_4$ composites, both in the acidic and alkaline environments (after [21.16])

the deposited metal phosphates, which results in the change of electrocatalytic properties of Au in the composites.

The $Au/AlPO_4$ nanocomposite was deposited on indium-tin oxide (ITO) coated glass by sputtering. The deposition was performed at room temperature (RT) under an Ar atmosphere with varying operating pressures of 5, 25, and 45 mTorr for $Au/AlPO_4$ nanocomposites and 25 mTorr for Au electrodes. All of the $Au/AlPO_4$ nanocomposites were annealed at 200 °C.

The transmission electron microscopy (TEM) image (Fig. 21.1a) represents the facets and cusps of several nanometer-sized gold grains in the $Au/AlPO_4$ nanocomposite. The gold grains have sizes of approximately 8.2, 6.7, and 10.9 nm, respectively, in the $Au/AlPO_4$ nanocomposites deposited at pressures of 5, 25, and 45 mTorr. The grain sizes of gold in the $Au/AlPO_4$ composites are smaller than those of the deposited gold alone ($\approx$ 19.8 nm). The change of grain size in the nanocomposites seems to result from the interposed $AlPO_4$ among the gold grains. The high-angle annular dark field (HAADF) image (Fig. 21.1b) indicates that gold nanocrystallites form a somewhat aggregated and interconnected geometry, demonstrating both the feasible electronic conduction of gold and suitable transport of the reactants.

To examine the catalytic activities of Au and the $Au/AlPO_4$ nanocomposites, their ORR currents were recorded with cyclic voltammetry in an oxygen-saturated 1 M NaOH solution. All of the potentials mentioned herein are presented versus reversible hydrogen electrode (RHE). As shown in Fig. 21.2a, Au catalysts generate approximately one-half of the limiting current density compared with that on the Pt surface at the given oxygen concentration. It implies that the oxygen reduction partially occurs on the bare Au surface with half the number of electrons involved ($O_2 + H_2O + 2e^- \leftrightarrow HO_2^- + OH^-$). Typically, complete oxygen reduction ($O_2 + 2H_2O + 4e^- \leftrightarrow 4OH^-$) occurs on Pt catalysts [21.32]. However, oxygen reduction on the $Au/AlPO_4$ nanocomposites occurs with the steeper reduction slope as well as a larger reduction-current density in the potential region of approximately 0.8−1.0 V. The enhanced oxygen reduction including a larger reduction current density is represented as the newly appeared peak at $\approx$ 0.85 V, and at the same time the oxidation peak at $\approx$ 0.95 V disappeared on the reverse sweep. Typically, oxygen reduction in an alkaline solution undergoes the hydrogen-peroxide intermediate state (step 1: $O_2 + H_2 + 2e^- \leftrightarrow HO_2^- + OH^-$; step 2: $HO_2^- + OH^- + H_2O + 2e^- \leftrightarrow 4OH^-$), according to *Anastasijevic* et al.'s model [21.33]. The hydrogen peroxides (HO_2^-) remain in the case of partial reduction of oxygen. In order to achieve the larger reduction current at the given oxygen concentration, the hydrogen peroxides should be further reduced to hydroxyl ions (OH^-). Therefore, the appeared peak at $\approx$ 0.85 V with a larger current density suggests that hydrogen peroxides (HO_2^-) are consumed, and more feasible oxygen reduction occurs [21.34]. As seen on the reverse sweep, the oxidation peak at $\approx$ 0.95 V is indicative of the oxidation of the residual HO_2^- [21.35]. The increased reduction of HO_2^- to OH^- on the $Au/AlPO_4$ nanocomposites leads to the decreased amount of HO_2^- oxidation in the cyclic voltammetry.

Oxygen reduction activities were also measured in an oxygen-saturated 0.5 M H_2SO_4 solution, as shown in Fig. 21.2b. The $Au/AlPO_4$ nanocomposites exhibit higher onset potential and a steeper reduction slope than that of the pure Au catalyst. The $Au/AlPO_4$ nanocom-

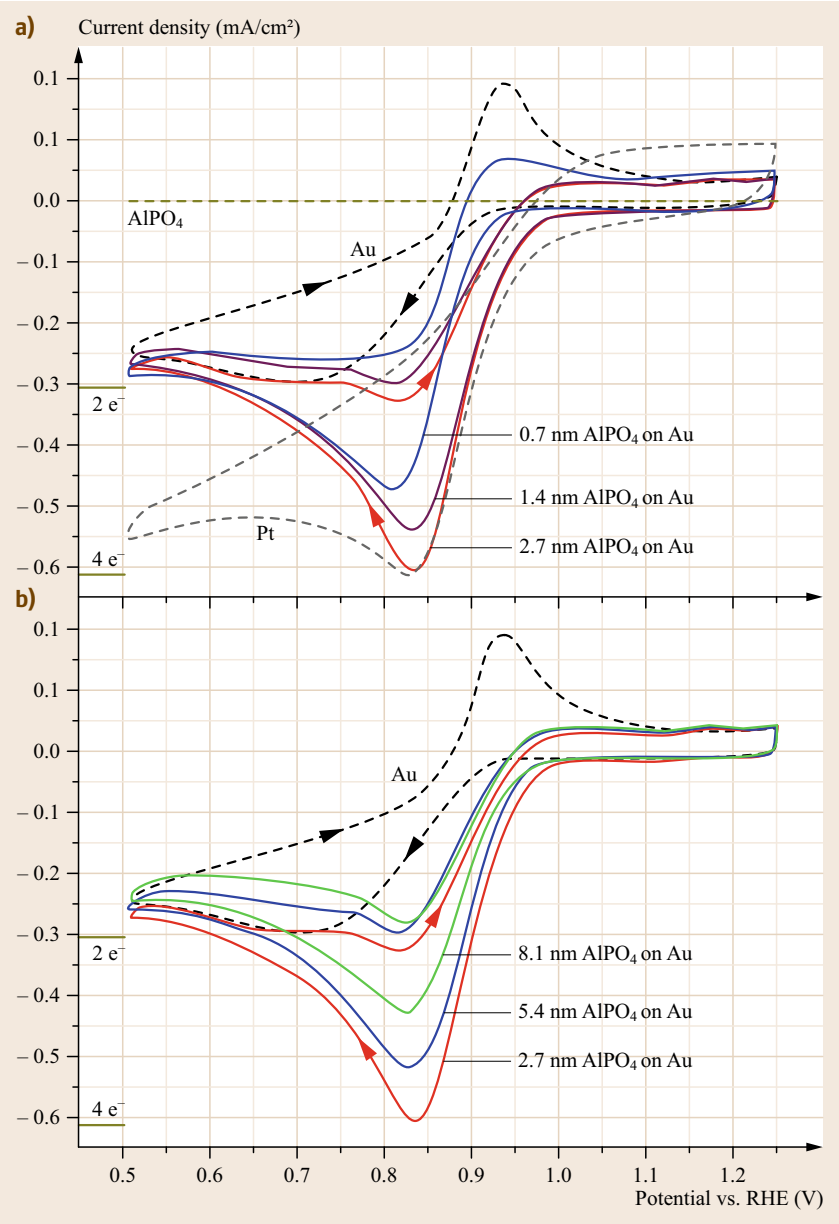


Fig. 21.4a,b Oxygen-reduction polarization curves on the Au thin-film electrodes with the $AlPO_4$ overlayer deposition of approximately **(a)** 0.7–2.7 nm and **(b)** 2.7–8.1 nm, in oxygen-saturated 0.1 M NaOH solution at a scan rate of 50 mV/s. The calculated current densities corresponding to the two-electron and four-electron paths are marked (after [21.15])

posite deposited at 25 mTorr presents higher activity than other nanocomposites. The enhanced oxygen-reduction activities were also identified with the electrochemical impedance spectroscopy at 0.38 V. It is noticeable that the overall activities of Au-based catalysts are low in an acidic environment. Typically, only partial oxygen reduction ($O_2 + 2H^+ + 2e^- \leftrightarrow H_2O_2$) occurs on the Au catalysts in an acidic solution [21.36]. An abundant proton environment enables the protonation of HO_2^- to H_2O_2, and the ORR does not proceed further. The negligible activities of pure $AlPO_4$ deposited at 25 mTorr in alkaline or acidic environment are presented in Fig. 21.2.

The schematics shown in Fig. 21.3 demonstrate that the electron transfer from $AlPO_4$ to Au plays an important role in controlling the Au catalytic activities with the modification of the electronic structure. The oxygen-reduction catalytic activities can be increased further by optimizing the nanostructures and interfaces of the Au/$AlPO_4$ nanocomposite.

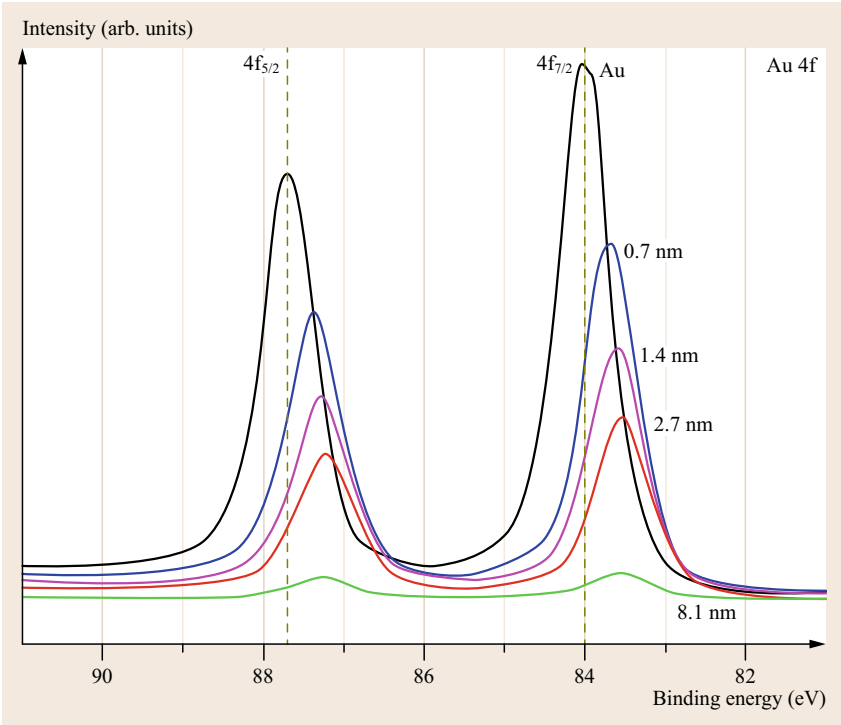


Fig. 21.5 XPS spectra for the pure Au, and the $AlPO_4$-overlayer-deposited Au electrodes with thicknesses in the range from 0.7 to 8.1 nm. The *dashed lines* are from the standard Au sample (after [21.15])

Au Thin-Film Catalyst with the Modification of the $AlPO_4$ Overlayer

As discussed before, composites have merits from tailored nanostructures and electronic structures. Here, as a model study, metal-phosphate overlayers are investigated in thin-film geometry [21.15]. Through the structures of the overlayer, the nanostructures of Au can remain successfully constant in order to decouple the charge-transfer effect from the morphological effects of Au in the composite structures.

The $AlPO_4$ overlayer permits both the access and release of the reactants, intermediates, and products, depending on the permeability of each chemical substance due to their porous structures. For this reason, they were adopted as overlayer materials in the $AlPO_4$/Au bilayer structures.

Gold was deposited on ITO-coated glass by sputtering before the deposition of the $AlPO_4$ overlayer. The deposition was performed at RT under an Ar atmosphere at 25 mTorr for both Au and $AlPO_4$. The deposition time of $AlPO_4$ was controlled in the range of 15–180 min for the purpose of obtaining $AlPO_4$ overlayers with various thicknesses.

In order to compare the ORR activities of the Au electrodes and $AlPO_4$-deposited Au thin-film electrodes, the voltammetric profiles of the electrodes in oxygen-saturated 0.1 M NaOH solution are summarized in Fig. 21.4. By increasing the amount of the phosphate overlayer, the shape of the voltammetric profile is changed, and the ORR is promoted within the potential region of approximately 0.7–1.0 V. Current densities are nearly doubled on the $AlPO_4$-deposited Au electrodes, as shown in Fig. 21.4a. This indicates that oxygen is nearly completely reduced within a certain potential range with the proper amount of $AlPO_4$ overlayer. As seen on the reverse sweep, the oxidation peak at ≈ 0.95 V is indicative of the oxidation of the residual HO_2^- and O_2^- ($O_2 + e^- \leftrightarrow O_2^-$), which are the intermediates in regard to incomplete oxygen reduction [21.35, 37]. The increase in the efficiency of the ORR decreases the oxidation currents of the residual intermediates. When the $AlPO_4$ overlayer becomes sufficiently thick, the oxygen accessibility becomes small, so that the equivalent effect of the extended diffusion layer is observed. As a result, the overall ORR current density gradually diminishes, once the $AlPO_4$ overlayer becomes thicker than ≈ 2.7 nm (Fig. 21.4b).

Figure 21.5 shows the XPS (x-ray photoelectron spectroscopy) spectra of the Au 4f region as a function of the growth time regarding the $AlPO_4$ overlayer on the Au electrodes [21.38, 39]. The shift of Au 4f toward a lower binding energy is observed with the increasing amounts of the $AlPO_4$ overlayers, which indicates

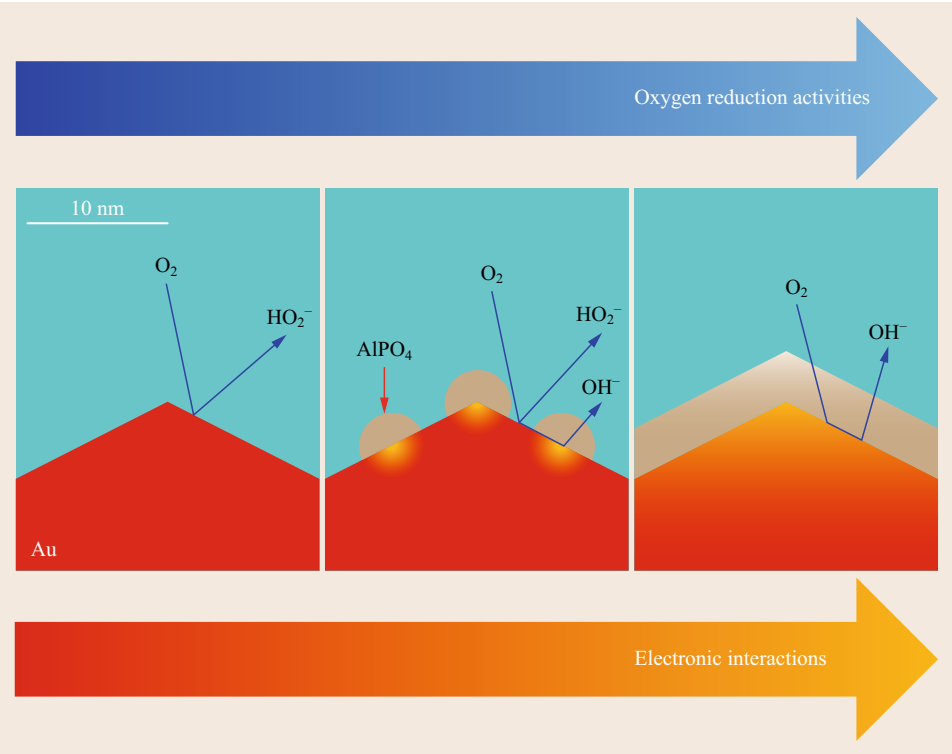


Fig. 21.6 Schematic illustrations showing possible reactions on Au thin film and $Au/AlPO_4$ with different overlayer thicknesses (after [21.15])

negatively charged Au. The observations by XPS are consistent with the activities of oxygen and hydrogen peroxide, as seen in Fig. 21.4. The electron transfer to Au induces alterations in the electronic structure of Au, and this can affect the adsorption state of oxygen and hydrogen peroxide on the electrodes, thereby changing the catalytic activities of the electrodes.

A brief conclusion of the work is proposed in Fig. 21.6. The surface properties of the Au layer are conserved before and after the deposition of the nanoscale $AlPO_4$ overlayer, in terms of the facet orientation and electrochemical surface area (ESA). However, the catalytic activities of Au are varied with the amount of the $AlPO_4$ overlayer. The potential region of the enhanced ORR (approximately 0.7−1.0 V) is associated with the reaction path including the decomposition (disproportionation) of hydrogen peroxide. These enhancements are attributed to the electronic effects on Au and the changed behaviors of the intermediate hydrogen peroxide.

21.1.2 Improved Structural Stability Against Pt Dissolution

In proton exchange membrane fuel cells (PEMFCs), protons generated in the anode are transferred to the cathode through a polymer electrolyte membrane, thereby forming water via the bonding of oxygen and electrons [21.40]. Since PEMFCs are operating at a low temperature, nanosized platinum-supported carbon is currently used as a catalyst in PEMFCs to increase the efficiency of the fuel cell [21.41].

However, since the platinum on a carbon support used as a catalyst for PEMFCs merely has a size of less than ≈ 5 nm, the catalysts are not stable. During the operation of fuel cells, especially, in the acidic medium, catalysts become more unstable, which results in the dissolution of platinum nanoparticles [21.42]. They can deposit on the polymer electrolyte blocking the ion diffusion path and/or agglomerate into larger nanoparticles, whose phenomena degrade the overall cell performance.

Applying the nanocomposite structures can be an effective solution for preventing this dissolution issue of the catalysts [21.17, 19]. The nanocomposite inorganic compounds can act as physical barriers to prevent direct contact between electrolyte and catalysts surface, thus, they can conserve the high activity of catalyst, and prohibit the agglomeration of catalysts. In addition, the catalytic activity can be tuned by the charge transfer between the inorganic matrix and the metal catalyst.

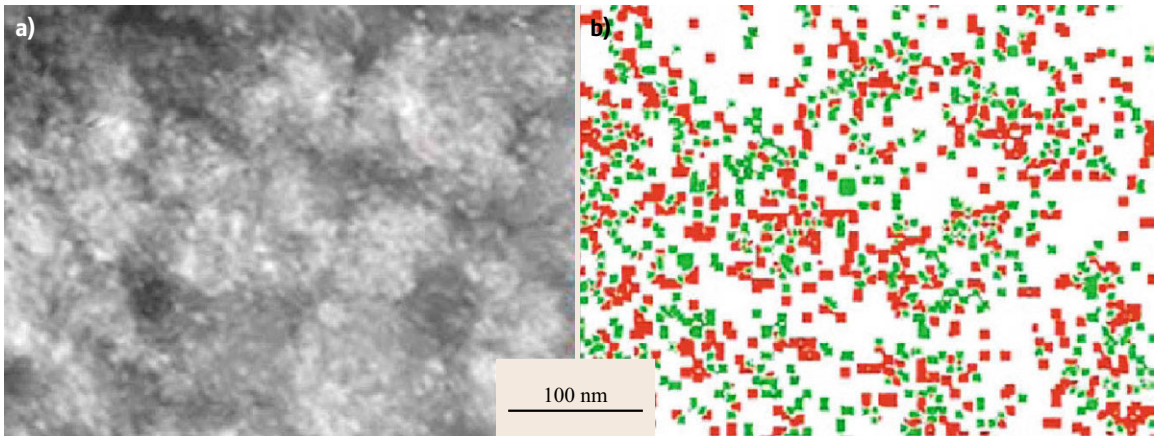


Fig. 21.7 (a) *Z*-contrast STEM image of $FePO_4$–Pt/C nanocomposite (at 0.1 mM with $FePO_4$: Pt = 1 : 1), and (b) the position of Pt (*red*) and Fe (*green*) from the EDS mapping confirm the relatively good dispersion of $FePO_4$ and Pt nanoparticles (after [21.17], courtesy of AIP)

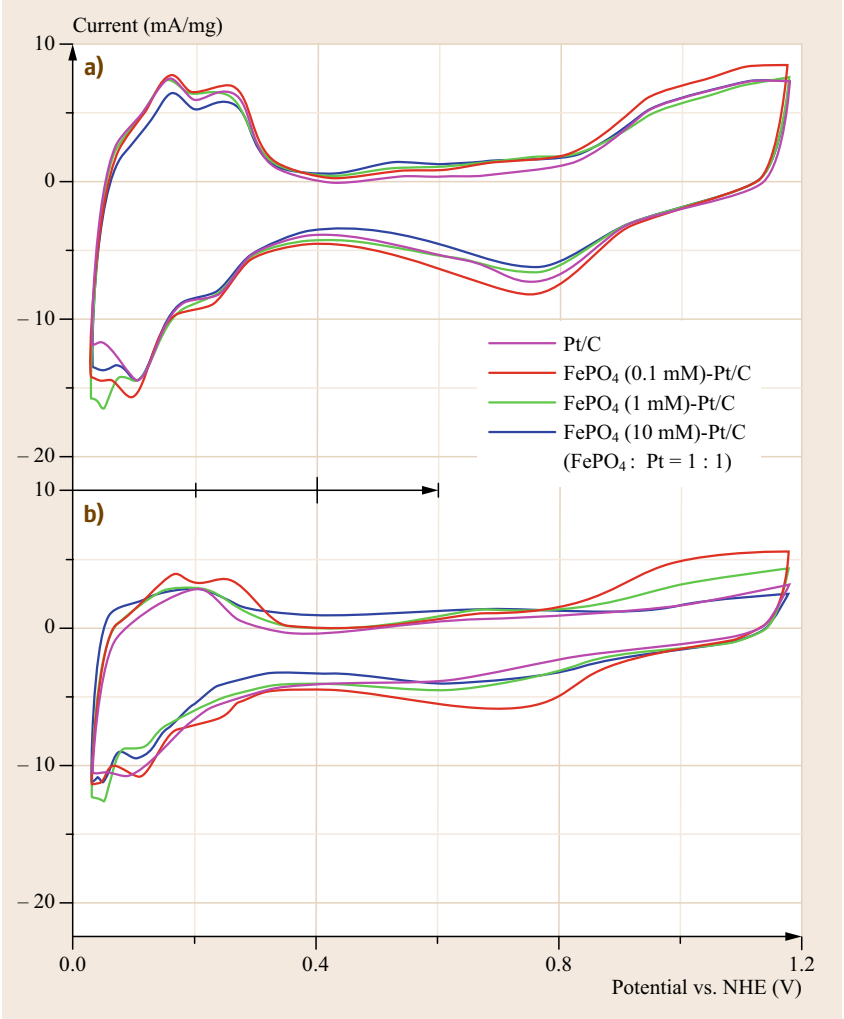


Fig. 21.8a,b Cyclic voltammograms of the Pt/C and $FePO_4$–Pt/C nanocomposites (a) before and (b) after 1000 accelerated cycles (after [21.17], courtesy of AIP)

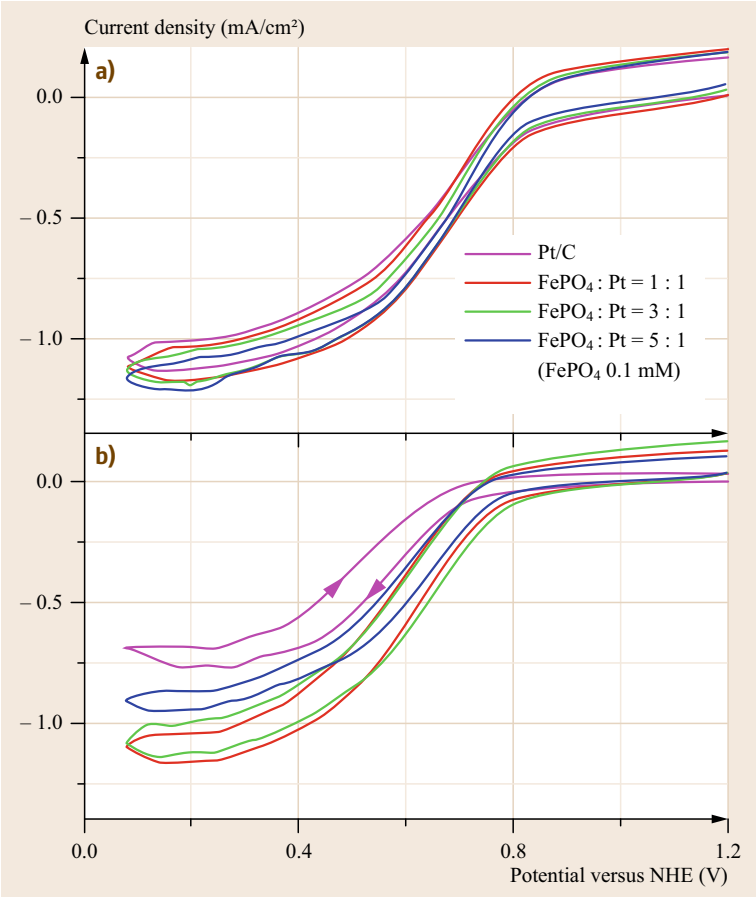


Fig. 21.9a,b ORR currents of Pt/C and $FePO_4$–Pt/C nanocomposites recorded by RDE with a rate of 400 rpm in oxygen-saturated solution **(a)** before and **(b)** after 1000 cycles (after [21.17], courtesy of AIP)

Enhanced Electrocatalytic Stability of Pt/$FePO_4$/Carbon Nanocomposites

Despite significant advancement in PEMFC research, serious issues still remain, such as the low cathode efficiency for the ORR, the loss of Pt activity by long-term operation, and easy poisoning by CO, in addition to the economic barrier [21.43]. In order to resolve these problems, nanostructured Pt-based electrodes have been intensively investigated for enhancing the performances of PEMFCs or reducing the amount of Pt loading. However, the decreased catalytic activity by long-term operation needs to be resolved. Although the catalytic performance of catalysts have been improved through several treatments, such as alloying Pt with transition/refractory/group-V metals, deposition of carbon around Pt, and surface oxidation of the carbon supports, the instabilities of Pt catalysts during long-term operation of fuel cells have not yet been fully resolved [21.42].

Recently, *Bouwman* et al. confirmed superior catalytic properties from Pt^{2+}/Pt^{4+}-dispersed $FePO_x$ [21.44]. Hydrous phosphate was selected as the matrix due to its suitable properties for co-catalysts, such as high ionic conductivity, thermal stability, and catalytic efficiency. Also, ≈ 3 nm Pt nanoparticles embedded in thin-film $FePO_4$ exhibited an enhanced electrocatalytic activity and stability compared with the Pt thin films [21.18].

In this chapter, the long-term stabilities of $FePO_4$/Pt/C nanocomposites for the application of cathodes in PEMFCs will be introduced. The $FePO_4$/Pt/C nanocomposites seem to be very effective in preventing both the dissolution and agglomeration of Pt nanoparticles without any initial degradation of the electrocatalytic activities, in addition to the d-band electronic control by the Fermi energy difference between Pt and $FePO_4$.

The commercial 20 wt% Pt-supported carbon catalysts were added to the solution with the desired molar ratios of synthesized $FePO_4$ nanoparticles to Pt. The resultant $FePO_4$/Pt/C nanocomposites were annealed in an Ar atmosphere at 200 °C for 6 h, and the catalyst inks for the electrochemical tests were prepared as reported elsewhere [21.45].

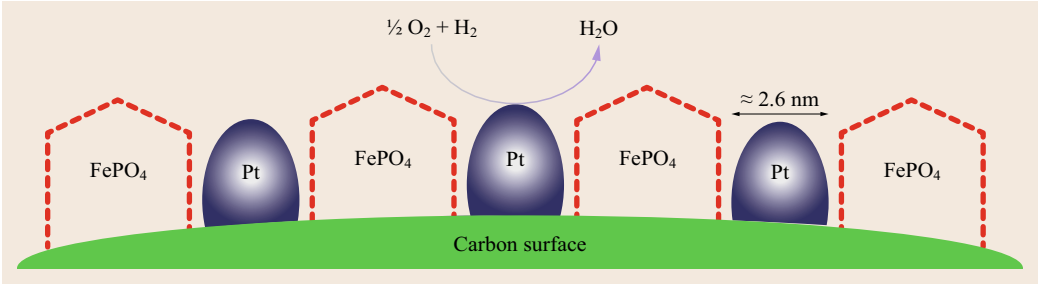


Fig. 21.10 Schematic of Pt/$FePO_4$ composite catalysts loaded on a carbon electrode

To confirm the existence and distribution of $FePO_4$ nanoparticles, energy-dispersive spectrometry (EDS) mapping was carried out (Fig. 21.7). The *Z*-contrast scanning transmission electron microscopy (STEM) image of $FePO_4$–Pt/C nanocomposites and the EDS mapping of Pt and Fe demonstrate a uniform distribution of $FePO_4$ nanoparticles without much aggregation, as shown in Fig. 21.7a. For the positions of Pt and Fe in Fig. 21.7b, the $FePO_4$ and Pt nanoparticles are relatively well dispersed as nanocomposites.

In order to observe the changes of the electrocatalytic surface area (ESA) in the $FePO_4$–Pt/C nanocomposites and Pt/C, cyclic voltammograms were carried out in H_2SO_4, before and after 1000 accelerated cycles (Fig. 21.8). Regardless of the synthetic concentrations of $FePO_4$, the $FePO_4$–Pt/C nanocomposites show nearly the same initial behavior as the untreated Pt/C catalysts, without any hindrance of the reactions on Pt. However, after 1000 cycles, the $FePO_4$ (0.1 mM)/Pt/C nanocomposites show the best long-term stabilities and the least dissolution of Pt [21.46]. No dissolution of Fe or P is observed in the $FePO_4$–Pt/C nanocomposites after long-term operation, while Fe ions can easily act as catalyst-like agents in the Nafion degradation by a Fenton reaction [21.47]. To optimize the $FePO_4$/Pt/C nanocomposites, the molar ratios of $FePO_4$ to Pt in the nanocomposites were varied from 1 to 5 at a fixed synthetic concentration of $FePO_4$ (= 0.1 mM). The $FePO_4$ (0.1 mM)/Pt/C nanocomposites with the molar ratio ($FePO_4$/Pt) of 3 and 1 show the most enhanced long-term stabilities after 1000 cycles.

For examining the catalytic stabilities as a cathode, the ORR currents of Pt/C and $FePO_4$ (0.1 mM)–Pt/C nanocomposites were recorded using a rotating disk electrode (RDE). Although the Pt^{2+}/Pt^{4+} dispersed $FePO_x$ facilitates ORR, most likely through the activations of oxygen sources to the prerequisite species (O_2^- or HOO^-) [21.44], the electrocatalytic behaviors of Pt/C and $FePO_4$/Pt/C before the accelerated tests are quite similar, as shown in Fig. 21.9a. The interactions between Pt and $FePO_4$ exert little effect on the initial catalytic properties, despite some interatomic charge transfer in the nanocomposites. The ORR currents in Fig. 21.9b clearly demonstrate that the limiting current of Pt/C ($\approx 0.75\,mA/cm^2$) is only $\approx 70\%$ of the $FePO_4$–Pt/C nanocomposites ($\approx 1.2\,mA/cm^2$) after 1000 cycles. Moreover, the onset potential of ORR in Pt/C (≈ 0.71 V) also significantly shifts to a lower potential compared to that in $FePO_4$–Pt/C nanocomposites (≈ 0.81 V). It is believed that the loss of ORR activities results from the irreversible oxidation/dissolution of the Pt surface. However, nanocomposites show negligible loss in the ORR activities. These enhanced long-term stabilities are attributed to the structural stability of $FePO_4$. The iron phosphate nanoparticles remain stable after long-term operation due to their high electrochemical/acidic stability compared with typical metal oxides, and the optimum nanoscale contact between $FePO_4$ and Pt stabilizes the activity of Pt nanoparticles.

The long-term stability of Pt by mixing metal phases with oxides or phosphates [21.44, 48] has not been discussed in many reports. However, the $FePO_4$/Pt/C nanocomposites show a clear enhancement of long-term stabilities over the repeated cycles, without any initial degradation, by the proper interfacial contact between Pt and $FePO_4$. It is believed that the well-dispersed $FePO_4$ nanoparticles serve important roles in preserving the Pt surface activities by impeding both the dissolution and agglomeration of Pt nanoparticles (Fig. 21.10).

Pt/$AlPO_4$ Nanocomposite Catalysts

A conventional catalyst including platinum is generally provided in the form of nanoparticles having a small diameter of several nanometers so as to show its excellent catalytic activities via an increased specific surface area. Such catalytically active particles become unstable as electrochemical reactions proceed, thereby causing the particles to coarsen as well as agglomerate with one another. Such coarsening significantly reduces the surface area of the catalyst particles needed for the reactions, resulting in the degra-

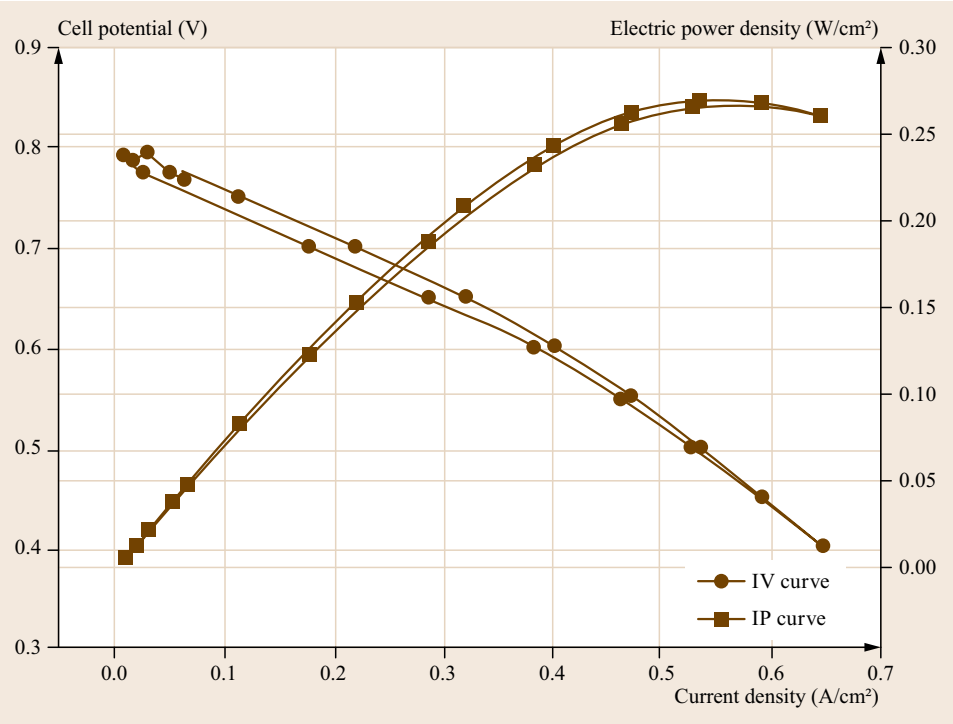


Fig. 21.11 Electrochemical characteristics of $Pt/AlPO_4$ in a full-cell configuration (after [21.48])

dation of the quality of a fuel cell using the catalyst.

To solve this problem, a certain compound (anticoarsening compound) has been introduced onto the surface of the catalyst particles. However, the presence of such anticoarsening compounds on the surface of metal catalyst particles causes an increase in electric resistance among the metal catalyst nanoparticles and a drop in proton conductivity to the surface of the metal-catalyst particles. In addition, the surface of the metal in catalytic reactions is poisoned by the anticoarsening compounds, and the catalyst shows a decreased reactive surface, resulting in the degradation of the quality of a fuel cell. The present chapter relates to an electrode catalyst, which provides a fuel cell with excellent lifespan characteristics by preventing metal catalyst components from coarsening while not adversely affecting the electrochemical quality.

The anticoarsening compound is not coated on the surface of metal nanoparticles, but rather, is coated onto and/or dispersed in specific sites capable of inhibiting coarsening. These include interstitial sites for metal atoms and contact points between the carbon support and catalyst nanoparticles. Therefore, even if the catalytically active surfaces become unstable during electrochemical reactions, it is possible to inhibit coarsening. Accordingly, it is possible to increase the thermal and structural stability of electrode catalysts, to minimize the degradation of fuel-cell quality, and thereby to improve the lifespan characteristics of the fuel cell.

Platinum-supported carbon compounds having an average Pt size of $\approx 2.5\,\text{nm}$ were mixed with aluminum phosphate in various molar ratios. The solution was completely dried at a temperature of 90 °C or less, and then heat treated at 200 °C for 2 h to cause the hydrous $AlPO_4$ to be properly bound on the surface of the Pt-supported carbon. Additionally, such heat treatment also serves to completely remove any trace impurities that may inhibit electrochemical reactions.

The Pt-supported carbon coated with aluminum phosphate was mixed with Nafion ink for the oxygen electrode. A Nafion electrolyte membrane was bonded thermally and mechanically between a cathode and an anode to provide a membrane electrode assembly (MEA), which, in turn, was used to manufacture a proton exchange membrane fuel cell. The membrane-electrode assembly is a monolithic unit having a catalyst electrode attached to an electrolyte membrane. Next, the assembly was inserted into the gap between two hot plates operated in a hydraulic manner while maintaining a temperature of

≈ 140 °C, and then pressurized to perform hot pressing.

The air and hydrogen were supplied at the cathode and anode side, respectively. The $AlPO_4$-coated Pt/C shows a current density of $0.27\,A/cm^2$ and an electric power density of $0.17\,W/cm^2$ at 0.65 V, in which the composite catalyst shows quality equivalent to the quality of MEA for general PEMFCs, when the amount of Pt on the oxygen electrode is 0.25 mg of Pt/cm^2, as shown in Fig. 21.11. Their long-term stabilities were evaluated under the real-cell operations, and also the reduced agglomeration of catalysts was confirmed by simple peak broadening in the x-ray diffraction of Pt.

The inorganic compound $AlPO_4$, which is capable of preventing a catalytic substance from coarsening, is coated/dispersed in the Pt-supported carbon catalysts. By successfully inhibiting the growth of nanoparticle, the structural stability of the catalytic substance is greatly enhanced. Therefore, it is possible to provide a fuel cell having excellent lifespan characteristics while not causing any degradation of electrocatalytic quality. In addition, this work is considered to be the most practical for industrial applications since metal phosphates are very inexpensive and abundant chemicals, and all experimental steps are incredibly mild.

21.1.3 Conclusions

Various types of catalyst/inorganic composite nanostructures were described, and their enhanced and prolonged catalytic activities are confirmed. Through the comprehensive review of the most recent advances in the nanocomposite structures for ORR, the physical/chemical effects of nanostructures can further be improved. Electron transfer between metals and inorganic compounds is confirmed to play a critical role in enhancing the catalytic properties in ORR. Nanocomposites are also beneficial to the structural stabilization of highly active nanometric metal catalysts by supplying the physical barriers for their dissolution and agglomeration. Indeed, metal-inorganic composites suggest a new way to achieve highly efficient catalysts for fuel cells. The mechanisms can become more unambiguous if both the detailed electronic structures and phase-transformation kinetics can be studied by in situ absorption/emission spectroscopy.

21.2 Methanol-Oxidation Reaction – Anodes

Since methanol is directly fed to the anode in direct-methanol fuel cells (DMFCs), effective methanol oxidation is one of the important issues in the development of DMFCs. In general, Pt is the most widely used for methanol oxidation with various intermediates formed during the reaction.

Some of these reaction intermediates have been found to poison the catalyst surface inhibiting further oxidation of methanol, and hence there should be an efficient kinetic path by which these strongly adsorbed intermediates are removed from the catalyst surface. The overall reaction of methanol oxidation liberating six electrons is quite slow on pure Pt. Especially, methanol oxidation is associated with both an unknown intermediate and CO_{ads} as a poison. In order to tackle this problem, many researchers have been looking for new Pt-based alloys with a high tolerance for this CO poisoning.

Among the Pt-based alloys, PtRu catalysts are considered as the most effective anode catalysts for DMFC. Two mechanisms have been proposed to improve the CO tolerance of PtRu catalysts. The first is the bifunctional mechanism. *Watanabe* and *Motoo* suggested that Ru acted as promoting centers for the generation of the Ru–OH species [21.49], and the Langmuir–Hinshelwood mechanism is

$$CO_{ads} + OH_{ads} \rightarrow CO_2 + H^+ + e^-$$

CO on Pt is oxidized into CO_2 recombining with oxygen species on Ru. Therefore, the adsorbed Ru–OH is active to oxidize the poisoning CO into CO_2. In addition, Ru transfers oxygen more effectively than Pt due to its ability to oxidatively adsorb water at less positive potentials.

The second mechanism involves the electronic or ligand mechanism, in which the electronic structure of Pt is modified through the formation of an alloy with Ru, resulting in the weakened adsorption of CO on Pt. In general, the CO–Pt bond is described in terms of electron donation from the CO 5σ to the Pt 5d and back donation from the Pt 5d to the CO $2\pi^*$. However, the 5σ contribution to the bond is quite small. Therefore, the interaction between Pt 5d and $2\pi^*$ is important to determine the bond strength of Pt–CO.

The change in the electronic properties of PtRu alloy electrodes was confirmed by the shift of the d-band center, as demonstrated by *Mukerjee* et al. with their XANES study [21.50]. Accordingly, Ru alloyed with Pt causes the increase in the d-band vacancy of Pt, and this

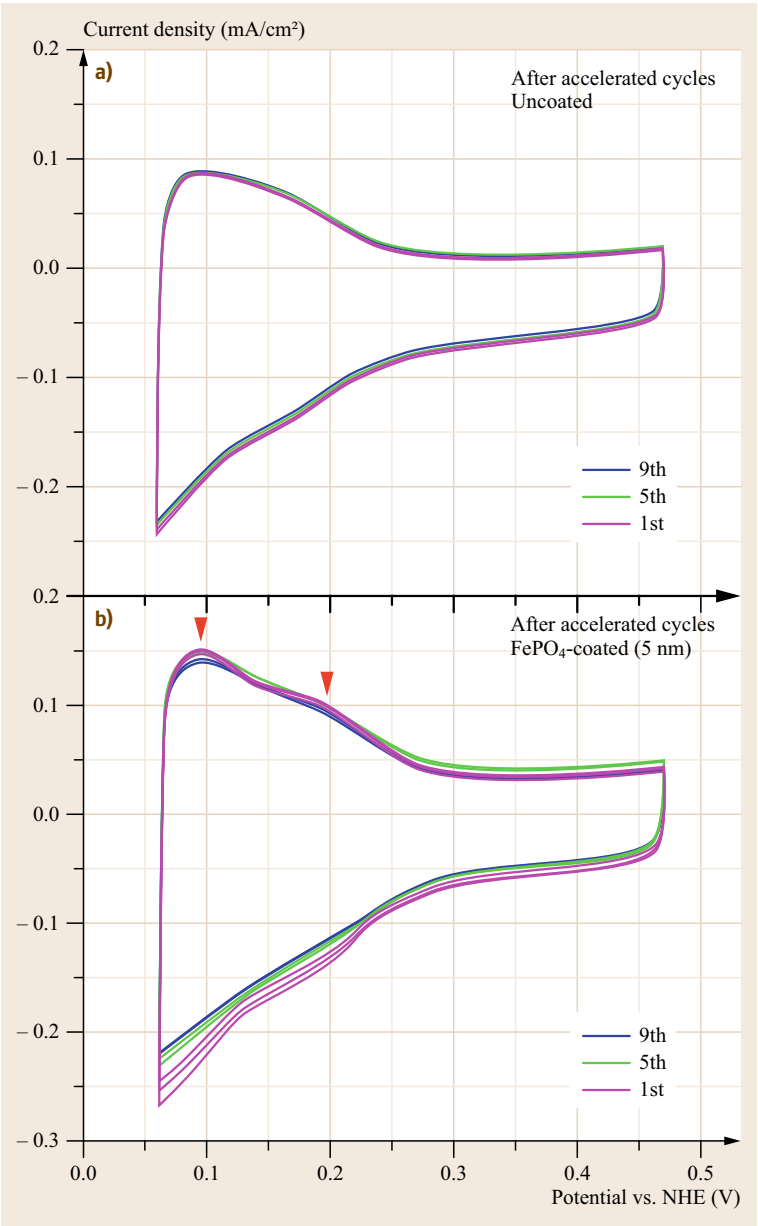


Fig. 21.12a,b Cyclic voltammograms (0.06–0.47 V) of **(a)** the uncoated and **(b)** $FePO_4$-coated PtRu thin-film electrodes in the fresh H_2SO_4 electrolyte after accelerated cycles between 0.4 and 1.05 V. The current densities were normalized by a 1 cm^2 sample area (after [21.19])

creates a lower density of states (DOS) on the Fermi level, reducing the $2\pi^*$ back donation and weakening the CO–Pt bonding. Therefore, PtRu electrodes show enhanced methanol-oxidation activities.

21.2.1 Suppression of Ru Dissolution in PtRu Catalyst

In recent years, the stability of electrocatalysts has received much attention because the catalytic properties deteriorate after long-term operation due to the dissolution of noble metal-based catalysts and the aggregation of catalyst nanoparticles [21.17]. Meanwhile, much effort has been made for PtRu catalysts due to its high tolerance for carbon monoxide. The formation of the surface-oxygenated species on Ru takes place at a potential lower than on Pt. Therefore, the presence of Ru adjacent to Pt diminishes the surface-poisoning of Pt by CO [21.51, 52]. However, though thermodynamics tell us that metallic Ru is stable within the operating potential range of DMFCs, the abnormal dissolution of Ru occurs during the oxidation of methanol by the

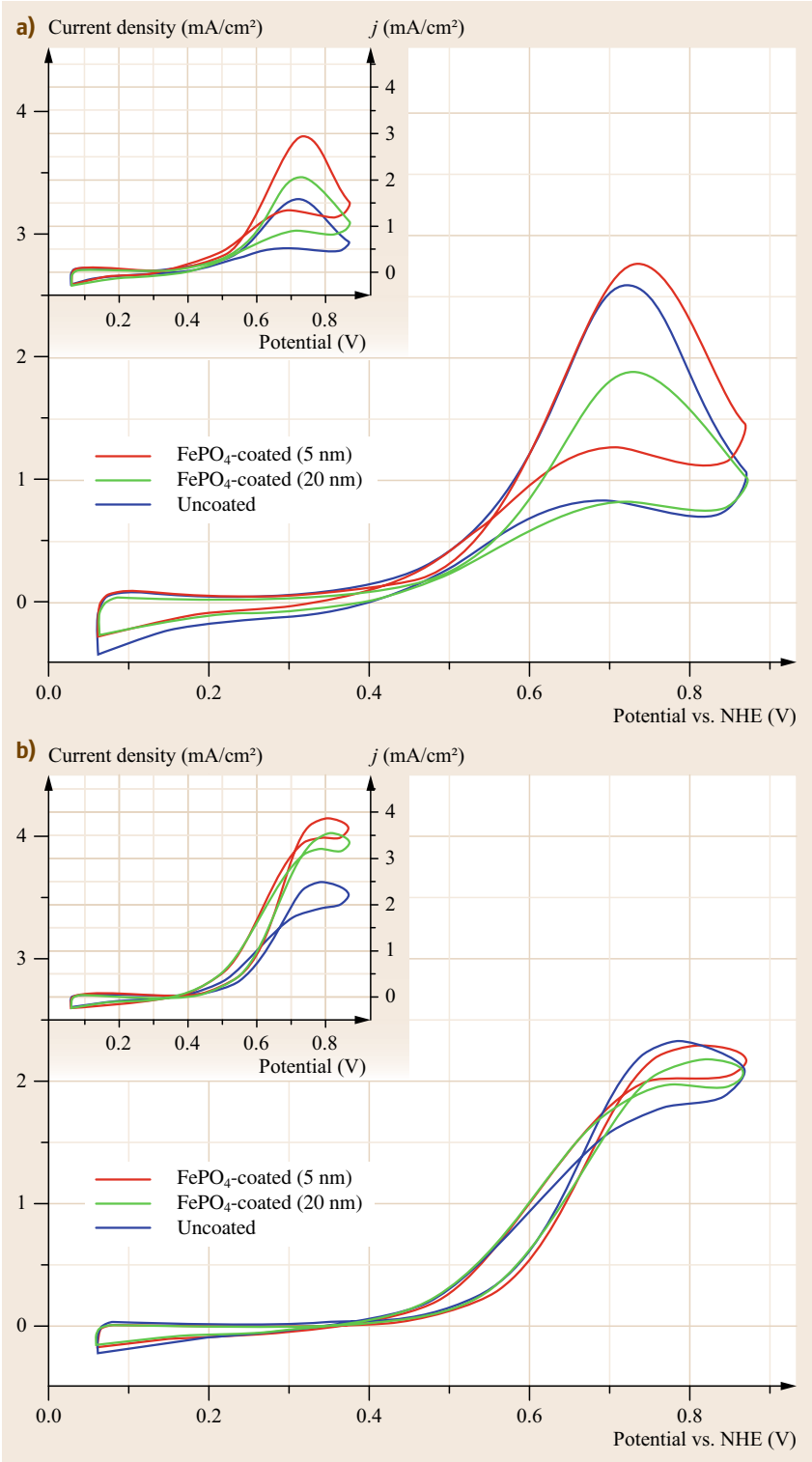


Fig. 21.13a,b Methanol-oxidation activities (normalized by ESA) of the uncoated and $FePO_4$-coated PtRu thin-film electrodes **(a)** before and **(b)** after accelerated cycles. The *insets* show the same oxidation data normalized by a 1 cm^2 sample area (after [21.19])

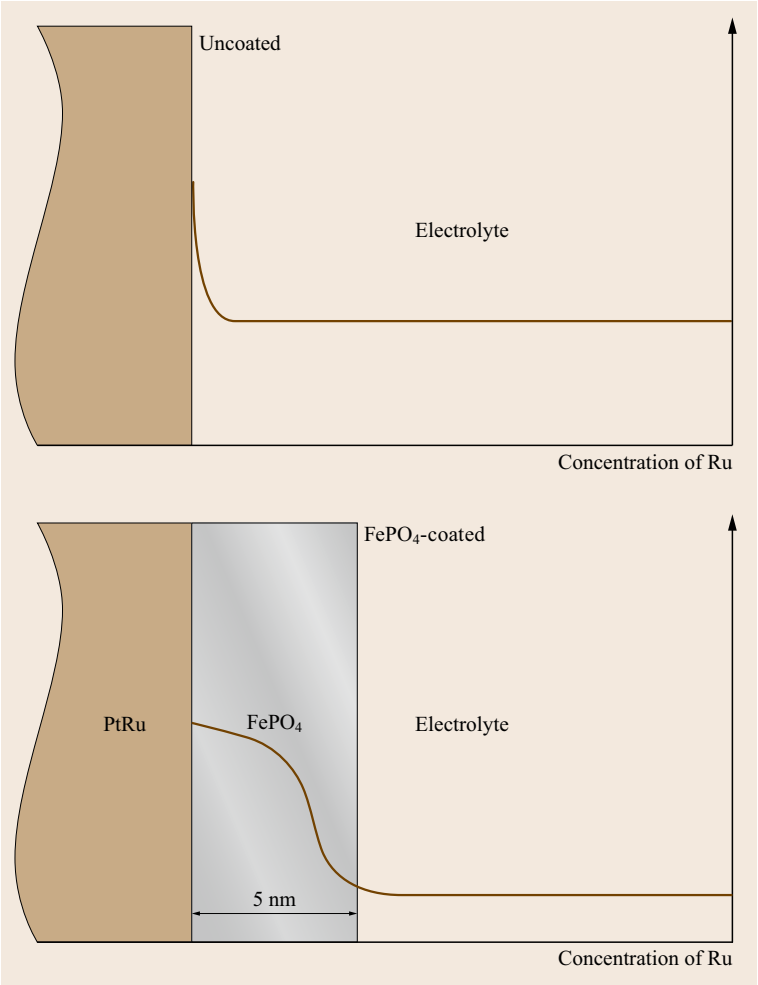


Fig. 21.14 Schematic figures for the possible role of $FePO_4$-coating layer for preventing the dissolved Ru species to diffuse into the electrolyte after accelerated cycles (after [21.19])

PtRu catalyst. In particular, *Piela* et al. [21.53] observed the Ru crossover where Ru crossed from the anode to the cathode through the proton-exchange membrane (Nafion). Accordingly, it is an important issue to block the dissolution of Ru for the practical utilization of the PtRu catalyst [21.19, 54].

Reduced Dissolution of Ru by $FePO_4$ Coating in PtRu Thin-Film Electrode

It was already reported that the electrochemical stabilities were greatly enhanced by nanoscale metal-phosphate coating on $LiCoO_2$ used in Li-ion batteries [21.28, 55, 56]. The enhanced stability with metal-phosphate is due to the reduced Co dissolution by avoiding direct contact between the $LiCoO_2$ electrode and carbonate-based electrolyte. This useful concept in the literatures is conveyed to the PtRu catalyst in the fuel cell. The porous characteristics of amorphous $FePO_4$ also have advantages in the effective transfer of protons, water, and methanol to the catalyst surface [21.18].

The effect of $FePO_4$ coating on the PtRu catalyst was investigated through the PtRu thin-film electrode with the subsequent coating of $FePO_4$. The thickness of coating layer was varied from ≈ 5 to ≈ 20 nm. The stability of the PtRu thin-film catalyst was tested by cyclic voltammograms after intentional accelerated cycles between 0.4 and 1.05 V. As seen in Fig. 21.12a, the uncoated PtRu thin-film electrodes exhibit Ru-depleted features inferred from the appearance of shoulder peak at ≈ 0.2 V due to dissolution of Ru, because the peak at ≈ 0.2 V is considered as the nature of Pt alone [21.4]. The Ru dissolution can also be confirmed by an increase in the ESA due to the surface roughness through the depletion of Ru. Ru dissolution is unavoidable even in the $FePO_4$-coated PtRu as shown in Fig. 21.12b. However, the dissolved Ru atoms from the $FePO_4$-coated PtRu are gradually redeposited onto the PtRu

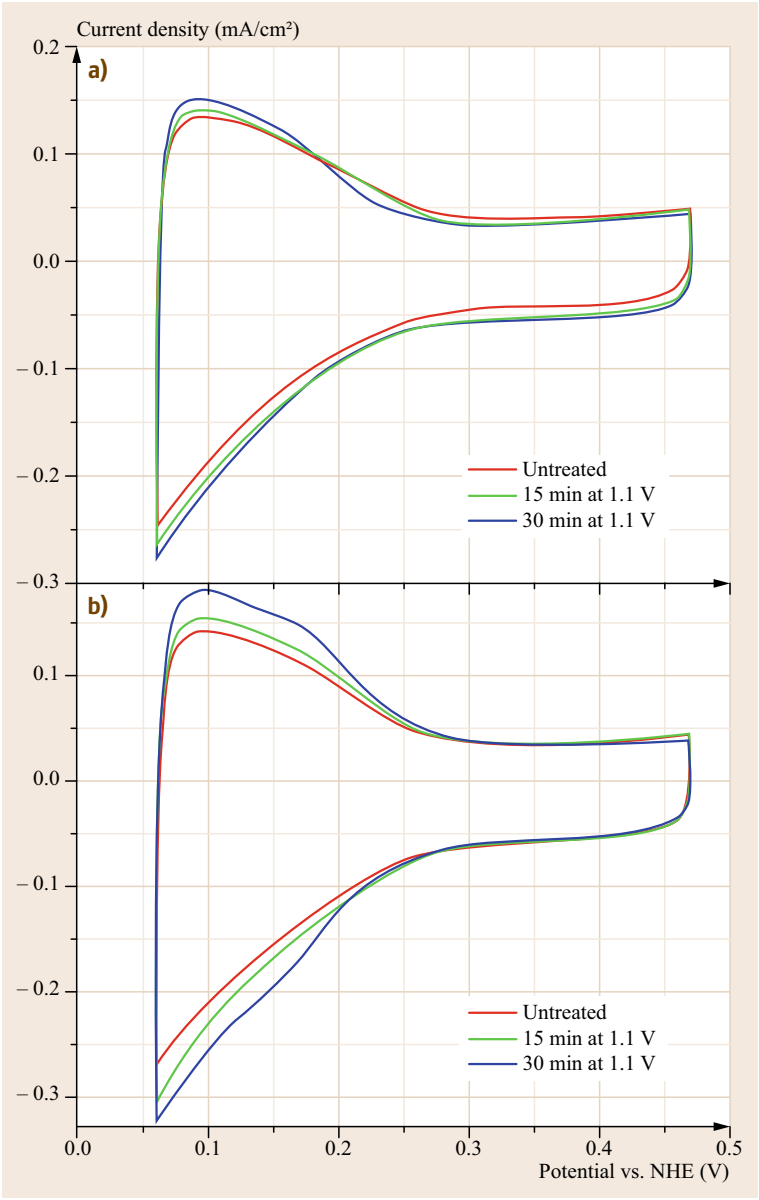


Fig. 21.15a,b Cyclic voltammograms of thin-film electrodes in a H_2SO_4 solution: **(a)** before and **(b)** after 200 cycles (after [21.54])

surface during the potential sweep after accelerated cycles. This observation is supported by the shape change of cyclic voltammograms, where the shoulder peak at ≈ 0.2 V becomes smooth indicating that the dissolved Ru species from the PtRu surface remains within the $FePO_4$-coating layer. It is likely that the retained Ru species is reduced onto the deteriorated PtRu surface. On the other hand, there is no change in the cyclic voltammogram during the nine cycles in the fresh electrolyte for the uncoated PtRu electrodes.

The activity of the uncoated and $FePO_4$-coated PtRu electrodes for methanol oxidation was evaluated before and after the accelerated cycles, as shown in Fig. 21.13. Prior to the accelerated cycles, the $FePO_4$-coated (≈ 5 nm) PtRu electrodes show a similar activity to that of the uncoated PtRu sample (Fig. 21.13a). The $FePO_4$-coated (≈ 20 nm) PtRu electrodes show a lower methanol-oxidation activity, indicating that too-thick coating layer interferes with the permeation of methanol through the phosphate layer. After 9 accelerated cycles, however, the uncoated and coated PtRu electrodes show decreased methanol-oxidation activity after 200 cycles. The relatively high oxidation current during the backward sweep also indicates the deterio-

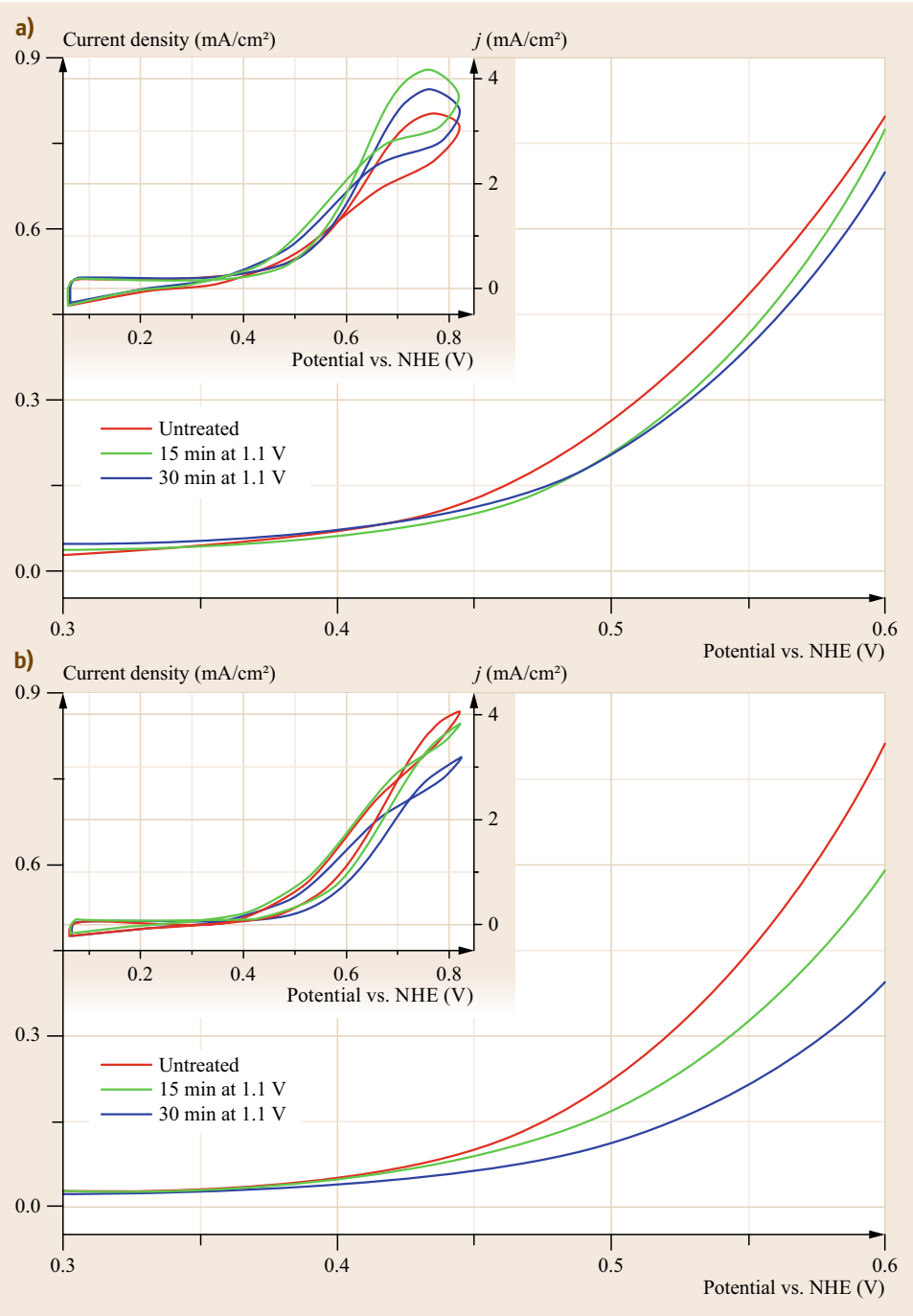


Fig. 21.16a,b Current densities versus applied potentials (normalized by ESA) for the untreated and anodic-treated PtRu thin-film electrodes in $H_2SO_4 + CH_3OH$: **(a)** before and **(b)** after 200 cycles. The *insets* show methanol oxidation normalized to the 1 cm^2 sample area (after [21.54])

ration of the original PtRu surface [21.57]. While the major role of the $FePO_4$ coating is to retain the dissolved Ru species, the redeposition of Ru does not influence much on the methanol-oxidation activities, probably by not forming the ideal PtRu solid-solution structure.

The schematic (Fig. 21.14) demonstrates the possible role of the nanoscale $FePO_4$-coating layer to prevent the dissolved Ru species from diffusing into the electrolyte. The dissolved Ru species measured by ICP-MS (inductively coupled plasma-mass spectroscopy) after accelerated cycles is found to be little

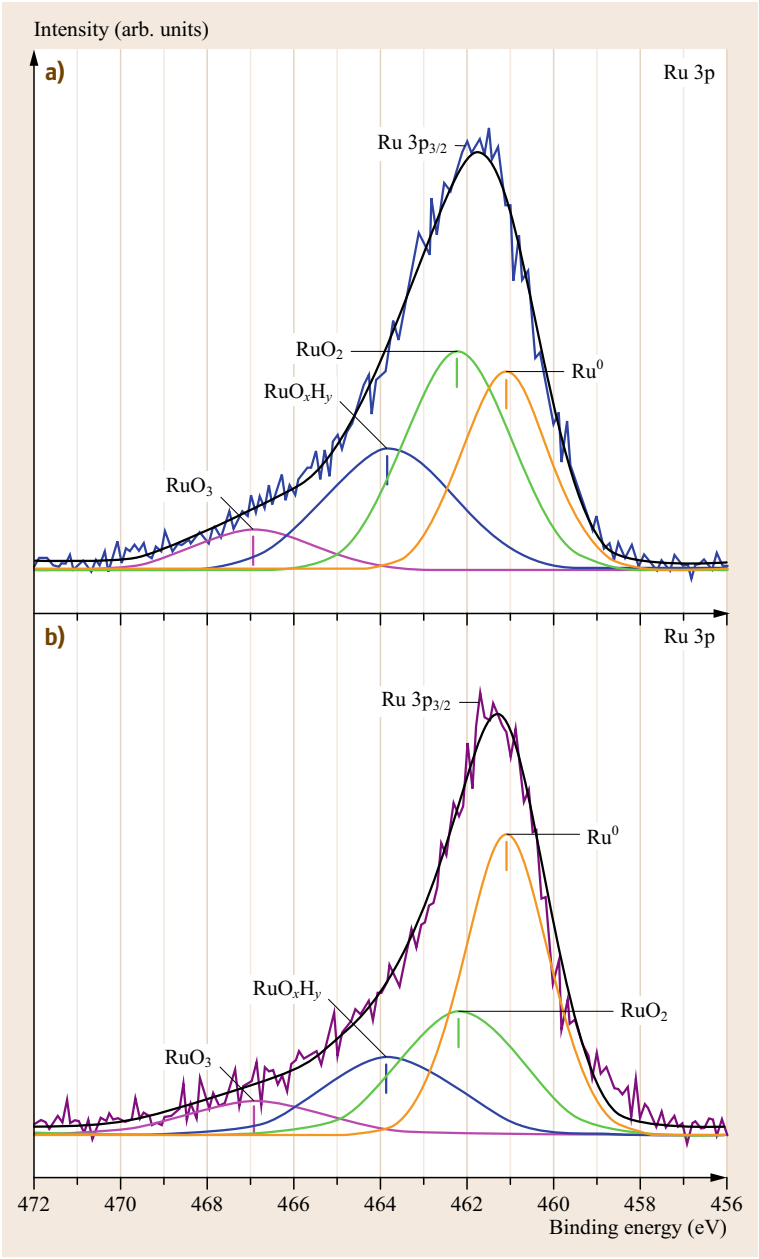


Fig. 21.17a,b XPS spectra of Ru for the anodic-treated PtRu electrodes at 1.1 V for 30 min: **(a)** before and **(b)** after 200 cycles (after [21.54])

in the $FePO_4$-coated PtRu electrodes [21.19], supporting the retained Ru species within the $FePO_4$-coating layer as a barrier.

Ru-Oxidation States on Ru Dissolution

Although many research groups observed dissolved Ru during cycles, the origin of Ru dissolution from the PtRu alloy was not completely elucidated. The identification of the involved mechanisms for Ru dissolution is important. Meanwhile, the oxophilic properties of Ru allow oxide species to form, and Ru oxides are present on the PtRu alloy surface at a significant fraction [21.58]. Enhanced proton transport in the hydrous Ru oxides (RuO_2 H_2O or RuO_xH_y) in Pt–RuO_2 was reported in this respect [21.59]. Recently, it has been reported that the mixture of the Pt metal and hydrous Ru-oxide phase shows better performance than a bimetallic alloy [21.60]. It can be thought that the oxidation state of ruthenium is associated with Ru dissolution from the PtRu catalyst.

The Ru-oxidation states of the PtRu thin films were modified with an anodic treatment at 1.1 V (versus NHE (normal hydrogen electrode)) for 15 or 30 min at 50 °C, and the Ru dissolution from the untreated and anodic-treated PtRu thin film was examined with a repeated potential cycling between 0.4 and 1.05 V for 200 cycles. Figure 21.15 shows the active surface areas of the untreated PtRu and the anodic-treated PtRu, from the cyclic voltammograms before and after 200 cycles [21.45]. The increase in the active surface area following the anodic treatments may be due to an increase in surface roughness, which results from the formation of irreversible Ru-oxide species. It should be noted that the anodic treatment of the PtRu alloy for 30 min at 1.1 V does not considerably alter the surface composition.

The efficiency of the untreated PtRu and the anodic-treated PtRu electrodes for methanol oxidation was evaluated before and after the 200 cycles, as shown in Fig. 21.16. Before the 200 cycles, the anodic-treated PtRu electrodes and the untreated PtRu electrodes have similar methanol-oxidation activities. On the other hand, the untreated PtRu electrodes after 200 cycles show a smaller decrease in methanol-oxidation activity than the anodic-treated PtRu electrodes. The Ru dissolution from PtRu after 200 cycles is confirmed by the increased surface area. This Ru dissolution was also identified by XPS analysis of the apparent composition of Pt and Ru in the PtRu surface (Fig. 21.17). The relative amounts of RuO_2 and hydrous RuO_2 decrease after the 200 cycles, implying that the Ru dissolution from PtRu is kinetically feasible when Ru occurs in the form of Ru-oxide species, namely, nonalloyed and segregated Ru oxides in the PtRu.

The oxidation of Ru occurs from the PtRu surface, and the oxide precipitates lead to a rougher surface than before. The size of the segregated Ru-oxide species is on a nanometer scale, as illustrated in Fig. 21.18. One plausible conclusion is that the Ru dissolution in the PtRu alloy is attributed to the segregated Ru-oxide species in the PtRu surface. It is, however, necessary to further identify various Ru oxides, especially the hydrous and anhydrous Ru oxide.

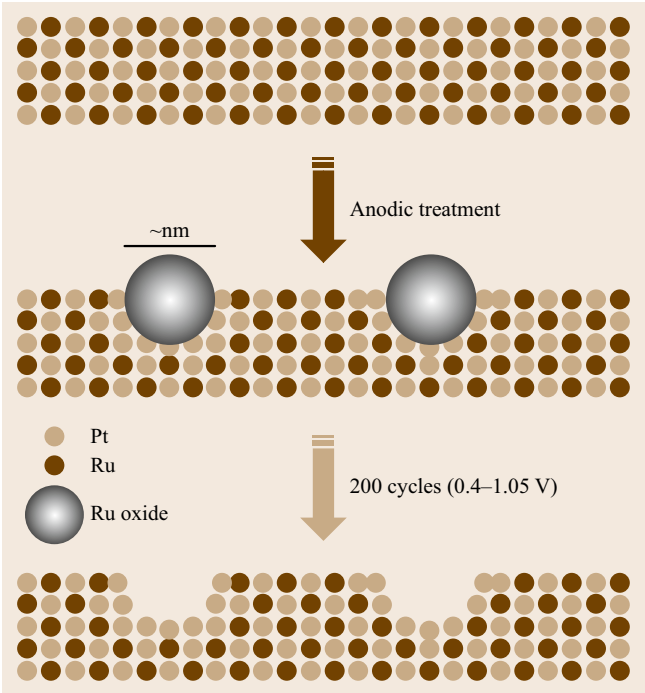


Fig. 21.18 Schematic illustration of the proposed mechanisms of Ru dissolution from the PtRu surface (after [21.54])

21.2.2 Enhancement from Various Nanostructured Catalysts

Several researches have been dedicated to nanostructure-controlled electrodes for the optimized utilization of catalysts [21.61]. In particular, platinum-based electrocatalysts with various nanostructures have been intensively investigated [21.17, 62]. In addition, either porous catalysts or embedded catalyst nanoparticles offer crucial benefits due to their enlarged surface area and short diffusion paths for efficient catalytic reactions [21.18, 41, 63–70].

Pt Nanoparticles Embedded in $FePO_4$ Matrix

Recently, nanostructured materials based on metal nanoparticles in an oxide matrix have been studied extensively for various applications on account of their attractive physical, chemical, and catalytic properties [21.71–73]. Above all, Pt/metal-oxide catalysts such as Pt–WO_3 and Pt–RuO_2 have been investigated by several groups for potential use as electrodes in DMFCs [21.74–76]. The improved catalytic activities of Pt/metal-oxide can be attributed to physical effects (increase in surface area) and/or catalytic effects, such as the bifunctional effects of the oxide matrix. The discovery of metal-oxide-support catalysts has accelerated the investigation of metal phosphates for catalytic applications due to their desirable properties, such as high proton conductivity, acid stability, open framework nanostructures, catalytic activity, etc. [21.27, 28, 77, 78]. Therefore, various nanostructures of metal/metal-phosphate electrodes were investigated, and their physical properties and catalytic activities were examined.

The nanostructured Pt–$FePO_4$ thin films were deposited by sputtering using the Pt and $FePO_4$ targets. The nanostructures of the Pt–$FePO_4$ thin-film elec-

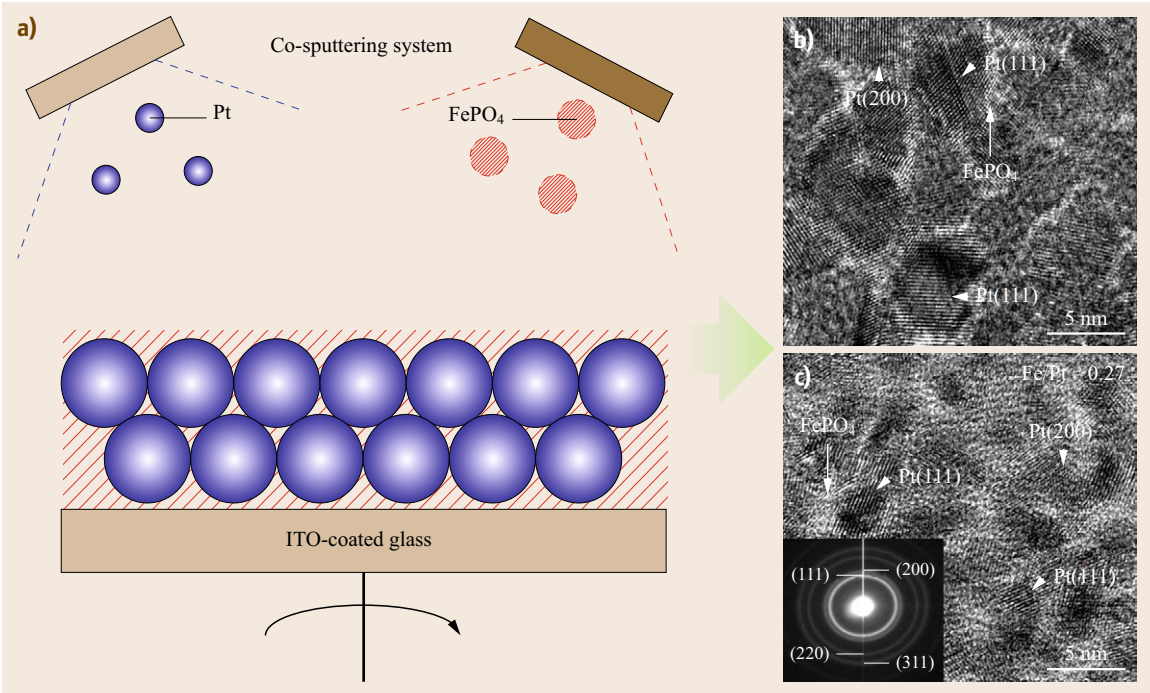


Fig. 21.19 **(a)** An experimental scheme of nanostructured Pt–$FePO_4$ thin films fabricated by cosputtering. **(b)** TEM images of the nanostructured Pt–$FePO_4$ thin films consisting of **(b)** ≈ 5 nm and **(c)** ≈ 3 nm Pt nanocrystalline phase and an amorphous $FePO_4$ matrix, with atomic ratios (Fe/Pt) of 0.12 and 0.27, respectively. The *inset* of **(c)** shows diffraction patterns of Pt–$FePO_4$ (Fe/Pt = 0.27) (after [21.18], courtesy of Electrochem. Soc.)

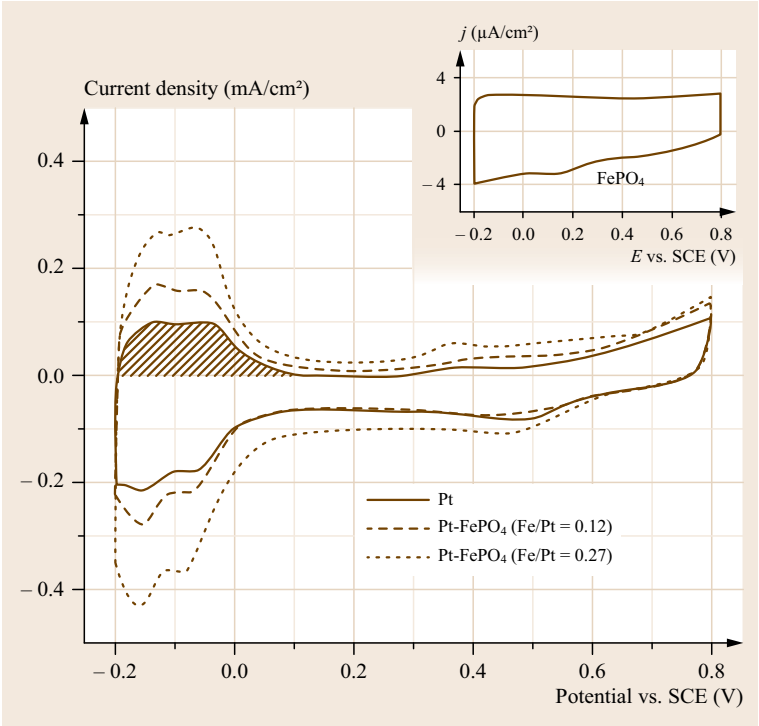


Fig. 21.20 Cyclic voltammograms of the Pt and Pt–$FePO_4$ thin-film electrodes in H_2SO_4 solution. The CV (cyclic voltammetry) data for pure $FePO_4$ is also shown in the *inset*, and the *shaded area* represents the oxidation of hydrogen chemisorbed on the Pt (after [21.18], courtesy of Electrochem. Soc.)

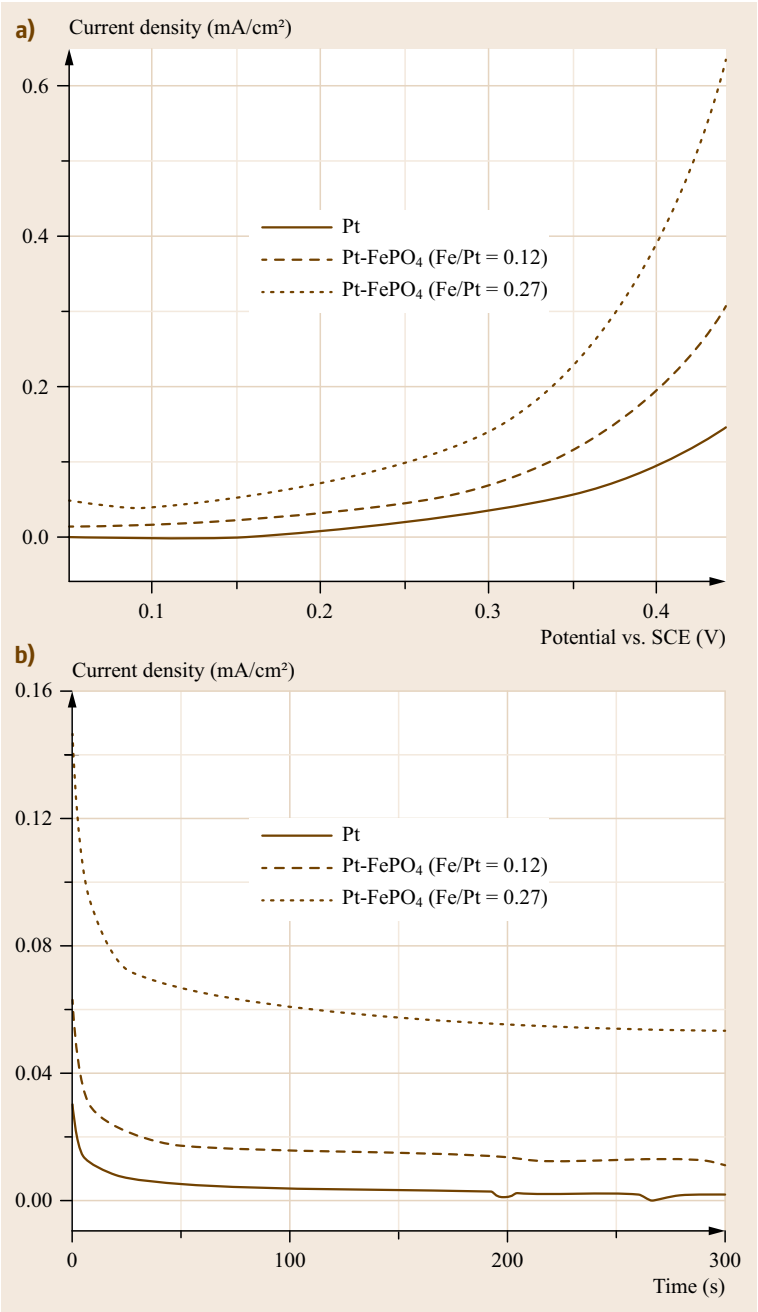


Fig. 21.21 **(a)** Current density versus potential for the Pt and Pt–$FePO_4$ thin-film electrodes in $H_2SO_4 + CH_3OH$, and **(b)** the decay of the current density at the oxidation potential of 0.3 V (after [21.18], courtesy of Electrochem. Soc.)

trodes were varied by tuning the sputtering power. The overall experimental setup is depicted in Fig. 21.19, with the TEM images of the nanostructured Pt–$FePO_4$ thin films. As shown in Fig. 21.19c, the Pt–$FePO_4$ thin films consist of $\approx$ 3 nm Pt crystalline nanoparticles with the $FePO_4$ matrix, and the atomic ratio (Fe/Pt) of this electrode is 0.27 as measured by ICP-AES (inductively coupled plasma-atomic emission spectroscopy) analysis. The formation of a Pt nanophase in the Pt–$FePO_4$ thin film was confirmed by diffraction, as shown in the inset of Fig. 21.19c. The tendency of minimizing the interfacial free energy gives rise to the embedded Pt nanoparticles in the $FePO_4$ matrix.

While the active surface area of the nanocomposite thin-film electrodes clearly becomes larger than pure Pt (Fig. 21.20), the efficiency of pure Pt and Pt–$FePO_4$

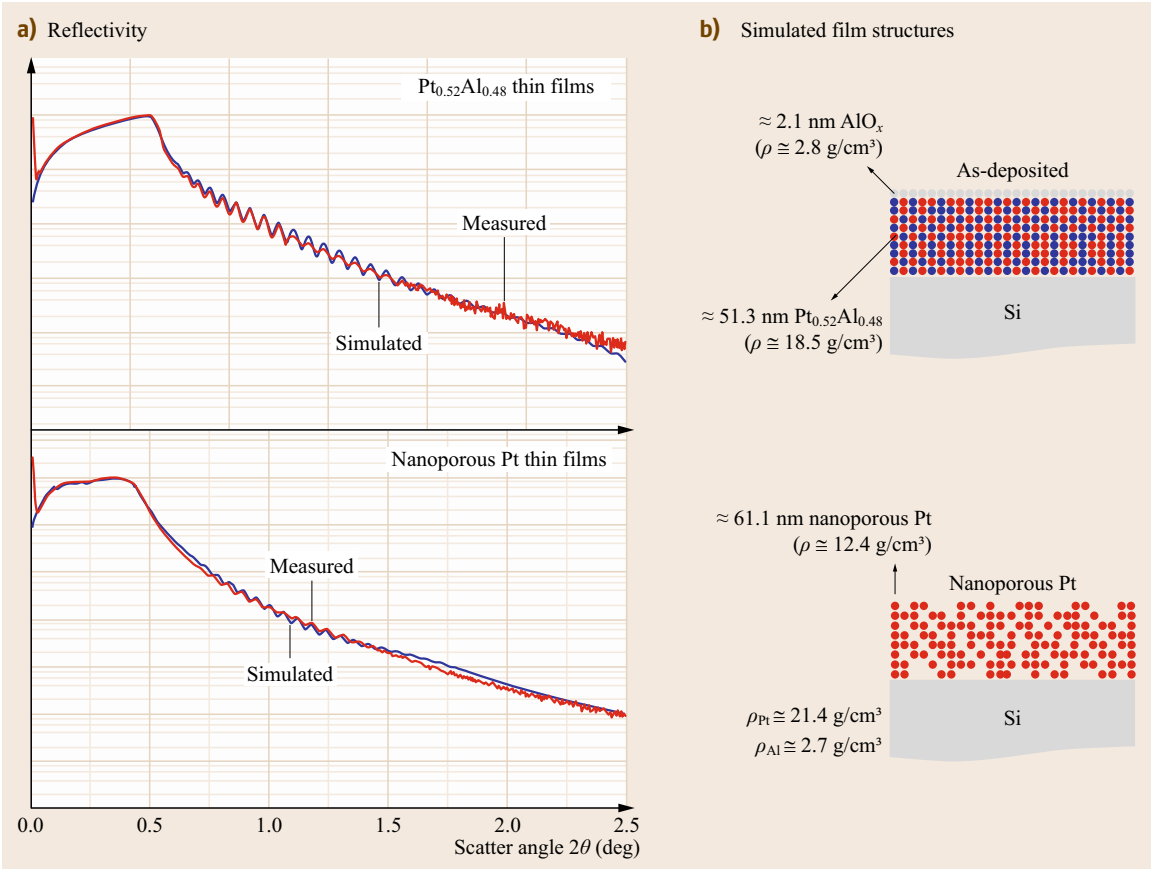


Fig. 21.22a,b Total-reflection x-ray diffraction of the **(a)** $Pt_{0.52}Al_{0.48}$ and **(b)** nanoporous Pt thin films, in comparison with the simulation (after [21.70], courtesy of Springer)

electrodes for methanol oxidation was evaluated. Compared with the pure Pt electrodes, the Pt–$FePO_4$ electrodes show a significantly high efficiency, stability, and low charge-transfer resistance for methanol oxidation (Fig. 21.21). The improved catalytic activities of the Pt–$FePO_4$ thin-film electrodes can be attributed to the possible ability of the $FePO_4$ matrix affecting the chemisorptive and catalytic properties of the Pt surface. The improvements in the methanol-oxidation activity for the Pt–$FePO_4$ electrodes are also partly attributed to the ability of the $FePO_4$ matrix to mediate proton transfer. It was reported that the proton conductivity of $FePO_4$ resulted in high value on the clean Pt sites [21.79]. Moreover, the increased activities indicate better tolerance to the reaction intermediate, CO, which blocks the active Pt sites and suppresses methanol oxidation [21.44].

Nanoporous Pt Catalysts by Electrochemical Dissolution of Al

Catalytic reactions occur only at the surface of catalysts, and it is one of the advantages of nanosized catalysts in that they have high surface-to-bulk ratio. Then, it can be thought that more surfaces can be available if porous morphology is obtained with the size of nanoparticles. The porous characteristic also provides a shorter diffusion path for catalytic reactions. In this section, nanoporous Pt thin films by selective dissolution of Al from PtAl alloy and their superior catalytic properties are introduced.

Pt_xAl_{1-x} thin films were obtained at 400 °C on Si(100) substrates by sputtering using Pt and Al targets. Pt nanoporous thin films were facilely synthesized through the selective dissolution of Al in the Pt_xAl_{1-x} thin films in the acidic environment. The changes of the ESA were measured by the hydrogen-desorption method (Pt–H) [21.45]. Figure 21.22 shows the total-reflection spectra of the $Pt_{0.52}Al_{0.48}$ and nanoporous Pt thin films. The thicknesses and densities of the thin films were simulated from the x-ray diffraction data. The nanoporous Pt thin films exhibit decreased density (≈ 50% of Pt thin film) by the dissolution of Al.

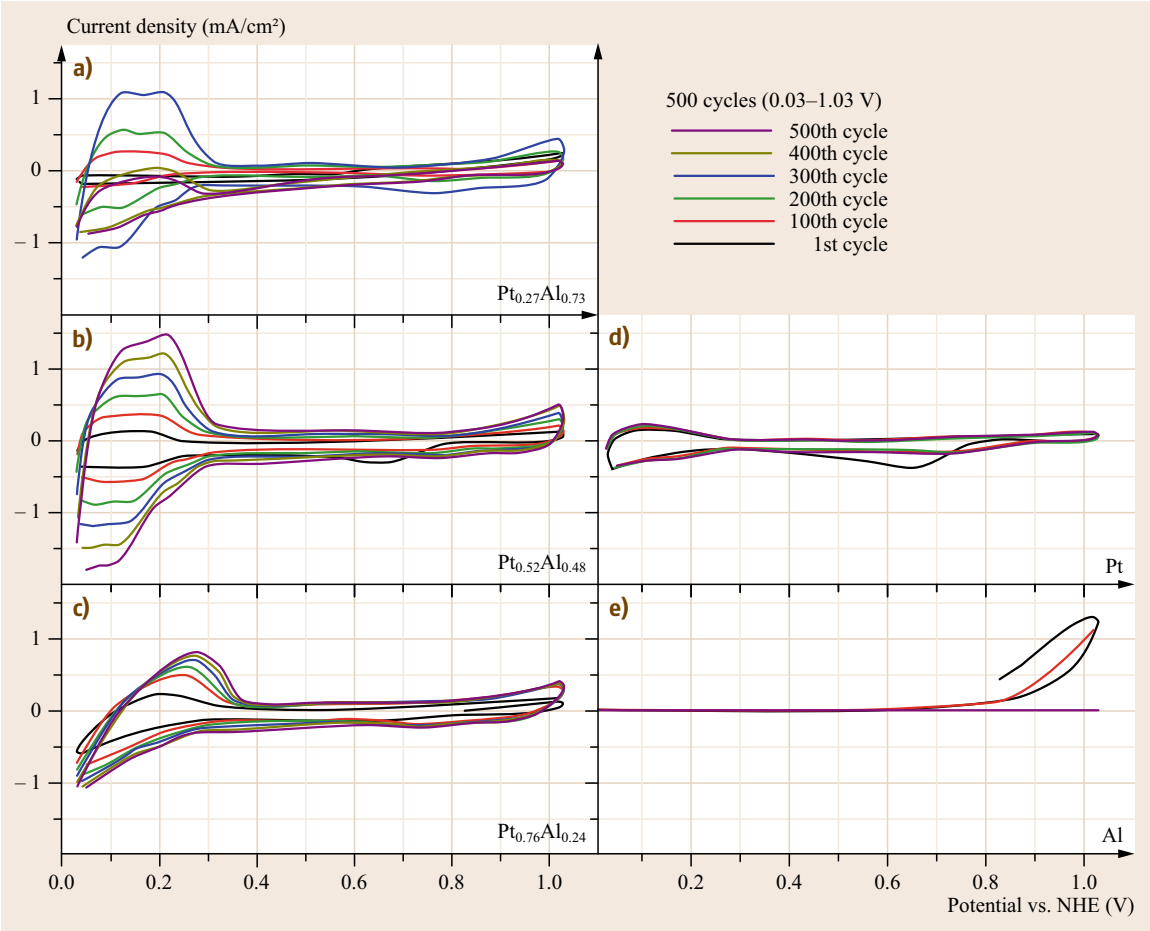


Fig. 21.23a–e Cyclic voltammograms of the **(a)** $Pt_{0.27}Al_{0.73}$, **(b)** $Pt_{0.52}Al_{0.48}$, **(c)** $Pt_{0.76}Al_{0.24}$, **(d)** Pt, and **(e)** Al thin films during 500 cycles in a H_2SO_4 solution (after [21.69], courtesy of Springer)

Electrocatalytic activities of Pt_xAl_{1-x}, Pt, and Al thin films were investigated during 500 electrochemical cycles (Fig. 21.23). At the initial state, there is no remarkable difference between Pt_xAl_{1-x} and Pt thin films. As the cycles proceed, the Pt_xAl_{1-x} thin films gradually exhibit an increase in catalytic activities, and in the case of $Pt_{0.52}Al_{0.48}$ thin films (Fig. 21.23), the ESA after 500 cycles increases approximately by 1 order of magnitude compared to the initial ESA. The increased ESA is attributed to the nanoporosity formed by the gradual dissolution of Al. The dissolution of Al from Pt_xAl_{1-x} and Al thin films is detected over 0.7 V due to low kinetics [21.80]; nevertheless the redox potential of Al is much lower than the operation voltage window ($Al \leftrightarrow Al^{3+} + 3e^-$, $E^0 = -1.676$ V versus NHE at pH 0).

The morphological changes in the nanoporous Pt thin films were also confirmed by SEM (scanning electron microscopy) and TEM. As shown in Fig. 21.24a, the nanoporous Pt thin films show a clear image due to surface roughening or dissolution of the Al-oxide layer, whereas the image of the as-deposited $Pt_{0.52}Al_{0.48}$ thin film is quite dim due to the flat surface and/or oxidized layer. While the as-deposited PtAl alloy reveals a gray color, likely due to the oxidation of Al, the nanoporous Pt thin films demonstrate metallic brightness, after the dissolution of Al. The surface morphology of the as-deposited Pt_xAl_{1-x} thin films, as indicated by AFM (atomic force microscopy) (Fig. 21.24b), is relatively smooth with a vertical roughness of ≈ 0.51 nm. After 500 cycles, the surface becomes rougher with a vertical roughness of ≈ 3.77 nm (Fig. 21.24c), due to the dissolution of Al and the subsequent agglomeration of Pt, thereby leading to the formation of nanoporous Pt thin films.

With the advantages of short effective diffusion lengths for reactants and large surface areas, the nanoporous Pt thin films show high oxidation activities (Fig. 21.25), compared with the untreated PtRu or Pt

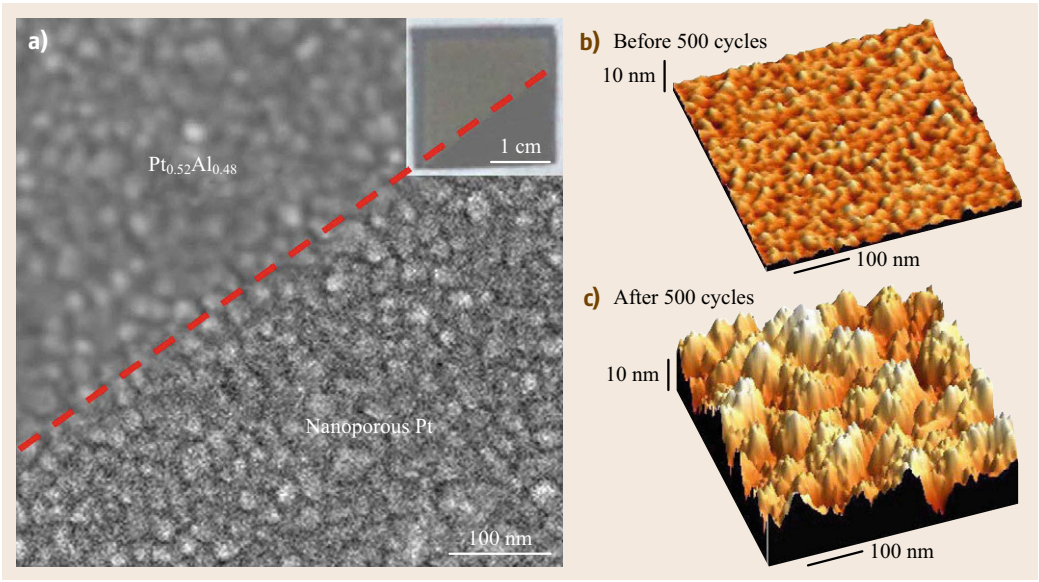


Fig. 21.24
(a) Plan-view SEM image of the $Pt_{0.52}Al_{0.48}$ and nanoporous Pt (after 500 cycles) thin films, with a photograph (*inset*). The AFM images of the **(b)** $Pt_{0.52}Al_{0.48}$ and **(c)** nanoporous Pt thin films, with a vertical roughness of 0.51 and 3.77 nm, respectively (after [21.69], courtesy of Springer)

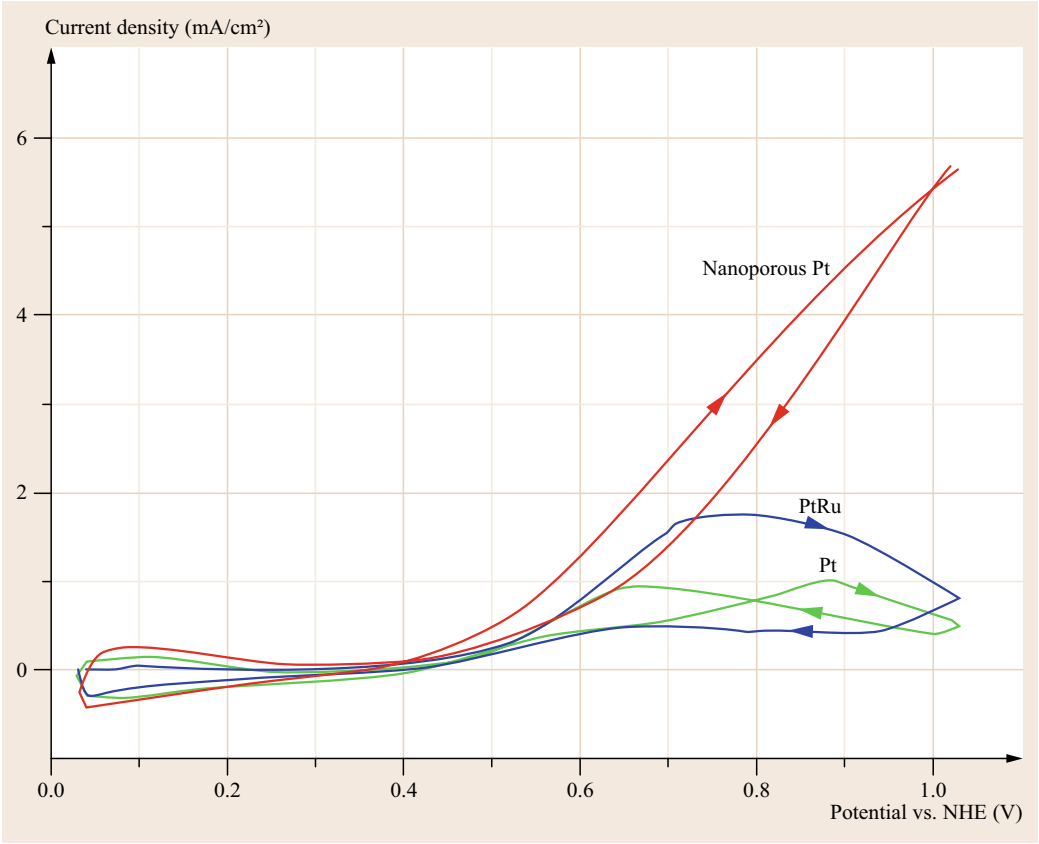


Fig. 21.25
Methanol-oxidation activities of nanoporous Pt (*red*), Pt (*green*), and PtRu (*blue*) thin films in a $H_2SO_4 + CH_3OH$ solution (after [21.69], courtesy of Springer)

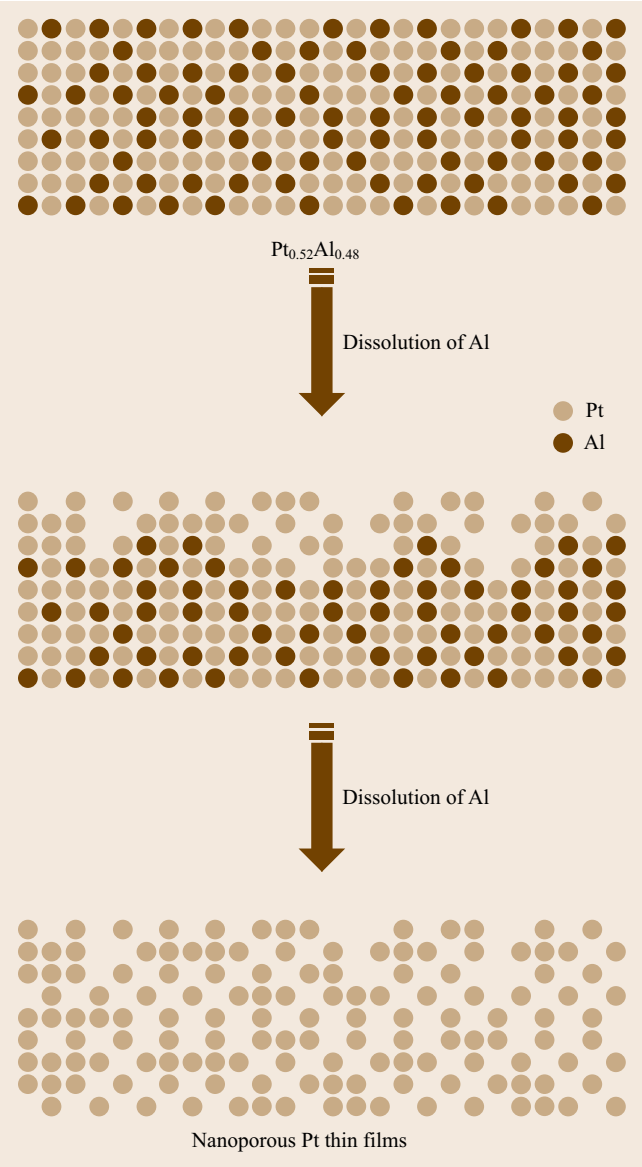


Fig. 21.26 Schematic of the mechanisms proposed to explain the formation of the nanoporous Pt thin films by the selective dissolution of Al (after [21.69], courtesy of Springer)

thin films. A schematic figure of the proposed mechanisms for nanoporosity is presented in Fig. 21.26.

$Pt/AlPO_4$ Nanocomposite Thin-Film Electrodes for Ethanol Electrooxidation

Other than methanol, ethanol is another promising fuel in that it can be produced easily from abundant biomass, and it has lower toxicity than methanol [21.81]. In addition, the high theoretical mass-energy density of ethanol ($\approx 8.0\,\mathrm{Wh/g}$) is appropriate for the rising demand for future energy [21.82]. Our group tried to investigate $Pt/AlPO_4$ nanocomposite thin-film electrodes as a potential catalyst for ethanol oxidation with various $Pt/AlPO_4$ ratios [21.14].

As shown in Fig. 21.27, all of the composite catalysts show higher catalytic activities for ethanol electrooxidation compared to the pure Pt. Among the various $Pt/AlPO_4$ nanocomposites, the electrode with Al/Pt = 0.57 shows the highest electrocatalytic activity for ethanol electrooxidation, and the activation enthalpy is 0.05 eV lower than that of pure Pt (not shown here). The enhanced electrocatalytic properties of the nanocomposites may be attributed to the electron transfer from the $AlPO_4$ matrix to the Pt catalysts.

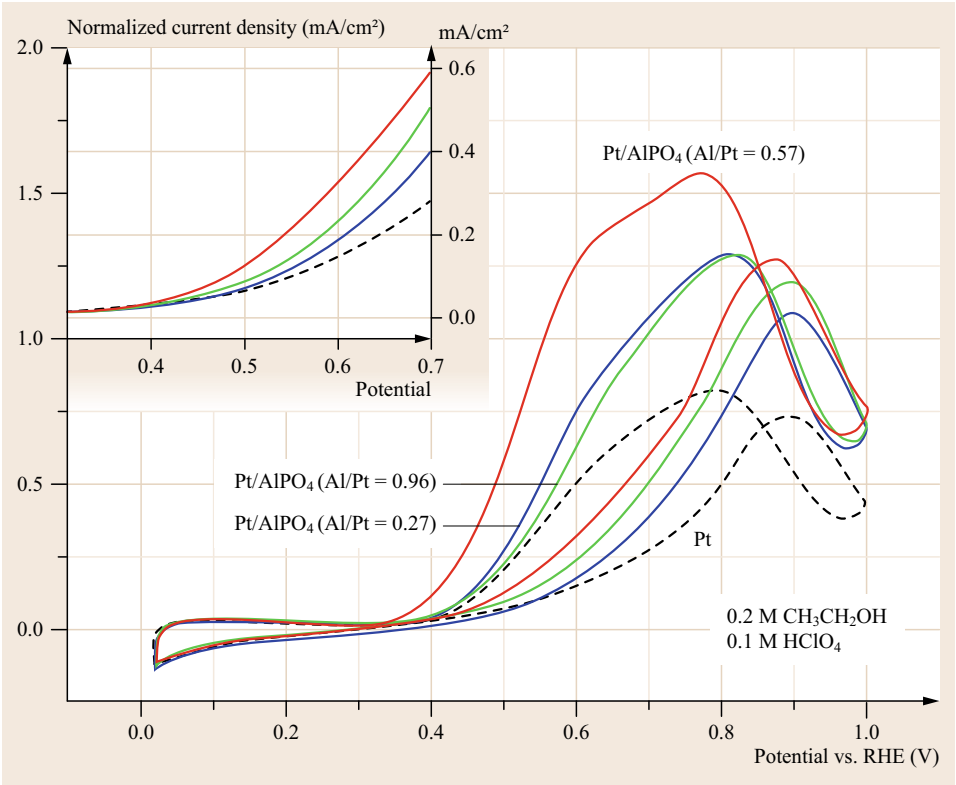


Fig. 21.27 Ethanol electrooxidation activities of the Pt and $Pt/AlPO_4$ nanocomposites at a scan rate of 50 mV/s. The polarization curves near the onset voltages are magnified in the *inset* (after [21.14], courtesy of Elsevier)

21.2.3 Conclusion

The dissolution of Ru is somewhat reduced by the nanoscale coating layer on PtRu alloy, and is closely associated with the formation of Ru-oxide species (oxidation state of Ru). Porous catalysts are beneficial due to the enlarged electrochemical surface area and well-percolated diffusion paths for efficient reactions. Furthermore, the catalytic properties can be enhanced by the metal-phosphate matrix, due to the high proton conductivity, acid stability, porous nanostructures, catalytic activity, and charge transfer to/from the metal catalysts [21.27]. Utilizing both the bifunctional and electronic effects can be optimized for the enhanced fuel-oxidation kinetics.

Acknowledgments. The researches were supported by the National Research Foundation of Korea. Grant funded through the Korean Government (MEST: NRF, 2010-0029065) and the World Class University (WCU, R31-2008-000-10075-0).

References

21.1 K.E. Martin, J.P. Kopasz, K.W. McMurphy: *Fuel Cell Chemistry and Operation* (American Chemical Society, Washington 2010)
21.2 B. Wang: Recent development of non-platinum catalysts for oxygen reduction reaction, J. Power Sources **152**, 1–15 (2005)
21.3 X.-Z. Yuan, H. Wang: *PEM Fuel Cell Electrocatalysts and Catalyst Layers Fundamentals and Applications* (Springer, London 2008)
21.4 W. Vielstich: *Handbook of Fuel Cells – Fundamentals, Technology and Applications* (Wiley, London 2003)
21.5 C.C. Liang, A.L. Juliard: The overpotential of oxygen reduction at platinum electrodes, J. Electroanal. Chem. **9**, 390–394 (1965)
21.6 T. Toda, H. Igarashi, H. Uchida, M. Watanabe: Enhancement of the electroreduction of oxygen on Pt alloys with Fe, Ni, and Co, J. Electrochem. Soc. **146**, 3750–3756 (1999)
21.7 L. Zhang, C. Song, J. Zhang, H. Wang, D.P. Wilkinson: Temperature and pH dependent oxygen reduction catalyzed by iron fluoro-porphyrin adsorbed on a graphite electrode, J. Electrochem. Soc. **152**, A2421–A2426 (2005)

21.8 A.B. Anderson: O_2 reduction and CO oxidation at the Pt-electrolyte interface. The role of H_2O and OH adsorption bond strengths, Electrochim. Acta **47**, 3759–3763 (2002)

21.9 D. Pillay, M.D. Johannes, Y. Garsany, K.E. Swider-Lyons: Poisoning of Pt_3Co electrodes: A combined experimental and DFT study, J. Phys. Chem. C **114**, 7822–7830 (2010)

21.10 M. Chen, Y.C. Xing: Polymer-mediated synthesis of highly dispersed Pt nanoparticles on carbon black, Langmuir **21**, 9334–9338 (2005)

21.11 R. Zeis, A. Mathur, G. Fritz, J. Lee, J. Erlebacher: Platinum-plated nanoporous gold: An efficient, low Pt loading electrocatalyst for PEM fuel cells, J. Power Sources **165**, 65–72 (2007)

21.12 R. Bashyam, P. Zelenay: A class of non-precious metal composite catalysts for fuel cells, Nature **443**, 63–66 (2006)

21.13 W. Chen, J. Akhigbe, C. Bruckner, C.M. Li, Y. Lei: Electrocatalytic four-electron reduction of dioxygen by electrochemically deposited poly{[meso-tetrakis(2-thienyl)porphyrinato]cobalt(II)}, J. Phys. Chem. C **114**, 8633–8638 (2010)

21.14 Y. Oh, J. Kang, S. Nam, S. Byun, B. Park: Pt/$AlPO_4$ nanocomposite thin-film electrodes for ethanol electrooxidation, Mater. Chem. Phys. **135**, 188–192 (2012)

21.15 Y. Park, S. Nam, Y. Oh, H. Choi, J. Park, B. Park: Electrochemical promotion of oxygen reduction on gold with aluminum phosphate overlayer, J. Phys. Chem. C **115**, 7092–7096 (2011)

21.16 Y. Park, B. Lee, C. Kim, J. Kim, S. Nam, Y. Oh, B. Park: Modification of gold catalysis with aluminum phosphate for oxygen-reduction reaction, J. Phys. Chem. C **114**, 3688–3692 (2010)

21.17 C. Kim, B. Lee, Y. Park, B. Park, J. Lee, H. Kim: Iron-phosphate platinum carbon nanocomposites for enhanced electrocatalytic stability, Appl. Phys. Lett. **91**, 113101 (2007)

21.18 B. Lee, C. Kim, Y. Park, T.-G. Kim, B. Park: Nanostructured platinum/iron phosphate thin-film electrodes for methanol oxidation, Electrochem. Solid-State Lett. **9**, E27–E30 (2006)

21.19 Y. Park, B. Lee, C. Kim, J. Kim, B. Park: Effects of iron-phosphate coating on Ru dissolution in the PtRu thin-film electrodes, J. Mater. Res. **24**, 140–144 (2009)

21.20 J. Zhang, Y. Mo, M.B. Vukmirovic, R. Klie, K. Sasaki, R.R. Adzic: Platinum monolayer electrocatalysts for O_2 reduction: Pt monolayer on Pd(111) and on carbon-supported Pd nanoparticles, J. Phys. Chem. B **108**, 10955–10964 (2004)

21.21 J.L. Zhang, M.B. Vukmirovic, Y. Xu, M. Mavrikakis, R.R. Adzic: Controlling the catalytic activity of platinum-monolayer electrocatalysts for oxygen reduction with different substrate, Angew. Chem. Int. Ed. **44**, 2132–2135 (2005)

21.22 L.M. Vracar, D.B. Sepa, A. Damjanovic: Palladium electrode in oxygen-saturated aqueous solutions: Reduction of oxygen in the activation controlled region, J. Electrochem. Soc. **133**, 1835–1839 (1986)

21.23 K. Kinoshita: *Electrochemical Oxygen Technology* (Wiley, New York 1992)

21.24 A. Morozan, B. Jousselme, S. Palacin: Low-platinum and platinum-free catalysts for the oxygen reduction reaction at fuel cell cathodes, Energy Environ. Sci. **4**, 1238–1254 (2011)

21.25 J. Zhang, K. Sasaki, E. Sutter, R.R. Adzic: Stabilization of platinum oxygen-reduction electrocatalysts using gold clusters, Science **315**, 220–222 (2007)

21.26 J. Guo, A. Hsu, D. Chu, R. Chen: Improving oxygen reduction reaction activities on carbon-supported ag nanoparticles in alkaline solutions, J. Phys. Chem. C **114**, 4324–4330 (2010)

21.27 A.K. Cheetham, G. Ferey, T. Loiseau: Open-framework inorganic materials, Angew. Chem. Int. Ed. **38**, 3268–3292 (1999)

21.28 J. Cho, Y.-W. Kim, B. Kim, J.-G. Lee, B. Park: A breakthrough in the safety of lithium secondary batteries by coating the cathode material with $AlPO_4$ nanoparticles, Angew. Chem. Int. Ed. **42**, 1618–1621 (2003)

21.29 A. Matsuda, T. Tezuka, Y. Nono, K. Tadanaga, T. Minami, M. Tatsumisago: Preparation of proton conducting composites by mechanical milling for phosphorus-containing solid acids, Solid State Ionics **176**, 2899–2904 (2005)

21.30 H. Yang, R.I. Walton, S. Biedasek, S. Antonijevic, S. Wimperis, A.J. Ramirez-Cuesta, J. Li, A.I. Kolesnikov: Experimental observations of water-framework interactions in a hydrated microporous aluminium phosphate, J. Phys. Chem. B **109**, 4464–4469 (2005)

21.31 Y. Yamamura, M. Ishida: Monte Carlo simulation of the thermalization of sputtered atoms and reflected atoms in the magnetron sputtering discharge, J. Vac. Sci. Technol. A **13**, 101–112 (1995)

21.32 N.M. Markovic, H.A. Gasteiger, P.N. Ross Jr.: Oxygen reduction on platinum low-index single-crystal surfaces in alkaline solution: Rotating ring disk Pt(hkl) studies, J. Phys. Chem. **100**, 6715–6721 (1996)

21.33 N.A. Anastasijevic, V. Vesovic, R.R. Adzic: Determination of the kinetic parameters of the oxygen reduction reaction using the rotating ring-disk electrode: Part I. theory, J. Electroanal. Chem. **229**, 305–316 (1987)

21.34 J. Hernandez, J. Solla-Gullon, E. Herrero, A. Aldaz, J.M. Feliu: Electrochemistry of shape controlled catalysts. Oxygen reduction reaction on cubic gold nanoparticles, J. Phys. Chem. C **111**, 14078–14083 (2007)

21.35 S. Strbac, R.R. Adzic: The influence of OH^- chemisorption on the catalytic properties of gold single crystal surfaces for oxygen reduction in alkaline solutions, J. Electroanal. Chem. **403**, 169–181 (1996)

21.36 M.H. Shao, R.R. Adzic: Spectroscopic identification of the reaction intermediates in oxygen reduction on gold in alkaline solutions, J. Phys. Chem. B **109**, 16563–16566 (2005)

21.37 E.I. Rogers, X.-J. Huang, E.J.F. Dickinson, C. Hardacre, R.G. Compton: Investigating the mechanism and electrode kinetics of the oxygen

vertical bar superoxide ($O_2|O_2^{\cdot-}$) couple in various room-temperature ionic liquids at gold and platinum electrodes in the temperature range 298–318 K, J. Phys. Chem. C **113**, 17811–17823 (2009)
21.38 K. Takahiro, S. Oizumi, A. Terai, K. Kawatsura, B. Tsuchiya, S. Nagata, S. Yamamoto, H. Naramoto, K. Narumi, M. Sasase: Core level and valence band photoemission spectra of Au clusters embedded in carbon, J. Appl. Phys. **100**, 084325 (2006)
21.39 J.F. Moulder, W.F. Stickle, P.E. Sobol, K.D. Bomben: *Handbook of X-Ray Photoelectron Spectroscopy* (Perkin-Elmer, Waltham 1992)
21.40 B.C.H. Steele, A. Heinzel: Materials for fuel-cell technologies, Nature **414**, 345–352 (2001)
21.41 Y.-S. Hu, Y.-G. Guo, W. Sigle, S. Hore, P. Balaya, J. Maier: Electrochemical lithiation synthesis of nanoporous materials with superior catalytic and capacitive activity, Nature Mater. **5**, 713–717 (2006)
21.42 T. Kinumoto, K. Takai, Y. Iriyama, T. Abe, M. Inaba, Z. Ogumi: Stability of Pt-catalyzed highly oriented pyrolytic graphite against hydrogen peroxide in acid solution, J. Electrochem. Soc. **153**, A58–A63 (2006)
21.43 M.L. Sattler, P.N. Ross: The surface structure of Pt crystallites supported on carbon black, Ultramicrosc. **20**, 21–28 (1986)
21.44 P.J. Bouwman, W. Dmowski, J. Stanley, G.B. Cotten, K.E. Swider Lyons: Low-Pt oxide-based catalysts for ORR in PEM fuel cells, J. Electrochem. Soc. **151**, A1989–A1998 (2004)
21.45 T.J. Schmidt, H.A. Gasteiger, G.D. Stäb, P.M. Uraban, D.M. Kolb, R.J. Behm: Characterization of high-surface-area electrocatalysts using a rotating disk electrode configuration, J. Electrochem. Soc. **145**, 2354–2358 (1998)
21.46 Y.J. Kim, H. Kim, B. Kim, D. Ahn, J.-G. Lee, T.-J. Kim, D. Son, J. Cho, Y.-W. Kim, B. Park: Electrochemical stability of thin-film $LiCoO_2$ cathodes by aluminum-oxide coating, Chem. Mater. **15**, 1505–1511 (2003)
21.47 A. Pozio, R.F. Silva, M. De Franseco, L. Giorgi: Nafion degradation in PEFCs from end plate iron contamination, Electrochim. Acta **48**, 1543–1549 (2003)
21.48 B. Park, C. Kim, M. Kang, J.-N. Park, H. Kim, M. Kim: Electrode catalyst with improved longevity properties and fuel cell using the same, US Patent 2007/0248862 (2007)
21.49 M. Watanabe, S. Motoo: Electrocatalysis by adatoms: Part I. Enhancement of the oxidation of methanol on platinum and palladium by gold adatoms, J. Electroanal. Chem. **60**, 267–273 (1975)
21.50 S. Mukerjee, S. Srinivasan, M.P. Soriaga, J. McBreen: Role of structural and electronic properties of Pt and Pt alloys on electrocatalysis of oxygen reduction an in situ XANES and EXAFS investigation, J. Electrochem. Soc. **142**, 1409–1422 (1995)
21.51 W.M. Martinez, T.T. Thompson, M.A. Smit: Characterization and electrocatalytic activity of carbon-supported polypyrrole-cobalt-platinum compounds, Int. J. Electrochem. Sci. **5**, 931–943 (2010)
21.52 A. Hamnett: Mechanism and electrocatalysis in the direct methanol fuel cell, Catal. Today **38**, 445–457 (1997)
21.53 P. Piela, C. Eickes, E. Brosha, F. Garzon, P. Zelenay: Ruthenium crossover in direct methanol fuel cell with Pt-Ru black anode, J. Electrochem. Soc. **151**, A2053–A2059 (2004)
21.54 Y. Park, B. Lee, C. Kim, Y. Oh, S. Nam, B. Park: The effects of ruthenium-oxidation states on Ru dissolution in PtRu thin-film electrodes, J. Mater. Res. **24**, 2762–2766 (2009)
21.55 J.-G. Lee, B. Kim, J. Cho, Y.-W. Kim, B. Park: Effect of AlPO4-nanoparticle coating concentration on high-cutoff-voltage electrochemical performances in LiCoO2, J. Electrochem. Soc. **151**, A801–A805 (2004)
21.56 J. Cho, J.-G. Lee, B. Kim, B. Park: Effect of P_2O_5 and $AlPO_4$ coating on $LiCoO_2$ cathode material, Chem. Mater. **15**, 3190–3193 (2003)
21.57 W.L. Holstein, H.D. Rosenfeld: In-situ x-ray absorption spectroscopy study of Pt and Ru chemistry during methanol electrooxidation, J. Phys. Chem. B **109**, 2176–2186 (2005)
21.58 H. Li, G. Sun, Y. Gao, Q. Jiang, Z. Jia, Q. Xin: Effect of reaction atmosphere on the electrocatalytic activities of Pt/C and PtRu/C obtained in a polyol process, J. Phys. Chem. C **111**, 15192–15200 (2007)
21.59 W. Dmowski, T. Egami, K.E. Swider-Lyons, C.T. Love, D.R. Rolison: Local atomic structure and conduction mechanism of nanocrystalline hydrous RuO_2 from x-ray scattering, J. Phys. Chem. B **106**, 12677–12683 (2002)
21.60 J.W. Long, R.M. Stroud, K.E. Swider-Lyons, D.R. Rolison: How to make electrocatalysts more active for direct methanol oxidation – Avoid PtRu bimetallic alloys!, J. Phys. Chem. B **104**, 9772–9776 (2000)
21.61 C. Nahm, C. Kim, Y. Park, B. Lee, B. Park: Iron-phosphate/Pt nanostructured electrodes for high-efficiency fuel cells, Electron. Mater. Lett. **4**, 5–7 (2008)
21.62 S.H. Joo, S.J. Choi, I. Oh, J. Kwak, Z. Liu, O. Teraski, R. Ryoo: Ordered nanoporous arrays of carbon supporting high dispersions of platinum nanoparticles, Nature **412**, 169–172 (2001)
21.63 K.-S. Choi, E.W. McFarland, G.D. Stucky: Electrocatalytic properties of thin mesoporous platinum films synthesized utilizing potential-controlled surfactant assembly, Adv. Mater. **15**, 2018–2021 (2003)
21.64 H.-P. Liang, H.-M. Zhang, J.-S. Hu, Y.-G. Guo, L.-J. Wan, C.-L. Bai: Pt hollow nanospheres: Facile synthesis and enhanced electrocatalysts, Angew. Chem. Int. Ed. **43**, 1540–1543 (2004)
21.65 J.C. Thorp, K. Sieradzki, L. Tang, P.A. Crozier, A. Misra, M. Nastasi, D. Mitlin, S.T. Picraux: Formation of nanoporous noble metal thin films by electrochemical dealloying of Pt_xSi1_x, Appl. Phys. Lett. **88**, 033110 (2006)
21.66 E. Kim, D. Son, T.-G. Kim, J. Cho, B. Park, K.S. Ryu, S.H. Chang: A mesoporous/crystalline composite material containing tin phosphate for use as the

anode in lithium-ion batteries, Angew. Chem. Int. Ed. **43**, 5987–5990 (2004)
21.67 Y. Oh, D. Ahn, S. Nam, C. Kim, J.-G. Lee, B. Park: Nanoscale interface control for high-performance Li-ion batteries, Electron. Mater. Lett. **4**, 103–105 (2008)
21.68 J.G. Lee, D. Son, C. Kim, B. Park: Electrochemical properties of tin phosphates with various mesopore ratios, J. Power Sources **172**, 908–912 (2007)
21.69 C. Nahm, C. Kim, Y. Park, B. Park: Nanoporous Pt thin films with superior catalytic activities by the electrochemical dissolution of Al, Met. Mater. Inter. **15**, 989–992 (2009)
21.70 C. Kim, Y. Park, C. Nahm, B. Park: Formation of nanoporous Pt thin films by electrochemical dissolution, Electron. Mater. Lett. **4**, 75–77 (2008)
21.71 M. Hirasawa, H. Shirakawa, H. Hamamura, Y. Egashira, H. Komiyama: Growth mechanism of nanoparticles prepared by radio frequency sputtering, J. Appl. Phys. **82**, 1404–1407 (1997)
21.72 W.-S. Ju, M. Matsuoka, K. Lino, H. Yamashita, M. Anpo: The local structures of silver(I) ion catalysts anchored within zeolite cavities and their photocatalytic reactivities for the elimination of N_2O into N_2 and O_2, J. Phys. Chem. B **108**, 2128–2133 (2004)
21.73 X.G. Yang, C.Y. Wang: Nanostructured tungsten carbide catalysts for polymer electrolyte fuel cells, Appl. Phys. Lett. **86**, 224104 (2005)
21.74 K.-W. Park, K.-S. Ahn, J.-H. Choi, Y.-C. Nah, Y.-M. Kim, Y.-E. Sung: Pt-WOx electrode structure for thin-film fuel cells, Appl. Phys. Lett. **81**, 907–909 (2002)
21.75 K.-W. Park, K.-S. Ahn, J.-H. Choi, Y.-C. Nah, Y.-E. Sung: PtRu-W03 nanostructured alloy electrode for use in thin-film fuel cells, Appl. Phys. Lett. **82**, 1090–1092 (2002)
21.76 H.M. Villullas, F.I. Mattos-Costa, L.O.S. Bulhoes: Electrochemical oxidation of methanol on Pt nanoparticles dispersed on RuO_2, J. Phys. Chem. B **108**, 12898–12903 (2004)
21.77 D. Son, E. Kim, T.-G. Kim, M.K. Kim, J. Cho, B. Park: Nanoparticle iron-phosphate anode material for Li-ion battery, Appl. Phys. Lett. **85**, 5875–5877 (2004)
21.78 K. Otsuka, Y. Wang: Direct conversion of methane into oxygenates, Appl. Catal. A **222**, 145–161 (2001)
21.79 K.D. Kreuer: Proton conductivity: Materials and applications, Chem. Mater. **8**, 610–641 (1996)
21.80 D.A. Jones: *Principles and Prevention of Corrosion*, 2nd edn. (Prentice Hall, Upper Saddle River 1996)
21.81 A. Demirbas: Progress and recent trends in biofuels, Prog. Energy Combust. Sci. **33**, 1–18 (2007)
21.82 F. Vigier, C. Coutanceau, F. Hahn, E.M. Belgsir, C. Lamy: On the mechanism of ethanol electrooxidation on Pt and PtSn catalysts: electrochemical and in situ IR reflectance spectroscopy studies, J. Electroanal. Chem. **563**, 81–89 (2004)

22. Methods in Biological Fuel Cells

Shelley D. Minteer

This chapter details the common analytical methods used to evaluate all types of biological fuel cells. These include in situ and ex situ techniques for studying the catalyst, the bioelectrodes, and the complete biological fuel cell. Spectroscopic methods include spectrophotometric kinetic assays, product analysis assays, and electrode characterization techniques. Electrochemical methods include methods for proving bioelectrocatalysis via voltammetry, studying biocatalyst kinetics via amperometry, and performing polarization and power curve measurements on complete biological fuel cells.

22.1 **Bioelectrocatalysis** 744
22.1.1 Microbial, Enzymatic, Nucleic Acid, and Organelle Catalysts 744
22.1.2 Mediated Versus Direct Bioelectrocatalysis 745
22.2 **Spectroscopic Methods** 746
22.2.1 Michaelis–Menten Kinetics 746
22.2.2 Specific Activity 746
22.2.3 Leaching Studies 746
22.2.4 XPS Surface Analysis 748
22.2.5 Infrared, Nuclear Magnetic Resonance, and Mass Spectrometry 748
22.3 **Electrochemical Methods** 749
22.3.1 Voltammetry 749
22.3.2 Amperometric Methods 750
22.3.3 Polarization Measurements 750
22.3.4 Stability Testing 752
22.3.5 Electrochemical Impedance Spectroscopy 752
22.4 **Engineering Considerations** 752
22.5 **Conclusions** 753
References 753

Biological fuel cells are a subset of fuel cells. Fuel cells are energy conversion devices that convert the chemical energy of a fuel into electrical energy via the use of electrocatalysts. Most fuel cells are classified by their electrolyte or their separator (phosphoric acid fuel cells, alkaline fuel cells, solid oxide fuel cells, polymer electrolyte membrane (PEM) fuel cells), but biological fuel cells are different. They can use a variety of separators and electrolytes, but they are classified by the type of biocatalyst used to catalyze the fuel oxidation or oxygen/peroxide reduction. Therefore, a biological fuel cell can be defined as a fuel cell where the catalyst at the anode and/or the cathode is a catalyst of biological origin, including living cells and their subcellular components. Figure 22.1 is an example of a biological fuel cell. It shows the most common anode and cathode schemes in biological fuel cells, utilizing the enzyme glucose oxidase to catalyze the oxidation of glucose to gluconolactone and the enzyme laccase to catalyze the reduction of oxygen to water.

Biological fuel cells are considered one of the youngest subsets of fuel cells, although biological fuel cells have celebrated a century of existence [22.1]. During that century, research has focused on the improvement in biocatalysts [22.2–5], improvement in materials for electrodes [22.6–9], and improvements in cell design [22.10–14], but until recently, there has not been a standardization of the techniques used to characterize and evaluate biofuel cells [22.9, 15–17]. This book chapter will introduce the reader to the field of biological fuel cells and then given detailed methods for characterizing biological fuel cells. These include standard electrochemical evaluation (i. e., polarization curves and cyclic voltammetry), as well as spectroscopic techniques for the catalysts and the electrodes.

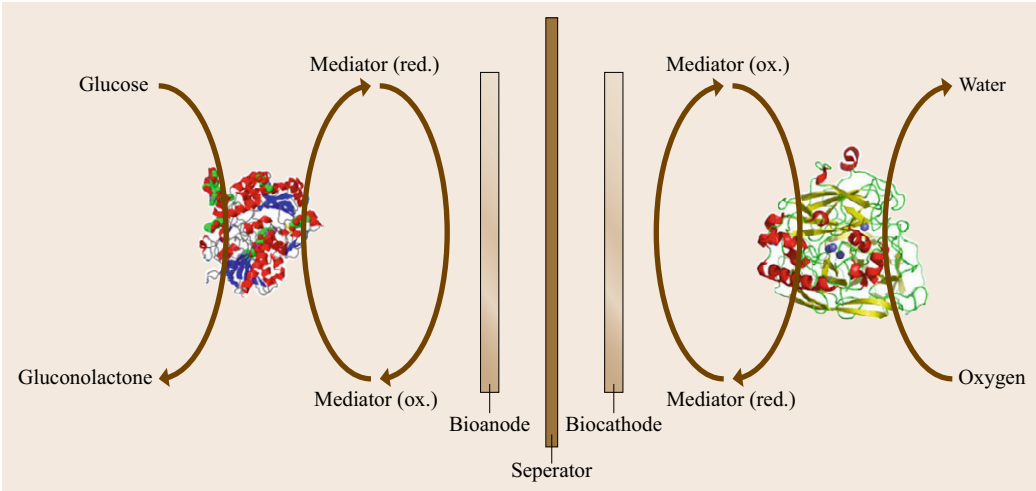


Fig. 22.1 Schematic of a glucose/oxygen biofuel cell

22.1 Bioelectrocatalysis

As described before, biological fuel cells are categorized by the type of biocatalyst used to catalyze oxidation at the anode and/or reduction at the cathode. The first biological fuel cells utilized complete living cells (microbes) to catalyze oxidation of fuel at the anode of a fuel cell [22.1]. Over half a century later, researchers realized that it was enzymes (catalytic proteins) in the living cells that were actually catalyzing the oxidation of fuel and proposed that enzymes could be used at the anode of a biological fuel cell [22.18]. Later, both enzymatic biofuel cell researchers and microbial fuel cell researchers realized that enzymes and microbes could also be used as catalysts for the cathode [22.19, 20]. Several decades later, three other classifications of biocatalysts have been utilized (whole tissue, organelles [22.21, 22], and nucleic acids [22.23]). These are extremely new classifications of biological fuel cells, but we are likely to see more research in all three of these areas. Tissue-based biofuel cells have been studied due to the fact that they allow for inexpensive sources of enzymes compared to the high cost of isolated enzymes.

22.1.1 Microbial, Enzymatic, Nucleic Acid, and Organelle Catalysts

The idea behind tissue-based biofuel cells is similar to microbial fuel cells in that you are using the enzyme in the living cells without destroying the living cell. A similar approach utilizing subcellular components (organelles) of living cells to catalyze oxidation of fuel has also been explored. The organelle that is most frequently used is the mitochondrion, as it is frequently considered the *powerhouse* organelle of the cell that is responsible for the vast majority of metabolism (i. e., oxidation of food/fuel) [22.24]. Finally, nucleic acid catalysts in the form of deoxyribozymes have been used to catalyze reactions in fuel cells. These oxidoreductase nucleic acids are similar in function to the oxidoreductase proteins (enzymes) that have been used for decades, but they are more stable in response to changes in ionic strength and pH [22.23]. In each case, the biological fuel cells are named and classified by the type of biocatalyst used for bioelectrocatalysis at the anode and/or cathode. In some instances, more than one type of catalyst is used and these are commonly referred to as *hybrid* systems [22.25]. This term is commonly used for a microbial anode and an enzymatic cathode or vice versa. However, the recent work of *Fishilevich* and coworkersusing microbes to produce surface-displayed enzymes for enzymatic bioelectrocatalysis at an anode would likely also be an example of a hybrid system, even though the bioelectrocatalysis is only coming from the enzyme [22.26]. Another term that is used in both the scientific and popular literature is *biobattery*. The term biobattery has not been easily defined, but is generally considered to be a biofuel anode or cathode that is used with the corresponding electrode of a battery. For instance, Zn/air biobatteries have an enzymatic biocathode and traditional Zn battery anodes [22.27], and alcohol biobatteries have alcohol dehydrogenase bioanodes and a Prussian blue battery cathode [22.28].

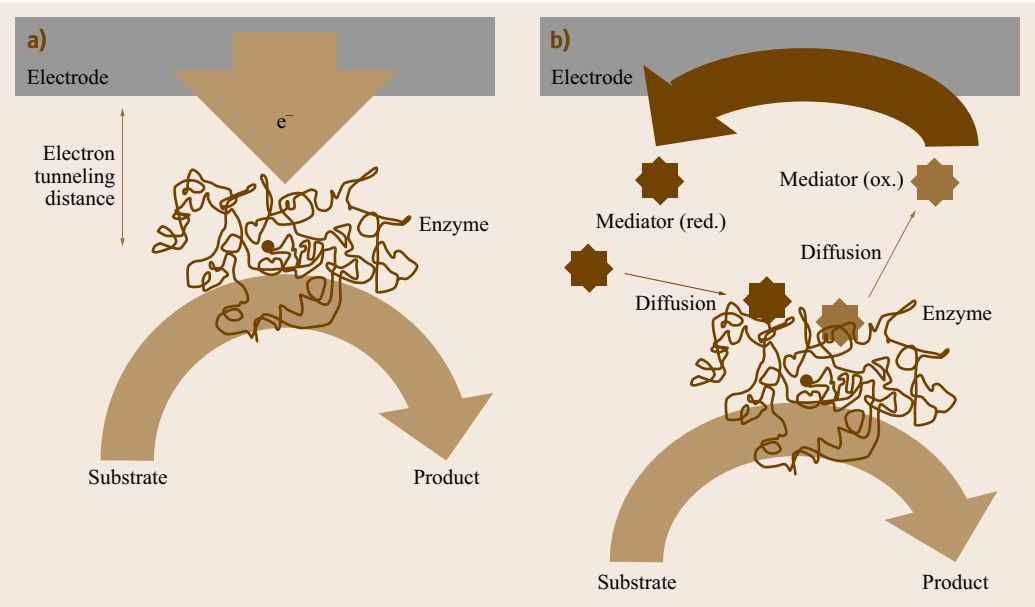


Fig. 22.2a,b Comparison of **(a)** direct bioelectrocatalysis and **(b)** mediated bioelectrocatalysis (after [22.29], courtesy of ACS)

22.1.2 Mediated Versus Direct Bioelectrocatalysis

Most bioelectrocatalysts are further classified by whether they are capable of directly communicating with electrodes (direct bioelectrocatalysis) or whether they require small molecule or polymeric mediators to shuttle electrons between the biocatalyst and the electrode surface, as shown in Fig. 22.2. Mediated bioelectrocatalysis is the most common and oldest mechanism [22.29], but transport limitations and instability of mediators have resulted in many researchers trying to transition from mediated bioelectrocatalysis to direct bioelectrocatalysis. In some systems, this is easier than others. For instance, some microbes are known to be able to communicate directly with carbon electrodes via surface cytochromes or pilli, while others require external mediators [22.30]. On the other hand, mitochondria have also been shown to communicate directly with carbon electrodes [22.24], but all tissue systems have required mediators. For enzymes, it is very dependent on the structure of the enzyme and how buried the redox sites of the enzymes are in the protein [22.31]. For instance, many heme-containing enzymes can do direct electron transfer [22.32–36], because the hemes are commonly close to the surface of the protein. Also, many multi-copper oxidases have shown direct electron transfer [22.37–39], because the copper sites are close to the surface. However, enzymes like glucose oxidase dependent on flavin adenine dinucleotide (FAD) do not readily do direct electron transfer, because the active site is buried deep in the protein [22.40]. Finally, many oxidoreductase enzymes have diffusional cofactors. The dehydrogenases dependent on nicotinamide adenine dinucleotide (NAD) and nicotinamide adenine dinucleotide phosphate (NADP) are likely the largest class of oxidoreductase enzymes having a diffusional cofactor. If they are utilized in a biological fuel cell, then the cofactor acts as the mediator and typically an additional electrocatalyst is added to the electrode surface to decrease the overpotential of NADH and NADPH oxidation at common current collectors (i. e., carbon, gold, platinum). These electrocatalysts include polyazines [22.41–43], nanomaterials [22.44], and organometallic species [22.45].

22.2 Spectroscopic Methods

Spectroscopic methods are frequently used for studying biocatalyst properties (i. e., stability, catalytic activity before and after immobilization, product determination, etc.). Therefore, this section of the text will discuss the common spectroscopic methods used to evaluate biological fuel cells. Some of these methods are designed to study the catalyst before the fabrication of the biological fuel cell, some of these techniques are in situ techniques that can be utilized during the operation of the biological fuel cell, and some of these techniques are used ex situ to evaluate the fuel cell or fuel cell components after operation.

22.2.1 Michaelis–Menten Kinetics

Kinetic analysis of biological systems is far more complex than traditional metal catalysts and is rarely performed for cellular-based bioelectrodes (i. e., tissue-based biofuel cells, microbial fuel cells, or organelle-based biofuel cells). However, kinetic analysis is common for understanding the kinetics of enzymes in enzymatic biofuel cells. There are a number of kinetic models for enzymes of different types. For instance, some enzymes catalyze single-substrate reactions. The Michaelis–Menten model is typically used to describe single-substrate reactions, where the substrate binds to the enzyme and catalyzes a reaction. Since enzyme-catalyzed reactions are saturable, then there is not a linear response with increasing substrate concentration like you would expect, but instead the enzyme saturates with substrate and the rate levels off to the enzyme's maximum rate (V_{max}). In an effort to linearize plots of rate versus concentration, a double reciprocal plot is commonly used. This is called the Lineweaver–Burk plot and although it is commonly used to find V_{max} and K_m (the Michaelis constant, which is defined as the substrate concentration that results in a reaction rate that is one half of V_{max}), it is not as accurate as simply using nonlinear regression methods for determining the V_{max} and K_m. Examples of Michaelis–Menten plots and Lineweaver–Burk plots are shown in Fig. 22.3 It is important to note that the rate of reaction can be either determined via a spectroscopic assay (typically a ultraviolet–visible (UV-Vis) assay described below) or via an electrochemical assay (Sect. 22.3.2).

Although Michaelis–Menten kinetic models are frequently applied to enzymatic bioelectrochemistry, not all oxidoreductase enzymes follow Michaelis–Menten kinetics. For instance, many oxidoreductases follow ping-pong mechanisms, where the substrate binds and changes the enzyme, and then the enzyme releases that substrate and another substrate binds and reacts with the modified enzyme to regenerate the original form of the enzyme.

22.2.2 Specific Activity

Another common kinetic analysis that is done to characterize an enzyme is to determine its specific activity. Specific activity is defined as the speed of the reaction per unit weight of the enzyme. Specific activity is normally represented in units/mg or units/g, where a unit is described as the ability to turnover 1 μmole of substrate per minute. Most oxidoreductase enzymes have an assay to allow for the determination of specific activity in whatever buffer or solution conditions are being used for the electrochemical cell. For instance, NAD-dependent enzymes will study either the production of NADH or the loss of NADH via a direct UV-Vis assay at 340 nm. On the other hand, enzymes dependent on pyrroloquinoline quinone (PQQ) don't have a cofactor that is easy to directly measure, so instead a dye-based assay is used employing dichlorophenolindophenol (DCIP) and phenazine methosulfate (PMS) [22.9, 46]. A dye-based assay is also used for FAD-dependent enzymes, as well as multi-copper oxidases typically used for oxygen reduction enzymes at the cathode of enzymatic biofuel cells [22.47]. There are a wealth of UV-Vis-based spectroscopic assays for PQQ-dependent dehydrogenase, FAD-dependent oxidoreductases, and multi-copper oxidases and most commercially purchased enzymes come with a specific activity assay. One important condition to keep in mind is that if the enzyme is being used for a biofuel cell, then it is critically important to carry out the kinetic assays in the appropriate buffer and fuel environment that will be used in the fuel cell.

22.2.3 Leaching Studies

Until recently, the effectiveness of immobilization of the biocatalyst has not been a concern. Recently, studies of the leaching of the biocatalysts (specifically enzyme catalysts) has become a test used to understand stability of the bioelectrodes [22.9]. For over a decade, scientists interested in immobilizing enzymes at surfaces for bioprocessing have been quite interested in leaching studies, but this has only recently been applied to bioelectrodes, because it has only been recently that scientists have been interested in understanding the mechanism of degradation of bioelectrodes (i. e., does electrochemical performance decrease because the mediator decomposes, the enzyme denatures, the enzyme leaches off the surface, etc.). Leaching studies are nor-

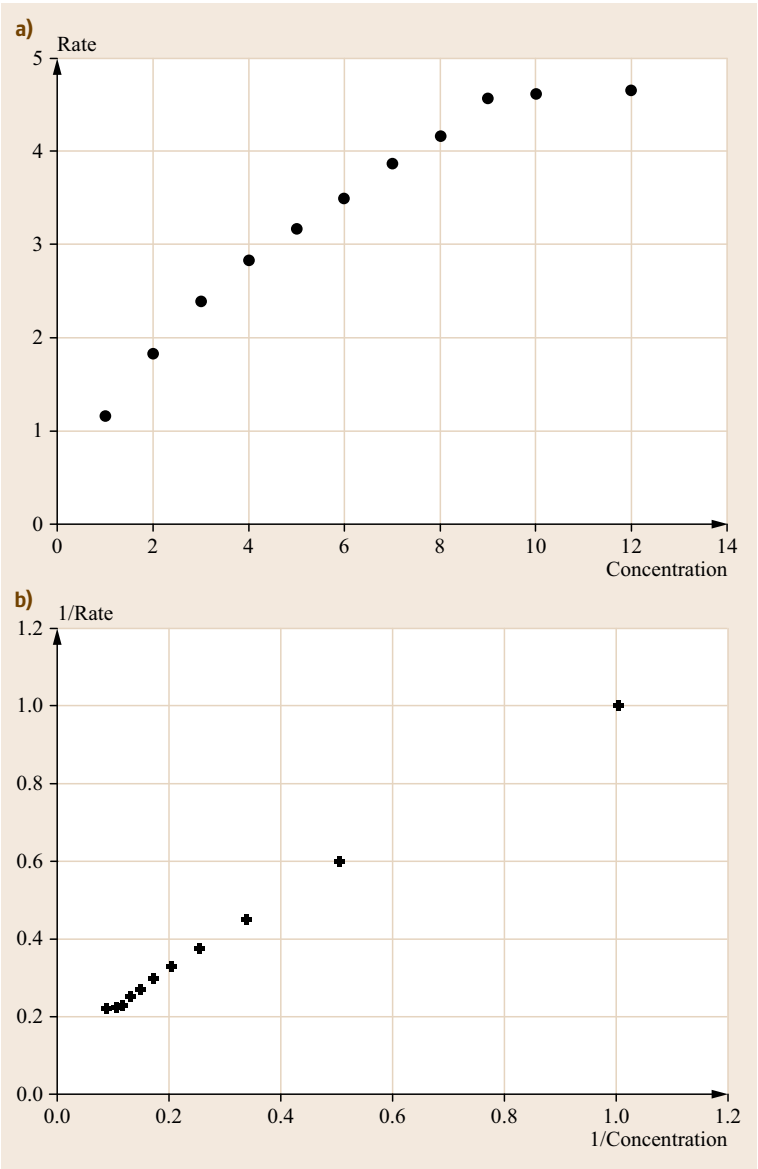


Fig. 22.3 **(a)** Plot of kinetic rate of enzyme versus concentration; **(b)** Lineweaver–Burk plot of inverse of kinetic rate of enzyme versus inverse of concentration

mally done by first determining the amount of enzyme that is immobilized on the electrode surface. This is commonly the milligrams or micrograms of enzyme that is used to coat the electrode, but is sometimes determined by quartz crystal microbalance (QCM) determination of immobilization or via an electrochemical technique. After the initial enzyme loading is done, the electrode is typically washed and the washed solution is tested via a spectroscopic protein assay (i. e., BCA assay) to determine the concentration of enzyme in the wash solution. Then, the electrode is typically allowed to soak in a solution for different periods of time and the same spectroscopic protein quantification assay is performed at those time aliquots to determine how much protein has leached. This is frequently presented as a percentage of leached protein.

The most common spectroscopic protein quantification assay is the nonlabeled UV assay that determines protein concentration via the protein peak from the tyrosine, tryptophan, and phenylalanine amino acids in the protein, which show up in the UV at 280 nm. This assay is common, because it doesn't use additional reagents, but the molar absorptivity of protein at 280 nm is quite low, so the sensitivity is low and the limits of detection are large. This may not be a problem if a lot of enzyme is leaching, but if the leaching percentage is small, then

this assay may not be practical. Other common assays are dye-based assays that require a dye that reacts with residues of the enzyme to turn colors and they also require a protein standard to compare color changes to (this is frequently either the protein of interest if you have purified protein or bovine serum albumin (BSA), because it is so inexpensive). There are three common dye-based protein quantification assays: BCA, modified Lowry, and the Bradford assay.

BCA stands for bicinchoninic acid, which is a ligand that binds to copper ions when they have been reduced by cysteine, tyrosine, and tryptophan amino acids in proteins. This organometallic complex when formed has an intense purple color and can be detected via a spectrophotometer at 560 nm. The Lowry (and modified Lowry assay) uses similar copper chelating chemistry, but it produces a blue complex that is measured at 750 nm. Finally, the Bradford assay uses the Coomassie blue dye, where the protein binds the dye and causes a spectral shift from the reddish/brown form of the dye to the blue form of the dye. The absorbance is typically measured with a spectrophotometer at a wavelengths between 575 and 615 nm. There are several variations to this dye and assay. Overall, there are interferences with all three main dye-based techniques and the 280 nm direct UV assay, so there is no one single perfect protein quantification assay, but the 280 nm direct UV assay and the BCA assay are the most common in the literature for studying bioelectrode-based protein leaching [22.9].

22.2.4 XPS Surface Analysis

X-ray photoelectron spectroscopy (XPS) is frequently used as a catalyst characterization tool for traditional metallic electrocatalysts. Recently, it has become a tool for studying bioelectrodes as well [22.48–50]. The most common use of XPS is for elemental analysis to determine composition. This is used in traditional fuel cell electrocatalysts to determine the portion of different metals in a catalyst, but is used for bioelectrodes to detect the presence of self-assembled monolayers and/or enzymes or other biocatalysts on electrode surfaces. XPS can also provide binding information, so it is commonly used to evaluate current collector materials and even polymeric mediators and electrocatalysts for bioelectrodes to determine their structure in an effort to correlate structure with function [22.51, 52]. Overall, these methods are ex situ methods that can be used to study the bioelectrodes of the biofuel cell before or after the operation of the biofuel cell.

22.2.5 Infrared, Nuclear Magnetic Resonance, and Mass Spectrometry

Fuel cell product analysis is quite useful to understand the degree of oxidation of fuel and to understand if toxic intermediates are being produced during oxidation. For instance, if glucose is being oxidized, then spectroscopic analysis can be performed to determine the concentration of glucose remaining, as well as the concentration of gluconolactone, gluconic acid, glucuronic acid, carbon dioxide, etc. For a fuel like methanol, methanol, formaldehyde, formate, and carbon dioxide are typically analyzed. There are a number of different methods for fuel cell product analysis that can be used for biofuel cells. One common analysis used in traditional fuel cells is ATR-FTIR (attenuated total reflection-Fourier transform infrared spectroscopy) to study product formation [22.53, 54]. Depending on the fuel and the system, this can be a semiquantitative method for determining product formation in traditional fuel cells, but is more complicated in biological fuel cells, because current densities are lower so product formation rates are typically considerably lower. Nuclear magnetic resonance spectroscopy (NMR) utilizing carbon-13 labeled fuels is typically used to qualitatively determine the identity of products that are formed [22.21, 55, 56], but if you are wanting to understand the kinetics of the process or to determine the product concentrations, then mass spectrometry (MS) is the preferred method. Mass spectrometry analysis is usually done in connection with a separation technique. Gas chromatography-mass spectrometry (GC-MS) is typically used for product analysis of volatile fuels, but many fuels used for biological fuel cells are not volatile, so either the products are derivatized to form volatile components or liquid chromatography-mass spectrometry (LC-MS) is used. Analysis is either done at the outlet of the fuel cell flow stream or done as a function of time at the electrode in order to determine kinetic information.

22.3 Electrochemical Methods

Electrochemical techniques are logically the most common set of methods used to characterize biological fuel cells. These methods range from single-electrode methods (i. e., voltammetry) to complete biological fuel cell operational tests (i. e., polarization and power curves).

22.3.1 Voltammetry

A variety of voltammetric techniques are used to study bioelectrocatalysis. Direct and mediated bioelectrocatalysis are typically verified via cyclic voltammetry, but the methods are slightly different. Mediated bioelectrocatalysis involves the study of the mediator cyclic voltammety in the presence and absence of the enzyme and substrate. The enzyme and substrate usually do not contribute individually to the cyclic voltammetry (no additional peak for the enzyme or for the substrate), but the cyclic voltammogram changes when the enzyme and substrate are present together, because the enzyme reacts with the substrate and then transfer electrons with the mediator. This results in *catalytic* cyclic voltammograms, where the forward peak increases in size and the background peak decreases (or disappears depending on the scan rate) in size. This is due to the fact that the enzyme is a regenerated mediator at the electrode surface, so the forward peak grows because of this cycling, but since the enzyme is consuming the product, then the backward peak decreases, because the enzyme decreases the effective concentration at the electrode surface. For direct bioelectrocatalysis, the voltammetry is different, because the enzyme communicates directly with the electrode. Therefore, there is an initial peak associated with the redox species in the enzyme communicating with the electrode. If direct bioelectrocatalysis happens, then the addition of a substrate causes an increase in the forward peak and a decrease in the backward peak. This is shown in Figure 22.4 and it is important to note that degassing solutions and performing denatured or inhibited enzyme controls are important.

Another type of voltammetry that is commonly used to study bioelectrodes is protein film voltammetry. Protein film voltammetry is a type of cyclic voltammetry that was invented by *Armstrong* and *Wilson* to study direct protein bioelectrochemistry [22.58]. This technique cannot always be used with biofuel cell electrodes, because usually proteins are adsorbed directly to electrode surfaces and characterized, so they must directly communicate with the electrode and they must adsorb. Not all enzymes will adsorb to all surfaces and not all proteins communicate directly, but if so, this subset of cyclic voltammetry can be used to determine kinetic values.

The final set of voltammetric techniques that are used for characterizing bioelectrodes are the hydrodynamic techniques of rotating disk voltammetry and rotating ring-disk voltammetry. They serve two different purposes. Rotating disk voltammetry involves rotating an electrode and studying the difference in

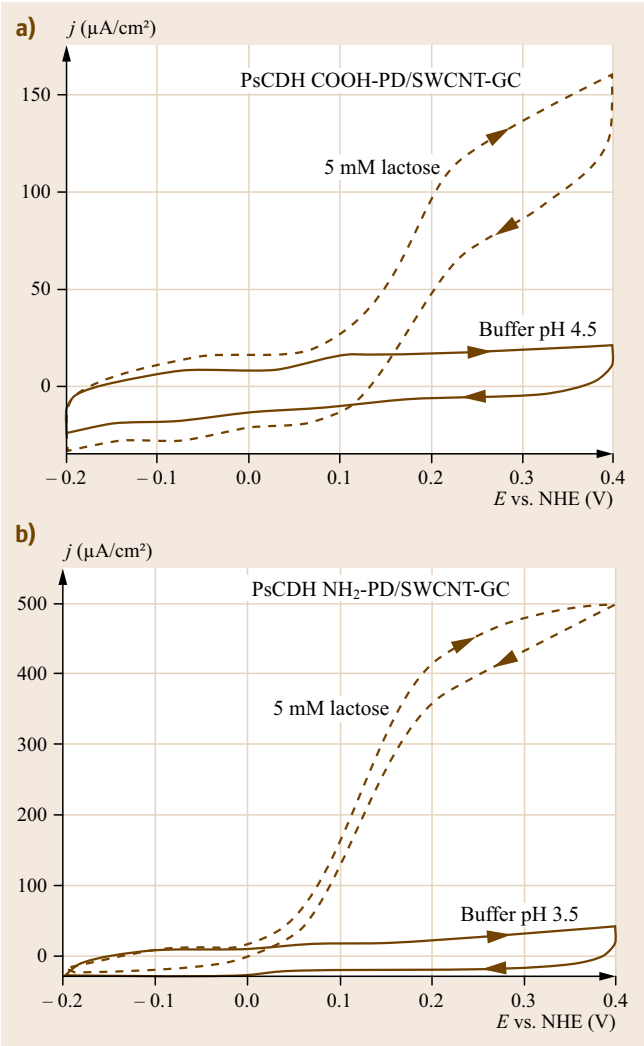


Fig. 22.4 **(a)** Cyclic voltammogram of a PsCDH COOH-PD/SWCNT-GC electrode in the presence of 5 mM lactose (*dashed line*) and in the absence of a substrate (*solid line*), 0.1 M acetate buffer, pH 4.5, scan rate 1 mV/s, **(b)** Cyclic voltammogram of a PsCDH NH_2-PD/SWCNTs-GC electrode in the presence of 5 mM lactose (*dashed line*) and in the absence of substrate, 0.1 M acetate buffer, pH 3.5, scan rate 1 mV/s (after [22.57], courtesy of ACS)

the voltammetric limiting currents as a function of the rotation rate. For simple systems, Koutecky–Levich analysis can be used to determine reaction rates and numbers of electrons transferred. For example, this analysis is frequently done with multi-copper oxidase cathode enzymes and other enzymes capable of simple direct electron transfer [22.59–61]. For more complex mediated systems or systems with complex kinetics, Saveant analysis is required to separate transport, kinetic, and catalytic components [22.62–64].

Rotating ring-disk electrochemistry is a similar technique, except that the central disk is surrounded by a ring that allows for the product of the disk electrochemistry to be measured at the ring. Rotating-ring disk electrochemistry is frequently used with cathodic catalysts to determine whether oxygen reduction is occurring as a 2-electron or a 4-electron process [22.65, 66].

22.3.2 Amperometric Methods

Amperometric methods are more common for biosensor investigations than biofuel cell investigations, but they provide integral kinetic information and can be used as the technique for evaluating Michaelis–Menten kinetics (as described above) [22.67]. Therefore, in recent years, it is common to see amperometric analysis of bioelectrodes to compare immobilized bioelectrode kinetics with enzyme solution kinetics that are typically evaluated via a UV-Vis assay. Amperometric experiments are one of the most difficult experiments to conduct in the laboratory. There are two main methods: (1) using a flow cell to inject different concentrations to the electrode and (2) using a stirred solution where the user pipettes increasing concentrations of fuel or substrate in the solution. The first method results in a series of increasing peaks and the peak height or peak area can be plotted against concentration to make a Michaelis–Menten plot. The second technique results in a staircase plot of current versus concentration and those limiting currents can be used to plot the same Michaelis–Menten plot. The advantage of the first method is that it normally results in less noise, but parallel flow cells may result in only a small portion of the fuel coming into contact with the electrode and wall-jet flow cells may result in instability of the bioelectrode. On the other hand, the use of a stirred solution can result in a great deal of noise due to turbulence, so efforts need to be made to ensure the stirbar is sufficiently far from the electrode and sufficiently small to minimize noise. An effort to use stirplates that cause minimal noise is also necessary.

22.3.3 Polarization Measurements

Polarization curves and power curves are one of the main techniques for evaluating a complete fuel cell. Polarization curves can be done potentiostatically or galvanostatically, but probably the most common technique in the biological fuel cell literature is to run a polarization curve at a very slow scan rate as a linear scan voltammogram. In theory, if performed correctly, all three techniques would provide the same data. The question becomes how to accurately make each measurement. In a potentiostatic polarization curve, the potential is stepped through a series of potentials (usually from open circuit potential to a near 0 potential (i. e.,

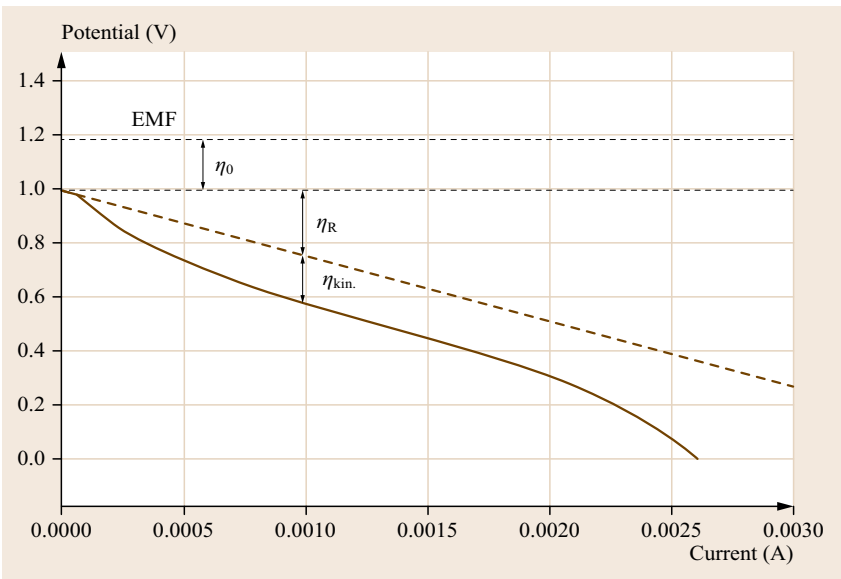


Fig. 22.5 Representative polarization curve showing the decrease from nonideality from thermodynamic losses associated with mediators and cofactors at the anode and the cathode(η_0), losses due to resistance (η_R), and losses due to kinetics (η_{kin}). emf is the electromotive force between the biofuel oxidation and oxygen reduction. Potential is measured as the potential difference between the anode and cathode (after [22.17], courtesy of ACS)

0.05 V) and the current is allowed to level out at each potential before a current-potential data point is taken. This is an effective technique if the user ensures that the current is stabilized, but frequently the user will assume a time to stabilization that may result in an inaccurate measurement of stabilized current. In a galvanostatic polarization curve, the current is stepped through a series of currents and the potential is allowed to stabilize before a current-potential data point is taken. Galvanostatic polarization curves are frequently considered to be preferable, but the same issue arises that it is critical to allow for stabilization of the potential before a measurement is taken. The third type of polarization curve is used infrequently for traditional fuel cells, but frequently for enzymatic and organelle-based biofuel cells. In this technique, a linear polarization is performed from open circuit potential to a near-0 V or 0 V. This requires the linear scan to be sufficiently slow to ensure steady state measurements and this speed is dependent on the system. Sometimes 5 mV/s is slow enough to be steady state, frequently 1 mV/s is slow enough for steady state, but sometimes 0.1 mV/s is needed to reach steady state. Each one of these techniques requires the user to ensure that accurate measurements are made. For scientists doing linear polarization curve techniques, the common method is to test more than one scan rate to ensure no change in the polarization curve. For scientists using galvanostatic or potentiostatic polarization curves, it is common for scientists to either do both a galvanostatic and potentiostatic polarization curve to ensure they are the same or to do a polarization curve in the forward and reverse direction to ensure they are the same. These validations are needed to ensure the accuracy of a polarization curve.

There is one more type of polarization curve that is used solely by researchers in the microbial fuel cell area. This involves using a series of resistors as loads and measuring the performance of the fuel cell under those loads. This is only applicable if you are accurately measuring both current and voltage at that load.

Polarization curves are useful for determining mechanisms of loss of performance (Fig. 22.5). Figure 22.5 shows that the use of mediators and cofactors at the anode and the cathode of a biological fuel cell decreases the potential from the theoretical potential of oxidation of the fuel and reduction of oxygen or peroxide (EMF). It also shows that you have deviations from ideality associated with the resistance of the electrochemical cells and the poor kinetics of the reactions. Finally, many fuel cells also have a deviation from ideality at high current densities associated with mass transport limitations.

Finally, polarization curves are used to calculate and plot power curves. The polarization curve is a plot of the potential as a function of current or the current as a function of potential, so the current and voltage can be multiplied to calculate the power. A power curve can be generated to show how the power changes as a function of potential or current. Some researchers plot as a function of potential and some as a function of current, but plotting a power curve as a function of current is preferential, because it shows fuel cell instabilities that are masked in the plot of power versus voltage. Figure 22.6 shows representative power curves for an unstable biological fuel cell that was evaluated via linear scan polarization at 1 mV/s. It is clear from the plot of power versus current that the power curve is unstable, but it is not clear from the plot of power versus potential. This shows the reason that biological fuel cell power curves should be plotted power versus current.

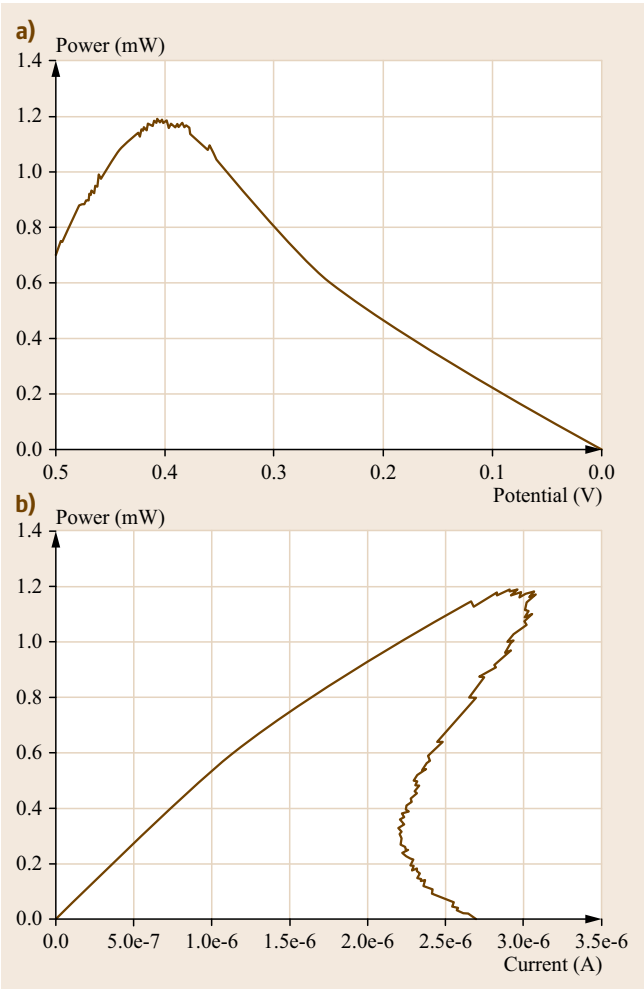


Fig. 22.6a,b Representative power curves for the same unstable biological fuel cell tested via linear scan polarization at 1 mV/s. **(a)** Plot of power versus potential. **(b)** Plot of power versus current

The polarization curve is a useful tool for understanding voltage efficiency, because it allows you to observe the voltage losses due to the mediators or cofactors, but also allows you to see what the operating voltage is compared to theoretical voltage (EMF) at any given operational current density. With biofuel cells, these losses in voltage range from 100 mV to 1 V or even greater, so studying voltage efficiency is important. However, in many enzymatic fuel cells, the loss in efficiency due to poor fuel utilization is a bigger issue than the loss in voltage efficiency. Most biological fuel cells use complex biological fuels. Microbial fuel cells have been shown to completely oxidize a variety of biofuel cell and efficiencies of $> 90\%$ have been discussed. However, enzymatic biofuel cells are different. Frequently, researchers use a single enzyme and most frequently that single enzyme is glucose oxidase to do a two-electron oxidation of the fuel. If the fuel is glucose, that means that even if the anode converts 100% of fuel to product before leaving the fuel cell, then the fuel efficiency is still quite low, because only 2 of the 24 electrons of glucose have been harnessed by the fuel cell. Therefore, product studies discussed above are important to understand fuel utilization and losses in efficiency due to poor fuel degree of oxidation.

22.3.4 Stability Testing

Stability testing of any fuel cell is important. Stability testing can be performed either as a half cell or a complete fuel cell. Both types of stability testing are important and the combination often allows the user to determine modes of decomposition in connection with leaching studies and enzyme activity studies. Half cell stability testing is usually performed via amperometry for long time periods, but it can be determined via chronopotentiometry at a constant current [22.9, 68]. Note that the stability is usually longer at lower current densities. Complete fuel cell stability tests can be done a variety of ways, including galvanostatically and potentiostatically. Stability is usually a function of potential or current density and longer lifetimes are usually observed for fuel cells operated at potentials closer to open circuit and current densities closer to 0 Amps. Stability testing is something that has not been standardized in the biological fuel cell area, but needs to be standardized in the coming years.

22.3.5 Electrochemical Impedance Spectroscopy

Electrochemical impedance spectroscopy (EIS) is a common technique for evaluating any electrochemical cell [22.69]. This technique involves overlaying a range of alternating-current (AC) perturbation signals onto an existing direct-current (DC) bias that is being placed on an electrochemical cell. This technique is used in microbial fuel cell testing a great deal to understand the internal resistance of the cell. However, it has also been used in enzymatic fuel cells to understand internal resistances associated with different designs as well as to gain insight on the limiting mechanisms associated with charge transfer.

22.4 Engineering Considerations

One of the problems with fuel cells and specifically biological fuel cells is that they are difficult to compare, because the cell design plays a vital role in the performance. For instance, early biological fuel cells were operated in a cell that is commonly referred to as a U-cell or an H-cell [22.70]. This cell design involved having the anode soaking in the anolyte and the cathode soaking in the catholyte and the anolyte and catholyte separated by a polymer exchange membrane. The resistance of this cell is going to be directly related to the ionic strength of the salts in the catholyte and the anolyte and the distance between the anode and cathode. Therefore, smaller H-cells are going to result in higher recorded performance, because the resistance of the cell is less. Microfluidic biofuel cells have been designed to decrease this distance [22.12, 13, 71, 72] and membraneless biofuel cells have been designed to decrease the resistance associated with the membrane [22.10, 11, 73, 74]. However, most of these designs have not allowed for scaling. Therefore, as evaluation methods are advancing, it is going to be critical to find techniques that allow researchers to more easily compare fuel cells from a variety of different cell designs, because right now researchers are essentially comparing *apples to oranges* when they try to compare the performance of one biological fuel cell in one cell design to a different biological fuel cell in a different cell design.

22.5 Conclusions

Overall, biological fuel cells are one of the youngest subsets of the fuel cell family and for that reason the characterization techniques are less standardized. However, it is generally agreed that bioelectrocatalysis must be established via cyclic voltammetry for both direct and mediated bioelectrocatalysis and that polarization curves must be evaluated. Careful attention to studying both blanks and controls for each of these methods is a necessity as well as careful evaluation of uncertainty or reproducibility of measurements, since there is some variability in biocatalyst, bioelectrode fabrication, and biofuel cell fabrication. Finally, over the next decade, more standardization is expected in the methods for characterizing stability.

References

22.1 M.C. Potter: Electrical effects accompanying the decomposition of organic compounds, Proc. R. Soc. Lond. Ser. **84**, 260–278 (1912)

22.2 V.A. Pedrosa, J. Yan, A.L. Simonian, A. Revzin: Micropatterned nanocomposite hydrogels for biosensing applications, Electroanalysis **23**, 1142–1149 (2011)

22.3 A. Kausaite-Minkstimiene, V. Mazeiko, A. Ramanaviciene, A. Ramanavicius: Enzymatically synthesized polyaniline layer for extension of linear detection region of amperometric glucose biosensor, Biosens. Bioelectron. **26**, 790–797 (2010)

22.4 D. Ivnitski, P. Atanassov, C. Apblett: Direct bioelectrocatalysis of PQQ-dependent glucose dehydrogenase, Electroanalysis **19**(15), 1562–1568 (2007)

22.5 A. Pothukuchy, N. Mano, G. Georgiou, A. Heller: A potentially insect-implantable trehalose electrooxidizing anode, Biosens. Bioelectron. **22**, 678–684 (2006)

22.6 I.R. Wheeldon, J. Gallaway, S.C. Barton, S. Banta: Bioelectrocatalytic hydrogels from electron-conducting metallo-polypeptides co-assembled with bifunctional enzymatic building blocks, Proc. Nat. Acad. Sci. **105**(40), 15275–15280 (2008)

22.7 S.R. Higgins, D. Foerster, A. Cheung, C. Lau, O. Bretschger, S.D. Minteer, K. Nealson, P. Atanassov, M. Cooney: Fabrication of macroporous chitosan scaffolds doped with carbon nanotubes and their characterization in microbial fuel cell operation, Enzyme Microb. Technol. **48**, 458–465 (2011)

22.8 D. Ivnitski, K. Artyushkova, R.A. Rincon, P. Atanassov, H.R. Luckarift, G.R. Johnson: Entrapment of enzymes and carbon nanotubes in biologically synthesized silica: Glucose oxidase-catalyzed direct electron transfer, Small **4**(3), 357–364 (2008)

22.9 K. Fujita, N. Nakamura, K. Murata, K. Igarashi, M. Samejima, H. Ohno: Electrochemical analysis of electrode-immobilized dehydrogenases in hydrated choline dihydrogen phosphate-type ionic liquid, Electrochim. Acta **56**, 7224–7227 (2011)

22.10 N. Mano, A. Heller: A miniature membraneless biofuel cell operating at 0.36 V under physiological conditions, J. Electrochem. Soc. **150**(8), A1136–A1138 (2003)

22.11 S. Nikolic, L. Mojovic, M. Rakin, D. Pejin: Bioethanol production from corn meal by simultaneous enzymatic saccharification and fermentation with immobilized cells of Saccharomyces cerevisiae var. ellipsoideus, Fuel **88**, 1602–1607 (2009)

22.12 C.M. Moore, S.D. Minteer, R.S. Martin: Microchip-based ethanol/oxygen biofuel cell, Lab on a Chip **5**(3), 218–225 (2004)

22.13 P. Santhosh, K.M. Manesh, S.-H. Lee, S. Uthayakumar, A.I. Gopalan, K.-P. Lee: Sensitive electrochemical detection of superoxide anion using gold nanoparticles distributed poly(methyl methacrylate)-polyaniline core-shell electrospun composite electrode, Analyst **136**, 1557–1561 (2011)

22.14 M. Abramson, O. Shoseyov, Z. Shani: Plant cell wall reconstruction toward improved lignocellulosic production and processability, Plant Sci. **178**, 61–72 (2009)

22.15 V. Svoboda, M. Cooney, B.Y. Liaw, S. Minteer, E. Piles, D. Lehnert, S. Calabrese-Barton, R. Rincon, P. Atanassov: Standardized characterization of electrocatalytic electrodes, Electroanalysis **20**(10), 1099–1109 (2008)

22.16 A.V. Lygin, J. Upton, F.G. Dohleman, J. Juvik, O.A. Zabotina, J.M. Widholm, V.V. Lozovaya: Composition of cell wall phenolics and polysaccharides of the potential bioenergy crop-Miscanthus, GCB Bioenergy **3**, 333–345 (2011)

22.17 M.J. Moehlenbrock, R.L. Arechederra, K. Sjoholm, S.D. Minteer: Analytical techniques for characterizing enzymatic biofuel cells, Anal. Chem. **81**, 9538–9545 (2009)

22.18 A.T. Yahiro, S.M. Lee, D.O. Kimble: Bioelectrochemistry. I. enzyme utilizing biofuel cell studies, Biochim. Biophys. Acta **88**(2), 375–383 (1964)

22.19 G. Palmore, G.M. Whitesides: Microbial and enzymatic biofuel cells, ACS Symp. Ser. **566**, 271–290 (1994)

22.20 Z. He, L.T. Angenent: Application of bacterial biocathodes in microbial fuel cells, Electroanalysis **18**(19–20), 2009–2015 (2006)

22.21 Y. Li, R. Yuan, Y. Chai, Z. Song: Electrodeposition of gold-platinum alloy nanoparticles on carbon nanotubes as electrochemical sensing interface for sensitive detection of tumor marker, Electrochim. Acta **56**, 6715–6721 (2011)

22.22 S.C. Wang, A. Patlolla, Z. Iqbal: Carbon nanotube-based, membrane-less and mediator-free enzymatic biofuel cells, ECS Transactions **19**, 55–60 (2009)

22.23 L. Deng, L. Shang, D. Wen, J.-F. Zhai, S.-J. Dong: A membraneless biofuel cell powered by ethanol and alcoholic beverage, Biosens. Bioelectron. **26**, 70–73 (2010)

22.24 R.L. Arechederra, K. Boehm, S.D. Minteer: Mitochondrial bioelectrocatalysis for biofuel cell applications, Electrochimica. Acta **54**(28), 7268–7273 (2009)

22.25 K. Mizutani, M. Toyoda, K. Sagara, N. Takahashi, A. Sato, Y. Kamitaka, S. Tsujimura, Y. Nakanishi, T. Sugiura, S. Yamaguchi, K. Kano, B. Mikami: X-ray analysis of bilirubin oxidase from myrothecium verrucaria at 2.3 Å resolution using a twinned crystal, Acta. Crystallogr. F **66**, 765–770 (2010)

22.26 C.M. Eggleston, J. Voeroes, L. Shi, B.H. Lower, T.C. Droubay, P.J.S. Colberg: Binding and direct electrochemistry of OmcA, an outer-membrane cytochrome from an iron reducing bacterium, with oxide electrodes: A candidate biofuel cell system, Inorg. Chim. Acta **361**, 769–777 (2008)

22.27 X. Wang, J. Wang, H. Cheng, P. Yu, J. Ye, L. Mao: Graphene as a spacer to layer-by-layer assemble electrochemically functionalized nanostructures for molecular bioelectronic devices, Langmuir **27**, 11180–11186 (2011)

22.28 P. Addo, R. Arechederra, S.D. Minteer: Towards a rechargeable alcohol biobattery, J. Power Sources **196**, 3448–3451 (2011)

22.29 S.C. Barton, J. Gallaway, P. Atanassov: Enzymatic biofuel cells for implantable and microscal devices, Chem. Rev. **104**, 4867–4886 (2004)

22.30 Z. Du, H. Li, T. Gu: A State of the art review on microbial fuel cells: A promising technology for wastewater treatment and bioenergy, Biotechnol. Adv. **25**, 464–482 (2007)

22.31 M.J. Cooney, V. Svoboda, C. Lau, G.P. Martin, S.D. Minteer: Enzyme catalysed biofuel cells, Energy Environ. Sci. **1**, 320–337 (2008)

22.32 E.F. Ferapontova, L. Gorton: Direct electrochemistry of heme multicofactor-containing enzymes on alkanethiol-modified gold electrodes, Bioelectrochem. **66**, 55–63 (2005)

22.33 L. Gorton, A. Lindgren, T. Larsson, F.D. Munteanu, T. Ruzgas, I. Gazaryan: Direct electron transfer between heme-containing enzymes and electrodes as basis for third generation biosensors, Analyt. Chimica. Acta **400**(1–3), 91–108 (1999)

22.34 K. Karnicka, K. Miecznikowski, B. Kowalewska, M. Skunik, M. Opallo, J. Rogalski, W. Schuhmann, P.J. Kulesza: ABTS-modified multiwalled carbon nanotubes as an effective mediating system for bioelectrocatalytic reduction of oxygen, Anal. Chem. **80**, 7643–7648 (2008)

22.35 L. Stoica, T. Ruzgas, R. Ludwig, D. Haltrich, L. Gorton: Direct electron transfer-A favorite electron route for cellobiose dehydrogenase (CDH) from trametes villosa. Comparison with CDH from phanerochaete chrysosporium, Langmuir **22**(25), 10801–10806 (2006)

22.36 M. Zhou, X. Zheng, J. Wang, S. Dong: A self-powered and reusable biocomputing security keypad lock system based on biofuel cells, Chemistry **16**, 7719–7724 (2010)

22.37 G. Gupta, C. Lau, B. Branch, V. Rajendran, D. Ivnitski, P. Atanassov: Direct bio-electrocatalysis by multi-copper oxidases: Gas-diffusion laccase-catalyzed cathodes for biofuel cells, Electrochim. Acta **56**, 10767–10771 (2011)

22.38 S. Shleev, J. Tkac, A. Christenson, T. Ruzgas, A.I. Yaropolov, J.W. Whittaker, L. Gorton: Direct electron transfer between copper-containing proteins and electrodes, Biosens. Bioelectron. **20**(12), 2517–2554 (2005)

22.39 W. Zheng, Q. Li, L. Su, Y. Yan, J. Zhang, L. Mao: Direct electrochemistry of multi-copper oxidases at carbon nanotubes noncovalently functionalized with cellulose derivatives, Electroanalysis **18**(6), 587–594 (2006)

22.40 H. Zhou, T.-H. Lu, H.-X. Shi, Z.-H. Dai, X.-H. Huang: Direct electrochemistry and electrocatalysis of catalase immobilized on multi-wall carbon nanotubes modified glassy carbon electrode and its application, J. Electroanal. Chem. **612**, 173–178 (2008)

22.41 R.A. Rincón, K. Artyushkova, M. Mojica, M.N. Germain, S. Minteer, P. Atanassov: Structure and electrochemical properties of electrocatalysts for NADH oxidation, Electroanalysis **22**(7–8), 799–806 (2010)

22.42 A.A. Karyakin, E.E. Karyakina, W. Schuhmann, H.L. Schmidt: Electropolymerized azines: Part II. In a search of the best electrocatalyst of NADH oxidation, Electroanalysis **11**(8), 553–557 (1999)

22.43 D.-M. Zhou, H.-Q. Fang, H.-Y. Chen, H.-X. Ju, Y. Wang: The electrochemical polymerization of methylene green and its electrocatalysis for the oxidation of NADH, Analyt. Chim. Acta **329**, 41–48 (1996)

22.44 Y. Wang, C. You, S. Zhang, J. Kong, J.L. Marty, D. Zhao, B. Liu: Electrocatalytic oxidation of NADH at mesoporous carbon modified electrodes, Microchim. Acta **167**, 75–79 (2009)

22.45 C.-X. Cai, H.-X. Ju, H.-Y. Chen: Catalytic oxidation of reduced nicotinamide adenine dinucleotide at a microband gold electrode modified with nickel hexacyanoferrate, Analyt. Chim. Acta **310**, 145–151 (1995)

22.46 B.L. Treu, D.S. Minteer: Isolation and purification of PQQ-dependent lactate dehydrogenase from gluconobacter and use for direct electron transfer at carbon and gold electrodes, Bioelectrochemistry **74**(1), 73–77 (2008)

22.47 Y. Tan, W. Deng, Y. Li, Z. Huang, Y. Meng, Q. Xie, M. Ma, S. Yao: Polymeric bionanocomposite cast thin films with in-situ laccase-catalyzed polymerization of dopamine for biosensing and biofuel cella Applications, J. Phys. Chem. B **114**, 5016–5024 (2010)

22.48 F. Durand, C. Stines-Chaumeil, V. Flexer, I. Andre, N. Mano: Designing a highly active soluble PQQ-glucose dehydrogenase for efficient glucose biosensors and biofuel cells, Biochem. Biophys. Res. Commun. **402**, 750–754 (2010)

22.49 J.L. Kerr, S.D. Minteer: Soybean oil biofuel cell: Utilizing lipoxygenase immobilized by modified Nafion to catalyze the oxidation of fatty acids for biofuel cells, ACS Symp. Ser. **986**, 334–353 (2008)

22.50 O. Courjean, N. Mano: Recombinant glucose oxidase from penicillium amagasakiense for efficient bioelectrochemical applications in physiological conditions, J. Biotechnol. **151**, 122–129 (2011)

22.51 T.K. Tam, M. Ornatska, M. Pita, S. Minko, E. Katz: Polymer brush-modified electrode with switchable and tunable redox activity for bioelectronic applications, J. Phys. Chem. C **112**, 8438–8445 (2008)

22.52 J.Y. Lee, H.Y. Shin, S.W. Kang, C. Park, S.W. Kim: Use of bioelectrode containing DNA-wrapped single-walled carbon nanotubes for enzyme-based biofuel cell, J. Power Sources **195**, 750–755 (2010)

22.53 I.T. Bae: Detection of reaction products at DMFC cathodes by ATR-IR spectroscopy and mass spectrometry, J. Electrochem. Soc. **153**(11), A2091–A2097 (2006)

22.54 P. Gao, I.C. Chang, Z. Zhou, M.J. Weaver: Electrooxidation pathways of simple alcohols at platinum in pure nonaqueous and concentrated aqueous environments as studied by real-time FTIR spectroscopy, J. Electroanal. Chem. **272**, 161–178 (1989)

22.55 A. Zebda, C. Gondran, G.A. Le, M. Holzinger, P. Cinquin, S. Cosnier: Mediatorless high-power glucose biofuel cells based on compressed carbon nanotube-enzyme electrodes, Nat. Commun. **2**, 370 (2011)

22.56 S. Xu, S.D. Minteer: Enzymatic biofuel cell for oxidation of glucose to CO2, ACS Catalysis **2012**(2), 91 (2012)

22.57 F. Tasca, W. Harreither, R. Ludwig, J.J. Gooding, L. Gorton: Cellobiose dehydrogenase aryl diazonium modified single walled carbon nanotubes: Enahnced direct electron transfer through a positively charged surface, Anal. Chem. **83**(8), 3042–3049 (2011)

22.58 F.A. Armstrong, G.S. Wilson: Recent developments in faradaic bioelectrochemistry, Electrochim. Acta **45**(15–16), 2623–2645 (2000)

22.59 R.L. Arechederra, S.D. Minteer: Kinetic and transport analysis of immobilized oxidoreductases that oxidize glycerol and its oxidation products, Electrochim. Acta **55**, 7679–7682 (2010)

22.60 N. Mano, H. Kim, Y. Zhang, A. Heller: An oxygen cathode operating in a physiological solution, J. Am. Chem. Soc. **124**(22), 6480–6486 (2002)

22.61 B. Su, J. Tang, H. Chen, J. Huang, G. Chen, D. Tang: Thionine/nanogold multilayer film for electrochemical immunoassay of alpha-fetoprotein in human serum using biofunctional double-codified gold nanoparticles, Anal. Methods **2**, 1702–1709 (2010)

22.62 C.P. Andrieux, J. Saveant: Kinetics of electrochemical reactions mediated by redox polymer films: Pre-activation mechanisms, J. Electroanal. Chem. **171**, 65–93 (1984)

22.63 C.P. Andrieux, O. Haas, J.M. Saveant: Catalysis of electrochemical reactions at redox-polymer-coated electrodes. Mediation of the iron(III)/iron(II) oxido-reduction by a polyvinylpyridine polymer containing coordinatively attached bisbipyridine chlororuthenium redox centers, J. Am. Chem. Soc. **108**(26), 8175–8182 (1986)

22.64 J. Leddy, A.J. Bard, J.T. Maloy, J. Saveant: Kinetics of film-coated electrodes, J. Electroanal. Chem. **187**, 205–227 (1985)

22.65 N.J. Forrow, S.J. Walters: Transition metal half-sandwich complexes as redox mediators to glucose oxidase, Biosens. Bioelectron. **19**(7), 763–770 (2004)

22.66 J.M. Ziegelbauer, T.S. Olson, S. Pylypenko, F. Alamgir, J. Jaye, P. Atanassov, S. Mukerjee: Direct spectroscopic observation of the structural origin of peroxide generation from co-based pyrolyzed porphyrins for ORR applications, J. Phys. Chem. **112**, 8839–8849 (2008)

22.67 M.J. Moehlenbrock, M.T. Meredith, S.D. Minteer: Bioelectrocatalytic oxidation of glucose in CNT impregnated hydrogels: Advantages of synthetic enzymatic metabolon formation, ACS Catalysis **2**, 17–25 (2012)

22.68 C. Tanne, G. Goebel, F. Lisdat: Development of a (PQQ)-GDH-anode based on MWCNT-modified gold and its application in a glucose/02-biofuel cell, Biosens. Bioelectron. **26**, 530–535 (2010)

22.69 I.Z. Kiss, V. Gaspar, L. Nyikos: Stability analysis of the oscillatory electrodissolution of copper with impedance spectroscopy, J. Phys. Chem. A **102**(6), 909–914 (1998)

22.70 N.L. Akers, C.M. Moore, S.D. Minteer: Development of alcohol/O_2 biofuel cells using salt-extracted tetrabutylammonium bromide/Nafion membranes to immobilize dehydrogenases enzymes, Electrochim. Acta **50**(12), 2521–2525 (2005)

22.71 K.G. Lim, G.T.R. Palmore: Microfluidic biofuel cells: The influence of electrode diffusion layer on performance, Biosens. Bioelectron. **22**(6), 941–947 (2007)

22.72 M. Vijay, R.M. Meyyappan: Electricity generation and effect of catholyte in a dual chambered microbial fuel cell using Klebsiella pneumoniae as biocatalyst, Indian J. Environ. Ecoplann. **15**, 9–14 (2008)

22.73 M. Armand, F. Endres, D.R. MacFarlane, H. Ohno, B. Scrosati: Ionic-liquid materials for the electrochemical challenges of the future, Nat. Mater. **8**, 621–629 (2009)

22.74 P. Du, P. Wu, C. Cai: A glucose biosensor based on electrocatalytic oxidation of NADPH at single-walled carbon nanotubes functionalized with poly (nile blue A), J. Electroanal. Chem. **624**, 21–26 (2008)

23. Energy Conversion Based on Bio(electro)catalysts

Tanja Vidaković-Koch

Redox enzymes can be efficiently coupled with an electrode surface giving prospect of highly efficient and selective bio(electrochemical) transformations for energy conversion and/or production of commodities or fine chemicals. One example is glucose oxidase that immobilized on the electrode surface and in the presence of glucose and oxygen reduction cathode generates electricity and D-glucono-1,5-lactone with applications in different industries. Other examples might comprise whole enzymatic cascades performing complex sequences of biochemical reactions, turning, for example, such inert and environmentally polluting substances (like CO_2) into useful commodities (e.g., methanol). These processes have a significant potential for development of new enzyme-based production systems, with electrochemistry playing an important role, especially regarding electrochemical regeneration of redox enzymes (redox cofactors). Although the electrochemical regeneration is feasible, its efficiency is still too low to be considered competitive for industrial applications. In this contribution we consider some important aspects of electrochemical regeneration of enzymes and common co-factors. At first, working principles of two typical representatives of bioelectrochemical systems will be described, followed by a short discussion of so-called cell free systems and their relationship to bioelectrochemical systems. For practical development of bioelectrochemical systems, the thermodynamics of related processes as well as kinetics are important. We give some examples of enzymes showing reversible electrode behavior, as an inspiration. Mathematical modeling will play a significant role in the design and optimization of bioelectrochemical systems. For this reason, we show how nonlinear mathematical models for studying the kinetics ofenzymatic processes can be developed. Finally, we discuss some practical aspects of biotransformation with redox enzymes, including examples of electron transfer mechanisms, enzyme adaptation on process conditions, development of electrodes etc.

23.1 **Working Principles of Bioelectrochemical Systems** 758
23.1.1 Enzymatic Fuel Cells 758
23.1.2 Electrolytic Biochemical Systems 758
23.2 **Bioelectrochemical Systems in Cell-Free Systems** 758
23.3 **General Aspects** 760
23.3.1 Thermodynamics 760
23.3.2 Mechanism of Bioelectrochemical Transformation 763
23.3.3 Reaction Kinetics 764
23.3.4 Balance Equations 766
23.3.5 Determination of Enzyme Coverage 767
23.3.6 Determination of Kinetic Parameters 769
23.4 **Biotransformation with Redox Enzymes** 770
23.4.1 Enzymes Showing DET 770
23.4.2 FAD- and NAD-Dependent Enzymes 771
23.5 **Conclusions and Outlook** 774
References 774

23.1 Working Principles of Bioelectrochemical Systems

Bioelectrochemical systems combine the high catalytic activity and selectivity of biological elements (e.g., enzymes, microorganisms) and the virtue of electrochemistry. Two typical representatives of these systems are an enzymatic fuel cell and a bioelectrochemical electrolytic system. The working principles of these two systems are shortly shown below.

23.1.1 Enzymatic Fuel Cells

Enzymatic fuel cells use fuel (e.g., glucose, methanol, H_2) and oxygen to *produce* energy in the form of electricity, CO_2, and water. The overall cell reaction is similar as in the case of cellular respiration (Fig. 23.1a), except that the chemical energy of a fuel is converted into electrical energy and not into adenosine triphosphate (ATP). In addition in technical system, CO_2 will appear as a product only if carbon-containing fuels are utilized and completely oxidized, while in the case of hydrogen the end product will be only water. In an enzymatic fuel cell for fuel oxidation, a single enzyme or an enzyme cascade might be employed. This choice will determine the level of fuel oxidation, partial or total.

For example, in case of glucose enzymatic fuel cell glucose-oxidase is typically employed, resulting in a partial glucose oxidation. Another example is a methanol enzymatic fuel cell, where a multienzyme cascade comprising methanol dehydrogenase, formaldehyde dehydrogenase, and format dehydrogenase can be employed leading to total methanol oxidation. During these later biotransformations, reduced nicotinamide adenine dinucleotide (NADH), acting as an intermediate electron donor will be formed. NADH governs its flow of electrons to the electrode–anode (Fig. 23.1b). These electrons are then transferred to the second electrode, that is, the cathode by means of an outer electrical circuit. Electron flow, that is, electricity, can be further utilized in different electrical devices (laptops, mobiles etc.). At the cathode electrons are recombined with protons from solution and oxygen (final electron acceptor) by the virtue of an electrochemical reaction. This reaction requires also a catalyst, for example, an redox enzyme.

23.1.2 Electrolytic Biochemical Systems

In contrast to cellular respiration, during photosynthesis (Fig. 23.2a) sun energy is transformed into chemical energy, which is then stored in different organic compounds. In a similar way in a bioelectrochemical electrolytic system, electrical energy is transformed into chemical energy of, in the simplest case, hydrogen (water electrolysis) or more complex organic compounds. In an example shown below (Fig. 23.2b) enzymatic cascade is utilized for biotransformation of CO_2, while necessary redox equivalents (NADH) are supplied by an electrochemical reactor.

23.2 Bioelectrochemical Systems in Cell-Free Systems

As seen before, in bioelectrochemical systems, biological elements (enzymes) are employed for a specific engineering task without limitations induced by requirements of cellular system viability, they are so-called cell-free systems [23.1]. The term cell free covers all kinds of systems, where the cell wall and the native genomic deoxyribonucleic acid (DNA) are removed and a direct access to the biochemical network of the cell is enabled. In general, this leads to an increase in engineering flexibility, allowing an easier transport of reactants and products and easier monitoring. In addition, enzyme concentrations can be freely adjusted, and the system can be compartmentalized in a smart way in order to increase productivity. Furthermore, synthetic biochemical networks comprising enzymes from different organisms can be created, which adds up to system productivity. As interesting example is a proposal of synthetic CO_2 fixation pathways [23.2]. By using approximately 5000 metabolic enzymes known to occur in nature, *Bar-Even* et al. [23.2] were able to identify a synthetic carbon fixation pathway, which is predicted to be two to three times faster than the Calvin cycle [23.3]. The implementation of this designed carbon fixation cycle will hopefully follow.

The cell-free systems have high potential, but this potential has still to be proven in praxis, especially regarding the industrial application of these systems. Major disadvantages on the way for industrial applications are low enzyme stability under in-vitro conditions and requirements on process energy. The first point can be possibly tackled by using some strategies for enzyme immobilization and also by the virtue of enzyme engineering. Regarding the requirements on process energy which is especially critical in the case of redox enzymes, due to necessity of their regeneration (or regeneration of their redox factors), bioelectrochemistry, and electrochemical enzyme regeneration can possibly offer a solution.

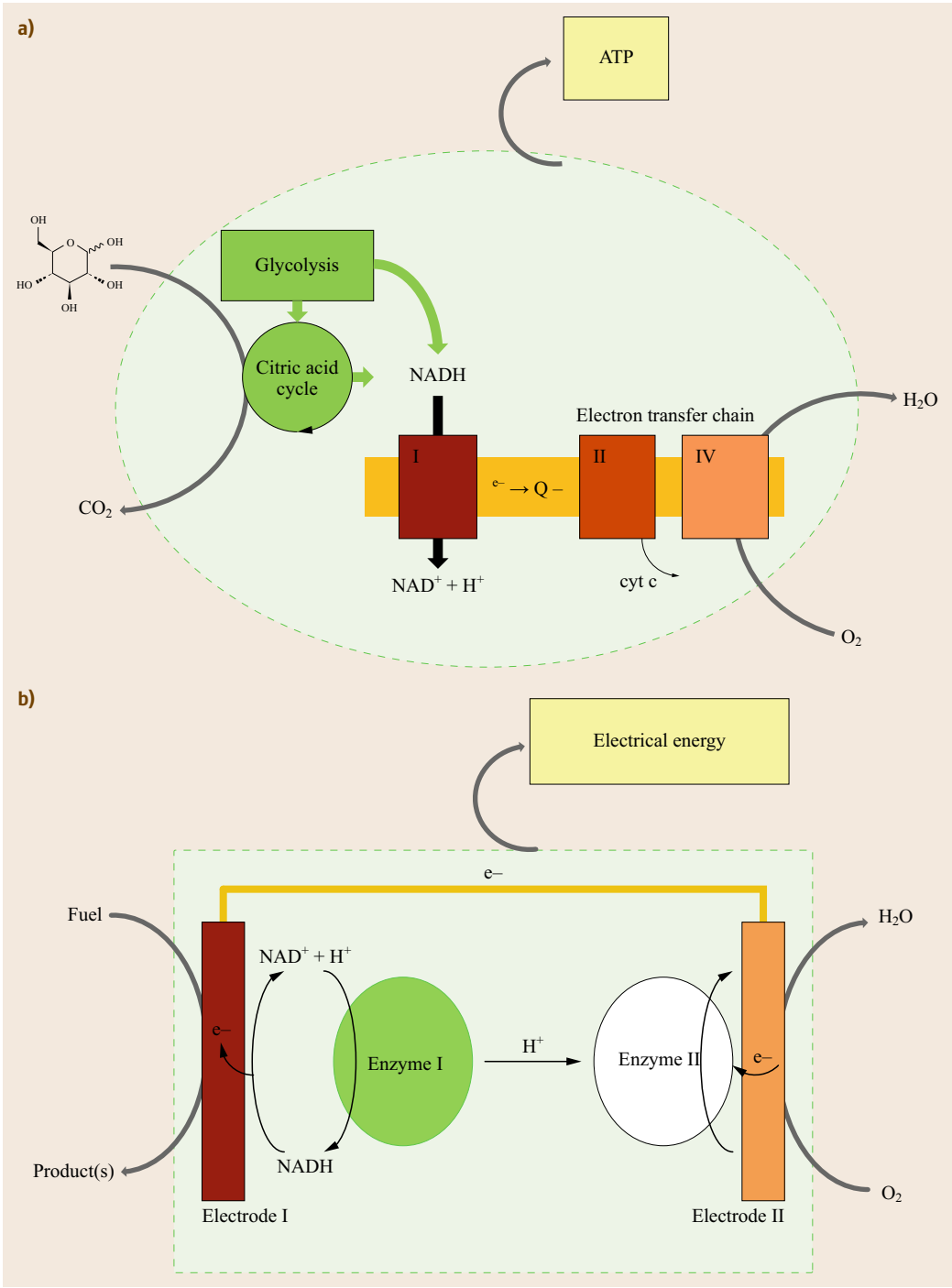


Fig. 23.1 (a) Schematic representation of a cellular respiration and (b) an enzymatic fuel-cell working principle

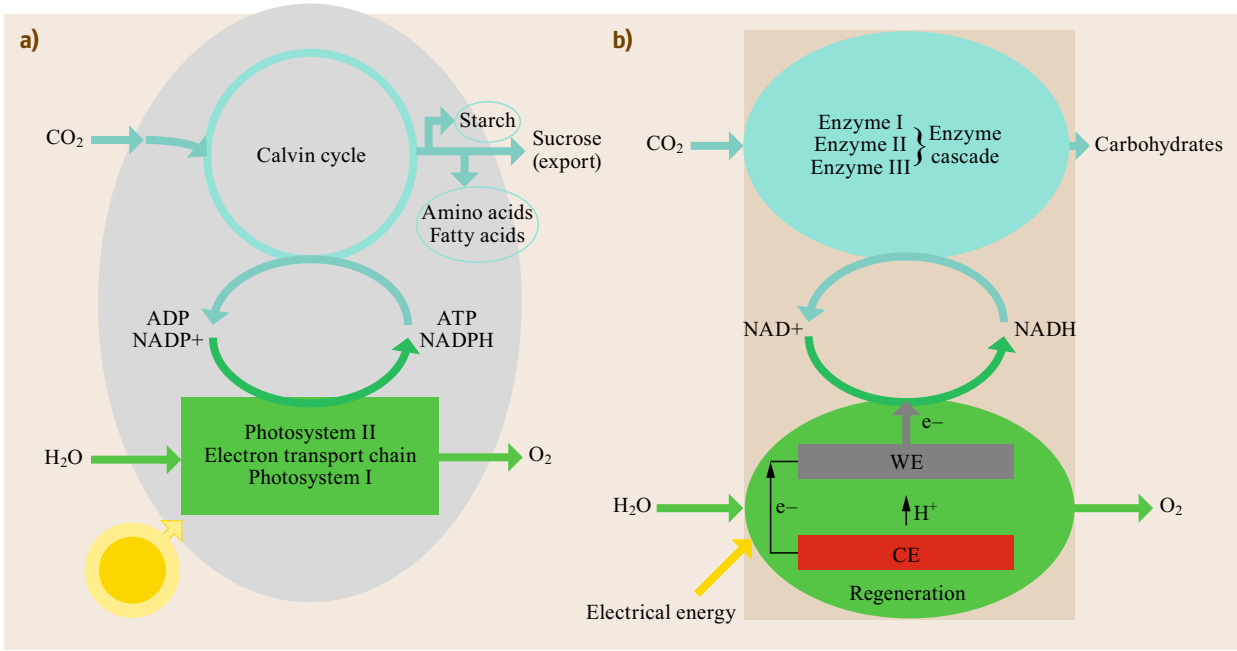


Fig. 23.2 **(a)** Schematic representation of photosynthesis and **(b)** a technical system employing multienzyme cascade for synthesis purpose

23.3 General Aspects

Electrochemical (bioelectrochemical) systems can be divided into two groups: galvanic and electrolytic. Galvanic systems are spontaneous. Enzymatic fuel cells belong obviously to this group. Electrolytic systems are not spontaneous and they require an energy input for an overall reaction to take place. These systems convert electrical energy into chemical energy. In this section, we give some examples regarding the thermodynamics of some enzymes. Clearly, all these examples consider enzymes or cofactors (NAD), which can exchange electrons directly with the electrode surface (so called direct electron transfer (DET)) mechanism. In the second part we show how a nonlinear model for studying of enzyme kinetics can be developed. Finally we discuss the importance of enzyme coverage determination for accurate kinetic constants estimation.

23.3.1 Thermodynamics

We consider the well-known reaction

$$H_2 + O_2 = H_2O(l) \qquad (23.1)$$

which is an overall cell reaction in different types of fuel cells. Examples are low-temperature polymer electrolyte fuel cell, phosphoric acid fuel cell, and alkaline fuel cell. These fuel cell types differ mainly in a type of electrolytes (e.g., solid polymer electrolyte, phosphoric acid, and alkaline electrolyte) and a type of catalysts. Usually noble metal catalysts like platinum or its alloys are employed. In the case of an enzymatic fuel cell, enzymatic catalysts like hydrogenase and bilirubin-oxidase can be employed. The choice of catalysts does not influence the fuel-cell thermodynamics. The standard Gibbs free energy change for reaction (23.1) is -237.1 KJ/mol. By using the relation between a Gibbs free energy change and an electrical work

$$\Delta G = -nFU_r\,, \qquad (23.2)$$

where ΔG is a Gibbs free energy change, n is number of electrons, and F is Faraday's constant, one can calculate the value of the theoretical cell voltage (U_r) for hydrogen oxidation. Under standard conditions this value is 1.23 V and it can be considered as an upper limit of the achievable cell voltage under real conditions. It should correspond to the experimentally measured value under conditions of zero current flow, so-called open-circuit voltage. In praxis this is rarely the case. Theoretical cell voltage or theoretical electrode potential has been experimentally obtained only in the case of very fast reactions or under high-temperature conditions. In the

case of hydrogen/oxygen fuel cell, hydrogen kinetics

$$2H^+ + 2e^- = H_2 \qquad (23.3)$$

is very fast and it establishes its equilibrium conditions, on some electrode materials, easily. The theoretical electrode potential of a hydrogen reaction depends on pH value, hydrogen gas pressure, and temperature in accordance to

$$E(H^+/H_2) = E^\theta(H^+/H_2) + \frac{RT}{2F}\ln\frac{a_{H^+}^2}{p_{H_2}} . \qquad (23.4)$$

If we consider unit hydrogen partial pressure and 25 °C, (23.4) will reduce to

$$E(H^+/H_2) = 0.0\,V - 0.059\,pH . \qquad (23.5)$$

In Fig. 23.3 the experimental data for a hydrogen reaction in a three-electrode electrochemical cell using platinum catalyst and in the presence of hydrogen dissolved in an acid aqua solution are shown. As can be seen, the reaction establishes easily its equilibrium which corresponds to the theoretically expected 0.0 V versus standard hydrogen electrode (SHE) under these experimental conditions (pH = 0). Similar has been observed for an enzymatically catalyzed hydrogen reaction. Open circuit potential value close to theoretically expected −0.354 V (pH 6, room temperature) have been measured in case of the enzyme *Escherichia coli* hydrogenase-2 physically adsorbed on the graphite electrode (Fig. 23.3b) [23.4].

This enzyme has a nickel–iron [Ni–Fe] active center and three [Fe–S] clusters, which are believed to be responsible for the electron transfer from the Ni–Fe center (where catalytic event occurs) to the electrode. In addition to electron channeling mechanism, another important condition for the reversibility of an enzyme catalyzed reaction seems to be an enzyme ability of bi-directional catalysis.

Although enzymes are by nature designated as bi-directional catalyst, some enzymes show significant difference between forward and backward reaction rates, they are so-called *one-way enzymes* [23.5]. This can be seen also in Fig. 23.3b, where the *E. coli* hydrogenase 1 behaves in such a way showing significant overpotential for hydrogen oxidation reaction. This asymmetry, was recently studied on an example of *Desulfovibrio fructosovorans* (Df) [Ni–Fe] hydrogenase and its mutants [23.5]. They showed that the wild type has symmetrical activity toward both hydrogen oxidation and evolution reaction, while mutants were more active toward hydrogen oxidation. Practically, the one-directional mutant showed more positive open-circuit potential, compared to the theoretical value. The authors discussed that the catalytic cycle of hydrogenase involves various steps (substrate binding, product release, proton and electron transfer active site chemistry). The reason for different activity of enzymes in forward and backward directions might be different nature of rate-determining step in these two directions. The authors concluded that other catalytic steps rather than the active site chemistry were responsible for ob-

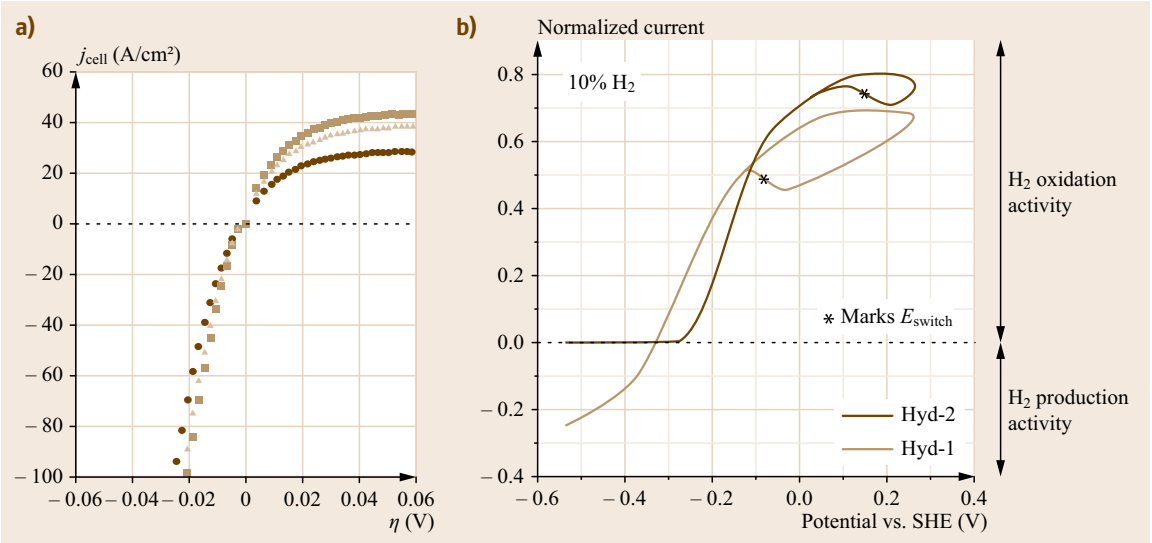


Fig. 23.3 **(a)** Steady-state polarization curves for hydrogen reaction on a platinum rotating disk electrode at three different rotation rates, and pH 0 and room temperature, **(b)** cyclic voltammograms of *E. coli* hydrogenase 1 and 2 at pH 6 and 30 °C (after [23.4])

served effects and they pointed out the necessity of studying whole mechanism and not only active site chemistry.

Another enzyme that shows reversible electrode behavior is *E. coli* fumarate reductase. This enzyme has a flavin adenine dinucleotide (FAD) active center and [Fe–S] clusters, which enable the electron transfer to the electrode surface [23.6]. This example demonstrates nicely the dependence of the FAD redox potential on the type of the enzyme. In addition, observed change of the FAD redox potential with concentration of reacting species, shows that the equilibrium of this reaction is dependent on the kinetics of preceding steps (enzymatic catalytic event).

To summarize, based on the mentioned examples, in the case of enzymatic catalysts the open-circuit potential depends not only on active site properties and electron channeling but also on concentration of reacting species and kinetics of all involved steps.

We consider further an example of nicotinamide adenine dinucleotide (NAD) dependent enzyme. Unlike before mentioned active centers, NAD is a soluble cofactor for large number of redox enzymes. An example is alcohol dehydrogenase (ADH), which catalyzes the ethanol oxidation

$$CH_3CH_2OH + ADH_{ox} = CH_3CHO + ADH_{red} \,. \tag{23.6}$$

Since the redox process takes place effectively at the NAD cofactor, (23.6) reaction can be rewritten as

$$CH_3CH_2OH + NAD^+ = CH_3CHO + NADH \,. \tag{23.7}$$

In the next step NAD can be regenerated at the electrode surface in accordance to

$$NADH = NAD^+ + H^+ + 2e^- \,. \tag{23.8}$$

According to thermodynamic data, the theoretical electrode potential for this reaction is $-0.32\,V$. This reaction proceeds on most known materials with significant overpotential. There are, however, some exceptions. For example a reversible NAD reaction was reported by *Karykin* et al. [23.8] using neutral red catalyst. It was also observed by using a hydrophilic domain of mitochondrial complex [23.7]. In both examples, the NAD reaction was not coupled with an enzymatic event (23.7).

Unlike previous examples, the oxygen reaction

$$O_2 + 4e^- + 4H^+ = H_2O \tag{23.9}$$

is rather slow on most electrode materials and does not establish its equilibrium conditions, neither in the presence of noble metal or enzymatic catalyst. The oxygen reaction is much more complicated than the previously

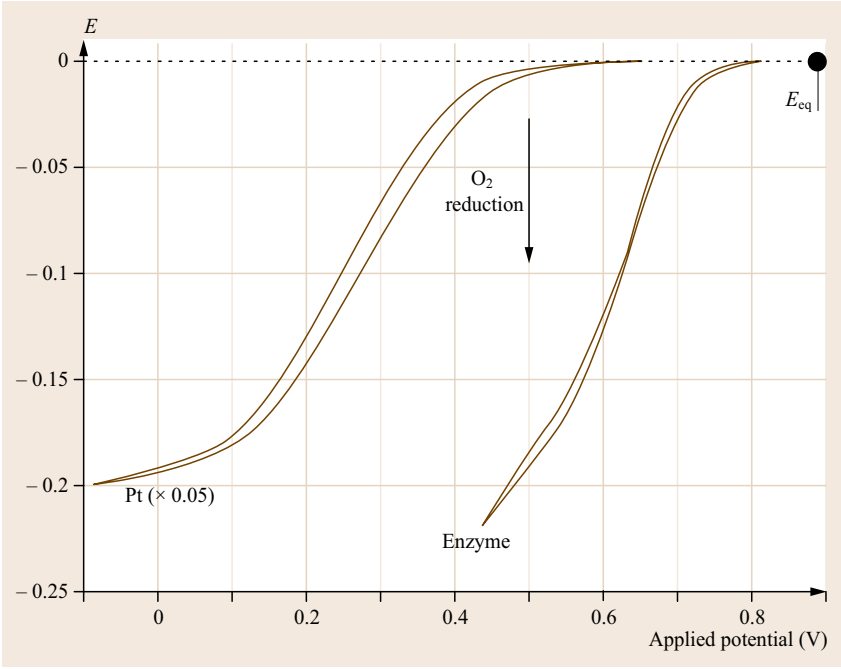


Fig. 23.4 Polarization curves for oxygen reduction in the presence of platinum and bilirubin oxidase electrocatalysts at pH 5.8 and 20 °C. The original Pt currents have been multiplied by 0.05 to facilitate comparison (after [23.7])

discussed examples since it involves the transfer of four electrons and four protons. It is still considered not completely understood in the electrochemical community. If one follows the same reasoning as in the case of hydrogen or succinate, an ideal catalyst for oxygen reaction should be able to catalyze equally fast both the forward reaction (formation of water) and the backward reaction (oxygen evolution). In praxis at all known catalysts this is not the case. One reason is that the usual metal catalysts are subjected to change their self under conditions where the theoretical equilibrium of this reaction is expected; for example, platinum in this region is covered by oxide, which has no activity for an oxygen reduction reaction. The reaction starts only after the oxide reduction. Enzymatic catalysts at neutral pH conditions can establish an open-circuit potential value closer to the theoretical equilibrium than the metal catalysts as shown in Fig. 23.4.

From this discussion, it is obvious that neither noble metal nor an enzymatic fuel cell can establish theoretical value of cell voltage.

23.3.2 Mechanism of Bioelectrochemical Transformation

In general, bioelectrochemical transformations comprise biochemical and electrochemical steps. A biochemical (enzymatic) step is commonly described by the *Briggs–Haldane* mechanism [23.9], which is more generalized formulation of Michaelis–Menten mechanism, including explicitly the rate constants of forward and backward reactions of enzyme substrate (ES) formation

$$E_{ox} + R \overset{k_1/k_{-1}}{\longleftrightarrow} ER\,, \tag{23.10}$$

$$ER \xrightarrow{k_2} E_{red} + P\,. \tag{23.11}$$

In a given example, the overall biotransformation (23.10) and (23.11) leads to oxidation of reactant (also called substrate) R to product P, while the enzyme (E_{ox}) is reduced to E_{red}. To regain its catalytic function, the enzyme has to be regenerated into its original state (E_{ox}). In nature, the enzyme regeneration is provided by a second biotransformation with a help of a so-called second substrate, for example, oxygen that oxidizes the enzyme (more precisely its catalytic center) and return it into its native state (Fig. 23.5).

The role of this second substrate in the case of a bioelectrochemical process is taken by an electrode itself. The action of the electrode on an enzyme is indirect (so-called mediated) or direct and depends on enzyme properties as well as on the catalytic properties of the electrode. Based on this, redox enzymes can be divided into two groups. The first group comprises the enzymes that cannot directly communicate with an electrode. These enzymes can be regenerated only in accordance to the mechanism presented in Fig. 23.5, that is, by

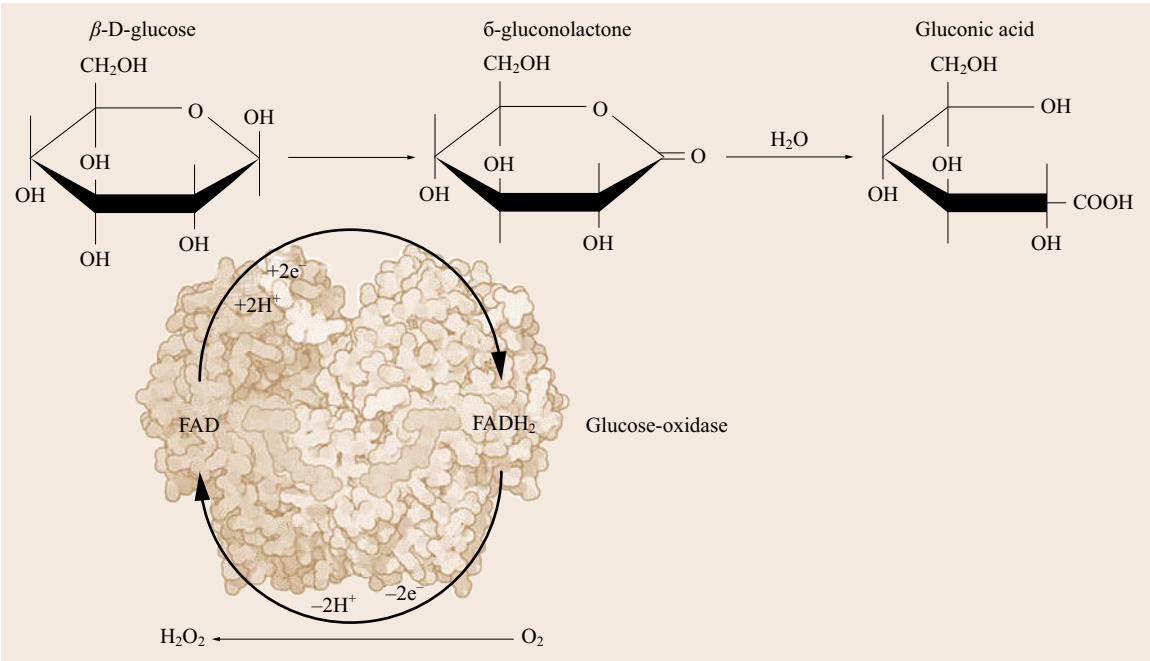


Fig. 23.5 Natural cycle of glucose-oxidase catalyzed glucose oxidation

a second substrate. The mechanism of this biotransformation follows also Briggs–Haldane proposal

$$E_{red} + M_{ox} \overset{k_3/k_{-3}}{\longleftrightarrow} EM \,, \tag{23.12}$$

$$EM \overset{k_4}{\longrightarrow} E_{ox} + M_{red} \,. \tag{23.13}$$

In the literature, these two steps are usually lumped together giving

$$E_{red} + M_{ox} \overset{k_4}{\longrightarrow} E_{ox} + M_{red} \,. \tag{23.14}$$

This second substrate might be an enzyme natural substrate, but more often it is a substance, so-called mediator which can easily react with an enzyme, but also can be efficiently regenerated in a subsequent electrochemical step

$$M_{red} \underset{k_M/k_{-M}}{\longleftrightarrow} M_{ox} + e^- \,. \tag{23.15}$$

This mechanism of enzyme regeneration is called mediated electron transfer (MET) mechanism.

The second group of enzymes in addition to the above-described mode of regeneration can also react directly with an electrode. As already mentioned, this mechanism of enzyme regeneration is DET. In this case, instead of reactions (23.12)–(23.15) the following step occurs

$$E_{red} \underset{k_D/k_{-D}}{\longleftrightarrow} E_{ox} + e^- \,. \tag{23.16}$$

It should be kept in mind that the DET mechanism described by (23.16) in reality can involve the transfer of several electrons, intraelectron transfer steps and might be also accompanied by a proton transfer.

To summarize, in general, the biotransformation involving redox enzymes comprise the following steps

$$R_{bulk} \overset{\text{diffusion}}{\longrightarrow} R \tag{23.17}$$

mass transfer of the reactant,

$$E_{ox} + R \overset{k_1/k_{-1}}{\longleftrightarrow} ER \tag{23.18}$$

enzymatic reaction,

$$ER \overset{k_2}{\longrightarrow} E_{red} + P \,, \tag{23.19}$$

$$E_{red} \underset{k_D/k_{-D}}{\longleftrightarrow} E_{ox} + e^- \tag{23.20}$$

enzyme regeneration step,

$$P \overset{\text{diffusion}}{\longrightarrow} P_{bulk} \tag{23.21}$$

product diffusion away from the electrode surface.

One should keep in mind that any of these steps can be rate determining or several of them can have similar rates. The influence of different steps in the reaction mechanism on the total electrode response has been nicely experimentally demonstrated on an example of *A. vinosum* [Ni–Fe]-hydrogenase [23.6]. As it was already discussed, hydrogenases show a fast reversible electrode electrochemical behavior. However, depending on operating conditions different rate-determining steps might become operative. In a first example one can see that the reaction reaches fast a limiting current behavior (Fig. 23.6a). The strong dependence of the limiting current on the electrode rotation rate indicates mass transfer limitations. In another example of the same enzyme but at elevated temperature, no limiting current behavior was observed. Instead, the current was increasing linearly in a broader potential range. The authors ascribed this phenomenon to the dispersion in enzyme orientation on the electrode surface and hence the dispersion of the rate constants determining the electron transfer rate between an enzyme and an electrode (Fig. 23.6b). If the enzyme coverage at the electrode surface was very low, a limiting current behavior was also observed (Fig. 23.6c). In this case, the reason for leveling off of the current was not mass transfer but the kinetics of the enzymatic reaction.

23.3.3 Reaction Kinetics

Based on the proposed mechanisms for MET and DET, one can formulate rate expressions for single-reaction steps. For the enzyme kinetic steps (23.10)–(23.11) it follows:

$$r_1 = k_1 E_{ox} R - k_{-1} ER \,, \tag{23.22}$$

$$r_2 = k_2 ER \,. \tag{23.23}$$

Similarly for enzyme mediator reaction steps (23.14) follows

$$r_4 = k_4 E_{red} M_{ox} \,. \tag{23.24}$$

To describe the electrochemical mediator regeneration kinetics, Butler–Volmer (BV) formalism can be used

$$r_5 = \underbrace{k_{M,0} \exp\left(\alpha \frac{\eta F}{RT}\right)}_{k_{M,\text{electro}}} M_{red} - \underbrace{k_{-M,0} \exp\left(-\beta \frac{\eta F}{RT}\right)}_{k_{-M,\text{electro}}} M_{ox} \,, \tag{23.25}$$

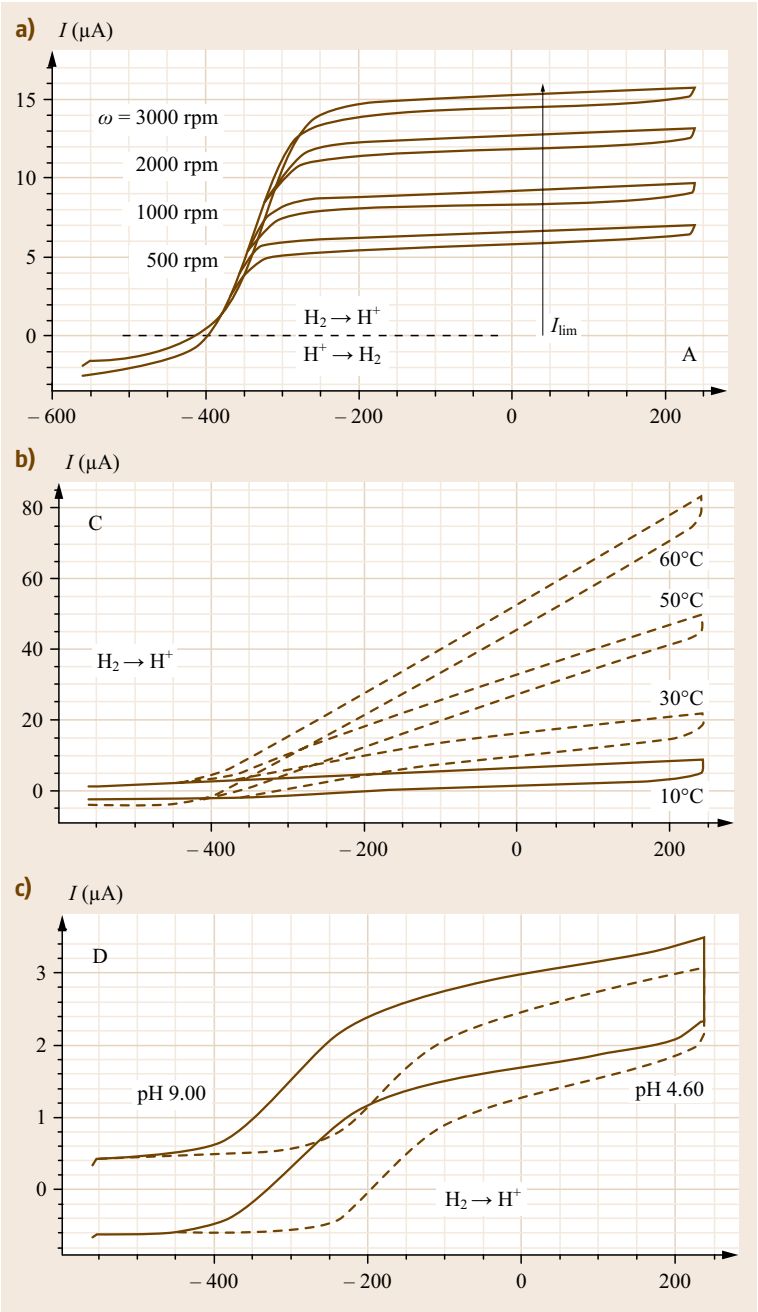


Fig. 23.6a–c Illustration of the different reaction step influence on overall kinetics: **(a)** mass transfer limitation (after [23.5]), **(b)** limitation by electrochemical step (after [23.6]), **(c)** limitation by enzymatic reaction; *x*-axis potential vs. SHE (after [23.6])

where $k_{M,0}$ and $k_{-M,0}$ are heterogeneous rate constants in m/s, M_{red} and M_{ox} are concentrations of reduced and oxidized forms of mediators in mol/m^3, α and β are transfer coefficients, η is the overpotential in V, R stands for universal gas constant in J/mol K, T for temperature, and F for Faraday's constant in C/mol. If the mediator is adsorbed in a thin layer at the electrode surface, the heterogeneous rate constants will have a unit of in s^{-1}, while the unit for concentration of mediator species will be mol/m^2.

Since the only electrochemical step is the mediator regeneration (23.15), the electrochemical current, expressed as a current density in A/m^2 will be defined as

$$j = Fr_5 \,. \tag{23.26}$$

If the transfer of more than one electron has been involved, the total number of exchanged electrons per mediator molecule will also appear in (23.26).

In the case of the DET (23.16), the rate expression can also be formulated in accordance with BV formalism

$$r_6 = \underbrace{k_{\mathrm{D},0}\exp\left(\alpha\frac{\eta F}{RT}\right)}_{k_{\mathrm{D,electro}}} E_{\mathrm{red}} - \underbrace{k_{-\mathrm{D},0}\exp\left(-\beta\frac{\eta F}{RT}\right)}_{k_{-\mathrm{D,electro}}} E_{\mathrm{ox}}\,, \tag{23.27}$$

where the constants have the similar meaning as already discussed for the mediator case. However, the electron transfer between an electrode and an enzyme is for obvious reasons more complicated than in the case of an electron transfer between relatively simple mediator molecules and the electrode. It has been shown that the DET kinetics can be simulated using BV approach but values of some parameters, like transfer coefficient, deviate a lot from typical values in electrochemical kinetics (e.g., transfer coefficient values about 0.2 and below have been reported). It is also known that the BV can be considered as a limiting case of the more theory sounded Markus relation for the electron transfer mechanism. According to Marcus theory, the two electrochemical constants in (23.27) can be expressed as follows [23.10]

$$k_{\mathrm{D,electro}} = k_{\mathrm{D},0}\exp\left(\frac{\eta F}{2RT} - \frac{\eta^2 F}{4\lambda RT}\right)\,, \tag{23.28}$$

$$k_{-\mathrm{D,electro}} = k_{-\mathrm{D},0}\exp\left(-\frac{\eta F}{2RT} - \frac{\eta^2 F}{4\lambda RT}\right)\,, \tag{23.29}$$

which can be rearranged into

$$k_{\mathrm{D,electro}} = k_{\mathrm{D},0}\exp\left[\frac{\eta F}{2RT}\left(1-\frac{\eta}{2\lambda}\right)\right]\,, \tag{23.30}$$

$$k_{-\mathrm{D,electro}} = k_{-\mathrm{D},0}\exp\left[-\frac{\eta F}{2RT}\left(1+\frac{\eta}{2\lambda}\right)\right]\,. \tag{23.31}$$

According to (23.30) and (23.31), the rate constants expressed in accordance to Marcus theory would reduce to BV case (23.27) if $\eta/\lambda << 1$. This condition is easily satisfied in the case of simple redox molecules like ferro/ferrycyanide. In the case of enzymes, reorganization energies are in the range of overpotential. For example, reorganization energies from 0.60–0.43 eV (pH 4.1–8.0) were determined for compound II of horseradish peroxidase (HRP) [23.11]. The further consequence of a low value of the reorganization energy is the dependence of the transfer coefficient α on potential, with values close to 0.5 only at overpotentials close to zero.

In (23.28)–(23.31), the distribution of the electronic states in the electrode was neglected. Taking this into account, following formulation of Marcus approach can be obtained [23.11]

$$k_{-\mathrm{D,electro}} = \frac{k_{-\mathrm{D},0}}{Y}\int_{-\infty}^{\infty}\frac{\exp\left(-\frac{(\xi_{\mathrm{F}}-\xi+e_0\eta+\lambda)^2}{4\lambda kT}\right)}{1+\exp\left(\frac{\xi-\xi_{\mathrm{F}}}{kT}\right)}\mathrm{d}\xi\,, \tag{23.32}$$

where Y is the value of the integral in (23.32) at $\eta = 0$, ξ is the energy of a given electronic state in the electrode, ξ_{F} is the energy of the Fermi level of the electrode, and k is the Boltzmann constant.

The Markus approach is mathematically more complicated than the BV approach and therefore commonly less used. One advantage of the Markus approach compared to BV is the possibility of the determination of the reorganization energy of the enzyme [23.11], which has more theoretical significance than the α value provided by BV.

In addition, the heterogeneous rate constant $k_{\mathrm{D},0}$ might show some dependence on enzyme orientation at the electrode surface [23.12], as was mentioned before. This effectively led to the distribution of the heterogeneous rate constant as

$$k_{\mathrm{D},0} = k_{\mathrm{D,max}}\exp(-\beta\, d)\,, \tag{23.33}$$

where d is the distance between the electrode surface and an enzyme-active center and β is a constant.

Similar to the case of MET the current in the DET case will be expressed as

$$j = F\, r_6\,. \tag{23.34}$$

23.3.4 Balance Equations

Still, to determine the current value in accordance to (23.26) (MET) or (23.34) (DET), one will have to determine the profiles of reduced and oxidized forms of the mediator (or enzyme) as a function of the electrode potential, which means that one has to add the balance equations to the model.

In the present case, there are two types of species to be balanced: at the electrode surface and in the solution. The material balance equations for adsorbed species is

$$\frac{\mathrm{d}A}{\mathrm{d}t} = r_i - r_{i+1}\,, \tag{23.35}$$

where A stands for the following species: ER, E_{red} and EM and index i for a number of a reaction step. Other balanced species (reactant R, product P, and mediator M) are usually present in solution and their concentration profiles can be obtained by solving the convection–diffusion equation. This equation has a very complicated form, but in case of some specific geometries like rotating disk electrode (RDE), which is often used to study the kinetics of electrochemical processes it simplifies to the one-dimensional form [23.13]

$$\frac{\partial c_i(z,t)}{\partial t} = D_i \frac{\partial^2 c_i(z,t)}{\partial z^2} - \upsilon_z \frac{\partial c_i}{\partial z} , \qquad (23.36)$$

where D_i is the diffusion coefficient, υ_z is the convective velocity in the direction perpendicular to the electrode surface, and the index i refers to R , P or M_{red}. Usually the convective contribution to mass transfer in (23.36) can be neglected. This approximation can be considered valid in the thin layer close to the electrode surface, the so-called Nernstian diffusion layer, where the υ_z velocity falls below 1% of its maximal value in the bulk and the diffusion becomes the main way of transport [23.13]. In this case, (23.36) simplifies to the second Fick's law

$$\frac{\partial c_i(z,t)}{\partial t} = D_i \frac{\partial^2 c_i(z,t)}{\partial z^2} . \qquad (23.37)$$

The boundary conditions for the solving of (23.37) are

$$z = 0 ,$$
$$D_i \left.\frac{\partial c_i(z,t)}{\partial z}\right|_{z=0} = r_i(t) , \qquad (23.38)$$

and $z = \delta_{D,i}$

$$c_i(\delta_{D,i}, t) = c_\infty ,$$

where

$$\delta_{D,i} = 1.61 D_i^{1/3} \nu^{1/6} \omega_r^{-1/2} \qquad (23.39)$$

is the thicknesses of the diffusion layer at rotation speed ω_r of the RDE in the solution of kinematic viscosity ν.

To complete the model, the charge balance at the electrode surface has to be formulated

$$C_{dl} \frac{dE(t)}{dt} = j(t) - Fr_5(t) , \qquad (23.40)$$

where C_{dl} is the double layer capacitance and $j(t)$ is the cell current density. In the case of DET instead of (23.25), (23.27) will be considered. In the case of steady-state conditions all derivate with time will become zero.

23.3.5 Determination of Enzyme Coverage

The model equations that we introduced can be further used to simulate the electrode response and for the determination of kinetic parameters. In this respect, the knowledge of the enzyme coverage at the electrode surface appears to be crucial, since all kinetic constants are dependent on the enzyme coverage. In most cases, there are no direct methods for the determination of the enzyme coverage. To circumvent this problem, basically two approaches regarding kinetic parameter determination were followed. In the first approach, an assumption on total enzyme concentration was made, while in the second one, kinetic parameter values were assumed. As an example in the case of HRP enzyme, *Ruzgas* et al. [23.14] approximated the total enzyme concentration, based on the literature results with proteins with similar molecular weight as HRP and an assumption of the electrode surface roughness. Similarly, *Ferapontova* and *Gorton* [23.15] also for HRP enzyme assumed total enzyme coverage of 23 pmol/cm^2 on Au electrode based on quartz crystal microbalance data. In the second approach, it was assumed that the enzyme activity at the electrode surface was the same as for the enzyme in the solution [23.11]. These different approaches resulted in different surface coverage, with

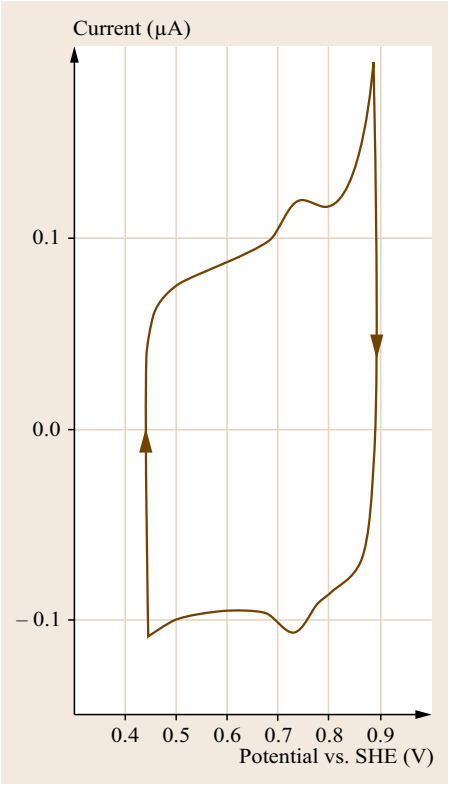


Fig. 23.7 Cyclic voltammogram of cytochrome c peroxidase modified pyrolithic graphite electrode in 20 mM phosphate buffer, pH 6.1, 4 °C (after [23.16])

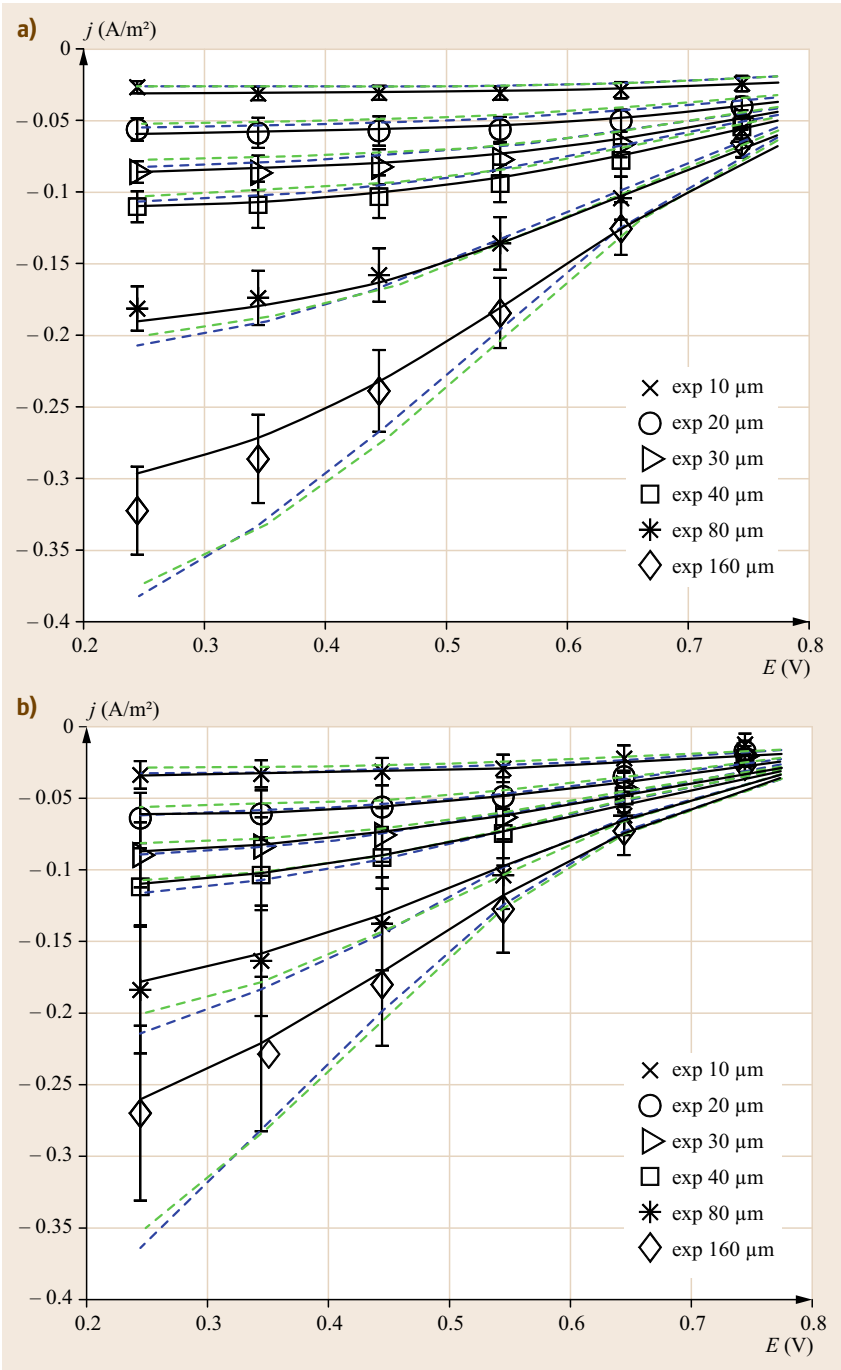


Fig. 23.8a,b Steady-state polarization curves at **(a)** pH 5 (after [23.17]) and **(b)** pH 6 (after [23.18]) for hydrogen peroxide reduction on HRP modified graphite electrode; *symbols*: experimental data; *lines*: simulated curves for three model variants (model 1–*blue dash dotted line*, model 2–*green dashed line* and model 3–*black solid line*). Conditions: fixed delay of 1 min, hydrogen peroxide concentrations from 10 to 160 µM, room temperature; rotation rate 400 rpm (after [23.18])

values ranging from ca. 40 pmol/cm^2 [23.14] to ca. 0.1 pmol/cm^2 [23.11] and significantly lower values of the kinetic parameters in the case of higher coverage.

If the redox process at the enzyme redox site(s) can be evidenced electrochemically, the determination of the surface coverage under electrochemical conditions appears possible. This is usually done by applying cyclic voltammetry, which is then termed non catalytic (nonturnover) cyclic voltammetry. In Fig. 23.7, a cyclic voltammogram of cytochrome c peroxidase modified pyrolithic graphite electrode is shown [23.16]. As can be seen, the almost reversible redox peak at potential

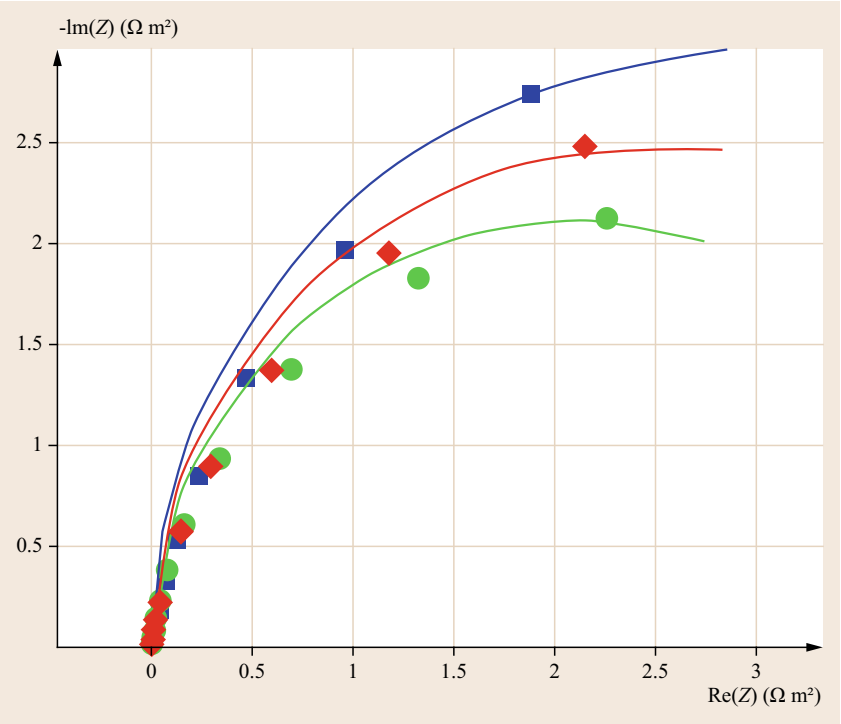


Fig. 23.9 Experimental EIS (*symbols*) vs. simulated (*lines-models* 3) with optimized parameters at three different potentials. Other conditions: pH 6, 80 μM hydrogen peroxide concentration room temperature, and rotation rate 400 rpm (after [23.18])

assigned to reduction potential of cytochrome c peroxidase compound I appears. In some examples, the contribution of the background current is significant and can mask the redox processes of the enzyme. This can be resolved by a baseline subtraction as shown, for example, in [23.17]. The enzyme coverage can be estimated by calculating the charge under the peak area and by assuming the number of exchanged electrons using

$$\text{Coverage} = \frac{\int_{E_1}^{E_2} I \, \mathrm{d}E}{nFv} , \qquad (23.41)$$

where E_1 and E_2 are potential limits, I is the current, n the number of exchanged electrons, F is Faraday's constant, and v is the sweep rate. In the mentioned example [23.16], the authors assumed a two-electron process and calculated a surface coverage of 6.2 pmol/cm^2.

23.3.6 Determination of Kinetic Parameters

Providing that the total enzyme coverage on the electrode surface is known, other kinetic parameters can be obtained by fitting of the experimental data using a suitable mathematical model (Sects. 23.3.3–23.3.4), which describes electrochemical response of an enzymatic electrode. Based on the existing knowledge of an enzyme reaction mechanism, different model variants can be formulated for a certain enzymatic reaction, as shown recently by *Vidakovic-Koch* et al. [23.18]. Starting from primary catalytic cycle of HRP catalyzed hydrogen peroxide reduction and by introducing different assumptions (e.g., by neglecting mass transfer limitations or by neglecting ES complex formation) three different model variants have been formulated. These mathematical models were further used to simulate enzymatic electrode responses under different operating conditions. It was shown that all three models were capable to describe electrode responses under steady-state conditions (Fig. 23.8). However, the best quantitative agreement was obtained for a model taking into account kinetics of *ER* complex formation (23.18) and mass transfer effects (Model 3 in Figs. 23.8 and 23.9). This was further confirmed by modeling of electrochemical impedance spectroscopy (EIS) responses where only that model was able to describe EIS experimental data under all studied conditions (Fig. 23.9). These findings are in accordance with our earlier studies on kinetics of other electrochemical reactions where we have shown that dynamic methods are more sensitive for parameter determination and model discrimination than steady-state methods [23.13, 19, 20]. Unlike steady-state conditions where some constants are lumped (e.g., k_1 and k_{-1} constants in (23.22) cannot be determined from steady-state experiments, but only Michaelis–Menten constant defined as $K_M = (k_{-1} + k_2)/(k_1)$) under dynamic conditions these further constants can be identified [23.18].

23.4 Biotransformation with Redox Enzymes

In this chapter, some electrochemical aspects of biotransformation with redox enzymes are reviewed. These aspects refer mainly to mechanism of the enzyme or common cofactors regeneration at the electrode surface. As shown earlier, some enzymes can be directly regenerated at the electrode surface. As an example from this group, hydrogenase enzymes have been chosen. Further examples relate to FAD- and NAD-dependent enzymes.

23.4.1 Enzymes Showing DET

Hydrogenases have been studied extensively in the last decade [23.6, 21, 22]. The interests in these enzymes are both fundamental and practical. Hydrogenases are highly active catalysts for hydrogen reaction. Its activity can be compared with platinum (at mild conditions and lower H_2 partial pressure), which opens up an interesting possibility of low-cost non-noble metal platinum like catalyst synthesis [23.21]. Hydrogenases can be also possibly utilized in some niche applications (like self-powered sensors), where shortcuts of enzymes are overate by their advantages.

Based on the metal content of the active site, two main classes of hydrogenases can be distinguished, that is, [Fe–Fe] and [Ni–Fe] hydrogenase. In addition, there are membrane-bound hydrogenases which are not water soluble due to the hydrophobic membrane anchor domain. All so far discovered hydrogenases have a Fe(CO)(CN)(RS) unit in common, which is bridged to either Ni or second Fe–S cluster, responsible for electron transfers to and from the enzyme surface.

Major aspects of hydrogenase electrochemistry have been summarized in several review papers, for example, electrochemical enzyme kinetics studied by protein film voltammetry has been reviewed by *Léger* et al. [23.6], electrochemical behavior of hydrogenases originated from different organisms with an emphasis of inhibition by small molecules (H_2, CO, H_2S, O_2) has been reviewed by *Armstrong* et al. [23.21], and different strategies for enzyme immobilization for fuel-cell applications by *Lojou* [23.22]. In this chapter, we focus on those aspects of hydrogenase electrochemistry which we believe are important for the process development, such as an enzyme adaptation on process conditions, reversibility of hydrogen reaction, as well as the development of electrodes.

An important prerequisite for the technical application of an enzyme is a high level of tolerance toward process conditions (e.g., temperature, pH, solvent, oxygen). This can be influenced by a careful choice of an organism as well as the conditions of its cultivation (anaerobic, aerobic, high temperature). It was shown that hydrogenases isolated from organisms cultivated under aerobic conditions are more oxygen tolerant (e.g., some [Ni–Fe]-hydrogenases; in contrast to [Fe–Fe]-hydrogenases, usually isolated from anaerobic organisms [23.21]). Also hydrogenases originated from thermophiles (like from hyperthermophilic bacterium *Aquifex aeolicus* [23.22]) show higher stability and also higher tolerance to oxygen, CO, and H_2S. These examples demonstrate nicely the high potential of further enzyme fine tuning by for example, protein engineering.

For practical applications, the open-circuit potential (OCP) (onset potential of the reaction) and its relationship to the theoretical electrode potential is very important. As we commented before, some hydrogenases show a reversible behavior (e.g., [Fe–Fe]-hydrogenase from *Desulfovibrio desulfuricans* [23.23] or *D. fructosovorans* [Ni–Fe]-hydrogenase [23.5]. Some others show certain preferences, also called catalytic bias for a forward or backward reaction. This catalytic bias influences the intensity of the catalytic current in backward and forward direction, but it might also influence the value of the OCP which, in the case of some *one-way-hydrogenases* (e.g., *Ralstonia eutropha* [Ni–Fe] membrane-bound hydrogenase [23.23], gives the OCP values, which deviate from the values expected by thermodynamics. This loss under open-circuit conditions will inherently reduce the available fuel-cell voltage (in the above-mentioned case for ca. 80 mV). In these respect enzymes behave like traditional noble metal catalysts, where reversible catalysis is more an exception than a rule. Logically for practical applications, reversible catalysts should be sought after. This point was also recently addressed by *Hamdan* et al. [23.5] who stressed that a reversible behavior of hydrogenase can be influenced by the efforts to generate more oxygen tolerant catalysts, more suitable for practical applications. This could induce some inherent losses due to the catalytic bias of the mutant catalysts.

Hydrogenase can be physically adsorbed at the surface of pyrolithic graphite electrode. The method is fast and efficient for studying of bioelectrochemistry of thin protein films as demonstrated by Armstrong et al., but the disadvantage is low film stability. It was shown that even within the same cycle at lower sweep rates, the current decreases due to the enzyme desorption [23.23]. In addition, the enzyme orientation at the electrode surface is random which can result in the dispersion of the heterogenous electrochemical rate constant between an enzyme and a surface [23.6].

Both problems of physical adsorption (low stability and the orientation) could be possibly tackled by co-

valent attachment of the enzyme to the surface. For an efficient covalent adsorption the distribution of charges at the enzyme surface, as well as the direction of the dipole moment of the enzyme are important [23.24]. In addition, the electrode surface should be adequately prepared and the ionic strength as well as the pH value for covalent adsorption should be carefully chosen. It was shown on an example of *Desulfovibrio gigas* [Ni–Fe]-hydrogenase that the so-called Fe–S distal cluster, where the electron exchange with the electrode surface probably takes place, carries a negative charge. For positively charged electrode surface (e.g., by modification with amino groups), a covalent attachment of the enzyme at the electrode surface (through carbodiimide coupling) can be expected. It was shown that a lower ionic strength of the solution and a lower pH value benefit the proper orientation of the enzyme. At higher ionic strength, it was assumed that the electrostatic interaction between the enzymes and the electrode was screened, which resulted in a random orientation of the enzymes and almost no catalytic current in the absence of a redox mediator. The immobilization procedure described by *Rüdiger* et al. [23.24] resulted in exceptional stability of electrodes with a 90% initial activity maintained after 1 week of continuous measurements.

In general, this method might be applicable to other redox enzymes, but it is not always possible to specifically orient enzymes using electrostatic interaction. As an example, no specific orientation of the enzyme using electrostatic interaction was obtained in the case of *A. aeolicus* [Ni–Fe]-hydrogenase, which have a high tolerance with respect to O_2, CO, and heat and therefore might be an enzyme of high technical relevance [23.25]. The reason is the absence of charged residues in the close vicinity of the distal Fe–S cluster and the presence of a transmembrane helix surrounded by neutral detergent. The authors showed that on hydrophilic surfaces no preferential orientation of enzymes were possible governing both MET and DET electron transfer. On the other hand, on hydrophobic surfaces only MET was possible.

For practical applications in addition to stable and oriented enzyme immobilization, it is important to increase the current density per geometrical surface area. This goal can be achieved by 3-D electrode structuring, which is a common strategy in electrochemical engineering. If one follows a fuel-cell example, one can see that the significant progress in this field has been achieved by the introduction of 3-D electrodes based on carbon and noble metal catalyst nanomaterials. However, the catalyst utilization despite progress in recent years is still not very high (currently only ca. 34%), showing potential for further improvements. Can a similar progress be made in enzymatic electrode field? In fuel-cell technology state-of-the-art electrodes are based on so-called gas diffusion electrodes incorporating ionic conducting phase (currently Nafion based), electron conducting phase (carbon nanoparticles plus metal catalyst) and catalytic phase (Pt nanoparticle). Although, in the field of enzymatic electrodes the *state-of-the-art* is not so easy to define due to the number of different strategies in the literature, there is a notable trend toward utilization of carbon nanomaterials.

A very stable and highly active electrodes based on multiwall carbon nanotubes (MWCNTs) were constructed by *Alonco-Lomillo* et al. [23.26]. MWCNTs were grown on gold support by chemical vapor deposition, which resulted in a highly oriented layer. The MWCNTs were further functionalized by amino groups and the enzyme was covalently attached by carbiimide coupling between amino groups at the MWCNTs surface and carboxylic groups at the enzyme surface, following conditions which were discussed above [23.24]. This resulted in enzymatic electrodes of a very high activity (ca. $2.5\,mA/cm^2$ for limiting current) and an exceptional stability (less than 10% loss of activity during 33 days of operation).

Lojou et al. [23.27] studied the immobilization of *D. fructosovorans* [Ni–Fe]-hydrogenase on long and cut single wall carbon nanotubes (SWCNTs). They found out that the DET between the electrode surface and the immobilized hydrogenase was controlled more by the geometry of the nanotubes than by the surface charge. Cut SWNTS created more disordered coatings than the long ones, which favored the DET. Similarly in the case of *A. aeolicus* [Ni–Fe]-hydrogenase, higher catalytic currents were obtained in the case of cut (up to $1\,mA/cm^2$) than long (up to $0.4\,mA/cm^2$) SWCNTs [23.28].

A very active enzymatic electrode based on pyrolitic graphite particles, *E. coli* [Ni–Fe]-hydrogenases 1 and 2 and pH-neutralized Nafion were constructed by *Healy* et al. [23.29]. The activity was up to $1.6\,mA/cm^2$ for *E. coli* hydrogenase 1.

23.4.2 FAD- and NAD-Dependent Enzymes

Hydrogen is a highly promising energy carrier, which can be electrochemically oxidized with a high efficiency both in traditional and those fuel cells based on enzymatic catalysts. The disadvantages of hydrogen are largely connected with its storage and transport as well as with the required level of purity (enzymatic catalysts are similar to platinum sensitive to impurities such as CO, H_2S, etc.). On the other hand, hydrogen is *stored* in nature abundantly in form of different carbon-containing compounds. These are, for example, different carbohydrates (like glucose, fructose, sucrose,

lactose, starch), alcohols (methanol, ethanol, glycerol), or organic acids (formic acid), which are also termed renewables, since it can be produced from renewable sources. These renewables can be utilized as fuels (e.g., in fuel cells) or as building blocks in chemical synthesis. Nowadays, most of the existing enzymatic fuel cells are so-called co-generation devices since they do not perform a total fuel oxidation, which would lead to total fuel utilization (in terms of its energy density and number of exchanged electrons), but rather only a partial oxidation, giving rise to a partial oxidation product and energy in form of electricity. As shown above, these partial oxidation products can be further used as building blocks in chemical industry. This latter aspect seems to be very attractive, since the process industry is currently looking for new synthesis routes based on renewables. In this respect, enzymatic catalysts performing only partial biotransformation (oxidation or reduction) might have some advantages over traditional catalysts which (by the rule) are less selective and causing higher costs of product purification as well as lower utilization.

The majority of enzymes that catalyse oxidative or reductive biotransformation of carbon containing compounds are cofactor dependent. The common cofactors (or coenzymes) are FAD, pyrroloquinoline quinone (PQQ) and NAD. While FAD and PQQ are parts of the enzyme, NAD is a soluble coenzyme. This has important consequences, namely the redox potential of FAD (PQQ) is dependent on protein (and therefore can be tuned in certain extent), while in the case of NAD the redox potential will be more protein independent. The standard values of the equilibrium potentials are $-0.219\,\mathrm{V}$ and $-0.323\,\mathrm{V}$ for FAD/$FADH_2$ and NAD^+/NADH couples, respectively, (conditions are: pH 7, 298.15 K, and the ionic strength of 0.1) [23.30]. In addition, in accordance to the Nernst equation the equilibrium potential will be dependent on the concentration of the redox species in the equilibrium. For multistep reactions the concentration of the redox species will depend on preceding steps as it was already discussed.

In some cases enzymes do not have only one, but several redox centers. *E. coli* fumarate reductase is such an example which contains covalently linked FAD, three different iron–sulfur clusters and at least two quinones [23.31]. Some other enzymes contain, in addition to the FAD or the PQQ redox center, heme as a second redox center. An additional redox center might add up an important benefit since it increases the number of possible electron transfer pathways between an enzyme and an electrode as it was shown in the case of *E. coli* fumarate reductase [23.6]. A further example is cellobiose dehydrogenase (EC. 1.1.99.18) which can establish DET through a heme domain or a MET through FAD as shown by *Tasca* et al. [23.32]. This second functionality can be introduced into the enzyme structure by protein engineering as demonstrated in the case of PQQ-glucose dehydrogenase (GDH) which become able of DET after fusion of a cytochrome c with PQQ-GDH [23.33].

Electrochemical Regeneration of FAD Dependent Enzymes

As shown before, FAD is a common cofactor that is tightly bonded to the enzyme and commonly deeply buried, for which reason it can be considered as a part of the enzyme. FAD is a catalytic center of these enzymes meaning that the reaction between a substrate and an enzyme involves changes on FAD. From the point of view of the electron transfer, it is important to know if the FAD is the only redox center or there are other redox centers. To exemplify the problem of electrochemical cofactor regeneration and its dependence on enzyme structure we consider the following three enzymes: glucose oxidase (GOx), cellobiose dehydrogenase, and *E. coli* fumarate reductase. All three enzymes possess FAD as an active center. Cellobiose dehydrogenase and *E. coli* fumarate reductase in addition to FAD contain subsidiary redox centers, heme, and iron sulfur clusters, respectively. As already discussed, these subsidiary redox centers might provide an important benefit to these enzymes. Unlike GOx which according to the most reports establishes only MET (exception was GOx which was deglycolized [23.34]), the other two enzymes are also able to establish DET. *E. coli* fumarate reductase, simply adsorbed at the surface of nonmodified pyrolithic graphite shows a well-defined reversible behavior in the presence of succinate and fumarate [23.35]. It was also shown that the cyclic voltammetry in the absence of a substrate (also termed nonturnover or noncatalytic voltammetry) shows evidences of DET between an enzyme and an electrode and according to the authors the redox potentials of all four catalytic centers (FAD and three iron sulfur clusters) can be determined in this way. Cellobiose dehydrogenase shows DET (through heme domain), but also MET in the presence of a suitable mediator [23.32]. Based on the above examples, it is clear that there will be no unique strategy for FAD regeneration. In the case of *E. coli* fumarate reductase it can be anticipated that the problem of enzyme regeneration will have some similarity with the electrochemical regeneration of hydrogenases (see discussion above), including a proper orientation of the enzyme to the electrode surface, an increase in the stability by, for example, covalent attachment and also an increase in the electrode surface area by application of carbon nanomaterials. In the case of cellobiose dehydrogenase, MET seems to be thermo-

dynamically and kinetically more favorable than DET, which means that the proper mediator might be sought after [23.32]. As commented earlier, GOx requires also a mediator.

Different mediators, soluble or immobilized, have been reported in the literature for FAD regeneration [23.36]. Recent efforts are more directed toward immobilization of the mediator due to some drawbacks of the soluble mediators like interferences during product purification, limited reusability and cost-intensive elimination from waste waters [23.37]. In this chapter, we also concentrate on immobilized mediator systems. For further reading regarding other type of mediators please consider [23.36].

The addition of a redox mediator adds up a new species into an enzyme electrode system, which is characterized by a certain redox potential. For an efficient mediator, this redox potential should be close to a redox potential of a redox site in the enzyme. In case of FAD-dependent enzymes -0.219 V vs. SHE (pH 7) [23.30] can be considered as a benchmark value, although (see above) this can deviate depending on the enzyme. If we consider a redox potential of the mediator as a prime criteria for its efficiency the Os-based redox hydrogels will take a lead compared to other systems [23.36]. This mediator in addition to the favorable redox potential (ca. 0.01 V SHE) shows also good kinetics. It was reported that the bioanode based on Os-polymer reaches the limiting current behavior at overpotential of only 0.19 V [23.38]. The further advantage of this mediator is the possibility of a further tuning of its redox potential, which can be done by a careful selection of residues forming Os-complexes [23.39]. The efficiency of Os-polymer has been demonstrated in a number of publications by *Heller*'s group [23.38, 40–44] who originally introduced this polymer as well as by a number of other research groups [23.39, 45, 46]. However, the procedure for synthesizing this mediator is complicated and involves a number of steps. In addition, in some applications (e.g., enzymatic biofuel cells as implantable power sources), some issues, associated with the toxicity of Os-containing compounds might arise [23.47] and references therein.

8-Hydroxyquinoline-5-sulfonic acid can be also employed as mediator for GOx [23.48–50]. The redox potential of this mediator is much more positive compared to Os-based mediators (ca. 0.3 V SHE) [23.36]. Also the kinetics of glucose oxidation in this example was not so favorable as with an Os-mediator showing a slow increase in the current without reaching the limiting current behavior [23.49].

Another group of mediators is based on tetrathiafulvalane (TTF), which can be used as a single compound or in form of a so-called charge transfer complex (CTC) combined with tetracyanoquinodimethan (TCNQ) [23.36, 47]. As we have shown recently, in both cases and at lower overpotentials TTF behaves as a mediator, showing a formal redox potential of ca. 0.419 V SHE [23.51]. The advantage of using CTC instead of TTF is the electronic conductivity of the former complex, which is not the case with TTF. It was demonstrated that TTF or CTC composite electrodes comprising a mediator, carbon nanomaterials and GOx show good performances (catalytic current under steady-state conditions of ca. 1.5 mA/cm^2 at 20 mM glucose), but the kinetics was slower than in the case of Os-polymer mediated systems [23.51].

Electrochemical Regeneration of NAD

Unlike FAD, NAD is a soluble cofactor. Its electrochemical regeneration is of high practical importance due to its involvement in catalytic cycles of a number of enzymes of practical interest [23.52, 53]. Electrochemical methods for NAD regeneration have been reviewed in several occasions, for example, *van der Dock* and *Zhao* [23.54] gave a broader overview of different methods, including an electrochemical for NAD(P) regeneration. *Hollmann* and *Schmid* [23.55] reviewed the electrochemical regeneration of oxidoreductases covering the literature up to 2004, while *Kochius* et al. [23.37] concentrated on immobilized redox mediators for the NAD regeneration. Without an emphasis to repeat previous efforts, we discuss in this chapter those methods which enable reversible NAD regeneration (both oxidation and reduction direction), as well as the recent progress in *one* directional NAD regeneration showing some improvements with respect to common problems in this field like overpotential, current efficiency with respect to enzymatically active NAD forms as well as electrode constructions resulting in higher current densities.

In the most favorable case, an electrode should be able to regenerate the NAD in a reversible manner, which indeed has been demonstrated by *Zu* et al. [23.56]. The authors modified a pyrolytic graphite edge electrode by a hydrophilic domain of mitochondrial NADH: ubiqinone oxidoreductase (subcomplex $I\lambda$). This subcomplex comprises a flavin mononucleotide (FMN) as the active site for NAD oxidation/reduction and iron sulfur (FeS) clusters and showed a reversible bioelectrochemical NADH/NAD$^+$ oxidation/reduction reaction. The use of this catalyst possibly circumvents the formation of enzymatically not active NADH forms, which are usual problems encountered with other electrochemical methods. However, the stability of the adsorbed protein layer as well as the catalytic currents were low. The question stays if this structure could become more practical.

Karyakin et al. [23.8] also reported a reversible NAD reaction using electropolymerized neutral red, which shows a fast kinetics reaching limiting current behavior at overpotential of ca. 50 mV (oxidation reaction). The application of this polymer was also reported recently in a rechargeable biobattery [23.57]. Furthermore, *Kim* and *Yoo* [23.58] showed that porous tin(IV) oxide electrodes can be used as a bidirectional catalysts for NAD oxidation and reduction reaction. Still, the NAD reduction required a higher overpotential than the oxidation reaction.

Aside of these procedures, other reported electrocatalysts do not support reversible NAD reaction. They behave predominantly as one-way catalysts showing a preference for the oxidation or the reduction direction and involving some intrinsic losses. *Karyakin* et al. [23.59] studied different electropolymerized azines as electrocatalysts for NAD oxidation emphasizing poly(methylene green) as the best one. *Li* et al. [23.60] showed recently that the modification of a carbon nanotubes (CNTs) with poly(methylene green) forms a highly active electrocatalysts for NADH oxidation (currents up to 5 mA/cm^2, at 0.25 V SHE). However, this activity was followed by a large overpotential (more than 0.5 V). Poly(methylene green) modified electrodes were also used recently for NADH regeneration in combination with different enzymes (e.g., malate dehydrogenase [23.61]).

Composite electrodes containing a Ru(III) complex and single-walled CNTs were reported to be active in regeneration of electrochemically active 1,4 NADH [23.62]. It can be estimated that the overpotential was larger than 200 mV and the reported currents were in mA/cm^2 range.

Traditional electrocatalysts (carbon or metal electrodes), as many times reported show a high overpotential for NAD reduction. In addition, they are prone to fouling and formation of enzymatically non active NADH form or dimers. However, recent reports demonstrate that on a glassy carbon electrode under suitable operating conditions (high overpotentials) enzymatically active 1,4-NADH forms almost exclusively (with a yield of 98%), but at the cost of a very high overpotential [23.63]. Very recently the same group of authors showed that a glassy carbon electrode modified with electrochemically deposited platinum and nickel nanoparticles regenerates up to 100% enzymatically active 1,4-NADH at a significantly lower overpotential (ca. 0.7 V less) than the nonmodified glassy carbon (GC) electrode [23.64].

23.5 Conclusions and Outlook

Enzymes as catalysts have several advantages. From the point of view of the electrochemistry, especially inspiring are enzymes catalyzing oxygen reduction under neutral conditions as well as reversible catalysis by hydrogenases and several other enzymes. For process applications multienzyme sequences are interesting. These reaction networks require an enzyme (redox cofactor) regeneration to operate continuously. It was shown that the electrochemical regeneration is mainly enzyme dependent. Some enzymes can be regenerated directly at the electrode surface (like hydrogenases), while others need a mediator (GOx). Especially, interesting are those enzymes containing several redox centers. These enzymes have several possibilities for electron transfer to the electrode surface, for example, DET and MET. Examples of hydrogenases show that enzymes from different organisms have a different catalytic activity, which gives the possibility for a further tuning of enzymes for process conditions. The catalytic currents that can be obtained using enzymatic catalysts are still low. Some improvements can be achieved by 3-D electrode structuring. Still, the carbon materials that are the most suitable electrode construction materials are hydrophobic, which usually results in low level of enzyme coverage. There is still a little information about enzyme distribution in the catalyst layer, which is important for the further development of such enzymatic electrodes. Also, the most examples of bioelectrochemical systems comprise single biotransformation. Here hopefully more exciting examples including more complex reaction sequences combined with electrochemical regeneration will follow. To design such systems both mathematical modeling and experimental work will be important.

References

23.1 C.E. Hodgman, M.C. Jewett: Cell-free synthetic biology: Thinking outside the cell, Meta. Eng. **14**(3), 261–269 (2012)

23.2 A. Bar-Even, E. Noor, N.E. Lewis, R. Miloa: Design and analysis of synthetic carbon fixation pathways, Proc. Natl. Acad. Sci. U.S.A **107**(19), 8889–8894 (2010)

23.3 C.A. Raines: The Calvin cycle revisited, Photosynth. Res. **75**(1), 1–10 (2003)

23.4 M.J. Lukey, A. Parkin, M.M. Roessler, B.J. Murphy, J. Harmer, T. Palmer, F. Sargent, F.A. Armstrong: How *Escherichia coli* is equipped to oxidize hydrogen under different redox conditions, J. Biol. Chem. **285**(6), 3928–3938 (2010)

23.5 A. Abou Hamdan, S. Dementin, P.-P. Liebgott, O. Gutierrez-Sanz, P. Richaud, A.L. De Lacey, M. Rousset, P. Bertrand, L. Cournac, C. Léger: Understanding and tuning the catalytic bias of hydrogenase, J. Am. Chem. Soc. **134**(20), 8368–8371 (2012)

23.6 C. Léger, S.J. Elliott, K.R. Hoke, L.J.C. Jeuken, A.K. Jones, F.A. Armstrong: Enzyme electrokinetics: Using protein film voltammetry to investigate redox enzymes and their mechanisms, Biochemistry **42**(29), 8653–8662 (2003)

23.7 F.A. Armstrong, J. Hirst: Reversibility and efficiency in electrocatalytic energy conversion and lessons from enzymes, Proc. Natl. Acad. Sci. U.S.A. **108**(34), 14049–14054 (2011)

23.8 A.A. Karyakin, Y.N. Ivanova, E.E. Karyakina: Equilibrium (NAD(+)/NADH) potential on poly (Neutral Red) modified electrode, Electrochem. Commun. **5**(8), 677–680 (2003)

23.9 G.E. Briggs, J.B.S. Haldane: A note on the kinetics of enzyme action, Biochem. J. **19**(2), 338–339 (1925)

23.10 S. Fletcher: Tafel slopes from first principles, J. Solid State Electrochem. **13**(4), 537–549 (2009)

23.11 R. Andreu, E.E. Ferapontova, L. Gorton, J.J. Calvente: Direct electron transfer kinetics in horseradish peroxidase electrocatalysis, J. Phys. Chem. B **111**(2), 469–477 (2007)

23.12 C. Léger, A.K. Jones, S.P.J. Albracht, F.A. Armstrong: Effect of a dispersion of interfacial electron transfer rates on steady state catalytic electron transport in NiFe-hydrogenase and other enzymes, J. Phys. Chem. B **106**(50), 13058–13063 (2002)

23.13 T.R. Vidaković-Koch, V.V. Panić, M. Andrić, M. Petkovska, K. Sundmacher: Nonlinear frequency response nalysis of the ferrocyanide oxidation kinetics. Part I. A theoretical analysis, J. Phys. Chem. C **115**(35), 17341–17351 (2011)

23.14 T.L.G. Ruzgas, J.G.M.-V. Emnéus: Kinetic-models of horseradish-peroxidase action on a graphite electrode, J. Electroanal. Chem. **391**(1/2), 41–49 (1995)

23.15 E.E. Ferapontova, L. Gorton: Effect of proton donors on direct electron transfer in the system gold electrode-horseradish peroxidase, Electrochem. Commun. **3**(12), 767–774 (2001)

23.16 M.S. Mondal, H.A. Fuller, F.A. Armstrong: Direct measurement of the reduction potential of catalytically active cytochrome c peroxidase compound I: Voltammetric detection of a reversible, cooperative two-electron transfer reaction, J. Am. Chem. Soc. **118**(1), 263–264 (1996)

23.17 M.S. Mondal, D.B. Goodin, F.A. Armstrong: Simultaneous voltammetric comparisons of reduction potentials, reactivities, and stabilities of the high-potential catalytic states of wild-type and distal-pocket mutant (W51F) yeast cytochrome c peroxidase, J. Am. Chem. Soc. **120**(25), 6270–6276 (1998)

23.18 T. Vidaković-Koch, V.K. Mittal, M. Varničić, Q.N. Do Thi, K. Sundmacher: Application of electrochemical impedance spectroscopy for studying of enzyme kinetics, Electrochim. Acta **110**, 94–104 (2013)

23.19 V.V. Panić, T.R. Vidaković-Koch, M. Andrić, M. Petkovska, K. Sundmacher: Nonlinear frequency response analysis of the ferrocyanide oxidation kinetics. Part II. Measurement routine and experimental validation, J. Phys. Chem. C **115**(35), 17352–17358 (2011)

23.20 B. Bensmann, M. Petkovska, T. Vidaković-Koch, R. Hanke-Rauschenbach, K. Sundmacher: Nonlinear frequency response of electrochemical methanol oxidation kinetics: A theoretical analysis, J. Electrochem. Soc. **157**(9), B1279–B1289 (2010)

23.21 F.A. Armstrong, N.A. Belsey, J.A. Cracknell, G. Goldet, A. Parkin, E. Reisner, K.A. Vincent, A.F. Wait: Dynamic electrochemical investigations of hydrogen oxidation and production by enzymes and implications for future technology, Chem. Soc. Rev. **38**(1), 36–51 (2009)

23.22 E. Lojou: Hydrogenases as catalysts for fuel cells: Strategies for efficient immobilization at electrode interfaces, Electrochim. Acta **56**(28), 10385–10397 (2011)

23.23 K.A. Vincent, A. Parkin, O. Lenz, S.P.J. Albracht, J.C. Fontecilla-Camps, R. Cammack, B. Friedrich, F.A. Armstrong: Electrochemical definitions of O_2 sensitivity and oxidative inactivation in hydrogenases, J. Am. Chem. Soc. **127**(51), 18179–18189 (2005)

23.24 O. Rüdiger, J.M. Abad, E.C. Hatchikian, V.M. Fernandez, A.L. De Lacey: Oriented immobilization of *Desulfovibrio gigas* hydrogenase onto carbon electrodes by covalent bonds for nonmediated oxidation of H_2, J. Am. Chem. Soc. **127**(46), 16008–16009 (2005)

23.25 A. Ciaccafava, P. Infossi, M. Ilbert, M. Guiral, S. Lecomte, M.T. Giudici-Orticoni, E. Lojou: Electrochemistry, AFM, and PM-IRRA spectroscopy of immobilized hydrogenase: Role of a hydrophobic helix in enzyme orientation for efficient H_2 oxidation, Angew. Chem. Int. Ed. **51**(4), 953–956 (2012)

23.26 M.A. Alonso-Lomillo, O. Rüdiger, A. Maroto-Valiente, M. Velez, I. Rodríguez-Ramos, F. Javier Muñoz, V.M. Fernández, A.L. De Lacey: Hydrogenase-coated carbon nanotubes for efficient H_2 oxidation, Nano Lett. **7**(6), 1603–1608 (2007)

23.27 E.X.L. Lojou, M.N.C. Brugna, S.M.T.G.-O. Dementin: Biocatalysts for fuel cells: Efficient hydrogenase orientation for H_2 oxidation at electrodes modified with carbon nanotubes, J. Biol. Inorg. Chem. **13**(7), 1157–1167 (2008)

23.28 X. Luo, M. Brugna, P. Tron-Infossi, M.T. Giudici-Orticoni, E. Lojou: Immobilization of the hyperthermophilic hydrogenase from *Aquifex aeolicus* bacterium onto gold and carbon nanotube electrodes for efficient H_2 oxidation, J. Biol. Inorg. Chem. **14**(8), 1275–1288 (2009)

23.29 A.J. Healy, H.A. Reeve, A. Parkin, K.A. Vincent: Electrically conducting particle networks in polymer electrolyte as three-dimensional electrodes

for hydrogenase electrocatalysis, Electrochim. Acta **56**(28), 10786–10790 (2011)
23.30 R.A. Alberty: Calculation of standard transformed formation properties of biochemical reactants and standard apparent reduction potentials of half reactions, Arc. Biochem. Biophys. **358**(1), 25–39 (1998)
23.31 T.M. Iverson, C. Luna-Chavez, G. Cecchini, D.C. Rees: Structure of the *Escherichia coli* fumarate reductase respiratory complex, Science **284**(5422), 1961–1966 (1999)
23.32 F.L.G. Tasca, W.D.H. Harreither, R.N.G. Ludwig: Comparison of direct and mediated electron transfer for cellobiose dehydrogenase from phanerochaete soridida, Analytical Chem. **81**(7), 2791–2798 (2009)
23.33 J. Okuda, T. Yamazaki, M. Fukasawa, N. Kakehi, K. Sode: The application of engineered glucose dehydrogenase to a direct electron-transfer-type continuous glucose monitoring system and a compartmentless biofuel cell, Anal. Lett. **40**(3), 431–440 (2007)
23.34 O. Courjean, F. Gao, N. Mano: Deglycosylation of glucose oxidase for direct and efficient glucose electrooxidation on a glassy carbon electrode, Ange. Chem. Int, Ed. **48**(32), 5897–5899 (2009)
23.35 C. Léger, K. Heffron, H.R. Pershad, E. Maklashina, C. Luna-Chavez, G. Cecchini, B.A.C. Ackrell, F.A. Armstrong: Enzyme electrokinetics: Energetics of succinate oxidation by fumarate reductase and succinate dehydrogenase, Biochemistry **40**(37), 11234–11245 (2001)
23.36 I. Ivanov, T. Vidakovic-Koch, K. Sundmacher: Recent advances in enzymatic fuel cells: Experiments and modeling, Energies **3**(4), 803–846 (2010)
23.37 S. Kochius, A.O. Magnusson, F. Hollmann, J. Schrader, D. Holtmann: Immobilized redox mediators for electrochemical NAD(P)(+) regeneration, Appl. Microbiol. Biotechnol. **93**(6), 2251–2264 (2012)
23.38 N. Mano, F. Mao, W. Shin, T. Chen, A. Heller: A miniature biofuel cell operating at 0.78 V, Chem. Commun. **4**, 518–519 (2003)
23.39 M.N.X.W. Zafar, C.R.L. Sygmund, D.L.G. Leech: Electron-transfer studies with a new flavin adenine dinucleotide dependent glucose dehydrogenase and osmium polymers of different redox potentials, Anal. Chem. **84**(1), 334–341 (2012)
23.40 N.A.H. Mano: A miniature membraneless biofuel cell operating at 0.36 V under physiological conditions, J. Electrochem. Soc. **150**(8), A1136–A1138 (2003)
23.41 N. Mano, F. Mao, A. Heller: A miniature membraneless biofuel cell operating at +0.60 V under physiological conditions, ChemBioChem **5**(12), 1703–1705 (2004)
23.42 N. Mano, F. Mao, A. Heller: Characteristics of a miniature compartment-less glucose-O_2 biofuel cell and its operation in a living plant, J. Am. Chem. Soc. **125**(21), 6588–6594 (2003)
23.43 F. Mao, N. Mano, A. Heller: Long tethers binding redox centers to polymer backbones enhance electron transport in enzyme wiring hydrogels, J. Am. Chem. Soc. **125**(16), 4951–4957 (2003)
23.44 V. Soukharev, N. Mano, A. Heller: A four-electron O_2-electroreduction biocatalyst superior to platinum and a biofuel cell operating at 0.88 V, J. Am. Chem. Soc. **126**(27), 8368–8369 (2004)
23.45 F.Y.F. Barrière, D.D.L. Rochefort: Targetting redox polymers as mediators for laccase oxygen reduction in a membrane-less biofuel cell, Electrochem. Commun. **6**(3), 237–241 (2004)
23.46 M.N. Zafar, F. Tasca, L. Gorton, E.V. Patridge, J.G. Ferry, N. Gilbert: Tryptophan repressor-binding proteins from *Escherichia coli* and *archaeoglobus fulgidus* as new catalysts for 1,4-dihydronicotinamide adenine dinucleotide-dependent amperometric biosensors and biofuel cells, Anal. Chem. **81**(10), 4082–4088 (2009)
23.47 I. Ivanov, T. Vidakovic-Koch, K. Sundmacher: Direct hybrid glucose-oxygen enzymatic fuel cell based on tetrathiafulvalene-tetracyanoquinodimethane charge transfer complex as anodic mediator, J. Power Sources **196**(22), 9260–9269 (2011)
23.48 L. Brunel, J. Denele, K. Servat, K.B. Kokoh, C. Jolivalt, C. Innocent, M. Cretin, M. Rolland, S. Tingry: Oxygen transport through laccase biocathodes for a membrane-less glucose/O_2 biofuel cell, Electrochem. Commun. **9**(2), 331–336 (2007)
23.49 A. Habrioux, G. Merle, K. Servat, K.B. Kokoh, C. Innocent, M. Cretin, S. Tingry: Concentric glucose/O_2 biofuel cell, J. Electroanal. Chem. **622**(1), 97–102 (2008)
23.50 G. Merle, A. Habrioux, K. Servat, M. Rolland, C. Innocent, K.B. Kokoh, S. Tingry: Long-term activity of covalent grafted biocatalysts during intermittent use of a glucose/O_2 biofuel cell, Electrochim. Acta **54**(11), 2998–3003 (2009)
23.51 I. Ivanov, T. Vidaković-Koch, K. Sundmacher: Alternating electron transfer mechanism in the case of high-performance tetrathiafulvalene–tetracyanoquinodimethane enzymatic electrodes, J. Electroanal. Chem. **690**, 68–73 (2013)
23.52 R. Devaux-Basseguy, A. Bergel, M. Comtat: Potential applications of NAD(P)-dependent oxidoreductases in synthesis: A survey, Enzyme Microb. Technol. **20**(4), 248–258 (1997)
23.53 P. Schenkels, S. De Vries, A.J.J. Straathof: Scope and limitations of the use of nicotinoprotein alcohol dehydrogenase for the coenzyme-free production of enantiopure fine-chemicals, Biocatal. Biotransform. **19**(3), 191–212 (2001)
23.54 W.A. van der Donk, H.M. Zhao: Recent developments in pyridine nucleotide regeneration, Curr. Opin. Biotechnol. **14**(4), 421–426 (2003)
23.55 F.A.S. Hollmann: Electrochemical regeneration of oxidoreductases for cell-free biocatalytic redox reactions, Biocatal. Biotransform. **22**(2), 63–88 (2004)
23.56 Y.B. Zu, R.J. Shannon, J. Hirst: Reversible, electrochemical interconversion of NADH and NAD(+) by the catalytic (I lambda) subcomplex of mitochondrial NADH: Ubiquinone oxidoreductase (complex I), J. Am. Chem. Soc. **125**(20), 6020–6021 (2003)
23.57 M.N. Arechederra, P.K. Addo, S.D. Minteer: Poly(neutral red) as a NAD+ reduction catalyst and a NADH oxidation catalyst: Towards the develop-

ment of a rechargeable biobattery, Electrochim. Acta **56**(3), 1585–1590 (2011)

23.58 Y.H. Kim, Y.J. Yoo: Regeneration of the nicotinamide cofactor using a mediator-free electrochemical method with a tin oxide electrode, Enzyme Microb. Technol. **44**(3), 129–134 (2009)

23.59 A.A. Karyakin, E.E. Karyakina, W. Schuhmann, H.L. Schmidt: Electropolymerized azines: Part II. In a search of the best electrocatalyst of NADH oxidation, Electroanalysis **11**(8), 553–557 (1999)

23.60 H. Li, H. Wen, S.C. Barton: NADH oxidation catalyzed by electropolymerized azines on carbon nanotube modified electrodes, Electroanalysis **24**(2), 398–406 (2012)

23.61 C.W. Narváez Villarrubia, R.A. Rincón, V.K. Radhakrishnan, V. Davis, P. Atanassov: Methylene green electrodeposited on SWNTs-based bucky papers for NADH and l-Malate oxidation, ACS Appl. Mater. Interfaces **3**(7), 2402–2409 (2011)

23.62 A. Salimi, M. Izadi, R. Hallaj, S. Soltanian, H. Hadadzadeh: Electrocatalytic reduction of NAD(+) at glassy carbon electrode modified with single-walled carbon nanotubes and Ru(III) complexes, J. Solid State Electrochem. **13**(3), 485–496 (2009)

23.63 I. Ali, B. Soomro, S. Omanovic: Electrochemical regeneration of NADH on a glassy carbon electrode surface: The influence of electrolysis potential, Electrochem. Commun. **13**(6), 562–565 (2011)

23.64 I. Ali, A. Gill, S. Omanovic: Direct electrochemical regeneration of the enzymatic cofactor 1,4-NADH employing nano-patterned glassy carbon/Pt and glassy carbon/Ni electrodes, Chem. Eng. J. **188**(0), 173–180 (2012)

24. Photoelectrochemical Conversion Processes

Stuart Licht

Society's electrical needs are largely continuous. However, clouds and darkness dictate that photovoltaic solar cells have an intermittent output. A photoelectrochemical solar cell (PEC) can generate not only electrical but also electrochemical energy, and provide the basis for a system with an energy storage component. Sufficiently energetic insolation incident on semiconductors can drive electrochemical oxidation/reduction and generate chemical, electrical or electrochemical energy. Aspects include efficient dye sensitized or direct solar to electrical energy conversion, solar electrochemical synthesis (electrolysis), including water splitting to form hydrogen, environmental cleanup and solar energy storage cells. The PEC utilizes light to carry out an electrochemical reaction, converting light to both chemical and electrical energy. This fundamental difference of the photovoltaic (PV) solar cell's solid/solid interface, and the PEC's solid/liquid interface has several ramifications in cell function and application. Energetic constraints imposed by single bandgap semiconductors have limited the demonstrated values of photoelectrochemical solar to electrical energy conversion efficiency to 16%, and multiple bandgap cells can lead to significantly higher conversion efficiencies.

24.1 **Overview and Historical Perspective** 779
24.2 **Photoelectrochemical Processes** 780
24.2.1 Semiconductor/Electrolyte Electrical Energy Conversion 780
24.2.2 Semiconductor/Electrolyte Electrochemical Energy Storage ... 781
24.2.3 Dye-Sensitized Solar Cell 785
24.2.4 Multi-Bandgap Semiconductor/Electrolyte Electrical Energy Conversion 787
24.2.5 Solar Thermal Electrochemical Photochemical Energy Conversion 791
24.3 **State-of-the-Art and Emerging Technologies** 795
24.4 **Summary** 796
References 796

Photoelectrochemical systems may facilitate not only solar to electrical energy conversion, but have also led to investigations in solar photoelectrochemical production of fuels and photoelectrochemical detoxification of pollutants, and efficient solar thermal electrochemical production (STEP) of metals, fuels, bleach and carbon capture [24.1].

24.1 Overview and Historical Perspective

A photoelectrochemical cell (PEC) utilizes light to carry out an electrochemical reaction, converting light to both chemical and electrical energy. This fundamental difference of the photovoltaic (PV) solar cell's solid/solid interface, and the PEC's solid/liquid interface has several ramifications in cell function and application. By generating not only electrical, but also electrochemical energy, PECs provide the basis for systems with an energy storage component. Sufficiently energetic insolation incident on semiconductors can drive electrochemical oxidation/reduction and generate chemical, electrical or electrochemical energy. Aspects include efficient dye sensitized or direct solar to electrical energy conversion, solar electrochemical synthesis (electrolysis), including water splitting to form hydrogen, environmental cleanup and solar energy storage cells. Energetic constraints imposed by single bandgap semiconductors have limited the demonstrated values of photoelectrochemical solar to electrical energy conversion efficiency to 16%, and multiple bandgap cells can lead to significantly higher conversion efficiencies.

Photoelectrochemistry and photovoltaics share a common history, dating back to the nineteenth century when in 1839, *Becquerel* discovered the photovoltaic

effect while experimenting with two metal electrodes in an aqueous solution [24.2]. Today, Becquerel's configuration would be called a photoelectrochemical PV cell. Up until the mid-twentieth century photoelectrochemistry was not an area of special interest, and was studied more through interest in related fields. The pioneering work of *Gerischer* on the fundamental energetics of photoelectrochemical systems formalized the science of photoelectrochemistry after the mid-twentieth century [24.3, 4]. In 1972, *Fujishima* and *Honda* demonstrated that a wide band gap E_g semiconductor such as titanium dioxide TiO_2 ($E_g = 3.4\,eV$), can use near-ultraviolet (UV) radiation to split water and form hydrogen [24.5]. This study has also been the basis for photoelectrochemical driven disinfectants and waste treatments [24.6].

With the discovery of sustained, efficient photoelectrochemical solar cells in the mid-1970s by research groups at the Weizmann Institute of Science [24.7], Bell Labs [24.8] and MIT [24.9], the field of photoelectrochemistry blossomed. These studies provided a basis for the wide exploration of a large variety of semiconductors and redox couples, as summarized in early reviews [24.10–12] and more recent monographs on photoelectrochemistry [24.13, 14] and solar-driven hydrogen fuel [24.15, 16].

A high efficiency photoelectrochemical solar cell with in situ storage was demonstrated (*the solar cell which works in the dark*) in the 1980s [24.7, 17]. During this period, photoelectrochemical etching as a useful surface treatment for the semiconductor industry was developed [24.18] and the understanding of solution effect limitations on photoelectrochemical charge transfer led to semiconductor-photoabsorber photoelectrochemical solar cells with increasing solar to electrical energy conversion efficiency [24.19–21].

Rather than a semiconductor as the photoabsorber, *Tributsch* and others demonstrated that a coating of dye on a semiconductor film (zinc oxide) can drive photoelectrochemical charge transfer [24.22, 23]. *O'Regan* and *Grätzel*'s discovery in 1991 of a low-cost, high-efficiency solar cell based on dye-sensitized colloidal TiO_2 films, led to intense interest in these systems [24.24, 25]. The solar to electrical efficiency of dye-sensitized solar cells remains lower than those of solid-state devices such as thin film, silicon and concentrator photovoltaics.

In 2002, *Licht* developed a theory of light driven endothermic electrochemical formation of energetic molecules [24.26], demonstrating that a small bandgap semiconductor such as Si ($E_g = 1.12\,eV$) could drive water splitting ($E^0(25\,^\circ C) = 1.23\,V$), when excess solar heat was used to decrease the electrolysis potential [24.27]. As summarized in Sect. 24.4, this STEP process was generalized, from water splitting, to all endothermic electrolytic processes in 2009 including solar efficient carbon capture, and the formation of carbon fuels, bleach and metals [24.28].

24.2 Photoelectrochemical Processes

Radiation incident on semiconductors can drive electrochemical oxidation/reduction and generate chemical, electrical or electrochemical energy.

24.2.1 Semiconductor/Electrolyte Electrical Energy Conversion

Light is absorbed by the semiconductor and drives charge formation. If charge recombination occurs, heat, rather than useful work, is the result. Useful work requires charge separation.

Photo-driven semiconductor/electrolyte processes maintain similarities with solid-state solar cells. In a traditional (photovoltaic, rather than photoelectrochemical) solar cells, light is absorbed, which induces formation of an electron/hole pair. Electron/hole separation occurs across a space charge field gradient formed at a pn junction (the intimate contact of p-doped and n-doped semiconductors). The photopotential of a single pn junction is

$$V_{pn} = \left(\frac{nkT}{e}\right) \ln\left(1 + \frac{j_{ph,pn}}{j_{o,pn}}\right) ,$$

where V_{pn} is constrained by the photocurrent density through the junction, $j_{ph,pn}$ and $j_{o,pn}$ is the saturation current (of a reversely polarized diode), and is described by the Shockley equation [24.12].

Rather than a pn junction, the space charge field may be formed by a single p or n type semiconductor in contact with another material, such as a metal or an electrolyte. In illuminated semiconductor systems the absorption of photons generates excited electronic states. These excited states have lifetimes of limited duration. Without a mechanism of charge separation their intrinsic energy would be lost through relaxation (recombination). Several distinct mechanisms of charge separation have been considered in designing

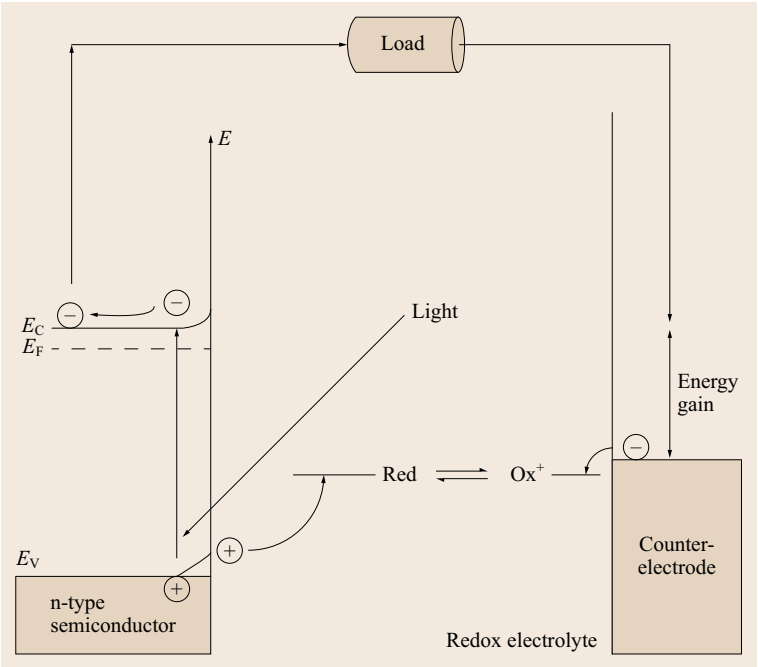


Fig. 24.1 Carrier generation under illumination arising at the semiconductor/liquid interface

efficient photoelectrochemical systems. At illuminated semiconductor/liquid interfaces, an electric field (the space charge layer) occurs concurrent with charge/ion redistribution at the interface. Upon photogeneration of electron/hole pairs this electric field impedes recombinative processes by oppositely accelerating and separating these charges, resulting in minority carrier injection into the electrolytic redox couple.

Depending on the relative rates of charge transfer, $j_{o,sh}$ (Shockley current) may be constrained by either solid state or electrochemical limitations, and is respectively termed the saturation current, or the equilibrium exchange current [24.12].

This concept of carrier generation is illustrated in Fig. 24.1 (for an n-type PEC) and has been the theoretical basis for several efficient semiconductor/redox couple PEC cells. Illumination of the electrode surface with light, whose photon energy is greater than the bandgap, promotes electrons into the conduction band leaving holes in the valance band. In the case of a photoanode, band bending in the depletion region drives electrons in the conduction band into the interior of the semiconductor and eventually to the contact and holes in the valence band towards the electrolyte, where they participate in an oxidation reaction. The electrons removed through the contact drive an external load and eventually reach the counter electrode (CE) or storage electrode, where they participate in a reduction process. Under illumination and open circuit, a negative potential is created in a photoanode and, as a result, the Fermi level for the photoanode shifts in the negative direction, thus reducing the band bending. Under illumination with increasing intensity, the semiconductor Fermi level shifts continually towards negative potentials until the band bending effectively reduces to zero, which corresponds to the flat band condition. At this point a photoanode exhibits its maximum photovoltage, which is equal to the barrier height.

Electrolyte modification, and an understanding of the distribution (speciation) and role of chemical species in the solution, can substantially impact photoelectrochemical charge transfer and lead to improved solar to electrical conversion efficiency. Fundamental understanding of the photo-oxidized species, the nature of the counter ion and competing reactions can overcome limits to photoelectrochemical charge transfer. Such effects have been shown in sulfide, selenide, iodide, and ferrocyanide electrolytes [24.29]. For example, as shown in Fig. 24.2, additions to a ferri/ferrocyanide electrolyte can increase the photopotential by 0.4 V of an immersed, illuminated n-CdSe photoelectrode, and cesium cation additions can also improve photoelectrochemical charge transfer [24.19].

24.2.2 Semiconductor/Electrolyte Electrochemical Energy Storage

PECs can generate not only electrical but also electrochemical energy. Figure 24.2 presents one configuration of a PEC combining in situ electrochemical storage

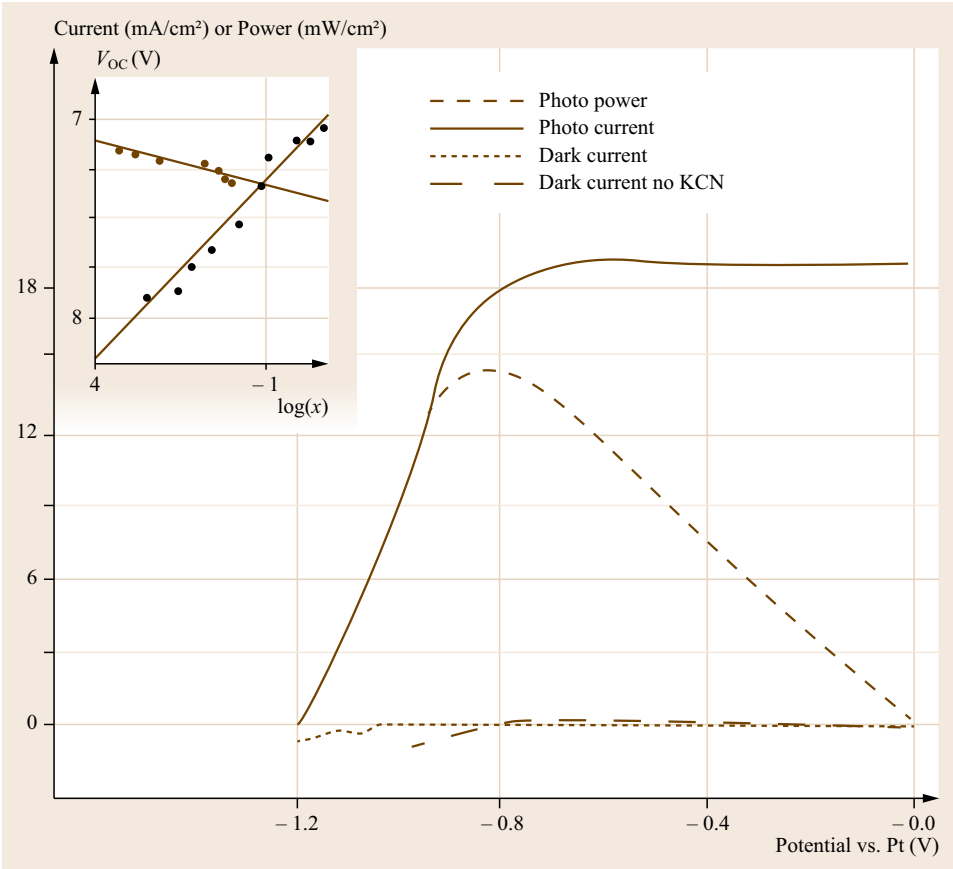


Fig. 24.2 Outdoor photoelectrochemical solar cell current–voltage characteristics for an illuminated, or dark, n-CdSe electrode in 0.25 M $K_4Fe(CN)_6$, 0.0125 M $K_3Fe(CN)_6$, 0.1 M KCN, 0.5 M KOH solar cell. Measured solar to electrical conversion efficiency was 16(±0.4)%. *Inset*: The variation of open circuit photovoltage (under 80 mW/cm^2 tungsten-halogen illumination) in such cells containing (i) varying concentrations of KCN (*black dots*) or $Cd(CN)_4^{2-}$ (*brown dots*, added as 4 : 1 [KCN] : [$CdCl_2$]) (after [24.20, 30])

and solar conversion capabilities; providing continuous output insensitive to daily variations in illumination. A high solar to electric conversion efficiency cell configuration of this type was demonstrated in 1987 and utilized a Cd(Se,Te)/S_x^{2-} conversion half cell and a Sn/SnS storage system resulting in a solar cell with a continuous output [24.17]. Under illumination, as seen in Fig. 24.3a, the photocurrent drives an external load. Simultaneously, a portion of the photocurrent is used in the direct electrochemical reduction of metal cations in the device storage half cell. In darkness or below a certain level of light, the storage compartment spontaneously delivers power, by metal oxidation, as seen in Fig. 24.3b.

A variety of two electrode configurations have been investigated as PEC storage systems. Important variations of these photoelectrochemical conversion and storage configurations are summarized in Table 24.1. In each case, and as summarized in Fig. 24.4 for two of the configurations, exposure to light drives separate redox couples and a current through the external load. There is a net chemical change in the system, with an overall increase in free energy. In the absence of illumination, the generated chemical change drives a spontaneous discharge reaction. The electrochemical discharge induces a reverse current in the storage electrode, but the same direction through the load as during light-induced charging. In each case in Table 24.1, exposure to light drives separate redox couples, and current through the external load.

Consistent with Fig. 24.1, in a regenerative photoelectrochemical solar cell (PEC), illumination drives work through an external load, without inducing a net change in the chemical composition of the system. This compares with the two-electrode PEC storage configurations shown in Fig. 24.4. Unlike a regenerative system, there is a net chemical change in the system, with an overall increase in free energy. In the absence of illumination, the generated chemical change drives a spontaneous discharge reaction. The electrochemical discharge induces a reverse current. Utilizing two quasi-reversible chemical processes, changes taking place in the system during illumination can be reversed in the dark. Similar to a secondary battery, the system

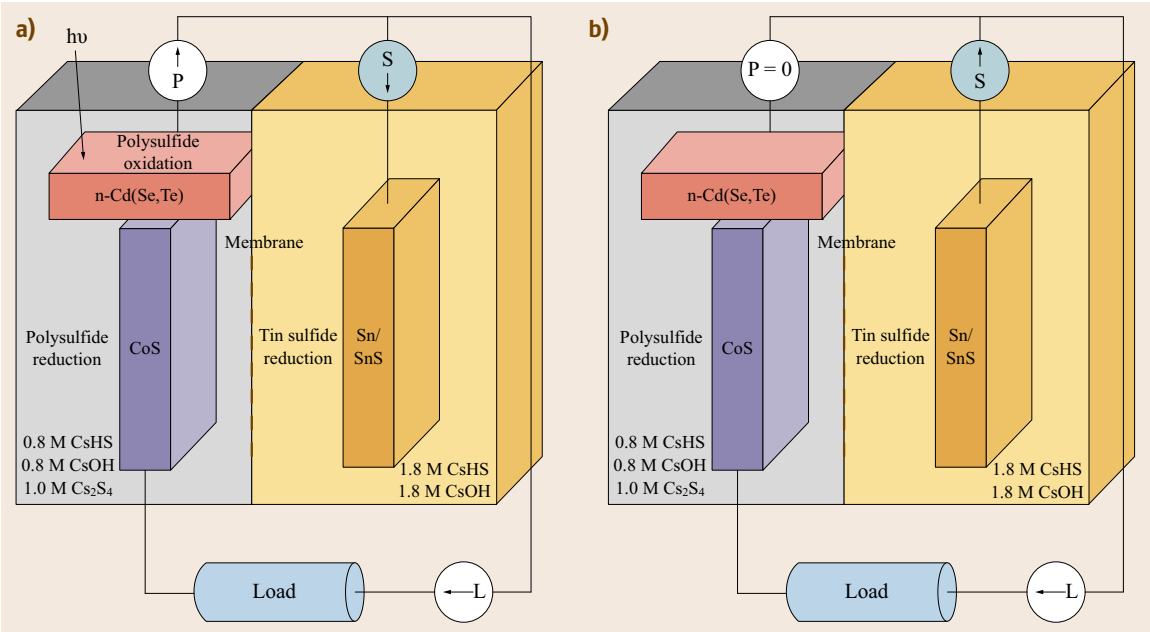


Fig. 24.3a,b Schematic of a photoelectrochemical solar cell combining both solar conversion and storage capabilities. **(a)** Under illumination; **(b)** in the dark

Table 24.1 Two electrode photoelectrochemical conversion and storage configurations. Components of these systems include a semiconductor photoelectrode (SPE) and counter electrode (CE). At the electrode/electrolyte interface, redox couples A or B are either in solution (|Redox|), counter electrode confined (|$Redox_{CE}$-CE|) or confined to the semiconductor photoelectrode (SPE -Redox A_{SPE}|)

Scheme	Electrode 1	Electrolyte(s)	Electrode 2
I	SPE	|Redox A Redox B	|CE
II	SPE	|Redox A -membrane- Redox B	|CE
Fig. 24.4a			
III	SPE	|Redox A	|Redox B_{CE} -CE 4-Left
Fig. 24.4b			
IV	SPE- Redox A_{SPE}	|Redox B	|CE
V	SPE	|Redox A -membrane- Redox B	|SPE

discharges producing an electric flow in the opposite direction and the system gradually returns to the same original chemical state.

Each of the cells shown in Fig. 24.4 have some disadvantages. For both bound (Fig. 24.4a) and soluble (Fig. 24.4b) redox couples, the redox species may chemically react with, and impair, the active materials of the photoelectrode. Furthermore, during the discharge process, the photoelectrode is kinetically unsuited to perform as a counter electrode. In the absence of illumination, the photoelectrode P, in this case a photoanode, now assumes the role of a counter electrode by supporting a reduction process. For the photoanode to perform efficiently during illumination (charging), this very same reduction process should be inhibited, to minimize photo-oxidation back reaction losses. Hence, the same photoelectrode cannot efficiently fulfill the duel role of being kinetically sluggish to reduction during illumination and yet being kinetically facile to the same reduction during dark discharge. The configuration represented in Fig. 24.4 has another disadvantage: the disparity between the small surface area needed to minimize photocurrent dark current losses, and the large surface area necessary to minimize storage polarization losses to maximize storage capacity. (3)dye-sensitized solar cell

Several of the two-electrode configuration disadvantages can be overcome by considering a three-electrode storage cell configuration as shown in Fig. 24.5, where the switches E and F are generally alternated

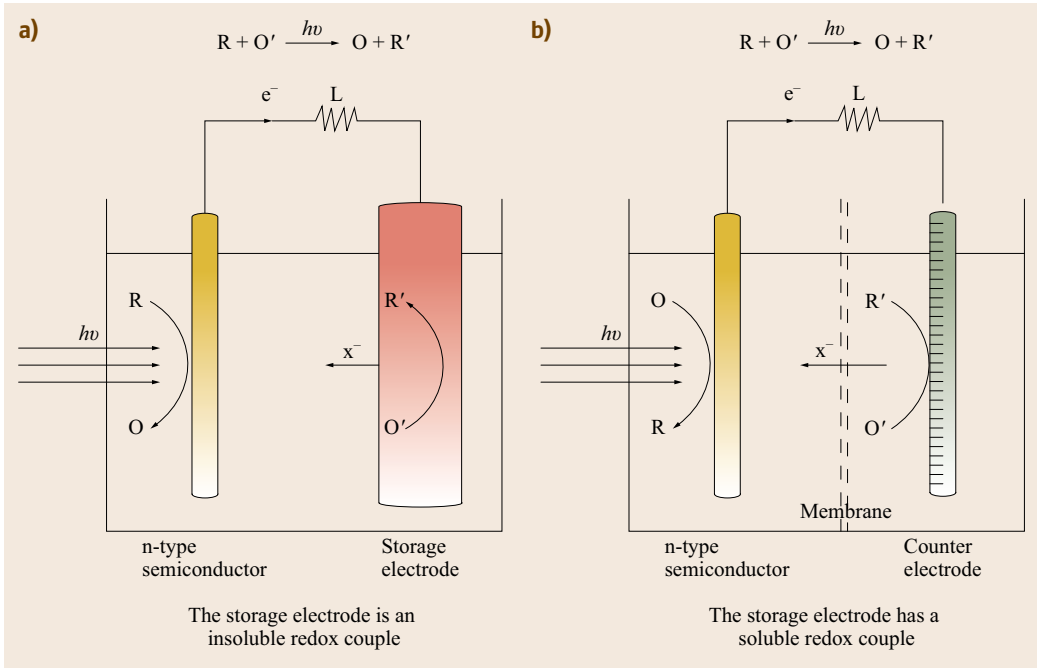


Fig. 24.4a,b Schematic diagrams of two electrode PEC storage cells with either **(a)** a insoluble or **(b)** soluble redox couple

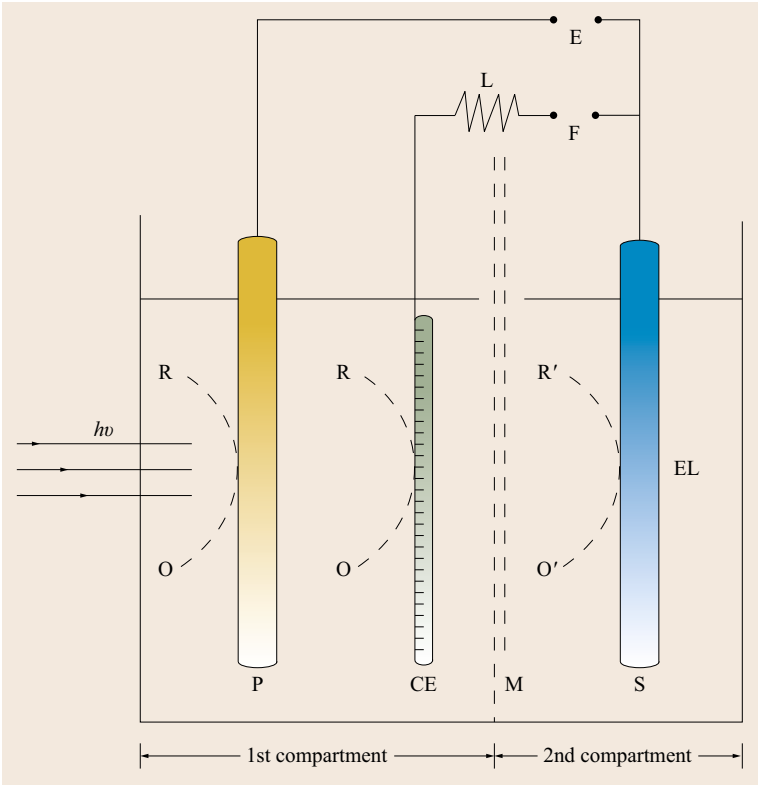


Fig. 24.5 Schematic diagram for a storage system with a third electrode (counter electrode) in the photoelectrode compartment. P = photoelectrode, CE = counter electrode, M = membrane, S = storage electrode, EL = electrolyte, E, F = electrical switch, L = load

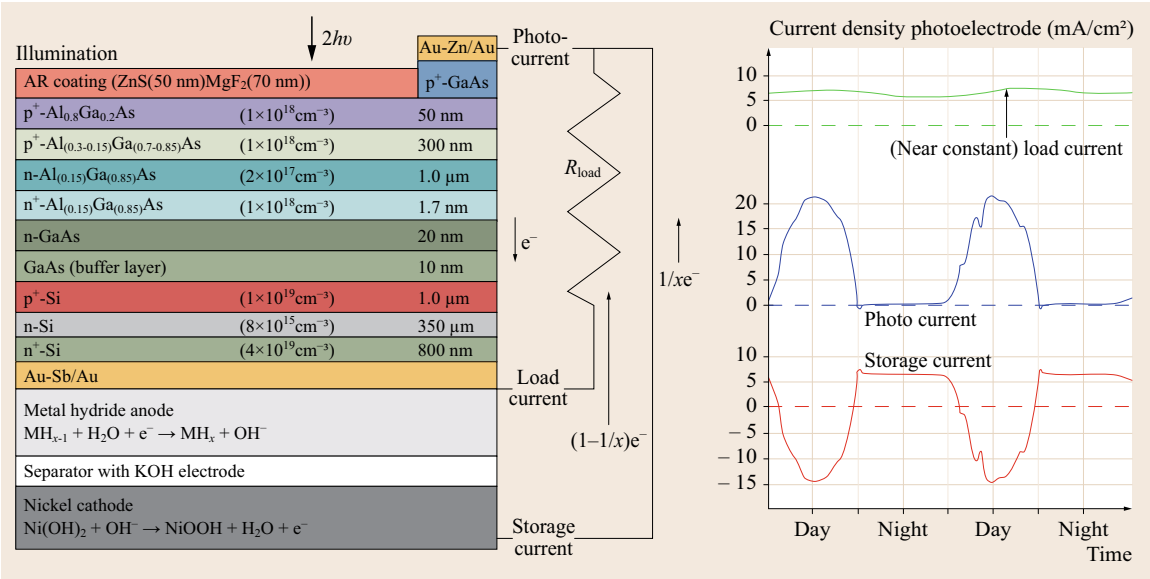


Fig. 24.6 High solar to electrical efficiency (18%) solar conversion and storage cell (after [24.31, 32])

during charge and discharge. During the charging, only switch E may be closed facilitating the storage process and during discharge E is kept open while F is closed. In this case, chemical changes that took place during the storage phase are reversed, and a current flow is maintained from the storage electrode to a third (counter) electrode (CE), which is kept in the first compartment. To minimize polarization losses during the discharge, this third electrode should be kinetically fast to the redox couple used in the first compartment.

Still an improved situation would be to have both switches closed all the time. In this case, electric current flows from the photoelectrode to both counter and storage electrodes. The system is energetically tuned such that when insolation is available, a significant fraction of the converted energy flows to the storage electrode. In the dark, or diminished insolation, the storage electrode begins to discharge, driving continued current through the load. In this system, a proper balance should be maintained between the potential of the solar energy conversion process and the electrochemical potential of the storage process. There may be residual electric flow through the photoelectrode during dark cell discharge, as the photoelectrode is sluggish, but not entirely passive, to a reduction process. This can be corrected by inserting a diode between the photoelectrode and the outer circuit.

A range of Scheme I to V (Table 24.1) systems for photoelectrochemical charge storage have been reviewed [24.33]. A logical evolution of Scheme I, is Scheme VI in Table 24.1, in which a photovoltaic cell drives a battery. This prevents any electrolytic corrosion of the semiconductor, as the semiconductor is only in electronic (wire) contact with the battery and never contacts the battery electrolyte. A high efficiency version of Scheme VI is shown in Fig. 24.6 and delivers a nearly constant power output, with little variation at night or under cloudy conditions.

The single cell in Fig. 24.6 contains both multiple bandgap and electrochemical storage, which unlike conventional photovoltaics, provides a nearly constant energetic output in illuminated or dark conditions [24.31], and exhibits excellent long-term stability [24.32]. The cell combines bipolar AlGaAs (E_g = 1.6 eV) and Si (E_g = 1.0 eV) and AB_5 metal hydride/NiOOH storage. Appropriate lattice matching between AlGaAs and Si is critical to minimize dark current, provide ohmic contact without absorption loss and maximize cell efficiency. The NiOOH/MH metal hydride storage process is near ideal for the AlGaAs/Si due to the excellent match of the storage and photocharging potentials. The electrochemical storage processes utilize MH oxidation and nickel oxyhydroxide reduction

$$\mathrm{MH + OH^- \rightarrow M + H_2O + e^-}$$
$$E_{\mathrm{M/MH}} = -0.8\ \mathrm{V\ vs\ SHE}$$
$$\mathrm{NiOOH + H_2O + e^- \rightarrow Ni(OH)_2 + OH^-}$$
$$E_{\mathrm{NiOOH/Ni(OH)_2}} = 0.4\ \mathrm{V\ vs\ SHE}$$

24.2.3 Dye-Sensitized Solar Cell

Excitation can also occur in molecules directly adsorbed and acting as a mediator at the semiconductor

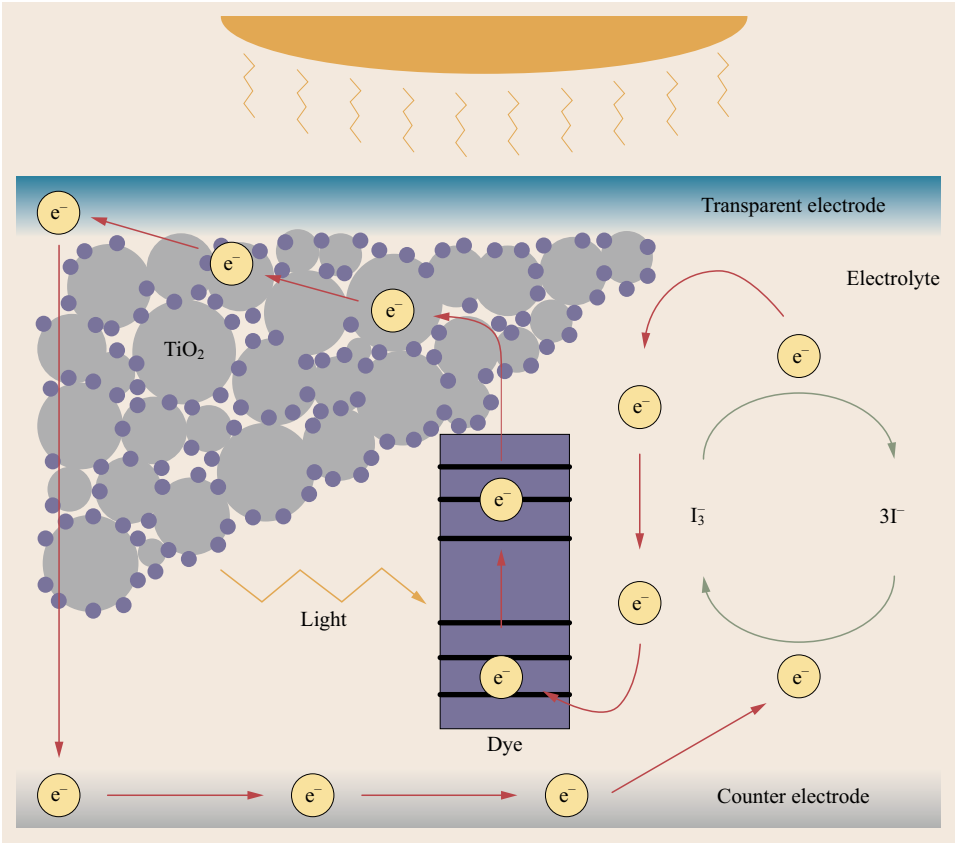


Fig. 24.7 Schematic operation of a dye-sensitized solar cell. Sunlight is shown striking (expanded) the dye on the TiO_2

interface. In this dye sensitization mode, the function of light absorption is separated from charge carrier transport. Photoexcitation occurs at the dye and photogenerated charge is then injected into a wide bandgap semiconductor. This alternative carrier generation mode can also lead to effective charge separation as illustrated in Fig. 24.7.

The first high solar to electric conversion efficiency example of a dye-sensitized solar cell was presented in 1991 [24.24], through the use of a high surface area (nanostructured thin film) n-TiO_2, coated with a well matched trimeric ruthenium complex dye immersed in an aqueous polyiodide electrolyte. The unusually high surface area of the transparent semiconductor coupled to the well matched spectral characteristics of the dye leads to a device which harvests a high proportion of insolation.

Functional components of a dye-sensitized solar cell are shown in Fig. 24.7. An electrically conducting transparent electrode is generally made of fluorine-doped tin dioxide (SnO_2) which is deposited on glass. This is coated with nanoporous, very high surface area TiO_2 on which a monolayer of dye is adsorbed. Sunlight enters the cell through the transparent electrode and strikes the dye. Photogenerated electrons are injected into the TiO_2 where they diffuse to the transparent electrode. The photoexcited dye removes electrons from iodide ions (injects holes to the iodide) to form triiodide (composed of iodine + iodide) ions I_3^-/I^-. The reverse redox process (the reduction of triodide back to iodide) occurs at the counter electrode. Hence, during solar to electrical conversion, the redox couple is regenerated and the concentration of the electrolyte remains unchanged.

This solar cell is made possible by the use of a high surface area nanoporous layer. The need to absorb more of the incident light was the driving force for the development of mesoscopic semiconductor materials with a very high surface area morphology. A single monolayer of the dye on the semiconductor surface was sufficient to absorb essentially all the incident light in a reasonable thickness (several um) of the nanoporous semiconductor film. TiO_2 became the semiconductor of choice as it is inexpensive, abundant and nontoxic. The original dye was tris(2,2′-bipyridyl-4,4′-carboxylate)ruthenium(II). The function of the carboxylate group in the dye is to attach the semiconductor oxide substrate by chemisorption. The dye must carry

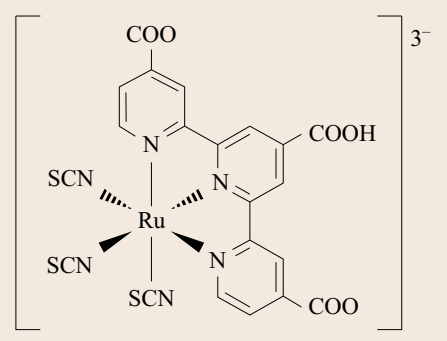


Fig. 24.8 The *Black Dye* has a wider spectral response than the original ruthenium bypyridine used in dye-sensitized solar cells (after [24.34])

attachment groups such as carboxylate or phosphonate to firmly graft onto the TiO_2 surface. The attachment group of the dye ensures that it spontaneously assembles as a molecular layer upon exposing the oxide film to a dye solution, and increases the probability that, once a photon is absorbed, the excited state of the dye molecule will relax by electron injection to the semiconductor conduction band. An alternative is the *Black Dye*, Fig. 24.8, tri(cyanato-2,2′,2″-terpyridyl-4,4′,4″-tricarboxylate)Ru(II) whose response extends 100 nm further into the infrared (IR).

As described by *Wei* [24.25], because of the encapsulation problem posed by the use of a liquid electrolyte, research is underway to form an enhanced stability, all solid-state dye-sensitized solar cell. In principle, a solid p-type conductor can replace the liquid electrolyte. The redox levels of the dye and p-type materials have to be adapted carefully, as Fig. 24.9 shows, to inject an electron into the conduction band of n-type semiconductors (e.g., TiO_2) and a hole into the valence band of the p-type conductor.

Wei has also reviewed recent efforts to form a conducting polymer dye-sensitized solar cell [24.25]. A conducting polymer, pyrrole, was electrochemically polymerized on dye-sensitized porous nanocrystalline TiO_2 electrode, and functions as a hole transport layer connecting dye molecules anchored on TiO_2 to the counter electrode. Conducting polyaniline has also been used in solid state solar cells sensitized with methylene blue with conducting polyaniline-coated electrodes sandwiched with a solid polymer electrolyte, poly(vinyl alcohol) with phosphoric acid. The prototype of this kind of conducting polymer dye-sensitized solar cell is shown in Fig. 24.10, and to date, these cells offer only ≈ 40% the output of comparable liquid electrolyte dye-sensitized solar cells [24.34]. The solar to electrical efficiency of dye-sensitized solar cells generally remains lower than those of solid-state devices such as

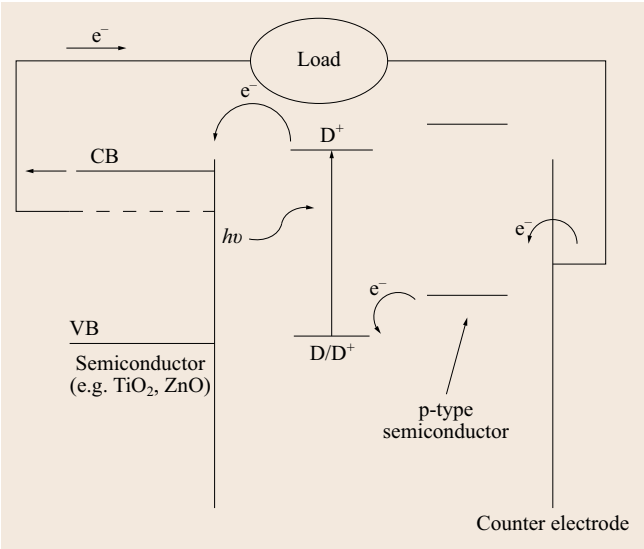


Fig. 24.9 The mechanism of a dye-sensitized solar cell with a p-type semiconductor to replace the liquid electrolyte containing redox couples in electrolyte. D: dye sensitizer, D*: electronically excited dye, D^+: oxidized dye, CB: semiconductor conduction band, VB: semiconductor valence band (after [24.25])

thin film, silicon and concentrator photovoltaics. Dye-sensitized solar cells were widely studied during the period from 1991 through 2010 and a variety of reviews are available [24.25, 35–39].

24.2.4 Multi-Bandgap Semiconductor/Electrolyte Electrical Energy Conversion

Energetic constraints imposed by single bandgap semiconductors limited values of photoelectrochemical solar to electrical energy conversion efficiency to date to 12–16% [24.20, 40]. Multiple bandgap devices can provide efficient matching of the solar spectra [24.41–45]. A two or more bandgap configuration will lead, per unit surface area, to more efficient solar energy conversion, and in the solid state multiple bandgap solar cells have achieved more than 40% conversion efficiency of solar energy [24.46].

A limited fraction of incident solar photons have sufficient (greater than bandgap) energy to initiate charge excitation within a semiconductor. Due to the low fraction of short wavelength solar light, wide bandgap solar cells generate a high photovoltage, but have low photocurrent. Smaller bandgap cells can utilize a larger fraction of the incident photons, but generate lower photovoltage. As shown in the Fig. 24.11 schematic, multiple bandgap devices can overcome these limitations. In stacked multijunction systems, the

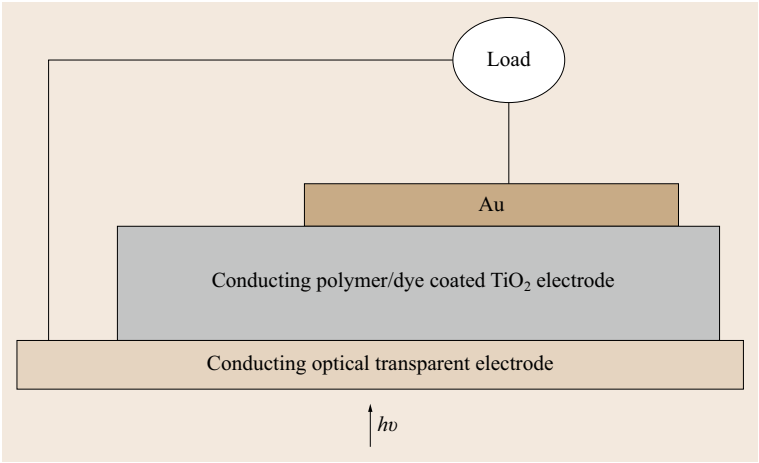


Fig. 24.10 The conducting polymer dye-sensitized solar cell (after [24.25])

topmost cell absorbs (and converts) energetic photons, but is transparent to lower energy photons. Subsequent layer(s) absorb the lower energy photons, and conversion efficiencies can be enhanced.

A variety of distinct multiple bandgap photoelectrochemical solar cell (MBPEC) configurations are possible, each with advantages and disadvantages [24.21]. The simplest MBPEC configurations contain two different bandgaps which can be aligned in the cell in either a bipolar (or *tandem*), or a less conventional inverted manner. In either configuration, the PEC solid/electrode interface can consist of either an ohmic or a Schottky interface. The ohmic interface can consist of either direct (semiconductor/electrolyte) or indirect (semiconductor/metal and/or electrocatalyst/electrolyte) interfaces. The bipolar arrangement provides a conceptually simpler PEC, and generates a large open circuit photopotential V_{oc}. The generated bipolar photovoltage V_{photo} is the sum of the potentials of the individual bandgap layers, minus cathodic and anodic polarization losses in driving a regenerative redox couple

$$V_{photo} = V_w + V_s - (\eta_{cathode} + \eta_{anode}) \, .$$

The energy diagram of a bipolar bandgap photocathodic electrochemical Schottky configuration is presented in Fig. 24.12. The scheme comprises a two photon/one electron photoelectrochemical process ($2h\nu \rightarrow e^-$), which may be generalized for an n bandgap configuration, to an n photon process ($nh\nu \rightarrow e^-$). Light shown incident from the left side of the configuration, first enters the wide bandgap layer(s) in which more energetic photons are absorbed; less energetic photons are transmitted through this upper layer, and are absorbed by the small bandgap layer. The resultant combined potential of the photodriven charge sustains reduction at the photocathode interface, and drives extractable work through the external load R_{load}. The wide (w) and small (s) bandgap layers are denoted with respective valence and conduction bands, E_V and E_C, and bandgap of

$$E_{Gw} = E_{Cw} - E_{Vw}; \quad E_{Gs} = E_{Cs} - E_{Vs} \, .$$

Wide bandgap layer charge separation occurs across a pn junction space charge field gradient, while charge separation in the small bandgap is maintained with a field formed by the Schottky semiconductor/electrolyte interface. In the bipolar Schottky MBPEC configuration, generated charge flows through all layers of the cell, providing the additional constraint [24.47]

$$j_{ph,pn} = j_{ph,sh} \, .$$

A bipolar gap direct ohmic photoelectrochemical system comprises either: a bipolar bandgap pnpn/electrolyte ohmic photoelectrochemical cell, with reduction occurring at the photoelectrode/electrolyte interface and regenerative oxidation occurring at the electrolyte/counter electrode (anode) interface, or alternately: a npnp/electrolyte bipolar bandgap with oxidation occurring at the semiconductor/electrolyte interface and regenerative reduction occurring at the electrolyte/counter electrode interface.

In an alternate bipolar regenerative configuration, the bipolar (or multiple) bandgap configurations may contain consecutive space charge field gradients generated only via solid state phenomena. For example, in the case of two consecutive bipolar pn junctions, the lowest semiconductor layer (the small bandgap n-type layer in Fig. 24.12) may remain in direct contact with the electrolyte, but the contact is ohmic, and is not the source of the small bandgap space charge field. In this case, the lowest semiconductor layer is restricted

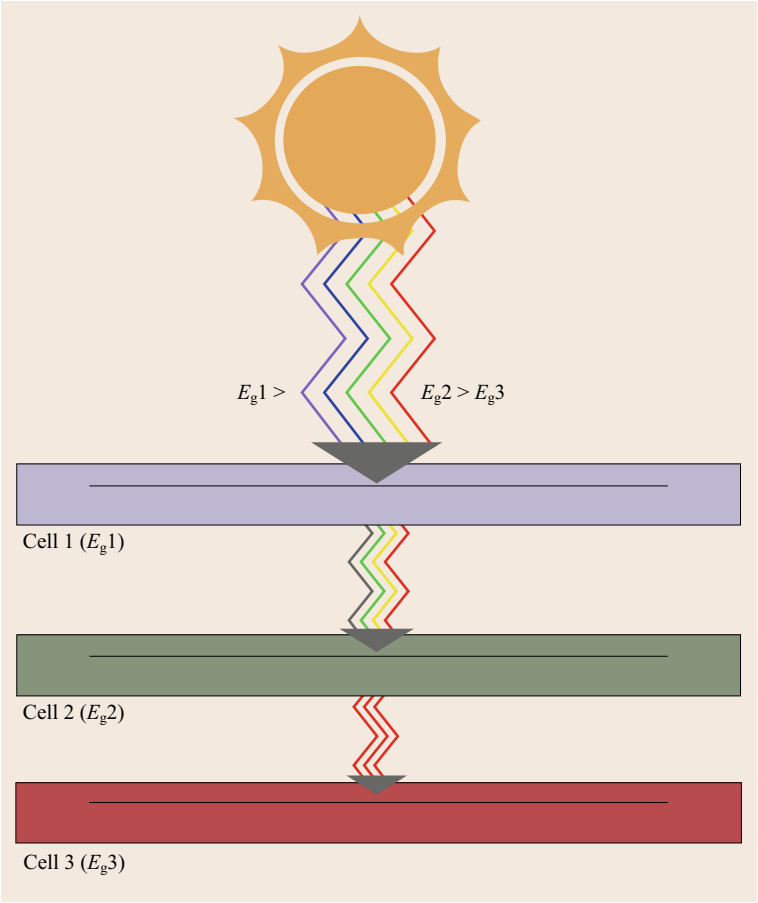


Fig. 24.11 In stacked multijunction solar cells, the top cell converts higher energy photons and transmits the remainder into layers, each of smaller bandgap cell than the layer above, for more effective utilization of the solar spectrum

to electronic, and not ionic contact with the electrolyte, through use of an intermediate (bridging) ohmic electrocatalytic surface layer. This can facilitate charge transfer to the solution phase redox couple, and prevent any chemical attack of the semiconductor. In the bipolar cases (including Schottky, direct or indirect ohmic configurations), the photopower generated by a bipolar regenerative MBPEC is given by the product [24.12]

$$P_{\text{bipolar regenerative}} = j_{\text{ph}}[V_{\text{w}} + V_{\text{s}} - (\eta_{\text{cathode}} + \eta_{\text{anode}})] \, .$$

The example presented here combines multijunction solid state layers consisting of a bipolar AlGaAs ($E_{\text{Gw}} = 1.6\,\text{eV}$) wide bandgap, overlaid on a Si ($E_{\text{Gs}} = 1.0\,\text{eV}$) small bandgap, and used in an electrolytic cell [24.21]. Light absorption by the electrolyte can interfere with the cell and should be avoided. Figure 24.13 overlays the optical characteristics of the solid and solution phase of the AlGaAs/Si solid state and $V^{3+/2+}$ electrolyte optimized components within a bipolar gap photoelectrochemical cell. Solution transmission is measured through a pathlength typical (1 mm) of many experimental front wall photoelectrochemical cells. As is evident, light transmission interference will occur for the top AlGaAs layers and bottom Si layers through this or substantially shorter electrolyte pathlengths. The solid state component includes a graded band emitter, varying from $Al_{(0.3-0.15)}Ga_{(0.7-0.85)}As$ with overlayers of p^+-$Al_xGa_{x-1}As$ on n-$Al_xGa_{x-1}As$. The growth sequence and graded band emitter layer improve collection efficiency. The Si bottom cell consists of a p^+-Si, n-Si and n^+-Si multijunction. The band edges observed in the figure at approximately 800 and 1100 nm are consistent with the respective AlGaAs and Si bandgaps.

For efficient electron/hole pair charge generation, incident photons need to be localized within the multiple bandgap semiconductor small and wide bandgap regions, rather than lost through competitive electrolyte light absorption. As seen in Fig. 24.13 the vanadium electrolyte can significantly block light, over a wide range of visible and near infrared wavelengths, from entering the wide and small bandgap layers of the multiple bandgap photoelectrochemical cell. This deleterious effect is prevented by use of the back wall

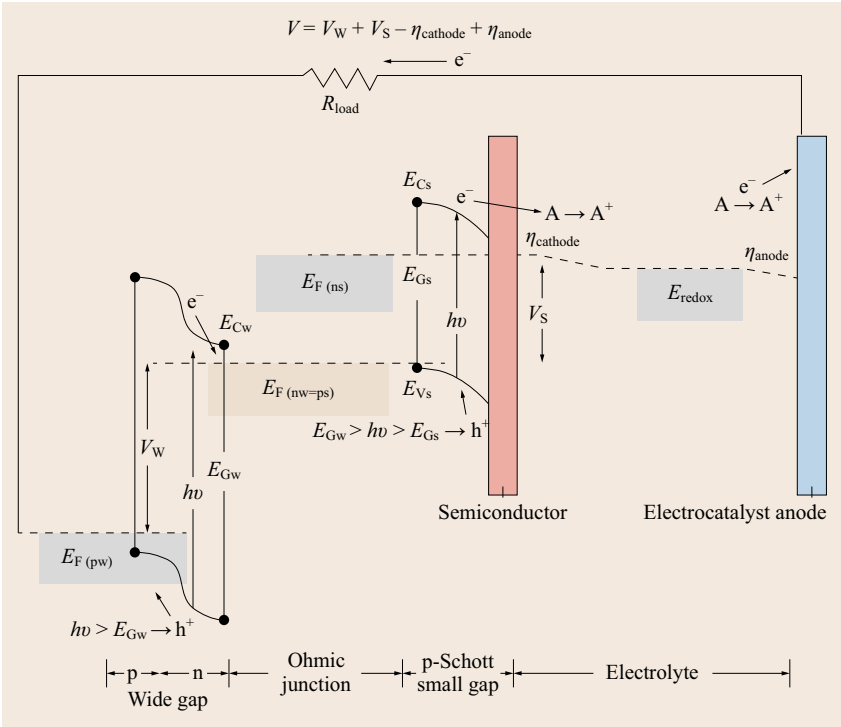


Fig. 24.12 Energy diagram for a bipolar bandgap Schottky regenerative MBPEC

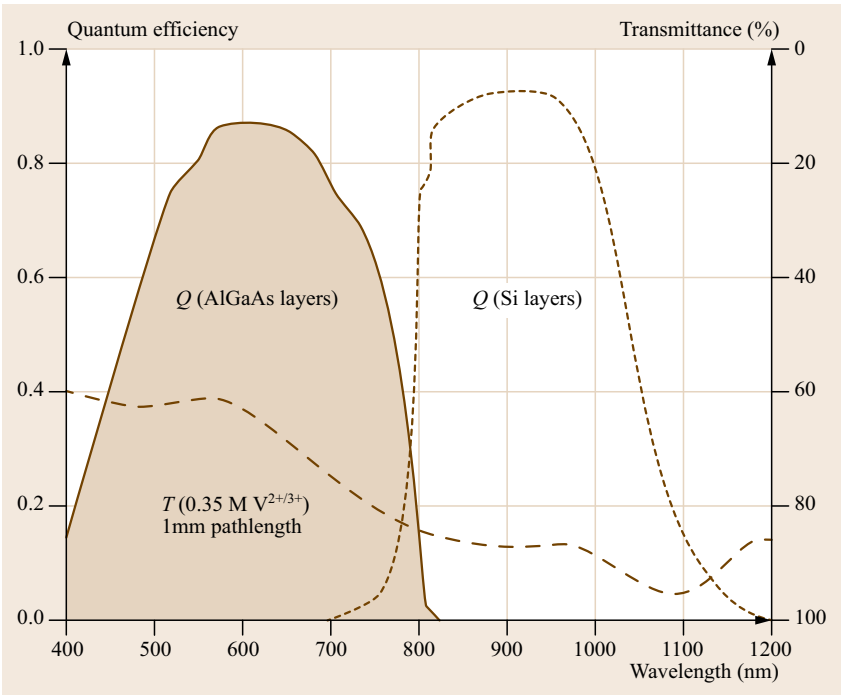


Fig. 24.13 Overlay of the optical characteristics of the solid and solution phase of the AlGaAs/Si solid state and $V^{3+/2+}$ electrolyte constituents within a bipolar gap photoelectrochemical cell. Transmission of the $V^{3+/2+}$ electrolyte is measured through a pathlength of 1 mm. As described in the text, the Si bottom cell consists of a p^+-Si, n-Si and n^+-Si multijunction. The $Al_{(0.3-0.15)}Ga_{(0.7-0.85)}As$ top cell utilizes a graded band emitter

multiple bandgap photoelectrochemical cell presented in Fig. 24.14. Light does not pass through the solution. As shown, illumination enters directly through anti reflection films of 50 nm ZnS situated on 70 nm MgF_2. An evaporated Au-Zn/Au grid provides electrical contact to the wide gap AlGaAs layers through a bridging p^+

= GaAs layer. Internally, a bridging GaAs buffer layer provides an ohmic contact between the wide bandgap AlGaAs junctions and the lower Si layers. An intermediate contact layer indicated as Au is used only for probing separated characteristics of the wide and small bandgap junctions, and is not utilized in the complete cell. Photo-generated charge at the indicated silicon electrolyte interface induces solution phase vanadium reduction, and a carbon counter electrode provides an effective (low polarization) electrocatalytic surface for the reverse process in a regenerative cell, in accord with

$$V^{3+}\ (+h\upsilon) \rightarrow V^{2+} + h^{+}; \quad V^{2+} \rightarrow V^{3+} + e^{-}\ .$$

Maximization of the photopower necessitates minimization of the anodic and cathodic polarization losses, η_{anode} and $\eta_{cathode}$ during charge transfer through the photoelectrode and counter electrode interfaces. In the current domain investigated, polarization losses are linear for both anodic and cathodic processes at 2.5–3.5 mV/(mA/cm^2) and can create small, but significant, losses on the order of 10–100 mV in the MBPEC.

Figure 24.15 presents the outdoor characteristics of the bipolar direct ohmic AlGaAs/Si/$V^{2+/3+}$ photoelectrochemical cell under solar illumination. The system comprises the individual components illustrated in Fig. 24.15 and uses an HF containing aqueous vanadium electrolyte to improve photocurrent stability (0.35 M V(II)+V(III), 4 M HCl, 0.2 M HF). As shown under 75 mW/cm^2 insolation, the AlGaAs/Si/$V^{2+/3+}$ electrolyte photoelectrochemical solar cell exhibits an open circuit potential $V_{oc} = 1.4$ V, a short circuit photocurrent $j_{sc} = 12.7$ mA/cm^2, a fill factor FF = 0.81, determined from the fraction of the maximum power P_{max} compared to the product of the open circuit potential and short circuit current. The multiple bandgap solar to electrical conversion efficiency of 19.1% compares favorably to the maximum 15–16% solar to electrical energy conversion.

A common disadvantage of photoelectrochemical systems is photoinduced corrosion of the semiconductor which originates at the semiconductor/solution interface. The corroded surface dissolves the semiconductor or inhibits charge transfer which diminishes photocurrent. A stable solid/solution interface which both facilitates charge transfer and impedes semiconductor photocorrosion, is provided by an electrocatalyst placed between the semiconductor and the electrolyte. The multiple bandgap photoelectrochemical cell can utilize this electrocatalyst interface, as well as a bipolar series arrangement of wide and small bandgap semiconductors to enhance energy conversion. In this indirect ohmic photoelectrochemistry, such as with a modified GaAs/Si-$V^{3+/2+}$ MBPEC, electrolyte-induced photocorrosion of the silicon is entirely inhibited by utilization of an electrocatalyst (a second carbon electrode) bridging charge transfer between the semiconductor and the electrolyte, while retaining a high solar to electrical conversion efficiency in excess of 19%.

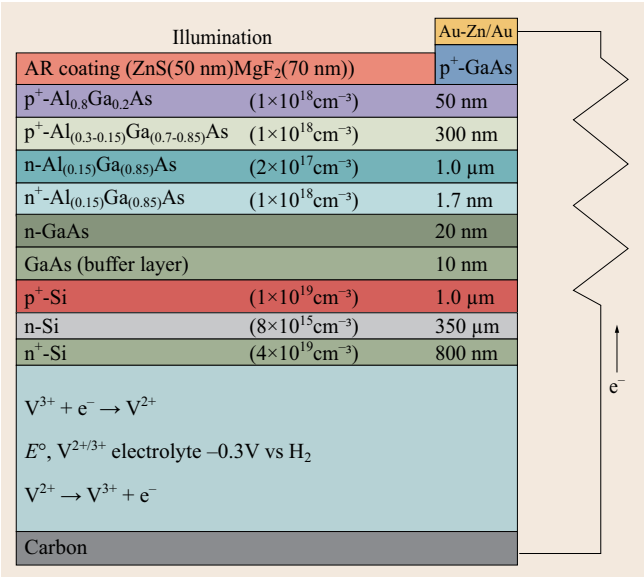


Fig. 24.14 Schematic description of the components in the bipolar gap direct ohmic AlGaAs/Si-$V^{3+/2+}$ photoelectrochemical solar cell

24.2.5 Solar Thermal Electrochemical Photochemical Energy Conversion

Rather than using solar generation to form electricity as a product, solar energy can be used to form chemicals. This section explores an electrochemical approach to efficiently generate useful chemicals using solar energy. The new process is synergetic, using both the visible and thermal components of sunlight, to achieve higher solar energy conversion efficiencies than processes that use only radiation used by the semiconductor, or thermal sunlight. The captured solar energy is stored within the generated energetically rich chemical products, including iron, bleach, lime, solar fuels, and to proactively convert anthropogenic CO_2 generated in burning fossil fuels [24.1, 28, 48–57].

With photovoltaic solar cells, charge transfer only occurs up to the semiconductor band edge, excluding the use of long wavelength (thermal) radiation. The new STEP (solar thermal electrochemical production) pro-

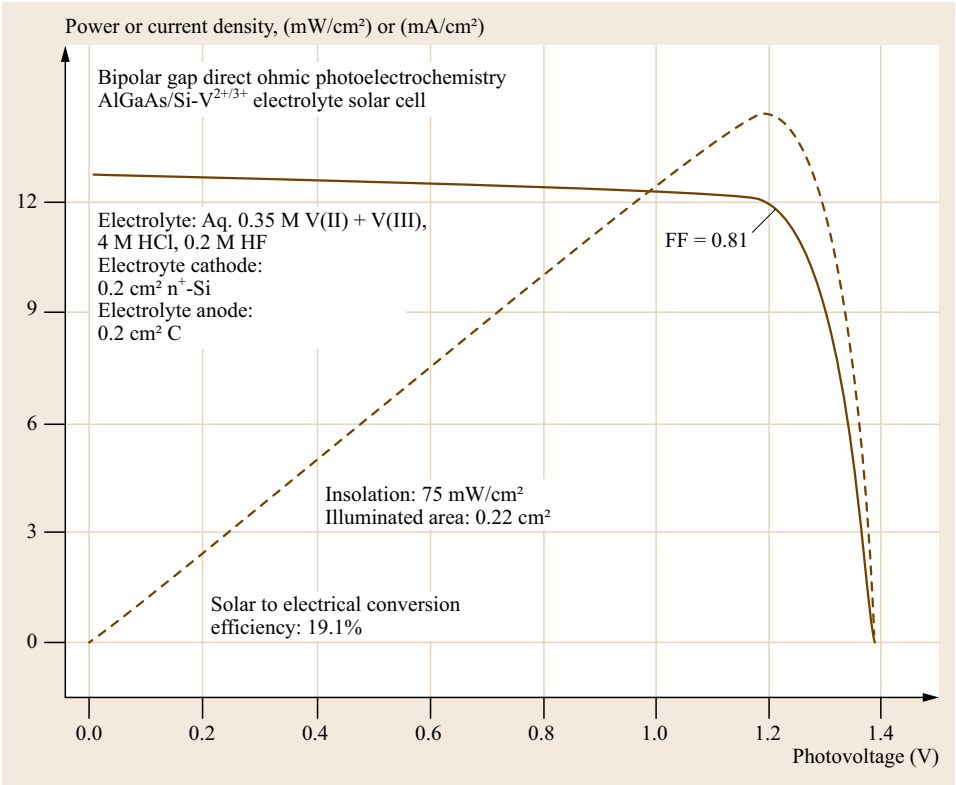


Fig. 24.15 Measured outdoor photocurrent/voltage characteristics of the bipolar gap direct ohmic AlGaAs/Si-$V^{3+/2+}$ photoelectrochemical solar cell (after [24.21])

cess of energetic molecules distinguishes radiation that has sufficient energy to drive photovoltaic charge transfer, and applies all excess energy to heat and to drive enodothermic electrolysis reactions (reactions chosen that require less energy at higher temperature). Examples of electrolysis reactions that are endothermic are presented in Fig. 24.16.

One example of the STEP process is the reduction of the greenhouse gas carbon dioxide back to carbon, or to carbon monoxide. The latter product is a useful starting point for the synthesis of a range of useful hydrocarbon products. CO_2 is a stable gas, and normally difficult to activate and utilize. However, as seen in Fig. 24.17a, CO_2 is readily electrically reduced to carbon in high temperature molten carbonates. As summarized in the figure, the principal product switches from C to CO at elevated temperatures, the rates of electrolysis are high (A/cm^2) and the electrochemical potential decreases with increasing temperature. Solar energy drives the process from 30 to over 50% conversion efficiency, depending on the efficiency of solar heat used to increase the temperature of the CO_2 reactant [24.48]. Similarly, iron oxide is readily reduced to iron metal and oxygen. In this latter example of STEP iron production process, visible light drives conventional PV electronic charge transfer, and all excess heat is used to increase the electrolysis temperature. Iron is produced at low electrolysis potential (less than 1 V), and without the CO_2 emissions associated with the industrial carbothermic process used to form iron [24.48, 50].

Light-driven water splitting to generate H_2 was originally demonstrated with TiO_2 (a seminconductor with a bandgap $E_g > 3.0\,eV$) [24.5]. However, only a small fraction of sunlight has sufficient energy to drive TiO_2 photoexcitation, and studies had sought to tune (lower) the semiconductor bandgap to provide a better match to the electrolysis potential [24.42], or to use multiple photons to drive the multiple bandgap water electrolysis [24.58]. The STEP process was used to demonstrate the first case in which a small bandgap semiconductor, such as silicon ($E_g = 1.12\,V$) can be used to directly spit hydrogen fuel from water splitting (E_{H_2O}) $= 1.23\,V$), with $> 30\%$ solar to hydrogen energy conversion [24.27, 59]. The key is that, rather than previous attempts to tune the bandgap of the semiconductor to make it more compatible with the water splitting energetics, the STEP approach tunes the water splitting potential to match the semiconductor bandgap. A single small band gap material, such as silicon, cannot generate the minimum potential required to drive many room temperature redox couples as illustrated in

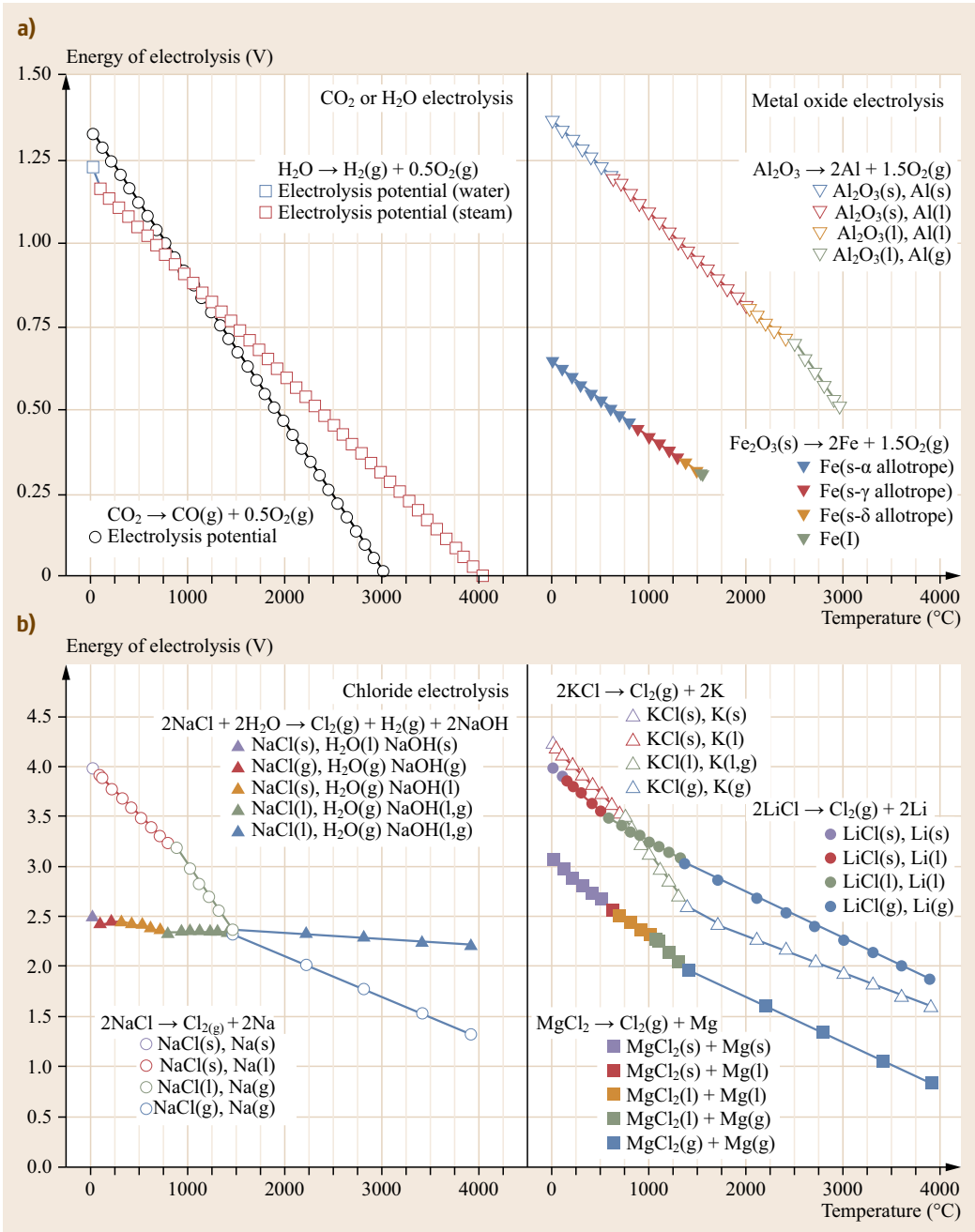


Fig. 24.16a,b The thermodynamic potential to electrolyze selected oxides **(a)** and chlorides **(b)**. The decrease in electrolysis energy, with increase in temperature, provides energy savings in the STEP process in which high temperature is provided by excess solar heat (after [24.28])

Fig. 24.18a. Rather than tuning the bandgap to provide a better energetic match to the electrolysis potential, the STEP process instead tunes the redox potential to match the bandgap. Figure 24.18b presents the energy diagram for a STEP process.

At any electrolysis temperature T_{STEP} and at unit activity, the reaction has electrochemical potential E_T^0. This may be calculated from consistent, compiled unit activity thermochemical data sets, such as the NIST condensed phase and fluid properties data sets, [24.14] as

$$E_T^0 = -\frac{\Delta G^\circ(T = T_{\mathrm{STEP}})}{nF} ,$$

$$E^\circ_{\mathrm{ambient}} \equiv E_T^0(T_{\mathrm{ambient}}) ,$$

here $T_{\mathrm{ambient}} = 298.15\,\mathrm{K} = 25\,^\circ\mathrm{C}$.

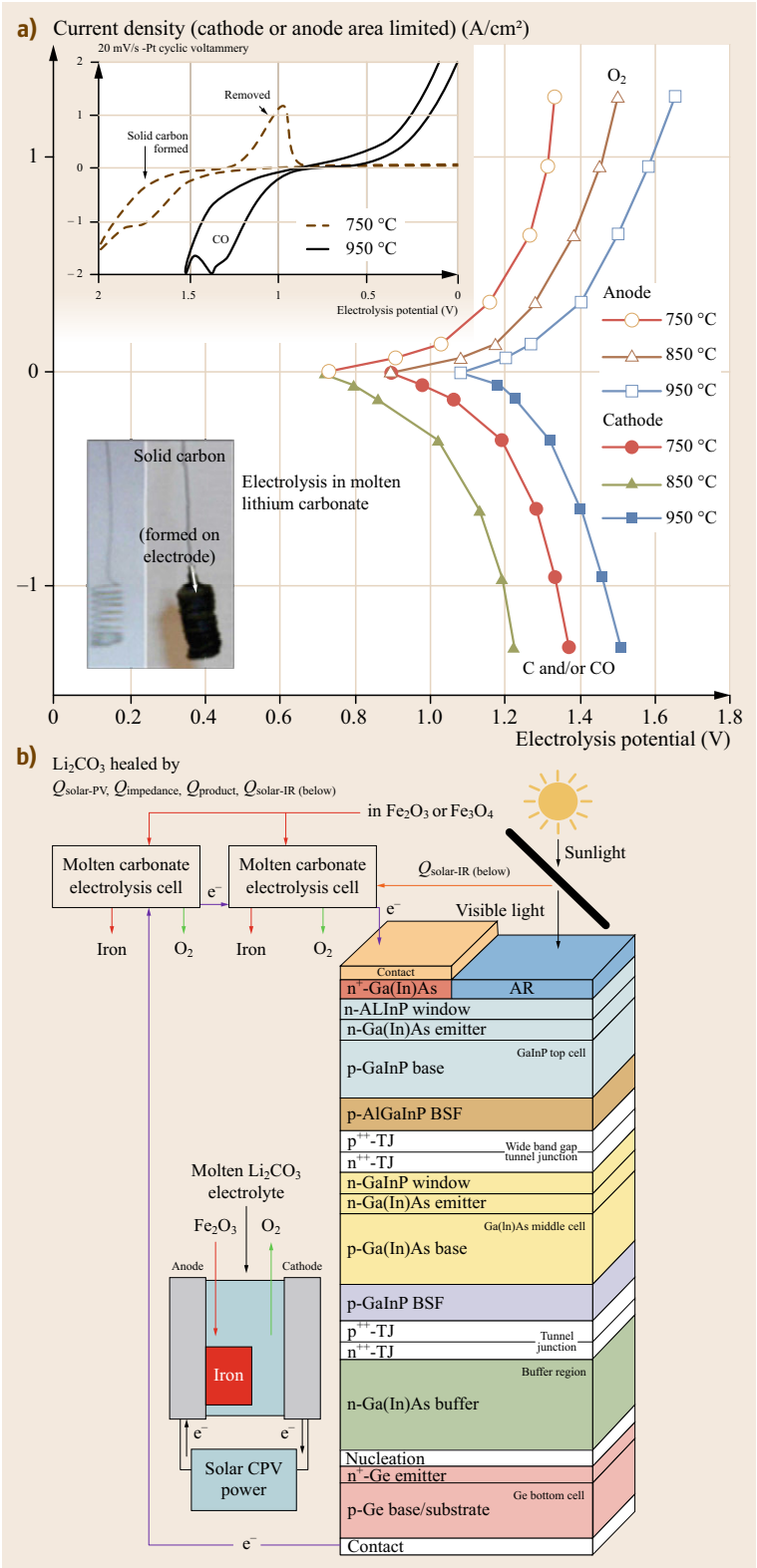


Fig. 24.17 **(a)** *Photograph inset*: electrode before (*left*), and after (*right*) carbon capture at 750 °C in molten carbonate. Carbon dioxide fed into the electrolysis chamber is converted to solid carbon in a single step. Main figure: The electrolysis full cell potential, in molten Li_2CO_3. *Figure inset*: cyclic voltammetry in molten Li_2CO_3 (after [24.48]). **(b)** In STEP iron production, solar thermal can be separated from visible sunlight using a cold mirror to provide one thermal component Q to heat a molten carbonate electrolysis chamber. Iron ore, such as hematite (Fe_2O_3) is added to the carbonate and is electrolyzed to iron metal using power from the CPV solar cell driven by visible sunlight (after [24.48, 50])

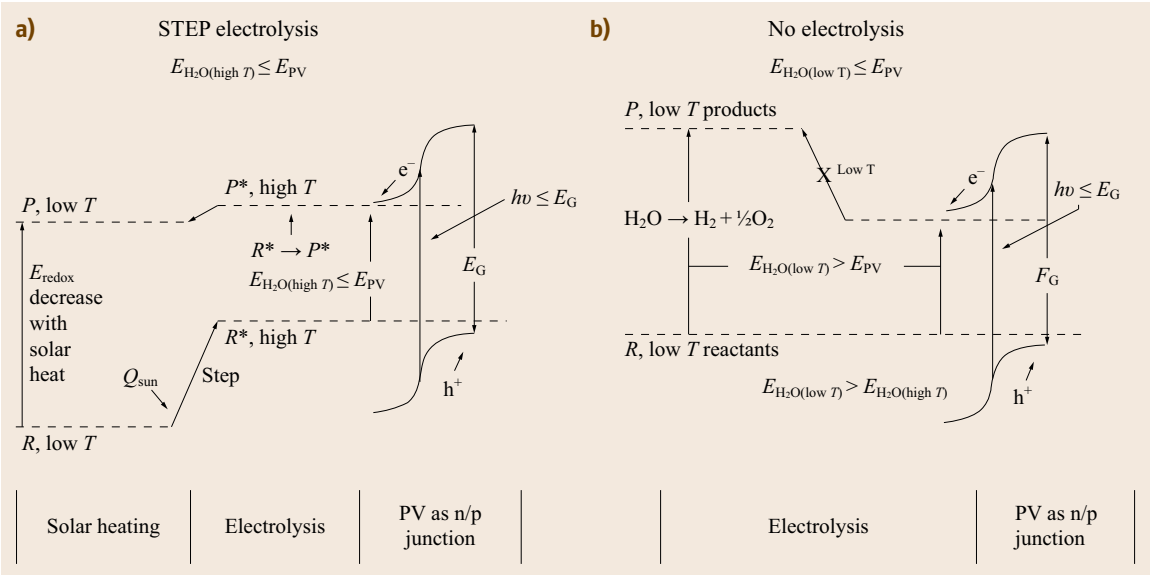


Fig. 24.18a,b Comparison of the STEP and ambient temperature solar driven water electrolysis energy diagrams. **(a)** A conventional efficient PV generates a voltage too low to drive the indicated generic redox transfer. **(b)** The STEP process uses both visible and thermal solar energy for higher efficiency. The process uses this thermal energy for the indicated step decrease of the necessary electrolysis energy and forms an energetically allowed pathway to drive electrochemical charge transfer

Given a stable high temperature electrolysis environment, the experimental STEP solar conversion efficiency is the product of the electrolysis efficiency and the electronic solar efficiency

$$\eta_{STEP} = \eta_{PV}\eta_{electrolysis} \,.$$

STEP's high temperature pathway decreases the thermodynamic energy requirements for processes whose electrolysis potential decreases with increasing temperature. The extent of the decrease in the electrolysis potential E_{redox} may be tuned (will vary) with the temperature.

24.3 State-of-the-Art and Emerging Technologies

The simplest mode of photoelectrochemical energy conversion occurs with illumination of a semiconductor immersed in an electrolyte. In this mode solar energy conversion efficiencies of up to 18% have been achieved. However, these systems remain a technological challenge due to corrosion and photocorrosion at the semiconductor/electrolyte interface which decreases the output over time. Though not commercialized as solar cells in this mode, related photoelectrochemistry methodologies have commercial applications including photoelectrochemical etching as a useful surface treatment for the semiconductor industry [24.18], and cesium improvements on photoelectrochemical charge transfer [24.19] to increase efficiencies in photovoltaic cells [24.60].

Another approach is to use TiO_2 as a highly stable photoabsorber/electrolyte interface, even though its wide bandgap ($E_g = 3.2$ eV) can only access the near UV, but not the visible or IR portions of sunlight. A range of commercial disinfectant products, which use the oxidizing power available at the illuminated TiO_2 aqueous surface, have been developed, including self cleaning tiles and headlights, air purifiers and drinking water sterilization [24.6, 61].

Another alternative to avoid electrolyte contact and the corrosion at the interface is to use a back-wall cell configuration, in which the semiconductor-as-photoabsorber layer does not contact the electrolyte [24.62]. The alternative, which has received the greatest deal of attention, is to replace the semiconductor-as-photoabsorber with a dye-as-the-photoabsorber. While solar efficiencies of these dye-sensitized solar cells have only improved modestly in nearly two decades, [24.24] the production of higher

surface area cells is improving and several companies claim low cost, effective cells, and are promising availability of the dye-sensitized solar cell in the near future including SolarPrint, G24innovations, Hydrogen Solay, Dyesol, Konarka, Aisin Seiki and Sony [24.34].

One third of the global industrial sector's annual emission of 1×10^{10} t (metric tons) of the greenhouse gas CO_2, is released in the production of metals and chlorine. The photoelectrochemical generation of these staple chemicals without carbon dioxide emission is viable [24.28]. This, together with the additional CO_2 emissions for electrical generation, heating and transportation, comprise the majority of anthropogenic CO_2 emissions. The STEP process proactively converts anthropogenic CO_2 generated in burning fossil fuels, as well as eliminates CO_2 emissions associated with the generation of hydrogen fuel, bleach, iron, aluminum, chlorine, magnesium, lithium and sodium, and carbon monoxide, and synthetic diesel and jet fuels. This process captures sunlight more efficiently than photovoltaics. STEP's synergistic coupling of endothermic electrolysis with photovoltaics is promising, and is intrinsically more efficient than photovoltaics alone. Photovoltaic efficiencies above 40% have been reported [24.46], which will provide impetus to develop new STEP technologies. STEP hydrogen generators are under development by Lynntech, Inc., College Station, TX for the US Airforce [24.63].

24.4 Summary

Society's electrical needs are largely continuous. However, clouds and darkness dictate that photovoltaic solar cells have an intermittent output. A photoelectrochemical solar cell (PEC) can generate not only electrical but also electrochemical energy, and provide the basis for a system with an energy storage component. Sufficiently energetic insolation incident on semiconductors can drive electrochemical oxidation/reduction and generate chemical, electrical or electrochemical energy. Aspects include efficient dye sensitized or direct solar to electrical energy conversion, solar electrochemical synthesis (electrolysis), including water splitting to form hydrogen, environmental cleanup and solar energy storage cells. The PEC utilizes light to carry out an electrochemical reaction, converting light to both chemical and electrical energy. This fundamental difference of the photovoltaic (PV) solar cell's solid/solid interface, and the PEC's solid/liquid interface has several ramifications in cell function and application. Energetic constraints imposed by single bandgap semiconductors have limited the demonstrated values of photoelectrochemical solar to electrical energy conversion efficiency to 16%, and multiple bandgap cells can lead to significantly higher conversion efficiencies. Photoelectrochemical systems may facilitate not only solar to electrical energy conversion, but have also led to investigations in solar photoelectrochemical production of fuels and photoelectrochemical detoxification of pollutants, and efficient Solar Thermal Electrochemical Production (STEP) of metals, fuels, bleach and carbon capture.

References

24.1 S. Licht, B. Cui, B. Wang, F.-F. Li, J. Lau, S. Liu: Ammonia synthesis by N_2 and steam electrolysis in molten hydroxide suspensions of nanoscale Fe_2O_3, Science **345**(6197), 637–640 (2014)

24.2 E. Becquerel: Memoires sur les effets electriques produits sous l'influence des rayons, C.R. **9**, 561–567 (1839)

24.3 H. Gerischer: Semiconductor electrode reactions, Adv. Electrochem. Electrochem. Eng. **1**, 139 (1961)

24.4 H. Gerischer: Semiconductor electrochemistry, Phys. Chem. **9**, 463–542 (1970)

24.5 A. Fujishima, K. Honda: Electrochemical photolysis of water at a semiconductor electrode, Nature **238**, 37–38 (1972)

24.6 T. Rao, D.A. Tryk, A. Fujishima: Applications of TiO_2 photocatalysis. In: *Semiconductor Electrodes and Photoelectrochemistry*, ed. by S. Licht (Wiley-VCH, Weinheim 2002), Chap. 6.1

24.7 G. Hodes, J. Manassen, D. Cahen: Photoelectrochemical energy conversion and storage using polycrystalline chalcogenide electrodes, Nature **261**, 402–404 (1976)

24.8 A.B. Ellis, S.W. Kaiser, M.S. Wrighton: Visible light to electrical energy conversion. Stable cadmium sulfide and cadmium selenide photoelectrodes in aqueous electrolytes, J. Am. Chem. Soc. **98**, 1635–1637 (1976)

24.9 B. Miller, A. Heller: Semiconductor liquid junction solar cells based on anodic sulphide films, Nature **262**, 680–681 (1976)

24.10 A.J. Nozik: Photoelectrochemistry: Applications to solar energy conversion, Annu. Rev. Phys. Chem. **29**, 18–222 (1978)

24.11 M.A. Butler, D.S. Ginley: Review principles of photoelectrochemical, solar energy conversion, J. Mater. Sci. **15**, 1–91 (1980)

24.12 R. Memming: Improvements in solar energy conversion. In: *Photochemical Conversion and Storage of Solar Energy*, ed. by E. Pelizzetti, M. Schiavello (Kluwer, Dordrecht 1991) pp. 139–212

24.13 S. Licht (Ed.): *Semiconductor Electrodes and Photoelectrochemistry* (Wiley-VCH, Weinheim 2002)

24.14 M. Archer, A. Nozik (Eds.): *Nanostructured and Photoelectrochemical Systems for Solar Photon Conversion*, Vol. 3 (World Scientific, Singapore 2008)

24.15 K. Rajeshwar, S. Licht, R. McConnell (Eds.): *The Solar Generation of Hydrogen: Towards a Renewable Energy Future* (Springer, New York 2008)

24.16 L. Vayssieres: Solar hydrogen and nanotechnology, SPIE Proc. **6340**, 641–664 (2010)

24.17 S. Licht, G. Hodes, R. Tenne, J. Manassen: A light variation insensitive high efficiency solar cell, Nature **326**, 863–864 (1987)

24.18 R. Tenne, G. Hodes: Improved efficiency of CdSe photoanodes by photoelectrochemical etching, Appl. Phys. Lett. **37**, 428–430 (1980)

24.19 S. Licht: A description of energy conversion in photoelectrochemical solar cells, Nature **330**, 148–151 (1987)

24.20 S. Licht, D. Peramunage: Efficient photoelectrochemical solar cells from electrolyte modification, Nature **345**, 330–333 (1990)

24.21 S. Licht: Multiple bandgap semiconductor/electrolyte solar energy conversion, J. Phys. Chem. B **105**, 6281–6294 (2001)

24.22 H. Tributsch: Reaction of excited chlorophyll molecules at electrodes and in photosynthesis, Photochem. Photobiol. **16**(4), 261–269 (1972)

24.23 H. Tsubomura, M. Matsumura, Y. Nomura, T. Amamiya: Dye sensitised zinc oxide: Aqueous electrolyte: Platinum photocell, Nature **261**, 402–403 (1976)

24.24 B. O'Regan, M. Grätzel: A low-cost, high-efficiency solar cell based on dye-sensitized colloidal TiO_2 films, Nature **353**, 737–740 (1991)

24.25 D. Wei: Dye sensitized solar cells, Int. J. Mol. Sci. **11**, 1103–1113 (2010)

24.26 S. Licht: Efficient solar generation of hydrogen fuel – A fundamental analysis, Electrochem. Commun. **4**, 789–794 (2002)

24.27 S. Licht: Electrochemical potential tuned solar water splitting, Chem. Commun. **2006**, 3006–3007 (2003)

24.28 S. Licht: STEP (solar thermal electrochemical photo) generation of energetic molecules: A solar chemical process to end anthropogenic global warming, J. Phys. Chem. C **113**, 16283–16292 (2009)

24.29 S. Licht: Optimizing photoelectrochemical solar energy conversion: Multiple bandgap and solution phase phenomenon. In: *Semiconductor Electrodes and Photoelectrochemistry*, ed. by S. Licht (Wiley-VCH, Weinheim 2002), Chap. 4.4

24.30 S. Licht, D. Peramunage: Rational electrolyte modification of n-CdSe/($[KFe(CN)_6]^{3-/2-}$) photoelectrochemistry, J. Electrochem. Soc. **139**, L23–L26 (1992)

24.31 S. Licht, B. Wang, T. Soga, M. Umeno: Light invariant, efficient, multiple bandgap AlGaAs/Si/metal hydride solar cell, Appl. Phys. Lett. **74**, 4055–4057 (1999)

24.32 B. Wang, S. Licht, T. Soga, M. Umeno: Stable cycling behavior of the light invariant AlGaAs/Si/metal hydride solar cell, Sol. Energy Mater. Sol. Cells **64**, 311–320 (2000)

24.33 S. Licht, G. Hodes: Photoelectrochemical storage cells. In: *Nanostructured and Photochemical Systems for Solar Photon Conversion*, Vol. 3, ed. by M. Archer, A. Nozik (World Scientific, Singapore 2008), Chap. 10

24.34 H. Snaith, A. Moule, C. Klein, K. Meerholz, R.H. Friend, M. Grätzel: Efficiency enhancements in solid-state hybrid solar cells via reduced charge recombination and increased light capture, Nano Lett. **7**, 3372–3376 (2007)

24.35 M.K. Naseeruddin, M. Grätzel: Dye-sensitized regenerative solar cells. In: *Semiconductor Electrodes and Photoelectrochemistry*, ed. by S. Licht (Wiley-VCH, Weinheim 2002), Chap. 5.2

24.36 J. Nelson: Charge transport in dye-sensitized systems. In: *Semiconductor Electrodes and Photoelectrochemistry*, ed. by S. Licht (Wiley-VCH, Weinheim 2002), Chap. 5.3

24.37 K. Uzaki, T. Nishimura, J. Usagawa, S. Hayase, M. Kono, Y. Yamaguchi: Dye-sensitized solar cells consisting of 3D-electrodes – A review: Aiming at high efficiency from the view point of light harvesting and charge collection, J. Solar Energy Eng.-Trans. ASME **132**, 021204 (2010)

24.38 J.H. Wu, Z. Lan, S.C. Hao, P. Li, J. Lin, M. Huang, L. Fang, Y. Huang: Progress on the electrolytes for dye-sensitized solar cells, Pure Appl. Chem. **80**, 2241–2258 (2008)

24.39 T.W. Hamann, R.A. Jensen, A.B.F. Martinson, H. Van Ryswykac, J.T. Hupp: Advancing beyond current generation dye-sensitized solar cells, Energy Environ. Sci. **1**, 66–78 (2008)

24.40 B. Miller, S. Licht, M.E. Orazem, P.C. Searson: Photoelectrochemical systems, Crit. Rev. Surf. Chem. **3**, 29 (1994)

24.41 C.H. Henry: Limiting efficiencies of ideal single and multiple energy gap terrestrial solar cells, J. Appl. Phys. **51**, 4494–4500 (1980)

24.42 D.J. Friedman, S.R. Kurtz, K. Bertness, A.E. Kibbler, C. Kramer, J.M. Olsen, D.L. King, B.R. Hansen, J.K. Snyder: 30.2% efficient GaInP/GaAs monolithic two-terminal tandem concentrator cell, Progr. Photovolt. **3**, 47–50 (1995)

24.43 J.P. Benner, J.M. Olson, T.J. Coutts: Recent advances in high-efficiency solar cells, Adv. Solar Energy **7**, 125–165 (1992)

24.44 M.A. Green, K. Emery, K. Bucher, D.L. King, S. Igari: Solar cell efficiency tables (version 8), Progr. Photovolt. **4**, 321–325 (1996)

24.45 T. Soga, T. Kato, M. Yang, M. Umeno, T. Jimbo: High efficiency AlGaAs/Si monolithic tandem solar cell grown by metalorganic chemical vapor deposition, J. Appl. Phys. **78**, 4196–4199 (1995)

24.46 R.R. King, D.C. Law, K.M. Edmondson, C.M. Fetzer, G.S. Kinsey, H. Yoon, R.A. Sherif, N.H. Karam: 40% efficient metamorphic GaInP/GaInAs/Ge multijunc-

tion solar cells, Appl. Phys. Lett. **90**, 183516–183518 (2007)

24.47 N. Alonso-Vante, H. Colell, U. Stimming, H. Tributsch: Anomalous low-temperature kinetic effects for oxygen evolution on ruthenium dioxide and platinum electrodes, J. Phys. Chem. **97**, 7381–7384 (1993)

24.48 S. Licht: Efficient solar-driven synthesis, carbon capture, and desalinization, STEP: Solar thermal electrochemical production of fuels, metals, bleach, Adv. Mater. **47**, 5592–5612 (2011)

24.49 S. Licht, H. Wu, C. Hettige, B. Wang, J. Lau, J. Asercion, J. Stuart: STEP cement: Solar thermal electrochemical production of CaO without CO_2 emission, Chem. Commun. **48**, 6019–6602 (2012)

24.50 B. Cui, S. Licht: Critical STEP advances for sustainable iron production, Green Chem. **113**, 881–884 (2013)

24.51 S. Licht: Solar water splitting to generate hydrogen fuel: Photothermal electrochemical analysis, J. Phys. Chem. B **107**(18), 4253–4260 (2003)

24.52 J. Ren, F.-F. Li, J. Lau, L. Gonzalez-Urbina, S. Licht: One-pot synthesis of carbon nanofibers from CO_2, Nano Lett. **15**, 6142–6148 (2015)

24.53 F.-F. Li, S. Liu, B. Cui, J. Lau, J. Stuart, S. Licht: A one-pot synthesis of hydrogen and carbon fuels from water and carbon dioxide, Adv. Energy Mat. **7**(7), 1401791–1401791 (2015)

24.54 F.-F. Li, J. Lau, S. Licht: Sungas instead of syngas: Efficient co-production of CO and H_2 from a single beam of sunlight, Adv. Sci. (2015), doi:10.1002/advs.201500260

24.55 J. Ren, J. Lau, M. Lefler, S. Licht: The minimum electrolytic energy needed to convert carbon dioxide by electrolysis in carbonate melts, J. Phys. Chem. C **119**, 23342–23349 (2016)

24.56 Y. Zhu, H. Wang, B. Wang, X. Liu, H. Wu, S. Licht: Solar thermoelectric field photocatlysis for efficient organic synthesis exemplified by toluene tobBenzoic acid, Appl. Cat. B **193**, 151–159 (2016)

24.57 S. Licht, A. Douglas, J. Ren, R. Carter, M.M. Lefler, C.L. Pint: Carbon nanotubes produced from ambient carbon dioxide for environmentally sustainable lithium-ion and sodium-ion battery anodes, ACS Cent. Sci. **2**, 162–168 (2016)

24.58 S. Licht, B. Wang, S. Mukerji, T. Soga, M. Umeno, H. Tributsch: Over 18% solar energy conversion to generation of hydrogen fuel; theory and experiment for efficient solar water splitting, Int. J. Hydrogen Energy **280**, 425–659 (1998)

24.59 S. Licht, O. Chitayat, H. Bergmann, A. Dick, H. Ayub, S. Ghosh: Efficient STEP (solar thermal electrochemical photo) production of hydrogen – An economic assessment, Int. J. Hydrogen Energy **35**, 10867–10882 (2010)

24.60 W.C. Butterman, W.E. Brooks, R.G. Reese: *Cesium*, US Publication Open-File Report, Vol. 2004–1432 (US Geological Service, Washington 2004), http://pubs.usgs.gov/of/2004/1432/2004-1432.pdf

24.61 J. Ng, X. Zhang, T. Zhang, J. Pan, A. Du Jian-Hong, D.D. Sun: Construction of self-organized free-standing TiO_2 nanotube arrays for effective disinfection of drinking water, J. Chem. Technol. Biotechnol. **85**(8), 1061–1066 (2010)

24.62 S. Licht, F. Forouzan: Solution modified n-GaAs/Aqueous polyselenide photoelectrochemistry, J. Electrochem. Soc. **142**, 1539–1545 (1995)

24.63 C.P. Rhodes, A. Cisar, H. Lee, Y. Fu, A. Anderson, A. Gonzales-Martin: Book of Abstracts, 215-th Electrochem. Soc. Meet., San Francisco (2008), abstract #398

Part E Electroch

Part E Electrochemical Processes

25 Advanced Extractive Electrometallurgy
Di Hu, Ningbo, China
George Z. Chen, Ningbo, China

26 Electrodeposition of Nanomaterials
I-Wen Sun, Tainan, Taiwan
Jeng-Kuei Chang, Taoyuan, Taiwan

27 Electrochemical Hydrogen Production
Ting He, Idaho Falls, USA
Mahaprasad Kar, Bartlesville, USA
Neal D. McDaniel, Bartlesville, USA
Bruce B. Randolph, Bartlesville, USA

28 Electrochemical Machining
Michael Schneider, Dresden, Germany
Manuel Lohrengel, Düsseldorf, Germany

25. Advanced Extractive Electrometallurgy

Di Hu, George Z. Chen

This chapter starts with a brief introduction of current technologies for metal extraction via chemical and electrochemical means. A focus is given to recent research and development of new methods for titanium extraction. The chapter is then devoted to describing the principle and methodology of the more recently proposed Fray–Farthing–Chen (FFC) Cambridge process, which is a molten salt-assisted solid-state electrochemical reduction process. Typical examples are highlighted for application of the FFC Cambridge process for extraction of titanium, silicon and other metals, and also the production of various metal alloys, and the related development of fundamental understanding of the proposed in situ reduction routes from physical, chemical, and electrochemical points of view. The unique ability of the FFC Cambridge process for near-net-shape production of metallic components directly from their metal oxide precursors is also discussed.

25.1 **Conventional Extractive Metallurgy** 801
25.1.1 Nonelectrolytic Extraction Techniques 802
25.1.2 Conventional Electrolytic Extraction Techniques 806
25.2 **Innovative Electrolytic Extraction Techniques for Titanium** 808
25.2.1 Electrolytic Extraction from Non-Oxide Compounds 808
25.2.2 Electrolytic Extraction from Solid Metal Oxides 809
25.2.3 Summary and Note 813
25.3 **Direct Electroreduction of Solid Metal Oxides to Metals: The FFC Cambridge Process** 814
25.3.1 History 814
25.3.2 Principle 814
25.3.3 Applications 824
25.4 **Summary** 829
References 830

There are different approaches to extraction of metals from their minerals, including metal oxide reduction which is traditionally achieved in several ways. The selection of these methods depends on the stability of the impurities contained in the metal oxide, and the relative stability of the oxide itself [25.1].

25.1 Conventional Extractive Metallurgy

When metal oxides exhibit lower stability, direct heating of the unstable metal oxides to their decomposition temperature to produce the pure metals is the simplest method for metal extraction. For example, mercuric oxide (HgO) can be decomposed in this way.

For oxides that exhibit greater stability, a reductant needs to be used to extract the metal from its oxide. As in the case of nickel extraction, hydrogen has been used to react with nickel oxide (NiO) to form pure nickel metal and water [25.1]. However, the most widely used reduction method is the carbothermic reduction process that uses carbon, either in the elemental state or as carbon monoxide (CO), as the reductant. In the case of iron oxide (Fe_2O_3) reduction, carbon has been used to reduce iron oxide to pure iron with the production of carbon dioxide (CO_2). Owing to the fact that the reaction of carbon and oxygen to form CO is positive in terms of entropy, and the stability of CO increases with temperature, whereas the stability of metal oxides decreases, carbon is theoretically capable of reducing all metal oxides [25.2]. However, carbon can form stable carbides with produced metals during the carbothermic reduction process, such as the formation of titanium carbide (TiC), which is even more stable than TiO_2 [25.3], thus carbon cannot be used for titanium extraction.

Another commonly used metal extraction method is the metallothermic reduction process, which substitutes carbon with a metal as the reductant. In the case of reduction of chromium oxide (Cr_2O_3), aluminum has been introduced as the reductant, and the process is therefore called aluminothermic reduction [25.4]

$$Cr_2O_3(s) + 2Al(l) = 2Cr(s) + Al_2O_3(s)\,. \qquad (25.1)$$

This technique requires two reduction stages, i. e., the production of the metallic reductant via a reduction process, and then the reduction of the target metal oxide using the produced metal, which dramatically increases the cost of extraction. In addition, for metals that are highly reactive with other elements, such as titanium, this process will lead to the formation of alloys or intermetallic compounds (e.g., formation of TiAl) [25.5] rather than producing the pure metal.

To reduce extremely stable compounds, such as Al_2O_3, molten salt electrolysis is most often employed. The following sections will give some examples of metal extraction using different conventional techniques.

25.1.1 Nonelectrolytic Extraction Techniques

Silicon is the second most common element in the Earth's crust by mass, and it plays essential roles in modern semiconductors, solar energy devices and traditional metallurgical processes [25.6]. According to its purity, silicon can be classified as solar-cell-grade (SoG 99.999%), metallurgical-grade-silicon (MG-Si, 98.5%) [25.6], and so on.

Direct Carbothermic Reduction of Silica to Silicon

St. Claire Deville was the first person to develop a method of preparing pure silicon in 1857, by electrolysis of a solution of SiO_2 in a KF/NaF melt [25.7]. Following his first success, electrodeposition of silicon has been extensively studied, using solutes of silica and fluorosilicates and solvents of alkali halides. Nevertheless, owing to the high capital cost, low output and difficulty in purity control of the product, this method has never been commercialized. Since 1905, when the first electric arc furnace was installed in the US, the modern silicon production industry has been established using the direct carbothermic reduction process [25.8]. By using this process, MG-Si can be produced.

The direct carbothermic reduction process for silicon production is illustrated in Fig. 25.1, which involves reactions between silica and carbonaceous reducing agents in an electric arc furnace at around 2173 K [25.9].

As shown in Fig. 25.1, lumpy quartz with appropriate sizes, for example 10 to 100 mm, is mixed with carbonaceous reducing agents consisting of metallurgical-grade coal and woodchips and/or charcoal and coke. This mixture of raw materials is then fed into the electric arc furnace, where it is heated to over 2173 K by taking advantage of an intense electric arc generated between the tips of three submerged carbon electrodes and the electrical ground of the furnace. The extracted silicon is in liquid form, and it is drained out from the bottom of the furnace.

The principal reactions occurring in the electric arc furnace can be described as

$$SiO_2 + 2C = Si + 2CO\,,$$
$$\Delta G^0_{2173\,K} = -23.040\,Wh\,, \qquad (25.2)$$
$$SiO_2 + 2C + O_2 = Si + 2CO_2\,,$$
$$\Delta G^0_{2173\,K} = -76.258\,Wh\,. \qquad (25.3)$$

Depending on the size of the electric arc furnace, the working electrical load is normally between 10 and 30 MW. Typically, the energy consumption for the production of 1 kg MG-Si is 12.5 to 14 kWh, which is only for heating via the electric arc. However, if the energy content in the carbon is considered, the overall energy consumption goes over 22 kWh. The world silicon production in 2010 was around 6.9 million tonnes [25.10], which means the annual energy consumption for silicon production was over 86 TWh (or 152 TWh considering the energy in carbon). It should also be noted here that the direct carbothermic reduction process for silicon production consumes huge amounts of carbonaceous reducing agents and carbon-based electrodes; therefore, the high emissions of greenhouse gas from the silicon production industry becomes a major concern. For example, the production of 6.9 million tonnes of silicon corresponds to releasing about 10.9 million tonnes of CO_2 into the atmosphere.

Moreover, the purity of MG-Si produced by the direct carbothermic reduction process is not satisfactory for high-end applications, such as semiconductor devices and solar panels. Therefore, further purification processes have to be adopted, involving the conversion of MG-Si into silicon compounds, and then the decomposition of these compounds back to silicon with a higher purity.

The Siemens process is most popular for silicon purification, which is based on the thermal decomposition of trichlorosilane ($SiHCl_3$) at around 1373 K on a heated silicon rod placed inside a deposition chamber (25.4) [25.11]

$$2SiHCl_3 = SiCl_4 + Si + 2HCl\,. \qquad (25.4)$$

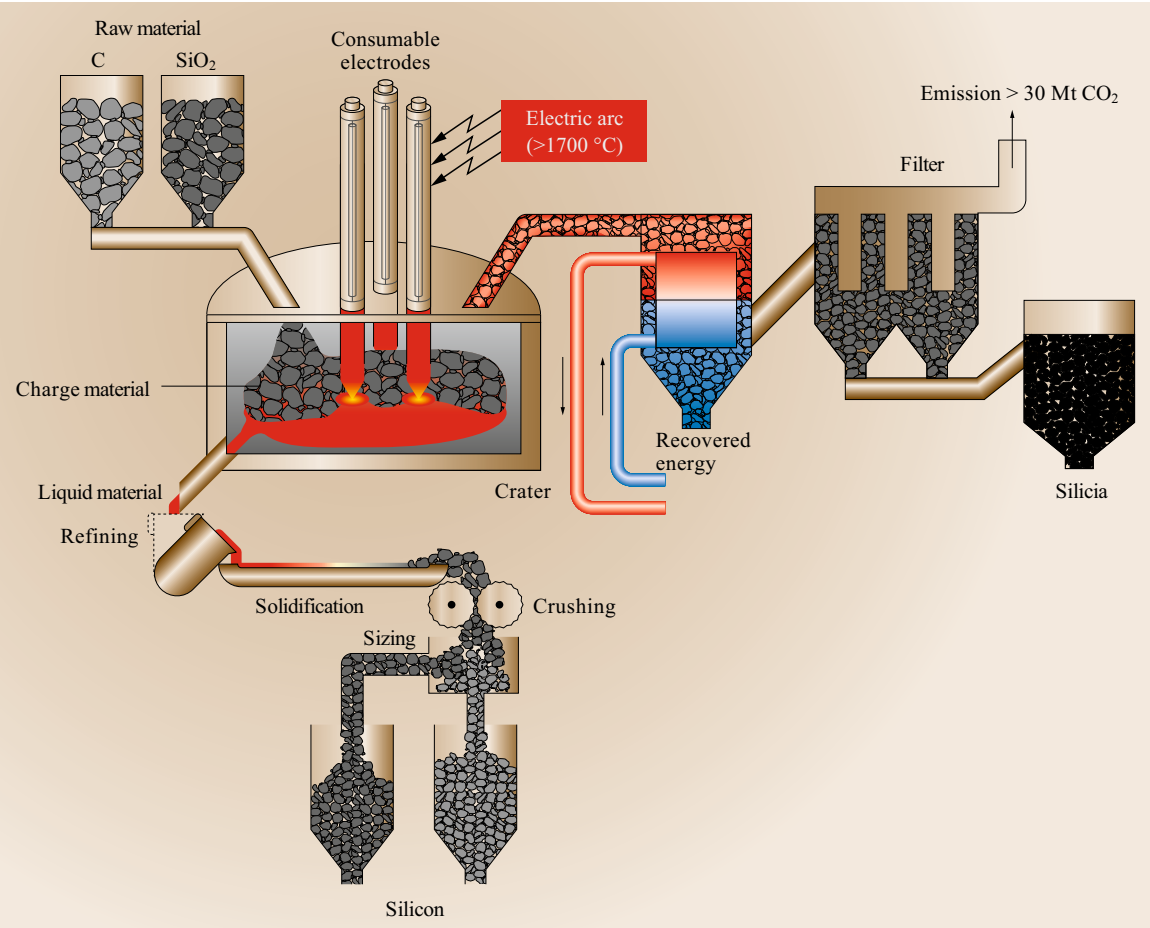


Fig. 25.1 Schematic representation of a furnace for production of MG-Si (after [25.9])

In a more recent development of the Siemens process, the trichlorosilane has been replaced by monosilane (SiH_4), as shown in (25.5) [25.8]

$$SiH_4 = Si + 2H_2 \,. \tag{25.5}$$

The direct carbothermic reduction process of silica to silicon is high in energy consumption and not environmentally friendly, and its downstream processes for further purification are complicated. For these reasons, new technologies for silicon production and purification with lower cost and environmental impact are in high demand.

Indirect Metallothermic Reduction of Titania to Titanium

As the ninth most plentiful element in the Earth's crust (after oxygen, silicon, aluminum, iron, calcium, sodium, potassium, and magnesium), and the fourth most prevalent structural metal (only exceeded by aluminum, iron, and magnesium), the current worldwide supply of feedstock ore for producing titanium metal is virtually unlimited. However, even today, it has not yet lost the mien of an exotic and expensive metal [25.12–14]. The difficult and costly extraction of titanium from its ore is one of the main reasons that severely inhibit wider application.

The Hunter Process. In 1910, *Hunter* successfully produced almost pure titanium using sodium to reduce titanium tetrachloride ($TiCl_4$) [25.15]. This process was therefore named after him as the Hunter process, which was the first industrial method for titanium production. In the Hunter process, the retort is sealed and filled with molten sodium. The retort is then heated to the reaction temperature (973–1073 K) and a certain amount of $TiCl_4$ is slowly fed into the retort to react with sodium. The Hunter process can be stated as

$$TiCl_4 + 4Na = Ti + 4NaCl \,. \tag{25.6}$$

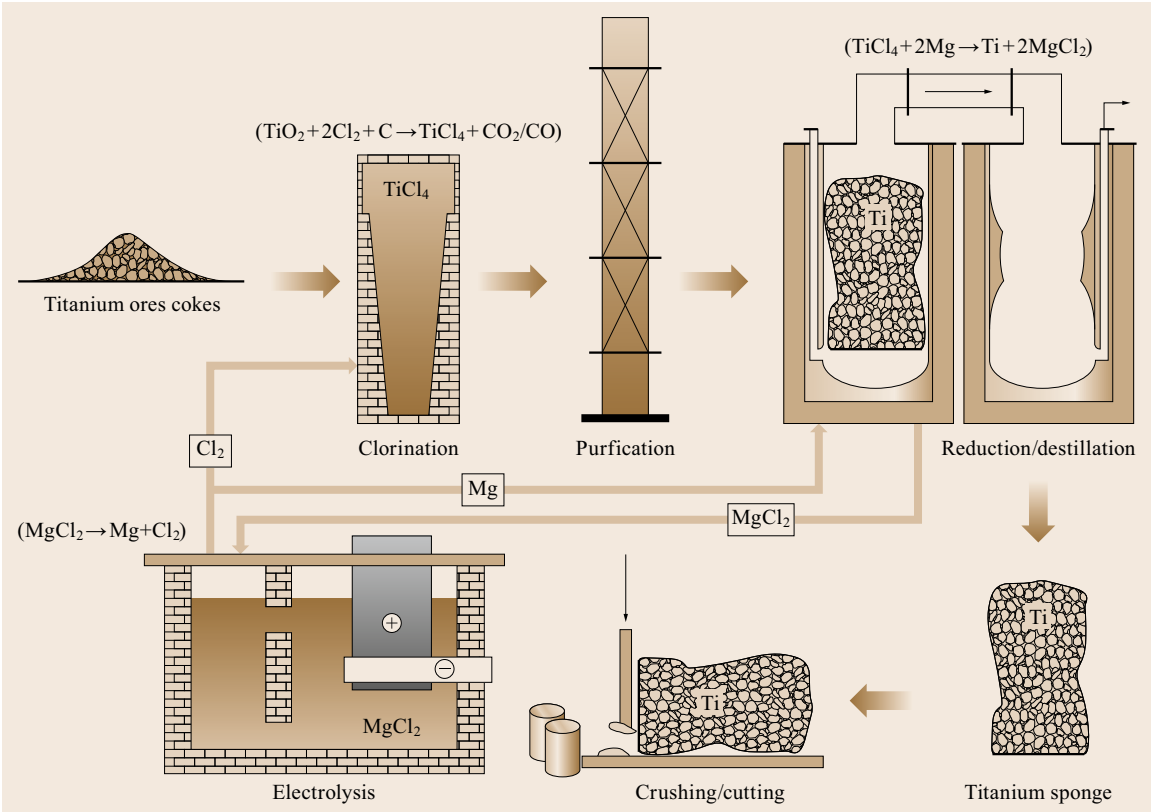


Fig. 25.2 Schematic of the Kroll process by TOHO Titanium (after [25.16])

When the reduction finishes, the retort is allowed to cool down, and then the NaCl-titanium mixture is chipped out and washed using hydrochloric acid to remove NaCl. The brine solution is discarded; thus no sodium can be recycled and sodium must be bought for every run [25.17].

Because the boiling point of sodium metal (1156 K) and the melting point of NaCl (1074 K) are quite close, the temperature range for operating the Hunter process is small, and it has to be controlled below the boiling point of sodium metal. However, the sodium reduction process is an extremely exothermic reaction, making temperature control even more difficult.

In 1938, *Kroll* found that calcium is a better reductant than sodium for the reduction of $TiCl_4$ [25.18]. The boiling point of calcium metal is at 1757 K and its chloride melts at 1045 K, which renders an increased permissible range of operating temperatures compared to that when using sodium and sodium chloride. However, the calcium metal is highly reactive with both oxygen and nitrogen, making it difficult to handle and purify. Subsequently, in 1940, *Kroll* successfully replaced the calcium reductant with magnesium [25.19], and found that magnesium can also offer a desirable operating temperature range since the boiling point of magnesium is at 1363 K and its chloride melts at 987 K. Moreover, magnesium was found to be inexpensive and available in an adequately pure form on a larger scale. Following the success of using magnesium as reductant to reduce $TiCl_4$, the industry of commercial titanium production using the Kroll process was established.

After dominating the titanium production market for around 30 years, the Hunter process was finally replaced by the Kroll process. It is worth mentioning here that in the US, the only Hunter process plant in operation today is that of the Alta Group (with a production capacity of 340 t/y in the year 2000) which provides titanium sponge fines and high purity powders for specialist markets, such as electronics industry [25.17, 20].

The Kroll Process. The Kroll process, as implemented by Dr. Kroll and the US Bureau of Mines (USBM), is based on the direct chlorination of titanium ore (i. e., rutile) to produce titanium tetrachloride, which is then reduced to titanium metal using the magne-

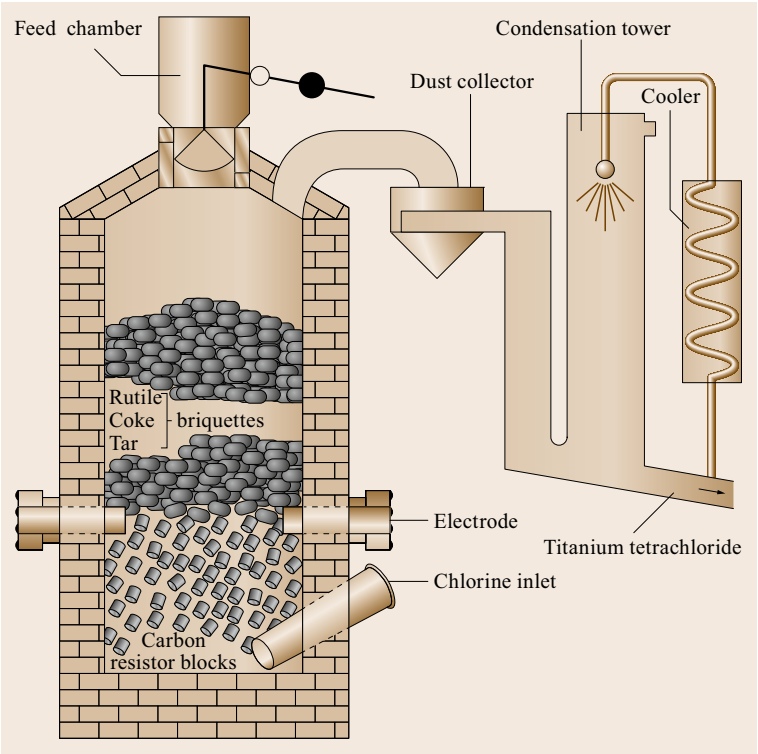


Fig. 25.3 Schematic of the carbochlorination process for producing $TiCl_4$ (after [25.21])

sium reduction process. Since the first establishment of this process for the commercial production of titanium, many different extraction processes have been developed for the production of titanium metal [25.17, 22, 23]. However, the Kroll process is still dominating today's titanium production industry due to its better economic performance compared to other methods. The Kroll process is a series of batch steps, as schematically illustrated in Fig. 25.2.

During the Kroll process for titanium production, the first step is to produce $TiCl_4$. Currently, most $TiCl_4$ is produced by carbochlorination using a fluidised bed reactor (as shown in Fig. 25.3).

The petroleum coke, which is low in ash and hydrogen content, is utilized to react with TiO_2 and chlorine in the fluidized bed reactor at approximately 1273 K to produce $TiCl_4$ and CO/CO_2

$$TiO_2 + 2Cl_2 + C = TiCl_4 + CO_2 \,. \qquad (25.7)$$

The carbochlorination process is an exothermic reaction; therefore it can be self-sustaining by taking advantage of the released heat. By careful control of the temperature, the carbochlorination of impurities in the feedstock, such as silica and zirconia, could be avoided to some extent. The $TiCl_4$ formed is in the gas state, which is spray-cooled after leaving the fluidized bed and is then subjected to purification.

The purification of the $TiCl_4$ begins in the chlorinator where chloride impurities that possess very high boiling points remain, such as those containing calcium, manganese, sodium and magnesium, while $TiCl_4$ and other impurities are released, which includes gases (CO and CO_2), medium-high-boiling-point chlorides (such as $SnCl_4$, $SiCl_4$, $FeCl_3$, and $AlCl_3$), and solid fines carried by the gas (including rutile, petroleum coke, and oxychlorides) [25.17]. The released mixtures are first condensed to the boiling point of $TiCl_4$ (409 K) to separate CO/CO_2 and to settle out solids. The remaining mixture is then fed to a fractional distillation column to precipitate medium-high-boiling-point chlorides such as $FeCl_3$ and $AlCl_3$ and to distil low-boiling-point impurities such as $SnCl_4$ and $SiCl_4$. The final purified $TiCl_4$ could reach a purity of $> 99.9\%$ after these process stages.

The magnesium reduction is then carried out to reduce $TiCl_4$ to pure titanium metal. In a typical run, enough magnesium metal to reduce all the $TiCl_4$ feed, plus 15–30% excess, is introduced into an argon-filled steel retort that is vacuum-pumped. The retort is then heated to approximately 1073 K to melt the magnesium whilst the $TiCl_4$ gas is slowly fed into the retort over a period of several days. The $TiCl_4$ reacts exothermically with magnesium via (25.8) to establish a temper-

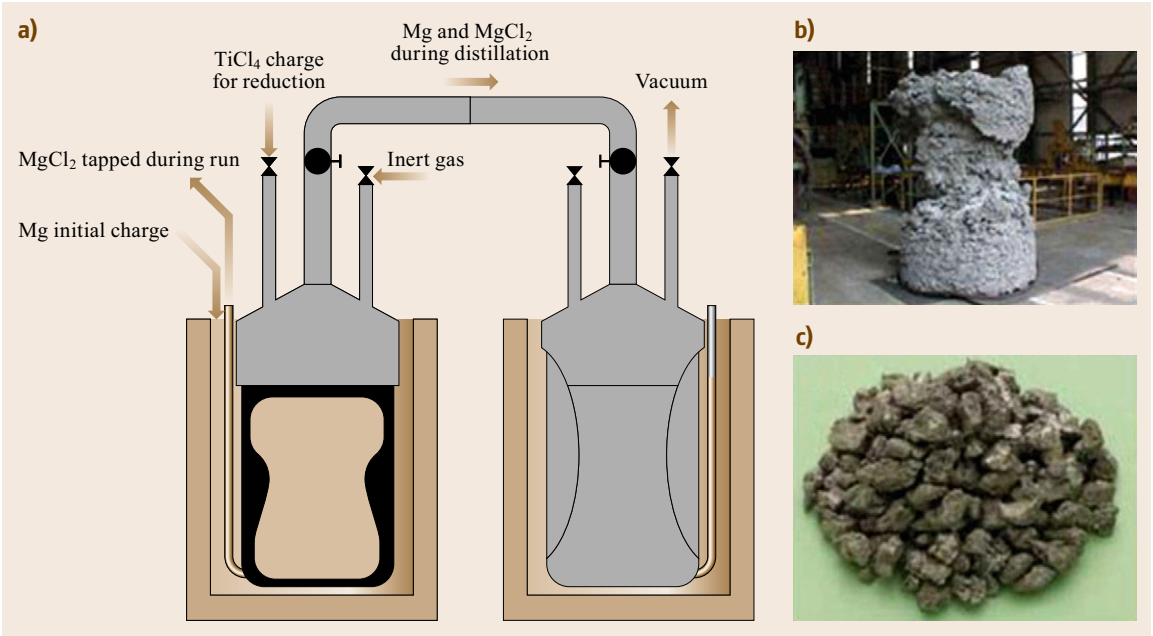


Fig. 25.4 (a) Schematic of a Kroll reaction vessel coupled with a collection vessel on the right for vacuum distillation to remove Mg and $MgCl_2$ (after [25.13]). Photos of titanium sponge produced from the Kroll process (b) before, and (c) after crushing (after [25.24])

ature between 1123 and 1223 K.

$$TiCl_4 + 2Mg = Ti + 2MgCl_2,$$
$$\Delta G^0_{1173\,K} = -103.363\,Wh\,. \qquad (25.8)$$

The $MgCl_2$ produced is tapped off several times during the reduction process. Electrolysis of $MgCl_2$ is then carried out in a separate molten salt electrolyzer to recover both Cl_2 at the anode for the carbochlorination process and magnesium metal at the cathode for the reduction.

The product of magnesium reduction of $TiCl_4$ is an intermingled solid mixture of metallic titanium, unreacted magnesium, and $MgCl_2$. Therefore, it is necessary to extract the metallic titanium from the sponge cake by removal of the residual Mg and $MgCl_2$. Although the cost of using vacuum distillation to purify titanium sponge is relatively high compared to acid leaching and inert gas sweeping, it is the most favored method as it can more effectively remove magnesium metal and $MgCl_2$ in situ during the Kroll process [25.13]. Figure 25.4a schematically illustrates the vacuum distillation process.

Following the completion of the magnesium reduction process, the retort is cooled, the seal is broken and the titanium sponge produced is pressed or jack hammered out, as shown in Fig. 25.4b. The titanium sponge mass is then crushed to produce granules of metallic titanium (Fig. 25.4c).

Table 25.1 compares the Kroll and Hunter processes. The ability to produce high-purity fine titanium powder is the main reason why the Hunter process is still in limited use nowadays [25.20].

25.1.2 Conventional Electrolytic Extraction Techniques

Molten salt electrolysis is most often employed for reducing extremely stable compounds, such as Al_2O_3. The most famous electroextraction process is the Hall–Héroult process, which is named after the inventors who

Table 25.1 A comparison of the Kroll process and the Hunter process (after [25.17])

The Kroll process	The Hunter process
Batch process	Batch or continuous followed by batch
15 to 30% excess magnesium	Small excess of $TiCl_4$
Little fine product	Up to 10% fine product
Product hard to grind	Product easy to grind
Substantial iron contamination from retort walls	Little iron contamination from retort walls
Sponge leached or vacuum distilled	Sponge leached
Retort contains mostly titanium	Retort contains four moles of NaCl for each mole of titanium

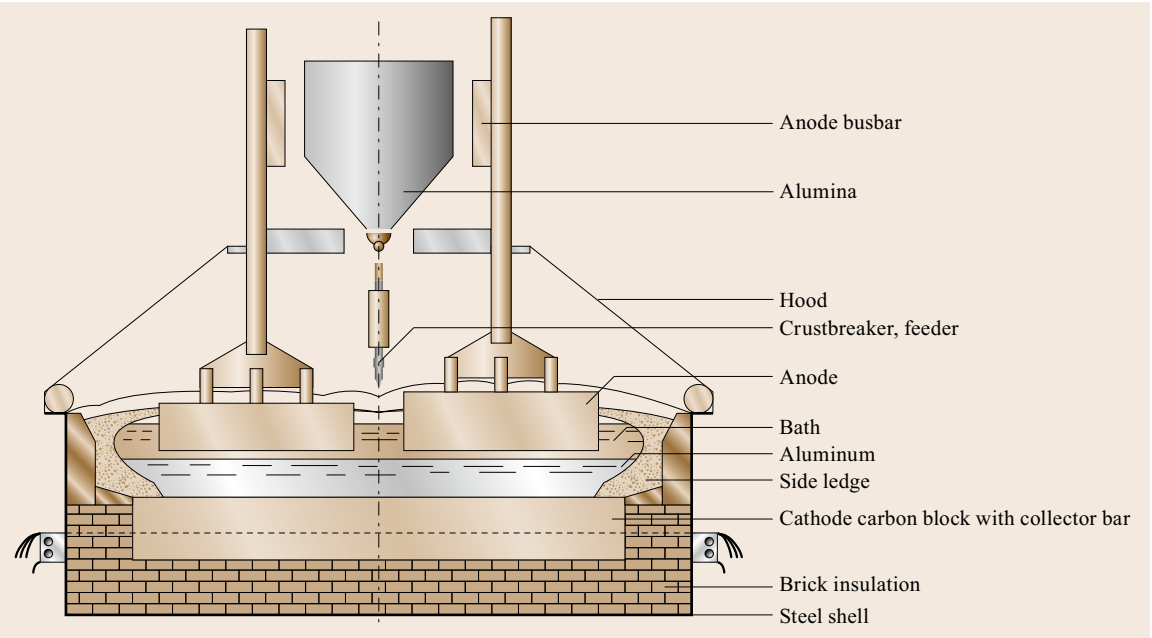


Fig. 25.5 Cross-section of aluminum cell (after [25.25])

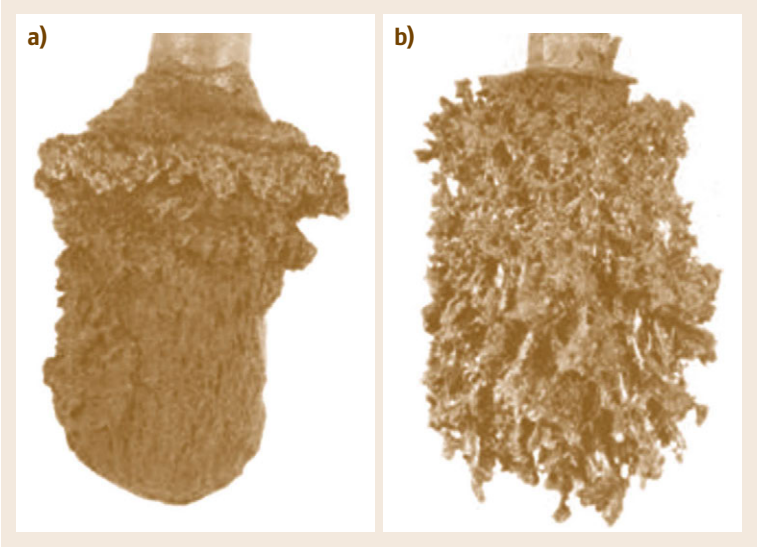


Fig. 25.6a,b Titanium dendrite deposited from a solution of **(a)** TiO in molten $CaCl_2$ (after [25.22]) and **(b)** K_2TiF_6 in molten NaCl (after [25.23])

simultaneously but independently discovered this process in 1886.

Electrolytic Extraction of Aluminum

This process involves dissolving aluminum oxide (Al_2O_3) in molten cryolite (Na_3AlF_6) and then carrying out the electrolysis above the melting temperature of the mixture (approximately 1243 K) using carbon as both the cathode and consumable anode. The molten aluminum electrodeposited at the cathode then flows, as a consequence of buoyancy difference between the metal and the salt, to the bottom of the carbon bath where it can be tapped off periodically [25.26]. In this process, a high current density ($> 10\,kA/m^2$) is required in order to achieve both high production rates and maintain the cell temperature via Joule heating. In addition, a frozen salt ledge is maintained around the inner wall of the electrolytic cell by carefully controlling heat input and loss, as shown in Fig. 25.5. This frozen salt ledge can prevent the cor-

rosion caused by the high-temperature cryolite-alumina mixture.

The current efficiency of the Hall–Héroult process is > 90%, and its energy consumption is at 13 to 14 kWh/kg. In 2006, the CO_2 emissions released during aluminum production was 0.2 Gt, which accounts for 0.7% of all global CO_2 emissions (i. e., 27 Gt) [25.27]. Despite the fact that this process was discovered more than a century ago, it remains the only industrial method for the electroextraction of aluminum metal from aluminum oxide.

Antecedent Attempts in Electrolytic Extraction of Titanium

The concept of electroextraction of titanium was proposed in the 1950s aiming to achieve a similar success to that of aluminum. These processes focused on dissolving titanium compounds (e.g., TiO or K_2TiF_6) in molten salts, and then electrowinning titanium from the molten salt solution [25.22, 23]. However, some lingering problems existed, such as the redox cycling of multivalent titanium ions (25.9)–(25.12), failure of diaphragms used to stop ion cycling or floating carbon impurities, and dendritic electrodeposition of titanium (Fig. 25.6) [25.22, 23].

$$\text{Cathode}: \ Ti^{4+} + e^- = Ti^{3+} \tag{25.9}$$

$$\text{Anode}: \ Ti^{2+} = Ti^{3+} + e^- \tag{25.10}$$

$$\text{Cathode}: \ Ti^{3+} + e^- = Ti^{2+} \tag{25.11}$$

$$\text{Anode}: \ Ti^{3+} = Ti^{4+} + e^- \tag{25.12}$$

25.2 Innovative Electrolytic Extraction Techniques for Titanium

Electrons with adjustable activities and desirable availability could be ideal green energy carriers (when electric energy is generated through solar or other renewable energy sources) for metallurgical processes. Although electrolytic processes have achieved enormous success in the aluminum extraction industry (i. e., the Hall–Héroult process), it still remains a challenge to extend this method to certain metals, such as titanium.

During recent years, some new attempts have been made to produce cost-affordable titanium and/or its alloys by taking advantage of electrolytic processes. The following sections will focus on some predominant electrolytic processes for titanium production and a brief summary will be given for each process.

25.2.1 Electrolytic Extraction from Non-Oxide Compounds

Ginatta Technologie Titanio (GTT) Process

The concept of the GTT process for titanium production is based on the fact that above 1100 K, when alkali and alkaline earth metals are present, the reduction of $TiCl_4$ to Ti metal can be completed with near zero equilibrium concentrations of lower chlorides in the electrolyte [25.29–31]. Further improvement of this process is made by increasing the temperature to 2000 K, and therefore liquid titanium can be produced. In this configuration, the produced liquid titanium can be used for casting directly.



Fig. 25.7 Solidified electrolyte and Ti cathode from the GTT process (after [25.28])

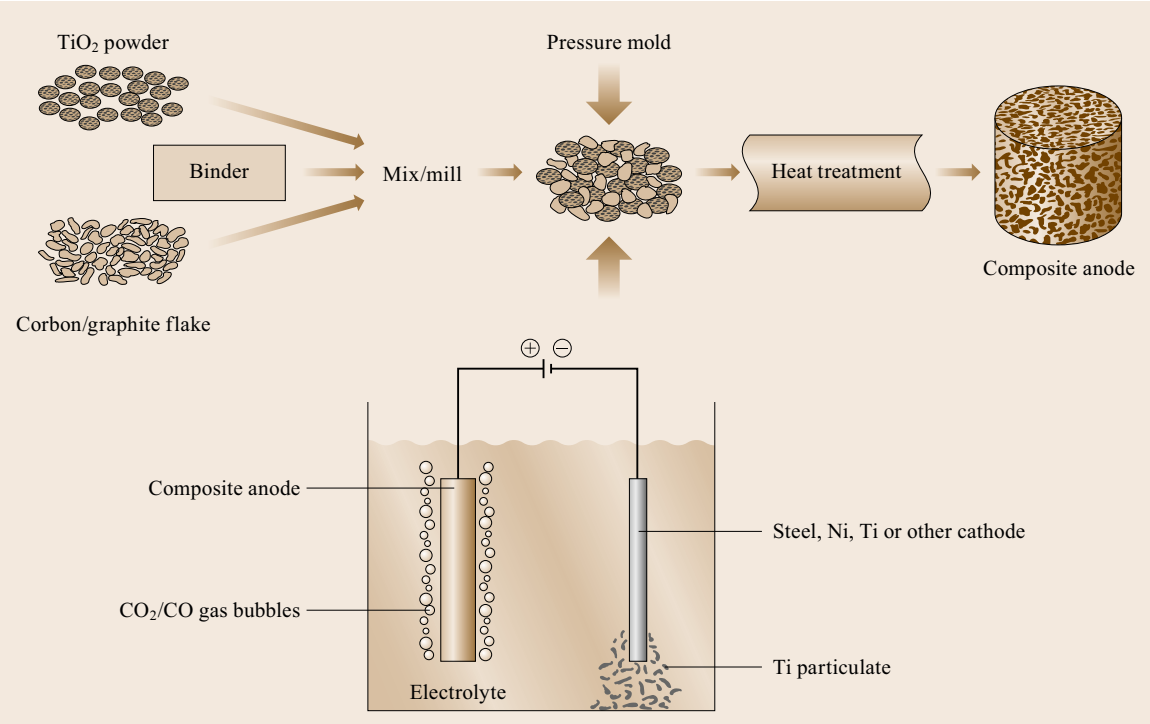


Fig. 25.8 Schematic of the MER composite anode process (after [25.28])

Moreover, in batch operation, the produced liquid titanium is contained by a water cooled copper crucible; therefore a solidified titanium slab and electrolyte can be formed at the bottom of the crucible (as shown in Fig. 25.7), which can be removed after reduction. The GTT process is quite complex, and alloy production appears difficult.

Materials and Electrochemical Research (MER) Process

The MER composite anode process involves dissolution of partially reduced titanium cations in the molten salt from a composite anode. The dissolved titanium cations are then transferred through molten salt to the cathode where they are reduced and deposited as titanium metal [25.32, 33]. The proposed reactions are as follows [25.34]

$$\text{At anode}: \ TiC_xO_y = Ti^{2+} + xCO/CO_2 + 2e^- , \tag{25.13}$$

$$\text{At cathode}: \ Ti^{2+} + 2e^- = Ti . \tag{25.14}$$

The composite anode is produced by firing a mixture of TiO_2 and carbon in an inert atmosphere or under vacuum in the temperature range of 1473–2373 K to give a partially reduced titanium compound (TiO_x where $x < 1.5$), followed by fabrication into a preform with additional carbon and a binder. The whole process is illustrated in Fig. 25.8.

It should be noted that the fabrication of the composite anode is relatively difficult, and the Ti^{2+} can still be anodically oxidised to higher oxidation states during the electrolytic process. Moreover, a dendritic deposition of titanium has been observed [25.32].

25.2.2 Electrolytic Extraction from Solid Metal Oxides

The EMR process, which is shown in Fig. 25.9, was invented by *T. Okabe* at the University of Tokyo [25.35].

Electronically Mediated Reaction/ Molten Salt Electrolysis (EMR/MSE)

The basic idea of this process is to pass the electrons that are generated from the oxidation of electrolytically produced calcium alloy via a conducting medium to TiO_2 where the reduction is initiated [25.35, 36].

A calcium alloy is selected here, as the electrodeposition of calcium into an alloy form exhibits a higher current efficiency than for the electrodeposition of pure calcium. Once the calcium alloy is electrolytically produced, it does not need the application of an external current as the reduction process is thermodynamically driven by the instability of the alloy.

Therefore, the calcium alloy can be produced during the off-peak time where the electricity price is low, and during the peak time the reduction of TiO_2 is employed.

However, the mechanism of the EMR process is still under discussion [25.36]. Another concern is that the current efficiency for alloy generation can be significantly reduced by the presence of dissolved calcium in the melt, which makes the melt highly conductive to electrons.

MIT Two-Year Titanium Initiative (Avanti Process)

The Avanti process distinguishes itself from the other electrolytic processes for titanium extraction through its use of molten oxide electrolysis (Fig. 25.10). Unlike the Hall–Héroult process, which uses cryolite to dissolve alumina for electrolysis, the difficulty with molten oxide electrolysis is that there is no proper salt for dissolving titanium dioxide. However, in the Avanti process, TiO_2 is dissolved in a high-temperature oxide melt (at 1998 K, which is above the melting point of Ti) and electrolyzed to give molten titanium and oxygen [25.38, 39].

This process is deemed to be able to reduce CO_2 emissions and produce oxygen using a proper anode. However, owing to the extremely high operation temperature of the Avanti process (1998 K for titanium extraction), an inert anode may be difficult to develop for use under this extreme condition. Furthermore, as the electrolytically produced titanium is in the liquid state and the melt contains molten titanium oxide, the feasibility for producing low-oxygen titanium needs to be verified [25.38].

Ono–Suzuki Process (OS)

As shown in Fig. 25.11a, the OS process utilizes the calciothermic reduction of TiO_2 or its metal oxide mixtures to produce titanium metal or its alloys, where the reductant Ca is in situ generated by electrolysis of CaO in molten $CaCl_2$ [25.41–45]. By taking advantage of molten $CaCl_2$ as a flux, which can dissolve 3.9 mol% Ca, but about 20 mol% CaO at 1173 K, the issue of CaO saturation during the calciothermic reduction process may be satisfactorily solved (Fig. 25.11b).

Moreover, continuous production of titanium by the OS process has been proposed and the schematic can be seen in Fig. 25.12.

Owing to the solubility of metallic Ca in the molten $CaCl_2$, backward reactions and parasitic reactions of Ca and carbon oxides ((25.15) and (25.16)) are the main problems with this process. Moreover, the formation of carbon crust layers in the upper part of the bath were observed as well [25.42].

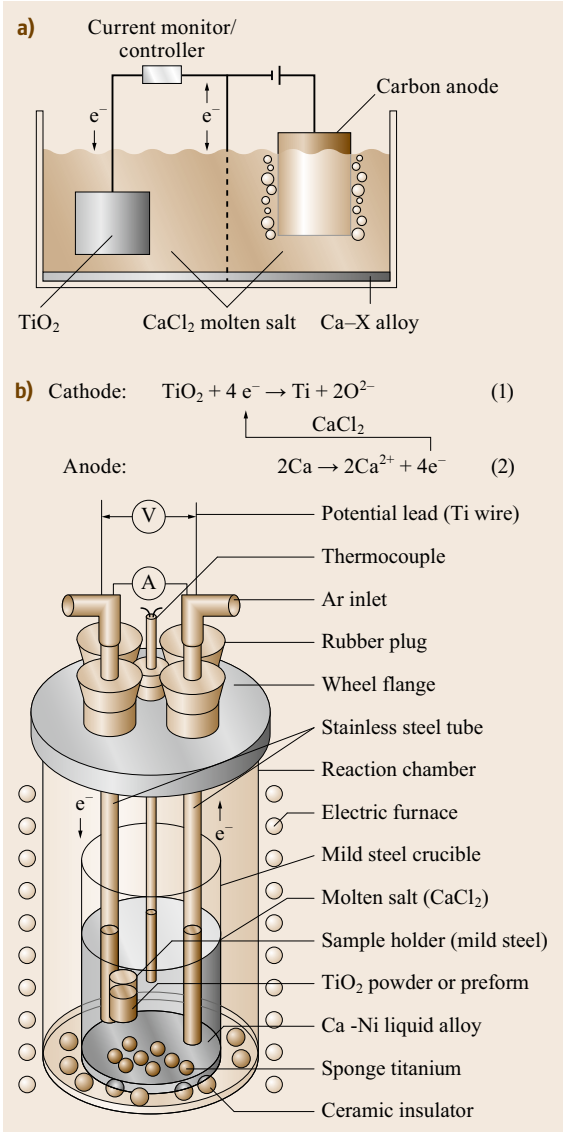


Fig. 25.9a,b Schematic of the EMR/MSE process **(a)** (after [25.37]) and its experimental setup **(b)** (after [25.35])

$$2Ca(l) + CO_2(g) = C(s) + 2CaO\,, \qquad (25.15)$$

$$Ca(l) + CO(g) = C(s) + CaO\,. \qquad (25.16)$$

Polar Titanium (BHP Billiton) Process

Little information has been publicly released on the BHP Billiton process [25.28, 47]. However, this process appears to also be based on the calciothermic reduction process using in situ generated Ca as a reductant to reduce TiO_2, which is similar to the OS process. The schematic of the Polar titanium process is shown

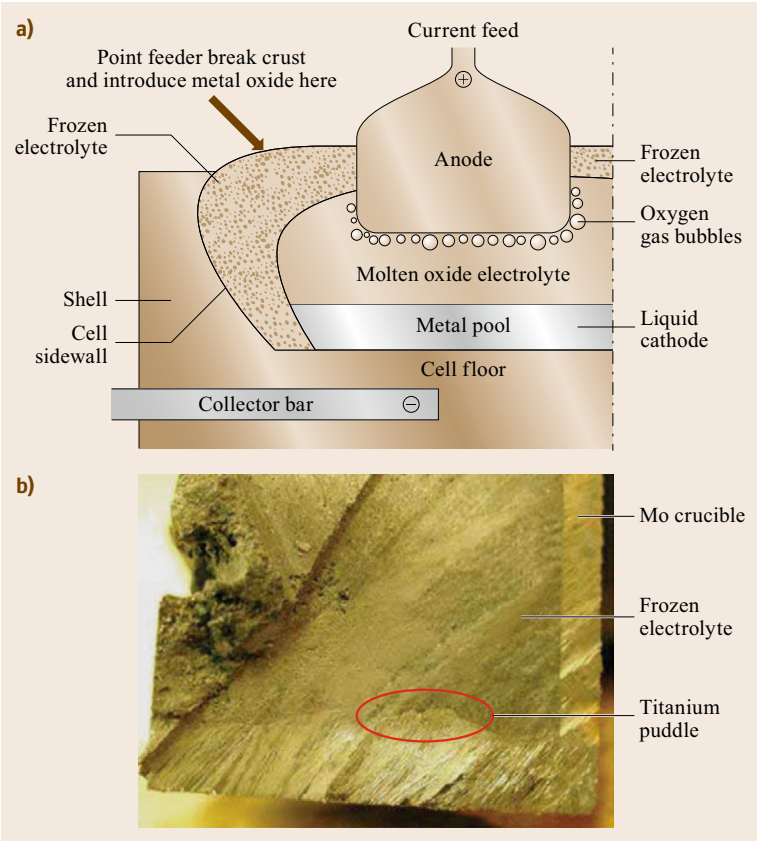


Fig. 25.10a,b Schematic of molten oxide electrolysis **(a)** (after [25.40]) and photo of cross-section of Mo crucible containing produced titanium **(b)** (after [25.39])

Table 25.2 Summary of emerging titanium electrolytic extraction processes

Name	Process	Products
Electronically mediated reaction (EMR/MSE) [25.36]	Electrolytic cell between TiO_2 and liquid Ca alloy reduces TiO_2	Highly porous Ti powder compact
Fray–Farthing–Chen Cambridge process (FFC Cambridge process)[a] [25.48]	Electrolytic reduction of TiO_2 electrode in molten salt	Powder block
Ginatta Technology Titanio (GTT) [25.28]	Electrolytic reduction of $TiCl_4$ vapor dissolved in molten electrolyte	Liquid Ti, either tapped or solidified as slab
Materials and electrochemical research (MER) [25.32]	Dissolution of titanium cations based composite anode, transport through mixed halide electrolyte and deposition on cathode	Powder, flake or solid slab
MIT two-year titanium initiative (Avanti process) [25.49]	Direct electrolysis of molten TiO_2	Liquid Ti
Ono–Suzuki process (OS)[a] [25.50]	Calciothermic reduction of TiO_2	Powder/sponge
Polar titanium (BHP Billiton) [25.28]	Limited information available	N/A
Quebec iron and titanium (QIT)[a] [25.28]	Electrolytic reduction of titania slag in calcium fluoride	Liquid Ti

[a] Method is capable of direct alloy production

in Fig. 25.13. The Polar titanium process has been scaled up to a pilot test of 10 kg titanium per day in 2005 [25.47].

Although a membrane is shown in the schematic of the process (Fig. 25.13), no further information is available about this.

Quebec Iron and Titanium (QIT) Process

As shown in Fig. 25.14, the QIT process involves the electrolytic conversion of molten titania slag to liquid titanium metal in the molten salt electrolyte, such as CaF_2 [25.51].

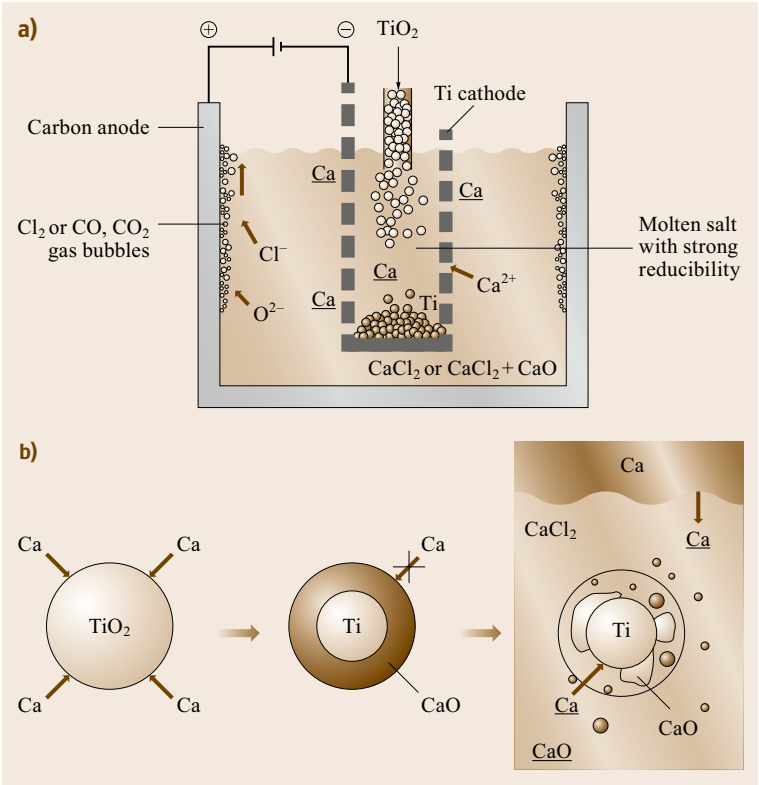


Fig. 25.11a,b Experimental arrangement of the OS process **(a)** (after [25.42]), and flux assisted calciothermic reduction **(b)** (after [25.46]), where Ca and CaO represent dissolved Ca and CaO in the flux of $CaCl_2$

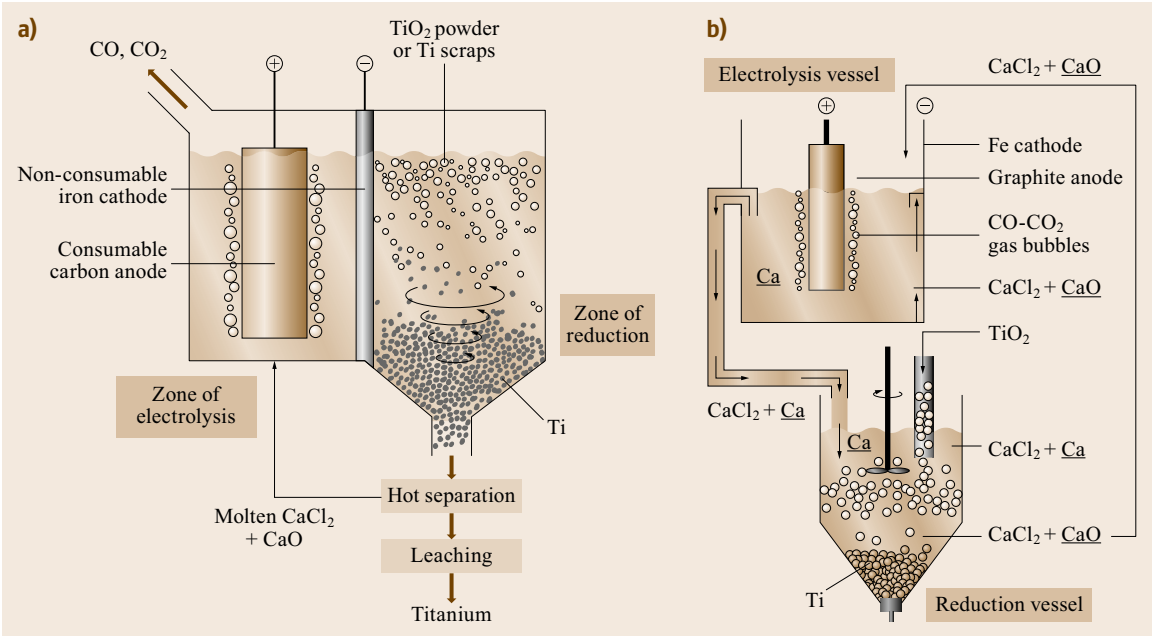


Fig. 25.12 Schematic of the concept for continuous production of titanium using the OS process (after [25.41])

The produced titanium is in the liquid state, which can be collected at the chamber floor and then periodically tapped off. When the process for removal of titanium is combined with continuous molten ti-

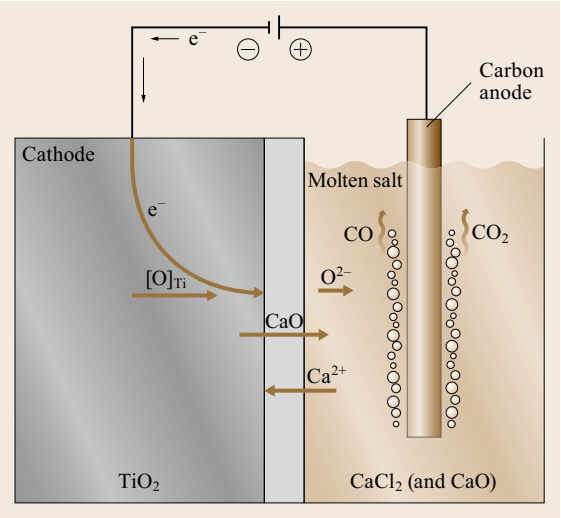


Fig. 25.13 Schematic of the Polar titanium process(after [25.47])

tania slag injection, it can produce titanium metal continuously [25.51, 52].

However, titania slag of high purity is required to produce pure titanium, otherwise a two-step process needs to be carried out. In the two-step process, the first electrolysis process is applied to purify the slag by removal of more electropositive elements such as Fe, Cr, Mn, V and so on. The electrolytic products fall to the chamber floor where they are removed through a tap hole. The second step is carried at a higher temperature to extract titanium from the purified titania slag. It should be mentioned here that the one-step process can be used for alloy production by adding other metal oxides into the chamber, such as Al_2O_3 and V_2O_5 in order to obtain Ti-6Al-4V [25.28].

The issue of oxygen contamination is a major concern, as the produced metal is in the liquid state and in contact with titania slag, which is similar to the Avanti process.

25.2.3 Summary and Note

Table 25.2 summaries some of innovative electrolytic extraction techniques for titanium.

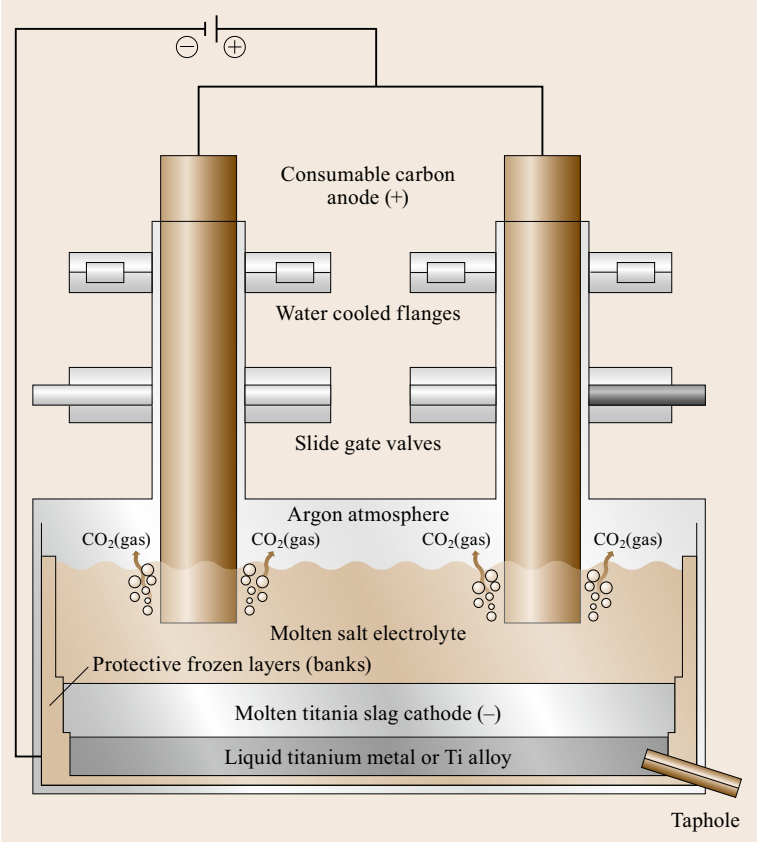


Fig. 25.14 Basic concept of the QIT process for Ti extraction (after [25.51])

The majority of these developments focus on the production of commercially pure titanium, with some having the capability to produce titanium alloys directly, and fewer still having done so. Notable among these, the FFC Cambridge process [25.48] has been successfully demonstrated to directly produce titanium metal and its alloys by the electrochemical reduction of a cathodic oxide precursor in a molten salt electrolyte [25.48, 53–61].

25.3 Direct Electroreduction of Solid Metal Oxides to Metals: The FFC Cambridge Process

25.3.1 History

The Fray–Farthing–Chen (FFC) Cambridge process, which is named after its inventors, Derek J. Fray, Tom W. Farthing, and George Z. Chen, was first developed at the University of Cambridge in 1996 following a discovery made when attempting to reduce the oxygen content of an oxygen-rich titanium alpha phase in molten calcium chloride ($CaCl_2$). It was found that, under the experimental conditions employed (at 1123 K with a cell voltage of 2.8–3.2 V against a graphite anode), it was possible to not only leach out the absorbed oxygen in the alpha phase, but also to reduce the oxide layer that had formed on the titanium. This discovery was surprising in that the oxide layer of titanium dioxide (TiO_2) was thought to be nonconductive, and therefore no reduction was expected. This work was extended to the electrolysis of porous TiO_2 cathodes for the express purpose of reducing pure oxide to pure titanium metal under the same experimental conditions. The resultant success in these studies was published [25.48] and outlined in several patents [25.62–67].

25.3.2 Principle

The basic principle of the FFC Cambridge process is to remove oxygen from a metal oxide feedstock by taking advantage of a direct electroreduction process (also known as the electrodeoxidation process), which is carried out at a voltage higher than that for oxygen ionisation but lower than that for electrolyte decomposition [25.48, 62–64, 66].

A schematic illustration of the FFC Cambridge process based on the direct electrochemical reduction of solid oxide in molten salt is presented in Fig. 25.15.

As shown in Fig. 25.15, the relatively simple operating procedure is one of the advantages of the FFC Cambridge process. First a feedstock, which is either a single or mixed metal oxide powder, is made into a porous preform by pressing or slip casting. After this, the sintering process is normally carried out to increase the strength of the preform for handling. The preform itself is made into the cathodic assembly by attaching it onto a metal substrate, and this assembly is then submerged in a molten salt (normally a $CaCl_2$ melt) that is able to dissolve the oxide ion, O^{2-}. A graphite anode is usually used that is also inserted into the melt to complete the circuit. By applying a predefined voltage that is below the decomposition voltage of the molten salt, but above that of the oxide preform, the electrodeoxidation process is carried out. During this process, the ionised oxygen atoms are transferred via the molten salt from the metal oxide cathode to the anode where they discharge as a mixture of CO/CO_2, or pure O_2 for graphite or inert anode materials (e.g., tin oxide), respectively, finally leaving the electrodeposited metal or alloy at the cathode.

The FFC Cambridge process can be represented by the following reactions.

Overall Reactions

$$MO_x(s) = M(s) + x/2O_2(g) \text{ (inert anode)}\,, \quad (25.17)$$

$$nMO_x(s) + xC(s) = nM(s) + xCO_n(g) \text{ (graphite anode, } n = 1 \text{ or } 2)\,. \quad (25.18)$$

Cathode Reaction

$$MO_x(s) + 2xe^- = M(s) + xO^{2-}\,. \quad (25.19)$$

Anode Reactions

$$xO^{2-} = x/2O_2(g) + 2xe^- \quad \text{(inert anode)}\,, \quad (25.20)$$

$$nO^{2-} + C(s) = CO_n(g) + 2ne^- \text{ (graphite anode, } n = 1 \text{ or } 2)\,, \quad (25.21)$$

where M represents metals.

Following the completion of the electrodeoxidation process, the cathode assembly is removed from the molten salt, cooled, washed, and dried. The electrolytic product can then be subjected to conventional metallurgical processes.

However, there was formerly a debate on the mechanism of the FFC Cambridge process: whether electrometallothermic reduction (e.g., calciothermic reduction in the OS process) or direct electrodeoxidation dominates the process [25.69].

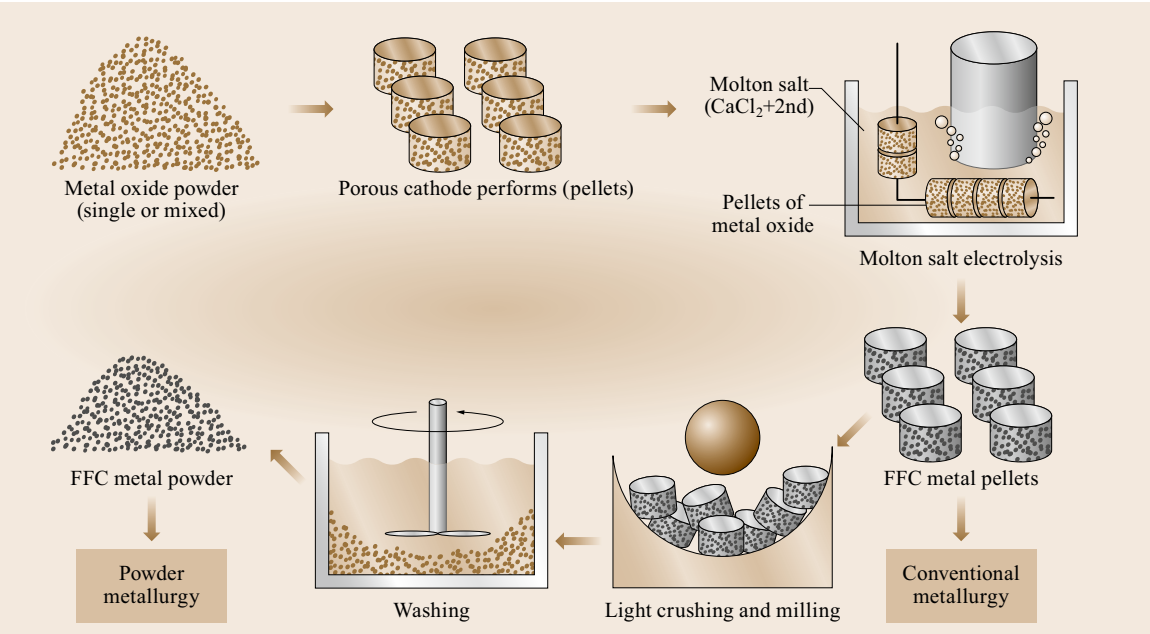


Fig. 25.15 A schematic representation of the FFC Cambridge process for the electroreduction of solid metal oxide to solid metal in molten salt (after [25.68])

These two mechanisms are summarized here:
Electrometallothermic Reduction

$$x\mathrm{Ca}^{2+} + 2x\mathrm{e}^- = x\mathrm{Ca}\,, \tag{25.22}$$

$$x\mathrm{Ca} + \mathrm{MO}_x = \mathrm{M} + x\mathrm{Ca}^{2+} + x\mathrm{O}^{2-} (\text{or } x\mathrm{CaO})\,. \tag{25.23}$$

Direct Electrodeoxidation

$$\mathrm{MO}_x + 2x\mathrm{e}^- (+x\mathrm{Ca}^{2+}) = \mathrm{M} + 2x\mathrm{O}^{2-} \text{ (or } x\mathrm{CaO})\,. \tag{25.24}$$

To verify the reduction mechanism of the FFC Cambridge process, several studies were carried out independently. In 2006, *Wang* et al. demonstrated the electrochemical metalization of solid terbium oxide (Tb_4O_7) using the FFC Cambridge process (Fig. 25.16) [25.70].

Based on this work, it has been confirmed that by increasing the cell voltage the reduction speed (indicated by reduction depth) will be accelerated until a plateau of reduction depth increase is reached at voltages well above that for decomposition of $CaCl_2$ (as shown in Fig. 25.16). The plateau can be attributed to the saturation of Ca metal that blocks the ionic pathway for further removal of oxygen. However, if the electrometallothermic reduction dominates, once the Ca activity reaches unity, the reduction speed will become constant and be independent of the cell voltage beyond the $CaCl_2$ decomposition voltage which is in theory 3.262 V at 850 °C. In Fig. 25.16 it can be seen that the reduction rate increases well beyond 3.3 V. Therefore, the reduction mechanism in this case must be the electrodeoxidation process, which can be accelerated by increasing the cell voltage, i. e., the driving force for the removal of oxygen.

In 2007, *Schwandt* and *Fray* further validated the direct electrodeoxidation mechanism by electrochemical reduction of chromium sesquioxide (Cr_2O_3) in molten salt (consisting of 98.0 mol% of $CaCl_2$ and 2.0 mol of CaO) using a potential at which the Ca deposition cannot be initiated [25.71].

In addition, a mechanism of three-phase interlines (3PIs) has been proposed for the explanation of the progression of electrodeoxidation through insulators (e.g., TiO_2, Cr_2O_3, etc.) [25.68], which is illustrated in Fig. 25.17.

During electroionisation, three factors are required to initiate the process, i. e., an electrical contact to the oxide, the metal, the oxide itself, and an electrolyte to transfer the ionised oxygen. The location where these three factors exist are thus defined as three-phase points, which subsequently extend to lines (i. e., 3PIs) with the progression of electrodeoxidation, as can be seen from Fig. 25.17. Once the surface of the metal oxide precursor is fully metalized, the generation of new conductive materials (e.g., metal and/or conductive suboxide) underneath permits the penetration of this 3PI into the pellet, leading to the final electrodeoxidation of the whole precursor.

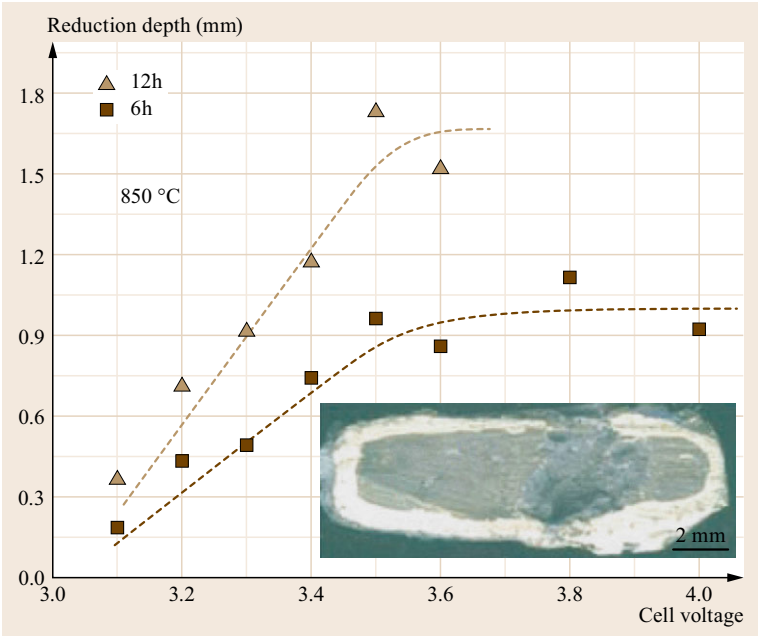


Fig. 25.16 Correlations between the reduction depth and cell voltage for 6 and 12 h of electrolysis. The inset shows the cross-section of a Tb_4O_7 pellet after electrolysis at 4.2 V for 6 h. The pellet was enclosed by a layer of Ca and Tb, but was only partly reduced inside (after [25.70])

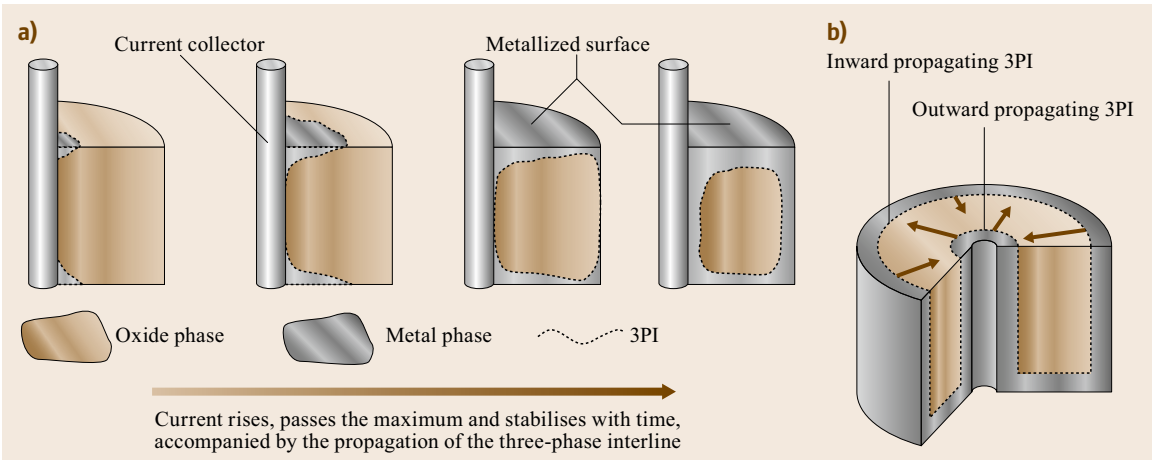


Fig. 25.17a,b 3PI propagation model; **(a)** cross-sectional view, and **(b)** overall view (after [25.68])

Experimental Setup

Cyclic Voltammetric (CV). Figure 25.18 shows a typical experimental set-up for laboratory study of the FFC-Cambridge process. The experimental setup can utilize either two- or three-electrode arrangements, depending on the purpose of the investigation. For reduction of bulk materials, a two-electrode arrangement is normally adopted, and a three-electrode arrangement with a reference electrode is always chosen when precise control or measurement of the cathodic potential and hence reactions is required, such as for cyclic voltammetric (CV) investigations. Figure 25.19 illustrates these two different electrode arrangements.

It is worth mentioning here that the graphite rod in Fig. 25.19 can be replaced by, for example, a tin oxide rod that functions as an inert anode for eliminating CO_2 emissions during the electrodeoxidation process (pure O_2 is the only off-gas) [25.72, 73]. The cathode assembly can also be set up according to different designs, such as suspending a metal oxide pellet on a metal wire, sandwiching pellets in between molybdenum meshes, and so on [25.48, 59, 68, 74]. Pure metal wire (e.g., titanium) or a graphite rod can be used as a pseudo-reference electrode for three-electrode electrolysis [25.75, 76]. Proper reference electrodes for the FFC Cambridge process have



Fig. 25.18 A typical experimental setup of the FFC Cambridge process

also been developed. Ag/AgCl based reference electrodes are the most commonly used type in molten chloride salts, which are normally fabricated by sealing AgCl and additional salts within a junction (membrane) material. Various junction materials have been tested for this purpose, including sodium glass [25.77], Pyrex [25.78], quartz [25.79], and Mullite. Figure 25.20 gives two examples of the construction of typical Ag/AgCl reference electrodes used in molten chloride salts [25.78, 79]. It is worth mentioning here that a robust alumina membrane reference electrode has been developed and investigated recently, which can withstand repeated (> 15 times) and prolonged continuous (seven days) uses in molten chloride and carbonate salts over a wide range of temperatures (773–1173 K) [25.80].

For CV investigations on powdery materials, metallic cavity electrodes (MCE) have been developed to load powders and form the working electrode [25.69, 81–83]. Figure 25.21 shows two kinds of MCEs, i. e.,

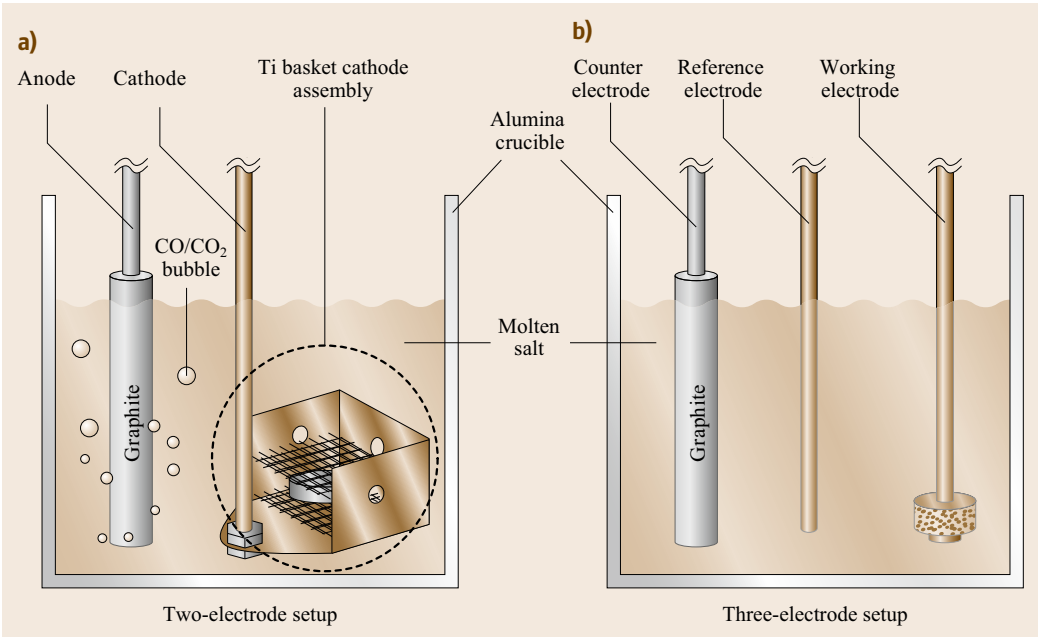


Fig. 25.19a,b Illustrations of a two-electrode setup for constant voltage or current electrolysis of an oxide precursor in a cathode basket **(a)** and a three-electrode setup for potentiostatic or galvanostatic electrolysis or cyclic voltammetry of an oxide pellet suspended on the cathode wire **(b)**

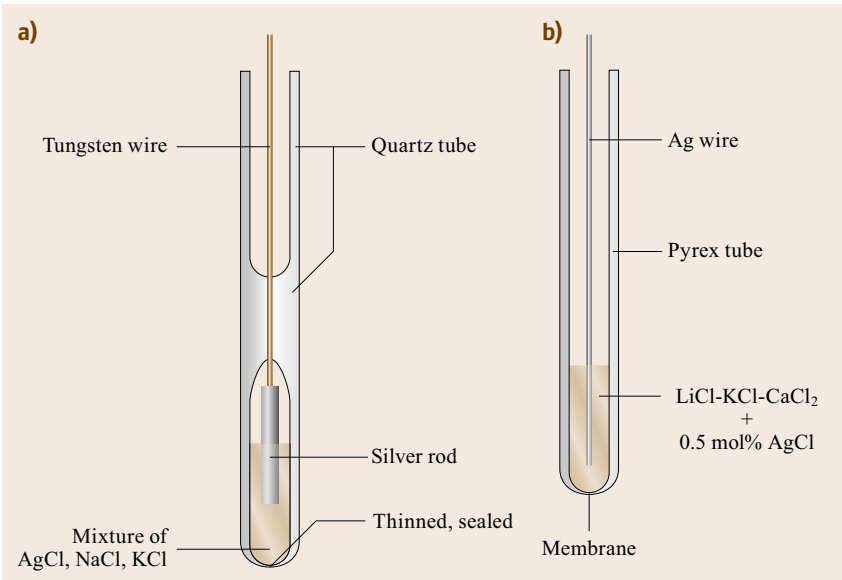


Fig. 25.20a,b Schematic illustrations of reference electrodes for molten chloride salts. The quartz sealed Ag/AgCl reference electrode; thinned and sealed lower end of the quartz tube as the ion conducing membrane **(a)** (after [25.79]). The Pyrex tube sealed Ag/AgCl reference **(b)** (after [25.78])

the crack cavity electrode and the through-hole cavity electrode [25.69, 81].

The crack cavity electrode is prepared by repeatedly bending and fracturing a metal wire at a prenotched location [25.83], and the hole made in the through-hole cavity electrode can be done by either laser or mechanical drilling [25.81]. The mass of the metal oxides loaded onto MCEs is normally of the order of submilligrams so that the response is quick and complete during CV and potentiostatic investigations.

Mechanism of Electrochemical Reduction of SiO_2

As described before, the carbothermic reduction of SiO_2 is the main method adopted by the silicon production industry, which is high in terms of energy consumption and CO_2 emissions. The FFC Cambridge process, which uses electrons as the reductant, has been considered as an alternative process to the conventional carbothermic reduction process.

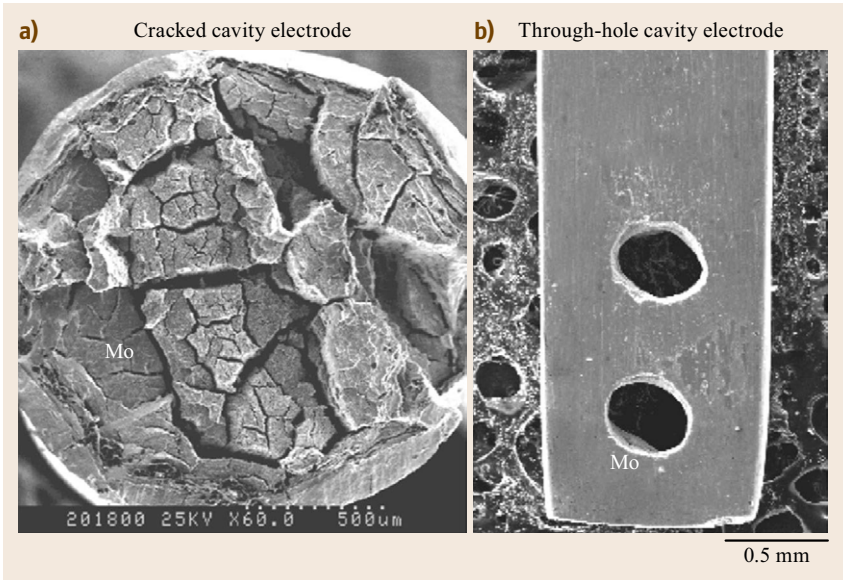


Fig. 25.21a,b Cracked end-face of a Mo wire **(a)** (after [25.69]) and a 0.5 mm thick Mo foil with two laser-drilled through-holes **(b)** (after [25.81])

The feasibility of the direct electroreduction of silica to silicon via the FFC Cambridge process has been confirmed in different laboratories [25.74, 84–86]. The electrochemical reduction of silica to silicon appears to be a one-step reaction, which can be described as

$$SiO_2 + 4e^- = Si + 2O^{2-} . \qquad (25.25)$$

Based on the results of CV investigations, reaction (25.25) occurrs at a far more positive potential (E_{Si/SiO_2}) than that for the deposition of Ca ($E_{Ca^{2+}/Ca}$) in molten $CaCl_2$ [25.84, 85] or the deposition of Ca-Li ($E_{Ca^{2+},Li^+/Ca\text{-}Li}$) in molten $CaCl_2$-LiCl-KCl [25.87]. Figure 25.22a,b show two CVs recorded to show the electroreduction of silica in pure $CaCl_2$ [25.84] and $CaCl_2$-LiCl-KCl [25.87] respectively.

Although the electrochemical reduction of silica to silicon appears to be a one-step reaction and it happens at potentials far more positive than that of salt decomposition, impurities including oxygen, $MgSiO_3$, $CaSiO_3$, and Si-Ca alloys in electrolytic products were reported [25.84, 86, 88]. The origins of these impurities were thought to arise from:

1. The electrolyte [25.84]
2. The contamination of the reaction vessel and electrodes [25.86]
3. The formation of Si-Ca alloys at more negative potentials [25.88].

Therefore, pre-electrolysis of the molten salt and keeping the potential window within a desired range are essential factors in order to produce silicon with high purity. It has been reported that the optimal potential window for the electroreduction of silica to silicon (< 0.5 wt% oxygen) in molten $CaCl_2$ at 1173 K is in the range of −0.6 to −0.95 V (versus a quartz sealed Ag/AgCl reference electrode) [25.89]. In addition, silicon ingots with a purity of 99.8% were produced through melting the electrolytic product under vacuumx [25.86, 90].

The morphology and crystallography of the silicon prepared by potentiostatic electrolysis of a silica contacting electrode at 1.10 V (versus $E_{Ca^{2+}/Ca}$) for 1 h were investigated by *Yasuda* et al., and the mechanism for the direct electroreduction of solid silica was interpreted as well [25.91]. Figure 25.23 shows the morphology of electrolytically produced silicon and the mechanism of its formation [25.91].

It was found that the silicon columns produced became arranged perpendicularly to the reaction interface between the electrolytic silicon and silica, as shown in Fig. 25.23a. The silicon columns basically had a hexagonal prismatic and stacking structure (Fig. 25.23b). It was proposed that during electroreduction, amorphous silicon was first formed and then transformed to crystalline silicon at a high temperature via the bond-breaking process [25.91].

Mechanism of Electrochemical Reduction of TiO_2

Following the first report on electrochemical reduction of solid-state TiO_2 to titanium metal [25.48], the FFC Cambridge process for titanium production has been successfully demonstrated by different groups [25.59, 76, 92–96]. In order to understand the mechanism of electrochemical reduction of TiO_2,

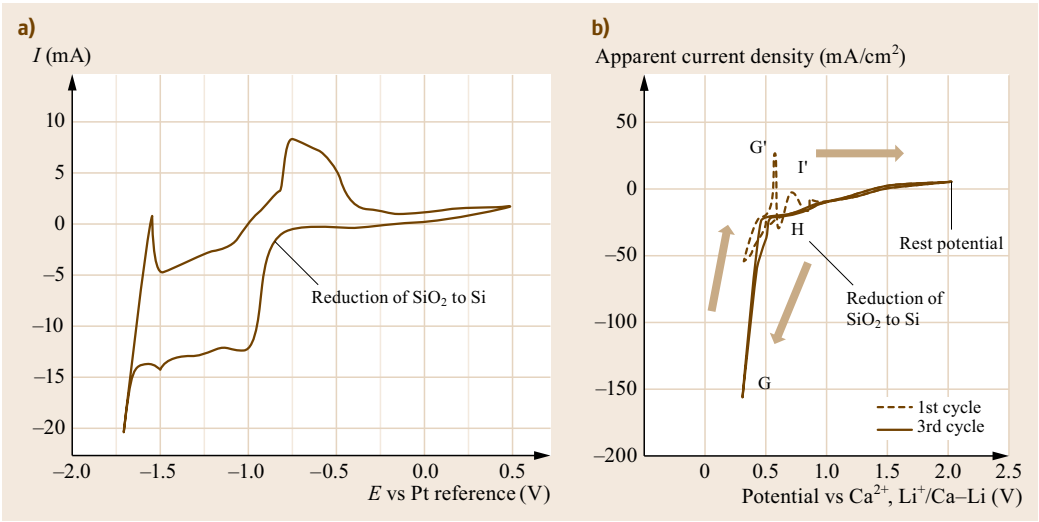


Fig. 25.22a,b CVs of **(a)** the W-SiO_2 electrode in molten $CaCl_2$ (200 mV/s, 1123 K) (after [25.84]), and **(b)** the SiO_2 contacting electrode in the LiCl-KCl-$CaCl_2$ eutectic melt (20 mV/s, 773 K) (after [25.87])

CV investigations were conducted by several researchers [25.75, 93, 97]. Figure 25.24 shows a typical CV recorded on a thermally grown scale of TiO_2 on titanium [25.75].

Four reduction peaks (C1 to C4) were observed on the CV (Fig. 25.24) as well as that of calcium deposition (C0). Different cathodic products were obtained by performing electrolysis of TiO_2 at these identified potentials, and products were then subjected to x-ray diffraction (XRD) analysis.

$$\text{C4}: \ 3TiO_2(s) + 2e^- = Ti_3O_5(s) + O^{2-} , \quad (25.26)$$

$$\text{C3}: \ 2Ti_3O_5(s) + 2e^- = 3Ti_2O_3(s) + O^{2-} , \quad (25.27)$$

$$\text{C2}: \ Ti_2O_3(s) + 2e^- = 2TiO(s) + O^{2-} , \quad (25.28)$$

$$\text{C1}: \ TiO(s) + 2e^- = Ti_{[O]} + O^{2-} . \quad (25.29)$$

It is worth mentioning here that between TiO_2 and Ti_2O_3 there are many intermediates, which are highly conductive, known as the Magneli phases. The composition of a Magneli phase varies according to the formula of Ti_nO_{2n-1} ($n \geq 2$) [25.48, 75, 97].

Moreover, it was found that the calcium ions play an active role in the process for the electrodeoxidation of TiO_2 [25.95].

Based on analysis of products from partial and complete reduction, *Schwandt* et al. have claimed that the electrochemical reduction of TiO_2 to titanium metal undergoes substantial changes in microstructure and composition, involving the formation and decomposition of calcium titanate ($CaTiO_3$) initially, and calcium titanite ($CaTi_2O_4$) later [25.95]. The suggested pathway for the electrodeoxidation of TiO_2 in molten $CaCl_2$ is presented in the following reactions

$$5TiO_2(s) + Ca^{2+} + 2e^- = Ti_4O_7(s) + CaTiO_3(s) , \quad (25.30)$$

$$4Ti_4O_7(s) + Ca^{2+} + 2e^- = 5Ti_3O_5(s) + CaTiO_3(s) , \quad (25.31)$$

$$3Ti_3O_5(s) + Ca^{2+} + 2e^- = 4Ti_2O_3(s) + CaTiO_3(s) , \quad (25.32)$$

$$2Ti_2O_3(s) + Ca^{2+} + 2e^- = 3TiO(s) + CaTiO_3(s) , \quad (25.33)$$

$$CaTiO_3(s) + TiO = CaTi_2O_4(s) , \quad (25.34)$$

$$CaTi_2O_4(s) + 2e^- = 2TiO(s) + Ca^{2+} + 2O^{2-} , \quad (25.35)$$

$$TiO(s) + 2(1-\delta)e^- = Ti_{[O]\delta} + (1-\delta)O^{2-} . \quad (25.36)$$

Based on these observations, the current-time curve with cathode composition obtained at different time intervals was plotted [25.95], and can be seen in Fig. 25.25a. Figure 25.25b–e shows the microstructure of products taken at different polarization times.

These findings provide further insight into the electrodeoxidation mechanism of the FFC Cambridge process for bulk electrolysis, which is accompanied by the formation and decomposition of calcium titanates. The formation of calcium titanates (i. e., in situ perovskitization) proceeds inevitably by both electrochemical and chemical reactions during the electrodeoxidation process of TiO_2 [25.93–95], which can be described by (25.37). On the other hand, the originally proposed reduction mechanism for TiO_2 is a more direct reaction

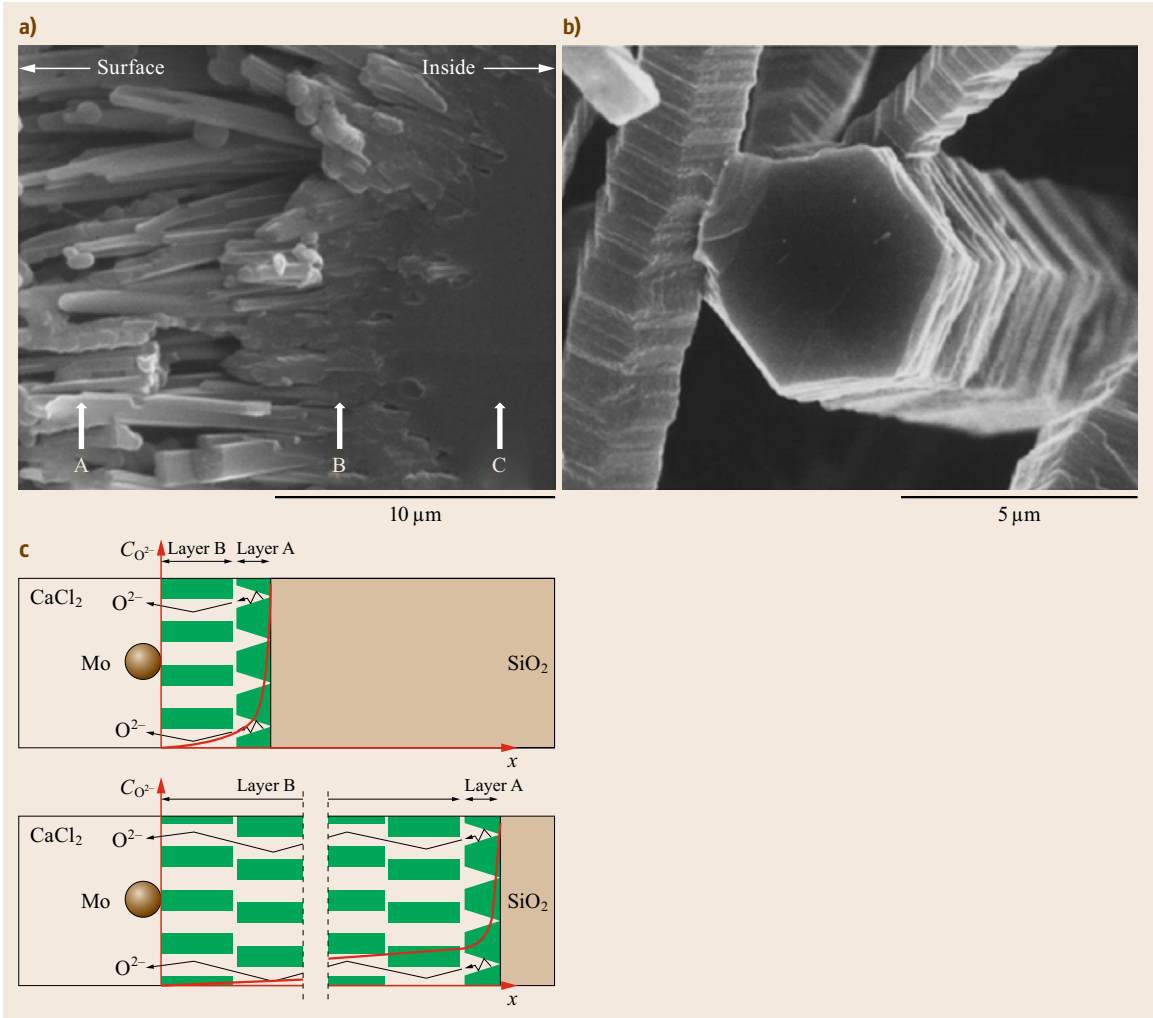


Fig. 25.23 **(a)** Cross-sectional SEM image of the reaction interface of the sample, and **(b)** field emission (FE)-SEM image of the silicon columns. Samples obtained by potentiostatic electrolysis of silica at 1.10 V (versus $E_{Ca^{2+}/Ca}$) for 1 h in molten $CaCl_2$ at 1123 K. **(c)** Conceptual drawing of Si layer formation and O^{2-} diffusion in initial period (*top image*) and last period (*bottom image*) during the electroreduction of silica in molten $CaCl_2$ (after [25.91])

sequence of [25.75, 97]

$$\begin{aligned} &TiO_2 \rightarrow Ti_3O_5 \rightarrow Ti_2O_3 \rightarrow TiO \rightarrow Ti\,, \\ &TiO_2 + \alpha Ca^{2+} + \beta O^{2-} + 2(\alpha-\beta)e^- \\ &\quad = Ca_\alpha TiO_{2+\beta}\,, \end{aligned} \tag{25.37}$$

where $1 \geq \alpha \geq \beta \geq 0$.

The reaction (25.37) is a chemical reaction for $\alpha = \beta$, but an electrochemical one for $\alpha > \beta$.

Recently, in 2011, *Alexander* et al. demonstrated that a more direct reduction pathway can be achieved by bulk electrolysis of more dense TiO_2 precursors, which is somewhat akin to the originally proposed direct reaction pathway [25.98]. The dense metal oxide precursor restricts the calcium-incorporation reactions by limiting the capacity of the porosity for the expansion of solid volume associated with the calcium titanates formation [25.98].

Other works carried out by *Jiang* et al. [25.93] and *Li* et al. [25.99] indicated that the electrodeoxidation efficiency of TiO_2 can be enhanced either by preventing in situ formation of calcium titanate using the ex situ *perovskitisation* [25.93] method or by increasing the porosity of metal oxide precursor [25.99].

It should be noted here that, another effect of the ex situ *perovskitisation* process (i. e., by mixing and sintering a pressed mixture of TiO_2 and CaO or $Ca(OH)_2$) is to increase the porosity of the metal oxide precur-

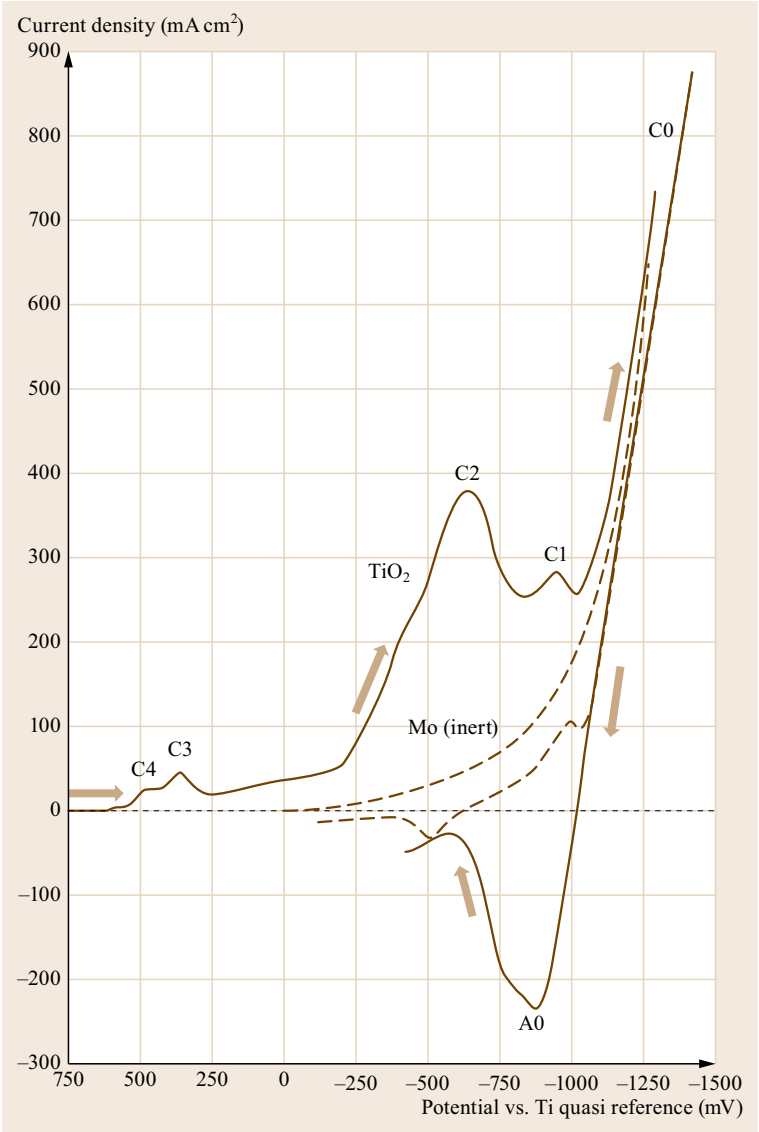


Fig. 25.24 CVs of TiO_2 scale in $CaCl_2$ at 1173 K (scan rate 50 mV/s) (after [25.75])

sor, when considering the net volume of TiO_2 in the bulk material. Therefore, porosity enhancement could be considered as a common method to boost the efficiency of electrodeoxidation processes. Most recently, a more fundamental insight into the rate-determining mechanism has been reported, which claims that diffusion of oxygen ions in the pores of the produced metal layer plays a decisive role in electrodeoxidation speed [25.100]. A theoretical model has therefore been developed that offers a more accurate prediction of the optimal cathode porosity (P_{opt}) (25.38) [25.100]

$$P_{opt} = \frac{3R + S - 1}{3R} \times 100\% \,, \qquad (25.38)$$

where P is the precursor porosity (in volume percentage), R the metal-to-oxide molar volume ratio, and S the cathode volume shrinkage (in volume fraction, experimentally determined) (the porosity ratio shrinkage (PRS [25.38]) model).

When compared with the Kroll process for titanium production, the FFC Cambridge process can use an inert, harmless, economical and readily accessible feedstock (i. e., TiO_2), rather than using expensive and potentially hazardous electrolytic preparation of the chlorine gas that is required in the carbochlorination process for the formation of the gaseous feedstock of $TiCl_4$ [25.19]. Furthermore, the FFC Cambridge process is capable of producing commercially pure

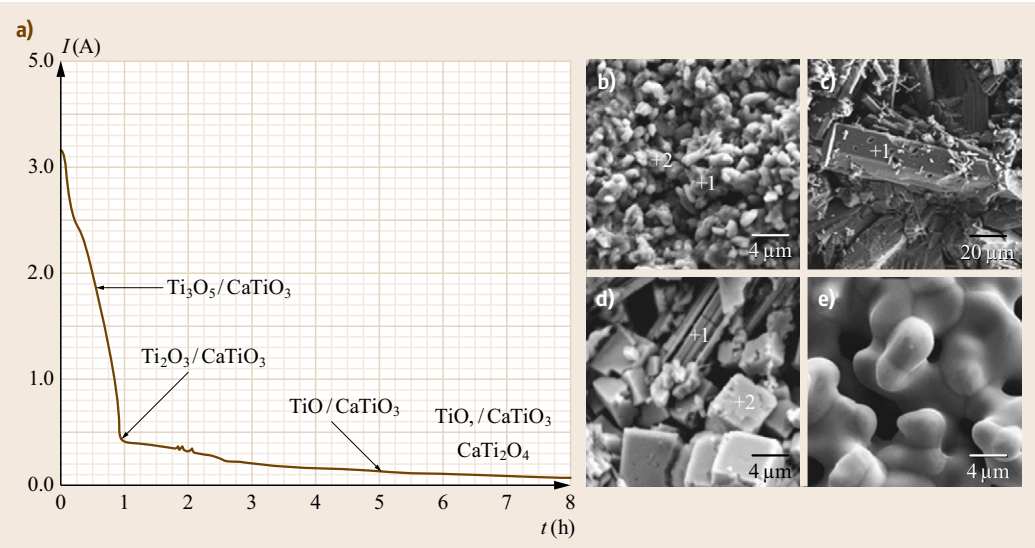


Fig. 25.25 **(a)** A particularly well-resolved current time curve with cathode composition given for various points in time during the first stage of reduction. SEM images of preform microstructure after **(b)** 1 h; **(c)** 12 h; **(d)** 52 h; **(e)** 120 h polarization. Composition: **(b)** $Ti_2O_3/CaTiO_3$; **(c)** $CaTi_2O_4$; **(d)** $CaTi_2O_4/TiO$; **(e)** Ti (after [25.95])

titanium sponge (oxygen content < 2000 ppm) at an energy consumption of 21.5 kWh/kg [25.99]; approximately 57% less than the conventional Kroll process (> 50 kWh/kg) [25.59].

Ability of Direct Production of Alloys from Metal Oxide Mixtures

It was found that, if a mixture of different metal oxides is subjected to the electrochemical reduction process, the oxides reduce in the order of increasing stability. However, rather than forming a mixture of individual elements, a homogenous alloy can be formed eventually [25.38, 55].

This special capability of the FFC Cambridge process can be utilized to produce alloys that are difficult or impossible to prepare using conventional technology, because the melting temperature of one metal may be greater than the boiling temperature of the other (Fig. 25.26) [25.101]. By taking advantage of the FFC Cambridge process, the electrochemical reduction of metal oxide mixtures can be controlled at a temperature lower than the melting points of each of the individual metal elements contained in the metal oxide mixture. Therefore, metal alloys can be directly produced in the solid state. In addition, density differences between different alloying elements could also cause difficulties with the alloy production process via melting and casting. For example, the relatively low density of titanium makes the process of fusion alloying difficult when alloying elements with a density greater than that of titanium. This issue can also be eliminated using the

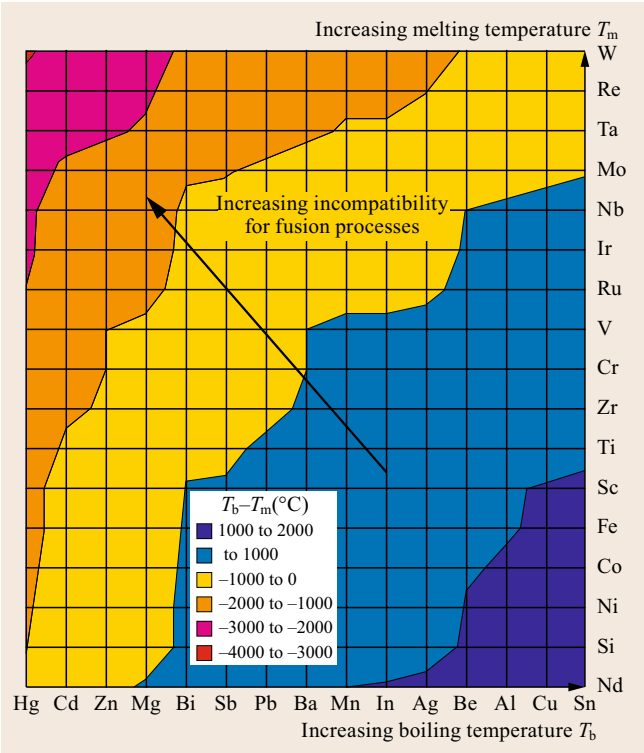


Fig. 25.26 The incompatibility of metals for fusion alloying processes (after [25.101])

FFC Cambridge process where metal extraction and alloy formation happen simultaneously in the solid state.

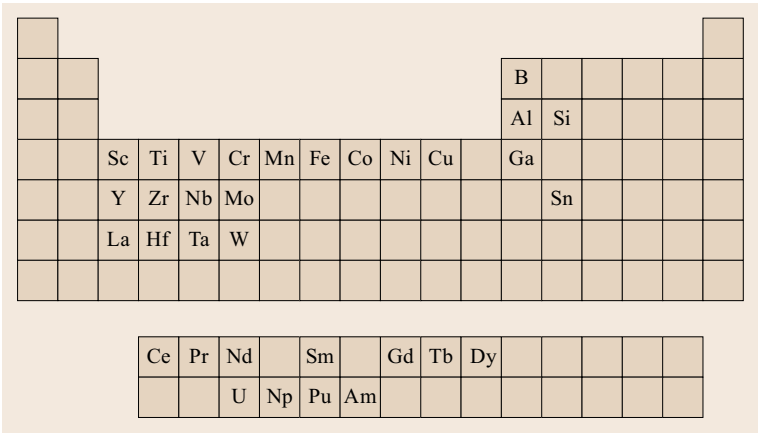


Fig. 25.27 Elements successfully extracted from solid compounds in the form of either pure metals or alloys using direct electrorduction in molten salt according to publicly available sources (after [25.102])

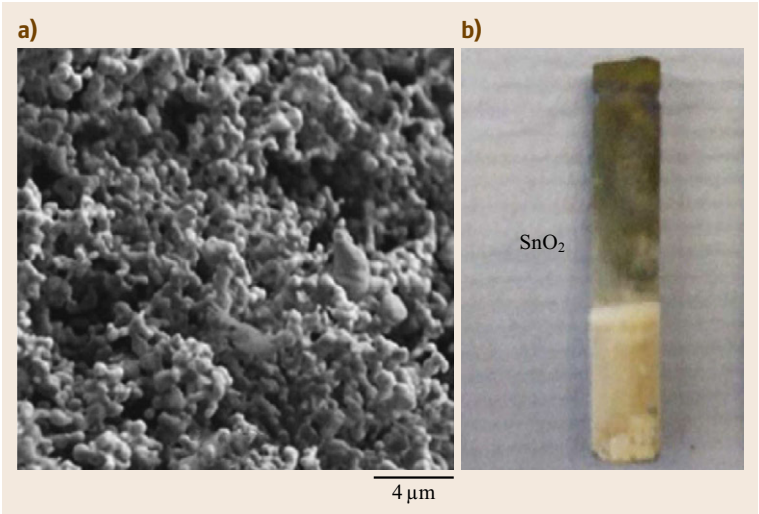


Fig. 25.28a,b SEM image of tantalum produced using a tin oxide anode **(a)**, and a photograph of a used tin oxide anode **(b)** (after [25.73])

25.3.3 Applications

The FFC Cambridge process has been successfully utilized for production of more than 30 metals or semimetals as single metal and/or alloy [25.102], as shown in the periodic table in Fig. 25.27. Titanium has been cited as the main development candidate for the FFC Cambridge process.

Extraction of Metals

Among these metals, the electrochemical reduction of chromium oxide powder (Cr_2O_3) to chromium metal (Cr) shows a relatively high current efficiency and a lower energy consumption (75% and 5 kWh/kg) [25.68]. It only took 6 h of electrolysis to produce chromium metal with an oxygen level of less than 0.2 wt% [25.68].

The use of a tin oxide rod as an inert anode for metal extraction has been demonstrated in the electrolytic extraction of tantalum metal (Ta) (with an oxygen content of less than 0.5 wt%) from tantalum oxide (Ta_2O_5). Figure 25.28 shows the SEM image of tantalum metal produced using a tin oxide anode, and the photograph of the tin oxide anode after use [25.73].

Apart from tin oxide, other materials that potentially could be used as an inert anode, such as the $CaRuO_3/CaTiO_3$ composite [25.103, 104], have been investigated as well [25.105]. Additionally, a novel solid oxide ion conducting membrane (SOM) process has been developed and reported [25.106]. Instead of using inert materials to assemble the anodes, in the SOM process, a yttria-stabilised zirconia membrane, which can only conduct oxygen ions, is utilized to separate the anode materials from the melt in order to inhibit the side reactions and decomposition of molten salts. Figure 25.29 shows the construction of an anodic assembly for uses in the SOM process [25.106].

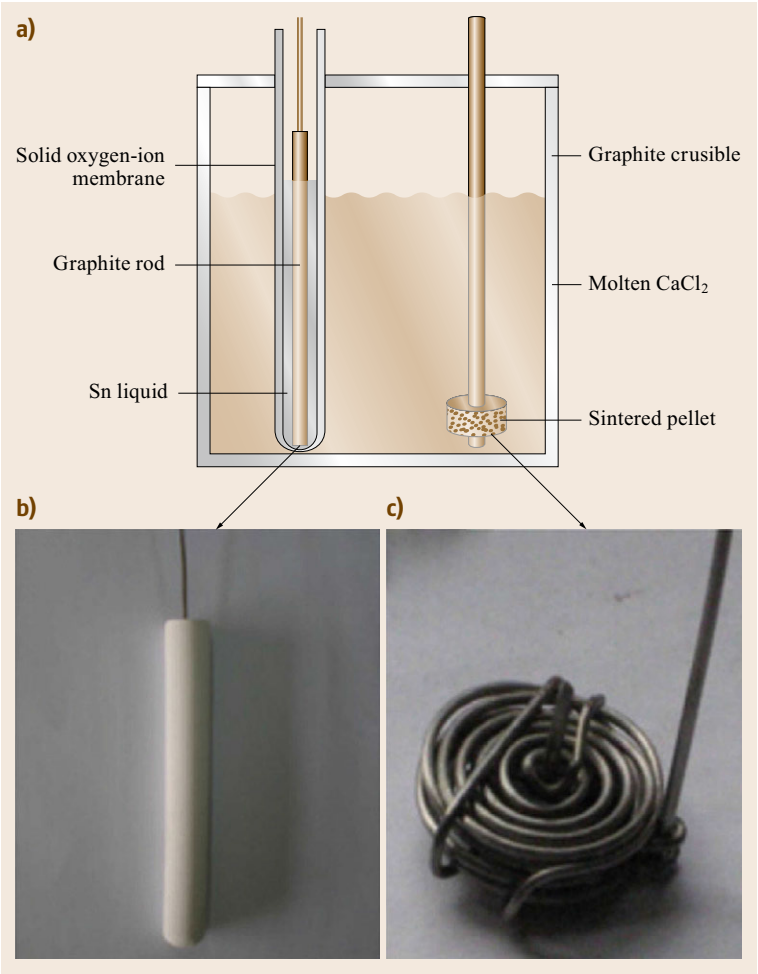


Fig. 25.29a–c Schematic diagram of electrodeoxidiation apparatus **(a)** with photos of **(b)** anode and **(c)** cathode for electrolysis (after [25.106])

In the SOM process, since only oxygen ions can be conducted to anodic materials, the evolution of chlorine gas and hence the decomposition of chloride salt can be prevented. This allows the electrolysis process to be operated at voltages even higher than those for salt decomposition. Consequently, a higher electroreduction rate can be anticipated.

The capability of the FFC Cambridge process to operate using an inert anode is a great advantage, as it can provide a much more environmentally friendly method for metal extraction, particularly if the electricity is generated from renewable sources. The off-gas evolved from an inert anode is pure oxygen, and the carbon contamination from conventional graphite anodes can be eliminated.

Synthesis of Metal Alloys

During the last decade, various metal alloys and intermetallics for structural uses and various functionalities, e.g. shape memory and magnetism, have been productively synthesized via the electrochemical reduction of mixtures of metal oxides [25.38, 53–58, 60, 61, 104, 107–110]. Among these, two kinds of alloys have drawn the most attention in research, i. e., hydrogen storage alloys and titanium-based alloys.

Different hydrogen storage alloy powders including $LaNi_5$-type alloys [25.106, 111], ferrotitanium alloys [25.61] and zirconium-based multiphase alloys [25.112] have been synthesized by the FFC Cambridge process. The morphologies of these alloys possess nodular particle shapes with sizes between 5−10 μm, similar to that of pure metals produced by the same method, (as shown in Fig. 25.30 [25.61, 113]).

This nodular morphology is of high surface-to-volume ratio and can be easily crushed into powder, which is highly desirable for the purpose of hydrogen absorption. Apart from being able to produce hydrogen storage alloys in powder form directly, the energy

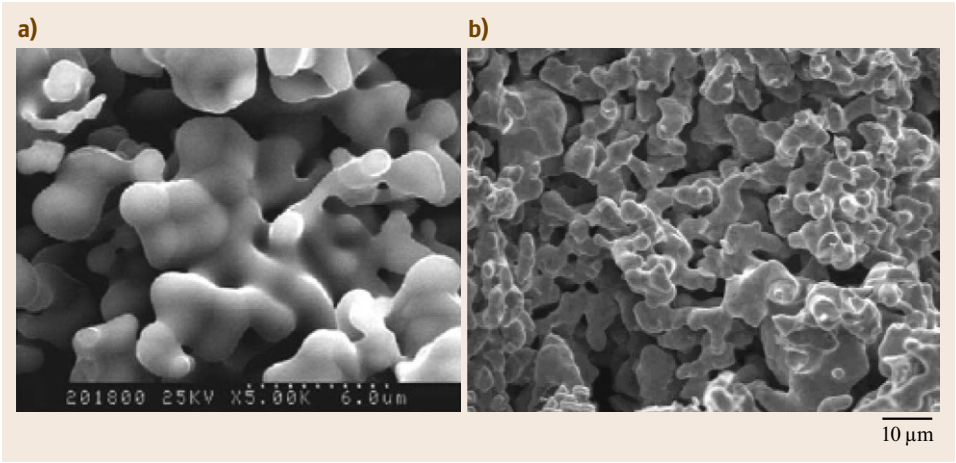


Fig. 25.30a,b SEM images of electrolytic hydrogen storage alloys: **(a)** $TiFe_{0.4}Ni_{0.6}$ (after [25.61]) and **(b)** $CeNi_5$ (after [25.106])

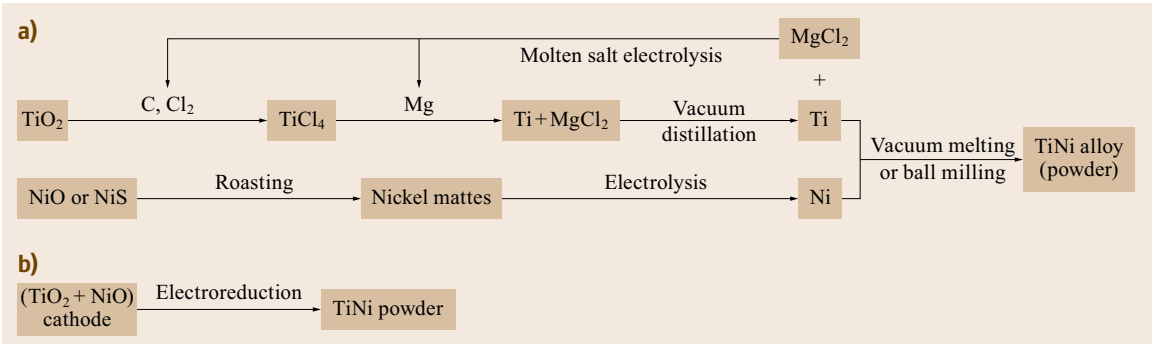


Fig. 25.31a,b Schematics of **(a)** Ti-Ni alloy production by conventional methods and **(b)** by the FFC Cambridge process (after [25.102])

consumption of the FFC Cambridge process is much less than that of conventional processes. For example, the total energy consumption of the current industrial process for $LaNi_5$ production includes energies for the extraction of each individual metal (i. e., Ni for approximately 10 kWh/kg, La for 11–20 kWh/kg), alloying, casting, homogenizing and crushing into powder form. In contrast, the energy consumption for $LaNi_5$ production is less than 5.5 kWh/kg using the FFC Cambridge process [25.111].

For titanium alloys, it should be noted the cost of the post-extraction alloying processes is significant because the wide differences in the melting points and densities of the alloying elements necessitates multiple remelting steps to ensure homogeneity of the final alloys.

The most significant advantage of the FFC Cambridge process over the Kroll process is its ability to directly produce titanium alloys. For example, when compared to the conventional process for Ti-Ni alloy production, the FFC Cambridge process is obviously greater in efficiency and simplicity, as shown in Fig. 25.31.

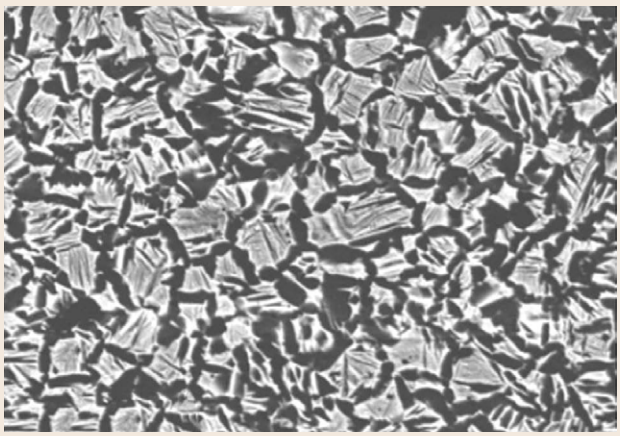


Fig. 25.32 Microstructure of Ti-10W alloy in as-produced condition by taking advantage of the FFC Cambridge process (after [25.56, 108]) ◄

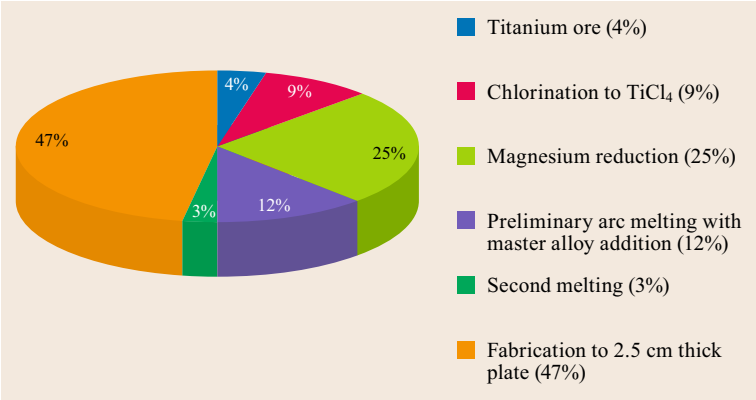


Fig. 25.33 Relative cost factors for conventional mill processing of a 2.54 cm thick Ti alloy plate (after [25.17, 28])

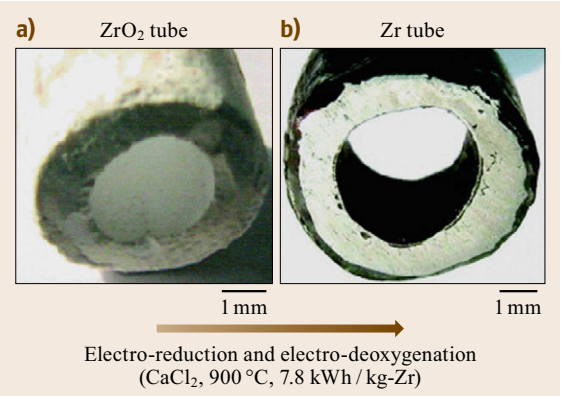


Fig. 25.34a,b Photos of a slip-cast ZrO_2 tube **(a)** and electrolytically produced Zr tube **(b)** (after [25.114])

This advantage has been successfully demonstrated for the synthesis of different titanium based alloys, such as alloys of Ti-Ni [25.58, 104, 115], Ti-10W [25.56], Ti-Mo [25.57], Ti-W [25.116], Ti-Fe [25.61], Ti-Zr [25.53] and [25.38, 54, 55, 108]).

Because there are no titanium alloys that have been specifically designed for casting, the microstructure of as-cast titanium alloy is usually poor, for example, grain sizes are large [25.12–14, 117]. However, as the FFC Cambridge process is a solid-state electrodeoxidation process, when a fine particle size is employed for the preparation of metal oxide precursors, titanium alloys with fine grain sizes (1–20 μm) can be easily obtained. The fine grain sizes of an electrolytic alloy of Ti-10W are shown in Fig. 25.32.

During the alloy production process, the oxides are reduced in the order of increasing stability but the final result is a homogenous alloy. The homogeneity of electrolytic alloys is thought to arise from the very short diffusion distances and the high reactivity of the electrolytic metals [25.38, 54]. Moreover, because almost all of the beta stabilizing elements are more noble than titanium, during the electrodeoxidation process, their oxides are metalized more readily than titanium oxides. The formed beta phase stabilizers can provide not only depolarization for reduction of TiO_2, but also more electrical pathways through the metal oxide precursor, leading to improved current distribution and reduction efficiency [25.55].

Near-Net-Shape Metallic Components

During the solid-state electrochemical reduction process, the preformed cathode material does not dissolve in the molten salt; consequently, the shape of the electrolytic product is essentially the same as the shape of the preform. This is of great importance because it has the potential to produce near-net-shape components that can avoid downstream processes significantly and hence reduce the cost [25.118].

The ability of the FFC Cambridge process to achieve near-net-shape production of metallic components is especially important for the production of titanium and its alloys. Compared to shaping processes employed for common metallic materials, the manufacturing of titanium and its alloys into their final components encounters more difficulties, arising from the unique physical and chemical properties of titanium [25.12, 119, 120]:

- The low thermal conductivity of titanium prevents quick dissipation of the heat generated from machining processes. This leads to increased wear of the cutting tools.
- The low modulus of elasticity of titanium results in a significant *spring-back* elastic effect after deformation under load. This results in premature flank wear of the cutting tools, vibration of titanium work piece, and a higher cutting temperature.
- The low hardness of titanium and its high chemical reactivity leads to a tendency for the titanium workpiece to bond with the cutting tool.

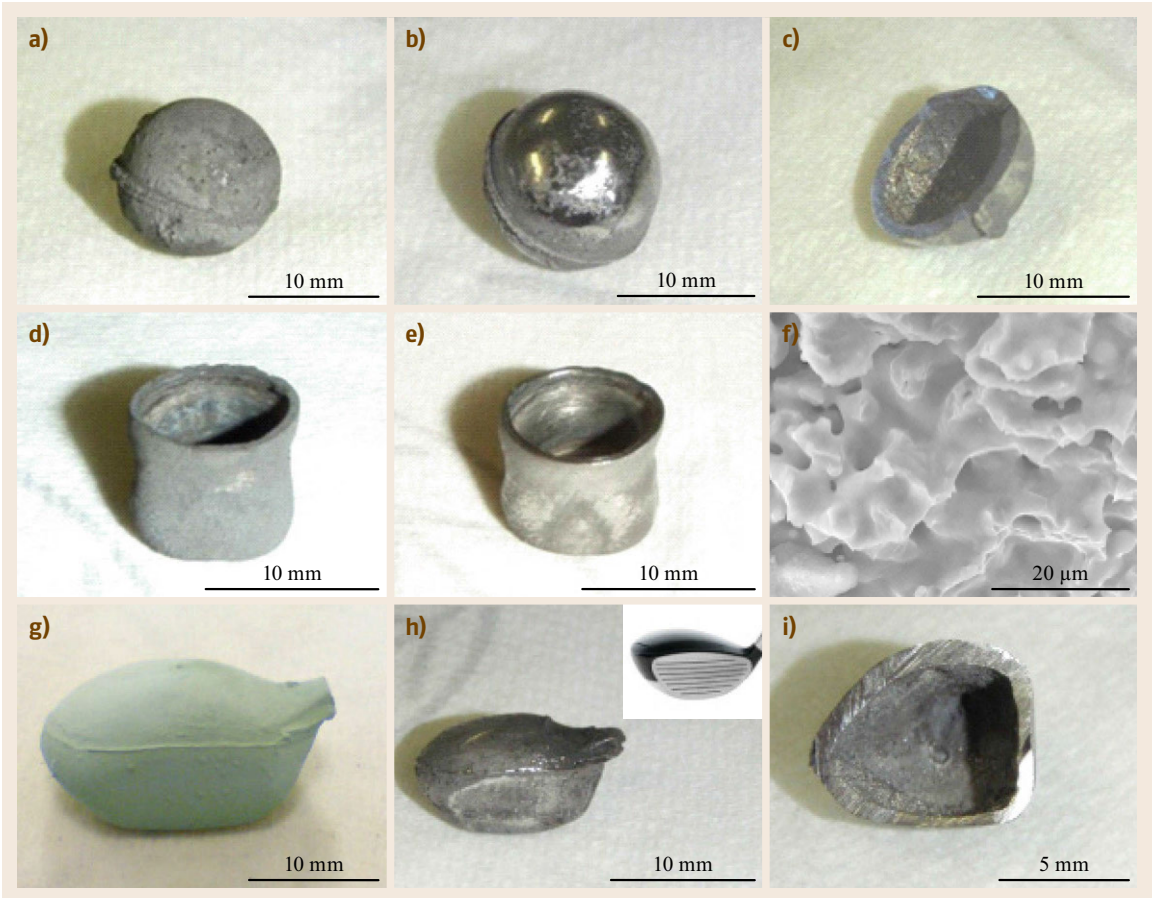


Fig. 25.35a–i Photographs of electrolytically produced **(a)** Ti-6Al-4V hollow sphere before and **(b)** after minor polishing, **(c)** cross-section of hollow sphere, **(d)** cup-shaped Ti-6Al-4V before and **(e)** after minor polishing, and **(f)** SEM image of the interior structure of the electrolytically produced Ti-6Al-4V alloy. **(g)** Golf-club-head-shaped metal oxide precursor, **(h)** electrolytically produced miniature Ti-6Al-4V hollow golf club head. The *inserted photo* is the commercial titanium golf club driver head. **(i)** Cross-section of produced miniature golf club head (after [25.121])

- The high chemical reactivity also causes titanium to readily react with atmospheric elements to form the so-called hard *alpha case* on the surface at elevated temperatures. Therefore, for those shaping operations requiring high temperatures, such as casting and forging, titanium has to be protected from normal atmospheric elements in some way.

Therefore, during titanium fabrication processes, extra care and special means are required. Additionally, the complex and expensive downstream processes (e.g., processes of double smelting, milling, forging, and machining) for the alloying and manufacturing of the final titanium alloy components dramatically increase its final cost [25.28, 122]. For instance, the cost of downstream processes for the production of a 2.54 cm thick titanium alloy plate accounts for 62% of the total cost [25.17, 28], as illustrated in Fig. 25.33; fabrication of more complex shapes is of course more expensive, constituting a commensurately greater proportion of the bottom-line figure.

As a result, the near-net-shape production of titanium and its alloy components has been attracting more and more research interests, owing to its ability to minimize machining, reduce part count, and avoid part distortion from fabrications [25.122]. Consequently, titanium and its alloy products could be produced by taking advantage of this concept.

The near-net-shape production of metallic components from metal oxide precursors to their metal or alloy counterparts was proposed in the early years of development of the FFC Cambridge process [25.123]. This advantage was recently demonstrated by *Peng* et al. in 2008 for zirconium tubes [25.114].

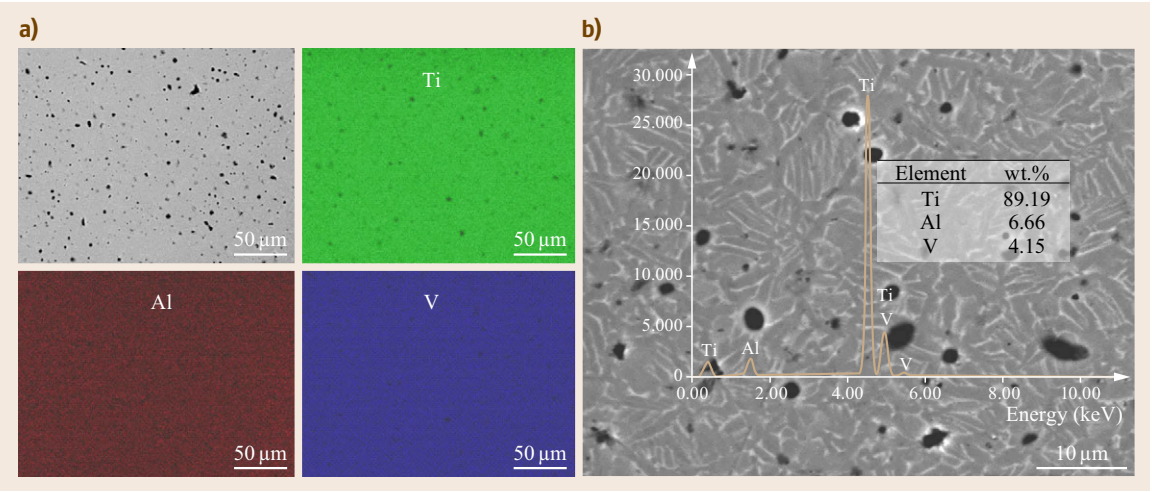


Fig. 25.36a,b BSE–SEM images of (a) polished electrolytic product together with Ti, Al, and V energy-dispersive x-ray spectroscopy (EDX) maps, (b) polished sample investigated under higher magnification with *insert* of the EDX spectrum and elemental composition (after [25.121])

In their work, porous tubular oxide precursors consisting of either pure ZrO_2 or a mixture of ZrO_2 and Nb_2O_5 were directly metalized to pure Zr or the Zr-2.5 Nb tubes through direct electrodeoxidation in molten $CaCl_2$ at approximately 1173 K [25.114]. Photographs of the ZrO_2 tube and its metalized counterpart are shown in Fig. 25.34.

Furthermore, near-net-shape production of titanium alloy (i. e., Ti-6Al-4V) components in more complicated shapes has been demonstrated as well (as shown in Fig. 25.35) [25.121].

The distribution of alloying elements across the electrolytically produced samples was investigated, and it revealed a homogeneous distribution of Ti, Al, and V elements (as shown in Fig. 25.36a). The image obtained using back-scattered electron imaging-scanning electron microscopy (BSE-SEM) at a higher magnification shows a fine α- (*dark part*) and β-phase (*bright part*) distribution across the electrolytic products (Fig. 25.36b). In addition, the elemental composition was analyzed and it was well within the range of that of commercial Ti-6Al-4V (insert of Fig. 25.36b) [25.121].

25.4 Summary

The use of electrons as the energy carrier for metal extraction is highly advantageous in comparison with the traditional pyrometallurgical extraction processes such as carbothermic and metallothermic reduction. The electrolytic extraction process possesses a relatively high efficiency, and can be a *green* process with no greenhouse gas emissions when electrons are generated from renewable energy sources and when inert anode materials are adopted. Furthermore, when compared to the traditional electrolytic extraction techniques, the innovative electrolytic extraction processes use mild electrolytes (e.g., molten $CaCl_2$ for the FFC Cambridge process and oxide melts for the Avanti process) rather than using aggressive and harmful electrolytes such as Na_3AlF_6 for the Hall–Héroult process. Most importantly, some of these innovative electrolytic processes (e.g., the EMR process and the FFC Cambridge process) can extract metals and alloys from solid metal oxides directly (solid-state electrochemical reduction), yielding either a powdery product that can be used for powder metallurgy directly or a product with the original shape of its metal oxide precursor (i. e., near-net-shape production of metallic components).

Reducing the cost of those metals and alloys that are difficult to extract and fabricate using conventional methods is the main driving force for the development of various innovative electrolytic extraction technologies. Cost-affordable production of titanium and its alloys is a classic example. In the titanium industry, the primary development focus has been the production of cost-affordable titanium and titanium alloy components rather than the development of alloys with enhanced properties [25.122, 124, 125]. The result is two research routes: devising novel methods for the extraction of ti-

tanium metal and developing creative techniques for the fabrication of titanium and its alloy components. Therefore, apart from innovative electrolytic extraction techniques, new metallurgical technologies (e.g., the near-net-shape process) have also been brought closer to commercialization, focusing on reducing the costs of downstream processes (e.g., alloying and shaping metallic components).

Among recently demonstrated or proposed innovative electrolytic metal extraction techniques, the FFC Cambridge process has the unique ability of combining the stages of extraction, alloying and near-net-shape production for fabricating metallic components. The near-net-shape conversion of metal oxide precursors to their metallic counterparts via the FFC Cambridge process has been successfully demonstrated in principle [25.114, 121].

As a typical example of the techniques for solid-state electrochemical production of metals and alloys, the favorable characteristics of the FFC Cambridge process can be summarized as follows:

1. Metal oxide can be used as feedstock directly, rather than using unusual compounds that are difficult to handle, such as $TiCl_4$ for titanium production, and hence requires less prereduction procedures.
2. Environment-friendly and mild electrolytes are used, such as $CaCl_2$, NaCl, LiCl, and salt mixtures, rather than using aggressive and toxic salts such as fluoride salts that are used in the Hall–Héroult process.
3. During the solid-state electrochemical reduction process, the metal oxide precursor does not dissolve in the molten salt and is electrochemically reduced in situ at the cathode. As a consequence there is no metal dendrite formation.
4. The porosity of the electrolytic product can be adjusted as desired; therefore the product can be either in a powdery form or in a well-consolidated form, with the shape similar to its metal oxide precursor. Thus the process can achieve near-net-shape production of metallic components.
5. When a metal oxide mixture is used as the feedstock, a variety of alloys and intermetallics can be produced directly.
6. Aside from the production of metals and alloys, by taking advantage of the versatile properties of the energy carrier, i. e., the electrons, the FFC Cambridge process can be used to attain a wide range of deoxidation levels, and hence to produce various kinds of lower oxides and oxide composites.

Overall, advances in the electrolytic extraction of metals and alloys from solid metal oxides have led to a wide spectrum of new academic and industrial opportunities. These include, but are not limited to, fundamental understanding of materials and chemistry in high temperature molten salts, and commercial development for the cost-affordable near-net-shape production of metallic engineering components with complex shapes, particularly those of titanium alloys.

References

25.1 F. Habashi: *Handbook of Extractive Metallurgy* (Wiley-VCH, Weinheim 1997)

25.2 G.Z. Chen, D.J. Fray: Electro-deoxidation of metal oxides, Proc. 130th TMS Annu. Meet. New Orleans (2000) pp. 1147–1151

25.3 A. Maitre, P. Lefort: Carbon oxidation at high temperature during carbothermal reduction of titanium dioxide, Phys. Chem. Chem. Phys. **1**, 2311–2318 (1999)

25.4 O. Kubaschewski, C.B. Alcock: *Metallurgical Thermo-Chemistry*, 5th edn. (Pergamon, New York 1979)

25.5 J.L. Murray (Ed.): *Phase Diagrams of Binary Titanium Alloys* (ASM, Materials Park 1987) p. 345

25.6 V. Dosaj, M. Kroupa, R. Bittar: Silicon and silicon alloys, chemical and metallurgical. In: *Kirk-Othmer Encyclopedia of Chemical Technology*, ed. by K. Othmer (Wiley, New York 2000)

25.7 D. Elwell, G.M. Rao: Electrolytic production of silicon, J. App. Electrochem. **18**, 15–22 (1988)

25.8 B.G. Gribov, K.V. Zinov'ev: Preparation of high-purity silicon for solar cells, Inorg. Mater. **39**, 653–662 (2003)

25.9 A. Schei, J.K. Tuset, H. Tveit: *Production of High Silicon Alloys* (Tapir, Trondheim 1998)

25.10 L.A. Corathers: Silicon. In: *Mineral Commodity Summaries*, ed. by E.K. Schnebele (US Geological Survey, Washington 2010) pp. 144–145

25.11 B. Ceccaroli, O. Lohne: Solar grade silicon feedstock. In: *Handbook of Photovoltaic Science and Engineering*, ed. by A. Luque, S. Hegedus (Wiley, New York 2011) pp. 169–217

25.12 C. Leyens, M. Peters: *Titanium and Titanium Alloys: Fundamentals and Applications* (Wiley-VCH, Weinheim 2003)

25.13 G. Lütjering, J.C. Williams: *Titanium*, 2nd edn. (Springer, Berlin, Heidelberg 2007)

25.14 M.J. Donachie: *Titanium: A Technical Guide* (ASM International, Materials Park 2000)

25.15 M.A. Hunter: Metallic titanium, J. Am. Chem. Soc. **32**, 330–336 (1910)

25.16 Toho Titanium Ltd: The Kroll process, http://www.toho-titanium.co.jp/en/products/sponge_en.html (2011)

25.17 P.C. Turner, A. Hartman, J.S. Hansen, S.J. Gerdemann: *Low Cost Titanium – Myth or Reality SciTech Connect* (DOE, Washington 2001), http://www.osti.gov/bridge/servlets/purl/899609-PMSrtc/899609

25.18 W. Kroll: Einige Eigenschaften des reinen Titans, Metallwirtschaft **18**, 77–80 (1938)

25.19 W. Kroll: The production of ductile titanium, J. Electrochem. Soc. **78**(1), 35–47 (1940)

25.20 A.D. Hartman, S.J. Gerdemann, J.S. Hansen: Producing lower-cost titanium for automotive applications, J. Min. Met. Min. Soc. **50**, 16–19 (1998)

25.21 A.D. Mcquillan, M.K. Mcquillan: *Titanium* (Butterworths, London 1956)

25.22 M.E. Sibert, Q.H. Mckenna, M. Steinberg, E. Wainer: Electrolytic reduction of titanium monoxide, J. Electrochem. Soc. **102**, 252–262 (1955)

25.23 M. Steinberg, S.S. Carlton, M.E. Sibert, E. Wainer: Preparation of titanium by fluoride electrolysis, J. Electrochem. Soc. **102**, 332–340 (1955)

25.24 Toho Titanium Ltd: Titanium sponge produced from the Kroll process, http://www.toho-titanium.co.jp/en/products/sponge_en.html (2011)

25.25 J. Thonstad: Some recent trends in molten salt electrolysis of titanium, magnesium, and aluminum, High Temp. Mater. Process. **9**, 135–146 (1990)

25.26 K. Grjotheim, M. Krohn: *Aluminum Electrolysis: Fundamentals of the Hall–Heroult Process*, 3rd edn. (Aluminum, Düsseldorf 2002)

25.27 J.M. Allwood, J.M. Cullen, R.L. Milford: Options for achieving a 50% cut in industrial carbon emissions by 2050, Environ. Sci. Technol. **44**, 1888–1894 (2010)

25.28 E.H.K. Technologies: *Summary of Emerging Titanium Cost Reduction Technologies* (EHK Technologies, Vancouver 2004) p. 59

25.29 M.V. Ginatt: Process for the electrolytic production of metals, U.S. Patent 6 074 543 (2000)

25.30 M.V. Ginatta: Why produce titanium by EW?, J. Min. Met. Miner. Soc. **52**, 18–20 (2000)

25.31 M.V. Ginatta: *Economics and Production of Primary Titanium by Electrolytic Winning* (EPD Congr., New Orleans 2001) pp. 1–17

25.32 J.C. Withers, J. Laughlin, R.O. Loufty: The production of titanium from a composite anode, Proc. Light Met. '07, Orlando (2007) pp. 117–125

25.33 J.C. Withers, J. Laughlin, R.O. Loufty: Processing routes to produce titanium from TiO_2, Proc. Light Met. '07, Orlando (2007) pp. 109–115

25.34 J.C. Withers, F. Cardarelli, J. Laughlin, R.O. Loufty: Recent Improvements for Electrowinning Titanium Metal from Composite Anodes, Int. Round Table Titanium Prod. Molten Salts (DLR German Aerospace Center, Cologne 2008)

25.35 I. Park, T. Abiko, T.H. Okabe: Production of titanium powder directly from TiO_2 in $CaCl_2$ through an electronically mediated reaction (EMR), J. Phys. Chem. Solids **66**, 410–413 (2005)

25.36 T. Okabe, Y. Waseda: Producing titanium through an electronically mediated reaction, J. Min. Met. Miner. Soc. **49**, 28–32 (1997)

25.37 T. Abiko, I. Park, T.H. Okabe: Reduction of titanium oxide in molten salt medium, Proc. 10th World Conf. Titanium, Hamburg (2003)

25.38 D.J. Fray: Novel methods for the production of titanium, Int. Mater. Rev. **53**, 317–325 (2008)

25.39 D.R. Sadoway: *Electrochemical Pathways Towards Carbon-Free Metals Production* (GCEP Carbon Management in Manufacturing Industries, Stanford 2008), Available from:http://gcep.stanford.edu/pdfs/2RK4ZjKBF2f71uM4uriP9g/SadowayGCEP_reduced.pdf

25.40 US Department of Energy: *Technical Feasibility Study of Steelmaking by Molten Salt Electrolysis* (US Department of Energy, Washington 2007) Available from: http://www1.eere.energy.gov/industry/steel/pdfs/moe_steelmaking.pdf

25.41 R. Suzuki, K. Ono, K. Teranuma: Calciothermic reduction of titanium oxide and in-situ electrolysis in molten $CaCl_2$, Met. Mater. Trans. B **34**, 287–295 (2003)

25.42 R.O. Suzuki: Calciothermic reduction of TiO_2 and in situ electrolysis of CaO in the molten $CaCl_2$, J. Phys. Chem. Solids **66**, 461–465 (2005)

25.43 K. Ono, R.O. Suzuki: A new concept for producing Ti sponge: Calciothermic reduction, J. Min. Met. Miner. Soc. **54**, 59–61 (2002)

25.44 R.O. Suzuki, Y. Matsuoka: Preparation of Ti-V-Cr hydrogen absorption alloy powder, Jt. Int. Conf. Sustain. Enegry Environ. (SEE), Hua Hin (2004) pp. 167–170

25.45 R.O. Suzuki, K. Tatemoto, H. Kitagawa: Direct synthesis of the hydrogen storage V-Ti alloy powder from the oxides by calcium co-reduction, J. Alloy. Compd. **385**, 173–180 (2004)

25.46 R. Suzuki, S. Inoue: Calciothermic reduction of titanium oxide in molten $CaCl_2$, Met. Mater. Trans. B **34**, 277–285 (2003)

25.47 G.D. Rigby, I.P. Ratchev, R.I. Olivares, K. Mukunthan, S.A. Bliznyukov, A.A. Shook: Polar titanium – Development of the BHP billiton titanium metal production process, Proc. 21st Annu. ITA Conf. Titanium, Scottsdale (2005)

25.48 G.Z. Chen, D.J. Fray, T.W. Farthing: Direct electrochemical reduction of titanium dioxide to titanium in molten calcium chloride, Nature **407**, 361–364 (2000)

25.49 D.R. Sadoway: New opportunities for metals extraction and waste treatment by electrochemical processing in molten salts, J. Mater. Res. **10**, 487–492 (1995)

25.50 T.H. Okabe, M. Nakamura, T. Oishi, K. Ono: Electrochemical deoxidation of titanium, Met. Mater. Trans. B **24B**, 449–455 (1993)

25.51 F. Cardarelli: Method for electrowinning of titanium metal or alloy from titanium oxide containing compound in the liquid state, Canadia Patent 2 363 647 (2004), pp. 18

25.52 F. Cardarelli: A method for the continuous electrowinning of pure titanium metal from molten titanium slag, ilmenite and other semiconductive titanium oxide compounds, Canadia Patent 2 363 648 (2001), pp. 27

25.53 J. Peng, H. Chen, X. Jin, T. Wang, D. Wang, G.Z. Chen: Phase-tunable fabrication of consolidated $(\alpha + \beta)$-TiZr alloys for biomedical applications through molten salt electrolysis of solid oxides, Chem. Mater. **21**, 5187–5195 (2009)

25.54 D.J. Fray, G.Z. Chen: Reduction of titanium and other metal oxides using electrodeoxidation, Mater. Sci. Technol. **20**, 295–300 (2004)

25.55 K. Dring, C. Rosenkilde: Production of titanium and titanium alloys by electrochemical reduction of oxide precursors, Mater. Technol. **22**, 4 (2007)

25.56 K. Dring, R. Bhagat, M. Jackson, R. Dashwood, D. Inman: Direct electrochemical production of Ti-10W alloys from mixed oxide preform precursors, J. Alloy. Compd. **419**, 103–109 (2006)

25.57 R. Bhagat, M. Jackson, D. Inman, R. Dashwood: The production of Ti–Mo alloys from mixed oxide precursors via the FFC Cambridge process, J. Electrochem. Soc. **155**, E63–E69 (2008)

25.58 J. Ben, J. Martin, D. David, I. Douglas, D. Richard: Production of NiTi via the FFC Cambridge Process, J. Electrochem. Soc. **155**, E171–E177 (2008)

25.59 M. Ma, D. Wang, W. Wang, X. Hu, X. Jin, G.Z. Chen: Extraction of titanium from different titania precursors by the FFC Cambridge process, J. Alloy. Compd. **420**, 37–45 (2006)

25.60 A.M. Abdelkader, D.J. Fray: Direct electrochemical preparation of Nb-10Hf-1Ti alloy, Electrochim. Acta **55**, 2924–2931 (2010)

25.61 M. Ma, D. Wang, X. Hu, X. Jin, G.Z. Chen: A direct electrochemical route from ilmenite to hydrogen-storage ferrotitanium alloys, Chemistry **12**, 5075–5081 (2006)

25.62 D.J. Fray: Electrochemical method and apparatus, US Patent WO 2004/18 735 A1 (2004), pp. 15

25.63 D.J. Fray, G.Z. Chen: Metal and alloy powders and powder fabrication, US Patent WO 02/40 725 A2 (2002)

25.64 D.J. Fray, G.Z. Chen: Metal and alloy powders and powder fabrication, US Patent US 2004/52 672 A1 (2004)

25.65 D.J. Fray, R.C. Copcutt, G.Z. Chen: Intermetallic compounds, US Patent US 2004/104 125 A1 (2004)

25.66 D.J. Fray, T.W. Farthing, G.Z. Chen: Removal of oxygen from metal oxides and solid solutions by electrolysis in a fused salt, US Patent WO 99/64 638 (1999)

25.67 D.J. Fray, T.W. Farthing, G.Z. Chen: Removal of substances from metal and semi-metal compounds, US Patent US 6,712,952 (2004)

25.68 G. Chen, E. Gordo, D. Fray: Direct electrolytic preparation of chromium powder, Met. Mater. Trans. B **35**, 223–233 (2004)

25.69 G. Qiu, K. Jiang, M. Ma, D. Wang, X. Jin, G.Z. Chen: Roles of cationic and elemental calcium in electro-reduction of solid metal oxides in molten calcium chloride, Z. Naturforsch. A **62a**, 292–302 (2007)

25.70 D. Wang, G. Qiu, X. Jin, X. Hu, G.Z. Chen: Electrochemical metallization of solid terbium oxide, Angew. Chem. Int. Ed. **45**, 2384–2388 (2006)

25.71 C. Schwandt, D.J. Fray: The electrochemical reduction of chromium sesquioxide in molten calcium chloride under cathodic potential control, Z. Naturforsch. A **62**, 655–670 (2007)

25.72 K.C.T. Kilby, L. Centeno, G. Doughty, S. Mucklejohn, D.J. Fray: *The Electrochemical Production of Oxygen and Metal via the FFC-Cambridge Process* (Space Resources Roundtable, Colorado School of Mines, Golden, 2006)

25.73 R. Barnett, K. Kilby, D. Fray: Reduction of tantalum pentoxide using graphite and tin-oxide-based anodes via the FFC-cambridge process, Met. Mater. Trans. B **40**, 150–157 (2009)

25.74 W. Xiao, X. Jin, Y. Deng, D. Wang, X. Hu, G.Z. Chen: Electrochemically driven three-phase interlines into insulator compounds: Electroreduction of solid SiO_2 in molten $CaCl_2$, Chem. Phys. Chem. **7**, 1750–1758 (2006)

25.75 K. Dring, R. Dashwood, D. Inman: Voltammetry of titanium dioxide in molten calcium chloride at 900 °C, J. Electrochem. Soc. **152**, E104–E113 (2005)

25.76 C. Schwandt, G.R. Doughty, D.J. Fray: The FFC-cambridge process for titanium metal winning, Key Eng. Mater. **436**, 13–25 (2010)

25.77 J.O.M. Bockris, G.J. Hills, D. Inman, L. Young: An all-glass reference electrode for molten salt systems, J. Sci. Instrum. **33**, 438 (1956)

25.78 K. Yasuda, T. Nohira, Y.H. Ogata, Y. Ito: Electrochemical window of molten LiCl-KCl-$CaCl_2$ and the Ag^+/Ag reference electrode, Electrochim. Acta **51**, 561–565 (2005)

25.79 P. Gao, X. Jin, D. Wang, X. Hu, G.Z. Chen: A quartz sealed Ag/AgCl reference electrode for $CaCl_2$ based molten salts, J. Electroanal. Chem. **579**, 321–328 (2005)

25.80 H. Wang, N.J. Siambun, L. Yu, G.Z. Chen: A Robust alumina membrane reference electrode for high temperature molten salts, J. Electrochem. Soc. **159**, H740–H746 (2012)

25.81 G. Qiu, M. Ma, D. Wang, X. Jin, X. Hu, G.Z. Chen: Metallic cavity electrodes for investigation of powders, J. Electrochem. Soc. **152**, E328–E336 (2005)

25.82 J. Peng, G. Li, H. Chen, D. Wang, X. Jin, G.Z. Chen: Cyclic voltammetry of ZrO_2 powder in the metallic cavity electrode in molten $CaCl_2$, J. Electrochem. Soc. **157**, F1–F9 (2010)

25.83 K. Jiang, X.H. Hu, H.J. Sun, D.H. Wang, X.B. Jin, Y.Y. Ren, G.Z. Chen: Electrochemical synthesis of $LiTiO_2$ and $LiTi_2O_4$ in molten LiCl, Chem. Mater. **16**, 4324–4329 (2004)

25.84 X. Jin, P. Gao, D. Wang, X. Hu, G.Z. Chen: Electrochemical preparation of silicon and its alloys from solid oxides in molten calcium chloride, Angew. Chem. Int. Ed. **43**, 733–736 (2004)

25.85 T. Nohira, K. Yasuda, Y. Ito: Pinpoint and bulk electrochemical reduction of insulating silicon dioxide to silicon, Nat. Mater. **2**, 397–401 (2003)

25.86 K. Yasuda, T. Nohira, R. Hagiwara, Y.H. Ogata: Direct electrolytic reduction of solid SiO_2 in Molten $CaCl_2$ for the production of solar grade silicon, Electrochim. Acta **53**, 106–110 (2007)

25.87 K. Yasuda, T. Nohira, Y.H. Ogata, Y. Ito: Direct electrolytic reduction of solid silicon dioxide in molten LiCl-KCl-$CaCl_2$ at 773K, J. Electrochem. Soc. **152**, D208–D212 (2005)

25.88 K. Yasuda, T. Nohira, R. Hagiwara, Y.H. Ogata: Diagrammatic representation of direct electrolytic reduction of SiO_2 in molten $CaCl_2$, J. Electrochem. Soc. **154**, E95–E101 (2007)

25.89 W. Xiao, X. Jin, Y. Deng, D. Wang, G.Z. Chen: Rationalisation and optimisation of solid state electro-reduction of SiO_2 to Si in molten $CaCl_2$ in accordance with dynamic three-phase interlines based voltammetry, J. Electroanal. Chem. **639**, 130–140 (2010)

25.90 K. Yasuda, T. Nohira, R. Hagiwara, Y.H. Ogata: Direct electrolytic reduction of solid SiO_2 in molten $CaCl_2$, Proc. Light Met. '07, Orlando (2007) pp. 5–11

25.91 K. Yasuda, T. Nohira, K. Amezawa, Y.H. Ogata, Y. Ito: Mechanism of direct electrolytic reduction of solid SiO_2 to Si in molten $CaCl_2$, J. Electrochem. Soc. **152**, D69–D74 (2005)

25.92 K. Dring: Direct electrochemical reduction of titanium dioxide in molten salts, Key Eng. Mater. **436**, 27–34 (2010)

25.93 K. Jiang, X. Hu, M. Ma, D. Wang, G. Qiu, X. Jin, G.Z. Chen: "Perovskitization" – Assisted electrochemical reduction of solid TiO_2 in molten $CaCl_2$, Angew. Chem. Int. Ed. **45**, 428–432 (2006)

25.94 C. Schwandt, D.T.L. Alexander, D.J. Fray: The electro-deoxidation of porous titanium dioxide precursors in molten calcium chloride under cathodic potential control, Electrochim. Acta **54**, 3819–3829 (2009)

25.95 C. Schwandt, D.J. Fray: Determination of the kinetic pathway in the electrochemical reduction of titanium dioxide in molten calcium chloride, Electrochim. Acta **51**, 66–76 (2005)

25.96 R. Centeno-Sánchez, D. Fray, G. Chen: Study on the reduction of highly porous TiO_2 precursors and thin TiO_2 layers by the FFC-Cambridge process, J. Mater. Sci. **42**, 7494–7501 (2007)

25.97 G.Z. Chen, D.J. Fray: Voltammetric studies of the oxygen-titanium binary system in molten calcium chloride, J. Electrochem. Soc. **149**, E455–E467 (2002)

25.98 D.T.L. Alexander, C. Schwandt, D.J. Fray: The electro-deoxidation of dense titanium dioxide precursors in molten calcium chloride giving a new reaction pathway, Electrochim. Acta **56**, 3286–3295 (2011)

25.99 W. Li, X. Jin, F. Huang, G.Z. Chen: Metal-to-oxide molar volume ratio: The overlooked barrier to solid-state electroreduction and a green bypass through recyclable NH_4HCO_3, Angew. Chem. Int. Ed. **49**, 3203–3206 (2010)

25.100 H. Chen, Y. Zeng, W. Li, J. Peng, X. Jin, G.Z. Chen: A PRS model for accurate prediction of the optimal solid oxide cathode structure for the preparation of metals in molten chlorides, Electrochem. Commun. **26**, 33–36 (2013)

25.101 A.J. Fenn, G. Cooley, D. Fray, L. Smith: Exploiting the FFC Cambridge process, Adv. Mater. Process. **162**, 51 (2004)

25.102 D. Wang, X. Jin, G.Z. Chen: Solid state reactions: An electrochemical approach in molten salts, Phys. Chem. **104**, 189–234 (2008)

25.103 S. Jiao, D. Fray: Development of an inert anode for electrowinning in calcium chloride-calcium oxide melts, Met. Mater. Trans. B **41**, 74–79 (2010)

25.104 S. Jiao, L. Zhang, H. Zhu, D.J. Fray: Production of NiTi shape memory alloys via electro-deoxidation utilizing an inert anode, Electrochim. Acta **55**, 7016–7020 (2010)

25.105 H. Yin, L. Gao, H. Zhu, X. Mao, F. Gan, D. Wang: On the development of metallic inert anode for molten $CaCl_2$-CaO System, Electrochim. Acta **56**, 3296–3302 (2011)

25.106 B. Zhao, X. Lu, Q. Zhong, C. Li, S. Chen: Direct electrochemical preparation of CeNi5 and LaxCe1-xNi5 alloys from mixed oxides by SOM process, Electrochim. Acta **55**, 2996–3001 (2010)

25.107 X.J. Liao, H.W. Xie, Y.C. Zhai, Y. Zhang: Preparation of Al_3Sc intermetallic compound by FFC method, J. Mater. Sci. Technol. **25**, 717–720 (2009)

25.108 M. Jackson, K. Dring: A review of advances in processing and metallurgy of titanium alloys, Mater. Sci. Technol. **22**, 881–887 (2006)

25.109 G. Qiu, D. Wang, X. Jin, G.Z. Chen: A direct electrochemical route from oxide precursors to the terbium-nickel intermetallic compound $TbNi_5$, Electrochim. Acta **51**, 5785–5793 (2006)

25.110 G. Qiu, D. Wang, M. Ma, X. Jin, G.Z. Chen: Electrolytic synthesis of $TbFe_2$ from Tb_4O_7 and Fe_2O_3 powders in molten $CaCl_2$, J. Electroanal. Chem. **589**, 139–147 (2006)

25.111 Y. Zhu, D. Wang, M. Ma, X. Hu, X. Jin, G.Z. Chen: More affordable electrolytic LaNi5-type hydrogen storage powders, Chem. Commun., 2515–2517 (2007)

25.112 J. Peng, Y. Zhu, D. Wang, X. Jin, G.Z. Chen: Direct and low energy electrolytic co-reduction of mixed oxides to zirconium-based multi-phase hydrogen storage alloys in molten salts, J. Mater. Chem. **19**, 2803–2809 (2009)

25.113 B.J. Zhao, L. Wang, L. Dai, G.G. Cui, H.Z. Zhou, R.V. Kumar: Direct electrolytic preparation of cerium/nickel hydrogen storage alloy powder in molten salt, J. Alloy. Compd. **468**, 379–385 (2009)

25.114 J. Peng, K. Jiang, W. Xiao, D. Wang, X. Jin, G.Z. Chen: Electrochemical conversion of oxide precursors to consolidated Zr and Zr-2.5Nb Tubes, Chem. Mater. **20**, 7274–7280 (2008)

25.115 Y. Zhu, M. Ma, D. Wang, K. Jiang, X. Hu, X. Jin, G. Chen: Electrolytic reduction of mixed solid oxides in molten salts for energy efficient production of the TiNi alloy, Chin. Sci. Bull. **51**, 2535–2540 (2006)

25.116 R. Bhagat, M. Jackson, D. Inman, R. Dashwood: Production of Ti–W alloys from mixed oxide precursors via the FFC Cambridge process, J. Electrochem. Soc. **156**, E1–E7 (2009)

25.117 M. Jolly: Castings. In: *Comprehensive Structural Integrity*, ed. by I. Milne, R.O. Ritchie, B. Karihaloo (Elsevier, Oxford 2003) pp. 377–466

25.118 V. Moxson, O. Senkov, F. Froes: Innovations in titanium powder processing, J. Min. Met. Mater. Soc. **52**, 24–26 (2000)

25.119 P.J. Bridges, B. Magnus: Manufacture of titanium alloy components for aerospace and military applications, Proc. RTO Appl. Veh. Technol. Panel (AVT) Specialists' Meet. (NATO Research and Technology Organisation, Oslo 2001)

25.120 E.O. Ezugwu, Z.M. Wang: Titanium alloys and their machinability – A review, J. Mater. Process. Technol. **68**, 262–274 (1997)

25.121 D. Hu, W. Xiao, G.Z. Chen: Near-net-shape production of hollow titanium alloy components via electrochemical reduction of metal oxide precursors in molten salts, Met. Mater. Trans. B **44**, 272–282 (2013)

25.122 F.H. Froes, M. Gungor, M. Ashraf Imam: Cost-affordable titanium: The component fabrication perspective, J. Min. Met. Mater. Soc. **59**, 28–31 (2007)

25.123 D.J. Fray, Z. Chen, T.W. Farthing, Fabrication of metal articles by electrolysis of preshaped metal compounds in a fused salt, EHR Patent EP1333110B1 (2010)

25.124 F.H. Froes, M.A. Iman, D.J. Fray (Eds.): *Cost affordable titanium*, *Proc. Light Metals*, *Charlotte* 2004)

25.125 F.H. Froes, M. Ashraf Imam: Cost affordable developments in titanium technology and applications, Key Eng. Mater. **436**, 1–11 (2010)

26. Electrodeposition of Nanomaterials

I-Wen Sun, Jeng-Kuei Chang

This chapter describes various processes for electrodeposition of nanomaterials including:

1. Template-free direct electrodeposition of nanoparticles with unique shapes, nanowires, nanotubes, and conducting polymer nanostructures
2. Fabrication of various templates for template-assisted electrodeposition, and electrodeposition of nanowires, -rods, -tubes using the templates
3. Electrodeposition of nanoparticles, -wires, -wire arrays on highly oriented pyrolytic graphite (HOPG)
4. Electrodeposition using lithographically patterned methods, such as photolithographic, interference lithographic, electron-beam lithography (EBL) methods, and electrochemical lithographic methods.

Finally, examples of using the electrodeposited nanomaterials for the lithium-ion batteries (LIBs), and pseudocapacitors are presented.

This chapter outlines the representative electrochemical strategies in the recent literature for the fabrication of nanostructured materials, such as metals, alloys, polymers, and semiconductors. In view of the fact, the electrodeposited nanomaterials have numerous applications; this chapter will focus on the applications of these nanomaterials for the energy storage and conversions.

26.1 **Processes for Electrodeposition of Nanomaterials** 836
26.1.1 Direct Electrodeposition Without Template 836
26.1.2 Template-Assisted Electrodeposition 848
26.1.3 Electrodeposition on HOPG 855
26.1.4 Lithographically Patterned Electrodeposition 861
26.2 **Electrodeposited Nanomaterials for Energy Storage/Conversion Devices** .. 865
26.2.1 Lithium-Ion Battery Applications 866
26.2.2 Pseudocapacitors 873
26.3 **Conclusions and Prospects** 882
References 882

The fabrication of nanostructured materials has received vast attention due to their interesting properties which can be applied to various fields including electronics, optical, magnetic, catalysts, sensors, and energy storage and conversion. Among the popular methods of fabricating nanomaterials, the electrodeposition approach is simple and less expensive. The electrodeposition basically involves applying a potential or current to a conducting substrate such that the desired materials are deposited at the surface. The deposition can be controlled by various techniques, include chronoamperometry (CA), cyclic voltammetry (CV), chronopotentiometry (CP), and pulsed plating. The composition, shape, and size of the nanomaterials can be readily controlled by varying the precursors in the plating solution and the electrodeposition conditions. The nanostructured materials can be electrodeposited either without or with the assist of a template. Without using a template, particles with interesting shapes, such as cubes, flowers, spikes, and dendrites are often produced. With the use of a template, the shape, and the size of the nanomaterial, such as nanowires, is defined by the template.

26.1 Processes for Electrodeposition of Nanomaterials

It is known that the shape of nanoparticles is determined by the difference in the growth rate (which is related to the surface energy) of the planes that causes specific facets to be exposed. The growth kinetics, however, can be manipulated by:

1. Adding capping agents or modifiers which adsorb on certain facets
2. Programming the deposition potential or current form
3. Varying the precursor concentration and
4. Varying the temperature.

26.1.1 Direct Electrodeposition Without Template

The electrochemical growth of metal nanocrystals (NCs) with various shapes has been achieved by carefully programming the applied potential during the electrodeposition process [26.1–7]. This was demonstrated by *Tian* et al. who synthesized high-index-facet Pt and Pd NCs by employing a two-step process (Fig. 26.1a) [26.1]. First, Pt or Pd metal nuclei were generated at a nucleation potential (E_N). A square-wave potential with lower (E_L) and upper (E_U) limits was then applied.

Electrodeposition of Nanoparticles With Unique Shapes

Some of the metal nanospheres that form at E_N were anodically dissolved at E_U and redeposited at E_L during each square-wave potential cycle. The periodic dissolution and deposition that accompany the periodic adsorption/desorption of hydrogen and oxygen allow the preferential growth of more stable high-index planes. Tetrahexahedral (THH) Pt from solution containing ascorbic acid, concave hexoctahedral Pt from solution containing sodium citrate, as well as tetrahex-

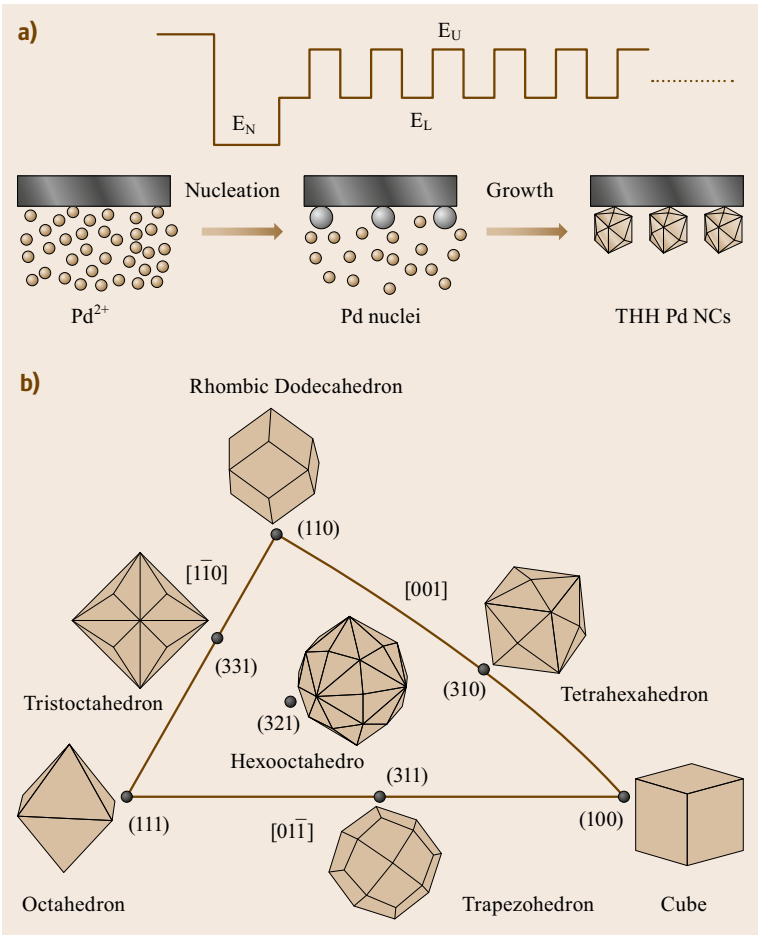


Fig. 26.1 **(a)** Illustration of the programmed electrodeposition method for preparation of tetrahexahedral Pd nanocrystals (THH Pd NCs) (after [26.1]); **(b)** Unit stereographic triangle of polyhedral NCs bounded by different crystal planes (after [26.2])

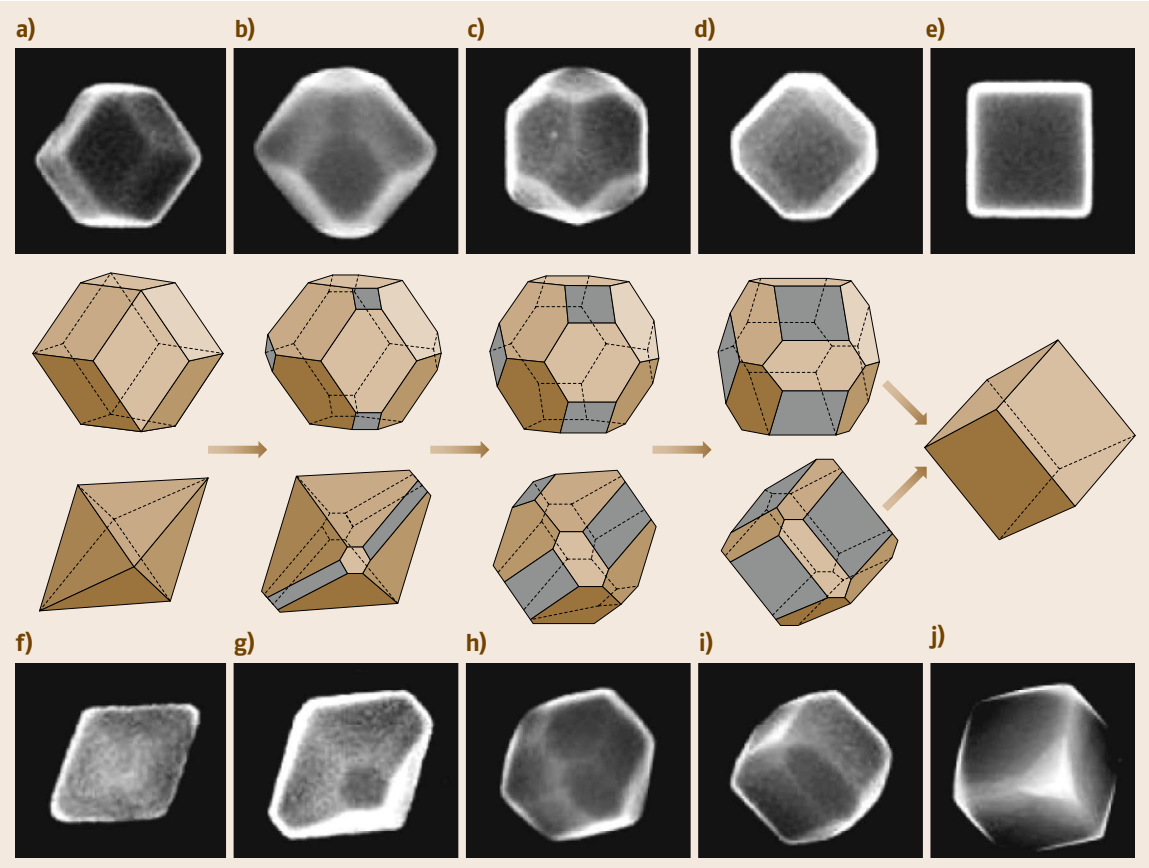


Fig. 26.2a–j SEM images of Fe nanoscrystals (NCs) and corresponding models. **(a–e)** Shape transformation of Fe NCs from RD to a series of 18-facet polyhedral shapes and finally to cubic in 0.002 M $FeSO_4$ + 0.1 M Na_2SO_4 (pH 3–3.5). **(f–j)** Shape transformation of Fe NCs from tetragonal bipyraidal (TB) to a series of 18-facet polyhedral shapes and finally to cubic in 0.02 M$FeSO_4$ + 0.1 MNa_2SO_4 (pH 3–3.5) (after [26.7])

ahedral, trapezohedral, and concave hexoctahedral Pd NCs with sizes ranging from 20 to 500 nm have been prepared by varying E_U, E_L, and the electrolyte content (Fig. 26.1b) [26.2]. With this method, nanorods were obtained when the concentration of the precursor, such as $PdCl_2$, was higher than 1.0 mM [26.4]. Because face-centered cubic (fcc) Pd and Pt can easily form alloys due to the very small lattice mismatch between them, square-wave programmed potential electrodeposition can be applied to the synthesis of THH Pd–Pt NCs with a tunable composition [26.6].

Chen et al. produced two series of Fe NCs with different shapes by varying the electrodeposition conditions. Fe nanoseeds with a size of 3–8 nm were first produced on a glassy carbon (GC) electrode surface at a nucleation potential E_N for a short period of time t_N in solution containing 0.1 M Na_2SO_4 and various concentrations of $FeSO_4$. The Fe nanoseeds were then grown slowly at a relatively positive growth potential E_G for a desired period of time t_G. As depicted by scanning electron microscopy (SEM) in Fig. 26.2 [26.7], in a dilute $FeSO_4$ (0.002 M) solution, the Fe NCs transformed from rhombic-dodecahedral (RD) to a series of 18-facet polyhedral shapes and finally to cubic as the E_G was changed from -1.03 to -1.07 V. In concentrate (0.02 M) $FeSO_4$ solutions, the Fe NCs changed from tetragonal bipyramidal (TB) to a series of 18-facet polyhedral shapes and finally to cubic as the E_G was varied from -0.97 to -1.025 V. The end result cubic for both approaches is in agreement with two-dimensional nuclei theory, which indicates that {100} facet cubic predominates at high overpotentials (-1.07 and -1.025 V) [26.8].

Additive-free electrochemical deposition has been applied to the synthesis of monodispered copper nanooctahedra on the gold film in a $CuSO_4$ solution at a low potential. The low deposition potential makes the difference in the growth rate of the various planes sig-

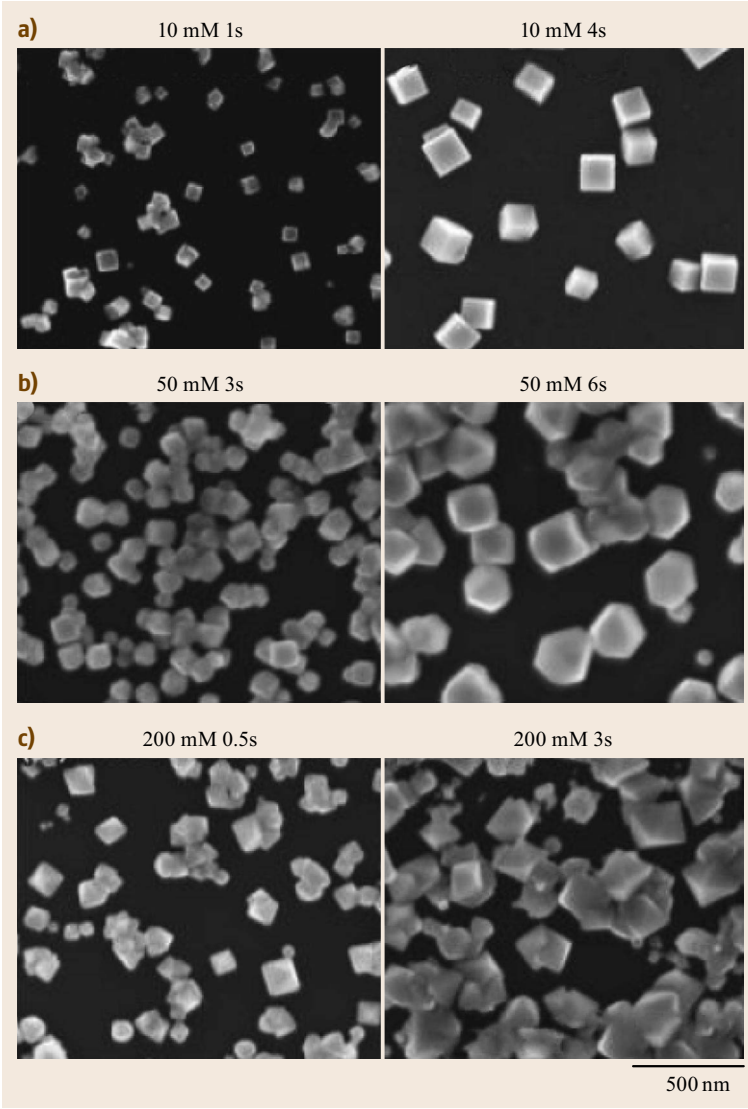


Fig. 26.3a–c SEM images of cubic, cuboctahedral, and octahedral Cu–Cu_2O core–shell nanoparticles electrodeposited on H-Si(100) at −1.0 V (versus Ag/AgCl) respective aqueous solutions of **(a)** 10 mM, **(b)** 50 mM, and **(c)** 200 mM [$CuSO_4 \cdot 5H_2O$] (and 10 mM [$NaClO_4$]), each for two different deposition times (after [26.9])

nificant enough to result in anisotropic growth of Cu from truncated octahedral to octahedral when the deposition time is increased from 20 to 180 s. A high deposition potential, however, destroys the anisotropic growth and results in a near-spherical shape [26.10]. Similarly, the electrochemical growth of Cu–Cu_2O core–shell NCs at an H-terminated Si(100) substrate without a template or capping agent was performed in aqueous solutions containing various concentrations of $CuSO_4$ and 1 mM $NaClO_4$. The shape of the NCs is highly affected by the concentration of $CuSO_4$ (Fig. 26.3) [26.9]. With low concentrations (5–10 mM), the particles grow faster in the [111] direction than in the [100] direction, resulting in cubic NCs. When the concentration is increased to 50 mM, the growth rate in the [100] direction becomes comparable with that in the [111] direction, so the cubic shape changes to truncated cubic and then to cuboctahedron. Further increasing the concentration to 200 mM makes the growth rate in the [100] direction faster than that in the [111] direction, and the NCs turn into truncated octahedral and then into octahedral. Increasing the deposition time increases the average size and the number density of the NCs until they coalesce into a thin film [26.9]. Capping agents (surfactants) were employed to control the morphology of electrodeposited Cu NCs by *Ko* et al. [26.11, 12]. Depending on their concentration and nature, the capping agents adsorb onto some surface of the deposited Cu, influencing the relative growth rates between the [111] and [100] directions, which in turn affect the final

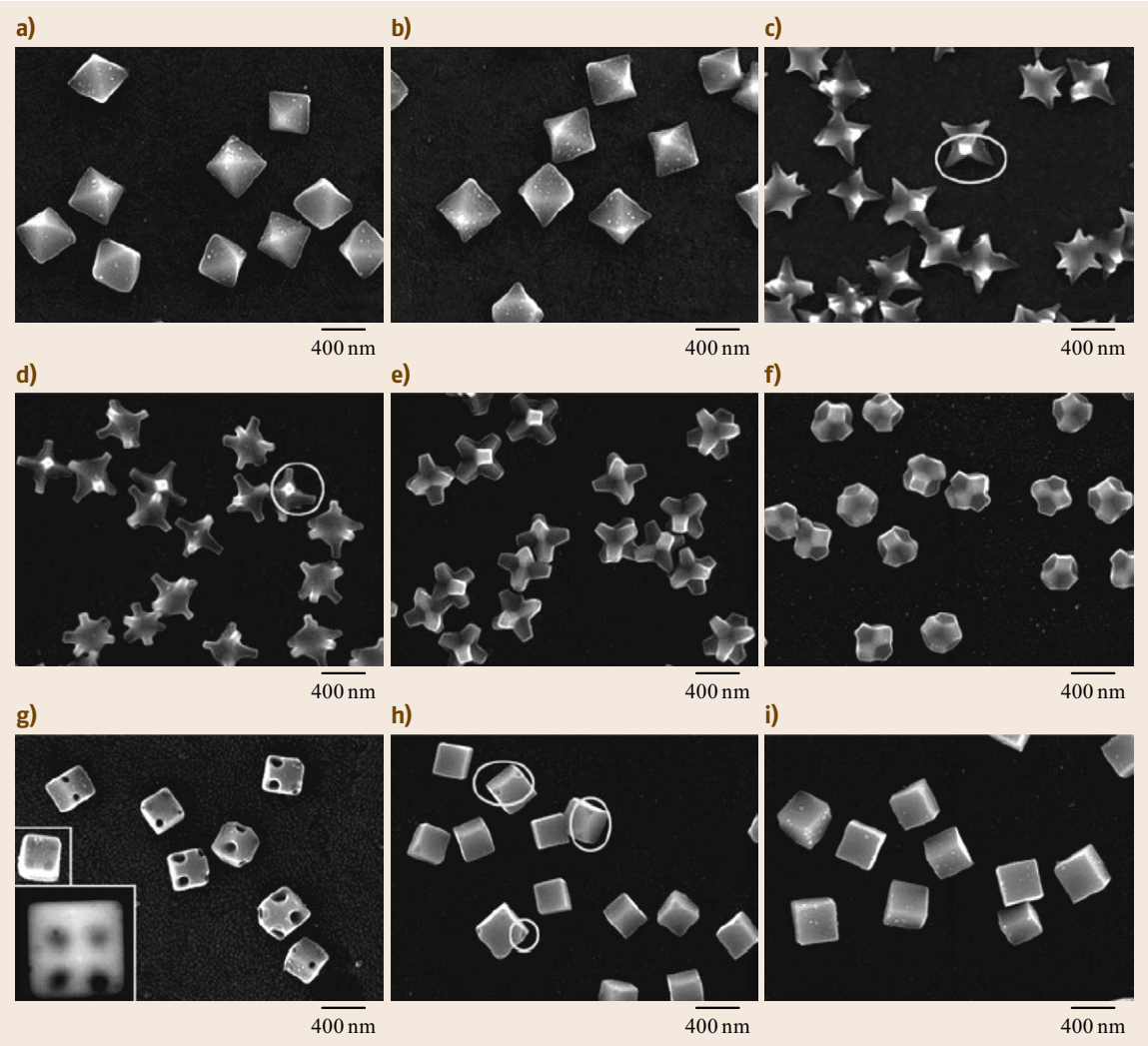


Fig. 26.4a–i The shape evolution of PbS crystals with decreasing $PbCl_2$ concentration at a constant deposition current of 0.2 mA and with deposition time of 75 s: **(a)** 0.027 g, octahedral without branching; **(b)** 0.025 g, octahedral with appearing branches; **(c)** 0.022 g, typical star shaped; **(d)** 0.020 g, star shaped with the appearance of (100) facets; **(e)** 0.018 g, star shaped with larger (100) facets but shorter branches; **(f)** 0.016 g, football-like shaped with even larger (100) facets and shorter branches; **(g)** 0.014 g, partially hollow cubic, with *inset* showing a typical PbS crystal and its backscattered electron image; **(h)** 0.012 g, cubic with incompletely formed apexes; **(i)** 0.010 g, well-defined solid cubic (after [26.13])

shape of the crystals. Pyramidal Cu NCs were obtained when the weight ratio of dodecylbenzene sulfonic acid (DBSA)/Cu^{2+} was 3, whereas cube-shaped Cu NCs were obtained when the DBSA/Cu^{2+} ratio was decreased to 2. Multipod Cu particles were obtained when DBSA was replaced by poly(vinylpyrrolidone) (PVP) under similar conditions.

The successive evolution of PbS NCs (400 nm) from octahedral to star-like, to football-like, and finally to cubic shape during galvanostatic electrodeposition from a 110 ml DMSO-H_2O mixture containing a sufficient amount of S and various amounts of $PbCl_2$ (0.027–0.012 g) without using any surfactant has been elucidated [26.13]. The morphology of PbS NCs is determined by both the mass transport of the reactants and the surface energy of the crystal facets. With a high $PbCl_2$ concentration (0.027 g), the diffusion of Pb^{2+} from the bulk solution to the growing sites was able to keep up with its consumption, and thus octahedral PbS crystals were obtained (highlight as circled in Fig. 26.4a). The formation of the octahedral shape can also be related to the preferential and efficient adsorp-

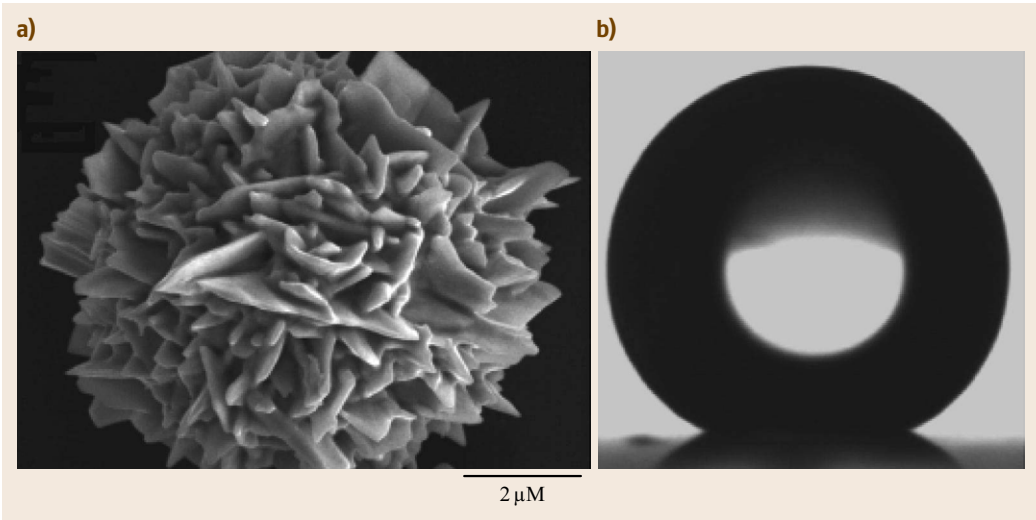


Fig. 26.5 **(a)** SEM images of the hierarchical flowerlike gold microstructures (HFGMs) located at ITO substrate prepared by square wave voltammetry for 72 times of repetitive run. $E_L = -0.2\,V$, $E_U = 0.8\,V$ (versus Ag/AgCl); the concentration of $HAuCl_4$ is 24.3 mM; **(b)** Shape of a water droplet on the surface of HFGMs modified with *n*-dodecanethiol (drop weight 5 mg) (after [26.14])

tion of Cl^- ions onto the (111) facets of PbS, which lowers the surface energy of the (111) facets. When the $PbCl_2$ concentration is reduced, a Pb^{2+} depletion zone forms around the growing sites and the apexes that protrude into the bulk solution grow faster than the rest of the facets, forming branches (highlight as circled in Fig. 26.4b). Due to such branching [26.15] star-shaped PbS NCs were obtained when the $PbCl_2$ concentration was lowered to 0.022 g. When the $PbCl_2$ concentration was further reduced, the depletion zone effect was enhanced and the effective adsorption of Cl^- onto the (111) facets decreased making the (100) facets increasingly dominant (highlight as circled in Fig. 26.4d–f), and finally allowing the formation of cubic PbS crystals when the $PbCl_2$ concentration was 0.010 g. When $PbCl_2$ was replaced with $Pb(NO_3)_2$, only cubic or irregular PbS was obtained regardless the $Pb(NO_3)_2$ concentration [26.13]. Branching has also been observed in the template-free electrodeposition of gold nanostructures from 0.1 M $HClO_4$ containing 40 mM $HAuCl_4$. At a mild potential of $-0.08\,V$ Ag/AgCl, the diffusion of Au^{3+} keeps up with its consumption, allowing the preferential growth of (111) facets, giving a pyramidal structure. When the potential is change to $-0.2\,V$, at which a concentration depletion zone forms, branching occurs at the apex and rod-like structures are obtained [26.16].

Under proper conditions, micro- and nanoflowers can be obtained by the template-free and surfactant-free electrodeposition of clustered nanoflakes or nanopricks. Examples including the square-wave potential deposition of Au flowers from $HAuCl_4$ solution and the potentiostatic deposition of Ag and Pt flowers from $AgNO_3$ solution and $HPtCl_6$ in H_2SO_4 solution, respectively (Fig. 26.5) [26.14, 17, 18]. These examples indicate that solutions containing a low precursor concentration are necessary for producing nanoflowers; a high precursor concentration results in polyhedral or irregular particles probably because the depletion zone does not form as easily at high concentration.

Intersectional plate and conifer-like cadmium sulfide (CdS) NCs on indium tin oxide (ITO) glass have been obtained by constant current electrodeposition from a dimethylsulfoxide (DMSO)-water (90–20 ml) mixture containing 0.10 g $CdCl_2$ 2.5 H_2O and 0.10 g elemental sulfur (Fig. 26.6) [26.19]. The x-ray diffraction (XRD) and SEM results show that the conifer-like crystals grow on a 200 nm-thick nonconifer-like underlayer. The formation of CdS nanoconifers is divided into three steps. First, CdS particles are deposited preferentially along the [001] direction, resulting in perpendicularly oriented nonconifer-like CdS NCs, which act as the seed layer. Next, new CdS grains are deposited on the seed layer; however, as the deposition continues, the preferential growth orientation of the NCs changes from the [001] direction to the [100] direction, and conifer-like CdS crystals begin to appear. The final CdS conifers form gradually. To obtain well-defined intersectional CdS nanoconifers with a length of 650 nm and a width of 250 nm with a typical deposition time of 60 min, the deposition conditions should be carefully controlled; the temperature must be higher than 110 °C, the current density should be kept between

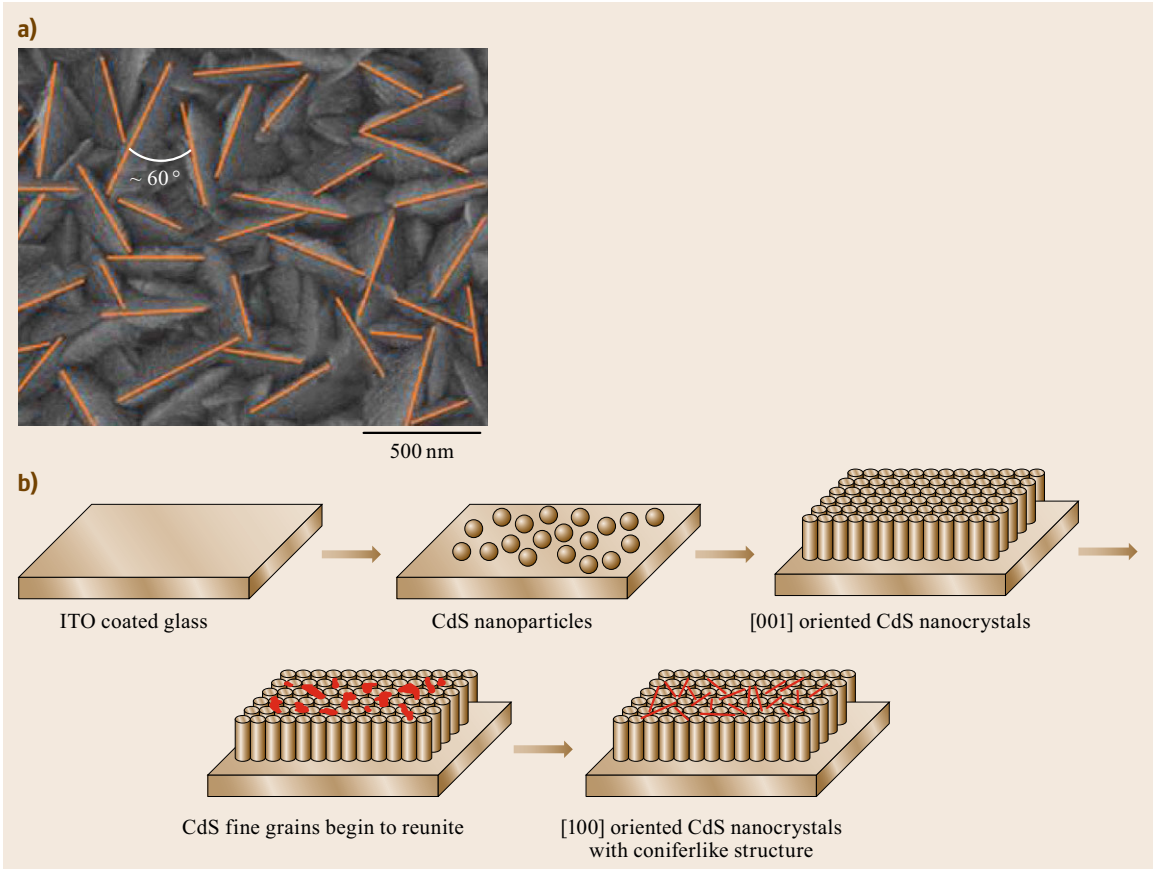


Fig. 26.6 **(a)** As indicated by the *orange lines*, the geometric distribution of the CdS nanoconifers with an intercross angle of $\approx 60\,^{\circ}$C, and **(b)** Schematic illustrations of the growth process of CdS nanocrystalline thin films with a coniferlike structure (after [26.19])

0.06 and 0.08 mA/cm^2. Galvanostatic electrodeposition (0.1 mA/mm^2) has also been employed for the preparation of aligned Co nanodiscs (50 nm thick and 500 nm wide) on a GaAs surface from surfactant-free aqueous solutions containing 0.1 M $CoSO_4$ and 1.0 M $(NH_4)_2SO_4$ within a temperature range of 22–2 °C. Removing $(NH_4)_2SO_4$ or adding H_2SO_4 or $(NH_4)OH$ destroyed the well-aligned growth morphology [26.20].

The template-free direct electrochemical synthesis of Pd nanoplates and nanotrees (dendrites) on a Au substrate through a cyclic deposition/dissolution route was performed with the assistance of surfactants, such as cetyltrimethyl ammonium bromide (CTAB) and PVP, respectively. The electrochemical preparation was carried out by cycling the potential at a rate of 100 mV/s between the low potential limit E_{low} of -1.0 V versus saturated calomel electrode (SCE) and the high potential limit E_{high} of 0.4 V versus SCE in a solution containing NH_3H_2O and K_2PdCl_4, in which Pd ions existed as the $Pd(NH_3)_4^{2+}$ complex. In the absence of a surfactant, however, only aggregated nanoparticles were obtained. If E_{low} is more negative than -1.4 V, only irregular particles form, whereas if E_{low} is less negative than -0.7 V, the growth rate becomes slow. At a more positive E_{high} (0.8 V) no special nanostructure was observed because the nanostructure that formed in the cathodic deposition scan was largely dissolved during the anodic scan [26.21, 22]. Vertically crosslinked Ag nanoplate array have also been electrochemically prepared in the presence of PVP. This procedure has two steps. First, chemically synthesized spherical Ag nanoparticles, 5–30 nm in size, were spin-coated onto an ITO electrode. Next, the Ag nanoplates were electrodeposited in 50 ml of aqueous solution of 0.05 g $AgNO_3$ and 0.25 g PVP. It is crucial to do the electrodeposition at a low current density of 5 μA/cm^2 because higher current densities produced mainly large particles [26.23]. The merit of this procedure is that the number density of the nanoplates could be controlled by the number of Ag seeds loaded on the electrode.

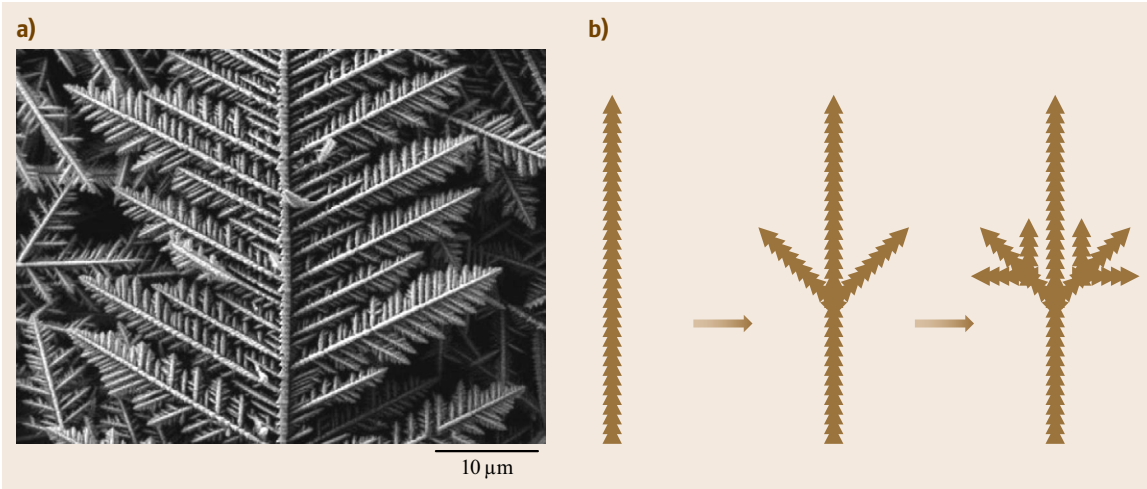


Fig. 26.7 (a) SEM images of PbTe dendritic structures, and (b) simple schematic description of the growth process of PbTe dendritic structures (after [26.24])

Super-hydrophobic films with metallic nanocone arrays of Ni and Co, respectively, were prepared by *Hang* et al. [26.25–27], who used the direct electrodeposition method with the addition of dihydrochloride and on inorganic salt with NH_4^+ ions, respectively, as the crystal modifier (CM). No cone-like structure was observed in the absence of the CM. Increasing the CM concentration increased the number and size of nanocones until whiskers appeared.

In electrodeposition, dendritic structures often form when the deposition process is far from the thermodynamic equilibrium conditions and the growth rate is diffusion limited. A typical dendrite consists of an elongated central trunk with secondary or tertiary branches comprising ordered particles. The formation of dendritic structures generally involves several stages, as indicated in Fig. 26.7 [26.24]. First, a large number of nuclei form upon the application of a sufficient deposition potential or current. Subsequently, the deposits grow with the incorporation of new adatoms onto the preformed nuclei. With time, the precursor concentration at the front of the growth interface quickly depletes, and the new deposited particles are more likely to attach on the tips of the cluster than on other parts of the cluster, leading to the outward growth of branches. As the deposition continues, tertiary branches grow out from the secondary branches, leading to the final dendritic structure. The trunk and branches often grow in a certain preferential direction.

The concentration of the precursor affects the formation of dendrites. It is generally recognized that for single-component systems, higher concentrations favor the formation of dendrites, whereas low concentrations result in particles [26.28, 29] However, the situation could be more complex for multicomponent systems. For example, in the deposition of Cu_7Te_4 from solution containing $Cu(CH_3COO)_2$, Na_2TeO_3, and HNO_3, the optimal concentration of $Cu(CH_3COOH)_2$ is 0.5 mM; increasing or decreasing the concentration produces spherical and aggregated nanorods, respectively. HNO_3 was used to prevent the formation of precipitates of the precursor [26.30].

Counter-anions may play important roles in the formation of dendrites. For example, Cu_7Te_4 dendrites were obtained when $Cu(CH_3COOH)_2$ and $Cu(SO_4)$ were employed as the Cu^{2+} source, but no dendrites were obtained when $Cu(NO_3)_2$ was used as the Cu^{2+} source. This was attributed to the stronger coordinating ability of CH_3COO^- and SO_4^{2-} ions compared to that of NO_3^- ions [26.30]. Dendritic Pd structures were obtained from $PdSO_4$ solution but not from $PdCl_2$ solution. It was proposed that this is due to the adsorption of SO_4^{2-} on the Pd (111) surface [26.31].

The influence of surfactants and complexing agents on the morphology of the deposits has been investigated. For example, in the deposition of Bi from a solution of BiO^+, dendritic structures were obtained when cationic surfactant cetyltrimethylammonium bromide (CTAB) was added. In contrast, aggregated nanoparticles were produced when anionic sodium dodecyl benzene sulfonate (SDBS) was added. The addition of nonionic PVP, however, resulted in spherical grains [26.32]. It has been shown that complexing agents such as tartaric acid and citric acid promote the formation of dendritic Bi nanostructures, but the strong complexing EDTA-2Na enhanced the morphology to flower-like structures constructed by microrods [26.32]. Tartaric acid has also been shown to be essential for

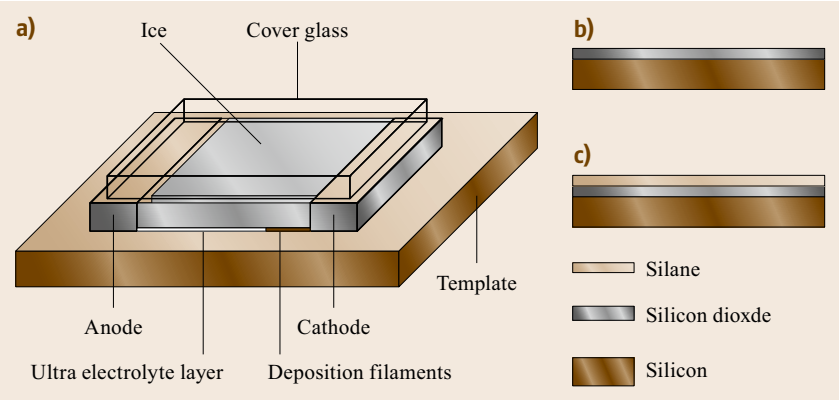


Fig. 26.8a–c Schematic diagrams showing the procedures used to prepare the substrate for electrodeposition. **(a)** The electrochemical cell; **(b)** the surface of a silicon wafer is first oxidized; **(c)** octadecyltrichlorosilane (OTS) molecules self-assemble on the silicon dioxide (after [26.33])

the electrodeposition of dendritic PbTe [26.24]. In addition to the common additives, cysteine (0.1 mM) has been used to control the electrodeposition of Au dendrites from $HAuCl_4$ and H_2SO_4 solutions. The cysteine molecules adsorbed on the (111), (110), and (100) facets of the initially grown Au nanoparticles through Au–S bonds. The cysteine molecules adsorbed on the (111) facet can be desorbed at a more negative potential. Consequently, the (111) facet is exposed to the solution, whereas the (100) and (110) facets are not, making the preferential growth along the ⟨111⟩ direction, eventually forming a threefold dendritic structure. However, it is noted that desorption is greatly retarded when the concentration of cysteine is too high, with no dendrite formed [26.34].

Electrodeposition of Inorganic Nanowires and Nanotubes

While the growth of branches is crucial for the electrodeposition of dendritic structures, branches prohibit the direct electrodeposition of nanowires. The branching rate can be, however, greatly reduced in an ultrathin electrolyte layer. In an ultrathin electrolyte layer, the mass transport of ions is dominated by electric migration while diffusion and convection are suppressed. In the beginning of the deposition, nuclei form on the cathode. Subsequent growth of the deposits prefers the front of the nuclei because, in accordance with migration, the electric potential driving force at the front is higher than that at the side. Therefore, branching is suppressed and wire-like structures form. This was demonstrated experimentally by *Fleury* et al. [26.33] and adopted by *Wang* et al. [26.35] in the electrode position of Cu wires. The original cell consisted of a graphite rod cathode surrounded by a circular anode made of a copper wire. The two electrodes and the electrolyte were sandwiched between two glass plates. The temperature beneath the cell was reduced to solidify the electrolyte, and a ultrathin electrolyte layer with a thickness of about 200 nm formed at −4 °C. Using this setup, the number of branches was greatly reduced. This cell configuration was improved by replacing the cathode and anode with two parallel straight electrodes, as depicted in Fig. 26.8 [26.36]. With this cell design, aligned, smooth wire arrays of Cu [26.36–40], and Co [26.39] have been obtained. It is noted that ion flux oscillation at the liquid–solid interface occurs during the deposition, leading to periodic component or density oscillation in the individual wires.

The electrodeposition of one-dimensional nanostructures also has been realized from a nonultrathin electrolyte layer. The most studied example is ZnO. The cathodic electrodeposition of ZnO has been achieved based on the reaction of electrochemically generated hydroxide ions (OH^-) with Zn^{2+} ions at the electrode surface according to [26.40, 41]

$$Zn^{2+} + 2OH^- \rightarrow ZnO + H_2O\,.$$

In the deposition, the cathodic potential is usually controlled at values (−1 V versus SCE) at which the direct electrochemical reduction of Zn^{2+} does not occur. ZnO has a wurtzite structure composed of a positive polar zinc face (0001) along the *c*-axis. It has been suggested that negative ions, such as OH^- and $Zn(OH)_4^{2-}$ are adsorbed on the (0001) face by electrostatic force, which allows anisotropic growth in the ⟨0001⟩ direction, promoting the formation of rod and wire structures. Although OH^- can be cathodically generated from NO_3^- [26.42, 43] and H_2O_2 [26.44], most studies have used O_2 [26.45–56]. $ZnCl_2$ and $Zn(NO_3)_2$ have been used as the Zn^{2+} sources. The morphology of the electrodeposited ZnO depends on the Zn^{2+} concentration. In a $ZnCl_2$ solution, it was found that compact ZnO films are obtained with a high Zn^{2+} concentration (> 5 mM), whereas nanorod or nanowire arrays are obtained when the Zn^{2+} concentration is reduced to below 0.5 mM [26.49]. Similar behavior was observed using $Zn(NO_3)_2$ solutions [26.50, 51]. The influence

of the anions (Cl^-, ClO_4^-, SO_4^{2-}, and CH_3COO^-) of the supporting electrolyte on the growth of aligned ZnO nanowire arrays from $ZnCl_2$ solutions has been investigated [26.52–54]. In general, the preferential adsorption of anions on the polar (0001) crystal plane of ZnO favors the lateral growth (diameter) of the crystals. Furthermore, the adsorption of anions inhibits OH^- production. The difference in adsorption behaviors of different anions (Cl^- exhibits the strongest the absorption) results in different OH^- production rates and different ZnO nanowire morphologies (length and diameter). For these reasons, the anion concentration should be kept lower than 1 M. To ensure the effective formation of ZnO, the deposition is usually performed at 70–90 °C. A study indicated that ZnO nanobelts were obtained by lowering the deposition temperature to 0 °C using a solution containing 0.1 M $Zn(NO_3)_2$ and 0.1 M KCl at -1.4 V versus Ag/AgCl [26.57].

Cadmium selenide (CdSe) nanowires have been fabricated by constant-current electrolysis with a current density of 0.22 mA/cm^2 at 147 °C from a dry dimethylformamide (DMF) solution of 10 mM $CdCl_2$ and 5 mM elemental Se in a two-electrode cell that contains an ITO working electrode and a Pt foil counter-electrode parallel to the ITO. The elemental Se is first reduced electrochemically to Se^{2-}, which reacts with Cu^{2+} to form CdSe. Because wurtzite CdSe comprises polar surfaces with different polarities and activities, the CdSe grows preferentially along the *c*-axis, resulting in a structure [26.58]. Similarly, preferential growth along the [001] direction is induced by the intrinsic anisotropic crystal structure of Te, and gives rise to the electrodeposition of single-crystalline one-dimensional (1-D) Te nanostructures on an ITO electrode from a 1 M KOH alkaline solution containing TeO_3^{2-} (introduced as TeO_2) at a stationary potential of -1.3 V (versus SCE) at 85 °C [26.59].

The electrodeposition of Co nanowires has been attempted from aqueous solutions prepared from $[Co(NH_3)_6]Cl_3$. The influence of the reduction potential, concentration, supporting electrolyte, and temperature on the morphologies of the deposits was investigated. Nanowires were obtained from 19 mM $[Co(NH_3)_6]Cl_3$ at -1.03 V (versus SCE) and 18 °C using Li_2SO_4 or K_2SO_4 as the supporting electrolyte. Dendrites were obtained when the concentration was reduced to 5 mM. When $[Co(NH_3)_6]Cl_3$ was replaced with $CoSO_4$, $CoCl_2$ failed to produce nanowires, indicating the important role of ammine ligands [26.60].

Copper sulfide nanowires have been grown electrochemically from quiescent aqueous solutions containing 1.0 mM $CuSO_4$ and 4.0 mM thiourea (TU) using square-wave potential electrolysis with a forward potential, $V_f = 0.85$ V, and a reverse potential, $V_r = 0.0$ V

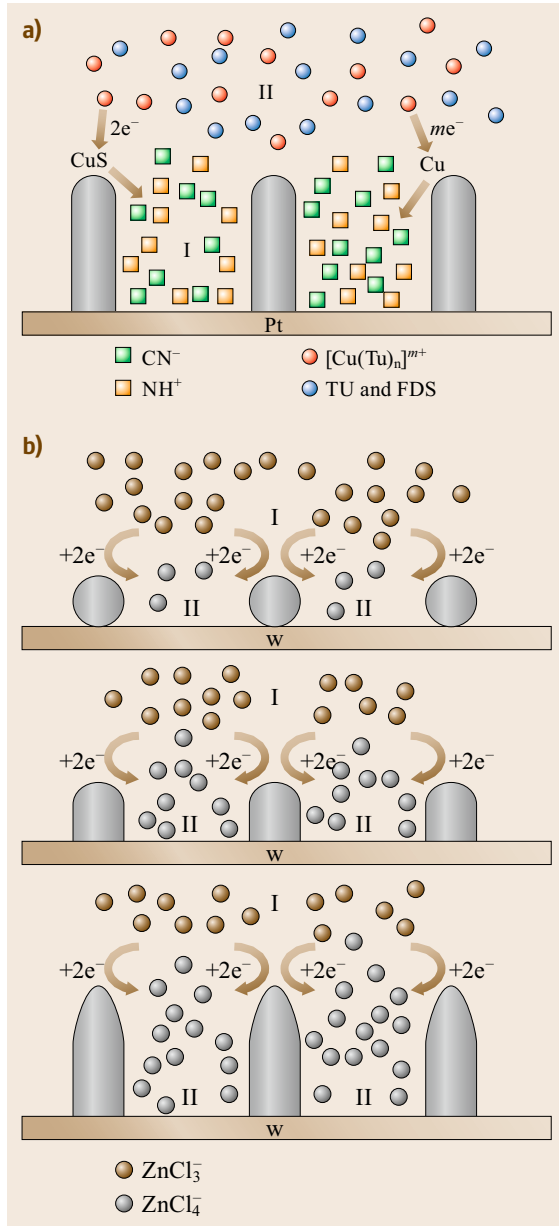


Fig. 26.9 **(a)** Schematic illustration for the growth mechanism of copper sulfide nanowires (after [26.61]); **(b)** Schematic illustration of the growth process of Ni–Zn filaments (after [26.62])

versus Ag/AgCl [26.61, 63]. The deposits contain CuS and Cu_2S resulting from the reduction of $Cu(TH)_n^{2+}$ complex ions according to the following overall equations

$$[CuTU]^{2+} + 2e^- \rightarrow CuS + CN^- + NH_4^+ ,$$
$$2[CuTU]^{2+} + 4e^- \rightarrow Cu_2S + CN^- + NH_4^+ + TU .$$

The Cu–TU complexes and TU are reduced at V_f, producing Cu and CuS nuclei and S^{2-}, CN^-, NH_4^+. Afterward, at V_r, the deposited Cu is dissolved, and the dissolved Cu^{2+} ions form CuS with S^{2-}. As shown in Fig. 26.9a [26.61], CN^- and NH_4^+ ions rapidly accumulate and adsorb on the surface between the deposited CuS particles (designated as Zone 1) during the forward and reverse steps, and inhibit further deposition in Zone 1. In addition, the electroactive Cu^{2+} ions near the surface are exhausted in the deposition process. Thus, the reducible Cu–TU ions must diffuse from the bulk solution (designated as Zone 2) toward the top of the deposited particles and deposit there, leading to the growth of the deposit in one direction, forming nanowires.

Arrays of aligned polycrystalline Ni–Zn alloy filaments have been electrodeposited by constant-potential electrolysis from a quiescent solution of Lewis acidic ionic liquid (IL), $ZnCl_2$-1-ethyl-3-methylimidazolium chloride ($ZnCl_2$-EMIC), containing $NiCl_2$ without using a template [26.62]. The growth of Ni–Zn filament arrays could be related to the speciation of the metal ions. In this Lewis acidic IL, the reducible Zn^{2+} species exist as $ZnCl_3^-$ (or $Zn_2Cl_6^{2-}$). As shown in Fig. 26.9b, upon the application of a cathodic potential, Ni and Zn atoms are deposited along with the release of chloride ions to the liquid–solid interface. The chloride ions turn Zn^{2+} and Ni^{2+} into fully coordinated complex ions such as $ZnCl_4^{2-}$, which are not reducible in this IL. Therefore, there are insufficient reducible metal ions between the growing Ni–Zn deposits (Zone 1) to continue the deposition. As a result, the filaments have to grow along the vertical direction as the reducible metal ions diffuse from the bulk solution (Zone 2) to the front of the growing filaments. Without $NiCl_2$, the same potential electrolysis method produced straight Zn biaxial microbelts from the same IL system [26.64].

Electrodeposition of Conducting Polymer Nanostructures

During electrochemical polymerization, monomers are oxidized into radical cations and then coupled into soluble oligomers. When the concentration of oligomers exceeds their solubility or the polymerization reaches a critical point, the polymers are deposited on the working electrode. Several factors, such as dopant, current density, and potential have great effects on the morphology of the electrodeposited conducting polymer.

Large arrays of oriented and aligned polyaniline (PANI) have been prepared by a stepwise electrochemical deposition in a solution of 0.5 M aniline and 1.0 M perchloric acid ($HClO_4$). In the first step, a large number of PANI nuclei are deposited on the substrate using a large current density of $0.08\,mA/cm^2$. The current is then reduced to $0.04\,mA/cm^2$ to limit the number of nucleation centers, which may induce branches. Finally, the current is reduced to $0.02\,mA/cm^2$ for the growth of PANI into nanowire arrays [26.65, 66]. The single-step synthesis of PANI nanowire arrays has been achieved in a solution containing 0.1 M aniline and 1 M $HClO_4$ using a low constant anodic current of $0.01\,mA/cm^2$ [26.67]. The one-step electrodeposition of oriented PANI nanorods has been studied in 0.5 M oxalic acid (pH = 1.5) solution containing aniline. The appropriate aniline monomer concentration is between 0.05 and 0.25 M, and the appropriate current density is $2\,mA/cm^2$. With a deposition time of 5 min, the diameter and length of the PANI nanorods could be controlled in the ranges of 50–60 nm and 150–250 nm, respectively [26.68]. In contrast to aligned PANI nanoiwres, PANI nanofibers with interconnected network-like structures were obtained by galvanoatatic electrodeposition at 25 °C in 0.5 M aniline solutions with various dopants, including H_2PO_4, H_2SO_4, HNO_3, and CH_3COOH. The dendrite degree of PANI nanofibers follows the order: PANI-H_3PO_4 > PANI-H_2SO_4 > PANI-HNO_3. Because PANI-CH_3COOH is highly soluble in water, no nanofibers are obtained [26.69]. Network-like PANI nanofibers were also prepared using cyclic voltammetry between −0.10 and 0.92 V (versus SCE) from aqueous solution containing 0.2 M, ferrocenesulfonic acid, and 0.3 M H_2SO_4. The average diameters of nanofibers increased from 80 to 130 nm when the potential scan rate was decreased from 60 to 6 mV/s. XDR indicated that the crystallinity of PANI nanofibers increased with decreasing diameter [26.70]. The growth of tangled PANI nanofibers during constant potential electrodeposition was studied in solutions containing H_2SO_4 and aniline. The results revealed that a compact two-dimensional layer of PANI nodules is formed in the initial state of aniline polymerization. After the two-dimensional (2-D) PANI layer is formed, the growth of PANI through an electrophilic substitution reaction at the *p*-position of aniline leads to linear nanowires (Fig. 26.10) [26.71]. The platinum tip of a scanning tunneling microscope (STM) has been employed for the nanometer-scale electrodeposition of PANI on a graphite surface immersed in an aniline-containing electrolyte. A negative voltage pulse (6.0 V × 5 μs) at the tip was first applied to cause the formation of a pit on the graphite surface, and a second negative voltage pulse (3.0 V × 50 μs) was applied to induce the oxidative polymerization of aniline at this pit to form a PANI particle smaller than 1 nm. In-

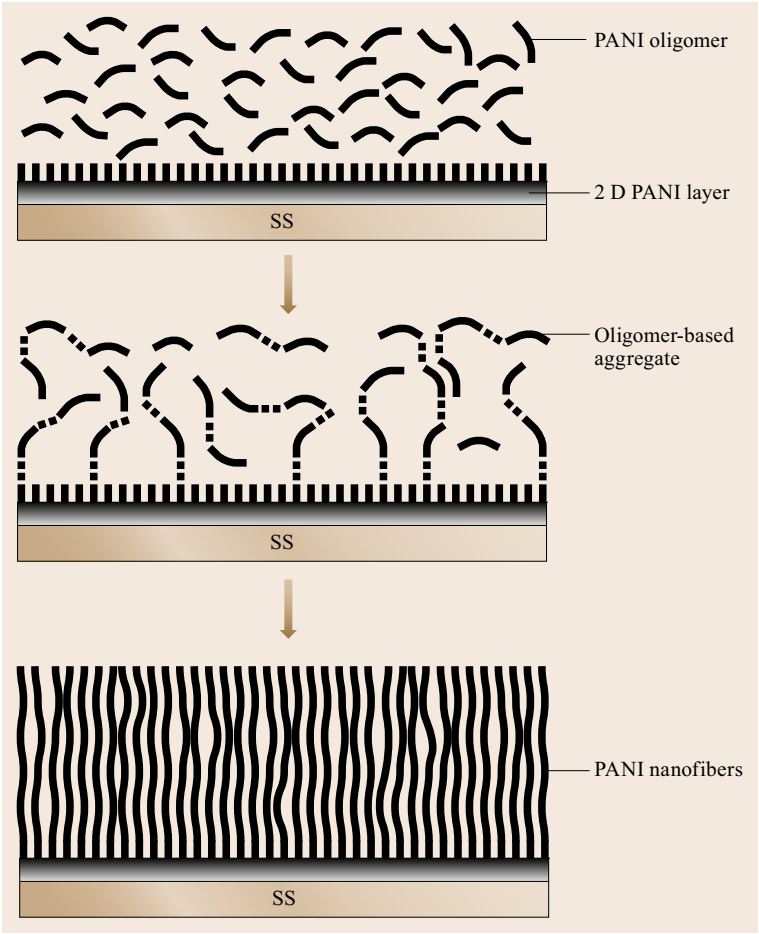


Fig. 26.10 The scheme of nanodimensional deposition for PANI nanofibers (after [26.71])

situ STM images revealed that the volume of the particle in the oxidized form is about 30% larger than that in the reduced form [26.72].

Another commonly studied conducting polymer is polypyrrole (PPy). Nanowires of PPY have been directly electrodeposited on a graphite/paraffin composite electrode in 0.2 M phosphate buffer solution (PBS) at a pH of 6.86 containing lithium perchlorate and pyrrole using cyclic voltammetric polymerization between 0.00 and 0.75 V or potential-step polymerization at 0.85 V (versus SCE). The pyrrole monomers adsorb on the composite electrode surface by hydrogen bonding and polymerize upon the application of a proper potential. The formation of PPY nanowires initiates with an instantaneous 2-D nucleation followed by 1-D growth [26.73]. The morphology of electrodeposited PPY can be influenced by the nature of the anion dopant in the electrolyte solution. Several studies have investigated the electrochemical polymerization of PPY in the presence of β-naphthalenesulfonic acid (β-NSA) surfactant. PPY nanotubes with diameters ranging from 50 nm to 2 μm were obtained on a steel plate electrode using a two-electrode cell at room temperature. The anodic polymerization was initiated by applying 1.2 V between the two electrodes for 1 min, followed by constant-current (0.36 mA/cm^2) polymerization. It was proposed that micelles, which are formed by the hydrotrope β-NSA surfactant, act like templates, leading to the formation of nanotubes [26.74, 75]. PPY micro/nanocup/bowl-like structures were fabricated from a solution containing 0.25 M pyrrole and 0.4 M β-NSA using electrogenerated H_2 gas bubbles as a template. The potential was scanned from −1.0 V to −1.4 V (versus Ag/AgCl) for the first cycle to generate H_2, which forms *soap bubbles* with β-NSA. The potential window was then set in a range of 0.5 to 1.1 V for subsequent cycles for the electropolymerization of pyrrole around the bubbles on the electrode surface at 10 mV/s. The size of the nanocup/bowl can be controlled by the number of potential cycles [26.76]. Similarly, PPY microcontainers have been synthesized using electrogenerated O_2 as a template [26.77–79].

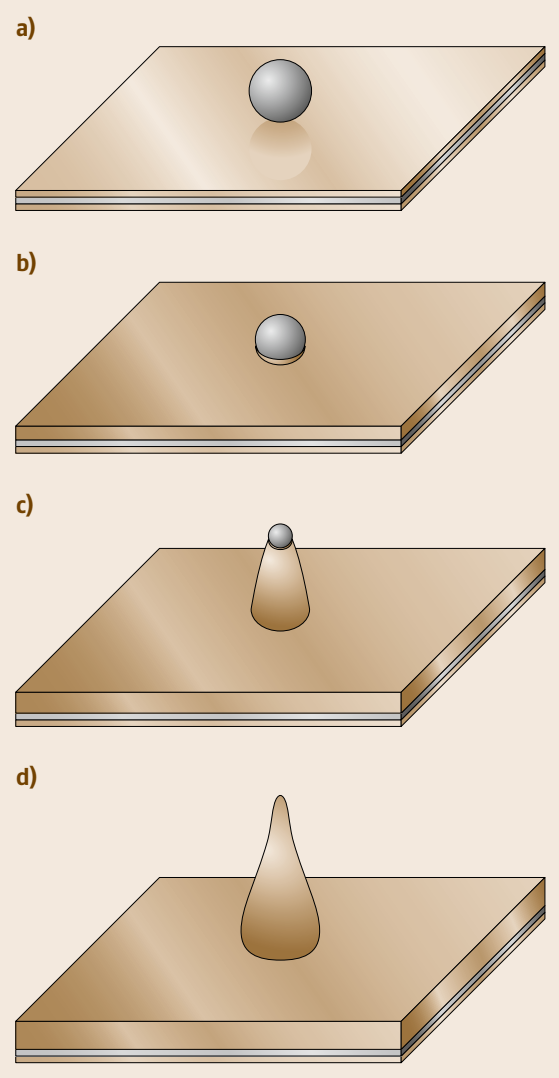


Fig. 26.11a–d Scheme showing the growth model of h-PPY, TOS^- micelle absorbed on the tantalum electrode **(a)**, initial formation of h-PPY with TOS^- micelle as *template* **(b)**, formation of h-PPY with open hollow horn **(c)**, formation of h-PPY with closed end horn **(d)**; silver gray: tantalum substrate, white: TOS^- micelle and gray: PPY (after [26.80])

PPY nanowires with diameters of 120–500 nm have been potentiostatically grown at 1.1 V (versus SCE) in the presence of 1-pyrenesulfonic acid (PSA), which acts as both surfactant and dopant. The electrolyte contained 16.7 mM pyrrole and 25–50 mM PSA. No PPY nanowires were obtained when the concentration of PSA was lower than 25 mM. The addition of a certain amount of NaCl (20–40 mM) in the electrolyte can reduce the diameters of the wires [26.81]. The electrodeposition of PPY nanotubes via a self-assembly process in an electrolyte containing 1.5 mM pyrrole, 0.75 mM KNO_3, and 5 mM methyl orange (MO), sodium 4[4′-(dimethylamino)phenyldiazo]phenylsulfonate MO, has been performed using a constant current of $1\,mA/cm^2$. Although MO is not a surfactant, it self-assembled into a fibrillar precipitate via electric flocculation on the electrode, and acted as a template to direct the growth of PPY into nanotubes [26.82]. Well-aligned nanocone arrays of PPY have been synthesized on an Au substrate by template-free, one-step electropolymerization at 0.85 V (versus Ag/AgCl) from an electrolyte containing 0.6 M pyrrole and 0.2 M PBS with pH 6.8. It is proposed that the hydrogen bonding introduced from PBS and the steric hindrance effect from the high concentration of pyrrole lead to the vertical growth of well-aligned nanocones [26.83]. A PPY nanofiber network is, however, obtained when ClO_4^- is added to this electrolyte [26.84].

It is known that OH^- hinders the polymerization of pyrrole by deprotonating the cation radicals to form neutral radicals that interfere with the coupling reaction. However, nano horn-like structures of PPY have been obtained galvanostatically from an alkaline (pH = 9) solution containing 0.3 M pyrrole and 0.3 M *p*-tolunensulfonate (TOS^-). It is proposed that micelles of TOS^- adsorb on the working electrode and act as templates in the formation of PPY-TOS hollow tubes. The inner diameter of micrortubes in PPY-TOS gradually decreases during the growth process as the TOS^- is consumed as a dopant. Finally, the ends of the horns close when TOS^- is exhausted (Fig. 26.11) [26.80]. In addition to single-phase electropolymerization, biphasic electrochemical synthesis of PPY nanofiber arrays has been reported [26.85]. The system contains a 0.1 M pyrrole chloroform organic phase and a 1 mM L-camphorsulfonic acid (L-CSA) aqueous phase (Fig. 26.12) [26.85]. The electropolymerization was performed using cyclic voltammetry in the potential range of −0.2–1.0 V (versus Ag/AgCl) at a scan rate of 20 mV/s. The polymerization takes place on the electrode in the aqueous phase, in which the concentration of pyrrole is controlled by diffusion from the organic phase to the aqueous phase, and is thus kept low near the electrode surface. The low pyrrole concentration and the L-CSA anions, which adsorbed on PPY nuclei during the deposition, minimize the branching effect, and ensure 1-D growth that leads to nanofibers. If L-CSA is replaced by sodium dodecyl sulfate (SDS), coral-like nanostructures are obtained. The length of the PPY nanofibers can be controlled from several hundred nanometers to several micrometers by the number of CV scanning cycles [26.85].

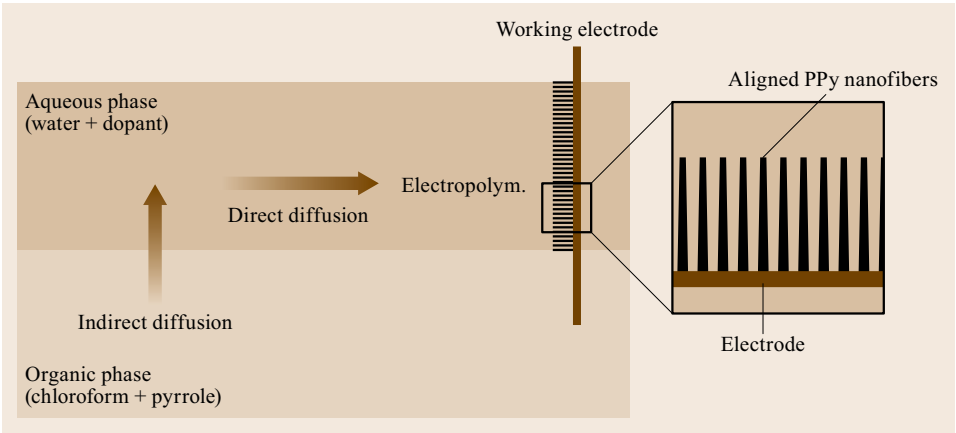


Fig. 26.12 Schematic illustration of biphasic electropolymerization in which the electrolysis contains two different phases (organic and aqueous). Pyrrole diffused from organic phase into aqueous phase slowly (indirect diffusion). Then PPY were deposited on the electrode by electropolymerization by the diffusion of pyrrole to the electrode (direct diffusion). Aligned PPY nanofibers were produced with successive CV electropolymerizations (after [26.85])

26.1.2 Template-Assisted Electrodeposition

Template assisted deposition is a popular procedure for the fabrication of nanomaterials [26.86]. The most popular porous templates for preparing nanowires include porous anodic aluminum oxide (AAO), track-etched polymeric membranes, and highly oriented pyrolytic graphite (HOPG). For more complicate patterned nanostructures, lithographic methods have been developed. This section describes these methods. The preparation of metal nanostructures using the porous created by self-assembly in block copolymer structures is described in another chapter of the handbook.

Fabrication of Nanoporous Alumina Templates

Porous AAO is produced by the anodization of aluminum in acidic electrolytes [26.87–92]. As shown in Fig. 26.13 [26.93], AAO film contains an array of noninterconnected parallel cylindrical nanopores. Each pore is surrounded by alumina, forming a hexagonal cell. The self-organization of these cells gives a honeycomb-like structure. It is generally accepted that the formation of the oxide pores is a result of the dynamic equilibrium between the simultaneous growth and dissolution of the alumina in the acidic electrolytes. Under proper conditions, porous AAO film with a uniform pore diameter in the range of 20–400 nm and with a pore density in the range of 1×10^{8}–1×10^{10} pores/cm^2 can be fabricated. The thickness of the porous AAO film can be varied from a few tens of nanometers to more than several hundred micrometers.

The early hard anodization (HA) process, which uses a high current density, generally produces AAO with low regularity in the pores, and thus the structure is unsatisfactory for use as a template for preparing well-defined nanostructures. The fabrication of ordered porous AAO is generally performed by the mild anodization (MA) process introduced by *Masuda* and *Fukuda* [26.91, 92]. The fabrication of self-organized porous AAO using the MA process has been studied in oxalic acid [26.89–91, 94–99], sulfuric acid [26.87, 89, 92, 100, 101], and phosphoric acid [26.88, 90, 102] solutions using potentiostatic methods. It has been revealed [26.103] that the structural parameters, such as the pore diameter (D_p), interpore spacing (D_{int}), and barrier layer thickness (t_b) of AAOs increase linearly with increasing anodization voltage (U) with proportionality constants of 2.5 nm/V, 1.2 nm/V, and 1.3 nm/V, respectively [26.93]. Highly ordered self-organized porous AAO has been obtained at individually specified self-ordering voltages, that is, sulfuric acid at 25 V, oxalic acid at 40 V, and phosphoric acid at 195 V, giving D_{int} of 63, 100, and 500 nm, respectively. *Ono* et al. [26.104] reported that for each electrolyte, the corresponding steady-state current density increased exponentially with increasing U. The current density at the self-ordering voltage regime is about 5 mA/cm^2. Lowering the current density by decreasing U results in irregular film growth, indicating the necessity of high current density during anodization for self-ordering. However, intense gas evolution occurs at the surface when U is higher than the self-ordering regimes, causing burning or breakdown of the AAO film. While the MA process for the fabrication of AAO is normally carried under low current density, *Chu* et al. [26.105] successfully fabricated ordered AAO in aged sulfuric acid electrolyte using an anodic potential and a current

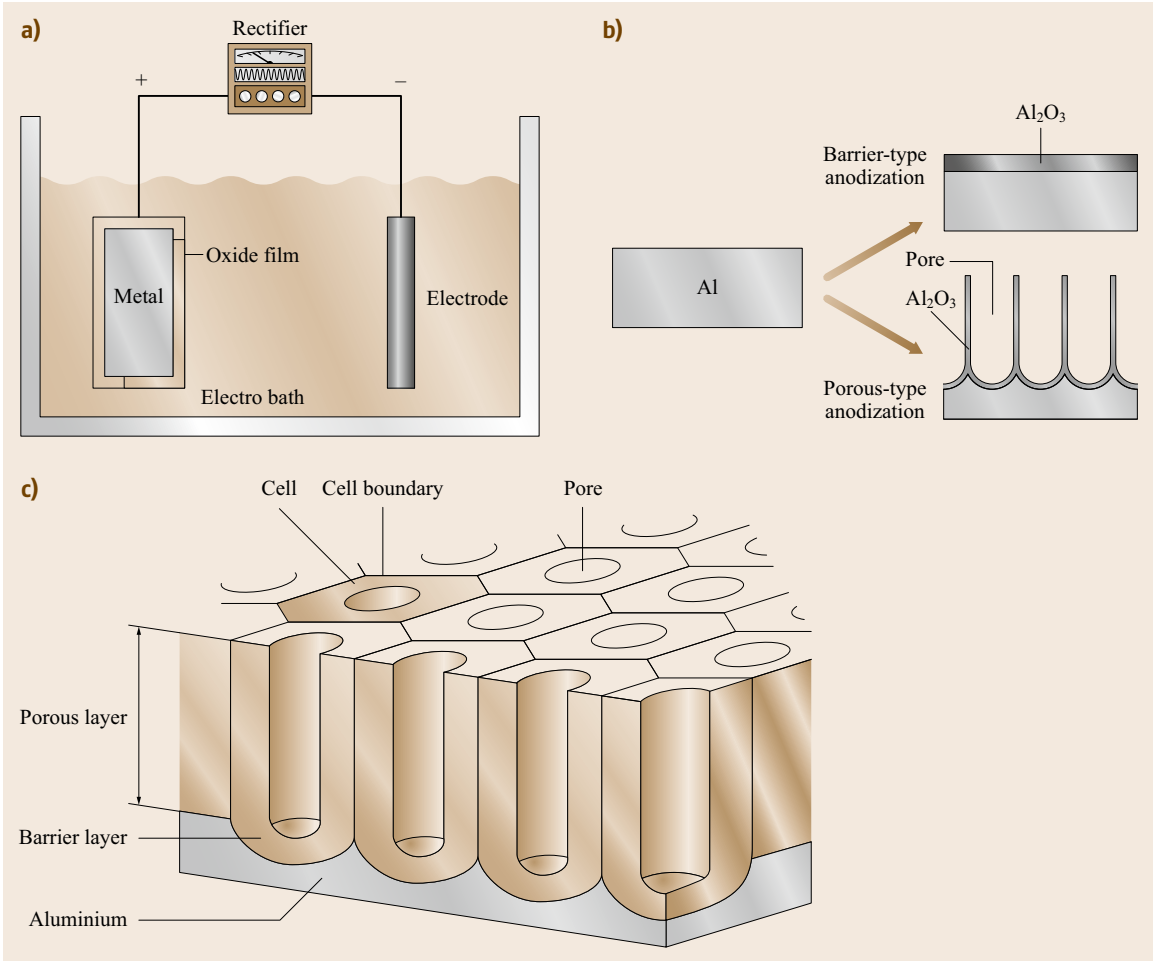


Fig. 26.13a–c Schematic illustrations showing **(a)** a simplified anodization setup, **(b)** two different types of aluminum anodization, and **(c)** an idealized structure of AAO produced by a porous-type anodization (after [26.93])

density of as high as 70 V and 2000 mA/cm^2, respectively.

Lee et al. [26.106] showed that the suppression of the breakdown effects and the formation of uniform AAO film at a rate higher than that in the MA process, that is, high voltage, could be achieved by introducing a thin protective oxide layer on aluminum before performing the HA process. A clean, polished aluminum substrate was first anodized at 40 V in 0.3 M oxalic acid (1–2 °C) for 8 min to produce the protective oxide layer. Then, the anodization voltage was gradually increased at a rate of 0.5–0.9 V/s until a target voltage (U_t) (100–160 V) was reached. The HA anodizationn was continued at this target voltage for the desired time period. With this modified HA process, long-range ordered porous AAO films with a widely tunable interpore spacing (D_{int} = 200–300 nm) and pore diameters (D_p = 49–59 nm) could be grown up to 70 μm thick on a time scale of 1 h. The oxide nanostructure growth rate in the modified HA process was 25–35 times faster than that in the typical MA process. This modified HA process was also applied to sulfuric acid (between −1.5 and 1 °C) [26.107]. In this process, the protective oxide layer was formed at 25 V for 10 min in 0.3 M sulfuric acid. The following HA process was then carried out in 0.03 M sulfuric acid by gradual increasing the voltage (at a rate of 0.1 V/s) to U_t (40–65 V). Note that HA is accompanied by a large heat evolution. The excess heat should be removed using an effective cooling system.

AAO with a periodically modulated pore diameter along the pore axes (Fig. 26.14) [26.108] has been fabricated by deliberately oscillating the current during HA, or by combining the MA and HA processes [26.108, 109]. The diameter-modulated AAO can be a template for the fabrication of interesting nanostructures.

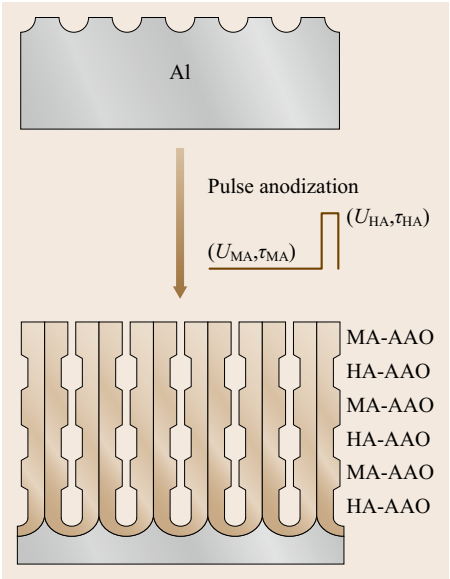


Fig. 26.14 Scheme for the fabrication of AAO with modulated pore diameters by pulse anodization. MA-AAO: mild anodization AAO; HA-AAO: Hard anodiztion AAO (after [26.108])

The structure of AAO is described as a closely packed array of columnar cells, each containing a central hole, and the configuration and shape of cells can be defined based on the mathematical expression known as the Voron tessellation. In naturally occurring self-ordered porous AAO, the columnar cells are hexagonal closely packed with a hole in the center of each cell. However, *Masuda* et al. showed that square- or triangular-shaped pore arrays in a close-packed square or hexagonal arrangement could be fabricated by the layout of the initiation nuclei sites in square- or graphite-structure lattice patterns (Fig. 26.15) [26.110]. The layout was achieved by a nanoindentation process. In this process, a SiC mold with arrays of a convex feature with the desired arrangement is prepared using conventional EBL. With indentation using the SiC mold, an array of shallow depressions is formed on the aluminum, which serves as the initiation sites for the hole generation at the initial stage of anodization. Then, the desired close-packed square or triangular nanoporous structures are obtained by anodization of the indented aluminum [26.110]. The nanoindentation or prepatterning method was also applied for the fabrication of ideally ordered AAO with a single-domain configuration over a few mm^2 [26.111, 112].

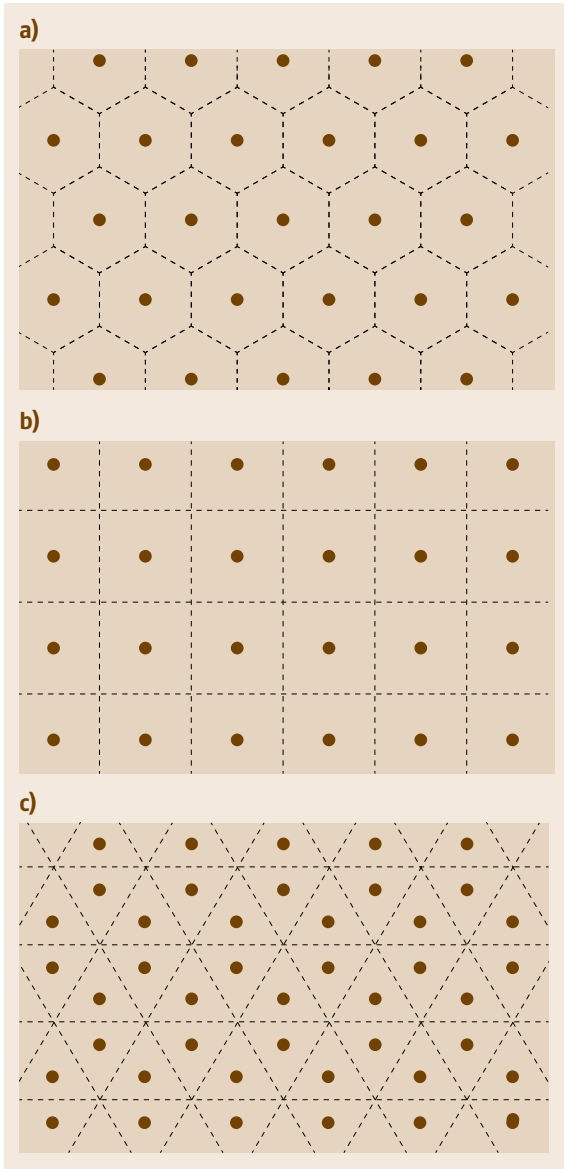


Fig. 26.15a–c Voronoi tessellation of two-dimensional space by uniformly sized cells of normal *hexagons*, *squares*, and *triangles*. *Dots* in each tessellation represent the initiation site for hole generation of *triangular* **(a)**, *square* **(b)**, and *graphite structure* **(c)** *lattices* (after [26.110])

Fabrication of Track-Etched Polymer Membrane Templates

Nanoporous polymeric membranes, such as polycarbonate (PC), poly(ethylene terephthalate) (PET), and polyimide (Kapton), can be fabricated using the track-etched method [26.113]. In this method, the polymer is irradiated with a beam of high-energy particles such as fragments from the fission of heavy nuclei (R18-33) or ion beams in accelerators (R18-29), creating latent tracks in the polymer film. Such tracks are then etched using alkaline (KOH or NaOH) etching solutions, generating nanopores into which desired materials are electrodeposited. The number of tracks and sizes of the pores can be manipulated by the tracking time and etch-

ing time. It should be noted that the pores produced with track-etched methods are randomly distributed. The pores are not always parallel to each other, and their shape is not always cylindrical.

Electrodeposition of Nanowires and -rods

Nanowires of single metals, metal oxides, alloys, multicomponent nonmetal compounds, and polymers have been fabricated by electrodeposition in the pores of AAO and polymer templates. Because of the nonconductive nature of AAO and polymer templates, one side of the membrane is generally coated with a metal film to serve as the working electrode during the electrodeposition of nanowires within a template. The nanowires are formed progressively from the bottom toward the top of the pores. The deposition can be conducted potentiostatically or galvanostatically under direct current (DC) or alternating current (AC) or pulsed modes. For DC deposition, a constant potential or current is applied continuously. For AC deposition, the potential or current is applied in the form of a sine wave or square wave. Pulsed deposition comprises potential or current pulses with desired duration and intensity. A constant growth rate is required for achieving uniform filling of the template pores. For DC deposition, a slow and uniform wire growth rate can be accomplished by controlling the applied overpotential at the minimum value required for the reduction of the reactants. When the applied overpotential is increased so that the electrodeposition rate is faster than the rate that the reactant can be transported from the bulk electrolyte to the wire growth front, severe depletion of the reactant concentration can led to nonuniform wire growth and poor pore filling. This difficulty can be circumvented by adopting AC and pulsed electrolysis [26.114–117]. Because the applied potential is varied between cathodic and anodic half-cycles during each AC cycle, the concentration depleted in the cathodic half-cycle can be recovered in the anodic half-cycle, leading to a steady concentration profile for uniform wire growth. Similarly, for pulsed deposition [26.118], a rest period, during which no current flows, is used between pulses to allow re-equilibrium of the electrolyte concentration in the pore. For AC and pulsed deposition, the wave form, frequency, and pulse period are important parameters for achieving successful fabrication of nanowires arrays.

The purity, crystallinity, and texture of metal nanowires are affected by thermodynamics and kinetics of the growth process, which can be controlled by various factors, such as the overpotential, temperature, concentration, pH, and additives. In addition to polycrystalline nanowires of typical metals, such as Pt [26.119], Pd [26.120–122], Cu [26.123], Ag [26.124], Fe [26.125–128], Co [26.129, 130], and Ni [26.131–134] single-crystalline nanowires have been electrodeposited using porous templates because the confinement of the nanopore structure in the template facilitates the formation of columnar grains and single-crystalline nanowires. It has been suggested [26.135] that for low-melting-point metals, such as Au [26.135], Ag [26.136, 137], Cu [26.135], Bi [26.138, 139], Zn [26.140], and Sn [26.141], single-crystals are obtained at a moderately high temperature (40 °C), which promotes surface diffusion of atoms and favors the growth of existing crystal nuclei, and a lower overpotential, which minimizes the nucleation rate. In contrast, for metals such as Ni and Co that have higher melting points, their stronger metal–metal bond energies inhibit surface diffusion. Nevertheless, the electrodeposition of single-crystalline nanowires of Ni [26.142] and Co [26.143, 144] has been achieved. It was suggested that lower temperature and higher overpotential decrease the thermal agitation and the critical dimension of the nuclei size, favoring the formation of single-crystalline Ni nanowires [26.142]. The orientation of single-crystalline Co nanowire arrays obtained from pulsed deposition can be controlled by varying the deposition conditions [26.143, 144].The type of AAO template may also affect the structure of the deposited nanowires. For instance, Fe nanowires grown in sulfuric anodized AAO pores are essentially single-crystalline, whereas Fe nanowires grown in oxalic anodized pores are polycrystalline [26.145].

Hydrogen bubbles generated during electrolysis may block the growth path, leading to nonuniform nanowires. Furthermore, hydroxide ions accompanied with the hydrogen generation may precipitate metal ions, introducing unwanted components into the nanowires. Therefore, controlling the pH of the electrolyte is important. H_3BO_3 has been used for this purpose [26.126, 127, 132].

When multicomponent nanowires are grown by electrodeposition performed in a single-electrolyte bath containing all the ingredients, the composition and microstructure of the resulting nanowires can be affected by the deposition parameters. For example, in the codeposition of NiCo alloy nanowires in an AAO template, single-crystalline, polycrystalline, bamboo, or layer structures have been obtained by varying the concentrations and deposition current density [26.146]. As demonstrated in the fabrication of polycrystalline Pt–Fe, Co–Pt, and Ni–Pt alloys using AAO, nanowires with uniform alloy compositions along the wires were obtained by maintaining stable growth rates of each component [26.147, 148]. However, when the deposition rate is increased by increasing deposition current density or overpotential, diffusion becomes the rate-

determining mechanism, and nonuniform composition along the growth axis is observed due to different diffusion rates of the constituent precursor ions. To avoid the formation of nanowires with nonuniform compositions, alternating potentials [26.149] and pulsed potentials [26.150] have been applied. The techniques decrease the concentration gradients of the constituent ions and lead to uniform composition along the wire. Single-crystalline semiconducting CuS nanorods have been synthesized by using ultrasonication during electrodeposition through AAO because ultrasonication greatly reduces mass-transfer resistance, leading to uniform concentration distribution [26.151]. Alternatively, agitation of the bath by a rotating electrode affords a nearly constant supply of electrolyte to the electrode surface, allowing the fast growth of Bi_2Te_3 nanowires with uniform composition [26.152]. A study on the electrodeposition of CdSe nanowire arrays through AAO in DMSO bath revealed that the growth orientation of the CdSe nanowires can be manipulated by varying either the nanopore diameter of the AAO or the deposition current density [26.153]. Single phase but polycrystalline ternary $CuInSe_2$ compound nanowire arrays have been successfully electrodeposited through AAO. The nanowires could be tuned from the Cu-rich p-type to the In-rich n-type by varying the electrodeposition potential [26.154].

In contrast to uniform composition nanowire arrays, segmented or layered multicomponent nanowires (Fig. 26.16) can be grown from a single bath containing different constituent ions by modulating the potential between different values [26.155]. The composition and length of each segment or layer are adjusted by varying the pulse potential and pulse width. Typically, the bath concentration of the component that is deposited at low overpotential is kept much lower than that of the component that is deposited at high overpotential so that the content of the former in the segment grown at high overpotential can be minimized. With this approach, Ni/Cu multilayer nanowires have been grown into a nanoporous polycarbonate template for a solution containing 0.5 M $NiSO_4$ and 0.005 M $CuSO_4$. Pure Cu was deposited at -0.16 V versus Ag/AgCl, whereas $Ni_{0.85}Cu_{0.15}$ was deposited at -1.0 V [26.155]. Similarly, multilayered CoPt/Pt [26.156] and Ni/Pt [26.157] nanowires have been deposited from solutions containing 2 M $CoSO_4$ and 0.2 M H_2PtCl_6, and 2 M $NiSO_4$ and 2 mM H_2PtCl_6, respectively. In these examples, Pt layers were deposited at more positive potential, and CoPt or NiPt layers were deposited at more negative potentials. Thermoelectric superlattice nanowires of Bi/Sb [26.158], $Bi_2Te_3/(Bi_{0.3}Sb_{0.7})_2Te_3$ [26.159], and Bi/BiSb [26.160] have been synthesized using the pulsed deposition approach. An alternative procedure to prepare segmented nanowire arrays is sequential electrodeposition. In this procedure, each component is deposited sequentially into the template pores by changing the corresponding electrolyte baths. The sequence is repeated to give the final segmented nanowires. Typical examples of sequential electrodeposition of nanowires containing segments of Au/Ag/Ni/Pd/Pt [26.161], Au/Pt [26.162], Au/Sn [26.163], and CoNiP/Au [26.164] have been studied for interconnects in nanodevices and barcode purposes. The sequential approach has been modified for fabricating free-standing aligned gold wires. First, wires of alternating Au–Ni layers are electrodeposited in the pores of AAO templates. After the templates are removed, the Au segments of the wires are linked to each other by a combination of thiols and Au nanoparticles. Subsequent removal of the Ni layers results in free-standing arrays of highly aligned Au wires [26.165]. A novel method for fabricating inorganic nanopeapods (Fig. 26.17) [26.166] has been developed using the sequential approach. First, Co/Pt multilayered nanowires are deposited into the porous AAO by pulsed potential electrodeposition. After the deposition, the Co/Pt wires together with the AAO template membrane are annealed at 700 °C in an ambient atmosphere for 1–5 h. During the heat treatment, $CoAl_2O_4$ nanoshells, or *pods* are formed from the reac-

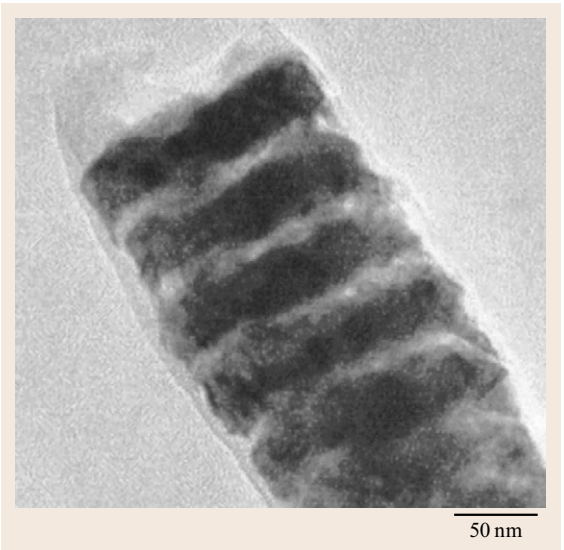


Fig. 26.16 Transmission electron microscope image of a 100 nm diameter nanowire with alternating 20 nm-thick Ni layers and 10 nm-thick Cu layers. The transmission electron microscopy (TEM) sample was prepared by placing a drop of a suspension of nanowires on a gold grid ≈ 400 mesh with holey carbon film (after [26.154], courtesy of Ted Pella Inc., Redding)

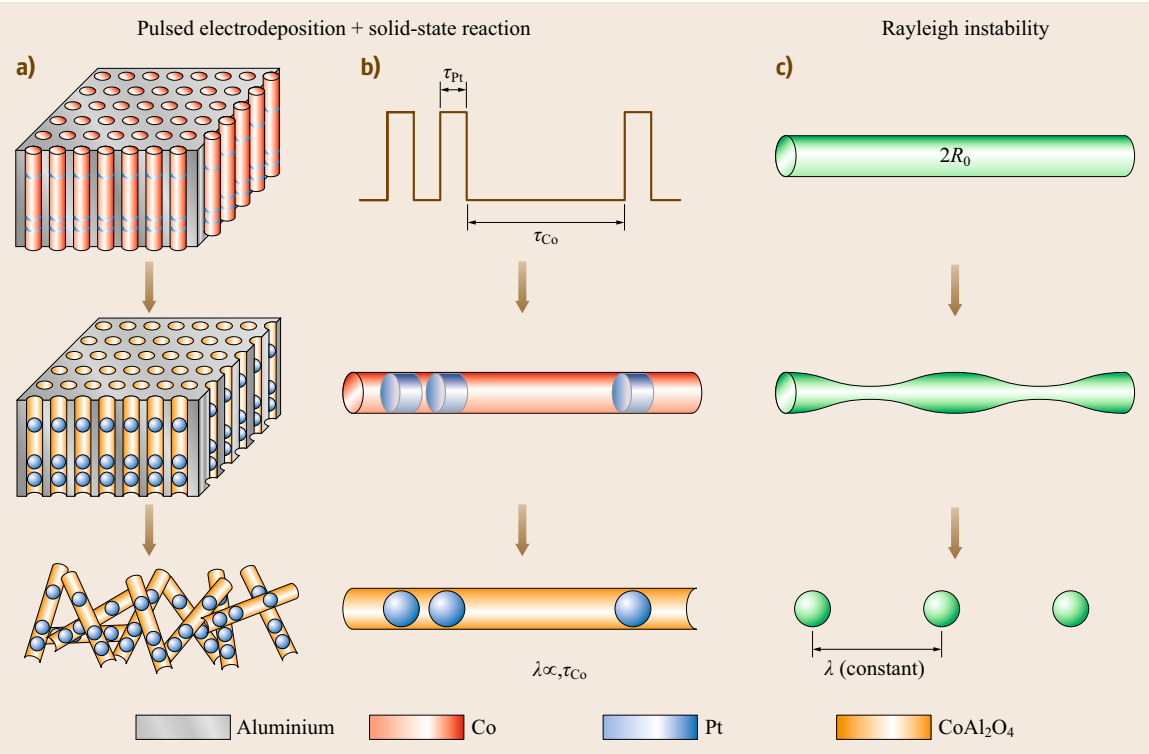


Fig. 26.17a–c Fabrication of peapod nanostructures. **(a,b)** Fabrication of Pt at $CoAl_2O_4$ inorganic nanopeapods (Pt nanoparticle chains encapsulated in $CoAl_2O_4$ nanoshells) by template-based pulsed electrodeposition and high-temperature solid-state reaction. The separation between Pt nanoparticles ($D_{c\text{-}c}$) is proportional to the pulse duration for Co electrodeposition τ_{Co} and can be changed at will. **(c)** Metal nanoparticle chains fabricated on the basis of the Rayleigh instability of metal nanowires (after [26.165])

tion between Co segments and alumina, while spherical Pt peas are formed from the agglomeration of the Pt segments to minimize their surface energy. Accordingly, peapod nanostructures are obtained. The size of the peas and pods can be manipulated by controlling the electrodeposition pulse sequence [26.166]. Recently, polycrystalline segmented all-Pt nanowires were fabricated using a template-assisted pulse-reverse electrodeposition. During the deposition, cathodic potential pulse ($U_c = -1.3\,V$) and anodic potential pulse ($U_a = +0.4\,V$) are applied repeatedly. The deposition of Pt occurs during the cathodic pulses but is retarded during the anodic pulses, resulting in the segmented nanostructure. The length of the segments can be varied by varying the cathodic pulse duration [26.167].

The template-assisted approach has easily adapted for the electrochemical fabrication of porous nanowires. As illustrated in (Fig. 26.18) [26.168], this can be achieved by the dealloying process in which two-component A_xB_{1-x} alloy is first electrodeposited into a nanoporous template followed by the selective dissolution of the less noble component B, creating pores on the nanowires of component A. The most well-known example is the preparation of porous Au nanowires by the electrodeposition of Au_x/Ag_{1-x} nanowires followed by the dissolution of Ag [26.169]. The surface morphology of the porous Au nanowires can be tailored by the ratio of the Au_x/Ag_{1-x} alloy components and the diameter of the nanowires [26.170, 171]. These porous Au nanowires have been found useful for various applications, including sensors [26.170, 172], localized surface plasmon (LSP) resonance [26.168], and surface-enhanced Raman scattering (SERS) [26.173]. Platinum-coated nanoporous Au nanowires can be obtained by first coating a layer of Cu through underpotential deposition (UPD), and then replacing the Cu layer by Pt via a chemical redox displacement reaction [26.174]. The dealloying approach has also been used for fabricating porous Pt nanowires by electrodepositing Pt/Cu alloy nanowires and dissolving the Cu component [26.175]. Another approach of fabricating porous nanowires arrays is the use of sphere-infiltrated membranes [26.176]. In this method, silica or polystyrene nanospheres are loaded in the pores of a membrane by vacuum filtra-

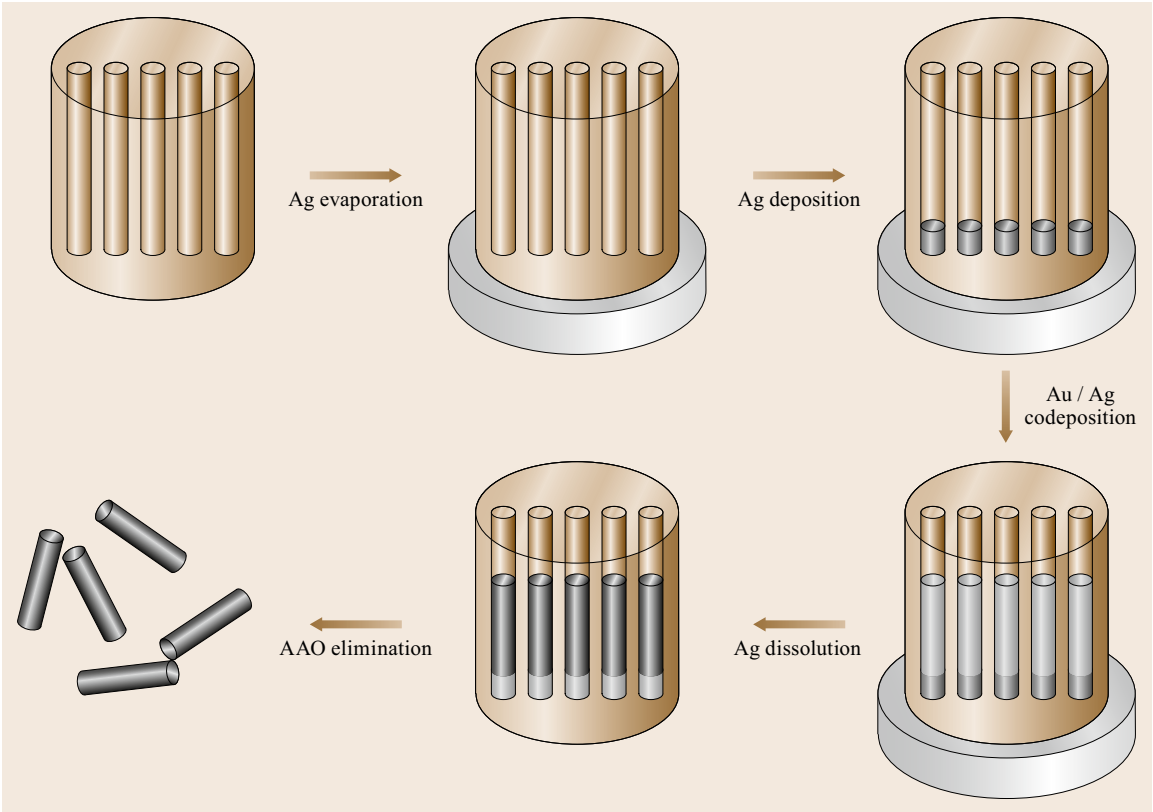


Fig. 26.18 Schematic representation of the template assisted synthesis of nanoporous Au nanorods (NRs). The electrochemical codeposition of Au/Ag results in alloy NRs in the interior of AAO templates. The Ag component is dissolved with concentrated nitric acid and the resulting nanoporous Au NRs were formed (after [26.168])

tion. The desired metal, such as Ni or Au, is electrodeposited in the sphere-loaded pores. After the removal of the spheres, porous nanowires are obtained. Porous Au nanowire arrays have been prepared by the direct electrodeposition of Au into an AAO membrane at a low current density, under which the nucleation is so difficult and slow that the nuclei are selectively deposited instead of covering the whole surface [26.177]. Hence, protrusions form, offering sites for preferential crystallization of Au deposits. As a result, dispersed Au particles are deposited and packed in the template, forming porous Au nanowire arrays.

Electrodeposition of Nanotubes

Many kinds of metal, semiconductor, and polymer nanotube structures have been synthesized by template-assisted electrodeposition. Similar to the deposition of nanowires using a porous template, a thin metal layer is sputtered on one side of the template membrane to serve as the conductive base for electrodeposition. However, this conducting metal layer should be so thin that it only partially covers the surface of the template, leaving the orifices open [26.178–180]. Some of the sputtered metal will diffuse into the nanopores and become deposited on the wall. Consequently, an annular base electrode forms at the bottom of the nanopores [26.181–184]. During the deposition, the conditions are controlled to ensure the preferential growth of the deposits along the direction parallel to the pore wall. In general, the preferential growth is promoted by a fast deposition rate resulting from high overpotential or current density and low precursor concentration. Otherwise, nanowires may form because precursors in bulk solution have sufficient time to diffuse into and fill the pores [26.185–187]. Under certain conditions, hydrogen gas bubbles are generated during electrodeposition. The generated gas bubbles grow and occupy the pore center until they diffuse to the top of the pore. Consequently, the deposition in the pore center is blocked, facilitating the formation of nanotubes. The nanotube walls can be made thinner by increasing the hydrogen gas evolution by lowering the pH of the electrolyte [26.188–192]. The use of a high deposition current density together with gas bubbles produced dispersed Pt nanoparticles in the

formed nanotubes, leading to a highly rough surface and greatly improved electrocatalytic activity [26.193]. Careful control of local pH is especially important for the electrodeposition of metal oxide nanotubes, such as ZnO [26.194], SnO_2 [26.195, 196], and IrO_2 [26.197] using porous AAO and polycarbonate templates, because the cathodic formation of metal oxide is highly pH dependent, as illustrated by the following examples [26.196]

$$NO_3^- + 2H^+ + 2e^- \rightarrow NO_2^- + H_2O\,, \tag{26.1}$$

$$Sn^{4+} + 4H_2O \rightarrow Sn(OH)_4 + 4H^+\,, \tag{26.2}$$

$$Sn(OH)_4 \rightarrow SnO_2(s) + 2H_2O\,, \tag{26.3}$$

$$\text{Net: } Sn^{4+} + 2NO_3^- + 4e^- \rightarrow SnO_2(s) + 2NO_2^-\,. \tag{26.4}$$

A study of the electrodeposition of binary Bi_2Te_3 nanotubes [26.198] in AAO indicated that the potentiostatic method is better than the galvanostatic method for precise control of the composition of the obtained binary nanotubes. In addition to homogenous alloy nanotubes, multisegmented metallic Au–Ni–Au–Ni nanotubes have been obtained in AAO using a multistep procedure [26.199]. Recently, a method for the electrodeposition of single-crystalline Cu nanotubes using an AAO template in the presence of a lateral rotating electric field, which is applied in addition to the longitudinal DC electrodeposition current was demonstrated [26.200]. The applied rotating field makes the ions graze the surface of the pores in helical paths and thus leads to the preferential deposition in the region near the pore wall. The thickness of the tubes increases with descending lateral field amplitude.

Besides the above-mentioned single-step direct deposition methods of nanotubes, multistep methods have been applied for the deposition of nanotubes. In one example [26.201], carbon nanotubes (CNTs) were first deposited onto the interior walls of AAO templates by the pyrolytic decomposition of ethyne. A gold thin film was then coated onto one side of the CNTs/AAO, and Ni was electrodeposited into the pores of CNTs/AAO, forming a nickel core and CNT shell rods. The CNTs in the Ni/CNTs/AAO structure were removed by heating, leaving nickel oxide rods inside the AAO pores, and thus annular nanochannels were obtained. Following this, metals, such as Pt, Au, Bi, In, and Ni were electrodeposited into the annular nanochannels. Finally, the nickel oxide core and AAO were chemically dissolved to expose the produced metal nanotubes. In another example [26.202], nickel nanorods were first electrodeposited into the pores of the AAO. After deposition, the exposed ends of the Ni nanorods were anodized in a KOH solution. Following this, the AAO template was removed by chemical etching, leaving an array of nickel nanorods. Then, gold was electrodeposited onto the surface of each nickel nanorod. After the removal of the nickel nanorods, gold nanotube arrays were obtained.

Electrodeposition of Core–Shell Nanowires

Evans et al. [26.203] fabricated Ni-coated Au-core nanorods by the electrodeposition of Au into thin film AAO. The AAO was then etched in NaOH solution to widen the pores around the Au nanorods. Subsequently, Ni was electrodeposited onto the Au nanorods contained in the widened AAO pores to produce the Au-core Ni-shell nanorods. Alternatively, *Wang* et al. [26.204] fabricated Pd/Pt core–shell nanowire arrays by the electrodeposition of Pd into AAO. The AAO template was then removed by immersion in 2 M NaOH solution and rinsed with pure water. Pt thin film was coated onto the surface of Pd nanowire using a magnetron sputtering method to produce the final Pd/Pt core–shell nanowires arrays. Recently, *Narayanan* et al. [26.205], fabricated Ni/Co core–shell nanorods by the electrodeposition of Co nanotubes into AAO followed by electrodeposition of Ni into the Co nanotubes. *Park* et al. [26.206] prepared hybrid double-walled nanotubes (HDWNTs) of ferromagnetic Ni encapsulated in conducting PPY through a sequentially electrochemical method. Conducting PPY nanotubes were electropolymerized in an AAO template with a nanopore diameter of 100–200 nm. Sequentially, Ni nanotubes were potentiostatically deposited on conducting PPY nanotubes within the AAO template. With this manner, arrays of HDWNT of PPY nanotube enveloped by Ni nanotube were obtained after the removal of the AAO template.

26.1.3 Electrodeposition on HOPG

As shown in Fig. 26.19 [26.207], an HOPG exhibits large atomically flat basal-plane terraces which are parallel to the graphite plane [26.208, 209]. The terraces are bounded by step defects of the edge-plane face of

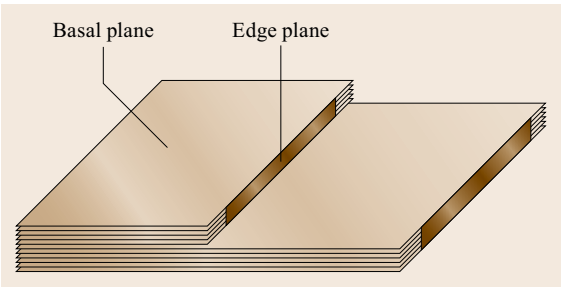


Fig. 26.19 Schematic of the surface of HOPG showing areas of differing electroactivity (after [26.206])

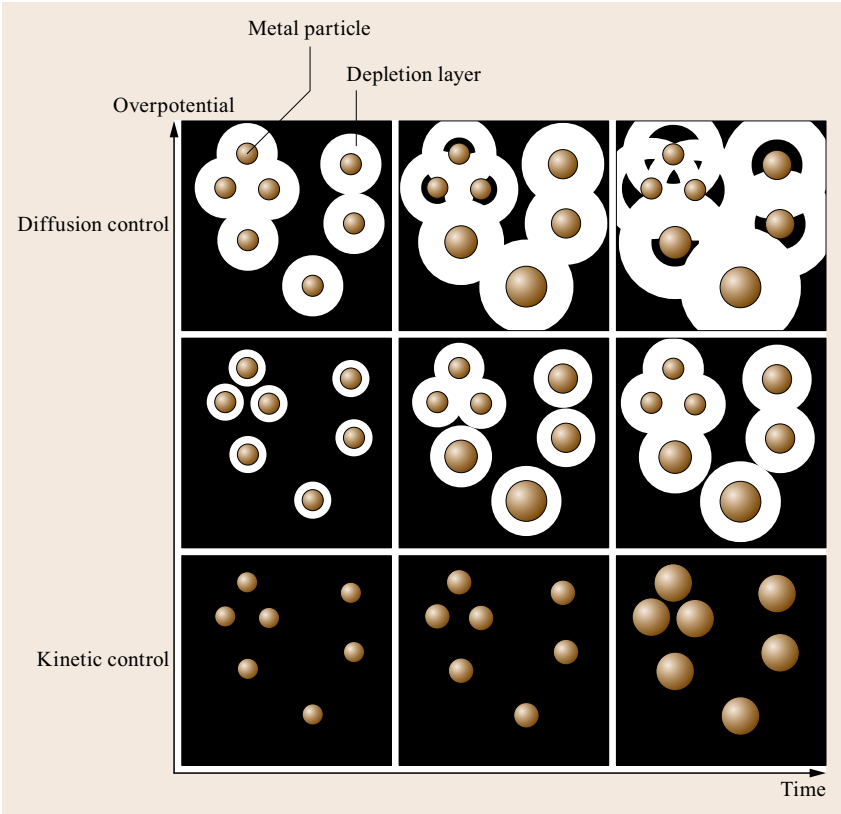


Fig. 26.20 Effect of deposition overpotential on extension of depletion layer from the surface of growing metal particles, and the effect on particle size dispersion (after [26.210])

the graphite crystal. The surface energy of the basal-plane differs from that of the edge-plan so that electrodeposition may occurs preferentially on the edge plane rather than the basal plane. As such, HOPG can be employed as a template for the deposition of nanowires arrays.

Electrodeposition of Nanoparticles on HOPG

Nanoparticles of various metals and metal oxides have been electrodeposited onto HOPG electrodes. An important issue related to the electrodeposition of nanoparticles on HOPG is the control of particle size distribution. The size distribution can be affected by the initial nucleation process. If progressive nucleation is involved, the individual particles are born and grown at different times, resulting in large size heterogeneity. In contrast, if the deposition involves instantaneous nucleation, the individual particles are initiated at the same time, and size homogeneity is expected. Nevertheless, instantaneous nucleation is not a sufficient condition for preparing dimensionally uniform nanoparticles using a constant deposition potential [26.211, 212]. According to *Fransaer* and *Penner* [26.213, 214], size heterogeneity can be rationalized by the interparticle diffusional coupling (IDC) as illustrated in Fig. 26.20 [26.210]. This figure shows that the metal ions near each of the growing particles are consumed as the deposition proceeds, resulting in concentration depletion layers. The rate of the concentration depletion increases with increasing applied overpotential and deposition time, and IDC occurs when the depletion layers surrounding neighboring metal particles overlap, causing a decrease in the growth rates of these particles relative to that for metal particles growing in isolated areas on the surface. Consequently, particles of diverse sizes are formed. Therefore, IDC should be avoided in order to improve the size uniformity of the deposited particles. Procedures based on multipulse deposition have been developed to implement this goal [26.215, 216]. A typical pulse program is shown in Fig. 26.21 [26.216]. First, a voltage pulse with sufficiently high overpotential is applied to generate the desired number of nuclei on the HOPG surface. Then, a pulse with a lower overpotential, at which no more nuclei would form, is applied to grow the metal particles obtained in the first pulse to the desired final diameter. The low growth overpotential slows down the particle growth rate as well as the concentration depletion rate, and effectively hinders the occurrence of IDC, leading to improved size uniformity.

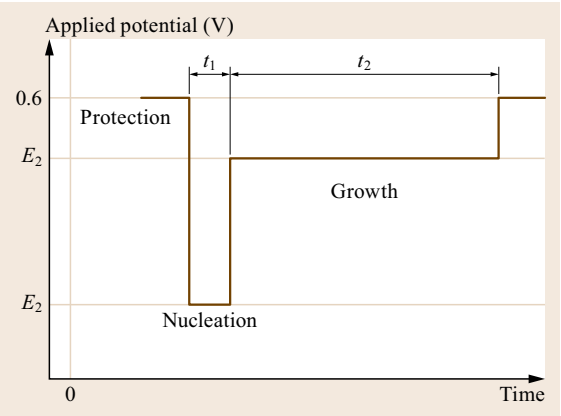


Fig. 26.21 Schematic representation of the double potential step profile employed (after [26.215])

Electrodeposition of Nanowires on HOPG

Penner [26.217] has shown that nanowires can be obtained on HOPG electrodes through the coalescence of nanoparticles that are selectively electrodeposited and grown at the step edges present on the HOPG surface, a process they termed electrochemical step-edge decoration (ESED). ESED is, however, overpotential dependent. At low deposition overpotential, nucleation occurs almost exclusively at the step edges on the HOPG, but nucleation density may be too low to yield satisfactory nanowires in a reasonable time period. On the other hand, nucleation take places also at the terraces with increasing overpotential, making it difficult to fabricate nanowires without co-deposition of nanoparticles on the HOPG surface. To enhance the preferential deposition of nanowires on step edges, constant-potential electrodeposition can be replaced by the triple voltage pulse procedure. First, an anodizing potential is applied to oxidize the step edges on HOPG for about 5 s at -0.8 V (versus SCE). Anodization produces carbonyls, ethers, hydroxyls, and other oxygen-containing functionalities preferentially at steps, making them more active subject to nucleation. Immediately after the oxidizing pulse, a short (5–100 ms) large overpotential ($\eta \approx -1.0$ V) pulse is applied to generate high nucleation density along step edges. Finally, a small amplitude ($\eta < 100$ mV) growth pulse is applied subsequently to grow the nanoparticles until they coalesce into nanowires. With this procedure, pure metal nanowires of palladium, nickel, copper, gold, silver, and Pd–Ni have been successfully prepared [26.218–223]. It was found that the nanowire growth is characterized by a pseudo-steady-state deposition current i_{dep} and that the nanowire radius $r(t)$ is proportional to the square root of the deposition duration t_{dep}. The minimum nanowire diameter is inversely proportional to the density of nuclei present on the step edges. The highest nuclei density seen in purely electrochemical growth of gold nanowires is in the 10–13 $1/\mu$m range, corresponding to the 80–100 nm minimum nanowire diameter obtained. Apparently, higher nuclei density is required in order to further reduce the minimum nanowire diameter. By replacing the electrochemical nucleation step with vapor deposition of one-dimensional nanoparticle arrays on HOPG at 670–690 K, the number density of 2–15 nm diameter gold particles at step edges was greatly increased to 30–40 $1/\mu$m. The vapor-deposited nanoparticles were then used as

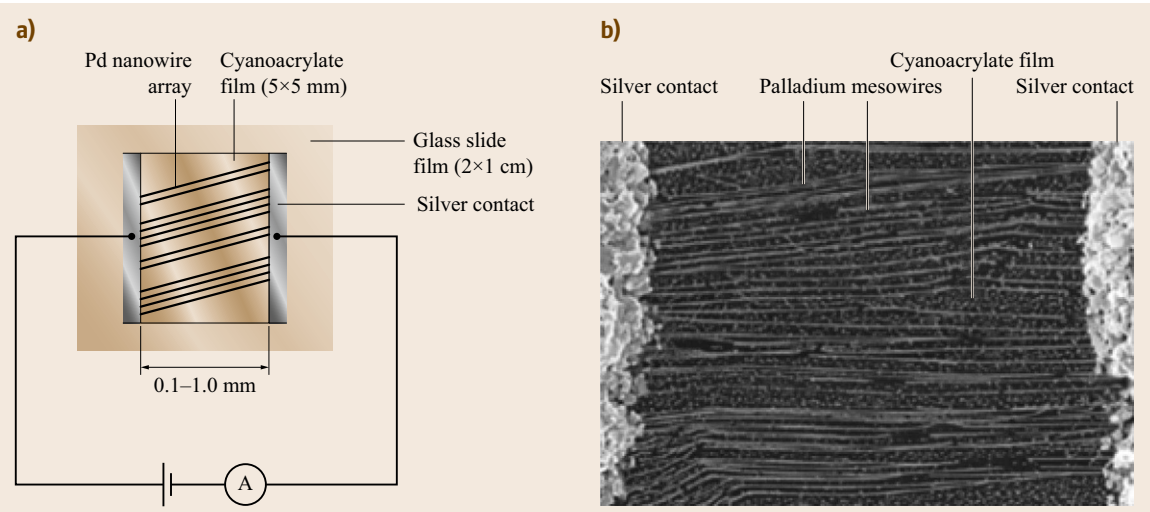


Fig. 26.22 **(a)** Schematic diagram of a PMA-based hydrogen sensor or switch. **(b)** SEM image (400 μm(h) by 600 μm(w)) of the active area of the PMA-based hydrogen sensor (after [26.218])

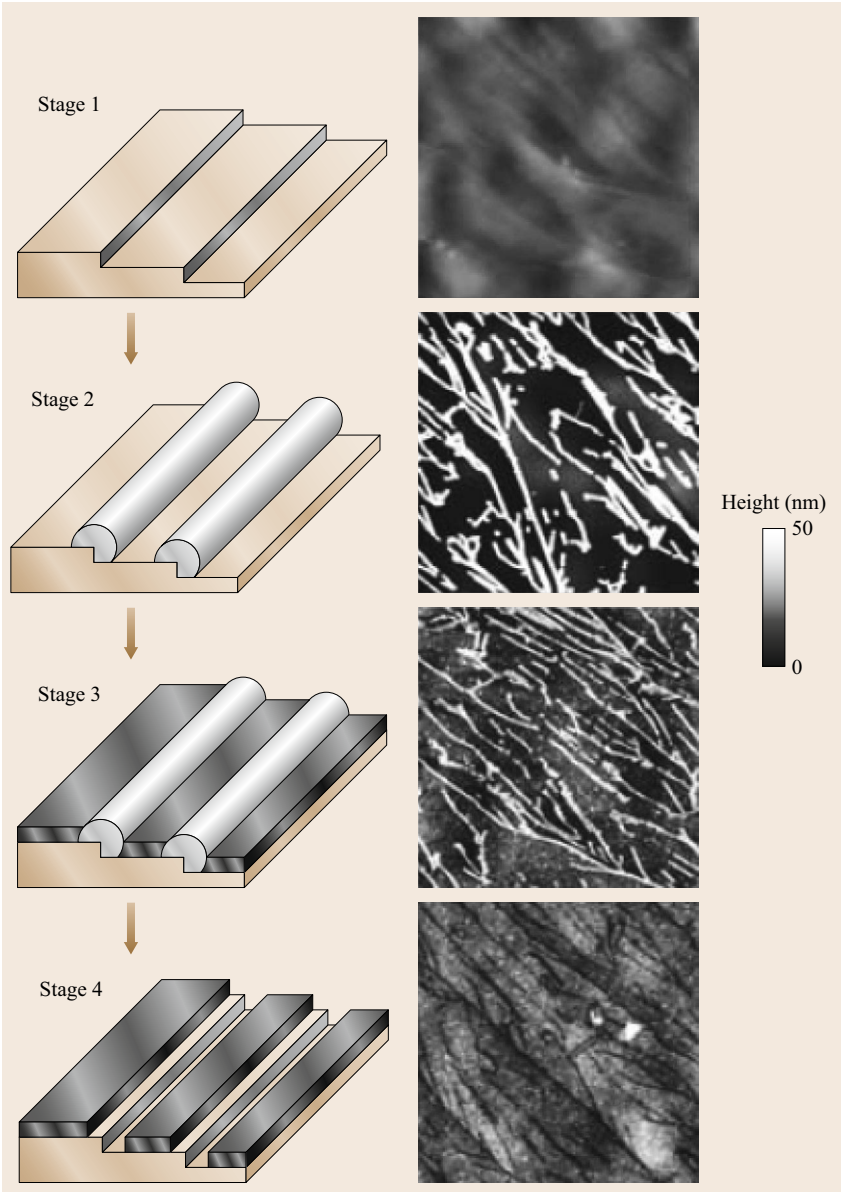


Fig. 26.23 Schematic diagram and corresponding AFM images ($5 \times 5\,\mu m^2$ each) of the four stages involved in nanotrench fabrication (after [26.224])

the seeds for further electrochemical growth of gold nanowires [26.225].

ESED has also been applied to fabricate multicomponent compounds, such as MoO_2 [26.226, 227]. The fabrication of MoO_2 is based on the reduction of MoO_4^{2-} through a single-step deposition at a proper potential (-0.6 V versus SCE) where MoO_2 particles can be selectively deposited at step edges. Metallic Mo nanowires can then be obtained by reducing the MoO_2 nanowires with hydrogen gas at 500 °C [26.226, 227]. Furthermore, MnO_2 nanowires can be converted to MoS_2 via exposure to H_2S either at 500–700 °C, producing MoS_2 nanowires, or above 800 °C, producing MoS_2 ribbons [26.228, 229]. Similar to MoO_2, MnO_2 nanowires have been prepared using ESED by the reduction of MnO_4^- employing a small overpotential (< 100 mV) or a small current density ($50\,mA/cm^2$) [26.230]. Photoconductive CdS nanowires were fabricated by first electrochemically reducing $Cd(EDTA)^{2-}$ to Cd nanowires on step edges and then converting the Cd wires into CdS by exposure to H_2S at 280–300 °C. Interestingly, the resulting CdS

nanowires had a hemicylindrical shell morphology due to the Kirkendall effect [26.231]. Nanowires composed of polycrystalline thermoelectric Bi_2Te_3 have been prepared using the ESED method from an aqueous solution containing Bi^{3+} and $HTeO_2^+$ [26.232, 233]. First, the HOPG surface is anodized at $+0.8$ V (versus SCE) to activate the step edges. Secondly, Bi_2Te_3 nuclei are produced at step edges by applying a potential of -0.6 V for 5 ms, and finally, the growth of Bi_2Te_3 nanowires is performed by cycling the potential between -0.05 V and -0.30 V at 20 mV/s. Bi-rich Bi_2Te_3 is electrodeposited during the negative going potential scan, and the extra Bi is stripped during the positive potential scan. The diameter of the Bi_2Te_3 nanowires can be varied from 100 to 300 nm by controlling the number of potential cycles and could be further reduced to 30 nm by electro-oxidizing the Bi_2Te_3 nanowires at $+0.37$ V under conditions of kinetic control.

Sensors Using Nanowire Arrays Electrodeposited on HOPG

Penner et al. have constructed sensing devices using metal nanowire arrays that were deposited on the step edges of an HOPG surface. The procedure is shown in Fig. 26.22a [26.218]. In the preparation, after the metal nanowire arrays were deposited (Step 1), they were transferred from the HOPG surface to another insulating surface (glass slide) in Step 2 by first casting a layer of adhesive such as cyanoacrylate on the nanowire-array-coated HOPG. After the adhesive was cured, the HOPG was removed, leaving the nanowire arrays embedded in the cured cyanoacrylate adhesive. Finally, metal contacts were applied to the ends of these nanowires arrays o form a sensor with the configuration shown in Fig. 26.22b [26.218]. Hydrogen [26.218, 219] and amine vapor [26.222] sensors have been made from palladium and Ag nanowire arrays, respectively, with this configuration.

Compton et al. demonstrated the formation of nanotrenches on an HOPG surface using the four steps shown in Fig. 26.23 [26.224]. First, edge-plane steps are produced on HOPG. Second, nanowires of MoO_2 are electrodeposited along the step edges. Thirdly, the electrode surface is covered with an insulating polynitrophenyl polymer by the electrodeposition of nitrophenyl diazonium salts. Finally, the MoO_2 nanowires are dissolved with dilute HCL, leaving nanotrenches of edge-plane graphite surrounded by polymer film. The nanotrench array can be further used as a template for developing metal nanoband electrodes [26.234]. In this procedure, nanotrenches are first formed using the above three-step process except that the insulating polynitrophenyl is replaced with divinylbenzene (DVB). After the formation of nanotrenches, a layer of the desired metal is then evaporated to cover the nanotrenches and the insulating polymer. Finally, the metal layer is cleaved from the HOPG. Because DVB binds much more strongly to the metal rather than does HOPG, it remains on the metal surface after cleavage. As a result, the metal nanoband electrode is obtained.

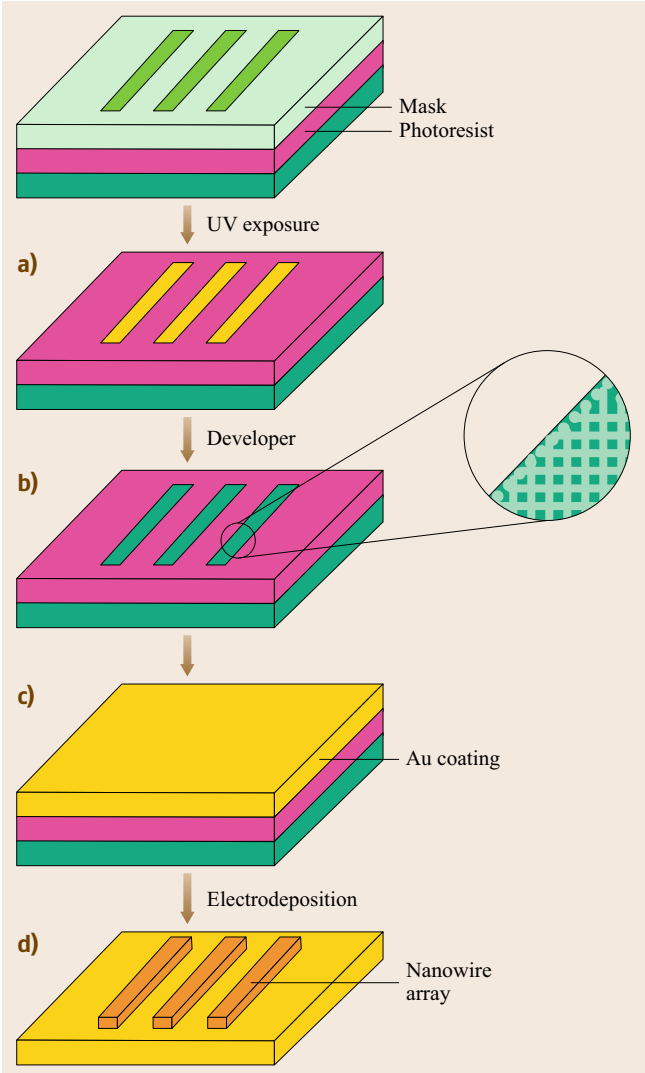


Fig. 26.24a–d Fabrication procedure of metal nanowire patterns. **(a)** Photoresist is coated on the surface of AAM, the composites are covered by mask, and exposed to UV; **(b)** the pores of AAM are then selectively opened by dissolving the exposed areas in a developer; **(c)** patterned nanowire arrays are then produced by electrochemical deposition; **(d)** nanowire arrays are released from the template with a NaOH solution (after [26.235])

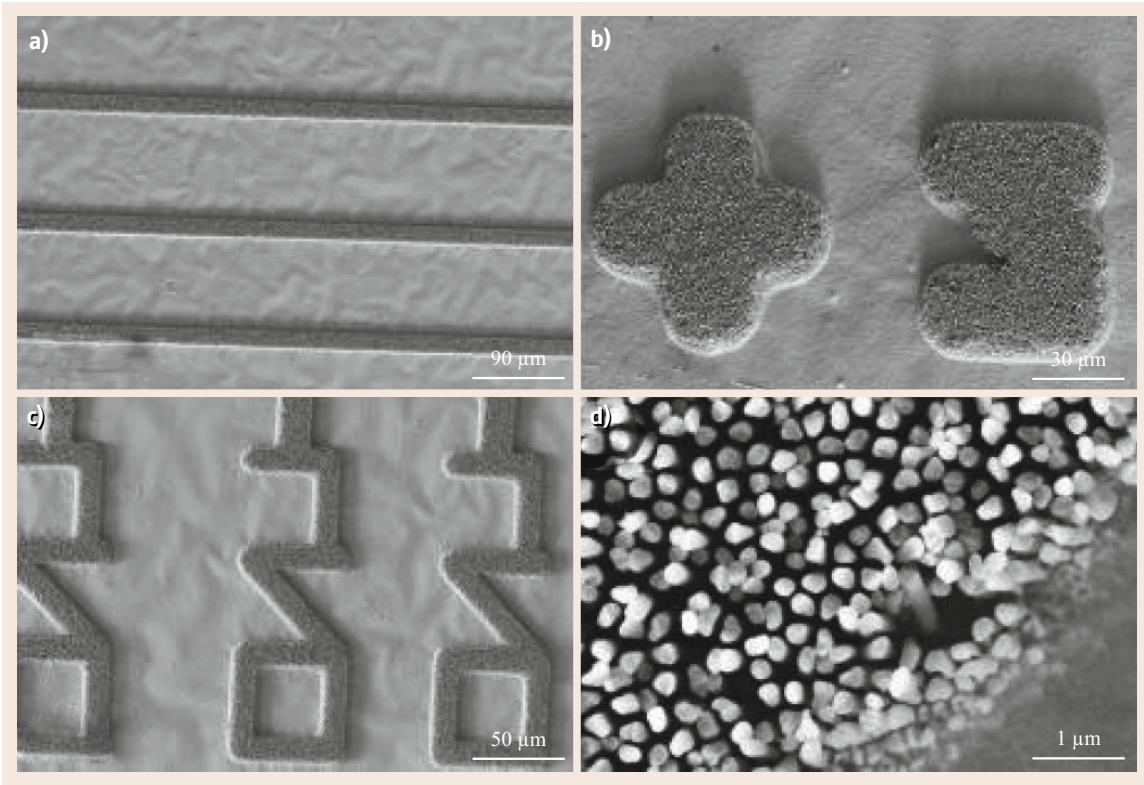


Fig. 26.25a–d Field emission scanning electron microscopy (FESEM) images of Au nanowire pattern with line width of 15 µm **(a–c)** nanowire patterns with different features can be fabricated; **(d)** higher magnification image shows the diameter of the nanowires is about 200 nm (length about 3 µm) (after [26.235])

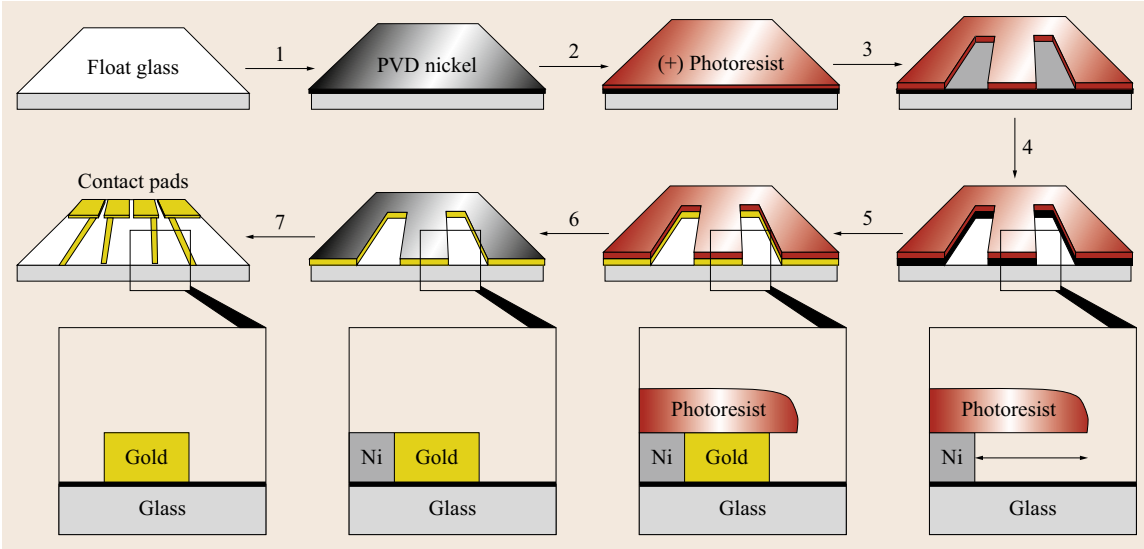


Fig. 26.26 Seven-step process flow for metal-nanowire fabrication using LPNE (after [26.236])

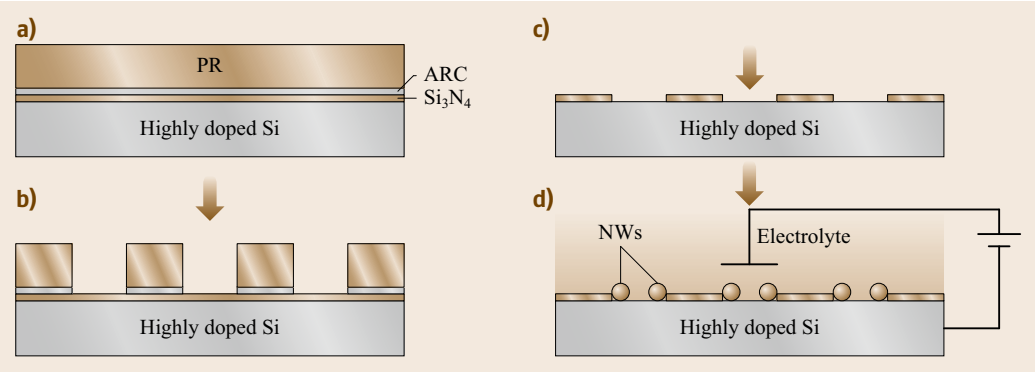


Fig. 26.27a–d Schematic illustration of lithographically guided electrodeposition of metallic nanowire (NW) or nanoring arrays; **(a)** resist stack on a substrate obtained by spin-coating; **(b)** laser interference lithographic exposure and development; **(c)** pattern transfer into the underlying Si_3N_4 and highly doped Si substrate by CHF_3 RIE, removal of polymer with O_2 plasma, and subsequent treatment of the resulting sample with HF; and **(d)** selective electrodeposition of metal along the step edges (ARC: antireflection coating. PR: photoresist) (after [26.237])

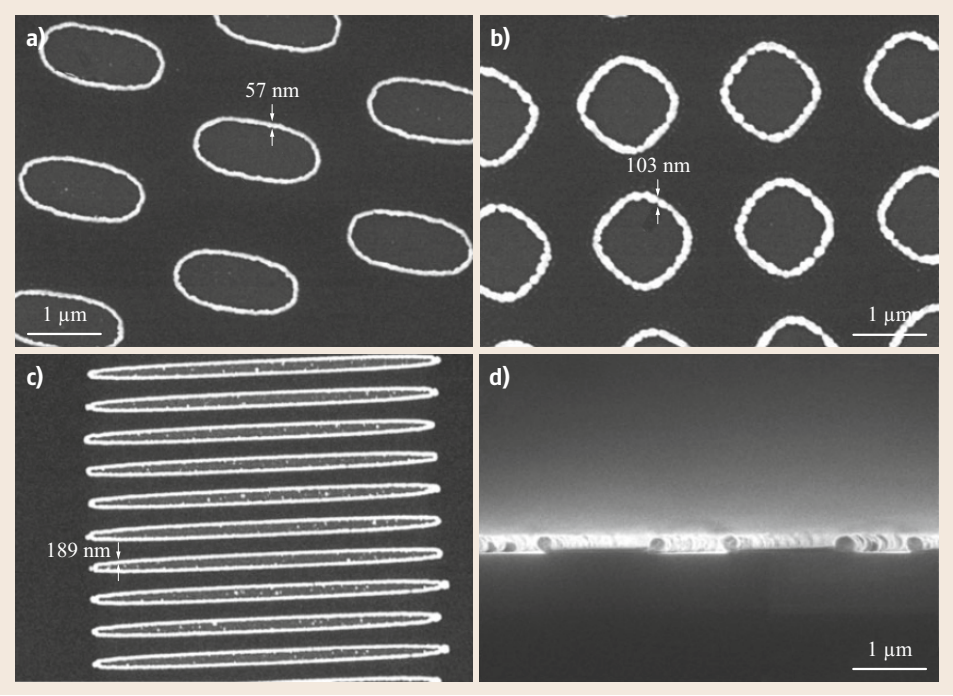


Fig. 26.28a–d Representative SEM images of arrays of gold rings with different geometries; **(a)** hexagonally arranged *elliptical rings* array with a 57 nm wire thickness, **(b)** *circular ring* array with 103 nm wire thickness, **(c)** top and **(d)** cross-sectional views of elliptical ring array with an aspect ratio of 11 : 1 (long-axis–short-axis) and a wire thickness of 189 nm (after [26.237])

26.1.4 Lithographically Patterned Electrodeposition

A large amount of research has been devoted to patterning nanomaterials for the fabrication of miniaturized devices, such as integrated circuits, sensors, data storage devices, biomedical devices, and displays [26.238]. In this regard, lithography techniques combined with electrodeposition methods have proven to be effective for preparing patterned nanomaterials.

Photolithographic Methods

Among the various lithographic techniques, photolithography has been widely used due to its simplicity and high throughput. As illustrated in Fig. 26.24 [26.235], the substrate, porous anodic alumina membranes (AAM), is initially coated with a layer of photoresist (PR). Then, this composite is covered with a photolithographic mask and exposed to ultraviolet (UV). Exposure to UV photons alters the solubility of the PR and transfers the patterns of the mask to

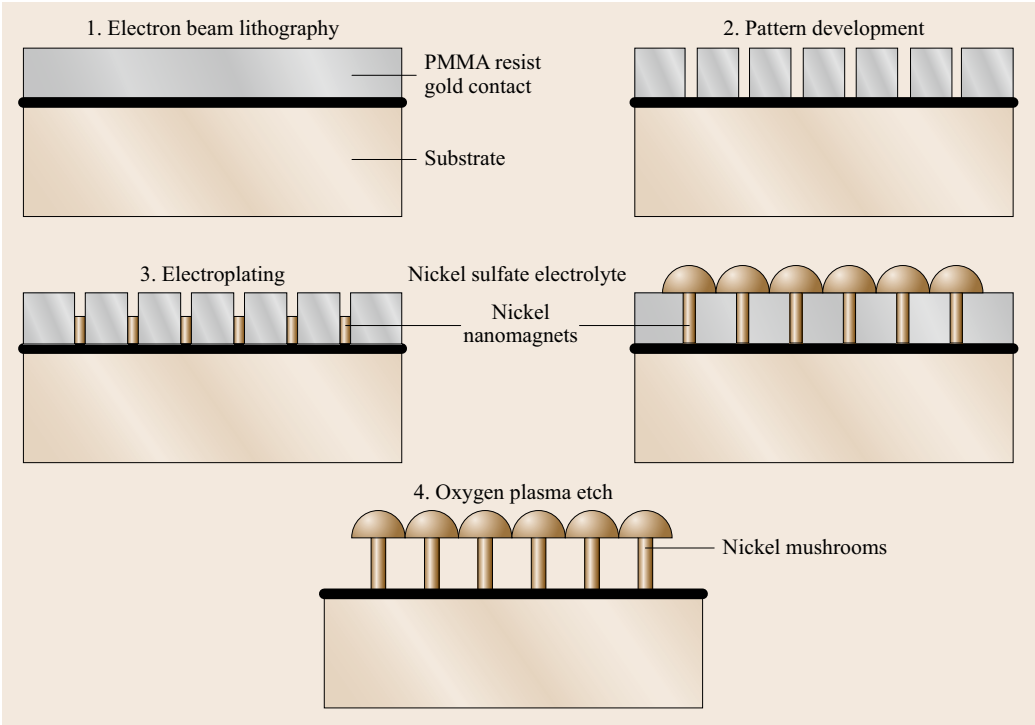


Fig. 26.29 Schematic of the fabrication procedure used to generate ultrasmall magnets (after [26.239])

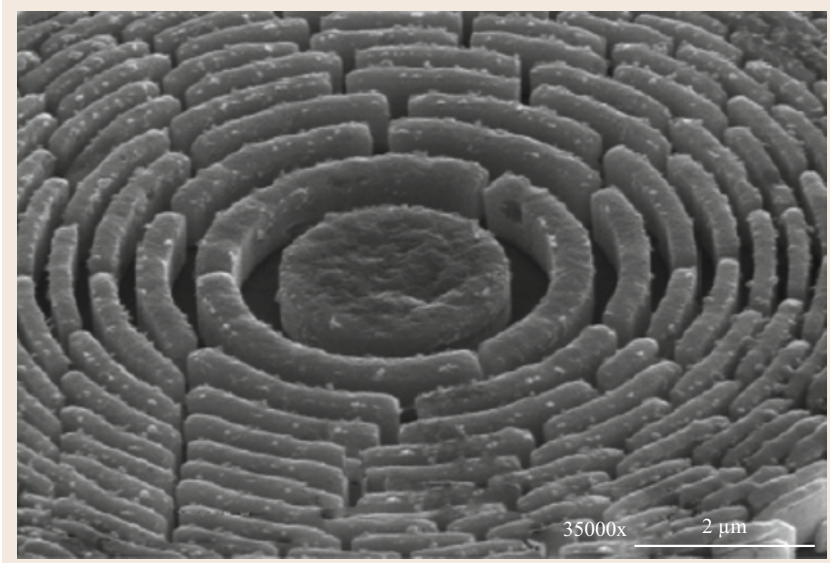


Fig. 26.30 Very thick zone plate ($> 1\,\mu m$) with an outermost zone width $< 100\,nm$ produced by EBL and electrodeposition (after [26.240])

the PR. The exposed PR is then dissolved in a developer solution, leaving the patterned structure on the substrate. Patterned nanostructures are then fabricated by electrodeposition using the patterned substrate as a template. *Li* et al. [26.235] demonstrated the electrochemical preparation of patterned metal nanowire arrays as shown in Fig. 26.25 [26.235], using a photolithographically patterned AAO template. While photolithography is a feasible technique for patterning, its resolution is constrained by the diffraction limit d which is related to the wavelength λ of the UV radiation $d = \lambda/2$. Typically, d is limited in the 100 nm range. This problem can be circumvented by the lithographically patterned nanowire electrodeposition (LPNE) method

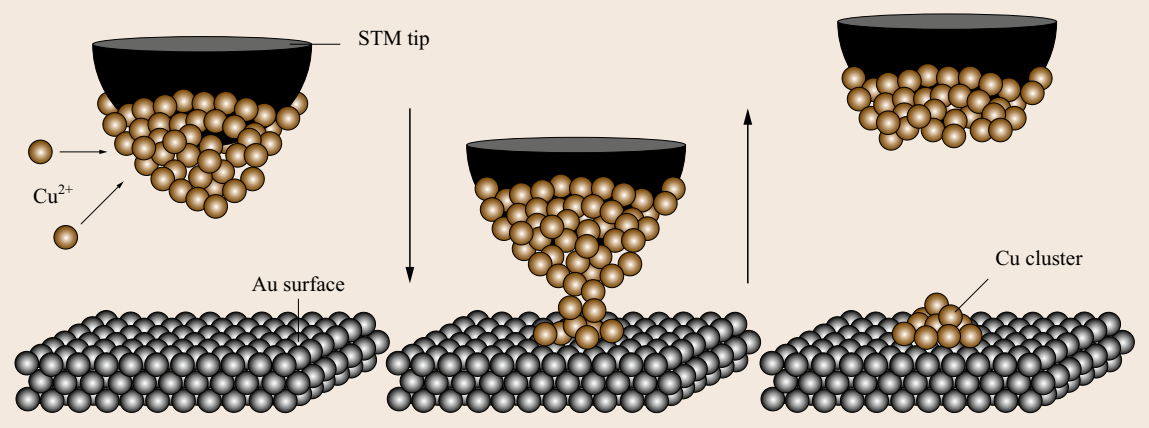


Fig. 26.31 Schematic diagram of the suggested mechanism of material transfer from a Cu-covered STM tip to the Au substrate, caused by an appropriate tip approach (after [26.241])

developed by *Penner* et al. [26.242]. As shown in Fig. 26.26 [26.242], this method involves seven steps. In Step 1, a 5–200 nm thick sacrificial metal film of Ni or Ag is deposited by physical vapor deposition (PVD) on a flat glass. In Step 2, a uniform layer of the positive PR layer is coated onto the metal film. In Step 3, the PR layer is patterned via exposure to 365 nm light through a contact mask. The pattern transferred to the PR layer is developed, rinsed in pure water, and dried in a stream of N_2. In Step 4, the exposed metal layer is removed by electrochemical anodization or an etching solution (0.8 M nitric acid for Ni, and 18% NH_4OH + 4% H_2O_2 for Ag). As the metal layer is removed, an undercut is produced at the perimeter of the exposed region, and a lithographically patterned, recessed metal edge is formed on the glass surface. In Step 5, nanowires are electrodeposited into this horizontal trench potentiostatically. In Step 6, the PR is removed by rinsing with acetone, methanol, and pure water in sequence. Finally, the sacrificial metal is removed as in Step 4. With this method, various nanopatterned structures, such as parallel nanowires, coiled nanowires, and nanowires, loops as long as several mm, have been fabricated with wire dimensions as low as 11 nm (w) ×5 nm (h) for Bi [26.242], Au [26.242–246], Pd [26.236, 242, 243, 245], Pt [26.242, 243, 245], Ag [26.247], and PbTe [26.248]. *Menke* et al. extended the LPNE method to the fabrication of Au/PbSe and Au/$CuInSe_2$ (CIS) core/shell nanowires by the electrodeposition of either PbSe or CIS onto Au nanowires fabricated by LPNE [26.249].

Interference Lithographic Methods

While conventional photolithography requires a mask for patterning, interference lithography (IL), also called holographic lithography, provides a maskless, facile, large-area nanolithography technique for the generation of two-dimensional periodic structures with sub-100 nm features [26.250]. Typically, a coherent laser source is split into two or more beams, which are incident on a PR-coated wafer at angles of $+\theta$ and $-\theta$, resulting in an interference pattern with a spatial period of $P = (\lambda/2)\sin\theta$. By selecting the laser source and adjusting the parameters, nanostructures with sizes lower than 100 nm can be fabricated. In addition to parallel lines, more complicated circular or elliptical patterns in the PR can be generated by multiple consecutive exposures and sample rotation between exposures. *Nielsch* et al. [26.237] demonstrated the electrochemical fabrication of gold nanowire and nanoring arrays using templates prepared by IL (Fig. 26.27) [26.237]. First, a negative-tone PR was spin-coated and then baked on highly *n*-doped Si wafers with a Si_3N_4 layer (ca. 35 nm). The polymer structures generated by IL served as etching masks for anisotropic reactive-ion etching (RIE) through the Si_3N_4 layer and over-etching into the Si substrate. The remaining polymer was subsequently removed by O_2 plasma. Constant-current electrodeposition of gold was then performed. When the deposition of metals occurred only along the edges of the RIE undercuts, arrays of nanowires and nanorings with various aspect ratios were obtained on samples with linear and circular or elliptical hole patterns (Fig. 26.28) [26.237]. The width of the nanowires could be controlled by the charges used in the electrodeposition. Typically, feature sizes ranging from 50 to 300 nm can be obtained.

Electro-Beam Lithography Methods

EBL [26.251, 252] uses a highly focused electron beam for direct-write patterning on electron-beam-sensitive resists. EBL easily allows one to achieve designed nanostructures with precise position and sizing down to

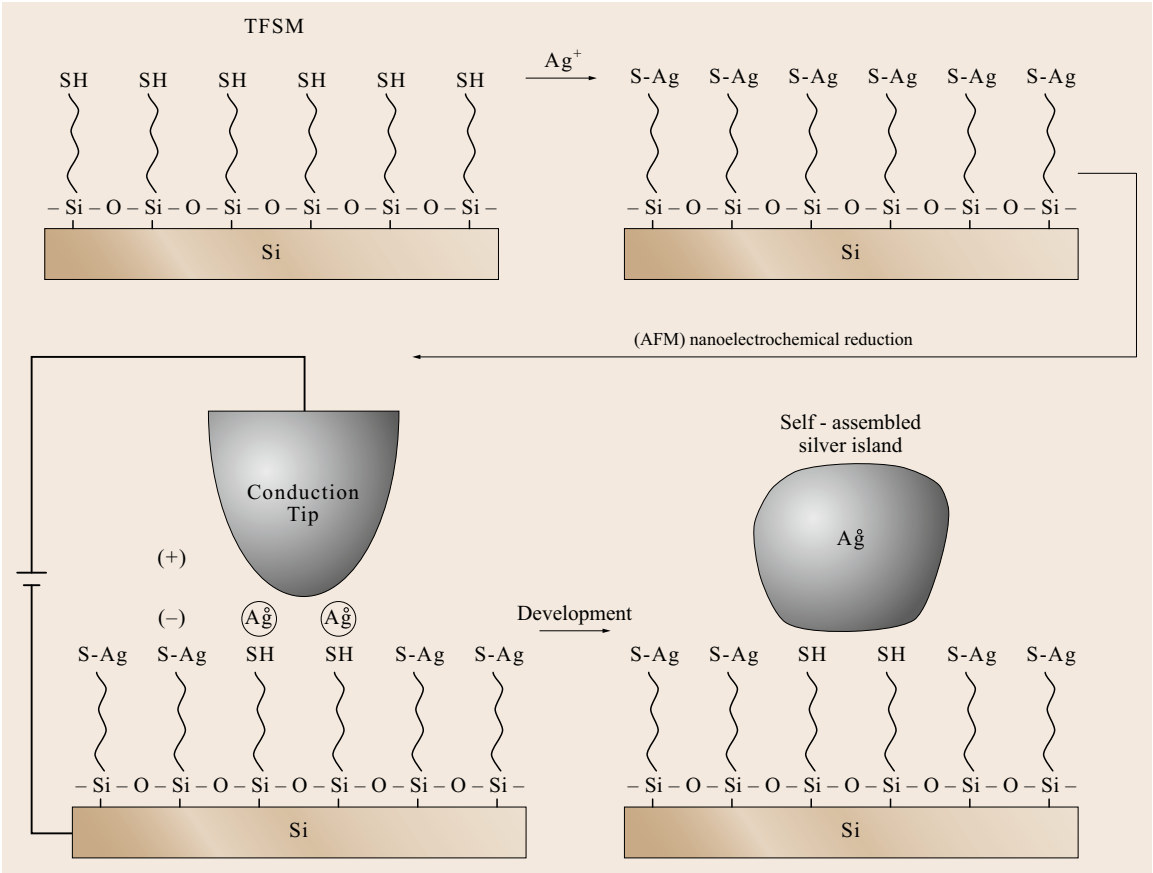


Fig. 26.32 Scheme of the site-defined self-assembly of silver metal on a thiol-top-functionalized silane monolayer (TFSM) preassembled on silicon. The silver-thiolate (–S–Ag) template surface obtained by the chemisorption of Ag^+ ions on the TFSM surface (*top left*) is nondestructively patterned using a nanoelectrochemical process involving the application of a DC voltage to a conducting AFM tip, the slightly conducting silicon substrate being biased negatively (reductive bias) with respect to the tip. Further development of the macro and, nanopatterns of reduced silver particles imprinted on the Ag^+–TFSM template is shown to result in self-assembled silver islands selectively grown at tip-defined sites (after [26.253])

the submicron scale. The general procedure for the electrodeposition of nanostructures using the EBL method is shown in Fig. 26.29 [26.239]. First, a conducting Au layer is vapor-deposited onto the substrate. A layer of polymethylmethacrylate (PMMA) resist is then spin-coated on the Au. The PMMA is then irradiated with the electron beam. The PMMA in the exposed area is then developed in a developer solution, such as a 3 : 7 cellosolve–methanol mixture [26.239] or 1 : 3 methyl isobutyl keton isopropanol (MIBK:IPA) [26.254]. The desired material is then electrodeposited into the cavities formed in the PMMA. After electrodeposition, PMMA is removed, leaving the desired nanostructures. With this method, *Xu* et al. [26.239] fabricated nanomagnet arrays of 20 nm Ni pillars with a 100 nm spacing. *Duvail* et al. [26.255] used pulse-potential deposition to produce multilayered Ni80Fe20/Cu nanopillars. Au and Cu nanoscale mechanical testing specimens were fabricated by *Bured* and *Greer* [26.256]. *Lo* et al. [26.257] fabricated Au nanostructures with a small line width (40 nm) and a high aspect ratio (> 12). High-speed fabrication of Au nanostructures with a 10 nm spatial resolution (Fig. 26.30) was reported by *Biring* et al. [26.240]. While PMMA is the mostly used resist for the EBL process, recently, *Ugo* et al. [26.258] demonstrated the use of polycarbonate as a resist for EBL and prepared ordered arrays of electrochemical nanoelectrodes.

Electrochemical Lithographic Methods

Electrochemical lithography (EL) based on scanning probe microscopy has been employed for the nanopat-

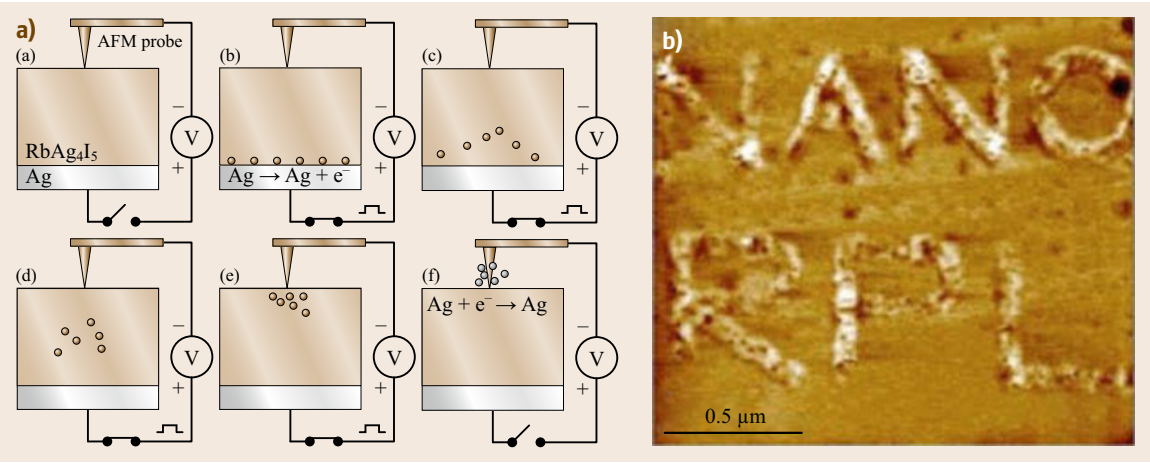


Fig. 26.33 **(a)** Simplified schematic diagram of the experimental setup for nanopatterning of Ag on RbAg4I5, showing the time evolution of Ag atoms and ions under the voltage bias. Oxidation and reduction processes are depicted in steps (b) and (f), respectively. The migration of silver ions in the ion conductor under the electric field is shown in steps between (b) and (e) (drawing not to scale); **(b)** AFM contact-mode deflection images of electrochemically induced Ag nanofeatures on RbAg4I5 Positive features generated by 200 mV pulses (dot spacing = 17 nm, pulse duration = 0.25 ms for upper letters, dot spacing = 22 nm, pulse duration = 0.30 ms for lower letters) (after [26.253])

terning fabrication [26.259]. Two widely used scanning techniques are STM and atomic force microscopy (AFM). While EL patterning can be achieved by either electrochemical etching or electrodeposition, only some representative examples of the electrodeposition methods will be described here. *Kolb* et al. demonstrate the nanofabrication of copper clusters on gold electrodes by an STM from solution containing H_2SO_4 + 1 mM $CuSO_4$ [26.241]. As illustrated in Fig. 26.31 [26.241]. First, Cu is deposited on the tip at a potential negative than the Cu/Cu^{2+} reference potential. Then an external voltage pulse forces the Cu-covered tip to approach the Au surface momentarily for a transfer of a small Cu clusters on the Au surface, while Cu will be reloaded from the solution on the tip when the tip is retracted. By using a microprocessor, which controls the moving of the tip from desired cluster position to the next, the electrodeposition of patterned nanostructures is achieved. As shown in Fig. 26.32 [26.253], *Maoz* et al. [26.253] showed the planned construction of hybride metal-organic surface nanostructure using an AFM. The fabrication starts with a thiol-top-functionalized silane monolayer (TFSM) with silver ions chemisorbed on its outer surface (Ag^+-TFSM). By moving the AFM tip, Ag nanoparticles are produced at selected surface sites by the tip-induced electrochemical reduction of the surface-bounded Ag^+ ions, and patterned nanostructure is obtained. The use of AFM for electrochemical nanopatterning of Ag on solid-state ionic conductor was reported by *Lee* [26.260]. The process is shown in Fig. 26.33a [26.260]; the electrodeposition of Ag was performed by applying potential pulses between the AFM probe and an Ag counter electrode attached on the back side of the $RbAg_4I_5$ film. Prior to patterning, the sample topology was scanned at a zero-current potential in order to avoid unintentional bias-induced topological change. After the topological image was stabilized, the tip was moved to the position where Ag deposition was desired. Silver electrodeposition was performed using negative tip-to-sample bias pulses of 50 mV–2 V lasting from 0.5 to 50 ms. A typical AFM image is shown in Fig. 26.33b [26.260].

26.2 Electrodeposited Nanomaterials for Energy Storage/Conversion Devices

Nanomaterials, such as nanoparticles, nanorods, nanowires, nanotubes, nanosheets, nanoflakes, and core–shell nanowires, can be created through electrochemical methods. These structures have received considerable attention because of their potential applications in the fields as diverse as optics [26.262, 263], magnetics [26.264–266], thermoelectrics [26.267, 268], catalysis [26.269, 270], sensors [26.271–273], semiconductor

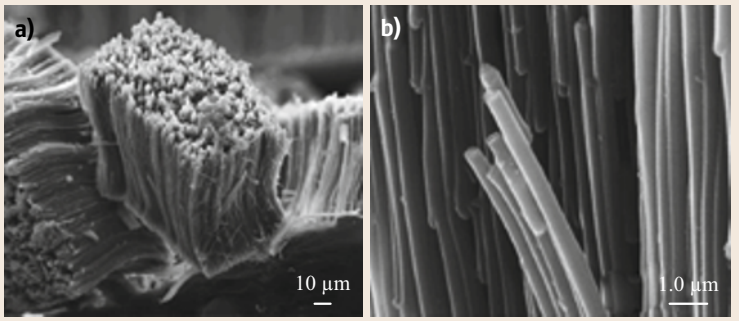


Fig. 26.34a,b SEM micrographs of electrodeposited manganese oxide nanowire arrays which the MnO_2 nanowires had a specific Li^+ capacity of 300 mAh/g after removing the AAO template. **(a)** Low magnification and **(b)** high magnification (after [26.261])

[26.159, 274], substrates for SERS [26.275], and surface modification layers [26.261, 276]. Covering all the applications of the electrodeposited nanostructures is beyond the scope of this chapter. Readers who are interested in the particular area can refer to the aforementioned reference paper for further information. In this section, we would focus on the nanosized electrodeposits used in energy-storage applications, including LIB and supercapacitors (SCs). The reasons why the nanostructures are desired, the strategies to fabricate the nanostructures, and the corresponding performance improvements (as compared to those without the nanostructures) are described in detail. Hopefully, based on these fundamental reviews, new applications of the electrodeposited nanostructures can be inspired.

26.2.1 Lithium-Ion Battery Applications

LIBs are the very important energy-storage systems which have been widely used in nowadays portable electronic devices and electric vehicles. To meet with the rapid increasing demand on energy–power density and safety of LIBs for diverse applications, the exploitation of new electrodes (including the materials and the architectures) of improved performances has become the key issue.

Electrodepostion is capable of preparing various cathodes and anodes for use in LIBs. This electrochemical process is simpler than the conventionally used electrode preparation method (involving powder synthesis, slurry preparation, and electrode pasting). Moreover, since the electroactive materials are directly electrodeposited on the current collectors, there is no need for any binder or conductive additives. Another significant advantage of electrodeposition is that the material characteristics of the deposits can be readily tuned by adjusting the plating parameters, such as potential, current, precursor concentration, bath recipe, plating temperature, etc.

Nanostructured cathodes and anodes prepared by electrodeposition are the main subjects of this section. The high surface area of the nanostructures provides the high electrochemical activity of the electrodes; the high electrolyte accessibility promotes the charge transfer at the electrode–electrolyte interface. Moreover, the small Li^+ diffusion lengths in the nanomaterials improve the utilization and rate capability of the electrodes. Accordingly, their energy-storage performances are considerably superior to those of the electrodes without nanoarchitectures.

The Cathodes

Various electrodeposited cathodes, anodes, and electrode current collectors in LIBs are reviewed as follows.

Manganese Oxide. Manganese oxide is a suitable candidate material for the LIB cathode. Its charge–discharge performance is highly dependent on the grain size, texture, surface area, and morphology of

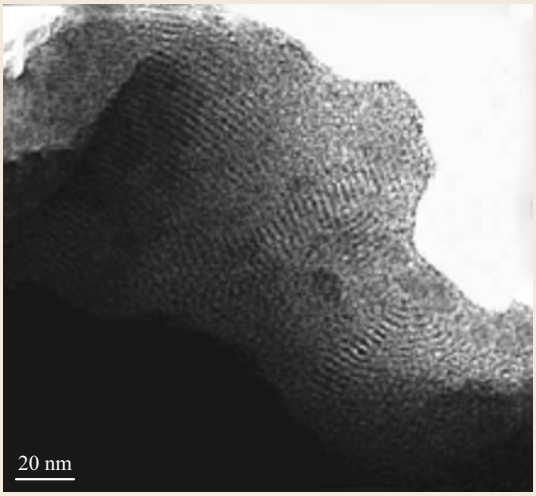


Fig. 26.35 TEM image of the mesoporous vanadium oxide electrodeposited using CTAB as a templating agent as a possible cathode material for Li-ion batteries (after [26.277])

the electrode. The ability to engineer an ordered and high-porosity structure of the oxide is of great importance. Arrays of manganese oxide nanowires have been electrodeposited (from aqueous solution consisting of $MnSO_4$) into AAO membranes [26.277]. After removing the template, the typical SEM micrographs are shown in Fig. 26.34. Without the use of binder and conductive additives, the nanostructured cathode was capable of multiple charge–discharge cycles with a specific capacity of approximately 300 mAh/g. Moreover, the electrode can be discharged at a current density up to 0.1 mA/cm^2 without any significant polarization.

Vanadium Oxide. Mesoporous vanadium oxide (V_2O_5), another potential cathode for LIBs, was electrodeposited from an aqueous solution of vanadyl sulfate using CTAB as a templating agent [26.278]. Figure 26.35 indicates the presence of mesoporosity with a well-ordered lamellar structure in the synthesized film. The mesoporous films prepared with CTAB had a much higher capacity and lithium-ion diffusion rate than the nonporous electrode prepared without CTAB.

Lithium vanadate (LiV_3O_8) nanostructures with flower-like nanosheets were successfully deposited by solvo-hydrothermal electrochemical route [26.279]. The typical structure observed is shown in Fig. 26.36. The organic solvents added were found to play a significant role in controlling the morphology of nanostructures. Especially, alcohols with long chain have promoted the oriented growth of nanosheets as soft templates. Some promising electrochemical performances as the LIB cathode were demonstrated.

$LiFePO_4$/Polypyrrole Composites. $LiFePO_4$ has emerged as a highly promising cathode for large LIBs because it is of low cost, environmentally benign, and highly safety. Typically, $LiFePO_4$ powder is required to blend with organic binder and conductive additives before being pasted on the electrode substrate. However, use of these electrochemically inactive materials has the drawback of reducing the energy and power densities of the electrodes. Recently, *Goodenough* et al. have developed a new method to co-electrodeposit $LiFePO_4$ powder and PPY on stainless steel mesh [26.280–282]. During the electrochemical oxidation of the monomers (pyrrole), PPY polymerization occurred at the electrode–electrolyte interface and $LiFePO_4$ particles were incorporated into the polymer matrix (as shown in Fig. 26.37) [26.282]. The conducting polymer PPY can overcome the poor electrical conductivity of $LiFePO_4$ and actively participate in the electrode charge–discharge process. The replacement of the inactive binder and additives by PPY enhances the capacity and rate capability of the composite electrodes.

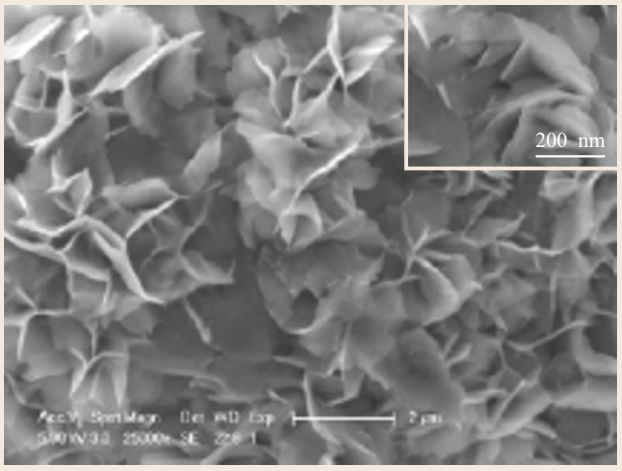


Fig. 26.36 Typical morphology of the carnation-like LiV_3O_8 prepared using a solvo-hydrothermal electrodeposition technique (after [26.278])

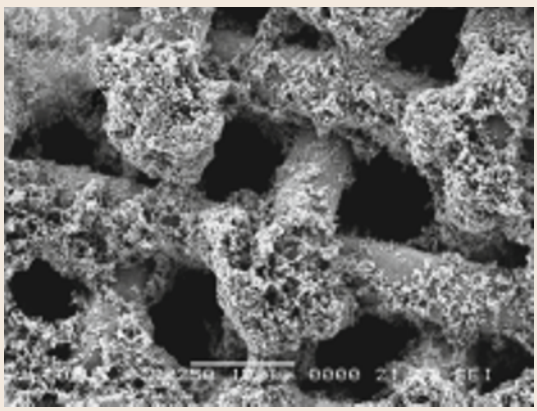


Fig. 26.37 SEM image of a co-deposited $LiFePO_4$/PPY composite on stainless steel mesh (after [26.281])

The Anodes

With the rapidly increasing application demands, high-performance LIBs are urgently needed. Generally, the high-energy LIBs depend intimately on the high capacity of electrode materials. For anode materials, the capacity of the traditionally used graphite is unlikely to increase much further due to its lower theoretical capacity of 372 mAh/g. Therefore, some metal anodes with high theoretic capacity, such as Si (4200 mAh/g), Sn (990 mAh/g), Sb (660 mAh/g), Al (2234 mAh/g) and their alloys have been studied. These metal electrodes can be prepared using electrodeposition, and their structures and morphologies can be tuned via controlling the deposition conditions. The electrodes with

nanostructured architectures have been found to possess promoted charge–discharge performance.

The Si-Based Materials. Si has a specific capacity as high as 4200 mAh/g, thus has attracted much attention as an LIB anode material. However, it exhibits drastic volume expansion–contraction during Li^+ insertion–extraction. Specifically, Si suffers a 310% volume increase after Li insertion (as the formation of $Li_{22}Si_5$). The large volume variation due to the lithiation–delithiation process leads to significant internal stresses within the Si particles, resulting in fracture of the Si electrode. Due to the loss of mechanical integrity, the electrode capacity is significantly reduced after the first few charge–discharge cycles. In order to deal with the large volume expansion of the Si anode, an effective way is to reduce the diameters of Si particles (or decrease the thickness of Si films) below the critical crack length, since the deformation mechanisms of nanoscale particles are less severe.

To obtain suitable thin-film Si electrodes with nanostructures, the preparation method of electroplating is convenient. Since the reduction potential of Si is too low to be conducted in aqueous electrolyte (beyond the hydrogen evolution potential), *Schmuck* et al. has attempted to electrodeposit Si in organic propylene carbonate (PC) or *N*-butyl-*N*-methylpyrrolidinium bis(trifluormethanesulfonyl)imide ionic liquid solution with $SiCl_4$ as a precursor [26.283]. The results showed that it is possible to deposit Si directly on a Cu current collector out of both the plating electrolytes, where the reduction of $SiCl_4$ occurred around 1.0 V versus Li/Li^+. Si particles with a size in the range of 100–500 nm can be clearly observed with SEM.

Recently, a porous-microspheres Li–Si film was prepared by multistep constant current electrodeposition on Cu foil [26.284, 285]. The plating electrolyte was a PC solvent containing $SiCl_4$ and $LiClO_4$. Figure 26.38 [26.285] shows the obtained nanostructure of the deposited Li–Si film. The authors have attributed the formation of the micropores to the gas bubbles (as soft templates) arising from the reductive decomposition of PC on the Li-rich electrode surface. The electrode can deliver a higher capacity than that of a Si film, which was relatively compact. Moreover, after 50 cycles, 96% of its initial capacity was retained.

Using a similar plating bath, which consisted of PC solvent, $SiCl_4$, and tetrabutylammonium perchlorate, *Osaka* et al. have claimed that a highly durable SiOC composite can be deposited by co-reduction of $SiCl_4$ and PC on the current collector [26.286, 287]. The organic–inorganic compounds formed by the reduction of the organic solvent, as in the formation of a resultant solid electrolyte interphase (SEI) layer on anodes

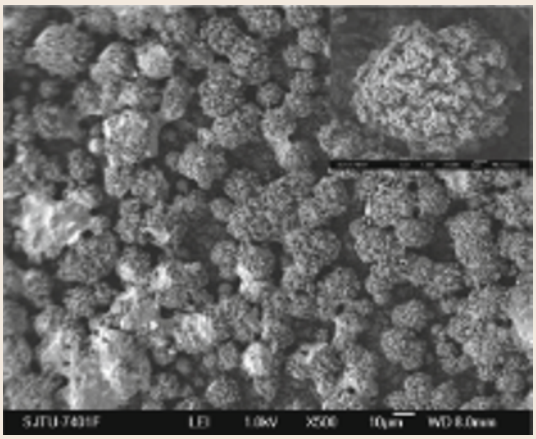


Fig. 26.38 Porous Li–Si film electrodeposited from propylene carbonate solution containing $SiCl_4$ and $LiClO_4$ (after [26.284])

in LIBs, are well known to exhibit permeability to Li^+ ions as well as chemical–electrochemical stability. Moreover, the existence of this compound can buffer the stress of the electrode during charging–discharging. The SEM image in Fig. 26.39a indicates that the deposit consisted of submicrometer clusters. The cross-sectional STEM image of the deposit (Fig. 26.39b) indicates the direct deposition on a Cu foil substrate. The SiOC composite anode can deliver a discharge capacity of 1045 mAh/g of Si at the 2000th cycle and 842 mAh/g even at the 7200th cycle. The results revealed that the excellent cyclability was achieved by the homogeneous dispersion of SiO_x and organic–inorganic compounds at the nanometer scale.

The Sn-Based Materials. Sn is another promising anode for LIBs since its theoretical capacity (≈ 990 mAh/g) is much higher than 372 mAh/g of a traditional graphite electrode. Similar to Si, a large volume change caused by the Li^+ insertion–extraction into/from Sn results in unsatisfactory cycle life. Therefore, the synthesis of nanosized Sn is also desired. Fortunately, electrodeposition of nanostructured Sn and its alloys can be readily performed in aqueous plating solution (in contrast to Si which must be deposited in aprotic electrolyte due to the low reduction potential). Some examples are described in the following.

Ui et al. have proposed a pulse electrodeposition method to prepare a Sn anode [26.288]. The aqueous plating bath was composed of $SnSO_4$, gelatin, and sulfuric acid. This method is effective for improving the adhesion strength between Sn and the substrate, and suitable for producing microcrystal grains of the Sn particles. Figure 26.40 indicates that the crystal grains of the

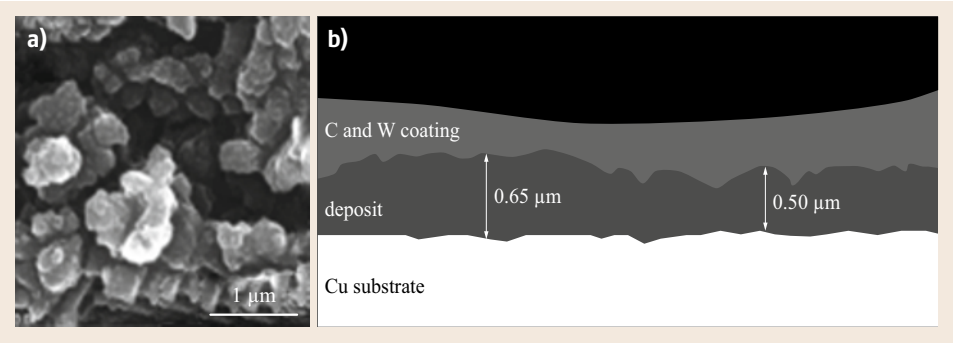


Fig. 26.39 **(a)** Plane view and **(b)** cross-sectional view of the electrodeposited SiOC composite film (after [26.286])

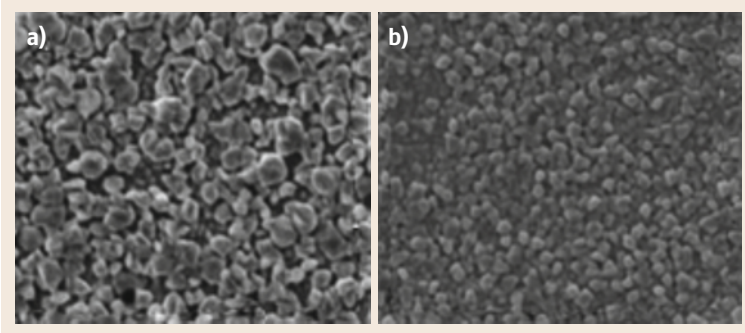


Fig. 26.40a,b Surface morphologies of the Sn film electrodes prepared by the **(a)** constant-current and **(b)** pulse-current electrodeposition methods (after [26.287])

Sn film deposited by the pulse method are more homogeneous and considerably smaller as compared to those on the Sn film prepared by constant current electrodeposition. By reducing the particle size and increasing the reaction surface area, the electrochemical characteristics of the electrode can be considerably improved.

Using the similar pulse electrodeposition technique, Sn and Co can be co-deposited to form a Sn–Co alloy [26.289]. The morphology and chemical composition are shown in Fig. 26.41. It was found that the grain size was less than 0.5 µm, which was smaller than that of the plain Sn film (ca. 1 µm). The incorporated Co can act as an inactive matrix, which can encapsulate the Sn particles and buffer the volume change of Sn during charging–discharging. It was confirmed that the cyclability of the alloy film was much better than that of the plain Sn film electrode.

A three-dimensional foam structure of Sn_5Cu_6 alloy was successfully created using an electrodeposition process [26.290]. As shown in Fig. 26.42, the walls of the foam structure are highly porous and consist of numerous small grains. This unique structure is attributed to the concurrent generation of hydrogen bubbles with extremely fast metal deposition at a high cathodic current density. The porous foam would allow not only fast transport of Li^+ through the electrolyte and the electrode (due to the short diffusion length) but also rapid electrochemical reactions (due to high surface area), resulting in a high-performance anode for LIBs with a superior rate capability.

A ternary Sn–Co–P alloy was also prepared by co-electrodeposition [26.291]. With a Cu foam current collector, the highly porous electrode with multiphases (including $SnP_{0.94}$, Sn, and Sn_2Co_3) was capable of showing a great charge–discharge capacity and excellent cycleability. Moreover, the reticular electrode can buffer the large volume variation caused by repeatedly charging–discharging, which led the ternary alloy anodes to exhibit a good cyclability.

Besides the metal alloying elements, carbon was also co-deposited with Sn to form a composite electrode [26.292]. To improve the cycle performance of a thick Sn electrode, *Park* et al. used two kinds of carbon particles, namely graphite and the acetylene black, to fabricate Sn–C nanocomposites. The carbon particles were crushed by high-energy ball milling before dispersion in the plating bath containing a $SnCl_2$ precursor. The Sn-acetylene black electrode was found to have a superior cyclability because acetylene black particles were better dispersed in the Sn matrix and acted as buffer zones for preventing the crumbling of the electrode.

SnO_2 meso-scale tubes were also synthesized (without using additional templates) by a one-step anodic deposition method [26.293]. The electrodeposition was performed in a plating solution containing $SnCl_2$,

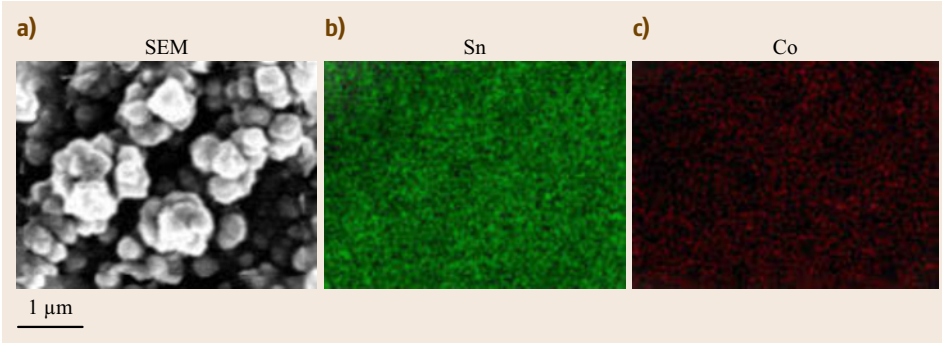


Fig. 26.41 (a) SEM image of the Sn–Co film prepared by a pulse electrodeposition method. (b) and (c) are the chemical mappings of Sn and Co on the electrode (after [26.288])

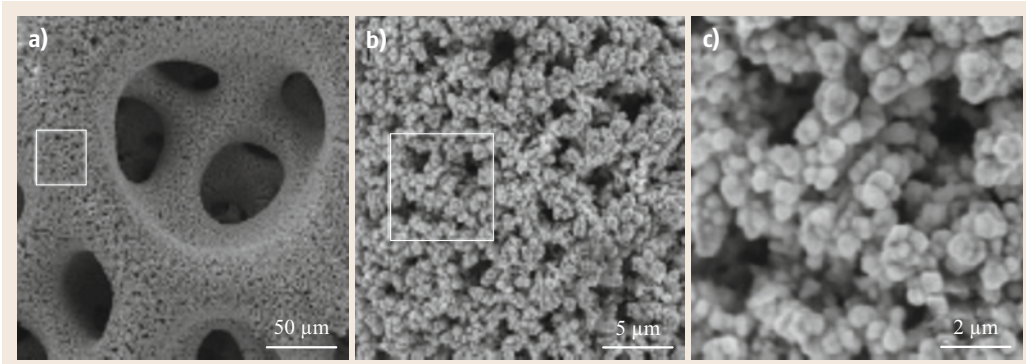


Fig. 26.42 Three-dimensional foam structure of a porous Cu-Sn alloy sample at different magnifications showing (a) the large pores formed due to evolution of H_2 from the substrate, (b) the detailed microstructure of the walls, and (c) the small pores within the walls formed by the evolution of H_2 from the deposited Cu-Sn particles (after [26.289])

HNO_3, and $NaNO_3$ at a potential higher than the O_2 evolution potential. Controlled self-bubbling O_2 acted as both the template and the oxidizing agent for obtaining the SnO_2 tubular structures. The schematic and the SEM micrographs of the electrodeposition process are shown in Fig. 26.43. Electrochemical testing results showed that the nanotubular SnO_2 was a promising anode for LIBs with enhanced cyclability and rate performance.

The other nanostructured Sn-based materials obtained from electrodeposited, such as plain Sn [26.294, 295], Sn–Co [26.296, 297], Sn–Cu [26.298–300], and Sn–Ni [26.301, 302] have also been reported in the literature.

The Other Anodes. Sb is another useful anode that can alloy with Li to form Li_3Sb. The theoretic capacity is around 660 mAh/g. The electrode cyclic stability is an issue that has to be improved. Sb/Sb_2O_3 nanocomposites were prepared by electrodeposition [26.303]. It was demonstrated that the cyclability of the deposits depended on the Sb_2O_3 concentrations as well as on the electrode microstructures, which were influenced by the deposition conditions (e.g., pH).

It is noted that $SbCu_2$ is an intermetallic that does not exhibit large volume change during charging–discharging. $SbCu_2$ intercalates Li to form Li_3Sb in a Cu matrix with relatively small volume variation and long cycle life. The Sb atoms are arranged in an fcc array that acts as a flexible framework for Li insertion. Metallic copper is then extruded to the surface of each crystallite, which is proposed to create a conducting matrix that maintains electrical contact from grain to grain. This kind of material has been successfully prepared by electrodeposition [26.304].

Poizot et al. have proposed a new type of anode materials, the nanosized transition-metal compounds, for LIBs [26.305]. The charge-storage mechanism in such anodes differs from the classical Li insertion–desertion in graphite anodes or Li-alloying processes in alloy anodes. Instead, these kinds of anodes can exhibit a reversible *conversion process* that can be summarized by the following generalized half-reaction [26.306]

$$M_xX_y + ne^- + nLi^+ \leftrightarrow xM^0 + Li_nX_y \,,$$

where M is a transition metal and X = O, S, F, or P. This electrode reaction involves two or even more

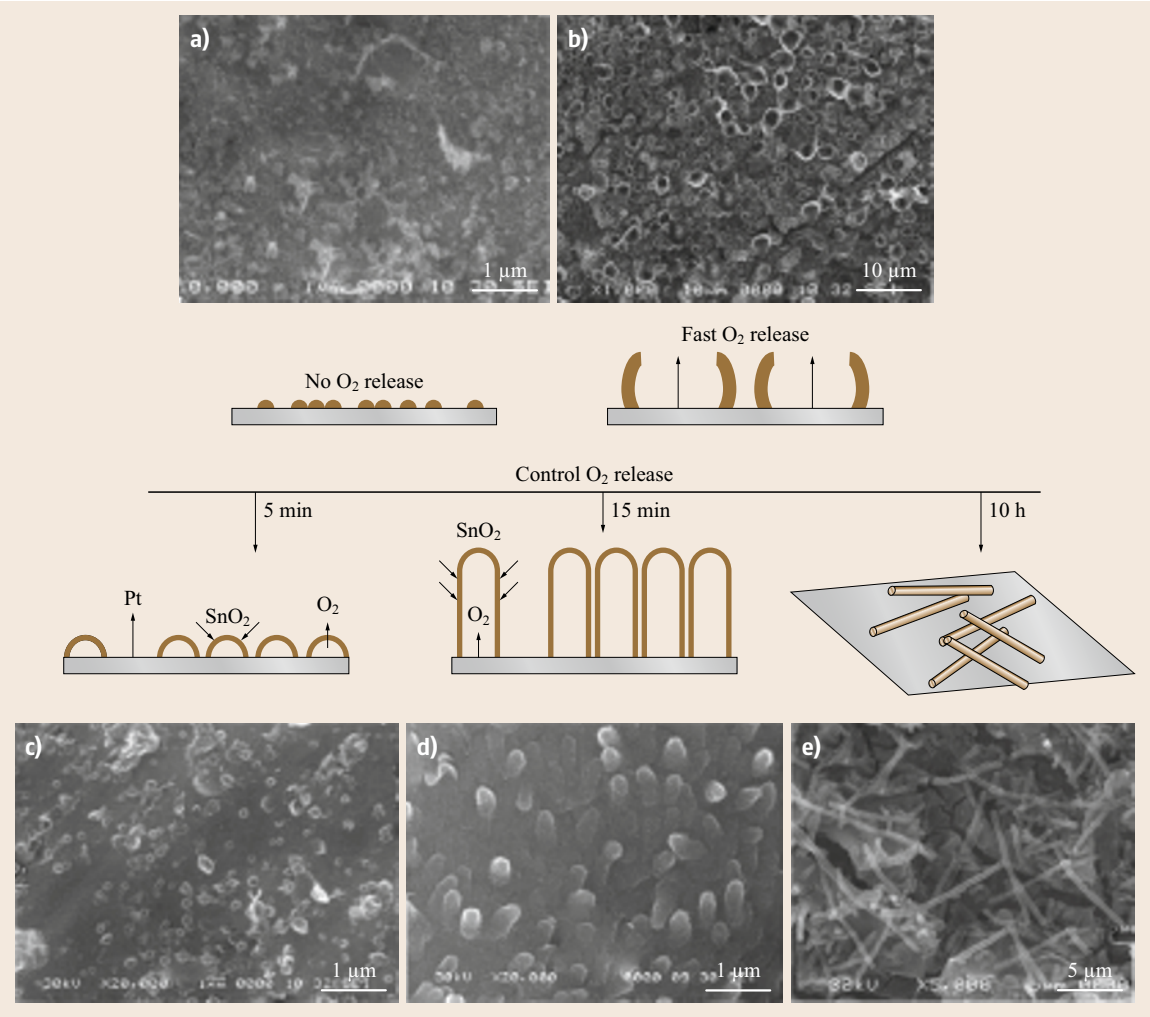


Fig. 26.43 Schematic of the formation mechanism for SnO_2 nanotubes and the corresponding SEM images **(a–e)** (after [26.292])

electrons per 3d metal, as compared to only one in today's commercial graphite electrodes, resulting in a higher charge-storage capacity. However, this reaction mechanism associates with the formation and decomposition of Li_nX_y, accompanying the reduction and oxidation of metal, respectively, indicating that the kinetic properties are of the great concerns. Nanosized transition-metal compounds play an important role in improving the reactivity and energy efficiency during charging–discharging. Nanostructured Fe_2O_3 [26.307] and CoO [26.308] were prepared by electrodeposition for use in LIBs; the morphologies are shown in Fig. 26.44. The electrodeposited Fe_3O_4 [26.306], Cu_2O [26.309, 310], and Fe–Sb–P anodes [26.311] were also reported.

The Current Collectors

Besides the nanoengineering on the electroactive materials, the nanostructured LIB electrodes can also be achieved by using nanoarchitectured current collectors. With the three-dimensional (3-D) configuration (rather than the traditional two-dimensional electrodes with flat substrates), the electrode charge storage performance can be improved [26.312]. The higher energy and power densities per footprint area and larger contact area between the current collector and the active material (thus lower electrical resistance and better mechanical adhesion) are realized. These 3-D nanostructured current collectors can be prepared by electrodeposition.

The typical anode current collector is Cu. Using an AAO template, *Taberna* et al. electrodeposited

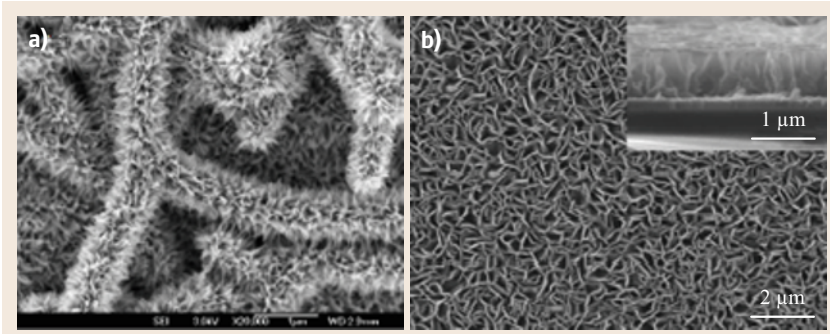


Fig. 26.44a,b Nanostructured Fe_2O_3 and CoO prepared by electrodeposition for the possible LIB anodes ((**a**) after [26.306], (**b**) after [26.307])

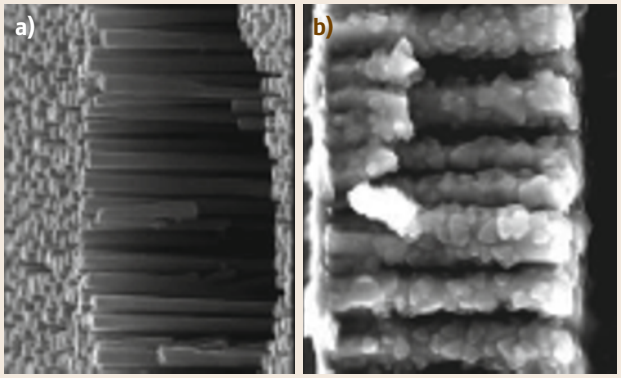


Fig. 26.45a,b Cross-sectional views of the Cu-nanopillar current collector (prepared using an AAO template) (**a**) before and (**b**) after electrodeposition of Fe_3O_4 (after [26.312])

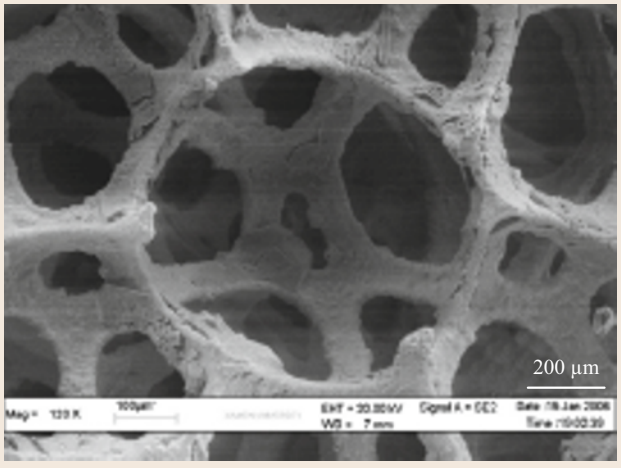


Fig. 26.46 Reticular Cu foam for an anode current collector (after [26.313])

vertically aligned Cu nanorods on a commercial Cu foil [26.314]. Figure 26.45a shows the cross-section view of the Cu pillars after the removal of the AAO. Obviously, the Cu foil is covered with well distributed nanorods with diameters of ≈ 200 nm, defined by the pore size of the AAO used, and of a uniform height. Subsequently, the electroactive material Fe_3O_4 was electrodeposited on the Cu nanorod array, as shown in Fig. 26.45b. Such a 3-D electrode demonstrated a factor of six improvement in power density over a planar electrode. The capacity at 8 C rate was 80% of the total capacity and was sustained over 100 charge–discharge cycles.

Based on the similar concept (using the Cu nanorod array as the anode current collector), the nanoarchitectured NiSn [26.315], Bi [26.316], and Sn [26.317] electrodes have likewise been investigated. Recently, *Perre* et al. [26.313] analogously electrodeposited Sb onto the Cu nanopillars. After a post annealing treatment, $SbCu_2$ formed. The cyclic stability of the electrode was greatly improved as compared with a plain Sb electrode due to the ability of Cu to accommodate the volume variations of Sb during charging–discharging. Direct alloying of Sb with the Cu substrate was profitable since the connection between the electroactive material and the current collector was enhanced.

In addition to the AAO-assisted deposition technique, *Huang* et al. [26.318] also proposed a 3-D Cu foam as the anode current collector (Fig. 26.46). The preparation procedure of the Cu foam consisted of coarsenization of polyurethane foam, sensitization and activation, electroless Cu deposition, electroplating of Cu, and thermal reduction at a hydrogen atmosphere. As shown in the following figure, the obtained Cu foam exhibits a 3-D reticular structure. A Sn–Ni alloy was then electrodeposited on this substrate. After an annealing at 200 °C in Ar, the electrode showed a promising battery performance.

Although suitable for use at the anode side, Cu cannot be used as the cathode current collectors because the high operating voltage (≈ 4 V versus Li/Li^+) would result in oxidation of Cu in contact with electrolyte. The corrosion-resistant Al is a commonly used

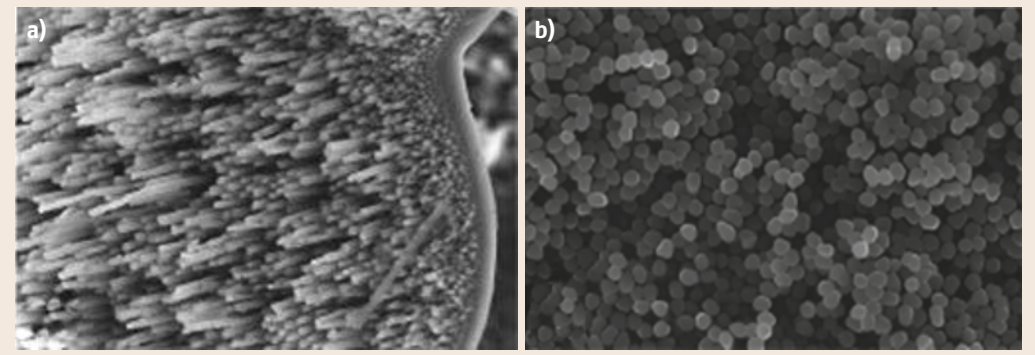


Fig. 26.47 **(a)** Oblique view and **(b)** top view of the Al-nanopillar current collector electrodeposited using an AAO template in an ionic liquid (after [26.318])

current collector material at the cathode side. Electrodeposition of Al nanorods on an Al substrate has been attempted using a similar AAO approach [26.319, 320]. However, due to the low reduction potential of Al and the instability of the $AlCl_3$ precursor in aqueous solution, the electrodeposition was carried out in 1-ethyl-3-methylimidazolium chloride/aluminium chloride ionic liquid. A careful removal of the AAO template unveiled the free standing arrays of Al nanorods, as shown in Fig. 26.47.

This nanorod array current collector was used to support a TiO_2 cathode material, which was grown by atomic layer deposition [26.321]. In Fig. 26.48a, the TEM micrograph shows that the whole surface of the Al pillar is covered by a conformal layer of TiO_2. Figure 26.48b reveals that even the narrow spacing between nanorods is also ideally filled. An order of magnitude increased discharge capacity was reported compared to the capacity for the corresponding planar electrode (for the same footprint area).

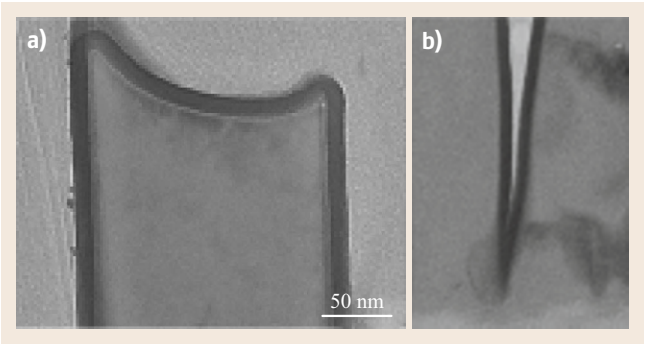


Fig. 26.48 The Al nanorods covered with a conformal TiO_2 layer prepared by atomic layer deposition (after [26.320])

26.2.2 Pseudocapacitors

SCs, also known as electrochemical capacitors or ultracapacitors, are energy-storage devices that have a greater power density and a longer cycle life than those of batteries and a higher energy density than those of conventional capacitors. Accordingly, they have been developed for a wide range of applications (especially for high-power and long-life demands), such as in electric vehicles, consumer electronics, medical electronics, and military missile systems. SCs can be classified, based on their operating mechanisms, into two categories: (i) electrochemical double-layer capacitors (EDLCs), which are based on non-faradic charge separation at the electrode–electrolyte interface (high surface area carbon is the common electrode material); and (ii) pseudocapacitors, which are based on faradic redox reaction of the electrode materials, including conductive polymer and metal oxides.

Characterized by the fast and reversible redox reaction, instead of only electrostatic adsorption–desorption of ions on the electrodes, pseudocapacitors have a higher energy density ($1-5\,F/m^2$ compared to $0.1-0.2\,F/m^2$ for EDLCs). Therefore, more and more attention has been given to these types of SCs. RuO_2 has been shown to exhibit ideal pseudocapacitive behavior. However, the high cost of Ru substantially limits its commercial application. Among the cheaper alternatives (e.g., oxides/hydroxides of Co, Ni, Fe, Mo, V, etc.), MnO_2 seems to be the most promising one. Therefore, MnO_2 is the focal subject in this section.

The MnO_2 electrode stores energy according to the following reversible equation

$$MnO_2 + xC^+ + yH^+ + (x+y)e^- \leftrightarrow MnOOC_xH_y\,, \tag{26.5}$$

where C^+ denotes the cations in the aqueous electrolyte (Li^+, Na^+, K^+). However, due to the low electrical conductivity ($\approx 1\times10^{-5}-1\times10^{-6}\,S/cm$) of MnO_2, to fully exploit its theoretical capacitance ($\approx 1100\,F/g$) is challenging. Because the redox reactions occur only in the top few nanometers near the electrode's surface, nanoengineering techniques play a significant role in

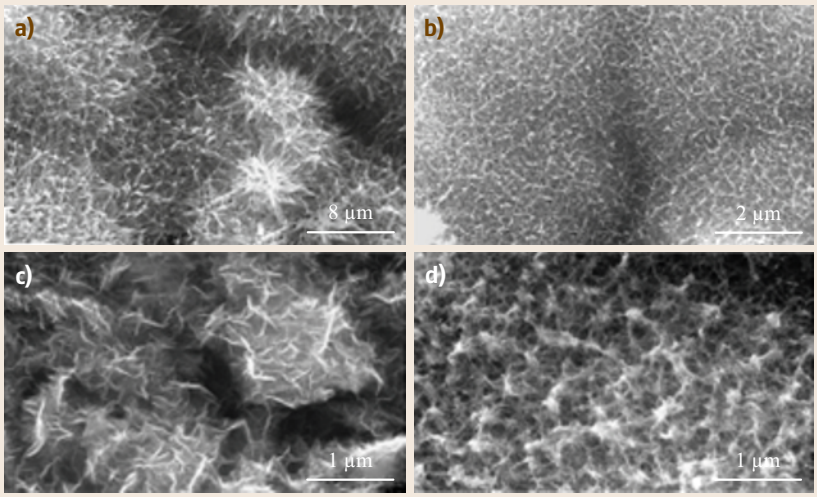


Fig. 26.49a–d Morphologies of MnO_2 anodic deposited at various temperatures **(a)** 25 °C and **(b)** 50 °C in 0.5 M Mn^{2+} plating solution) and various precursor concentrations **(c)** 0.05 M and **(d)** 1 M of Mn^{2+} in 25 °C plating solution) (after [26.322])

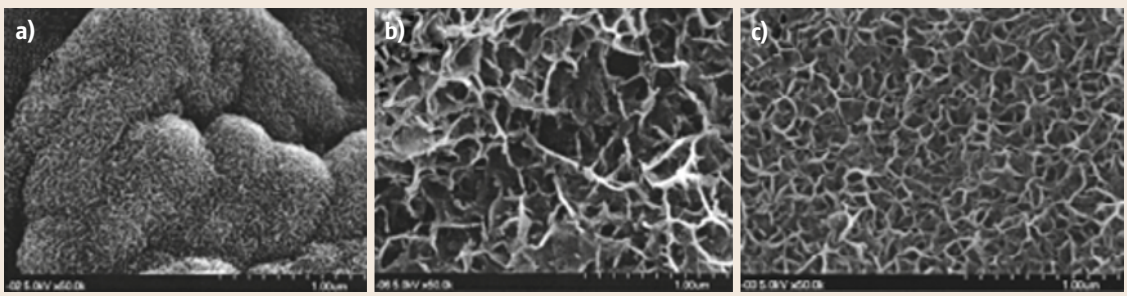


Fig. 26.50a–c Morphologies of MnO_2 elecrodeposited using the **(a)** potentiostatic, **(b)** galvanostatic, and **(c)** potentiodynamic modes (after [26.323])

enhancing pseudocapacitive properties (even more critical than that in the case of battery electrodes where the bulk redox reaction takes place). The nanoengineering idea is to decrease both the electronic and ionic transport distances, trying to improve the electrochemical utilization.

Preparation of Nanostructured MnO_2

There are at least eight types of approaches to obtain nanostructured MnO_2 electrodes incorporating electrodeposition techniques, which are reviewed as follows:

1. *Controlling the plating parameters during the anodic and cathode deposition processes.*
   Direct electrodeposition of MnO_2 on the electrode substrates can avoid the addition of an organic insulating binder, not only increasing the electrical conductivity, but simplifying the electrode manufacture. In general, there are two types of plating processes, including anodic deposition and cathodic deposition. The former can be expressed as follows

$$Mn^{2+} + 2H_2O \rightarrow MnO_2 + 4H^+ + 2e^- , \quad (26.6)$$

whereas the latter involves electro-reduction of Mn(VII) species on the cathode surface as

$$MnO_4^- + 2H_2O + 3e^- \rightarrow MnO_2 + 4OH^- . \quad (26.7)$$

The other cathodic process can be realized by electrogeneration of the base, including reactions that consume H^+ ions or electrolysis of water. Consequently, Mn ion deposits in the form of hydroxide on the cathode as

$$Mn^{2+} + 2(OH)^- \rightarrow Mn(OH)_2 . \quad (26.8)$$

Subsequent heat treatment will convert the manganese hydroxide into stable MnO_2 by a dehydration process.

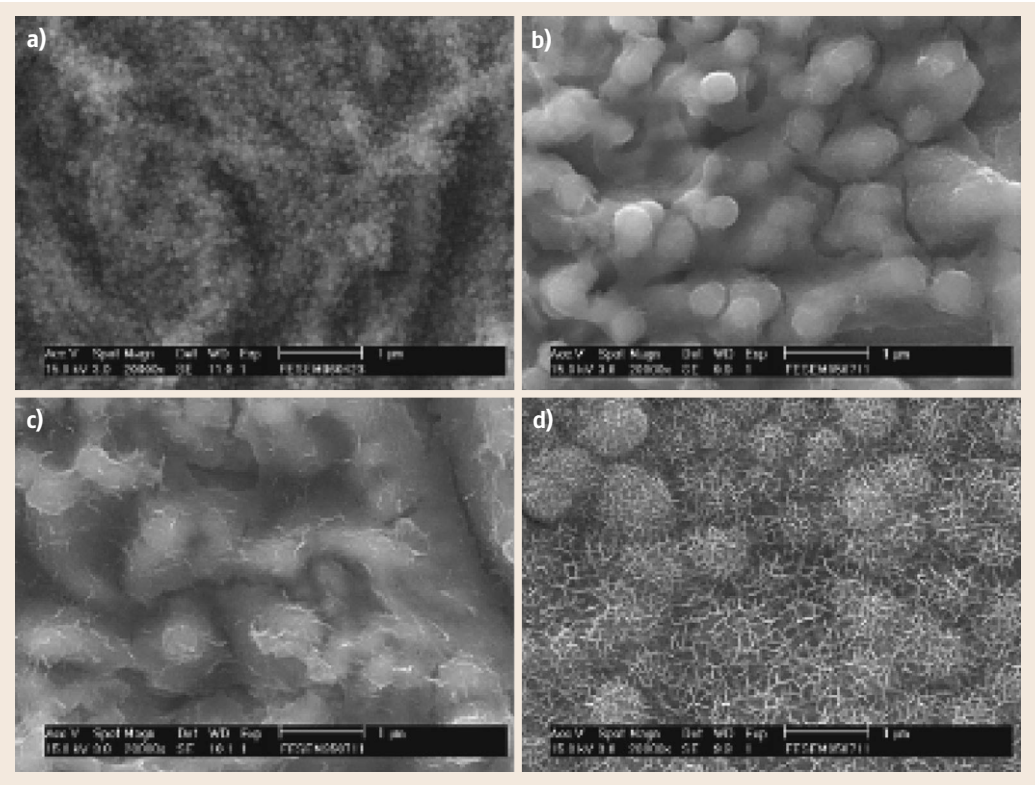


Fig. 26.51a–d Morphologies of the electrodeposited metallic Mn film **(a)** before and after oxidized using the **(b)** potentiostatic, **(c)** galvanostatic, and **(d)** potentiodynamic modes (after [26.324])

A great advantage of electrodeposition is that the morphologies and microstructures of the deposits can be readily controlled by adjusting the plating parameters, such as potential, current, precursor concentration, and bath temperature. The galvanostatic, potentiostatic, and pulse electrodeposition techniques have been used. Porous and 3-D MnO_2 nanostructures prepared by anodic deposition [26.322, 325–331], cathodic deposition from Mn(VII) [26.332–335], and cathodic deposition from Mn(II) [26.323] have been reported. Figure 26.49 shows an example of how the deposition temperature (Fig. 26.49a,b) and the precursor concentration (Fig. 26.49c,d) affect the nanostructures of the anodic deposited MnO_2 (from Mn(II) acetate aqueous solution).

2. *Using a potentiodynamic deposition technique*.
It has been found that the electrodeposition modes (e.g., potentiostatic, galvanostatic, and potentiodynamic techniques) play an important role of determining the nanostructure of the MnO_2 deposits [26.337]. As shown in Fig. 26.50, the ox-

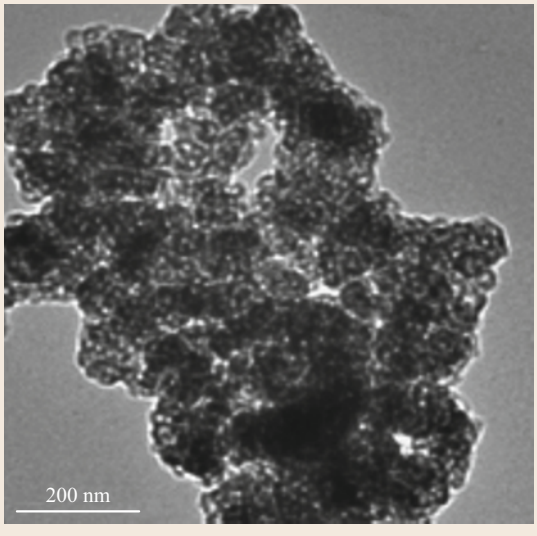


Fig. 26.52 Mesoporous MnO_2 electrodeposited from hexagonal structured lyotropic liquid crystalline phases with polyoxyethnlene surfactant (after [26.336]) ►

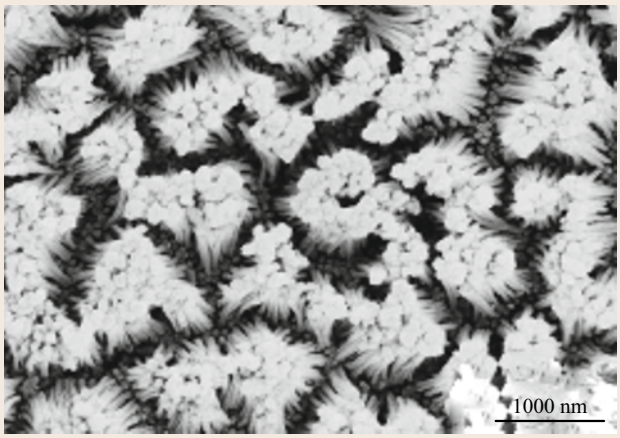


Fig. 26.53 MnO_2 nanowire arrays fabricated using an electrodeposition technique with the aid of an AAO template (after [26.338])

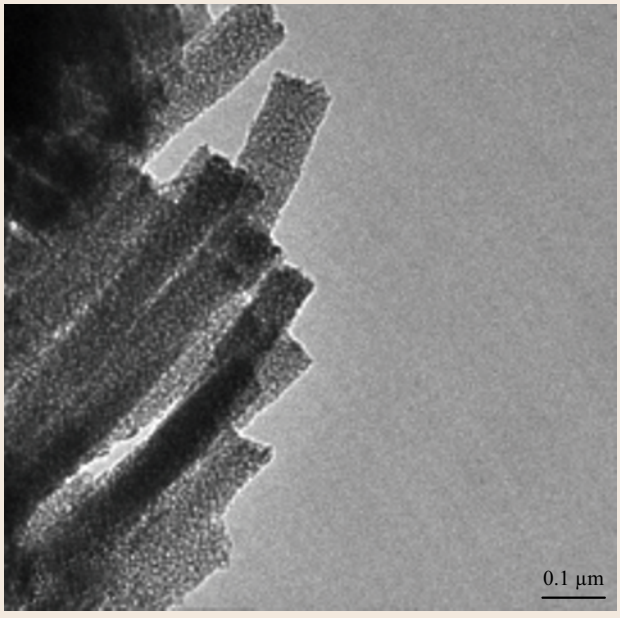


Fig. 26.54 Mesoporous MnO_2 nanowires prepared by electrodeposition using both the AAO and lyotropic liquid crystal templates (after [26.339])

ide deposited using a potentiodynamic method has a more uniform and porous three-dimensional structure.

The morphology and porosity of the oxide can be further controlled by adjusting the deposition parameters, such as potential scanning rate and potential scanning range [26.341–344]. The promoted SC performance can be obtained when the nanostructures of the oxide electrodes were well tailored.

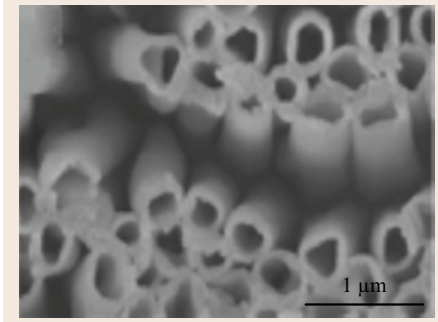


Fig. 26.55 MnO_2 nanotube arrays prepared using an electrodeposition technique with the aid of an AAO template (after [26.340])

3. *Controlling the oxidation procedures for the electrodeposited metallic Mn films*.
   Nanostructured MnO_2 was also prepared by electrochemically anodizing a metallic Mn film, which can be obtained from electrodeposition in butylmethylpyrrolidinium bis(trifluoromethylsulfony)imide ionic liquid. An advantage of this approach is that the nanostructures of MnO_2 can be electrochemically manipulated both at the Mn deposition and at the anodizing stages.
   It was confirmed that the deposition potential and temperature caused a strong influence on the morphology of the deposited Mn [26.324]. Moreover, when the metallic Mn films were anodized in Na_2SO_4 aqueous solution by various anodizing routes, such as potentiostatic, galvanostatic, and CV methods, they transformed to Mn oxide with different nanostructures (as shown in Fig. 26.51 [26.336, 345]. The electrode anodized with the CV method, which had the largest surface area and a suitable chemical state, showed the most promising pseudocapacitive performance.
4. *Using lyotropic liquid crystalline phases*.
   Mesoporous MnO_2 (≈ 5 nm of the pore diameter) was successfully electrodeposited from hexagonal structured lyotropic liquid crystalline phases with polyoxyethnlene surfactant [26.338]. The high surfactant concentrations (≈ 60 wt%) formed a homogeneous self-assembled liquid crystal template. Then, MnO_2 were deposited in the domains of the template. A typical TEM image of the resulting MnO_2 is shown in Fig. 26.52. The bright regions were attributed to pores left after removing the liquid crystalline template from the deposit and the dark area was the mesoporous MnO_2.
5. *Using anodic aluminum oxide (AAO) templates*.
   MnO_2 nanowire arrays were fabricated using an electrodeposition technique with the aid of an AAO

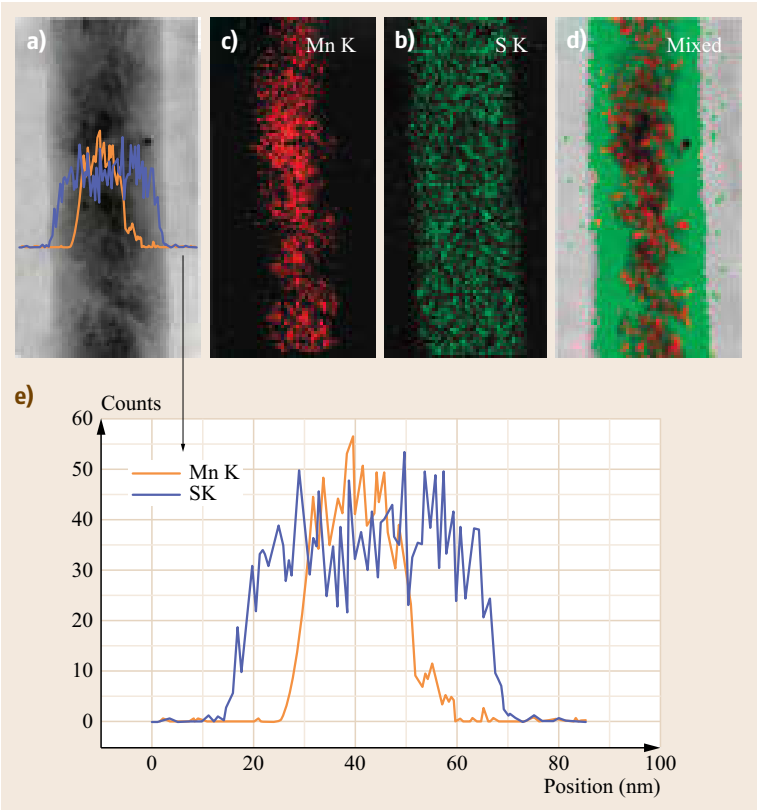


Fig. 26.56 **(a)** TEM image of a MnO_2/PEDOT coaxial nanowire synthesized in an AAO template. **(b)** Mn, **(c)** S, and **(d)** mixed Mn and S EDS mapping of the same coaxial nanowire in **(a)**. **(e)** Mn (*orange*) and S (*blue*) elemental EDS line scan profile across the same coaxial nanowire in **(a)** (after [26.346])

template [26.339]. First, a pure Al film was deposited on a Si substrate coated with a Ti film by radio frequency sputtering. The Al was anodized in oxalic acid solution to develop pores of ≈ 40 nm in diameter. After removing the alumina barrier layer, MnO_2 was deposited into the pores. The AAO template can be dissolved in NaOH solution, leaving behind the oxide nanowire arrays. Figure 26.53 shows the SEM observation result.

A combination of the AAO and lyotropic liquid crystal templates has also been attempted [26.340]. As shown in Fig. 26.54, the mesoporous MnO_2 nanowire array is successfully prepared using the dual-templates assisted electrodeposition method. Due to the intriguing architecture (consisting of mesopores and nanowire arrays), enhanced capacitance and charge–discharge performance were obtained.

To further increase the reaction area and shorten the electronic and ionic transport distances within MnO_2, nanotubes are the more desirable structures than nanowires. *Xia* et al. have indicated that with short electrodeposition time (into AAO) homogeneous nanotubular arrays are found (Fig. 26.55), whereas prolonged deposition leads to a wire-like structure [26.349]. The nanotubular structure was originated from the ring structure of the plasma-deposited Pt on the bottom surface of the AAO template. In addition to high specific capaci-

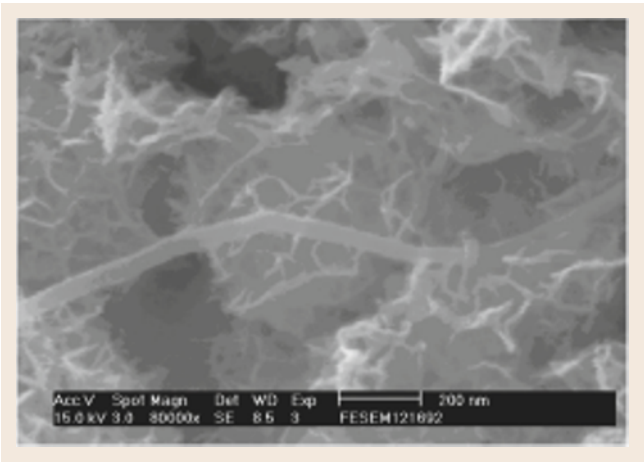


Fig. 26.57 The MnO_2/CNTs composite electrode prepared by co-electrodeposition (after [26.347])

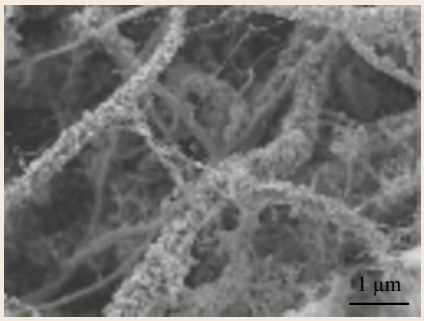


Fig. 26.58 The MnO_2/CNTs composite electrode prepared by electrodeposition of MnO_2 on CVD-grown CNTs (on a steel substrate) (after [26.348])

tance, the MnO_2 nanotube array electrode exhibited good rate capability and good cycling stability, which make it a promising candidate for use in SCs.

The PEDOT (MnO_2/poly(3,4-ethylenedioxythiophene)) coaxial nanowires were also prepared using a similar AAO method [26.346, 347]. Anodic codeposition of the composite wires was performed in a plating solution containing Mn^{2+} and EDOT monomers. In the coaxial nanowires, the core MnO_2 provides high energy-storage capacity, while the highly conductive, porous, and flexible PEDOT shell facilitates the electron transport and ion diffusion into/from the core MnO_2 and protects it from structurally significant collapsing and breaking. Figure 26.56 shows the TEM image and the energy dispersive x-ray spectroscopy (EDS) data, confirming the coaxial nanostructure. The resulting core–shell nanowires exhibited ideal pseudocapacitive performance.

6. *Incorporating with CNTs*.

CNTs are one-dimensional tubular nanostructures, which have high electrical conductivity, high mechanical strength, high chemical stability, and high surface area. Incorporation of CNTs into MnO_2 not only helps create nanoarchitectures but also improves the overall electrical conduction of the electrodes.

Co-electrodeposition of CNTs and MnO_2 on a graphite substrate has been attempted [26.351]. As shown in Fig. 26.57, CNTs are surrounded by numerous MnO_2 nanoflakes. The highly porous structure would favor the diffusion of electrolyte into the oxide electrode.

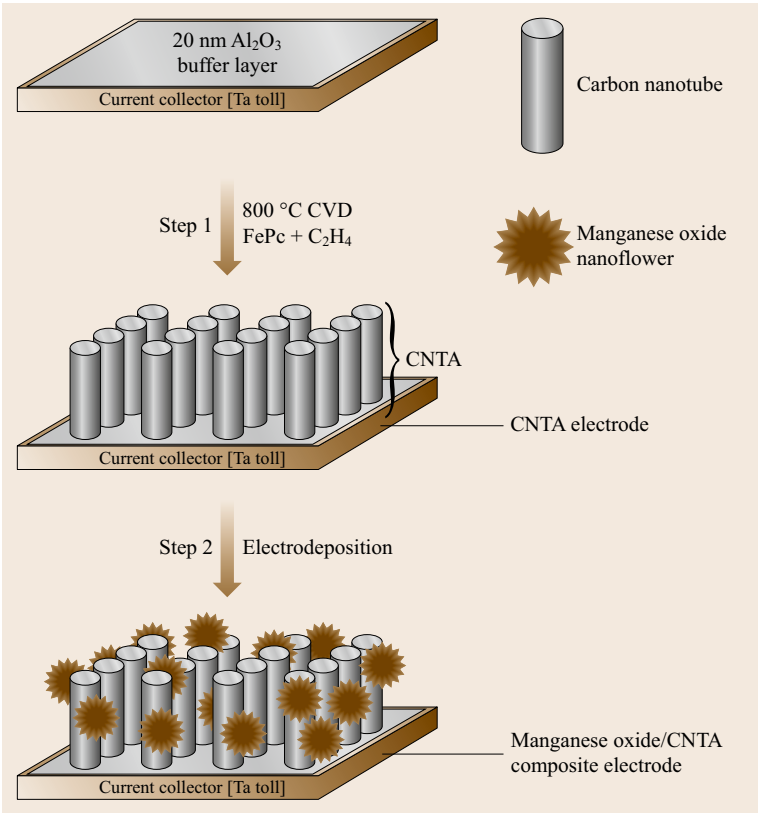


Fig. 26.59 Schematic for preparation of a MnO_2/aligned-CNT nanocomposite electrode (after [26.350])

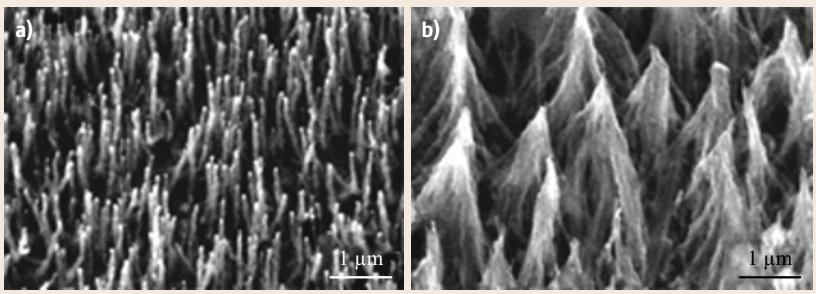


Fig. 26.60a,b SEM images of the well-aligned carbon nanotube arrays **(a)** before and **(b)** after electrodeposition of γ-MnO_2 (after [26.352])

Besides the above-mentioned co-deposition method, many efforts were dedicated to electrodeposit MnO_2 onto CNT architectures. In these cases, CNTs were first deposited by electrophoresis [26.353] or directly grown by chemical vapor deposition (CVD) [26.348, 350] on the electrode substrates. Then, MnO_2 was synthesized on the interwoven CNTs either by anodic or cathodic deposition. Figure 26.58 shows a typical morphology of the MnO_2/CNT nanocomposite electrode, which exhibited better energy-storage capability than that of MnO_2 deposited on a flat substrate (without CNTs).

To further improve the SC performance, vertically aligned CNTs were recently developed to load the electrodeposited MnO_2. *Zhang* et al. have proposed a procedure to synthesize a MnO_2/aligned-CNT nanocomposite [26.352]. This strategy, as shown in Fig. 26.59, mainly involves (1) growing vertically aligned CNTs on a Ta foil by CVD and (2) electrodepositing MnO_2 nanoflowers on the aligned-CNT scaffold by potentiodynamic electrodeposition.

In this geometry, each oxide particle is directly connected to the current collector without binders, which add extra contact resistance and weight. This superior conducting network allows for efficient charge transport within the composite electrode. The high surface area of the nanostructure, which reduces the diffusion length of ions within MnO_2 during the charge–discharge process, ensures a high utilization of the electroactive material. In addition, the use of CNTs can suppress the cycle degradation caused by mechanical problems or volume changes of MnO_2 and can overcome nanoparticle aggregation. As a result, the MnO_2/aligned-CNT composite electrode is capable of presenting an ideal SC performance.

A similar approach was used to prepare a γ-MnO_2/aligned-CNT on a graphite substrate [26.355]. The plasma-enhanced hot filament CVD was employed to grow the vertically aligned CNTs (Fig. 26.60a). Subsequently, γ-MnO_2 was added using a cathodic deposition technique; the resulting microstructure of the electrode is shown in Fig. 26.60b.

It is noted that the electrodeposition of MnO_2 nanowires on free-standing CNT paper, prepared by a simple filtration method, has also been reported in [26.354]. The resulting nanocomposite electrode has a great potential for commercial applications in totally flexible SCs.

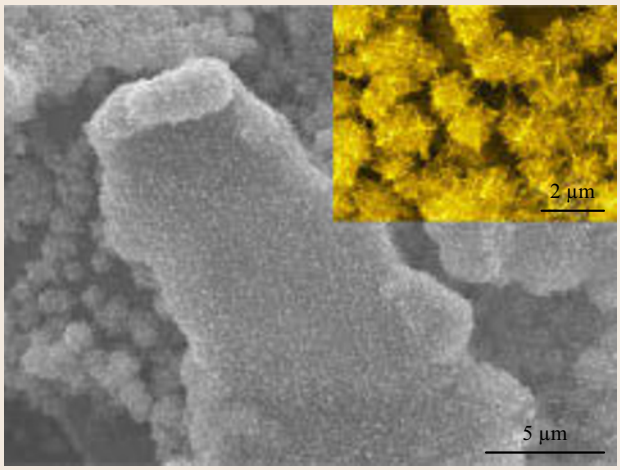


Fig. 26.61 Morphology of MnO_2 nanoflowers electrodeposited on graphene (after [26.354])

7. *Incorporating with graphene*.

Besides CNTs, graphene nanosheets are another promising material for incorporating with MnO_2 in SCs, because of their unique two-dimensional structure, high surface area, remarkable chemical stability, and excellent electrical conductivity.

Cheng et al. prepared a graphene paper by vacuum filtering [26.358]. Afterward, the graphene paper was cut into pieces of specific dimensions as electrodes and was ready for the anodic electrodeposition of MnO_2. The morphology of the obtained composite electrode is shown in Fig. 26.61. The graphene nanosheets were covered by the MnO_2 nanoflow-

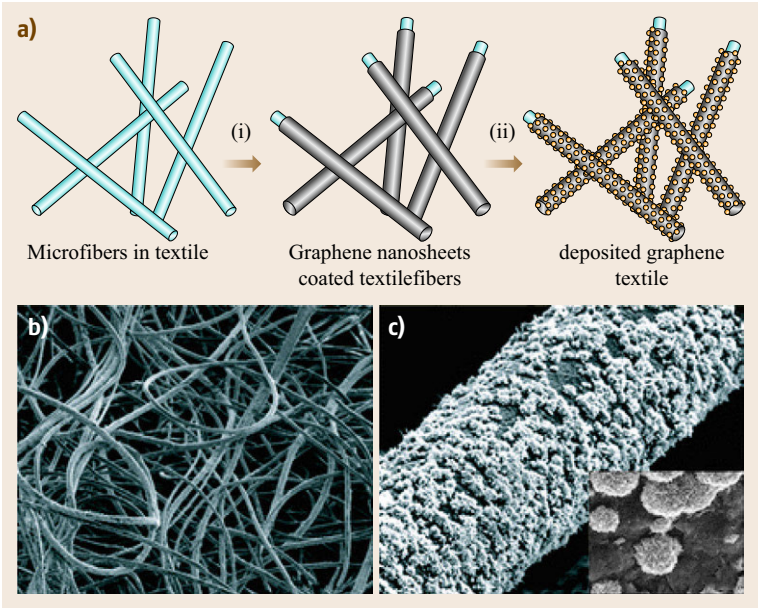


Fig. 26.62 **(a)** Schematic illustration of two key steps for preparing hybrid MnO_2/graphene nanostructured textiles. **(b)** and **(c)** SEM micrographs of the real electrode prepared at different magnifications (after [26.356])

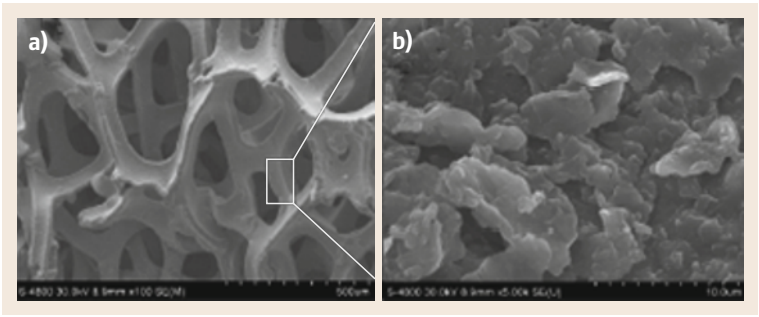


Fig. 26.63a,b Morphologies of **(a)** the bare Ni foam and **(b)** the electrodeposited MnO_2/graphene composite on the Ni foam (after [26.357])

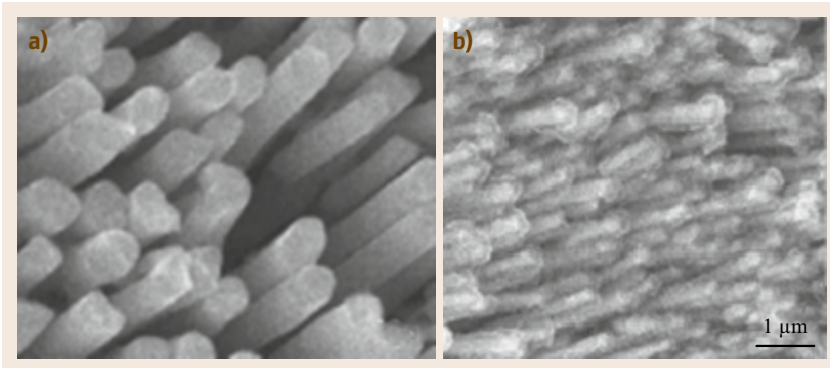


Fig. 26.64a,b SEM micrographs of Ni nanorod arrays (prepared using AAO); **(a)** before and **(b)** after electrodeposition of MnO_2 (after [26.357])

ers. The deposited MnO_2 was suggested to serve as a spacer to prevent re-stacking of graphene and facilitate the electrolyte diffusion within the electrode. This nanostructured electrode possessed high energy density and power density, thus was claimed to be promising for electrical vehicle applications.

Instead of using graphene paper as the electrode substrate, *Yu* et al. demonstrated that graphene nanosheets can be conformably coated from solution on three-dimensional, porous textiles for high loading of electrodeposited MnO_2 and to facilitate the accessibility of electrolyte [26.356]. Fig-

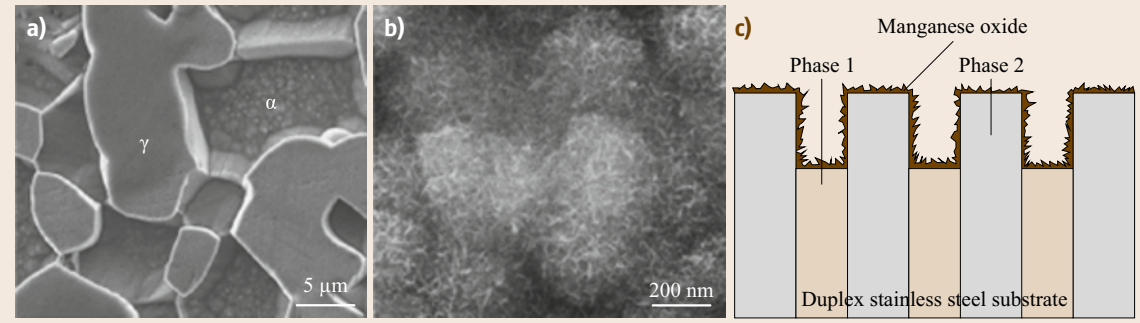


Fig. 26.65 **(a)** Preferential etching of α phase in a duplex stainless steel. **(b)** Morphology of the MnO_2 nanofibers electrodeposited on the steel substrate. **(c)** Schematic of the high-surface-area MnO_2 electrode prepared (after [26.359])

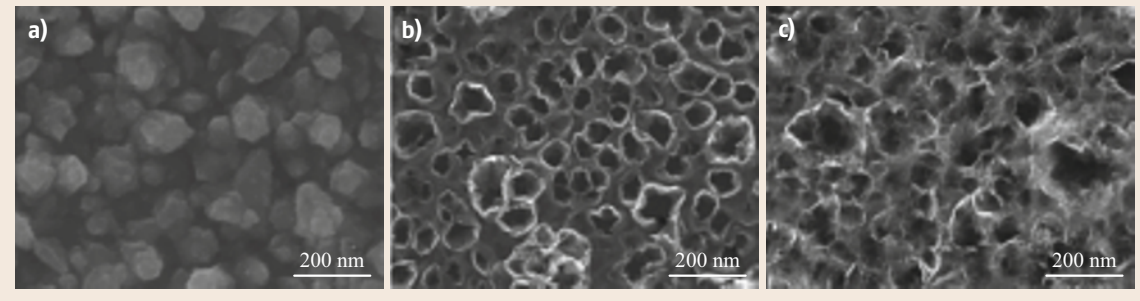


Fig. 26.66a–c Morphologies of **(a)** as-deposited Ni–Cu film, **(b)** nanoporous Ni film after selective dissolution of Cu, and **(c)** the resulting high-porosity electrode after electrodeposition of MnO_2 (after [26.360])

ure 26.62a schematically illustrates the two key steps for preparing the hybrid MnO_2/graphene nanostructured electrode. Figure 26.62b,c shows the morphologies of a real sample. Uniform decoration of MnO_2 nanoflowers on graphene-wrapped textile fibers was clearly observed. This nanocomposite electrode has been confirmed to have high specific capacitance, good rate capability, and remarkable cycling performance.

An analogic ideal was performed on a Ni foam substrate, whose microstructure is shown in Fig. 26.63a [26.357]. The approach includes the electrophoretic deposition of graphene on Ni foam and subsequent electrodeposition of MnO_2 on the top (Fig. 26.63b).

8. *Using electrochemically derived nanostructured current collectors to support MnO_2.*

The nanostructured electrodes can also be created by using desirable nanoarchitectures as the supports for MnO_2 (besides the nanoengineering performed directly on the oxide). The electrode substrates with nanoarchitectures can be readily manufacture by electrochemical routes.

Lei et al. prepared Ni nanorods by electrodeposition through an AAO membrane and used them as the electrode substrate [26.359]. The SEM micrograph, shown in Fig. 26.64a, depicts the perfect and dense array of Ni nanorods (≈ 200 nm in diameters) after the dissolution of the AAO template. Using a pulse potentiostatic deposition technique, a MnO_2 layer was homogeneously loaded on the array (Fig. 26.64b).

High-porosity substrates can also be obtained from the electrochemically selective dissolution of one constituent phase in a duplex stainless steel (with α and γ phases) [26.360]. Due to the chemical composition and crystal structure differences, preferential etching in either α or γ phase can be controlled by choosing the particular applied potential. Figure 26.65a shows an electrode, on which α phase is selectively etched. After the anodic deposition of MnO_2, the electrode surface morphology is revealed as Fig. 26.65b. The idea of constructing the large surface area MnO_2 electrode is illustrated in Fig. 26.65c.

Along the similar concept, an entirely electrochemical process has been further developed to create even smaller pores (≈ 100 nm compared to ≈ 5 µm of the above duplex stainless steel electrode) [26.361]. The proposed procedure is quite

simple and efficient and mainly includes three steps:

a) Co-electrodeposition of a Ni–Cu alloy film on a conductive electrode (Fig. 26.66a)
b) Selective dissolution of Cu from the alloy film and hence the formation of a nanoporous Ni structure (Fig. 26.66b)
c) Anodic deposition of fibrous MnO_2 onto the porous Ni substrate (Fig. 26.66b).

The obtained nanostructured electrode can deliver a superior specific capacitance, which is 85% higher than that deposited on a flat Ni substrate. Moreover, the capacitance retained ratio after 500 charge–discharge cycles was also significantly improved from 75% to 93% due to the use of the nanoporous architecture.

In this section, the MnO_2 electrodes are taken as the examples to demonstrate how the nanostructures can be prepared via various electrochemical approaches. According to the similar strategies mentioned above, syntheses of other pseudocapacitive materials (such as oxides and hydroxides of Fe, Co, Ni, Cu, Mo, V, Ru, etc.) with nanoarchitectures and thus with promoted charge–discharge performances can also be achieved.

26.3 Conclusions and Prospects

As highlighted in this chapter, nanostructured materials can be created by electrodeposition at planar electrodes either with or without the assist of a template. Nanostructured materials with a variety of different shapes, structure sizes, and compositions can be created for specific application. In particular, the area of energy storage and conversion is well suited for the application of the electrodeposited materials. It is expected that further studies into development of new technique for the electrodeposition of nanostructured materials will continually improve their applications in various fields.

References

26.1 N. Tian, Z.-Y. Zhou, N.-F. Yu, L.-Y. Wang, S.-G. Sun: Direct electrodeposition of tetrahexahedral Pd nanocrystals with high-index facets and high catalytic activity for ethanol electrooxidation, J. Am. Chem. Soc. **132**, 7580–7581 (2010)

26.2 Z.-Y. Zhou, N. Tian, Z.-Z. Huang, D.-J. Chen, S.-G. Sun: Nanoparticle catalysts with high energy surfaces and enhanced activity synthesized by electrochemical method, Faraday Discuss. **140**, 81–92 (2009)

26.3 N. Tian, Z.-Y. Zhou, S.-G. Sun, Y. Ding, Z.L. Wang: Synthesis of tetrahexahedral platinum nanocrystals with high-index facets and high electrooxidation activity, Science **316**, 732–735 (2007)

26.4 N. Tian, Z.-Y. Zhou, S.-G. Sun: Electrochemical preparation of Pd nanorods with high-index facets, Chem. Commun. **12**, 1502–1504 (2009)

26.5 L. Wei, Y.-J. Fan, N. Tian, Z.-Y. Zhou, X.-Q. Zhao, B.-W. Mao, S.-G. Sun: Electrochemically shape-controlled synthesis in deep eutectic solvents – A new route to prepare Pt nanocrystals enclosed by high-index facets with high catalytic activity, J. Phys. Chem. C **116**, 2040–2044 (2012)

26.6 Y.-J. Deng, N. Tian, Z.-Y. Zhou, R. Huang, Z.-L. Liu, J. Xiao, S.-G. Sun: Alloy tetrahexahedral Pd–Pt catalysts: Enhancing significantly the catalytic activity by synergy effect of high-index facets and electronic structure, Chem. Sci. **3**, 1157–1161 (2012)

26.7 Y.-X. Chen, S.-P. Chen, Z.-Y. Zhou, N. Tian, Y.-X. Jiang, S.-G. Sun, Y. Ding, Z.L. Wang: Tuning the shape and catalytic activity of Fe nanocrystals from rhombic dodecahedra and tetragonal bipyramids to cubes by electrochemistry, J. Am. Chem. Soc. **131**, 10860–10862 (2009)

26.8 Y.-X. Chen, S.-P. Chen, Q.-S. Chen, Z.-Y. Zhou, S.-G. Sun: Electrochemical preparation of iron cuboid nanoparticles and their catalytic properties for nitrite reduction, Electrochim. Acta **53**, 6938–6943 (2008)

26.9 A. Radi, D. Pradhan, Y. Sohn, K.T. Leung: Nanoscale shape and size control of cubic, cuboctahedral, and octahedral Cu–Cu20 core–shell nanoparticles on Si(100) by one-step, templateless, capping-agent-free electrodeposition, ACS Nano **4**, 1553–1560 (2010)

26.10 S.C. Tang, X.K. Meng, S. Vongehr: An additive-free electrochemical route to rapid synthesis of large-area copper nano-octahedra on gold film substrates, Electrochem. Commun. **11**, 867–870 (2009)

26.11 W.-Y. Ko, W.-H. Chen, C.-Y. Cheng, K.-J. Lin: Architectural growth of Cu nanoparticles through electrodeposition, Nanoscale Res. Lett. **4**, 1481–1485 (2009)

26.12 W.-Y. Ko, W.-H. Chen, S.-D. Tzeng, S. Gwo, K.-J. Lin: Synthesis of pyramidal copper nanoparticles on gold substrate, Chem. Mater. **18**, 6097–6099 (2006)

26.13 W. Qiu, M. Xu, F. Chen, X. Yang, Y. Nan, H. Chen: Morphology evolution route of PbS crystals via environment-friendly electrochemical deposition, Cryst. Eng. Comm. **13**, 4689–4694 (2011)

26.14 L. Wang, S. Guo, X. Hu, S. Dong: Facile electrochemical approach to fabricate hierarchical flowerlike gold microstructures: Electrodeposited superhydrophobic surface, Electrochem. Commun. **10**, 95–99 (2008)

26.15 M.J. Siegfried, K.-S. Choi: Elucidation of an overpotential-limited branching phenomenon observed during the electrocrystallization of cuprous oxide, Angew. Chem. Int. Ed. **47**, 368–372 (2008)

26.16 Y. Tian, H. Liu, G. Zhao, T. Tatsuma: Shape-controlled electrodeposition of gold nanostructures, J. Phys. Chem. B **110**, 23478–23481 (2006)

26.17 S. Tang, X. Meng, C. Wang, Z. Cao: Flower like Ag microparticles with novel nanostructure synthesized by an electrochemical approach, Mater. Chem. Phys. **114**, 842–847 (2009)

26.18 H. Zhang, W. Zhou, Y. Du, P. Yang, C. Wang: One-step electrodeposition of platinum nanoflowers and their high efficient catalytic activity for methanol electro-oxidation, Electrochem. Commun. **12**, 882–885 (2010)

26.19 Y.-X. Nan, F. Chen, L.-G. Yang, H.-Z. Chen: Electrochemical synthesis and charge transport properties of CdS nanocrystalline thin films with a conifer-like structure, J. Phys. Chem. C **114**, 11911–11917 (2010)

26.20 Z.L. Bao, K.L. Kavanagh: Aligned Co nanodiscs by electrodeposition on GaAs, J. Cryst. Growth **287**, 514–517 (2006)

26.21 F.K. Jia, K.W. Wong, R. Du: Direct growth of highly catalytic palladium nanoplates array onto gold substrate by a template-free electrochemical route, Electrochem. Commun. **11**, 519–521 (2009)

26.22 F. Jia, K.-W. Wong, L. Zhang: Electrochemical synthesis of nanostructured palladium of different morphology directly on gold substrate through a cyclic deposition/dissolution route, J. Phys. Chem. C **113**, 7200–7206 (2009)

26.23 G. Liu, W. Cai, L. Kong, G. Duan, F. Lue: Vertically cross-linking silver nanoplate arrays with controllable density based on seed-assisted electrochemical growth and their structurally enhanced SERS activity, J. Mater. Chem. **20**, 767–772 (2010)

26.24 G.-R. Li, C.-Z. Yao, X.-H. Lu, F.-L. Zheng, Z.-P. Feng, X.-L. Yu, C.-Y. Su, Y.-X. Tong: Facile and efficient electrochemical synthesis of PbTe dendritic structures, Chem. Mater. **20**, 3306–3314 (2008)

26.25 T. Hang, M. Li, Q. Fei, D. Mao: Characterization of nickel nanocones routed by electrodeposition without any template, Nanotechnology **19**(3), 035201 (2008)

26.26 T. Hang, A. Hu, M. Li, D. Mao: Structural control of a cobalt nanocone array grown by directional electrodeposition, Cryst. Eng. Comm. **12**, 2799–2802 (2010)

26.27 T. Hang, A. Hu, H. Ling, M. Li, D. Mao: Superhydrophobic nickel films with micro-nano hierarchical structure prepared by electrodeposition, Appl. Surf. Sci. **256**, 2400–2404 (2010)

26.28 W. Ye, J. Yan, Q. Ye, F. Zhou: Template-free and direct electrochemical deposition of hierarchical dendritic gold microstructures: Growth and their multiple applications, J. Phys. Chem. C **114**, 15617–15624 (2010)

26.29 X. Qin, Z. Miao, Y. Fang, D. Zhang, J. Ma, L. Zhang, Q. Chen, X. Shao: Preparation of dendritic nanostructures of silver and their characterization for electroreduction, Langmuir **28**, 5218–5226 (2012)

26.30 Y. Zhang, Y. Ni, X. Wang, J. Xia, J. Hong: Polycrystalline Cu7Te4 dendritic microstructures constructed by spherical nanoparticles: Fast electrodeposition, influencing factors, and the shape evolution, Cryst. Growth Des. **11**, 4368–4377 (2011)

26.31 Y.-J. Song, J.-Y. Kim, K.-W. Park: Synthesis of Pd dendritic nanowires by electrochemical deposition, Cryst. Growth Des. **9**, 505–507 (2009)

26.32 Y. Ni, Y. Zhang, L. Zhang, J. Hong: Mass synthesis of dendritic Bi nanostructures by a facile electrodeposition route and influencing factors, Cryst. Eng. Comm. **13**, 794–799 (2011)

26.33 V. Fleury, J.H. Kaufman, D.B. Hibbert: Mechanism of a morphology transition in ramified electrochemical growth, Nature **367**, 435–438 (1994)

26.34 T.-H. Lin, C.-W. Lin, H.-H. Liu, J.-T. Sheu, W.-H. Hung: Potential-controlled electrodeposition of gold dendrites in the presence of cysteine, Chem. Commun. **47**, 2044–2046 (2011)

26.35 M. Wang, S. Zhong, X.B. Yin, J.M. Zhu, R.W. Peng, Y. Wang, K.Q. Zhang, N.B. Ming: Nanostructured copper filaments in electrochemical deposition, Phys. Rev. Lett. **86**, 3827–3830 (2001)

26.36 M. Zhang, G. Zuo, Z. Zong, H. Cheng, Z. He, C. Yang, G. Zou: Self-assembly of copper micro/nanoscale parallel wires by electrodeposition on a silicon substrate, Small **2**, 727–731 (2006)

26.37 M.Z. Zhang, G.H. Zuo, Z.C. Zong, H.Y. Chen, Z. He, C.M. Yang, D.M. Li, G.T. Zou: Self-assembly from the branch pattern to parallel wire array in electrodeposition, Appl. Phys. Lett. **88**, 203106 (2006)

26.38 S. Zhong, T. Koch, M. Wang, T. Scherer, S. Walheim, H. Hahn, T. Schimmel: Nanoscale twinned copper nanowire formation by direct electrodeposition, Small **5**, 2265–2270 (2009)

26.39 X.-P. Huang, W. Han, Z.-L. Shi, D. Wu, M. Wang, R.-W. Peng, N.-B. Ming: Electrodeposition of periodically nanostructured straight cobalt filament arrays, J. Phys. Chem. C **113**, 1694–1697 (2009)

26.40 S. Peulon, D. Lincot: Mechanistic study of cathodic electrodeposition of zinc oxide and zinc hydroxychloride films from oxygenated aqueous zinc chloride solutions, J. Electrochem. Soc. **145**, 864–874 (1998)

26.41 T. Yoshida, D. Komatsu, N. Shimokawa, H. Minoura: Mechanism of cathodic electrodeposition of zinc oxide thin films from aqueous zinc nitrate baths, Thin Solid Films **451**, 166–169 (2004)

26.42 M. Izaki: Electrolyte optimization for cathodic growth of zinc oxide Films, J. Electrochem. Soc. **143**, L53–L55 (1996)

26.43 M. Izaki, T. Omi: Transparent zinc oxide films prepared by electrochemical reaction, Appl. Phys. Lett. **68**, 2439–2440 (1996)

26.44 M. Lai, D.J. Riley: Templated electrosynthesis of zinc oxide nanorods, Chem. Mater. **18**, 2233–2237 (2006)

26.45 T. Pauporté, D. Lincot: Heteroepitaxial electrodeposition of zinc oxide films on gallium nitride, Appl. Phys. Lett. **75**, 3817–3819 (1999)

26.46 S. Peulon, D. Lincot: Cathodic electrodeposition from aqueous solution of dense or open-structured zinc oxide films, Adv. Mater. **8**, 166 (1996)

26.47 R. Liu, A.A. Vertegel, E.W. Bohannan, T.A. Sorenson, J.A. Switzer: Epitaxial electrodeposition of zinc oxide nanopillars on single-crystal gold, Chem. Mater. **13**, 508–512 (2001)

26.48 T. Pauporte, R. Cortes, M. Froment, B. Beaumont, D. Lincot: Electrocrystallization of epitaxial zinc oxide onto gallium nitride, Chem. Mater. **14**, 4702–4708 (2002)

26.49 T. Pauporte, D. Lincot, B. Viana, F. Pelle: Toward laser emission of epitaxial nanorod arrays of ZnO grown by electrodeposition, Appl. Phys. Lett. **89**(23), 233112–233112 (2006)

26.50 D. Pradhan, S. Sindhwani, K.T. Leung: Parametric study on dimensional control of ZnO nanowalls and nanowires by electrochemical deposition, Nanoscale Res. Lett. **5**, 1727–1736 (2010)

26.51 J. Lee, Y. Tak: Electrodeposition of ZnO on ITO electrode by potential modulation method, Electrochem. Solid State Lett. **4**, C63–C65 (2001)

26.52 R. Tena-Zaera, J. Elias, G. Wang, C. Levy-Clement: Role of chloride ions on electrochemical deposition of ZnO nanowire arrays from O-2 reduction, J. Phys. Chem. C **111**, 16706–16711 (2007)

26.53 J. Elias, R. Tena-Zaera, C. Levy-Clement: Effect of the chemical nature of the anions on the electrodeposition of ZnO nanowire arrays, J. Phys. Chem. C **112**, 5736–5741 (2008)

26.54 T. Pauporte, E. Jouanno, F. Pelle, B. Viana, P. Aschehoug: Key growth parameters for the electrodeposition of ZnO films with an intense UV-light emission at room temperature, J. Phys. Chem. C **113**, 10422–10431 (2009)

26.55 T. Pauporte, G. Bataille, L. Joulaud, F.J. Vermersch: Well-aligned ZnO nanowire arrays prepared by seed-layer-free electrodeposition and their cassie-wenzel transition after hydrophobization, J. Phys. Chem. C **114**, 194–202 (2010)

26.56 O. Lupan, T. Pauporte, B. Viana, I.M. Tiginyanu, V.V. Ursaki, R. Cortes: Epitaxial electrodeposition of ZnO nanowire arrays on p-GaN for efficient UV-light-emitting diode fabrication, ACS Appl. Mater. Interfaces **2**, 2083–2090 (2010)

26.57 D. Pradhan, Z. Su, S. Sindhwani, J.F. Honek, K.T. Leung: Electrochemical growth of ZnO nanobelt-like structures at 0 °C: Synthesis, characterization, and in-situ glucose oxidase embedment, J. Phy. Chem. C **115**, 18149–18156 (2011)

26.58 Z. Feng, Q. Zhang, L. Lin, H. Guo, J. Zhou, Z. Lin: Preferential growth of CdSe nanowires on conducting glass: Template-free electrodeposition and application in photovoltaics, Chem. Mater. **22**, 2705–2710 (2010)

26.59 G. She, W. Shi, X. Zhang, T. Wong, Y. Cai, N. Wang: Template-free electrodeposition of one-dimensional nanostructures of tellurium, Cryst. Growth Des. **9**, 663–666 (2009)

26.60 K. Hoshino, Y. Hitsuoka: One-step template-free electrosynthesis of cobalt nanowires from aqueous [Co(NH)]Cl solution, Electrochem. Commun. **7**, 821–828 (2005)

26.61 A. Ghahremaninezhad, E. Asselin, D.G. Dixon: Electrodeposition and growth mechanism of copper sulfide nanowires, J. Phys. Chem. C **115**, 9320–9334 (2011)

26.62 J.-M. Yang, S.-P. Gou, I.W. Sun: Single-step large-scale and template-free electrochemical growth of Ni–Zn alloy filament arrays from a zinc chloride based ionic liquid, Chem. Commun. **46**, 2686–2688 (2010)

26.63 A. Ghahremaninezhad, E. Asselin, D.G. Dixon: One-step template-free electrosynthesis of 300 μm long copper sulfide nanowires, Electrochem. Commun. **13**, 12–15 (2011)

26.64 J.-M. Yang, Y.-T. Hsieh, T.-T. Chu-Tien, I.W. Sun: Electrodeposition of distinct one-dimensional Zn biaxial microbelt from the zinc chloride–1-ethyl-3-methylidazolium chloride ionic liquid, J. Electrochem. Soc. **158**, D235–D239 (2011)

26.65 L. Liang, C.J. Liu, F. Windisch Jr., G.J. Exarhos, Y. Lin: Direct assembly of large arrays of oriented conducting polymer nanowires, Angew. Chem. Int. Ed. **41**, 3665–3668 (2002)

26.66 J. Liu, Y. Lin, L. Liang, J.A. Voigt, D.L. Huber, Z.R. Tian, E. Coker, B. Mckenzie, M.J. McDermott: Templateless assembly of molecularly aligned conductive polymer nanowires a new approach for oriented nanostructures, Chemistry **9**, 604–611 (2003)

26.67 K. Wang, J. Huang, Z. Wei: Conducting polyaniline nanowire arrays for high performance supercapacitors, J. Phys. Chem. C **114**, 8062–8067 (2010)

26.68 L. Jiang, Z. Cui: One-step synthesis of oriented polyaniline nanorods through electrochemical deposition, Polym. Bull. **56**, 529–537 (2006)

26.69 Y. Guo, Y. Zhou: Polyaniline nanofibers fabricated by electrochemical polymerization: A mechanistic study, Eur. Polym. J. **43**, 2292–2297 (2007)

26.70 S. Mu, Y. Yang: Spectral characteristics of polyaniline nanostructures synthesized by using cyclic voltammetry at different scan rates, J. Phys. Chem. B **112**, 11558–11563 (2008)

26.71 H. Zhang, J. Wang, Z. Wang, F. Zhang, S. Wang: Electrodeposition of polyaniline nanostructures: A lamellar structure, Synth. Met. **159**, 277–281 (2009)

26.72 R.M. Nyffenegger, R.M. Penner: Nanometer-scale electropolymerization of aniline using the scan-

ning tunneling microscope, J. Phys. Chem. **100**, 17041–17049 (1996)
26.73 D. Ge, J. Wang, Z. Wang, S. Wang: Electrochemical synthesis of polypyrrole nanowires on composite electrode, Synth. Met. **132**, 93–95 (2002)
26.74 Y. Yang, M. Wan: Microtubules of polypyrrole synthesized by an electrochemical template-free method, J. Mater. Chem. **11**, 2022–2027 (2001)
26.75 Y.S. Yang, J. Liu, M.X. Wan: Self-assembled conducting polypyrrole micro/nanotubes, Nanotechnology **13**, 771–773 (2002)
26.76 S. Gupta: Template-free synthesis of conducting-polymer polypyrrole micro/nanostructures using electrochemistry, Appl. Phys. Lett. **88**(6), 0631081 (2006)
26.77 L.T. Qu, G.Q. Shi: Electrochemical synthesis of novel polypyrrole microstructures, Chem. Commun. **2**, 206–207 (2003)
26.78 L.T. Qu, G.Q. Shi, F. Chen, J.X. Zhang: Electrochemical growth of polypyrrole microcontainers, Macromolecules **36**, 1063–1067 (2003)
26.79 V. Bajpai, P.G. He, L.M. Dai: Conducting-polymer microcontainers: Controlled syntheses and potential applications, Adv. Funct. Mater. **14**, 145–151 (2004)
26.80 J. Wang, Y. Xu, F. Yan, J. Zhu, J. Wang: Template-free prepared micro/nanostructured polypyrrole with ultrafast charging–discharging rate and long cycle life, J. Power Sources **196**, 2373–2379 (2011)
26.81 G.W. Lu, C. Li, G.Q. Shi: Polypyrrole micro- and nanowires synthesized by electrochemical polymerization of pyrrole in the aqueous solutions of pyrenesulfonic acid, Polymer **47**, 1778–1784 (2006)
26.82 X. Yang, T. Dai, Z. Zhu, Y. Lu: Electrochemical synthesis of functional polypyrrole nanotubes via a self-assembly process, Polymer **48**, 4021–4027 (2007)
26.83 J. Zang, S.-J. Bao, C.M. Li, H. Bian, X. Cui, Q. Bao, C.Q. Sun, J. Guo, K. Lian: Well-aligned cone-shaped nanostructure of polypyrrole/RuO_2 and its electrochemical supercapacitor, J. Phys. Chem. C **112**, 14843–14847 (2008)
26.84 J. Zang, C.M. Li, S.-J. Bao, X. Cui, Q. Bao, C.Q. Sun: Template-free electrochemical synthesis of superhydrophilic polypyrrole nanofiber network, Macromolecules **41**, 7053–7057 (2008)
26.85 M. Li, Z. Wei, L. Jiang: Polypyrrole nanofiber arrays synthesized by a biphasic electrochemical strategy, J. Mater. Chem. **18**, 2276 (2008)
26.86 J.C. Hulteen, C.R. Martin: A general template-based method for the preparation of nanomaterials, J. Mater. Chem. **7**, 1075–1087 (1997)
26.87 K. Wada, T. Shimohira, M. Yamada, N. Baba: Microstructure of porous anodic oxide-films on aluminum, J. Mater. Sci. **21**, 3810–3816 (1986)
26.88 R.C. Furneaux, W.R. Rigby, A.P. Davidson: The formation of controlled-porosity membranes from anodically oxidized aluminium, Nature **337**, 147–149 (1989)
26.89 A.P. Li, F. Muller, A. Birner, K. Nielsch, U. Gosele: Hexagonal pore arrays with a 50–420 nm interpore distance formed by self-organization in anodic alumina, J. Appl. Phys. **84**, 6023–6026 (1998)
26.90 F.Y. Li, L. Zhang, R.M. Metzger: On the growth of highly ordered pores in anodized aluminum oxide, Chem. Mater. **10**, 2470–2480 (1998)
26.91 H. Masuda, K. Fukuda: Ordered metal nanohole arrays made by a 2-step replication of honeycomb structures of anodic alumina, Science **268**, 1466–1468 (1995)
26.92 H. Masuda, F. Hasegwa, S. Ono: Self-ordering of cell arrangement of anodic porous alumina formed in sulfuric acid solution, J. Electrochem. Soc. **144**, L127–L130 (1997)
26.93 W. Lee: The anodization of aluminum for nanotechnology applications, JOM **62**, 57–63 (2010)
26.94 P. Bocchetta, C. Sunseri, A. Bottino, G. Capannelli, G. Chiavarotti, S. Piazza, F. Di Quarto: Asymmetric alumina membranes electrochemically formed in oxalic acid solution, J. Appl. Electrochem. **32**, 977–985 (2002)
26.95 J.H. Yuan, F.Y. He, D.C. Sun, X.H. Xia: A simple method for preparation of through-hole porous anodic alumina membrane, Chem. Mater. **16**, 1841–1844 (2004)
26.96 J.M. Montero-Moreno, M. Sarret, C. Muller: Influence of the aluminum surface on the final results of a two-step anodizing, Surf. Coat. Technol. **201**, 6352–6357 (2007)
26.97 Z. Su, W. Zhou: Formation mechanism of porous anodic aluminium and titanium oxides, Adv. Mater. **20**, 3663–3667 (2008)
26.98 J.M. Montero-Moreno, M. Belenguer, M. Sarret, C.M. Mueller: Production of alumina templates suitable for electrodeposition of nanostructures using stepped techniques, Electrochim. Acta **54**, 2529–2535 (2009)
26.99 T.T. Xu, R.D. Piner, R.S. Ruoff: An improved method to strip aluminum from porous anodic alumina films, Langmuir **19**, 1443–1445 (2003)
26.100 G.D. Sulka, K.G. Parkola: Temperature influence on well-ordered nanopore structures grown by anodization of aluminium in sulphuric acid, Electrochim. Acta **52**, 1880–1888 (2007)
26.101 M.L. Tian, S.Y. Xu, J.G. Wang, N. Kumar, E. Wertz, Q. Li, P.M. Campbell, M.H.W. Chan, T.E. Mallouk: Penetrating the oxide barrier in situ and separating freestanding porous anodic alumina films in one step, Nano Lett. **5**, 697–703 (2005)
26.102 Y. Li, M. Zheng, L. Ma, W. Shen: Fabrication of highly ordered nanoporous alumina films by stable high-field anodization, Nanotechnology **17**, 5101–5105 (2006)
26.103 J.M. Montero-Moreno, M. Sarret, C. Mueller: Some considerations on the influence of voltage in potentiostatic two-step anodizing of AA1050, J. Electrochem. Soc. **154**, C169–C174 (2007)
26.104 S. Ono, M. Saito, M. Ishiguro, H. Asoh: Controlling factor of self-ordering of anodic porous alumina, J. Electrochem. Soc. **151**, B473–B478 (2004)
26.105 S.Z. Chu, K. Wada, S. Inoue, M. Isogai, A. Yasumori: Fabrication of ideally ordered nanoporous alumina films and integrated alumina nan-

otubule arrays by high-field anodization, Adv. Mater. **17**, 2115–2119 (2005)
26.106 W. Lee, R. Ji, U. Goesele, K. Nielsch: Fast fabrication of long-range ordered porous alumina membranes by hard anodization, Nat. Mater. **5**, 741–747 (2006)
26.107 K. Schwirn, W. Lee, R. Hillebrand, M. Steinhart, K. Nielsch, U. Goesele: Self-ordered anodic aluminum oxide formed by H_2SO_4 hard anodization, ACS Nano **2**, 302–310 (2008)
26.108 W. Lee, K. Schwirn, M. Steinhart, E. Pippel, R. Scholz, U. Gosele: Structural engineering of nanoporous anodic aluminium oxide by pulse anodization of aluminium, Nat. Nanotechnol. **3**, 234–239 (2008)
26.109 W. Lee, J.-C. Kim, U. Goesele: Spontaneous current oscillations during hard anodization of aluminum under potentiostatic conditions, Adv. Funct. Mater. **20**, 21–27 (2010)
26.110 H. Masuda, H. Asoh, M. Watanabe, K. Nishio, M. Nakao, T. Tamamura: Square and triangular nanohole array architectures in anodic alumina, Adv. Mater. **13**, 189–192 (2001)
26.111 H. Masuda, H. Yamada, M. Satoh, H. Asoh, M. Nakao, T. Tamamura: Highly ordered nanochannel-array architecture in anodic alumina, Appl. Phys. Lett. **71**, 2770–2772 (1997)
26.112 H. Asoh, K. Nishio, M. Nakao, T. Tamamura, H. Masuda: Conditions for fabrication of ideally ordered anodic porous alumina using pretextured Al, J. Electrochem. Soc. **148**, B152–B156 (2001)
26.113 A. Apel: Tracketching technique in membrane technology, Radiat. Meas. **34**, 559–566 (2001)
26.114 N.J. Gerein, J.A. Haber: Effect of ac electrodeposition conditions on the growth of high aspect ratio copper nanowires in porous aluminum oxide templates, J. Phys. Chem. B **109**, 17372–17385 (2005)
26.115 A.L. Friedman, L. Menon: Optimal parameters for synthesis of magnetic nanowires in porous alumina templates – Electrodeposition study, J. Electrochem. Soc. **154**, E68–E70 (2007)
26.116 F. Maurer, J. Broetz, S. Karim, M. Eugenia, T. Molares, C. Trautmann, H. Fuess: Preferred growth orientation of metallic fcc nanowires under direct and alternating electrodeposition conditions, Nanotechnology **18**(13), 135709 (2007)
26.117 D. Borissov, S. Isik-Uppenkamp, M. Rohwerder: Fabrication of iron nanowire arrays by electrodeposition into porous alumina, J. Phys. Chem. C **113**, 3133–3138 (2009)
26.118 K. Nielsch, F. Muller, A.P. Li, U. Gosele: Uniform nickel deposition into ordered alumina pores by pulsed electrodeposition, Adv. Mater. **12**, 582–586 (2000)
26.119 M. Qu, G. Zhao, Q. Wang, X. Cao, J. Zhang: Fabrication of superhydrophobic surfaces by a Pt nanowire array on Ti/Si substrates, Nanotechnology **19**(19), 055707 (2008)
26.120 K. Kim, M. Kim, S.M. Cho: Pulsed electrodeposition of palladium nanowire arrays using AAO template, Mater. Chem. Phys. **96**, 278–282 (2006)
26.121 C. Xu, H. Wang, P.K. Shen, S.P. Jiang: Highly ordered Pd nanowire arrays as effective electrocatalysts for ethanol oxidation in direct alcohol fuel cells, Adv. Mater. **19**, 4256–4259 (2007)
26.122 F. Cheng, H. Wang, Z. Sun, M. Ning, Z. Cai, M. Zhang: Electrodeposited fabrication of highly ordered Pd nanowire arrays for alcohol electrooxidation, Electrochem. Commun. **10**, 798–801 (2008)
26.123 S. Shin, B.S. Kim, K.M. Kim, B.H. Kong, H.K. Cho, H.H. Cho: Tuning the morphology of copper nanowires by controlling the growth processes in electrodeposition, J. Mater. Chem. **21**, 17967–17971 (2011)
26.124 J. Choi, G. Sauer, K. Nielsch, R.B. Wehrspohn, U. Gosele: Hexagonally arranged monodisperse silver nanowires with adjustable diameter and high aspect ratio, Chem. Mater. **15**, 776–779 (2003)
26.125 D.J. Sellmyer, M. Zheng, R. Skomski: Magnetism of Fe, Co and Ni nanowires in self-assembled arrays, J. Phys. Condens. Matter **13**, R433–R460 (2001)
26.126 J.H. Lim, W.S. Chae, H.O. Lee, L. Malkinski, S.G. Min, J.B. Wiley, J.H. Jun, S.H. Lee, J.S. Jung: Fabrication and magnetic properties of Fe nanostructures in anodic alumina membrane, J. Appl. Phys. **107**, 09A334 (2010)
26.127 V. Haehnel, S. Faehler, P. Schaaf, M. Miglierini, C. Mickel, L. Schultz, H. Schloerb: Towards smooth and pure iron nanowires grown by electrodeposition in self-organized alumina membranes, Acta Mater. **58**, 2330–2337 (2010)
26.128 J. Qin, J. Nogues, M. Mikhaylova, A. Roig, J.S. Munoz, M. Muhammed: Differences in the magnetic properties of Co, Fe, and Ni 250–300 nm wide nanowires electrodeposited in amorphous anodized alumina templates, Chem. Mater. **17**, 1829–1834 (2005)
26.129 F.S. Li, T. Wang, L.Y. Ren, J.R. Sun: Structure and magnetic properties of Co nanowires in self-assembled arrays, J. Phys. Condens. Matter **16**, 8053–8060 (2004)
26.130 P. Wang, L. Gao, Z. Qiu, X. Song, L. Wang, S. Yang, R.-I. Murakami: A multistep ac electrodeposition method to prepare Co nanowires with high coercivity, J. Appl. Phys. **104**, 064304 (2008)
26.131 M. Zheng, L. Menon, H. Zeng, Y. Liu, S. Bandyopadhyay, R.D. Kirby, D.J. Sellmyer: Magnetic properties of Ni nanowires in self-assembled arrays, Phys. Rev. B **62**, 12282–12286 (2000)
26.132 R. Inguanta, S. Piazza, C. Sunseri: Influence of electrodeposition techniques on Ni nanostructures, Electrochim. Acta **53**, 5766–5773 (2008)
26.133 J.K. Lee, Y. Yi, H.J. Lee, S. Uhm, J. Lee: Electrocatalytic activity of Ni nanowires prepared by galvanic electrodeposition for hydrogen evolution reaction, Catal. Today **146**, 188–191 (2009)
26.134 A. Gambirasi, S. Cattarin, M. Musiani, L. Vazquez-Gomez, E. Verlato: Direct electrodeposition of metal nanowires on electrode surface, Electrochim. Acta **56**, 8582–8588 (2011)
26.135 J.G. Wang, M.L. Tian, T.E. Mallouk, M.H.W. Chan: Microtwinning in template-synthesized single-

crystal metal nanowires, J. Phys. Chem. B **108**, 841–845 (2004)
26.136 G. Sauer, G. Brehm, S. Schneider, K. Nielsch, R.B. Wehrspohn, J. Choi, H. Hofmeister, U. Gosele: Highly ordered monocrystalline silver nanowire arrays, J. Appl. Phys. **91**, 3243–3247 (2002)
26.137 M.L. Tian, J.U. Wang, J. Kurtz, T.E. Mallouk, M.H.W. Chan: Electrochemical growth of single-crystal metal nanowires via a two-dimensional nucleation and growth mechanism, Nano Lett. **3**, 919–923 (2003)
26.138 F.Y. Yang, K. Liu, K.M. Hong, D.H. Reich, P.C. Searson, C.L. Chien: Large magnetoresistance of electrodeposited single-crystal bismuth thin films, Science **284**, 1335–1337 (1999)
26.139 L. Li, Y. Zhang, G.H. Li, L.D. Zhang: A route to fabricate single crystalline bismuth nanowire arrays with different diameters, Chem. Phys. Lett. **378**, 244–249 (2003)
26.140 J.G. Wang, M.L. Tian, N. Kumar, T.E. Mallouk: Controllable template synthesis of superconducting Zn nanowires with different microstructures by electrochemical deposition, Nano Lett. **5**, 1247–1253 (2005)
26.141 M.L. Tian, J.G. Wang, J. Snyder, J. Kurtz, Y. Liu, P. Schiffer, T.E. Mallouk, M.H.W. Chan: Synthesis and characterization of superconducting single-crystal Sn nanowires, Appl. Phys. Lett. **83**, 1620–1622 (2003)
26.142 H. Pan, B.H. Liu, J.B. Yi, C. Poh, S. Lim, J. Ding, Y.P. Feng, C.H.A. Huan, J.Y. Lin: Growth of single crystalline Ni and Co nanowires via electrochemical deposition and their magnetic properties, J. Phys. Chem. B **109**, 3094–3098 (2005)
26.143 X. Huang, L. Li, X. Luo, X. Zhu, G. Li: Orientation-controlled synthesis and ferromagnetism of single crystalline Co nanowire arrays, J. Phys. Chem. C **112**, 1468–1472 (2008)
26.144 X.H. Huang, G.H. Li, X.C. Dou, L. Li: Magnetic properties of single crystalline Co nanowire arrays with different diameters and orientations, J. Appl. Phys. **105**, 084306 (2009)
26.145 J.M. Baik, M. Schierhorn, M. Moskovits: Fe nanowires in nanoporous alumina: Geometric effect versus influence of pore walls, J. Phys. Chem. C **112**, 2252–2255 (2008)
26.146 S. Thongmee, H.L. Pang, J.B. Yi, J. Ding, J.Y. Lin, L.H. Van: Unique nanostructures in NiCo alloy nanowires, Acta Mater. **57**, 2482–2487 (2009)
26.147 S.Z. Chu, S. Inoue, K. Wada, Y. Kanke, K. Kurashima: Fabrication and characterization of integrated ultrahigh-density Fe–Pt alloy nanowire arrays on glass, J. Electrochem. Soc. **152**, C42–C47 (2005)
26.148 S.Z. Chu, S. Inoue, K. Wada, K. Kurashima: Fabrication of integrated arrays of ultrahigh density magnetic nanowires on glass by anodization and electrodeposition, Electrochim. Acta **51**, 820–826 (2005)
26.149 V. Haehnel, S. Faehler, L. Schultz, H. Schloerb: Electrodeposition of Fe70Pd30 nanowires from a complexed ammonium-sulfosalicylic electrolyte with high stability, Electrochem. Commun. **12**, 1116–1119 (2010)
26.150 A. Ramazani, M.A. Kashi, S. Kabiri, M. Zanguri: The influence of asymmetric electrodeposition voltage on the microstructure and magnetic properties of Fe_xCo_{1-x} nanowire arrays, J. Cryst. Growth **327**, 78–83 (2011)
26.151 K.V. Singh, A.A. Martinez-Morales, G.T.S. Andavan, K.N. Bozhilov, M. Ozkan: A simple way of synthesizing single-crystalline semiconducting copper sulfide nanorods by using ultrasonication during template-assisted electrodeposition, Chem. Mater. **19**, 2446–2454 (2007)
26.152 W.-L. Wang, C.-C. Wan, Y.-Y. Wang: Investigation of electrodeposition of Bi_2Te_3 nanowires into nanoporous alumina templates with a rotating electrode, J. Phys. Chem. B **110**, 12974–12980 (2006)
26.153 H. Sun, X. Li, Y. Chen, D. Guo, Y. Xie, W. Li, B. Liu, X. Zhang: Diameter- and current–density-dependent growth orientation of hexagonal CdSe nanowire arrays via electrodeposition, Nanotechnology **20**, 425603 (2009)
26.154 E.A. Hernandez-Pagan, W. Wang, T.E. Mallouk: Template electrodeposition of single-phase p- and n-type copper indium diselenide ($CuInSe_2$) nanowire arrays, ACS Nano **5**, 3237–3241 (2011)
26.155 M. Chen, P.C. Searson, C.L. Chien: Micromagnetic behavior of electrodeposited Ni/Cu multilayer nanowires, J. Appl. Phys. **93**, 8253–8255 (2003)
26.156 Y.K. Su, D.H. Qin, H.L. Zhang, H. Li, H.L. Li: Microstructure and magnetic properties of bamboo-like CoPt/Pt multilayered nanowire arrays, Chem. Phys. Lett. **388**, 406–410 (2004)
26.157 H.P. Liang, Y.G. Guo, J.S. Hu, C.F. Zhu, L.J. Wan, C.L. Bai: Ni–Pt multilayered nanowire arrays with enhanced coercivity and high remanence ratio, Inorg. Chem. **44**, 3013–3015 (2005)
26.158 F.H. Xue, G.T. Fei, B. Wu, P. Cui, L.D. Zhang: Direct electrodeposition of highly dense Bi/Sb superlattice nanowire arrays, J. Am. Chem. Soc. **127**, 15348–15349 (2005)
26.159 B. Yoo, F. Xiao, K.N. Bozhilov, J. Herman, M.A. Ryan, N.V. Myung: Electrodeposition of thermoelectric superlattice nanowires, Adv. Mater. **19**, 296–299 (2007)
26.160 X. Dou, G. Li, H. Lei, X. Huang, L. Li, I.W. Boyd: Template epitaxial growth of thermoelectric Bi/BiSb superlattice nanowires by charge-controlled pulse electrodeposition, J. Electrochem. Soc. **156**, K149–K154 (2009)
26.161 S.R. Nicewarner-Pena, R.G. Freeman, B.D. Reiss, L. He, D.J. Pena, I.D. Walton, R. Cromer, C.D. Keating, M.J. Natan: Submicrometer metallic barcodes, Science **294**, 137–141 (2001)
26.162 B.R. Martin, D.J. Dermody, B.D. Reiss, M.M. Fang, L.A. Lyon, M.J. Natan, T.E. Mallouk: Orthogonal self-assembly on colloidal gold-platinum nanorods, Adv. Mater. **11**, 1021–1025 (1999)
26.163 J.G. Wang, M.L. Tian, T.E. Mallouk, M.H.W. Chan: Microstructure and interdiffusion of template-

synthesized Au/Sn/Au junction nanowires, Nano Lett. **4**, 1313–1318 (2004)
26.164 S. Anandakumar, V.S. Rani, T.S. Ramulu, H.-J. Yang, B.H. Lim, J. Kim, S.S. Yoon, C. Kim: Electrodeposition of multi-segmented CoNiP-Au nanowires for bio-barcodes, J. Electrochem. Soc. **158**, E124–E127 (2011)
26.165 F. Li, J.B. Wiley: Preparation of free-standing metal wire arrays by in situ assembly, J. Mater. Chem. **18**, 3977–3980 (2008)
26.166 L. Liu, W. Lee, R. Scholz, E. Pippel, U. Gosele: Tailor-made inorganic nanopeapods: Structural design of linear noble metal nanoparticle chains, Angew. Chem. Int. Ed. **47**, 7004–7008 (2008)
26.167 M. Rauber, J. Broetz, J. Duan, J. Liu, S. Mueller, R. Neumann, O. Picht, M.E. Toimil-Molares, W. Ensinger: Segmented all-platinum nanowires with controlled morphology through manipulation of the local electrolyte distribution in fluidic nanochannels during electrodeposition, J. Phys. Chem. C **114**, 22502–22507 (2010)
26.168 H.-M. Bok, K.L. Shuford, S. Kim, S.K. Kim, A.S. Park: Multiple surface plasmon modes for a colloidal solution of nanoporous gold nanorods and their comparison to smooth gold nanorods, Nano Lett. **8**, 2265–2270 (2008)
26.169 C.X. Ji, P.C. Searson: Fabrication of nanoporous gold nanowires, Appl. Phys. Lett. **81**, 4437–4439 (2002)
26.170 Z. Liu, P.C. Searson: Single nanoporous gold nanowire sensors, J. Phys. Chem. B **110**, 4318–4322 (2006)
26.171 L. Liu, W. Lee, Z. Huang, R. Scholz, U. Goesele: Fabrication and characterization of a flow-through nanoporous gold nanowire/AAO composite membrane, Nanotechnology **19**, 335604 (2008)
26.172 D. van Noort, C.F. Mandenius: Porous gold surfaces for biosensor applications, Biosens. Bioelectron. **15**, 203–209 (2000)
26.173 H.-O. Lee, E.-M. Kim, H. Yu, J.-S. Jung, W.-S. Chae: Advanced porous gold nanofibers for highly efficient and stable molecular sensing platforms, Nanotechnology **20**, 325604 (2009)
26.174 S.-H. Yoo, S. Park: Platinum-coated, nanoporous gold nanorod arrays: Synthesis and characterization, Adv. Mater. **19**, 1612–1615 (2007)
26.175 X. Zhang, W. Lu, J. Da, H. Wang, D. Zhao, P.A. Webley: Porous platinum nanowire arrays for direct ethanol fuel cell applications, Chem. Commun. **2**, 195–197 (2009)
26.176 F. Li, J.B. He, W.L.L. Zhou, J.B. Wiley: Synthesis of porous wires from directed assemblies of nanospheres, J. Am. Chem. Soc. **125**, 16166–16167 (2003)
26.177 X. Zhang, D. Li, L. Bourgeois, H. Wang, P.A. Webley: Direct electrodeposition of porous gold nanowire arrays for biosensing applications, Chem. Phys. Chem. **10**, 436–441 (2009)
26.178 Y.H. Wang, C.H. Ye, X.S. Fang, L. Zhang: A simple method for synthesizing copper nanotube arrays, Chem. Lett. **33**, 166–167 (2004)
26.179 X. Zhang, H. Wang, L. Bourgeois, R. Pan, D. Zhao, P.A. Webley: Direct electrodeposition of gold nanotube arrays for sensing applications, J. Mater. Chem. **18**, 463–467 (2008)
26.180 L. Soleimany, A. Dolati, M. Ghorbani: A study on the kinetics of gold nanowire electrodeposition in polycarbonate templates, J. Electroanal. Chem. **645**, 28–34 (2010)
26.181 Y. Zhao, Y.G. Guo, Y.L. Zhang, K. Jiao: Fabrication and characterization of highly ordered Pt nanotubule arrays, Phys. Chem. Chem. Phys. **6**, 1766–1768 (2004)
26.182 W. Lee, M. Alexe, K. Nielsch, U. Gosele: Metal membranes with hierarchically organized nanotube arrays, Chem. Mater. **17**, 3325–3327 (2005)
26.183 L. Li, Y.W. Yang, X.H. Huang, G.H. Li, R. Ang, L.D. Zhang: Fabrication and electronic transport properties of Bi nanotube arrays, Appl. Phys. Lett. **88**, 103119 (2006)
26.184 L. Liu, W. Zhou, S. Xie, L. Song, S. Luo, D. Liu, J. Shen, Z. Zhang, Y. Xiang, W. Ma, Y. Ren, C. Wang, G. Wang: Highly efficient direct electrodeposition of Co-Cu alloy nanotubes in an anodic alumina template, J. Phys. Chem. C **112**, 2256–2261 (2008)
26.185 H. Cao, L. Wang, Y. Qiu, Q. Wu, G. Wang, L. Zhang, X. Liu: Generation and growth mechanism of metal (Fe, Co, Ni) nanotube arrays, Chem. Phys. Chem. **7**, 1500–1504 (2006)
26.186 R. Xiao, S. Il Cho, R. Liu, S.B. Lee: Controlled electrochemical synthesis of conductive polymer nanotube structures, J. Am. Chem. Soc. **129**, 4483–4489 (2007)
26.187 D. Mo, J. Liu, H.J. Yao, J.L. Duan, M.D. Hou, Y.M. Sun, Y.F. Chen, Z.H. Xue, L. Zhang: Preparation and characterization of CdS nanotubes and nanowires by electrochemical synthesis in ion-track templates, J. Cryst. Growth **310**, 612–616 (2008)
26.188 Q. Huang, D.P. Young, J.Y. Chan, J. Jiang, E.J. Podlaha: Electrodeposition of FeCoNiCu/Cu compositionally modulated multilayers, J. Electrochem. Soc. **149**, C349–C354 (2002)
26.189 Q. Huang, E.J. Podlaha: Simulation of pulsed electrodeposition for giant magnetoresistance FeCoNiCu/Cu multilayers, J. Electrochem. Soc. **151**, C119–C126 (2004)
26.190 D.M. Davis, E.J. Podlaha: CoNiCu and Cu nanotube electrodeposition, Electrochem. Solid State Lett. **8**, D1–D4 (2005)
26.191 Y. Fukunaka, M. Motoyama, Y. Konishi, R. Ishii: Producing shape-controlled metal nanowires and nanotubes by an electrochemical method, Electrochem. Solid State Lett. **9**, C62–C64 (2006)
26.192 M. Motoyama, Y. Fukunaka, Y.H. Ogata, F.B. Prinz: Impact of accompanying hydrogen generation on metal nanotube electrodeposition, J. Electrochem. Soc. **157**, D357–D369 (2010)
26.193 X. Zhang, D. Dong, D. Li, T. Williams, H. Wang, P.A. Webley: Direct electrodeposition of Pt nanotube arrays and their enhanced electrocatalytic activities, Electrochem. Commun. **11**, 190–193 (2009)

26.194 L. Li, S. Pan, X. Dou, Y. Zhu, X. Huang, Y. Yang, G. Li, L. Zhang: Direct electrodeposition of ZnO nanotube arrays in anodic alumina membranes, J. Phys. Chem. C **111**, 7288–7291 (2007)

26.195 M. Lai, J.A.G. Martinez, M. Gratzel, D.J. Riley: Preparation of tin dioxide nanotubes via electrosynthesis in a template, J. Mater. Chem. **16**, 2843–2845 (2006)

26.196 M. Lai, J.-H. Lim, S. Mubeen, Y. Rheem, A. Mulchandani, M.A. Deshusses, N.V. Myung: Size-controlled electrochemical synthesis and properties of SnO_2 nanotubes, Nanotechnology **20**, 185602 (2009)

26.197 E. Mafakheri, A. Salimi, R. Hallaj, A. Ramazani, M.A. Kashi: Synthesis of iridium oxide nanotubes by electrodeposition into polycarbonate template: fabrication of chromium (III) and arsenic (III) electrochemical sensor, Electroanalysis **23**, 2429–2437 (2011)

26.198 X.-H. Li, B. Zhou, L. Pu, J.-J. Zhu: Electrodeposition of Bi_2Te_3 and Bi_2Te_3 derived alloy nanotube arrays, Cryst. Growth Des. **8**, 771–775 (2008)

26.199 W. Lee, R. Scholz, K. Niesch, U. Gosele: A template-based electrochemical method for the synthesis of multisegmented metallic nanotubes, Angew. Chem. Int. Ed. **44**, 6050–6054 (2005)

26.200 M.V. Kamalakar, A.K. Raychaudhuri: A novel method of synthesis of dense arrays of aligned single crystalline copper nanotubes using electrodeposition in the presence of a rotating electric field, Adv. Mater. **20**, 149–154 (2008)

26.201 C. Mu, Y.X. Yn, R.M. Wang, K. Wu, D.S. Xu, G.L. Guo: Uniform metal nanotube arrays by multistep template replication and electrodeposition, Adv. Mater. **16**, 1550–1553 (2004)

26.202 M.S. Sander, H. Gao: Aligned arrays of nanotubes and segmented nanotubes on substrates fabricated by electrodeposition onto nanorods, J. Am. Chem. Soc. **127**, 12158–12159 (2005)

26.203 P.R. Evans, W.R. Hendren, R. Atkinson, R.J. Pollard: Nickel-coated gold-core nanorods produced by template assisted electrodeposition, J. Electrochem. Soc. **154**, K79–K82 (2007)

26.204 H. Wang, C. Xu, F. Cheng, M. Zhang, S. Wang, S.P. Jiang: Pd/Pt core-shell nanowire arrays as highly effective electrocatalysts for methanol electrooxidation in direct methanol fuel cells, Electrochem. Commun. **10**, 1575–1578 (2008)

26.205 T.N. Narayanan, M.M. Shaijumon, P.M. Ajayan, M.R. Anantharaman: Synthesis of high coercivity core-shell nanorods based on nickel and cobalt and their magnetic properties, Nanoscale Res. Lett. **5**, 164–168 (2010)

26.206 D.H. Park, Y.B. Lee, M.Y. Cho, B.H. Kim, S.H. Lee, Y.K. Hong, J. Joo, H.C. Cheong, S.R. Lee: Fabrication and magnetic characteristics of hybrid double walled nanotube of ferromagnetic nickel encapsulated conducting polypyrrole, Appl. Phys. Lett. **90**, 093122 (2007)

26.207 K.R. Ward, N.S. Lawrence, R.S. Hartshorne, R.G. Compton: The theory of cyclic voltammetry of electrochemically heterogeneous surfaces: Comparison of different models for surface geometry and applications to highly ordered pyrolytic graphite, Phys. Chem. Chem. Phys. **14**, 7264–7275 (2012)

26.208 H.P. Chang, A.J. Bard: Observation and characterization by scanning tunneling microscopy of structures generated by cleaving highly oriented pyrolytic-graphite, Langmuir **7**, 1143–1153 (1991)

26.209 R.L. McCreery: Advanced carbon electrode materials for molecular electrochemistry, Chem. Rev. **108**, 2646–2687 (2008)

26.210 H. Liu, F. Favier, K. Ng, M.P. Zach, R.M. Penner: Size-selective electrodeposition of mesoscale metal particles: A general method, Electrochim. Acta **47**, 671–677 (2001)

26.211 J.V. Zoval, J. Lee, S. Gorer, R.M. Penner: Electrochemical preparation of platinum nanocrystallites with size selectivity on basal plane oriented graphite surfaces, J. Phys. Chem. B **102**, 1166–1175 (1998)

26.212 C.J. Boxley, H.S. White, T.E. Lister, P.J. Pinhero: Electrochemical deposition and reoxidation of Au at highly oriented pyrolytic graphite. Stabilization of Au nanoparticles on the upper plane of step edges, J. Phys. Chem. B **107**, 451–458 (2003)

26.213 J.L. Fransaer, R.M. Penner: Brownian dynamics simulation of the growth of metal nanocrystal ensembles on electrode surfaces from solution. I. Instantaneous nucleation and diffusion-controlled growth, J. Phys. Chem. B **103**, 7643–7653 (1999)

26.214 R.M. Penner: Brownian dynamics simulations of the growth of metal nanocrystal ensembles on electrode surfaces in solution: 2. The effect of deposition rate on particle size dispersion, J. Phys. Chem. B **105**, 8672–8678 (2001)

26.215 H. Liu, R.M. Penner: Size-selective electrodeposition of mesoscale metal particles in the uncoupled limit, J. Phys. Chem. B **104**, 9131–9139 (2000)

26.216 M. Bayati, J.M. Abad, R.J. Nichols, D.J. Schiffrin: Substrate structural effects on the synthesis and electrochemical properties of platinum nanoparticles on highly oriented pyrolytic graphite, J. Phys. Chem. C **114**, 18439–18448 (2010)

26.217 R.M. Penner: Mesoscopic metal particles and wires by electrodeposition, J. Phys. Chem. B **106**, 3339–3353 (2002)

26.218 F. Favier, E.C. Walter, M.P. Zach, T. Benter, R.M. Penner: Hydrogen sensors and switches from electrodeposited palladium mesowire arrays, Science **293**, 2227–2231 (2001)

26.219 E.C. Walter, F. Favier, R.M. Penner: Palladium mesowire arrays for fast hydrogen sensors and hydrogen-actuated switches, Anal. Chem. **74**, 1546–1553 (2002)

26.220 V.C. Diculescu, A.-M. Chiorcea-Paquim, O. Corduneanu, A.M. Oliveira-Brett: Palladium nanoparticles and nanowires deposited electrochemically: AFM and electrochemical characterization, J. Solid State Electrochem. **11**, 887–898 (2007)

26.221 E.C. Walter, B.J. Murray, F. Favier, G. Kaltenpoth, M. Grunze, R.M. Penner: Noble and coinage metal nanowires by electrochemical step edge decoration, J. Phys. Chem. B **106**, 11407–11411 (2002)

26.222 B.J. Murray, E.C. Walter, R.M. Penner: Amine vapor sensing with silver mesowires, Nano Lett. **4**, 665–670 (2004)

26.223 Y.K. Xiao, G. Yu, J. Yuan, J.Y. Wang, Z.Z. Chen: Fabrication of Pd-Ni alloy nanowire arrays on HOPG surface by electrodeposition, Electrochim. Acta **51**, 4218–4227 (2006)

26.224 T.J. Davies, M.E. Hyde, R.G. Compton: Nanotrench arrays reveal insight into graphite electrochemistry, Angew. Chem. Int. Ed. **44**, 5121–5126 (2005)

26.225 C.E. Cross, J.C. Hemminger, R.M. Penner: Physical vapor deposition of one-dimensional nanoparticle arrays on graphite: Seeding the electrodeposition of gold nanowires, Langmuir **23**, 10372–10379 (2007)

26.226 M.P. Zach, K.H. Ng, R.M. Penner: Molybdenum nanowires by electrodeposition, Science **290**, 2120–2123 (2000)

26.227 M.P. Zach, K. Inazu, K.H. Ng, J.C. Hemminger, R.M. Penner: Synthesis of molybdenum nanowires with millimeter-scale lengths using electrochemical step edge decoration, Chem. Mater. **14**, 3206–3216 (2002)

26.228 Q. Li, J.T. Newberg, E.C. Walter, J.C. Hemminger, R.M. Penner: Polycrystalline molybdenum disulfide (2H-MoS2) nano- and microribbons by electrochemical/chemical synthesis, Nano Lett. **4**, 277–281 (2004)

26.229 Q. Li, E.C. Walter, W.E. van der Veer, B.J. Murray, J.T. Newberg, E.W. Bohannan, J.A. Switzer, J.C. Hemminger, R.M. Penner: Molybdenum disulfide nanowires and nanoribbons by electrochemical/chemical synthesis, J. Phys. Chem. B **109**, 3169–3182 (2005)

26.230 Q.G. Li, J.B. Olson, R.M. Penner: Nanocrystalline alpha-MnO_2 nanowires by electrochemical step-edge decoration, Chem. Mater. **16**, 3402–3405 (2004)

26.231 Q.G. Li, R.M. Penner: Photoconductive cadmium sulfide hemicylindrical shell nanowire ensembles, Nano Lett. **5**, 1720–1725 (2005)

26.232 E.J. Menke, Q. Li, R.M. Penner: Bismuth telluride (Bi_2Te_3) nanowires synthesized by cyclic electrodeposition/stripping coupled with step edge decoration, Nano Lett. **4**, 2009–2014 (2004)

26.233 E.J. Menke, M.A. Brown, Q. Li, J.C. Hemminger, R.M. Penner: Bismuth telluride (Bi_2Te_3) nanowires: Synthesis by cyclic electrodeposition/stripping, thinning by electrooxidation, and electrical power generation, Langmuir **22**, 10564–10574 (2006)

26.234 M.E. Hyde, T.J. Davies, R.G. Compton: Fabrication of random assemblies of metal nanobands: A general method, Angew. Chem. Int. Ed. **44**, 6491–6496 (2005)

26.235 F. Li, M. Zhu, C. Liu, W.L. Zhou, J.B. Wiley: Patterned metal nanowire arrays from photolithographically-modified templates, J. Am. Chem. Soc. **128**, 13342–13343 (2006)

26.236 F. Yang, D.K. Taggart, R.M. Penner: Fast, sensitive hydrogen gas detection using single palladium nanowires that resist fracture, Nano Lett. **9**, 2177–2182 (2009)

26.237 R. Ji, W. Lee, R. Scholz, U. Gösele, K. Nielsch: Templated fabrication of nanowire and nanoring arrays based on interference lithography and electrochemical deposition, Adv. Mater. **18**, 2593–2596 (2006)

26.238 H.M. Saavedra, T.J. Mullen, P. Zhang, D.C. Dewey, S.A. Claridge, P.S. Weiss: Hybrid strategies in nanolithography, Rep. Prog. Phys. **73**, 036501 (2010)

26.239 W. Xu, J. Wong, C.C. Cheng, R. Johnson, A. Scherer: Fabrication of ultrasmall magnets by electroplating, J. Vac. Sci. Technol. B **13**, 2372–2375 (1995)

26.240 S. Biring, K.-T. Tsai, U.K. Sur, Y.-L. Wang: High speed fabrication of aluminum nanostructures with 10 nm spatial resolution by electrochemical replication, Nanotechnology **19**, 355302 (2008)

26.241 D.M. Kolb, R. Ullmann, T. Will: Nanofabrication of small copper clusters on gold(111) electrodes by a scanning tunneling microscope, Science **275**, 1097–1099 (1997)

26.242 E.J. Menke, M.A. Thompson, C. Xiang, L.C. Yang, R.M. Penner: Lithographically patterned nanowire electrodeposition, Nat. Mater. **5**, 914–919 (2006)

26.243 C. Xiang, S.-C. Kung, D.K. Taggart, F. Yang, M.A. Thompson, A.G. Gueell, Y. Yang, R.M. Penner: Lithographically patterned nanowire electrodeposition: A method for patterning electrically continuous metal nanowires on dielectrics, ACS Nano **2**, 1939–1949 (2008)

26.244 C. Xiang, A.G. Guell, M.A. Brown, J.Y. Kim, J.C. Hemminger, R.M. Penner: Coupled electrooxidation and electrical conduction in a single gold nanowire, Nano Lett. **8**, 3017–3022 (2008)

26.245 C. Xiang, Y. Yang, R.M. Penner: Cheating the diffraction limit: Electrodeposited nanowires patterned by photolithography, Chem. Commun. **8**, 859–873 (2009)

26.246 C. Xiang, J.Y. Kim, R.M. Penner: Reconnectable Sub-5 nm nanogaps in ultralong gold nanowires, Nano Lett. **9**, 2133–2138 (2009)

26.247 S.C. Kung, W. Xing, K.C. Donavan, F. Yang, R.M. Penner: Photolithographically patterned silver nanowire electrodeposition, Electrochim. Acta **55**, 8074–8080 (2010)

26.248 Y. Yang, S.C. Kung, D.K. Taggart, C. Xiang, F. Yang, M.A. Brown, A.G. Guell, T.J. Kruse, J.C. Hemminger, R.M. Penner: Synthesis of PbTe nanowire arrays using lithographically patterned nanowire electrodeposition, Nano Lett. **8**, 2447–2451 (2008)

26.249 S. Ghosh, J.E. Hujdic, A. Villicana-Bedolla, E.J. Menke: Gold core-semiconductor shell nanowires prepared by lithographically patterned nanowire electrodeposition, J. Phys. Chem. C **115**, 17670–17675 (2011)

26.250 D. Xia, Z. Ku, S.C. Lee, S.R.J. Brueck: Nanostructures and functional materials fabricated by interferometric lithography, Adv. Mater. **23**, 147–179 (2011)

26.251 D.F. Spicer, A.C. Rodger, G.L. Varnell: Computer-controlled pattern generating system for use with electron-beam writing instruments, J. Vac. Sci. Technol. **10**, 1052–1055 (1973)

26.252 G.L. Varnell, D.F. Spicer, A.C. Rodger: E-beam writing techniques for semiconductor-device fabrication, J. Vac. Sci. Technol. **10**, 1048–1051 (1973)

26.253 R. Maoz, E. Frydman, S.R. Cohen, J. Sagiv: Constructive nanolithography: Site-defined silver self-assembly on nanoelectrochemically patterned monolayer templates, Adv. Mater. **12**, 424–429 (2000)

26.254 H. Duan, J. Zhao, Y. Zhang, E. Xie, L. Han: Preparing patterned carbonaceous nanostructures directly by overexposure of PMMA using electron-beam lithography, Nanotechnology **20**, 135306 (2009)

26.255 J.L. Duvail, S. Dubois, L. Piraux, A. Vaures, A. Fert, D. Adam, M. Champagne, F. Rousseaux, D. Decanini: Electrodeposition of patterned magnetic nanostructures, J. Appl. Phys. **84**, 6359–6365 (1998)

26.256 M.J. Burek, J.R. Greer: Fabrication and microstructure control of nanoscale mechanical testing specimens via electron beam lithography and electroplating, Nano Lett. **10**, 69–76 (2010)

26.257 T.N. Lo, Y.T. Chen, C.W. Chiu, C.J. Liu, S.R. Wu, I.K. Lin, C.I. Su, W.D. Chang, Y. Hwu, B.Y. Shew, C.C. Chiang, J.H. Je, G. Margaritondo: E-beam lithography and electrodeposition fabrication of thick nanostructured devices, J. Phys. D **40**, 3172–3176 (2007)

26.258 L.M. Moretto, M. Tormen, M. De Leo, A. Carpentiero, P. Ugo: Polycarbonate-based ordered arrays of electrochemical nanoelectrodes obtained by e-beam lithography, Nanotechnology **22**(18), 185305 (2011)

26.259 F.C. Simeone, C. Albonetti, M. Cavallini: Progress in micro- and nanopatterning via electrochemical lithography, J. Phys. Chem. C **113**, 18987–18994 (2009)

26.260 M. Lee, R. O'Hayre, F.B. Prinz, T.M. Gur: Electrochemical nanopatterning of Ag on solid-state ionic conductor $RbAg_4I_5$ using atomic force microscopy, Appl. Phys. Lett. **85**, 3552–3554 (2004)

26.261 X. Zhang, F. Shi, J. Niu, Y. Jiang, Z. Wang: Superhydrophobic surfaces: From structural control to functional application, J. Mater. Chem. **18**, 621–633 (2008)

26.262 M. Chang, X. Cao, H. Zeng: Electrodeposition growth of vertical ZnO nanorod/polyaniline heterostructured films and their optical properties, J. Phys. Chem. C **113**, 15544–15547 (2009)

26.263 Z.-L. Wang, G.-R. Li, Y.-N. Ou, Z.-P. Feng, D.L. Qu, Y.-X. Tong: Electrochemical deposition of Eu^{3+}-doped CeO_2 nanobelts with enhanced optical properties, J. Phys. Chem. C **115**, 351–356 (2011)

26.264 O. Azzaroni, P.L. Schilardi, R.C. Salvarezza: Templated electrodeposition of patterned soft magnetic films, Appl. Phys. Lett. **80**, 1061–1063 (2002)

26.265 X. Yu, C. Cao, X. An: Facile conversion of Fe nanotube arrays to novel alpha-Fe_2O_3 nanoparticle nanotube arrays and their magnetic properties, Chem. Mater. **20**, 1936–1940 (2008)

26.266 L. Xu, S. Zhang, W. Liu, Z. Du: Vertically cobalt nanoplate arrays based on one-step electrochemical growth and their magnetic properties, J. Phys. Chem. C **116**, 2801–2806 (2012)

26.267 F. Xiao, C. Hangarter, B. Yoo, Y. Rheem, K.-H. Lee, N.V. Myung: Recent progress in electrodeposition of thermoelectric thin films and nanostructures, Electrochim. Acta **53**, 8103–8117 (2008)

26.268 Y. Zhao, J.S. Dyck, C. Burda: Toward high-performance nanostructured thermoelectric materials: The progress of bottom-up solution chemistry approaches, J. Mater. Chem. **21**, 17049–17058 (2011)

26.269 C. Wang, M. Waje, X. Wang, J.M. Tang, R.C. Haddon, Y.S. Yan: Proton exchange membrane fuel cells with carbon nanotube based electrodes, Nano Lett. **4**, 345–348 (2004)

26.270 Y. Li, X.-Y. Yang, Y. Feng, Z.-Y. Yuan, B.-L. Su: One-dimensional metal oxide nanotubes, nanowires, nanoribbons, and nanorods: Synthesis, characterizations, properties and applications, Crit. Rev. Solid State Mater. Sci. **37**, 1–74 (2012)

26.271 B.J. Plowman, S.K. Bhargava, A.P. O'Mullane: Electrochemical fabrication of metallic nanostructured electrodes for electroanalytical applications, Analyst **136**, 5107–5119 (2011)

26.272 A.M. Kumar, S. Jung, T. Ji: Protein biosensors based on polymer nanowires, carbon nanotubes and zinc oxide nanorods, Sensors **11**, 5087–5111 (2011)

26.273 S. Guo, E. Wang: Functional micro/nanostructures: Simple synthesis and application in sensors, fuel cells, and gene delivery, Acc. Chem. Res. **44**, 491–500 (2011)

26.274 X. Dou, G. Li, H. Lei: Kinetic versus thermodynamic control over growth process of electrodeposited Bi/BiSb superlattice nanowires, Nano Lett. **8**, 1286–1290 (2008)

26.275 Y.-C. Yang, T.-K. Huang, Y.-L. Chen, J.-Y. Mevellec, S. Lefrant, C.-Y. Lee, H.-T. Chiu: Electrochemical growth of gold nanostructures for surface-enhanced Raman scattering, J. Phys. Chem. C **115**, 1932–1939 (2011)

26.276 I. Gurrappa, L. Binder: Electrodeposition of nanostructured coatings and their characterization-A review, Sci. Technol. Adv. Mater. **9**, 043001 (2008)

26.277 W.C. West, N.V. Myung, J.F. Whitacre, B.V. Ratnakumar: Electrodeposited amorphous manganese oxide nanowire arrays for high energy and power density electrodes, J. Power Sources **126**, 203–206 (2004)

26.278 J.-K. Lee, G.-P. Kim, I.K. Song, S.-H. Baeck: Electrodeposition of mesoporous V_2O_5 with enhanced lithium-ion intercalation property, Electrochem. Commun. **11**, 1571–1574 (2009)

26.279 X. Li, P. Li, M. Luo, X. Chen, J. Chen: Controllable solvo-hydrothermal electrodeposition of lithium vanadate uniform carnation-like nanostructure and their electrochemical performance, J. Solid State Electrochem. **14**, 1325–1332 (2010)

26.280 Y.-H. Huang, K.-S. Park, J.B. Goodenough: Improving lithium batteries by tethering carbon-coated $LiFePO_4$ to polypyrrole, J. Electrochem. Soc. **153**, A2282–A2286 (2006)

26.281 K.-S. Park, S.B. Schougaard, J.B. Goodenough: Conducting-polymer/iron-redox-couple composite cathodes for lithium secondary batteries, Adv. Mater. **19**, 848–851 (2007)

26.282 I. Boyano, J. Alberto Blazquez, I. de Meatza, M. Bengoechea, O. Miguel, H. Grande, Y. Huang, J.B. Goodenough: Preparation of C-$LiFePO_4$/polypyrrole lithium rechargeable cathode by consecutive potential steps electrodeposition, J. Power Sources **195**, 5351–5359 (2010)

26.283 M. Schmuck, A. Balducci, B. Rupp, W. Kern, S. Passerini, M. Winter: Alloying of electrodeposited silicon with lithium-a principal study of applicability as anode material for lithium ion batteries, J. Solid State Electrochem. **14**, 2203–2207 (2010)

26.284 R.-G. Lue, J. Yang, J.-L. Wang, Y.-N. Nuli: Electrodeposition and electrochemical property of porous Li-Si film anodes for lithium-ion batteries, Acta Phys. Chim. Sin. **27**, 759–763 (2011)

26.285 R. Lv, J. Yang, J. Wang, Y. NuLi: Electrodeposited porous-microspheres Li-Si films as negative electrodes in lithium-ion batteries, J. Power Sources **196**, 3868–3873 (2011)

26.286 T. Momma, S. Aoki, H. Nara, T. Yokoshima, T. Osaka: Electrodeposited novel highly durable SiOC composite anode for Li battery above several thousands of cycles, Electrochem. Commun. **13**, 969–972 (2011)

26.287 H. Nara, T. Yokoshima, T. Momma, T. Osaka: Highly durable SiOC composite anode prepared by electrodeposition for lithium secondary batteries, Energ. Environ. Sci. **5**, 6500–6505 (2012)

26.288 K. Ui, S. Kikuchi, Y. Kadoma, N. Kumagai, S. Ito: Electrochemical characteristics of Sn film prepared by pulse electrode position method as negative electrode for lithium secondary batteries, J. Power Sources **189**, 224–229 (2009)

26.289 K. Ui, S. Kikuchi, Y. Jimba, N. Kumagai: Preparation of Co-Sn alloy film as negative electrode for lithium secondary batteries by pulse electrodeposition method, J. Power Sources **196**, 3916–3920 (2011)

26.290 H.C. Shin, M.L. Liu: Three-dimensional porous copper-tin alloy electrodes for rechargeable lithium batteries, Adv. Funct. Mater. **15**, 582–586 (2005)

26.291 L. Huang, Y. Yang, L.-J. Xue, H.-B. Wei, F.-S. Ke, J.-T. Li, S.-G. Sun: Electrodeposition and electrochemical properties of novel ternary tin-cobalt-phosphorus alloy electrodes for lithium-ion batteries, Electrochem. Commun. **11**, 6–9 (2009)

26.292 J. Park, J. Eom, H. Kwon: Fabrication of Sn-C composite electrodes by electrodeposition and their cycle performance for Li-ion batteries, Electrochem. Commun. **11**, 596–598 (2009)

26.293 S.-L. Chou, J.-Z. Wang, H.-K. Liu, S.-X. Dou: SnO2 meso-scale tubes: One-step, room temperature electrodeposition synthesis and kinetic investigation for lithium storage, Electrochem. Commun. **11**, 242–246 (2009)

26.294 J. Park, S. Rajendran, H. Kwon: Effects of substrate morphology and ageing on cycle performance of a Sn-anode fabricated by electroplating, J. Power Sources **159**, 1409–1415 (2006)

26.295 H. Zhao, C. Jiang, X. He, J. Ren, C. Wan: Advanced structures in electrodepo sited tin base anodes for lithium ion batteries, Electrochim. Acta **52**, 7820–7826 (2007)

26.296 N. Tamura, A. Fujimoto, M. Kamino, S. Fujitani: Mechanical stability of Sn-Co alloy anodes for lithium secondary batteries, Electrochim. Acta **49**, 1949–1956 (2004)

26.297 F.-S. Ke, L. Huang, H.-B. Wei, J.-S. Cai, X.-Y. Fan, F.-Z. Yang, S.-G. Sun: Fabrication and properties of macroporous tin-cobalt alloy film electrodes for lithium-ion batteries, J. Power Sources **170**, 450–455 (2007)

26.298 S.D. Beattie, J.R. Dahn: Single bath, pulsed electrodeposition of copper-tin alloy negative electrodes for lithium-ion batteries, J. Electrochem. Soc. **150**, A894–A898 (2003)

26.299 W. Choi, J.Y. Lee, H.S. Lim: Electrochemical lithiation reactions of Cu_6Sn_5 and their reaction products, Electrochem. Commun. **6**, 816–820 (2004)

26.300 F.-S. Ke, L. Huang, J.-S. Cai, S.-G. Sun: Electroplating synthesis and electrochemical properties of macroporous Sn-Cu alloy electrode for lithium-ion batteries, Electrochim. Acta **52**, 6741–6747 (2007)

26.301 H. Mukaibo, T. Sumi, T. Yokoshima, T. Momma, T. Osaka: Electrodeposited Sn-Ni alloy film as a high capacity anode material for lithium-ion secondary batteries, Electrochem. Solid State Lett. **6**, A218–A220 (2003)

26.302 J. Hassoun, S. Panero, B. Scrosati: Electrodeposited Ni-Sn intermetallic electrodes for advanced lithium ion batteries, J. Power Sources **160**, 1336–1341 (2006)

26.303 H. Bryngelsson, J. Eskhult, K. Edstroem, L. Nyholm: Electrodeposition and electrochemical characterisation of thick and thin coatings of Sb and Sb/Sb_2O_3 particles for Li-ion battery anodes, Electrochim. Acta **53**, 1062–1073 (2007)

26.304 J.M. Mosby, A.L. Prieto: Direct electrodeposition of Cu_2Sb for lithium-ion battery anodes, J. Am. Chem. Soc. **130**, 10656–10661 (2008)

26.305 P. Poizot, S. Laruelle, S. Grugeon, L. Dupont, J.M. Tarascon: Nano-sized transition-metaloxides as negative-electrode materials for lithium-ion batteries, Nature **407**, 496–499 (2000)

26.306 S. Mitra, P. Poizot, A. Finke, J.-M. Tarascon: Growth and electrochemical characterization versus lithium of Fe_3O_4 electrodes made via elec-

trodeposition, Adv. Funct. Mater. **16**, 2281–2287 (2006)
26.307 M.-S. Wu, Y.-H. Ou, Y.-P. Lin: Electrodeposition of iron oxide nanorods on carbon nanofiber scaffolds as an anode material for lithium-ion batteries, Electrochim. Acta **55**, 3240–3244 (2010)
26.308 A. Xiao, J. Yang, W. Zhang: Mesoporous cobalt oxide film prepared by electrodeposition as anode material for Li ion batteries, J. Porous Mater. **17**, 583–588 (2010)
26.309 J. Morales, L. Sanchez, S. Bijani, L. Martinez, M. Gabas, J.R. Ramos-Barrado: Electrodeposition of Cu_2O: An excellent method for obtaining films of controlled morphology and good performance in Li-ion batteries, Electrochem. Solid State Lett. **8**, A159–A162 (2005)
26.310 S. Bijani, M. Gabas, L. Martinez, J.R. Ramos-Barrado, J. Morales, L. Sanchez: Nanostructured Cu_2O thin film electrodes prepared by electrodeposition for rechargeable lithium batteries, Thin Solid Films **515**, 5505–5511 (2007)
26.311 L. Huang, X.-M. Zheng, Y.-S. Wu, L.-J. Xue, F.-S. Ke, G.-Z. Wei, S.-G. Sun: Electrodeposition and lithium storage performance of novel three-dimensional porous Fe-Sb-P amorphous alloy electrode, Electrochem. Commun. **11**, 585–588 (2009)
26.312 J.W. Long, B. Dunn, D.R. Rolison, H.S. White: Three-dimensional battery architectures, Chem. Rev. **104**, 4463–4492 (2004)
26.313 E. Perre, P.L. Taberna, D. Mazouzi, P. Poizot, T. Gustafsson, K. Edstrom, P. Simon: Electrodeposited Cu_2Sb as anode material for 3-dimensional Li-ion microbatteries, J. Mater. Res. **25**, 1485–1491 (2010)
26.314 L. Taberna, S. Mitra, P. Poizot, P. Simon, J.M. Tarascon: High rate capabilities Fe_3O_4-based Cu nano-architectured electrodes for lithium-ion battery applications, Nat. Mater. **5**, 567–573 (2006)
26.315 J. Hassoun, S. Panero, P. Simon, P.L. Taberna, B. Scrosati: High-rate, long-life Ni-Sn nanostructured electrodes for lithium-ion batteries, Adv. Mater. **19**, 1632–1635 (2007)
26.316 A. Finke, P. Poizot, C. Guery, L. Dupont, P.-L. Taberna, P. Simon, J.-M. Tarascon: Electrochemical method for direct deposition of nanometric bismuth and its electrochemical properties vs Li, Electrochem. Solid State Lett. **11**, E5–E9 (2008)
26.317 L. Bazin, S. Mitra, P.L. Taberna, P. Poizot, M. Gressier, M.J. Menu, A. Barnabe, P. Simon, J.M. Tarascon: High rate capability pure Sn-based nano-architectured electrode assembly for rechargeable lithium batteries, J. Power Sources **188**, 578–582 (2009)
26.318 L. Huang, H.B. Wei, F.S. Ke, X.Y. Fan, J.T. Li, S.G. Sun: Electrodeposition and lithium storage performance of three-dimensional porous reticular Sn-Ni alloy electrodes, Electrochim. Acta **54**, 2693–2698 (2009)
26.319 E. Perre, L. Nyholm, T. Gustafsson, P.-L. Taberna, P. Simon, K. Edstrom: Direct electrodeposition of aluminium nano-rods, Electrochem. Commun. **10**, 1467–1470 (2008)
26.320 G. Oltean, L. Nyholm, K. Edstrom: Galvanostatic electrodeposition of aluminium nano-rods for Li-ion three-dimensional micro-battery current collectors, Electrochim. Acta **56**, 3203–3208 (2011)
26.321 S.K. Cheah, E. Perre, M. Rooth, M. Fondell, A. Harsta, L. Nyholm, M. Boman, T. Gustafsson, J. Lu, P. Simon, K. Edstrom: Self-supported three-dimensional nanoelectrodes for microbattery applications, Nano Lett. **9**, 3230–3233 (2009)
26.322 J.K. Chang, W.T. Tsai: Material characterization and electrochemical performance of hydrous manganese oxide electrodes for use in electrochemical pseudocapacitors, J. Electrochem. Soc. **150**, A1333–A1338 (2003)
26.323 W. Xiao, H. Xia: J.-Y.-H. Fuh, L. Lu: Electrochemical synthesis and supercapacitive properties of epsilon-MnO_2 with porous/nanoflaky hierarchical architectures, J. Electrochem. Soc. **156**, A627–A633 (2009)
26.324 J.-K. Chang, C.-H. Huang, W.-T. Tsai, M.-J. Deng, I.W. Sun, P.-Y. Chen: Manganese films electrodeposited at different potentials and temperatures in ionic liquid and their application as electrode materials for supercapacitors, Electrochim. Acta **53**, 4447–4453 (2008)
26.325 S.C. Pang, M.A. Anderson, T.W. Chapman: Novel electrode materials for thin-film ultracapacitors: Comparison of electrochemical properties of sol-gel-derived and electrodeposited manganese dioxide, J. Electrochem. Soc. **147**, 444–450 (2000)
26.326 C.C. Hu, T.W. Tsou: Capacitive and textural characteristics of hydrous manganese oxide prepared by anodic deposition, Electrochim. Acta **47**, 3523–3532 (2002)
26.327 C.C. Hu, T.W. Tsou: Ideal capacitive behavior of hydrous manganese oxide prepared by anodic deposition, Electrochem. Commun. **4**, 105–109 (2002)
26.328 J.K. Chang, C.T. Lin, W.T. Tsai: Manganese oxide/carbon composite electrodes for electrochemical capacitors, Electrochem. Commun. **6**, 666–671 (2004)
26.329 J.K. Chang, W.T. Tsai: Effects of temperature and concentration on the structure and specific capacitance of manganese oxide deposited in manganese acetate solution, J. Appl. Electrochem. **34**, 953–961 (2004)
26.330 B. Babakhani, D.G. Ivey: Anodic deposition of manganese oxide electrodes with rod-like structures for application as electrochemical capacitors, J. Power Sources **195**, 2110–2117 (2010)
26.331 W. Wei, X. Cui, X. Mao, W. Chen, D.G. Ivey: Morphology evolution in anodically electrodeposited manganese oxide nanostructures for electrochemical supercapacitor applications-Effect of supersaturation ratio, Electrochim. Acta **56**, 1619–1628 (2011)
26.332 I. Zhitomirsky, M. Cheong, J. Wei: The cathodic electrodeposition of manganese oxide films for

electrochemical supercapacitors, J. Min. Met. Mater. Soc. **59**, 66–69 (2007)
26.333 J. Wei, N. Nagarajan, I. Zhitomirsky: Manganese oxide films for electrochemical supercapacitors, J. Mater. Process. Technol. **186**, 356–361 (2007)
26.334 J. Wei, I. Zhitomirsky: Electrosynthesis of manganese oxide films, Surf. Eng. **24**, 40–46 (2008)
26.335 G.M. Jacob, I. Zhitomirsky: Microstructure and properties of manganese dioxide films prepared by electrodeposition, Appl. Surf. Sci. **254**, 6671–6676 (2008)
26.336 J.-K. Chang, C.-H. Huang, M.-T. Lee, W.-T. Tsai, M.-J. Deng, I.W. Sun: Physicochemical factors that affect the pseudocapacitance and cyclic stability of Mn oxide electrodes, Electrochim. Acta **54**, 3278–3284 (2009)
26.337 C.C. Hu, C.C. Wang: Nanostructures and capacitive characteristics of hydrous manganese oxide prepared by electrochemical deposition, J. Electrochem. Soc. **150**, A1079–A1084 (2003)
26.338 B. Dong, T. Xue, C.-L. Xu, H.-L. Li: Electrodeposition of mesoporous manganese dioxide films from lyotropic liquid crystalline phases, Microporous Mesoporous Mater. **112**, 627–631 (2008)
26.339 C.L. Xu, S.J. Bao, L.B. Kong, H. Li, H.L. Li: Highly ordered MnO_2 nanowire array thin films on Ti/Si substrate as an electrode for electrochemical capacitor, J. Solid State Chem. **179**, 1351–1355 (2006)
26.340 C. Xu, Y. Zhao, G. Yang, F. Li, H. Li: Mesoporous nanowire array architecture of manganese dioxide for electrochemical capacitor applications, Chem. Commun. **8**, 7575–7577 (2009)
26.341 K.R. Prasad, N. Miura: Potentiodynamically deposited nanostructured manganese dioxide as electrode material for electrochemical redox supercapacitors, J. Power Sources **135**, 354–360 (2004)
26.342 M.S. Wu: Electrochemical capacitance from manganese oxide nanowire structure synthesized by cyclic voltammetric electrodeposition, Appl. Phys. Lett. **87**, 153102 (2005)
26.343 M.S. Wu, P.C.J. Chiang: Fabrication of nanostructured manganese oxide electrodes for electrochemical capacitors, Electrochem. Solid State Lett. **7**, A123–A126 (2004)
26.344 T. Shinomiya, V. Gupta, N. Miura: Effects of electrochemical-deposition method and microstructure on the capacitive characteristics of nanosized manganese oxide, Electrochim. Acta **51**, 4412–4419 (2006)
26.345 J.-K. Chang, C.-H. Huang, W.-T. Tsai, M.-J. Deng, I.W. Sun: Ideal pseudocapacitive performance of the Mn oxide anodized from the nanostructured and amorphous Mn thin film electrodeposited in BMP-NTf_2 ionic liquid, J. Power Sources **179**, 435–440 (2008)
26.346 R. Liu, S.B. Lee: MnO_2/Poly(3,4-ethylenedioxythiophene) coaxial nanowires by one-step coelectrodeposition for electrochemical energy storage, J. Am. Chem. Soc. **130**, 2942–2943 (2008)
26.347 R. Liu, J. Duay, S.B. Lee: Electrochemical formation mechanism for the controlled synthesis of heterogeneous MnO_2/Poly(3,4-ethylenedioxythiophene) nanowires, ACS Nano **5**, 5608–5619 (2011)
26.348 Z. Fan, J. Chen, B. Zhang, F. Sun, B. Liu, Y. Kuang: Electrochemically induced deposition method to prepare gamma-MnO_2/multi-walled carbon nanotube composites as electrode material in supercapacitors, Mater. Res. Bull. **43**, 2085–2091 (2008)
26.349 H. Xia, J. Feng, H. Wang, M.O. Lai, L. Lu: MnO_2 nanotube and nanowire arrays by electrochemical deposition for supercapacitors, J. Power Sources **195**, 4410–4413 (2010)
26.350 Y. Wang, H. Liu, X. Sun, I. Zhitomirsky: Manganese dioxide-carbon nanotube nanocomposites for electrodes of electrochemical supercapacitors, Scr. Mater. **61**, 1079–1082 (2009)
26.351 Y.T. Wu, C.C. Hu: Effects of electrochemical activation and multiwall carbon nanotubes on the capacitive characteristics of thick MnO_2 deposits, J. Electrochem. Soc. **151**, A2060–A2066 (2004)
26.352 H. Zhang, G. Cao, Z. Wang, Y. Yang, Z. Shi, Z. Gu: Growth of manganese oxide nanoflowers on vertically-aligned carbon nanotube arrays for high-rate electrochemical capacitive energy storage, Nano Lett. **8**, 2664–2668 (2008)
26.353 C.Y. Lee, H.M. Tsai, H.J. Chuang, S.Y. Li, P. Lin, T.Y. Tseng: Characteristics and electrochemical performance of supercapacitors with manganese oxide-carbon nanotube nanocomposite electrodes, J. Electrochem. Soc. **152**, A716–A720 (2005)
26.354 S.-L. Chou, J.-Z. Wang, S.-Y. Chew, H.-K. Liu, S.-X. Dou: Electrodeposition of MnO_2 nanowires on carbon nanotube paper as free-standing, flexible electrode for supercapacitors, Electrochem. Commun. **10**, 1724–1727 (2008)
26.355 Z. Fan, J. Chen, B. Zhang, B. Liu, X. Zhong, Y. Kuang: High dispersion of gamma-MnO_2 on well-aligned carbon nanotube arrays and its application in supercapacitors, Diam. Relat. Mater. **17**, 1943–1948 (2008)
26.356 G. Yu, L. Hu, M. Vosgueritchian, H. Wang, X. Xie, J.R. McDonough, X. Cui, Y. Cui, Z. Bao: Solution-processed graphene/MnO_2 nanostructured textiles for high-performance electrochemical capacitors, Nano Lett. **11**, 2905–2911 (2011)
26.357 Y.-Q. Zhao, D.-D. Zhao, P.-Y. Tang, Y.-M. Wang, C.-L. Xu, H.-L. Li: MnO_2/graphene/nickel foam composite as high performance supercapacitor electrode via a facile electrochemical deposition strategy, Mater. Lett. **76**, 127–130 (2012)
26.358 Q. Cheng, J. Tang, J. Ma, H. Zhang, N. Shinya, L.-C. Qin: Graphene and nanostructured MnO_2 composite electrodes for supercapacitors, Carbon **49**, 2917–2925 (2011)
26.359 Y. Lei, B. Daffos, P.L. Taberna, P. Simon, F. Favier: MnO_2-coated Ni nanorods: Enhanced high rate behavior in pseudo-capacitive supercapacitor, Electrochim. Acta **55**, 7454–7459 (2010)
26.360 S.-J. Pan, Y.-J. Shih, J.-R. Chen, J.-K. Chang, W.-T. Tsai: Selective micro-etching of duplex stainless steel for preparing manganese oxide superca-

pacitor electrode, J. Power Sources **187**, 261–267 (2009)
26.361 J.-K. Chang, S.-H. Hsu, W.-T. Tsai, I.W. Sun: A novel electrochemical process to prepare a high-porosity manganese oxide electrode with promising pseudocapacitive performance, J. Power Sources **177**, 676–680 (2008)

27. Electrochemical Hydrogen Production

Ting He, Mahaprasad Kar, Neal D. McDaniel, Bruce B. Randolph

The electrochemical–photoelectrochemical production of hydrogen has been widely investigated for decades, largely driven by the potential to reduce environmental impact, satisfy distributed demand, and enhance public perception. As an alternative to steam methane reforming for hydrogen production, these approaches have enjoyed renewed vigor over the last several years. This chapter reviews recent progress in low-temperature electrolysis, high-temperature electrolysis, and photoelectrochemical techniques. Perspectives are given on the electricity consumption, carbon dioxide emission, costs of hydrogen production, and competitive landscape in the future hydrogen market.

27.1 **Theoretical Aspects of Electrochemical Hydrogen Production** 899
27.1.1 Thermodynamics of Water Electrolyzers 899
27.1.2 Chemical Kinetics at Electrodes ... 901
27.1.3 Transport in Electrolytes 901
27.1.4 Temperature Effect 902
27.1.5 Photoelectrochemistry 904
27.2 **Electrochemical Hydrogen Production Methods** 905
27.2.1 Low-Temperature Electrolysis 905
27.2.2 High-Temperature Electrolysis 912
27.2.3 Photoelectrolysis 923
27.3 **Development Perspectives** 929
27.4 **Conclusions** 933
References 934

The modern hydrogen market is almost entirely satisfied by steam methane reforming (SMR). Originating in the 1920s, hydrogen production by SMR involves the well understood, thermally driven oxidation of methane by steam, producing hydrogen gas and carbon dioxide. Owing to the maturity of the field, the material and energy efficiencies of SMR have been extensively optimized. In addition, SMR has a long track record of reliable operation, which is of utmost importance to the commodity industries that rely heavily on it for a steady supply of hydrogen. The feedstock, methane, is currently in plentiful supply due in large part to recent implementation of shale gas technology, making it difficult to envision competing with this inexpensive source of both hydrogen and energy [27.1].

However, some key drawbacks must also be acknowledged when considering SMR to supply hydrogen. Chief among these is the low cost-scaling factor (≈ 0.7) of a conventional reformer [27.2]. Optimized for refinery-scale production volumes, these reformers scale up much more affordably than they scale down. For distributed or small-scale applications, SMR is a relatively expensive option. This problem is exacerbated by the necessity for operating at high temperatures (700–850 °C) [27.3], requiring reliable material performance and also significant fuel consumption for process heat. Additionally, the hydrogen produced by SMR is accompanied at $\approx 20\%$ volume by carbon dioxide and trace carbon monoxide. If the downstream, hydrogen-consuming process requires pure hydrogen, the product of an SMR must first be purified (conventionally using a pressure-swing adsorber or amine-based solvent) and cleaned up, and then delivered to the consumer. Finally, SMR produces carbon dioxide both as part of the stoichiometric process and in the generation of heat necessary to drive the reaction. In a hypothetical economic environment that penalizes carbon dioxide emission, SMR-derived hydrogen could be significantly disadvantaged relative to low-carbon, competing technologies. Electrolysis of water may prove to be a viable alternative to SMR in specific applications. First, most methods of electrochemical hydrogen production have cost-scaling factors that are closer to unity (≥ 0.85) [27.4]. This may enable them to compete fiscally against the conventional SMR when production scale is small, for instance in neighborhood or otherwise distributed production. Second, electrolytic hydrogen production usually generates pure hydrogen, requiring little or no downstream gas separation. The most anticipated impurity is water, which can

be conveniently and inexpensively removed. Most electrochemical hydrogen production methods are capable of operating over a wide range of pressures, and water can be removed from the products without necessitating a pressure drop. Also, the oxygen byproduct of water electrolysis, collected separately from the hydrogen, is a useful co-product that can be sold for use in a variety of industrial processes, such as welding, oxy-firing, and chemical oxidation. Finally, electrolysis is not directly accompanied by carbon dioxide. Because the vast majority of the power is being supplied electrically (a small amount is thermal, but $\approx 25\%$ thermal energy in high-temperature electrolysis (HTE)), electrolysis of water potentially has a flexible carbon budget. It may be powered by conventional coal, emerging wind and/or solar, or any intermediary power source. The carbon footprint associated with hydrogen from electrolysis is due in very large part to the carbon associated with electricity generation.

The first instance of water electrolysis is credited to an experiment performed by van Troostwijk and Deiman in 1789, powered by an electrostatic generator [27.5, 6]. In 1800, Alessandro Volta invented the first battery [27.7], allowing Nicholson and Carlisle to repeat the electrolysis of water 11 years after it was first reported, this time powered by several batteries in series [27.8]. Michael Faraday, one of the founders of electrochemistry, published in 1834 the laws of electrolysis and popularized the terms anode, cathode, electrode, and ion [27.9]. The first industrial electrolyzer based on a filter-press design was presented in Zurich in 1900 [27.10]. By 1902, there were more than 400 industrial water electrolyzers in operation. The increasing demand for ammonia in the fertilizer industry continued to expand electrolyzer service into the 1920s and 1930s, at which time steam reforming was only just starting to be commercialized. Norway and Canada built numerous hydropower-based electrolysis plants exceeding 100 MW of installed power [27.11]. In 1939, the first large-scale water electrolysis plant was built, with a hydrogen generation capacity of $10\,000\,\mathrm{Nm^3/h}$. Pressurized electrolysis was developed and patented by *Noeggerath* in the early 1930s [27.12, 13]. In 1948, Zdansky designed the first pressurized industrial electrolyzer. Following Zdansky's technology, a German company called Lurgi produced and distributed high-pressure electrolyzers (3 MPa) starting in 1951 [27.14]. Currently, there are five major commercial vendors providing high-pressure alkaline electrolyzers: StatOil (Norsk Hydro, Stavanger, Norway), Hydrogenics (Stuart, Mississauga, Canada), ELT, Teledyne (CA, USA), and Avalence (CT, USA) [27.15].

A different methodology toward electrolysis was unlocked in the development of solid electrolytes by General Electric (CT, USA) as part of the space program in 1966 [27.16]. This breakthrough gave birth to the field of proton exchange membrane (PEM) or solid polymer electrolysis. Sulfonated polystyrene and subsequently Nafion, a sulfonated perfluorinated material patented by DuPont [27.17], were developed for the purpose with the latter prevailing in PEM research up to the present day. Small-scale PEM water electrolyzers were used for military and space applications in the early 1970s. In 1987, the first 100 kW PEM electrolyzer was built by BBC (now ABB). Currently, there are a few manufacturers that offer commercial PEM electrolyzers with hydrogen production rates as high as $30\,\mathrm{Nm^3/h}$, namely Proton Energy Systems, StatOil, and Hydrogenics.

HTE is most often accomplished by the use of solid oxide-based electrolysis cells and stacks (SOEC). SOEC technology emerged from the development of solid oxide fuel cells (SOFC), with the idea that, rather than utilizing a fuel to make electrical power, the reverse operation of using electrical power to produce a fuel (H_2) is possible. This process normally uses steam as the feed, and performed at temperatures of 750–900 °C. Pioneering work in this area dates back to the late 1960s [27.18] in Germany and the United States. In the 1980s, *Doenitz* and coworkers reported results from the *Hot Elly* project [27.19] and Westinghouse researchers also published work with tubular cell designs [27.20]. These early forays into SOEC technology development waned due to a combination of lower energy prices and technical challenges. However, in the past decade, interest has renewed in this area, due to significant technical progress using planar cells based on SOFC technology [27.21].

HTE using SOECs provides several benefits over low-temperature electrolysis technologies. high-temperature operation requires decreased electricity consumption. This lower electricity demand is offset by higher heat demand required to maintain the high temperature. However, when high-temperature heat is available at low cost, HTE offers a favorable energy balance compared to low-temperature alternatives. Additionally, operating an electrolyzer at high temperatures favors the reaction kinetics and therefore less noble (less expensive) materials such as Ni and conductive oxides can be used instead of Pt as electrocatalysts.

Recently, a new field of study has emerged in which water electrolysis is powered by light. This is a photoelectrochemical (PEC) process, originated from *Becquerel's* 1839 discovery that electrodes covered in a layer of silver halide exhibit an electrical response to illumination [27.22]. The first physical explanation for this *Becquerel effect* is attributed to Brattain and Garrett of Bell Labs, 1955. Studying germanium and silicon

electrodes, *Brattain* and *Garrett* were able to elucidate the underlying photovoltaic process behind the operation of PEC for the first time [27.23]. This work led into the investigation of PEC for chemicals production and power generation over the following decades [27.24]. Hydrogen production from the PEC decomposition of water was first proposed in 1972 by *Fujishima* and *Honda* who observed that the electrical component of water electrolysis could be greatly reduced by the utilization of ultraviolet light [27.25]. Since the time of that finding, the pursuit of PEC hydrogen production has grown into a vast body of research.

The water electrolysis technologies can be divided into three distinct categories, based on commercial availability. The first of these, referred to herein as low-temperature electrolysis, is already commercial and is the most mature of all the electrolysis categories. The second, HTE, is approaching the crossroads of commercialization, but challenges remain. The third of these technologies, photoelectrolysis, is the youngest and farthest from commercialization. This chapter reviews the recent development of electrochemical hydrogen production technologies, particularly in these three areas.

27.1 Theoretical Aspects of Electrochemical Hydrogen Production

Electrochemical energy conversion takes place from electrical to chemical energy in electrolyzers, and from chemical to electrical energy in power sources. The consumption of electric power in the former case, and the production of electric power in the latter, are proportional to $U \times I$, where U is the potential difference (voltage) applied to or existing at the terminals of the cell as current I flows across the cell. Generally, the goal is to minimize U in electrolyzers and maximize U in power sources, for a given I. The efficiency and rate of energy conversion are governed by two controlling factors: the first of these is the kinetics of chemical reactions occurring at the electrode–electrolyte interface, and is subject to the activity of catalysts used. Situations in which slow chemical reactions limit overall energy conversion fall under the so-called Tafel regime. The second controlling factor is the availability and mobility of ionic species throughout the electrolyte. Scenarios in which the slow transport of ions limits overall energy conversion fall under the Ohmic regime. In the case of photoelectrochemistry, overall energy conversion is also affected by a third factor, namely the photovoltaic efficiency of the electrode. The limitations and characterization of these essential processes are discussed in this section.

27.1.1 Thermodynamics of Water Electrolyzers

Water electrolyzers convert electrical energy directly into chemical fuels, namely hydrogen, by the decomposition of water in acidic, basic, or neutral media. An electric power source is connected to two electrodes that are placed in water. Hydrogen evolves at the cathode (the negatively charged electrode), and oxygen is produced at the anode (the positively charged electrode). The amount of hydrogen generated is proportional to the total electrical charge conducted by the solution, with two electrons yielding one molecule of hydrogen in the ideal Faradaic case. The thermodynamic efficiency of an electrolyzer depends on the energy needed to overcome kinetic barriers, known as overpotential, as well as the thermal energy required for elevated temperature operations.

Every electrolyzer must contain two electrodes separated by an electrolyte and be connected to an external power source (aside from photoelectrolysis). Ions flow through the electrolyte from one electrode to the other, and electrons travel through the external conducting circuit, requiring electromotive force to drive the process. For water electrolysis in acidic media (e.g., using a PEM), a water oxidation reaction takes place at the positively charged anode, generating oxygen gas and giving electrons to the anode; whereas at the negatively charged cathode, a reduction of protons occurs, forming hydrogen gas and completing the external conducting circuit. At the interface between the electrode and electrolyte, the flow of current is continuous, but the identity of the charge-carrying species changes from an electron to a proton (H^+). The half-cell reactions at anode and cathode are

$$2H_2O \rightarrow O_2 + 4H^+ + 4e^- \quad \text{(anode)}\,, \tag{27.1}$$

$$2H^+ + 2e^- \rightarrow H_2 \quad \text{(cathode)}\,. \tag{27.2}$$

Combining these half-cell reactions yields the overall decomposition of water into oxygen and hydrogen

$$2H_2O \rightarrow 2H_2 + O_2\,. \tag{27.3}$$

For water electrolysis in alkaline media (either liquid alkaline solution or a solid anion exchange membrane), the corresponding half-cell reactions at the anode and

cathode are

$$4OH^- \rightarrow O_2 + 2H_2O + 4e^- \quad \text{(anode)}\,, \tag{27.4}$$
$$2H_2O + 2e^- \rightarrow H_2 + 2OH^- \quad \text{(cathode)}\,, \tag{27.5}$$

where hydroxide anions (OH^-) are now the charge-carrying species in the electrolyte. In the neutral case where a solid oxide membrane is used as the electrolyte (in HTE), the half-cell reactions at anode and cathode can be described as

$$2O^{2-} \rightarrow O_2 + 4e^- \quad \text{(anode)}\,, \tag{27.6}$$
$$2H_2O + 2e^- \rightarrow H_2 + O^{2-} \quad \text{(cathode)}\,. \tag{27.7}$$

It should be noted that, in practice, the electrochemical reactions in water electrolysis are more complicated than those described by the equations above. It is commonly agreed that each electrochemical reaction step involves only one electron and each reaction above involves multiple reaction steps and energy barriers.

The decomposition of water into hydrogen and oxygen is not thermodynamically favorable at standard temperature and pressure. The change of Gibbs free energy for the reaction in (27.3) has an ideal standard potential of −1.23 V at 25 °C, which means that the reactions cannot occur without providing the necessary energy, usually supplied by an external electric power source. The 1.23 V is the minimum voltage needed to perform the water electrolysis, with the hydrogen production rates approaching zero. The actual cell voltage is much higher than this equilibrium value due to various irreversible losses, known as overpotentials, and depends on the hydrogen production rate as shown in Fig. 27.1.

The efficiency of any energy conversion device is defined as the ratio between useful energy output and energy input. In the case of an electrolyzer, the useful energy output is the enthalpy of hydrogen, that is, hydrogen's higher heating value (HHV) (W_{H_2}), and the energy input is the electrical (W_{el}) and thermal energies (W_{th}) used in electrolysis

$$\eta = \frac{\eta_{el}}{\left(1 + \frac{\eta_{el}}{\eta_{th}}\right)}\,, \tag{27.8}$$

where $\eta_{el} = W_{H_2}/W_{el}$ is the electrical efficiency and $\eta_{th} = W_{H_2}/W_{th}$ is the thermal contribution. If the amount of thermal energy input is very small (low-temperature electrolysis), the system efficiency is equivalent to the electrical efficiency. However, for the case of HTE, the thermal contribution term has to be taken into account. If a Faradaic efficiency of 100% is assumed for an electrolyzer operating at ambient

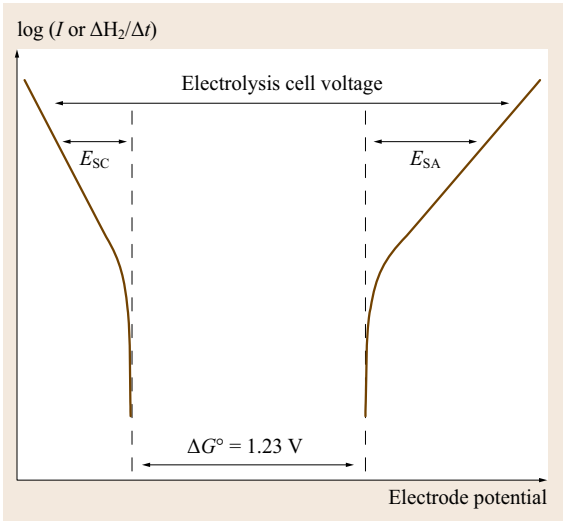


Fig. 27.1 The relationship between the hydrogen production rate and the overpotentials at the cathode and anode, where E_{SC} and E_{SA} are the surface overpotentials on the cathode and anode, respectively

conditions, the electrical efficiency can be defined as $1.482/U$, where U is the voltage applied to the cell and 1.482 is the thermoneutral voltage of water electrolysis at ambient conditions. It is noted that the maximum theoretical efficiency would be of no practical value, since an electrolysis cell operating at theoretical efficiency would generate negligible hydrogen.

Faraday's law relates the rate of reaction to the applied current. It states that the rate of production of a species is proportional to the current, and the total mass produced is proportional to the amount of charge passed multiplied by the equivalent weight of the species. For water electrolysis, Faraday's law can be written as

$$M_{H_2}(\mathrm{g/(A\,s)}) = \frac{WI}{nF}\,, \tag{27.9}$$

where W is the formula weight of hydrogen (2.0159 g/mol), I is total current (in A), n is the number of electrons required to produce a molecule of hydrogen (27.2), and F is the Faraday constant (96 487 C/mol). The behavior of electrochemical systems is determined by the current density rather than by the total current, which is the product of the current density and the cross-sectional area (electrode area). From (27.9), the hydrogen production rate will be ≈ 9 kg hydrogen per day for every ampere of current (106 Nm^3 hydrogen (Nm^2/Ad)).

The hydrogen production rate from water electrolysis (27.9) is based on the assumption that the Faradaic efficiency for the cell is 100%. In the case of electrode

or membrane corrosion, charges are consumed without producing hydrogen, resulting in a lower Faradaic efficiency (η_F) and, hence, a lower system efficiency

$$\eta = \frac{\eta_{el}\eta_F}{\left(1+\frac{\eta_{el}}{\eta_{th}}\right)} . \tag{27.10}$$

Under high operating potential and in aqueous solution, electrode corrosion can occur through a direct electrical dissolution of the metals or by an oxide formation and chemical dissolution of the oxide layers. The preference for one process over the others is a function of cell voltage and solution pH. Due to the instability of most metals and oxides at high electrochemical potentials, electrode corrosion is a chief concern in low-temperature electrolysis.

27.1.2 Chemical Kinetics at Electrodes

In electrochemical systems of practical importance, including corrosion, it is critical to understand the processes that occur at the electrode–electrolyte interface. Electrochemical reactions at an electrode involve both a transfer of electrical charge and a change in Gibbs free energy. The rate of electrochemical reaction is determined by the speed at which the electrons are consumed or released at the electrode surface, and is controlled by an energy barrier that the charge must overcome in order to transfer from a solid electrode to reactant species or vice versa. The rate of reagent consumption is proportional to their surface concentration. In the case of hydrogen reduction, (27.2), the flux J_{red} (mol/(s cm^2)) for the forward reaction and the flux J_{ox} for the backward reaction can be described by

$$J_{red} = k_{red}\,[H^+]^2 , \tag{27.11}$$

$$J_{ox} = k_{ox}\,[H_2] , \tag{27.12}$$

where k_{red} and k_{ox} are the reduction and oxidation rate coefficients that are functions of the Gibbs free energy, $k = k_B T/\hbar \exp(-\Delta G/RT)$, where k_B and $\hbar$ are Boltzmann's and Planck's constants, and $[H^+]$ and $[H_2]$ are the concentrations of the protons and hydrogen, respectively. The net charge transferred q (C/mol) is the difference between the electrons consumed and released

$$q = 2F\left(k_{red}[H^+]^2 - k_{ox}[H_2]\right) . \tag{27.13}$$

At equilibrium, the net charge transferred is equal to zero, although the reaction proceeds in both directions simultaneously. Therefore, for water electrolysis, a potential has to be applied to the hydrogen electrode to force current to flow; and the potential difference between the hydrogen and oxygen electrodes is the driving force for the reactions shown in (27.1), (27.2), and (27.4)–(27.7). This driving force is termed the surface overpotential E_s. The rate of the reaction can often be related to the surface overpotential by

$$j = j_0\left[\exp\left(\alpha_{ox}F\frac{E_s}{RT}\right) - \exp\left(\frac{-\alpha_{red}FE_s}{RT}\right)\right] , \tag{27.14}$$

where j_0 is the exchange current density, analogous to the rate constant used in chemical kinetics, and α is the transfer coefficient that is an additional parameter relating to how an applied potential favors one direction of the reaction over the other. Equation 27.14 is known as the Butler–Volmer equation, that is, a relationship between current and surface overpotential for an electrode. From the Butler–Volmer equation, the surface overpotential (E_s) at a given current density can be calculated, resulting in the overpotential plot shown in Fig. 27.1. For small values of E_s, the current density varies linearly with E_s, whereas the current density varies exponentially for large values of E_s. By plotting surface overpotential as a function of logarithm of current density, the well-known Tafel plot can be created.

The Butler–Volmer equation (27.14) can also be regarded as a result of cathodic and anodic reactions taking place independently, each with an exponential dependence on the corresponding surface overpotential. Generally speaking, the surface overpotential of a particular electrode reaction is related to the electrochemical potentials of reactants and products, for example, the surface overpotential for the reaction in (27.2) can be written as

$$E_s = -\frac{(\mu_{ec,H_2} - 2\mu_{ec,H^+} - 2\mu_{ec,e^-})}{2F} , \tag{27.15}$$

where $\mu_{ec,k}$ is the electrochemical potential of the species k consisting of chemical potential ($\mu_{c,k}$) and electrical potential (ϕ) by $\mu_{ec,k} = \mu_{c,k} + z_k F\phi$.

27.1.3 Transport in Electrolytes

The potential applied to an electrode creates a driving force for reactions at the electrode. The potential difference across two electrodes also creates a driving force for the flow of ionic species inside electrolyte. The driving force is the electric field ($\boldsymbol{E}$), which is related to the gradient of potential ϕ by $\boldsymbol{E} = -\nabla\phi$. The current density in electrolyte is the net flux of various charged species

$$j = \sum z_k F j_k , \tag{27.16}$$

where z_k and j_k are charge number and flux density of the ionic species k, respectively. While electrons in a conductor flow only in response to an electrical field, ionic species in an electrolyte move in response to an electric field (migration) and also in response to concentration gradients (diffusion) as well as bulk fluid motion (convection). The net flux of an ion is therefore the sum of the migration, diffusion, and convection terms. Very often, the transport of ionic species in electrolytes and/or the removal of product gases from electrodes are the rate-limiting processes.

The electric field, which creates a driving force for the movement of ionic species, drives cations toward the cathode and anions toward the anode, that is, cations move in the direction opposite to the gradient in potential. The flux density of a species is given by

$$j_{k,\mathrm{mig}} = -z_k u_k F[c_k]\nabla\phi \,, \tag{27.17}$$

where u_k is the mobility and $[c_k]$ is the concentration of the species k. Often, a transference number of an ion is reported for ionic species in electrolyte, which is defined as the fraction of the current that is carried by that ion in a solution of uniform composition $t_k = z_k F j_k / J$. For the case that the transference number of the reacting ion is less than unity, there will be fluxes of the other ions in solution that will create a concentration gradient; this is particularly true for solution electrolytes. These concentration gradients drive mass transport by the process of diffusion, which occurs in addition to the process of migration above. The diffusional transport is a nonconvective flow that tends to equilibrate the concentrations in inhomogeneous nonequilibrium systems. The flux density of the diffusion can be described by the concentration gradient $\nabla[c_k]$

$$j_{k,\mathrm{dif}} = -D_k \nabla[c_k] \,, \tag{27.18}$$

where D_k is the diffusion coefficient of the species k. Equation (27.18) is incomplete for not specifying the reference frame of transport and neglecting the cross terms. The last one to be discussed is the convection term. Convection is the bulk movement of a fluid. The flux density of a species by convection is given by (27.19), where v is the velocity of the bulk fluid

$$j_{k,\mathrm{con}} = [c_k] v \,. \tag{27.19}$$

Convection includes natural convection which is caused by density gradient and forced convection caused by mechanical stirring or a pressure gradient. The latter is often used in practice to remove gases from electrodes to avoid electrode poisoning and to serve as an effective means to bring reactants to the electrode surfaces. However, in an electrically neutral solution, bulk convection alone does not cause a net current except affecting concentration profiles. Combining the migration (in *electrical units*; (27.17)) and diffusion (in *thermal units*; (27.18)) terms results in (27.20), where the term $\mu_{c,k} + z_k F\phi$ is the electrochemical potential of the species k ($\mu_{ec,k}$)

$$j_k = \frac{-D_k[c_k]}{RT}\nabla(\mu_{c,k} + z_k F\phi) \,. \tag{27.20}$$

Again, the interactions between ionic and electronic fluxes have been neglected by assuming that the cross coefficients in the matrix of the transport coefficients take zero value. By using (27.20), one can calculate the transport properties of charged species in electrolytes.

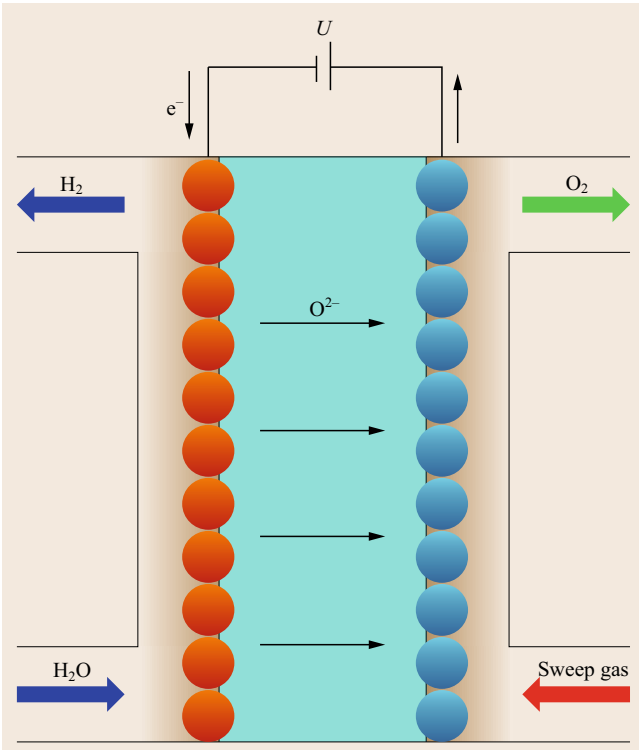


Fig. 27.2 Schematic of SOEC cell, with cathode on the *left* and anode on the *right*

27.1.4 Temperature Effect

High-temperature steam electrolysis is most often accomplished with SOEC technology. At a very high level, SOEC operation is simply the reverse of SOFC operation. Instead of burning a fuel to provide electricity, electricity is used to produce hydrogen and oxygen from water splitting. A basic schematic of the process is shown in Fig. 27.2.

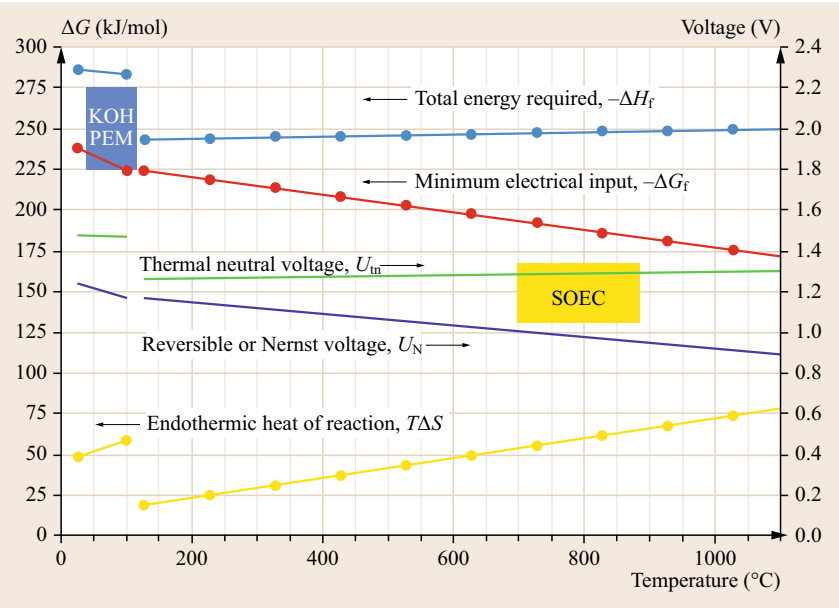


Fig. 27.3 Water-splitting thermodynamics (courtesy of Ceramatec)

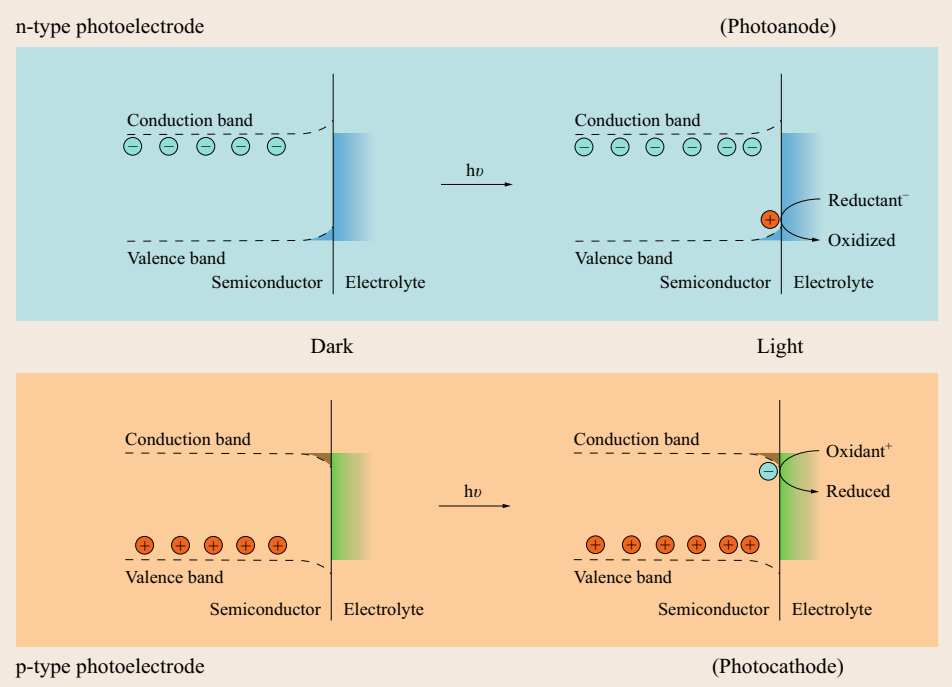


Fig. 27.4 The photoresponses of an n-type and p-type photoelectrode

As in SOFC technology, there is a nonporous, dense, gas-tight electrolyte, sandwiched between an anode and a cathode. The electrolyte ideally has high oxygen anion (O^{2-}) conductivity, but low or no electronic conductivity. Both the anode and cathode are usually porous and have mixed ionic and electronic conduction. This allows gas reactants into the reaction sites and establish a triple-phase boundary (TPB), where gas reactants, oxide ions, and electrons can react.

In SOEC mode, the cathode and anode reactions for hydrogen and oxygen production, respectively, are shown in (27.6) and (27.7). The overall water decomposition reaction (27.3) is governed by the Nernst equation (27.21), where ΔG^{o} is the Gibbs energy at standard

pressure and temperature, P_x are partial pressures of the gases, n is the number of electrons involved, and F is Faraday's constant

$$V = -\frac{\Delta G^{\circ}}{nF} - \left(\frac{RT}{nF}\right) \ln\left(\frac{\left(P_{H_2}^2 P_{O_2}\right)}{P_{H_2O}^2}\right) . \qquad (27.21)$$

At elevated temperatures, by taking into account the thermal energy, the minimum energy input required for water splitting is given by

$$\Delta G = \Delta H - T\Delta S , \qquad (27.22)$$

where ΔH and ΔS are the enthalpy and entropy for the water splitting reaction, respectively. It can be seen that the overall energy requirement decreases with increasing temperature. There are three basic operating regimes for SOEC: endothermic, exothermic, and thermoneutral [27.26] (Fig. 27.3). By virtue of electrical current passing through the cell, heat is generated due to internal resistances. When the electrical energy supplied to the cell is equal to the reaction enthalpy, the thermoneutral point is achieved, and this voltage is termed the thermoneutral voltage (U_{tn})

$$U_{tn} = \frac{\Delta H}{nF} . \qquad (27.23)$$

At the thermoneutral point, the gas outlet temperature is equal to the steam inlet temperature, and the electricity-to-hydrogen conversion efficiency is 100%. Entropy required for water splitting matches the heat generated by resistances and losses in the cell.

For the endothermic regime, the electrical potential applied to the system is below V_{tn}. As a result, additional energy (in the form of heat) must be supplied to maintain the desired temperature. Conversely, exothermic operations are those in which a potential greater than U_{tn} (energy input $> \Delta H$) is supplied.

27.1.5 Photoelectrochemistry

Water electrolysis using solar energy occurs through a PEC process, whereby a semiconductor–electrolyte junction replaces the p–n junction of photovoltaic cell for charge separation. When a neutral, doped semiconductor is immersed in an electrolyte solution, its surface becomes charged. For positively doped (p-type) materials, equilibrium charge is reached when a small number of electrons are injected from the electrolyte into the easily accessible holes of the semiconductor's valence band, yielding a net negative charge in the solid. In contrast, the electrolyte removes a small number of easily accessible electrons from the conduction band of negatively doped (n-type) materials, leading to a net positive charge in the solid.

Polarization of the electrolyte then occurs at the surface of the electrode, resulting in band bending at the semiconductor–electrolyte interface in Fig. 27.4 [27.27]. This Schottky barrier, generated by bringing a doped semiconductor into contact with an appropriate electrolyte, is capable of separating electron/hole exciton pairs as they are formed, and therefore supplants the need for a solid-state p–n junction.

Under illumination, electrons begin to populate the conduction band of p-type semiconductors; meanwhile the number of holes in the valence band does not change appreciably considering the large number of holes that already existed under dark conditions. The converse is true when photons are absorbed by an n-type material: Accessible holes begin to appear in the valence band, meanwhile the number of electrons in the conduction band is largely unaltered. For all these reasons, p-type photoelectrodes thus exhibit a cathodic photoresponse (photocathodes) while n-type photoelectrodes exhibit an anodic response (photoanodes), as depicted in Fig. 27.4 [27.28].

For the water-splitting reaction, electrolyte pH is a controlling parameter. The electron affinity of an aqueous solution increases linearly with pH. For n-type materials, the semiconductor–electrolyte Schottky junction is therefore expected to be of greatest magnitude under acidic conditions, and to diminish as the pH increases. Meanwhile, the opposite behavior is expected for p-type electrodes. For this reason, it is important to note the reported conditions of operation for each study; from a survey of the most outstanding reports of PEC solar conversion efficiency for both photocathode [27.29] and photoanode [27.30], a minimal Schottky barrier appears to be favored (alkaline conditions are preferred for photoanodes, acidic conditions for photocathodes).

27.2 Electrochemical Hydrogen Production Methods

Three technologies define the scope of this chapter: low temperature, high temperature, and photo-driven electrolysis. Low-temperature electrolysis can be further dissected into that which uses a liquid electrolyte (usually referred to as alkaline electrolysis due to the preferred use of strongly alkaline conditions) and that which uses a solid, PEM electrolyte (usually referred to as PEM or acidic electrolysis, due to the acidic nature of the polymer membrane). HTE also operates using a solid electrolyte membrane, though utilizing very different materials for high-temperature compatibility. Finally, in photoelectrolysis there is negligible electrical power input, with the catch that the electrodes must now be photoactive in addition to electrocatalytic. Each of these practices faces a unique set of technical merits and challenges; the states of these fields are herein discussed.

27.2.1 Low-Temperature Electrolysis

Alkaline Electrolysis

Industrial scale electrolyzers may be broadly classified into unipolar (tank type) electrolyzers and bipolar (filter-press type) electrolyzers. In the tank-type electrolyzers, each cell consists of anodes and cathodes that are alternated and separated by diaphragms (Fig. 27.5). The electrodes are electrically connected outside the cell in parallel sets. This leads to a very simple design that provides easy maintenance, even during operation [27.11].

In filter-press electrolyzers, the electrodes are bipolar, with one face serving as an anode in one cell and the other as a cathode in the next cell (Fig. 27.5). A separator (binder) is present between the two cells. Diaphragms are used to separate gas collection spaces. By applying back pressure to the gas collection lines, filter-press electrolyzers can be operated to generate hydrogen and oxygen at pressures [27.14] For similar H_2 production rates, a filter-press electrolyzer is more compact and lightweight than a tank type electrolyzer. Moreover, less wiring is required as the current flows through the cells that are connected in series, (Fig. 27.5) [27.31–34].

Earlier designs exhibit the use of two separate electrodes with a separator or diaphragm in between. The ohmic loss associated with passing current through the electrolyte was reduced by appending the electrodes to the separator in the *zero-gap* electrode design introduced by *Costa* and *Grimes* in 1967 [27.35]. The design is a modified filter-press electrolyzer with porous nickel electrodes attached directly to a diaphragm (Fig. 27.6). For identical external dimensions, porous electrodes provide a higher specific surface area than nonporous electrodes for the electrochemical reactions. Furthermore, gas bubbles produced during electrolysis are pressurized to traverse the porous electrodes; hence the space between electrodes can be virtually kept free of bubbles. The electrolyte conductance is also increased as a result of the increase in operational temperature to about 110 °C. These operational features reduce various types of overpotentials and thus allow the electrolyzers to be operated at higher current density with improved electrical efficiency (Table 27.1) [27.31].

Materials. To attain low ohmic overpotentials, 25–30 wt% KOH solution is typically used as the electrolyte in alkaline electrolyzers. Hence, the materials used require high corrosion resistance. Most of the electrolyzers also operate at slightly elevated temperatures (70–90 °C). Under these conditions, nickel-plated steel provides adequate corrosion resistance as a containment material. The electrodes are typically made of a nickel or nickel-plated steel substrate with a catalyst coating.

Diaphragms are required to perform multiple functions: They keep hydrogen and oxygen from mixing, allow the electrolyte to permeate through, and have acceptable mechanical and electrochemical corrosion stability. Before being banned in all European countries, asbestos was considered as the most suitable candidate as a diaphragm. Recently, asbestos has been substituted by polymer-reinforced ceramic oxide composites. Zirfon is an example of a porous composite separator material composed of a polysulfone matrix and zirconia [27.37].

Table 27.1 Example operating parameters and performance data of different types of alkaline electrolyzers (after [27.31])

	Tank type	Filter press	Advanced zero-gap
Operating temperature (°C)	80–85	65–80	110
Operating pressure (atm)	–	30	20
Current density (A/cm^2)	0.04–0.06	0.07–0.3	0.85/1.7
Cell voltage (V)	1.90–2.40	–	1.78/1.99
Energy consumption (kWh/Nm^3H_2)	4.15–4.90	4.30–4.75	4.1
Efficiency (%)	60–70	63–70	73/83

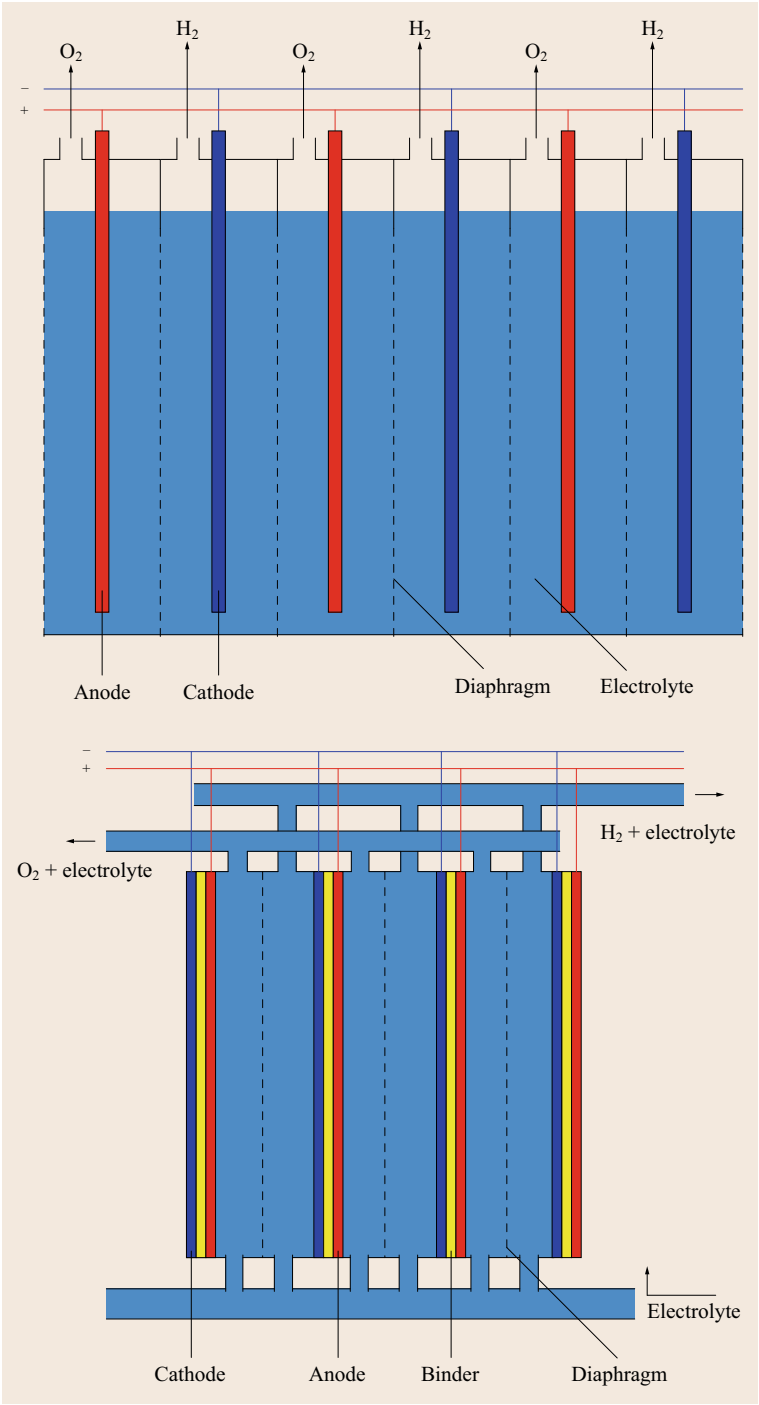


Fig. 27.5 Illustration of tank-type electrolyzer and filter-press type electrolyzer

Cathodic catalysts are primarily nickel based. Raney nickel has proven to be a good long-term stable catalyst at 80 °C. High surface-area nickel catalysts developed by *Raney* in 1925 are considered noteworthy contributions to the field of catalysis [27.39, 40]. The use of such catalysts in electrolyzers was patented by *Justi* et al. in 1954 [27.41]. Raney nickel was later used in a matrix of another metal (e.g., aluminum, zinc) to

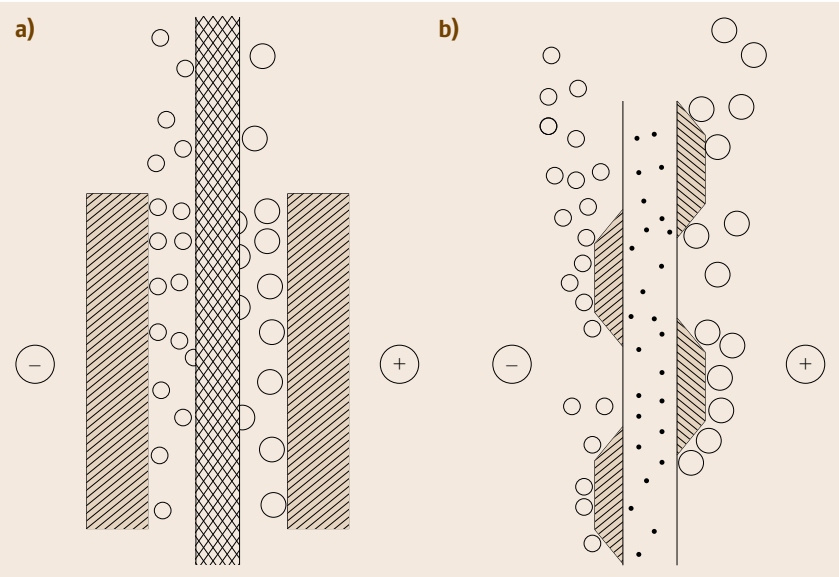


Fig. 27.6 (a) Conventional electrolyzer configurations for gas-evolving electrodes, (b) zero-gap configuration with perforated plate electrodes pressed to either side of the diaphragm (after [27.36], courtesy of Wiley)

Table 27.2 Hydrogen overpotentials of different electrode materials (after [27.38], courtesy of Elsevier)

Composition formula	Method	T (°C)	Electrolyte	C (mol/dm^3)	j (A/m^2)	η_{hyd} (mV)
Ni–Fe–Mo–Zn	Codeposition	80	KOH	6	1350	83
Ni–S–Co	Electrodeposition	80	NaOH	28 wt%	1500	70
Ni50%-Zn	Electrodeposition	N/A	NaOH	6.25	1000	168
$MnNi_{3.6}Co_{0.75}Mn_{0.4}Al_{0.27}$	Arc melting	70	KOH	30 wt%	1000	39
Ti_2Ni	Arc melting	70	KOH	30 wt%	1000	16
Ni50%Al	Melting	25	NaOH	1	1000	114
Ni75%Mo25%	Codeposition	80	KOH	6	3000	185
Ni80%Fe18%	Codeposition	80	KOH	6	3000	270
Ni73%W25%	Codeposition	80	KOH	6	3000	280
Ni60%Zn40%	Codeposition	80	KOH	6	3000	225
Ni90%Cr10%	Codeposition	80	KOH	6	3000	445

improve the mechanical stability and the electrical conductivity of the electrode, consequently reducing the overpotentials.

Raney-type catalysts are synthesized by first preparing an alloy of the catalytically active catalyst (Ni, Co, Cu) with another support metal (Al, Zn). The support metal is then leached out in an alkaline solution, leaving behind a high surface area catalyst. Alternatively, high surface area Ni foams [27.42] and whiskers [27.43] have also been investigated as the cathode catalyst. Other compounds studied thus far include iron molybdates [27.44] and nickel molybdates [27.45], nickel borides, nickel sulfides, and nickel–cobalt thio-spinels. Adding 13% Mo to Ni improves the catalytic activity, and when doped with ceramics such as TiO_2 and ZrO_2 exhibits enhanced stability [27.46]. Applying these measures, the cathodic (hydrogen) overpotential at 1000 A/m^2 and 90 °C was reduced from 0.35 V down to 0.15–0.2 V. Non-nickel-based cathode catalysts such as PdTi, Hf_2Fe, Hf_2Co, $PtMo_3$, NbPd, and other transition metal alloys represent an important step toward the development of novel water reduction catalysts. Table 27.2 lists the hydrogen overpotentials (η_{hyd}) corresponding to various cathode catalysts.

Identifying efficient and stable anode catalysts has proven to be more challenging than cathode catalysts. The anode material has traditionally been made from nickel or nickel-coated steel, as it is inexpensive and corrosion resistant at positive potentials. However, a wide variety of materials have been investigated, as the overpotential associated with a Ni electrode can be as high as 20% (300–400 mV) of the overall cell voltage. At the end of 1970s, overpotentials of 150 mV less than Ni were achieved with polytetrafluoroethylene (PTFE)-bonded $NiCo_2O_4$; but the material exhibited long-term stability issues. In the 1980s, mixed oxides such as perovskites and spinels were examined. Nickel anodes with 2–3 mg/cm^2 of cobalt spinel demonstrated

Table 27.3 Oxygen overpotentials of different electrode materials

Composition formula	Method	T (°C)	Electrolyte	C (mol/dm^3)	j (A/m^2)	η_{oxy} (mV)
Ni + Spinel-type Co_3O_4	Thermodecomposition	25	KOH	1	1000	235± 7
Ni + La-doped Co_3O_4	Thermodecomposition	25	KOH	1	1000	224± 8
MnOx-modified Au	Electrodeposition	25	KOH	0.5	100	300
Li10% doped CO_3O_4	Spray pyrolysis	RT[a]	KOH	1	10	550
Ni	N/A	90	KOH	50 wt%	1000	300
$La_{0.5}Sr_{0.5}CoO_3$	Spray-stiner	90	KOH	50 wt%	1000	250
$Ni_{0.2}Co_{0.8}LaO_3$	Plasma jet projection	90	KOH	50 wt%	1000	270

[a] Room temperature

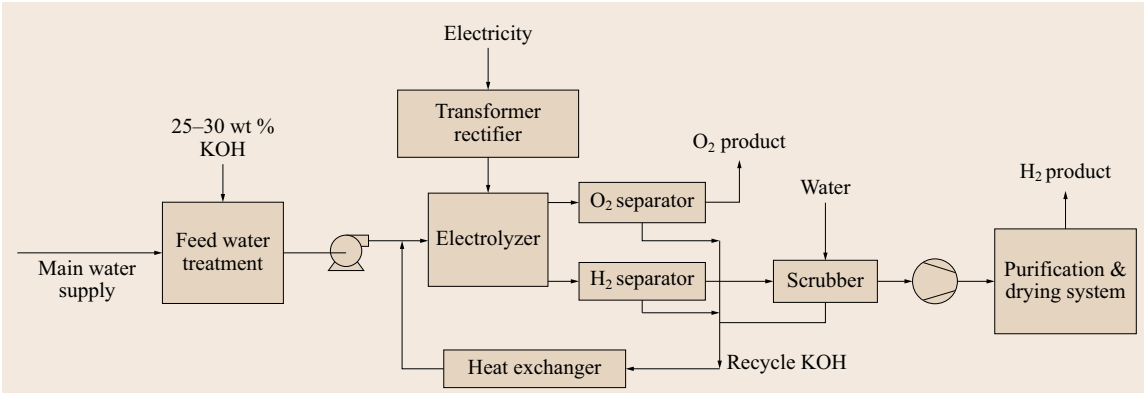


Fig. 27.7 Schematic of an alkaline water electrolysis plant (after [27.31–34])

80 mV lower overvoltage compared to plain Ni. In the mid 1980s, perovskites and spinels containing transition metals such as Ni_2Co_4, $La_{0.2}Sr_{0.8}CoO_3$, and Co_3O_4 were identified as promising catalysts owing to their activity, long-term stability, and affordability. To date, these transition metals based oxides have proven to be the most successful anode catalysts in operation. Table 27.3 lists the oxygen overpotentials (η_{oxy}) corresponding to various anode catalysts and electrolysis conditions.

Process Flow and Operating Conditions. The electrolyte, a 25–30 wt% aqueous KOH solution, is pumped into the electrolyzer. The transformer–rectifier converts the AC high-voltage supply into DC current input that is applied across the electrodes. Hydrogen and oxygen are produced in the electrolyzer via water electrolysis. The gases bubble up through the electrolyte to be conveyed by internal ducts into separation tanks at the front of the electrolyzer. This module consists of two gas separators, one each for O_2 and H_2, and the electrolyte recirculation system. In the separators, the electrolyte is recovered and is then chilled in the heat exchanger and recycled into the cell block.

The separated H_2 gas is sent to the scrubber to remove residual traces of the electrolyte and to reduce the temperature of the gas. The liquid from the scrubber containing the electrolyte is recycled into the electrolyzer. The hydrogen gas is compressed to the required level by one or more compressors. After the gas scrubber, the hydrogen has a purity of 99.9%. If higher purity is desired, the gas is further treated in the purification and drying system. The impurities primarily consist of oxygen and water (in addition to nitrogen). The oxygen is removed by a catalytic recombination with hydrogen in a deoxidizer. The gas is dehydrated by twin absorption towers packed with desiccant to absorb the water. One tower is always in operation, while the other one is being regenerated. The result is very high purity hydrogen – up to 99.993%, depending on the plant configuration. Optionally, a pressurized hydrogen storage system can be installed. A generic schematic is given in Fig. 27.7.

The applied voltage is a key parameter as it establishes the electrical efficiency and the power consumption of the electrolyzer. Current density is another important parameter that affects the efficiency directly. A higher current density directly results in an increased hydrogen generation rate. However, the rapid bubble formation raises the overpotential owing to increased bubble resistance, resulting in a lower efficiency. Therefore, alkaline electrolyzers are typically operated be-

tween 1000 and 3000 A/m^2 to compromise between hydrogen generation rates and electrical efficiencies. Most conventional alkaline water electrolyzers operate around 80–90 °C. Increasing the temperature of electrolysis decreases the equilibrium voltage, hence reducing the electrical power input. However, operating at elevated temperatures also affects the structural integrity of the materials and heat management issues [27.47]. To sustain long-term service, operating temperatures above 150 °C have been abandoned.

Another key parameter is the working pressure of the electrolyzer. Alkaline electrolyzers can be operated either at atmospheric pressures or higher depending on the end use of the hydrogen. High pressures are generated by controlling the exit valve of the evolving product gases. Operating at elevated pressures reduces the size and volume fraction of gas bubbles, minimizing the overpotentials due to them. However, the increase in efficiency at higher pressures is not significant when compared to atmospheric cells [27.16]. Yet, alkaline pressure electrolyzers save substantially on gas compression costs in systems where gaseous storage is applied.

Proton Exchange Membrane Electrolysis

PEM electrolyzers offer a number of advantages over traditional alkaline electrolysis technologies, while still avoiding the formation of explosive hydrogen–oxygen gas mixtures. First, only pure water with no added electrolyte is used in the electrolyzer. Second, a shorter electron path through the electrolyte (< 250 µm) results in reduced ohmic loss, allowing higher current densities (> 1000 mA/cm^2) and hence a more compact design [27.49, 50]. However, the high cost and compromised longevity of polymer membranes make the electrolyzers too expensive for general applications [27.51]. Further, the prerequisites to use noble metal catalysts and special current collectors, due to the acidic nature of the polymer electrolyte, are disadvantages compared to alkaline electrolyzers [27.52].

The general design of a PEM electrolyzer is analogous to that of a PEM fuel cell. The electrolyzer consists of an anode and a cathode separated by a membrane as shown in Fig. 27.8. The catalysts are deposited on either side of the membrane, forming the membrane electrode assembly (MEA). Purified water is fed to the anode structure of the cell. The membrane conducts hydrated protons from the anode to the cathode side. Individual cells are stacked into modules with bipolar plates providing the manifolds for water feed and gas evacuation. The bipolar plates include flow-field structures to enhance the transport of water to the electrodes, and product gases out of the cell.

Anode. In PEM electrolyzers, the oxygen evolution electrode, or anode, has a higher overpotential than the cathode [27.53]. Oxygen evolution occurs on noble metal catalysts such as Pt, Au, Ir, Rh, Ru, and Ag, but oxides of noble metals such as IrO_2 and RuO_2 have gained considerable interest over the last few decades. Several factors influence the electrocatalytic evolution of oxygen, namely the crystal-field stabilization energy, mixed and doped oxides, dispersion, crystallinity, and crystallite size [27.54]. Ruthenium oxide is known to be

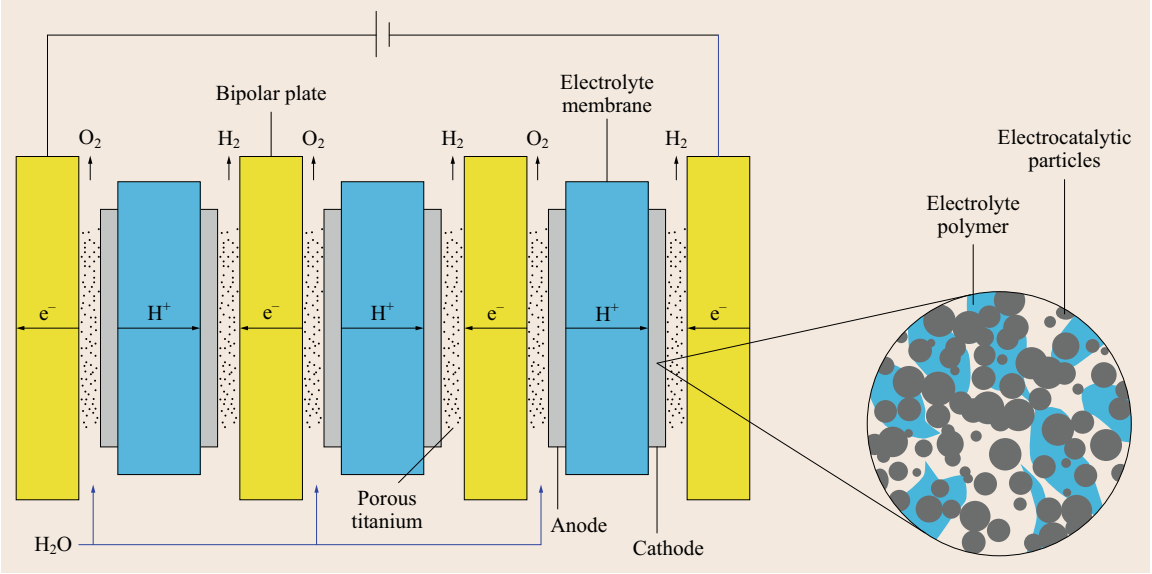


Fig. 27.8 Schematic of a PEM electrolysis cell (after [27.48], courtesy of ECS)

the most active oxide for the oxygen evolution reaction (OER) [27.55]; however, it suffers from instability and therefore needs to be stabilized with another oxide such as IrO_2. IrO_2 exhibits better corrosion resistance but is more expensive and has slightly lower electrocatalytic activity than RuO_2.

Addition of non-noble metal oxides has been reported to improve the stability of the IrO_2- and RuO_2-based electrodes in acidic media. Ir–Ta oxides have been suggested as the most efficient electrocatalysts for oxygen evolution in acidic electrolytes due to their high activity and stability [27.56]. Industrial anodes have been customarily based on a RuO_2 and TiO_2 mixture, where RuO_2 is the active component and TiO_2 the stabilizing agent. It has also been shown that SnO_2 improves the stability of IrO_2–RuO_2 anodes without reducing the activity significantly [27.57]. CeO_2 is also often added in order to enhance the selectivity for the desired reaction or to increase the anodic stability. Table 27.4 compares the performance (applied voltage) of PEM electrolyzers with different anode catalysts and loadings.

Among the parameters affecting the anodic overpotential are the catalytic activity and electrical conductivity of the electrocatalyst, which in turn relates to the composition and loading of the active component. The stability is related to the crystal growth and corrosion properties. Also, it is known that the development of efficient and less expensive electrodes (by reducing the loading of noble metal oxides or replacing them with cheaper alternatives) for the OER will make the electrolysis process more economical. The field is still open to new developments and improvements because many parameters must be optimized.

Cathode. Metallic platinum is typically used at the cathode for the promotion of the hydrogen evolution reaction (HER). The use of platinum is made necessary due to the highly acidic environment encountered in a solid polymer electrolyte, which promotes the corrosion of non-noble metal catalysts. Cost considerations require a significant reduction of noble metal loadings, at both the electrodes, from a few mg/cm^2 (current state of the art) down to around $0.1\,mg/cm^2$. Low Pt contents ($0.3–0.5\,mg/cm^2$) have been used at cathodes by depositing Pt nanoparticles onto high surface area carbons; for example, Vulcan XC 72 carbon black [27.58], carbon nanofibers [27.59], and carbon nanotubes.

Pd is almost as active as Pt for the HER and significantly less expensive. Using Pd–Pt mixtures, cell efficiencies close to 85% (1.7 V at $1000\,mA/cm^2$) have been demonstrated at the lab-scale with $0.7\,mg/cm^2$ metal loadings. Efforts are still required to further reduce Pt loadings down to $0.1\,mg/cm^2$ range. However, the cost of the noble metal is not only due to the metal itself, but also due to the cost of the precursor salts used in the synthesis. The chemistry required to produce the most appropriate precursor may have a significant impact. Thus, the overall cost can be significantly different from one process to another, even with a similar final metal loading.

However, the ultimate goal is to eliminate the need for noble metals. Carbon-supported cobalt clathrochelate catalysts [27.60] have been developed for the HER. In these compounds, the metal ion is locked in a close-knit structure, inhibiting ligand exchange in the more labile oxidation states of the encapsulated metal ion. This, in turn, explains the low chemical activity of this family of stable complexes. A cell efficiency of 80% at a current density of $500\,mA/cm^2$ was obtained at 90 °C. Additional encouraging results have been obtained with polyoxometallates [27.61]. Commercially available tungstosilicic acid hydrate (α-$H_4SiW_{12}O_{40}$) adsorbed at the surface of the cathodic titanium current collector yielded an efficiency of 70% at a current density of $1000\,mA/cm^2$.

Membranes. Perfluorosulfonic acid (PFSA) membranes have found use in modern PEM electrolyzers and fuel cells [27.62]. These membranes have excellent proton conductivity, mechanical strength, and chemical stability. They serve three basic functions:

1. Conduct protons between the anode and the cathode
2. Provide electrical insulation
3. Provide a barrier that prevents the produced gases from mixing.

Implicit in this list is the additional requirement that the membranes have a suitably long lifetime for the desired application. This usually means that the polymers must have hydrolytic and oxidative stability and have good mechanical integrity. In addition to these basic requirements, modern PFSA membranes need to be humidified in order to achieve maximum performance (conductivity) and durability. This requirement has several drawbacks such as the additional expense of humidifiers and parasitic power losses from the operation. Hence, there is a need for membranes that depend less on water for conductivity, allowing hotter and drier operating conditions.

Up to now, proton-conducting perfluorinated sulfonic acid membranes, in the form of DuPont's Nafion or Dow Chemical's materials, have been used as the gas-separator and the electrolyte simultaneously. They contain sulfonic acid groups ($-SO_3H$) attached to perfluorinated carbon backbones, which upon contact with water produce polar hydrated sulfonic groups ($H^+SO_3^-$). They allow the mass and charge transfer in

Table 27.4 Summary of PEM water electrolyzer performance at an operating current density of 1000 mA/cm^2 and temperature of 80 °C using Nafion 115 membrane

Anode	Cathode	Noble metal loading (mg/cm^2)	ΔE_{app} (V)
Ir	40% Pd/C	3.36	1.697
Ir–Ru oxide (70 : 30)	20% Pt/C	2.4	1.623
Ir-oxide	10% Pt/C	2.4	1.645
Ir–Ta oxide	10% Pt/C	2.4	1.572
Ru oxide	Pt	8	1.675
Ir	Pt	3–6	1.620
Ir-oxide	Pt black	7	1.620
Pt–Ir	Pt	1	1.750
Ir oxide	Pt black	3	1.680

a PTFE insulator. The conductivity of the membranes increases with the acid content of the polymer, which is realized by lowering its equivalent weight (nonsulfonic group content). However, lowering the equivalent weight increases the solubility of the polymer in water making it mechanically unstable. Hence there is a compromise between performance and durability.

Recently, Ballard Power Systems developed low-cost nonperfluorinated polymer-based electrolytes. A series of sulfonated polyaromatic polymers were synthesized, and fabricated into membranes via solution casting. A comparison of the performance of the membranes in single solid polymer fuel cells showed that sulfonated polyaromatic membranes performed equally well or better than the standard Nafion membrane [27.63]. Some other nonperfluorinated membranes have been developed more widely for fuel cell applications. It is expected that the development of this new generation of low-cost solid polymer membranes will have a beneficial impact on industrial acid electrolyzers.

Bipolar Plates. Current collectors are porous structures located between the membrane–electrode assembly and bipolar plates to allow a uniform distribution of the electric current. Carbon-based materials such as carbon paper or felts can be used on the cathode side of PEM electrolyzers. However, carbon undergoes electrochemical oxidation on the anode side at voltages greater than 0.9 V [27.64]. Hence, porous structures made from titanium are used on the anode side. The main drawbacks of Ti are the formation of a resistive oxide layer at the surface and the high cost of the material. The performance of sintered Ti is superior to that of other structures, but it is also the most expensive choice followed by felt and expanded mesh.

A well-designed bipolar plate must have a high electrical conductivity, high gas permeability, and permit water flow to the electrode. In single electrolysis cells, the MEA and current collectors are sandwiched between two electrically conductive endplates. Several single cells are connected electrically in series and hydraulically in parallel as a stack. A bipolar plate separates two adjacent cells so that it acts as an anode of one and cathode of the adjacent cell simultaneously. As for current collectors, bipolar plates have to be constructed from corrosion-resistant materials, such as expensive titanium, stainless steel, or cheaper graphite composite materials. In order to reduce the contact resistance between a bipolar plate and the adjacent current collector, the plate is coated with precious metals such as gold or platinum [27.65].

System and Operating Conditions. The system configuration of a PEM electrolyzer is similar to that of an alkaline unit (Fig. 27.9). However, the system is simpler due to the absence of caustic as the liquid electrolyte. The power is supplied through a transformer and a rectifier to convert the AC voltage to the required DC voltage. The feed water pump supplies water to the circulation loop on the oxygen side of the electrolyzer. The water is pumped through a heat exchanger, ion-exchange resin, and gas–water separator. The circulation pump in the loop is used to cool the stack. On the hydrogen side, the product gas is separated by a gas–water separator, followed by a demister to remove droplets, heat exchanger and condensate trap to reduce the dew point to room temperature.

PEM electrolysis stacks offer very high power densities at similar voltage efficiencies compared to alkaline electrolysis stacks. At present, current densities from 500 to 2000 mA/cm^2 and cell voltages from 1.7 to 2.1 V are usual. In most cases, PEM electrolyzer stacks operate at temperatures between 50 and 90 °C, and at pressures in the range of 0.8–20 MPa [27.67]. In terms of operating hours and lifetime, considerable progress has been made over the years. Due to the endothermic reaction, higher efficiencies, and efficient cooling by the water recirculation, thermal management is facilitated compared with PEM fuel cells. However, mechanical

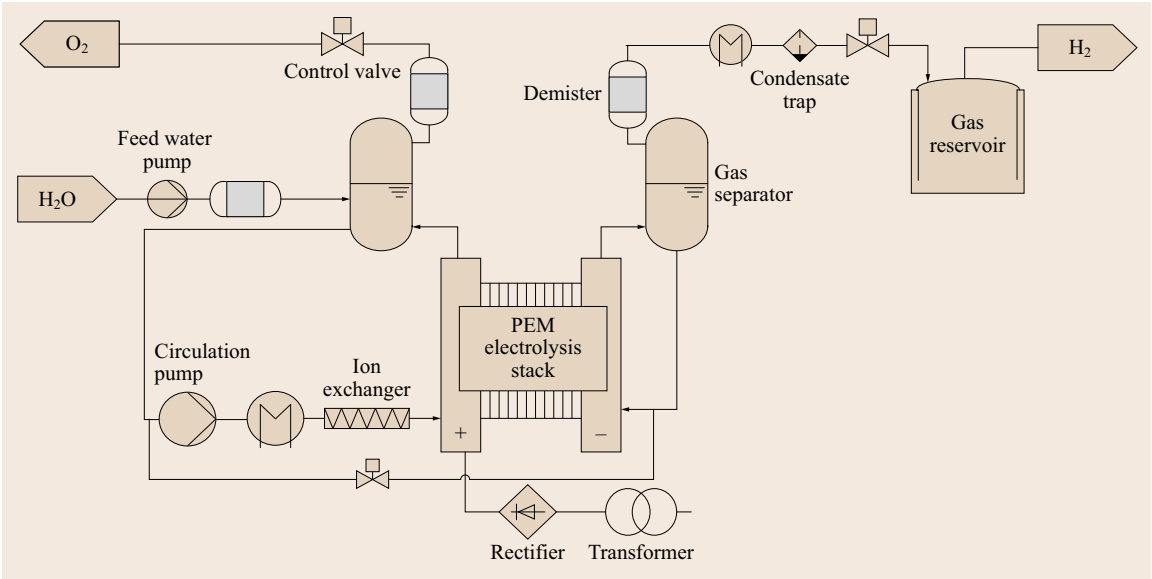


Fig. 27.9 Schematic of a PEM water electrolysis plant (after [27.66], courtesy of Wiley-VCH)

stress could be higher, as the stacks are operated under high pressures, with fluctuations caused during startup and shutdown. The most critical component of a PEM electrolyzer is the membrane, with thinning and ultimately failure leading to the mixing of gases. The lifetime of a well-designed and correctly operated PEM electrolyzer stack can reach up to several tens of thousands of hours. Water quality also has a strong effect on the degradation of the MEA, and typically deionized water with resistance values higher than 10 MΩcm should be used.

27.2.2 High-Temperature Electrolysis

High-temperature electrolysis using SOEC is capable of operation at extremely high electrical efficiency, near 100%. Similar to SOFCs, high operating temperatures, typically 800–900 °C, are required due to the limited electrolyte conduction at low temperatures. As the resistance decreases (and ΔG decreases, Fig. 27.3) with increasing temperature, the current density will increase if the cell voltage is at the thermoneutral voltage. Since hydrogen production is stoichiometric with current density (which is limited by the cell resistance), it is apparent that optimum current density and cell resistance values are critical variables for the most efficient production of hydrogen.

Common Electrolytes and Electrodes

The most common electrolyte by far used in SOEC application is YSZ or yttria-stabilized zirconia. Most often, yttria is present in about 6–8% concentration. Such materials have very good oxygen ion conductivities, but these conductivities are only achieved at high temperatures (> 750 °C). The maximum conductivity of YSZ is reported to occur at 7% loading, but significant differences (factor of 1.5) in conductivity measurements on samples with Y levels of 6–8% are not due to dopant levels [27.68]. Yttria (and other dopants) is used to stabilize the cubic fluorite phase of zirconia as well as to increase the concentration of oxygen vacancies [27.69]. Scandium is also reported to be an effective dopant for scandia-stabilized zirconia (ScSZ) and the conductivity of ScSZ is comparable to, or slightly higher than, YSZ at temperatures of interest for fuel cell or electrolysis cell applications.

Doped ceria also has a fluorite structure and is a common electrolyte in fuel cells. It has a higher *conductivity* than zirconia, especially at lower temperatures, but possesses electronic conductivity at low oxygen partial pressures [27.70]. Ceria is often doped with gadolinium (GDC) or samarium (SDC) to generate oxygen vacancies, which increases ionic conductivity [27.71–73]. Similar to the YSZ–ScSZ system, the conductivity is maximized with dopant ions that have the lowest size mismatch. Conductivity increases with Gd content, reaching a reported maximum at ≈ 10 mol% Gd, and then decreases [27.74]. *Fergus* [27.69] summarizes comparative conductivity data for YSZ, ScSZ, and GDC samples. The GDC samples consistently show higher conductivity than the zirconia species below 600 °C, and the level of Gd has a sensitive effect on stability toward low oxygen partial pressures.

A notably different approach is the use of strontium-doped zirconate and cerate as proton conductors for SOEC [27.75]. These materials, which are perovskite-type oxides, exhibit proton conduction at intermediate temperatures ($\approx 400\,^{\circ}C$). However, the cell design is such that protons, produced at the anode, are *pumped* through the electrolyte to the cathode, where they are reduced to form H_2. This eliminates the need to separate H_2 from steam, which simplifies the process, and lowers the overall costs for stacks and system. In addition, the intermediate temperature will potentially allow a greater selection of materials for flow channels, interconnects, etc. (i. e., balance of plant materials). The ceria derivatives are reportedly hydrothermally unstable, reacting with water vapor to form $Sr(OH)_2$ and CeO_2.

Electrodes. By far, the most common cathodic (produce hydrogen) materials are nickel cermets (ceramic–metallic blends). Most commonly, this is nickel mixed with zirconia [27.76] or YSZ [27.26, 77, 78]. It has been reported that Ni–YSZ electrodes have lower activity in electrolysis mode versus fuel-cell mode, and a diffusion-limited process was proposed to account for this behavior [27.79]. In addition, the aging of Ni–YSZ electrodes in a steam-rich environment has been reported, and ascribed primarily to coarsening of Ni particles [27.80]. This effect can be overcome to a large extent by ensuring that a reducing atmosphere over the electrode is maintained. Maintaining some hydrogen partial pressure with the steam feed can accomplish this. *Kim-Lohsoontorn* and coworkers have reported the performance of gadolinium doped ceria (GDC)-impregnated Ni–YSZ cathodes [27.81]. Addition of GDC to Ni–YSZ-enhanced performance, and the addition of 0.5 wt% Rh to the GDC led to significant improvement in the performance of both electrolysis and fuel-cell mode as compared to Ni–YSZ and Ni–GDC electrodes. The latter showed decreasing performance as the steam–H_2 ratio increased from 50/50 to 90/10, but the GDC-Ni YSZ analogue was relatively insensitive to these changes.

Anodic materials for O_2 generation (27.6) are commonly composites of YSZ and perovskites such as lanthanum manganite ($LaMnO_3$), ferrite ($LaFeO_3$), and cobaltite ($LaCoO_3$) which have been partially substituted with strontium [27.82]. Very commonly the strontium-substituted lanthanum manganite is used, termed LSM. However, there is a very wide range of oxide materials used, usually in combination (i. e., LSM with LSCF (lanthanum strontium cobalt ferrite). The composites are referred to as YSZ–LSM, YSZ–LSCM, YSZ–LSF, etc.

The use of LSM and LSM-derived anodes for SOEC is common, due to cost (relative to noble metals), ease of anode preparation, and thermal expansion characteristics [27.71, 76, 77]. It has been reported that LSF–YSZ composite exhibited higher catalytic activity for the oxidation on O^{2-} to O_2 [27.76]. LSM can be sintered together with YSZ at relatively high temperatures without forming insulating layers comprised of zirconates [27.83]. However, it is known that anodes based on LSCo and LSF exhibit much lower polarization losses than LSM, but LSCo–YSZ electrodes are reported to deactivate slowly due to solid-state reactions [27.77].

Marina et al. have reported a study on electrode performance in fuel cell and electrolysis modes; in both half- and full-cell mode [27.84]. The authors report that Ni-YSZ has higher losses than a La-substituted strontium titanate–ceria composite in electrolysis mode, but similar performance in fuel-cell mode. The titanate–ceria electrode performance was diminished at high steam partial pressure. Anode materials also showed higher losses in electrolysis mode, particularly for mixed conductor electrodes made from LSCuF and LSCoF. With fuel cells using a thin electrolyte, polarization losses were higher in electrolysis mode. The anodic polarization arising from O_2 evolution operation is expected to decrease oxygen vacancy concentrations, which would then give rise to higher polarization losses [27.84]. *Singh* and coworkers have reported a study on the effect of O_2 partial pressure on the stability of LSM–YSZ composite [27.85]. They report that the unit cell volume for LSM increases during exposure to lower O_2 partial pressures (1×10^{-7} MPa), but YSZ unit cell volume is unchanged. Lower O_2 partial pressure also results in grain growth and formation of $La_2Zr_2O_7$ and MnO_x compounds, which lower the stability, but the reaction was shown to be reversible upon sintering at O_2 partial pressure of 0.021 MPa.

Cells and Stacks

Leung's team has published a relatively recent review on SOEC technology development [27.77]. Electrolytes, electrodes, and cell–stack designs are covered. Although the earlier work by *Doenitz* [27.19] and *Isenberg* [27.20] utilized tubular cells, planar cells have received much more attention recently, due to better manufacturability and also more uniform distribution of gas species on the planar cells [27.71]. The latter characteristic improved the performance relative to tubular cells.

Mogensen and coworkers at the Riso National Laboratory in Denmark have published a number of papers over the last several years describing the develop-

ment of planar SOEC cells [27.78, 86, 87]. Ceramatec, Inc. and collaborators have also published a number of papers on stack production and testing [27.76, 88–90]. The work by Mogensen and coworkers describe planar, Ni–YSZ-supported cells (5 × 5 cm) with active electrode areas of 16 cm^2, which are produced at the Riso National Lab for Sustainable Energy at the Technical University of Denmark. Typically, the cells have a 300 μm thick NiO–YSZ porous support layer prepared by tape casting, a 10−15 μm thick YSZ electrolyte, spray painted onto the support tape. After these half cells are stamped and sintered, a 10−15 μm thick LSM–YSZ (50 : 50) composite oxygen electrode (anode) is spray painted onto the cells followed by re-sintering. The cell construction consists of aluminum housing, Ni foil current collector, gas sealing, and a gas distributor based on Ni-YSZ. The air distributor is based on LSM, and another current collector (gold foil) and remaining alumina housing are placed on top to prove a cross flow for the gases. Ceramatec also uses a planar cell design. The cells are electrolyte-supported, using ScSZ electrolytes (≈ 140 μm thick), Ni-cermet cathodes, and manganite-based anodes [27.70]. The cells are slightly larger (10 × 10 cm) than those reported by Mogensen, with an active area of 64 cm^2 per cell. Interconnects are made from ferritic stainless steel. Stacks are assembled from single cells, and for laboratory testing commonly contain 10 or 25 individual cells [27.88, 89]. The Idaho National Laboratory (INL) in the United States established a significant program on HTE coupled with nuclear energy. Ceramatec was a partner in this effort. As part of the scale up and demonstration activities, INL commissioned a 15 kW HTE test facility, termed the integrated laboratory scale (ILS) HTE test facility [27.91]. The ILS includes three electrolysis modules, each consisting of four stacks with 60 cells, yielding 240 cells per module and 720 cells total. The cells are planar cells based on Ceramatec's technology. Each module has an independent support system, which supplies electrical power, feedstock (steam with some H_2), sweep gas for removal of produced O_2, and exhaust gas handling. Other equipment includes dewpoint measurement for inlet and outlet feeds, steam generators, condensers for residual steam, and H_2 vent. All three modules were housed in a single hot zone.

Bo and coworkers at the Institute of Nuclear and New Technology (INET), Tsinghua University, Beijing, have also reported on their efforts for HTE process development [27.92]. Again, a major thrust of the work was the utilization of nuclear-based heat. This group also uses planar cells and designs, using Ni–YSZ cathodes, YSZ electrolyte, and both LSM and BSCF ($Ba_{0.5}Sr_{0.5}Co_{0.8}Fe_{0.2}O_{3-\delta}$) anodes. The BSCF gave improved performance (lower cell resistance, higher H_2 production) compared to LSM.

Kim and coworkers at the Korea Institute of Energy Research recently reported a three-cell flat-tubular solid oxide electrolysis stack [27.93, 94]. The NiO-YSZ cathode supports were extruded in the shape of flat tubes by a well-defined process. After heat treating the tubes for 3 h at 1150 °C, gas channels were formed by machining one side. The other side was used for a ceramic interconnector. After dip coating into a YSZ slurry, the ceramic interconnector was applied via spray coating of perovskite-type ceramic powders. Tubes were then calcined at 1400 °C for 3 h. Lastly, the anode catalyst was spray-coated onto the gas channel using a LSM slurry, followed by heat treatment again at 1150 °C for 3 h. A Ba–Si-based glass ceramic sealant was used for gas seals and stack manufacturing. The seals were cured via a two-step process, first at 900 °C for 1 h (spreading and adhesion), then 800 °C for 3 h for complete fixation and sealing.

Other workers have also recently reported studies on microtubular electrolysis cells. *Lagunna-Bercero* et al. [27.95] fabricated a cathode-supported Ni-YSZ/YSZ/LSM cell, with a 20 μm electrolyte thickness. The Ni–YSZ tube was 2.4 mm diameter and 10−15 cm in length, fabricated by cold isostatic pressing at 200 MPa. The gas-tight electrolyte was applied by wet powder spraying, then fired at 1400 °C. After firing, the LSM anode (LSM and 50/50 LSM–YSZ) was applied via dip coating, then re-sintered at 1250 °C. Researchers from the Energy Research Center of The Netherlands recently reported their progress on planar SOEC technology [27.96]. These cells used Sc–Ce-doped zirconia (ScCeZ) as electrolytes made by conventional tape casting. The anode was a 5 μm thick layer of YDC ($Y_{0.2}$,$Ce_{0.8}O_{2-\delta}$), applied via screen printing. After firing at 1400 °C for 1 h, the cathode layer was applied. This cathode had three layers, 5 μm thick layer of GDC, then a ≈ 15 μm thick NiO–GDC (65/35) layer was applied, followed by a 20 μm thick NiO layer. After firing the cathode at 1250 °C for 1 h, a final layer of LSCF was applied to the anode and the assembly given a final heat treatment at 1100 °C for an hour.

Kerafol GmbH has also reported its efforts with ScYZ electrolytes [27.97] These newer electrolyte-supported cells, developed with HC Stark, utilize a YSZ–LSM cathode and GDC–NiO anode. The electrolyte thickness is ≈ 150 μm. Optimum cathode sintering temperature was determined to be 1100 °C. Kerafol also describes its efforts in developing ceramic glass sealing tapes and processes to improve reliability and lower costs.

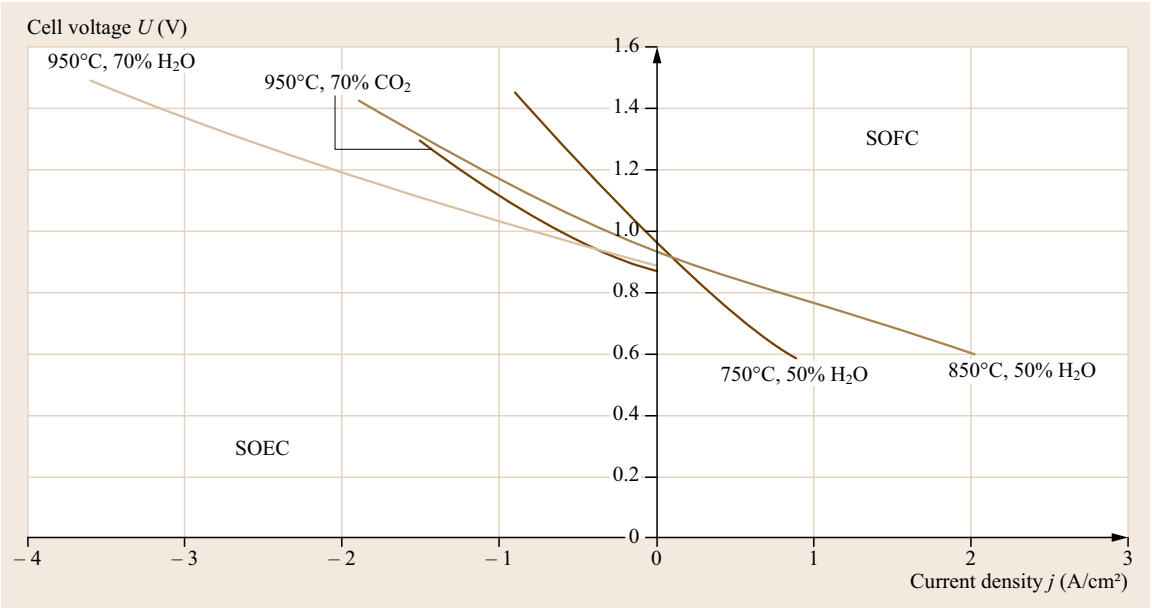


Fig. 27.10 Current–voltage curve from a planar cell (after [27.86])

Cell and Stack Performance. Current density versus cell voltage (I/V) curves are most often used to demonstrate performance characteristics of cells and stacks. Figure 27.10 shows cell voltage versus current density from a planar cell produced at Riso Laboratory described above. The positive current density is fuel-cell mode, and negative current density is electrolysis mode. (Current densities in this section will be reported without the negative sign, but it should be understood where these lay with respect to fuel-cell mode.) Note that the various curves (corresponding to different temperatures and gas partial pressures) have a similar *y*-intercept at zero current density. This is the opens-circuit voltage (OCV) and is often around 0.9 to 1.0 V for SOEC-type devices (the exact OCV can be calculated with the Nernst equation for a given gas composition and temperature). Note that very high current density ($\approx 3600\,\mathrm{mA/cm^2}$) is achieved at 950 °C with 70% steam/30% H_2 feed (and steam utilization of 37%). Typically, some fraction of the feed stream is H_2 to keep the Ni cathode from oxidizing and coarsening. *Jensen* et al. believed that this was the highest current density reported at that time (2007) for SOEC operation [27.86]. It is certainly much more common to find current densities in the $200–600\,\mathrm{mA/cm^2}$ range especially for longer term testing. However, the microtubular cell reported by *Lagunna-Bercero* et al. is claimed to withstand $6000\,\mathrm{mA/cm^2}$ current density at 895 °C without apparent cell damage [27.95].

A similar *I–U* curve has been published by *Schiller* et al. and is shown in Fig. 27.11 [27.21]. Here, both voltage (U) and power density (p) are plotted against current density. In this case, a single cell was operated in both electrolysis and fuel-cell modes at temperatures between 750 °C and 850 °C. The negative current density indicates electrolysis mode. A 70/30 steam–hydrogen feed was used in these tests. Note here that the OCV again is near 0.95 V. The effect of temperature is readily apparent: At 750 °C, a voltage of 1.2 V gives a current density of $\approx 375\,\mathrm{mA/cm^2}$, whereas at 850 °C, the same voltage results in a current density of $800\,\mathrm{mA/cm^2}$.

Another representation is shown in Fig. 27.12. This graph (with calculated values) shows heat flux versus voltage and current density for a planar-type stack. It illustrates that the heat generation in the stack can be negative, zero, or positive, depending on the voltage. Again, the open-circuit voltage (or open cell potential) is about 0.86 V. The calculation assumed an operating temperature of 927 °C, H_2 mole fractions of 0.1 and 0.95 at the inlet and outlet, respectively, and a R_{ASR} (area-specific resistance) of $1.25\,\Omega\mathrm{cm^2}$. The ohmic heat flux is given by

$$q_\Omega = j^2 R_{ASR} = j(V_{op} - V_N) \qquad (27.24)$$

where j is the current density, V_N is the mean Nernst potential for the cell, and R_{ASR} is the area-specific resistance. The reaction heat flux is given by

$$q_{rxn} = \frac{j}{2F}(T\Delta S_e)\,, \qquad (27.25)$$

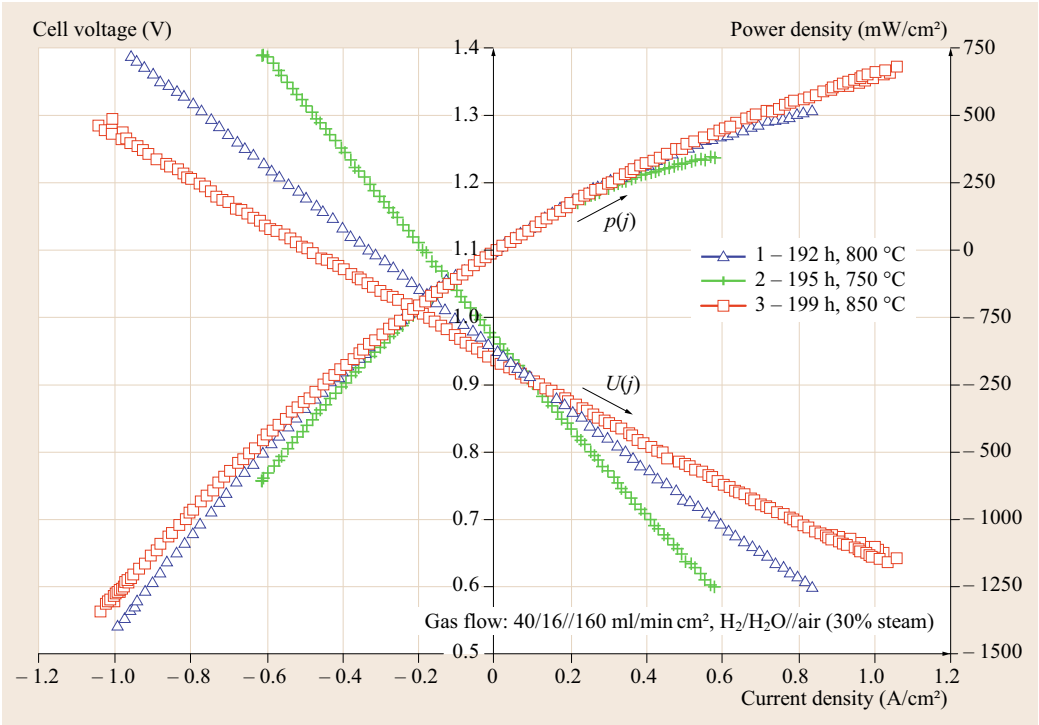


Fig. 27.11 I/U and j/p characteristics of a metal-supported cell (after [27.21])

where ΔS_e is the entropy change for the electrolysis process, accounting for the reactant and product partial pressures.

In fuel-cell mode, the net heat flux is always positive, and increases with operating voltage and current density [27.91]. In electrolysis mode, the net heat flux is negative at low current densities, increases to zero, then is positive at the higher current densities. The point at which the net heat flux is *zero* is the thermoneutral voltage (Sect. 27.1.4 and (27.23)) [27.91].

The thermoneutral voltage increases only slightly in magnitude over the typical operating temperature range for SOEC devices (1.287 V at 800 °C to 1.292 V at 1000 °C) [27.91]. At typical SOEC temperatures and R_{ASR} values, operation at the thermoneutral voltage will give rise to current densities in the 200–600 mA/cm^2 range [27.91]. The very high current density reported by Mogensen et al. may result from very low internal resistance associated with their cell (0.17 Ωcm^2). For example, the Riso cell achieved the −3600 mA/cm^2 current density at 1.48 V. With an OCV of 0.88, the internal resistance is

$$\frac{1.48-0.88\,\mathrm{V}}{3.6\,\mathrm{A/cm^2}} = 0.17\,\Omega\,\mathrm{cm^2}\,.$$

If the resistance were in the range of 1.0 to 1.5, the current density would be 400–600 mA/cm^2.

In order to produce large volumes of hydrogen, individual cells must be assembled into stacks. Figure 27.13 shows a schematic of a stack assembly.

Commonly, a lab scale stack will contain 10 identical electrolyte-supported cells (less frequently there are 25). A *cell* is defined as one anode–electrolyte–cathode assembly. The individual cells have been described in Sect. 27.2.2 and are also discussed in [27.76].

The stack is assembled by layering the cells with metallic interconnect assemblies. The interconnects comprise a metallic separator plate sandwiched between two metallic flow-field layers (Fig. 27.13). These conductive metal layers provide electrical contact between the anode and cathode of adjacent cells, connecting the cells in series. Interconnects can be fabricated from low-Cr ferritic stainless steel. It includes an impermeable separator plate approximately 0.46 mm thick, with edge rails and two corrugated/perforated flow fields. The flow-field layers provide channels for gas flow to the anode and cathode with which they were in contact (the cells were arranged in parallel with respect to gas flow). The steam–H_2 flow field is fabricated from Ni foil; same for the air side is ferritic stainless steel. To improve performance, the air-side separator plates have the surface pretreated to form a rare-earth conductive oxide scale. A perovskite rare-earth coating is also applied to the separator-plate oxide scale by screen printing or plasma spraying; a thin (≈ 10 μm) nickel

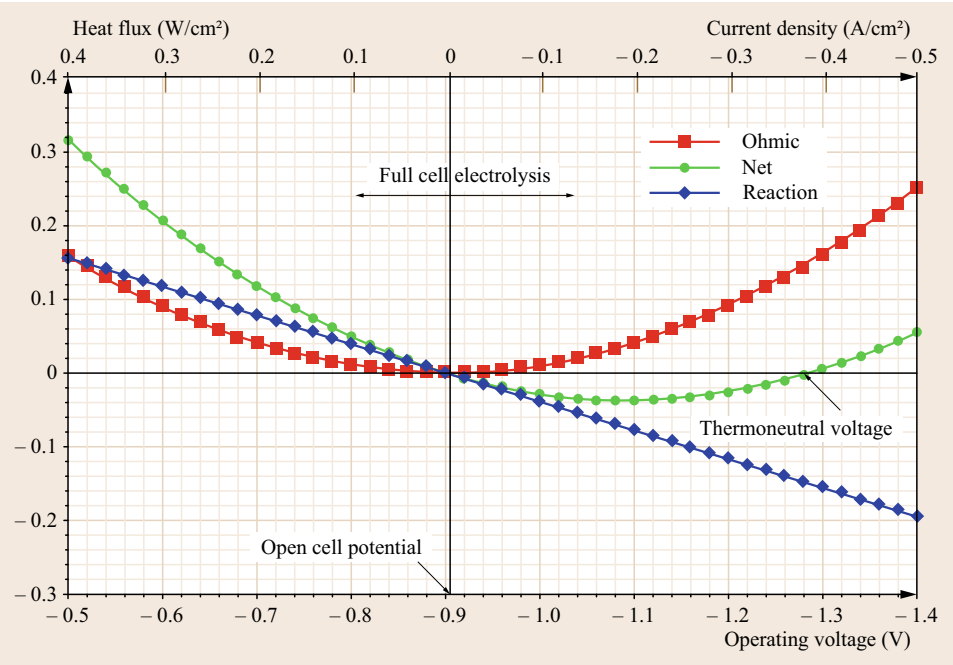


Fig. 27.12 Thermal contributions in electrolysis and fuel cell operations (after [27.91], courtesy of INL)

metal coating is applied to the steam–H_2 side of the separator plate.

Gas inlet and outlet manifolds were added to the sides of the stack assemblies. Two sets of manifolds were used, one to provide steam–H_2 to the stack cathodes and one to provide sweep gas (air) to the stack anodes. The sweep gas is not a reactant; rather, it is used to ensure a constant oxygen partial pressure at the stack anodes. Stack operating voltages are measured by spot-welding wires onto power lead attachment tabs that were integral to the upper and lower interconnect separator plates. Since the stack air outlet plane is open, the small air-flow channels are accessible for small leads to provide intermediate cell voltages. Additionally, four miniature thermocouples were inserted into the air-flow channels to monitor internal stack temperature. The entire stack assembly is then placed into a stack holder inside a large furnace or kiln.

The process test system included automated dew point sensors on the steam–hydrogen inlet and process outlet streams. Typical flow rates in the system were 2000 sccm (standard cubic centimeters per min) N_2, 400 sccm H_2, and 4000 sccm water (corresponds to an inlet dew point temperature of 83 °C). Air flow rate was 3500 sccm. Figure 27.14 provides data from such a stack test. In each of the tests shown in Fig. 27.14, the furnace temperature and gas flows were held constant, and the power supply programmed to vary the applied stack voltage between 8 and 14 V. The sweep rate was $\approx 8\,\mathrm{mV/s}$; thus each sweep in the figure was approximately 25 min in duration. The curves labeled *FLUENT* were calculated with the FLUENT modeling package. The OCV values were calculated values. The simulation empirically adjusted gap contact resistances to yield overall R_{ASR} values that matched experiment. The area-specific contact resistance values for sweep 4 were reported to be $0.74\,\Omega\mathrm{cm}^2$ between the electrodes and flow channels, and $0.18\,\Omega\mathrm{cm}^2$ between flow channels and the separator plate.

Sweep 1 was performed with low inlet steam content, and had a large ASR value as inferred from I–V curves. This behavior is an example of a mass-transfer-limited overpotential. Sweep 2 was an intermediate steam content test, and is nearly linear over the range of current densities tested. Sweeps 3 and 4 (inlet dew point of $\approx 83\,^\circ\mathrm{C}$) show linear behavior at lower current densities, then become concave-down at the higher values. Herring et al. suggested that the lower slope in these sweeps is related to the mean electrolyte temperature as the operating voltage increases (as the ionic conductivity of the electrolyte increases with temperature). Sweep 5 has a shallower slope than the others, reflective of the higher furnace temperature.

The internal temperatures measured in the stack at four different locations showed lower temperatures than the stack inlet temperature. At voltages between OCV and thermoneutral, the endothermic reaction heat requirement is less than the ohmic heating and a net stack cooling occurs. The thermal minimum was reached at 11.2 V and full thermal recovery (internal stack temper-

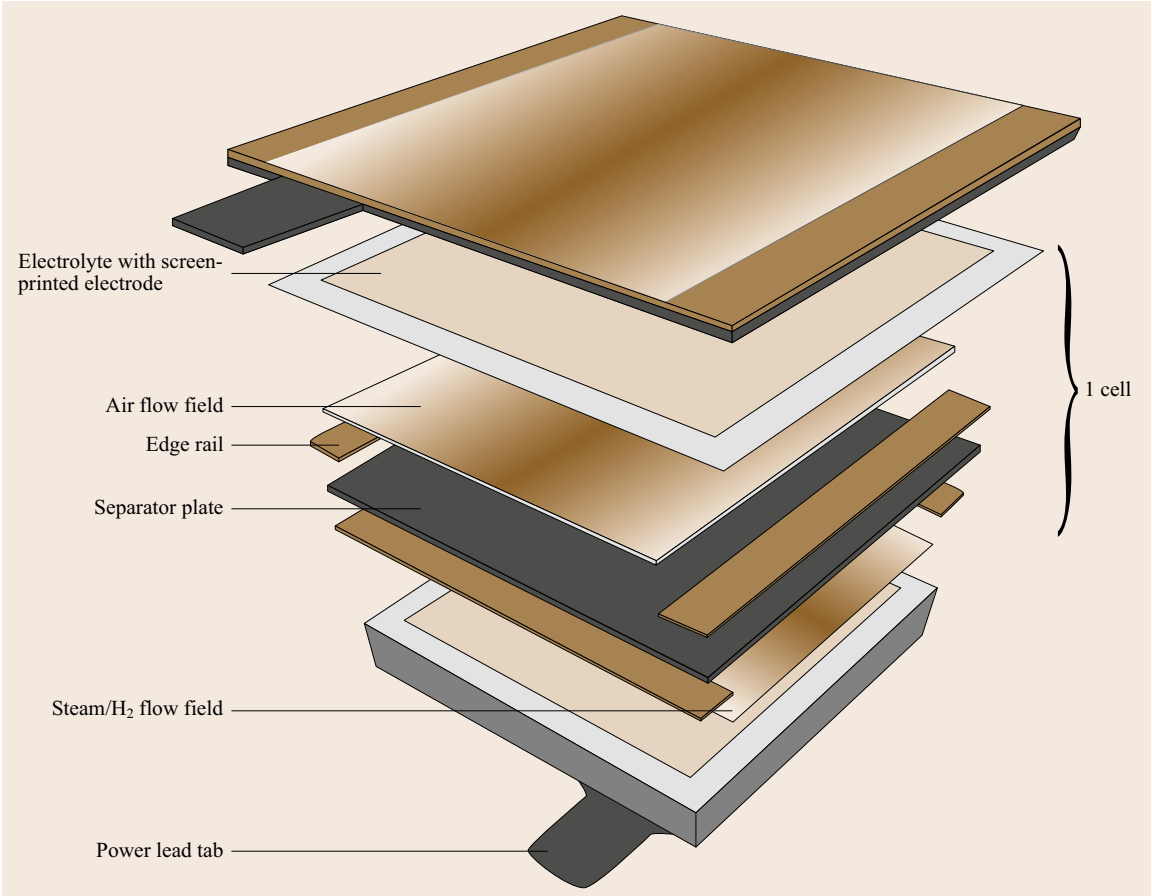


Fig. 27.13 SOEC stack diagram (courtesy of INL and Ceramatec)

atures near the inlet temperature) was realized near the thermoneutral voltage of 12.9 V.

Hydrogen production rates can be calculated from the stack current according to

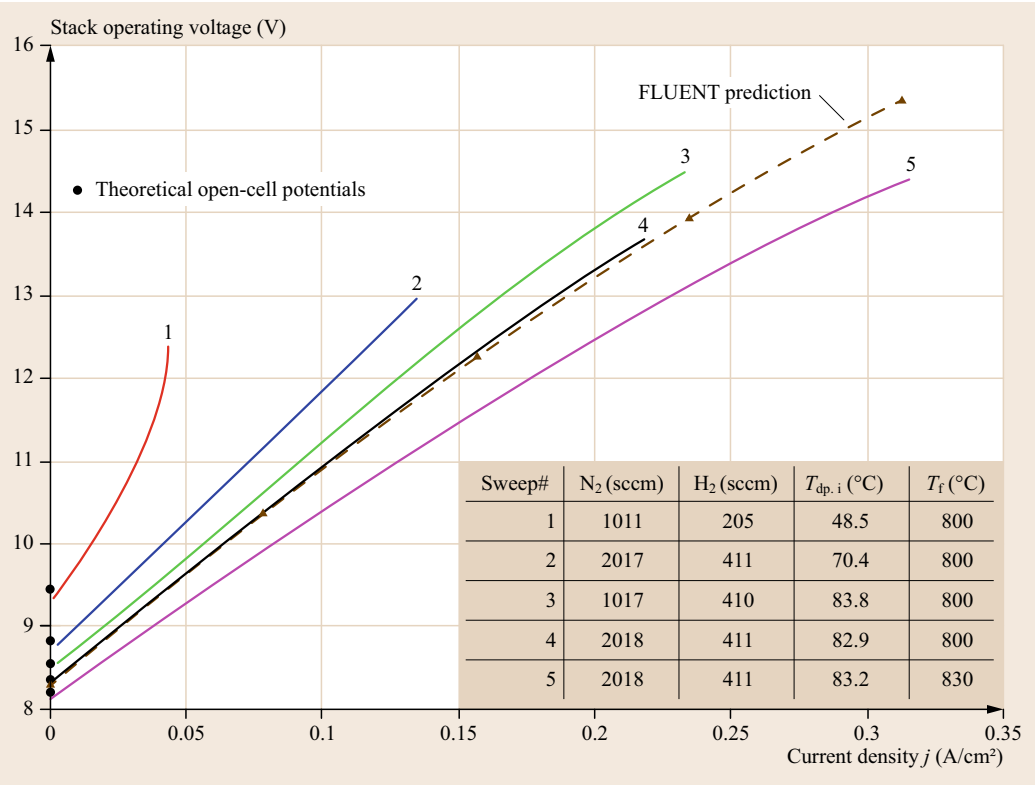
$$\text{H}_2 \text{ molar flow rate} = \frac{I}{2F}(\text{no. of cells}) \,, \qquad (27.26)$$

where I is current (A) and F is the Faraday number. The product of the electrical current and number of cells is the total ionic current. In addition, the hydrogen production rate can be calculated independently from the inlet and outlet dewpoint temperatures. The production rates from sweep 2 in Fig. 27.14 are shown in Fig. 27.15.

Note that both methods are in good agreement, although there is a bit more noise in the values based on dewpoint. The production rate of H_2 is linear since it is directly proportional to stack current. The authors indicate that up to 0.09 Nm^3/h H_2 production was achieved with this stack.

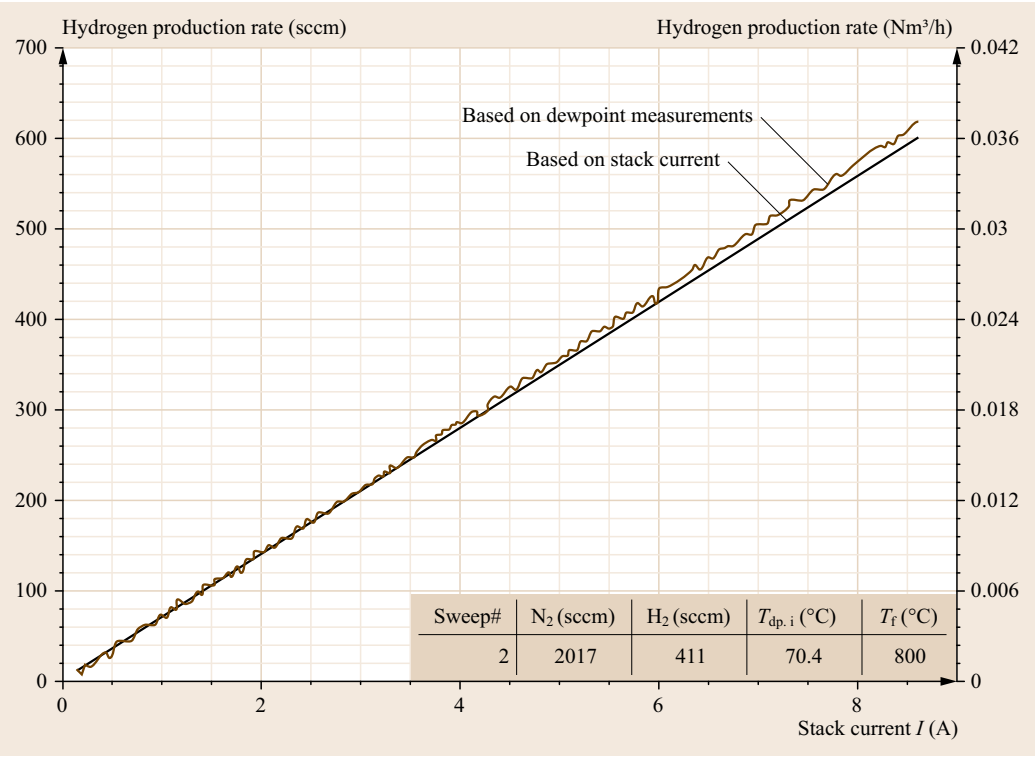
Researchers at the Korea Institute of Energy Research have published results from a three cell flat-tubular solid oxide stack. The details of the cell assembly were described above. Figure 27.16 shows the gas flows, stack voltage, current, and H_2 production rate from an 80 h test at 750 °C. The stack was operated at 3.9 V (1.3 V per cell), and stack current was monitored. The average current flow was 3.23 A, and the equivalent H_2 production rate was 0.004 Nm^3/h. The authors report a total of 0.144 Nm^3 of H_2 produced over 37.1 h of operation. At an average 0.004 Nm^3/h, and the 30 cm^2 cell area, a production rate of 2.95 kg H_2/d per square meter cell area can be calculated.

Lifetime and Degradation Testing. Operation at higher current density offers the possibility of producing a given volume of H_2 with less cell/stack area. In turn, the expected overall stack investment will be lower. These savings may be offset by more rapid degradation at the higher current density. Invariably, SOE cells and stacks will degrade with time. If this degradation rate can be managed to an acceptably slow rate (i. e., < 1%/1000 h), a sufficient lifetime can be an-



Sweep#	N_2 (sccm)	H_2 (sccm)	$T_{dp,i}$ (°C)	T_f (°C)
1	1011	205	48.5	800
2	2017	411	70.4	800
3	1017	410	83.8	800
4	2018	411	82.9	800
5	2018	411	83.2	830

Fig. 27.14 Stack operating potential as a function of current density (after [27.76])



Sweep#	N_2 (sccm)	H_2 (sccm)	$T_{dp,i}$ (°C)	T_f (°C)
2	2017	411	70.4	800

Fig. 27.15 H_2 production rates during DC potential sweep (after [27.76])

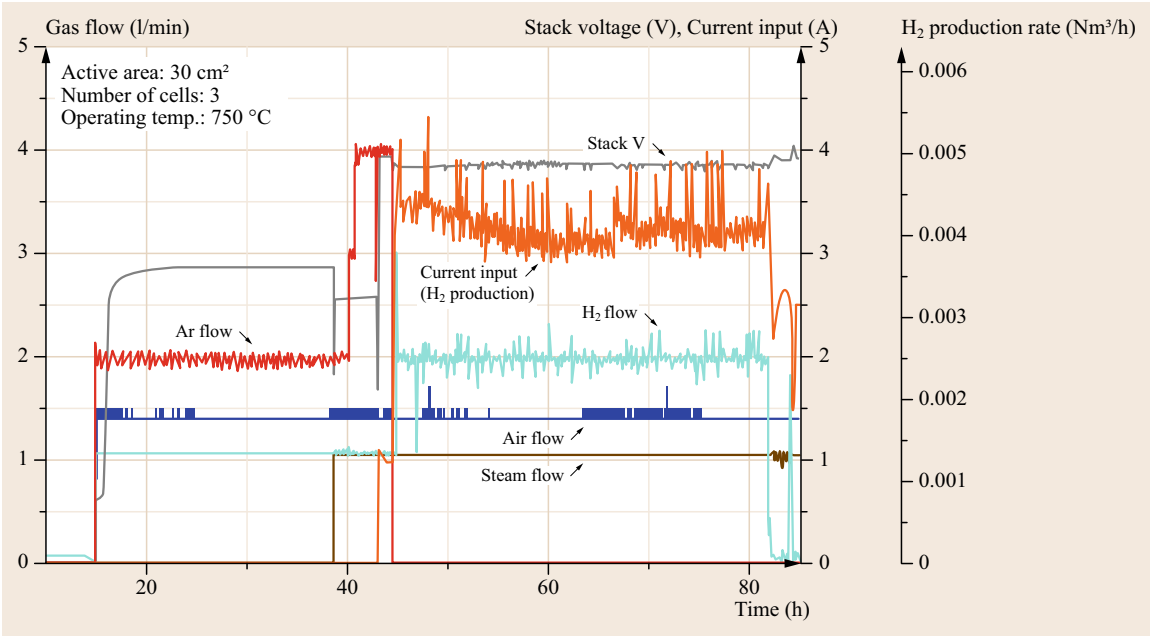


Fig. 27.16 Performance of a three-cell flat-tubular solid oxide electrolysis stack at 750 °C (after [27.93])

ticipated. Commonly, targets of 4.5–5 years stack life are targeted in the literature as *acceptable*, based in part on the relative insensitivity of H_2 production price to the lifetime longer than 3–4 years [27.98]. Operational integrity and reliability (up-time) are always essential characteristics.

However, while many researchers have reported good initial performance over short periods of time, demonstrating the maintenance of such performance over thousands of hours is much more challenging. There are multiple pathways for SOEC degradation, both *chemical* (impurities, Cr, Mn poisoning, etc.) and *mechanical* (bonding, sealing, electrode adhesion, metallurgy, etc.). In addition, long-term testing is not always possible due to resource and time constraints. There is much less information available regarding long-term (thousand's of hours) operation of SOEC cells and stacks than the short-term testing and performance characterization data. Nevertheless, a few groups have reported such studies.

Schiller et al. [27.21] reported the performance characteristics of the metal-supported cell described above. Over 2000 h, at 300 mA/cm^2, the voltage loss was 3.2%/1000 h. The Riso National Lab results show a similar result, but initial periods ($\approx$ 100 h) have voltage increases, then begins to decrease. They reported tests of > 700 h.

One of the longest term test periods has been reported by *Schefold* et al. in Germany [27.99]. This 9300 h test (387 d) was performed on an anode-supported SOEC (45 cm^2 area) at 780 °C and 1000 mA/cm^2 current density. The cell consisted of a YSZ electrolyte, Ni–YSZ cathode, and LSCF anode.

This report also provides an excellent summary of the degradation studies to date for both cells and stacks. At current densities between 300 and less than 500 mA/cm^2 in SOEC mode, the lowest rates for voltage losses were in the range of 2–3%/1000 h. These authors also document studies where degradation rates of up to 10%/1000 h were noted. When the current density was increased to $\approx$ 1000 mA/cm^2, drastic acceleration in degradation was documented, owing to an increasing resistance of YSZ electrolyte as well as increases in ohmic resistances.

Such long-term tests are not without process upsets. Such upsets are commonly encountered in most labs, pilot plants, and operating facilities. Mechanical shocks, unstable steam supply, impacts from evaporator purging, blocked evaporator, and loss of gas flow are all documented [27.93]. Nevertheless, the test duration represents about double the longest stack test and about an order of magnitude longer than cell tests. In addition, the high current density is significantly above most long term test studies. Remarkably, the voltage loss over the entire test was 3.8%/1000 h, corresponding to 40 mV. During the initial 5600 h, the loss was lower (2.5%/1000 h) and, during an incident-free period, it was even lower at 1.7%/1000 h.

These authors also correctly point out that SOEC degradation data are not based on standardized test-

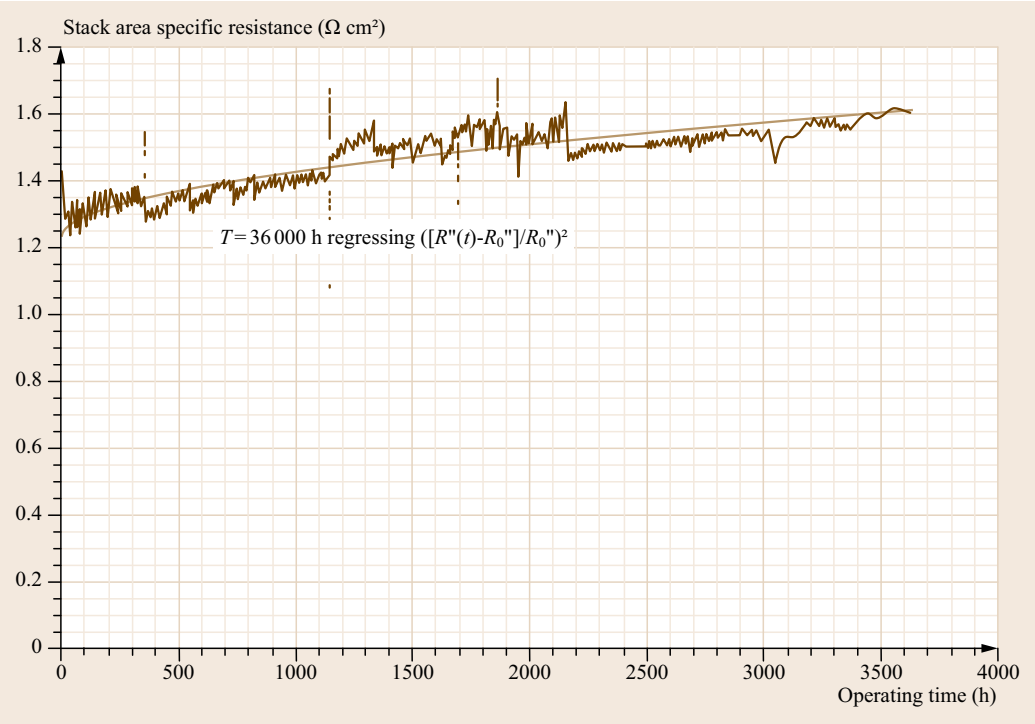


Fig. 27.17 Regression fit in stack with low degradation (after [27.100], courtesy of Ceramatec)

ing conditions. Steam content, current density, steam utilization, constant current versus constant voltage operation, etc., are all different in many of these studies. Degradation could be defined as an increase in voltage (if operating at constant current), a decrease in current (if operating at constant voltage, as in this experiment), or an increase in resistance. These quantities are all related as shown in (27.27)

$$R_{\mathrm{ASR}} = \frac{U - U_0}{nj} \,, \tag{27.27}$$

where R_{ASR} is the average ASR, U is the stack voltage, U_0 is the stack open-circuit voltage, j is the current density, and n is the number of cells. If U, U_0, and n are held constant, the ASR is simply proportional to the reciprocal of current density (j). Essentially, lower current density at a given operating voltage means a higher resistance.

One challenge in using the 1000 h percent degradation metric is that it is sometimes difficult and somewhat arbitrary to choose an appropriate baseline or initial value, particularly in a specific case where there is a relatively high level of noise in the data. Ceramatec [27.100] has reported that long-term degradation follows a square root dependence with time, as shown in

$$R_{\mathrm{ASR}} = R_0 \left(1 + \sqrt{\frac{t}{\tau}}\right) \,, \tag{27.28}$$

where R_0 is the initial resistance, t is time, and τ is a time constant, which is defined as the time required to double the initial ASR. This represents another way to quantify the long-term performance of a cell or stack of cells. An example of Ceramatec's approach is given in Fig. 27.17. The resulting τ value is 36 500 h, or just over 4 years, for this stack to double the resistance.

Degradation Mechanisms. At present, a complete understanding of, and complete agreement upon the causes of degradation and the electrochemical mechanisms behind them does not exist. However, this has been the focus of much work in the SOEC community, and certain degradation routes are well-characterized. *O'Brien* et al. [27.89] have suggested three main categories for degradation:

1. Progressive, constant rate degradation
2. Degradation corresponding to transients caused by thermal or redox cycling phenomena
3. Degradation resulting from a sudden failure or malfunction of a component.

Degradation data is available for both individual cells as well as stacks. Degradation routes in stacks are not the same as those for individual cells [27.101]. Stack degradation is faster than cell degradation. Degradation in SOECs is more rapid than the same cell run in SOFC mode, as much as five times faster. Thus, the body of work that exists for SOFC technology can be used as a starting point and reference, but the development of SOEC technology will require study of SOEC components and stacks. In early work, *Jensen* and *Mogensen* reported cells that showed lifetimes of a hundred hours or so [27.102]. A second-generation design showed limited degradation over a 1 year test. The authors reported that the degradation in SOFC mode was far less than in SOEC mode for the same system. More recently, they have reported that degradation (or passivation) of their cells occurs mainly over the first 100 h, and can be partially reactivated by *I–U* scanning in fuel-cell mode. Additionally, after the initial degradation, some reactivation occurred by operation at constant galvanostatic electrolysis conditions. Very recently, *Mogensen* and coworkers have reported the degradative effect of very low levels of impurities in the feed gases (≈ 5 ppb) on SOEC performance [27.87, 103, 104]. Treatment of the inlet gases to remove impurities fed to the Ni–YSZ electrode and LSM–YSZ electrode led to essentially no degradation over 600 h, at current densities up to $-750\,\mathrm{mA/cm^2}$. Presumably, trace levels of sulfur compounds were responsible.

Sohal et al. have summarized degradation issues in SOECs during HTE [27.105]. The total polarization loss (degradation) consists of three dominant parts: Activation (or charge transfer) polarization (η_{act}), concentration (or diffusion) polarization which includes chemical reaction effects (η_{conc}), and ohmic resistance polarization (η_{ohm}). At the same temperatures and current densities, the η_{act} and η_{ohm} are likely to be very similar. The η_{conc} is different because the gas transport mechanisms through the electrodes are different. A nonexhaustive list of leading causes for SOEC degradation is as follows:

- Microstructural changes in bond layer on the anode (O_2 electrode)
- Cr poisoning and dissociation of the bond layer on the anode
- Resulting delamination of the anode
- Loss of electrical–ionic conductivity of the electrolyte
- Generation of contaminants from the interconnects.

Delamination of the anode and the resulting degradation has been a significant problem, especially related to LSM-type materials [27.79, 91]. *Chen* and *Jiang* [27.106] recently reported the degradation of an LSM anode in SOEC mode over 48 h ($-500\,\mathrm{mA/cm^2}$ current density, 800 °C) [27.106]. Significant increases in electrode polarization and ohmic resistances were observed. In the delaminated cell, the formation of nanoparticles at the electrode–electrolyte interface was noted, caused by local disintegration of LSM grains at the interface. One proposed mechanism for the delamination is the incorporation of O^{2-} ions from the YSZ electrolyte into the LSM grain, leading to shrinkage of the LSM lattice. This, in turn, creates local tensile strains, resulting in microcracks and subsequent nanoparticle formation. O'Brien et al. have also raised the possibility that the high rate of O_2 production can exert high pressure at the electrolyte–electrode interface, increasing chances for delamination.

Many authors make use of electrochemical impedance spectroscopy (EIS) as a tool to characterize the degradation [27.21, 26, 76, 77, 83, 96, 99, 104, 106]. *Kong* et al. noted that after thermal cycling, polarization resistances increased on the anode, indicating degradation of the TPB [27.82]. *Ebbesen* et al. [27.103] reported extensive EIS data for Ni–YSZ–YSZ–LSM–YSZ cells. At current densities up to $-500\,\mathrm{mA/cm^2}$ at 850 °C, these researchers only observed polarization degradation (no ohmic degradation). They divide the polarization degradation into two mechanisms, one located at the Ni–YSZ electrode (100–200 Hz in the impedance spectra), and one minor mechanism located either at the Ni–YSZ or LSM–YSZ electrodes with a frequency of 1000–3000 Hz. The low-frequency mechanism is heavily influenced by feed impurities. An additional detailed EIS study, with an equivalent circuit, for SOEC is given by *Ouweltjes* et al. [27.96].

Impurities and Poisons. Chromium (Cr) and silica (Si) have also been reported as poisons in SOEC systems [27.91, 103]. Silica can be present at low levels in the steam, but can also be produced from glass seals used in stack manufacturing. Cr can arise from the materials used for interconnects and other balance of plant components, which liberate Cr vapor at electrolysis conditions [27.91, 103]. These contaminants often migrate to grain boundaries, blocking the active TPB, and increasing the polarization resistance. *Hauch* and coworkers in Denmark reported the formation of a glassy phase containing Si impurities developed at the TPB of the Ni–YSZ electrode in their cells [27.107]. The majority of the increased polarization resistance was confirmed by EIS to be due to this electrode.

Virkar has recently reported on the mechanism of oxygen electrode delamination in SOEC [27.109]. An electrochemical model was developed, which indicates

Table 27.5 Solar conversion efficiencies and other related data for solar photolysis of water using global AM1.5 solar radiation (after [27.108])

Scheme	Conditions	η_P (%)	η_C (%)	U_{loss} per photon (eV)	Threshold wavelengths (nm)	
					λ_0 or λ_1	λ_2
S1	Ideal limit	5.3	–	0.49	420	–
S2	Ideal limit	30.7	–	0.37	775	–
S2	Chemical conversion	–	23.5	0.60	680	–
S2	Chemical conversion	–	17.4	0.80	610	–
S2	Chemical conversion	–	12.7	1.00	555	–
S4	Ideal limit	30.6	–	0.31	1340	–
D2	Ideal limit	42.4	–	0.38[a]	655	930
D4	Ideal limit	41.0	–	0.31[a]	910	2610
D4	Chemical conversion	–	32.3	0.60	785	1465
D4	Chemical conversion	–	27.1	0.80	720	1120
D4	Chemical conversion	–	21.6	1.00	655	925

In schemes D2 and D4, it is assumed that equal photon fluxes are used by the two photosystems
[a] Average U_{loss} per photon

oxygen electrode delamination arises via high internal oxygen pressure within the electrolyte. Particularly noteworthy findings from this modeling are that modest changes in the *electronic* conductance can cause orders of magnitude changes in the oxygen pressure, and a small amount of electronic conduction through the electrolyte is actually preferred from a stability standpoint. Thus, addition of ceria (or other metal oxides comprised of metals with multiple valence states) should decrease the delamination tendency [27.109].

27.2.3 Photoelectrolysis

There are two parts to the efficiency of photoelectrolysis: the photovoltaic (η_{pv}) and Faradaic (η_F) efficiencies. The overall efficiency, often referred to as the solar-to-hydrogen (STH) efficiency of a cell (η_{sth}), is defined as the product of these quantities

$$\eta_{sth} = \eta_{pv} \times \eta_F \, .$$

Challenges and Strategies in Cell Design

Even in the case of the most quickly degrading photoelectrodes, the Faradaic efficiency is nearly unity [27.110]. Implicit in this observation are the conclusions that (1) even the smallest measurable Faradaic inefficiency is extremely important to the long-term success of the PEC cell, and (2) discussion of the overall STH efficiency is dominated by the photovoltaics half of the problem.

Efficiency Limits. The photovoltaic efficiency limits of PEC processes have been evaluated for various cell-operating scenarios [27.108, 111].

Reproduced in Table 27.5 is a summary of the conclusions from *Bolton* et al. [27.108], who investigated the photovoltaic-based efficiency limits of PEC cells in both the 1-junction and 2-junction scenarios. In all cases there is a necessary loss of energy, relative to the band gap of the light harvester, which is required to drive the charge separation and electrochemical processes. Without knowing exactly what those losses will be for a real system, the authors give efficiencies for a realistic range of values in each case, either ignoring (U_{loss} under *ideal limit*) or taking into account (U_{loss} under *chemical conversion*) the overpotential for electrolysis. The scheme abbreviations are defined as follows: S1 is a single junction cell that converts 1 photon into 2 electron–hole pairs (requires 1 photon for each molecule of hydrogen produced); S2 is a single junction cell that converts 2 photons into 2 electron–hole pairs (requires 2 photons for each molecule of hydrogen produced); D2 is a stacked double junction cell that converts 2 photons into 2 electron–hole pairs (requires 2 photons for each molecule of hydrogen produced); and D4 is a stacked double junction cell that converts 4 photons into 2 electron–hole pairs (requires 4 photons for each molecule of hydrogen produced). In the case of a double junction (type *D*) cell, the efficiency limits depend on the bandgaps of both junctions, as shown in Fig. 27.18, and are maximized when the achievable photocurrents of the two junctions are equivalent (i. e., when the top junction absorbs the same number of short-wavelength photons as the underlying junction absorbs penetrating, longer wavelength photons). The most physically realistic designs are S2 and D4, which are reported to have theoretical efficiency maxima in the ranges of 13–24% and 22–32%, respectively.

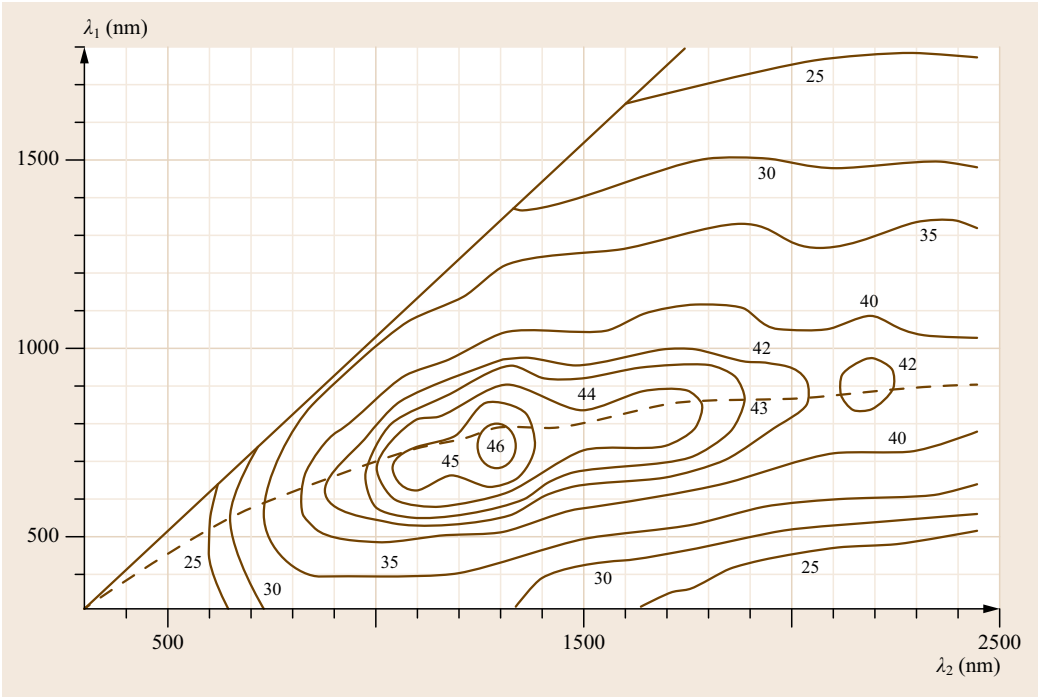


Fig. 27.18 Contour diagram showing the ideal limiting efficiencies η_P, in a layered dual-bandgap system with bandgap wavelengths λ_1 and λ_2. *Dashed line*: Path of equal effective photon fluxes used in two photosystems as required for use of the two halves in series (after [27.108])

Electrochemical Stability. It has been recognized that materials known to possess good photovoltaic properties, for example, transition metal chalcogenides and pnictogenides, are poorly suited for use in PEC due to electrochemical instability [27.112, 113]. Meanwhile, electrochemically stable materials typically exhibit poor photovoltaic efficiency. The two strategies that research has adopted in response to this significant challenge are (1) an attempt to imbue stable semiconductors (metal oxides) with better photovoltaic properties and (2) an effort to electrochemically stabilize known photovoltaic materials. As a result, the main thrust in this field has been in the direction of material discovery [27.114, 115] and novel photoelectrode design [27.116].

Photoelectrolysis presents a significant material challenge. Conventional solar cells are typically encapsulated to prevent exposure to moisture and oxygen, either of which can lead to photocorrosion problems over time. When immersed in water and used to generate oxygen under high illumination, temperature, and pressure, extreme electrochemical stability is required from the light absorber. Typical materials used in photovoltaics, particularly group IV elements, III–V compounds [27.114, 117–119], II–VI materials [27.120–123], $Cu(In,Ga)Se_2$ [27.124], and other metal chalcogenides [27.125], are especially susceptible to PEC degradation in aqueous environment. Because these materials are more vulnerable to anodic rather than cathodic degradation, it was universally found that their stability is enhanced at low pH under cathodic protection.

The same is not always true for metal oxide semiconductors, where photodegradation is often caused by cathodic stress. Unconventional in the field of photovoltaics due to their generally poor charge transport and often large bandgaps compared to nonoxide semiconductors, metal oxide materials are often employed as photoanodes for hydrogen production due to the promise of enhanced stability. However, even the most stable of these materials can have problems in the harsh environments of photoelectrolysis. Strontium titanate, for example, is known to be indefinitely stable in alkaline electrolyte, but photodegrades very quickly at low and neutral pH [27.110]. Similarly, the stability of most metal oxide semiconductors prefers a specific pH range, the value of which can vary tremendously. In Table 27.6 a survey of common metal oxides and mixed oxides can be found, with stable pH range, reproduced from a thorough review of metal oxide stabilities by *Scaife* [27.126].

Peripheral Challenges. In addition to the chemical challenges involved with achieving efficient PEC hydrogen evolution, there are also several engineering obstacles to consider. The impracticality of storing or transporting large amounts of near-atmospheric pressure hydrogen gas necessitates its compression. Pres-

Table 27.6 Thermodynamic stability of oxides toward photoanodic decomposition (after [27.126])

Oxides stable pH 0–14	Oxides unstable pH 0–14	Oxides stable over some pH rangewith pH range for stability			
Fe_2O_2	MnO	CoO (6.8–14) Al_2O_3 (2.9–14)	$MgTiO_3$ (4.7–14)	$CrNbO_4$ (0–4.3)	$MgNb_2O_6$ (1.9–14)[a]
TiO_2	SnO	NiO (6.2–14) In_2O_3 (2.2–14)	$CaTiO_3$ (6.5–14)	Co_2TiO_4 (4.4–14)	$FeNb_2O_6$ (0.2–11.9)[a]
SnO_2	PbO	CuO (3.7–14) Ga_2O_3 (0.9–14)	$SrTiO_3$ (5.9–14)	Zn_2TiO_4 (4.2–14)	$ZnNb_2O_6$ (0.2–13.9)[a]
ZrO_2	Cr_2O_3	ZnO (5.8–14) Bi_2O_3 (1.5–14)	$Sr_{0.5}Ba_{0.5}TiO_3$ (6.8–14)	Cd_2SnO_4 (5.3–14)	$FeTa_2O_6$ (3.2–10.7)
Ta_2O_5	La_2O_3	CdO (7.6–14) Y_2O_3 (8.5–14)	$Ca_{0.2}Ba_{0.8}TiO_3$ (7.3–14)	Zn_2SnO_4 (3.5–14)	$CrTi_2O_7$ (1.0–4.8)
$NaNbO_3$	Ti_nO_{2n-1}[b]	HgO (1.2–14) Nb_2O_5 (0–12.2)	$BaTiO_3$ (7.4–14)	$CdFe_2O_4$ (1.6–14)	$La_2Ti_2O_7$ (3.0–14)[a]
$KNbO_3$	NbO_2	WO_3 (0–2.4)	$FeTiO_3$ (4.9–14)	$CdIn_2O_4$ (3.4–14)[a]	Sr_2FeNbO_6 (5.1–14)[a]
$FeNbO_4$	U_3O_8		$CoTiO_3$ (1.7–14)	$CdGa_2O_2$ (2.4–14)	
$LaNbO_4$	$MnTiO_3$		$NiTiO_3$ (2.1–14)	Al_2TiO_5 (2.0–14)	
$FeTaO_4$	$CdTiO_3$		$PbTiO_3$ (1.1–2.3)	$MgTi_2O_5$ (3.5–14)	
Fe_2TiO_5	Mn_2TiO_4		$LiNbO_3$ (1.1–14)		
$CaNb_2O_5$	Fe_2TiO_4		$YFeO_3$ (4.2–14)		
$SrNb_2O_6$[a]			$CdSnO_3$ (0.4–14)[a]		
$BaNb_2O_6$[a]			$BaSnO_3$ (0.4–14)[a]		
$CoNb_2O_6$[a]					
$NiNb_2O_6$[a]					
$TiNb_2O_7$					
$Hg_2Nb_2O_7$					
$Hg_2Ta_2O_7$					
$Pb_4Ti_3WO_{13}$[a]					
$PbFe_{12}O_{19}$					

[a] Using estimated values of ΔG_f (298.15); [b] where $n = 4–8$

surization of hydrogen is more challenging than that of other gases due to its small mass. While it contains the largest energy density of any possible fuel, it also results in the largest pressure density of any possible product gas. A multiple stage hydrogen compressor is required to affordably bring hydrogen to significant pressure. While this equipment contributes significantly to the one-time expense of a hydrogen-producing facility, its energy requirement is also nonnegligible in the long run. Figure 27.19 from the work of *Bossel* is a diagram depicting the power requirement of hydrogen compression [27.127]. For viewing convenience, the energy axis was herein normalized by the combustion energy of the hydrogen product under standard conditions, rather than reported in the originally published megajoules per kilogram.

This thermodynamic requirement of compression, along with the large capital cost of the compressor, both highlight the advantages possible in producing hydrogen electrochemically at already-elevated pressure. However, such a task becomes very difficult when the other requirements of PEC hydrogen production are put into place:

1. Light is required to efficiently penetrate the pressurized cell.
2. The compressed hydrogen and oxygen products must be kept separate from each other, requiring either a low-resistance membrane or laminar flow-cell design.
3. In designs that rely on both a photocathode and photoanode operating in series, the incoming light must be distributed to both halves of the reaction, or, in the ideal case the two electrodes would make use of different spectral regions of sunlight, and be situated on top of each other in a monolithic arrangement.

Owing to the underdeveloped technical state of PEC hydrogen production, these future issues surrounding cell design are rarely discussed in detail.

Electrode Design. Module design plays a major role in determining a conventional solar cell's efficiency limit [27.128]. Analogously PEC hydrogen generation, which is strongly limited by the photovoltaics side of the process, has been shown to benefit from the use of advanced cell designs [27.129]. Discussed in this section are several common strategies that have been explored.

The most straightforward PEC cell design consists of a single photoelectrode connected in series with a counter electrode. This system possesses the

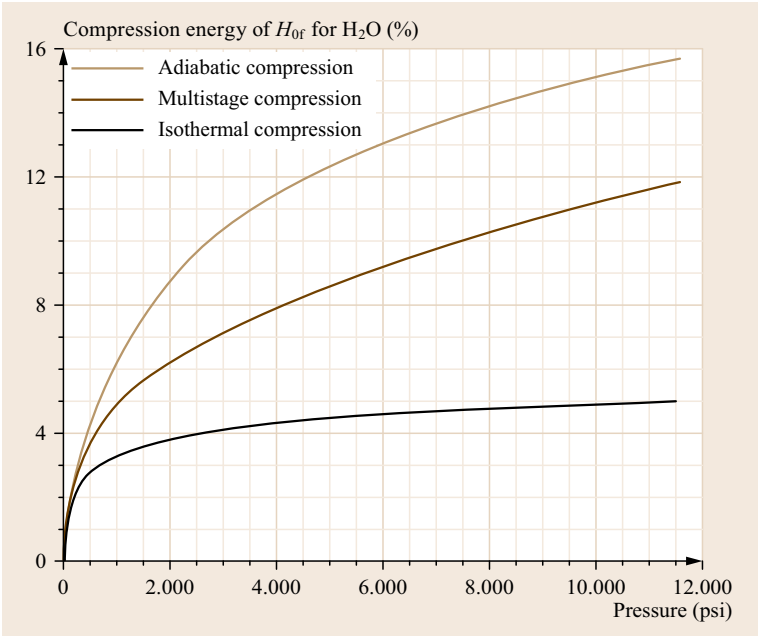


Fig. 27.19 The energy cost of hydrogen compression starting from ambient atmosphere, given in units of hydrogen combustion energy as a function of final pressure (after [27.127])

advantage of simplicity; the study of individual photoelectrodes is facilitated when only one light-sensitive electrode is present. A voltage bias between the two electrodes, from a power supply, is often used to mimic the contribution from a second photoactive junction. In this way, the study of single junctions enables the careful study of photoelectrodes that are intended ultimately for use in multiple-junction PEC cells. However, photoelectrodes intended for self-sufficient (unbiased) use in single-photoelectrode cells are not known to reach solar-to-hydrogen efficiencies beyond 1% [27.130]. The explanation is a deficit of photovoltage. In addition to the 0.4 V energy drop required to drive exciton separation [27.131], an additional 0.3 V of overpotential is necessary to drive each of the electrode processes (anodic and cathodic) at reasonable current, on top of the 1.23 V thermodynamic requirement [27.132]. Each photon usable by a single, unbiased photoelectrode must therefore contain energy in excess of ≈ 2.2 eV, limiting the efficiency to 12.7% and narrowing the list of usable semiconductors. In practice, it is observed that closer to 3 eV band gaps are necessary to achieve measurable performance, limiting η_{sth} to 2% [27.108, 116, 130, 133, 134].

A photoanode–photocathode combination has the capacity to be more efficient than a single photoelectrode. The critical difference lies in their respective absorption of the solar spectrum. Two photoelectrodes in series can have small band gaps, yet still be capable of driving electrolysis using the sum of their photovoltages. This allows their absorption to extend much further into the visible wavelengths of the solar spectrum, improving η_{pv}. It should be noted, however, that because the two junctions operate in series, their photocurrents are by definition identical. The implication is that two photons are now absorbed to generate each electron that is ultimately passed around the external circuit, limiting the external quantum efficiency (EQE) to 50% of what can be expected from a single junction. Overall, the improved light absorption outweighs this limitation in the theoretical efficiency limit. The first tandem PEC cell was reported in 1975 by *Yoneyama* et al. [27.113]. Similar to the single photoelectrode cell demonstrated by *Fujishima* and *Honda* [27.25], the Yoneyama cell used a p-GaP photocathode in series with n-TiO_2 to provide the additional photovoltage needed to split water, with a rapidly degrading η_{STH} starting at 1.2%. Similar cells were described shortly thereafter by *Nozik* [27.135] and then later more efficiently by *Bockris* and *Kainthla* (8.2% solar-to-hydrogen efficiency) [27.136] and others.

The concept of biasing photoelectrodes with standard p–n junctions has also been explored. When the p–n junction lies monolithically beneath (i. e., absorbing from the same pool of light as) the photoelectrode, the device is referred to as a buried junction. Khaselev and Turner reported 12.4% solar-to-hydrogen efficiency under 11 suns illumination from a platinum-catalyzed p-$GaInP_2$ photocathode biased with a GaAs p–n buried junction. It was stated to be essential for device performance that the absorption of light by the underlying GaAs layer limit the overall photocurrent generated

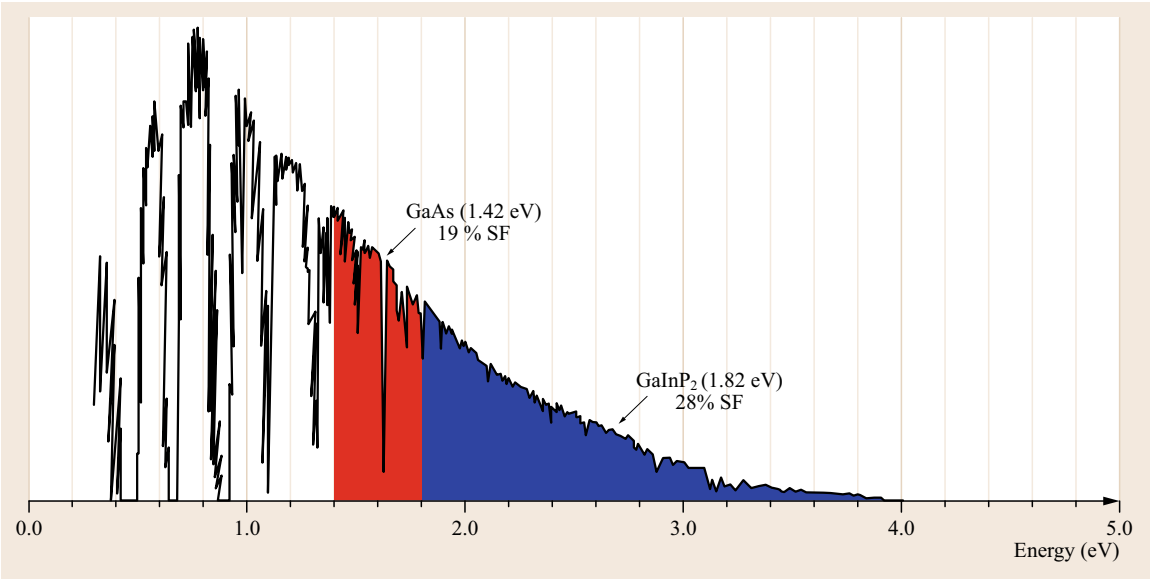


Fig. 27.20 Solar spectrum utilization from the photocathode reported by *Khaselev* and *Turner*, broken down by layer (after [27.29]). The photocurrent generated by the GaAs layer limits that of the overall device

by the device. The spectral utilization of each layer is shown in Fig. 27.20. As with many examples of III–V light harvesters, this efficient photocathode suffered from electrochemical instability.

Notable Photoelectrode Materials

Most of the photoactive materials common to photovoltaics have been studied as cathodes in PEC cells.

Conventional for PV. There are examples demonstrating appreciable and sometimes extraordinary performance from photocathodes based on silicon [27.137], group III–V materials [27.29, 113, 138], group II–VI materials [27.139, 140], $Cu(In,Ga)Se_2$ [27.141], and Cu_2ZnSnS_4 [27.142].

The use of these semiconductors as photoanodes, however, is less common due to problems with electrochemical corrosion under oxidative stress. There are nevertheless a few examples in which researchers have enhanced the stability of these materials, generally by coating the photoactive layer with a very thin film of stable metal oxides [27.143–146].

Unconventional for PV. A wide variety of mixed metal oxide semiconductors have been explored for favorable electrochemical and photovoltaic properties, namely a reasonably small band gap, good charge mobility in both the conduction and valence band, appropriate band edge potentials, electrochemical stability, and photochemical stability. No single material, oxide or otherwise, has yet been reported to embody all these qualities. A noncomprehensive survey of nonconventional (oxide) semiconductors studied for PEC, reproduced from the work of *Scaife* [27.126], is presented in Fig. 27.21. The most commonly studied classes of material include zinc oxides [27.147], tantalates [27.148, 149], tungstates [27.150], chromates [27.151], ferrites, and titanates [27.152–154].

One of the key challenges when working with metal oxides is the movement of charge throughout the solid. Hematite, Fe_2O_3, has been widely recognized as an interesting PEC challenge [27.155]. Despite being abundant, stable, and good at absorbing light [27.156], hematite has poor electron and hole conductivity, rampant charge recombination (as a consequence), nonideal band-edge potentials, and poor catalytic activity toward water decomposition [27.157, 158]. Much work has been done by the *Grätzel* group to compensate for the drawbacks of Fe_2O_3 by doping it with other elements [27.159], as well as reducing the dimensions of the photoactive layer [27.160, 161]. Photovoltages achieved by hematite-based photoanodes are on the order of 0.8 V, with photocurrents reaching a maximum of $\approx 3\,mA/cm^2$ when biased externally [27.162].

It is far rarer to find reports of metal oxide photocathodes. There have been a handful of studies related to photocathodes based on cuprates [27.163] and ferrites [27.164], though with stability issues in each case. The cathodic degradation mechanism is different than anodic. Instead of material dissolution from the photoactive layer, the metal atoms in the cathodes tend to reduce, forming splinters of conductive metal within

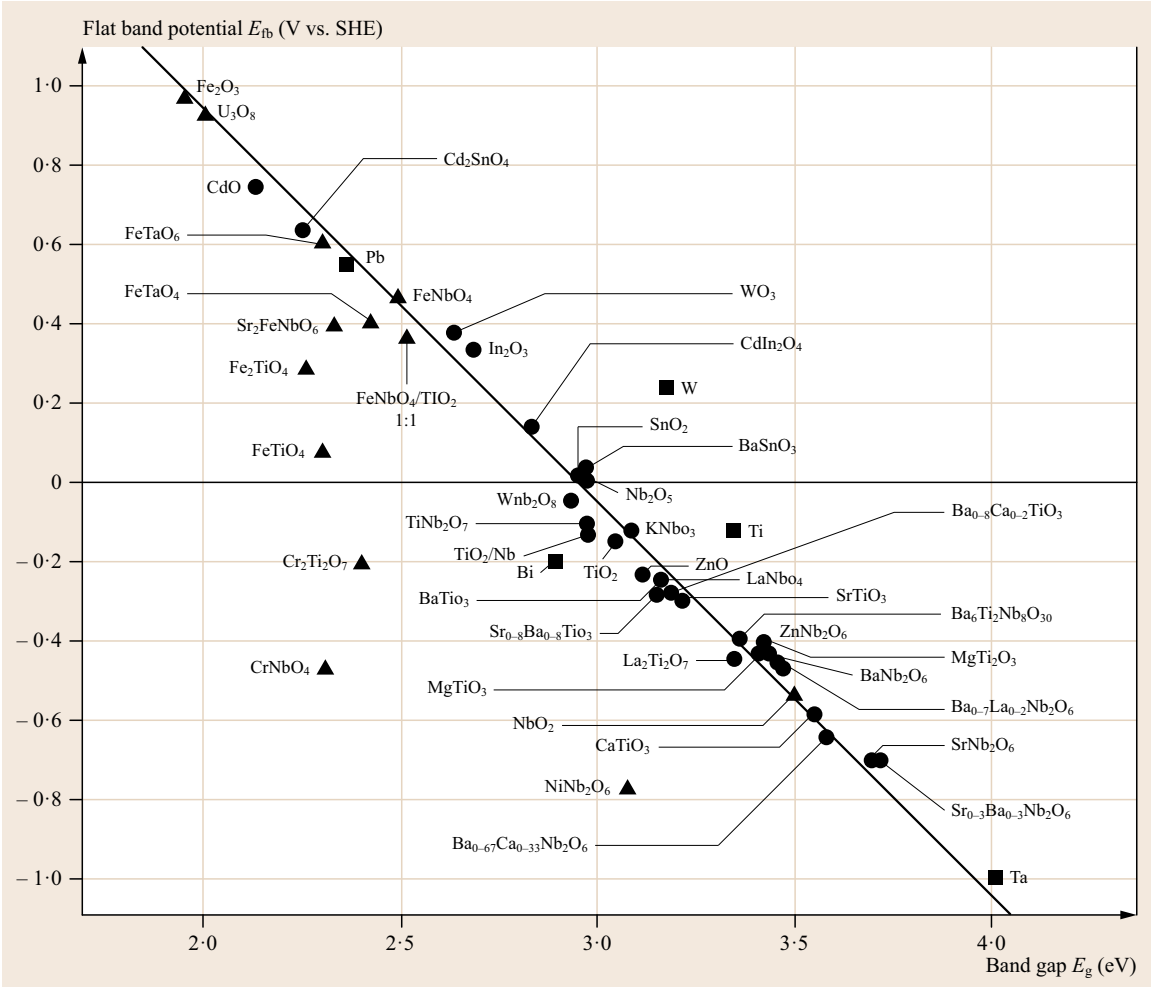


Fig. 27.21 Measured flat band potentials and effective band gaps in semi-conducting oxides. *Circles*: Oxides without partially filled d-levels. *Triangles*: Oxides with partially filled d-levels. *Squares*: Oxides formed anodically on metals (after [27.126])

the oxide semiconductor. When this happens, the electrolyte interface can short circuit with the underlying conductive support, rendering charge separation ineffective.

Performance-Enhancing Surface Modification. It has become more widely recognized in recent years that electrode surfaces can be modified with submicron features, or with performance-enhancing additives, to enable unexpected photo- or electrocatalytic properties [27.165]. As an illustrative example, the surface modification of TiO_2 to achieve ordered nanotube arrays has received much recent attention [27.166–173]. It was found by the Bard and Misra groups that anodically prepared TiO_2 nanotube arrays exhibit dramatically enhanced photovoltaic characteristics over typical TiO_2 wafers. The *Bard* group reported more than a factor of 10 improvement in photocurrent from carbon-doped TiO_2 nanotubes as compared to a 15 μm, featureless film of the same material [27.174]. Using catalyst-enhanced TiO_2 nanotube arrays for both the photoanode (carbon doped) and cathode, the *Misra* group reports a PEC cell efficiency for water splitting of 8.5% [27.175, 176].

Addition of submicron catalyst particles to the surface of photoelectrodes is also known to strongly affect performance. An example of the powerful effect that electrochemical catalysis can have on the activity and stability of a photoelectrode is presented by the *Domen* group [27.177]. In their study of a tantalum oxynitride photoelectrode (TaON), it was discovered that $\approx 1\,\mathrm{mA/cm^2}$ photocurrent diminished to zero very

quickly during operation (on the order of seconds), due to the photocorrosion of the electrode to form Ta_2O_5. It was found that addition of an IrO_2 oxygen evolution catalyst to the surface of the TaON electrode had a profound effect on the electrode's performance. First, the photocurrent generated by the electrode was improved by a factor of 3 over uncatalyzed TaON. In addition, incorporation of IrO_2 as a charge collector prevented anodic leaching of nitrogen out of the electrode surface. The result was an electrode that sustained its photocurrent on the order of hours instead of seconds.

A final way in which surface additives can aid solar-to-hydrogen efficiency is by enhancing the absorption of light by the semiconductor. An area of growing interest is the addition of plasmonic metal nanostructures to the surface of semiconductors [27.178]. Surface plasmon resonance describes the storage of photonic energy in the form of a standing wave within a metal body. It has been shown by *Ingram* and *Linic* that photovoltaic enhancement of a PEC cell can be achieved with visible wavelengths by the addition of silver nanostructures to a n-TiO_2 photoanode [27.179]. The authors saw significant, sustained photocurrent enhancement (roughly an order of magnitude) over the silver-free control electrode. They attribute this effect to an enhanced probability of photonic absorption at the semiconductor's surface, due to the presence of the silver, as opposed to more general absorption within the bulk of the TiO_2 (where the charge-separating electric field is much weaker).

27.3 Development Perspectives

Findings from a technoeconomic analysis of today's commercial electrolyzers suggest that electricity costs are a major contributor to the cost of hydrogen, regardless of the system size [27.15]. It was also found that capital cost reduction is needed for smaller scale electrolyzers to reduce H_2 costs. Figure 27.22 shows the status of current-day commercial electrolyzers in terms of the electricity consumption as a function of the electrolyzer capacity. The HHV of hydrogen is $3.5\,kWh/Nm^3$ and the system efficiency is defined as the ratio of the HHV and the electricity consumption (y-axis of Fig. 27.22).

System efficiencies of large-scale alkaline electrolyzers ($> 100\,Nm^3/h$) such as those made by StatOil (previously Norsk Hydro) and ELT are in the range of 75–80%. Medium-sized electrolyzers ($10–100\,Nm^3/h$) by Teledyne (PEM) and Hydrogenics (alkaline) have lower system efficiencies (60–70%). Small-scale electrolyzers ($< 10\,Nm^3/h$) manufactured by Proton Energy Systems and PIEL (ILT Technologies) have system efficiencies in the range of 50–60%. Electrolyzers with high production capacities achieve lower power consumption or higher efficiency. This can be mainly attributed to the improved efficiency of ancillary components with increasing size. Existing commercial alkaline electrolyzers spans three orders of magnitude in capacity. All these electrolysis units are sized to meet the demands of current nonrefinery hydrogen markets. Only electrolyzers 10–100 times the size of today's largest units could meet the minimum capacity requirement of a typical refinery.

The cost of the electricity will have a dominant effect on the H_2 price, accounting for $> 75\%$ of the total cost in SOEC-based systems. Researchers at the National Renewable Energy Laboratory reported in 2007 the boundary electricity cost effect on H_2 costs. The electricity price would have to be less than \$0.01/kWh for H_2 to be produced at \$2/kg (\$0.18/Nm^3). This is less than the cost to produce electricity from coal. For a production target of \$3/kg, electricity costs were estimated to be \$0.04 to \$0.055/kWh for electrolyzer efficiencies of 72–58%, respectively. In another estimate, the electricity cost of \$0.075 was needed to meet the \$3/kg H_2 target even at 100% efficiency [27.180].

Floch et al. [27.181] reported a study on using off-peak grid power for an alkaline electrolyzer. Various production capacities up to $\approx 7200\,Nm^3$ H_2/h were modeled. Their results show a minimum in production cost of 2.56 €/kg at 48 €/MWh electricity cost (2005 basis). This corresponded to a 64.3% uptime, mainly operation at nights and on weekends. Savings by using the off-peak power were said to be significant, but varied enormously in different markets.

In addition to the efficiency limitation and cost of grid electricity, the associated CO_2 emission (a reasonable US value is $\approx 0.59\,kg$ CO_2/kWh) [27.182] is a significant barrier to the adoption of electrolysis as a low-carbon hydrogen production technology. The only meaningful choice for comparison of carbon intensity is the SMR technology. Praxair has published a white paper indicating that historical SMR units produce $\approx 10.8\,kg$ CO_2/kg H_2 [27.183]. Modern units are closer to $9.5\,kg$ CO_2/kg H_2. With credits for the high-quality steam that is typically exported in refineries, a 22% reduction is found for historical units ($\approx 8.7\,kg$ CO_2/kg H_2). This CO_2 is produced during water gas shift (process related) and from burning natural gas/fuel to provide heat (combustion-related).

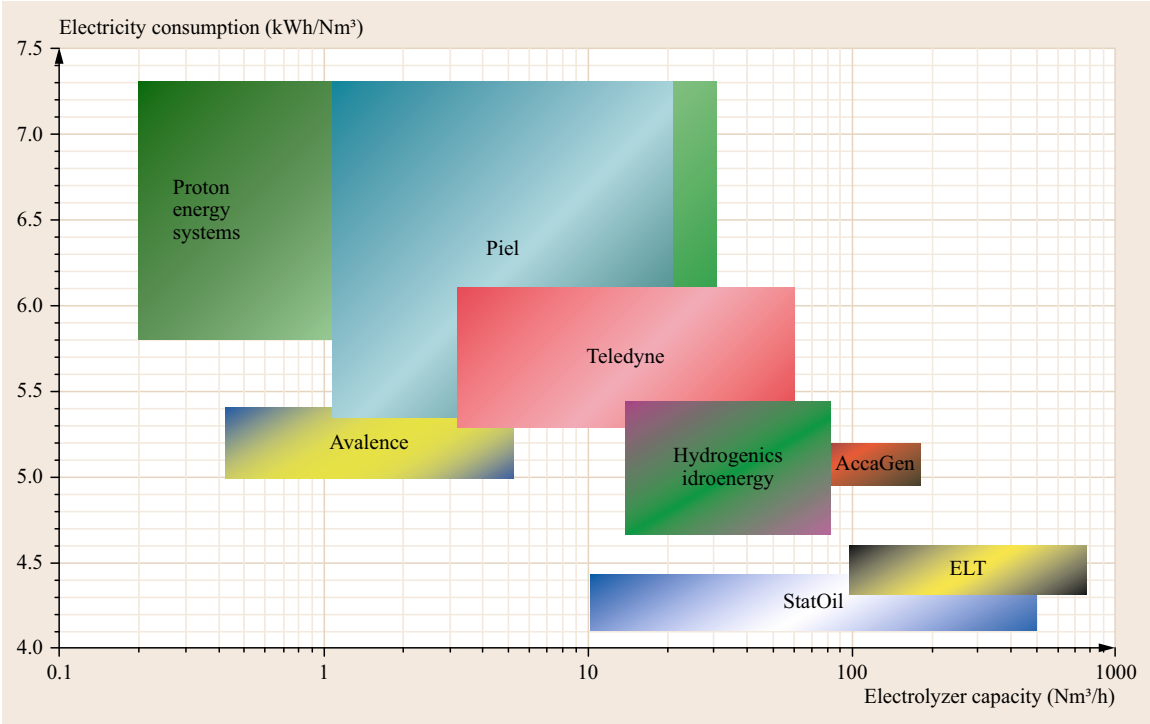


Fig. 27.22 Status of current commercial water electrolyzers in terms of the electricity consumption as a function of the electrolyzer capacity ($Nm^3 \equiv$ normal cubic meter $= 0.09\,kg\ H_2$)

For the purpose of comparison, a CO_2 production rate of 10.8 kg CO_2/kg H_2 can be used as a reasonable upper boundary for SMR technology. If one assumes an electricity demand of 33 kWh/kg H_2 (thermodynamic limit, V_N for low-temperature electrolysis), a CO_2 intensity of 19 kg CO_2/kg H_2 is easily calculated based on the assumed grid power CO_2 footprint given above (Fig. 27.23). This ignores any other source of CO_2 emissions for SOEC operations. At \$0.07/kWh, the electricity costs are seven times as expensive as natural gas on an energy basis, using a natural gas price of \$3 per gigajoule. Thus, using the lowest reasonable expected power consumption for electrolytic H_2 production, grid-powered electrolysis has double the amount of CO_2 relative to SMR.

Renewable and low-carbon electricity sources, such as solar, wind, and nuclear power, also play a critical role in the development of renewable H_2 production. Spanish researchers [27.184] have published a study on the performance of an alkaline electrolyzer (1 Nm^3/h rated H_2 production) working under emulated wind conditions. Wind speed data from a wind farm were used to establish a power profile for a wind turbine of some rated power that was emulated by a power supply designed and built in house. Their results indicated a narrow range of specific energy consumption of 3.60–4.05 kWh/Nm^3 H_2 (40–45 kWh/kg H_2) over variable emulated wind energy input. The stack voltage matched the electric current–time profile, which the authors suggest is essentially ohmic behavior governed by internal resistances of the electrolyte (30% KOH) and cell components. No costs were provided, but good electrolyzer performance was noted.

In a recent report, researchers from National Renewable Energy Laboratory (NREL) the Colorado School of Mines and Xcel Energy in Colorado offered a technical report on opportunities for electrolysis for electric power utilities [27.185]. Hydrogen delivered costs as a function of electricity price were modeled where the electrolyzer farm was sized to the maximum wind farm capacity. With a capacity factor of 41% (an intermediate factor in their study), costs were about \$12/kg H_2 (2005 basis) at an electricity cost of \$0.10/kWh, using given economic assumptions. Some benefits (in addition to storage of intermittent wind energy) were to use electrolyzers in off-peak periods to run the power system closer to rated capacity (and raise its overall efficiency). Additionally, when off-peak power is inexpensive, H_2 can be produced and stored for later use via fuel cell or H_2-engine generator to produce power.

The NREL authors concluded that ample resources of solar and wind-derived power exist in the US for

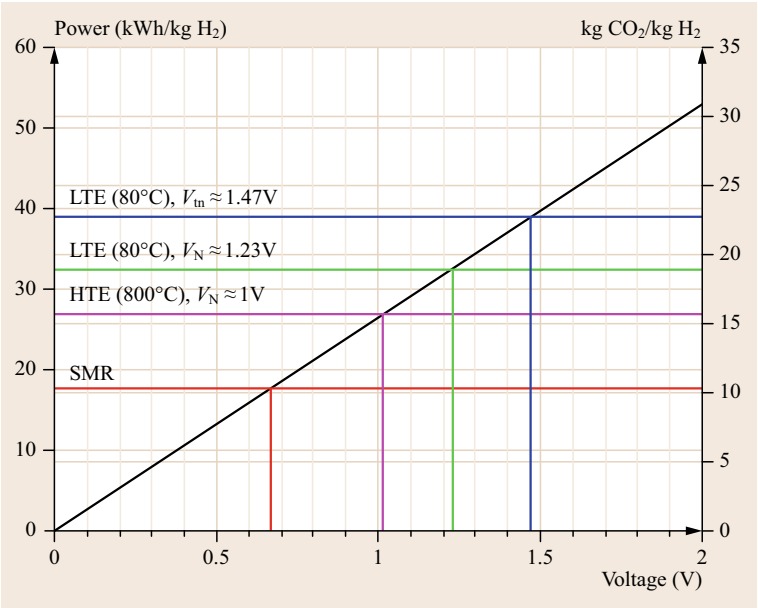


Fig. 27.23 Power requirements and CO_2 footprint as a function of the applied voltage for water electrolysis and comparison with SMR

electrolysis of H_2. Currently, electricity from these sources typically commands a premium price, although efforts are showing progress for *grid parity* of these clean power technologies. To produce H_2 electrolytically with a CO_2 footprint less than SMR, then using the hypothetical electrolysis system above the supply of electricity should have a carbon intensity of ≈ 0.32 kg CO_2/kWh or less. Natural gas supplied power plants approach this value, but still exceed it. A mix of wind, hydroelectric, nuclear, and/or solar, with natural gas, could conceivably produce a power supply with the appropriate CO_2 footprint. However, the power costs can prove challenging. Abbasi and Abbasi recently published estimates for *renewable* H_2 costs [27.186]. They report SMR costs at \$1.03/kg, coal gasification at \$0.96/kg, but wind electrolysis at \$6.64/kg. Both biomass pyrolysis (\$3.8/kg) and biomass gasification (\$4.63) are less than the wind-powered case. For reference, the authors report gasoline production cost of \$0.93/gallon refined.

For a solar-powered electrolysis process, the PV module costs must be reduced by one-third over the present cost. The National Research Council (NRC) in the United States estimated that the H_2 produced from a solar-powered electrolysis process would exceed \$28/kg at \$3.28/W_{Peak} (installed) and electricity cost of \$0.32/kWh [27.187]. The NRC projected that H_2 costs could be reduced to \$6.18/kg (assuming improvements in PV technology and electricity costs of \$0.098/kWh).

HTE of steam requires less electricity than conventional low-temperature electrolysis. However, there are still significant barriers to large-scale implementation. The largest factors impacting the potential economics of HTE are:

1. The cost of electricity
2. Capital expense (CAPEX)
3. Cell degradation
4. Uncertainties with scale up of new technology.

INL has been involved with a detailed program on HTE for large-scale H_2 and syngas production from nuclear energy. A report on the simulation and economics in 2010 showed the potential for a 2.2 million Nm^3/d (≈ 200 t H_2/d) plant with a 600 MW reactor [27.188]. Production cost using the H2A Analysis Methodology developed by Department of Energy H_2 program was estimated to be \$3.23/kg (leaving the plant gate at 5 MPa pressure). The estimated price was shown to be most sensitive to the assumed after-tax internal rate of return (typically 10%) and unplanned replacement costs. In this case, 70% of the H_2 price was due to capital costs (high costs for nuclear reactors). The authors report a commodity price of \$2.50/kg for H_2 from SMR technology for comparison, but this is probably too high at current natural gas prices. Nevertheless, these transparent and documented procedures likely result in a reasonable estimate of H_2 production cost from a *world scale* SOEC plant.

A dated but informative life cycle analysis (LCA) by NREL on wind-powered electrolysis shows a remarkably low 0.97 kg CO_2/kg of net produced H_2 [27.190]. The bulk of the CO_2 was associated with turbine production and operation (78%) with a lesser fraction for compression and storage (17.6%) and very

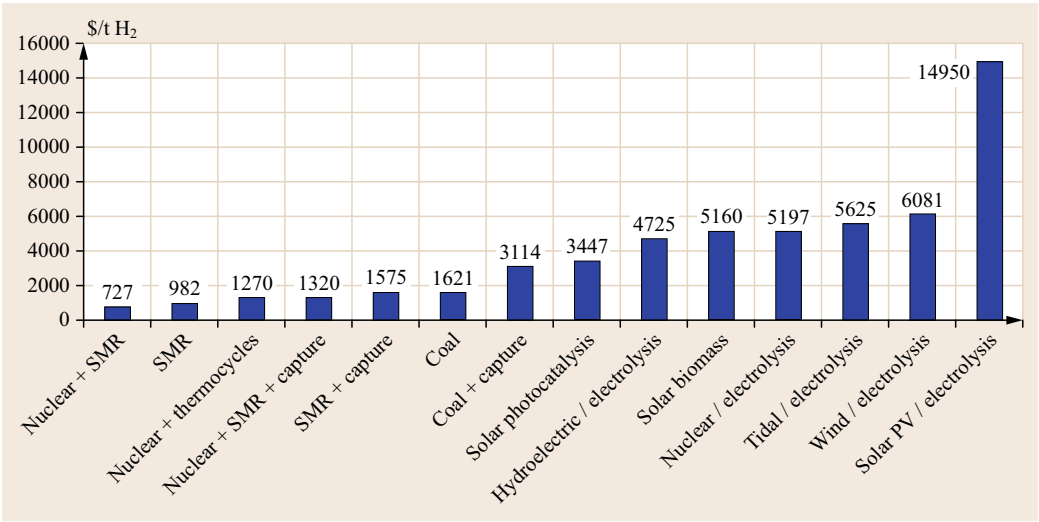


Fig. 27.24 H_2 production costs from different sources (after [27.189])

low emissions for electrolysis production and operations (4.4%). In addition, the energy balance was very favorable, with considerably more energy in the H_2 produced relative to the amount of fossil energy consumed.

Koroneos and coworkers [27.191] have published the results of an LCA for electrolysis powered by various renewable sources (PV, solar thermal, wind, hydroelectric, biomass) along with SMR from methane as a comparison. Impacts in addition to CO_2 (i. e., smog, acidification, eutrophication, carcinogens, ozone depletion, solid waste, and heavy metals) were considered in their analysis following generally accepted LCA methodology. Their conclusion was that wind, solar-thermal, and hydroelectric-based power for electrolysis were the most environmentally friendly options. *Ewan* and *Allen* assigned figures of merit for several different routes to H_2, and electrolysis was a common step in several approaches [27.189]. SMR, SMR + CO_2 capture, coal and other integrated nonelectrolysis processes were included (Fig. 27.24). Four feasibility criteria used in their analysis were CO_2 reduction, land use impacts, power limitations with the primary energy source, and production costs. A figure of merit (FOM) for each criteria was calculated. In turn, an overall FOM was then calculated from the individual FOM values. The results (not unexpectedly) showed processes based on SMR and coal had the best economics, but nuclear/thermocycle and coal + CO_2 capture scored reasonably high. The best score for an electrolysis-related process was the combination with nuclear energy. Solar PV, wind, and hydroelectric sources for electrolysis all had relatively low overall scores, primarily due to higher production costs. Interestingly, the hydroelectric case had the lowest overall score.

Lemus and *Duart* have provided a detailed cost analysis study for various H_2 production methods that include both electrolytic and bio-based technologies [27.192]. These authors have taken literature data for production costs, accounted for inflation, and provided some estimates for future costs. Their results for renewable energy/electrolysis processes show estimated H_2 production costs of \$5–15/kg, in reasonable agreement with Fig. 27.24.

A recent LCA on various hydrogen production strategies found that, among SMR, coal gasification, water electrolysis via wind and solar power, and a Cu–Cl thermochemical water-splitting cycle, the wind and solar powered electrolysis had the lowest global warming potentials [27.193]. In terms of CO_2 equivalent emissions, the wind/electrolysis route was the lowest, at < 1 kg CO_2 e/kg of net produced H_2, in agreement with *Spath* and *Mann* [27.188]. However, the authors pointed that out the production capacities for these processes were 4 orders of magnitude lower than the coal gasification example used in their study. The thermochemical Cu–Cl cycle also had very low reported CO_2 equivalent emissions, and was advantaged over the electrolysis options in view of greater production capacity opportunity. This study has a detailed and comprehensive set of economic inflows, emissions, and global warming potential (GWP).

A high-level review of water electrolysis technologies for hydrogen production has appeared recently, which includes possible configurations for coupling renewable energy systems to electrolysis in both autonomous and grid-connected systems [27.194]. The autonomous systems are separate from the grid and the hydrogen is completely renewable. Two types of au-

tonomous, or off-grid, systems were identified by *Ursua* et al. [27.194]. In one, the wind or solar PV system is coupled to the electrolyzer and H_2 (as well as O_2) is the only product. Such systems are subject to variable production, since the availability of wind and solar power fluctuates. The second off-line system incorporates H_2 storage and fuel cells, such that surplus renewable energy is stored as H_2, then converted to power in areas where the main grid is not accessible.

In grid-connected systems, three configurations were identified. In one, all electricity generated by the wind or solar system is continuously injected onto the grid. The electrolyzer is driven by a constant operating profile derived from the average of the renewable energy system, but does not include the variations. A second type uses the renewable energy directly, and excess renewable energy is supplied to the grid. In this case, the electrolyzer is subject to renewable energy variability. Under most circumstances, such an electrolyzer would be underutilized. The third configuration for grid-connected system allows the electrolyzer to participate in the instantaneous adjustment between the renewable energy generated by wind or solar units and the energy demanded by loads connected to the grid.

Demonstration projects integrating renewable energy and electrolysis were also noted for the United States, Canada, Germany, Italy, Norway, Finland, UK, Japan, and Spain [27.192]. Most were autonomous systems, isolated from the grid or microgrids. The use of solar PV energy is more common than wind, but some consider both options. Alkaline electrolyzers are typically employed but PEM-based systems are utilized as well.

The Wind2H2 project, led by NREL and Xcel Energy, integrates wind turbines and photovoltaic (PV) arrays with electrolyzer stacks to produce hydrogen (and oxygen) with renewably generated electricity [27.195]. The system uses two variable speed wind turbines with 100 and 10 kW capacity. Two PEM electrolyzers (1.05 Nm^3/h each) and one alkaline electrolyzer (5.6 Nm^3/h) produce the hydrogen. Integration of these technologies as well as the operation of electrolyzers with different gas output pressures are part of the study. The H_2 is compressed and stored for later use in a hydrogen internal combustion engine where it is converted to electricity and fed into the utility grid during peak demand hours. Refueling of a passenger car was demonstrated in 2009. Base-line production price for the hydrogen was 6.25/kg.

Another demonstration project in Spain has been described recently [27.196]. In this project, excess energy from the large Sotovento wind farm (17.56 MW) is used to power an alkaline electrolyzer to produce hydrogen at a rate of 60 Nm^3/h. The hydrogen is compressed to 200 bar, then used as fuel for a 55 kW engine to supplement power when wind energy falls below targeted levels.

The demonstration projects described here and elsewhere [27.134, 197] clearly show that renewable hydrogen via electrolysis is feasible, but cost challenges remain. Technical improvements in all system components are documented, and cost reduction targets are identified.

27.4 Conclusions

As discussed in this chapter, the use of electrolysis for large scale, centralized hydrogen production is challenged by component costs and high electricity costs without assuming an unrealistic regulatory incentive. These technologies are unlikely to replace the mature and low-cost SMR in the foreseeable future, due largely to the contemporary expansion in the supply of natural gas in the United States (and Eurasia/Middle East) that has suppressed the costs of SMR-derived hydrogen.

However, the electrochemical hydrogen production technologies do offer potential advantages in a distributed hydrogen market, especially when the technologies are combined with renewable or low-carbon electricity sources. At smaller production capacities, the cost of H_2 from SMR increases due to the unfavorable economy of scale down. In anticipation of demand for renewable hydrogen (i. e., for greenhouse gas reduction and renewable fuels production), the coupling of low-carbon power sources to different electrolysis technologies has been demonstrated. In addition, electrochemical hydrogen production offers an opportunity to store energy from intermittent power sources such as wind and solar. As improvements and cost reductions in system components are realized, truly renewable hydrogen may emerge as a cost-effective commodity.

References

27.1 US Department of Energy: US Crude Oil, Natural Gas, and Natural Gas Liquids Proved Reserves 2009 (US Department of Energy, Washington 2010) http://www.eia.gov/pub/oil_gas/natural_gas/data_publications/crude_oil_natural_gas_reserves/current/pdf/arrsummary.pdf

27.2 C. Yang, J.M. Ogden: *H_2 Production via Natural Gas Reforming, Task 4.1 Technology Assessments of Vehicle Fuels and Technologies* (California Energy Commission, Sacramento 2007)

27.3 J.M. Ogden: *Agreement on the Production and Utilization of Hydrogen Task 16, Hydrogen from Carbon-Containing Materials* (International Energy Agency, Paris 2001)

27.4 National Research Council: *Front Matter. The Hydrogen Economy: Opportunities, Costs, Barriers, and R and D Needs* (National Academies Press, Washington 2004)

27.5 R. De Levie: The electrolysis of water, J. Electroanal. Chem. **476**(1), 92–93 (1999)

27.6 S. Trasatti: Water electrolysis: who first?, J. Electroanal. Chem. **476**(1), 90–91 (1999)

27.7 S. Trasatti: Alessandro Volta's electric pile: Two hundred years, but it doesn't seem like it, J. Electroanal. Chem. **460**(1), 1–4 (1999)

27.8 W. Kreuter, H. Hofmann: Electrolysis: The important energy transformer in a world of sustainable energy, Int. J. Hydrogen Energy **23**(8), 661–666 (1998)

27.9 K.J. Laidler: The chemical history of a current, Can. J. Chem. **75**(11), 1552–1565 (1997)

27.10 G. Sandstede: Status of the technology and development in water electrolysis, Dechema Monogr. **125**, 329–355 (1992)

27.11 R.L. Le Roy: Industrial water electrolysis: Present and future, Int. J. Hydrogen Energy **8**(6), 401–417 (1983)

27.12 J.E. Noeggerath: Electrolytic apparatus, US Patent 1 799 116 (1931)

27.13 J.E. Noeggerath: Electrode vessel for electrolytic apparatus, US Patent 1 896 718 (1933)

27.14 H. Vandenborre: New developments in alkaline water electrolysis, Dechema Monogr. **98**, 313–328 (1985)

27.15 J. Ivy: Summary of electrolytic hydrogen production. In: *Milestone Completion Report* (National Renewable Energy Laboratory, Golden 2004)

27.16 D. Pletcher, F.C. Walsh: *Industrial Electrochemistry* (Blackie Academic Professional, London 1990)

27.17 K.A. Mauritz, R.B. Moore: State of understanding of Nafion, Chem. Rev. **104**(10), 4535–4585 (2004)

27.18 B.V. Tilak, P.W.T. Lu, J.E. Colman, S. Srinivasan: Electrolytic production of hydrogen. In: *Comprehensive Treatise of Electrochemistry*, Vol. 2, ed. by J.M. Bockris, B. Conway, E. Yeager, R. White (Plenum, NY 1981) pp. 1–104

27.19 W. Doenitz, R. Schmidberger, E. Steinheil, R. Streicher: Hydrogen production by high temperature electrolysis of water vapour, Int. J. Hydrogen Energy **5**, 55–63 (1980)

27.20 A. Isenberg: Energy conversion via solid oxide electrolyte electrochemical cells at high temperatures, Solid State Ion **3–4**, 431–437 (1981)

27.21 G. Schiller, A. Ansar, M. Lang, O. Patz: High temperature water electrolysis using metal supported solid oxide electrolyser cells (SOEC), J. Appl. Electrochem. **39**, 293–301 (2009)

27.22 A.E. Becquerel: Mémoire sur les effets électriques produits sous l'influence des rayons solaires, Comptes Rendus **9**, 561–567 (1839)

27.23 W.H. Brattain, C.G.B. Garrett: Physical theory of semiconductor surfaces, Phys. Rev. **99**, 376–387 (1955)

27.24 C.N.R. Rao, J. Gopalakrishnan: *New Directions in Solid State Chemistry* (Cambridge Univ. Press, Cambridge 1997) pp. 416–419

27.25 A. Fujishima, K. Honda: Electrochemical photolysis of water at a semiconductor electrode, Nature **238**, 37–38 (1972)

27.26 A. Brisse, J. Schefold, M. Zahid: High temperature water electrolysis in solid oxide cells, Int. J. Hydrogen Energy **33**, 5375 (2008)

27.27 H. Gerischer: Electrochemical photo and solar cells – Principles and some experiments, Electroanal. Chem. Interf. Electrochem. **58**, 263–274 (1975)

27.28 J.O. Bockris, K. Uosaki: Photoelectrochemical production of hydrogen, ACS Adv. Chem. **163**, 33–70 (1977)

27.29 O. Khaselev, J.A. Turner: A monolithic photovoltaic-photoelectrochemical device for hydrogen production via water splitting, Science **280**, 425–426 (1998)

27.30 S.U.M. Kahn, M. Al-Shahry, W.B. Ingler Jr.: Efficient photochemical water splitting by a chemically modified n-TiO_2, Science **297**, 2243–2245 (2002)

27.31 M.S. Casper (Ed.): *Hydrogen Manufacture by Electrolysis, Thermal Decomposition and Unusual Techniques* (Noyes, Park Ridge 2007)

27.32 C.L. Mantell: *Electrochemical Engineering*, 4th edn. (McGraw Hill, New York 1960)

27.33 D.H. Smith: Industrial water electrolysis. In: *Industrial Electrochemical Processes*, ed. by A.T. Kuhn (Elsevier, Amsterdam 1971), Chap. 4

27.34 B. Kroposki, K. Harrison, P.K. Sen, J. Levene, F. Novachek: *Electrolysis: Information and Opportunities for Electric Power Utilities* (National Renewable Energy Laboratory, Golden 2006)

27.35 R.L. Costa, P.G. Grimes: Electrolysis as a source of hydrogen and oxygen, Chem. Eng. Prog. **63**(4), 56–58 (1967)

27.36 J. Fischer, H. Hofmann, G. Luft, H. Wendt: Fundamental investigations and electrochemical engineering aspects concerning an advanced concept for alkaline water electrolysis, AIChE J. **26**(5), 794–802 (1980)

27.37 P. Vermeiren, W. Adriansens, J.P. Moreels, R. Leysen: Evaluation of the Zirfon separator for use in alkaline water electrolysis and Ni-H2 batteries, Int. J. Hydrogen Energy **23**(5), 321–324 (1998)

27.38 K. Zeng, D. Zhang: Recent progress in alkaline water electrolysis for hydrogen production and applications, Prog. Energ. Combust. Sci. **36**(3), 307–326 (2010)

27.39 M. Raney: Method of preparing catalytic nickel, US Patent Application 1 563 587 (1925)

27.40 M. Raney: Method of producing finely-divided nickel, US Patent Application 1 628 190 (1927)

27.41 E. Justi, W. Scheible, A. Winsel: Doppelskelett-Katalysator-Elektrode, German Patent Application DE1 019 361 (1954)

27.42 I. Abe, T. Fujimaki, M. Matsubara: Hydrogen production by high-temperature high-pressure water electrolysis; results of test plant operation, Int. J. Hydrogen Energy **9**(9), 753–758 (1984)

27.43 W. Vielstich, E. Knauf: Investigation of nickel whisker networks as electrodes for hydrogen and oxygen evolution comments, J. Electrochem. Soc. **129**(6), 1273 (1982)

27.44 J. De Carvalho, G. Tremiliesi-Filho, L.A. Avaca, E.R. Gonzalez: Iron-based coatings for hydrogen evolution in alkaline solutions, Adv. Hydrogen Energ. **5**, 250–257 (1986)

27.45 I.A. Raj, V.K. Venkatesan: Investigations on the adoptability of electrocatalytic nickel-molybdenum-iron alloy cathode to industrial water electrolysis, Trans. SAEST **22**(4), 189–197 (1987)

27.46 H. Wendt, G. Imarisio: Nine years of research and development on advanced water electrolysis. A review of the research program of the Commission of the European Communities, J. Appl. Electrochem. **18**(1), 1–14 (1988)

27.47 K. Kinoshita: *Electrochemical Oxygen Technology* (Wiley, New York 1992)

27.48 R. Tunold, A.T. Marshall, E. Rasten, M. Tsypkin, L.E. Owe, S. Sunde: Materials for electrocatalysis of oxygen evolution process in PEM water electrolysis cells, ECS Trans. **25**(23), 103–117 (2010)

27.49 S.A. Grigoriev, V.I. Porembsky, V.N. Fateev: Pure hydrogen production by PEM electrolysis for hydrogen energy, Int. J. Hydrogen Energy **31**(2), 171–175 (2006)

27.50 A. Marshall, B. Borresen, G. Hagen, M. Tsypkin, R. Tunold: Hydrogen production by advanced proton exchange membrane (PEM) water electrolysers-reduced energy consumption by improved electrocatalysis, Energy **32**(4), 431–436 (2006)

27.51 P.W.T. Lu, S. Srinivasan: Advances in water electrolysis technology with emphasis on use of the solid polymer electrolyte, J. Appl. Electrochem. **9**(3), 269–283 (1979)

27.52 F. Barbir: PEM electrolysis for production of hydrogen from renewable energy sources, Sol. Energ. **78**(5), 661–669 (2005)

27.53 O. Savadogo: Water electrolysis in acid medium, Hem. Ind. **54**(3), 95–101 (2000)

27.54 A. Di Blasi, C. D'Urso, V. Baglio, V. Antonucci, A.S. Arico, R. Ornelas, F. Matteucci, G. Orozco, D. Beltran, Y. Meas, L.G. Arriaga: Preparation and evaluation of RuO_2-IrO_2, IrO_2-Pt and IrO_2- Ta_2O_5 catalysts for the oxygen evolution reaction in an SPE electrolyzer, J. Appl. Electrochem. **39**(2), 191–196 (2009)

27.55 A. Marshall, B. Borresen, G. Hagen, S. Sunde, M. Tsypkin, R. Tunold: Iridium oxide-based nanocrystalline particles as oxygen evolution electrocatalysts, Russ. J. Electrochem. **42**(10), 1134–1140 (2006)

27.56 A.T. Marshall, S. Sunde, M. Tsypkin, R. Tunold: Performance of a PEM water electrolysis cell using Ir_x Ru_y Ta_z O_2 electrocatalysts for the oxygen evolution electrode, Int. J. Hydrogen Energy **32**(13), 2320–2324 (2007)

27.57 A. Marshall, B. Borresen, G. Hagen, M. Tsypkin, R. Tunold: Preparation and characterization of nanocrystalline Ir_xSn_1-xO_2 electrocatalytic powders, Mater. Chem. Phys. **94**(2–3), 226–232 (2005)

27.58 P. Millet, N. Mbemba, S.A. Grigoriev, V.N. Fateev, A. Aukauloo, C. Etiévant: Electrochemical performances of PEM water electrolysis cells and perspectives, Int. J. Hydrogen Energy **36**(6), 4134–4142 (2010)

27.59 S.A. Grigoriev, P. Millet, V.N. Fateev: Evaluation of carbon-supported Pt and Pd nanoparticles for the hydrogen evolution reaction in PEM water electrolyzers, J. Power Sources **177**(2), 281–285 (2008)

27.60 O. Pantani, E. Anxolabehere-Mallart, A. Aukauloo, P. Millet: Electroactivity of cobalt and nickel glyoximes with regard to the electro-reduction of protons into molecular hydrogen in acidic media, Electrochem. Commun. **9**(1), 54–58 (2006)

27.61 P. Millet, R. Ngameni, S.A. Grigoriev, N. Mbemba, F. Brisset, A. Ranjbari, C. Etiévant: PEM water electrolyzers: From electrocatalysis to stack development, Int. J. Hydrogen Energy **35**(10), 5043–5052 (2010)

27.62 M.A. Yandrasits, S.J. Hamrock: Membranes for PEM fuel cells, ACS Symp. Ser. **1040**, 15–29 (2010)

27.63 A.E. Steck: *Membrane Materials in Fuel Cells* (Editions de l'Ecole Polytechnique de Montreal, Montreal 1995)

27.64 L.M. Roen, C.H. Paik, T.D. Jarvi: Electrocatalytic corrosion of carbon support in PEMFC cathodes, Electrochem. Solid-State Lett. **7**(1), A19–A22 (2004)

27.65 H.-Y. Jung, S.-Y. Huang, P. Ganesan, B.N. Popov: Performance of gold-coated titanium bipolar plates in unitized regenerative fuel cell operation, J. Power Sources **194**(2), 972–975 (2009)

27.66 T. Smolinka, S. Rau, C. Hebling: PEM water electrolysis. In: *Hydrogen and Fuel Cells*, ed. by D. Stolten (Wiley-VCH, Weinheim 2010)

27.67 A.B. LaConti, L. Swette: Special application using PEM-technology. In: *Handbook of Fuel Cells*, Vol. 4, ed. by W. Vielstich, A. Lamm, H.A. Gasteiger (Wiley, Chichester 2003)

27.68 J. Van Herle, A.J. McEvoy, K. Ravindranathan Thampi: Conductivity measurements of various yttria-stabilized zirconia samples, J. Mater. Sci. **29**, 3691 (1994)

27.69 J. Fergus: Electrolytes for solid oxide fuel cells, J. Power Sources **162**, 30 (2006)

27.70 B. Dalslet, P. Blennow, P.V. Hendriksen, N. Bonanos, D. Lybye, M. Mogensen: Assessment of doped ceria as electrolyte, J. Solid State Electrochem. **10**, 547–561 (2006)

27.71 K. Schwarz: Materials design of solid electrolytes, Proc. Nat. Acad. Sci. **103**(10), 3497 (2006)

27.72 D.A. Andersen, S.I. Simak, N.V. Skorodumova, I.A. Abrikosov, B. Johansson: Optimization of ionic conductivity in doped ceria, Proc. Nat. Acad. Sci. **103**(10), 3518–3521 (2006)

27.73 H, Yahiro, K. Eguchi, H. Arai: Electrical properties and reducibilities of ceria-rare earth oxide systems and their application to solid oxide fuel cell, Solid State Ion. **36**(1–2), 71–75 (1989)

27.74 D.J. Seo, K.O. Ryo, S.B. Park, K.Y. Kim, R.-H. Song: Synthesis and properties of $Ce_{1-x}Gd_xO_{2-x/2}$ solid solution prepared by flame spray pyrolysis, Mater. Res. Bull. **41**, 359–366 (2006)

27.75 T. Sakai, S. Matsushita, H. Matsumoto, S. Okada, S. Hashimoto, T. Ishihara: Intermediate temperature steam electrolysis using strontium zirconate-based protonic conductors, Int. J. Hydrogen Energy **34**, 56–63 (2009)

27.76 J.S. Herring, J.E. O'Brien, C.M. Stoots, G.L. Hawkes, J.J. Hartvigsen, M. Shahnam: Progress in high-temperature electrolysis for hydrogen production using planar SOFC technology, Int. J. Hydrogen Energy **32**, 440–450 (2007)

27.77 M. Ni, K.H. Leung, D.Y.C. Leung: Technological development of hydrogen production by solid oxide electrolyzer cell (SOEC), Int. J. Hydrogen Energy **33**, 2337–2354 (2008)

27.78 A. Hauch, S.H. Jensen, S. Ramousse, M. Mogensen: Performance and durability of solid oxide electrolysis cells, J. Electrochem. Soc. **153**(9), A1741–A1747 (2006)

27.79 A. Momma, T. Kato, Y. Kaga, S. Nagata: Polarization behavior of high temperature solid oxide electrolysis cells (SOEC), J. Ceram. Soc. Jpn. **105**, 369–373 (1997)

27.80 A. Hauch, S.H. Jense, M. Mogensen: Ni/YSZ electrodes in solid oxide electrolyser cells, Proc. 26th Risø Int. Symp. Mater. Sci.: Solid State Electrochem., ed. by S. Linderoth, A. Smith, N. Bonano, A. Hagen, L. Mikkelson, K. Kammer, D. Lybye, P.V. Hendriksen, F.W. Poulsen, M. Mogensen, W.G. Wang (Risø National Laboratory, Roskilde 2005) p. 203

27.81 P. Kim-Lohnsoontorn, Y.-M. Kim, N. Laosiripojana: Gadolinium doped ceria-impregnated nickel–yttria stabilised zirconia cathode for solid oxide electrolysis cell, Int. J. Hydrogen Energy **36**, 9420–9427 (2011)

27.82 J. Kong, Y. Zhang, C. Deng, J. Xu: Synthesis and electrochemical properties of LSM and LSF perovskites as anode materials for high temperature steam electrolysis, J. Power Sources **186**, 485–489 (2009)

27.83 W. Wang, Y. Juang, S. Jung, J. Vohs, J. Gorte: A Comparison of LSM, LSF, and LSCo for solid oxide electrolyzer anodes, J. Electrochem. Soc. **153**(11), A2066–A2070 (2006)

27.84 O.A. Marina, L.R. Pederson, M.C. Williams, G.W. Coffey, K.D. Meinhardt, C.D. Nguyen, E.C. Thomsen: Electrode performance in reversible solid oxide fuel cells, J. Electrochem. Soc. **154**(5), B452–B459 (2007)

27.85 M.K. Mahapatra, S. Bhowmick, N. Li, P. Singh: Role of oxygen pressure on the stability of lanthanum strontium manganite–yttria stabilized zirconia composite, J. Eur. Ceram. Soc. **32**(10), 2341–2349 (2012)

27.86 S.H. Jensen, P. Larsen, M. Mogensen: Hydrogen and synthetic fuel production from renewable energy sources, Int. J. Hydrogen Energy **32**, 3253–3257 (2007)

27.87 S. Ebbesen, M. Mogensen: Exceptional durability of solid oxide cells, Electrochem. Solid-State Lett. **13**(9), B106–B108 (2010)

27.88 J.E. O'Brien, J.S. Herring, C.M. Stoots, G.L. Hawkes, J.J. Hartvigsen, M. Shahnam: Progress in high-temperature electrolysis for hydrogen production using planar SOFC technology, Proc. AIChE Spring Nat. Meet. '05 (2005), Idaho National Laboratory (INL)/CON-05-00078 Rep.

27.89 J. O'Brien, C. Stoots, J. Herring, G. Hawkes, J. Hartvigsen: Thermal and electrochemical performance of a high-temperature steam electrolysis stack, Fuel Cell Seminar, Idaho National Laboratory (INL) (2006), /CON-06-11716 Rep.

27.90 J.E. O'Brien, J.S. Herring, C.M. Stoots, M.G. McKellar, E.A. Harvego, K.G. Condie, G.K. Housley, J.J. Hartvigsen: Status of the INL high-temperature electrolysis research program – Experimental and modeling, Proc. 4th Information Exchange Meeting on the Nuclear Production of Hydrogen (2009), Idaho National Laboratory (INL)/CON-09-15618 Rep.

27.91 J.E. O'Brien, C.M. Stoots, J.S. Herring, M.G. McKellar, E.A. Harvego, M.S. Sohal, K.G. Condie: High temperature electrolysis for hydrogen production from nuclear energy – Technology summary, Proc. Idaho National Laboratory (INL) (2010), EXT-09-16140 Rep.

27.92 Y. Bo, Z. Wenqiang, X. Jingming, C. Jing: Status and research of highly efficient hydrogen production through high temperature steam electrolysis at INET, Int. J. Hydrogen Energy **35**, 2829–2835 (2010)

27.93 S.-D. Kim, J.-H. Yu, D.-W. Seo, I.-S. Han, S.-K. Woo: Hydrogen production performance of 3-cell flat-tubular solid oxide electrolysis stack, Int. J. Hydrogen Energy **37**, 78–83 (2012)

27.94 S.D. Kim, S.H. Hyun, J. Moon, J.-H. Kim, R.H. Song: Fabrication and characterization of anode-supported electrolyte thin films for intermediate temperature solid oxide fuel cells, J. Power Sources **139**, 67–72 (2005)

27.95 M.A. Laguna-Bercero, R. Campana, A. Larrea, J.A. Kilner, V.M. Orera: Steam electrolysis using a microtubular solid oxide fuel cell, J. Electrochem. Soc. **157**(6), B852–B855 (2010)

27.96 J.P. Ouweltjes, L. Berkeveld, B. Rietveld: Recent progress in the development of solid oxide electrolyzers at ECN, Proc. 18th World Hydrogen Energy Conference, Essen '10 (2010)

27.97 A. Glauche, T. Betz, M. Ise: Product development for SOFC and SOE, App. ECS Trans. **35**(1), 157–165 (2011)

27.98 A. Hauch, S.J. Jensen, S.D. Ebbesen, M. Mogensen: Durability of solid oxide cells for hydrogen production. In: *Energy Solutions for Sustainable Development*, ed. by L.S. Petersen, H. Larsen (Risø National Laboratory, Risø 2007) pp. 327–338

27.99 J. Schefold, A. Brisse, F. Tietz: Nine thousand hours of operation of a solid oxide cell in steam electrolysis mode, J. Electrochem. Soc. **159**(2), A137–A144 (2012)

27.100 E. Elangoven, J. Hartvigsen: Progress in the conversion of CO_2 to liquid fuel, Proc. 220th ECS Meeting and Electrochemistry Summit, Boston (2011) p. 1509

27.101 A.V. Virkar: A model for solid oxide fuel cell (SOFC) stack degradation, J. Power Sources **172**, 713–724 (2007)

27.102 S.H. Jensen, M. Mogensen: *Perspectives of high Temperature Electrolysis Using SOEC* (European Institute of Energy Research (EIfER), Karlsruhe 2015), http://www.hi2h2.com/perspectives.htm

27.103 S.D. Ebbesen, J. Hogh, K.A. Nielsen, J.U. Nielsen, M. Mogensen: Durable SOC stacks for production of hydrogen and synthesis gas by high temperature electrolysis, Int. J. Hydrogen Energy **36**, 7363–7373 (2011)

27.104 S.D. Ebbesen, C. Graves, A. Hauch, S. Jensen, M. Mogensen: Poisoning of solid oxide electrolysis cells by impurities, J. Electrochem. Soc. **157**(10), B1419–B1429 (2010)

27.105 M.S. Sohal, J.E. O'Brien, C.M. Stoots, V.I. Sharma, B. Yildiz, A. Virkar: Degradation issues in solid oxide cells during high temperature electrolysis, J. Fuel Cell Sci. Technol. **9**(1), 011017 (2012)

27.106 K. Chen, S.P. Jiang: Failure mechanism of $(La,Sr)MnO_3$ oxygen electrodes of solid oxide electrolysis cells, Int. J. Hydrogen Energy **36**, 10541–10549 (2011)

27.107 A. Hauch, S.D. Ebbesen, S.H. Jensen, M.J. Mogensen: Highly efficient high temperature electrolysis, Mater. Chem. **18**, 2331–2340 (2008)

27.108 J.R. Bolton, S.J. Strickler, J.S. Connolly: Limiting and realizable efficiencies of solar photolysis of water, Nature **316**, 495–500 (1985)

27.109 A.V. Virkar: Mechanism of oxygen electrode delamination in solid oxide electrolyzer cells, Int. J. Hydrogen Energy **35**, 9527–9543 (2010)

27.110 C.W. De Kreuk, J.L.B. De Groot: Photocorrosion of strontium titanate photoanodes, Solar Energy Mater. **5**(4), 437–444 (1981)

27.111 M.C. Hanna, A. Nozik: Solar conversion efficiency of photovoltaic and photoelectrolysis cells with carrier multiplication absorbers, J. Appl. Phys. **100**(074510), 1–8 (2006)

27.112 R. Memming, G. Schandt: Electrochemical properties of gallium phosphide in aqueous solutions, Electrochimica Acta. **13**, 1299–1310 (1968)

27.113 H. Yoneyama, H. Sakamoto, H.A. Tamura: Photoelectrochemical cell with production of hydrogen and oxygen by a cell reaction, Electrochimica Acta. **20**, 341–345 (1975)

27.114 B.A. Parkinson: Combinatorial identification and optimization of new oxide semiconductors. In: *Photoelectrochemical Hydrogen Production*, ed. by V. De Krol, R.M. Grätzel (Springer, Berlin 2012) pp. 173–203

27.115 Y. Matsumoto: Energy positions of oxide semiconductors and photocatalysis with iron complex oxides, J. Solid State Chem. **126**, 227–234 (1996)

27.116 M.G. Walter, E.L. Warren, J.R. McKone, S.W. Boettcher, Q. Mi, E.A. Santori, N.S. Lewis: Solar water splitting cells, Chem. Rev. **110**, 6446–6473 (2010)

27.117 O. Khaselev, J.A. Turner: Electrochemical stability of p-$GaInP_2$ in aqueous electrolytes toward photoelectrochemical water splitting, J. Electrochem. Soc. **145**(10), 3335–3339 (1998)

27.118 B. Miller: Charge transfer and corrosion processes at III-V semiconductor/electrolyte interfaces, J. Electroanal. Chem. Interf. Electrochem. **168**(1), 91–100 (1984)

27.119 T.G. Deutsch, C.A. Koval, J.A. Turner: III-V Nitride epilayers for photoelectrochemical water splitting: GaPN and GaAsPN, J. Phys. Chem. B **110**, 25297–25307 (2006)

27.120 H. Gerischer: On the stability of semiconductor electrodes against photodecomposition, J. Electroanal. Chem. Interf. Electrochem. **82**(1), 133–143 (1977)

27.121 D. Meissner, R. Memming, B. Kastening: Fundamental problems of water splitting at cadmium sulfide, Chem. Phys. Lett. **127**, 419–422 (1986)

27.122 D. Meissner, C. Benndorf, R. Memming: Photocorrosion of cadmium sulfide: Analysis by photoelectron spectroscopy, Appl. Surf. Sci. **27**, 423–436 (1987)

27.123 D. Meissner, R. Memming: Photoelectrochemistry of cadmium sulfide. 1. Reanalysis of photocorrosion and flat-band potential, J. Phys. Chem. **92**, 3476–3483 (1988)

27.124 R.C. Valderrama, P.J. Sebastián, M. Miranda-Hernandez, J. Pantoja Enriquez, S.A. Gamboa: Studies on the electrochemical stability of CIGS in H_2SO_4, J. Photochem. Photobiol. A **168**(1), 75–80 (2004)

27.125 W. Kautek, H. Gerischer: Anisotropic photocorrosion of n-type MoS_2 $MoSe_2$, and WSe_2 single crystal surfaces: The role of cleavage steps, line and screw dislocations, Surf. Sci. **119**(1), 46–60 (1982)

27.126 D.E. Scaife: Oxide semiconductors in photoelectrochemical conversion of solar energy, Solar Energy **25**(1), 41–54 (1980)

27.127 U. Bossel: The physics of the hydrogen economy, Eur. Fuel Cells News **10**(2), 1–16 (2003)

27.128 K. Tanabe: A review of ultrahigh efficiency III-V semiconductor compound solar cells: Multijunction tandem, lower dimensional, photonic up/down conversion and plasmonic nanometallic structures, Energies **2**, 504–530 (2009)

27.129 S. Licht: Multiple band gap semiconductor/electrolyte solar energy conversion, J. Phys. Chem. B **105**, 6281–6294 (2001)

27.130 B. Neumann, P. Bogdanoff, H. Tributsch: TiO_2-protected photoelectrochemical tandem Cu(In,Ga)Se_2 thin film membrane for light-induced water splitting and hydrogen evolution, J. Phys. Chem. C **113**, 20980–20989 (2009)

27.131 W. Shockley, H.J. Queisser: Detailed balance limit of efficiency of p–n junction solar cells, J. Appl. Phys. **32**, 510–519 (1961)

27.132 N.D. McDaniel, S. Bernhard: Solar fuels: thermodynamics, candidates, tactics, and figures of merit, Dalton Trans. **39**, 10021–10030 (2010)

27.133 J.M. Bolts, M.S. Wrighton: Correlation of photocurrent-voltage curves with flat-band potential for stable photoelectrodes for the photoelectrolysis of water, J. Phys. Chem. **80**(24), 2641–2645 (1976)

27.134 J. Maclay, J. Brouwer, G.S. Samuelsen: Experimental results for hybrid energy storage systems coupled to photovoltaic generation in residential applications, Int. J. Hydrogen Energy **36**(19), 12130–12140 (2011)

27.135 A.J. Nozik: p–n photoelectrolysis cells, Appl. Phys. Lett. **29**, 150–153 (1976)

27.136 J. o'M. Bockris, R.C. Kainthla: The conversion of light and water to hydrogen and electric power, Int. J. Hydrogen Energy **13**(6), 375–383 (1988)

27.137 D.C. Bookbinder, N.S. Lewis, M.G. Bradley, A.B. Bocarsly, M.S. Wrighton: Photoelectrochemical reduction of N,N′-dimethyl-4,4′-bipyridinium in aqueous media at p-type silicon: Sustained photogeneration of a species capable of evolving hydrogen, J. Am. Chem. Soc. **101**(26), 7721–7723 (1979)

27.138 E. Aharon-Shalom, A. Heller: Efficient p-InP(Rh-H alloy) and p-InP(Re-H alloy) hydrogen evolving photocathodes, J. Electrochem. Soc. **129**, 2865–2866 (1982)

27.139 K. Ohashi, J. McCann, J.O.M. Bockris: Stable photoelectrochemical cells for the splitting of water, Nature **266**, 610–611 (1977)

27.140 H.S. Gurev, R.E. Hahn, K.D. Masterson: High temperature; stable, spectrally selective solar absorbers for thermochemical hydrogen production, Int. J. Hydrogen Energy **1**(3), 259–265 (1977)

27.141 B. Marsen, B. Cole, E.L. Miller: Photoelectrolysis of water using thin copper gallium diselenide electrodes, Sol. Energ. Mater. Sol. Cells **92**, 1054–1058 (2008)

27.142 D. Yokoyama, T. Minegishi, K. Jimbo, T. Hisatomi, G. Ma, M. Katayama, J. Kubota, H. Katagiri, K. Domen: H_2 evolution from water on modified Cu_2ZnSnS_4 photoelectrode under solar light, Appl. Phys. Express **3**(10), 101202–101204 (2010)

27.143 M. Kaneko, G.J. Yao, A. Kira: Efficient water cleavage with visible light by a system mimicking photosystem II, J. Chem. Soc. Chem. Commun. **18**, 1338–1339 (1989)

27.144 J. Hensel, G. Wang, Y. Li, J.Z. Zhang: Synergistic effect of CdSe quantum dot sensitization and nitrogen doping of TiO_2 nanostructures for photoelectrochemical solar hydrogen generation, Nano Lett. **10**, 478–483 (2010)

27.145 H. Hashiguchi, K. Maeda, R. Abe, A. Ishikawa, J. Kubota, K. Domen: Photoresponse of GaN: ZnO Electrode on FTO under visible light irradiation, Bull. Chem. Soc. Jpn. **82**, 401–407 (2009)

27.146 S. Yamane, N. Kato, S. Kojima, A. Imanishi, S. Ogawa, N. Yoshida, S. Nonomura, Y. Nakato: Efficient solar water splitting with a composite n-Si/p-CuI/n-i-p a-Si/n-p GaP/RuO_2, semiconductor electrode, J. Phys. Chem. C **113**(32), 14575–14581 (2009)

27.147 S. Shet, K.-S. Ahn, T. Deutsch, H. Wang, N. Ravindra, Y. Yan, J. Turner, M. Al-Jassim: Synthesis and characterization of band gap-reduced ZnO:N and ZnO:(Al,N) films for photoelectrochemical water splitting, J. Mater. Res. **25**(1), 69–75 (2010)

27.148 J. Ye, Z. Zou, H. Arakawa, M. Oshikiri, M. Shimoda, A. Matsushita, T. Shishido: Correlation of crystal and electronic structures with photophysical properties of water splitting photocatalysts $InMO_4$ (M=V5+,Nb5+,Ta5+), J. Photochem. Photobiol. A **148**, 79–83 (2002)

27.149 Z.G. Zou, J.H. Ye, K. Sayama, H. Arakawa: Direct splitting of water under visible light irradiation with an oxide semiconductor photocatalyst, Nature **414**, 625–627 (2001)

27.150 G. Hodes, D. Cahen, J. Manassen: Tungsten trioxide as a photoanode for a photoelectrochemical cell (PEC), Nature **260**, 312–313 (1976)

27.151 Y. Shimodaira, H. Kato, H. Kobayashi, A. Kudo: Investigations of electronic structures and photocatalytic activities under visible light irradiation of lead molybdate replaced with chromium (VI), Bull. Chem. Soc. Jpn. **80**, 885–893 (2007)

27.152 M.S. Wrighton, A.B. Ellis, P.T. Wolczanski, D.L. Morse, H.B. Abrahamson, D.S. Ginley: Strontium titanate photoelectrodes. Efficient photoassisted electrolysis of water at zero applied potential, J. Am. Chem. Soc. **98**(10), 2774–2779 (1975)

27.153 H.P. Maruska, A.K. Ghosh: Transition-metal dopants for extending the response of titanate photoelectrolysis anodes, Sol. Energ. Mater. **1**(3–4), 237–247 (1978)

27.154 L.G.L. De Haart, A.J. De Vries, G. Blasse: On the photoluminescence of semiconducting titanates applied in photoelectrochemical cells, J. Sol. State Chem. **59**(3), 291–300 (1985)

27.155 K. Sivula, F. Le Formal, M. Grätzel: Solar water splitting: progress using hematite (α-Fe(2) O(3)) photoelectrodes, Chem. Sus. Chem. **4**(4), 432–449 (2011)

27.156 P.C. Bailey: Absorption and reflectivity measurements on some rare earth iron garnets and alpha-

iron oxide, J. Appl. Phys. **31**, S39–S40 (1960)
27.157 L.A. Marusak, R. Messier, W.B. White: Optical absorption spectrum of hematite, α Fe_2O_3 near IR to UV, J. Phys. Chem. Solids **41**, 981–984 (1980)
27.158 J.H. Kennedy, K.W. Frese: Photo oxidation of water at α-Fe_2O_3 electrodes, J. Electrochem. Soc. **125**, 709–714 (1978)
27.159 A. Kay, I. Cesar, M. Grätzel: New benchmark for water photooxidation by nanostructured α -Fe_2O_3 films, J. Am. Chem. Soc. **128**(49), 15714–15721 (2006)
27.160 K. Sivula, F.L. Formal, M. Grätzel: WO_3-Fe_2O_3 photoanodes for water splitting: a host scaffold, guest absorber approach, Chem. Mater. **21**(13), 2862–2867 (2009)
27.161 K. Sivula, R. Zboril, F. Le Formal, R. Robert, A. Weidenkaff, J. Tucek, J. Frydrych, M. Grätzel: Photoelectrochemical water splitting with mesoporous hematite prepared by a solution-based colloidal approach, J. Am. Chem. Soc. **132**(21), 7436–7444 (2010)
27.162 S.D. Tilley, M. Cornuz, K. Sivula, M. Grätzel: Light-induced water splitting with hematite: Improved nanostructure and iridium oxide catalysis, Angew. Chem. Intl. Ed. **49**(36), 6405–6408 (2010)
27.163 A. Paracchino, V. Laporte, K. Sivula, M. Gräzel, E. Thimsen: Highly active oxide photocathode for photoelectrochemical water reduction, Nature Mater. **10**, 456–461 (2011)
27.164 Y. Matsumoto, M. Omae, K. Sugiyama, E.-I. Sato: New photocathode materials for hydrogen evolution: Calcium iron oxide ($CaFe_2O_4$) and strontium iron oxide ($Sr_7Fe_{10}O_{22}$), J. Phys. Chem. **91**, 577–581 (1987)
27.165 A.J. Nozik: Nanoscience and nanostructures for photovoltaics and solar fuels, Nano Lett. **10**(8), 2735–2741 (2010)
27.166 O.K. Varghese, D. Gong, M. Pailose, C.A. Grimes, E.C. Dickey: Crystallization and high-temperature structural stability of titanium oxide nanotube arrays, J. Mater. Res. **18**, 156–165 (2003)
27.167 K.S. Raja, M. Misra, K. Paramguru: Formation of self-ordered nano-tubular structure of anodic oxide layer on titanium, Electrochimica. Acta. **51**, 154–165 (2005)
27.168 C.-C. Chen, J.-H. Chen, C.-G. Chao, W.C. Say: Electrochemical characteristics of surface of titanium formed by electrolytic polishing and anodizing, J. Mater. Sci. **40**, 4053–4059 (2005)
27.169 J. Zhao, X. Wnag, R. Chen, L. Li: Fabrication of titanium oxide nanotube arrays by anodic oxidation, Sol. State Commun. **134**, 705–710 (2005)
27.170 S. Bauer, S. Kleber, P. Schmuki: TiO_2 nanotubes: Tailoring the geometry in H_3PO_4/HF electrolytes, Electrochem. Commun. **8**(8), 1321–1325 (2006)
27.171 P.S. Albu, A. Ghicov, J.M. Macak, P. Schmuki: 250μm long anodic TiO_2 nanotubes with hexagonal self-ordering, Phys. Status Solidi **1**, R65–R67 (2007)
27.172 W.-J. Lee, M. Alhoshan, W.H. Smyrl: Titanium dioxide nanotube arrays fabricated by anodizing processes – Electrochemical properties, J. Electrochem. Soc. **153**, B499–B505 (2006)
27.173 Y.-C. Nah, A. Ghicov, D. Kim, S. Berger, P. Schmuki: TiO_2-WO_3 Composite nanotubes by alloy anodization: Growth and enhanced electrochromic properties, J. Am. Chem. Soc. **130**, 16154–16155 (2008)
27.174 J.H. Park, S. Kim, A.J. Bard: Novel carbon-doped TiO_2 nanotube arrays with high aspect ratios for efficient solar water splitting, Nano Lett. **6**(1), 24–28 (2005)
27.175 K.S. Raja, M. Misra, V.K. Mahajan, T. Gandhi, P. Pillai, S.K. Mohapatra: Photo-electrochemical hydrogen generation using band-gap modified nanotubular titanium oxide in solar light, J. Power Sources **161**, 1450–1457 (2006)
27.176 S.K. Mohapatra, M. Misra, V.K. Mahajan, K.S. Raja: Design of a highly efficient photoelectrolytic cell for hydrogen generation by water splitting: Application of $TiO_{2-x}C_x$ nanotubes as a photoanode and Pt/TiO_2 nanotubes as a cathode, J. Phys. Chem. C **111**, 8677–8685 (2007)
27.177 R. Abe, M. Higashi, K. Domen: Facile fabrication of an efficient oxynitride TaON photoanode for overall water splitting into H_2 and O_2 under visible light irradiation, J. Am. Chem. Soc. **132**(34), 11828–11829 (2010)
27.178 S. Linic, P. Christopher, D. Ingram: Plasmonic-metal nanostructures for efficient conversion of solar to chemical energy, Nature Mater. **10**, 911–921 (2011)
27.179 D.B. Ingram, S. Linic: S: Water splitting on composite plasmonic-metal/semiconductor photoelectrodes: Evidence for selective plasmon-induced formation of charge carriers near the semiconductor surface, J. Am. Chem. Soc. **133**, 5202–5205 (2011)
27.180 J.I. Levene, M.K. Mann, R.M. Magrolis, A. Milbrandt: An analysis of hydrogen production from renewable electricity sources, Solar Energ. **81**, 773–780 (2007)
27.181 P.-H. Floch, S. Gabriel, C. Mansilla, F. Werkoff: On the production of hydrogen via alkaline electrolysis during off-peak periods, Int. J. Hydrogen Energy **32**, 4641–4647 (2007)
27.182 IEA: *CO_2 Emissions from Fuel Combustion* (International Energy Agency, Paris 2011)
27.183 D. Bonhaquist: *Emissions, Reductions, and Capture for Large-Scale Hydrogen Production Plants*, Praxair White Paper (Praxair, Danbury 2010)
27.184 L.M. Gandia, R. Orosz, A. Ursua, P. Sanchis, P. Diegueuz: Renewable hydrogen production: Performance of an alkaline water electrolyzer working under emulated wind conditions, Energy Fuels **21**, 1699–1706 (2007)
27.185 B. Kroposki, J. Levene, K. Harrison, P.K. Sen, F. Novachek: *Electrolysis: Information and Opportunities for Electric Power Utilities* (National Renewable Energy Laboratory, Golden 2006), NREL Tech. Rep. NREL/TP-581-40605
27.186 T. Abbasi, S.A. Abbasi: Renewable hydrogen: Prospects and challenges, Renew. Sust. Energ.

Rev. **15**, 3034 (2011)
27.187 National Research Council: *The Hydrogen Economy. Opportunities, Costs, Barriers, and R and D Needs* (National Academies, Washington 2004)
27.188 J.E. O'Brien, M.G. McKellar, E.A. Harvego, C.M. Stoots: High-temperature electrolysis for large-scale hydrogen and syngas production from nuclear energy – Summary of system simulation and economic analyses, Int. J. Hydrogen Energy **35**, 4808–4819 (2010)
27.189 B.C.R. Ewan, R.W.K. Allen: A figure of merit assessment of the routes to hydrogen, Int. J. Hydrogen Energy **30**, 809–819 (2005)
27.190 P.L. Spath, M.K. Mann: *Life Cycle Assessment of Renewable Hydrogen Production via Wind/Electrolysis* (National Renewable Energy Laboratory, Golden 2004), NREL Milestone Rep. MP-560-35404
27.191 C. Koronos, A. Dompros, G. Roumbas, N. Moussiopoulos: Life cycle assessment of hydrogen fuel production processes, Int. J. Hydrogen Energy **29**, 1443–1450 (2010)
27.192 R.G. Lemus, J.M.M. Duart: Updated hydrogen production costs and parities for conventional and renewable technologies, Int. J. Hydrogen Energy **35**, 3929–3936 (2010)
27.193 E. Cetinkaya, I. Dincer, G.F. Naterer: Life cycle assessment of various hydrogen production methods, Int. J. Hydrogen Energy **37**, 2071–2080 (2012)
27.194 A. Ursua, L.M. Gandia, P. Sanchis: Hydrogen production from water electrolysis: Current status and future trends, Proc. IEEE, Vol. 100 (2012) pp. 410–426
27.195 K.W. Harrison, G.D. Martin, T.G. Ramsden, W.E. Kramer, F.J. Novachek: *The Wind-to-Hydrogen Project: Operational Experience, Performance Testing, and Systems Integration* (National Renewable Energy Laboratory, Golden 2009), NREL TP/550-44082 Tech. Rep.
27.196 M. Rey Porto, T. Carretero, M. Aguado, R. Garde: H_2 production in Sotavento wind farm, Proc. 18th World Hydrogen Energy Conf., Vol. 78, ed. by D. Stolten, T. Grube (2010)
27.197 K.W. Harrison, R. Remick, G.D. Martin, A. Hoskin: *Hydrogen Production: Fundamentals and Case Study Summaries* (National Renewable Energy Laboratory, Golden 2010), NREL CP-550-47302 Tech. Rep.

28. Electrochemical Machining

Michael Schneider, Manuel Lohrengel

Electrochemical machining (ECM) is an interesting and effective technique to shape metals by controlled anodic dissolution at extremely large current densities. The process avoids mechanical stress to workpiece and tool and yields shiny surfaces without further processes. The hardness of the material has no influence on the process. A compact overview with focus on the fundamental electrochemical interface kinetics is presented. After a brief introduction and a historical abstract, the electrochemical processes of anodic dissolution are discussed (Sect. 28.2). The common interface models developed over the last decades are introduced and compared. Experimental research concepts in lab-scale with partly unique equipment are described in Sect. 28.3 which focuses on the principles of interface process due to the extremely high current densities which are typical for ECM. Further information comes from in situ techniques to analyze the reaction products in the electrolyte and to monitor the anode surface. Extensively discussed is the formation of supersaturated product films close to the anode as a consequence of the high dissolution rate during the process. In Sect. 28.5 the authors propose a classification of the ECM processes based on the individual metal properties and structures of surface films (oxides) or the types of product complex ions. The interplay between anodic dissolution, metal microstructure and crystallography is intensively described in the second part of the chapter. Side reactions such as anodic oxygen evolution and the corresponding aspects of electronic conductivity are separately discussed in Sect. 28.7. Pulse ECM is an improved technique which means more complex kinetics of dissolution and is described in Sect. 28.8. The overview is completed by a discussion about *difficult-to-machine* materials such as titanium and carbides or nitrides (Sect. 28.9).

28.1 **Introduction and History** 942
28.1.1 History 942

28.2 **Fundamentals of Electrochemical Machining** 943
28.2.1 The Fundamental Process 943
28.2.2 Passivity, Transpassivity and Transition to ECM Conditions 943
28.2.3 Side Reactions 944
28.2.4 Common Interface Models 945

28.3 **Experimental Techniques** 946
28.3.1 Laboratory Setup for Quantitative Investigations 946
28.3.2 Product Analysis 948
28.3.3 Gaseous Products 948
28.3.4 Surface Characterization Electron Backscatter Diffraction (EBSD) 948

28.4 **The Interface Process During ECM** 949
28.4.1 Cyclic Voltammetry and Surface Layers 949
28.4.2 Supersaturated Product Films 950

28.5 **Classification of ECM Processes** 952

28.6 **Surface Topography, Crystallographic Effects and Surface Quality** 952
28.6.1 Theory 953
28.6.2 Grains in Experiments 954
28.6.3 Grain Boundaries and Other Crystal Defects 955
28.6.4 Surface Brightening 957

28.7 **Oxygen Evolution** 958

28.8 **Pulse ECM** 959

28.9 **Too Difficult-to-Machine: Hard Metals, Carbides and Nitrides** 962
28.9.1 Titanium 963
28.9.2 Cemented Carbides 964

References 967

28.1 Introduction and History

ECM is a fast and effective technology to shape products of high quality from steel and other metals. Parts of the metal are dissolved by controlled anodic dissolution in neutral solutions (e.g., aqueous sodium nitrates or chlorides) at extremely large current densities of up to some 100 A/cm^2. An especially formed cathode, the so-called tool, defines the final shape of the workpiece. The gap between workpiece and tool must be small to realize such large current densities at moderate potentials and to guarantee high precision. The electrolyte is moved in a closed circuit to remove dissolution products which finally deposit as hydroxides and must be removed in special filter setups.

The frequently stressed advantages of ECM are [28.1]:

- An almost forceless machining, and, thus, no mechanical stress impact into the workpiece.
- No significant thermal impact and thermal stress (less than 100 K).
- The removal rate is not determined by mechanical material properties. If the hardness of the material exceeds 450 HB, the material removal rate of ECM exceeds shape cutting technologies [28.2].
- No relevant tool wear (with the exception of bipolar processing).
- Great versatility for machining of geometrical complex shapes.
- No burr formation.
- High surface quality without additional processes.

In comparison with conventional machining processes the disadvantage of ECM should not be suppressed:

- The equipment requires high investment costs.
- High energy consumption, expenses for electric energy.
- Waste management costs (hydroxides of heavy metals).
- Corrosion exposure of the machine equipment.
- A relative slow dissolution rate of less than 0.02 mm/s.

Many high quality parts are prepared by ECM, such as shaver caps (Fig. 28.1), medical implants, gears, or turbine blades. The hardness of the workpiece is not relevant. Therefore, ECM is also a perfect choice for industrial shaping of extremely hard materials such as so-called *hard metals* which consist of carbide particles, embedded in a softer matrix of Co, Fe, Ni or alloys.

ECM is an extremely complex process – interpretation, modeling and further development requires knowledge of completely different aspects such as chemistry and physics, or, in more detail, corrosion, passivation, interface kinetics, material science, crystallography, fluidics and electronics. The present work is exclusively focused on the electrochemical basics and some material specific features. Hybrid technologies or production-technical details will be disregarded. The authors refer to corresponding monographs or journals.

28.1.1 History

In the 1920s of the last century, electrochemical machining was developed in the former Soviet Union [28.3]. Admittedly, *Pirani* and *Schröter* published an electrochemical method to shape and drill tungsten carbide [28.4]. This work is an indication that especially *difficult-to-machine alloys* [28.5] initiated the development of technologies aside mechanical machining. However, only the crucial intention of *Gusev* [28.6–8] laid the foundation of the ECM. Gusev moved one electrode in direction to the other and added a streaming electrolyte to remove the process heat [28.9]. In fact, since the work of Gusev a number of decades had to pass before ECM was established in industry. From the 1950s, ECM started to get established induced by an increasing interest in *difficult-to-machine alloys* such as hard metals, nickel based alloys or titanium alloys. *Stanek* [28.10] showed that the number of these materials continuously increased and, in parallel, the number of electrochemically machinable

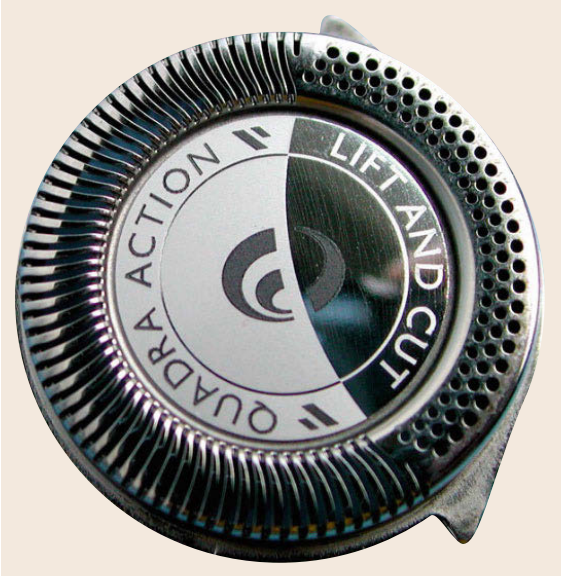


Fig. 28.1 Top view of cap of an electric shaver. Slots, holes and shiny surface are results of ECM

alloys. This suggested, according to *Degner* [28.9], that material development is strictly associated with the development of treatment and machining technologies. To put it straight, the tensile strength of materials seem to be doubled over the last 20 years which is associated with a slowing-down of metalworking. Therefore, a machining technology which is independent of the hardness of the workpiece is absolutely necessary [28.3]. The economic aspect of ECM depends mainly on the complexity or difficulty to shape the workpiece [28.3] and requirements on the surface quality.

Altogether, ECM is a well-established technology for shaping metals, mainly steel and hard alloys [28.11–13].

ECM is frequently combined with mechanical processes. An overview of hybrid technologies and their special applications is given by *Degner* [28.9].

28.2 Fundamentals of Electrochemical Machining

28.2.1 The Fundamental Process

The equilibrium state of base metals in the common environment (air, humidity) according to thermodynamics is cations such as (diluted) salts, oxides or hydroxides. The dissolution reaction

$$\mathrm{Me} \rightarrow \mathrm{Me}^{n+} + n\,\mathrm{e}^- \qquad (28.1a)$$

is the fundamental process of corrosion of metals. In the presence of water, low energy aquo complexes are formed as ionization of nonhydrated ions requires energies up to 20 eV

$$\mathrm{Me} + 6\,\mathrm{H_2O} \rightarrow [\mathrm{Me(H_2O)_6}]^{n+} + n\,\mathrm{e}^- \,. \qquad (28.1b)$$

This process is normally hindered by so-called passive layers, in most cases oxide films, which inhibit the transfer of cations into the environment. Corrosion according to (28.1b) is normally unwanted, but an electrochemically accelerated dissolution is well known as ECM.

The workpiece to be shaped is connected as an anode. The cathode, the so-called tool, is especially formed and represents in some way a negative of the final shape of the workpiece. The tool works without mechanical contact.

ECM requires extremely large current densities around $100\,\mathrm{A/cm^2}$. These current densities are at least 5 decades lager than in common electrochemical experiments and require suitable dc power supplies.

The tool (cathode), which is a negative of the intended workpiece shape, is narrowed to the workpiece (anode). Those parts of the tool which are closest to the workpiece (typically 10 to 50 µm) develop the largest current densities and, thus, the largest dissolution rates (Fig. 28.2). The complementary reaction at the cathode is hydrogen evolution. All products, mainly hydroxides of the dissolved metals, are removed by the flowing electrolyte. The tool should never touch the workpiece to avoid short circuit conditions with destruction of tool and workpiece.

Many types of electrolytes were tested, initially sodium chloride solutions were used, but nowadays mainly neutral $NaNO_3$ solutions are common to yield high quality products. The concentrations are close to saturation to guarantee high conductivity which is necessary at such large current densities. Typical potential drops across commercial cells are around 20 V.

The process requires large electrolyte flow rates up to some m/s to remove the products from the surface. The metal cations can be dissolved in the beginning, but then precipitate in the neutral electrolytes and form hydroxides. The only exception is chromium, it forms chromates in the electrolyte which remain dissolved and must be reduced by special techniques. The electrolyte is pumped in a closed circuit and the precipitated hydroxides are removed in filter systems.

Electrochemical reaction rates depend strongly on the temperature. The energy losses in the gap between tool and workpiece are large (Joule heating, some $100\,\mathrm{W/cm^2}$), but heat can be removed by the high flow and, thus, depends on the local geometry. Accordingly, the temperature at the anode interface is not exactly known, it can be up to approximately 80 °C [28.14].

28.2.2 Passivity, Transpassivity and Transition to ECM Conditions

Most metals form dense oxide films with thicknesses of some nm during anodization, at least at pH values around 7. These oxide films are ceramic-like insulators, but get some ionic conductivity at very large electric field strengths (up to some MV/cm) to enable their growth [28.15]. The films should disable redox processes, i. e., electron transfer from the metal to the electrolyte or back. Some metals such as iron or nickel, however, develop oxygen at potentials > 1.6 V, which means electronic conductivity at these potentials.

This was sometimes interpreted as partial destruction of the oxide film, an idea which was supported

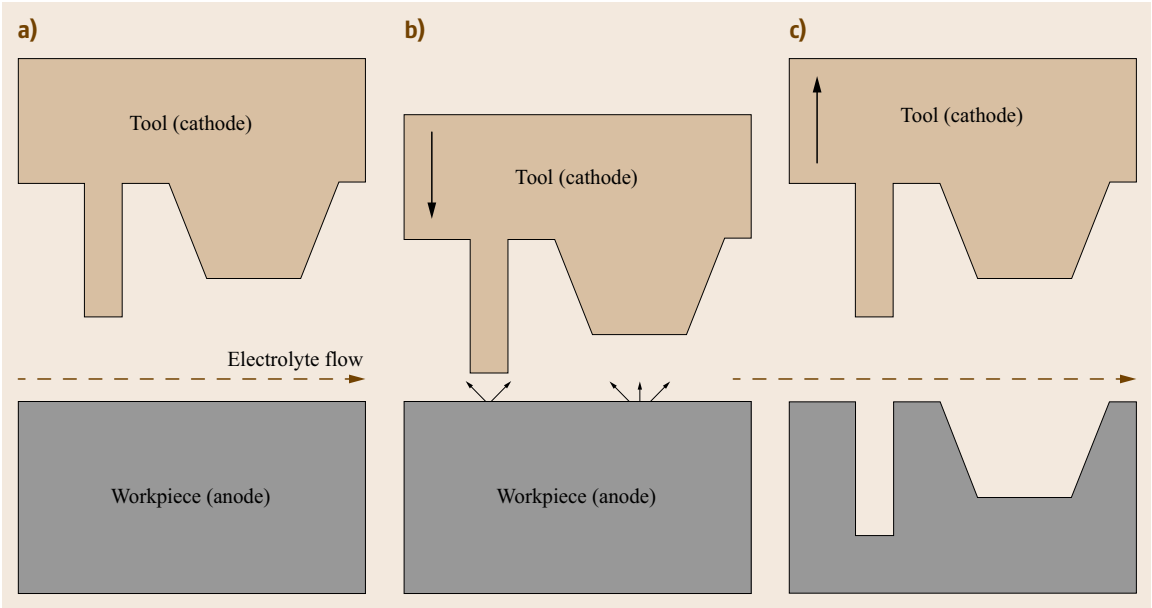


Fig. 28.2a–c Scheme of ECM process. Initial conditions **(a)**, process starts **(b)**, process has finished **(c)**

by the acidification (28.10) due to oxygen evolution. In fact, oxygen evolution is possible only on oxide covered metals. This is easily understood as thermodynamics predict an oxide formation before oxygen evolution as equilibrium potentials of oxide electrodes of base metals are much smaller ($< 0\,\mathrm{V}$) than that of oxygen evolution (1.23 V). Furthermore, even noble metals form oxide layers before oxygen evolution [28.16, 17].

Oxygen is evolved at the interface oxide/electrolyte, otherwise the oxide film must flake off. This requires a sufficient electronic conductivity of the film, which can be explained by semiconductor models [28.18].

A further increase of potential and, therefore, current density, means a complete change in mechanism from transpassivity to ECM conditions. This starts around $1\,\mathrm{A/cm^2}$ in solvents such as mixtures of highly concentrated perchloric acid, acetic acid and alcohols (commonly used for electropolishing of metals) or in many other electrolytes around $5\,\mathrm{A/cm^2}$. The increasing amount of corrosion products is not removed by diffusion, but form precipitates or supersaturated surface films.

28.2.3 Side Reactions

The fundamental anodic reaction during ECM was already presented in (28.1a). The cathodic part of the total cell reaction is hydrogen evolution at the cathode

$$2\mathrm{H_2O} + 2\mathrm{e^-} \rightarrow \mathrm{H_2} + 2\mathrm{OH^-}\,. \qquad (28.2)$$

Unfortunately, many systems behave in a more complex way. The oxidation number of the metal ion can be unknown or several oxidation states can coexist, e.g.,

$$2\mathrm{Me} \rightarrow \mathrm{Me}^{n+} + \mathrm{Me}^{m+} + (n+m)\mathrm{e^-}\,. \qquad (28.3)$$

This is true for iron which forms Fe^{2+} and Fe^{3+}. Lower oxidation states can be chemically oxidized by oxygen developed as a side reaction (28.10), e.g.,

$$4\mathrm{Me}^{n+} + \mathrm{O_2} + 4\mathrm{H^+} \rightarrow 4\mathrm{Me}^{(n+1)+} + 4\mathrm{OH^-}\,, \qquad (28.4)$$

or react chemically with water somewhere in the electrolyte

$$2\mathrm{Me}^{n+} + 2\mathrm{H_2O} \rightarrow \mathrm{H_2} + 4\mathrm{Me}^{(n+1)+} + 2\mathrm{OH^-}\,. \qquad (28.5)$$

These processes hinder simple calculations of efficiency.

So far, the formation of cations was assumed. Some metals, e.g., Cr or Mn, form anions (chromates or permanganates) according to

$$\mathrm{Me} + 4\mathrm{H_2O} \rightarrow \mathrm{MeO_4^{n-}} + 8\mathrm{H^+} + (8-n)\mathrm{e^-}\,. \qquad (28.6)$$

This means a more complex, two-step mechanism which will be discussed later.

Other anodic processes which must be considered are oxide formation (passivation) according to

$$\mathrm{Me} + \left(\frac{z}{2}\right)\mathrm{H_2O} \rightarrow \mathrm{MeO}_{z/2} + z\mathrm{H^+} + z\mathrm{e^-} \qquad (28.7)$$

which is true for most metals in neutral solutions. These oxide films can dissolve in a nonelectrochemical, purely chemical reaction, especially at low pH values

$$\mathrm{MeO}_{z/2} + \left(\frac{z}{2}\right)\mathrm{H_3O^+} \rightarrow \mathrm{Me}^{z+} + z\mathrm{H_2O}\,. \qquad (28.8)$$

If the rates of (28.7) and (28.8) are equal, the oxide thickness remains constant while metal is continuously dissolved and, in total, (28.1a) is fulfilled. This means, the oxide amount remains constant from a macroscopic point of view; this state is called stationary corrosion.

Most cations will precipitate in neutral electrolytes according to

$$\mathrm{Me}^{z+} + z\mathrm{H_2O} \rightarrow \mathrm{Me(OH)}_z + z\mathrm{H}^+ \qquad (28.9)$$

and must be removed by filter systems. Further processes are side reactions such as oxygen evolution

$$2\mathrm{H_2O} \rightarrow \mathrm{O_2} + 4\mathrm{H}^+ + 4\mathrm{e}^-\,. \qquad (28.10)$$

Oxygen evolution becomes dominant at higher potentials around 2 V with current densities up to some $\mathrm{A/cm^2}$. This means an acidification at the interface as current densities $\gg 1\,\mathrm{A/cm^2}$ will produce pH values below zero and accelerates oxide film dissolution according to (28.8).

In chloride solutions, chlorine formation becomes possible

$$2\mathrm{Cl}^- \rightarrow \mathrm{Cl_2} + 2\mathrm{e}^-\,. \qquad (28.11)$$

Another nonelectrochemical, purely chemical dissolution of metal under hydrogen evolution was discussed in [28.19], especially if the oxide films dissolve at low pH values

$$\mathrm{Me} + z\mathrm{H_2O} \rightarrow \mathrm{Me}^{z+} + \left(\frac{z}{2}\right)\mathrm{H_2} + z\mathrm{OH}^-\,. \qquad (28.12)$$

This is active dissolution and becomes possible if the oxide film locally breaks down. Such types of reactions were discussed for the first time during hydrogen evolution [28.20].

Further side products are formed at the cathode (tool); hydrogen, which completes the cell reaction, and, if present, artifacts of nitrate reduction such as $\mathrm{NO_2}$, NO, $\mathrm{N_2O}$ or ammonia (Sect. 28.3.3).

28.2.4 Common Interface Models

Interpretation started with simple electrostatic models [28.21], but most authors assumed a more complex interface structure, dependent on electrolyte composition, current density or potential, temperature and substrate, e.g.:

- Model A: Supersaturated viscous films with limited water diffusion ($\mathrm{Cu/H_3PO_4}$ [28.22]; Fe-Cr/$\mathrm{H_3PO_4}$, $\mathrm{H_2SO_4}$ [28.23]).
- Model B: Passive films ($\mathrm{Ni/NaNO_3}$ [28.24]).
- Model C: Precipitated compact salt films ($\mathrm{Ni/NaNO_3}$ [28.25]; $\mathrm{Fe/NaNO_3}$ [28.26]; Ni, Fe/NaCl [28.27]; Fe, $\mathrm{Ni/NaNO_3}$, $\mathrm{NaClO_3}$ [28.28]; Ni/NaCl [28.29]).
- Model D: Duplex (compact and porous salt) films (Fe-Cr/NaCl [28.30]).

and variants (Fig. 28.3). Recent investigations favored a modified combination of Model A and B.

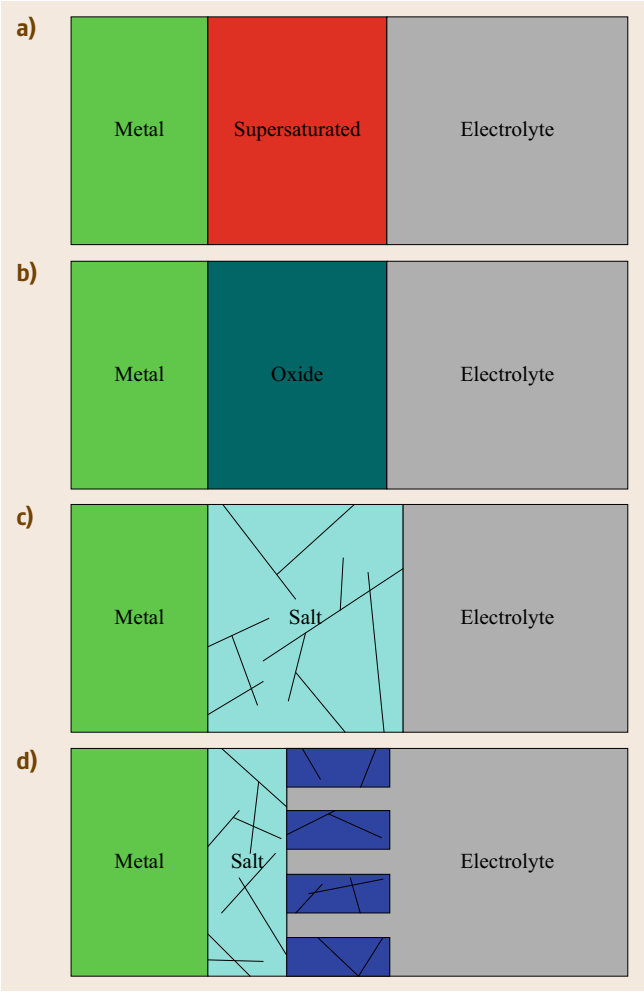


Fig. 28.3a–d Models of the interface workpiece/electrolyte. **(a)** Supersaturated viscous film; **(b)** Passive film; **(c)** Precipitated compact salt film; **(d)** Compact and porous salt film

Landolt [28.31] proposed different models to localize the rate determining step:

- A salt precipitation model where the diffusion/migration of dissolved cations is rate limiting.
- A model of rate limited anion diffusion to the surface.
- A model of rate limited water diffusion to the surface.

Rotating cylinder experiments with a direct comparison of aqueous $NaNO_3$ and NaCl solutions [28.32] indicated an active dissolution in NaCl and passive dissolution in $NaNO_3$. As a result, model B is not always true. Investigations of product nitrates showed that all these nitrates form supersaturated metastable solutions (Sect. 28.4.2) and cannot crystallize in the ECM process [28.33], accordingly, model A is favored.

The extremely large current densities, the large amounts of electrolyte in technical systems and the fast electrolyte movement, which is necessary to remove dissolution products, hindered fundamental electrochemical investigations and quantitative product analysis for many years. Accordingly, suitable laboratory equipment had to be developed.

28.3 Experimental Techniques

28.3.1 Laboratory Setup for Quantitative Investigations

An effective setup for quantitative investigations of fundamental ECM kinetics should avoid large absolute currents (up to several 1000 A in commercial systems) and large amounts of electrolytes (some 1000 l in commercial systems) to reduce efforts. Precise electric control (potential and current density), flow control, optical monitoring and product control including gases were required. Electrochemical microtechniques such as capillary based flow-through droplet cells [28.34] or channel flow microcells were promising.

Capillary Based Flow-Through Droplet Cells

Capillary based droplet cells [28.35, 36] were used to limit the extreme absolute currents necessary for ECM. The typical spot diameters of about 100 µm or less and means affected areas of about 10^{-3} cm^2, i. e., the interesting range of current density requires absolute currents < 1 A only. With this equipment, current densities of 100 A/cm^2 were reached, but only for short periods of time, from µs to 10 ms. After that period the anodic products (oxygen and iron hydroxide) blocked the capillary. Therefore, a new concept to remove the products of anodic dissolution had to be developed.

Hence, *Moehring* and coworkers designed a flow-through microcell with a double barreled capillary [28.34]. So-called theta capillaries, small glass tubes of 1 mm in diameter with a partition inside were used (Fig. 28.5). The tips were prepared in a professional capillary puller. The partition wall was removed close to the mouth (Fig. 28.6) and, thus, a flow-through of electrolyte could be realized: one channel is the inlet, the other one the outlet (Fig.28.7). Flow rates up to 10 m/s in the tip avoided troubles with oxygen bubbles. A precise continuous electrolyte flow is guaranteed by a computer controlled gear pump. The electrolyte is supplied from a thermostatted vessel of about 1 l. The product solution was collected at the outlet for further analysis (Sect. 28.3.2).

The concept with working electrode (workpiece, anode), counter electrode (tool, cathode) and a reference electrode enables potentiostatic control with all common techniques in microscale, e.g., cyclovoltammetry, pulse transients, microimpedance spectroscopy [28.37, 38] or galvanostatic experiments.

Channel Flow Cells

As already mentioned, ECM is characterized by high current densities, small electrode gaps and high electrolyte flow speed. In common electrochemistry research the application of so-called channel flow cells is well known. Channel flow cells are so designed that the mathematic description of the hydrodynamic inside the cell is in a simple manner. The type of flow (laminar or turbulent) can be easily distinguished by the Reynolds number *Re* according to

$$Re = \frac{2hv_0}{v}\,, \tag{28.13}$$

where v_0 is the electrolyte speed in the center of the channel, h is the half height of the cell and v is the kinematic viscosity. It can be said that the electrolyte flow became turbulent at $Re > 2000$. A very helpful introduction in this technique is given by *Compton* and *Banks* [28.40]. The electrolyte almost always flows turbulent under near-ECM conditions. Flow channel cells specially applied to investigate ECM were already described by *Datta* and *Landolt* [28.27], later on by *Hoogsteen* et al. [28.41] and *Haisch* et al. [28.32, 42]. The working and counter electrode were arranged in op-

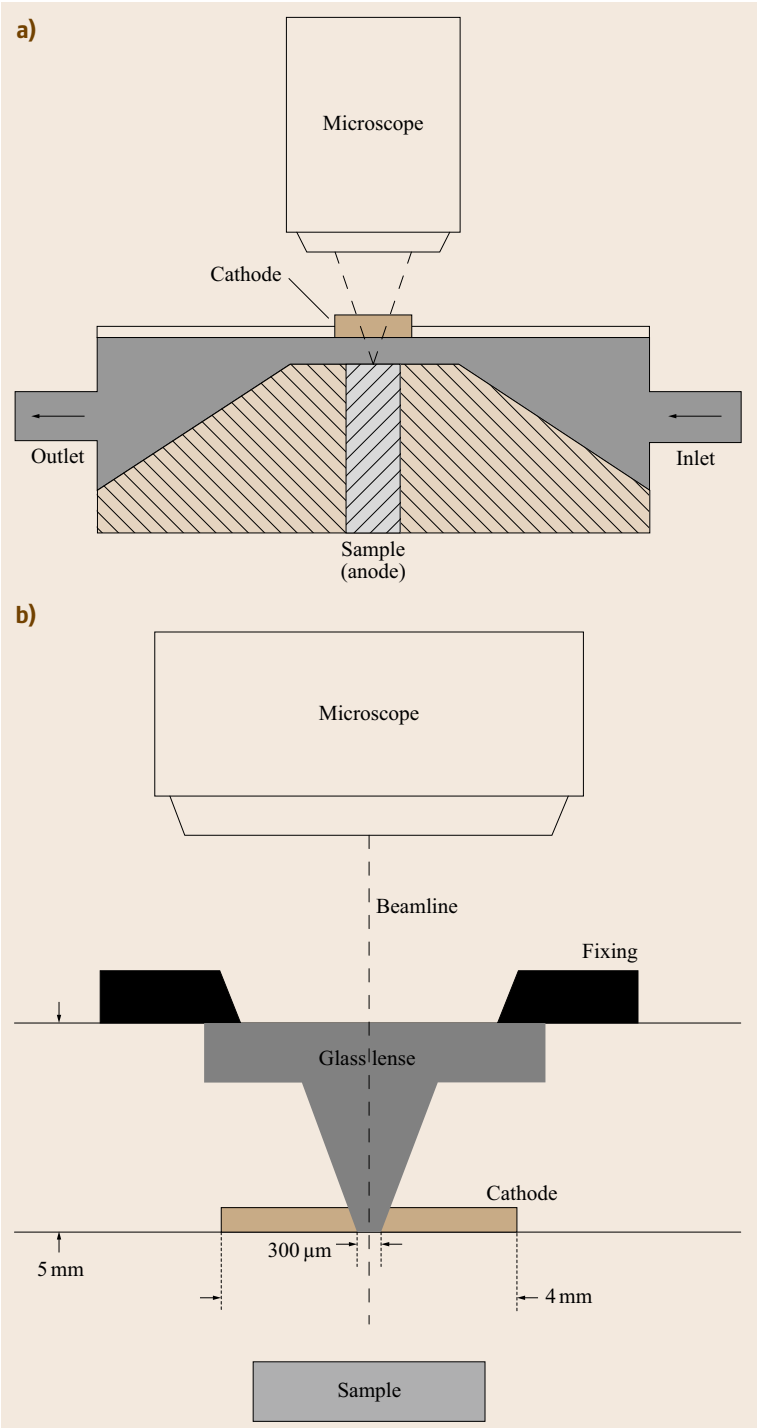


Fig. 28.4 **(a)** Schematic view of the channel flow cell. The cell is an in-house design and allows the in situ observation of the surface topography (after [28.39]). **(b)** Detailed schematic view of the cell lid with the embedded cathode and the glass lens which allows the beam passage (after [28.39])

posite (*parallel plate reactor* [28.42]) and represented the situation in ECM equipment very well. Unfortunately, an electrode arrangement in opposite blocks the view on the anode or workpiece during the experiment. Therefore, *Schneider* et al. [28.39] designed a modified channel flow cell which allows light microscopic observation of a sample during the anodic dissolution under near-ECM conditions (Fig. 28.4).

28.3.2 Product Analysis

The most detailed information was taken from quantitative online analysis of products, e.g., by UV-vis spectroscopy [28.34, 43] and enabled a quantitative interpretation of the processes at the interface. UV-vis spectroscopy was realized in a flow-through cuvette, connected to the electrolyte outlet of the microcell (Fig. 28.8). Some products were sufficiently colored, e.g., chromate or permanganates, in other cases the color had to be intensified, e.g., by addition of complexing agents such as Alizarin or phenanthroline derivates [28.43]. This individual analysis had to be tailored for all metals and is described together with the results. Common for all systems were only oxygen and chlorine detection (Sect. 28.3.3).

Products in Solution

A comparison of electrochemical and analytical data is important. The corresponding charges should be equal to the anodic charge q_a

$$q_a = q_{Me^{z+}} + q_{O_2} + q_{Cl_2} \qquad (28.14)$$

with the charges of metal dissolution $q_{Me^{z+}}$, oxygen formation q_{O_2} (and chlorine formation in chloride solutions q_{Cl_2}), where these data where calculated from spectroscopy. If (28.18) is not fulfilled, further side reactions, mixed valencies or chemical dissolution must be expected.

28.3.3 Gaseous Products

Some special techniques were necessary to quantify dissolved gases.

Oxygen was quantified by fluorescence quenching of Ru complexes [28.44, 45]. Illuminated by blue light these complexes show an orange fluorescence which is quenched by dissolved oxygen. It is necessary to keep all oxygen dissolved as bubbles would not be respected. Hence, the pressure in the system had to be enlarged to keep all gas dissolved. This could be easily controlled as bubbles produced blue stray light. A special high-pressure flow-through cuvette had to be developed [28.46].

Products at the Cathode

In aqueous electrolyte the general cathodic reaction is also a hydrolysis of water according to (28.2). However, especially in sodium nitrate as the most common ECM-electrolyte, the reduction of nitrate anions is evident [28.47–50]. Regarding the very low potentials and the pH value at the cathode under ECM-conditions, the following reduction reactions were assumed [28.51]

$$NO_3^- + 6H_2O + 8e^- \rightarrow NH_3 + 9OH^- , \qquad (28.15)$$

$$NO_3^- + 7H_2O + 8e^- \rightarrow NH_4OH + 9OH^- . \qquad (28.16)$$

A number of other reduction products or intermediates (e.g., NO_2^-, NO_2, NO, N_2, NH_2OH, NH_3, N_2H_4) are discussed in [28.52–55]. *Reyter* and coworkers reported on the interplay of cathode material, process parameters (e.g., pH value, potential) and the activity as well as the selectivity of the nitrate reduction [28.52].

A reduction and deposition of the anodic dissolved metals on the cathode is negligible because the diffusion of metal ions in the electrolyte is very slow in comparison with the usual electrolyte speed. Metal ions are wick away from the electrode gap before a deposition is probably on the cathode.

28.3.4 Surface Characterization Electron Backscatter Diffraction (EBSD)

The texture of many polycrystalline samples was characterized by EBSD [28.56].

The sample was adjusted under an angle of 70°. A focused electron beam hit a small area of the specimen (spot mode) and primary electrons were scattered diffusely (inelastic scattering). These electrons served as new primary rays at the inside of the sample and suffered reflections at the lattice atoms of the sample. The backscattered electrons (information depth: 40–70 nm at 25 keV) provided characteristic diffraction patterns (Kikuchi lines), when they collided with a phosphor screen. By analyzing these diffraction lines, the position of the unit cell towards the surface of the specimen can be described by the Euler angles ϕ_1, Φ and ϕ_2.

This technique is well established. Together with capillary microcells it becomes possible to address single (monocrystalline) grains by electrochemical techniques (cyclovoltammetry [28.57], microimpedance spectroscopy [28.37]) and to correlate crystallographic orientation with anodic behavior [28.57–60].

28.4 The Interface Process During ECM

Cyclic voltammetry up to potentials around 10 V, which corresponds to current densities up 50 or 100 A/cm^2, is a powerful tool for fundamental characterization of the ECM process.

28.4.1 Cyclic Voltammetry and Surface Layers

Figure 28.9 shows two examples with Fe electrodes in aqueous NaCl and $NaNO_3$ solutions of almost the same conductivity. The ECM process starts at some A/cm^2 and the current density increases linearly with potential for currents > 5 A/cm^2.

This is characteristic for ohmic resistances; the inverse slope in Fig. 28.9 is 0.6 Ωcm^2, which fits to the electrolyte resistance between working and reference electrode in the capillary cell (distance some 10 μm). The conductivity of the supersaturated film is > 1 mS/cm, which means values < 0.1 Ωcm for an estimated thickness around 1 μm^2. The electrolyte resistance is not of interest, but it indicates that the potential drop at the interface workpiece/electrolyte is mainly determined by the electrolyte resistance.

Surprising, however, is the anodic shift in nitrate solutions. This means an additional potential drop of almost 3 V and, thus, an additional layer with negligible influence of current density. Most probable is an oxide film with a thickness of some nm. The influence of this layer has to be discussed.

Adding an oxide film, the potential drop at the surface ΔU (between tool and reference electrode) is given by

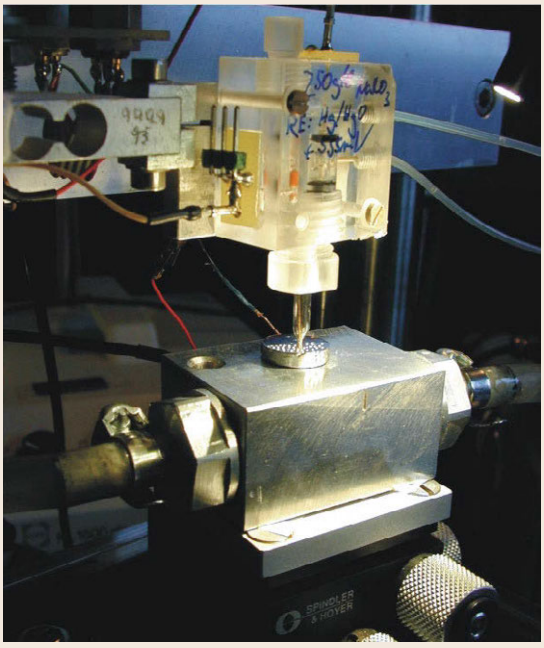
$$\Delta U = \Delta U_{\mathrm{Me/ox}} + \Delta U_{\mathrm{ox}} + \Delta U_{\mathrm{ox/el}} + \Delta U_{\mathrm{ssat}} + \Delta U_{\mathrm{el}} \quad (28.17)$$

with the potential drops at the interface metal/oxide $\Delta U_{\mathrm{Me/ox}}$, within the oxide ΔU_{ox}, at the interface $\Delta U_{\mathrm{ox/el}}$, within the supersaturated product film ΔU_{ssat} and in the electrolyte up to the reference electrode ΔU_{el}. A linear behavior is expected only for ΔU_{ssat} and ΔU_{el}, as already mentioned.

This means, $\Delta U_{\mathrm{Me/ox}} + \Delta U_{\mathrm{ox}} + \Delta U_{\mathrm{ox/el}}$ are almost constant for changes from 5 to 50 A/cm^2. This may be true, if the corresponding potential drops depend on

Table 28.1 Crystalline salts

Nitrate	T_m
$Fe(NO_3)_2\ 6\ H_2O$	60.5 °C
$Fe(NO_3)_3\ 9\ H_2O$	47 °C
$Mn(NO_3)_2\ 6\ H_2O$	26 °C
$Cr(NO_3)_3\ 9\ H_2O$	37 °C
$Ni(NO_3)_2\ 6\ H_2O$	56.7 °C
$Cu(NO_3)_2\ 6\ H_2O$	114 °C



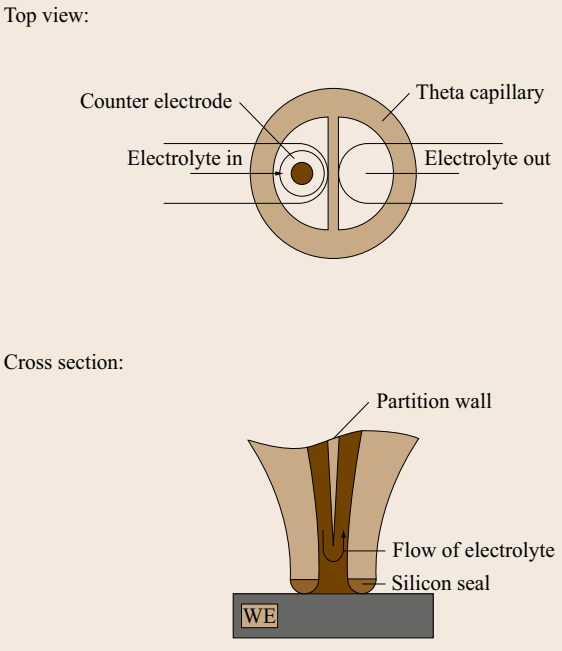


Fig. 28.5 Capillary based flow-through microcell

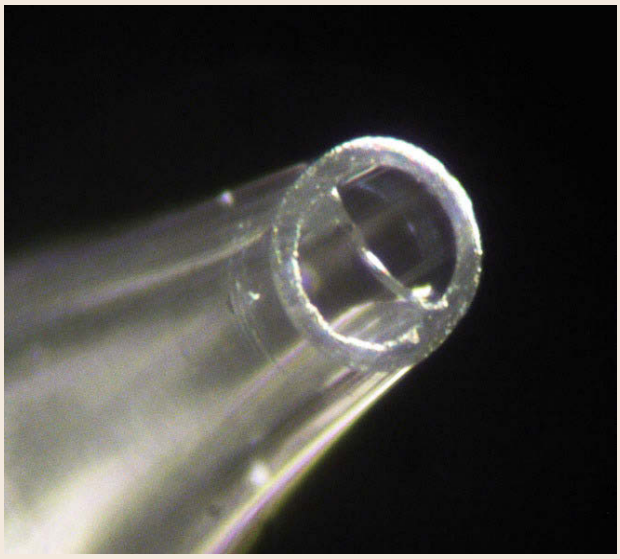


Fig. 28.6 Capillary tip with partition, pulled and ground [28.33]

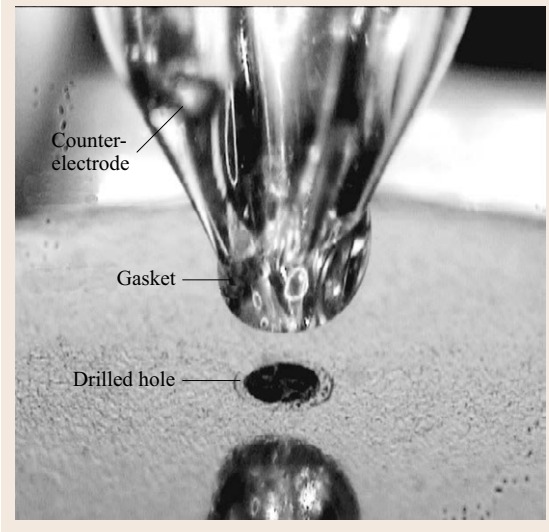


Fig. 28.7 Capillary over ECM-drilled hole

the logarithm of current density only. This is typical for Butler–Volmer kinetics of interfaces [28.61] or the mechanism of ionic conductivity in high-field oxides [28.15]. Values around 100 mV per decade of current are typical and, thus, negligible in Fig. 28.9.

The oxide model corresponds to a linear extrapolation to current zero. This yields chloride solution values in the active range of Fe (28.1a) and much higher values in nitrate, which indicate passive dissolution (28.7). Accordingly, these cyclovoltammograms enable separation of active and passive dissolution.

28.4.2 Supersaturated Product Films

The formation of solid precipitates is much less probable than expected in the former literature. Base metal nitrates, perchlorates and some chlorides crystallize

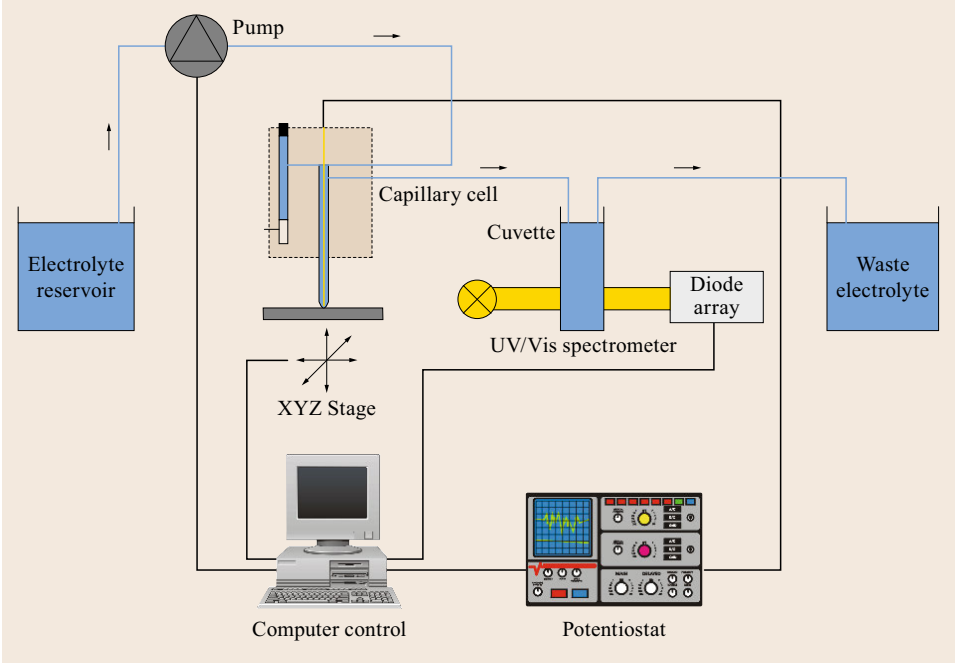


Fig. 28.8 Scheme of the experimental setup with capillary flow-through microcell and UV-vis spectrometer for product analysis

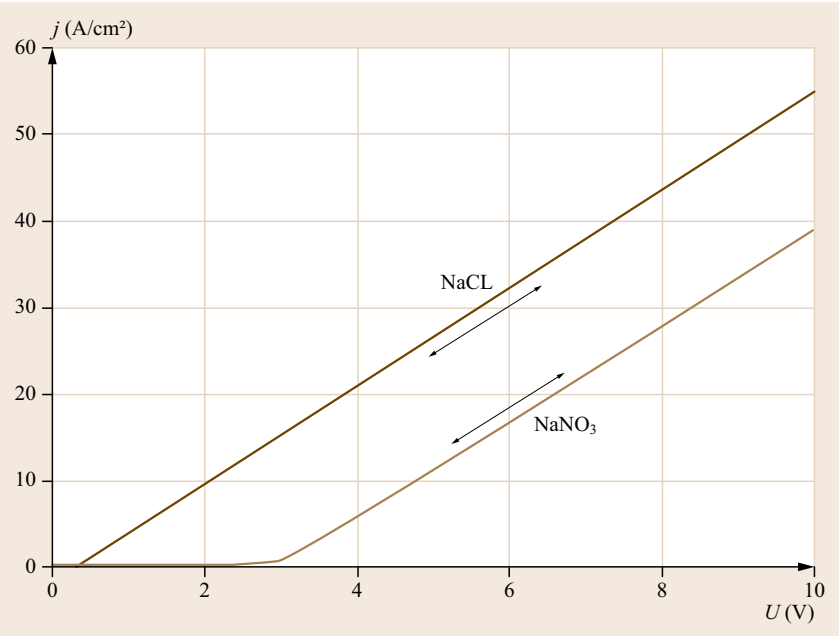


Fig. 28.9 Schematic cyclovoltammograms of Fe in aqueous solutions, 200 g/l NaCl and in 250 g/l $NaNO_3$, respectively; sweep rate 0.5 V/s

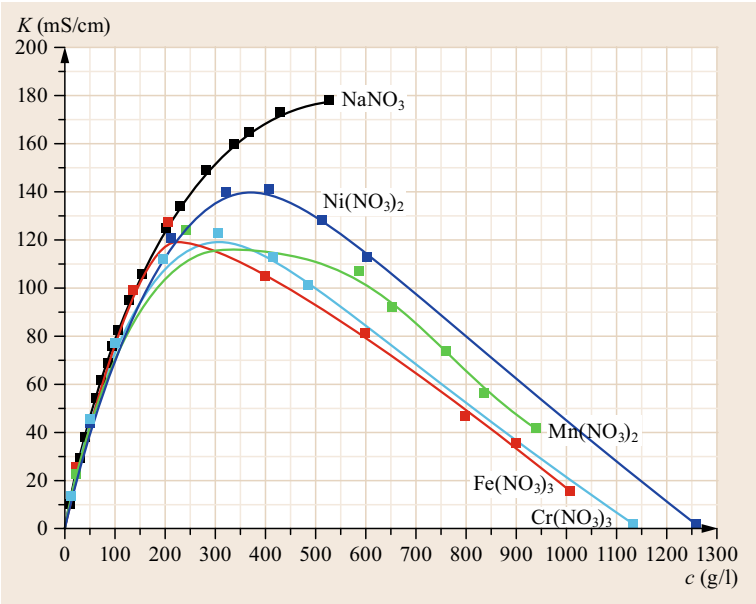


Fig. 28.10 Conductivity of aqueous nitrate solutions. Supersaturation starts at around 400 g/l

very slowly and form metastable supersaturated solutions. Crystallization requires seconds or days, which is much longer than the presence of products within the surface layer, which is < 0.3 s [28.43].

This was proved in simple experiments [28.33]. Crystalline salts (as in Table 28.1), which are commercially available, were heated to about 60 °C and melted. No crystallization was observed after cooling down to room temperature for at least some 10 s. Due to this long life time of supersaturation, it was possible to determine their physical properties, such as conductivity (Fig. 28.10) or viscosity.

The properties of these supersaturated films are unique; they are viscous, often intensely colored, and just in between solutions and melted salts. They are highly soluble in water and, thus, partly dissolved by movement of the electrolyte down to stationary values of some µm. Some chlorides form slurries [28.62] in-

stead of supersaturated solutions. Slurries are mixtures of nano crystals and electrolyte. Therefore, surface quality is much better in nitrates as viscous films are responsible for polishing effects.

The thickness of the supersaturated film can be estimated from the charge necessary to start the ECM process or from finite element simulations, both methods yield thicknesses around some μm. The exact value is determined by the electrolyte flow; the film is formed at the metal interface and washed off by the electrolyte, resulting in a stationary layer thickness.

The concentration of free water in the supersaturated film is low as almost all water is consumed for hydration of cations; the number of water molecules per ion is in fact < 3. Hence, the oxygen evolution is reduced (28.10), typically to values around 10% of total charge. The conductivity, however, remains similar to common electrolytes (Ohmic behavior).

28.5 Classification of ECM Processes

The models in Sect. 28.2.4 indicated a common mechanism for the dissolution of different metals at large current densities, but, altogether, detailed investigations at many metal showed that the behavior is as complex as for small current densities. Nevertheless, some more common characteristics were found [28.63, 64]. This led to classifications which are not exclusive as some metals belong to several groups.

Some metals dissolve in passive state and form oxide films obviously not different from the common passive films. They belong to the *High-field oxide group*, a typical example is Al.

Many metals dissolve as cations. Others, such as Mo or V, dissolve in passive state and form oxo complexes, e.g., MoO_4^{2-} or VO_4^{3-}, so-called *one-step anion makers*. The oxidation numbers in oxide and electrolyte are equal, i. e., the dissolution at the interface oxide/electrolyte is a purely chemical process. In chloride solutions chloro complexes may be formed, e.g., well-defined anions such as $Au(Cl)_4^-$.

Some other metals such as Cr or Mn are *two-step anion makers* and cannot form stable oxides and anions with the same oxidation number. Therefore, a two-step oxidation is required, the first at the metal interface to form Cr_2O_3 or MnO_2, and a second one during dissolution at the interface oxide/electrolyte under formation of anions (CrO_4^{2-} or MnO_4^-).

Metals or alloys in the *spinel group* form special oxides of the spinel type. Spinels are homogeneous oxides with compositions close to Me_3O_4. The valences of the different cations are $+2$ and $+3$, accordingly, spinels can also be described as mixed oxides of the type $Me^{II}O \cdot Me_2^{III}O_3$. Some metals (Cr, Mn, Fe, Co and Ni) exist in both oxidation states, in some cases even in the same oxide, e.g., magnetite Fe_3O_4 and Hausmannite Mn_3O_4. Many spinels are known as gemstones and are resistant against chemical and mechanical attacks.

The common passive oxides can transform to spinels at larger current densities and the valences of the cations can adapt to form spinels. A typical example is Fe in nitrate solutions: The common anodic oxide is Fe_2O_3 which changes into Fe_3O_4 under ECM conditions.

Some metals such as Ta or Zr, the so-called *inert metals*, show no significant dissolution in common electrolytes such as nitrate or chloride solutions. In other electrolytes, e.g., after addition of complex formers or at other pH values, machining can become possible.

Few metals dissolve in active state without formation of oxide films and form the *active dissolution group*. This is true for Fe in chloride solutions, the product is Fe^{2+}.

Metals such as Co or Cu, the *weak oxide group*, cannot form stable oxides under ECM conditions. Parts of the surface oscillate between an active and passive state, accompanied by product precipitation. As a result, the ECM process is not stable and experimental data are less reproducible.

28.6 Surface Topography, Crystallographic Effects and Surface Quality

Most technical materials are used in polycrystalline state which implies a wide variation of microstructure (e.g., phase composition, grain orientation). Additionally, the materials contain submicrostructures or lattice defects such as grain boundaries, stacking faults and dislocations. Even single crystals have crystal defects (e.g., dislocations or point defects). Consequently, surfaces are nonhomogeneous and processes such as electrochemical machining or corrosion will be nonhomogeneous reactions. This results in a complex

Table 28.2 Surface energy of iron and copper taken from the literature (after [28.65, 66])

Metal	(111)	(110)	(100)
Iron (bcc) (J/m^2) [28.65]	2.73	2.43	2.22
Iron (bcc) (J/m^2) [28.66]	–	3.09	2.66
Copper (fcc) (J/m^2) [28.65]	1.95	2.24	2.17
Copper (fcc) (J/m^2) [28.66]	1.96	2.31	2.09

Table 28.3 Energy to remove iron from the lattice (kJ/mol)

lattice	{111}	{110}	{100}
Fe	140.37	189.62	265.56

interaction between surface quality and machining parameters.

28.6.1 Theory

The elementary step of the active dissolution is the transfer of a metal atom from solid state into the electrolyte. The kinetic of this step depends on atomic structure and the energetic situation of the metal. Consequently, the dissolution kinetic depends on the crystallographic orientation as well as the various kinds of crystal defects. This fact is utilized in metallography e.g., to visualizing dislocation arrangements [28.68, 69] and even well known in corrosion research under comparatively low anodic current densities as demonstrated in [28.70–75].

The creation of a free surface needs a work per unit area [28.76]. Accordingly, surface atoms have a potential energy called surface energy γ, which depends on the number of near neighbors and corresponds to the number of bonds. Generally, it can be assumed that the higher the surface energy the easier the transformation of metal atoms to metal ions. *Landolt* estimates the energy γ_{hkl} of an {111}-surface of a face-centered cubic metal to approximately $2\,J/m^2$ [28.77]. In case of face-centered material (fcc) the {111} planes are close-packed with 9 near neighbors, followed by the {100} planes with 8 near neighbors and the {110} planes with 6 near neighbors. Consequently, the lower the number of next neighbors the higher the surface energy γ_{hkl} ($\gamma_{111} < \gamma_{100} < \gamma_{110}$) and therefore {111} planes should be the most stable ones [28.77]. In case of body-centered materials (bcc) (e.g., iron) $\gamma_{100} < \gamma_{110} < \gamma_{111}$ and the {111} will be preferably dissolved.

Table 28.2 shows theoretical calculated surface energies of iron (bcc) and copper (fcc) depending on Miller indices hkl [28.65, 66].

The difference between, e.g., γ_{111} and γ_{100} of copper according to [28.65] is about 11%. *Chan* et al. [28.78] reported a difference 14–16% between the surface energy of {100}- and {111}-orientated planes of copper.

Similar results can be found by quantum mechanical calculations. Quantum mechanical calculation by solving the Schrödinger equation for all electrons within the external potential of the atomic nuclei for some 100 atoms were performed by *Amkreutz* and coworkers [28.67] (Fig. 28.11). The corresponding atom densities of iron are {111} $1.88\times10^{15}\,cm^{-2}$, {101} $1.73\times10^{15}\,cm^{-2}$, {100} $1.22\times10^{15}\,cm^{-2}$.

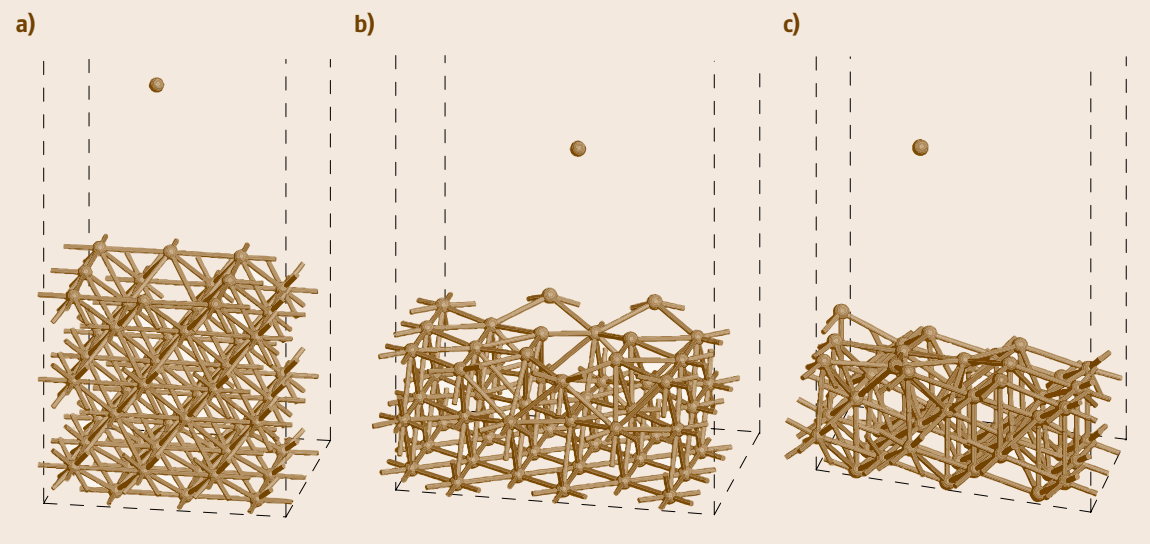


Fig. 28.11a–c Quantum mechanical simulation of removal of one Fe atom from {100} **(a)**, {100} **(b)** and {111} **(c)** (after [28.67])

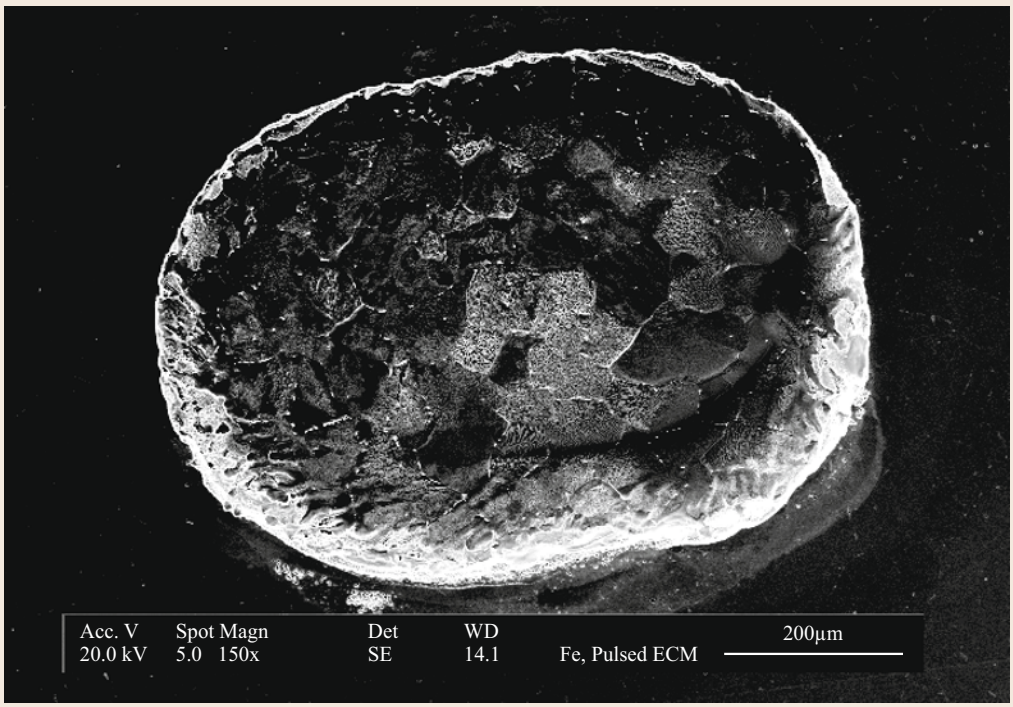


Fig. 28.12 Scanning electron microscopy (SEM) image of a flat hole on large grain Fe formed by an ECM simulation; 250 anodic pulses of 10 ms at 33 A/cm^2, 5 ms pauses, electrolyte aqueous $NaNO_3$, 250 g/l (after [28.79])

The energy to remove one surface atom from the lattice increases in the sequence {111} < {110} < {100} (Table 28.3). Moreover, according to simulations of Amkreutz, the relaxation of lattice atoms after removal decreases in the sequence {111} > {110} > {100}. These data, however, exclude all effects of water or ion adsorption and corresponding field effects.

28.6.2 Grains in Experiments

The relation between microstructure and dissolution rate at higher current densities is probable if kinetics are mainly controlled by charge transfer. *Landolt* [28.47] reported the crystallographic influence on copper dissolution at high current densities. They observed different topography development and etching effects on the sample surface depending on the crystallographic orientation. Recently, *Schneider* et al. [28.80] investigated the dissolution of copper at a current density of 15 A/cm^2 and 17.5 A/cm^2. Their results confirmed the influence of the crystallography on the surface topography [28.47] and the prediction in [28.77] that less dense packed surfaces dissolve faster than closed packed surfaces.

Detailed investigations on large grain iron at lower current densities $\ll$ 1 A/cm^2 showed, that the height of

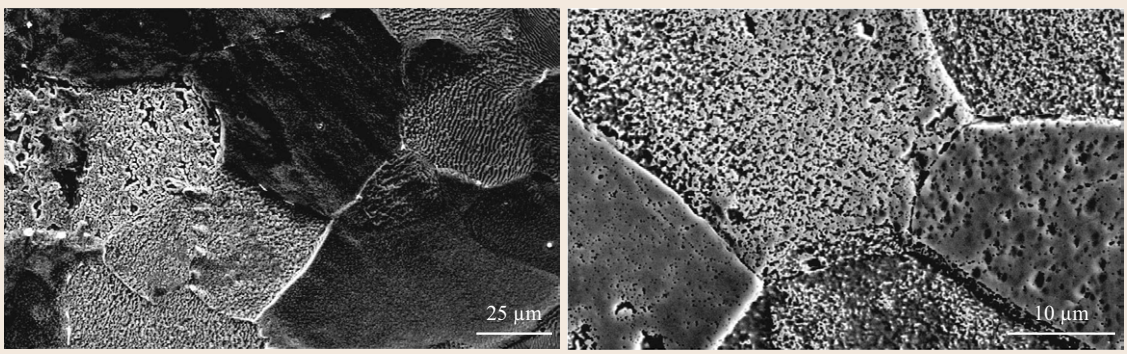


Fig. 28.13 Magnified areas from Fig. 28.12 (after [28.79])

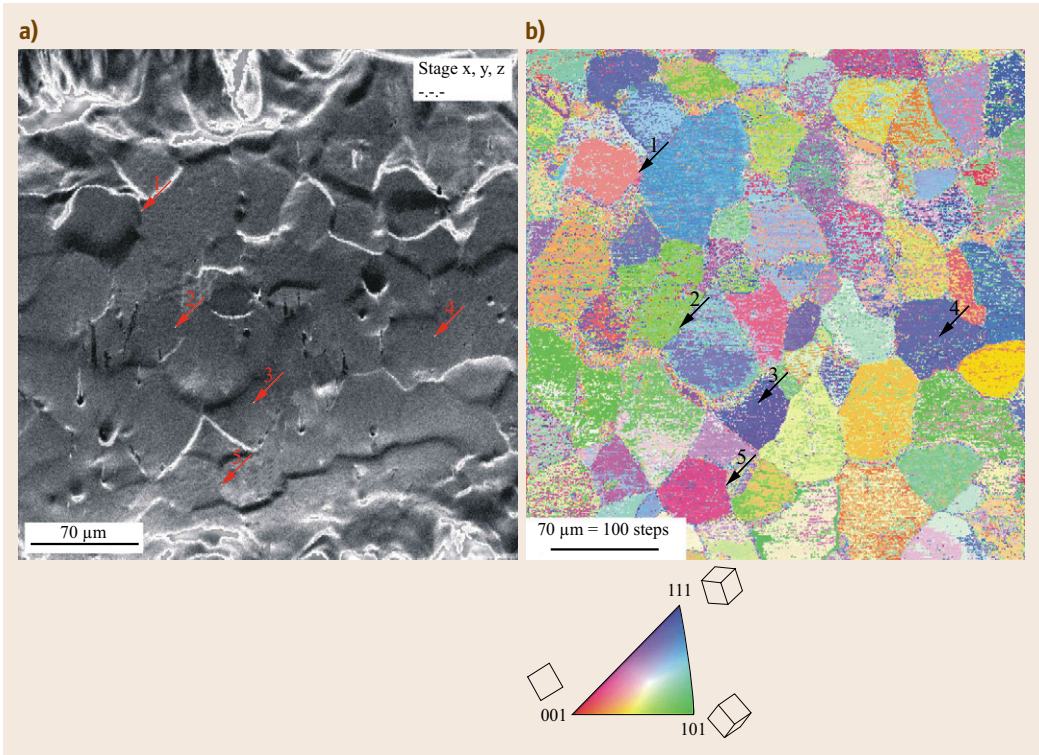


Fig. 28.14 **(a)** SEM image and **(b)** corresponding EBSD image of an iron sample, machined at 33 A/cm^2 for 1 s, electrolyte aqueous $NaNO_3$ (after [28.79])

the Flade peak, which is a measure of the active dissolution rate just before passivation, follows {101} > {111} ≫ {100}. The oxide formation charge varies up to a factor of about 5 with a maximum at low values of Φ, i. e., orientations close to {100}. {101} and {111} differ much less. These results contradict the discussion above in detail. However, a {100} plane of bcc material has the lowest surface energy and therefore the lowest dissolution rate. This fact is also valid for hexagonal close-packed (hcp) metals like titanium [28.81] or cobalt [28.82] where {0001} orientated grains and their vicinal grains show the lowest reactivity.

In contrast to this, *Heusler* [28.83] and *Bockris* et al. [28.84] assumed homogeneous active dissolution in the lateral direction of the surface, independent of crystallographic orientation.

The crystallographic influence is determined by single crystal investigations. Experiments with macroscopic single crystals are possible but expensive, requires time consuming preparation and is limited to a small number of specimens and, thus, few orientations. More effective is a combination of large grain samples and electrochemical microtechniques.

Fig. 28.12 shows the surface after a special ECM experiment [28.79] (250 anodic pulses of 10 ms at 33 A/cm^2) with the flow-through capillary cell (Sect. 28.8). A flat hole was formed. The grain structure is clearly visible and the surface image differs from grain to grain. Fig. 28.13 shows these effects in more detail. The grains differ in height and in surface shape; some are smooth and shiny, others are black or covered by pits. Macroscopically, the latter grains seem to be white. The reasons for this different image are discussed in detail in Sect. 28.8.

The crystallographic characterization by EBSD (Sect. 28.8) requires smooth and planar surfaces, but, surprisingly, even these machined samples yield sufficient patterns. Fig. 28.14 shows a sample with significantly differing heights of the grains. The dissolution rate increases in the sequence {100} < {101} < {111} at extremely large current densities, i. e., crystal planes with larger densities such as (101) and (111) are dissolved with higher rates.

28.6.3 Grain Boundaries and Other Crystal Defects

So far, the interaction of neighboring grains and grain boundaries has not been discussed. Grain boundaries accumulate impurities which can dominate the electrochemical properties. Impurities can inhibit the removal of material which results in the formation of walls or accelerates the dissolution and forms trenches. Furthermore, the properties of the grain boundaries depend on

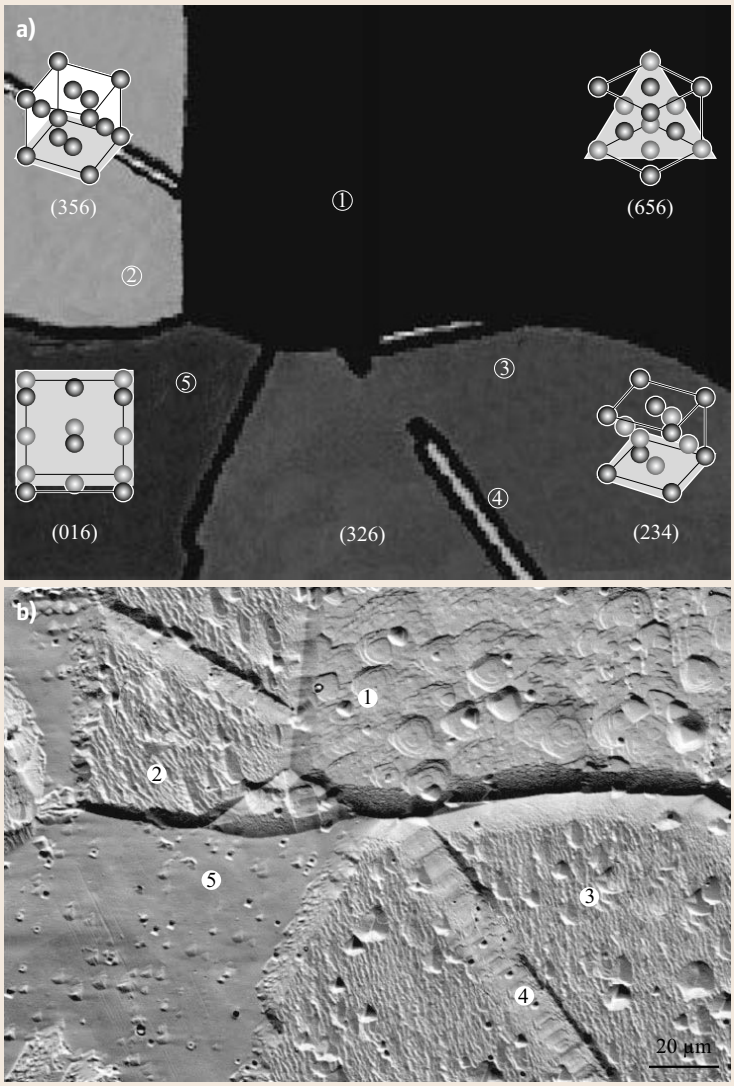


Fig. 28.15 **(a)** EBSD mapping of a copper surface after ECM. EBSD pattern with the orientation of the unit cells (after [28.80]). **(b)** SEM image of the same area as shown in Fig. 28.15a. The sample was machined at 17.5 A/cm^2 and 4 m/s electrolyte flow (after [28.80])

the combination of neighbored orientations, which add a contribution independent of the presence of impurities.

The grain energy γ_{gb} depends on the short range order of the grain boundary and is expressed by the misorientation angle θ between adjacent grains and the reciprocal density of coincidence sites Σ [28.86–89]. Consequently, atoms located at grain boundaries are less bound in the crystal lattice and dissolve more easy [28.77, 78]. This is clearly illustrated in Fig. 28.15. The topography shows the highest dissolution rate on grains vicinal to {001} in comparison with other grains. According to *Landolt* [28.77], a still higher dissolution rate can be expected only for {110} planes. However, such crystallite orientations were out of the observation area in Fig. 28.15. All grains of other orientations obviously show a lower rate of material removal and a surface texture or roughness is visible. Furthermore, parts of grain boundaries are preferentially attacked and appear as trenches. Additionally, the visible triangular or quadrangular etch patterns in grain 1, 3 or 5, e.g., are caused by penetration points of dislocations on the surface. Again, dislocations such as crystal defects are naturally preferential sites of anodic dissolution due to the energy of the dislocation core [28.68]. This phenomenon is well known as dislocation etching in the literature [28.68, 69, 90].

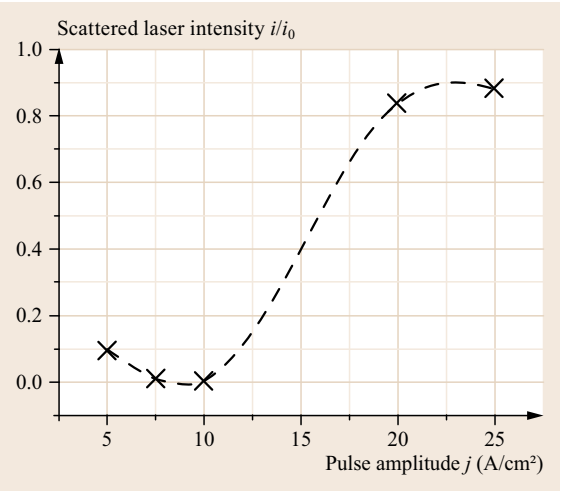


Fig. 28.16 Semi-quantitative roughness measurement of the machined surface by laser light scattering (after [28.85])

By the way, it may be of interest to compare crystallographic and grain boundary effects of ECM with electropolishing or chemical etching [28.79]. Electropolishing leads to an occurrence of positive, barely visible or step-like grain boundaries, but trenches were never observed. Neighboring grains with orientations close to {100} form grain boundaries with the shape of walls in most cases. Almost invisible grain boundaries were found between {111} grains and step-like boundaries between grains with greater differences in the orientation. In the majority of cases the {100}-oriented crystal faces show the largest rate of metal removal after electropolishing or chemical polishing. The metal removal from the faces {100} and {111} seems to be similar in most cases.

The Sect. 28.6.1 to 28.6.3 have shown that real structures (including crystal defects or other deviations from the ideal structure) enhance the anodic dissolution of metals according to their stored energy. Only if the dissolution rate is so high that an interphase of reaction products is formed (salt layers, supersaturated viscous films), smoothing effects overwhelm the influence of the crystallography. This will be shown in the following Sect. 28.6.4.

28.6.4 Surface Brightening

If the metal dissolution leads to a strong formation of surface films, the kinetic changes from charge transfer controlled to mass transport controlled dissolution. Now, the surface films determine the transport of educts and products to and from the interface. Consequently, the surface topography is less affected by the crystallographic structure and appears bright. The role of mass transport on the surface brightening is intensively investigated by *Landolt* et al. in the 1960s–1970s [28.27, 28, 92].

A simple laser scattered measurement of a copper sample machined at various current density confirms the increase of the surface roughness at current densities $\leq 10\,\mathrm{A/cm^2}$ in comparison to the mechanical polished initial state. At higher current densities $\geq 20\,\mathrm{A/cm^2}$ the material removal is associated with high surface finishing [28.85]. In many cases (Cu in $NaNO_3$) the transition of the kinetic and the surface brightening is associated with increasing current densities as shown in Fig. 28.16.

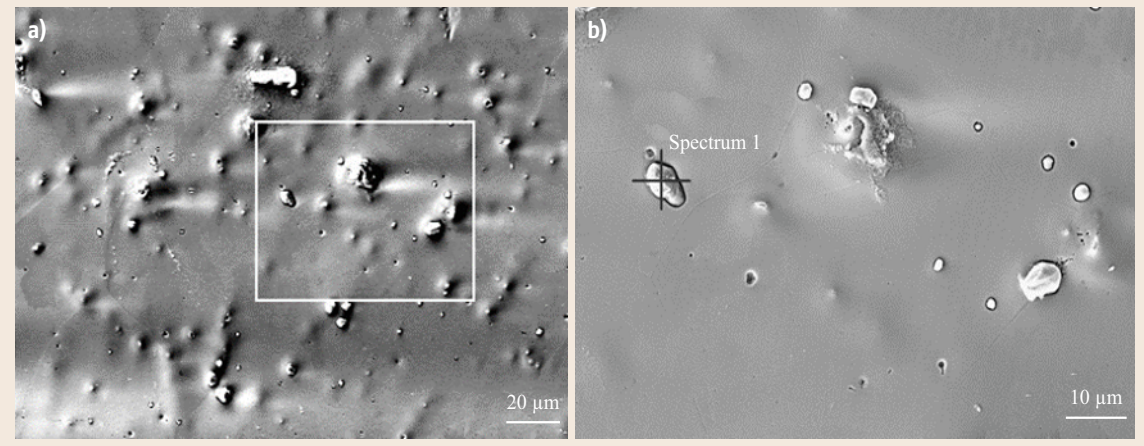


Fig. 28.17 **(a)** SEM image of the same area as shown in the EBSD image. The sample is machined at $25\,\mathrm{A/cm^2}$ and 4 m/s (after [28.91]). **(b)** Zoom of the white framed part in **(a)** showing inclusions in copper surface (after [28.91])

However, bright surfaces do not have to be obligatory perfect, preferential dissolution of or at inclusions and hydrodynamic instabilities can cause a roughness on microscale [28.93].

Fig. 28.17 shows a copper surface machined at 25 A/cm^2 [28.91]. Visually the sample surface was bright and shiny, however, on microscale, small particles (copper oxide, verified by electron diffraction x-ray analysis (EDX)) are visible. On the one hand, these particles create hydrodynamic turbulences and flow strikes and, on the other hand, pits will be created by undermining and drop out of these particles. Finally, the surface is polished but not really smooth and flat.

28.7 Oxygen Evolution

Oxygen evolution was already mentioned as a possible side reaction (28.10). In fact, bubbles were observed at the workpiece (anode). The sum charges for ion formation (products) and oxygen evolution should be equal to the total anodic charge q_a, which is easily measured

$$q_a = q_{ions} + q_{O_2} \,. \tag{28.18}$$

Therefore, the amount of oxygen can be calculated by Faraday's law from q_a and product analysis.

Bubble formation, however, can also indicate hydrogen evolution. This is impossible at the anode as an electrochemical process, but can be discussed as a purely chemical process (28.19) Cu as an example

$$Cu + 2H_2O \rightarrow Cu^{2+} + H_2 + 2OH^- \,. \tag{28.19}$$

Moreover, a complex electrochemical/chemical mechanism can be discussed

$$2Cu \rightarrow 2Cu^+ + 2e^- \,, \tag{28.20a}$$

$$2Cu^+ + 2H_2O \rightarrow 2Cu^{2+} + H_2 + 2OH^- \,. \tag{28.20b}$$

A direct quantification of this hydrogen is almost impossible as much hydrogen is produced at the cathode (tool) which must be very close to the workpiece to enable the extreme current densities for ECM conditions. A direct quantification of oxygen by microanalysis is much better, as described in Sect. 28.3.3. Most results in this work were validated by direct oxygen analysis.

Some hydrogen formation was expected for metals from the weak oxide group (Sect. 28.5), e.g., Co or Cu. If base metals such as Co are in direct contact with acids, they form hydrogen similar to (28.19). Accordingly, some chaotic local reaction cycles can be imagined: passivation – oxygen evolution and acidification – corrosion of oxide – active dissolution and hydrogen evolution – and finally, perhaps, repassivation. This scenery can explain less reproducible ECM experiments with Co or Cu.

Oxygen evolution is possible only on oxide-covered metals. This is easily understood as the equilibrium potential of oxide electrodes is much smaller for base metals (< 0 V) than that of oxygen evolution (1.23 V) but noble metals also form oxide layers before oxygen evolution, which can be easily proved by cyclic voltammetry. Obviously, the oxide film acts similar to a catalyst.

Oxygen is evolved at the interface oxide/electrolyte. This requires:

- A sufficient electronic conductivity of the oxide in parallel to ionic transport during growth, and
- An adequate potential drop at this interface. This increasing potential drop accelerates oxide dissolution (corrosion) according to (28.8), and, as a result, the oxide thickness is reduced.

Oxygen evolution under ECM conditions (current densities around 40 A/cm^2) depends on the material. The following results are taken from [28.94, 95]:

- No or negligible oxygen evolution ($< 3\%$ of charge) was observed with Al, CrC, Mg, Mo_2C, NbC, Ni, TaC, TiC, VC, WC, ZrC
- Oxygen evolution up to 10% of charge: Ag, Al_3Fe, Al_3Mg_2, $Al_{12}Mg_{17}$, Mo, Mo_2C, VC
- Oxygen evolution around 20% of charge: Al_2CuMg, Al_4Mn, Co, Cr, Cr_3C_2, Cu, Fe, ZrC
- Oxygen evolution around 40% of charge: Al_2Cu, Fe_3C, $Fe_{64}Ni_{36}$ (Invar), Mn
- Oxygen evolution almost 100% of charge: Au, Pt
- No oxygen evolution and no machining in aqueous nitrate solutions: Nb, NbC, Ta, TaC, Ti, V, W, WC, Zr.

28.8 Pulse ECM

Modern Electrochemical Machining is not based on direct currents, but uses special pulse techniques to improve the process efficiency, accuracy and surface quality [28.96–99]. Most common are rectangular anodic pulses which require special fast switching power supplies, which requires some electronic efforts due to the large absolute currents. The development of bipolar devices which deliver sequences of anodic and cathodic pulses is more sophisticated. The cathodic pulses are in most cases shorter and of smaller amplitude.

The fundamental parameters are:

- The transformation from stationary electrode state to machining conditions during the first anodic pulse
- The amplitude and length of the anodic pulses
- The length of the pauses in on-off techniques or amplitude and length of the cathodic pulses
- The frequency and the on-off ratio or the length of pauses.

The amplitude of anodic pulses defines the dissolution rate, but has almost no influence on the fun-

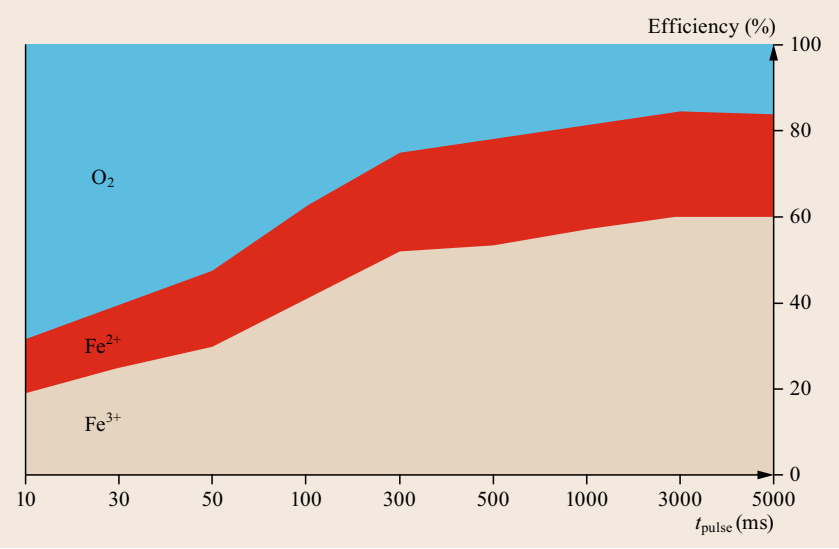


Fig. 28.18 Product composition for single anodic pulses of 33 A/cm^2 and different lengths t_{pulse}, pure Fe electrode, active state before pulse at −0.2 V, electrolyte $NaNO_3$, 250 g/l, 25 °C (after [28.100])

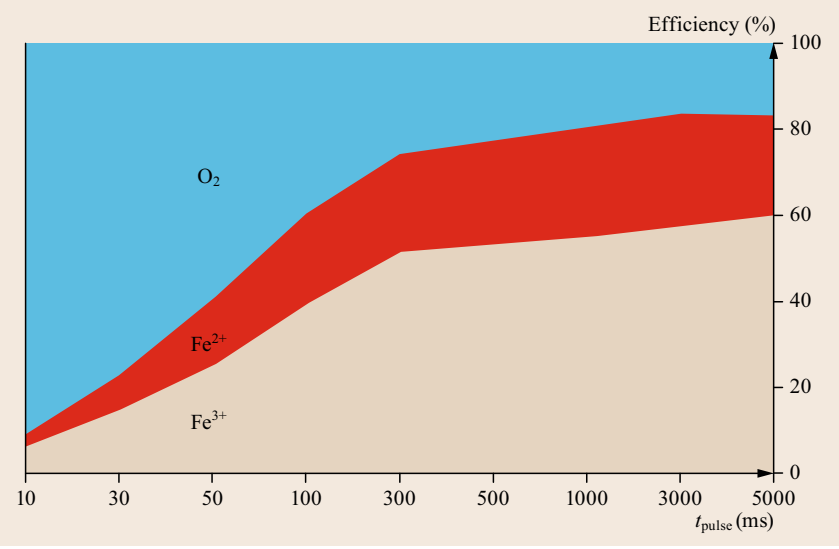


Fig. 28.19 Product composition for single anodic pulses of 33 A/cm^2 and different lengths t_{pulse}, pure Fe electrode, passive state before pulse at 1 V, electrolyte $NaNO_3$, 250 g/l, 25 °C (after [28.100])

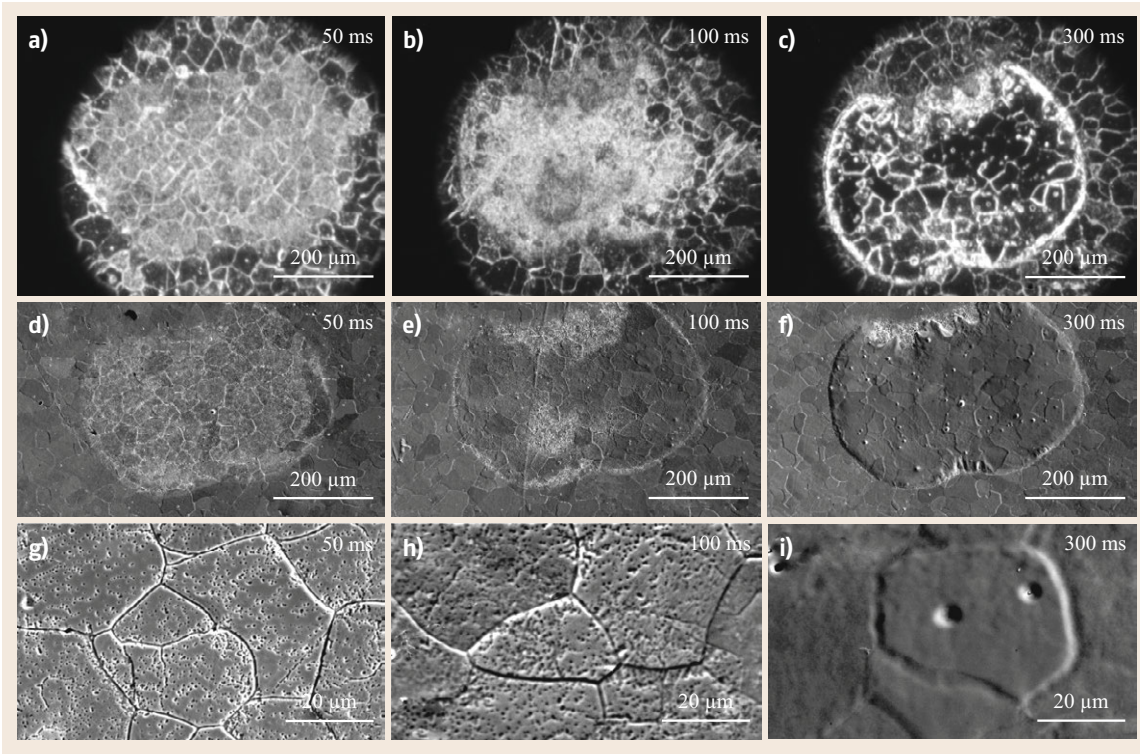


Fig. 28.20 (a–c) Optical and (d–i) SEM images of the machined area after single anodic pulses of 33 A/cm^2 and different lengths, pure Fe electrode, initially passive state at 1 V), electrolyte $NaNO_3$, 250 g/l, 25 °C (after [28.100])

damental machining process provided that machining conditions were reached, i. e., if the current densities were larger than 5 or 10 A/cm^2.

To investigate the transition to machining and to see the influence of the initial electrode state, which means the difference between passive and an active start, we used single pulses of different lengths from 10 ms to 5 s [28.101].

For short pulses and active start (Fig. 28.18), the dissolution begins with an efficiency of 30%. Iron is dissolved as ferric and ferrous ions in a molar ratio of $Fe^{3+}/Fe^{2+} \approx 1:1$. Main product is oxygen. Then, up to 300 ms, a transition occurs. The current efficiency increases up to 80% at 300 ms. The product composition changes to a bigger share of Fe^{3+} while the Fe^{2+} amount remains almost constant. Finally, current efficiency and product composition remain constant and independent of the length of the applied pulse. The current efficiency reaches its maximum around 85% with a molar ratio of $Fe^{3+}/Fe^{2+} \approx 2:1$. This corresponds to dissolution of Fe_3O_4. Small amounts of oxygen are still evolved.

The dissolution efficiency for passive starts (Fig. 28.19) is very low in the beginning (< 10% for 10 ms). Most charge is consumed for oxygen evolution. Iron dissolves mainly as ferric ions, indicating the dissolution of Fe_2O_3. For pulses > 30 ms the share of ferrous ions increases and oxygen evolution reduces.

Finally, conditions as for active start are obtained. There is no influence of the initial potential on the ECM performance after 300 ms.

Hence, ECM conditions are reached in both cases after 300 ms, but the amount of dissolved Fe is larger starting in active state. Both experiments show oxygen evolution, but passive electrodes develop more oxygen, indicating a thicker oxide film (Fe_2O_3), as oxides are a prerequisite of O_2 formation. Obviously, few Fe_2O_3 are formed in the first ms after pulse start.

Oxygen evolution means an acidification and, thus, increasing dissolution of the oxide which enforces a transformation into a thin Fe_3O_4 layer.

Optical microscopy and scanning electron microscopy (SEM) were used to visualize changes of microstructure with the pulse length for passive start (Fig. 28.20).

The 50 and 100 ms pulses form a dull surface (Fig. 28.20a,b), while for 300 ms the affected area is bright and proves machining conditions. The SEM images (Fig. 28.20d,e) give similar results. For the 50 ms

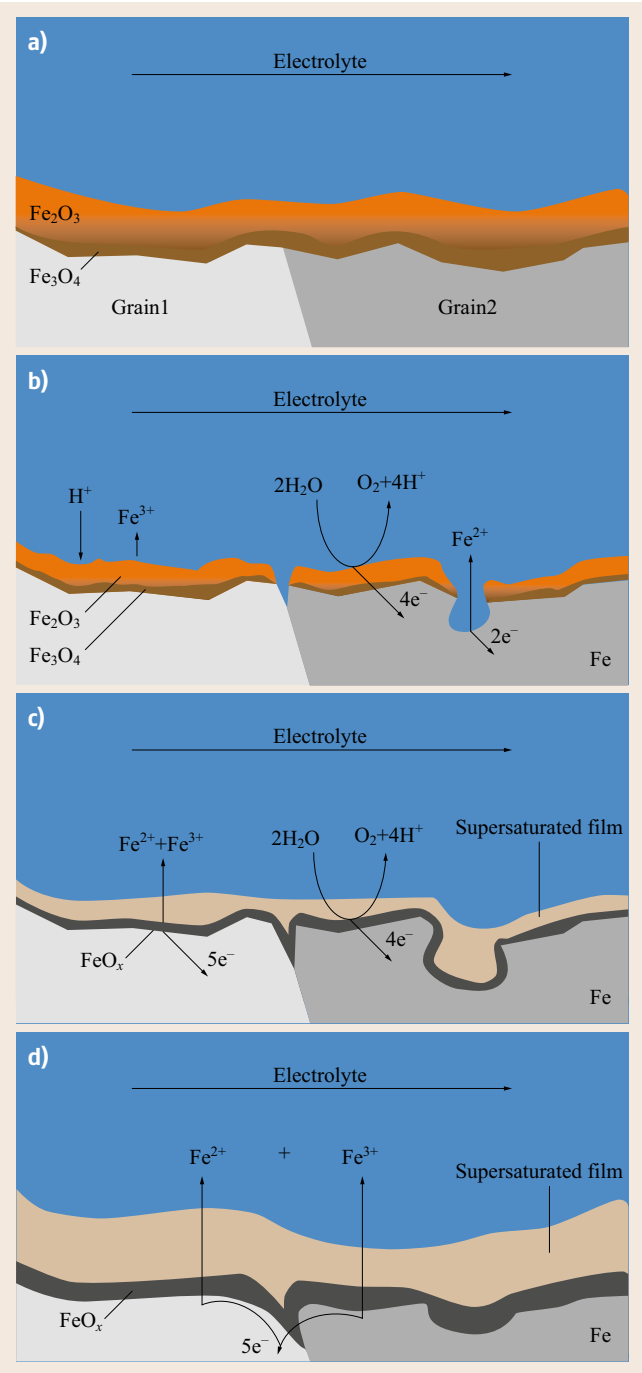


Fig. 28.21a–d Time resolved scheme of ECM start. Passive electrode before pulsing **(a)**, after 10 ms **(b)**, after 100 ms **(c)**, after some s **(d)**. The film thicknesses are not to scale (after [28.100])

pulse the surface appears completely white; higher magnification shows severe pitting due to the acidification by oxygen evolution and a strong attack of the grain boundaries (Fig. 28.20g). Effects of crystallographic orientation and grain boundaries were already discussed in Sect. 28.6.

Fig. 28.21 tries to summarize all these transient effects. Passive iron is initially covered with a natural oxide layer of Fe_2O_3 (some nm) and a thin underlying Fe_3O_4 (about 1 nm).

Short pulses mainly form oxygen and pitting is observed due to the pH-shift; grain boundaries are at-

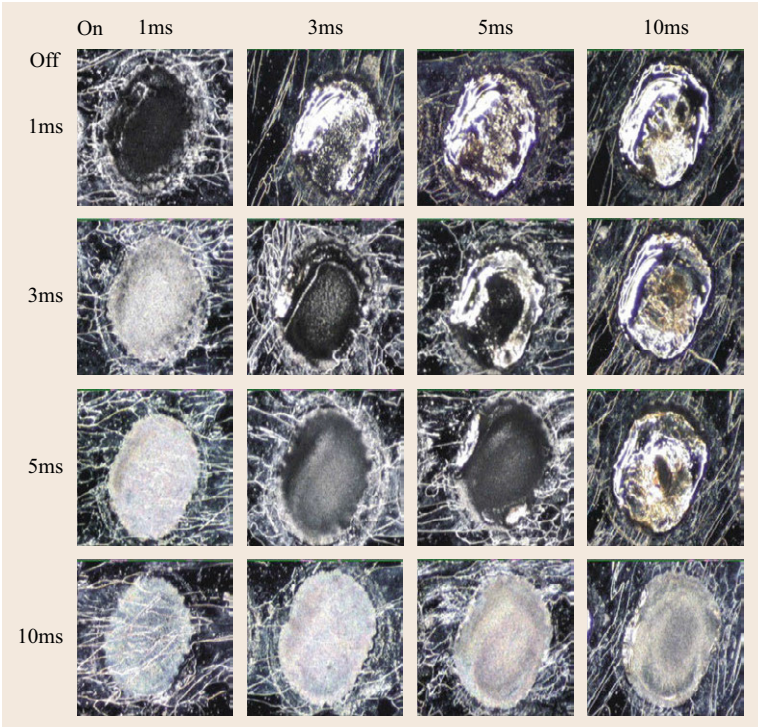


Fig. 28.22 Optical images for different pulse/pause ratios after some 100 pulses at 26 A/cm^2

tacked (Fig. 28.21b). The supersaturated polishing film develops with increasing pulse length (Fig. 28.21c). As a result, the pits vanish with time. The composition of the oxide underneath the film changes to Fe_3O_4 due to the limited water diffusion through the film. For longer pulses the surface becomes polished (Fig. 28.21d). For very long pulses the crystallographic orientation of the grains becomes relevant due to an anisotropic dissolution determined by the different dissolution speeds of the individual grains (Fig. 28.21e).

Fig. 28.22 shows the surface quality after several hundred pulses for different combinations of pulse and pause. The surface becomes shiny if the pulses are longer than the pauses. The supersaturated film is reduced in the pause but not completely removed and ECM conditions are maintained.

If the pause is much longer than the pulse, the black Fe_3O_4 layer, which is formed under the supersaturated film, transforms to Fe_2O_3 and oxygen evolution starts with the next pulse. Accordingly, the pH decreases (28.10), pitting corrosion starts and forms dull, white surfaces.

In between, if pulse and pause are almost equal in length, the film is washed off, but time is too short to transform Fe_3O_4 to Fe_2O_3; it accumulates and forms dull, dark gray surfaces.

28.9 Too Difficult-to-Machine: Hard Metals, Carbides and Nitrides

In the late 1960s *DeBarr* and *Olivier* [28.5] created the synonym *difficult-to-machine* alloys for a number of materials which could not be efficiently machined by mechanical techniques. There is no clear assignment which alloys are *difficult-to-machine* but the synonym is doubtless still qualified for some high-tensile steels, titanium, cemented carbides and cermets. Some of them are still *too difficult-to-machine* but nevertheless currently under investigation.

Too difficult-to-machine are materials of special interest such as hard metals, carbides and nitrides. Hard metals consist of hard particles, e.g., carbides, embedded in a softer matrix of metals or alloys of Co, Fe and Ni. ECM of these materials is complex due to the nonhomogenous structure. The components dissolve and passivate differently, depending on the electrolyte composition (e.g., Cr_3C_2/Ni [28.103], TiC [28.104, 105], TiC/Ni [28.103], WC/Co [28.106–112], ZrC [28.113]). A fundamental understanding of the technology requires separate investigations. To focus on fundamental processes, ECM of pure metals such as W and Ti and some carbides and nitrides is presented.

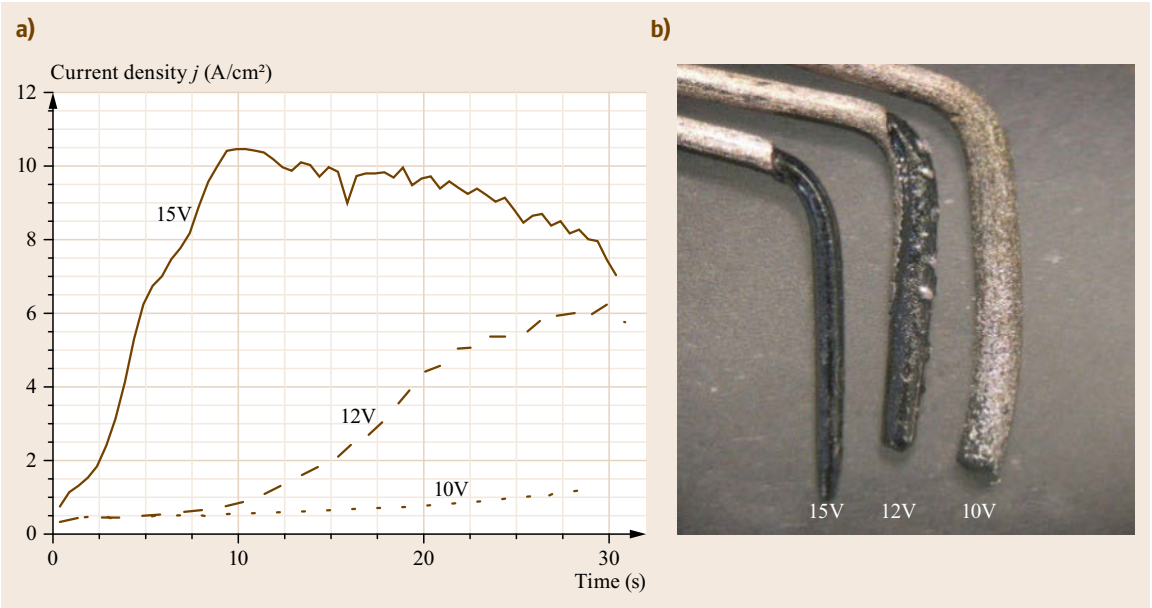


Fig. 28.23 **(a)** Machining of pure Ti in a mixture of choline chloride and ethylene glycol at different potentials, current response versus time (after [28.102]). **(b)** Ti wires machined at various potentials according to **(a)** (after [28.102])

28.9.1 Titanium

Titanium and its alloys are mainly used in aircraft manufacturing and medical engineering caused by the outstanding corrosion protective properties [28.114–117]. Moreover, titanium alloys are lightweight materials with excellent strength to weight ratio [28.118]. Titanium forms outstanding passive layers which are highly stable under oxidizing conditions [28.119]. However, the high corrosion resistance is a drawback concerning electrochemical machining. The anodic polarization does not lead to an active or transpassive dissolution but rather to a oxide growth according to

$$\mathrm{Ti} + 2\mathrm{H_2O} \rightarrow \mathrm{TiO_2} + 4\mathrm{H^+} + 4\mathrm{e^-} \,. \qquad (28.21)$$

In electrolytes free of specific pit initiating anions, the anodic breakdown does not take place until very high potentials (about 100 V) are reached [28.120]. In the past, various halides-containing electrolytes were used to machine titanium and its alloys electrochemically [28.121, 122]. Unfortunately, such electrolytes are problematic in view of the machining equipment, safety and environment. A promise approach is the combination of specific aggressive anions which destabilize the passive layer on titanium and the suppression of the anodic oxide film formation. Recently, an electrolyte mixture consisting of choline chloride and ethylene glycol was investigated [28.102].

Fig. 28.23a shows voltage-controlled pulse experiments on titanium in a mixture of choline chloride and ethylene glycol. The dissolution of titanium takes place in the transpassive range and needs an incubation time. Already 15 V are sufficient to machine titanium after a short incubation time. Fig. 28.23b shows the associated samples. The sample machined at 15 V shows a clear material removal associated with a bright and shiny surface. The efficiency of approximately 80% is in a typical range of ECM processes. The mechanism of the titanium dissolution in a deep eutectic solvent consisting of choline chloride and ethylene glycol is still under discussion. A similar electrolyte was used by *Fushimi* et al. [28.124, 125]. They investigated the anodic dissolution of titanium in nonaqueous electrolytes consisting of ethylene glycol and varying metal chlorides. They assume that due to the absence of water an anodic oxide formation on titanium is prevented. At high voltages titanium cations as well as chloride anions migrate through the thin surface film of native oxide and the following reaction is assumed

$$\mathrm{Ti} + 4\mathrm{Cl^-} \rightarrow \mathrm{TiCl_4} \,. \qquad (28.22)$$

Fushimi and *Habazaki* and *Fushimi* et al. further postulate that $\mathrm{TiCl_4}$ is stable in water-free electrolytes and forms a viscose film on the anode. The further reaction of titanium dissolution is controlled by the transport through the viscous film [28.124, 125].

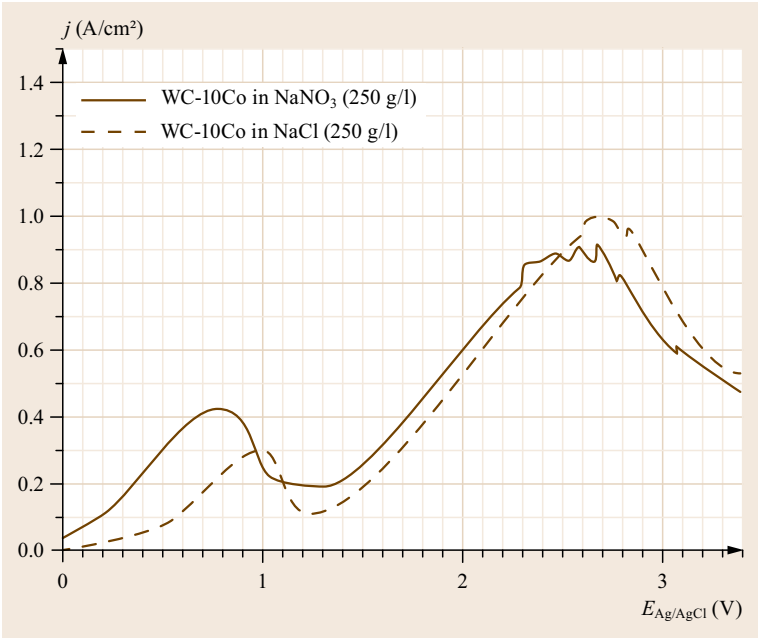


Fig. 28.24 Current density versus potential curves on WC-10Co in various electrolytes ($dU/dt = 100\,mVs^{-1}$) (after [28.123])

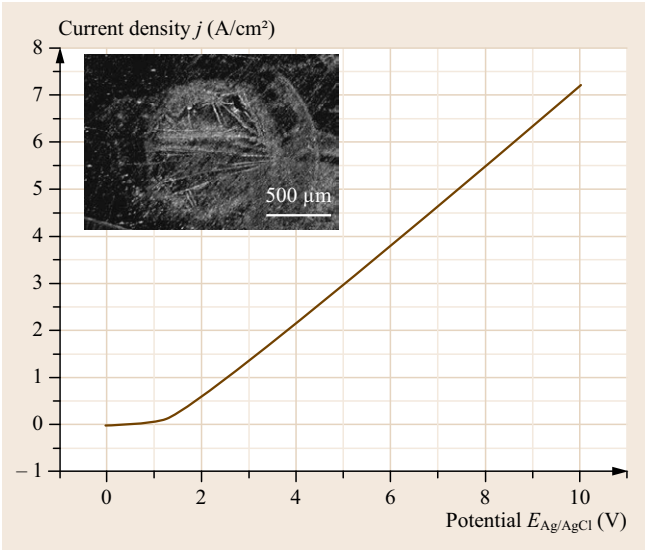


Fig. 28.25 Anodic behavior of Co in 0.75 M NaOH ($dU/dt = 200\,mV/s$) (after [28.126])

28.9.2 Cemented Carbides

Cemented carbides is a common name of a composite material consisting of tungsten carbide as hard phase and a softer binder phase. Most common is a combination with cobalt as binder phase (e.g., WC-10Co or WC-6Co). However, the electrochemical machining of these prevalent cemented carbides is exceedingly difficult. Under acidic or neutral conditions, commonly used electrolytes ($NaNO_3$, NaCl), Co is the only one that dissolves anodically whereas WC forms very stable oxides. Fig. 28.24 shows a cyclovoltammogram of WC-10Co in sodium nitrate as well as in sodium chloride up to 3 V [28.123].

The graphs in Fig. 28.24 show two current peaks followed by a decreasing current density. Subsequent microscopic investigations have shown that the first peak can be interpreted as cobalt dissolution, followed by a depletion of cobalt, and the second peak is associated with the active-passive transition of tungsten carbide and the formation of a protective oxide film on the sample surface. The situation is vice versa under alkaline conditions. *Schroth* et al. [28.126] have shown that cobalt in 0.75 M NaOH beyond 1 V is passive and the complete current density is consumed by the anodic oxygen evolution. Material removal could not be observed (Fig. 28.25). Tungsten carbide can be easily removed under alkaline conditions as shown in Fig. 28.26.

Despite the described problems, the efforts to machine tungsten carbides electrochemically is as old as the ECM technology. In 1924 already, *Pirani* and *Schröter* [28.4] published a method to drill holes in the hard phase tungsten carbide using sodium hydroxide or potassium hydroxide, respectively. In the 1960s–1970s Russian scientists particularly investigated the possibility of ECM of cemented carbides. *Parshutin* et al. reported successful machining of cemented carbide in a mixture of sodium hydroxide and sodium nitrate [28.111, 112]. *Kondrateev* and *Vodyanov* inves-

tigated the behavior of cemented carbides in phosphate electrolytes [28.127]. Alternatively, *Levin* and *Nechaev* [28.108] and *Davydov* et al. [28.109] suggested alternating or pulse currents for effective machining of cemented carbides.

Unfortunately, these works are focused on technologic aspects and a clear hint of the success evidenced by micro or macro images, e.g., are missing. *Iliev* and *Mitikov* reported the efforts to machine several cemented carbides in various electrolytes [28.128]. They used sodium chloride and potassium nitrate electrolytes with and without additives such as phosphates or tartrates and postulated partially successful machining. However, the presented current-potential curves are rather similar to Fig. 28.26. The additives seemed to be supported the depassivation of the surface oxides. A similar effect was postulated for cathodic polarization, however, the surface roughness increased significantly. Furthermore, the cathodic polarization involved the risk of dissolution of the cathode [28.11]. *Schroth* et al. [28.126] have investigated the dissolution behavior of WC-10Co in mixed electrolytes of sodium nitrate and sodium hydroxide. Indeed, a machining of the cemented carbide alloys was possible using an 1 : 1 electrolyte mixture of 1.2 M $NaNO_3$/2.6 M NaOH. The dissolution was associated with a slurry formation which was easily removed by the hydrodynamic of the electrolyte stream flow. Recently, extensive investigation of the ECM of cemented carbides was published by *Lohrengel* et al. [28.129]. The authors demonstrate the anodic dissolution of a WC-6Co-alloy in an electrolyte mixture consisting of 1.2 M $NaNO_3$ and 0.6 M NaOH at pH $\approx$ 14. An overview of the behavior is given by the cyclovoltammogram shown in Fig. 28.27. It can be seen that a high current density of $\approx 25\,A/cm^2$ is achieved at ≈ 30 V. The linear increasing graph suggested only an ohmic limitation of the dissolution by the electrolyte. The visible temporary current drops at (e.g., ≈ 15 V and ≈ 25 V) are explained by the formation of different poly-tungstates depending on the concentration of tungstate in the electrolyte [28.130, 131].

Additionally, the authors used a new, near-to-use technology for ECM of cemented carbides – jet-ECM. The special hydrodynamics of a free electrolyte jet enhances the hydro-mechanical removal of the cobalt oxide layers from the surface. Unfortunately, the surface quality after the machining is low caused by the different dissolution mechanism of WC (active) and Co (transpassive).

An interesting approach to solve the problem of the simultaneous dissolution of hard phase and binder phase of WC-6Co was recently published by *Schubert* et al. [28.132], using an electrolyte consisting of sodium hydroxide and ammonia at pH $\approx$ 12. The

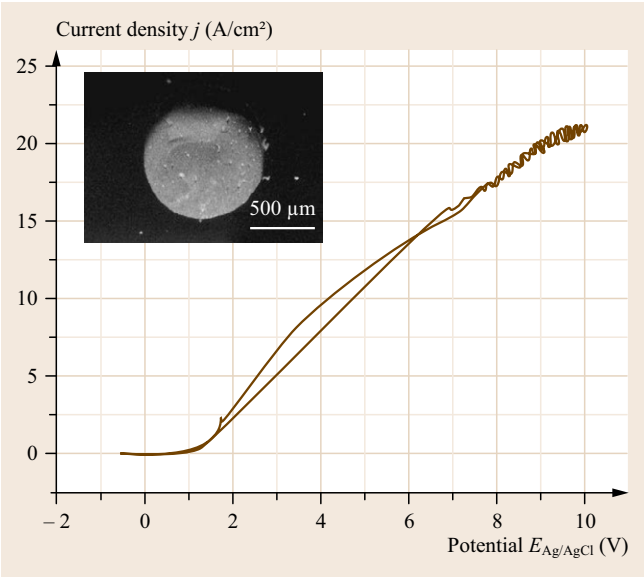


Fig. 28.26 Anodic behavior of WC in 0.75 M NaOH ($dU/dt = 200\,mV/s$) (after [28.126])

consideration was that ammonia works as complex agents for cobalt to suppress the formation of cobalt oxide films, which were found in previous investigations [28.133]. Cobalt forms soluble ammonia complexes according to *Vu* and *Han* [28.134]

$$Co(OH)_2 + 6NH_3 \rightarrow [Co(NH_3)_6]^{2+} + 2OH^- \,. \tag{28.23}$$

It is well known that tungsten dissolves anodically to tungstate ions in alkaline solutions whereas carbon forms carbonate ions [28.135]. Therefore, *Schubert* et al. [28.132] assume the dissolution of WC under alkaline conditions (pH 12) according to

$$WC + 7H_2O \rightarrow WO_4^{2-} + CO_3^{2-} + 14H^+ + 10e^- \,. \tag{28.24}$$

However, the carbonate ions can further react with the resulting protons (from oxygen evolution, if possible) under the formation of water and carbon dioxide.

$$CO_3^{2-} + 2H^+ \rightarrow CO_2 + H_2O \,, \tag{28.25}$$

Alternatively, one can discuss the formation of carbon monoxide [28.44] or elementary carbon according to (28.26) and (28.27)

$$WC + 5H_2O \rightarrow WO_4^{2-} + CO + 10H^+ + 8e^- \,, \tag{28.26}$$

$$WC + 4H_2O \rightarrow WO_4^{2-} + C + 8H^+ + 6e^- \,. \tag{28.27}$$

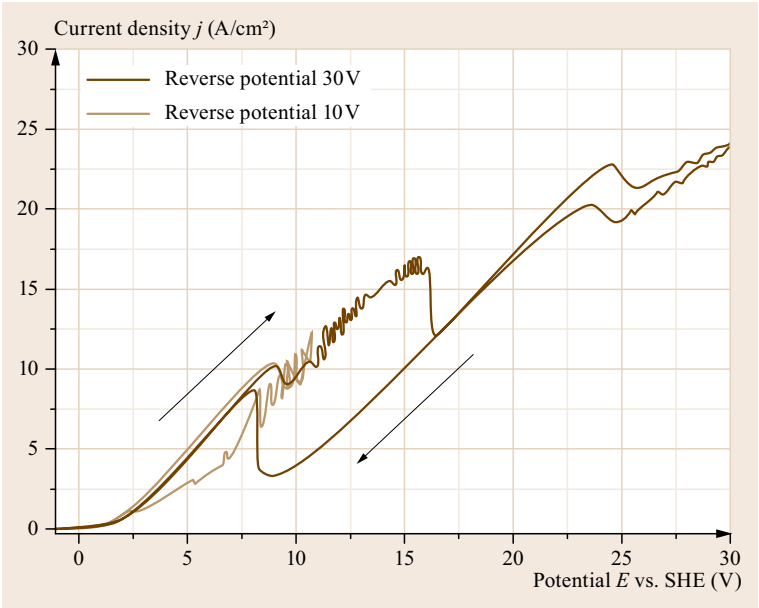


Fig. 28.27 Cyclovoltammogram of CTM12A in $NaOH/NaNO_3$, $dU/dt = 500\,mV/s$ (after [28.129])

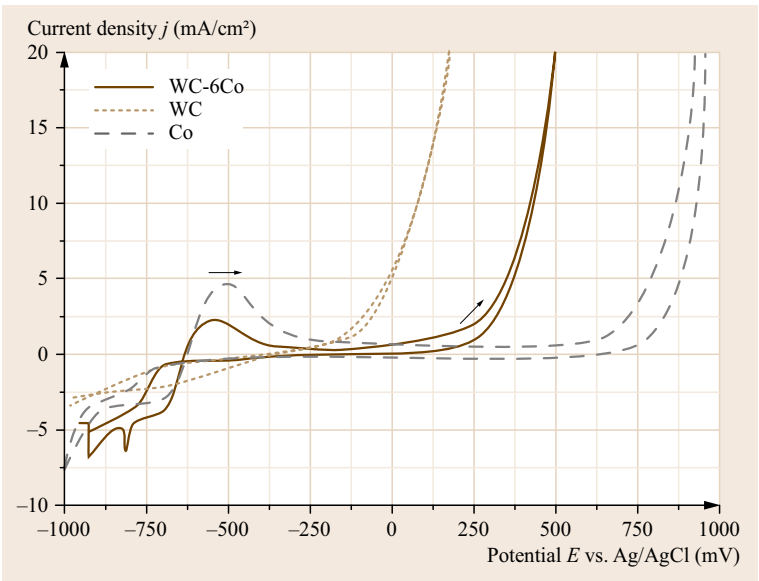


Fig. 28.28 Cyclovoltammograms, $U = -0.90 - 1.00\,V$, $dU/dt = 50\,mV/s$, $NH_3/NaNO_3$ (2.0 M/2.9 M), *gray dashed line*: Co ($dU/dt = 0.5\,V/s$) (after [28.132])

The protons lower the pH value close to the electrode and suppress the dissolution rate of WC. However, ammonia acts as a buffer and keeps the pH value in the bulk electrolyte constant. Fig. 28.28 shows the cyclovoltammogramm of WC-6Co as well as of the individual phases WC and Co in the aforementioned electrolyte mixture. The cyclovoltammogram of WC-6Co can be interpreted as superposition of the voltammograms of the individual phases. The initial dissolution of Co takes place under formation of hydroxides which are dissolved by the formation of the cobalt ammonia complexes as described in (28.23). The dissolution of WC needs a slightly higher overvoltage and the dissolution takes place. The current efficiency is close to 100% at low current densities and decreases with increasing current density to approximately 75% (Fig. 28.29). Anodic oxygen evolution becomes possible due to the intermediate formation of cobalt oxides.

Fig. 28.30 shows the result of post experimental analysis of the waste electrolyte. Both cobalt ions as

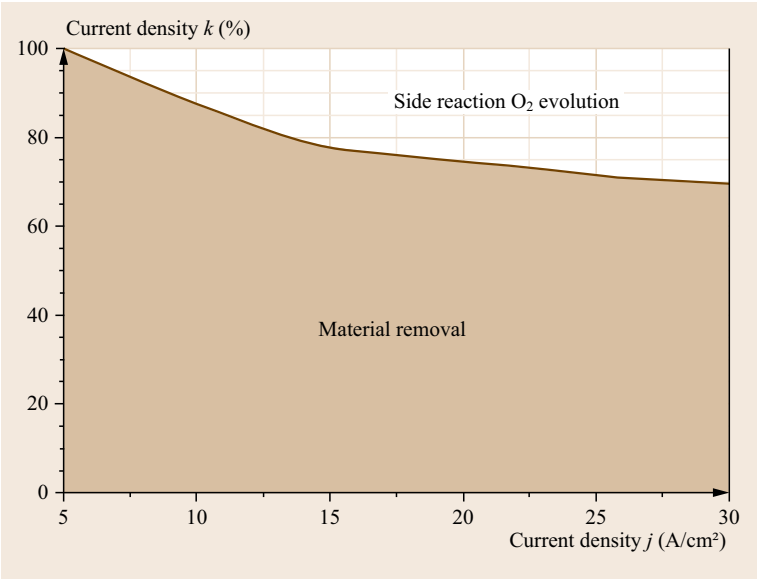


Fig. 28.29 Current efficiency of ECM of WC-Co6 in $NH_3/NaNO_3$ electrolyte as a function of the current density (after [28.132])

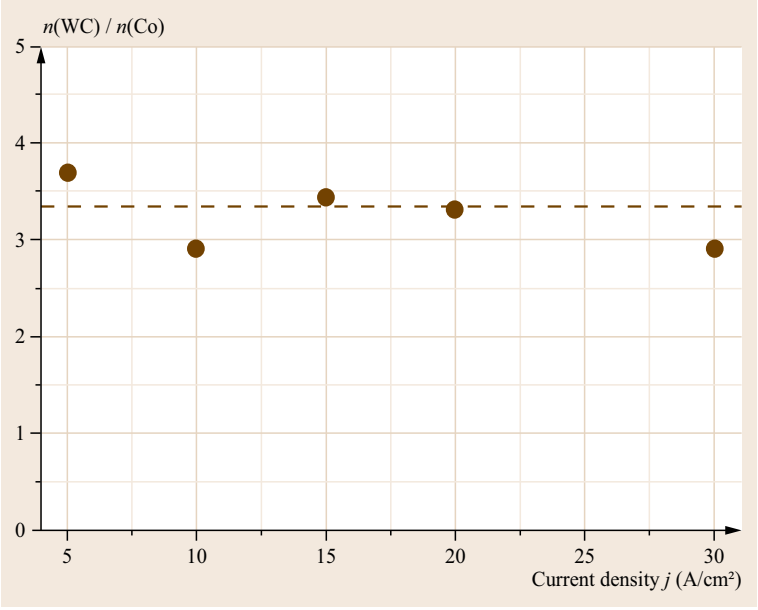


Fig. 28.30 Relation of WC and Co analyzed in the waste electrolyte (after [28.132])

well as tungsten ions could be detected. Thereby, the relation between the dissolved tungsten carbide and cobalt is more or less constant and independent of the applied current density.

References

28.1 M. Datta: Anodic dissolution of metals at high rates, IBM J. Res. Develop. **37**, 207–222 (1993)

28.2 W. Forker, L. Franke: Über einige verfahrenstechnischen Grundlagen der Metallbearbeitung, Technik **2**(3), 19 (1968), in German

28.3 E. Rummyantsev, A. Davidov: *Electrochemical Machining of Metals* (Mir, Moscow 1989)

28.4 M. Pirani, K. Schröter: Elektrolytische Formgebung von harten metallischen Gegenständen, Z. Metallkd. **16**, 132–133 (1924), in German

28.5 A.E. De Barr, D.A. Oliver: *Electrochemical Machining* (Macdonald, London 1968)

28.6 V.N. Gusev, L.A. Rozkov: Method of metal tube etched, Soviet Union Patent SU 19280 025 470 19 280 321 (1928)

28.7 V.N. Gusev: Method and Apparatus for the Electrolytic Treatment of Metals, British Patent Nr. 335 003 (1930)

28.8 V.N. Gussev: Verfahren und Vorrichtung zur elektrolytischen Bearbeitung von Metallen, German Patent Nr.565 765 (1932)

28.9 W. Degner: *Elektrochemische Metallbearbeitung* (VEB Technik, Berlin 1984), in German

28.10 J. Stanek: Perspektiven der Entwicklung der EDM – und ECM-Technik, Symp. Elektrobearbeitungstechnik, Vienna (1970), in German

28.11 J.A. McGeough: *Principles of Electrochemical Machining* (Chapman Hall, London 1974)

28.12 J. Bannard: Electrochemical machining, J. Appl. Electrochem. **7**, 1–29 (1977)

28.13 D. Landolt, P.F. Chauvy, O. Zinger: Electrochemical micromachining, polishing and surface structuring of metals: Fundamental aspects and new developments, Electrochim. Acta **48**, 3185–3201 (2003)

28.14 D. Deconinck, W. Hoogsteen, J. Deconinck: A temperature dependent multi-ion model for time accurate numerical simulation of the electrochemical machining process. Part III: Experimental validation, Electrochim. Acta **103**, 161–173 (2013)

28.15 M.M. Lohrengel: Thin anodic oxide layers on aluminium and other valve metals: High field regime, Mater. Sci. Eng. R **11**, 243–294 (1993)

28.16 M.M. Lohrengel, J.W. Schultze: Electrochemical properties of anodic gold oxide layers – I: Potentiostatic oxide growth and double layer capacity, Electrochim. Acta **21**, 957–965 (1976)

28.17 J.W. Schultze, M.M. Lohrengel: Ageing effects in monomolecular oxide layers on gold, Ber. Bunsenges. Phys. Chem. **80**, 552–556 (1976)

28.18 U. Stimming, J.W. Schultze: A semiconductor model of the passive layer on iron electrodes and its application to electrochemical reactions, Electrochim. Acta **24**, 859–869 (1979)

28.19 M.E. Straumanis: Valency of ions formed during anodic dissolution of metals in acids, J. Electrochem. Soc. **108**, 1087–1092 (1961)

28.20 A.R. Despic, J. Radosevic, P. Dabic, M. Kliskic: Abnormal yields of hydrogen and the mechanism of its evolution during cathodic polarization of aluminium, Electrochim.ica Acta **35**, 1743–1746 (1990)

28.21 R.R. Cole, Y. Hopenfeld: An investigation of electrolytic jet polishing at high current densities, J. Eng. Ind. **85**, 395–401 (1963)

28.22 S.H. Glarum, J.H. Marshall: The anodic dissolution of copper into phosphoric acid, I. Voltammetric and oscillatory behavior, J. Electrochem. Soc. **132**, 2872–2878 (1985)

28.23 M. Matlosz, S. Magaino, D. Landolt: Impedance analysis of a model mechanism for acceptor-limited electropolishing, J. Electrochem. Soc. **141**, 410–418 (1994)

28.24 M. Datta, H.J. Mathieu, D. Landolt: Anodic film studies on nickel under high rate transpassive dissolution conditions, Electrochim. Acta **24**, 843–850 (1979)

28.25 M. Datta, D. Landolt: Surface brightening during high rate nickel dissolution in nitrate electrolytes, J. Electrochem. Soc. **122**, 1466–1472 (1975)

28.26 M. Datta, H.J. Mathieu, D. Landolt: AES/XPS study of transpassive films on iron in nitrate solution, J. Electrochem. Soc. **131**, 2484–2489 (1984)

28.27 M. Datta, D. Landolt: On the role of mass transport in high rate dissolution of iron and nickel in ECM electrolytes – I. Chloride solutions, Electrochim. Acta **25**, 1255–1262 (1980)

28.28 M. Datta, D. Landolt: On the role of mass transport in high rate dissolution of iron and nickel in ECM electrolytes – II. Chlorate and nitrate solutions, Electrochim. Acta **25**, 1263–1271 (1980)

28.29 M. Datta, D. Landolt: Electrochemical machining under pulsed current conditions, Electrochim. Acta **26**, 899–907 (1981)

28.30 R.D. Grimm, D. Landolt: Salt films formed during mass transport controlled dissolution of iron-chromium alloys in concentrated chloride media, Corros. Sci. **36**, 1847–1868 (1994)

28.31 D. Landolt: Fundamental aspects of electropolishing, Electrochim. Acta **32**, 1–11 (1986)

28.32 T. Haisch, E. Mittemeijer, J.W. Schultze: Electrochemical machining of the steel 100Cr6 in aqueous NaCl and $NaNO_3$ solutions: Microstructure of surface films formed by carbides, Electrochim. Acta **47**, 235–241 (2001)

28.33 M.M. Lohrengel, I. Klüppel, C. Rosenkranz, H. Bettermann, J.W. Schultze: Microscopic investigations of electrochemical machining of Fe in $NaNO_3$, Electrochim. Acta **48**, 3203–3211 (2003)

28.34 M.M. Lohrengel, C. Rosenkranz, I. Klüppel, A. Moehring, H. Bettermann, J. Deconinck, B. Van den Bossche: A new microcell or microreactor for material surface investigations at large current densities, Electrochim. Acta **49**, 2863–2870 (2004)

28.35 M.M. Lohrengel, A. Moehring: Electrochemical microcells and surface analysis, New Trends Electrochem. Technol. **2**, 104–121 (2002)

28.36 M.M. Lohrengel, A. Moehring, M. Pilaski: Capillary-based droplet cells: limits and new aspects, Electrochim. Acta **47**, 137–141 (2001)

28.37 M. Pilaski, T. Hamelmann, A. Moehring, M.M. Lohrengel: Impedance spectroscopy in micro systems, Electrochim. Acta **47**, 2127–2134 (2002)

28.38 M.M. Lohrengel, S. Heiroth, K. Kluger, M. Pilaski, B. Walther: Microimpedance – Localized material analysis, Electrochim. Acta **51**, 1431–1436 (2006)

28.39 M. Schneider, S. Schroth, N. Schubert, A. Michaelis: In-situ investigation of the surface-topography during anodic dissolution of copper under near-ECM conditions, Mater. Corros. **63**(2), 96–104 (2012)

28.40 R.G. Compton, C.E. Banks: *Understanding Voltammetry* (World Scientific, Singapore 2007) p. 306

28.41 W. Hoogsteen, S. Kuindersma, B.P. Minks, A.D. Davydov: High-rate electrochemical dissolution of Ni–Cu alloys in nitrate electrolyte, J. Appl. Electrochem. **32**, 1029–1037 (2002)

28.42 T. Haisch, E. Mittemeijer, J.W. Schultze: Influences of material inhomogeneities in 100Cr6 steel on the electrochemical metal dissolution process, Z. Metallkd. **92**, 417–422 (2001)

28.43 M.M. Lohrengel, C. Rosenkranz: Microelectrochemical surface and product investigations during electrochemical machining (ECM) in $NaNO_3$, Corros. Sci. **47**, 785–794 (2005)

28.44 B. Walther, J. Schilm, A. Michaelis, M.M. Lohrengel: Electrochemical dissolution of hard metal alloys, Electrochim. Acta **52**, 7732–7737 (2007)

28.45 C. Hammer, B. Walther, H. Karabulut, M.M. Lohrengel: Oscillating oxygen evolution at Ta anodes, J. Solid State Electrochem. **15**, 1885–1891 (2011)

28.46 K.P. Rataj, C. Hammer, B. Walther, M.M. Lohrengel: Quantified oxygen evolution at microelectrodes, Electrochim. Acta **90**, 12–16 (2013)

28.47 D. Landolt, R.H. Müller, C.W. Tobias: Crystallographic factors in high-rate anodic dissolution of copper, J. Electrochem. Soc. **118**, 36–40 (1971)

28.48 I. Katsounaros, D. Ipsakis, C. Polatides, G. Kyriacou: Efficient electrochemical reduction of nitrate to nitrogen on tin cathode at very high cathodic potentials, Electrochim. Acta **52**, 1329–1338 (2006)

28.49 M.S. El-Deab: Electrochemical reduction of nitrate to ammonia at modified gold electrodes, Electrochim. Acta **49**, 1639–1645 (2004)

28.50 D. Landolt, R. Acosta, R.H. Müller, C.W. Tobias: An optical study of cathodic hydrogen evolution in high-rate electrolysis, J. Electrochem. Soc. **117**, 839–845 (1970)

28.51 M. Pourbaix: *Atlas of Electrochemical Equilibria in Aqueous Solutions* (Pergamon, Oxford 1966) p. 493

28.52 D. Reyter, G. Chamoulaud, D. Belanger, L. Roue: Electrocatalytic reduction of nitrate on copper electrodes prepared by high-energy ball milling, J. Electroanal. Chem. **596**, 13–24 (2006)

28.53 J.O.M. Bockris, J. Kim: Electrochemical treatment of low-level nuclear wastes, J. Appl. Electrochem. **27**, 623–634 (1997)

28.54 S. Ureta-Zanartu, C. Yanez: Electroreduction of nitrate ion on Pt, Ir and on 70:30 Pt:Ir alloy, Electrochim. Acta **42**, 1725–1731 (1997)

28.55 J.F.E. Gootzen, L. Lefferts, J.A.R. van Veen: Electrocatalytic nitrate reduction on palladium based catalysts activated with germanium, Appl. Catal. A **188**, 127–136 (1999)

28.56 A.J. Schwartz, M. Kumar, B.L. Adams: *Electron Backscatter Diffraction in Materials Science* (Kluwer Academic/Plenum, New York 2000)

28.57 J.W. Schultze, M. Pilaski, M.M. Lohrengel, U. König: Single crystal experiments on grains of polycrystalline materials: Oxide formation on Zr and Ta, Faraday Discuss. **121**, 211–227 (2002)

28.58 C.-J. Park, M.M. Lohrengel, T. Hamelmann, H.-S. Kwon: Grain-dependent passivation of surfaces of polycrystalline zinc, Electrochim. Acta **47**, 3395–3399 (2002)

28.59 A. Schreiber, J.W. Schultze, M.M. Lohrengel, F. Kármán, E. Kálmán: Grain dependent electrochemical investigations on pure iron in acetate buffer pH 6.0, Electrochim. Acta **51**, 2625–2630 (2006)

28.60 M. Schneider, S. Schroth, J. Schilm, A. Michaelis: Micro-EIS of anodic thin oxide films on titanium for capacitor applications, Electrochim. Acta **54**, 2663–2671 (2009)

28.61 K.J. Vetter: *Electrochemical Kinetics: Theoretical and Experimental Aspects* (Academic, New York 1967)

28.62 A.J. Davenport: Developing corrosion prediction models from x-ray measurements, Proc. 10th Symp. Electrochem. Methods Corrosion Res. (EMCR), Maragogi (2012) p. 10

28.63 M.M. Lohrengel: On the fundamental interface kinetics during ECM, Proc. Int. Symp. Electrochem. Mach. Technol. INSECT, Vienna (2011) p. 10

28.64 T. Münninghoff, B. Walther, C. Rosenkranz, M.M. Lohrengel: Electrochemical Machining – Formgebung harter Werkstoffe durch anodische Auflösung, Galvanotechnik **100**, 436–442 (2009), in German

28.65 L. Vitos, A.V. Ruban, H.L. Skriver, J. Kollar: The surface energy of metals, Surf. Sci. **411**, 186–202 (1998)

28.66 H.L. Skriver, N.M. Rosengaard: Surface energy and work function of elemental metals, Phys. Rev. B **46**, 7157–7168 (1992)

28.67 M.M. Lohrengel, M. Amkreutz, A. Schreiber: Influence of crystallographic orientation on the anodic dissolution of iron, Int. Symp. Electrochem. Mach. Technol. (INSECT), Dresden (2006)

28.68 W. Schaarwächter: Zum Mechanismus der Versetzungsätzung I. Die Bildung zweidimensionaler Lochkeime an den Enden von Versetzungslinien, Phys. Status Solidi **12**, 375–382 (1965), in German

28.69 L. Jasper, W. Schaarwächter: Versetzungsätzung an Kupfereinkristallen durch potentiostatische Elektrolyse, Z. Metallkd. **57**, 661–668 (1966), in German

28.70 W.R. Buck, H. Leidheiser: The corrosion of single crystals and recrystallized single crystals of iron and steel in citric acid, J. Electrochem. Soc. **104**, 474–481 (1957)

28.71 H.-J. Engell: Elektrochemische Untersuchungen der Korrosion von α-Eisen-Einkristallen in verdünnten Säuren, Arch. Eisenhüttenwes. **7**, 393–404 (1955), in German

28.72 G.P. Camorata, L. Felloni, G. Palombarini, S.S. Traverso: Optical microscopy studies of anodic dissolution of iron in sulfuric and hydrochloric acid solutions: Influence of metal purity, structure, and heat treatment, Corrosion **26**, 129 (1970)

28.73 H. Roßwag, G. Eichkorn, J.W. Lorenz: Einfluß des Metallsubgefüges auf den anodischen Auflösungsmechanismus von Eisen, Werkst. Korros. **25**(2), 86–92 (1974), in German

28.74 M. Seo, M. Chiba: Nano-mechano-electrochemistry of passive metal surfaces, Electrochim. Acta **47**, 319–325 (2001)

28.75 M. Chiba, M. Seo: Mechanoelectrochemical properties of passive iron surfaces evaluated by an in situ nanoscratching test, J. Electrochem. Soc. **150**, B525–B529 (2003)

28.76 K.-H. Näser, D. Lampe, O. Regen: *Physikalische Chemie für Techniker und Ingenieure*, 19th edn. (VEB, Leipzig 1990), in German

28.77 D. Landolt: *Corrosion and Surface Chemistry of Metals* (EPFL Press, Lausanne 2007) pp. 59–61

28.78 H.S.O. Chan, P.K.H. Ho, L. Zhou, N. Luo, S.C. Ng, S.F.Y. Li: In situ atomic force microscopy of the electrochemical dissolution of a copper grain, Langmuir **12**, 2580–2586 (1996)

28.79 A. Schreiber, C. Rosenkranz, M.M. Lohrengel: Grain-dependent anodic dissolution of iron, Electrochim. Acta **52**, 7738–7745 (2007)

28.80 M. Schneider, S. Schroth, S. Richter, S. Höhn, N. Schubert, A. Michaelis: In-situ investigation of the interplay between microstructure and anodic copper dissolution under near-ECM conditions – Part 1: The active state, Electrochim. Acta **56**, 7628–7636 (2011)

28.81 A.W. Ruff: Grain orientation dependence of reactivity in polycrystalline titanium after anodic polarization, Metall. Trans. **5**, 601–603 (1974)

28.82 M. Schneider, N. Schubert, S. Höhn, A. Michaelis: Anodic dissolution behaviour and surface texture development of cobalt under electrochemical machining conditions, Electrochim. Acta **106**, 279–287 (2013)

28.83 K.E. Heusler: Der Einfluß der Wasserstoffionenkonzentration auf das elektrochemische Verhalten des aktiven Eisens in sauren Lösungen Der Mechanismus der Reaktion $Fe \rightleftharpoons Fe^{++} + 2e$, Z. Elektrochem. **62**, 582–587 (1958), in German

28.84 J.O'.M. Bockris, D. Drazic, A.R. Despic: The electrode kinetics of the deposition and dissolution of iron, Electrochim. Acta **4**, 325–361 (1961)

28.85 M. Schneider, S. Schroth, N. Schubert, C. Lämmel, A. Michaelis: A novel approach of in-situ investigation of the surface topography under near ECM-conditions, Proc. 5th Int. Symp. Electrochem. Technol. (INSECT), Dresden (2009) pp. 81–87

28.86 G. Gottstein: *Physikalische Grundlagen der Materialkunde* (Springer, Berlin, Heidelberg 1998) pp. 73–92

28.87 F. Erdmann-Jesnitzer: Interkristalline Korrosion und Korngrenzenangriff, Werkst. Korros. **9**, 7–16 (1958), in German

28.88 P. Lin, G. Palumbo, U. Erb, K.T. Aust: Influence of grain boundary character distribution on sensitization and intergranular corrosion of alloy 600, Scr. Metall. Mater. **33**, 1387–1392 (1995)

28.89 V. Randle: The coincidence site lattice and the 'sigma enigma', Mater. Charact. **47**, 411–416 (2001)

28.90 C. Nanev, K. Dicheva: Electrochemical etching, Acta Phys. Hung. **57**, 271–283 (1985)

28.91 M. Schneider, S. Schroth, S. Richter, S. Höhn, N. Schubert, A. Michaelis: In-situ investigation of the interplay between microstructure and anodic copper dissolution under near-ECM conditions – Part 2: The transpassive state, Electrochim. Acta **70**, 76–83 (2012)

28.92 D. Landolt, R.H. Müller, C.W. Tobias: High rate anodic dissolution of copper, J. Electrochem. Soc. **116**, 1384–1390 (1969)

28.93 D. Landolt: The role of surface films in electrochemical machining, Proc. 5th Int. Symp. Electrochem. Technol. (INSECT), Dresden (2009) pp. 9–14

28.94 K.P. Rataj: Elektrochemische Charakterisierung technisch relevanter anodischer Oxidschichten bei niedrigen und höchsten Stromdichten, Ph.D. Thesis (Heinrich-Heine-University, Düsseldorf 2013), in German

28.95 T.R. Münninghoff: Mechanismus der anodischen Auflösung von Metallen und Legierungen bei extrem hohen Stromdichten, Ph.D. Thesis (Heinrich-Heine-University, Düsseldorf 2012), in German

28.96 M. Datta, D. Landolt: Electrochemical saw using pulsating voltage, J. Appl. Electrochem. **13**, 795–802 (1983)

28.97 A.D. Davydov, V.S. Shaldaev, A.N. Malofeeva, I.V. Savotin: Electrochemical dissolution of tungsten under pulsed conditions, J. Appl. Electrochem. **27**, 351–354 (1997)

28.98 A.K.M. De Silva, H.S.J. Altena, J.A. McGeough: Precision ECM by process characteristic modelling, CIRP Ann. **49**, 151–155 (2000)

28.99 K.P. Rajurkar, D. Zhu, J.A. McGeough, J. Kozak, A. De Silva: New Developments in electro-chemical machining, CIRP Ann. **48**, 567–579 (1999)

28.100 C. Rosenkranz, M.M. Lohrengel, J.W. Schultze: The surface structure during pulsed ECM of iron in $NaNO_3$, Electrochim. Acta **50**, 2009–2016 (2005)

28.101 M.M. Lohrengel: Pulsed electrochemical machining of iron in $NaNO_3$: Fundamentals and new aspects, Mater. Manufact. Proc. **20**, 1–8 (2005)

28.102 M. Schneider, S. Schroth, S. Richter, N. Schubert, A. Michaelis: Elektrochemische Bearbeitung (ECM) von Titan in einer ionischen Flüssigkeit, Galvanotechnik **103**, 744–750 (2013), in German

28.103 A.D. Davydov, R.P. Klepikov, A.N. Malofeeva, I.I. Moroz: Anodic dissolution and electrochemical machining of hard alloys based on chromium and titanium carbides, Elektron. Obrab. Mater. **4**, 11–14 (1985)

28.104 C.A. Coughanowr, B.A. Dissaux, R.H. Muller, C.W. Tobias: Electrochemical machining of refractory materials, J. Appl. Electrochem. **16**, 345–356 (1986)

28.105 N.A. Amirkhanova, L.G. Rafikova, O.M. Tatarinova: Anodic solution of transition-metal carbides at high current densities, Zashchita Metallov **19**, 412–414 (1983)

28.106 S. Malkin, R. Levinger: Electrochemical grinding and surface damage for cemented carbides, NBS Spec. Publ. **562**, 305–315 (1979)

28.107 R. Levinger, S. Malkin: Electrochemical grinding of WC-Co cemented carbides, J. Eng. Ind. **101**, 285–294 (1979)

28.108 A.I. Levin, A.V. Nechaev: Electrochemical machining of WC-Co carbides with an assymetrical alternating current, Elektronnaya Obrab. Materialov **1**, 12–15 (1971)

28.109 A.D. Davydov, R.P. Klepikov, I.I. Moroz: Electrochemical machining of tungsten carbide based hard alloys in neutral solution with application of anodic pulses, Elektronnaya Obrab. Materialov **1**, 23–26 (1981)

28.110 A.D. Davydov, E.Y. Grodzinskii, A.N. Kamkin: Depassivation of solid alloys based on tungsten carbide during electrochemical dimensional machining, Elektrokhimiya **9**, 518–520 (1973)

28.111 V.V. Parshutin, Yu.N. Petrov, A.I. Loskutov: Special futures of the anodic dissolution of hard alloys of type VK in nitrate alkaline electrolytes, Elektronnaya Obrab. Materialov **3**, 15–20 (1970)

28.112 V.V. Parshutin, Y.N. Petrov: Selecting an electrolyte for electrochemical dimensional machining of VK hard alloys, Elektronnaya Obrab. Materialov **6**, 17–21 (1969)

28.113 B.A. Dissaux, R.H. Muller, C.W. Tobias: Electrochemical Machining of Carbides and Borides, M.S. Thesis (Univ. Berkley, Berkley 1978)

28.114 V.N. Moiseyev (Ed.): *Titanium Alloys: Russian Aircraft and Aerospace Applications* (CRC, Boca Raton 2006)

28.115 R.R. Boyer: An overview on the use of titanium in the aerospace industry, Mater. Sci. Eng. A **213**, 103–114 (1996)

28.116 T.M. Brunette, P. Tengvall, M. Textor, P. Thomsen: *Titanium in Medicine* (Springer, Berlin, Heidelberg 2001) pp. 13–24

28.117 M. Niinomi: Recent research and development in titanium alloys for biomedical applications and healthcare goods, Sci. Technol. Adv. Mater. **4**, 445–454 (2003)

28.118 J. Bannard: On the electrochemical machining of some titanium alloys in bromide electrolytes, J. Appl. Electrochem. **6**, 477–483 (1976)

28.119 K. Schwabe: *Korrosion und Korrosionsschutz* (VEB, Berlin 1971), p. 22; in German

28.120 K.D. Allard, M. Ahrens, K.E. Heusler: Wachstum und Auflösung anodisch erzeugter Oxidschichten auf Titan, Werkst. Korr. **26**, 694–699 (1975)

28.121 R.D. Dyaminov, A.N. Maltsev, G.V. Kargin: Electrochemical machining of titanium-rotor cast blades for vortex pumps, Khimicheskoe I Neftyanoe Mashinostroenie **9**, 29–30 (1977)

28.122 J. Bannard: Effect of surface finish obtained by electrochemical machining on the fatigue life of some titanium alloys, J. Appl. Electrochem. **4**, 229–234 (1974)

28.123 D. Hänig: *In-situ Untersuchung der Topographieentwicklung von Werkstoffen bei elektrochemischer Parametervariation unter ECM-nahen Bedingungen, Diploma Thesis* (TU, Dresden 2008), in German

28.124 K. Fushimi, H. Habazaki: Anodic dissolution of titanium in NaCl-containing ethylene glycol, Electrochim. Acta **53**, 3371–3376 (2008)

28.125 K. Fushimi, H. Kondo, H. Konno: Anodic dissolution of titanium in chloride-containing ethylene glycol solution, Electrochim. Acta **55**, 258–264 (2009)

28.126 S. Schroth, M. Schneider, A. Michaelis: Investigation oft the anodic dissolution on cemented carbides under near ECM conditions, Proc. 5th Int. Symp. Electrochem. Technol. (INSECT) (VUB, Brussels 2010) pp. 67–73

28.127 V.P. Kondrateev, Y.M. Vodyanov: The anodic behaviour of WC-Co, group hard alloys in phosphate electrolyte, Elektronnaya Obrab. Materialov **72**, 10–12 (1978)

28.128 K. Iliev, C. Mitikov: Hartmetalle bei elektrochemischer Bearbeitung, Werkzeugmasch. Int. **2**, 47–49 (1974), in German

28.129 M.M. Lohrengel, K.P. Rataj, N. Schubert, M. Schneider, S. Höhn, A. Michaelis, M. Hackert-Oschätzchen, A. Martin, A. Schubert: Electrochemical machining of hard metals – WC/Co as example, Powder Metall. **57**, 21–29 (2014)

28.130 K. Andersson, L. Bergström: Oxidation and dissolution of tungsten carbide powder in water, Int. J. Refract. Met. Hard Mater. **18**, 121–129 (2000)

28.131 M. Anik: Effect of concentration gradient on the anodic behavior of tungsten, Corros. Sci. **48**, 4158–4173 (2006)

28.132 N. Schubert, M. Schneider, A. Michaelis: Electrochemical machining of cemented carbides, Int. J. Refract. Met. Hard Mater. **47**, 54–60 (2014)

28.133 N. Schubert, M. Schneider, A. Michaelis: The mechanism of anodic dissolution of cobalt in neutral and alkaline electrolyte at high current density, Electrochim. Acta **113**, 748–754 (2013)

28.134 C. Vu, K.N. Han: Leaching behavior of cobalt in ammonia solutions, Trans. Inst. Min. Metall Sec. C **86**, C119–125 (1977)

28.135 M. Pourbaix: *Atlas of Electrochemical Equilibria in Aqueous Solutions* (Pergamon, Oxford 1974) p. 282

About the Authors



Jan Allen

US Army Research Laboratory
Sensors and Electron Devices Directorate
Adelphi, USA
jan.l.allen8.civ@mail.mil

Chapter D.15

Dr. Jan Allen is a Research Chemist at the US Army Research Laboratory in Adelphi, Maryland. His current research interests focus primarily on Li-ion battery materials including electrode materials and electrolytes. He received the BS in Chemistry from Truman State University in 1989 and the MS and PhD degrees in Chemistry from Northwestern University in 1990 and 1993, respectively.

Michael Angelo

University of Hawaii – Manoa
Hawaii Sustainable Energy Research
Facility, Hawaii Natural Energy Inst.
Honolulu, USA
mangelo@hawaii.edu



Chapter D.19

Michael Angelo received his BS in Chemical Engineering from the University of Delaware in 2004 and MS in Mechanical Engineering from the University of Hawaii in 2013. He is currently research faculty at the University of Hawaii where he has worked since 2005. His research interests include fuel cells and optimization of electrical grids with renewable energy.

Dick Bedeaux

Norwegian University of Science and Technology
Dept. Chemistry
Trondheim, Norway
dick.bedeaux@chem.ntnu.no



Chapter A.4

Dick Bedeaux received his Doctorate degree in Theoretical Physics from the University of Utrecht in 1969. He is Professor emeritus of Physical Chemistry at the Norwegian University of Science and Technology. His current research is in non-equilibrium statistical mechanics and thermodynamics of heterogeneous systems. He has co-authored 3 books, 270 journal papers and several book chapters. He is a Fellow of the American Physical Society, a member of the Norwegian Academy of Science and Letters and of the Norwegian Academy of Science and Technology. He was appointed to the honorary position of Onsager Professor at the Norwegian University of Science and Technology.



Daniel Bélanger

University Quebec at Montreal (UQAM)
Dept. Chemistry
Montreal, Canada
belanger.daniel@uqam.ca

Chapter D.16

Daniel Bélanger is Professor in the Département de Chimie of the Université du Québec à Montréal. He received his PhD in Sciences de l'Énergie from the Institut National de la Recherche Scientifique of the Université du Québec, Canada, in 1985. His post doctoral studies were at the MIT (1986–1987). His current research interests include chemical modification of surfaces, developing new materials for energy storage and environmental applications. He has published more than 150 papers.



Keith Bethune

University of Hawaii – Manoa
Hawaii Sustainable Energy Research
Facility, Hawaii Natural Energy Inst.
Honolulu, USA
bethune@hawaii.edu

Chapter D.19

Keith Bethune received his BS and MS in Ocean Engineering with a specialization in marine corrosion from Florida Atlantic University. He is currently the lead test engineer at the Hawaii Sustainable Energy Research Facility of the University of Hawaii at Manoa. His current research focus is advanced diagnostic techniques for batteries and fuel cells.

Nils Brandau

Volkswagen AG
Fuel Cell Research
Wolfsburg, Germany
nils.brandau@volkswagen.de



Chapter B.10

Nils Brandau received two Diplomas in Electrical Engineering from the University of Kassel as well as a Dr. degree in Mechanical Engineering from the University of Braunschweig. He has been with the Fuel Cell Department at the Volkswagen AG since 2009. For the Fuel Cell Automotive Research Program in collaboration with Ballard Power Systems, he moved to Vancouver for two years. His work is focused on the operation strategy of automotive PEM Fuel Cell Systems.

Cornelia Breitkopf Chapters 1, 2 For biographical profile, please see the section "About the Editors".



Thierry Brousse Chapter D.16

Université de Nantes
Inst. des Matériaux Jean Rouxel IMN, UMR CNRS 6502/Polytech Nantes
Nantes Cedex 3, France
thierry.brousse@univ-nantes.fr

Thierry Brousse is a Professor of Materials Science at the University of Nantes. He received his engineer degree in 1987 and his PhD degree in 1991. He joined the University of Nantes in 1994 and is a Full Professor since 2005. He is a researcher at Institut des Matériaux Jean Rouxel (IMN), where he focuses on materials for electrochemical energy storage with particular emphasis on alternative materials for batteries, Li-ion capacitors and innovative and/or modified materials for electrochemical supercapacitors.



Colin G. Cameron Chapter D.17

Defence Research and Development Canada
Atlantic Research Centre
Dartmouth, Canada
colin.cameron@drdc-rddc.gc.ca

Colin G. Cameron received his PhD in Electrochemistry from Memorial University of Newfoundland. Following a postdoctoral appointment at Caltech, he has worked as a scientist with Canada's Department of National Defence since 2002. His research interests include electrochemical energy storage and polymer failure investigations.

Jeng-Kuei Chang Chapter E.26

National Central University
Inst. Material Science and Engineering
Taoyuan, Taiwan
jkchang@ncu.edu.tw



Jeng-Kuei Chang received his PhD in Materials Science and Engineering from the National Cheng Kung University, Tainan City, Taiwan, in 2005. He is Associate Professor in the Institute of Materials Science and Engineering at National Central Universityin Taoyuan. His current research is in supercapacitors, batteries, and electrochemical sensors. Professor Changhas twice received the Outstanding Young Scientist Award from National Science Council of Taiwan.

George Z. Chen Chapter E.25

University of Nottingham Ningbo China
Dept. Chemical and Environmental Engineering
Ningbo, China
george.chen@nottingham.ac.uk



George Zheng Chen (FRSC, FRSA, FIMMM) obtained his Diploma from Jiujiang Teacher Training College (1981), MSc from Fujian Normal University (1985) China, and his PhD from Imperial College, University of London (1992). He worked in Oxford, Leeds, Cambridge and Wuhan and is now Professor at the University of Nottingham doing research on electrochemical technologies and liquid salts innovation for materials, energy and environment.



Kazumi Chiba Chapter D.16

Tokyo University of Agriculture and Technology
Laboratory of Bio-organic Chemistry
Tokyo, Japan
chiba@carlit.co.jp

Kazumi Chiba earned his Doctorate in Engineering from the Tokyo University of Agriculture and Technology in 2011. In 1999 he joined the Ministry of International Trade and Industry and in 2002 the Japan Carlit Co., Ltd., whre he is engaged in the research of electrolytes for EDLC. He received the Technology Award from the Electrochemical Society of Japan.



Kevin Cooper Chapter D.20

Scribner Associates, Inc.
Southern Pines, USA
kevin@scribner.com

Kevin Cooper received his Doctorate degree from the Department of Materials Science and Engineering in the University of Virginia in 2001. He is Principal Scientist at Scribner Associates, Inc. His current interests include fuel cell and battery testing, fuel cell education, novel electrochemical power sources, diagnostic techniques in electrochemical systems, corrosion science, and sensor arrays.

Minato Egashira

Nihon University
College of Bioresource Sciences
Fujisawa, Japan
egashira.minato@nihon-u.ac.jp



Chapter D.16

Minato Egashira received his engineer degree in 1994 and his doctor (Engineering) degree in 1998. He joined Yamaguchi University from 2004 to 2013, Presently, he is an Associate Professor in the College of Bioresource Sciences at Nihon University. His research focuses on materials for electrochemical energy storage with particular emphasis on alternative non-aqueous electrolytes for the use in batteries and electrochemical capacitors.

Frédéric Favier

Université Montpellier II
Inst. Charles Gerhardt (ICG)
Montpellier Cedex 05, France
fredf@um2.fr



Chapter D.16

Frédéric Favier is CNRS Director of Research and Vice-Director of the Chimie Balard Carnot Insitute, He joined the CNRS at the University of Montpellier in 1993 at, what is now, the Charles Gerhardt Institute. His research activities lie in the synthesis and the characterization of nanostructured materials for electrochemical systems, including electrochemical capacitors, gas sensors, electrocatalysis and Li-ion/Li-air battery.



James M. Fenton

University of Central Florida
Florida Solar Energy Center
Cocoa, USA

Chapter D.20

James M. Fenton is the Director of the University of Central Florida's Florida Solar Energy Center (FSEC). Prior to joining FSEC, Dr. Fenton spent 20 years as a Chemical Engineering Professor at the University of Connecticut. He received his PhD in Chemical Engineering from the University of Illinois in 1984 and his BS from UCLA in 1979. He is an Electrochemical Society Fellow.



Robert J. Forster

Dublin City University
School of Chemical Sciences
Dublin 9, Ireland
robert.forster@dcu.ie

Chapter C.13

Robert Forster holds a Personal Chair within the School of Chemical Sciences at Dublin City University (DCU). Forster's research focuses on the creation of novel materials that have useful electronic or photonic properties because they are highly ordered on the molecular length scale. He obtained a PhD from Dublin City University in 1990 before moving to the University of Illinois as a Postdoctoral Fellow. He is the author/co-author of more than 200 papers and reviews.

Yannick Garsany

Excet Inc./US Naval Research Laboratory
Chemistry Division
Washington, USA
yannick.garsany.ctr@nrl.navy.mil



Chapter C.14

Dr. Yannick Garsany is a senior scientist for Excet, Inc. working in the Alternative Energy Section in the Chemistry Division at the Naval Research Laboratory (NRL) in Washington, DC. He specializes in electrochemistry and presently studies Pt-based fuel cell electrocatalysts plus works on the development and understanding of membrane electrode assemblies (MEAs).

Isaí Gonzalez Martínez

ThyssenKrupp Electrolysis GmbH
Process Engineering
Dortmund, Germany
isai.gonzalez-martinez@thyssenkrupp.com



Chapter B.9

Isai Gonzalez Martinez works for ThyssenKrupp Electrolysis GmbH in the Process Engineering Department. His main area of work is plant engineering for the chlorine industry, with special focus on the chlor-alkali electrolysis and hydrochloric acid electrolysis processes employing membrane technology.



Richard Hanke-Rauschenbach

Leibniz University Hannover
Institute for Electric Power Systems,
Electric Energy Storage Systems
Hannover, Germany
hanke-rauschenbach@ifes.uni-hannover.de

Chapter B.9

Richard Hanke-Rauschenbach obtained his Diploma in Energy Engineering from Leipzig University of Applied Sciences, Germany. In 2007, he received a PhD degree from the Otto-von-Guericke University, Magdeburg, Germany. Since then he is a team leader at the Max Planck Institute for Dynamics of Complex Technical Systems, Magdeburg. His research focus is on the analysis, design and operation of renewable energy systems.



Ting He

Idaho National Laboratory
Energy and Environment Science and Technology
Idaho Falls, USA
ting.he@inl.gov

Chapter E.27

Ting He is a Director at Phillips 66, in charge of the development of clean energy technologies. He received his PhD in Physical and Electrochemistry from the Leibniz University Hannover, Germany. His research interests include the application of electrochemistry and nanotechnology in energy conversion, storage and efficient utilization. He is the inventor/author of over 120 patents and refereed journal articles.

Dietrich Hebecker

Martin-Luther-University
Halle-Wittenberg
Engineering Science Center
Halle (Saale), Germany
dietrich.hebecker@iw.uni-halle.de



Chapter A.3

Dietrich Hebecker received his PhD in Chemical Engineering in 1972 from the Moscow Institute of Chemical Engineering under the supervision of Prof. S. N. Shorin. Since 1985 he has been Professor of Energy Engineering at the Technical University Leuna-Merseburg and later at the Martin-Luther-University Halle-Wittenberg, Germany. His research focuses on the thermodynamic and thermoeconomic analysis of chemical processes. It also includes energy transformation and thermodynamic cycles for refrigeration as well as for heat and power production.

Matthias Heim

BMZ GmbH
Karlstein, Germany
heimmatthias@hotmail.com



Chapter B.6

Matthias Heim received his Diploma in Materials Science from the Friedrich-Alexander University in Erlangen, Germany in 2007 and his PhD degree from the University of Bordeaux, France in 2011 working on different aspects of porous electrodes. Currently he carries out research on batteries as a Postdoctoral Fellow in at the University of St. Andrews, UK.



Rudolf Holze

Technische Universität Chemnitz
Institut für Chemie
Chemnitz, Germany
rudolf.holze@chemie.tu-chemnitz.de

Chapter D.18

Professor Rudolf Holze received his PhD in 1983 from the University of Bonn, Germany. In1987 he moved to Oldenburg University as associate professor in Physical Chemistry. Since 1993 he is full Professor of Physical Chemistry and Electrochemistry at Technical University Chemnitz, Germany. His research is focused on spectroelectrochemistry, self-assembled monolayers, lithium ion batteries, electrochemical energy conversion and storage, materials science and corrosion. He is member of the Saxon Academy of Sciences. He is the author of more than 335 articles in refereed international journals and eleven books.



Di Hu

University of Nottingham Ningbo China
Dept. Chemical and Environmental Engineering
Ningbo, China
di.hu@nottingham.edu.cn

Chapter E.25

Di Hu received the BEng degree from the China University of Mining Technology (Beijing) and the MSc (Hons) and PhD degrees from the University of Nottingham, UK. He is currently a postdoctoral research fellow in the Department of Chemical and Environmental Engineering, University of Nottingham. His current work focuses on molten salt electrometallurgy and energy storage systems.

Jack Huizingh

University of Hawaii – Manoa
Hawaii Sustainable Energy Research Facility, Hawaii Natural Energy Inst.
Honolulu, USA
huizingh@hawaii.edu



Chapter D.19

Jack Huizingh is a graduate of the University of Michigan in Naval Architecture/Marine Engineering and Mechanical Engineering. He received his MS degree from New York University. He is currently a project engineer for the Hawaii Natural Energy Institute and facility manager for the Hawaii Sustainable Energy Research Facility.

Greg Jackson

Colorado School of Mines
Dept. Mechanical Engineering
Golden, USA
gsjackso@mines.edu



Chapter B.8

Prof. Greg Jackson has served as Head of Mechanical Engineering at the Colorado School of Mines since 2013. He leads a research group in fuel cell systems, catalysis, and thermochemical energy storage. Before CSM, Jackson was on faculty for 15 years at the University of Maryland. He also worked at Precision Combustion until 1997 on catalytic reactors for low-NO_x combustion.



Michelle D. Johannes

US Naval Research Laboraty
Center for Computational Materials Science
Washington, USA
michelle.johannes@nrl.navy.mil

Chapter B.11

Dr. Johannes's work centers around the use of density functional theory to understand and predict materials properties for strongly correlated systems, including battery materials, superconductors and magnetic compounds. She currently leads a highly intertwined theoretical/experimental nanoscience battery group. She has a PhD in Physics from UC Davis and is a fellow of the American Physical Society.



T. Richard Jow

US Army Research Laboratory
Sensors and Electron Devices Directorate
Adelphi, USA
t.r.jow.civ@mail.mil

Chapter D.15

T. Richard Jow received his Doctorate degree in Materials Science and Engineering from Northwestern University in 1977. He is an ARL Fellow and Team Lead for Energy Storage Materials at the US Army Research Laboratory in Adelphi, MD. His research focuses on the development of energy storage materials and devices, including high-energy and high-power density rechargeable lithium batteries and dielectric capacitors. Dr. Jow has co-edited one book, co-authored over 120 papers and 28 patents. He is a member of the Electrochemical Society and the IEEE Dielectric and Electrical Insulation Society.

Mahaprasad Kar

Phillips 66 Research Center
Sustainability Technologies
Bartlesville, USA
prasad.kar@p66.com



Chapter E.27

Mahaprasad Kar received his Bachelor degree in Chemical Engineering from the University of Mumbai, India (2005) and his PhD in Chemical Engineering from Purdue University, Indiana (2010). He is a research engineer in the sustainability technologies division at the Phillips 66 Research Center, Bartlesville, OK. His research interests include thin film photovoltaics, electrochemical hydrogen generation and acid gas capture.

Tia E. Keyes

Dublin City University
School of Chemical Sciences
Dublin 9, Ireland
tia.keyes@dcu.ie



Chapter C.13

Tia Keyes is a Professor at the School of Chemical Sciences Dublin City University, where she has been a member of faculty since 2002. Her research interests lie in photoactive coordination compounds and supramolecular and interfacial chemistry. Tia coordinates a multi-disciplinary research team which is based between and the National Biophotonics and Imaging Platform Ireland and the National Centre for Sensor Research.



Chunjoong Kim

Chungnam National University
Department of Materials Science and Engineering
Daejeon, Republic of Korea
ckim0218@cnu.ac.kr

Chapter D.21

Professor Chunjoong Kim received his PhD in Materials Science and Engineering under the guidance of Prof. Byungwoo Park from Seoul National University. He is an Assistant Professor at Chungnam National University after having had positions at Samsung Fine Chemicals, Lawrence Berkeley National Laboratory, and University of Illinois at Chicago. His research interests include the understanding of reaction mechanisms in electrode materials for energy storage/conversion devices.



Signe Kjelstrup

Norwegian University of Science and Technology
Dept. Chemistry
Trondheim, Norway
signe.kjelstrup@ntnu.no

Chapter A.4

Kjelstrup graduated cum laude at Norwegian University of Science and Technology (NTNU) in 1974 and became Professor of Physical Chemistry in 1985. Since 2005, she has held a part-time chair at the Technical University of Delft. Her research concerns transport at interfaces, electrochemical cells, membrane separation and entropy production minimisation in process equipment. She has authored, co-authored and edited several books.

Jürgen Köhler

University of Braunschweig
Thermal Science Laboratory
Braunschweig, Germany
juergen.koehler@tu-braunschweig.de



Chapter B.10

Jürgen Köhler is a Full Professor and Head of the Thermal Science Laboratory at the University of Braunschweig, Germany. His research focuses on thermal sciences, heat and mass transfer, and thermal and refrigeration processes. In 2007, he received the German Environmental Award of the German Environmental Foundation.

Andriy Kovalenko

University of Alberta
National Inst. Nanotechnology
Edmonton, Canada
andriy.kovalenko@nrc-cnrc.gc.ca



Chapter A.5

Andriy Kovalenko is Senior Research Officer at the National Institute for Nanotechnology since 2003, and Adjunct Professor in the Department of Mechanical Engineering at the University of Alberta, Edmonton, Canada. He earned his PhD degree (1993) in Theoretical and Mathematical Physics from Lviv State University, Bogolyubov's Institute. Dr. Kovalenko has been developing methodology and software implementation of statistical-mechanical, molecular theory of solvation, coupling it with electronic structure theories, molecular simulations, and docking protocols in a platform of predictive multiscale theory and modeling.



Alexander Kuhn

Université de Bordeaux
Ecole Nationale Supérieure de Chimie,
Biologie et Physique
Pessac, France
kuhn@enscbp.fr

Chapter B.6

Alexander Kuhn obtained a MS in Chemistry from the Technical University of Munich and a PhD in Physical Chemistry from the University of Bordeaux in 1994. After a post-doc position at CALTEC, he moved to the University of Bordeaux (1996) as an Assistant Professor and holds a Full Professor since 2000. His main research interests are in electrochemistry, surface modification and nanoscience. He obtained the Electrochemistry Award of the French Chemical Society, and has been nominated in 2013 as a Senior Member of the Institut Universitaire de France (IUF).

H. Russel Kunz (deceased)

Chapter D.20

Stuart Licht

George Washington University
Dept. Chemistry
Washington, USA
slicht@gwu.edu



Chapter D.24

Stuart Licht is a Professor of Chemistry at the George Washington University in Washington, DC, USA. He has published more than 300 peer reviewed studies and patents on renewable energy, climate change, batteries, photoelectrochemistry, analytical chemistry, environmental chemistry and fundamental physical electrochemistry. He was a National Science Foundation Program Director in Chemistry, was previously a Professor at the Technion Institute, Israel. He received the PhD from the Weizmann Institute and was a Postdoc at MIT. His awards include the Electrochemical Society Energy Technology prize.

Manuel Lohrengel

Heinrich-Heine-Universität Düsseldorf
Inst. Physikalische Chemie
Düsseldorf, Germany
manuel.lohrengel@uni-duesseldorf.de



Chapter E.28

Manuel M. Lohrengel received his Doctorate degree in Physical Chemistry from the Free University Berlin in 1977. He is Head of the working group Microelectrochemistry of Heinrich-Heine-University Düsseldorf. His research covers electrochemical machining, passivity, grains and intermetallics, microcells, transients and electronic equipment which was presented in over 120 papers and over 100 lectures at international conferences.



Jeffrey Long

Naval Research Laboratory
Surface Chemistry Branch
Washington, USA
jeffrey.long@nrl.navy.mil

Chapter D.16

Jeffrey Long joined the US Naval Research Laboratory in Washington, DC in 2000 as a staff scientist after receiving a PhD in Chemistry from the University of North Carolina, Chapel Hill in 1997 and finishing a National Research Council postdoctoral fellowship at the NRL (1997–2000). His research focuses on the design, synthesis, and evaluation of nanostructured materials (metals, metal oxides, and carbons) and advanced electrode architectures; with the primary goal of improving the performance of electrochemical power sources (Li-ion batteries, metal–air batteries, electrochemical capacitors).



Corey T. Love

US Naval Research Laboratory
Chemistry Division
Washington, USA
corey.love@nrl.navy.mil

Chapter B.11

Dr. Corey T. Love is a materials research engineer in the Alternative Energy Section in the Chemistry Division at the Naval Research Laboratory in Washington DC. He currently leads basic and applied research programs enabling the safe implementation of lithium-ion batteries through materials discovery and development and advanced diagnostic and monitoring techniques.

Cynthia A. Lundgren

US Army Research Laboratory
Sensors and Electron Devices Directorate
Adelphi, USA
cynthia.lundgren@us.army.mil



Chapter D.15

Cynthia Lundgren is currently Chief of the Electrochemistry Branch at the Army Research Laboratory. Her research interests include electrochemical energy storage and conversion to include batteries, fuel cells, catalysis and electrochemical energy transduction. Previously, she was a Senior Research Scientist at DuPont's Central Research and Development Depatment, where she worked on a variety of electrochemical programs.

Neal D. McDaniel

Phillips 66 Research Center
Sustainability Technologies
Bartlesville, USA
neal.d.mcdaniel@p66.com



Chapter E.27

Neal McDaniel (PhD 2010 Princeton) is a Senior Scientist at Phillips 66 with research background in inorganic synthesis, electrochemistry, carbon/polymer composites, and photochemistry.



John R. Miller

JME, Inc.
Beachwood, USA
jmecapacitor@att.net

Chapter D.16

John R. Miller, President and founder of JME, Inc. and Adjunct Professor in Electrical Engineering & Computer Science at Case Western Reserve University. He has 34 years experience in advancing electrochemical capacitor technology. He developed an electric double-layer capacitor that operates up to kHz frequencies using vertically-oriented graphene nanosheets. Dr. Miller earned BS and PhD degrees in Physics from MIT.



Shelley D. Minteer

University of Utah
Dept. Chemistry and Dept. Materials Science and Engineering
Salt Lake City, USA
minteer@chem.utah.edu

Chapter D.22

Dr. Shelley Minteer is a USTAR Professor in both the Departments of Chemistry and Materials Science and Engineering at the University of Utah. She received her PhD in Chemistry from the University of Iowa in 2000 under the direction of Johna Leddy. After receiving her PhD, she spent 11 years as a Faculty Member at Saint Louis University before moving to the University of Utah in 2011. She has expertise in bioelectrocatalysis for biosensors and biofuel cells.

Masayuki Morita

Yamaguchi University
Graduate School of Sciences and Technology for Innovation
Ube, Japan
morita@yamaguchi-u.ac.jp



Chapter D.16

Masayuki Morita is a Professor of Applied Fine Chemistry Division at Yamaguchi University. He graduated and received PhD degree from Osaka University at 1980. He joined Yamaguchi University as a Research Associate in 1980, and was promoted to Full Professor in 1996. His research interest focuses on materials for electrochemical energy conversion, including electrochemical capacitors. He is an active member of the Electrochemical Society and the International Society of Electrochemistry.

Seunghoon Nam

Korea Institute of Machinery & Materials (KIMM)
Dept. of Nano Mechanics, Nano Mechanical Systems Research Division
Daejeon, Republic of Korea
kwek14@kimm.re.kr



Chapter D.21

Dr. Seunghoon Nam received PhD degree in Materials Science and Engineering under the supervision of Prof. Byungwoo Park from Seoul National University. He is a senior researcher at Samsung Advanced Institute of Technology (SAIT). His research is associated with the development of electrode materials and solid electrolytes for solid-state Li-ion batteries as well as the control of the electrolyte/electrode interface.



Katsuhiko Naoi

Tokyo University of Agriculture and Technology
Japan Institute of Symbiotic Science and Technology
Tokyo, Japan
naoi2@cc.tuat.ac.jp

Chapter D.16

Katsuhiko Naoi is Executive Professor and Vice Dean at Tokyo University of Agriculture & Technology. He obtained his PhD from Waseda University. He serves as the Chair of The Capacitor Technology Committee of The Electrochemical Society of Japan. He is currently the leader of the Global Innovation Research(GIR)-Supercap team and the Director of Advanced Capacitor Research Center(ACC) at Tokyo University of Agriculture & Technology. His research interests are advanced supercapacitors, high-power Li-ion batteries, and other EES for automotive/stationary applications.



Yuhong Oh

Samsung Electro-Mechanics
LCR Materials Group
Suwon, Republic of Korea
yuhong.oh@samsung.com

Chapter D.21

Dr. Yuhong Oh received his PhD degree in Materials Science and Engineering under the supervision of Prof. Byungwoo Park from Seoul National University. He is currently a senior engineer at Samsung Electro-Mechanics. His research interests lie in the synthesis of various inorganic nanomaterials for energy devices.

Byungwoo Park

Seoul National University
Dept. Materials Science and Engineering, and Research Institute of Advanced Materials
Seoul, Republic of Korea
byungwoo@snu.ac.kr



Chapter D.21

Professor Byungwoo Park received his PhD in Applied Physics from Harvard University (1989). After post-doc at IBM T. J. Watson Research Center, CALTEC (research fellow), and Georgia Institute of Technology (assistant professor), he joined the faculty of the Department of Materials Science and Engineering at Seoul National University in 1997. His current research interests include the development of nanoscale coating, novel nanocomposites, quantum-dot sensitized solar cells, and nanophase control of thin-film electrodes for energy applications.

Vijay K. Ramani

Washington University in St. Louis
Dept. Energy, Environmental and Chemical Engineering
St. Louis, USA
ramani@wustl.edu



Chapter D.20

Vijay Ramani holds the Roma B. and Raymond H. Wittcoff Professorship in Energy, Environmental and Chemical Engineering at Washington University in St. Louis. His research interests lie at the confluence of electrochemical engineering, materials science, and renewable energy technologies. Current research directions in his group include multi-functional electrolyte and electrocatalyst materials for polymer-based electrochemical systems, analyzing the source and distribution of overpotential in electrochemical systems, mitigating component degradation in electrochemical devices, and in-situ diagnostics to probe electrochemical systems.



Bruce B. Randolph

Phillips 66 Research Center
Sustainability Technologies
Bartlesville, USA
bruce.b.randolph@p66.com

Chapter E.27

Bruce Randolph is a Research Fellow at Phillips66. His research interests include alkylation, corrosion and emulsions, water treating, trace metal management, and hydrogen production. He currently holds 50 US patents and has co-authored 26 publications. Randolph earned a BS degree in Chemistry from Southwestern Oklahoma State University, and a PhD degree in Chemistry from the University of Oklahoma.



Tatyana Reshetenko

University of Hawaii – Manoa
Hawaii Sustainable Energy Research Facility, Hawaii Natural Energy Inst.
Honolulu, USA
tatyanar@hawaii.edu

Chapter D.19

Tatyana V. Reshetenko received her Master's degree in Catalysis and Adsorption from Novosibirsk State University and PhD degree from Boreskov Institute of Catalysis, Russia. She has been with the Hawaii Natural Energy Institute since December 2007. Her research interests are in studies of spatial PEMFC performance under different operating conditions and fuel/air/system contaminants exposure using a segmented cell system.

Hans-Hermann Rüttinger

Martin-Luther-University
Halle-Wittenberg
Dept. Pharmacy
Halle, Germany
ruettinger@pharmazie.uni-halle.de



Chapter B.7

Hans-Hermann Rüttinger graduated as Diplomchemiker in 1970 at Martin-Luther-University in Halle. After PhD degree (1973) in Organic Chemistry he joined the electrochemical group of Prof. Matschiner for cooperation with chemical industry in electrolysis. Parallel work on organic electrosynthesis resulted in his Habilitation 1988. Since 1997 he has been the Leader of the Analytical Laboratory in the Department of Pharmacy. Main interests in the last years were in capillary electrophoresis and electrochemical instrumentation.

Michael Schneider

Fraunhofer IKTS
Dept. Electrochemistry
Dresden, Germany
michael.schneider@ikts.fraunhofer.de



Chapter E.28

Michael Schneider studied at the Mining Academy Freiberg, Germany. He graduated as Dipl.-Ing. in Materials Science in 1989 and as Dr.-Ing. at the Technical University Dresden, Germany, in 1993. Since 2006 he is Group Manager Electrochemistry at Fraunhofer IKTS, Dresden. Currently, he is dealing with functional oxide films, corrosion, electroplating, energy storage systems, and electrochemical machining.



Patrice Simon

Université Paul Sabatier
Centre Inter-universitaire de Recherche et d'Ingénierie des Matériaux
Toulouse, France
simon@chimie.ups-tlse.fr

Chapter D.16

Patrice Simon is Professor of Materials Science at the Université Paul Sabatier, Toulouse, France. His research is focused on the characterization of nanostructured materials for electrochemical energy storage sources, including electrochemical capacitors and Li-ion batteries. He is Director of the Alistore European Research Institute focused on Li-ion battery research and Deputy Director of the French network on Electrochemical Energy Storage.
He holds the Chair of Excellence from the Airbus Group Foundation *Nanomaterials for embedded energy storage sources*.



Richard O. Stroman

US Naval Research Laboratory
Chemistry Division
Washington, USA
richard.stroman@nrl.navy.mil

Chapter B.8

Rick Stroman has been an Engineer at the US Naval Research Laboratory since 2004, where his research involves the simulation, design, and development of power systems, primarily for autonomous vehicles and soldier applications. He received his PhD in Mechanical Engineering from the University of Maryland in 2013, for which he developed a transport-focused direct borohydride-hydrogen peroxide fuel cell model.

Wataru Sugimoto

Shinshu University
Dept. Fine Materials Engineering, Faculty of Textile Science and Technology
Ueda, Japan
wsugi@shinshu-u.ac.jp



Chapter D.16

Wataru Sugimoto is a Professor of Materials and Chemical Engineering at Shinshu University. He received his PhD degree in 1999 from Waseda University and has been a faculty member of the Faculty of Textile Science and Technology, Shinshu University since then. His research focuses on nanomaterials for electrochemical charge storage and conversion with particular emphasis on the synthesis and application of nanosheets and nanoparticles. He is also Vice-Director of the Center for Energy and Environmental Science, Shinshu University.

I-Wen Sun

National Cheng Kung University
Dept. Chemistry
Tainan, Taiwan
iwsun@mail.ncku.edu.tw



Chapter E.26

I-Wen Sun received the PhD degree in Chemistry from the University of Mississippi in 1989. He was Research Associate at the University of Tennessee 1989–1992 and is currently Professor of Chemistry at National Cheng Kung University, Taiwan. His research interests are in the electrochemistry in ionic liquids, electrochemical fabrication of nanomaterials, and energy storage devices.



Kai Sundmacher

Max Planck Institute for Dynamics of Complex Technical Systems
Process Systems Engineering
Magdeburg, Germany
sundmacher@mpi-magdeburg.mpg.de

Chapter B.9

Kai Sundmacher is Director of the Max-Planck-Institute for Dynamics of Complex Technical Systems, Professor of Process Systems Engineering at Otto-von-Guericke University in Magdeburg, Germany and Einstein Professor of the Chinese Academy of Sciences. His research focuses on the model-based analysis and synthesis of complex (bio-)chemical production systems, energy conversion processes, electrochemical reactors, fuel cells, and particulate processes.

Karen Swider-Lyons Chapters 1, 2, B.11, C.14 For biographical profile, please see the section "About the Editors".

YuYe J. Tong

Georgetown University
Dept. Chemistry
Washington, USA
yyt@georgetown.edu



Chapter C.12

YuYe J. Tong received BS (1983) and MS (1986) in Nuclear Physics from Fudan University, Shanghai China and PhD degree (1994) in Experimental Condensed Matter Physics from the Swiss Federal Institute of Technology in Lausanne, Switzerland. He currently is a Professor and Chair in the Department of Chemistry at Georgetown University, Washington DC, USA. His research focuses on fuel cell electrocatalysis and charge transfer in metal nanoparticles-based nanomaterials by in situ NMR/IR/Raman, SPM, and ab initio DFT calculations.

Tanja Vidaković-Koch

Max Planck Institute for Dynamics of Complex Technical Systems
Process Systems Engineering
Magdeburg, Germany
vidakovi@mpi-magdeburg.mpg.de



Chapters B.9, D.23

Dr.-Ing. Vidaković-Koch's research focus is on low-temperature electrochemical processes. Examples are direct methanol fuel cell, enzymatic fuel cells/reactors and chlorine recycling. She graduated in Chemical Engineering from the University of Belgrade, Serbia and received her PhD from the Otto-von-Guericke University (OvGU), Magdeburg, Germany. Since 2005 she is a team leader in the research group of Professor Sundmacher, Max-Planck-Institute for Dynamics of Complex Technical Systems.



James J. Walsh

University of Liverpool
Stephenson Institute for Renewable Energy
Liverpool, UK
jjwalsh@liv.ac.uk

Chapter C.13

Jamie received his BSc (2007) and PhD (2011) degrees from Dublin City University. He subsequently undertook postdoctoral work in analytical biospectroscopy at DCU and at Queen's University, Belfast, on photoelectrocatalysis. He is currently working at the Stephenson Institute for Renewable Energy, University of Liverpool, on photoelectrochemical solar fuels production. His research interests include solar fuels, (photo)electrochemistry, polyoxometalates and spectroscopic studies of complex systems.



Kang Xu

US Army Research Laboratory
Sensors and Electron Devices Directorate
Adelphi, USA
conrad.k.xu.civ@mail.mil

Chapter D.15

Kang Xu is a chemist at the US Army Research Laboratory. He received his PhD from Arizona State University and his work on electrolytes has received world-wide attention. In addition to the new salts, solvents and additives he invented, he is best known in the field for the two comprehensive reviews published in Chemical Reviews in 2004 and 2014, respectively.

Yunfeng Zhai

University of Hawaii – Manoa
Hawaii Sustainable Energy Research
Facility, Hawaii Natural Energy Inst.
Honolulu, USA
yunfeng@hawaii.edu



Chapter D.19

Yunfeng Zhai received a PhD degree in Chemical Engineering from the Chinese Academy of Sciences. He is now a Junior Researcher at the University of Hawaii. He is working on contamination effects and degradation in PEMFCs. He is a member of The Electrochemical Society and the American Chemical Society.

Sheng S. Zhang

US Army Research Laboratory
Sensors and Electron Devices Directorate
Adelphi, USA
shengshui.zhang.civ@mail.mil



Chapter D.15

Shengshui Zhang received his PhD in Physical Chemistry from the University of Science and Technology Beijing, China, in 1993. He currently is a Research Chemist in the Electrochemistry Branch, US Army Research Laboratory. He has more than 20 years of experiences in rechargeable lithium and lithium-ion batteries. His most recent researches are on lithium-air and lithium-sulfur batteries. He has authored 131 papers, holds 28 patents, and has edited two books. His publications have received over 7400 citations with an h-index of 49.

Detailed Contents

List of Abbreviations XXI

1 **Electrochemical Science – Historial Review**
Cornelia Breitkopf, Karen Swider-Lyons 1
References 9

2 **Modern Electrochemistry**
Cornelia Breitkopf, Karen Swider-Lyons 11
2.1 Fundamental Components of Electrochemistry 11
2.1.1 General References 12
2.1.2 Electrochemistry Journals 14
2.1.3 Electrochemistry Conferences 14
2.2 Thermodynamics 14
2.3 Kinetics 17
2.4 Mass Transport 19
2.5 The Charged Electrode Interface/Electrochemical Double Layer 21
2.6 Ionic and Electronic Resistance 23
2.7 Experimentation 24
2.8 Subtopics in Electrochemistry 26
2.8.1 Solid-State Ionics 26
2.8.2 Ionic Liquids 26
2.8.3 Corrosion at Liquid Interfaces 27
2.8.4 Chlor–Alkali Process 27
2.9 Summary 28
References 29

Part A Thermodynamics

3 **Thermodynamical Aspects of Electrochemical Reactions**
Dietrich Hebecker 33
3.1 Electrochemical Reactions for Energy Conversion 33
3.1.1 Unity of Material and Energy Conversion 34
3.1.2 Energy Balance of Electrochemical Reactions 35
3.1.3 Equilibrium and Equilibrium Temperature 36
3.1.4 Availability of Chemical Reactions 37
3.1.5 Temperature–Energy Diagram of Chemical Reactions 47
3.1.6 Exotropic Reactions 50
3.1.7 Endotropic Reactions 52
3.2 Electrochemical Reactions and Energy Transformation 54
3.2.1 Systematics of Energy Transformation 54
3.2.2 Chemical Energy Transformation 57
3.2.3 Electrochemical Thermodynamic Cycles 60
References 67

4 **Thermodynamics of Electrochemical Systems**
Signe Kjelstrup, Dick Bedeaux 69
4.1 Scope and Premises 69
4.1.1 The Core Postulates of Non-Equilibrium Thermodynamics 70
4.1.2 Perspectives of NET on Electrochemical Systems 70
4.1.3 Symmetry Rules in Heterogeneous Systems 71
4.1.4 The Basic Assumption: Local Equilibrium 71
4.2 Thermodynamic Properties of the Total Cell 72
4.3 Example Cells 73
4.4 Entropy Production in Three- and Two-Dimensions 74
4.5 Alternative Variable Sets 75
4.5.1 Mass Balance and Entropy Production 76
4.5.2 Transference Coefficients and Transport Numbers 77
4.5.3 Externally Controlled Fluxes. The Measurable Electric Potential 78
4.5.4 Ionic Fluxes and Forces: The Planck Potential 79
4.6 Cell Potentials 80
4.6.1 An Isothermal Formation Cell with a Concentration Gradient 80
4.6.2 A Nonisothermal Formation Cell 80
4.6.3 The Liquid Junction 82
4.6.4 The Butler–Volmer Equation 83
4.6.5 Power from Reverse Electrodialysis 85
4.6.6 Electrochemical Cells as Thermoelectric Generators 86
4.7 The Polymer Electrolyte Fuel Cell 87
4.8 Transport at Interfaces. Perspectives and Conclusion 90
References 91

5 **Multiscale Modeling of Solvation**
Andriy Kovalenko 95
5.1 Integral Equation Theory of Molecular Liquids 96
5.2 Statistical–Mechanical, Molecular Theory of Solvation 99
5.2.1 3D-RISM-KH Integral Equations for the Solvation Structure 99
5.2.2 Analytical Expressions for the Solvation Thermodynamics 102
5.2.3 Analytical Treatment of Electrostatics 103
5.2.4 Examples of 3D-RISM-KH Calculations of Solvation Structure 103
5.2.5 Molecular Recognition and Protein–Ligand Binding 112
5.2.6 Post-Processing of the Thermodynamics of MD Trajectories 112
5.3 Multiscale Coupling of the 3D-RISM-KH Molecular Theory 113
5.3.1 Self-Consistent Field Coupling of KS-DFT with 3D-RISM-KH 113
5.3.2 Example of Multiscale KS-DFT/3D-RISM-KH Calculations .. 115
5.4 Multi-Time-Step Molecular Dynamics of Biomolecules 116
5.4.1 Molecular Dynamics Coupled with 3-D Molecular Theory of Solvation 116
5.4.2 Calculation of Solvation Forces by 3D-RISM-KH MTS-MD .. 118
5.4.3 MTS-MD/SFCE/3D-RISM-KH Method for Biomolecular Solvation 120

5.5 Electrical Double Layer in Nanoporous Materials 123
5.6 Replica Formalism for Fluid Sorbed in a Disordered Matrix 123
5.7 Replica DRISM-KH-VM for Electrolyte Solution Sorbed in Nanoporous Material 124
5.7.1 Thermodynamics of Sorbed Solution 126
5.7.2 Electric Double Layer in the Nanopores of Host Matrix 127
5.7.3 Molecular Mechanism of Electrosorption and Capacitance 128
5.7.4 Illustration for a Supercapacitor 129
5.8 Conclusions 133
References 134

Part B Electrodes and Electrode Processes

6 **Highly Ordered Macroporous Electrodes**
Alexander Kuhn, Matthias Heim 143
6.1 Macroporous Electrodes by Infiltration of Colloidal Templates 144
6.1.1 Assembly of Colloidal Crystals 144
6.1.2 Overview over Different Infiltration Techniques 151
6.1.3 Electrodeposition of Metals in Colloidal Templates 156
6.1.4 Electrodeposition of Conducting Polymers in Colloidal Crystals 165
6.2 Macroporous Materials with a Gradient in Pore Diameter 172
6.2.1 Gradient Pore Diameter Template Fabrication 173
6.2.2 Electrodeposition of Metals and Conducting Polymers 176
6.3 Macroporous Microelectrodes with Cylindrical Geometry 181
6.3.1 Fabrication of Colloidal Crystal Templates on Gold Wires . 182
6.3.2 Electrodeposition of Metals and Conducting Polymers 183
6.3.3 Characterization of Macroporous Gold Cylinders 188
6.4 Applications of Macroporous Electrodes 188
6.4.1 Electrocatalysis 189
6.4.2 Energy Storage 189
6.4.3 Sensing Applications 190
6.4.4 Electrosynthesis 191
6.4.5 Optical Applications 193
6.5 Conclusion 197
References 197

7 **Ion-Sensitive Electrodes**
Hans-Hermann Rüttinger 207
7.1 Fundamentals of Potentiometry 207
7.1.1 Reference Electrodes 208
7.1.2 Simple Indicator Electrodes 210
7.1.3 Membrane Electrodes 210
7.1.4 Characterization of Ion-Selective Electrodes 217
7.1.5 Direct Potentiometric Determination of Concentrations 218
7.1.6 Models of ISE Response 218
7.1.7 All Solid-State Electrodes 222
7.1.8 Ion-Selective Field Effect Transistor (ISFET) 225
7.1.9 Drug Sensitive Electrodes 226

7.2 Application of ISE 226
7.2.1 Gas-Sensitive Electrodes and Biosensors 226
7.2.2 Detectors in Flow Systems 227
7.3 Amperometric and Voltammetric Methods 227
7.3.1 Experimental Methods 227
7.3.2 Electrochemical Reaction Mechanisms 233
References 237

8 **Transport in Liquid-Phase Electrochemical Devices**
Richard O. Stroman, Greg Jackson 239
8.1 A General Transport Model for Liquid-Fed Electrochemical Cells 240
8.1.1 Governing Equations in Liquid Electrolytes 241
8.1.2 Transport in Liquid Electrolytes 242
8.1.3 Transport of Liquids in Porous Media 243
8.1.4 Common Boundary Conditions and Interfaces 244
8.1.5 Reaction Fluxes at the Electrode–Channel Interfaces 245
8.2 Practical Considerations 246
8.2.1 Grid Development and Gradient Approximations 246
8.2.2 Implementation of the Governing Equations 246
8.2.3 Numerical Approaches 247
8.2.4 Model Calibration and Validation 248
8.3 Example Cell: Direct Borohydride–Hydrogen Peroxide Fuel Cell 248
8.3.1 DBFC Overview 248
8.3.2 Transport in the Channels 250
8.3.3 Transport at the Membrane–Channel Interfaces 250
8.3.4 DBFC Transport Model Calibration 251
8.3.5 Results from the DBFC Transport Model 253
8.4 Conclusions 256
8.5 Nomenclature 256
References 257

9 **Catalyst Layer Modeling**
Tanja Vidaković-Koch, Richard Hanke-Rauschenbach, Isaí Gonzalez Martínez, Kai Sundmacher 259
9.1 Gas Diffusion Electrodes 259
9.2 Catalyst Layer Physical Structure 261
9.2.1 Catalyst and Electron Conducting Network 261
9.2.2 Ionic Conducting Network 262
9.2.3 Void Fraction 262
9.3 Governing Equations 262
9.3.1 Porous Electrode Models 263
9.3.2 Interface Models – Neglecting Spatial Gradients 267
9.3.3 Agglomerate Models 269
9.4 Macroscale Models 273
9.4.1 Interface Models 273
9.4.2 Porous Electrode Models 276
9.4.3 Agglomerate Models 277
9.5 Conclusions and Outlook 282
References 283

10 **Water Management in Proton Exchange Fuell Cells**
Nils Brandau, Jürgen Köhler 287
10.1 Water Management in PEMFC 287
10.2 Thermodynamics and Electrochemistry 289
10.3 Polarization Curve 290
10.4 Gas Humidification 294
10.4.1 Model of Mass Exchanger 294
10.4.2 Operating Characteristics of Humidifier 301
10.5 Sensorless Humidification 302
References 311

11 **Calculations in Li-Ion Battery Materials**
Michelle D. Johannes, Corey T. Love, Karen Swider-Lyons 313
11.1 Using DFT to Calculate the Voltage of Layered Materials 315
11.1.1 Background 315
11.1.2 Computational Methods 316
11.1.3 Experimental Methods 317
11.1.4 Experimental and DFT Results for NCM and $NCA_{1/3}$ 317
11.1.5 Conclusions 323
11.2 PDOS Calculations of Oxygen Stability and Cycling Safety 323
11.2.1 DFT Methods 324
11.2.2 PDOS of $LiCoO_2$ 324
11.2.3 PDOS of NCA 326
11.2.4 Conclusions 326
11.3 Summary 326
References 327

Part C Electrochemistry Probes

12 **Electrochemical Energy Generation and Storage as Seen by In-Situ NMR**
YuYe J. Tong 331
12.1 Spatially-Resolved ^{195}Pt NMR Spectroscopy of Pt-Based Electrocatalysts 336
12.1.1 ^{195}Pt NMR of Pt Nanoparticles 336
12.1.2 Study of Ru@Pt Versus Au@Pt M (Ru/Au) Core-Pt Shell NPs 338
12.2 NMR/MRI Studies of Energy Storage (Batteries) Materials 342
12.2.1 Toroid Resonator: Near-Electrode Imager Versus Compression Coin Cell 344
12.2.2 Bellcore-Like Flexible NMR Cells 347
12.2.3 NMR/MRI Studies of Formation of Li Dentrites 350
12.3 MRI of Water Distribution in Fuel Cells 352
12.3.1 In-Plane Water Distribution 353
12.3.2 Through-Plane Water Distribution 356
12.4 Conclusion and Future Perspectives: Sensitivity, Sensitivity and Sensitivity 357
References 360

13 **Spectroscopy of Electrochemical Systems**
James J. Walsh, Robert J. Forster, Tia E. Keyes 365
13.1 General Experimental Considerations 366
13.1.1 Interaction of Light with Electrode Materials 366
13.2 Electronic Spectroscopy 368
13.2.1 Optically Transparent Electrodes for Transmittance Spectroscopy 368
13.2.2 Thin-Layer Spectroelectrochemistry 370
13.2.3 Reflectance Spectroscopy 381
13.3 Spectroelectrochemistry of the Excited State 385
13.3.1 Steady-State Emission Spectroelectrochemistry 386
13.3.2 Transient Luminescence Spectroelectrochemistry 391
13.4 Vibrational Spectroelectrochemistry 393
13.4.1 IR Spectroelectrochemistry 393
13.4.2 External Reflectance 399
13.4.3 Vibrational Circular Dichroism SEC 403
13.5 Raman Spectroelectrochemistry 404
13.5.1 Resonance Raman Spectroelectrochemistry 407
13.5.2 Surface-Enhanced Raman Spectroscopy 409
13.6 Sum Frequency Generation Spectroelectrochemistry 413
13.7 Conclusions and Outlook 414
References 415

14 **Kinetic Activity in Electrochemical Cells**
Yannick Garsany, Karen Swider-Lyons 423
14.1 Evaluation of Pt/VC Electrocatalysts for the ORR 428
14.1.1 Glassware Cleaning 428
14.1.2 Electrocatalyst Ink Formulation, Preparation of Glassy Carbon Electrode Substrate, and Electrocatalyst Thin-Film Electrodes 429
14.1.3 Electrochemical Test Protocol for Evaluation of the Thin-Film Electrocatalyst Electrodes 433
14.2 Electrochemical Characterization of the Pt/VC Electrocatalyst Thin-Film Electrodes by RDE and RRDE 435
14.2.1 Influence of Pt/VC Thin-Film Electrodes Quality 435
14.2.2 Pt ECSA Calculation in Acid 435
14.2.3 Pt ECSA Calculation in Base 436
14.2.4 ORR Polarization Curves Versus Film Morphology in Acid Electrolyte by RDE 437
14.2.5 ORR Measurements of Pt/C in Acid Electrolyte by RRDE 438
14.2.6 Calculation of Electrocatalyst Mass and Specific Activities 439
14.3 Electrochemical Characterization of Mn_xO_y Thin-Film Electrodes ... 440
14.3.1 Mn_xO_y/VC INK#1 Preparation 440
14.3.2 Mn_xO_y/VC INK#2 Preparation 441
14.3.3 Comparison ORR Measured for Mn_xO_y/VC INK#1 to ORR Measured Mn_xO_y/VC INK#2 441
14.4 Conclusions 443
References 444

Part D Energy Conversion and Storage

15 **Lithium-Ion Batteries and Materials**
Cynthia A. Lundgren, Kang Xu, T. Richard Jow, Jan Allen, Sheng S. Zhang 449
15.1 Overview – Electrochemical Evaluation of Li-Ion Batteries 449
15.2 Evaluation of Materials and Components in Li-Ion Batteries 451
15.2.1 Electrode Evaluation 451
15.2.2 Electrolytes and Interphases 454
15.2.3 Separators 470
15.2.4 Advanced/In Situ Spectroscopy 471
15.3 Evaluation at the Cell–Battery Level 481
15.3.1 Cell Configurations 481
15.3.2 Performance Characteristics 481
15.3.3 Energy Density 483
15.3.4 Power Capability 483
15.3.5 Cycle Life and Storage Life (or Calendar Life) 485
15.3.6 Safety 486
15.4 Beyond Li-Ion 487
15.4.1 Li–S Battery 487
15.4.2 Li–Air Battery 489
15.5 Conclusions 490
References 491

16 **Materials for Electrochemical Capacitors**
Thierry Brousse, Daniel Bélanger, Kazumi Chiba, Minato Egashira, Frédéric Favier, Jeffrey Long, John R. Miller, Masayuki Morita, Katsuhiko Naoi, Patrice Simon, Wataru Sugimoto 495
16.1 Batteries and Electrochemical Capacitors – Basic Concepts 496
16.1.1 Electrochemical Characterization of Electrochemical Capacitors 497
16.1.2 Basic Concept of Hybrid Electrochemical Capacitor 500
16.2 Carbon 504
16.2.1 Activated Carbons 505
16.2.2 Carbon Aerogels and Related Sol-Gel-Derived Nanoarchitectures 506
16.2.3 Templated Mesoporous Carbons (TMCs) 507
16.2.4 Microporous Carbons 507
16.2.5 Carbon Nanotubes 508
16.2.6 Enhanced Charge Storage 509
16.3 Manganese Dioxide 510
16.3.1 Fundamental Structural Properties 510
16.3.2 Pseudocapacitance Mechanisms for Manganese Oxides 511
16.3.3 Thin-Film Electrodes 513
16.3.4 *Bulk* Composite MnO_2 Electrodes 516
16.3.5 Advanced MnO_2-Carbon Electrode Architectures 518
16.3.6 MnO_2-Based Devices 520
16.3.7 Future Outlook 522
16.4 Ruthenium Oxide 523
16.4.1 Synthesis, Chemical, and Physical Properties 523
16.4.2 Composites and Other Ruthenium Oxides 524
16.4.3 Charge Storage Mechanism 525

16.5 Other Pseudocapacitive Materials 529
16.6 Electrolytes 529
16.6.1 Aqueous 529
16.6.2 Organic Solvent Solutions 529
16.6.3 Ionic Liquids 530
16.6.4 Polymer and Gel Electrolytes 531
16.6.5 Stability of the Electrolyte in High Voltage EC 534
16.7 Applications of Electrochemical Capacitors 537
16.7.1 Copiers 537
16.7.2 Power Tools 538
16.7.3 Transportation 538
16.7.4 Secondary Uses in Transportation 540
16.7.5 Industrial Applications 541
16.7.6 Stationary Applications for Power and Power Quality 543
16.8 Electrochemical Capacitor Prospective View 543
References 545

17 **Electrochemical Capacitors**
Colin G. Cameron 563
17.1 The Nature of Capacitance 563
17.1.1 Important Capacitor Relationships 565
17.1.2 Double-Layer Capacitance 565
17.1.3 Pseudocapacitance 566
17.1.4 The Role of the Electrolyte 567
17.2 Test Methods 568
17.2.1 Constant Current Discharge 568
17.2.2 Cyclic Voltammetry 571
17.2.3 Impedance 573
17.2.4 Self-Discharge and Leak Currents 578
17.3 Configuration 578
17.3.1 Three- and Two-Electrode Cells 578
17.3.2 Hybrid Electrochemical Capacitors 581
17.3.3 Two-Electrode Cell Designs 581
17.3.4 Electrode Construction 582
17.3.5 Separators 583
17.3.6 Current Collectors 583
17.4 Further Practical Concerns 584
17.4.1 Electrode Area and Pore Size 584
17.4.2 Minimizing Series Resistance 585
17.4.3 Standard Testing 585
17.5 Summary and Conclusions 586
17.6 Symbols 586
References 587

18 **Kinetics of Fast Redox Systems for Energy Storage**
Rudolf Holze 591
18.1 Overview and Introduction 591
18.1.1 Flow Batteries and Redox Flow Batteries 592
18.1.2 Chemistry of Redox Batteries 593
18.1.3 Hybrid Systems 595

18.2 Flow Batteries – Basic Components 597
18.2.1 Electrodes 597
18.2.2 Separators 597
18.3 Redox Reactions and their Kinetics 598
18.3.1 Diffusion, Transport and Flow of Reactants 599
18.3.2 Transport in Porous Electrodes 599
18.3.3 Charge Transfer Reactions 600
18.4 Acceleration of Redox Reactions 600
18.4.1 Catalysis by Chemical Surface Treatment 601
18.4.2 Catalysis by Chemical Surface Modification 601
18.5 Materials for Electrodes in Flow Batteries 601
18.5.1 Modified Carbons and Graphites 602
18.5.2 Non-Carbon Materials 605
18.6 Catalysis and Surface Enlargement Effects 605
18.7 Future Directions 606
References 606

19 **Modern Fuel Cell Testing Laboratory**
Jean St-Pierre, Michael Angelo, Keith Bethune, Jack Huizingh, Tatyana Reshetenko, Mebs Virji, Yunfeng Zhai 611
19.1 Fuel Cell Laboratory Evolution 611
19.1.1 Background 612
19.1.2 Fuel Cell Laboratory Overview 614
19.2 Safety and Test Stations 614
19.2.1 Safety 614
19.2.2 Test Stations 616
19.3 Fuel Cell Stack Components and Assembly 621
19.3.1 Hardware Design and Manufacturing 621
19.3.2 Cell and Stack Components Cleaning 621
19.3.3 Single Cell Assembly 623
19.3.4 Cell Assembly Verification 625
19.3.5 Installation into the Test Station 625
19.4 Testing and Diagnostic Techniques 626
19.4.1 Conditioning 627
19.4.2 In Situ Tests 628
19.4.3 Ex Situ Tests 638
19.5 Conclusion 640
References 641

20 **Polymer Electrolyte Fuel Cells**
Vijay K. Ramani, Kevin Cooper, James M. Fenton, H. Russel Kunz 649
20.1 Experimental Methods 650
20.1.1 Fuel Cell Testing Safety and Good Lab Practices 651
20.1.2 Handling Instructions for Membrane Electrode Assemblies (MEA) 651
20.1.3 Single Cell PEM Fuel Cell Components 651
20.1.4 Fuel Cell Assembly Instructions 653
20.1.5 Calculation of Pinch 655
20.1.6 Fuel Cell Test System Instrumentation 656
20.1.7 Reactant Humidification in Fuel Cell Testing 656

20.2 H_2/O_2 or Air Fuel Cell Performance Testing 662
20.2.1 Effects of Oxygen Partial Pressure 663
20.2.2 Temperature and Relative Humidity Effects 672
20.3 Application of a Fuel Cell Empirical Model 679
20.3.1 Model Application and Analysis 680
20.3.2 Summary 683
20.4 Fuel Crossover and Electrochemical Surface Area 683
20.4.1 Hydrogen Crossover and Internal Short Circuit 683
20.4.2 Hydrogen Crossover Test via LSV 686
20.4.3 Electrochemically Active Surface Area and Catalyst Utilization Evaluation 687
20.5 Impedance Spectroscopy of PEM Fuel Cells 689
20.5.1 Impedance Theory and Practice 690
20.5.2 Results and Discussion 699
20.5.3 Impedance of a H_2 PEM Fuel Cell 701
20.5.4 Effect of Reactant Humidification 704
20.5.5 Electrode Proton Transport Resistance 708
References 710

21 **Next-Generation Electrocatalysts**
Seunghoon Nam, Chunjoong Kim, Yuhong Oh, Byungwoo Park 713
21.1 Oxygen-Reduction Reaction – Cathodes 713
21.1.1 Enhancement from Electronic Interactions 714
21.1.2 Improved Structural Stability Against Pt Dissolution 719
21.1.3 Conclusions 724
21.2 Methanol-Oxidation Reaction – Anodes 724
21.2.1 Suppression of Ru Dissolution in PtRu Catalyst 725
21.2.2 Enhancement from Various Nanostructured Catalysts 731
21.2.3 Conclusion 738
References 738

22 **Methods in Biological Fuel Cells**
Shelley D. Minteer 743
22.1 Bioelectrocatalysis 744
22.1.1 Microbial, Enzymatic, Nucleic Acid, and Organelle Catalysts 744
22.1.2 Mediated Versus Direct Bioelectrocatalysis 745
22.2 Spectroscopic Methods 746
22.2.1 Michaelis–Menten Kinetics 746
22.2.2 Specific Activity 746
22.2.3 Leaching Studies 746
22.2.4 XPS Surface Analysis 748
22.2.5 Infrared, Nuclear Magnetic Resonance, and Mass Spectrometry 748
22.3 Electrochemical Methods 749
22.3.1 Voltammetry 749
22.3.2 Amperometric Methods 750
22.3.3 Polarization Measurements 750
22.3.4 Stability Testing 752
22.3.5 Electrochemical Impedance Spectroscopy 752

22.4 Engineering Considerations 752
22.5 Conclusions 753
References 753

23 **Energy Conversion Based on Bio(electro)catalysts**
Tanja Vidaković-Koch 757
23.1 Working Principles of Bioelectrochemical Systems 758
23.1.1 Enzymatic Fuel Cells 758
23.1.2 Electrolytic Biochemical Systems 758
23.2 Bioelectrochemical Systems in Cell-Free Systems 758
23.3 General Aspects 760
23.3.1 Thermodynamics 760
23.3.2 Mechanism of Bioelectrochemical Transformation 763
23.3.3 Reaction Kinetics 764
23.3.4 Balance Equations 766
23.3.5 Determination of Enzyme Coverage 767
23.3.6 Determination of Kinetic Parameters 769
23.4 Biotransformation with Redox Enzymes 770
23.4.1 Enzymes Showing DET 770
23.4.2 FAD- and NAD-Dependent Enzymes 771
23.5 Conclusions and Outlook 774
References 774

24 **Photoelectrochemical Conversion Processes**
Stuart Licht 779
24.1 Overview and Historical Perspective 779
24.2 Photoelectrochemical Processes 780
24.2.1 Semiconductor/Electrolyte Electrical Energy Conversion 780
24.2.2 Semiconductor/Electrolyte Electrochemical Energy Storage 781
24.2.3 Dye-Sensitized Solar Cell 785
24.2.4 Multi-Bandgap Semiconductor/Electrolyte Electrical Energy Conversion 787
24.2.5 Solar Thermal Electrochemical Photochemical Energy Conversion 791
24.3 State-of-the-Art and Emerging Technologies 795
24.4 Summary 796
References 796

Part E Electrochemical Processes

25 **Advanced Extractive Electrometallurgy**
Di Hu, George Z. Chen 801
25.1 Conventional Extractive Metallurgy 801
25.1.1 Nonelectrolytic Extraction Techniques 802
25.1.2 Conventional Electrolytic Extraction Techniques 806
25.2 Innovative Electrolytic Extraction Techniques for Titanium 808
25.2.1 Electrolytic Extraction from Non-Oxide Compounds 808
25.2.2 Electrolytic Extraction from Solid Metal Oxides 809
25.2.3 Summary and Note 813

25.3 Direct Electroreduction of Solid Metal Oxides to Metals: The FFC Cambridge Process 814
25.3.1 History 814
25.3.2 Principle 814
25.3.3 Applications 824
25.4 Summary 829
References 830

26 **Electrodeposition of Nanomaterials**
I-Wen Sun, Jeng-Kuei Chang 835
26.1 Processes for Electrodeposition of Nanomaterials 836
26.1.1 Direct Electrodeposition Without Template 836
26.1.2 Template-Assisted Electrodeposition 848
26.1.3 Electrodeposition on HOPG 855
26.1.4 Lithographically Patterned Electrodeposition 861
26.2 Electrodeposited Nanomaterials for Energy Storage/Conversion Devices 865
26.2.1 Lithium-Ion Battery Applications 866
26.2.2 Pseudocapacitors 873
26.3 Conclusions and Prospects 882
References 882

27 **Electrochemical Hydrogen Production**
Ting He, Mahaprasad Kar, Neal D. McDaniel, Bruce B. Randolph 897
27.1 Theoretical Aspects of Electrochemical Hydrogen Production 899
27.1.1 Thermodynamics of Water Electrolyzers 899
27.1.2 Chemical Kinetics at Electrodes 901
27.1.3 Transport in Electrolytes 901
27.1.4 Temperature Effect 902
27.1.5 Photoelectrochemistry 904
27.2 Electrochemical Hydrogen Production Methods 905
27.2.1 Low-Temperature Electrolysis 905
27.2.2 High-Temperature Electrolysis 912
27.2.3 Photoelectrolysis 923
27.3 Development Perspectives 929
27.4 Conclusions 933
References 934

28 **Electrochemical Machining**
Michael Schneider, Manuel Lohrengel 941
28.1 Introduction and History 942
28.1.1 History 942
28.2 Fundamentals of Electrochemical Machining 943
28.2.1 The Fundamental Process 943
28.2.2 Passivity, Transpassivity and Transition to ECM Conditions 943
28.2.3 Side Reactions 944
28.2.4 Common Interface Models 945
28.3 Experimental Techniques 946
28.3.1 Laboratory Setup for Quantitative Investigations 946
28.3.2 Product Analysis 948
28.3.3 Gaseous Products 948

28.3.4 Surface Characterization Electron Backscatter Diffraction (EBSD) 948
28.4 The Interface Process During ECM 949
28.4.1 Cyclic Voltammetry and Surface Layers 949
28.4.2 Supersaturated Product Films 950
28.5 Classification of ECM Processes 952
28.6 Surface Topography, Crystallographic Effects and Surface Quality 952
28.6.1 Theory 953
28.6.2 Grains in Experiments 954
28.6.3 Grain Boundaries and Other Crystal Defects 955
28.6.4 Surface Brightening 957
28.7 Oxygen Evolution 958
28.8 Pulse ECM 959
28.9 Too Difficult-to-Machine: Hard Metals, Carbides and Nitrides 962
28.9.1 Titanium 963
28.9.2 Cemented Carbides 964
References 967

About the Authors 973
Detailed Contents 985
Subject Index 999

Subject Index

1H NMR 334
1-palmitoyl-2-oleoyl-*sn*-glycero-3-phosphocholine (POPC) 122
1-pyrenesulfonic acid (PSA) 847
3,5-bis(2-pyridyl)-1,2,4-triazole (HQBpt) 406
3-D distribution function 122
3-D molecular theory 121
3D-HNC bridge-corrected closure (3D-HNC) 100
3-D-profilometry 430
3D-RISM theory 104
4-carboxy-(2,5,7-trinitro-9-fluorenylidene) malonitrile (CTNFM) 191
7Li-NMR 476
13C NMR 336
195Pt NMR 335

A

absorbance unit (AU) 368
AC (alternating current) 454, 633, 752, 851
– dielectrophoresis 148
– impedance 459, 462
accelerated dissolution 943
accelerated test 629, 630
accelerated-rate calorimetry (ARC) 486
accurate transport model 240
acetonitrile (AN) 498
– health concern 568
acoustic emission (AE) 475
acoustic measurement 478
acousto-optic modulator (AOM) 385
activation
– energy 232
– enthalpy barrier 84
– overpotential 290
– polarization 665, 678
active
– dissolution 945
– electrode area 162
– membrane area 303
– surface area 144
activity coefficient 83
actuator 194
adenosine triphosphate (ATP) 758
adenosine-5′-triphosphate (ATP) 190
advanced battery energy density 451
advanced solvation force extrapolation (ASFE) 119
aerogel 519
– electrode 506
Ag/AgCl reference electrode 817
agglomerate model 267, 280
aggregated nanoparticle 841
air–stoichiometric ratio 306
alanine dipeptide 120
alcohol dehydrogenase (ADH) 762
alkaline fuel cell (AFC) 424, 460
alkaline water electrolysis 908
aluminum
– anodization 849
– cell 807
– metal electrolytic process for 7
American Society for Testing and Materials International (ASTMI) 618
amperometric method 227, 750
amperometry 752
amphiphilic molecule 148
Amsterdam density functional (ADF) 98
anion exchange membrane (AEM) 594
anode 280
– composite 809
– humidification 674
– humidifier temperature (AHT) 663
– inert 824
– surface 81
– tin oxide 824
anodic
– alumina membrane (AAM) 861
– aluminum oxide (AAO) 848
– dissolution 946
– process 944
anodization setup 849
anthraquinone (AQ) 580
antimony-doped tin oxide (ATO) 155
aqueous electrolyte 502
– solution 104
area-specific activity (SA) 427
area-specific impedance (ASI) 484
Arrhenius
– behavior 85
– equation 17, 45
– relationship 484
ascending–descending sequence 178
assembly 621
– verification 625
asymmetric capacitor 502, 520
atomic
– force microscopy (AFM) 368, 450, 475, 640, 735, 865
– fraction 339
– layer deposition (ALD) 153
attenuated
– internal reflectance (AIR) 381
– total reflectance infrared (ATR-FTIR) 368
– total reflection (ATR) 380, 748
Au@Pt NP 341
auxiliary electrode (AE) 227, 369, 408
availability 38
avalanche photodiode (APD) 390
Avanti process 810
averaged electrostatic potential 131
Avrami plot 454

B

$Ba_{0.5}Sr_{0.5}Co_{0.8}Fe_{0.2}O_{3-\delta}$ (BSCF) 914
back diffusion 360
back-scattered electron (BSE) 829
bacteria fuel cell 613
balance equation 766

Ballone–Pastore–Galli–Gazzillo (BPGG) 100
Barrett, Joyner, and Halenda theory (BJH) 584
battery 73, 189, 331, 496
– discharge time scale 564
– hybrid with electrochemical capacitor 564
– lead acid 564
– lithium-based 460
– lithium-ion 24, 835
– material 449
– redox 591
– transport property 456
beam splitter (BS) 390
Becquerel 779
Beer–Lambert law 368
Bellcore-like flexible NMR cell 347
beta phase stabilizer 827
bicinchoninic acid (BCA) 748
bicontinuous cathode 190
bifunction 738
Billiton process 810
biobattery 744
bioelectrocatalysis 744
– direct 745
– mediated 745
bioelectrochemical electrolytic system 758
bioelectrochemical system
– working principle 758
bioelectrochemistry 165
biofuel cell 24, 181, 744, 750
– tissue-based 744
biomedical device 861
biomolecular
– process 119
– solvation 120
biosensor 190, 226
biphasic electropolymerization 848
bipolar
– bandgap MBPEC 790
– gap 791
– plate 911
birdcage resonator 360
bis(oxalato)borate (BOB) 463
bis(trifluoromethanesulfonyl)imide (TFSI) 463
Bode plot 633, 695
borohydride fuel cell 613
boron-doped diamond (BDD) 369
bottle humidifier 661
boundary conditions 244
– dynamic 71, 87
– electrode surfaces 77
bovine pancreatic trypsin inhibitor (BPTI) 100
bovine serum albumin (BSA) 748
brackish water 85
Bradford assay 748
Bragg diffraction 193
Brandau number 298, 301
Broken Hill proprietary (BHP) 810
bromine 594
Brownian motion 146
Brunauer–Emmett–Teller (BET) 279, 513, 566, 584
Brunauer–Emmett–Teller (BET) theory
– Barrett, Joyner, and Halenda theory (BJH) 584
Buckingham theory 297
bulk
– electrolysis 370
– electrolyte resistance 460
– liquid 116
– magnetic susceptibility (BMS) 345
– movement 902
Butler–Volmer (BV) 764
– equation 18, 71, 290, 424, 901
bypass (BP) 310, 617

C

cadmium selenide (CdSe) 844
cadmium sulfide (CdS) 840
calcination 152
calciothermic reduction 812
calcium
– incorporation 821
– titanate ($CaTiO_3$) 820
– titanite ($CaTi_2O_4$) 820
calculation of pinch 654
calculation of solvation forces 118
calibration 620
calomel electrode 82
calorimetry
– accelerated-rate 486
capacitance 128
– specific 568
capacitor 24
– asymmetric 502, 520
– double layer 496, 565
– hybrid 503
capacity loss 322
capillary
– method 151
– pressure 357
– water permeation 357
capital expense (CAPEX) 931
capping agent 838
carbide 962
carbochlorination 805
– process 805
carbon 505–509
– aerogel 506
– dioxide (CO_2) 801
– dioxide electrolysis 794
– electrode 501
– fiber 334
– fiber electrode 602
– graphene 585
– monoxide (CO) 685, 801
– morphology 584
– nanoparticle 131
– nanotube (CNT) 106, 508, 585, 602, 774, 855
– nanotube array 879
– supported RuO_2 524
– surface area 585
– surface-modified 566, 580
carbon/carbon capacitor 500
carbon-derived carbons (CDC) 507
carbonized polyvinylidene chloride (PVDC) 129
carbonized PVDC 129
carbothermic reduction process 803
Carnot factor 38
Car–Parrinello molecular dynamics (CPMD) 115
carrier generation 781
$CaRuO_3/CaTiO_3$ composite 824
Castner–Kellner process 28
catalysis 601
– heterogeneous 336
catalyst
– biocatalyst 743
– coated membrane (CCM) 621
– ink 639
– utilization 689
catalytic protein 744
catalyzed glucose oxidation 763
cathode 353
– bicontinuous 190
– catalyst layer 281
– humidification 674
– humidifier temperature (CHT) 663

– lithiated 454
– optimal 280
– surface 82
cathodic
– polarization 965
– reaction 945
cation exchanger 215
cation-exchange membrane 79
cavity ring down spectroelectrochemistry (CRDS) 384
cell
– channel flow 946
– coin 481
– concentration 73
– configuration 481
– degradation 922
– design 752
– droplet 946
– dye-sensitized solar (DSC) 195
– electrochemical 74, 241, 428
– flow 750
– formation 73
– galvanic 449
– humidification 672
– long optical path thin layer 378
– Ohmic photoelectrochemical 788
– performance 249, 354
– planar 915
– plastic flexible battery 344
– potential 80
– pouch 481
– reflective thin layer 381
– single 624
– solar 786
– solid oxide electrolysis 898
– solid oxide fuel 898
– temperature (CT) 663
– thin layer 367
– three electrode 578
– three-electrode storage 783
– two electrode 578
– voltage loss 680
– wound 482
cell (DSC)
– dye-sensitized solar 779, 784
cell-free system 758
cellular respiration 759
cellulose nanocrystal (CNC) 106
cemented carbide 964
ceramic separator 471
cetyltrimethyl ammonium bromide (CTAB) 841
channel flow
– cell 946
Chapman layer 44
characteristics mass exchanger 299
charge
– balance 11, 264
– cycle 322
– production density 265
– storage 525
– storage mechanism 528
– transfer 210, 232
– transfer complex (CTC) 773
– transfer overpotential 599
– transfer resistance 577
charge–discharge cycle 347
charging current 635
chemical
– energy transformation 57
– equilibrium 129
– etching 957
– kinetics 901
– potential 96, 128
– shift 351
– shift imaging (CSI) 351
– substance availability 39
– vapor deposition (CVD) 152, 368, 879
chemical reaction
– availability 37
– energy diagram 47
– temperature 47
chlor–alkali process 27
chloride electrolysis 793
chlorine–alkali electrolysis 54
choice of variables 75
chronoabsorptometry 375
chronoamperometry (CA) 835
chronopotentiometry (CP) 835
circular dichroism (CD) 380
cleaning agent 624
closed electrochemical cycle 60
clustered nanoflake 840
CO adsorption 436
CO_2 footprint 931
coated microwire 187
coated wire electrode 226
coaxial nanowire 877
cobalt 964
coefficient of performance (COP) 33, 43, 57
coflow 297
– operation 292
coin cell 481
colloidal
– assembly 151
– sphere 146
– stacking 182
– template 156
– templating 152
colloidal crystal 145, 146
– assembly 147
– fabrication 152
– gold-filled 185
– planar defect 173
– single-gradient 173
– template 182
– thickness 150
complementary metal-oxide-semiconductor (CMOS) 537
complementary reaction 943
complete active space self-consistent field (CASSCF) 98
complexing agent 842
composite
– anode 809
– electrode 516
– polypyrrole 168
– structure 165
comprising catalyst (CL) 259
computational fluid dynamics (CFD) 240
concentration
– cell 73
– cell potential 78
– distribution curve 296
– field 264
– gradient 80
– overpotential 599
– polarization 669
– profile 632
concentrator photovoltaic cell (CPV) 794
conducting polymer (CP) 143, 165, 170, 222, 566
– capacitance 566
– nanostructure 845
– polypyrrole 180
– stability 566
conductivity
– of the electron conductor 265
– of the ion conductor 265
confocal Raman spectroelectrochemistry 406
conifer-like structure 841

constant
– current discharge 453
– phase element (CPE) 576, 634, 692
consumption of reactant 637
contact angle 196
contact ion pair (CIP) 104
contaminant 615
convection 19
conventional cycle comparison 64
conversion efficiency 782
Coomassie blue 748
copper
– grid 345
– sulfide 844
– sulfide nanowire 844
core–shell
– nanowire 855
– particle 151
correlation function 101
corrosion 27, 953
– at liquid interface 27
– protection 165
– resistance 261
cost-scaling factor 897
coulomb counting 450
coulombic efficiency (CE) 486
coulometry 486
counter electrode (CE) 155, 370, 407, 428, 635, 685, 781
counterflow
– case 296
– operation 293, 299
counterion 165
coupled transport 69, 74, 81, 90
coupling
– at interfaces 71
– in homogeneous phases 71
crack formation 147
cracked cavity electrode 819
crane 542
creactive protein (CRP) 190
crossflow operation 299
crossover current density 688
crystal
– membrane electrode 213
– modifier (CM) 842
– orbital hamiltonian population (COHP) 341
– quality 146
– structure 451
crystallization overpotential 599
crystallographic characterization 955
crystallographic effect 952
Cu UPD 436
cubo-octahedral cluster 340
Cu-Cu_2O core–shell nanoparticle 838
Curie principle 71
Curie temperature 194
current
– density 46, 943
– discharge 453
– efficiency 967
– interrupt technique 676
– oscillation 157
– yield 601
current collector 357, 871, 872
– nanoarchitectured 871
current-voltage distribution 636–638
cycle life 522
cyclic voltabsorptometry (CVA) 378
cyclic voltammetry (CV) 231, 373, 427, 434, 526, 527, 571, 684, 732, 816, 835
– capacitance 572
cyclic voltammogram (CV) 162, 634
cycling life 485
cylindrical symmetry 345
cytochrome c peroxidase 767

D

data acquisition 620
data storage 861
DC electrophoresis 148
DC polarization 462
Debye–Hückel law 243
deep discharge 598
defect
– grain boundary 150
degradation 311, 918
– mechanism 921
dehydration 353
dehydrogenase 746
dendritic structure 842
density
– functional theory (DFT) 313, 340, 404
– of state (DOS) 315, 725
– probability distribution 83
deoxyribonucleic acid (DNA) 758
deposition overpotential 856
depth of discharge (DOD) 594
descending stack 178
desulfovibrio fructosovorans (Df) 761
dew point temperature 658
diagnostic
– imaging 352
– method 611
– technique 626
diaphorase (DI) 192
dichlorophenolindophenol (DCIP) 746
dielectrically consistent reference interaction site model (DRISM) 124
diethylmethyl(2-methoxyethyl) ammonium (DEME) 530
difference frequency generation (DFG) 413
differential
– cyclic voltabsorptometry (DCVA) 378
– pulse technique 190
– reflectance 381
– scanning calorimetry (DSC) 454, 640
diffraction electrode 451
diffuse reflectance (DR) 381
diffusion
– back 360
– coefficient 302
– Fick's law 19
– layer model (DLM) 220
– overpotential 599
diffusion element
– Warburg 694
dimensionally stable electrode (DSE) 28
dimethyl carbonate (DMC) 456, 530
dimethylformamide (DMF) 533, 844
dimethylsulfone (DMS) 530
dimethylsulfoxide (DMSO) 840
direct
– borohydride fuel cell (DBFC) 240
– current (DC) 458, 696, 752, 851
– electron transfer (DET) 760
– methanol fuel cell (DMFC) 53, 240, 662, 713, 724
discharge capacity 453
disordered matrix 123
disproportionation 55

dissipated energy 73, 83, 91
dissolution
– kinetic 953
– rate 942
– reaction 943
divinylbenzene (DVB) 859
dodecylbenzene sulfonic acid (DBSA) 839
Donnan equilibrium 86
double layer 44
– capacitance 265, 508
– capacitance predicting 565
– capacitor 496
– capacity 166, 606
– effect 21
double-gradient gold electrode 179
down field 348
droplet cell 946
drug sensitive electrode 226
dry air mass flow rate 306
dry bulb temperature 658
d-sorbitol dehydrogenase (DSDH) 192
dual-bandgap system 924
durability 630
dye-sensitized solar cell (DSC) 195, 779, 784
dynamic hydrogen electrode (DHE) 432
dynamic nuclear polarization (DNP) 332, 360

E

edge-induced shearing 151
effective mass transfer coefficient 296, 299, 304
effective surface area 281
effectiveness factor 271
efficiency 752
– conversion 782
elastic photonic crystal (EPC) 195
electric
– double layer (EDL) 11, 24, 96, 123
– potential 78
– potential profile 89
– vehicle (EV) 450, 537
electrical
– conduction 352
– efficiency 900
– energy conversion 780
– misuse 486
– short 616
– work 15
electro motoric force (EMF) 220
electroactive integrated optical waveguide (EA-IOW) 384
electro-assisted deposition (EAD) 191
electrocatalysis 165, 338
electrocatalyst 423, 745
– ink 429
– loading 431
electrocatalytic surface area (ESA) 722
electrochemical
– process 767
– quartz crystal microbalance (EQCM) 512
electrochemical (EC) 331, 897
– active surface area 427, 636, 684
– availability 41
– characterization 162, 497
– cycle 61
– deposition 155
– device 240
– device modeling 240
– double layer 268
– double layer capacitor 496, 565, 873
– energy storage 781
– lithography 864
– quartz crystal microbalance 512
– reaction 33, 54, 233, 262, 713
– stability 923
– step-edge decoration 857
– storage 594
– strain microscopy 475
– surface area 719
– thermodynamic cycle 60
electrochemical capacitor (EC) 496, 563
– area from BET 584
– binary solvent system 568
– bipolar stack 582
– capacitance 568
– cell design 581
– charge 565
– charge transfer resistance 576
– coin cell 581
– constant current discharge 568, 578
– construction 582
– current collector 583
– cyclic voltammetry 571
– de Levie pore model 576
– discharge time scale 564
– double-layer capacitance 565
– electrode 581
– electrolyte 567
– energy 565
– ESR 569, 585
– hybrid 500
– hybrid with battery 564
– impedance spectroscopy (IS) 573
– leak current 578
– low frequency capacitance 576
– maximum power 571
– Nyquist plot 574
– pore 576
– potential drift 580
– power 565
– pseudocapacitance 566
– Ragone plot 568
– resistance 576
– self-discharge 578
– separator 578
– series resistance 585
– source of ESR 570, 577, 584
– specific capacitance 568
– specific energy 568, 578
– specific power 568
– stability 573
– standard test method 585
– three electrode cell 578
– transmission line model 576
– two electrode cell 578
– two- versus three-electrode 579
electrochemical cell
– three-electrode 761
electrochemical impedance spectroscopy (EIS) 4, 25, 274, 454, 498, 573, 632, 752, 922
electrochemical machining (ECM) 941
– side reaction 944
– simulation 954
electrochemical potential 902
– definition 76
electrochemically active surface area (EASA) 602
electrochemiluminescence (ECL) 389
electrode 597
– Ag/AgCl reference 817
– architecture 185
– auxiliary 227, 369, 408
– calomel 82
– coated wire 226
– crystal membrane 213

– design 925
– dimensionally stable 28, 596
– drug sensitive 226
– electrochemical technique 453
– electrolyte interface 901
– evaluation 451
– gas diffusion 259, 621, 651
– gas-evolving 907
– gas-sensitive 226
– glass 211
– glassy carbon 429
– gold 178
– graphene 585
– hydrogen 209
– inert 210
– intercalation 477
– interface 21
– kinetics 668
– material 451, 497
– membrane 210
– metal-based 605
– model 262
– nanoarchitecture 507
– nanoporous 125
– normal hydrogen 402, 731
– optically transparent 368
– overpotential 69
– performance 671
– pseudo reference 332
– saturated calomel 432, 841
– sheet resistance 708
– Si 478
– silver sulfide 213
– sodium-selective 212
– solid-state 222
– spectroscopic study 452
– storage 785
– surface 74
– symmetric 127
– thermal study 454
– thin-film 368, 429
– thin-film RDE 431
– working 155, 407, 425, 460, 634, 683
– W-SiO_2 820
electrode (DHE)
– dynamic hydrogen 432
electrodeposited paint (EDP) 192
electrodeposition 156, 176, 340
– nanoparticle 836
– template-assisted 848, 854
electro-Fenton's reagent 603
electrolysis 897
– alkaline water 908
– cell 73
– rate 370
– temperature 793
– water 5
electrolyte 454, 529
– additive 468
– aqueous 502
– binary solvent system 568
– conductivity 567, 951
– distributed resistance (EDR) 576
– electrochemical capacitor 567
– freezing point 568
– ion depletion 568
– solution 124
electrolytic 449, 808
– NMR cell 332, 335
– system 760
electrolyzer 24, 907
electromagnetic (EM) 368, 411
electromagnetic interference (EMI) 697
electromotive force (emf) 15, 82, 750
electron
– backscatter diffraction (EBSD) 948, 956
– beam lithography (EBL) 835, 863
– conducting network 261
– diffraction x-ray analysis (EDX) 958
– paramagnetic resonance (EPR) 366
– transfer (ET) 375
electroneutrality 127
electronic interaction 738
– Au/$AlPO_4$ 715
– Pt/Au 714
electronic resistance 23
electronically mediated reaction (EMR) 809
electronic-orbital-specific (EOS) 341
electroosmosis 86–88
electroosmotic
– drag 353
electrophoresis nuclear magnetic resonance (eNMR) 463
– tube 463
electrophoretic forces 146
electropolishing 190, 957
electropolymerization 165
electrosorption 128
electrostatic 103
– model 945
– potential 132
– repulsion 145
elemental composition 829
emulsion polymerization 145
endergonic reaction 35, 49
endothermic electrolytic process 780
endothermic reaction 35
endotropic reaction 48
– endothermic 53
– example 53
– exoenergetic 52
energy
– balance 35
– conversion 33, 34, 779
– disproportionation 55
– dissipated 73, 83, 91
– of electrolysis 793
– reorganization 766
– specific energy 568
– storage 165
– storage materials 342
– surface 953
– synproportionation 57
– transformation 54, 58
energy density
– advanced battery 451
energy-dispersive
– spectrometry (EDS) 722
– spectroscopy (EDS) 878
– x-ray analysis spectrometer (EDAX/EDS) 640
– x-ray spectroscopy (EDX) 829
engine cranking 541
entropy balance 73
entropy creation 46
entropy production 70, 87
– from calorimetric measurements 73
– homogeneous systems 74
– interfaces 74
– mesoscopic level 84
environmental compound 39
environmental scanning electron microscopy (ESEM) 640
enzymatic catalyst 762
enzymatic fuel cell 758
enzyme 744
– coverage 767
– linked immunosorbant assay 227
– substrate (ES) 763
equation
– Nernst 16, 46, 291, 449

equilibrium 36
– constant 36
– global 72
– local 71
– temperature 36
– zero entropy production 72
equivalent
– circuit model 703
– electrical circuit (EEC) 632, 634
– serial resistance (ESR) 129, 498, 522, 565
– temperature 37
ethanol oxidation 737
ethyl-3-methylimidazolium chloride (EMIC) 845
ethylene carbonate (EC) 456
ethylenediaminetetraacetate (EDTA) 210, 600
ethylmethyl carbonate (EMC) 456, 530
ethylmethylimidazolium (EMI) 530
ethyl-methyl-immidazolium-trifluoro-methane-sulfonylimide (EMI,TFSI) 508
evanescent wave (EW) 384
evanescent wave broadband cavity-enhanced absorption spectroscopy (EW-BBCEAS) 385
evanescent wave cavity ring down spectroelectrochemistry (EW-CRDS) 384
evaporation humidifier 661
exergeric COP 43
exergonic reaction 35
exergy 38
– loss 43, 73, 91
exoenergetic reaction 48
exothermic reaction 35
exotropic reaction 49
– endoenergetic 51
– example 51
– exoenergetic 50
experimental consistency check 70
experimental design 70
exponential recovery function 336
extended x-ray absorption fine structure (EXAFS) 450, 640
external cavity diode laser (ECDL) 385
externally controlled flux 78
externally controlled variable 78
extractive electrometallurgy
– calciothermic reduction 810
– constant voltage electrolysis 818
– continuous production of titanium 811
– direct electrodeoxidation 815
– direct electroreduction 814
– direct production of alloys 823
– electrochemical reduction of SiO_2 818
– electrochemical reduction of TiO_2 819
– electrolytic extraction 808, 809
– molten oxide electrolysis 811
– polar titanium process 813
– titanium electrolytic extraction process 811
– titanium production 808
extractive metallurgy
– carbothermic reduction 802
– electrolytic extraction 806
– electrometallothermic reduction 815
– electrometallurgy 801
– Hall–Héroult process 808
– Hunter process 804
– indirect metallothermic reduction 803
– Kroll process 804
– magnesium reduction 805
– metallothermic reduction 802

F

Fabry–Pérot fringes 175
face-centered cubic (fcc) 146, 837
faradaic efficiency 900
Faraday constant 15
Fe nanocrystal 837
Fenton's reagent 603
ferrocene (Fc) 396
fiber optic spectroelectrochemical sensor (FOSEC) 383
Fick's law 46, 291, 426
– of diffusion 19
field effect transistor (FET) 225
field emission (FE) 821
– scanning electron microscopy (FESEM) 860
field homogeneity 334
figure of merit (FOM) 449, 932
filling ratio 153
filling-factor 348
filter-press type electrolyzer 906
fingerprint sensor 194
finite element (FE) 239
finite volume (FV) 239
flammable materials 651
flash photolysis 391
flavin adenine dinucleotide (FAD) 745, 762
flavin mononucleotide (FMN) 773
flooded agglomerate model 281
flow battery 591, 640
– cell 598
– lithium-based 592
flow cell 750
flow field 598
fluctuation
– hydrodynamic 72
fluctuation-dissipation theorem 72
fluoride sensitive electrode 213
fluorine-doped tin oxide (FDTO) 367
flux density 902
flux equation 82
foreseeable misuse 486
forklift 542
formation cell 73
– mass balance 76
– non-isothermal 80
formation reaction 39
formic acid oxidation reaction (FAOR) 341
fouling 595
Fourier's law 88
Fourier-transform (FT) 394
Fourier-transform electrochemically modulated infrared spectroscopy (FT-EMIRS) 397
Fourier-transform infrared (FTIR) 376, 640, 748
frame of reference 75
Fray–Farthing–Chen (FFC) 801, 815
– Cambridge process 814
frequency response analyzer (FRA) 633, 697
fresh water 85
friction electricity 86
Frumkin/Temkin (FT) 274
Frumpkin 21
FTIR spectroscopy 394
fuel
– channel 249
– crossover 683
– efficiency 752

fuel cell (FC) 73, 189, 352, 423, 617, 640, 713, 910
– alkaline 424, 460
– bacteria 613
– biological 743, 744
– borohydride 613
– component fabrication 640
– conditioning 627
– design 623
– enzymatic 758
– high-temperature 276
– humidification 294
– hybrid 744
– hydrogen 615
– limiting current density 666
– methanol 53, 240, 662, 713, 724
– microbial 752
– microfluidic 752
– moisture content 659
– operation 287, 916
– oxygen 615
– performance 353, 651, 661
– polymer electrolyte 87
– proton 460
– proton-exchange membrane 23, 248, 352, 423, 656
– regenerative 591
– stack 621
– support component 629
– system 294, 310
– test stand 619
– test station 616, 657
– test station control 618
– thin layer 613
fuel cell laboratory 611
– facility planning 614
– regulation 614
– test station 614
full cell potential 78
full width at half maximum (FWHM) 334, 373
fusion alloying process 823

G

gadolinium-doped ceria (GDC) 912
Galvani potential 21
galvanic cell 449
galvanic system 760
galvanostatic
– discharge 568
– polarization 750
gap identification 626, 627
gas chromatography-mass spectrometry (GC-MS) 748
gas diffusion electrode (GDE) 259, 621, 651
gas diffusion layer (GDL) 259, 288, 352, 489, 624, 651
gas flow field plate 624
gas-evolving electrode 907
gas-sensitive electrode 226
Gaussian de-convolution 339
gel electrolyte 470, 531
gel polymer electrolyte 531
generalized
– gradient approximation (GGA) 317
– minimal residual (GMRes) 103
– SFE (GSFE) 98
– solvation force extrapolation (GSFE) 119
generalized Born (GB) 97
– solvent accessible surface area (GBSA) 97
germanium inverse opal 155
Gibbs
– energy 36, 80
– excess density 71
– free energy 14, 243, 760, 900
Ginatta Technologie Titanio (GTT) 808
glass electrode 211
glassy carbon (GC) 428, 774, 837
– electrode 429
global warming potential (GWP) 932
glucose 40
– dehydrogenase (GDH) 772
– oxidase (GOx) 743, 772
Gouy–Chapman
– diffuse layer 96
– model 21
grain boundary 955
graphene
– based optically transparent electrode 368
– oxide 602
– paper 879
graphite 602
– intercalation compound (GIC) 467
– oxide (GO) 368
– surface area 585
– wax electrode (GWE) 378
gravitational force 146
grid development 246
grid-related storage 592
Grothuss-like transportation mechanism 469

H

half-cell reaction 899
hard
– and soft templates 144
– anodization (HA) 848
– metal 962
hardware in the loop 631, 639
Hartree potential 114
heat of transfer 87, 88
heat transformation 58
heat-treated carbon fiber 602
helical rosette nanotube (HRN) 112
Helmholtz
– layer 21, 44
– model 508
heterogeneous catalysis 336
heterogeneous system 69, 90
hexagonal close-packed (hcp) 146, 955
hierarchical flowerlike gold microstructure (HFGM) 840
hierarchical porosity 164
high
– angle annular dark field (HAADF) 716
– frequency resistance 632
– precision coulometry (HPC) 486
– resolution transmission electron microscopy (HRTEM) 473
– solar to electric efficiency 784
– surface area carbon (HSC) 423, 429
– voltage 616
higher heating value (HHV) 900
highest occupied molecular orbital (HOMO) 470
high-field oxide 952
high-frequency resistance (HFR) 698
highly ordered pyrolytic graphite (HOPG) 534, 605, 835, 856
high-performance liquid chromatography (HPLC) 226, 381
high-temperature electrolysis (HTE) 898
high-temperature fuel cell 276
hollow
– fiber humidifier 301

– golf club head 828
– sphere 828
homogeneous anode phase 80
horseradish peroxidase (HRP) 766
HPLC-detector 236
human neuroglobin (hNb) 375
humidification 287, 309, 660
– control 618
– method 660
humidifier 287
– calculation 307
– development 303
– efficiency 307
– operation characteristic 307
humidity 292, 357
Hunter process 803
hybrid
– capacitor 503
– double-walled nanotube (HDWNT) 855
– drive technology 539
– electric vehicle (HEV) 450, 537
– pulse power characteristic (HPPC) 484
– truck 538
– vehicle 539
hydrodynamic electrochemistry 425
hydrogel
– electrolyte 531
– inverse opal 194
hydrogen 615
– adsorption/desorption (H_{upd}) 436
– adsorption/desorption (HAD) 684
– chloride electrolysis 52
– crossover rate 636, 637
– electrode 209
– evolution reaction (HER) 910
– fuel 780
– oxidation reaction (HOR) 634
– production 897
– sensor 857
hydrogen fuel cell 43, 65, 615
– closed circuit 64
hydrogenase 770
hydrophobic solvent 109
hypernetted chain (HNC) 100

I

ideal electrochemical processes 249
impedance spectra 702
impedance spectroscopy (IS) 25, 460, 471, 633, 699
– constant phase element 576
– diffusion region 576
– Nyquist plot 574
– porous region 576
– principle 632
– transmission line model 576
indicator electrode 210
indium tin oxide (ITO) 148, 367, 513, 716, 840
inductively coupled plasma-atomic emission spectroscopy (ICP-AES) 733
inductively coupled plasma-mass spectroscopy (ICP-MS) 729
industrial shaping 942
inert
– anode 824
– electrode 210
– metal 952
infiltration of colloidal crystal 153
infrared (IR) 366, 787
– reflection absorption spectroscopy (IRRAS) 394, 397
inorganic
– crystal structure database (ICSD) 315
– nanotube 843
– nanowire 843
integrated laboratory scale (ILS) 914
intensified CCD (iCCD) 392
intercalated Li 343
intercalation electrode 477
interface
– model 267, 273, 945
– modeling 276
– process 949
interference lithography (IL) 863
internal
– DC resistance 483
– short circuit 683
– variable 71, 83
interparticle diffusional coupling (IDC) 856
interphase 455
– additive 468
– formation 463
inter-valence charge transfer (IVCT) 372
inverse opal 155
ion
– etching 603
– selective sensor (ISS) 222
ion exchange 172
– membrane (IEM) 85, 86, 239, 596
ionic
– conductivity 458, 459
– mobility 315
– resistance 23
– transference number 464
ionic liquid (IL) 26, 98, 115, 508, 530, 845
– electrochemical capacitor 567
– voltage range 567
ionomer phase 282
ionomer-to-carbon ratio (I/C) 429
ion-selective
– electrode (ISE) 217
– field-effect transistor (ISFET) 225
iron oxide electrolysis 794
irreversibility 45
isobaric gas 292

J

Jahn–Teller symmetry breaking 319
J-coupling 337
junction material 817

K

Kapton tube 181
Kauranen model 274
Ketjen Black (KB) 524
Kikuchi lines 948
kinetic 17
– limitation 678
– loss 631
Knight shift 336, 352
Kohn–Sham density functional theory (KS-DFT) 98
Koutecky–Levich equation 426, 639
Kovalenko and Hirata (KH) 97
Kroll process 806

L

laboratory scope 626
laccase 743

Langevin (LN) 117
Langmuir or Frumkin/Temkin adsorption 274
Langmuir–Blodgett technique (LB) 148
lanthanum manganite (LSM) 913
lanthanum strontium cobalt ferrite (LSCF) 913
law of mass action 72
layer-by-layer
– assembly 174
– deposition 149
layered oxide compound 316
L-camphorsulfonic acid (L-CSA) 847
lead acid accumulator 596
Lennard-Jones cross-term 114
Levich 20
– equation 426
Leyden jar 1
Li
– battery 74
– dentritic structure 350
– diffusion 454
– insertion 345
– microstructure 350
– NMR 342
$LiCoO_2$ 452, 453
life cycle analysis (LCA) 931
$LiFePO_4$ 451–453
ligand charge transfer transition 408
ligand-gated ion channel (GLIC) 97
Li-ion
– battery 23, 315, 470, 866
– cell 483
– technology 450
limiting current 632
– density 292, 666
line circuit model 705
linear
– flux–force relations 69, 81
– polarization 751
– sweep voltammetry (LSV) 230, 650
Lineweaver–Burk plot 746
$LiNi_{1/3}Co_{1/3}Al_{1/3}O_2$ ($NCA_{1/3}$) 313
$LiNi_{1/3}Co_{1/3}Mn_{1/3}O_2$ (NCM) 313
liquid
– ion exchanger 214
– junction potential 82
– membrane electrode 213
– precursor 154
liquid chromatography-mass spectrometry (LC-MS) 748
liquid electrolyte 460
– governing equations 241
– separator 470
– transport 242
liquid-phase electrolyte 239
lithiated cathode 454
lithiation 324, 466
lithium-based battery 460
lithium-ion battery (LIB) 24, 835
lithium-sulfur (Li-S) 487
– battery 487
lithographic method 864
lithographically
– guided electrodeposition 861
– patterned nanowire electrodeposition (LPNE) 862
load leveling 592
local density approximation (LDA) 317
local density of state (LDOS) 338
local equilibrium
– chemical 71
– evidence for 72
– model 220
– thermodynamic 71
localized surface plasmon (LSP) 853
long optical path thin layer cell (LOPTLC) 378
long-range correlation 72
long-term performance 921
long-term stability 722
loss coefficient 43
lost work 73
low humidity condition 705
low temperature (LT) 617
low-carbon electricity source 930
lowest unoccupied molecular orbital (LUMO) 470
Lowry assay 748
low-temperature electrolysis 905
Luggin capillary 227
luminescence spectrometer 386

M

macropore 143, 505
macroporous
– conducting polymer 180
– electrode 181
– hydrogel PC 194
– material 172
– metal electrode 156, 161
– platinum 164
macroporous gold
– cylinder 181
– electrode 160, 177
– film 196
macroscale modeling 269, 282
magic angle spinning (MAS) 342, 348, 475
Magneli phase 820
magnetic circular dichroism (MCD) 376
magnetic resonance imaging (MRI) 331
magnetohydrodynamic (MHD) 61
manganese dioxide 510, 518–522
– polymorph 516
manganese dioxide/carbon composite electrode 518
manganese oxide 566
manganese-carbon nanoarchitecture 522
Marcus theory 766
Martynov–Sarkisov (MS) 100
mass
– activity (MA) 435
– balance 263
– detection sensitivity 331
– exchanger 294, 298
– flow controller (MFC) 656
– spectrometry (MS) 748
mass transfer
– coefficient 287, 303
– efficiency 298
– loss 631
mass transport 11
– correction 439
– limitations 678
– loss 667
mass-specific activity (MA) 427
material
– balance 266, 269
– characterization 640
– safety data sheet (MSDS) 616
materials and electrochemical research (MER) 809
matrix nanoparticle 127
Maxwell potential 77
Maxwell-Stefan diffusion coefficient 266
Mayer diagram 124
mean spherical approximation (MSA) 100

measuring humidity 658
mechanochromic photonic crystal 195
mediated electron transfer (MET) 764
mediator 764
melting point 471
membrane
– diffusion 87
– humidifier 660
– resistance 664
– template 850
– thermal conductivity 87
membrane electrode 210
– crystalline 213
membrane–channel interface 247
membrane–electrode assembly (MEA) 288, 425, 612, 651, 723, 909
mercury intrusion porosimetry (MIP) 640
mesh electrode 369
mesopore 143, 505
mesoporous carbon microbead (MCMB) 605
mesoporous vanadium oxide 866
metal
– air battery 423
– electrode 210
– nanoparticle 192
– nanowire 851
– nanowire fabrication 860
– phosphate matrix 738
– to-ligand charge transfer (MLCT) 372
metal alloy
– hydrogen storage 825
– $LaNi_5$-type alloy 825
– synthesis 825
– Ti-6Al-4V 829
– Ti-10W alloy 826
– $TiFe_{0.4}Ni_{0.6}$ 826
– Ti-Ni alloy 826
– titanium-based alloy 825
metal oxide 313
– chromium oxide (Cr_2O_3) 802
– electrolysis 793
– iron oxide (Fe_2O_3) 801
– mercuriy oxide (HgO) 801
– mixture 823
– nickel oxide (NiO) 801
– structure 314
metal-adsorbate bonding 340
metal-based electrode 605
metallic
– cavity electrode (MCE) 817
– component 827
– Li 343
metallothermic 814
metallurgical-grade-silicon (MG-Si) 802
methanol (MeOH) 341
– fuel cell 62
methanol oxidation
– CO poisoning 724
– reaction (MOR) 341
methyl
– isobutyl keton isopropanol (MIBK:IPA) 864
– orange (MO) 847
– viologen 369
methylmethyl-imidazolium ($mmim^+$) 110
Michaelis constant 746
Michaelis–Menten
– kinetic 746
– plot 746
micro analytical system 223
microbe 744
microbial fuel cell 752
microcell 946
microdrop technique 387
microelectrode 232
microfluidic fuel cell 752
micropore 505
microporous carbon 507
microscale 269
migration 19
mild anodization (MA) 848
MnO_2-based devices 521
mobility
– along reaction coordinate 84
– ionic 79
model
– application 680
– discrimination 274
– parameter 279
– porous electrode 263, 268
modeling impedance data 703
modified
– carbon 602
– direct inversion in the iterative subspace (MDIIS) 103
– Verlet (VM) 100
moisture-exchange device 660
molar
– electric work 289
– electrostatic potential energy 15
– flow rate 289, 298, 918
– mass 306
molecular
– building block 110
– dynamics (MD) 97, 116
– Langmuir film 148
– liquid 96
– mechanics (MM) 109, 115
– orbital (MO) 341
– recognition 112
– theory 99
molten oxide electrolysis 811
molten salt electrolysis (MSE) 809
monodispersity 145
monolayer 149
Mössbauer effect 453
multienzyme cascade 760
multilayered template 184
multiple bandgap
– device 787
– photoelectrochemical solar cell (MBPEC) 788
multiple time step (MTS) 117
– molecular dynamics (MTS-MD) 97
multiscale coupling 113
multistage reduction 487
multiwall carbon nanotube (MWCNT) 580, 602, 771

N

N,*N*-diethyl-*N*-methyl-*N*-methoxyethyl ammonium (DEME) 531
Nafion 262
– film 429
– membrane 359
– transport property 250
nano
– conifer 841
– crystal (NC) 836
– fabrication 144
– flake 878
– flower 879
– foam 506
– patterning 865
– peapod 852
– pillar current collector 873
– pore 127
– prick 840
– rod 854
– scale catalyst 336

– sphere lithography 149
– void 196
nanocomposite
– $AlPO_4$–Pt/C methanol 724
– $FePO_4$–Pt/C 720–722
– Pt/$AlPO_4$ 737
– Pt/$FePO_4$ 734
nanocrystal (NC) 836
– Fe 837
nanoparticle (NP) 336, 856
– aggregated 841
– chain 853
– electrodeposition 836
nanoporous
– Au 854
– carbon 133
– carbonized PVDC 131
– confinement 99
– electrode 125
– material 123
– matrix 130
– morphology 96
nanoporous Pt 734
– thin film 733
nanostructure 96
– conducting polymer 845
– thin film 515
nanotrench 859
– fabrication 858
nanotube
– array 876
– electrodeposition 854
nanowire (NW) 844, 861
– array 859, 876
– coaxial 877
– electrodeposition 851
– multicomponent 852
– segmented 852
naphthalenesulfonic acid (NSA) 846
natural graphite (NG) 605
Navier–Stokes equation 241
near-infrared (NIR) 366
near-net-shape metallic component 827
Nernst
– behavior 635
– diffusion layer 767
– Einstein relation 242
– equation 16, 46, 291, 449
– Planck equation 79, 242
– potential 82, 604
net flux 902
neural engineering 165
neutral component 80
neutral red catalyst 762
neutron depth profiling 479
neutron diffraction 479
Ni/Cu nanowire 852
Ni/Pd/Pt 852
nickel
– chelating nitrilo-triacetic acid (Ni(II)-NTA) 376, 401
– inverse opal 155
– metal hydride (NiMH) 538, 585
nickel–zinc deposit 845
nicotinamide adenine dinucleotide (NAD) 745, 762
– phosphate (NADP) 745
NiO-YSZ cathode 914
nitrate reduction 948
nitride 529, 962
Ni–YSZ electrode 913
NMR cell
– Bellcore-like flexible 347
nonaqueous electrolyte 460
nonaqueous RFBs 595
nonequilibrium thermodynamic description
– concentration cell 73, 74
– formation cell 73, 74
nonequilibrium thermodynamics (NET) 69–75
nonlinear
– flux–force relations 69, 84, 90
– frequency response analysis (NFRA) 275
– system coupling 85
non-oxide compound 808
normal hydrogen electrode (NHE) 402, 731
normalized exergy 38, 42
Nosé–Hoover (NH) 117
nuclear magnetic resonance (NMR) 115, 331, 366, 450, 475, 748
– spectroscopy 335
– tube 332
number of transfer units (NTU) 298
Nyquist plot 633, 695
– ideal electrochemical capacitor 574

O

O_2 flow rate 354
octadecyltrichlorosilane (OTS) 843
Ohmic loss 632, 666
Ohmic photoelectrochemical cell 788
one-step anion maker 952
Ono–Suzuki (OS) process 810
Onsager relation 70
opal 145
opaline film 151
open circuit
– potential (OCP) 386, 578, 770
– voltage (OCV) 314, 346, 452, 635, 664, 760, 915
– voltage crystalline Si 346
open electrochemical cycle 63
optical sensor 194
optically transparent
– electrode (OTE) 368
– thin layer electrode (OTTLE) 370
optimal cathode 280
– porosity 822
optimized catalyst layer 280
optimized isokinetic Nosé–Hoover (OIN) 98
orbital-free embedded (OFE) 98
ordinary pyrolytic graphite (OPG) 605
organelle 744
organic
– electrolyte 501
– Rankine cycle (ORC) 61
– solvent 529
Ornstein–Zernike (OZ) 97
outdoor photoelectrochemical cell 782
outer membrane cytochrome (OMC) 412
overpotential 17, 83, 290, 424, 900
– deposition 856
– diffusion 599
– effective driving force 85
– metal deposition (opd) 604
– surface 901
oxidant composition 668
oxidation 724
– reaction 11
oxidative and reductive cycle (ORC) 411
oxide 338, 529
oxide-containing matrix 145
oxidizer channel 249
oxidoreductase enzyme 746
oxygen 615
– cathode 276
oxygen evolution 958
– reaction (OER) 490, 910

oxygen reduction reaction (ORR) 341, 423, 489, 634, 662, 713
– four-electron reduction 713
– hydrogen peroxide 716
– two-electron reduction 713

P

packing density (PD) 338
packing factor 150
pair-density function (PDF) 528
PANI nanorod 845
parasitic current 460
partial density of states (PDOS) 319
– calculation 326
partial series expansions of order *n* (PSE-n) 100
patterned electrodeposition 861
PbS 839
PbTe 843
peak current 634
peak potential difference 634
peapod nanostructure 853
Peltier
– coefficient 73
– cooling 87
– effect 75, 86
PEM fuel cell
– operating conditions 678
– performance 628
– polarization curve 631
– resistance 658
– stack 294
Percus–Yevick (PY) 100
perfluorosulfonic acid (PFSA) 23, 261, 910
periodic table 358
perovskitisation 821
phase diagram 457
phenazine methosulfate (PMS) 746
phosphate buffer solution (PBS) 846
photo-activated localization microscopy (PALM) 415
photoanode 903
photoelectrochemical (PEC) 779, 898
– conversion efficiency 782
– PV cell 780
– storage cell 782–784
photoelectrochemistry 779, 904
photoelectrode 903
photoelectrolysis 923
photolithographic method 861
photomultiplier tube (PMT) 385
photonic bandgap (PBG) 145, 193
photonic crystal (PC) 145
photoresist (PR) 861
photosynthesis 760
photovoltaic (PV) 779, 927
– array 933
physical damage 486
physical vapor deposition (PVD) 153, 863
pinch 655
– calculation of 654
planar cell 915
planar membrane humidifier 301
Planck potential 78, 86
plasma enhanced CVD (PECVD) 153
plastic flexible battery cell 344
platinum film 161
platinum/carbon (Pt/C) 423
plot
– Avrami 454
– Bode 633, 695
– Lineweaver–Burk 746
– Nyquist 633, 695
– Ragone 500
– Tafel 45
Poisson–Boltzmann (PB) 97
– solvent accessible surface area (PBSA) 97
Poisson's electrostatic equation 241
polarization curve 290, 631, 664, 749
– composition 632
polarization modulated (PM) 398
poly(3,4-ethylenedioxythiophene) (PEDOT) 155, 378, 566, 878
poly(3-octyl thiophene) (POT) 223
poly(dimethyldiallylammonium chloride) (PDDA) 192
poly(ethylene glycol) dimethyl ether (PEGDE) 532
poly(ethylene terephthalate) (PET) 850
poly(methyl methacrylate) (PMMA) 145, 532, 864
poly(tetrafluoroethylene) (PTFE) 533, 581, 652, 907
poly(vinylidene difluoride) (PVdF) 532
poly(vinylpyrrolidone) (PVP) 839
polyaniline (PANI) 156, 566, 845
polybithiophene (PBT) 169
polycarbonate (PC) 850
polyethylene (PE) 470
polymer aerogel 506
polymer electrode membrane fuel cell (PEMFC) 287, 713
polymer electrolyte 531, 909
– fuel cell 87
– membrane (PEM) 260, 294, 743
polymer fuel cell 82
polymer inverse opal 154
polyolefin membrane 471
polyoxometalate (POM) 369
polypyrrole (PPy) 156, 846
– deposition 165
– film 167
polystyrene (PS) 145
polysulfide (PS) 487
polythiophene (PT) 156
polyvinyl chloride (PVC) 213
polyvinylpyridine (PVP) 393
pore
– gradient architecture 172
– layer 177
– size gradient 180
porosity ratio shrinkage (PRS) 822
porous
– electrode 482, 599
– electrode model 263, 268
– media 243
– nanowire 853
– type anodization 849
postulates of nonequilibrium thermodynamics 70
potassium ferrocyanide 433
potential
– averaged electrostatic 131
– chemical 96, 128
– concentration cell 78
– electrostatic 79
– energy level 132
– field 46, 264
– Galvani 21
– Hartree 114
– isothermal formation cell 80
– liquid junction 82
– Maxwell 77
– non-isothermal formation cell 80
– of mean force (PMF) 97, 104
– Planck 78
potentiometric measurement 227
potentiostatic
– deposition 840

– intermittent titration (PITT) 454
– polarization 750
pouch cell 481
power
– curve 749
– quality 592
– specific power 568
– tool 538
PPY nanowire 847
precursor infiltration 152
primary
– battery 449
– particle 482
– solvation sheath 457
process time scale 626
product
– analysis 948
– composition 959
– identification 637
production reaction (PR) 39
programmed electrodeposition 836
propylene (PP) 470
propylene carbonate (PC) 467, 506
– replacement for acetonitrile 568
protection additive 468
protein quantification 747
protein–ligand binding 112
proton
– conductivity 288
– diffusion 513
– fuel cell 460
– nuclear magnetic resonance (^{1}H-NMR) 528
proton-exchange membrane (PEM) 23, 53, 352, 649, 898
– fuel cell (PEMFC) 23, 352, 423, 613, 656
proton-exchange membrane fuel cell (PEMFC) 244
pseudo reference electrode 332
pseudocapacitance (PC) 511, 565
pseudocapacitive material 529
pseudocapacitor 496, 873
pseudo-inductive response 695
Pt dissolution 719
Pt electrochemical surface area (Pt ECSA) 427
Pt island 340
Pt/C 435
– electrocatalyst 427
Pt/metal oxide catalyst
– Pt–RuO_2 731
– Pt–WO_3 731
Pt/Ru catalyst 724
Pt-based electrocatalyst 331
PtRu catalyst
– $FePO_4$ coating 727
– $FePO_4$-coated PtRu 727, 728
– Ru crossover 727
– Ru dissolution 725, 730
pulse ECM 959
pulse field gradient (PFG) 463
pump storage power plant 591
pyramidal Cu nanocrystal 839
pyrroloquinoline quinone (PQQ) 746, 772

Q

Q-factor 332
q-reaction 36
quadrupolar interaction 343
quantum
– chemistry (QC) 464
– mechanical simulation 953
– mechanics (QM) 115
– size effect (QSE) 336
quartz crystal microbalance (QCM) 747
quasi metallic 348
quasi-equilibrium solvation 97
Quebec iron and titanium (QIT) 811
– process 813

R

radial distribution function (RDF) 126, 130
radio frequency (RF) 335
– chokes 332
– coil 335
– radiation 350
– resonator 359
Ragone plot 500
Raman spectroelectrochemical emersion cell 407
Raman spectroscopy 404
Randles circuit 695
rate-determining mechanism 822
rate-limiting process 902
reactant
– humidification 661
– humidity 676
– purity 617
– supply 617
– utilization 666
reaction
– coordinate 83
– endergonic 35
– endothermic 35
– endotropic 48
– exoenergetic 48
– exothermic 35
– exotropic 49
– flux 245
– formation 39
– formic acid oxidation 341
– Gibbs energy 80
– half-cell 899
– kinetics 271
– overpotential 599
– oxygen reduction 341, 423, 489, 634, 662, 713
reactive-ion etching (RIE) 863
recovery braking 540
redox
– couple 784
– enzyme 770
– flow battery (RFB) 591
– process 170
– shuttle 470
redox battery 591
– all-vanadium system 594
– bromine/polysulfide system 594
– chemistry 593
– iron/chromium system 593
– vanadium/bromine system 595
– zinc/bromine system 596
– zinc/cerium system 595
redox reaction
– acceleration 600
– heterogeneous 600
reduced nicotinamide adenine dinucleotide (NADH) 758
reduction
– depth 816
– metal oxide reduction 801
– of titaniametallothermic 803
reference
– electrode (RE) 155, 208, 370, 428, 634, 653, 818
– interaction site model (RISM) 95
– system propagator algorithm (RESPA) 117
reflectance spectroscopy 381
reflective thin layer cell 381
refractive index change 194
regeneration kinetic 764
regenerative fuel cell 591
regions of interest (ROI) 354

relative humidity (RH) 356, 649
remote area power supply (RAPS) 591
reorganization energy 766
replica formalism 123
resonance Raman spectroscopy 407
reverse electrodialysis 85
– power density 86
reversible
– charge-transfer reaction 14
– deionization 15
– hydrogen electrode (RHE) 426, 716
revolution per minute (rpm) 426
Reynolds number 946
rhombic-dodecahedral (RD) 837
Rietveld refinement 451
ring disk collection efficiency 427
Robin-Day classification 373
room temperature (RT) 716
root mean square (RMS) 484, 585
rosette nanotube (RNT) 110
– surface self-assembly 111
rosette ring 110
rotating ring-disc 750
– electrode (RRDE) 426, 638, 639
rotating ring-disc electrode (RRDE) 423
rotating-disk electrode (RDE) 20, 423–425, 639, 722, 761, 767
– hydrodynamic flow 425
– methodology 424
rotating-disk voltammetry 749
roughness factor 164, 268
rules of coupling 71
RuO_2 523–528
Ru@Pt NP 341
ruthenium
– dioxide 524–528
– oxide 523, 566

S

safety 486, 611
– data sheet (SDS) 651
– Li-ion battery 486
– plan 614
– regulation 614
safety-trigger additive 468
saline power plant 85
salt bridge 82
samarium-doped ceria (SDC) 912
saturated calomel electrode (SCE) 432, 841
scandia-stabilized zirconia (ScSZ) 912
scanning
– electron microscopy (SEM) 144, 278, 348, 640, 735, 821, 837, 954
– near field optical microscopy (SNOM) 415
– probe microscopy (SPM) 475
– probe microscopy (SPM) probe 477
– transmission electron microscopy (STEM) 722
– tunneling microscopy (STM) 475, 640, 845
Sc–Ce-doped zirconia (ScCeZ) 914
Schottky barrier 904
sea water 85
secondary
– electrode interface (SEI) 22
– electrolyte interphase (SEI) 449
– electrolyte interphase (SEI) layer 465
Seebeck coefficient 86
selective dissolution 734
selectivity coefficient 218
self discharge 593
self-assembled monolayer (SAM) 144
self-heating 487
self-humidification 660
semiconductor 86
– photoelectrode (SPE) 783
semi-infinite linear diffusion (SILD) 370
sensitivity 358
sensitized solar
– cell 786
– mechanism of a dye 787
sensor
– fingerprint 194
sensorless humidification 302
separator 358, 595
shaping metal 943
shear alignment 151
Shockley current 781
short lived transient species 344
shrinkage 154
Si cluster 346
Si electrode 478
Si-based electrode 477
side reaction 944, 967
Siemens process 802
signal enhancement technique 332
signal-over-noise ratio 348
silicon
– column 821
– metallurgical-grade-silicon (MG-Si) 803
– purification 802
silver sulfide electrode 213
simple energy conversion 54
single
– carbon sphere (SCS) 130
– electrode heats 86
– molecule (SM) 412
– wall carbon nanotube (SWCNT) 771
single cell 622, 624
– PEM fuel cell 655
– testing 656
single-electrode method 749
singly occupied molecular orbital (SOMO) 380
six-membered supermacrocycle 110
skin-depth effect 350
slab optical waveguide spectroscopy (SOWG) 379
slow beat 339
small angle x-ray scattering (SAXS) 640
smoothly deposited (SD) 347
sodium dodecyl benzene sulfonate (SDBS) 842
sodium dodecyl sulfate (SDS) 160, 847
sodium-selective electrode 212
software and hardware control 620
solar
– conversion 782
– to electrical efficiency 785
solar cell 786
– dye sensitized 786
– multiple bandgap 787
– stacked multijunction 789
solar thermal electrochemical production (STEP) 779, 792
– energy pathway 795
– iron production 792
– solar efficiency 795
solar-cell-grade (SoG) 802
solar-powered electrolysis 931
solar-to-hydrogen (STH) 923
solenoid coil 348
sol–gel process 154

sol–gel-derived nanoarchitecture 506
solid
– metal oxide 809
– polymer electrolyte 787
solid electrolyte
– interphase (SEI) 343, 868
– membrane 259
solid oxide
– electrolysis cell (SOEC) 898
– fuel cell (SOFC) 23, 276, 614, 898
– membrane (SOM) 824
solid-state electrode 222
solid-state ionic 26
solvation 99
– chemical potential 102
– structure 99, 116, 131
– thermodynamics 102
solvation force 118
– calculation of 118
– coordinate extrapolation (SFCE) 117
– extrapolation (SFE) 98
solvation-free energy 102
– density (SFED) 102
solvent
– diffusion flux 243
– distribution 123
– evaporation 147
– separated ion pair (SSIP) 104
sorbed electrolyte solution species 125
sorbed solution 126
Soret equilibrium 81
sorption capacity 133
spatial decomposition analysis (SDA) 103
species flux 246
specific
– activity (SA) 435, 746
– humidity (SH) 657
– surface area (SSA) 505
spectroelectrochemical 335
– cell 638
– quartz crystal microbalance measurement (SECQM) 378
spectroelectrochemistry (SEC) 366
– circular dichroism 380
– quantitative 375
– steady-state luminescence 386
– thin layer 370
– vibrational 393
spectroscopy 640, 748
spin echo sequence 338
spinel group 952
spin-lattice relaxation 336
spin-spin relaxation 337
spirobipyrrolydinium tetrafluoroborate (SBP-BF_4) 530
stability
– testing 752
– window 534–537
stack 623, 911
– plot 358
standard
– calomel electrode (SCE) 513
– electrode 208
– hydrogen electrode (SHE) 593, 761
standard hydrogen electrode (SHE) 411
standardization 627
starting, lighting and ignition (SLI) 591
state of charge (SOC) 450
stationary corrosion 945
steady-state 360
– current 462
steam injection 661
steam methane reforming (SMR) 897
step-like grain boundaries 957
Stern layer 98
stochastic optical reconstruction microscopy (STORM) 415
storage electrode 785
storage life 485
stress-annealed pyrolytic graphite (SAPG) 605
structural transition 107
subtractively normalized interfacial Fourier transform infrared spectroscopy (SNIFTIRS) 394
sulforane (SL) 530
sum frequency generation (SFG) 393, 413
supercapacitor (SC) 129, 189, 496, 592, 866
– electrochemical capacitor 563
super-hydrophobic 842
supersaturated film 949
surface
– area (SA) 97
– brightening 957
– charge distribution 108
– electrochemistry 27
– finishing 957
– layer 949
– overpotential 901
– plasmon polariton (SPP) 196
– plasmon resonance (SPR) 414
– potential drop 82
– redox reaction 378
– topography 952
surface energy 953
– minimization 152
surface-catalytic mechanism 468
surface-enhanced infrared absorption (SEIRA) 400
– spectroscopy (SEIRAS) 400
surface-enhanced Raman
– scattering (SERS) 853
– spectroscopy (SERS) 196, 401
surface-enhanced resonance Raman (SERR) 376, 412
surface-templated material 169
surface-templating 155
sustainability 612
symmetric electrode 127
symmetry rules 71
synproportionation 55
system
– cleaning 617, 618
– development 311
– efficiency 311

T

Tafel
– equation 19
– plot 45
– slope 670
tank-type electrolyzer 906
tantalum oxynitride (TaON) 928
temperature control 619
temperature effect 902
temperature–energy-diagram 47
template 143
– free direct electrochemical synthesis 841
– mesoporous carbon (TMC) 507
terbium oxide (Tb_4O_7) 816
ternary phase diagram 457
tert-butyl alcohol (TBA) 104
test station 616
– control system 618
– diagnostic technique 626
tetrabutylammonium tetrafluoroborate (TBA BF_6) 169

tetracyanoquinodimethan (TCNQ) 773
tetraethyl orthosilicate (TEOS) 145
tetraethylammonium (TEA) 392, 530
tetraethylenepentamine 601
tetragonal bipyramidal (TB) 837
tetrahexahedral (THH) 836
tetrathiafulvalane (TTF) 773
thermal characterization 486
thermal power station 66
thermochemical
– cycle 61
– data 16
thermodynamic
– cycle 61
– integration 102
thermodynamics 14, 899
– of small systems 72
thermoelectric energy conversion 87
thermoelectric power generation 86
thermogravimetric analysis (TGA) 640
thermoneutral voltage 904
thermostat 134
theta capillaries 946
Thiele modulus 271
thin electrolyte shell 272
thin layer
– cell 367
– fuel cell 613
– SEC redox probe 375
thin-film 516
– battery 479
– electrode 368, 429, 513
– RDE electrode 431
thiol-top-functionalized silane monolayer (TFSM) 865
thiourea (TU) 844
three-compartment electrochemical cell 428
three-electrode electrolysis 816
three-electrode storage cell 783
three-phase interline (3PI) 815
through-hole cavity electrode 819
through-plane water distribution 356
time-correlated single-photon counting (TCSPC) 390
time-resolved luminescence spectroelectrochemistry (TRLS) 391
tin oxide anode 824
titania slag 813
titanium 963
– carbide (TiC) 801
– dendrite 807
– tetrachloride ($TiCl_4$) 803
titration potentiostatic intermittent 454
total
– analytical system (TAS) 223
– cell 72
– internal reflectance fluorescence microscopy (TIRF) 414
– ion strength adjustment buffer (TISAB) 218
tracer species 615
transference coefficient 73
– of salt 77
– position dependent 77
transference number 460
transformation
– characteristics 58
– efficiency 57
– ratio 57
transmission
– electron microscopy (TEM) 165, 336, 463, 473, 640, 716, 733, 852
– line model (TLM) 576
– line model-pore size distribution (TLM-PSD) 576
– spectroscopy 366
transport 901
– equation 240
– loss 241
– model 240
– number 77
transportation 538–541
transported entropy 81
triethylmethyl ammonium (TEMA) 530
triple phase boundary (TPB) 903
tungsten carbide 964
tungsten inverse opal 154
two-band model 338
two-electrode PEC 782
two-step anion maker 952

U

ultracapacitor 496
– electrochemical capacitor 563
ultracentrifugation 524
ultrasmall magnet 862
ultraviolet (UV) 780, 861
ultraviolet–visible (UV-Vis) 746
underpotential deposition (UPD) 604, 853
uninterruptible power supply (UPS) 543, 591
United States Department of Energy 630
unity of material and energy 34

V

Van der Waals force 145
vanadium electrolyte 791
vapor-grown carbon fiber (VGCF) 602
Verlet correction 126
vertical 345
– deposition (VD) 146
vibrational circular dichroism (VCD) 403
vibrational spectroscopy 393
Vienna ab initio simulation package (VASP) 315
vinylene carbonate (VC) 469
voltage
– current control 620
– efficiency 752
– profile 321
voltaic pile 5
voltammetric method 227
voltammetry 634, 749
– protein film 749
volume-templating 154
Voronoi tessellation 850
vulcan carbon (VC) 440

W

w, q-reaction 36
Warburg
– diffusion element 694
– impedance 692
water 357
– brackish 85
– content 528
– distribution 353
– electrolysis 64, 793, 898
– electrolyzer 899
– fresh 85
– management 287, 309
– sea 85
– transport 288
– transport mechanism 288

water–alcohol mixtures 104
water-splitting 903
wavelength dispersive x-ray spectrometer (WDS) 640
weak oxide group 952
Wilhelmy plate 149
workforce 612
working electrode (WE) 155, 407, 425, 460, 634, 683
wound cell 482
W-SiO_2 electrode 820

X

x-ray absorption
– near-edge spectroscopy (XANES) 512, 640
– near-edge structure 527
– spectroscopy (XAS) 511
x-ray diffraction (XRD) 317, 463, 511, 566, 640, 820, 840
– data 473
– profile 474
x-ray photoelectron spectroscopy (XPS) 368, 452, 511, 566, 640, 718, 748
x-ray radial electron density distribution (REDD) 640

Y

$Y_{0.2}Ce_{0.8}O_{2-\delta}$ (YDC) 914
yttria-stabilized zirconia (YSZ) 912

Z

zinc oxide (ZnO) 843

Recently Published Springer Handbooks

Springer Handbook of Electrochemical Energy (2017)
ed. by Breitkopf, Swider-Lyons, 1016 p., 978-3-662-46656-8

Springer Handbook of Ocean Engineering (2016)
ed. by Dhanak, Xiros, 1345 p., 978-3-319-32550-7

Springer Handbook of Robotics (2nd) (2016)
ed. by Siciliano, Khatib, 2227p., 978-3-319-32550-7

Springer Handbook of Computational Intelligence (2015)
ed. by Kacprzyk, Pedrycz, 1633 p., 978-3-662-43505-2

Springer Handbook of Marine Biotechnology (2015)
ed. by Kim, 1512 p., 978-3-642-53970-1

Springer Handbook of Acoustics (2nd) (2015)
ed. by Rossing, 1286 p., 978-1-4939-0754-0

Springer Handbook of Spacetime (2014)
ed. by Ashtekar, Petkov, 887 p., 978-3-642-41991-1

Springer Handbook of Bio-/Neuro-Informatics (2014)
ed. by Kasabov, 1230 p., 978-3-642-30573-3

Springer Handbook of Nanomaterials (2013)
ed. by Vajtai, 1222 p., 978-3-642-20594-1

Springer Handbook of Lasers and Optics (2nd) (2012)
ed. by Träger, 1694 p., 978-3-642-19408-5

Springer Handbook of Geographic Information (2012)
ed. by Kresse, Danko, 1120 p., 978-3-540-72678-4

Springer Handbook of Medical Technology (2011)
ed. by Kramme, Hoffmann, Pozos, 1500 p., 978-3-540-74657-7

Springer Handbook of Metrology and Testing (2nd) (2011)
ed. by Czichos, Saito, Smith, 1229 p., 978-3-642-16640-2

Springer Handbook of Crystal Growth (2010)
ed. by Dhanaraj, Byrappa, Prasad, Dudley, 1816 p., 978-3-540-74182-4

Springer Handbook of Nanotechnology (3rd) (2010)
ed. by Bhushan, 1961 p., 978-3-642-02524-2

Springer Handbook of Automation (2009)
ed. by Nof, 1812 p., 978-3-540-78830-0

Springer Handbook of Mechanical Engineering (2009)
ed. by Grote, Antonsson, 1576 p., 978-3-540-49131-6

Springer Handbook of Experimental Solid Mechanics (2008)
ed. by Sharpe, 1096 p., 978-0-387-26883-5

Springer Handbook of Speech Processing (2007)
ed. by Benesty, Sondhi, Huang, 1176 p., 978-3-540-49125-5

Springer Handbook of Experimental Fluid Mechanics (2007)
ed. by Tropea, Yarin, Foss, 1557 p., 978-3-540-25141-5

Springer Handbook of Electronic and Photonic Materials (2006)
ed. by Kasap, Capper, 1406 p., 978-0-387-26059-4

Springer Handbook of Engineering Statistics (2006)
ed. by Pham, 1120 p., 978-1-85233-806-0

Springer Handbook of Atomic, Molecular, and Optical Physics (2nd) (2005)
ed. by Drake, 1506 p., 978-0-387-20802-2

Springer Handbook of Condensed Matter and Materials Data (2005)
ed. by Martienssen, Warlimont, 1120 p., 978-3-540-44376-6